Forschungszentrum Jülich
in der Helmholtz-Gemeinschaft
50 Jahre / Zukunft

**J. Lecomte-Beckers, M. Carton,
F. Schubert and P. J. Ennis (Editors)**

Materials for Advanced Power Engineering 2006

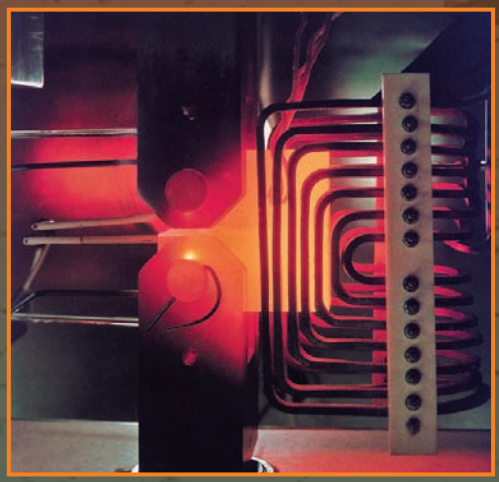

Proceedings Part I

**Energietechnik
Energy Technology**

Schriften des Forschungszentrums Jülich
Reihe Energietechnik / Energy Technology Band / Volume 53, Part I

Forschungszentrum Jülich GmbH
Institut für Energieforschung

Jacqueline Lecomte-Beckers, Marc Carton,
Florian Schubert and Philip J. Ennis (Editors)

Materials for Advanced Power Engineering 2006

Proceedings of the 8th Liège Conference

Part I

Université de Liège
European Commission
COST
European Science Foundation

Schriften des Forschungszentrums Jülich
Reihe Energietechnik / Energy Technology Band / Volume 53, Part I

ISSN 1433-5522 ISBN 3-89336-436-6

Bibliographic information published by Die Deutsche Bibliothek.
Die Deutsche Bibliothek lists this publication in the Deutsche Nationalbibliografie; detailed bibliographic data are available in the Internet at <http://dnb.ddb.de>.

Publisher and Distributor: Forschungszentrum Jülich GmbH
Zentralbibliothek, Verlag
D-52425 Jülich
Telefon (02461) 61-5368 · Telefax (02461) 61-6103
e-mail: zb-publikation@fz-juelich.de
Internet: http://www.fz-juelich.de/zb

Cover Design: Grafische Medien, Forschungszentrum Jülich GmbH

Printer: Grafische Medien, Forschungszentrum Jülich GmbH

Copyright: Forschungszentrum Jülich 2006

Schriften des Forschungszentrums Jülich
Reihe Energietechnik / Energy Technology Band / Volume 53, Part I

ISSN 1433-5522
ISBN 3-89336-436-6

Neither this book nor any part may be reproduced or transmitted in any form or by any means, electronic or mechanical, including photocopying, microfilming, and recording, or by any information storage and retrieval system, without permission in writing from the publisher.

FOREWORD

The European Co-operation in the field of Scientific and Technical Research (COST) is a well-established organisation for the co-ordination of national research and development programmes on the European level. The series of Liège conferences began in 1978 with the aim of disseminating the results of the COST Action 50 in which materials for gas turbines were investigated. Since then, a Liège Conference has been held every four years and the results of COST Actions 501 and 522, which were concerned with materials for power generation plant, reported. At this, the Eighth Liège Conference, the materials research and development work being carried out in the current COST Actions 536 'Alloy Development for Critical Components of Environmentally Friendly Steam Power Plant' with the acronym ACCEPT and 538 'High Temperature Plant Lifetime Extension' will be reported.

Reliable energy supply at reasonable cost is one of the most important factors in the development and maintenance of the modern industrial society, but there are increasing concerns about the environmental impact of energy production as well as about the need to conserve valuable energy resources for future generations. New and emerging energy technologies are of great interest, but fossil fuels will continue to make a considerable contribution to energy requirements into the foreseeable future. The emphasis in this field is therefore on the most efficient use of fossil fuels, which can be achieved by increasing the thermal efficiency of the energy conversion process. For steam power plant and gas turbines, this means raising the temperature and pressure of the process. This in turn requires the application of improved materials that are able to withstand the increasingly arduous service conditions.

In the COST Actions, the materials research and development activities that are necessary for the critical components of advanced, highly efficient power generation plant have been based on the principle of work-sharing, bringing together materials scientists and engineers, plant designers, alloy producers, component manufacturers, plant constructors and plant operators. This constellation of expertise reflects the need to match materials properties to component behaviour.

In order to put the European efforts into a world-wide scenario, there are in this conference a number of invited papers that will discuss the energy perspectives and the development of power plant materials in the USA, Japan, India and China.

The Conference Proceedings are organised as follows:

Part I: INAUGURAL SESSION
Invited papers

EUROPEAN ENERGY MATERIALS RESEARCH
Invited papers

ENERGY PERSPECTIVES
Invited papers

ADVANCED GAS TURBINE MATERIALS
Invited papers
Contributed papers
Mechanical properties
Microstructure

Part II: ADVANCED GAS TURBINE MATERIALS
Contributed papers
Modelling
Joining technology
Oxidation and hot corrosion
Coating technology
Intermetallics and ceramics

ADVANCED STEAM TURBINE MATERIALS
Invited papers
Contributed papers
Mechanical properties

Part III: ADVANCED STEAM TURBINE MATERIALS
Contributed papers
Microstructure
Modelling and alloy design
Welding technology
Steam oxidation and coatings
Austenitic and nickel-base alloys

ADDENDUM

The Technical and Editorial Board members would like to express their gratitude to all the members of the COST 536 and COST 538 Management Committees, for their supervision and support of the considerable research and development efforts, both in their own countries and across national borders. Those who were involved in the reviewing of the submitted papers are also sincerely thanked for their important contribution to the production of the Proceedings.

Research Centre Jülich - 50 Years of Innovation

Addressing society's challenges, questions and expectations and delivering solutions with the aid of excellent, strategically positioned research: this is the mission that Research Centre Jülich has been involved in ever since its foundation 50 years ago. Over the course of the years, it has undergone a huge transition, moving from research focused on the peaceful uses of nuclear energy to a research enterprise run on a multi-programmatic and interdisciplinary basis with an internationally unrivalled profile.

The key to this profile is the close linking of Jülich's traditional core competence, physics, to the other sciences. The basic insights gained in physics contribute decisively to a better understanding of the complex systems in energy, chemistry, biology, medicine and the geosciences, while the questions encountered in these fields extend the approaches adopted in physics. A further core competence that has evolved in Jülich with a remarkable momentum over the last few years is scientific computing. The operation of medium and large-scale equipment and a well-developed scientific and technical infrastructure round off the profile. This leads to the co-operation between and mutual enrichment of the different areas of expertise in Jülich, which remains internationally unparalleled in both nature and intensity. The positive effect of this cross-linking is further enhanced through strategic alliances with other centres in the Helmholtz Association, as well as with universities, industrial companies and research institutions worldwide.

The Research Centre Jülich will use this profile as a focal point for its research over the next two decades, making thus significant future contributions to the following four grand challenges: responsible management of the environment's natural resources, sustainable and comprehensive energy supply, securing food for and the health of a growing world population, and the provision and solutions-orientated linking of large quantities of information.

TABLE OF CONTENTS

Part I

Foreword iii
Table of Contents vii

INAUGURAL SESSION

ENGINEERING SUSTAINABILITY 5
Wall G

THE EU RESEARCH STRATEGY TOWARDS ZERO EMISSION FOSSIL FUEL POWER PLANTS 25
Dechamps P

EUROPEAN ENERGY MATERIALS RESEARCH

MATERIALS DEVELOPMENT FOR BOILERS AND STEAM TURBINES OPERATING AT 700 °C I 41
Blum R, Vanstone R W

THE EUROPEAN WAY TO 700°C COAL FIRED POWER PLANT I 61
Tschaffon H

MATERIALS ASPECTS OF SOLID OXIDE FUEL CELLS I 69
Steinbrech R, Menzler N H, Batfalsky P, Blum L

MATERIALS FOR EXTREME ENVIRONMENTS IN FUSION APPLICATIONS I 81
Bolt H, Maier H

DEVELOPMENT AND CURRENT STATUS OF ECCC CREEP PROPERTY DATA SHEETS I 91
Holdsworth S R

(see also Part III 1722, Addendum)

ENERGY PERSPECTIVES

EVALUATION OF THE MATERIALS TECHNOLOGY REQUIRED FOR A 760ºC POWER STEAM BOILER I 107
Shingledecker J P, Wright I G

CURRENT AND 2050 ENERGY PERSPECTIVES IN INDIA: OPPORTUNITIES FOR MATERIALS SCIENTISTS AND TECHNOLOGISTS I 121
Baldev Raj, B S Rao Kota

MATERIALS CHALLENGES IN CO_2 CAPTURE AND STORAGE I 143
Mathieu P

THE HYDROGEN ECONOMY I 161
Birnbaum U, Hake J-F, Linssen J, Walbeck M

ADVANCED POWER PLANT DEVELOPMENTS AND MATERIAL EXPERIENCES IN JAPAN I 175
Masuyama F

DEVELOPMENT OF HIGH TEMPERATURE MATERIALS FOR ENERGY MARKET IN CHINA I 189
Hu Z Q, Guo J T

ADVANCED GAS TURBINE MATERIALS

Invited papers

DEGRADATION IN SINGLE CRYSTAL NICKEL-BASE SUPERALLOYS – A REVIEW I 205
Nazmy M, Epishin A, Link T, Staubli M

RECENT ADVANCES IN NDT TECHNIQUES FOR GAS TURBINE COATINGS I 217
Osgerby S, Rinaldi C, De Maria L

GAS TURBINE ISSUES IN ADVANCED GASIFICATION SYSTEMS I 233
Wenglarz R, Oakey J

MATERIALS PROBLEMS AND SOLUTIONS IN BIOMASS FIRED PLANTS I 245
Larsen O H, Montgomery M

RE-QUALIFICATION OF BOILER DRUMS IN THERMAL POWER PLANT I 261
Brziak P, Bernasovský P

(see also Part III 1696, Addendum)

Contributed papers: Mechanical properties

DEVELOPMENT OF NI-BASED SINGLE CRYSTAL SUPERALLOYS FOR POWER-GENERATION GAS TURBINE BLADES I 273
Hashizume R, Yoshinari A, Kiyono T, Murata Y, Morinaga M

A 5TH GENERATION NI-BASE SINGLE CRYSTAL SUPERALLOY WITH SUPERIOR ELEVATED TEMPERATURE PROPERTIES I 287
Sato A, Yeh A C, Kobayashi T, Yokokawa T, Harada H, Murakumo T, Zhang J

EFFECT OF PLASTIC ANISOTROPY ON CREEP STRENGTH OF SINGLE CRYSTAL NI-BASED SUPERALLOYS I 299
Koyabu H, Tsuno N, Kakehi K

DEVELOPMENT OF CO-FREE NI-BASE SINGLE CRYSTAL SUPERALLOY I 309
Yokokawa T, Kobayashi T, Suzuki T, Koizumi Y, Harada H

THE EFFECT OF HIGH TEMPERATURE CREEP DAMAGE ON LOW CYCLE FATIGUE IN CMSX-4 I 317
Epishin A, Link T, Brückner U, Klingelhöffer H, Portella P

THE LONG-TERM CREEP PROPERTY OF NICKEL-BASE SINGLE-CRYSTAL SUPERALLOYS I 327
Koizumi Y, Harada H, Yokokawa T, Kobayashi T

INFLUENCE OF SOLIDIFICATION CONDITIONS ON HOMOGENISATION HEAT TREATMENT AND MECHANICAL PROPERTIES IN SINGLE CRYSTAL NICKEL-BASE SUPERALLOYS I 335
Lamm M, Volek A, Luesebrink O, Singer R F

PREDICTION OF THERMAL MECHANICAL FATIGUE PROPERTIES OF NI-BASE SINGLE CRYSTAL SUPERALLOYS I 347
Ohata H, Yokokawa T, Kobayashi T, Ro Y, Harada H

DEVELOPMENT OF A HIGH STRENGTH NI-BASED SUPERALLOY FOR CONVENTIONAL CASTING I 355
Tamaki H, Yoshinari A, Doi H

HIGH TEMPERATURE PROPERTIES OF SELECTED NI-BASE SUPERALLOYS I 365
Hakl J, Vlasák T

HOT ISOSTATIC PRESSING PROCESS TO REJUVENATE SERVICED CAST NICKEL-BASE SUPERALLOY IN738 TURBINE BLADES I 377
Wangyao P, Zrnik J, Polsilapa S, Nisaratanaporn E, Homkrajai W

DEVELOPMENT OF NEW SUPERALLOYS FOR TURBINE DISK APPLICATIONS I 385
Gu Y, Cui C, Ping D, Harada H, Sato A, Fujioka J

INFLUENCE OF CARBIDES AND OXIDATION ON THERMAL FATIGUE BEHAVIORS OF TWO NICKEL-BASE SUPERALLOYS I 393
Li Y L, Yuan C, Guo J T, Hou J S

LOW CYCLE FATIGUE BEHAVIOR OF WROUGHT NICKEL BASED SUPERALLOY GH413 I 403
Guo X G, Guo J T, Yuan C, Yang H C

EFFECT OF CARBIDES ON THERMAL FATIGUE PROPERTY OF K465 CAST SUPERALLOY I 413
Guan H R, Yang J X, Zheng Q, Wang Y L, Sun X F, Hu Z Q

ENVIRONMENTAL EFFECT ON HIGH TEMPERATURE FATIGUE BEHAVIOUR OF A NICKEL BASE SUPERALLOY FOR TURBINE DISCS I 423
Marchionni M, Onofrio G, Osinkolu G A

INFLUENCE OF SOLUTION HEAT TREATMENT CONDITIONS ON GAMMA PRIME CHARACTERISTICS IN A HOT CORROSION RESISTANT SUPERALLOY I 435
Hou J S, Guo J T, Zhou L Z, Li J Z, Qin X Z, Li Y L, Ye H Q

Contributed papers: Microstructure

MORPHOLOGICAL EVOLUTION OF GAMMA PRIME AND $M_{23}C_6$ CARBIDE IN A CAST NI-BASE SUPERALLOY IN THE DIFFERENT TREATMENT CONDITIONS I 447
Qin X Z, Guo J T, Yuan C, Hou J S, Ye Q H

DISLOCATION SUBSTRUCTURE IN γ-CHANNEL OF SINGLE CRYSTAL NICKEL-BASED SUPERALLOY, CMSX-4, CREPT AT 1273 K, 160 MPA I 455
Kondo Y, Miura N, Matsuo T

DISLOCATION SUBSTRUCTURE AT γ/γ' INTERFACE OF SINGLE CRYSTAL NICKEL-BASED SUPERALLOY CMSX-4 CREPT AT 1273 K, 250 MPA I 465
Miura N, Tanaka F, Kurita K, Kondo Y, Matsuo T

MODELLING OF RAFTING AND ITS INFLUENCE IN NI-BASE SUPERALLOYS I 475
Fedelich B, Künecke G, Epishin A

TEM MICROSTRUCTURAL ANALYSIS OF CREEP DEFORMED CM186LC SINGLE CRYSTAL NI-BASE SUPERALLOY I 485
Dubiel B, Blackler M, Barnard P M, Czyrska-Filemonowicz A

ATOM PROBE MICROANALYSIS OF FIFTH-GENERATION NI-BASE SINGLE-CRYSTAL SUPERALLOYS I 495
Kitashima T, Ping D H, Harada H, Kobayashi T

MICROSTRUCTURAL STABILITY OF CMSX-4 AND CMSX-10 UNDER HIGH TEMPERATURE CREEP CONDITIONS I 507
Epishin A, Link T, Brückner U

X-RAY TOMOGRAPHY FOR POROSITY ANALYSIS IN SINGLE-CRYSTAL NI-BASE SUPERALLOYS I 521
Link T, Zabler S, Haibel A, Epishin A

DEFORMATION BEHAVIOR AND MICROSTRUCTURE EVOLUTION DURING HOT WORKING PROCESS OF NICKEL-BASE ALLOY GH742 I 533
Zhang B, Zhao G, Xu G, Feng D

ORIENTATION DEPENDENCE OF SECONDARY REACTION ZONES IN SURFACE MODIFIED NI-BASED SINGLE CRYSTAL SUPERALLOYS I 541
Murakami H, Sakai T, Shibata M, Yamaguchi A, Kuroda S

STUDY ON THE INVESTMENT CASTING PROCESS OF K418 SUPERALLOY TURBINE I 549
Li J, Zhao M, Shao C, Kong S, Wu J, Li W

STUDY ON CASTING PROCESS OF K4537 SUPERALLOY GAS TURBINE I 555
Shao C, Li J, Zhao M, Li W, Wu J, Kong S

DIFFUSION COEFFICIENT OF REFRACTORY ELEMENTS IN MULTI-COMPONENT NI-ALLOY I 561
Murata Y, Hattori M, Efendi, Goto N, Koyama T, Morinaga M

MICROSTRUCTURAL DEGRADATION OF HAYNES 230 COMBUSTOR HARDWARE I 571
Marchant G, McColvin G, Strang A

SHOT PEENING INDUCED RECRYSTALLIZATION IN A DIRECTIONALLY SOLIDIFIED NI-BASE SUPERALLOY I 583
Zhang J, Wang L, Xie G, Sun C, Lou L H

AUTHOR INDEX I

KEYWORD INDEX VII

Part II

ADVANCED GAS TURBINE MATERIALS

Contributed papers: Modelling

MICRO-MECHANICAL MODELLING OF THE SINGLE CRYSTAL NICKEL-BASE SUPERALLOY CMSX-4 II 595
Tinga T, Geers M G D, Brekelmans W A M

MODELLING THE CONSTANT AND VARIABLE LOADING / TEMPERATURE CREEP BEHAVIOUR OF UDIMET 720LI II 607
Maldini M, Lupinc V

A GENERAL APPROACH TO MICROSTRUCTURAL MODELLING OF CREEP II 619
Pein C, Kozeschnik E

Contributed papers: Joining technology

THE CREEP RUPTURE BEHAVIOUR OF A NICKEL-BASE SINGLE-CRYSTAL SUPERALLOY AFTER TLP BONDING II 627
Liu J D, Jin T, Zhao N R, Wang Z H, Sun X F, Guan H R, Hu Z Q

NANOINDENTATION AND ORIENTATION MEASUREMENTS IN SINGLE CRYSTALLINE BRAZING JOINTS OF NICKEL – BASE SUPERALLOYS II 633
Dinkel M, Pyczak F, Göken M, Heinz P, Volek A, Singer R F, Ott M, Affeldt E, Vossberg A

Contributed papers: Oxidation and hot corrosion

LONG-TIME HIGH-TEMPERATURE OXIDATION OF MA 6000 AND PM 3030 ODS SUPERALLOYS II 645
Maresca P, Pratesi F, Terzigli V, Innocenti M, Giorni E

OXIDATION RESISTANCE OF SILICON-CONTAINING 5TH GENERATION NICKEL-BASE SINGLE CRYSTAL SUPERALLOYS II 655
Sato A, Harada H, Ang J, Yutaka K, Toshiharu K, Kawagishi K, Imai H

ESTIMATION OF THE RISK OF HOT CORROSION IN GAS TURBINES BY THERMODYNAMIC MODELLING II 665
Müller M

Contributed papers: Coating technology

MICROSTRUCTURAL INVESTIGATIONS AND MODELLING OF INTERDIFFUSION BETWEEN MCRALY COATING AND IN738 SUPERALLOY II 675
Dahl K V, Hald J

DEVELOPMENT OF EQ COATINGS FOR A NEW TBC COATING SYSTEM IN NI-BASE SUPERALLOYS II 691
Kawagishi K, Sato A, Matsumoto K, Ang J, Harada H

COATINGS BY LASER CLADDING AGAINST LIQUID DROPLET EROSION II 699
Giannozzi M, Giorni E, Giovannetti I, Pratesi F, Zonfrillo G

A NEW DEVICE FOR TESTING COATINGS UNDER THERMAL SHOCK II 707
Zonfrillo G, Giannozzi M, Pratesi F, Giorni E

CHARACTERIZATION OF THERMAL BARRIER COATINGS BY MEANS OF FURNACE CYCLE TESTING II 717
Cappuccini F, Zonfrillo G, Pratesi F, Giannozzi

ACOUSTIC EMISSION ANALYSIS USED AS MONITORING TOOL FOR BURNER RIG TESTS OF THERMAL BARRIER COATINGS II 727
Mack D E, Casu A, Traeger F, Vaßen R, Stöver D

PRACTICAL APPLICATIONS OF TEMPERATURE ESTIMATION MODELS BASED ON SUPERALLOY BASE METAL AND MCRALY COATING MICROSTRUCTURE EVOLUTION IN SERVICE GAS TURBINE COMPONENTS II 737
Hussain K, Daleo J A

NUMERICAL SIMULATION OF TBC DELAMINATION UNDER THERMAL CYCLIC LOADING II 747
Białas M, Bednarz P, Herzog R

OXIDATION AND HOT CORROSION BEHAVIOUR OF ALUMINIZED PT-IR COATINGS ON NI-BASED SUPERALLOYS TMS-82+ II 757
Yamaguchi A, Wu Y N, Suzuki A, Murakami H, Kuroda S, Imai H

Contributed papers: Intermetallics and ceramics

CREEP BEHAVIOR OF ORTHORHOMBIC Ti_2AlNb-BASED ALLOYS II 767
Hagiwara M, Emura S, Mao Y

COMPARISON OF THE ISOTHERMAL FATIGUE BEHAVIOUR OF TIMETAL 6242 AND γ-TIAL ALLOYS AT 700°C II 773
Cempura G, Penkalla H J, Schubert F, Czyrska-Filemonowicz A

TIAL OXIDATION PROTECTION IMPROVEMENTS USING THE HALOGEN EFFECT II 783
Masset P, Zschau H-E, Schütze M

THERMAL EXPOSURE EFFECTS ON THE MECHANICAL PROPERTIES OF TIAL INTERMETALLIC II 793
Holdway P, Lucas K, Wisbey A

DIRECTIONALLY SOLIDIFIED MULTIPHASE NI_3AL-BASED INTERMETALLICS FOR HIGH TEMPERATURE APPLICATIONS II 803
Lapin J, Pelachová T, Mareček J

SUPERPLASTIC DEFORMATION AND MECHANISM OF EXTRUDED EUTECTIC NIAL/CR(MO) ALLOY DOPED WITH DY II 819
Guo J T, Du X, Li G

FEM STUDY OF A CMC SHROUD II 829
Del Pugliaa P, Lanese N, Zonfrilloa G

ADVANCED STEAM TURBINE MATERIALS

Invited papers

THE EUROPEAN EFFORT IN DEVELOPMENT OF NEW HIGH TEMPERATURE ROTOR MATERIALS – COST 536 II 843
Kern T -U, Staubli M, Mayer K H, Donth B, Zeiler G, DiGianfrancesco A

THE EUROPEAN EFFORTS IN DEVELOPMENT OF NEW HIGH TEMPERATURE CASING MATERIALS – COST 536 II 855
Staubli M, Hanus R, Weber T, Mayer K H, Kern T-U

WELDABILITY AND PROPERTIES OF NEW CREEP RESISTANT MATERIALS FOR USE IN ULTRA SUPERCRITICAL COAL FIRED POWER PLANTS II 871
Bauné E, Cerjak H, Caminada S, Jochum C, Mayr P, Pasternak J

US PROGRAM ON MATERIALS TECHNOLOGY FOR ULTRASUPERCRITICAL STEAM-COAL FIRED POWER PLANTS II 893
Viswanathan R, Henry J F, Tanzosh J, Stanko G, Shingledecker J P, Vitalis B

METALLOGRAPHY AND ALLOY DESIGN IN THE COST 536 ACTION II 917
Hald J

MATERIALS DEVELOPMENT FOR ADVANCED STEAM BOILERS II 931
Helmrich A, Chen Q, Stamatelopoulos G, Scarlin B

COATINGS FOR PROTECTION OF HIGH TEMPERATURE NEW GENERATION STEAM PLANT COMPONENTS: A REVIEW II 949
Aguero A

METALLURGY FOR LONG-TERM STABILIZATION OF FERRITIC STEELS FOR THICK SECTION BOILER COMPONENTS IN USC POWER PLANT AT 650^{O}C II 965
Abe F

Contributed papers: Mechanical properties

CONTRIBUTION TO THE INVESTIGATION OF ADVANCED LOW-ALLOY P23 STEEL CREEP BEHAVIOUR II 985
Hakl J, Vlasák T, Brziak P, Zifcak P

EFFECT OF TEMPERING TIMES ON CREEP STRENGTH IN ASME GR 23 (2 25CR-1 6W STEEL) II 997
Komai N, Imazato T

CREEP OF 0.5CrMoV STEEL AT VERY LOW STRAIN RATES II 1011
Kloc L, Sklenica V

IMPROVEMENT IN CREEP STRENGTH OF HEAT RESISTANT FERRITIC STEEL STRENGTHENED BY INTERMETALLIC COMPOUND II 1019
Toda Y, Kushima H, Kimura K, Abe F

SUPERIOR LONG-TERM CREEP BEHAVIOUR AND MICROSTRUCTURAL EVOLUTION OF 9%CR-STEELS WITH BORON II 1031
Kager F, Böck N, Spiradek-Hahn K, Höfinger S, Brabetz M, Zeiler G

ALLOY DESIGN AND CREEP STRENGTH OF ADVANCED 9%CR USC BOILER STEELS CONTAINING HIGH BORON II 1041
Semba H, Abe F

IMPROVEMENT OF CREEP STRENGTH OF 650 °C FERRITIC/MARTENSITIC SUPER HEAT RESISTANT 11-12 % CR STEELS II 1053
Mayer K-H, Berger C, Scholz A, Wang Y

STATUS OF DEVELOPMENT OF THE VM12 STEEL FOR TUBULAR APPLICATIONS IN ADVANCED POWER PLANTS II 1065
Gabrel J, Bendick W, Vandenberghe B, Lefebvre B

MICROSTRUCTURAL DEVELOPMENT OF VM12 STEEL CAUSED BY CREEP DEFORMATION AT 625ºC II 1077
Zielińska-Lipiec A, Bendick W, Cempura G, Vandenberghe B, Ennis P J, Czyrska-Filemonowicz A

REGENERATIVE HEAT TREATMENT OF L21HMF CAST STEEL AFTER LONG TERM OPERATION II 1087
Golanski G, Kupczyk J, Stachura S, Gajda B

LONG TERM CREEP STRENGTH DEGRADATION IN T122/P122 STEELS FOR USC POWER PLANTS II 1095
Igarashi M, Yoshizawa M, Iseda A, Matsuo H, Kan T

DEGRADATION BEHAVIOUR AND LONG-TERM CREEP STRENGTH OF 12CR FERRITIC CREEP RESISTANT STEELS II 1105
Kimura K, Sawada K, Kushima H, Toda Y

CREEP CURVE ANALYSIS USING THE MODIFIED Ω METHOD II 1117
Yin Y F, Faulkner R G

EFFECT OF NON STEADY LOADING ON CREEP BEHAVIOUR OF ADVANCED 9-12 % FOSSIL POWER PLANT STEELS II 1127
Sklenicka V, Kucharova K, Svoboda M, Kloc L, Kudrman J

CREEP AND CREEP FATIGUE PROPERTIES OF TURBINE STEELS FOR APPLICATION TEMPERATURES UP TO 625 °C II 1137
Berger C, Schwienheer M, Scholz A

LOW CYCLE FATIGUE BEHAVIOUR OF SANDWICH STRUCTURES OF P92 AND NICROFER 6025 HT II 1147
El-Magd E, Stuhrmann J, Gebhard J

CAUSES OF CREEP FRACTURE MECHANISM CHANGE IN 9CR-1 8W-0 5Mo-VNb STEEL II 1157
Lee J S, Arnaki H G, Maruyama K, Muraki T, Asahi H

AUTHOR INDEX I

KEYWORD INDEX VII

Part III

ADVANCED STEAM TURBINE MATERIALS

Contributed papers: Microstructure

MICROSTRUCTURAL CHARACTERIZATION OF MODERN BORON CONTAINING 9-11 % CR STEELS DEVELOPED IN THE FRAMEWORK OF THE COST PROGRAM III 1171
Kauffmann F, Mayer K H, Straub S, Zies G, Scheu C, Willer D, Ruoff H, Maile K

QUANTITATIVE MICROSTRUCTURAL ANALYSIS ON THE STABILITY OF MX AND M2X IN 9-12 % CR STEELS BY AFM, SEM, TEM III 1181
Seibert T, Durst K, Chilukuru H, Göken M

SIMULATION OF THE PRECIPITATION KINETICS DURING HEAT TREATMENT AND SERVICE OF CREEP RESISTANT MARTENSITIC 9-12% CR STEEL III 1191
Holzer I, Rajek J, Kozeschnik E, Cerjak H

MICROSTRUCTURAL ANALYSIS ON A CREEP RESISTANT MARTENSITIC 9-12% CR STEELS USING THE EBSD METHOD III 1199
Sonderegger B, Mitsche S, Cerjak H

DISLOCATION MOBILITY IN 9% CHROMIUM STEELS EXPOSED TO CREEP III 1207
Böck N

EFTEM INVESTIGATIONS ON PRECIPITATES IN A CREEP RESISTANT 9-12% CR STEEL III 1217
Sonderegger B, Kothleitner G, Rechberger W, Cerjak H

PRECIPITATION BEHAVIOR OF Z PHASE AFTER LONG-TERM CREEP IN HIGH CHROMIUM FERRITIC HEAT RESISTANT STEELS III 1227
Sawada K, Kushima H, Kimura K

ON THE ROLES OF M2X AND Z-PHASE IN TEMPERED MARTENSITIC 9-12% CR-STEELS III 1241
Chilukuru H, Durst K, Göken M, Blum W

ELECTRON DIFFRACTION STUDIES ON (Nb,V)CrN PARTICLES IN 12CrMoVNbN STEELS III 1251
Vodarek V, Danielsen H, Grumsen F, Hald J, Strang A

AN EFTEM STUDY OF Z-PHASE NUCLEATION IN MARTENSITIC CHROMIUM STEELS III 1267
Golpayegani A, Andren H O

Z-PHASE IN 9-12%CR STEELS - OBSERVATIONS AND THERMODYNAMIC MODELLING III 1275
Danielsen H K, Hald J

MICROSTRUCTURE AND STEAM OXIDATION RESISTANCE OF LAVES PHASE FORMING 12%CR STEELS AT 600-650°C III 1285
Pirón Abellán J, Ennis P J, Singheiser L, Quadakkers W J

Contributed papers: Modelling

CDM MODELLING OF POWER PLANT FERRITIC STEELS III 1299
Yin Y F, Faulkner R G

AN EFFECTIVE PARAMETRIC STRAIN MODEL FOR CREEP III 1309
Holmström S, Auerkari P, Holdsworth S

ADVANCED ALLOY DESIGN TOOLS APPLIED TO THE DEVELOPMENT OF VANADIUM NITRIDE STRENGTHENED HIGH-TEMPERATURE STEELS III 1319
Gaude-Fugarolas D, Yardley V, Lardon J-M, Montagnon J, De Carlan Y

Contributed papers: Welding technology

APPLICATION OF BAINITIC CREEP RESISTING STEELS FOR SUPERCRITICAL PARAMETERS AND PROPERTIES OF WELDED JOINTS III 1331
Brózda J, Zeman M, Pasternak J

INVESTIGATIONS ON OPTIMISATION OF WELD CREEP PERFORMANCE IN MARTENSITIC STEELS III 1341
Bauer M, Klenk A, Maile K, Roos E, Jochum C

STRUCTURAL STABILITY AND PROPERTIES OF WELD JOINTS OF NEW CREEP-RESISTANT STEEL GRADES WITH 9 OR 12% CR CONTENTS APPLIED IN OPERATION OF POWER GENERATIONS SECTOR OVER 30000 h III 1357
Moskal G, Hernas A, Pasternak J

WELDABILITY AND HIGH TEMPERATURE BEHAVIOR OF 12% CR-STEEL FOR TUBES AND PIPES IN POWER PLANTS WITH STEAM TEMPERATURES UP TO 650 °C III 1369
Vekeman J, Dhooge A, Huysmans S, Vandenberghe B, Jochum C

EXPECTED CREEP LIFE OF WELDED 9-12% CR STEELS III 1381
Auerkari P, Holmström S, Salonen J

STUDY OF THE SIMULATED HAZ OF A BORON ALLOYED CREEP RESISTANT 9% CHROMIUM STEEL III 1393
Mayr P, Cerjak H

MICROSTRUCTURAL STUDIES OF SIMILAR AND DISSIMILAR WELDS OF P91 III 1401
Jandova D, Kasl J, Folkova E, Kanta V

PHYSICAL SIMULATION AND NUMERICAL MODELLING OF X10CRMOVNB 9 10 (P91) STEEL REPAIR WELDING III 1417
Lomozik M, Tasak E

DISSIMILAR WELDED JOINTS WITHOUT A BUFFER AREAS OF STEEL TYPE 9CR WITH 1CRMOV TO BE USED FOR STEAM BOILER PIPELINES III 1427
Tasak E, Hernas A, Pasternak J, Fudali S

CREEP PROPERTIES OF HETEROGENEOUS P91/P23 WELDS AT 550 AND 600 °C III 1437
Kuboň Z, Vodárek V, Toušová D

STRUCTURAL STABILITY OF HETEROGENEOUS WELD JOINT OF 6CRMOV 8-3-2 AND X12CRMOV 10-1 STEELS WITH INCREASED NITROGEN CONTENT III 1449
Foret R, Zlámal B, Sopoušek J, Buršík J

Contributed papers: Oxidation and coatings

OXIDATION OF CANDIDATE CHROMIUM STEELS IN STEAM ENVIRONMENT III 1461
Cizner J, Hakl J

OXIDE SCALE GROWTH AND SPALLATION IN STEAM ENVIRONMENTS – AN ASSESSMENT OF DIFFERENT MODELLING APPROACHES III 1469
Fry A T, Osgerby S

THE INFLUENCE OF OXIDATION ON LONG TERM CREEP RUPTURE STRENGTH DATA III 1479
Allen D J, Harvey B

NEW EXPERIENCE IN THE FIELD OF APPLICATION OF CORROSION RESISTANCE PROTECTION IN FLUE GAS DESULPHURISATION PLANT ABSORBERS III 1491
Hernas A, Imosa M, Pasternak J, Fudali S

CORROSION AND OXIDATION EXPERIENCES IN AVEDØRE II MULTIFUEL BOILER III 1503
Montgomery M, Jensen S A, Biede O, Larsen O H, Andersson A

HEAT EXCHANGER CORROSION IN BIOMASS AND COAL CO-FIRED POWER PLANTS III 1513
Simms N J, Kilgallon P J, Oakey J E

HOT CORROSION MONITORING OF ALLOY 617 IN MOLTEN CHLORIDES USING ELECROCHEMICAL TECHNIQUES III 1523
Pérez, F J, Hierro M P, Nieto J

METAL WASTAGE IN LOW ALLOY STEELS UNDER ALTERNATING ATMOSPHERES AT ELEVATED TEMPERATURE III 1533
Osgerby S, Gohil D D

DEVELOPMENT OF ALUMINIDE DIFFUSION COATINGS FOR HEAT EXCHANGER MATERIALS AND THEIR CREEP-CORROSION RESISTANCE IN SIMULATED COAL FIRING ENVIRONMENT III 1543
Rohr V, Weber T, Schütze M, Ennis P J, Quadakkers W J

DEVELOPMENT AND VALIDATION OF ADVANCED OXIDATION PROTECTIVE COATINGS FOR SUPER CRITICAL STEAM POWER PLANT III 1553
Henderson M B, Scheefer M, Aguero A, Allcock B, Norton B, Tsipas D N, Durham R

IMPROVEMENT OF OXIDATION RESISTANCE OF TUBES BY PULSED SILICONISING III 1571
Maile K, Berreth K, Lyutovich A

INFLUENCE OF SURFACE TREATMENT ON THE OXIDATION KINETICS OF ADVANCED STEELS IN FLOWING STEAM AT 650 °C III 1581
Knoedler R, Straub S

LONG TERM STEAM OXIDATION RESISTANCE OF SHOT-BLASTED STAINLESS STEEL TUBING III 1589
Minami Y, Fukui T

Contributed papers: Austenitics and Ni-base alloys

QUALIFICATION OF NI-BASED MATERIAL FOR TUBES AND PIPING OF 700°C POWER PLANT III 1597
Klenk A, Maile K, Theofel H, Helmrich A, Husemann R U, Lüdenbach G

AN INVESTIGATION ON STRUCTURE STABILITY AND ITS IMPROVEMENT ON A NEW DEVELOPMENTAL NI-CR-CO-MO-NB-TI-AL SUPERALLOY FOR USC POWER PLANT APPLICATION AT TEMPERATURE ABOVE 750ºC III 1609
Xie X, Zhao G, Dong J, Smith G D, Baker B A, Patel S J

CHEMISTRY MODIFICATIONS OF INCONEL 706 FOR IMPROVED MICROSTRUCTURAL STABILITY III 1619
Del Genovese D, Mukherji D, Rösler J, Kindratschuk V, Wabderka N, Banhart J

CRACK GROWTH BEHAVIOUR OF WASPALOY AT 700°C IN DIFFERENT ATMOSPHERES III 1629
Penkalla H J, Schubert F, Singheiser L

ASSESSMENT OF THE INFLUENCE OF LASER-DRILLED HOLES ON THE DAMAGE BEHAVIOUR OF ALLOY 617 III 1639
Mülders B, Wessel E, Schubert F

DEFORMATION BEHAVIOUR OF ALLOY INCONEL 617 TUBES IN THE TEMPERATURE RANGE 600°C TO 850°C III 1651
Makhele-Lekala L, Ennis P J, Schubert F

FIELD TESTING OF TP 347H FG AT ULTRA SUPERCRITICAL STEAM CONDITIONS III 1663
Hansson A N, Montgomery M

AN IMPROVED METHOD TO CALCULATE THE CREEP-FATIGUE ENDURANCE OF TYPE 316H STAINLESS STEEL III 1673
Spindler M

WEB-ENABLED DATABASES OF JRC PETTEN-EFFECTIVE TOOLS FOR EUROPEAN KNOWLEDGE MANAGEMENT III 1683
Over H H, Dietz W

ADDENDUM
These papers arrived too late for reviewing and are reproduced as received

ADVANCED COATINGS FOR GAS TURBINES III 1696
Nicholls J R, Bordenet B

APS-TBC FOR GAS TURBINES: FAILURE MODES, DAMAGE EVOLUTION AND LIFE-TIME ASSESSMENT III 1722
Herzog R, Bednarz P, Trunova O, Steinbrech R W, Wessel E, Quadakkers W J, Schubert F, Singheiser L

AUTHOR INDEX I

KEYWORD INDEX VII

Part I

Inaugural Session

European Energy Materials Research

Energy Perspectives

Advanced Gas Turbine Materials

Part I

Inaugural Session

Invited papers

ENGINEERING SUSTAINABILITY

Göran Wall

International Exergy Institute, Sweden, http://exergy.se

Abstract

Humankind faces the most serious challenge ever – sustainable development. This is described from a physical and ecological perspective. A new engineering paradigm based on increasing nature's capital instead of exploiting it is presented, as well as fundamental ecological principles and exergy based concepts and methods in order to understand, analyze and optimize engineering processes towards sustainability.

Keywords: Sustainable development, Environmental sciences, Ecological engineering, Energy and Natural resources, Exergy

Introduction

The ongoing depletion of nature's capital must come to an end before it is too late. Values are lost and substances are spread in the environment when nature's capital is exploited and consumed in our economies. The physical conditions in nature change and create instability. New life forms that are better fitted to these new conditions will appear, i.e. survival of the fittest. Some of these new organisms will not support present higher forms of life, e.g. homo sapiens. We see this as new diseases. The bird flu virus is just but one example of an ongoing creation of new organisms that will go on as long as suitable conditions are offered. Thus, present industrial society is fertilizing its own extinction. The only solution to sustainable development for humankind is to restore and preserve nature's capital. This enforces a new paradigm based on increasing the capital of nature instead of exploiting it. Present technology and social management are founded, to a large extent, on the knowledge offered by science. Yet it is precisely these structures and their impact, which we know to be unsustainable. This implies tremendous efforts from science, which gradually adopts the new situation. In some areas of science this even relates to a complete change of paradigm. Science is partly the problem as well as a part of the solution for a sustainable development.

The evolution of knowledge is essential to human cultures. Every human culture carries a unique cultural paradigm—the soil for knowledge to grow and flourish. The diversity of cultures in our world is essential to the evolution of human knowledge—our creative diversity. This diversity is the wellspring of our progress and creativity.

Present focus must be on relationships; between humans and with nature. Today these relationships are characterized by greed and violence fostered by the present cultural paradigm, or arrogance and ignorance instead of friendship and compassion. This must change into a culture of peace. Peace within us, peace among us and peace with nature are essential for happiness, harmony and knowledge to flourish.

We, the people of the world, are also children of earth with a common goal to care for life itself. We were given intelligence, emotions and possibilities, but also responsibilities. With these gifts we have created a world of prosperity, but also of poverty. The world has brought us together, but also apart and away from nature. We face a future of threats and limitations, but also possibilities. These challenges demand careful and responsible actions from everyone, based on a better understanding together with moral obligations.

Nature's Engineering

Nature is the only creature and holder of life, as far as we know. From our understanding there are some fundamental conditions that maintain this unique capacity of nature.

Contrast, Motion, Exergy, and Time

In order for things to happen, i.e. motion to occur, there must be a driving force: something that can create action. A force is created by a difference in space of some kind, i.e. a contrast. This is a physical quantity such as temperature, pressure or tension. When this force, due to a contrast, is acting, it also "eats up" its source of power. The depletion of power into action is the creator of time. By allowing a contrast that is enclosed into the three-dimensional space to act, a new fourth dimension is created, i.e. time.

Exergy is the physical concept of contrast, which quantifies its power of action. A system in complete equilibrium with itself and the environment does not have any exergy, i.e. no power of action. Exergy is defined as work, i.e. ordered motion, or ability to perform work. If there is exergy then time can be experienced, however, only if exergy is destroyed. This is an irreversible process, which creates a motion in a specific direction, i.e. in the direction of time.

The limited speed of light is also of essential importance for the life support systems. If light could move at infinite speed, the sun could, in principal, release all its stored exergy immediately, thus, there would be no time for life to appear. The light from other stars in the universe brings also with it the history, due to the limited speed of light. When we look into space, we look into the history of the universe. The border of the universe gives us its time of birth, or the so-called "big bang," perhaps the birth of time. However, if the universe is infinite, then also time would be infinite.

Energy, Matter, Exergy, and Entropy

Energy and matter cannot be created, destroyed, produced or consumed. Energy and matter can only be converted into different forms. This occurs by the consumption of contrast. Locally, the contrast may increase, but this can only occur at the expense of an even greater deterioration of the contrast elsewhere. On the whole it is a question of continuous deterioration of contrast, thus, pointing out the existence and direction of time, see Fig. 1.

Energy and/or matter flow through a system. The motive force of the flow of energy and/or matter through the system is the contrast or the level of order. Energy and/or matter are falling from high order, i.e. low entropy, in the inflow into low order, i.e. high entropy, in the outflow. This is also expressed as a destruction of exergy [1].

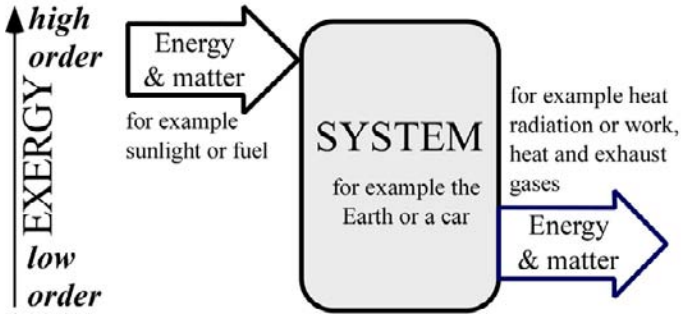

Fig. 1 The flow of energy and matter through a system.

Energy and matter only serve as carriers of contrast, which is partly consumed when it flows through a system. When energy and matter flow through a system, a very small part of this may sometimes be stored in or removed from the system. If there is a balance between inlets and outlets of energy and matter, the system will remain unchanged, a kind of steady state that is described in Fig. 1. Such steady state systems are the moon and a car. The moon offers us moonlight and a car is a mean of transport, however, the systems remain in principal unchanged.

If exergy is stored in the system we may have a viable state, i.e. life may occur. Logic would suggest therefore that the existence of life and the evolution of life imply that exergy from the sun must be stored on the earth.

The Earth, the Sun, and Space

Fig. 2 The sun-earth-space system.

The source of exergy on the earth is secured from the contrast between the sun and space, see Fig. 2. The exergy on the earth, exists through the conversion of energy from sunlight into heat radiation, which flows from the earth back into space. Due to this, all flows of energy and matter are carried forward through systems on the earth's surface, and life can be created and maintained.

Life

Life in nature relates to three fundamental processes: production, consumption, and decomposition. These maintain the circulation of matter by using the incoming solar exergy in a sustainable and evolutionary way, see Fig. 3.

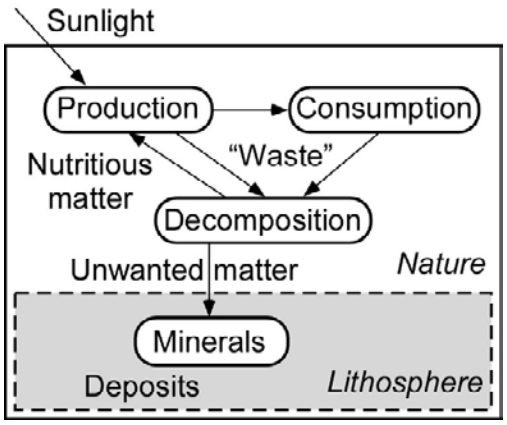

Fig. 3 The circulation of matter in nature is powered by sunlight.

Green plants, which represent the production process, convert exergy from sunlight into the exergy-rich matter of biomass, via photosynthesis. The exergy as biomass then passes through different food chains in the ecosystems. At every trophic level exergy is consumed and decomposition organisms dominate the last level in this food chain. There is no waste, however a removal of "unwanted" substances. Nature operates a unique machinery of development on the earth by capturing and sealing certain substances into minerals in the earth's crust. A fraction of the exergy from the sun-space contrast is stored as an increase of the exergy capital on the earth. This appears as a net-flow of "unwanted" substances from the biosphere into the lithosphere as well as a redistribution of other substances in the environment, e.g. oxygen to the atmosphere. Thus, the exergy capital on the earth is increasing, which is a key element in nature's process of evolution.

Society's Engineering

Resource Use in the Society

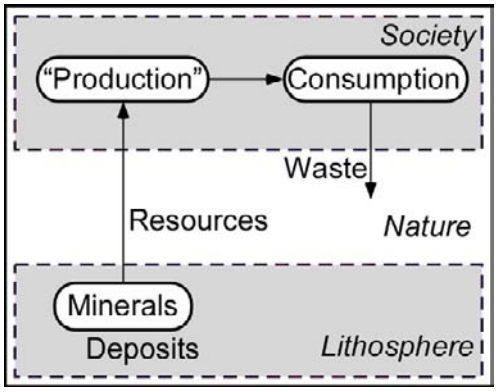

Fig. 4 Society depletes nature's capital and returns waste.

Present industrial society, is built on an unsustainable resource use, see Fig. 4. Fossil fuels and metals that originate from deposits of minerals in the lithosphere are unsealed and spread in the environment, which is exactly the opposite of what is done by nature (Fig. 3). This is obviously not sustainable, at least not for a very long time. Resource depletion and environmental destruction are two consequences of the use of deposits. In a closed system "nothing disappears and everything disperses" which state that these substances will unavoidably end up in the environment.

In Fig. 5, we see how the resource use in the society is maintained. The greater part of the exergy requirements are utilized from the terrestrial exergy stocks, i.e. funds and deposits. Only a very small part of the exergy flow from the sun is used directly. Through society we see an almost continuous exergy loss. Some exergy flows, such as flows of metals, initially increase their exergy when passing through society. However, other flows decrease their exergy all the more. A tank, which contains the funds and the deposits, indicates the limited amount of exergy stocks or capital on the earth. As long as the levels are kept stable, i.e. the output of resources does not exceed the input from the sun and the biological processes, then we have a sustainable situation. However, if the level is dropping, i.e. the exergy capital is depleting then we have an unsustainable situation and substances will be contaminated in the environment. As long as these substances are under control this may not be a serious problem. Large amount of substances are accumulated in the society as constructions, e.g. buildings and machines, and, as long as these remain, their substances may not effect the environment. However, when they are allowed to decompose some of them may pose a serious threat, e.g. old nuclear, chemical, and biological arms that are not safely stored or destroyed. This also relates to harmful substances that are accumulated by a purification system, e.g. used filters and sediments from sewage treatment works, cyclone separators and scrubbers. However, human constructions and buildings will not last forever. Sooner or later they will deteriorate and their substances will end up in the environment. Thus, environmental pollution is an inevitable consequence of the use of deposits. The depletion of the resource may not be the most serious problem, but rather the emission of pollutant and unwanted substances into the environment. The concern for an eventual lack of non-renewable resources must be combined by a similar concern for the environmental impact and its consequences from the emission of these substances. Presently, only nature offers the machinery to put these substances back into the lithosphere (Fig. 3). However, the present damage may take nature millions of years to repair, and in the meantime there will be a serious impact on the living conditions for all forms of life.

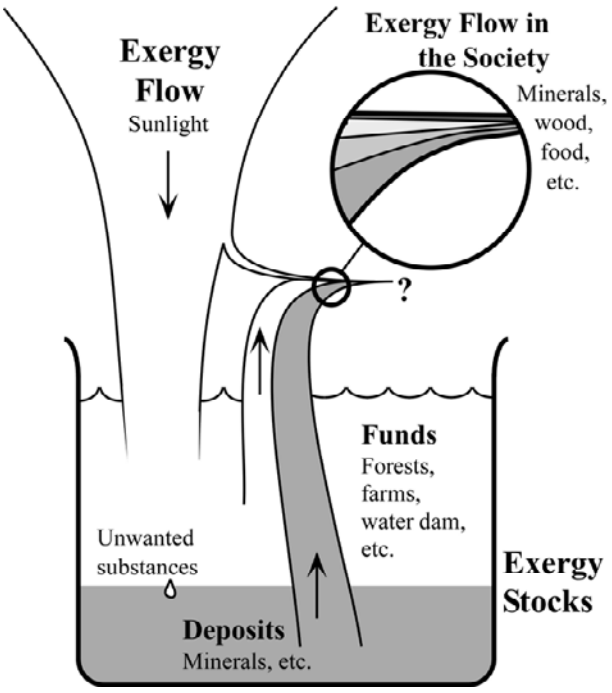

Fig. 5 Exergy flows to the society.

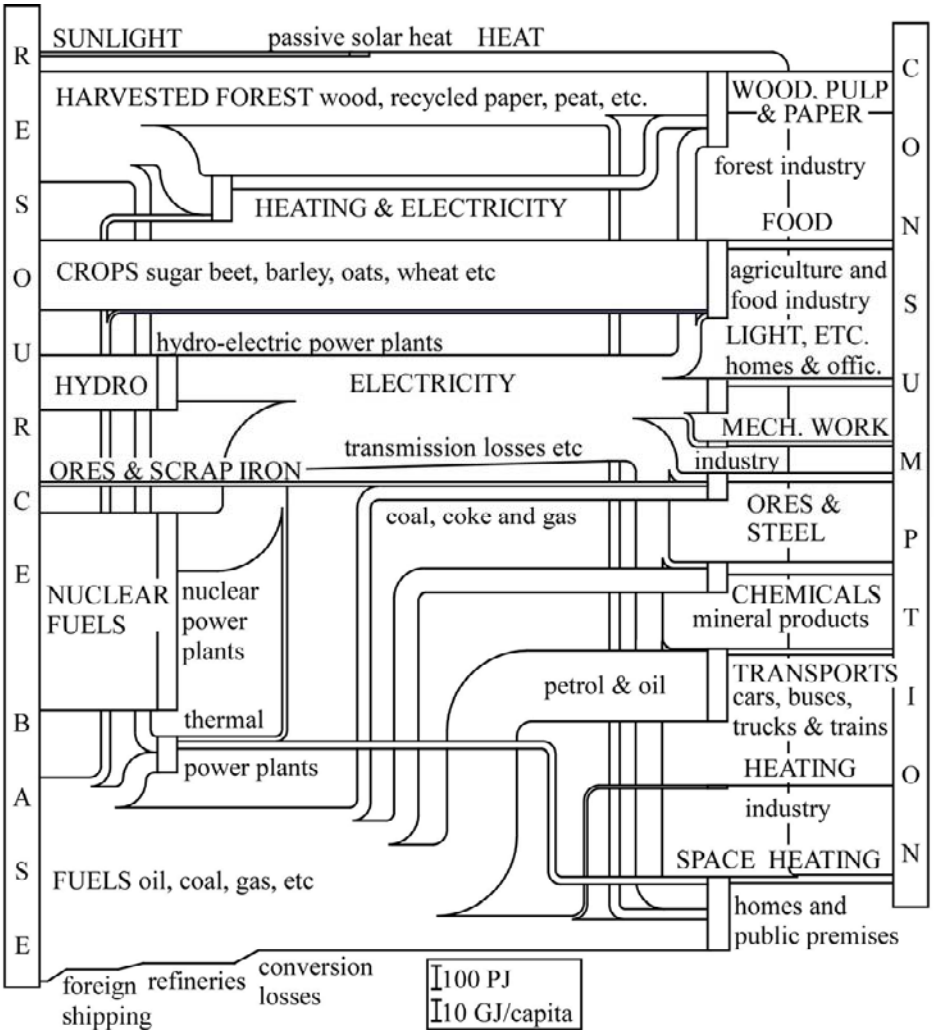

Fig. 6 Exergy use in the Swedish society in 1994.

Figure 6 shows the exergy flow in the society in more detail, in this case the main conversions of energy and materials in Sweden in 1994 [2]. The flows go from the resource base to the consumption sector. Thus, the diagram basically represents the resource supply sector where resources such as crops and minerals are turned into consumer goods such as food, transport and thermal comfort. The inflows are ordered according to their origins. Sunlight is thus a renewable natural flow. Besides a minor use of wind power, far less than 5 PJ, this is the only direct use of a renewable natural flow. Harvested forests, agricultural crops, and hydropower are renewable exergy flows derived from funds. Iron ore, nuclear fuels, and fossil fuels are flows from deposits, which are exhaustible and also carry with them toxic substances. The

unfilled boxes represent exergy conversions, which in most cases represent a huge number of internal conversions and processes. The total inflow of resources during 1994 amounts to about 2720 PJ or 310 GJ per capita and the net output becomes 380 PJ or 40 GJ per capita. Thus, the overall efficiency of the supply sector can be estimated at less than 15%. As we can see, some sectors are extremely inefficient. Some resource conversion systems have a ridiculously poor efficiency. For nuclear fuel to space heating through short circuit heaters the utilization becomes less than 0.025% [2].

The emission of unwanted substances from the industrial society is likely to produce diverse and unpredictable consequences in the biosphere. New microorganisms adapted to new environments will appear, see Fig. 7. Existing microorganisms, i.e. bacteria, fungi and viruses, provide the conditions on which present forms of life are founded. All forms of life are built on the existence of a specified mixture of certain microorganisms.

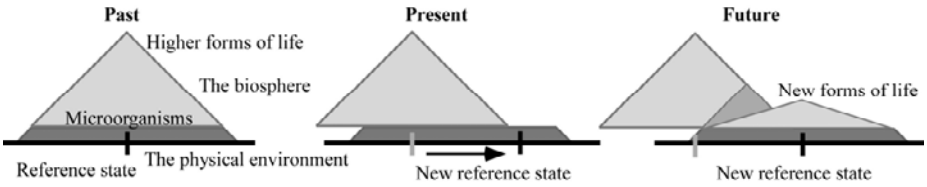

Fig. 7 “Survival of the Fittest” is a driving force in the evolution .

The incredible power of these tiny organisms must not be ignored. One single bacterium could in theory fill out the entire solar system within a few weeks if it were able to multiply without limitations. This describes the power of the living foundation of nature’s life support system and the danger of interfering with this. By changing the physical environment it becomes unfavorable for existing microorganisms as well as for higher forms of life. This may be recorded as a reduction in the number of species. However, the new physical environment that is offered will also encourage new forms of life to appear, initially by new microorganisms that are better fitted to the new conditions, e.g. bacteria that develop immunity to antibiotics. Later new insects or insects with new characteristics will appear, such as the malaria mosquito that is resistant to DDT. This is what Darwin expresses as “the survival of the fittest.” Toxicity is a condition that can be reversed when transferred to different biological systems. A toxic substance is of course harmful for some organisms but at the same time it offers a new ecological niche that soon will be occupied by new organisms. This is a dangerous consequence of environmental pollution and an important perspective on the bird flu virus.

Thus, industrial society may nourish its own extinction by degrading the biological foundations of human existence. It would be very naive to believe that new microorganisms will only live in harmony with the present higher forms of life. The immediate signs of this are the appearance of new diseases as the bird flu virus, less resistance against existing diseases due to a weakened immune system and the increasing rate of chronic allergy.

Sustainable Engineering

Sustainable Development

There are more than hundred definitions of sustainable development, however, the most widely-used was coined in 1987 by the Brundtland Commission in their report, Our Common Future: “to meet the needs of the present without compromising the ability of future generations to meet their own needs.” This may sound very attractive since everyone will get what they “need”, now and forever. However, this does not free the rich from dealing very concretely with the problems associated with redistribution of current wealth to those who are in greater need. Still, need must be treated with global justice to remain its meaning. United Nations Development Programme Human Development Report has stated that the annual income of the poorest 47 percent of the earth’s people is less than the combined assets of the richest 225 people in the world. Given this obscenely unequal distribution of wealth and income, the top fifth of the world’s people consume 86 percent of all the goods and services while the bottom one-fifth must subsist on a mere 1.3 percent. Sustainable development must not become a mantra used as an excuse and justification to sustain economic growth at the expense of continued human suffering and environmental destruction. Thus, it must incorporate explicit and well-founded notion of the globe’s carrying capacity and an awareness of the consequences of exceeding this. However, since the Brundtland report was presented, resource depletion and environment destruction have only proceeded and worsen. The poor are still ignored and left out with a catastrophe. Thus, the time of lip service must be replaced with action and true change. This implies the fulfillment of moral obligations concealed for generations.

Exergy is a suitable scientific concept in the work towards sustainable development. Exergy accounting of the use of energy and material resources provides important knowledge on how effective and balanced a society is in the matter of conserving nature’s capital. This knowledge can identify areas in which technical and other improvements should be undertaken, and indicate the priorities, which should be assigned to conservation measures. Thus, exergy concept and tools are essential to the creation of a new engineering paradigm towards sustainable development.

Exergy

The exergy concept originates from works of Carnot [3], Gibbs [4] Rant [5] and Tribus [6]. Exergy of a system is [1]

$$E = U + P_0 V - T_0 S - \sum_i \mu_{i0} n_i \tag{1}$$

where U, V, S, and n_i denote extensive parameters of the system (energy, volume, entropy, and the number of moles of different chemical materials i) and P_0, T_0, and μ_{i0} are intensive parameters of the environment (pressure, temperature, and chemical potential). Analogously, the exergy of a flow can be written as:

$$E = H - T_0 S - \sum \mu_{i0} n_i \tag{2}$$

where H is the enthalpy.

All processes involve the conversion and spending of exergy, thus high efficiency is of most importance. This implies that the exergy use is well managed and that effective tools are applied.

Exergy Losses

Energy is always in balance, however, for real processes exergy is never in balance due to irreversibilities, i.e. exergy destruction that is related to the entropy production by

$$E_{\text{in}}^{\text{tot}} - E_{\text{out}}^{\text{tot}} = T_0 \Delta S^{\text{tot}} = \sum_i (E_{\text{in}} - E_{\text{out}})_i > 0 \tag{3}$$

where ΔS^{tot} is the total entropy increase, $E_{\text{in}}^{\text{tot}}$ is the total exergy input, $E_{\text{out}}^{\text{tot}}$ is the total exergy output, and $(E_{\text{in}} - E_{\text{out}})_i$ is the exergy destruction in process *i*.

The exergy loss, i.e. destruction and waste, indicates possible process improvements. In general "tackle the biggest loss first" approach is not always appropriate since every part of the system depends on each other, so that an improvement in one part may cause increased losses in other parts. As such, the total losses in the modified process may in fact be equal or even larger, than in the original process configuration. Also, the use of renewable and non-renewable resources must be considered. Therefore, the problem needs a more careful approach.

Exergy Efficiencies

A simple definition of efficiency expresses all exergy input as used exergy, and all exergy output as utilized exergy. So the exergy efficiency $\eta_{\text{ex},1}$ becomes:

$$\eta_{\text{ex},1} = \frac{E_{\text{out}}}{E_{\text{in}}} = 1 - \frac{E_{\text{in}} - E_{\text{out}}}{E_{\text{in}}} \tag{4}$$

However, this efficiency does not always provide an adequate characterization of the thermodynamic efficiency of processes, such as heat transfer, separation, expansion etc. Often, there exists a part of the output exergy that is unused, i.e. an exergy waste E_{waste} to the environment. Thus, the utilized exergy is given by $E_{\text{out}} - E_{\text{waste}}$, which we call the exergy product E_{pr}. The output consists of two parts.

$$E_{\text{out}} = E_{\text{pr}} + E_{\text{waste}} \tag{5}$$

The exergy efficiency $\eta_{\text{ex},2}$ now instead becomes

$$\eta_{\text{ex},2} = \frac{E_{\text{out}} - E_{\text{waste}}}{E_{\text{in}}} = \frac{E_{\text{pr}}}{E_{\text{in}}} = \eta_{\text{ex},1} - \frac{E_{\text{waste}}}{E_{\text{in}}} \tag{6}$$

Sometimes a part of the exergy going through the system is unaffected. This part of the exergy has been named the transit exergy E_{tr}, see Fig. 8. Example of transit exergy is the

exergy which goes unaffected through a production process, e.g. the exergy of crude oil being refined into petroleum products.

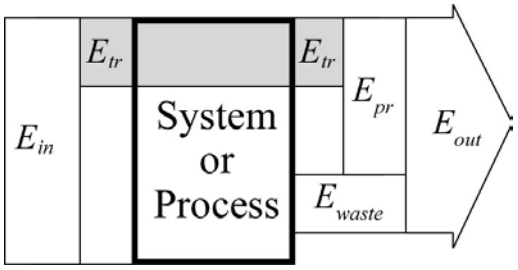

Fig. 8 Process flows.

If the transit exergy E_{tr} is deducted from both the input and the output exergy (or rather from exergy product), the exergy efficiency $\eta_{\mathrm{ex},3}$ becomes

$$\eta_{\mathrm{ex},3} = \frac{E_{\mathrm{out}} - E_{\mathrm{waste}} - E_{\mathrm{tr}}}{E_{\mathrm{in}} - E_{\mathrm{tr}}} = \frac{E_{\mathrm{pr}} - E_{\mathrm{tr}}}{E_{\mathrm{in}} - E_{\mathrm{tr}}} \tag{7}$$

These latter definitions are compared by applying them to a system with two different processes A and B (Fig. 9) The exergy efficiencies are for process A: $\eta_{ex,2}$=91% and $\eta_{ex,3}$=10%, and for process B: $\eta_{ex,2}$= $\eta_{ex,3}$=50%. Thus, determining which is the most efficient process is a matter of defining efficiency. In addition, the exergy destruction of process A is larger than that of process B, 9 versus 5.

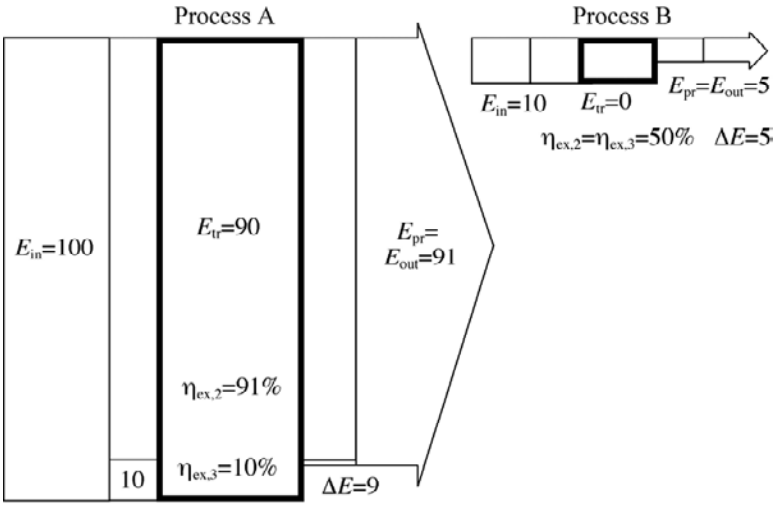

Fig. 9 Comparing exergy efficiencies.

A better insight is offered by using exergy flow diagrams since it shows: (1) the exergy efficiencies of the various parts of a system, (2) the different exergy inputs and outputs, (3) where the various exergy flows come from and go to, (4) the amount of transit exergy, (5) how much exergy is destroyed in each processes.

Exergy diagrams

Exergy flow diagrams

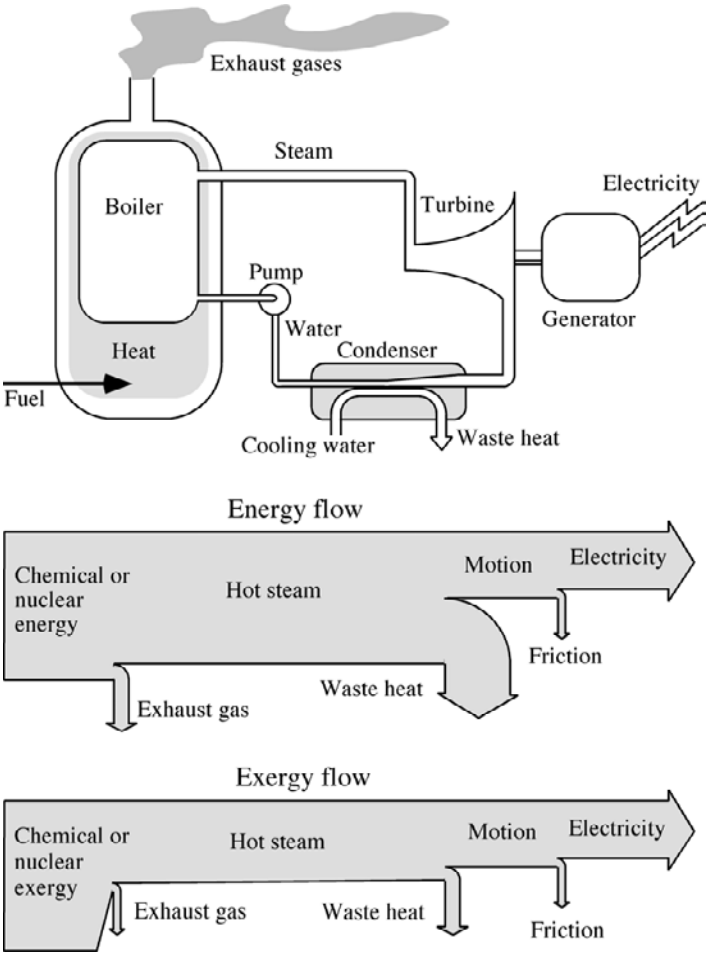

Fig. 10 Energy and exergy flow diagrams of a heat power plant.

From the above it is clear that ambiguity reduces if an exergy flow diagram is used to demonstrate an exergy transfer instead of a ratio. In engineering, these diagrams are often used to describe the energy or exergy flows through a process.

Figure 10 shows a typical heat power plant, its main components and roughly the main energy and exergy flows of the plant. This diagram shows where the main energy and exergy losses occur in the process, and also whether exergy is destroyed from irreversibilities or whether it is emitted as waste to the environment. In the energy flow diagram energy is always conserved, the waste heat carries the largest amount of energy into the environment, far more than is carried by the exhaust gases. However, in the exergy flow diagram the temperature of the waste heat is close to ambient so the exergy becomes much less. The exergy of the exhaust gas and the waste heat are comparable.

Figure 11 illustrates the energy and exergy flows of an oil furnace, an electric heater, an electric heat pump and a combined power and heat plant, i.e. a co-generation plant. The produced heat is used for space heating. In the oil furnace the energy efficiency is assumed to be typically about 85%, losses being due mainly to the hot exhaust gases. The exergy efficiency is very low, about 4%, because the temperature difference is not utilized when the temperature is decreased, to a low of about 20°C, as a comfortable indoor climate.

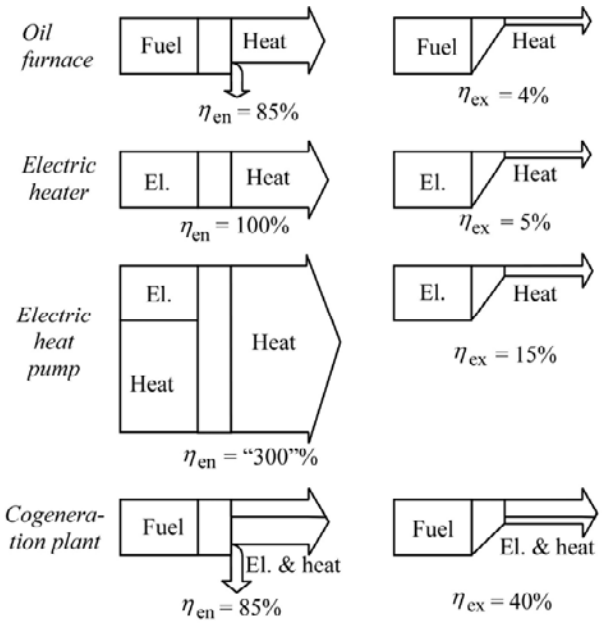

Fig. 11 Energy and exergy flows through some typical energy systems.

Electric heating by short-circuiting in electric resistors has an energy efficiency of 100%, by definition of energy conservation. The energy efficiency of an electric heat pump is not limited to 100%. If the heat originating from the environment is ignored in the calculation of the efficiency, the conversion of electrical energy into indoor heat can be well over 100%, e.g. 300% as in Fig. 11. The exergy flow diagram of the heat pump looks quite different. The exergy efficiency for an electric heater is about 5% and for the heat pump, 15%.

In Fig. 10 the energy and exergy efficiencies are the same because the inflow of fuels and the outflow of electricity both have an exergy factor of about or exactly 1 respectively. For a combined power and heat plant, i.e. a cogeneration plant (Fig. 11) the exergy efficiency is about the same as for a thermal power plant (Fig. 10). This can be better understood from the exergy diagrams. The main exergy loss occurs in the conversion of fuel into heat in the boiler. Since this conversion is practically the same in both the condensing and the combined power plants, the total exergy efficiency will be the same, i.e. about 40%. However, it may be noted that the power that is instead converted into heat corresponds to a heat pump with a coefficient of performance (COP) of about 10. Thus, if there is a heating need a cogeneration plant is far superior to a condensing power plant. The maximum energy efficiency of an ideal conversion process may be over 100%, depending on the definition of efficiency. The exergy efficiency, however, can never exceed 100%.

Total Exergy input/output Analysis

Exergy Analysis

To estimate the total exergy input that is used in a production process it is necessary to take all the different inflows of exergy to the process into account. This type of budgeting is often termed Exergy Analysis [1]. There are basically three different methods used to perform an Exergy Analysis: a process analysis, a statistical analysis or an input-output analysis. The latter is based on an input-output table as a matrix representation of an economy. Every industrial sector is represented by a row and column in the matrix. The main advantage of this method is that it can quickly provide a comprehensive analysis of an entire economy. The main disadvantages results from the use of financial statistics and from the degree of aggregation in the table. In order to obtain a more detailed disaggregation than used in input-output tables it may be sufficient to make use of the more detailed statistics from which input-output tables are usually compiled. The method is called statistical analysis, which is basically a longhand version of input-output analysis. This method has two advantages over the input-output method: firstly, it can achieve a more detailed analysis, and secondly, it can usually be executed directly in physical units, thus avoiding errors due to preferential pricing, price fluctuations, etc. However, its disadvantage compared to the input-output method is that the computations usually have to be done manually. Process analysis, see Fig. 12, focuses on a particular process or sequence of processes for making a specific final commodity. It evaluates the total exergy use by summing the contributions from all the individual inputs, in a more or less detailed description of the production chain.

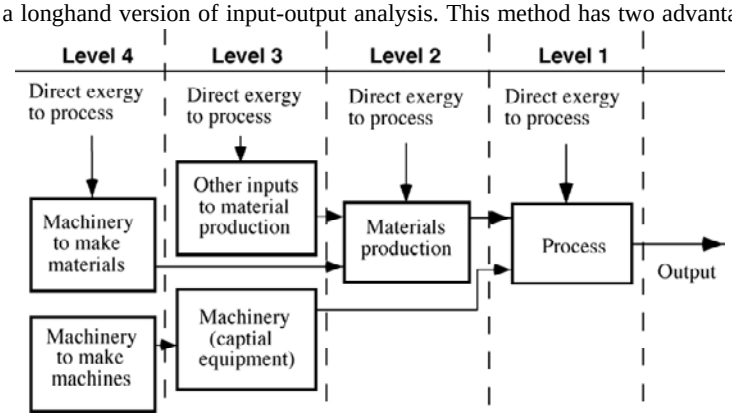

Fig. 12 Levels of an exergy process analysis.

Net Exergy Analysis has also been introduced, see Fig. 13. All exergy being used, directly or indirectly, in the production of the product will be deducted from the exergy of the product, in order to define the net exergy product.

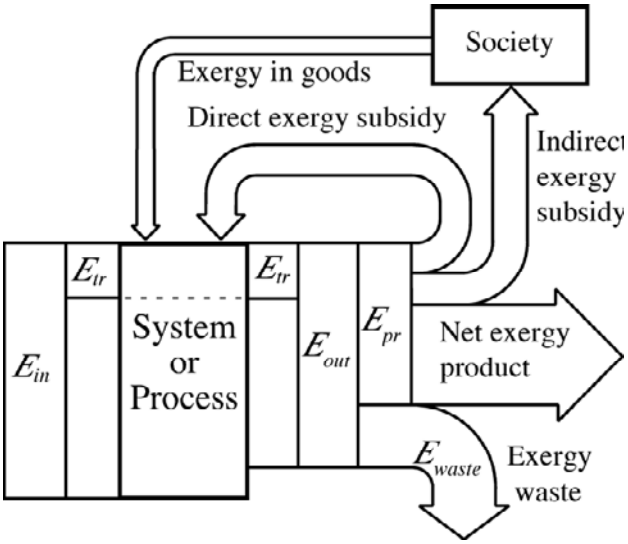

Fig. 13 Net exergy analysis.

Life Cycle Analysis or Assessment

Environmentally oriented Life Cycle Analysis or Assessment (LCA) has become very popular in the last decade to analyze environmental problems associated with the production, use and disposal or recycling of products or product systems, see Fig. 14. Every product is assumed to be divided into these three "life processes", or as it is sometimes named "from cradle to grave".

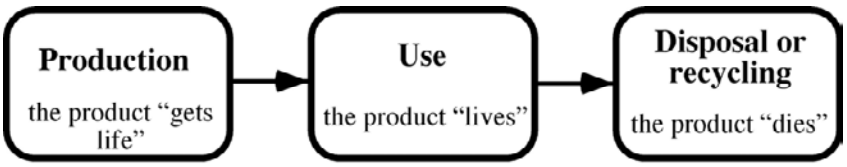

Fig. 14 The life cycle "from cradle to grave".

For every "life process" the total inflow and outflow of energy and material is computed, thus, LCA is similar to Exergy Analysis. In general Exergy Analysis and LCA have been developed separately even though they are strongly linked. This inventory of energy and material balances is then put into a framework as described in Fig. 15. Four stages in the LCA can be distinguished: (1) Aims and limits, (2) Inventory, (3) Environmental impact, and (4) Measures. These four main parts of an LCA are indicated by boxes, and the procedure is shown by arrows. Solid arrows show the basic steps and dashed arrows indicates suitable next steps, in order to further improve the analysis.

In LCA the environmental burdens are associated with a product, process, or activity by identifying and quantifying energy and materials used, and wastes released to the environment. Secondly one must assess the impact on the environment, of those energy and material uses and releases. Thus it is divided into several steps (Fig. 15).

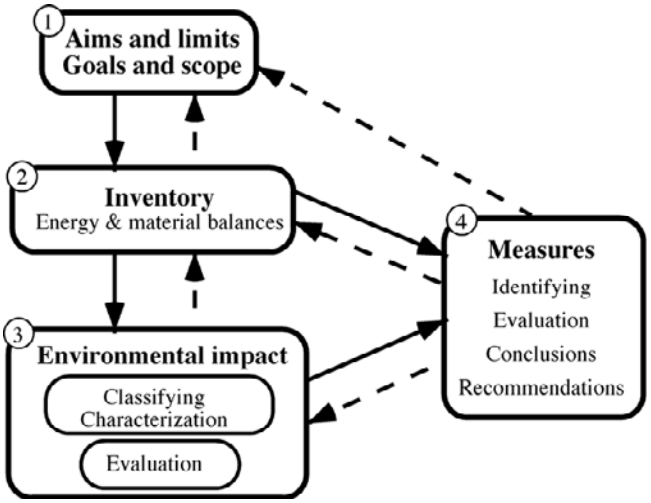

Fig. 15 Main steps of an LCA.

Life Cycle Exergy Analysis

The multidimensional approach of LCA causes large problems when it comes to comparing different substances, and general agreements are crucial. This problem is avoided if exergy is used as a common quantity, which is done in Life Cycle Exergy Analysis (LCEA) [2].

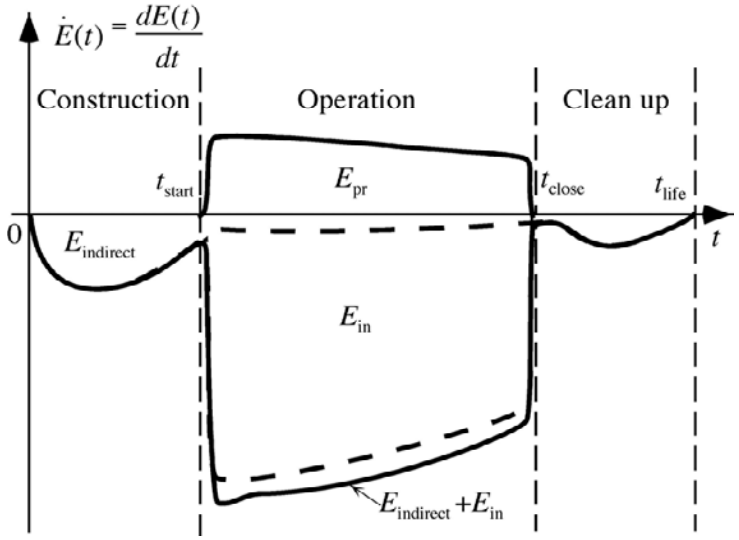

Fig. 16 LCEA of a fossil fueled power plant.

In this method we distinguish between renewable and non renewable resources. The total exergy use over time is also considered. These kinds of analyses are of importance in order to develop sustainable supply systems of exergy in society. The exergy flow through a supply

system, such as a power plant, usually consists of three separate stages over time (Fig. 16). At first, we have the construction stage where exergy is used to build a plant and put it into operation. During this time, $0 \le t \le t_{\text{start}}$, exergy is spent of which some is accumulated or stored in materials, e.g. in metals etc. Secondly we have the maintenance of the system during time of operation, and finally the clean up stage. These time periods are analogous to the three steps of the life cycle of a product in an LCA. The exergy input used for construction, maintenance and clean up we call indirect exergy E_{indirect} and we assume this originates from non renewable resources. When a power plant is put into operation, it starts to deliver a product, e.g. electricity with exergy power E_{pr}, by converting the direct exergy power input E_{in} into demanded energy forms, e.g. electricity. In Fig. 16 the direct exergy is a non-renewable resource, e.g. fossil fuel and in Fig. 17 the direct exergy is a renewable resource, e.g. wind.

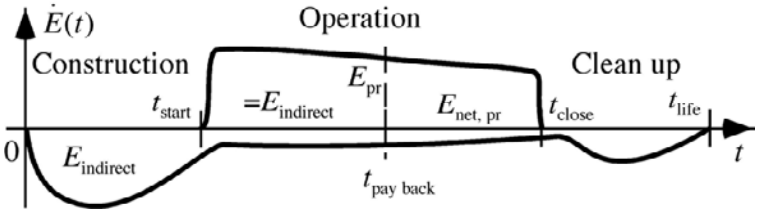

Fig. 17 LCEA of a wind power plant.

In the first case, the system is not sustainable, since we use exergy originating from a non-sustainable resource. We will never reach a situation where the total exergy input will be paid back, simply because the situation is powered by a depletion of resources, we have $E_{\text{pr}} < E_{\text{in}} + E_{\text{indirect}}$. In the second case, instead, at time $t = t_{\text{payback}}$ the produced exergy that originates from a natural flow has compensated for the indirect exergy input, see Fig. 17, i.e.

$$\int_{t_{\text{start}}}^{t_{\text{pay back}}} \dot{E}_{\text{pr}}(t)dt = \int_{0}^{t_{\text{life}}} \dot{E}_{\text{indirect}}(t)dt = E_{\text{indirect}} \tag{8}$$

Since the exergy input originates from a renewable resource we may not account for it. By regarding renewable resources as free then after $t = t_{\text{payback}}$ there will be a net exergy output from the plant, which will continue until it is closed down, at $t = t_{\text{close}}$. Then, exergy has to be used to clean up and restore the environment, which accounts for the last part of the indirect exergy input, i.e., E_{indirect}, which is already accounted for (Eq. 8). By considering the total life cycle of the plant the net produced exergy becomes $E_{\text{net,pr}} = E_{\text{pr}} - E_{\text{indirect}}$. These areas representing exergies are indicated in Fig. 17. Assume that, at time t=0, the production of a wind power plant starts and at time $t = t_{\text{start}}$ it is completed and put into operation. At that time, a large amount of exergy has been used in the construction of the plant, which is indicated by the area of E_{indirect} between t=0 and $t = t_{\text{start}}$. Then the plant starts to produce electricity, which is indicated in Fig. 17 by the upper curve $E_{\text{pr}} = E_{\text{indirect}} + E_{\text{net, pr}}$. At $t = t_{\text{payback}}$ the exergy used for construction, maintenance and clean up has been paid back. For modern

wind power plants this time is only some months. Then the system has a net output of exergy until it is closed down, which for a wind power station may last for decades. Thus, these diagrams could be used to show if a power supply system is sustainable.

LCEA is very important in the design of sustainable systems, especially in the design of renewable energy systems. Take a solar panel, made of mainly aluminum and glass, that is used for the production of hot water for household use, i.e. about 60°C. Then, it is not obvious that the exergy being spent in the production of this unit ever will be paid back during its use, i.e., it might be a misuse of resources rather than a sustainable resource use. The production of aluminum and glass require a lot of exergy as electricity and high temperature heat or several hundred degrees Celsius, whereas the solar panel delivers small amounts of exergy as low temperature heat. LCEA must therefore be carried out as a natural part of the design of sustainable systems in order to avoid this kind of misuse. Another case to investigate is the production of biofuels in order to replace fossil fuels in the transport sector. This may not necessarily be sustainable since the production process uses a large amount of fossil fuels. Thus, it may well turn out to be better to use the fossil fuels in the transport sector directly instead.

Sustainable engineering could be defined as systems which make use of renewable resources in such a way that the input of non-renewable resources will be paid back during its life time, i.e. $E_{\text{pr}} > E_{\text{in}} + E_{\text{indirect}}$. In order to be truly sustainable the used deposits must also be completely restored or, even better, not used at all. Thus, by using LCEA and distinguishing between renewable and non-renewable resources we have an operational method to define sustainable engineering.

Exergy and economics

Exergy measures the physical value of a natural resource. Thus, it is also related to the economic value, which reflects the usefulness or utility of a resource.

In order to encourage the use of sustainable resources and to improve resource use, an exergy tax could be introduced. The use of non-renewable resources and its waste should be taxed by the amount of exergy it accounts for, since this is related to the environmental impact. In addition to this, toxicity and other indirect environmental effects must also be considered. In the case of irreversible environmental damage, a tax is not suitable, instead restrictions must be considered.

A system could be regarded as a part of two different environments, the physical and the economic environment. The physical environment is described by pressure P_0, temperature T_0, and a set of chemical potentials μ_{i0} of the appropriate substances i, and the economic environment by a set of reference prices of goods and interest rates. These two environments are connected by cost relations, i.e. cost as a function of physical quantities (Fig. 18).

With the system embedded in the physical environment, for each component there are mass and energy balances needed to define the performance of the system. In addition, these balances describe the physical behavior of the system.

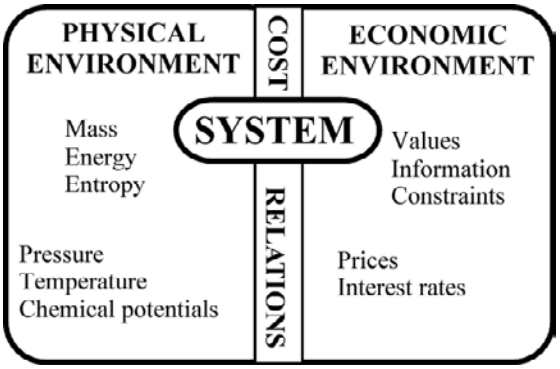

Fig. 18 The system surrounded by the physical and the economical environments, which are linked through cost relations.

If the cost relations are known, then the physical and economic environments could be linked. The cost equations can sometimes be simplified to a scale effect, times a penalty of intensity. Then the system of lowest cost, which is physically feasible, can be found. Usually the maintenance and capital costs of the equipment are not linear functions, so in many cases these costs have more complex forms. If, by some reason, it is not possible to optimize the system, then at least cost could be linked to exergy by assuming a price of exergy. This method is called Exergy Economy Accounting (EEA).

Exergy Economy Accounting

Since exergy measures the physical value, and costs should only be assigned to commodities of value, exergy is thus a rational basis for assigning costs, both to the interactions that a physical system experiences with its surroundings and to the sources of inefficiency within it. The exergy input is shared between the product, and the losses, i.e. destruction and waste.

EEA simply means determining the exergy flows and assigning economic value to them. When there are various inflows and outflows, the prices may vary. If the price per exergy unit does not vary too much, an “average price” can be defined. This method allows comparison of the economic cost of the exergy losses of a system. Monetary balances are formulated for the total system, and for each component of the system, being investigated. EEA gives a good picture of the monetary flows inside the total system and is an easy way to analyze and evaluate very complex installations.

EEA does not, however, include consideration of internal system effects. It does not describe how the capital investments in one part on the system affect exergy losses in other parts of the system. In the EEA method the exergy losses are numbers and not functions. However, this simple type of analysis sometimes gives ideas for, otherwise, not obvious improvements, and a good start of an optimization procedure, in which the exergy losses would be functions.

Exergy Economy Optimization

When constructing a system, the goal is often to attain the highest possible technical efficiency at the lowest cost, within the existing technical, economical and legal constrains. The analysis also includes different operating points (temperatures, pressures, etc.), configurations (components, flow charts, etc.), purpose (dual purpose, use of waste streams, etc.), and environments (global or local environment, new prices, etc.). Usually, the design and operation of systems have many solutions, sometimes an infinite number. By optimizing the total system, the best system under the given conditions is found. Some of the general engineering optimization methods could be applied, in order to optimize specific design and operation aspects of a system. However, selecting the best solution among the entire set requires engineering judgment, intuition and critical analysis. Exergy Economy Optimization (EEO) is a method that considers how the capital investments in one part of the system affect other parts of the system, thus optimizing the objective function. The marginal cost of exergy for all parts of the system may also be calculated to find where exergy improvements are best paid off.

Optimization, in a general sense, involves the determination of a highest or lowest value over some range. In engineering we usually consider economic optimization, which in general means minimizing the cost of a given process or product, i.e. we need a well defined objective function. It is also important not to be misled by a local optimum, which may occur for strongly non linear relations. It is only the global optimum that truly optimizes the objective function.

Conclusions

From a sustainable development point of view, present industrial resource use is a dead-end technology, leading to nothing but resource depletion and environmental destruction in the long run. The exergy capital is used and become waste in a one-way flow (Fig. 4). Instead we need to develop a vital and sustainable society, similar to what is practiced by nature.

Nature has so far generated life and awareness by means of natural evolution. Present social evolution is instead governed by increased wealth in terms of money, often indicated by Gross Domestic Production (GDP). This is when asphalt, smokestacks and color TVs replace rain forests, or when rice fields, cultivated for more than 5000 years, are converted to golf courses. This myth of progress must be questioned if we are serious in our efforts for sustainable development. At first we must find the roots to the problem. The reason for our failure is a consequence of our deep-rooted weakness of building empires. The so-called human civilizations appearing some 10,000 years ago may be characterized as the beginning of an empire builder era of humankind. This empire building era must come to an end in order to reestablish a sustainable development. Then, we must work for a change through education, true actions, practical exercises, and precaution. Finally we must secure a guidance based on morals and responsibility.

Exergy is an excellent concept to describe the use of energy and material resources in the society and in the environment. A society that consumes the exergy resources at a faster rate than they are renewed is not sustainable. From the description of the conditions of the present industrial society, we may conclude that this culture is not sustainable. One may argue about

details, such as how or when, but not that a culture based on resource depletion and environmental destruction is doomed. The educational system has a crucial role to play to meet this change towards sustainable development. This must be based on a true understanding of our physical conditions. Exergy is a concept that offers a physical description of the life support systems as well as a better understanding of the use of energy and other resources in society. Thus, exergy and descriptions based on exergy are essential for our knowledge towards sustainable development.

Time to turn is here. Time to learn and time to unlearn has come. Education must practice true democracy and morals to enrich creativity and knowledge by means of joy in learning. Culture of peace must replace cultures of empire building, violence and fear. The torch of enlightenment and wisdom carried through the human history must be shared within a spirit of friendship and peace.

Acknowledgement

The permission to use my work for the UNESCO's Encyclopedia of Life Support Systems (www.eolss.net) for this paper is hereby gratefully acknowledged. I also want to express my gratitude to the organizers of this conference to invite me to have this presentation.

References

1 Wall, G. Exergy — a Useful Concept. Ph.D. Thesis, 1986, Chalmers University of Technology, Sweden, http://www.exergy.se/goran/thesis/index.html.
2 Gong, M. and Wall, G. "On Exergy and Sustainable Development − Part 2: Indicators and methods." *Exergy, an International Journal*, 2001, 1(4), 217-233.
3 Carnot, S. Réflections sur la puisance motrice du feu et sur les machines propres a dévelopeer cette puissance (Ed R. Fox), 1978 (Bachelier, Paris).
4 Gibbs, J.W. A Method of Geometrical Representation of the Thermodynamic Properties of Substances by Means of Surfaces. Trans. Conn. Acad., 1873, II, 382-404.
5 Rant, Z. Exergie, ein neues Wort für 'technische Arbeitsfähigkeit'. (Exergy, a New Word for Technical Available Work). Forschungen im Ingenieurwesen, 1956, 22(1), 36-37.
6 Tribus, M. Thermostatics and Thermodynamics, 1961 (Van Norstrand, New York).

THE EU RESEARCH STRATEGY TOWARDS ZERO EMISSION FOSSIL FUEL POWER PLANTS

Pierre Dechamps
European Commission
Directorate General for research
Energy Conversion and Transport Unit
Brussels – Belgium
e-mail : pierre.dechamps@ec.europa.eu

Abstract

This paper describes the research strategy put in place by the Directorate General for Research of the European Commission in the field of the mitigation of CO_2 emissions. This is first placed in the general context of the Commission energy policies. This section covers the main policy actions and instruments relevant to energy policy, that is namely the climate change issue, the introduction of renewable energy sources, the security of energy supply, the promotion of energy efficiency and the opening of energy markets.
The paper then concentrates on the research policies of the Commission, mainly the European Research Area concept and its number one instrument, the Framework Programmes for research and technological development. The rational and the analysis supporting the ERA are covered, as well as the structure and the implementation modalities of the Framework Programmes. Initial ideas for the 7th framework programme covering the years 2006-2013 are debated.
The paper then goes into some details of past and present projects in CO_2 capture and sequestration and shows how they are organised and how they fit into the above-mentioned research policy, while contributing to the successful deployment of the Commission energy policies. These projects represent a portfolio of the order of 130 m€ of research and technological development.
Emphasis is put on the new integrated projects and networks of excellence resulting from the calls for proposal of FP6 in this field.
The new technology platform on zero emission fossil fuel power plants is presented, in its organisation, working methods, objectives and achievements – mainly its vision and the corresponding strategic research agenda and strategic deployment agenda.

Keywords : European Commission, research, energy, fossil fuels, CO2

Introduction

Sustainable development and world-class economic competitiveness are central objectives for the European Union. These overriding needs are reflected in the European Union's research priorities in order to implement sustainable development, with energy as a key aspect. Three key strategic objectives for energy are:

- to reduce greenhouse gas and pollutant emissions,
- to secure a future sustainable and diversified energy supply, with the increased use of new and renewable energy sources
- to ensure a competitive European industry
-

In order to achieve an impact in the medium to long term, considerable RTD effort is required to implement a sustainable energy system with clean energy sources, carriers and conversion technologies that are economically attractive and technically robust. Within this scenario, fossil fuel use will be required to fulfil a long-term transitional role prior to the increasing introduction of new and renewable energy sources. However, if fossil fuels are to be part of

this sustainable energy scenario, then near-zero emissions fossil fuel systems will be required. Accordingly, the development of CO_2 capture and sequestration systems associated with fossil fuel power plants is a key priority within the RTD Framework Programmes of the European Union (EU).

Within the context of global environmental policy issues and initiatives, this paper provides an overview of such RTD activities together with comments on the complementary international cooperation and coordination actions by the EC.

Global Environmental Policy Issues

Worldwide, there is increasing concern regarding climate change issues related to Green House Gas (GHG) emissions. It is also recognised that global issues require global responses. This approach has been reflected in the Kyoto Protocol, with many major nations agreeing to limit greenhouse gas emissions in the period up to 2012. Thus the European Union intends to decrease its GHG emissions by 8% in 2008-2012 compared to 1990 under the Kyoto Protocol. This will be achieved through a burden sharing agreement between Member States taking into account the fuel mix and situation pertaining within each State. The EU is making reasonable progress so far, although there is still uncertainty on whether a reduction by 8% will be achieved in the designated timescale. Entry into force of the Protocol is subject to the ratification by countries representing at least 55% of total CO_2 emissions. After the US withdrawal, this means that Russia should ratify and thus has in effect the future of the Protocol in its hands.

The European Climate Change Programme (ECCP) was also established to identify the most promising and cost-effective routes. With regard to the practicalities of reducing GHG emissions, this will be achieved through a combination of the more rational use of energy in all sectors together with a switch to lower carbon fuels including a greater introduction of (zero carbon) renewable energy sources. A second phase of the ECCP has started in early 2006, has a working group on carbon dioxide capture and storage and will give birth to a Commission Communication to the Council and the Parliament on carbon dioxide capture and storage.

Indeed at the Johannesburg World Summit on sustainable development, it was reaffirmed that increasing the use of clean renewable energy will have multiple benefits for developed and developing countries alike, with a positive outcome likely to arise from increasing the global share of renewable energy sources. However, as is noted below, the use of fossil fuels will continue to dominate the energy mix for a variety of reasons and as such there is a need to ensure that fossil fuel systems become more energy efficient and have a less adverse environmental impact.

For fossil fuel utilisation systems, the drive will be towards near zero emission power plant and for such units the currently proposed way forward is to introduce CO_2 Capture and Sequestration techniques with the existing systems. Such techniques are not yet cost effective in the Kyoto horizon, but the results so far are promising. Thus, further RTD is worthwhile. Mitigation costs are high although they vary according to the technology to be used and even within the same technology there may be differences in costs (1), as shown in Figure 1.

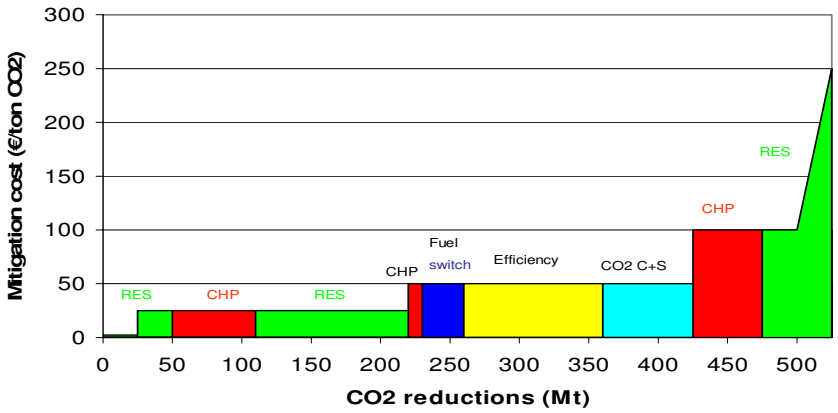

Figure 1: Cost effectiveness of CO_2 reduction technology (source: ECCP)

With regard to GHG, since the 1st of January 2005, mandatory emissions limits are placed on all big industrial and energy intensive businesses on a continent-wide scale. The EU-wide emissions trading scheme is tailored to suit the Kyoto Protocol. This draws in five industry sectors across 25 EU Member States and the three EEA States (Iceland, Lichtenstein and Norway). The scheme covers power generation over 20 MW, including industrial installations, such as refineries, coke ovens, cement, metals, minerals and the pulp and paper industries (but not the chemicals sector) except for hazardous or municipal waste burners. A Linking Directive has been developed to bring CDMs and Joint Initiatives credits within the emissions trading umbrella.

For CO_2 capture and sequestration, it is deemed essential that the use of such technologies can receive credits in the context of these two directives. It would appear that this should be the case since neither directive refers to any particular technology while defining emissions as releases to atmosphere. However, the position needs to be clarified and in particular, guidelines are required for the storage. About half of the EU's total CO_2 emissions are covered by the scheme, with 5,000 firms taking part. It covers all greenhouse gases but only CO_2 will be traded in the first instance as it accounts for 80% of emissions in the EU. The other gases will be traded from 2008 onwards when the scheme will be extended to other sectors and chemicals will almost certainly be brought in.

In the post-Kyoto scenario, more significant reductions of CO_2 will be needed. On the basis of current climate models, it has been suggested that a maximum 2°C increase in global temperatures could be accommodated, which would equate to an atmospheric CO_2 concentration level of some 450 ppmv. On the basis of 1990 levels this would require 50% to 60 % less emissions of CO_2 by 2050 and a path going through -20 to -30% by 2020, as recently approved by the Council. This would need to come not only from developed economies but also from economies in transition since in the latter case even if per capita

emissions are relatively low, total emissions will become ever more significant. Any post-Kyoto negotiation process will need to recognise the right to development of less developed and transitional economies.

International Projections and Comparisons for Energy Use

Following on from the previous point, various scenarios and projections have been made. A key study is the so called WETO Report (2), supported by the EU, which examined the world energy, technology and climate policy outlook in order to provide assistance to decision makers in defining their long term policies. Two of the key results arising from this work are as follows:

- If no specific policy initiatives and measures are taken, world CO_2 emissions are expected to double by 2030 and, with a share of 90%, fossil fuels will continue to dominate the energy system.
- As the largest growing energy demand and CO_2 emissions originate from developing countries, Europe will have to intensify its cooperation, particularly in terms of technology transfer.

The former point is shown in Figure 2, taken from the WETO study (2). Complementary work by the IEA (3) also indicates that on a global scale, coal demand for power generation is expected to double over the period to 2030, with the major increase arising within economies in transition. The IEA estimates that 4500 GW of new power plant will be required, of which coal fired plant is expected to be 40% of this with natural gas providing the very great of the remaining capacity. These projections arise from the recognition that the use of renewables can only be accelerated in the medium to long term both in developed and developing countries.

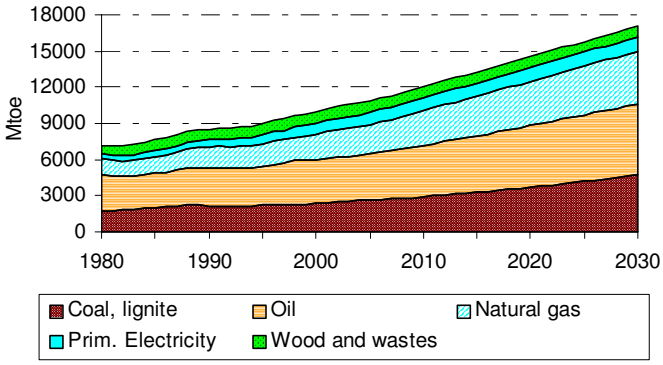

Figure 2: Scenarios and projections – fuels (source : WETO)

With regard to carbon intensity compared to GDP, the WETO report indicates that the EU is amongst the lowest, as shown in Figure 3.

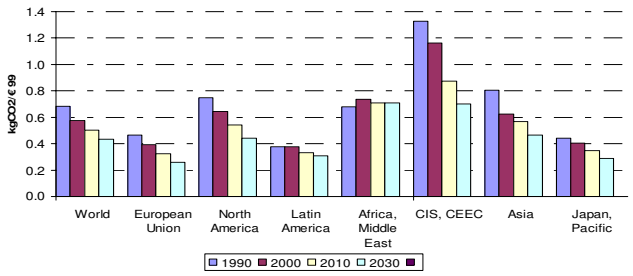

Figure 3: Scenarios and projections (source : WETO) - Carbon intensity of GDP

There are also scenarios and projections for CO_2 emissions per capita. Here, the EU is above the world average but below some other continents, as shown in Figure 4

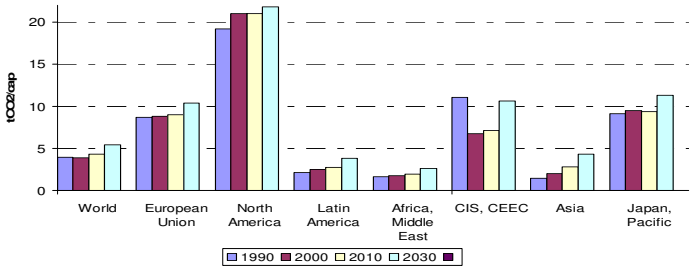

Figure 4: Scenarios and projections (source : WETO) - CO2 emissions per capita

Key Energy Considerations within the EU

Within the European vision of energy sustainability, key issues include the need for security of energy supply and the need to ensure EU industrial competitiveness in a post Kyoto scenario. These key issues must also be reconciled with environmental protection.

Thus, in this context, within Europe, the EC Green Paper (4) identifies the need to establish a sustainable approach to energy use and management. There is a focus on ensuring diversity of supply while meeting environmental standards and limits through increased use of indigenous renewable energy sources. At the same time, the Green Paper explicitly recognises that doubling the renewables share in the energy supply quota from 6 to 12% and raising their part in electricity production from 14 to 22% is an ambitious objective. Indeed a prevailing view amongst EU energy experts is that the future energy needs of the enlarged EU will require the full range of available fuels (including renewables, nuclear, natural gas, oil and coal) to be utilised on an environmentally acceptable basis to meet the projected overall needs. Such an approach is considered sustainable as it will ensure the necessary diversity and security of supply, provided adequate environmental performance can be achieved. Consequently fossil energy usage will require advanced technologies with near zero emissions. This will mean the use of CO_2 capture and sequestration technologies integrated with the advanced fossil fuel power plant.

The other key issue is EU industrial competitiveness. EU industry needs to be placed in a position to compete globally in a post-Kyoto scenario. Since the expectation is that there will be a major upsurge in new and retrofit power station construction, based on fossil fuels (and subsequently renewables), the need is to ensure that the EU power generation and associated equipment manufacturers can remain competitive for the supply of fossil energy utilisation systems and components, both for EU markets and on a global basis. This will also help ensure a cheap and secure energy supply to all the citizens of Europe. Such systems will, in the medium to long term, need to be equipped with CO_2 capture and sequestration techniques. In the electricity sector alone, 4500 GW of new generating plant will be required by 2030 to meet the increased demand. This represents a major market opportunity for EU industry to supply such export markets, particularly in Eastern Europe, Asia and Australasia, provided that the necessary technology has been developed and proven. Historically, EU industry has supplied close to 50% of the global market and to date has had an enhanced reputation for innovation in the development of advanced systems and components, much of which has arisen from RTD projects supported by the EU. There will be significant competition from industry in the USA and Japan, where Government support for the development of carbon management techniques is significant, with the recognition that the return on such investment is expected to come from increased export of advanced technology.

The other key point to stress is that the introduction of renewables and fossil fuels with CO_2 capture and sequestration are complementary from a timing point of view, from a generation mix point of view and to ease the penetration of hydrogen as an energy vector.

There are also synergies between CO_2 capture and sequestration applied to fossil fuel and renewables (in this instance biomass) plants. For example, biomass utilisation in itself is seen as CO_2 neutral. Consequently, should CO_2 capture and sequestration be applied to biomass plants, this would in effect result in negative CO_2 emissions. There are also technical

synergies in the co-utilisation of biomass with solid fossil fuels in large scale power plant, which again can also result in CO_2 credits in a tax /trading environment.

EU Carbon Management RTD Policy Issues

Within Europe, the challenge is to establish a sustainable energy system that will allow the preservation of equilibrium for ecosystems while also encouraging economic development. The medium to long term objective is to develop and establish new and renewable energy sources and energy vectors, such as hydrogen and electricity, which are affordable, clean and can be readily integrated into a long-term sustainable energy supply and demand structure. It is also recognised that the RTD necessary to achieve such objectives requires resources beyond the capacity of any one Member State. Indeed, the pressure of international competition necessitates an integrated European response. Work toward this goal started within the EU Fifth Framework Programme and this will be taken forward and consolidated within the Sixth Framework Programme that is now implemented.

Within this vision, it is recognised that fossil fuels will continue to be used for the foreseeable future and it is therefore imperative that cost effective solutions are required to establish near zero emissions technologies of a high environmental standard. Accordingly, the capture and sequestration of CO_2 associated with cleaner fossil fuel power plants is deemed to be an essential factor for fossil fuels to be part of the sustainable energy scenario. The approach, which is a priority topic within FP6 (2002-2006), will include both cost effective, safe and environmentally compatible disposal options together with the technology for CO_2 capture thereby enabling cleaner and more efficient fossil fuel plants (5).

The plans for FP7 also include a priority on CO_2 capture and storage, with a view towards zero emission fossil fuel power generation.

There are significant costs involved in CO_2 capture and sequestration, of which capture represents 70-80% of total costs. Therefore, the primary RTD objective for the EU is to decrease the cost of capture. The target is to reduce the costs of CO_2 capture from 50-60 € down to 20-30 € per tonne of CO_2 captured, whilst aiming at achieving capture rates above 90%. Methods include pre-combustion capture (applicable to gasification systems); post-combustion capture and oxyfuels combustion.

There is also a strong need to assess both the reliability and long term stability of CO_2 sequestration in order to map geological storage potential, determine safety aspects and to build public confidence to ensure acceptability. CO_2 sequestration options of interest to the EU include geological based storage in aquifers, depleted oil and gas reservoirs (with the possibility of enhanced oil recovery) and deep un-mined coal beds (that offer the benefit of enhanced coal bed methane recovery). In addition, there are certain chemical techniques and other innovative ways that appear to be promising. At present, the EU's Sixth Framework Programme supports research on oceans and biospheric sinks such as forests and algues, but does not support the development of storage techniques in these sinks, because of the risk potential associated with the degrees of uncertainty in such techniques.

It is also recognised that while the sustainable energy economy is under development, for a transition period, hydrogen is likely to be mostly produced from fossil fuels. For fossil fuel

based gasification technologies, when CO_2 is removed from the gas stream the fuel that remains is hydrogen. Thus within the FP6 RTD Programme, there is strong complementarity between the work on capture and sequestration of CO_2 from fossil fuels and another strategic priority, namely the development of new technologies for future energy carriers and converters such as hydrogen and fuel cells (5).

The Current and Proposed EU RTD Portfolio on Carbon Capture and Sequestration

The current portfolio of EU funded research projects is summarised in Table 1.

European project acronym	**Topic**	**Total cost (m €)**	**EC funding (m €)**	**Coordinator**
AZEP	Advanced membrane cycles	9.3	3.4	Siemens
GRACE	Capture in processes	3.2	2.1	BP
GESTCO	Sequestration potential	3.8	1.9	GEUS
CO2STORE	SACs2 follow up on land	2.4	1.2	Statoil
NASCENT	Natural storage analogues	3.3	1.9	BGS
RECOPOL	Enhanced coal bed methane	3.4	1.7	TNO
WEYBURN	Weyburn monitoring	2.2	1.2	BGS
SACS2	Monitoring of Sleipner	2.1	1.2	Statoil
CO2NET	Thematic Network	2.1	1.4	Technology Initiatives

Table 1. The portfolio of EU funded research projects under FP5

This indicates that the EU is contributing some 16 m€ to support nine projects, worth over 30m€ of total investment. This contains two projects on CO_2 capture, six projects covering CO_2 sequestration and sequestration monitoring and one Thematic Network.

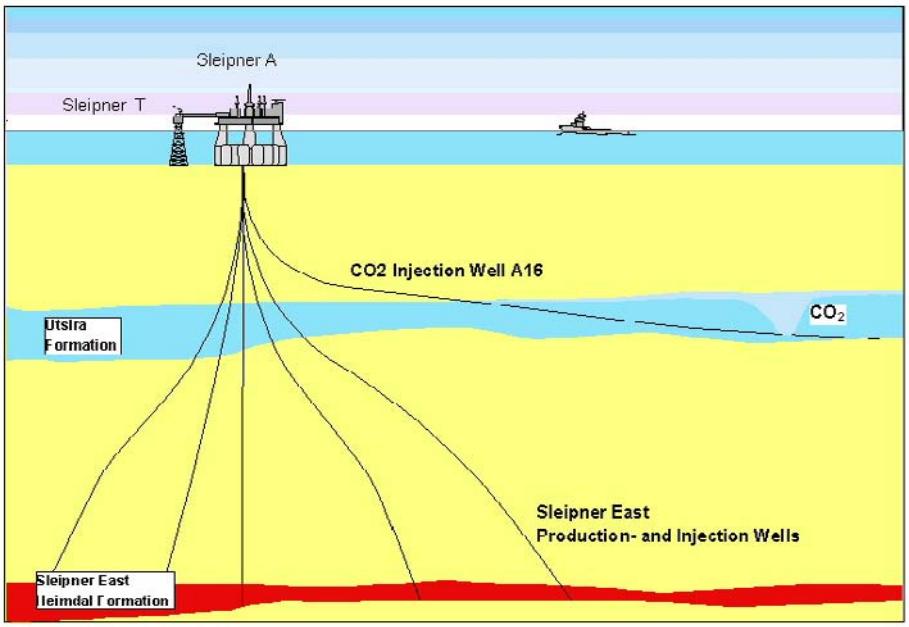

Fig. 5 – Sleipner – CO_2 injection into the Utsira formation - courtesy of Statoil.

The projects listed above are supported within the Fifth RTD Framework Programme of the EU. In addition, there is funding available for this priority RTD area within FP6. The first FP6 call was published in December 2002, with a budget of 198 million € for medium to long-term energy research. These projects are summarised in Table 2.

Project acronym	**Project type**	**Topic**
ENCAP	IP – Integrated Project	Enhanced capture of CO_2
CASTOR	IP – Integrated Project	CO_2 from capture to storage
CO2SINK	IP – Integrated Project	In-situ laboratory for capture and sequestration of CO_2
CO2GeoNet	NoE – Network of Excellence	Network of excellence on geological sequestration of CO_2
ISSC	STREP – Scientific Technical Research Project	Innovative in-situ CO_2 capture technology for solid fuel gasification

Table 2. RTD projects from the first half of FP6

The proposed support for these projects reflects the commitment by the EU to continue to create and develop the European Research Area. A short description of each project is given below. These projects represent a total EC funding of the order of 35 m€ and a total cost of the order of 60 m€.

ENCAP
This project has been put forward by major players within the EU power industry to establish the basis for the integration of enhanced CO_2 capture techniques within fossil fuel power plant concepts.

CASTOR
This project builds on earlier work to develop effective, innovative techniques for post-combustion CO_2 capture.

CO2SINK
This project offers the prospect of a large-scale land based detailed study of CO_2 sequestration, with the basis for an in-situ laboratory being established at the demonstration site.

CO2GeoNet
This Network of Excellence is designed to bring together the key research institutes to rationalise and share their resources in order to create a critical mass capable of responding positively to the European challenges for geological sequestration of CO_2.

ISCC
This project will undertake RTD to develop innovative techniques for in-situ capture of CO_2 appropriate for solid fuel gasification technologies.

The second half of FP6

The second half of the budget for FP6 has been made available to a number of projects described below, which are now started. These brings the total commitment under FP6 up to 68 m€, for a total research cost well in excess of 120 m€.

CACHET

CO2 capture and hydrogen production from gaseous fuels (IP)

CO2REMOVE

The monitoring and verification of CO2 geological storage (IP)

DYNAMIS

Preparing for large scale H2 production from decarbonised fossil fuels including CO2 geological storage (IP) (HYPOGEN PHASE1)

CLC GAS POWER, C3-Capture, DeSANNS, HY2SEPS

Advanced separation techniques (STREP)

EU GeoCapacity

Mapping geological CO2 storage potential matching sources and sinks (STREP)

A Technology Platform

Zero emission power generation is in the process of becoming the topic of an industry-lead technology platform grouping all the stakeholders getting together to define a Strategic Research Agenda on a number of strategically important issues with high societal relevance where achieving Europe's future growth, competitiveness and sustainable objectives is dependent upon major research and technological advances in the medium to long term.

This platform is clearly expected to build a roadmap towards the vision of a zero emission power generation plant.

International Cooperation and Coordination Activities

Within the EC, there is a clear recognition that the need to deal with environmental challenges requires an international approach. Accordingly the EC is involved in a wide range of international cooperation and coordination activities that complement the RTD activities that they manage directly.

Thus, the EC takes an active role in the International Energy Agency (IEA) of the OECD. It participates in the "Committee of Energy Research and Technology - CERT" and in the "Working Party on Fossil Fuels - WPFF", with a particular role in the "Zero Emission Technologies - ZETS" strategy.

It also sponsors and participates in the IEA "Greenhouse Gas" Implementing Agreement and in the IEA "Clean Coal Centre" Implementing Agreement.
In addition, the EU, via the EC, has Science and Technology Cooperation Agreements with many countries such as Argentina, Australia, Brazil, Canada, China, India, Russia, South Africa and the USA. The EC has also signed a Memorandum of Understanding with the US Department of Energy (DoE) and is a Member of the Carbon Sequestration Leadership Forum (CSLF), which is an initiative led by the USA.

At the EU level, within the European Initiative for Growth, a number of "*quick start*" projects will probably be launched to stimulate the European economy. Among the research projects considered is HYPOGEN, a full size demonstration plant for the production of hydrogen from fossil fuels with CO_2 capture and storage. This initiative also underlines the link between CO_2 capture and storage and the future hydrogen economy.

Within the European Union, the EC is involved in the open co-ordination of Member State activities as part of the process for the creation of the European Research Area. At the policy strategy definition level, co-operation may be done through open co-ordination in which Member States voluntarily agree to coordinate amongst themselves in an informal way. With regard to structuring EU RTD work, co-ordination is carried out at the project level through STREPs, IPs, Networking and Co-ordination actions that are the instruments of the EU Framework Programmes . It may also be carried out at the Programme level through ERA-NET activities. Of relevance here is a project in an exploratory phase (FENCO) to undertake a

specific support action for Fossil Energy Concerted Actions. The intention is to establish the feasibility for a subsequent co-ordination action that could create the basis for a unified approach within Europe for the development of near zero emissions technologies and carbon management strategies for fossil fuel power generation.

Conclusions

The European Union's research priorities include the need to establish sustainable development, with energy as a key aspect, while ensuring EU industrial competitiveness. The future fuel mix is expected to be diverse, thereby ensuring security of supply, and fossil fuels will be part of that mix provided that environmentally acceptable techniques can be established, with the emphasis on carbon management. Accordingly, when considering a post Kyoto scenario, the development of CO_2 capture and sequestration systems associated with fossil fuel power plants is a key priority within the RTD Framework Programmes of the EU.

There is now a significant RTD Programme that is designed to ensure both cost effective, safe and environmentally compatible disposal options together with the technology for CO_2 capture thereby enabling cleaner and more efficient fossil fuel plants. This is being undertaken by EU industry in collaboration with research institutes and universities. The involvement of EU industry is critical since they are the technology stakeholders that will subsequently have to compete in the global market place.
In addition, there is a clear recognition that the need to deal with global environmental challenges requires an international approach. Accordingly the EC is involved in a wide range of international cooperation and coordination activities that complement the RTD activities that they manage directly.

A great deal of additional information on the European Union is available on the internet.
It can be accessed through the Europa server (http://europa.eu.int).

Legal notice

Neither the European Commission, nor any person acting on behalf of the Commission is responsible for the use which might be made of the information contained in this publication. The views expressed here are those of the authors and do not necessarily reflect those of the European Commission.

References

1 European Climate Change Programme, European Commission Report June 2001.
2 World Energy, Technology and climate policy Outlook 2030, WETO. Official Publication
of the EC, Report EUR 20366, Luxembourg 2003.
3 World Energy Outlook, IEA 2002
4 Towards a European Strategy for the Security of Energy Supply, COM(2000) 769 final
5 Calls for FP6 RTD, Official Journal of the EC, 2002 to 2006

Part I

European Energy Materials Research

Invited papers

MATERIALS DEVELOPMENT FOR BOILERS AND STEAM TURBINES OPERATING AT 700°C

R.Blum[1] and R.W.Vanstone[2]
[1]Elsam Engineering A/S, [2]ALSTOM Power ltd

Abstract

In Europe development of boilers and steam turbines for plant operating at temperatures in excess of 700°C is being carried out within the EU supported AD700 project. This collaborative project involves all of the major European power plant manufacturers supported by utilities and research institutes. The first phase of the project began in 1998 and was extended to run until the end of 2003. A second phase began in 2002 and runs until the end of 2006. The objective has been the development of all technology necessary for the construction and operation of such plant.

This paper describes the development of the high temperature materials technology essential to underpin the development of the AD700 power plant technology. It describes the factors influencing alloy design and selection and the scope and results of investigations on candidate alloys carried out within the project. It then goes on to describe the programme of full-scale prototype component manufacture which is currently in progress. These prototype components are being characterised through extensive long term testing programmes. The development of joining procedures for these materials is also described.

Keywords: Materials, boiler, steam turbine, AD700

The AD700 project

The overall objective of the AD700 project is to develop and demonstrate a new generation of pulverised coal-fired power plants featuring advanced steam conditions [1]. This is being achieved through the application of nickel-based superalloys to bring the live steam temperature up to about 700°C, resulting in an increase in efficiency from around 47%, representing the current state-of-the-art plant, to around 55%, an increase yielding reductions in fuel consumption and carbon dioxide emission of almost 15%. The plant will have an output within the range of 400-1000MW, making it suitable for the range of utility scale generation. The project involves nearly all the major European power plant manufacturers and their material suppliers, the largest European utilities and major research organisations.

The principal innovation which underlies this development is the replacement of iron-based alloys by nickel-based alloys for the highest temperature components. These alloys are already used in the aerospace and gas turbine industries so that the project has been to some extent one of technology transfer. However much larger components are required for boilers and especially for steam turbines than are currently produced for gas turbines and significant technical challenges have been overcome to achieve the manufacture of larger components. In addition, these components will be required to operate under significantly different conditions of environment, stress and temperature. Therefore demonstration of manufacturing capability and appropriate material characteristics as been required. Nickel-based alloys are much more expensive than alloy steels and this aspect has motivated further innovations to minimise the requirement for these alloys. This challenge has been addressed through radical new concepts in plant architecture and innovation in turbine construction and also through material developments to maximise the strength of austenitic and ferritic steels.

The first phase of the project began in 1998 and was extended until the end of 2004 to allow the continuation of long term creep tests. A second phase began in 2002 and will run until the end of 2006. The objective has been the development of all technology necessary for the construction and operation of such plant. The success of the AD700 project has underpinned the COMTES 700 project, an in-plant demonstration of critical boiler and turbine components which was launched in 2004 [2].

Material selection

Development and demonstration of appropriate materials and their properties, especially in the case of the nickel based alloys, is critical to establishing the technical feasibility of the new power plant concept. As well as creep strength sufficient for long term operation at these high temperatures (typically 100,000 hour rupture strength of around 100MPa at the metal temperature is required), materials requirements include corrosion resistance in boiler flue gases and under conditions of steam oxidation, resistance to thermo-mechanical cycling and the ability to be manufactured and welded in thick section.

Most modern-day nickel based alloys have been developed from a relatively simple Ni20%Cr alloy. In order to achieve the required creep properties, further strengthening through solid solution strengthening or dispersion strengthening is necessary. Additions of elements like Mo, W and Co confer solid solution strength. Alloys relying principally on this mechanism, such as alloys 230 and 617, are used in the solution treated condition and have the advantage of being relatively easy to weld with no requirement for complex post weld heat treatment. However their proof strengths are relatively low and where this property is important additions of Ti and Al to form dispersions of the gamma prime precipitate, conferring high proof strength as well as improved creep strength, can be made. Alloys such as these, for example alloy 263 and waspaloy, must be aged after solution treatment to produce the strengthening dispersion and thus post weld heat treatment requirements are more complex. Additions of Ti and Al are limited by the requirement for weldability: where these additions are too high the kinetics of gamma prime precipitation become such that precipitation occurs in the heat affected zone (HAZ) during welding, the reduced ductility resulting from which leads to the potential for HAZ cracking. An alternative approach to dispersion strengthening is by alloying with Nb, leading to the more sluggishly precipitated gamma double prime. With regard to corrosion resistance, where flue gas corrosion resistance is required, increased levels of Cr may be necessary. Finally the economic aspects of material selection cannot be neglected so, in order to mitigate the high cost of nickel-based alloys, significant additions of Fe, such as are made in the case of alloys 718 and 901, may be considered.

Boiler materials

In order to realise a 700 °C USC boiler, extensive materials development and qualification is necessary, including the use of Ni based superalloys in the most severely exposed components. These developments can be categorized into three groups reflecting the key components of such plant, i.e:

- Furnace panels
- Superheaters
- Thick section components and steam lines

Furnace panels

The behaviour of water and steam in the furnace panels changes rapidly as steam pressure increases from sub to super critical conditions, and in particular, at constant enthalpy increase (constant heat input) the rise of water/steam temperature also grows rapidly. Therefore, the water/steam temperature at the outlet of the furnace panels of super critical boilers grows constantly, as steam parameters moves towards the advanced conditions of 350 bar and 700 °C planned for the AD700 technology.

Typically, the enthalpy at the outlet of the furnace panels would be in the range of 2600-2700 kJ/kg, and Figure 1 indicates how temperature grows from ~375 °C to ~450 °C as steam pressure increases, which means growing problems with the strength of conventional well proven low alloyed steel like 13CrMo 44. On the other hand the cooling characteristics of single phased super critical water/steam are good as no evaporation takes place.

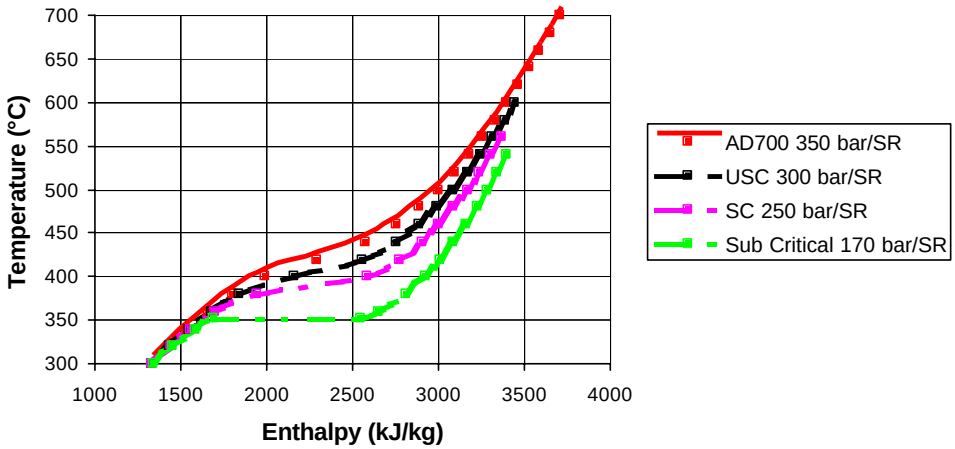

Figure 1. Water/steam temperature versus enthalpy

However, also increased steam temperatures, which rise from 540-560 °C into the range of 700 °C add to the temperature rise of water/steam in the furnace panels, as feed water and live steam flows are reduced. In these circumstances the steam temperature in the furnace outlet panels will grow to around 525 °C, resulting in a calculated mid wall temperature of 575 °C at start of service. Further, due to the growth of magnetite on the internal tube surface, mid wall temperatures could increase to about 600 °C, if low alloy steels were used. Therefore more oxidation resistant and stronger furnace tube materials are needed than the 1Cr 0.5Mo used at present.

Three newly developed steels have been selected as candidate materials for furnace panels in future boilers with advanced steam parameters. The high alloyed 12%Cr tube steel HCM12 developed by Sumitomo Metal Industries and Mitsubishi Heavy Industries has excellent creep strength, oxidation and corrosion resistance and, due to a duplex microstructure of approximately 30% d-ferrite and 70% tempered martensite, it is possible to weld this steel without preheat and post weld heat treatment (PWHT) [3]. The lower alloyed 2½%Cr tube steel HCM2S developed

by Sumitomo Metal Industries and Mitsubishi Heavy Industries and the Mannesmann developed 2½%Cr tube steel 7CrMoVTiB1010 both have sufficient high temperature strength and a metallurgy which makes it possible to omit PWHT [4,5]. The chemical composition and mechanical properties for all three steels are given in Figure 2.

Testing of HCM12, HCM2S and 7CrMoVTiB1010 is in progress in Europe to establish practical experience with the handling of these steels. In the furnace panels of an existing subcritical once through boiler, test sections of all three steels have been installed, and service under cycling conditions has been tested for several years. For the HCM2S and 7CrMoVTiB1010 tube materials no problems have been encountered during the production of the test panels or during operation at steam temperatures up to 500 °C. For the tube steel HCM12 which has a rather complicated microstructure, lack of sufficient filler material has caused problems with cracks after welding due to embrittlement, and further development of suitable filler material is required before a reliable welding procedure can be established. Test panels of HCM12 have been service exposed with steam temperatures up to 530 °C under cycling conditions. A full size wood chip fired boiler furnace construction operating with steam temperatures up to 540 °C for more than five years demonstrates that HCM12 could be a candidate for furnace tubes in future advanced USC boilers.

Chemical composition, mass %

	C	Cr	Mo	W	Others
1Cr½Mo	0.13	0.9	0.5		
HCM2S	0.06	2.25	0.3	1.6	V,Nb,N,B
7CrMoTiB1010	0.07	2.4	1		V,Ti,N,B
HCM12	0.1	12	1	1	V, Nb

Creep rupture strength

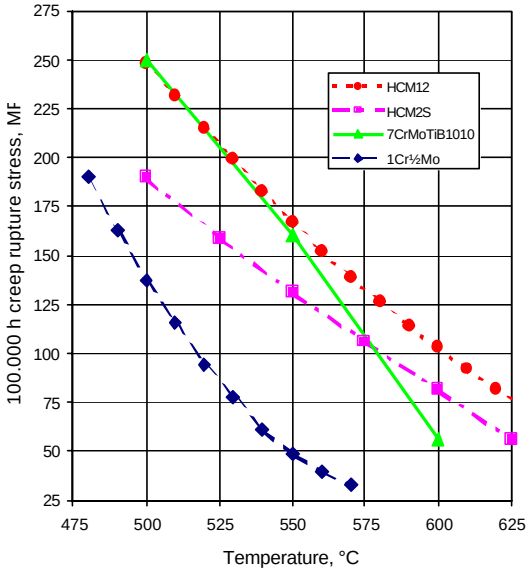

Figure 2. Materials for furnace panels

In connection with the in-plant test and the construction of the wood chip boiler, a computer furnace panel calculation programme has been set up by Elsam to simulate the service exposure and life consumption of a furnace panel in a USC boiler during operation [6]. Calculations first of all demonstrate that at media temperatures higher than around 450°C the temperature rise during operation is strongly dependent on the rate of self oxidation and on the deposition rate of oxides from the feed water. High quality feed water chemistry assuring minimum oxide in feed water is therefore essential if USC plants with advanced steam parameters are to be realised.

Based on these calculations it can be demonstrated that the use of either HCM2S or 7CrMoVTiB1010 is sufficient for media temperatures up to 475°C. For higher media temperatures, only the 12% Cr-steel HCM12 should be considered due to the need for better oxidation resistance. In 2005, however, it was realised that a major reduction in long-term creep rupture strength at temperatures above 550°C must be foreseen. This reduction is due to the formation of Z-phase in this steel not intentionally alloyed with nitrogen. Any future use of HCM12 for furnace panels operating at elevated temperatures must wait for a thorough assessment of the creep rupture strength of this steel.

In COMTES700, fabrication trials leading to in-plant exposure testing have just been finished and in-plant testing began in July 2005. The possible use of the INCONEL® alloy 617 is investigated in parallel as an alternative to HCM12. Of course, alloy 617 has much better mechanical properties and does not generate any significant internal oxide, and therefore it can be exposed to much higher temperatures than HCM12. The fact that alloy 617 tubes cost roughly 10 times more than HCM12 and call for a far more expensive fabrication means, however, that the whole boiler economy must be carefully considered before such a choice of material is taken.

Superheater tubing

For superheater tubing the aim has been to develop an improved austenitic tube material with sufficient strength and flue gas corrosion resistance to operate at steam temperatures around 650 °C, and to develop a Ni base superalloy to fill the gap up to 700 °C steam temperature. Intensive development work has been undertaken in the AD700 project to demonstrate a suitable austenitic tube material with 100,000 hour rupture strength of about 100 MPa at 700 °C and a Ni based tube material with 100,000 hour rupture strength of 100 MPa at 750 °C - both materials to demonstrate a flue gas corrosion resistance better than 2 mm metal loss during an exposure of 200,000 hours.

Austenitic tube material

30 trial melts were manufactured based on the following alloy design principles:

- Precipitate strengthening through the precipitation of Nb(C, N), NbCrN and Cu-rich precipitates.
- The precipitation of fine M(C, N) to induce the precipitation of fine and stable $M_{23}C_6$.
- Addition of W to improve the high temperature strength and stabilise carbonitrides. The creep rupture strength of W alloyed steels is much higher than that of the Mo alloyed steels at higher temperatures.
- Addition of a large amount of Ni, approximately 25 wt%, together with a relatively high amount of N and low amounts of Mn, Mo and Si to suppress the precipitation of sigma phase.

- A Cr content of approximately 23-25 wt% and low Mo content to improve the corrosion resistance in coal-fired boilers.

All trial melts were forged to bars simulating a tube production. After appropriate heat treatment, fourteen of the samples were tested for mechanical properties as well as steam oxidation and flue gas corrosion resistance up to 5,000 hours. This screening test indicated that four of the fourteen tested trial melts might be able to meet the targets. After another 10,000 hour testing one of the four alloys showing the best properties was selected. The chemical composition and room temperature mechanical properties of this alloy called Alloy 174 are shown in tables 1 and 2.

C	Cr	Ni	W	Co	Cu	Nb
0.08	22.2	24.9	3.5	1.5	3	0.49

Table 1. Chemical composition for alloy 174

Tensile strength (MPa)	Yield strength (MPa)	Elongation (%)	Reduction of area (%)	Hardness (HV)	Charpy impact value (J/cm^2)
785	345	55	70	195	216

Table 2. Mechanical properties at room temperature for alloy 174

Figure 3 demonstrates the improvements in creep rupture strength compared with some of the best commercial austenitic superheater tube alloys. The extrapolated rupture data of alloy 174 are based on 20,000 hours of testing. Ongoing steam oxidation and flue gas corrosion test demonstrate properties comparable to or slightly better than those obtained for a large variety of 22 - 25% Cr austenitic superheater steels. So far all targets are fulfilled. Full scale tube production has been successfully demonstrated by the production of 50 m superheater tubes with dimensions 41.4 mm OD x 8 mm wall thickness, and fabricability trials including welding and bending have been completed successsfully. Different filler materials were considered for similar and dissimilar welds. So far, Inconel alloy 617 has been chosen due to its excellent mechanical properties, comparable to alloy 174.

Long term creep rupture properties for base material as well as cross-weld specimens and microstructural stability test are ongoing and will complete the characterisation of this super austenite which will be launched in the market under the name Sanicro 25.

Nickel base tubing

A literature survey conducted by Special Metals concluded that an existing alloy, viz. NIMONIC® alloy 263, had adequate strength to meet the creep requirement, but, from previous work, it was felt that its corrosion resistance would be inadequate. Hence it was decided to develop a new alloy based on alloy 263 for the superheater and reheater tubular components, which would be exposed to corrosive flue gas/ash conditions. The alloy optimisation process considered creep strength and corrosion resistance. Over thirty trial compositions were produced in 22 kg heats which were worked to bars. Improvement of the coal ash corrosion resistance of the alloy was developed in a series of coal ash corrosion tests at different

temperatures employing samples with a systematic variation in alloy constituents. The tests used an atmosphere of 15 vol % CO_2 + 10 vol % H_2O + 1 vol % SO_2 with balance N_2 , and the test specimens were coated with a synthetic coal ash, K_2SO_4 + (Fe_2O_3/Al_2O_3/SiO_2) in the ratio 1:1:1.

Chemical composition, mass%

	Cr	Ni	W	Nb	Cu	Others
Super 304H	18	9		0,4	3	N
NF709	20	25		0,25		Mo, Ti, N
HR3C	25	20		0,4		N
SAVE 25	23	20	1,5	0,4	3	N
Alloy 174	22	25	3,5	0,5	3	N

Creep rupture strength

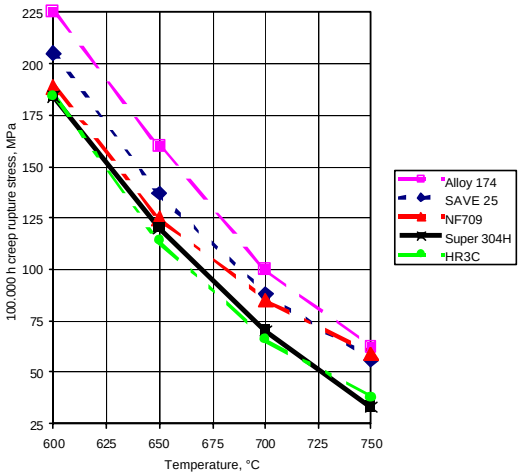

Figure. 3. Materials for superheater tubes

The resultant optimised chemical composition which was selected is given in Table 3. The new alloy INCONEL® alloy 740, based on alloy 263, is a nickel chromium cobalt alloy which is age hardenable by the precipitation of gamma prime but also benefits from solid solution hardening. Table 4 gives the ash corrosion results for this alloy.

A large creep test programme is presently underway covering two major test temperatures, 725 °C and 775 °C, with some shorter term tests at 700, 750 and 800 ºC. Test durations up to 65,000 hours are being targeted, and the results to date are shown in Figure 4.

C	Ni	Cr	Mo	Co	Al	Ti	Nb	Mn	Fe	Si
0.03	Bal	25.0	0.5	20.0	0.9	1.8	2.0	0.3	0.7	0.5

Table 3. Composition of INCONEL alloy 740

Ageing trials are underway with target times up to 70,000 hours. Up to now, 1,000, 3,000 and 15,000 hours have been completed at 700 °C, 750 ºC and 800 °C. The long term ageing trials are being carried out on material which has been given the initial strengthening/ageing treat-

ment of 4 hours at 800ºC. After 1,000 hours at 700 °C, the Charpy impact values dropped to some 45% of the values after the initial ageing/strengthening treatment, and further exposure to 3,000 hours exhibited a reduction to around 27% (of the initial aged/strengthened values). The absolute values after 3000 hours are around 25 J.

Time (hours)	Metal loss (m)	Depth of attack (m)
116	0	4
500	4	14
1000	5	19
1984	16	33
5008	39	60

Table 4. Penetration results for INCONEL alloy 740 in coal ash corrosion tests at 700°C

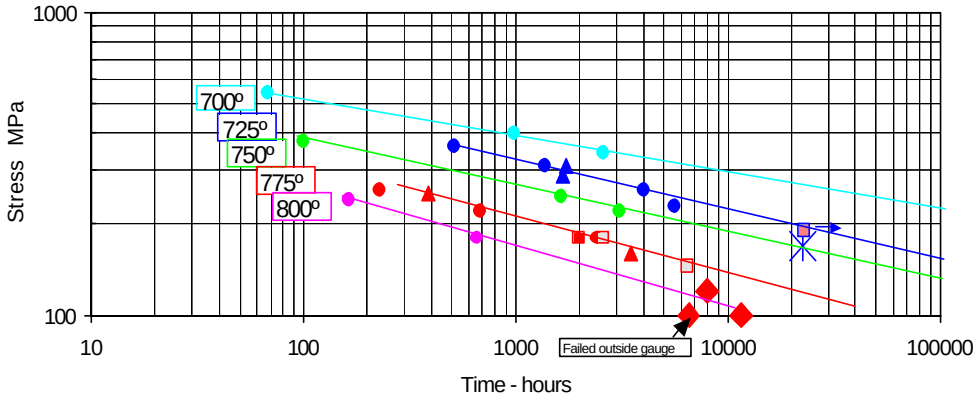

Figure. 4. Inconel alloy 740 creep results

Welding trials have been initiated and have demonstrated that alloy 740 is readily fabricated in the annealed condition. Joining is accomplished with the gas tungsten-arc welding (GTAW) process using both INCONEL Filler Metal 740 and NIMONIC Filler Metal 263. If a high joint strength is required, the deposited weldment may be precipitation hardened. The need for repair of boiler tubes is inevitable and successful welding on aged material has been undertaken although the mechanical test results are not yet available.

A commercial size cast of the alloy has been produced and put through the normal tube production route to produce 100 m superheater tubes with dimensions 38.1 mm OD x 7.7 mm wall thickness. Welding trials and fabrication trials – i.e. tube bending - have been successfully performed and long term creep rupture data for base material as well as cross-weld specimens and microstructural stability tests are ongoing and will complete the characterisation of this nickel alloy.

In the framework of work sponsored by major European generators known as the Emax initiative, fabrication trials of superheater sections partly made of Sanicro 25 and alloy INCONEL®

alloy 740 leading to in-plant exposure testing have been finished successfully. In-plant tests taking these superheater tube materials to temperatures above 700 °C began in September 2004 at the power plant Esbjergværket [7] and in July 2005 at the power plant Scholven as part of the COMTES 700 project.

Thick section components and steam lines

For thick section boiler components and steam lines there were two goals for the materials development. An improved ferritic/martensitic 9-12%Cr steel is desirable to expand the present temperature range for ferritic steels up to app. 650 °C. A Ni-based superalloy with a 100,000 hour rupture strength of 150 MPa at 700 °C is needed to allow construction of outlet headers and main steam lines with acceptable wall thicknesses.

Ferritic pipe steels

The task of improving the 9-12%Cr steels on top of the impressive developments in the last two decades has proved to be very difficult. In the last five years worldwide research has resulted in a large number of new alloys being announced, and from short-term tests they seemed very promising. However, in long-term tests the steels show sigmoidal creep behaviour and so far no ferritic alloy has demonstrated long-term creep strength better than steel P92. In AD700 an attempt was made to improve the creep rupture strength of 9-12% Cr steels. Seven trial melts were manufactured and mechanical properties were obtained up to 12,000 hours. Six of the seven melts turned out to be weaker than P92 and only one melt, a 9%Cr5Co2WVNbN, showed creep rupture data similar to P92. In parallel, tests were made on steel NF12. Short-term data demonstrated a major improvement, but longer term data showed a dramatic drop in strength also for this steel (Figure 5).

Systematic microstructure investigations of new ferritic steels showing sigmoidal creep behaviour have demonstrated that precipitation of the complex Z-phase nitride (Cr(V,Nb)N) takes place in the steels at the expense of the strengthening MX carbonitrides, which dissolve. This mechanism is responsible for the reduction in creep strength, and it seems that high Cr steels are more prone to Z-phase formation than low Cr steels. In order to be able to improve the strength, a fine-tuning of the composition is needed based on a thorough understanding of recent developments. Recent advances in microstructure characterisation techniques and thermodynamically based microstructure models may prove to be the only way to go further in the development of improved ferritic steels [8].

A potentially interesting new ferritic steel is the low carbon 9Cr3Co3WVNbN steel currently under development at the NIMS in Japan. This steel is strengthened only by nitrides and Laves phase precipitates, and the unstable $M_{23}C_6$ carbides are not present. Creep tests up to about 10,000 hours at 650°C show no signs of sigmoidal creep behaviour, see fig. 5. If the low C steels can maintain microstructure stability up to long times, this idea may serve as an important platform for future developments of ferritic steels. The low Cr content will, however, lead to poor steam oxidation resistance, and a surface coating will be needed. At the moment, it does not seem to be possible to obtain high creep strength together with high oxidation resistance at the same time in ferritic steels.

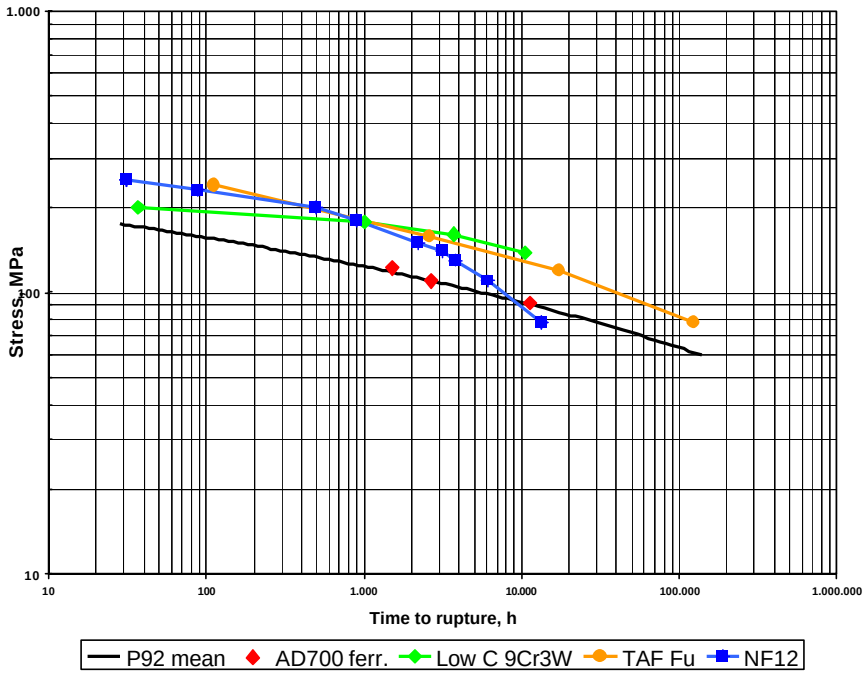

Figure. 5. Ferritic steels 650 °C

Nickel base piping

NIMONIC® alloy 263 or an improved version of INCONEL® alloy 617 meet the demands for outlet headers and steam lines at 700 °C steam temperature. However longer term creep data and demonstration of fabricability – pipe production, hot bending and welding – are needed before a 700°C power plant can be realised. Alloy 263 is under investigation in the AD700 project, and the improved version of alloy 617 is investigated by the German national project MARCKO DE2. Alloy 617 pipes were successfully manufactured in late 2002.

The precipitation hardened Nimonic alloy 263 chemical composition, see table 5, had only limited stress rupture data available as its designed purpose was for industries that do not require 100,000 hour creep data. Therefore, the biggest experimental effort expended on this alloy is in creep testing of commercially available 15 mm diameter bar.

C	Ni	Cr	Mo	Co	Al	Ti	Mn	Fe	Cu	B
0.04 0.08	Bal	19.0 21.0	5.6 6.1	19.0 21.0	0.6 Max	1.9 2.4	0.60 Max	0.7 Max	0.2 Max	0.0005 Max

Table 5. Composition of Nimonic alloy 263 (Note: Ti + Al : 2.4 – 2.8)

The failed tests up to now along with running tests are shown in Figure 6. These data suggest that the alloy will easily meet the creep criteria. This will enable the design of components with relatively small thicknesses and thereby reduce production costs.

A vital demonstration of the viability of this alloy in the context of the AD700 programme is the ability to manufacture in thick section. A NIMONIC® alloy 263 ingot has been put through the normal pipe production route to produce 4.5 meter steam pipe with dimensions 310 mm OD x 66 mm wall thickness shown in Figure 7. Welding trials have been successfully performed and long term creep rupture data for base material as well as cross-weld specimens and microstructural stability test are ongoing and will complete the characterisation of this nickel alloy.

In the German MARCKO DE2 project, mechanical testing and welding trials are established on alloy 617. Both tube and pipe products are available and a review of the existing creep data base, covering creep rupture data for more than 20 heats with testing times above 100,000 h, resulted in an update of creep strength values for both tube and pipe products. Figure 8 shows the ASME creep rupture data of alloy 617 and the proposed revised data obtained in the MARCKO DE2 project as well as the extrapolated creep rupture data of alloy 263 based on 20,000 hours testing.

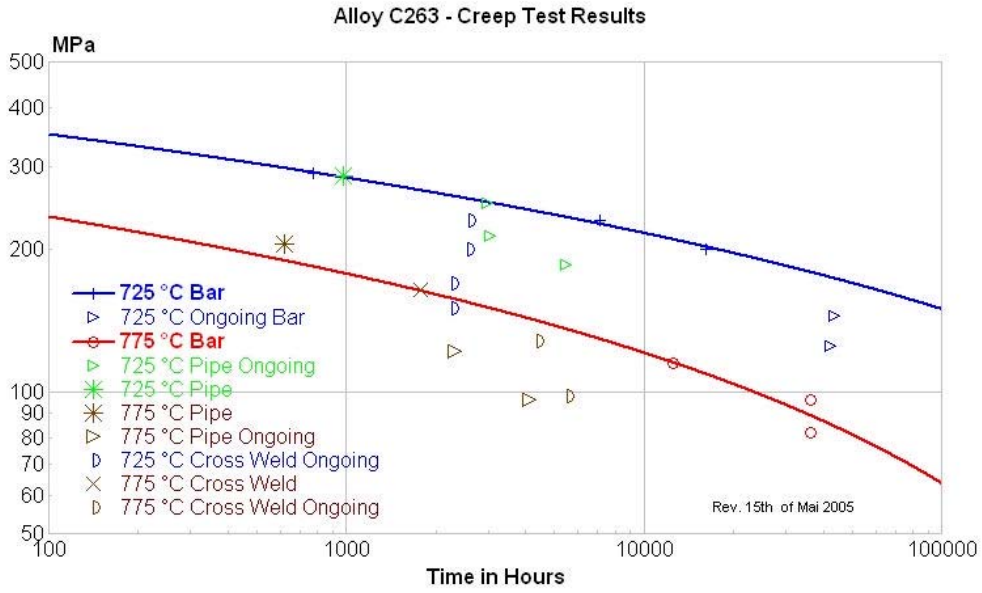

Figure. 6. Nimonic alloy 263 creep results

Figure. 7. Extruded NIMONIC® alloy 263 steam pipe

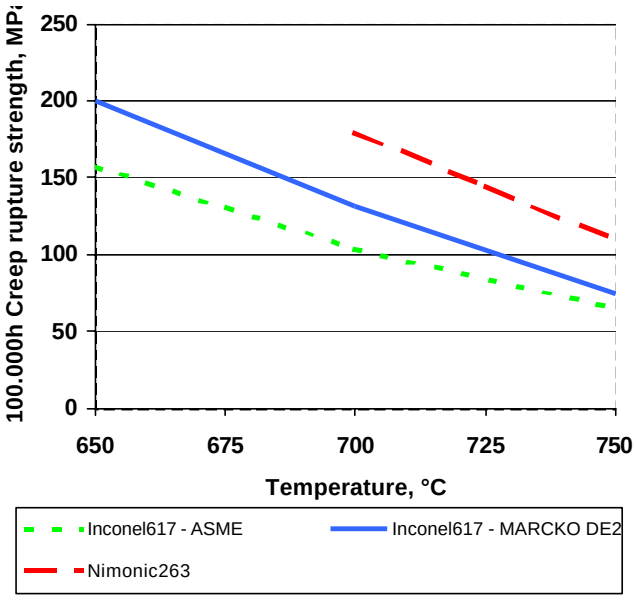

Figure. 8. Super alloy rupture strength

Turbine materials

In addition to the factors already described, the selection of a first generation of candidate alloys in the AD700 project was influenced by the requirement to produce very large components so that experience of the project participants in producing large forgings in, for example alloys 706 and 718, and large castings in, for example, alloy 625 was taken into account. The selection was also influenced by the extent of data already available on the alloy, albeit generally not in the appropriate product form, for example the large body of data on tubes and pipes in alloy 617.

All these considerations, a review of the literature and of other data available to the project, led to the selection of nine alloys for investigation: alloys 155, 230, 263, 617, 625, 706, 718, 901 and waspaloy. In a couple of cases, alloys were selected in more than one heat treatment condition.

Investigation of candidate alloys

The main focus of the initial investigation was the identification of the best candidate alloys for the large rotor and casing components. The smaller components such as blading and bolting are equally important, but it was recognised that the product forms required for these components, bar and possibly investments castings, were already available for the gas turbine industry and could be applied to steam turbines with relatively little effort, perhaps limited to additional materials characterisation to establish those materials parameters required for steam turbine design. The nine candidate alloys were produced in various product forms, conventional castings, centri-spun castings, and bar or forgings. One alloy was also investigated in a powder metallurgy form.

A first series of investigations was intended to confirm reported or expected short-term properties and to gain indications of response to ultrasonic testing and welding. These investigations included room temperature and elevated temperature tensile testing, creep testing at 700°C to target durations of 300-3,000 hours, and ageing trials at 650 and 700°C. The ageing trials involved impact and tensile testing after exposure for durations of 300, 1000 and 3000 hours. Welding trials were carried out on testpieces in each alloy. The weldments were around 35mm in thickness and all were made with the same, alloy 617, consumable. Ultrasonic inspection was carried out on samples of the test materials to establish attenuation properties. Where possible, these investigations were carried out on already available materials but in many cases materials were manufactured specifically for the project.

The mechanical property investigations yielded results which were generally consistent with expected values. In terms of tensile properties castings were generally weaker than wrought products. The properties of centri-spun castings were similar to those of conventional castings. There was some concern that the low proof strength of the castings might lead to poor resistance to thermal cycling. A low cycle fatigue test programme mounted on these alloys has indicated that although relatively low strains lead to endurances of around 100 cycles, the gradient of the endurance curves is shallow so that the strains for endurance of around 5000 cycles are acceptable for steam turbine applications (Figure 9). Nearly all of the alloys responded to long term ageing through increased tensile strength but reduced impact strength. The reductions in impact strength were large enough to be of concern and prompted further investigation. In alloy 617, values of Charpy-V impact strength were observed to fall to as

low as 10J. However when fracture toughness tests were carried out on this embrittled material, values of fracture toughness in excess of 70MPam$^{0.5}$ were measured, values which are considered acceptable for steam turbine applications. The kinetics of embrittlement were very similar in all of the alloys. There was little difference in ageing response at 650 and 700°C and most of the embrittlement appears to be complete after 1000 hours so that the differences between properties measured after ageing for 1000 hours and 3000 hours were relatively small (Figure 10). The creep tests indicated properties generally in line with expectations. However the creep properties of the powder metallurgy product, in alloy 625, were disappointing. Investigation showed that premature, low ductility creep failures occurred at prior particle boundaries due to the presence of nitrides. However process improvements were identified with potential to overcome this problem. One notable success was the development of a modified heat treatment for alloy 718. The alloy normally undergoes a two-stage ageing treatment involving ageing at around 720°C and then 620°C. An increase in the temperature of these ageing treatments by 30-40°C has resulted in a significant increase in long term creep strength. Figure 11 shows the creep master curve of the modified heat treatment [9].

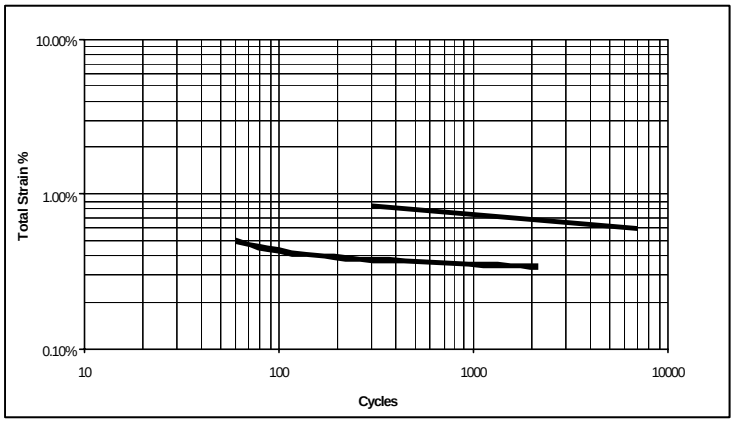

Figure 9. Upper and lower bounds to low cycle fatigue endurance data obtained from tests on cast alloys 263, 617 and 625

The welding trials indicated potential weldability for all of the alloys. No heat affected zone cracking was observed in any case. The ultrasonic investigations showed that the wrought alloys could be inspected by ultrasonics but very clearly showed this would not be possible in cast components. Attenuation levels were so high that in some cases no back wall echo was observed even after ultrasonic path lengths less than 100 mm. Therefore volumetric inspection of castings will be carried out by radiography.

Alloy selection for full scale or model component prototype demonstration

The first round of investigations confirmed that a number of alloys were potentially suitable for application to steam turbine components. The next stage in the project was the selection of alloys for manufacture of full scale prototypes or of components which realistically simulate full scale components.

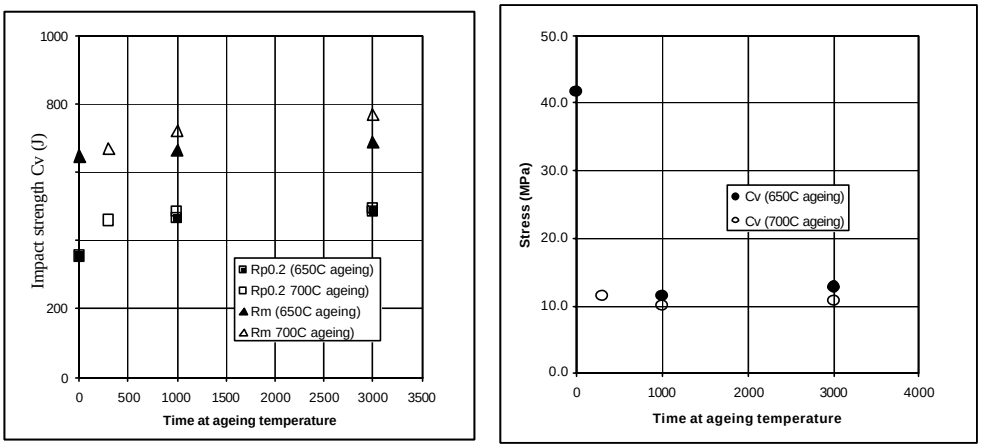

Figure 10. Kinetics of long term ageing in alloy 617

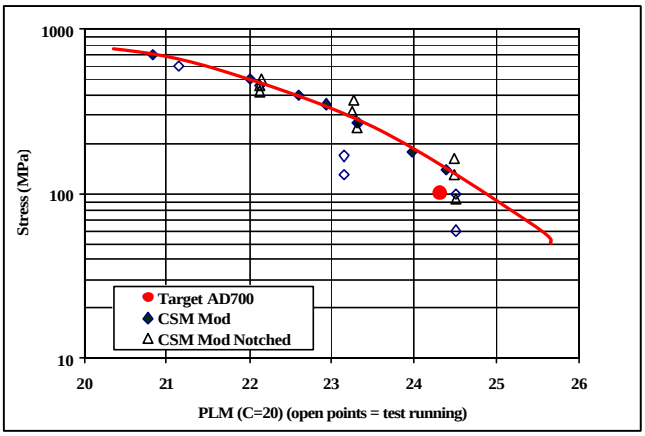

Figure 11. Larson-Miller master curve of modified heat treatment alloy 718 [9]

Even if the properties of castings are poorer than those of forgings, there are strong drivers for their application to valve chest and turbine casings arising from their lower costs and more flexible geometries. Castings require good weldability for the upgrading process arising from defects in the casting itself, but also due to the requirement to join castings to other components. This is especially true in the AD700 concept where the limited size of nickel alloy castings, coupled with the desire to restrict their application to the highest temperature parts of the turbine, means that welded joints in turbine casings, either between two nickel alloy castings, or between nickel alloy castings and steel castings, will be required. The weldability of alloys used in the solution treated condition is generally high due to the relatively low levels of hardening elements such as Ti and Al. Furthermore the absence of phase changes during the welding process means that these nickel alloys require no PWHT to modify the microstructure in the heat affected zone and that they can tolerate any PWHT that is appropriate to the steel base material in dissimilar joints. Taking into account all available data and experience, alloys 617 and 625 were selected for further casting development.

Very similar factors drove the selection of alloys for forging development. Again limited size and high cost mean that welded constructions will be necessary, again favouring the solution treated alloys. For these reasons alloys 617 and 625 were also selected for further forging development. However two additional alloys were also selected. It is unlikely that alloy 718 in its standard form has adequate long term creep strength, but, with the heat treatment modification developed in the first round of investigations, it may provide a lower cost alternative to 617 and 625. Therefore this alloy was also selected for continued development. Finally, in case longer term testing showed unexpected reductions in the creep strength of these first three alloys, a fourth alloy, expected to have even higher strength, alloy 263, was also selected.

The initial round of investigations had also revealed that waspaloy is an excellent alloy for application to smaller, non-welded components such as blading and bolting.

Casting manufacture

Model castings (step blocks with sections up to 200mm) were successfully manufactured in alloys 617 and 625 (Table 6). Additional blocks were also cast for the manufacture of similar metal joints. Joints 70mm in depth and 500mm long were successfully manufactured and inspected using dye pentrant and radiographic techniques. In the case of both alloys, the joints were manufactured using matching consumables. These castings and welded joints were sectioned and are currently being subjected to an extensive and long term testing programme. Investigation of dissimilar joints is also in progress.

617 and 625 casting geometry: Stepped block 300mm in length with sections of 50, 100 and 200mm

617 and 625 casting weight: 750kg

Heat treatment: 617: 1170C/water quench
625: 1200C/water quench

Cast analysis:

Alloy	C	Ni	Fe	Cr	Mo	Co	Nb	Ti	Al	Mn	Si	P	S	Others
617	0.06	bal	0.6	21.6	9.2	12.2	<0.01	0.53	1.09	0.27	0.34	<0.01	0.001	N, 0.021 Cu, 0.02
625	0.02	bal	0.5	21.9	8.4	0.2	3.59	0.3	0.3	0.16	0.18	0.005	0.002	N, 0.033 Cu, 0.08

Table 6: Details of castings for long term property investigation

Full scale valve chests (delivery weight about 3.5 tonnes) have also been manufactured in alloys 617 and 625 (Figure 12). Further work is in progress to confirm the properties of these full scale castings are similar to those of the model castings and a valve chest casting in alloy 625 has been incorporated in the COMTES 700 service exposure project as part of the demonstration of a turbine valve [10].

Figure 12. 617 valve chest casting after removal from mould and shot peening (courtesy of Goodwin Steel Castings)

Figure 13. 617 forging during automatic ultrasonic inspection (courtesy of Saarschmiede)

Rotor forging manufacture

In both of the principal candidate alloys, 617 and 625, full scale HP and IP rotor forgings, repectively 700mm and 900-1000mm in diameter have been successfully manufactured (Figure 13). Careful selection and control of heat treatment parameters is necessary to avoid excessive grain growth which leads to poor ultrasonic inspectability. A first attempt to manufacture the 617 HP forging was unsuccessful but success was achieved on the second attempt after further heat treatment trials and adoption of a modified heat treatment practice. The final result has been sound forgings in a fully solution treated condition but with minimum detectable defect sizes of better than 3mm diameter flat bottomed hole equivalent. These forgings have been sectioned and are currently being tested in a long term test programme.

Model forgings have been manufactured in alloys 718 and 263, heat treatment parameters being controlled to simulate as far as possible the larger forgings manufactured in alloys 617 and 263. These forgings have also been sectioned for investigation. Details of all forgings investigated in this testing programme are given in Table 7.

Welding development has focussed on the two primary candidates and on the requirement for dissimilar joints. Different welding processes and filler metals have been investigated and an optimum solution has been defined. This involves manufacture of the joint using a narrow-gap TIG process and a nickel based filler metal. Manufacture of full scale joints to demonstrate this solution have been successfully completed and a full investigation of weldment properties is in progress.

Candidate materials for blading, bolting and valve components

As previously stated, the identification of the optimum alloy selection and manufacturing route for blading and bar products such as bolts received a lower priority in the early stages of the programme. It is clear there are many alloys with properties more than sufficient for the requirements of steam turbine applications. However a significant decision was required over the manufacturing route for blading. The conventional route involves machining of blades from bar. However as the value of the alloy and the difficulty of machining rises, then the

attraction of a near-net shape process grows. For example, investment castings have been applied very successfully in gas turbines. However cost estimates showed that this route was marginally less attractive than the conventional route, at least for the relatively low volumes anticipated during the early stages of exploitation of this technology. Therefore work is now focussing on development of all the properties needed for application of blades machined from bar.

Alloy	C	Ni	Fe	Cr	Mo	W	Co	Nb	Ti	Al	B	Zr	Mn	Si	P	S	Others
263	0.052	bal	0.34	19.5	5.8		19.5		2.21	0.48	<0.005		0.04	0.09	<0.005	<0.002	Cu, <0.10
617	0.060	bal	0.35	22.8	9.0	0.02	11.9	0.003	0.48	1.15	0.0002	0.005	0.02	0.05	0.005	0.001	Cu, 0.013; N, 0.004; V, 0.005
625	0.030	bal	2.17	21.9	9.1	0.03	0.02	3.7	0.20	0.19	0.004	0.010	0.01	0.02	0.002	0.001	Cu, 0.012; N, 0.006; V, 0.01
718	0.023	54.1	bal	18.8	3.0	<0.01	0.04	5.0	0.93	0.46	0.004		0.01	0.09	0.009	0.0006	

Alloy	Dimensions	Heat treatment (Hold temp, C/ hold time, h/ cooling medium)		
		Solution treatment	Ageing 1	Ageing 2
263	600mm diameter x 100mm	1150/10/air	800/8/air	
617	700mm diameter x 800mm	1100/3/water		
625	725mm diameter x 1230mm	1100/6/water		
718	730mm diameter x 320mm	1065/1/air	760/8/furnace	650/12/air

Alloy	Rp0.2	Rm	A	Z
	MPa	MPa	%	%
263	615	912	21	18
617	359	772	48	45
625	363	763	57	52
718	1155	1340	19	21

Table 7: Details of forgings for long term property investigation

Bolting materials will inevitably be machined from bar and materials with appropriate properties are already available.

Wear resistance is an important issue for valve components and hard-facing solutions are applied in conventional steam turbines. The wear performance of these conventional solutions, as well as more advanced solutions, has been investigated.

Investigation of rotor forging and casting model and full-scale prototypes

The materials manufactured as full scale prototypes or as model components for rotor forgings or castings have been sectioned and are currently under investigation. The objective is to provide a basis for full validation of all allowable stresses used in steam turbine design and to investigate all potential failure mechanisms. In the as-received condition tensile, fracture toughness, long term creep (>30,000 hours), fatigue crack growth, creep crack initiation and growth, low cycle fatigue, creep-fatigue and steam oxidation properties have all been investigated. To investigate the influence of service exposure on properties, tensile, fracture toughness, fatigue crack growth, low cycle fatigue and creep-fatigue tests have been repeated on material aged for 1000 hours at 650°C.

Weldments are being investigated to define cross-weld, heat affected zone and weld metal properties. Cross-weld tensile, long term creep and low cycle fatigue tests have been undertaken. The heat affected zone fracture toughness, creep crack initiation and growth and fatigue crack growth properties have also been investigated. Finally the weld metal properties have been assessed through fracture toughness, creep crack initiation and growth, fatigue crack growth, low cycle fatigue, creep-fatigue and steam oxidation tests.

This programme of testing has been in progress for over 35,000 hours. The results already available have revealed no unexpected behaviours or parameters which would create major difficulties for steam turbine design.

Conclusions

Alloys have been identified which meet the requirements for boilers and steam turbines operating at 700-720°C. Manufacture of a series of prototype components in these alloys has successfully demonstrate the feasibility of manufacture. A comprehensive materials testing programme has been carried out to investigate these prototype components and has addressed all critical properties and potential failure mechanisms. Currently the test programme is confirming the expected properties and has identified no technical obstacles to design and manufacture of boiler and steam turbines.

The results of this project have placed the European power generation industry and its supply chain in a powerful position for exploitation of this technology which on its own has a significant potential for mitigation of carbon emissions. When coupled with emerging technologies for carbon capture and storage, this technology can also facilitate the transition to zero-emission coal-fired power generation.

Acknowledgement

The authors wish to acknowledge the efforts of all of their partners in the AD700 project. There are around 50 partners in the two phases of the project and we regret that space does not allow them all to be mentioned in this paper. The authors also acknowledge the financial support of the European Commission through its Framework IV Thermie programme under contract SF/1001/97/DK and through its Framework V Energy programme under contract ENK5-CT2001-00511, and of the Swiss and UK governments for the support provided to participants from their countries.

References

1) S. KJAER, F. KLAUKE, R. VANSTONE, A. ZEIJSEINK, G. WEISSINGER, P. KRISTENSEN, J. MEIER, R. BLUM, K. WEIGHARDT, The advanced supercritical 700°C pulverised coal-fired power plant, Powergen Europe 2001, Brussels, May 2001.
2) C. FOLKE, U. FRANKE, H. TSCHAFFON, Integration of a component test facility into a 700MW coal-fired power station, 2nd Int Conference on Clean Coal Technologies, 10-12 May 2005, Castiadas, Italy.
3) A. ISEDA, Y. SAWARAGI, H. TERANISHI, M. KUBOTA, Y. HAYASE, Development of New 12%Cr Steel Tubing (HCM12) for Boiler Application, The Sumitomo Search, No. 40, November 1989, pp.41-56.
4) F. MASUYAMA, T. YOKOYAMA, A. SAWARAGI, A. ISEDA, Development of tungsten strengthened low alloy steel with improved weldability, Materials for Advanced Power Engineering 1994, Liege, October 3-6, 1994.
5) W. BENDICK, M. RING, Stand der Entwicklung neuer Rohrwerkstoffe für den Kraftwerksbau in Deutschland und Europa, VGB-Konfernz "Werkstoffe und Schweisstechnik im Kraftwerk 1996" 8. - 9. Oktober 1996, Cottbus.
6) N. HENRIKSEN, O. H. LARSEN, T. VILHELMSEN, Lifetime Evaluation of Evaporator Tubes Exposed to Steam Oxidation, Magnetite deposition, High Temperature Corrosion and Creep in Super Critical Boilers, Int. conf. Power Plant Chemical Technology 1996, 4-6 September 1996, Kolding, Denmark.
7) Q. CHEN, G. STAMATELOPOULOS, A. HELMRICH, S. KJAER, C. STOLZENBERGER, Investigations on oxidation and corrosion characteristics of the advanced boiler materials at steam temperatures up to 720 °C, 1st Int. conf. Super-High Strength Steels, 2-4 November 2005, Rome.
8) J. HALD, Creep resistant 9-12% Cr steels - long-term testing, microstructure stability anddevelopment potentials, 1st Int. conf. Super-High Strength Steels, 2-4 November 2005, Rome.
9) A. FINALI, A. DI GIANFRANCESCO, O. TASSA, L. CIPOLLA, R. MONTANI, Mechanical and microstructural qualification of a prototype IN718 forged disk, PARSONS 2003 6th International Charles Parsons Turbine Conference, 16-18 September 2003, Dublin.
10) K. WIEGHARDT, J. MEIER, C. FOLKE, H. TSCHAFFON, R. VANSTONE, COMTES 700 turbine valve – the world's first 700°C steam turbine component, Powergen Europe 2005, 28-30 June 2005, Milan, Italy.

61

THE EUROPEAN WAY TO 700°C COAL FIRED POWER PLANT

Helmut Tschaffon E.ON Energie

D-80333 München, Brienner Straße 40

Abstract

Coal will remain an indispensable major source of energy for European power generation in the coming decades (today: 30%). There will be a considerable demand for new power plants in the EU-25 beginning in the year 2010. 200,000 MW are estimated to be replaced due to the age structure of the current power plant park in the next 20 years, additionally 100,000 MW will be needed according to rising electricity consumption. Sustainable technologies for coal-fired power plants have to be developed to optimise environmental protection and to save valuable resources. Future coal fired steam power plants aim at elevated steam temperatures of 700 °C to reach an efficiency of minimum 50%. The paper gives an overview over the main projects started and planned in Europe to meet this goal.

The main running project is a Component Test Facility named COMTES700 which was integrated into the E.ON power plant Scholven in Germany to demonstrate how advanced, mainly nickel based materials and power plant components can pave the way towards future optimised and efficient coal-fired power plant. The operation started on 15th July 2005. A flow diagram, the used materials and components and same characteristic photos of COMTES700 are content of the presentation. In an overview additional material and component tests in Europe are pointed out. The next steps towards a demonstration plant with 400 MW are shown and scheduled.

1. COMTES700 in Power Plant Scholven

a) Description of the Project

The objective of the COMTES700 project is to design, manufacture, erect and operate a Component Test Facility (COMTES700) to test high temperature durable new materials needed to realise a coal based power plant with efficiencies above 50 %.

Within COMTES700 (Component Test Facility for a 700 °C Power Plant) designing and testing of a smaller scale evaporator panel and superheater banks in an existing boiler is included. But whereas the new materials have already been used in gas turbines and experience in manufacturing exists, there is a strong need to gain experience in handling the new materials in bigger scale on the boiler side including valves and pipelines.

So in the COMTES700 the following components are tested:

- an evaporator panel operated as superheater
- a number of superheater banks including a steam header
- a long steam line
- a HP bypass valve
- a safety valve and
- the necessary shut off and control valves.

During a four year operation period beginning with the 15 July 2005 with at least approximately 20,000 hours it is planned to carry out after two-year operation a preliminary evaluation and at the end a detailed evaluation over about half a year.

As it is expected that a lot of aged coal-fired capacity has to be replaced by new capacity in the period 2010-2030 the COMTES700 technology fits well into this time frame as the first commercial projects may be in service in 2015, and they will offer more than 20% reduction of CO_2 emissions compared with the plants, which are replaced.

The generating companies behind this project are EDF, ELECTRABEL, Elsam Kraft, EnBW Kraftwerke, ENERGI E2, E.ON Energie and E.ON Kraftwerke respectively, PPC, RWE Power and Vattenfall Europe Generation (see Figure 1).

The manufacturing side with Alstom Power Boiler, Babcock-Hitachi Europe, Burmeister & Wain Energy and Siemens also counts the most important European suppliers of power plant equipment and share the engineering and the manufacturing of the components.

The overall project co-ordination and management including the relation towards the European Commission (EC) Research Fund for Coal and Steel (RFCS) is taken over by the VGB. VGB is a voluntary association of companies for which the operation of power stations and heating plants and the associated technology form an important basis of their corporate activity.

The total project budget exceeds 15 M€, herein about 6 M€ from RFCS.

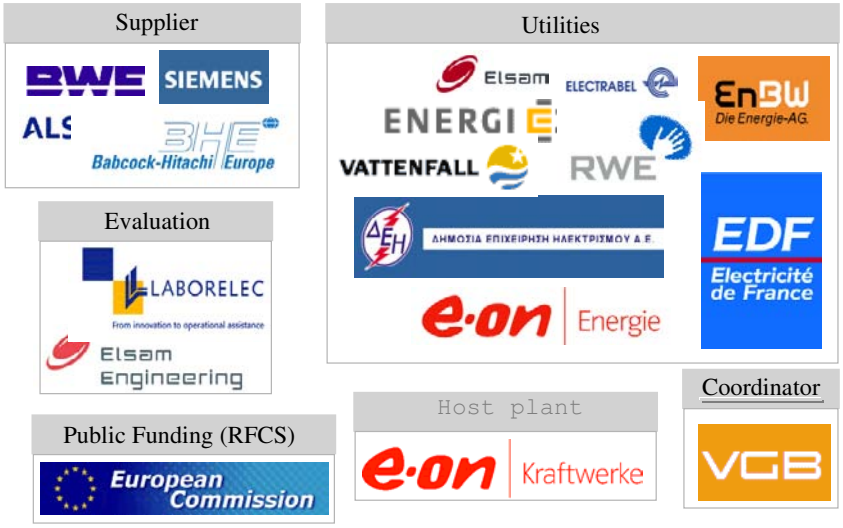

Figure 1: Parties involved in the COMTES700 Project

b) E.ON Kraftwerk's Power Plant Scholven F

Headquartered in Hanover, Germany, E.ON Kraftwerke GmbH operates the E.ON Energie Group's conventional power stations (30 coal, gas, and oil-fired power stations) with a total generation capacity of approximately 15,000 megawatts (MW). These power stations generate around 50 billion kilowatt-hours (kWh) of electric power each year. This amounts to around 11% of Germany's entire electricity consumption and makes E.ON Kraftwerke one of Europe's largest conventional electricity generators.

E.ON Kraftwerke operates 17 hard-coal power stations and seven lignite-fired generating facilities with an aggregate installed capacity of approximately 10,300 megawatts. The Scholven plant is E.ON Kraftwerke's most powerful coal-fired generating station, with a net capacity of 2,254 megawatts (see Table 1 and Figure 2).

Table 1: Year of commissioning and capacity of the units of Scholven

Units	Commissioned	Net output capacity in MW(el)
B – E	1968 - 1971	1,440
F	1979	676
FWK	1985	138
Sum		2,254

Figure 2: Plan of the Scholven Site

Unit F with a net capacity of 676 MW(el) and a firing thermal capacity of 1,860 MW (see Table 2) is the largest unit at the Scholven site. It is a bituminous coal-fired supercritical plant with a once-through boiler and a natural draught wet cooling tower commissioned in 1979. The boiler was manufactured by EVT Energie- und Verfahrenstechnik Stuttgart (now Alstom Power Boiler GmbH) and the steam turbine was delivered by KWU (now Siemens Power Generation).

Table 2: Scholven F design data

Fuel	Hard coal
Firing thermal capacity	1,860 MW
Steam production	2,200 t/h
HP- / IP- temperature	537 °C
HP- /IP- pressure	191 / 37 bar
Coal consumption at full load	280 t/h
Net heat rate	9,900 kJ/kWh
Number of pulverized coal/oil burners	32

c) COMTES700 Design

The steam for the testing purpose (12 kg/s approx. 40 t/h) is taken from the inlet header of the SH1 and is led to the evaporator panel, where it is heated up to 610 °C (see Figure 3). Between the evaporator panel and the superheater an injection is placed, which can quickly control the temperature level before the test superheater inlet. The evaporator consists of tubes made of T24, HCM12 and Alloy 617. The steam is heated in the test superheater (material selection see Table 3) up to 705 °C and enters then either the HP bypass test valve, or will pass through the turbine valve and be cooled down at SH4 temperature level and mixed with the main superheater steam. In the first case the steam after leaving the HP bypass test valve will be cooled down and led to the RH2 outlet header.

Table 3: COMTES700 - Material Selection

	Temperature	**Material**
Evaporator	410 - 610°C	T24, HCM12, Alloy 617
Superheater	580 - 705°C	DMV310N, HR3C, Alloy 617, Alloy 740, Sanicro25 (Alloy 174)
Header, pipes	410 - 705°C	13CrMo44, 10CrMo910, P91, P92, Alloy 617
Turbine valve[1]	705°C	Alloy 625

The test evaporator is located between 56.5 m and 66.2 m with the superheater above. The main components of COMTES700 listed in Table 3 and shown in Figure 3 were delivered by the suppliers listed in Figure 1. COMTES700 required a lot of additional piping and components for venting and draining which were delivered by E.ON Kraftwerke. Therefore the integration of COMTES700 into the existing system and boiler house was a complex task.

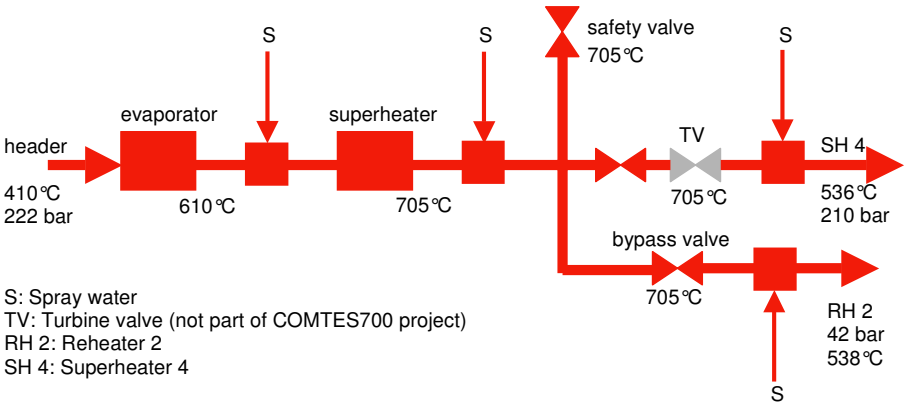

Figure 3: COMTES700 - Principal flow chart

d) Time Schedule

The project COMTES700 started in July 2004. COMTES700 should have been integrated into the Scholven F unit during a planned big inspection between 23rd April 2005 and 1st July 2005. Due to problems during the manufacturing process begin of operation was delayed by 14 days.

e) First Results

Connecting a complex research and developing project with a big electrical power producing unit is a very challenging task. Outages of the test facility are very cost intensive and therefore the test facility gets a high importance. Project costs may be influenced by this factor.

Manufacturing of components of nickel-based alloys can only be done by a few companies in Europe, because special machines, allowances and a lot of experience are needed. For example it was not so easy to find a company which was prepared to cast the housing of the big turbine valve which is out of alloy material for commercial operation. In the end Goodwin in UK delivered it. Up to now it is operating very well.

Forging of thick walled components must be planned due to possible problems with increasing grains. Choosing the false normalising temperature or time can cause unacceptable big grains. A lot of experience is needed to get the right conditions for optimised forgings.

Manufacturing of Alloy tubes and pipes in high quantities is also not so easy because of the ductility of Alloy materials. It is important to optimise all boundary conditions so that cracks can be avoided. In this context I have to mention that a reliable non-destructive testing method for a bigger amount of tubes and pipes would be an invaluable advantage.

Starting operation in July 2005 there was a problem with fouling in the steam system, because due to lack of time it was not possible to blow out the system in advance. 700 °C steam temperature is a big challenge for sealings. Leakages can occur and cause a lot of noise. A lot of know how is necessary to seal up the valves permanently. Perhaps new

research project must be launched to develop better sealings. Another way can be to put the sealings as possible at a place with lower temperatures.

2. Important Material Projects on the Way to the 700°C Power Plant

Beside the COMTES700 project there are a lot of additional material and component projects in Europe where materials are qualified and manufacturing processes are optimised. Some important of them shall be mentioned here.

AD 700 was the first project on the way to the 700°C power plant. It started in 1998 and is still ongoing. The development of materials, components and concepts were also in the focus of this project like the first planning of a demo plant. Although this project will end soon the purpose of AD 700 will be continued.

In the German research and development project MARCKO 700 material values, producibility of tubes and pipes and proving methods in laboratory up to 700/720 °C are examined. The programme started in 2004. Results are expected in 2008.

Two test rigs with temperatures until 720 °C in the hard coal fired power plant Esbjerg and the lignite fired power plant Weisweiler began operation in 2004 and will deliver additional operation experience. The tube and pipe materials are almost the same than in COMTES700. Therefore the projects started one year before COMTES700 operational problems oxidation and corrosion can be determined in advance.

In the German COORETEC research and development programme that will start in 2006 and last until 2010 several projects for the 700 °C power plant were launched. In one project corrosion behaviour of nickel-based alloys under high temperature and as a function of oxygen content in the flue gases is examined. Caking of melting ashes on the tubes and their influence on corrosion must also be checked. Material values of promising alloys and coatings which are improving the corrosion resistance must be determined. Reliable non-destructive testing during the manufacturing process and the outages are a very important precondition for the building of 700 °C power plants. Therefore another project shall evaluate and improve these methods.

3. Pre-Engineering Study for the 400 MW Demonstration Plant

In spring 2006 the participants of the COMTES700 project launched the pre-engineering study for the 400 MW coal fired demonstration plant. Aim of the study is to get the best concept for the demonstration plant and to improve the manufacturing processes which were used in COMTES700.

To achieve this goal the basic engineering for three designs for the tower boiler were started. Burmeister & Wain, Babcock Hitachi and Alstom Power are working out the variants. End of 2006 the detail engineering for the chosen design for the boiler and the turbine island will start. At the same time the manufacturing processes have to be examined and proposals for improving them will be worked out. Membrane wall arrangements and material interferences are also in the focus of the project. Last but not least a scale-up to a 1000 MW hard coal and lignite power plant will be examined. The study will last 18 months and will end at the beginning of 2008.

4. Erection and Operation of the Demonstration Plant

In 2008 we can do the next step on the way to the 700 °C power plant. It is planned

- to choose a site for the demonstration plant,
- find the partners for the project
- and begin with the call for tenders for the demonstration plant.

In 2009 the permit procedure can be started. Erection of the plant should be possible in 2010, so that operation is expected to begin in 2015. But to reach this goal, a lot of difficulties must be overcome.

MATERIAL ASPECTS OF SOLID OXIDE FUEL CELLS

R.W. Steinbrech, N.H. Menzler, P. Batfalsky* and L. Blum

Institute for Materials and Processes in Energy Systems
*Central Department of Technology
Forschungszentrum Jülich GmbH, 52425 Jülich, Germany
r.w.steinbrech@fz-juelich.de

Abstract

Solid Oxide Fuel Cells (SOFCs) with electrical efficiencies above 50 % are considered as very promising option for future decentralized energy conversion. At the Research Centre Jülich (FZJ) planar SOFC stacks are currently being developed and tested at 800°C and up to 10000 h using H_2 and methane as fuel. Stacks in the kW class routinely reach power densities of 600 W/cm². Typically the layered material composite of the FZJ-stack consists of cells with yttria stabilized zirconia (YSZ) electrolyte, Ni-YSZ anode and a cathode of lanthanum strontium manganite. The cells are mounted between ferritic steel interconnects. The fuel and air compartment are sealed by glass ceramic. With this material combination significant progress in reliable stack operation has been achieved over the past decade. However, problems with thermo-chemical and thermo-mechanical compatibility still remain a major challenge. To illustrate the complexity of material interactions in SOFCs, selected problems related to the degradation of electrochemical performance and mechanical failure processes are presented and solution strategies are discussed. As examples, short circuiting due to interaction between glass-ceramic and ferritic steel, Cr-poisoning of the cathode, and electrolyte fracture triggered by Ni-oxidation in the anode are addressed.
The examples emphasize the importance of an in-depth understanding of the interaction processes of the composite materials in SOFC stacks for further progress in this advanced energy conversion technology.

Keywords: Solid oxide fuel cell, material compatibility, Ni-YSZ cermet, glass ceramics, ferritic steel

1. Introduction

The basic ideas of solid oxide fuel cells (SOFCs) have their origin in the high temperature conductivity of stabilized zirconia, first observed more than a century ago by Nernst [1]. Today, with considerable advances in theory and experiment, the SOFC is considered as the most efficient device for converting chemical fuels directly into electrical energy. The electrical efficiency (~ 50%) even increases when coupled with a gas turbine in a power plant. The SOFCs also offer multi-fuel capability (e.g. hydrogen, carbon monoxide, methane etc.). In particular, in the past decade SOFC development has made significant progress as evident in a tenfold increase of power density [2].
There are essentially two main concepts under development, the tubular and the planar design. As far as proof of long term stability and demonstration of plant technology are concerned, the tubular concept is far more advanced whereas the planar design offers higher volumetric and gravimetric power density [2]. Standard SOFC cells comprise yttria stabilised zirconia (YSZ) as electrolyte, porous Ni-YSZ cermet as anode and lanthanum-strontium-

manganite (LSM) as cathode [3]. Typical operation temperatures are in the range between 600°C and 1000°C. In order to operate the SOFC in the lower temperature regime (700 – 800°C) either thin YSZ electrolytes and/or oxides with higher ionic conductivity, such as CeO, Sc stabilized zirconia, are used. Recent progress in electrochemical performance has also been achieved with improved cathodes. Composite cathodes (LSM + YSZ) increase the number of electrochemically active sites for oxygen reduction (three phase boundaries of electrolyte/cathode/air) [4]. Also new cathode materials of $(La,Sr)(Co,Fe)O_3$ composition (LSCF) reveal superior performance [5].

In planar designs, larger power units of SOFCs require stacking of the cells and their connection in serial mode with intermediate bipolar plates via contact layers. Moreover, the fixation of the cells and the sealing of anode and cathode compartment need appropriate material solutions [6]. The development of a robust, reliable SOFC stack with such a complex multilayer composite arrangement still poses various problems. They are related with the different high temperature behaviour of the involved materials and their partial lack of thermo-chemical and thermo-mechanical compatibility in the stack composite.

It is the aim of the present work to highlight some of the critical material aspects at high temperature. The interaction effects are demonstrated with results obtained within the SOFC project of the Research Centre Jülich (FZJ). Since planar SOFCs are being developed at FZJ the focus is directed to this design concept.

First the current status of planar SOFC development is outlined. Thereafter three selected aspects of material interaction are presented, which have emanated at FZJ from stack tests and their routine post-operation "autopsies". The examples are related with sealing, degradation by Cr-poisoning of the cathode and cell failure by anode re-oxidation.

2. Current status of planar SOFC development

Planar SOFC concepts distinguish between electrolyte and electrode-supported cell designs. In the first variant the electrolyte with a thickness of 100 – 200 µm serves as the load supporting layer of the cell (Fig. 1). Operation temperatures are typically between 850°C and 1000°C due to the relatively high ohmic resistance of the thick electrolyte. In this temperature regime ceramic interconnects are advantageous because of negligible corrosion and therefore low stack degradation.

The electrode-supported variant allows the use of a much thinner electrolyte layer (5 – 10 µm) and thus decreases the ohmic resistance. Accordingly the operation temperature can be reduced to 700 – 800°C, whilst retaining the same power density as electrolyte-supported cells at 950°C. An anode- rather than cathode-supported cell is most frequently used (Fig. 1). The better electrical conductivity of the Ni-YSZ anode cermet compared to the perovskite materials of the cathode favours the design of mechanically more rigid cell geometries. At lower operation temperature also metallic interconnects become attractive. Ferritic steels with higher chromium content (>16%) form conductive oxide scales and can be furthermore compositionally adjusted to the thermal expansion of the mechanically dominating anode [7].

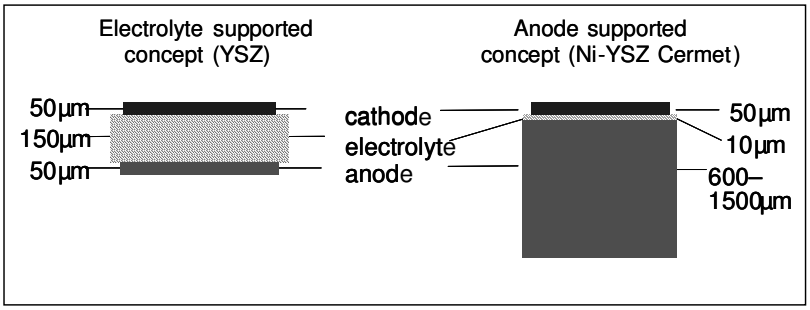

cathode LSM – $(La_{1-x}\ Sr_x)_{1-y}\ Mn_yO_3$ electrolyte YSZ (yttria-stabilised ZrO_2)
anode Ni/YSZ

Fig. 1: Schematic of planar SOFC design concepts. Standard materials are indicated [2].

Starting more than a decade ago, FZJ was one of the first research institutions to focus the planar SOFC activities on anode-substrate supported cells. To date in more than 200 stack tests, new approaches with respect to materials, fabrication of components and stack design have been investigated. The current standard experimental "short"-stack contains 2-cells of 100 x 100 mm² size. Larger stacks with a larger number of planes (10, 20, 40 and 60) are typically assembled with cells of 200 x 200 mm² in size. A 60 plane power stack is shown in Fig. 2. Both experimental "short"-stack and power stack are considered to enhance the development of SOFCs for stationary application.

Fig. 2: SOFC stack with 60 planes (200 x 200 mm² cells) [8].

Recently the development of light-weight stacks for mobile auxiliary power application (APU) has also been started. As one option pre-fabricated cassettes are used in the APU stacks as repeating unit [9]. The development of planar SOFCs has matured to a level that long term experience can be based on several stacks each operated for more than 5000 h.

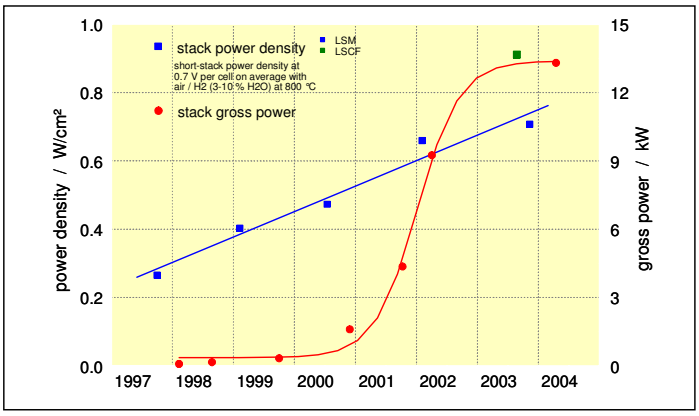

Fig. 3: Improvements of power density and net gross power of FZJ stacks between 1998 and 2004 [8].

The increase in power density which has been achieved at FZJ between 1998 and 2004 with the stack variants for stationary application is shown in Fig. 3. In addition the increase in stack gross power is plotted. The maximum power densities of 0.7 W/cm² obtained in stack tests with LSM cathodes are in good agreement with the respective values measured in single tests [4]. The data in Fig. 3 also indicate a higher power density when using LSCF cathodes. Note that the power density can be more than twice as high for single cells with LSCF cathodes [5].

A benchmark survey of worldwide SOFC technology shows on average similar results. The degradation rates of the stacks are always significantly higher than the single cell results [4]. Also single cell tests at FZJ exhibit degradation rates below 0.4% / 1000 h, whereas the lowest long term (~ 8200 h) stack degradation measured to date was not better than 1% / 1000 h. Since both values represent state of the art performance, the need of further improvement for long term application of planar SOFCs in stacks is obvious. However, in order to analyze the origin of the long term degradation behaviour, the possible competing short term failure mechanisms need to be eliminated in the first place.

Three examples of material related stack degradation or failure are presented in the subsequent sections.

i) First, as a short term effect, the material interaction between a specific combination of glass-ceramic sealant and ferritic steel is addressed.

ii) Cr-poisoning of the cathode is generally considered to be one of the major degradation effects during stack operation with chromia-forming ferritic steel as interconnect. In a

second case study results of microstructural investigations are presented, which illustrate the Cr deposition at the cathode / electrolyte interface after 8200 h stack operation.

iii) Finally the detrimental re-oxidation problem of anode supported cells with Ni-YSZ anodes is demonstrated and discussed.

3. Chemical interaction between glass-ceramic sealant and ferritic steel

Standard joining and sealing concepts of the dissimilar and similar materials of planar SOFC stacks are often based on electrically isolating glass-ceramics. At FZJ the rigid fixation of the cell in the metallic frames and the sealing of anode and cathode compartment are typically provided by glass-ceramics of the BCAS (BaO-CaO-Al_2O_3-SiO_2) system [10]. Compositional variations and the selection of minor additives allow adjustment, within certain limits, of the thermal expansion of the sealant to the metallic interconnect and the anode substrate of the cell. Good adherence to the metallic and ceramic joining partners can then be obtained [11,12]. However, considering the complexity of possible high temperature material interactions, chemical compatibility problems may occur. As an example, rapid degradation of stack performance has been observed with special variants of the BCAS glass ceramic and the ferritic steel [13]. Short circuiting effects after stack operation times of only ~ 200 h could be attributed to the chemical interactions along the seals between interconnect and cell frame [13]. In addition pronounced differences between the air and fuel side of the seal occurred. Near the three phase boundary of oxidant (air), glass ceramic and ferritic steel internal and surface oxidation of the metal was observed [13]. The voluminous outward growth of highly conductive iron-containing oxide nodules provided material bridges, which short-circuited the metallic cell frame and the interconnect, otherwise separated and isolated by the sealant.

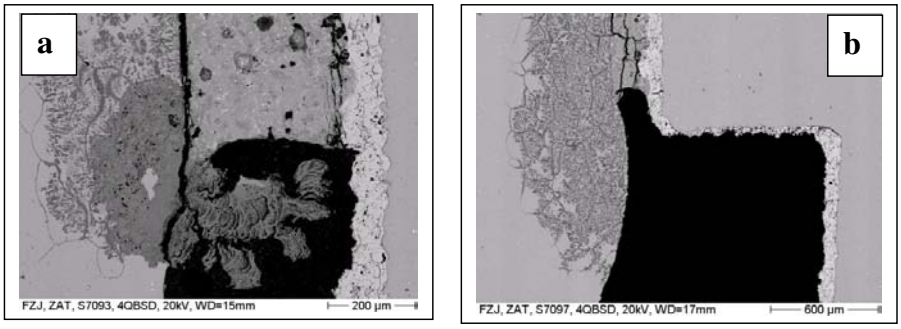

Fig. 4: Corrosion reaction of glass ceramic with unprotected ferritic steel (left) at a stack seal. Plasma sprayed YSZ coating on steel surface (right) suppresses the corrosion. a) Formation of Fe-oxide nodules at air side, which can bridge the seal gap and can cause short-circuiting. b) Internal oxidation at fuel side of seal with surface uplift of steel.

The basic effect is demonstrated in a cross-section of a glass ceramic seal between coated and uncoated ferritic steel (Fig. 4). Note that the specimen was prepared after short term stack operation at 800°C. The SEM micrograph in Fig. 4a shows the effect of massive outward oxidation from the unprotected ferritic steel, whereas the plasma sprayed YSZ coating completely suppresses the reaction. Under the conditions of the fuel atmosphere at the other end of the seal, the unprotected ferritic steel exhibits excessive internal oxidation accompanied by a substantial volume increase (Fig. 4b). Bulging of the steel is manifest in surface uplifts up to several hundred microns [13]. Again no corrosion is visible at the YSZ coated steel surface.
Model experiments on laboratory scale with the unprotected ferritic steel reproduced the rapid, massive internal oxidation at the fuel side and the formation of Fe-oxide nodules on the air side [14,15]. Both effects only occurred in BCAS sealants with PbO additive. The rate of corrosion attack increased with increasing Si-content in the ferritic steel. Accordingly compositional modifications of the glass-ceramic and the steel were carried out yielding the same positive results like the protective YSZ coating. Thereafter successful long term operation (>5000 h) of stacks could be demonstrated with seals comprising BCAS glass ceramics without PbO and/or ferritic steels with low Si-content [13].

4. Cr-poisoning due to deposition at cathodic triple phase boundaries

Chromia-forming metallic interconnects are favourably used for SOFC stacks with lower operation temperature (600-850°C). They satisfy to a certain extent key functional and structural requirements of the interconnect, such as high electrical conductivity, chemical stability in fuel and air, thermo-chemical and thermo-mechanical compatibility with the other stack materials.
In particular, chromia-forming ferritic steels have conductive oxide scales and exhibit a decreasing thermal expansion with increasing Cr-content [7]. The ferritic interconnect steel developed at FZJ matches well in thermal expansion coefficient with the Ni-YSZ cermet of the anode substrate and forms a conductive double layered oxide scale of chromia and Cr-Mn-spinell at the surface [7]. Based on this development the commercial ferritic steel Crofer22APU (ThyssenKrupp) is now available.
However, despite the progress with chromia-forming materials, there are two main disadvantages of these metallic interconnects. The formation of the oxide scales during stack operation leads to ohmic losses and the metallic interconnects release volatile Cr-species, which affect cathode performance and cell voltage.
Several studies of the Cr-effect revealed that the evaporation of volatile Cr-oxide and oxyhydroxide species gave rise to a rapid degradation of the electrical properties of SOFCs [16,17,18]. Cr-containing species (e.g. Cr-Mn-spinells) were observed in LSM cathodes with preferential localisation near the electrolyte/cathode interface in case of applied current density. One of the proposed degradation mechanisms [19] is based on the electrochemical reduction of the gaseous, higher valent CrO_3 and $CrO_2(OH)_2$ at the triple-phase boundaries (TPBs) between LSM cathode, YSZ electrolyte and air. The solid reaction products from the electrochemically active sites (TPBs) inhibit the oxygen reduction and thus degrade SOFC performance. As an alternative Cr-poisoning mechanism also the reaction of

Mn^{2+} species, generated in the cathode under cathodic polarization or at high temperature, with the gaseous Cr species in discussed [19]. Ultimately both mechanisms can lead to the formation of Cr-Mn-spinels.

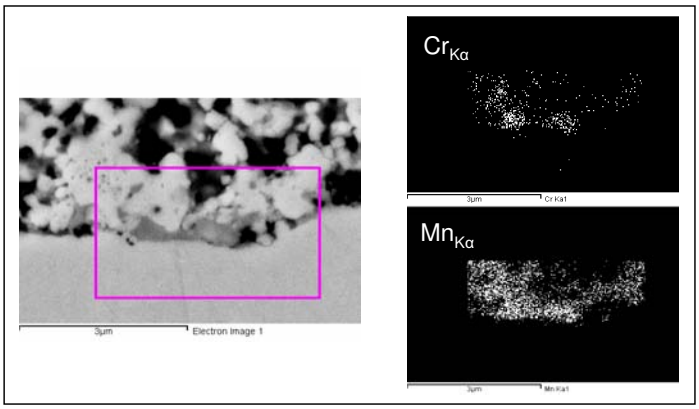

Fig. 5: SEM analysis of Cr-poisoning near interface between LSM cathode and YSZ electrolyte. Specimen has been prepared from a cell after 8200 h stack test. Isolated Cr-Mn spinell formation is observed.

Various strategies have been developed to reduce the chromium poisoning effect. Although the chromium volatilization is reduced with lower temperature, a reduction of the SOFC operation temperature does not lead to a significant improvement of the stack performance. Material options rely on minimising the chromium transport in the cathode compartment. Either "Cr-getter" materials such as La_2O_3 [20] can be used on the cathode or additional protective layers can be coated on the surface of the ferritic interconnect. Lanthanum chromites, manganites and cobaltites have been tested [21]. A two layer system of proprietary composition which is currently used as contact and protective coating in the SOFC stacks of FZJ has proved good Cr-retention [22]. Over 8200 h operation time the degradation of stack performance at 300 mA/cm² and 8 % fuel utilization was only about 1 %/1000 h. Post-operation examination of the electrolyte/cathode interface was performed using SEM with the analytical tools. The analyses revealed only limited and isolated grains of Cr-Mn spinel in the TPB regime (Fig. 5) emphasizing the good Cr-retention of the protective FZJ interconnect layers.

5. Re-oxidation of Ni in anode substrate

The planar SOFCs with a relative thick, load supporting Ni-YSZ cermet as anode substrate (600 – 1500 µm) and a thin YSZ electrolyte (5 -10 µm) take advantage of good electrochemical operation at lower temperature. However, in case of any (unintended) oxygen access to the anode compartment, such anode supported cells are very prone to mechanical

failure. Material aspects related to the irreversible transition from the oxidised to reduced and re-oxidised state of the Ni play the key role for the failure behaviour.

The standard fabrication procedure of FZJ for planar anode supported SOFCs follows a ceramic route, where a porous anode (NiO and YSZ) is co-fired at 1400°C with a thin YSZ electrolyte film [23]. Due to the thermo-elastic mismatch between anode and electrolyte layer of $\Delta\alpha \sim 2 \cdot 10^{-6} K^{-1}$, residual stresses develop upon cooling.

At room temperature they are highly compressive in the electrolyte (~ 500 MPa [24]), which is advantageous for the required mechanical integrity of the electrolyte. After deposition of the mechanically less important LSM cathode and new co-firing, the cells are assembled, fixed and sealed in the stacks. The cells are still in oxidised state during sealing with glass-ceramics. After sealing the stack is kept at operation temperature (800°C) and the anode is reduced with the H_2 fuel. Although the residual stresses are lower at operation temperature compared to RT, a compressive stress is still maintained in the electrolyte [24]. The NiO-reduction shifts the compressive electrolyte stress only slightly [24]. However, the residual stress situation in the electrolyte changes considerably when re-oxidation of the Ni takes place [25].

The microstructural changes within the sequence of NiO reduction and Ni re-oxidation have been studied in laboratory experiments [25]. Fig. 6 displays in a sequence of SEM micrographs from exactly the same location the microstructural changes of an anode supported FZJ half cell. Obviously the reduction step of Ni is not reversible by a subsequent re-oxidation. The microstructure of the re-oxidised Ni requires a larger volume (~0.5 % strain increase) compared to the initial oxidised state [25]. In model experiments the kinetics and geometrical implications of the re-oxidation have been studied [25].

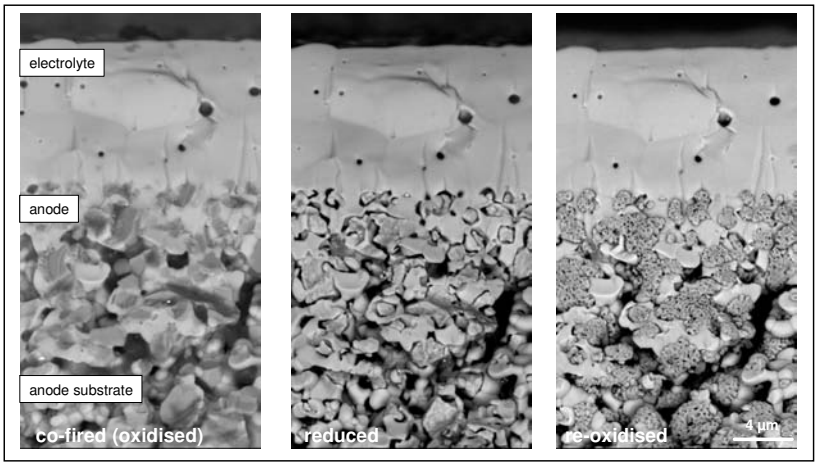

Fig. 6: Microstructural changes in anode and anode substrate during sequence from co-firing via reduction to re-oxidation. The NiO reduction is not reversible. The porous re-oxidized NiO requires a larger volume, causing compressive stresses in the anode and tension in the electrolyte [25].

The movement of a re-oxidation zone, propagating from the free anode substrate surface towards the electrolyte is reflected in an unconstrained half cell by changes in curvature as shown in Fig. 7. The material expansion related with the anode re-oxidation causes global tensile stresses in the electrolyte. Mechanical modelling of the effect [25] reveals that complete anode re-oxidation yields tensile stresses in the electrolyte which may exceed the combined material resistance of residual and fracture stress. Similar to the model experiments (Fig. 8) electrolyte fracture is typically observed after complete anode re-oxidation of the cell in stacks [26].

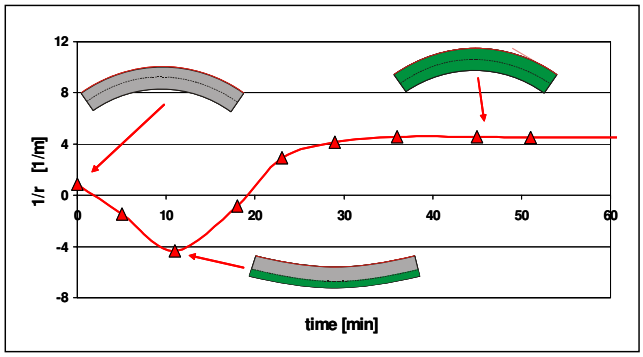

Fig. 7: Change of curvature (1/r) in unconstrained half cell due to anode re-oxidation. The curvature depends on the position of the re-oxidized material compared to the neutral axis of the specimen [25].

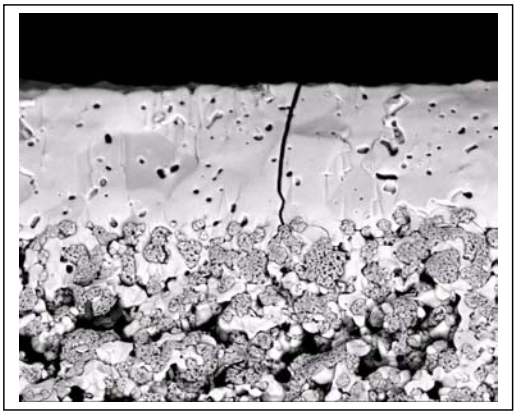

Fig. 8: Complete re-oxidation causes electrolyte fracture [25].

Various geometrical and material approaches are being considered so solve this detrimental problem. Thicker electrolytes and/or mechanically weaker anodes with higher porosity have been proposed [25], but also materials which serve as oxygen getter and the replacement of Ni by alloys are options currently discussed and examined.

Conclusions

In the past decade the development of planar SOFCs with metallic interconnects for operation temperatures between 700°C and 800°C has matured to a level such that increasingly long term operation can be realized with power densities of 0.7 W/cm² and degradation rates of a few percent / 1000 h. Both design and material solutions contributed to the remarkable progress.
The three presented case studies from the planar SOFC stack development at FZJ give some insight into the solved and still existing problems with materials interaction. Identifying further critical material aspects and developing solutions with respect to thermo-chemical and thermo-mechanical compatibility remain as on going tasks for reliable, long term operation of the multi-layered composite of a planar SOFC stacks.

Acknowledgements

The paper addresses complex material aspects of planar SOFCs. Specific results from many colleagues of the SOFC project at FZJ have been considered. The authors gratefully acknowledge the scientific and technical support they got. In particular the authors would like to thank the “autopsy” group to make the case studies available.

References

[1] W. Nernst, Über die Elektrolytische Leitung fester Körper bei sehr hohen Temperaturen, Z. Elektrochem. 6 (1899) 41 – 43.
[2] L. Blum, W.A. Meulenberg, H. Nabielek, and R. Steinberger-Wilckens, Worldwide SOFC technology overview and benchmark, Int. J. Appl. Ceram. Technol. 2 (2005) 482.
[3] R.N. Basu, G. Blass, H.-P. Buchkremer, D. Stöver, F. Tietz, E. Wessel, and I.C. Vinke, Simplified processing of anode-supported thin film planar solid oxide fuel cells, J. Europ. Ceram. Soc. 25 (2005) 463-471.
[4] V.A.C. Haanappel, J. Mertens, D. Rutenbeck, C. Tropartz, W. Herzhof, D. Sebold, and F. Tietz, Optimisation of processing and microstructural parameters of LSM cathodes to improve the electrochemical performance of anode-supported SOFCs, J. Power Sources 141 (2005) 216-226.
[5] F. Tietz, V.A.C. Haanappel, A. Mai, J. Mertens, and D. Stöver, Performance of LSCF cathodes in cell tests, J. Power Sources, in press.
[6] J.W. Fergus, Sealants for solid oxide fuel cells, J. Power Sources 147 (2005) 46-57.

[7] P. Huczkowski, N. Christiansen, V. Shemet, L. Singheiser, and W.J. Quadakkers, Growth rates and electrical conductivity of oxide scales on ferritic steels proposed as interconnect materials for SOFC, in: Proc. Sixth Europ. SOFC Forum, Mogensen (Ed.), Lucerne, Switzerland, 2004, 1594–1601.

[8] R. Steinberger-Wilckens, L. G. J. de Haart, H-P. Buchkremer, H. Nabielek, W. J. Quadakkers, U. Reisgen, R. Steinbrech, F. Tietz, and I. Vinke, Recent Results of Solid Oxide Fuel Cell Development at Forschungszentrum Juelich, Proc. Fuel Cell Seminar, San Antonio, TX, USA, 2004.

[9] P. Lamp, J. Tachtler, O. Finkenwirth, S. Mukerjee, und S. Shaffer, Development of an Auxiliary Power Unit with Solid Oxide Fuel Cells for Automotive Applications, Fuel Cells 3 (2003) 1-7.

[10] S.M. Gross, T. Koppitz, J. Remmel, and U. Reisgen, Glass-ceramic materials of the system BaO-CaO-SiO_2 as sealants for SOFC applications, Ceram. Eng. Sci. Proc. 26/4 (2005) 239.

[11] J. Malzbender, R.W. Steinbrech, and L. Singheiser, Determination of the Interfacial Fracture Energies of Cathodes and Glass/Ceramic Sealants in a Planar Solid Oxide Fuel Cell Design, J. Mater. Res. 18 (2003) 929.

[12] J. Malzbender, R.W. Steinbrech, and P. Batfalsky, Fracture Energies of Brittle Sealants in Planar Solid Oxide Fuel Cells, Ceram. Eng. Sci. Proc. 26/4 (2005) 285.

[13] P. Batfalsky, V.A.C. Haanappel, J. Malzbender, N.H. Menzler, V. Shemet, I.C. Vinke, and R.W. Steinbrech, Chemical interaction between glass–ceramic sealants and interconnect steels in SOFC stacks, J. Power Sources, 155 (2006) 128-137.

[14] V.A.C. Haanappel, V. Shemet, I.C. Vinke, S.M. Gross, Th. Koppitz, N. Menzler, M. Zahid, and W.J. Quadakkers, Evaluation of the suitability of various glass sealant-alloy combinations under SOFC stack conditions, J. Mater. Sci. 40 (2005), pp. 1583–1592.

[15] V.A.C. Haanappel, V. Shemet, S.M. Gross, Th. Koppitz, N. Menzler, M. Zahid, and W.J. Quadakkers, Behaviour of various glass–ceramic sealants with ferritic steels under simulated SOFC stack conditions, J. Power Sources 150 (2005), pp. 86–100.

[16] S.P.S. Badwal, R. Deller, K. Foger, Y. Ramprakash, and J.P. Zhang, Interaction between chromia forming alloy interconnects and air electrode of solid oxide fuel cells, Solid State Ionics 99 (1997), pp. 297–310.

[17] S.P. Jiang, S. Zhang, and Y.D. Zhen, A fast method for the investigation of the interaction between metallic interconnect and Sr-doped $LaMnO_3$ of solid oxide fuel cells, Mater. Sci. Eng. B 119 (2005), pp. 80–86.

[18] M.C. Tucker, H. Kurokawa, C.P. Jacobson, L.C. De Jonghe, and S.J. Visco, A fundamental study of chromium deposition on solid oxide fuel cell cathode materials, J. Power Sources, in press.

[19] K. Hilpert, E. Konysheva, H. Nabielek, R. Steinberger-Wilckens, F. Tietz, I.C. Vinke, E. Wessel, and M. Zahid, A Semi-quantatative Analysis of Chromium Poisoning in Planar SOFC**,** Fuel Cell Seminar 2005, Abstract 666, presentation available under www.fuelcellseminar.com/2005_presentations.asp.

[20] K. Fujita, K. Ogasawara, Y. Matsuzaki, and T. Sakurai, Prevention of SOFC cathode degradation in contact with Cr-containing alloy, J. Power Sources 131 (2004) 261-269.

[21] E. Konysheva, J. Laatsch, E. Wessel, F. Tietz, N. Christiansen, L. Singheiser, and K. Hilpert, Influence of different perovskite interlayers on the electrical conductivity between $La_{0.65}Sr_{0.3}MnO_3$ and Fe/Cr-based steels, Solid State Ionics, 177 (2006) 923-930.

[22] L. Blum, H.-P. Buchkremer, S.M. Gross, S.M., B. De Haart, J.W. Quadakkers, U. Reisgen, R. Steinberger-Wilckens, R.W. Steinbrech, F. Tietz, Overview of the Development of Solid Oxide Fuel Cells at Forschungszentrum Jülich, Proc. Electrochem. Soc. PV 2005-07, 39-47.

[23] H.P. Buchkremer, U. Diekmann, and D. Stöver, Components manufacturing and. stack integration of an anode supported planar SOFC system, in: B. Thorstensen Editor, Proc. 2nd Eur. SOFC Forum, Oslo 1 (1996) 221.

[24] W. Fischer, J. Malzbender, G. Blass, and R.W. Steinbrech, Residual stresses in planar solid oxide fuel cells, J. Power Sources 150 (2005) 73.

[25] J. Malzbender, E. Wessel, R.W. Steinbrech, and L. Singheiser, Reduction and Re-oxidation of Anodes for Solid Oxide Fuel Cells (SOFC), Ceram. Eng. Sci. Proc. 25/3 (2004) 387.

[26] M. Molinelli, D. Larrain, N. Autissier, R. Ihringer, J. Sfeir, N. Badel, O. Bucheli, and J. Van Herle, Dynamic behaviour of SOFC short stacks, J. Power Sources 154 (2006) 394-403.

MATERIALS FOR EXTREME ENVIRONMENTS IN FUSION APPLICATIONS

H. Bolt and H. Maier

Max-Planck-Institut für Plasmaphysik, EURATOM Association,
Boltzmannstr. 2, D-85748 Garching, Germany

Abstract

According to current knowledge and understanding, nuclear fusion can be developed to a sustainable energy technology. Fuel is abundant and key points as fusion power production and alpha particle heating have already been demonstrated. The next-step device ITER is designed to demonstrate net power production and to address all relevant technological issues on the way to a power reactor. There is, however, a series of materials problems to be addressed in the frame of the ITER project and by a long-term development programme. A survey of the current status of materials development for fusion applications is given, emphasizing low-activation structural materials and on the development of plasma-facing materials and components. To provide materials which can sustain the severe loading conditions in a fusion environment is a key issue in developing fusion as a nuclear technology without long-lived radioactive waste.

Keywords: nuclear fusion, low activation materials, plasma-facing materials, high heat flux materials, ExtreMat Integrated Project

1. Introduction

Controlled nuclear fusion of hydrogen isotopes has been a research topic in the world since around 1950. Among many attractive features are the abundance of fuel for the reaction, the high specific energy release per reaction, and - in contrast to nuclear fission techniques - the inherent safety of the process due to its thermonuclear nature. To achieve controlled nuclear fusion on earth various schemes have been proposed, among which the magnetic confinement in the so-called tokamak arrangement has been the most successful one up to now.

The principal problem to overcome in the fusion of two atomic nuclei is the repulsive electrostatic force, which acts in between them. The highest probability to achieve the fusion process, i. e. the highest reaction rate can be met when the two hydrogen isotopes deuterium (D) and tritium (T) are employed at a temperature in the range of 10...20 keV, one to two hundred million K:

$$D + T \longrightarrow {}^4He\ (3.5\ MeV) + n\ (14\ MeV)$$

The released energy of 17.5 MeV is distributed between a neutron and a charged ^{4}He nucleus, an alpha particle. In a magnetic confinement scheme, the neutron is not confined and escapes from the plasma. The charged ^{4}He particle, however, is confined by the magnetic field. Its energy must be thermalized to sustain the high plasma temperature.

The availability of these two fuel components on earth is very different: Deuterium is abundant in nature, its concentration in natural hydrogen is about 0.015%. Therefore it is

practically inexhaustibly available from seawater. Tritium, however, does not occur naturally in sufficient quantities because it is radioactive with a half-life of about 12 years. The concept for a fusion power plant is that the fusion reactor produces its own supplies of tritium in a self-sustained fashion. The neutrons produced by the fusion reaction are employed for producing tritium from the two naturally occurring lithium isotopes:

$$^{6}\mathrm{Li} + \mathrm{n} \longrightarrow {}^{4}\mathrm{He} + \mathrm{T} + 4.8\ \mathrm{MeV}$$
$$^{7}\mathrm{Li} + \mathrm{n} \longrightarrow {}^{4}\mathrm{He} + \mathrm{T} + \mathrm{n}' - 2.5\ \mathrm{MeV}$$

This is achieved by surrounding the plasma vessel with a so-called blanket, a structure that absorbs the neutrons and contains the tritium breeding fuel. It is this blanket which also absorbs the energy released with the neutron. Therefore it must contain coolant channels. The coolant carries the produced tritium to an extraction stage and the tritium is finally injected into the plasma as new fuel. In this way radioactive tritium is handled only inside a closed system of a fusion reactor facility.

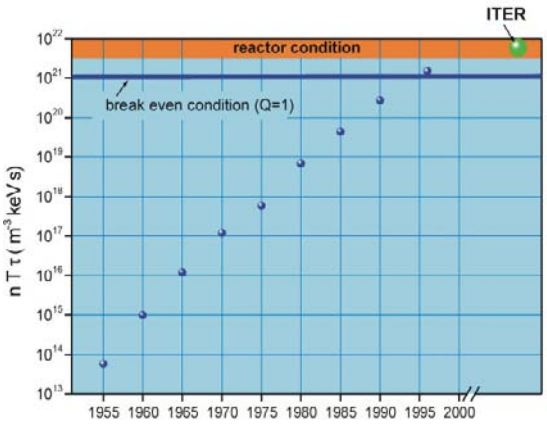

Figure 1: Development of the fusion product of plasma density (n), plasma temperature (T) and energy confinement time(τ) (after [1]).

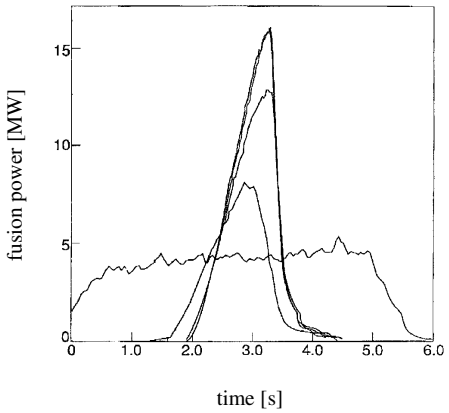

Figure 2: Achieved fusion power in the JET tokamak during the 1997 deuterium/tritium experiment (after [2]). The peaked profiles refer to special transient discharge scenarios.

2. The status of fusion research

Magnetic confinement of fusion plasmas has been widely investigated in various field configurations. Nowadays two toroidally closed configurations are mainly pursued: The tokamak and the stellarator. Since a purely toroidal magnetic field configuration does not yield a stable plasma confinement, an additional twist of the field lines is necessary. In the tokamak configuration this is achieved by using an external toroidal field and additionally driving a current through the plasma in the toroidal direction. The stellarator concept, on the other hand,

does not employ current drive inside the plasma, but instead uses external magnetic fields of complex shapes. Tokamaks nowadays produce the better results concerning the so-called fusion product of plasma density, temperature, and energy confinement time. Stellarators have no necessity for current drive and therefore have a general advantage concerning stability and continuous operation. Figure 1 shows the progress of the fusion product that has been made over the last decades. Today's large devices are close to the breakeven condition Q=1, which means fusion power equals input heating power. Since the fusion product also scales with the volume of the plasma, reactor conditions can only be met in a next step device.

Present day fusion research facilities generally do not operate with deuterium/tritium mixed plasmas. The breakeven condition of a D-T plasma, however, has already been reached. Only a few experiments on realistic mixtures producing fusion power have been done. In its 1997 deuterium/tritium experiment the Joint European Torus tokamak JET has achieved the substantial amount of 16 MW of fusion power corresponding to Q=0.62 [2] (see Figure 2). Significant alpha particle heating of the confined plasma has been demonstrated in the Princeton tokamak fusion test reactor TFTR [3] as well as in JET [4].

3. The ITER project

Recognizing the importance of the next step to a rector-scale fusion device, in 1987 the European Union, Japan, the Russian Federation, and the United States initiated the so-called Conceptual Design Activities for ITER, the International Thermonuclear Experimental Reactor. It was agreed that the overall objective of ITER would be "to demonstrate the scientific and technical feasibility of fusion energy for peaceful purposes"[5].

The scientific and technical performance specifications were reformulated in 1998. Now the ITER design envisages the demonstration of extended burn of deuterium-tritium plasmas with a fusion power of 500 MW and a ratio of fusion power to input heating power Q at least ten [6]. Another target is the demonstration of technologies essential to a reactor in an integrated fusion technology system. ITER will allow to study the science of self-heated plasmas in power plant relevant regimes. Prototypes of key components have already been manufactured and tested: Central Solenoid for inductive current drive, superconducting toroidal field coils, complete blanket module mock-ups as well as full scale modules of the vacuum vessel [6].

In 2005 the decision was made to build ITER in Cadarache (France) as a joint project of the European Community, Japan, Russia, US, Rep. Korea, China and India.

In conjunction with further materials development, modelling and neutron irradiation experiments of these materials, ITER is supposed to provide a sufficient scientific and technological basis for a "first of its kind" fusion reactor [7]. The Power Plant Conceptual Study has evaluated different options for a commercial fusion power plant based on varying degrees of technological extrapolation from the present state [8]. These variants include a water-cooled reactor design, and several Helium cooled reactor designs. The availability of suitable materials and the achievable progress in plasma engineering dictates which of these variants will become a realistic base for the design of a fusion reactor.

4. Material issues in fusion energy systems

4.1 Structural materials

One of the main features of fusion reactor material issues is the intense irradiation with neutrons. This immediately brings about two of the key problems in the development of structural materials:

- The materials must not suffer strong radiation-induced embrittlement or other degradation
- Radioactive waste must be minimized: The half-life of neutron-induced activation products should be as short as possible

In order to meet these requirements, three lines of development are being pursued [9]: Reduced activation ferritic-martensitic steels are currently the furthest developed technology. Vanadium alloys based on the V-Cr-Ti system have a great potential for high-temperature operation in combination with a liquid lithium breeder system. Finally, SiC-fiber-reinforced SiC composite ceramic materials (SiC-SiC) would have a great potential for very low radioactivity and for very high operating temperature, corresponding to a high degree of efficiency. This system, however, surely constitutes the most difficult technological challenge of the three groups. The aim is to arrive at materials which allow operation at reactor relevant coolant temperatures and, at the end of the life, recycling or disposal under strongly relaxed conditions.

The mainstream of this work has resulted in a ferritic-martensitic steel with 9% Cr and substitution of the elements which cause the strongest activation like Mo and Nb. Data regarding the properties after neutron irradiation hint that embrittlement can be reduced when this material is being irradiated above 250°C to 300°C. Of highest importance in this respect is the irradiation induced shift of the ductile to brittle transition temperature (DBTT). Irradiation data of this material group as a function of the displacement damage are shown in Figure 3. Recently developed grades like F82H and the European EUROFER grade, which is not yet included in Figure 3, show only a moderate shift of the ductile to brittle transition temperature DBTT. In a recent irradiation experiment to a high dose of 32 dpa at 300°C irradiation temperature EUROFER showed an increase of the DBTT by 200 degrees from -100°C to +100°C [10]. However, this shift will be enhanced by irradiation with high energy neutrons typical for the fusion neutron energy spectrum. Under fusion conditions the high energy neutrons will cause He production from transmutation reactions on the order of 10 appm/dpa in steel. The He will interact with the displacement-induced damage and increase the embrittlement at low temperatures. EUROFER is currently in a state of development, where due to the low activation composition the neutron-induced radioactivity would have decreased to the hands-on level after a storage time on the order of one hundred years.

Further development is being carried out on oxide dispersion strengthened 9%Cr and 12/14% Cr steels to increase the upper temperature limit for operation from 550°C for EUROFER V to higher values [10].

In addition to this the properties of SiC-SiC especially in terms of thermal conductivity and resistance to neutron irradiation are being improved. The use of SiC-SiC either as structural material or as heat insulation liner material would allow coolant temperatures in a range up to 1000°C [11].

The specific neutron energy spectrum which includes a large portion of high energy neutrons up to 14 MeV leads to different neutron damage in materials as compared to the neutrons from fission reactors. This is caused by the additional production of He and H in the bulk of the materials due to transmutations. In order to test materials for a fusion power reactor in a relevant neutron environment, an intense high energy neutron source is needed. Such a source based on the D-Li stripping reaction, the International Fusion Materials Irradiation Facility (IFMIF) is presently under international planning [9].

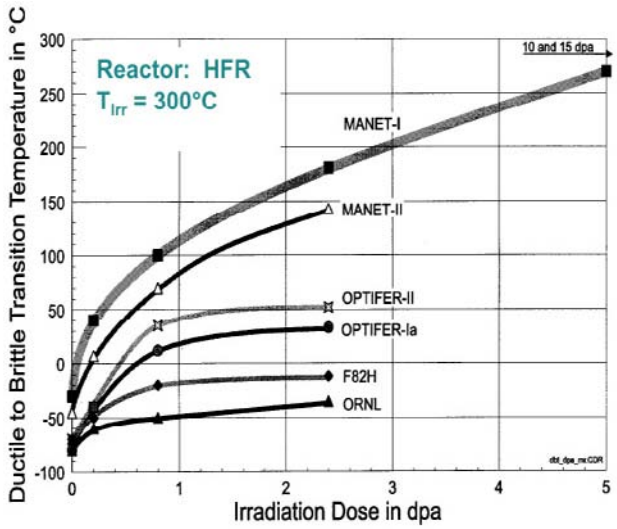

Figure 3: DBTT shift of reduced activation steels under neutron irradiation (fission reactor spectra) (after [9]).

4.2 Plasma-facing materials and components

The loading conditions of the materials for the plasma-facing components in ITER and a fusion reactor are listed in Table 1 [13].

In addition to the neutron damage, very high heat loads to the divertor under steady state operation the effect of heat flux transients has major impact on the materials selection. Experimental investigations on the materials damage resulting from thermal transients have been carried out in plasma, electron and ion beam facilities [14]. Concerning a fusion reactor, it is expected that the effect of thermal transients has to reduced very strongly to allow the operation of components with reasonable lifetime, since the erosion and fatigue of the plasma-facing materials would be excessively large.

	ITER		**reactor**	
	First Wall	**Divertor target**	**First Wall**	**Divertor target**
component replacements	none	up to 3	5 year cycle	5 year cycle
av. neutron fluence (MWa/m^2)	0.3	max.0.15*	10	5
displ./transmut. product. dpa / appm (He); (dpa / %Re for W)	Be 1 / 1000 Cu 3 / 30 SS 3 / 30	CFC 0.7 / 230 W 0.7 / 0.15% Re Cu 1.7 / 16 SS 1.6 / 16	W 30 / 6% Re RAFM steel 120 / 1200	W 15 / 3% Re Cu 60 / 600 RAFM st. 60 / 600
normal operation				
No. of cycles	30000	10000	< 1000	< 1000
Peak particle flux ($10^{23}/m^2s$)	0.01	~10	0.02	~10
Surface heat flux (MW/m^2)	< 0.5	~10** / 3	< 1	...10...
PFM operational temp. (°C)	Be: 200...300	W: 200...1000 CFC: 200...1500	W: 550...700	W: 350...500
ELM energy density (MJ/m^2)	-	< 1	–	reduced
ELM duration (ms)/ {Frequency}	-	0.2/ {few Hz}	–	"grassy"?
off-normal operation				
Peak energy density (MJ/m^2)	60 (VDEs)	30 (Disr.)	-	?
Duration (ms)/ {Frequ. (%)}	300 {1%} (VDEs)	1-10 {<10%} (Disr.)	-	1-10, max. 10 events

* without replacement;
** slow transients 20 MW/m^2 lasting 10 s (10% frequency)

Table 1: Operation conditions for the plasma-facing components of ITER and a of DEMO-like fusion reactor [13]

Regarding the development of plasma-facing materials and high heat flux components, the ITER project is currently representing the most advanced status. The components facing the plasma will consist of carbon-fibre reinforced carbon, tungsten and beryllium as plasma facing material and CuCrZr as high thermal conductivity heat sink. The selection of these materials has been driven mainly by the need to furnish the ITER first wall with low-Z plasma facing material in order to provide maximum operational flexibility with coincides with the high tolerance of the plasma towards influxes of low Z impurities. The use of carbon on the first wall, as applied in most present day experiments, has been avoided, since the first wall is subject to erosion processes. The eroded carbon would eventually redeposit in the form of amorphous hydrocarbon

films with high fractions of tritium and thus lead to a rapid build-up of a high tritium inventory. This is undesirable from a radiological point of view for ITER, but it must also be avoided in a fusion reactor because tritium must be produced on site and must not get permanently bound in hydrocarbon films.

Regarding the divertor, the component of a fusion reactor receiving the highest heat flux, the materials selection has been mainly driven by highly peaked transient heat fluxes which would lead to excessive erosion of most materials during e.g. disruptions. In divertor target areas with highest transient heat loads, carbon-fiber reinforced carbon material (CFC) with 3-d fiber reinforcement and very high thermal conductivity will be applied. In order to minimize the amount of carbon used as plasma facing material, the less highly loaded regions of the divertor will be furnished with tungsten. A concise review on the selection of the plasma-facing materials for ITER can be found in [15].

The joining technology of the plasma facing materials has been developed to a standard allowing the removal of stationary surface heat loads on the order of 20 MW/m^2. This is of special importance, since divertor heat loads in ITER can reach 20 MW/m^2 under quasi-stationary conditions. Joining methods for dissimilar bonds of Be-Cu and W-Cu are high temperature brazing and hot isostatic pressing. CFC-Cu bonds can be also joined by active metal casting (AMC). The heat removal capability under thermal cycling conditions of CFC-CuCrZr model components with active cooling has been subject of a review [16]. For ITER a detailed Materials Assessment Report has been issued which compiles the fusion relevant aspects of the Be, W and CFC materials [17].

Beryllium to cover the major part of the plasma-facing wall will not be a suitable option for an economic fusion reactor concept. Therefore an alternative must be identified. Plasma material interaction studies in the tokamak ASDEX Upgrade indicate that tungsten may be a plasma-facing material which can provide sufficient lifetime of the first wall components [14,15]. The use of tungsten in this tokamak on large surface areas resulted in low plasma impurities, well below the tolerable limit of 10^{-5} and very little tungsten erosion from energetic neutrals. ITER will allow the achievement of a conclusive result on the selection and use of plasma-facing materials for a fusion power reactor. Plasma-facing materials issues related to the application in a reactor are described in more detail in [20].

Hydrogen isotopes as the fuel of the fusion reaction constitutes a very general problem for metallic materials, especially for ferritic-martensitic steels because of the low solubility and for vanadium alloys because of exothermic hydride formation, leading to embrittlement [21,22]. Furthermore, the transport of tritium through the heat sink materials into the reactor coolant has to be limited. Thin film technology is employed to deposit hydrogen permeation barrier coatings with μm thickness and below. These coatings are to be applied as a sandwiched barrier between the plasma-facing material and the metallic heat sink material as well as at the breeding blanket walls. Work on α-crystalline alumina (Al_2O_3) films which were deposited by low temperature PVD techniques on EUROFER steel showed that permeation reduction factors of 1000 can be reached [23]. The issue of tritium breeding and handling, however, puts a special emphasis on coatings technology regarding the concepts for breeding blankets. Some design concepts, which employ lithium containing liquid metals, must rely on coatings for the purpose of corrosion protection as well as their hydrogen barrier function [24,25]. Here, work on thin erbia (Er_2O_3)

coatings has demonstrated that at the same time a good corrosion resistance and a permeation reduction by a factor of 200 can be obtained [26].

5. Relation of the development of materials for fusion reactors with regard to other applications

Besides the highly specific materials issues related to fusion energy development, at least partly similar loading conditions can be identified for other applications. In space applications the chemical reactivity of composite protection materials for reentry use has to be reduced. The underlying processes are widely similar to the passivation mechanisms explored for carbon-based composite materials in fusion. The thruster wall of rocket engines is subjected to very high heat fluxes with extreme temperature gradients between the heated surface and the liquid hydrogen coolant. In electronics, the heat fluxes to be removed from modern devices are comparable to those in fusion as items related to the bonding technology of heat sink materials to the devices have similarities to the fusion application. In advanced fission reactor concepts, esp. the VHTR a need for self-passivation against water impurities in the He coolant and against erosion under accidental air ingress need to be investigated. Parts of the requirements for VHTR control rod composite materials are very similar to the PFC loading conditions in fusion and thus are a field for joint development activities. The cross-cutting relations between subjects for research into new materials across different applications are listed in table 2. The European Integrated Project "ExtreMat" (New Materials for Extreme Environments" is performing materials development which is relevant to different applications, such that each single application can carry off a benefit from this concentrated joint activity [27]. The R&D subjects of this Integrated Project are those listed in table 2.

	Space	**Electronics**	**Fusion**	**Advanced Fission**	**Spin-Offs**
Protection Materials	x		x	x	x
Heat Sink Materials	x	x	x	(x)	x
Radiation Res. Materials			x	x	(x)
Compound Technologies	x	x	x	x	x

Spin-offs: - gas turbines: diffusion barriers
- very high temperature heat exchangers
- new brake materials

Table 2: Relevance of materials R&D subjects with regard to different applications as pursued in the ExtreMat Project

6. Conclusion

The physics and technology of hot fusion plasmas have already reached a very elaborate stage. Key features of energy production by magnetic confinement thermonuclear fusion have already been demonstrated: Alpha particle heating, necessary for self-sustained burn, has been demonstrated in the USA and in Europe and a substantial amount of fusion power has been produced. Solutions for the materials problems are currently being worked out, some being already at hand. The preparations for ITER, for example, have brought the issue of high heat flux components a big step forward. The key topic of low-activation structural materials is being addressed as well as the further development of the technologies required for the plasma-facing components of a fusion reactor.

Paths towards the development of new materials for fusion applications are also investigated in the framework of the European Integrated Project "ExtreMat" which aims at the concerted development of new materials for applications with comparable loading conditions.

Acknowledgement

A part of this review has been performed within the framework of the European Integrated Project "ExtreMat" (Contract NMP-CT-2004-500253) with financial support by the European Community. It only reflects the view of the authors and the European community is not liable for any use of the information contained therein.

References

1. U. Schumacher, Naturwissenschaften **88**, 102 (2001).
2. M. Keilhacker, M. Watkins, the JET Team, Europhys. News **29**, 230 (1998).
3. G. Taylor, J. D. Strachan, R. V. Budny, D. R. Ernst, Phys. Rev. Lett **76**, 2722 (1996).
4. P. R. Thomas et al., Phys. Rev. Lett **80**, 5548 (1998)
5. ITER Physics Basis, Nucl. Fusion **39**, Vol. 12 (1999)
6. ITER-FEAT Outline Design Report, IAEA ITER Documentation Series No. 18, Vienna (2001)
7. R. Toschi et al., Fusion Engineering and Design **56-57**, 163 (2001)
8. D. Maisonnier et al., A Conceptual Study of Commercial Fusion Power Plants; Final Report; EFDA-RP-RE-5.0; 13 April 2005
9. K. Ehrlich, E. E. Bloom, T. Kondo, J. Nucl. Mater **283-287**, 79 (2000)
10. N. Baluc, D.S. Gelles, S. Jitsukawa et al., ICFRM-12, J. Nucl. Mater, in print
11. K. Ehrlich, Phil. Trans. R. Soc. Lond. **A 357**, 595 (1999)
12. M. Victoria, N. Baluc, P. Spätig, Nucl. Fusion **41**, 1047 (2001)
13. H. Bolt, V. Barabash, F. Federici et al., J. Nucl. Mater. **307**, 43 (2002)
14. J. Linke, I.V. Mazul, R. Nygren, J. Schlosser, S. Suzuki, ICFRM-12, J. Nucl. Mater., in print

15. G. Janeschitz, ITER Joint Central Team and Home Teams, J. Nucl Mater. **290-293**, 1 (2001)
16. V. Barabash et al., J. Nucl. Mater. **283-287**, 1248 (2000)
17. ITER Materials Assessment Report, ITER DO. No. G 74 MA 1001-07 W0.2
18. K. Krieger, H. Maier, R. Neu, ASDEX Upgrade Team, J. Nucl. Mater. **266-269**, 207 (1999)
19. R. Neu et al., Plasma Phys. Contr. Fusion **44**, 811 (2002)
20. H. Bolt, V. Barabash, W. Kraus et al., J. Nucl. Mater. **329**, 66 (2004)
21. P. Jung, Fusion Technology **33**, 63 (1998)
22. G. W. Hollenberg, E. P. Simonen, G. Kalinin, A. Terlain, Fusion Eng. Des. **28**, 190 (1995)
23. D. Levchuk, F. Koch, H. Maier, H. Bolt, J. Nucl. Mater. **329**, 1403 (2004)
24. J. H. Park, T. Domenico, G. Dragel., R. Clark, Fusion Eng. Des. **27**, 682 (1995)
25. H. Nishimura; A. Suzuki;T. Terai; M. Yamawaki; S Tanaka;.A Sagara; O. Motojima, Fusion Eng. Des. 58-9, 667 (2001)
26. D. Levchuk, F. Koch, H. Maier, H. Bolt, A. Suzuki, ICFRM-12, J. Nucl. Mater., in print
27. ExtreMat, European Integrated Project, Contract NMP-CT-2004-500253, www.extremat.org

DEVELOPMENT AND CURRENT STATUS OF ECCC CREEP PROPERTY DATA SHEETS

S R Holdsworth
EMPA, Dübendorf, Switzerland

Abstract

The European Creep Collaborative Committee (ECCC) was formed in 1992 to provide European industry with a means of influencing the creep rupture strength values required for the large number of European Product and Design Standards in preparation during the early 1990s. The objective was and continues to be achieved through the publication of ECCC Creep Property Data Sheets.

The predicted creep rupture strength values contained in ECCC Data Sheets are based on duplicate expert assessments of the largest possible multi-cast datasets comprising the longest duration data available from all possible sources. The paper describes the development of procedures to ensure minimum uncertainty of the predicted long time strength values contained in the Data Sheets and reviews their current status. Practical implications associated with strength values recommended in new Data Sheets for Grade 92 steel and the Alloy-80A nickel base alloy are also examined.

Keywords: ECCC Data Sheets, Grade 92, Alloy-80A

Introduction

The European Creep Collaborative Committee (ECCC) was originally formed to provide the means for European industry to combine its resources to influence the content of the new European high temperature Product and Design Standards in preparation during the early 1990s [1]. Initially, the principal aims of ECCC were:[1]
- to co-ordinate the generation of creep data throughout Europe,
- to interact with, and supply information to European Standards organisations and their technical committees,
- to mutually exchange technical information relating to current and future activities on material developments, and
- to develop common rules for creep data generation, collation/exchange and assessment.

The defined objectives were, and continue to be achieved through the efforts of a number of working groups whose activities are steered by the ECCC Management Committee (Fig. 1). The WG3x groups co-ordinate the main creep data generation (testing), collation and assessment activities directed towards influencing the content of European Standards/Codes. The results of WG3x assessments underpin the ECCC Data Sheets [2]. The respective WG3x areas of responsibility are presently:
- WG3A: Low and high alloy ferritic steels
- WG3B: Low and high alloy austenitic steels
- WG3C: Nickel base alloys

[1] A list of terms and symbols is given in the Nomenclature Section

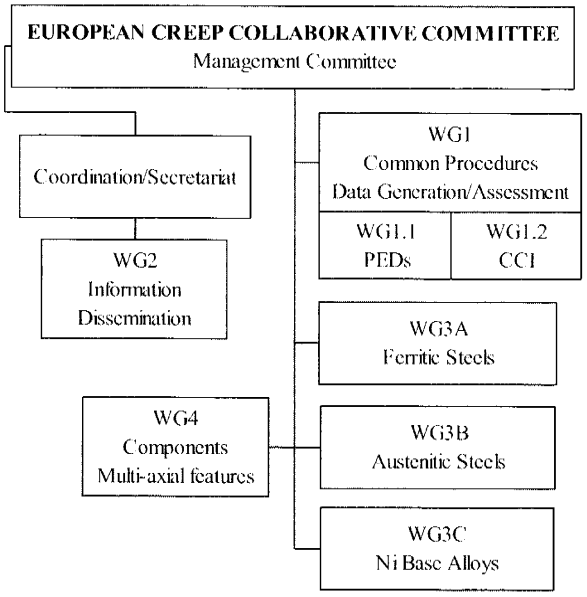

Fig. 1 Structure of European Creep Collaborative Committee (ECCC)

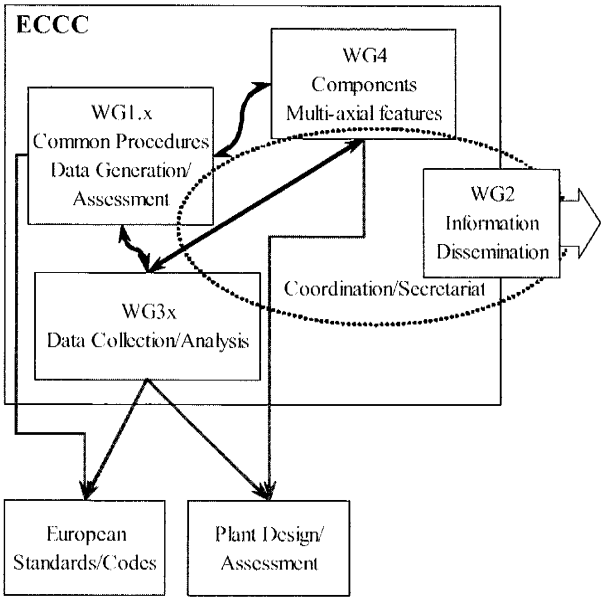

Fig. 2 Relationship between ECCC and external organisations

Technical support is provided by working group WG1 and its sub-groups. The main role of WG1 is to provide recommendations on procedures for data generation, collation and

assessment to form the basis of common practices followed within ECCC [3]. These recommendations are published and are thereby available to other users. They are acknowledged to have influenced several important Standards [4-6]. Two WG1 sub-groups focus specifically on the provision of testing and assessment procedures relating to post service exposed materials (WG1.1) and creep crack initiation (WG1.2), Fig. 1.

More recently, WG4 was formed to focus on the assessment of high temperature components and multi-axial features. When ECCC was first founded, its main activities were driven by the requirements of the alloy producers and plant manufacturers [3b-e]. Subsequently, the requirements of plant operators have become increasingly important [3f-i]. This is reflected by the creation of WG1.1 in 1997 and in particular by the formation of WG4 in 2001 to provide support for plant design and assessment functions (Fig. 2).

The following paper reviews the data assessment procedure adopted to ensure that there is minimum uncertainty associated with the predicted long time creep-rupture strength values contained in the ECCC Data Sheets, reviews their current status, and examines the practical implications associated with strength values recommended in new Data Sheets for Grade 92 steel and the Alloy-80A nickel base alloy.

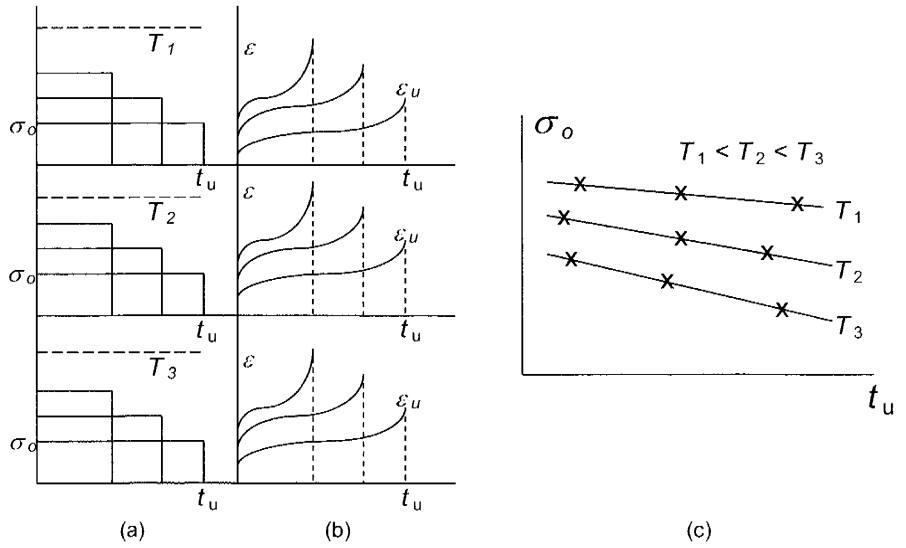

Fig. 3 Schematic representations of (a) the T,σ_o (dependent variable) conditions for 3 creep-rupture tests each at 3 temperatures, (b) the corresponding $\varepsilon(t)$ (response variable) test records, and (c) the resulting $t_u(T,\sigma_o)$ data points

Creep-Rupture Strength

Background

At elevated temperatures, metallic structures deform with time under the influence of applied stress. In the limit, the accumulation of such plastic deformation leads to fracture by a creep-rupture mechanism (Fig. 3a,b). The consideration of this damage process is a key part of the

design assessment of critical components for high temperature applications, with the necessary engineering calculations requiring a knowledge of the creep-rupture strength of the material from which the structure is manufactured.

In ideal circumstance, creep-rupture strength values for design purposes are determined from an assessment of the results of sufficient tests on a variety of casts of the specified material to ensure that its true property variance has been fully characterised for an appropriate range of stresses and temperatures. In practice, this means the assessment of the largest possible multi-cast $t_u(T,\sigma_o)$ datasets comprising the longest duration data available from all possible sources. Such full-size datasets for traditional materials may comprise up to ~1,000 observations for ~100 casts covering several temperatures with test durations up to >100,000h (e.g. Fig. 4).

The large international creep-rupture datasets collated in the early 1990s originated from an era when national groups from the main industrial nations had the resources to independently generate the long term results required to adequately characterise the behaviour of their strategic alloys to design life durations. ECCC provided the means by which these could be exchanged in an equitable way. At the present time, there are fewer opportunities for the generation of full-size international datasets, except on new advanced alloys (e.g. in COST).

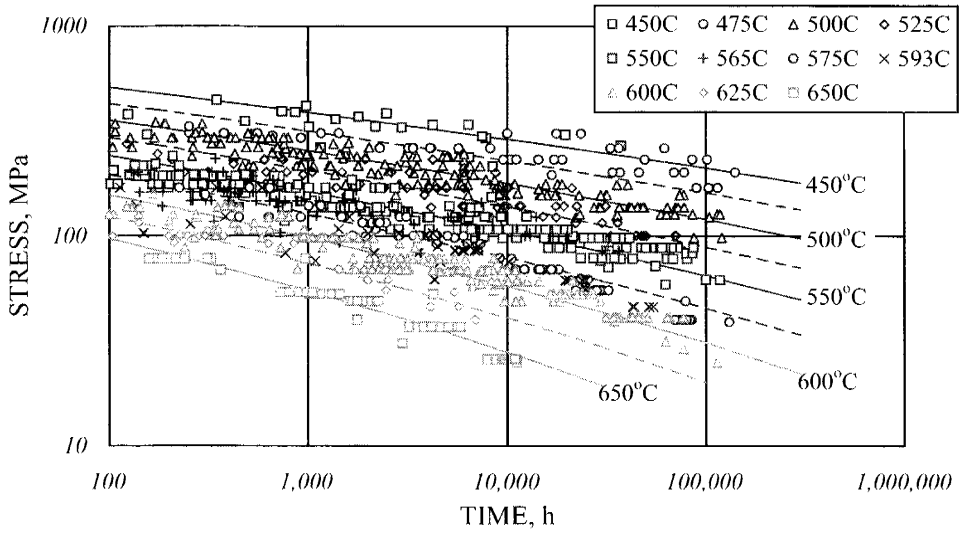

Fig. 4 Large multi-temperature, multi-cast, multi-source creep-rupture dataset for 2¼CrMo

Assessment Procedure

The ECCC creep rupture data assessment procedure was primarily developed to predict long time creep-rupture strength values for European Product and Design Standards, and for this reason is extremely rigorous by intention. It comprises a number of analysis stages (Fig. 5), of which three are of particular importance and worthy of further mention:

- pre-assessment
- $t_u^*(T,\sigma_o)$ model selection (main assessment)
- post assessment tests

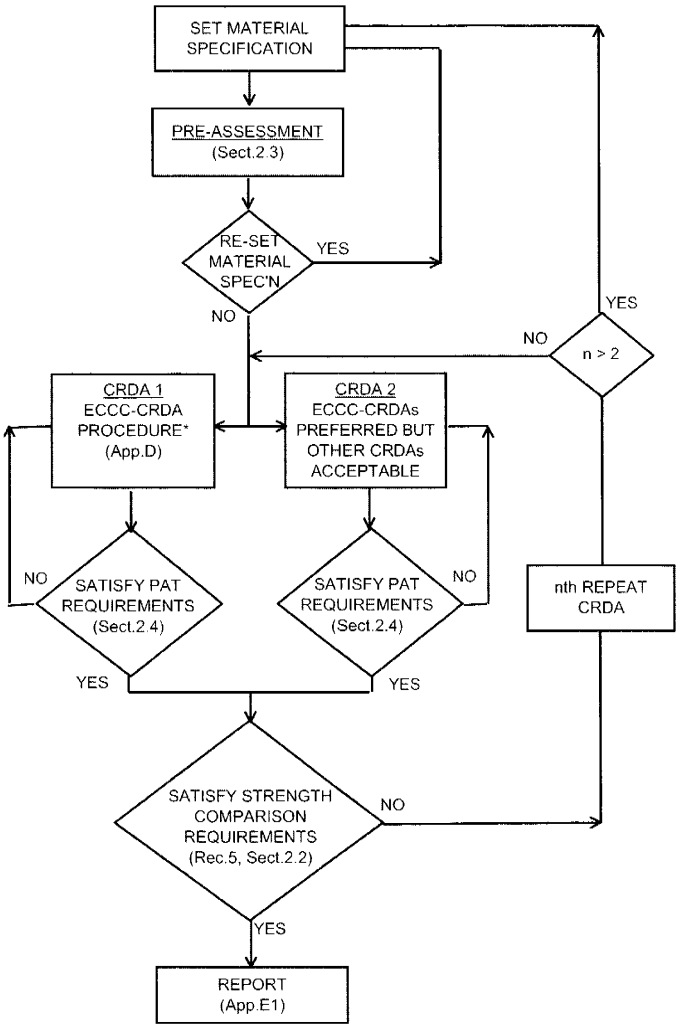

Fig. 5 Steps in the ECCC creep rupture data assessment procedure
The references in parentheses refer to sections in the ECCC Recommendations Volume 5 Part Ia [3e]

Pre-assessment
Pre-assessment is undertaken to confirm that all $t_u(T,\sigma_0)$ data meet the material pedigree and testing information requirements recommended in [3c]. In particular, it is intended to confirm that the material pedigree of all casts (for which $t_u(T,\sigma_0)$ data is being considered) meet the set specification.

Pre-assessment is also used to provide a first visual examination of all broken and unbroken test data plotted in log t_u(log σ_0) diagrams to characterise trends and scatter in the data (e.g.

Fig. 4 [3c]). This gives a first indication of the scope of the data, the presence of any clear outliers, any dominance by specific casts, and the need for data re-organisation (e.g. in the event of clear product related sub-populations). Data interrogation at this stage also reveals the presence of data point duplication.

Model Selection
The main assessment phase employs an ECCC recognised creep-rupture data assessment (CRDA) procedure [3e]. In principle, these are procedures which are formally defined, and include:
- the German graphical method [7]
- the ISO method [8]
- the DESA procedure (fully software implemented) [9], and
- the PD-6605 procedure (software implemented) [4]

A CRDA procedure is one which determines the optimum $t_u^*(T,\sigma_o)$ model (master equation), with the exception of the German graphical method. There are a wide range of $t_u^*(T,\sigma_o)$ model options from which to make a selection for the master equation (e.g. [10-15]).

Post Assessment
ECCC developed the post assessment tests (PATs) to provide an independent check on the reliability and credibility of results from any CRDA procedure [3c,16]. Three categories of tests are employed to examine:
- the physical realism of predicted isothermal log $t_u(\log \sigma_o)$ data lines
- the effectiveness of the model prediction within the range of the $t_u(T,\sigma_o)$ assessment input data, and
- the repeatability and stability of the extrapolations

The detail of their development and validation are given elsewhere [3e,16]. Since their introduction, the ECCC PATs have proved to be highly effective. Nevertheless, their main drawback has been the time needed for their full implementation. This task has now been alleviated by the development of ePAT software which significantly reduces implementation time [17].

Strength Comparison Requirements
A main feature of the ECCC flow diagram (Fig. 5) is that following definition of the material specification and data pre-assessment, at least two main (model selection) assessments are performed, ideally involving different procedures by different assessors. Moreover, the reliability and credibility of the outcome of each of the model selection assessments has to be demonstrated by means of the post assessment tests.

For the overall assessment to be acceptable, the results of two CRDAs should predict $R_{u/100kh/T}$ strength levels to within 10% at $T_{min,10\%}$, T_{main} and $T_{max,10\%}$. Only $R_{u/t/T}$ strength values from a creep-rupture data assessment activity meeting these requirements are regarded as being acceptable to be published in ECCC Data Sheets.

ECCC Data Sheets

Format of Data Sheets
ECCC Data Sheets typically comprise four parts, providing details of the material pedigree characteristics, the assessed data characteristics, the recommended creep-rupture strength values and the master equation from which the strength values were determined.

Material Pedigree Characteristics
A table defines the condition of the specified alloy in terms of:
- chemical composition,
- product form,
- heat treatment details, and
- tensile properties

Importantly, it compares the requirements of the specified alloy and product form with a summary of the characteristics of the individual casts of material providing the creep-rupture data which had been assessed.

Assessed Data Characteristics
A second table summarises, for all test temperatures, the scope of the data in terms of:
- number of casts, and
- tests within specific time regimes

Creep-rupture strength values are qualified when extrapolation has been required and is regarded as extended [3e,4,8]. Strength values are deemed extended in terms of stress if they are in the range $0.9.\sigma_{o,min}$ to $\sigma_{o,min}$ (or $\sigma_{o,max}$ to $1.1.\sigma_{o,max}$). Time extrapolations are deemed extended when they are $\geq$3 times the duration at which there are individual data points from at least five casts at, and within 25°C, of the given temperature. The assessed data characteristics table provides an indication of why creep rupture strength values have been qualified in the following (third) table.

Creep-Rupture Strength Values
A third table summarises the recommended creep-rupture strength values for temperatures within the material's high temperature application regime or within a more restricted range of temperatures if dictated by the scope of the available data. Creep-rupture strength values are typically tabulated for 10kh, 30kh, 100kh and, if appropriate, 200kh.

These creep-rupture strength values are also illustrated in a $R_{u/t}(T)$ diagram (e.g. Fig. 6).

Master Equation
Apart from a number of the earliest Data Sheets, the $t_u^*(T,\sigma_o)$ master equation determined from the formal data assessment procedure and used to determine the tabulated creep-rupture strength values is given.

Status of Data Sheets
The first issue of published ECCC Data Sheets was in 1999, although many had been prepared and supplied to the appropriate ECISS technical committee at a much earlier date. The 1999 issue contained data sheets for 53 low and high alloy ferritic and austenitic steels

(App. A). A number of these contained strength values which had not been derived by the 'formal' ECCC CRDA procedure described above. In those cases (indicated in Table A1) strength values were based on those already existing in National and/or International Standards for which it was known that no additional long term data had become available since the original assessment.

The second issue of Data Sheets was published in 2005, and contained 59 Data Sheets of which six were completely new, three were revisions following a new assessment and one had been amended to correct an error (Table A1). Practical implications associated with strength values recommended in new Data Sheets for Grade 92 steel and the Alloy-80A nickel base alloy are examined in the following sections.

Steel Grade 92

ASTM Steel Grade 92 (P92/T92) is a relatively new martensitic 9%Cr steel containing 2% tungsten and 1% molybdenum (X10CrWMoVNb9-2) and is being increasingly adopted for critical high temperature pipe and tubing applications in the construction of advanced power plant.

The first ECCC assessments of Grade 92 led to the strength values published in the 1999 issue of the Data Sheet for the steel. The assessments were performed on a large dataset comprising information from 42 casts gathered at temperatures in the range 550 to 700°C (Table 1). However, despite the large number of $t_u(T,\sigma_o)$ data points and the total accumulated testing hours exceeding 4 million, maximum test durations for ruptured and unbroken testpieces were only in the range 40 to 60kh. This meant that 100kh was the practical limit for creep-rupture strength predictions with acceptable levels of uncertainty.

Table 1 Summary Statistics of Datasets used for Grade 92 Data Assessments

Year of ECCC assessment	1999	2005
No. of casts	42	48
No. of temperatures	15	15
Temperature range covered by test data	550-700°C	550-700°C
T_{main}	600/650°C	650°C
$T_{min,10\%}$	550°C	550°C
$T_{max,10\%}$	700°C	700°C
No. of $t_u(T,\sigma_o)$ data points	733	802
$t_{u,max}$	43,514h	110,450h
No. of unbroken $t(T,\sigma_o)$ data points	65	29
t_{max}	59,136h	111,912h
Total accumulated testing hours	4,161kh	6,159kh

In view of the strategic importance of the alloy, the ECCC dataset was updated and re-assessed in 2005. By this time, more tests had been mounted and completed on more casts of the material resulting in a 50% increase in the total testing hours, and test durations exceeding 110kh (Table 1). Significantly, whereas the early test data were mainly for material originating from relatively small section product forms, by 2005 many more results were available for the steel in larger section product forms.

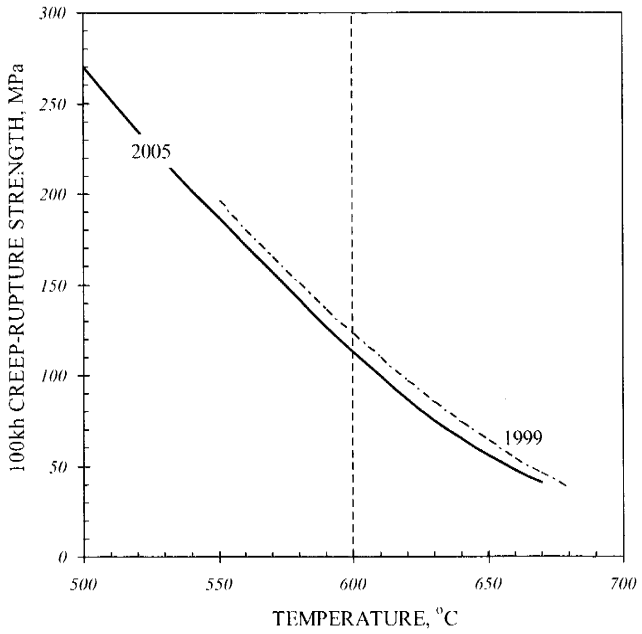

Fig. 6 Comparison of 1999 and 2005 ECCC Data Sheet 100kh creep-rupture strength values for Grade 92 steel.

The difference between the $R_{u/100kh/T}$ strength values determined for the ECCC Data Sheets in 1999 and 2005 is shown in Fig. 6. The latest assessment indicates a discernable reduction in 100kh creep-rupture strength, which for example at 600°C is from 123 to 113MPa. While this reduction is relatively small (<10%), it does have a significant influence on practical ruling section size requirements.

The assessed strength reduction is not obviously due to a significant metallurgical instability of the steel revealed by the availability of longer duration rupture data in 2005 (e.g. Fig. 7). The explanation for the lower $R_{u/100kh/T}$ strength values is more likely to be a consequence of the availability of longer duration rupture and unbroken test data in 2005 giving rise to a more representative model fit in the long time regime, and to the higher number of data points being the result of tests on material from larger section product forms. There is evidence to indicate that rupture data for Grade 92 material from larger section product forms consistently fall in the lower half of the 1999 $t_u(T,\sigma_o)$ data scatter-bands.

Alloy-80A

Two new Data Sheets covered Alloy-80A, the NiCr20TiAl nickel base alloy, in the 3-stage and 2-stage heat treated conditions.[2,3] 3-stage heat treated Allo-80A is traditionally used for applications to ~650°C, e.g. steam turbine bolts and blades, whereas 2-stage heat treated

[2] 3-stage heat treatment for Alloy-80A: 8h,1080°C,AC + 24h,850°C + 16h,700°C,AC

[3] 2-stage heat treatment for Alloy-80A: 8h,1080°C,AC + 4h,700°C,AC

Alloy-80A is usually employed for applications above ~650°C, i.e. for aero and land-based gas turbine parts.

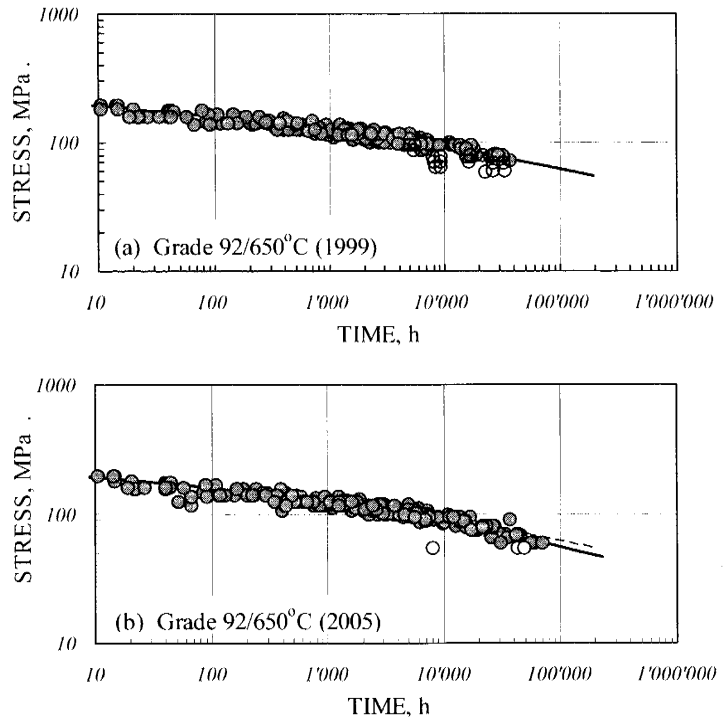

Fig. 7 Comparison of $t_u(650°C,\sigma_o)$ and $t(650°C,\sigma_o)$ unbroken (unfilled) data points for Grade 92 steel with ECCC assessed $t_u^*(650°C,\sigma_o)$ data lines (a) 1999, (b) 2005
The broken line in (b) is the 1999 assessed line for comparison

Table 2 Summary Statistics of Datasets used for Alloy-80A Data Assessments

Heat treatment	3-stage	2-stage
No. of casts	31	13
No. of temperatures	11	10
Temperature range covered by test data	475-850°C	500-900°C
T_{main}	550°C	820°C
$T_{min,10\%}$	550°C	700°C
$T_{max,10\%}$	750°C	820°C
No. of $t_u(T,\sigma_o)$ data points	147	131
$t_{u,max}$	55,096h	77,762h
No. of unbroken $t(T,\sigma_o)$ data points	41	14
t_{max}	71,152	101,000h
Total accumulated testing hours	2,049kh	1,358kh

The characteristics of the 2 datasets used for the assessment of the nickel base alloy in its two standard heat treatment conditions are summarised in Table 2. There were data for significantly more casts of the 3-stage heat treated material, although the two datasets were similar in size in terms of $t_u(T,\sigma_0)$ data point number. The temperature range over which data had been collected for the 2-stage heat treated material was higher than that for the 3-stage heat treated material reflecting the respective practical application temperature regimes for the two conditions. While the maximum test durations for the 2-stage heat treated alloy were significantly longer, the total accumulated testing hours for this condition were much lower then for the 3-stage heat treated material.

The ECCC Data Sheet $R_{u/100kh/T}$ strength values for the two heat treated conditions of Alloy-80A are shown in Fig. 8. The long time strength advantage of Alloy-80A in the 3-stage heat treated condition at temperatures below ~650°C is clearly evident. Similarly, at high temperatures, the long time strength advantage of the alloy in the 2-stage heat treated condition is demonstrated. It is also clear that the $R_{u/100kh/T}$ strength values given for 3-stage heat treated Alloy-80A in the EN 10269 Product Standard [18] are excessively conservative and should be revised.

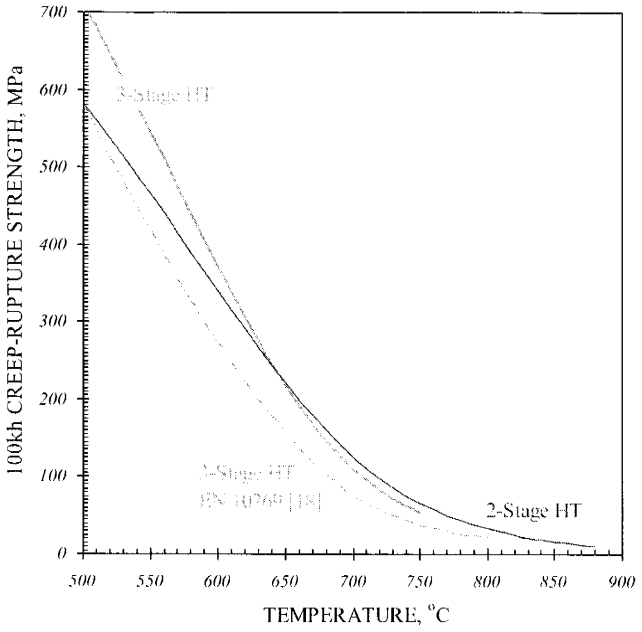

Fig. 8 Comparison of ECCC Data Sheet 100kh creep-rupture strength values for 3-stage and 2-stage heat treated Alloy-80A

Concluding Remarks

Procedures developed by the European Creep Collaborative Committee to ensure minimum uncertainty in the predicted long time creep-rupture strength values contained in the ECCC Creep Property Data Sheets have been described.

The current status of the ECCC Creep Property Data Sheets is also reviewed, and practical implications associated with new creep-rupture strength values recommended in the 2005 issue for Grade 92 and Alloy-80A are examined.

The $R_{u/t/T}$ strength values given for Grade 92 in a new ECCC Data Sheet (2005) are lower than those recommended previously in 1999 in the light of the latest $t_u(T,\sigma_0)$ data. While the recommended strength reductions are <10%, the significant influence on allowable ruling section thicknesses for plant components is acknowledged.

The $R_{u/t/T}$ strength values given for Alloy-80A in two new ECCC Data Sheets (2005) confirm the superiority of the material in the 3-stage heat treated condition at temperatures below ~650°C and the advantage of using the alloy in the 2-stage heat treated condition at higher temperatures. The ECCC strength values for 3-stage heat treated Alloy-80A indicate that the values given in the EN 10269 Product Standard are excessively conservative and should be revised.

References

1 D.V. Thornton, 'Activities of the European Creep Collaborative Committee', Proc. 5th Intern. Parsons Conf. on Advanced Materials for 21st Century Turbines and Power Plant, Cambridge, 3-7/7/00, A. Strang et al. eds., IOM London, 2000, 123-128.

2 ECCC Data Sheets, 'Rupture strength, creep strength and relaxation strength values for carbon-manganese, low alloy ferritic, high alloy ferritic and austenitic steels, nickel base alloys and high temperature bolting steels/alloys', eds. D.G. Robertson & S.R. Holdsworth, publ. ETD Ltd, http://www.ommi.co.uk/etd/eccc/advancedcreep/open.htm, 2005.

3 ECCC Recommendations, 'Creep data validation and assessment procedures', eds. S.R. Holdsworth et al., publ. ETD Ltd, 2005, a) Vol.1: Overview, b) Vol.2: Terms and terminology, c) Vol.3: Data acceptability criteria, Data generation, d) Vol.4: Data exchange and collation, e) Vol.5: Data assessment, f) Vol.6: Characterisation of microstructure and physical damage for remaining life, g) Vol.7: Data assessment – Creep crack initiation, h) Vol.8: Data assessment – multi-axial, i) Vol.9: Component assessment, http://www.ommi.co.uk/etd/eccc/advancedcreep/open.htm.

4 BS PD6605, Guidance on Methodology for the Assessment of Stress-Rupture Data, British Standards Institution, 1998.

5 EN 10291, Metallic Materials, Uniaxial Creep Testing in Tension, Method of Test, European Norm, 2000.

6 EN 10319, Metallic Materials, Tensile Stress Relaxation Testing, European Norm, 2000.

7 J. Granacher & M. Schwienheer, 'Assessment procedure document for graphical multi-heat averaging and cross-plotting method', App.D4 in ECCC Recommendations Vol.5 Part Ia (see [3c]).

8 ISO 6303, Annex: 'Method of extrapolation used in analysis of creep rupture data', 1981.

9 J. Granacher & M. Monsees, 'Assessment procedure document for DESA', App.D2 in ECCC Recommendations Vol.5 Part Ia (see [3c]).

10 F.R. Larson & J. Miller, 'A time-temperature relationship for rupture and creep stress', Trans ASME, 74, 1952, 765.

11 S.S. Manson, & A.M. Haferd, 'A linear time-temperature relation for extrapolation of creep and stress rupture data', NASA-TN-2890, 1953.

12 R.L Orr, O.D. Sherby & J.E. Dorn, 'Correlation of rupture data for metals at elevated temperatures', Trans ASM, 46, 1954, 113.

13 A. Mendelson, E. Roberts & S.S. Manson, 'Optimisation of time-temperature parameters for creep and stress rupture, with application to data from German cooperative long time creep program', NASA-TN-D-2975, August, 1965.

14 I.I. Trunin, N.G. Golobova & E.A. Loginov, 'New method of extrapolation of creep test and long time strength results', Proc. 4th Int. Symp. on Heat Resistant Metallic Materials, Mala Fatra, CSSR, 1971, 168.

15 S.S. Manson & U. Muraldihan, 'Analysis of creep-rupture data for the five multi-heat alloys by the minimum commitment method using double heat term centering techniques', Final Report of Res. Proj. 638-1, EPRI CS-3171, 1983, July.

16 S.R. Holdsworth, 'Recent developments in the assessment of creep-rupture data', Proc. 8th Intern. Conf. on Creep and Fracture of Engineering Materials and Structures, Tsukuba, 1-4/11/99, JSME, 1999, 1-8.

17 A. Scholz, M. Schwienheer & R. Znajda, 'Scatter band assessment methods for creep and fatigue data', Proc. 8th Intern. Conf. on Operating Pressure Equipment, Melbourne, April 2005.

18 EN 10269, 'Steels and nickel alloys for fasteners with specified elevated and/or low temperature properties', European Norm, 1999.

Nomenclature

CRDA	Creep rupture data assessment
ECCC	European Creep Collaborative Committee
PATs	Post assessment tests
$R_{u/t}(T)$	Rupture strength for a given time as a function of temperature
$R_{u/t/T}$	Rupture strength for a given time and temperature
$R_{u/100kh/T}$	100kh rupture strength for a given temperature
t, t_u, t_u*	Time, observed time to rupture, predicted time to rupture
t_{max}	Maximum unbroken testpiece duration
$t_{u,max}$	Maximum time to rupture
$t_u(T,\sigma_0)$	Observed time to rupture as a function of temperature and stress
t_u*(T,σ_0)	Predicted time to rupture as a function of temperature and stress
T	Temperature
T_{main}	Main temperature at which there are the most $t_u(T,\sigma_0)$ data points
$T_{min,10\%}$	Minimum temperature at which there are 10% of $t_u(T,\sigma_0)$ data points
$T_{max,10\%}$	Maximum temperature at which there are 10% of $t_u(T,\sigma_0)$ data points
σ, σ_0	Stress, initial stress
$\sigma_{0,min}$, $\sigma_{0,max}$	Minimum initial test stress, maximum initial test stress
ε	Strain

Appendix A ECCC Creep Property Data Sheets

An overview of the currently published ECCC Creep Property Data Sheets [2] is given in Table A1. They are reviewed in five categories, i.e.

a) Carbon-manganese and low alloy ferritic steels
b) High alloy ferritic steels
c) Austenitic steels
d) Nickel base alloys, and
e) High temperature bolting steels

Table A1a Overview of Data Sheets for Carbon-Manganese and Low Alloy Ferritic Steels

Steel	ECISS Grade	Formal CRDA	Release Date
C, Si/Al killed (normalised)	Steel P195	N	1996
C, Si/Al killed (normalised)	Steel P235	N	1996
C, Si/Al killed (normalised)	Steel P265	N	1996
CMnNb (normalised)	Steel P355	N	1996
0.3%Mo (normalised)	16Mo3	N	1996
MoB (normalised)	8MoB5-4	N	1996
1%CrMo (normalised + tempered)	13CrMo4-5	N	1996
1%CrMo (hardened + tempered)	25CrMo4	N	1996
1¼CrMo (normalised + tempered)	13CrMo5-5	N	1996
½Cr¼Mo¼V (normalise + tempered)	12MoCrV6-2-2, 14MoV6-3	Y	1996
2¼CrMo (normalised + tempered)	11CrMo9-10+NT	N	1996
2¼CrMo (quenched + tempered)	11CrMo9-10+QT	N	1996
3CrMoV (hardened + tempered)	20CrMoV13-5	N	1996
5CrMo (annealed)	X11CrMo5+I	N	1996
5CrMo (normalised + tempered)	X11CrMo5+NT1, +NT2	N	1996
1NiMoCuNb (Normalise + tempered)	9NiMoCuNb5-6-4	N	1996

Table A1b Overview of Data Sheets for High Alloy Ferritic Steels

Steel	ECISS Grade	Formal CRDA	Release Date(s)
9Cr1Mo (annealed)	X11CrMo9-1+I1	N	1996
9Cr1Mo (annealed)	X11CrMo9-1+I2	N	1996
9Cr1Mo (normalised + tempered)	X11CrMo9-1+NT	N	1996
Steel 91 (P91/T91)	X10CrMoVNb9-1	Y	1995
Cast steel 91	GX12CrMoVNbN-1	Y	2005
Steel E911	X11CrMoWVNb9-1-1	Y	2005
ASTM Grade 92 (P92/T92)	X10CrWMoVNb9-2	Y	1999, 2005
12CrMoV (hardened + tempered)	X20CrMoNiV11-1	N	1996 (2004)

Date in parentheses represents an amendment to correct an error in the original version of the Data Sheet

Table A1c Overview of Data Sheets for Austenitic Steels

Steel	ECISS Grade	Formal CRDA	Release Date(s)
TP 304L	X2CrNi18-9	N	1999
TP 304LN	X2CrNiN18-10	N	1999
TP 304H	X6CrNi18-10	N	1999
Super 304H		N	1999
TP 316L	X2CrNiMo17-12-2	Y	1998
TP 316	X5CrNiMo17-12-2	Y	1998
TP 316Ti	X6CrNiMoTi17-12-2	Y	1999
TP 316LN	X2CrNiMoN17-13-3	N	1999
TP 316L(N)	X2CrNiMo17-12-2	Y	1999
TP 316LNB	X3CrNiMoBN17-13-3	N	1999
TP 321H (1070-1150°C)	X7CrNiTi18-10	N	1999
TP 321H (950-1070°C)	X7CrNiTi18-10	Y	1999
TP 347 (1070-1150°C)	X6CrNiNb18-10	Y	1999
TP 347 (950-1070°C)	X6CrNiNb18-10	Y	1999
TP 347H (fine grained)		N	1999
16-13Nb	X8CrNiNb16-13	N	1999
Alloy 800	X5NiCrAlTi31-20	N	1999
Alloy 800H	X8NiCrAlTi32-21	Y	1998
Alloy 800HT (restricted Al + Ti)	X8NiCrAlTi32-21	Y	1998
Alloy 800 (recrystallised)	X5NiCrAlTi31-21 RK	N	1999
TP AC66	X6NiCrNbCe32-27	N	1999
Steel 253MA	X7CrNiSiNCe21-11	Y	1998
Esshete 1250	X10CrNiMoMnNbVB15-10-1	Y	1999
TP 310		Y	1999
Steel HR3C		Y	1999, 2005
Steel NF709		Y	1999, 2005
Steel NF709R		Y	2005

Table A1d Overview of Data Sheets for Nickel Base Alloys

Alloy	ECISS Grade	Formal CRDA	Release Date
Alloy-617	NiCr23Co12Mo	Y	2005
Alloy-80A (3-stage heat treated)	NiCr20TiAl	Y	2005
Alloy-80A (2-stage heat treated)	NiCr20TiAl	Y	2005

Table A1e Overview of Data Sheets for High Temperature Bolting Steels

Steel	ECISS Grade	Formal CRDA	Release Date
Durehete 900	42CrMo5-6	Y	1998
Durehete 1050	20CrMoVTiB4-10	Y	1996[+]
1%CrMoV	21CrMoV5-7	Y	1998*

Additional Data Sheets for stress relaxation strength (+) and 1% creep strength (*)

Part I

Energy Perspectives

Invited papers

EVALUATION OF THE MATERIALS TECHNOLOGY REQUIRED FOR A 760ºC POWER STEAM BOILER

John P. Shingledecker and Ian G. Wright

Oak Ridge National Laboratory
Oak Ridge, TN, USA
shingledecjp@ornl.gov

Abstract

The U.S. Ultra-supercritical (USC) Steam Boiler Consortium, funded by the U.S. Department of Energy and the Ohio Coal Development Office, has been working to develop the necessary materials technology to construct a steam power boiler with maximum steam conditions of 760ºC and 35MPa. One large component of this work is to evaluate the properties of the materials chosen for such a boiler. While long-term creep strength of base metal is initially used to set temperatures, stresses, and simple design rules, it is clear that base metal creep strength is not always the material property of most importance when selecting an alloy. The fabrication issues (typically weldability), the properties of materials after fabrication, the corrosion resistance of the material, and material cost all need to be considered in addition to baseline mechanical properties. Work is ongoing at Oak Ridge National Laboratory to evaluate the material technologies being developed by the USC Steam Boiler Consortium and perform additional advanced research activities in areas where new materials developments and better fundamental understanding are needed to ensure the long-term success of a 760ºC power steam boiler.

Keywords: ultrasupercritical, creep, oxidation, 9-12 Cr ferritic steels, Ni-based alloys

Introduction

Global demand for high-efficiency pulverized coal-fired (PC) power plants has markedly increased in the past ~15 years. Environmental concerns, cost of fuel, energy need, and an aging energy infrastructure are all factors driving the need for the construction of efficient powerplants. Main/reheat steam temperature in recently-constructed power steam boilers have increased from ~566/566ºC in standard supercritical technology to 600/620ºC in the current state-of-the-art plants [1]. The ability to build and operate these new ultrasupercritical (USC) power plants has only been possible through the use of new, higher-strength materials – namely creep-strength-enhanced ferritic steels. However, these newer steels cannot be used at the highest temperatures needed to further increase the efficiency of PC powerplants, so that new materials technology is needed. To respond to these material needs, a U.S. USC Steam Boiler Consortium was formed to develop the materials technology necessary to construct and operate a USC power steam boiler with maximum steam conditions of 760ºC and 35MPa. The consortium is made up of the U.S. boiler manufactures (Alstom, Babcock and Wilcox, Foster Wheeler, and Riley Power), the Electric Power Research Institute (EPRI), Energy Industries of Ohio (EIO), and Oak Ridge National Laboratory (ORNL), and is funded by the U.S. Department of Energy (DOE) and the Ohio Coal Development Office (OCDO) [2]. Through its role as the mechanical properties task leader on the consortium, ORNL is providing analysis of the materials technology being developed by the consortium. Additionally, ORNL is performing longer-term advanced materials research activities to study new materials developments, and to provide improved scientific understanding (microstructural analysis, thermodynamic modelling, etc.) of PC powerplant materials to ensure DOE's long-term success at the development and implementation of a 760ºC power steam boiler.

Background

A plot of stress for rupture in 100kh as a function of temperature, by materials class, is shown in Fig. 1. Since a 760ºC steam boiler will see a large range of temperatures from the waterwall to the superheater, the temperature limits of materials, particularly relatively inexpensive ferritic steels, is of primary importance. Using as the initial discriminator 100kh rupture strength at 100MPa (which allows the use of relatively thin walled tubes and pipes, so minimizing thermal fatigue issues), we can see that ferritic steels can be used up to ~620ºC, austenitic stainless steels up to ~690ºC, primarily solid solution-strengthened nickel-based alloys (based on a recent CCA617 analysis [3]) up to ~720ºC, and age-hardenable nickel-based alloys beyond 720ºC.

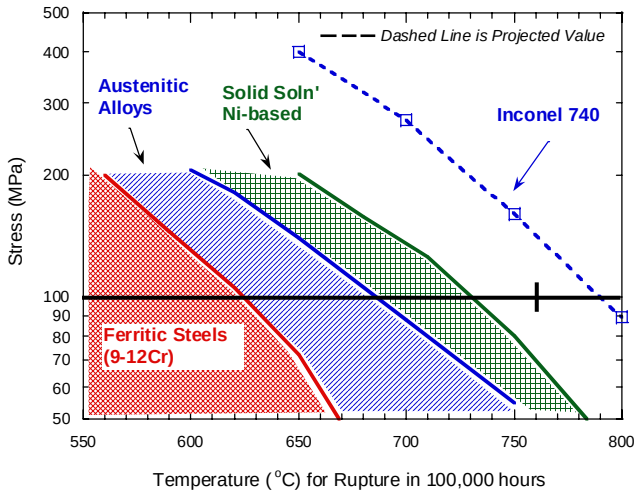

Figure 1. Stress for rupture in 100,000 hours as a function of temperature by materials class. Solid line at 100MPa gives estimation of maximum use temperature for boiler materials. For boilers operation at ~720ºC and above, age-hardenable Ni-based alloys (including Inconel 740) will be required.

Consideration also must be given to factors that may decrease the useful temperature limit of a given material, which include fabricability (welding, forming, etc.), resistance to high-temperature corrosion (typically oxidation on the steam-side and oxidation/deposit-related corrosion on the fireside), and strength after thermal treatment (welding, aging, etc.). In this paper we will only consider these issues as they pertain to ferritic steels and Ni-based alloys. In austenitic stainless steels, the combination of high thermal expansion and low thermal conductivity can generate large stresses during thermal transients in thick-section components. Thus, creep-fatigue and thermal shock is a concern for these alloys. However, thick-walled pipes made from austenitic stainless steels have been successfully used in Eddystone, which has been operating at USC conditions above 600ºC for over 40 years [4]. Thus, based on creep strength and in-plant experience, austenitic stainless steels represent an important class of materials for bridging the gap between 620 and 700ºC. Further improvements in the properties of these alloys, including fatigue resistance, are possible, and significant research is ongoing elsewhere [5].

From Fig. 1, we see that to raise the steam temperature, and thus efficiency, of the current USC boiler technology (~620ºC), either new ferritic steels are needed, or austenitic steels followed by Ni-based alloys must be used. The preferred configuration would be to avoid the use of austenitic steels, but this would depend on minimizing the amount of high-cost Ni-based alloy needed. It is also clear that current solid solution-strengthened Ni-based alloys (including alloy 230 and 617 which are pressure vessel code approved) have the necessary strength to reach to 700 to 720ºC. This, not coincidentally, is the temperature goal of the European AD700 program [6]. To reach 760ºC (vertical line intersecting the 100MPa line in Fig. 1), an age-hardenable nickel-based alloy will be required. The U.S. Steam Boiler program is unique in that it is the first research program to consider the factors outlined earlier (oxidation, weldability, etc.) as they pertain to the usage of thick-section age-hardenable nickel-based alloys (Inconel 740) in a boiler.

Ferritic Steels

Ferritic steels are important alloys for a 760ºC power steam boiler for a number of factors. First, since they are relatively inexpensive compared to austenitic and nickel-based alloys, boiler designers would like to utilize ferritic steels as much as possible to reduce the cost of the boiler. Second, the fabrication technology for ferritic steels is well developed so that there is no learning curve associated with implementing this technology. Third, extensive welding is used to construct waterwall panels, and austenitic steels and nickel-based alloys are not commonly used for water-touched tubes because of concerns about stress corrosion cracking.

Strength Limitations

The strength of creep strength enhanced ferritic steels appears to be limited to ~620ºC. These steels include grade 91, 911, and 92, and their creep resistance is due to the precipitation of very fine MX (mainly VN) carbonitrides [7]. These steels also contain W and/or Mo for solid solution and laves phase strengthening. Hald [8] has discussed the role of W and Mo in these alloys, and has concluded that, in fact, little strengthening contribution is due to these elements. In terms of long-term microstructural stability, B appears to have a large effect in these alloys, apparently slowing the coarsening of grain boundary carbides [9, 10, and 11].

In an effort to make steels with improved temperature performance, steels with higher chromium levels have been developed, including 122 (HCM12A), NF12, and SAVE12. Initial strength of these alloys is higher than the nominally 9Cr steels, but long-term creep strength is comparable or even inferior. P/T122 failures at ~10% of life have occurred in test superheaters operating at 610 and 650ºC [8] and after 30,000 hours service in a utility power steam boiler in Japan [12]. This latter failure led to the re-evaluation of allowable stress values in Japan for P/T122, which were subsequently lowered close to grade 91 strength values [12]. Z-phase, which consumes large amounts of the MX carbonitrides after long-term exposure in some ferritic steels, has been identified as one of the primary factors affecting the microstructural stability of the 12Cr steels. Z-phase precipitation kinetics appear to be highly accelerated at higher Cr levels above 10% [8, 13]. If a 12Cr ferritic steel is to be developed for service above 620ºC, new strengthening mechanisms need to be explored, backed by fundamental research to ensure long-term structural stability of these alloys.

Further complicating the strengthening issues of advanced ferritic steels is the strength of weldments. During welding and subsequent post-weld heat-treatment (PWHT), a fine-grained (FG) heat-affected zone (HAZ) forms in the base metal, adjacent to the weld metal of ferritic steels. The creep strength of this HAZ is inferior to the base metal. Based on long-term creep data, the reduction in strength due to this 'type IV' failure can be very significant. Efforts within the European Creep Collaborative Committee (ECCC) to quantify a reduction in strength have shown that between 550 and 600ºC, the weld strength factors for advanced ferritic steels can vary between 0.95 and 0.65 [14]. Considering a strength reduction factor of 0.65, designing a new alloy for weldment strength may be more important than base metal strength.

Steam-Side Oxidation Limits

In the development of the 9-12Cr ferritic steels, consideration also has been given to the alloying and microstructural needs for maximizing oxidation resistance in steam. It is well known that progressively increasing the Cr level in ferritic steels confers increased resistance to oxidation, and ferritic steels with Cr levels in the 9-12% range can form Cr-rich scales that are (at least, initially) very protective. Consequently, it is important to understand the factors that promote such scales, and if they can provide long-term protection. Extensive studies in Japan and Europe have defined the roles of alloy composition on oxidation behavior in steam. Of the minor elements typically found in this class of alloys (Si, Mn, Mo, V, W, Nb, Pd, Cu, C, and S), Si forms a more stable oxide than Cr; some oxides of Nb have a similar thermodynamic stability to Cr_2O_3; and Mn can form mixed oxides (spinels) which can exhibit reduced transport properties for Fe, so that these three elements can exert a beneficial effect on protective scale behavior under some circumstances. Studies using tightly-controlled alloy compositions have defined the optimum levels of minor elements for maximizing oxidation resistance. Silicon and S have been found to be particularly effective; several groups have suggested that Si additions have a greater effect than does Cr on the oxidation rate of ferritic steels (in the range up to 12%Cr) in steam [15-19]; Fukuda et al. [16] suggested that 1 wt% Si is approximately equivalent to 4 wt% Cr; Fujikawa and Otsuka [17] ranked Si more than 5 times as effective as Cr, especially at temperatures above 600°C in steam. Sulfur additions greater than 50 ppmw have been shown to significantly reduce the oxidation rate of 10Cr steels at 600-650°C in steam, independent of the Si content [20]. This effect apparently is associated with accumulation of S at the alloy-oxide interface [21-23], although the mechanism involved has not yet been fully explained.

The effectiveness of optimizing the alloy Cr, Si and S contents on the oxidation behavior at 650°C in 17 bar steam is illustrated in Fig. 2. The influence of increased Cr content is evident for T122 (10.6Cr-0.12Si-0.001S) compared to T91 (8.3Cr-0.13Si-0.001S), T92 (9.2Cr-0.16Si-0.005S), and SAVE 12 (9.25Cr-0.28Si-0.001S). An experimental alloy (shown as a single line) with a higher Cr content but significantly lower than optimum Si and S levels (11Cr-CoMnWVMo-0.06Si-0.002S) exhibited an even lower oxidation rate to 2.5kh, after which it suffered extensive scale loss. In contrast, the MAR alloys [11] with only 9Cr, but with optimized levels of Si (0.7%) and S (0.005%), exhibited significantly lower oxidation rates. It should be noted, however, that even the slowest oxidation kinetics measured extrapolate to 300 µm-thick scales (approximately the thickness at which scale exfoliation is expected) after only 34-39kh, compared to 5-6kh for P91 and P92 (assuming parabolic behavior). Thus, it

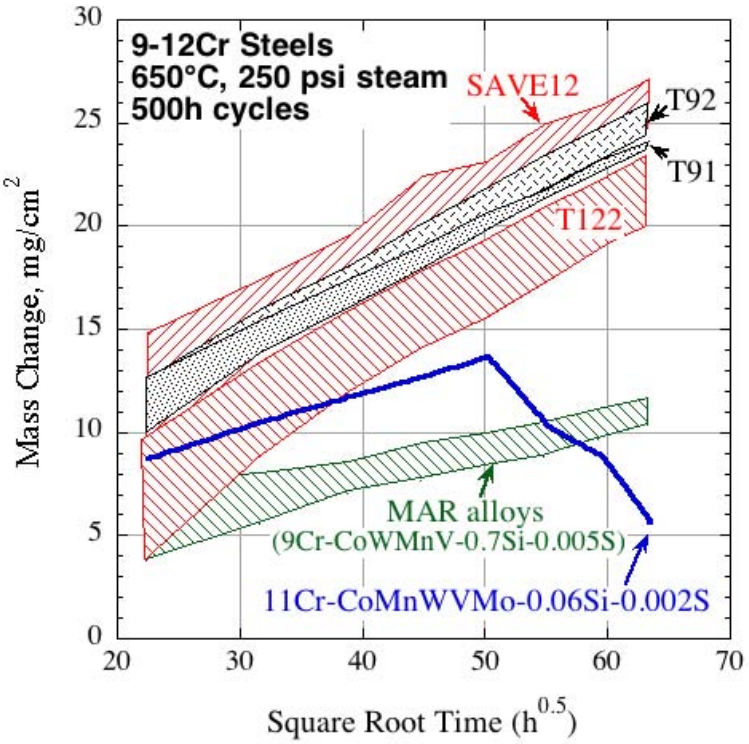

Figure 2. Comparison of the oxidation kinetics of 9-12Cr steels in 4kh exposures in 17 bar steam at 650°C.

appears that the maximum oxidation-limited service temperature of nominally 9Cr steels such as P/T92 will be significantly less than 650°C, unless protective coatings can be applied. A major issue with coatings is the need to avoid a heat treatment schedule that would interfere with that required to fully develop the martensitic microstructure in the alloy. Coating approaches involving low-temperature processing were studied in the European COST 522 program [24] and appear to be very promising. In addition, an extensive evaluation of available coatings is in progress in the US USC Steam Boiler Consortium [25], and a small effort at ORNL is aimed at quantifying the effects of the application of typical high-temperature coatings on the creep behavior of alloy T92 [26].

Overall experience of the steam oxidation behavior of this class of alloys (mostly in laboratory or rig tests) has been that the scale formed typically consists mainly of magnetite, with an outer layer of essentially pure magnetite, and an inner layer of magnetite containing oxides of alloying elements (especially Cr). In the 9-10Cr steels, these elements also tend to accumulate at the base of the inner layer next to the alloy, where they may interfere with the outward movement of iron ions, and so modify the oxidation behavior. Figure 3 illustrates the complex nature of the inner oxide layer formed on T112, in which multiple, incomplete layers

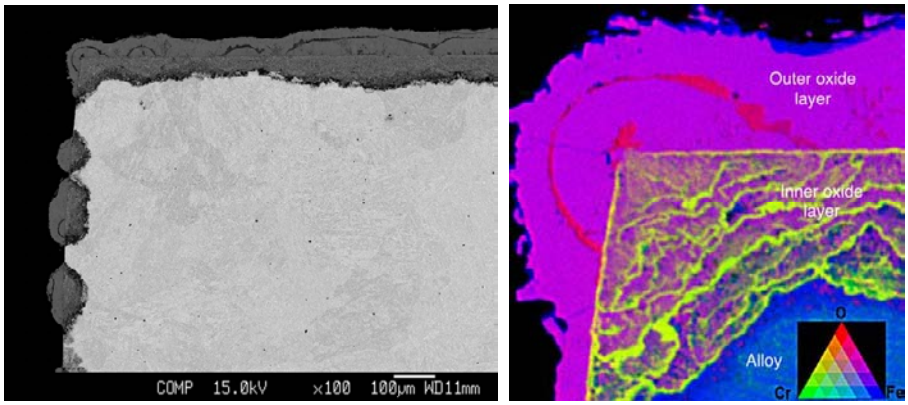

(a) *(b)*

Figure 3. Cross sections of the scale formed on alloy T122 (10.6%Cr) oxidized for 2kh in 17 bar steam at 700°C. (a) overall view of specimen corner, showing double-layered scale and irregular scale thickness; (b) composite X-ray images of specimen corner, in which the bright-appearing, incomplete layers are remnants of Cr-rich subscales that have been incorporated as the inner layer grows into the alloy.

of Cr-rich subscale have been incorporated as the inner layer continues to grow. Each of these incomplete layers can serve to modify the local diffusion paths for iron ions involved in the growth of the overall scale. As a result, the oxidation behavior of the 9-10Cr steels can be highly variable, and it appears sensitive to minor changes in levels of both Cr and minor elements. This means, that not only the thickness and but also the morphology of the scales formed can differ substantially. Other factors found to influence the oxidation behavior are test temperature, duration, and surface treatment; in addition, anomalous temperature dependence has been reported, since the initially-formed scale may control subsequent oxidation behavior for long times. Such variability is not apparent in steels containing more than approximately 12.5%Cr, which typically exhibit excellent oxidation resistance, forming scales in which the inner layer is Cr-rich (up to 40wt%Cr) with an outermost layer of Fe_2O_3. The oxidation behavior of the 9-12Cr class of alloys has been discussed extensively in the literature, and Zurek, et al. [27] have proposed a way of rationalizing the behavior, using a classification based largely on alloy Cr content.

Fabrication of Waterwalls

The fabrication of waterwall panels requires extensive welding of low-alloy steels such as T22/T23. For a 760ºC steam boiler, design studies have indicated that an advanced ferritic steel, such as T91/92 may be required, as the pressure and temperature in the waterwall will be higher than current designs [28]. This creates significant fabrication issues because the current waterwall materials do not require a PWHT, whereas advanced ferritic steels, including T91, do. Not only is applying a PWHT to a panel difficult (requiring a large furnace), but it will cause distortion of the part. In the field, this part will need to be assembled and welded, requiring a localized PWHT.

Recent materials developments in Japan by Abe at NIMS [29] have shown the absence of a fine-grained HAZ after welding of an advanced ferritic steel with highly-controlled B and N

levels. Creep-rupture studies have confirmed that weldments in these developmental alloys do not fail by a type IV mechanism [29]. It is unclear why these steels do not form the FG-HAZ. ORNL are collaborating with NIMS to better understand this potentially significant phenomenon.

Using high-intensity synchrotron radiation, real-time diffraction experiments are being conducted to examine the ferrite-austenite-ferrite phase transformations during simulated weld heat-affected zone thermal histories. Figure 4 shows the variations in amounts of austenite and ferrite (martensite) during the cooling portions of a thermal history for an experimental 9 Cr steel developed at NIMS, N130B, and P92. The steels were heated to peak temperatures near 900°C, which is well above the A_3 transformation temperatures for both steels. These data indicate that the formation of austenite during heating was much more sluggish for the experimental steel. The maximum amount of austenite in the N130B reached about 40% compared to about 85% for the P92. In addition, retained austenite was only detected after this thermal history in the P92. These results are consistent with metallographic evidence on

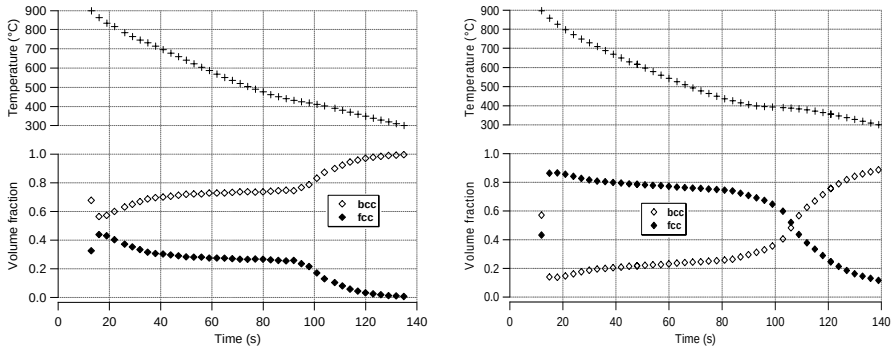

Figure 4. Variations of temperature and peak area fractions, i.e., amounts of bcc ferrite and fcc austenite, measured by synchrotron diffraction experiments on a NIMS steel (a) and P92 (b) during cooling for a simulated welding cycle [30]

HAZ grain structures that suggest austenite nucleation is more sluggish in the N130B steel than in P92. Their implications in determining HAZ microstructures and weldments creep properties are still being analyzed. Elimination of FG-HAZ type IV failures and/or PWHT of advanced steels could significantly reduce the fabrication cost of a 760ºC steam boiler.

Ni-Based Superalloys

Nickel-based superalloys are necessary for the construction of a 760ºC power steam boiler. Extensive fabrication efforts have been carried out by the USC Steam Boiler Consortium. Thick-section weldments have been successfully produced in Haynes 230 and CCA617, and other fabrication technologies (forming, machining, etc.) have been demonstrated [see ref. 31 in this proceedings]. However, these alloys are limited by base metal strength to ~700ºC. To reach 760ºC, Inconel 740 was chosen by the consortium as the alloy of study. The progress on Inconel 740, to date, indicates that the alloy has the necessary properties for 760ºC steam, but more effort is needed on this alloy before a 760ºC steam boiler can be constructed.

Strength and Long-Term Microstructural Stability

In general, solid solution-strengthened nickel-based alloys derive their high-temperature strength from a combination of solid solution elements and carbides, and a major feature is that their microstructures do not change significantly with time. However, alloy 617 and, in particular, CCA617 do contain appreciable levels of Ti and Al which, with Ni and Nb, can form intermetallics such as gamma prime. One study conducted by ORNL and the University of Cincinnati showed that the creep strength differences in CCA617 and 617 were due to the precipitation of an appreciable amount of gamma prime at 700 to 750ºC in CCA617 [32]. However, aging for 3,000 hours at 800ºC resulted in dissolution of the gamma prime indicating that its effectiveness for strengthening is limited. In agreement with these microstructural observations, the experimental creep data indicate a strength advantage of CCA617 over 617 up to ~720ºC but no difference at 750ºC and above [33].

In contrast to solid solution-strengthened alloys, high-temperature creep strength in Inconel 740 depends, in part, on gamma prime precipitation. Studies at ORNL on early experimental heats of Inconel 740 identified the different phases in Inconel 740, including gamma prime, eta phase, g-phase, MX carbides, and $M_{23}C_6$ carbides [34]. Some of these grain boundary precipitates contribute to relatively poor creep-rupture ductility in the alloy, and control of these precipitates can increase creep ductility [35]. Further studies on the production heats of Inconel 740 are being carried out by ORNL and the University of Cincinnati. Figure 5 shows the variations of gamma prime precipitate size with aging time and temperature [36]. After 3,000 hours, there was little coarsening of the precipitates at 700 and 750ºC, but significant coarsening was observed at 800ºC. Creep-rupture data on Inconel 740 reported by the AD700

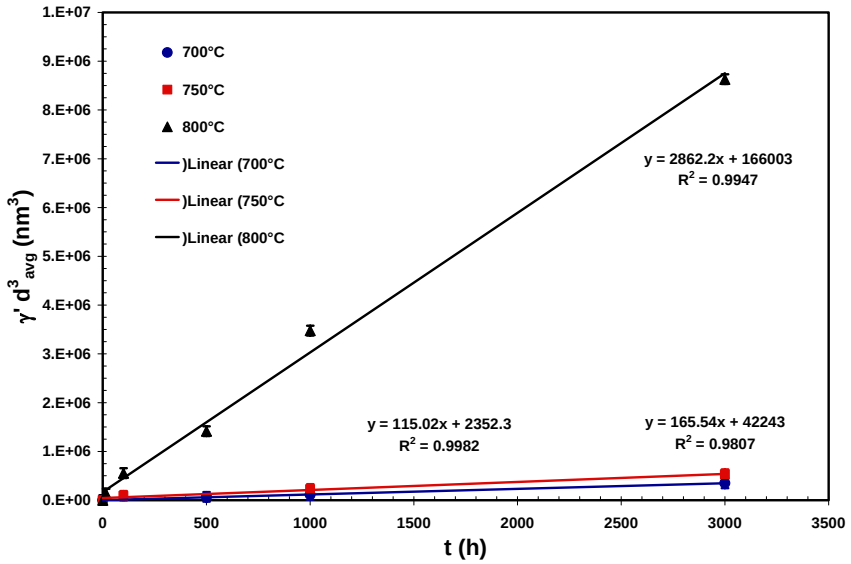

Figure 5. Gamma prime precipitate size (nm^3) as a function of aging time for Inconel 740 at 700, 750, and 800ºC [32]. There was little to no difference in coarsening at 700 and 750ºC but a large change in size and coarsening was observed at 800ºC.

program showed different stress dependencies at 725ºC and 775ºC, but no attempt was made to explain this observation [37]. Based on Fig. 5, it is clear that the gamma prime growth kinetics are highly dependent on temperature and, based on Orowan hardening, one would expect Inconel 740 to show different creep behaviour at 750 and 800ºC based on microstructural observations. Microstructural studies are continuing to fully describe the long-term microstructural stability of Inconel 740.

Internal Oxidation

At temperatures up to 700°C, the external oxides formed in steam on Ni-base alloys containing >16%Cr usually are described as being very thin (difficult to observe), uniform, and protective, and apparently consist of Cr_2O_3 with some $MnCr_2O_4$ [18, 38, 39]. Of the elements used for strengthening Ni-base alloys, Ti and Al form oxides that have increased thermochemical stability compared to Cr, while some of the oxides of Nb and Ta have stabilities similar to that of Cr_2O_3, so that these elements can exert a beneficial effect on protective scale behavior under some circumstances. At 700°C and above, alloys with appreciable levels of elements such as Al and Ti (Inconel 617; IN718) are observed increasingly to form a subscale of (usually) discrete, internal oxide particles. Often, such internal precipitates take the form of a jumbled layer immediately beneath the continuous, protective Cr-rich layer. In some cases the precipitates may form a band that thickens with time, often progressing more rapidly along alloy grain boundaries than in grain bodies. The consumption of elements such as Al by the formation of a subscale is considered detrimental to alloy performance, not only because the Al then is not available for participation in precipitate strengthening, but also because the subscale represents either an effective loss of load-bearing section or a preferred crack initiation site. Adjustments of the levels of the minor alloying additions to modify the type and morphology of the subscale formed is possible, but the requirements for improved oxidation behavior and optimum strengthening often conflict, and may limit the range of options.

Welding of Ni-based Alloys

For solid solution-strengthened Ni-based alloys, welding technology has been demonstrated both in Europe and the U.S. for thin and thick section sizes. Cross-weld creep-rupture tests on tube butt welds (50mm O.D., 10mm wall) and cross-weld and weld metal tests on plates (6.3mm thick) of Haynes 230 (Haynes 230 filler metal) have been performed. Using the Haynes 230 database, weld strength factors (WSF = stress for rupture of the weldment / stress for rupture of the base metal at a given time and temperature) were calculated. The results are shown in Fig. 6 as a function of test temperature; an average WSF of 0.8 was observed. No

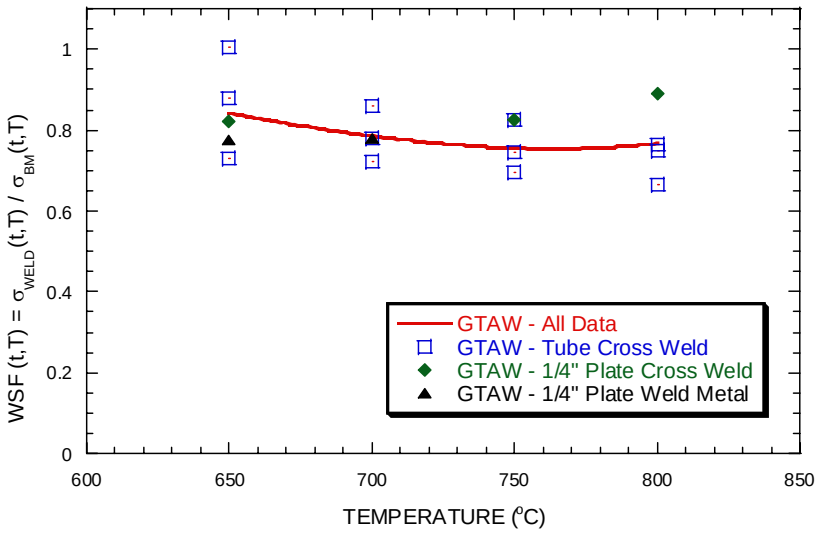

Figure 6. Calculated weld strength factors for creep-rupture life of Haynes 230 weldments (cross-weld and weld metal specimens) as a function of test temperature. All ruptures were in the weld metal.

trend with temperature, test time, weld type, or specimen geometry was observed, and all specimens failed in the weld metal. Thus, for Haynes 230 the weld metal was consistently weaker than the base metal. A 75mm plate of Haynes 230 has been produced by the US Boiler Consortium [2], and cross-weld testing of large specimens will be performed at ORNL to compare with the tube and plate data.

Weld development of Inconel 740 has focused on the end result of welding a 75mm thick plate. Plates 12.5mm thick have been welded and subjected to short-time creep-rupture tests (~2000 hours). Optimization of the process has produced 37mm plate weldments of 740 without any visible weld defects. ORNL has provided input to the boiler manufacturers using thermodynamically-based solidification modelling, microstructural analysis, short-term testing, and hardness mapping. Differences between a matching 740 filler metal and an alloy 263 filler metal are currently being evaluated. Based on the scale-up results, welding of a 75mm thick plate of Inconel 740 is anticipated within the year, followed by testing and analysis at ORNL.

Conclusions

Ferritic steels will be used extensively in a 760ºC USC boiler. Recent alloy developments (12Cr steels) have shown that a better fundamental understanding of these alloys is needed in order to improve the temperature capability of the entire alloy class. Potentially significant developments, such as the NIMS steel, which may eliminate type IV failure and the need for a PWHT, must be understood. Steam oxidation of alloys such as P/T92 is considered to be too fast at 650°C, but it is not clear where the limiting temperature should be set, since the oxidation behavior of alloys in this Cr range is significantly affected by many factors, including relatively small changes in alloy Cr content, and the levels of minor alloying additions. The oxidation rate (and its variability) of these alloys can be minimized by judicious adjustment of alloying additions such as Si and S, but this has not yet been accomplished in production heats. Ferritic steels with improved temperature capability may significantly reduce the overall cost of a USC boiler making it a more attractive technology. ORNL is studying these issues because, without these developments, the implementation of 760ºC boiler technology may be limited by factors other than the creep strength of Ni-based alloys.

Developing the Ni-based materials technology for construction of a 760ºC steam boiler is one of the critical activities for the USC Steam Boiler Consortium. Base metal creep strength differences between CCA617 and 617, and the stress dependency as a function of temperature in Inconel 740, have been explained in terms of the microstructural evolution of each alloy. Further microstructural studies are being conducted on Inconel 740 to evaluate long-term stability of this class of materials. In terms of oxidation behaviour, the Ni-based alloys appear to be nominally capable of developing very protective surface oxides. However, internal oxidation of alloying additions of, for instance, Al and Ti can result in the formation of a subscale which may, with time, result in a surface layer denuded in these elements, as well penetration into the alloy along grain boundaries. The welding technology for solid solution alloys (Haynes 230 and CCA617) has been successfully demonstrated by the US Boiler Consortium, and testing of these weldments is ongoing at ORNL. Thinner section rupture tests show the Haynes 230 weld metal strength to be ~80% that of the base metal. For Inconel 740, ORNL is providing support to the welding development efforts of the consortium. Plate weldments 75mm thick are expected within the year for analysis at ORNL.

To reach the goal of 760ºC power steam boiler, fabrication and welding studies on thick sections of Inconel 740 need to be completed. Long-term creep testing (>20,000 hours) will be used to evaluate the welding technology and compare to current long-term creep-rupture tests. Research on ferritic steel technologies, oxidation/coating evaluations, and long-term microstructure stability will still be needed (even if the 740 studies are successful) to make a 760ºC power steam boiler an economic reality. Finally, a U.S. USC Steam Turbine Consortium has been formed and the materials issues have been defined [40]. ORNL is actively involved in research and development activities that will enable the materials for both these applications.

Acknowledgements

The authors would like to thank Udaya Rao and Robert Romanosky of the NETL, Fred Glaser of the DOE, Robert Purgert of the EIO, and R. Viswanathan of the EPRI for their support and guidance of the USC Steam Boiler Consortium. This research was supported by the U.S. Department of Energy, Office of Fossil Energy, Advanced Research Materials Program, under Contract DE-AC05-00OR22725 with UT-Battelle, LLC.

References

[1] R. Viswanathan, R. Purgert, U. Rao. "Materials for Ultra-Supercritical Coal-Fired Power Plant Boilers." *Materials for Advanced Power Engineering 2002, Proceedings Part II.* Forschungszentrum Julich GmbH, 2002. 1109-1129

[2] R. Viswananthan, J.F. Henry, J. Tanzosh, G. Stanko, J. Shingledecker, B. Vitalis, R. Purgert. "U.S. Program on Materials Technology for Ultra-Supercritical Coal Power Plants." *Journal of Materials Engineering and Performance.* Vol. 14 (3) June 2005. 281-292.

[3] F.V. Ellis, P.J. Maziasz, I.G. Wright, J.P.Shingledecker. "Analysis of Creep and Stress Relaxation Data for Ultra-Supercritical Steam Turbine Materials." *Proceedings of the 2006 ASME Pressure Vessels and Piping Division Conference*, July 23-27, 2006, Vancouver, BC, Canada. Paper: PVP2006-ICPVT11-93110 .

[4] J.F. Henry, J.D. Fishburn, I.J. Perrin, E.S. Sadlon, C.T. Ward. "Advanced Supercritical Technology: Back to the Future." Proceedings to the Fourth International Conference on Advances in Materials Technology for Fossil Power Plants (Hilton Head, SC, Oct. 25-28, 2004). ASM-International, Materials Park, OH, 2005.

[5]J. P. Shingledecker, P. J. Maziasz, N. D. Evans, M.L. Santella, and M. J. Pollard. "CF8C-Plus: A New High Temperature Austenitic Casting for Advanced Power Systems." *Energy Materials: Materials Science and Engineering for Energy Systems*. Accepted 23/12/2005.

[6] S. Kjaer. "Advances in PF Plant, 1990 to 2010." *Parsons 2003 - Proceedings of the Sixth International Charles Parsons Turbine Conference*, Institute of Materials, Minerals, and Mining, London, 2003. 57-67.

[7] R.L. Klueh. "*Boiler Materials for Ultrasupercritical Coal Power Plants – Task 2, An Assessment of Candidate Materials – A review of Literature; Part II: Advanced Ferritic Martensitic Steels."* NETL/DOE, 2004. USC T-8.

[8] J.Hald. "Microstructure and Long-Term Creep Properties of 9-12%Cr Steels." *Proceedings to the ECCC Conference on Creep and Fracture in High Temperature Components – Design and Life Assessment Issues (London, UK, September 12-14, 2005).* DEStech Publications, Inc.

[9] M. Hattestrand, M. Schwind, H.-O. Andren. "Microanalysis of two creep resistant 9-12% chromium steels." *Materials Science and Engineering* A250 (1998) 27-36.

[10] M. Hattestrand, H.-O. Andren. "Boron Distribution in 9-12% chromium steels." *Materials Science and Engineering* A270 (1999) 33-37.

[11] F. Abe. "Alloy Design of Creep and Oxidation Resistant 9Cr Steels for Thick Section Boiler Components Operating at 650ºC." *Proceedings to the Fourth International Conference on Advances in Materials Technology for Fossil Power Plants (Hilton Head, SC, Oct. 25-28, 2004).* ASM-International, Materials Park, OH, 2005. 202-216.

[12] K.Kimura. "Review of Allowable Stress and New Guidelines of Long-term Creep Strength Assessment for High Cr Ferritic Creep Resistant Steels" *Proceedings to the ECCC Conference on Creep and Fracture in High Temperature Components – Design and Life Assessment Issues (London, UK, September 12-14, 2005).* DEStech Publications, Inc.

[13] H. Danielsen, J. Hald. " Z-Phase in 9-12%Cr Steels." *Proceedings to the Fourth International Conference on Advances in Materials Technology for Fossil Power Plants (Hilton Head, SC, Oct. 25-28, 2004).* ASM-International, Materials Park, OH, 2005. 999-1012.

[14] J.Schubert et. al "Determination of Weld Strength Factors for the Creep-Rupture Strength of Welded Joints" *Proceedings to the ECCC Conference on Creep and Fracture in High Temperature Components – Design and Life Assessment Issues (London, UK, September 12-14, 2005).* DEStech Publications, Inc.

[15] N.J. Cory and T.M. Herrington, *Oxidation of Metals*, 28 (5/6), 237-258 (1987).

[16] Y. Fukuda, K. Tamura, and K. Suzaki, *Int. Symp. on Plant Aging and Life Prediction of Corrodible Structures*, Sapporo, Japan, 1995.

[17] H. Fujikawa and N. Otsuka, "Effect of Si content on the oxidation behavior of Cr-Mo steels in steam," *Nippon Kagaku Kaishi*, No. 1, 53-59 (1998).

[18] N. Otsuka and H. Fujikawa, *Corrosion*, 47 (4), 240-248 (1991).

[19] T. Ishitsuka, Y. Inoue, and H. Ogawa, "Effect of silicon on the steam oxidation resistance of a 9% Cr heat-resistant steel," *Oxidation Met.*, 61 (1-2): 125-142 (2004).
[20] Y. Murata, M. Morinaga, R. Hashizume, Y. Sawaragi, and M. Nakai, "Role of an impurity element on improvement in steam oxidation resistance on high-Cr ferritic steels," paper 9.1, presented at the *3rd EPRI Conference on Advances in Materials Technologies for Fossil Power Plants*, Swansea, 2001.
[21] M. Morinaga, Y. Murata, R. Hashizume, and Y. Sawaragi, "Remarkable improvement in steam oxidation resistance due to the presence of sulfur in high-Cr ferritic steels," *ISIJ Intl*., 41 (3), 314-316 (2001).
[22] Kutsumi, T. Itagaki, and F. Abe, "Effect of trace amount of S on the steam oxidation behavior for Mod. 9Cr-1Mo steels," *Tetsu-to-Hagane*, 86 (9), 42-47 (2002).
[23] M. Nakai, Y. Murata, M. Morinaga, and R. Hashizume, "Dependence of high-temperature steam oxidation resistance on the stability of the chromium sulfide in high-Cr, heat-resistant steels," pp. 420-427 in *Proc. 4th Intl. Conf. on Advances in Materials Technology for Fossil Power Plants*, R. Viswanathan, D. Gandy, and K. Coleman, Eds., ASM International (2005); also, EPRI Report No. 1011381.
[24] A. Agüero, R. Muelas, B. Scarlin, and R. Knodler, "Coatings for steam power plants under advanced conditions," pp. 1143-1158 in Materials for Advanced Power Engineering 2002, J. Lecomte-Beckers, M. Carton, F. Schubert, and P. J. Ennis, Eds., Forschungszentrum Jülich GmbH (2002).
[25] S.L. Goodstine and J.C. Nava, "Use of Surface Modification of Alloys for Ultrasupercritical Coal-fired Boilers," *Proceedings to the Fourth International Conference on Advances in Materials Technology for Fossil Power Plants (Hilton Head, SC, Oct. 25-28, 2004).* ASM-International, Materials Park, OH, 2005. 428-440.
[26] S. Dryepondt, Y. Zhang and B.A. Pint, "Creep and corrosion testing of aluminide coatings on ferritic substrates," to be published in Surface and Coatings Technology 2006.
[27] J. Zurek, L. Nieto-Hierro, P.J. Ennis, L. Singheiser, and W.J. Quadakkers, "Oxidation behavior of ferritic and austenitic steels in simulated steam environments," *Proceedings to the Fourth International Conference on Advances in Materials Technology for Fossil Power Plants (Hilton Head, SC, Oct. 25-28, 2004).* ASM-International, Materials Park, OH, 2005. 371-387
[28] "*Boiler Materials for Ultrasupercritical Coal Power Plants – Task 1A, Conceptual Design – Alstom Approach*, NETL/DOE USC T-2.
[29] M. Kondo, M. Tabuchi, S. Tsukamoto, F. Yin, F. Abe. "Suppression of Type IV Failure in High-B Low-N 9Cr-3W-3Co-NbV Steel Welded Joint." *Proceedings to the Fourth International Conference on Advances in Materials Technology for Fossil Power Plants (Hilton Head, SC, Oct. 25-28, 2004).* ASM-International, Materials Park, OH, 2005. 987-998
[30] M.L. Santella, J.P. Shingledecker, and F. Abe, unpublished research, 2005
[31] R. Viswanathan, et al. This proceedings
[32] Q. Wu, V. K. Vasudevan, J. P. Shingledecker, and R.W. Swindeman. "Microstructural Characterization of Advanced Boiler Materials for Ultra Supercritical Coal Power Plants." *Proceedings to the Fourth International Conference on Advances in Materials Technology for Fossil Power Plants (Hilton Head, SC, Oct. 25-28, 2004).* ASM-International, Materials Park, OH, 2005. 748-761.
[33] J. P. Shingledecker, R. W. Swindeman, Q. Wu, and V. K. Vasudevan. "Creep Strength of High-Temperature Alloys for Ultrasupercritical Steam Boilers." *Proceedings to the Fourth International Conference on Advances in Materials Technology for Fossil Power Plants (Hilton Head, SC, Oct. 25-28, 2004).* ASM-International, Materials Park, OH, 2005. 1198-1212.
[34] N.D. Evans, P.J.Maziasz, R.W. Swindeman, and G.D. Smith. "Microstructure and Phase Stability in Crept INCONEL Alloy 740." *Scripta Materialia.* 51 (2004) 503-507.
[35] J.P. Shingledecker, et al. *"Effect of Heat Treatment and Chemistry on the Creep Properties of Inconel ® Alloy 740."* Submitted for publication, 2006
[36] Q. Wu, J.P. Shingledecker, V.K. Vasudevan. *"Age Hardening Behavior in the Nickel-Base Superalloy IN 740."* Submitted for publication, 2006.
[37] R. Blum, R.W. Vanstone. "Materials Development for Boilers and Steam Turbines Operating at 700°C." *Parsons 2003 - Proceedings of the Sixth International Charles Parsons Turbine Conference*, Institute of Materials, Minerals, and Mining, London, 2003. 489-510.
[38] H.E. McCoy and B. McNabb, *Oak Ridge National Laboratory Report No. ORNL/TM-5781* (1977).
[39] J.C. Griess and W.A. Maxwell, "The Long-Term Oxidation of Selected Alloys in Superheated Steam at 482 and 538°C," *Oak Ridge National Laboratory Report No. ORNL-5771* (1981).
[40] P.J. Maziasz, I.G. Wright, J.P. Shingledecker, T.B. Gibbons, and R.R. Romanowsky. "Defining of the Materials Issues and Research for Ultrasupercritical Steam Turbines." *Proceedings to the Fourth International Conference on Advances in Materials Technology for Fossil Power Plants (Hilton Head, SC, Oct. 25-28, 2004).* ASM-International, Materials Park, OH, 2005. 602-622.

CURRENT AND 2050 ENERGY PERSPECTIVES IN INDIA: OPPORTUNITIES FOR MATERIALS SCIENTISTS AND TECHNOLOGISTS

Baldev Raj* and K. Bhanu Sankara Rao#

*Distinguished Scientist & Director
#Head, Mechanical Metallurgy Division
Indira Gandhi Centre for Atomic Research, Kalpakkam 603 102, INDIA
dmg@igcar.ernet.in

Abstract

Nuclear technology can provide an essentially inexhaustible supply of energy to meet the world energy needs in an environmentally sustainable manner. In order to utilise the available uranium resources effectively, India has been successfully pursuing the construction and operation of Pressurized Heavy Water Reactors (PHWRs) and Liquid Metal (sodium) Cooled Fast Breeder Reactors (FBRs). In PHWR systems, the main factors responsible for shortening the life of in-core components are irradiation damage, in-reactor creep and growth, stress corrosion cracking and hydrogen pick up during service life. The materials used for manufacturing fuel tubes, pressure tubes and calendria tubes must meet stringent requirements of various properties in order to perform reliably in nuclear reactor environments. While Zirconium alloys have proven to be successful in their designed usage, a desire for longer life time of components and duty cycle puts more demand on the development of newer compositions for zirconium alloys, their processing and fabrication, and their evaluation for critical applications. In the next two decades, the progress made in the development and operation of PHWRs will depend on how well the performance of the existing structural materials can be improved under the extreme conditions prevailing in the reactor. The crucial constraint in the development of FBRs is the need for high temperature structural materials for reactor structural components, primary heat exchanger tubes, steam generator tube sheets and piping, and radiation resistant high temperature materials for reactor core components. For economic viability of FBRs, the target fuel burn-ups required are more than 20 atom % of heavy metal (200,000 MWd/t), and this can be achieved only by the availability of materials resistant to void swelling, irradiation creep and irradiation embrittlement, as well as satisfying the high temperature mechanical properties. There are several challenging tasks ahead for material scientists and technologists in developing materials with high creep strength and yet resistant to void swelling and irradiation embrittlement. Equally challenging task is the development of materials that can resist type IV cracking in the weldments of steam generator components and develop austenitic stainless steels for structural components that can resist hot cracking. It is a challenging task to develop structural materials and coatings for components in the reprocessing of the fast reactor spent fuel as they use highly concentrated nitric acid in boiling condition. The environment is highly aggressive as it contains noble fission products and high activity. All these issues have been overcome by developing Ti-Ta-Nb alloys for dissolver tanks and evaporators of fuel reprocessing plants. Safe operating window for processing, corrosion and weldability characteristics for these materials have been established. The future challenge is to develop nuclear technologies to meet energy needs through emissions-free production of electricity and in the longer-term transportation fuels such as hydrogen. High temperature reactors hold promise in this regard. The paper high lights the technologies, processes, and materials research relevant to PHWR and FBR programmes in India. Thorium based reactors and Fusion Reactors are important for energy security beyond 2050. Materials challenges in fusion reactors are briefly outlined. India's dream of self sufficient in energy can be realized by expeditious and efficient harvesting of her limited uranium and vast thorium resources.

Energy Scenario in India

At the time of independence in 1947, the total installed electricity generation capacity was a meager 1,363 MWe. It rose to 30,214 MWe in 1980-81 and to 66,086 MWe in 1990-91. It stood at 136,973 MWe as on 31st March 2003, the corresponding growth rates being 9.54 %/yr, 8.14 %/yr and 6.26 %/yr. The average growth rate over the entire period thus has been an impressive 8.6 %/yr [1]. Electricity is a primary pre-requisite for development in today's

industrial world. Per capita gross national product is directly related to the per capita electricity consumption in the country. Quality of life and health are also closely linked to the per capita electricity consumption: any additional electricity generation in the country will lead to a sharp increase in life expectancy (Fig. 1). India is on the right path to provide energy security commensurate with fast pace of economic growth by adequately planning for the envisaged power requirements.

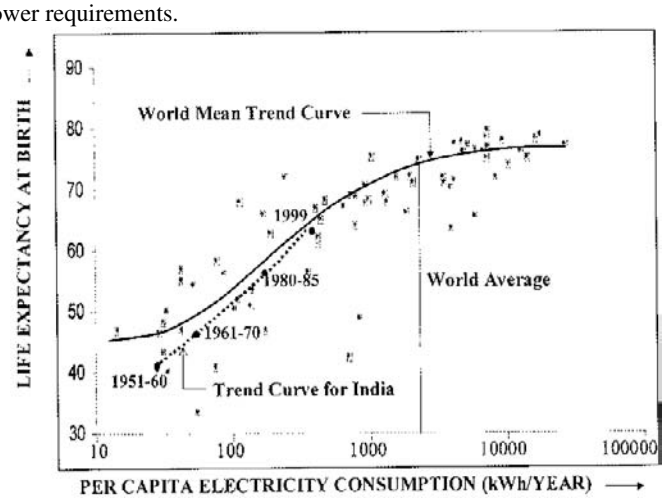

Fig. 1: Dependency of average life expectancy on per capita electricity consumption.

In spite of over hundredfold increase in the installed capacity since independence, the average per capita consumption presently is only about 610 kWhr per year. This is only about one sixth of the world average. In addition, the share of non-commercial energy resources continues to be much higher than in the developed countries. Domestic production of commercial energy has registered an average growth of about 5.9 %/yr during the period 1981-2000. Various constraints, particularly the poor coal and hydrocarbon resource base, have forced an increased reliance on energy imports, which has grown at the rate of about 7.1%/yr. The electricity sector has also experienced severe shortages during the above period despite an impressive growth. During the year 2000-01, there was an average electricity shortage of 7.8 % and a peak power shortage of 13%. There is a need for careful energy planning to ensure growth based on future demands and projected scale of population growth during the coming decades. It is expected that India's population would stabilise at about 1.5 billion by the year 2050. If we consider continuously improving energy intensity of GDP and the fact that India has a tropical climate, we would need per capita electricity generation at a modest level of about 5000 kWhr per year to reach the status of a developed nation by 2050. Toward achieving this, we would need a total electricity generation capacity of 8000 billion kWhr by 2050. Raising the electricity availability by about 8 times in the next 5 decades calls for a careful examination of all issues related to sustainability including abundance of available energy resources, diversity of sources of energy supply and technologies, security of supplies, self sufficiency, security of energy infrastructure, effect on local, regional and global environment and demand side management [2]. It is true that energy policy is the central issue with India attracting highest level of attention at political level and focused attention by technologists and scientists.

Energy Alternatives

The primary energy resources presently are based on coal, natural gas, oil, hydel and nuclear. Wind, solar and fuel cell technology is currently possible only for distributed energy systems of smaller power rating. Fusion and hydrogen based energy resources are still in the technology development stage and are not expected to be available for large-scale deployment at least for the next two decades. India has around 16% of the world's population, but has only about 6% of the worlds coal reserves and less than 1% of oil and gas. However, India has about 32% of the world's thorium reserves. Considering the unique distribution of available fuel resources, large-scale development of nuclear power becomes inevitable for energy planning of our country. Table 1 summarises [1] various fuel resources, availability, electricity potential and maximum Potential capacity that can be used for 100 year sustainability of fuel. The expected electricity installed generation capacity in India by the middle of the century is about 1500 GWe-yr. As can be seen from the table, this requirement can be met with a three-stage nuclear power programme.

Table 1: Availability of various fuel resources and their electricity potential

Fuel	Amount available	Electricity Potential GWe-Yr
Coal	38 BT	7614
Hydrocarbon	12 NT	5833
Uranium metal in PHWR in FBR	61,000 T	 328 42,231
Thorium Metal in Breeders	2,25,000 T	1,55,502
Hydro	150 GWe	69
Non- Conventional Renewable	100 GWe	20

Three-stage Nuclear Power Programme

India's power strategy is based on the present status of implementation of the Three Stage Nuclear Power Programme that has been the key-driver propelling the activities of the Department of Atomic Energy in the five decades of its existence (Fig. 2). The three-stage programme was planned based on a closed fuel cycle concept, meaning reprocessing of spent fuel from every reactor, to judiciously reutilise all available fissile material for peaceful purposes. ^{238}U the dominant isotope of uranium is a fertile material and cannot make the reactor critical by itself. It has to be converted to fissile ^{239}Pu. The process of conversion takes place in a nuclear reactor and the spent fuel from thermal reactors contains ^{239}Pu, which is most efficiently burned in a fast reactor. Similarly, thorium is a fertile material and has to be converted to a fissile material, viz. ^{233}U. To ensure long term energy security for the country, a closed cycle approach, involving reprocessing of spent fuel to separate the useful ^{239}Pu and ^{233}U isotopes from ^{238}U and ^{232}Th has been adopted as a guiding principle for our nuclear energy programme [1, 2].

The first stage comprising setting up of Pressurised Heavy Water Reactors (PHWRs) and associated fuel cycle facilities is already in the industrial domain. Nuclear Power Corporation of India Limited (NPCIL) is presently operating fourteen nuclear power units at six locations and is implementing construction of eight on-going nuclear power projects and handling other related activities consistent with the policies of the Government of India. The commercial viability of first stage owes its success amongst others to the multi-faceted mission oriented materials research programme. The Nuclear Fuel Complex, Hyderabad indeed was based on the intense materials research programme on Zirconium and its alloys conducted at BARC, Mumbai.

The commissioning of Fast Breeder Test Reactor (FBTR)-the flagship of Indira Gandhi Centre for Atomic Research, in October, 1985 marked the birth of the second stage of India's nuclear programme. Again, in this stage also, materials research has been to a good extent, responsible for its success. The confidence to proceed with carbide fuel, for the first time in the world, was gained from the expertise on the thermodynamics of various fuels. The experience in construction, commissioning and satisfactory operation of FBTR for the past twenty years have demonstrated the mastering of the multi-disciplinary technology for energy production using a fast reactor and provided sufficient feedback to enable the launch of the work on building a Fast Breeder Reactor Project (PFBR) of 500 MWe capacity.

The third stage will be based on the Th-^{233}U cycle. ^{233}U is obtained by irradiation of thorium in PHWRs and FBRs. India has vast resources of thorium. It is the endeavour of DAE to develop suitable technologies for utilization of this resource to bridge the gap between the country's energy needs and energy resources. An advanced Heavy Water Reactor (AHWR) is being planned at BARC to gain useful experience in using thorium-based fuels and to expedite the transition to thorium-based systems. AHWR is a 300 MWe, vertical, pressure tube type boiling light water cooled, and heavy water moderated reactor and is designed to achieve large-scale use of thorium. The design of AHWR has been developed to a level needed for initiating a detailed safety review followed by construction of a nuclear power plant. In addition, it will enable us to sustain some of the PHWRs. Simultaneously work is in progress at BARC on the development of Compact High Temperature Reactor (CHTR) that will operate on thorium based fuel with low fissile inventory. CHTR provides a source of heat at temperatures close to 1000 ^{o}C for application in production of hydrogen for use as clean fuel and enables to develop compact nuclear power stations for supplying non-grid-based electricity in remote areas, which are difficult to access [1].

India plans to have an installed nuclear capacity of 20 GWe by the year 2020 and it is envisaged that 7 GWe of this will be based on Light Water Reactor (LWR) technology. As the presently known economically extractable coal reserves would have been nearly exhausted by 2050, it is necessary to ensure that nuclear power generation through fast breeder reactors and thorium fuelled reactors gains enough maturity by then to replace some of the coal based plants. Fast breeder reactors have the potential to ensure that generation by the middle of the present century is about a quarter of the total electricity generation. This path would enable us to limit the primary energy import to about 30%. Development of U-Pu fuel based FBRs of requisite breeding characteristics and associated fuel reprocessing technologies should be completed in the next 15-20 years. Use of metallic fuels would ensure faster doubling time, resulting in quicker generation of fissile isotope inventory to sustain continuous growth of the FBRs. It is expected that metal-fuelled FBRs of 4 GWe capacity or more will be installed

annually from 2021 till the plutonium inventory from PHWR discharged fuel lasts. Similarly FBRs will be installed from the plutonium generated in PHWRs and also from the plutonium bred in FBRs themselves. The combination of power reactors from all the three stages would ensure long-term energy security for the country.

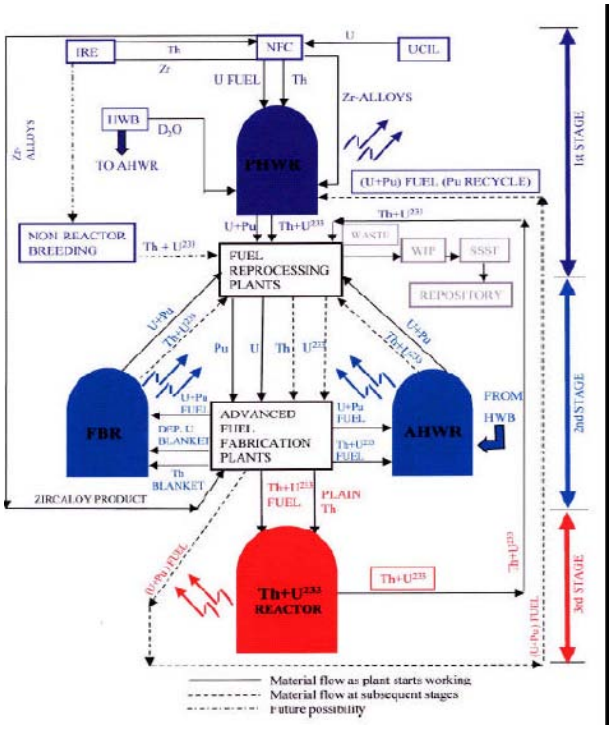

Fig. 2: Three stages of the Indian Nuclear Programme

Issues in the Development of FBR materials

Materials play a very crucial role for the successful development of fast reactor technology. Fast breeder reactor (FBR) components operate at high temperatures under complex loading and environmental conditions which include sodium coolant, water and superheated steam and high fast neutron flux depending on the component. These materials are broadly classified as core, structural and steam generator materials. Core components consist of the fuel pins and wrapper tubes which together form the fuel subassemblies. They have a limited design life of about two years. The use of liquid metal (sodium) cooled fast breeder reactors for energy production poses a challenge to the metallurgists and the designers on development of suitable structural and cladding materials. The materials inside the reactor core have to withstand intense neutron irradiation and temperatures upto 923 K. These hostile environments introduce materials problems unique to fast reactors, like void swelling, creep and embrittlement which determine the permissible life of core components. For economic viability, the target burn-up required for FBRs is large, more than 20 atom% of heavy metal (~ 200,000 MWd/t) and this can be achieved only by the availability of materials resistant to

void swelling, irradiation creep and irradiation embrittlement, as well as satisfying high temperature mechanical properties [2-4]. The residence time of fuel sub-assembly and hence the achievable fuel burn-up is limited by either void swelling of the hexagonal sheath material or creep strength of clad. Since fuel cycle cost is strongly linked with burn-up, development of materials resistant to void swelling and irradiation embrittlement is very important and a challenging task. Structural components operate at moderate temperatures upto 823 K and should be compatible with flowing sodium. These components are exposed to low levels of neutron irradiation and are designed for 40 years of operation. Mechanical properties such as creep and low cycle fatigue strength at these temperatures, corrosion resistance and weldability, are important considerations in the choice of materials for structural components. The heat generated through nuclear fission is extracted by liquid sodium and is converted into steam in the steam generator. In the steam generator, hot sodium and water/steam are separated by thin walled tubes. Any leak in the tubes would lead to violent sodium-water reaction and affect other tubes in their vicinity. Therefore, austenitic stainless steels resistant to aqueous and caustic corrosion are selected. Ferritic steels are employed for steam generator components in view of their good mechanical properties and excellent resistance to stress corrosion cracking. IGCAR has set up a comprehensive range of facilities and evaluated the metallurgical properties of variety of materials selected for PFBR.

Indigenous Development of FBR Materials

While most of the core and structural materials used in the Fast Breeder Test Reactor (FBTR) were imported, all the materials required for PFBR have been developed within the country. IGCAR has played a leading role in the collaborative efforts carried out with other units of the DAE as well as public sector and private industries. In FBTR, modified type 316 SS has been chosen as the fuel clad and wrapper material. It is now well recognized that swelling of these steels would be too high at displacement doses of 100-200 dpa and these steels would not be acceptable for the economical viability of commercial breeder reactors. Alloy composition, level of cold work and second phase precipitates are reported to influence the irradiation resistance of these steels. The compositional adjustments in terms of decreasing chromium and increasing nickel and addition of titanium to improve the resistance to void swelling culminated in the development of a 15Cr-15Ni-2.2Mo-Ti modified austenitic stainless steel (Alloy D-9) conforming to ASTM A771/UNS S38660 as the reference cladding and wrapper material for fast breeder reactors [5]. In this context, a systematic programme has been pursued towards indigenous development and characterisation of Alloy D-9 which is intended for use in a 500 MWe proto type fast breeder reactor (PFBR), at IGCAR Kalpakkam.

The indigenous development of alloy D9 started with a large number of laboratory melts made at IGCAR to optimise the melting, casting, forging and heat treatment conditions followed by industrial production of Alloy D-9 ingots with Ti/C ratios of 4, 6 and 8, with a fixed carbon content of 0.05% at MIDHANI, Hyderabad. Using these ingots, clad and wrapper tubes have been successfully produced at NFC. The processing technology has been fully developed to produce the estimated 50,000 fuel clad tubes of 2.7 metre long and 0.45 mm wall thickness required for PFBR. Whereas alloy D9 will be used for the initial core of PFBR, efforts are underway to develop modified grades of alloy D9 called D9I for clad tubes. Improved D9I version includes specific alloy additions P and Si to improve void swelling resistance. As alloy D9 would be used in the cold worked condition for high resistance to void swelling, and also be subjected to prolonged exposure at elevated temperatures, stability of

the microstructure has been carefully evaluated at various Ti/C ratios as a function of the amount of PCW in the range of 2.5 to 30% [6, 7]. The optimum level of cold work that would not lead to softening of the material due to recrystallization was estimated to be 20% by employing the Larson – Miller parametric approach. Using a thermodynamic model the amount of primary carbide which remains undissolved after solution annealing treatment, and the secondary TiC precipitates which form during ageing, were estimated. The amount of primary coarse precipitates increased with an increase in Ti/C ratio which facilitated early onset of recrystallisation. Secondary TiC precipitates were fine in the alloy with Ti/C ratio of 4 and this is beneficial to retard recovery and recrystallisation. This composition provided the best resistance against recrystallisation of the cold worked structure and hence also the highest creep strength (Fig. 3) [8]. Creep rupture strength of Alloy D9 clad tubes was found to be higher than that of 316 SS in the range 923 to 1073K [9].

Modified 9Cr-1Mo steel is selected for PFBR steam generators based on superior corrosion resistance and high temperature mechanical properties compared with 2.25Cr-1Mo used in FBTR... The creep-rupture strength of indigenously developed modified 9Cr-1Mo steel in rolled, forged and tube product forms were found to be higher than the average strength values reported in RCC-MR design code (Fig. 4) [10, 11].The seamless tubes of Modified 9Cr-1Mo steel in the sizes required by PFBR (23 meters long) have been produced through a collaborative programme between IGCAR, MIDHANI and NFC. Steel meeting stringent requirements was produced by electro slag refining process at MIDHANI and the forged rounds were then converted into long seamless tubes at NFC. Strict quality control was carried out at all stages including development of innovative non-destructive testing techniques. Microalloying with B and Ce has been found to increase the short term creep rupture life of Mod.9Cr1Mo steel.

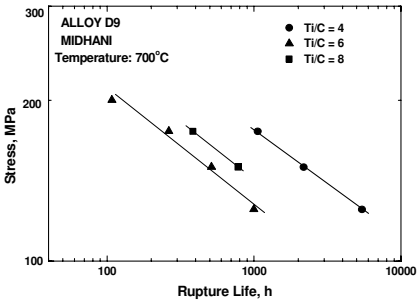

Fig. 3

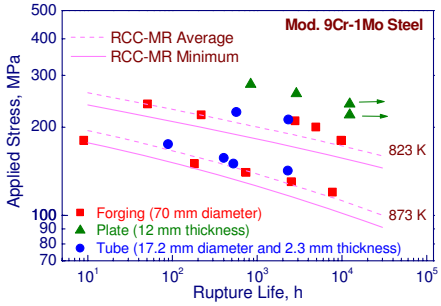

Fig. 4

Fig. 3: Influence of Ti/C on creep life of 20% cold worked D9 bars at 973 K
Fig. 4: Comparison of creep rupture strengths of tube, plate and forging of modified 9Cr-1Mo steel with the design curves

Structural components of FBTR have been made using nuclear grades of 304 and 316 SS. In order to reduce the susceptibility of welds to corrosion and stress corrosion cracking, low carbon grades of 304 and 316 SS strengthened by nitrogen alloying called 304(L)N and 316(L)N SS, have been selected for PFBR. Another strategy has been to eliminate the number of welds by using large size plates and long size tubes. All plates in sizes required for 304L(N) and 316(L)N SS have been produced within the country for the first time and the evaluation of their creep properties gave very promising results compared to the imported materials [12]. The successful indigenous development of PFBR structural materials

necessitated constant interaction at various stages between IGCAR, SAIL and private sector industries.

In order to design PFBR for 40 years of lifetime with a load factor of 75%, detailed investigations have been performed to obtain creep allowable stresses for Mod. 9Cr-1Mo steel at a life of 2,63,000 h. Allowable stress values predicted by Larsen-Miller parametric approach and multilayer perception ANN lie very close to those obtained by extrapolating RCC-MR (French Code) data at a creep rupture life value of 2,63,000 h [13]. These investigations gave the confidence that LMP and ANN can be used as complimentary techniques for extrapolating creep rupture lives for service conditions of PFBR steam generator

Low Cycle Fatigue, Creep-Fatigue Interaction and Thermomechanical Fatigue and life Prediction of Structural Materials of PFBR

The components in PFBR operate for extended periods of time at temperatures between 0.3 to 0.5 T_m and have design lives that have limited by creep. Service conditions experienced by components would also involve cyclic loading during start-up and shut down or during power transients leading to fatigue. The combination of cyclic loading and steady state operation of the reactor at elevated temperatures introduces a special phenomenon known as creep-fatigue interaction damage that can have a detrimental effect on the performance of components. When temperatures are high enough, time-dependent creep strains as well as cyclic (fatigue) strains can be present, interpretation of the effect that one has on the other becomes extremely important. A detailed characterization of high temperature fatigue in different metallurgical conditions under the relevant operating conditions of PFBR has been carried out. The relevant time and temperature dependent damage processes and the synergistic interactions affecting the LCF behaviour of 304SS, nitrogen alloyed 316SS and modified 9Cr-1Mo have been established. In these alloys the LCF lives were shown to be significantly affected by dynamic strain ageing (DSA), inelastic deformation, deformation ratcheting, slip character, mean stress, oxidation, creep damage and phase instabilities in the temperature range of their operation. These time dependent mechanisms have been found to act either independently or synergistically depending on the test conditions and caused premature failure when compared with fatigue failure under time-independent conditions. DSA has been noticed to be particularly harmful in austenitic stainless steels at moderately elevated temperatures where creep and oxidation damage effects were not operative [14, 15]. The negative strain rate sensitivity of half-life cyclic stress is established as a potent indicator of DSA effects in fatigue [14, 15].

LCF and creep-fatigue interaction data generated in house on 316L(N) stainless steel has been used to assess the capability of Artificial Neural Network (ANN) approach for life prediction. LCF and creep-fatigue life prediction carried out by ANN approach gave values very close to the actual lives [15]. These investigations revealed that the success and accuracy of prediction depends upon (i) quality of data, (ii) extent of coverage of training data in the domain of prediction, (iii) selection of appropriate input variables, (iv) transformation of input variables and (v) optimization of neural network parameters. The detailed investigations on thick section forged 9Cr-1Mo steel have shown that the total strain controlled LCF resistance and creep properties are inferior to those of hot rolled thin sections. The fatigue lives at very low strain ranges that were not covered by laboratory testing were successfully predicted by

employing suitable life prediction models and fatigue design curves for different temperatures were formulated using the appropriate safety factors. The forged Mod. 9Cr1Mo alloy exhibited lower cyclic stress response than extruded or rolled material under strain controlled LCF conditions [16].

The heating and cooling cycles during start-up and shutdown operations, such as those expected in main vessel of PFBR, cause thermal stresses that often occur in combination with mechanical loads. The resulting thermo-mechanical fatigue (TMF) cycles lead to material degradation mechanisms and failure modes typical of service conditions. It is recognized that the synergism between the combined thermal and mechanical loads cannot be reproduced by means of isothermal fatigue tests. In view of this detailed investigations have been performed to evaluate TMF behaviour of 316L(N) Stainless Steel under in-phase and out-of-phase conditions. The out-of-phase TMF tests were established to be more deleterious in the sub-creep range while in-phase tests were found to be more detrimental in the creep range [17].

Radiation Damage Studies at IGCAR on FBR Materials

Radiation induced dimensional changes resulting from void swelling and creep in fuel cladding and wrapper of FBR impose severe limits on the achievable fuel burn up. Detailed investigations on radiation damage are currently under progress at IGCAR for understanding the basic phenomenon and develop core structural materials with better radiation resistance. Void swelling behaviour of Alloy D9 simulated by heavy ion irradiation was evaluated using step height and positron annihilation measurements [18]. . Alloy D9 samples in 18% cold-worked condition were pre-implanted with helium at 170 keV and 275 keV energies to create a uniform helium concentration of 100 appm around 588 nm depth region. Subsequently the samples were subjected to 2.5 MeV Ni ion irradiation to create a peak damage of ~ 84 dpa at various irradiation temperatures between 700 and 970 K. Defect-sensitive positron annihilation line shape S-parameter revealed clear changes consequent to void formation as a function of sample depth. From the variation of average S-parameter as a function of irradiation temperature, the peak swelling temperature has been deduced. The results obtained by the step height profilometry and positron annihilation are in good agreement and the peak swelling temperature as determined by two techniques differed by 50 K. Currently the screening of indigenously produced D9I steel is in progress under 5MeV Ni ion irradiation in order to optimize the chemical composition with respect to minor alloying element concentration.

Weldability of Austenitic Stainless Steels

Failures in FBR components have generally been associated with the welds. Weldability studies are conducted for ensuring that components are welded without defects and that the welded components possess adequate mechanical and other engineered properties to perform satisfactorily during their design life. Detailed weldability evaluation of PFBR materials was carried out to obtain clear quantitative guidelines for excluding the possibility of hot cracking. Weld metal and heat affected zone (HAZ) cracking propensity, quantified in terms of the brittleness temperature range (BTR), has been studied in 316L(N) and D9 [19]. The D9 alloys, despite having low P+S (0.014 wt-%), showed high susceptibility to solidification and HAZ cracking because of the fully austenitic microstructure and segregation of Ti, S, N and C to the grain boundaries. The study showed that a Ti/C of about 4 showed least susceptibility to solidification as well as HAZ cracking and highlighted the importance of controlling weld metal N to minimise cracking. Studies on effect of N on cracking in 316L(N) base metal and

modified 316 weld metals showed that N has no detrimental effect on cracking, if Cr_{eq}/Ni_{eq} is maintained to obtain a ferritic solidification mode (FA) during welding. Based on these studies, a Ferrite content of 3-7 FN is specified for the modified E316-15 welding electrodes that would be used for welding all 316L(N) components of PFBR. Studies on nickel alloy 718 revealed that weld metal cracking could be minimised by using lower heat input and by using alloy 82 filler metal rather than consumable of matching composition.

Weldability of Cr-Mo Ferritic Steels

The major technological issues in weldability of modified 9Cr-1Mo (grade 91) steel are the determination of critical preheat temperature to avoid hydrogen assisted cracking (HAC) and achievement of adequate toughness in the weld metal. Weldability studies on grade 91 revealed that susceptibility to HAC is a strong function of composition. Backing of electrodes and control of preheat temperature were found to be critical steps in the control of HAC. Achieving good toughness in the weld metal produced by processes that involve fluxes (like SMAW, SAW and FCAW) in grade 91steel is a challenging task due to the higher inclusion content compared to flux less welding such as GTAW. To improve weld metal toughness, the chemical composition of welding electrodes was optimized by controlled additions of Ni, Mn, Nb and Si and by avoiding delta-ferrite in the deposited weld metal [19]

Mechanical Behaviour of Welds and Weldments for Component Design

High temperature nuclear design codes did not contain adequate design data for welds; instead design has been largely based on properties of the base metal. In the absence of sufficient guidelines in the codes extensive studies on the creep behaviour of the modified 316 SS and 316L(N) SS weld metals and weldments were performed. It is noticed that the creep strength of the weld metal is significantly lower than that of the base metal. The delta ferrite in the as welded 316SS which is essential for avoiding hot cracking during welding undergoes transformation to brittle intermetallic phases during creep,, thereby lowering weld metal creep strength and ductility. These studies enabled arriving at appropriate creep strength reduction factors for welds at different temperatures for realistic design of components. A comparative evaluation of LCF lives and cyclic stress-strain properties and fracture behaviour of type 304SS base, 3O8SS welds and 304/308 weldments (as well as 316LN base, 316 welds and 316LN/316 weldments) has been carried out at various temperatures. The inferior properties of stainless steel weldments in LCF have been shown to arise from the presence of coarse grain and residual stresses in the heat affected zone [20]. Optimization of stress relieving treatments has been carried out to improve the fatigue resistance of weldments. Influence of weld discontinuities on LCF properties have been assessed. It has been found that the type and location of the flaw determine the LCF life of austenitic stainless steel welds; these studies provided much needed information for the acceptance and performance of welds containing defects and realistic life assessment procedures.

Extensive analysis on creep deformation and fracture was conducted on the base, weld, weldments and the simulated HAZ structures of 2.25Cr-1Mo, 9Cr-1Mo and Mod. 9Cr-1Mo steels with a view to optimizing performance of the weldments. In Mod.9Cr1Mo Creep rupture lives of weld joints were found to be significantly inferior compared to the base metal (Fig. 5a) [21]. The failure location changed from base metal to intercritical region of HAZ with increase in test temperature and decrease in applied stress (Fig. 5b). The type IV cracking in (craking in intercritical HAZ) weld joint occurred as a result of preferential accumulation of creep strain with associated creep cavitation. Poor creep strengths in weld

joints have been attributed to the microstructural degradation in this region. These investigations have identified that the reduction in width of intercritical zone has to be controlled to improve the performance of ferritic steel weldments

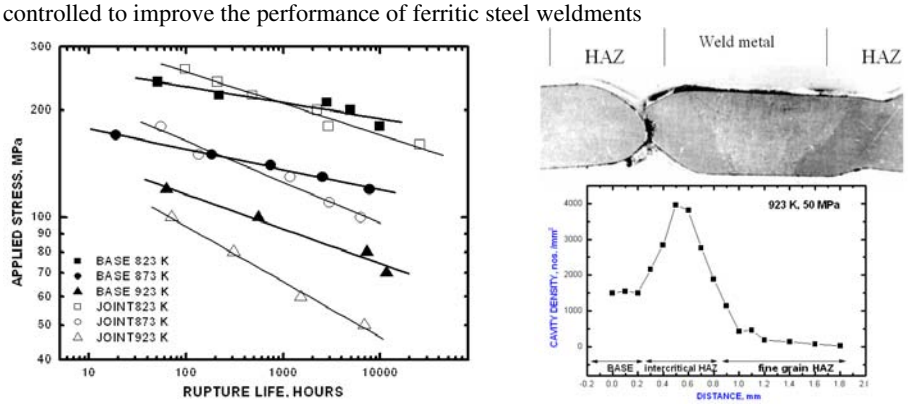

Fig. 5: (a) Variation of rupture life of modified 9Cr-1Mo base metal and weld joint with applied stress and (b) Creep failure location of the weld joint and creep cavity density with distance of modified 9Cr-1Mo similar weld joint failure location of the weld joint at 823 K, 120 MPa.

Welding of Dissimilar Metals

Welding of dissimilar-metals becomes a necessity, as different materials have to be chosen for different components operating under different service conditions. Differences in physical and mechanical properties of base metals and their influence on the in-service behaviour of the weld joint as also alloying between the base metals and filler metal are major considerations. In the steam generator circuit of PFBR, 316L(N) SS pipes from the intermediate heat exchangers have to be welded to the modified 9Cr-1Mo steel pipes of the steam generators. These dissimilar metal welds in steam generators are prone to large-scale premature service failures, leading to expensive plant outages, due to the difference in thermal expansion coefficients between the ferritic steel base metal and weld metal. The problem was circumvented by engineering a gradient in the thermal expansion coefficients along the joint by using an Alloy 800 transition piece. For welding 316L(N) SS to Alloy 800 and Alloy 800 to modified 9Cr-1Mo steel, ER16-8-2 and Inconel 82/182 welding consumables, respectively, have been chosen. Thermal cycling performance tests have shown that this tri-metallic transition joint has at least four times superior service life than the joints presently in use [22].

Metal Forming

The demanding and hostile environment in the PFBR necessitates the components from special materials are to be processed by judicious selection of hot, warm or cold forming methods. To achieve the required service properties, it is essential that the microstructural development during hot working should be carefully controlled and defects and flow instabilities are avoided. The processing maps and instability maps have been generated for the materials used in reactor systems such as stainless steel 304, 316, 304LN, 316LN and Mod. 9Cr-1Mo steel [23, 24]. The “safe” processing windows delineated by dynamic recrystallisation (DRX) and dynamic recovery (DRY) are identified. In certain regimes of temperature and strain rate, austenitic stainless steels exhibited flow localization and these “unsafe” domains need to be avoided during mechanical working. The usefulness of these

maps for controlling the industrial processes such as press forging, extrusion and hammer forging has been validated under industrial process conditions with a considerable reduction in the rejection rates. This has generated full confidence that the PFBR components can be produced within the country at a competitive cost.

Development of Materials for dissolver tank assemblies of Fuel Reprocessing Plants

Demands on structural materials for reprocessing spent fuel of fast reactor assembly are stringent due to its high concentration of plutonium, which has forced the conventional PUREX process to be changed to electro-oxidative process. In this process, the structural materials are exposed to high molality of boiling Nitric acid, which is orders of magnitude more corrosive than the environment in PUREX process. Hence, replacement of the conventional materials by more corrosion resistant materials would increase the lifetime of the component in addition to reducing the radio-active waste. The perspective corrosion rate of 304 L is not satisfactory for long life of reprocessing plants. Hence, a Ti-5Ta-2Nb alloy has been fabricated and examined for its fabricability, weldability, optimization of thermo-mechanical treatments and corrosion behaviour in boiling Nitric acid [25,26]. The fabrication of Ti based alloys is known to be easier in the duplex phase field of high temperature bcc β and low temperature hcp α. Since the transition temperatures of this alloy are not known, these have been evaluated using metallography, differential scanning calorimetry (DSC) and computational methods. The flow chart for the thermo-mechanical processing is also developed. Physical metallurgy data base for this alloy was established and the thermo-mechanical treatments yielding desirable and detrimental structures with respect to corrosion behaviour were identified. Controlled treatments were carried out based on experience of commercial $\alpha+\beta$ Ti alloys to identify the optimum microstructure for best performance. Evaluation of mechanical and corrosion properties show that the average corrosion rate is below 1mpy in liquid and vapor state, while it is 2.5-3 mpy in condensate phase. These studies showed that this alloy exhibits a superior corrosion resistance as compared to the presently used SS 304 and Grade 2 Ti. The measured Yield strength and UTS are in the range of 300-340 MPa and 410- 440 MPa respectively with 30-35% ductility, which are comparable to that of commercial Ti alloys. Weldability studies on 3mm plates of Ti-Ta-Nb alloys enabled the selection of welding and weld qualification procedures. Since most of the failures in Ti alloys during service occurred in the weld, simulated weld and HAZ structures were studied in detail and a microstructural map was generated. This can be used to predict the microstructures that would result for various cooling rates.

Hardfacing

All components in static/dynamic surface contact in liquid sodium are prone to adhesive wear (self-welding) or fretting wear. Hence, suitable hardface coatings on the contact areas are necessary for imparting adequate high-temperature in-sodium wear-resistance. Cobalt-base alloys and other designation ERCoCr-A, B and C as per AWS A5.21 (Stellites) are the most commonly used hardfacing materials in nuclear reactors, and have been used in the FBTR as well. However, for in-core components, where radiation dose is very high, activation products, primarily Co^{60}, formed in cobalt-base Stellites result in additional activity in the primary circuit. Such induced radioactivity during maintenance, component handling and decommissioning must be minimized. Hence, based on detailed induced radioactivity and shielding calculations, nickel-base cobalt-free ERNiCr-B has been chosen to replace the cobalt-base alloys as the hardfacing material for all nuclear steam supply system components of PFBR made of 316L(N) and 304L(N) SS. While ERNiCr-B hardface coatings were used satisfactorily in fast breeder reactors, but there are at least a few reports of failures in some

hardfaced components operating at 823 K. Hence, to address this concern regarding reduction in hot-hardness of ERNiCr-B above 723K, the hardness degradation in long-term aged ERNiCr-B deposits was characterized [27]. Based on time-temperature correlation, the estimated hot-hardness after exposure at 823 K showed that these hardface deposits would retain adequate hardness even after 40 years of service.

For hardfacing of PFBR components with ERNiCr-B, deposition procedures using the plasma transferred-arc welding (PTAW) process, instead of the conventional GTAW process, has been developed in collaboration with industry. The PTAW deposition procedures minimize dilution of the coating by the austenitic SS substrate thereby ensuring adequate hardness in the hardface coating. These PTAW deposition procedures have been successfully implemented for hardfacing (with ERNiCr-B) of some critical PFBR components, such as the roller bearings of the transfer arm and most significantly on the inner surface of grid plate sleeves at a location 450 mm away from the ends. High-temperature wear-resistant ERNiCr-B bushes are required in various components for in-sodium service in PFBR. These ERNiCr-B bushes, conventionally manufactured by precision casting, are not available in India and have to be imported at very high costs. As an import substitution measure, these bushes have been fabricated using a novel procedure involving GTA deposition of ERNiCr-B on austenitic SS rods followed by precision machining of the hardface deposits. These bushes were found to meet the dimensional tolerance and surface-finish requirements and have excellent dimensional stability on high-temperature ageing. This procedure has been successfully implemented for fabricating ERNiCr-B bushes for the transfer arm gripper assembly of PFBR.

For minimising fretting wear of tube bundle support structures under flow-induced vibrations of steam generator tubes, aluminised Inconel 718 was chosen based on international experience. Either pack cementation process or vapour-phase aluminising process, both of which require special equipment and proprietary procedures and reagents, were used to produce aluminide coatings on Inconel 718 strips in different FBRs. A highly cost-effective and efficient process technology was indigenously developed and implemented for aluminizing of Inconel 718 steam generator bundle support structures of FBRs. This technology uses a procedure involving thermal spraying of aluminum followed by diffusion heat treatment in vacuum to obtain the desired coating.

Design of FBR Components and Structural Integrity Evaluation

PFBR is designed for a plant life of 40 y (extendable to 60 y) in compliance with design codes viz. RCC-MR (2002) [28, 29] and ASME-Section III (2003) [30], respecting all the safety criteria stipulated by Atomic Energy Regulatory Board. The design was done ‘by analyses and hence necessitated detailed structural mechanics investigations of all possible failure modes (Fig. 6). The creep-fatigue damage is assessed for the high temperature components, viz. main vessel, control plug, inner vessel and intermediate heat exchangers (IHX) as well as steam generator shell-skirt support, as per RCC-MR (1993) code. For the main vessel and inner vessel the stresses and strains are computed using viscoplastic analysis, since it is not possible to respect the creep fatigue damage limits through elastic analysis route for these components. For the viscoplastic analysis, the Chaboche model was employed [31]. For other components viz. control plug, IHX and SG shell-skirt support, elastic analysis route was followed. The summary of computed creep fatigue damage assessment of hot pool components is presented in Table 3.

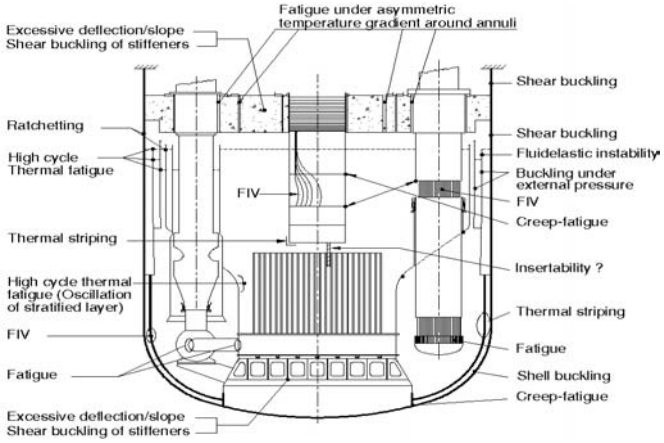

Fig. 6: High temperature failure modes in FBR

Table 3 : Creep fatigue damage for PFBR Components [30]

Component	Analysis	30 y			45 y		
		D_c	D_f	D_{eff}	D_c	D_f	D_{eff}
Main vessel	Viscoplastic	0.01	0.004	0.020	0.02	0.007	0.036
Inner vessel	Viscoplastic	0.03	0.010	0.053	0.05	0.015	0.086
Control plug	Elastic	0.24	0.003	0.250	0.36	0.005	0.370
IHX	Elastic	0.29	0.002	0.300	0.45	0.003	0.460
SG	Elastic	0.20	0.020	0.250	0.30	0.030	0.310

These results indicate that the maximum creep-fatigue damage estimated based on design load cycles (D_{eff}) is less than 50 % of code allowable value (unity). Hence structural mechanics considerations permit a design life of 45 y with a comfortable margin. This analysis has formed a basis for the selection of higher operating temperature (820 K) and longer plant life (40 y) for PFBR

Fracture mechanics studies were conducted mainly for the LBB analysis of main vessel, sodium piping and SG shell [31]. The critical parameters required to demonstrate LBB are asymptotic crack length ($2C_s$), detectable crack length ($2C_L$) and critical crack length ($2C_G$). $2C_s$ is the crack length of a particular surface whose crack front touches the opposite wall surface, i.e. crack depth (a) is equal to wall thickness (h). $2C_L$ is the crack length, which can produce detectable leak (Q_d) of sodium in the pipe. Q_d is equal to the sensitivity of leak detection system (Q_s) multiplied by a factor of safety 10. $2C_G$ is the crack length, with which the structure becomes unstable under the design basis loads, such as safe shutdown earthquake (SSE) or large sodium water reaction (LSWR). For demonstrating LBB, $2(C_s+C_L)$ should be less than $2C_G$ with a factor of safety (α). The value for α depends upon the procedure followed for determining C_G parameter and material. Figure 7 depicts the C_s, C_L and C_G, pictorially.

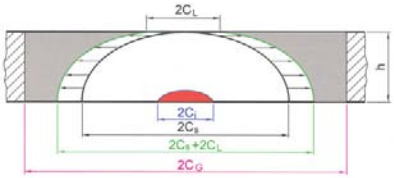

Fig. 7:LBB Parameters

Creep-fatigue and fracture analyses completed for PFBR components are validated by systematically planned experiments. Tests were conducted on models of shells subjected to axially varying temperature gradients to simulate thermal ratcheting which happens on the vessels subjected to free level variations of sodium. Creep-fatigue damage assessment methodology was validated based on tests on specimens having component features. The rolled and welded tube -to-tubesheet joints of IHX were qualified by carrying out tests for pull out strength after simulating creep relaxation. The SG tubes made of Mod.9Cr1Mo were tested at high operating temperature under internal pressure with axial deformations to simulate the creep rupture. All these tests have provided results that assure the operation of components at high temperature, for the design life of 40 yr. Reactor vessels are basically large diameter thin walled shells, which are prone to buckle. Geometrical imperfections imposed during manufacturing stage and subsequently by progressive deformations during operation, plastic deformations, seismic loadings and their dynamic effects reduce the buckling strength significantly. Buckling of vessels have been investigated extensively with the help of numerical analysis and validated thoroughly based on tests on scaled down models. Tests were conducted on 1/30 and 1/8 scale down models of main vessel under bending moment and shear forces and on 1/13 models of inner vessel under internal pressure and concentrated loads transmitted through stand pipes. Fracture assessment including analysis for LBB justification and crack propagation behaviour has been studied on 316LN and G91 plates by subjecting them to bending loads. Also a series of fatigue and fracture tests conducted on 1/5 scale modes of primary sodium pipe and SG tube bends, subjected to internal pressure and bending moment, confirmed the applicability of RCC-MR:A16(2002) rules and validated the design. Fatigue and fracture tests were conducted on typical large size tees, bends and SG nozzle junctions with the objective of demonstrating LBB.

Non-destructive Testing for Quality Control of FBR Clad Tubes

Non-destructive testing (NDT) methods were developed for stringent quality control of fuel cladding tubes [32, 33]. The quality of the tubes could be comprehensively assessed using complementary NDT techniques such as ultrasonic (UT) and eddy current (ECT). For the indigenous development of cladding tubes, an advanced eddy current testing methodology has been developed to detect banding (fabrication defect) of tubes, and also defects in the presence of banding, with high sensitivity and reliability. Procedures based on laser scattering technique were developed to characterize the surface of the tubes. A close correlation between the roughness outside surface and thickness variation has been established which enabled 100% assessment of the tubes for detecting unacceptable variations in thickness and surface conditions. As the tube thickness is only 375 microns with close tolerances, it is crucial that all such unacceptable variations are detected. For actual inspection of the tubes, the basis for comparison of the severities of the defects was the defect depths as percentages of the tube wall thickness. Tubes having no defects or defects less than 7% wall thickness

were accepted. The significant percentage of unacceptable tubes after the tubes were tested ultrasonically, underscored the importance and the essential nature of eddy current testing for the pre-service quality control. Random checks by metallography indicated that both ECT and UT are complementary for detection of different types of defects. For example, ECT detected localized dispersion of fine inclusions, while UT successfully detected large inclusions. The outside surface defects could be detected by ECT with high reliability and sensitivity, while the inside defects could be detected by UT. The standard ASTM procedure was followed for ultrasonic testing, and the complete procedure along with suitable probes has been developed at IGCAR for the eddy current testing.

Future Directions in the Development of FBR Core and Structural Materials

Since fuel cycle cost is strongly linked with burn-up, development of materials resistant to void swelling and irradiation embrittlement is very important and a challenging task. In FBRs, ferritic and martensitic steels are contemplated for use as possible structural and/or fuel cladding and other incore component applications. Ferritic steels, HT9 and Mod.9Cr1Mo are of interest because they display low swelling compared to conventional austenitic stainless steels 304 and 316 when irradiated. However, the irradiation hardening in these steels affects their toughness and fatigue properties. The embrittlement effect in these steels is reflected through the increase in ductile-brittle transition temperature and reduction in upper shelf energy. Development of ferritic steel compositions which are less prone to irradiation hardening effects is urgently needed and it is a great challenge to alloy designers. An improved version of Mod.9Cr-1Mo steel with superior impact toughness, as compared to the standard grade, is being developed for wrapper applications in the later cores of PFBR. In the first phase of this programme, the influence of nitrogen and silicon on the swelling behaviour, impact and tensile properties, formability and weldability will be investigated on the heats produced by a combination of Vacuum Induction Melting and Electro Slag Refining.

Oxide dispersion strengthened ferritic/martensitic (9-12% Cr) steels (ODS) show the potential to be used as cladding material in FBRs with the ability of operating temperatures beyond 650C. The major problem that hindered their widespread application is the anisotropy of mechanical properties owing to the processing procedures. These alloys show bamboo-like grain structure and a strong deformation texture which are responsible for their anisotropic mechanical properties, especially an inferior biaxial creep –rupture strength. Research and development programmes are needed to produce equi-axed structure and to explore new alloy compositions. There are other problems with ODS steels besides anisotropy. At present, there is no information on the production of thick-walled parts or large-diameter tubing. Fabrication processes for these materials for heavy sections still need to be established, and this includes the problem of joining these materials. Therefore, even if the anisotropy problems are solved, much research and development is required for establishing the commercial acceptance of ODS steels for structural applications.

In order to ensure the longer design life of structural components in future FBRs, materials with superior creep strength and high temperature LCF properties are being developed. Several heats of 316L SS with varying nitrogen content (0.06% to 0.22%) have been produced. A comprehensive programme to evaluate the effects of nitrogen on mechanical properties, weldability and corrosion behaviour is currently under progress at IGCAR..

Zirconium Alloys for PHWR Applications

Zirconium based alloys are the natural choice for both fuel element cans and in-core structural components such as pressure tubes, calendria tubes, garter springs etc. in the water cooled thermal reactors [34]. The general requirements for these components include low thermal neutron absorption cross section, adequate strength, ductility and toughness at ambient and reactor operating temperatures, good corrosion resistance, low hydrogen absorption, long term dimensional stability in irradiation environments, compatibility with fuel and coolant under service conditions, good heat conductivity and resistance to fracture [35]. Pure zirconium undergoes uniform surface oxidation in high pressure water at 573 K. after a certain time interval, however, film cracking occurs leading to breakaway corrosion. It was found that the presence of impurities like nitrogen, carbon, aluminium, titanium and silicon are associated with the above phenomenon. Further it was noticed that additions of iron, chromium, nickel or tin, combined with restriction of nitrogen content reduces the tendency for film cracking. This led to the development of zircaloy-2 alloy, with 1.5%Sn, 0.12% Fe, 0.1% Cr and 0.05% Ni. ZIrcaloy-2 was widely used as clad, wrapper, pressure tube (PT) and calandria tube (CT) materials for PHWR. The major problems associated with this alloy are hydriding, stress corrosion cracking and irradiation creep. Hydriding can result either from attack by coolant or by reacting with the moisture in the fuel. Since nickel is known to increase the hydrogen absorbing tendency in zirconium, zircaloy-4 (1.5% Sn,-0.18-0.24 Fe, 0.1Cr, Ni<0.007) in which the hydrogen absorption rates are reduced top about half of that in ziorcaloy-2 have been developed for clad applications.

The requirements for pressure tube alloys differ from those for fuel cladding, largely because of the fact that an improvement in the strength of the material can significantly reduce the quantity of parasitic material within the core and that the pressure tube, unlike the fuel cladding, is expected to have a long service life preferably extending up to the design life of a reactor. Pressure tubes being the final pressure boundary containment structures in PHWRs, their integrity is to be maintained during reactor operation and safety demands that leak before break (LBB) criterion is met with. During service, all the zirconium alloy core components in general and pressure tubes in particular are subjected to very slow aqueous corrosion, hydride induced embrittlement and radiation damage. Zr-Nb based alloys are known to exhibit superior irradiation creep and hydriding resistance compared to zircaloy-4. Zr-2.5 Nb is a precipitation hardened alloy and thereby the irradiation creep rate is significantly low. Also Zr-Nb alloys show slower hydrogen pick up rate, resulting in lower build-up stress around the blisters. Crack initiation is therefore delayed. Zr-2.5Nb alloy has therefore been chosen as the construction material for pressure tube and calandria tube of PHWRs under construction. India has indigenously developed zirconium production technologies and NFC is producing components of zircaloy-2, zircaloy-4 and Zr-2.5Nb [1]. In PHWR systems, various zirconium products are used in the form of tubes either to clad the fuel or to contain the pressurized heavy water coolant. The structural components like fuel tubes, pressure tubes and calendria tubes are exposed to highly aggressive environments during reactor operation. The main factors responsible for shortening the life of in-core components are irradiation damage, in-reactor creep and growth, corrosion and hydrogen pick up during service life. Therefore, the materials used for manufacturing these components must meet stringent requirements of various properties in order to perform reliably in nuclear reactor environments.

Calandria tube is exposed to low temperature and low stress and hence excessive deformation and creep is not of much significance. But irradiation growth does pose some concern. Garter spring possesses high strength and is subjected to complex loading at relatively lower temperature. Due to exposure to relatively lower temperature, hydrogen pick up is not of concern. The major concern for Garter spring is their displacement from their designed location, which is also greatly reduced by employing tight fit springs. Moreover, these components are not the final pressure boundary containment structures. The pressure tube poses the major challenge for PHWR safety. Two main life limiting factors associated with fuel tubes were hydride embrittlement and Iodine induced stress corrosion cracking (SCC) as a result of pellet-clad interaction. Excessive hydriding could lead to performance limiting embrittlement. The extent to which the hydrides embrittle the clad also depends on the orientation of the hydrides. Formation of radial hydrides is an undesirable situation as it greatly reduces the ductility while circumferentially oriented hydrides have only marginal effect. Crystallographic texture has therefore an important influence in determining the orientation of hydrides. For a favourable hydride orientation, it is necessary that the alpha grains of zircaloy be oriented with the basal plane normals close to the radial direction. The development of texture is influenced by the strain history of the cladding tubes during fabrication. Careful optimization of process parameters at NFC involving cold pilgering to final dimensions, has led to the development of clad tubes with desired texture. Stress corrosion cracking is also one of the important problems associated with clad tubs. This occurs when a fuel element, which has been exposed to prolonged irradiation at relatively low power, has its power increased. The resulting thermal expansion of the fuel stresses the cladding while fission product iodine released from the fuel is the likely corrodant. This problem has been solved by incorporating a thin layer of graphite on the inner surface of the cladding. After carrying out considerable developmental work at NFC the production process for graphite coating of zircaloy tubes was standardized. An automatic coating equipment has been designed and fabricated with a high capacity vacuum backing unit. With this equipment the graphite coating process could be taken up on a production scale and it has become a part of the flow sheet since 1990.

Fabrication of Zr-Nb Tubes

India occupies a distinguished position among countries that have developed the total technology for the processing, fabrication, characterization and use of zirconium alloy components in the nuclear industry [1]. While the zirconium alloys have proven to be successful in their designed usage, a desire for longer lifetime of components and increased duty cycle puts more demand on materials performance. This demand has led to more in-depth studies of phenomena associated with zirconium alloy composition, development of fabrication techniques and to the evaluation of newer zirconium alloys for critical applications. Although zircaloy-2 was used as a pressure tube material in the very early versions of CANDU- PHWRs, there has been mounting evidence that these zircaloy-2 tubes showed accelerated oxidation and hydrogen-up take over longer exposures in reactors. These led to the development of Zr-2.5 Nb alloy. Based on the extensive development work done , a fabrication route was evolved at NFC for production of thin walled larger diameter tubes through seamless route. NFC has established advanced facilities to manufacture the seamless tubes with close dimensional tolerances with required quality and stringent mechanical properties. It was found that the fracture toughness of Zr-2.5Nb pressure tube alloy can be improves substantially by reducing the level of trace element impurities like hydrogen (from 25 ppm to 5 ppm), chlorine (From >2.5 ppm to 0.5 ppm), carbon and phosphorous. Such

refining is achieved by multiple consumable vacuum arc melting. It was demonstrated that such purity can be routinely achieved by qudraplate vacuum arc melting practice at NFC. These are very significant development since the reduction in trace elements gives a substantial increase in the coolant channel life. During the last three decades, NFC has acquired industrial scale experience on manufacturing grade zirconium sponge, using zircon sand as starting material. A number of zirconium alloys and components have been successfully manufactured and utilized in all the 14 operating water-cooled reactors in India.

Cold Reduction of Large Diameter Thin Wall Tubes

Normally large diameter thin wall tubes are rolled in cold pilger mills using 2 roll dies. NFC has designed both rolling and auxiliary toolings for 150 VMR cold pilger mill and successfully rolled tubes with outer diameter to all thickness ratio of around 100. This development resulted in successfully producing calandria tubes for PHWRs, which were earlier fabricated by seam welding process but are now produced by seamless process giving better integrity and uniform stress during expansion of mouth ends and subsequent rolling of joints in the reactor. This innovating seamless pilgering process developed has resulted in achieving superior texture and consequent mechanical properties and dimensional tolerances over long lengths. NFC has also recently manufactured seamless zirconium alloy calandria tubes and coolant tubes for PHWR-540 MWe at Tarapur. The PHWR 540 is the first in the series of 500 MWe type PHWR units in the country. Each PHWR 540 core has 392 co-axial assemblies of zircaloy-4 tubes and Zr-2.5 Nb coolant tubes inside which the uranium fuel assemblies are loaded. Such long and thin walled seamless calandria tubes have been manufactured for the first time in the world [1].

Nuclear Fusion Technology

In India, a road map for future technologies is envisioned in terms of on-going basic research work on fusion devices at the Institute of Plasma Research (IPR), Ahmedabad, as well as development of accelerator driven sub-critical reactor system (ADS) at BARC. In the case of fusion research, apart from detailed studies on fundamental aspects of plasma physics i.e., generation and confinement of plasma, diagnostic tools for characterization have been well studied using the Mark-1 TOKOMAK, ADITYA since 1989 [1]. A steady state superconducting tokomak SST-1 is presently in the final stage of assembly at IPR [36]. It is a large aspect ratio tokomak configured to run elongated plasma with pulse duration of 1000s. Superconducting magnetic field coils are deployed to produce the toroidal and poliodal fields in SST-1.The plasma facing components (first wall) of SST-1 comprises of diverters, limiters, passive stabilizers, baffles and auxiliary baffles. Fabrication works of all the PFC components has been completed successfully. The major breakthrough in the PFC fabrication is in the process of brazing copper alloy modules to SS cooling tubes [34]. The chosen high strength copper alloy materials are the Cu-Cr-Zr for diverters and baffles and Cu-Zr for passive stabilizers. The brazing cycle normally deteriorates the electrical, mechanical and thermal properties of copper alloy material. Hence a suitable heat treatment needs to be applied in order to retrive the deteriorated properties. A new method of brazing combined with heat treatment cycle is selected and thereby, strength of 310 MPa is regained for CuCrZr alloy after brazing with 83% IACS .

International Thermonuclear Experimental Reactor (ITER) Project

In June 2005 the European Union, USA, Russia, Japan, Chaina and South Korea committed to build a new fusion reactor known as International Thermonuclear Experimental Reactor

(ITER), at Cadarache in southern France. Once operational, in 2015, ITER will become the main focus of world fusion research.. India is now one of the seven partners of International Thermonuclear Experimental Reactor (ITER) project. A critical element in the ITER mission since its inception has been testing integrated blanket modules in special ports. The principal objectives of ITER Test Blanket Module (TBM) programme include the development of technology necessary to install breeding capabilities to supply ITER with the tritium necessary for operation in its extended phase, and the acquisition of experimental data vital to evaluating the feasibility , constraints, and potential D-T cycle for fusion systems. TBMs will be installed in ITER from the beginning of its operation with the aim of obtaining information on (i) demonstration of structural integrity of TBM structures and attachments during disruption and vertical displacement events, (ii) assessment of the impact of Ferritic/Martensitic steel, used as a structure for most TBMs, on magnetic fields deformation in static conditions; (iv) testing of fluid flow, particularily MHD, in the complex magnetic field environment, (iv) establishment of TBM first wall requirements and (v) screening of flaws in TBMs so that they can be fixed prior to D-T operation. Maximum utilization of ITER for blanket and material testing is essential for the advancement of energy related fusion technology that in turn provides essential feedback to possible plasma physics operating regimes and boundary conditions.

Fusion can only fulfill its promise of providing safe, economical, and environmentally acceptable energy if materials science and engineering can develop and deliver new materials for the first wall, blanket and diverter systems. To realize the potential safety and environmental advantages of fusion the materials must have low neutron activation characteristics. This limits the practical choices of material systems from which a structural material can be developed. Low activation goals limit the choice of alloying elements from which structural material can be synthesized and require that certain elements which are often present as impurities be maintained at ppm levels. The fusion programmes have focused on alloys having 7-10%Cr with W substituted for Mo and V and Ta as carbide forming elements as low activation counterparts to the commercial 9Cr-1Mo and 12Cr-1Mo alloys. Properties of the low activation alloys are similar to those of their commercial counterparts with the exception of the fracture behaviour, as measured by Ductile to Brittle Transition Temperature, both before and after irradiation, which is superior[37-39]. Specific challenges identified but awaiting in-depth research include the effects of transmutation-generated helium on many facets of irradiation response, development of plasma diagnostic materials and insulators to limit MHD power losses in liquid metal systems, design methods for ceramic composite structures, development of vacuum vessel and superconducting magnetic materials and the feasibility of using ferromagnetic steels in magnetic confinement concepts. India has unique capabilities and strong base in materials development for fast breeder reactors, the design and operation of safety critical nuclear systems and vast experience in experimental and theoretical research in the physics of magnetically confined hot plasmas and non-linear plasma phenomena.

Accelerator Driven Sub-critical Reactor System (ADS)

ADS is one of the emerging technologies, which can have a major impact on the nuclear energy scenario, It is a sub-critical reactor device for producing nuclear power, which would operate with high neutron economy and safety. In ADS, a high energy proton beam generates neutrons directly through spallation reaction in a non-fertile/non-fissile element like lead [1]. A sub-critical blanket can further amplify this external source as well as produce energy.

Development of such a system offers the promise of a short doubling time with Th-^{233} U systems, incineration of long-lived actinides and fission products and can provide robust technology for large scale thorium utilization. Major activities in ADS are in progress at BARC, Raja Ramanna Centre for Advanced Technology, Indore, Variable Energy Cyclotron Centre, Kolkata.

Acknowledgements

The authors wish to thank Dr. Anil Kakodkar, Chairman, Atomic Energy Commission, Government of India, for the encouragement and guidance. The authors also wish to place on record their appreciation to a large number of their colleagues for many useful contributions and discussions and whose work has been cited in this manuscript. The help rendered by Shri R. Kannan, during the preparation of the manuscript is gratefully acknowledged.

References

[1]. Atoms with Mission, A Golden jubilee Commemorative Volume on Nuclear Technology Development, Department of Atomic Energy, Government of India, Vol.2, 2005.
[2] Baldev Raj, Energy Security of India – A Challenge to Materials Scientists and Technologists, Presidential Address, The Indian Institute of Metals, 43rd National Metallurgists' Day, Chennai, 14th November 2005.
[3] Baldev Raj, Structural Materials: Achievements and Future Developments, Proc. Seminar "Materials R & D for PFBR", (Eds) S.L. Mannan and M.D. Mathew, January 1-2, 2003, Kalpakkam, pp 1-8.
[4] S.L. Mannan, S.C. Chetal, Baldev Raj and S.B. Bhoje, Selection of Materials for Prototype Fast Breeder Reactor, ibid, pp 9-43
[5]. J.L. Seran, V. Levy, P. Debuisson, D. Gilbon, A. Maillard, A. Fissolo, h. Touron, R. Cauvin, A. Chalony and E. Le. Boulbin, in "Effects of Radiation Materials: 15th International Symposium ASTM STP 1125" (Eds) R.E. Stopller, A.S. Kumar, D.S. Gelles, ASTM, Philadelphia, (1992) pp1209-1233.
[6]S. Venkadesan, P.V. Sivaprasad, M. Vasudevan, S. Venugopal and P. Rodriguez, "Effect of Ti/C Ratio and Prior Cold Work on the Tensile Properties of 15Cr-15Ni-2.2Mo- Ti Modified Austenitic Stainless Steel", Trans. Indian Inst. Met., 45, (1992) pp 57-68.
[7] M. Vasudevan, S. Venkadesan, P.V. Sivaprasad and S.L. Mannan, J. Nucl. Mat. 211 (1994) 251.
[8] S. Latha, M.D. Mathew, K. Bhanu Sankara Rao and S.L. Mannan, Creep & Fracture of Engineering Materials and Structures, (Ed) J.D. Parker, The Institute of Materials, London (2001) pp 507-513.
[9] S. Latha, M.D. Mathew, K. Bhanu Sankara Rao and S.L. Mannan, " Thermal Creep Properties of Alloy D9 Fuel Clad Tubes of Fast Breeder Reactor", Trans. Indian Inst. Met., 58 (2005) pp 343-346.
[10] E. Isaac Samuel, B.K. Choudhary , K. Bhanu Sankara Rao and S.L. Mannan, "Creep Rupture Properties of Indigenously Developed Modified 9Cr-1Mo Steam Generator Tube Steel", Ibid, pp 297-301.
[11] B.K. Choudhary, K. Laha, A. Nagesha, E. Isaac Samuel, V.S. Srinivasan, K.S. Chandravathi, M. Valsan, R. Kannan, K. Bhanu Sankara Rao and S.L. Mannan, "Creep and Fatigue Behaviour of Modified 9Cr-1Mo Steel, Base Metal, Weld Metal and Weld Joint", Proc. Seminar "Materials R & D for PFBR", (Eds) S.L. Mannan and M.D. Mathew, January 1-2, 2003, Kalpakkam, pp 121-136.
[12] C. Girish Sastry, M.D. Mathew, K. Bhanu Sankara Rao and S.L. Mannan, "Creep Deformation and Fracture Behaviour of Type 316L(N) Stainless Steel", Trans. Indian Inst. Met., 58 (2005) pp 275-279.
[13] V.S. Srinivasan, K. Laha, K. Bhanu Sankara Rao, S.L. Mannan and Baldev Raj, "Prediction of Long-term Creep Rupture Strength for Modified 9Cr-1Mo Ferritic Steel" ibid, pp 255-259.
[14] V.S. Srinivasan, M. Valsan, R. Sandhya, K. Bhanu Sankara Rao, S.L. Mannan and D.H. Sastry, Int. J. Fat. 21(1) (1999) p11.
[15] V.S. Srinivasan, M. Valsan, R. Sandhya, R. Kannan, K. Bhanu Sankara Rao and S.L. Mannan, "Low Cycle Fatigue and Creep-Fatigue Interaction Behaviour of 316L(N) Stainless Steel", Proc. Seminar "Materials R & D for PFBR", (Eds) S.L. Mannan and M.D. Mathew, January 1-2, 2003, Kalpakkam, pp 77-90.
[16] B.K. Choudhary, K. Bhanu Sankara Rao and S.L. Mannan, Mater. Sci Eng A 148 (1991) p 267.
[17] A. Nagesha, M. Valsan, K. Bhanu Sankara Rao, R. Kannan and S.L. Mannan, " Thermomechanical Fatigue Behaviour of Type 316L(N) Austenitic Stainless Steel", Trans Indian Inst. Met., 58 (2005) 373-378.
[18] C.David, B.K. Panigrahi, G.Amarendra, S. Abhaya, S. Balaji, A.K. Balamurugan, K.G.M. Nair, B. Viswanathan and Baldev Raj, Void swelling studies in ion irradiated (15Ni-14Cr), Ti-modified stainless

steel using positron annihilation and step height measurements, Communicated to J. Nuclear Materials (2006)

[19] V. Shankar, S.K. Albert, G. Srinivasan, C.R. Das, V. Ramasubbu, A.K. Bhadhuri, S.K. Ray and S.L. Mannan, " Weldability Studies on PFBR Materials", Proc. Seminar "Materials R & D for PFBR", (Eds) S.L. Mannan and M.D. Mathew, January 1-2, 2003, Kalpakkam, pp 233-248.

[20] M. Valsan, A. Nagesha, K. Bhanu Sankara Rao and S.L. Mannan, "Low cycle fatigue and creep-fatigue behaviour of 316(N) stainless steel weld metal and weld joints", ibid pp 91-104.

[21] K. Laha, K.S. Chandravathi, K. Bhanu Sankara Rao and S.L. Manann," Creep Behaviour of Modified 9Cr-1Mo Forged Steel and Its Weld Joints" Trans Indian Inst. Met., 58 (2005) pp 379-385.

[22] A.K. Bhadhuri, S. Venkadesan, P. Rodriguez and P.G. Mukunda, "Performance of Trimetallic Transition Joint", Mater. High. Temp., 10 (1992) pp 45-50.

[23] S. Venugopal, P.V. Sivaprasad and S.L. Mannan, "Optimisation of Workability and Control of Microstructure during Deformation Processing of Various Grades of Austenitic Stainless Steels – An Overview" Trans. Indian Inst. Met. 58 (2005) pp 1-17.

[24] P.V. Sivaprasad, S.L. Mannan and Y.V.R.K. Prasad, "Processing Parameters for Mechanical Working of 9Cr-1Mo Steel: Processing Maps Approach" Mater. Sci. Tech 20 (2004) pp 1545-1550.

[25] Baldev Raj, R. Natarajan and V.S. Raghunathan, "Development of Ti-5Ta-1.8Nb for Dissolver Tank in Fast Reactor Fuel Reprocessing Applications – An Overview" Proc. conf. *Materials and Technologies for Nuclear Fuel Cycle,* 15-16 Dec. 2003, Chennai pp 1-8.

[26] R. Mythili, V. Thomas Paul, S. Saroja, M. Vijayalakshmi and V.S. Raghunathan, Mater. Sci. Engng. A (2003).

[27] A.K. Bhadhuri, S.K. Albert, C.R. Das, Hemant Kumar, V. Ramasubbu, V. Balasubramaniyan, B.P.S. Rao and S.K. Ray, "Development of Hardfacing Technology for 500 MWe Fast Breeder Reactor" Proc. Conf. National Welding Seminar, December 2005, Bhilai, India.

[28] RCC-MR subsection NB for class 1 components, *Design and construction rules for mechanical components of FBR Nuclear Islands,* 2002, AFCEN, Paris, France

[29] RCC-MR subsection Z, Technical Appendix A16, *Guide for Leak Before Break analysis and Defect assessment*, 2002 AFCEN, Paris, France.

[30] ASME Sec III, *Appendix II -1000: Experimental Stress Analysis*, 2001

[31] P. Chellapandi, A. Biswas, R. Srinivasan, S.C. Chetal and S.B. Bhoje, " Qualification of Creep, Fatigue and Fracture Design of PFBR Components based on Tests" Trans Indian Inst. Met., 58 (2005) pp 207-219

[32] Baldev Raj, T. Jayakumar, B.P.C. Rao, " Nondestructive Test Techniques for Assessment of Cracks", J. Aeronatut. Soc. India, 46 (1994) pp 101-115

[33] Baldev Raj, T. Jayakumar, B.P.C. Rao, "Nondestructive Testing and Evaluation of Structural Integrity", Sadhana 20 (1995) pp 5-38.

[34] C.V. Sundaram and S.L. Mannan, " Nuclear Fuels and Development of Nuclear Fuel Elements", SADHANA, 14 (1989) pp 21-57.

[35] Anil Kakodkar, "Life Management of PHWR Coolant Channel", Proc. Int. Symp. *Materials Ageing and Life Management,* (Eds) Baldev Raj, K. Bhanu Sankara Rao, T. Jayakumar and R.K. Dayal, October 3-6, 2000, Kalpakkam, India, pp 1109-1121.

[36] Institute for Plasma Research, Annual Report 2004 – 2005.

[37] M. Abdou, D. Sze, C. Wong, M. sawan, A. Yung, N.B. Morley and S. Malang, U.S. Plans and strategy for ITER blanket testing, Fusion Science and Technology, Vol.47 (2005) pp.475-487

[38] E.E. Bloom, The challenge of developing structural materials for fusion power systems, J. Nuclear Materials, 258-263 (1998) pp.7-17.

[39] E.E. Bloom, S.Z. Zinkle and F.W. Wiffen, Materials to deliver the promise of fusion power-progress and challenges, J. Nuclear Materials, 329-333(2004)pp.12-19.

MATERIALS CHALLENGES IN CO_2 CAPTURE AND STORAGE

Philippe MATHIEU
University of Liège, Chemin des Chevreuils,1 ,B52/3- 4000 Liège (Belgium)
Pmathieu@ulg.ac.be

Abstract

In order to achieve deep reductions in CO_2 emission from power generation, the implementation of technologies for CO_2 capture and storage are required can complement the other options used to reduce generation such as the improvement of fuel use efficiencies, the switch to low carbon fuels, the use of renewable energies and of nuclear energy. Capturing CO_2 consists in its separation from other components in gaseous or liquid mixtures. Three main options are currently developed for that purpose: removal of CO_2 from the flue gas or flue gas decarbonisation; removal of carbon from the fuel or fuel gas decarbonisation; oxyfuel combustion systems using pure oxygen as fuel oxidizer. The performance and environmental impacts of the CO_2 capture and storage technologies are discussed in this paper with a special focus on the materials issues. On the transport and storage side, the materials issues come from corrosion and may be solved by a proper treatment of the CO_2 stream, which is dried and from which oxygen and impurities have to be removed. On the capture side, there are no specific issues on the materials used in the different technologies such as chemical absorption of CO_2 in an appropriate solvent (usually amines). Advances on materials are only needed in the oxyfuel combustion systems using high temperature membranes for separation of oxygen from nitrogen in air in relation to their ion conduction properties, to their thermal and mechanical stability and to their lifetime when integrated in boilers, fluidized beds and gas turbine systems. In general, the performance of the systems integrating oxygen separating ceramic membranes is largely depending on the operating temperature so that the behaviour of these materials at higher and higher temperatures is a real technical challenge.

Key words : CO_2 emissions mitigation, oxyfuel, ceramic membranes, CO_2 capture, advanced power plants

Introduction

International framework

In Kyoto, in 1997, a protocol was adopted as a first step towards the world reduction of greenhouse gases emissions by around 5 % compared to the 1990 emissions taken as the baseline by 2008-2012. Today and in the near future, however, the world is not on a way of greenhouse gases concentration stabilization and certainly not of reduction of the emissions. Europe will not be able to comply with the Kyoto target by 2012. As an illustration, if the current emissions are projected up to 2010, Europe-15 will be 7.5 % pts below the target (reduction by 0.5% below 1990 level instead of 8%) [1]. In addition, the real environmental target is asking for a seriously deeper reduction than that considered in the Kyoto protocol. In many of the models that IPCC has considered, stabilization at a level of 550 ppmv of CO_2 in the atmosphere would require a reduction in global emissions by 2100 of 7–70% compared with current rates and the emissions should start to decrease by 2030. If the target were to be lower (450 ppmv), even deeper reductions of 50-60% y 2050 would be required [2, 3].

For deep reduction, capture and storage technologies (CCS) offer a particularly well suited option for power generation and other heavily polluting industrial sectors in order to fill the gap between the Kyoto scenario and a 50% and more emissions reduction. Within the Kyoto protocol, technological options for reducing net CO_2 emissions to the atmosphere include:

increasing the efficiency of energy conversion and/or utilization;. switching to less carbon intensive fuels, for example natural gas instead of coal;. increasing the use of renewable energy sources; and sequestering CO_2 by enhancing biological absorption in forests and soils. All these measures taken with their maximal economic potential are not able to reduce the emissions. In order to achieve a stabilization of the CO_2 concentration at 450 ppmv and decrease the emissions accordingly, new tools have to be implemented, among which are the capture and storage of CO_2.

Materials development

Regarding the materials development and characterisation in the power plants themselves, it is well known that new alloys for supercritical power plants are developed to achieve higher temperatures and consequently higher efficiencies. Demonstration of their use in forgings and castings is needed. Improved welding procedures and weld failure prediction methods are required. This is especially important because of the current small number of new advanced coal-fired plants.

As far as CCS is concerned, there is no specific need to develop new materials in 2 links of the CCS chain, namely transport and storage of CO_2. Transport is a mature technology whereas storage still requires more demonstration at large scale. Apart the usual corrosion issues due to existing oxygen and water in CO_2, there is no need to develop new materials. In capture techniques based on the use of solvents to absorb CO_2, the technology is well known and mature from other engineering sectors but the new materials are new solvents themselves. On the other hand, in oxy-fuel combustion systems, there is a need to develop new materials such as high temperature membranes for oxygen production as an alternative to conventional cryogenic systems. Ion transport membrane systems promise indeed higher purity of separated oxygen with lower energy consumption and lower capital costs than existing systems. Work is needed to scale-up to the capacity required in power generation. There is also a need to assess other developing options such as the oxygen transport in chemical looping combustion. There is still a need for work to assess the possible corrosion of and deposition on boiler heat transfer surfaces as well as component development and to identify the best materials for membranes in oxyfuel systems and metallic particles in chemical looping combustion.

CO_2 capture and storage (CCS) chain

As fossil fuels are predicted to remain the dominant form of primary energy used worldwide (about 85%) and are responsible for about 75% of anthropogenic CO_2 emissions for the next decades [4] , the CCS technology allows to continue using them in a clean way and to make the bridge towards an economy based on carbon free energy carriers such as hydrogen and electricity production from renewable sources . Power plants are the best candidates for CCS since they are large centralized sources contributing for around 35% of the world emissions in 2001. A storage of the total flue gas can not be cost-effective because of the high amount of N_2 , together with existing pollutants, to compress and store . The removal of CO_2 from flue gases , as well as from fuel gas, for storage is hence unavoidable.

Capturing the CO_2 arising from the combustion of fossil and renewable fuels, as in power generation, or from the preparation of fossil fuels, as in natural gas processing, the production of hydrogen, ammonia, iron and steel, or cement, involves separating the CO_2 from some other

components in a mixture. The CO_2 having then to be transported to a storage site where it will be stored away from the atmosphere for several centuries, it is compressed to supercritical conditions (73 bar, 30°C) in which it is in a 'dense phase' and occupies around 0.2% of the volume in the gaseous phase at standard conditions. Storage reservoirs must ideally be large relative to annual emissions, be tight and safe for a very long time. The averaged leakage rate should be less than 0.01% per year giving a fraction retained of 99% over 100 years.

The concept of CCS is based on a combination of known technologies applied to the new purpose of mitigating climate change. CO_2 capture techniques were developed 60 years ago in connection with the production of town gas involving scrubbing CO_2 from the gas stream with a chemical solvent [5]. Subsequently they were adapted for capturing CO_2 from the flue gas streams of coal- or gas-burning plants for the carbonation of drinks and for enhancing oil recovery.

Considering storage, the world capacity of CO_2 storage sites is much larger than the CO_2 production for the predicted lifetime of the fossil fuels. Possible storages are in the deep ocean, in carbonate minerals or in geological reservoirs such as deep saline formations, depleted gas and oil reservoirs, un-minable coal beds, with possible enhancement of oil and methane recovery from oil fields and coal seams respectively using CO_2 instead of water injection. The single existing storage at commercial scale at present is a deep saline aquifer under the North Sea operated by Statoil (Norway) since 1996 with a CO_2 injection rate of 1 Mton per year [6]. From this experiment, the permanence, the leakage rate and safety of the storage should be demonstrated. Transport and storage are comparatively less expensive than capture (typically 20-25% of capture and compression cost, but this is very much site dependent) and are both economically feasible, transport by pipelines being in a mature market while enhanced coal bed methane recovery is still in a demonstration phase.

Although CO_2 is routinely separated today at some large industrial plants, CO_2 capture has only been applied to several small power plants. However, there are no current applications at large-scale power plants that are the major source of CO_2 emissions. For power plant applications, the main options for CO_2 capture may be divided into 3 categories [3, 7, 8].

- Removal of CO_2 from the flue gas or de-carbonization of the flue gas from energy-intensive industry: power generation, refinery, chemistry, cement…
- Removal of carbon from the fuel or de-carbonization of the fuel gas
- Oxy-fuel combustion or near ZERO EMISSION TECHNOLOGIES in boilers, fluidized beds and gas turbine systems

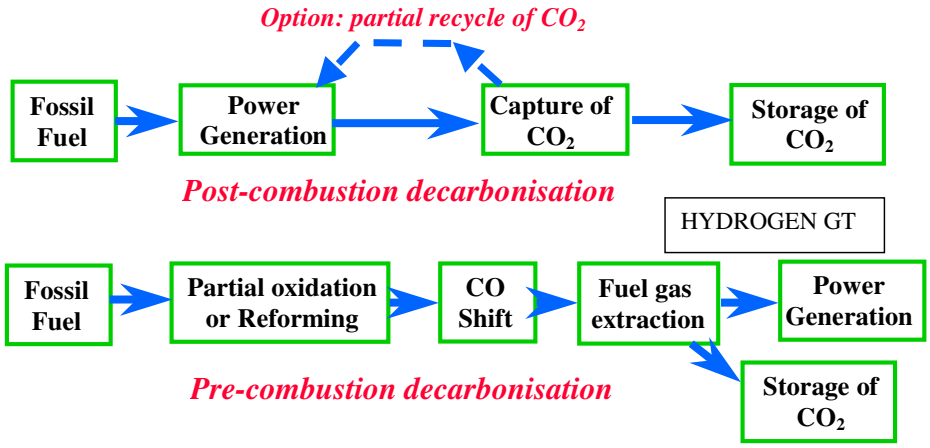

Fig 1 Post- and pre-combustion CO_2 capture

The 2 first options are based on a de-carbonisation process as shown on fig 1, that is on the removal of a large amount of carbon atoms injected via the fuel in the system, either before or after the combustion, that is to say, either from the flue gas or from the fuel itself, generally in the form of CO_2. The third option is based on the de-nitrification of air, that is, on the separation of oxygen from nitrogen in air. Separation of components from mixtures, either CO_2 from N_2 in the flue gas de-carbonisation, or CO_2 from hydrogen in fuel de-carbonisation or O_2 from N_2 in an air separation unit, is of course at a cost. From thermodynamics, these separation processes induce large penalties on the performance as well as significant additional capital and operation and maintenance costs. So removing CO_2 means increasing the fuel consumption and thus the generation of CO_2 as well as of other pollutants and increasing the energy costs.

Flue gas de-carbonisation

In post-combustion capture or flue gas decarbonisation, a large fraction of the CO_2 generated in the combustion process is removed from the flue gas (air+water+ pollutants). CO_2 is at a low partial pressure in the flue gas, namely 3-5% vol and 10-15% vol for natural gas and coal fired power plants respectively, in mixture with 85-97% N_2 so that the separation will be costly both in energy and money. Among several techniques, namely chemical absorption, membranes, cryogenic distillation, selective adsorption, the first one is the best suited to power plants, that is, to small CO_2 concentrations at atmospheric pressure and large flue gas mass flow rates. It will be the first one available in the near term (possibly within this decade) for large centralized sources. The other 3 techniques are not well adapted to large power plants because they require higher CO_2 partial pressures and smaller throughputs. CO_2 scrubbing is just like flue gas de-sulphurisation, and as such can be used in retrofit of existing (coal) boilers, at low capital cost. This technique 'saves' the boiler (no change of the plant itself). The CO_2 retention rate is typically 80-85% but with large scrubbers may reach 90% of the amount of CO_2 generated in combustion. Most of the acid gases NO_x and SO_2, as well as particulates, have to be removed at a high level of retention from the flue gas before entering the absorber to minimize consumption of solvent. The separated CO_2 being at atmospheric pressure, CO_2 has still to be compressed up to 110-135 bar where it is liquid (critical point: 73 bar; 30°C).

The heat requirement for solvent regeneration and CO_2 de-sorption from the solvent in the form of steam extracted from the steam turbine is high (typically 4-5 GJ/t CO_2 captured) so that the performance is heavily penalized, namely around 25% decrease of efficiency, which means 10-13 % points efficiency drop for coal and gas fired power plants. The chemical scrubbing commonly used for CO_2 removal from natural gas (separation from methane) and syngas is not yet at commercial scale for removal from flue gas of power plants, except in a few small units.

For post-combustion capture, absorption technology is a leading option but its implementation in a power station will decrease the efficiency of generation by 25% and increase the cost of the generated electricity above 50% [3,9,10,11,12,13]. In a EU funded project called CASTOR (CAPture and STORage) running from 2004 to 2008, the objectives are on the one hand to cut the capture costs by a factor 2 and raise the retention rate up to 90% and on the other hand to demonstrate the feasibility of the new CO_2 capture/storage technologies during the 2 next years. A pilot plant has been commissioned in March 2006 at the Esbjerg coal fired power plant (Denmark), operated by Elsam. One tonne CO_2 per hour (7 kton instead of 2.1 Mt/y) is captured in a fraction of the flue gases mass flow rate diverted from the existing plant on a sufficiently large scale to ensure reliable industrial extrapolation. In this largest installation in the world, the captured CO_2 from a fraction of the diverted flue gas is fixed into a calcium cycle, yielding calcium carbonate (limestone) while the remaining flue gas is passed over a special solid to adsorb CO_2. The final product is thus either limestone or gaseous CO_2 for geological storage

Regarding the materials, various novel solvents are developed for achieving a reduced energy consumption for solvent regeneration. In addition, novel process designs are also currently under development such as a hybrid system [14;15].

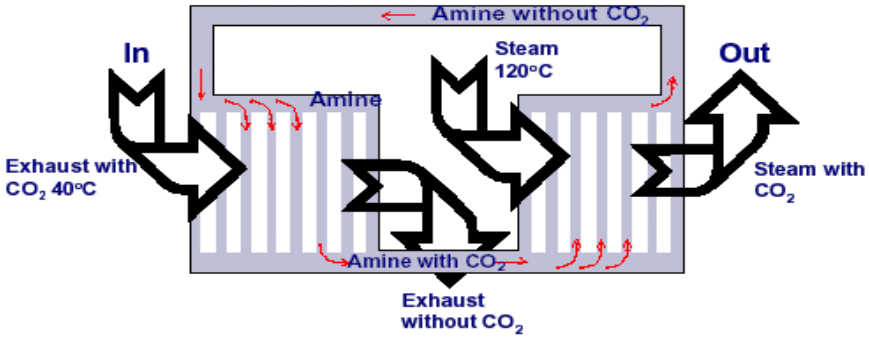

Figure 1: Schematic of a membrane contactor absorber/stripper system.

Fig 2 *Scheme and basic principle of a membrane contactor. The flue gas enters the absorber section at 40°C and after having given up a large fraction of its* CO_2 *leaves the absorber towards the stack while the amine solution loaded in* CO_2 *goes inside a stripper section where heat brought by steam at 120°C bled from the steam turbine liberates the absorbed* CO_2 *and regenerates the amine. The steam leaving the stripper with* CO_2 *is condensed out and recycled with the amine while* CO_2 *is compressed for transport.*

Fig 2 shows that the membrane forms a gas permeable barrier between a liquid and a gaseous phase and enhances the mass transfer rate between gas and solvent thanks to the very high surface area to volume ratio resulting in a compact system. When it is a porous medium, gaseous CO_2 in the flue gas diffuses selectively through the pores under a partial pressure gradient and is absorbed by the liquid solvent on the other side. When the membrane is non-porous, it ensures the contact between gas and liquid phases by dissolving the gaseous CO_2 inside it and diffusing it through. Membrane/solvent systems avoid several operational problems (such as foaming, flooding entrainment and channelling) occurring in conventional solvent absorption systems where gas and liquid flows are in direct contact. Furthermore, the use of compact membranes result in smaller equipment sizes with capital cost reductions. The choice of a suitable combination of solvent and membrane material is a key point. The material characteristics should be such that the transfer of gas is favoured at operating pressure gradients of typically 50–100 kPa, while the transfer of solvent is hindered. Membrane/solvent systems can be both used in the absorption as well as in the desorption step [15,16] .

Fuel gas de-carbonisation

In pre-combustion capture or fuel de-carbonisation, a large fraction (around 90%) of carbon is extracted from the fuel before its combustion [3]. This technique is based either on natural gas reforming using steam or on the gasification of fossil and renewable fuels, and their conversion in a synthetic gas, mixture of mainly CO and hydrogen. CO may be shifted with water into CO_2 and H_2. The components of the mixture may then be efficiently separated by physical absorption in a solvent, leaving H_2 as a fuel and CO_2 for possible re-use and storage. This technology is also available from chemical engineering. However its adaptation at the power generation scale still requires further R&D efforts [3,17,18]. On the other hand, the best adapted power plants (integrated gasification combined cycle or IGCC) are not commercially available yet so that this mitigation option is expected in the medium term (15 to 20 years). Many commercial H_2 and ammonia plants based on gasification are in operation and produce pure H_2 and CO_2. Gas turbines firing H_2 rich fuel gas (H_2 + N_2) are currently under development and near to commercial availability for advanced heavy duty gas turbines (GE's experience is however mostly on older low power gas turbines) [19]. CO_2 removal from the fuel is less penalizing than flue gas de-carbonization, with around 15% capacity decrease, which means 5-7% pts efficiency drop. The challenge is that gasification based chemical plants and IGCC, even without CO_2 capture, are complex processes and thus expensive and not suitable to off-design and transients. They also require much space on the ground and are still at the demonstration level (Buggenum, NL and Puertollano, SP in Europe). A significant asset is the opening of the pathway towards a H_2 economy.

In Europe, the EU project called ENCAP (ENhanced CAPture) running from 2004 to 2009 has the objective of demonstrating the feasibility of IGCC with pre-combustion capture and, in particular, the development of H_2 gas turbine. In USA, the FutureGen Industrial Alliance project consists also of a coal-fuelled IGCC co-generating electricity and H_2 while pre-combustion capturing and permanently storing CO_2 with EOR but is still at the design level today. 9 states (22 sites) have expressed in 2006 their interest in hosting the project. Recently BP has announced its decision to build a demonstration plant rated at 350 MWe and based on natural gas reforming with pre-combustion capture of 1.3 Mt CO_2/ year used for EOR in one of its platform in the North Sea and ultimate storage in the depleted oil field. No special development of new materials different from those involved in post-combustion is needed. However the development of a GT operating on H_2 instead of NG is required.

Oxy-fuel combustion

Oxy-fuel combustion uses oxygen instead of air for combustion, producing a flue gas that is mainly H_2O and CO_2 , which is readily captured either in a simple condenser or in a cooler/separator. This concept is currently under development. Because fuel combustion in pure O_2 generates very high temperatures, the combustion or exhaust products are partly recycled back to the upstream combustion process in order to control the flame temperature and to meet temperature limitations of equipment materials. Because CO_2 or H_2O replaces the nitrogen of air as a thermal ballast, the production of thermal NOx is practically zero. Despite the avoidance of costly chemical absorption in the flue gas, there is however a high energy penalty due to O_2 production by cryogenic distillation and O_2 compression amounting to some 13%pts . In other words, separation of CO_2 from N_2 after the combustion or separation of O_2 from N_2 before combustion results roughly in the same efficiency drop [3,20,21,22].

There are 4 main oxyfuel options under consideration today: oxyfuel combustion in atmospheric boilers; oxyfuel combustion in circulating fluidized beds under pressure or not; oxyfuel combustion in gas turbine cycles; and chemical looping combustion. Their performance is expected to increase with advancements both in oxygen production techniques based on membranes and in gas turbine technology.

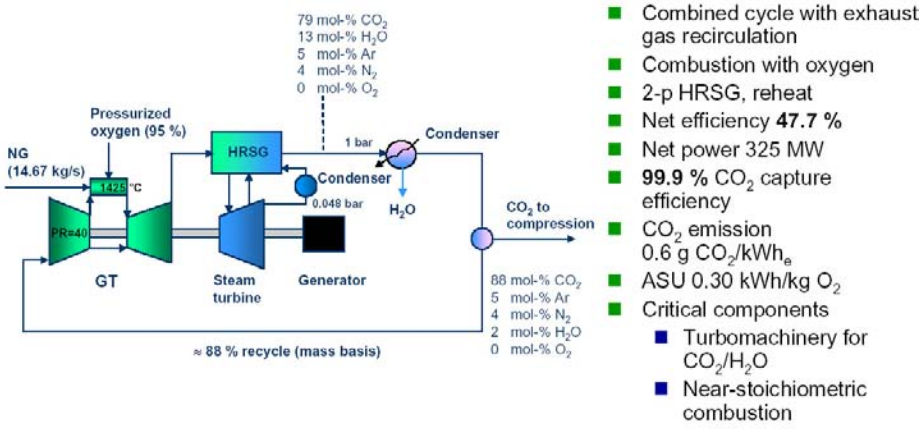

Fig 3 *Scheme of an oxyfuel combustion gas turbine with* CO_2 *recycling in a combined cycle configuration*

Fig 3 shows a CO_2 gas turbine in a combined cycle configuration (Matiant cycle) with O_2 produced in a separate cryogenic air separation unit. Water is extracted in a cooler/separator while the CO_2 generated in the combustion (10%vol of total flow) is extracted through a simple valve. 90%vol of the flow is recycled back to the compressor inlet for a flame temperature control and travels along the cycle in a closed loop. The heat of the turbine exhaust gas is given up to a steam cycle in a heat recovery boiler. Some water (~2%) and the excess O_2 flow together with the CO_2 working fluid. An example of such an oxycombustion cycle has been developed at the University of Liège (Belgium) and is called the Matiant cycle in the literature [3,23,24,25,26]. Fig 4 shows a T-s diagram of an oxyfuel (Matiant) combined cycle with a reheat in the CO_2 gas cycle and two pressure levels and reheat in the steam cycle.

With a 1300°C at turbine inlet and 700°C at the steam generator inlet, the efficiency is about 49-50%. Other oxyfuel options such as the water cycle [27], the Graz cycle [28] and the AZEP cycle [29] are currently under development.

In oxy-fuel combustion, while nearly 100% of CO_2 from combustion can theoretically be removed, the other acid oxides (NOx, SO_2) may be left in the « raw » CO_2 product together with other impurities (Ar; N_2; O_2; H_2O). If pure CO_2 is needed for enhanced oil recovery or storage for example, purification of the raw CO_2 gas, its compression and liquefaction and stripping of acid oxides and inert gases require more power and capital. Then some 3% of the combustion CO_2 escapes from the system with inert gases. Also, NOx and SOx could be removed by the purification of the raw CO_2 flow instead of the flue gas.

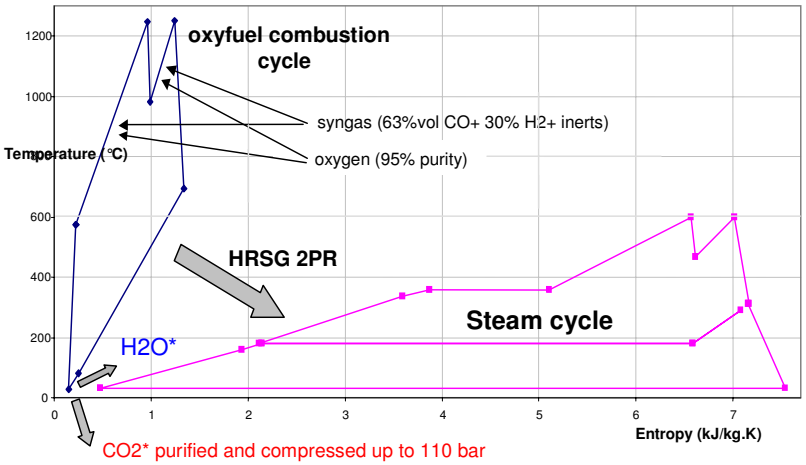

Fig 4 *T-s diagram of an oxyfuel combustion combined cycle (Matiant cycle)*

Oxygen production

Oxygen is the key requirement for any oxy-fuel combustion system. It is also a key technology for pre-combustion CO_2 capture. On top of advances in conventional cryogenic distillation of air, emerging concepts aimed at reducing the energy consumption and cost are analyzed here under.

Separation with membranes

High temperature oxygen ion transport membranes or ITM

Ceramic mixed metal oxides have been developed which exhibit simultaneous oxygen ion and electron conduction at temperatures above 500°C and preferably above 700°C [30-37]. Typical crystal structures which exhibit these properties include the perovskites and the brownmillerites. The selectivity of these materials for oxygen is theoretically infinite. The

oxygen permeability is primarily controlled by the oxygen ion vacancies in the metal oxide lattice. The flow of oxygen through the membrane is usually driven by the partial pressure difference across the membrane. When oxygen molecules are ionized on the ceramic surface, the ions travel through the crystal structure by jumping from vacancy to vacancy and give up their electrons when leaving the ceramic. The electron conduction path is through the metal ions in the lattice. As the membrane is a dense, impermeable ceramic, no gas can pass through, so that it is permeable to oxygen and no other substance. Fig 5 shows the O_2 production by a pressure-driven ceramic membrane with ionic and electronic conductivity at 800-1000°C and 6-20 bar. The O_2 flux is proportional to the log of partial pressure ratio and inversely proportional to the thickness.

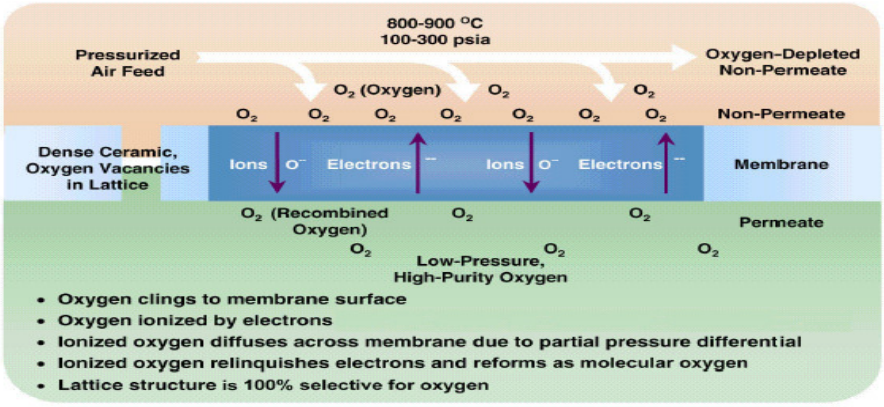

Fig 5 *Ceramic conducting membrane with air feed (retentate or non-permeate side) and sweep gas (permeate side)*

In the technical literature, the engineered structures (plain tubes or hollow fins on a central collector tube) of these ceramic mixed metal oxides are referred to as ion transport membranes, ITM or oxygen transport membranes, OTM. Among the many design problems of ITM/OTM reactors, thermal and mechanical stability is a crucial one because it determines both the performance and the lifetime. Since the oxygen flux is inversely proportional to the thickness, thin dense membranes with a thickness of a few tens of micrometers are currently manufactured. These membranes must be supported on a porous ceramic substrate which may sinter at high temperatures, reducing the porosity and decreasing the performance. Porous perovskite are reported to resist at some 30 bar absolute pressure difference and some 900 °C (above a non-negligible sinter activity develops [34]).

There are many different types of membrane materials (polymeric, metallic, ceramic) that may find application in CO_2 capture systems to preferentially separate H_2 from a fuel gas stream, CO_2 from a range of process streams or O_2 from air. Although membrane separation finds many current commercial applications in industry (some at a large scale, like CO_2 separation from natural gas) they have not yet been applied at the scale of large CO_2 capture systems. A large worldwide R&D effort is in progress aimed at the manufacture of more

suitable membrane materials with the reliability and low costs required for CO_2 capture in large scale applications.

As an illustration, the AZEP cycle shows how an ITM may be integrated in a GT cycle. The compressed air is feeding the ITM reactor on one side of a ceramic membrane while the other side is swept with the flue gas (CO_2+ H_2O) from the combustion chamber (~1250°C). O_2 is conducted from air to the flue gas through the membrane and the depleted air, after been heated by the hot flue gas, is expanded and then gives up its heat to a steam cycle in a steam generator. The flue gas enriched in O_2 (~90%vol of total flow) and cooled through a preheating of the compressed air is recycled back to the combustion chamber for temperature control. The extracted CO_2 (~10%vol of total flow) is either expanded in a CO_2 turbine or sent to the steam generator for more steam production (avoiding so the development of a CO_2 turbine). To adjust the amount of O_2 required for the combustion (with a slight excess), a by-pass of part of the air from the compressor towards the turbine is introduced. The authors claim an efficiency of 52%. In order to increase it, a supplementary firing is installed in the exhaust gas (still containing O_2) and then the efficiency rises to 55% but now 15% of the combustion CO_2 is released at the stack, resulting in a trade-off between efficiency and CO_2 retention rate.

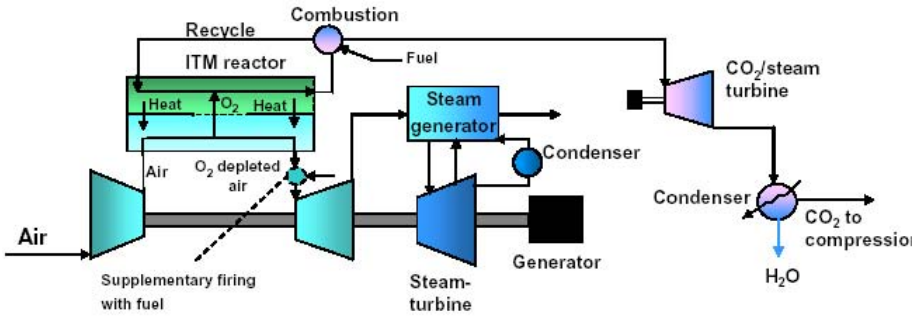

Fig 6 *AZEP cycle integrating a membrane in an ITM reactor*

The membrane reactor is a large mixed oxide ceramic module (ITM reactor) operating at temperatures as high as 1250ºC while the membrane operation temperature is limited to some 900 °C. Air heaters for pulverized coal-fired air turbines are another example of large ceramic components at high temperatures. After many decades of work, these air heaters are still a problem. Two designs exist with combustion chamber incorporating an ITM module into the same vessel or as shown in the figure a combustion chamber and an ITM module separated. When the combustion takes place in the ITM reactor itself, the temperature is controlled by the temperature of combustion. Due to a possible embrittlement of the materials, the temperature of the combustion must remain relatively low (<1250°C). Such a low temperature results in a relatively low efficiency. In addition to this, the AZEP designers have studied a staged combustion using partial catalytic oxidation as the best method of achieving low temperature complete combustion [29,38,39]. This method of combustion brings its own engineering challenges. The authors claim efficiencies close to 50% and in order to increase the efficiency, which is limited by the membrane operation temperature, a supplementary firing has been introduced. In this configuration the efficiency climbs up to 52 -55% but now the CO_2 retention rate decreases down to 85%.

Ceramic Autothermal Recovery (CAR)

An alternative to ceramic membrane technology, referred to as Ceramic Autothermal Recovery (CAR), utilises oxygen storage properties on perovskite type materials at high temperature (600-800°C) based on an adsorption process rather than oxygen transport based on ionic conduction. Perovskite is alternately exposed to oxidizing / reducing conditions in two beds containing spherical perovskite pellets similar to well known adsorbent or catalyst materials. In a cyclic operation using partial pressure swing (using a sweep gas such as steam and CO_2 to reduce the O_2 partial pressure), one bed is fed with a high temperature air stream (250-300°C) and the oxygen is stored in the material at 600-800°C while in the other bed the oxygen is released by reduction of partial pressure due to the sweep gas , which is the recycled working fluid CO_2 + H_2O in a power plant, and is removed. The two beds exchange their function in cyclic form resulting in the generation of an nitrogen rich gas or an oxygen rich gas in mixture with steam and carbon dioxide with internal heat regeneration at constant temperature .

Regarding the materials, composite materials are developed to increase their capacity to store oxygen from a current 0.5 wt% to 1.6 wt%. Also manufacturing techniques of pellets (extrusion, granulation and dry pressing) are developed to decrease the costs. In an oxyfuel PC boiler with a 38% net efficiency and a thermal power of 1866 MWth, the CO_2 capture rate amounts typically to 96%, so that 4% are released with N_2 -rich stream.

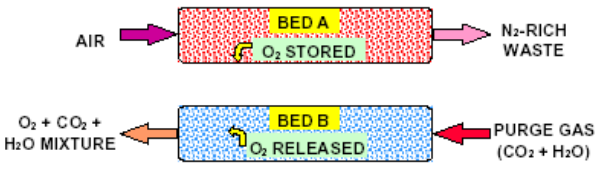

Fig 7 *Ceramic Autothermal Recovery Systems*

Chemical looping combustion

Originally proposed by [40] and with subsequent significant contributions by[41] , the main idea of chemical looping combustion is to split combustion of a fossil or renewable fuel into separate oxidation and reduction reactions by introducing a suitable metal oxide as an oxygen carrier to circulate between two reactors (Figure 7). Separation of oxygen from air is accomplished by fixing the oxygen as a metal oxide. Consequently no air separation plant is required. The reaction between fuel and oxygen is accomplished in a second reactor by the release of oxygen from the metal oxide in a reducing atmosphere caused by the presence of a fuel. The recycle rate of the solid material between the two reactors controls the temperature levels in each reactor. The effect of having combustion in two reactors compared to conventional combustion in a single stage is that the CO_2 is not diluted with nitrogen gas, but is almost pure after separation from water, without requiring any extra energy demand and costly external equipment for CO_2 separation.

The chemical looping combustion principle in a gas turbine cycle shown on Fig 8 is similar to a circulating fluidized bed except that here the particles are moving in a loop are the fuel. Possible metal oxides are some oxides of common transition-state metals, such as iron, nickel, copper and manganese [42]. The metal/metal oxide may be present in various forms, but most studies so far have assumed the use of particles with diameter 100-500 microns. In order to move particles between the two reactors, the particles are fluidized. This method also ensures efficient heat and mass transfer between the gases and the particles. A critical issue is the long-term mechanical and chemical stability of the particles that have to undergo repeated

cycles of oxidation and reduction, to minimize the make-up requirement. When a chemical looping cycle is used in a gas turbine cycle, the mechanical strength and the filtration system are important to avoid damage to the turbine. The temperature in the reactors may be in the range 800℃-1200℃. NO_x formation at these typical operating temperatures will always be low. The fuel conversion in the reduction reactor may not be complete, but it is likely that the concentrations of methane and CO when burning natural gas are very small [43]. In order to avoid deposit of carbon in the reduction reactor, it is necessary to use some steam together with the fuel.

The chemical looping principle may be applied either in a gas turbine cycle with pressurized oxidation and reduction reactors, or in a steam turbine cycle with atmospheric pressure in the reactors. In the case of a gas turbine cycle, the oxidation reactor replaces the combustion chamber of a conventional gas turbine.

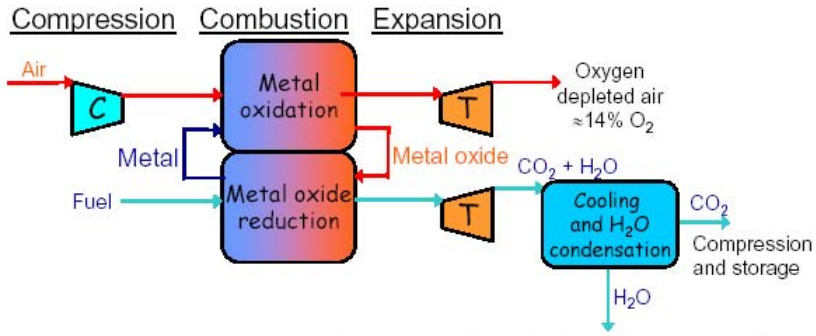

Fig 8 *Chemical Looping Combustion system*

The exothermic oxidation reaction provides heat for increasing the air temperature entering the downstream expansion turbine. In addition, the reduction reactor exit stream may also be expanded in a turbine together with steam production for power generation. The cooled low pressure CO_2 stream will then be compressed to pipeline pressure. Another option is to generate steam using heat transfer surfaces in the oxidation reactor. Current circulating fluidized bed combustion technology operating at atmospheric pressure in both the oxidation and reduction stages necessitates the use of a steam turbine cycle for power generation. For a chemical looping combustion cycle which uses natural gas as fuel and supplies a gas turbine combined cycle power plant and delivers CO_2 at atmospheric pressure, the efficiency is estimated to be in the range 45-50% [3,44] . Work on chemical looping combustion is currently in the pilot plant and materials research is carried out on the appropriate metallic carriers.

Status and outlook

From studies by the IEA GHG R&D Programme [8], it turns out that the efficiency penalty due to capture is around 8-9 % points for post-combustion capture both with coal and natural gas as well as for pre-combustion capture in an IGCC fed with a dry coal (much less for a coal slurry) . The results show that the efficiency penalty is also around 9 % pts for an oxyfuel combustion steam boiler, equipped with an air separation unit, a recycling of the flue gas CO_2 + steam and a CO_2 compressor, when compared to an air based boiler without capture

whereas the efficiency penalty is higher, around 11 % pts, for an oxyfuel combustion gas turbine combined cycle compared to a standard natural gas combined cycle.

In conclusion, there is no clear winner (if any) among the 3 options post- and pre-combustion capture and oxyfuel coal boiler. Each option might have its own niche of application. As projections to the 2010-2020 time frame are predicting efficiencies above 50% [44;45] for coal plants using ultra-supercritical steam conditions (45% today), an increase in efficiency of more than 5% points can therefore be expected for future oxy-fuel capture systems based on coal firing that could potentially match the best efficiencies realisable today for pulverized coal-fired plants without CO_2 capture.

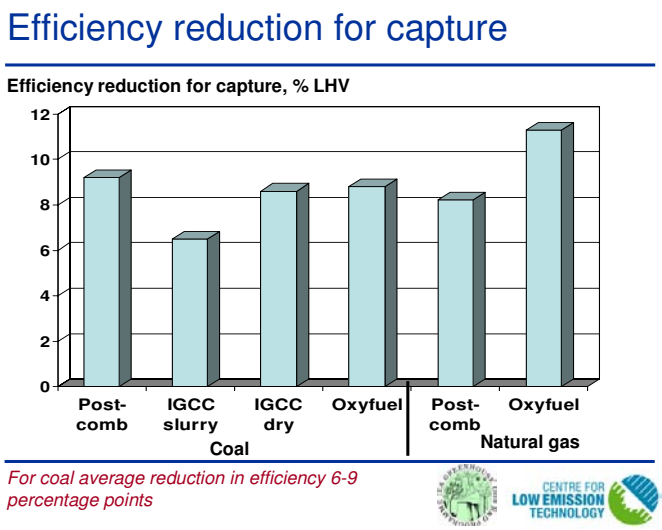

Fig 9 *Efficiency penalty in % points (LHV) due topost and pre- combustion capture compared to efficiency of the same plant without capture for coal and natural gas based power plants. Oxyfuel coal boiler and oxyfuel gas turbine are compared with air based boiler and gas turbine.*

Similarly, natural gas fired combined cycles will have efficiencies of 65% in 2020 [8] from current efficiencies between 55 and 58%, which will enable plant efficiencies for natural gas fired oxy-fuel cycles with CO_2 capture above 50%. In addition, these options involve the minimal modification of technologies and infrastructure that have hitherto been already developed for the combustion of fossil and renewable fuels in air. The energy penalty for producing oxygen is by far the most important cause for reduced efficiency in an oxy-fuel cycle compared to a conventional power plant.

Oxy-fuel combustion is feasible since no technical barriers for its implementation have been identified. However, several novel applications proposed for oxyfuel combustion steam and gas turbine cycles still require the development of new components such as oxy-fuel combustors, higher temperature tolerant components such as CO_2- and H_2O-based turbines with blade cooling, CO_2 compressors and high temperature ion transport membranes for oxygen separation. As for Chemical Looping Combustion, it is currently still at an early stage

of development. Current technology development envisages very high efficiency separation of NO_x, SO_x, and Hg, as part of the CO_2 compression and purification system. Improved separation efficiencies of these contaminants are possible based on further process and heat integration in the power cycle. Current cryogenic oxygen technology is showing continuing cost reduction based on improved compressor efficiencies, more efficient process equipment and larger scale plants. The new high temperature oxygen membrane could significantly improve power generation efficiency and reduce capital cost.

Future oxy-fuel demonstration plants could be based on new designed boilers or retrofits to existing boilers, in order to minimize development costs and achieve early market entry. Several demonstration units may be expected within the next few years particularly in Europe, USA, Canada and Australia where active research initiatives are currently underway. As these developments proceed and the technologies achieve market penetration they may become competitive relative to alternate options based on pre- and post-combustion CO_2 capture. t present, only tests on pilot plant boilers and retrofit of existing boilers and heaters have been carried out. This option « saves » the boiler but needs compression of CO_2 to the supercritical state (typically at or above 110 bar) and an air separation unit. Vattenfal has recently decided to implement a pilot plant of an oxyfuel boiler with CO_2 recycling and capture next to its lignite fired plant in Berlin (Schwarze Pumpe) and the commissioning is expected in 2008. Other similar projects are under development [47-51].

Conclusion

Proven post-combustion CO_2 capture technologies based on absorption processes are commercially available today. However, they require a large scale up of the current unit capacities for deployment in large-scale power plants in the 500 MW_e capacity range. The intense development efforts on novel solvents for improved performance and reduced energy consumption during regeneration, as well as process designs incorporating new contacting devices such as hybrid membrane-absorbent systems (but also solid adsorbents and high temperature regenerable sorbents not considered here) may lead to the use of more energy efficient post-combustion capture systems. However, all these novel concepts still need to prove their lower costs and reliability of operation on a commercial scale. The same considerations also apply to other advanced CO_2 capture concepts with oxy-fuel combustion and pre-combustion capture. Oxygen production is a key element and advances on high temperature ceramic membranes strongly depend on the development of new materials both for conducting and storing membranes integrated to oxyfuel combustion systems and for metallic particles in chemical looping combustion.

It is generally not yet clear which of these emerging technologies, if any, will succeed as the dominant commercial technology for energy systems incorporating CO_2 capture. Each option could find its own niche application so that it is not necessarily wished to identify an absolute winner option.

.

References

1. EEA, European Environment Agency 2003b. Greenhouse Gas Emissions Trends and Projections in Europe., Environmental Issue Report 36, Copenhagen
2. IPCC, 2001a: Climate Change 2001 – Mitigation. The Third Assessment Report of the Intergovernmental Panel on Climate Change. B. Metz, O. Davidson, R. Swart, J. Pan (eds.). Cambridge University Press, Cambridge, UK

3. IPCC special report on CO_2 capture and storage, 2005, B. Metz, O. Davidson, H. de Coninck, M. Loos, L. Meyer eds, IPCC Working Group III, Cambridge University Press
4. IPCC, 2001c. Climate Change 2001 – the Scientific Basis. The Third Assessment Report of the Intergovernmental Panel on Climate Change. Houghton, J.T., Ding, Y., Griggs, D.J., Nogouer; M., van der Linden, P.J., Dai, X., Maskell, K., Johnson, C.A. (eds). Cambridge University Press, Cambridge, UK
5. IEA GHG, 2002b: Opportunities for early application of CO2 sequestration technologies, report PH4/10, Sept. 2002, IEA Greenhouse Gas R&D Programme, Cheltenham, UK.
6. Gale JJ, Christensen NP, Cutler A and Torp TA, 2001, Demonstrating the potential of geological storage of CO_2 : the Sleipner and GESTCO projects, Environmental Geosciences 8(3)
7. Hendriks CA, Blok K, Turkenburg WC, 1989, The recovery of CO2 from power plants, Proceedings of the Symposium on Climate Energy, Utrecht (NL)
8. IEA GHG: Leading options for the capture of CO2 emissions at power stations", Report No. PH3/14, IEA Greenhouse Gas R&D Programme, Cheltenham UK February 2000
9. Bolland O., 2004b, "CO2 capture technologies-an overview," The Second Trondheim Conference on CO2 Capture, Transport and Storage, 25-26 Oct., Trondheim, Norway.
10. Bolland, O., Undrum, H., "Removal of CO2 from gas turbine power plants: Evaluation of pre-and post combustion methods," 4 th International Conference on Greenhouse Gas Control Technologies, Interlaken, Switzerland, 30 August – 2 September 1998
11. Rao, A, Rubin E., 2002: A technical, economic, and environmental assessment of amine-based CO2 capture technology for power plant greenhouse gas control. Environmental Science and Technology, 36, 4467-4475.
12. Stromberg, L., Options for CO2 free coal based power generation - timing, technology and economics, in Euro-CASE Workshop: CO2 Management in Europe. Oslo, May 16.
13. Mimura, T., T. Nojo, M. Iijima, T. Yoshiyama and H. Tanaka, 2002: Recent developments in flue gas CO2 recovery technology. 6 th International Conference on Greenhouse Gas ControlTechnologies , Kyoto, Japan, October 2002, Elsevier publishers.
14. Feron, P.H.M., 1992: Carbon dioxide capture: The characterisation of gas separation/removal membrane systems applied to the treatment of flue gases arising from power plant generation using fossil fuel, IEA/92/08, IEA Greenhouse Gas R&D programme, Cheltenham, UK
15. Feron, P.H.M and A.E. Jansen, 2002: CO2 Separation with polyolefin membrane contactors and dedicated absorption liquids: Performances and prospects, Separation and Purification Technology, 27(3), 231-242.
16 . Falk-Pedersen, O., H. Dannström, M. Grønvold, D.-B. Stuksrud, and O. Rønning, 1999: Gas Treatment Using Membrane Gas/Liquid Contractors, Greenhouse Gas Control Technologies. B. Eliasson, P. Riemer and A. Wokaun (eds.), Elsevier Science, Ltd., United Kingdom 115-120.
17. Chiesa, P., S. Consonni, T. Kreutz, and R. Williams, 2005: Co-production of hydrogen, electricity and CO2 from coal with commercially ready technology. Part A: Performance and emissions, International Journal of Hydrogen Energy, 30 (7): 747-767.
18. IEA GHG, 2003: Potential for Improvement in IGCC with CO2 Capture, report PH4/19, May 2003, IEA Greenhouse Gas R&D Programme, Cheltenham UK, 788 pp.
19. Todd DM; Battista RA "Demonstrated Applicability of Hydrogen Fuel for Gas Turbines", 4th European Gasification Conference 11-13th April 2001, Noordwijk Norw
20. P. Mathieu, 2005, Zero Emission Technologies : An Option for Climate Change Mitigation, International Jl of Green Energy,Taylor & Francis ed, Vol 2, n°2, pp 193-200, April-June 2005

21. P. Mathieu , Towards the hydrogen era using near-zero CO2 emissions energy systems, ECOS 2002, Berlin (Germany), July, 2002 published in Energy, International Journal, Elsevier, Vol 29, 2004
22. Panesar, R., Gibbins, J., Allam, R.J., White,V., Wall, A., "Oxy-combustion processes for CO2 capture from power plant'' 7th International greenhouse gas control technologies conference,Vancouver 2004
.23. Dechamps P, Distelmans M, Mathieu P, Pirard N, 1994, Performances of combined cycle power plants using CO2 gas turbines, Flowers'94 conf, ppp 671-682
24. Mathieu P., 1998, "Presentation of an innovative Zero-Emission cycle for mitigation the global climate change.," Int. Journ. of Applied Thermodyn., Vol. 1, No.1-4. www.ulg.ac.be/genienuc/publicat.htm
25. S Houyou, P Mathieu and R Nihart, "Techno-economic comparison of different options of very low CO2 emission technologies", Fifth International Conference on Greenhouse Gas Control Technologies, Cairns, Australia, 13-16 Aug. 2000
26. Ruether J, Le P, White C, Electricity generation from coal with CO_2 capture by means of a novel power cycle, 25th Int Technical Conf on Coal Utilization and fuel Systems, Clearwater, Florida, March 2000. and "A Zero-CO2 Emission Power Cycle Using Coal." Technology, Vol.7S, pp.95-101
27. Anderson R.E., Doyle S.E., Pronske K.L., 2004, "Demonstration and Commercialization of Zero-Emission Power Plants," 29th International Technical Conference on Coal Utilization & Fuel Systems, April 18-22, Clearwater, FL, USA.
28. Jericha, H., Göttlich, E., Sanz, W., Heitmeir, F., 2003, "Design Optimisation of the Graz Cycle Prototype Plant", ASME Paper 2003-GT-38120, ASME Turbo Expo 2003, Atlanta, USA, ASME Journal of Engineering for Gas Turbines and Power, Oct. 2004, Vol. 126, pp. 733-740
29. Griffin, T., S.G. Sundkvist, K. Aasen, and T. Bruun, 2003: Advanced Zero Emissions Gas Turbine Power Plant, ASME Turbo Expo Conference, paper# GT-2003-38120, Atlanta, USA.
30. Bouwmeester H., Burggraaf A., 1996, "Dense Ceramic Membranes for Oxygen Separation," Ch. 11 in the CRC Handbook of Solid state Electrochemistry, CRC Press, Boca Raton.
31. Van der Sluijs, J.P, C.A. Hendriks, and K. Blok, 1992: Feasibility of polymer membranes for carbon dioxide recovery from flue gases, Energy Conversion Management, 33(5-8), 429-436.
32. Feron, P.H.M., 1994: Membranes for carbon dioxide recovery from power plants. In Carbon Dioxide Chemistry: Environmental Issues. J. Paul, C.M. Pradier (eds.), The Royal Society of Chemistry, Cambridge, United Kingdom, 236-249.
33. Armstrong, P.A., D.L. Bennett, E.P. Foster, and V.E. Stein, 2002: Ceramic membrane development for oxygen supply to gasification applications. Proceedings of the Gasification Technologies Conference, San Francisco, CA, USA
34. Dyer P., Richards R., Russek S., Taylor D., 2000, "Ion transport membrane technology for oxygen separation and syngas production," Solid State Ionics, Vol. 134, pp. 21-33.
35. Bouwmeester, H.J.M., L.M.Van Der Haar, 2002: Oxygen permeation through mixed-conducting perovskite oxide membranes. Ceramic Transactions, 127, Materials for Electrochemical Energy Conversion and Storage, 49-57.
36. Jordal, K., R. Bredesen, H.M. Kvamsdal, O. Bolland; 2002 Integration of H2-separating membrane technology in gas turbine processes for CO2 sequestration. Proceedings of GHGT-6, Kyoto,Japan
37. Shockling L., Huang K., Christie G., 2001, "Zero Emission Power Plants Using Solid Oxide Fuel cell and Oxygen transport Membranes," Vision 21 Program Review meeting, Nov.6, US DOE, NETL

38. Bill, A., Span, R., Griffin, T., Kelsall, G., Sundkvist, S G., "Technology options for 'Zero Emissions' gas turbine power generation," International Conference Power Generation and Sustainable Development, Liège, Belgium, 8 – 9 October 2001.
39. Sundquist S., Klang A. Sjödin M., Wilhelmsen K., Asen K., Tintinelli A., McCahey S., Ye H., 2004, "AZEP gas turbine combined cycle power plants," GHGT-7, Uni Regina, Canada,
http://uregina.ca/ghgt7/PGF/papers/peer/079.pdf
40. Richter, H.J., K. Knoche 1983: Reversibility of Combustion processes, Efficiency and Costing -Second Law Analysis of Processes, ACS Symposium series, 235, p. 71-85.
41. Ishida M., Jin H., 1998, "Greenhouse gas control by a novel combustion: no separation equipment and energy penalty," 4th Int. Cong. GHGT, Interlaken, ENT-13.
42. Zafar, Q., T. Mattisson, and B. Gevert, 2005: Integrated Hydrogen and Power Production with CO2 Capture Using Chemical-Looping Reforming-Redox Reactivity of Particles of CuO, Mn2O3, NiO, and Fe2O3 Using SiO2 as a Support, Industrial and Engineering Chemistry Research, 44(10), 3485-3496.
43. Cho, P., T. Mattisson, and A. Lyngfelt, 2002: Reactivity of iron oxide with methane in a laboratory
fluidised bed - application of chemical-looping combustion, 7th International Conference on Circulating Fluidised Beds, Niagara Falls, Ontario, May 5-7, 2002, 599-606.
44. Brandvoll, Ø. and O. Bolland, 2004: Inherent CO2 capture using chemical looping combustion in a
natural gas fired power cycle. ASME Paper No. GT-2002-30129, ASME Journal of Engineering for Gas Turbines and Power, 126, 316-321
45. IEA WEO, 2004: IEA World Energy Outlook 2004, International Energy Agency, Paris France.
46. IEA, 2004: Prospects for CO2 capture and storage, ISBN 92-64-10881-5.
47. Chatel-Pelage, F., M. Ovidiu, R. Carty, G. Philo, H. Farzan, S. Vecci, 2003: A pilot scale demonstration of oxy-fuel combustion with flue gas recirculation in a pulverised coal-fired boiler, Proceedings 28th International Technical Conference on Coal Utilization & Fuel Systems, Clearwater, Florida, March 10-13.
48. Croiset, E. and K.V. Thambimuthu, 2000: Coal combustion in O2/CO2 Mixtures Compared to Air.
Canadian Journal of Chemical Engineering, 78, 402-407.
49. Dillon, D.J., R.S. Panesar, R.A.Wall, R.J. Allam, V. White, J. Gibbins, and M.R. Haines, 2005:
Oxy-combustion processes for CO2 capture from advanced supercritical PF and NGCC power plant, In: Rubin, E.S., D.W. Keith, and C.F. Gilboy (eds.), Proceedings of 7th International Conference on Greenhouse Gas Control Technologies. Elsevier Science, Oxford, UK (in press).
49. Abanades, J.C., E.J. Anthony, D. Alvarez, D.Y. Lu, and C. Salvador, 2004a: Capture of CO2 from
Combustion Gases in a Fluidised Bed of CaO. AIChE J, 50, No. 7, 1614-1622.
50. Alstom Power Inc., ABB Lummus Global Inc., Alstom Power Environmental Systems and
American Electric Power, 2001: Engineering feasibility and economics of CO2 capture on an existing coal-fired power plant. Report no. PPL-01-CT-09,USDOE/NETL Pittsburg,PA
51. Energy news Europe, Vattenfall newsletter " Vattenfall builds CO2-free power plant" Platts Commodity News, 19 May 2005 www.vattenfall.com
52. European projects CASTOR www.CO2castor.com and www.ifp.fr and ENCAP www.encapCO2.org

THE HYDROGEN ECONOMY

U. Birnbaum, J.-F. Hake, J. Linssen, M. Walbeck

Forschungszentrum Jülich, Systems Analysis and Technology Evaluation (STE),
D-52425 Jülich, Germany
jfh@fz-juelich.de

Abstract
This paper focuses on the current discussion on the contribution of the hydrogen economy to a "sustainable energy system". It discusses whether advantages for the environmental situation and energy carrier supply can be expected from the already visible future characteristics of hydrogen as a new secondary energy carrier.
Possible production paths for hydrogen from hydrocarbon-based, renewable or carbon-reduced/-free primary energy carriers are evaluated with respect to primary energy use and CO_2 emissions from the fuel cycle. Whether generated by electrolysis or by reforming, and even if produced locally at filling stations, the gaseous or liquid hydrogen has to undergo different processes before it can be used by the customer as a product. Hydrogen has to be packaged by compression or liquefaction, transported by surface vehicles or pipelines, stored and transferred to the end user. In order to provide an idea of possible markets, a technical systems analysis of possible hydrogen applications is performed for the stationary and mobile sector.
Hydrogen may represent an option for clean energy use if hydrogen can be produced with carbon-reduced or -free primary energy carriers like renewable energy, biomass or nuclear energy. It can be produced from fossil primary energy carriers, too, if the CO_2 emissions during processing are captured and stored. So far the energetic use of hydrogen competes with the direct use of clean primary energy and/or with the use of electric energy which is produced without CO_2 emissions. As a substitute for other secondary energy carriers hydrogen must have advantages in comparison to the use of traditional energy carriers, especially electricity

Keywords
Hydrogen generation, distribution, storage, application, energy supply chain

I Introduction

Energy represents a fundamental resource for economic and societal development. Energy is needed for agriculture, industrial production, transportation and for mobility.

For centuries, the energy history was dominated by biomass in form of wood. The discovery of coal and the invention of the steam engine have substituted the horse-drawn vehicles by steam locomotives whereby large distances became fast bridgeable and have led to industrialisation. In the second half of the 20^{th} century coal lost its dominant role and was displaced by oil or better by oil products in several energy sectors. Especially the transportation systems benefited from liquid fuels as they were easier to handle (storage and use), which was also an advantage for stationary applications in industry or households. Since three to two decades, natural gas is favourite for heating systems if a connection to the gas grid exists. Again the simple handling of this continuously delivered energy carrier and the omission of storage room were/are motivation for users to substitute oil.

The wide use of coal, oil and gas for thermal combustion can have severe impacts on the environment and on living conditions. Moreover, climate change most likely results from CO_2 emissions. Another concern is raised from finiteness of the global oil and gas reserves and resources. Increased prizes for oil and gas are expected.

The discussion on sustainable development in the energy sector so far has pointed out the dependency of industrialized countries and regions like the EU on fossil energy carriers. Figure 1 shows, that the energy supply is based at a high amount on fossil fuels, 37% oil,

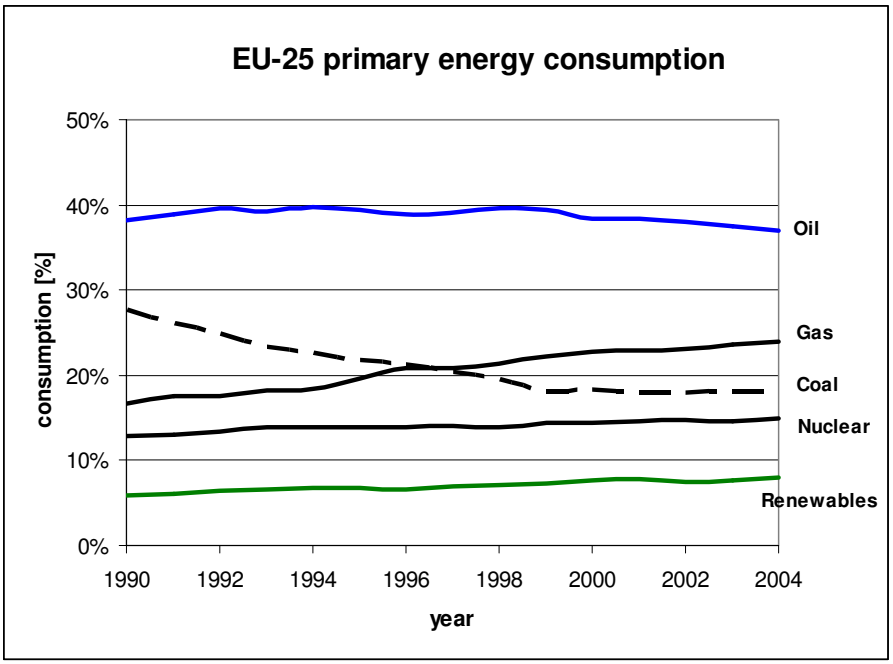

Figure 1: Consumption of primary energy in EU 25 up to 2004 [1]

24% gas and 17% coal, which set free a large amount of greenhouse gas (GHG) emissions. Though there are ambitious programs in several countries to push the use of renewables, their share at the energy mixture is actually not more than 8%.

Figure 2 shows the development of the GHG emissions of EU countries since 1990, the year when the Kyoto protocol was signed with the commitment to reduce the GHG emissions by 6% by 2008 - 2012. The linear line symbolises the reduction pathway towards the Kyoto target and at the first view the results seem not to be so bad. But between 2003 and 2004 the emission increased by 18 million tonnes, whereas 11.5 million tonnes are caused by the EU-15 countries, see the little graph. Main reasons for that development were the increasing road transport and the manufacturing of iron and steel [2].

In the mean time it is commonly held that the large amount of the world wide anthropogenic greenhouse gas (GHG) emissions, especially carbon dioxide and nitrous oxide, must be seen as important reasons for the observed global warming. As the effect is appraised as a significant threat, current political and social intentions are to develop strategies towards a “sustainable development” with less emission and less resource consumption.

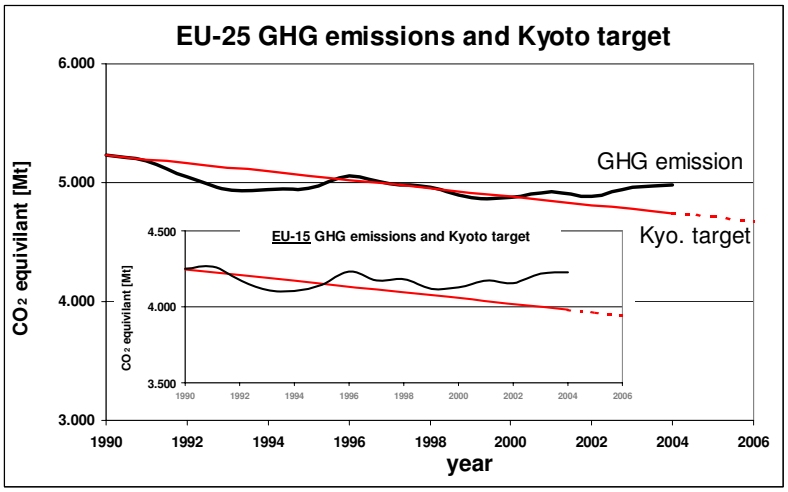

Figure 2: EU greenhouse gas emissions and Kyoto target [3]

The scientific cognition about the reasons for the observed climatic change and its velocity raised the question how to transform present energy systems into ones which can provide affordable energy services to a broad public accompanied by strongly reduced emissions. Additional pressure arises if a country decides to withdraw from using specific energy forms like nuclear energy for instance. [4]

The European Commission has given high political priority to sustainable development. In the context with sustainable development the EU evaluates several options. The hydrogen economy represents one of them because the use of hydrogen as a secondary energy carrier offers a huge potential with respect to emissions. [5]

The strategies for sustainable development involve at the supply side new technologies for the environmentally friendly conversion of coal as well as the provision of low or zero emission secondary energy carriers and at the demand side the availability of suitable devices and the acceptance of the consumer of new secondary energy carriers, such as bio-fuels or/and hydrogen [6, 7, 8, 9]. Figure 3 shows the coherences and dependencies between the different stages and levels of modern energy supply systems. They form the framework into which new fuels have to fit and to grow.

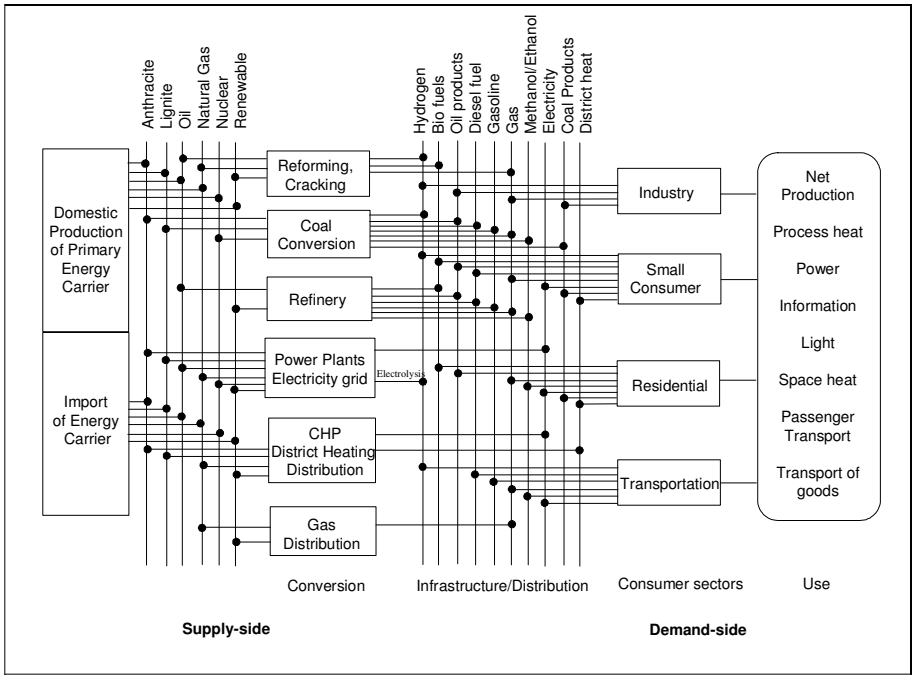

Figure 3: Scheme of a today's energy supply system

Challenges for the supply side are

- the development of decarbonisation technologies combined with carbon dioxide capture and storage to use the fossil primary energy carriers, especially the large coal reserves
- the development and introduction of accepted and low or zero emission secondary energy carriers, such as hydrogen for the multifaceted application in the consumer sectors.

No problems should be expected at the generation and conversion side. The technologies for carbon dioxide capture and storage are under demonstration, coal conversion technologies to produce clean fuels are well proven and technologies for the use and conversion of biomass are also practised.

On the demand side an adjustment of the existing infrastructure and of the application devices to the new challenges seem to be necessary. The properties of oil-, coal- or biomass-based liquid fuels on one hand and of natural gas and hydrogen on the other hand differ significantly, so that it is doubtful whether the effectiveness of the current distribution systems and application devices could be preserved without improvements. The problems which occurred with the conversion from town gas to natural gas in the Ruhr district in Germany in the 1960s can be seen as an example for necessary modifications. Even if the today's pipeline material and fittings are more suitable, questions remain: Are the TM steel pipelines or the PVC respectively PE pipelines suitable for a hydrogen rich gas or for pure hydrogen; can the safety standards be fulfilled; are the application units (heating vessels or

stoves, for example) suitable for a hydrogen-rich gas or for a gas with a varying hydrogen content?

A similar situation can already be observed in the transportation sector, where biomass based fuels shall substitute petroleum products. Actually car manufactures give no guarantee, if modern diesel engines are operated with pure bio-fuels. Up to now they are added with a share of only 5 to 10 percent to the oil-based fuels. Two reasons are addressed by the car manufacturers; the first one has to do with the aggressiveness of bio-diesel against some materials which are used for pumps, fuel feed pipes or others in the car and the second one is the probability of exceeding the stringent emission standards, if fuels with no fixed specification are used. It is fact that the specification of bio-fuels varies corresponding to the variability of the biomass feedstocks.

II Supply side: Hydrogen production

Hydrogen does not occur in nature in its elementary form, which could be used as a clean energy carrier without giving off harmful emissions. It is linked in chemical compounds such as water and hydrocarbon carriers (oil, natural gas, coal, biomass and others) [10]. These feedstocks must be reformed or refined to generate hydrogen, which is not an exotic or unknown product. The current world consumption amounts to ~ 550x 10^9 Nm^3, of which about 50% are used for ammonia production and about 37 % in petroleum refineries for sulphur removal and others [10]. So far hydrogen is a very common crude material with well established production routes. About 60% are produced from fossil fuels and 40 % as by-product in the petrochemical industry and by the chlor-alkali electrolysis from water [11].

In principle there are two main routes to produce hydrogen. The first one is the thermal reforming of hydrocarbons, such as oil or natural gas, and the second one is the electrolytic dissociation of water. [12, 13]

The most effective thermal process is the steam reforming of natural gas, a production form with relatively little environmental impact, as a good part of the produced hydrogen comes from the reactant water vapour [14].
A further production process is the partial oxidation of heavy hydrocarbons with the theoretical advantage of a more compact technical construction but with the disadvantage of a product flow with more inert components or, better said, with a more diluted hydrogen product gas [15].
Hydrogen can also be produced by thermal gasification and partial oxidation of coal and biomass such as wood, energy plants, straw and others. In principle the biomass generation processes are comparable to the conventional ones, but they are not yet in commercial use, as the processing is not yet profitable. The research and developing activities target to more efficient catalysts and cheap materials that will increase the yield and reduce the costs. Nevertheless it is expected that biomass processing will complete the hydrogen production possibilities. In the case of a sustainable hydrogen production from coal, one has so separate and to store the accompanying carbon dioxide (CCS = Carbon Dioxide Capture & Sequestration). The first demonstration plants are designed and under construction, so that they can start within the next 5 years.

The European Well-to-Wheels study [16] analysed a couple of today's and future automotive fuels to calculate the energy effort for the well to wheel chain. Figure 4 shows for seven fuel-routes the energy requirements along the whole chain. The results include the production (mining), the conversion and the distribution and the consumption with a modern car.

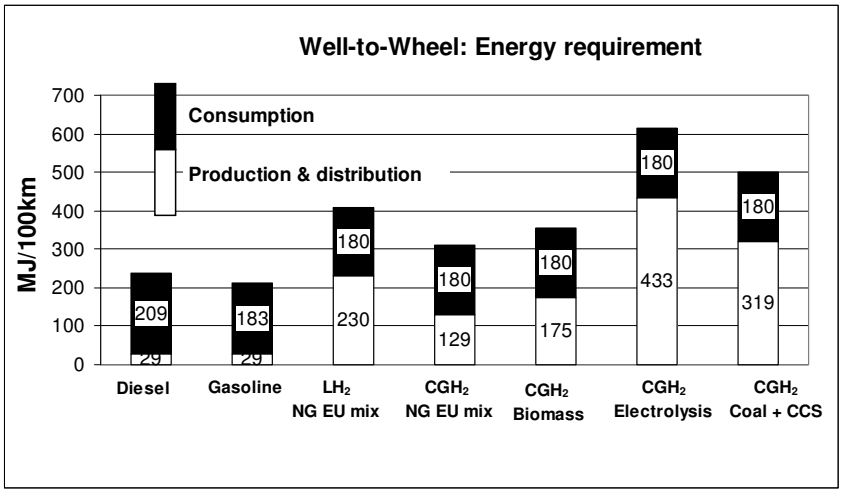

Figure 4: Energy demand for secondary energy carrier routes [16]

The process chains for diesel and gasoline (petrol) refined from crude oil have the smallest energy requirements with 29 MJ/100 km (or with 0.16 MJ/MJ_{diesel} and 0.14 $MJ/MJ_{gasoline}$). The energy consumption for motion is 209 MJ/100 km for a direct injection spark ignition internal combustion engine. The production of hydrogen for any considered pathway amounts to essentially more energy. In the case of electrolysis, no CCS technology is considered. The proportional energy demand for production and for distribution is the highest of the shown pathways. The hydrogen consumption of the direct injection spark ignition hydrogen internal combustion engine is calculated at 180 MJ/100 km. Comparing all cases, the diesel and gasoline pathways show the lowest energy demand along the well to wheel chain, as the production is relatively easy and efficient.

Figure 5 gives the GHG emission results for the fuel routes of figure 4. The lowest GHG-emission shows the compressed hydrogen from biomass (in this case planted wood). The second best solution is hydrogen from coal gasification using the CCS technology. No essential differences can be addressed between diesel, hydrogen from natural gas and gasoline; their emissions are calculated to 164, 177 and 183 gCO_{2equ}/km respectively. The electrolysis-hydrogen pathway is burdened by an emission of 364 gCO_{2equ}/km so that it seems to be the most unfavourable route. The reason is the chosen European power generation mix without CCS or, better said, the emissions of the coal power generation and the high coal power share at the European electricity mix.

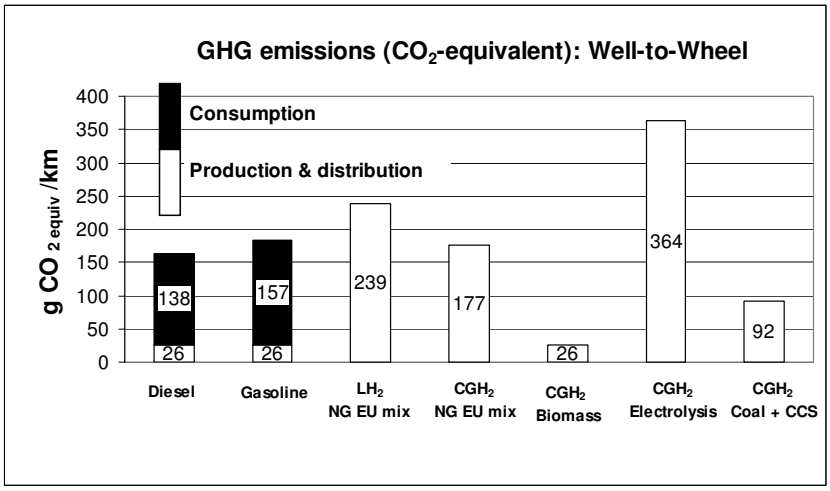

Figure 5: Specific GHG emission of production chains of energy carriers [16]

If the generation mix were modified in favour of electricity from hydropower, which is done on a large scale in Norway, Switzerland and Austria, the result would be completely different. Hydropower is free of emissions, so that the electrolysis would not be burdened by the coal power plant emissions. Additionally this production pathway would have economic advantages, as the electricity generation costs are obviously lower than those of coal power plants. The electricity price for Norwegian industrial consumers was ~ 3,5 cent/kWh in 2005. On the base of such an electricity price, the hydrogen generation cost can be calculated to ~ 27 cent/Nm^3H_2 following the assumptions of Norsk Hydro for a 230 MW electrolysis facility (that 27 cents corresponds to 2.5 cent/MJ H_2 or ~ 79 cent/litre gasoline equivalent), see figure 6 [17].

Other green power generation technologies, such as wave and tidal power, are not yet available and even wind power, which has an essential contribution to the power generation of several European countries, is still so expensive, that its consideration has only a theoretical character, but they are zero emission.

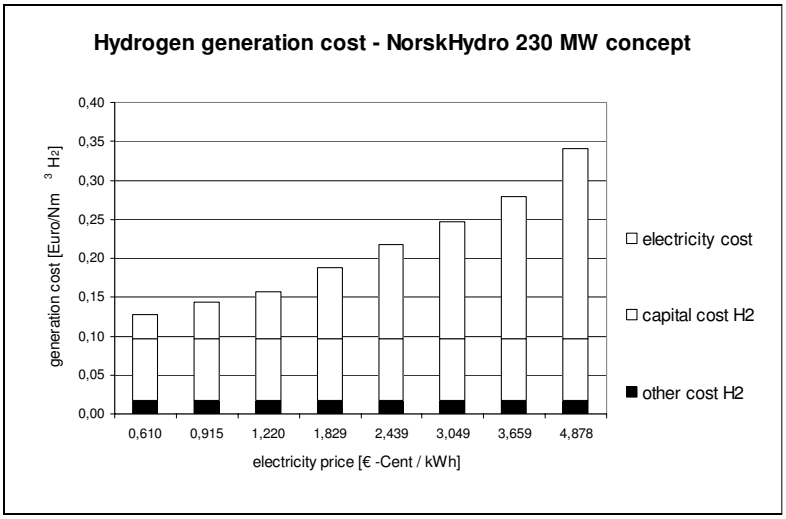

Figure 6: Importance of the electricity price to the hydrogen generation cost [17]

Especially the cost aspect shows the gap between the expectations or hope and the reality. But this discrepancy describes the necessities too: low cost generation technologies have to be developed. Their realisation is a question of simple and cheap materials, which only can be used if the processing causes less material stress. That means that process optimisation has to take place. The same can be said for physical/chemical processes (reformation), whose efficiency must be increased and for which more efficient catalysts have to be explored whereby they have to be cheaper at the same time. As an example can be seen the research activities on catalysts for the Fischer-Tropsch synthesis to produce fuels from coal as well as from biomass, which is a research topic in many institutions and companies.

III Distribution system for the secondary energy carriers

Figure 7 shows in principle the linkages between the secondary energy carriers and the consumer, which belong to the four main energy consumption sectors, transportation, industry, small consumer and household. The four central icons symbolise the two distribution philosophies: on one hand not grid bounded and discontinuous delivery of storable energy carriers such as oil products, on the other hand the grid bounded and continuous delivery of such not storable energy carriers as gas or electricity.

In certain limits gas can and must be buffered to balance daily and seasonal load curves. But that means investment costs and efficiency losses caused by varying the grid pressure or by charging/discharging storages (underground caverns and gasometers).

The storing of electricity is strictly limited to batteries or has to be done indirectly, for example, via pumped storage plants. Normally the electricity generation orientates itself to the expected consumption curve and reacts by a high sophisticated combination of generation units with different operation characteristics. The electricity grid can be seen as a lake with a

continuous flow in and a corresponding take off at the same time as otherwise an overflow would occur (= system blackout).

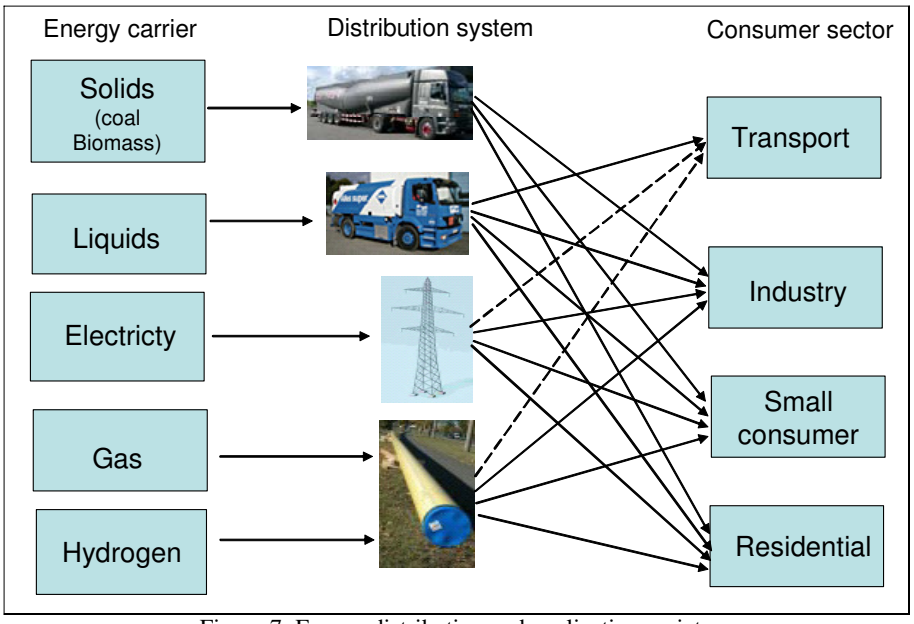

Figure 7: Energy distribution and application variety

Other secondary energy carriers such as heating oil, gasoline or diesel can be handled more easily and stored without problems; they do not need a grid connected distribution system. The distribution is based on a fleet of tanker trucks, which can be operated around-the-clock to supply the consumers. In Germany circa 9,000 trucks distribute the ~ 50 Mio t diesels and gasoline as well as the ~ 20 Mio t heating oil, which are consumed per year in the sectors transportation, household and small consumer. The trucks have a high transportation (=supply) velocity and a high variability into the area so that consumers can be supplied, which have no connection to a gas or even electricity grid. In earlier times, also railway tank-wagons were used, but as it takes too long to reach a consumer, their use is rare today.

The discontinuous distribution system requires storage at the consumer side to enable the operation of machineries, heating vessels or others for a certain time. The properties of heating oil or even gasoline and diesel make it easy and uncomplicated.

The supply of the transportation sector has a special position. The distribution chain ends at filling stations, where the consumers have to reload the fuel tanks of their vehicles, trucks or passenger cars. In Germany 15,000 filling stations, distributed over the whole federal territory, form the area-wide infrastructure.

The existing distribution infrastructures and systems for the secondary energy carriers were developed over a long time and they were optimised with regard to the fuels and the

applications respectively devices. The successful introduction and integration of a new fuel into a high developed energy economy takes place without problems, if the existing infrastructure and logistic can be used without the necessity of costly retrofitting or upgrading measurements. As example can be seen the substitution of leaded by unleaded gasoline or the introduction of bio-diesel.

Though the properties of hydrogen differ obviously from those of gas, diesel or gasoline, the transportation and storage systems are very similar: Pipelines are used as well as road trailers. The safety requirements for the hydrogen systems are very high and find their expression in the materials and construction for pipelines, seals and tanks. There exist many national and international (European) guidelines and directives for production, storage, transportation and use.

The handling is state of the art, which is proven by the operation of around 22 hydrogen pipelines worldwide with a total length of 2,300 km [18]. For the mobile transportation of liquefied hydrogen, cryogenic-tank trailers are used, while gaseous compressed hydrogen is delivered with tube or cylinder package trailers. The different components are shown with figure 8, a hydrogen product pipeline, a scheme of the H_2-pipeline in the Rotterdam area and trailer tank types.

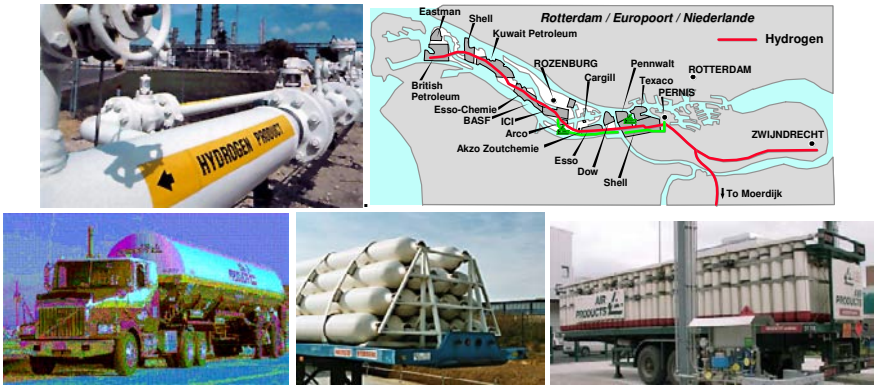

Figure 8: Pipeline, LH_2-trailer, tube and cylinder packages trailer for CGH_2 [19, 20, 21]

But the currently operated H_2-pipeline grids are not designed to supply the energy demand of a large number of consumers like thousands of households, neither with regard to the possible capacity (flow-rate) nor with regard to the required distribution density. Therefore it is a question, whether the existing gas pipeline systems can be used for the hydrogen supply. The high costs of around 700,000 USD/km [22] for a new pipeline are motivation to analyse that challenge. Prerequisite for such a plan is

- the qualification of the pipeline material, its condition with regard to the special hydrogen properties as any metallic component may be susceptible to hydrogen effects,
- the status of the welds, valves and flanges, if they can hold hydrogen,
- the qualification of the fittings and other aspects which have to be regarded by a risk analysis,
- the availability of suitable compressors.

These requirements describe the main areas of the research. It is the question of the condition and the applicability of the material if existing pipeline systems can be used/retrofitted at low cost or not. If they cannot be converted to hydrogen, the research activities have to concentrate on the development of highly qualified but cheap material and embedding technologies to reduce to cost for new pipelines.

IV Stationary and mobile application of hydrogen

If one speaks today of the energy carrier hydrogen, then one thinks of the fuel cell technology too. Except for the methanol direct fuel cell, all fuel cells need hydrogen though the high temperature fuel cells – solid oxide fuel cell (SOFC) and molten carbonate fuel cell (MCFC) – can be fuelled with natural gas which has to be reformed to hydrogen and carbon monoxide. Hydrogen can be oxidised electrochemically and reactions start at the boundary layer of the electrode. Natural gas does not react electrochemically.

For the existing situation, fuelling the fuel cells with natural gas, the electrical efficiency$_{net}$ is calculated to ~30% for the polymer electrolyte fuel cell (PEFC) including pre-reforming, to ~45% for the MCFC and to ~50% for the SOFC. The researchers, who are engaged in developing and optimising fuel cells, calculate that the efficiency of the PEFC would be raised obviously (to ~50%) if it were fuelled with pure hydrogen, as the effort for the reforming would be cancelled and as the whole PEFC system would have more favourable reaction kinetics.

Though a couple of fuel cell systems have operated over thousands of hours, the development has not yet reached the expectations. The degradation of the electrode units is too high, the life time too short. Systems have problems with the size, the volume and the weight. The used material for the cell and the auxiliary components such as heat exchangers are very costly, as is the manufacturing too, so that the economy compared to other technologies is not yet achieved. Actually it is spoken of costs of ~ 14,000 EUR/kW for the PEFC, 8,000 EUR/kW for the MCFC and of ~20,000 EUR/kW for the tubular SOFC. Nearly 60% of the costs are caused by the balance of plants, so that many activities aim at new materials for and at simplification of the auxiliary components. Those aspects are barriers for the broad successful introduction of fuel cells up to now.

It was already mentioned that the storage of hydrogen is an important point. It is a key function for the transportation sector or, better said, for the application in vehicles. Hydrogen can be used in modified internal combustion engines, as demonstrated by the car manufacturer BMW with the hydrogen concept car H2R and the dual-mode version of the current 7-Series (hydrogen and gasoline). Other car manufacturers use hydrogen with a fuel cell which delivers power for an electric propulsion of the vehicle.
Apart from the technical challenge of the realisation the fuel cell/electric propulsion, the hydrogen storage is a further serious task. Hydrogen has a low density (0.0899 kg/Nm^3) and the energy content of 1 Nm^3 hydrogen corresponds to 0.34 l gasoline or diesel. Today the vehicles have only limited space for the fuel tank system so that the tank volume is as small as possible, whereas conventional driving ranges must be achieved. In the case of long-distance trucks ~3,000 km and more are demanded, which can be met with ~1,000 litre diesel as the modern long distance trucks have a specific consumption of ~30 litres/100 km. The minimum

range for passenger cars is seen at 500 - 600 km, so that the tank volume has to be of ~50 - 70 litres, whereas the more frugal cars come along with a smaller tank volume, which reduces the weight of the vehicle too.

Today's state-of-the-art for hydrogen storage includes 3,000 psi (~200 bar) compressed gas tanks and cryogenic liquid hydrogen tanks for on-board hydrogen storage. The current status in terms of weight, volume and cost of various hydrogen storage technologies is shown with the upper part of the two schemes of figure 9 [9].

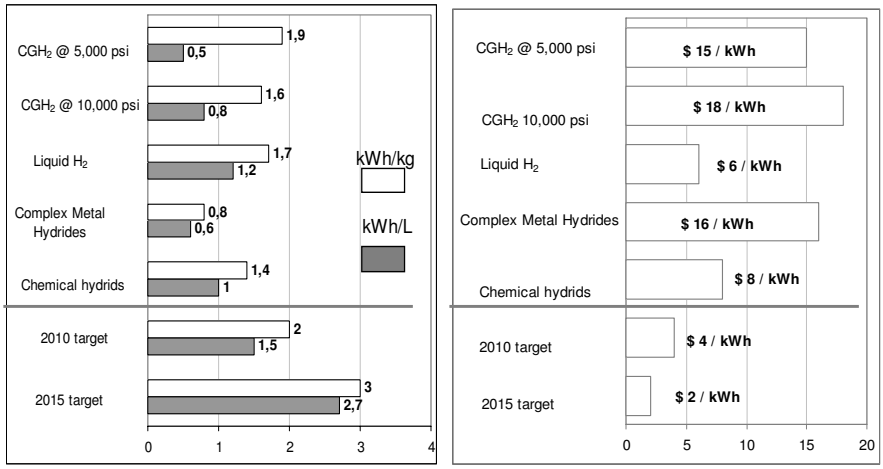

Figure 9, left: volumetric & gravimetric energy capacity; right: system cost [19]

The DOE, the U.S. Council for Automotive Research (USCAR) and the energy companies established those values as targets for on board storage systems, which can be seen at the lower parts in figure 9 [19]. And none of the today's hydrogen storage systems meets the combined gravimetric, volumetric and system cost targets.

Research into new materials of construction such as metal ceramic composites, improved resins, and engineered fibers is needed to meet cost targets without compromising performance. Materials to fulfil performance and cost requirements for hydrogen delivery and off-board storage are also needed.

V Summary

With regard to the today's use of hydrogen in the chemical or petroleum industry it can be said, that a hydrogen economy already exists. But it is a closed society that is using it and they use it normally not as energy carrier.

The main difference between the industrial and an energetic use is the fact that at the one side people handle that product who have long experience with it, while at the other side people must handle it who are neither trained nor educated. So it will be necessary to reach a high level of safety for all forms of applications.

It can be expected that natural gas or/and coal will not suffice to make available the amount of hydrogen that is necessary to deliver an essential contribution to the energy supply. It will be inescapable to activate all available feedstocks, including renewable and electrolysis. The realisation depends on the technological advance, if it will be possible to develop efficient and cheap processes.

The economical use of hydrogen as energy carrier, compared to petroleum products or natural gas is not yet achieved. With respect to the vision of a common hydrogen economy, it is a strong challenge to the research and developing activities, to meet the targets with regard to distribution and application systems. The targets for all components of the hydrogen are: high safety, high reliability, high efficiency, low cost, easy handling and consistency with the principles of a sustainable development.

VI References

[1] Eurostat, 2006
[2] European Environment Agency; EU greenhouse gas emissions increase for second year in row; Press release – Copenhagen, 22nd June, 2006
[3] European Environment Agency, Annual European Community greenhouse gas inventory 1990–2004 and inventory report 2006, EEA Technical report No 6/2006, final version
[4] W. Fischer, R. Eich, J.-F. Hake: Die ökologische Weltlage und die Gefährdung des Klimas, Naturschutzblätter, Vol. 1/2006 (Teil 1) und Vol. 2/2006 (Teil 2)
[5] J.-F. Hake; J. Linßen; M. Walbeck: Perspectives of Hydrogen in the German Energy System; Energy Policy, Volume 34, Issue 11, Pages 1271-1283
[6] Hake, J.-Fr. und R. Eich: Anforderungen an eine in die Zukunft gerichtete Energieforschung. In: et – Energiewirtschaftliche Tagesfragen. Zeitschrift für Energiewirtschaft, Recht, Technik und Umwelt. Januar/Februar 2005. Heft 1/2, Seite 8-12.
[7] Eich, R.; Hake, J.-Fr.: Sustainable Development and Energy – Presenting Connections between these two Concepts. In: Hake, J.-Fr.; Kuckshinrichs, W.; Eich, R. (Ed.): Energy Systems Analysis for Political Decision-Making. Schriften des Forschungszentrums Jülich, Reihe Energietechnik/Energy Technology, Band/Volume 32. Jülich 2004.
[8] Martinsen, D.; Müller, M.; Wagner, H.-J.; Walbeck, M.; Jülich; Belyaev, L.S.; Kaganovich, B.M.; Krutov, A.N.; Filipov, S.P.; Irkutsk: Wege zu einer umweltfreundlichern Energieversorgung – zwei methodische Lösungsansätze, BWK Bd. 39 (1987) Nr. 3, S. 80-85
[9] Walbeck, M.; Wagner, H.-J.; Martinsen, D.; Bundschuh, V.: Energie und Umwelt als Optimierungsaufgabe – Das MARNES-Modell, Springer Verlag, ISBN 3-540-18489-9, 1988
[10] Kazimi, M.S.: Energy in the year 2030 and Implications for the Arab World, MIT; June 23, 2004
[11] Energy Economics Group, TU Wien, National Project, Wasserstoff aus erneuerbarer Energie in Österreich - Ein Energieträger der Zukunft?
[12] Birnbaum, U.; Martinsen, D.; Walbeck, M.: Wasserstoff aus fossilen Energietraegern; Studie A.5.2.b (2), in Band 6 Energiespeicherung und Energiesysteme, in Energie und Klima, Studie der Enquete Kommission "Vorsorge zum Schutz der Erdathmosphaere"

[13] Birnbaum, K. U.: “Offshore Hydrogen Electrolysis - Fuel Production for Fuel Cells?” Presentation, IEA Advanced Fuel Cells ANNEX XIX Stationary Fuel Cells, Meeting 3, ECN, Petten , The Netherlands, April 4-5, 2005
[14] Linde Gas Division: The cleanest energy carrier ever; Hydrogen Solutions from Linde Gas
[15] Aicher, T; Fraunhofer ISE, Hydrogen Technology, personal information 2006
[16] Well-to-Wheels Analysis of Future Automotive Fuels and Powertrains in the European Report Version, May 2006, Joint Research Centre, European Commission
[17] Norsk Hydro; Bulk Supplies - Athmospheric Electrolysers; Norsk Hydro Electrolysers AS, 2004
[18] Vinjamuri, G. K.; Development of US-DOT Regulations for Hydrogen Transportation Systems, US Department of Transportation, Hydrogen portal; International Pipeline Conference and Exposition Calgary, Alberta Canada, October 5, 2004
[19] DOE, Energy Efficiency and Renewable Energy, http://www1.eere.energy.gov/hydrogenandfuelcells/
[20] AirLiquide, personal information 2006
[21] PLANET GbR, 2003, in CUTE Brochure “Hydrogen Supply Infrastructure and Fuel Cell Bus Technology”, Evo Bus GmbH, Ulm, 2004, http://www.fuel-cell-bus-club.com
[22] Campbell, J.; Conversion of Existing Hydrocarbon Pipelines for Hydrogen Service**,** Pipeline Construction, Air Liquide Process & Construction, Houston, Texas; Challenges of Hydrogen Pipeline Transmission, Pipeline Systems Division, ASME, international Pipeline Conference, Calgary, Alberta Canada, October 5, 2004

ADVANCED POWER PLANT DEVELOPMENTS AND MATERIAL EXPERIENCES IN JAPAN

Fujimitsu Masuyama

Graduate School of Engineering
Kyushu Institute of Technology
1-1, Sensui-cho, Tobata, Kitakyushu 804-8550,
Japan

Abstract

In order to reduce CO_2 emissions for environmental protection and to conserve energy, improved efficiency has been sought in power plant design through higher temperature and pressure. About twenty modern ultra super critical coal-fired power plants are already in service in Japan that were commissioned from 1995 to date employing newly developed high strength ferritic steels and austenitic steels, and recently studies on the advanced 700℃ class power plants has been started. However during the last decade many material-related issues have arisen due to increased temperature and uncertainty in terms of the properties of fabricated metal of new alloys for high temperature components. The maximum use temperature have been greatly elevated through the achievement thus far of high strength ferritic and austenitic steels, but the stability of their properties in the vicinity of their temperature limits must be ascertained, and new materials must be developed with an appropriate balance between strength and cost for practical application in 700℃ class plants.

***Keywords*:** Power plant, heat resistant alloy, creep failure, thermal fatigue, steam oxidation

Introduction

Higher temperature and pressure steam conditions for fossil-fired power plants are essential in the quest for reductions in CO_2 as well as conservation of resources and energy[1)]. To achieve this, Japan began to aggressively develop heat-resistant steels for thermal power plants from the 1970s, resulting in ferritic and austenitic steels that could be used at higher temperatures. Currently, ferritic steels are used for high-temperature components in boilers and turbines, with 600°C class plants realized from 1995 onward[2)], and all newly designed plants feature steam temperatures of over 600°C. Even higher temperatures are now being considered so as to achieve a jump in thermal efficiency for coal-fired plants, which face a disadvantage in terms of CO_2 reduction, and there is an increasing need for research and development work on high-temperature materials, and studies on the integrity assessment of components made of these newly developed materials used under higher temperature and pressures for long period of operation. Higher strength and greater corrosion resistance is also required in order to address the various materials-related issues associated with higher temperature and pressure steam conditions surpassing those found in the latest 600°C class USC (ultra super critical) plants. The following paper describes higher temperature trends in Japanese coal-fired power plants and materials-related issues accompanying higher temperatures, in addition to noting materials development progress to date, the current state of development for 700°C class boiler materials, and future directions.

Trends in Power Plant Development

Let us review Japan's recent history of power supply. Looking at trends in the capacity of power generating facilities, thermal power overtook hydro in 1963, followed by substantial progress in larger capacity facilities and higher efficiency, with a shift from coal to cheaper oil for fuel. However, the oil crisis of 1973 sparked active pursuit of energy sources to subsitute for oil, and diversified fuel sources came to include nuclear, coal, and LNG. At present, the composition of electrical generating capacity is 20% nuclear, 26% LNG, 15% coal, 20% oil, and 19% hydro. Nevertheless, as indicated in Fig. 1[3], the composition of electrical power generation is 26% nuclear, 28% LNG, 24% coal, 12% oil, and 9% hydro, such that coal-fired generation occupies a very strong position in terms of the ratio of electricity generated to facilities capacity. This is related to the fact that all coal-fired power plants constructed since 1993 have featured ultra high temperature and pressure, and these plants now account for roughly half of all coal-fired output. Table 1 presents the steam conditions and materials utilized for plants built in Japan from 1995 to 2004. The steam temperatures currently adopted are to a maximum of 613°C, and the materials used to achieve these temperatures consist universally of high-stength, heat-resistant steels developed over the last two decades.

Coal-fired generation systems currently under development include ultra super critical pressure steam turbines (USC), pressurized fluidized-bed combustion boilers (PFBC), and integrated gasification combined cycle generation (IGCC), and these face competition from LNG-powered gas turbine combined cycle generation (GTCC) and solid oxide fuel cells (SOFC) in terms of efficiency and construction costs. Comparison between USC and IGCC is attracting considerable attention, and steam temperatures elevated to over 700°C would potentially deliver USC efficiency of approximately 48%, thus becoming the stronger candidate.

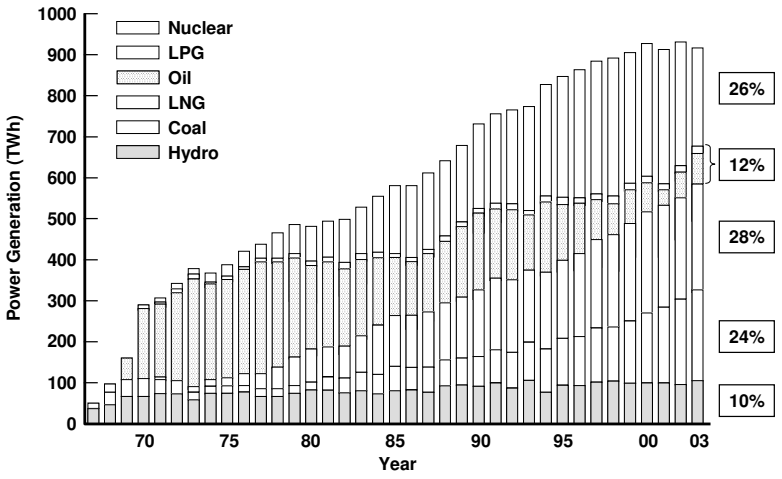

Fig. 1 Power generation and construction in Japan

Table 1 Recent coal-fired USC power plants in Japan

Power Station		Capacity	Steam Parameter		Fuel	Comm.	Eff. (%)	Boiler / Steam Line Material	Turbine Material
			Press. (MPa)	Temp. SH/RH (℃)					
Reihoku 1	Kyushu	700	24.1	566/566	PC	1995	42.1	TP347H/P91	TOS107
Haramachi 1	Tohoku	1000	24.1	566/593	PC	1997	41.0	TP347H, HR3C/P91	TOS110
Matsuura 2	EPDC	1000	24.1	593/593	PC	1997	41.7	Super304H/P91	TMK1
Misumi 1	Chugoku	1000	24.5	600/600	PC	1998	43.0	Super304H, HR3C/P91	TMK2, TMK1
Nanao-Ohta 2	Hokuriku	700	24.1	593/593	PC	1998	41.5	TP347H/P91	TOS107
Haramachi 2	Tohoku	1000	24.5	600/600	PC	1998	43.0	Super304H/P91	HR1100
Tachibanawan	Shikoku	700	24.1	566/593	PC	2000	42.7	Super304H/P91	TOS107
Tachibanawan 1	EPDC	1050	25.0	600/610	PC	2000	42.1	Super304H/P91	TOS107
Tsuruga 2	Hokuriku	700	24.1	566/593	PC	2000	43.7	Super304H, HR3C/P122	TOS110
Tachibanawan 2	EPDC	1050	25.0	600/610	PC	2000	42.1	Super304H/P122, P92	TMK2, TMK1
Hekinan 4	Chubu	1000	24.1	566/593	PC	2001	42.2	Super304H/P91	TOS107
Tomato-Atsuma 4	Hokkaido	700	25.0	600/600	PC	2002	44.2	Super304H/P122, P91	HR1100
Hekinan 5	Chubu	1000	24.1	566/593	PC	2002	42.2	Super304H/P91	TOS107
Isogo New 1	EPDC	600	28.0	605/613	PC	2002	42.0	Super304H/P122, P91	COST501E
Reihoku 2	Kyushu	700	24.1	593/593	PC	2003		Super304H, HR3C/P122	TOS107
Hitachi-Naka	Tokyo	1000	24.5	600/600	PC	2003	43.1	Super304H/P122	HR1100
Maizuru 1	Kansai	900	24.5	595/595	PC	2004		Super304H/P122	TMK1
Hirono 5	Tokyo	600	24.5	600/600	PC	2004	43.0	Super304H, HR3C/P122	TMK1

PC :Pulverized Coal. SH/RH :Superheater/Reheater

Fig. 2 shows the past, present, and future utilization ranges for ferritic steels, austenitic steels, and Ni-base alloys, plotted in a diagram indicating steam temperature and pressure for USC developed in the 1950s and USC as currently operated or under development. Both the European Thermie and US DOE projects aimed at 700°C conditions show clearly that Ni-base alloys would have to be utilized even with future progress in materials development. The economic viability of such plants requires consideration, but maximum generating efficiency (HHV) of 48% is anticipated.

USC development has thus far been undertaken in the Europe, US, and Japan. In the case of Japan, as shown in Fig. 3, project-based research was conducted from 1981 to 1993, culminating in steam temperatures of 593°C for ferritic steel and 649°C for austenitic steel. A subsequent project was launched in 1994 for the realization of a 30Mpa, 630°C /630°C class plant using ferritic steel, and this was successfully concluded in 2001. At the R&D level, then, a 630°C class plant using ferritic steel is considered possible. However, the reliability of ferritic steel, including weldments and fabricated components must be carefully considered, and the highest temperature yet achieved in an actual plant remains at approx. 610°C. While materials R&D work aimed at realizing 650°C with ferritic steel has been undertaken, the temperature limit in terms of actual utilization has yet to be determined. R&D work in Japan on 700°C class USC plants is at the feasibility level, and full-scale research has not been attempted. In 2005, however, a group of Japanese experts came together to prepare for a new project. Research is also being pursued on 700°C high-temperature materials, and it is expected that affordable heat-resistant steels and Ni-base alloys will be developed for use at 700°C and above.

Although Ni-base alloys would be utilized for the highest temperature components of 700°C class thermal power plants, there have been relatively few examples in Japan of Ni-base alloy development for steam turbine power plants to date, and data on material

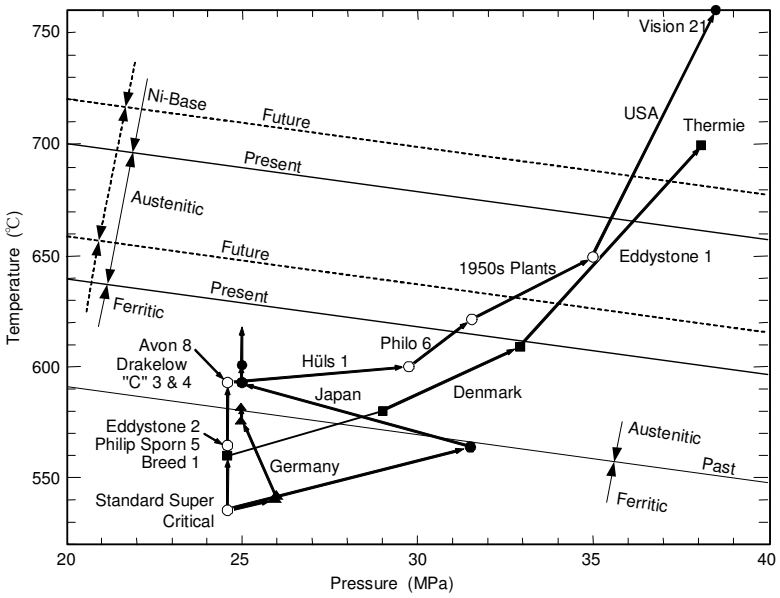

Fig. 2 Steam parameter plots for USC power plants

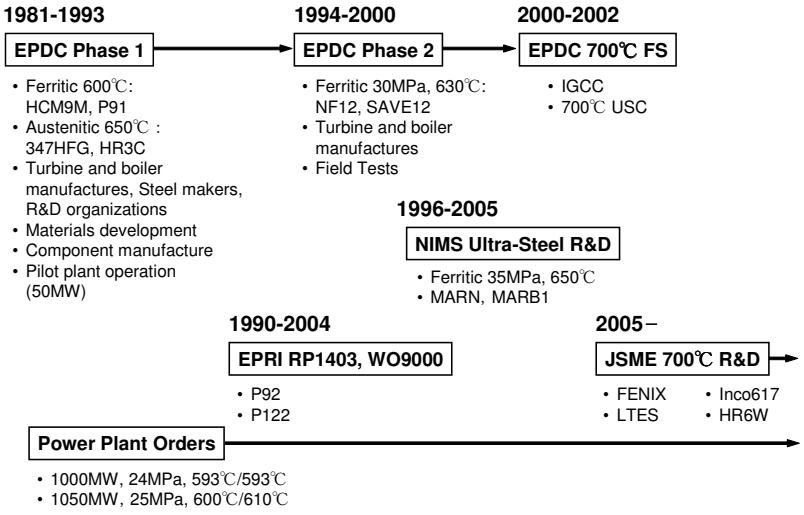

Fig. 3 R&D project on USC power plants in Japan

properties are insufficient. Furthermore, little progress is being made on standardization, which would be required for boiler materials. If Ni-base alloys were to be used for large-diameter, thick-walled components, problems would arise with currently available materials in terms of welding and fabricability, and improvements would be required. On

the other hand, ferritic and austenitic candidate steels have been developed in Japan that would be suitable for the mid-temperature range in 700°C class facilities, although consideration is certainly needed with respect to further elevation of the utilization limit temperature and the stability of strength in the vicinity of that limit. In particular, accurate prediction is required for long-term creep strength in the range of 600~650°C for ferritic steels, and for long-term structural change and precipitation behavior in the range of 650~700°C for austenitic steels.

Material Experience with Increasing Steam Temperature

If ferritic steels are to be used at temperatures of about 600°C and greater, and if austenitic steels are to be used at temperatures higher than presently, important materials-related issues will include the degradation of weldments and fabricated parts in comparison to base metal properties, as well as the impact on plant reliability due to thermal fatigue, high-temperature corrosion, and steam oxidation.

Degradation in fabricated metal

Degradation in creep strength as a result of cold working is well known in austenitic steels, and ASME Sec.I PG-19 provides standardized countermeasures[4]. This problem continues to affect even recently developed creep-strength enhanced (high-strength) ferritic steels.

Another issue is that the creep strength of the fine-grained heat affected zone (HAZ) of high-strength ferritic steel weldments tends to degrade increasingly severely as the temperature increases, meaning that weldment strength reduction factors setting and system stress evaluation are important factors. Fig. 4 presents the results of 655°C internal pressure (65MPa hoop stress) creep rupture testing performed on a header made of high-strength ferritic P122 (11Cr-0.4Mo-2W-Cu-V-Nb) steel, exhibiting Type IV failure at the HAZ after

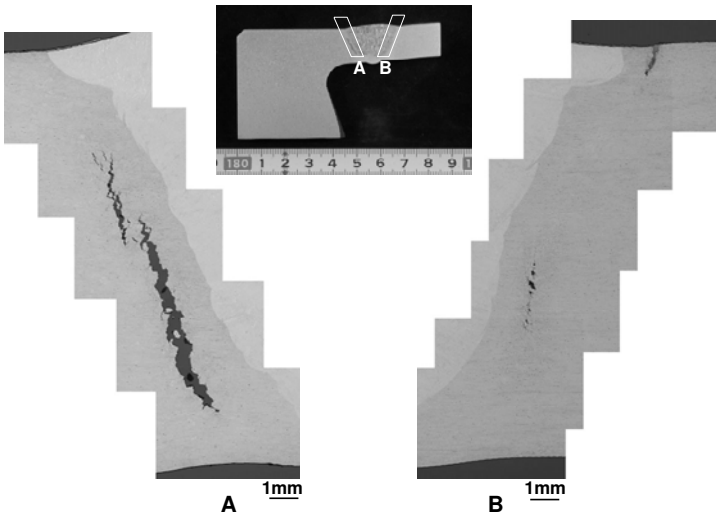

Fig. 4 Type IV failure in P122 pressure vessel test

approximately 8000h. This type of rupture has been experienced recently in 600°C class USC power plants in Japan, suggesting the need to reconsider allowable stresses and extrapolation methods for determining the long-term strength of high-strength ferritic steels[5]. Fig. 5 shows a comparison among three grades of high-strength ferritic steels in terms of the creep rupture strength of base metal and welded joints. Although the Larson-Miller parameter dependency of stress-to-rupture differs among the three grades, the strength of the welded joint (ruptured at the HAZ) compared to that of the base metal is consistently low. The 10^5h extrapolated strength is about 20% lower than for the parent metal, and the rate of decline increases with higher temperature. Accordingly, it is necessary to set creep strength reduction factors appropriately for welded joints of high-strength ferritic steel.

Thermal fatigue

Thermal fatigue is an inescapable problem in the case of austenitic steels, and the development of materials having a small thermal expansion coefficient is required if plant operation with few startups and shutdowns cannot be specified. Fig. 6[6] shows an example of thermal fatigue cracking in a control valve made of TP316 (17Cr-12Ni-2.5Mo) austenitic steel and used for about 20000h at 650°C in Eddystone power station No. 1 unit. Ni-base alloys have smaller thermal expansion coefficients than austenitic steels, serving to reduce stress from that source, but thermal conductivity is low (as is the case with austenitic steels) making for a large thermal gradient and therefore the potential for substantial thermal stress.

Hot corrosion and steam oxidation

High-temperature (hot) corrosion is not a particularly major issue when coal with low sulfur content is used, but corrosion-induced thinning occurs more easily at high temperatures in the superheater and reheater tubes in the boiler furnace. However, material corrosion resistance generally depends heavily on the amount of Cr content, with substantial improvement seen when the amount is over 20%. High-Cr austenitic steels and Ni-base alloys are therefore often used in these applications. Notwithstanding, the Ni element itself contained in Ni-based alloys reacts with the S in molten ash, and caution is required with respect to sulfide corrosion. The corrosiveness of combustion ash and gas in coal-fired boilers is determined

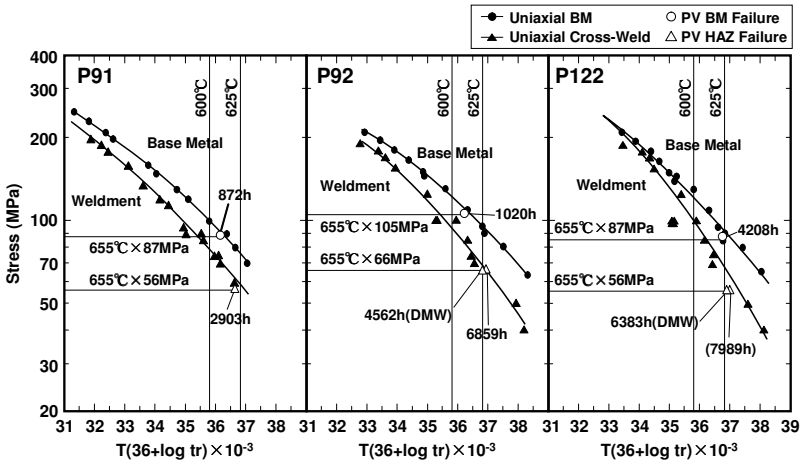

Fig. 5 Creep rupture strength of base metal and welds for P91, P92, and P122

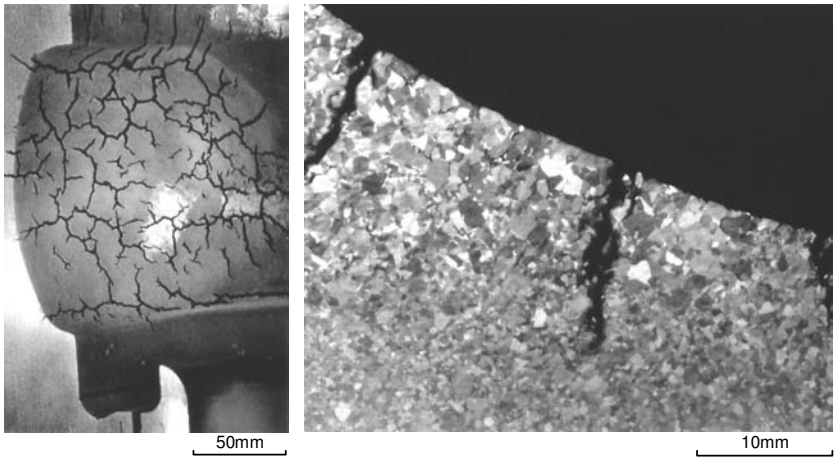

Fig.6 Thermal fatigue cracks on the inside surface of Type 316 stainless steel control valve used at 650°C

by the presence of N_2SO_4 and K_2SO_4 in the ash and the concentration of SO_2 in the gas. Accordingly, particular attention must be paid to the type of coal used for fuel and the amount of S contained.

The problem of steam oxidation becomes increasingly serious as the temperature increases, and the only countermeasure currently available for ferritic steels is the selection of a material with high Cr content. For austenitic steels, shot-blasted, fine-grained, and high-Cr materials can be selected, although the effective temperature limits have not yet been clarified for the respective options available. However, the limit for recently developed 9-12% Cr high-strength ferritic steels is considered to be over 600°C, and this type of material has become widely used in 600°C class USC plants, although it has also been reported that oxidation behavior differs from that of conventional ferritic steels[7]. For example, Mod.9Cr-1Mo (9Cr-1Mo-V-Nb) steel (T91) is a ferritic steel, but differs from conventional ferritic steels in that exfoliation often occurs from the interface between the scale inner and outer layers (as with austenitic steels) rather than from the interface between the scale and the metal. Fig. 7[7] indicates the state of exfoliation of oxidation scale on the inner surface of T91 reheater tube. Cracks occur in the scale in the circumferential direction at intervals of about 30 mm, with the scale outer layer separating from the tube surface. However, the scale does not detach easily, and can become a cause of heat transfer insulation and overheating, leading to creep rupture. This type of phenomenon may also occur in other high-strength ferritic steels, and further research is required. Problems induced by steam oxidation scale, as have been known for some time, are essentially 1) tube blockage due to exfoliated scale, leading to overheating and creep rupture, and 2) erosion of turbine parts due to dispersion of exfoliated scale. Both of these occur more frequently in conjunction with higher temperature.

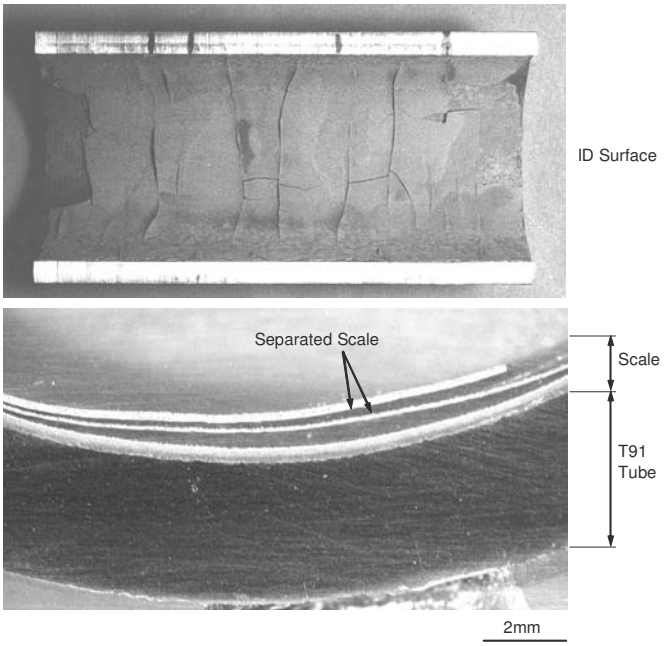

Fig. 7 Typical appearances of inner surface of damaged T91 tube

Alloy Development for Advanced Power Plants

Steam turbines

The steam temperatures of fossil-fired power plants in Japan have conventionally been elevated in 50°F intervals, to 538°C (1000°F), 566°C (1050°F), 593°C (1100°F), 623°C (1150°F), and 649°C (1200°F), but in modern plants with operations based on load changing, the maximum temperature is approximately 600°C. In demonstration tests, steam temperatures of 623°C and 649°C have been realized for ferritic steels and austenitic steels respectively. Now, however, research is being considered that would propel steam temperatures in a leap past 650°C to arrive at 700°C. 1CrMoV steel or conventional 12Cr steel can be used through 566°C for turbine rotors, the most important components of steam turbines, but the limits for these materials are considered to be 570°C and 590°C respectively. 12Cr steel for which 1.5% W is added in substitution for the equivalent amount of Mo can be used through approximately 610°C, but higher temperatures require 12Cr steel with the addition of W and Co. While the limit has not been clearly defined, safety considerations suggest a temperature of around 630°C. The appearance of ferritic steels that can withstand 650°C is awaited, but advanced materials development is needed since rotors require not only high-temperature strength, but also good tensile strength and toughness. Austenitic superalloys such as Discaloy (Fe-13Cr-25Ni-3Mo-Al-Ti) and A286 (Fe-15Cr-26Ni-1.5Mo-Al-Ti) have demonstrated performance at the 650°C level, but temperatures over

700°C would require Ni-base alloys such as Inco617 (Ni-22Cr-13Co-9Mo-Al-Ti) or Waspaloy (Ni-19Cr-14Co-4.5Mo-Al-Ti), or Fe-Ni base alloys with improved creep strength. From the standpoint of practical application, fabricability would need to be improved to enable the manufacture of large components. Fig. 8 presents the relationship between 10^5h creep rupture strength and temperature for various materials, based on the results of research to date. In Japan, along with consideration of Inco617, efforts are also being made to improve Inco706 (Ni-16Cr-36Fe-3Nb-Al-Ti) and to develop alloys modifying the low thermal expansion Inver-type Ni alloy. Of these, LTES700 (Ni-12Cr-18Mo-Al-Ti)[8] is an austenitic alloy featuring a low thermal expansion coefficient similar to ferritic steels, and having creep strength equivalent to that of Refractaloy26 (Fe-18Cr-38Ni-20Co-3Mo-Al-Ti). Utilization is anticipated for turbine rotors and various other turbine components.

Boiler tube and pipe work

Figs. 9 and 10 show the latest development progress diagrams for ferritic and austenitic steels used for power boiler tubing and main steam piping respectively, while Fig. 11[9] presents a comparison of allowable stresses for various materials. If materials developed thus far were utilized, ferritic steels could be used to approximately 630°C, austenitic steels to approximately 700°C, and Ni-base alloys for higher temperatures. With the substantial gains in strength delivered by 9-12%Cr steels, the conventional 538°C limit on steam temperature has been elevated to 600°C at present. Research aimed at development of ferritic steels for use at 650°C is being actively pursued, but, given the requirements of toughness, fabricability, and weldability for the thick-walled, large-diameter critical boiler components such as main steam piping and headers, a 9-12%Cr tempered martensite structure would likely be adopted. There are a number of points to be clarified with respect to the stability of the strength and structure of such materials in the temperature range over 600°C, and the limit for ferritic steels has yet to be determined. TP316 steel has been used for 650°C class plants in the past, but various newly developed high-strength austenitic steels can also be applied within this class.

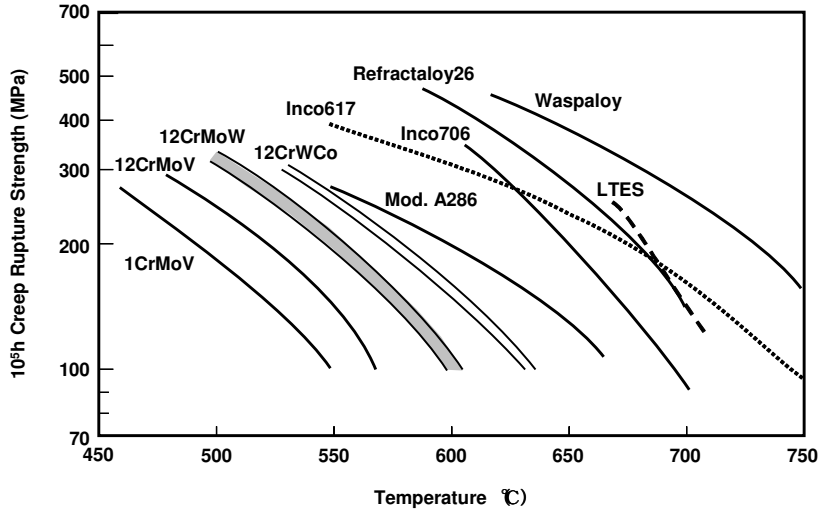

Fig. 8 Comparison of 10^5h creep rupture strength turbine of rotor alloys

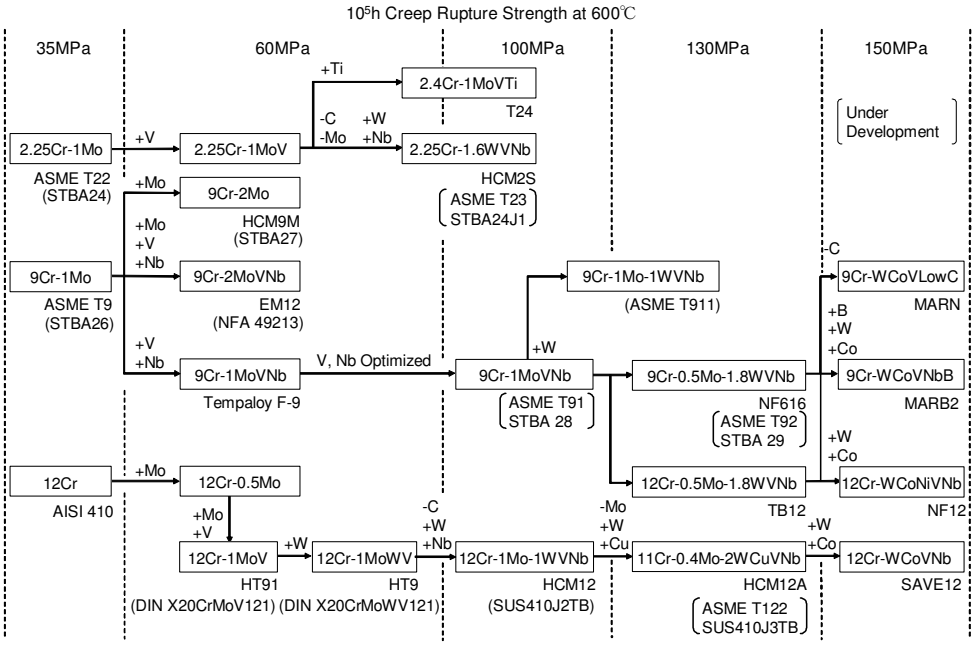

Fig. 9 Development progress of ferritic steels for boiler

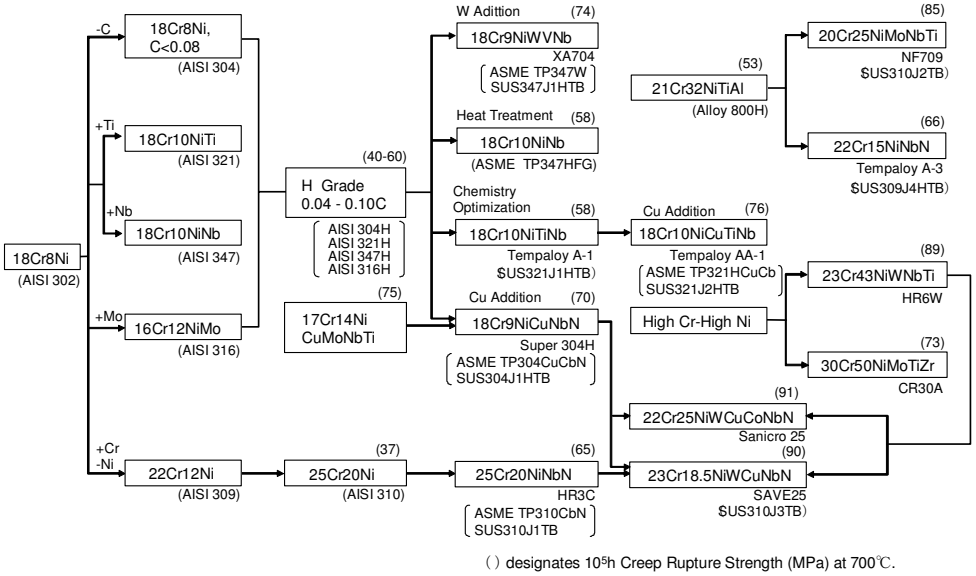

Fig. 10 Development progress of austenitic steels for boiler

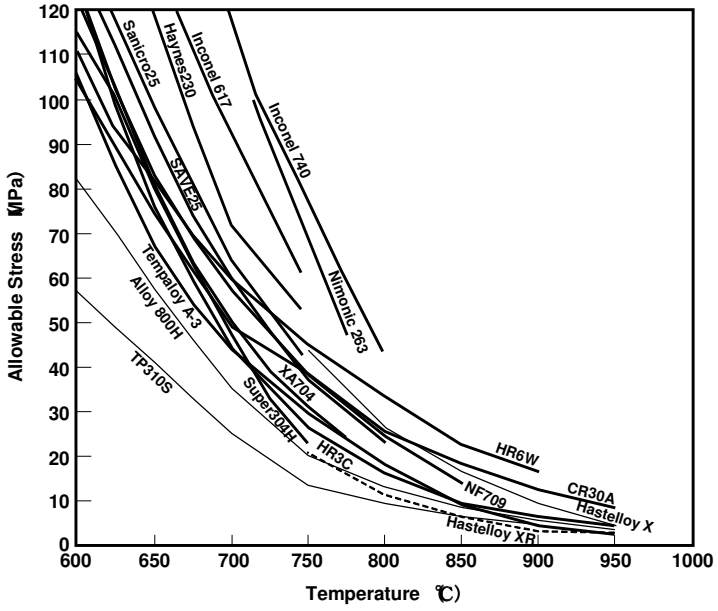

Fig. 11 Comparison of maximum allowable stresses for boiler alloys

Currently, the greatest 700°C, 10^5h creep rupture strengths available are 70MPa for 18%Cr materials and 90MPa for 25%Cr materials. As 100MPa is thought to be required for high-temperature, high-pressure plants, the limits for application of 18%Cr and 25%Cr steels in 35MPa plants would be approximately 660°C and 680°C respectively. Ni-base alloys could be used as is or improved, but data is insufficient for most of these, and 10^5h creep rupture strength cannot be accurately predicted. Table 2 lists the austenitic steels and Ni-base alloys that can be used at temperatures over 620°C.

700°C class plant design is possible using Ni-base alloys, but prices for these materials ranging from several times to an order of magnitude higher than those for austenitic steels would necessarily impact on the economic viability of such a plant. As indicated in Fig. 12, the logarithmic cost ratios for various boiler materials increase with temperature limit (strength). The limit for austenitic steels is approximately 700°C (in a 24MPa plant). On the other hand, while Ni-base alloys can be applied at temperatures in excess of 700°C, the cost rises quite steeply. As a result, and as shown by the figure, no currently available material occupies the region of balance between cost and strength (named as the "alloy lack triangle")[9]. In the future, continued search and development is needed for Ni-base alloys that can be applied at temperatures over 700°C, cost around the same as austenitic steels, and have superior fabricability, or alternatively for austenitic steels that can be used at over 700°C.

Summary

Past development of new high-strength ferritic steels allowed the realization of 600°C class USC plants, but the temperature limits for ferritic materials remain unclear, and it

Table 2　Candidate alloys for USC power boiler

Trade Designation		Nominal Composition	ASME Code /Code Case	Preferred Application	Temp. of Application (metal)
Austenitic Steels (18%Cr)	347HFG	18Cr-10Ni-Nb	2159	T	620℃～660℃
	Super304H	18Cr-8Ni-Cu-Nb-N	2328	T	
	XA704	18Cr-9Ni-W-V-Nb	2475	T	
	Temp. AA-1	18Cr-10Ni-Nb-Ti	2512	T	
Austenitic Steels (20-25%Cr)	HR3C	25Cr-20Ni-Nb-N	2115	T	620℃～680℃
	NF709	20Cr-25Ni-Nb-Ti-N	—	T	
	800HT	21Cr-32Ni-Al-Ti	1325	T	
	SAVE25	23Cr-18Ni-W-Cu-Nb-N	—	T	
	Sanicro25	23Cr-18.5Ni-W-Cu-Nb-N	—	T	
	HR120	25Cr-42Ni-N	—	T	
	HR6W	23Cr-43Ni-6W-Nb-Ti	—	P. T	
Ni-Base Alloys	Haynes230	22Cr-5Co-3Fe-14W-2Mo-La	2063	P. T	680℃～770℃
	Inco617	22Cr-13Co-9Mo-Al-Ti	1956	P. T	
	Inco625	22Cr-5Fe-9Mo-Nb-Al-Ti	1409	P. T	
	Inco740	25Cr-20Co-Mo-Nb-Al-Ti	—	P. T	
	45TM	27Cr-23Fe-2.75Si	2188	P. T	

T :Superheater/Reheater Tubes
P :Pipes and Headers

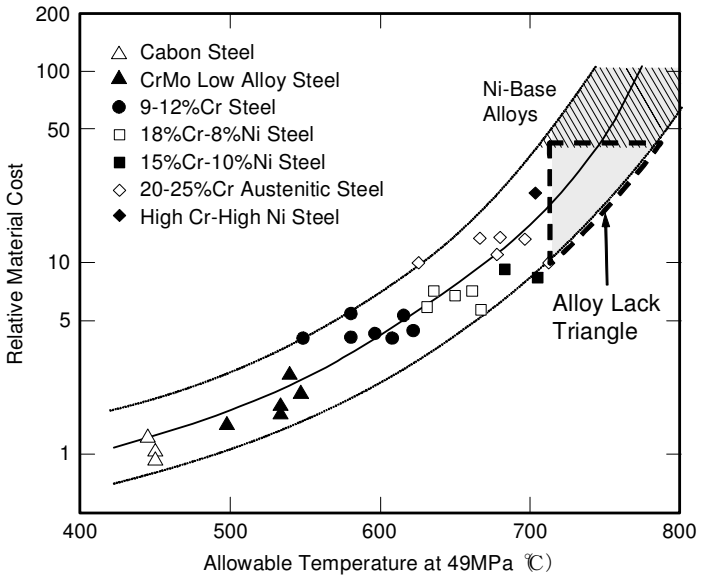

Fig. 13　Relation between allowable metal temperature at the allowable stress of 49MPa and the relative material cost

appears unlikely that these materials will be applicable in plants over 630°C. For 700°C class plants, USC is considered to be economically superior to IGCC, but actual realization depends on practically applicable materials. Higher temperatures are also accompanied by substantial declines in the strength of weldments and fabricated components of newly developed high-strength materials, and countermeasures are needed. Higher temperatures also mean that issues affecting safe operations such as thermal fatigue and steam oxidation take on a new dimension of importance. The maximum use temperatures have been greatly elevated through the achievement thus far of higher strength ferritic and austenitic steels, but the stability of their properties in the vicinity of their temperature limits must be ascertained, and new materials must be developed with an appropriate balance between strength and cost for practical application in 700°C class plants.

References

1) F. Masuyama: J. Lecomte-Beckers, et al. (eds.), Materials for Advanced Power Engineering, Part III, Forshungszentrum Juelich GmbH, Germany, (2002), p.1767
2) F. Masuyama: ISIJ Int., 41, (2001), p.612
3) Ministry of Economy, Trade and Industry of Japan: An Energy White Paper, (2005)
4) The American Society of Mechanical Engineers: ASME Boiler and Pressure Vessel Code, (2004)
5) K. Kimura: I. A.Shibli, et al. (eds.), Creep and Fracture in High Temperature Components –Design and Life Assessment Issues-, (2005), p.1009
6) F. Masuyama, K. Setoguchi, H. Haneda and F. Nanjo: Trans, ASME, J. of Pressure Vessel Tech., 107, (1985), p.260
7) N. Nishimura, H. Komai, Y. Hirayama and F. Masuyama: EPRI/NPL Workshop on Scale Growth and Exfoliation in Steam Plant, London, U.K., Sep.3-5, (2003)
8) R. Yamamoto, Y. Kadoya, S. Ueta, T. Node, R. Magoshi, S. Nishimoto and T. Nakano: R. Viswanathan et al. (eds.), Advances in Material Technology for Fossil Power Plants, (2005), p.623
9) F. Masuyama: R. Viswanathan et al. (eds.), Advances in Material Technology for Fossil Power Plants, (2005), p.35

DEVELOPMENT OF HIGH TEMPERATURE MATERIALS FOR ENERGY MARKET IN CHINA

Zhuangqi HU, Jianting GUO

Institute of Metal Research
Chinese Academy of Sciences
Eamil: zqhu@imr.ac.cn, jtguo@imr.ac.cn

Abstract

The power industry is a forerunning industry for the sustained development of national economy. In the past half century after the establishment of new China, the China power industry already climbed to a very high level. Up to 2002, not only the total installed capacity of electricity, but also the annual overall electricity generation, jump to the second place in the world, next to the United States, Among the energy resources, the coal deposit is the highest, In 2000, the coal consumption occupied 67% of the total energy consumption in China, among which 40% of the energy consumption is used for electricity generation; besides, the installed capacity using coal reaches 67.3% of the total installed capacity. China has abundant hydropower, but its installed consumption only occupies 24.8% of the total. The nuclear power and gas power now are in the initiative stage, occupying 0.7% and 0.3% respectively. In the next one or two decades, China will pay great attention to raise the coal utility and develop highly efficient、clean、supercritical and ultra-supercritical power stations, to build up large scale hydropower stations, natural gas power stations and 1000MW nuclear power stations. After the energy structure gradually by increasing the proportion of hydro, natural gas and nuclear power stations in the energy structure, the future China energy structure is demonstrated in Table 1 [1].

Table 1. Energy structure in 2000~2020 period

	Year		
	2000	2010	2020
installed capacity （MW）	319320	590000	960000
hydropower（%）	24.8	25.8	27.1
coal power（%）	69.3	63.3	58.6
nuclear power（%）	0.7	2.3	7.5
natural gas power（%）	0.3	5.4	4.2
new energy resources（%）	0.1	0.7	0.1
other fuels (%)	4.8	2.5	2.5

Except hydropower, all the developments of coal power, natural gas power and nuclear power needs various high temperature structural materials, such as high quality heat resistant steels and superalloys.

Keywords: High temperature materials, GH2984 superheater alloy, Hot corrosion resistant superalloys, GH690 alloy tube, Gas turbine

1. Coal power

1.1 Progress of coal power in China.

China is the largest country by using coal burning for electricity generation, and coal power is still a major one in the following decades. Recently the average capacity of coal power generators is less than 100 MW, and the capacity of subcritical 300 MW coal power generators only occupies less than 50% of the total coal power capacity with an average coal

consumption of 399 g/kW·h, 25% higher than the advanced record from foreign countries, that makes the resource waste and the exhaust gas exhalation serious. Develop the supercritical and ultra-supercritical power generators is an efficient and economic way to raise the coal utility percentage and lower the environment pollution as shown in Table 2[2]. The higher the vapor temperature, the higher the net efficiency and the lower the coal consumption. The world level reaches 33.5 MPa and 630℃ for the ultra-supercritical coal power generator and the next target will be 40 MPa and 720℃. In the Chinese high tech plan, the proposed targets are 30 MPa vapor pressure, 600°C vapor temperature and 43-45% net efficiency.

Table 2. Net efficiency and coal consumption of various coal power generators [2]

Vapor parameter	Net efficiency (%)	Coal consumption ($g(kW·h)^{-1}$)
Subcritical (17MPa, 538℃)	37-38	330-340
Supercritical (24MPa, 538℃)	40-41	310-320
Ultra-supercritical(30MPa,566℃)	44-45	290-300

Because the vapor pressure and vapor temperature become higher, the requirement of the supreme quality high temperature material is urgent. Particularly, the superheater and reheater in boiler are the parts suffering severely in corrosive medium due to higher pressure and temperature. In this case, the alloys must possess good creep, oxidation resistant and corrosion resistant properties.

For the subcritical set, low alloying ferritic heat-resistant steel is traditionally used, nearly up to the service limit. For supercritical and ultra-supercritical sets, better heat-resistant steels and superalloys should be used. When the vapor temperature is lower than 600-620°C, the ferritic heat-resistant steels, such as T91 or T92 are selected for the superheater and reheater materials. If the vapor temperature reaches 650°C, the ferritic steel is not satisfied due to poor oxidation resistance, and the austenitic stainless steels are preferred, such as TP347HFG, TP310CbN and Super 304H steels. When the vapor temperature exceeds 700°C, it is necessary to use superalloy. In the world advanced ultra-supercritical sets developed in USA and European Community in twenty first century, the vapor parameters are 700°Cand 37.5 MPa, some nickel-base superalloys, for example, Inconel 617, Inconel 690 and Inconel 671 alloys, are selected, but these alloys cannot satisfy simultaneously all the requirements of high temperature strength and hot corrosion resistance for the superheater tube[3]. In 2003 the Special Metals Co, USA, announced a new alloy Inconel 740 [4, 5], developed on the base of Nimonic 263 alloy, that can satisfy all the requirements. Up to now, China cannot produce all the key high temperature materials for the supercritical and ultra-supercritical sets, a new Ni-Fe-base superalloy GH2984 used for the superheater and reheater tube material of ultra-supercritical boiler has been developed [6].

1.2 GH2984 Ni-Fe-base superalloy

The Institute of Metal Research, Chinese Academy of Sciences started to develop GH2984 alloy for superheater tube materials in 1969, which was successfully finished in 1978, that was used for the superheater tube for marine application. After ten-year service, GH2984 tubes were well in shape without any damage which can be continuously used[6] that proves GH2984 alloy is an excellent superheater tube material, which main properties are at the same level as Inconel 740 alloy. Following are the important characteristics of GH2984 alloy.

1.2.1 Chemical composition with high Fe and Co-free

GH2984 alloy contains high Fe content and without Co. Table 3 lists the chemical compositions of GH2984 and related alloys. It can be seen that Inconel 740, Inconel 617 and Nimonic 263 alloys contain 19.8%, 12% and 20% Co respectively, but there is no Co in GH2984 alloy; secondly, GH2984 alloy contains low Ni and Fe as high as 32-34%, but other three alloys contains high Ni and very low Fe. Co and Ni are the strategic metallic materials, so to save them has important strategic significance as well as magnificent economic benefit.

Table 3 Chemical compositions of superalloys used for superheater tube (%) [6]

Alloys	C	Cr	Co	Mo	Nb	Ti	Al	Fe	Si	Mn	Ni
GH2984	0.04/0.08	18-20	–	1.8/2.2	0.9/1.2	0.9/1.2	0.2/0.5	32/34	≤0.5	≤0.5	Bal
lnconel 740	0.06	24.97	19.80	0.58	2.01	1.69	0.87	0.71	0.47	0.30	Bal
lnconel 617	0.09	21.65	12.0	8.72	–	0.31	1.16	≤2.50	0.58	0.54	Bal
Nimonic 263	0.04/0.08	19/21	19/21	5.6/6.1	–	1.9/2.4	≤0.60	≤0.70	≤0.4	≤0.6	Bal
lnconel 625	≤0.10	20/23	≤1.0	8.0/10.0	3.15/4.15	≤0.40	≤0.40	≤5.0	≤0.5	≤0.5	Bal

1.2.2 Better mechanical properties

GH 2984 alloy has promising mechanical properties, particularly the tensile strength from room temperature to high temperature and the stress rupture at 650-750°C. From Table 4 and Fig 1 the room temperature and 700°C tensile strengths are higher than those of Inconel 625 and Nimonic 263, but lower than Inconel 740[7]. The elongation and area reduction maintain at high levels, completely in accordance with the designers′ requirement. Due to the long service life of the marine boiler, the 30 000h stress rupture property is minimum requirement. Comparing the stress rupture data of 30 000h and 100 000h at 700℃ between GH 2984 and Inconel 740 alloys, they are at the same level, Besides, the stress rupture properties at 650 and 750°C, they also nearly the same. The minimum requirement of stress rupture strength for 100 000h is 110 MPa for the ultra-supercritical set, so GH2984 and Inconel 740 alloys satisfy the designers' requirement, but Nimonic 263 cannot.

Table 4 Mechanical properties of some superalloys used for boiler tube [6]

Alloys	R.T.				700℃				700℃ stress rupture strength（MPa）	
	UTS (MPa)	0.2YS (MPa)	EL (%)	RA (%)	UTS (MPa)	0.2YS (MPa)	EL (%)	RA (%)	30000h	100000h
GH2984	1107	686	26.6	46.6	745	539	34.4	52.3	149	130
Inconel740	1150	705	30.0	39.0	905	650	37.0	44.5	149	130
Inconel625	960	514	48.0	-	651	398	40.0	-	162	-
Nimonic263	960	580	43.0	46.0	740	490	26.0	34.0	120	100

Note: The standard heat treatment of GH2984 alloy is :1100℃, 1h, AC+760℃, 8h, $\underline{50^0 C/h}$ 650℃, 16h, AC

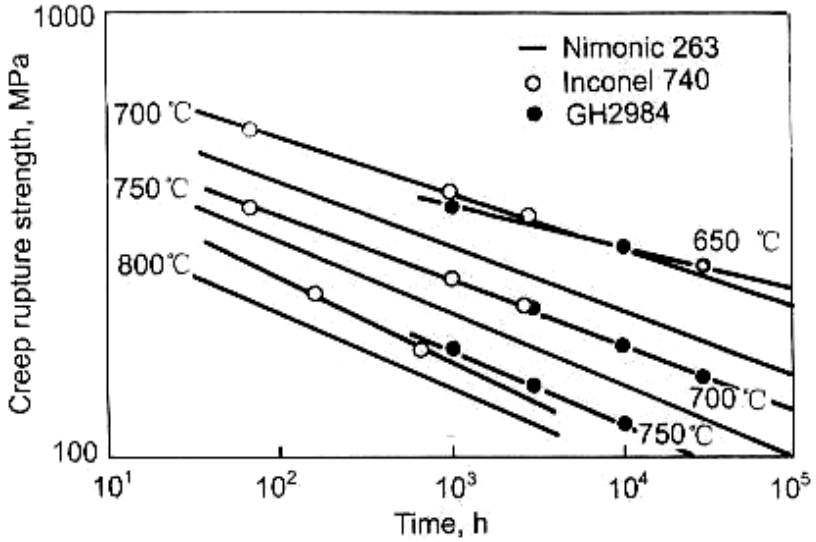

Fig 1 Stress rupture properties of GH2984, Inconel 740 and Nimonic 263 alloys

1.2.3 Good corrosion resistance

The chemical property usually consists of oxidation resistance and corrosion resistance. One of the advantages of GH 2984 alloy is that the alloy possesses excellent oxidation resistance as well as corrosion resistance, because the alloy contains 18-20%Cr, which can form a tight and adherent Cr_2O_3 film, that guarantees the alloy having better oxidation resistance. Table 5 lists the oxidation rate of GH2984 alloy, which is better than the oxidation rates of GH2135 and GH1140 alloys. The latter two alloys are also Fe-Ni-base alloys developed in China.

Table 5 Average oxidation rates of GH2984 alloy at 700-900℃ for 100h ($g/m^2 \cdot h$)[8]

Alloy	700℃	800℃	900℃
GH2984	0.0058	0.020	0.0738
GH2135	0.019	0.042	0.095
GH1140	0.014	0.028	0.139

The hot corrosion of superalloy is caused by the surface sulfate attack that is formed by the interaction of S in the fuel gas and salt in the environment. The attack by the hot corrosion on the superalloy machine parts is stronger than that by pure oxidation. The hot corrosion resistance of GH2984 alloy was studied by crucible method and burner rig test. The corrosion medium in the crucible method was 25% NaCl+ 75%Na_2SO_4 at 650℃-820℃ for 3h, The corrosion weight loss data are compiled in Table 6. The hot corrosion of GH2984 alloy at 750 ℃ is best. In the burner rig test, the diesel oil and artificial sea-water were selected. The high salt concentration was preferred for accelerating the test. The test temperature was 900℃ and corrosion time is 25h. Table 6 lists the hot corrosion resistance of GH2984 alloy.

Table 6 Hot corrosion resistance of GH2984 alloy (weight loss： mg/cm^2·h)

Alloy	Crucible method				Burner rig test
	650℃	700℃	750℃	820℃	900℃
GH2984	0.40	1.29	1.63	1.24	0.28
GH1140	0.63	0.85	3.50	152.0	0.19
GH2135	0.94	1.92	3.16	46.23	0.94
GH403	-	-	-	-	6.24

GH2984 alloy also has good anti-intergranular corrosion property, which is free both after various heat treatments or welding. By immersing the GH2984 alloy tube with 25 mm in diameter and 2mm in thickness in sea-water for 21 months, the outer and inner tube surfaces were not corroded [8].

1.2.4 Stable microstructure

The microstructure stability test was carried at 700°C from 1000 to 18000 h . After prolonged aging, it was proved that GH2984 alloy is fairly stable, that satisfies the requirement of long-term service for large ships and ultra-supercritical boiler.

After standard heat treatment, the spherical γ′ strengthening phase particles with an average diameter of 23μm and an amount of 5.74 wt% uniformly distributed in the austenitic γ matrix. Besides, there is also minor MC phase, including NbC and Ti(N,C) locating inside the grains as well as at the grain boundary and having a size of 1-10μm and an amount of 0.52 wt%.

After 700°C prolonged exposure, the radius of γ′ particles increases linearly with the third root of aging time and obeys the diffusion –controlled coarsening kinetics that governing the growth rate of γ′ phase. The amount of γ′ phase gradually increases to 7.23 wt% after 18000h. The strengthening effect due to the increase of γ′ amount compensates the loss of strength caused by the γ′ particle growth. The change of γ′ composition also proves that γ′ phase is rather stable during the prolonged aging[9].

1.2.5 Easy formability

Besides excellent mechanical properties and corrosion resistance, a superalloy for producing tube should have good formability. Otherwise, it cannot be easily formed into tubes and loses its real application. GH2984 alloy exhibits very good cold or hot workability and can be easily deformed into tube products; the tendency of grain growth is low[10].

The temperature of hot billet piercing is 1100°C and increases to 1160-1180°C during piercing. The rate of finished product can reach 100%. The technical property of cold rolling or cold extrusion is similar to that of 1Cr18Ni9Ti stainless steel. The surface quality and size tolerance are in accordance with the tube standard. The tube reaming is easy up to 38% .The tubes with a radius of 65mm can be bent with perfect quality. The tube expansion is also easy particularly fitting the manufacture of expansion type of superheater.

Finally from the understanding of comprehensive properties, GH 2984 alloy is a promising tube candidate for the superheater and reheater of ultra-supercritical boiler.

2. Development of gas turbine and application of superalloy

2.1 Development of gas turbine in China

In the years between sixty to seventy last century, China began to self-design the gas turbine with a gas inlet temperature of 700°C, and the typical turbine sets are 1 MW, 1.5 MW and 6 MW electricity generators, 6 MW marine turbine, 3500 hp and 4500 hp locomotive

engines. In the middle of seventh decade, 23000 kW gas turbine with a gas inlet temperature of 990°C has been built. A total of three sets have been put in service for electricity generation. Up to now, more than twenty sets have been produced [I1].

In order to reuse the coal gas generated in the blast furnace, the cooperation was continued to manufacture gas turbine by burning fuel of low calorific value. In 2003 China started to produce heavy gas turbine of 100 MW and 200 MW. These joint projects run smoothly.

China medium size gas turbines were mainly manufactured in the aviation industry. Beginning from seventh decade, a series of gas turbines more than 100 sets have been produced, such as WJ5G, WJ6G, WP6G, and WZ6G. Another example is the cooperation with Pratt & Whitney Co, to manufacture FT-8 type gas turbine, having a power of 25 MW and efficiency of 38.4%. China side is responsible for the production of low pressure compressor and turbine, combustion chamber, case etc. roughly about 30% of the work load. Up to now more than 100 sets of FT 8 gas turbines have been produced[11].

At the end of year 1999, installed capacity of gas turbines for electricity generation in China main land reaches 5939 MW, about 2% of the total installed capacity for electrical generation in China. Among them, the installed capacity of large gas turbines is 4735 MW, about four fifth of the total installed capacity.

There are 42 sets of gas turbines that have above 30 MW capacity, and 4 sets even reach 300 MW level [11]. It is sure that China gas turbine electricity stations enter a stage of large capacity and high efficiency. According to the 2003 statistics, the installed capacity of gas turbines for generating electricity goes up to 7000 MW, and about 3% of the total. In the coming five to ten years. China requires a total of 34000 MW gas turbines, for the hot parts of gas turbines, superalloys with good comprehensive properties are necessary. China already develops a series of superalloys possessing high mechanical properties, excellent oxidation and hot corrosion resistance.

2.2 Superalloys for gas turbine

2.2.1 Hot corrosion resistant superalloys

Materials for blades and vanes in gas turbine are always the hot corrosion resistant superalloys. Beginning from 1973, the Institute of Metal Research, Chinese Academy of Sciences developed K438 conventional cast Ni-base superalloy, used in the 23000kW gas turbine. Recently other five hot corrosion resistant cast superalloys (K435, K444, K452, K4537, K438G), one wrought superalloy (GH413) one directionally solidified Ni-base alloy (DZ38G) and one single crystal Ni-base alloy(DD8) have been developed [12-18], and their chemical compositions are compiled in Table 7.

Table 7 Chemical compositions of hot corrosion resistant superalloys developed by IMR

Allooy	C	Cr	Co	W	Mo	Al	Ti	Nb	B	Zr	Hf	Ta	V	Y	La	Ce	Ni
GH413	0.07	15.0	–	6.0	3.3	2.7	2.0	–	0.02	–	–	–	0.6	–	–	0.02	bal
K435	0.09	16.0	11.0	5.5	2.0	2.8	4.6	0.2	0.02	0.05	–	–	–	0.05	0.01	–	bal
K444	0.07	16.0	11.0	5.5	2.0	3.0	4.6	0.2	0.08	0.05	0.3	–	–	0.03	–	0.02	bal
K452	0.10	21.0	11.0	3.5	0.6	2.5	3,5	0.3	0.02	0.04	–	–	–	0.03	0.02	–	bal
K4537	0.10	15.5	9.5	5.0	1.5	3.0	3.5	2.0	0.02	0.05	–	–	–	–	–	–	bal
K438	0.15	16.0	8.5	2.6	1.7	3.5	3.2	0.9	0.01	0.1	–	1.8	–	–	–	–	bal
K438G	0.15	16.0	8.5	2.6	1.7	4.0	3.6	0.7	0.01	–	–	1.8	–	–	–	–	bal
DZ38G	0.10	16.0	8.5	2.6	1.7	4.0	3.9	0.7	0.01	–	–	1.8	–	–	–	–	bal
DD8	0.02	16.0	8.5	6.0	–	4.0	4.0	–	0.004	0.005	1.0	–	–	–	–	–	bal

The common characteristics of the above –mentioned alloys are as following:

(i) High Cr content

Cr is usually higher than 15% in order to form tight and dense Cr_2O_3 film to protect the alloy against hot corrosion. Of course too much Cr addition will accelerate the σ phase precipitation that impairs the mechanical property.

(ii) Appropriate Al and Ti contents

Addition of Al and Ti can form the main strengthening γ′ phase to keep the high temperature strength at a high level. From Table 7, it can be seen that most of the alloys contain 6-8% (Al+Ti). The amounts of γ′ phase are around 37-50%.

(iii) Moderate addition of refractory metals

The refractory metals (Mo, W, Ta etc) are usually added in the hot corrosion resistant alloys to improve the mechanical properties, but too much refractory metals, particularly Mo, will deteriorate the hot corrosion resistance. In K435, K452, K444 and GH413 alloy, there is no Ta addition that can cut down the alloy price. Their stress rupture and 900°C tensile properties are listed in Table 8 and 9, respectively.

Table 8. Stress rupture properties at 900°C of hot corrosion resistant alloys(MPa)

Alloys	100h	1000h	2000h	5000h	10000h
K435	300	200	169	129	99
K444	330	200	–	–	–
K452	186	160	136	104	80
GH413*	259	158	–	91	59
K438	265	177	147	123	108
DZ38G	334	245	205(3000h)	-	-
DD8	385	220	170	-	-

* 850℃ stress rupture data

Table 9. 900°C tensile properties of hot corrosion resistant alloys

Alloys	UTS (MPa)	0.2YS (MPa)	EL(%)	RA(%)
K435	692	541	16.9	26.0
K444	728	514	17.0	30.0
K452	556	417	17.0	35.0
GH413	570	505	24.0	30.0
K438	485	375	23.0	34.0
DZ38G	807	724	16.2	22.8
DD8	853	762	17.8	

The newly developed K435 alloy has no σ phase precipitation after 800-900°C prolonged aging for 1000 h, but γ′ phase has a little growth. The influence of prolonged aging on stress rupture is not pronounced, which can be proved in Table 10. K452 and GH413 alloys also have good phase stability similar to K435 alloy, but K444 alloy has very small σ precipitation after 3000 h prolonged aging at 900°C.

Table 10. 900℃ tensile and 900°C/245 MPa stress rupture properties of K435 alloy after prolonged aging

Aging temp. (℃)	Aging time(h)	UTS (MPa)	0.2YS (MPa)	EL (%)	RA (%)	Stress rupture life (h)
800	1000	705	505	20.3	42.8	513.6
	3000	713	482	19.2	39.5	460.1
	5000	645	454	21.6	42.5	337.8
	10000	644	449	16.4	22.9	362.4
850	1000	663	465	20.0	46.1	467.2
	3000	665	479	21.6	42.5	385.0
	5000	623	443	26.4	51.2	161.6
	10000	627	417	–	–	140.0
900	1000	618	438	25.2	46.0	417.4
	3000	640	412	19.2	36.1	277.3
	5000	592	425	23.6	33.0	160.4
	10000	599	387	17.6	22.9	88.8
Standard heat treatment	0	692	542	16.1	25.6	369.0

Table 11 shows the hot corrosion results of some alloys tested by crucible method in a corrosive medium of 75% Na_2SO_4 +25%NaCl, that proves the hot corrosion resistances of K435, K444, and K452 alloys are better than K438 alloy.

Table 11. Corrosion resistance of K435,K444 and K452 alloys

Alloys	Temp.(℃)	Time(h)	Average corrosion rate ($mg/cm^2 \cdot h$)
K435	900	200	0.281
K444	900	100	0.116
K452	900	100	0.190
K438	900	100	1.904

2.2.2 Disk superalloy

There are four superalloys used for gas turbine disk materials in China and their chemical compositions are listed in Table 12.

Table 12 Chemical compositions of disk superalloys for gas turbine.

Alloys	C	Cr	Ni	Co	Mo	Al	Ti	Nb	B	Ce	La	Fe	Zr	V
GH2132	0.06	15	26	–	1.3	–	2.1	–	0.007	–	–	bal	–	0.3
GH738	0.06	19.5	bal	14	4.2	1.4	3.0	–	0.007	–	–	–	0.05	–
GH4698	0.06	14.5	bal	–	3.0	1.5	2.6	2.0	0.005	0.005	–	–	0.05	–
GH742	0.06	14	bal	10	5.0	2.6	2.6	2.6	0.01	0.01	0.10	–	–	–

Now we choose GH4698 alloy as an example, which is recently used for the disk material of large gas turbine[19]. The disk size of gas turbine is usually larger than that of jet engine. The disk diameter of GH4698 alloy reaches 1200 mm and a weight of 1300 kg, which is the largest disk size ever made in China. The alloy was first melted in a vacuum induction furnace of 6t capacity, and remelted in a vacuum consumable electrode furnace into an ingot with a diameter of 660 mm. The γ' amount was 27% by controlling the Al, Ti, Nb contents at their upper levels. Afterwards the ingot was homogenized at high temperature to reduce the dendritic segregation. Table 13 proves that the ingot segregation after homogenization treatment is not serious.

Table 13 Chemical compositions at different locations in GH4698 alloy ingot (diameter 660mm)

Location in ingot	Al	Ti	Nb	Mg	C
Center	1.70	2.70	2.11	0.003	0.046
Half of radius	1.70	2.69	2.09	0.003	0.046
periphery	1.70	2.70	2.12	0.003	0.047

The ingot was forged into ϕ435×1115 mm rod in a 2000 t quick forging machine between 1140-1170°C, which was finally deformed into disk cake in a 30000 t hydraulic press. The mechanical properties of GH4698 alloy specimens taken from the disk cake are collected in Table. 14.

Table 14 Mechanical properties of GH4698 alloy specimens taken from disk cake

RT tensile				RT impact	650℃ stress rupture	
UTS (MPa)	0.2YS (MPa)	EL (%)	RA (%)	a_K (J/cm^2)	σ (MPa)	τ (h)
1230	860	21	23.5	77.5	720	469

3. Superalloy exchanger for nuclear power

China already held the advanced technology to manufacture 300 MW and 600 MW nuclear power stations. In the future, a 1000 MW pressurized water nuclear power station will be constructed. In China long term programme, the nuclear generated electricity will reach 12700–14000 MW in 2010 and 30000~40000 MW in 2020[20].

In the pressurized water nuclear reactor, one of the most important high temperature materials is the superalloy used for heat exchanger tubes. In the early years, 304 and 316 stainless steels were used for exchanger tubes, but they had serious stress corrosion cracking during the service. Afterwards these stainless steels were replaced by Inconel 600 or Inconel 800 superalloys. But their corrosion resistance is still not good. In order to enhance the reactor reliability, Inconel 690 superalloy was developed to replace the old one[21]. The Inconel 690 alloy tubes used in Dayawan nuclear power station were supplied by France. China started to produce GH690 alloy tube by own effort, which composition is similar to Inconel 690 alloy.

3.1 GH690 alloy tube production

GH690 alloy was produced by VIM+ ESR duplex smelting process. The sulfur content can be dropped to less than 20 μg/g (ppm) that made the area reduction higher than 50%. If the S content was higher than 20 μg/g, the ductility was worsened, as shown in Fig.2 [22]. When the area reduction was larger than 50%, it was easy to produce the tubes [23]. Of course it is better to control the S content below 10 μg/g.

In the VIM smelting process, slag as well as desulfurizer were added; the slag composition was 50 CaO-25CaF_2-25Al_2O_3 and the desulfurizer was Ca-containing. The S content can be lowered from original 35 to 18 μg/g. After electroslag remelting, the S content was further dropped to 10-12 μg/g. Such very low S content can completely eliminate the hot shortness, raise the high temperature ductility and increase the tube productivity to higher than 42% [24].

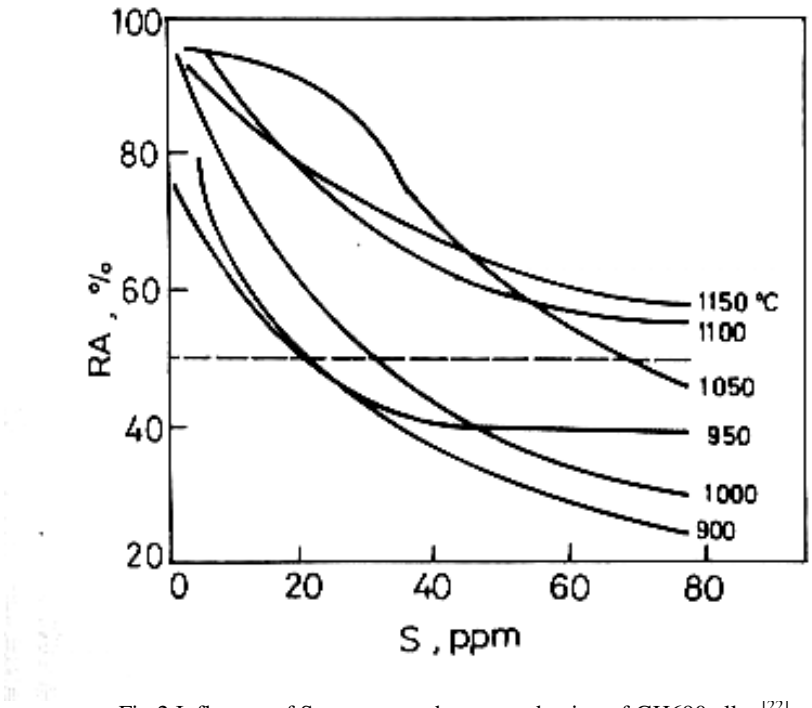

Fig.2 Influence of S content on the area reduction of GH690 alloy[22]

3.2 Corrosion resistance of GH690 alloy

The Cr content of GH690 alloy is 30%, that guarantees the alloy to have excellent corrosion resistance. However, if the heat treatment system was not appropriate, there happened severe intergranular corrosion or alkali stress corrosion. It was found the intergranular corrosion became smaller, if the solution treatment was between 1000°C and 1100°C. At the same time the stress corrosion in 50% NaOH high concentration solution was also not heavy. Therefore the best heat treatment system is 1050°C solutioning plus 715°C aging[25].

Why this heat treatment system can improve the corrosion resistance? Careful microstructural observation can give the answer [21]. With the rise of solution temperature, the matrix grains enlarge and carbide dissolves more. After aging, the $M_{23}C_6$ with fcc. structure precipitates in the grain boundary. In the vicinity of grain boundary, there appears an obvious Cr-poor region, which width can reach 200nm, as shown in Fig。3. After 715°C/205 h aging, the Cr solutes adjacent to the Cr-poor region diffuse into this region. At the same time, the carbide particles appear in grain boundary in a chain-like mode that will enhance the anti-corrosion property.

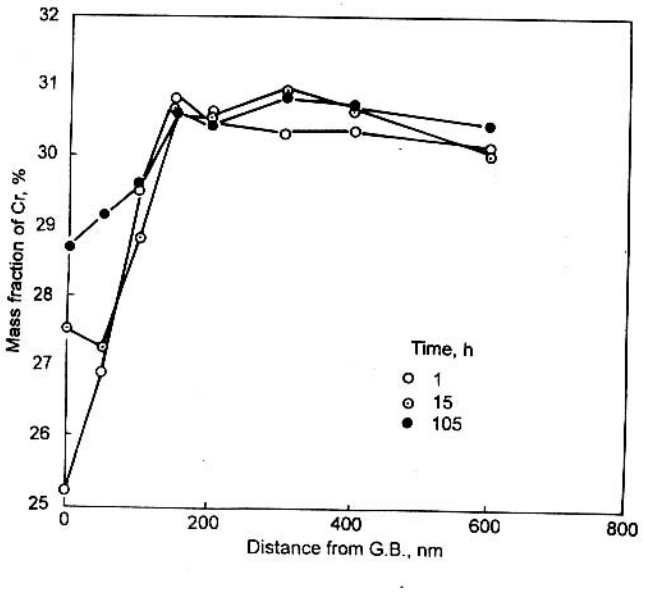

Fig. 3 Cr content adjacent to the grain boundary after 715 ℃ aging for various time[21].

4. Conclusion

1) China will pay great attention to overcome the energy shortage due to rapid progress of economic reconstruction.
2) In coal power generator, China will put great effort to set up supercritical and ultra-supercritical electricity generator.
3) In order to change the energy structure, China will continuously reinforce the manufacture of large gas turbines and build new nuclear power station.
4) Recently China will plan the future research and development on superalloys having better high temperature strength and corrosion resistance to meet the need of new power stations.

References

[1] Yansun Lu, The principal developments in the 11th five-year plan and prospects for 2020 of the power generation, transmission and transforming industry. Power Engineering, 23(5) (2003)2115
[2] Xiaojun Bian, Nana Wang, Yunjuan Chao, Zhejiang development and application of supercritical units. Electricity, (2)(2003)21
[3] Smith GD, Patel SJ, Farr NC, et al, Corrosion99, Houston; NACE International, (1999) 12
[4] Blum R., Advanced (700) PF Power Plant, EC Contract No SF/1001/97/DK(1997)

[5] Smith GD,Sizek HW,Corrosion 2000,Houston:NACE International(2000), 00256,1.
[6] Guo J.T., Du X.K., A superheater tube superalloy GH2984 with excellent properties, Acta Metall. Sinica, 41(2005)1221.
[7] Zhao S Q, DongJX, Zhang MC, Xie XS., Inconel 740 used for superheater tube of new ultra-supercritical Boiler, Journal of Iron and Steel Research,15(7)(2003) 160.
[8] Wang S H, Du XK,GuoJT,Xu HZ., Anticorrosion performance of GH984 alloy under various environmental conditions, Corrosion Science and Protection Technology, 14(5)(2002)284.
[9] Institute of Metal Research, CAS, Mechanical Properties and Microstucture Stability of GH2984 Superalloy after Long-time Thermal Exposure at 700 ,(1991).
[10] Institute of Metal Research, CAS, Shanghai N0.5 Steel Plant, Harbin 703 Institute, The Investigation of GH2984 Superalloy,(1991).
[11] Fupei Xue, Recent Status and Development of Gas Turbine in China, Institute of Metal Research, Chinese Academy of Science, Report, (2003)
[12] Lanzhang Zhou, Yong Wang, Jianting Guo, Research report on K444 superalloy , Institute of Metal Research, (2003).
[13] Lanzhang Zhou, Jieshan Hou, Jianting Guo, Research report on K435 superalloy, Institute of Metal Research, (2003).
[14] Chao Yuan, Gusong Li, Jianting Guo, Research report on K452 superalloy, Institute of Metal Research, (2003)
[15] Chao Yuan, Weiyong He, Jianting Guo, Research report on GH 413 superalloy, Institute of Metal Research, (2003)
[16] Zhuangqi Hu, Yajun Tang, Jishan Zhang, Jinghua Zhang, Ying'ao Li, Yang Yu, Yaoxiao Zhu, Influence of minor elements on the directionally solidified IN 738 alloy (Development of DZ38G alloy) J. Mater Eng., (7/9)(1992)102
[17] Zhuangqi Hu, Jinghua Zhang, Tao Jin, Xiaofeng Sun, Hengrong Guan, Research report on DD8 single crystal superalloy, Institute of Metal Research, (1996).
[18] Guanliang Zeng, Hengrong Guan, Xiaofeng Sun, Zhuangqi Hu, Hot corrosion of DD8 and DZ38G superalloys, Corrosion Sci. & Prot. Technique, 5(1993)81.
[19] Guangpu Zhao, Jianting Guo, Research report on large size forged disk made of hard deformed wrought superalloy, Institute of Metal Research, (2004).
[20] Research and development of China energy science and technology in 2020, Special group of science and technology of energy sources, China Association of Science and Technology, (2004).
[21] Qiang Li, Bangxin Zhou, A study of microstructure of alloy 690, Acta Metall. Sin., 37(2001)8
[22] Bingda Zhang, Kui Liu, Chuiping Hou, Shunnan Zhang, Effect of sulfur and magnesium on hot ductility of Inconel 690 alloy, Acta Metall. Sin., (suppl.), 31(1995)S258
[23] Yamaguchi S, et al, Effect of minor elements on hot workability of nickel-base superalloys, Met Technol, (1979)171
[24] Shoujun Li, Yaohe HU, Hongshen Mei, Xishan Xie, Yunhua He, Hongbin Zhang, Desulphurization of Ni-base superalloy GH690, J. Iron & Steel Research, 15(7)(2003)317
[25] Shaoyu Qiu, Xing Su, Yan Wen, Fuguang Yan, Yinhua Yu, Yanchun He, Effect of heat treatment on corrosion resistance of alloy 690, Acta Metall. Sin., 16(1995)336.

Part 1

Advanced Gas Turbine Materials

Invited Papers

DEGRADATION IN SINGLE CRYSTAL NICKEL - BASE SUPERALLOYS –A REVIEW

M. Nazmy, Alstom (Switzerland) Ltd., Baden, Switzerland
A. Epishin, Federal Inst. for Mat. Research & Testing (BAM), Berlin, Germany
T. Link, Technical University, Berlin, Germany
M. Staubli, Alstom (Switzerland) Ltd., Baden, Switzerland

Abstract

Single crystal Nickel-base superalloys are in use for the front rows of blading in advanced land-based gas turbines. This is for their higher creep capabilities as well as outstanding low cycle fatigue properties as compared with conventionally cast Nickel-base superalloys. The continuous efforts to improve the high temperature creep properties of SX superalloys resulted in the development of the fourth generation of these alloys. Nevertheless, this improvement in the high temperature capability of these materials required the use of higher contents of Re and Ru which increased their densities and costs. The application of SX superalloys at higher temperatures results in microstructural changes called rafting and a topological inversion of their γ/γ` phases. These two microstructural features reduce the tensile and low cycle fatigue properties of the SX superalloys. The extent of degradation in the microstructure and mechanical properties, in a certain SX superalloy, depends on the exposure temperature, duration and to a lesser extent on the applied stress. The consequences of these changes in microstructure and properties should be taken into consideration in the evaluation of the mechanical properties of SX superalloys.

Keywords: Single crystals, superalloys, degradation, gamma prime, blading

Introduction

Modern land-based gas turbine designs have been employing single crystal (SX) superalloys in high-pressure turbine vanes and blades to achieve high operation performance and life cycle objectives as well. The benefits of using SX components have been well documented and can be summarized as improved creep-rupture properties, low cycle fatigue (LCF) strength and oxidation resistance [1-5].
In addition, SX superalloys retain a higher fraction of their thick section rupture life as wall thickness is reduced [5]. Four generations of SX superalloys have been developed with the goal of improving the high temperature capability under creep and fatigue conditions [6-8]. Directional coarsening or "rafting" of γ' precipitates in SX superalloys has been reported in different alloy systems [9-13]. Though it has been extensively studied experimentally and theoretically, the exact nature of the driving force, the associated kinetics and its consequences on the mechanical properties, are controversial and still discussed [14-18]. Nevertheless, it is generally agreed that the rafting morphology and its kinetics are governed by two key parameters, namely the lattice misfit between the two phases γ and γ', and the sign and magnitude of the uniaxial applied stress. Additionally, it has been reported that plastic pre-strain and residual internal stresses can induce rafting of γ' in SX superalloys [18,19].

The aims of the present investigation are:

(a) Review the status of SX superalloys development
(b) Present recent results on the effect of the different parameters on the rafting kinetics in different SX superalloys
(c) Present results on the effect of the microstructural degradation on the mechanical behaviour of different SX superalloys, i.e. tensile and LCF properties.

Status of SX Superalloys Development

The main goal of developing Nickel–base SX superalloys has been the increase in their creep strength [20]. This improvement of the temperature capabilities of the SX superalloys has been achieved by increasing the volume fraction of γ' up to 70-75% and using potent solid solution hardening refractory elements such as Re and Ru [8, 20]. At present, there are four generations of SX superalloys developed for blade applications in aero jet engines and land–based gas turbines. Table 1, gives the nominal chemical compositions of selected SX superalloys of the 1st, 2nd, 3rd and 4th generations.
A comparison of the creep strength of selected SX Superalloys from the four generations is given in Figure 1.
The improvements in the creep strength of the 3rd and 4th generations of SX superalloys are accompanied by an increase in density and a significant reduction in Cr content necessary to suppress the precipitation of topologically closed packed phases.

Rafting Process

The microstructure of SX superalloys consists of two phases, the ordered intermetallic γ' precipitates coherently embedded in the disordered γ matrix. Under the combined influence of stress and temperatures above 800°C, the initially cuboidal γ' precipitates coalesce into extended rafts [9, 15]. This phenomenon of rafting or directional coarsening has been observed in several SX superalloys [13,33]. An example of a rafted microstructure in N5 is shown in Figure 2.

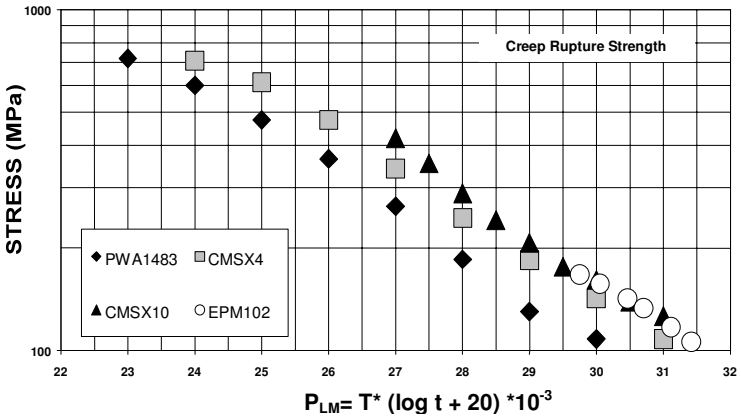

Figure 1
Creep rupture strength of selected SX superalloys

Alloy	Ni	Cr	Co	Mo	W	Ta	Re	Nb	Al	Ti	Hf	Ru	Ir	Density g/cm^3	Ref.
1st Generation															
PWA1480	bal.	10	5	-	4	12	-	-	5	1.5	-	-	-	8.7	1
PWA1483	bal.	12.8	9	1.9	3.8	4	-	-	3.6	4	-	-	-	8.2	21
René N4	bal.	9	8	2	6	4	-	0.5	3.7	4.2	-	-	-	8.56	22
SRR99	bal.	8	5	-	10	3	-	-	5.5	2.2	-	-	-	8.56	23
CMSX-2	bal.	8	5	0.6	8	6	-	-	5.6	1	-	-	-	8.56	24
CMSX-6	bal.	10	5	3	-	2	-	-	4.8	4.7	0.1	-	-	7.98	25
CMSX-11B	bal.	12.5	7	0.5	5	5	-	0.1	3.6	4.2	0.04	-	-	8.44	26
2nd Generation															
CMSX-4	bal.	6.5	9	0.6	6	6.5	3	-	5.6	1	0.1	-	-	8.7	27
PWA1484	bal.	5	10	2	6	9	3	-	5.6	-	0.1	-	-	8.95	2
MC2	bal.	8	5	2	8	6	-	-	5	1.5	0.1	-	-	8.63	28
René N5	bal.	7	8	2	5	7	3	-	6.2	-	0.2	-	-	8.64	29
3rd Generation															
CMSX-10	bal.	2	3	0.4	5	8	6	0.1	4.7	0.2	0.03	-	-	9.05	30
René N6	bal.	4.2	12.5	1.4	6	7.2	5.4	-	5.75	-	0.15	-	-	8.98	31
TMS75	bal.	3	12	2	6	6	5	-	6	-	0.1	-	-	8.82	32
4th Generation															
EPM-102	bal.	2.5	16.5	2	6	8.25	5.95	-	5.55	-	-	3	-	9.2	20
MC645	bal.	5	-	-	6	5	4	-	6	0.5	0.1	5	-	8.78	8
TMS-138	bal.	2.9	5.9	2.9	5.9	5.6	4.9	-	5.9	-	0.1	2	-	8.87	32
TMS-139	bal.	2.9	11.6	1.9	5.8	5.8	4.9	-	5.8	-	0.1	-	3	8.81	32
TMS-162	bal.	2.9	5.8	3.9	5.8	5.6	4.9	-	5.8	-	0.1	6	-	8.96	32

Table I: Nominal compositions of selected SX superalloys of the 1st, 2nd, 3rd and 4th generations

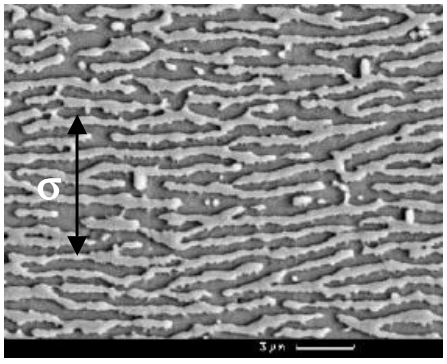

Figure 2:
Rafted microstructure of N5 (T=1000°C, t=2999 h, σ=90 MPa)

The evolution of the microstructure of the SX superalloys leads finally to an effect called topological inversion: the γ'–phase surrounds the γ-phase and becomes topologically the matrix [13, 34]. At high temperatures this topological inversion takes place within few hundred hours [13]. It is evident from numerous experimental and theoretical investigations that rafting is strongly controlled by the sign and magnitude of applied stress, lattice misfit δ, and the difference between the elastic constants of γ and γ' phases [13, 18]. The definition of lattice misfit δ is:

$$\delta = (a\gamma' - a\gamma)/0.5(a\gamma' + a\gamma) \quad (1)$$

Most of SX superalloys have negative lattice misfit δ at service temperatures. This is because the thermal expansion coefficient of γ-phase is larger than that of γ'-phase. One-way to explain the rafting process is to consider a typical γ/γ' structure with a negative lattice misfit as illustrated in Figures 3-a & 3-b [35, 36]. They show the internal stresses in γ and γ' phases, in absence and presence of an external stress, respectively. Figure 3-a assumes that in the absence of external stress, the chemical potentials of the phases at points 1 and 2 are equal. Under this condition, normal non-directional coarsening is expected. When an external stress is applied as in Figure 3-b, a situation characterised by un-equal stress components and

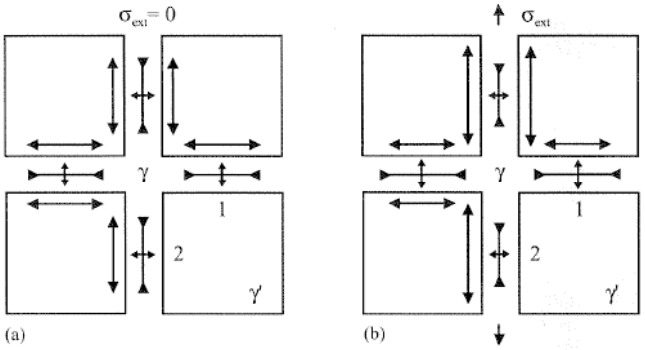

Figure 3
Schematic illustrations of the roles of lattice misfit and external stress σ_{ext} on γ/γ' structure.
(a) $\sigma_{ext}=0$
(b) $\sigma_{ext}>0$

hydrostatic pressures at positions 1 and 2 will develop. The major effect of the external applied stress as shown in Figure 3-b is that the local stresses are modified and hence the chemical potentials of the phases at the positions 1 and 2. This will result in a stress directed diffusion flux [37] producing the rafting effect and inducing the topological γ/γ' inversion [13, 18, 35, 36].

Effect of Rafting in SX Superalloys on Mechanical Properties

Effect of Rafting on Tensile Properties

Tien and Gamble were the first to report on the effect of rafting on the yield stresses, at various temperatures, of UDIMET 700 [11]. They observed an enhancement in the yield stresses in the samples rafted under compressive stress at 954°C to produce a rod structure of the γ'-phase parallel to the stress axis as compared with the samples rafted under tensile stress to produce a plate structure of γ'-phase perpendicular to the stress axis. Nevertheless, no topological inversion of γ/γ' was reported since the volume fraction of γ' in UDIMET 700 is less than 50%.

Recently, it has been reported that rafting by tensile creep in the SX superalloys N5, CMSX-2, CMSX-6, CMSX-11B and PWA1483 caused a marked drop in the yield stress at room temperature RT [38]. The rafting in these SX superalloys was accompanied by a topological inversion of γ/γ', i.e. γ' matrix surrounding elongated rafts of γ [38].

A significant drop in the tensile ductility in these rafted SX superalloys was also observed. Additionally, a {100} type of cleavage cracking was found in all of the five SX rafted superalloys tested at strain rates $<7x10^{-6}$ s^{-1} and under moist environment [39]. This behaviour was explained on the basis of a hydrogen embrittlement mechanism similar to that reported in Ni_3Al intermetallic [39]. This environmental effect in Ni_3Al can be simply explained by the following chemical reaction:

$$2Al + 3H_2O \rightarrow Al_2O_3 + 6H \quad (2)$$

The Aluminium atoms in γ' react with moisture during testing at RT resulting in the generation of atomic hydrogen that penetrates into the γ' by moving dislocations causing {100} type of cleavage fracture [39].

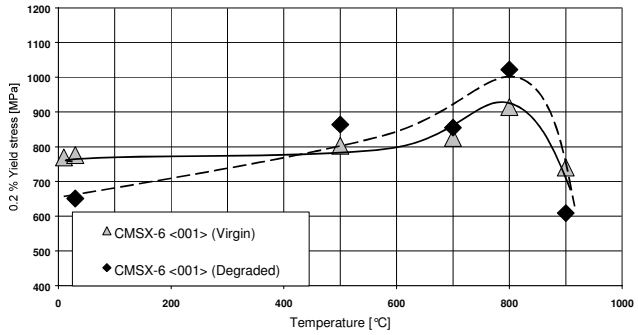

Figures 4-6
Yield stress vs. temperature of <001> specimens, virgin and degraded conditions.

Fig.4: CMSX-6

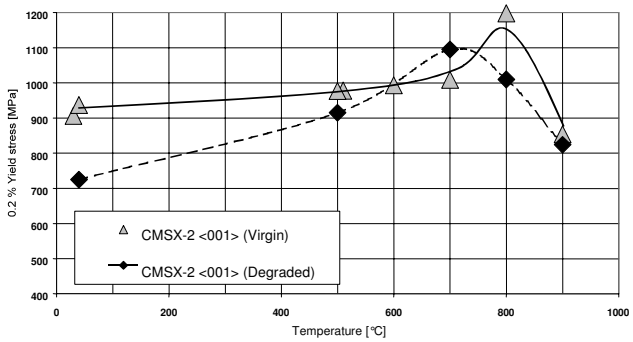

Fig.5 CMSX-2

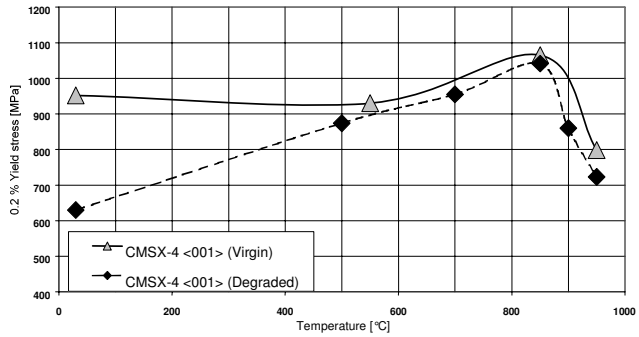

Fig.6: CMSX-4

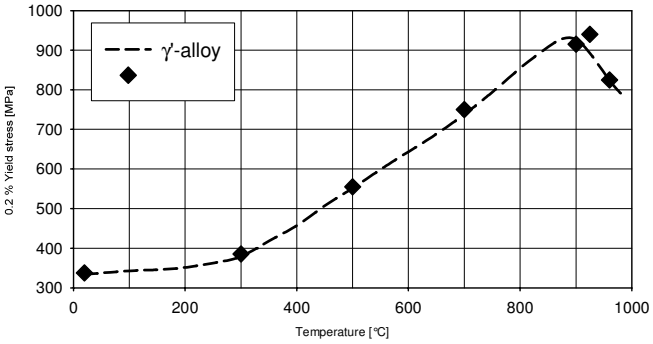

Fig. 7: γ'-alloy Ni-Cr-Al [40].

In the present investigation, tensile tests of a number of SX superalloys were carried out at various temperatures on <100> orientated specimens pre-rafted by tensile creep. The results on yield stress $\sigma_{0.2}$ vs. temperature, of the pre-rafted specimens and the fully heat treated ones, i.e. in virgin condition, are given in Figures 4-6 for CMSX-6, CMSX-2 and CMSX-4, respectively. Figure 7 shows $\sigma_{0.2}$ vs. T for the γ'-alloy Ni-Cr-Al, for comparison [40]. The yield stress of the pre-rafted specimens of the three SX superalloys exhibited positive temperature dependence similar the well-known behaviour of Ni_3Al intermatallic as shown in Figure 7 and later reported in ref. [41]. This behaviour of the pre-rafted specimens can be attributed to the topological inversion of the γ/γ` microstructure since all of these SX superalloys have a γ` volume fraction > 60%. Several factors can influence the strengthening mechanism, to different extents, in the pre-rafted specimens. These factors are: - lattice misfit at RT, volume fraction of γ`, antiphase boundary energy APBE of γ`matrix, stacking fault energy SFE of γ rafts, thickness and inter-rafts spacing of γ and the refractory elements content in the superalloy. The lattice misfit, depending on its sign at RT, can induce a tensile or compressive internal stress in γ` matrix of the pre-rafted specimen. Both of the thickness and inter-raft spacing of γ depend on the degree of the microstructural degradation, which in turn depends on the temperature, time and to a lesser extent on the stress [18]. During tensile tests of pre-rafted material the dislocations enter the γ'-phase as it is seen in TEM image presented in Figure 8.

In the present study, CMSX-4 specimens, degraded by tensile creep at different temperatures and different durations, were tensile tested at RT. Figure 9 shows the yield stresses of the degraded specimens vs. a degradation parameter "D".

$$D = (T-800)t^{1/2}\sigma^{1/5} \quad (3)$$

Where T=creep temperature in °C, t= creep time, i.e. duration of degradation in h, and σ=creep stress in MPa. This degradation parameter reflects the influence of temperature, time and applied stress. The effect of temperature in inducing the microstructural evolution is relevant, at T > 800°C. The time dependence in the degradation parameter D was taken as $t^{1/2}$ This time dependence was found to give a better correlation of the data than the typical time dependence of $t^{1/3}$ found in LSW theory [42, 43]. Additionally, this selected time dependence of $t^{1/2}$ agrees well with the reported results on the channel widening of γ in CMSX4 [44]. The performed quantitative SEM analysis of the microstructure of degraded specimens of CMSX-4 showed a clear correlation between the reduction of $\sigma_{0.2}$(RT) and the increase of γ-channel width.

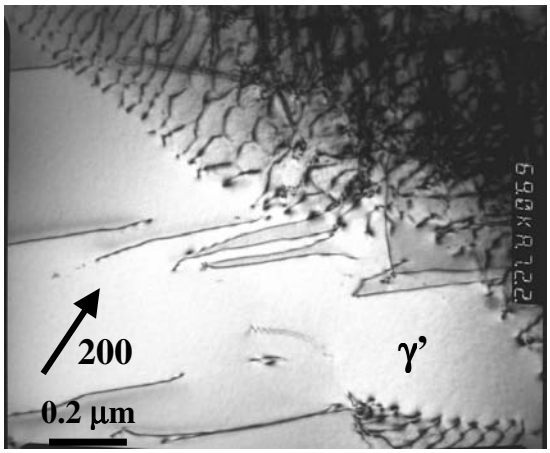

Figure 8. Dislocations enter the γ' -phase and then move as a tongue-like loops in pre-rafted single-crystal of CMSX-4 after tensile testing.

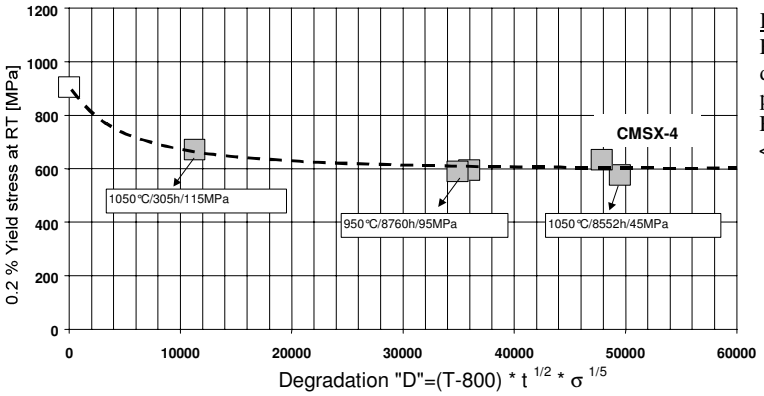

Figure 9
Effect of degradation i.e. pre-rafting on the RT yield stress of <100> CMSX-4.

Effect of Rafting on Low Cycle Fatigue

It has been reported that pre-rafted specimens of CMSX-6, exhibited lower LCF lives at 950°C as compared with specimens with cuboidal γ/γ' microstructure [45]. The reason for that is the fast growth of fatigue cracks along the γ/γ'-interfaces extended perpendicular to applied load as shown in Figure 10 [46]. This is a general effect in all materials with the plate-like structure.

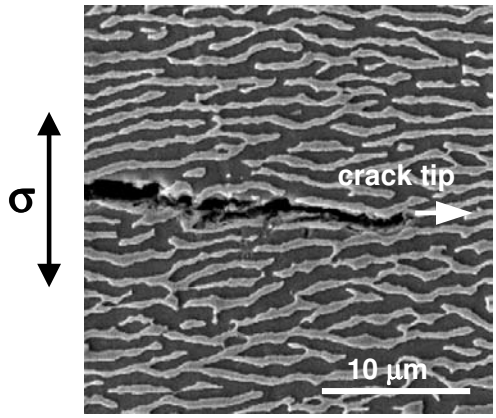

Figure 10. Growth of LCF cracks along extended semi-coherent γ/γ'-interfaces in the pre-rafted microstructure of CMSX-4 [46].

In the present investigation, LCF specimens of CMSX-4 were degraded by creep at high temperature before fatigue testing at 950°C. The pre-rafted specimens exhibited lower lives as compared with those with normal γ/γ' microstructure as shown in Figure 11. These results are in agreement with the LCF results reported in [47] on the same alloy.

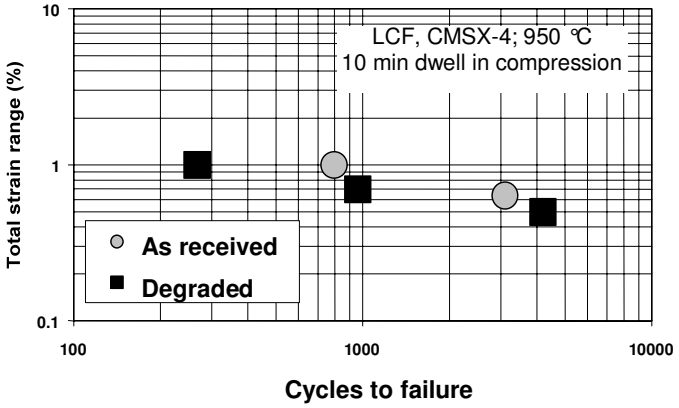

Figure 11
Effect of degradation on LCF of <100> CMSX-4 specimens at 950°C

Recently, it has been reported that the rafting of the γ/γ'-microstructure causes a significant deterioration in the RT LCF properties of SX superalloys, PWA1483 and N5 [48].
In the present investigation, pre-rafted specimens of CMSX-4 were tested under LCF at RT in moist environment. The results are shown in Figure 12. The reduction in LCF lives of the degraded specimens was accompanied by a cleavage failure of {100} type.
This behaviour of the degraded specimens was attributed to the effect of moisture on the ductility of the intermetallic Ni_3Al, i.e. γ'-matrix of the inverted microstructure [48].

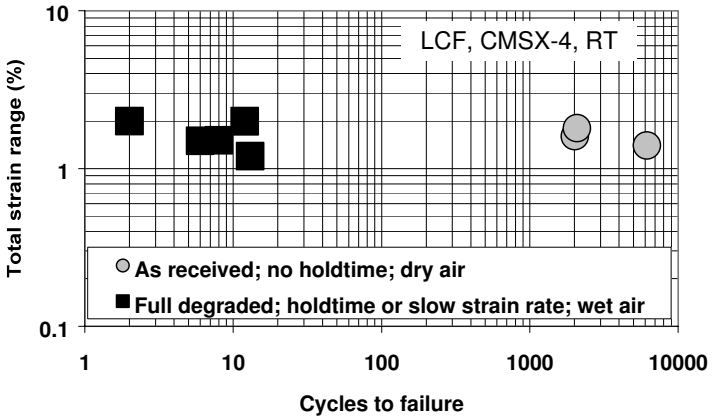

Figure 12
Effect of degradation on LCF behaviour of <100> CMSX-4 specimens at RT in moist environment

Effect of Rafting on Creep Properties:

In literature, there is a large volume of experimental data on the creep behaviour of SX superalloys [46, 47, 50]. However, the influence of rafting on the creep properties of SX superalloys is not well understood. For example, it was reported that the coarsening of γ'-phase in SX superalloys increases the creep resistance during creep because the rafted morphology suppresses the dislocation by pass mechanism which slows down the recovery process resulting in improved creep resistance [9]. On the other hand, it was reported that rafting of CMSX-4 specimens by prior-creep, increases the creep rate, i.e. decreases the creep resistance [33]. Recently, it has been shown that the pre-rafted specimens of SRR99 exhibited a tendency for improved creep lifetime at 1050°C and stresses lower than 150 MPa [50]. Based on the referred results on SRR99, two creep mechanisms were proposed to explain the effect of rafting on creep resistance [50]. The first mechanism was related to low temperature and high stresses and the second one was concerned with the low stresses and high temperatures conditions.

However, it is noteworthy to point out that the experimental data presented in [50] was obtained for relatively short creep durations, less than few hundred hours. Hence, it is essential to examine the validity of such mechanisms at longer creep durations as well as on different SX superalloys.

Conclusions

1. The development of SX superalloys, starting from the 1st to the 4th generation, resulted in an improved creep capability, which was achieved by alloying with Re and Ru.
2. The degradation of SX superalloys under high temperature creep conditions results in a topologically inverted γ/γ' microstructure with high dislocation density and inverted internal stresses.
3. The degraded SX superalloys with inverted γ/γ' structure exhibit lower yield stress at RT accompanied by {001} cleavage fracture and lower LCF strength at all temperatures.
4. The consequences of the microstructural changes on the mechanical properties of SX superalloys, exposed to high temperature loadings, should be taken into consideration in the evaluation of mechanical properties of SX superalloys.

Acknowledgements

The skilful works in testing by A. Künzler of ALSTOM, as well as the financial support by the Swiss government (EDI SBF C05.0075) are highly appreciated. The authors gratefully acknowledge the permission of ALSTOM to publish this paper.
The financial support of the German Research Society (DFG), project Li 494/4-1, Po 405/10-1, is acknowledged.

References

(1) M. Gell, D. N. Duhl and A. F. Giamei, " The Development of Single Crystal Superalloy Turbine Blades", in "Superalloys 1980", Eds. J. K. Tien et al., p.205-214, ASM publication (1980).
(2) A. D. Cetel and D. N. Duhl, "Second-Generation Nickel-Base Single Crystal Superalloy", in "Superalloys 1988", Eds. D. N. Duhl et al., p.235-244, TMS publication (1988).
(3) R.Kehlhofer, "Power Engineering-Status and Trends", in "Materials for Advanced Power Engineering 1998" Liege, Eds. J. Lecomte-Beckers et al., p.3-17, Forschungszentrum Juelich publication, (1998).
(4) T. Schulenberg, "New Development in Land-Based Gas Turbine Technology", in "Materials for Advanced Power Engineering 1998" Liege, Eds. J.Lecomte-Beckers et al., p.849-859, Forschungszentrum Juelich publication, (1998).
(5) D.N. Duhl, " Directionally Solidified Superalloys", in "Superalloys II", Eds. C. Sims et al., p189-214, J. Wiley & Sons, (1987).
(6) G. L. Ericson, "The Development of the CMSX-11B and CMSX11-C Alloys for Industrial Gas Turbine Application", in "Superalloys 1996", Eds. R. D. Kissinger et al., p.45-52, TMS publication, (1996).
(7) Y. Koizumi et al., "Third Generation Single Crystal Superalloys with Excellent Processability and Phase Stability", in "Materials for Power Engineering 1998" Liege, Eds. J. Lecomte-Beckers et al., p. 1089-1098, Forschungszentrum Juelich publication, (1998).
(8) P. Caron, " High γ` Solvus New Generation Nickel-Based Superalloys for Single Crystal Turbine Blade Applications", in " Superalloys 2000", Eds. T. M. Pollock et al., p.737-746, TMS publication, (2000).
(9) D. D. Pearson et al., "Stress Coarsening of γ` and its Influence on Creep Properties of a Single Crystal Superalloy", in "Superalloys 1980", Eds. J. K. Tien et al., p.513-520, ASM publication (1980).
(10) J. K. Tien and S. M. Copley, "The Effect of Uniaxial Stress on the Periodic Morphology of Coherent Gamma Prime Precipitates in Nickel-base Superalloys Crystals", Metall. Trans. A, vol. 2A,p. 215-219, (1971).
(11) J. K. Tien and R. P. Gamble, "Effects of Stress Coarsening on Coherent Particle Strengthening", Metall. Trans. A, vol. 3A,p. 2157, (1972).
(12) T. M. Pollock and A. S. Argon, "Directional Coarsening in Nickel-Based Single Crystals with High Volume Fractions of Coherent Precipitates", Acta Metall. Mater, vol. 42, p. 1859, (1994).
(13) W. S. Walston et al, "René N6: Third Generation Single Crystal Superalloy", in " Superalloys 1996", Eds. R. D. Kissinger et al., p. 27-34, TMS publication, (1996).
(14) A. Pineau, "Influence of Uniaxial Stress on the Morphology of Coherent Precipitates During Coarsening", Acta Metall., vol. 24, p. 559-564, (1976).
(15) A. Fredholm and J. L. Strudel, " On the Creep Resistance of Some Nickel Base Single Crystals", in " Superalloys 1984 ", Eds. M. Gell et al., p.211-220, TMS publication, (1984).
(16) R. A. MacKay and L. J. Ebert, "The Development of γ/γ` Lamellar Structures in a Nickel-Base Superalloy During Elevated Mechanical Testing", Metall. Trans. A, vol. 16A, p.1969-1982, (1985).

(17) T. M. Pollock and A. S. Argon, " Creep Resistance of CMSX-3 Nickel-Base Superalloy Single Crystals", Acta Metall. Mater.vol.40, p.1-30, (1992).
(18) M. Veron et al., "Directional Coarsening of Nickel Based Superalloys: Driving Force and Kinetics", in " Superalloys 1996 ", Eds. R. D. Kissinger et al., p. 181-190,TMS publication, (1996).
(19) H. Biermann et al., " Investigations on the Origin and Effect of Anomalous Rafting", in " Superalloys 2000", Eds. T. M. Pollock et al., p.525-534, TMS publication (2000).
(20) S. Walston et al., "Joint Development of a Fourth Generation Single Crystal Superalloy", in "Superalloys 2004", Eds. K. A. Green et al., p.15-24, TMS publication (2004).
(21) C. S. Wukusick(Final Report NAVAIR/N62269-78-C-0315,25 August 1980)
(22) D. N. Duhl and M. L. Gell, GB patent 2112812 A.
(23) M. J. Goulette et al., „Cost Effective Single Crystals", in „Superalloys1984", p.167-176, Eds. M. Gell et al.,TMS publication,(1984).
(24) K.Harris and G. L. Ericson, US patent 4,582,548.
(25) K. Harris and G. L. Ericson, US patent 4,721,540.
(26) G. L. Ericson, US patent 5,489,346.
(27) K. Harris and G. L. Ericson, US patent 4,643,782.
(28) P. Caron and T. Khan, "Development of a New Nickel-Base Single Crystal Turbine Blade Alloy for Very High Temperatures", in "Euromat 89", p.333-338,(1989).
(29) C. S. Wukusick and L. Buchakjian Jr, patent application GB 2,235,697.
(30) G. L. Ericson, US patent 5,366,695.
(31) W. S. Walston et al., US patent 5,455,120.
(32) Y. Koizumi et al., „Development of Next-Generation Nickel-Base Single Crystal Superalloys", in "Superalloys 2004", Eds. A. K. Green et al., p.35-43, TMS publication,(2004).
(33) Y. Kondo et al., "Effect of Morphology of γ` Phase on Creep Resistance of a Single Crystal Nickel-Based Superalloy, CMSX-4", in "Superalloys 1996 ", Eds. R. D. Kissinger et al., p. 297-304, TMS publication, (1996).
(34) A. Epishin et al., "Kinetics of the Topological Inversion of the γ/γ` Microstructure During Creep of a Nickel-Based Superalloy", Acta Mater.vol.49, p.4017-4023, (2001).
(35) F. R. N. Nabarro and H. L. Villiers, in " The Physics of Creep", p.241-245, publisher Taylor & Francis (1995)
(36) M. Kamaraj, "Rafting in Single Crystal Nickel-Base Superalloys-An Overview", Sadhana vol. 28, parts 1 & 2 p.115-128, (2003)
(37) I.L. Svetlov et al, "Diffusional Mechanism of γ`-Phase Particles Coalescence in Single Crystals in Nickel-Base Superalloys", Scripta Metallurgica and Materiali vol. 26, pp. 1353-1358 (1992)
(38) M. Nazmy et al., "The Effect of Strain Rate on the Room Temperature Tensile Properties of Single Crystal Superalloys", Scripta Mater. Vol.47, p. 521-525, (2002).
(39) C. T. Liu, "Moisture-Induced Environmental Embrittlement of Ordered Intermetallic Alloys at Ambient Temperatures", in Ordered Intermetallics-Physical Metallurgy and Mechanical Behavior, Eds. C. T. Liu et al., p. 321-334, NATO ASI series E: applied sciences-vol.213, Kluwer Academic Publishers, (1992).
(40) P. Beardmore, R. G. Davies and T. L. Johnston, "On the temperature dependence of the flow stress of nickel-base alloys", Trans. Of AIME, vol. 246, pp. 1537-1545 (1969).
(41) A. F. Giamei et al.,"γ/γ`: The Key to Superalloy Behavior", in High-Temperature Ordered Intermetallic Alloys, MRS proceedings vol. 39,Eds. C. C. Koch et al., p.293-308, (1985).
(42) C. Wagner, Z.Elektrochem., 65, p.581(1961).
(43) M. I. Lifshits and V. V. Slyozof, J. Phys. Chem. Solids, 19, p.35,(1961)
(44) K. Serin and G. Eggeler, "Kinetics of γ-Channel Widening in Superalloy Single Crystals under Conditions of High Temperature and Low Stress Creep", in Creep & Fracture of Engineering Materials & Structures, editor J.D. Parker, p.385-392, publication of the Inst. Of Materials, (2001).

(45) H. Mughrabi et al., “Specific Aspects of Isothermal and Anisothermal Fatigue of the Monocrystalline Nickel-Base Superalloy CMSX-6”, in “Superalloys 1996”, Eds.R.D.Kessinger et al., p 335-344,TMS publication,(1996).
(46) A. Epishin, T. Link, U. Brückner, H. Klingelhöffer and P. D. Portella, “The effect of high temperature creep damage on low cycle fatiuge of CMSX-4”, submitted to the Liege conference on Materials for Advanced Power Engineering, 2006.
(47) U. Tetzlaff and Mughrabi, “Enhancement of the High-Temperature Tensile Creep Strength of Monocrystalline Nickel-Base Superalloys by Pre-rafting in Compression”, in”Superalloys 2000”, Eds.T. M. Pollock et al., p.273-282, TMS publication,(2000).
(48) M. Nazmy et al.,”Environmental Effects on Tensile and Low Cycle Fatigue Behavior of Single Crystal Nickel-Base Superalloys”, Scripta Mater. Vol.48, p.519-524,(2003).
(49) M. Feller-Kniepmeier and T. Link, “Correlation of Microstructure and Creep Stages in the <100> Oriented Superalloy SRR 99 at 1253K”, Metall. Trans. A, vol.20A, p.1233-1238,(1989)
(50) H. Mughrabi, “γ/γ' Rafting and its Effect on the Creep and Fatigue Behavior of Monocrystalline Superalloys”, in The Johannes Weertman Symposium Proceedings, p.267-278, TMS publication, (1996).

RECENT ADVANCES IN NDT TECHNIQUES FOR GAS TURBINE COATINGS

S. Osgerby*, C. Rinaldi**, L. De Maria**

* National Physical Laboratory, Teddington, Middlesex, TW11 0LW UK
** CESI RICERCA, Milan, Italy
steve.osgerby@npl.co.uk

Abstract

The quality and endurance of metallic and thermal barrier coatings used on gas turbine components is a key issue for life management. As a consequence there is increasing industrial interest in techniques that assess coating condition not only prior to introduction into service but also after operation ie to monitor the actual degradation level of the metallic coating (bond coat) and the integrity of TBCs.
Recently there has been increasing interest in the development of reliable non-destructive techniques that are able to evaluate the condition of coatings, thus avoiding irreversible component damage. In this paper a range of non-destructive techniques applicable to such complex coatings are reviewed. Examples are drawn from work contributed to COST522 and COST538; activities with the authors' Institutes; and from published literature.
This review describes the complementary capabilities and peculiar characteristics (eg spatial resolution) of the following techniques: frequency scanning eddy-current technique (F-SECT); photo-luminescence piezospectroscopy (PLPS); pulsed thermography; laser back scattering; impedance spectroscopy and acoustic emission.
The potential for each of these techniques for in-situ monitoring of component condition is also discussed.

Keywords: Coatings, gas turbines, NDE, Frequency-Scanning Eddy Current, Photo-Luminescence Piezospectroscopy, Laser Back-Scattering

Introduction

Initially coatings were applied to hot parts in gas turbines to increase resistance to high temperature oxidation and hot corrosion. More recently the possibility to increase inlet temperatures and thus significantly increase turbine efficiency came with the introduction of ceramic thermal barrier coatings (TBCs) on combustion chambers and rotating blades. The endurance of such coatings is a key concern for both manufacturers and operators as very variable lifetimes can be registered. As a consequence it is important both to assess the condition of the coating prior to introduction into service and to monitor the actual degradation level of the metallic coating (or bond coat, BC) and the integrity of TBCs after operation.

Detailed description of the composition, processing and subsequent microstructure of individual coating systems is beyond the scope of this review, which will focus on the use of non-destructive techniques to monitor the evolving condition of coatings after service exposure. However a distinction will be made between ceramic layers produced by electron-beam plasma vapour deposition (EB-PVD) and air-sprayed plasma (APS) techniques. Both the residual protective capability of the metallic

coating from oxidation and hot corrosion, and the detection of incipient failure of TBCs before macroscopic spallation will be considered.

Industrial needs

Gas turbine users usually follow the maintenance schedule suggested by the OEM, which is usually based on very conservative criteria to increase plant reliability. In practice, after a defined operation period the coatings of hot parts in each specific plant could have a different residual life, depending on the particular operation history experienced. Even if life prediction modelling of metallic coatings is nowadays well developed, the actual coating durability reduction due to fuel changes and/or higher degradation due to cycling is still less known. Moreover the problem of coating assessment (both in the as produced situation and after service) is even more critical for ceramic thermal barriers, as the endurance of such coatings is still a key issue and very variable lifetimes are registered.

As a consequence both the OEMs and the utilities have a common interest in the development of non destructive techniques able to evaluate both initial coating quality and the actual coating situation after an operation period, on several respects:

- thickness measurement;
- incipient defects and detachments;
- protective capability deterioration of the bond coat (BC);
- internal oxidation and interdiffusion at the interface with the substrate;
- growth of the thermally grown oxide (TGO) at the metallic/ceramic interface, with the development of high compressive stresses at the bottom of the TBC;
- sintering of the ceramic layer (TBC) and consequent thermal conductivity and stiffness increase;
- microcracking of TGO and TBC

All these aspects of coating degradation are happening inside a multi-layer system and non-destructive techniques should be able to detect the different damage mechanisms that contribute in an interactive way to the final TBC failure. Recent development of such techniques are both in the direction of higher reliability and sensitivity and also in the direction of the applicability in situ during scheduled inspections, without dismounting the blades.

A further step highly desirable in perspective for industry could be the possibility to use such non destructive techniques directly on blades mounted in the gas turbine, even without opening the turbine case. New methodologies could implement the inspections based today only on the visual inspection with the aid of optical fibres and video cameras and give a more complete coating assessment. Such data could be a starting point for more precise residual life evaluations, permitting optimised inspection intervals and reduced maintenance costs.

Individual Techniques:

Frequency scanning eddy-current technique (F –SECT)

The degradation level of the protective capability of metallic coatings, which are used for protective against environmental attack or as bond coats, is the first issue to be

considered in coating life assessment of hot parts. It depends on the residual content of the aluminium-rich β phase, which is gradually reduced due to interdiffusion of Al with the substrate on one side and the formation of alumina on the other. Modelling of these phenomena is well developed [1-4] and allows residual life estimates based on coating thickness and residual phase content, using inverse problem solution techniques [5].

The Frequency Scanning Eddy Current method (F-SECT) [6-10] is a special application of the eddy current technique. It is based on the principle of scanning the frequency of the sinusoidal currents applied to the transmitter coil of the probe, held near the surface of the component. The magnetic field produced at each frequency penetrates in the material at a depth inversely proportional to the square root of the frequency. The receiver coil inside the probe detects the field "reflected" by the material in the form of an induced voltage at its terminals. The probe output voltage vs. frequency is influenced by the small differences in electrical conductivity between adjacent layers of electrically conductive multiple-layer materials, such as the metallic coating-substrate system of hot parts. From these raw data the physical parameter "normalised impedance" is obtained, by a computerised system. As shown in Figure 1, different shapes of the impedance vs frequency plot are associated to different damage levels of an MCrAlY coating. [6].

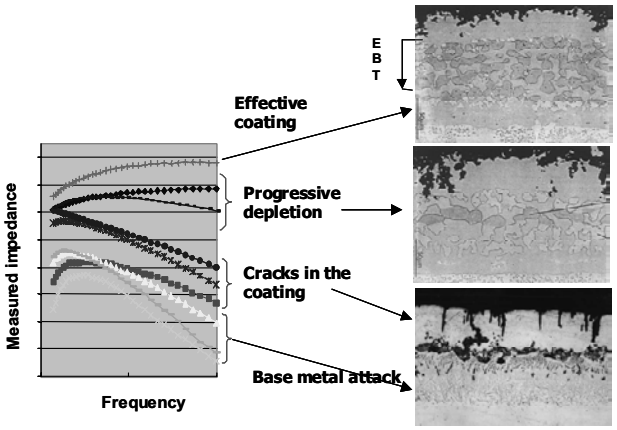

Figure 1 Examples of impedance vs frequency plots associated to different damage levels of an MCrAlY coating. The parameter EBT is also indicated [6].

An inter-comparison exercise, organised by EPRI, verified the capability to measure the thickness of new MCrAlY coatings [7]. On service exposed components the total thickness of the metallic coating can be measured and also the diagnostic parameter called EBT (effective β thickness (see Figure 1)), indicating the thickness of the residual protective layer inside the coating (see Figure 2) [7, 9].

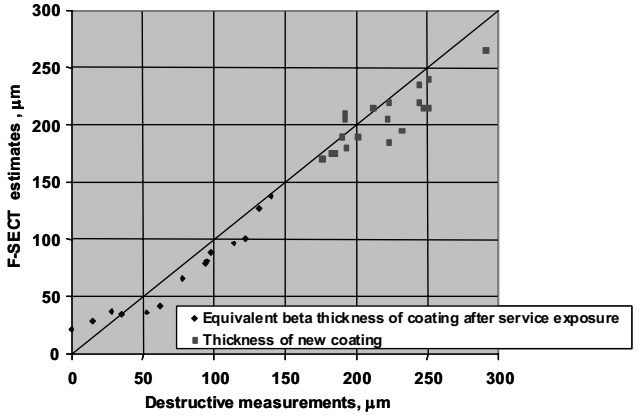

Figure 2 Demonstated agreement between the coating thickness and EBT values estimated by F-SECT and measured by metallographic analyses [7, 9].

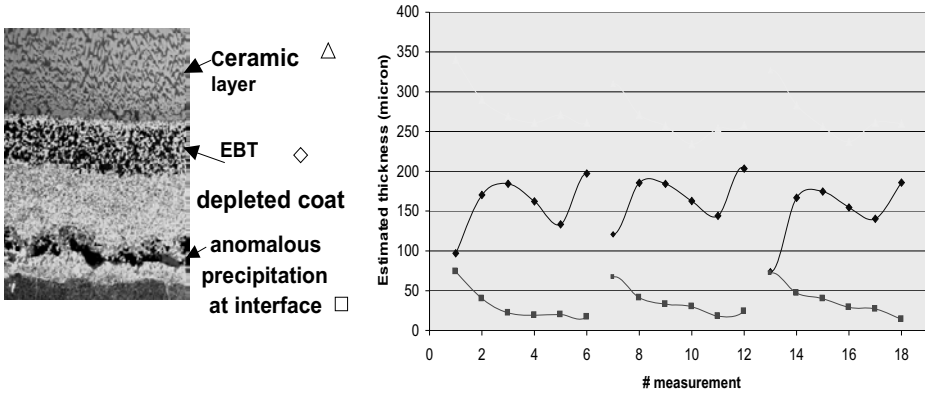

Figure 3 Example of F-SECT results on 18 points of an operated component with EB-PVD TBC and NiCoCrAlYRe bond coat: thickness of TBC (Δ), residual protective layer of the metallic coating (◆) and anomalous precipitation layer at the interface with the base material (■), [8].

In modern gas turbines a metallic layer is present under the ceramic thermal barrier and is subjected to similar aluminium depletion. Figure 3 shows an example [8] of the application of the F-SECT system to evaluate the degradation of the NiCoCrAlYRe bond coat on an operated V94.3A2 gas turbine. An additional benefit of the F-SECT technique is that the thickness of the TBC can also be measured, through the lift-off signal, if the distance of the probe is kept always at a fixed distance from the component surface, as in the case of the probe developed by CESI. This sensor is applicable *in situ* on mounted blades in the turbine after service exposure [8], as shown in Figure 4. On the first blade several measurements are taken to find out the hottest region; then in that position measurements are performed on all the blades (or on a statistically significant number of blades of the same wheel), to

obtain a representative assessment of blade coating degradation, to support maintenance decisions.

Finally examples were recently published of the possibility to estimate the mean operation temperature of the measured region of the component [11, 12] using coating degradation models and inverse analysis methods applied to F-SECT results.

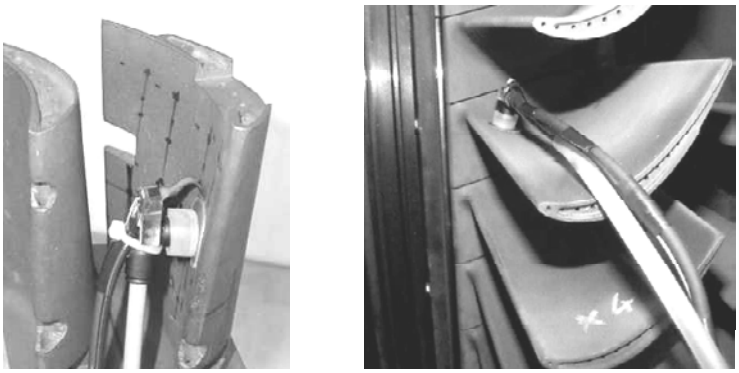

Figure 4 New F-SECT sensor for in situ measurements on mounted blades.

Photo-Luminescence Piezospectroscopy (PLPS)

PLPS is used to monitor residual stress in the thermally grown oxide (TGO) within the TBC system. The principle of the technique is that laser excitation of small amounts of Cr^{3+} ions in the TGO causes fluorescence to occur and the spectral response is pressure (stress) dependent [13,14]. Thus should the TGO become detached the stress would be reduced and would be detected by a peak shift in the fluorescent spectra. The surface of a laboratory specimen or component can be scanned to determine a spatial distribution of TGO stress and hence (potentially) delaminations.

There are however many subtleties in interpreting the luminescence signal to determine the TGO stress. For a single homogenous stress state at a given temperature a well-defined doublet is observed which requires at least eleven parameters to describe its R1/R2 spectrum. [15,16]. These are the peak positions of the R1 and R2 line and their separation, the intensities of the R1 and R2 lines and their ratio, the halfwidths of the R1 and R2 lines and their ratio, and the shape of the R1 and R2 lines conventionally expressed as the fraction of Lorentzian versus Gaussian character for each R line (Figure 5).

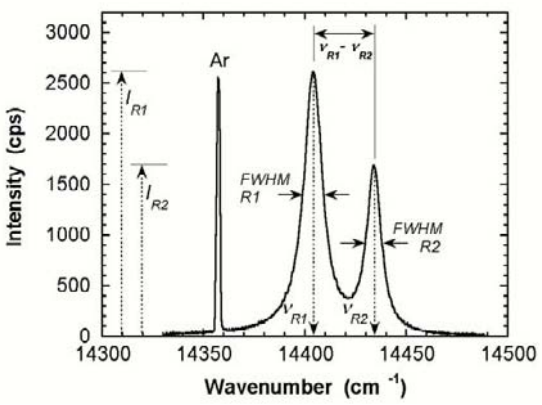

Figure 5 Representative spectrum from luminescence of Cr^{3+} ions showing the parameters required to define the peak fully

In practice the spectra obtained from aged TBC systems often contain more than a single stress state and two or more R1/R2 doublets must be used to interpret the signal. In this case a fit to two doublets is implemented, with the parameters from the fit to a single doublet utilised to obtain an initial estimate of the parameters for the optimisation routine. Occasionally even two doublets are insufficient to fit the experimental data and in this case the signal cannot be interpreted. Examples of fitting experimental data are shown in Figure 6.

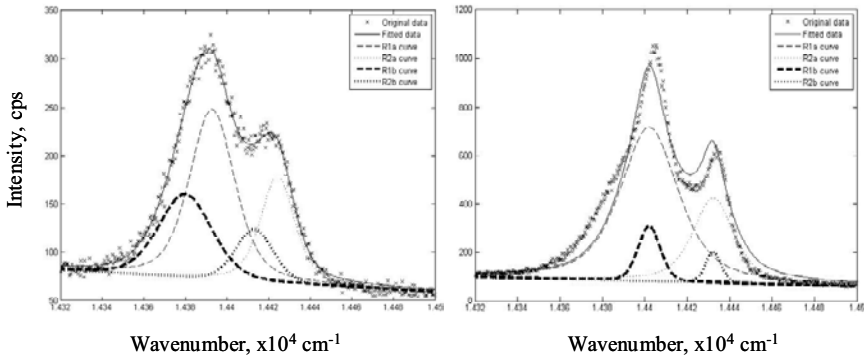

Figure 6 Fitted spectra obtained from two different regions of IN738/Amdry 997/ EB-PVD coating system after exposure for 1200 h at 1000 °C (a) good fit obtained (b|) poor fit

A selection of spectral collection and fitting procedures were compared [16]. The exercise had two components – spectra collection and spectral analysis and involved University of California, Santa Barbara (UCSB), University of Connecticut (UConn), Oak Ridge National Laboratory (ORNL), University of Trieste (U Trieste), National Physical Laboratory (NPL) and Imperial College (IC). Four institutes carried out measurements on TBC samples aged for various times. The results showed good consistency as demonstrated in Figure 7.

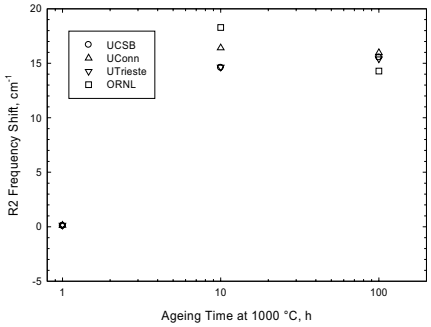

Figure 7 Comparison of PLPS measurements from different laboratories carried out on TBC specimens aged at 1000 °C for various times (data from ref [16]).

A similar comparison was carried out for spectral fitting where the dataset was distributed electronically to five institutes for fitting using their 'in-house' procedures. Again good agreement was obtained when the spectrum was analysed using procedures that fitted the data to a pair of doublets rather than assuming a single stress state (Figure 8).

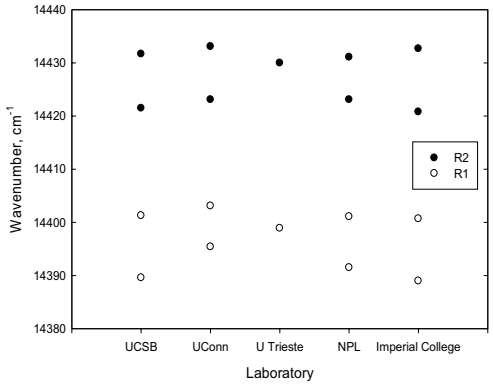

Figure 8 Comparison of R1 And R2 wavenumbers derived by different institutes from a common dataset obtained from a TBC system after ageing for 100 h at 1000 °C (Data from Ref [16]).

The evolution of TGO stress with time at temperature has been studied by several researchers on EB-PVD [17,18] and APS [17, 19] systems. A typical pattern of stress evolution with exposure for an EB-PVD system is shown in Figure 9 – the specimen failed completely before 700 cycles had been completed. It can be seen that for the majority of the coating life the mean stress derived from the two R2 peaks (see Figure 6 for explanation) remains effectively constant but that just prior to failure the mean compressive stress decreases and the scatter between points measured on the same specimen increases.

Detailed analysis of the data obtained after each exposure time show that early warning of failure may be obtained. Figure 10 shows individual data points from each of the above conditions, plotted on a probability diagram. It can be seen that the stress

values indicate a significant event, attributable to the initiation of failure, after 500 h exposure. The technique has potential use for inspection without dismantling the gas turbine. Towards this aim a portable system, incorporating a small probe that can be inserted through the inspection ports of the engine is presented in [20]. The limitations of this technique are that the attenuation of the signal is very high, particularly in APS TBC systems. Subsequently the technique at the moment is effectively limited to EB-PVD TBCs, even if a recent application of PLPS to pseudo-columnar APS TBCs seems to give positive results [21], worthy of further investigation.

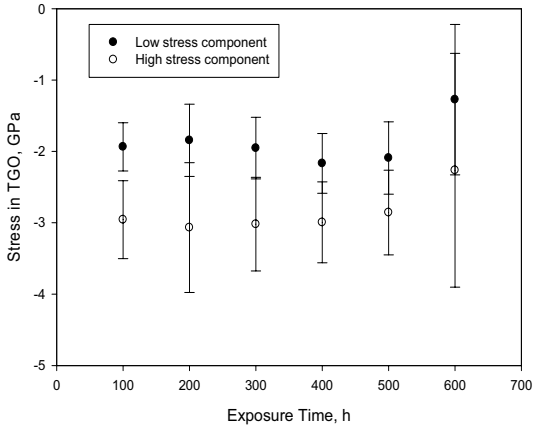

Figure 9 Evolution of TGO stress with exposure time for EB-PVD\ MCrAlY Coating on IN738 aged at 1000 °C

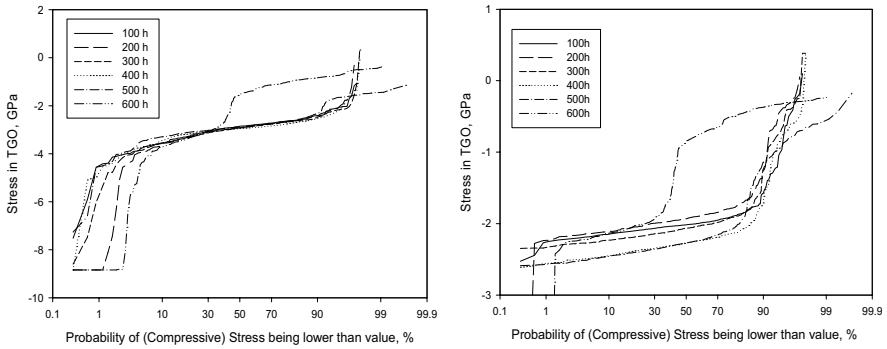

(a) (b)

Figure 10 Probability plots of TGO stress as a function of exposure time (a) high stress component (b) low stress component

Laser Back Scattering (LBS)

LBS is a non contact optical technique recently developed at Argonne National laboratories [22,23] and based on the transparency of ceramic materials at visible and near infrared radiation. Figure 10 shows the principle of the technique: a polarised

He-Ne laser beam is scanned along the ceramic surface, partially transparent to it. The radiation backscattered by the metal/ceramic interface or by defects in the ceramic layer is collected in real time and sent to two detectors (A and B in Figure 10). A reflecting surface with a small hole (typical diameter 100 μm) is placed in front of the first detector, so that it collects only the low angle back scattered beam; the high angle fraction is collected by the second detector; one fraction of the back scattered light is also sent to a video camera to form the image of the inspected area.

Computerised 3D scanning of the surface is performed; in each point the signals of the two detectors are collected and used to form two images: a grey scale image of the surface and an image obtained with the ratio between the two signals, containing information about the lateral extension of the area containing defects. Dedicated software performs a statistical analysis of the grey levels distribution of the two images, obtaining quantitative information about the type of defect (e.g. size of small cracks, detachments) [24].

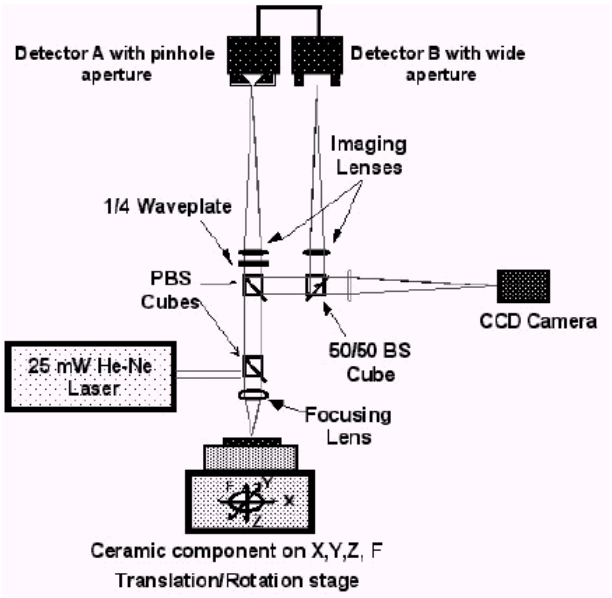

Figure 11 Schematic of the laser backscattering technique, developed by Ellingson [22]

This technique has been applied to the analysis of the degradation of thermal barrier coatings used on blades and vanes of gas turbines [24]. Back scattered light images were measured on specimens of CMSX4 with an MCrAlY bond coat and a 7-8 wt% YSZ ceramic layer (APS or EB-PVD), which had been exposed to thermal cycling in a cycling oxidation test. One of the most important results is that the shape of the grey levels histogram changes during the thermal cycling of the specimen, as shown in Figure 11. The peak position is correlated with the number of thermal cycles and consequently to the increase of the interface between the bond coat and the zirconia layer. These preliminary results are promising but further studies are needed to better evaluate the reliability of the indications relative to the damage level of the thermal barrier.

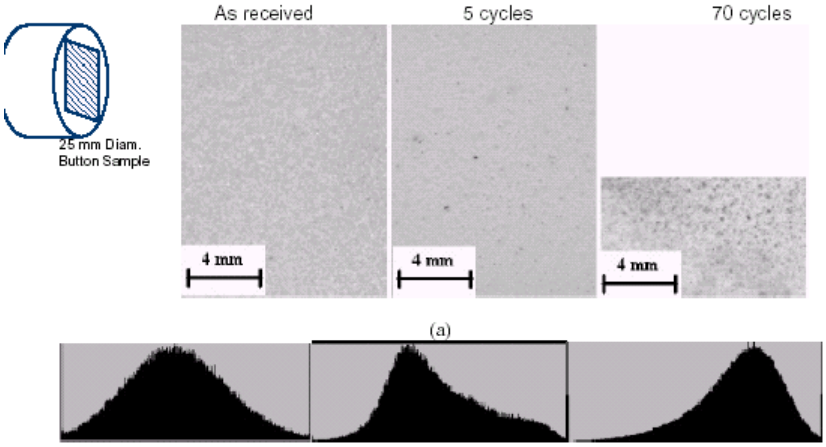

Figure 12 Laser back scattering technique applied to CMSX-4 specimens with MCrAlY bond coat and YSZ thermal barrier. Change of the grey level histogram with number of thermal cycles and roughening of the metallic/ceramic interface.

Impedance spectroscopy (IS)

IS is a non-destructive technique, based on the measurement of electrical impedance at different frequencies; it is extensively used to identify the microstructural changes of ceramic materials which induce variations of electrical properties (as densification and microcracking associated to phase transformation) [25]. In the last years [26-28], this technique has been applied to characterise Thermal Barrier systems and to assess the TGO growth in TBCs after exposure at high temperatures. Impedance measurements are possible only at temperatures where the ceramic coating has a sufficient conductivity due to oxygen ions transport. As a consequence the specimen under test has to be heated, in air, at temperatures higher than 200 °C.

To perform the IS measurements, the metal side of the coated specimen acts as one electrode; the ceramic TBC side is coated with a silver paint, to serve as the other electrode. During the application of an alternating current (a.c.) with varying frequency (typically in the range 1 Hz-1x10^7 Hz), the voltage and current responses related to YSZ, TGO and mixed oxide layers are measured and presented in the impedance spectra [24,25]. These spectra are acquired by measuring the magnitude and phase shift of the resulting current.

The most frequently used presentations of impedance data are as Nyquist and Bode plots [25-27]. In a Nyquist plot, also termed the complex plane impedance plot, the impedance is represented by a real part Z' and an imaginary part Z'' with the formula $Z(\omega)=Z'+jZ''$, where ω is the angular frequency and j=the square root of (-1). For a simple resistor-capacitor (R-C) circuit, the Nyquist plot is characterised by a semicircle. If the physical system is more complicated, few semicircles could be present, as shown in Figure 10, relating to as-sprayed and oxidised specimens [26,27]. These spectra have to be fitted with an equivalent circuit, using proper Equivalent Circuit software, which corresponds to a physical model of the multi-layer system.

The equivalent circuit represents the main electrical features of the model when fitting measured spectra [27,28].

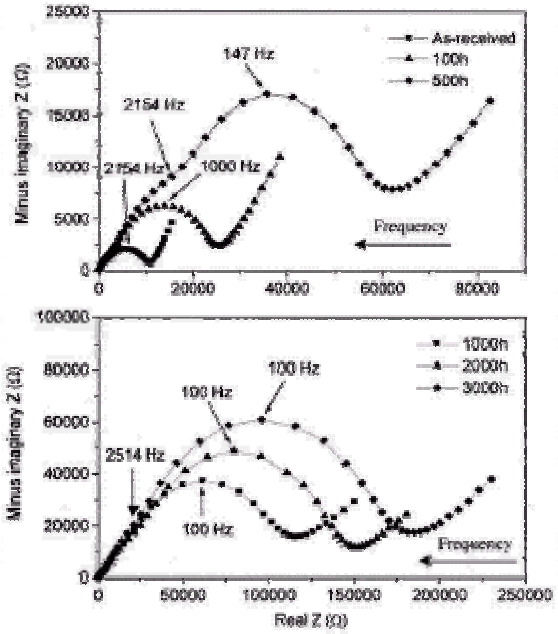

Figure 13 Typical Nyquist plots for the specimens as-received and oxidised at 950°C for different times: IS measurements at 400°C [25].

In a Bode plot, the modulus of the impedance and the phase angle are both plotted as a function of frequency. The phase angles as function of frequency are represented in Figure 14. In this diagram the relaxation frequencies of each layer of the system are evidenced. Changes of the relaxation processes are related to the changes in material microstructure (porosity, densification, micro-cracks) and microchemistry (mixed oxides). In Figure 14, for instance, two relaxation processes are evidenced for the as-sprayed and 100h oxidised specimens, while for the specimens oxidised for 1000 h or more there are three processes [27]. The two relaxation processes of the as received material in the impedance spectra correspond to the alumina and to Yttria Stabilised Zirconia (YSZ) topcoat, when a discontinuous alumina layer is formed between the top and bond coats. Instead, three relaxation processes were found in the impedance spectra, corresponding to the alumina layer, the mixed oxide layer, and the YSZ layer, when a continuous alumina layer and a mixed oxide layer were formed between the top and the bond coats.

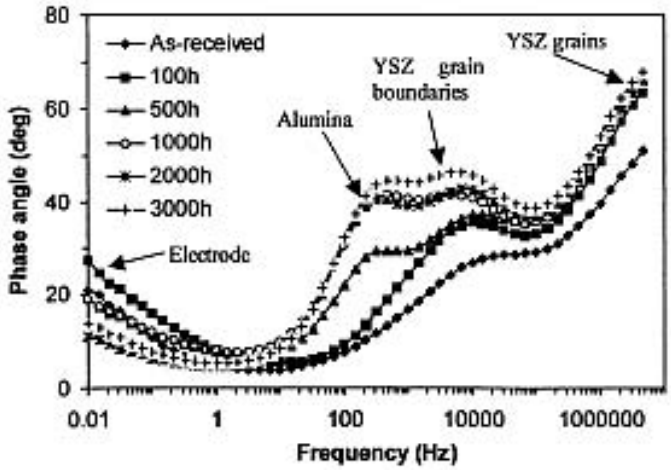

Figure 14 Phase angle as a function of frequency at 400 °C for the specimens as received and after oxidation at 950°C for different times.

Recently, using the IS technique and SEM/EDX, Anderson et al [30] have characterised a range of isothermally heat-treated plasma sprayed (PS) and electron beam physical vapour deposited (EB-PVD) thermal barrier coatings.

Overall IS seems to be a powerful non-destructive tool to monitor TGO growth, mixed oxide formation and, in general, for the analysis of the whole TBC systems. Nevertheless, its application, for the practical requirements (high temperature operation, electrode), is still confined to laboratory assessment.

Recently a new implementation of this technique, named Electrochemical Impedance spectroscopy (EIS), has been pressed in literature to perform in electrolyte solution [29,30], room temperature assessment of both free-standing TBC samples and multi-layered Thermal Barrier. The feasibility of this technique is still under investigation.

Acoustic Emission (AE)

AE is well known as a non-destructive method for detection of damage initiation and growth induced for example by thermal or mechanical stresses. Energy release during damage processes generates ultrasound waves inside the material that can be easily detected with appropriate transducers. Recently AE has been used during mechanical tests performed on TBC coated specimens to determine the deformation level at which delamination occurred [31-35]. The use of two or more sensors allows the location of the damage to be defined, thus permitting only those of interest to be analysed.

Moreover in some laboratories acoustic emission is also applied to detect both oxide spallation and TBC detachments during cyclic oxidation tests [31]. In such case a metallic guideline welded to the testing specimen is necessary to preserve the sensor from the high temperatures experienced by the specimen.

A recent development in AE analysis is the use of wavelets to differentiate between different damage mechanisms. To date the authors are not aware of any direct

application of this analysis to gas turbine coating but the technique has been used to determine fracture features in scratch testing of coated steels [36].

Finally it must be noticed that the applicability of this technique is presently limited to laboratory tests.

Thermography

Thermography can be used to inspect coating systems in several ways. In the simplest case the area of to be inspected is heated either through conduction or radiation and the surface temperature monitored using a suitable imaging system such as a scanning infra-red camera with mK resolution. Areas of cracking/delamination are detected as cool or hot spots respectively. This is illustrated in Figure 11 for a IN738/MCrAlY/EB-PVD system. The thermographs in Figure 11a and 11b show the image obtained from conduction and radiation heating respectively. Figure 11c shows a cross-section of the coated specimens and clearly shows the delamination causing the thermal contrast.

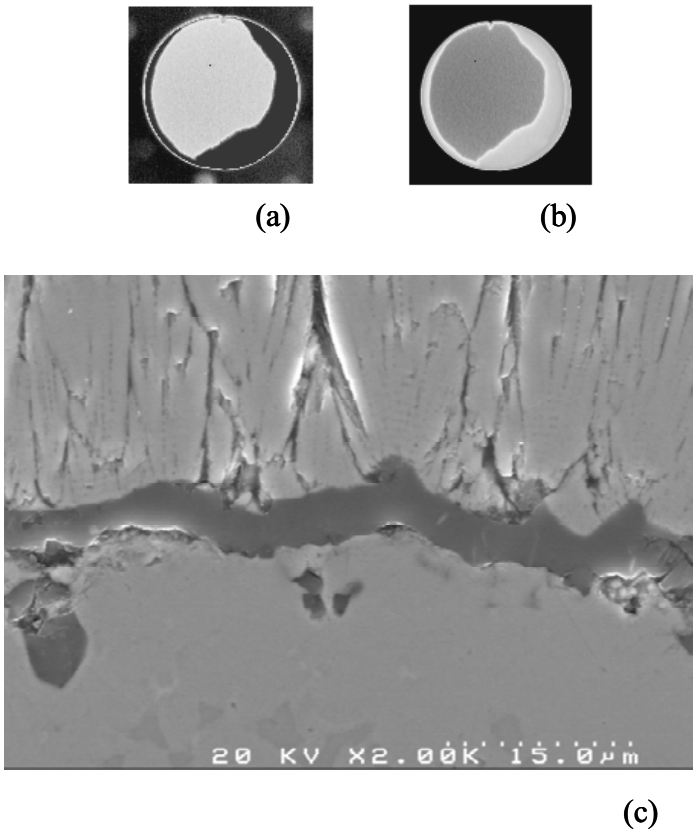

Figure 15 Example of application of thermography in a IN738/MCrAlY/EB-PVD coating system (a) Conduction heating mode (b) Radiation heating mode (c) Metallographic cross section

The theory of thermal wave imaging is well established [37,38] and has been used to demonstrate that the technique will not detect cracks that are normal to the surface [37]. In addition the theory allows other characteristics of the coating to be determined eg thickness and thermal properties [38].

Conclusions

Several NDE techniques exist for assessment of the condition of gas turbine coatings both prior to entry into service and after exposure. Each technique produces complementary information and for a full assessment of coating condition a combination of NDE techniques is recommended.

The capabilities, limitations and applicability of the techniques are summarised in Table I.

Table I Comparison of Available Techniques

Technique	Detection capabilities	Limitations	In Field applicability
F-SECT	♦ MCrAlY or bond coat degradation (quantitative parameters) ♦ TBC thickness	Requires preliminary calibration on each type of metallic coating	also on mounted blades - open turbine case
PLPS	♦ Very early stages of damage at TBC/BC interface can be detected ♦ TGO residual stress level (quantitative)	Only EB-PVD Application to Pseudo-segmented APS is under study	Portable instrument with optical fibre – dismounted blades
Thermography	Detachment at TBC/BC or metallic coating/substrate Interfaces	An air layer must be formed at interfaces, several mm wide	YES if component accessibility exists
Laser BKS	Interface TBC/BC Roughness increase		Only laboratory
IS – EIS	Evolution processes and TGO growth		Only laboratory
AE	Initial delamination of TBC During laboratory testing (active technique)		Only laboratory

References

[1] K.S. Chan, N.S. Cheruvu, G. R. Leverant, Trans. ASME: Journal of Eng. for Gas Turbines and Power, 120, (1998) 609-614.

[2] K. S. Chan, Metall. and Mater. Trans. A, 28A, (1997) 411-422.

[3] H.B. Probst, C.E. Lowell, Journal of Metals, (1988) 18-21.

[4] J.A.Nesbitt in Life Time Modelling of High Temperature Corrosion Processes, ed. M. Schuetze, W.J. Quadakkers and J.R. Nicholls, EFC pub. N°34, 2001, 359-378

[5] P. Krukovsky, V Kolarik et al., in Life Time Modelling of High Temperature Corrosion Processes, ed. M. Schuetze, W.J. Quadakkers and J.R. Nicholls, EFC pub. N°34, 2001, 231-245.

[6] G. Antonelli, M. Ruzzier, F. Necci, ASME Journal of Engineering for Gas Turbines and Power 120(3) (1998) pp 537-542

[7] G.Antonelli, G. Tirone, Power Gen. Europe, Helsinki, Finland (2000).

[8] G. Antonelli and L. De Maria, Proc. Turbine Forum – Advanced Coatings for High Temperatures, Nice/France, Apr. 21-23 (2004).

[9] C. Rinaldi and G. Antonelli, Special Issue Paper Proc. Imech E, J. Power and Energy, 219 Part A (2005) 93-99.

[10] C. Rinaldi, L. de Maria, G. Antonelli and F. Cernuschi, ASME ESDA Turin July 4-7, (2006), paper 2006-95555.

[11] C Rinaldi, M Mandelli and D Colombo, La Metallurgia Italiana, 5/2005 (2005) 58-66.

[12] C. Rinaldi and M. Mandelli, 2005 " Residual life assessment of coating with F-SECT technique and a predictive model", Proc. of AIPND Conference, Milan Oct. 2005.

[13] D M Lipkin and D R Clarke, Oxid. Met. **45** (1996) 267.

[14] R.J Christensen, D.M Lipkin, D.R. Clarke, K.S. Murphy, Appl. Phys. Lett., 69 [24] (1996) 3754-3756.

[15] A Nychka, D R Clarke, S Sridharan, E Jordan, M. Gell, M J Lance, C J Chunnilall, I M Smith, S R J Saunders, R. Pillan, V. Sergo, A. Selçuk, A. Atkinson, and K S Murphy, Surface and Coatings Technology, 163-164 (2003) 87-94

[16] S R J Saunders, J P Banks, G Chen and C J Chunnilall, Materials Science Forum, 461- 464 (2001) 383-390.

[17] M Bartsch, C Leyens and W Kaysser, in Life Time Modelling of High Temperature Corrosion Processes, eds M Schutze, W J Quadakkers and J R Nicholls, EFC Publication N° 34, Institute of Materials, London, (2001) pp. 313-323

[18] L. De Maria, C. Rinaldi and V. Sergo, "Portable optical system for in situ thermal barrier assessment of service operated blades", Proc. ASME TURBO EXPO Barcellona May 8-11 (2006), paper GT2006-90551.

[19] C. Rinaldi, L. De Maria, F. Cernuschi and G. Antonelli, Proc. ASME ESDA 2006, Torino, July 4-7 (2006), paper ESDA2006-95555.

[20] J A Nychka and D R Clarke Surf. and Coatings Techn. 146-147 (2001) 110-116.

[21] M. Gell, S. Sridharan, M. Wen, Int. J. Appl. Ceram. Technol., 1 [4] (2004) 316-329.

[22] W.A. Ellingson et al. Patent n° US 5,689,332 Nov.1997

[23] W.A. Ellingson et al. Patent n° US 6,285,449 B1 Sep.4,2001

[24] W.A.Ellingson et al. in First International Conference on Industrial Gas Turbine Technologies 10-11 July 2003 Brussels

[25] J.R. MacDonald (Ed.), Impedance Spectroscopy, Wiley, Chichester, 1987.

[26] Shenhua Song, Ping Xiao, Mater. Sci. Eng. B97 (2003) 46–53

[27] X. Wang, J.F. Mei, P. Xiao, J. Eur. Ceram. Soc. 21 (2001) 855.

[28] Xin Wang, Junfa Mei, Ping Xiao Journal of Materials Science Letters 20, 2001, 47– 49

[29] M.S. Ali, S.-H. Song, P. Xiao, J. Eur. Ceram. Soc. 22 (2002)101

[30] P.S. Anderson, X. Wang, P. Xiao, Surface & Coatings Technology 185 (2004) 106–119

[31] V Voyer, F Gitzhofer, M I Boulos, Journal of Thermal Spray Technology; 1998; Vol. 7 (2); 181-190

[32] C-K Lin and C C Berndt, Surface and Coatings Technology; 102 (1998) 1-7

[33] D J Andrews, J A T Taylor, Journal of Thermal Spray Technology; 9 (2000) 181-190

[34] M. Białas; P. Majerus; R. Herzog; Z. Mróz, Mater. Sci. Eng. 412 (2005) 241-251

[35] A Kucuk, C C Berndt, U Senturk, and R S Lima, Mater. Sci. Eng. 284 (2000) 41-50.

[36] A Gallego, J F Gil, J M Vico, J E Ruzzante and R Piotrkowski, Scripta Materialia. 52 (2005) pp. 1069-1074

[37] K R Grice, L J Inglehart, L D Favro, P K Kuo and R L Thomas, J. Appl. Phys. **54** (1983) pp 6245-6255

[38] A C Bento and D P Almond, Meas. Sci. Technol. **6** (1995) pp 1022-1027

GAS TURBINE ISSUES IN ADVANCED GASIFICATION SYSTEMS

Richard Wenglarz,
South Carolina Institute for Energy Studies; Clemson SC, USA

John Oakey
Cranfield University; Cranfield, Bedfordshire, UK

Abstract

Gasification of feedstock such as coal, petroleum coke, refinery residuals, biomass, waste and their blends is an emerging technology to produce syngas as a fuel for gas turbines and for chemical processing. More than twenty syngas-fired turbine plants have been constructed world wide and many more are being considered for the future. Although these plants utilize multiple stages of cleanup of the product gas, limited quantities of impurities pass the cleanup systems; these enter the gas turbine hot section flow path after combustion leading to a risk of damage to the vane and blade materials. Since the turbines used in these plants and their hot gas path materials have typically been designed to operate with natural gas (the purest of fuels), materials performance associated with operation with syngas fuels is of concern.

This paper discusses materials experience and issues related to gas turbines operating with fuels produced by gasification systems. Operational requirements that affect the hot section materials environments are reviewed. These include injection of diluents (such as steam) for the control of NO_x emissions and increased hot section mass flow due to the relatively low energy content of syngas. Levels and composition of impurities in syngas produced at an Integrated Gasification Combined Cycle (IGCC) plant are discussed along with potential compositions of impurity compounds resulting from the combustion of gasification product gas. Available information on corrosion, erosion, and deposition degradation of turbine alloys and coatings from pilot plant tests and IGCC turbine experience is described. Remaining materials issues for syngas turbines are presented, including the effects of higher inlet temperatures in future turbines to increase efficiency and power output, and thereby improve the economics of IGCC plants.

Keywords: syngas, turbine, materials, issues

Introduction

In recent years, more than twenty commercial plants have been constructed that utilize gas turbines operated with synthetic gases (syngas). Because of decreasing availability of low cost fuels and other factors, many more syngas turbine plants are being considered for the future. The wide range of feedstock to the gasifiers that produce the syngas has included coal, petroleum coke (petcoke), biomass, waste, and blends of these feedstock. The gasifier product gases are typically processed by many stages of cleanup to remove environmental pollutants and to protect the components in turbine hot section from corrosion, erosion, and deposition due to feedstock ash impurities. The combustible products (H2/CO) in the syngas and overall level feedstock ash carryover to the turbine combustor are well controlled by the gasification and syngas treatment processes. However, the composition of the remaining limited level of impurities in the syngas combustion products and their effects on turbine hot section materials can potentially vary greatly between different plants, depending on the wide variety of feedstock, gasifier configurations, types and number of syngas processing stages, and operating conditions. This paper considers the effects of several of these many factors affecting hot section materials

performance to identify potential materials issues and needs for turbines operating in advanced gasification systems. Since relatively little in-depth information is available in the open literature on syngas impurity compositions, severity of syngas turbine materials environments, and characterization of the extent and nature of materials degradation, the information discussed in this paper represents an initial perspective on materials issues for syngas turbines and potential solutions.

Syngas turbine operational factors

Low heating values typical of syngas and injection of diluents (to control combustion temperatures and therefore thermal NOx) have resulted in higher mass flows (~14%, Ref. [1]) through the turbine hot section than for operation with natural gas. This produces 20-25% higher turbine output power compared to natural gas but also tends to increase the heat transfer to the hot section vanes and blades. Accordingly, syngas turbines have been operated at reduced firing temperatures to maintain hot gas parts at temperatures similar to those of the same model turbines operated with natural gas (Ref. [1]). Future higher inlet temperature turbines produced for operation with syngas may need higher temperature TBC/alloy designs and/or increased cooling of the upstream rows of the hot section and also higher temperature alloys for the uncooled downstream rows.

Both steam and nitrogen have been used as syngas diluents in IGCC plants to control NOx emissions. For example, a representative nitrogen diluted syngas fired in the turbine combustor at one IGCC plant contains about 53 % N2 for dilution with about 11% H2 and about 4% H20 (Ref. [2]). A representative steam diluted syngas fired in the turbine combustor at another IGCC plant (Ref. [2]) contains 22% H20 and 28% H2 (all of the above are expressed as volume %). Consequently, the diluent used (steam vs. nitrogen) and water vapor formed from H2 in the combustion process along with differences in water input for various gasification processes result in significant differences in possible in water vapor levels in the combustion gases flowing through IGCC turbine hot sections. This may result in differences in hot section component degradation since increased water vapor levels have increased oxidation rates in laboratory tests of turbine materials (Ref. [3]).

Syngas turbine inlet temperature is another important operational factor affecting materials performance, as to be discussed in some detail in a later section.

Impurities in syngas

The levels and composition of the limited impurities that are carried after cleanup into the turbine depend not only on the specific cleanup processes and equipment at the syngas plant but also on the gasifier feedstock. For coal feedstock (and coal blends with other fuels such as petcoke), the potential range of impurity concentrations and composition are large along with the potential variation in impurities that might enter IGCC turbines, as suggested by Table 1 below.

Element	Range (%)		
Na	0	—	0.20
Mg	0.1	—	0.25
Al	0.43	—	3.04
Si	0.58	—	6.09
Cl	0	—	0.56
K	0.02	—	0.43
Ca	0.05	—	2.67
Ti	0.002	—	0.32
Fe	0.32	—	4.32
Zn	0	—	0.56
		(ppm)	
Be	0	—	31
B	1.2	—	356
F	10	—	295
P	5	—	1430
Sc	10	—	100
V	0	—	1281
Cr	0	—	610
Mn	6	—	181
Co	0	—	43
Ni	0.4	—	104
Cu	1.8	—	185
Ga	0	—	61
Ge	0	—	819
As	0.5	—	106
Se	0.4	—	8
Br	4	—	52
Y	<0.1	—	59
Zr	8	—	133
Mo	0	—	73
Cd	0.1	—	65
Sn	0	—	51
Sb	0.2	—	9
La	0	—	98
Hg	0.01	—	1.6
U	<10	—	1000
Pb	4	—	218

Table 1. Trace Element Range in US Coals (Ref. [4])

Element	Particulate	Gaseous
Arsenic	< 16E-6*	<0.00023*
Calcium	0.0024	0.063
Iron	0.0021	0.0049
Mercury	< 3.9E-6*	0.0048
Nickel	0.000026	0.00011
Potassium	0.00053	0.0051
Sodium	0.0128	0.095
Carbonyl sulfide		173.0
Hydrogen sulfide		1.6
Ammonia		0.116
HCl		0.036

Table 2. Syngas Impurity Levels (ppmw) (*indicates levels below detection limit values shown)

Impurities in the cleaned syngas entering an IGCC turbine combustor can be in gaseous or particulate form. Very little data on IGCC syngas impurities appear to be available in the literature. However, Table 2 gives data on impurities (Ref. [5] data converted to ppmw) that have been measured in the undiluted syngas immediately upstream of the turbine combustor at the Polk Power Station IGCC Plant operated with a the gasifier feedstock consisting of a blend of coal and petcoke. The total particulate loading is 0.41 ppmw, which is substantially greater (by about 20x) than the sum of the listed particulate elemental concentrations in Table 2. This is due to several factors including:

i) The mass of silicon and aluminum are not given in the analyses above. Expressed as oxides, silica and alumina constitute about 49.2% and 20.5% (by weight) of the ash minerals in a typical coal/petcoke blend feedstock used at the plant. Presumably, a large fraction of the syngas particulate would consist of compounds of silicon and aluminum, which were not measured.

ii) The masses of the other elements (e.g., S, Cl and possibly F) that form the ash particulate compounds in the syngas are not given in Table 2.
iii) Since coal ash contains a large range and variety of elements (Table 1), the syngas particulate (and also gaseous) impurities very likely contain significant quantities of other elements not measured.

Materials environments in syngas turbine hot sections

The addition of N2 or H20 for NOx control and the air used in the turbine combustion processes dilute the concentrations of particulate and gaseous impurities entering the turbine hot section. For example, the total particulate concentration of impurities entering the turbine hot section is estimated to be reduced by about a factor of ten (to about 0.04 ppmw) for the syngas (diluted with N2) which impurities are listed in Table 2. A GE turbine fuel specification (Ref. [6]) limits total sodium plus potassium (Na +K) in conventional fuels to less than 1 ppmw. At a typical 40:1 air to fuel ratio in turbine combustion of conventional fuels results in a maximum allowable limit of <0.024 ppmw in the turbine hot section expansion gases. The factor of ten dilution of impurities just discussed for the syngas of Table 2 (due to addition of NOx diluents and combustion air) results in a calculated particulate and gaseous Na+K value of about 0.01 ppmw, about 40% of the limit implied by the GE standard. Note that the more stringent ASTM Standard (Ref. [7]) of <0.5 ppmw Na+K in the fuel implies an allowable syngas turbine hot section Na+K limit <0.012 ppmw which is only slightly higher than calculated for the syngas which impurities are listed in Table 2. The calcium levels (particulate plus gaseous) in Table 2 correspond to about 13% of the limit implied by the GE standard of 2 ppmw (Ref. [6]).

Since the above discussed fuel impurity standards are based on experience related to past fuels (e.g., residual oils), their applicability is not certain for gasified solid fuels which have a broader range and different relative concentrations of impurities than oil-derived fuels. Also, the flow path impurities produced by oil-derived fuels typically enter the hot section as gaseous phases that condense as very small particles which experience very low rates of delivery to turbine flow path surfaces. Table 2 of syngas impurities shows particulate in addition to gaseous phases. If these particulate do not vaporize in the turbine combustion process and enter the hot section, rates of delivery of some critical impurities to turbine surfaces could be significantly higher than for oil-derived fuels, even at lower concentrations in the syngas than corresponding to the fuel specifications.

Assuming sufficient reaction time in the burner, the combustion process oxidizes impurities that existed in the syngas under reducing conditions. Thermal-chemical analyses representing the transformations of syngas impurities and hot section materials environments resulting from turbine combustion do not appear to be available in the literature. Such analyses would be useful to identify critical impurities (e.g., those resulting in molten phases) for laboratory tests to evaluate turbine alloys and coatings for syngas turbine conditions.

Turbine materials experience

IGCC plant experience

Information in the literature on turbine materials experience at IGCC plants is very limited. Deposits (attributed to pipe scale) formed on turbine combuster liners and hot section vanes and blades during early operation of one US IGCC Plant. Installation of a syngas filter immediately upstream of the combustor significantly reduced the deposition. Even after installation of the filter, coatings on first stage vanes and blades had to be refurbished after each scheduled periodic inspection at least through early 2001 (Ref. [8]). Figure 1 shows a first stage rotor blade (GTD-111 DS, CoCrAlY coating with over-aluminide) taken from the turbine after about 24,000 hours of service operating with syngas produced from coal and petcoke and #2 distillate fuel (for startup). The airfoil had experienced erosion on the leading edge and on the downstream pressure surface extending to the trailing edge at the tip regions. Some areas of the airfoil were not significantly affected while in other areas the coating were significantly degraded.

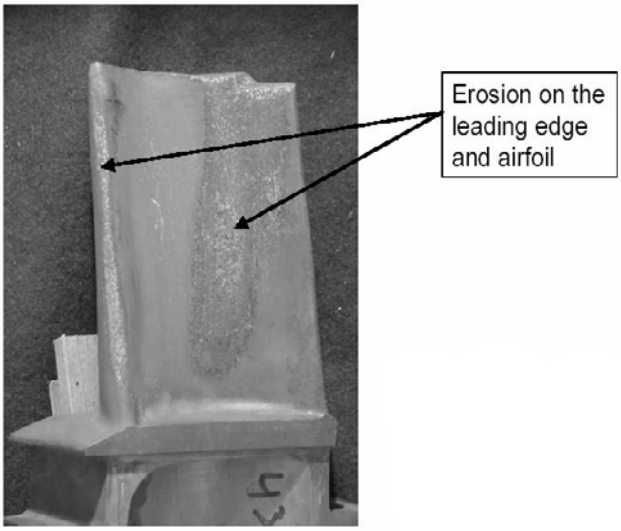

Figure 1. First Stage Syngas Turbine Blade

Fig. 2 (Ref. [9]) shows a section of the blade and the range of surface conditions at the nose and downstream regions. The coating in the eroded nose region had been completely removed and the underlying alloy substrate was oxidized with internal particles of alumina and some nitrides. Cracking of the coating is seen immediately downstream of the leading edges on both the concave and convex surfaces of the airfoil. Other analyses (Ref. [5]) show sulfides and the absence of a continuous alumina layer in areas of the leading edge.

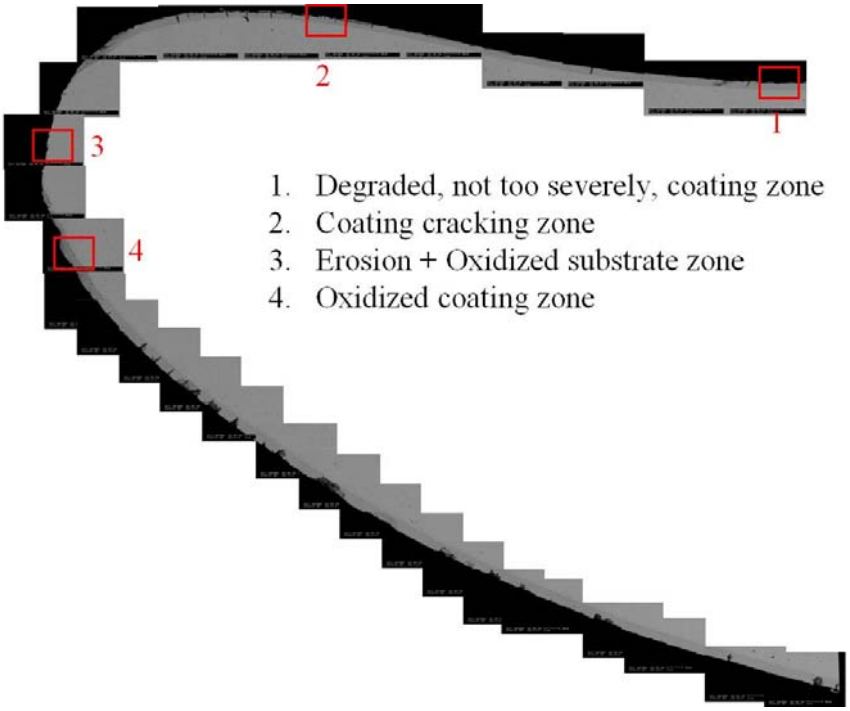

Figure 2. Cross Section of First Stage Syngas Turbine Blade

At another IGCC plant during one period of operation well after the plant was commissioned, the first stage vanes and blades of the turbine needed replacement at a much shorter interval than for a natural gas turbine. At a later inspection (and less than 12,000 operating hours after the vane/blade replacement), spalled TBC coating and deposits fragments were obtained from the first stage vanes of the turbine. The turbine had operated with syngas (produced from coal and later from petcoke) in addition to startup with fuel oil and natural gas. The spalled TBC and deposits from the vanes were analyzed at the University of Pittsburgh (Ref. [9]). X-ray diffraction analyses of the spalled TBC coating indicated the presence of NiFe2O4. EDS analyses confirmed the presence of Ni and Fe in the spalled TBC. Analyses of the vane deposits indicated Fe2O3 and possibly FeS2. EDS analyses of the deposits also showed the presence of Fe and S in addition to Ca and Ni. Other analyses showed that the deposit penetrated into the porosity of the TBC and appearance suggested that the deposit might have been molten.

Hot section parts from other syngas turbines at IGCC plants have also been analyzed (Ref. [10]). Analyses of a NiCoCrAlY coated syngas turbine first stage blade showed a spinel (Ni/Co-rich) oxide scale on the coating and some internal sulfidation. Analyses of TBC coated turbine part (from another IGCC plant) that had experienced deposition and regions of spallation showed Fe2O3 as the primary constituent of the deposit with also the presence of Si, Al, Ca, Mg, Na, K, and sulfate ions. Oxides of Co, Cr, Si and Mg were observed throughout the depth of the 8YSZ

coating thickness. Significant presence of spinel compounds (e.g., NiFe2O4, NiCr2O4, CoCr2O4) was observed in the analyses of surfaces exposed by the spallation of the coating.

Although Si and Al are typically the impurity elements of highest concentrations in coal ash and petcoke ash, Fe sometimes appeared to occur at relatively higher concentrations in the analyses of deposits adjacent to areas of turbine coating/alloy degradation described above. As indicated earlier, spalled scales from upstream piping has been considered as a source of iron in deposits on hot section components in at least one IGCC turbine. Also, a well know laboratory method for extraction of iron involves flowing carbon monoxide over an ore to produce iron carbonyl (Fe(CO)5). Consequently, iron extracted from upstream piping by syngas CO might potentially be another the source of the higher relative concentrations of iron in turbine component deposits compared to other elements in gasifier feedstock ash.

Significant deposition typically requires molten phases for attachment/sticking of particles delivered to surfaces from the high velocity flow stream. This often results in higher deposit concentrations of elements involved in the molten phases that attach the deposits than their concentrations in the fuel ash. Molten phases are also usually implicated in corrosion. Consequently, although Fe is usually not implicated in corrosion of turbine materials, lower melting point compounds containing iron might be involved in some of the syngas turbine materials degradation described above. For example, even without the presence of alkali or sulfur, oxide eutectics of Fe and other ash elements (e.g., Ca and Si) can be molten in the vicinity of 1200 C and lower (Ref. [11]).

Materials test data

A materials program in Japan exposed specimens of turbine alloys and coatings for periods up to 350 hours and temperatures of 850, 950, and 1050 C to the combustion products from a cleaned syngas produced by a Texaco type, entrained bed coal gasifier pilot plant (Ref. [12]). Syngas cleanup included a zinc oxide process to remove sulfur and a hot gas filter to remove particulate. This resulted in less than 150 ppm H2S, 300 ppm COS, and under 5 mg/m3N particulate in the cleaned syngas. Analyses of the cleaned syngas indicated Na, K, and Ca levels of 0.05mg/m3N, 0.03 mg/m3N, and 0.12 mg/m3N, respectively. At the same time as the materials tests, deposition results were obtained for a row of small airfoils exposed to the flow of the combusted syngas.

In the corrosion tests, the uncoated alloys Rene 80H and FSX414 experienced depth of corrosion penetration up to 100 microns and greater in 350 hours. Initial depth of penetration through 100 hours was low for the CoCrAlY and CoNiCrAlY coated specimens but they appeared to experience the start of breakaway degradation by 350 hours. The 8YSZ TBC experienced the least depth of damage (less than 30 microns in 350 hours) of any of the materials tested.

Although the syngas cleanup system produced an ash loading mostly under 1 micron in diameter, delivery of particles was sufficient to produce deposits in the airfoil test. Si, Fe, and Ni were the highest detected level elements on the concave (pressure) surfaces and Al, Si, and Ni were detected at the highest levels on the convex (suction) surfaces. Although P was not listed in the

minor element analysis of the syngas, significant levels of P were measured at all nine analyzed concave and convex surface locations. Since oxides of P can form relatively low melting point compounds with oxides of other ash elements (e.g., Fe and Si), molten compounds involving P likely contributed to sticking of particles delivered to the airfoil surfaces and bonding of the deposits. Molten phases involving P might also contribute to corrosion.

Another element often not detected in corrosion for turbines using conventional fuels is Ca. However, coal ash typically contains significant levels of Ca and combustion rig tests under conditions of turbines operated with coal-water fuels showed two atypical forms of very aggressive corrosion involving Ca for CoCrAlY coated specimens (Ref. [13]). Recent cyclic oxidation laboratory tests (Ref. [14]) for platinum aluminide coatings on Rene N5 in dry and wet air (0.1 atm. H2O partial pressure) have shown substantial attack due to CaO deposits at temperatures of 950 and 1150 C. At these temperatures, CaO deposits caused more severe degradation than either Na2SO4 or CaSO4 deposits, and CaO attack was more severe in wet compared to dry air.

Effects of higher inlet temperatures for future syngas turbines

Among other factors, the high capital cost and lower plant efficiency compared to natural gas fired combined cycle plants have been deterrents to the commercialization of IGCC plants. For most turbine applications, increased inlet temperature is used to improve power output and efficiency and therefore economics. Consequently, turbines with higher inlet temperatures than those for which materials experience is described above might be expected in future syngas turbine plants. Although no materials data at higher gas temperature conditions of future syngas turbines appears to be available, past turbine materials test experience might provide some insights concerning the effects of increased syngas turbine inlet temperatures. This is because common materials degradation factors associated with increased gas temperatures have been experienced in turbine materials tests with a wide range of coal-derived and other alternate fuels. These factors are probably also significant for turbine operation with fuels produced by gasification.

Before natural gas became the land based turbine fuel of choice, extensive rig tests in the 1970's and 1980's were conducted with alternate fuels to assess the effects on turbine materials degradation of increased turbine temperatures. Refs. [15] and [16] describe results from a number of past materials rig tests which are summarized here. These observations were consistent from materials test results using coal water fuels, coal derived liquids, residual oils, and deposition from pulverized coal. In summary, the past tests indicated that even extremely low levels of gas stream ash and impurities are capable of producing significant materials corrosion, deposition, and erosion degradation (as shown again by the degradation described above for IGCC components). The most critical factors affecting the type and rate of degradation are the size distribution of particulate (affecting the rates of delivery to surfaces) and levels of molten phases arriving at materials surfaces. Relatively low levels of corrosion and deposition along with weak deposits occur for low levels of molten phases delivered to surfaces. However, there is a transition temperature above which corrosion and deposition rates can drastically

increase (by an order of magnitude and more) as gas temperatures increase to a point where a significant fraction (probably only a few percent by mass) of the larger (order of 0.5 micron diameter and larger) gas stream particles are molten. Not only does the level of corrosion and deposition greatly increase above the transition temperature, but also the nature of degradation substantially changes. Above the transition temperature, additional and higher levels molten phases with different reactivity affect the modes of corrosion attack. Above the transition temperature deposits are very strong, tend to dominate greatly on upstream surfaces (protecting those surfaces from erosion) and grow approximately linearly with time. Below the transition temperature, deposits (if they occur) are relatively weak, have thickness of the same order of magnitude or less on upstream compared to downstream surfaces and deposit growth rates tend to decrease with time, often to a near limiting deposit thickness.

Consequently, as syngas turbine inlet temperatures increase in the future, levels of materials corrosion and deposition may be at higher levels than experienced to date, unless additional approaches are taken to protect flow path components. These approaches might include selection of more corrosion resistant coatings and alloys, additional syngas cleanup, fuel feedstock ash specifications, or possibly even increased hot section component cooling. Development of these approaches for future higher temperature syngas turbines would probably require significant test programs, for example, to identify the most resistant coatings/alloys or define syngas impurity specifications for feedstock selection and/or cleanup specifications to limit levels of specific aggressive impurities.

Identification of the turbine inlet temperature range above which a transition to extreme corrosion and deposition might be anticipated also requires testing. This temperature range is determined by the levels and composition of the ash particulate and vapor phase constituents that enter the turbine hot section. These are affected by the gasification feedstock ash chemistry and also by the plant syngas cleanup system. However, since combustion is an oxidation process, an initial criterion on an inlet temperature range where significant additional testing might be considered is temperatures above which oxide eutectics of primary ash elements (usually Si, Al, Fe, and Ca) can exist as molten phases. At these temperatures, sodium, potassium and sulfur (primary contributors to corrosion in past turbine experience) are no longer needed to produce molten ash phases. The much higher levels of the primary ash constituents in the fuel feedstock (compared to Na and K) might also be expected to result in relatively higher levels of these oxides carried into the turbine in a larger particle size range that results in substantially greater delivery rates to flow path surfaces than for the smaller size range of condensed alkali compounds. A review of phase diagrams (Ref. [11]) involving oxides of Si, Al, Fe, and Ca suggests the potential for a variety of molten ash phases significantly increases starting at temperatures above 1250 C and that Ca appears to be the element most involved in the eutectics with the lowest melting points.

Syngas turbine materials issues - summary and conclusions

This paper has reviewed limited available data related to syngas turbines to present a perspective on hot section materials issues for turbines operated in advanced gasification systems. Greater materials degradation (corrosion, erosion, and deposition) has occurred in at least some syngas turbines to date than for the same model turbines operated with conventional fuels such as natural gas. For properly designed and operated syngas cleanup systems, no forced turbine outages resulting from hot section materials degradation associated with syngas appear to be reported at IGCC plants. However, at least in some cases, hot section coatings, vanes, and blades have needed replacement during routine maintenance shutdowns at more frequent intervals than for natural gas fired turbines. The hot section materials degradation experienced to date may well be alleviated by using field experience to refine the selection of turbine coatings and alloys and syngas cleanup equipment. However, the basic mechanisms and impurity sources of the degradation do not currently appear to be well understood and fundamental considerations suggest a potential for much more severe of turbine hot section degradation in future higher temperature turbines than experienced to date at IGCC plants. Consequently, considering the lack of understanding of the fundamental processes of syngas turbine materials degradation, the variability of plant equipment and feedstock ash properties, and the potential for more severe degradation for higher temperature syngas turbines, additional materials testing (preferably on a slip stream at an existing syngas plant) is recommended. These tests would help define impurity specifications for syngas cleanup system performance and possibly feedstock selection, and for coating/alloy selection or refinement for turbines operating at gasification plants.

References

[1] Brdar, R.D., and R.M. Jones, “GE IGCC Technology and Experience with Advanced Gas Turbines”, GE Report GER-4207, Oct. 2000, pp. 4-5.

[2] CRE Group Ltd., “Migration of Gas Turbine Problems and Performance for Biomass IGCC: Experiences in Europe and US. Lessons Learnt for Coal IGCC”, CRE Report No. 7996/3, April 1999, p.13.

[3] Onal, K., Maris-Sida, M.C., Meier, G.H. and Pettit, F.S., "The Effects of Water Vapor on the Oxidation of Nickel-Base Superalloys and Coatings at Temperatures from 700°C to 1100°C", pp. 607-616 in Superalloys 2004, K.A. Green, H. Harada, T.W. Howson, T.M. Pollock, R.C. Reed, J.J. Scherra and S. Walston, editors, TMS, September 19, 2004.

[4] Valkovic, V., Trace Elements in Coal, CRC Press Inc., Raton, Florida, 1983.

[5] GE Energy, “Enabling Technology for Monitoring and Predicting Gas Turbine Health and Performance in Coal IGCC Powerplants”, Technical Progress Report to the US Department of Energy for Semi-Annual Period April 1, 2004 through August 31, 2004, September 30 2004.

[6] Pareek, V., and Wilkes, C., "Fuels in Gas Turbines", in proceedings of Materials and Practices to Improve Resistance to Fuel Derived Environmental Damage in Land-and Sea-Based Turbines, EPRI Report 1009173, October 2003, pp. 3-1 to 3-21.

[7] ASTM, Standard D-2880, "Standard Specification for Gas Turbine Fuel Oils".

[8] Wolk, R. H., "Study of Gas Turbine and Fuel Cell R&D Needs for Integration with Coal Gasification", Draft Final Report, July, 2001.

[9] Meier, G., and Pettit, F., "Investigation of Materials Performance in High Moisture Environments Including Corrosive Contaminants Typical of Those Arising by Using Alternate Fuels in Gas Turbines", Semi-Annual Report for August 1, 2004-January 31, 2005, UTSR Project 04-01-SR116.

[10] Sohn, Y., and Desai, V., "Degradation of Thermal Barrier Coatings with Syngas Combustion", Proceedings of UTSR Peer Review Workshop III, Poster Session, October 18-20, 2005.

[11] Tabakoff, W., Hamed, A., and Wenglarz, R. A., Particulate Flows and Blade Erosion, von Karman Institute for Fluid Dynamics Lecture Series, Rhode-Saint-Genese, Belgium; Lecture 2, 1988.

[12] Wada, K., Yan, L., Takahashi, M., Takaishi, K., and Furukawa, T., "Degradation of Gas Turbine Blade Materials In Integrated Coal-Gasification Combined Cycle Plant", Materials at High Temperatures, Vol. 18, No. 2, 2001, pp. 131-138.

[13] Wenglarz, R., Sethi, V., and Gonzalez, R., "Atypical Corrosion from Coal-Water Fuels", Materials at High Temperatures, Vol. 9, No. 3, August 1991, pp. 145-152.

[14] Meier, G., Pettit, F., and Jung, K., "Investigation of Materials Performance in High Moisture Environments Including Corrosive Contaminants Typical of Those Arising by Using Alternate Fuels in Gas Turbines", Proceedings of UTSR Peer Review Workshop III, October 18-20, 2005.

[15] DeCorso, M., Anson, D., Newby, R., Wenglarz, R., and Wright, I., "Coal/Biomass Fuels and the Gas Turbine", ASME Paper 96-GT-76, 1996.

[16] Wenglarz, R., and Wright, I., "Alternate Fuels for Land-Based Turbines", in proceedings of Materials and Practices to Improve Resistance to Fuel Derived Environmental Damage in Land-and Sea-Based Turbines, EPRI Report 1009173, October 2003, pp. 4-45 to 4-64.

MATERIALS PROBLEMS AND SOLUTIONS IN BIOMASS FIRED PLANTS

O.H. Larsen[1], M. Montgomery[2]

[1]ELSAM A/S, Kraftværksvej 53, Skærbæk, 7000 Fredericia, Denmark.
[2]IPL/Energi E2/Elsam, DTU, Building 204, 2800 Lyngby, Denmark

Abstract

Due to Denmark's pledge to reduce carbon dioxide emissions, biomass is utilised increasingly as a fuel for generating energy. Extensive research and demonstration projects especially in the area of material performance for biomass fired boilers have been undertaken to make biomass a viable fuel resource. When straw is combusted, potassium chloride and potassium sulphate are present in ash products, which condense on superheater components. This gives rise to specific chlorine corrosion problems not previously encountered in coal-fired power plants. The type of corrosion attack can be directly ascribed to the composition of the deposit and the metal surface temperature. In woodchip boilers, a similar corrosion rate and corrosion mechanism has on some occasions been observed. Co-firing of straw (10 and 20% energy basis) with coal has shown corrosion rates lower than those in straw-fired plants. With both 10 and 20% straw, no chlorine corrosion was seen. This paper will describe the results from in situ investigations undertaken in Denmark on high temperature corrosion in biomass fired plants. Results from 100% straw-firing, woodchip and co-firing of straw with fossil fuels are summarised and compared.

Keywords: biomass, straw, woodchip, co-firing, high temperature corrosion, chlorination,

Introduction

In Scandinavia, there have been serious efforts to reduced carbon dioxide emissions by using carbon dioxide neutral fuels which do not contribute to the greenhouse effect. The Danish government has pledged to reduce carbon dioxide emissions to 80% of the 1988 levels, by the year 2005. This resulted in the biomass agreement from 1993 between the utility operators (Elsam and Energy E2) and the government, where power plants have to utilise 1.4 million tonnes biomass for power production. The extensive research and development programme in the area of biomass firing is a direct result of this agreement. Therefore, in Denmark, straw or woodchip has a growing utilisation as a fuel for generating energy. Denmark has concentrated its efforts on straw since it does not have large forest areas like the other Scandinavian countries. There are currently seven straw-fired CHP (combined heat and power) plants in operation and one woodchip boiler. Two co-firing plants (Studstrup with straw and coal and Avedøre II with oil + gas + wood pellets) have recently commenced operation.

Many field investigations have been undertaken into corrosion due to straw combustion in Denmark over the past decade, and more detailed discussion of the results can be found in these publications [1-10]. This paper will highlight the significant results and compare the corrosion mechanisms and rates from straw, woodchip and co-firing with straw and fossil fuels. The results included in this paper are from field investigations in various plants: a summary of the data from the plants and the investigations conducted is given in Table 1. Three types of corrosion investigations have been undertaken: a) exposure of metal rings on air/water cooled probes, b) exposure of test tubes in the test superheater c) exposure of test tubes in existing superheaters. The aim of the corrosion programme has been to i) measure accurately corrosion rates in existing superheaters, ii) measure corrosion rates of possible alternative materials at other temperatures and iii) measure corrosion rates at higher steam temperatures (increase efficiency). The exposure

temperature are measured with thermocouples on corrosion probes, or calculated based on inlet and outlet steam temperatures and steam flow. The latter calculations are associated with some uncertainties, mainly due to lack of knowledge of heat flux distribution on superheaters. Corrosion rate is calculated based on residual metal thickness which is metal loss + internal corrosion subtracted from the original metal thickness. For low corrosion rates, oxide thickness measurements are used.

Table 1: Summary of in situ investigations

Plant Description	Steam Temp. °C	Pressure MPa	Size MW_{th}	Investigations
Rudkøbing CHP grate-fired 100% straw	450	6.1	10.7	Deposit studies: probe and matured deposits. Corrosion studies: probes.
Masnedø CHP - grate-fired: Almost 100% straw	520	9.2	33	Deposit studies: probe and matured deposits. Aerosol measurements. Corrosion studies: probes, test tubes in existing superheaters and in test superheater (up to 600°C).
Maribo Sakskøbing CHP grate-fired: 100% straw	540	9.3	33	Mature deposit studies. Corrosion studies: test tubes in existing superheaters.
Ensted CHP grate fired - 100% straw boiler - 100% woodchip	 470 470-540	 20.1 20.1	 99.4 16.3	Deposit studies: probe and matured deposits. Aerosol measurements. Corrosion studies: test tubes in existing superheaters. Additive
Studstrup suspension fired coal plant modified for coal + 10-20% straw	540	14.3	380	Deposit studies, aerosol measurements, gaseous emission. Corrosion studies: probes and test tubes in existing superheaters.
Avedøre II -Biokedel: straw firing -main boiler: oil+gas+wood	 540-580 540-580	30	600	Deposit studies, probe measurements, test tubes in existing superheaters in main boiler, test superheater loop in biomass boiler. Additive

Straw firing

The four plants from which results are included in this section are Rudkøbing, Ensted, Masnedø and Maribo Sakskøbing. Rudkøbing and Ensted are plants of the Elsam power company, and Masnedø and Maribo Sakskøbing are plants of Energy E2 power company. Specific areas which will be included in this section are alloy composition, weld performance, steam and flue gas temperature.

Sulphur dioxide and potassium chloride are released when straw is combusted, and these compounds result in the deposition of potassium chloride and potassium sulphate on superheater components. This gives rise to chlorine corrosion problems.

Alloy Composition

In conventional coal-firing, an alloy with high chromium content results in lower corrosion rates, however the contrary is the case for straw-firing plants. The results from three separate in situ investigations[1,2,4] where a variety of steels have been tested show that at high temperatures, high chromium steels are rapidly attacked. Figure 1 shows one set of results where a range of alloys from a 2½% Cr to a 30% Cr steel were investigated [4]. The graph shows total corrosion rate with respect to chromium percent, and additionally shows the contribution of internal corrosion (selective corrosion + grain boundary attack) and material loss as a function of corrosion rate. The low chromium steels exhibit a high material loss whereas the higher chromium steels are characterized by severe internal corrosion in the form of chromium depletion.

Iron is also depleted however nickel has a higher corrosion resistance in this environment. These results indicate a minimum in total corrosion rate of steels at an intermediate chromium content of 12-18% Cr.

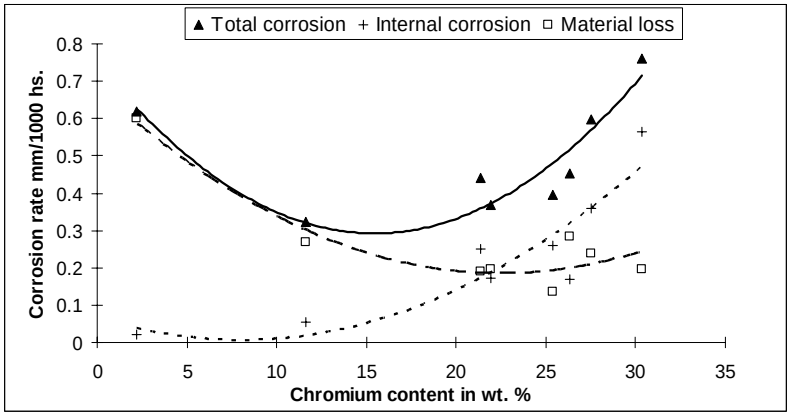

Figure 1: Corrosion rate with various chromium contents in the alloys at approx. 580°C.

Figure 2 shows the different types of corrosion attack for a TP347H (18Cr 12Ni Nb) type steel. Selective removal of chromium resulting in a porous metal structure and grain boundary attack is observed. For austenitic steels, grain-boundary corrosion is a precursor to corrosion within the grains. The corrosion products formed are chromium oxides and iron oxides; these are present at the surface of the specimen. In many cases, nickel is also present in the outer corrosion product as non-reacted nickel. If chlorine is detected, it is close to or at the corrosion front. Exposure of a 13%Cr-13%Mn steel in the test superheater at Masnedø revealed both manganese and chromium depletion [5].

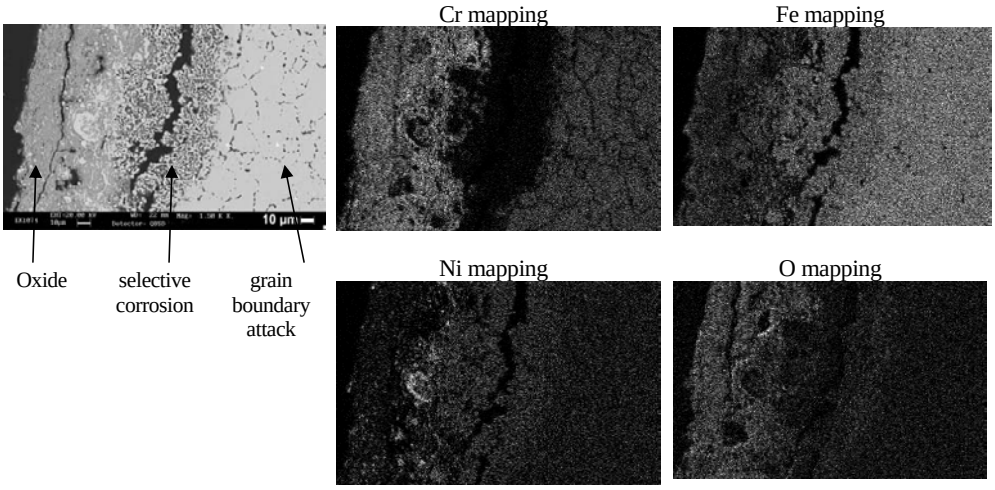

Figure 2: TP347H FG exposed for 3500 hours at Masnedø: steam temperature 567°C, calculated metal temperature 613°C.

Preferential corrosion attack of chromium-rich austenite grains in martensitic steel has been observed for HCM12 (12Cr1Mo1W) at high temperatures. Even at low temperatures (below 500°C), after a three year exposure preferential attack was seen, however, at low temperatures the corrosion rate was minimal due to the formation of a protective chromium-rich iron oxide.

For weld overlay specimens, there is no grain boundary attack, but a slight tendency to preferential attack in the interdendritic zone [10]. Investigation of a Sanicro 63 (9%Mo, 3.5% Nb, 22% Cr, <5% Fe, rest Ni) specimen also indicates other elements that are preferentially attacked. Figure 3 shows the outer oxide of the specimen and the depleted metal. As previously mentioned, the metal is chromium depleted but as can be observed, niobium and titanium have also formed oxides and therefore are also susceptible to attack. Molybdenum and nickel are not attacked. Niobium is not completely depleted from the alloy and therefore it is suggested that niobium carbides are more susceptible to attack similar to that seen by us and other workers with chromium carbides.

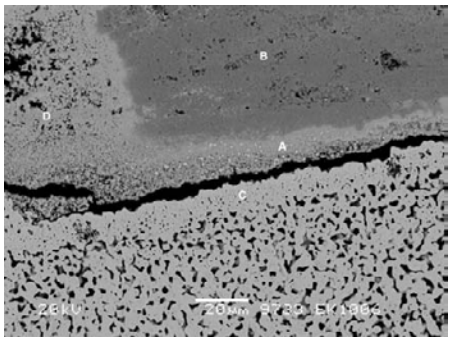

	O	Si	Cl	Ti	Cr	Fe	Ni	Nb	Mo
9733 A	16		1	5	14	1	7	56	
9733 B	16	1	1		74	2	2	3	1
9733 C					3		77	1	19
9733 D	18		<1	5	19			56	

Figure 3: SEM analysis of corrosion products on Sanicro 63 exposed at 1400 hours at Masnedø at an approximate temperature of 580°C. Analysis in wt.%.

Based on these observations, it is concluded that the elements having a high affinity for oxygen and therefore also chlorine are more likely to be attacked. Thus the reason why chromium, manganese, titanium and to a lesser extent niobium are preferentially attacked lies in their thermodynamic stabilities with respect to chlorine.

Performance of welds

A test loop fabricated by welding different test tubes of iron based alloys together with the weld filler Nibas 625 was exposed for 3500 hours at 500-600°C steam temperature [7]. The 18% Cr and 12% Cr tube sections incurred severe corrosion attack in the area adjacent to the Nibas welds. Such attack was not observed for the same material welded with an 18Cr-8Ni weld filler material. The extent of localised attack decreased with temperature and distance from the Nibas weld as shown in Figure 4 such that at the steam temperature of 514°C, this type of attack was not seen. This type of attack is believed to be a type of high temperature galvanic corrosion such that the nickel rich Nibas is the cathode and the 18-8 stainless steel tube is the anode. The electrolyte which has not been positively identified could be a metal-chloride: alkali-chloride mixture. As the

tubes steam temperature increases, the electrolyte becomes more molten and the depth of galvanic attack increases. In addition, the amount of attack decreases with greater distance from the cathode. Thermal stresses due to the different thermal expansion coefficients of the tube and weld may also contribute to this attack.

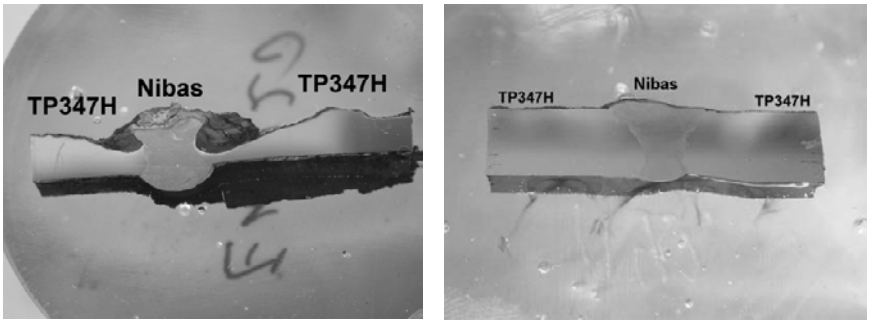

(a) (b)

Figure 4: Macrographs of cross-sections of Nibas welds exposed for 3500 hours in Masnedø test loop showing corrosion adjacent to weld at steam temperatures a) 570°C and b) 514°C.

Replacing the welds with a weld of similar composition to the tube reduced the problems with this type of attack however preferential chromium carbide attack was observed, i.e. attack of the interdendritic zone as shown in Figure 5. Figure 5b is a backscattered micrograph showing darker precipitates in the preferentially attacked interdendritic zone of the welded area. It is assumed that the precipitates in the weld are chromium carbides although a positive analysis of these is difficult. This type of corrosion attack needs to be monitored but is not as severe as the attack observed in Figure 4.

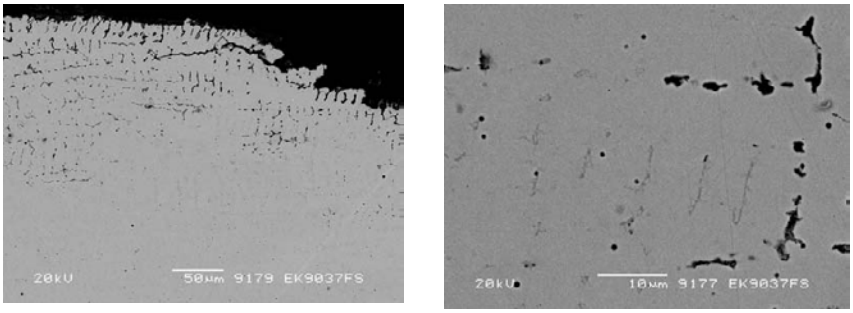

(a) (b)

Figure 5: 18-8 welds exposed at Maribo Sakskøbing at steam temperature 540°C for 4 years.

Influence of steam and flue gas temperature

For the austenitic alloys investigated, a gradual change in the corrosion product morphology as a function of temperature is observed as seen in Figure 6. A protective oxide is formed at surface metal temperatures below 500°C. At around 500-520°C, both grain boundary attack and protective oxides can be observed for the same specimen. This indicates that at this temperature region, there is a transition in the type of corrosion attack. Above this temperature, chromium depletion and grain boundary attack are always observed and at estimated metal temperatures of 600°C, it can be over 0.5 mm in depth.

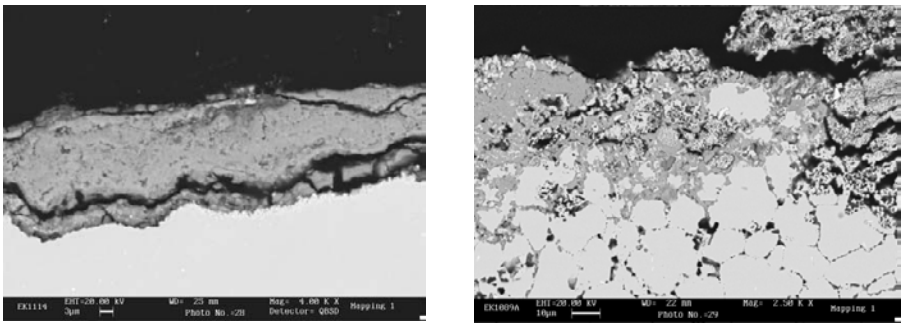

a b

Figure 6: TP347H exposed at Masnedø for 3500 hours with a calculated metal temperature of a) 462˚C and b) 525˚C.

In Figure 7, the corrosion rate of 12-18% Cr steels is plotted against temperature [5]. Corrosion rates are modest at 460°C, where as shown in Figure 6, a relatively protective oxide can be formed. With increase in temperature up to 525°C, then corrosion rates become more linear with respect to temperature. For the steels for 12-18% chromium content, similar corrosion rates are measured and they all increase steeply with increase in metal temperature.

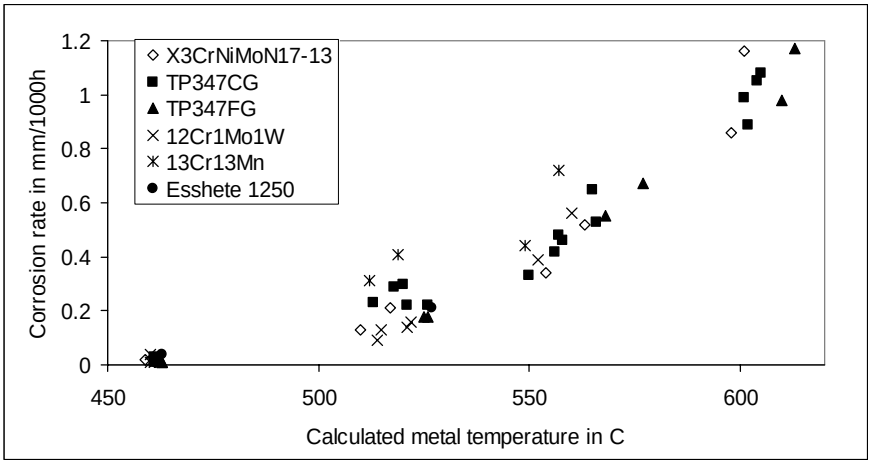

Figure 7: Corrosion rate of specimens in one investigation in Masnedø straw-fired plant relating metal temperature to corrosion rate.

In Figure 8, corrosion rates for TP347H (both fine and coarse-grained) from various straw-fired plants are collated. The results are illustrated on an Arrhenius type plot, with natural log of corrosion rate in mm/1000h on the y-axis and metal temperature as 1/T in Kelvin on the x-axis. For test tubes in existing superheaters, the metal surface temperature is taken to be steam temperature plus 20 °C, if more accurate data cannot be obtained. For TP347H, the corrosion rates fit into a broad band. The variations observed could be due to an effect of flue gas temperature. In the high flue gas temperature areas, heat flux will be higher and hence the temperature increase from steam to tube surface might be higher than the assumed 20 °C. The flue gas temperature will also affect the thickness of the deposit and the morphology and composition of the deposit.

These factors influence the possibility of melt deposit formation that may lead to faster corrosion rates. Flue gas temperatures have been classified into high flue gas (over 900 °C) and low flue gas temperature. Corrosion rates of actual superheaters are also given which are generally lower than those for test superheaters and probes. The specimens from actual superheaters at the higher steam temperature end have low flue gas temperature, since the boilers are designed with superheaters cocurrent, that is, with the final superheater located at lower steam temperatures. There can be great variation in corrosion from a specific tube depending on its location in the superheater bank, i.e. leading tube or shielded tube, heat flux from combustion chamber, close to walls or ceilings where there is less heat flux - these are important parameters but difficult to quantify [6].

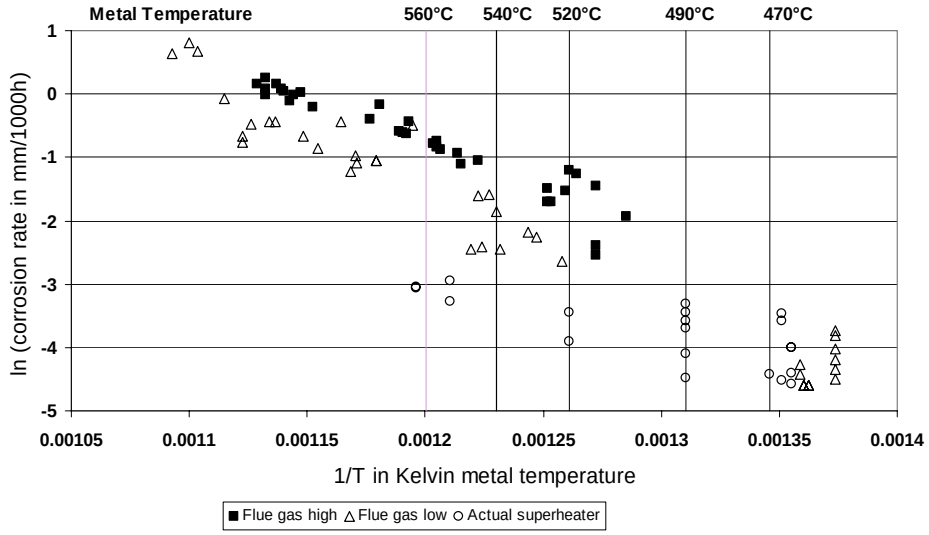

Figure 8: Arrhenius type plot of corrosion rates for TP347H steels in straw-fired plants.

Corrosion Mechanism

The following mechanism explains the preferential attack of certain elements such as chromium and the linear increase of corrosion rates with temperature. Initially, an outer oxide of magnetite and haematite and an inner oxide of chromium-rich iron oxide is formed at the surface of the metal. Short-term deposition experiments show that potassium chloride constitutes the initial condensate on the probes [11]. Thus chlorine has to be released from these condensed deposits to result in corrosion. The initiation reaction due to the presence of potassium chloride deposits can be one or a combination of the following three reactions, depending on the presence of sulphur dioxide and water vapour.

$$2KCl + ½O_2 + SO_2 + H_2O \rightarrow K_2SO_4 + 2HCl \quad (1)$$

$$2KCl + O_2 + SO_2 \rightarrow K_2SO_4 + Cl_2 \quad (2)$$

$$2KCl + Fe_2O_3 + ½O_2 \rightarrow K_2Fe_2O_4 + Cl_2 \quad (3)$$

Eq. (1) releases HCl and Eq. (2) and (3) result in the release of chlorine gas. The released chlorine then migrates through the protective oxide to react at the metal-oxide interface (Eq. 4).

$$Cr + 1½Cl_2 \rightarrow CrCl_3 \quad (4)$$

A similar reaction for $CrCl_2$ would also apply. Chlorine is observed to preferentially attack chromium; this is due to chromium's greater affinity for chlorine than iron and nickel (more negative Gibbs free energy). In the same way, manganese and titanium are also preferentially attacked due to their high affinity for chlorine.

The metal chloride migrates out to an area of higher oxygen partial pressure and is converted to metal oxychloride or metal oxide and chlorine (Eq. 5 and 6). Although chromium chloride has lower volatility compared to iron chloride, a temperature gradient due to the difference in metal temperature and gas temperature encourages the evaporation of metal chlorides. Thus a higher flue gas temperature will give a greater corrosion rate. In addition, chromium chloride oxidises partially to chromium oxychloride which has a high volatility. The released chlorine then migrates back to the corrosion front to form metal chlorides again.

$$2CrCl_2 + O_2 \rightarrow CrO_2Cl_2 \quad (5)$$

$$2CrCl_3 + 1½O_2 \rightarrow Cr_2O_3 + 1½Cl_2 \quad (6)$$

This behaviour explains the voids seen at grain boundaries at the corrosion front due to evaporation of metal chlorides, and also explains the presence of oxides at grain boundaries or within the grains where the partial pressure of oxygen is higher than at the corrosion front. The precipitated chromium and iron oxide is non-protective and therefore spalls off with the ash.

For austenitic materials, it is noted that grain boundaries are the initial course of attack, followed by attack of chromium within the grains. Grain boundaries present fast short-circuit diffusion paths for chlorine into the metal and chromium out of the metal. Attack of chromium may also be due to preferential chlorine attack of chromium carbides that are present at grain boundaries. For a number of austenitic steels exposed to an oxygen-chlorine environment at 500-600°C, chromium carbides were preferentially attacked to form chromium chlorides and carbon dioxide[12]. For weld overlays, there is an indication that chromium carbides and niobium carbides present in the interdendritic zone are preferentially attacked.

Thus at higher temperatures, it is primarily the metal affinity for chlorine that governs the selective and grain boundary corrosion. Accordingly, chromium does not form a protective oxide at high temperatures. As the temperature decreases, the volatility of the metal chlorides becomes more significant.

An expression for the corrosion rate incorporating the important parameters can be given as:

$$c = \exp\left[\left(\frac{A.b}{T_m}\right) + C(T_g - T_m) + d\right] \quad (7)$$

where
c is corrosion rate in mm/1000h
T_m is metal temperature in K
T_g is gas temperature in K
A is a constant related to the alloy composition, e.g. amount of chromium etc.
C is a constant related to the flue gas temperature
b and d are empirical constants.

Woodchip firing

As straw-fired boilers demonstrated high corrosion rates, it was expected that woodchip would be a less corrosive biomass alternative. A comparison of the two fuels shows that woodchip has less ash and corrosive compounds [13]. The content of potassium and chlorine in straw is about an order of magnitude higher than in woodchip. There has been no investigation program for woodchip firing, as it was believed that the lower ash and chlorine content would not give corrosion problems. Ensted CHP plant, commissioned in 1998, consists of a straw-fired and a woodchip boiler [8]. The straw-fired boiler has an outlet steam temperature of 470°C. This steam is led into the woodchip boiler which has an outlet steam temperature of 540°C. The woodchip boiler is fabricated from HCM12 steel (12Cr 1Mo 1W).

Analysis of the ash from high temperature components in the boiler has revealed the presence of potassium sulphate and calcium sulphate close to the oxide, and in some cases potassium chloride closer to the flue gas-deposit interface. Potassium and chlorine have been detected at and near the corrosion front, which indicates that a mechanism similar to that in straw-fired boilers can occur. Two adjacent TP347H FG tubes were exposed simultaneously in the plant for 2000 hours. In most positions on both tubes, the formation of a protective oxide was observed; however, on one specimen there were areas of grain boundary attack and unprotective oxide.

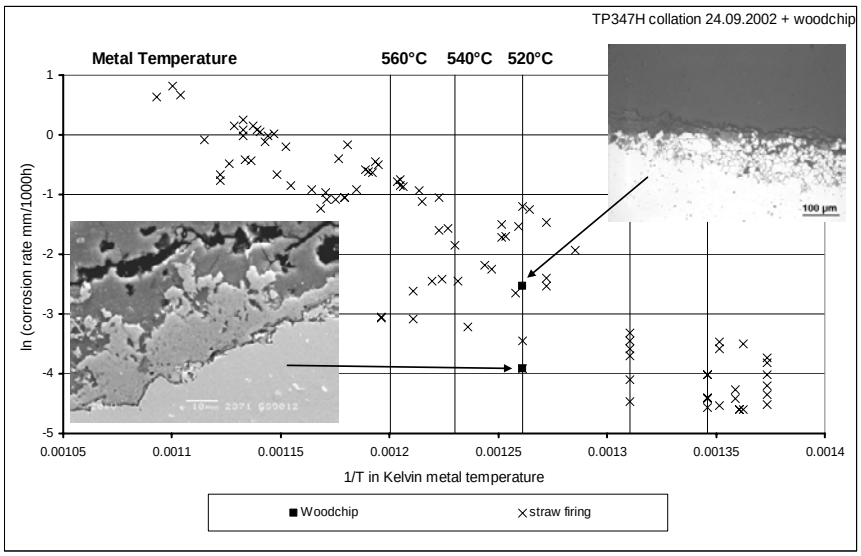

Figure 9: Two similar specimens of TP347H FG exposed for 2000h at Ensted woodchip boiler with a surface metal surface temperature of 520°C.

In Figure 9 which compares corrosion rates in straw fired boilers with those from Ensted woodchip boiler, a difference in corrosion attack is also reflected in the corrosion rates. It is suggested that in areas with potassium chloride present in the deposit, high corrosion rates will be observed. In the case of TP347H this occurs as grain boundary attack similar to that in straw-fired boilers. The variability of the deposit composition leads to variable corrosion mechanisms and corrosion rates.

Corrosion problems were encountered on the membrane panels of Ensted constituting the final superheater and having an exit steam temperature of 540 °C. An extensive repair procedure was carried out, consisting of weld overlay with Inconel 625 (approx. 60% Ni, 21% Cr, 9% Mo). The calculated surface metal temperature in the corrosion affected areas was up to 580 °C. During a boiler inspection after 6 months, a chip of Inconel 625 was removed. This chip revealed that a zone below the oxide-metal interface was depleted in chromium. The corrosion attack is similar to that in straw-fired plants i.e. the depletion of chromium from the surface of the alloy by the formation of chromium chloride. The chromium chloride is then oxidized to chromium oxide. Nickel and chlorine together with oxygen were found on the surface of the material. Nickel also reacts with chlorine, however not as readily as chromium. In addition, the formation of nickel and chlorine-rich corrosion products is more stable since nickel chloride is not readily oxidized when the partial pressure of oxygen increases. It is suggested that nickel binds the aggressive chlorine and slows down the active oxidation mechanism.

Despite the use of Inconel 625, there were still unacceptable high corrosion rates with steam outlet temperatures of 540 °C which is the design temperature of the plant. Therefore the plant is now limited to operating with a steam outlet temperature of 520 °C and reduced load. The chromium content of 23% results in chromium depletion of the Inconel 625 which increases rapidly at higher temperatures.

How to decrease corrosion rates in biomass combustion

As described in the previous section, combustion of biomass results in corrosion problems which are difficult to overcome with normal material solutions, such as higher chromium content in steel. The formation of metal chlorides and metal oxychlorides and their increased volatility at temperatures approaching 600°C results in extremely high corrosion rates. From investigation of the Nibas welds, there is also the indication that a molten phase is becoming more stable at higher temperatures. Therefore due to the corrosiveness of straw, possibilities to increase electricity production from straw combustion by increasing the steam temperature is limited as this leads to unacceptable corrosion rates. Thus to achieve higher temperatures when burning biomass, it is necessary to hinder potassium chloride produced in the gas phase from condensing on metallic surfaces. Various methods to achieve this will be described in the following sections.

Co-firing of straw with coal

Elsam has carried out on-site investigations at the Studstrup power plant into the feasibility of co-firing straw with coal with respect to corrosion, ash deposition and aerosol formation. On the basis of the positive results obtained, two co-firing plants are now in operation. The results described in this section are from long-term exposures in a suspension-fired boiler with 10 and 20 % straw (% energy basis) [9,14]. The results are compared with those from straw-firing.

Corrosion Morphology

The ash adjacent to the corrosion products on corrosion test tubes was investigated with SEM-EDS and the trend in Figure 10 was observed. The main elements detected in the ash are aluminium, silicon, sulphur, potassium, calcium and iron. Whilst aluminium and silicon decrease as the percentage of straw in fuel increases, the percentage of sulphur and potassium increases. Deposition studies support this observation. No chlorine was detected in the deposits or corrosion product, or at the corrosion front.

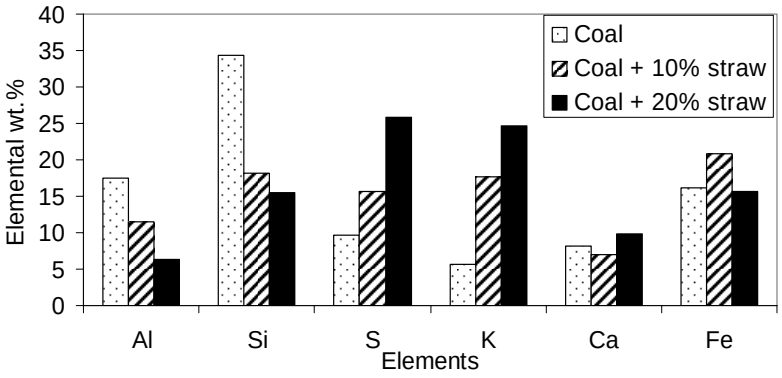

Figure 10: Average composition of main elements in ash adjacent to corrosion products for TP347H FG. (Analysis has been undertaken with SEM-EDS where elements below sodium could not be analysed).

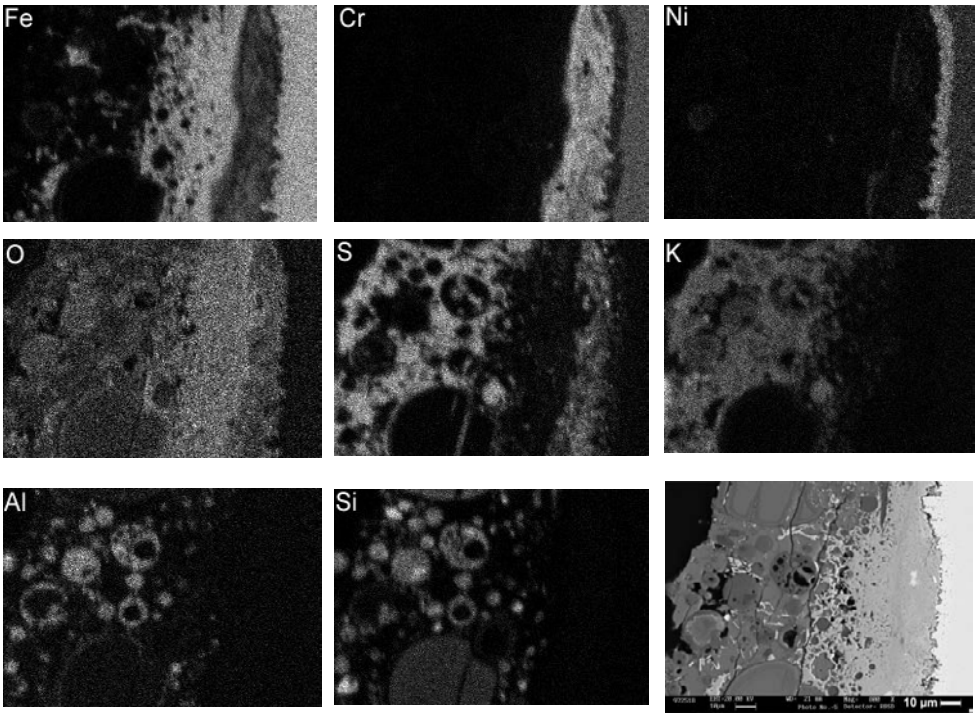

Figure 11: TP347H FG steel located in platen superheater at Studstrup – metal temperature 525°C with 20% straw co-firing.

EDS analysis of the composition of the ash (Figure 11) showed particles rich in aluminium, silicon, potassium and oxygen in a matrix rich in potassium, sulphur and oxygen, i.e. potassium sulphate. Iron oxide precipitates were also present within this potassium sulphate matrix.

The corrosion morphology for 10% straw and 20% straw co-firing at low metal temperatures is similar to that seen in coal-firing plants, i.e. an outer layer of iron oxide, and an inner layer of iron chromium oxide. For the higher alloyed steels, a thin chromium rich oxide is formed. The lower alloyed steels had thicker oxides. Sulphur in the form of sulphates or sulphides are present within the oxide.

With 20% straw co-firing at high temperatures (approx. 580°C), as well as the corrosion morphology described above, large shallow oxide pits are present, especially for the austenitic steels. Figure 12 shows a thin and thick oxide on the same specimen of HR3C steel (niobium modified 310 stainless steel). The thin oxide is similar to that seen with 10% co-firing for this high alloyed steel. In the base regions of the oxide pit, sulphates or sulphides are detected.

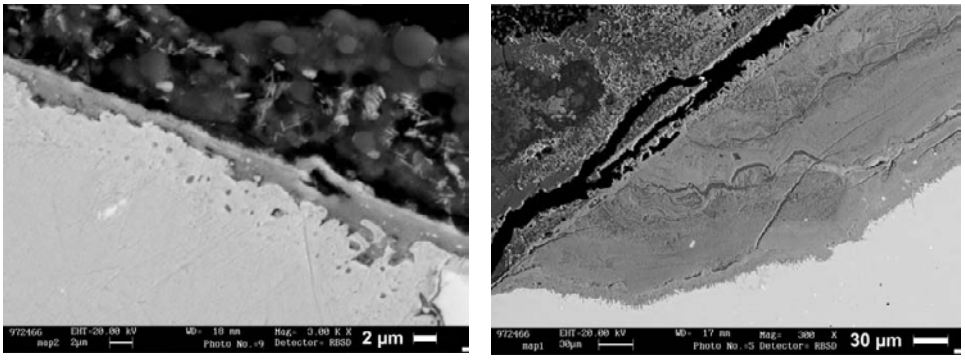

Figure 12: Two different areas on HR3C (niobium modified 310 steel) specimen with a metal temperature of 586°C exposed at Studstrup to 20% straw co-firing for 3000 hours.

Corrosion Mechanism

The following corrosion mechanism is proposed. Potassium chloride from straw combustion reacts in the combustion chamber (Eq. 8 and 9) to form potassium aluminium silicates and potassium sulphate. Chlorine is released as hydrogen chloride according to the following reactions.

$$2KCl + Al_2O_3 + 6SiO_2 + H_2O \rightarrow K_2O \cdot Al_2O_3 \cdot 6SiO_2 + 2HCl \quad (8)$$

$$2KCl + SO_2 + H_2O + ½O_2 \rightarrow K_2SO_4 + 2HCl \quad (9)$$

Potassium sulphate is deposited on the metallic components together with potassium aluminosilicates. Hydrogen chloride gas is released into the flue gas. An increase in straw content from 10% to 20% results in a greater amount of potassium chloride in the combustion chamber. This is converted to more potassium sulphate (Eq. 9) which is deposited on the superheaters. In addition, hydrogen chloride emission from the stack increases due to increase in straw percentage [14].

In contrast to the above finding, severe chloride attack was experienced in a circulating fluidized bed (CFB) plant firing 18% straw with coal [1,2]. This difference was attributed to the differences in combustion temperature, since CFB combustion takes place at 850°C whereas in a suspension-fired boiler, combustion temperatures are in the region of 1400-1700°C. Thus in the CFB plant, most potassium is found in the form of KCl. Also lower content of sulphur is available for sulphation of KCl due to the in-bed desulphurization by addition of limestone. The lower heat-up

rates and lower sulphur dioxide partial pressures are not favourable for incorporation of potassium in insoluble silicates, or for major sulphation in the flue gas.

At 10% straw co-firing and at 20% straw co-firing at low temperatures in pulverised fuel boilers, sulphidation and oxidation occur according to Eq. 10 and 11 where the oxidants are supplied from potassium sulphate present in the deposit. Similar oxidation and sulphidation are observed in coal firing.

$$2Fe + 1½O_2 \rightarrow Fe_2O_3 \quad (10)$$

$$2Fe + S_2 \rightarrow 2FeS \quad (11)$$

When there is more sulphur and potassium in the deposit, i.e. with 20% co-firing, increased corrosion due to a greater amount of potassium sulphate salt in contact with the metal is observed.

At 20% straw co-firing at higher metal and gas temperatures, both formation of large shallow pits and thin chromium rich oxide is observed for high alloy steels. This indicates a more corrosive environment in some localized regions. The deposit adjacent to the oxide is highly heterogeneous with aluminate and silicate particles surrounded by potassium sulphate (Figure 14). Corrosion increases with potassium sulphate concentration indicating that potassium sulphate is the corrosive species in the deposit. Iron oxide at the oxide-salt interface can react with sulphur trioxide to form iron sulphate (Eq. 12).

$$Fe_2O_3 + 3SO_3(g) \rightarrow Fe_2(SO_4)_3 \quad (12)$$

The phase diagram of a eutectic melt of iron sulphate and potassium sulphate gives a melting point of 621°C and contains approximately 90 mol.% potassium sulphate [15]. It must be noted that the presence of sodium which could come from other coal types will decrease this melting point. There are two criteria that have to be fulfilled to result in the presence of a ferric sulphate-potassium sulphate eutectic melt. The ash must have a high potassium sulphate concentration and the temperature of the melt must be close to the eutectic melting point. At 20% co-firing at metal temperatures of 580°C, there is a high concentration of potassium sulphate, and it is assumed that the temperature at the oxide-deposit interface is sufficient to form a eutectic melt. It is therefore suggested that low temperature hot corrosion occurs at the higher temperatures with 20% straw co-firing. Thus iron sulphate forms a melt with potassium sulphate, and due to SO_3 gradients, iron sulphate will migrate to the outer part of the melt and precipitate haematite. The net result is that at high temperatures of 580-600°C, the presence of potassium sulphate leads to acidic fluxing of iron oxide.

Corrosion Rates

Co-firing in a suspension-fired boiler with either 10% or 20% straw removes the danger of catastrophic chlorine corrosion. The corrosion rate is much lower than that seen in straw-fired power plants and is closer to that in coal-fired power plants. For comparison purposes, the corrosion rates for TP347H FG have been plotted on an Arrhenius type plot (Figure 13) assuming parabolic kinetics according to Eq. 13. Here *x* is the thickness of corroded away material, t is the duration of exposure, and the natural logarithm of the parabolic rate constant (ln k_p) is plotted on the y-axis.

$$x^2 = 2k_p t \quad (13)$$

These corrosion rates are compared with coal-firing and straw-firing. Parabolic kinetics is assumed for the three types of corrosion although it is apparent that linear kinetics is more applicable for corrosion in 100% straw-fired boilers at high temperatures. Corrosion rates in straw co-firing lie in the same region as those for coal-firing and significantly below the results for straw-firing. For specimens with 10% straw co-firing, corrosion rates can be considered as similar to coal-firing for all temperature ranges. For 20% straw co-firing at low temperatures, the corrosion rate is also in the same range as coal-firing. There is an increase in the corrosion rate at high temperatures due to the change in corrosion mechanism as iron sulphate-potassium sulphate melt is formed. Recent results from a newly built power plant from Studstrup show that long term corrosion rates with 10% straw are in the upper end of the 10% straw area on Figure 13 [16]. This is attributed to the greater amount of internal sulphidation observed after much longer exposures of up to 3 years. However the rates are still much lower than the straw-firing corrosion rates.

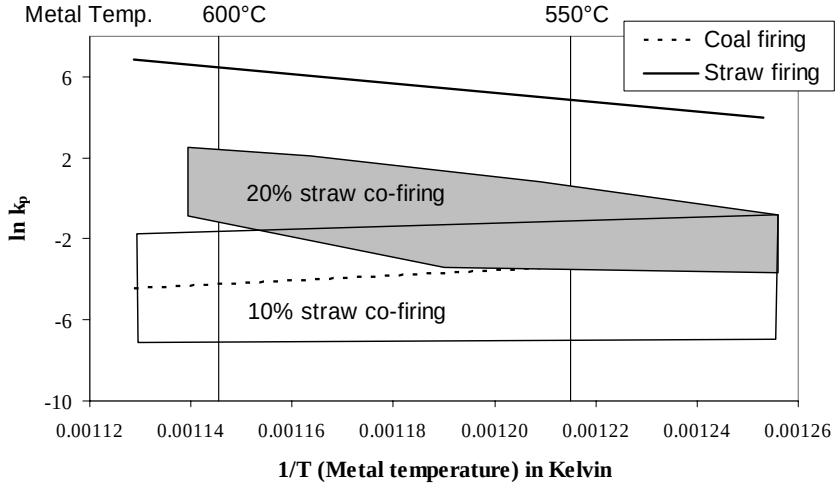

Figure 13: Arrhenius type plot showing corrosion of TP347H FG in co-firing of straw and coal compared to 100% coal-firing and 100% straw-firing.

Co-firing of wood pellets with heavy fuel oil

The main boiler at the Avedøre 2 power plant currently uses heavy fuel oil and gas together with wood pellets at steam outlet temperatures of 540°C [17]. From the extensive amount of research on straw-firing, the risk of potassium chloride deposit corrosion was known. In order to monitor this, potassium chloride in the gas phase was measured using an IACM system (In situ alkali continuous Monitor System) developed by Vattenfall - a system based on differential optic absorbance spectroscopy. This showed that combustion of wood pellets together with natural gas results in high potassium chloride concentration in the flue gas. However the addition of heavy fuel oil containing sulphur removes potassium chloride at a specific oil to wood ratio. Potassium chloride from the wood pellets reacts with sulphur dioxide from the heavy oil in the combustion chamber resulting in potassium sulphate as in equation 9. The type of deposit formed is shown in Figure 14. The corrosion morphology is similar to that for coal/straw co-firing (c.f. Fig 11) where there are iron oxide needles within an alkali sulphate matrix. In addition localised internal corrosion was also observed after 19,000 hours exposure. However an added problem with heavy oil is the presence of vanadate compounds which can also lead to severe vanadate corrosion. Trials using coal flyash as an additive indicate that this might reduce vanadate corrosion and in

any case will help alleviate chloride corrosion [18]. The corrosion rate thus needs to be monitored with future increase in temperature with respect to internal sulphidation and vanadate corrosion.

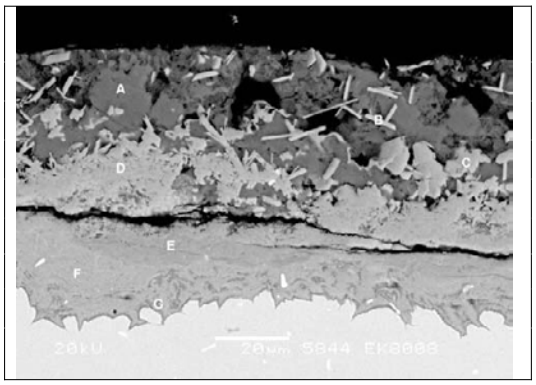

	Main elements	Minor elements
A	S O K	Ca Ni
B	Fe O	S
C	Fe V Ni O	
D	Fe O	
E	Cr Fe O Ni	S
F	Cr Fe O S	Ni
G	Cr Fe O S	Ni Mn

Figure 14: Composition of fireside oxide on TP347H FG tubes after 2 years exposure at Avedøre II main boiler.

Use of additives

Another way to reduce deposition of potassium chloride is the use of additives. In the same way that the components of fossil fuels, such as sulphur, silicates and aluminates react with potassium chloride to produce less corrosive deposits, then additives can also be used. Trials with sulphur and alumina and silica additives have been conducted at two straw fired plants (Ensted and Avedøre biomass boiler) and at Ensted wood chip plant [19,20]. At Ensted and Avedøre straw-fired boilers, the addition of additives showed modest decrease of potassium chloride levels however a total elimination is required to ensure that there is no risk for corrosion. Due to the high amount of potassium content in straw, large amounts of additive (5% of dry fuel weight) are required to obtain significant KCl conversion. Additives must be fed in so they can react with the gaseous potassium chloride in the correct temperature window for the additive concerned and before the potassium chloride condenses on the vulnerable components. This is different for both sulphate and aluminium silicate additives. In addition there are certain practical problems in feeding in such large amounts of additive. Thus it was concluded that dosing with additives in straw firing, although theoretically a possibility is practically not a viable solution. However there was success with additive dosing for woodchip firing because the potassium and chloride content of the woodchip is markedly lower.

Conclusions

In straw-fired boilers, high corrosion rates are observed due to the presence of potassium and chlorine rich deposits. At high temperatures, a chlorination reaction occurs where the alloy is attacked first at the grain boundaries followed by chromium depletion within the grains. Experience from woodchip fired boilers also indicates the threat of chlorine corrosion due to a similar mechanism as in straw-fired plants. However, there are variations in corrosion rates, which probably relates to the heterogeneous character of the deposits. The solution to the corrosion problem is to react gas-phase KCl in the combustion chamber such that the non corrosive potassium aluminium silicate or less corrosive potassium sulphate are the only alkali-containing species that can come in contact with the vulnerable high temperature metallic components. This

has been undertaken in two full-scale plants in Denmark by co-firing with coal and 10 - 20 % straw (on energy basis), co-firing wood pellets and heavy fuel oil, and by using additives. Co-firing with coal is by far the most viable way to avoid corrosion problems when using straw as the biomass fuel. This is due to the large amounts of potassium chloride in the fuel which need to be neutralised. Due to the lower amount of potassium and chloride in woodchip, use of additives is a possibility in boilers using this fuel.

Acknowledgements: Some of this work has been funded by PSO (public service obligations) through ELTRA and Elkraft Systems.

References

[1] O.H. Larsen and N. Henriksen, "Ash Deposition and High Temperature Corrosion at Combustion of Aggressive Fuels" Proc. Power Plant Technology, Kolding 4-6 Sept. pp 7.1-7.18. (1996)
[2] N. Henriksen, OH, Larsen, R. Blum, S. Inselmann, "High temperature corrosion at co-firing of coal and straw in pc boiler and CFB boilers" VGB Conference Corrosion and Corrosion Protection in Power Plants 1995.
[3] N. Henriksen and O.H. Larsen, "Corrosion in ultra supercritical boilers for straw combustion" Materials at High Temperatures, 14 (3) pp. 227-236 1997
[4] M. Montgomery, A. Karlsson, "In situ Corrosion Investigation at Masnedø CHP Plant" Materials and Corrosion, 50 579-584 (1999)
[5] M. Montgomery, A. Karlsson , O.H. Larsen, "Field test corrosion experiments in Denmark with biomass fuels Part I: Straw firing" Materials and Corrosion 53 pp. 121-131 (2002).
[6] M. Montgomery, O. Biede and OH Larsen, "High Temperature Corrosion in straw fired power plants: Influence of steam/metal temperature on corrosion rates for TP347H" Materials for Advanced Power Engineering 2002 Part II pp 957-966 (2002).
[7] M. Montgomery, B. Carlsen, O. Biede and OH Larsen, "Superheater corrosion in biomass fired power plants: investigation of welds" Proc. NACE Conference CORROSION/2002, paper 02379.
[8] N. Henriksen, M. Montgomery, O.H. Larsen, Korrosion in energieerzeugenden Anlagen VDI-Berichte 1680. VDI Verlag GmbH Düsseldorf pp. 111-133 (2002).
[9] M. Montgomery and O.H. Larsen, "Field test corrosion experiments in Denmark with biomass fuels Part II: Co-firing" Materials and Corrosion, 53 pp185-194 (2002).
[10] M. Montgomery, O. Biede, O.H. Larsen " Experiences with Inconel 625 in biomass and waste incineration plants" Proceedings ISHOC 2005 conference, Nara, Japan.
[11] H.P. Nielsen, Ph.D Thesis, Technical University of Denmark, (1998).
[12] D.A. Berztiss. A. Zahs, A. Schneider, M. Spiegel, H. Viefhaus, HJ Grabke HJ, "Role of carbides in the high temperature corrosion of steels in HCl containing atmospheres" Z. Metallkd. 90 pp.4-12 (1999).
[13] B. Sander, "Properties of Danish biofuels and the requirements for Power production" Biomass and Bionergy, 12 3 pp177-183, (1997)
[14] K. Wieck Hansen, P. Overgaard, O.H. Larsen, "Co-firing coal and straw in a 150MWe Power boiler experiences" Biomass and Energy, 19 pp.395-409 (2000).
[15] A. Rahmel "Beitrag zur Frage des Zunderverhaltens von Kesselbaustählen" VGB Mitteilungen 74 October (1961).
[16] R.B. Frandsen, M. Montgomery, O.H. Larsen "Field test corrosion experiences when co-firing straw and coal: Ten years status within Elsam" 4th International Workshop "Materials Issues Governing the Performance of Advanced 21st Century Energy Systems" held in Wellington, New Zealand in February 2006.
[17] M. Montgomery, SA Jensen, O. Biede, O.H. Larsen C. Andersson "Corrosion and oxidation experiences in Avedøre II multifuel boiler" Poster at this conference.
[18] J.P. Jensen, K. Nielsen, M. Montgomery, C. Andersson "Ash chemistry, corrosion and heavy metal emissions from a 800MW wood pellet + oil+natural gas fire power plant" Proc of 14th European biomass conference 17-20th October 2005, Paris.
[19] O.H. Larsen, J.P. Jensen, O. Biede, M. Montgomery, C. Andersson "Relations between combustion, deposition, flue gas temperatures and corrosion in straw-fired boilers" Proc. 2nd World Conference and Technology Exhibition on Biomass for Energy and Industry, paper OD7.2 Rome 10-14th May 2004.
[20] J. Knudsen, J.P. Jensen, O. Biede, M. Montgomery, O.H. Larsen, J. Zeuthen, J. Hansen, P.A. Jensen, S. Clausen "Full-scale evaluation of additives for the reduction of chlorine-rich deposits in a 100MW straw-fired boiler" Proc of 14th European biomass conference 17-20th October 2005, Paris.

RE-QUALIFICATION OF BOILER DRUMS IN THERMAL POWER PLANT

Peter Brziak, Peter Bernasovský
Welding Research Institute – Industrial Institute of Slovak Republic

Abstract

The technical condition and serviceability of boiler drum operating in thermal power plant Zemianske Kostolany (Slovakia) with exhausted design life were determined.
Fulfillment of conditions stated by the Slovak acts on safety and health protection at work & safety of technical equipment was approved.

1. Introduction, legislative framework

Servicing of pressure components of power equipment with exhausted design life is usual practice not only in the East European countries but also in the countries of Western Europe. The key factors of prolonging the life are the economical reasons leading the user to effort to postpone the demanding investment connected with replacement of equipment or some its components. On the other hand servicing of equipment which has exhausted its design life is connected with several technical and also legislative problems. In European measure, a unified legislation does not exist, neither unambiguous criterion, which could be applied in decision making process on possible prolonging of equipment life. Thus it is on the user proper, how he would approach to the given problem.

In general, any legal instrument that would strictly order to the user to shutdown the equipment with exhausted design life there does not exist. In case of selected dedicated technical equipment (DTE) the equipment user on Slovak territory is obliged to prove by documents the safety in the sense of several relevant laws, decrees and regulations [1, 2, 3]. In practice this concerns the compulsory periodical (or exceptional in case of interference to pressure system, for example owing to repair or replacement of several components) performance of constructional and pressure test of the DTE in the sense of Slovak technical standards.

In Slovak Power Plant Inc. the issue of servicing the pressure components of equipment is solved in the form of plant standards (PS). The issue of prolonging the service of boiler drums is included in plant standard: „Re-qualification of boiler drums and selected stationary pressure vessels with exhausted design life“ [4].

The above-mentioned plant standard regulates the procedure of determination of technical condition (re-qualification) and serviceability of the selected dedicated pressure equipment up to service temperature of the wall of 350 °C after exhausting the design life according to an approved set of technical guidelines for the conditions of Slovak Power Plant, Inc. The technical guidelines were agreed by the Technical Inspection[1] in the issued special binding standpoint as the safety – technical requirements for assessment of condition of the selected

[1] The Technical Inspection (thereinafter "TI") was in order to perform state technical supervision on occupational safety. The TI is public contributory organization. The Director of TI is appointed and recalled by the Minister of Labour, Social Affairs and Family of the Slovak Republic.

pressure equipment [5]. The re-qualification of boiler drum in sense of (4) was performed by Welding Research Institute - Industrial Institute of Slovak Republic (WRI) as an authorized assessor (just assessor in next) on the basis of request. The WRI has met the requirements laid on the authorized assessor in such a manner that it showed its professional competence to the customer, by acquiring the certificate of TI for performing the re-qualification [6].

2. Information about boiler drum

The boiler drum was constructed in the years 1962 – 1964 according to the standard valid at that time. The shell consists of four welded bent rings and two cups. The main dimensions are as follows: length: 15.25m (11.65 m without cups), outer diameter: 1.8 m, wall thickness: 94 mm.

The working parameters are 15.86MPa/344°C. The design life is 200 000 h. Total operating time is 214 000 h. Total amount of start-ups: 1656, cold shut-downs: 1543, hot shut-downs 113, pressure tests: 16 (performed at working pressure multiplied by 1.25).

The chemical composition of base metal (BM) is seen in Table I. The Mo-Mn according STN 41 5233 steel devoted for temperature range up to 400°C is concerned. This steel has no foreign equivalent. The base material was delivered in quenched + tempered condition. Another tempering was performed after circumferential welds were manufactured.

Table I Chemical composition of boiler drum compared with standards.

	Chemical composition (weight %)								
	C	**Mn**	**Si**	**P**	**S**	**Cu**	**Ni**	**Cr**	**Mo**
15 223 STN standard	0.7 ↓ 0.23	1.2 ↓ 1.6	0.15 ↓ 0.4	↓ 0.04	↓ 0.04	↓ 0.3	↓ 0.25	↓ 0.2	0.3 ↓ 0.5
Boiler drum	0.228	1.54	0.21	0.021	0.012	0.11	0.058	0.082	0.43

3. Re-qualification program

The re-qualification in sense of [4] consists of the following procedure:

1. Specification of re-qualification documentation.
2. Specification of inspections, mechanical and non-destructive tests.
3. List of inspected zones. Requirements on treatment of the inspected surface.
4. Specification of zones and sampling procedure for the material from the boiler drum.
5. Assessment of technical condition of boiler drum and classification of its serviceability.
6. Schedule of tests.
7. Requirements for assuring the work safety.

The re-qualification procedure is given in **Fig. 1**. The collaboration with customers was crucial to get proper information about device and its history. Some parts of re-qualification are in details mentioned as follows:

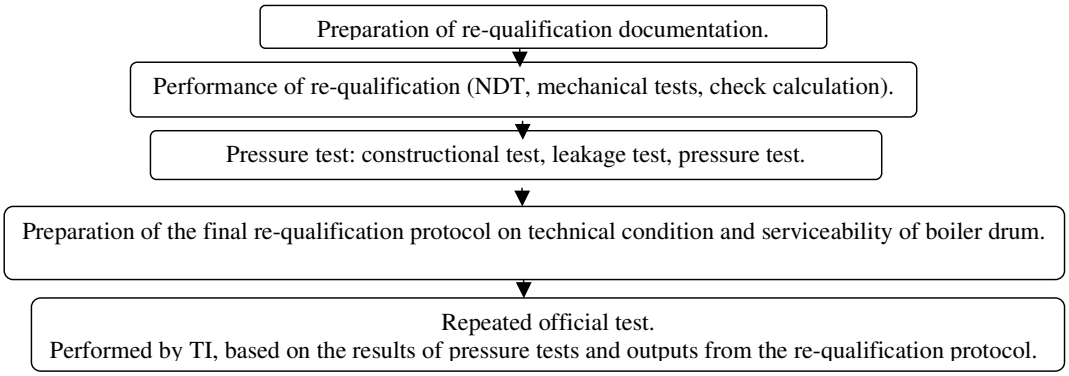

Fig. 1 Sequence of re-qualification process

3.1 Specification of re-qualification documentation

Boiler drum was specified on the basis of following data which were provided by the user to assessor:

1. Evidence data and boiler drum passport.
2. Data about the design life. Documents on quality.
3. Constructional and accompanying documentation.
4. Service regimes and parameters necessary for calculation of residual life (extent given by the assessor's specification).
5. List of materials and their mechanical characteristics at +20°C and at the service temperature.
6. Data on results of periodic inspections and test. Map of the found out defects. Really measured thickness of shell and bottom, thickness at welded joint of shell with bottom, thickness of nozzles.
7. Survey of failure occurrence and reproving measures.
8. Data on modifications and repairs that were done on the boiler drum.

3.2 Specification of inspections, non-destructive and mechanical tests and their scope

3.2.1 Non-destructive tests

NDT tests were used for:

- identification and location of flaws – material defects caused by the service thermal and mechanical loading or environment aggresiveness,
- determination of damage range (depths of defects) and their quantification.

The following NDT tests were performed on the boiler drum in the following scope:

- visual inspection of the inner and outer surface according to EN ISO 58-17, EN ISO 6520-1, EN 12062, EN 970
- 100 % magnetic inspection of all weld joints (circumferential and longitudinal) according to EN 1291/A1
- 100 % ultrasonic inspection of all weld joints (circumferential and longitudinal) according to EN 12062, EN 1712, EN 1714
- measurement of wall thickness according to EN 14 127
- metallographic examination by means of replica for a brief microstructure comparison.

For the needs of NDT the insulation and building-in had to be removed from the boiler drum. The surrounding of welded joints was ground to metallic gloss at minimum 10 cm distance on both sides.

3.2.2 Mechanical tests

The mechanical tests of BM were performed on drilled off material in the range given by dimensions of the sampled material (cylinder ϕ 102 mm, height app. 90 mm):

- tensile test, 2 pieces at +20 °C, 1 piece at + 350°C,
- CVN test,
- fracture toughness test.

The measured values were compared with the WRI database. A cylinder 102 mm in diameter was drilled off from the boiler drum – rolled ring 4. The location of bore is shown in **Fig. 2**. The opening was then blinded. The layout of specimens in cylinder is seen in **Fig. 3**. For performing the drilling off and blinding, the assessor contracted the by Slovak boiler producer SES Tlmace, Inc. which determined the location and size of bore, performed the strength calculation and designed the blinding technology. Whole documentation was then agreed by the manufacturer of drum – Vitkovice Steel Inc. (Czech Republic) and approved by the TI, what enabled to apply this procedure during re-qualification.

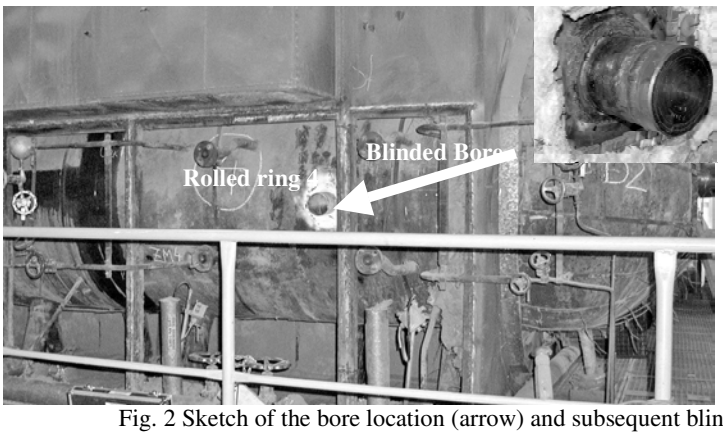

Fig. 2 Sketch of the bore location (arrow) and subsequent blinding.

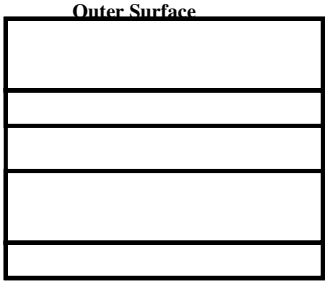

Fig.3 Layout of specimens in cylinder removed from boiler drum.

4. Results of re-qualification

4.1 Visual inspection and NDT testing

Visual inspection and NDT testing of boiler drum have shown that from the last inspection of drum done in the year 2001 none new crack-like defects were found out. Neither other defects were found in the locations detected at previous inspection of the drum.

4.2 Mechanical properties

Some data attained about the real mechanical properties are as follows:

The strength characteristics are summarized in **Tab. II**. The values of strength characteristics of the serviced base metal type are comparable to those measured in virgin material.

Table II Tensile properties of boiler drum.

Material	**Testing temp.** (°C)	$\mathbf{R_e}$ (MPa)	$\mathbf{R_m}$ (MPa)	**A** (%)	**Z** (%)	**Note**
Boiler drum	+20	min. 373	539 to 735	min. 16.0	–	According to standard STN 41 5223
	+350	min. 314	-	-	-	
Boiler drum (year 1962) virgin	+20	548	656	20.0	62.8	Rolled ring 4, Data selected from passport. Specimen direction (Y)
	+350	490	643	17.0	30.3	
Boiler drum (year 2005) 214 307 hours	+20	529 ± 3.0	674 ± 3.0	23.9 ± 1.6	66.6 ± 0.5	Rolled ring 4, Tested at WRI Specimen direction (Y)
	+350	485	635	19.8	62.5	
	+350	562.4 ± 19.7	692.0 ± 14.7	22.6 ± 2.2	62.0 ± 2.1	

Notch toughness of base metal was compared to virgin materials. As it can be seen from **Fig.4**, the base material embrittled during service. The transition temperature is high, the 40 J value is achieved at +65°C, comparing with virgin material, where T40 value is achieved at -35°C.

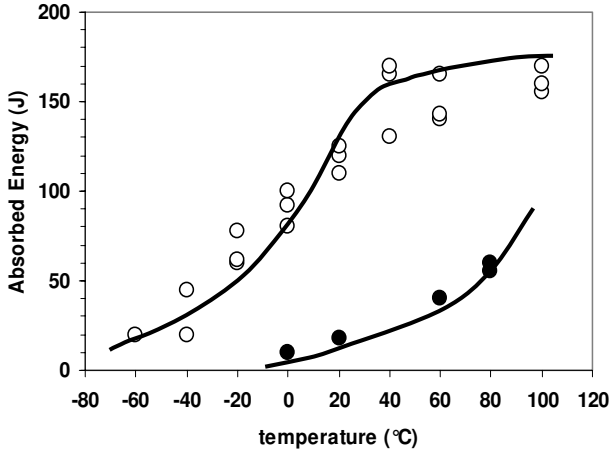

Fig.4 The absorbed energy of base metal: open symbols-virgin base metal, solid symbols – base metal serviced for 214 307 h (rolled ring No.4).

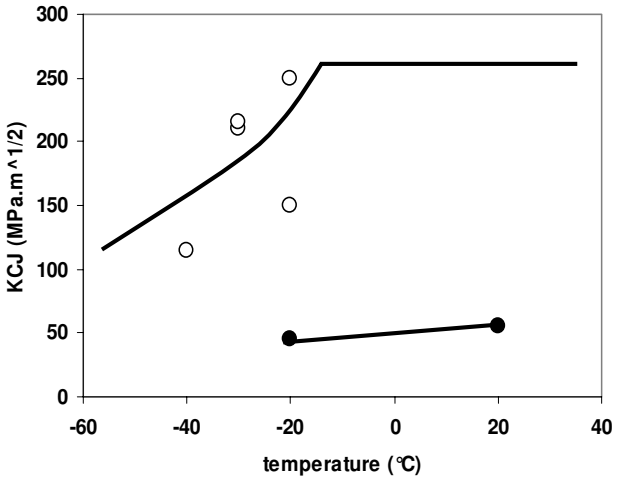

Fig.5 The fracture toughness of base metal: open symbols-virgin base metal, solid symbols – base metal serviced for 214 307 h (rolled ring No.4).

The deterioration of toughness was also proved by static fracture toughness tests. For the thickness of 25 mm, very low valid K_{IC} values were measured. The steel will attain the criterion value of notch toughness K_{IK}(base metal) = 100 MPa$\sqrt{m}$ just above the temperature of $T_{K100} \geq 115$, eventually 125 °C. The KCJ measurements are summarized in **Fig.5**.

Based on the attained data it was stated that the base metal of boiler drum is embrittled and the several measures have to be done to fulfill the safe operation. Besides all, the temperature of obligatory pressure tests was increased; and acoustic emission was recommended.

4.3 Microstructural analysis

The microstructure testing by means of small sampling was applied to compare the microstructure of ring 4 (from which the cylinder for mechanical test was removed) to other parts of drum shell.

The microstructure of base metal of bent ring 4 is bainitic with a low proportion of ferrite and pearlite, see **Figs. 3 – a, b**. Direct comparison with microstructures of other rings (identified by NDT metallography – not documented) was impossible, since their surface layers are decarburized to greater depth than the depth of surface preparation at current NDT techniques.

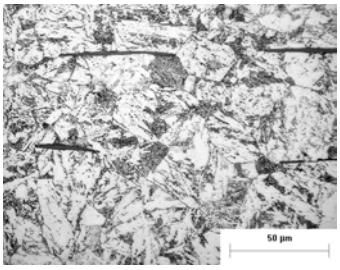

a) wall centre

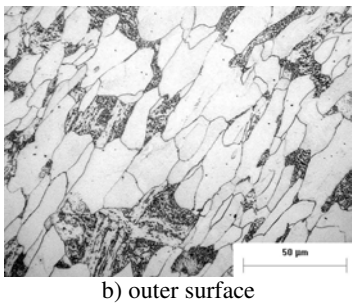

b) outer surface

Fig. 3 Microstructure of base metal of boiler drum, ring No. 4.

However, from comparison of surface layer of ring No. 4 and other studied zones it follows that those are principally the same; therefore we suppose that also the non-decarburized microstructures are similar. It is therefore possible to conclude that the mechanical properties of BM of the ring No. 4 are representative for BM of the entire boiler drum.

4.4 Check calculation of strength and life

Based on the check calculation[2] it can be stated for that:

Calculation of static strength: **acceptable**

Calculation of fatigue damage at cyclic loading: **acceptable**

[2] The calculations are based on Slovak standards and finite element analysis. This article is not focused on this issue.

The residual life up to attaining the admissible value of low-cycle fatigue damage**:** 42 311 h (about 8 years)

4.5 Pressure tests

The pressure test at wall temperature around 65 °C (estimated ductile – brittle transition of base metal) - was performed with the result: Acceptable for the requirements of Slovak standard STN 07 0624: 1979.

4.6 Acoustic emission

The acoustic emission was performed in parallel with the pressure test with the result: no indications of "living" cracks.

5. Conclusions

Based on above mentioned results the Welding Research Institute elaborated the final re-qualification protocol, which was used as one of the documents for TI at issuing the positive binding expert standpoint about the repeated official test.

The result of binding expert standpoint is the certificate stating that the boiler drum meets the basic requirements laid on safety of technical equipment. Regarding the legislative viewpoint, all assessments of service safety regarding the dedicated pressure equipment, available in the Slovak Republic, were thus performed on the boiler drum.

References

[1] Act No. 330/1996 on safety and health protection at work
[2] Regulation No. 718/2002 for assuring the safety and health protection at work and safety of technical equipment
[3] Decrees of Slovak government No. 159/2001 and No. 470/2003
[4] Company standard 07 – 04/2000 „ Re-qualification of boiler drums and selected stationary pressure vessels with exhausted design life"
[5] Technical Inspection certificate No. 141/5/2000-TZ on technology for performing the re-qualification of selected dedicated pressure equipment with exhausted design life
[6] Technical Inspection certificate No. 588/2005 on technology for performing the re-qualification of selected dedicated pressure equipment with exhausted design life

Part 1

Advanced Gas Turbine Materials

Contributed Papers

Mechanical Properties

DEVELOPMENT OF NI-BASED SINGLE CRYSTAL SUPERALLOYS FOR POWER-GENERATION GAS TURBINE BLADES

Ryokichi .Hashizume [1)], Akira.Yoshinari [2)] ,Takamasa Kiyono[3)] ,Yoshinori.Murata [4)] and Masahiko.Morinaga [4)]

1) The Kansai Electric Power Company Inc., Amagasaki , JAPAN
e-mail: hasizume@rdd.kepco.co.jp
2) Hitachi Research Laboratory, Hitachi Co. Ltd., Ibaraki, JAPAN
3) Thermal & Hydroelectric Systems Div, Hitachi Co. Ltd., Tokyo, JAPAN
4) Department of Materials Science and Engineering, Nagoya University, Nagoya JAPAN

Abstract

In advanced industrial gas-turbine systems, there has been a great demand for new single crystal (SC) superalloys with an excellent combination of high-temperature creep strength, hot-corrosion resistance and oxidation resistance. In this study, twelve nickel-based SC superalloys were designed with the aid of the d-electrons concept. Their chemical compositions were in the range of 1.2-1.5%Ti, 3.8-6.5%Cr, 11%Co, 0-1.4%Mo, 0-3.0%Ru,6.5-7.4%Ta, 5.0-6.4%W, 3.6-5.4%Re, 5.1-5.5%Al, 0.12-0.14%Hf and balanced Ni in wt%. A series of experiments such as creep rupture tests, burner rig tests and cyclic oxidation tests were conducted with the heat-treated SC specimens of these alloys. Almost all the designed alloys were found to be superior in creep rupture life to a 2nd generation superalloy currently used in the world. In the hot-corrosion resistance estimated from the burner rig tests, any designed alloys were similar or even superior to a 2nd generation superalloy. The oxidation resistance was very different among the designed alloys, but some of them showed better resistance than the 2nd generation superalloy. Thus the SC alloys containing about 4-5 wt% Re had about 30℃ or more higher temperature capability than the 2nd gene-ration superalloy, while exhibiting excellent hot-corrosion resistance and good oxidation resistance.

Keywords: Ni-based superalloy, d-electrons concept, creep strength, oxidation resistance, hot corrosion resistance

1. Introduction

There has been a strong need to develop new superalloys with excellent heat resistant properties, but no 3rd generation SC superalloys have been used for power plants commercially despite their excellent creep strength at high temperatures.
The reasons can be summarized as follows:
1) It is difficult to grow a large single crystal blade for power plants with no grain defects in conventional casting experiments. .

2) The oxidation resistance at high temperatures is much lower than that of the 2nd generation superalloys.
3) The phase stability is also poor at high temperatures, so that the TCP phases tend to form in the alloy, resulting in the degradation of long time properties, which are critical for power generation gas turbines.
In this study, we have designed twelve different superalloys using the d-electrons concept to solve these problems, and conducted a series of experiments to examine their creep strength, hot corrosion resistance and oxidation resistance as well. We have previously succeeded in finding alloys with high creep strength and good hot-corrosion resistance [1]. So, this time we have tried to develop nickel-based superalloys which possess higher oxidation resistance than the 2nd generation superalloys. For this purpose, the contents of Cr, Mo, W and Ta were optimised in the 4-5 wt% Re containing superalloys. Some alloys did not contain Mo, because Mo is known to deteriorate oxidation resistance. Also a Ru-containing alloy was tested so as to examine the effect of Ru on the creep strength. It will be shown that some of the designed SC alloys had an excellent combination of high creep strength, hot corrosion resistance, extremely good oxidation resistance and good castability.

2. Experimental Procedure

2.1. Alloy chemistry

Twelve Nickel-based SC superalloys containing Ti-(3.8-6.5)Cr-Co-Hf(-Mo,Ru)-Ta-W-(3.6-5.4)Re-Al-Ni,were designed with the aid of the d-electrons concept. Their chemical compositions are listed in Table1. The d-electrons concept has been devised on the basis of the molecular orbital calculation of electric structures [2]. In this concept both the Md and Bo parameters are used, where Md is the d-orbital energy level of alloying element and Bo is the bond order between alloying element and Ni atom. Both the $\overline{Md}$ and the $\overline{Bo}$ values for the designed alloys are

Table1 Chemical compositions and alloying parameters of experimental alloys（mass%）

	Ti	Cr	Co	Ni	Ru	Mo	Hf	Ta	W	Re	Al	$\overline{Md}$	$\overline{Bo}$
TA	1.4	6.0	11.0	Bal.	3.0	--	0.12	6.8	6.0	4.8	5.4	1.000	0.690
SA	1.4	6.0	11.0	Bal.	--	--	0.12	6.8	6.0	4.8	5.4	0.991	0.672
A	1.4	4.0	11.0	Bal.	--	--	0.12	6.8	5.5	4.4	5.4	0.978	0.650
B	1.4	6.0	11.0	Bal.	--	--	0.12	6.8	5.5	4.4	5.4	0.987	0.668
C	1.4	6.0	11.0	Bal.	--	--	0.12	6.8	5.5	3.6	5.4	0.984	0.664
D	1.4	5.0	11.0	Bal.	--	--	0.12	7.4	5.5	3.6	5.4	0.984	0.658
E	1.4	6.5	11.0	Bal.	--	--	0.12	7.4	5.0	3.6	5.4	0.988	0.669
F	1.4	5.0	11.0	Bal.	--	--	0.12	6.8	6.4	4.4	5.3	0.985	0.664
G	1.4	5.0	11.0	Bal.	--	0.5	0.12	6.5	5.6	4.4	5.3	0.982	0.662
H	1.2	4.0	11.0	Bal.	--	0.8	0.12	6.8	6.0	5.2	5.5	0.987	0.661
I	1.5	4.0	11.2	Bal.	--	0.6	0.14	6.7	5.5	5.4	5.3	0.985	0.661
J	1.5	3.8	11.0	Bal.	--	1.4	0.14	6.7	5.3	5.4	5.1	0.988	0.667
K	1.0	6.5	9.0	Bal.	--	0.6	0.10	6.5	6.0	3.0	5.6	0.984	0.664
L	0.7	6.6	9.2	Bal.	--	0.5	1.40	3.2	8.5	3.0	5.7	0.983	0.664
M	--	3.0	12.0	Bal.	--	2.0	0.10	6.0	6.0	5.0	5.7	0.971	0.666

shown in the Table1. They were obtained from the compositional average of the d-electron parameters, Md and Bo of each alloying element. The compositions of the refractory elements such as Cr, Mo, W and Ta in the alloys were adjusted so that the $\overline{Md}$ and $\overline{Bo}$ values lay in the range of :(0.97-1.00),:(0.65-0.69), since the target region for alloy design is located in this range] [3]. Also, in the $\overline{Md}$ - $\overline{Bo}$ map shown in Fig. 1, the twelve designed alloys are located nearer to the 2nd generation SC superalloys than the 3rd generation SC superalloys. In Table 1, eight alloys of TA,SA,A thru F are Mo-free alloys, designed so as to raise the oxidation resistance.

Alloys K, L, and M are reference alloys, i.e., the chemical compositions of K, L and M are the same as CMSX-4, CM186LC and TMS75, respectively.

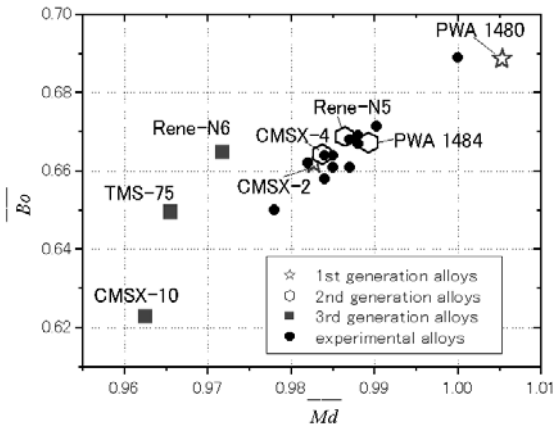

Fig.1 Bo-Md Map of the designed alloys and the references

Table2 Heat treatment conditions employed in this study

Alloy	Solution	1st Step aging	2nd Step aging
TA	1583K/10h+1593K/12h	1433K/4h, AC	1144K/20h, AC
SA	1583K/10h+1593K/12h +1598K/12h	1453K/4h, AC	1144K/20h, AC
A	1573K/4h+1583K/6h +1588K/12h	1433K/4h, AC	1144K/20h, AC
B		1413K/4h, AC	
C		1433K/4h, AC	
D			
E			
F	1573K/8h+1583K/4h +1588K/8h	1433K/4h, AC	1144K/20h, AC
G			
H	1593K/12h+1598K/12h +1603K/24h	1393K/4h, AC	1144K/20h, AC
I			
J	1573K/12h+1583K/12h +1593K/24h	1433K/4h, AC	1144K/20h, AC

2.2 Alloy Preparation and Heat Treatments

First, the master ingots of the experimental alloys were made in a vacuum induction furnace by controlling the contents of gas elements to be as low as possible. Then, using those ingots, single crystals 15mm in diameter and 180mm in length were grown by a directionally solidified method. The conditions of solution heat treatment and aging heat treatment are listed in Table 2. Every specimen was first heat treated following the parameters given in Table 2 and then supplied for a series of experiments

2.3 Microstructural Observation

The microstructures in the SC alloys were examined with SEM before and after the creep rupture tests. The cross section of the specimens after a hot corrosion test and oxidation tests were also investigated using a SEM equipped with the EDX analyzer. For these micro-structural analyses, the specimen surface was first polished mechanically with emery papers and then with a buff dripping water containing Al_2O_3 powders. Subsequently, the surface was etched chemically in an HCl-HNO_3 solution

2.4 Creep Rupture and Tensile Test

The heat-treated SC alloys were machined mechanically into the specimens for the creep rupture tests and the tensile tests. The gauge length of the specimen was 6mm in diameter and 30mm in length. These tests were performed following the standard of ASTM-E139. The tensile tests were carried out at room temperature and 973K with the strain rate of 5.56×10^{-5}/s. The creep rupture tests were performed under the temperature/stress conditions of 1313K/137MPa, 1255K/206MPa, 1193K/314MPa, 248MPa, 206MPa, and 1123K/441MPa.
The additional creep rupture tests of 1373K/137MPa were carried out for the three designed alloys-TA,SA,B and the reference 2nd generation alloy.

2.5 Oxidation and Hot Corrosion Test

The plate specimens with the size 10x25x1.5 mm were cut from the SC alloys by an electro-spark machine. Two kinds of oxidation tests were realized in this study. One was the cyclic oxidation test, in which the specimen was held in air at 1373K for 20 hours followed by air cooling in each cycle. This cycle was repeated 12 times, so the total exposure time at 1373K was 240hours. The other was the continuous oxidation test at 1313K for 3,600 hours and at 1193K for 10,000 hours. In order to examine the hot corrosion resistance of the SC alloys, a burner-rig test was carried out at 1173K for 35 hours with specimens of 8 mm in diameter and 30 mm in length. The burning gas was prepared by using a fuel containing 0.04% sulfur and the atomized brine of 80 ppm NaCl.

2.6 Single Crystal Casting of a Model Bucket

The casting test was carried out with a model bucket for the first stage of 25MW class gas turbine. The model bucket was 170 mm long, and there was a return-flow type cooling structure inside it.

3. Experimental Results

3.1 Microstructure

The microstructures of some of the designed alloys after the 2nd step aging are shown in Fig. 2. While every alloy appeared to have a similar uniform γ/γ' phase microstructure, but still

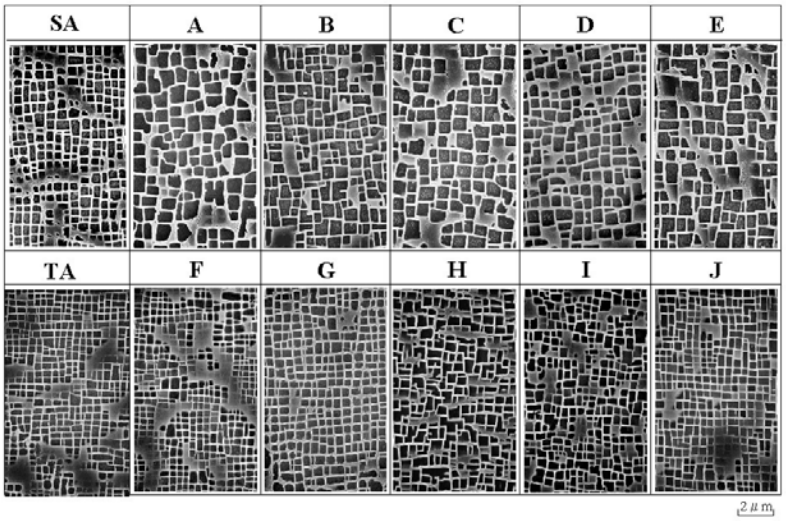

Fig.2 SEM micrographs of typical specimens of the investigated alloys after the heat treatment

there was a little difference in the aspect and the size of the γ' phase among the alloys. The shape of the γ' phase in the alloys A and H was partially irregular. The size of the γ'phase was about 0.5μm in alloys A through E, and about 0.3-0.4μm in alloys F through J and SA. Thus, the Mo-free alloys A through E (except for alloy SA and F) had the larger γ' phase as compared to the Mo-containing alloys G and H. Also, the size of the γ' phase was larger in the alloy SA than in the Ru- containing alloy TA. Thus, the Ru addition was effective in making the fine precipitates of the γ' phase in the alloy. Besides this, no correlation was found between the micro structure and the chemical compositions of the alloys

3.2 Creep Strength

The results of the creep rupture tests are given in Fig. 3. The measured creep strength of the designed alloys varied to some degree depending on the chemical compositions. As for the creep condition of 1313K, 137Mpa, the creep rupture life of the designed alloys TA, SA, B,E through I exceeded 1000 hours, much longer than the rupture life, 726 hours, of the second generation superalloy(alloy K). Among them, alloys TA and SA had the longest rupture life of 2050 and 2016 hours, respectively. As for the creep condition of 1255K, 206MPa, the creep rupture life of all the designed alloys were longer than that of the 2nd generation superalloy, and the life of alloy TA (1504 hours) was better than the rupture life (1215 hours) of the 3rd generation SC superalloy (alloy M). Thus, it can be said that the creep rupture strength of the designed alloys was at a very high level. Although alloys TA,SA, A through F contained no Mo, the creep strength was superior or comparable to that of alloy G containing

0.5%Mo. Also, alloys SA, B and C contained 4.8%,4.4%and 3.6% Re respectively and the rest of the alloy compositions were almost same among them. So, the difference in the measured creep strengths between them is mainly attributable to the differences in the Re content. It was stressed here that the alloy TA showed the longer creep rupture life in every condition compared to the alloy SA, indicating that the addition of 3%Ru was beneficial to the improvement of the creep strength even in the alloy without Mo. Alloys H, I and J showed relatively higher creep strength among the designed alloys. This result may also be interpreted as due to the Re content, since these alloys contained 5.2-5.4%Re but the other alloys contained 3.6-4.4% Re. In addition, alloy J had the highest Mo and Re contents (e.g., 1.4% Mo and 5.4% Re) among alloys H, I and J, but it showed weaker creep strength than alloys H and I. In this case, it seemed that Mo played no significant role on the improvement of the creep strength at high temperatures.

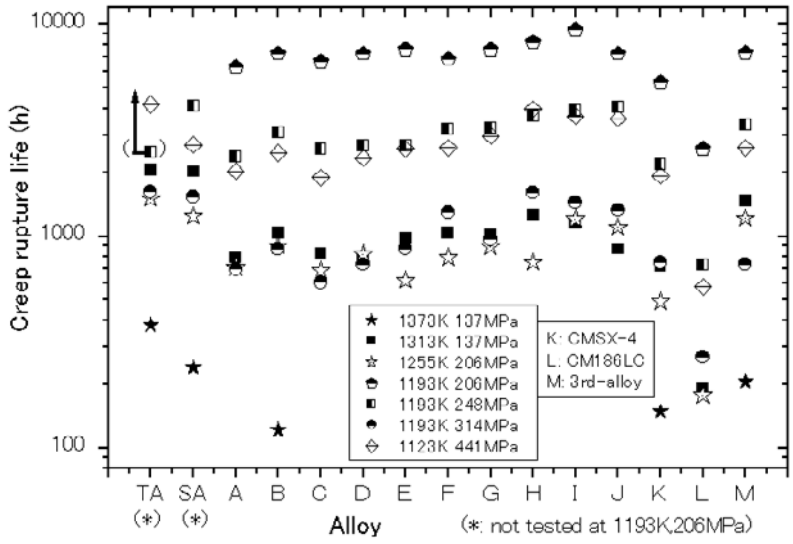

Fig.3 Results of creep rupture tests.

3.3 Hot Corrosion Resistance

The results of mass changes in the hot corrosion test are shown in Fig. 4 for the designed alloys and the reference alloys. This burner rig test was performed at 1173K for 35 hours. Every designed alloy exhibited good hot-corrosion resistance, and their mass change was similar to or even smaller than that of 2nd generation alloy-K(CMSX-4.) Among the experimental alloys, Alloy D exhibited the largest mass change, 1.86mg/cm^2, but still its

magnitude was similar to that of alloy-K(CMSX-4). On the other hand, the mass changes of the two reference alloys, L(CM186LC) and M(TMS-75), were larger than 10mg/cm^2. In case of the 14% CrCC alloy, which is a practically used material for the first stage blade of 1300℃ TRIT(Turbine rotor inlet temperature) power generation gas turbine, the mass change was –1.9 mg/cm^2 , because the corroded scale that formed on the surface flaked off. The appearance of the specimens after the burner rig test are shown in Fig.5 for the six designed alloys, TA, SA, A, B, F, H, and also the four reference alloys. In contrast to these designed alloys, two of the reference alloys, L(CM186LC) and M(TMS-75), showed a very rough surface covered with thick and ragged corroded scales, indicating that the hot-corrosion resistance was extremely low in these alloys

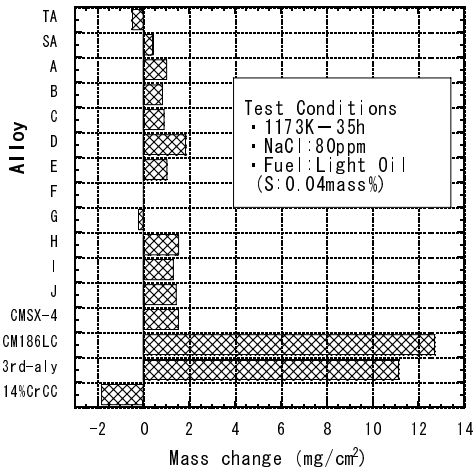

Fig.4 Results of hot corrosion burner rig tests

Fig.5 Photos of test specimens after hot corrosion burner rig tests

3.4 Oxidation Resistance

The results of the continuous oxidation tests at 1193K and 1313K and the cyclic oxidation tests at 1373K are shown in Figs. 6,7 and 8, respectively. At all tested temperatures , it was found that the mass changes were smaller in the Mo-free alloys than the Mo-containing alloys. Thus, as might be expected from the detrimental effect of Mo, the Mo-free alloys had better oxidation resistance than the Mo-containing alloys. Also, judging from the result of oxidation test of the alloy TA at 1313K, Ru has probably a detrimental effect on the oxidation resistance to some degree. In addition, the reference alloy K (CMSX-4) and alloy L (CM186LC) exhibited very good oxidation resistance. In general the oxidation reaction becomes more active with

increasing temperature, so that the cycle of forming oxidation scale, flaking off, and then forming new oxidation scale, will be accelerated with temperature, resulting in significant mass reduction. However, there was little mass change in alloys B and D, although these alloys showed a little mass gain in the beginning of the oxidation test. As shown in Table 1, the chemical compositions are quite similar among the Mo-free alloys, SA,A through F, for example, their Ti, Co and Al contents are equal, but only alloys B and D exhibited almost no mass change in the oxidation test at every temperature. The reason why the oxidation resistance was so different among these alloys despite a little difference in the chemical compositions, still remains unclear. But the present results will provide us a clue to the improvement of the oxidation resistance, so it is necessary to investigate the cause of this phenomenon in the future.

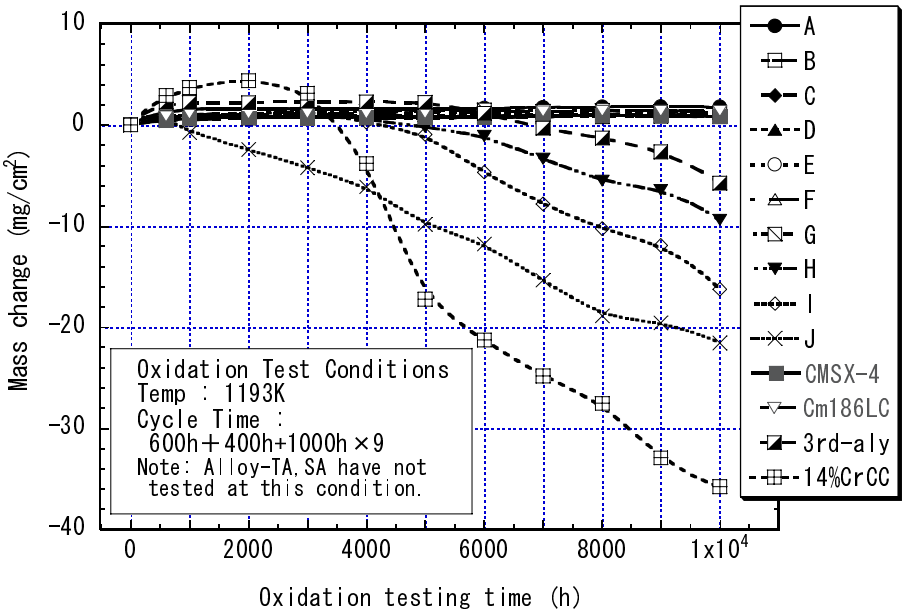

Fig.6 Results of continuous oxidation tests at 1193K

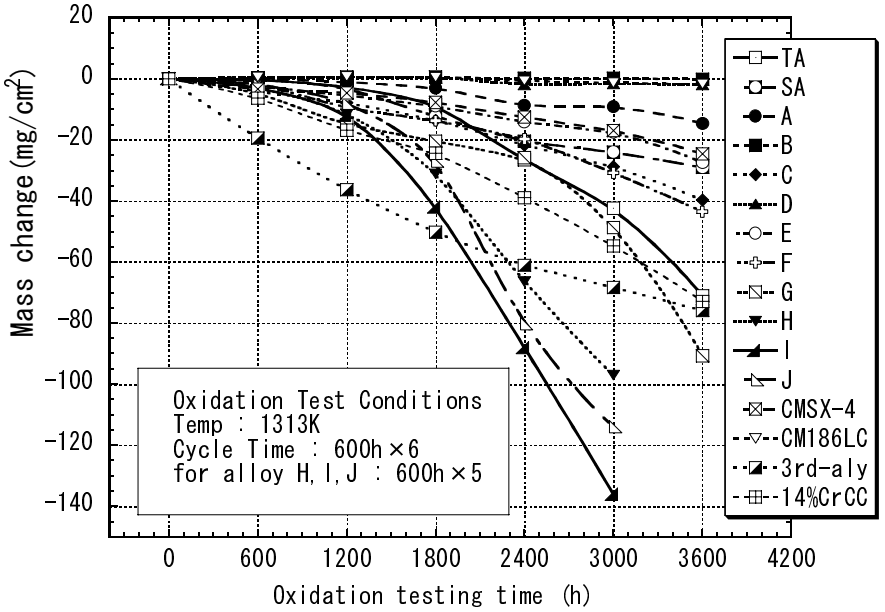

Fig.7 Results of continuous oxidation tests at 1313K

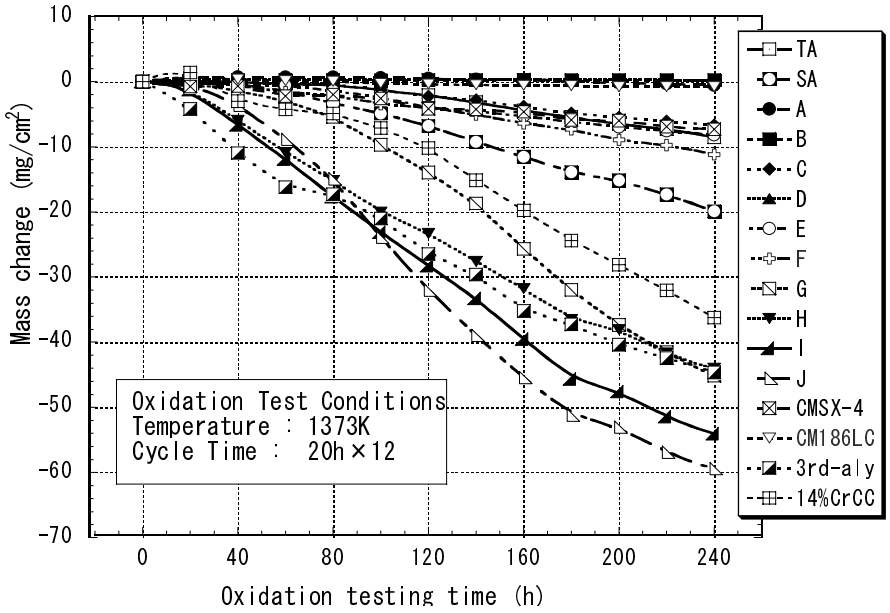

Fig.8 Results of cyclic oxidation tests at 1373K

3.5. Single crystal casting of a model Bucket

It is well known that there is great difficulty in casting 3rd generation superalloys in a large size, gas turbine blades. In order to evaluate single crystal bucket castability, a casting test of alloy F and TA was carried out using a model bucket for the first stage blade in the 25MW class gas turbine. We have successfully cast a SC model bucket with the length of 170mm. The photo is shown in Fig. 9. The model bucket was heat-treated following the aging condition of each alloy shown in Table 2, and test pieces were cut from the single crystal bucket. The microstructure is shown in Fig. 10 together with the one obtained from the round bar specimen. Although the size of the γ'phase of the model bucket was slightly larger than that of the round bar specimen, the microstructure still consisted of uniform γ + γ' phases. The reason why the γ'phase in the model bucket tended to be large is probably due to the fact that as the bucket was larger and thicker than the round bar specimen, and hence the cooling rate of the bucket after the heat treatment was slower than that of the round bar specimen. It is, however, supposed that the

Fig.9 Photo of the single-crystal model bucket (length : 170 mm)

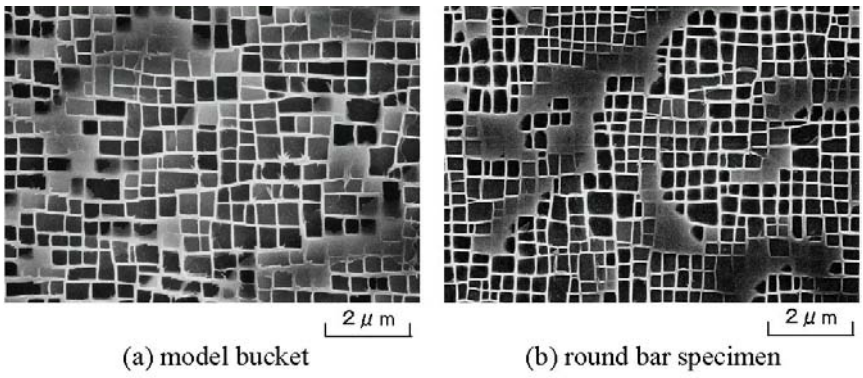

Fig.10. SEM micrographs showing the γ/γ' microstructure of the model bucket and the round bar specimen after aging

creep strength of the bucket is nearly the same as the round bar specimen, since the creep test results and the sizes of γ'phase of the bucket and the round bar specimen of alloy H were almost the same [1].

4. Discussion

4.1. Creep strength

Great efforts have been made to enhance the creep strength of the superalloys by controlling the volume fraction of the γ'phase and also by increasing the contents of refractory elements such as Mo, W, Re and Ta in the alloy. In fact, the total wt% of (Mo+W+Re) in 3rd generation superalloys is typically more than 10%. In addition, the lattice misfit between the γ and γ'phases is controlled to be a proper value (ie:－0.2%)[4] and several SC superalloys have been developed along this approach [5]. The chemical compositions of the designed alloys in this study were first optimized by the d-electron theory and then the contents of Cr, Mo, Ta, W and Re were varied by about 0.5% to optimize the oxidation resistance and the castability as well. Although it was found that the addition of Re yielded a beneficial effect on the creep strength, there was no extremely large difference in the creep strengths among the same Re content alloys except alloy SA. The difference in chemical composition between alloy SA and B is only 0.5%W and 0.4%Re, the rests are completely the same. The reason of this big difference in creep strength is still remain unclear.

Furthermore, the alloying of Mo has been believed to be effective in improving the creep

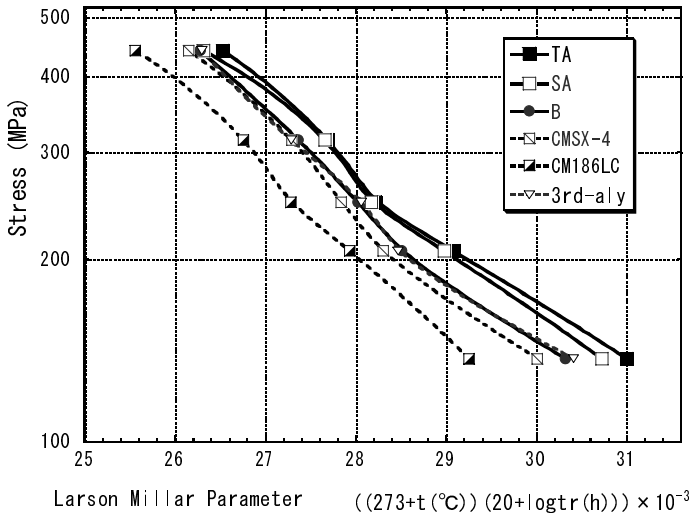

Fig.11. Creep rupture strength of alloy TA,SA and alloy B

strength, but this was not necessarily true according to the present results. This knowledge is probably very important to develop new SC superalloys with an excellent combination of high creep strength and very good oxidation resistance. Further, by comparing the rupture life between the alloy TA and alloy SA, it is evident that the Ru addition yields a beneficial effect on the creep-strengthening as reported in Superalloy2004 [9]. We also investigated the microstructures of alloy-SA,TA and B after the creep tests. No TCP phase was observed in it, which was in contrast to CMSX-10 [6] and MC2 [7]. Thus, the phase stability of alloy-SA,TA and B was excellent indeed. It was noted here that alloy-SA,TA possessed much higher creep strength than the 2nd generation superalloy, CMSX-4, as shown in Fig. 11. Alloy-SA and alloy-TA had about 30-40°C higher temperature capability than CMSX-4, while exhibiting excellent hot corrosion resistance and good oxidation resistance as shown in Fig. 4,Fig.7 and Fig.8 .

4.2 Oxidation resistance

According to our previous study, it is important to control the Ti/Al compositional ratio in order to keep oxidation resistance good. In this study, all the designed alloys had almost the same Ti/Al compositional ratio, so it was supposed that the oxidation resistance was similar among the alloys. However, this was not the case. The results of oxidation tests varied greatly among the alloys. This is partially due to the presence of a large amount of Re, 3.6%- 5.4%,

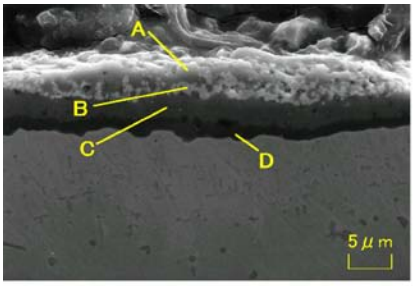

Elements	A	B	C	D
O	44.1	24.9	35.6	40.1
Al	5.4	1.5	23.4	44.1
Ti	1.6	1.9		
Cr	22.4	6.2	5.1	1.9
Co	9.9	3.1	6.6	2.3
Ni	14.5	10.7	26.9	9.4
Ta	1.4	46.2	1.7	0.2
W	0.7	5.6	0.7	2.0

(a) Alloy- B (mass%)

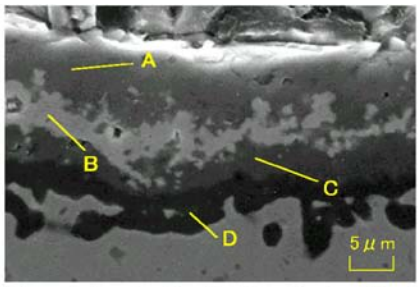

Elements	A	B	C	D
O	33.4	21.6	35.5	42.4
Al	3.0	0.6	23.5	45.5
Ti	0.6	5.5	0.3	
Cr	35.9	8.2	4.6	1.0
Co	15.8	1.9	8.3	1.6
Ni	11.3	6.8	25.0	7.6
Ta		45.4	2.3	0.3
W		10.0	0.6	1.5

(b) Alloy- F (mass%)

Fig. 12. SEM micrographs and the corresponding semi-quantitative EDX analyses of surface scale taken from the cross section of alloy B and alloy F after the continuous oxidation test at 1313K for 3600 hours

in the alloys, because Re is an element that can deteriorate oxidation resistance due to the formation of the volatile oxides of Re [8]. Also, it was found from the present experiments that the oxidation resistance changed depending on the contents of Mo, Cr, W and Re in the alloy

It is well known that Mo is an element to form volatile MoO_3 at high temperatures. In accordance with this Mo effect, as shown in Fig. 6,7 and Fig. 8, any Mo-containing alloys had lower oxidation resistance than Mo-free alloys, nearly independent of the contents of the refractory elements in the alloys. SEM micrographs and the corresponding semi-quantitative EDX analyses of surface scale are shown in Fig.11 for the alloy B and the alloy F. Despite that both alloys were Mo-free, alloy-B had the highest oxidation resistance, whereas alloy-F had relatively low resistance among the designed alloys.

The differences in their chemical compositions were mainly the Cr and W contents between them. But the appearance of the oxidation scale was very different between them. In case of the alloy F, the most inner scale of Al_2O_3 eroded the base alloy without forming the dense layer. On the other hand, in the case of alloy B, the most inner Al_2O_3 scale was formed in a condensed way, so it worked as a barrier to the oxidation, resulting in the high oxidation resistance of alloy B.

Concerning the Ru, it has been said that the Ru addition is not harmful to the oxidation resistance. However, this is not the case in the oxidation for a long term. As shown in Fig. 7, the alloy TA exhibited the largest mass reduction among the Mo-free alloys, and its reduction rate was similar to that of the 3rd generation superalloy. However, the oxidation resistance of the Ru-containing, Mo free alloys would be improved to a practical-use level by adding a trace amount of some elements (e.g., Ce) [1].

5. Conclusions

Ni-based single crystal superalloys were designed in order to develop single crystal alloys which are usable for the first stage blades in the 1500℃ or even higher class industrial gas turbine with high efficiency. The results are summarized as follows :

1. Most of the designed alloys had high tensile strength, excellent creep strength, hot corrosion resistance and stable microstructure. No TCP phases or undesirable phases were observed even after a long term creep test. It was also found that Mo is not a critical element to enhance the creep strength of the superalloy.

2. Mo-free alloys had higher oxidation resistance than Mo-containing alloys. Also, it was possible to improve oxidation resistance greatly even in the alloys containing more than 4% Re by optimizing the contents of the other refractory elements such as Cr, W and Ta.

3. There was no inherent problem of castability in the Mo-free alloys. A single crystal model bucket 170 mm in length was grown for use in the first stage blade of 25MW class industrial gas turbine.

4. The designed alloys, SA and TA, possessed about 30°C~ 40°C higher temperature capabilities than the 2nd generation superalloys.

6. References

[1] A.Yoshinari, R.Hashizume, Y.Murata and M.Morinaga "Development of the third generation single crystal superalloy for power generation gas turbines": Proc.8th Int.Gas.Turbine. Conf.2003 Tokyo(IGTC2003), ed . by Toshinori Watanabe, Gas Turbine Society of Japan, Tokyo.

[2] M.Morinaga, N.Yukawa and H.Adachi, "Alloying Effect on the Electronic Structure of Ni3Al(γ ')", J. Phys. Soc. Japan, 53 (1984), 653-663.

[3] K.Matsugi, Y.Murata, M.Morinaga and N.Yukawa,
"Realistic Advancement for Nickel-Based Single Crystal Superalloys by the d-Electrons Concept",
Superalloys 1992, edited by S.D.Antolovich et al., The TMS, 2000, pp.307-316.

[4] H.Harada, "Materials Design", Report of the 123 Committee on Heat-Resisting Metals and Alloys, JapanSociety for the Promotion of Science, 28(1997),185-196.

[5] T.Hino, Y.Yoshioka, Y.Koizumi, T.Kobayashi and H.Harada, "TMS-82+: A High Strength Ni-Base Single Crystal Superalloy", Materials for Advanced Power engineering 2002, ed. by J.Lecomte-Beckers et al., Forchungszentrum, Julich GmbH, 2002, pp.303-312.

[6] W. S. Walston et al., "Rene N6: Third Generation Single Crystal Superalloy", Superalloys 1996, Eds. R.D. Kissinger et al., TMS, Warrendale, 1996, pp.27-34

[7]: M. Pessah et al., "Effect of μ phase on the mechanical properties of a nickel-base single crystal superalloy", Superalloys 1992, Eds. R.D. S. D. 5 Antolovich et al., TMS, Warrendale, 1992, pp.567-576

[8] Md.Moniruzzaman, M.Maeda, Y.Murata and M. Morinaga, "Degradation of High-Temperature Oxidation
Resistance for Ni-Based Alloys by Re Addition and the
Optimization of Re/Al Content", ISIJ International, 43 (2003), 386-393.

[9] W. S. Walston et al., "Joint development of a fourth generation Single Crystal Superalloy", Superalloys 2004, Eds. K.A. Green et al., TMS, Warrendale, 2004, pp.15-23

A 5th GENERATION NI-BASE SINGLE CRYSTAL SUPERALLOY WITH SUPERIOR ELEVATED TEMPERATURE PROPERTIES

Akihiro Sato[1, 2], An-Chou Yeh[1], Toshiharu Kobayashi[1], Tadaharu Yokokawa[1], Hiroshi Harada[1], Takao Murakumo[1] and Jianxin Zhang[1]

[1]High Temperature Materials Group, Materials Engineering Laboratory, National Institute of Materials Science, Tsukuba, 305-0047
[2]Materials Technology Department, Research & Engineering Division, Aero-Engine & Space Operations, Ishikawajima-Harima Heavy Industries Co., Ltd., Tokyo, 188-8555

Abstract

The National Institute of Materials Science (NIMS) has utilized the in-house alloy design program to develop a 5th generation Ni-base single crystal superalloy, TMS-196 with superior high temperature creep, thermo mechanical fatigue (TMF) and oxidation resistance by incorporating further ruthenium (Ru) and chromium (Cr) content over the compositions of 4th generation superalloys. With Ru additions in advanced superalloys to enhance phase stability, higher content of refractory elements can be accommodated to provide further strengthening; the associated oxidation resistance can be improved by the increase in Cr additions.

In present article, TMS-196 has been subjected to cyclic/isothermal oxidation tests at 1100°C and 900°C, creep at conditions between 800°C~1100°C/137MPa~735MPa and TMF cycles. Preliminary studies indicate that the surface of oxidized TMS-196 can exhibit continuous alumina layer attributing good oxidation resistance similar to that of Rene'N5. The high refractory content in this class of superalloy has attributed large negative lattice misfits and formation of fine interfacial dislocation networks between γ and γ' at elevated temperatures resulting strong resistance against creep and TMF.

In conclusion, TMS-196 is a promising candidate alloy for turbine blade applications in future jet engines, because it possesses a balance of excellent properties desired by gas turbine engine manufacturer to further enhance performances of the turbine section. TMS-196 possesses good microstructural stability and shows significant improvement in creep resistance/TMF properties over the current commercial superalloys, such as CMSX-4, CMSX-10, PWA1484 and Rene'N5.

Keywords: Ni-base Single Crystal Superalloys, Lattice Misfit, Oxidation Resistance, Creep, Thermo Mechanical Fatigue

Introduction

Alloy development for turbine blade materials with higher temperature capability is crucial in order to improve the thermal efficiency in gas turbine systems and meet Kyoto Protocol at mitigating CO_2 emission. The turbine blade experiences continuous radial loading from the rotation of the turbine in a harsh environment behind the combustor, so high temperature properties of the material, such as creep strength and oxidation resistance can dictate the performance of the gas turbine engine. Through the "High Temperature Materials 21 Project" initiated by the National Institute of Materials Science (NIMS) in Japan, two 5th generation Ni-base single crystal superalloys, TMS-162 and TMS-173 [1] have already been successfully developed to supersede the high temperature creep resistance of all reported Ni-base materials, including the recent 4th generation alloys (EPM-102 and TMS-138) [2, 3].

To design an advanced Ni-base superalloy with improved strength while retaining a balance of properties is a challenging task. Additions of rhenium (Re) and other refractory elements

such as tungsten (W) and molybdenum (Mo) have allowed the development of multiple generations of superalloys due to their ability to provide high degrees of solid solution strengthening. However, the addition of refractory elements can also promote the formation of topologically close packed (TCP) phases, which are detrimental to mechanical properties, when the alloy is exposed to elevated temperature environments [4]. As the ability to incorporate high levels of refractory content into these alloys has been limited due to the tendency to result in the formation of TCP phases, ruthenium (Ru) additions become critical to the development of new generations of superalloys by further improving the phase stability and creep resistance [5, 6]. The partitioning characteristics of alloying elements into γ and γ' phases not only influence their intrinsic properties such as lattice parameters, solid solution strengthening, stacking fault and anti phase boundaries energies, but also associated volume fraction of γ' and lattice misfit, which can influence the evolution of the microstructure during high temperature creep [7]. Due to increasing amount of refractory elements additions that partitions into γ in modern alloys [8], the lattice misfit has been increased toward more negative and result the formation of fine γ/γ' interfacial dislocation network that can attribute to certain degree of strengthening [1, 6, 9]. Morphological evolution of the coherent γ/γ' microstructure into directional formation of the γ' raft perpendicular to the applied stress direction is strongly determined by the magnitude of γ/γ' misfit [10]. Under certain loading conditions, the rafted microstructure can be an effective barrier to deformations [7, 8, 11].

TMS-162 and TMS-173 are the first two 5th generation Ni-base single crystal superalloys developed within the "High Temperature Materials 21 Project" of NIMS; both alloys are shown to exhibit excellent creep resistance [1]. Based on the composition of TMS-138, higher Ru content (≥5.0wt%) allows higher Mo and Re additions in TMS-162 and TMS-173, respectively. Additional Mo and Re in conjunction with high Ru concentration for these alloys aim at refining the γ/γ' interfacial dislocation network. So, further solid solution strengthening, improved phase stability and higher lattice misfit can all attribute its superiority in creep resistance over previous generations [1, 7]. However, high Ru and Re content in both low Cr bearing TMS-162 and TMS-173 have resulted poor oxidation resistance at elevated temperatures due to vaporization of Ru and Re oxides [12], so a much improved oxidation resistance would be required for their practical applications. During oxidation at temperatures above 700°C, scales of Al_2O_3, Cr_2O_3, NiO, spinel $Ni(Cr, Al)_2O_4$ can form on advanced superalloys. For alloys upon which scale of Al_2O_3 are formed can exhibit better oxidation resistance, because diffusion transport through Al_2O_3 is slow [13]; formation of continuous Al_2O_3 scale, which is resistant to cracking and spalling, would render the alloy to be more oxidation resistant [14].

In this article, we introduce TMS-196, the flagship alloy in the 5th generation category. TMS-196 has gone through extensive evaluation programmes on its ability to against high temperature creep, thermo mechanical fatigue, phase instability and oxidation. The alloy design process along with test results are summarised and compared with current commercial superalloys.

Alloy Design

The in-house alloy design programme (NIMS-ADP) [15] for high temperature materials development has been established by multiple regression analysis of a large number of empirical data based on statistical valid and systematic experiments; the programme is

capable in estimating elemental effects and interactions. Its application can assist alloy designers to derive compositions by manipulating parameters, such as γ' volume fraction, lattice misfit, alloy density, phase stability and creep rupture life.

Compositions of recent NIMS superalloys and some other commercial alloys are summarised in Table I. To improve the oxidation resistance of TMS-162 and TMS-173, Cr content in TMS-196 was increased to 4.6wt% [16]. Cr additions could promote the formation of protective scales against oxidation [17]. By calculations based on NIMS-ADP, the additional 1.6wt% Cr with fine adjustment of Mo, W and Re concentrations can retained the γ' volume fraction and lattice misfit of TMS-173 in TMS-196.

Table I. Some examples of 2nd, 3rd and 4th generations of superalloys compositions (wt%), associated alloy density ρ(g/cm^3) estimated by NIMS alloy design programme.

Alloy Generations		Cr	Co	Mo	W	Ta	Re	Al	Ti	Ru	Hf	ρ
2nd	CMSX-4	6.5	9.0	0.6	6.0	6.5	3.0	5.6	1.0	-	0.1	8.70
	PWA1484	5.0	10.0	2.0	6.0	9.0	3.0	5.6	-	-	0.1	8.95
	Rene' N5	7.0	8.0	2.0	5.0	7.0	3.0	6.2	-	-	0.2	8.63
3rd	Rene' N6	4.2	12.5	1.4	6.0	7.2	5.4	5.75	-	-	0.15	8.98
	CMSX-10	2.0	3.0	0.4	5.0	8.0	6.0	5.7	0.2	-	0.03	9.05
4th	EPM-102	2.0	16.5	2.0	6.0	8.3	6.0	5.6	-	3.0	0.15	9.20
	TMS-138	3.2	5.8	2.9	5.9	5.6	5.0	5.8	-	2.0	0.1	8.95
	TMS-138A	3.2	5.8	2.9	5.6	5.6	5.8	5.7	-	3.6	0.1	9.01
5th	TMS-162	3.0	5.8	3.9	5.8	5.6	4.9	5.8	-	6.0	0.1	9.04
	TMS-173	3.0	5.6	2.8	5.6	5.6	6.9	5.6	-	5.0	0.1	9.11
	TMS-196	4.6	5.6	2.4	5.0	5.6	6.4	5.6	-	5.0	0.1	9.01

Through NIMS-ADP, TMS-196 has been designed to possess maximum phase stability while retaining strong creep and acceptable oxidation resistance. A derivative composition of TMS-196 is currently ongoing to further optimise microstructural parameters and process conditions.

Casting and Heat Treatment Processes

The master ingots of TMS-196 were vacuum induction melted by Ishikawajima Master Metal (IMM), Japan. Evaluations on high temperature creep, TMF and oxidation of TMS-196 were based on single crystal bars (10mm diameter and 130mm length) fabricated at NIMS using conventional Bridgman technique (200mm/hour withdraw rate) with pigtail grain selector.

As-cast bars of TMS-196 were subjected to solution heat treatment at 1340°C for 10hours. To determine the optimal primary ageing temperature, as-solutioned samples were heat-treated for 4hours at 1100°C, 1125°C, 1150°C, 1175°C and 1200°C, followed by secondary ageing at 870°C for 16hours. Microstructures were examined for chemical homogeneity, γ/γ' morphology and volume fractions. As the ageing temperature increased, the average size of γ' also increased. 1100°C primary ageing resulted regular and cuboidal γ' structures (64% γ' volume fraction with γ' size ~ 0.2μm), Figure 1(a). However, some lost of coherency between γ and γ' was detected in samples aged at higher temperatures, Figure 1(b). Samples aged at 1175°C and 1200°C exhibited severe widening of the γ channels and coarse γ' particles in the dendrite areas.

Specimens subjected to different primary ageings were creep tested at temperatures between 800°C and 1100°C, results indicated that TMS-196 aged at 1100°C possessed the optimal γ/γ' microstructure and performed best against creep. So, the 1100°C / 4hours primary ageing was chosen as the standard process condition for samples analyzed in the following sections.

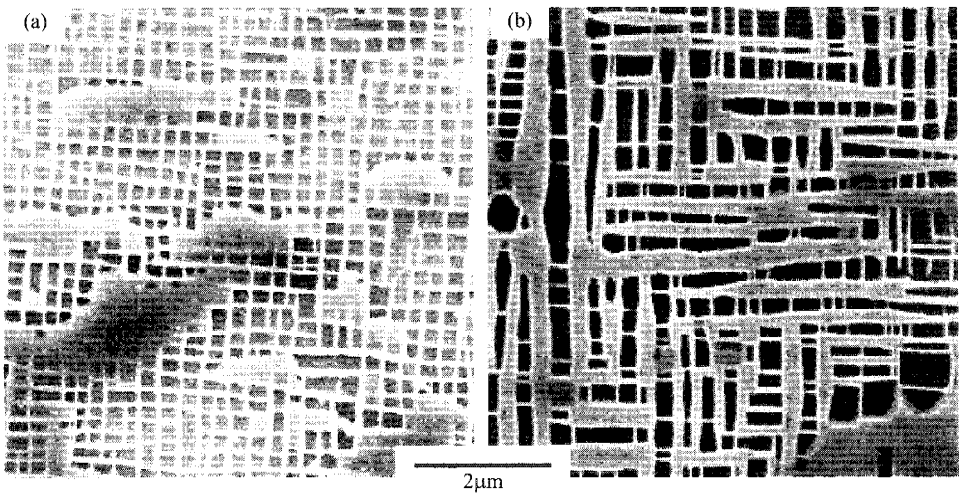

Figure 1. SEM images of γ/γ' microstructures taken at the dendrite cores, solutioned TMS-196 after (a) 1100°C primary ageing for 4 hours, γ/γ' are regular with γ' size ~ 0.2μm (b) 1175°C primary ageing for 4 hours, incoherent γ/γ' and severe widening of γ channels. (γ is the brighter phase and γ' is the darker phase)

TMS-196 is currently undergoing castability trials at a Japanese heavy industries company, the alloy is in the process to be cast into actual turbine blades for evaluations.

Mechanical Properties

Bars of as-cast single crystal TMS-196 were solution-treated at 1340°C for 10hours followed by a primary age of 4 hours at 1100°C and a secondary age of 16 hours at 870°C. Samples of orientations within 9 degrees of the <001> were chosen and machined into standard creep specimens and TMF samples for testing.

Creep behaviours

A wide range of temperature and stress conditions was covered to creep test TMS-196, and creep data was used to plot the Larson-Miller diagram along with other alloys for comparisons, Figure 2. TMS-196 clearly exhibited superior creep strength over current commercial superalloys - Rene'N5, CMSX-4 and CMSX-10; the plot indicated an impressive 47°C improvement over CMSX-4 at 1000°C/245MPa. Since TMS-196 was designed for maximum strength with acceptable phase stability and oxidation resistance, this alloy possessed high negative misfit, especially at elevated temperatures.

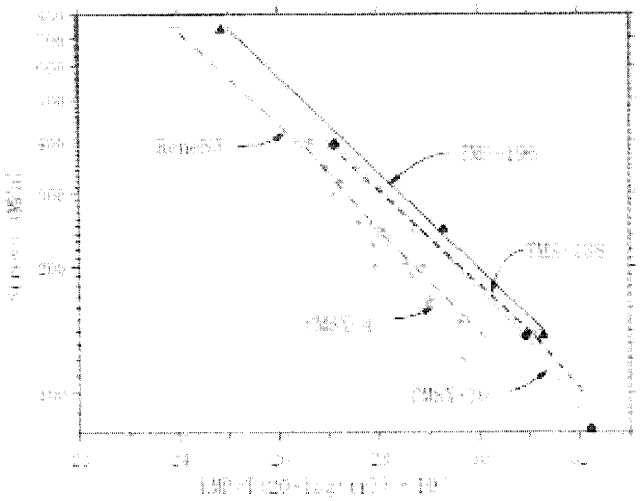

Figure 2. Larson-Miller plot shows significant creep advantage of TMS-196 over other commercial alloys.

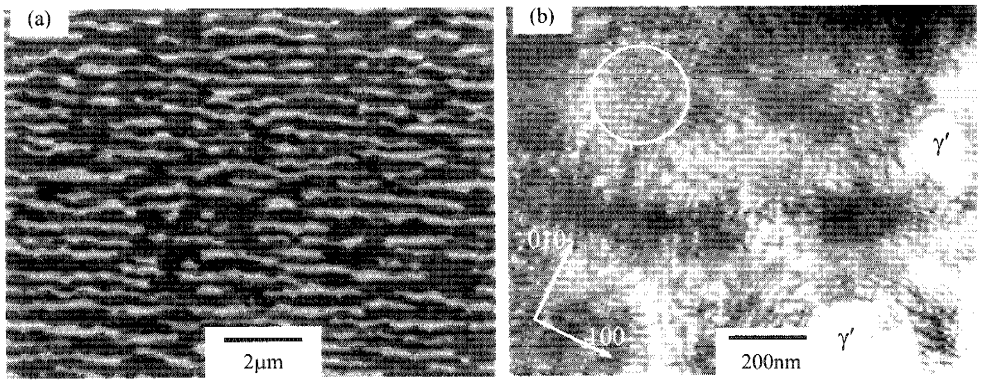

Figure 3. Microstructures of TMS-196 after creep at 1000°C/245MPa. (a) SEM images shows formation of raft structure. (b) TEM bright field image shows the formation of fine γ/γ′ interfacial dislocation network (an example is shown in the circled region).

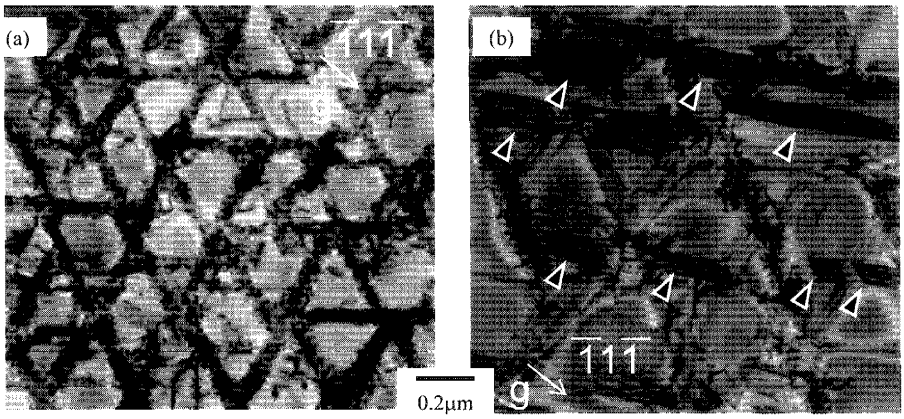

Figure 4. (a) TEM bright field image of TMS-196 interrupted creep until 1% strain at 800°C/735MPa. Time taken to reach 1% creep strain was 727hours, the TEM micrograph indicates dislocations were mainly confined at the γ/γ′ interface. (b) For a typical 3rd generation alloy, TMS-75, 1% creep strain at 800°C/735MPa only took less than an hour and resulted many super stacking faults (indicated by arrows) in γ′.

The high negative misfit promoted formations of raft γ/γ′ microstructure during creep at temperatures ≥900°C, Figure 3(a) and the fine interfacial dislocation network, Figure 3(b). Both features attributed the excellent creep resistance of this alloy. During creep at 800°C/735MPa, the γ/γ′ of TMS-196 appeared to be very resistance to deformation, as dislocations were mainly confined at the γ/γ′ interfaces, Figure 4(a). In comparison to a third generation alloy crept at the same condition, γ′ sheared by super stacking faults could be observed throughout the microstructure, Figure 4(b).

Studies conducted at NIMS to characterise detailed creep deformations of TMS-196 have suggested that this alloy could be further optimised for even greater creep resistance, hence efforts are being initiated to optimise the compositions of TMS-196 by reducing segregations and further manipulating in lattice misfits.

Thermo-Mechanical Fatigue (TMF) Property

TMF tests were performed on testpieces in air to failure on a hydraulic-servo system fatigue machine (MTS type 810). Figure 5 showed schematic drawings of the TMF experimental procedure. The temperature was varied between 400°C and 900°C, which corresponded to the points of maximum tensile and compressive stresses, respectively (i.e. out-of-phase). The strain was controlled with a total range ε_t = 1.28% (±0.64%), and a triangular waveform was adopted with a frequency of 6 minutes per cycle with 1hour holding time in between at 900°C.

This TMF test cycles was designed to simulate thermal and stress fluctuations experienced by the actual turbine blade during service.

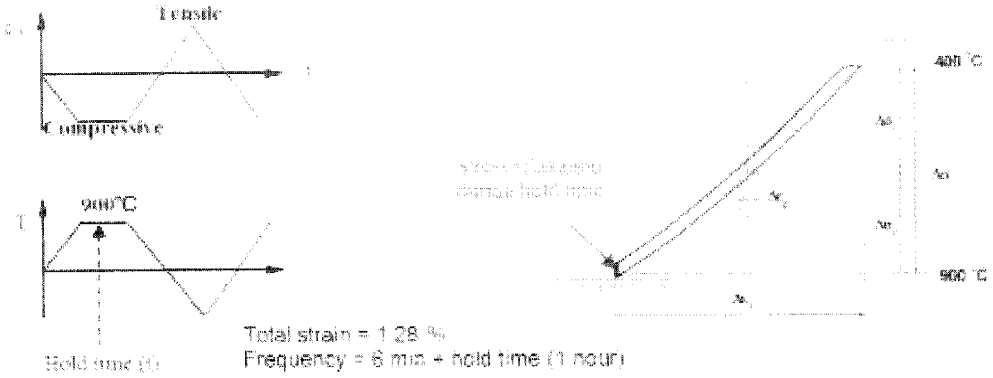

Figure 5. Thermo Mechanical Fatigue test cycle

The results of TMF tests were summarized in Table II. TMS-196 exhibited better TMF property than other alloys. Especially the number of cycles to failure for TMS-196 was over two times the cycles of Rene'N5, Table II. As the TMF cycles increased, magnitude of stress relaxation also increased. However, stress relaxation for TMS-196 was relatively small in comparison to the other two alloys, and it resulted much less plastic deformations.

Table II. TMF test results of TMS-196 in comparisons with other alloys

Alloy	Cycles to Failure, Nf	Stress Relaxation (MPa) – (the smaller, the better)		
		N=1	N=Nf/2	N=Nf
Rene'N5	92	150	140	290
TMS-138A	124	140	60	140
TMS-196	198	20	10	70

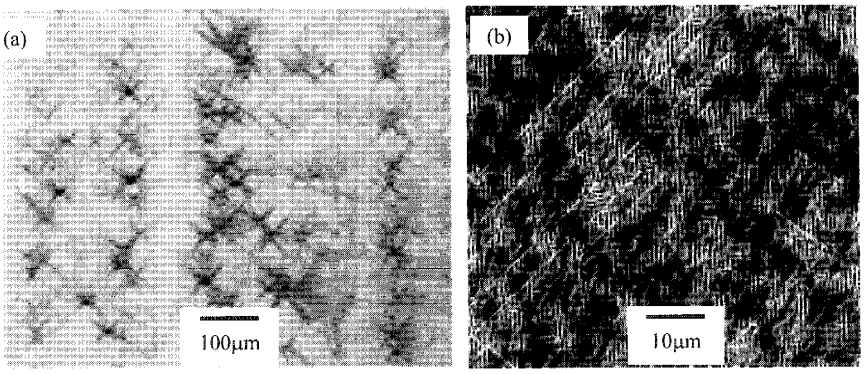

Figure 6. Microstructures of TMS-196 after thermal mechanical fatigue tests to rupture. (a) The optical image showed homogeneous twinning traces throughout the microstructure. (b) SEM image with higher magnification showed high density of deformation twins.

The microstructures of TMF ruptured TMS-196 exhibited homogeneous distribution of deformation twins, which could be attributed by an alloy system with low stacking fault

energy, Figure 6. This was in contrast to the large deformation twins distributed heterogeneously as observed in some 3rd generation alloys [18].

High Temperature Phase Instability

Thermodynamically stable TCP phases can form in Ni-based single crystal superalloys after exposures at high temperatures. The precipitation is more pronounced during elevated temperature creep due to the increase in the number of stress induced vacancies and accelerated diffusion rates, the associated formation of γ' envelope surrounding the TCP phases can result localised stress concentrations at the junction of TCP linkage during creep. The presence of brittle TCP precipitates in the microstructure is detrimental to mechanical properties, because its absorption of critical elements (Re, W, Mo and Cr) from the matrix and its disruption on the morphology of the rafted and unrafted microstructures can lead to the onset of tertiary creep. So, it is critical to hinder the phase instability associated with the formation of TCP precipitates for optimal creep performance. TMS-196 contains 5.0wt% Ru to counteract the tendency for phase instability attributed by high Re, Mo and W content.

Samples of TMS-196 were capsulated and then subjected to isothermal exposures at 1100°C for various length of time up to 3000hours, microstructures along the (100) plane were examined for presence of TCP phases and the onset of those precipitates were used as indicators for comparisons with current commercial superalloys. Although the number of TCP phases increased with the length of time during isothermal ageing, TCP precipitates were detected within the dendritic regions due to residual chemical segregations and the coarsening rate appeared to be sluggish.

For the current commercial superalloy, CMSX-10, a 1% area fraction of TCP precipitates plus γ' envelopes was detected after 100hours exposure at 1100°C [19]. In comparison, after 600hours exposure at 1100°C, only 0.85% area fraction of TCP phases was measured in the microstructure of TMS-196, and it showed little or no formation of γ' envelope surrounding TCP precipitates. Due to high refractory content, TMS-196 exhibited slight tendency to form TCP precipitates. Since its relevance to creep responses, further improving the phase stability could attribute to greater creep resistance.

Research activity is currently on-going in NIMS to optimise the chemical composition of TMS-196 by systematic addition of Ni-8.5wt%Al, which would allow the γ' volume fraction to be retained (according to NIMS-ADP calculations) while diluting the refractory content slightly to improve its phase stability. As a result, derivative compositions of TMS-196 are being developed and currently going through extensive creep and stability tests. Figure 7 shows the microstructure instability occurred in CMSX-10 and a derivative composition of TMS-196 after isothermal exposure at 1100°C for 600hours. It is clear that TMS-196 alloy system possesses superior high temperature microstructural stability than a current commercial superalloy – CMSX-10.

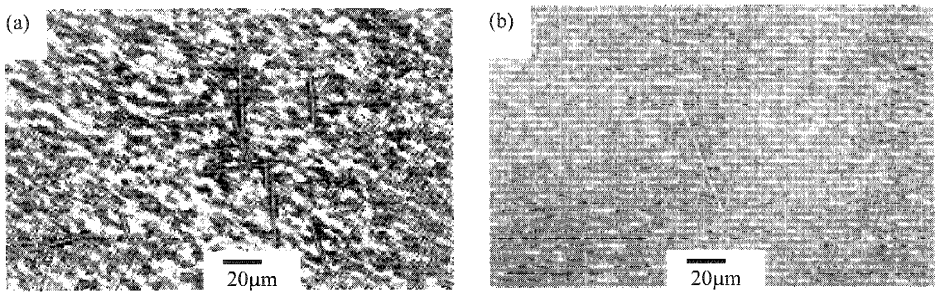

Figure 7. Phase instability occurred in the microstructures after isothermal exposure at 1100°C for 600hours, representative back scattered images were taken at the cores of dendrites, where TCP phases would precipitate initially. (a) CMSX-10, and (b) TMS-196 derivative composition.

Oxidation Resistance

One hour cyclic oxidation tests were performed at 1100°C in air, and the weight change of each sample was measured by analytical balance. Other commercial single crystal superalloys were also tested for comparative study. PWA1484, CMSX-4 and Rene'N5 compositions were cast and heat treated at NIMS by same procedure as TMS-196. The weight changes of TMS-173, TMS-196, CMSX-4 and Rene'N5 during 50 cycles of 1hour cyclic oxidation tests were shown in Figure 8. Large weight gain during the first 5 cycles followed by severe weight loss was observed in TMS-173. On the other hand, TMS-196 exhibited good resistance to oxidation. The weight change behaviours of TMS-196 was almost identical to that of Rene'N5 and slightly more severe than CMSX-4 and PWA1484.

Mass changes were also measured on samples of PWA1484, TMS-173, CMSX-10 and TMS-196 after isothermal exposure at 900°C for various amount of time up to 1000hours. Results again indicated that TMS-196 exhibited strong oxidation resistance, similar to that of PWA-1484 and much better than TMS-173 and CMSX-10, Figure 9.

Cross sectional SEM images of TMS-196 and TMS-173 after 1 hour cycle test at 1100°C were shown in Figure 10 (a) and (b). The average oxide layer thickness of TMS-173 and TMS-196 were measured to be around 26μm and 7μm, respectively. The oxide layer in both alloy consisted of NiO, $Ni(Cr,Al)_2O_4$ and Al_2O_3. Particle-like Al_2O_3 layer was observed in TMS-173, and continuous Al_2O_3 layer was observed in TMS-196 attributing better oxidation resistance.

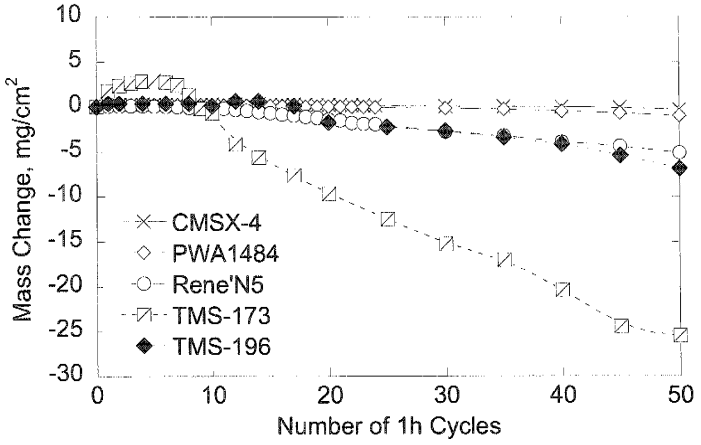

Figure 8. Cyclic oxidation test results at 1100°C

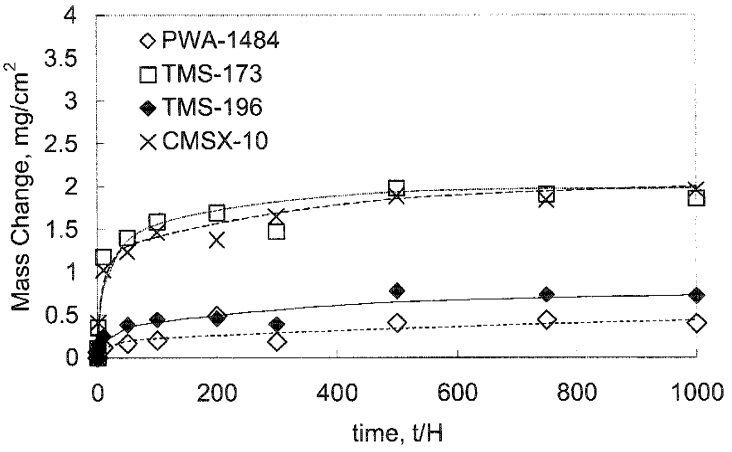

Figure 9. Isothermal oxidation test results at 900°C

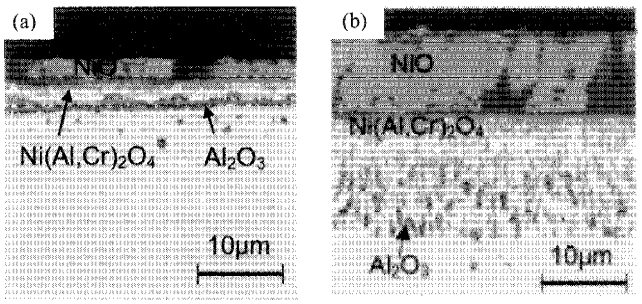

Figure 10. SEM micrographs of (a) TMS-196 and (b) TMS-173 after 1hour oxidation at 1100°C. TMS-196 exhibited continuous Al_2O_3 scale on the surface.

Summary

The present article has demonstrated that TMS-196 is a potential candidate alloy as turbine blade materials for applications in future jet engines. This alloy possesses a balance of excellent properties, which are desired by gas turbine engine manufacturer in order to further enhance the efficiency of gas turbine engines. TMS-196 with a density of 9.01g/cm^3 possesses significant advantage in elevated temperature properties over the current commercial superalloys, such as CMSX-4, CMSX-10, PWA1484 and Rene'N5. The highlights of alloy design concept for the 5th generation Ni-base single crystal superalloy (TMS-196) and its evaluations are as followings:

- By increasing the Ru content to further enhance the phase stability, manipulations in refractory elements content allow the development of the 5th generation superalloys. TMS-196 contains higher Ru, Re and Cr over the 4th generation alloys
- High misfit of TMS-196 has attributed formation of raft structure and finer interfacial dislocation network to inhibit dislocation motions and result excellent creep resistance. A 47°C improvement on creep over CMSX-4 at 1000°C has been achieved.
- TMS-196 exhibits more than two times the thermo mechanical fatigue life cycles of Rene'N5.
- TMS-196 possesses superior phase stability than current commercial alloy, CMSX-10.
- Moderate amount of Cr in TMS-196 allows the alloy to retain acceptable oxidation resistance, which is similar to that of Rene'N5.
- Evaluations on the derivative compositions of TMS-196 are currently ongoing and greater creep resistances are expected.

Acknowledgements
The authors would like to thank Mr. S. Masaki, Mr. M. Hosoya, Mr. M. Arai and Dr. Y. Aoki of Ishikawajima Harima Heavy Industries for the collaboration of the development of 4th and 5th generation alloys. Many thanks also to Mr. S. Nakazawa for his support with the experiments.

References

[1]. Y. Koizumi, T. Kobayashi, T. Yokokawa, J. Zhang, M. Osawa, and H. Harada. in *Superalloys2004*. (2004). Warrendale, Pennsylvania TMS p. 35-43.
[2]. S. Walston, A. Cetel, R. MacKay, K. O'Hara, D. Duhl, and R. Dreshfield. in *Superalloys2004*. (2004). Warrendale, Pennsylvania TMS p. 15-24.
[3]. T. Kobayashi, Y. Koizumi, T. Yokokawa, and H. Harada, Journal of the Japan Institute of Metals, (2002). **66**(9): p. 897-900.
[4]. T. Hino, Y. Yoshioka, K. Nagata, H. Kashiwaya, T. Kobayashi, Y. Koizumi, H. Harada, and T. Yamagata. in *Materials for Advanced Power Engineering*. (1998) p. 1129-1137.
[5]. K.S. O'Hara, W.S. Walston, E.W. Ross, and R. Darolia. in. Nickel base superalloy and article. USA General Electric Co. Patent: US5482789. 9 Jan. 1996
[6]. J.X. Zhang, T. Murakamo, H. Harada, Y. Koizumi, and T. Kobayashi. in *Superalloys2004*. (2004). Wrrendale, Pennsylvania TMS p. 189-195.
[7]. F.R.N. Nabarro and H.L.d. Villiers, *The Physics of Creep*. (1995): Taylor & Francis Ltd.

[8]. T. Yokogawa, M. Osawa, K. Nishida, T. Kobayashi, Y. Koizumi, and H. Harada, Scripta Materialia, (2003). **49**: p. 1041-1046.
[9]. J.X. Zhang, T. Murakamo, Y. Koizumi, T. Kobayashi, H. Harada, and S. Masaki, Metallurgical and Materials Transactions A (USA), (2002). **33**: p. 3741-3746.
[10]. T. Ichitsubo, D. Koumoto, M. Hirao, K. Tanaka, M. Osawa, T. Yokogawa, and H. Harada, Acta Materialia (USA), (2003). **51**: p. 4033-4044.
[11]. A.C. Yeh, C.M.F. Rae, and S. Tin. in *Superalloys 2004*. (2004). Champion, Pennsylvania p. 677-685.
[12]. K. Kawagishi, H. Harada, A. Sato, A. Sato, and T. Kobayashi, JOM, (2006). **58**: p. 43-46.
[13]. J.L. Smialek and G.H. Meier, in *Superalloys II*. (1987), New York, NY: John Wiley & Sons.
[14]. F.S. Pettit and G.W. Goward, Metallurgical Treatises, (1981): p. 603-619.
[15]. H. Harada, K. Ohno, T. Yamagata, T. Yokokawa, and M. Yamazaki. in *Superalloys1988*. (1988). Warrendale, Pennsylvania TMS p. 733-742.
[16]. A. Sato, H. Harada, T. Kobayashi, T. Murakumo, J.X. Zhang, and T. Yokokawa. in *Japan Institute of Metals*. (2005) p. 70.
[17]. C.S. Giggins and F.S. Pettit, J. Electrochem. Soc., (1971). **118**: p. 1782-1790.
[18]. J.X. Zhang, Y. Ro, H. Zhou, and H. Harada, Scripta Materialia, (2006). **54**: p. 655-660.
[19]. G.L. Erickson. in *Superalloys1996*. (1996). Warrendale, Pennsylvania TMS p. 35-44.

EFFECT OF PLASTIC ANISOTROPY ON CREEP STRENGTH OF SINGLE CRYSTAL Ni-BASED SUPERALLOYS

H. Koyabu, N. Tsuno and K. Kakehi

Department of Mechanical Engineering, Tokyo Metropolitan University,
6-6 Asahigaoka, Hino, Tokyo 191-0065, JAPAN
kkakehi@cc.tmit.ac.jp

Abstract

The effect of crystallographic orientation, alloy elements and heat treatment on the creep rupture strength of single crystals of a nickel-base superalloy was examined at 750 °C in detail. Two initial tensile orientations were selected on the standard stereographic triangle. CM186LC, CMSX4 and TMS75 showed distinct primary creep, and the {111}<112> slip system was activated during the creep deformation. Whereas, in PWA1480, the operation of {111}<112> slip was found to be difficult to occur because the small primary creep strain and no lattice rotation were observed. It was revealed that Re and Co promoted the <112> slip, and that Ta and Ti prohibited it during primary creep stage. In CM186LC, solution heat treatment promoted <112> slip because the eutectic and irregular shape γ' were dissolved into the matrix and reprecipitated as coherent cuboidal γ' particle. The grain boundary strengthening elements did not reduce the anisotropy in creep strength at 750 °C.

Keywords: Ni-based superalloys, single crystal, creep, anisotropy, primary creep

Introduction

In single crystal Ni-based superalloys, [001] orientation provides better creep strength and a low Young's modules that enhanced thermal fatigue resistance. Therefore, the longitudinal direction of single crystal turbine blades are designed within 10 ° to 15 ° of the [001] axis. However, the strength property of single crystal superalloys varies widely in this orientation range at temperatures between 700 °C and 850 °C. For example, in the tensile orientation with about 15 degrees off the [001] along the [001] - [$\bar{1}$11] boundary of the stereographic triangle, creep strength of single crystal superalloys are very weak [1]. The reason is that the orientation is single slip orientation for {111}<112> slip system, and there is the maximum Schmid factor near the orientation. The extent of primary creep strain correlates well with the activation of secondary slip systems, thus high primary creep strain causes the short creep rupture life [2]. The majority load of the turbine blade is borne by the cooled webs of the blade calculated to be as low as 700 °C to 850 °C [3], therefore the {111}<112> slip systems would be active in this environment. Furthermore, this {111}<112> slip would decrease low cycle fatigue strength with increase of compressive stress hold time [4,5]. In air cooled blade and vane of gas turbine, the external surface of high temperature regime is compressive stress state, and the cooled core is tensional stress state because of these temperature difference. This compressive stress in outer surface is held during rated operation of gas turbine. Consequently, the external superficial layer is compressive strain controlled low cycle fatigue condition during start-and-stop of gas turbine [6]. Ni-based superalloys does not deform plastically in normal test condition because of high proof stress alloy, so only the stress relaxation arises. When the number of cycles increases, the tensile residual stress increases. The compressive creep strength of single crystal superalloys is lower than tensile one due to the deformation twin associated with the {111}<112> slip operation on [001] loading [7]. That is, the high tensile residual stress occurred by large stress relaxation would decreased low cycle fatigue strength of single crystal superalloy. Therefore, it is important to clarify the

influence factors on {111}<112> slip to control it. It is known that the addition of C, B, Zr, and Hf into a single crystal superalloy reduces the anisotropy in the creep rupture lives [8]. However, the effect and the mechanism have not been clarified yet. Therefore, we investigated the effect of alloy elements including the grain boundary strengthening elements, tensile orientation, and heat treatment on creep anisotropy at the temperature where the operation of {111}<112> is active.

Experimental procedures

The composition and heat treatment are listed in Table 1 and Table 2, respectively. The specimens for creep rupture tests were cut from the single crystal rods by a spark cutter. The misorientation of tensile direction in each specimen was within 2 °. The specimens were cut from the same single-crystal bar. The rectangular-cross-sectional specimens had a gage section of 2.7 mm × 3.0 mm × 18.5 mm. First, in order to investigate the most remarkable temperature of {111}<112> slip, creep test was performed at temperatures between 700 °C and 800 °C under a nominal stress of 750 MPa. Then creep test was performed under the same resolved shear stress for {111}<112> slip system between the different tensile orientation samples (Fig. 1). One is [001] orientation and another is the easy glide orientation which has the maximum Schmid factor. The specimens of the [001] orientation having the Schmid factor of 0.46 were tested under 750 MPa. The specimens having the maximum Schmid factor of 0.50 were tested under 708 MPa. The effects of grain boundary strengthening elements and solution treatment on creep strength were investigated in CM186LC. The solution treatment was performed at 1274 °C for 8 hours, which condition corresponds to the solution index (SI) of 70 % [9]. The SI value is defined as the volume percent of the region where γ' phase completely dissolved into the γ phase during solution heat treatment [9]. Following the treatment, they were aged at 1080 °C for 4 hours and 871 °C for 20 hours. For the determination of the lattice rotations which occurred upon deformation,

Table 1 Chemical composition of alloys (mass %)

Alloy	Co	Cr	Mo	W	Al	Ti	Ta	Re	C	B	Zr	Hf	Ni
PWA1480	5	10	-	4	5	1.5	12	-	-	-	-	-	bal.
CMSX-4	9	6.5	0.6	6	5.6	1	6.5	3	-	-	-	0.1	bal.
TMS75	12	3	2	6	6	-	6	5	-	-	-	0.1	bal.
CM186LC	9.3	6	0.5	8.3	5.74	0.73	3.4	2.9	0.072	0.016	0.005	1.4	bal.

Table 2 Heat treatment condition of alloys

Alloy	Solution heat treatment[a]	Aging treatment
PWA1480	1282°C/1 hr + 1287°C/2 hr + 1294°C/1 hr/GFC	1080°C/4 hr/AC+ 870°C/32 hr/AC
CMSX-4	1277°C/2 hr + 1288°C/2 hr + 1296°C/3 hr + 1304°C/3 hr + 1313°C/2 hr + 1316°C/2 hr + 1318°C/2 hr + 1321°C/2h/GFC	1140°C/4 hr/GFC + 870°C/20 hr/GFC
TMS75	1240°C/1 hr + 1280°C/2 hr + 1300°C/2 hr + 1320°C/8 hr/GFC	1150°C/4 hr/GFC + 870°C/20 hr/GFC
CM186LC	As Cast	1080°C/4 hr/GFC + 871°C/20 hr/GFC

[a]GFC – Gas Fan Cooling.

electron-backscattered patterns (EBSPs) were taken within 100 μm × 100 μm squares near the fracture surface. The specimens were interrupted on primary creep stage for TEM analysis. The interrupted specimens were cut along {111} plane.

Results

The outstanding primary creep strains were observed between 700 °C and 750 °C under 750 MPa (Fig. 2). {111}<112> slip would be most active in this temperature range. In this study, the temperature of 750 °C was selected as creep test temperature. The creep curves are shown in Fig. 3. In CMSX4, TMS75 and CM186LC, the amount of primary creep strain in orientation A is almost three times larger than those of [001], but difference between these orientations was hardly observed in PWA1480. Moreover, only in PWA1480, the creep life of orientation A was longer than that of [001] (Fig. 3(a)). The extremely high creep strain rates with the strain softening at primary creep and correspondingly short creep rupture lives were

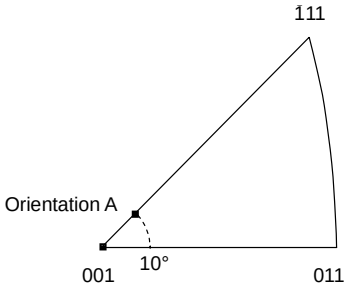

Fig. 1. The initial tensile axis of the single crystals on the standard stereographic triangle

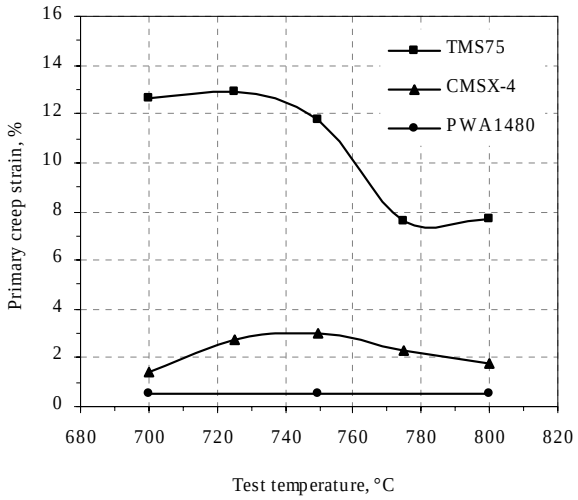

Fig. 2. Influence of temperature on primary creep strain in <001> oriented single crystal superalloys at 750 MPa

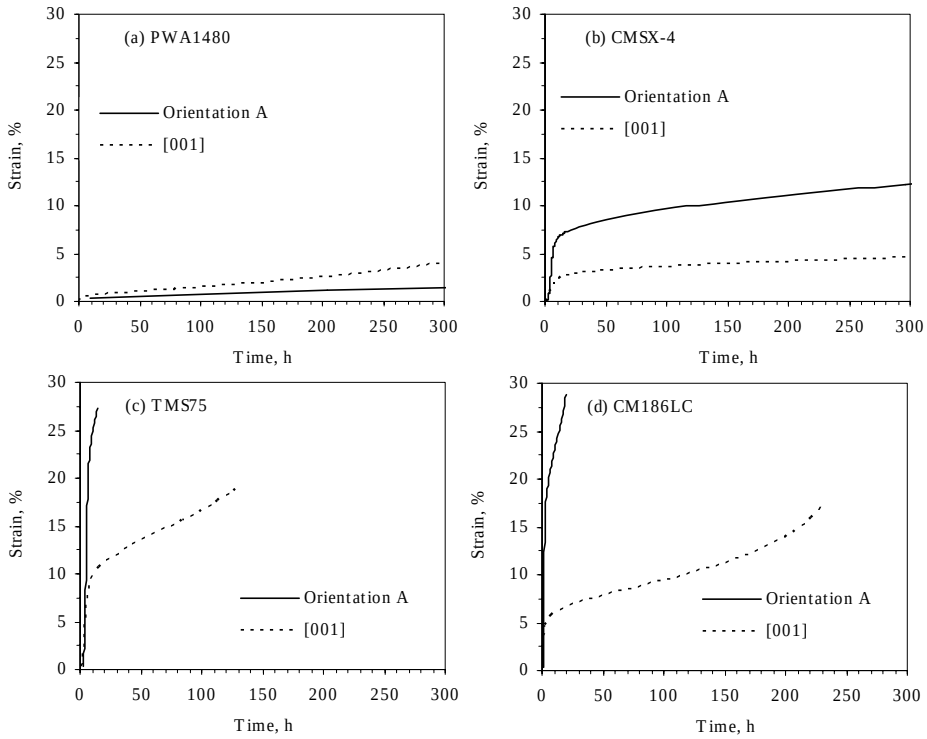

Fig. 3. Creep curves of four kinds of superalloys under the same resolved shear stress for {111}<112> slip at 750 °C: (a) PWA1480; (b) CMSX-4; (c) TMS75; (d) CM186LC. Test stresses of orientation A and [001] were 708 MPa and 750 MPa respectively

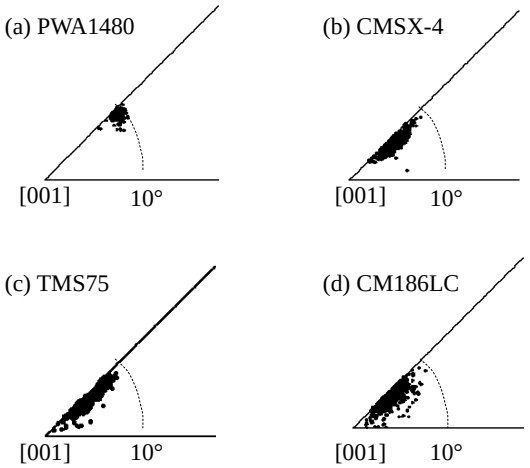

Fig. 4. Lattice rotation measurement by EBSP in orientation A

observed in orientation A of TMS75 and CM186LC (Fig. 3(c) and (d)). The lattice rotation for orientation A during creep was followed by EBSP and the orientation is plotted in the standard stereographic triangle (Fig. 4). The eutectic of CM186LC would cause the dispersion of the dots of the lattice orientation. The lattice rotations toward the $[\bar{1}\bar{1}2]$ pole were observed in CMSX4, TMS75 and CM186LC. On the contrary, the lattice rotation was not observed in PWA1480. Fig. 5 showed the influence of solution heat treatment on microstructure of CM186LC. The specimens subjected to both solution and aging treatments showed higher

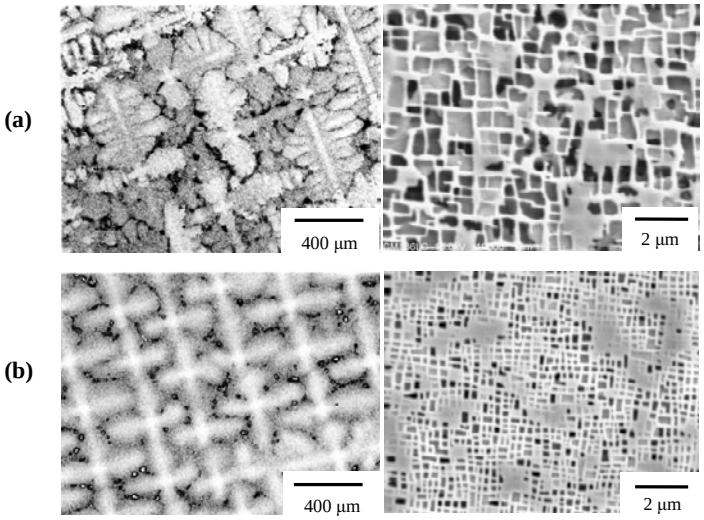

Fig. 5. Optical photograph (left), and SEM photograph (right) of CM186LC specimen after (a) cast and aging treatment and (b) solution heat treatment

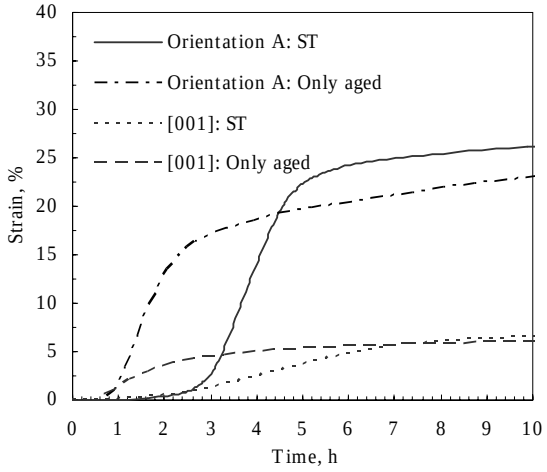

Fig. 6. Creep curves of CM186LC at 708 MPa (orientation A) and 750 MPa ([001]) for solution heat treated and only aged specimens tested at 750 °C

primary creep strain and longer incubation periods prior to primary creep on each orientation (Fig. 6). Fig. 7 is the micrograph taken from the sample tested to 0.8 % strain and sectioned on the (111) plane. As for PWA1480 (Fig. 7(a)), the stacking faults in γ' were rarely observed, and the Burger's vector of dislocation which was concentrated in γ matrix was determined a/2<110> using the analysis of the dislocation contrast for various two-beam diffraction conditions [10,11]. Fig. 7 (b) and (c) shows the TEM micrographs of CMSX4 and TMS75 crept at 1.4 % strain respectively. The Burger's vector of the dislocation which sheared the γ' was identified a/3<112> by the two-beam method.

Discussion

In CMSX4, TMS75, and CM186LC, the large primary creep strain with incubation period was observed. In addition, the lattice rotation towards [$\bar{1}$12] was indicated by the analysis by EBSP and the Burgers vector of the dislocation which shear the γ' was identified a/3<112> by TEM observation. Therefore, {111}<112> slip would be activated during primary creep in CMSX4, TMS75, and CM186LC. Re and Co [12], which preferentially partition into the matrix and are originally hexagonal close packed elements, will lower the stacking fault energy and hence may facilitate the formation of a/2<112> type widely dissociated dislocations which are required for the intrinsic/extrinsic shearing of the γ' particles during creep [13]. Thus the dislocations are able to pass through both γ and γ' phases without the

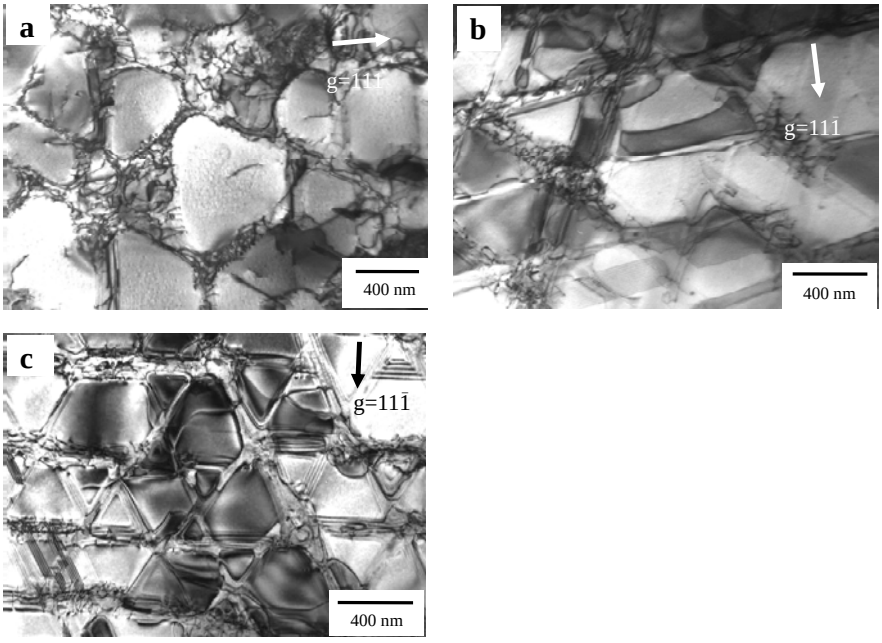

Fig. 7. TEM micrograph of the [001] samples deformed to the start of secondary creep at 750 °C and 750 MPa: (a) PWA1480; (b) CMSX4; (c) TMS75. The specimens were sectioned on the (111) plane

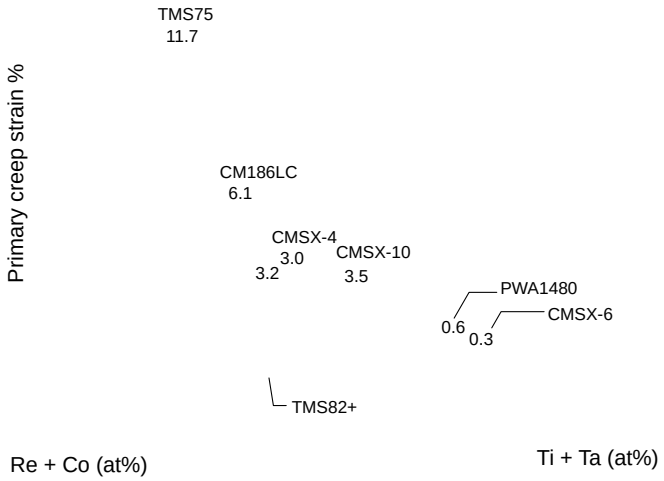

Fig. 8. The effect of alloy elements on primary creep strain at 750 °C under 750 MPa in [001]

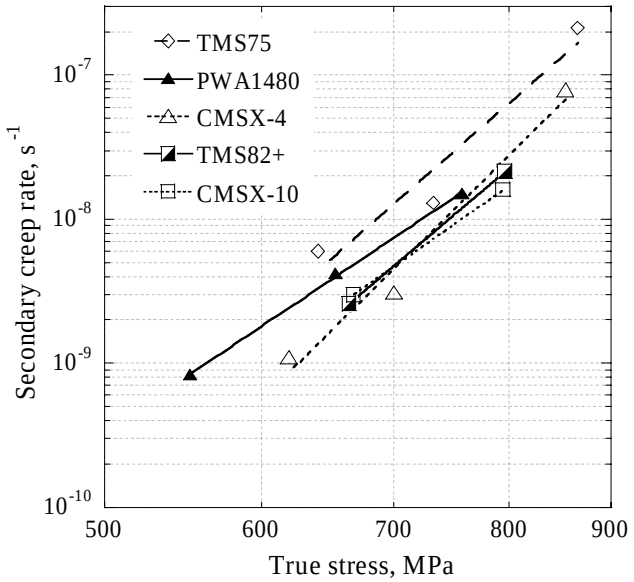

Fig. 9. Relationship between the true stress and the secondary creep rate at 750 °C

constriction of the stacking faults. Furthermore, Re is solid solute hardening element for the matrix and would prohibit a/2<110> dislocations from bowing and gliding in the matrix channel. As a result, the generation of interfacial dislocation network in matrix would be restricted. The loss of coherency of the γ-γ' interface might prohibit partial dislocations from shearing cuboidal precipitates. Link and Feller-Kniepmeier [14] have shown that the shearing of γ' precipitates by the {111}<112> slip requires coherent interfaces, because (i) coherency stresses allow the energetically favorable deposition of a/6<112> dislocation in the interface, and (ii) dislocation networks in the interface inhibit the partial dislocation from entering into γ' precipitates and the propagation of the triple dislocation node. The formation of interfacial dislocation networks destroys these conditions. Thus {111}<112> slip was promoted by the impediment of interfacial dislocation network formation in the Re-bearing alloys, i.e., CMSX4, TMS75, and CM186LC, and caused the large primary creep strain. The amount of primary creep strain was promoted more by solid solution treatment in CM186LC. The solid solution treatment causes eutectic and large irregular-shape precipitates to go back into solution and reprecipitate as cuboidal coherent precipitates with the coherent ineterface.

The creep behavior of PWA1480 is quite different from other three alloys. In the alloy, a/2<110> dislocations were concentrated in the matrix at 0.8 % strain (Fig. 7(a)). However, assuming that only the {111}<110> slip operated, the Schmid factors of orientation A and [001] are 0.452 and 0.409 respectively. Creep life in orientation A was longer than that of [001], although the resolved shear stress of 320 MPa in orientation A is higher than that of 307 MPa in [001] orientation. Thus creep mechanism of PWA1480 cannot be explained only by operation of {111}<110> slip. The dominant deformation mode should be a combination of both dislocation's bowing in matrix and its climbing along γ/γ’ interface. Both Ta and Ti will prohibit {111}<112> slip by the solid solution strengthening of the γ’ phase resulted from (i) lattice parameter changes [15,16], (ii) increase of APB energy on (111) [16] and (iii) promoting a Suzuki locking effect of {111}<112> slip resulted from segregation of Ta to the superlattice stacking fault (SSF) [13]. The deformation mechanism during primary creep is shear of the γ and γ' by dislocations separated by intrinsic and extrinsic stacking faults and a narrow anti-phase boundary fault in the γ' [17]. Thereby, it would be effective against the activation of {111}<112> slip to increase the energy of stacking fault and anti-phase boundary, and to produce the incoherent γ/γ’ interface.

It follows from what has been said that both Re and Co promote the primary creep which is the reflection of {111}<112> slip, and that both Ta and Ti prohibit that as shown Fig. 8. The figure also includes the experimental reference dates of CMSX6, CMSX10 and TMS82+. CM186LC contains the grain boundary strengthening elements that are more than the amount provided by the patent [8], but, outstanding decrease of primary creep could not be observed. It seem reasonable that conclude the grain boundary strengthening elements do not decrease the anisotropy occurred by {111}<112> slip.

Fig. 9 showed the stress dependence of secondary creep rate. The primary creep deformation terminates only after the occurrence of sufficient strain hardening because of the interaction of {111}<112> type slip system, and the {111}<101> slip system by the slip of a/2<110> dislocation pairs becomes the dominant deformation mechanisms during the secondary creep region [2,18]. The slope of PWA1480 was smaller than other alloys. This suggests that the mechanism is different between the alloy and others. The dominant deformation mode should be combination of both a/2<110> dislocation's bowing on {111} plane in matrix and climb

process along γ/γ’ interface as well as primary creep region, that is to say, the creep rates would be controlled by the dislocation climb process throughout primary and secondary creep regions. The dominant deformation mechanism in the other alloys would be a diffusive slip of a/2<110> dislocation pairs. However TMS75, which showed the remarkable {111}<112> slip during primary creep region, resulted in the highest creep rate among the alloys, therefore, {111}<112> slip system would be partly operative even during secondary creep region. In the alloys deformed by a{111}<112> slip in primary creep stage, the principal deformation mechanism during secondary creep is the shearing of the γ' by partial dislocations trailing stacking fault, and rate determining process is the formation of dislocation configurations able to enter the γ' [19].

Conclusions

1. The {111}<112> slip system was activated during creep at 750 °C under 750 MPa in CMSX4, TMS75 and CM186LC. As for TMS75, {111}<112> slip would be operative throughout primary and secondary creep regions. It was promoted by solution treatment in CM186LC due to the increase of coherent interface by cuboidal γ' reprecipitation.
2. The {111}<112> slip was not activated in PWA1480 due to the solid solution strengthening of the γ’ phase by Ti and Ta.
4. The amount of primary creep strain could be explained by the elements of Ti, Ta, Re and Co. Both Re and Co promote the {111}<112> slip, whereas both Ta and Ti inhibit it.
5. The influence of C, B, Zr, and Hf on the plastic anisotropy occurred by {111}<112> slip was found to be neglected.

References

[1] B.H. Kear and B.J. Piearcey, Trans. TMS-AIME. 239 (1967), pp.1209-1215.
[2] R.A. MacKay and R.D. Maier, Metall. Trans. A 13A (1982), pp. 1747-1754.
[3] D.W. MacLachan and D.M. Knowles, Fatigue Fract. Eng. Mater. Struct. 25 (2002), pp. 399-409.
[4] H. Zhou, M. Osawa, H. Harada, T. Yokokawa, Y. Koizumi, T. Kobayashi, M. Waki, Y. Ro and I. Okada, Superalloy 2004, TMS, Warrendale, PA, 2004, pp. 225-231.
[5] Y. Sakon, Proc. 1st Innovative Casting Simulation Technology, Tokyo, (2001) pp. 6-11.
[6] N. Matsuda, K. Ichikawa, Y. Fukuda, A. Yoshinari and H. Toritani, Journal of the Gas Turbine Society of Japan 23 (1995), pp. 84-91.
[7] K. Kakehi, Scripta Mater., 41 (1999), pp. 461-465.
[8] D.M. Shah and D.N. Duhl, US Patent, No. 4915907, (1990).
[9] H. Tamaki, A. Okayama, B. Önay and A. Yoshinari, Proc. 7th Liege Conference on Materials for Advanced Power Engineering 2002, (2002), pp.355-364.
[10] B.H. Kear, G.R. Leverant and J.M. Oblak, Trans. ASM 62 (1969), pp. 639-650.
[11] D.B. Williams and C.B. Carter, Transmission Electron Microscopy, III imaging, Plenum Press, New York, 1996.
[12] H. Murakami, T. Yamagata, H. Harada, M. Yamazaki, Mater. Sci. Eng. A223 (1997), pp. 54-58.
[13] C.M. Rae, K. Kakehi and R.C. Reed, Proc. 7th Liege Conference on Materials for Advanced Power Engineering 2002, (2002), pp.207-216.
[14] T. Link and M. Feller-Kniepmeier, Metall. Trans. A., 23A (1992), pp. 99-l05.
[15] Y. Mishima, S. Ochiai and T. Suzuki, Acta Metall., 33 (1985), pp. 1161-1169.

[16] B.H. Kear and D.P. Pope, Superalloys, Supercomposites and Superceramics, San Diego: Academic Press, (1989), pp. 558-561.
[17] C.M.F. Rae, N. Matan and R.C. Reed, Mater. Sci. Eng., A300 (2001), pp. 125-134.
[18] G.R. Leverant, B.H. Kear and J.M. Oblak, Metall. Trans., 4 (1973), pp. 355-362.
[19] G.L. Drew, R.C. Reed, K. Kakehi and C.M.F. Rae, Superalloy 2004, TMS Warrendale, PA, (2004), pp. 127-136.

DEVELOPMENT OF A CO-FREE NI-BASE SINGLE CRYSTAL SUPERALLOY

*Tadaharu Yokokawa, *Toshiharu Kobayashi, **Takanobu Suzuki,
*Yutaka Koizumi and *Hiroshi Harada

*National Institute for Materials Science (NIMS)
1-2-1 Sengen, Tsukuba Science City, Ibaraki 305-0047, Japan
**Shibaura Institute of Technology
3-9-14 Shibaura, Minato-ku, Tokyo 108-8548, Japan
yokokawa.tadaharu@nims.go.jp

Abstract

Increased attention is being paid to the Pebble Bed Modular Reactor (PBMR) as a mean of nuclear electric power generation. PBMR generates electricity by a gas turbine that uses He-gas as a reactor coolant. If conventional Ni-base superalloys were to be used for PBMR, the presence of Co, which produces ^{60}Co, a radioactive isotope, will make turbine maintenance cumbersome and dangerous. As part of the "High Temperature Materials 21" project, the authors are developing a Co-free Ni-base single crystal superalloy for PBMR. Creep rupture tests were performed on the developed alloy; furthermore, the relationships between creep strength and micro-structural parameters such as lattice misfit, etc. were investigated.

Keywords
Ni-base single crystal superalloy, PBMR, Co-free, Lattice misfit, Partitioning ratio

1. Introduction

As a new-type of nuclear power generation system, attention is paid to the Pebble Bed Modular Reactor (PBMR)[1] as shown in **Figure 1**. The PBMR essentially comprises a steel pressure vessel which contains about 450,000 fuel spheres. The fuel consists of low enriched uranium triple-coated isotropic particles embedded in a molded graphite sphere. The PBMR is cooled with helium (He) gas. The heat that is transferred by He-gas to the power conversion system, is converted into electricity through a He-gas turbine. The He-gas turbine of PBMR is designed as a system with an inlet gas temperature at 900°C and non-cooling blades/vanes. Ni-based superalloys are the primary materials used in industrial turbines. In addition, the requirement of creep strength for the blade material should exceed that of CMSX-4[2]. However if conventional Ni-base superalloys are to be used for the turbine materials of PBMR system, turbine maintenances will be difficult due to the presence of Co, as it can produce the isotope, ^{60}Co, which is dangerously radioactive and possesses a long half-life. Therefore, Co-free Ni-base superalloys[3] are required for PBMR system.

The addition of Rhenium (Re) has recently received attention because of its contribution toward improvement of creep and hot corrosion. However, there is a problem of raising the manufacturing cost of the blades/vanes for the land-base turbines. TMS-82+[4], developed

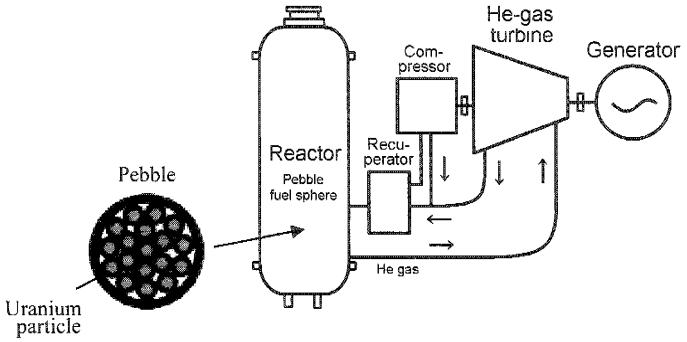

Fig.1 Schematics of Pebble Bed Module Reactor (PBMR) system.
The PBMR uses particles of enriched uranium dioxide coated with silicon carbide and pyrolitic carbon. The particles are encased in fuel encapsulated in graphite pebble.

under NIMS-Toshiba collaborative work, has excellent creep strength. In TMS-82+[3], the content of Re is less than that in CMSX-4 and therefore it was chosen to be the base alloy for developing the Co-free Ni-base SC superally of TMS-82R.

In this work, creep strength and structural parameters such as lattice misfit and partitioning ratios of alloying elements in both phases, γ and γ', of TMS-82R were investigated.

2. Experimental procedure

The chemical composition of three alloys investigated is shown in **Table 1**. These alloys were cast by the directional solidification method to a SC bar of 10mm in diameter and 130mm in length. The heat-treatment conditions for these alloys are given in **Table 2**.

Table 1. Chemical composition of three alloys investigated.

Alloy	Composition in wt%, Ni balanced								
	Co	Cr	Mo	W	Al	Ti	Ta	Hf	Re
CMSX-4	9	6.5	0.6	6	5.6	1	6.5	0.1	3
TMS-82+	7.8	4.9	1.9	8.7	5.3	0.5	6	0.1	2.4
TMS-82R	0	4.6	1.8	8.6	5.3	0.5	6.4	0.1	2.5

Table 2. Heat treatment conditions for three alloys investigated.

Alloy	Solution treatment	1st aging	2nd aging
CMSX-4	1277°C~1318°C (6steps) /18h,AC	1140°C/6h,AC	872°C/20h,AC
TMS-82+	1300°C/1h + 1320°C/5h,AC	1150°C/4h,AC	870°C/20h,AC
TMS-82R	1300°C/1h + 1330°C/5h,AC	1100°C/4h,AC	870°C/20h,AC

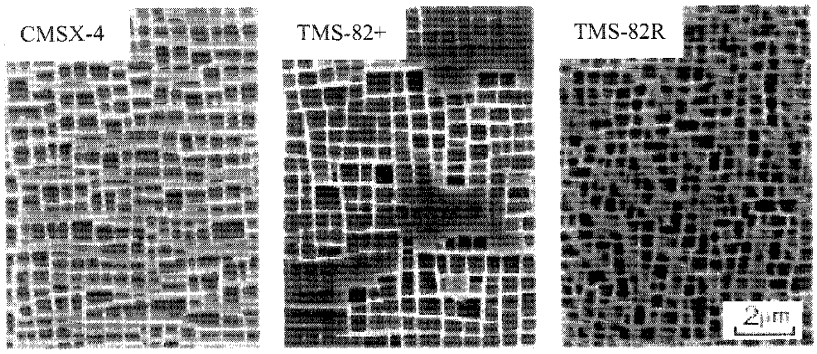

Fig. 2 SEM micrographs of CMSX-4, TMS-82+ and TMS-82R alloys after fully-heat treatment.

Typical SEM micrographs of CMSX-4, TMS-82+ and TMS-82R alloys after fully-heat treatment are shown in **Figure 2**. As shown in Fig. 2, all of the alloys investigated have γ' precipitates of an $L1_2$ structure based on Ni_3Al in a γ matrix (fcc). The γ' volume fraction of these alloys were determined by image analysis, and were almost the same, 65% for CMSX-4, 63% for TMS-82+, and 64% for TMS-82R.

The high temperature X-ray diffractometer (HT-XRD)[5-7] having a parallel and monochromatic X-ray beam is used to determine the lattice parameters and the lattice misfit under R.T. to 1100°C. The specimens for the XRD were prepared as follows. The crystal directions of SC bars were determined by X-ray Laue method, and the SC bars were cut parallel to <100> crystal direction in circular platelet of 10mm in diameter and 0.5mm in thickness.

To investigate the influence of Cobalt (Co) on the partitioning ratios of the alloying elements, the equilibrium compositions of γ and γ' phases in TMS-82+ and TMS-82R at 1100°C were measured by the energy dispersive spectroscopy (EDS). Since the size of γ and γ' phases obtained with the heat treatment described above were below the spatial resolution of the EDS analysis, as shown in Fig. 2, a coarsening heat treatment[8] was performed. After heat treatment, SC bars were cut into disks with 10mm diameter and 5mm thickness. The disks were cold-worked and annealed at 1240°C for 30 hours. Under stress annealing, fine γ and γ' two-phase structures coarsened. In order to achieve the equilibrium state at 1100°C, the specimens were slowly cooled from 1240°C to 1100°C, and aged at that temperature for 500 hours. Lamellar structures with a thickness of 3 to 5μm were finally obtained; these structures were large enough for EDS analysis. Finally, the disks were cut into halves; the cross sections were polished and analyzed with the EDS.

From heat-treated SC bars, creep specimens of 4mm diameter and 22mm length as gauge part were machined out and carefully finished by grinding. Creep tests were carried out at 800°C/735MPa, 900°C/392MPa, 1000°C/245MPa and 1100°C/137MPa. At 1000°C and higher, a non-contact extensometer[9] was used to obtain precise creep curves.

3. Results and discussion

Lattice misfit

The lattice misfit between γ and γ' phases is defined as follows,

$$\delta = (a_\gamma - a_{\gamma'}) / a_\gamma \quad \text{x100\%} \qquad (1)$$

where, a_γ and $a_{\gamma'}$ are lattice parameters of the γ and γ' phase, respectively.

The temperature dependence of lattice misfits of CMSX-4, TMS-82+ and TMS-82R is represented in **Figure 3**. All alloys investigated have negative lattice misfit from R.T. to 1100°C, and lattice misfits tend to be more negative values, in the order of CMSX-4, TMS-82+ and TMS-82R. The lattice misfit of TMS-82R became more negative than that of TMS-82+, although the nominal compositions are similar with the exception of Co, which has been reported to preferably partition into the γ phase[10-12].

Interestingly, the lattice misfit of TMS-82R changes toward the positive direction at 1000°C and 1100°C. This is probably due to the formation of topologically close packed (TCP) phase during HT-XRD experiment, as shown in **Figure 4**. The TCP phase usually contains high Re, W, and Mo, which are preferably allocated to the γ phase. Thus, contents of these elements in γ phase were decreased due to TCP precipitates, it results the lattice misfit shifting toward the positive direction.

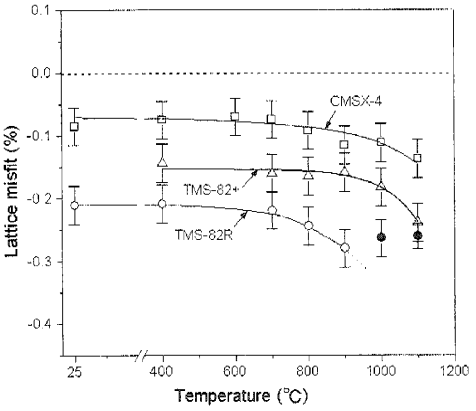

Fig. 3 Temperature dependence of lattice misfit for CMSX-4, TMS-82+ and TMS-82R.

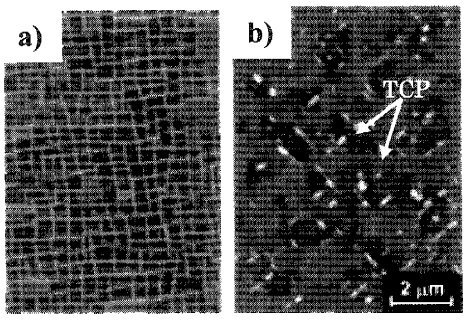

Fig. 4 SEM micrograph of specimen surface for TMS-82R.
(a) before and (b) after HT-XRD.

Partitioning ratios of alloying elements

The partitioning behavior of alloying elements was examined by the analysis of the equilibrium composition of γ and γ' phases in TMS-82+ and TMS-82R at 1100°C.

The partitioning ratio k_i is defined as shown in Eq. (2):

$$k_i = X_{i\gamma} / X_{i\gamma'} \qquad (2)$$

where $X_{i\gamma}$ and $X_{i\gamma'}$ are the compositions of the alloying element i in the γ and γ' phases, respectively.

Thus, for example, when $k_i > 1$, the element i has a tendency to partition into the γ phase, while it prefers to partition into the γ' phase when $k_i < 1$.

The partitioning ratios of the alloying elements into γ and γ' phases of TMS-82+ and TMS-82R at 1100°C are given in **Figure 5**. In this figure, it is clear that (1) Co, Cr, Mo, W, and Re have a preference to partition into the γ phase, and the order of partitioning ratios is Re > Cr > Mo > Co > W; (2) Al, Ti and Ta have a preference to partition into the γ' phase, while Ta strongly partitions into the γ' phase. Furthermore, the partitioning ratio for each element is affected by the absent of Co, **Table 3**; the change in partitioning ratio is denoted as Δk_i $\{= (k_i^{TMS\text{-}82R} - k_i^{TMS\text{-}82+}) / k_i^{TMS\text{-}82R} \}$. Cr, Mo and W partition more into the γ phase, while Al and Ti segregate more into the γ' phase in the Co-free alloy in comparison with those observed in TMS-82+. However, the effects are less pronounced for strongly partitioned elements, such as Ta and Re. We can assume that more Cr, Mo and W can be accommodated into the γ phase due to the elimination of Co from the alloy system; this might have attributed decreases in the amounts of Cr, Mo, W and increases in the Al, Ti contents in the γ' phase.

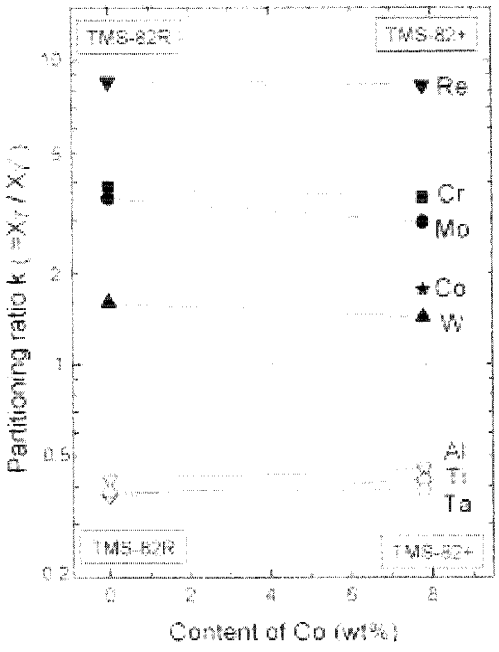

Fig. 5 partitioning ratios of alloying elements in TMS-82+ and TMS-82R at 1100°C.

Table 3. Partitioning ratios of alloying elements in TMS-82+ and TMS-82R.

	k_{Co}	k_{Cr}	k_{Mo}	k_W	k_{Al}	k_{Ti}	k_{Ta}	k_{Re}
TMS-82+	1.7	3.5	2.9	1.4	0.45	0.42	0.39	8.3
TMS-82R	-	3.9	3.5	1.6	0.42	0.37	0.38	8.5
Δk_i(%)	-	8.0	16.5	11.0	7.7	11.8	1.3	2.9

Creep property

Creep rupture tests were carried out for TMS-82+ and TMS-82R at 800°C/735MPa, 900°C/392Mpa, 1000°C/245MPa and 1100°C/137MPa conditions.

A comparison of the creep strength by means of the Larson-Miller parameters is presented in **Figure 6**. Creep strength of TMS-82R exceeds that of CMSX-4 in all of stress/temperature conditions tested, and TMS-82R has strongest creep strength at higher stress/lower temperature regime. TMS-82+ exhibits better creep resistance at 1000°C and 1100°C creep conditions. J.X.Zhang, *et al*[13] have reported that when creep takes place under high temperature / low stress, the large γ/γ′ lattice misfit in the negative leads to the formation of a dense interfacial dislocation network, and it guarantees a superior creep property by preventing glide dislocations from cutting the rafted γ/γ′ structure. Although TMS-82R possesses larger negative lattice misfit comparing to TMS-82+, its phase instability associated with the formation of TCP phases has degraded the creep resistance at 1000°C and 1100°C. Crept microstructures of TMS-82R at 1000°C/245Mpa and 1100°C/137Mpa are shown in Figure 7; the microstructural instability might be related to the absent of Co in the alloy system.

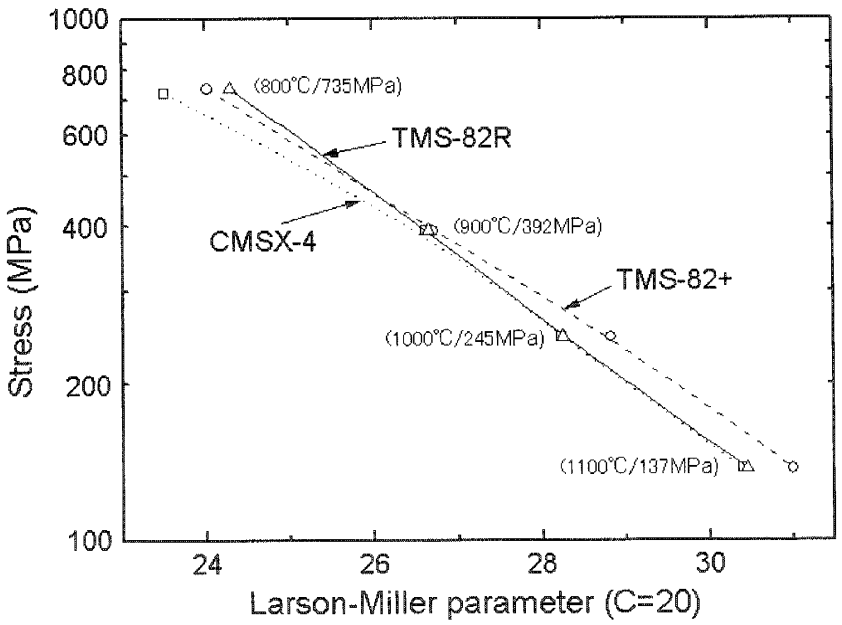

Fig. 6 Comparison of creep strength among CMSX-4, TMS-82+ and TMS-82R.

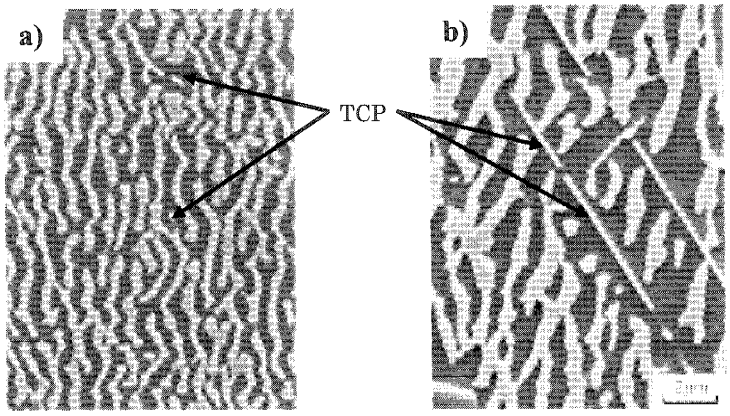

Fig. 7 SEM micrographs of TMS-82R after creep tests at
a) 1000°C/245MPa and b) 1100°C/137MPa.

4. Conclusions

A Co-free Ni-base SC superalloy TMS-82R, based on 2nd generation SC superalloy TMS-82+, has been developed. Creep rupture tests were performed on the newly developed alloy. Furthermore, the relationship between creep strength and structural parameters such as lattice misfit and partitioning ratio of alloying elements were investigated.

The following results were obtained,

1. Creep strength of TMS-82R exceeds that of CMSX-4 in all of stress/temperature conditions tested, and TMS-82R has strongest creep strength at higher-stress/ lower-temperature condition.
2. The partitioning ratios were affected by the Co elimination. For example, Cr, Mo and W tend to partition more into the γ phase, while Al and Ti tend to partition more into the γ' phase in TMS-82R.
3. The absent of Co has rendered TMS-82R to have larger negative lattice misfit. However, it also makes TMS-82R more susceptible to phase instability at temperatures above 1000°C.

TMS-82R displayed excellent creep-rupture life in comparison with CMSX-4 in all creep tests. Further improvement in the microstructural stability will enable TMS-82R to be utilized to the PBMR.

Acknowledgment

This work was performed as a part of the research activities of "High Temperature Materials 21 project", being conducted at NIMS under collaborations with Japanese and overseas private companies and research organisations. The authors would also like to thank Mr. S. Nakazawa for creep test, Dr. T.Kimura and Mr. T.Awane for EDS analysis.

References

[1] *ex.* WWW address; http://www.pbmr.co.za

[2] G.L.Erickson: Superalloys 1996 (Warrendale, PA, USA, Minerals, Metals and Materials Society), 35 (1996).

[3] T.Kobayashi, H.Harada, M.Osawa and A.Sato: J. Japan. Inst. Metals, **69**, 8, 707 (2005).

[4] T.Hino, T.Kobayashi, Y.Koizumi, H.Harada and T.Yamagata: Superalloys 2000 (Warrendale, PA, USA, Minerals, Metals and Materials Society), 729 (2000).

[5] T.Yokokawa, M.Osawa, T.Kobayashi, Y.Koizumi T.Yamagata and H.Harada: Proc. 6th on Materials for Advanced Power Engineering 1998 (Liege, Belgium, European Committee), 1121 (1998).

[6] T.Yokokawa, K.Ohno, H.Murakami, T.Kobayashi, T.Yamagata and H.Harada: Adv. in X-ray Analysis, **39**, 449 (997).

[7] K.Ohno, T.Yokokawa and T.Yamagata: Advances in X-ray Analalysis, **36,** 515 (1993).

[8] H.Harada, K,Ohno, T.Yamagata, T.Yokokawa and M.Yamazaki: Superalloys 1988, (TMS-AIME) 733 (1988).

[9] Y.Koizumi, H.Harada, T.kobayashi and T.Yokokawa: J. Japan. Inst. Metals, **69**, 8, 743 (2005).

[10] G.E.Maurer, L.A.Jackman and J.A.Domingue: Superalloys 1980 (TMS-AIME), 43 (1980).

[11] M.V.Nathal: Supealloys 1984 (TMS-AIME), 125 (1984).

[12] C.H.Lund, M.J.Woulds and J.Hockin: Superalloys 1968 (TMS-AIME), 25 (1968).

[13].J.X.Zhang, T.Murakumo, Y.Koizumi, T.Kobayashi, H.Harada and S.Masaki Jr.: Metal. Mater. Trans. **33A**, 3741 (2002).

[14] T.Hino, Y.Yoshioka, K.Nagata, H.Kashiwaya, T.Kobayashi, Y.Koizumi, H.Harada and T.Yamagata: Proc. 6th on Materials for Advanced Power Engineering 1998 (Liege, Belgium, European Committee), 1129 (1998).

Dedicated in memory of our colleague Professor D. S. Tchankov

THE EFFECT OF HIGH TEMPERATURE CREEP DAMAGE ON LOW CYCLE FATIGUE OF CMSX-4

A. Epishin[1], T. Link[1], U. Brückner[2], H. Klingelhöffer[2] and P. D. Portella[2]

[1]Technical University Berlin, Berlin, Germany
[2]Federal Institute for Materials Research and Testing, Berlin, Germany
e-mail: alex_epishin@yahoo.de

Abstract

Creep damage reduces fatigue strength and therefore this degradation of the material properties has to be considered in lifetime modelling of turbine blades. Investigation of the influence of high temperature creep on low cycle fatigue (LCF) of the single-crystal superalloy CMSX-4 showed, that a short primary creep at 1100-1150°C reduces LCF lifetime for several times, while further creep has nearly no degrading effect. Metallographic analysis of creep deformed specimens showed that the reduction of LCF lifetime correlates with rafting of the γ/γ'-microstructure. To remove this microstructural damage a "rejuvenation heat treatment" was applied dissolving the γ'-rafts. CMSX-4 deformed up to 0.5% creep strain showed no recrystallization after this heat treatment. The γ/γ'-microstructure attained again cuboidal morphology and the LCF lifetime was several times longer compared with creep deformed material, however shorter than in virgin condition. Consequently the main high temperature creep damage is rafting, but also other damage accumulated during high temperature creep contributes to the LCF lifetime reduction.

Keywords: Superalloys, CMSX-4, single crystal, creep, fatigue

Introduction

A reduction of fatigue strength due to creep damage is an important effect, which has to be considered in lifetime modelling of engineering components operating at high temperatures under static and cyclic loadings. Such components are blades of gas turbines operating under centrifugal force, pressure of the gas jet, thermal stresses and vibrations. Two types of creep damage should be distinguished:

- "Plastic damage" based on dislocation mechanisms. This is typical for short creep deformation under high applied stresses, resulting in large plastic strain.
- "Microstructural damage" based on diffusion processes, which is typical for long-term annealing under low applied stresses, resulting in a degradation of the microstructure.

Plastic creep damage is investigated for different materials, usually by performing relatively short mechanical tests (creep+LCF) under cyclic loading with dwells [e.g. 1-4]. Phenomenological theories describe this type of damage and allow to take it into account in mechanical engineering [e.g. 5, 6]. Investigations of microstructural creep damage are quite rare as they are very time consuming. They need long-term load annealing experiments followed by LCF tests (creep→LCF) and accompanied by the characterisation of the microstructure. For gas turbine blades operating at high temperatures for thousands of hours (aircraft engines) or tens of thousands of hours (power plants), the relevance of microstructural creep damage is great. Under these service conditions the γ/γ'-microstructure

of rotor blades made out of nickel-base superalloys transforms from cuboidal into rafted microstructure [7, 8], loses phase stability (precipitation of topologically close packed (TCP) phases [9]) and porosity grows [10, 11]. These structural processes influence the LCF lifetime, e.g. γ/γ'-rafting increases the rate of fatigue crack propagation [12] and hereby decreases the LCF lifetime [13]. The aim of this work was to determine the kinetics of microstructural creep damage of the single-crystal nickel-base superalloy CMSX-4 during long-term annealing at high temperature and low applied stresses. The question was, how the duration such tests influences the LCF lifetime. Additionally the effect of a heat treatment, which rejuvenates the creep deformed CMSX-4 by restoring the cuboidal γ'- morphology, was investigated.

Experimental

Single-crystal cylindrical bars (∅19 mm, length 175 mm) of CMSX-4 were solidified in [001] direction and heat treated by Howmet Alcoa, USA. Creep specimens with total length 170 mm were machined from these bars (Fig. 1b). The gauge length was 32 mm, the gauge diameter 12 mm. The specimens were tested in constant load machines equipped by short two zone furnaces (ATS Inc.). The temperature gradient along the gauge length was less than 7°C. The screw specimen heads were placed outside the furnace to reduce the risk of welding between specimen heads and grips which often occurs at such high temperatures. Additionally, the specimens and grips were slightly oxidized before the tests. These measures allow the destruction free removal of the specimens from the grips which is important for combined creep→LCF tests.

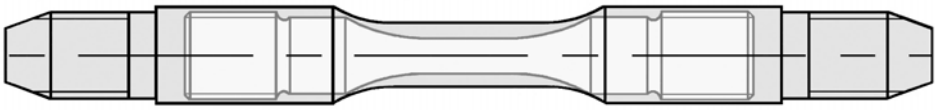

a

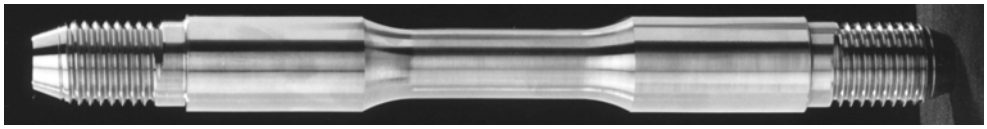

b

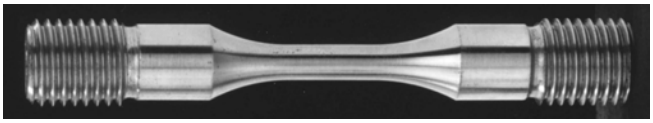

c

Fig. 1: Specimens used for combined creep→LCF tests.
Technical drawing (a) shows, how from the creep specimen (b) the LCF-specimen (c) is machined.

The interrupted creep tests were performed under a stress level of 90 MPa at two temperatures: 1100°C for 100 h, 640 h, 1240 h and 1800 h; 1150°C for 25 h and 420 h. At

these testing conditions [001] single-crystals of CMSX-4 show classical creep curves with extended secondary creep (Fig. 2). Stresses and testing times were dimensioned in such a way, that deformation proceeds slowly and the tests cover the creep stages from primary to accelerated creep. For all tests, except a test at 1150°C for 420 h, the creep strains did not exceed 0.5%, which is close to the creep strain limit for gas turbine blades.

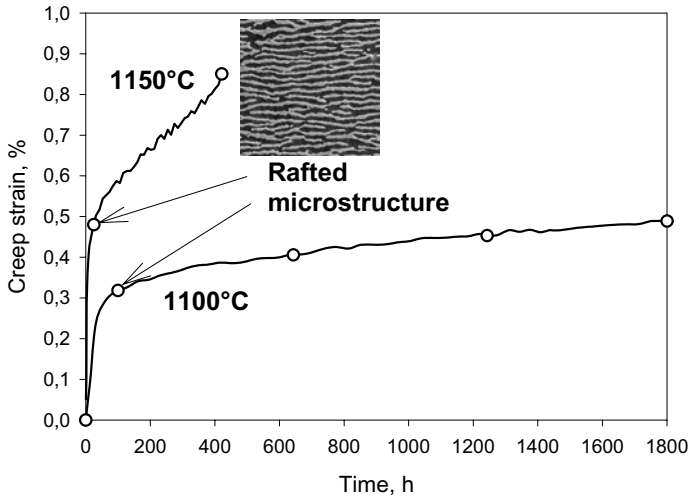

Fig. 2: Creep curves of CMSX-4 at 1100°C and 1150°C, 90 MPa. The lifetimes are about 2000 h and 500 h respectively. Dots show the durations of the different tests.

After the creep tests the LCF specimens were machined out of the creep specimens (Figs 1a, c). The diameter of the LCF specimens (∅6 mm, gauge length 16 mm) is much smaller than that of the creep specimens, to be sure that the oxidized surface layer having formed during the preceding creep test is totally removed. After machining the LCF specimens the surfaces were ground and subsequently polished using diamond abrasive down to 1 μm. The LCF rupture tests were performed in a hydraulic universal testing machine (MFL) at 700°C under strain controlled loading with reversible straining cycle $R=\varepsilon_{\min}/\varepsilon_{\max}=-1$ with a total strain range $\Delta\varepsilon=\varepsilon_{max}-\varepsilon_{min}=1.25\%$ and strain rate $\dot{\varepsilon}=10^{-3}$/s. The LCF testing temperature of 700°C was chosen, because at this temperature surface oxidation is greatly reduced and the effect of microstructural damage should therefore be clearer to observe.
After LCF tests the fracture surfaces of the specimens were investigated in scanning electron microscope (SEM), then the specimens were cut and investigated metallographically.

Results

The results of the LCF tests of the creep deformed specimens are shown in Fig. 3. After a short primary creep (100 h) at 1100°C the LCF lifetime has decreased dramatically from about 16000 down to about 2000 cycles (circular dots in Fig. 3). Further steady creep up to 1200 h has no remarkable effect on the LCF lifetime, however after 1800 h creep some increase of the LCF life up to about 3500 is observed. A similar result was found for the

specimens deformed for creep at 1150°C: the LCF life strongly decreases due to creep deformation (square dots in Fig. 3). The finding, that lifetime reduction is less at higher temperatures has to be investigated by additional experiments.

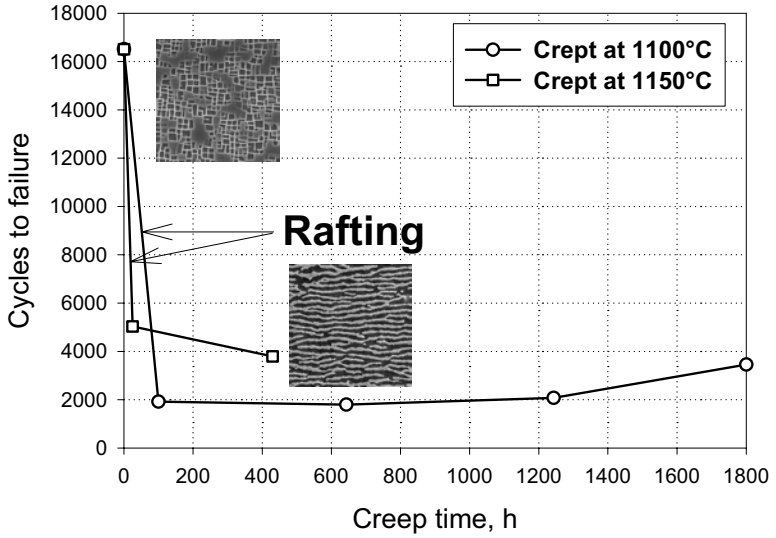

Fig. 3: Influence of high temperature creep on LCF life of CMSX-4.
LCF test at 700°C, $\Delta\varepsilon$=1.25%, R=–1. SEM images show the initial and rafted structure.

Analysis of the fracture surface showed that in all specimens (undeformed and pre-deformed) LCF fracture started in the interdendritic region from the largest cluster of solidification pores (Fig. 4a, b). Usually only one fracture nucleus was observed. The position of the fracture nucleus relative to the cylindrical surface differs from specimen to specimen. Generally it was close to the surface, in a range from about 0.1 mm up to 1 mm. Three zones of crack development could be distinguished in the fracture surface (Fig. 4a). The first zone has a circular shape (so-called “fish eye”, Fig. 4a) and smooth topography. The radius of this zone is equal to the distance between the fracture nucleus and the specimen surface. Within this zone the fatigue crack grows very slowly, perpendicular to the load direction. The second zone shows fatigue striations (Fig. 4c). Each line belongs to one cycle, giving an increased crack propagation rate of about 2 μm/cycle. The third zone corresponds to the final rupture, where the crack grows very fast. Here the fracture surfaces are {111} planes indicating {111} shearing as crack growth mechanism. In general the fracture surface was found to be similar for all specimens tested under the given conditions.
SEM analysis of the microstructure showed that after primary creep CMSX-4 attained a rafted γ/γ’-microstructure (see Fig. 2). By visual inspection no remarkable difference in the γ/γ’-microstructure of the different specimens could be observed. In earlier investigations [14] however it was shown by quantitative metallography that under similar creep conditions (1100°C, 120 MPa) the γ/γ’-microstructure of CMSX-4 rapidly becomes rafted during primary creep and then coarsens slowly during steady creep.

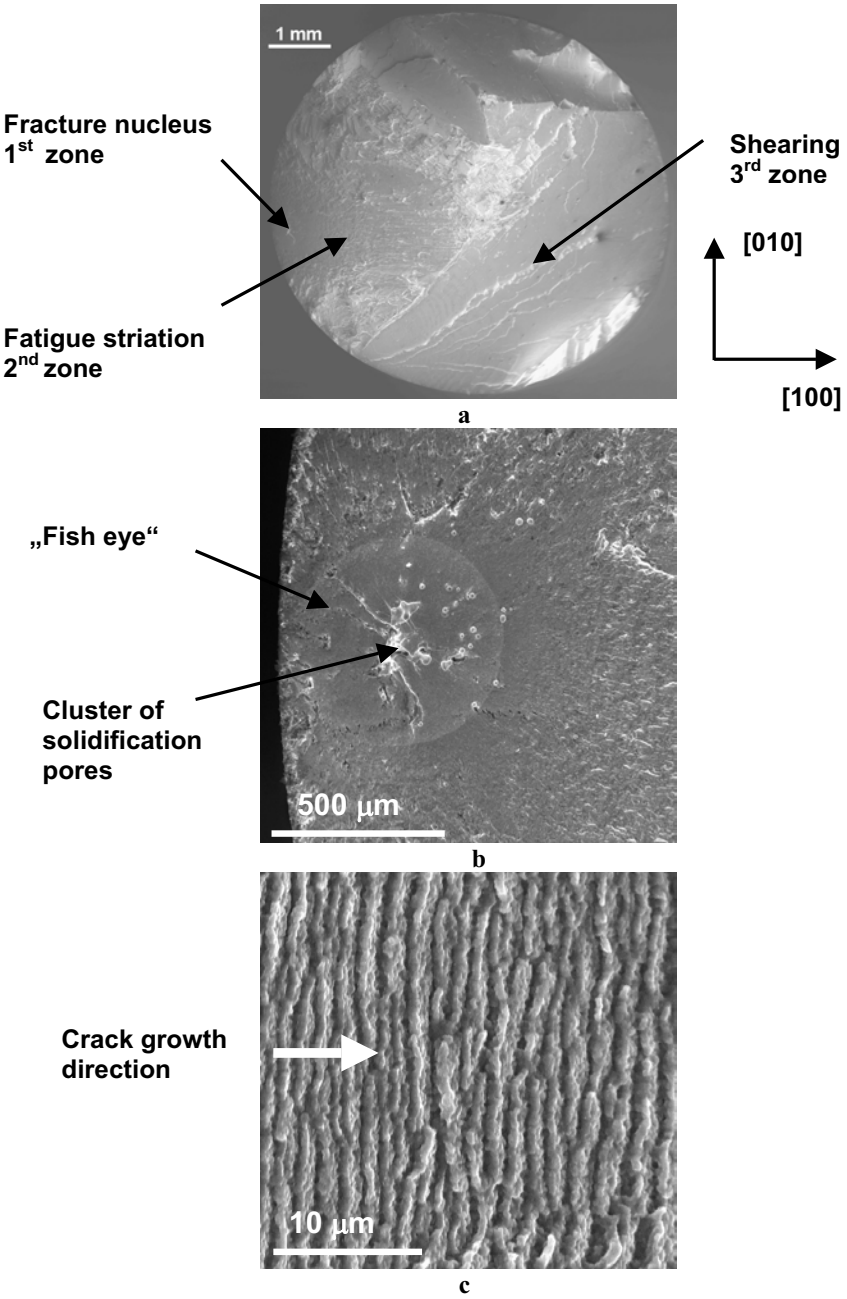

Fig. 4: Fracture surface after a LCF test at 700°C, $\Delta\varepsilon$=1.25%, R= –1.
a - Overview of the fracture surface.
b - Fracture nucleation from a cluster of solidification pores in the centre of a "fish eye" placed about 300 µm from the specimen surface (1st zone).
c - Fatigue striations in 2nd zone.

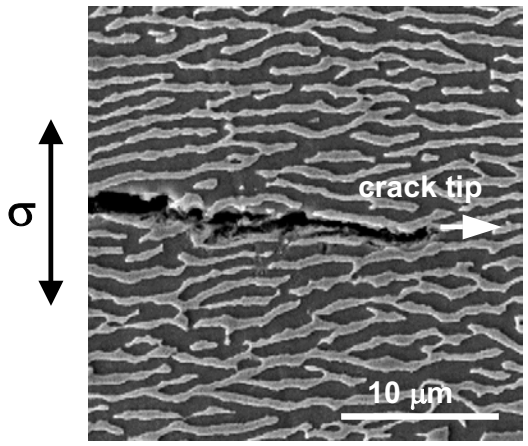

Fig. 5: Growth of LCF cracks along extended semi-coherent γ/γ'-interfaces in the rafted microstructure of CMSX-4.

Fig. 5 shows that the fatigue cracks grow along the extended semi-coherent γ/γ'-interfaces, indicating that the interfaces facilitate the crack propagation by their defects and their geometry. Analysis of longitudinal cuts of the specimens showed no additional fracture nuclei. Only a few small cracks were found at pores near the fracture surface, probably by-products of the growth of the main primary crack. So fractography confirms the metallographic findings: the crack nucleates at just one centre. It propagates from this centre resulting in specimen fracture. Precipitation of TCP phases was found to be moderate, after 600 h creep at 1100°C the TCP phase volume fraction is about 0.1%.

Assuming that rafting of the γ/γ'-microstructure is the main reason for the observed reduction of LCF lifetime after creep we tried to recover the LCF strength of creep deformed CMSX-4 by application of a "rejuvenation heat treatment" as applied by some commercial companies on turbine blades after service. A creep specimen deformed for 640 h at 1100°C, 90 MPa was held at 1305°C for 30 min to dissolve the γ'-rafts (γ'-solvus for CMSX-4 is 1280±2°C, measured by electrical resistivity method [15]). Then an annealing process according to the standard heat treatment of CMSX-4 was applied, i.e. 1140°C/6 h + 870°C/16 h. Afterwards the specimen surface was etched by a grain boundary selective agent (HCl + 10% of H_2O_2). No indication of recrystallization was found in this specimen deformed up to about 0.5% creep strain. The γ/γ'-microstructure attains again the cuboidal morphology typical for undeformed material. A LCF specimen was machined from the rejuvenated creep specimen and tested under the same conditions as the previous specimens. The LCF lifetime was found to be 8279 cycles compared to 1800 cycles for a not rejuvenated creep deformed specimen (1100°C, 90 MPa, 640 h) and 16511 cycles for undeformed material, so the rejuvenation heat treatment increased the LCF lifetime of the creep deformed specimen by about 4.5 times. Compared with the virgin material rejuvenated material is only half as good. The ruptured specimen (crept + rejuvenated + LCF tested) was investigated by fractography, showing the fracture surface to be similar to those of the other specimens.

Discussion

It is seen in Fig. 2 that primary creep at high temperatures and low stresses results in a strong reduction of the strain rate (work hardening) but on the other hand it dramatically reduces the LCF strength (Fig. 3). It is unambiguous that this effect is mostly caused by rafting, i.e. by the formation of extended semi-coherent γ/γ'-interfaces orientated perpendicular to the applied load direction. In [12] it was found for CMSX-2 that the formation of a rafted γ/γ'-microstructure accelerates fatigue crack growth by about 3-5 times, which is comparable to our results. Obviously the effect of rafting is stronger when the rafts are long and when the interfaces are densely covered by interfacial dislocation networks. Such a microstructure forms in superalloys with a high γ/γ'-misfit. After heat treatment CMSX-4 has a well aligned cuboidal γ/γ'-microstructure, which allows the formation of very regular rafts. The rafts are the longest and the interfacial networks are the densest in the middle of the creep process when the creep rate is slow and steady. According to Fig. 3 the LCF lifetime has a minimum between 100 h and 1200 h (1100°C). Coarsening of the rafted γ/γ'-microstructure during creep is connected with the effect of topological inversion: neighbouring rafts become interconnected. For the crack propagation this means a reduction of the mean free path length, which is probably the reason for the slight increase of the LCF life at 1800 h.
Because the recovering of the γ/γ'-microstructure (dissolution of the γ'-rafts and the formation of the cuboidal γ/γ'-microstructure) did not fully restore the LCF properties one can conclude that there is additional creep damage besides rafting, reducing LCF lifetime. Such damage could be the growth of porosity during creep and the precipitation of the TCP phases. Investigation of the porosity growth by measuring the material density showed that during primary and steady creep at 1100°C, 90 MPa the porosity volume fraction increases by about 0.1 vol.% (Fig. 6).

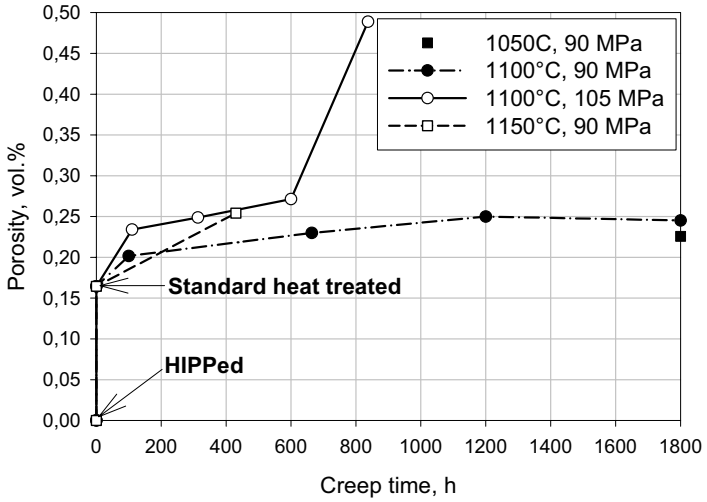

Fig. 6: Increase of porosity in CMSX-4 during creep at high temperatures.
Porosity was determined by density measurements in water.

This porosity growth is comparable with the initial porosity 0.16 vol.% determined by comparison of the densities of standard heat treated and hot isostatically pressed (HIPPed) CMSX-4 (see Fig. 6). This relative increase of the porosity volume fraction is about 60-70%, whereas the relative increase of the pore diameter is significantly smaller, not more than 20% (absolute increase few microns). It is assumed that such a pore enlargement is not enough to be the main reason for the observed dramatic reduction of the LCF life, but it could contribute to the lifetime reduction too.
It should be mentioned that according [13] rafting decreases the LCF lifetime of CMSX-4 by a factor of two, whereas the present investigation shows a 4-8 fold decrease in life time. In [13] the creep specimens were pre-deformed at 950°C and then tested for LCF at the same temperature. Three reasons could be proposed for this discrepancy. First: the quality of the rafted γ/γ'-microstructure depends on the testing conditions and consequently can be different after creep at 950°C and 1100-1150°C. Second: with LCF tests at 950°C the surface oxidation during testing can somewhat smooth the effect of rafting, while at 700°C the surface oxidation effect is very small. Third: during creep at 1100-1150°C there are additional types of creep damage besides rafting.

Conclusions

1. The LCF lifetime of CMSX-4 is dramatically reduced (4-8 times) after primary creep at 1100-1150°C. The main reason is rafting of the γ/γ'-microstructure. For reliable prediction of LCF lifetime under creep-LCF conditions the kinetics of raft formation has to be considered.
2. The LCF lifetime of creep deformed CMSX-4 specimens can be significantly improved by application of a rejuvenation heat treatment dissolving the γ'-rafts and recovering the initial cuboidal γ/γ'-microstructure. After rejuvenation CMSX-4 shows a shorter LCF lifetime than in virgin condition, which could be due to creep induced porosity or TCP phases.

Acknowledgements

Authors are grateful to Dr. K. Harris, Vice-President of the Cannon Muskegon Corporation, USA for providing the master alloy of CMSX-4 free of charge and the German Research Society (DFG) for funding of this work (project Po. 405/7-1, Re 688/41-1).

References

[1] D. S. Tchankov, J. Xu, H. Schlums and W. Rothkegel, "Mean stress effect on high temperature low cycle fatigue of a single crystal alloy", *ESIA 2002, 6th International Conference on Engineering Structural Integrity Assessment*, Manchester, UK, 7-9 October 2002.
[2] L. J. Chen, G. Yao, J. F. Tian, Z. G. Wang and H. Y. Zhao, "Fatigue and creep-fatigue behavior of a nickel-base superalloy at 850°C", *Int. J. Fatigue*, 20, (7) (1998), 543-548.
[3] J. Zrink, J. Semeňák, V. Vrchovinský and P. Wangyao, "Influence of hold period on creep-fatigue behaviour of nickel base superalloy", *Mat. Sci. Eng*., A-319-321 (2001), 637-642.
[4] T. Yokobori and A. T. Yokobori Jr, "High temperature creep, fatigue and creep-fatigue interaction in engineering materials", *International Journal of Pressure Vessels and Piping*, 78 (2001), 903-908.

[5] H. Mao and S. Mahadevan, "Reliability analysis of creep-fatigue failure", *International Journal of Fatigue*, 22 (2000), 789-797.
[6] K. Nikbin, "A unified European approach to high temperature defect assessment code and its incorporation in a knowledge base system", *International Journal of Pressure Vessels and Piping*, 78 (2001), 929-935.
[7] J. K. Tien and S. M. Copley, "The Effect of Uniaxial stress on the Periodic Morphology of Coherent Gamma Prime Precipitates in Nickel-Base Superalloys Crystals", *Metall. Trans.*, 2 (1971), 215-219.
[8] J. K. Tien and S. M. Copley, "The Effect of Orientation and Sense of Applied Stress on the Morphology of Coherent Gamma Prime Precipitates in Stress Annealed Nickel-Base Superalloy Crystals", *Metall. Trans*., 2 (1971), 543-553.
[9] R. Darolia, D.F. Lahrman and R.F. Field, "Formation of topologically closed packed phases in nickel base single crystal superalloys", *Superalloys 1988*, ed. D.N. Duhl, G. Maurer, S. Antolovich, C. Lund, S. Reichman (TMS, 1988), 255-264.
[10] J. Komenda and P.J. Henderson, "Growth of pores during the creep of a single crystal nickel-base superalloy", *Scripta mater*. 37 (1997), 1821-1826.
[11] A. Epishin, T. Link, U. Brückner and P. D. Portella, "Investigation of the porosity in single-crystal nickel-base superalloys", *Proceedings of the 7th Conference on Materials for Advanced Power Engineering*, 30 Sept.-2 Oct. 2002, Liège, Belgium, Part 1, ed. J. Lecomte-Beckers, M. Carton, F. Schubert and P. J. Ennis (Jülich, Forschungszentrum Jülich GmbH, 2002), 217-226.A
[12] S.H. Ai, V. Lupinc and G. Onofrio, "Influence of precipitate morphology on high temperature fatigue crack growth of a single crystal nickel base superalloy", *Scripta Metall. Mater.*, 29 (1993), 1385-1390.
[13] M. Ott and H. Mughrabi, "Dependence of the high-temperature low-cycle fatigue behaviour of the monocrystalline nickel-base superalloys CMSX-4 and CMSX-6 on the γ/γ'-morphology", *Mater. Sci. and Engineering A*, 272 (1999), 24-30.
[14] A. Epishin and T. Link, "Mechanisms of high temperature creep of nickel-base superalloys under low applied stresses", *Philosophical Magazine*, 84 (2004), No. 19, 1979-2000.
[15] A. Epishin, T. Link, U. Brückner and P. D. Portella, "Influence of dendritic inhomogeneity on the creep behaviour of single-crystal superalloys of the 3rd generation", (Interim report of the German Research Society (DFG), BAM-TUB, Berlin, 2002).

THE LONG-TERM CREEP PROPERTIES OF NICKEL-BASE SINGLE-CRYSTAL SUPERALLOYS

Yutaka Koizumi, Hiroshi Harada, Tadaharu Yokokawa and Toshiharu Kobayashi

National Institute for Materials Science (NIMS)
1-2-1 Sengen, Tsukuba Science City 305-0047
Japan

Absract

Long component-life of at least two years under a daily start and stop condition is required on turbine blades and vanes in land-based power plants. For this reason, creep rupture life of 10,000 hours or longer is required for the application of Ni-base superalloys. In this paper, long –term creep property of more than 15,000 hours was analyzed for a second-generation Ni-base single crystal superalloy, TMS-82+. Consequently, Larson-Miller parameters in the range of C=12–14 resulted in good fits over the short-to-long-term creep rupture life, even though C=20 is conventionally used for Ni-base superalloys. In addition, the creep strength of TMS-82+ exceeds that of CMSX-4 under wide range of stress / temperature conditions, especially under the higher temperature and lower stress condition.

The creep data obtained is input in the material database of the virtual jet engine simulation program that is currently under development.

Keywords: single-crystal, second generation, Ni-base superalloy, long-term creep, Larson-Miller parameter

1. Introduction

Creep rupture tests lasting 1000h are sufficient for the proper evaluation of Ni-base superalloys for use as aero-jet engine components. The time at maximum load lasts merely several minutes during takeoff, and even if 10,000 flights are assumed, the time at maximum load would not exceed 1000h. However, in the case of the industrial gas turbine used for power generation, it must operate at maximum load for two years or more, under daily start-stop conditions. Thus, creep rupture tests lasting 10,000 hours or longer are required.

In this paper, the long–term (>15,000 hours) creep properties of a second-generation Ni-base single crystal (SC) superalloy, TMS-82+, have been analyzed.

2. Experimental procedure

TMS-82+[1], a second generation Ni-base SC superalloy, has been developed through a joint research venture between Toshiba Corporation and the National Institute for Materials Science (NIMS), as part of the "High temperature Materials 21 project"[2]. A computer-aided Alloy Design Program (ADP)[3], based on empirical equations derived from a database of SC superalloys developed at NIMS, was used for developing this alloy. ADP can estimate various mechanical and microstructural properties of an alloy, such as creep rupture life, heat-treatment window, phase stability, concentrations of solid solution elements in γ and γ' phases, γ' phase volume fraction, and lattice misfit between γ and γ' phases.

TMS-82+ has superior creep strength, especially at high temperature, and also has excellent microstructural stability, although a small amount of topologically close packed (TCP) phases would precipitate during long-term high temperature exposure. Additionally, its good castability allows it to be cast as large SC blades with lengths of up to 300mm. The

Table 1: Nominal compositions (mass% Ni-bal.) of the alloys.

	Co	Cr	Mo	W	Al	Ti	Ta	Hf	Si	Re
TMS-82+	7.8	4.9	1.9	8.7	5.3	0.5	6.3	0.1	0.4	2.4
CMSX-4	9.6	6.4	0.6	6.4	5.6	1.0	6.5	0.1	-	3.0

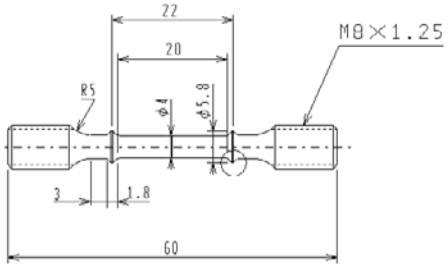

Figure 1: Schematic draw of creep test piece.

composition of TMS-82+ is shown together with a commercial 2nd generation SC superalloy, CMSX-4, in Table 1.

SC bars, 10mm in diameter and 130mm in length, were cast with a directional solidification furnace at NIMS. All bars used in this experiment were within 10° of the [001] orientation along their longitudinal axes. Heat treatment conditions were as follows: the bars were held for 1 h at 1300°C, followed by a hold for 5 h at the solution temperature of 1320°C, and air-cooled. A two-step aging treatment, 1100°C for 4 h, followed by air-cooling, then 870°C for 20 h, followed by air-cooling, was performed. Creep test specimens, 4mm in diameter and 22mm gage section length, were machined from these heat treated SC bars (Figure 1). Creep tests were carried out under various conditions; experiment temperatures ranged from 800°C to 1150°C, and applied stresses ranged from 78MPa to 392MPa.

Two types of extensometers were used for the strain/elongation measurements of creep tests in the experiment temperature range; one is the conventional extensometer, and the other is a newly developed, non-contact extensometer. Usually, the conventional extensometer is used in creep tests of metals. The creep specimen is supported by a jig with rods, and the dial gauge through the rods measures specimen elongation during creep testing. From this, specimen creep strain is determined. At temperatures beyond 900°C, the accuracy of elongation measurement decreases, as jig and rod deformation can occur (Figure 2).

A non-contact extensometer[4)] has been newly developed for creep tests at higher temperatures. This is a collaboration between Toshin Kogyo and NIMS. As shown in Figure 3, the CCD camera is put outside of the furnace with a small quarts window, so that the sample can be observed through the window. We need a sample with two projections as shown in Figure 1 to detect the strain. Prior to a creep test, the CCD camera memorizes the projection's initial shape and position. During a creep test, the CCD camera records the changes in projection position due to specimen elongation. Creep tests at temperatures above 1000°C were carried out by using the non-contact extensometer. This was the first usage of this non-contact extensometer to measure the results of a long-term (>15000h) creep test.

3. Results and discussion

Figure 4 shows the creep curve of TMS-82+ obtained from a creep test at 1000°C/98MPa. The specimen strain/elongation could be measured by the non-contact extensometer that was positioned outside of the furnace, although it was a long-term (>15000h) creep test at a relatively higher temperature of 1000°C. Occasionally, the quartz window through which the extensometer uses to detect becomes cloudy during a test. Typically, the experiment temperature needs to be lowered if this quartz window has to be changed, and this leads to experiment inaccuracy. However, the window used in this paper has been designed to be easily changeable, such that experiment conditions would not be affected.

TMS-82+ has a long steady-state creep region and took over 13000 hours to reach 1% of creep strain. Figure 5 is the Larson-Miller parameter (LMP) results for TMS-82+ obtained from short-term and long-term creep tests. The horizontal axis is plotted as the value P:

$$P = (T+273)\cdot(C+\log t) \times 10^{-3}$$

where T is test temperature (°C), t is creep rupture life (h), and C is a coefficient.

The trend lines obtained by applying various C values to previous short-term creep data were plotted together with the short and long-term creep test results acquired in this paper (Figure 5). Typically, the coefficient value C= 20 is applied for nickel-base superalloy creep test specimens. The trend line for C= 20 had a good fit with the short-term higher stress data, but not with the long-term lower stress data. Substantial deviation was seen for the LMP values calculated in the lower stress region of 98-245MPa. Thus, this trend line cannot be

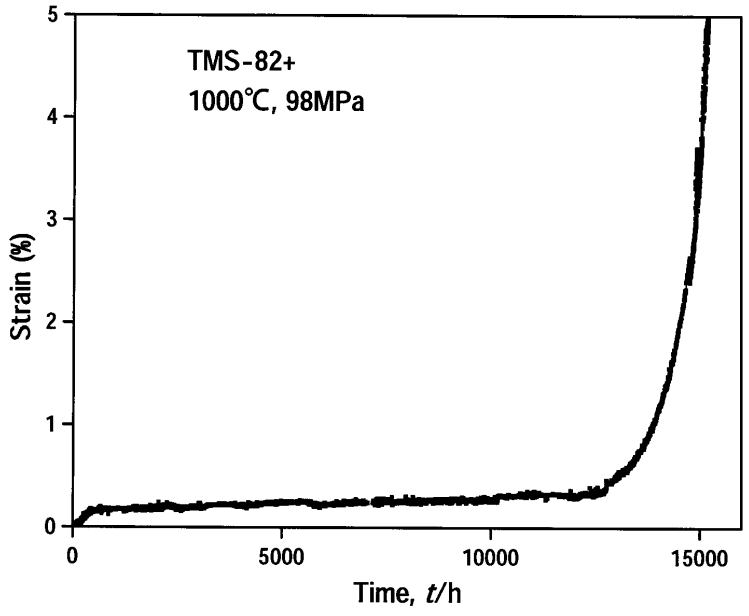

Figure 4: The prolonged creep-test result of 15000 hours or more. Strain deformation is measured by non-contact extensometer. Result of long-term creep test for TMS-82+ under the condition of 1000℃,98MPa.

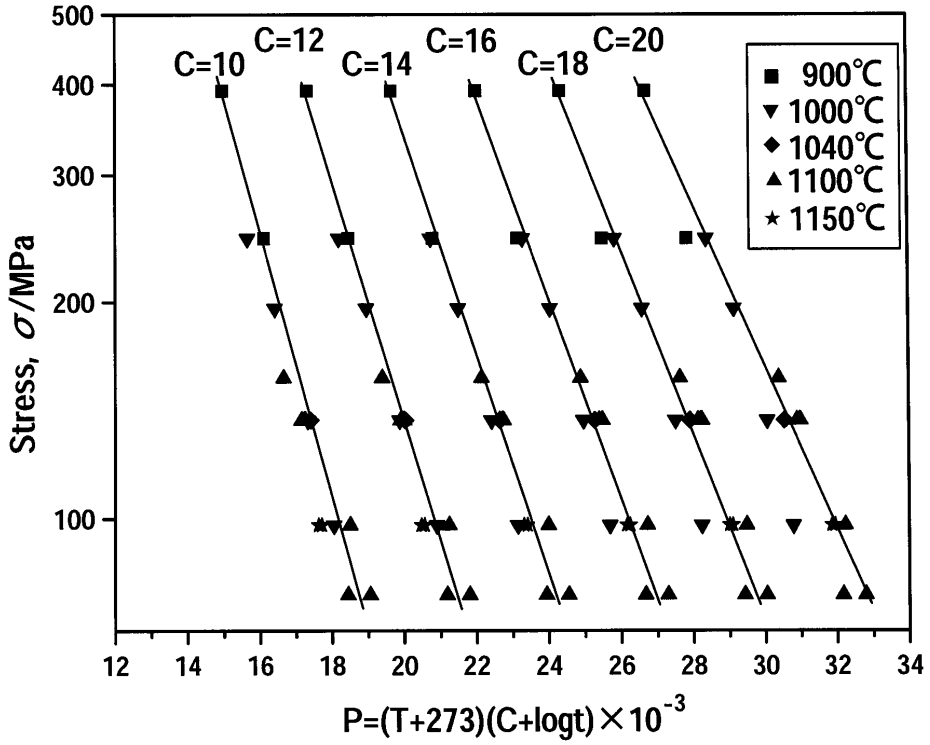

Figure 5: Optimization of coefficient C of the Larson-Miller parameter for low-term creep.

used to estimate the creep rupture life of a specimen under long-term lower stress; instead, actual long-term creep data must be collected. This deviation tendency of the LMP values reduces with decreasing C values. The minimum deviation occurs at C= 12 and 14, but increases again at C=10.

In order to clarify this tendency in detail, standard deviations about the stress of 245MPa, 137MPa, and 98MPa were plotted in Figure 6, respectively. It can be seen that the C-value is strongly related to the applied stress during creep testing. For instance, when C= 14.5 was applied to the data obtained at 245MPa, the standard deviation was minimum; therefore C= 14.5 is optimal for an applied stress of 245MPa. Similarly, C= 11.7 was the optimum value for an applied stress of 137MPa; and for a lower stress of 98MPa, C= 12.5 was optimum. Accordingly, the value C= 20 should not be applied to the results of long-term creep tests of Ni-base superalloys, even though the estimation of creep rupture life becomes better when a small value of C is applied. Several reasons for this tendency have been postulated. The Larson-Miller method[5] tends to over-estimate specimen creep rupture life for long-term, low stress creep. Moreover, during long-term creep, the stresses and temperatures experienced by the creep test specimen are lower compared to short-term creep, and the principal mechanism

of creep rupture might have changed from the cutting mechanism to the climbing mechanism[6].

The optimum C-value for CMSX-4 was determined by COST 501 program[7] to be 14.07. Figure 7 shows creep strengths of TMS-82+ and CMSX-4 used the coefficient C of 14 for the Larson-Miller parameter. Creep strength of TMS-82+ exceeds that of CMSX-4 in all of temperatures and stresses examined. TMS-82+ shows excellent creep strength, especially at lower stress / higher temperature condition. TMS-82+ has a more negative lattice misfit than that of CMSX-4; thus, the former formed the rafted structure of γ/γ' phases more easily at higher temperature. The dense interface dislocation network created at the γ/γ' interfaces resulted in the superior creep strength of TMS-82+ at higher temperatures[8].

In Figure 7, creep data of TMS-82+ under examination were also plotted with arrows. Although long-term creep tests require about a decade to complete, collection of such data is crucial for gas turbine design,

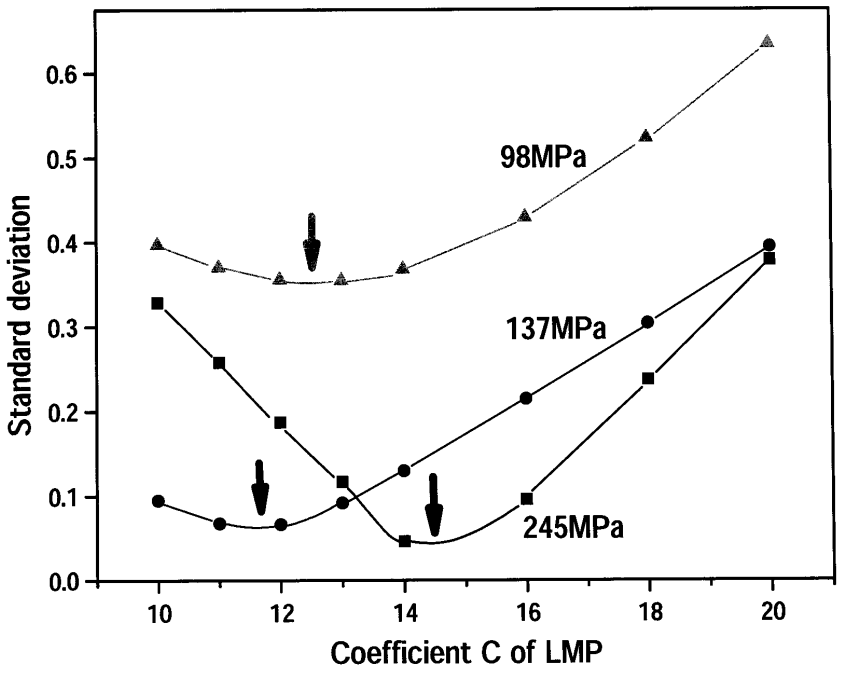

Figure 6: The optimal value of Larson-Miller Parameter.

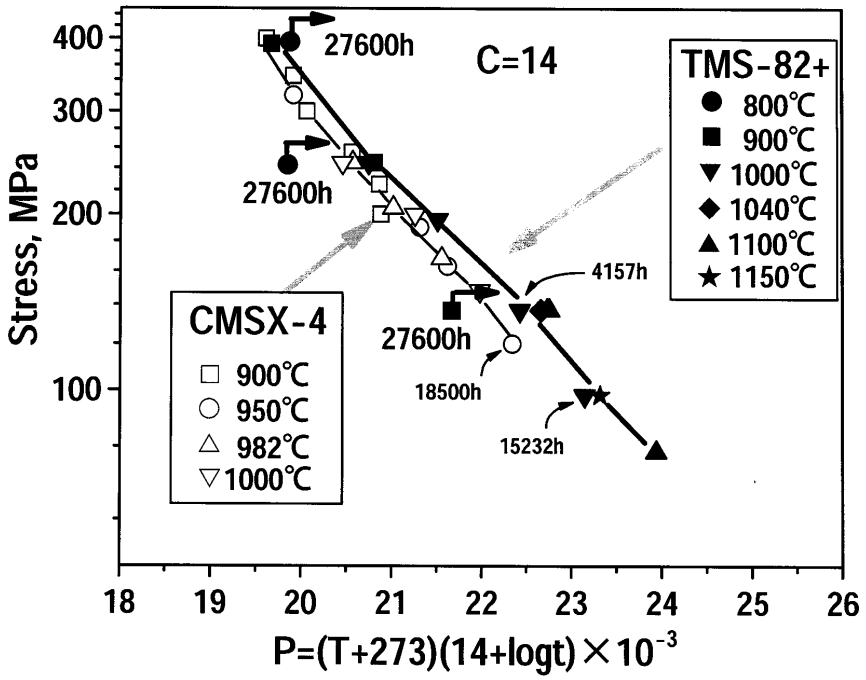

Figure 7: Larson-Miller plot (C=14) for the evolution of creep rupture strength of TMS-82+ compared with CMSX-4.

4. Conclusions

The long-term creep data of the superalloys developed at NIMS superalloys need to be acquired in order to use these alloys as the blade material of land-based gas turbines. Acquiring long-term (>15000h) creep data of these superalloys allows for examination and clarification of their creep characteristics. In this paper, the second-generation nickel-base single crystal superalloy, TMS-82+, was used. The following conclusions can be drawn from this study:

(1) Specimen creep strain / elongation during a long-term (15000h) creep test at 1000°C can be accurately measured by the newly developed non-contact extensometer.

(2) The coefficient value C= 20 for the Larson-Miller parameter is accurate for short-term creep tests, but not for long-term creep tests.

(3) For TMS-82+, C=12-14 are the optimum values to evaluate short-term and long-term creep test results together.

(4) By using C=14 as the Larson-Miller parameter, it can be seen that the creep strength of TMS-82+ exceeds that of CMSX-4 in all temperature/stress conditions examined.

References

1) T.Hino, Y.Yoshioka, Y.Koizumi, T.Kobayashi and H.Harada: Proc. Sixth International Conference on Materials for Advanced Power Engineering 2002, European Committee, (2002) pp. 303-312.
2) http://sakimori.nims.go.jp
3) H.Harada, K.Ohno, T.Yamagata, T.Yokokawa and M.Yamazaki: *Superalloys 1988*,(TMS AIMA, 1988) pp.733-742.
4) S.Nakazawa, Y.Koizumi, H.Harada and N.Nakayasu: *Report of the 123rd committee on Heat-Resisting Materials and Alloys*, (Japan Society for the Promotion of Science, **37**, 1996)pp.263-266.
5 E.Nakajima, K.Maruyama *ed.*: "Materials Science of High Temperature Strength", Uchida-Roukaku-ho, (1997), pp.251-264.
6 J.X.Zhang, T.Murakumo, K.Koizumi, T.Kobayashi and H.Harada: Acta Mater. 52, (2003)pp.5073-5081.
.7) C.K.Bullough, M.Toulios. M.Oehl and P.Lukas: Proc. *Sixth International Conference on Materials for Advanced Power Engineering 1998*, (European Committee, 1998) pp. 861-878.
8) T.Hino, Y.Yoshioka, Y.Koizumi, T.Kobayashi and H.Harada: *Superalloys 2000*, (TMS AIMA, 2000) pp.729-736.

INFLUENCE OF SOLIDIFICATION CONDITIONS ON HOMOGENISATION HEAT TREATMENT AND MECHANICAL PROPERTIES IN SINGLE CRYSTAL NICKEL-BASE SUPERALLOYS

M. Lamm[1], A. Volek[1], O. Luesebrink[2], R.F. Singer[1]

[1]University of Erlangen-Nuremberg, Department of Materials Science and Engineering, Institute of Metals Science and Technology, Martensstr. 5, 91058 Erlangen, Germany
E-mail: matthias.lamm@ww.uni-erlangen.de
[2]Doncasters Precision Castings, Bessemerstr. 80, 44793 Bochum, Germany

Abstract

The state of the art technique for the production of industrial gas turbine blades is the high rate solidification casting method (HRS process). The new liquid metal cooling technique (LMC process) offers great potential for cost reduction and microstructure improvement due to higher temperature gradients and cooling rates.
In the present study, high-cycle fatigue tests were performed on samples of the single crystal alloy PWA 1483 at elevated temperature. Primary dendrite arm spacings studied comprised 400 microns in the LMC process and 600 microns in the HRS process due to the different solidification conditions. In terms of stresses, the fatigue strength is found to be improved by 20 % in the LMC samples. The origin of fatigue failure is found to be casting pores as they are the largest microstructural defect present in the samples. Casting porosity in the LMC samples is smaller which can be attributed to the smaller dendrite arm length as well as the more regular structure, resulting in improved conditions for feeding.

Keywords: Directional solidification, liquid metal cooling, single crystal superalloy, homogenisation, fatigue

Introduction

The increase in turbine inlet temperature leads to an increased demand for directionally solidified and single crystal turbine blades for industrial gas turbines (IGT). Also the size of the turbine blades increases with the development of larger gas turbines with higher power output. This trend to larger and more complex blades reveals the limits of the established Bridgman (high rate solidification, HRS) casting technique. Especially for large blades the necessary temperature gradient at the solidification front for a directionally solidified microstructure cannot be established. This is due to the heat transfer by radiation to the ambiance being less efficient for large components and cluster castings. A promising alternative is the liquid metal cooling process (LMC) where the cooling conditions are improved. Earlier work suggests that due to larger temperature gradients a refined microstructure is produced leading to enhanced mechanical/fatigue properties and improvements with respect to homogenization treatment [1-3]. However, the argument was largely based on heat balance considerations and the experimental evidence presented has been limited. The present study aims to reiterate the advantages of the liquid metal cooling process, in particular for the properties of large scale single crystals from Ni-based superalloys. Special emphasis will be put on the homogenization of the as-cast segregation pattern and the improvement of the fatigue behaviour.

Materials and experimental procedures

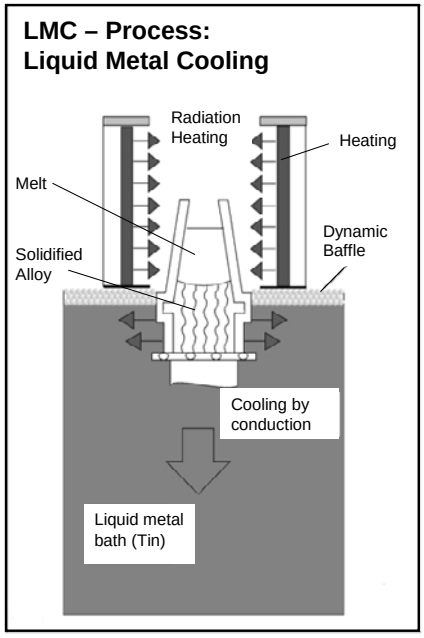

Figure 1: LMC Process [2]. The mould is withdrawn into a liquid tin bath after pouring the superalloy melt. Cooling by conduction gives an increased temperature gradient.

The alloys used in this study comprise the first generation single crystal Ni-based superalloy PWA 1483 and the second generation single crystal Ni-based superalloy CMSX-4. The nominal compositions of the two superalloys are listed in Table 1. To vary the solidification conditions two casting setups were used. Single crystals were grown in the world's largest LMC casting unit at Doncasters Precision Castings in Bochum. A schematic drawing of the casting set up is shown in Figure 1. It comprises a heating zone were the ceramic mould is heated and the molten superalloy is poured. After pouring the mould is withdrawn into the liquid tin bath where the heat is led away by conduction cooling. A dynamic, floating baffle separates the heating from the cooling chamber and helps to establish the longitudinal temperature gradient. For comparison purposes the well established HRS/Bridgman technique was used. Here the main heat transfer is done by radiation cooling to the ambiance.

Table 1: Nominal compositions of the investigated Ni-based superalloys in wt.-% [4].

Alloy	Cr	Co	Mo	Al	Ti	Ta	W	Re	C	Hf	Ni
CMSX-4	6.5	9.0	0.6	5.6	1.0	6.5	6.0	3.0	-	0.1	bal.
PWA 1483	12.2	9.0	1.9	3.6	4.1	5.0	3.8	-	0.07	-	bal.

Homogenization treatment

As-cast CMSX-4 slabs and bars were cut to cubical and cylindrical samples with a volume of approximately 350 mm^3. The homogenization experiments were conducted in a high temperature furnace in air. The heat treated specimens were cut perpendicular to [001] for further microstructural studies. For analysing the element distribution microprobe measurements (JEOL JXA-8100) were performed on a 1250 μm by 1250 μm square grid at a spacing of 5 μm. The probe diameter was 10 μm.

In order to characterize the change of the element concentration in the dendrite core and in the interdendritic areas with proceeding homogenization time the residual segregation index δ_i is used [5], see eqn. (1). The concentration values c with the superscript 0 represent the initial concentration of the element i. Maximal concentrations are denoted with a M and minimal values with a m. c_M and c_m are the maximum and the minimum concentrations at time t, respectively.

$$\delta_i = \frac{c_M - c_m}{c_M^0 - c_m^0} = \frac{\Delta c}{\Delta c^0} \quad (1)$$

Mechanical properties

Solution heat treated single crystal PWA 1483 slabs (140 x 100 x 20 mm^3) were used for the determination of the mechanical properties. After casting a standard heat treatment was applied to remove the γ/γ' eutectic that is known to have an important effect on fatigue strength [6]. In this way we made sure that the microstructural condition investigated is representative of standard gas turbine blades in service. Laue orientation measurements were employed to determine the [001] direction of the slabs. Testing in the high cycle fatigue regime at elevated temperature was conducted using a resonance testing machine (Roell Amsler 2 HFP 421) exciting the sample with an electromagnet.

Experimental Results

Microstructure

Primary dendrite arm spacing

Optical microscopy pictures are presented in Figure 2 representing the two different microstructures obtained by changing the casting setup from radiation cooling (HRS) to conduction cooling (LMC). In the HRS case dendrite crosses can be identified due to cutting perpendicular to the primary dendrite trunk. Large secondary dendrite arms originating from the middle of the crosses are also visible. Furthermore well developed tertiary arms grown from the secondary arms are observed. The LMC microstructure shows dendrite crosses but they are standing closer together with secondary arms attached. In contrast to the coarse HRS microstructure nearly no tertiary arms are found.

To obtain a first impression of the solidification conditions the primary dendrite arm spacing λ_1 was analysed. The dendrite arm spacing for the HRS process is 600 μm whereas for the LMC process a dendrite arm spacing of 400 μm is found at a withdrawal rate of v=3.5 mm/min.

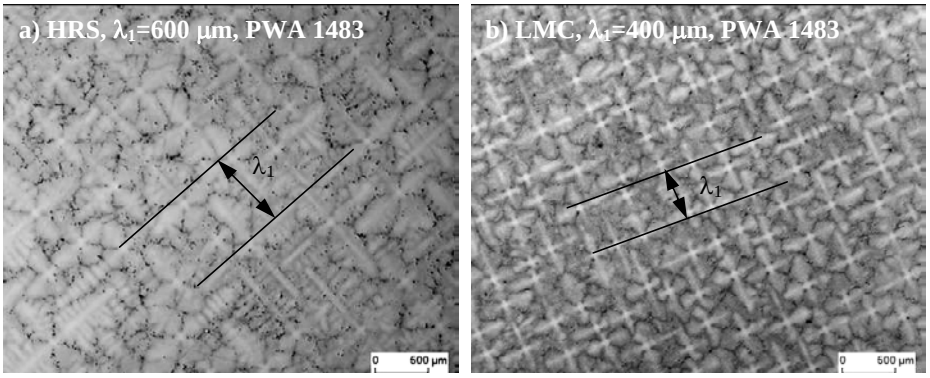

Figure 2: Optical microscopy pictures of the two different sample materials after solution heat treatment. Dendrite crosses appear in both pictures with different spacing. Figure 2 a): HRS microstructure with well developed secondary and tertiary dendrite arms. Figure 2 b): LMC microstructure with secondary and no or less pronounced tertiary dendrite arms.

Porosity

The microporosity content and size was determined by light optical microscopy on a sufficient number of polished samples. The results for solution heat treated PWA 1483 are shown in Figure 3. The upper diagram shows the overall microporosity content over the primary dendrite arm spacing for the two investigated microstructures. For the Bridgman casting technique (mean value λ_1 = 600 µm) a mean microporosity content of 0.28 percent is observed. For the liquid metal cooling technique (mean value λ_1 = 400 µm) the microporosity content is determined to be about 0.15 percent. Furthermore the standard deviation of the microporosity is smaller when using LMC casting conditions. In the lower diagram of Figure 3 the microporosity size distribution is plotted. The number of pores per measured area is shown over the pore size classes ranging from 100 µm^2 to sizes greater than 1000 µm^2. It can be seen that for the large dendrite arm spacing in HRS an increased number of pores is found for all pore classes. The difference is particularly notable in the largest pore size class (pore sizes greater than 1000 µm^2). The samples produced by liquid metal cooling show a smaller number of pores for all sizes. It is also important to notice that there is a reduced number of large pore sizes.

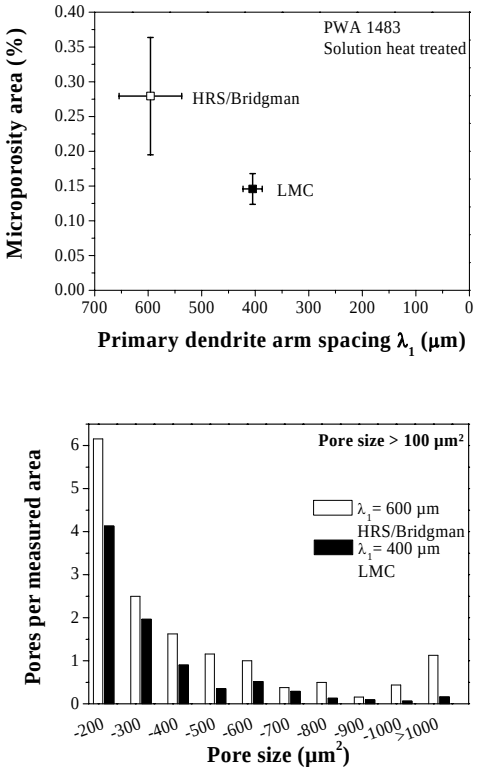

Figure 3: Microporosity content (area percent) over the dendrite arm spacing and number of pores over pore size classes. LMC gives reduced overall porosity, smaller and fewer pores than the HRS casting setup.

Carbides

As carbides may also play a dominant role in the high-cycle fatigue fracture behaviour their content and size is analysed. The carbides are found in the interdendritic region of the samples. From the two dimensional cuts it seems that the carbides are not interconnected and do not form any kind of carbide network. Also no sharp edges which may act as stress raisers are observed. The overall carbide content is about 0.55 percent for the examined samples. The mean carbide size is shown in Figure 4 for the two employed solidification conditions. A slight decrease of the mean carbide size from 7.7 μm^2 to 6.4 μm^2 in the LMC microstructure is found. The scatter of the results of the carbide content and size is nearly the same if the two solidification processes are compared.

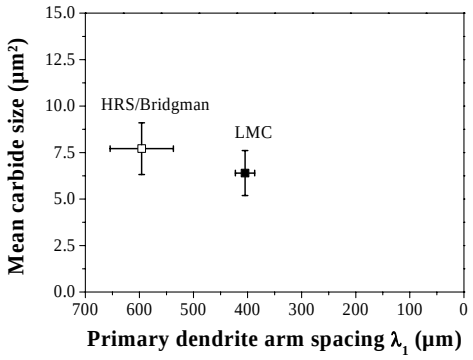

Figure 4: Carbide size for the two casting setups. The carbide content remains constant for different thermal conditions at 0.55 percent. But the carbide size is sensitive to the heat extraction method.

Fatigue properties

One main purpose of this study was the determination of the high cycle fatigue properties for microstructures typically found in large industrial gas turbine blade castings at completely reversed stresses (stress ratio R = minimum stress/maximum stress = -1). The results of the high cycle fatigue testing at elevated temperature T = 800°C are presented in Figure 5. Therefore the applied stress amplitude is plotted over the number of cycles to failure for the two examined solidification conditions labelled as HRS and LMC. The applied stress amplitudes range from 340 to 500 MPa. The two examined microstructures show remarkable differences in their fatigue behaviour. For example at a stress amplitude of 400 MPa the HRS microstructure sustains $1x10^5$ cycles until failure whereas the LMC microstructure has a fatigue life of $2x10^6$ cycles. Averaged over the whole stress range an enhancement of fatigue life of one order of magnitude for the microstructure obtained by the liquid metal cooling solidification condition is found. In terms of stresses, the fatigue limit is found to be 20 % higher approximately.

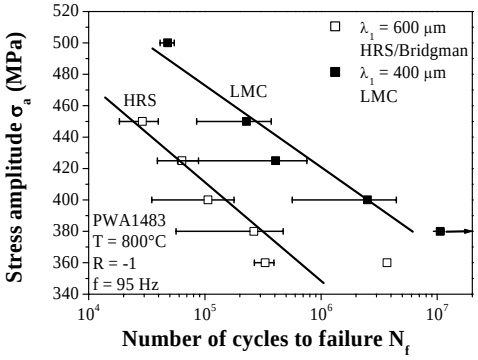

Figure 5: Fatigue life dependence of the two microstructures for different applied stress amplitudes in the high cycle fatigue regime. The finer microstructure produced by liquid metal cooling shows a by approximately one magnitude improved fatigue life.

Fracture behaviour

The fracture surface is inclined by approximately 45° to the sample [001] direction. The fractured surface and the facets associated with fracture are shown in Figure 6. A SEM picture of the whole fracture surface and a magnified insert of the origin of failure are presented. The origin of failure is found to be porosity with very few exceptions, perhaps caused by unsuitable sample preparation. The fatigue life determining casting pore is surrounded by a

smooth fracture initiation zone. The next zone attached is the transition zone which shows some broken carbides. Its appearance is rougher than the fracture initiation zone. Finally, in most cases, the overload fracture zone follows. The appearance of this zone is rough and similar to the one found after static tensile testing.

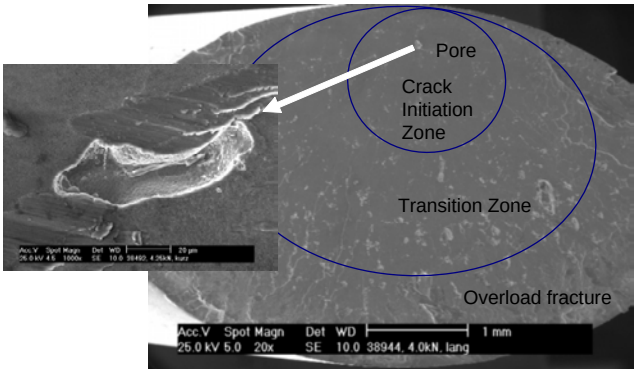

Figure 6: Fracture surface in the SEM. Fracture is initiated at a casting micro pore (see magnified picture). The pore is surrounded by a flat fracture initiation zone. A transition zone follows which passes over to the rough overload fracture zone.

Possible fracture sites

It was shown before that the fatigue life is improved comparing the liquid metal cooling technique with the HRS/Bridgman technique and that fracture originates from pores. Now the question arises what is the reason for this. In Fig. 7 the size of the potential fracture relevant microstructural features is plotted for the two casting setups. The equivalent radius is calculated by assuming a circular defect area in the cross section. It is obvious from the diagram that pores are indeed the largest defects present in our case. The pores found to initiate the fracture observed on the fracture surface by SEM were found to be larger than the largest pore observed with light optical microscopy (OM). This shows that fatigue is more efficient to detect the largest pore in the sample than metallography with its very limited volume of material investigated.

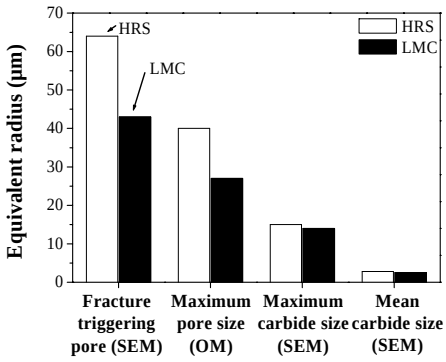

Figure 7: Size comparison for possible fracture initiation sites. Casting pores are the largest microstructural defect present. Therefore it is concluded that micropores determine the fatigue life of the samples in this study.

Change of microstructure during heat treatment

As shown above, porosity plays a defining role in high cycle fatigue. In order to understand the origins of casting porosity better, the change of the microstructure during heat treatment was investigated. Unfortunately, for this set of experiments a different set of samples made from a different alloy had to be used. The as-cast microstructure of CMSX-4 in this case shows again a dendritic pattern with eutectic islands separating the dendrites when cutting perpendicular to [001]. Microporosity is observed in the space between the dendrites. The mean primary dendrite arm spacing was determined to be λ_1 = 470 µm for the HRS setup and λ_1 = 345 µm for the LMC setup.

Porosity growth

The area fraction and size of micropores for various heat treatment periods at 1315°C of CMSX-4 samples is presented in Figure 8 a) and b). With increasing time at homogenization temperature the microporosity increases. The major increase is seen up to eight hours of homogenization. At longer times the slope of the microporosity increase flattens. The porosity

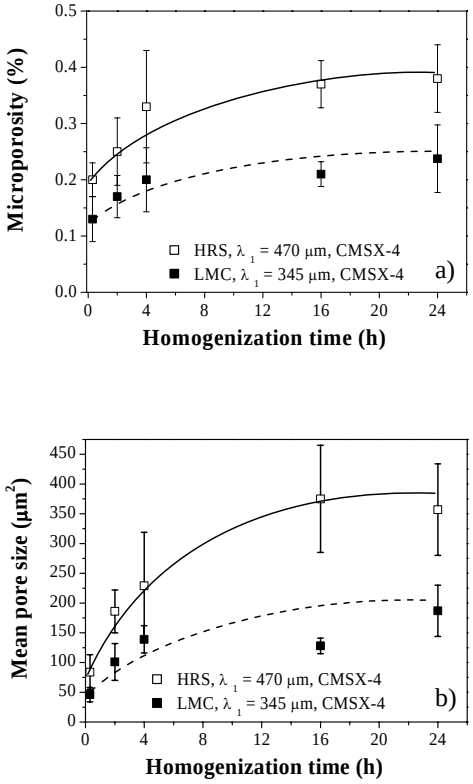

Figure 8: Overall microporosity content (area percent) and mean pore size for different homogenization times at 1315°C. The LMC samples show less microporosity and smaller pore sizes at all homogenization times.

for the LMC microstructure is significantly reduced compared with the HRS microstructure. The difference between the two microstructures remains for all homogenization times.

Change of elemental segregation

Figure 9 shows the residual segregation index δ for various homogenization times at 1315°C heat treatment temperature. The results for the LMC and HRS microstructure with special emphasis on rhenium Re and tungsten W are plotted. In the as-cast condition the residual segregation index δ is 1. For complete homogenization it drops to 0. The largest change in residual segregation is observed at short homogenization times. After long homogenization heat treatment the segregation index changes only slightly. It is observed that the homogenization of W occurs more readily than for Re. But there is also a difference between the two different casting setups. The LMC microstructure with a primary dendrite arm spacing of λ_1 = 345 μm shows a better homogenization than the HRS case being characterized by a dendrite arm spacing of λ_1 = 470 μm.

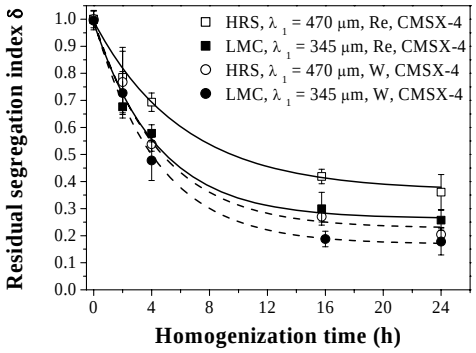

Figure 9: Residual segregation index δ for different homogenization times. For the chosen elements W and Re the refined microstructure produced by the liquid metal cooling technique shows a better homogenization as the coarse Bridgman microstructure.

Discussion

Porosity in the as-cast condition

The microporosity found in vacuum casting is generated due to the volume decrease during solidification (shrinkage porosity). During mushy zone freezing liquid pools are trapped in the space between already solidified dendrites. Furthermore these pools may be more or less isolated from the feeding of the remaining liquid. Due to solidification contraction and hindered feeding a pressure drop occurs which finally leads to porosity nucleation and growth. The extent of microporosity is directly related to the solidification parameters like dendrite arm spacing or development of secondary and tertiary dendrite arms, temperature gradient and solidification velocity which is coupled with the withdrawal rate [7, 8]. The dendrite morphology influences the feeding where smooth dendrite morphologies (no tertiary arms) favour low microporosity content. The lower microporosity content of the LMC microstructure is explained in the following way. The smaller dendrite arm spacing and the less pronounced appearance of tertiary dendrite arms lead to an increased feeding in the mushy zone. Furthermore a large temperature gradient helps feeding by reducing the mushy zone length. As the withdrawal rate was kept constant in the present case there should be no

influence of the solidification velocity at the end of the solidification on the microporosity content.

Porosity growth during annealing

An important result of the heat treatment experiments is that porosity increases during annealing, both in the HRS and LMC microstructures. A study [9] on porosity growth during heat treatment suggests four pore growth mechanisms. At first there may be coalescence of dissolved gas, secondly pores formed by carbon reaction products. These two mechanisms can be excluded here due to vacuum casting conditions and the absence of carbon in CMSX-4. Furthermore vacancy formation by the molar volume difference of the constituent phases γ and γ' and vacancy creation within the crystal through a diffusional mechanism (Kirkendall effect) are mentioned. Diffusional porosity growth is due to asymmetric diffusion fluxes mainly caused by the asymmetric distribution of the slow diffusing elements Re and W between dendrite core, interdendritic area and eutectic. It is believed that the last mechanism generates vacancies in our case. The microporosity content increases in the two used microstructures by a factor of 2. This increase in microporosity content is observed in LMC and HRS microstructures. LMC conditions show that low initial microporosity content is beneficial for a reduced extent of microporosity after homogenization treatment. With the content increase also a size increase is observed. The LMC microstructure shows a smaller pore size at all homogenization times leading to improved fatigue properties as discussed below.

Advantages of the LMC casting process

The fatigue life determining microstructural feature is the casting microporosity in this study. The carbides present are too small to cause fracture in the studied range of dendrite arm spacing or thermal gradients acting. The fatigue life diagram together with the analysis of the possible fracture sites shows clearly that the smaller pore size found in LMC castings leads to an enhancement of fatigue life of one order of magnitude. One might argue that hot isostatic pressing could be employed to close casting porosity and improve fatigue strength. It should be remembered though that HIP is not straightforward in a single crystal because of recrystallisation.

Another advantage of the finer microstructure in LMC castings is seen in an improved homogenization especially for the slow diffusing alloy constituents W and Re. This leads to more homogeneous properties of the heat treated microstructure. Furthermore heat treatment time can be shortened which is an enormous economic effect with respect to heat treatment times up to 24 h for modern superalloys. The reason for the more homogeneous microstructure or reduced heat treatment time respectively is seen in the shorter diffusion distance between the dendrites.

Other advantages of the LMC technique that have been pointed out earlier include the shorter cycle time due to the potential for higher withdrawal rate and larger clusters.

Acknowledgements

The author gratefully acknowledges the financial and sample support from Doncasters Precision Castings, Bochum. Also we like to thank the German Federal Ministry for Education and Research (Grant Nr. 03N2021) for financial support.

References

[1] R.F. Singer, Advanced Materials and Processes for land-based Gas Turbines, In: Materials for advanced power engineering, Part II, edited by D. Coutsouradis et al., 1994, pp. 1707-1729

[2] A. Lohmueller, W. Eßer, J. Großmann, M. Hoerdler, J. Preuhs, R.F. Singer, Improved Quality and Economics of Investment Castings by Liquid Metal Cooling – The Selection of Cooling Media, Superalloys 2000, edited by T.M. Pollock et al., 2000, pp. 181-187

[3] A.F. Giamei, J.G. Tschinkel, Liquid Metal Cooling: A New Solidification Technique, Metallurgical Transactions A, Volume 7A, 1976, pp. 1427-1434

[4] R. Bürgel, Handbuch Hochtemperaturwerkstoffe, 1998, p. 526

[5] M.C. Flemings, Solidification Processing, 1978, p. 328

[6] P. Caron, T. Khan, Evolution of Ni-based superalloys for single crystal gas turbine applications, Aerospace Science and Technology, Vol. 3, 1999, pp. 513-523

[7] J. Lecomte-Beckers, Study of Microporosity Formation in Nickel-Base Superalloys, Metallurgical Transactions A, Vol. 19A, 1988, pp. 2341-2348

[8] J. Lecomte-Beckers, Relations between Chemistry, Soldification Behaviour, Microstructure and Microporosity in Nickel-Base Superalloys, Superalloys 1988, edited by D.N. Duhl et al., 1988, pp. 371-721

[9] D.L. Anton, A.F. Giamei, Porosity Distribution and Growth During Homogenization in Single Crystals of a Nickel-base Superalloy, Materials Science and Engineering, Volume 76, 1985, pp. 173-180

PREDICTION OF THERMAL MECHANICAL FATIGUE PROPERTIES OF NI-BASE SINGLE CRYSTAL SUPERALLOYS

Hirofumi Ohata[1、2], Tadaharu Yokokawa[2],Toshiharu Kobayashi[2],
Yoshikazu Ro[2] and Hiroshi Harada[2]

[1] Kiguchi Technics Corporation, Shimane 692-0057
[2]High Temperature Materials Group, Materials Engineering Laboratory,
National Institute for Materials Science, Tsukuba, 305-0047

Abstract

Thermal mechanical fatigue (TMF) of a number of nickel-base single crystal superalloys has been studied in an effort to assess the factors which affect TMF life. Based on the experimental data, multiple regression analysis has been performed for the correlation between the number of TMF cycles to failure and the alloy compositions. The multiple correlation coefficient is found to be R=0.84, indicating that the alloy composition has a close relationship with the number of TMF cycles to failure. Especially the addition of Co, Ru and Al can effectively improve the TMF properties. In addition, the TMF life is also related to the high temperature mechanical property and microstructural parameters.

Keywords: nickel-base single crystal superalloys, thermal mechanical fatigue, regression analysis, alloy composition, mechanical properties, microstructural parameter

1. Introduction

Nickel-base single crystal superalloys are widely used for turbine blades of aircraft engines and stationary gas turbines with increased temperature for higher thermal efficiency. In the case of turbine blade of gas turbine for power generation, external surface temperature is about 900℃ at the time of operation, and the inside is about 600℃ by cooling. At the time of a pause, the temperature of the whole blade drops to about 400℃. The big temperature difference due to alternate operation and pause will cause thermal mechanical fatigue (TMF).

The strength evaluation of Ni-base single crystal superalloys has mainly been performed by creep test. In fact, the TMF properties are also very important for practical application. However, TMF evaluation of nickel base single crystal superalloys was seldom done systematically [1)]. So far the factors, which may influence TMF properties, have not been clarified.

In this paper, two kinds of multiple regression analysis are carried out on the basis of TMF test. One kind is done for the correlation between TMF and alloy composition. The other is tried to understand the effect of microstructural parameters and mechanical properties.

2. Experimental

The alloys were designed and cast at National Institute for Materials Science (NIMS, Japan). A total of 28 kinds of the Ni-base single crystal superalloys were tested and their range of composition is listed in **Table 1**.

Table.1 Range of chemical compositions in this study (mass%,Ni-bal.)

Co	Cr	Mo	W	Al	Ti
0~16.5	2~10	0~2.8	4~12.9	3.7~6.2	0~4.2

Nb	Ta	Hf	Re	Ru	Ir
0~0.5	4~12	0~0.2	0~6.9	0~6	0~9.1

After cast, heat treatments including solution treatment and aging were performed for all the alloys. Cylindrical specimens as shown in Figure 1 were machined from single crystal bars in [001] orientation. TMF testing was carried out on a hydraulic-servo system fatigue machine (MTS type 810) with a capacity of ±50 kN. The test piece was heated by the high frequency heating method. The temperature range is from 400 to 900℃ and the strain range is ±0.64%. The frequency is 66 min/cycle. The load was applied in the out of phase mode to simulate the practical working condition of gas turbines for power generation.

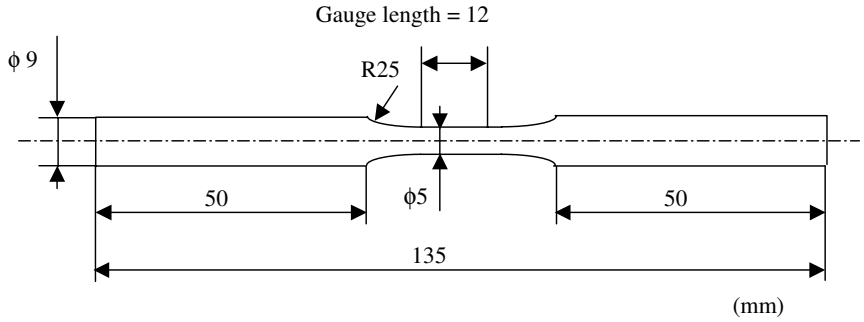

Fig.1 Schematic diagram of TMF specimen.

Figure 2 shows typical stress-strain hysteresis loop of the TMF test. Stress relaxation happens during hold time (1 hour) in compression. The amount of the stress relaxation in the first cycle was assumed to be σ_R. Moreover, work hardening happens during the tension. The difference (ultimate tensile strength (UTS)－0.2% proof stress) was assumed to characterize a work hardening tendency in this study. And the work hardening tendency (UTS－0.2% proof stress) was used for multiple regression analysis. The UTS and 0.2% proof stress were obtained from high temperature tensile test (Figure 3) at 400℃ with a strain rate of 0.3%/min (5x10-5s^{-1}).

Two kinds of multiple linear regression analysis were carried out to investigate the effect of chemical composition, microstructural parameters, and mechanical properties. Lattice misfit (%), volume fraction of γ' phase and stacking fault energy (SFE)(J/m^2) were employed as the microstructural parameters. For the mechanical properties, the ultimate tensile strength (UTS)

and 0.2% proof stress (MPa) were used. The formula in the reference [2] was utilized for calculation of SFE as follows.

$$\text{SFE}\quad (\Gamma/Gb\times10^{3})=12.914-0.224X_{Cr}-0.356X_{Mo}-0.0826X_{Fe}-0.271X_{Nb}$$
$$-0.822X_{Ti}-0.238X_{Al}-0.113X_{Co}-0.720X_{W}-0.271X_{Ta}.$$

where, X_i is the i element concentration in an alloy.

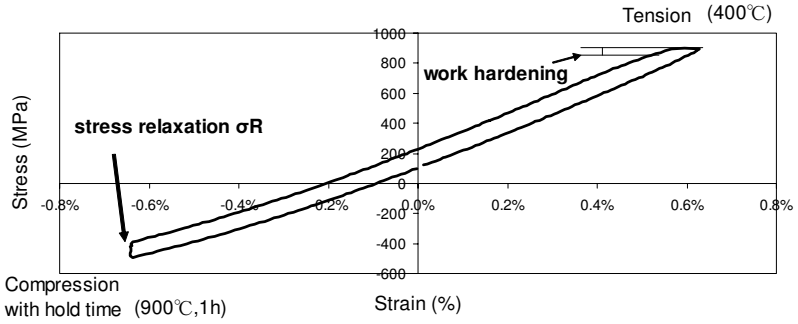

Fig.2 Typical stress-mechanical strain hysteresis loop.

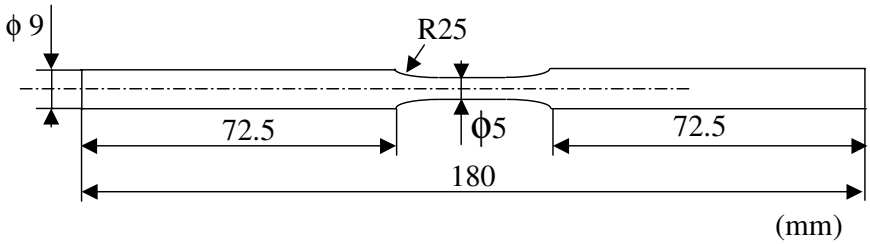

Fig.3 Schematic diagram of tensile test specimen.

3. Results and discussions

Multiple regression analysis by alloy composition

The multiple regression analysis is first carried out by alloy. The regression equation is shown below:

$$\log(Nf) = a_0 + \sum_i a_i X_i \qquad (1)$$

Where, X_i is i element concentration in an alloy composition. a_i is the regression coefficient.

The coefficient and error probability of each element in regression equation (1) are shown in Table 2. The multiple correlation coefficient is R= 0.84. The scatter chart of TMF life (Nf) tested and calculated by regression equation (1) is shown in Figure 4. The experimental

values are distributed along a regression line. Therefore, the prediction of the regression equation is considerably accurate. It is suggested that addition of Co, Ru, and Al increase the number of TMF cycles to failure from the sign (+/-) of the coefficient and the error probability in Table 2.The element Co is effective in promoting miniaturization of γ/γ′ microstructure. [3)]

Table 2 Coefficients of the regression equation (1) explained by the alloy compositions. multiple correlation coefficient R=0.84

	Term of constant	Co	Ru	Al	Re	Ti	Mo
coefficient	-0.338	0.045	0.147	0.506	-0.165	0.108	0.057
Probability of error (%)	5	5	5	5	20	50	60
	W	Cr	Ta	Nb	Hf	Ir	
Coefficient	-0.013	-0.013	-0.011	-0.157	-2.581	0.061	
Probability of error (%)	80	90	90	50	5	20	

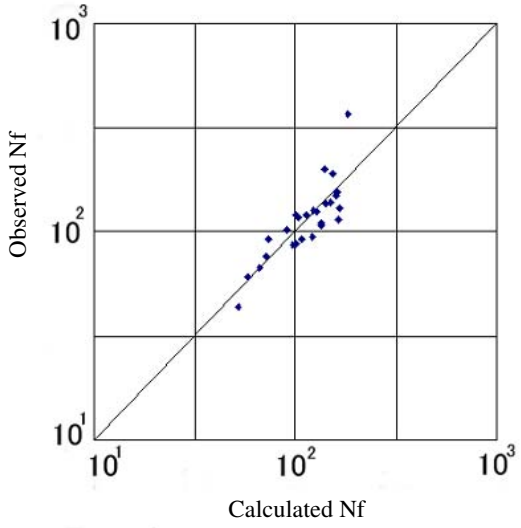

Fig.4 Relationship between observed and calculated number of cycles to failure (Nf). Calculated values were obtained by the regression equation (1).

So the dislocations accompanying modification during TMF test can be controlled in some degree. Al is one of the alloying elements in γ′ and its addition can increase the volume

fraction of γ′ phase, which is harder than γ phase. As to the addition of Ru, it maybe lower stacking fault energy of the alloys. Formation of stacking faults will prevent the motion of dislocations. Thus work hardening is promoted.

On the other hand, both Hf and Ir have error probability as low as 5% and 20%, respectively. The two elements seem to have an influence on TMF life. However, the composition range of Hf is very narrow (0～0.2mass%). Therefore, it is difficult to evaluate the influence of Hf on TMF life at this stage. Since one alloy of the total 28 contains Ir, its effect on TMF life in the alloy cannot be judged.

Multiple regression analysis by microstructural parameter and mechanical properties

The multiple regression analysis shows that the microstructural parameters and mechanical properties also bear a relationship with TMF life. The regression equation is produced as follows:

$$\log(Nf) = b_0 + \sum_i b_i (Vf, SFE, Misfit, UTS - 0.2, \sigma_R, 0.2\%proof, R.A) \qquad (2)$$

Where, b_i is the regression coefficient.

Table 3 Coefficients of the regression equation (2) explained by the mechanical and microstructural properties.

multiple correlation coefficient R=0.62

	Term of constant	Vf	SFE (J/m^2) ×10^{-1}	Misfit (%)
Coefficient	0.859	1.622	-0.532	0.194
Probability of error (%)	40	10	40	80
	UTS-0.2 (MPa) ×10^{-2}	σ_R (MPa)	0.2%proof (MPa) ×10^{-4}	Reduction in area (%)
Coefficient	0.072	-0.435	3.673	0.009
Probability of error (%)	30	80	70	40

The coefficient and error probability of each microstructural parameters and mechanical properties in regression equation (2) are shown in **Table 3**. The scatter chart of TMF life (Nf) tested and calculated by regression equation (2) is shown in Figure 5. The multiple correlation

coefficient is R= 0.62, which marks the effect of the considered factors on TMF life. From Table 3, the volume fraction of γ′, the stacking fault energy and the work hardening tendency are related to the TMF life. An increase of the γ′ volume fraction can raise the number of TMF cycles to failure. If the stacking fault energy is small, the number of TMF cycles to failure will increase. This result is consistent with the above analysis based on chemical compositions. Increase of the volume fraction of γ′ is directly concerned with the aluminum addition. On the other hand, it is reported that addition of Co and Ru is effective in lowering stacking-fault energy. [4)5)] If stacking-fault energy is small, it will become easy for the dislocations to extend accompanying modification. When a dislocation becomes an extended one, its existence increases the resistance for a gliding dislocation to intersect with it. Therefore, work hardening takes place to an alloy and the number of TMF cycles to failure increases. Considering the mechanical property factor, the TMF life can be improved if work hardening tendency is strong.

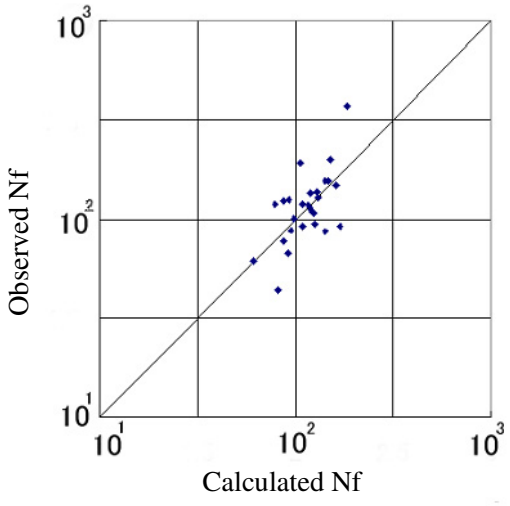

Fig.5 Relationship between observed and calculated number of failure Nf .
Calculated values were obtained by the regression equation (2).

4. Summary

The TMF test has been done for a number of Ni-base single crystal superalloys. The influence on the TMF life of several factors, such as chemical composition, mechanical property and microstructural parameter, is examined on the basis of multiple regression analysis. The following conclusions can be drawn in the present study.

1) The prediction of TMF life can be made accurately only based on the alloy composition.
2) Of all the alloying elements in superalloys, Al, Co and Ru can increases the TMF life effectively.

3) The microstructural parameter (stacking fault energy or volume fraction of γ′) and mechanical property (UTS or 0.2% roof stress) have a close relationship with the TMF life of superalloys.

Acknowledgements
Authors acknowledge greatly Dr.J.XZang, Dr. J.Fujioka and Mr.A.Sato at NIMS, for their participation in helpful discussion.

References

1) Y.Ro, H.Zhou, Y.Koizumi, T.Yokokawa, T.Kobayashi, H.Harada and I.Okada: Mater. Trans. **45** (2004) pp.396-398.
2) H.Harada and M.Yamazaki: Tetsu-to-Hagane **65**,7 (1979) pp.1059-1068.
3) M.V.Nathal and L.J.Ebert: Superalloys (1984) pp.125-133.
4) G.E.Maurer, L.A.Jackman and J.A.Domingue: Superalloys (1980) pp.43-52.
5) J.X.Zhang, H.Harada, Y.Ro, Y.Koizumi and T.Kobayashi: Collected Abstracts of the 2005 Autumn Meeting of The Japan Institute of Metals p.173.

DEVELOPMENT OF A HIGH STRENGTH NI-BASED SUPERALLOY FOR CONVENTIONAL CASTINGS

Hideki Tamaki, Akira Yoshinari and Hiroyuki Doi

Hitachi Research Lab., Hitachi, Ltd., MD#840 7-1-1 Omika, Hitachi, Ibaraki, 319-1292, Japan (hidekit@hrl.hitachi.co.jp)

Abstract

In this paper, a new Ni-based superalloy for conventional castings (CCs) is proposed as one of contribution to increase efficiency of turbomachineries such as gas turbines and microturbines. When developing a high strength Ni-based superalloy for CCs, it has been a challenging task to increase its creep, tensile and fatigue strength without decreasing its ductility. Experimental alloys were designed based on a single crystal superalloy YH61 which contains some grain boundary strengthening elements to increase tolerance for grain defects. Increases in W/W+Ta ratio and Co,C and Hf contents from YH61 base were found to increase high temperature strength with a minimum of decrease in ductility. The developed alloy (YH101) realized 20 °C higher temperature capability (137MPa-10^5h) than Mar-M247LC which is one of the highest strength commercial Ni-based superalloys for CCs. Oxidation resistance of the alloy was comparable to Mar-M247LC while hot corrosion resistance of the alloy was higher than that of a 14% Cr containing blade alloy.

Keywords: Superalloy, Conventional Casting (CC), Directionally solidified (DS), YH61

1. Introuction

After electricity deregulation, distributed power generation systems such as microturbines have been paid attention as efficient, reliable, clean and easy-to-use power generation systems. However, their lower efficiencies and higher costs than those expected have prevented their markets from spreading rapidly. In this study, as one of contribution to increase efficiency of turbomachineries such as gas turbines and microturbines, a high strength Ni-based superalloy for conventional castings (CCs) has been developed. In the case of under about 200kW turbines, centrifugal-type wheels are commonly used for their turbine wheels. Because the latest directionally solidified (DS) or single crystal (SC) castings are not easily introduced to centrifugal-type wheels due to their shape, a high strength Ni-based superalloy for CCs has been required to increase firing temperatures of microturbines. Meanwhile in axial gas turbines, a higher strength CC alloy has been demanded for their rear stages' blades to decrease casting cost by replacing conventional DS blades. CM681LC [1], which contains about 3% Re, has been developed as a higher strength superalloy for CCs. However, lower contents of expensive elements such as Re would be favourable for microturbine's wheel materials because (a) non-Rhenium containing superalloys, such as alloy713LC [2] or Mar-M247 [3], are still mainstream alloys for microturbines and (b) microturbines have been subjected to sever price competition against other power generation systems such as gas engines. In the case of the rear stages' blades of axial gas turbines, lower Re content would also be preferable unless strength is significantly decreased. YH61 [4] shows high temperature strength equivalent to the second-generation SC superalloys (Re=3%) while YH61 contains

only 1.5% Re. As shown in Figure 1, around 1.5% Re can be considered as the most effective region to achieve higher strength with a lower Re content, which means a lower cost. Therefore, the goal was determined to provide a lower cost material for microturbine wheels than the second-generation CC alloys and lower cost and higher strength blades for the rear stages' blades of axial gas turbines than DS castings of the first-generation alloys even though a master ingot price of the alloy would be higher than that of the first-generation alloys.

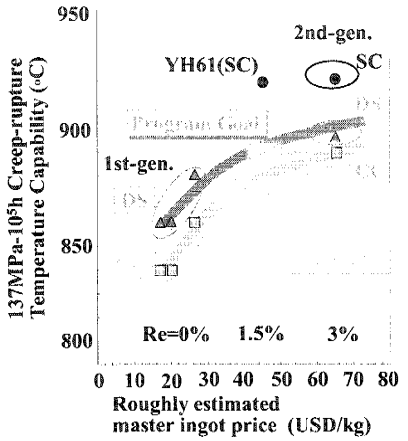

Fig. 1 Relationship between master ingot price and creep-rupture strength for CC and DS superalloys

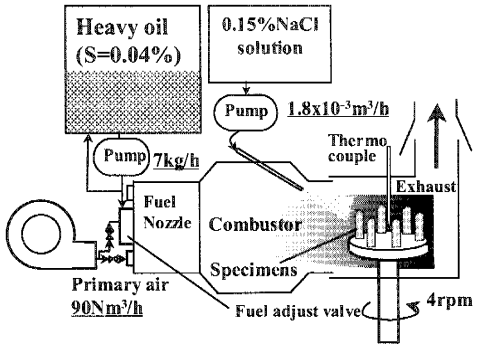

Fig. 2 A schematic view of the burner rig test apparatus

2. Experimental

In the preliminary examination, DS castings were used for investigating effects of Hf and Co contents and W/W+Ta ratio on some important properties for Ni-based superalloys. Although it was result of cooperation with another DS alloy development program, it also help to minimize effects of casting defects on strength of the alloys without HIP (Hot Isostatic Pressing). In the examination, DS-L (DS longitudinal direction) strength was considered as substitute for the grain strength of CCs and DS-T (DS transverse direction) strength was considered as that for the grain boundary strength of CCs. Finally, Hf and carbon contents were optimised by using CCs because their essential effects on grain boundary strength of CCs should not be evaluated by DS-T strength precisely.

All experimental CC specimens were HIPed at 1205°C, 147.5MPa for 4 hours. All experimental specimens including CC specimens after HIP as well as as-cast DS specimens were solution-heat-treated at 1220-1260°C for 4-6 hours and then gas-flow-quenched. The aging condition for all specimens was 1080°C / 4hours / air cool followed by 871°C / 20hours / air cool. Creep tests were carried out based on ASTM E 139. Hot corrosion resistance of the alloys was evaluated by a burner rig test. Figure 2 shows a schematic view of the burner rig test apparatus used in this study. The fuels used were heavy oil which contained about 0.04% sulfur. 0.15 mass% NaCl solutions were sprayed into the combustion gases at the rate of $1.8 \times 10^{-3} m^3/h$. The test temperature was monitored at the centre of the specimen holder. A single test

cycle was 10 hours and the weight change of the specimens was measured after either one or two cycles. Before each measurement, the specimens were washed by hot water to remove combustion products other than the scale.

3. Results and discussion

3.1 Effects of Hafnium and Cobalt on high temperature strength

First of all, creep strength of CC YH61 was evaluated. As shown in Figure 3, creep-rupture life of CC YH61 was significantly inferior to that of Mar-M247LC and the two creep curves indicate that lower rupture ductility, which could be caused by lower grain boundary strength, brought about lower creep-rupture life of CC YH61. It can be concluded from the above result that amount of grain boundary strengthening elements of YH61 is insufficient for a CC use of YH61 while it is actually sufficient to allow larger tolerance of grain defects in SC castings than that allowed for conventional SC alloys.

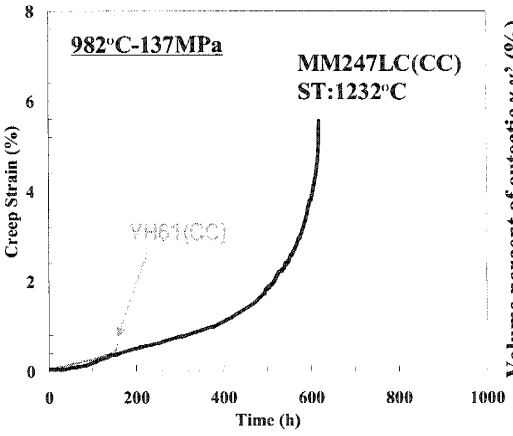

Fig. 3 A creep curve for YH61 (CC) compared with that for Mar-M247LC(CC)

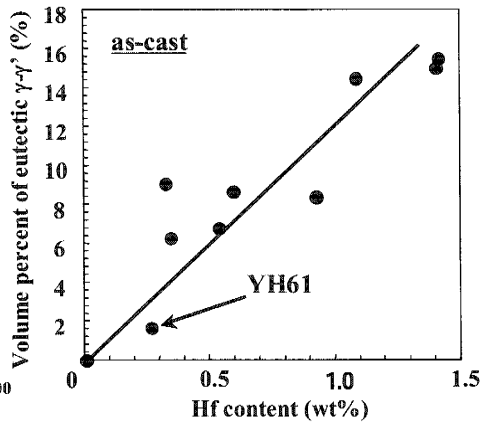

Fig. 4 Relationship between Hf content and volume percent of eutectic γ-γ' phases

Increase in Hf content from YH61 base (Ni-7Cr-5Al-8.8W-8.9Ta-0.8Mo-0.8Nb-1.4Re-1Co-0.25Hf-0.07C-0.02B, wt%) was examined to increase grain boundary strength of YH61. As shown in Figure 4, Hf is expected to increase amount of eutectic γ-γ' phases which causes increasing of grain boundaries surrounded with non-solutioned γ' phases during solution heat treatment. These grain boundaries can be considered to show higher grain boundary strength because of their waving shape and higher boron content after solution heat treatment [5]. Grain boundaries, surrounded with solutioned γ' phases, which could move during solution heat treatment, can be thought to show lower grain boundary strength because of their linear shape and lower boron content after solution heat treatment [5]. Figure 5 represents effect of Hf content on grain boundary morphology of Ni-based cast superalloys after solution heat treatment.

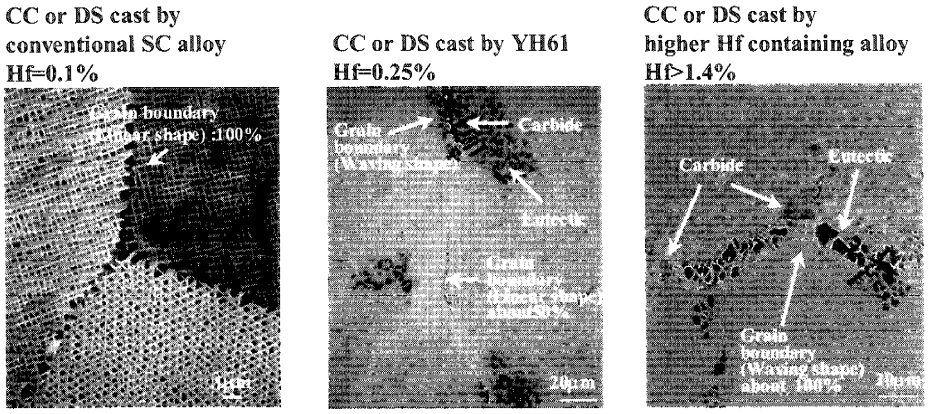

Fig. 5 Effect of Hf content on grain boundary morphology of Ni-based cast superalloys after solution heat treatment

Table 1 Co and Hf contents for YH61 modified alloys (wt%)

No.		Co	Hf
YH61	base	1.00	0.25
YH62	YH61-5Co	4.72	0.25
YH63	YH61-10Co	9.48	0.25
YH64	YH61-10Co-1Hf	9.48	1.03
YH65	YH61-10Co-1.5Hf	9.48	1.55
YH66	YH61-10Co-2Hf	9.48	2.07

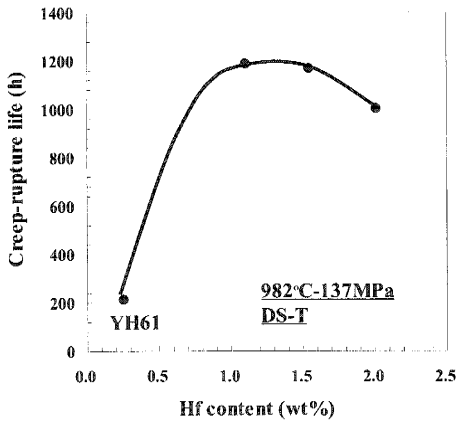

Fig. 6 Effect of Hf content on creep-rupture life of DS-T

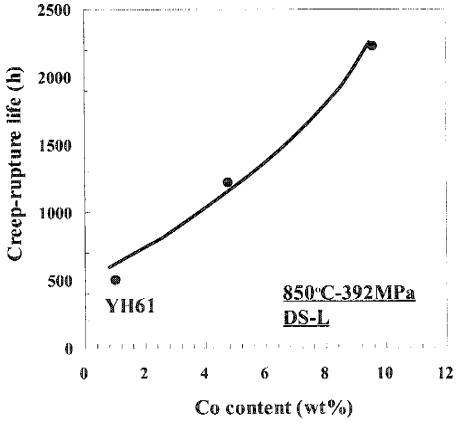

Fig. 7 Effect of Co content on creep-rupture life of DS-L

Table 1 shows Co and Hf contents for YH61 modified alloys. In these alloys, Ni was replaced by Co and Hf. Higher Hf content tends to decrease region where γ' phases were completely solutioned into a γ phase during solution heat treatment. Increase in volume percent of the region (volume percent of solutioned γ') is know to improve high temperature strength of cast superalloys [4], therefore, higher Co content than YH61 was examined to compensate for decreasing of the volume percent due to increasing of Hf. Co is expected to increase the volume percent without increasing solution heat treatment temperature.

Figure 6 shows effect of Hf content on creep-rupture life of DS-T or grain boundary strength. Increase in Hf content significantly improved grain boundary strength. As mentioned above, increase in volume percent of γ-γ' eutectic phases can be considered to cause this improvement. Figure 7 shows effect of Co content on DS-L creep-rupture life. Increase in Co content improved creep-rupture life of DS-L. Figure 8 shows that higher Co content also realizes higher volume percent of solutioned γ'. This higher volume percent can be thought to cause longer creep-rupture life of DS-L for the higher Co alloys.

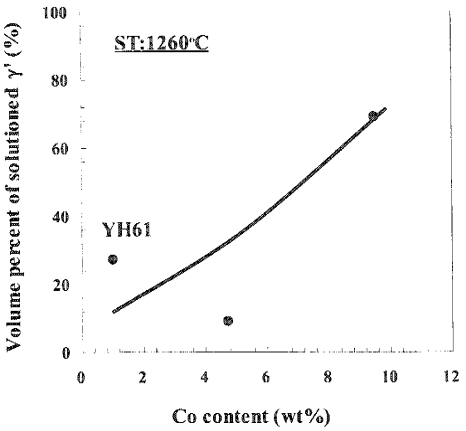

Fig. 8 Effect of Co content on volume percent of solutioned γ'

3.2 Effects of Tungsten and Tantalum on high temperature strength

From the above results, effects of W and Ta on high temperature strength of DS castings were examined by using experimental alloys based on YH65 (Tabale 2). In these alloys, W/W+Ta atomic percentage ratio was varied with keeping amount of W and Ta by atomic percentage 5.1at%, which is decreased from YH61 (6.1at%) to compensate increase in Hf content.

Table 2 Tungsten and Ta contents for the experimental alloys (wt%)

No.	W/W+Ta at% ratio	W	Ta
YH61	0.49	8.80	8.90
YH65	0.54	8.15	6.95
YH71	0.42	6.25	8.55
YH72	0.65	9.90	5.32
YH73	0.75	11.48	3.72

Figure 9 shows creep-curves of experimental alloys for DS-L. Figures 10 and 11 describe relationship between W/W+Ta atomic percentage ratio and creep-rupture life for DS-L and DS-T, respectively. Creep-rupture life for DS-L increased with increasing of W/W+Ta atomic percentage ratio. Creep-rupture life of the alloy (YH73) whose ratio is the highest in these alloys was longer than that of SC YH61. Figure 12 shows optical and secondary electron micrographs for these alloys. From optical micrographs, volume percent of solutioned γ' increased with increasing of the atomic percentage ratio and secondary electron micrographs show that morphologies of γ' for these alloys were changed from spherical to cuboidal shape with increasing of the ratio. This morphology-change of γ' from unstable to stable shape could be caused by decreasing of lattice misfit between γ and γ' with increasing of the ratio. It can be concluded that these two important factors (higher volume percent of solutioned γ' and lower misfit with increasing of W/W+Ta at% ratio) caused higher creep strength of YH73 DS-L. Creep-rupture life of DS-T was also improved with increasing of the ratio. Because the above two factors cannot be considered to contribute to the improvement of grain boundary strength, improvement of DS-T life could also be caused by higher grain strength due to increasing of the W/W+Ta atomic percentage ratio.

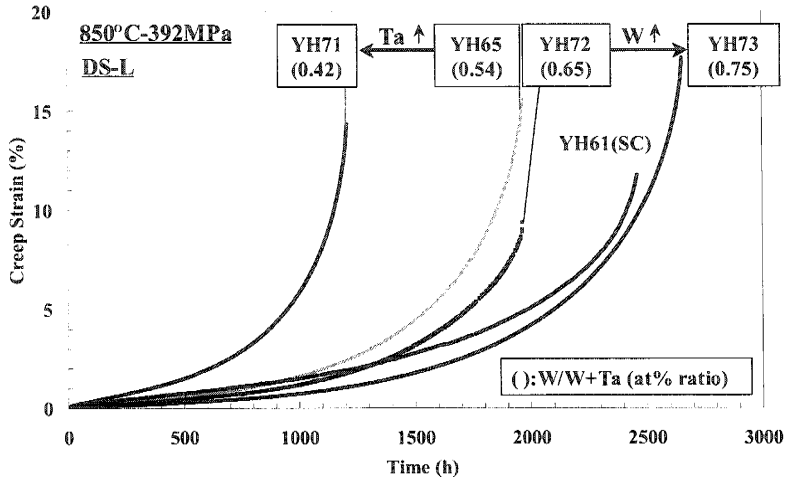

Fig. 9 Creep curves for DS experimental alloys for evaluating Tungsten and Ta contents compared with SC YH61.

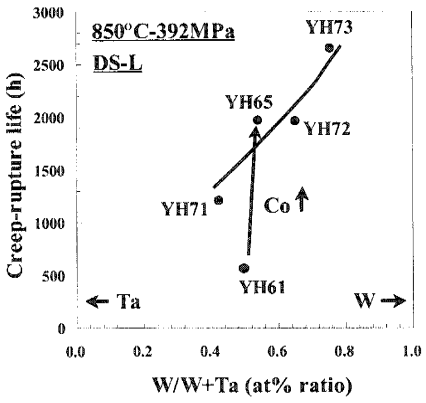

Fig. 10 Effect of W/W+ Ta at% ratio on creep-rupture life of DS-L

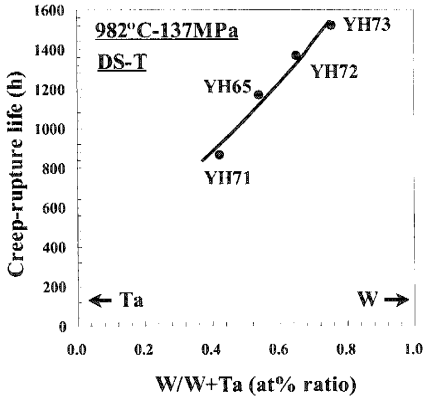

Fig. 11 Effect of W/W+ Ta at% ratio on creep-rupture life of DS-T

It can be concluded from the above results that higher W/W+Ta atomic percentage ratio realized higher both DS-L and DS-T strength. Next, based on YH72 and YH73, the following alloys (Table 3) were examined to achieve higher strength with practical phase stability. Figure 13 shows relationship between amount of refractory elements (W+Ta+Mo+Nb+Re, at%) and creep-rupture life (850°C-392MPa). Phase stability of the alloys was evaluated by investigating microstructure after aged by 1100°C-40h. 1100°C-40h corresponds to the Time-Temperature-Precipitation nose of TCP (Topologically close-packed) phases in YH61, therefore, this aging condition is intended to expect phase stability after aged more than 10^5h at about 900°C. From the results of both creep and phase stability tests, YH92 can be considered as the most promising alloy because it showed the longest creep-rupture life in the alloys which suffered from no severe TCP phase precipitation after the accelerated aging.

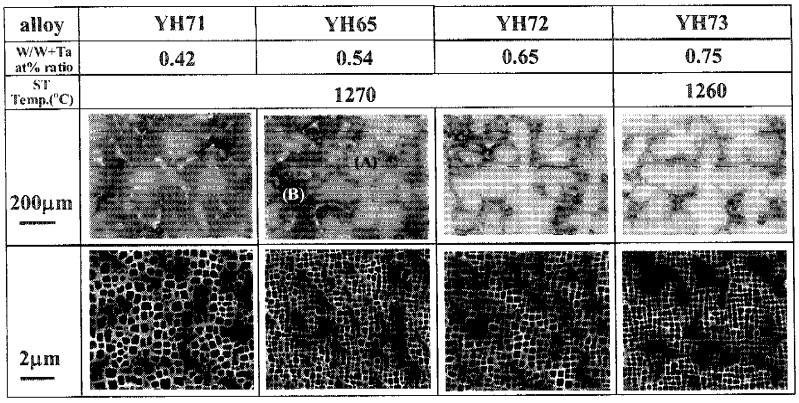

Fig. 12 Optical and secondary electron micrographs for experimental alloys for evaluating W and Ta contents, (A) indicates the region where γ' was completely solutioned and (B) is the region where γ' was not solutioned into γ during solution heat treatment

Table 3 Chemical compositions of the second experimental alloys for evaluating Tungsten and Ta contents (wt%)

No.		W	Ta
YH72	Base 1	9.90	5.32
YH86	Base 1+W	10.59	5.30
YH87	Base 1+W,Ta	10.54	5.99
YH89	Base 1+Ta	9.85	6.02
YH73	Base 2	11.48	3.72
YH92	Base 2+W	12.16	3.70
YH93	Base 2+Ta	12.10	4.41
YH95	Base 2+W,Ta	11.42	4.43

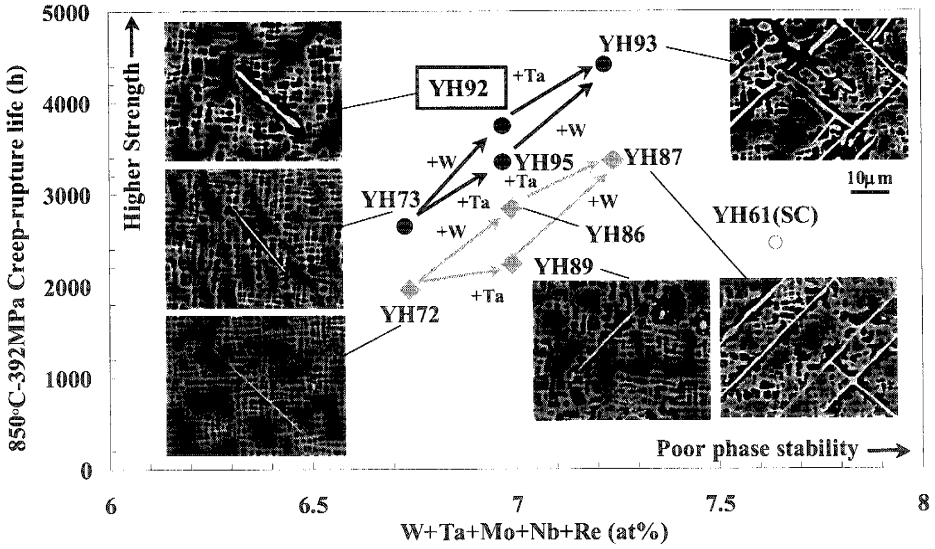

Fig. 13 Relationship between amount of refractory elements (W+Ta+Mo+Nb+Re, at%) and creep-rupture life (850°C-392MPa), secondary electron micrographs show microstructures after aged by 1100°C-40h

3.3 Effects of Hafnium and Carbon on high temperature strength of a CC

Finally, by casting CCs actually, effects of Hf and carbon on high temperature strength of a CC were examined. YH96 CC has same composition as YH92 DS and only Hf and carbon contents were varied from YH96 for other alloys (Table 4).

Table 4 Hf and carbon contents of CC experimental alloys (wt%)

No.		Hf	C
YH61		0.25	0.07
YH92	Base	1.54	0.07
YH96	Base CC	1.54	0.07
YH97	YH96 +Hf	2.04	0.07
YH98	YH97:0.15C	2.04	0.15
YH99	YH97:0.20C	2.04	0.20
YH101	YH99 +Co	2.04	0.20

Figure 14 shows creep curves for these alloys when the test condition was 982 °C-137MPa. YH96, whose chemical composition is same as DS YH92, showed about three times longer creep-rupture life against CC YH61. As discussed in the above sections, longer creep-rupture life of YH96 could be realized by higher Co and Hf contents and W/W+Ta atomic percentage ratio compared with YH61. Moreover, increase in Hf content from 1.5% (YH96) to 2.0% (YH97) improved creep-rupture life from 497h to 853h. Effect of carbon on high temperature strength of a CC was examined by YH97, 98 and 99.

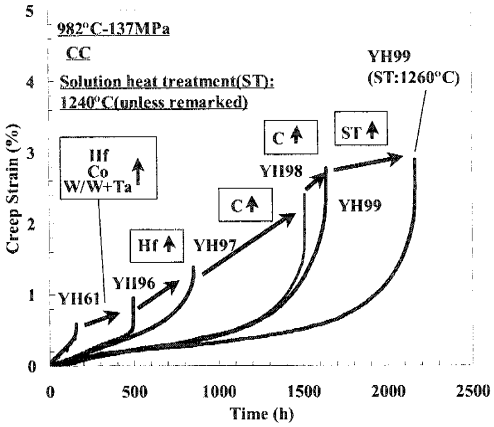

Fig. 14 Creep curves for CC experimental alloys for evaluating Tungsten and Ta

Increase in carbon content from 0.07% (YH97) to 0.15% (YH98) also significantly improved creep-rupture life of CCs. Higher carbon content alloy YH99 (0.20%) showed longer creep-rupture life than YH98 and increase in solution heat treatment temperature from 1240°C to 1260°C improved the life of YH99 from 1638h to 2164h. This creep-rupture life corresponds to 898°C as creep-rupture temperature capability at 10^5h-137MPa, which is about 25 °C higher than that of CC Mar-M247LC. The above improvement of creep-rupture life is described as a faction of Hf and carbon content in Figures 16.17, respectively. Figure 18 shows a creep-curve for YH101 (ST=1240 °C), which is a higher Co content version of YH99, compared to conventional superalloys. Creep-rupture temperature capability at 10^5h-137MPa for YH101 was 20°C higher than Mar-M247LC and it should be noted that it was also 10°C higher than DS Mar-M247LC. It means that YH101 (CC) could be low cost alternative to DS Mar-M247LC.

A stress-strain curve of a tensile test at room temperature for YH99 is shown in Figure 19. Elongation after a tensile test for YH99 was larger than 5% while poor ductility (Elongation < 4%) at temperature below about 700°C is major concern for high strength CC superalloys.

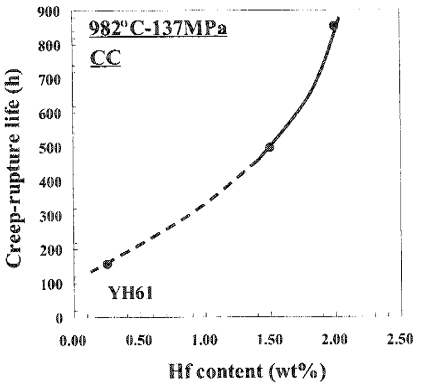

Fig. 16 Effect of Hf content on creep-rupture life of CCs

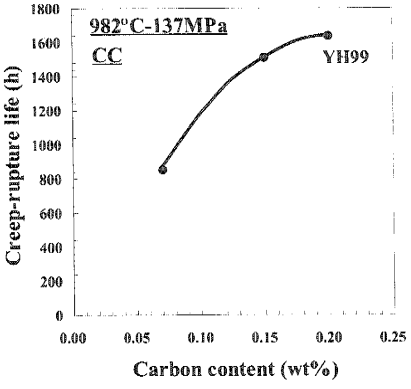

Fig. 17 Effect of carbon content on creep-rupture life of CCs

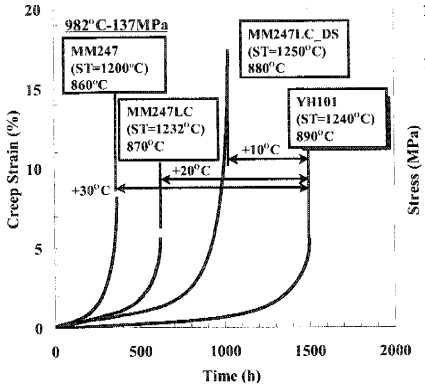

Fig. 18 Creep-rupture temperature capability at 10^5h-137MPa for the developed alloy compared with conventional CC/DS alloys

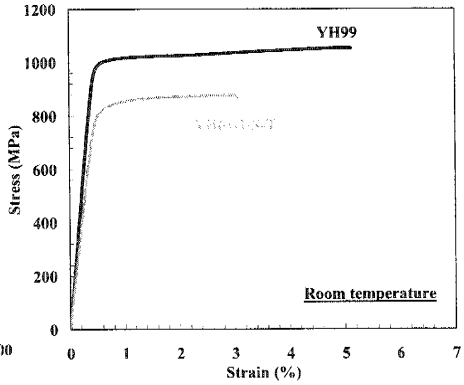

Fig. 19 A stress-strain curve of a tensile test at room temperature for YH81 compared to YH61 (DS-T)

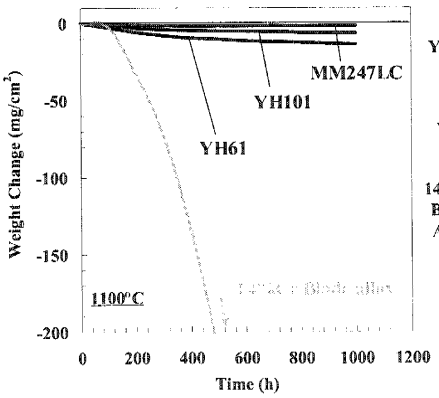

Fig. 20 Oxidation resistance of the developed alloy compared to conventional alloys

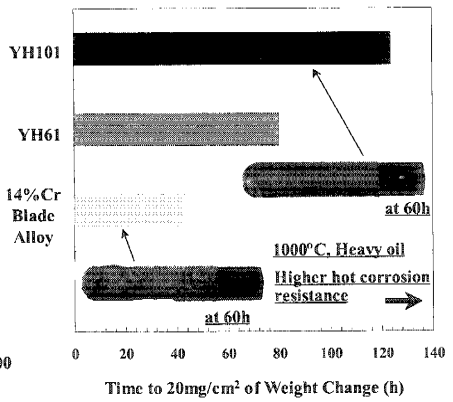

Fig. 21 Hot corrosion resistance of the developed alloy compared to conventional alloys

Figure 20 shows oxidation resistance of YH101 at 1100°C compared to a 14% Cr containing blade alloy and YH61. Oxidation resistance of YH101 was significantly superior to the 14% Cr containing blade alloy and comparable to YH61 and Mar-M247LC. Hot corrosion resistance of YH101 at 1000°C was shown in Figure 21. While hot corrosion resistance was examined by using heavy oils which contained about 0.04% sulfur, YH101 shows evidently higher hot corrosion resistance than the 14% Cr containing blade alloy and YH61 in this condition. It can be concluded from these results that not only creep strength but also hot corrosion and oxidation resistance of YH101 was confirmed practical for gas turbine blade use.

Conclusions

A new Ni-based superalloy for conventional castings (CCs) has been developed.

1. Increases in Hf and Co contents and W/W+Ta atomic percentage ratio from YH61 have been realized a high strength and low cost (Re=1.5% class) DS superalloy YH92.
2. High strength CC alloy YH101 has been obtained by increasing Hf and carbon contents form YH92. Temperature capability (137MPa-10^5h) of the alloy was 20 °C higher than that of Mar-M247LC which is one of the highest strength commercial Ni-based superalloys for CCs and also 10 °C higher than that of DS Mar-M247LC.
3. Oxidation resistance of the alloy was comparable to Mar-M247LC while hot corrosion resistance of the alloy was higher than that of 14% Cr containing blade alloy.

Acknowledgements

One of the authors would like to acknowledge Dr. Noriaki Matsuda for his helpful discussions. This work has been subsidized by New Energy and Industrial Technology Development Organization (NEDO).

References

[1] R. C. Helmink, R. A. Testin, A. R. Price , R. Pachman, G. L. Ericksont, K. Harris, J. A. Nesbittt and J. F. Radavich, "Advanced Superalloys and Tailored Microstructures for Integrally Cast Turbine Wheels", Proceedings, Superalloys 2000, T.M. Pollock et al., ed., TMS, Warrendale, PA, pp.757-766.

[2] J. Milne, ""Green" Power Possible with Micro-turbines", Nickel, 8 (1999), p. 16.

[3] S. Guo, "Blade Vibration of Radial Inflow Micro Gas Turbine", Proceedings, The 10th International Symposium on Transport Phenomena and Dynamics of Rotating Machinery, (2004), ISROMAC10-2004-097.

[4] H. Tamaki, A. Yoshinari, A. Okayama, S. Nakamura, K. Kageyama, K. Sato and T. Ohno, "Development of A Low Angle Grain Boundary Resistant Single Crystal Superalloy YH61", Proceedings, Superalloys 2000, ed. T.M. Pollock et al., (Warrendale, PA: TMS, 2000), 757-766.

[5] H. Tamaki, A. Yoshinari, A. Okayama, S. Nakamura, K. Kageyama, and T. Ohno, "Development of A New Ni-Based Single Crystal Superalloy for Large Sized Buckets", Materials for Advanced Power Engineering 1998, J. Lecomte-Beckers et al., ed., Forschungszentrum Jülich GmbH, Jülich, Germany, pp.1099-1110.

HIGH TEMPERATURE PROPERTIES OF SELECTED Ni-BASE SUPERALLOYS

Jan Hakl
Tomáš Vlasák

SVUM a.s., Prague, Czech Republic, hightempmat@svum.cz

Abstract

For advanced methods of remaining lifetime predictions of hot parts in gas turbines and turbosuperchargers it is necessary to evaluate dependencies of creep plastic characteristics on temperature, stress and time adequately. Quantitative relations of this type will be presented for the widely used cast superalloys IN 713 LC, IN 738 LC and IN 792 5A.

Key words: turbines, superalloys, creep properties, mathematical models, lifing.

1. INTRODUCTION

The term superalloy has been used since the end of the fifties of the past century as a designation of complex alloyed Fe-, Ni- or Co-base materials used primarily for the production of the most stressed high-temperature parts of gas turbines or turbochargers. The basic requirements for these materials are:

- Resistance to complex mechanisms of damage due to mechanical stress at high temperatures
- Resistance to the corrosion effects of working media
- Satisfactory technological properties.

Due to their strategic importance, primarily in aviation, superalloys became the most investigated group of metallic materials. The result of this development is a large number of these materials and many new technologies [1] that are available today (certainly due to commercial and patent applications). Relatively frequently used superalloys, including examples of applications by the foremost world producers, are reviewed in paper [2].

Manufacturers of aviation and stationary turbines and turbochargers in our country (primarily MOTORLET – now WALTER Engines a.s., Prague, PBS Brno, PBS Velká Bíteš a.s.) were primarily using materials from the former USSR and from POLDI Kladno. For processing these materials, adequate technologies were mastered (vacuum metallurgy, investment casting – including casting of blades with hollow channels, crystallization refinement of investment castings, transient liquid-phase bonding, electron-beam welding, friction welding, etc.).

A serious problem occurred after political and economical changes at the end of the 20th century. As a consequence of the interruption of production in Poldi Kladno and breaking links to traditional suppliers of special materials from Russia, it was necessary to find an alternative solution.

In this context, the objective of this contribution is to present basic information on the high-temperature properties of selected supperalloys of western origin that meet the

requirements of the current technological environment and the level or requirements of design engineers expected in the nearest future. We will discuss typical blade materials IN 713 LC, IN 738 LC and IN 792 5A, whose frequent application in designs is reviewed in [2]. The IN 713 LC alloy is the best known in our country and has been already used in domestic designs (various parts of turbochargers and gas turbines). We will be using this alloy as a reference material for the characterization of two further materials.

2. GENERAL CHARACTERISTICS OF THE EVALUATED ALLOYS

All the alloys discussed in this paper are complex alloyed precipitation-hardenable Ni-base alloys. A typical technology for those alloys is vacuum investment casting. The nominal chemical composition and some physical characteristics of these alloys are indicated in Table I and II.

Table I Nominal chemical composition of the discussed alloys (wt.%, Ni – base)

Alloy	C	Cr	Co	Mo	W	Nb	Ta	Ti	Al	Zr	B
IN 713 C	0.12	12.5	-	4.2	-	2.0	-	0.8	6.1	0.10	0.012
IN 713 LC	0.05	12.0	-	4.5	-	2.0	-	0.6	5.9	0.10	0.010
IN 738	0.17	16.0	8.5	1.7	2.6	0.9	1.7	3.4	3.4	0.10	0.010
IN 738 LC	0.10	16.0	8.5	1.75	2.6	0.85	1.75	3.4	3.4	0.05	0.010
IN 792	0.12	12.4	9.0	1.9	3.8	-	3.9	4.5	3.1	0.10	0.020
IN 792 5A	0.08	12.5	9.0	1.9	4.17	-	4.17	3.97	3.37	0.03	0.015

Table II Some physical properties

Alloy	**Temperature [°C]**		**Density [g.cm^{-3}]**
	Solids	Liquids	
IN 713 C	1260	1288	7,91
IN 713 LC	1288	1321	8,01
IN 738	1230	1315	8,11
IN 792	1235	1320	8,25

The IN 713 LC alloy is a low-carbon modification of IN 713 C (LC – low carbon). It is one of the cast alloys of the so-called 1st generation, where vacuum metallurgy was applied during production. Lowering the C content shifted the solid and liquid toward higher temperatures and improved some material characteristics (primarily plasticity). The alloy is commonly used in the cast condition and is considered to be structurally stable from the point of view of the precipitation of the topologically close-packed phases during operational exposure. In our country, the equivalent of this alloy was formerly produced under the LVN-10 designation.

The IN 738 alloy and its IN 738 LC modifications are higher materials of the 2nd generation in comparison with IN 713 LC. The heat resistance of the more frequently used IN 738 LC version is comparable to IN 713 LC, however, thanks to a higher Cr content and other alloying materials, it is more resistant to high temperature corrosion. With respect to more complex alloying (see Table I), it is more expensive and technologically demanding. In the event of unsuitable combination of the content of the alloying elements, there is a danger of the formation of the undesired σ phase during operational exposure. Precipitation of this

phase can be prevented by optimizing the chemical composition by the PHACOMP method. The alloy is used in a state heat treated, in most cases by the 1120°C/2h/air + 845°C/24h/air procedure.

From the discussed alloys, IN 792 is the youngest one from the point of view of development and has the highest creep resistance and corrosion resistance is comparable to IN 738 LC; however, it is the most expensive. It also belongs to the cast alloys of the 2nd generation. It is produced in several modifications that slightly differ in chemical composition. We will focus on the IN 792 5A alloy that is, obviously, the most frequently used. Contrary to the basic composition (see Table I), modifications denoted as 5B and 5C contain 0.5 or, as the case may be, 0.9 % Hf and are more expensive than the 5A alternative. In the same manner as in the case of IN 738 LC, the chemical composition must be optimized using the PHACOMP method in order to avoid the formation of the σ phase. The optimum properties of the IN 792 5A alloy are achieved by a two-stage heat treatment, identical to the above-indicated process for IN 738 LC, or by a three-stage procedure 1120°C/2h/air + 845°C/4h/air + 760°C/16h/air.

During the production of castings, the foundry primarily guarantees the chemical composition (and in the case of IN 738LC and IN 792 5A, also documents the mean value of the μNv electron vacancies as a criterion of the optimum composition from the point of view of sigmatization). Apart from the control of shapes, dimensions and the interior and surface quality of castings, the alloy quality is usually declared by the result of a short term test of creep strength. These tests are routinely carried out by the accredited test laboratory of SVUM for a number of customers. According to the experience of this test laboratory, various examples of the acceptance requirements are indicated for the discussed materials in Table III.

Table III Conditions of creep acceptance tests and minimum required properties.

Alloy	Temperature [°C]	Stress [MPa]	Acceptance requirements		
			Time to rupture [h]	Elongation [%]	Reduction of area [%]
IN 713 LC	980	150	30	4	-
	760	530	50	2	-
	870	353	29	3.5	-
IN 738 LC	760	545	60	-	-
	930	230	20	-	-
	982	152	35	5	10
IN 792 5A	950	230	16	5	5

3. EXPERIMENTS

All the evaluated heats were cast by a standard technology in the foundries of precision casting either in PBS Velká Bíteš a.s. or PCS a.s. Prague. During the production of castings, master heats were used that were delivered from foreign producers that specialize in Ni-base high temperature alloys. The chemical composition of the heats was satisfactory in all the cases (see Tab.IV.). In the case of the IN 738 LC and IN 792 5A alloys, admissible values of the μNv electron vacancies were found. In the case of these alloys, the material of these casts was subject to standard heat treatment. All the details of the technological character are indicated in [3,4]. Creep experiments were carried out on air during a permanent load.

Table IV Chemical composition of tested alloys (wt.%, Ni base)

Element	IN 713 LC		IN 738 LC			IN 792 5A
	RCL 433/09	009H16/027	Q197/15	RC 443/18	C3873	RC 458/24
C	0.045	0.05	0.10	0.093	0.10	0.078
Cr	11.63	12.00	15.74	15.83	16.09	12.28
Mo	4.24	4.42	1.74	1.66	1.75	1.81
Nb	1.90	1.91	0.82	0.76	0.83	<0.10
Ta	-	-	1.75	1.74	1.61	4.12
Al	6.04	6.0	3.45	3.55	3.39	3.36
Ti	0.75	0.72	3.29	3.25	3.26	3.98
B	0.01	0.008	0.008	0.009	0.008	0.015
Zr	0.081	0.094	0.04	0.023	0.041	0.031
Si	<0.10	<0.02	0.04	<0.05	0.04	<0.10
Mn	<0.05	0.01	0.01	<0.05	<0.02	<0.10
Fe	0.12	0.04	0.31	0.07	0.30	0.16
Co	<0.05	0.05	8.42	8.32	8.36	8.87
W	-	-	2.4	2.60	2.63	4.10
Hf	-	-	-	-	0.04	-
Cu	<0.02	<0.01	<0.01	<0.02	<0.02	-
S	<0.003	<0.001	0.002	<0.003	0.005	<0.002
P	-	<0.005	0.03	0.003	<0.005	<0.002
ppm N_2	8.00	10.0	14.0	-	18.0	-
ppm O_2	4.00	3.0	11.0	-	5.0	-
ppm Ag	-	-	<5.0	<0.1	-	<0.1
ppm As	-	-	<15.0	<5.0	-	<5.0
ppm Bi	-	-	<0.5	<0.1	-	<0.1
ppm Cd	-	-	-	<0.1	-	<0.1
ppm Ga	-	-	<20.0	<15.2	-	<10.0
ppm In	-	-	-	0.1	-	<0.1
ppm Mg	-	-	<50.0	-	-	8.4
ppm Th	-	-	-	-	-	<1.0
ppm Pb	-	-	<5.0	<0.3	-	0.3
ppm Sb	-	-	<2.0	<1.0	-	<1.0
ppm Se	-	-	<1.0	<2.0	-	<2.0
ppm Sn	-	-	<20.0	<5.0	-	<5.0
ppm Te	-	-	<0.5	<1.0	-	<1.0
ppm Tl	-	-	<0.5	<2.0	-	<0.2
ppm Zn	-	-	<4.0	<1.0	-	<1.0
µNv	-	-	2.29	2.30	2.30	2.26

3.1 Methodology of the evaluation of experiments

For the evaluation of the dependence between the time to rupture, temperature and stress, the following relation was chosen according to [5] in the form

$$\log\sigma = A_1 + A_2 \cdot P_{LM} + A_3 \cdot P_{LM}^2, \qquad (1)$$

where $P_{LM} = T \cdot (\log t_r + A_4)$,

T	is temperature,	t_r	is the time to fracture,
σ	is stress,	A_1 - A_4	are the material constants.

For the evaluation of the deformation characteristics, individual creep curves were assessed by means of a model [7]

$$\varepsilon_c = \varepsilon_0 \cdot \left[\left[\frac{\varepsilon_m}{\varepsilon_0} \right]^{[g(\pi(t))]} - 1 \right] \tag{2}$$

$$g(\pi(t)) = \pi^N \cdot \left[\frac{1+\exp(-2\cdot\pi^K)}{1+\exp(-2)} \right]^M \tag{2a}$$

$$\pi = \frac{t}{t_r} \tag{2b}$$

$$\varepsilon_0 = \frac{\sigma}{E(T)} \cdot 10^2 \tag{2c}$$

$$E(T) = E_1 + E_2 \cdot \exp\left(\frac{E_3}{T} \right) \tag{2d}$$

where

ε_c	is the overall plastic deformation,	t	is time,
ε_0	is the initial deformation,	σ	is stress,
T	is temperature,	K, M, N, ε_m, $E_{1\text{-}3}$	are the material constants.

Examples of some creep curves evaluated by the indicated procedure are in Fig. 1.

The temperature and stress dependencies of the creep limit and creep rate were expressed from the processed data. A regression model formally identical to (1) was used for the evaluation of the creep limit,

$$\log\sigma = B_1 + B_2 \cdot P_{LM} + B_3 \cdot P_{LM}^2 \quad , \tag{3}$$

where $P_{LM} = T \cdot (\log t_1 + B_4)$,

T	is temperature,
σ	is stress,
t_1	is the time to 1% plastic deformation
B_1 - B_4	are the material constants.

A model was used for the evaluation of the creep rate according to [6] in form

$$\log\dot{\varepsilon} = C_1 + C_2 \cdot \log\left| \frac{1}{T} - \frac{1}{C_5} \right| + C_3 \cdot \log[\sinh(C_6 \cdot \sigma \cdot T)] + C_4 \cdot \log\left| \frac{1}{T} - \frac{1}{C_5} \right| \cdot \log[\sinh(C_6 \cdot \sigma \cdot T)] \tag{4}$$

where

$\dot{\varepsilon}$	is the minimum creep rate (%/h),	σ	is stress (MPa),
T	is temperature (K),	C_1-C_6	are the material constants.

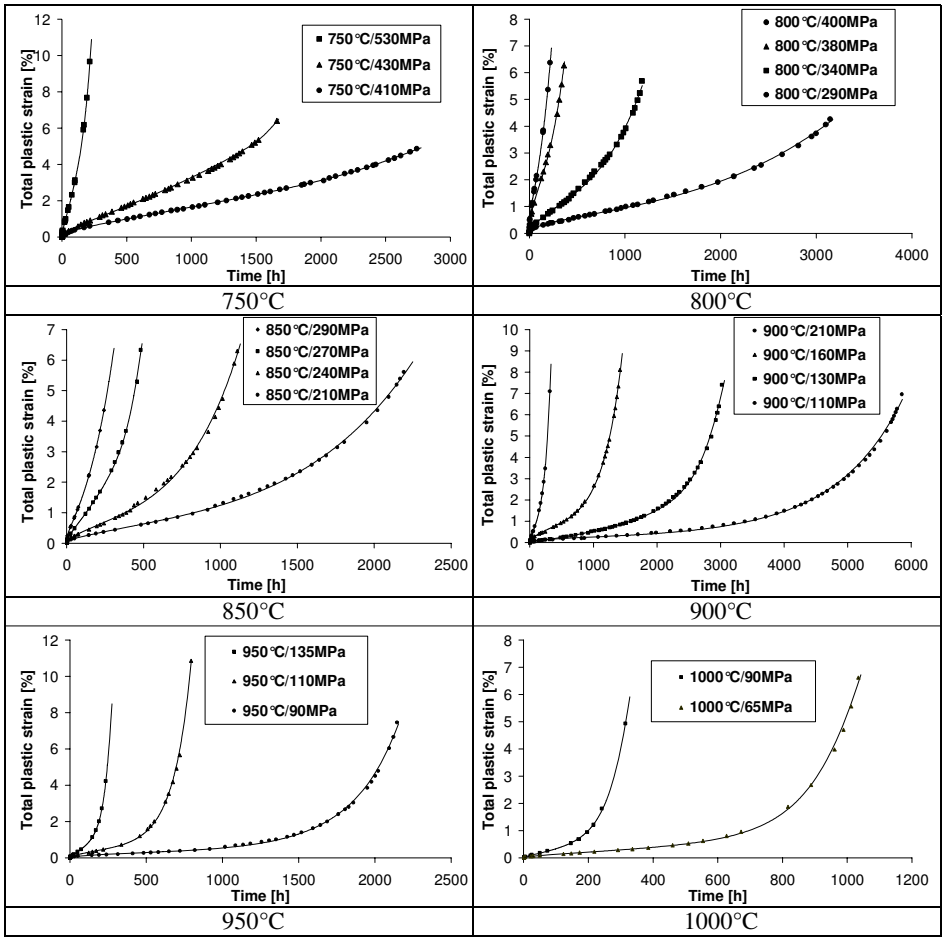

Fig. 1 Creep curves of the IN 738 LC alloy

3.2 Evaluation of the creep characteristics

3.2.1 IN 713 LC

Altogether 55 tests were used for the evaluation from two heats (chemical composition see Table IV). The tests were carried out in the 80-480 MPa range of stress, 730-950°C temperature range and times to fracture 29-6776 h. The total time of the carried out experiments was 114235 h. Detailed information on the experiments is in paper [4]. The results of the evaluation are show in Fig.2.

Material constants from relation (1) valid for R_{mT} [MPa], T [K], t_r [h]			
A_1	3,41051917E+00	A_3	-3,96133382E-09
A_2	5,59013351E-05	A_4	1,88884956E+01

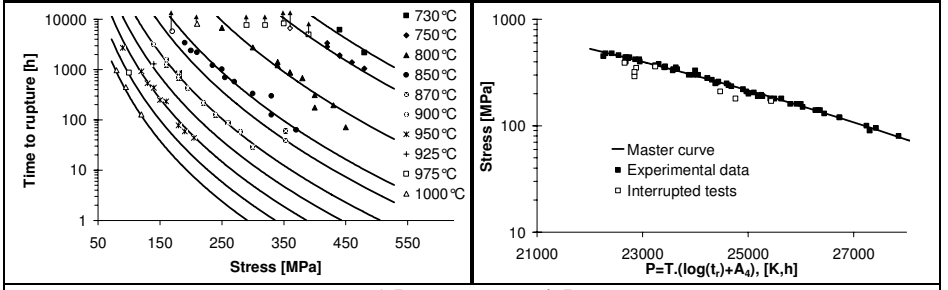

a) Rupture strength R_{mT}

Material constants from relation (3) valid for R_{mT} [MPa], T [K], t_r [h]			
B_1	1,10913690E+00	B_3	-6,52773577E-09
B_2	2,19648275E-04	B_4	2,06036529E+01

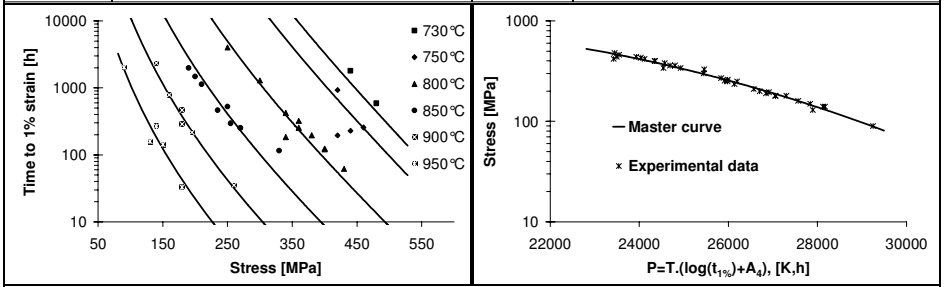

b) Strength for 1% creep strain $R_{1\%/T}$

Material constants from relation (4)	
C_1	-1,31999909E+02
C_2	-4,40592396E+01
C_3	1,42050861E+01
C_4	4,88454774E+01
C_5	-7,95396959E+03
C_6	1,32548306E-06

$\dot{\varepsilon}$ [$\%h^{-1}$], σ [MPa], T [K]

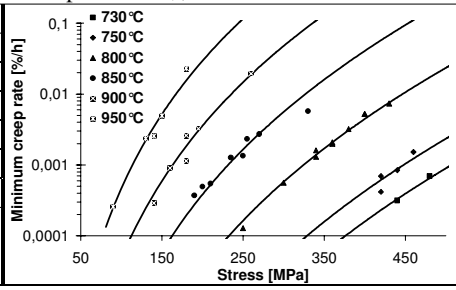

c) Minimum creep strain rate $\dot{\varepsilon}$

Fig. 2 Creep properties of the IN 713 LC alloy

3.2.2 IN 738 LC

These characteristics were determined on the basis of the evaluation of 58 tests of the material from three heats (chemical composition see Tab IV). The tests were carried out in the 65-530 MPa range of stress, 750-1000°C temperature range and 65-5862 h range of times to fracture The total time of the carried out experiments was 76265 h. Detailed information on

the experiments is in paper [4]. The results of the evaluation of the experimental data are obvious from Fig.3.

Material constants from relation (1) valid for R_{mT} [MPa], T [K], t_r [h]			
A_1	3,94363667E-01	A_3	-9,42817312E-09
A_2	3,10429148E-04	A_4	1,85422591E+01

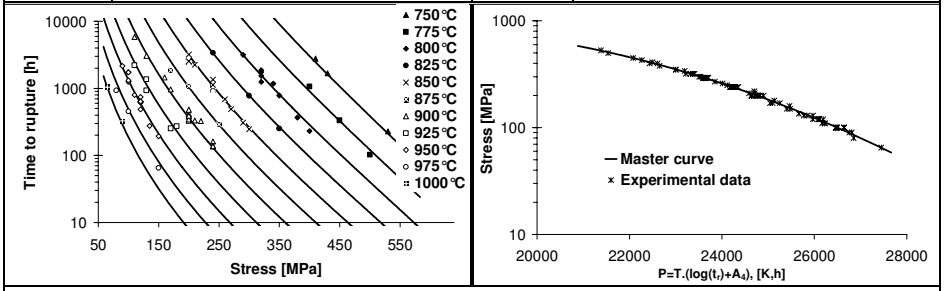

a) Rupture strength R_{mT}

Material constants from relation (3) valid for R_{mT} [MPa], T [K], t_r [h]			
B_1	-2,82039086E-01	B_3	-8,07777944E-09
B_2	3,14852133E-04	B_4	2,10941619E+01

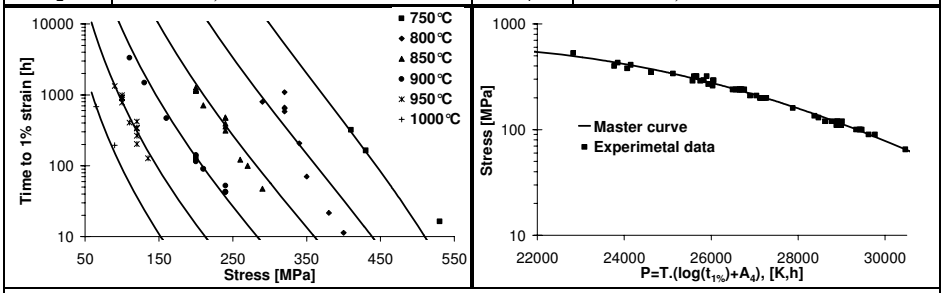

b) Strength for 1% creep strain $R_{1\%/T}$

Material constants from relation (4)	
C_1	9,56308425E+01
C_2	3,04703938E+01
C_3	-1,69707424E+01
C_4	-4,89543766E+01
C_5	6,76138414E+02
C_6	3,34390031E-06

$\dot{\varepsilon}$ [$\%h^{-1}$], σ [MPa], T [K]

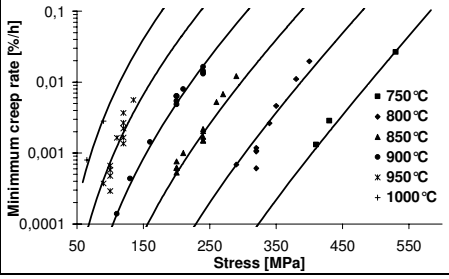

c) Minimum creep strain rate $\dot{\varepsilon}$

Fig. 3 Creep properties of the IN 738 LC alloy

3.2.3 IN 792 5A

These characteristics were determined on the basis of the evaluation of 45 tests of the material from one heat which chemical composition is in Tab.IV. The tests were carried out in

the 80-540 MPa range of stress, 750-975°C temperature range and 36-10495 h range of time to fracture The total time of the carried out experiments was 81718 h. Detailed information on the experiments is in paper [4]. The results of the evaluation are summarized in Fig.4.

Material constants from relation (1) valid for R_{mT} [MPa], T [K], t_r [h]			
A_1	-4,68657401E-01	A_3	-9,39400294E-09
A_2	3,56137884E-04	A_4	1,99733928E+01

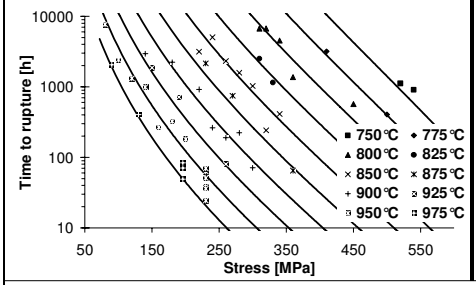

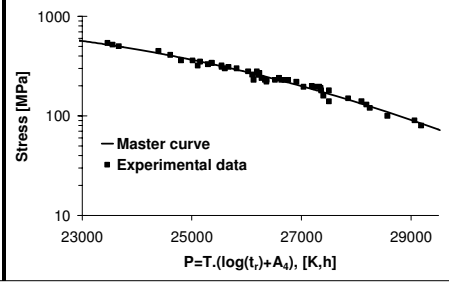

a) Rupture strength R_{mT}

Material constants from relation (3) valid for R_{mT} [MPa], T [K], t_r [h]			
B_1	-2,32361121E-01	B_3	-6,23516284E-09
B_2	2,78827287E-04	B_4	2,46893793E+01

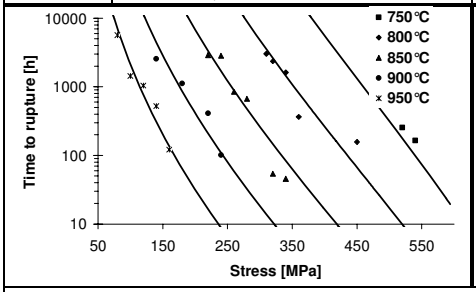

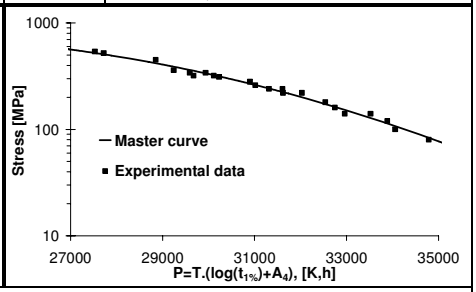

b) Strength for 1% creep strain $R_{1\%/T}$

Material constants from relation (4)	
C_1	-2,13513420E+01
C_2	-3,86464846E+00
C_3	-6,26871693E-01
C_4	-1,95308164E+00
C_5	1,35048670E+03
C_6	6,20537446E-05
$\dot{\varepsilon}$ [%h^{-1}], σ [MPa], T [K]	

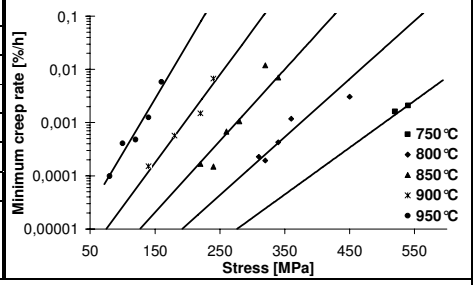

c) Minimum creep strain rate $\dot{\varepsilon}$

Fig. 4 Creep properties of the IN 792 5A alloy

3.3 Comparison of the creep properties of the evaluated alloys

For the comparison of the high temperature properties of the investigated alloys, model (1) was used in which the uniform coefficient was used for all the alloys.

The dependence of the creep strength limit on the Larson-Miller parameter (LMP) is displayed graphically in Fig.5. A similar comparison is given in Fig.6, where the dependence of the 1% creep limit is illustrated. For illustration, the corresponding stresses are evaluated for the chosen LM parameters, corresponding to the chosen temperatures of the creep exposition and the rapture times (Fig. 5) or, as the case may be, times for achieving 1% permanent deformation (Fig.6). While there is no much difference between IN 713 LC and IN 738 LC from the point of view of the load-carrying capacity, it is obvious from both figures that the IN 792 5A alloy exhibits the highest values.

Another evaluation, carried out on the basis of the calculation according to relation (1), is illustrated graphically in Fig.7; it compares alloys from the point of view of their durability. The corresponding times to rupture are plotted for the chosen temperatures and stress. It is obvious that in comparison with IN 713 LC and IN 738 LC, the IN 792 5A application increases durability approximately three times. Fig.8 offers a similar interpretation; in this figure, the limit temperature of the application is determined for the chosen strengths and times to rupture.

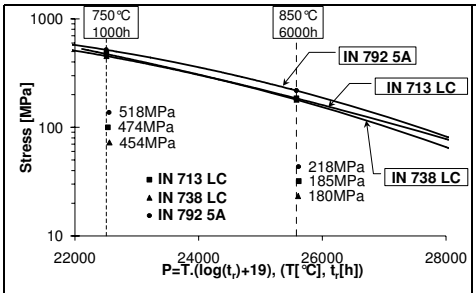

Fig.5 Comparison of the creep strength of the IN 713 LC, IN 738 LC and IN 792 5A alloys.

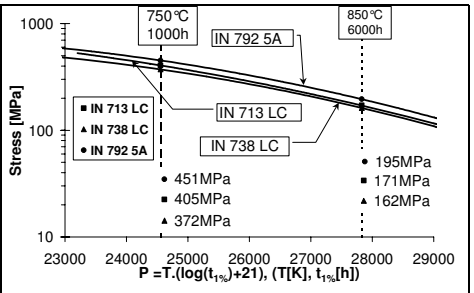

Fig. 6 Comparison of the creep strength for 1% creep strain of the IN 713 LC, IN 738 LC and IN 792 5A alloys.

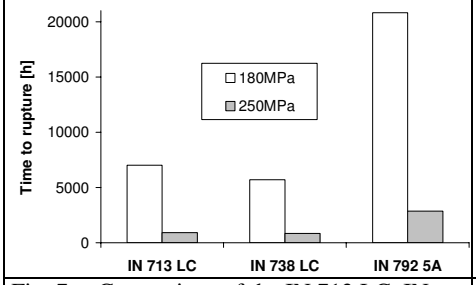

Fig. 7 Comparison of the IN 713 LC, IN 738 LC and IN 792 5A alloys at a temperature of 850°C and the given stress.

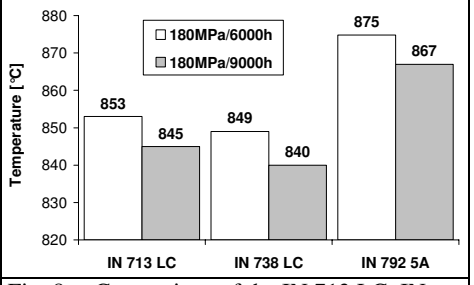

Fig. 8 Comparison of the IN 713 LC, IN 738 LC and IN 792 5A alloys at a selected stress and time to rupture in relation to temperature.

4. DISCUSSION

The IN 713LC alloy is historically the oldest one. However, it has a number of advantages due to which it remains the most often produced and used cast Ni alloy from the point of view of quantity. It has a relatively simple alloying and is not prone to sigmatization, has a short solidification interval (see Table II) and castings can be used in a cast state. IN 713 LC is technologically undemanding, the level of its high temperature properties is good and in most cases, there are no problems with achieving the required properties during creep tests (see, e.g., [7]).

With high temperature properties comparable to those of IN 713 LC, the advantage of IN 738 LC is increased resistance to high temperature corrosion, primarily in the sulphuric environment [8,9]. This is achieved by more complex alloying, which, however, increases its specific mass (see Table II) and the price of the alloy (in comparison with IN 713 LC, it is approximately half more expensive). IN 738 LC is prone to sigmatization during operation and for this reason, its composition must be optimized. In comparison with IN 713 LC, the temperature interval of solidification is approximately two and half wider, which must be taken into account when choosing the risering of castings in order to avoid microporosity. Heat treatment is necessary for achieving the required use properties of the alloy.

The IN 792 5A alloy is also a material with high resistance to high temperature corrosion in a sulphuric environment. Its main advantage is that it has the best high temperature properties of all the evaluated alloys. However, it is obvious from Table II that is also has the highest specific mass and the same solidification interval as IN 738 LC. It has the same procedure of thermal treatment and is prone to sigmatization. The disadvantage of the IN 792 5A alloy is that it is approximately three times more expensive.

5. CONCLUSION

The main application sphere of the IN 713LC, IN 738 LC and IN 792 5A alloys are the cast high temperature parts of gas turbines and turbochargers. Creep characteristics are important material documents for the construction design of these parts. In the present paper, creep strengths, 1% creep limits and creep rates are given for all the above-indicated alloys and some technological aspects that may be helpful in choosing the optimum material solution.

6. LITERATURA

[1] SHAFRIK,R.-SPRAGUE,R.: Gas Turbine Materials. Advanced Materials and Processes,162 (2004), No.3,pp.33-36, 162(2004),No.4, pp. 27-30, 162 (2004), No.5, pp. 29-33.

[2] WAHL,J.B.-HARRIS,K.: Superalloys in Industrial Gas Turbines – an Overview. Proc. 9th World Conference on Investment Casting. Paper No 12, San Francisco, California, Oct. 13-16,1996.

[3] HAKL,J.-VLASÁK,T.: Vyhodnocení výsledků creepových zkoušek slitin IN 713 LC, IN 738 LC a IN 792 5A. Výzkumná zpráva SVUM a. s., č. 2 31 0053/6, Praha, 2004.

[4] HAKL,J.-VLASÁK,T.: Materiálové charakteristiky superslitin IN 713 LC, IN 738 LC, IN 792 5A, ŽS6W. Výzkumná zpráva SVUM a.s. č. 2 31 0053/7, Praha, 2004

[5] SEIFERT,W.-MELZER,B.: Rechnerische Auswertung von Zeitstandversuchen am Beispiel des Stahles 13CrMo4-4. 15.Vortragsveranstaltung „Langzeitverhalten warmfester Stähle und Hochtemperaturwerkstoffe“, Düsseldorf, 06.11.1992.
[6] BÍNA, V.-HAKL, J.: Relation between creep strength and strength for specific creep strain at temperatures up to 1200°C, Mat. Sci. Eng. A234-236 (1997), pp. 583-586.
[7] HAKL,J.-VLASÁK,T-KOVAŘÍK.P.: Zkouška pevnosti při tečení jako kritérium jakosti odlitků pro vysokoteplotní aplikace. Slévárenství, LII (2004),č.11-12, s.461-464.
[8] Nickel-base, Vacuum-cast, High-temperature ALLOY IN-738. Technical Data. International Nickel, London, September 1968.
[9] PECH,R.-HAKL,J.-KUDRMAN,J.: Vývoj niklových slitin pro nejnáročnější použití u leteckých turbinových motorů. Výzk. zpráva SVUM Z 89-6060. SVUM Praha, 1989.

This work was supported by Ministry of Education, Youth and Sports of Czech Republic – COST 538 (1P05 OC022).

HOT ISOSTATIC PRESSING PROCESS TO REJUVENATE SERVICED CAST NICKEL BASE SUPERALLOY IN738 TURBINE BLADES

[1]P. Wangyao, [2*]J. Zrnik, [3]S. Polsilapa, [4]E. Nisaratanaporn, [5]W. Homkrajai

[1] Metallurgy and Materials Science Research Institute (MMRI), Chulalongkorn University, Bangkok, Thailand

[2*]Dept. of Materials Science, Faculty of Metallurgy, Technical University of Kosice, Kosice, Slovak Republic, e-mail: jzrnik@comtesfht.cz

[2] Dept. of Materials Engineering, Engineering Faculty, Kasetsart University, Bangkok, Thailand

[3] Dept. of Metallurgical Engineering, Engineering Faculty, Chulalongkorn University, Bangkok, Thailand

[5]Electricity Generating Authority of Thailand (EGAT), Nonthaburi, Thailand

Abstract

Many of land base gas turbines for power plants are already long-time operating and lots of efforts were brought to evaluate the remnant life of turbine components. The aims is to assess the actual conditions of the material used for critical components are sustainable with respect to remaining life judgement. The present work provides information on land-base gas turbine first-stage turbine blade structure degradation due to long-term thermomechanical and environmental exposure. The virgin blade was of cast and heat treated nickel base superalloy IN 738 and prior examination it was exposed more than 70 000 hours at turbine inlet temperature, operating by Electricity Generating Authority of Thailand (EGAT) company. The pieces, differently localized along the blade, were cut off for microstructural analyses, which were performed using light and scanning electron microscopy. After long-term service the gamma prime coarsening, re-precipitation of finer gamma prime precipitates and grain boundary carbide precipitates dissolving were observed. The most degraded microstructure was found at top part of trailing edge and at the middle leading edge of blade where small cracks, pores and nests of voids were observed. In order to find proper condition to recover the microstructure the attempt of rejuvenation involving hot isostatic pressing (HIP) followed by standard heat treatment of IN 738 alloy was employed to pieces of the blade. The series of HIP treatments at two different temperatures and at different holds have been conducted. This process appeared to be successful in healing of micro voids and pores in interior of blade, but no restoration of surface defects was observed. Increasing the HIP temperature and extending the HIP time higher efficiency for micro voids and porosity closing were observed.

Keywords: Nickel base superalloy, long term exposure, structure degradation, hot isostatic pressing (HIP), structure analysis.

Introduction

Nickel base superalloys are used within the industrial gas turbine (IGT) engines for electricity generating leading to the need of the high temperature path components. These materials can be exposed to very severe operating conditions where high tensile strength, good fatigue and creep resistance as well as oxidation and hot corrosion resistances are all required. A range of nickel base superalloys, from dilute, solid solution strengthened alloys to the highly alloyed precipitation hardened materials are available for high temperature loading performance and

environmental resistance. For optimal performance, high pressure/high temperature turbine blades are generally made of nickel base superalloys. The choice of precipitation temperatures governs not only the type but also the size, distribution and volume fraction of precipitate. Multiple precipitation treatments are usually common in wrought alloys but uncommon in cast alloys [1]. Usually, selection of a single aging temperature may result in obtaining optimal amounts of multiple precipitating phases. In case higher hardening is expected, alternatively, a double-aging treatment at different temperatures, which produces different sizes and types of gamma prime precipitate, may be utilized [2]. A principle reason for a need of double aging, in addition of gamma prime precipitation, is carbides precipitation, and/or grain boundary carbide morphology control [3].

Superalloys normally respond to heat treatment, and thus, exposure of these alloys to elevated temperatures, with or without stress, can cause microstructural changes and resultant changes in properties. Generally, the higher the exposure temperature, the more rapid the structure changes [4]. At the highest exposure temperatures, an alloy may be subject to incipient melting. As exposure temperature decreases, the type of microstructural degradation may change. In addition, oxidation and surface corrosion may take place at all temperatures for which these alloys are normally specified.

Some superalloys are exposed to extremely high temperatures in furnace and petrochemical applications, but loads are not very high. Alloys for gas turbine applications generally are exposed to the most demanding combination of high temperature and stress. The approximate metal temperature for airfoils of some cast superalloys may range as high as 1093°C. Within the range of about 727 to 1093°C microstructural changes readily occur with time at temperature. Furthermore when stress is applied, the changes may be accelerated. The break down of primary carbides, primary geometrically closed-packed phases agglomeration and formation of topologically closed-packed (tcp) phases could appear.

IN-738LC, a cast nickel base superalloy was originally developed as a material for turbine blade applications. It was specially designed for long-term service in excess of 100000 hours at temperature up to 980°C with surface coating. The chemical composition of alloy was proposed to provide an excellent combination between mechanical and physical properties such as high temperature tensile and fatigue strength, creep strength, fracture toughness, thermal fatigue, structural stability including hot corrosion and hot oxidation resistance. The IN-738 superalloy is used as a material for gas turbine in power plants of Electricity Generating Authority of Thailand (EGAT) in a present days.

In present study, as the first step, the assessment of structural degradation of the first-stage turbine blade exposed long-term in land base gas turbine was carried out. The airfoil was exposed in actual operational conditions for 70000 hours and as effect a consequence of the exposure the structure degradation should result. The extent of microstructure changes due to long-term exposure was evaluated. In order to restore the structure, consequently, the series of hot isostatic pressing, where pressing time and temperature were variables, followed by standard heat treatment process were applied with aim to restore the structure. The microstructure changes resulting form HIP process have been evaluated and the results of are presented in this work.

Experimental material and procedures

The nickel base superalloy Inconel 738 was the material the airfoils were cast from. This superalloy is frequently used for the investment casting of turbine airfoils of gas turbine engines in power plants, where the operational temperature is up to 980°C. The chemical composition of the alloy in weight % is shown in Table 1.

Table 1. Chemical composition of IN 738 in weght %.

Cr	Co	Ti	Al	W	Mo	Ta	Nb	Fe	Zr	B	Ni
15,8	8,5	3,5	3,5	2,5	1,9	1,7	0,9	0,07	0,04	0,12	bal.

The IN-738 is a γ' precipitation-strengthened nickel base superalloy, which is widely used as turbine blades in hot sections of gas turbine engines due to its outstanding strength properties at high temperature as well as excellent hot corrosion resistance. Inconel 738 contains substantial amount of Al and Ti together more than 6 wt%, which provides abundant precipitation strengthening of ordered $L1_2$ intermetallic Ni_3 (Al, Ti) γ' phase [5]. The size distribution and, sometimes, the type of γ' precipitate are affected by aging temperature. Usually, selection of a single aging temperature may result in obtaining optimal amounts of multiple precipitating phases.

The nominal two steps heat treatment applied to airfoil prior exposure was as follow:

- Solution heat treat at 1125°C for 2 hours, air cooling
- Aging at 845°C for 24 hours, air cooling

The airfoil serviced for 70000 hours was received from EGAT, Thailand is documented in Fig. 1. About 1 cm^2 rectangular plates were cut from the most severe degradation zone of turbine blades. Metallography investigation was carried out along the blade in a plane perpendicular to the longitudinal blade axis. The study of microstructure characteristics of the initial heat treated alloy and those of thermomechanically exposed was conducted by means of light and scanning electron microscopy (SEM). The plates cut off the blade have been subjected to HIP treatment. All plates were isostatically pressed by identical pressure of 100 MPa. Two homogenization temperatures of 1100°C and 1200°C and four different hold times in range of 1 to 4 hours at each temperature were conducted. The HIP-ed plates were then heat treated according to the standard heat treatment procedure of IN738 alloy. The merit of applied HIP process was investigated using SEM of unetched samples where the size of voids and pores and their frequency were measured and related to the HIP condition.

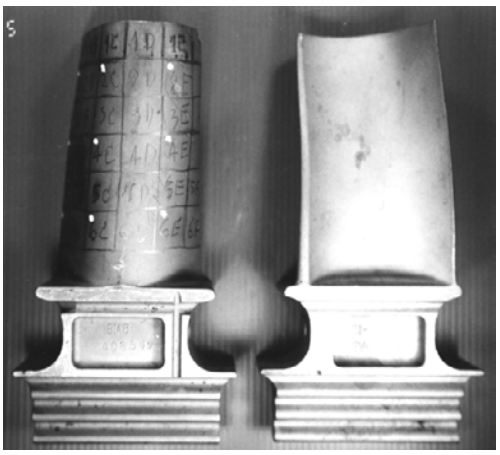

Fig. 1. The exposed airfoils delivered for structure analysis and hot isostatic pressing.

Experimental results and discussion

Microstructure of virgin material

The microstructure of virgin IN738 cast superalloy subjected to two-steps heat treatment is documented in Fig. 2. The structure consists of large dendritic grains with irregular grain boundaries. Eutectic islands, accidentally scattered in grains, of irregular gamma prime were found accidentally scattered within the grains. The fine carbides precipitates are embedded along the grain boundaries, Fig. 3. Scarcely inside the grains and also deposited along the boundaries were found the course irregular in shape the most probably MC carbides. The microstructure of as-cast and heat treated alloy consists of extensive precipitation of ordered gamma prime precipitates, which are of cuboidal morphology and of high volume fraction. The size of these intermetallic precipitates is in range of 500- 700 nm.

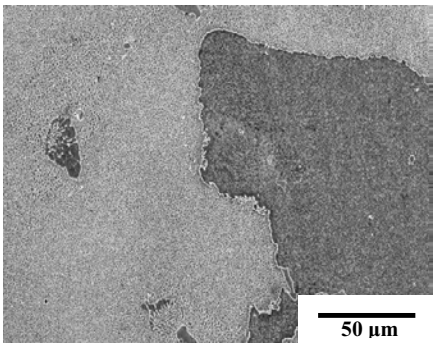

Fig. 2. SEM micrograph of blade structure after nominal heat treatment.

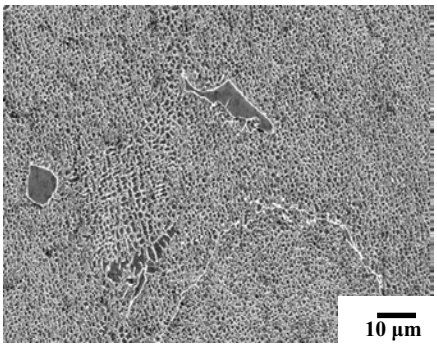

Fig. 3. Gamma prime homogeneous distribution together with fine carbides along grain boundary and eutectic area in IN738 after nominal heat treatment.

Microstructure of exposed blade

SEM micrograph, obtained from the transverse section at about mid-blade height of the exposed airfoil, is shown in Fig. 4. The changes in gamma prime distribution and grain boundary carbides modification is apparent. Service exposure at about 980°C caused extensive degradation of structure. The reduction of the amount of gamma prime phase, the form modification and increasing irregularity of particles are due to long term operation. If

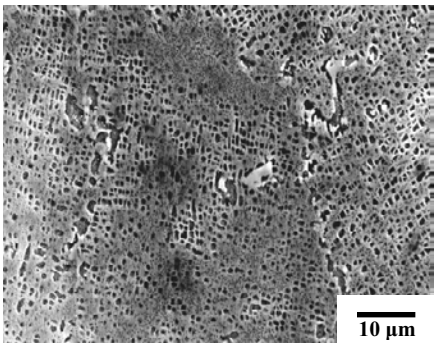

Fig. 4. SEM micrograph of degraded blade structure after exposure of 70000 h.

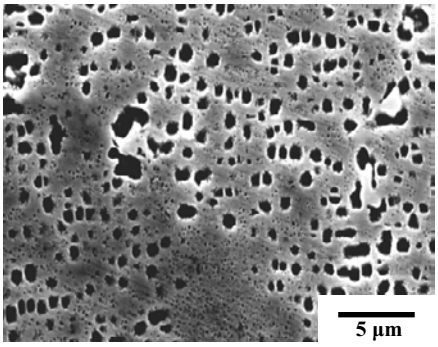

Fig. 5. Morphology of degraded gamma prime and carbides residue.

gamma prime dissolved, the re-precipitation of fine gamma prime, as can be seen in Fig. 5, is possible during subsequent shut down periods of gas turbine. Carbide phases behave somewhat like gamma prime, but subsequent re-precipitation is not reversible process in time of exposure. As regards carbides, they can dissolve or agglomerate during exposure, resulting in substantial variation in amount, morphology and distribution. In Fig. 5 in vicinity of these carbide residues the presence of pores was observed. It can evoke the suggestion that a reason for pores appearance is either creep process, either incipient melting or as-cast porosity.

In order to compare an extent of microstructure degradation in area of blade leading edge and in area of airfoil locks the investigation was carried out. It is expected that that temperature and stress level in the blade root is not as severe as for leading edge of blade and structure changes should be less. The representative structures corresponding to root of blade are presented in Fig. 6 and Fig.7. The noticeable difference in structure obtained from different locations can be easily distinguished in term of gamma prime degradation, size and volume fraction, and carbides changes. This indicates that the microstructure changes along blade edge are on a much greater scale. The structure in lock is well-preserved and only negligible changes of carbides on grain boundaries were observed.

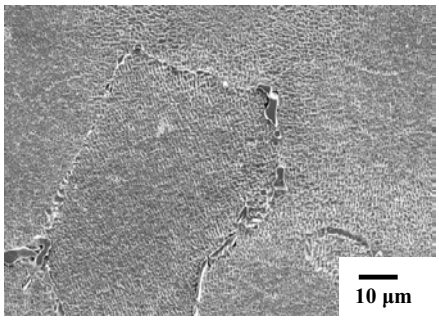

Fig. 6. Carbides decoration of grain boundaries in blade root .

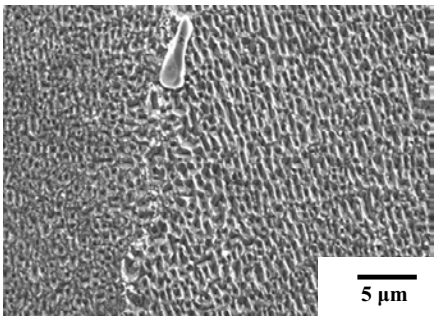

Fig. 7. Uniform gamma prime in matrix and fine carbides along grain boundary.

This study showed that extensive changes resulted from long-term thermomechanical exposure of airfoil extracted from the first stage of high pressure gas turbine section. Service exposure not only modified the morphology of gamma prime but also sufficiently reduced the amount of gamma prime phase and thereby can reduce the alloy creep strength. On the other side some small gamma prime precipitates have been re-precipitated but they can not recover the original properties of blade. In addition to these changes the modification of grain boundaries carbides could deteriorate the alloy creep strength as well. Moreover, dissolution of coarse MC carbide nucleated the microvoids and pores in vicinity of carbide remainings. All these blade structure changes observed can then consequently influenced creep behaviour.

Microstructure of hot isostatic pressed blade

Under prolonged application at elevated temperature, even the most well-designed component will exceed its service life. If the life is exceeded, then failure could occur. The microstructure analysis of exposed airfoil unambiguously confirmed that long term exposure caused degradation of microstructure, however the failures likewise surface cracks were not

observed. On the other side the presence of various internal defects including pores, voids, cavities, and also cracks close to MC carbides have been observed, Fig. 8 a Fig. 9. As previous results showed the restoration of these defects by using solution heat treatment was not effective [4,6]. Therefore it was expected that by applying hot isostatic pressing almost complete recovery of internal structural defects would be possible. After conducting the HIP treatment according to the condition stated, the SEM structure analysis of processed plates

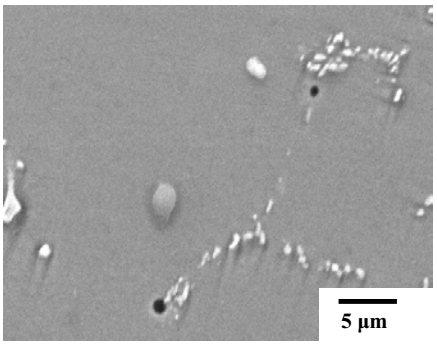

Fig. 8. Microvoids located at matrix and at carbides.

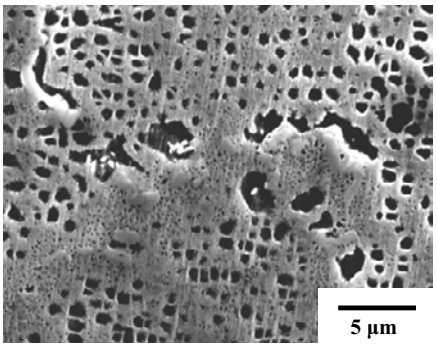

Fig. 9. SEM micrograph of voids and cracks in structure of exposed superalloy.

was performed. After conducting HIP process, accepting all testing conditions, apparent recovery of the defects was observed. The SEM analysis of unetched samples confirmed the effective defects healing by rejuvenation. HIP is successful to almost remove internal voids and cavities and promote diffusion welding. This indicates that defects in the structure can be restored, as can be seen in Fig. 10. Evaluating the HIP processing the amount of internal defects decreased by an increased of HIP temperature and time. The higher temperature and longer time provides the significant beneficial effect in sintering of defects. The relationship between the internal voids diameter and HIP parameters are shown in Fig. 11. It was found that amount of remain microvoids decreased as HIP time and temperature increased.

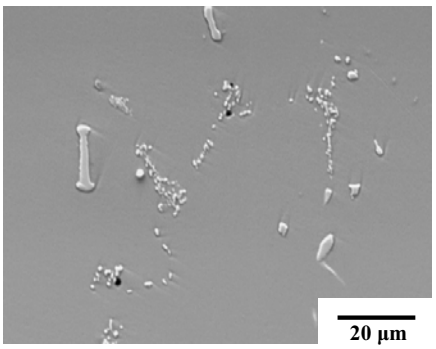

Fig. 10. SEM micrograph of resulted structure after HIP at 1200°C for 4 hours.

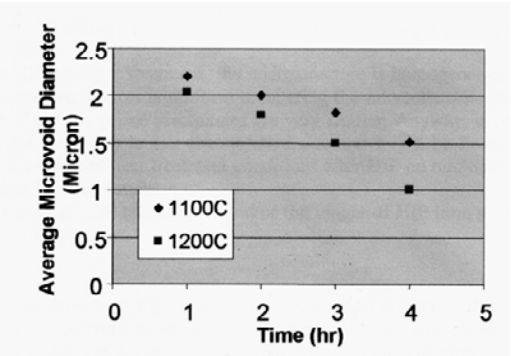

Fig.11. Relationship between internal void diameter and HIP parameters.

An aspect of microstructural and creep degradation that has received some attention, with limited commercial application, is the reported ability to heat treat exposed alloys to recover

creep strength. The damage however depends on time of exposure and the possible recovery can be maintained by using a combination of HIP process and solution heat treatment. The concept was investigated in this study and effect of post HIP heat treatment was analysed with aim to identify the deviations of structure development with respect to IN 738 superalloy virgin structure. The HIP-ed blade pieces, prior exposed at 1200°C for 4 hours, were subjected to standard heat treatment as stated earlier in this work. The resulted microstructure recovery observed after applying such combined treatment is documented in Fig. 12. Comparing this restored structure with that one observed in blade after long term exposure (see Figs. 4 and 5) the progress in microstructure restoration is evident. On the other side the structural characteristics of resulted structure suggested that full recovery was not obtained. Especially the characteristics of the gamma prime morphology and its volume fraction are apparently different. Concerning also the precipitation of fine carbide precipitates $M_{23}C_6$ along the grain boundary it is insufficient. Instead of that the carbide clustering and agglomeration is surviving. The obtained results suggest that full recovery was partial with respect to virgin superalloy. All these microstructure achievements suggest that the resulted structure degradation process has been preceded to such extent that complete recovery of structure would be difficult to maintain.

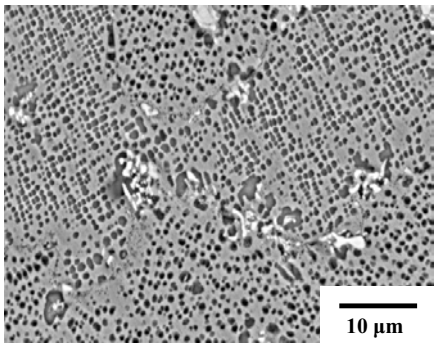

Fig. 12. Microstructure resultıng trom rejuvenation process.

According to the previous studies [7,8,9] it was reported that very few procedures concerning rejuvenation heat treatment have been developed and carried out in Thailand. Usually repairing process for degraded gas turbine components should be modified mainly concerning the solution part of thermal treatment, for next gamma prime and carbide precipitation in appropriate morphology and distribution and subsequently receive qualification tests, including microstructural examination and mechanical testing to ensure rejuvenated materials meet the original materials specification. However, to complete microstructure recovery is for as-cast components very rare due to complex alloying of blade materials. Therefore, the re-heat treatment can restore the microstructure to some extent, but if considering the recovery of the creep properties it will resulted in their limitation.

Hot isostatic pressing process offers the possibility of eliminating closed porosity, voids and creep cavities in cast components. HIP process is able also to improve the homogeneity of the microstructure, both by dissolution of segregates and by elimination of porosity, as well as the material properties. This is especially important in the case of cast parts, which are subjected to high stresses, such as turbine blades cast of nickel base superalloys. Turbine blades for aircrafts and stationary gas turbines are among the first applications of HIP process to cast products [6,10,11]. Furthermore, HIP process, as was shown, may significantly accelerate the healing process, at least for voids and creep cavities, which are locked inside structure. However, as results of experimental showed applied combination of HIP followed by standard heat treatment used for serviced IN 738 superalloy only partially restored the degraded structure of blade. This study showed that microstructure to some extent was recovered when compared to that of long term exposed, but neither gamma prime morphology

nor volume fraction nor grain boundary carbides re-precipitation was such quality that they could guarantee safety run of gas turbine for further long period.

Conclusions

The experimental was carried out with an aim to evaluate the structural degradation of turbine blade cast from IN 738 nickel base superalloy that has been exposed for long term in working condition of land base gas turbine. The state of structure degradation was compared with virgin material. The series of HIP treatments combined with standard heat treatment, ordinary applied for blades prior installing, were carried out to with purpose to restore the structure of exposed blade material. The results obtained are as follow:

- Structure degradation of exposed blade was of great extent considering the change of gamma prime morphology, its volume fraction and grain boundary carbides dissolving.
- The defects in structure including pores, voids and cavities resulting from long thermomechanical exposure were found in structure.
- Hot isostatic pressing was used with success to restore all flaws present in structure.
- Standard heat treatment applied after hot isostatic pressing restored the structure characteristics to some extent. The further investigation is needed to optimise the structure characteristics of exposed blade material.

Acknowledgment

This research was supported by Grant of Ratchada Research Fund, Chulalongkorn University, Bangkok, Thailand. Special thanks are also extending to Electricity Generating Authority of Thailand (EGAT) for experimental material and their technical support. One of the authors (J. Zrnik) is grateful to the Ministry of Education, Slovak Republic for their support concerning the COST 538 Action.

References

[1] J.R. Davis, Nickel, Cobalt, and their alloys, ASM Specialty Handbook, ASM International, 2000.
[2] E.F. Bradley, Superalloys: A Technical Guide, ASM International, 1989.
[3] D.J. Tillack, J.M. Manning, J.R. Hensley, Heat treating of nickel and nickel alloys in: ASM Handbook, Vol. 4, 1994, 907.
[4] O.A. Ojo, N.L. Richards, M.C. Chaturvedi, Scripta Materialia,Vol. 50, 2004, 641.
[5] J. Zrnik, P. Hornak, P. Pinke, M. Zitnansky, Metals Alloys Technologies (Kovine Zlitine Technologie) 3, 1996, 179.
[6] M.J. Donachie, S.J. Donachie, SUPERALLOYS: A Technical Guide, 2nd edition, ASM International 2002.
[7] J.A. Daleo, H.A. Ellison, D.H. Boone, Journal of Engineering for Gas Turbines and Power, July 2002, Vol. 124, 571.
[8] G.W. Meetham, M.H. Van de Voorde: Materials for High Temperature Application, Springer, 2000.
[9] J. Zrnik, P. Strunz, P. Hornak, Metalurgija/Metallurgy, 41, 3, 2002, 232.
[10] www.liburdi.com
[11] P. Wangyao, T. Korath, T. Harnvirojkul, W. Homkarai, Journal of Metals, Materials and Minerals, 14, 1, 2004, 49.

Development of new superalloys for Turbine Disk Applications

Y. Gu, C. Cui, D. Ping, H. Harada, A. Sato, and J. Fujioka
National Institute for Materials Science
1-2-1 Sengen, Tsukuba Science City, Ibaraki, 305-0047, Japan
GU.Yuefeng@nims.go.jp

Abstract

There is always a need to increase the upper temperature limit of turbine disks to allow higher operating temperatures in the design of high efficiency engine. We recently proposed a new concept to design disk alloy. This concept is based on combining the characters of two kinds of γ- γ' two-phase alloys (Ni-base and Co-base alloys). The preliminary results show that this design concept leads up to some promising candidate alloys that can be processed by normal cast & wrought (C&W) route and have 50 °C up in temperature capability compared with C&W U720LI superalloy.

Keywords: Ni-base superalloy, Ni-Co-base superalloy, Disk application, U720Li

1 Intoduction

Higher engine performance can be achieved by higher turbine inlet gas temperature and compression ratio, which mainly depend on the development of the materials with higher temperature capabilities for the key components of turbine engines, such as the turbine blades and the disks.

For enhancing the turbine entry temperature, much work has been done on the improvement of the temperature capability of turbine blades. Figure 1 shows a perspective for the alloy and process improvement in the temperature capabilities of the superalloys for turbine blade components [1-3]. We choose the creep performance (here taken as the highest temperature at which rupture occurs at no less than 1000 hours at 137 MPA) as a measure for the progress. There is about 400 °C improvement in the latest 60 years and the latest target temperature indicated in Figure 1 is the objective of the High Temperature Materials 21 Project (HTM21) led by the Japanese National Institute for Materials Science in collaboration with gas-turbine industries.

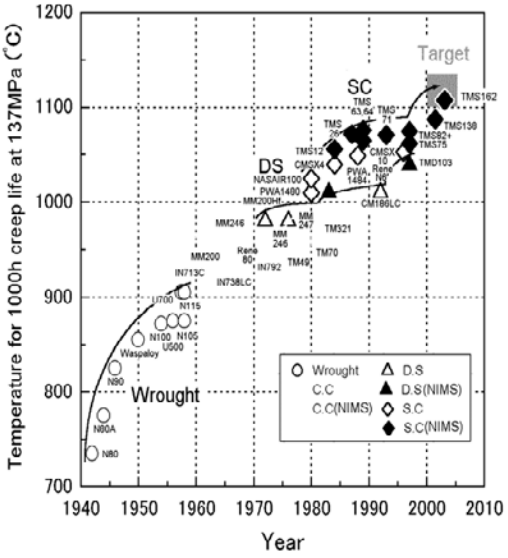

Figure 1. Improvement in temperature capability of Ni-base superalloys for blades.

Comparatively speaking, the thermal capability of disk materials is not subjected to such extreme temperatures as blades but has higher requirements for strength, creep and dwell fatigue crack growth properties for increasing in the compression ratio. Figure 2 shows the progress of turbine disk superalloys ranked by creep/rupture performance (the stress for 1000 h life at 630 MPa) [4-10]. For the latest 30 years, there are about 50 °C increase in the thermal capability for the disk superalloys produced by C&W process route and 60 °C improvement by P/M process route.

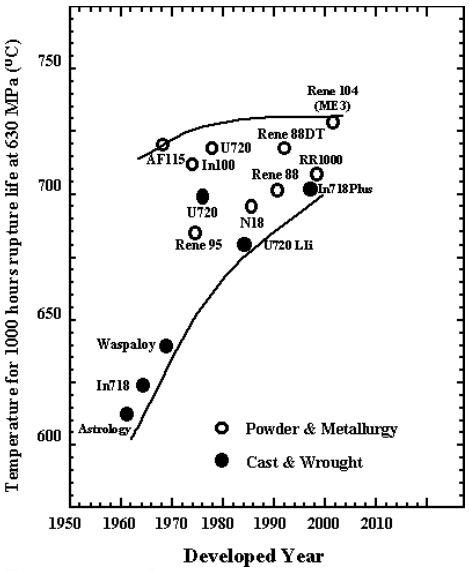

Figure 2. Improvement in temperature capability of Ni-base superalloys for disks.

2 Alloy design

Ni-base superalloys are the typical materials for the hot parts such as blades and disks of either aircraft engines or land-based gas turbines because of their excellent properties, which include high-temperature strength, resistance to creep and fatigue, hot corrosion and oxidation resistance. Most Ni-base disk alloys contain 10-20 wt.% Cr, up to 8 wt.% Al and Ti, 5-23 wt.% Co, and small amounts of B, Zr, and C. Other common additions are Mo, W, Ta, Hf, and Nb [4-10].

In the HTM21, recently, we proposed a new concept to design new disk alloy. This concept is based on combine the characters of two kinds of γ/γ' two phase superalloys (Ni-base and Co-base superalloys) as shown in Figure 3.

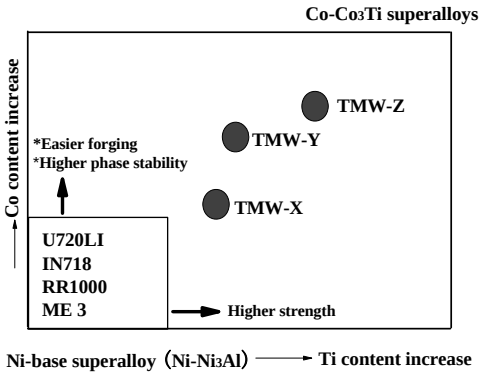

Figure 3. New concept to design disk alloys

Based on our new concept, some Ni-Co base superalloys, called TMW alloys, are designed for the first trial property investigations. The nominal chemical compositions of these TMW alloys are listed in Table 1. Here we refer U720LI

Table 1. The chemical Compositions of TMW alloys, wt%

Alloy No.	Co	Cr	Mo	W	Al	Ti	C	B	Zr	Ni
TMW-1 (U720LI)	**14.8**	**16.3**	**3.06**	**1.29**	**2.36**	**4.79**	**0.032**	**0.016**	**0.03**	Bal.
TMW-2	**21.8**	**14.4**	**2.75**	**1.19**	**2.28**	**5.92**	**0.033**	**0.015**	**0.033**	Bal.
TMW-3	**23.1**	**16.8**	**3.12**	**1.25**	**1.87**	**5.44**	**0.03**	**0.018**	**0.022**	Bal.
TMW-4	**26.3**	**14.9**	**2.81**	**1.09**	**1.93**	**6.02**	**0.017**	**0.017**	**0.019**	Bal.
TMW-5	**28.6**	**12.8**	**2.42**	**1.0**	**2.0**	**7.4**	**0.03**	**0.013**	**0.021**	Bal.
TMW-6	**30.0**	**14.6**	**2.7**	**1.08**	**1.78**	**6.35**	**0.029**	**0.015**	**0.020**	Bal.
TMW-7	**31.1**	**15.6**	**3.0**	**1.05**	**1.58**	**5.65**	**0.032**	**0.017**	**0.022**	Bal.

alloy as TMW-1 alloy as a comparative and other six new disk alloys are named as TMW-2 to -7 alloy respectively. In the TMW disk alloys, the contents of Co and Ti are higher than that of normal disk alloys, and Co content is varied from about 22 to 31wt% and Ti content is varied from 5.1 to 7.4 wt%.

3 Microstructure

For these seven TMW alloys, 50-kg ingots were cast and then hot rolled in the Special Metals Corporation. The hot rolling was conducted smoothly at about 1100 °C with reduction of 75% (from 50.8 mm to 12.7 mm). For microstructures investigation, small samples were cut from as-rolled plates and heat treated at 1100°C/4h + air cooling (AC)

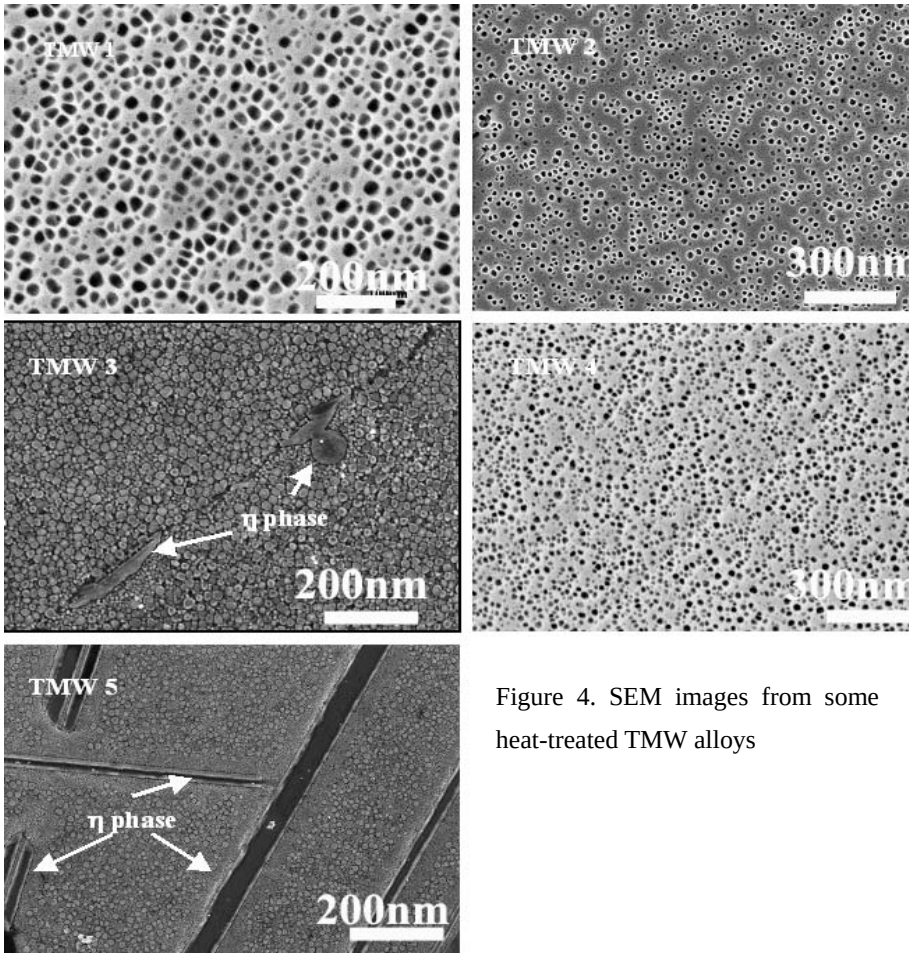

Figure 4. SEM images from some heat-treated TMW alloys

+ 650 °C /24h AC + 760 °C/16h AC. The grain sizes for all heat treated alloys are about 5 to 10 μm. Figure 4 shows some SEM images of the microstructures. For TMW-1 (U720LI), TMW-2 and TMW-4 alloys, γ-γ' two-phase structure was identified and the morphology and size of γ' phase are almost the same. For TMW-3 and TMW-5 alloys, some plate-shape phase was found. EDS results indicated that the plate-shape phase was rich in Ti and Ni.

4 Property assessment

The properties requirements for disk alloys are complex but high yield (0.2% offset) and ultimate tensile strengths with good tensile ductility, high creep resistance are major ones.

The tensile yield strengths as a function of the tested temperatures for tested alloys are shown in Figure 5. At room temperature, all tested TMW alloys showed high yield strength at about 1200 MPa. However, the yield strength of TMW-1 alloy (U720LI) dropped quickly than TMW-2 to -4 alloys at temperatures below 750 °C. At 650 °C, there was about 70 °C up to the strengths of TMW-2 and -4 comparing with TMW-1 (U720LI). At 750 °C, the yield strength of TMW 2 and 4 alloys still kept at about 950 MPa, which was about 100 MPa higher than that of TMW-1 alloy (U720LI). Meanwhile,

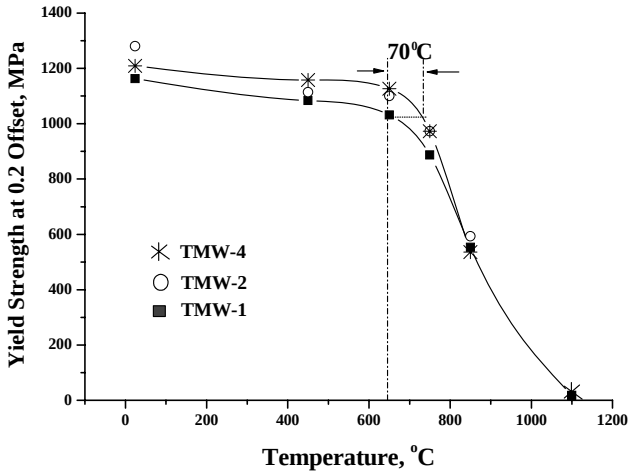

Figure 5. The tensile yield strengths of the tested alloys.

at temperatures above 1100°C, the yield strengths of all tested TMW alloys were almost the same, which indicates that TMW alloys may be processed by hot forge like TMW-1 (U720LI) alloy.

Another important critical property that must be considered is creep resistance of new disk superalloys. Tensile creep tests were conducted at 650 °C and 725 °C under initial applied stresses of 628 or 630 MPa. Figures 6 and 7 display the strain-time curves.

At 650 °C and 628 MPa (Figure 6), TMW-2 and -6 alloys had better primary creep resistance as illustrated by a lower creep strain for the first 300 hours. Time to 0.2% creep strain was about 810 hours for TMW-1 alloy (U720LI) and was over 1000 hours for the other tested TMW alloys. It was noted that 1000-hour creep strain was only about 0.05% for the TMW-2 alloy.

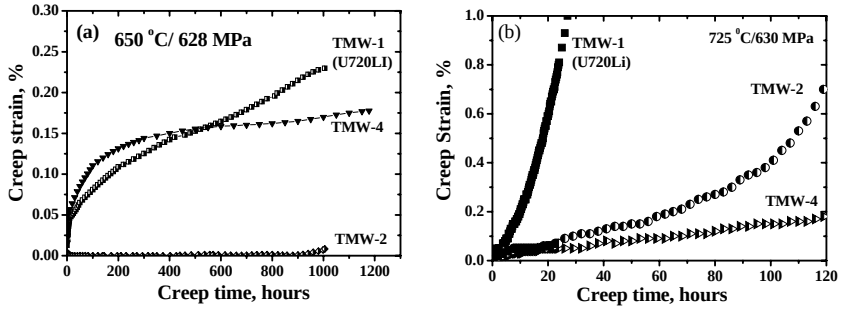

Figure 6. Tensile creep curves at (a) 650 °C/628 MPa and (b) 725 °C/630 MPa.

At 725 °C and 630 MPa (Figure 7), time to 0.2% creep strain was about 10 hours for TMW-1 alloy (U720LI), 62 hours for TMW-2 alloy and over 120 hours for -4 alloy. So there is 12 times improvement in creep resistance of TMW-4 alloys compared with TMW-1 alloys (U720 LI) at such high temperature and stress.

5 Summary

All above results show that our new design concept leads up to some promising candidate alloys, such as TMW-2 and -4 alloys, which have γ-γ' two-phase structure, can be processed by cheap "cast & wrought" (C&W) route and have at least 50°C increase (compared with C&W 720Li superalloy) in temperature capability.

Achknowledgement

The authers would like to thank Dr. M. Fahrmann and Dr. S. Patel at Special Metals Corporation for their useful discussion and the support of alloy process.

6. Reference

[1] H. Harada, et al.: High Temperature Alloys for Gas Turbines 1982, (1982).
[2] H. Harada, et al.: High Temperature Alloys for Gas Turbines 1990, (1990)1319.
[3] H. Harada: IGTC2003Tokyo, (2003) KS2.
[4] M. Durand-Charre: The Microstructure of Superalloys, Amsterdam B. V. Publisher, (1997).
[5] M. J. Donachie and S. J. Donachi: Superalloys, ASM International Publisher, (2002).
[6] P. R. Bhowal, E. F. Wright and E. L. Raymond: Metall. Trans. A, 21A(1990)1709.
[7] W. D. Chao and R. kennedy: Superalloys 2004, (2004)91.
[8] T. P. Gabb, et al.: NASA/TM-2002-211796.
[9] T. P. Gabb, et al.: NASA/TM-2004-213066.
[10] J. R. Groh and D. P. Mourr: Superalloys 2004, (2004)101.

INFLUENCE OF CARBIDES AND OXIDATION ON THERMAL FATIGUE BEHAVIORS OF TWO NICKEL-BASE SUPERALLOYS

Y.L. Li, C. Yuan, J.T. Guo*, J.S. Hou

Department of Superalloys, Institute of Metal Research, Chinese Academy of Sciences,
72 Wenhua Road, Shenyang 110016, China
*Email: jtguo@imr.ac.cn

Abstract

An experimental study of thermal fatigue (TF) behaviors of two polycrystalline nickel-base superalloys K445 and K438 was conducted between the temperatures ranging from 800 to 900 °C and 25 °C, using plate specimens notched to induce crack initiation. Conventional optical microscopy (OM), scanning electron microscopy (SEM) and transmission electron microscopy (TEM) examinations were conducted to investigate crack development and TF damage mechanisms. Almost all of the primary fatigue cracks at elevated temperatures propagate intergranularly and the secondary crack is transgranular. At 800 °C, crack propagation is carbide-predominant, where small blocky $M_{23}C_6$ discretely precipitating at grain boundaries (GBs) can effectively impede crack initiation in alloy K438. On the other hand, coarse MC carbides either at GBs or within the grain interior, as well as decohesion of MC/matrix interface, are the preferential sites of crack initiation and propagation in alloy K445. At 900 °C, crack propagation is an oxidation-dominant and carbide-assisted process. Stress assisted grain boundary oxygen (SAGBO) embrittlement is the principle mechanism of the environmental degradation to the alloy at the crack-tip region in two alloys.

Keywords: superalloys, thermal fatigue, crack, carbide, oxidation.

Introduction

Thermal fatigue (TF) caused by thermal strains and stresses which are associated with heating and cooling of components in the absence of external loads is one of the primary life limiting factors of nickel-base superalloys for turbine blades and vanes in advanced gas turbine [1]. Glenny and co-workers introduced a fluidized bed technique using tapered disc specimens [2]. Wedge-type specimens and a burner rig were widely applied to evaluate the TF resistance of candidate materials for turbine components by some researchers [3-6]. Influence of test conditions (temperature, environment etc.), specimen geometry and microstructures on TF behavior of superalloys has been determined in detail in references [3-4, 7]. In addition, short crack initiation and growth mechanisms were also discussed in some detail [8, 9]. The oxidation-fatigue interaction was found to be the main mechanism of TF failure, thus oxidation damage models were developed favored by a finite element computation of the temperature field and a uniaxial calculation of the stress-strain cycle [4, 10].

Carbides, in the form of MC, $M_{23}C_6$, M_6C, M_7C_3 etc., play a crucial role in determining high-temperature mechanical properties of superalloys, though the behavior is quite complex. Some researchers devote themselves to modify the MC morphology in order to enhance the creep and fatigue properties of superalloys at elevated temperatures by adding carbon, hafnium and magnesium [11-13]. The influence of grain boundary (GB) precipitates (for example, $M_{23}C_6$) on the properties of Ni-base superalloys has also been recognized [11, 14-15]. Both globular grain-boundary M_6C and massive acicular interdendritic M_6C are detrimental to fatigue life [7]. Generally, carbide strengthening is controlled by the size, morphology and distribution, as well as the mismatch.

Hence, in this study much attention is paid to the effects of microstructure (distribution, morphology and categories of carbides), environment and maximum temperatures on TF resistance of two cast nickel-base superalloys K445 (a newly developed superalloy by IMR) and K438 (a superalloy exhibiting a variety of excellent properties) respectively, using notched plate-like specimens.

Experimental procedures

Nominal compositions of tested materials are listed in Table 1. This two materials, in the form of cast discs as received, were heat treated simultaneously in the muffle furnace after a solution treatment at 1120 °C for 2 hours and subsequent an aging heat treatment at 850 °C for 24 hours, both followed by cooling to room temperature in still air.

Table 1. Nominal compositions of K445 and K438 alloys (wt.%)

Alloy	C	Cr	Co	W	Mo	Al	Ti
K445	0.07-0.12	13.7-14.1	9.5-10.5	4.0-4.6	1.2-1.8	3.7-4.3	2.4-3.0
K438	0.10-0.20	15.7-16.3	8.0-9.0	2.4-2.8	1.5-2.0	3.2-3.7	3.0-3.5
Alloy	Nb	Ta	B	Zr		Ni	
K445	-	4.4-5.0	0.01-0.04	0.025-0.125		Balance	
K438	0.6-1.1	1.5-2.0	0.005-0.015	0.05-0.15		Balance	

Specimens for TF tests were machined from the as-heat-treated discs according to the dimensions demonstrated in Fig.2. Two main faces of each sample were ground up to 1500-grit of water SiC paper and then mechanical-polished in order that the influence of nicks on the initiation and growth of cracks could be reduced to a negligible extend. Thermal shocks of TF specimens were simulated by heating them in a furnace at maximum temperatures ranged from 800 to 900 °C for about 15 minutes and cooling them immediately for 5 seconds in water controlled at 25 °C constantly. Tests were periodically interrupted to check for crack initiation, inspect specimen surfaces and measure the length of most cracks on both surfaces of every specimen using a binocular microscope with a graduated eyepiece. Only evolution of major cracks, which generally formed first, is reported in this paper. The final magnitude of the length of cracks after a certain thermal cycles was obtained by averaging all the lengths of major cracks observed on three similar specimens applied to every

testing temperature at the same time. Besides, isothermal oxidation experiments were carried out at 800 and 900 °C to determine the oxidation effect.

Metallographic observations were made on the etched specimen surfaces using optical microscope (OM) and scanning electron microscope (SEM) equipped with energy dispersive spectroscopy (EDS) system.

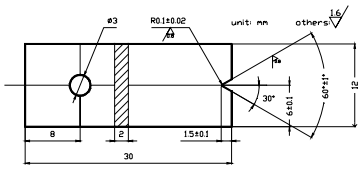

Figure 1: Geometry and dimensions of thermal fatigue test specimens.

Results

The heat-treated microstructures for both alloys consist of γ matrix, γ′ precipitate, γ+γ′ eutectic and carbides, distribution of which is shown in Fig.2 and summarized in Table 2. Alloy K445 has mostly a few large, blocky or rod-like (Ti, Ta)C type carbides at the grain boundaries (GBs) (Fig. 2b) as well as in the matrix (Fig. 2a) according to the EDS analysis in Fig. 2e. In alloy K438, (Ti, Nb, Ta)C has a propensity to situate within the grain (Fig. 2c and f), but small blocky $M_{23}C_6$ carbides are located discretely only along the GB (Fig. 2d). However, when GB passes through eutectic regions in alloy K438, MC carbide tends to precipitate in these areas.

Several cracks were observed to initiate and propagate during tests in all examples. As described above, only the length of the major crack (the longest) is plotted as a function of TF cycles in Fig. 3. With the exception of the constant growth rate at 900 °C, which is 8.32μm/cycle and 9.42μm/cycle for K445 and K438 alloys respectively, the TF resistance of K438 is somewhat superior to that of K445 at all tested temperatures. This is verified by activation energy calculations in the constant-rate crack propagation period following the classic Arrhenius equation, i.e. Q_p=108.95kJ/mol for alloy K445 and Q_p=130.94kJ/mol for alloy K438 in this testing condition. Furthermore, almost all of the major cracks progressed following a kind of similar course, initiating from the notches within the first few shock cycles at a pretty high rate in the successive 10 to 30 cycles, and then propagating at a constant but lower growth rate.

From metallurgical observations, it can be noticed that in all the specimens tested in the temperature range, especially at 800 °C, fatigue cracks are predominantly initiated from

cracked primary carbides or carbide/matrix interface along GBs. As shown in Fig. 4, large MC carbides always lead to early crack initiation, and connection of the cracks initiated at or along the carbides is contributed to the crack's propagation. It should be noticed that oxidation does not seem to influence the initiation process at 800 ℃， because only a quite thin oxide scale was visible in the specimens.

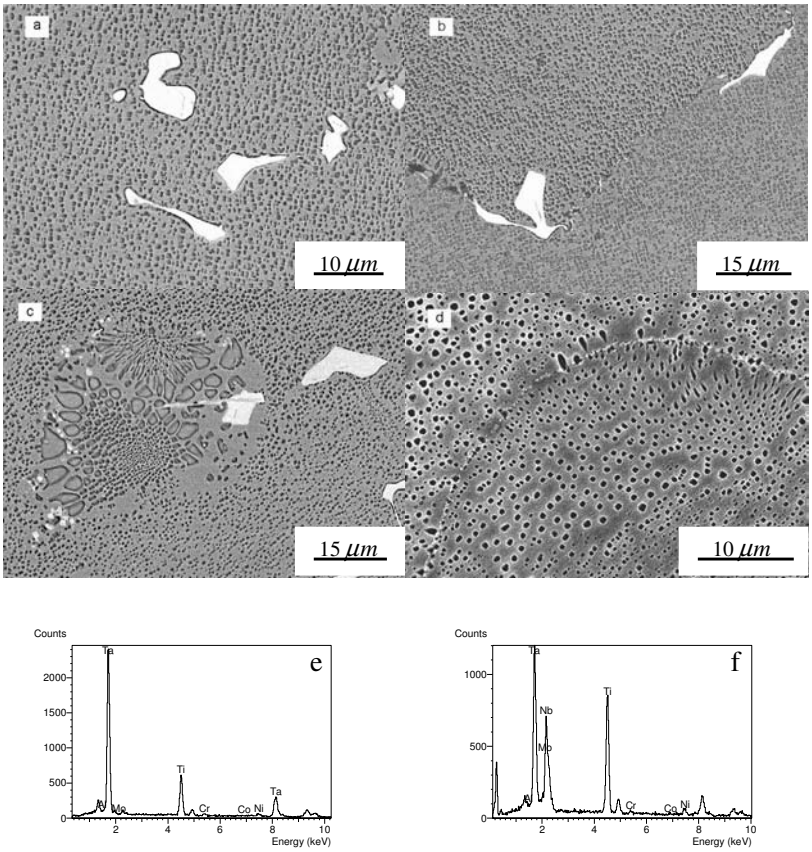

Figure 2: SEM images showing carbides distributions of K445 and K438: (a) K445, grain interior; (b) K445, grain boundary; (c) K438, grain interior; (d) K438, grain boundary; (e) Typical EDS analysis of MC in (a) and (b); (f) EDS analysis of MC in (c).

The crack propagation path has also been studied on the surface of thermal-fatigued specimens. Almost all of the primary cracks propagate along the GBs, although some secondary cracks grow into the grain interior. A major crack with a secondary crack developed is shown in Fig. 5. It is worth noting that this secondary crack passes through a MC carbide

distributed in the interdendritic area in the vicinity of the primary crack, ahead of which occurrence of de-cohesion of carbide/matrix interface is detected. Further observation shows that cracks in alloy K438 have more inclination to propagate along GBs where γ+γ′ eutectic exists (Fig. 4b).

Table 2. Carbide distributions of K445 and K438.

Alloy	grain boundaries	grain interior	proximate to γ+γ′ eutectic
K445	MC (coarse, dominant) $M_{23}C_6$ (coarse, few)	MC (coarse)	$M_{23}C_6$, M_6C (coarse, few)
K438	$M_{23}C_6$ (fine, dominant) MC (coarse)	MC (coarse)	MC (coaarse)

On the other hand, oxidation begins to become important as testing temperature increases though the influence of carbides still has to be taken into account considerably. Fig. 6a shows a typical view of a TF crack on a specimen surface. Obviously, a much thicker oxide scale with internal oxidation occurring is formed at the crack flanks along the grain boundary far from the tip where the crack opening is rather narrow. The EDS analysis (Fig. 6b) demonstrates that the internal oxide is Al_2O_3, which is affirmed by an oxidation experiment at 900 °C carried out in this study. It is well worth noting some individual carbides in the matrix as well as those at the crack are fractured and oxidized. And this is in a good agreement with that discussed in reference [16].

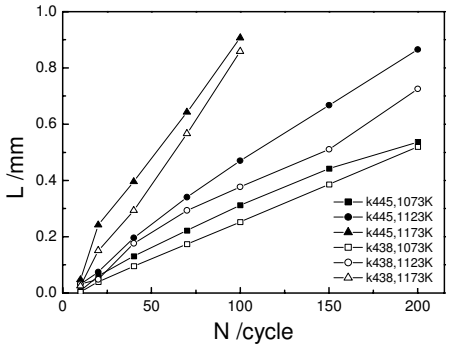

Figure 3: Plot of the longest fatigue crack length L as a function of number of thermal cycles N at various temperatures

Discussion

Effect of carbides in TF behaviors

In thermal fatigue, stresses and strains resulting from temperature gradients cycle between maximum and minimum values, so that some studying methods of LCF or creep can be applied to TF investigations [7].

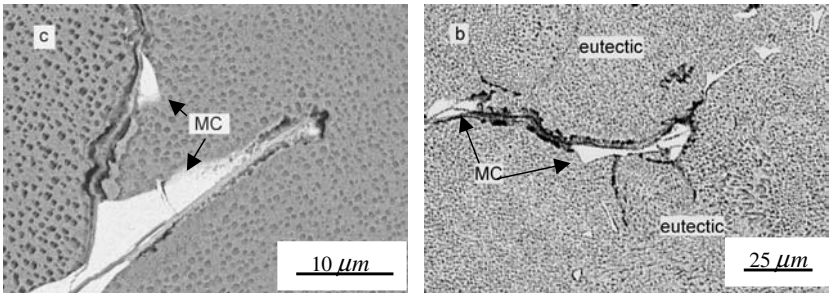

Figure 4: SEM images showing the cracking of primary MC carbides at 800℃ for 200 cycles: (a) K445; (b) K438.

Based on the curves in Fig. 3, alloy K438 is a little better than K445 in terms of crack initiation and propagation generally. Previous investigations [14] on superalloys have shown that high temperature strength is strongly affected by carbide morphology and distribution at GBs. It has been widely reported that blocky, discrete $M_{23}C_6$ particles at GBs can improve creep properties [11]. Thus, small, discrete $M_{23}C_6$ precipitates at the GBs in all K438 (Fig. 2d) are undoubtedly responsible for its superior resistance to TF failure. The much finer GB $M_{23}C_6$ carbide can effectively prevent GB migration during deformation, strengthening GB, and be beneficial to the fatigue property of the alloy.

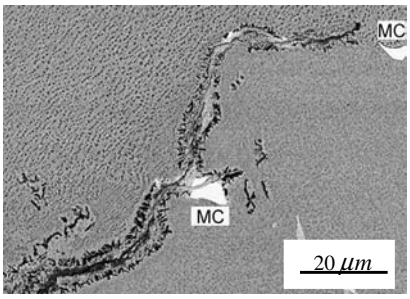

Figure 5: SEM image showing the propagation path of a primary crack with a secondary crack developed, K445 at 850℃, 200 cycles.

On the contrary, coarse MC carbide, either precipitates at GBs or within grain interior, can serve as origins of crack initiation and propagation by de-cohesion of the MC/matrix interface or the cracked MC carbide, as shown in Fig. 4, 5 and 6. This is consistent with the results obtained in references [15]. Large irregular MC carbide particles are often observed at GBs in alloy K445 and correspondingly contributed to its weakness of TF property. It is also the case for MC carbides along GBs near eutectic regions in alloy K438, though it has been reported that eutectic MC carbides along GBs will enhance creep performance through inhibiting GB sliding [11]. Besides, as described above MC precipitates within the grains enable easy

transgranular cracks propagation both in alloy K445 and K438.

Effects of oxidation

Influence of oxidation either on TF behaviors [4, 10] or mechanical fatigue [17-19] of superalloys has been discussed, which suggested that a longer fatigue life can be obtained as the oxygen partial pressure increases. It is necessary to mention that merely a negligibly thin oxide scale can be observed at 800 °C. As a result, a conclusion can be drawn that it is only at higher temperatures that oxidation has to be taken into consideration to analyze crack initiation and propagation mechanisms [20].

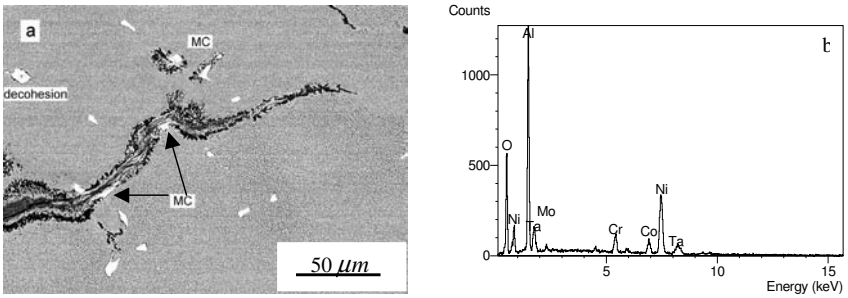

Figure 6: (a) SEM image showing a typical view of TF crack with sever oxidation occurring, K445 at 900℃ for 100 cycles; (b) EDS analysis of internal oxide.

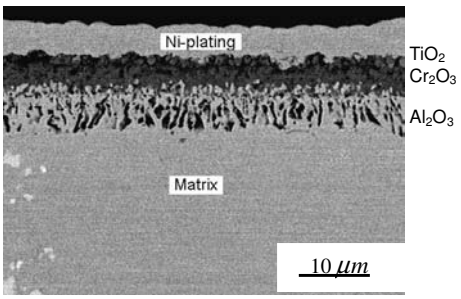

Figure 7: SEM image showing the cross-sectional micrograph of scales formed on K445 at 900℃ for 25 hours.

As discussed above, primary cracks along the GBs are in good agreement with that under atmospheric pressure intergranular crack is predominant [17, 19]. During the process of TF, stresses are induced due to the sudden change of temperature field distribution. Stress assisted grain boundary oxygen (SAGBO) embrittlement [20] may be the principal mechanism at the region of high stress concentration such as at the crack-tip region, because environment did not produced significant attack in unstressed materials [21]. According to the results of simple oxidation experiments at the same temperature (Fig. 7), an outermost surface scale consists of

$NiCr_2O_4$ and TiO_2 is formed firstly, which is porous and pervious to oxygen. Thus, at this stage the crack growth rate is higher. Later the formation of a dense Cr_2O_3 and Ta-contained oxide sub-layer can prevent oxygen penetration along the GB effectively leading to the reduction of crack growth rate. Moreover, internal stress is a ubiquitous phenomenon to damage oxide scale, which is severest when temperature decreases. As a result, internal stress may also play an assisted role in the cracking and opening of oxide scale at GB as the specimen is cooled. The narrowest crack tip in both Fig. 5 and Fig. 6 show that crack initiates and grows in the cooling period. Simple oxidation tests at 900 °C demonstrate that oxidation resistance ability of alloy K445 is better than that of alloy K438. This may be contributed to a lower crack propagation rate of alloy K445, though its crack length is shorter.

Nevertheless, it is rather difficult to conclude whether the oxidation of GBs occurs before their cracking or the cracking occurs before oxidation. It seems that both cases are possible to take place. In terms of the former, GB tends to be oxidized preferentially in comparison with the grain interior. Thus, under the exposure of thermal fatigue, the GB probably becomes susceptible enough to crack due to the cycled impact of thermal stresses. As for another case, GB cracks firstly because of the existence of MC carbides. Then oxidation takes place at the crack flanks. Consequently, the influence of oxidation, as well as the carbides, accelerates the crack propagation together. Besides, it is necessary to mention that carbide oxidation is not discussed in this paper though it can also influence the thermal fatigue behavior.

Conclusions

This study has focused on the TF behaviors of two polycrystalline Ni-base superalloys K445 and K438 using notched specimens machined from bulk castings. The investigation of K445 and K438 under TF cycling has shown the following results:

1. Alloy K438 displays a better TF resistance than K445 at all tested temperatures in general.
2. Primary TF cracks usually propagate intergranularly, while the secondary TF cracks are transgranular mostly.
3. Crack propagation is a carbide-predominant process at 800 °C, but oxidation-dominant and carbide-assisted at 900 °C.
4. Small blocky $M_{23}C_6$ particles discretely precipitating at grain boundaries of alloy K438 can effectively prevent crack initiation. On the other hand, cracked coarse MC carbides as well as decohesion of MC/matrix interface are the preferential sites of crack initiation and propagation in both alloys.
5. Stress assisted grain boundary oxygen (SAGBO) embrittlement is the principle mechanism of the environmental degradation to the alloy at the crack-tip region and can be attributed to the bigger crack propagation rate of the alloy K438.

References

[1] C.T. Sims, in: M. Cell, et al. (Eds.), Superalloys 1984, The Metallurgical Society of AIME, Pennsylvania, 1984, p. 411.

[2] E. Glenny, in: Thermal and High Strain Fatigue, Institute of Metals, Iron Steel Institute, London, 1967, p. 346-363.

[3] F. Rézaï-Aria, M. François, L. Rémy，Fatigue Fract. Eng. Mater. Struct. 11 (1988) 277-289.

[4] M. François, L. Rémy，Metall. Trans. A 21 (1990) 949-958.

[5] M. Blümm, B. deMestral, G. Eggeler, F. Rézaï-Aria, Scr. Metall. Mater. 33 (1995) 719-725.

[6] L. Felberbaum, K. Voisey, M. Gäumann, B. Viguier, A. Mortensen, Mater. Sci. Eng. A 299 (2001) 152-156.

[7] J.D. Varin, in: W.C. Hagel, C.T. Sims (Eds.), Superalloys, John Wiley and Sons Inc., New York, NY, 1972, p. 242-251.

[8] J.C. Healy, L. Grabowski, C.J. Beevers, Int. J. Fatigue 13 (1991) 133-138.

[9] T. Connolley, P.A.S. Reed, M.J. Starink, Mate. Sci. Eng. A 343 (2003) 139-154.

[10] F. Rézaï-Aria, B. Dambrine, L. Rémy, Fatigue Fract. Eng. Mater. Struct. 11 (1988) 291-302.

[11] Q.Z. Chen, C.N. Jones, D.M. Knowles, Mate. Sci. Eng. A 385 (2004) 402-418.

[12] Q.Z. Chen, C.N. Jones, D.M. Knowles, Acta Mater. 50 (2002) 1095-1112.

[13] H.Y. Bor, C.G. Chao, C.Y. Ma, Metall. Mater. Trans. A 30 (1999) 551-561.

[14] E.W. Ross, K.S. O'hara, René N4: a first generation single crystal turbine airfoil alloy with improved oxidation resistance, low angle boundary strength and superior long time rupture strength, in: Kissinger, D.J. Deye, D.L. Anton, A.D. Cetel, M.V. Nathal, T.M. Pollock, D.A. Woodford (Eds.), Superalloy 1996. TMS, Warrendale, PA, 1996, p. 19-25.

[15] A. K. Koul, W. Wallace, Metall. Trans. A 13 (1982) 673-675.

[16] J. Reuchet, L. Rémy, Mater. Sci. Eng. 58 (1983) 33-42.

[17] R. Molins, G. Hochstetter, J.C. Chassaigne, E. Andrieu, Acta Mater. 45 (1997) 663-674.

[18] C.F. Miller, G.W. Simmons, R.P. Wei, Scripta Mater. 44 (2001) 2405-2410.

[19] B. Kang, X.B. Liu, C. Cisloiu, K. M. Chang, Mater. Sci. Eng. A 347 (2003) 205-213.

[20] J. Reuchet, L. Rémy, Mater. Sci. Eng. 58 (1983) 19-32.

[21] S. Florren, R. Kane, Met. Trans. A 10 (1979) 1745-1751.

LOW CYCLE FATIGUE BEHAVIOR OF WROUGHT NICKEL BASED SUPERALLOY GH413

X.G. GUO [a, b, c], J.T. GUO [b,*], C. Yuan [b], H. C, YANG [a]

[a] The College of Material and Metallurgy, NEUT. Shenyang 110016 China.

[b] Institute of Metal Research. Chinese Academy of Sciences.72 Wenhua Road,.Shenyang 110016 China

[c] Shenyang University. Shenyang 110044, China.

Abstract

The low cycle fatigue behavior of wrought nickel based superalloy GH413 had been examined both at room temperature and 850℃ in laboratory air. A cyclic hardening had been observed at both temperatures. The fatigue properties can be rationalized in term of the Manson and Coffin equation relating the total strain range with the number of cycles to failure. For given total strain range the fatigue life of GH413 alloy at 850℃ is substantially less than that at room temperature. The fracture surface of the fatigue specimens was studied using scanning electron microscopy and transmission electron microscopy. It was found that the fatigue crack initiation is transgranular, the fatigue crack propagation is transgranular, and the mixed mode of transgranular and intergranular. The cyclic deformation, creep and oxidation are regarded as the main causes of fatigue life reduction and intergranular cracks propagation.

Keywords: Low cycle fatigue; Wrought Ni-based superalloy; Crack initatation; Crack propagation, Cyclic strain

*Corresponding Author: J.T. GUO

Department of Superalloys， Institute of Metal Research，The Chinese Academy of Sciences. Shenyang,.110016, China.
Tel: +86-24-23971917. Fax: +86-24-83978045. E-mail: jtguo@imr.ac.cn

1. Introduction

GH413 alloy is a new researched solid –solution strengthened Ni based superalloy that possesses excellent strength at elevated temperature, and combines with very good resistance to heat corrosion. This alloy is being used in gas turbines of sea ships. Due to cyclic thermal and mechanical stresses applied to these parts in service, failure can often be related to fatigue. In order to obtain satisfactory service for engineering applications, it is necessary to characterize the fatigue behavior of GH413 alloy, not only under loading at a design temperature but also under the start-up condition at room temperature.

A great deal of attention has been paid to the low cycle fatigue performance of superalloys. It has been well documented that low-cycle fatigue properties of superalloys, such as cyclic stress responses, cyclic stress–strain curves, and low-cycle fatigue lives, could be affected by different parameters relating to microstructure and testing conditions [1-7]. Concerning the low-cycle fatigue life data analysis, the well-known Manson–Coffin equation was often used to describe the relationship between the strain range and fatigue life and to predict the fatigue life of structural materials, especially for new materials [8-10].

The purpose of this paper is to study experimentally the low-cycle fatigue behavior of GH413 alloy in order to obtain reliable and useful data of this new superalloy for engineering applications,

2. Experimental

The alloy was supplied as hot-rolled bar of 23 mm diameter. Its nominal chemical composition of the GH413 alloy is listed in Table 1. Solution-annealing was carried out at 1210℃ for 2 hours followed by air cooling to room temperature, firstly precipitated at 1050℃ for 4 hours followed by air cooling, then secondly precipitated at 850℃ for 16 hours followed by air cooling to room temperature. The material is mainly composed of face-center-cubic austenitic grains with annealing twins. The tensile properties of the alloy after the heat treatment are in Table 2.

Table1. The composition of GH413 alloy (wt.%)

C	Cr	W	Mo	V	Al	Ti	Fe	Mn	B	Si	Mg	Ni
0..04	14.82	6.05	3.27	0.5	2.48	2.0	0.18	<0.01	0.013	0.11	0.004	Bal

Table2. The tensile properties of GH413 alloy

Temperature(℃)	Yield strength (MPa)	Ultimate strength (MPa)	Elongation (%)	Reduction of area (%)
R T	745	1060	11.0	10.5
850	653	769	20.0	26.0

Push-pull cylindrical fatigue specimens, with a gauge length of 12 mm and a diameter of 6 mm, were machined after heat treatment. Fatigue tests were carried out at room temperature and 850°C in air on a computer-controlled MTS 810 closed-loop servo-hydraulic test machine under different fully reversed strain amplitudes ranging. The stress stain hysteresis loops for selected cycles were recorded by a computer. A triangular strain waveform with zero mean strain and with frequent f = 0.125 Hz was used for all the tests conducted between room temperature and 850°C. The temperature fluctuation over the gauge length area was maintained within ±2°C. All specimens were run to failure. The fracture surfaces of failed specimens were examined by a scanning electron microscope to determine the fatigue crack initiation and propagation modes. The microstructure of GH413 alloy after fatigue testing was examined by a transmission electron microscope. The samples for TEM were obtained from thin slices of 0.5 mm in thickness, and cut from the regions adjacent to the fracture surface. Thin foils were prepared by initially grinding the slices down to 0.1mm and then electro polishing in a solution containing 5 volumes percentage (vol. %) of perchloric acid and 95 vol.% of ethanol using a twin jet apparatus.

3. Results and discussion

3.1. Low-cycle fatigue life behavior

From the viewpoint of engineering applications, the best way to describe the low-cycle fatigue behavior of the GH413 alloy is to use the fatigue life of the alloy as a function of total strain amplitudes at different temperatures, as shown in Fig. 1. It was found that temperature had a significant influence on the low cycle fatigue life. The low-cycle fatigue life of the alloy at room temperature is longer than that of the alloy at 850℃ at a given total strain amplitudes. The total strain amplitudes that the alloy received at room temperature is larger than that of the alloy at 850 ℃ at a given cyclic life.

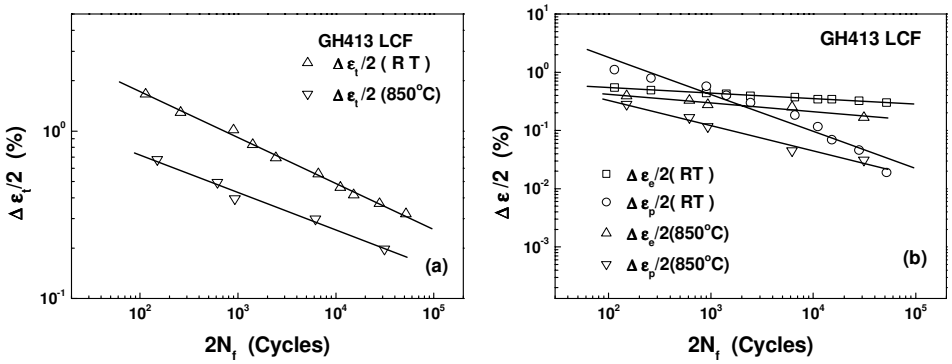

Fig.1 Strain amplitudes – life curves of GH413 alloy at 850℃ and room temperature. (a) Total strain amplitudes – life curve, (b) elastic and plastic strain amplitudes – life curve.

A better knowledge of low cycle fatigue behavior of the alloy is generally obtained by separating the total strain amplitudes into the plastic and elastic strain amplitudes. Based on the Coffin–Manson relationship [11], the total strain amplitudes can be expressed as

$$\frac{\Delta\varepsilon_t}{2}=\frac{\Delta\varepsilon_e}{2}+\frac{\Delta\varepsilon_p}{2}=\frac{\sigma_f^{'}}{2E}(2N_f)^{b^{'}}+\frac{\varepsilon_f^{'}}{2}(2N_f)^{c^{'}} \quad (1)$$

where $\Delta\varepsilon_t$, $\Delta\varepsilon_p$,and $\Delta\varepsilon_e$ are the total, plastic and elastic strain amplitudes, respectively, N_f is the number of cycles to failure, E is Young's modulus, $o_f^{'}$, $\varepsilon_f^{'}$, $c^{'}$ and $b^{'}$ are the fatigue parameters.

The cyclic stress-strain curves for various testing temperatures are shown in Fig. 2. The stress amplitude is obtained at half of fatigue life. The variation of the stress amplitude with plastic strain amplitude is generally represented by a power law

$$\frac{\Delta\sigma}{2}=k_f^{'}(\frac{\Delta\varepsilon_p}{2})^{n^{'}} \quad (2)$$

Where Δo is the stress range, $\Delta\varepsilon_p$ the plastic strain range, $k_f^{'}$ the cyclic strength coefficient and $n^{'}$ the cyclic strain hardening exponent. Using an apparent linear fit program, the strain amplitudes – life curve and the cyclic stress-strain data are analyzed according to Eq (1) and (2). The results of the analysis are given in Table 3.

Extensive studies [4-6, 12, 13] have clearly shown that at elevated temperatures, cyclic plastic deformation mode, creep and oxidation are the most important factors which influence the fatigue life of various materials. In this investigation, a combination of the three kinds of damage can be used to interpret the changes in fatigue life with testing temperature and total strain amplitude. It is obvious that if the imposed total strain amplitude is lower, the corresponding plastic strain component is very small and thus damage resulting from creep can be essentially neglected. Thus, a time-dependent damage process, i.e. oxidation, may contribute to the substantial reduction of low-cycle fatigue lives due to the increased temperature.

Table 3 Strain fatigue parameters of GH413 at different temperatures

Temperature	$\sigma_f^{'}(MPa)$	$b^{'}$	$\varepsilon_f^{'}(\%)$	$c^{'}$	$k_f^{'}(MPa)$	$n^{'}$
R T	1668	-0.092	0.306	-0.622	1701	0.116
850℃	1383	-0.1497	2.4319	-0.4343	4497	0.33

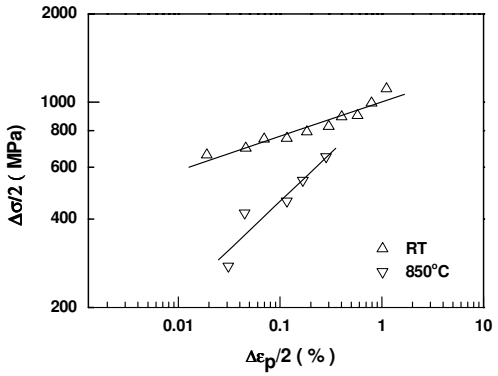

Fig .2 The cyclic stress-strain curves for different temperatures.

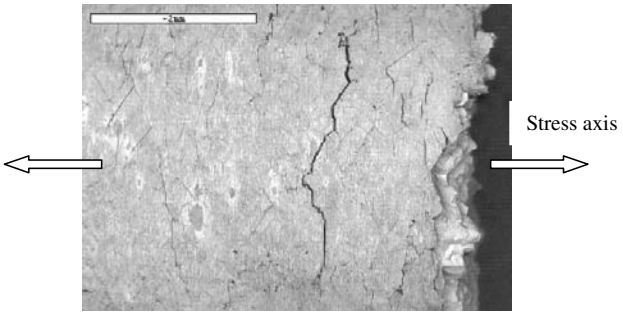

Fig. 3 The SEM micrograph of the surface of the fatigue sample failed at 850℃ ($\Delta\varepsilon_t/2 = 0.32\%$,, $N_f = 814$ cycles)

Obviously, a higher temperature could enhance the oxidation damage, and thus the alloy gave shorter fatigue lives at higher temperatures at the lower strain amplitudes, because it tends to assist intergranular cracking. Figure 3 is the surface micrograph of the fatigue sample failed at 850℃ which is lightly oxidative and filled with cracks. At intermediate total strain amplitudes, however, damages induced by creep, oxidation and cyclic plastic deformation processes are associated with the loss of fatigue life. The decrease in fatigue life resulted from creep is generally attributed to the fact that creep taking place during fatigue loading at higher

temperatures can promote intergranular crack propagation. At the high total strain amplitudes, the time at elevated temperatures is shorter because the fatigue life of the alloy is relatively low, and hence the effect of oxidation is relatively weak. The reduction in fatigue life can be taken as the consequence of damage induced by the cyclic plastic deformation process and creep.

3.2. Cyclic Stress response behavior

The cyclic stress response curves of the alloys, cycled under different total strain amplitudes at room temperature and 850℃, are depicted in Fig.4. In all the tests at room temperature and 850°C, the stress amplitudes were obtained by averaging for corresponding compressive and tensile reversals. It is clear from Fig. 4 (a) that the cyclic stress response behavior of the GH413 alloy is closely related to the imposed total strain amplitudes. Generally, the alloy exhibited higher cyclic stress amplitude with increasing total strain amplitudes at room temperatures. At room temperature, an initial cyclic hardening, followed by cyclic softening was observed at higher total strain amplitudes equal to or above 1.27 %, while the total strain amplitudes is equal to 0.9% after a short cyclic hardening the stress saturation stage begins and is maintained until the sample failed. After a short cyclic hardening, the gradually cyclic softening was noted at the low total strain amplitudes of 0.34% and 0.6%.

At 850℃, the cyclic stress response behavior of the GH413 alloy is depended on the total strain amplitudes from Fig. 4(b). At the 0.67% total strain amplitude the cyclic stress response behavior is similar with that of the higher total strain amplitude at room temperature. While the total strain amplitude is equal to 0.39% after a short cyclic softening the cyclic hardening was observed and then the cyclic softening again. At the 0.29% total strain amplitude, the gradually cyclic softening is maintained after a short initial softening. The cyclic hardening was arrived at the peak value at almost 200 cycles, and then gradually cyclic softening at the 0.19% until the sample failed.

The cyclic stress response behavior can be rationalized based on the individual or combined effects of (i) the interaction between dislocations and solute atoms (dynamic strain aging, DSA), (ii) dislocation–dislocation interactions and (iii) precipitation of fine carbides on dislocations during testing [14-17].In this investigation, the cyclic hardening at two testing temperature can be attributed to the interactions between dislocations and the interactions between the dislocations and the precipitates. With the plastic deformation exceeding, the slip bands generated at the local strain zone, as shown in Fig. 5. The number and density of slip bands related to the total strain amplitude imposed. The cyclic hardening is caused by the density of slip bands at beginning of cycling. At the high total strain amplitude the multi-slip systems start up synchronously, the interactions between two or three {111}slip systems form the tangles of the dislocations and retard the motion of dislocation. The hardening relates to the reduction of the mean free slip length of a dislocation on {111} slip plane by other interacting {111} slip systems [18].

The γ' precipitates cumber the movement of dislocation too. After the initial cyclic hardening the cyclic softening was observed, the intermediate softening stage was not due to crack nucleation, which generally occurred later in the fatigue life. The γ' precipitates are sheared and softening occurs through the continual reduction of the mean precipitates diameter in the slip plane, as shown in Fig. 5(a). At the intermediate total strain amplitude at room temperature, the cyclic stress saturation stage is due to the component of the plastic strain. The total strain amplitude is lower; the component of the plastic strain is lower, too. The rate of dislocation

multiplication equals to the rate of dislocation annihilation, the effect of hardening counteracts the effect of softening. The cyclic stress saturation stage can be maintained until the sample failed.

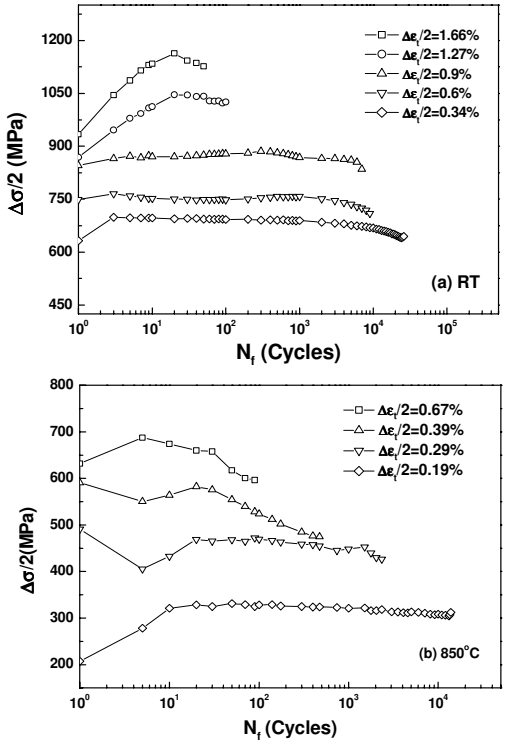

Fig. 4 The cyclic stress response curves of GH413 at different temperature

3.3 The initiation and propagation of the fatigue cracks

SEM examination of fracture surfaces on fatigued specimens reveals that the fatigue cracks initiate transgranularly at the free surface of specimens under all testing conditions, as shown in Fig. 6(a). Moreover, the micrograph at low magnification shows that there exist multiple fatigue crack initiation sites on all fracture surfaces and the machining marks around the entire specimen circumference are the most likely crack initiation sites. The arrows indicate the initiation sites of the fatigue cracks in the Fig. 6(a) and the propagation range of the fatigue crack is larger if the lower total strain amplitude is applied, as shown in Fig. 6(a) (850℃, $\Delta\varepsilon_t/2$ = 0.198%). The cleavage-type marking is often observed in the crack initiating region at two temperatures. However, the fatigue cracks grow by a mixture of transgranular and intergranular modes at the adjacent regions of the crack initiating region at both temperatures, as pointed out in Fig. 6(c). The fatigue striations and the cleavage steps are obviously seen in the fatigue crack propagation

regions at both the test temperature. The arrows in Fig. 6(c) and (d) indicate the directions of the fatigue striations propagation. It is easy to find that the modes of crack propagation are intergranular in the instantaneous fracture zones in Fig. 6(a). Fig. 6(e) is the amplifying image of the boundary failed at room temperature and Fig. 6(f) is the back scattered image of Fig. 6(e) at the same place; the arrows indicate discontinuous precipitate on the boundary. Although the crack propagation modes of the instantaneous fracture zones are intergranular, the large amount of dimple indwelling on the grain boundary indicate that the crack propagation modes of the instantaneous fracture zones are intergranular ductile fractures.

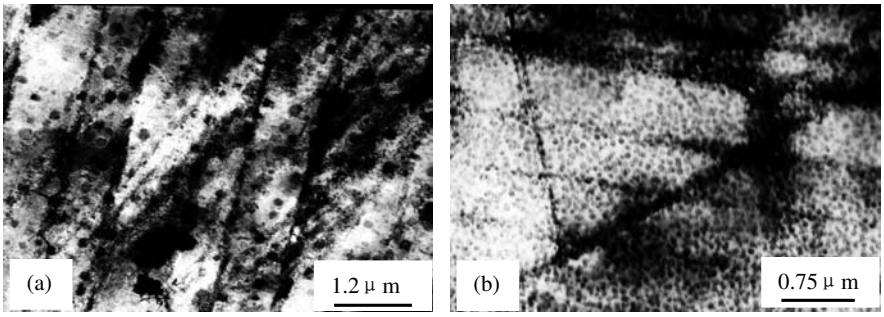

Fig.5 TheTEM micrograph of the fatigue samples failed. (a) RT, $\Delta\varepsilon_t/2 = 1.05\%$; (b) 850℃, $\Delta\varepsilon_t/2 = 0.67\%$.

The typical cleavage character in the region of fatigue crack initiation should be attributed to the concentration of plastic deformation in slip planes. Fracture usually occurs on crystallographic slip planes as a result of the concentration of plastic deformation in these planes. The component of the shear stress on the slip planes, which lie at an angle of about 45 degree with the direction of the imposed load, is larger than the critical value, the slip systems start up. When the local strain at the crack tip exceeds a critical value, cyclic cleavage takes place. So the fatigue cracks always initiate in a transgranular mode at all temperatures. With the crack propagation the slip system moved take place turning and the angle between the slip systems and the direction of the load imposed will be changed, the mode of fatigue crack propagation change from the transgranular mode to the mixed mode of transgranular and intergranular , as shown in Fig. 6(c). The area of the fatigue sample decreases and the stress of the sample imposed increases with the crack propagation. The instantaneous fracture zones display intergranular fatigue fracture. Obviously the high stresses promote the boundary failure in the propagation process. The discontinuous precipitates on the boundary play an important role in the intergranular fatigue fracture. With the plastic deformation increasing the cavities generate at the interfaces between the discontinuous precipitates and the boundary. Moreover, at high temperature, the creep strain component is enhanced and grain boundary cavities become easy to form. The generated grain boundary cavities grow up and combine with each other, which finally results in intergranular fracture. Another important reason resulting in intergranular crack propagation is the air environment, and specifically oxygen. In case the formation of fatigue crack, the grain boundary connecting to the crack tip will be exposed in air, the grain boundaries will become the favorable sites for oxygen penetration and oxidation. Those oxidized grain boundaries are apparently

weakened and have lower strength than the matrix. Consequentially, micro-scale plastic deformation and final fracture will be localized on these inherently weak grain boundaries, causing intergranular cracking.

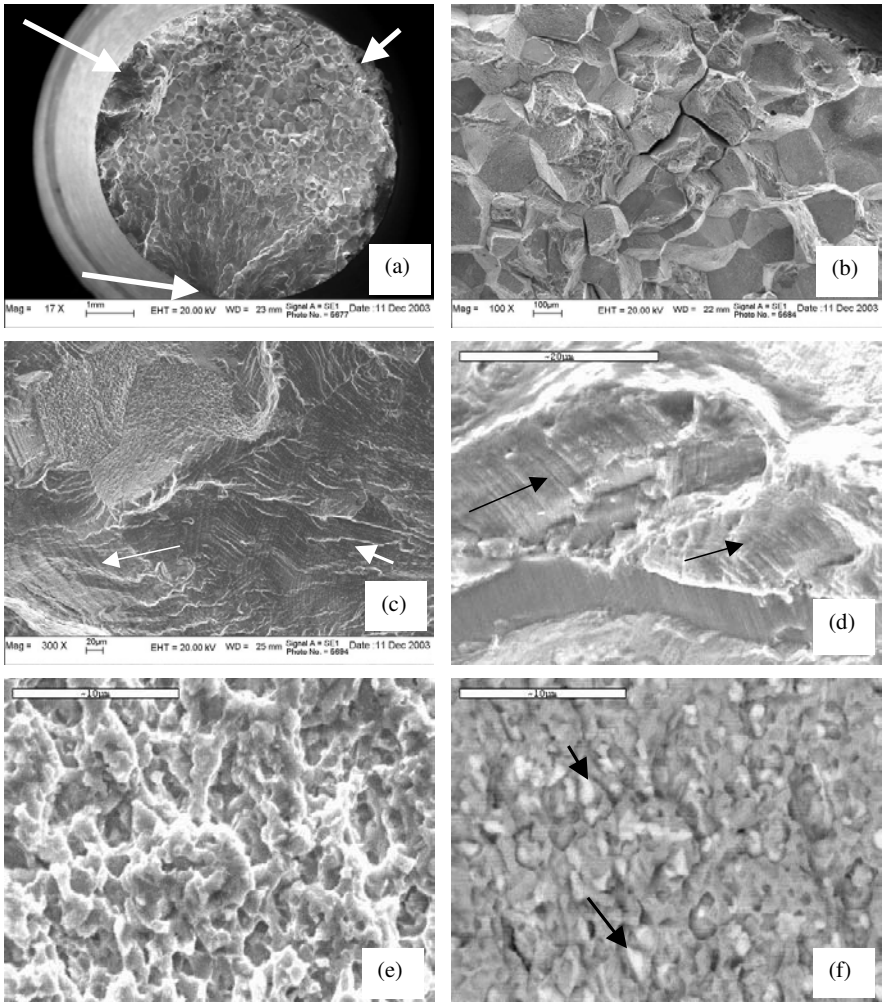

Fig. 6 The SEM micrograph of the fracture surface of the fatigue samples failed. (a) 850℃, $\Delta\varepsilon_t/2$=0.199%, (b) 850℃, $\Delta\varepsilon_t/2$=0.197%, (c) 850℃, $\Delta\varepsilon_t/2$=0.3%, (d) RT, $\Delta\varepsilon_t/2$=0.32%, (e) and (f) RT, $\Delta\varepsilon_t/2$=1.66%, (f) is the back-scattered electronic image of (e) at the same place.

4. Conclusions

To summarize this investigation of the low cycle fatigue behavior of the alloy GH413, the following conclusions can be drawn:

1.The Coffin–Manson equation and fatigue parameters were obtained for the GH413 alloy at room temperatures and 850℃. The Coffin–Manson equation fitted the experimental results well, which indicated that these equations could be used to predict the low-cycle fatigue lives of the GH413 alloy at the various strains and temperatures investigated. The low cycle fatigue life of the alloy shows strong dependence on both total strain amplitude and temperature.

2. At all testing temperatures, the fatigue cracks initiate transgranularly. The fatigue cracks propagation modes are transgranular. At two temperatures, the fatigue striations and the cleavage steps can be observed. The large amount of dimple indwelling on the grain boundary indicates that the crack propagation modes of the final fracture zones are intergranular ductile fractures.

3. The behavior of the cyclic stress response of GH413 alloy relates to the temperature and the total strain imposed. The hardening can be explained based on the reduction of the mean free slip length of a dislocation on {111} slip plane by other interacting {111} slip systems and the interactions between dislocation and the precipitates.

4. A combination of the cyclic plastic deformation, creep and oxidation is responsible for the substantial reduction in fatigue life and the transition from transgranular to intergranular fracture.

5. References

[1] M Cell, G R Leverant and C H Wells. In: Fatigue strength of nickel-base superalloys. ASTM STP 467. Philadelphia (PA): ASTM; 1970. p. 113-53.

[2] W J Plumbridge and E G Ellison. Low cycle fatigue behavior of superalloy blade materials at elevated temperature. Materials Science and Technology. 1987; 3(9):706-15.

[3] D Fournier and A Pineau. Low cycle fatigue behavior of Inconel 718 at 298K and 823K. Metallurgical Transactions A. 1977, 8A: 1095-105.

[4] M Regeand L Remy. High temperature low cycle fatigue of In-100 superalloy. Materials Science and Engineering A.1988; 101: 47-63.

[5] K B S Rao, H Schiffers, H Schuster and G R Halford. Temperature and strain-rate effects on low-cycle fatigue behavior of alloy 800H. Metallurgical Transactions A. 1996; 27A: 255-67.

[6] M Valsan, P Parameswaran, K B S Rao, M Vijayalakshmi, S L Mannan and D H Shastry. High temperature low cycle fatigue behavior of a NIMONIC PE-16 superalloy correlation with deformation and fracture. Metallurgical Transactions A. 1992; 23A: 1751-61.

[7] V S Sarma, M Sundaraman and K A Padmanabhan. Effect of γ' size on room temperature low cycle fatigue behavior of a nickel based superalloy. Materials Science and Technology.1998; 14: 669-75.

[8] America Society for Testing and Material, Annual book of standards, vol. 03.01. Philadelphia (PA): ASTM; 1996. p. E606.

[9] V Recina and B Karlsson. High temperature low cycle fatigue properties of Ti-48Al-2W-0.5Si gamma titanium aluminide. Materials Science and Engineering A. 1990; 262:70-81.

[10] L E Pierre and S B Guarro. In: PWB plated through hole thermal fatigue analysis and

reliability test development. New York: ASME; 1996. p8.
[11] Standard E606.In:Annual book of ASTM Standards, Philadelphia1,PA, ASTM, 1996; 03.01.
[12] L J Chen, Z G Wang, G Yao and J F Tian. The influence of temperature on low cycle fatigue behavior of nicklel base superalloy GH4049. International Journal of Fatigue.21 (1999) 791-799.
[13] J T Guo, D. Ranucci and E Picco. Low cycle fatigue behaviour of cast nickel-base superalloy IN-738LC in air and in hot corrosive environments. Materials Science and Technology.58 (1983); 127-133.
[14] K B S Rao, H Schiffers, H Schuster and H Nickel. Influence of time and temperature dependent processes on strain controlled low cycle fatigue behavior of alloy 617. Metallurgical Transactions A.19A (1988) 359-371.
[15] K B S Rao, M G Castelli and J R Ellis. On the low cycle fatigue deformation of HAYNES 188 superalloy on the dynamic strain aging regime. Scripta Metallurgica et Materiaia. 33 (6) (1995) 1005-1012.
[16] R.V. Miner, and M.G. Castelli. Hardening mechanisms in a dynamic strain aging alloy, HASTELLOY X, during isothermal and themomechanical cyclic deformation. Metallurgical Transactions A.23A (1992) 551-561.
[17] M Valsan, D H Sastry, K B S. Rao and S L Mannan. Effect of strain on the high temperature low-cycle fatigue properties of a Nimonic PE-16 superalloy. Metall. Trans. A. 25A (1994) 159-171.
[18] B A Lerch and V Gerold. Cyclic hardening mechanisms in NIMONIC 80A. Metallurgical Transactions A.18A (1987) 2135-2141.

EFFECT OF CARBIDES ON THERMAL FATIGUE PROPERTY OF K465 CAST SUPERALLOY

H.R. Guan[1], J.X. Yang, Q. Zheng, Y.L. Wang, X.F. Sun, Z.Q.Hu

Institute of Metal Research, Chinese Academy of Sciences, Shenyang, 110016, P. R. China
hrguan@imr.ac.cn

Abstract

Thermal fatigue (TF) tests on nickel-base K465 superalloy in as-cast and solution treated conditions were conducted from 1050℃ to 20℃ repeatedly. Main experimental results showed that thermal fatigue crack of as-cast K465 alloy propagated faster than that of solution treated K465 alloy, and the rise of holding time at the maximum temperature accelerated TF crack propagation. Metallographic observations depicted that the TF cracks were nucleated at Chinese script MC carbide and propagated along the cracked MC carbide in as-cast condition, whereas most M_6C carbide particles obstructed TF crack growth in solution treated condition. Chinese script MC carbide was responsible for the reduction of TF life in as-cast condition.

Keywords: K465 cast superalloy; thermal fatigue；crack growth；oxidation；carbides

1 Introduction

A nickel-base cast superalloy, K465, containing many refractory metal elements, such as tungsten, molybdenum, niobium, etc., is strengthened by precipitates, solute elements and carbides, and is being used for gas turbine blades and vanes operating at high temperatures where thermal fatigue (TF) is very easy to occur[1]. Therefore, the knowledge of the TF properties of this alloy is very important for prediction the service life of this alloy.

There were many factors effecting on the TF property including alloy variables, such as compositions and microstructure, and testing parameters, especially, the testing temperature and holding time[1-4]. This paper was focused on the effects of carbides on the TF property under different alloy conditions.

The carbides precipitated at grain boundaries played an important role in the strengthening of grain boundaries at elevated temperature[5,6]. Uniformly distributed fine carbides inhibited grain sliding and enhanced elevated temperature strength; however, coarse or continuous script-like carbides were detrimental because they served as crack initiation sites and propagation paths[7,8]. On the other hand, primary MC type carbide mainly containing Ti, Ta

[1] Corresponding author. Tel.: 86 24 23971807; Fax.: 86 24 23891320

and Nb was oxidized at high temperature and acted as crack source and propagation passage[9,10]. In addition, the TF cracks were produced and proceeded along networks of fine $M_{23}C_6$ carbide or carbides colonies[1].

The effects of M_6C and MC carbides on crack initiation and propagation were emphasized on the above investigation. However, the role of M_6C carbide in the TF property was unclear up to now. In this paper, the influences of MC and M_6C carbides on the TF property were illustrated in detail.

2. Experimental

Table 1 Nominal composition of the alloy (wt.%)

Alloy	C	Cr	Al	Ti	Mo	W	Co	Nb	Ni
K465	0.17	10	5.5	2.8	2.2	10.5	11	1.1	Bal.

The tested specimens in as-cast and solution-treated conditions (1210℃ holding for 4 hours, air cooling) which chemical composition (wt%) is provided in Table1, were machined according to Fig.1, and quenched into 20℃ recycling water for 10s after having held at 1050℃ (respectively for 100s and 300s) in electric resistance furnace. Measurement of crack length was made on the longest cracks on both surfaces using a microscope having reading-scale lens with a resolution of 1μm. The measured data were the averages of six readings of the two longest cracks on both surfaces. The samples for the optical microscope (OM) and scanning electron microscope(SEM) were sectioned around the main TF cracks, then were ground and polished, finally were etched in the $CuSO_4$ mixing with HCl and H_2O. These etched samples were observed by SEM and OM. Semi-quantitative analysis was performed using energy diffraction spectrum (EDS).

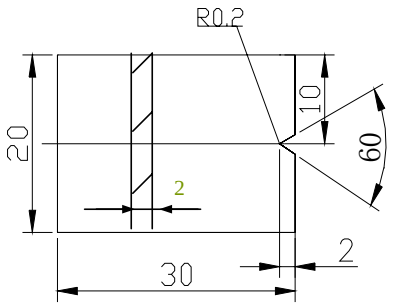

Fig.1 Specimen size in mm and angle

3 Results and discussion

3.1 Initial carbides and their changes during thermal fatigue

In as-cast K465 alloy, most Chinese script MC carbide particles are distributed in interdendritic region besides a small part of blocky MC carbide particles as shown in Fig.2(a).

Their chemical compositions are listed in Tab.2 using EDS, showing higher amounts of W 、Ti and Nb. The value of O element in Tab.2 only shows its existence and the relative amount.

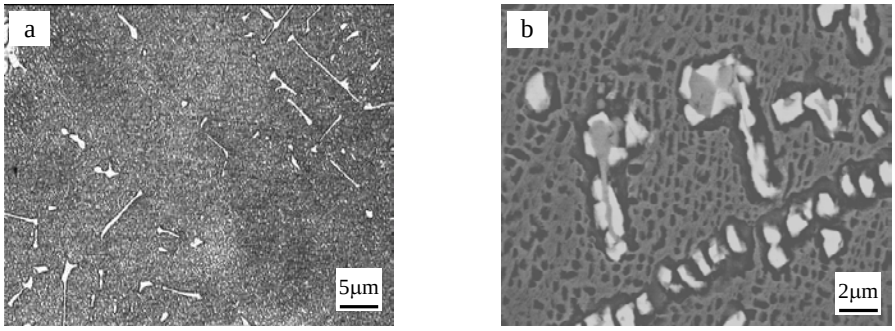

Fig.2 Carbides in K465 alloy: (a) the Chinese script MC carbide (white) in as-cast condition and (b) the MC (gray) and M_6C (white) carbides in solution treated condition

MC carbide is partly decomposed into another type white carbide after solution treated (Fig.2(b)). EDS analysis shows that this carbide is rich in W、Mo and Cr (Tab.2), which is identified to be M_6C carbide based on the previous investigation[4,5,9]. Further, script MC carbide networks are fractured into more small fragments and islands in morphology, and thinned out in size (Fig.2(b)).

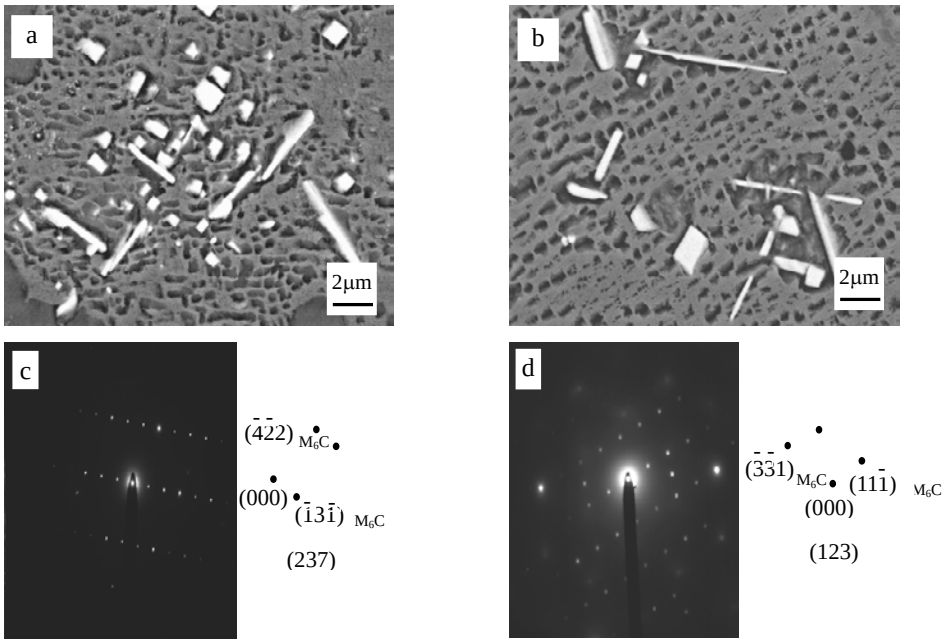

Fig.3 The carbide precipitates during thermal fatigue：(a) the rod-shaped and cuboidal M_6C carbides in interdendritic region and (b) dendritic arm; (c) the selective area diffraction pattern of rod-like M_6C carbide; (d) the selective area diffraction pattern of cuboidal M_6C carbide

The carbides have significant changes during TF. The short rod-like and cubic carbides are precipitated in interdendritic region(Fig.3(a)) and dendritic arm(Fig.3(b)) besides the transformation of MC carbide into M_6C carbide. EDS analysis indicates that this new carbide is rich in W、Mo and Cr(Tab.2). The TEM and selective area diffraction analysis demonstrate that these precipitates are M_6C carbide (Fig.3(c)-(d)). He[5] also discovered the cubic M_6C carbide precipitated at dendritic core regions during creep tests.

Table 2 Chemical compositions of carbides given by EDS (wt.%)

	O	W	Mo	Nb	Ti	Ni	Al	Cr	Co
MC in Fig.2(a)		45.96	5.20	16.48	28.82	2.23		1.31	
M_6C in Fig.2(b)		68.64	4.19	3.44	1.30	3.12	0.48	13.24	5.60
Cubic M_6C in Fig.3(a)		65.76	4.41	4.98	0.56			19.09	6.90
Rod-like M_6C in Fig.3(a)		65.32	4.49	4.93	0.57	4.57		18.85	1.27
Region1 in Fig.6(b)	19.74	15.57	4.26	1.46	1.64	26.25	1.50	18.79	3.90
Blocky M_6C in Fig.7(b)-1		75.15	7.80	3.28	2.18	13.22	0.60	10.86	

3.2 TF crack growth kinetics in two conditions

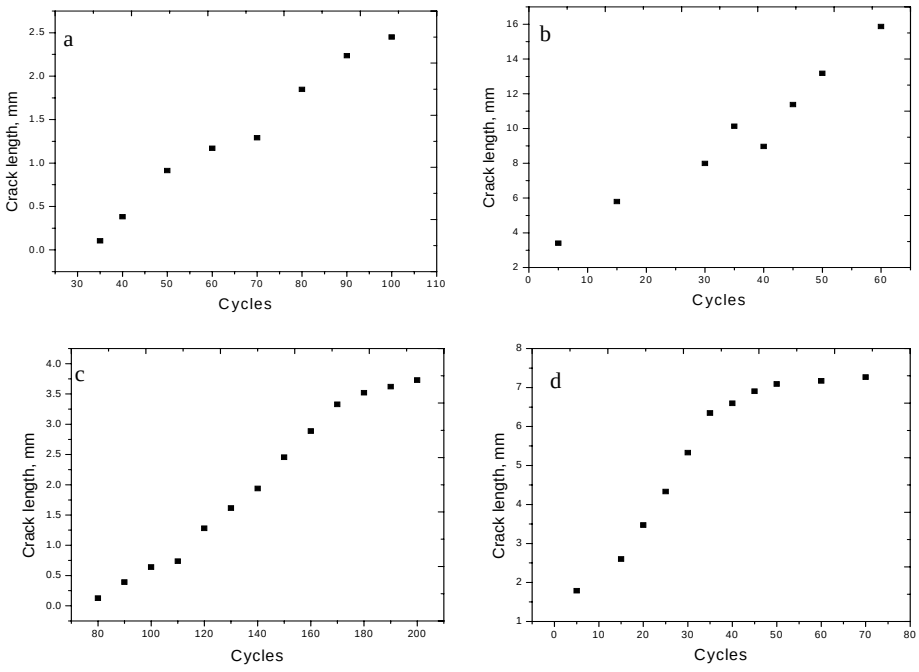

Fig.4 Crack growth kinetics curves: (a) for 100s and 300s (b) for as-cast K465 alloy; (c) for 100s and 300s (d) for solution treated K465 alloy

Crack growth kinetics curves are plotted respectively in Fig.4(a) and (b) for as-cast K465 alloy, and Fig.4(c) and (d) for solution treated K465 alloy. Comparing with these curves, the TF cracks in as-cast condition propagate faster than in solution treatment condition, and the increment of holding time at the maximum temperature accelerates crack propagation in two conditions.

For as-cast K465 alloy, there is considerable scatter in the overall TF crack lengths indicating the complexity of TF crack formation. Moreover, TF cracks are not retarded in final propagation stage when holding 300s at 1050℃, which is catastrophic to TF property of the alloy, but when holding 100s, the propagation rate of TF cracks becomes slowly after 80 cycles. Therefore, the increment of holding time not only promotes TF crack growth, but also makes crack propagation become more complex.

For solution treated specimens, there is a small scatter band in crack lengths indicating the higher stability of microstructure. In addition, crack bluntness is pronounced in final stage of crack propagation, which is advantageous to resisting crack growth.

The above analysis indicates that there are many factors resulting in TF damage, and it is very difficult to define single factor effect, respectively. However the microstructure influences are dominant[1,11-13], especially the carbides in this alloy[5.13].

3.3 Metallographic observation and analysis

In as-cast K465 alloy, TF crack nucleation is predominantly dependent on Chinese script MC carbide as shown in Fig.5(a). Further, interfacial debonding and MC carbide fracture led to TF crack initiation[14]. Interfacial cracking (Fig.5(b)-1) between γ matrix and MC carbide might be induced by oxidation of MC carbide because EDS analysis indicates the existence of O element in MC carbide(Fig.5(c)) and γ matrix(Fig.5(d)). Expansion and contraction of γ matrix and MC carbide, their cohesive stress and thermal fatigue stress are related to interfacial cracking, but are secondary of importance.

Cracking of MC carbide(Fig.5(b)-2) is mainly caused by its strength and thermal fatigue stress. In contrast to γ matrix and γ′ precipitates, these MC type carbide particles have lower ductility and higher toughness at high temperature where stress concentration is prone to occur, in particular, the MC carbide particles nearly perpendicular to thermal fatigue stress, must lead to earlier crack initiation. In addition, EDS analysis shows that the fractured MC carbide particles are oxidized because it contains O element(Fig.5(d)) that is only a semiquantitative result because of its low atomic number.

TF crack propagation is more dependent on Chinese script MC carbide, which have been broken at multi-sites as shown in Fig.6(a), subsequently, TF cracks propagate by linking up these cracked paths(Fig.6(b)). The evidences from EDS analysis show that the MC carbide and matrix might be oxidized (Tab.2 and Fig.6(b)). The oxidized carbide particles were prone to fracture and separate from matrix. Many previous investigations[1,8] proved that primary MC carbide was preferently oxidized and served as crack initiation site and propagation path.

As a result, the TF cracks are zigzag having considerable bendings and branchings which are formed due to the distribution of script MC carbide. However these bendings and branchings can not reduce crack propagation energy at crack tip, and inversely, provide the easy paths for crack advancement, which makes TF cracks propagate very rapidly.

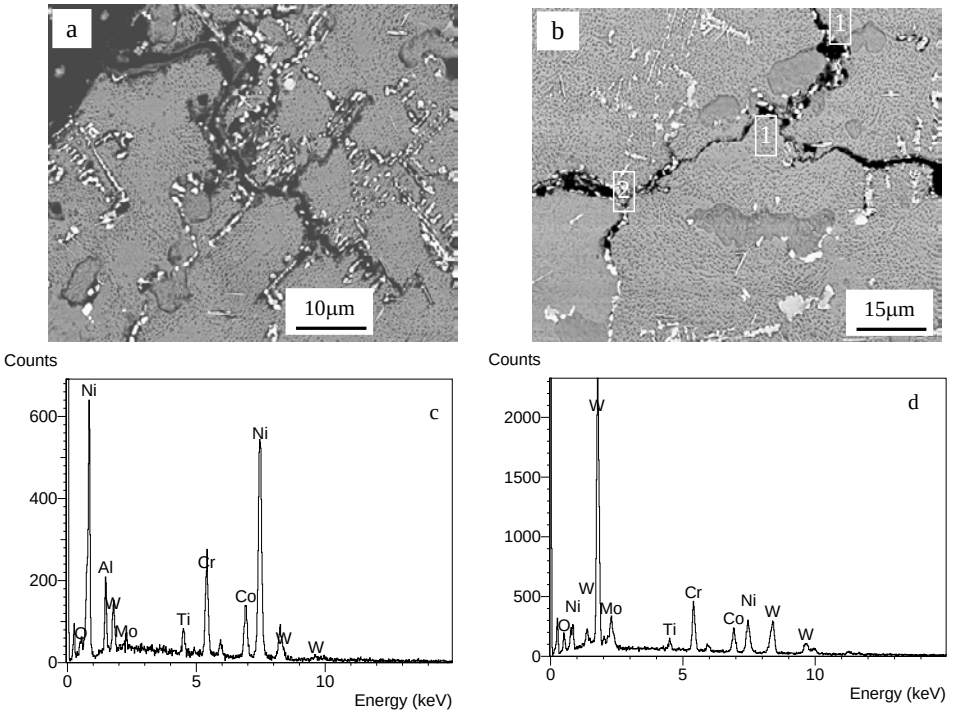

Fig.5 TF cracks in as-cast condition: (a) initiating; (b) propagating along the cracked script MC carbide particles; and the energy diffraction spectrum of region 1 (c) and 2 (d)

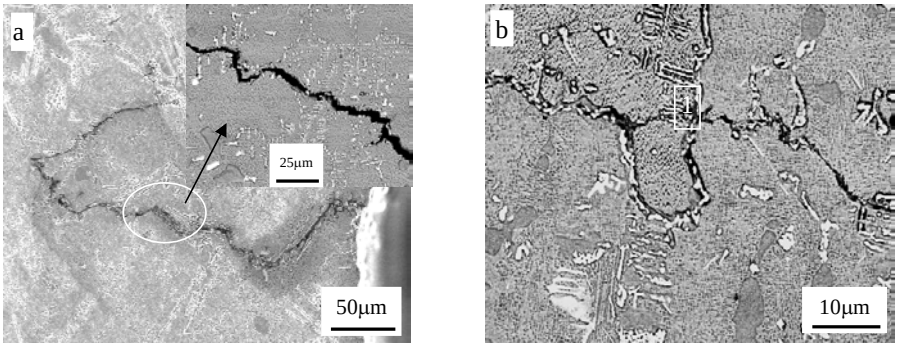

Fig.6 TF cracks in as-cast condition: (a) the zigzag TF crack; (b) propagating along the cracked script MC carbide

Under solution treated condition, carbides play double roles in crack growth. On one hand, the size and amount of script MC carbide are decreased, which weakens the detrimental

effects of MC carbide on TF property. Meantime, the M_6C carbide transformed from script MC carbide and perpendicular to crack propagation direction causes crack bending, which consumes a part of propagation energy at crack tip as shown in Fig.7(a), that leads to crack retardness. Further, the M_6C carbide colonies produced by the decomposition of MC carbide do not act as crack propagation path, whereas obstruct crack advancement and lead to the bluntness at crack tip(Fig.7(b)-1). These M_6C carbide particles are not oxidized based on their EDS results(Tab.2). The above analysis explains the obstruction of crack growth in this condition(Fig.4(c) and (d)).

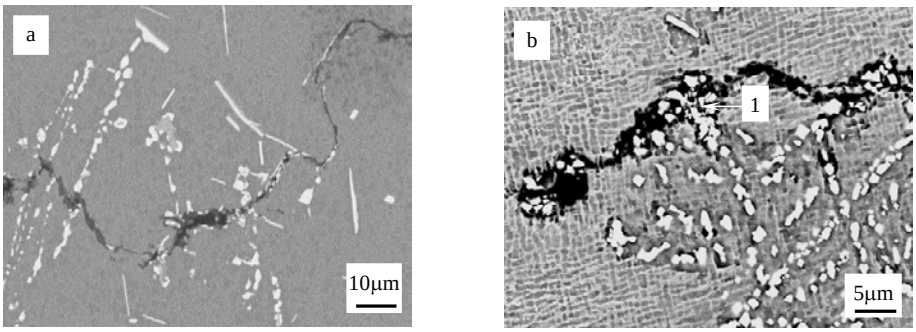

Fig.7 TF cracks in solution treatment condition: (a) bending and (b) bluntness at crack tip induced by M_6C carbide

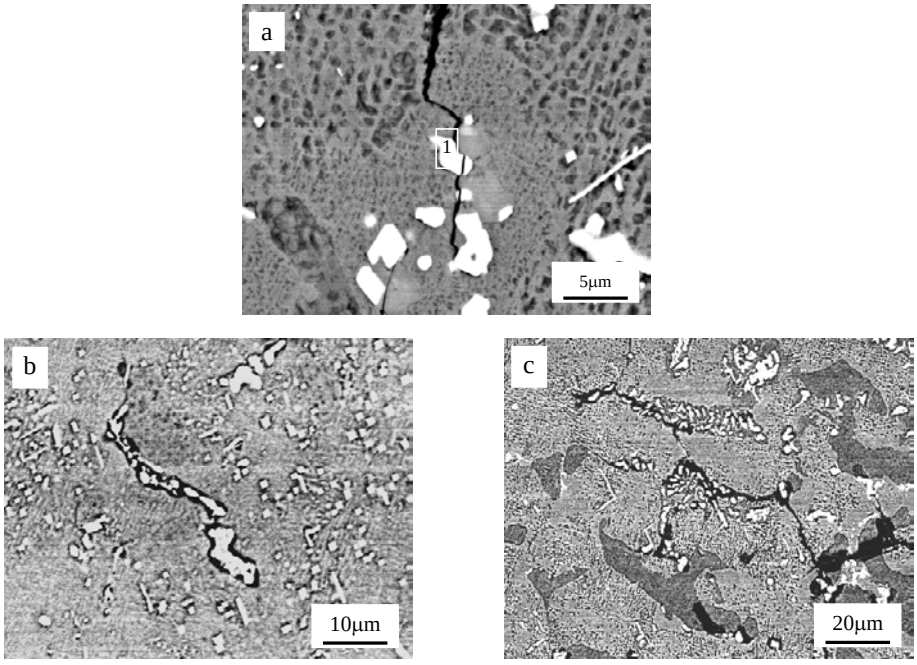

Fig.8 TF cracks in solution treated condition: (a) crossing M_6C carbide; (b) cracked blocky M_6C carbide and (c) fractured M_6C colonies at crack tip

On the other hand, TF cracks can penetrate the larger blocky M_6C carbides locating in interdendritic regions (Fig.8(a)-1). The M_6C carbide particles are cracked earlier when its fracture strength is lower than TF stress.

In addition, secondary cracks are produced around the large blocky M_6C carbide particles (Fig.8(b)) and the cracked M_6C carbide colonies (Fig.8(c)). The decohesion at carbide/γ matrix interface is formed at the site where TF stress is above the interfacial cohesive stress. Meantime, the different expansion and contraction of carbides and γ matrix are possibly responsible for the decohesion, also, but it is not detrimental because γ matrix around M_6C carbide is enough "soft" at high temperature to cooperate the interaction between two phases. Furthermore, these secondary cracks may have no effect on TF property because they are too tiny to connect with the principal crack. Totally, M_6C carbide increases the resistance to TF crack propagation.

Besides the MC and M_6C carbides transformed from MC carbide, the short rod-like and cubic M_6C carbide particles are precipitated during TF as shown in Fig.9. Because these precipitates stengthen the region which the M_6C carbide particles are precipitated. As a result, TF cracks are very difficult to invade this region. This means that the M_6C carbide precipitates inhibit TF crack propagation by the strengthening of small rod-like and cubic M_6C carbide particles.

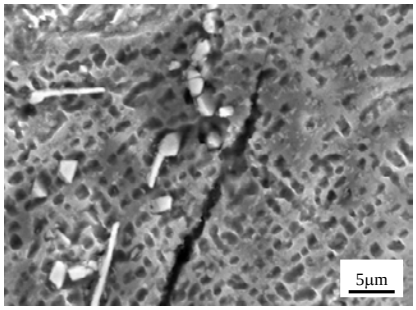

Fig.9 Crack tip morphology near the short rod and cubic M_6C carbide

MC carbide is partly decomposed into M_6C and some M_6C carbide particles are precipitated in as-cast K465 alloy during TF. However, these reactions are much slower than in solution treatment. As a result, the bluntness of crack growth induced by M_6C carbide is very late to take place (Fig.4(c)), even not to occur till material failure (Fig.4(d)).

4. Conclusions

1 Thermal fatigue crack of as-cast K465 alloy propagates faster than that of solution treated K465 alloy, and the rise of holding time at the maximum temperature accelerates TF crack propagation.

2 TF cracks are nucleated at Chinese script MC carbide and propagated along the cracked MC carbide in as-cast condition, whereas most M_6C carbide particles obstruct TF crack growth in solution treatment condition.

3 Chinese script MC carbide is responsible for the reduction of TF life in as-cast condition.

References

[1] D.A. Wood, D.F. Mowbray, Effect of material characteristics and test variables on thermal fatigue of cast superalloys, Mater.Sci.Eng., 16,1974,5-43.

[2] J. Reuchet, L. Remy, High temperature low cycle fatigue of MAR-M509 superalloy Ⅰ: The influence of temperature on the low cycle fatigue behaviour from 20 to 1100℃, Mater.Sci.Eng., 58,1983,19-32.

[3] Y.L. Lu, P.K. Liaw, G.Y. Wang, et al. Fracture modes of HAYNES 230 alloy during fatigue-crack-growth at room and elevated temperatures, Mater.Sci.Eng.A, 397, 2005,122-131.

[4] M. Reger and L. Remy, High temperature, low cycle fatigue of IN-100 superalloy: Influence of frequency and environment at high temperature, Mater.Sci.Eng.A, 101A,1988, 55-59.

[5] L.Z. He, Q. Zheng, X.F. Sun, et al., Effect of carbides on the creep properties of a Ni-base superalloy M963, Mater.Sci.Eng.A, 397,2005, 297-304.

[6] K.A. Al-Jarba, G.E. Fuchs, Effect of carbon additions on the as-cast microstructure and defect formation of a single crystal Ni-based superalloy, Mater.Sci.Eng.A,373,2004, 255-267.

[7] J.S. Bae, J.H. Lee, S.S. Kim, et al., Formation of MC-γ/γ′ eutectic fibers and their effect on stress rupture behaviour in D/S MAR-M247 superalloy, Scr. Mater.,45,2001,503-508.

[8] Q.Z. Chen, N. Joves, D.M. Knowles, The microstructures of base/modified RR2072 SX superalloys and their effects on creep properties at elevated temperatures, Acta Mater.,50,2002,1095-1112.

[9] J. Reuchet, L. Remy, High temperature low cycle fatigue of MAR-M509 superalloy Ⅱ: The influence of oxidation at high temperatures, Mater.Sci.Eng., 58,1983,33-42.

[10] L.Z. He, Q. Zheng, X.F. Sun, et al., Low ductility at intermediate temperature of Ni-base superalloy M963, Mater.Sci.Eng.A, 380,2004, 340-348.

[11] L. Lanes, Y. Torres, M. Anglada, On the fatigue crack growth behaviour of WC-Co cemented carbides: Kinetics description, microstructural effects and fatigue sensitivity, Acta Mater.,50,2002,2381-2393.

[12] D. Chen, C.J. Gilbert, X.F. Zhang, High-temperature cycle fatigue-crack growth behavior in an IN SITU toughened silcon carbide, Acta Mater., 48,2000,659-674.

[13] L.Z. He, Q. Zheng, X.F. Sun, et al., High temperature low cycle fatigue behaviour of Ni-base superalloy M963, Mater.Sci.Eng.A, 380,2005, 340-348.

[14] T.Denda, P.L. Bretz, J.K. Tien, Inclusion size effect on the fatigue crack propagation

mechanism and fracture mechanics of a superalloy, Metall. Trans.A,23A,1992,519-526.

ENVIRONMENT EFFECT ON HIGH TEMPERATURE FATIGUE OF A NICKEL BASE SUPERALLOY FOR TURBINE DISCS

M.Marchionni[1], G. Onofrio[1], G.A.Osinkolu[2]

[1]CNR-IENI, via Cozzi 53, 20125 Milano, Italy
[2]CERD Division of Materials Science and Electronics
Obafemi Awolowo University, Ile-Ife, Nigeria
marchionni@ieni.cnr.it

Abstract

The low cycle fatigue behaviour of UDIMET 720 Li has been investigated at 700°C in vacuum and air environments under strain control tests. Hold times have been introduced at peak tensile strain in order to determine the effects of creep and fatigue interactions. The fatigue life of the alloy is practically independent of hold time in both environments at high strain ranges while hold time has beneficial effect at low strain ranges. The main factor that adversely affects the life of the alloy is oxidation as the fatigue life is reduced in air compared to vacuum especially at high strain ranges. The increase in fatigue due to hold time at lower strain ranges is attributed to stress relaxation.

The fatigue crack growth rate has been investigated at 700°C in vacuum and air environments using corner crack specimens. The crack growth rate was considerably low in vacuum and remained practically unchanged with increase in hold time at maximum load until about 120 s. The crack growth rate was considerably high in air compared to vacuum tested specimens and the crack growth rate increased as the loading frequency decreased. The fracture surfaces then showed evidence of micro-cavity formation that was attributed to damages resulting from creep deformation.

Keywords: Nickel base superalloys, gas turbine, low cycle fatigue, fatigue crack propagation, environmental effect.

Introduction

There is a continuous effort to develop new materials that can withstand the demand of high service temperatures and stresses encountered by structural components such as blades and discs for turbine engines. Ni-base superalloys have performed satisfactorily well as turbine blade and disc materials because of their excellent mechanical and corrosion resistance properties at high temperatures [1]. However the life of these components is usually limited by initiation and subsequent growth of cracks that often occur at stress concentration regions due to thermal gradients or pre-existing flaws under the action of cyclic loading [2]. The reduction in the service life of these alloys is even more remarkable when cyclic loading is applied at low frequency or is combined with static load and in the presence of an oxidising environment [3, 4]. Under such conditions, time dependent microstructural damages evolve and produce a cumulative effect with cyclic deformation that can result into considerable loss in fatigue life. The effect of oxidation on fatigue life of superalloys has been largely discussed and plays a significant role in the mechanism of fatigue failure [5, 6]. Oxygen can, for example, react with the carbides at the grain boundaries to cause microcrack formation and therefore lead to increase in growth rate of an advancing crack. On the contrary oxidation may also play a beneficial role at extremely high temperatures by blunting the crack tip so

that crack growth rate is reduced and retardation effect of oxide-induced crack closure has been reported [7, 8].

In the present work the low cycle fatigue and fatigue crack propagation behaviour of a polycrystalline superalloy UDIMET 720 Li at 700°C in both vacuum and air environments has been examined in order to determine the factors limiting the fatigue life of the alloy. The tests under vacuum allow prediction of the alloy behaviour when cracks are embedded in the interior of the component and then propagate in the absence of air. The fatigue parameters of the Coffin – Manson life prediction relationship have been calculated and discussed.

Material and experimental technique

The UD720Li alloy has been supplied by Thyssen Umformtechnik (D) in form of a forging to disc size. The microstructure consists of rather uniform grain size, from ASTM 9 to 10, with uniform gamma prime distribution (Fig. 1). The chemical composition of the material is shown in table 1. The button head specimens for LCF and the CC (corner crack) specimens for FCG have been cut directly from the disc.

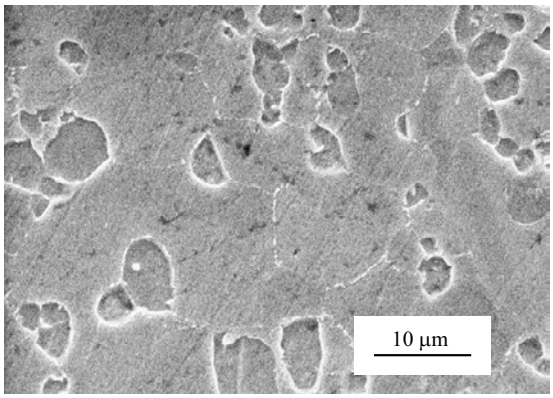

Fig.1 - SEM microstructure of U720 Li: the primary γ' precipitates in the grain boundaries were etched away.

In all the experiments specimens have been heated by induction coil and the temperature controlled by type K thermocouples spot-welded outside the gauge length to avoid crack initiation in correspondence of the welding.

LCF tests have been performed in strain controlled conditions with trapezoidal wave shape (R=0) and defined as the time in seconds to follow the cycle shape: for example 1-1-1-1 indicates respectively the time to go from 0 to the maximum strain, the hold time, the time to return to zero strain and finally the hold time at zero strain. In the case of 1-120-1-1 a hold time of 120 s is introduced at the maximum strain.

Fatigue crack propagation rate (FCPR) tests were carried out in load control (R=0.1) at the temperature of 700°C in air and in vacuum (P O_2 =10^{-3} Pa) at the frequency of 5 Hz. The

influence of wave shape of the applied load has been analysed adding a hold time of 120 s at maximum load, to the triangular wave. Corner crack specimens (CC) with a square gauge cross section of 7 x 7 mm^2 and a 0.2 mm deep starter notch were used.

Table 1 – Chemical composition (wt %) of UDIMET 720 Li alloy.

Al	Co	Cr	Mo	Ti	W	Zr	Fe	Ni
2.5	14.7	16	3.0	5.0	1.25	0.4	0.5	Bal.

Experimental Results

Low cycle fatigue.

The LCF results are shown in Fig. 2. In air test for the higher strains a low influence of hold time on the fatigue life is apparent, and no influence at all is observed for strain below 1%. When tests are performed in vacuum there is a small increasing of fatigue life at high strain, no influence of hold time and the same fatigue life of air tests for strains below 1%. The low influence of hold time can be ascribed to the 120 s hold time that is not long enough to introduce sensitive creep effects at the temperature of 700°C.

The fatigue results have been analysed by the following Basquin and Coffin – Manson relationships:

$$\Delta\varepsilon_e = A * N^{-\alpha} \quad (1)$$

$$\Delta\varepsilon_p = B * N^{-\beta} \quad (2)$$

where $\Delta\varepsilon_e$ and $\Delta\varepsilon_p$ are the elastic and plastic strain components evaluated at half life, N the number of cycles to failure, A, B, α and β constants of the material. The parameters obtained for both materials are reported in table 2, where R^2 is the confidence parameter (R^2=1 is the best fit).

Table 2 – Fatigue parameters according to (1) and (2) equations.

Wave shape and environment	A	α	R^2	B	β	R^2
1-1-1-1, air	0.018	0.096	0.65	0.153	0.62	0.98
1-120-1-1, air	0.019	0.116	0.87	0.084	0.49	0.95
1-1-1-1, vacuum	0.032	0.148	0.84	0.235	0.62	0.72
1-120-1-1, vacuum	0.018	0.070	0.74	0.824	0.76	0.75

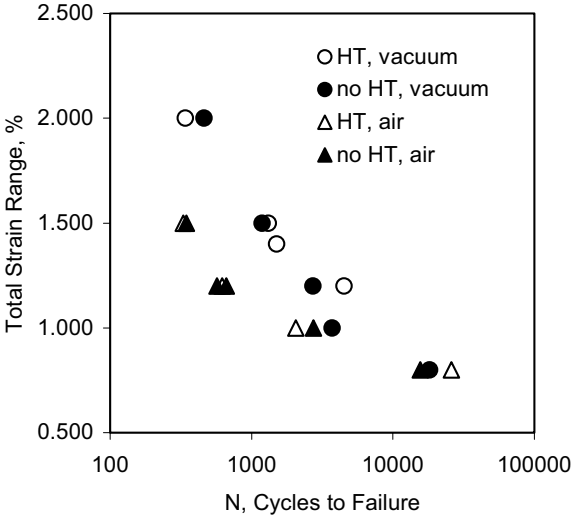

Fig. 2 - Influence of hold time (HT=120 s) and environment on fatigue life.

Fig. 3 shows the plot of the elastic and plastic strain components in function of the number of cycles to failure for air tests. The plastic strain component is higher when the 120 s hold time is applied as it can be expected, showing a creep component induced by hold time. The elastic strain component is almost the same in both cases. The correspondent strain components for vacuum tests are reported in Fig. 4. In this case the hold time has no influence on elastic and plastic strain components that are not substantially different.

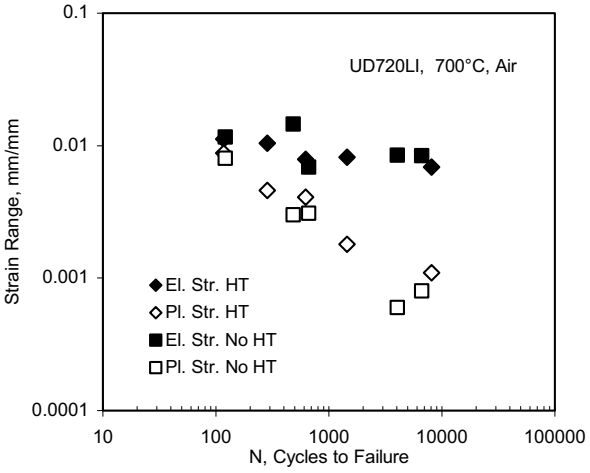

Fig. 3 - Elastic and plastic strain range components vs. N for air tests.

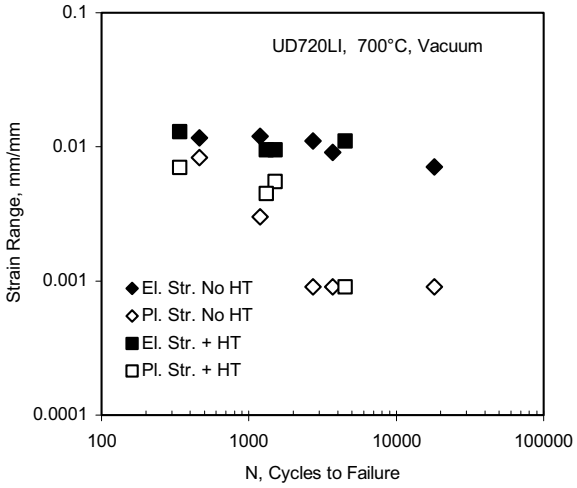

Fig. 4 - Elastic and plastic strain range components vs. N for vacuum tests.

Fatigue crack propagation

Fig. 5 shows the influence of hold time (HT) as well as the environment on the fatigue crack propagation rate at the temperature of 700°C. Under vacuum condition, da/dN versus ΔK curves do not result into any appreciable difference for 0.1–0–0.1–0 and 1–1–1–1 wave

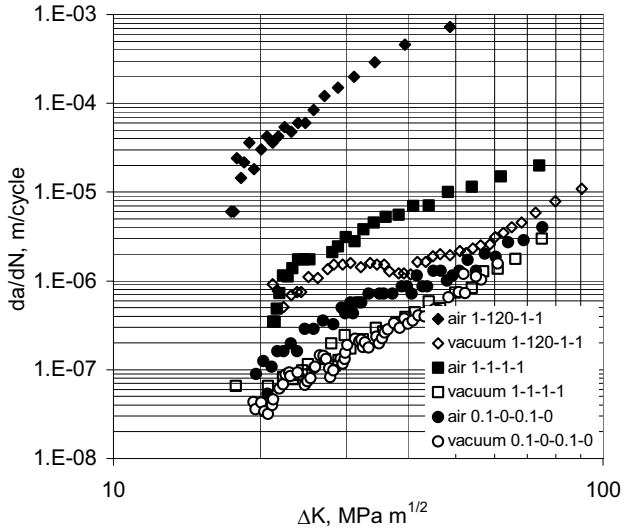

Fig. 5 - Influence of loading waveform and environment on FCGR, R = 0.05, 700°C.

shapes, whereas the crack growth rate is increased by a factor of about 7 when the hold time at maximum tensile load is increased from 1 to 120 s. In air environment, crack growth rate increases with the hold time, in all cases, as evidenced by the comparison between da/dN versus ΔK curves for 0.1–0–0.1–0 and 1–1–1–1 wave shapes (Fig. 5) even though no difference was observed for these two wave shapes under vacuum condition. When hold time increases to 120 s, the crack growth rate increases by a factor of about 600 above the 0.1–0–0.1–0 wave shape showing that the influence of hold time in air environment is more pronounced than in vacuum

Fracture surfaces

In the LCF experiments the crack initiation occurs at the specimen surface and subsequently propagates inwards as shown typically in Fig. 6. When polycrystalline materials are subjected to LCF, the crack initiation may occur at a grain boundary intercepting the

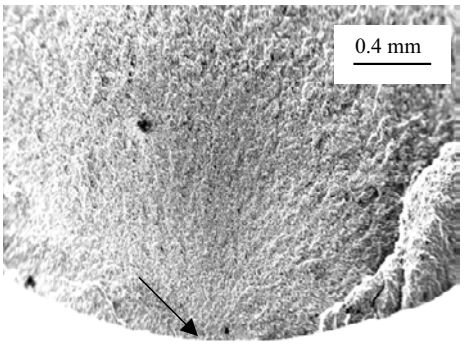

Fig. 6 – Typical micrograph of the fracture surface showing crack initiation at the specimen surface. Arrow indicates crack starting: vacuum, 1-120-1-1, $\Delta\varepsilon_t$=1.5%.

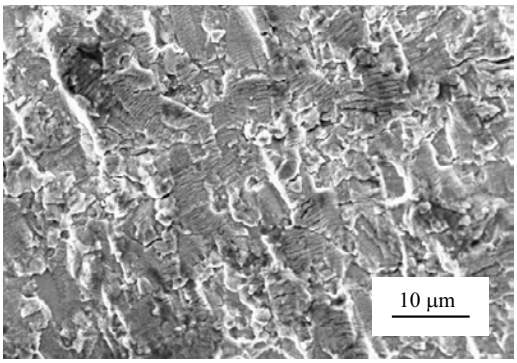

Fig. 7 – SEM micrograph of the fracture surface showing fatigue striations and secondary cracks: vacuum, 1-1-1-1, $\Delta\varepsilon_t$= 1%.

specimen surface. Attempts were made to examine closely the area of crack initiation. There was no evidence that the crack initiated at a grain boundary. In vacuum tested specimens, the salient features on the fracture surface are easily discernible since the surface is less oxidised. At low strain range the fracture mode was transgranular with the presence of fatigue striations as shown on scanning electron micrograph in Fig. 7.

Similar fracture mode was observed even when static loading is combined with cyclic deformation and there is no evidence of cavity formation on the fracture surface. This suggests that creep damage does not play a significant role in the overall material failure.

In an air environment at high strain range the mode of fracture is intergranular as shown in Fig. 8, which implies that the loss of fatigue life is due to grain boundary oxidation effects.

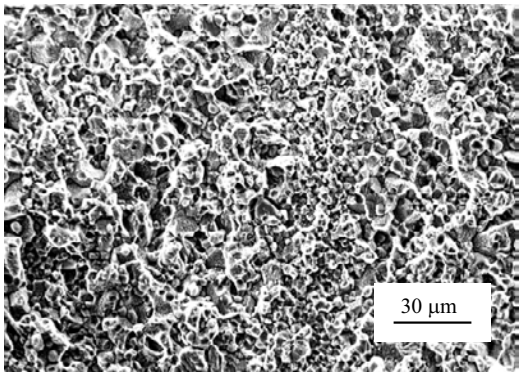

Fig. 8 – SEM micrograph of the fracture surface showing intergranular fracture: air, 1-1-1-1, $\Delta\varepsilon_t$= 1.2 %.

When the fractographic results are correlated with FCPR results, it is possible to identify two different fracture mechanisms of crack growth depending on the frequency of loading. The first is when the damage is purely of fatigue origin as typified by the 0.1–0–0.1–0 and 1–1–1–1 wave shapes. The results show clearly that the fracture mode is transgranular and the stress field ahead of the crack tip can be adequately described by the stress intensity factor K. The mechanism of crack growth under pure cyclic deformation is well known and it is usually explained in terms of blunting and re-sharpening of the crack tip or due to shear de-cohesion mechanism [9].

The second case is identified with low frequency of loading or when creep and fatigue deformations occur simultaneously, as typified by 1–120–1–1 wave shape where cavities or micro-voids are observed on the fracture surface (Fig. 9).

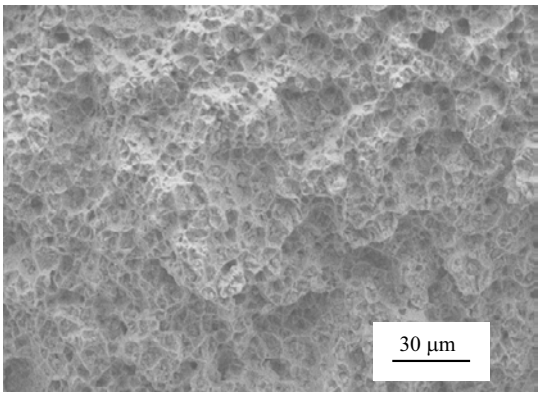

Fig.9 - SEM micrograph of the fracture surface after 1-120-1-1 FCPR test in vacuum at 700°C

The mechanism of crack growth can be explained with the aid of the schematic representation shown in Fig. 10, where voids are nucleated ahead of the crack tip and stress field ahead of the crack is characterised by a C*-parameter analogous to the Rice's J-integral [10].

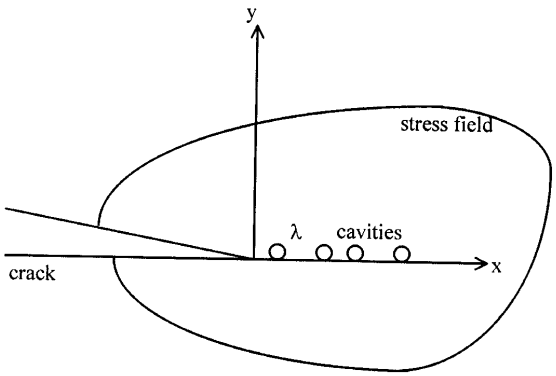

Fig. 10 - Schematic representation of the mechanism of crack growth

The subsequent growth of the crack will therefore be due to the growth and coalescence of the micro-voids ahead of the main crack in addition to the cyclic deformation. The origin of these cavities, as observed on the fracture surface, is not well known, but it may be due to vacancy condensation during the tensile hold time or due to plastic deformation ahead of the crack tip [11]. The interaction between slip and gamma prime precipitates on the grain boundaries can also lead to void or micro-cavity formation. However it should be remarked that cavity formation arising from diffusion process usually produces round shape cavity

unlike those observed in the present study, but the loading and reloading could modify the shape of the crack as well as to enhance the crack growth rate.

Discussion

The crack growth rate under the combined influence of creep and fatigue deformation can be expressed as the summation of damages arising from pure fatigue and from pure creep such that [12]

$$\frac{da}{dt} = \left(\frac{da}{dt}\right)_{creep} + \left(\frac{da}{dt}\right)_{fatigue} \tag{3}$$

where a is the crack length and t is the time. When the specimens are pre-cracked, we are concerned with fatigue crack propagation rate and the crack initiation period is not involved. However under static loading stress concentration is induced at the crack-tip with the consequences that cavity formation due to vacancy condensation or other time-dependent processes can occur so that the initiation period of the creep related damages must be taken into consideration. The damages arising from the creep effect involve cavity nucleation process, its subsequent growth and coalescence. The nucleation of cavities based on thermodynamics approach has been treated theoretically by several authors and the time for critical cavity size can be expressed as [13]:

$$t_i = \left(\frac{r_c^3 F_v}{\Omega}\right)\left[\frac{6\Omega^{4/3}}{\pi r_c^2 D_v + D_b(\pi\delta / r_c)}\right] \tag{4}$$

where r_c = radius of curvature of the cavity of critical size, Ω = atomic volume, F_v = geometric factor for cavity, D_v and D_b are volume and grain boundary diffusion coefficients. The contribution of the creep to the overall crack growth rate will depend therefore on the time for cavity initiation. When hold time at maximum load is below t_i it is plausible to suggest that the creep damage will not make any contribution to the overall crack growth rate. This could explain why hold time does not have any significant effect on the crack growth rate, under vacuum condition, below 120 s of hold time at maximum load (Fig. 4), but it is difficult to estimate the time required for cavity nucleation. Although the incubation period for cavity nucleation could determine the hold time necessary for the creep and fatigue interaction to occur, the rate at which cavities grow and coalescence will eventually determine the crack growth rate. Again, several models have been proposed for the growth of cavities under creep loading [14,15] and for the particular case where creep cavities are formed ahead of main crack the criterion for crack growth has been related to a critical value of strain given by [16]:

$$\varepsilon_f = 0.4\lambda / d(\sigma_e / \sigma_I) \tag{5}$$

where σ_e is the equivalent stress, σ_I the principal stress respectively, λ the interparticle spacing and d is the cavity diameter. This critical strain can be easily attained when both static loading and cyclic loading act together, although it is difficult to specify the exact contribution of pure fatigue damage from the total crack growth rate. The specimen tested with 1–120–1–1 wave shape spends a large proportion of its life under static loading but the imposition of cyclic loading could lead to re-sharpening of the micro-cavities that have been formed ahead of the major crack. This can increase the rate of material transport from the cavities and consequently increase the crack growth rate.

The LCF results on UD720Li have shown a low influence of hold time on fatigue life either in air or in vacuum. On the other side also the effect of environment is not strong mainly at higher endurance and lower strain. This behaviour is correlated to the good oxidation resistance of the alloy and to the fact that at the testing temperature creep plays a secondary role for the fatigue life. As observed in FCG tests, the FCGR is usually dependent on hold time and environment [17, 18]. In our case a strong influence of hold time on FCPR is observed in air tests, but not in vacuum tests [19]. This is not in contrast with the LCF results described above. In fact the LCF total life can be seen as a combination of crack incubation time and crack propagation time. As observed also in other nickel base superalloys [20, 21], the first is largely prevailing at lower strains and long lives, while the second is predominant at higher strains and shorter lives. Therefore the environment influences the fatigue life mainly at high strains while it is less effective when strain is progressively reduced.

These effects have been studied in detail in a previous work [22] on the same material in which a model is derived. This model has the advantage of providing the proportion of the life consumed under each phase of crack nucleation and crack propagation and more so the constants involved are material constants or parameters that can be derived from experiment. As a consequence at higher strains, where the propagation portion of life is prevailing the environment reduces fatigue life, while at lower strains where the initiation portion represents most of the life the environment is less important.

Conclusions

LCF and FCG testing on UDIMET 720Li in air and in vacuum at 700°C has shown a good resistance of the alloy to environment effect and a small influence of hold time on fatigue life.

Fracture surface examination of specimens tested in air at higher strain rate or without hold time has shown that fatigue crack (or cracks) starts on the external surface and propagates in transgranular mode for both the alloys. Fatigue striations are also apparent. At lower strain rate or in presence of hold time the fracture becomes mixed transgranular – intergranular without striations and with secondary cracks. In vacuum the aspect of the fracture surfaces is similar.

The Coffin – Manson relationship describes the fatigue life in air with good accuracy and confirms the good fatigue resistance of the UD720 Li alloy.

In vacuum environment the fatigue crack growth rate of UDIMET 720 Li superalloy remains practically unchanged for hold time up to 1 s, while a little increase is observed when the hold time is increased up to 120 s. The lack of influence of hold time on FCPR is rationalised in terms of the incubation period necessary for the creep related damages to occur. The fatigue crack growth rates in air environment increase with increasing in the hold time period and is considerably higher than those obtained in vacuum, indicating the adverse effect of oxidation.

The fracture mode is predominantly transgranular of cleavage type when frequency of loading is high, whereas the fracture mode changes to a dimple ductile type, suggestive of microcavity formation when the hold time was about 120 s. The crack growth rate reaches the highest level when both static and cyclic loading are combined in air environment. The proposed mechanism of fracture takes into consideration the role of oxygen and the form of damage resulting from creep and cyclic deformation.

Acknowledgement

The authors thank G.Grossi, T.Ranucci and E.Signorelli for their skilful technical assistance. One of the authors (G.A. Osinkolu) undertook this work with the associateship award of the "ICTP Programme for Training and Research in Italian Laboratories", Trieste, Italy.

References

1. Sims C T, and Hagel W C: The superalloys, Wiley, New York, 1987.
2. Gabrielli F, Marchionni M, Onofrio G. Advances in Fracture Research, 7th International Conf. on Fracture, Houston, K.Salama et al. Eds., 1989, 1149-1163.
3. Chen L J, Wang Z G, Yao G, Tian J F. The influence of temperature on low cycle fatigue behaviour of nickel base superalloy GH4049, Intern. J. Fatigue, 21 (8), 1999, 791-797.
4. Vasseur E, Rèmy L. High temperature low cycle fatigue and thermal-mechanical fatigue behaviour of an oxide dispersion strengthened nickel base superalloy, Mat. Sc. & Eng. , A184, 1994, 1-15.
5. Lu H M, Delph T, Dwyer D J, Gao M, Wei R P. Environmentally-enhanced cavity growth in nickel and nickel-based alloys, Acta Mater. , 44, 8, 1996, 3259-3266.
6. Andrieu E, Henon, J P. Effect of the environment on high temperature embrittlement of Inconel 718, Mater. Sci. Engng., 1987, 88, 191.
7. Suresh S. Fatigue of materials, 2nd ed. Cambridge (UK) Cambridge University Press, 1998.
8. Connolly T, Starink M J, Reed P A S. Effect of oxidation on high temperature fatigue crack initiation and short crack growth in INCONEL 718, Superalloys 2000, Eds, Pollock T M, Kissinger R D and Bowman R R (TMS), 2000, 435-444.
9. B. Tomkins, Phil. Mag. 1968,18,1041.
10. J.R. Rice, ASME J. Appl. Mech., 35, 1968, 379-386.
11. R. Raj, Acta Metall., 1978, 26, 1007
12. I. A. Saxena, Fat. Engng. Mater. Struct., 1988, 3, 247
13. S. Xu, X.J. Wu, A.K. Koul, J.1. Dickson, Metall. Mater. Transc. A. 1999, 30A 1039-1045

14. Jin Yu, J.0. Chung, Acta Metall. Mater., 38, No 8,, 1423–1434.
15. B.F. Dyson, Scripta Metall., 1983, 17, 31.
16. H. Riedel: Fracture at High Temperatures, Spring -Verlag, Berlin, 1987.
17. Hide N. J. et al., Proc. of Superalloys 2000, 2000, 495.
18. King J. E., Mat. Sci. Tech., Vol. 3, 1987, 750.
19. Onofrio G., Osinkolu G.A., Marchionni M.,"Fatigue crack growth of UDIMET 720LI superalloy at elevated temperature", International J. of Fatigue, 23, 2005, 887–895.
20. Runkle J. C. and Pelloux R. M., Fatigue Mechanisms, 1979, 50
21. Marshall P., Fatigue at high temperature, 1983, 259.
22. Marchionni M, Osinkolu G.A, Onofrio G, "High Temperature Low Cycle fatigue behaviour of UDIMET 720 Li superalloy", International J. of Fatigue, 24, 2002, 1261 – 1267.

INFLUENCE OF SOLUTION HEAT TREATMENT CONDITIONS ON GAMMA PRIME CHARACTERISTICS IN A HOT CORROSION RESISTANT SUPERALLOY

J.S.Hou, J.T.Guo, L.Z.Zhou, Z.J.Li, X.Z.Qin, Y.L.Li, H.Q.Ye
Institute of Metal Research, The Chinese Academy of Sciences, 72 Wenhua Raod, Shenyang 110016, China

Abstract

The evolution of γ' features of a nickel base superalloy is investigated in solution heat treatment conditions. In the 1170 ℃/*t*/air-cooled solution heat treatment, a single fine-size precipitate microstructure is developed after t = 1 and 3 h, an ideal cubical precipitate microstructure is yielded after t = 4 h while after t = 7 h, a morphological instability phenomenon (solid state dendrite structure) of the coarse precipitates that is related to the point effect of diffusion, occurs. In the heat treatment of 1170 ℃/4 h/*C.R* (specimens were cooled from 1170 ℃ to 900 ℃ with cooling rate *C.R.* = 5, 10, 20, 40, and 100 ℃/min) followed by 1050 ℃/4 h/AC and 850 ℃/16 h/AC, the morphological evolution of γ' undergoes splitting, alignment, and normal distribution. In addition, faster cooling rate is helpful for the refinement of the precipitate microstructure. In the solution heat treatments *T*/4 h/AC with *T* in the range of 1170 -1240℃ followed by 1050 ℃/4 h/AC and 850 ℃/16 h/AC, higher solution temperature is benefit to enhance the average size of γ' precipitates.

Keywords: Superalloy, Heat treatment, γ' precipitate, Morphology instability, Microhardness
E-mail: jshou@imr.ac.cn

1. Introduction

Nickel base Superalloys are widely used in gas turbine engines because of their good high temperature mechanical properties, which are due to characteristics of the γ' precipitates such as volume fraction, distribution, particle size, morphology and composition [1, 2]. The parameters (temperature, time, cooling rate) of the heat treatment can modify the γ' characteristics. Therefore, it is necessary to investigate the effect of heat treatment conditions on γ' evolution.

The experimental alloy, which consists of γ matrix, γ' precipitates, γ/γ' eutectic, carbides, and minor borides, is a cast nickel base superalloy [3]. To possess excellent hot-corrosion resistance and high temperature oxidation resistance capability, the alloy contains 16% Cr and 10% Co in weight percent. To possess a relatively high volume fraction of γ' precipitate, the alloy contains 7.5% precipitation strengthening elements (Al、Ti). In the present study, the influence of various solution and aging heat treatments on microstructural evolution of this alloy is considered with respect to the morphological instability and growth kinetics of γ' precipitate. Particular attention is paid to the characteristic of γ' particle size since it is a main factor to influence the strength. The variation of hardness exhibited by the alloy after different heat treatments is considered on the basis of particle hardening theories.

Table 1 Chemical composition of the alloy in wt.%

Al	Ti	B	C	Hf	Co	Cr	Mo	Nb	W	Ni
3.10	4.40	0.075	0.073	0.35	10.80	15.40	2.07	0.24	5.58	Bal.

Table 2 Heat Treatment Schedules for the alloy

Solution treatment	Aging treatment
1170 ℃/1 h/AC	
1170 ℃/3 h/AC	
1170 ℃/4 h/AC	
1170 ℃/5 h/AC	
1170 ℃/7 h/AC	
1170 ℃/4 h/*C.R.* (cooled to 900 ℃ with *C.R.* (cooling rate) = 5, 10, 20, 40, 100 ℃/min)	1050 ℃/4 h/AC + 850 ℃/16 h/AC
1180 ℃/4 h/AC	1050 ℃/4 h/AC + 850 ℃/16 h/AC
1200 ℃/4 h/AC	1050 ℃/4 h/AC + 850 ℃/16 h/AC
1220 ℃/4 h/AC	1050 ℃/4 h/AC + 850 ℃/16 h/AC
1240 ℃/4 h/AC	1050 ℃/4 h/AC + 850 ℃/16 h/AC

2. Experimental

The chemical composition of the alloy prepared by vacuum casting is reported in Table 1. Samples 8mm×5mm×5mm were cut from cast rod and were applied various heat treatments using a vertical electrical furnace with SiC heating elements. The temperature error was controlled within 5 ℃.The optimum dissolution of the particles was obtained by applying various solution treatment temperatures between 1170℃ and 1240℃ for 1 to 7 h followed by air cooling. A double aging treatment was then applied to the samples to observe the precipitate growth. Table 2 shows the various heat treatments used in the present investigation. The ground and polished specimens were etched with a solution of 10% perchloric acid, 2% distilled water and 88% methanol. A JSM-6301 or SUPRA 35 type scanning electron microscope (SEM) was used to characterize the morphology of the γ′ precipitates. Quantitative measurements of γ′ size were made directly on the SEM micrographs using a semi-automatic image analyzer. The reported values for γ′ size were the average values from the measurements made on ten SEM micrographs of each sample. The magnifications, 10000 and 20000×, were selected so that at least 60 γ′ particles presented in each picture. Hardness testing was carried out under a load of 5 kg using a calibrated Vickers hardness indentation machine. The results presented were the average of 6-15 measurements.

3.Results and discussion

3.1 Effect of solution holding time

The formation of the single cubical microstructure was determined through heat treatments at 1170℃ for different holding time. Figure 1 shows the γ′ microstructures after holding time from 1 to 7 h. With increasing holding time, the size of γ′ in dendrite cores becomes more inhomogeneous, while the average size of γ′ precipitate increases within 1-4 h and decreases when the time exceeds 4 h. After solution for 7 h (Fig. 1(e)), the coarse precipitates exhibit a morphological instability phenomenon (butterfly structure). In these treatments, the γ′ precipitate possesses a single regular cubic shape only at the holding time of 4 h (Fig.1(e)). The precipitates in interdendritic regions (Fig.1 (b), (d), (f), (h) and (j)) exhibit flowerlike or butterflylike morphology.

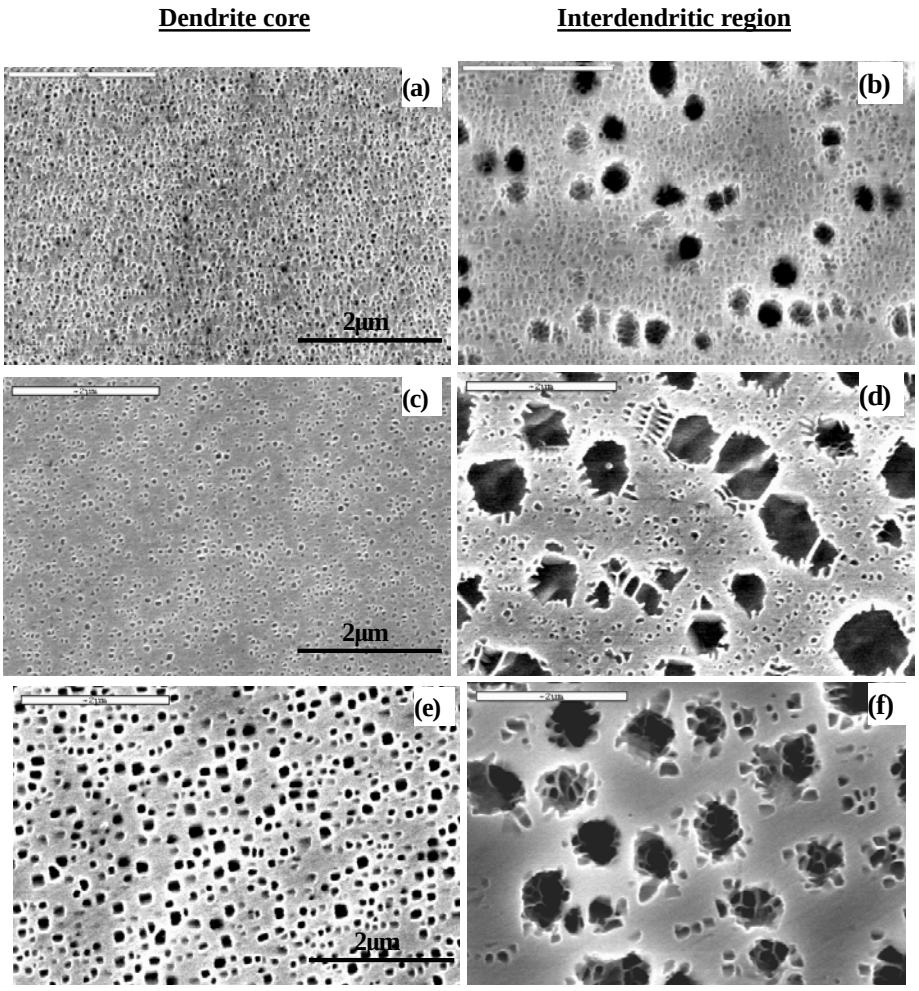

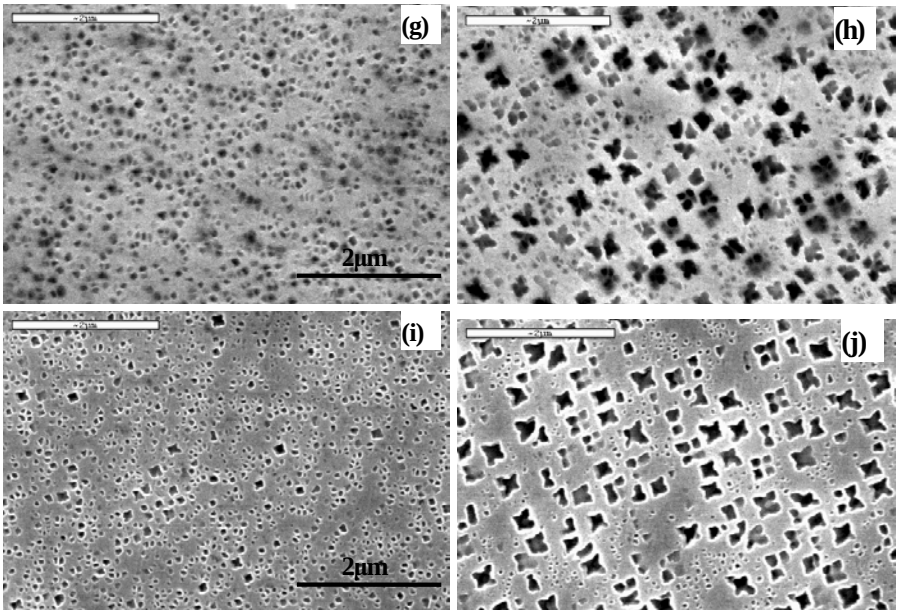

Fig.1 Morphologies of γ′ phases after solution treatment at 1170 ℃ for different holding times. (a, b) 1 h; (c, d) 3 h; (e, f) 4 h; (g, h) 5 h; (i, j) 7 h.

3.2 Effect of solution cooling rate

Microstructures obtained after solution treatment at 1170 ℃/4h with cooling rate of 5-100 ℃/min followed by double agings have much difference in γ′ morphology and size, as can be seen in Fig. 2. Under these heat treatment conditions, the alloy exhibits duplex-size γ′ microstructure and morphological evolution of coarse γ′ undergoes splitting, alignment, and normal distributing with increasing cooling rate (Fig. 2 (a), (c), (e), (g) and (i)). Moreover, precipitate refinement is observed, which is always reported in thermal processes [4,5]. With cooling rate increasing from 5 to100 ℃/min, the average edge length for coarse cuboidal γ′ precipitates in dendrite cores decreases from 523 nm to 110 nm indicating that fast cooling rate is helpful for the refinement of the precipitate. Furthermore, the fine precipitates keep a constant size, i.e. 30 nm, although their quantity decreases with increasing cooling rate. In interdendritic regions, the average size of coarse precipitates decreases with increasing cooling rate. There is no remarkable difference in the morphology of these coarse precipitates.

Dendrite core **Interdendritic region**

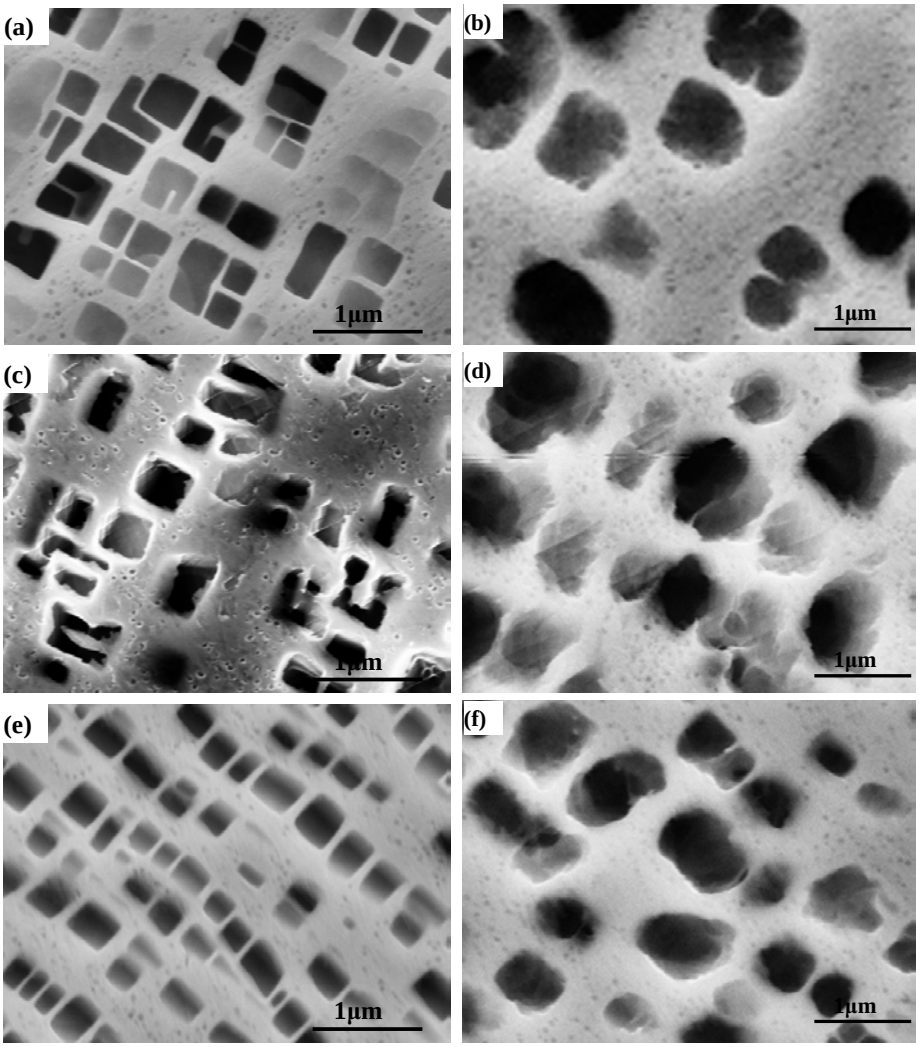
(a)
1μm
(b)
1μm
(c)
1μm
(d)
1μm
(e)
1μm
(f)
1μm

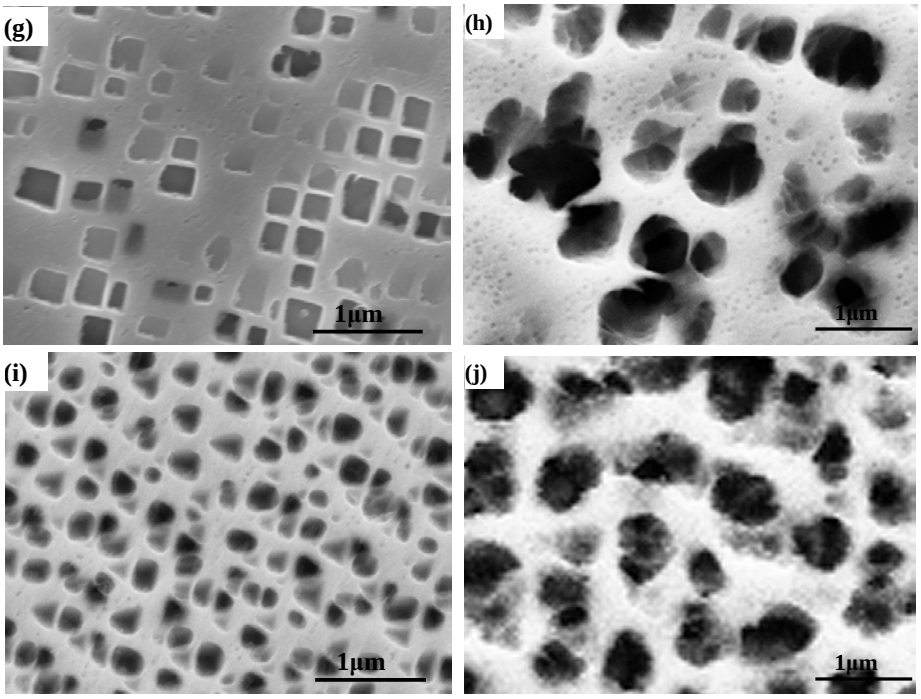

Fig.2 Morphologies of γ′ phases after heat treatment of 1170 ℃/4 h/C.R (specimens were cooled from 1170 ℃ to 900 ℃ with different cooling rate C.R.) followed by 1050 ℃/4 h/AC and 850 ℃/16 h/AC. (a, b) 5 ℃/min; (c, d) 10 ℃/min; (e, f) 20 ℃/min; (g, h) 40 ℃/min; (i, j) 100 ℃/min

There are two types of morphological instabilities of γ′ in Ni base superalloys, which can be found in both low misfit case and high misfit case [6-8]. One is in equilibrium shape such as splitting of cuboidal γ′ precipitates in two-phase coherent superalloy, which is determined by the total energy minimization condition. The other is in growth shape such as solid-state dendrites and flower-like unstable structure of γ′ determined by the fast growth conditions, which is developed normally in a low misfit superalloy with spherical γ′ precipitates.

At low cooling rate (5-10 ℃/min), the splitting patterns of the γ′ particles (Fig.2(a) and (c)) which can be observed commonly in superalloys, are schematically shown in Fig.3. When the γ′ particles splits or fissions into two or more smaller particles, the decrease of the elastic energy resulting from the transition more than compensates for the accompanying increase in the interfacial energy, thus, the total energy is preserved minimum.

Fig.3 The various split-patterns of γ′ precipitates observed in the alloy

At the cooling rate of 20 ℃/min, alignment or selective coarsening phenomena is observed. Ardell *et al*. [9] and Doi *et al*. [10] point out that the aligned particles would grow at the expense of the unfavorably located particles, so the particles aligned along a certain direction. Similar phenomena can also be observed in Fig. 2(e). When the cooling rate is higher (more than 40-100 ℃/min), the precipitated γ′ particles distribute dispersedly in matrix (Fig. 2(g) and (i)).

Figure 1(i) and the precipitates in interdendritic regions (Fig.1 (b), (d), (f), (h), (j)) show the examples of morphological instability in growth shape. The large particles exhibit a morphological instability (solid-state dendrites), which is related with point effect of diffusion. Ricks *et al.* [11] pointed out the mechanism of this phenomenon. When the γ′ grows in supersaturated γ phase in a diffusion controlled manner, the point effect of diffusion competes with stabilizing factors like surface energy, surface diffusion or anisotropy of surface tension. If point effect of diffusion is dominant, morphological instability occurs. High supersaturation is essential to this type of instability. With prolonged solution time, the precipitates formed during cast stage can dissolve sufficiently, which is benefit to enhance the supersaturation.

3.3 Effect of solution temperature

Figure 4 shows the morphologies of γ′ phases after heat treatment at five different temperatures (1180℃, 1200℃, 1220℃, and 1240℃) followed by double agings. At these heat treatment conditions, dendrite core and interdendritic region are not distinguishable. With increasing temperature, the γ′ precipitate size increases. There are several precipitate patterns observed in Fig. 4. Cuboidal / triangular precipitate shape is observed in Fig. 4(a), and trapeziform / triangular, and triangular / triangular precipitate shapes are observed in Fig. 4(c). Similar morphologies were reported in IN738LC [4]. The observed morphology difference should be due to the difference in grain orientations [5,6]. On the {100} plane of f.c.c superlattice, cuboidal morphology can be observed, and on the {111} plane, the octahedral morphology (triangle and trapezium) can be observed. These observations also suggest that the possibly splitting of γ′ precipitates occurs along a certain plane or direction, although it is seldom reported.

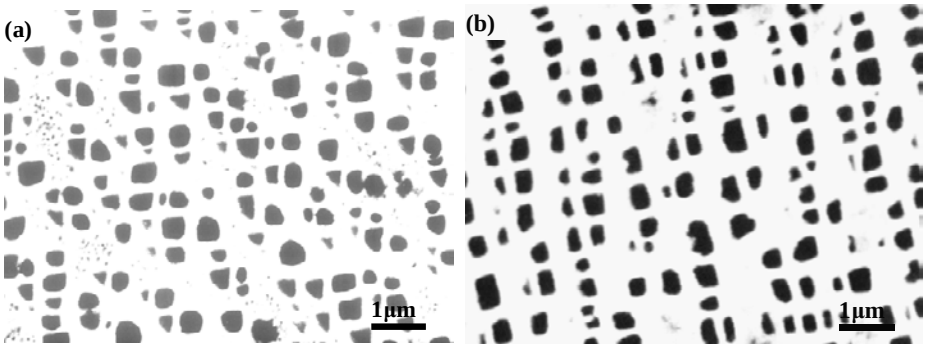

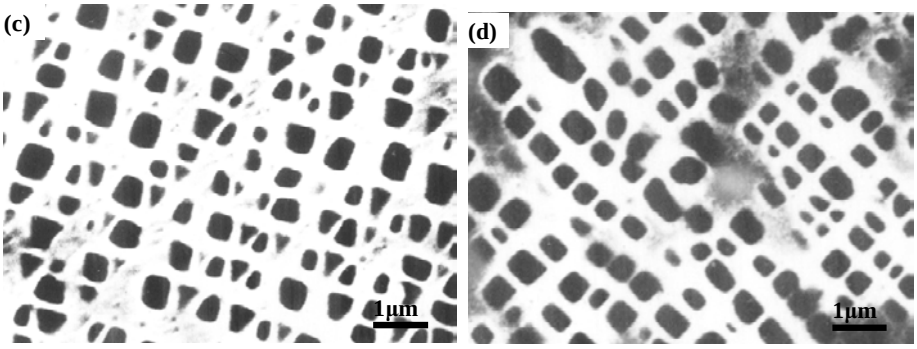

Fig.4 Morphologies of γ′ phases after solution at different temperatures for 4 h and air cooled, followed by 1050 ℃/4h/AC and 850 ℃/16 h/ AC. (a) 1180 ℃; (b) 1200 ℃; (c) 1220 ℃; (d) 1240 ℃.

Precipitates sizes were measured after solution heat treatments at different temperatures (*T*/4 h/AC +1050 ℃/4 h/AC + 850 ℃/16 h/AC) using the SEM micrographs. Precipitate growth data obey the following well-known growth equation:

$$d^n - d_0^n = Kt \qquad (1)$$

where $K = K_0 \exp(-Q/\mathrm{R}T)$, T is the absolute temperature. d_0 and d are the initial and final precipitate size, respectively. t is the time, n is the growth exponent, and K is a growth-rate parameter involving the interface energy between matrix and precipitate. From the plot of precipitate growth data in Fig. 5, the activation energy for the γ′ precipitate growth, is caculated to be 224 kJ/mol in the range of 1170 ℃ to 1240 ℃ by taking $d_0 = 0$ and n = 3. It should be noticed that in the above studies for the calculation of the activation energy Q, the concentration of γ′ forming elements in equilibrium (C_e) is considered as a constant at the first approximation, which may take a deviation of the activation energy. Considering the C_e term as a variable with temperature, the parameter K should be expressed as:

$$K = K_0 (C_e/T) \exp(-Q/\mathrm{R}T) \qquad (2)$$

where K_0 is a constant. It is reasonable to consider that the γ′ phases consist of Al and Ti atoms, so the term C_e is the sum of Al and Ti contents of the matrix. The atomic percentages of Al + Ti in the matrix evaluated with CALPHAD method were 5.8, 6.2, and 6.4 at.% for solution temperature of 1170 ℃, 1220 ℃, and 1240 ℃ respectively. Based on these data and formulae (2) and (1), the activation energy for γ′ growth is evaluated to be 199 kJ/mol, which is close to the calculated value 224 kJ/mol when C_e is considered as a constant. According to the formulae (2) and (1), the coarsening kinetics of γ′ in high temperature aging can be estimated by:

$$[(\frac{d}{2})^3 - (\frac{d_0}{2})^3]^{1/3} = 2.1\times10^5 t^{1/3} (\frac{C_e}{T})^{1/3} (\frac{-199000}{3RT}) \qquad (3)$$

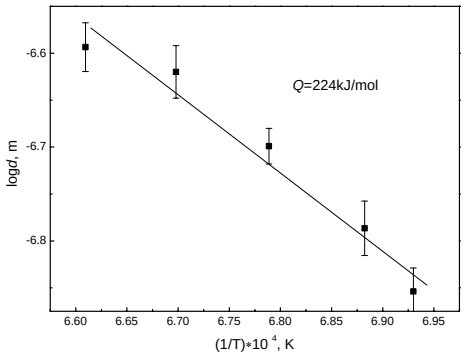

Fig.5 Plot of log d vs. 1/T derived from average diameter of γ′ precipitates d at different solution temperatures

4. Conclusions

The evolution of γ′ morphology, size, and distribution at solution heat treatment conditions has been investigated. With increasing solution cooling rate, the morphological evolution of γ′ undergoes splitting, alignment, and normal distributing. Faster solution cooling rate is helpful for refinement of the precipitate microstructure. At the same solution temperature and cooling rate, longer solution holding time is benefit to enhance the supersaturation in γ matrix which promotes the formation of γ′ morphological instability. With increasing solution temperature, the average size of γ′ precipitates after a solution and double agings increases.

5. References

[1] Benjamin Flageolet, Patrick Villechaise, Mustapha Jouiad, and José Mendez, Ageing Characterization of the Powder Metallurgy Superalloy N18, in: *K.A. Green*,et al. (Eds.), Superalloys 2004. The Minerals, Metals and Materials Society, 2004, p. 371.

[2] M.P. Jackson and R.C. Reed, Heat Treatment of UDIMET 720Li ,Mat. Sci. Eng. A, 259 (1999) 85.

[3] J.S.Hou, J.T.Guo, L.Z.Zhou, and H.Q.Ye, Effects of γ′-precipitate coarsening on tensile properties during long-term aging in a Ni base superalloy, Acta metal. sinica (in press)

[4] Ercan Balikci, A. Raman, and R. A. Mirshams, Influence of Various Heat Treatments on the Microstructure of Polycrystalline IN738LC, Metall. Mater. Trans. A, 28 (1997) 1993.

[5] M. Tanaka, Grain refinement by utilizing grain-boundary reaction in heat resistant allloys, J. Mater. Sci., 29 (1994) 4093.

[6] M. J. Kaufman, P. W. Voorhees, W. C. Jonshon, and F.S. Biancaniello, Consistent with an arrangement of four cubes and two rods, Metall. Mater. Trans., A, 20 (1989) 2171.

[7] M. F. Henry, Y. S. Yoo, D. Y. Toon, and J. Choi, The Dendritic Growth of γ′ Precipitates and Grain Boundary Serration in a Model Nickel-Base Superalloy, Metall Trans., 24A (1993) 1733.

[8] Y. S. Yoo, D. Y. Yoon, and M. F. Henry, The Effect of Elastic Misfit Strain on the

Morphological Evolution of gamma prime precipitates in a Model Ni-Base Superalloy, Metals. Mater., 1 (1995) 47.
[9] A. J. Ardell and R. B. Nicholson, On the modulated structure of aged Ni-Al alloys Acta Metal., 14 (1966) 1295.
[10] M. Doi, M. Fukaya, and T. Miyazaki, Inhomogeneity in a coherent precipitate distribution arising from the effects of elastic interaction energies, Phil Mag. A, 57(1988) 821.
[11] R. A.Ricks, J.A. Porter, and R.C. Ecob, The growth of γ′ precipitates in Nickel-base superalloys Acta Metal., 31 (1983) 43.

Part I

Advanced Gas Turbine Materials

Contributed Papers

Microstructure

MORPHOLOGICAL EVOLUTIONS OF γ' AND $M_{23}C_6$ CARBIDE IN A CAST NI-BASE SUPERALLOY IN THE DIFFERENT TREATMENT CONDITIONS

X. Z. Qin, J. T. Guo*, C. Yuan, J. S. Hou, H.Q. Ye

Superalloy Division, Institute of Metal Research, Chinese Academy of Sciences, 72 Wenhua Road, Shen Yang 110016, China
*E-mail address: jtguo@imr.ac.cn (J. T. Guo)

Abstract

An investigation has been made into the effects of heat treatment and long-term aging on the microstructural stability of a cast Ni-base superalloy K452. Specimens after heat treatment were aged at temperatures of 800, 850 and 900℃ for different times up to 10000 h, respectively. The microstructure examination indicated that the morphologies of γ' precipitates and $M_{23}C_6$ carbide exhibited the similar evolution laws. γ' precipitates were dendrite like in shape in the as-cast condition, then became cuboidal after heat treatment and finally spheroidal during long-term aging. $M_{23}C_6$ carbide dendritically precipitated from supersaturated γ solid solution in the initiation of aging, and then grew octahedral with increasing aging temperature or time. A conclusion was drawn that not only the minimization of the total free energy of the system but also the interfacial character, isotropic or anisotropic, are the root reasons of the morphological evolutions of the γ' precipitate and $M_{23}C_6$ carbide. The three-dimensional morphologies of the γ' precipitate and $M_{23}C_6$ carbide in the different condition were displayed with different etching technologies.

Keywords: long-term aging; γ' precipitate; $M_{23}C_6$ carbide; morphological evolution; free energy

1. Introduction

γ' phase is the focus of all industrial heat treatment, and is the most important strengthening phase in Ni-base superalloys. Its quantity, size and morphology have a great influence on the property [1].

The equilibrium shapes of γ' precipitates depend on the competition between the interfacial and elastic energies [2-4]. When γ' precipitates are small, they are spheres for the interfacial energy is minimized; however, as γ' precipitates coarsen during aging, they become sequentially cubes, doublets of plates, octets of cubes and finally platelets (dendrites) as the elastic energy is minimized [5-8].

In fact, the shape evolution of γ' precipitates is determined by the requirement that the sum of the elastic and interfacial energies be minimum. For example, when γ' splits, the decrease in the elastic energy resulting from the shape transition more than compensates for the accompanying increase in the interfacial energy [8].

Carbide is another important strengthening phase, even though it is a minor phase relative to γ' phase. Carbide mostly exists in the forms of M(CN), MC, M_7C_3, $M_{23}C_6$ and M_6C in Ni-base superalloys [9-11]. M(CN) and MC are generally primary carbides while M_7C_3, $M_{23}C_6$ and M_6C carbides precipitate from γ matrix.

The precipitation of carbides in Ni-base superalloys has been extensively studied [12-19].

Isothermal changes in shape of $M_{23}C_6$ carbide in austenitic steels were also investigated [20,21]. However, the precipitation and evolution of $M_{23}C_6$ carbide in γ matrix in Ni-base superalloys has never been systemically reported.

The present work exhibits the morphological evolutions of the γ' precipitate and $M_{23}C_6$ carbide during long-term aging. Micro mechanisms are also revealed. The three-dimensional displays of the γ' precipitate and $M_{23}C_6$ carbide in the different condition facilitate and visualize the morphological observations.

2. Experimental procedure

The nominal chemical composition of the alloy investigated in the present paper is given in Table 1. Raw material was rinsed to remove oil and oxide stains and was vacuum induction melt. Cast sample was machined into specimens, three groups of four, for heat treatment. The heat treatment was designed to obtain different size γ' particle, so the sample was solution heat-treated at 1170 ℃ for 4 h followed by a furnace cooling down to 900 ℃ and then air cooling. It was subsequently aged at 1050 ℃ for 4 h and 850 ℃ for 16 h. After heat treatment, specimens were heat exposed at temperatures of 800, 850 and 900℃ for times of 1000, 3000, 5000 and up to 10000 h, respectively.

Table 1. Composition of K452

	Cr	Co	Al	Ti	Nb	Mo	W	C	Ni
wt.%	20.9	11.15	2.5	3.5	0.25	0.6	3.5	0.11	Balance

The microstructure was examined using scanning electron microscopy (SEM) equipped with an energy dispersive X-ray spectroscopy (EDX) system. Specimens for SEM observation of $M_{23}C_6$ carbide were chemically etched using a solution containing 20 g $CuSO_4$, 50 ml HCl and 100 ml H_2O. Transmission electron microscopy (TEM) was used for phase identification. Foils for TEM were prepared on a twin-jet electropolisher with a solution of 10% perchloric acid and 90% ethanol at – 20 ℃.

The three-dimensional morphology of the γ' precipitate was clearly shown with deep etching technology. The etching was carried out in a solution of 200 g KCl, 50 g citric acid, 200 ml HCl and 1000 ml H_2O with 0.1-1 A/cm^2 at 0 ℃.

3. Results and discussions

3.1 Morphological evolution of γ' phase

After the alloy melt has solidified completely, the γ' phase precipitates from the supersaturated γ solid solution if the solid alloy is further cooled [22]. The γ' precipitate is spherical owing to its small size at the early stage of the precipitation. When a small perturbation impacts on the spherical γ' surface, dendritic growth is induced for the growth rate at the perturbed point accelerates relative to the rest of the precipitate (Fig. 1). The steep concentration gradient in the supersaturated γ solid solution is also in favor of the dendritic growth. The occurrence of dendritic growth needs three necessary conditions to be met [23]: (1) isotropic γ/γ' interface; (2) low diffusion rate within the precipitates; (3) low lattice misfit

between the γ and γ' phases.

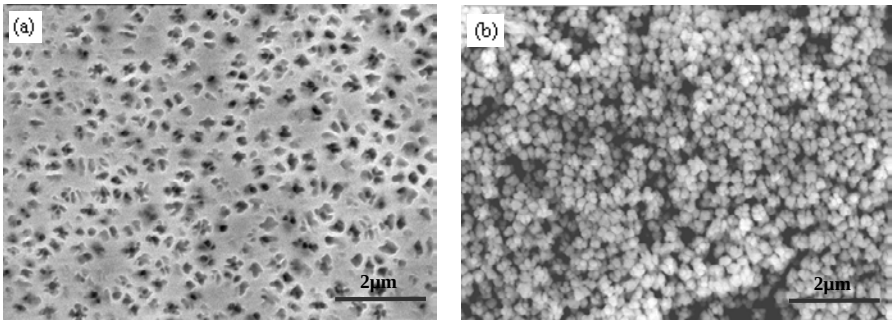

Fig.1 γ' phase in the cast condition: (a) chemically etched; (b) deeply etched.

The dendritic γ' precipitate contains a large surface area or interface energy to volume rate. The interfacial energy makes the precipitate apt to change its shape with a smaller surface area. Therefore during the standard heat treatment, the dendritic γ' precipitate agglomerates into cuboidal blocks (Fig. 2). The morphological transition depends not only on the interfacial energy whose decrease is the driving force but also on the elastic energy (mainly the misfit strain energy) whose anisotropy ultimately determines γ' to be cuboidal not spheroidal. In Fig. 2b and 2c, the duplex distribution of γ' is clearly shown: the bigger in

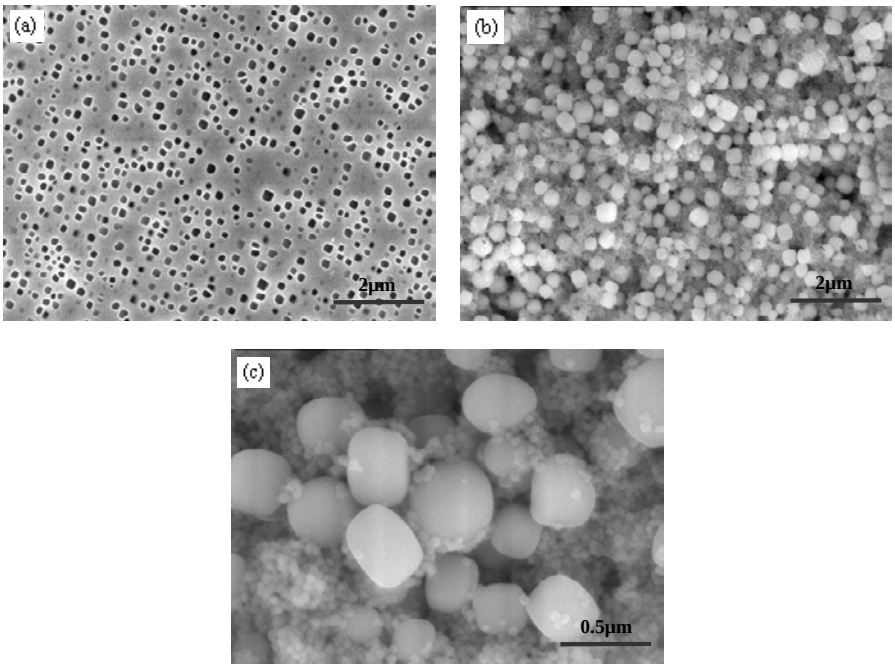

Fig.2 γ' precipitates in the heat treatment: (a) chemically etched; (b) and (c) deeply etched.

cuboidal shape is the primary γ' whose origin is the dendritic γ' mentioned above while the much smaller in spherical shape is the secondary γ' which precipitates during heat treatment and has an inappreciable misfit strain energy [24].

Completely different from the previous references [3-7], in the present study the cuboidal γ' precipitates do not split into so-called doublet or octet after experiencing coarsening at the different temperatures of 800, 850 and 900℃ with different times up to 10000 h. On the contrary, they become spherical in shape at all the temperatures. Due to the similarity, only the morphological evolution of the γ' precipitates at 900℃ is shown in Fig. 3. During long-term aging, as the γ' phase and $M_{23}C_6$ carbide much precipitate from the γ solid solution

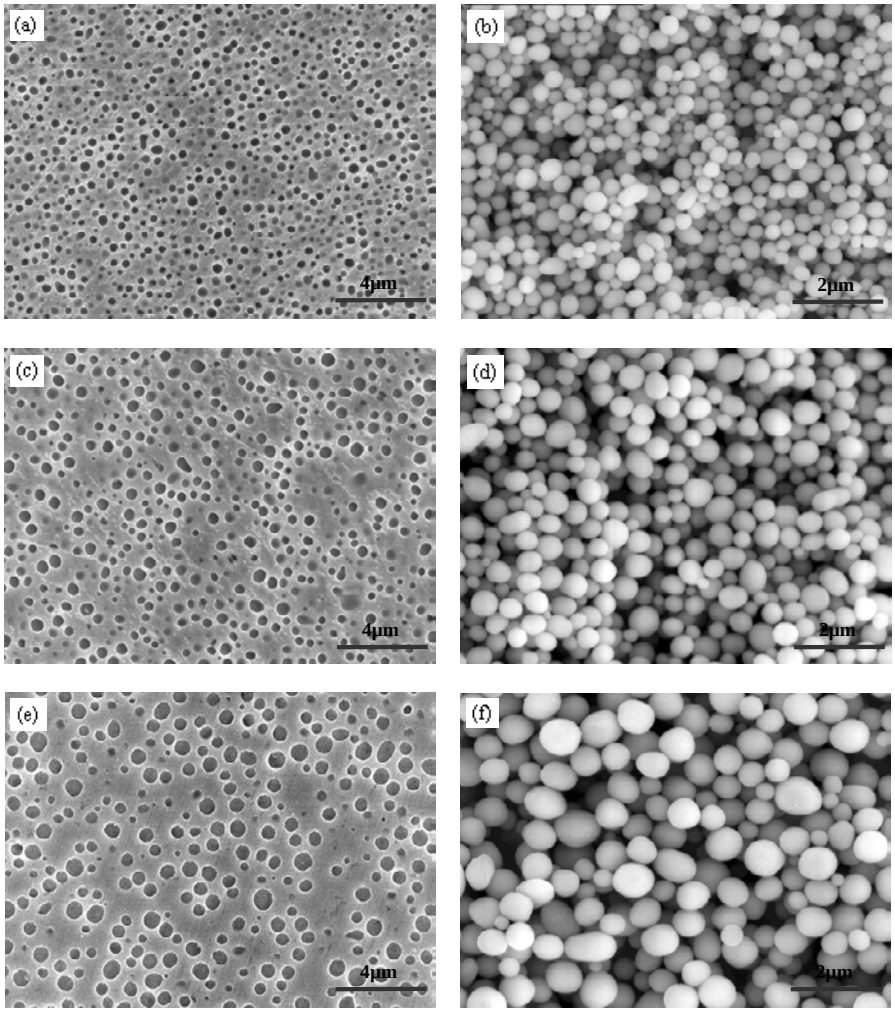

Fig.3 Morphologies of γ' phases: (a) and (b) 900℃/1000h; (c) and (d) 900℃/5000h; (e) and (f) 900℃/10000h.

in grain interior and at grain boundary, the γ/γ' lattice misfit $\delta = \frac{2(a_{\gamma'} - a_{\gamma})}{a_{\gamma'} + a_{\gamma}}$ decreases owing to the reduction of a_{γ} which the equilibrium redistribution of elements results in. A small lattice misfit corresponds to a low elastic energy. Therefore relative to the elastic energy, the interfacial energy dominates the total free energy and makes the shape of the γ' precipitates spherical [2]. Khachaturyan [4] defined the coarsening process driven by the decrease in the interfacial energy of the system during long-term aging as an "interface-controlled" coarsening.

3.2 Morphological evolution of $M_{23}C_6$ carbide during long-term aging

At the aging temperatures of both 800 and 850 ℃, the morphologies of $M_{23}C_6$ carbide particles basically remain dendrite-like. They begin to precipitate from the supersaturated γ solid solution at the aging time of 1000 h and then grows bigger and thicker with increasing aging time up to 10000 h. However, at 900 ℃ the morphology of $M_{23}C_6$ carbide particles changes more remarkably with the aging time.

The morphological evolution of $M_{23}C_6$ carbide particles at 900 ℃ with different time is shown in Fig. 4. Two important phenomena can be observed: first, the morphology of $M_{23}C_6$ carbide particles evolves sequentially from a small dendrite to a big and thick dendrite to an irregular block to a regular octahedron; second, the γ' precipitate embed in the $M_{23}C_6$ dendrite migrates outwards and gradually forms a thick γ' envelope around the octahedral $M_{23}C_6$ particle.

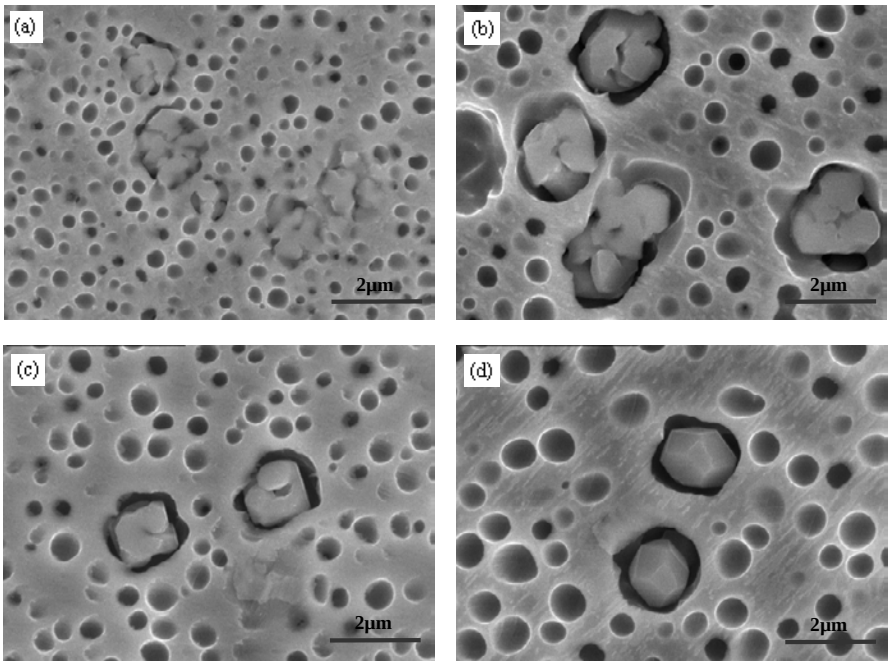

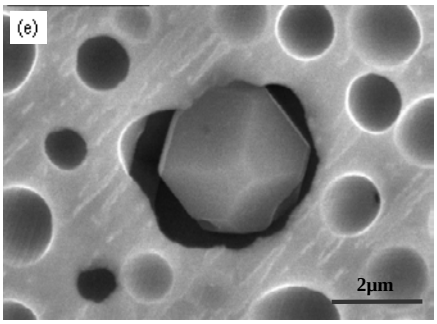

Fig.4 Morphological evolution of $M_{23}C_6$ carbide during long-term aging: (a) 900℃/1000h; (b) 900℃/3000h; (c) 900℃/5000h; (d) and (e) 900℃/10000h.

According to the above observations, several important viewpoints can be drawn. The decrease in the interfacial energy is the driving force of breaking-down of the γ'/$M_{23}C_6$ dendritic cell. The breaking-down minimizes the γ'/$M_{23}C_6$ interface and the γ' shell enveloped outside the $M_{23}C_6$ particle has a spherical shape with a low interfacial energy. $M_{23}C_6$ carbide has an excellent crystallographic relationship with γ (or γ'), that is, $\{111\}_{M_{23}C_6} // \{111\}_{\gamma}$ with $\langle 110\rangle_{M_{23}C_6} // \langle 110\rangle_{\gamma}$, which tends to make $M_{23}C_6$ particles octahedral in shape (Fig. 5). That is, the crystallographic relationship determines the most stable morphology of $M_{23}C_6$ carbide to be an octahedron whose surfaces are the {111} planes.

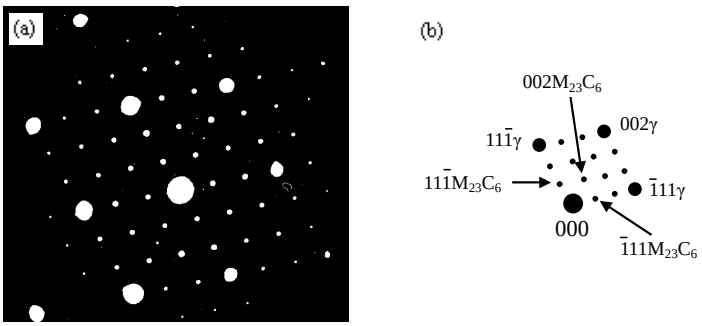

Fig.5 Diffraction patterns of $M_{23}C_6$ carbide and γ matrix: (a) diffraction patterns; (b) indexing.

4. Conclusions

In the present study, the morphology of the γ' precipitate changes from dendrite to cube to sphere, orderly corresponding to the conditions of as-cast, heat treatment and long-term aging. $M_{23}C_6$ particle evolves from small dendrite to large dendrite to octahedron in shape. Obviously, the two processes both begin with dendrite and end with regular gyometry. The similarity is determined not only by the minimization of the total free energy of the system but also by the interfacial character, isotropic or anisotropic. The isotropic interface makes the ultimate form of the γ' precipitate be spherical while the ultimate morphology of $M_{23}C_6$ particle is an octahedron bounded by {111} surfaces which is lowest-energy.

Acknowledgement

The authors would like to thank Prof. X. X. Jiang and PhD. Y. Wang, Institute of Metal Research, Chinese Academy of Sciences, for their useful discussion.

References

[1] Guo JT. Material Science of Superalloy, to be published. (in Chinese)
[2] W. C. Johnson, T. A. Abinandanan and P. W. Voorhees. The coarsening kinetics of two misfitting particles in an anisotropic crystal. Acta Metall. 38 (1990): 1349 - 1367.
[3] W. C. Johnson, J. W. Cahn. Elastically induced shape bifurcations of inclusions. Acta Metall. 32 (1984): 1925 - 1933.
[4] A. G. Khachaturyan, S. V. Semenovskaya and J. W. Morris Jr. Theoretical analysis of strain-induced shape changes in cubic precipitates during coarsening. Acta Metall. 36 (1988): 1563 - 1572.
[5] S. J. Yeom, D. Y. Yoon and M. F. Herry. The morphological changes of γ' precipitates in a Ni-8Al (Wt Pct) alloy during their coarsening. Metall. Trans. 24A (1993): 1975 - 1981.
[6] R. A. Ricks, A. J. Porter and R. C. Ecob. The growth of γ' precipitates in Ni-base superalloys. Acta Metall. 31 (1983): 43 - 53.
[7] Minoru Doi, Toru Miyazaki and Teruyuki Wakatsuki. The effects of elastic interaction energy on the precipitate morphology of continuously cooled Nickel-base alloys. Mater. Sci. Eng., 74 (1985): 139 - 145.
[8] M. J. Kaufman, P. W. Voorhees, W. C. Johnson and F. S. Biancaniello. An elastically induced morphological instability of a misfitting precipitates. Metall. Trans. 20A (1989): 2171 - 2175.
[9] H. E. Collins. Relative long-time stability of carbide and intermetallic phases in Ni-base superalloys. Trans ASM, 62 (1969): 82 - 104.
[10] C. Hammond and J. Nutting. The physical metallurgy of superalloys and titanium alloys. Metal Sci, 10 (1977): 474 - 490.
[11] H. J. Beattie, F. L. Versnyder. Microconstituents in high temperature alloys. Trans ASM, 45 (1952): 397 - 428.
[12] P. S. Kotval and H. Hatwell. Discontinuous precipitation of $M_{23}C_6$ carbide in a Nickel-base superalloy. Trans. Metall. Soc. AIME 245 (1969): 1821 - 1823.
[13] R. G. Faulkner and J. Caisley. The kinetics of grain boundary carbide precipitation in Nimonic PE16. Metal Sci. (1977): 200 - 207.
[14] F. T. Furillo, J. M. Davidson and J. K. Tien. The effect of grain boundary carbides on the creep and back stress of a Nickel-base superalloy. Mater. Sci. Eng. 39 (1979): 267 - 273.
[15] R. Maldonado and E. Nembach. The formation of precipitate free zones and the growth of grain boundary carbides in the Nickel-base superalloy Nimonic PE16. Acta Metall. 45 (1997): 213 - 224.
[16] B. J. Piearcey and R. W. Smashey. The carbide phases in Mar-M200. Trans Metall Soc AIME, 239 (1967): 451 - 457.
[17] H. J. Beattie and F. L. Versnyder. The influence of molybdenum on the phase relationships of a high temperature alloy. Trans ASM 49 (1957): 883 - 904.
[18] H. J. Beattie and W. C. Hagel. Intragranular precipitation of intermetallic compounds in complex austenitic alloys. Trans Metall Soc AIME, 221 (1961): 28 - 35.
[19] W. C. Hagel and H. J. Beattie. Aging reactions in certain superalloys. Trans ASM, 49 (1957): 978 - 1004.
[20] E. M. Mahla and N. A. Nielsen. Carbide precipitation in type 304 stainless steel – an electron microscope study. Trans ASM 43 (1951): 290 - 322.
[21] A. B. Kinzel. Chromium carbide in stainless steel. J. Metals, 4 (1952): 469 - 488.
[22] F. Zupanič, T. Bončina, A. Križman, B. Markoli and S. Spaić. Microstructural constituents of the Ni-based superalloy GMR 235 in the as-cast condition. Scripta Materialia, 46 (2002): 667 - 672.
[23] S. R. Summerfelt and C. B. Carter. Morphology of $NiFe_2O_4$ precipitation in NiO. Acta Metall. 40 (1992): 1051 - 1067.
[24] J. G. Conley, M. E. Fine and J. R. Weertman. Effect of lattice disregistry variation on the late stage phase transformation behavior of precipitates in Ni-Al-Mo alloys. Acta Metall. 37 (1989): 1251 - 1263.

DISLOCATION SUBSTRUCTURE IN γ-CHANNEL OF SINGLE CRYSTAL NICKEL-BASED SUPERALLOY, CMSX-4, CREPT AT 1273K, 160MPa

Yoshihiro Kondo*, Nobuhiro Miura* and Takashi Matsuo**

*National Defense Academy, 1-10-20 Hashirimizu Yokosuka, Kanagawa 239-8686, Japan
**Tokyo Institute of Technology, 2-12-1 Ookayama Meguro, Tokyo 152-8552, Japan
kondo@nda.ac.jp

Abstract

The Burgers vectors and the slip planes of dislocations in the γ channels were identified on the [001] oriented single crystal nickel-based superalloy, CMSX-4, crept at 1273K and 160MPa. The creep curve consisted of two stages, that is, the transient and the accelerating creep stage. The plates of the rafted γ' precipitates were arrayed perpendicular to the stress axis at the time of the minimum creep rate, but the regularity of the rafted γ' precipitates was lost at the accelerating creep stage. The change in the slip systems during creep deformation was discussed. The slip systems at the beginning of the transient creep stage were characterized by <101> and <011>, irrespective of the slip planes. With further creep deformation during the transient creep stage, the operation of the <110> slip systems was confirmed. After the time of the minimum creep rate, the slip systems were restricted to two directions on one slip plane. At the end of the accelerated creep stage, the ratio of the above two slip systems became larger. From above results, the twelve slip systems acted uniformly during the transient creep stage, but during the accelerating creep stage, the crystal began to rotate and the two specific slip systems, for example (111)[-101] and (111)[0-11], acted in preference to the other slip systems. Further creep deformation promotes the crystal rotation and the action of these two specific slip systems becomes larger.

Key words: Creep, Single crystal, Nickel-based superalloy, γ channel, Slip system

Introduction

It is well known that crystal orientations of single crystal nickel-based superalloys, in general, vary during creep deformation and the final orientations after creep tests are different from the initial ones[1-4]. McLean et al. reported crystal rotations during creep deformation of SRR99 with different initial orientations in the standard stereographic triangle at 1123K with an applied stress of 450MPa[1]. Miyazawa carried out creep tests at 1173K and 29.4MPa up to creep strains of 50% on single crystal Ni-20Cr alloys with tensile orientations of [001], [011], [111] and within the standard stereographic triangle, and suggested that rotations of crystals with orientations of [011], [111] and within the standard stereographic triangle during creep deformation, might be caused by preferentially activated specific slip systems[3]. On the other hand, the reason why a crystal with the orientation of [001] didn't rotate during creep deformation was assumed to result from the uniform operations of all eight slip systems. Crystal orientations at the gauge portions near the ruptured surface of a [001] oriented single crystal nickel-based alloy, CMSX-4, creep-ruptured at 1273K and 100 to 400MPa, were compared with those at the grip ends, and crystal rotations were detected on crystals crept at the applied stresses in excess of 130MPa by the current authors and co-workers[5]. Therefore, crystal rotations of single crystals during creep deformation seem to be related closely to the changes in slips systems. In these studies on crystal rotations of single crystals, the Burgers vectors and the slip planes of dislocations were not identified, so

that the change in the slip systems during creep deformation was not clear.
The objective of this study is to investigate the change in the slip systems during creep deformation by identifying the Burgers vectors and the slip planes of dislocations in the γ channels of a single crystal nickel-based superalloy crept at 1273K and 160MPa.

Experimental procedure

Single crystal specimens of CMSX-4 (Ni-6.4Cr-9.3Co-5.5Al-0.9Ti-6.3Mo-6.2Ta-6.2W-2.8Re-0.1Hf) were cast as the 13mm diameter cylindrical bars with orientations within 5 degrees of the <001> orientation. The bars were solution treated and aged using the standard CMSX-4 heat treatment. The solution treated and aged bars were machined into creep specimens with a gauge portion of 6mm in diameter and 30mm in length. The creep test of CMSX-4 with the stress axis of the [001] orientation was conducted up to rupture at 1273K and 160MPa (3.60×10^6s creep rupture strength). In addition, creep tests were interrupted at the times up to 3.24×10^6s using the specimens with a gauge portion of 8mm in diameter and 50mm in length to perform the microstructural observations. The creep strain was recorded automatically through the linear variable differential transformers (LVDT's) attached to the extensometers on the ridge of the gauge portion. Microstructural observations by the scanning electron microscope (SEM) and the transmission electron microscope (TEM) were carried out on the specimens cut parallel to the (100) plane determined by the Laue X-ray diffraction. Samples for SEM observations were metallographically prepared by polishing and electro-etched with a super-saturated solution of oxalic acid in water. The TEM discs with 0.15mm in thickness and 3mm in diameter were machined, then mechanically polished, followed by twin-jet electro-polishing with a solution of 10% perchloric acid in ethanol.

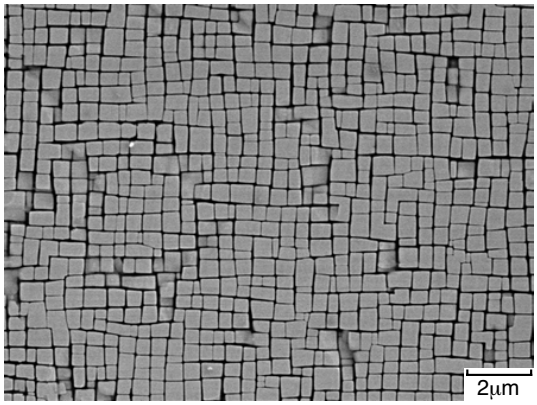

Fig. 1. Scanning electron micrograph of a single crystal nickel-based superalloy, CMSX-4.

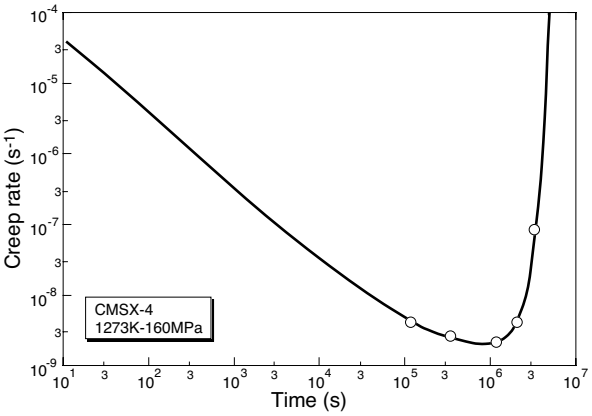

Fig. 2. Creep rate-time curve of solution treated and aged CMSX-4 at 1273K and 160MPa. Open circles depict the times when creep tests are interrupted to perform microstructure observations.

Experimental results and discussion

Microstructure of solution treated and aged specimen

A typical microstructure of a solution treated and aged CMSX-4 is shown in Fig. 1. The cuboidal γ' precipitates are arrayed uniformly through the γ channels. The eutectic γ' phases could not be detected. The average edge length of the cuboidal γ' precipitates is controlled to be about 0.5μm and the average width of the γ channels is estimated as 0.09μm.

Interrupted creep tests

The creep rate-time curve of a solution treated and aged CMSX-4 at 1273K and 160MPa is shown in Fig. 2. Open circles depict the times when creep tests are interrupted for the microstructural observations. This creep rate-time curve is consisted of the transient and accelerating creep stage. The minimum creep rate is attained at about 10^6s and creep tests are interrupted from the latter half of the transient creep stage to the end of the accelerating creep stage.

Microstructure of interrupted creep specimens

The scanning electron micrographs of the specimens crept for $1.08x10^5$, $1.08x10^6$ and $3.24x10^6$s are shown in Fig. 3. Most of the cuboidal γ' precipitates remain unchanged at $1.08x10^5$s, whereas some of the cuboidal γ' precipitates connect to each other (Fig. 3(a)). On the other hand, the directional coarsening of the γ' precipitates, which is called as rafting, is observed perpendicular to the applied stress axis at $1.08x10^6$s (Fig. 3(b)). The γ' precipitates coarsen in a direction parallel to the applied stress, as well as perpendicular to the applied stress, and then some of the γ channels turn their shapes to granular, as mounted within the γ' matrix at $3.24x10^6$s (Fig. 3(c)).

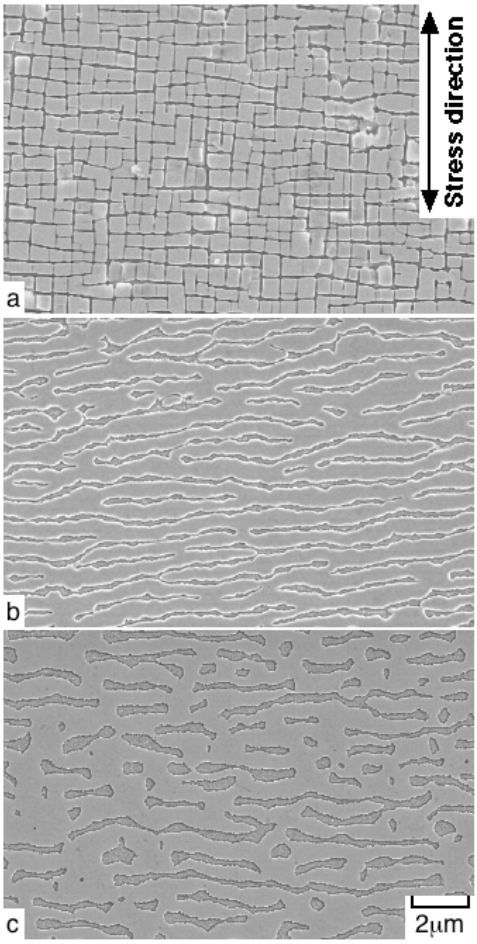

Fig. 3. The scanning electron micrographs of the specimens crept for $1.08x10^5$(a), $1.08x10^6$(b) and $3.24x10^6$s(c).

The transmission electron micrograph of the specimen crept for $1.08x10^5$s when the γ' precipitates remain cuboidal, is shown in Fig. 4, where the incident beam direction, **B**, was close to [100]. A few bowed-out dislocations are observed in the γ channels and a small number of dislocations are present at the γ/γ' interfaces. However, there are no dislocations in the γ' precipitates.

The transmission electron micrograph of the specimen crept for $1.08x10^6$s when the well developed rafted γ/γ' structures are formed, is shown in Fig. 5, where **B**= [100]. The number of bowed-out

dislocations in the γ channels is small, similar to that of the specimen crept for $1.08x10^5$s, but the radius of these bowed-out dislocations becomes larger. Furthermore, the dislocation density at the γ/γ' interfaces becomes higher.

The transmission electron micrograph of the specimen crept for $3.24x10^6$s when the regularity of the rafted γ' precipitates is lost, is shown in Fig. 6, where **B**= [100]. The number of bowed-out dislocations in the γ channels is still small, similar to that of the specimens crept for $1.08x10^5$ and $1.08x10^6$s, and these bowed-out dislocations have the larger radius. A large number of dislocations are observed at the γ/γ' interfaces. Therefore, the radius of bowed-out dislocations in the γ channels and the dislocation density at the γ/γ' interfaces increase with increasing creep-testing time.

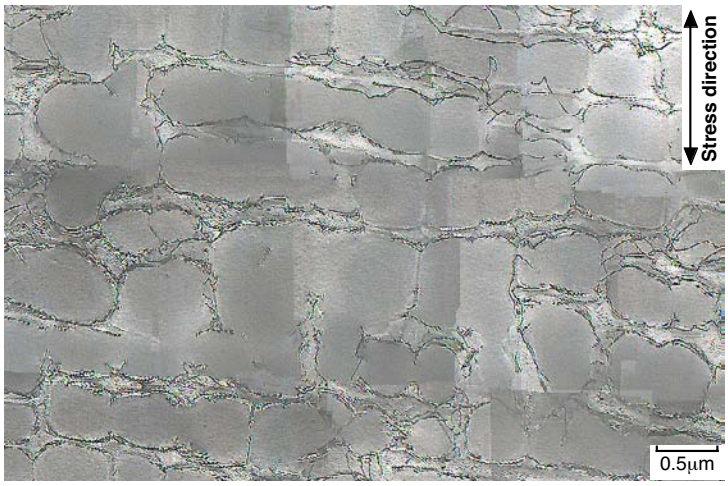

Fig. 4. The transmission electron micrograph of the specimen crept for $1.08x10^5$s, where **B**= [100].

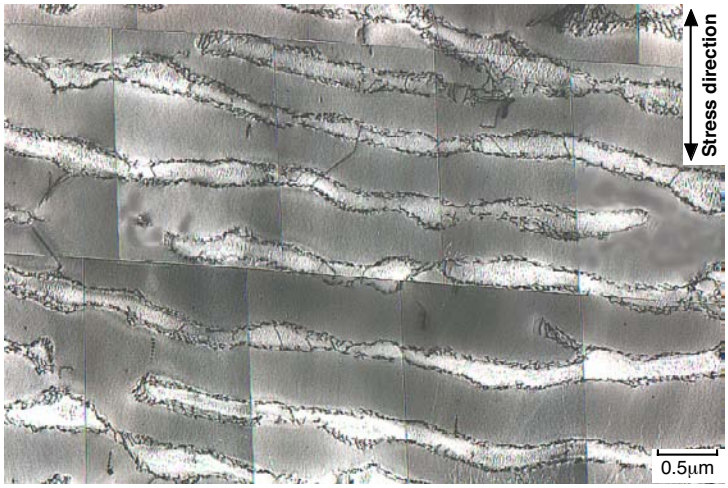

Fig. 5. The transmission electron micrograph of the specimen crept for $1.08x10^6$s, where **B**= [100].

Slip planes of dislocations in γ channels of interrupted creep specimens

In this section, the slip planes of dislocations in the γ channels will be identified on the interrupted creep specimen. The TEM observations on the same region are performed with five incident beam directions, B=[100], [211], [2-11], [21-1] and [2-1-1], so as to make the slip plane edge-on[6,7] and the bowed-out dislocation straight. That is to say, the incident beam direction, **B**=<211>, where the bowed-out dislocation is observed to be straight, is examined on the specimens cut parallel to the (100) plane, and the {111} plane which is parallel to this incident electron beam, **B**=<211>, is identified as the slip plane.

Fig. 7 shows examples of the transmission electron micrographs on the dislocation in the γ channel of the specimen crept for $3.24x10^6$s to identify the slip plane of this dislocation. The dislocation which is observed with an incident beam direction, **B**=[100](Fig. 7(a)), is straight only with [21-1] (Fig. 7(d)), but curved with the other incident beam directions (Figs. 7(b), (c) and (e)), and then the slip plane of this dislocation is identified as (1-11). The identification of the slip plane is performed on more than 40 dislocations and an area of over $100\mu m^2$ of each interrupted creep specimen.

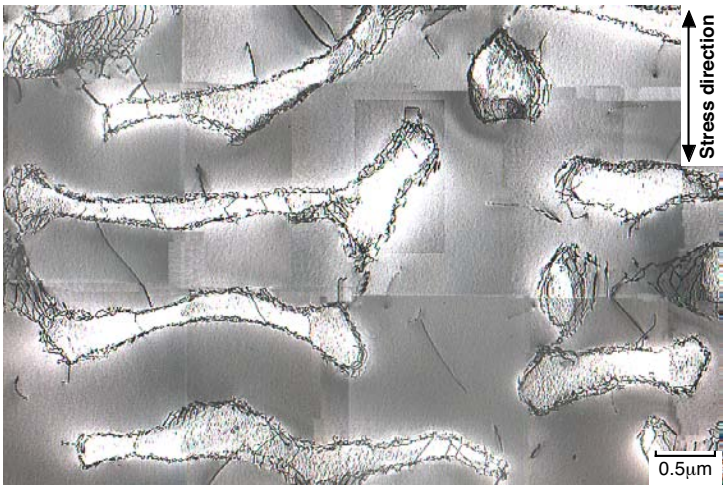

Fig. 6. The transmission electron micrograph of the specimen crept for $3.24x10^6$s, where **B**= [100].

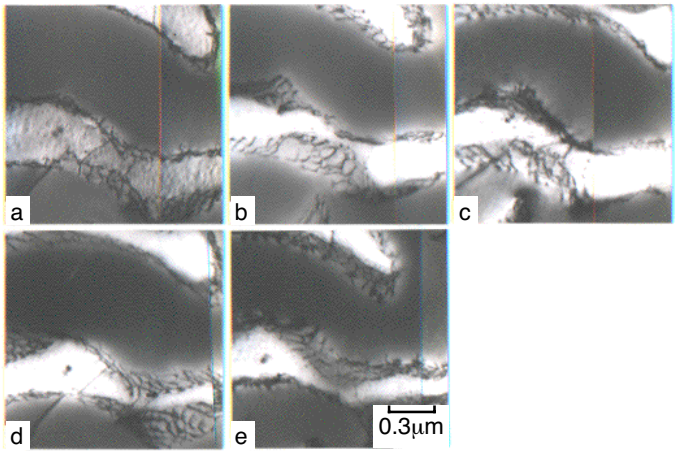

Fig. 7. Examples of the transmission electron micrographs on dislocation in the γ channel of the specimen crept for $3.24x10^6$s to identify the slip plane of the dislocation. (a) **B**= [100], g=[020], (b) **B**= [211], g=[02-2], (c) **B**= [2-11], g=[022], (d) **B**= [21-1], g=[022], (e) **B**= [2-1-1], g=[02-2]

The slip planes of dislocations in the γ channels of the specimen crept for $1.08x10^5$s are given in Fig. 8. This figure is the same image as Fig. 4. Dislocations, whose slip planes could not be identified, are designated as UK. Most of dislocations stay equally on four slip planes, that is, (111), (-111), (1-11) and (11-1).

The slip planes of dislocations in the γ channels of the specimen crept for $1.08x10^6$s are given in Fig. 9. This figure is the same image as Fig. 5. Many dislocations stay on the specific slip plane of (-111), and this result is different from that at $1.08x10^5$s (Fig. 8).

The slip planes of dislocations in the γ channels of the specimen crept for $3.24 x10^6$s are given in Fig. 10. This figure is the same image as Fig. 6. Most of dislocations stay on a specific slip plane of (111),

similar to the result at $1.08x10^6$s (Fig. 9).

Fig. 11 shows the ratio of the number of dislocations on {111} to that of all dislocations of the interrupted creep specimens.

Dislocations in the γ channels of the interrupted creep specimens at the transient creep stages, that is, $1.08x10^5$ and $3.60x10^5$s, stay equally on four slip planes. However, dislocations in the γ channels of the interrupted creep specimens at the time of the minimum creep rate, that is, $1.08x10^6$s, and the accelerating creep stages, namely, $1.80x10^6$ and $3.24x10^6$s, stay on the specific slip plane. And the ratio of the number of dislocations on the specific slip plane to that of all dislocations increases with increasing creep-testing time. From these results, it is confirmed that dislocations migrate equally on four slip planes during the transient creep stage of a [001] oriented single crystal nickel-based superalloy, but during the accelerating creep stage, the crystal rotation allows dislocations migration on the specific slip plane, and further creep deformation promotes a crystal rotation and dislocations glide on the specific slip plane.

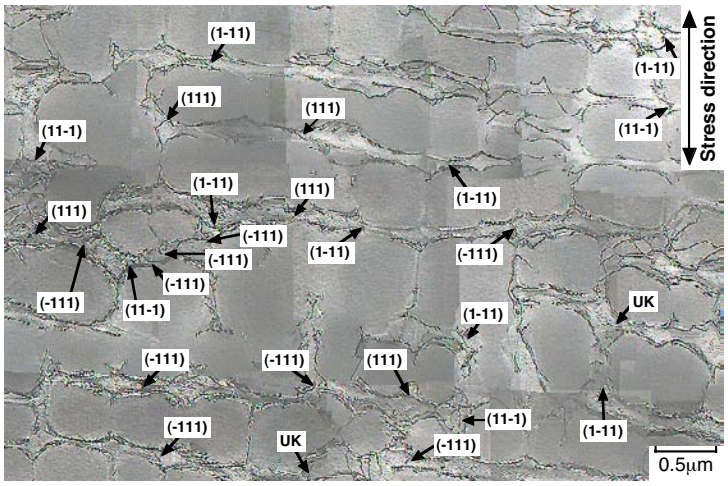

Fig. 8. The slip planes of dislocations in the γ channels of the specimen crept for $1.08x10^5$s. This figure is the same image as Fig. 4.

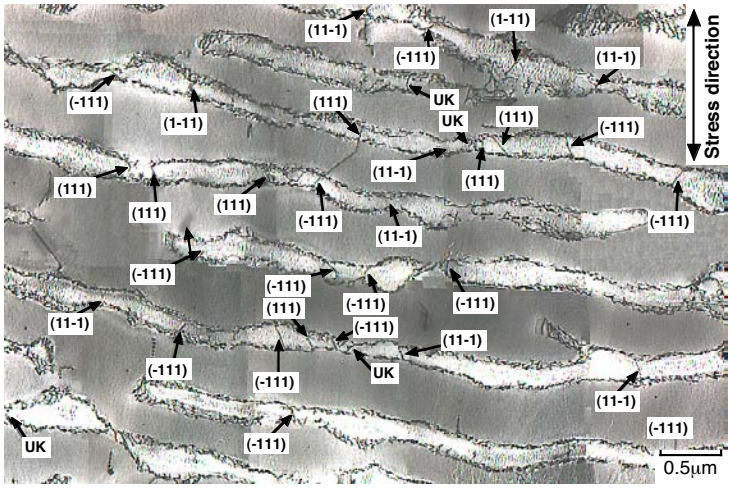

Fig. 9. The slip planes of dislocations in the γ channels of the specimen crept for $1.08x10^6$s. This figure is the same image as Fig. 5.

Burgers vectors of dislocations in γ channels of interrupted creep specimens

In this section, the Burgers vectors of dislocations whose slip planes were already identified in the

previous section, will be determined by finding the reflection in which the dislocation becomes invisible. Six invisibility conditions where required for determining a Burgers vector using the **g**·**b**=0 invisibility criterion[8, 9]. The TEM observations on the same region are performed with four incident beam directions, B=<211>, and six **g** vectors, **g**=<111> and <022>, so as to make the dislocation invisible. The Burgers vector is determined by examining whether the invisible dislocation lies on the slip plane which was identified in the previous section. The determination of the Burgers vector is performed on more than 40 dislocations and an area of over 100μm^2 of each specimen.

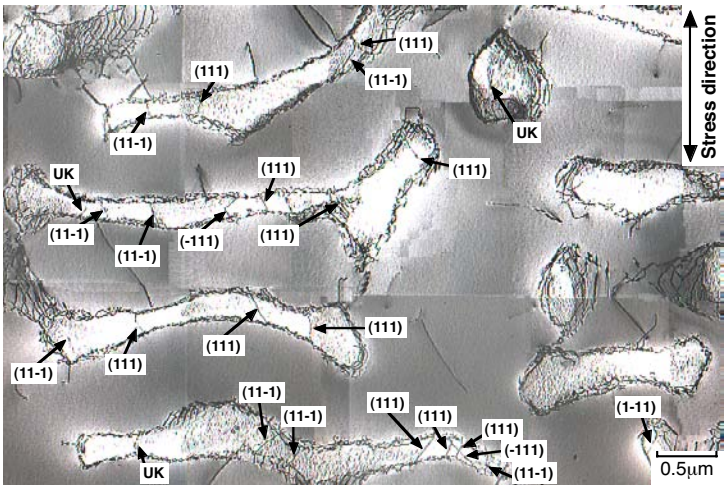

Fig. 10. The slip planes of dislocations in the γ channels of the specimen crept for 3.24x10^{6}s. This figure is the same image as Fig. 6.

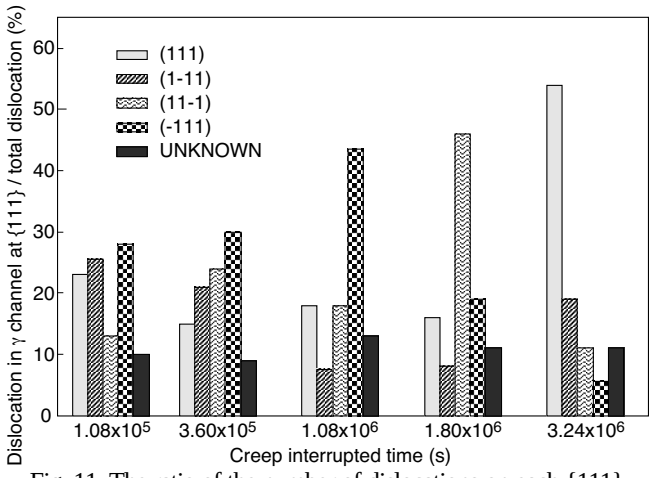

Fig. 11. The ratio of the number of dislocations on each {111} to that of all dislocations of the interrupted creep specimens.

The Burgers vectors and the slip planes of dislocations in the γ channels of the specimen crept for 1.08x10^{5}s are shown in Fig. 12. This figure is the same image as Figs. 4 and 8. Dislocations, whose Burgers vectors could not be identified, are designated as UK. Most of dislocations with three types of the <110> Burgers vectors stay equally on each {111} slip plane.

The Burgers vectors and the slip planes of dislocations in the γ channels of the specimen crept for 1.08x10^{6}s are shown in Fig. 13. This figure is the same image as Figs. 5 and 9. There are many dislocations with only two types of the <110> Burgers vectors on the specific slip plane, in this case, having the Burgers vectors of [101] and [01-1] on the (-111) slip plane, and this result is different from that at 1.08x10^{5}s (Fig. 12).

The Burgers vectors and the slip planes of dislocations in the γ channels of the specimen crept for $3.24x10^6$s are shown in Fig. 14. This figure is the same image as Figs. 6 and 10. Most of dislocations with only two types of the <110> Burgers vectors stay on the specific slip plane, in this case, having the Burgers vectors of [10-1] and [01-1] on the (111) slip plane, similar to the result at $1.08x10^6$s (Fig. 13). The Burgers vectors of dislocations of all interrupted creep specimens, are normal to the line directions at the bowed-out segments, and then these segments seem to be edge dislocations.

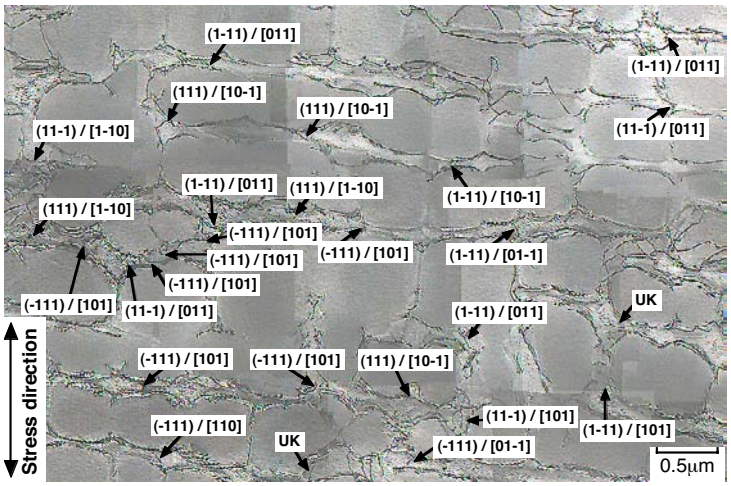

Fig. 12. The Burgers vectors and the slip planes of dislocations in the γ channels of the specimen crept for $1.08x10^5$s. This figure is the same image as Figs. 4 and 8.

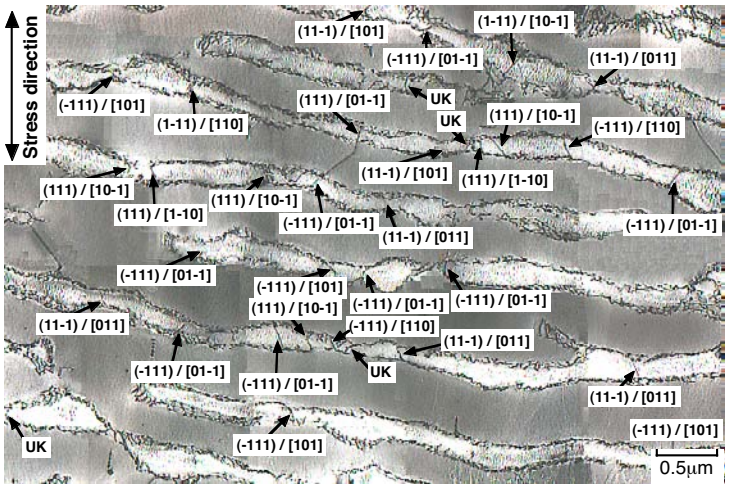

Fig. 13. The Burgers vectors and the slip planes of dislocations in the γ channels of the specimen crept for $1.08x10^6$s. This figure is the same image as Figs. 5 and 9.

Fig. 15 shows the ratio of the number of dislocations with three types of the <110> Burgers vectors on each {111} to that of all dislocations of the interrupted creep specimens. Dislocations with two types of the <101> and <011> Burgers vectors exist at the beginning of the transient creep stage, that is, $1.08x10^5$s, independent of the slip planes. And dislocations with three types of the <110> Burgers vectors stay equally on each of four slip planes at the transient creep stages, that is, $3.60x10^5$s. However, dislocations have the Burgers vectors of [101] and [011] types on the specific slip plane at the time of the minimum creep rate, that is, $1.08x10^6$s, and the accelerating creep stage, namely, $1.80x10^6$ and

$3.24x10^6$s. The ratio of the number of dislocations with these Burgers vectors on the specific slip plane to that of all dislocations increases with increasing creep-testing time. Consequently, it is assumed that twelve slip systems are equally activated during the transient creep stage of a [001] oriented single crystal nickel-based superalloy, but at the accelerating creep stage, the crystal rotation allows two preferential activated slip systems, such as (111)[10-1] and (111)[01-1], and further creep deformation promotes a crystal rotation and two preferential slip systems activation, and inhibits the other slip systems operation.

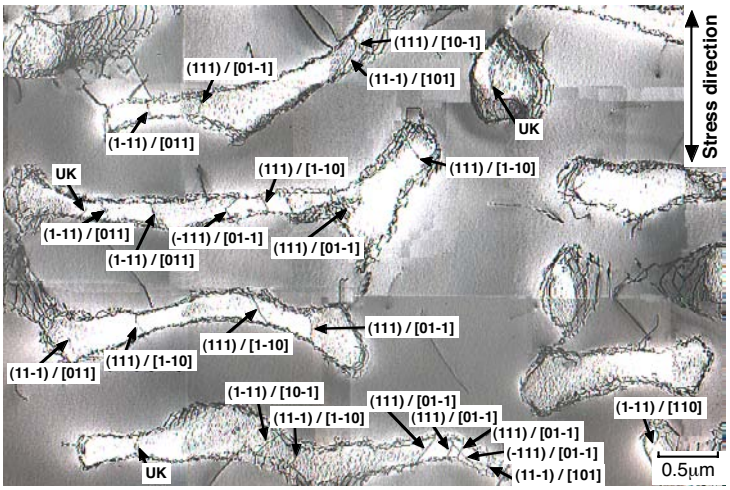

Fig. 14. The Burgers vectors and the slip planes of dislocations in the γ channels of the specimen crept for $3.24x10^6$s. This figure is the same image as Figs. 6 and 10.

Conclusion

The change in the slip systems during creep deformation is investigated by characterizing the Burgers vectors and the slip planes of dislocations in the γ channels of a single crystal nickel-based superalloy crept at 1273K and 160MPa. The results can be summarized in the following:

1) Directional coarsening of the γ' precipitates is observed perpendicular to the applied stress axis at the time of the minimum creep rate. Further creep deformation allows the γ' precipitates to coarsen in a direction parallel to the applied stress, as well as perpendicular to the applied stress, and then some of the γ channels turn their shapes to granular, as mounted within the γ' matrix.
2) Dislocations glide equally on four slip planes at the transient creep stage, but at the accelerating creep stage, the crystal rotation allows the dislocation migration on a specific slip plane, and further creep deformation promotes a crystal rotation and the dislocation glide on a specific slip plane.
3) Dislocations with three types of the <110> Burgers vectors are equally present on four slip planes at the transient creep stages. However, dislocations in the γ channels have the Burgers vectors of [101] and [011] types on the specific slip plane at the time of the minimum creep rate and the accelerating creep stage. The ratio of the number of dislocations with these Burgers vectors on the specific slip plane to that of all dislocations increases with increasing creep-testing time.
4) It is concluded that twelve slip systems are equally activated at the transient creep stage, but at the accelerating creep stage, the crystal rotation allows two preferential activated slip system, such as

(111)[10-1] and (111)[01-1], and further creep deformation promotes a crystal rotation and two preferential slip systems activation, and inhibits the other slip systems operation.

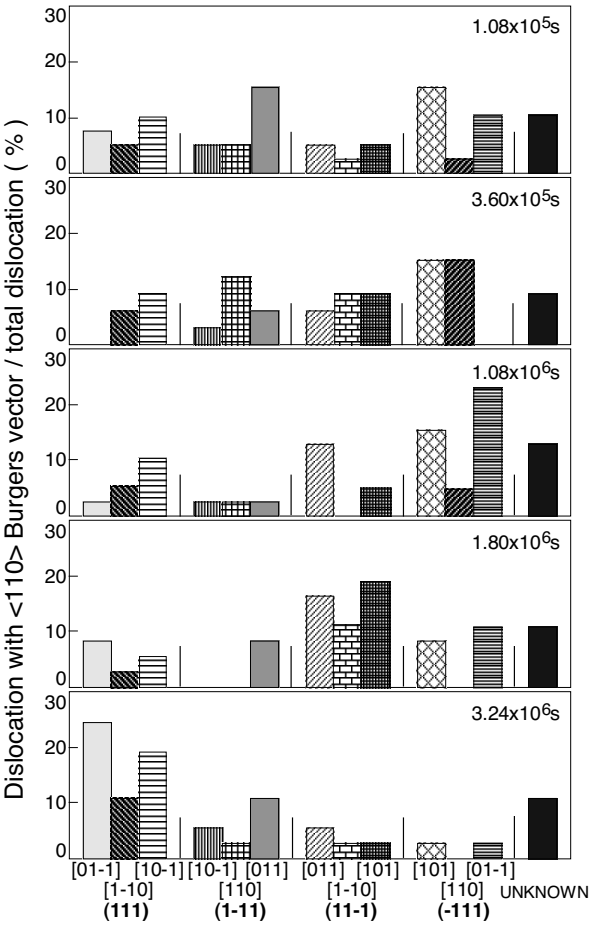

Fig. 15. The ratio of the number of dislocations with three types of the <110> Burgers vectors on each {111} to that of all dislocations of the interrupted creep specimens.

Reference

[1] M. McLean, R. N. Ghosh, R. V. Curtis, U. Basu-Conlin and M. R. Winstone, Anisotropy of High Temperature Deformation of Single Crystal Superalloys – Constitutive Laws, Modelling and Validation, Proc. of the 7th int'l Symp. Superalloys 1992, (1992), p.609

[2] R. N. Ghosh, R. V. Curtis and M. McLean, Creep Deformation of Single Crystal Superalloys – Modelling the Crystallographic Anisotropy, Acta Metall., 38(1990), p.1977

[3] Y. Miyazawa, Master thesis, Tokyo Institute of Technology, (1995), p.70

[4] K. Kakehi, Infuluence of γ' – particle Size, Interfacial Dislocation Networks and Orientation on Creep Strength of Single Crystals of Ni-Base Superalloy, 123rd Committee on Heat Resisting Metals and Alloys Rep., 35(1994), p.31

[5] K. Ishibashi, Y. Kondo, J. Namekata, N. Ohi and H. Hattori, Long Time Creep Rupture Properties of Single Crystal Nickel-based Superalloy, CMSX-4, 123rd Committee on Heat Resisting Metals and Alloys Rep., 37(1996), p.1

[6] A. Suzuki, T. Matsuo and M. Takeyama, Microstructure Control of Ni Base Alloys With High Volume Fraction of DO_{22} Compound, Proc. of the 10th int'l Symp. Superalloys 2004, (2004), p.115

[7] G. B. Viswanathan, P. Sarosi, M. Henry, D. Whitis and M. Mills, Deformation Mechanisms at Intermediate Creep Temperatures in Rene88 DT, Proc. of the 10th int'l Symp. Superalloys 2004, (2004), p.173

[8] Electoron Microscopy of Thin Crystals, Butterworths, London, (1965), p.171

[9] M. H. Loretto and R. E. Smallman, Defect Analysis in Electron Microscopy, Science Paperbacks, London, (1975), p.51

DISLOCATION SUBSTRUCTURE AT γ/γ' INTERFACE OF SINGLE CRYSTAL NICKEL-BASED SUPERALLOY, CMSX-4, CREPT AT 1273K, 250MPa

Nobuhiro Miura*, Futoru Tanaka*, Kazunori Kurita*, Yoshihiro Kondo* and Takashi Matsuo**

*National Defense Academy, 1-10-20 Hashirimizu Yokosuka, Kanagawa 239-8686, Japan
**Tokyo Institute of Technology, 2-12-1 Oookayama Meguro, Tokyo 152-8552, Japan
nmiura@nda.ac.jp

Abstract

The dislocation substructures at the γ/γ' interfaces of a single crystal nickel-based superalloy, CMSX-4, after the interrupted creep tests at the stages when the γ' precipitates were still cuboidal, were observed to investigate the correlation between creep deformation and the rafting of the γ/γ' structures. The interrupted creep tests were conducted at 1273K and 250MPa using the CMSX-4 with the stress axis of the [001] orientation, at the times from the transient creep stage to the beginning of the accelerating creep stage. Microstructural observations by a TEM were carried out on the γ/γ' interfaces parallel to the (010) and (001) planes of the interrupted creep specimens cut parallel to the (130) and (103) planes, respectively. The γ' precipitates were still cuboidal at the beginning of the accelerating stage. The numbers of dislocations at the γ/γ' interfaces parallel to both the (010) and (001) planes increased during creep deformation. The number of dislocations at the γ/γ' interfaces parallel to the (001) plane was larger than that at the γ/γ' interfaces parallel to the (010) plane. The Burgers vectors of all dislocations were identified. Dislocations at the γ/γ' interfaces have six kinds of the <110> Burgers vectors equally, independent of the creep strain and the interfaces. Consequently, dislocations at the γ/γ' interfaces may not be misfit dislocations, but the traces of mobile dislocations which led to creep deformation.

Keywords : Single crystal, Nickel-based superalloy, γ' pricipitates, Dislocation substructure, Burgers vectors

1 Introduction

The cuboidal γ' precipitates of the single crystal nickel-based superalloys with the stress axis of the [001] orientation turn their shapes into the plate like ones perpendicular to the stress axis during high temperature creep deformation [1-8]. This drastic morphological change in the γ' precipitates is called as rafting. Many papers discussed the rafting mechanisms during creep deformation. However, the rafting mechanism has not been elucidated. In our previous works, the creep tests in the wide stress range from 100 to 400MPa at 1273K were carried out by using a single crystal nickel-based superalloy, CMSX-4, with the stress axis of the [001] orientation [9-11]. The changes in the aspect ratios of the γ' precipitates with increasing creep testing time and the creep strain were investigated at each stress. At the stresses less than 200MPa, the maximum aspect ratios were attained at a strain of 1%, independent of the stress. This result suggested that the formation of the rafted γ/γ' structures was strongly related to the dislocation substructures at the γ/γ' interfaces. However, at the stresses more than 250MPa, the maximum aspect ratios was attained at a strain of 10% or more, and the γ' precipitates were still cuboidal at a strain of 1% [11]. At these stress conditions, it was assumed that there was not enough time for the solute elements, such as Al and Ti, to diffuse, even though the dislocation substructures were fully induced by creep deformation at a strain of 1%. To confirm this assumption, the simple aging was conducted on the samples on which the creep tests were interrupted at the strains less than 1%

under the stresses more than 250MPa [12]. The γ' precipitates of the interrupted creep specimens coarsened directionally only by conducting the simple aging, and then the complete rafted γ/γ' structures perpendicular to the stress axis was confirmed in the interrupted creep specimen at a strain of 0.74%. From these results, it was suggested that the formation of the rafted γ/γ' structures required the dislocation substructures at the γ/γ' interfaces corresponded to the creep strain. However, the dislocation substructures at the γ/γ' interfaces have not observed on the interrupted creep specimens, yet. The correlation between the dislocation substructures at the γ/γ' interfaces and creep deformation must be investigated to clarify the rafting mechanism.

In this study, the creep tests at 1273K and 250MPa on the single crystal nickel-based superalloy, CMSX-4, with the stress axis of the [001] orientation are interrupted at the strains less than 0.74%, and the changes in the dislocation substructures at the γ/γ' interfaces with increasing creep strain was investigated.

2 Experimental procedure

A single crystal of the nickel-based suprealloy of CMSX-4, (with a chemical composition in weight per cent ; 6.4Cr, 9.3Co, 5.5Al, 0.9Ti, 6.3Mo, 6.2Ta, 6.2W, 2.8Re, 0.1Hf, balance Ni), were prepared in the form of bars with 13mm in diameter and 160mm in length by a directional precision casting. The orientations of the longitudinal direction of the specimens were determined by Laue X-ray back-reflection technique; the angles between the [001] orientation and the longitudinal axis of single crystals were within 5 degrees. The eight steps solution treatment was employed as follows, 1550K-7.20x10^3s → 1561K-7.20x10^3s → 1569K-1.08x10^4s → 1577-1.08x10^4s → 1586K-7.20x10^3s → 1589K-7.20x10^3s→1591K-7.20x10^3s→1594K-7.20x10^3s→GFC, then the three steps aging treatment was conducted as follows, 1413K-2.16x10^4s→1353K-2.16x10^4s→1144K-7.20x10^4s→AC. The as-heat treated single crystals were machined into the creep specimen with a gauge portion of 6mm in diameter and 30mm in length. The creep test was carried out at 1273K and 250MPa under a constant load. Furthermore, the creep tests were interrupted at the strains less than 0.74% on the specimens with a gauge portion of 8mm in diameter and 40mm in length. The creep strain was measured automatically through the linear variable differential transformers (LVDT's) attached to the extensometer. Microstructural observations were carried out by a field emission scanning electron microscopy (FE-SEM) and a transmission electron microscopy (TEM) on the specimens sectioned parallel to the (010), (001), (130) and (103) planes determined by Laue X-ray

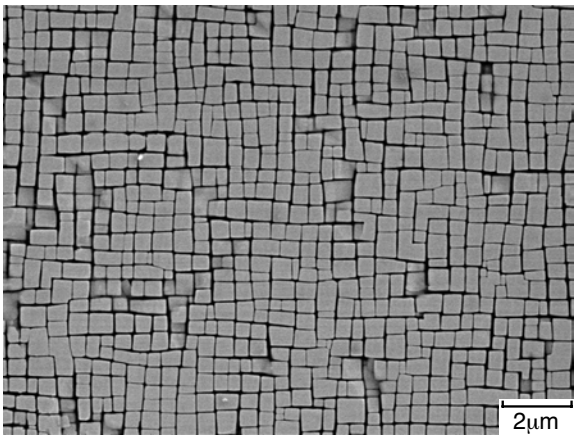

Fig.1. Scanning electron micrograph of a single crystal nickel-based superalloy, CMSX-4.

back-reflection technique. The specimens for the SEM observation were prepared metallographically and electroetched with a supersaturated oxialic acid aqueous solution. TEM foils were prepared by electropolishing using a twin jet polisher with the 10% perchloric acid-alcohol solution. The Burgers vector, b, of dislocations at the γ/γ' interfaces were identified by the g·b=0 contrast invisibility criterion [13, 14].

3 Results and discussion

3.1 Microstructure of as-heat treated specimen

The scanning electron micrograph of the as-heat treated CMSX-4 is shown in Fig.1. The cuboidal γ' precipitates are regularly arrayed in the γ matrix. The average edge length of the cuboidal γ' precipitates is about 0.5 μm. The average width of the γ channels is approximately 0.1 μm. The volume fraction of the γ' precipitates is estimated as 78 %. No eutectic γ' precipitates were detected after the heat treatment.

The transmission electron micrograph of the as-heat treated CMSX-4, where the incident beam direction, B, is closed to [010], as shown in Fig.2. Few dislocations are observed at the γ/γ' interfaces and there are no dislocations within the γ' precipitates.

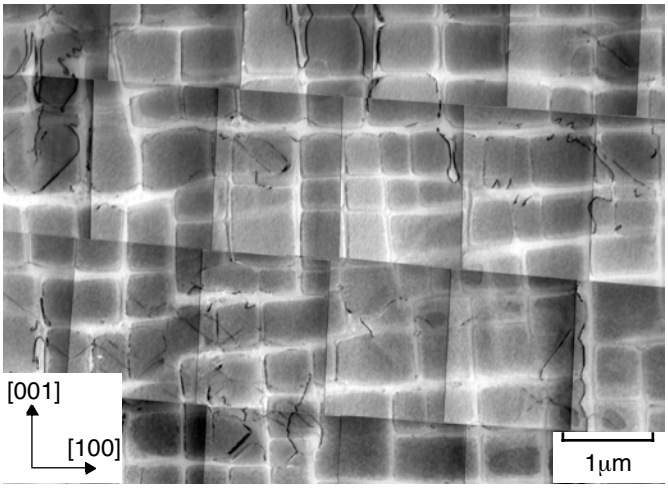

Fig.2. Transmission electron micrograph of a single crystal nickel-based CMSX-4, where the incident beam direction, B, is closed to [010].

3.2 Creep rate-time curve of CMSX-4 at 1273K and 250MPa

The creep rate-time curve of CMSX-4 at 1273K and 250MPa consists of the transient creep stage and the accelerating creep stage, as

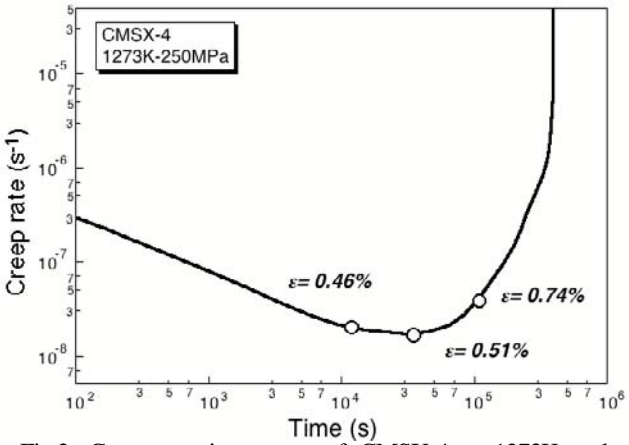

Fig.3. Creep rate-time curve of CMSX-4 at 1273K and 250MPa. The open circles on the curve show creep testing times at which the creep tests are interrupted.

shown in Fig.3. The open circles on the curve indicate creep testing times at which the creep tests are interrupted. Creep tests are interrupted at the times showing the end of transient stage, the minimum creep rate and the beginning of the accelerating creep stage.

3.3 Morphological change in γ' precipitates

The SEM observations are carried out on the specimens cut parallel to the (010) plane. The scanning electron micrographs of the interrupted creep specimens at the strains of 0.42, 0.51 and 0.74% are shown in Fig.4. The γ' precipitates of the interrupted creep specimen at a strain of 0.74% at 1273K and 250MPa, remain still cuboidal (Fig.4 (c)).

3.4 Dislocation substructures at γ/γ' interfaces

The TEM observations are carried out by using the interrupted creep specimens cut parallel to the (130) and (103) planes, to investigate the changes in the dislocation substructures at the γ/γ' interfaces parallel to the (010) and (001) planes, respectively with creep deformation.

The transmission electron micrograph of the interrupted creep specimen at a strain of 0.46%, the end of the transient creep stage, is shown in Fig. 5, where the incident beam direction, B, is closed to [010]. A few dislocations are observed at the γ/γ' interfaces parallel to the (010) plane.

The transmission electron micrograph of the interrupted creep specimen at a strain of 0.74%, corresponding to the beginning of the accelerating creep stage, is shown in Fig. 6, where B=[010]. There are a number of dislocations at the γ/γ' interfaces parallel to the (010) plane, compared with the interrupted creep specimen at a strain of 0.46%

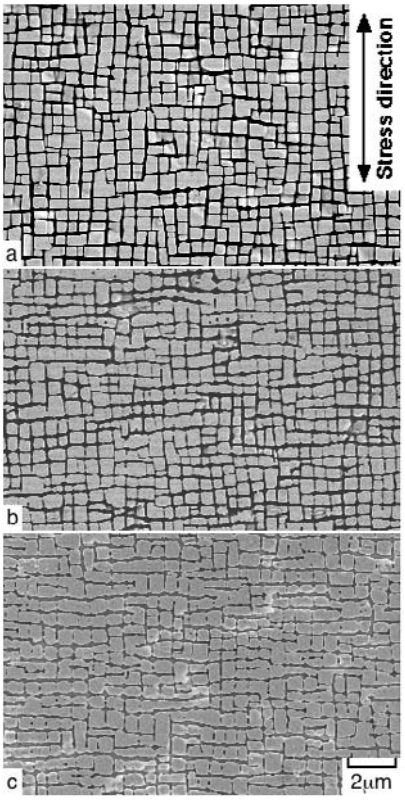

Fig.4. Scanning electron micrographs of the interrupted creep specimens at the strains of (a) 0.42, (b) 0.51 and (c) 0.74%.

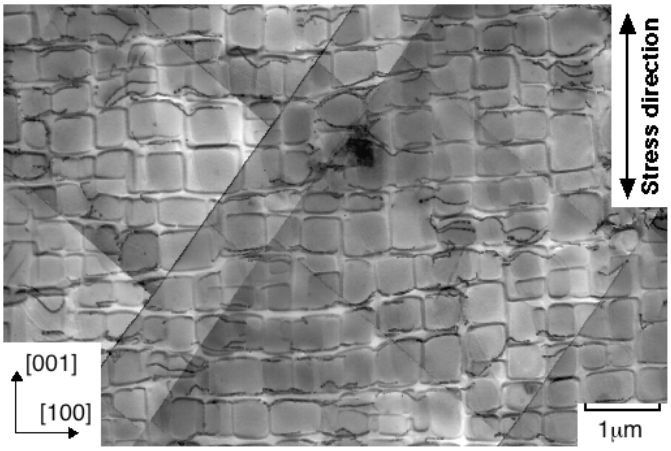

Fig.5. Transmission electron micrograph of the interrupted creep specimen at a strain of 0.46%, B= [010].

(Fig.5).

The transmission electron micrograph of the interrupted creep specimen at a strain of 0.46%, is shown in Fig. 7, where B=[001]. A few dislocations are observed at the γ/γ' interfaces. The number of dislocations at the γ/γ' interfaces parallel to the (001) plane is larger than that at the γ/γ' interfaces parallel to the (010) plane (Fig.5).

The transmission electron micrograph of the interrupted creep specimen at a strain of 0.74%, is shown in Fig. 8, where B=[001]. There are a lot of dislocations which are tangled with each other at the γ/γ' interfaces parallel to the (001) plane. Therefore, the number of dislocations at the γ/γ' interfaces parallel to the (001) plane is larger than that at the γ/γ' interfaces parallel to the (010) plane, and these numbers seem to increase during creep deformation.

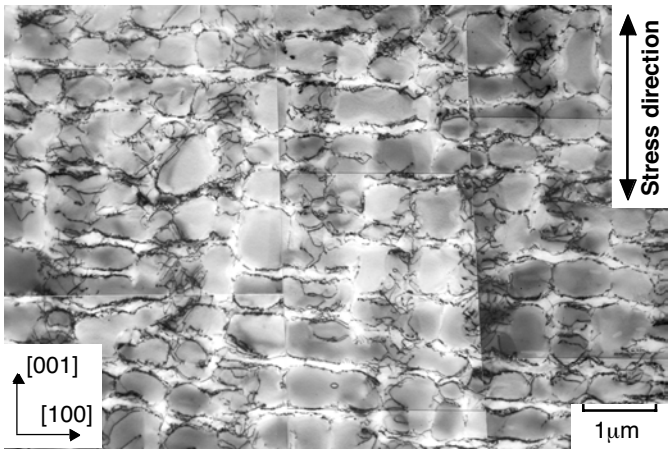

Fig.6. Transmission electron micrograph of the interrupted creep specimen at a strain of 0.74%, B= [010].

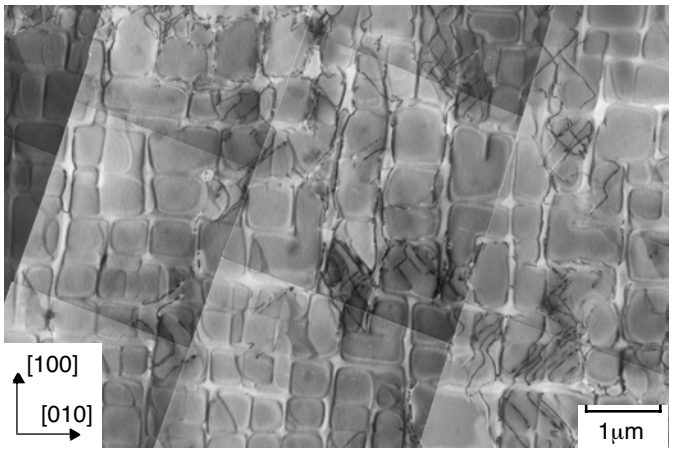

Fig.7. Transmission electron micrograph of the interrupted creep specimen at a strain of 0.46%, B= [001].

3.5 Dislocation density at the γ/γ' interfaces

The dislocation density at the γ/γ' interfaces is estimated by using the interrupted creep specimens in order to quantify the change in the dislocation substructures at the γ/γ' interfaces during creep deformation. Two invisibility conditions on the basis of the g·b=0 invisibility criterion, as shown in Table.1. For example, when the TEM observations are performed with the incident beam directions, B=[010], and the

Table.1. Two invisibility conditions on the basis of the g·b = 0 invisibility criterion.

Incident beam directions	010		001	
b \ g	002	200	020	200
110	Invisible	Visible	Visible	Visible
$1\bar{1}0$	Invisible	Visible	Visible	Visible
$10\bar{1}$	Visible	Visible	Invisible	Visible
101	Visible	Visible	Invisible	Visible
011	Visible	Invisible	Visible	Invisible
$01\bar{1}$	Visible	Invisible	Visible	Invisible

g-vector, g=[002], dislocations with the Burgers vectors of [10-1], [101], [011] and [01-1] are visible, but the ones with the Burgers vectors of [110] and [1-10] are invisible. Based on this criterion, all dislocations cannot be detected by using only one g-vector and then the accurate dislocation density cannot be estimated. The TEM observations should be carried out with two different g-vectors on the same region and the image with one g-vector should be superimposed on the other to express the accurate dislocation substructures at the γ/γ' interfaces.

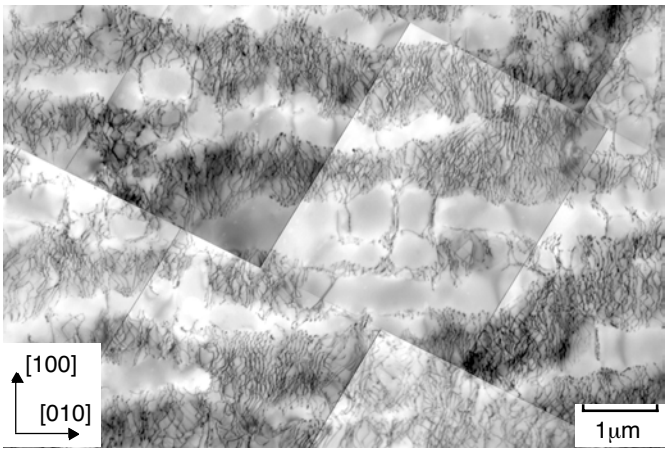

Fig.8. Transmission electron micrograph of the interrupted creep specimen at a strain of 0.74%, B= [001].

The TEM observations where B=[010], g=[002] and [200], are performed in the same region at the γ/γ' interfaces parallel to the (010) plane, by using the interrupted creep specimen at a strain of 0.74%, and these two images are superimposed, as shown in Fig.9. This figure corresponds to a part of the TEM image of Fig.6. The number of dislocations in this figure is larger than that in Fig.6 and it is possible to express all dislocations at the γ/γ' interfaces.

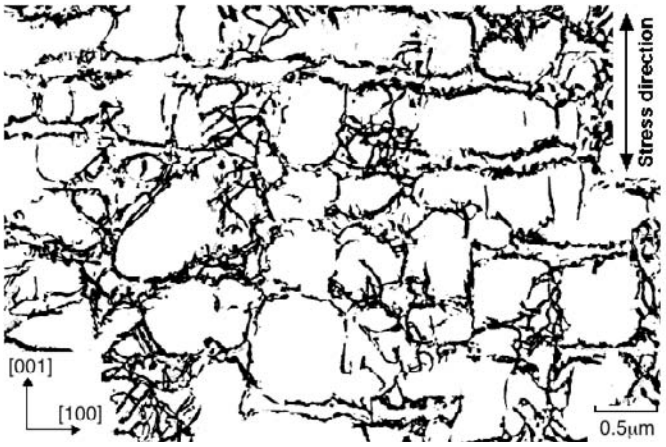

Fig.9. Superimposed image of transmission electron micrographs where B=[010], g=[002] and [200], on the same region at the γ/γ' interfaces parallel to (010) plane of the interrupted creep specimen at a strain of 0.74%.

The TEM observations where B=[001], g=[020] and [200], are performed in the same region at the γ/γ' interfaces parallel to the (001) plane, by using the interrupted creep specimen at a strain of 0.74%, and these two images are superimposed, as shown in Fig.10. This figure corresponds to a part of the TEM image of Fig.8. The number of dislocations at the γ/γ' interfaces parallel to the (001) plane seems to be larger than that parallel to the (010) plane. The accurate expression of all dislocations at the γ/γ' interfaces parallel to the (010) and (001) planes can be attained by using with the two different g-vectors on the same area.

The changes in the dislocation densities at the γ/γ' interfaces parallel to both the (010) and (001) planes with the creep strain are shown in Fig. 11. The dislocation density at the γ/γ' interfaces parallel to the (001) plane is larger than that parallel to the (010) plane, and the dislocation densities at the γ/γ' interfaces parallel to the (010) and (001) planes increase with increasing creep strain.

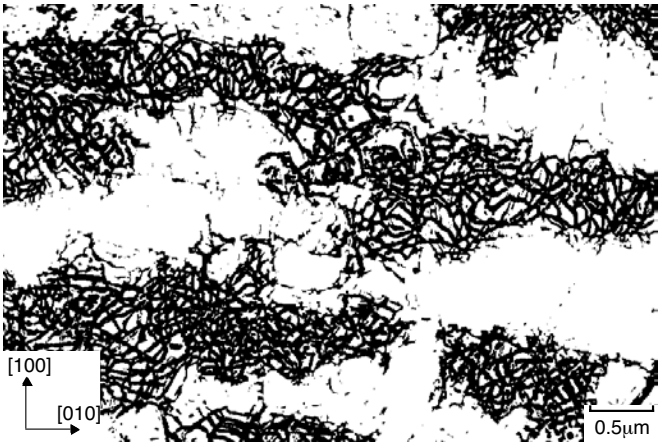

Fig.10. Superimposed image of transmission electron micrographs where B=[001], g=[020] and [200], on the same region at the γ/γ' interface parallel to the (001) plane of the interrupted creep specimen at a strain of 0.74%.

It is well understood that the lattice constant at the room temperature of the γ' phase of a single crystal nickel-based superalloy is smaller than that of the γ phase, and the elastic constant of the γ' phase is larger than that of the γ phase [15, 16]. Under an applied tensile stress, the lattice mismatch between the γ and γ' phases at the γ/γ' interfaces parallel to the stress axis is expanded, but that at the γ/γ' interfaces perpendicular to the stress axis is reduced. And the interfacial dislocations will be introduced to relief the lattice mismatch between the γ and γ' phases at the γ/γ' interfaces. From these assumptions, the dislocation density at the γ/γ' interfaces parallel to the tensile axis will be larger than that at the γ/γ' interfaces perpendicular to the tensile axis. Furthermore, in the case the interfacial dislocations are regarded as the misfit ones, the interfacial dislocation density will saturate at the higher strain during creep deformation because of the constant lattice misfit. However, these assumptions are exactly different from the results in this study. That is, the dislocation density at the γ/γ' interfaces parallel to the stress axis is smaller than that of the γ/γ' interfaces perpendicular to the stress axis, and the dislocation densities at the γ/γ' interfaces increase with increasing creep strain (Fig.11). Therefore, dislocations introduced at the γ/γ' interfaces may not be the misfit ones.

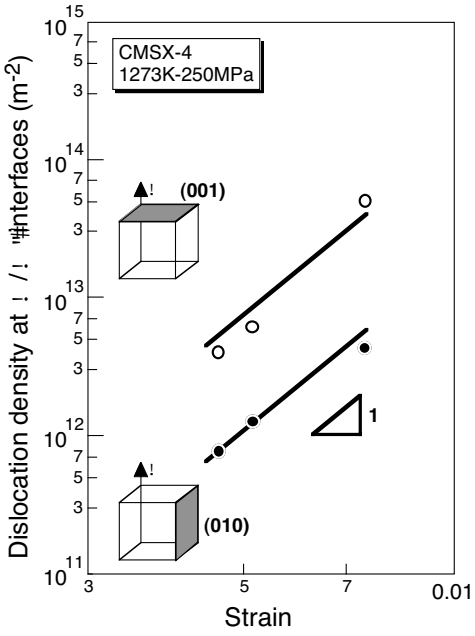

Fig.11. Changes in the dislocation density at the γ/γ' interfaces parallel to the (010) and (001) planes with the creep strain.

3.6 Burgers vectors of dislocations at γ/γ' interfaces

The correlation between the strain, ε, and the mobile dislocation density, ρ, are represented as Orowan's equation as follows, $\varepsilon = \rho b l$, where b is the Burgers vector and l is the average migration length of the dislocation [17]. That is, the creep strain is proportional to the dislocation density. In this study, the dislocation densities at the γ/γ' interfaces parallel to the (010) and (001) planes are directly proportional to the creep strain, as shown in Fig.11. Dislocations at the γ/γ' interfaces seem to be the traces of mobile dislocations in the γ channels which led to creep deformation. Therefore, the Burgers vectors of dislocations at the γ/γ' interfaces are identified in this section. In general, mobile dislocations of FCC metals have six kinds of the <110> Burgers vectors [18]. If dislocations at the γ/γ' interfaces are the traces of mobile dislocations, dislocations at the γ/γ' interfaces with six kinds of the <110> Burgers vectors, will be detected. Four invisibility conditions where required for identifying a Burgers vector using the g·b=0 invisibility criterion. The TEM observations on the same region are carried out with two incident beam directions, B={110} and {001} and four g-vectors, g =<-111> and <200>, as shown in Table.2.

Table.2. Four invisibility conditions on the basis of the g·b = 0 invisibility criterion for identifying a Burgers vector.

Incident beam directions	010		110	
b \ g	002	200	$\bar{1}1\bar{1}$	$\bar{1}11$
110	Invisible	Visible	Invisible	Invisible
$1\bar{1}0$	Invisible	Visible	Visible	Visible
$10\bar{1}$	Visible	Visible	Invisible	Visible
101	Visible	Visible	Visible	Invisible
011	Visible	Invisible	Invisible	Visible
$01\bar{1}$	Visible	Invisible	Visible	Invisible

Incident beam directions	001		101	
b \ g	020	200	$\bar{1}\bar{1}1$	$\bar{1}11$
110	Visible	Visible	Visible	Invisible
$1\bar{1}0$	Visible	Visible	Invisible	Visible
$10\bar{1}$	Invisible	Visible	Visible	Visible
101	Invisible	Visible	Invisible	Invisible
011	Visible	Invisible	Invisible	Visible
$01\bar{1}$	Visible	Invisible	Visible	Invisible

The Burgers vectors of dislocations at the γ/γ' interfaces parallel to the (010) plane of the interrupted creep specimen at a strain of 0.46% are shown in Fig.12. All dislocations at the γ/γ' interfaces with six kinds of the <110> Burgers vectors are detected. The Burgers vectors of all dislocations at the γ/γ' interfaces parallel to both the (010) and (001) planes of the interrupted creep specimens are identified in same way (Fig.12). Based on this identification procedure, quantitative comparisons between the ratio of six kinds of the <110> Burgers vectors to all dislocations and the creep strain are examined.

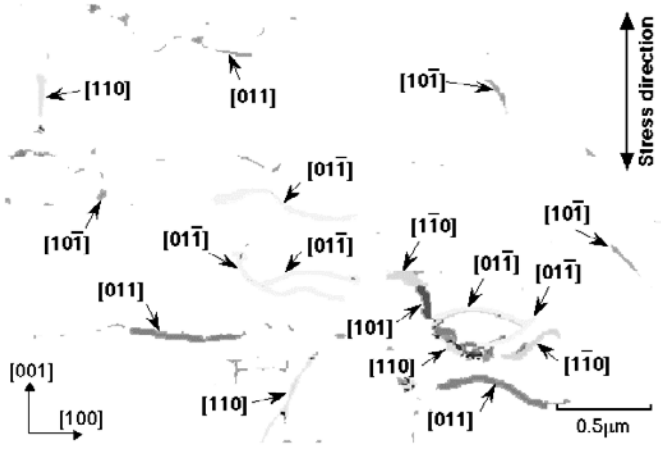

Fig.12. The Burgers vectors of dislocations at the γ/γ' interfaces parallel to the (010) plane of the interrupted creep specimen at a strain of 0.46%.

The ratios of dislocations at the

γ/γ' interfaces parallel to the (010) and (001) planes with six kinds of the <110> Burgers vectors to all dislocations of the interrupted creep specimens at the strains of 0.46, 0.51 and 0.74% are shown in Figs.13 and 14, respectively. Dislocations at the γ/γ' interfaces with six kinds of the <110> Burgers vectors are detected equally, independent of the creep strain and the interfaces. Consequently, it is suggested that dislocations at the γ/γ' interfaces may not be misfit ones, but the traces of mobile dislocations in the γ channels which led to creep deformation.

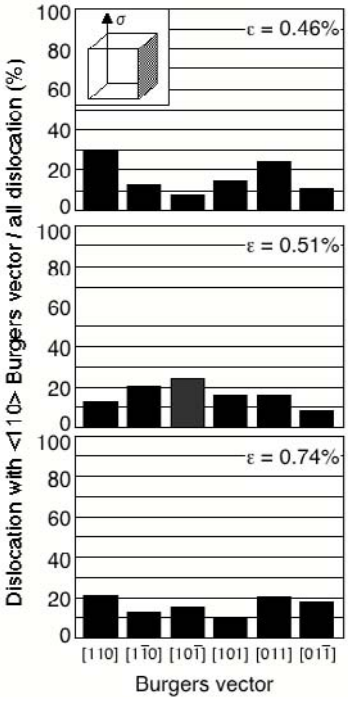

Fig.13. The ratio of dislocations at the γ/γ' interfaces parallel to the (010) plane with six kinds of the <110> Burgers vectors to all dislocations of the interrupted creep specimens at the strains of less than 0.74%.

4. Conclusions

The creep test and the interrupted creep tests are carried out on the [001] oriented single crystal nickel-based superalloy, CMSX-4, at 1273K and 250MPa, and the changes in the dislocation substructures at the γ/γ' interfaces parallel to the (010) and (100) planes with increasing creep strain is discussed. The following conclusions are obtained.

1) The accurate dislocation substructures at the γ/γ' interfaces parallel to the (010) and (001) planes can be express with the two different g-vectors on the same region.

2) The dislocation density at the γ/γ' interfaces parallel to the (001) plane is larger than that at the γ/γ' interfaces parallel to the (010) plane independent of the creep strain, and the dislocation densities at the γ/γ' interfaces parallel to the (010) and (001) planes increase with increasing creep strain.

3) All dislocations at the γ/γ' interfaces with six kinds of the <110> Burgers vectors are detected equally, independent of the creep strain and the interfaces.

4) From these results, it is concluded that dislocations at the γ/γ' interfaces may not be misfit ones, but the traces of mobile dislocations in the γ channels which led to creep deformation.

5. References

[1] A. Pineau, Influence of Uniaxial Stress on the Morphology of Coherent Precipitates during Coarsening – Elastic Energy Considerations, Acta Metall., 24(1976), p. 559

[2] F. R. N. Nabarro, Rafting in Superalloys, Metall. Mater. Trans., 27A(1996), p. 513

[3] M. Fahrmann, E. Fahrmann, O. Paris, P. Fratzl and T. M. Pollock, An Experimental Study of the Role of Plasticity in the Rafting Kinetics of a Single Crystal Ni-base Superalloy, Proc. of the 8th Int'l Symp. on Superalloysl996, (1996), p. 191

[4] J. K. Tien and R. P. Ganble, Effects of Stress Coarsening on Coherent Particle Strengthening, Metall. Trans, 3A(1972), p.2157
[5] D. Mukhherji, H. Gabrisch, W. Chen, H. J. Fecht and R. P. Wahi, Mechanical Behavior and Microstructural Evolution in the Single Crystal Superalloy SC16, Acta Mater., 44 (1997), p.3143
[6] R. A. MacKay and L. J. Ebert, The Development of γ / γ' Lamellar Structures in a Nickel-base Superalloy during Elevated Temperature Mechanical Testing, Metall. Trans. A, 16A(1985), p.1969
[7] M. V. Nathal and L. J. Ebert, Elevated Temperature Creep-Rupture Behavior of the Single Crystal Nickel-base Superalloy NASAIR 100, Metall Trans. A, 16A(1985), p.427
[8] T. M. Pollock and A. S. Argon, Creep resistance of CMSX-3 Nickel Base Superalloy Single Crystals, Acta Metall. Mater., 40(1992)1, p.1
[9] N. Miura, Y. Kondo and T. Matsuo, Stress Dependence of Strain Attained to Rafting of γ' phase in Single Crystal Nickel-based Superalloy, CMSX-4, Proc. of 9th Int'l. Conf. on Creep and Fracture Engineering Materials and Structures, (2001), p. 437.
[10] K. Ishibashi, Y. Kondo, J. Namekata, N. Ohi and H. Hattori, Long Time Creep Rupture Properties of Single Crystal Nickel-based Superalloy, CMSX-4, 123rd Committee on Heat Resisting Metals and Alloys Rep., 37(1996), p.1

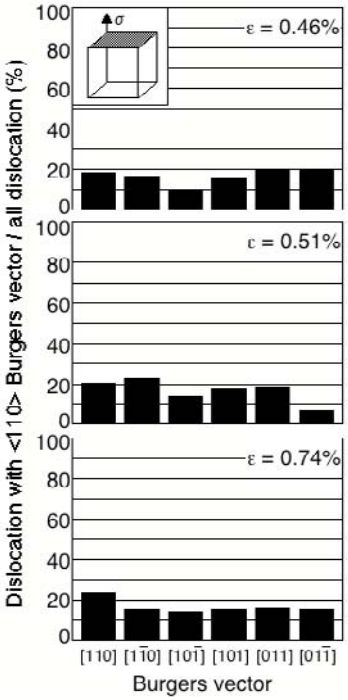

Fig.14. The ratio of dislocations at the γ/γ' interfaces parallel to the (001) plane with six kinds of the <110> Burgers vectors to all dislocations of the interrupted creep specimens at the strains of less than 0.74%.

[11] Y. Kondo and T. Matsuo, Creep of Single Crystal Superalloys, 123rd Committee on Heat Resisting Metals and Alloys Rep., 38(1997)3, p.269
[12] N. Miura, F. Tanaka, N. Harada and Y. Kondo, Change in Morphology of γ' phase of Prior-crept Single Crystal Nickel-based Superalloy, CMSX-4, with Simple Aging, CMSX-4, 123rd Committee on Heat Resisting Metals and Alloys Rep., 43(2002), p.243
[13] Electron Microscopy of Thin Crystals, Butterworths, London, (1965), p.171
[14] M. H. Loretto and R. E. Smallman, Defect Analysis in Electron Microscopy, Science Paperbacks, London, (1975), p.51
[15] T. Miyazaki and H. Mori, 123rd Committee on Heat Resisting Metals and Alloys Rep., 19(1978), p.257
[16] H. Harada, Materials Design, 123rd Committee on Heat Resisting Metals and Alloys Rep., 28(1997), p.185
[17] M. Kato, Introduction to the Theory of Dislocations, Shokabo, Tokyo, (1999), p.11
[18] M. Kato, Introduction to the Theory of Dislocations, Shokabo, Tokyo, (1999), p.78

MODELLING OF RAFTING AND ITS INFLUENCE IN NI-BASE SUPERALLOYS

Bernard Fedelich*, Georgia Künecke*, Alexander Epishin**

*Bundesanstalt für Materialforschung und -prüfung (BAM, Berlin)
** Technical University Berlin

Abstract

Rafting i.e., directional coarsening of the γ' precipitates usually occurs in Ni-base superalloys under high temperature creep loading and has been often observed in turbine blades after service. This instability of the microstructure can also lead to a significant degradation of the monotonous and the cyclic strength of these alloys. Hence, modelling tools to predict the occurrence of rafting in blades under service condition are highly desirable. A constitutive model that represents rafting has been developed. It is argued that the driving force for rafting can be best described by the back stress, which can be identified by the usual testing methods at the macroscopic level. The developed constitutive model has been validated for the alloy SRR99 at 980°C.
Keywords: Ni-base superalloys, rafting, modelling, creep, single crystals

1. Introduction

Advanced single crystal superalloys, as nowadays used in blades for gas turbines or aero engines, have a high volume content of the γ' phase (>40%). This second phase initially consists in quasi-periodically arranged cubic precipitates. Its predominant influence on the mechanical behavior and on the strength of these alloys is now well understood [1-3]. During high temperature deformation, the precipitate phase loses its stability and various morphology types may appear, depending on the local stress state and on the alloy characteristics. Typically, under uniaxial tension, the γ' precipitates coalesce to form plates perpendicular to the load axis, a phenomenon usually referred to as rafting. This microstructural transformation may significantly affect the subsequent monotonous or cyclic strength of the considered alloy. Reported effects of the plate morphology include reduction of the fatigue life [4,5] or creep/tensile strength [6-9].

For a reliable mechanical analysis of turbine blades it is thus necessary to estimate the kinetics of rafting and its influence on the mechanical behaviour of the alloy. The main objective of this work is thus the development of a constitutive law with the following features:

- The anisotropy of the behaviour is taken into account.
- The main high temperature deformation mechanisms are represented.
- The driving force for rafting can be estimated.
- The kinetics of rafting can be predicted.
- The effect of rafting on the alloy strength can be evaluated.
- The model can be used for structural analysis as a constitutive law in a FE code.

The present model originates from previous analyses of the mechanical behaviour of the γ/γ'-microstructure at the dislocation level [10,11]. This former work enables an analysis of the driving force for rafting and confirms the paramount role of the channel width in controlling the mechanical strength of those alloys. In this paper, the new constitutive model is presented and calibrated with test data from the single crystal superalloy SRR9.

2. Model presentation

2.1. General frame

The proposed model has been designed to describe the behavior of arbitrary oriented crystals under temperatures higher than 750°C, so that dislocation glide in the channels is the controlling deformation mechanism. It relies on the small strain assumption with the usual additive strain decomposition

$$\boldsymbol{\varepsilon} = \boldsymbol{\varepsilon}^e + \boldsymbol{\varepsilon}^p, \quad \boldsymbol{\sigma} = \mathbf{C} : \boldsymbol{\varepsilon}^e, \tag{1}$$

where the cubic stiffness tensor is denoted by **C.** The octahedral and the cubic slip systems will be throughout denoted with the superscript *o*, respectively *c.* In particular, the total plastic strain rate can be written as function of the shear rates on the octahedral and cubic systems $\dot{\gamma}_g^o$, resp. $\dot{\gamma}_g^c$

$$\dot{\boldsymbol{\varepsilon}}^p = \frac{1}{2}\sum_{g=1}^{12}\left(\mathbf{n}_g^o \otimes \mathbf{m}_g^o + \mathbf{m}_g^o \otimes \mathbf{n}_g^o\right)\dot{\gamma}_g^o + \frac{1}{2}\sum_{g=1}^{6}\left(\mathbf{n}_g^c \otimes \mathbf{m}_g^c + \mathbf{m}_g^c \otimes \mathbf{n}_g^c\right)\dot{\gamma}_g^c, \tag{2}$$

where $\mathbf{m}_g^o, \mathbf{m}_g^c =$ Slip direction and $\mathbf{n}_g^o, \mathbf{n}_g^c =$ Slip plane.

Thereby, the 12 octahedral slip systems $\{111\} < \bar{1}10 >$ and the 6 cubic slip systems $\{001\} < \bar{1}10 >$ are taken into account. The resolved shear stresses on both families of slip systems are as usual defined as $\tau_g^o = \mathbf{m}_g^o \cdot \boldsymbol{\sigma} \cdot \mathbf{n}_g^o, \quad \tau_g^c = \mathbf{m}_g^c \cdot \boldsymbol{\sigma} \cdot \mathbf{n}_g^c$.

2.2 Estimate of the Orowan stress for dislocation glide in the channels

For the octahedral systems, the plastic shear rate is supposed to be mainly controlled by the magnitude of the Orowan stress given by

$$\tau^{orowan} = \beta \frac{Kb}{w}, \tag{3}$$

where the current channel width is denoted by w and the magnitude of the Burgers vector is b. The factor K depends on the elastic constants and on the orientation of the trailed dislocation segments [10]. In the simplest case of elastic isotropy it is just the shear modulus. To simplify things, we take in the following $K = C_{1212}$. The numerical factor β is often assumed to be approximately one. However, there exist large uncertainties concerning the exact value of the Orowan stress (core energy, shape of the loop). Furthermore, one should also mention the large scatter in the actual channel width. In practice, it turns out that the value $\beta = 1$ is much too high, as demonstrated by the following discussion:

In the case of the alloy SRR99 at room temperature, the γ' volume fraction $f_{\gamma'}$ is about 0.7. At 980°C, this volume fraction is somewhat lower, i.e. $f_{\gamma'} \approx 0.62$. Taking the size of the initially cubic γ' particles as $2c_0 = 466nm$, the size of the periodic cell $2L$ can be obtained from

$$\left(\frac{2c_0}{2L}\right)^3 = f_{\gamma'}, \tag{4}$$

which gives $L = 272.5nm$. Hence, the initial channel width is $w_0 = 2L - 2c_0 = 79nm$. With the Burgers vector given by $b = 0.25nm$ and $C_{1212} = 93000MPa$ at 980°C, we can estimate of the Orowan stress for the initial cubic morphology without its corrective factor

$$\tau^{Orowan} = \frac{C_{1212}b}{w_0} = 294MPa\,. \tag{5}$$

However, [001] specimens already creep at 980°C under a tensile stress as low as 170MPa, which corresponds to a resolved shear stress of 68MPa. This makes clear the necessity to introduce the corrective factor β in (3). The later will be treated as an adjustable parameter of the model.

The final channel width w_∞ after rafting due a long term uniaxial positive pre-deformation will be estimated from the following assumptions:

- The γ' volume fraction $f_{\gamma'}$ is not altered by the rafting process.
- The raft structure consists of infinite plates perpendicular to the load axis.
- The periodicity length $2L$ remains constant in the direction perpendicular to the plates. This is only true during the initial stage of rafting. Subsequently, the rafts coarsen and the periodicity length significantly increases [12].

Accordingly, after completed rafting the relationship between the width of the γ plates $2c_\infty$ and the volume fraction of the γ' phase is

$$\frac{2c_\infty}{2L} = f_{\gamma'}, \tag{6}$$

from which follows the following estimate of the channel width $w_\infty = 2L - 2c_\infty = 204nm$.

2.3. Octahedral systems

The deformation mechanisms are assumed to be thermally activated. This is achieved by using a sinh law of the form

$$\begin{aligned} \dot{\gamma}_g^o &= \dot{v}_g^o \ \operatorname{sign}\left(\tau_g^o - x_g^o\right), \\ \dot{v}_g^o &= \rho_g^o \ \sinh\left[\frac{V_f^o}{kT}\hat{\tau}_g\left\{1-\left[\frac{1}{1+\left(\frac{\hat{\tau}_g}{\tau^{orowan}}\right)^n}\right]^{1/n}\right\}\right], \end{aligned} \tag{7}$$

where $\hat{\tau}_g = \left|\tau_g^o - x_g^o\right|$, x_g^o is the back stress on the slip system g and V_f^o is an activation volume. The Boltzmann constant is denoted by k and T is the absolute temperature. Note that the use of an exponent function inside the sinh allows the description of a smooth elastic-plastic transition. The degree of smoothness of the elastic-plastic transition is controlled by the exponent n. By this means, fluctuations like those due to the scatter in the channel width can be accounted for. The quantity ρ_g^o is assumed to be proportional to the dislocation density of the corresponding slip system. We assume for it a law with saturation, i.e.

$$\rho_g^o = \rho_0^o + \left(\rho_\infty^o - \rho_0^o\right)\left[1 - \exp\left(-\nu_g^o / b^o\right)\right], \tag{8}$$

where ν_g^o is the cumulated glide on the octahedral system *g*. Kinematic hardening is assumed to be described by a tensor variable denoted by $\mathbf{X}^o$, as resulting from the calculations of the internal stresses in the γ/γ' compound performed in [10]. The back-stresses at the level of the slip system are then obtained by

$$x_g^o = \mathbf{n}_g^o \cdot \mathbf{X}^o \cdot \mathbf{m}_g^o . \tag{9}$$

The internal stress $\mathbf{X}^o$ depends on a strain-like internal variable $\boldsymbol{\alpha}^o$ through a structural cubic fourth order tensor, here taken as isotropic for simplicity

$$\mathbf{X}^o = \boldsymbol{\Omega}^o : \boldsymbol{\alpha}^o, \quad \boldsymbol{\Omega}^o = c^o\, \mathbf{1} \Rightarrow \mathbf{X}^o = c^o \boldsymbol{\alpha}^o, \tag{10}$$

where c^o is a numerical constant homogeneous to a stiffness. Physically, $\mathbf{X}^o$ originates from the dislocations deposited on the γ/γ' interfaces. Its saturation is due to precipitate shearing at high stresses or dislocation climb during long term deformation processes, as explained in [10]. In accordance, a phenomenological evolution law is formulated as follows: The evolution of $\boldsymbol{\alpha}^o$ is obtained by adding the contributions $\dot{\alpha}_g^o$ of each slip system

$$\dot{\boldsymbol{\alpha}}^o = \frac{1}{2}\sum_{g=1}^{12}\left(\mathbf{n}_g^o \otimes \mathbf{m}_g^o + \mathbf{m}_g^o \otimes \mathbf{n}_g^o\right)\dot{\alpha}_g^o . \tag{11}$$

The pseudo shear rates $\dot{\alpha}_g^o$ are assumed to take the form

$$\dot{\alpha}_g^o = \dot{\gamma}_g^o - \dot{\nu}_g^o\, d^o \sinh\left[\frac{V_d^o x_g^o}{kT}\right] - h^o \sinh\left[\frac{V_s^o x_g^o}{kT}\right] \tag{12}$$

The second and the third terms on the right hand side of equ. (12) correspond to thermally activated dynamic and static recovery, respectively.

2.4 Cubic systems

The plastic shear rate for the cubic systems is supposed to follow a similar thermal activation law (without exponent) of the form

$$\dot{\gamma}_g^c = \dot{\nu}_g^c \;\; \mathrm{sign}\left(\tau_g^c - x_g^c\right), \quad \dot{\nu}_g^c = \rho_g^c \;\; \sinh\left[\frac{V_f^c \left\langle \left|\tau_g^c - x_g^c\right| - r_0^c \right\rangle}{kT}\right]. \tag{13}$$

According to the observations on <111> specimens reported in [13], macroscopic cubic slip is due to alternating cross-slip of $<01\bar{1}>$ dislocations on two conjugate octahedral planes. Accordingly, the dislocation density for cubic slip is driven by the intensity of octahedral slip. This is acknowledged by taking the dislocations density for the cubic system *g* as

$$\begin{aligned} &\rho_g^c = \rho_0^c + \left(\rho_\infty^c - \rho_0^c\right)\sum_{i=1}^{12}\varepsilon_{gi}\left[1 - \exp\left(-\nu_i^o / b^c\right)\right] \\ &\varepsilon_{gi} = 1 \quad \textit{if } g \textit{ and } i \textit{ have the same Burgers vector} \\ &\varepsilon_{gi} = 0 \quad \textit{if } g \textit{ and } i \textit{ have a different Burgers vector} \end{aligned} . \tag{14}$$

In accordance, ν_i^o is the cumulated slip on the octahedral system *i*, see equ.(7). In a similar way to octahedral systems, the internal stresses generated by cubic slip are also represented by a tensor stress variable, i.e.

$$x_g^c = \mathbf{n}_g^c \cdot \mathbf{X}^c \cdot \mathbf{m}_g^c, \tag{15}$$

The evolution of the internal stress $\mathbf{X}^o$ is assumed to follow similar laws to those of the octahedral systems, i.e.

$$\begin{aligned} &\mathbf{X}^c = \mathbf{\Omega}^c : \boldsymbol{\alpha}^c, \quad \mathbf{\Omega}^c = c^c\, \mathbf{1} \Rightarrow \mathbf{X}^c = c^c \boldsymbol{\alpha}^c, \\ &\dot{\alpha}_g^c = \dot{\gamma}_g^c - \dot{\nu}_g^c\, d^c \sinh\left[\frac{V_d^c x_g^c}{kT}\right] - h^c \sinh\left[\frac{V_s^c x_g^c}{kT}\right], \\ &\dot{\boldsymbol{\alpha}}^c = \frac{1}{2}\sum_{g=1}^{12}\left(\mathbf{n}_g^c \otimes \mathbf{m}_g^c + \mathbf{m}_g^c \otimes \mathbf{n}_g^c\right)\dot{\alpha}_g^c \end{aligned} \tag{16}$$

where c^c is a numerical constant homogeneous to a stiffness. The second and the third terms on the right hand side of $(16)_2$ correspond to dynamic and static recovery, respectively.

2.5 Modelling of rafting

The thermodynamic driving forces for the morphology change have been extensively analysed during the last twenty years (see, e.g. [14]). From FE calculations [15], dislocation models [16] and energy calculations [17-19] a coherent picture has emerged, in which the dominant part of the driving force for rafting originates from the anisotropic relaxation of the coherency stresses through the deformation induced dislocations. This conclusion is also supported by several recent observations [20-21], according to which the onset of measurable rafting coincides with the formation of misfit-relieving dislocation networks.

To illustrate this point, the elastic energy stored in the periodic cell of the γ/γ' microstructure under uniaxial tensile stress has been calculated for the alloy SRR99, which has an unconstrained misfit ratio $\delta_u \simeq -0.15\%$. It is assumed that only the channels V_3 perpendicular to the load axis [001] are plastically deformed and that the local plastic strain tensor in these channels has the form $\boldsymbol{\varepsilon}_3^p = \sqrt{\frac{2}{3}}\begin{bmatrix} -1/2 & 0 & 0 \\ 0 & -1/2 & 0 \\ 0 & 0 & 1 \end{bmatrix}\varepsilon_3^p$. The average density of the elastic energy stored in a periodic cell of the microstructure W can be evaluated following the procedure described in [10] for homogeneous elastic constants. It consists of a macroscopic part W^{macro}, which is independent of the morphology and a microscopic part W^{micro}

$$\begin{aligned} &W = W^{macro} + W^{micro}, \\ &W^{macro} = \frac{1}{2}\boldsymbol{\varepsilon}^e : \mathbf{C} : \boldsymbol{\varepsilon}^e, \quad W^{micro} = \frac{1}{2}\boldsymbol{\varepsilon}_3^p : \mathbf{\Omega}_{33} : \boldsymbol{\varepsilon}_3^p + \boldsymbol{\varepsilon}_3^p : \mathbf{\Omega}_{34} : \boldsymbol{\varepsilon}^* + \frac{1}{2}\boldsymbol{\varepsilon}^* : \mathbf{\Omega}_{44} : \boldsymbol{\varepsilon}^* \end{aligned} \tag{17}$$

where $\boldsymbol{\varepsilon}^e$ is the macroscopic elastic strain, $\varepsilon_{ij}^* = \delta_u\, \delta_{ij}$ is the eigenstrain of the precipitates in the unconstrained state and $\mathbf{\Omega}_{ij}$ are fourth order tensors strongly dependent on the underlying γ/γ' morphology. If the volume fraction of the channels V_3 is f_3, the macroscopic plastic strain is just $\boldsymbol{\varepsilon}^p = f_3\, \boldsymbol{\varepsilon}_3^p$. Its magnitude is proportional to the dislocation density on the γ/γ' interfaces perpendicular to [001]. The relevant part W^{micro} of W is plotted in Fig. 1 as function of the macroscopic creep strain for the cubic and for the plate microstructures.

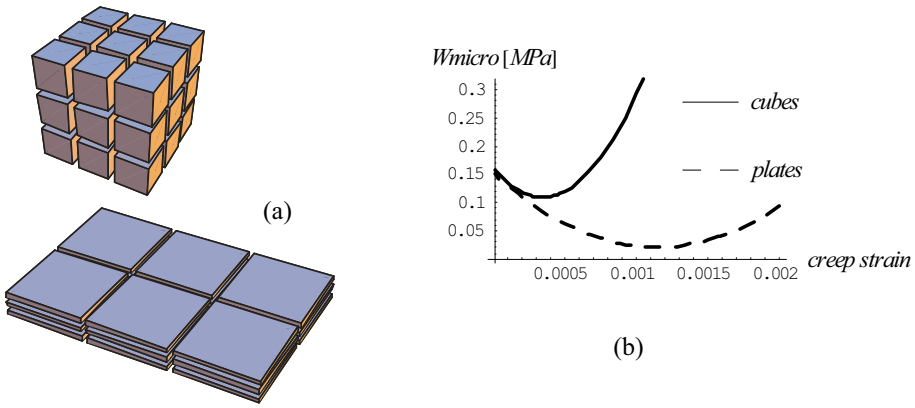

Fig.1. Cubic and plate morphologies (a). Elastic microscopic energy versus creep strain (b).

It can be concluded that plastic strain initially relieves the misfit stresses. If straining continues, the elastic energy increases again. This energy can be either decreased by shearing the γ' particles, by dislocation climbing or by rafting. From the theory of dissipative processes, the driving force X_i for a transformation parameterized by p_i is given by

$$X_i = -\frac{\partial W}{\partial p_i} = -\frac{1}{2}\boldsymbol{\varepsilon}_3^p : \frac{\partial \boldsymbol{\Omega}_{33}}{\partial p_i} : \boldsymbol{\varepsilon}_3^p - \boldsymbol{\varepsilon}_3^p : \frac{\partial \boldsymbol{\Omega}_{34}}{\partial p_i} : \boldsymbol{\varepsilon}^* - \frac{1}{2}\boldsymbol{\varepsilon}^* : \frac{\partial \boldsymbol{\Omega}_{44}}{\partial p_i} : \boldsymbol{\varepsilon}^* . \tag{18}$$

In particular, it remains unaltered by removal of the applied stress. This result is in agreement with the detailed observations of rafting after pre-deformation reported in [20]. Even after complete unloading, rafting still continues if a threshold pre-strain has been exceeded. Within this micro-mechanical analysis, the back-stress in the channels V_3 is obtained as

$$\mathbf{B}_3 = \frac{\mathbf{1}}{f_3}\left(\boldsymbol{\Omega}_{33} : \boldsymbol{\varepsilon}_3^p + \boldsymbol{\Omega}_{34} : \boldsymbol{\varepsilon}^*\right). \tag{19}$$

For creep strains larger than 0.1%, the first term on the right hand side of equ. (18) becomes predominant. From this analysis, it becomes clear that the driving force for rafting (18), the local plastic strain $\boldsymbol{\varepsilon}_3^p$ and the local back stress (19) in V_3 are strongly correlated. Moving back to our more phenomenological present model, we thus conjecture that the macroscopic counter-part to (19), i.e. the back-stress $\mathbf{X}^o$ that is given by equ. (10) essentially controls the rafting process.

Finally, simulations of tensile tests with a (stable) raft microstructure have been performed in [11]. They reveal that for sufficiently high stresses, the main mechanical consequence of rafting is a strength decrease, which can be rationalised by the reduction of the Orowan stress due to channel broadening. In the presented model, the degree of advancement of rafting is defined by the scalar value $\lambda(t), 0 \le \lambda(t) \le 1$ such that at any stage, the current channel width is given by

$$w = w_0(1-\lambda) + w_\infty \lambda \tag{20}$$

For the kinetics of rafting, a simple linear evolution law is assumed, with a driving force proportional to the magnitude of $\mathbf{X}^o$, so that

$$\dot{\lambda} = f_{raft}\left\|\mathbf{X}^o\right\|(1-\lambda), \tag{21}$$

where f_{raft} is a model parameter.

3. Results

The model parameters have been calibrated for the alloy SRR99 at 980°C. The test data basis included tensile, cyclic and creep tests for various specimen orientations. Some of the test simulations, which have been used to identify the model parameters, are presented in the Figures 2-4. Note the progressive increase of the strain rate during creep due to the broadening of the matrix channels in Fig. 4.

The decrease of the alloy tensile strength can also be observed in Fig. 5. Firstly, specimens have been pre-deformed at 980°C under 200MPa until 0.4% creep strain to generate a fully formed raft structure. In a second step, the specimens have been submitted to tensile loading. The same loading sequence has been simulated, demonstrating that the model is able to represent the strength decrease due to rafting.

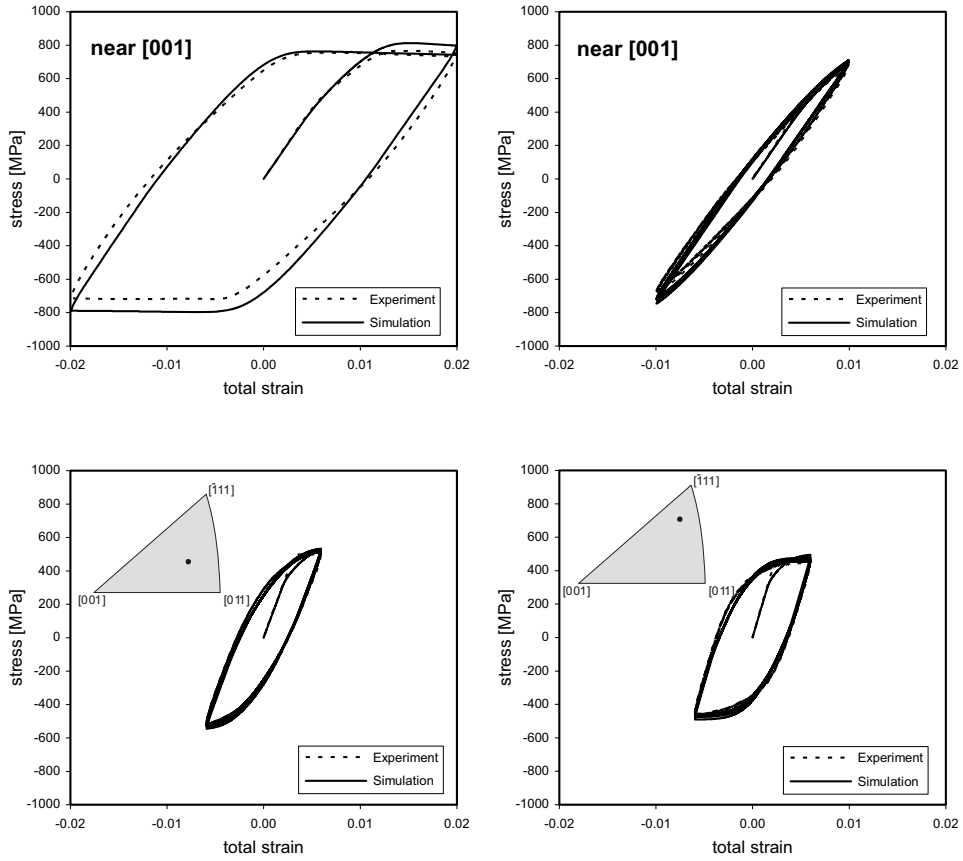

Fig. 2. Simulation of LCF tests with various orientations and strain amplitudes.

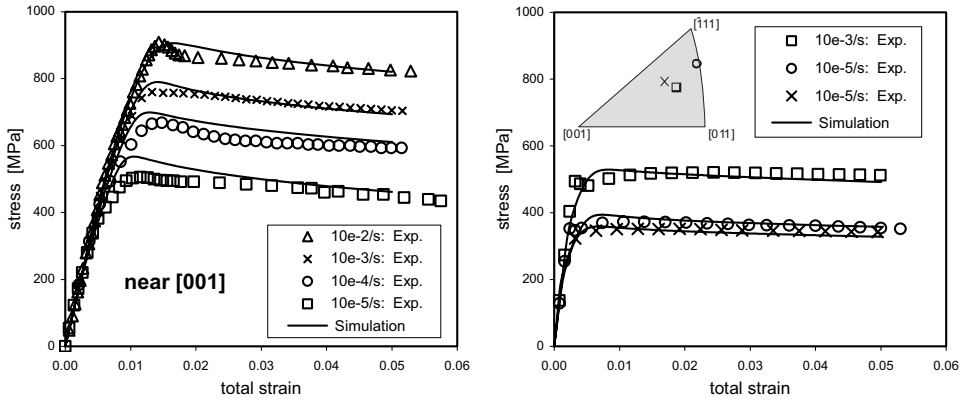

Fig. 3. Simulation of monotonous tensile tests with different strain rates and orientations

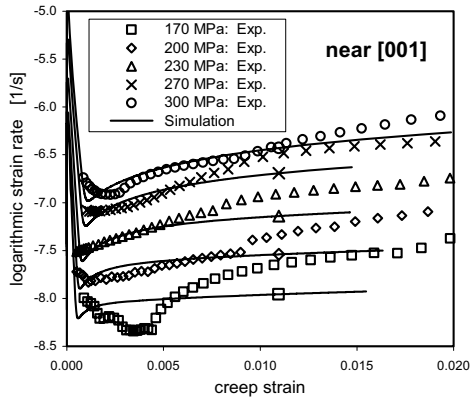

Fig. 4. Simulation of creep tests at 980°C.

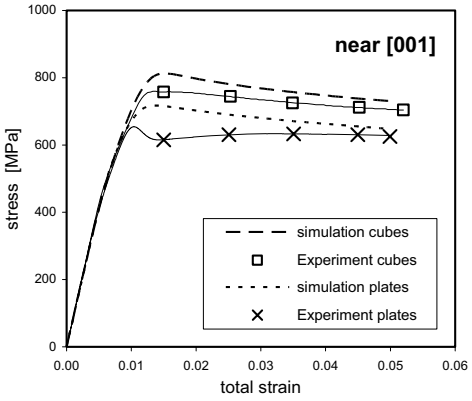

Fig. 5. Comparison of the behaviour of the initial cubic structure with the raft structure. The strain rate is $10^{-3}/s$ in all cases.

Finally, the degree of advancement of rafting λ defined in (20) has been plotted in Fig. 6 for a creep loading with a [001] oriented specimen and $\sigma = 200MPa$. The results are compared with micrographs of the microstructure in crept specimens examined after interrupting the tests at different stages. A reasonable qualitative agreement can be observed, the plates are already formed after about 0.4% creep strain.

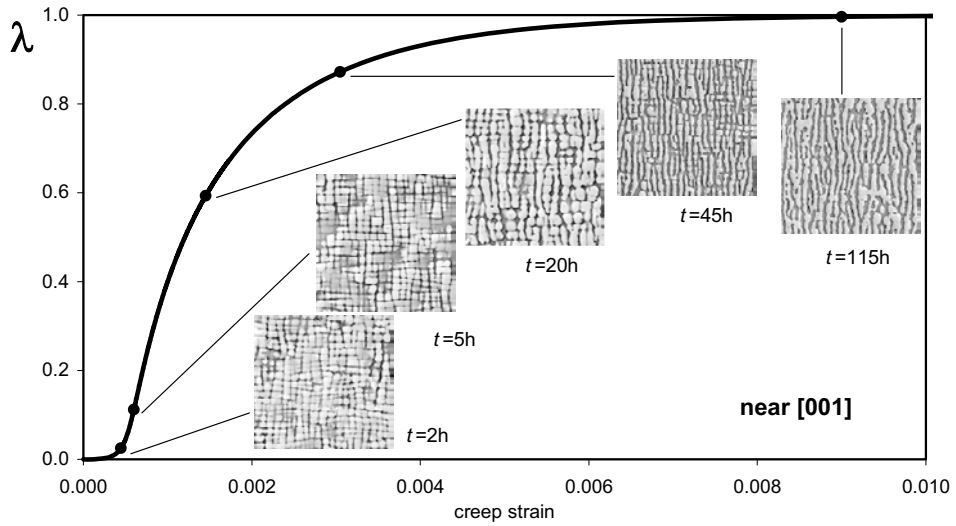

Fig. 6. Comparison between the computed rafting advancement degree during creep at 980°C, σ=200MPa and SEM micrographs of several crept specimens.

4. References

[1] Anton, D.: Ni_3-Al in Nickel-Based Superalloys. *Intermetallic Compounds, vol. 2.* Edited by J. H. Westbrook and R. L. Fleisher, John Wiley & Sons, New York, 1994.

[2] Pollock, T.M.; Argon, A.S.: Creep resistance of CMSX-3 nickel base superalloy single crystals. *Acta metall*., vol. 40, 1992, pp. 1-30.

[3] Feller-Kniepmeier, M.; Link, T.; Poschmann, L.; Scheunemann-Frerker, G.; Schulze, C.: Temperature dependence of deformation mechanisms in a single crystal nickel-base alloy with high volume fraction of γ' phase. *Acta mater*., vol. 44, 1996, pp. 2397-2407.

[4] Ai, S.H.; Lupinc, V.; Onofrio, G.: Influence of precipitate morphology on high temperature fatigue crack growth of a single crystal nickel base superalloy, *Scripta Metall. Mater*., vol. 29**,** 1993, pp. 1385-1390.

[5] Ott, M.; Mughrabi, H.: Dependence of the high-temperature low-cycle fatigue behaviour of the monocrystalline nickel-base superalloys CMSX-4 and CMSX-6 on the γ/γ'-morphology, *Mater. Sci. and Engineering A*, vol. 272, 1999, pp. 24-30.

[6] Nathal, M.V.; MacKay, R.A.; Miner, R.V.: Influence of precipitate morphology on intermediate creep properties of a nickel-base superalloy single crystal. *Metall. Trans. A,* vol. 20A, 1989, pp. 133-141.

[7] Pessah-Simonetti; Caron, P.; Khan, T.: Effect of a long-term prior aging on the tensile behavior of high-performance single crystal superalloy. *Journal de Physique III, C7*, vol. 3, 1993, pp. 347-350.

[8] Mughrabi, H.: γ/γ' rafting and its effect on the creep and fatigue behavior of monocrystalline superalloys. In: Arsenault, R.J., Cole, D., Gross, T., Kostorz, G., Liaw, P.K., Parameswaran, S., Sizek, H., (Herausgeber), The Johannes Weertman Symposium, 1996.

[9] Mukherji, D.; Gabrisch, H.; Chen, W.; Fecht, H.J.; Wahi, R.P.: Mechanical behaviour and microstructural evolution in the single crystal superalloy SC16. *Acta mater.*, vol. 45, 1997, pp. 3143-3154.

[10] Fedelich, B.: A microstructural model for the monotonic and the cyclic mechanical behavior of single crystals of superalloys at high temperatures. *Int. J. of Plasticity*, vol.18, 2002, pp. 1-49.

[11] Fedelich, B.: Modelling at the dislocation level the reinforcement of alloys by hard precipitates: The example of Ni-base superalloys, *J. Phys. IV France*, vol. 105, 2003, pp. 131-138.

[12] Epishin, A.; Link, T.; Portella, P.; Brückner, U.: Evolution of the γ/γ'-Microstructure during High Temperature Creep of a Nickel-Base Superalloy, *Acta mater*., vol. 48, 2000, pp. 4169-4177.

[13] Bettge, D.; Österle, W.: Cube slip in near [111] oriented specimens of a single-crystal nickel base superalloy. *Scripta Mater*., vol. 40, 1999, pp. 389-395.

[14] Biermann, H.: Ursachen und Auswirkungen der gerichteten Vergröberung ("Floßbildung") in einkristallinen Nickelbasis Superlegierungen, VDI Verlag, Düsseldorf,1999.

[15] Socrate, S.; Parks, D. M.: Numerical Determination of the Elastic Driving Force for Directional Coarsening in Ni-Superalloys, *Acta Metall. Mater*., vol. 41, 1993, pp. 2185-2209.

[16] Buffiere, J.-Y.; Ignat, M.: A Dislocation Based Criterion for the Raft Formation in Nickel-Based Superalloys Single Crystals, *Acta Metall. Mater*., vol. 43, 1995, pp. 1791-1797.

[17] Nabarro, F.R.N.; Cress, C.M.; Kotschy, P.: The thermodynamic driving force for rafting in superalloys. *Acta mater*., vol. 44, 1996, pp. 3189-3198.

[18] Ichisubo, T.; Koumoto, D.; Hirao, M.; Tanaka, K.; Osawa, M.; Yokokawa, T.; Harada, H.: Rafting mechanism for Ni-base superalloy under external stress: elastic or elastic-plastic phenomena? *Acta mater*., vol. 51, 2003, 4033-4044.

[19] Svoboda, J.; Lukas. P.: Modelling of kinetics of directional coarsening in Ni-superalloys. *Acta mater.*, vol. 44, 1996, pp. 2557-2565.

[20] Matan, N.; Cox, D. C.; Rae, C. M.; Reed, R.C.: On the kinetics of rafting in CMSX-4 superalloy single crystals, *Acta mater.*, vol. 47, 1999, pp. 2031-2045.

[21] Paris, O.; Fährmann, M.; Fährmann, E.; Polock T.M.; Fratzl, P.: Early stages of precipitate rafting in a single-crystal Ni-Al-Mo model alloy investigated by small-angle X-ray scattering and TEM, *Acta mater*., vol. 45, 1997, pp. 1085-1097.

TEM MICROSTRUCTURAL ANALYSIS OF CREEP DEFORMED CM186LC SINGLE CRYSTAL NI-BASE SUPERALLOY

B. Dubiel[1], M. Blackler[2], P. M Barnard[3] and A. Czyrska-Filemonowicz[1]

[1]AGH University of Science and Technology, 30-059 Kraków, Al. Mickiewicza 30, Poland
[2]Howmet Ltd., Kestrel Way, Sowton Industrial Estate, Exeter EX2 7LG, UK
[3]ALSTOM Power Turbo-Systems Technology Centre, Newbold Rd, Rugby, CV21 2NH, UK
e-mail: bdubiel@agh.edu.pl

Abstract

The nickel based single crystal superalloy CM186LC was extensively investigated as a potential low cost material for industrial gas turbine vanes within the COST522 programme. The alloy exhibits inhomogenous structure consisting of dendritic regions and eutectic colonies. In the present work attention is focused on microstructural changes observed in single crystal CM186LC following creep deformation at 750°C. Creep tests were conducted at 750°C with an applied stress of 560 or 675 MPa for up to 11440 hours. The microstructure of ruptured and terminated specimens was investigated by scanning (SEM) and transmission (TEM) electron microscopy. TEM analysis revealed the microstructural changes in the CM186LC at primary and secondary creep as well as after creep rupture.

Keywords: Single Crystal, CM186LC, Creep, Industrial Gas Turbine

Introduction

Manufacturing of large blades and vanes for industrial gas turbines (IGT) requires single crystal (SC) superalloys that are less susceptible to casting defects. Many different types of defects can be formed during casting of large single crystals in commercial production. IGT blades with orientations not exactly parallel to the preferred axis must be accepted because it is impossible to maintain perfect [001] orientation. It is also very difficult to avoid grain boundaries in large single crystal castings. To ensure high temperature strength of blades it is necessary to avoid formation of high angle grain boundaries and minimise the level of low angle grain boundaries [1]. Therefore there is still a need for development of new single crystal superalloys that are less susceptible to casting defects. Such requirements are fulfilled by second generation single crystal CM186LC alloy [2]. Although the alloy contains small amount of grain boundary strengthening elements (C, B, Zr and Hf), it is less susceptible to grain boundary defect formation. The single crystal blades and vanes of CM186LC are either used as-cast or approximately 50% partial solution treated, thus component costs can be considerably less than that of a high purity SC superalloys like CMSX-4. The creep properties of CM186LC were studied in detail within COST522 programme [3].
It was shown that during high temperature creep deformation at temperature above 850°C CM186LC generally exhibits a pronounced tertiary creep stage, while the primary and secondary stages are negligible. At lower temperature range 750-800°C, typical for core of a 1st stage turbine blade, the primary creep strain is relatively high, in the order of several percent. It considerably influences the lifetime of the material, because of shortening of time to reach 0.1% creep strain, used as the designers' criterion.

Therefore in this paper there is an attempt to examine in detail the microstructural changes in CM186LC superalloy during creep at 750°C.

Material

<001> solid bars of CM186LC superalloy investigated were supplied by Howmet Ltd, Great Britain, in the frame of European COST522 programme. The nominal chemical composition of the alloy is as follows: Ni- 9.3Co- 8.4W- 6.1Cr- 5.7Al- 3.4Ta- 2.9Re- 1.4Hf- 0.73Ti- 0.51Mo- 0.062C- 0.016B- 0.004Zr (wt %, manufacturer data). The alloy was solution annealed at 1080°C for 4 h and subsequently aged at 870°C for 20 h.

Figure 1 shows the SEM image of CM186LC superalloy microstructure in as-received condition. The addition of grain boundary strengtheners makes it difficult to fully solution heat treat and therefore the microstructure of as-received CM186LC superalloy retains a pronounced dendritic structure. Dendrite arms consist on cuboidal γ' precipitates, separated by narrow channels of γ matrix. Interdendritic regions contain of eutectic γ-γ' areas with large γ' particles of irregular morphology as well as MC carbides rich in Ta and Hf.

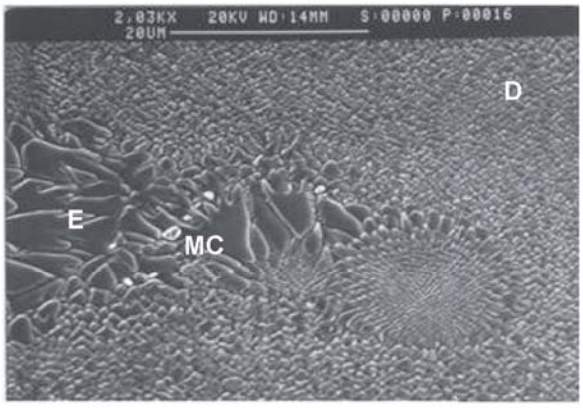

Figure 1. SEM micrograph of the as-received CM186LC, section parallel to (100) plane, showing dendritic region (D) and eutectic (E) with MC carbides.

The quantitative microstructural analysis of as-received CM186LC alloy showed that depending on the bar diameter the alloy contains of 70-80% volume fraction of γ' phase and the mean size of the precipitates calculated as the mean edge length of γ' cubes is 300-400 nm with γ matrix channels of 100 nm mean width. The volume fraction of γ-γ' eutectic is 20-25% [4].

Experimental methods

Creep tests of CM186LC were performed in air at temperature 750°C and at stresses 560 and 675 MPa with load direction parallel to [001]. All the creep specimens had the deviations from the [001] direction less than 10°. Specimens subjected to microstructural analysis were ruptured as well as terminated at primary and secondary creep. In the interrupted tests the specimens were cooled under load.

The details of the creep specimens investigated are given in Table 1.

Table 1. Details of the creep tested specimens

Specimen	T [°C]	σ [MPa]	Duration [h]	ε [%]	Status[#]
D	750	560	75	1.2	T
E	750	560	275	2.2	T
M	750	560	7 837	6.8	T
N	750	560	11 440	15.3	R
A	750	675	6	8.8	T
B	750	675	25	11.6	T
C	750	675	350	12.9	T
W	750	675	1 184	16.3	R

[#]T-*test terminated before rupture*, R-*ruptured*

Microstructural investigations were performed by SEM and TEM. Specimens used for the SEM investigations were mechanically polished and chemically etched in a solution of 4g $CuSO_4$+20 ml HCl+20 ml C_2H_5OH. Thin foils for TEM investigations were mechanically ground to about 50 μm, then dimpled to a thickness less then 25 μm. Double-jet polishing was performed in a solution of 450 ml $CH_2OHCH_2OC_4H_9$+ 450 ml CH_3COOH+ 100 ml $HClO_4$ at temperature range –2° to -5°C and a constant current of 30 mA. Thin foils were prepared from {001} longitudinal sections of creep deformed specimens. Microstructural investigations were carried out using STEREOSCAN 120 scanning and JEM 2010 ARP transmission electron microscopes. Stacking fault nature was determined by comparison of the contrast in bright and dark field images.

Results and discussion

Figure 2 shows the points indicating the strain and time data of tested specimens. The creep curves of ruptured specimens **N** and **W** are shown in Figure. 3. The shape of the strain versus time creep curves of CM186LC alloy tested at 750°C and stress of 560 and 675 MPa shows pronounced primary, secondary and tertiary stages. It is apparent that magnitude of primary

creep strain increases with increasing of the stress applied. For the lower stress of 560MPa the primary creep strain is around 2.5%, what gives 0.16 of the total creep strain, while at the higher stress of 675 MPa primary creep strain of 12% gives 0.75 of the total creep strain.

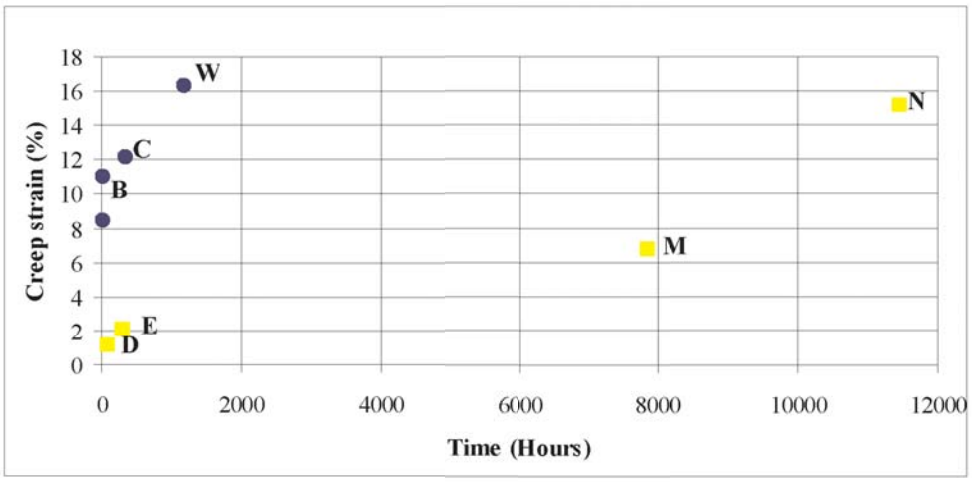

Figure 2. Strain versus time data of creep tested specimens.

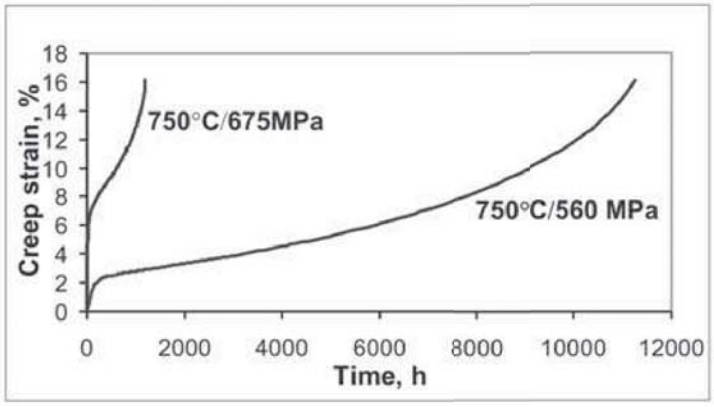

Figure 3. Creep curves of CM186LC alloy tested at 750°C and at stresses 675 MPa (specimen **N***) and 560 MPa (specimen* **W***).*

Due to the pronounced inhomogeneity, microstructural examinations of creep deformed CM186LC were confined to both dendritic and eutectic regions.

Dendritic regions

In the specimen **D** terminated at primary creep stage at 750°C/560MPa shearing of γ' particles by stacking faults was observed. Both extrinsic and intrinsic character stacking faults were identified (Figure 4, 5). The stacking faults observed were strongly aligned in one direction. TEM images observed in ~[112] beam direction revealed that the stacking faults are incorporated within extended dislocation ribbons passing through γ matrix and γ' particles. An example of such a ribbon with stacking faults inside γ' particles is shown in Figure 6. When the ribbon passes through γ' particles, two types of partial dislocations are visible: one remaining on the γ-γ' interface (marked as 1), and second, gliding inside γ' particle (marked as 2). The dislocations lying in the horizontal γ channel are also visible.

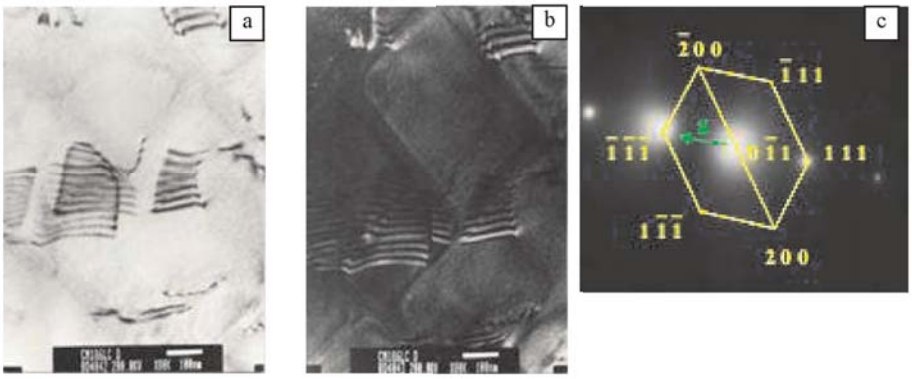

Figure 4. Identification of stacking fault SF in specimen **D**. *The beam direction ~ [0 $\bar{1}$ 1]; a) bright field image* **g**[$\bar{1}$ $\bar{1}$ $\bar{1}$], *b) dark field image, c) corresponding diffraction pattern. The analysed stacking fault is intrinsic.*

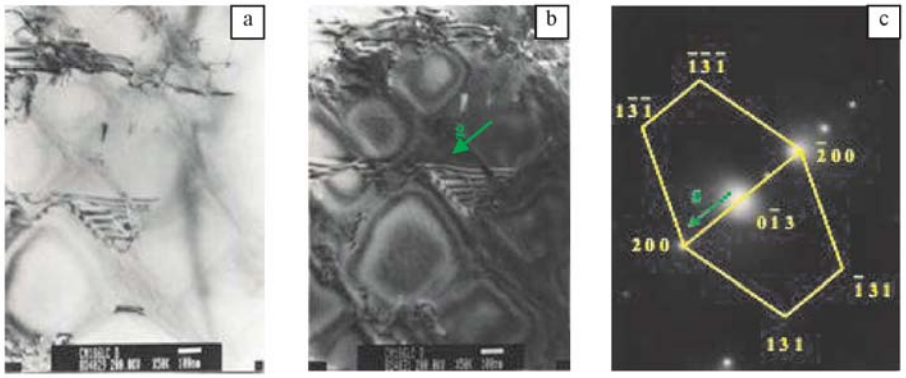

Figure 5. Identification of stacking fault SF in specimen **D**. *The beam direction ~ [0 $\bar{3}$ 1; a) bright field image* **g** *[200], b) dark field image, c) corresponding diffraction pattern. The analysed stacking fault is extrinsic.*

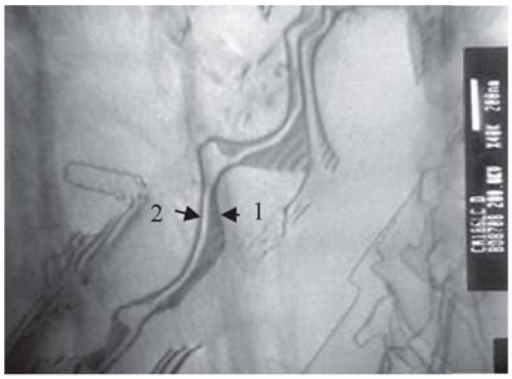

*Figure 6. Dislocation ribbon going through γ/γ' microstructure and dislocations in horizontal γ channel the specimen **D** terminated during primary creep. The beam direction ~[1 1 2], **g** [1 1 $\bar{1}$].*

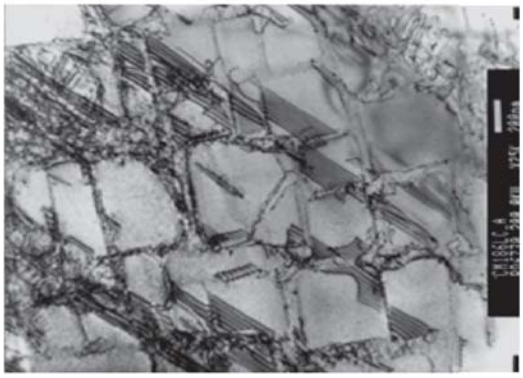

*Figure 7. Stacking fault ribbons in the specimen **A**.*

A higher density of ribbons with stacking faults was observed in the specimen **A** interrupted at the end of primary creep after 8% strain at 750ºC/675 MPa, as shown in Figure 6. It indicates that it was easier to shear the γ' particles under these higher stress conditions. The image shows also high density of dislocations in horizontal γ channels where the foil was thicker.

There is a general consensus [5] that the shearing of the γ and γ' by dislocations separated by intrinsic and extrinsic stacking faults is the dominant mechanism of primary creep of single crystal superalloys. According to this mechanism, single crystal superalloys of near <001> orientation at temperature 750-850ºC and stress ≥ 550 MPa, two a/2<110> dislocations, both gliding on the same (111) plane in the γ phase, can combine to form a/6<211> partial remaining at the γ-γ' interface and a/3 <211> partial gliding across the γ' particle, creating a stacking fault [6]. When the loading direction is oriented to [001], eight {111}<110> (Schmid factor =0.41) and four {111}<112> (Schmid factor = 0.47) slip systems are potentially active [7]. However the macroscopic deformation occurs by <112>{111} shear [8]. The reason is

that a <112> dislocation can slip both through the γ phase and γ' particles. Such dislocations form long ribbons moving easily through γ/γ' microstructure, leading to more extensive primary creep.

Specimens from tests that reached secondary creep (**M** and **C**) showed a comparable density of stacking fault ribbons at both stress levels. At this stage of creep deformation, dislocation networks are present inside the γ channels, as shown in Figure 8.

Formation of dislocation networks is connected with reactions between dislocations gliding on different slip systems in the γ phase during primary creep. This leads to relaxing of misfit stresses caused by the precipitate-matrix coherency, and in consequence results in decreasing the creep rate [9]. Additionally, in the specimens terminated at secondary creep stage, two slip systems of stacking faults ribbons were observed within γ' particles (Figure 9). Shearing of γ' particles by two operating slip systems can be related with the rotation of the orientation during creep deformation and generation of the new slip system. The activation of second stacking fault slip systems leads to reduced creep rate during secondary creep [10].

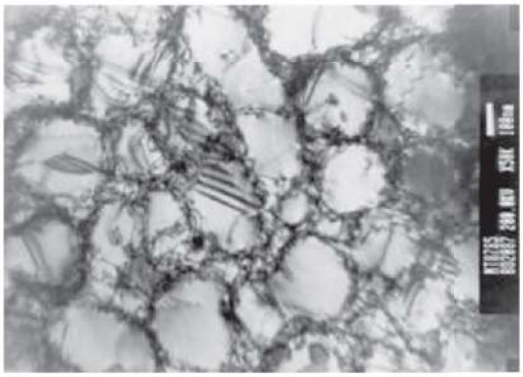

Figure 8. Dislocation networks inside the γ channels and stacking faults in the γ' particles in the specimen **M**.

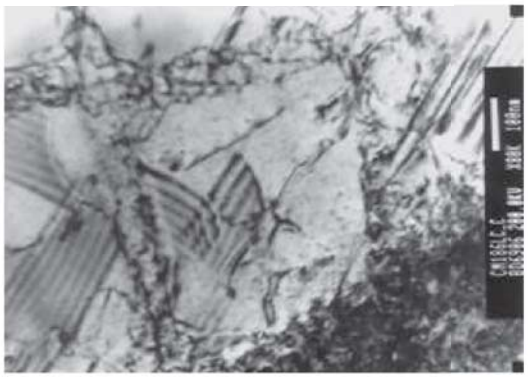

Figure 9. Stacking faults in two slip systems in the specimen **C**.

Stacking faults in two operating slip systems were also observed after creep rupture at lower stress of 560 MPa (specimen **N**). Increasing the applied stress to 675 MPa caused the formation of deformation twins, which cut both γ and γ' phases, as was found in specimen **W** (Figure 10). Diffraction pattern shows the extra spots arising from twins. The angles between twins are 60°. It suggests that they are formed on <111> planes. It was reported by Knowles et al. [11] that during creep deformation along the [001] axis, a twinning process is accompanied by rapid strain evolution close to rupture and requires the passage of a/3 112 dislocations through both the γ matrix and γ' particles on adjacent {111} planes.

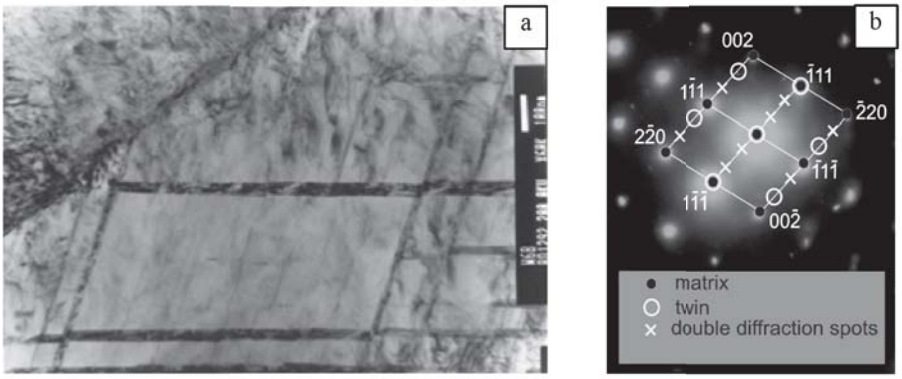

*Figure 10. Twins in specimen **W** creep ruptured at 750°C/675MPa, a) bright field image, beam direction ~(110), b) corresponding diffraction pattern with extra spots arising from twins.*

Eutectic regions

In the eutectic regions of the specimens creep deformed at 750°C, independent of the creep stage and stress applied, beside dislocations within γ channels and stacking faults, separate dislocations inside large γ' precipitates were observed (Figure 11). Similar observations were also made by Lukáš et al in eutectic areas of CM186LC creep deformed at 850°C [12]. It can be concluded that the deformation of large γ' particles in the eutectic areas takes place independent on the deformation in the dendritic regions. The easier formation of dislocations in eutectic γ' precipitates can be influenced by the weaker solution strengthening of γ', caused by differences in chemical composition between dendrites and eutectics.

In the eutectic areas of ruptured specimens, beside MC carbides, the precipitates of σ phase were found (Figure 12). The presence of brittle σ phase induces microcracks initiation, what results in the loss of ductility and decrease of creep strength, thus deteriorates the creep properties of CM186LC superalloy.

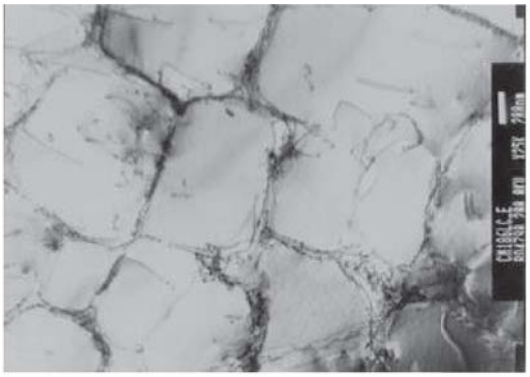

Figure 11. Dislocations in large γ' particles in the eutectic area of specimen **E**.

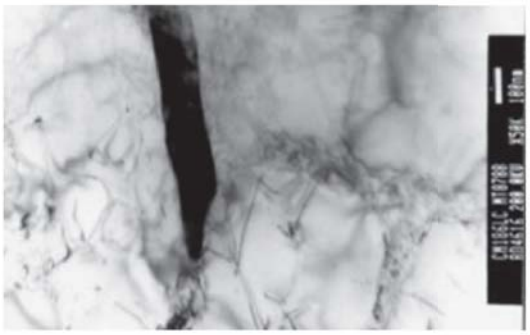

Figure 12. Precipitation of σ phase in eutectic area of specimen **N**.

Conclusions

1. The microstructure of CM186LC consists on dendritic regions and 20-25% volume fraction of eutectic colonies. This inhomogeneity influences the creep behaviour of the alloy.
2. At the primary creep stage at temperature 750ºC, shearing of γ' particles by intrinsic and extrinsic stacking faults formed inside dislocation ribbons occurred.
3. In the specimens terminated at the secondary creep stage, two slip systems of stacking faults ribbons and dislocation networks inside γ channels were formed.
4. After creep rupture at 750ºC and 675 MPa deformation twins cutting both γ and γ' phases were observed.
5. Independent deformation of large γ' particles in the eutectic areas is detrimental for creep properties of CM186LC.

Acknowledgements

The study was performed within COST522 and COST538 Actions. The co-operation of COST partners is gratefully acknowledged.
The authors from AGH University of Science and Technology gratefully acknowledge the support of the Ministry of Education and Science (project nr SPB_22.22.110.662). They also wish to thank their colleagues, A. Zielinska-Lipiec and J. Stepinski for their valuable contributions to the SEM investigations.

References

[1] B.B. Seth, Superalloys - the utility gas turbine perspective, in: Superalloys 2000, T.M Pollock et al (eds), TMS 2000, 3-16
[2] M. Toulios, D.H Allen, The mechanical behaviour of a class rhenium based SX superalloys for industrial gas turbine applications, Proceedings of 7th Int. Conf. on Materials for Advanced Power Engineering, 30.09-2.10.2002, Liége, Belgium, Lecomte-Beckers J. et al (eds), Schriften des Forschungszentrum Jülich, Energy Technology, 21, 2002, 5-21
[3] I.M. Wilcock, P. Lukáš, M. Maldini, J. Klabbers, B. Dubiel, M.B. Henderson, The creep behaviour of as-cast SX CM186LC at industrial gas turbine operating conditions, ibid, 21, 2002, 149-158
[4] B. Dubiel, A. Czyrska-Filemonowicz, Determination of Microstructural Parameters of CM186LC Nickel-Base Superalloy using Quantitative TEM Metalography Methods, Materials Chemistry and Physics, 81, 2003, 427-429
[5] D.H. Shah, S.Vega, S.Woodard, A.D. Cetel, Primary creep in nickel-base superalloys, in: Superalloys 2004, K.A. Green et al (eds), TMS 2004, 197-206
[6] G.R. Leverant, B.H. Kear, Metallurgical Transactions, 1, 1970, 491
[7] P. Caron, Y. Ohta, Y.G. Nakagawa, T. Khan, Creep deformation anisotropy in single crystal superalloys, in: Superalloys 1988, D.N. Duhl et al (eds), TMS 1998, 215-224
[8] N. Matan, D.C. Cox, P. Carter, M.A. Rist, C.M.F. Rae, R.C. Reed, Creep of CMSX-4 superalloy single crystals: effect of misorientation and temperature, Acta Materialia, 47, 1999, 1549-1563.
[9] T.M. Pollock, A.S. Argon, Creep resistance of CMSX-3 nickel- base superalloy single crystals, Acta Metallurgica et Materialia, 40, 1992, 1-30
[10] G.L. Drew, R.C. Reed, K. Kakehi, C.M.F. Rae, Single crystal superalloys: the transition from primary to secondary creep, in: Superalloys 2004, K.A. Green et al (eds), TMS 2004, 127-136
[11] D.M. Knowles, S. Gunturi, The role of <112>{111} slip in asymmetric nature of creep of single crystal superalloy CMSX-4, Materials Science and Engineering A, 328, 2002, 223-237
[12] P. Lukáš, J. Čadek, L. Kunz, M. Svoboda, J. Klusak, Creep resistance of single crystal superalloys CMSX-4 and CM186LC, Kovove Materialy-Metallic Materials, 43, 2005, 5-19

ATOM PROBE MICROANALYSIS OF FIFTH-GENERATION NICKEL-BASE SINGLE-CRYSTAL SUPERALLOYS

T. Kitashima, D.H. Ping, H. Harada and T. Kobayashi

High Temperature Materials Group,
National Institute for Material Science (NIMS)
1-2-1 Sengen, Tsukuba Science City, Ibaraki 305-0047, Japan
kitashima.tomonori@nims.go.jp

Abstract

The fifth-generation Ni-base single crystal superalloys containing Ruthenium or Iridium have been developed in National Institute for Materials Science (NIMS), Japan. The precipitation of topologically-closed-packed (TCP) phases in these superalloys was suppressed due to the Ru/Ir additions, resulting in the superior creep resistance. To determine the underlying mechanism of such improvement in phase stability in the atomic scale, the present article has investigated short-range ordering, the effects of Ru/Ir additions on elemental distributions in gamma phase by using 3-dimensional atom probe field-ion microscopy. The concentration frequencies of Re, W and Mo within Ru/Ir centered spheres including 100 atoms in gamma phases were analyzed statistically. The results showed that the concentration frequencies of Re, W and Mo within Ru/Ir centered spheres corresponded to binomial distributions. This indicated that the effects of Ru/Ir additions on elemental distributions in the gamma phase were not able to be detected so far under the condition employed in the present study.

Keywords: Nickel-base single-crystal superalloy, Ruthenium or Iridium addition, atom-probe field-ion microscopy, short-range ordering

Introduction

Ni-base single-crystal superalloys are used in the turbine blades of aero engines for superior creep resistance at high temperature. In recent years, the additional amount of Re in Ni-base single-crystal superalloys has been increased, resulting in improving the creep strength [1-3]. However, the excessive additional amount of Re acts as a trigger for the precipitation of TCP (Topologically-Closed-Packed) phase which is detrimental to the creep strength of Ni-base single-crystal superalloys.

In 1996, the improvement of the phase stability due to Ru addition in the 4th generation Ni-base single-crystal superalloys was reported by O'hara et al [4]. They showed that the addition of Ru to Ni-base superalloys caused elements to partition to the gamma phase or the gamma prime phase in a reverse direction that normally experienced in Ni-base superalloys, resulting in inhibiting the formation of undesirable TCP phase. However, Yokokawa et al.[5] reported that the suppression of TCP phase was not caused by the reverse partitioning behaviour of alloying additional elements to gamma/gamma prime phases due to Ru addition, but by the existence of Ru itself. In 1997, Kobayashi et al.[6] carried out creep tests to show that Ir addition instead of Ru addition also contributed to the phase stability.

Moreover, Yokokawa et al.[5] showed that not only Ru and Ir but also PGMs (Platinum Group Metals) suppress the precipitation of TCP phase. Volck et al.[7] and Reed et al.[8] demonstrated by atom-probe microanalysis that the reverse partitioning of elements due to Ru addition could not been confirmed. Few studies have been carried out on the atomic-scaled underlying mechanism of the phase stability due to PGMs addition. In this study, the following hypothesis was made for that mechanism.

It's thought that the atoms in the solid solution have short-range ordering to some extent[9]. The atomic radii of PGMs are large. Therefore, the strain field is locally formed around the lattice points of added PGM elements in gamma phase, as well as around those of Re, W and Mo, which are abundant in TCP phase. Each PGM element and Re, W and Mo migrates towards one another to first- or second-nearest neighbour lattice site in gamma phase to share the strain fields. These phenomena result in the low free energy of gamma phase and enlarging the solid solubility limit of Re, Mo and W. Therefore, the precipitation of TCP phase is suppressed due to PGMs additions.

In order to confirm the above hypothesis, short-range ordering and elemental distributions in gamma phase were estimated by three-dimensional atom-probe analysis. Moreover, there have been few reports about partitioning behaviour of substitutional alloying elements in fifth-generation Ni-base single crystal superalloys containing Ru or Ir. Therefore, that was also investigated in this study.

Materials and Experimental Procedure

The fifth-generation Ni-base single crystal superalloys TMS-173(Ir) and TMS-173(Ru), which were developed in National Institute for Materials Science (NIMS), were analysed in this study. The nominal compositions of TMS-173(Ir) and TMS-173(Ru) are shown in Table 1. The bar samples were cast into single crystal form by directional solidification with its longitudinal axis within 5 degree of <100>.

These samples were solution-heat treated for 1 hour at 1310°C for TMS-173(Ir) and 1300°C for TMS-173(Ru), and secondly for 10 hours at 1340°C for TMS-173(Ir) and 1330°C for TMS-173(Ru), and then air-cooled. They were followed by two aging heat treatments, the first at 1100 °C for 4 hours, the second at 870 °C for 20 hours. These heat treatment conditions are shown in table 2. Scanning electron micrographs of heat-treated (a)TMS-173(Ir) and (b)TMS-173(Ru) are shown in Figure 1. These photos proved that the heat-treated microstructures have a coherent gamma and gamma prime two phase structure.

Square rods of approximately 0.2mm×0.2mm ×10mm were cut out from the heat-treated bar samples. These rods were then electropolished to sharp needle-shape specimens with 25% perchloric acid and 75% acetic acid in first stage, and 2% perchloric acid in butoxyethanol in the second stage. Atom-probe analyses were performed at tip temperatures of about 65K under ultrahigh vacuum (<1×10-8Pa) with a pulse fraction of 0.2 and a pulse repetition rate of 1500Hz.

Alloy	Co	Cr	Mo	W	Al	Ta	Hf	Re	Ru	Ir	Ni
TMS-173(Ir)	6.09	3.45	1.87	1.95	13.38	1.98	0.04	2.38	0.0	3.18	Bal.
TMS-173(Ru)	6.09	3.45	1.87	1.95	13.38	1.98	0.04	2.38	3.18	0.0	Bal.

Table 1 Chemical compositions of TMS-173(Ir) and TMS-173(Ru) in atomic%.

TMS-173(Ir)	1310°C 1h → 1340°C 10h, Air cooling → 1100°C 4h, Air cooling → 870°C 20h, Air cooling
TMS-173(Ru)	1300°C 1h → 1330°C 10h, Air cooling → 1100°C 4h, Air cooling → 870°C 20h, Air cooling

Table 2 Heat treatment conditions of TMS-173(Ir) and TMS-173(Ru).

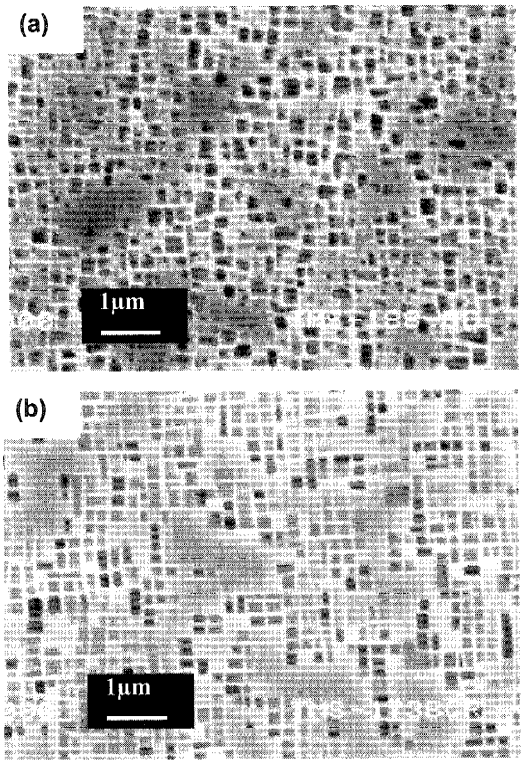

Fig. 1 SEM images of heat-treated (a)TMS-173(Ir) and (b)TMS-173(Ru).

Results and Discussion

Phase composition analysis of 5th generation Ni-base single-crystal superalloys

Murakami et al.[10] originally carried out the phase composition analysis of Ni-base single-crystal superalloys containing Ir by atom-probe field-ion microscopy. However, Re was not added into that alloy to analyze the effect of Ir addition of Re substitution. Then, Murakami et al.[11] investigated the partitioning behaviour of subsitutional alloying elements in Ni-base single-crystal superalloys containing both Ir and Re. They showed that Ir addition did not affect the partitioning behaviour of other alloying elements, and concluded the partitioning preferences of alloying elements as Re > Cr > (Mo, Ru, Co) > W > Ir.

On the other hand, several investigations have been conducted on the effect of Ru addition into Ni-base single-crystal superalloys. O'hara et al.[4] showed that the addition of Ru to Ni-base superalloys caused elements to partition to the gamma phase or the gamma prime phase in a reverse direction that normally experienced in Ni-base superalloys. However, Yokokawa et al.[5], Volek et al.[7] and Reed et al.[8] demonstrated experimentally that the reverse partitioning of elements due to Ru addition had not been confirmed.

In this study, the partitioning behaviours of alloying elements of 5th generation Ni-base single-crystal superalloys TMS-173(**Ir**) and TMS-173(**Ru**) were analyzed.

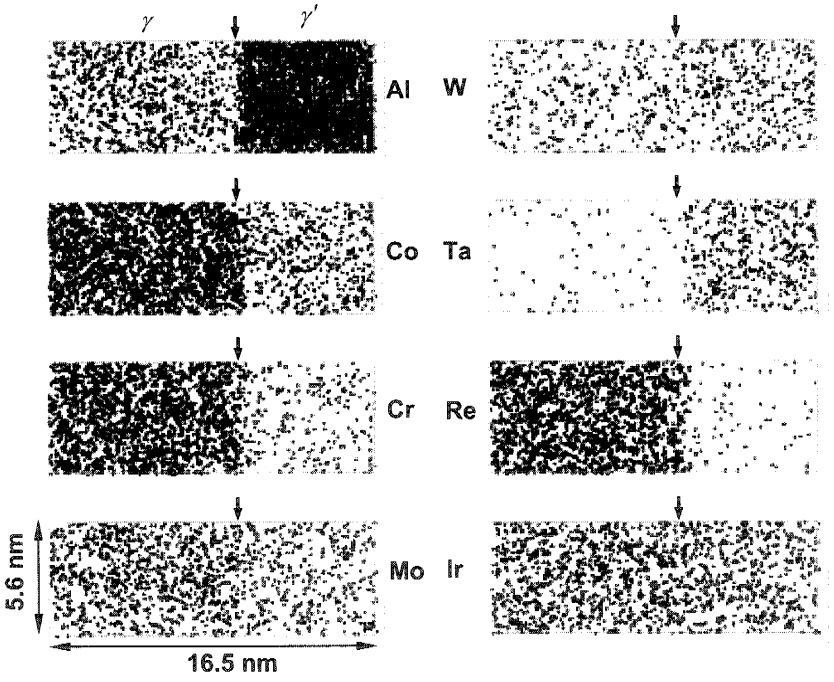

Fig. 2 3DAP elemental maps of Al, Co, Cr, Mo, W, Ta, Re and Ir through a γ/γ' phase of TMS-173(**Ir**).

Figure 2 shows the elemental maps of TMS-173(**Ir**) within the analysis volume containing the interface between the gamma and gamma prime phase. The size of this volume is 5.6nm×5.8mm ×16.5nm. The position of the interface between the gamma and gamma prime phase, which was determined by the change of the number density of Al atoms between gamma/gamma prime phase, is shown in Figure 2. Both Al and Ta are abundant in the gamma prime phase. On the other hand, Co, Cr and Re are enriched in the gamma phase. The concentration profiles across the interface determined from this selected region are shown in Figure 3. From the arrangement of Al atoms in gamma prime phase in Fig. 2, it was found that Al atomic layers were almost parallel to the interface between the gamma and gamma prime phase. Therefore, Al composition profile in gamma prime phase in Fig. 3 oscillated widely by 20 %, and the Al composition at each layer was large.

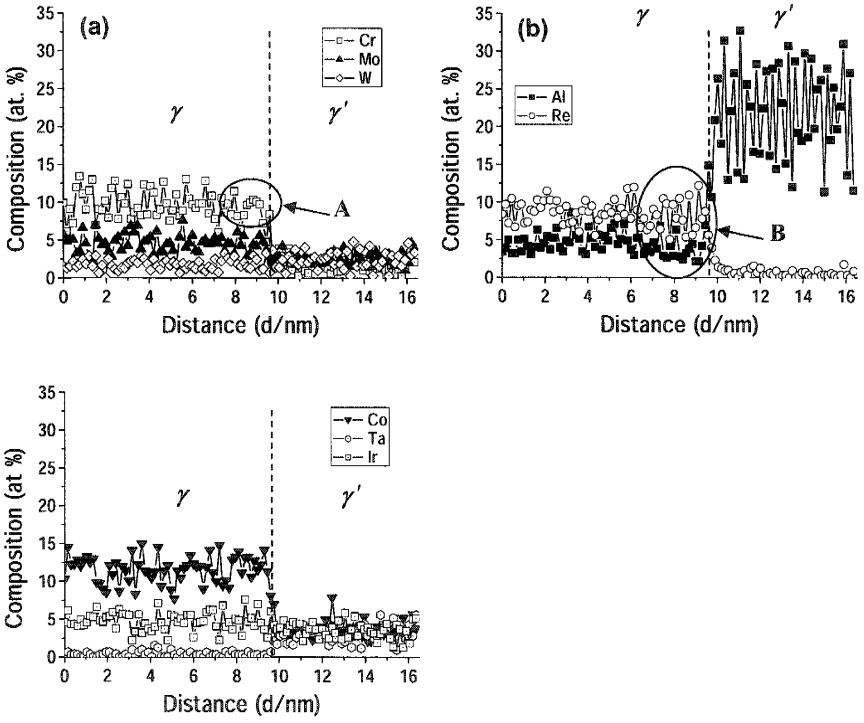

Fig. 3 Concentration profiles of (a)Cr, Mo, W, (b)Al, Re, (c)Co, Ta and Ir across the γ/γ' phase calculated from the elemental maps of Fig. 2 [TMS-173(Ir)].

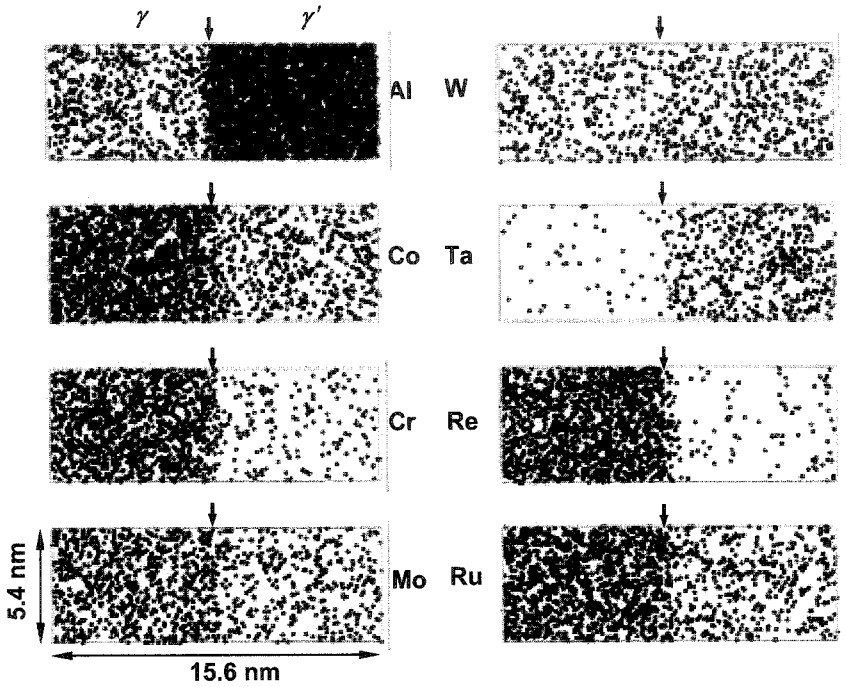

Fig. 4 3DAP elemental maps of of TMS-173(**Ru**).

In gamma phase near the gamma/gamma prime interface, the amplitude of Cr composition is small as shown by an arrow A in Fig. 3. The amplitude of Re composition is large between the interface and the region about 3 nm away from the interface as shown by an arrow B in Fig. 3. There has been reported that the amplitude of Cr composition in gamma phase near the interface is small[12], and that Re tends to segregated at the interface[13]. However, few studies have been reported about the oscillation of Re composition at the interface. The mechanism of that oscillation has not been clarified in this study yet.

The elemental maps of TMS-173(**Ru**) within the analysis volume containing the interface between the gamma and gamma prime phase is shown in Figure 4. The composition profiles of elements in that selected volume is shown in Figure 5. The size of this volume is 5.4nm × 5.2mm × 15.6nm. The tendency of partitioning behaviour of alloying elements in TMS-173(**Ru**) is similar to those in TMS-173(**Ir**) except for PGMs i.e. Ir and Ru. Ru is abundant in gamma phase compared to Ir in gamma phase.

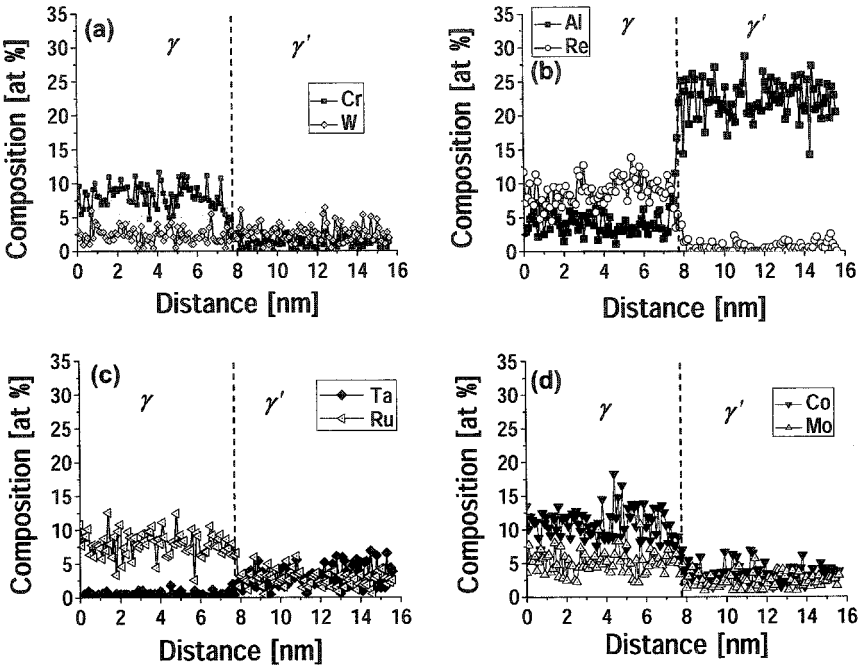

Fig. 5 Concentration profiles of (a)Cr, W, (b)Al, Re, (c) Ta, Ru, (d)Co and Mo across the γ/γ' phase calculated from the elemental maps of Fig. 4 [TMS-173(Ru)].

The partitioning behaviour of alloying elements in TMS-173(**Ir**) and TMS-173(**Ru**) were compared with TMS-80 and TMS-91 which were developed in late 1990's in NIMS, Japan, as shown in Figure 6. TMS-80 does not contain Ru but 1.0at%Ir. On the other hand, TMS-91 does not contain Ir but 0.9at%Ru. The nominal compositions of TMS-80 and TMS-91 are shown in Table 3. From fig. 6, recent fifth-generation superalloys TMS-173(**Ir**) and TMS-173(**Ru**) tend to have the larger absolute values of partitioning coefficients of Al, Co, Cr, Ta and Re compared to those in TMS-80 and TMS-91. Moreover, W in TMS-173(**Ir**) and TMS-173(**Ru**) slightly prefers to partition into gamma prime phases, while Ir in TMS-173(**Ir**) is slightly abundant in gamma phase contrary to the gamma prime phases in TMS-80. These differences are mainly attributed to the differences of the additional amounts of Re and Co, which have strong partitioning preferences to gamma phase[11].

Short-range ordering and elemental distributions around Ru and Ir in gamma phase

The precipitation of TCP phase was suppressed due to Ru or Ir addition. However, few studies have been reported about that underlying mechanism in atomic scale. In order to clarify the effect of Ru and Ir additions on the atomic configuration, the short-range ordering in gamma phase was investigated.

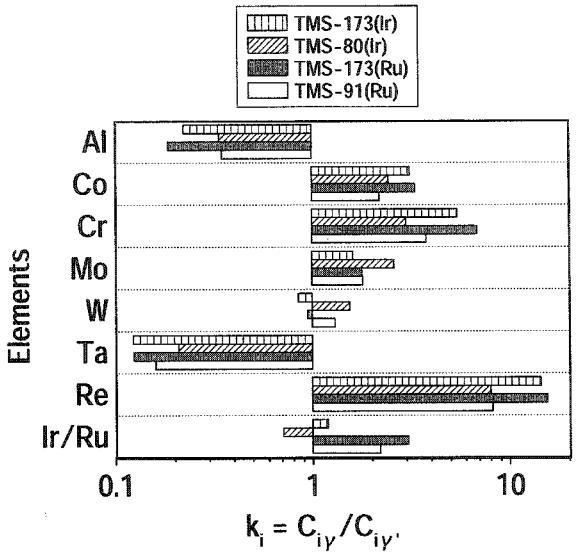

Fig. 6 Partitioning coefficients of TMS-173(Ir), TMS-173(Ru), TMS-80[11] and TMS-91[11].

Alloy	Co	Cr	Mo	W	Al	Ta	Re	Ru	Ir	Ni
TMS-80	12.4	3.5	1.3	2.0	13.6	2.0	1.7	0.0	1.0	Bal.
TMS-91	12.3	3.5	1.2	1.95	13.3	2.0	1.6	0.9	0.0	Bal.

Table 3 Chemical compositions of TMS-80[11] and TMS-91[11] in atomic%.

To clarify the short-range ordering in the disordered phase, use of the radial distribution function is helpful. By using that function, the existing probability of elements around particular element in the phase can be estimated. The radial distribution function is defined as follows;

$$g(r) = \frac{N(r,\Delta r)}{\frac{1}{2}N\rho V(r,\Delta r)} \quad (1)$$

where $N(r,\Delta r)$ is the total number of the specified element pair of which one element is at the center of the sphere, and the other is within the spherical shell between the radius of $r-\Delta r/2$ and $r+\Delta r/2$ as shown in Figure 7, N is the total number of the atoms of the specified element, ρ is the number density of phase,

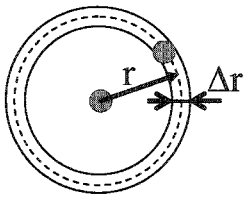

Fig. 7 Schematic of the specified element pair

and

$$V(r,\Delta r)=\int_{-\Delta r/2}^{r+\Delta r/2}4\pi r^2 dr=4\pi r^2\Delta r+\frac{1}{3}\pi(\Delta r)^3. \quad (2)$$

The lattice parameter of Ni-base single-crystal superalloys is about 0.36nm[14]. Therefore, the radial distribution function of the pair Ni-Ni in the face-centered-cubic structure can be predicted from the equation (1), (2) as shown in Figure 8. That calculation was performed within the sphere of the radius 0.5nm around each Ni atom. The positions of peaks can be confirmed at about 0.26, 0.36 and 0.44 nm in Fig. 8(a).

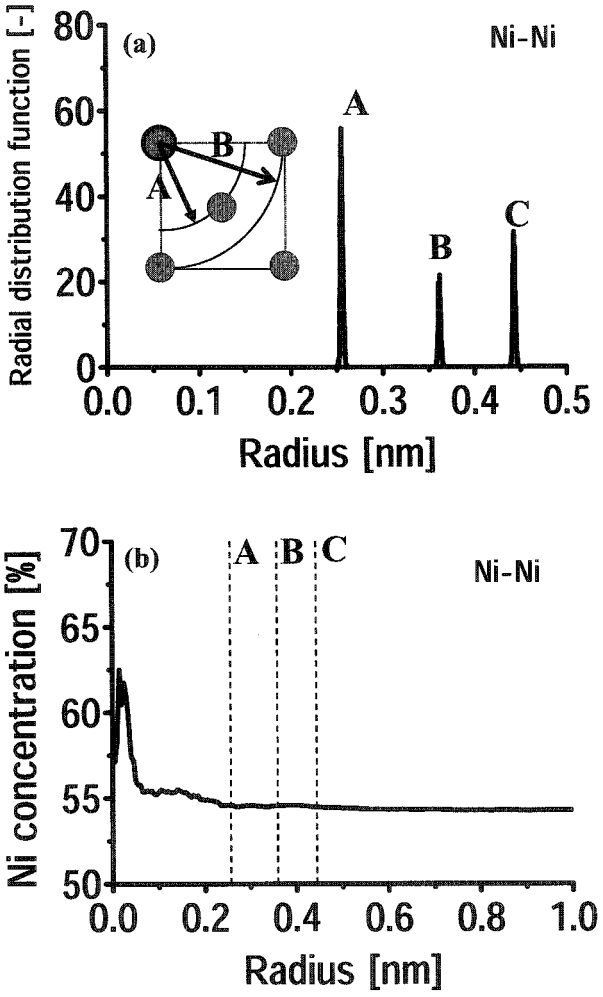

Fig. 8(a) Calculated radial distribution function of Ni-Ni in the face-centered-cubic structure which lattice parameter is 0.36nm. (b) Radial concentration distribution of Ni-Ni, which was calculated by using atom-probe data.

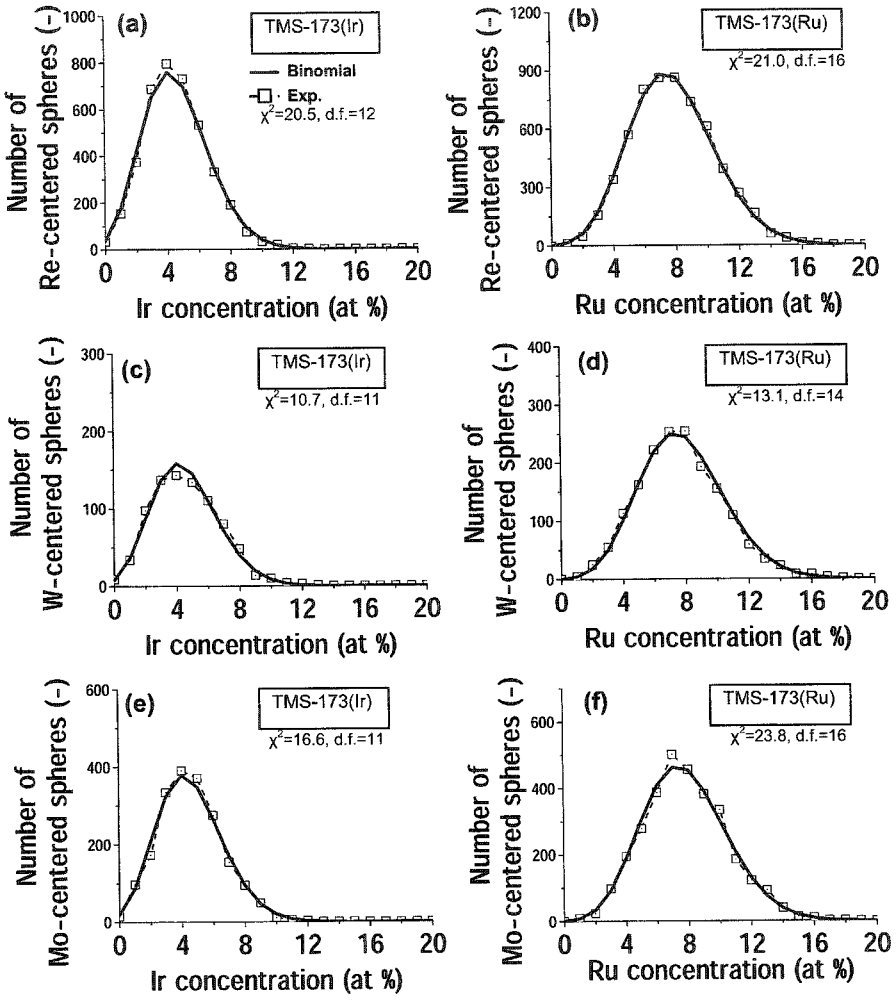

Fig. 9 Frequencies of Ir concentration within (a)Re-, (c)W- and (e)Mo-centered spheres including 100 atoms in a γ phase of TMS-173(Ir). Frequencies of Ru concentration within (b)Re-, (d)W- and (f)Mo-centered spheres including 100 atoms in one γ phase in TMS-173(Ru).

The radial concentration distribution of Ni in the experimentally detected atom-probe structure were also calculated as shown in Fig. 8(b). The positions of the peaks in Fig. 8(a) was shown by A, B and C in Fig. 8(b). Then, the positions of the peaks were compared between Fig. 8(a) and Fig. 8(b). As a result of that, only one peak was confirmed in Fig. 8(b). Moreover, the position of that peak is about 0.02nm, which is far away from A, B and C. From this result, it's difficult to estimate the distance difference between the first-nearest-neighbour lattice point and the second-nearest-neighbour lattice point in the detected structure because the subnanometer lateral resolution of atom-probe analysis largely affects the reconstruction of detected atom.

As the next step to find the effect of Ru or Ir addition on the phase stability in atomic scale, elemental distributions around Ru and Ir in gamma phase were estimated statistically. There has been reported that Re, W and Mo are abundant in the TCP phase[15]. Therefore, Re, W and Mo distributions around Ru and Ir in gamma phase were focused in this study. The concentration frequency distributions of Re, W and Mo within Ru/Ir centered spheres including 100 atoms in gamma phases were analyzed. Those distributions were compared with the binomial distributions. When the concentration frequency distribution corresponds to the binomial distribution, the elements are distributed randomly. The expected number of blocks with i solute atoms, F(i) (the binomial distribution), is defined as follows[16];

$$F(i) = N_A \frac{100!}{i!(100-i)!} f_A^i (1-f_A)^{100-i} \quad (3)$$

where N_A is the total number of element A (such as Re, Mo or W) -centered sphere including 100 atoms. f_A is the nominal composition of element A.

The hypothesis that there is no interaction between the atoms was tested with the use of a chi-squared statistical test, which is defined as[16];

$$\chi^2 = \sum_{i=0}^{n'-1} \frac{(O(i)-E(i))^2}{E(i)} \quad (4)$$

where E(i) is the expected number of observations of a class, O(i) is the experimentally observed number of occurrences of a class, and n' is the number of classes $n' \leq 99$. The sizes of the analysed regions in gamma phase are 8.2nm×9.6mm ×14.7nm for TMS-173(Ir) and 13.3nm×13.1mm ×10.5nm for TMS-173(Ru), respectively. The concentration frequency distributions of Re, W and Mo around Ru and Ir in gamma phase, and binomial distributions F(i) are shown in Figure 9. The values of chi-square and the degree of freedom are also shown in Fig. 9. From the values of chi-square, the experimental results correspond to the binomial distribution with probability 99.99%. It indicated that the elements in gamma phase are distributed randomly. As the results of this study, the effects of Ru/Ir additions on elemental distributions in the gamma phase were not able to be detected under the present condition that the size of each observation block is 100 atoms. However, use of the size of the smaller observation block to analyze the smaller region, such as 30 or 50 atoms, makes lager statistical errors [16]. Therefore, it's necessary to use the different analytical method, such as Extended X-ray Absorption Fine Structure (EXAFS), for further investigations of short-range ordering in gamma phase which may cause the improvement in the phase stability in atomic scale.

Conclusion

Three-dimensional atom-probe microanalysis was carried out to estimate partitioning behaviours of alloying elements of fifth-generation Ni-base single crystal superalloys TMS-173(Ir) and TMS-173(Ru), short-range ordering and elemental distributions in the gamma phase of TMS-173(Ir) and TMS-173(Ru). The conclusions are as follows;

1. TMS-173(**Ir**) and TMS-173(**Ru**) tend to have the larger absolute values of partitioning coefficients of Al, Co, Cr, Ta and Re compared to TMS-80 and TMS-91.
2. W in TMS-173(**Ir**) and TMS-173(**Ru**) slightly prefers to partition into gamma prime phase, while Ir in TMS-173(**Ir**) is slightly abundant in gamma phase.
3. The effects of Ru/Ir additions on elemental distributions in the gamma phase were not able to be detected so far under the condition employed in the present study.

Acknowlegdgments

The authors thank Dr. Y. Koizumi, Dr. M. Osawa, Dr. Yeh An-Chou, Dr. T. Murakumo for experimental assistance and discussing the results.

References

[1] J. X. Zhang, T. Murakumo, Y. Koizumi, T. Kobayashi, H. Harada and S. Masaki Jr., *Metallurgical and Materials transactions A*, **33A** (2002) 3741-3746.
[2] Y. Koizumi, T. Kobayashi, T. Yokokawa, J. X. Zhang, M. Osawa, H. Harada, Y. Aoki and M. Arai, *Superalloys 2004*, (Warrendale, PA, USA, Minerals, Metals and Materials Soc., 2004), pp.35-43.
[3] T. Kobayashi, Y. Koizumi, H. Harada, T. Yokokawa, J. X. Zhang, Atsushi Sato and Akihiro Sato, *J. Japan Inst. Metals*, **69** (2005) 241-244.
[4] K. S. O'hara W. S. Walston, E. W. Ross and R. Darolia, "Nickel Base Superalloy and Article", U. S. Patent 5,482,789A (1996).
[5] T. Yokokawa, M. Osawa, K. NishidaT. Kobayashi, Y. Koizumi, H. Harada, *Scripta Materialia*, **49** (2003) 1041-1046.
[6] T. Kobayashi, Y. Koizumi, S. Nakazawa, T. Yamagata and H. Harada, *4rd International Charles Parsons Turbine Conference Materials Engineering in Turbines and Compressors*, (The Institute of Materials, 1997), pp.766-773.
[7] A. Volek, F. Pyczak, R.F. Singer, H. Mughrabi, *Scripta Materialia*, **52** (2005) 141-145.
[8] R.C. Reed, A.C. Yeh, S. Tin, S.S. Babu, M.K. Miller, *Scripta Materialia*, **51** (2004) 327-331.
[9] Tomonori Kitashima, De-Hai Ping, Hiroshi Harada, Toshiharu Kobayashi, *J. Japan Inst. Metals*, (2006) **in press**.
[10] Murakami, Y. Koizumi, T. Yokokawa, Y. Yamabe-Mitarai, T. Yamagata, H. Harada: *Materials Science and Engineering*, **A250** (1998) 109-114.
[11] H. Murakami, T. Honma, Y. Koizumi and H. Harada, *Superalloys 2000*, (Warrendale, PA, USA, Minerals, Metals and Materials Soc., 2000), pp.747-756.
[12] D. Blabette, P. Caron and T. Khan, *Superalloys 1998*, (Warrendale, PA, USA, Minerals, Metals and Materials Soc., 1998), pp.305-314.
[13] H. Murakami, P.J. Warren and H. Harada, *3rd International Charles Parsons Turbine Conference Materials Engineering in Turbines and Compressors*, (The Institute of Materials, 1995), pp.343-350.
[14] Tadaharu Yokokawa, Katsumi Ohno, Hideyuki Murakami, Toshiharu Kobayashi, Yoshihiro Yamagata and Hiroshi Harada, *Advances in X-Ray Analysis*, **39** (1997) 449-456.
[15] Atsushi Sato, Hiroshi Harada, Tadaharu Yokokawa, Takuro Murakumo, Yutaka Koizumi, Toshiharu Kobayashi and Hachiro Imai, *Scripta Materialia*, **in press**.
[16] M.K. Miller, A. Cerezo, M.G. Hetherington, G. D.W. Smith, *Atom Probe Field Ion Microscopy*, (Clarendon press, Oxford, 1996).

MICROSTRUCTURAL STABILITY OF CMSX-4 AND CMSX-10 UNDER HIGH TEMPERATURE CREEP CONDITIONS

A. Epishin[1], T. Link[1], U. Brückner[2]

[1]Technical University Berlin, Berlin, Germany
[2]Federal Institute for Materials Research and Testing, Berlin, Germany
e-mail: alex_epishin@yahoo.de

Abstract

The structural stability of the nickel-base superalloys CMSX-4 and CMSX-10 during creep at 1100°C was investigated by scanning electron microscopy, X-ray diffraction and transmission electron microscopy. The microstructural processes responsible for the deformation behaviour of these superalloys were identified. In CMSX-4 the γ/γ'-microstructure rapidly takes a stable rafted morphology and then slowly coarsens during the creep process, therefore this superalloy shows a creep curve with extended slow secondary creep. In CMSX-10 the γ/γ'-microstructure becomes rafted after a delay and forms short unstable rafts, which results in an incubation before primary creep followed by a monotonically accelerating deformation. In spite of the lower structural stability CMSX-10 shows a lifetime nearly two times longer than CMSX-4 because of a much longer tertiary creep. This effect is caused by a more effective solid solution hardening of the γ-phase because of the two times higher concentration of rhenium in CMSX-10.

Keywords: superalloys, CMSX-4, CMSX-10, creep, microstructure

Introduction

For high temperature alloys stability of the microstructure is an important factor determining the mechanical properties under service conditions. Therefore the microstructural stability has to be investigated to predict the mechanical behaviour and to model it with sufficient reliability. The microstructure of single-crystal (SC) nickel-base superalloys consists of two phases: the γ-matrix hardened by small cuboidal precipitates of γ'-phase. Under high temperature creep conditions the γ/γ'-microstructure first becomes rafted, then slowly coarsens and becomes irregular. In superalloys with a high concentration of refractory elements additionally topologically closed packed (TCP) phases precipitate in the dendrite arms. Coarsening of the γ/γ'-microstructure and precipitation of the TCP phases result in the deterioration of the mechanical properties of superalloys. In the work presented the above microstructural processes were investigated in two SC superalloys, CMSX-4 and CMSX-10, creep deformed at 1100°C. The results show a clear correlation between the kinetics of microstructure evolution and the kinetics of creep deformation. Comparison of CMSX-10 (6 wt% Re) with its direct predecessor CMSX-4 (3 wt% Re) allows to understand the effect of rhenium on the mechanical and structural behaviour of modern nickel-base superalloys.

Experimental

SC bars of CMSX-4 and CMSX-10 (see composition in Table 1) with axial orientation close to [001] were solidified by Doncasters Precision Castings (DPC), Bochum, Germany. The bars were standard heat treated, CMSX-4 by DPC, CMSX-10 by Cannon&Muskegon, Muskegon, USA. Cylindrical specimens with gauge length 60 mm and diameter 6 mm were machined from these bars and tested for creep at 1100°C, 120 MPa in a constant load testing

machine. Creep tests were performed for different times to obtain the microstructures corresponding to the characteristic stages of the creep process: CMSX-4 for 4 h, 25 h, 75 h, 150 h, 292 h and until rupture at 393 h[1] and 692 h[1]; CMSX-10 for 25 h, 60 h, 200 h, 330 h and until rupture at 552 h. To check the influence of the TCP phases on creep lifetime a specimen of CMSX-4 and one of CMSX-10 were pre-annealed at 1100°C for 500 h (to precipitate TCP phases) and then tested for creep at 1100°C, 120 MPa until rupture. The microstructural changes during creep deformation were investigated by scanning electron microscopy (SEM), evolution of the γ/γ'-interface by X-ray diffraction (XRD) and transmission electron microscopy (TEM). Loss of the interface coherency was characterised by the change of γ/γ'-misfit measured by XRD. Detailed analysis of the interfacial dislocation networks was performed in TEM. Care was taken to identify the area in the dendritic structure, i.e. the primary dendrite arm (PDA), the secondary dendrite arm (SDA) and the interdendritic region (IR), before analysing it by SEM, XRD and TEM. To allow the positioning of the SEM frame and the X-ray spot at these defined areas the specimens were cut along planes deviating from the PDA axis by a few degrees, a method described in [1, 2].

Table 1. Compositions of investigated superalloys according to certificate (in wt%).

Alloy	Al	Ti	Cr	Co	Ni	Mo	Hf	Ta	W	Re
CMSX-4	5.7	1.0	6.5	9.7	Base	0.6	0.1	6.5	6.4	3.0
CMSX-10	5.6	0.2	2.3	3.3	Base	0.4	0.02	8.3	5.5	6.3

Results

Creep curves. The creep behaviour of CMSX-4 and CMSX-10 at 1100°C, 120 MPa up to 300 h is compared in Fig. 1. CMSX-4 shows the classical creep behaviour: fast primary creep starting immediately after loading, followed by extended secondary creep with slow nearly constant creep rate, which transits into accelerated creep after about 60% of lifetime. The creep behaviour of CMSX-10 is more complex. Creep starts with a very fast and short plastic deformation with a strain smaller than 0.1% and a duration of about 1 h, then the creep process slows down but after about 30 h it accelerates again.
The following secondary creep is remarkably shorter and faster than in CMSX-4: deformation starts to accelerate already after about 35% of lifetime. However at given testing conditions CMSX-10 shows a lifetime nearly two time longer than CMSX-4. The reason is, that the creep acceleration during tertiary stage is much slower in CMSX-10, thus reaching the rupture strain later. A similar difference in creep behaviour was found in [3] for the superalloys AM1 (no rhenium) and MC-NG (4 wt.% rhenium) at 1050°C and 150 MPa. Moreover the rupture strain of the CMSX-10 specimen is larger than for CMSX-4, which fits with the observation, that CMSX-4 shows a very localized necking in the rupture zone, while the cross section reduction in CMSX-10 is homogeneous.
Pre-annealed specimens of CMSX-4 and CMSX-10 showed remarkably smaller primary creep strain and shorter lifetimes than after standard heat treatment (see Fig. 2). The relative reduction of lifetime was found to be higher for CMSX-4 (about 42%) than for CMSX-10 (about 30%).
SEM. Kinetics of the morphological transformation of the γ/γ'-microstructure of CMSX-4 and CMSX-10 during creep is shown in Fig. 3. After standard heat treatment the initial

[1] These 2 ruptured specimens were tested at 117 MPa and 105 MPa respectively, all others at 120 MPa.

microstructure in CMSX-10 is much finer than in CMSX-4. Within the first 25 h the microstructure in CMSX-4 rapidly becomes rafted, while in CMSX-10 it remains still cuboidal. Rafts in CMSX-4 are regular, long and stable (see Fig. 3, 25 h and 150 h), in CMSX-10 they are irregular and short (Fig. 3, 200 h). In both superalloys TCP phases precipitate after long-term creep (see Fig. 3, 393 h for CMSX-4 and 552 h in CMSX-10), but their morphology is different: in CMSX-4 globular, in CMSX-10 elongated. In the (010) longitudinal sections of CMSX-10 the TCPs are visible as fine lines close to $[101]$ and $[10\bar{1}]$ directions, which means that they are thin plates (thickness about 0.5 μm) with orientation close to {111}.

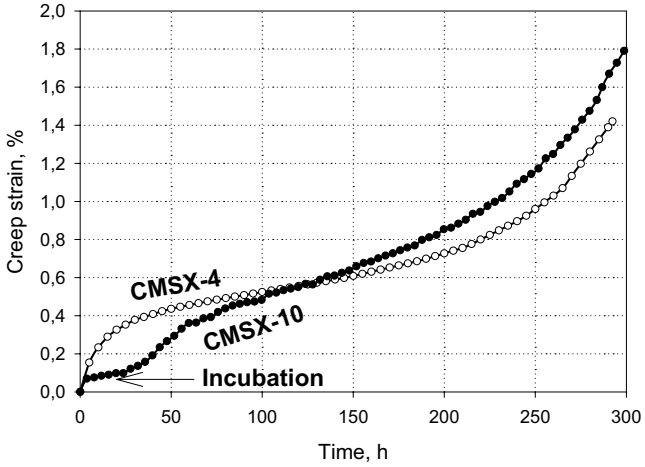

Fig. 1. Creep curves of CMSX-4 and CMSX-10 at 1100°C, 120 MPa. Both tests were interrupted. Under these testing conditions lifetime of CMSX-4 is about 335 h, of CMSX-10 about 575 h.

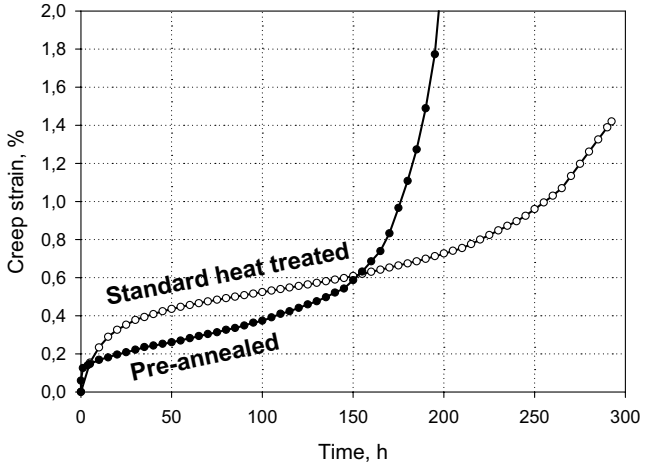

Fig. 2. Creep curves of CMSX-4 at 1100°C. Two material conditions: after standard heat treatment and pre-annealed at 1100°C for 500 h.

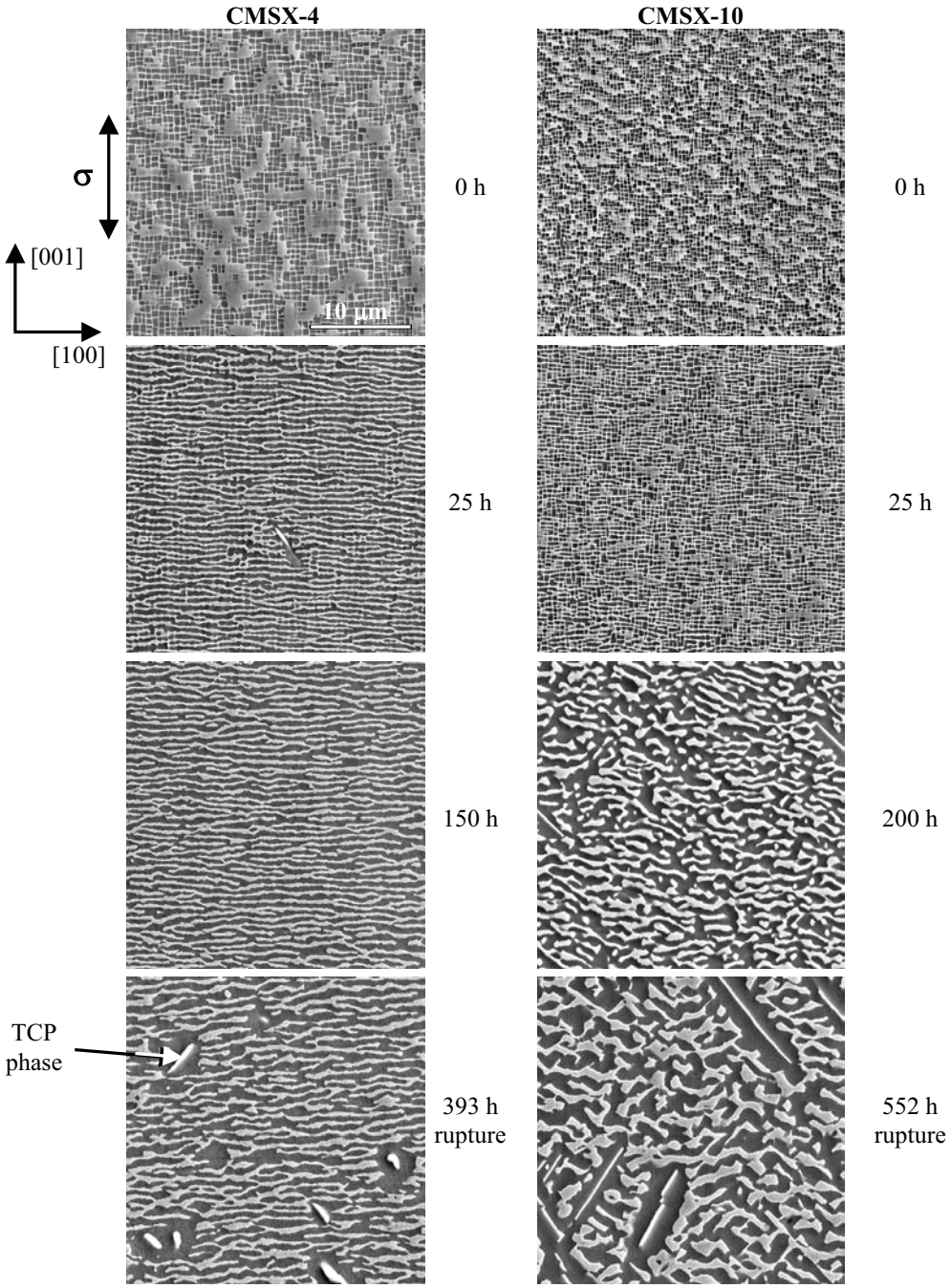

Fig. 3. Change of the γ/γ'-morphology in CMSX-4 and CMSX-10 during creep at 1100°C, 120 MPa. (The ruptured CMSX-4 specimen was tested at 117 MPa). All images are taken at the same magnification in the SDA. γ'-phase is dark.

The TCP precipitates are surrounded by a γ'-halo because during growth they absorb the γ-forming elements rhenium, tungsten, cobalt and chromium [4] from the surrounding, which results in a γ→γ' phase transformation around the TCP precipitates.
Coarsening of the γ/γ'-microstructure was characterized by the increase of the structure period λ in load direction [001]. For cuboidal γ'-morphology λ is the sum of the γ-channel width and the γ'-cube edge length, for rafted morphology the sum of the widths of the γ- and γ'-lamellae. λ was measured by Fourier analysis of SEM images as described in [5]. The results are presented in Fig. 4 and Table 2. They show that the rate of microstructure coarsening $d\lambda/dt$ measured in the SDA, which represents most of the material, is about 2.9 times higher in CMSX-10 than in CMSX-4. This ratio is nearly the same as the ratio 2.6 between the minimal creep rates for these alloys (see Table 2). This result fits with [5], where it was found that $\dot{\varepsilon} \sim d\lambda/dt$ for exponential-like creep curves of the SC superalloy SRR99 at 980°C, 200 MPa.

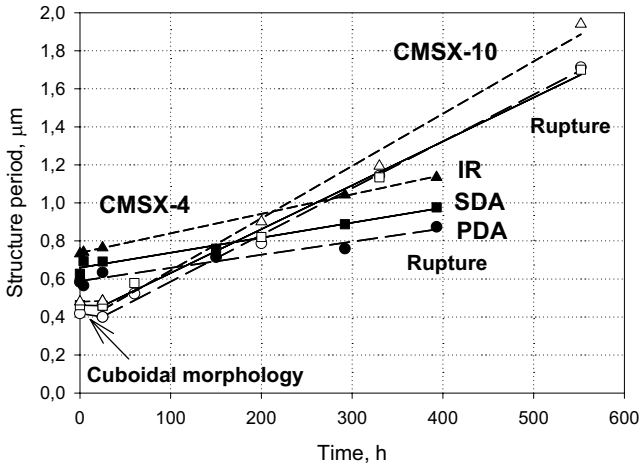

Fig. 4. Kinetics of the coarsening of the γ/γ'-microstructure during creep at 1100°C, 120 MPa. Black symbols: CMSX-4, white symbols: CMSX-10. Circles and long-dashed lines: PDA; squares and solid lines: SDA; triangles and short-dashed lines: IR. The ruptured CMSX-4 specimen was tested at 117 MPa.

The amount of the TCP phases was characterized by the precipitate area fraction A measured in backscatter electron images with an area of 46×46 µm^2 taken in the central parts of PDA and SDA. SEM results for the kinetics of the TCP precipitation are presented in Fig. 5 and Table 2. During precipitation the rate dA/dt is nearly constant. In CMSX-4 the TCP precipitation reaches saturation after about 400 h[2], while in CMSX-10 saturation is not attained within the investigated time interval, probably reaching saturation after 552 h. dA/dt is about three times higher in the PDA than in the SDA, obviously because of a higher level of the refractory elements. No TCP phases were observed in the IR. The difference in the precipitation rates between CMSX-4 and CMSX-10 was found to be small.

[2] Precipitation kinetics in CMSX-4 (monotonic growth followed by saturation) is in accordance with classical kinetics of phase precipitation in solid state [6].

Fig. 5 shows that after exposure at 1100°C for about 500 h the TCP volume fractions in CMSX-4 and CMSX-10 are nearly equal, however the relative reduction of the lifetime after pre-annealing 1100°C/500 h was found to be higher for CMSX-4 (about 42%) than for CMSX-10 (about 30%). One reason could be that the morphologies of the TCP phases forming in these alloys are different. According to [7] the elongated TCP morphology is less detrimental for the mechanical properties than the globular shape, probably due to a better cohesion with the matrix and a reinforcing effect. A second reason could be the different γ'-morphologies. It was found in [8] that after annealing at 1100°C for 300 h the γ/γ'-microstructure in CMSX-4 is completely rafted but with different raft orientations in the PDA, SDA and IR. In CMSX-10 however the γ'-morphology is still cuboidal except for a slight rafting in the PDA. Third, the reduction of rhenium in the matrix by TCP precipitation should weaken more strongly the solid solution hardening effect in CMSX-4, because both alloys have the same amount of TCP precipitates, but CMSX-4 contains half as much rhenium as CMSX-10.

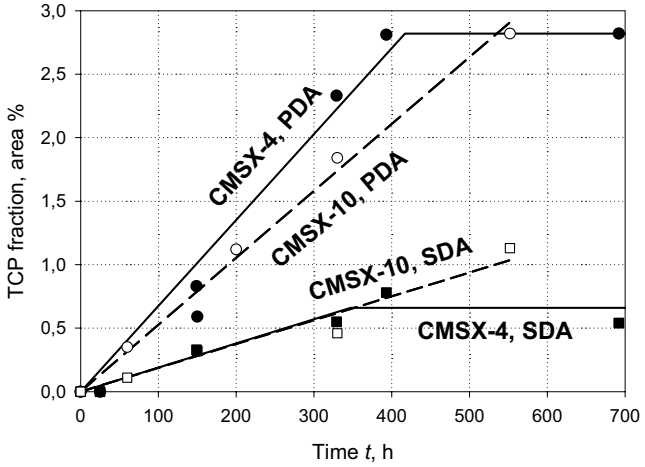

Fig. 5. Kinetics of the TCP precipitation in PDA and SDA during creep at 1100°C, 120 MPa. Black symbols and solid lines: CMSX-4, white symbols and dashed lines: CMSX-10. Circles: PDA; squares: SDA. The last two points for CMSX-4 at 393 h and 692 h were measured in specimens tested at 117 MPa and 105 MPa respectively.

XRD. Fig. 6 shows the kinetics of misfit change in CMSX-4 and CMSX-10 during creep measured by XRD. This constrained misfit δ is measured on lattice planes, which are perpendicular to the γ/γ'-interface, therefore δ is zero as long as the interface is fully coherent. In CMSX-4 the misfit deviates from the zero level indicating the loss of coherency of the γ/γ'-interface almost immediately after loading. Already after 4 h primary creep the X-ray reflections measured in the PDA and SDA show a pronounced asymmetry, giving misfit values of about -0.14% and -0.11% respectively. In the IR the X-ray reflection is symmetrical meaning that the phases are still coherent. After 100-150 h, which is the middle of steady creep, $|\delta|$ in the PDA and SDA reaches a maximum. At this time the difference in misfit between PDA (–0.34%), SDA (–0.31%) and IR (–0.26%) is the most pronounced. The absolute values decrease from PDA to IR as for the unconstrained misfit in undeformed

CMSX-4 at room temperature (RT) given in Table 2[3]. It is remarkable that the maximum of $|\delta|$, which means according to the Brooks formula the highest density of interfacial networks, corresponds to the minimal creep rate (see Fig. 6a and b). During further creep deformation $|\delta|$ in PDA and SDA becomes smaller which indicates a relaxation process resulting in a decrease of the dislocation density in the γ/γ'-interface.

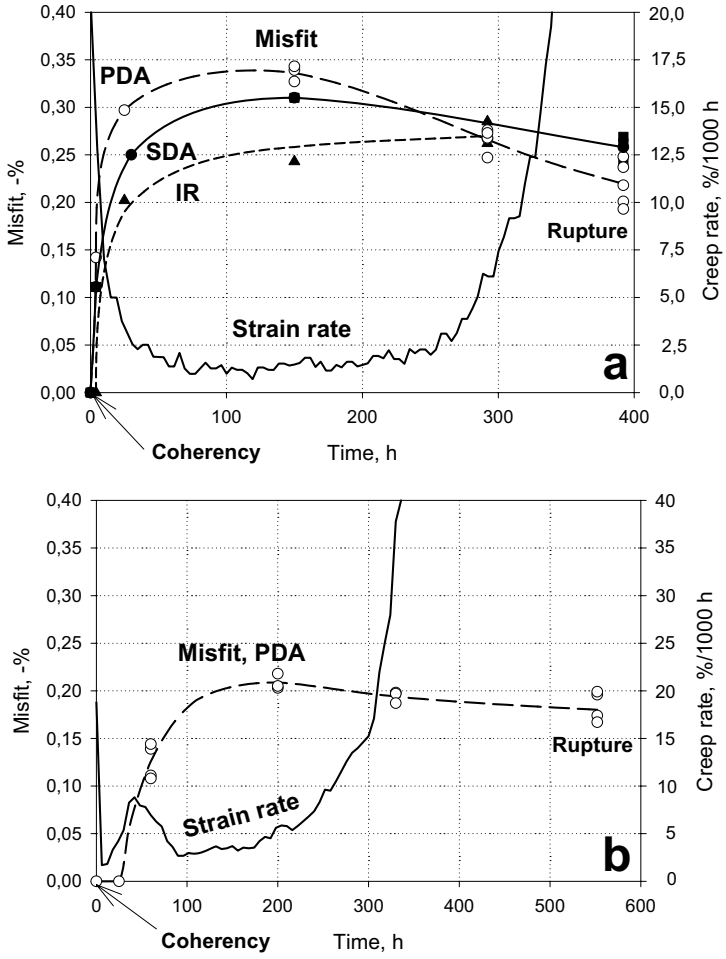

Fig. 6. Misfit change during creep at 1100°C and 120 MPa in comparison with the strain rate for CMSX-4 (a) and CMSX-10 (b). White circles and long-dashed lines: PDA; black squares and solid lines: SDA; black triangles and short-dashed lined: IR.
Last points for CMSX-4 at 393 h were measured in a specimen tested at 117 MPa.

[3] The constrained misfit in undeformed CMSX-4 and CMSX-10 was measured by XRD in [1] and [8] respectively. The unconstrained misfit one gets by dividing the constrained misfit by the factor 2.3 [9], considering the coherency strains of the γ-lattice.

Table 2. Minimum creep rate, γ/γ'-coarsening rate, TCP precipitation rate and unconstrained misfit measured separately in PDA, SDA and IR.

Superalloy	Minimal creep rate $\dot{\varepsilon}_{min}$, %/1000 h	Position in dendritic structure	γ/γ'-coarsening rate $d\lambda/dt$, μm/1000 h	TCP precipitation rate dA/dt, area %/1000 h	Unconstrained γ/γ'-misfit δ_{un} at RT, %
CMSX-4	1.2	**PDA**	0.69	6.8	-0.17
		SDA	0.79	1.9	-0.13
		IR	1.02	0	+0.02
CMSX-10	3.1	**PDA**	2.46	5.3	-0.04
		SDA	2.31	1.9	≈0
		IR	2.75	0	+0.03

After about 300 h the misfit scatters strongly exceeding the misfit difference between PDA, SDA and IR. Such kinetics of the misfit change (fast increase, followed by slow decrease) fits with the results of TEM measurements regarding the dislocation spacing in interfacial networks for the superalloy NASAIR 100 crept at 1000°C and 207 MPa [10].

In CMSX-10 the misfit change was investigated in the PDA only. Similar kinetics was found as in the PDA and SDA of CMSX-4. However the maximal absolute misfit in the PDA of CMSX-10 is remarkably smaller than in CMSX-4 (for about 0.13%) which corresponds to the difference in the unconstrained misfit in the undeformed superalloys (see Table 2).

A remarkable difference in the kinetics of the misfit change is, that the loss of coherency in CMSX-4 starts immediately, whereas in CMSX-10 it has a delay of about 25 h. This delay has the same reason as the observed incubation of creep deformation in CMSX-10 (see Fig. 1), namely the preservation of the cuboidal γ/γ'-microstructure for the first 25 h (see Fig. 3).

TEM. Plastic deformation in superalloys starts by dislocation movement in the γ-matrix. The dislocation segments deposited in the γ/γ'-interface are an indication for this process (Fig. 7).

In the PDA of CMSX-4 many interfacial dislocations are found already after 4 h creep (Fig. 7), whereas in the IR it is difficult to find some dislocations at all, which is in accordance with XRD investigations, showing that the loss of coherency starts in the PDA, in CMSX-4 immediately, in CMSX-10 delayed. This inhomogeneous plastic deformation is explained by the misfit inhomogeneity and residual stresses in the dendritic structure [11], both effects of the dendritic segregation. At the end of primary creep, in CMSX-4 at about 25 h, when the γ/γ'-microstructure is totally rafted all over the dendritic cell, the γ/γ'-interfaces are covered completely by dislocation networks (Fig. 7, 150 h). The networks are homogeneous and remain quite stable almost until rupture. In CMSX-10 a 25 h incubation period precedes primary creep. The dislocation configuration after this time is shown in Fig. 7, 25 h. As in CMSX-4 much more dislocations are observed in the PDA than in the IR. In CMSX-10 primary creep ends at about 60 h. The microstructure in the PDA and the SDA is now rafted, but in the IR it still is cuboidal. The γ'-rafts are covered by inhomogeneous dislocation networks, which soon lose stability and planar configuration (see bowing segments in Fig. 7, 200 h). *a*[001] dislocations having formed in the γ/γ'-interface due to dislocation reactions enter the γ'-lattice and climb through the γ'-rafts. This lowers the absolute misfit value, as found by XRD both in CMSX-4 and CMSX-10 (see Figs 6a and b) and accelerates the deformation process as seen in the creep curve of CMSX-10 after 200 h (see Fig. 1). A detailed description of this TEM investigation is given in [12].

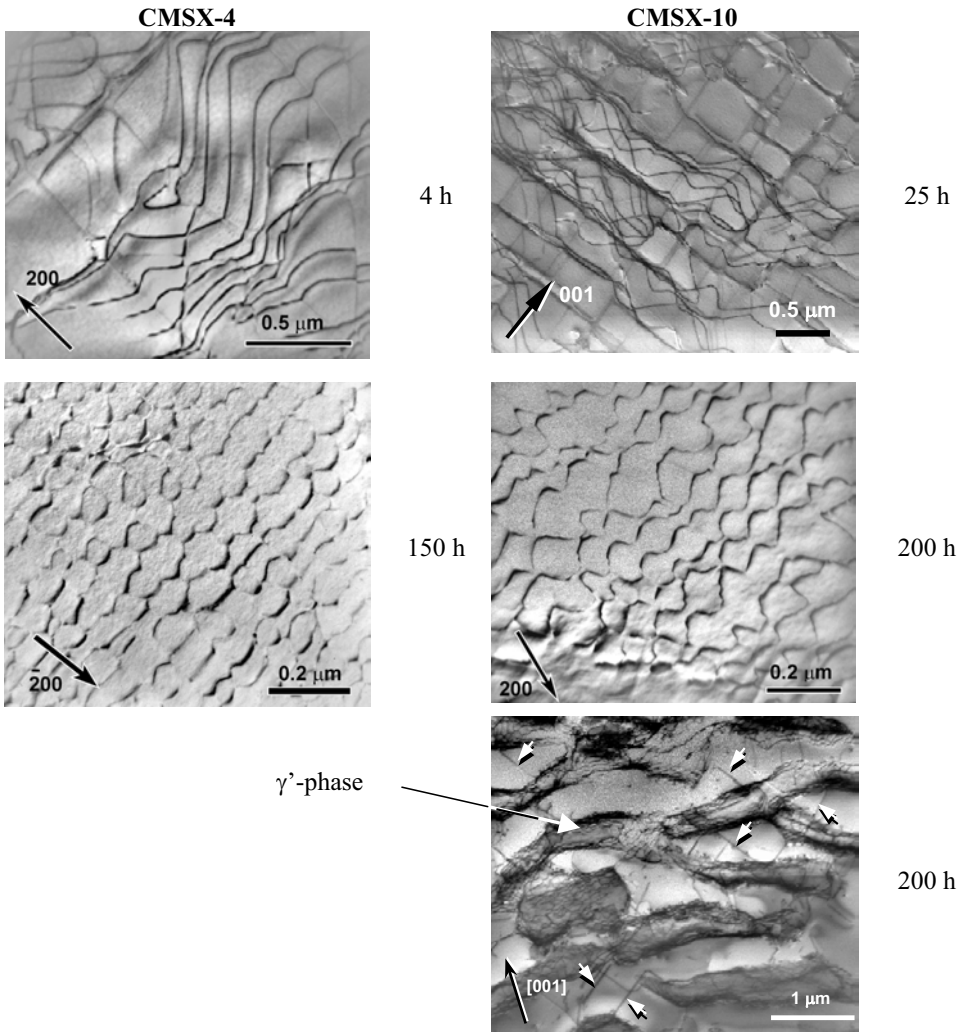

Fig. 7. Dislocation structures in the PDA of CMSX-4 and CMSX-10 after creep at 1100°C and 120 MPa.
Left side: CMSX-4. Cross sections, showing interfacial dislocation networks during primary creep (4 h, ε=0.10 %) and steady creep (150 h, ε=1.3 %).
Right side: CMSX-10. Interfacial dislocation networks during primary creep (25 h, ε=0.12 %) and transition from steady to accelerated creep (200 h, ε=1.6 %). Bottom: Longitudinal section of the CMSX-10 specimen tested for 200 h: prismatic loops of *a*[001] dislocations climbing through the γ'-rafts marked by arrows.

Discussion

To understand the effect of rhenium on the high temperature creep behaviour of superalloys, comparison of the two superalloys CMSX-4 (3 wt.% Re) and CMSX-10 (6 wt.% Re) showed to be helpful. The first striking difference in the creep behaviour is the incubation period found for CMSX-10. Such an incubated creep is reported for many superalloys [e.g. 3, 13-15] and it is assumed that it is related to the initial γ'-size. Detailed investigations of the effect of γ'-size on creep properties was performed by Nathal [13] for superalloys of the MAR-M200 type. He found that a quenched superalloy with small unaligned γ'-precipitates shows at 1000°C, 124 MPa a creep curve with incubation period and fast, short secondary creep very similar to CMSX-10 in the work presented. The γ'-size effect was found to be dependent on the magnitude of the γ/γ'-misfit. Similar results on the γ'-size effect are reported by Caron and Khan [14] and by Gabb et al. [15].

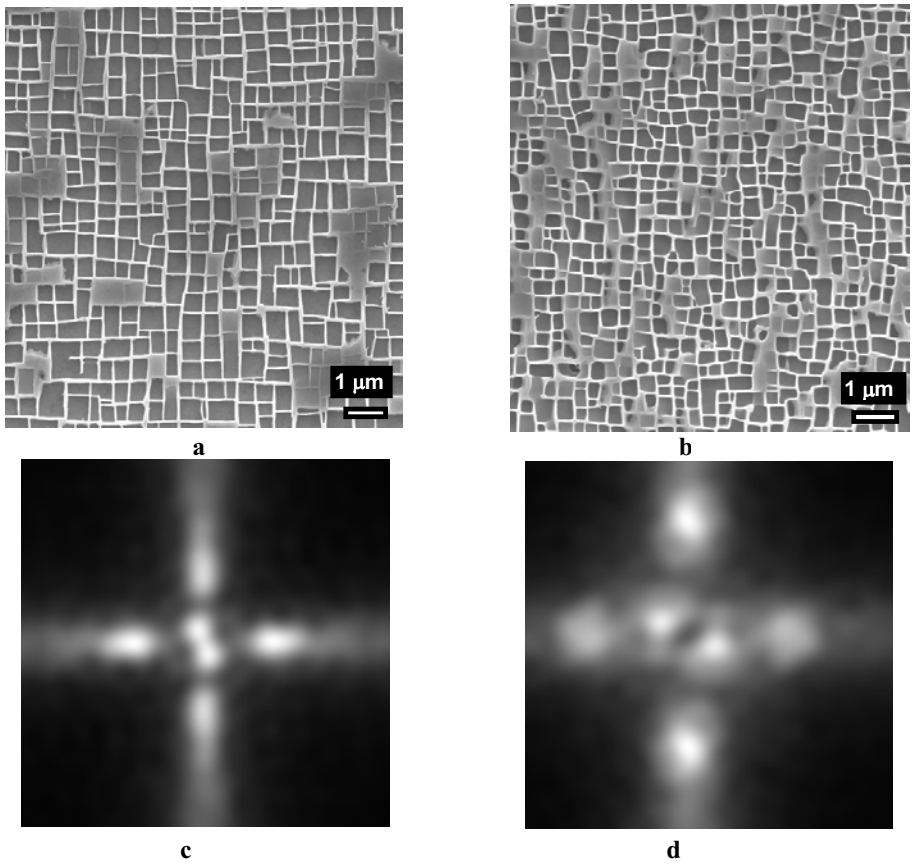

Fig. 8. Undeformed microstructure of CMSX-4 (left) and CMSX-10 (right) as seen in the SEM (top) or in the reciprocal space (bottom). The half width of the reflections in azimuth direction gives $\Delta\varphi$.

In our case the unconstrained misfit at RT is nearly zero in CMSX-10 and about −0.13% in CMSX-4. The lower absolute misfit of CMSX-10 is caused by the reduction of Cr (from 6.5 wt% to 2.3 wt%), Co (from 9.7 wt% to 3.3 wt%) and W (from 6.4 wt% to 5.5 wt%) necessary to suppress the tendency of CMSX-10 to TCP phase precipitation when the concentration of refractory elements is very high. According to data from [16] a side effect should be the decrease of the γ-lattice spacing lowering the absolute γ/γ'-misfit. Consequently the alignment of the γ'-cuboids, which is driven by coherency stresses [17], becomes worse. Another effect of rhenium results from the fact, that rhenium is nearly not compatible with the ordered γ'-lattice. So the transformation γ→ γ' can take place only after the Re-atoms have left the matrix area. The slow rhenium diffusion however retards this removal, which results in the reduction of the mobility of the γ/γ'-interface and consequently a slower coarsening rate. This explains the finer microstructure of CMSX-10. Both effects (misalignment and smaller γ'-size) can be clearly seen on SEM images (Fig. 8, top and quantified by Fourier analysis of these images (Fig. 8, bottom). The Fourier analysis gives the microstructure period λ and the deviation of the interface from the {100} orientation $\Delta\varphi$. For CMSX-4 one gets λ=0.63 μm, $\Delta\varphi$=±13°, for CMSX-10 λ=0.46 μm, $\Delta\varphi$=±17°.

Summarising the findings of [3, 10, 13-15] and our results leads to the following conclusions. In the fine γ/γ'-microstructure as in our case in CMSX-10 the γ-channels are thin and the Orowan stress, which is inversely proportional to the channel width, blocks the dislocation movement in the γ-matrix. Under high temperature creep conditions plastic deformation starts only after some microstructural coarsening accompanied by widening of the γ-channels.

The finer microstructure however is connected with a worse alignment of the γ'-precipitates. Therefore during creep the γ' cuboids form short rafts, which are less effective for blocking the dislocation movement in load direction. Moreover short rafts are morphologically less stable because of the short diffusion paths between the raft edges and centre, allowing a faster microstructure coarsening and degradation [18]. Caron and Khan [14] come to the same conclusion after investigation of the influence of different heat treatments on the creep behaviour of CMSX-2. The γ'-sizes after heat treatment were either 0.35 μm or 0.45 μm. The finer microstructure showed about two times faster and shorter secondary creep, which they explained by better alignment of the larger γ'-cuboids resulting in longer stable rafts. Therefore secondary creep is fast and rapidly turns into accelerated creep

The advantage for creep lifetime resulting from the incubation period in CMSX-10 is small compared with the disadvantage of a short fast secondary creep. The most beneficial effect of rhenium in CMSX-10 is solid solution hardening. The large rhenium atoms strongly distort the nickel lattice and form clusters as well. This becomes important in tertiary creep, when precipitation strengthening is much less effective because the γ/γ' microstructure has become degraded. Now the mechanical behaviour is no more that of a compound but rather that of single phase material. The γ-phase is weaker but the rhenium is concentrated there and therefore in tertiary creep the mechanical properties of CMSX-10 suddenly become much better than these of CMSX-4.

The general effects of rhenium and the structural and mechanical effects alternatively for CMSX-4 or CMSX-10 are summarized in the graphic, shown in Fig. 9.

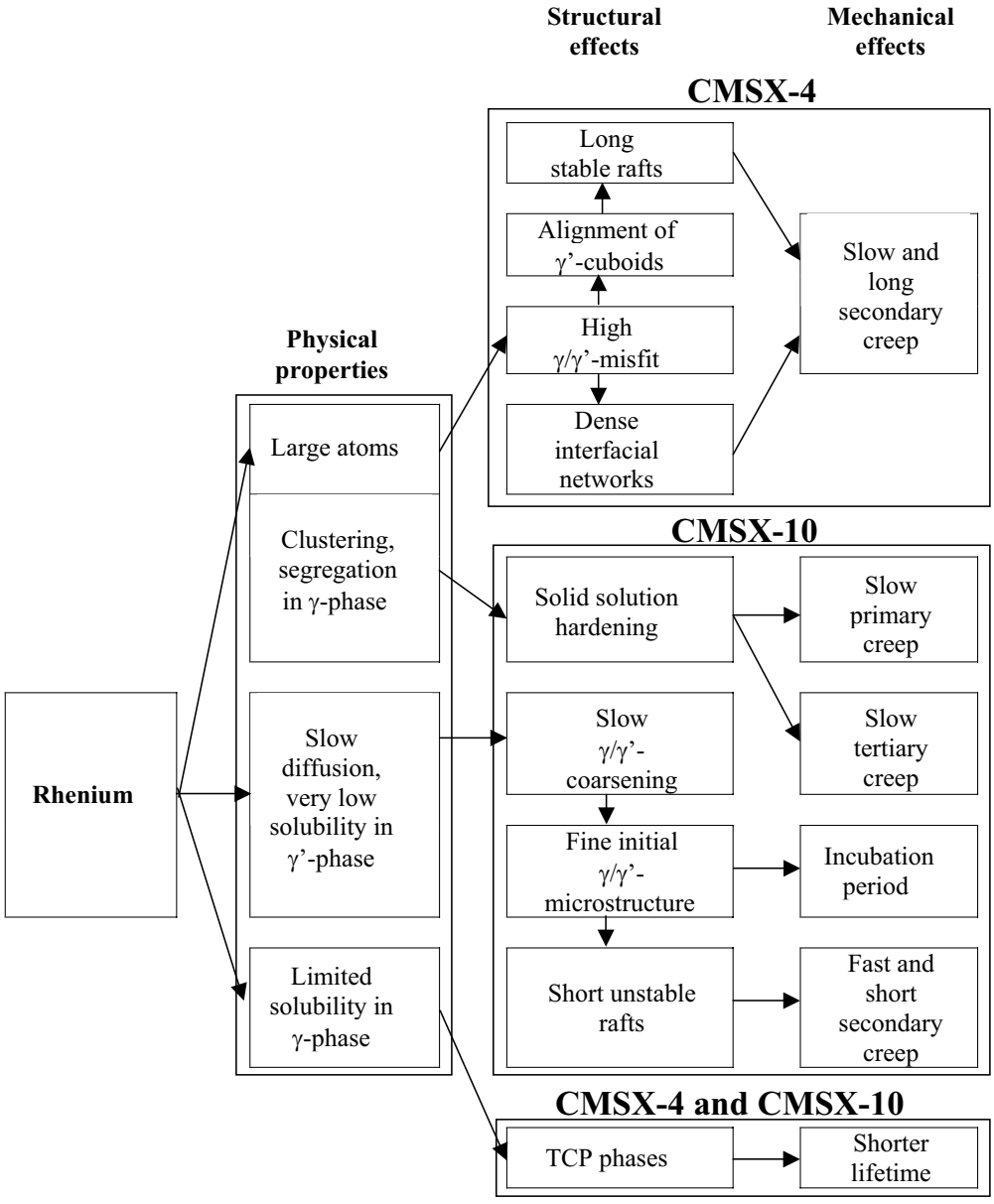

Fig. 9. Effect of rhenium on the structural and mechanical behaviour of superalloys.

Conclusions

From creep tests, SEM, X-ray diffraction- and TEM investigations it can be concluded:

- At 1100°C, 120 MPa , CMSX-10 has an about two times longer creep lifetime than CMSX-4. The creep curve of CMSX-4 shows the classical shape with extended steady creep. In CMSX-10 creep starts with an incubation period, followed by primary and short secondary creep which turns after 35% of lifetime into an exponential tertiary creep.
- In standard heat treated condition the microstructure of these two materials is different. In CMSX-4 the γ'-cuboids are larger and better aligned than in CMSX-10. During creep CMSX-4 forms quickly long rafts which are stable till the end of steady creep, while rafting starts later in CMSX-10 but degradation sooner.

These differences can be explained by the different rhenium concentrations in the alloys.

- In CMSX-4 rhenium causes a high misfit. The resulting misfit stresses lead to the aligned γ/γ'-microstructure in the virgin material, allowing the formation of long rafts during creep. The high misfit results in dense misfit dislocation networks, preventing dislocations from entering the rafts. This regular stable raft structure explains the extended secondary creep.
- In CMSX-10 the rhenium concentration is higher, but the misfit lower than in CMSX-4. This results from a reduction of the elements chromium, cobalt and tungsten, necessary to avoid the strong TCP precipitation. The high rhenium concentration retards the growth of the γ'-cuboids, but because of the low misfit they are worse aligned. The fine cuboids are effective at the beginning of creep by blocking the dislocation movement in the matrix channels, which is the reason for the creep incubation. The rafts forming during creep however are short and therefore not stable. The degradation proceeds very fast. In the degraded microstructure the γ/γ'-compound hardening is less effective compared with the rhenium solid solution hardening effect of the γ-matrix. At this stage of creep, which amounts to 2/3 of total life time, the higher rhenium concentration of CMSX-10 is advantageous.
- The volume fraction of TCP phases precipitating in CMSX-4 and CMSX-10 is nearly identical. The resulting reduction of creep lifetime is stronger in CMSX-4, supposedly because precipitation leads to a stronger reduction of rhenium in the matrix of CMSX-4, having less rhenium already before.

Acknowledgements

Authors are grateful to Dr. K. Harris, Vice-President of the Cannon Muskegon Corporation, USA for providing the master alloy of CMSX-4 free of charge and the German Research Society (DFG) for funding of this work (project Po 405/4-2, Li 494/3-2).

References

1. U. Brückner, A. Epishin, T. Link, Local X-ray diffraction analysis of the structure of dendrites in single-crystal nickel-base superalloys, *Acta mater.,* Vol. 45, No. 12 (1997), pp. 5223-5231

2. U. Brückner, A. Epishin, T. Link and K. Dressel, The influence of the dendritic structure on the γ/γ'-lattice misfit in the single-crystal nickel-base superalloy CMSX-4, *Mater. Sci. and Eng. A*, 19, Vol. A247 (1998), pp. 23-31

3. F. Diologent, P. Caron, A. Jacques and P. Bastie, Creep behavior at 1050°C of a new generation single crystal superalloy, *Creep Deformation: Fundamentals and Applications*, Ed.

by R. S. Mishra, J. C. Earthman and S. V. Raj, TMS (The Minerals, Metals & Materials Society), 2002, pp. 361-370
4. R. Darolia, D.F. Lahrman, R.F. Field, Formation of topologically closed packed phases in nickel base single crystal superalloys, *Superalloys 1988*, edited by D.N. Duhl, G. Maurer, S. Antolovich, C. Lund, S. Reichman, TMS 1988, pp. 255-264
5. A. Epishin, T. Link, P. D. Portella and U. Brückner, Evolution of the γ/γ'-microstructure during high temperature creep of a nickel-base superalloy, *Acta mater.,* Vol. 48 (2000), pp. 4169-4177
6. R. D. Doherty, Diffusive phase transformations in solid state, In: Physical Metallurgy, Part 2, ed. by R. W. Cahn and P. Haasen, North-Holland Physics Publishing, 1983
7. M. Simonetti and P. Caron, Role and behaviour of γ' phase during deformation of a nickel-based single crystal superalloy, *Mater. Sci. and Eng. A*,Vol. A254 (1998), pp. 1-12
8. A. Epishin, T. Link, B. Brückner and P. Portella, The influence of dendritic inhomogeneity on the creep behaviour of a single-crystal superalloy of the 3rd generation, Interim report on the German Research Society (DFG) project Po 405/4-1, Li 494/3-1, BAM - TU Berlin, 2002
9. U. Glatzel, Microstructure and Internal Strains of Undeformed and Creep-Deformed Samples of a Nickel-Base Superalloy, Verlag Dr. Köster, Berlin, 1994
10. T. P. Gabb, S. L. Draper, D. R. Hull, R. A. MacKay and M. V. Nathal, The role of interfacial dislocation networks in high temperature creep of superalloys, *Mat. Sci. Eng.,* Vol. A118 (1989), pp. 59-69
11. A. Epishin, T. Link, U. Brückner, B. Fedelich and P. Portella, Effects of segregation in nickel-base superalloys: dendritic stresses, *Superalloys 2004*, ed. by K. A. Green, H. Harada, T. E. Howson, T. M. Pollock, R. C. Reed, J. J. Shira and S. Walston, TMS, 2004 , pp. 537-543
12. T. Link, A. Epishin, M. Klaus, U. Brückner, A. Reznicek, <100> dislocations in nickel-base superalloys: formation and role in creep deformation, *Mat. Sci. and Eng.,* A 405 (2005), pp. 254-265
13. M. V. Nathal, Effect of initial gamma prime size on the elevated temperature creep properties of single crystal nickel base superalloys, *Met. Trans*., Vol. 18A (1987), pp. 1961-1970
14. P. Caron and T. Kahn, Improvement of creep strength of a nickel-base single-crystal superalloy by heat treatment, *Mater. Sci. and Eng.,* Vol. 61 (1983), pp. 173-184
15. M. V. Nathal and L. J. Ebert, The influence of cobalt, tantalum, and tungsten on the elevated temperature mechanical properties of single crystal nickel base superalloys, *Met. Trans.*, Vol. 16A (1985), pp. 1863-1870
16. Y. Mishima, S.Ochiai, T.Suzuki, Lattice parameters of Ni(γ), Ni_3Al(γ') and Ni_3Ge(γ') solid solutions with additions of transition and B-subgroup elements, *Acta metall.*, Vol. 33 (1985), pp. 1161-1169
17. Minoru Doi and Toru Miyataki, Effect of elastic interaction energy on the distribution of coherent precipitate particles in nickel-base alloys, *Superalloys 92*, ed. S. D. Antolovich et al, The Minerals, Metals and Materials Society, Warrendale, PA, 1992, pp. 537-546
18. A. Epishin, T. Link, U. Brückner and P. D. Portella, Kinetics of Topological Inversion of the γ/γ'-Microstructure during High Temperature Creep of a Nickel-Base Superalloy, *Acta Mater.*, Vol. 49 (2001), pp. 4017-4023

X-RAY TOMOGRAPHY FOR POROSITY ANALYSIS IN SINGLE CRYSTAL NICKEL-BASE SUPERALLOYS

T. Link[1], S. Zabler[2], A. Haibel[2], A. Epishin[1]

[1]Technical University Berlin, Berlin, Germany
[2]Hahn-Meitner-Institute, Berlin, Germany

Abstract

Porosity in single crystal nickel-base superalloys has 3 different reasons, represented by 3 types of pores: pores generated during solidification (S-pores), during homogenisation (H-pores) and during high temperature deformation (D-pores). These pores can be distinguished by their shapes: S-pores have irregular shape, H-pores are spheres and D-pores polyhedrons. Therefore the pore shape provides information about the pore formation. The pore distribution is inhomogeneous. Shape, size and spatial distribution were analysed with X-ray tomography at the European synchrotron radiation facility ESRF in Grenoble.
The method was applied to characterize the porosity in undeformed CMSX-6, SRR99, CMSX-4 and CMSX-10, showing clearly, that pore number and size increase with the content of refractory elements. Analysis of CMSX-4 specimens crept for different times at 1100°C, 120 MPa gave that during creep the pre-existing pores transform into polyhedrons and that a second fraction of small pores (about 5 μm) is formed. The spatial distribution of these D-pores depends on the creep rate.

Keywords: Superalloys, microporosity, tomography, creep.

Introduction

Porosity in superalloys has different reasons as shown in [1]. First the dendritic solidification impedes the melt flow in the interdendritic region (IR). The result are irregularly shaped solidification pores (S-pores) [2, 3]. Second, the homogenisation heat treatment causes diffusion fluxes: Al, Ti and Ta diffuse from the IR into the dendrite arms and centre but the flux of the refractory elements W, Re, Cr and Co into the opposite direction is much slower [4]. Consequently homogenisation pores (H-pores) form with characteristic spherical shape. This effect is pronounced in modern superalloys [1] with high content of refractory elements, making necessary an extensive heat treatment [5]. The third reason is high temperature creep, which causes a diffusion flux too but in this case by dislocations climbing in the γ channels perpendicular to the [001] tension axis, thus producing vacancies. Climb along [001], which would absorb these vacancies, is blocked by the γ'-rafts [6]. Therefore the vacancies condense in pores, having polyhedral shape due to the fact that surface energy is anisotropy at creep temperature [1, 7]. Such deformation pores, reported in [1, 7, 8], are designated as D-pores.
Characterisation of these pores is not trivial, because they are small (down to few μm), complex in shape and inhomogeneous in spatial distribution. Therefore it needs a 3D visualisation with high spatial resolution, which can be attained by synchrotron tomography at the European synchrotron radiation facility (ESRF).

Experimental

Single crystal superalloys with [001] orientation of CMSX-6, SRR99, CMSX-4 and CMSX-10 were solidified and heat treat by Doncasters Precision Casting, Bochum. Creep tests were performed at 1100°C with tensile stresses between 105 MPa and 135 MPa at the Federal Institute of Material Research and Testing (BAM), Berlin. The tomograms were taken at the ESRF, beamline ID 19. The high density of superalloys (8 ÷9 g/cm^3) requires a high photon energy (50 keV) but anyhow the high spatial resolution [about 1μm] restricts the cross-section area to about 0.5 mm$\times$0.5 mm. Therefore thin bars with 0.5 mm thickness along the secondary dendrite arm directions [100] and [010] were cut with the bar axis pointing in primary dendrite arm direction and being 14 mm long. One tomogram consists of 1000 slices of the (001) plane with a slice distance of 1 μm, so the scanned volume is about 0.5$\times$0.5$\times$1.0 mm^3.
Details about collecting and processing of the tomograms are reported in [6].

Results

Fig. 1 shows tomograms of the different pore types. Fig. 1a is taken in a CMSX-4 specimen, creep deformed at 1100°C, 135 MPa for 149 h. 3 pores are obviously much bigger than the rest and irregular in shape. These are S-pores. A closer look at the smaller pores of the same specimen shows that they are polyhedral, representing the D-pores (Fig. 1b). On contrary in heat treated undeformed material the H-pores are nearly spherical with the size strongly scattering (Fig. 1c).

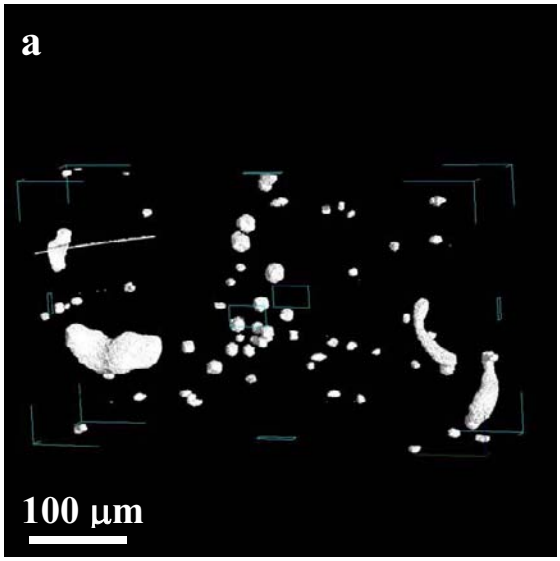

Fig. 1. Different pore types in single crystal superalloys. Notice the different scales!
a. S-pores in CMSX-4 deformed at 1100°C, 135 MPa, 149 h.

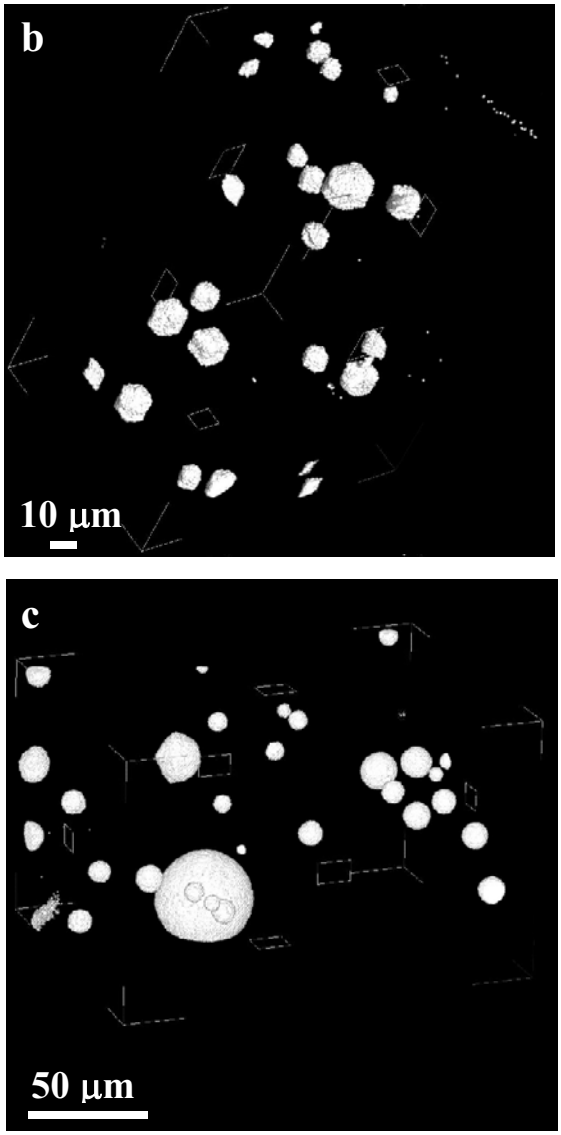

Fig. 1. Different pore types in single crystal superalloys. Notice the different scales!
b. D-pores in the same specimen as in Fig. 1a.
c. H-pores in undeformed CMSX-10.

The spatial pore distribution is illustrated by Fig. 2. In a three dimensional view of the porosity in CMSX-4 after 392 h creep deformation at 1100°C, 117 MPa, the pores seem to be distributed randomly (Fig. 2a). A projection of the pores along the primary dendrite axis [001] (Fig. 2b) however reveals that they are concentrated in the IR. A projection along the secondary dendrite arms (Fig. 2c) shows a pore depleted zone in [001] direction.

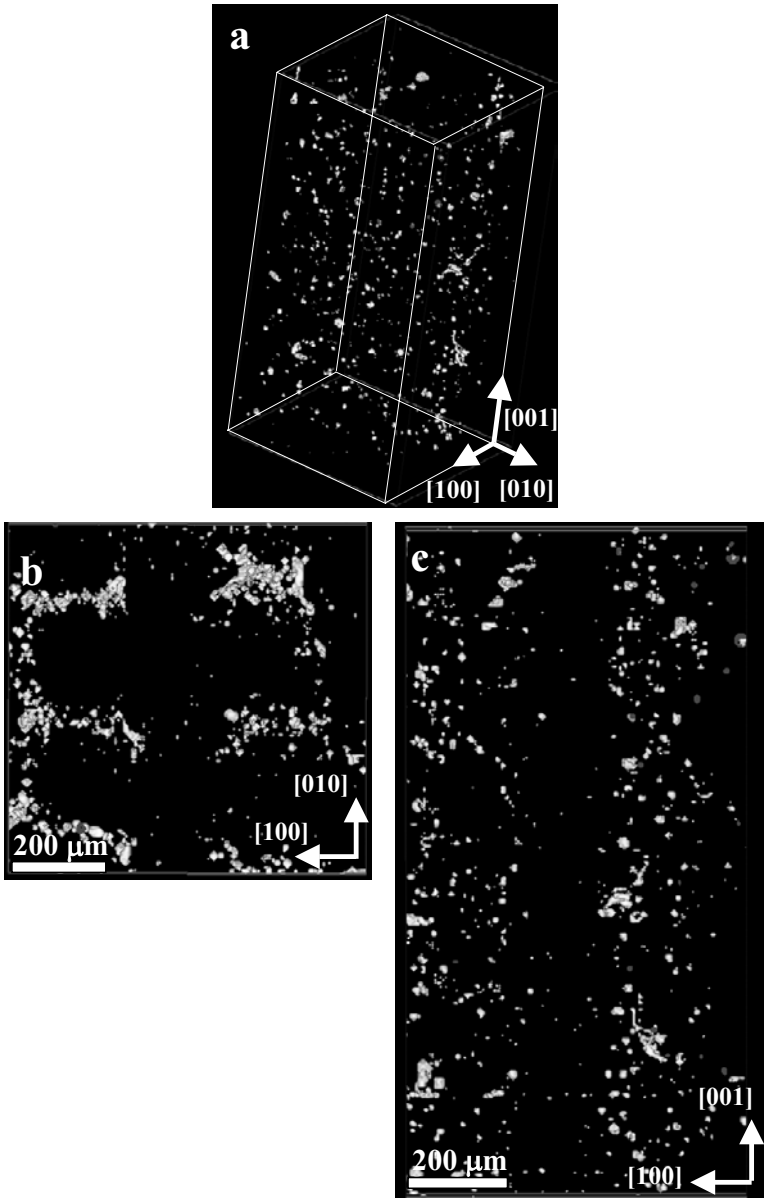

Fig. 2. Pore distribution in CMSX-4, crept at 1100°C, 117 MPa, 392 h.
a. 3D projection of the pores in the scanned volume. The dendrite axis is along [001].
b. All pores projected into the (001)-plane ("dendrite cross section").
c. Same for the (100) plane ("dendrite longitudinal section").

This interpretation is confirmed by scanning electron microscope (SEM) images (Fig. 3) allowing to visualize simultaneously the dendrites and the pores. Orientation differences between the dendrites cause different grey levels. The small black pores are strictly positioned

in these low angle boundaries, visible in cross sections (Fig. 3a) and longitudinal sections (Fig. 3b). The higher image brightness in the dendrite arms is caused by the segregation of the refractory elements to these areas.

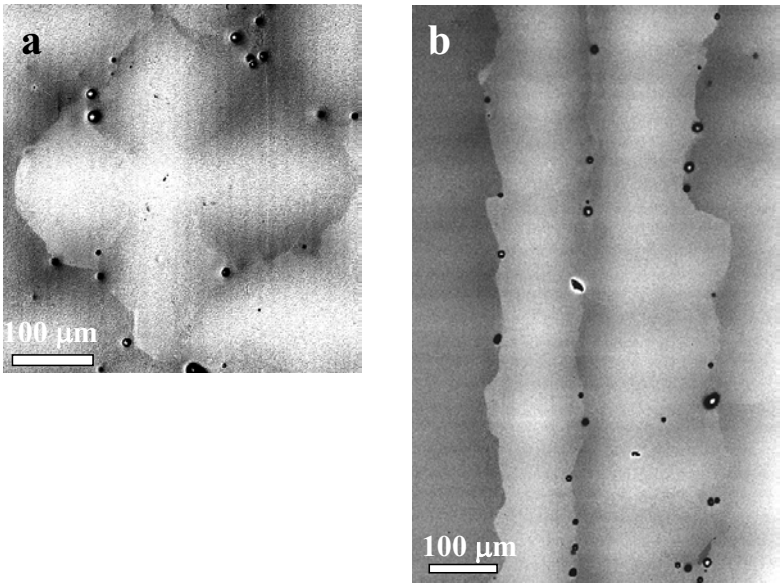

Fig. 3. Pores in the interdendritic regions of undeformed CMSX-4.
SEM back scatter electron images.
a. Cross section. b. Longitudinal section

Undeformed material: For quantitative analysis of the porosity first the total porosity in 4 standard heat treated single crystal superalloys was measured (Fig. 4). It confirmed previous metallographic measurements [1], where an increase of the porosity with the concentration of refractory elements Mo, Ta, W and Re was observed.
In hot isostatic pressed (HIP) CMSX-4 no pores could be detected at all.

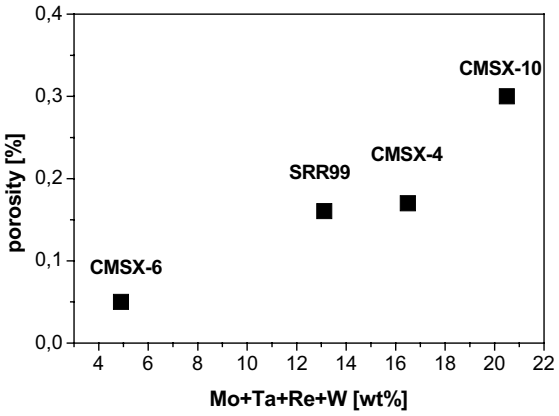

Fig. 4. Porosity in different superalloys, measured by tomography.

Tomography allowed to determine the volume of each pore. In Fig. 5 it is shown, how much pores with a certain size contribute to the total porosity. The big peaks between 7 µm and 15 µm are caused by H-pores, peaks further right by S-pores. So H-pores cause most of the microporosity in undeformed superalloys, whereas the pore size and number increases with the content of refractory elements.

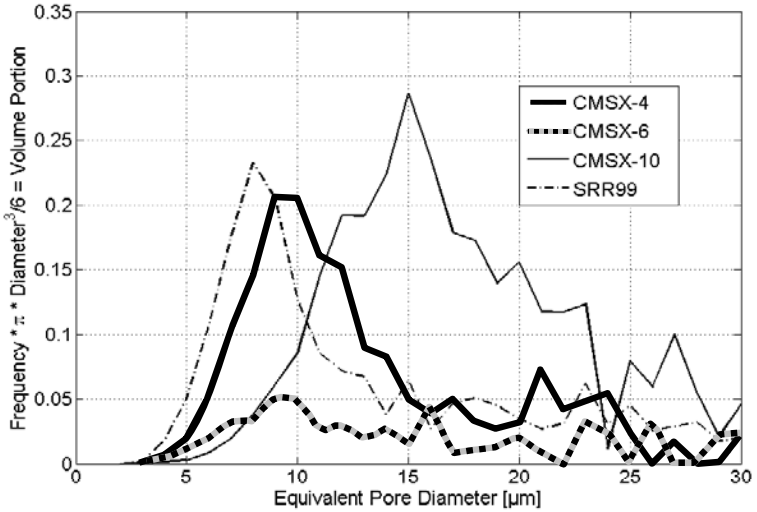

Fig. 5. Contribution of pores with a certain size to the total porosity. Equivalent pore diameter means the diameter of a sphere having the identical volume as the respective pore.

Creep deformed material: The dynamics of creep strain and porosity growth are correlated at high temperatures as shown in Fig. 6. Further results about porosity growth under different temperatures and stresses are reported in [7].

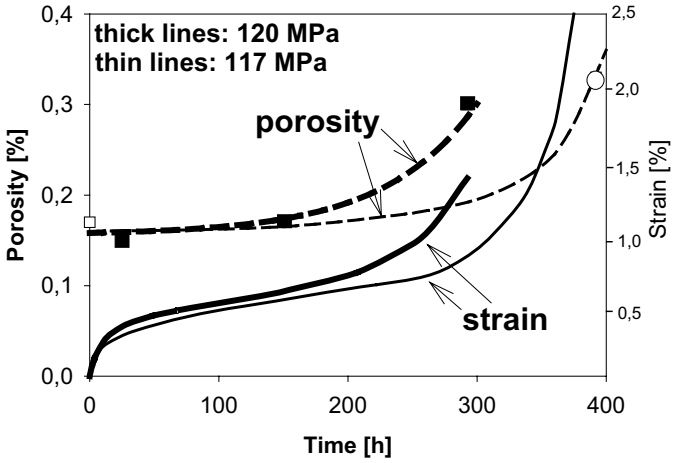

Fig. 6. Correlation between creep curve and porosity increase in CMSX-4 at 1100°C. The white square symbol at 0 h gives the porosity in undeformed material.

In Fig. 7 the change of porosity in CMSX-4 during creep at 1100°C is analysed again for each pore size separately. The peaks become higher and shift to the right during creep as expected from Fig. 6. The change of the shape of the histogram is unexpected. The most pronounced it is in the 392 h specimen, where a second peak appears at about 7 µm, but already the curve for 150 h shows a small peak on the left. This additional peak corresponds to the D-pores.

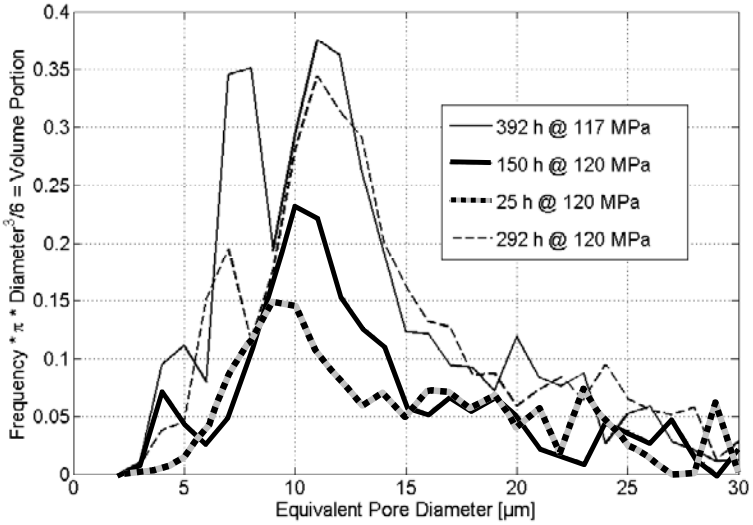

Fig. 7. Porosity-diameter histogram for CMSX-4, crept at 1100°C for different times. The main peak grows and shifts to the right while a second peak develops on the left.

SEM observations of these small pores gave that D-pores have {100} and {110} faces or both. Fig. 8 shows an example of such a pore in the 150 h specimen. The 4 triangles pointing towards the bottom of the pore are formed by {110} faces.

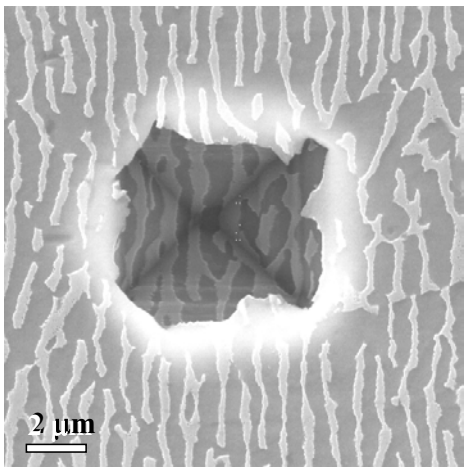

Fig. 8 SEM image of a typical D-pore in CMSX-4, creep deformed at 1100°C, 120 MPa, 150 h.

Tomography allowed to characterize the shape of each pore by a geometrical parameter [9]. It showed that the pore shape presented in Fig. 8 is typical for the D- pores. In total the surface consists of 12 {110} faces, forming an regular dodecahedron.
The stress dependence of the pore formation is shown in Fig. 9.

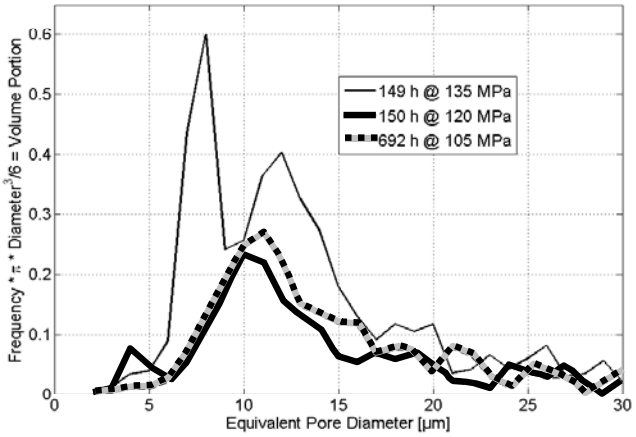

Fig. 9. Porosity-diameter histogram for CMSX-4 crept at 1100°C at different stresses and times. The development of the second peak strongly depends on the stress.

All 3 CMSX-4 specimens are crept at 1100°C. At 105 MPa D-pores are not found even after 692 h creep, whereas they become visible in the 120 MPa specimen already after 150 h. At the highest stress of 135 MPa however they are very pronounced at that time. The tomogram of this specimen (Fig. 10) shows, that the pores are no more confined to the IR but that small pores have developed everywhere.

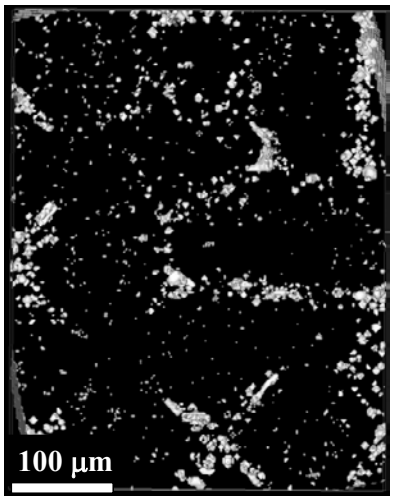

Fig. 10 Pore distribution in CMSX-4, creep deformed at 1100°C, 135 MPa, 149 h. Small pores have developed everywhere.

Discussion

The investigations show, that porosity in nickel-base superalloys has different reasons. It is not sufficient to take into account just the porosity of the undeformed material, because pore growth and pore generation during high temperature creep increase the total porosity considerably (Fig. 6). It is expected that the effect of this porosity growth on the mechanical properties is most pronounced for hot isostatical pressed materials. In such a case creep transforms a practically pore free material (as shown for CMSX-4) into a porous condition, whereas in unhipped material porosity just increases. Porosity growth however is only one aspect of microstructural degradation during high temperature creep, other important aspects are the formation of topologically close packed phases [11] and rafting [12]. First investigations, quantifying simultaneously the development of porosity and rafting during creep and the effect on low cycle fatigue properties [10] indicate, that the change of the γ'-morphology from cubes to rafts is more relevant, probably because it facilitates crack propagation [13, 14].
A reduction of porosity in undeformed materials is expected for casting technologies with higher thermal gradients, reducing the dendrite spacing [15]. The shorter distances for melt flow during solidification and diffusion during homogenisation should reduce S-porosity and H-porosity as well.
In deformed superalloys the porosity increase is correlated with creep strain, as illustrated by Fig. 9 and quantified in previous publications [1, 6]. The polyhedral shape of the D-pores is a clear indication for their formation at a temperature lower than the homogenisation temperatures (which is close to the solidus temperature), because with decreasing temperature the specific energy of the pore faces becomes anisotropic.
With rising applied load more D-pores develop (Fig. 9) and their distribution becomes more homogeneous (Fig. 10). This supports the D-pore formation mechanism, as described in detail in [6]. It is based on the climb of matrix dislocations in the γ/γ' interfaces of the γ'-rafts perpendicular to the stress axis. Such an interfacial climb and thus creep pore formation takes part everywhere in the material. The low angle boundaries distributed densely over the IR [16] however provide diffusion paths where the vacancies meet and condense. The consequence is, that pores preferably form in the interdendritic areas. When at higher strain rates vacancy generation becomes fast, this vacancy migration process has less time. Therefore D-pores are less uniformly distributed and more pronounced.

Conclusions

By synchrotron tomography it is possible to analyse the size and shape of micropores and their spatial distribution in single crystal nickel-base superalloys. Combination of the tomography results with the detailed inspection of selected pores by SEM allows the microstructural interpretation of the statistical tomography data.
In the superalloys under investigations, CMSX-6, SRR99, CMSX-4 and CMSX-10 porosity increases with the content of refractory elements. The reason are pores forming and growing during homogenisation.
During HT creep deformation additional small pores are formed, having polyhedrical shape. Their volume fraction and distribution depends on the applied load in accordance with a model of anisotropic creep in superalloys with rafted microstructure.

Acknowledgements

This work was financially supported by DFG-grant RE 688/41-1, PO 405/7-1. The tomography measurements were performed and financed by the ESRF, project ME-375. Both supports are gratefully acknowledged.

References

[1] A. Epishin, T. Link, U. Brückner and P.D. Portella, Investigation of porosity in single-crystal Nickel-base superalloys, Proc. of the 7th Conf. on Materials for Advanced Power Engineering, Liege, edited by J. Lecomte-Beckers, M. Carton, F. Schubert, P.J. Ennis, Forschungszentrum Jülich, (2002), pp. 217-226

[2] J. Lecomte-Beckers, Study of microposity formation in nickel-base superalloys, Metall. Trans. A, Vol. 19A, No. 9 (1988), pp. 2341-2348

[3] V. N. Toloraja, A. G. Zuev and I. L. Svetlov, Influence of regimes of directional solidification and heat treatment on porosity in single-crystal nickel-base superalloys, Izv. AN. USSR, Metalls, No. 5 (1991), pp. 70-76

[4] D. L. Anton and A.F. Giamei, Porosity distribution and growth during homogenization in Single Crystals of a Nickel-base superalloy, Mater. Sci. and Eng., Vol. 76, (1985), pp. 173-180

[5] G. E. Fuchs, Solution heat treatment response of a third generation single crystal Ni-base superalloy, Mater. Sci. and Eng., Vol. 300 (2001), pp. 52-60

[6] A. Epishin and T. Link, Mechanisms of high-temperature creep of Nickel-based superalloys under low applied stresses, Phil. Mag., Vol. 84, No. 19 (2004), pp. 1979-2000

[7] A. H. Sherry and R. Pilkington, Pore morphology changes in a single crystal superalloy during creep at high temperatures, Proceedings of the Fourth International Conference on Creep and Fracture of Engineering Materials and Structures, edited by Wilshire, B., and Evans, R. W. (London: the Institute of Metals), (1990), pp. 333-344.

[8] J. Komenda and P. J. Henderson, Growth of pores during the creep of a single crystal Nickel-base superalloy, Scripta Mat., Vol. 37, No. 11, (1997), pp. 1821-1826

[9] T. Link, S. Zabler, A. Epishin, A. Haibel, M. Bansal and X. Thibault, Synchrotron tomography of porosity in single-crystal Nickel-base superalloys, submitted to Mat. Sci. Eng. A (2005)

[10] A. Epishin, T. Link, U. Brückner, H. Klingelhöffer and P. Portella: The effect of high temperature creep damage on low cycle fatigue in CMSX-4, Proc. of the 8th Conf. on Materials for Advanced Power Engineering, Liege, (2006), to be published

[11] R. Darolia, D. F. Lahrman and R. D. Fields, Formation of topologicall closed packed phases in Nickel base single crystal superalloys, Superalloys 1988, edited by . Reichman, D.N. Duh, G. Maurer, S. Antolovich and C. Lund, The metallurgical society, (1988), pp. 255-264

[12] N. Matan, D.C. Cox, C.M.F. Rae and R.C. Reed, On the kinetics of rafting in CMSX-4 superalloy single crystals, Acta mater. Vol. 47, No.7 (1999) pp. 2031-2045

[13] S.H. Ai, V. Lupinc and G. Onofrio, Influence of precipitate morphology on high temperature fatigue crack growth of a single crystal nickel base superalloy, Scripta Metall. Mater. Vol. 29**,** (1993), pp. 1385-1390.

[14] H. Mughrabi, γ/γ' rafting and its effect on the creep and fatigue behaviour of monocrystaline superalloys, The Johannes Wertman symposion, edited by R.J. Arsenault, D. Cole, T. Gross, G. Kostorz, P.K. Liaw, S. Parameswaran and H. Sizek, The minerals, metals & materials soc., (1999), pp. 267-278

[15] R. F. Singer, Advanced materials and processes for land-based gas turbines, Materials for advanced power engineering, part II, Kluwer Academic Publishers, Printed in the Netherlands, (1994) pp. 1707-1729
[16] U. Brückner, A. Epishin and T. Link, Local X-ray diffraction analysis of the structure of dendrites in single-crystal Nickel-base superalloys, Acta mater. Vol. 45, No. 12, (1997), pp. 5223-5231

DEFORMATION BEHAVIOR AND MICROSTRUCTURE EVOLUTION DURING HOT WORKING PROCESS OF NI-BASE ALLOY GH742

Beijiang Zhang*, Guangpu Zhao, Guohua Xu, Di Feng
High Temperature Materials Division, Central Iron & Steel Research Institute, Beijing China
*Correspondence: zhangbeijiang@hotmail.com

Abstract

Deformation behavior and microstructure evolution in hot working process of highly alloyed nickel base superalloy GH742, have been experimentally and theoretically investigated. Isothermal compressive deformation test was conducted on MTS machine, and low stress data at various temperatures between 950℃ to 1150℃ and strain rates between $0.001s^{-1}$ to $1s^{-1}$ were obtained, microstructure evolution during deformation under the above conditions was also investigated. The results show that when deformation was performed at single phase region above 1075℃，rather low flow stress is exhibited, the apparent activation energy approach activation energy of grain boundary diffusion, the deformation mechanism is controlled by grain growth rate and fully recrystallized structures can be achieved. In two phase region, GH742 alloy presents considerably high activation energy, with decreasing temperature and increasing strain rate, the flow stress increases swiftly, while the dynamic recrystallization was strongly prohibited. At transition temperature between single and two phase region, a discontinuous change in flow stress was observed, and apparent activation energy sharply increased, strain induced dynamically precipitated γ′ inhibit the migration of grain boundaries, therefore diameter of recrystallized grain is drastically reduced with increase of plastic strain, and the microstructure was effectively refined.

Keyword: hot working, flow behavior, dynamic recrystallization, nickel base superalloy, activation energy

1 Introduction

Progressive enhancement of gas turbine engine performance has required increases in the compressor pressure ratio and the overall operating temperature, both of which have driven the development of materials. Turbine disk is one of critical component in land based heavy-duty gas turbine, just as its counterparts in aero gas turbine and rocket engine. Specifically, GH742 (EP742 in Russia), a precipitated strengthened Ni-based superalloy, has long been demonstrated as an excellent material for turbine disk. This alloy presents excellent mechanical properties below 800℃, nonetheless, this highly alloyed material exhibit narrow processing window, poor formability and high flow stress during hot working process. Both flow behavior and resultant microstructures have a strong dependence on deformation conditions, especially temperature. Therefore, comprehensive evaluation of the role of various processing parameters (temperature, strain rate and strain) on the deformation characteristics (flow behavior) and the microstructural evolution remains a matter of an extended investigation [1-5]. Extra difficulty is the extension of disk size, in order to meet the necessary of heavy land based gas turbine. Additionally for hot working practitioners of GH742 alloy, knowledge of the stress-strain relationships for specific values of strain, strain rate and temperature is instrumental for the development of finite element models that simulate various stages of the manufacturing process [6-14]. Hence, the objective of the present paper is to study the influence of the processing temperature, strain rate and deformation degree on the flow stress behavior and to perform constitutive modeling of the hot working process for GH742.

2 Experimental procedures

Chemical composition of experimental alloy GH742 was given in table 1. The material was manufactured via vacuum induction melting and vacuum arc re-melting process, all specimens was taken from as-forged bar. Cylindrical specimens with length of 15mm and diameter of 10mm were machined form the bar with the specimen axes parallel to that of bar, the two-end surfaces of specimen were lubricated with glass powder in order to reduce friction. All specimens undergone a solution treatment for 30min at 1150℃, then were cooled to the test temperatures at 5℃/s. After 20s of soaking at the test temperature, the specimens were compressed at constant strain rates.

Table 1 Chemical composition of experimental alloy (Mass fraction %)

	C	Co	Cr	Mo	Al	Ti	Nb	Ni
GH742	0.054	10.40	14.15	5.03	2.51	2.56	2.62	Bal.

Isothermal compression tests were conducted on a servo-hydraulic MTS machine, Transducer signals for load were obtained using a load cell and cross-head displacement was measured using a linear variable differential transformer system. Specimen strains were computed from the cross-head displacement after correcting for machine compliance. Si_3N_4-ZrO_2 platens which can be heated synchronized with specimen were applied to guarantee the homogenization of specimen temperature during deformation.

Flow stress data at various temperatures between 950℃ to 1150℃ and strain rates between 0.001 and 1 s^{-1} were recorded, the strains were in the range of 0 to 1.2 true strains. All specimens were water quenched immediately after deformation to study the microstructure. Specimens were polished and etched for optical and SEM investigation, Electropolished TEM specimens were used for TEM observations on a JEOL 2010 operated at 200kV.

3 Results and discussion

3.1 Flow behavior of alloy GH742

Initial yield stress and peak stress of GH742 alloy at various deformation temperature and strain rate were presented in figure 1(a)(b), respectively. The results show that when deformation was performed at single phase region above 1075℃, rather low flow stress is exhibited, while in two phase region, with decreasing temperature and increasing strain rate, the flow stress increases swiftly. At transition temperature between single and two phase region, flow stress undergoes a steep variation. Flow stress, temperature and strain rate can be express by the hyperbolic sine law given in function 1 as follow[15-19]:

$$Z = \dot{\varepsilon} \exp\left(\frac{Q}{RT}\right) = A[\sinh(\alpha\sigma)]^n \quad (1)$$

where A, α, n and Q are material dependent coefficients, Z the Zener-Hollomon parameter. Apparent activation energies of GH742 alloy corresponding to initial yield stress and peak stress were presented in figure 2 (a)(b). The calculation shows that, in temperature range of hot working process, apparent activation energy varies in a large-scale. When deformation was conducted in two phase region, apparent activation energy was significantly higher than that in single phase region. When temperature was confined in two phase region or single phase region, apparent activation energy hold a stable value. Activation energy was also found undergoes a drastically variation at boundary temperature between two phase and single phase regions. Therefore a mean value of apparent activation energy cannot describe the deformation behavior very well in the whole temperature regime of hot working process.

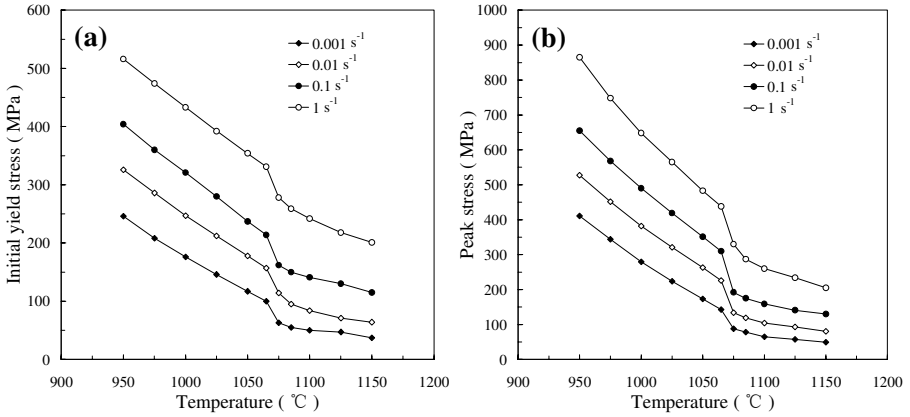

Fig. 1 Initial yield stress (a) and peak stress (b) of GH742 alloy at various deformation temperature and strain rate.

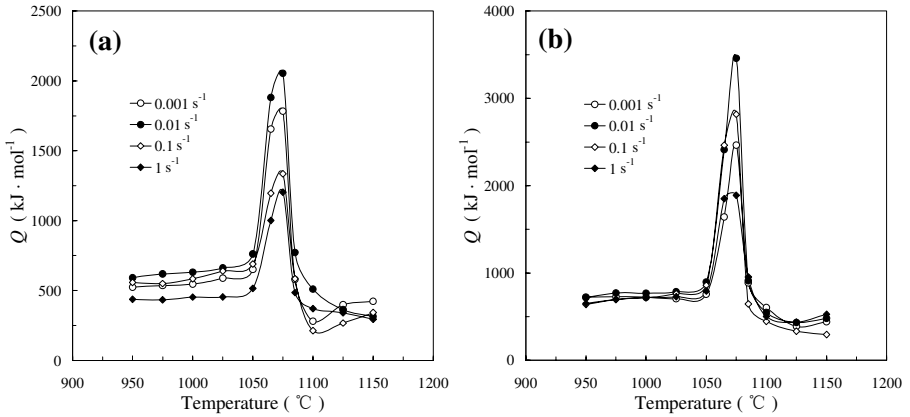

Fig. 2 Apparent activation energies of GH742 alloy corresponding to initial yield stress (a) and peak stress (b) respectively.

In single phase region, GH742 alloy exhibit relatively low apparent activation energy, under circumstance of high temperature and low strain rate, the value of apparent activation energy fall into the regime of self diffusion activation energy, and microstructure was controlled by grain boundary migrate. When deformation was conducted in two phase region, apparent activation energy reach a high level, a high level of apparent activation energy indicate that the flow softening mechanism was greatly inhibit, and the temperature and strain rate sensitivity of flow stress also increase greatly. Briottet's work[20] revealed that the fluctuation of apparent activation energy at certain temperature region during deformation indicate a particular mechanism of microstructure development, for instance, dynamic strain aging effect, will be discussed in following section.

3.2 microstructure evolution during hot deformation

Optical images of GH742 alloy deformed at various temperatures and strain rates were presented in figure 3(a)(b) and (c). When deformation was performed at single phase region above 1075℃，coarse grained, equiaxed structures were exhibited. As discussed in section 3.1, the apparent activation energy approach activation energy of grain boundary diffusion, the deformation mechanism is controlled by grain growth rate therefore fully recrystallized structures can be achieved. When deformation was performed at the conditions as follow: true strain of 0.51 at 1065℃ and $0.001s^{-1}$, fine recrystallized grain was obtained as shown in figure 3(b).

In two phase region, GH742 alloy presents considerably high activation energy, with decreasing temperature and increasing strain rate, the flow stress increases swiftly, while the dynamic recrystallization was strongly prohibited. Figure 3(c) is deformed to strain of 0.51 at 1000℃ and $0.1s^{-1}$, unrecrystallized, elongated original grains can be observed, (d) the corresponding structure of (c) after standard heat treatment, presents typical necklace structure. Fine, recrystallized grains can be observed on original grain boundaries, twin boundaries and surface of coarse primary carbides, dynamic recrystallization was controlled by nuclear process[21-23].

When alloy was deformation at the temperature of above 1075℃, microstructure was a single phase austenitic matrix, as shown in figure 4(a), curvature of grain boundary was small, which indicated a low grain boundary energy. Strain induced precipitated γ′ can be observed in figure 4(b), inhomogeneous distributed coarse γ′ have not significant affect dynamic recrystallization process of matrix. Figure 4(c) revealed that these coarse γ′ preferentially precipitate near large primary NbC, and figure 4(d) presents solid state dendrite of γ′ can well developed during deformation process.

TEM micrographs of as-deformed GH742 alloy was given in figure 5, (a): deformed to true strain of 1.2 at 1050℃ and $0.1s^{-1}$, dense dislocation interact with γ′, (b): deformed to true strain of 0.51 at 1065℃ and $0.1s^{-1}$, curving grain boundary indicate the influence of γ′, (c): deformed to true strain of 0.51 at 1065℃ and $0.001s^{-1}$, large γ′ can be observed at grain boundary, (d): dark field image of location C indicated in (c) shows the fine and dispersed γ′

in grain interior. At certain deformation temperature, strain induced dynamically precipitated γ′ inhibit the migration of grain boundaries, therefore diameter of recrystallized grain is drastically reduced with increase of plastic strain, therefore the microstructure was effectively refined, as shown in figure 3(b).

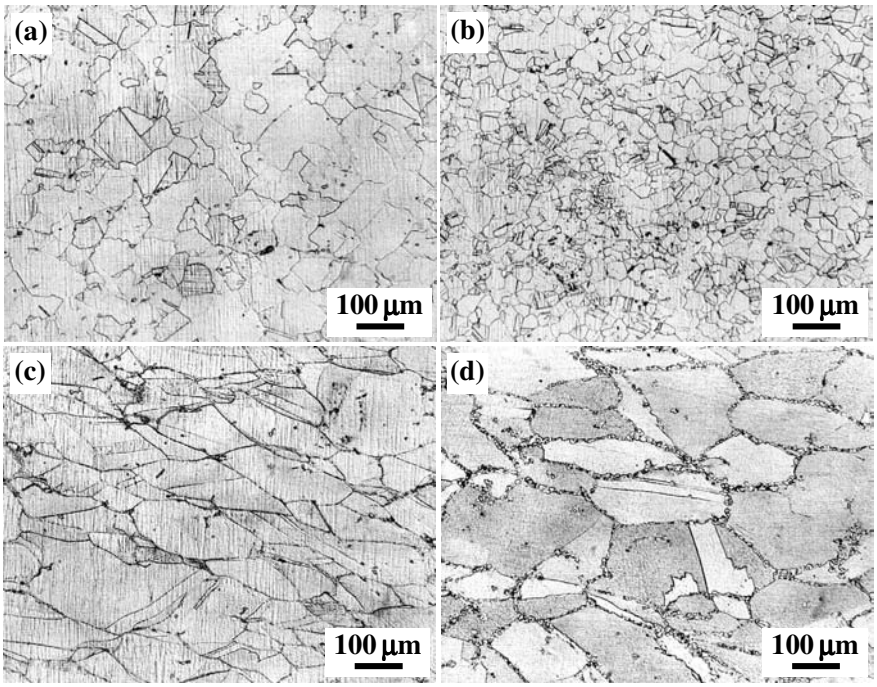

Fig. 3 Optical images of GH742 alloy (a): deformed to true strain of 0.51 at 1150℃ and $0.1s^{-1}$, showing fully recrystallized structure, (b): deformed to true strain of 0.51 at 1065℃ and $0.001s^{-1}$, exhibiting fine recrystallized grain, (c): deformed to strain of 0.51 at 1000℃ and $0.1s^{-1}$ and (d): corresponding structure of (c) after standard heat treatment, presents typical necklace structure.

4 conclusions

(1) High temperature and strain rate sensitivity of deformation behavior and microstructure evolution of highly alloyed superalloy was exhibited.
(2) When deformation was performed at single phase region, low flow stress is exhibited and microstructure evolution was controlled by grain boundary migrate, fully dynamic recrystallized structures can be easily achieved. Grain size exhibit close relationship with deformation parameter, decrease with decrease of temperature and increase of strain rate.
(3) In two phase region, dynamic recrystallization was inhibited by γ' precipitates and secondary carbides, fully dynamic recrystallized structures can only be obtained by

application of sufficient plastic strain. Various types of abnormal structure will revealed when dynamic recrystallized was inhibit.

(4) For alloys that possess of high volume fraction of γ' precipitates, such as GH742 alloy, precipitation behavior of γ' play a predominant role in structure evolution.

(5) For highly alloyed superalloy, such as GH742, a mean value of apparent activation energy can not describe the deformation behavior very well in the whole temperature regime of hot working process.

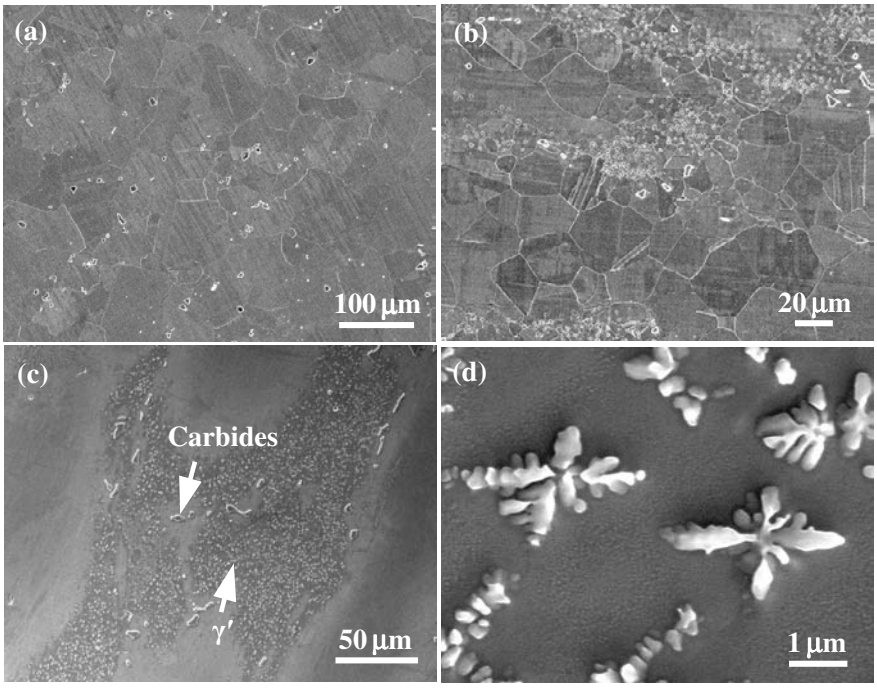

Fig. 4 SEM micrographs of as-deformed GH742 alloy, (a): deformed to true strain of 0.51 at 1150℃ and $0.1s^{-1}$, (b): deformed to true strain of 0.51 at 1075℃ and $0.1s^{-1}$, (c): deformed to true strain of 1.2 at 1075℃ and $0.001s^{-1}$, presents inhomogeneous distribution of γ′, (d): high magnification of (c), exhibiting well developed solid state dendrite of γ′.

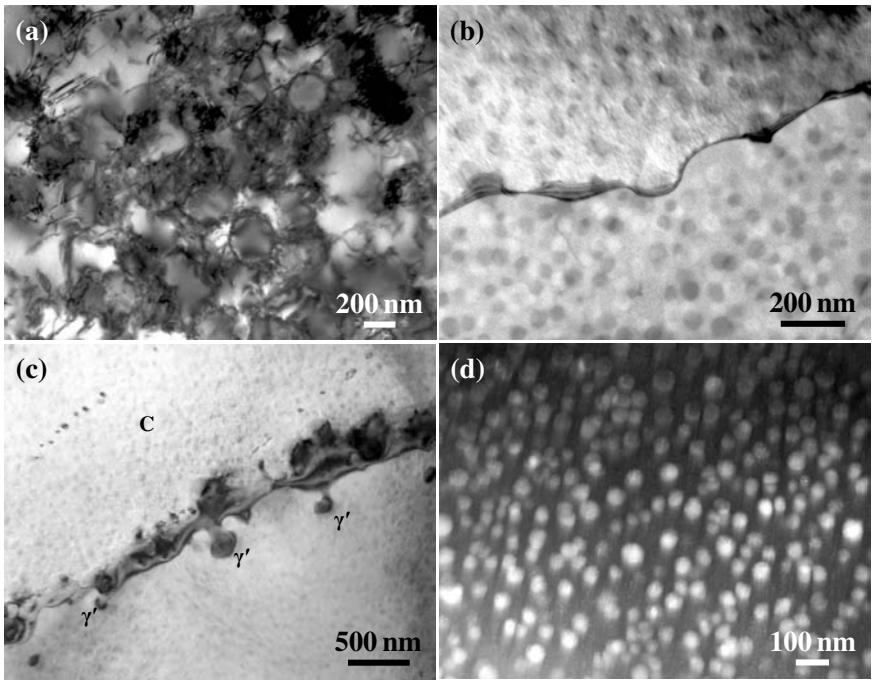

Fig. 5 TEM micrographs of as-deformed GH742 alloy, (a): deformed to true strain of 1.2 at 1050℃ and $0.1s^{-1}$, (b): deformed to true strain of 0.51 at 1065℃ and $0.1s^{-1}$, curving grain boundary indicate the influence of γ′, (c): deformed to true strain of 0.51 at 1065℃ and $0.001s^{-1}$, large γ′ can be observed at grain boundary, (d): dark field image of location C indicated in (c) shows the fine and dispersed γ′ in grain interior.

Reference

[1] Long Z D, Zhuang J Y, Deng B, Zhong Z Y. *Acta Metall Sin*, 1999; 35: 1211
[2] Meyers M A, Benson D J, Vohringer O, Kad B K, Xue Q, Fu H H. *Mater Sci Eng*, 2002; 322A: 194
[3] Semiatin S L, Weaver D S, Fagin P N, Glavicic M G. *Metall Mater Trans*, 2004; 35A: 679
[4] Hayes R W. *Acta Metall*, 1983; 31: 365
[5] Doherty R D, Hughes D A, Humphreys F J, Jonas J J. *Mater Sci Eng*, 1997; 238A: 219
[6] Prasad Y, Seshacharyulu T. *Inter Mater Rev*, 1998; 43: 243
[7] Shen G S, Semiatin S L, Shivpuri R. *Metall Mater Trans*, 1995; 26A: 1795
[8] Verdier M, Brechet Y, Guyot P. *Acta Mater*, 1999; 47: 127
[9] Sakai T, Ohashi M, Jonas J J. *Acta Metall*, 1988; 36: 1781
[10] Verdier M, Brechet Y, Guyot P. *Acta Mater*, 1999; 47: 127

[11] Speer J G, Hasen S S. *Metall Trans*, 1989; 20A: 25
[12] Simmons J P, Wen Y, Shen C, Wang Y Z. *Mater Sci Eng*, 2004; 365A: 136
[13] Gourdet S, Montheillet F. *Acta Mater*, 2003; 51: 2685
[14] Song X Y, Markus R, Zhang J X. *Acta Metall Sin*, 2004; 40: 1009
[15] McQueen H J, Ryan N D. *Mater Sci Eng*, 2002; 322A: 43
[16] Weertman J. *J Appl Phys*, 1957; 28: 362
[17] Bruni C, Forcellese A, Gabrielli F. *Mater Sci Technol*, 2002; 125: 242
[18] Siddall R J, Eggar J W. *Mater Sci Technol*, 1986; 2: 728
[19] Wahabi M E, Cabrera J M, Prado J M. *Mater Sci Eng*, 2003; 343A: 116
[20] Briottet L, Jonas J J, Monthellet F. *Acta Mater*, 1996; 44: 1665
[21] Gottstein G, Kocts U. *Acta Metall*, 1983; 31: 175
[22] Sakai T, Jonas J J. *Acta Metall*, 1984; 32: 189
[23] Crespo D, Pradell T, Clavaguera N. *Mater Sci Eng*, 1997; 238A: 160

ORIENTATION DEPENDENCE OF SECONDARY REACTION ZONES IN SURFACE MODIFIED Ni-BASED SINGLE CRYSTAL SUPERALLOYS

Hideyuki Murakami[1], Takashi Sakai[1,2], Mitsuhiro Shibata[1,3], Akihiro Yamaguchi[1,4] and Seiji Kuroda[1]

[1] Thermal Spray Group, Materials Engineering Laboratory, National Institute for Materials Science; 1-2-1, Sengen, Tsukuba-City, Ibaraki, Japan
[2]Department of Materials Engineering, Graduate School of Engineering, The University of Tokyo; 7-3-1, Hongo, Bunkyo-ku, Tokyo, Japan.
[3] Department of Mechanical Science and Engineering, Graduate School of Engineering, Chiba Institute of Technology; 2-17-1, Tsudanuma, Narashino, Japan
[4]Department of Materials Science and Engineering, Faculty of Engineering, Shibaura Institute of Technology; 3-9-14 Shibaura, Minato-ku, Tokyo, Japan

Abstract

Effects of surface treatments and coating conditions on microstructure changes of Ni-based superalloy substrates were investigated, with special attention to the orientation dependence. CoNiCrAlY (AMDRY 9954) powder was coated on Ni-based single crystal superalloy TMS-82+ by low pressure plasma spraying (LPPS). It was found that grit-blasted treatment drastically distorted the coherent γ / γ' microstructure of substrates, which accordingly promoted the uniform and accelerated the formation of secondary reaction zones (SRZ) by the post heat treatment at 1273K for 30 min, where precipitation of topologically close-packed (TCP) phases was observed. On the other hand, specimens without the grit-blast treatment had less amount of TCP precipitates, but showed preferred precipitation orientation along <011>{100} direction. Similar orientation dependence of SRZ formation was observed in the aluminized single crystal superalloy TMS-75. This orientation dependence of SRZ can occur in associate with the recrystallization of the substrate surface and subsequent interdiffusion of alloying elements.

Keywords: LPPS, CoNiCrAlY, TCP phase, aluminizing, Ni-based superalloy

Introduction

Nickel based single crystal superalloys constitute the major structural materials for turbine blades in jet engines and gas turbines. Superalloys have fcc structured γ and γ' two phase structure, where the $L1_2$ ordered γ' phase precipitates, in which Al atoms are located at cubic corners and Ni located at face centers, were distributed in the Ni-solid solutioned disordered γ phase matrix. Superior mechanical properties at elevated temperatures of Ni-based superalloys are caused by the coherent, uniform and fine (300-500nm in size) precipitation of γ' phase in the γ matrix.

As the inlet gas temperature in a current gas turbine system has already reached 1773K (which is well above the melting points of Ni-based superalloy substrates)[1], thermal barrier coatings (TBCs) on the substrate materials are essential in sustaining the turbine blades. TBCs consist of two layers, that is, a metallic bond coat layer on substrate materials for where an aluminum-enriched layer such as MCrAlY (Metal +Cr + Al+ Y) alloy coatings, or chemical aluminizing treatments were applied, and a ceramic top coat layer for which yttria stabilized zirconia (YSZ) is generally used.

The main roles of these coatings are respectively bond coats for preventing oxidation of substrates and top coat for insulating heat conduction. Due to this complex system applied for turbine blades, various factors should be taken into account to prolong the lifetime of turbine blades. Retarding the deterioration in mechanical properties of substrate materials should also be considered.

However, when the blades are exposed at high temperature, microstructural change of bondcoats and substrates, caused by the interdiffusion of alloying elements would be accelerated. For instance, inward diffusion of Al from the bondcoat to the superalloy substrate and outward diffusion of Ni vice versa would destroy the γ/γ' coherent two phase microstructure. In addition, since the diffusivities of refractory elements such as W, Re, Mo and Cr are low [2], these elements tend to segregate in the substrate and thus the precipitation of deleterious topologically close packed (TCP) phase would occur. The TCP precipitates can also destroy the γ/γ' coherent two phase microstructure, which accordingly deteriorate the creep properties of substrates.

While some defects of the coated blades, such as peeling of top the coat layer, can be repaired by recoating, degradation of substrate materials can only be solved by the replacement of the blade itself. Therefore, retarding the microstructural changes of substrates by controlling the chemistry of interfaces is one of the most important keys to prolonging the lifetime of turbine blades. It is thus of utmost importance to understand the effects of surface treatments and coating conditions on microstructure change of substrates.

There are several reports focusing on the microstructural changes of substrate materials exposed at high temperatures, such as aluminized[3], Pt[4,5] or Ir[6,7] - modified aluminized Ni-based single crystal superalloys, or MCrAlY coated polycrystal superalloys[8]. However, to the best of our knowledge, there are very few reports investigating the effects of surface morphology of substrates on microstructural changes [9]. This study investigates the effect of surface treatments and crystal orientation, on microstructural changes of CoNiCrAl Coated Ni-based single crystal superalloys prepared by the low pressure plasma spraying (LPPS) method, and aluminized Ni-based superalloys, with focusing on precipitation kinetics of TCP phases.

Experimental

LPPS deposition

Ni-based superalloy TMS-82+[10] (Ni - 7.8Co - 4.9Cr - 1.9Mo - 8.7W - 5.3Al - 0.5Ti - 6.0Ta - 0.1Hf - 2.4Re in mass %) was supplied as fully solutioned and aged single crystal bars with 25mm diameter, grown close to a <100> axis. Crystal orientation of the single crystal bars was further checked by the X-ray Laue back-reflection method, and then <100> oriented cylindrical bars (5 mm diameter x 25 mm), used as substrate specimens, were prepared by an electric discharge machine (EDM). The specimens were mechanically polished with emery paper up to #1200 followed by cleaning with acetone in the ultrasonic bath. In order to investigate the effect of surface treatment on subsequent microstructural changes, a conventional grit-blast treatment was applied to a part of specimens, in which Al_2O_3 powder, 500 -595 μm in size, was blown to the specimen with a 0.5 MPa compressed air for approximately 10 s. CoNiCrAlY powder, AMDRY9954 (Co - 32Ni - 21Cr - 8Al - 0.5Y in mass%, average particle size being

23 μm), was then coated on the side face of the specimens by the LPPS method, where the samples were clamped by the rotating jig. CoNiCrAlY deposition by LPPS was conducted in Ar atmosphere under the following conditions, arc current: 400 A, arc voltage: 50 V, Ar gas flow: 50 L/min, H_2 gas flow: 8 L/min, pressure: 150 Torr, deposition time: 10 s, powder feeding rate: 30 g/min. After the deposition, heat treatment was carried out at 1273K for 0.5 h in air with a muffle furnace.

Pack aluminizing treatment

For aluminizing, Ni-based single crystal superalloy TMS-75 [10] whose nominal composition is Ni - 12Co - 3Cr - 2Mo - 6W - 6Al - 6.0Ta - 0.1Hf - 5Re in mass % was used as a substrate material. From a fully heat treated single crystal bar with 12 mm in diameter, a <100> oriented round bar, 7.5 mm in diameter was prepared in the same manner as preparing LPPS specimens. A conventional Al pack cementation process was carried out where samples were embedded in a retort consisting of 24.5Al -24.5Fe - 49Al_2O_3 - 2NH_4Cl (mass%) powder mixture, and heated at 1273K for 5 hours in atmospheric pressure under flowing Ar. After the aluminizing treatment, samples were heated at 1273 K for 0.5 h in air.

Microstructure observation

Microstructural evolution of the samples was investigated by Philips XL 30 scanning electron microscopy (SEM) equipped with an energy dispersive spectroscope (EDS) and backscattered electron (BSE) detector. For observation, treated samples were cut along {001} followed by the mechanical polishing finished with 0.05 μm colloidal silica. In order to investigate the orientation relationship between the substrate, coated layer, and newly precipitated phases, JEOL JSM-7000F field emission SEM equipped with TSL-OIM electron back scattered diffraction (EBSD) analyzer was also used.

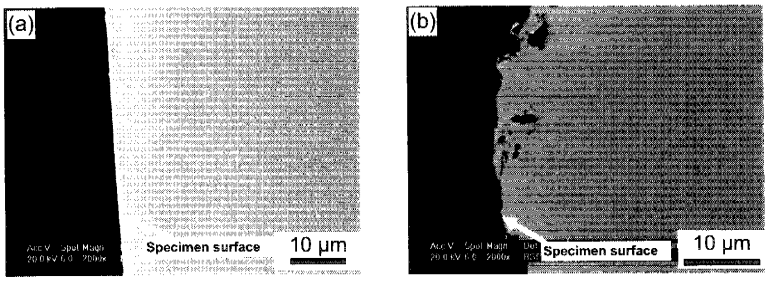

Fig. 1: Cross-sectional BSE micrographs of (a) as-polished and (b) grit blasted specimens.

Results

Microstructural change of CoNiCrAlY coated substrates[9]

In order to investigate the pre-surface treatment on microstructural changes of substrates, a grit blast treatment was conducted on the mechanically polished surface for a part of specimens. Figure 1 shows the cross-sectional backscattered electron (BSE) images of the (a) as-polished and (b) grit-blasted substrates, respectively. In fig. 1(a), the brightly contrasted γ matrices are observed as straight lines up to the vicinity of specimen surface, suggesting that the surface distortion, often induced by the mechanical surface finish, was not severely introduced in the as-polished

specimens. On the other hand, the grit blasted treatment not only roughened the surface, but also dramatically damaged the γ/γ' coherent two phase structure up to 5 μm in depth. Distortion of crystal orientation was further observed up to 5~15 μm in depth (Fig.1(b)), which is clear from the distorted lines of γ matrices.

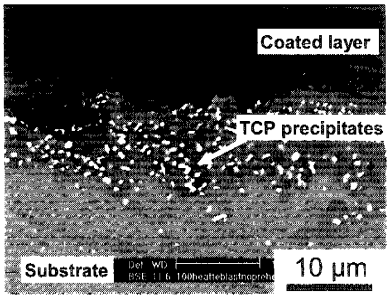

Fig. 2: Cross sectional images of grit blasted and CoNiCrAlY coated specimen after heat treated at 1273 K for 30 min.

Post-heat treatment at 1273 K for 0.5 h after the CoNiCrAlY deposition drastically changed the microstructure of substrates in the vicinity of substrate / coating interface as shown in Fig. 2, where whitely contrasted precipitates are observed with approximately 10 μm thick. These precipitates are known as the detrimental TCP phase enriched in refractory elements such as W, Mo, Re etc. In the grit-blasted substrate, the TCP precipitates are uniformly distributed from the substrate / coating interface, which is independent of crystal orientation of substrates. Hereafter, the TCP precipitation zones in the vicinity of substrate/coating interfaces are termed as secondary reaction zones (SRZ).

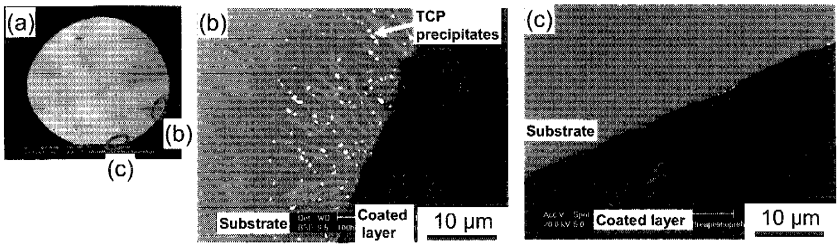

Fig.3: BSE cross sectional images of as-polished and CoNiCrAlY coated specimen after heat treated at 1273 K for 30 min, (a) whole view, (b) TCP precipitation zone and (c) no reaction zone.

In the case of as-polished substrates, on the other hand, SRZ are irregularly distributed. Precipitates are observed in Fig. 3(b), but no precipitates in Fig. 3(c). In order to understand the relationship between crystal orientation of substrates and TCP precipitation, OIM was conducted. Figure 4 shows the cross sectional SEM images of heat treated coatings and corresponding crystal orientation map, where (a) TCP precipitation was observed and (b) not observed, respectively. In the figure, the upper region of an image is the single crystal substrate and orientation maps are displayed from the Reference Direction (RD) that is normal to the substrate / coating interface, as shown in Fig. 5. Therefore, the upper set of images was taken where the substrate is oriented along <100>{001} direction whereas the lower set was taken where the substrate is oriented along <110>{001}, respectively (Note that the observation surface is {001}). The OIM investigation clearly showed that when the crystal orientation of substrate is <100>{001}, there is very little precipitation of TCP phase, while clear precipitation of TCP phase is observed along <110>{001} direction. It

should also be noted that recrystallization of substrate took place along <110>{001} direction and some of TCP precipitates were located on grain boundaries.

Orientation dependence of TCP phase precipitation kinetics was examined on the {100} plane. Figure 6 shows the thickness of TCP phase precipitation zones (SRZ) in the as-polished and grit-blasted substrates, as a function of crystal orientation. It is indicated that the grit-blasted specimen, thickness of TCP precipitate region is rather uniform, not dependent on orientation, while the as-polished samples showed clear orientation dependence of precipitation, ie. almost no precipitates along <100>{001}, but developed precipitation zones along <110>{001}. It is also found from this figure that the average thicknesses of TCP phase precipitation zones were estimated to be 8.3 μm for the grit-blasted specimen and 6.5 μm for the un-blasted specimens, respectively, indicating that the grit blasted sample exhibited more accelerated precipitation of TCP phase.

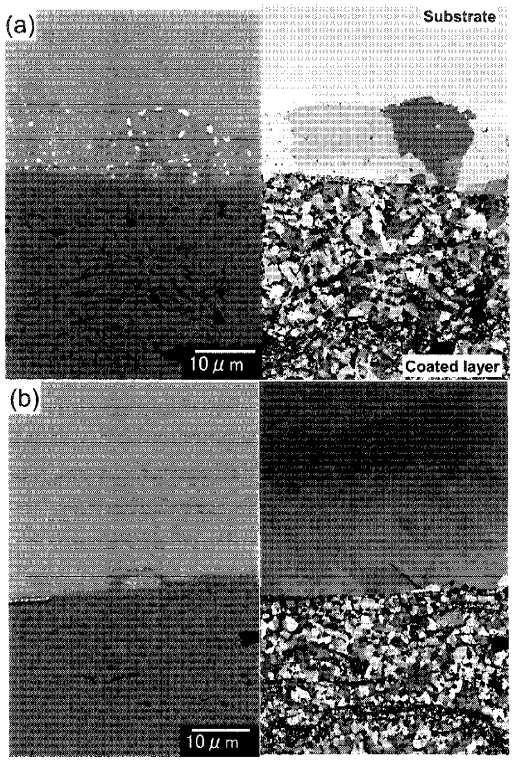

Fig. 4: Cross sectional SEM images of heat treated coatings (left) and corresponding orientation map (right), where (a)TCP is observed and (b)not observed.

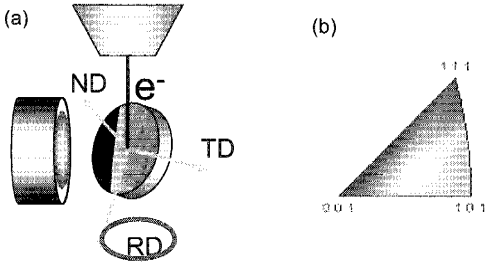

Fig. 5: (a) Crystal orientation direction and (b) orientation color map used in this study.

Microstructural change of aluminized substrates

Microstructural changes in the aluminized samples proceeded in a very similar manner to CoNiCrAlY deposited, as-polished specimens. Figure 7 shows the cross sectional SEM images of aluminized and heat treated specimens and corresponding crystal orientation map, where (a) SRZ was well developed and (b) SRZ was not

observed. Similar to Fig. 4, the upper region of an image is the single crystal substrate and orientation maps are displayed from the Reference Direction that is normal to the substrate / coating interface. It is again confirmed that when the crystal orientation of substrate is <100>{001}, there is very little precipitation of TCP phase, while clear precipitation of TCP phase is observed along <110>{001} direction were the recrystallization of the substrate took place.

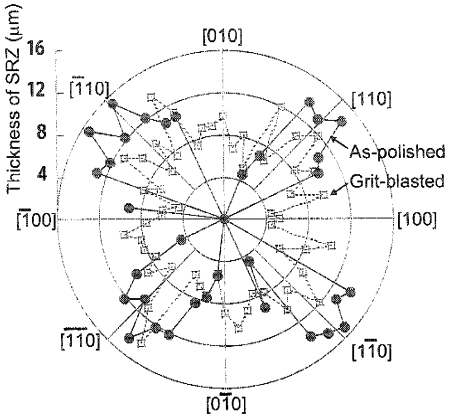

Fig.6 Thickness of TCP precipitation zone (SRZ) as a function of crystal orientation.

Discussions

Effect of pre-surface treatment

The difference in formation kinetics of TCP phase precipitation zones between the grit blasted and as-polished specimens could be explained in the following manner. In the case of grit blasted specimens, deformation of surface was so severe that a regular crystal orientation of the substrate was completely destroyed as shown in Fig. 1(b), leading to the random and uniform distribution of TCP precipitation. Heavy deformation may also promote the precipitation of additional phases which are thermodynamically stable. Indeed, current Ni-based superalloys contain large fraction of refractory elements such as Re, W, Mo, Cr, Ta in order to enhance the creep properties. However, addition of these elements in turn destabilizes the coherent and fine γ/γ'

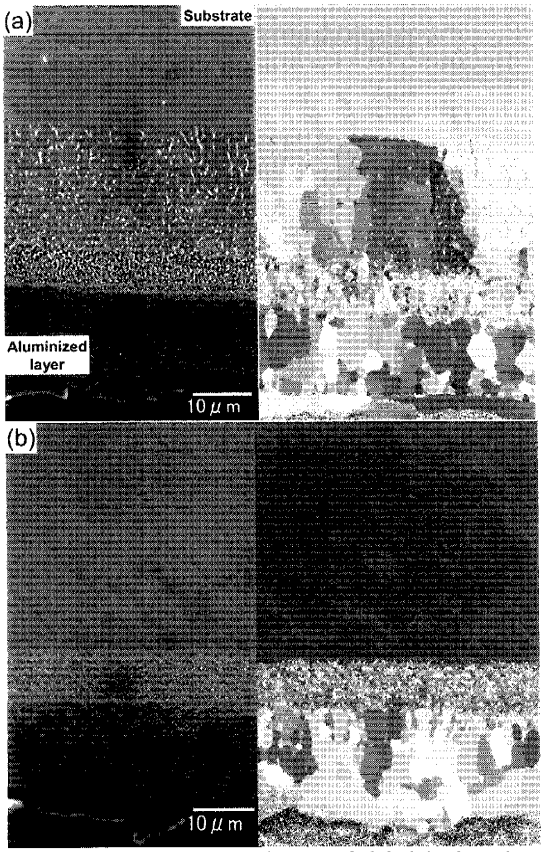

Fig. 7: Cross sectional SEM images of alulminized coatings (left) and corresponding orientation map (right), where (a)TCP is observed and (b)not observed.

two phase structure. In addition, the internal stress applied to the substrate could accelerate the interdiffusion of alloying elements. EDX analysis revealed slight enrichment of Al in the TCP precipitation zones in Figs. 2, 3(b) and 5(a). This result may have been caused by the inward diffusion of Al and outward diffusion of Ni, which could also be accelerated by the relaxation of internal stress in the initial stage. Combination of these factors discussed above may be attributed to the uniform and rapid formation of TCP phase in the grit blasted specimens. In the as-polished specimens, precipitation of TCP phase was slower than that in the grit-blasted ones, which may be attributable to the less deformation of surface.

Although the grid blast treatment is essential in order to increase the adhesion between substrates and coating layers, this study revealed that severe surface deformation accelerates the TCP precipitation, resulting in the deterioration of mechanical properties of substrates. Novel surface treatment which keeps the adhesion but without heavy surface deformation will be one of the key factors in increasing the lifetime of coating layer, which would be further study.

Orientation dependence of secondary reaction zone

In the as-polished and CoNiCrAlY coated TMS-82+ and aluminized TMS-75, orientation dependence of TCP precipitation was observed. To explain this phenomenon, following reasons can be taken into account; i) preferred precipitation orientation of TCP phases in relation to the single crystal substrates, ii) orientation dependence of interdiffusivity of alloying elements such as Al, Ni, and iii) anisotropy of strain or residual stress applied during process. As for the first hypothesis, Rae et al. [5,12]showed that the σ phase, one of the TCP phase group, formed coherently on {111} planes in the aluminized Ni-based single crystal substrates. However, in this study, no such orientation relationship between the substrate and TCP phase is observed. It is thus likely that the preferred precipitation orientation can be caused by the latter two reasons. It is clear from Figs. 4 and 7 that recrystallization accommodates with SRZ formation, resulting in the acceleration of interdiffusion via grain boundaries and subsequent precipitation of TCP phases. In addition, stress has been shown to both enhance and delay the formation of TCP phase, depending on Ni-base superalloy substrates[13]. It is well known that the dominant slip system in fcc crystals is <110>{011} and the orientation image maps in Figs. 4 and 7 show the slight misorientation along the slip system on the substrate surface, suggesting that strain along the slip system may have played important role in promoting the recrystallization. In fact, recrystallized grain boundaries can be seen along <110>{001} but not along <100>{001}, which may support our hypothesis. Further study is nevertheless necessary to understand whether precipitation of TCP phase is followed by or preceded by the recrystallization.

Orientation dependence of mechanical properties of N-based alloys is well studied and it is well known that single crystal alloys have the strongest creep resistance along <111> tensile direction, <100> comes next and <110> direction is the weakest. This study showed that detrimental phase precipitation easily occurs along <110> direction. Turbine blades are generally cast along <100>, however, if the "secondary orientation" of the blade can be controlled such as to avoid {011} surface for the high temperature or high stress zones, there is a possibility of prolonging the lifetime of the blades. This study suggested the importance in "secondary orientation" for designing and fabricating blades.

Conclusions

- For CoNiCrAlY coating prepared by LPPS, grit-blast treatment accelerates TCP phase precipitation.
- Crystal orientation dependence of TCP phase precipitation in the as-polished, CoNiCrAlY coated and aluminized substrates is observed, that is, no precipitation along <100>{001} while accelerated precipitation along <110>{001}.

References

[1] Y. harada, J. Turbine Soc. Jpn. **31**(2003) 97-107
[2] C.C.Jia, K.Ishida, T.Nishizawa, Metall.Trans **A25**(1994)473-485
[3] Silke Wollmer , Stefan Zaefferer , Mathias Goken , Thomas Mack , Uwe Glatzel, Surf. Coat Tech. **167** (2003) 83-96
[4] F.Pedraza, A.D. Kennedy, J. Kopecek, P. Moretto, Surf. Coat. Tech., in press, available on line (2006).
[5] C.M.F. Rae, M.S.Hook, R.C. Reed, Mater. Sci. Eng. **A396**(2005), 231-239
[6] Feng Wu, Hideyuki Murakami and Hiroshi Harada, Mater. Trans. **44**(2003) 1675-1678.
[7] P. Kuppusami and H. Murakami, Surf. Coat. Tech. **186** (2004) 377– 388.
[8] B.Baufeld, M.Schmucker, Surf. Coat. Tech., **199**(2005)49-56
[9] T. Sakai, M. Shibata, H. Murakami and S. Kuroda, submitted to Mater. Trans., (2006).
[10] T. Hino, T. Kobayashi, Y. Koizumi, H. Harada and T. Yamagata: *Superalloys 2000*, Ed. by K. A. Green, T. M. Pollock and R. D. Kissinger, (The Minerals, Metals, Materials Society, Warrendale, Pittsburg, 2000) pp. 729-736.
[11] T.Kobayashi, Y.Koizumi, S.Nakazawa, T.Yamagata and Harada, H; Advances in Turbine Materials, Design and Manufacturing; Newcastle upon Tyne, UK, (1997), 766-773.
[12] C.M.F. Rae, R.C. Reed, Acta Mater. **49**(2001)4110-4125.
[13] M.V.Acharya, G.E. Fuchs, Scr. Mater., **54**(2006)61-64.

STUDY ON THE INVESTMENT CASTING PROCESS OF K418 SUPERALLOY TURBINE

Juntao Li, Minghan Zhao, Chong Shao, Shengguo Kong, Jiantao Wu, Wei Li
Central Iron & Steel Research Institute, Beijing 100081, China, juntaoli@tom.com

Abstract: K418 superalloy turbine is a pivotal component in advanced small engines requiring high metallurgical quality and mechanical properties. The turbine includes blades, turbine disk and shaft. It is a near net shaped, thin wall superalloy investment casting. The blades are long and thin, thus they are difficult to fill; the shaft is long and thin, which is apt to form porosity and shrinkage cavities. So it has great difficulties in casting this turbine. Numerical simulation was adopted to simulate the solidification course and casting defects of the turbine under various process conditions. According to the results of simulation, non-conventional sand case was designed to control and strengthen the cooling condition of turbine shaft, at the same time, proper parameters of casting process were adopted. As a result, the turbine has excellent mechanical properties, high metallurgical quality and high percent of qualified products, which satisfies the requirements of usage and design well.

Keywords: K418 superalloy turbine, numerical simulation, non-conventional sand case

1 introduction

The K418 superalloy turbine is a high speed, high temperature and high loading rotating pivotal component in advanced small engine requiring high metallurgical quality and good mechanical properties. The turbine is composed of blades, turbine disk and shaft. Blade is thin and long, which trailing edge thickness is only about 0.4mm and the length is up to 56mm, thus cause mis-run easily. The diameter of disk is about 220mm and the thickness is about 16mm, which is apt to form porosity defect. The length of shaft is up to 140mm, while the diameter is only about 16mm, which is apt to form porosity and shrinkage cavities for solidification feeding difficultly. So it has great difficulties in casting this thin wall and complex integral precision K418 superalloy turbine. It is hard to acquire best cooling condition during solidification and achieve best casting process parameters for this casting. The casting process parameters were studied systematically and numerical simulation for solidification was adopted to guide and optimize the casting process design.

2 Experimental procedures

The material is K418 Ni-base superalloy [1], which major chemical weigh fractions are: C: 0.08～0.16, Cr: 11.5～13.5, Mo: 3.8～4.8, Al: 5.5～6.4, Ti: 0.5～1.0, Nb: 1.8～2.5, B: 0.008～0.02, Zr: 0.06～0.15. The 800℃ tensile and 800℃/490MPa endurance tests were carried out to examine the mechanical properties of turbine. The microstructure and porosity

were observed by optical metallographic microscope. CASTsoft[2] was adopted to simulate the solidification course.

3. Design of casting process and discuss

Big pouring cup was designed for pouring melt rapidly to fill mold and form high static pressure quickly to avoid the long and thin blades mis-run. The pouring system with spherical feeding head was adopted to gain good feeding capacity. In order to gain high mold temperature, the mold was stuffed with dry quartz sand and roasted in electrical resistance furnace at 1000℃.

The result of casting indicates that spherical feeding head has good feeding capacity, leading to high interior metallurgic quality of the turbine disk, while serious micro-porosities formed in the long and thin shaft which causes great difficulties in solidification feeding. Although different tests were done through adjusting the pouring and mold temperatures and other casting process parameters, serious micro-porosities in shaft exist all along. So it is hard to eliminate the serious micro-porosities in shaft by conventional casting process.

A large amount of time would be cost and many experiments should be done to ascertain feasible casting process for such complex structure casting according to the method of traditional trial and error. In order to save time and cost and gain optimum casting process, numerical simulation was adopted to simulate the solidification course under different process conditions and predict the porosity defect and so on. The casting process was adjusted and optimized according to the result of simulation.

The numerical simulation soft of solidification adopted is CASTsoft. Three-dimensional entity sculpting was done by UG soft firstly, and then the three-dimensional entity sculpting was output to CASTsoft through sterolithography style, and mesh subdivision was carried out with finite difference calculus method. All physical and casting process parameters were properly set respectively according to different casting process and casting solidification condition. The Niyam criterion to porosity defect was employed for CASTsoft[2].

The solidification courses of different casting process were simulated at various pouring and mold temperatures. The simulation results show that the turbine disk has high metallurgic quality, but serious porosity defect exist in the shaft when using traditional stuffing dry quartz sand around mold, as it could be seen from Fig.1. At the same time, the porosity in the interior of the shaft can be reduced to a certain extent and the distributing area also can be shifted through adjusting the pouring temperature, mold temperature and other casting process parameters. While the thin and long shaft causes limited feeding entryway and inferior feeding capacity [3], it is difficult to realize sequential solidification in the area of

shaft. As a result, the interdendritic area in the shaft cannot be feeding effectively and form serious porosity defect during solidification. It is hard to increase temperature gradient and decrease feeding distance through adjustment of pouring and mold temperatures and other casting parameters with conventional method only, which was consistent with the practical casting .

Casting solidification courses with different solidification conditions were simulated. The results show that the porosity in the interior of shaft can be eliminated only under the condition of controlling and strengthening the solidification cooling in the area of shaft, which forms high temperature gradient and proper solidification cooling direction to intensify feeding capacity and realize the sequential solidification from the end to the root of shaft.

The controlling and strengthening solidification cooling is needed to meet the numerical simulation requirement for sequential solidification and obtain high metallurgical quality at the area of shaft. It is hard to meet this requirement by adjusting pouring and mold temperatures and placing iron chill under shaft conventionally because the cooling intensity is much lower than the requirement of simulation. Non-conventional sand case with special cooling equipment was designed to meet the requirement of strengthening solidification cooling for the area of shaft. Solidification cooling condition was improved greatly through strengthening cooling of non-conventional sand case, at the same time, pouring and mold temperatures were adjusted through numerical simulation to achieve good matching. At last, the serious porosities in the shaft were eliminated. The simulation of porosity evident defect of turbine using non-conventional sand case could be seen from Fig.2. It was seen that there was no porosity in the disk and shaft, shrinkage cavity and porosity were removed from casting and distributed in the running channel and gate riser. The simulation of solidification course of turbine using non-conventional sand case could be seen from Fig.3. It was seen that the solidification of turbine was from the end to the root of shaft and from the edge to the center of disk, so it was the ideal sequential solidification. At the same time, the runner system with spherical riser using wrapping heat insulation material has high feeding capacity. At the end of casting solidification the riser has enough melt to offer feeding static pressure ensuring the casting has compact-grain structure.

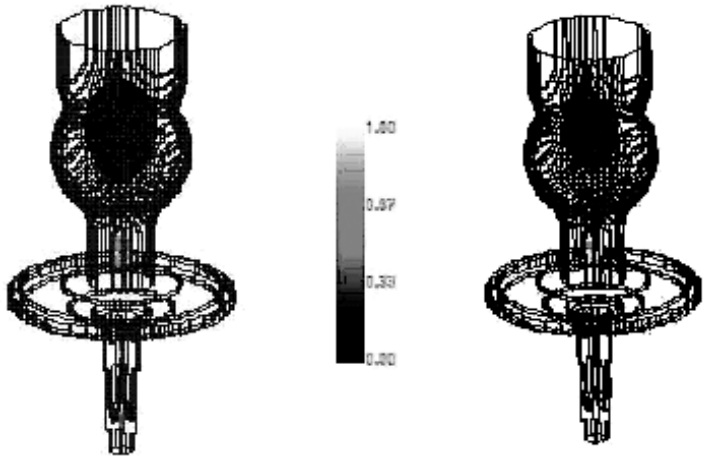

Fig1 Micro-porosity appeared when normal sand box is adopted

Fig2 Micro-porosity was disappeared when non-conventional type sand box is adopted

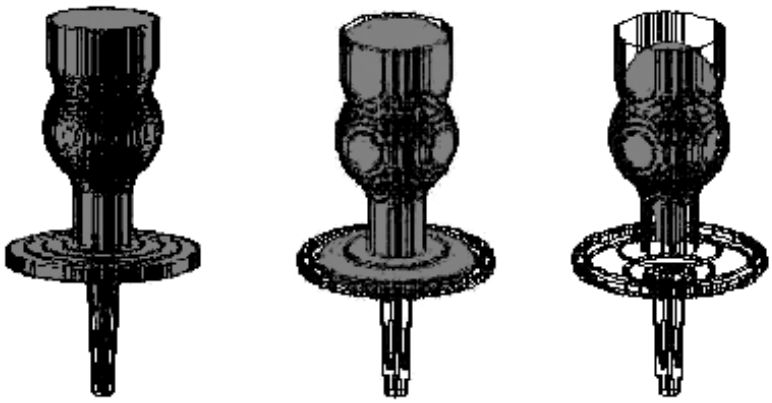

Fig3 process of solidification when non-conventional type sand box is adopted

4 The result of casting tests with non-conventional sand case

4.1 The micro-porosity in the interior of casting

It is necessary to know the inner metallurgical quality and the design rationality of non-conventional sand case with special cooling equipment, mold temperature, pouring temperature and other casting process parameters to ensure the safe and credible usage of K418 superalloy turbine casting. The turbine casting was sectioned along axial line to examine micro-porosity. The checking samples were got from disk and shaft respectively.

The results show that the disk and shaft have compact-grain structure and high metallurgical quality. The micro-porosity in the interior of the disk and shaft were shown in Fig.4. It was seen that the result of practical casting was in accordance with the numerical simulation well.

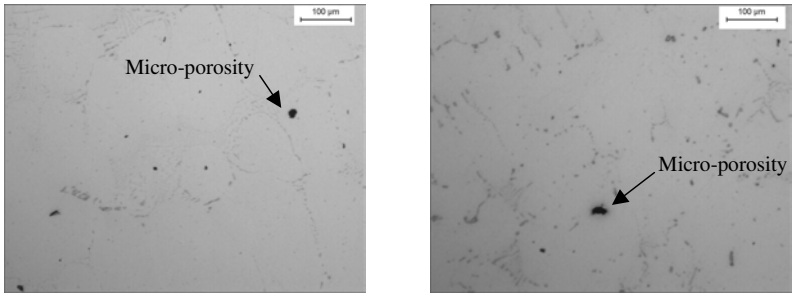

Fig4 Micro-porosity in turbine disk and shaft when non-conventional type sand box is adopted

4.2 Mechanical properties of K418 superalloy turbine

In order to examine the mechanical properties of K418 superalloy turbine using non-conventional sand case with special cooling equipment, two turbines was cut by linear cutting and made into standard mechanical testing samples with working diameter 5mm.

Because the solidification feeding capacity of casting is lower than that of standard mechanical testing sample generally, the mechanical properties of samples cutting from casting is lower than standard mechanical testing sample obviously. The testing results of mechanical properties were shown in Table.1. The 800℃ tensile strength is above 800 MPa and the 800℃ creep rupture life at 490 MPa exceeds 70 hours. At the same time, the mechanical properties keep high stability. It was seen that 800℃ tensile and endurance properties of samples cut from the two turbines all reach or(and) exceed the requirement of standard mechanical testing sample.

Table1 mechanical performance of turbine rotor

state	Tensile properties				Endurance properties		
	temperature (℃)	σb (MPa)	δ_5 (%)	Ψ (%)	temperature (℃)	σ (MPa)	T (h)
Samples cut from turbine castings	800	825	6.5	6.5	800	490	76:50’
	800	820	7.0	9.5	800	490	69:08’

5. Summary

1. The numerical simulation was adopted to select and optimize the casting process parameters of K418 superalloy turbine. The result shows it is difficult to achieve high interior metallurgical quality of the shaft through adjustments of pouring and mold temperatures only. It is necessary to control and strengthen the solidification cooling of shaft.

2. The non-conventional sand case with special cooling equipment was designed to meet the requirement of solidification cooling. Sequential solidification of turbine disk and shaft were achieved well and porosity and shrinkage defects were avoided effectively.

3.The K418 superalloy turbine casting has high metallurgical quality and good mechanical properties. The 800℃ tensile strength is above 800 MPa and the 800℃ creep rupture life at (under) 490 MPa exceeds 70 hours, which satisfies the requirements of usage and design well.

Reference:

[1] Yan minggao et al, K418 casting superalloy, Engineering material handbook, 2002 8, 612:621

[2] Xu hong, Cheng jun, Zhong xueyou, Summary of casting CAE integrated technology, Material guide, Vol.16 No.6, 2002, 6:8

[3] Li ri Liu baicheng Li wenzhen, The Importance of Temperature Gradient on Thick-wall Steel Casting, MECHANICAL SCIENCE AND TECHNOLOGY, Vol.23 No.1, 2004, 92:95

STUDY ON CASTING PROCESS OF K4537 SUPERALLOY GAS TURBINE

Chong Shao, Juntao Li, Minghan Zhao, Wei Li, Jiantao Wu, Shengguo Kong
Central Iron & Steel Research Institute, Beijing, 100081, China,yzxmy@sohu.com

Abstract

The production process of adopting computer aided investment casting technology (CAICT) to develop and produce K4537 superalloy gas turbine was introduced, and the casting process was studied systematically in this paper. Through computer aided investment casting technology, rapid shaping of investment pattern, numerical simulation of casting process and defect prediction were realized, the research cycle of precision casting was shortened greatly, and the cost of development was reduced. By adopting grain refining technology and proper casting technology, the blade surface of turbine casting has even and tiny equiaxed grain, and the casting had good mechanical properties and high product percent of qualified products.

Keywords: K4537 turbine, numerical simulation, mechanical properties

1. Introduction

The K4537 superalloy gas turbine works at about 850℃and the rotational speed reaches 60000r/min, which is a high speed, high temperature, high loading rotating part, bears high stress and serious gas corrosion for a long time. The turbine is a key part in engine. The nickel-based casting superalloy K4537 which has good heat corrosion resistance is selected [1], and the alloy composition is C0.07-0.12, Cr15.0-16.0, Co9.0-10.0, W4.7-5.2, Mo1.2-1.7, Al2.7-3.2, Ti3.2-3.7, Nb1.7-2.2, B0.01-0.02, Zr0.03-0.07(in weight%).

The integral casting K4537 turbine consists of central disk and 13 blades. The central disk of the casting is thick and large, and is apt to form porosity and shrinkage cavity because of difficult solidification feeding. The blade profile is complicated, large and thin. It is 50mm long, 70mm high, and the thinnest of trailing edge is only 0.6mm, so the casting is difficult in shaping. Because the turbine is a high speed, high temperature and high loading rotating part, the casting does not allow to repairing welding and require fine metallurgical quality, high comprehensive mechanical properties and blade profile dimensional precision. It is difficult to cast this K4537 superalloy turbine. After original design is determined, the design department demands to get first casting as soon as possible for using in the verifying test. If traditional casting method was adopted, it will take very long cycle to machine mould and trial-produce casting. If the experimental result of appraisal is unsatisfactory and the design needs to be changed, then the mould will be discarded basically and the losses will be very great. In order to accelerate development progress and economize the cost, advanced computer aided investment casting technology-CAICT has been adopted during the development and production of this turbine. The technological process and production process of adopting

CAICT to develop and produce K4537 superalloy turbine was introduced systematically in this paper. CAICT was adopted to realize rapid shaping of investment pattern and numerical simulation of casting process and quality controlling at different stages of casting, which has significant influence on investment casting.

CAICT adopts integrated mode of “design, material, technology”, which integrates some advanced technologies together, such as CAD/CAM technology, rapid prototyping manufacturing (RPM), and casting process numerical simulation (CPS) etc., to apply to producing the precision casting with high dependability and high percent of qualified products [2]. CAICT can realize whole quality control on the production process of casting. The process flow of CAICT is shown in Fig.1. The two-dimensional drawing is transformed into three-dimensional geometry model in the computer, and then the three-dimensional geometry information is input into the rapid prototyping equipment to make investment pattern directly. At the same time, the numerical simulation is carried on in the course of solidifying, predicts the defect of casting, optimizes casting process parameters, shortens development cycle greatly and reduces development cost. CAICT is one of the advanced manufacturing technologies with the fastest developing speed in the world.

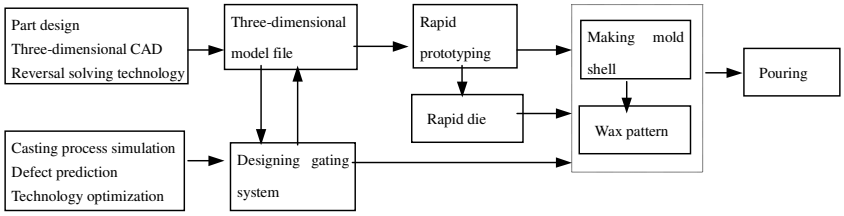

Fig.1 CAICT process flow diagram

2. Study on casting technique of casting

2.1 The manufacturing of rapid prototyping investment pattern

Traditional investment casting method needs to make metal die for pressing wax mould in advance. Because the structure of this gas turbine is very complicated and the requirement of size precision is very high, making die is very difficult and the designing and machining cycle is quite long. Moreover, the blade profile precision is high and the die is even machined repeatedly, so it needs a large amount of time and cost. As a rule, the making of metal die is the bottleneck in the course of investment casting to produce such complicated casting.

In order to solve this difficult problem, the rapid prototyping technique of investment pattern is adopted. At first, the casting three-dimensional modeling is established, then the entity model is changed into the format of STL (Sterolithography) with RP file standard and the bugs arising during file transferring is mended. After ensuring that files are free from these mistakes such as cracks, cavities, suspending surface, overlapping surface and cross surface etc., layered treatment is carried out. The thickness of layered tablets is chose between

0.10mm and 0.15mm. After complex treatment, the files are transferred to molding equipment. The method of district selecting laser sintering (SLS) is adopted to sinter wax mold. After certain surface treatment is done for the investment pattern manufacturing, the roughness of surface can reach Ra6.3, which has guaranteed the dimensional precision and surface quality of investment pattern well. So the fusible vanishing mould instead of traditional wax mould is used directly for investment casting, not requiring making metal die or pressing wax mould. Three-dimensional modeling and rapid prototyping mould of K4537 superalloy gas turbine are shown in Fig.2.

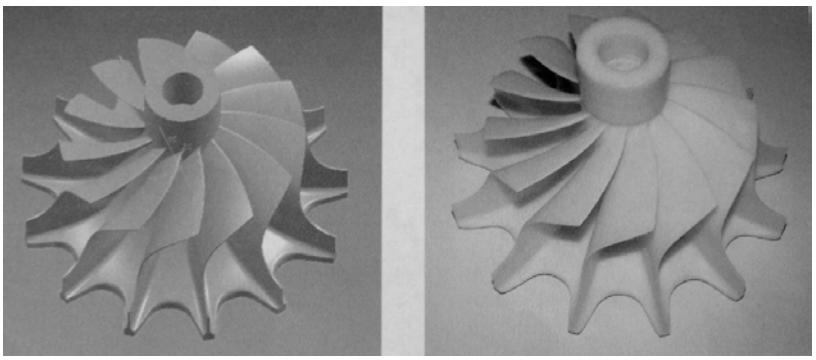

Fig.2 Three-dimensional modeling and rapid prototyping mould of K4537 superalloy gas turbine

2.2 Mold making

The gas turbine, which works under the conditions of high temperature, formidable circumstance, high stress and alternating fatigue stress, needs high fatigue resistance. In order to improve the fatigue resistance of turbine blade, the crystal grains of the blade should be controlled as tiny equiaxed crystal grains for the best. Grain refinement of casting surface is adopted, and zirconite powder is selected as surface fire resisting material because of its high melting point and good chemical stability. The slurry of cobalt aluminate-silica sol-zirconite powder is used as primary surface layer, and gangue is used for secondary layer because of its moderate high-temperature intensity and good concession and dispersion performance.

Because the fusing temperature range of the sintering powder material used is 178~196℃ and the flowability of fusing powder is bad, prototype cannot be taken off completely if steam stripping is adopted. Studies have shown that prototype can be separated smoothly by toasting at high temperature. In order to prevent mold from splitting, hollowed-heart treatment is adopted while fritting prototype to reserve some interval for buffering the expanding of the prototype during toasting. The material of prototype is toasted at high temperature and is apt to leave some ash. Through roasting at high temperature, the majority of ash can be oxidized, and the residual ash can be cleared by reaction in the high pure oxygen environment.

2.3 Casting process design

The solidifying temperature interval of K4537 superalloy is1255～1335℃[1]. In order to reduce the crystal grain size of the casting and improve the heat fatigue resistance of the turbine impeller blade, it needs to decrease the pouring temperature and avoid big crystal grains. However, the blade of the casting is big and thin, it is difficult to shape while the pouring temperature is too low, so the pouring temperature is chosen at the temperature interval of 1420～1450℃. The numerical simulation is adopted to simulate the solidifying course. The simulation result shows that the casting is apt to form serious porosity and shrinkage cavity near the gate when pouring at upper limit temperature, as shown in Fig.3. Pouring at lower temperatures helps to realize the sequential solidification and improve the internal metallurgical quality of casting.

In order to guarantee that the casting has good metallurgical quality, pouring should be controlled at lower temperatures. But adopting low pouring temperatures is unfavorable to shape the blade trailing edge in practice. On the other hand, the pouring speed has significant effect on filling capability of casting and rapid speed is favorable to the filling of casting. In order to guarantee good shaping of casting at lower pouring temperatures, gating system with big pouring cup that can fill the liquid rapidly is adopted to ensure that the time of filling the liquid into gating system is less than 2 seconds. Through the rapid filling of liquid, the hydrostatic head has been erected rapidly on one hand, and on the other hand, the distributary of liquid has been avoided, which prevents casting from producing cold shut and misrun.

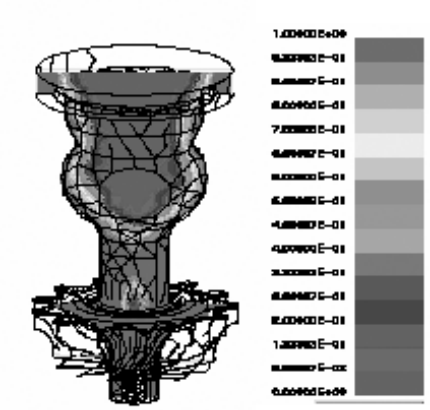

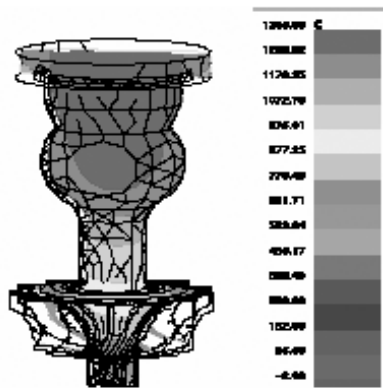

Fig.3 porosity and shrinkage when pouring at upper limit temperature

Fig.4 the progressive solidification of the casting with strengthening solidification cooling

In order to prevent mis-run of blade, higher mold shell temperature has been adopted, and the temperature is selected as 1050℃. On one hand higher mould shell temperature can improve the filling capability of the blade, because for thin wall casting, the main factor influencing filling capability of casting is mold shell temperature [3]. Increasing mold shell temperature is to reduce the shock cooling on melt, which improves the filling capability of casting effectively.

Because the turbine disk is thick and big, it needs to realize the sequential solidification of the disk in order to obtain high metallurgical quality, and it also needs to improve temperature gradient effectively to strengthen feeding capacity of central position [4]. Studies have shown that it is difficult to obtain comparatively ideal solidification cooling condition on the turbine position just by adjusting mould shell temperature and pouring temperature, and there are serious microporosity existing on the central department of the disk. Through strengthening solidification cooling partially under the turbine to increase temperature gradient and adopting heat insulation measure at the gate to delay the solidification time of gate, the feeding capacity has been improved effectively. After strengthening solidification cooling partially, the sequential solidification of the casting has been realized well, as shown in Fig.4.

3. Micro-structure, mechanical properties and experimental appraisal

To ensure the secure and reliable use of casting, the average crystal grain size on the blade surface of casting is limited to 2.0mm.The average size of crystal grains on the blade surface of the casting is about 1.0mm, and the grains on the blade surface are tiny and even, as shown in Fig.5.

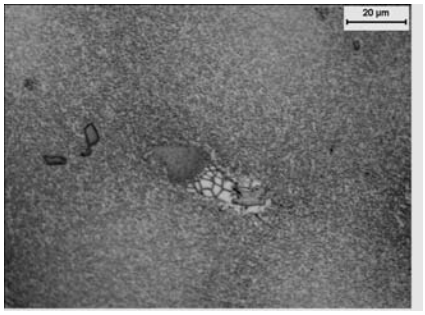

Fig.5 crystal grains on the blade surface of K4537 superalloy gas turbine
Fig.6 microstructure of K4537 superalloy gas turbine

In order to master the rationality of casting process parameters, such as gating system, mold temperature, pouring temperature, molding condition, etc., samples are cut from the disk and blade of the casting to observe the microstructure. The results show that the microstructure of alloy is mainly consists of γ matrix phase, γ' strengthening phase, massive (γ + γ') eutectic and MC carbide. They distribute thinly and evenly, as shown in Fig.6.

Because the solidifying cooling condition of precision casting is generally worse than that of shaping samples, the mechanical properties of the samples cut from precision casting are worse than the shaping samples obviously. The mechanical properties testing results of samples taken from the turbine casting of K4537 superalloy gas turbine are shown in Table 1. The high-temperature tensile and endurance properties all reach the mechanical properties

requirement of K4537 superalloy shaping samples [1], which shows that the casting has high metallurgical quality and comprehensive mechanical performance.

Table 1 mechanical properties of K4537 gas turbine casting

	Tensile properties				Endurance properties		
	Test temperature (℃)	σ b (MPa)	δ_5 (%)	Ψ (%)	Test temperature (℃)	σ (MPa)	T (h)
Shaping sample requirement	800	⩾784	⩾3	⩾3	850	363	⩾50
Sample of casting (average)	800	820	6.0	10.0	850	363	55

The K4537 superalloy gas turbine which is developed and produced by computer aided investment casting technology (CAICT) has passed long-time testing appraisal, and each performance index has reached the designing requirement.

4. Conclusions

1. Through computer aided investment casting technology, rapid shaping of investment pattern, numerical simulation of casting process and defect prediction are realized, the research cycle of precision casting is shortened greatly, and the cost of development is also reduced.

2. The K4537 superalloy gas turbine has high metallurgical quality and good mechanical properties. The 800℃ tensile strength reaches 820MPa and 850℃ creep rupture life at 363MPa exceeds 50 hours, which satisfy the requirements of usage and design well.

References

[1] Yan minggao, K4537 casting superalloy, Engineering material handbook, 8, 2002, 693:697.

[2] Li juntao, Wu jiantao, Computer aided investment casting technology for cast superalloy, Journal of iron and steel research, Vol.15 No.7, 2003, 298:302.

[3] Li juntao, The study on mechanical properties and casting process of Ti-46.5Al-2.5V-1Cr alloy, Postdoctoral report, 2001, 39.

[4] Li ri, Liu baicheng, Li wenzhen, The importance of temperature gradient on thick-wall steel casting, Mechanical science and technology, Vol.23 No.1, 2004, 92:95.

DIFFUSION COEFFICIENT OF REFRACTORY ELEMENTS IN MULTI-COMPONENT Ni ALLOYS

Y.Murata[1], M. Hattori[1], Efendi[1], N.Goto[1], T.Koyama[2] and M. Morinaga[1]

[1]Department of Materials, Physics and Energy Engineering,
Graduate School of Engineering, Nagoya University,
Furo-cho, Chikusa, Nagoya 464-8603, Japan
[2]National Institute for Materials Science, Tukuba 305-0047, Japan
e-mail: murata@numse.nagoya-u.ac.jp

Abstract

Interdiffusion coefficients of the refractory elements in Ni-X-Y (X, Y=W, Re, Ru, Al) ternary systems, which are the fundamental systems of Ni-based superalloys, were estimated by a series of experiments using diffusion couples. The modified ternary Boltzmann-Matano method was employed for analyzing the experimental data. The cross interdiffusion coefficients were smaller than the main interdiffusion coefficients in all systems. Especially, the cross interdiffusion coefficient $\tilde{D}^{\mathrm{Ni}}_{\mathrm{ReRu}}$ is much smaller by an order of magnitude than the main interdiffusion coefficient $\tilde{D}^{\mathrm{Ni}}_{\mathrm{ReRe}}$ in Ni-Ru-Re system. This result implies that the thermodynamical interaction parameter (Wagner's interaction parameter) between Ru and Re is negligible.

Keywords: diffusion coefficient, nickel-based alloy, rhenium, tungsten, ruthenium

Introduction

Refractory elements such as W and Re play an important role in improving the strength of Ni-based superalloys at elevated temperatures [1, 2]. But an excess amount of refractory elements leads to the formation of the brittle TCP (topologically close-packed) phases [3], resulting in shortening of the creep rupture life. It is also known that Ru suppresses the formation of the TCP phases, but the mechanism is still not clear [4].

Diffusion coefficients in multi-component alloys are known to correlate with the thermodynamic interaction parameters of the component atoms [5]. Thus it is important to examine the diffusion of alloying elements in superalloys [6] in order to make it clear the behaviour of these elements in the alloys. However, there is no available data on diffusion even in Ni-Al-X (X: Re, W, Ru) ternary systems, which are very important fundamental systems of advanced Ni-based single crystal superalloys. Furthermore, the examination of the diffusion coefficients of Ru, Re and W in Ni-Ru-X (X: Re, W) ternary system is also important in order to discuss the thermodynamical interaction between Ru and the refractory elements in Ni alloys.

The purpose of this study is to measure the diffusion coefficients of Ru, Re and W in Ni-X-Y (X, Y: Re, W, Ru, Al) ternary systems, which are fundamental systems of Ni-based superalloys.

Theory

In this study, the modified ternary Boltzmann-Matano method was employed to estimate the interdiffusion coefficients. This method enables to calculate the interdiffusion coefficients without determination of the Matano plane, and hence the diffusion coefficients of multi-component alloys can be estimated with accuracy [7]. According to Whittle *et al*. [8], interdiffusion coefficients relate to the experimental values obtained from the concentration profiles as the following equations.

$$\tilde{D}_{ii}^{k} + \left(dC_j / dC_i\right)\tilde{D}_{ij}^{k} = \left(1/2t\right)\left(dx/dY_i\right)\left[\left(1-Y_i\right)\int_{-\infty}^{x} Y_i dx + Y_i \int_{x}^{\infty}\left(1-Y_i\right)dx\right], \quad (1)$$

$$\tilde{D}_{jj}^{k} + \left(dC_i / dC_j\right)\tilde{D}_{ji}^{k} = \left(1/2t\right)\left(dx/dY_j\right)\left[\left(1-Y_j\right)\int_{-\infty}^{x} Y_j dx + Y_j \int_{x}^{\infty}\left(1-Y_j\right)dx\right], \quad (2)$$

$$Y_i = \left(C_i - C_i^{-}\right)/\left(C_i^{+} - C_i^{-}\right), \quad (3)$$

where both $\tilde{D}_{ii}^{k}$ and $\tilde{D}_{jj}^{k}$ are the major interdiffusion coefficients which represent the influence of concentration gradients of *i* and *j* elements upon their own fluxes, and $\tilde{D}_{ij}^{k}$ and $\tilde{D}_{ji}^{k}$ $(i \neq j)$ are the cross diffusion coefficients which represent the influence of the concentration gradients of *i* and *j* elements on the fluxes of *j* and *i* elements, respectively. Here, the superscript symbol *k* represents the host element, i.e. Ni in this case. These diffusion coefficients represent the diffusivity of the solute elements, *i* and *j*, in the host element *k*. C_i is the mole fraction of *i* element, and C_i^{+} and C_i^{-} are the values of the mole fraction at the positions, $x = +\infty$ and $x = -\infty$ (corresponding to the two terminal alloys), respectively. The duration for interdiffusion is denoted by the symbol *t*.

From Eqs. (1), (2) and (3) adopting the experimental data obtained from the two different diffusion couples composed in the same alloying system, we can calculate the interdiffusion coefficients at the chemical composition of the cross point of the two different diffusion paths which are obtained by tracing the concentration profiles measured from the two diffusion couples on the isothermal phase diagram of the employed ternary system.

Experimental Procedure

Pure Ni, Ni-5Al, Ni-8Al, Ni-5W, Ni-5Re, Ni-8Ru, Ni-5Al-5W, Ni-5Al-5Re, Ni-8Al-8Ru, Ni-8Ru-5W, and Ni-8Ru-5Re (mol%) were arc-melted into the button shape ingots in high

purity argon atmosphere. Materials used in this study were 4N Ni, 4N Al, 2N W, 2N Re and 3N Ru. The compositions of the ternary alloys are selected so that the alloys are in the solid solution state at 1250℃. The compositional homogenization and grain growth in each specimen cutting from the ingots were accomplished by cold rolling followed by annealing at 1250℃.

Table 1 Design of diffusion couples and the duration of diffusion annealing.

Diffusion couple	Duration, *t*/h
Ni-Al-W system	
Ni-5Al/Ni-5W	48
Ni/Ni-5Al-5W	110
Ni-Al-Re system	
Ni-5Al/Ni-5Re	192
Ni/Ni-5Al-5Re	192
Ni-Al-Ru system	
Ni-8Al/Ni-8Ru	48
Ni/Ni-8Al-8Ru	48
Ni-Ru-W system	
Ni-8Ru/Ni-5W	48
Ni/Ni-8Ru-5W	48
Ni-Ru-Re system	
Ni-8Ru/Ni-5Re	72
Ni/Ni-8Ru-5Re	72

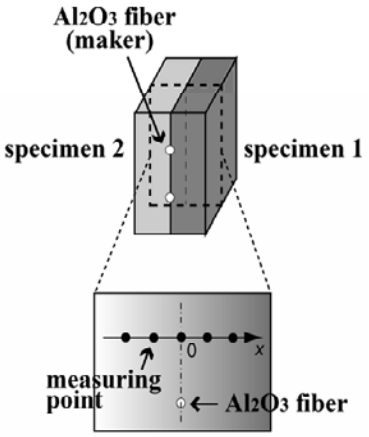

Fig.1 Schematic illustration showing assembly of the diffusion couples.

Diffusion couples were prepared in the following way. Surface of the plate specimen was mechanically ground using the emery papers followed by polishing using 0.25μm diamond slurry, and then the specimen was washed in acetone with an ultrasonic cleaner. The diffusion couples were assembled as shown in Table 1. These couples were held tightly with molybdenum holders. At that time, as shown in Fig.1, alumina fibers were sandwiched between the specimens of the couple as a marker indicating the initial interface.

Each diffusion couple was encapsulated in a quartz tube with argon and annealed at 1250℃. The duration employed in each diffusion couples are also listed in Table 1. After this annealing, the section of each diffusion couple was examined with a scanning electron microscope (SEM) equipped with an energy dispersive X-ray spectrometer (EDX) so as to

measure concentration profiles across the diffusion interface. The origin of the concentration profile is set at the position of the alumina fiber (see Fig.1).

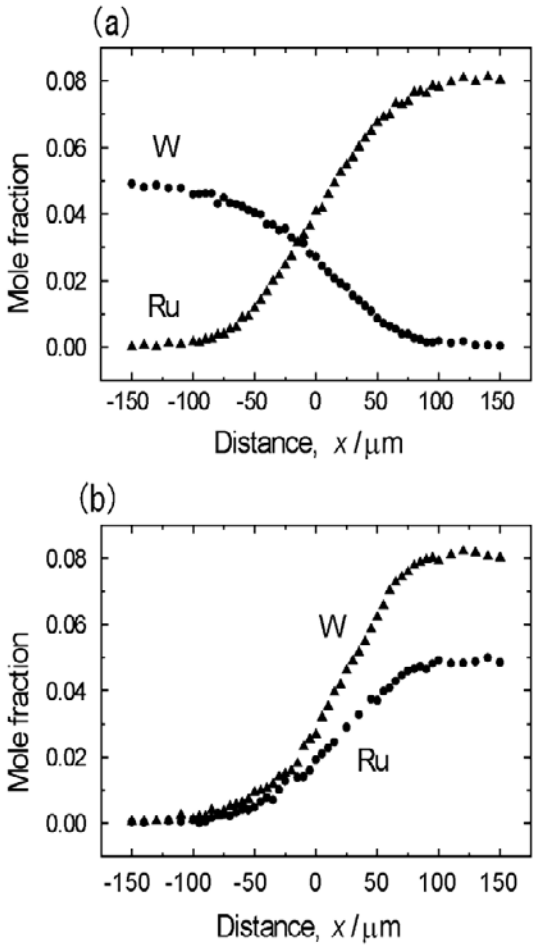

Fig.2 Concentration profiles of W and Ru obtained from (a) Ni-8Ru/Ni-5W and (b) Ni/Ni-8Ru-5W diffusion couples annealed at 1250℃

Results and Discussion

Concentration profiles and diffusion paths

As the representative examples, the solute concentration profiles obtained from the diffusion couples are shown in Fig.2 for Ni-Ru-W system and in Fig.3 for N-Ru-Re system. The profiles exhibit sigmoidal curves without any discontinuity, indicating that the atomic diffusion occurred in the solid solution region of each alloying system. The diffusion paths

can be obtained by replotting the data of Figs.2 and 3 into the Gibbs triangle. The results are shown in Figs.4 and 5**,** respectively. The chemical composition obtained from the cross point of the two diffusion paths was Ni-4.0Ru-2.6W (mol%) in Ni-Ru-W system and Ni-3.8Ru-2.6Re(mol%) in Ni-Ru-Re system. In a similar way, chemical composition at the cross point was obtained in each alloying system employed in this study. The results are summarized in Table 2. The composition at the cross point was used for calculating interdiffusion coefficients by the modified Boltzmann-Matano method as will be shown in the next section.

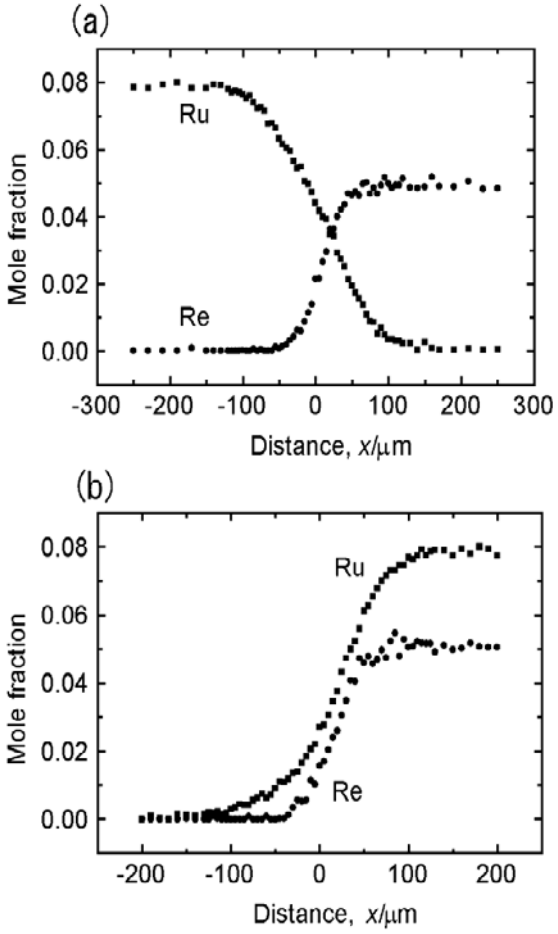

Fig.3 Concentration profiles of Re and Ru obtained from (a) Ni-8Ru/Ni-5Re and (b) Ni/Ni-8Ru-5Re diffusion couples annealed at 1250℃

Interdiffusion coefficients

On the basis of the modified ternary Boltzmann-Matano method represented by Eqs. (1), (2)

and (3), the interdiffusion coefficients were obtained in the following way. Firstly, Y_i values are calculated using Eq.(3) from the experimental data on the concentration profiles and then they are plotted against x. Also, the relationship between C_i and C_j was obtained from the experimental data. Secondly, in order to obtain suitable functions representing the Y_i-x profile and the C_i-C_j profile, the least square fitting was carried out. Thirdly, both the derivative terms and the integration terms in Eqs.(1) and (2) were calculated using the functions determined by the least square fitting. Here, the x value as the integration range of Eqs.(1) and (2) was determined from the composition at the cross point of the two diffusion paths. The procedure using the data obtained from the two different diffusion couples gave a set of simultaneous equations. Then the interdiffusion coefficients were obtained by solving the simultaneous equations. The calculated results are shown in Table 2. The values in the table are the interdiffusion coefficients at the compositions of the cross points of the diffusion paths in the solid solution phase.

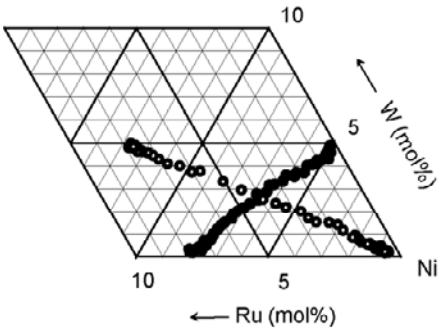

Fig. 4 Diffusion paths obtained from concentration profiles of diffusion couples in Ni-Ru-W system.

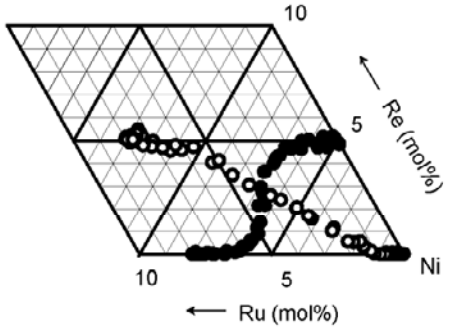

Fig. 5 Diffusion paths obtained from concentration profiles of diffusion couples in Ni-Ru-Re system.

Effective Interdiffusion Coefficients

Dayananda and Behnke introduced the effective interdiffusion coefficient $\tilde{D}_i^{\text{eff}}$ [9], and this is defined in a ternary system as the following equation,

$$\tilde{D}_i^{\text{eff}} \equiv \tilde{D}_{ii}^{k} + \tilde{D}_{ij}^{k} \frac{\partial C_j / \partial x}{\partial C_i / \partial x} \quad . \tag{4}$$

This means the sum of the main interdiffusion coefficient and the cross interdiffusion coefficient weighted by the proportion of concentration gradients, i.e., the effective interdiffusion coefficient involves the effect of cross interdiffusion coefficient. The effective interdiffusion coefficients in each diffusion couple of this study are summarized in Table 3.

Also, interdiffusion coefficients reported previously in Ni-W, Ni-Re and Ni-Ru binary systems are shown in Table 4 [10,11]. Comparing the results on the refractory elements in Table 3 to those in Table 4, it can be said that the effective interdiffusion coefficients of both W and Re are similar to those of the binary interdiffusion coefficients. This fact suggests that the cross interdiffusion coefficients of the two refractory elements are smaller than the main interdiffusion coefficients. In other words, the effect of Al or Ru on the diffusivity of both W and Re in Ni is small. In particular, the effect of Ru on the diffusivity of Re in Ni, $\tilde{D}^{Ni}_{ReRu}$, is much smaller by an order of magnitude than the main interdiffusion coefficient of Re in Ni, $\tilde{D}^{Ni}_{ReRe}$, as shown in Table 2.

Table 2 Chemical composition of the cross point of diffusion paths and interdiffusion coefficients in each alloying system.

System	Cross point (mol%)	Variety of coefficients	Interdiffusion coefficient, $\tilde{D}^{Ni}_{ij}$ / m^2s^{-1}
Ni-Al-W	Ni-2.7Al-3.3W	$\tilde{D}^{Ni}_{WW}$	9.3×10^{-15}
		$\tilde{D}^{Ni}_{WAl}$	-2.6×10^{-15}
		$\tilde{D}^{Ni}_{AlW}$	6.2×10^{-15}
		$\tilde{D}^{Ni}_{AlAl}$	8.6×10^{-14}
Ni-Al-Re	Ni-2.9Al-4.2Re	$\tilde{D}^{Ni}_{ReRe}$	2.0×10^{-15}
		$\tilde{D}^{Ni}_{ReAl}$	-1.2×10^{-15}
		$\tilde{D}^{Ni}_{AlRe}$	7.7×10^{-15}
		$\tilde{D}^{Ni}_{AlAl}$	6.2×10^{-14}
Ni-Al-Ru	Ni-5.0Al-5.3Ru	$\tilde{D}^{Ni}_{RuRu}$	8.5×10^{-15}
		$\tilde{D}^{Ni}_{RuAl}$	-2.3×10^{-15}
		$\tilde{D}^{Ni}_{AlRu}$	5.6×10^{-15}
		$\tilde{D}^{Ni}_{AlAl}$	1.2×10^{-13}
Ni-Ru-W	Ni-4.0Ru-2.6W	$\tilde{D}^{Ni}_{WW}$	6.9×10^{-15}
		$\tilde{D}^{Ni}_{WRu}$	-5.2×10^{-16}
		$\tilde{D}^{Ni}_{RuW}$	-1.4×10^{-15}
		$\tilde{D}^{Ni}_{RuRu}$	6.3×10^{-15}
Ni-Ru-Re	Ni-3.8Ru-2.6Re	$\tilde{D}^{Ni}_{ReRe}$	1.3×10^{-15}
		$\tilde{D}^{Ni}_{ReRu}$	9.0×10^{-17}
		$\tilde{D}^{Ni}_{RuRe}$	-1.0×10^{-15}
		$\tilde{D}^{Ni}_{RuRu}$	5.3×10^{-15}

Table 3 Effective interdiffusion coefficients.

Diffusion couple	Element, *i*	Effective interdiffusion coefficient, $\tilde{D}_i^{\text{eff}}$ / m^2s^{-1}
Ni-5Al/Ni-5W	W	1.0×10^{-14}
	Al	7.1×10^{-14}
Ni/Ni-5Al-5W	W	8.4×10^{-15}
	Al	1.0×10^{-13}
Ni-5Al/Ni-5Re	Re	2.4×10^{-15}
	Al	4.0×10^{-14}
Ni/Ni-5Al-5Re	Re	1.8×10^{-15}
	Al	1.0×10^{-13}
Ni-8Al/Ni-8Ru	Ru	9.3×10^{-15}
	Al	1.0×10^{-13}
Ni/Ni-8Al-8Ru	Ru	7.9×10^{-15}
	Al	1.4×10^{-13}
Ni-8Ru/Ni-5W	W	7.8×10^{-15}
	Ru	7.1×10^{-15}
Ni/Ni-8Ru-5W	W	6.0×10^{-15}
	Ru	5.5×10^{-15}
Ni-8Ru/Ni-5Re	Re	1.2×10^{-15}
	Ru	6.9×10^{-15}
Ni/Ni-8Ru-5Re	Re	1.4×10^{-15}
	Ru	4.1×10^{-15}

Table 4 Interdiffusion coefficient in binary system [10,11]

Composition (mol%)	Interdiffusion coefficient, $\tilde{D}$ / m^2s^{-1}
Ni-xW (0<x<3.4)	7.1×10^{-15}
Ni-xRe (0<x<3.4)	1.5×10^{-15}
Ni-xRu (0<x<6.06)	9.0×10^{-15}

According to the work done by Kirkaldy et al. the relationship between the major interdiffusion coefficient and the cross interdiffusion coefficient can be expressed by the

following equation if the alloy is assumed as a dilute solution [5].

$$\tilde{D}_{ij}^{k} / \tilde{D}_{ii}^{k} = \left(1 + \varepsilon_{ij}\right) C_i \quad , \tag{5}$$

where ε_{ij} is the Wagner's interaction parameter between *i* and *j* elements. The fact that $\tilde{D}_{\mathrm{ReRu}}^{\mathrm{Ni}}$ is much smaller than $\tilde{D}_{\mathrm{ReRe}}^{\mathrm{Ni}}$ implies that the thermodynamic interaction between Ru and Re is negligible. Therefore, it can be concluded that Ru scarcely changes the distribution behaviour of Re into the γ and the γ' phases, although the influence of Ru on the distribution of the refractory elements in nickel-based superalloys was a matter of debate.

In Table 2, all cross interdiffusion coefficients, $\tilde{D}_{X\mathrm{Al}}^{\mathrm{Ni}}$, for Al concentration gradient exhibited negative values, although each main interdiffusion coefficient, $\tilde{D}_{XX}^{\mathrm{Ni}}$, was positive value. This indicates that x elements diffuse against Al concentration as shown in Fig.5.

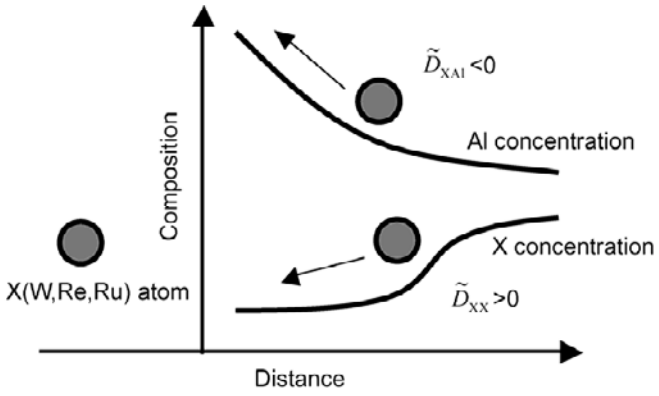

Fig.6 Schematic illustration showing the concentration distribution and X(W, Re, Ru) diffusion in Ni-based alloys.

Conclusion

The interdiffusion coefficients in the solid solution phase of Ni-X-Y (X,Y: Re, W, Ru, Al) ternary systems as the fundamental systems of Ni-based superalloys were estimated by a series of experiments.

The interdiffusion coefficients obtained in this study are summarized in Table 2. In these ternary systems, the cross interdiffusion coefficients of refractory elements (W, Re, Ru) were smaller than the main interdiffusion coefficients. In particular, $\tilde{D}_{\mathrm{ReRu}}^{\mathrm{Ni}}$ was much smaller than $\tilde{D}_{\mathrm{ReRe}}^{\mathrm{Ni}}$.

Acknowledgements

This work was supported in part by the Grant-in-Aid for Scientific Research of Japan Society for the Promotion of Science (JSPS), Japan. Also, a part of this work was supported by "Nanotechnology Support Project of the Ministry of Education, Culture, Sports, Science and Technology (MEXT), Japan" in the Research Center for Ultrahigh Voltage Electron Microscopy, Osaka University.

References

[1] M.Morinaga, R.Hashizume and Y.Murata: "An Electronic Approach to the Design of Ferritic Steels for Power Plants", Materials for Adv. Power Engineering 1994, Eds. D.Coutsouradis et al., Kluwer Academic Pub., Netherlands, (1994), 319-328.

[2] K.Matsugi, Y.Murata, M.Morinaga and N.Yukawa: "Realistic Advancement for Nickel-Based Single Crystal Superalloys by the d-Electrons Concept", Superalloys 1992, Eds. S.D.Antolovich et al., The TMS, (1992), 307-316.

[3] T.Hino, Y.Yoshioka, Y.Ishiwata, K.Nagata, T.Kobayashi, Y.Koizumi. H.Harada and T.Yamagata: "Effect of Re Content in Ni-base Single Crystal Superalloys on TCP Phase Precipitation and Creep Rupture Life", Report of the 123rd Committee on Heat-Resisting Materials and Alloys (Japan Society for the Promotion of Science) **40**(1999), 141-150.

[4] T.Yokokawa, M.Osawa, K.Nishida, Y.Koizumi, T.Kobayashi and H.Harada: "Effect of Ru Addition to Partitioning Behavior of Alloying Elements into γ and γ' Phases of Ni-Base Superalloys", J. Japan. Inst. Metals **68**(2004), 138-141.

[5] J.S.Kirkaldy, Z.U.Haq and L.C.Brown: "Diffusion in Ternary Substitutional Systems", Trans. ASM, 56(1963), 834-849.

[6] M.Hattori, N.Goto, Y.Murata, T.Koyama and M.Morinaga: "Diffusion of Refractory Elements in Ni-Al-X (X: Re, W) Ternary Alloys", Mater. Trans. **46**(2005)163-166.

[7] M.S.A.karunaratne, P.Carter and R.C.Reed: "On The Diffusion of Aluminium and Titanium in the Ni-Rich Ni-Al-Ti System between 900 and 1200℃", Acta Mater. **49**(2001), 861-875.

[8] D. P. Whittle and A. Green: "The Measurement of Diffusion Coefficients in Ternary System", Scr. Metall. **8**(1974), 883-884.

[9] M. A. Dayananda and D. A. Behnke: "Effective Interdiffusion Coefficients and Penetration Depths", Scr. Metall., **25**(1991)2187-2191.

[10] M. S. A. Karunaratne, P. Carter and R. C. Reed: Mater. "Interdiffusion in the Face-Centred Cubic Phase of the Ni-Re, Ni-Ta and Ni-W Systems between 900 and 1300℃", Mater. Sci. Eng. **A281**(2000), 229-233.

[11] M.S.A.Karunaratne and R.C.Reed: Acta Mater. "Interdiffusion of the Platinum-Group Metals in Nickel at Elevated Temperatures", **51**(2003), 2905-2919.

MICROSTRUCTURAL DEGRADATION OF HAYNES 230 COMBUSTOR HARDWARE.

G. Marchant[1]; G. McColvin[1] and A. Strang[2].

{1 - Siemens Industrial Turbomachinery Ltd, Lincoln, UK}
{2 - Department of Engineering, University of Leicester, Leicester, UK.}

Abstract

Haynes 230 is a sheet material used for combustor components in a number of small industrial gas turbines manufactured by Siemens. During service the material is subjected to high temperatures and stresses, which lead to degradation of the microstructure and mechanical properties, and hence limit the life of the component. A long-term programme has been initiated to investigate the effects of thermal and creep exposure on this material. The aim of this evaluation is to characterise the microstructural and hardness changes that the solid solution alloy undergoes during high temperature (stressed and unstressed) exposure. This involves optical microscopy, SEM and Analytical TEM metallographic studies as well as hardness determinations on both thermally and thermo-mechanically degraded material to enable characterisation of the microstructural changes. The final objective will be to produce a microstructural model to enable the assessment of component operating temperatures and remnant life evaluation.

This paper covers the first phase of the work being carried out as part of the COST 538 project, which has concentrated on initial studies of the effects of long-term high temperature exposure on hardness and microstructural changes of creep rupture tested and thermally exposed samples of HA230.

Keywords: HA230, Degradation, Hardness, Microstructure.

Introduction

Haynes® alloy 230™ is a nickel base alloy that combines excellent high-temperature strength and outstanding resistance to oxidising and nitriding environments for prolonged service applications up to 1150°C. It is a solid solution and carbide strengthened alloy that offers excellent long-term thermal stability. In addition, it has good formability and is readily weldable making it ideal for the manufacture of gas turbine sheet metal combustion hardware such as combustion cans, transition ducts etc.

The alloy is derived from the Ni-Cr-Mo-W system in which the high nickel content gives it a stable austenitic matrix. Additions of tungsten and molybdenum, in the presence of carbon and boron, result in the alloy's high temperature strength. Tungsten provides very effective solid solution strengthening whilst the presence of carbon promotes the formation of $M_{23}C_6$ carbides, which precipitate on and pin glide dislocations at service temperatures and thereby improve creep strength. Tungsten was chosen instead of molybdenum as a major alloying element, since it diffuses more slowly in nickel as well as increasing the elastic moduli and decreasing the stacking fault energy by impeding cross-slip, all of which promote high-temperature creep strength. Environmental resistance is provided by additions of chromium in combination with manganese, silicon and lanthanum, which promote excellent resistance to surface attack in oxidising environments.

The material is normally supplied in a solution heat-treated condition, which is carried out at about 1230°C followed by rapid cooling resulting in an equiaxed microstructure with an average grain size in the range of ASTM 4-6. In this condition the microstructure contains tungsten rich primary M_6C carbides, which resist solutioning during heat-treatment and thereby help to control the grain

® - Registered trademark of Haynes International Inc

size. The controlled grain size achieved helps to achieve a good balance between high temperature creep rupture strength favoured by a coarse grain size and LCF - properties favoured by a fine grain size. [1,2]. In addition to the primary M_6C precipitates some chromium rich $M_{23}C_6$ may also be present in the annealed condition precipitated at the grain boundaries and on annealing twins within the microstructure, Figs 1a and b.

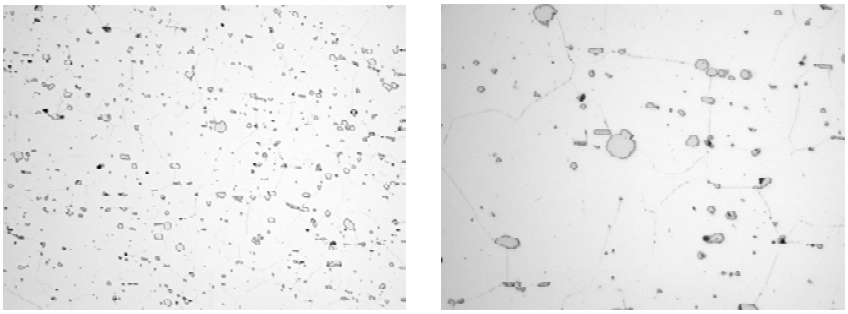

a) x155 b) x385

Fig 1. Microstructure of solution annealed HA230 showing distribution of primary M_6C particles

In service, the material is exposed to high temperatures for extended periods, during which it undergoes microstructural changes that will significantly affect its mechanical properties. These changes involve precipitation of secondary phases such as carbides and possibly intermetallic compounds, which may impair the fracture resistance of the material. The thermal and microstructural stability of the alloy is therefore of primary concern, since it may determine the life limiting parameters of design.

Programme and procedures

A three-year study aimed at characterising the microstructural and hardness changes that the solid solution alloy undergoes during high temperature thermal and creep exposure has been initiated as part of the COST 538 technology programme which commenced in September 2004. The primary thrust of this study is to evaluate the microstructural changes which occur in HA230 samples which have been exposed for durations of up to 20,000 hours at temperatures in the range 600°C to 1050°C and compare these with changes which occur in material taken from the same HA230 heat which has been creep tested at temperatures between 600°C to 1000°C for durations of up to 50,000 hours.

Advanced optical, analytical scanning and transmission electron microscopy, X-ray diffraction and other metallographic techniques will be used to identify phase evolution due to long-term thermal and creep exposure. The information gathered will be used to help in understanding the effects of thermal exposure on the microstructure and mechanical properties, for the purposes of developing a microstructural model to enable estimation of component operating temperatures and, through this, remnant life assessment. The effects of the microstructural degradation on the mechanical properties of the alloy such as hardness, tensile strength, ductility etc., will also be assessed.

This report covers the work carried out in the first phase of the project, which has concentrated on initial studies on the effects of long-term high temperature exposure on hardness and microstructural changes of creep rupture tested and thermally exposed samples of HA230.

Materials

The programme of thermal exposure tests is being carried out on coupons of HA230, approximately 30mm x 1000 mm in size. These are being exposed for durations of up to 20,000 hours, at temperatures in the range 600°C to 1050°C, for the purposes of determining the effects of unstressed long-term exposure on the hardness, microstructure and mechanical properties of this alloy.

In addition similar studies are being carried out on a series of creep samples which have been tested at temperatures in the range 650°C to 1000°C for durations of up to 50,000 hours to determine the combined effects of long-term thermal exposure and creep deformation on the hardness and microstructure of the material.

Both the thermal exposure and creep rupture tests have been carried out on material taken from a single heat of HA230 supplied by Haynes International Ltd to AMS 5878 in the form of 2 mm thick sheet in the solution treated and quenched condition. Details of the chemical composition, heat treatment and mechanical properties of heat 8305-5-7170 taken from the test certificate are shown in Tables 1 and 2, where they are compared with the requirements of AMS 5878.

Heat	Ni	Cr	W	Mo	Fe	Co	Mn	Si	Al	C	La	B	Ti	Cu	S	P
8305-5-7170	**Bal**	**21.75**	**13.96**	**1.32**	**1.40**	**0.37**	**0.49**	**0.36**	**0.29**	**0.12**	**0.013**	**0.004**	**<0.03**	**0.03**	**<0.002**	**<0.005**
AMS 5878	**Bal**	**20.0 to 24.0**	**13.00 to 15.00**	**1.00 to 3.00**	**3.00 max**	**5.00 max**	**0.30 to 1.00**	**0.25 to 0.75**	**0.20 to 0.50**	**0.05 to 0.15**	**0.005 to 0.05**	**0.015 max**	**0.01 max**	**0.05 max**	**0.015 max**	**0.03 max**

Table 1 - Chemical Analysis

Properties	Heat no 8305-5-7170	AMS 5878
Heat Treatment	Solution Annealed at 1230°C and quenched	Solution treat between 1177°C and 1246°C and cool rapidly
0.2% Yield Strength	345 MPa min	448 MPa
UTS	859 MPa	793 MPa min
% Elongation	45	40 min
Hardness	92 HRB	25 HRc max
Rupture Life at 69 MPa and 927°C	50 hrs	36 hrs min
% Elongation	34	10 min
ASTM Grain Size	5.5	3 max

Table 2. Heat Treatment and Mechanical Properties

Results and Discussion

Thermal exposure tests

The results of Vickers hardness measurements conducted at a load of 20 kg on HA230 coupons, exposed for durations of 1000, 3000 and 5000 hours in the temperature range 750°C to 1050°C are

shown in Table 3 and in the form of a parametric Larson-Miller plot, using a C-value of 20 for the Larson-Miller constant, in Fig 2.

Exposure	Hardness Values - Hv20				% Changes in hardness		
Temperatures	Exposure Duration in Hours				Exposure Duration in Hours		
°C	0	1000	3000	5000	1000	3000	5000
750	221.4	250.5	244.3	243.9	13.14	10.34	10.16
810	221.4	239.5	233.7	232.1	8.18	5.56	4.83
870	221.4	233.1	216.1	214.5	5.28	-2.39	-3.12
930	221.4	221.9	208.9	210.2	0.23	-5.65	-5.06
990	221.4	214.6	207.0	207.4	-3.07	-6.50	-6.32
1050	221.4	216.3	209.9	212.8	-2.30	-5.19	-3.88

Table 3. Hardness measurements on thermally exposed HA230

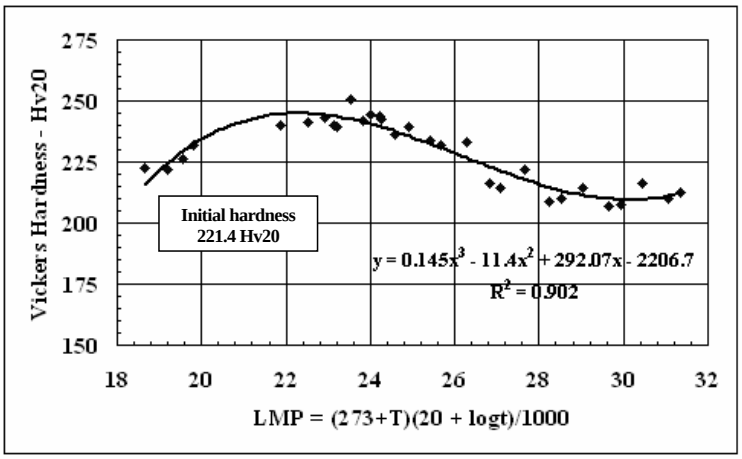

Fig 2. Hardness data on HA230 coupons thermally exposed in the temperature range 750°C-1050°C

The results indicate that systematic changes in the hardness of the HA230 occur with increasing temperature and exposure durations following thermal exposure of the alloy. As is evident from Fig 2 the hardness of the alloy initially increases from the original solution annealed value of 221.4 Hv20 to a peak value of about 250 Hv20 after exposure for 1000 hours at 750°C, viz., an increase of just over 13% compared with the material in the as-received solution annealed condition.

The relative effects of temperature and exposure durations of 1000, 3000, and 5000 hours are shown in the form of percentage changes in hardness relative to that of the material in the as-received solution annealed condition in Fig 3. The 1000 hours data curve indicates that following an initial hardening phase, re-softening of the alloy occurs reaching its original hardness level at an exposure temperature of about 930°C, with the curve reaching a minimum of about 215 Hv20 at 990°C. Exposure for 3000 hours and 5000 hours follow similar patterns with the curves being almost superimposed. In this case the original hardness is regained at an exposure temperature of just over 840°C after which softening continues once more reaching a minimum at a temperature

about 990°C. However the degree of re-softening at 990°C in the case of the 3000 hour and 5000 hour exposed samples is over twice that observed for the 1000 hour exposed material, viz., -6.5% and –6.32% compared to –3.07%. In addition to this the data plotted in Fig 2 suggests that the initial increases in hardness must occur at exposure times and temperatures of less than 1000 hours and 750°C respectively while a C-curve plot of the data suggests that the maximum softening temperature for the alloy is close to 1000°C, Fig 4.

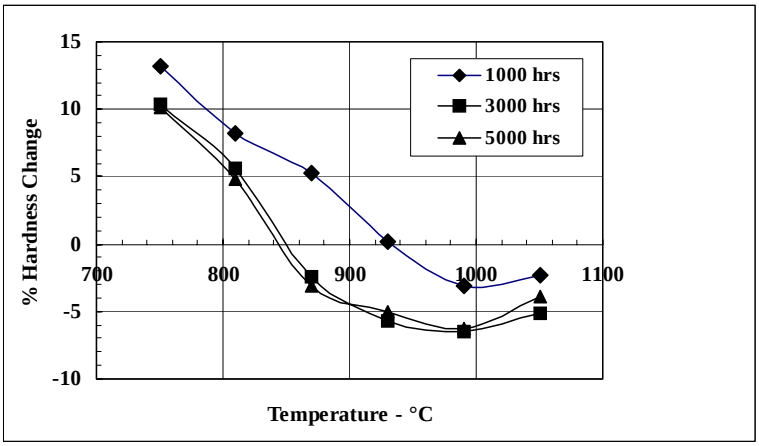

Fig 3. Effect of exposure temperature and duration on the % change in hardness relative to that of HA230 in the as-received solution annealed condition

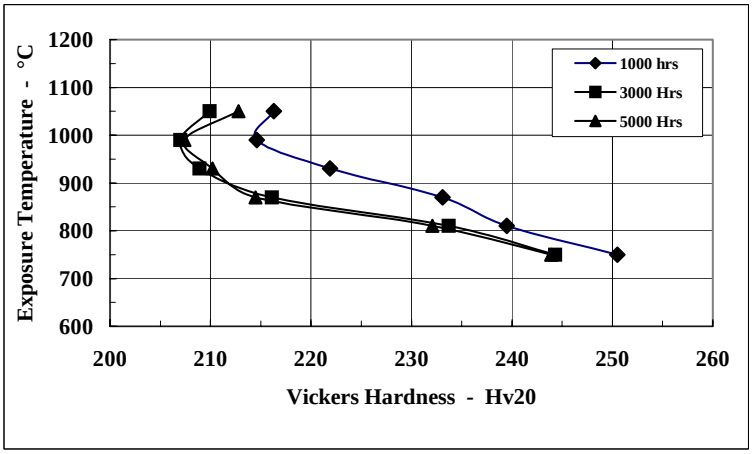

Fig 4. C-curve plot for thermally exposed HA230

Creep Exposure Tests

The results of Vickers hardness tests conducted at a load of 20kg on sections taken from unstressed areas in the creep specimen heads follow the same trends as in the case of the thermally exposed

test coupons. As before increases in hardness are observed reaching a maximum value of approximately 253Hv20 (corresponding to a Larson-Miller parameter value of 23.5), i.e. about 14% higher than the original 221.4 Hv20 solution annealed hardness value. These data are shown as a parametric Larson-Miller plot using a C-value of 20 for the Larson-Miller constant in Fig 5. A similar plot for the combined hardness data indicates that the results obtained for the thermal and creep exposed materials are closely matched with the maximum and minimum in the hardness v Larson-Miller plot occurring at Larson-Miller parameter values of approximately 23 and 29 respectively, Fig 6.

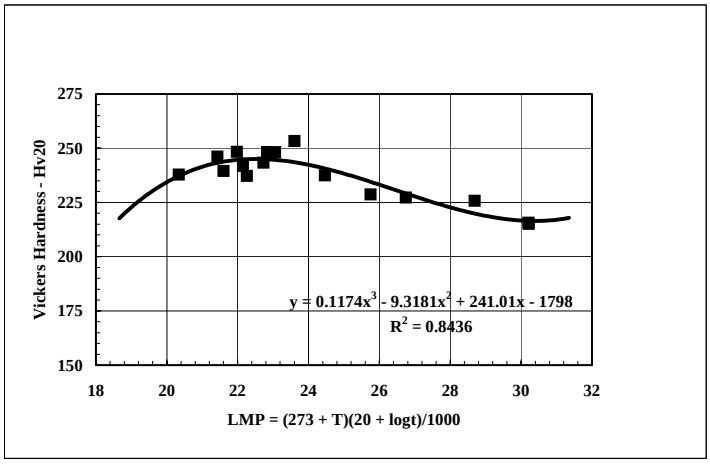

Fig 5. Hardness data on HA230 samples from unstrained regions in the heads of creep specimens tested in the temperature range 650°C-1000°C

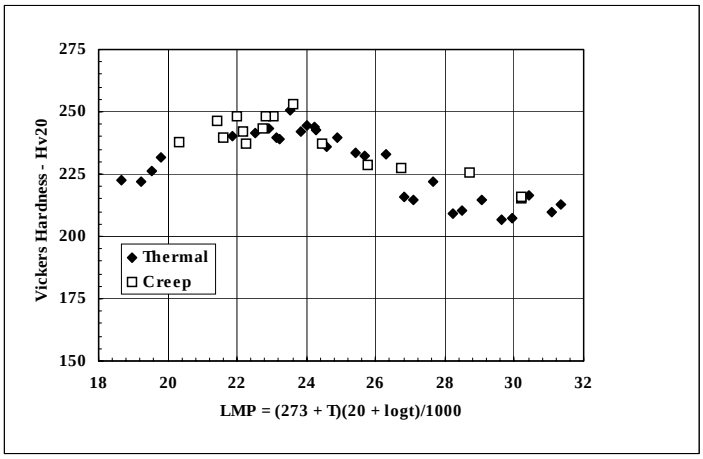

Fig 6. Combined hardness data on unstrained thermally and creep exposed HA230 material tested in the temperature range 600°C-1050°C

Data Analysis

Regression analyses on the hardness data on the thermally exposed material shown in the parametric shown in Fig 1 indicates that a good fit is obtained for the data set using a cubic polynomial of the form,

$$Hv = aP^3 + bP^2 + cP + d$$

Where, a, b, c, and d are constants, Hv is the thermal exposed hardness value and P is the Larson-Miller parameter defined as P = (273 + T)(20 + logt)/1000

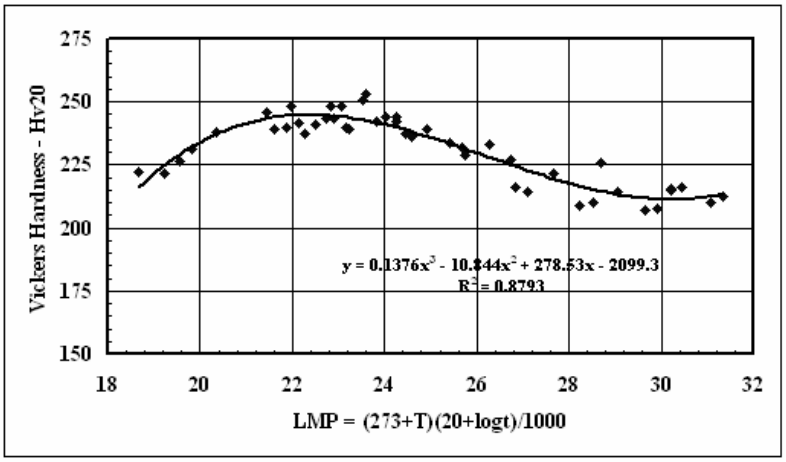

Fig 7. Combined hardness data on unstrained thermally and creep exposed HA230 material tested in the temperature range 600°C-1050°C

Analyses of the data plotted in Figs 1 and 4 results in the regression equations shown in Table 4 with respective R^2 values of 0.902 and 0.8436.

On the basis of these analyses and the closeness of the hardness data shown in Fig 7 it is concluded that the data from the thermal and creep exposure tests can reasonably be combined for the purposes of analysis to produce a Master hardness v Larson-Miller parametric plot for this alloy. The results of a regression analysis of the combined data indicates that a cubic polynomial once more results in a good fit with an R^2 value of 0.8793 and the following master Hardness v Larson-Miller equation.

$$Hv = 0.13P^3 - 10.8P^2 + 278.5P - 2099$$

Sample	Values of regression constants and R^2				
	a	b	c	d	R^2
Thermal Exposure	0.145	-11.40	292.07	-2206.7	0.902
Creep Heads	0.117	-9.32	241.01	-1798	0.8436
Combined Data	0.137	-10.84	278.53	-2099.3	0.8793

Table 4. Regression constants and values for thermally exposed HA230 hardness data

Metallographic Studies - Thermally Exposed HA230

Optical microscopy studies on HA230 coupons which have been exposed for 1000, 3000, and 5000 hours at temperatures in the range 750°C to 1050°C have revealed changes in the microstructure which can be related to the results obtained on the hardness studies on these samples described above. The preliminary results indicate that the initial increases in hardnesses, above that of the material in the as-received solution annealed condition of 13.14%, 10.345 and 10.16% following exposure at 750°C for 1000, 3000 and 5000 hours respectively, are due to precipitation of $M_{23}C_6$ type carbides, at the grain boundaries and original solution treatment annealing twins within the grains. Subsequent exposure for the same durations at the higher temperatures of 810°C, 870°C, 930°C, 990°C and 1050°C result in softening of the material due to progressive coarsening of these precipitates, with the microstructure of the alloy tending to approach that of the original as-received condition. Typical micrographs illustrating the effects of thermal exposure at 750°C, 870°C and 1050°C are shown in Fig 8. Similar conclusions have been proposed by Jordan, et al in studies of unstrained HA230 exposed for 10,000 hours at temperatures in the range 750°C to 1050°C [3].

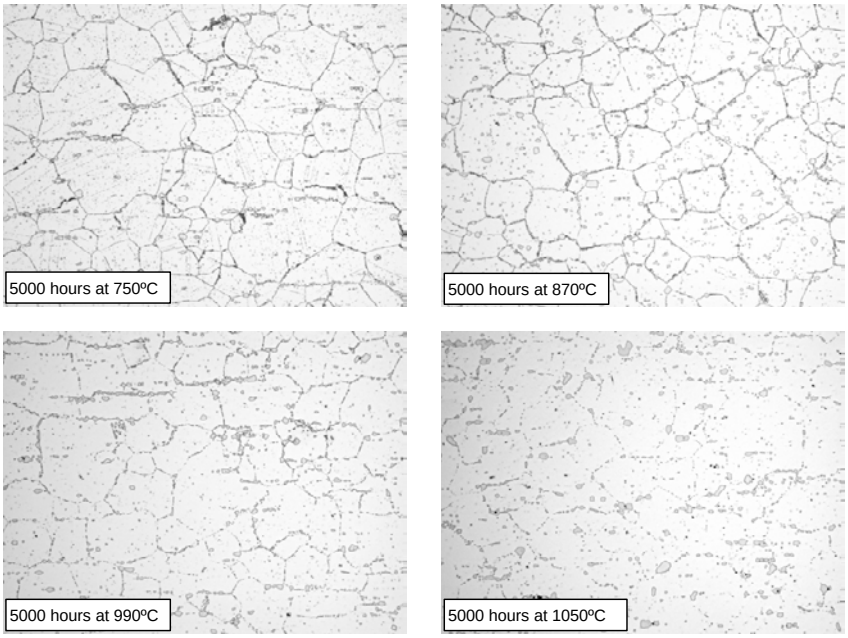

Fig 8. Microstructures of the 5000 hour thermal exposure samples (Magnifications x155)

Optical studies on the 1000 hour thermally exposed samples indicated that below the oxide scale there was increasing oxide finger penetration with increasing exposure temperature. In addition to this the depth of the precipitate free zone below the surface oxide scale also increased. Fig 9.

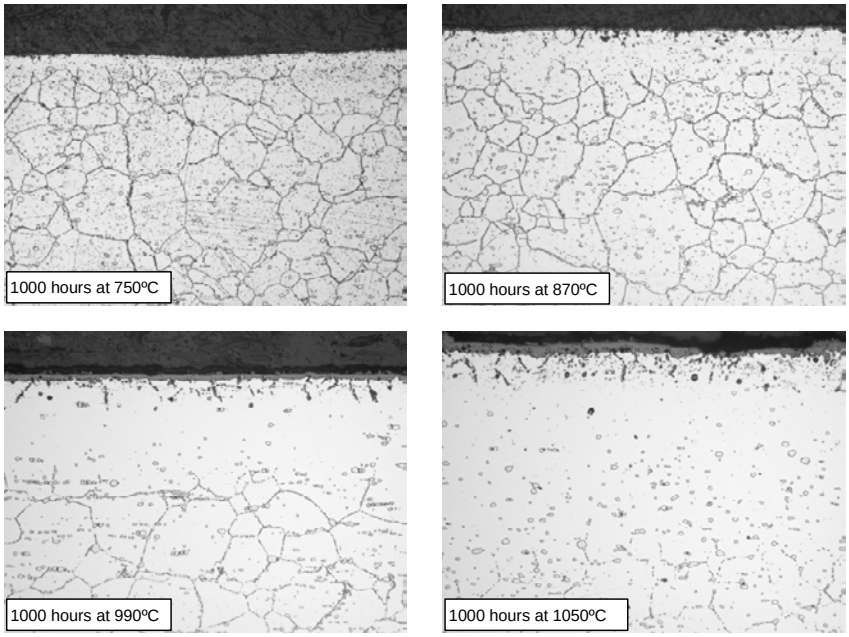

Fig 9. Microsections showing depleted zone at the material surface (Magnifications x155)

Metallographic Studies - Creep Tested HA230

Similar optical microscopy studies have been carried out on sections taken from areas in the gauge lengths close to the final fracture zones of selected creep rupture testpieces, and the microstructures compared with those found in the solution annealed and thermally exposed material described above. Details of the creep rupture testpieces examined are shown in Table 5

Testpiece	Temp °C	Rupture Life Hours	% Elong$^{n.}$
DKX	650	6577	20.7
DLA	700	18160	17.2
DLB	700	4995	
DLH	900	28776	~ 35
COG	1000	5366	70.8

Table 5. Creep rupture test results on HA230

In all instances the fractures were intergranular with the damage being present all along the testpiece gauge length. In addition the creep cracks tended to occur normal to the axial load on the testpiece. In the case of testpieces DKX, DLA and DLB the creep damage was mainly in the form of transverse intergranular cracks, while in specimens DLH and COG the damage was mainly in the form of large voids located on the grain boundaries normal to the applied stress, Figs 10a - e.

The general microstructure observed in gauge length regions of testpieces DKX, DLA and DLB was similar to that observed in the thermally exposed HA230 samples consisting of equiaxed grains with chromium rich $M_{23}C_6$ type carbides precipitated at the grain boundaries as well as along original twin boundaries. In addition, large rounded primary M_6C carbides, which are rich in tungsten and molybdenum, were present randomly distributed throughout the matrix, Figs 10 a-e. As Vecchia et al have shown, these phases are easily distinguished by their unique chemical signatures [4]. Typical EDX analyses results showing the compositions of the matrix as well as $M_{23}C_6$ and M_6C carbides in DLH are shown in Figs 11a-d and Table 6. Both the grain and twin boundary precipitation appeared to be more pronounced in testpieces DLA and DLB compared with that observed in DKX. This may be due to these tests having been carried out at 700°C compared with 650°C in the case of testpiece DKX and further supports the observations already made regarding the effects of temperature on the microstructures of the thermal exposed HA230 specimens.

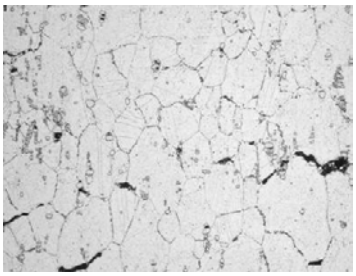

a) DKX - 6577 hrs at 650°C

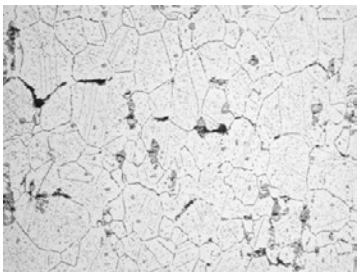

b) DLA - 18160 hrs at 700°C

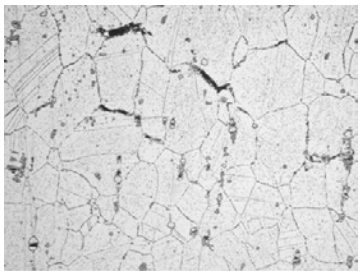

c) DLB - 4995 hrs at 700°C

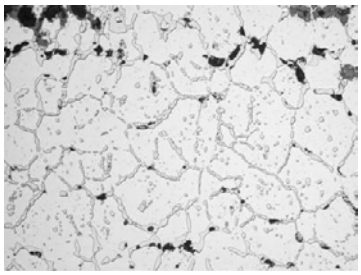

d) DLH - 28777 hrs at 900°C

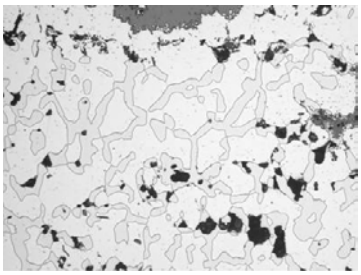

e) COG - 5366 hrs at 1000°C

Figs 10 a – e. Microstructures of gauge lengths in HA230 creep rupture testpieces. (Magnifications x155)

The microstructures observed in testpieces DLH and COG were totally different from those found in the gauge lengths of DKX, DLA and DLB. In the case of test DLH, which ruptured after 28777 hours at 900°C, the precipitation was almost continuous along the grain boundaries with coarse particles being also randomly present within the grains, Fig. 10d. Whereas it was possible to differentiate between the primary and grain boundary carbide types in testpieces DKX, DLA and DLB, this was not possible optically in testpiece DLH since the particles were very similar in both size and shape. The microstructural differences were even more pronounced in COG, which had fractured after 5366 hours at 1000°C. In this case the grain boundary precipitation was continuous with no evidence of discrete particles being present, Fig.10e.

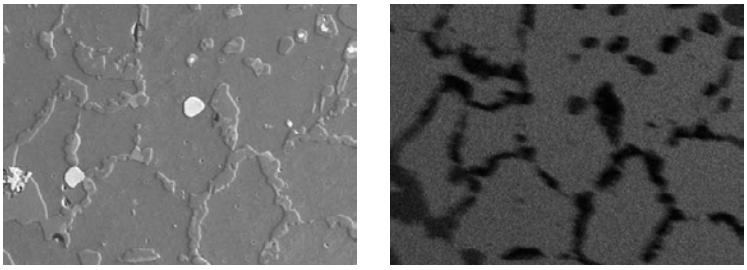

a) Backscattered electron image b) Nickel distribution - NiKα

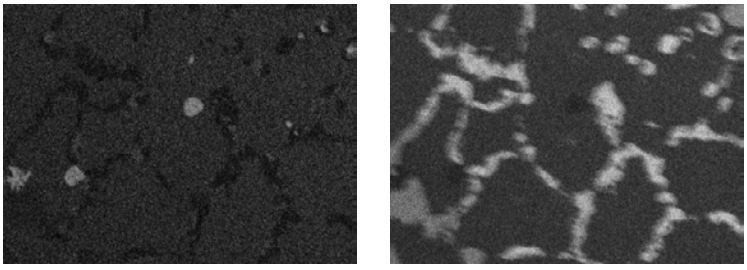

c) Tungsten distribution - WLα d) Chromium distribution - CrKα

Figs 11 a – d. FEGSEM and EDX images of carbides present in gauge length of creep testpiece DLH

Microstructural Features	Compositions – wt%			
	Cr	W	Mo	Ni
Primary M_6C carbides	10.95	65.79	5.03	18.23
Grain Boundary $M_{23}C_6$	41.37	22.79	4.88	30.96
Matrix	17.22	17.13	2.63	63.02

Table 6. EDX analyses of matrix, grain boundary and primary particles in creep tested HA230

Conclusions

The results to date have shown that the hardness data from the thermal and creep exposure tests can reasonably be combined to produce a single master hardness v Larson-Miller parametric plot for this alloy. The regression analysis of these data indicates that a cubic polynomial results in a good fit with an R^2 value of 0.8793.

Optical microscopy studies on the thermally exposed coupons have revealed changes in the microstructure which can be related to the hardness results. The initial increase in hardness above that of the material in the as-received solution annealed condition, are due to precipitation of $M_{23}C_6$ type carbides, at the grain boundaries and original solution treatment annealing twins within the grains. Subsequent exposure (longer times/higher temperatures) result in softening of the material due to progressive coarsening of these precipitates

The microstructures observed in the lower temperature (creep) strained testpieces were found to be similar to the thermally exposed test pieces. However, the effects of strain at higher temperatures results in almost continuous precipitation along the grain boundaries with coarse particles being also randomly present within the grains. The effects of creep strain on the microstructure were most pronounced at the highest test temperature where the grain boundary precipitation was continuous with no evidence of discrete particles being present.

References

1) D L Klastrom, Thermal Stability of a Ni-Cr-W-Mo Alloy, NACE Corrosion 94, Paper 407, NACE International, Housten, TX, 1994

2) D L Klarstrom, Heat Treatment/Property Relationships for Solid Solution Strengthened Heat Resisting Alloys, 1st International Conference on Heat Resistant Materials, Lake Geneva, September 22-26, 1991

3) C E Jordan et al, Thermal Stability of High Temperature Structural Alloys, Lockheed Martin, Schenectady, NY, March 1999

4) K S Vecchio et al, Met and Matls Trans A, vol 26A, pp 673 - 689

Acknowledgements.

The authors would like to thank their respective organizations for their support in this work and kind permission to publish this paper.

The authors are also grateful to the COST538 consortium for facilitating the programme that this work forms part of.

SHOT PEENING INDUCED RECRYSTALLIZATION IN A DIRECTIONALLY SOLIDIFIED NI-BASE SUPERALLOY

J. Zhang, L. Wang, G. Xie, C. Sun, L. H. Lou
Superalloys Division, Institute of Metal Research, Chinese Academy of Sciences,
Wenhua Road 72, Shenyang 110016, China

Abstract

This paper studied the effect of shot peening induced recrystallization (RX) on microstructure and creep properties of a directionally solidified (DS) nickel-base superalloy. It was shown that the depth of surface RX induced by shot peening is about 40 μm including a cellular RX layer after heat treatment. The RX grows slowly during 980°C, 235MPa creep test. However, cellular RX layer developed during creep. Little effect of the surface RX on the creep rupture life of the experimental DS alloy was observed since the recrystallized volume is small compared to the overall thickness of the creep rupture specimen. Methods that may reduce the RX were explored according to the present results. Surface coating was found to be one of the most effective ways to partially reduce the RX induced by spot peening.

Keywords: Shot peening, Nickel-base superalloy, Recrystallization (RX), Coating

1. Introduction

Directionally solidified (DS) turbine blades made from Ni-base superalloys with columnar grain or single crystal structures are critical components in modern aero engines and power generating plants. Shot peening is a standard treatment after DS casting of the blades. It is well known that shot peening will introduce strain to the component surface and may lead to surface recrystallization (RX) during the following heat treatment.

Shot peening induced RX has been characterized in several single crystal superalloys [1-3]. Two types of RX were observed depending on the heat treatment temperature: (I) a relatively homogeneous surface RX layer can be found after standard heat treatment; and (II) cellular recrystallization formed when ageing at temperatures below the γ' solvus temperature for longer time. Much attention has been paid to type I RX since it is readily formed in the "new" components.

It is generally agreed that RX has detrimental effect on mechanical properties of DS alloys since reinforcement-free grain boundaries probably perpendicular to the loading direction may form. For example, a reduction of fatigue life by local cellular RX was reported in single crystal superalloy CMSX-4 by Okazaki et al. [4]. In an experimental DS alloy, only ~5-50% of the creep rupture life can be achieved if a surface RX layer was introduced by shot peening

[5]. However, Bűrgel et al. [2] observed that the number of cycles to crack initiation is not influenced by surface RX in CMSX-6, although a higher crack density occurred during fatigue. Jo and Kim [6] also reported that surface RX does not reduce the creep rupture life of CMSX-4 at 982^{o}C, 240MPa in air. Therefore, as pointed out by Khan [7] et al., the influence of RX on mechanical properties of an alloy was probably a thickness dependent process. For samples with thicknesses of 1.5 mm or more, the reduction in rupture strength is due to the recrystallized layer. For thin plate samples (≤1 mm) however, there is a combined "thin wall" and RX effect.

Many efforts have been made to suppress the detrimental RX. It was reported that prior heat treatment [8], coating [4,9,10], carburization [11,12], and removing the surface layer [13] may all be effective to control the RX. However, these methods can only partially avoid or reduce the RX [2,14]. No conclusive technique has been developed so far to solve the RX problem in modern DS superalloys.

The present paper is focused on the shot peening induced surface RX in an experimental DS alloy, in both heat treated and creep conditions. The effect of RX on mechanical properties was studied. Methods that may reduce the RX were also explored.

2. Experimental

A DS nickel-base superalloy with a nominal composition in weight percent of 9Cr, 10Co, 7W, 2Mo, 5Al, 2.2Ti, 3.5Ta, 0.1C, and balance Ni was prepared using a Bridgman furnace. All samples for property test were machined along the DS direction. For creep rupture property tests, sheet specimens with 2 mm in thickness were used. Column specimens with gauge diameter of 5 mm and gauge length of 25 mm were prepared for the observation of microstructural evolution during creep. Shot peening was applied to one surface of the sheet samples and on the surface of column samples with 200 mesh SiO_2 ball at a pressure of 0.3-0.4MPa for 1 min. As comparison, sheet samples containing local RX were also used in creep rupture tests. (These samples were first indented by using Brinell hardness tester, then carefully removing the indentation after full heat treatment. A local RX within the gauge length was therefore produced [14].) All samples were heat treated in vacuum in sealed silica tubes as follows: 1220^{o}C/2h/air cooling, 1080^{o}C/4h/air cooling, and 900^{o}C/16h/air cooling. Creep rupture tests were conducted at 980^{o}C, 235MPa. Several creep rupture tests using column specimen were interrupted for microstructure observation before sample failure.

Several types of surface coating were deposited using MIP-8-800 arc ion plating equipment before solution heat treatment. The depositing was carried out with a working pressure of 7×10^{-2}Pa in argon. Detailed depositing parameters were described elsewhere [15].

Specimens were observed using optical microscopy and scanning electron microscopy (SEM). Depth of RX was measured using optical microscopy. The mean depth of RX was obtained by

averaging 10 measurements from different locations in each sample.

3. Results

3.1 Recrystallization after heat treatment

After full heat treatment surface recrystallization was created as shown in Fig. 1. The surface RX was about 40 μm in depth. A thin lamellar γ/γ′ layer (cellular RX) on tips of some RX grains with maximum thickness around 2 μm was also observed (Fig. 1b).

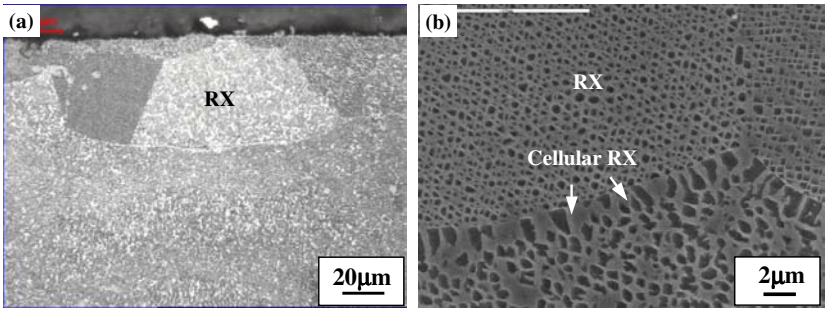

Fig. 1 (a) Surface recrystallization in shot peened samples after standard heat treatment, and (b) lamellar γ/γ′ layer (cellular RX) in front of the surface RX.

3.2 Change of surface recrystallization during creep

The depths of surface RX in samples before and after creep tests were measured and compared in table 1. One can see that surface RX, but not the cellular RX developed during ageing heat treatment since the maximum cellular RX observed was only around 2 μm. The RX depth decreases abruptly in creep rupture specimens due to oxidation of the surface and deformation. However, it is clear that RX layer developed further into the matrix during creep. The value of RX depth in 60h crept sample is still higher compared to that in 40h crept sample even there is more oxidation and deformation. Detailed observation shows that the cellular RX grows gradually but slowly into the matrix during creep (Fig. 2).

Table 1 Depth of surface recrystallization in heat treated and crept samples (μm).

Solution treatment	38.69 ± 5.79
Full heat treatment	43.21 ± 7.5
980°C/235MPa, 40h	31.22 ± 8.9
980°C/235MPa, 60h	34.1 ± 5.49

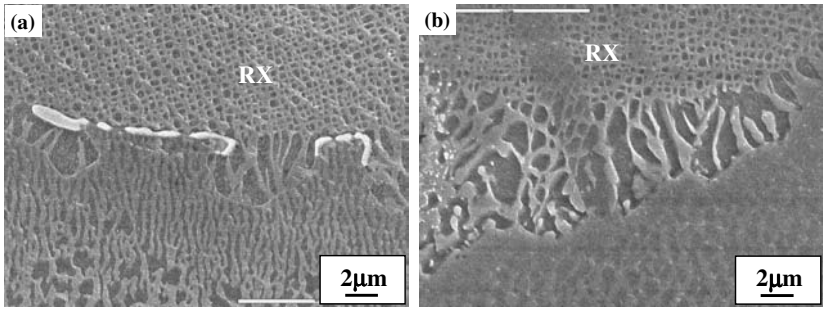

Fig. 2 Growth of cellular RX during creep in columnar specimens. After shot peening, the samples were heat treated and then crept at 980°C, 235MPa for (a) 40 h, and (b) 60 h.

3.3 Effect of surface recrystallization on creep rupture life

A surface RX layer around 40 μm in thickness (about 2% of the overall sheet thickness of the sample tested) results in no reduction of the creep rupture life at 980°C, 235MPa in the present tests (45h rupture life, 17% elongation compared to good specimens with 40h rupture life and 13% elongation). However, in the specimens with local RX produced by hardness indentation, the creep rupture life shows a significant drop when the maximum RX depth exceeds ~10% of the overall sample thickness [14]. The present results are in good agreement with the work reported by Khan et. al [7], i.e. the effect of RX is probably following a thickness dependent process.

3.4 Control of recrystallization

Surface coating before solution heat treatment were applied to explore the possible techniques that may reduce the surface RX produced by shot peening. It is interesting to note that different coatings show significantly different roles in preventing the development of surface RX (Fig. 3). Comparing with samples without coating, C2 coating gives the best result. The microstructure of the surface RX layer was compared in Fig. 4.

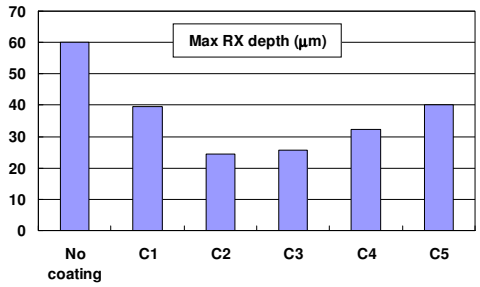

Fig. 3 Maximum RX depth measured in samples without and with different coatings.

To look at the RX kinetics in coated specimens, samples without coating and with C3 coating were heated to the solution heat treatment temperature for various time and quenched in air.

Similar nucleation kinetics was observed. Samples heated for 1 min and 2 min show no detectable RX layer. RX begins to form in samples heated for 3 min. A continuous RX layer formed on surface of the uncoated sample (Fig. 5b). On the contrary, RX grains were constrained locally under the C3 coating.

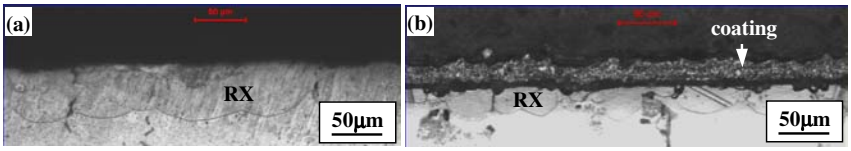

Fig. 4 Morphology of surface RX in samples with (a) no coating and (b) C2 coating.

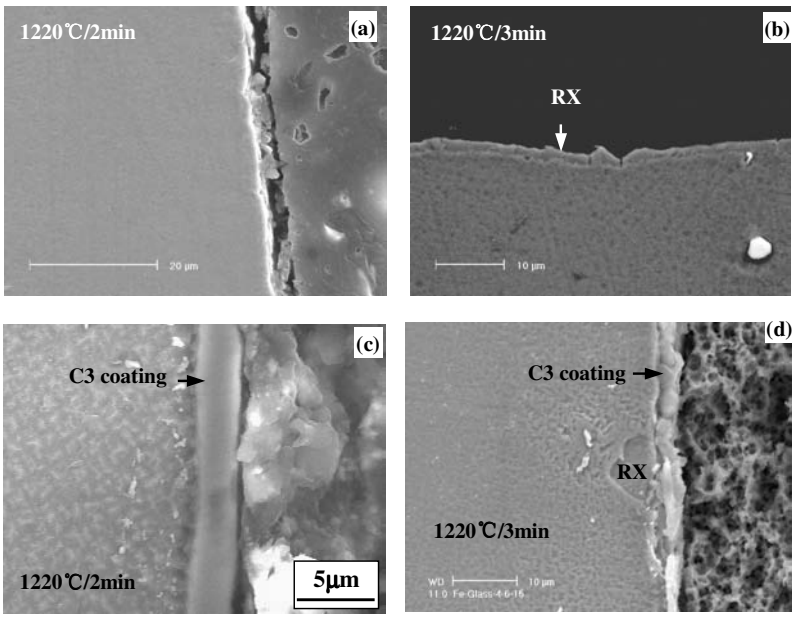

Fig. 5 Surface RX formation in samples without coating (a) and (b), and with C3 coating (c) and (d). Samples were heated to solution heat treatment temperature for various times. No RX formed for samples heated to 1220°C for 2 min. RX began to form in both coated and uncoated samples when heated to 1220°C for 3 min.

4. Discussion

4.1 Formation of cellular recrystallization (RX)

It is generally accepted that RX forms on the surface after shot peening during solution heat treatment, while cellular RX will only occur under the condition of low heat treatment temperature (below the solution temperature of γ′) and large residual strains [2]. It is interesting to note in our present observation that cellular RX formed in front of the surface RX after a three steps heat treatment. Several factors may contribute to the formation of this cellular RX layer: (a) residual strain may still remain in the matrix although most of the residual strain will be consumed during the high temperature heat treatment (solution heat treatment); (b) grain boundary diffusion is faster than the diffusion in the lattice. For instance, high solubility and diffusivity at the recrystallization interface in wrought superalloys (Nimonics PE16, Nimonics 80A, Nimonics 115, and Udimet 720) was observed by Porter and Ralph [16]; and (c) the existed RX grain boundary is still migrating into the matrix during ageing according to the data shown in table 1, and diffusion at migrating grain boundaries is much faster than that at stationary boundaries [17].

The development of cellular RX during creep can be contributed to the existence of stress that further accelerates the grain boundary diffusion. Carbides were observed to be very effective in preventing the formation of cellular RX as shown in Fig. 2.

4.2 Reduction of shot peening induced RX by surface coating

Several previous works have been reported that surface coating could be a very effective way to reduce or eliminate the surface RX in DS superalloy components [4,9,10]. The mechanism is thought to be that the threshold of RX formation is increased since no more free surface for nucleation is available. Our present observation confirmed this argument, i.e. the population of nuclei of RX is probably reduced by coating. However, the thickness of local RX layer is quite similar when comparing the coated and uncoated samples in Fig. 5(b) and (d). Since the final thickness of the RX layer is significantly reduced in coated sample (Fig. 4), it seems that the growth of RX is also influenced by surface coating. Different coatings containing different elements may have different interactions with the superalloy matrix. Therefore, diffusion was constrained to different level and various thickness of the surface RX resulted.

5. Summary

1. Depth of surface recrystallization (RX) induced by shot peening is about 40 μm after heat treatment. In front of the surface RX grains there are a very thin layer of the lamellar γ/γ′ structure (cellular RX).
2. The cellular RX layer developed during creep probably by the accelerated grain boundary diffusion aided by stress.
3. The surface RX (~40 μm) has little effect on the creep rupture life in the present experiments. Comparing with previous results, the effect of RX is probably following a thickness dependent process. When the RX volume is small compared to the whole specimen, there is little detrimental effect of RX on the creep rupture life.
4. Coating is an effective method in suppressing the surface RX induced by shot peening. However, the efficiency of coating strongly depends on the composition. Preliminary analysis reveals that both nucleation and growth of RX is delayed by certain surface coating.

References

[1] C. Y. Jo and H. M. Kim, Effect of recrystallization on microstructural evolution and mechanical properties of single crystal nickel based superalloy CMSX-2 Part 1 - Microstructural evolution during recrystallization of single crystal, Mater. Sci. Technol., 19, 2003, 1665

[2] R. Bűrgel, P. D. Portella, and J. Preuhs, Recrystallization in single crystals of nickel base superalloys, Superalloys 2000, 2000, 229

[3] S. D. Bond and J. W. Martin, Surface recrystallization in a single crystal nickel-based superalloy, J. Mater. Sci., 19, 1984, 3867

[4] M. Okazaki, I. Ohtera and Y. Harada, Prevention of fatigue life reduction relating to cellular microstructure in single crystal Ni-base superalloy, CMSX-4, subjected to previous local damage, Advanced Materials and Processes for Gas Turbines, TMS, 2003, 63

[5] Y. R. Zheng, Z. C. Ruan, and S. C. Wang, Recrystallization in surface layer and its effect on stress rupture properties for DZ22 alloy, Acta Metall. Sinica, 31, 1995, S325

[6] C. Y. Jo and H. M. Kim, Effect of recrystallization on microstructural evolution and mechanical properties of single crystal nickel based superalloy CMSX-2 Part 2—Creep behavior of surface recrystallised single crystal, Mater. Sci. and Technol., 19, 2003, 1671

[7] T. Khan, P. Caron and Y. G. Nakagawa, Mechanical behavior and processing of DS and single crystal superalloys, J. Met., 7, 1986,16

[8] W. J. Gostic, Cyclic Recovery Heat Treatment, UNITED STATES PATENT, Patent Number: 5551999, 1996

[9] M. Okazaki, I. Ohtera and Y. Harada, Damage repair in CMSX-4 alloy without fatigue life reduction penalty, Metall. Mater. Trans. A, Vol.35A, 2004, 535-542

[10] M. Keiichi, Ni-Based single crystal alloy having coating film for preventing recrystallization fracture, EU PATENT, EP 1036850 A1, 1999

[11] J. Corrigan, R. G. Vogt, J. R. Mihalisin, and D. L. Schmiedeknecht, Single crystal superalloy articles with reduced grain recrystallization, EU PATENT, EP 1038982 A1, 2000

[12] J. R. Mihalisin, J. Corrigan, G.t M. Gratti, and R. G. Vogt, Casting of single crystal superalloy articles with reduced eutectic scale and grain recrystallization, US PATENT, Pub. No.: 2002/0007877 A1, 2002
[13] R. W. Salkeld, T. T. Field, and E. A. Ault, Preparation of single crystal superalloys for post-casting heat treatment, UN PATENT, 5413648, 1983
[14] G. Xie, Effect of recrystallization on mechanical properties of DS superalloys, Master Thesis, Institute of Metal Research, Chinese Academy of Sciences, 2005
[15] Q. M. Wang, Y. N. Wu, P. L. Ke, H. T. Cao, J. Gong, C. Sun, and L. S. Wen, Hot corrosion behavior of AIP NiCoCrAlY(SiB) coatings on nickel base superalloys, Surf. Coat. Technol., 186, 2004, 389
[16] A. Porter and B. Ralph, The recrystallization of nickel-base superalloys, J. Mater. Sci., 16, 1981, 707
[17] Y. Mishin and C. Herzig, Grain boundary diffusion: recent progress and future research, Mater. Sci. Eng. A, 260, 1999, 5

AUTHOR INDEX

A

Abe F, II 965, II 1019, II 1041
Affeldt E, II 633
Aguero A, II 949, III 1553
Allcock B, III 1553
Allen D J, III 1479
Andersson C, III 1503
Andren H O, III 1267
Ang J, II 655, II 691
Armaki H G, II 1157
Asahi H, II 1157
Auerkari P, III 1309, III 1385

B

Baker B A, III 1609
Banhart J, III 1651
Barnard P M, I 485
Batfalsky P, I 69
Bauer M, III 1341
Baune E, II 871
Bednarz P, II 747, III 1722
Bendick W, II 1065, II 1077
Berger C, II 1053, II 1137
Bernasovský P, I 261
Berreth K, III 1571
Bhanu Sankara Rao K, I 121
Białas M, II 747
Biede O, III 1503
Birnbaum U, I 161
Blackler M, I 485
Blum L, I 69
Blum R, I 41
Blum W, III 1241
Böck N, II 1031, III 1207
Bolt H, I 81
Bordenet B, GT103
Brabetz M, II 1031
Brekelmans W A M, II 595
Brózda J, III 1331
Brückner U, I 317, I 507
Brziak P, I 261, II 985
Buršík J, III 1449

C

Caminada S, II 871
Cappuccini F, II 717
Casu A, II 727
Cempura G, II 773, II 1077
Cerjak H, II 871, III 1191, III 1199, III 1217, III 1393
Chen Q, II 931
Chilukuru H, III 1181, III 1241
Cizner J, III 1461
Cui C, I 385
Czyrska-Filemonowicz A, I 485, II 773, II 1077

D

Dahl K V, II 675
Daleo J A, II 737
Danielsen H K, III 1251, III 1275
De Carlan Y, III 1319
De Maria L, I 217
Dechamps P, I 25
Del Genovese D, III 1651
Del Puglia P, II 829
Dhooge A, III 1369
Dietz W, III 1683
DiGianfrancesco A, II 843
Dinkel M, II 633
Doi H, I 355
Dong J, III 1609
Donth B, II 843
Du X, II 819
Dubiel B, I 485
Durham R, III 1553
Durst K, III 1181, III 1241

E

Efendi, I 561
El-Magd E, II 1147
Emura S, II 767
Ennis P J, III 1285, II 1077, III 1543, III 1651

Epishin A, I 205, I 317, I 475, I 507, I 521

F

Faulkner R G, II 1117, III 1299
Fedelich B, I 475
Feng D, I 533
Folkova E, III 1401
Foret R, III 1449
Fry A T, III 1469
Fudali S, III 1427, III 1491
Fujioka J, I 385
Fukui T, III 1589

G

Gabrel J, II 1065
Gajda B, II 1087
Gaude-Fugarolas D, III 1319
Gebhard J, II 1147
Geers M G D, II 595
Giannozzi M, II 699, II 707, II 717
Giorni E, II 645, II 699, II 707
Giovannetti I, II 699
Gohil D D, III 1533
Göken M, II 633, III 1181, III 1241
Golanski G, II 1087
Golpayegani A, III 1267
Goto N, I 561
Grumsen F, III 1251
Gu Y, I 385
Guan H R, I 413, II 627
Guo J T, I 189, I 393, I 403, I 435, I 447, II 819
Guo X G, I 403

H

Hagiwara M, II 767
Haibel A, I 521
Hake J F, I 161
Hakl J, I 365, II 985, III 1461
Hald J, II 917, II 675, III 1251, III 1275
Hansson A N, III 1663
Hanus R, II 855
Harada H, I 287, I 309, I 327, I 347, I 385, I 495, II 655, II 691
Harvey B, III 1479
Hashizume R, I 273
Hattori M, I 561
Heinemann J, III 1597
Heinz P, II 633
Helmrich A, II 931, III 1597
Henderson M B, III 1553
Henry J F, II 893
Hernas A, III 1357, III 1427, III 1491
Herzog R, II 747, III 1722
Hierro M P, III 1523
Höfinger S, II 1031
Holdsworth S R, I 91, III 1309
Holdway P, II 793
Holmström S, III 1309, III 1385
Holzer I, III 1191
Homkrajai W, I 377
Hou J S, I 393, I 435, I 447
Hu Z Q, I 189, I 413, II 627
Husemann R U, III 1597
Hussain K, II 737
Huysmans S, III 1369

I

Igarashi M, II 1095
Imai H, II 655, II 757
Imazato T, II 997
Imosa M, III 1491
Innocenti M, II 645
Iseda A, II 1095

J

Jandovà D, III 1401
Jensen S A, III 1503
Jin T, II 627
Jochum C, II 871, III 1341, III 1369

K

Kager F, II 1031
Kakehi K, I 299
Kan T, II 1095
Kanta V, III 1401
Kasl J, III 1401
Kauffmann F, III 1171
Kawagishi K, II 655, II 691
Kern T -U, II 843, II 855
Kilgallon P J, III 1513
Kimura K, II 1019, II 1105, III 1227

Kindratschuk V, III 1619
Kitashima T, I 495
Kiyono T, I 273
Klenk A, III 1341, III 1597
Klingelhöffer H, I 317
Kloc L, II 1011, II 1127
Knoedler R, III 1581
Kobayashi T, I 287, I 309, I 327, I 347, I 495
Koizumi Y, I 309, I 327
Komai N, II 997
Kondo Y, I 455, I 465
Kong S, I 549, I 555
Kothleitner G, III 1217
Koyabu H, I 299
Koyama T, I 561
Kozeschnik E, II 619, III 1191
Kuboň Z, III 1437
Kucharova K, II 1127
Kudrman J, II 1127
Kunecke G, I 475
Kupczyk J, II 1087
Kurita K, I 465
Kuroda S, I 541, II 757
Kushima H, II 1019, II 1105, III 1227

L

Lamm M, I 335
Lanese N, II 829
Lapin J, II 803
Lardon J M, III 1319
Larsen O H, III 1503, I 245
Lee J S, II 1157
Lefebvre B, II 1065
Li G, II 819
Li J, I 549, I 555
Li W, I 549, I 555
Li Y L, I 393, I 435
Li Z J, I 435
Link T, I 205, I 317, I 507, I 521
Linssen J, I 161
Liu J D, II 627
Lomozik M, III 1417
Lou L H, I 583
Lucas K, II 793
Lüdenbach G, III 1597
Luesebrink O, I 335
Lupinc V, II 607
Lyutovich A, III 1571

M

Mack D E, II 727
Maier H, I 81
Maile K, III 1171, III 1341, III 1571, III 1597
Makhele-Lekala L Z, III 1651
Maldini M, II 607
Mao Y, II 767
Marchant G, I 571
Marchionni M, I 423
Mareček J, II 803
Maresca P, II 645
Maruyama K, II 1157
Masset P, II 783
Masuyama F, I 175
Mathieu P, I 143
Matsumoto K, II 691
Matsuo H, II 1095
Matsuo T, I 455, I 465
Mayer K H, II 843, II 855, II 1053, III 1171
Mayr P, III 1393
McColvin G, I 571
Menzler N H, I 69
Meyr P, II 871
Minami Y, III 1589
Mitsche S, III 1199
Miura N, I 455, I 465
Montagnon J, III 1319
Montgomery M, I 245, III 1503, III 1663
Morinaga M, I 273, I 561
Moskal G, III 1357
Mukherji D, III 1619
Mülders B, III 1639
Müller M, II 665
Murakami H, I 541, II 757
Muraki T, II 1157
Murakumo T, I 287
Murata Y, I 273, I 561

N

Nazmy M, I 205
Nicholls J R, III 1696
Nieto J, III 1523
Nisaratanaporn E, I 377
Norton B, III 1553

O

Oakey J, I 233, III 1513
Ohata H, I 347
Onofrio G, I 423
Osgerby S, I 217, III 1469, III 1533
Osinkolu G A, I 423
Ott M, II 633
Over H H, III 1683

P

Pasternak J, II 871, III 1331, III 1357, III 1427, III 1491
Patel S J, III 1609
Pein C, II 619
Pelachová T, II 803
Penkalla H J, II 773, III 1629
Pérez F J, III 1523
Ping D, I 385, I 495
Pirón Abellán J, III 1285
Polsilapa S, I 377
Portella P, I 317
Pratesi F, II 645, II 699, II 707, II 717
Pyczak F, II 633

Q

Qin X Z, I 435, I 447
Quadakkers W J, III 1285, III 1543, III 1722

R

Raj B, I 121
Rajek J, III 1191
Rechberger W, III 1217
Rinaldi C, I 217
Ro Y, I 347
Rohr V, III 1543
Roos E, III 1341
Rösler J, III 1619
Ruoff H, III 1171

S

Sakai T, I 541
Salonen J, III 1385
Sato A, I 287, I 385, II 655, II 691
Sawada K, II 1105, III 1227
Scarlin B, II 931
Scheefer M, III 1553
Scheu C, III 1171
Scholz A, II 1053, II 1137
Schubert F, II 773, III 1629, III 1639, III 1651, III 1722
Schütze M, II 783, III 1543
Schwienheer M, II 1137
Seibert T, III 1181
Semba H, II 1041
Shao C, I 549, I 555
Shibata M, I 541
Shingledecker J P, I 107, II 893
Simms N J, III 1513
Singer R F, II 633, I 335
Singheiser L, III 1285, III 1629, III 1722
Sklenicka V, II 1011, II 1127
Smith G D, III 1609
Sonderegger B, III 1199, III 1217
Sopoušek J, III 1449
Spindler M W, III 1673
Spiradek-Hahn K, II 1031
Stachura S, II 1087
Stamatelopoulos G, II 931
Stanko G, II 893
Staubli M, I 205, II 843, II 855
Steinbrech R, I 69, III 1722
Stöver D, II 727
Strang A, I 571, III 1251
Straub S, III 1171, III 1581
Stuhrmann J, II 1147
Sun C, I 583
Sun X F, I 413, II 627
Suzuki A, II 757
Suzuki T, I 309
Svoboda M, II 1127

T

Tamaki H, I 355
Tanaka F, I 465
Tanzosh J, II 893
Tasak E, III 1417, III 1427
Terzigli V, II 645
Theofel H, III 1597
Tinga T, II 595
Toda Y, II 1019, II 1105
Toshiharu K, II 655

Toušová D, III 1437
Traeger F, II 727
Trunova O, III 1722
Tschaffon H, I 61
Tsuno N, I 299
Tsipas D N, III 1553

V

Vandenberghe B, II 1065, II 1077, III 1369
Vanstone R W, I 41
Vaßen R, II 727
Vekeman J, III 1369
Viswanathan R, II 893
Vitalis B, II 893
Vlasák T, I 365, II 985
Vodarek V, III 1251, III 1437
Volek A, I 335, II 633
Vossberg A, II 633

W

Wabderka N, III 1651
Walbeck M, I 161
Wall G, I 5
Wang L, I 583
Wang Y, II 1053
Wang Y L, I 413
Wang Z H, II 627
Wangyao P, I 377
Weber T, II 855, III 1543
Wenglarz R, I 233
Wessel E, III 1639, III 1722
Willer D, III 1171
Wisbey A, II 793
Wright I G, I 107
Wu J, I 549, I 555
Wu Y N, II 757

X

Xie G, I 583
Xie X, III 1609
Xu G, I 533

Y

Yamaguchi A, I 541, II 757
Yang H C, I 403
Yang J X, I 413
Yardley V, III 1319
Ye H Q, I 435, I 447
Yeh A C, I 287
Yin Y F, II 1117, III 1299
Yokokawa T, I 287, I 309, I 327, I 347
Yoshinari A, I 273, I 355
Yoshizawa M, II 1095
Yuan C, I 393, I 403, I 447
Yutaka K, II 655

Z

Zabler S, I 521
Zeiler G, II 843, II 1031
Zeman M, III 1331
Zhang B, I 533
Zhang J, I 287, I 583
Zhao G, I 533
Zhao M, I 549, I 555
Zhao N R, II 627
Zhao S, III 1609
Zheng Q, I 413
Zhou L Z, I 435
Zielińska-Lipiec A, II 1077
Zies G, III 1171
Zifcak P, II 985
Zlámal B, III 1449
Zonfrillo G, II 699, II 707, II 717, II 829
Zrnik J, I 377
Zschau H E, II 783

KEYWORD INDEX

(Nb,V) CrN particles: III.1251
10Cr steels: II.843
12% Cr steel: II.1077, III.1285, III.1369
12CrMoVNbN steels: III.1251
3DAP: III.1619
5th generation Ni-base superalloys: II.655
6025HT: II.1147
9% Cr steels: III.1393, III.1553
9% Cr cast steel: II.855
9% Cr martensitic steel: II.1041
9-12% Cr steels: II.917, III.1207, II.1031, II.1065, II.1127, II.1137, III.1181, III.1199, III.1241, III.1267, III.1275, III.1357, III.1543
9-12Cr ferritic steels: I.107
Acoustic emission: II.727
Activation energy: I.533
AD700: I.41
Advanced creep laws: III.1341
Advanced power plant materials: III.1479
Advanced power plants: I.143
AFM: III.1181
Allowable stress: II.1095
Alloy 617 welds: III.1597
Alloy 617: III.1597, III.1639
Alloy composition: I.347
Alloy design: II.917
Alloy-80A: I.91
Alloys: III.1683
Alternating atmospheres: III.1533
Aluminising: I.541, II.757, III.1553
Analysis routines: III.1683
Analytical TEM: II.1077
Anisotropy: I.299
Application: I.161, II.855
APS: II.717
Atom-probe field-ion microscopy: I.495
Bainitic structure: II.1087
Biomass: I.245, III.1513
Blading: I.205
Boiler tube: III.1589
Boiler: I.41, II.931
Boron alloyed: III.1393
Boron: II.917, II.965, II.1031
Brazing: II.633
Burgers vectors: I.465
Burner rig test: II.727
Carbides: I.393, I.413, II.985
Carbon and nitrogen redistribution: III.1449
Cast steel: II.1087
CDM modelling: III.1299
Ceramic matrix composites: II.829
Ceramic membranes: I.143
Chemistry modification: III.1619
Chlorination: I.245
Chromium steel: III.1461, III.1469
CM186LC: I.485
CMSX-10: I.507
CMSX-4: I.317, I.507
CO_2 capture: I.143
CO_2 emissions mitigation: I.143
CO_2: I.25
Coal: III.1513
Coarsening of laves phase: II.1157
Coatings: I.217, I.583, II.707, II.737, II.893, II.949
Co-firing: I.245, III.1503, III.1513
Co-free: I.309
Cohesive zone modelling: II.747
Compositional modification: II.767
Conceptual design: II.893
CoNiCrAlY: I.541
Constitutive equation: II.607, III.1341, III.1651
Constitutive model: II.595, III.1207
Conventional Casting (CC): I.355
Cooling time: III.1417
Corrosion resistance: II.893, III.1427, III.1491
Corrosion: III.1533, III.1683
COST536: II.843, II.855
CPFBC: II.665
Crack growth: I.413
Crack initiation: I.403, III.1639
Crack propagation: I.403

Crack: I.393
Cr-diffusion: III.1663
Creep behaviour 11-12%CrWCo(Cu)B(V,Ta,T) steels: II.1053
Creep behaviour: II.1127
Creep damage: II.1117, III.1299, III.1673
Creep equations: II.1137
Creep failure: I.175
Creep fatigue: II.1137
Creep properties: I.365, II.871, II.985, II.1065
Creep rate: II.1117
Creep resistance: II.855, III.1171
Creep resistant steel: II.1011, III.1217, III.1449
Creep resisting steels: III.1331
Creep rupture: II.627, II.1137
Creep strain: II.1117
Creep strength: I.273, II.843, III.1267
Creep testing: III.1401
Creep: I.107, I.287, I.299, I.317, I.455, I.475, I.485, I.507, I.521, II.607, II.619, II.767, II.965, II.1019, II.1031, II.1041, II.1077, II.1105, III.1309, III.1319, III.1369, III.1381, III.1437, III.1479
Creep-fatigue: III.1673
Creep-resistance: III.1357
Cr-steel: III.1319
Crystal growth: II.803
Crystal plasticity: II.595
CVD: III.1571
Cyclic strain: I.403
Damage parameter: III.1341
Damage: III.1639
De-cohesion: II.747
Deformation mechanism: II.819
Degradation: I.205, I.571
D-electrons concept: I.273
Delta ferrite: II.1105, III.1393
Development of FBR materials: I.121
DICTRA: II.675
Diffusion coatings: III.1543
Diffusion coefficient: I.561
Diffusion: II.619, II.633
Directional solidification: I.335
Directionally solidified (DS): I.355
Disk application: I.385
Dislocation dynamics: III.1207
Dislocation Substructure: I.465
Distribution: I.161
Document management system: III.1683
Documentation database: III.1683
Dynamic recrystallisation: I.533
EBSD: II.633, III.1199
ECCC Data sheets: I.91
ECCC: III.1309
Ecological engineering: I.5
EFTEM: III.1217
Electrochemical impedance: III.1523
Electron diffraction: III.1251
Energy alternatives: I.121
Energy and natural resources: I.5
Energy supply chain: I.161
Energy: I.25
Energy-filtered TEM: III.1267
Environmental effect: I.423
Environmental sciences: I.5
Equilibrium: II.691
Esshete 1250: III.1503
European Commission: I.25
Exergy: I.5
Experience: II.855
Experimental data: III.1683
ExtreMat Integrated Project: I.81
Fatigue and creep fatigue crack growth: III.1629
Fatigue crack propagation: I.423
Fatigue: I.317, I.335, II.793
Ferrite matrix: II.1019
Ferritic steel: I.69, II.985, III.1299, III.1309, III.1401
Ferritic/austenitic steels: II.949
Filler metals matching to T/P 23, T/P 24, VM 12, Cost CB 2: II.871
Fireside corrosion: III.1503, III.1513
Flame thermal cycling: II.707
Flow behaviour: I.533
Flue gas desulphurisation plants: III.1427, III.1491
Fossil fuels: I.25
Free energy: I.447
Frequency-Scanning Eddy Current: I.217
Furnace cooling: II.1019

Gamma channel: I.455
Gamma prime: I.205, II.737
Gamma prime precipitate: I.435, I.447, I.465
Gamma TiAl: II.773, II.793
Gas turbine: I.189, I.217, I.423, II.665, II.737
GH2984 superheater alloy: I.189
GH690 alloy tube: I.189
Glass ceramics: I.69
Grade 92 steel: I.91, II.1157
Grain boundary sliding: II.819
Growth stresses: III.1663
HI.2530: I.571
Halogen effect: II.783
Hardness: I.571
Hastelloy alloys: III.1427
HAZ-toughness: III.1393
HCM12: II.1095
Heat affected zone: III.1417
Heat exchanger materials: III.1543
Heat exchanger: III.1513
Heat resistant alloy: I.175
Heat treatment: I.435, II.803, II.997, III.1191
Heterogeneous creep: II.1095
Heterogeneous weld: III.1437
High alloy steel: III.1479
High chromium ferritic steel: II.1105
High efficiency power plant: III.1597
High heat flux materials: I.81
High temperature corrosion: I.245, III.1543
High temperature materials: I.189
High temperature properties: II.655
High temperature: I.61, II.645, II.707, II.717, II.949
High-temperature application: II.843
Homogenisation: I.335
Hot corrosion resistance: I.273
Hot corrosion resistant superalloys: I.189
Hot corrosion: II.665
Hot isostatic pressing (HIP): I.377
Hot working: I.533
Hydrogen effects: III.1663
Hydrogen generation: I.161
Impact energy: II.1087
Implantation: II.783
IN706: III.1619
Inconel 617: III.1651
Inconel 740: III.1609
Industrial gas turbine: I.485
Influence of multiaxiality of the stress state: III.1341
In-situ observation in SEM: III.1639
Interdiffusion: II.675, II.691
Intergranular fracture: II.1157
Intermetallic compound: II.1019
Intermetallic: II.773
Intermittent heating: II.1127
Issues: I.233
K418 superalloy turbine: I.549
K4537 turbine: I.555
K465 cast superalloy: I.413
Laminate: II.829
Larson-Miller parameter: I.327
Laser back-Scattering: I.217
Laser cladding: II.699
Lattice misfit: I.287, I.309
Laves phases: III.1285
LCF: II.773
Life prediction: II.1105
Life: III.1381
Lifetime extension: I.261
Lifing: I.365
Liquid erosion: II.699
Liquid metal cooling: I.335
Long term aging: I.447
Long term exposure: I.377
Long-term creep strength: II.1105
Long–term creep: I.327, III.1227
Low activation materials: I.81
Low alloy steel: II.997, II.1011
Low alloy steels: III.1533
Low cycle fatigue: I.403, I.423, II.1147
Low stress creep: II.1011
LPPS: I.541
M23C6 carbide: I.447, II.965, II.1041
MA 6000: II.645
Martensite: III.1199, III.1417
Martensitic microstructure: II.965
Martensitic phase: II.1019
Material compatibility: I.69

Material development: II.843
Materials database: III.1683
Materials properties data: III.1683
Materials: I.41, I.233, II.931
Mathematical models: I.365
MCrAlY: II.675
Mechanical properties data: III.1683
Mechanical properties of weld joints: III.1357
Mechanical properties: I.347, I.555, II.803, II.871, II.893
Microhardness: I.435
Micromechanics: II.595
Microporosity: I.521
Microstructural changes: II.1127
Microstructural evolution: III.1299
Microstructural parameter: I.347
Microstructural stability: II.1041
Microstructure and modelling: II.917
Microstructure evolution: III.1191
Microstructure: I.507, I.571, II.619, II.767, II.803, II.985, II.1031, II.1077, III.1181, III.1393, III.1401, III.1427, III.1437, III.1491, III.1619
Minimum creep rate: II.997
Mismatched weld materials: III.1341
Mod. Z-phase: III.1217
Model: III.1309
Modelling: I.261, I.475, II.619, III.1469
Modified Z phase: III.1251
Molten salt corrosion: III.1523
Morphological evolution: I.447
Morphology instability: I.435
Multiphase nickel aluminides: II.803
MX and M2X Phase: III.1241
MX carbonitride: II.965
MX precipitates: III.1285
MX: II.1041
Nanoindentation: II.633
NDE: I.217, I.261
Neural network: III.1319, III.1469
Ni-31Cr-3 Mo (Dy) alloy: II.819
Ni-base single crystal superalloy: I.287, I.309, I.347
Ni-base superalloy: I.327, I.385, II.757
Ni-based alloy: I.107, I.561
Ni-based superalloy: I.273, I.299, I.377, I.423, I.455, I.465, I.475, I.533, I.541, I.583
Nickel alloys: III.1491
Nickel based materials: I.61
Nickel content: II.1019
Nickel-base single-crystal superalloy: I.495
Ni-Co-base superalloy: I.385
Ni-YSZ cermet: I.69
Non-conventional sand case: I.549
Non-destructive evaluation: II.1157
Nuclear fission: I.81
Nuclear power programme: I.121
Nuclear technology: I.121
Numerical simulation: I.549, I.555
ODS: II.645
Omega method: II.1117
Outlet header: III.1597
Oxidation resistance: III.1571, I.273, I.287, II.691, II.949
Oxidation: I.107, I.393, I.413, II.645, II.655, II.783, II.793, II.997, III.1461, III.1479
Oxide growth: III.1469
Oxide scale: III.1581
Oxyfuel: I.143
P122: II.1095
P23 steel: III.1437
P91 steel: III.1417, III.1437
P92 steel: II.1147
Pack cementation: III.1543
Partitioning ratio: I.309
PBMR: I.309
Phase computation: III.1609
Photo-luminescence piezospectroscopy: I.217
Plasma facing materials: I.81
Plastic properties: III.1417
PM 3030: II.645
Porosity: III.1319
Power generation: III.1331, III.1357
Power plant: I.61, I.175, III.1369, II.985
PPCC: II.665
Precipitates: III.1217
Precipitation analysis: III.1171
Precipitation kinetics: III.1191
Precipitation site: III.1227

Premature breakdown of creep strength: II.1157
Primary creep: I.299, II.1011
Processing: II.1065
Protective coatings: III.1553
Pt-Ir alloy: II.757
R5: III.1673
Rafting: I.475
Recovery: II.1019
Recrystallization (RX): I.583
Regenerative heat treatment: II.1087
Regression analysis: I.347
Remanent life: II.1117
Research: I.25
Rhenium: I.561
Ruthenium or Iridium addition: I.495
Ruthenium: I.561
SAGBO effect: III.1629
Sandwich-structures: II.1147
Second generation: I.327
SEM and TEM: III.1629
SEM: III.1181, III.1619
Short-range ordering: I.495
Shot peening: I.583, III.1581
Shot-blasted tube: III.1589
Shroud: II.829
Si: II.655
Siliconising: III.1571
Simulation of diffraction patterns: III.1251
Simulation: III.1191, III.1207
Single crystal superalloy: I.335
Single crystal: I.205, I.299, I.317, I.327, I.455, I.465, I.475, I.485, II.737
Single crystalline: II.633
Single-crystal superalloy: II.627
Size distribution: III.1217
Slip system: I.455
SNMS: III.1285
Solid oxide fuel cell: I.69
Spallation: III.1581
Sputtering: II.757
SRZ: II.691
Stainless steel: III.1589
Steam environment: III.1461
Steam oxidation: I.175, III.1285, III.1553, III.1581, III.1589, III.1663
Steam power plant: I.261, II.931, II.949
Steam side oxidation: II.1065
Steam turbine: I.41
Steam: III.1469
Steamside oxidation and resistance: II.893
Steamside oxidation: III.1503
Steel tubes: III.1571
Steel: III.1381
Stellite: II.699
Storage: I.161
Strain rate: III.1651
Strain: III.1309
Straw: I.245
Strength: III.1381
Stress analysis: II.829
Stress and/or strain effect: III.1227
Stress exponent: II.1011
Stress: II.619
Structural analyses: II.773, III.1449
Structural stability: III.1357
Structure analysis: I.377
Structure degradation: I.377
Structure stability: III.1609
Superalloy: I.205, I.317, I.355, I.365, I.393, I.435, I.507, I.521, II.595, II.607, II.645, II.675, II.699, III.1609
Supercritical: II.931
Superheater tubes: III.1597
Superplasticity: II.819
Surfaces: III.1581
Sustainable development: I.5
Syngas: I.233
T/P23: II.997
T122: II.1095
TBC: II.717
TCP phase: I.541
TEM: III.1171, III.1181, III.1401, III.1619
Temperature estimation: II.737
Tensile test: III.1651
Testing: III.1479
Thermal analysis: II.829
Thermal barriers: II.707
Thermal barrier coating: II.727
Thermal cycles: II.717
Thermal cycling: II.727, II.747
Thermal exposure: II.793

Thermal fatigue: I.175, I.393, I.413
Thermal mechanical fatigue: I.347
Thermal shock: II.707
Thermal spraying: III.1553
Thermal welding cycle: III.1417
Thermo mechanical fatigue: I.287
Thermodynamic and kinetic modelling: III.1449
Thermodynamic modelling: II.665
Thermo-physical properties data: III.1683
Ti2AlNb: II.767
Ti6242: II.773
TiAl: II.783
Titanium alloy: II.767
TLP bonding: II.627
Tomography: I.521
TP347H FG: III.1503
Tungsten: I.561
Turbine: I.233, I.365, II.699
Type 316H: III.1673
U720Li: I.385
Ultrasupercritical: I.107
USC plant: III.1589
USC: III.1609
Variable creep loading: II.1127
VM12: II.1065, II.1077, III.1369
VN precipitation: III.1319
Wallpapering: III.1491
Waspaloy: III.1629
Waste incineration: III.1523
Water quenching: II.1019
Web-enable data: III.1683
Web-services: III.1683
Weld joints: III.1449
Weld: III.1381
Weldability: II.855, II.893, III.1331
Welded joints: III.1331
Welding of pipe E911: II.871
Welding: III.1369, III.1401
Woodchip: I.245
Wrought Ni-based superalloy: I.403
YH61: I.355
Z phase: II.917, III.1171, III.1227, III.1241, III.1267, III.1275
Zirconia: II.717

Schriften des Forschungszentrums Jülich
Reihe Energietechnik / Energy Technology

1. **Fusion Theory**
   Proceedings of the Seventh European Fusion Theory Conference
   edited by A. Rogister (1998); X, 306 pages
   ISBN: 3-89336-219-3

2. **Radioactive Waste Products 1997**
   Proceedings of the 3rd International Seminar on Radioactive Waste Products
   held in Würzburg (Germany) from 23 to 26 June 1997
   edited by R. Odoj, J. Baier, P. Brennecke et al. (1998), XXIV, 506 pages
   ISBN: 3-89336-225-8

3. **Energieforschung 1998**
   Vorlesungsmanuskripte des 4. Ferienkurs „Energieforschung“
   vom 20. bis 26. September 1998 im Congrescentrum Rolduc und
   im Forschungszentrum Jülich
   herausgegeben von J.-Fr. Hake, W. Kuckshinrichs, K. Kugeler u. a. (1998),
   500 Seiten
   ISBN: 3-89336-226-6

4. **Materials for Advances Power Engineering 1998**
   Abstracts of the 6th Liège Conference
   edited by J. Lecomte-Beckers, F. Schubert, P. J. Ennis (1998), 184 pages
   ISBN: 3-89336-227-4

5. **Materials for Advances Power Engineering 1998**
   Proceedings of the 6th Liège Conference
   edited by J. Lecomte-Beckers, F. Schubert, P. J. Ennis (1998),
   Part I XXIV, 646, X pages; Part II XXIV, 567, X pages; Part III XXIV, 623, X
   pages
   ISBN: 3-89336-228-2

6. **Schule und Energie**
   1. Seminar Energiesparen, Solarenergie, Windenergie. Jülich, 03. und
   04.06.1998
   herausgegeben von P. Mann, W. Welz, D. Brandt, B. Holz (1998), 112 Seiten
   ISBN: 3-89336-231-2

7. **Energieforschung**
   Vorlesungsmanuskripte des 3. Ferienkurses „Energieforschung“
   vom 22. bis 30. September 1997 im Forschungszentrum Jülich
   herausgegeben von J.-Fr. Hake, W. Kuckshinrichs, K. Kugeler u. a. (1997),
   505 Seiten
   ISBN: 3-89336-211-8

8. **Liberalisierung des Energiemarktes**
   Vortragsmanuskripte des 5. Ferienkurs „Energieforschung“
   vom 27. September bis 1. Oktober 1999 im Congrescentrum Rolduc und
   im Forschungszentrum Jülich
   herausgegeben von J.-Fr. Hake, A. Kraft, K. Kugeler u. a. (1999), 350 Seiten
   ISBN: 3-89336-248-7

9. **Models and Criteria for Prediction of Deflagration-to-Detonation Transition (DDT) in Hydrogen-Air-Steam-Systems under Severe Accident Conditions**
   edited by R. Klein, W. Rehm (2000), 178 pages
   ISBN: 3-89336-258-4

10. **High Temperature Materials Chemistry**
    Abstracts of the 10th International IUPAC Conference, April 10 - 14 2000, Jülich
    edited by K. Hilpert, F. W. Froben, L. Singheiser (2000), 292 pages
    ISBN: 3-89336-259-2

11. **Investigation of the Effectiveness of Innovative Passive Safety Systems for Boiling Water Reactors**
    edited by E. F. Hicken, K. Verfondern (2000), X, 287 pages
    ISBN: 3-89336-263-0

12. **Zukunft unserer Energieversorgung**
    Vortragsmanuskripte des 6. Ferienkurs „Energieforschung“
    vom 18. September bis 22. September 2000 im Congrescentrum Rolduc und
    im Forschungszentrum Jülich
    herausgegeben von J.-Fr. Hake, S. Vögele, K. Kugeler u. a. (2000),
    IV, 298 Seiten
    ISBN: 3-89336-268-1

13. **Implementing Agreement 026**
    For a programme of research, development and demonstration on advances fuel cells
    Fuel Cell Systems for Transportation
    Annex X. Final Report 1997 - 1999
    edited by B. Höhlein; compiled by P. Biedermann (2000), 206 pages
    ISBN: 3-89336-275-4

14. **Vorgespannte Guß-Druckbehälter (VGD) als berstsichere Druckbehälter für innovative Anwendungen in der Kerntechnik**
    Prestressed Cast Iron Pressure Vessels as Burst-Proof Pressure Vessels for Innovative Nuclear Applications
    von W. Fröhling, D. Bounin, W. Steinwarz u. a. (2000) XIII, 223 Seiten
    ISBN: 3-89336-276-2

15. **High Temperature Materials Chemistry**
    Proceedings of the 10th International IUPAC Conference
    held from 10 to 14 April 2000 at the Forschungszentrum Jülich, Germany
    Part I and II
    edited by K. Hilpert, F. W. Froben, L. Singheiser (2000), xvi, 778, VII pages
    ISBN: 3-89336-259-2

16. **Technische Auslegungskriterien und Kostendeterminanten von SOFC- und PEMFC-Systemen in ausgewählten Wohn- und Hotelobjekten**
    von S. König (2001), XII, 194 Seiten
    ISBN: 3-89336-284-3

17. **Systemvergleich: Einsatz von Brennstoffzellen in Straßenfahrzeugen**
    von P. Biedermann, K. U. Birnbaum, Th. Grube u. a. (2001), 185 Seiten
    ISBN: 3-89336-285-1

18. **Energie und Mobilität**
    Vorlesungsmanuskripte des 7. Ferienkurs „Energieforschung“
    vom 24. September bis 28. September 2001 im Congrescentrum Rolduc und im Forschungszentrum Jülich
    herausgegeben von J.-Fr. Hake, J. Linßen, W. Pfaffenberger u. a. (2001),
    205 Seiten
    ISBN: 3-89336-291-6

19. **Brennstoffzellensysteme für mobile Anwendungen**
    von P. Biedermann, K. U. Birnbaum, Th. Grube u. a. (2002)
    PDF-Datei auf CD
    ISBN: 3-89336-310-6

20. **Materials for Advances Power Engineering 2002**
    Abstracts of the 7th Liège Conference
    edited by J. Lecomte-Beckers, M. Carton, F. Schubert, P. J. Ennis (2002),
    c. 200 pages
    ISBN: 3-89336-311-4

21. **Materials for Advanced Power Engineering 2002**
    Proceedings of the 7th Liège Conference
    Part I, II and III
    edited by J. Lecomte-Beckers, M. Carton, F. Schubert, P. J. Ennis (2002),
    XXIV, 1814, XII pages
    ISBN: 3-89336-312-2

22. **Erneuerbare Energien: Ein Weg zu einer Nachhaltigen Entwicklung?**
    Vorlesungsmanuskripte des 8. Ferienkurs „Energieforschung“
    vom 23. bis 27. September 2002 in der Jakob-Kaiser-Stiftung, Königswinter
    herausgegeben von J.-Fr. Hake, R. Eich, W. Pfaffenberger u. a. (2002),
    IV, 230 Seiten
    ISBN: 3-89336-313-0

23. **Einsparpotenziale bei der Energieversorgung von Wohngebäuden durch Informationstechnologien**
    von A. Kraft (2002), XII, 213 Seiten
    ISBN: 3-89336-315-7

24. **Energieforschung in Deutschland**
    Aktueller Entwicklungsstand und Potentiale ausgewählter nichtnuklearer Energietechniken
    herausgegeben von M. Sachse, S. Semke u. a. (2002), II, 158 Seiten, zahlreiche farb. Abb.
    ISBN: 3-89336-317-3

25. **Lebensdaueranalysen von Kraftwerken der deutschen Elektrizitätswirtschaft**
    von A. Nollen (2003), ca. 190 Seiten
    ISBN: 3-89336-322-X

26. **Technical Session: Fuel Cell Systems of the World Renewable Energy Congress VII**
    Proceedings
    edited by D. Stolten and B. Emonts (2003), VI, 248 pages
    ISBN: 3-89336-332-7

27. **Radioactive Waste Products 2002 (RADWAP 2002)**
    Proceedings
    edited by R. Odoj, J. Baier, P. Brennecke and K. Kühn (2003), VI, 420 pages
    ISBN: 3-89336-335-1

28. **Methanol als Energieträger**
    von B. Höhlein, T. Grube, P. Biedermann u. a. (2003), XI, 109 Seiten
    ISBN: 3-89336-338-6

29. **Hochselektive Extraktionssysteme auf Basis der Dithiophosphinsäuren: Experimentelle und theoretische Untersuchungen zur Actinoiden(III)-Abtrennung**
    von S. A. H. Nabet (2004), VI, 198 Seiten
    ISBN: 389336-351-3

30. **Benchmarking-Methodik für Komponenten in Polymerelektrolyt-Brennstoffzellen**
    von Matthias Gebert (2004), 194 Seiten
    ISBN: 3-89336-355-6

31. **Katalytische und elektrochemische Eigenschaften von eisen- und kobalthaltigen Perowskiten als Kathoden für die oxidkeramische Brennstoffzelle (SOFC)**
    von Andreas Mai (2004), 100 Seiten
    ISBN: 3-89336-356-4

32. **Energy Systems Analysis for Political Decision-Making**
edited by J.-Fr. Hake, W. Kuckshinrichs, R. Eich (2004), 180 pages
ISBN: 3-89336-365-3

33. **Entwicklung neuer oxidischer Wärmedämmschichten für Anwendungen in stationären und Flug-Gasturbinen**
von R. Vaßen (2004), 141 Seiten
ISBN: 3-89336-367-X

34. **Neue Verfahren zur Analyse des Verformungs- und Schädigungsverhaltens von MCrAlY-Schichten im Wärmedämmschichtsystem**
von P. Majerus (2004), 157 Seiten
ISBN: 3-89336-372-6

35. **Einfluss der Oberflächenstrukturierung auf die optischen Eigenschaften der Dünnschichtsolarzellen auf der Basis von a-Si:H und µc-Si:H**
von N. Senoussaoui (2004), 120 Seiten
ISBN: 3-89336-378-5

36. **Entwicklung und Untersuchung von Katalysatorelementen für innovative Wasserstoff-Rekombinatoren**
von I.M. Tragsdorf (2005), 119 Seiten
ISBN: 3-89336-384-X

37. **Bruchmechanische Untersuchungen an Werkstoffen für Dampfkraftwerke mit Frischdampftemperaturen von 500 bis 650°C**
von L. Mikulová (2005), 149 Seiten
ISBN: 3-89336-391-2

38. **Untersuchungen der Strukturstabilität von Ni-(Fe)-Basislegierungen für Rotorwellen in Dampfturbinen mit Arbeitstemperaturen über 700 °C**
von T. Seliga (2005), 106 Seiten
ISBN: 3-89336-392-0

39. **IWV-3 Report 2005. Zukunft als Herausforderung**
(2005), 115 Seiten
ISBN: 3-89336-393-9

40. **Integrierter Photodetektor zur Längenmessung**
von E. Bunte (2005), XI, 110 Seiten
ISBN: 3-89336-397-1

41. **Microcrystalline Silicon Films and Solar Cells Investigated by Photoluminescence Spectroscopy**
by T. Merdzhanova (2005), X, 137 pages
ISBN: 3-89336-401-3

42. **IWV-3 Report 2005. Future as a challenge**
(2005), 115 pages
ISBN: 3-89336-405-6

43. **Electron Spin Resonance and Transient Photocurrent Measurements on Microcrystalline Silicon**
by T. Dylla (2005), X, 138 pages
ISBN: 3-89336-410-2

44. **Simulation und Analyse des dynamischen Verhaltens von Kraftwerken mit oxidkeramischer Brennstoffzelle (SOFC)**
von M. Finkenrath (2005), IV, 155 Seiten
ISBN: 3-89336-414-5

45. **The structure of magnetic field in the TEXTOR-DED**
by K.H. Finken, S.S. Abdullaev, M. Jakubowski, M. Lehnen, A. Nicolai, K.H. Spatschek (2005), 113 pages
ISBN: 3-89336-418-8

46. **Entwicklung und Modellierung eines Polymerelektrolyt-Brennstoffzellenstapels der 5 kW Klasse**
von T. Wüster (2005), 211 Seiten
ISBN: 3-89336-422-6

47. **Die Normal-Wasserstoffelektrode als Bezugselektrode in der Direkt-Methanol-Brennstoffzelle**
von M. Stähler (2006), VI, 96 Seiten
ISBN: 3-89336-428-5

48. **Stabilitäts- und Strukturmodifikationen in Katalysatordispersionen der Direktmethanolbrennstoffzelle**
von C. Schlumbohm (2006), II, 211 Seiten
ISBN: 3-89336-429-3

49. **Eduktvorbereitung und Gemischbildung in Reaktionsapparaten zur autothermen Reformierung von dieselähnlichen Kraftstoffen**
von Z. Porš (2006), XX, 182, XII Seiten
ISBN: 3-89336-432-2

50. **Spektroskopische Untersuchung der poloidalen Plasmarotation unter dem Einfluß statischer und dynamischer Ergodisierung am Tokamak TEXTOR**
von C. Busch (2006), IV, 81 Seiten
ISBN: 3-89336-433-1

51. **Entwicklung und Optimierung von Direktmethanol-Brennstoffzellstapeln**
von M. J. Müller (2006), 167 Seiten
ISBN: 3-89336-434-X

Schriften des Forschungszentrums Jülich
Reihe Energietechnik / Energy Technology

52. **Untersuchung des reaktiven Sputterprozesses zur Herstellung von aluminiumdotierten Zinkoxid-Schichten für Silizium-Dünnschichtsolarzellen**
von J. Hüpkes (2006), XIV, 170 Seiten
ISBN: 3-89336-435-8

53. **Materials for Advanced Power Engineering 2006**
Proceedings of the 8th Liège Conference
Part I, II and III
edited by J. Lecomte-Beckers, M. Carton, F. Schubert, P. J. Ennis (2006),
Getr. Pag.
ISBN: 3-89336-436-6

COST is supported by the EU framework programme

COST is an intergovernmental European framework for international cooperation between nationally funded research activities. COST creates scientific networks and enables scientists to collaborate in a wide spectrum of activities in research and technology. COST activities are administered by the COST Office.

ESF provides and manages the scientific and technical secretariat for COST

Forschungszentrum Jülich
in der Helmholtz-Gemeinschaft

50 Jahre / Zukunft

Band / Volume 53, Part I
ISBN 3-89336-436-6

Energietechnik
Energy Technology

Forschungszentrum Jülich
in der Helmholtz-Gemeinschaft
50 Jahre / Zukunft

**J. Lecomte-Beckers, M. Carton,
F. Schubert and P. J. Ennis (Editors)**

Materials for Advanced Power Engineering 2006

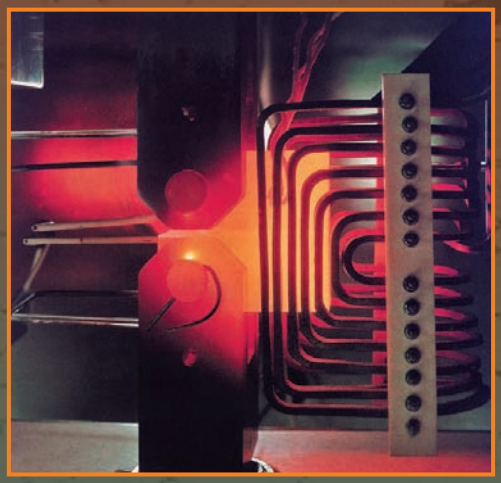

Proceedings Part II

**Energietechnik
Energy Technology**

Schriften des Forschungszentrums Jülich
Reihe Energietechnik / Energy Technology Band / Volume 53, Part II

Forschungszentrum Jülich GmbH
Institut für Energieforschung

Jacqueline Lecomte-Beckers, Marc Carton,
Florian Schubert and Philip J. Ennis (Editors)

Materials for Advanced Power Engineering 2006

Proceedings of the 8th Liège Conference

Part II

Université de Liège
European Commission
COST
European Science Foundation

Schriften des Forschungszentrums Jülich
Reihe Energietechnik / Energy Technology Band/Volume 53, Part II

ISSN 1433-5522 ISBN 3-89336-436-6

Bibliographic information published by Die Deutsche Bibliothek.
Die Deutsche Bibliothek lists this publication in the Deutsche Nationalbibliografie; detailed bibliographic data are available in the Internet at <http://dnb.ddb.de>.

Publisher and Distributor: Forschungszentrum Jülich GmbH
Zentralbibliothek, Verlag
D-52425 Jülich
Telefon (02461) 61-5368 · Telefax (02461) 61-6103
e-mail: zb-publikation@fz-juelich.de
Internet: http://www.fz-juelich.de/zb

Cover Design: Grafische Medien, Forschungszentrum Jülich GmbH

Printer: Grafische Medien, Forschungszentrum Jülich GmbH

Copyright: Forschungszentrum Jülich 2006

Schriften des Forschungszentrums Jülich
Reihe Energietechnik / Energy Technology Band / Volume 53, Part II

ISSN 1433-5522
ISBN 3-89336-436-6

Neither this book nor any part may be reproduced or transmitted in any form or by any means, electronic or mechanical, including photocopying, microfilming, and recording, or by any information storage and retrieval system, without permission in writing from the publisher.

FOREWORD

The European Co-operation in the field of Scientific and Technical Research (COST) is a well-established organisation for the co-ordination of national research and development programmes on the European level. The series of Liège conferences began in 1978 with the aim of disseminating the results of the COST Action 50 in which materials for gas turbines were investigated. Since then, a Liège Conference has been held every four years and the results of COST Actions 501 and 522, which were concerned with materials for power generation plant, reported. At this, the Eighth Liège Conference, the materials research and development work being carried out in the current COST Actions 536 'Alloy Development for Critical Components of Environmentally Friendly Steam Power Plant' with the acronym ACCEPT and 538 'High Temperature Plant Lifetime Extension' will be reported.

Reliable energy supply at reasonable cost is one of the most important factors in the development and maintenance of the modern industrial society, but there are increasing concerns about the environmental impact of energy production as well as about the need to conserve valuable energy resources for future generations. New and emerging energy technologies are of great interest, but fossil fuels will continue to make a considerable contribution to energy requirements into the foreseeable future. The emphasis in this field is therefore on the most efficient use of fossil fuels, which can be achieved by increasing the thermal efficiency of the energy conversion process. For steam power plant and gas turbines, this means raising the temperature and pressure of the process. This in turn requires the application of improved materials that are able to withstand the increasingly arduous service conditions.

In the COST Actions, the materials research and development activities that are necessary for the critical components of advanced, highly efficient power generation plant have been based on the principle of work-sharing, bringing together materials scientists and engineers, plant designers, alloy producers, component manufacturers, plant constructors and plant operators. This constellation of expertise reflects the need to match materials properties to component behaviour.

In order to put the European efforts into a world-wide scenario, there are in this conference a number of invited papers that will discuss the energy perspectives and the development of power plant materials in the USA, Japan, India and China.

The Conference Proceedings are organised as follows:

Part I: INAUGURAL SESSION
Invited papers

EUROPEAN ENERGY MATERIALS RESEARCH
Invited papers

ENERGY PERSPECTIVES
Invited papers

ADVANCED GAS TURBINE MATERIALS
Invited papers
Contributed papers
Mechanical properties
Microstructure

Part II: ADVANCED GAS TURBINE MATERIALS
Contributed papers
Modelling
Joining technology
Oxidation and hot corrosion
Coating technology
Intermetallics and ceramics

ADVANCED STEAM TURBINE MATERIALS
Invited papers
Contributed papers
Mechanical properties

Part III: ADVANCED STEAM TURBINE MATERIALS
Contributed papers
Microstructure
Modelling and alloy design
Welding technology
Steam oxidation and coatings
Austenitic and nickel-base alloys

ADDENDUM

The Technical and Editorial Board members would like to express their gratitude to all the members of the COST 536 and COST 538 Management Committees, for their supervision and support of the considerable research and development efforts, both in their own countries and across national borders. Those who were involved in the reviewing of the submitted papers are also sincerely thanked for their important contribution to the production of the Proceedings.

Research Centre Jülich - 50 Years of Innovation

Addressing society's challenges, questions and expectations and delivering solutions with the aid of excellent, strategically positioned research: this is the mission that Research Centre Jülich has been involved in ever since its foundation 50 years ago. Over the course of the years, it has undergone a huge transition, moving from research focused on the peaceful uses of nuclear energy to a research enterprise run on a multi-programmatic and interdisciplinary basis with an internationally unrivalled profile.

The key to this profile is the close linking of Jülich's traditional core competence, physics, to the other sciences. The basic insights gained in physics contribute decisively to a better understanding of the complex systems in energy, chemistry, biology, medicine and the geosciences, while the questions encountered in these fields extend the approaches adopted in physics. A further core competence that has evolved in Jülich with a remarkable momentum over the last few years is scientific computing. The operation of medium and large-scale equipment and a well-developed scientific and technical infrastructure round off the profile. This leads to the co-operation between and mutual enrichment of the different areas of expertise in Jülich, which remains internationally unparalleled in both nature and intensity. The positive effect of this cross-linking is further enhanced through strategic alliances with other centres in the Helmholtz Association, as well as with universities, industrial companies and research institutions worldwide.

The Research Centre Jülich will use this profile as a focal point for its research over the next two decades, making thus significant future contributions to the following four grand challenges: responsible management of the environment's natural resources, sustainable and comprehensive energy supply, securing food for and the health of a growing world population, and the provision and solutions-orientated linking of large quantities of information.

TABLE OF CONTENTS

Part I

Foreword iii
Table of Contents vii

INAUGURAL SESSION

ENGINEERING SUSTAINABILITY 5
Wall G

THE EU RESEARCH STRATEGY TOWARDS ZERO EMISSION FOSSIL FUEL POWER PLANTS 25
Dechamps P

EUROPEAN ENERGY MATERIALS RESEARCH

MATERIALS DEVELOPMENT FOR BOILERS AND STEAM TURBINES OPERATING AT 700 °C I 41
Blum R, Vanstone R W

THE EUROPEAN WAY TO 700°C COAL FIRED POWER PLANT I 61
Tschaffon H

MATERIALS ASPECTS OF SOLID OXIDE FUEL CELLS I 69
Steinbrech R, Menzler N H, Batfalsky P, Blum L

MATERIALS FOR EXTREME ENVIRONMENTS IN FUSION APPLICATIONS I 81
Bolt H, Maier H

DEVELOPMENT AND CURRENT STATUS OF ECCC CREEP PROPERTY DATA SHEETS I 91
Holdsworth S R
(see also Part III 1722, Addendum)

ENERGY PERSPECTIVES

EVALUATION OF THE MATERIALS TECHNOLOGY REQUIRED FOR A 760ºC POWER STEAM BOILER I 107
Shingledecker J P, Wright I G

CURRENT AND 2050 ENERGY PERSPECTIVES IN INDIA: OPPORTUNITIES FOR MATERIALS SCIENTISTS AND TECHNOLOGISTS I 121
Baldev Raj, B S Rao Kota

MATERIALS CHALLENGES IN CO_2 CAPTURE AND STORAGE I 143
Mathieu P

THE HYDROGEN ECONOMY I 161
Birnbaum U, Hake J-F, Linssen J, Walbeck M

ADVANCED POWER PLANT DEVELOPMENTS AND MATERIAL EXPERIENCES IN JAPAN I 175
Masuyama F

DEVELOPMENT OF HIGH TEMPERATURE MATERIALS FOR ENERGY MARKET IN CHINA I 189
Hu Z Q, Guo J T

ADVANCED GAS TURBINE MATERIALS

Invited papers

DEGRADATION IN SINGLE CRYSTAL NICKEL-BASE SUPERALLOYS – A REVIEW I 205
Nazmy M, Epishin A, Link T, Staubli M

RECENT ADVANCES IN NDT TECHNIQUES FOR GAS TURBINE COATINGS I 217
Osgerby S, Rinaldi C, De Maria L

GAS TURBINE ISSUES IN ADVANCED GASIFICATION SYSTEMS I 233
Wenglarz R, Oakey J

MATERIALS PROBLEMS AND SOLUTIONS IN BIOMASS FIRED PLANTS I 245
Larsen O H, Montgomery M

RE-QUALIFICATION OF BOILER DRUMS IN THERMAL POWER PLANT I 261
Brziak P, Bernasovský P

(see also Part III 1696, Addendum)

Contributed papers: Mechanical properties

DEVELOPMENT OF NI-BASED SINGLE CRYSTAL SUPERALLOYS FOR POWER-GENERATION GAS TURBINE BLADES I 273
Hashizume R, Yoshinari A, Kiyono T, Murata Y, Morinaga M

A 5TH GENERATION NI-BASE SINGLE CRYSTAL SUPERALLOY WITH SUPERIOR ELEVATED TEMPERATURE PROPERTIES I 287
Sato A, Yeh A C, Kobayashi T, Yokokawa T, Harada H, Murakumo T, Zhang J

EFFECT OF PLASTIC ANISOTROPY ON CREEP STRENGTH OF SINGLE CRYSTAL NI-BASED SUPERALLOYS I 299
Koyabu H, Tsuno N, Kakehi K

DEVELOPMENT OF CO-FREE NI-BASE SINGLE CRYSTAL SUPERALLOY I 309
Yokokawa T, Kobayashi T, Suzuki T, Koizumi Y, Harada H

THE EFFECT OF HIGH TEMPERATURE CREEP DAMAGE ON LOW CYCLE FATIGUE IN CMSX-4 I 317
Epishin A, Link T, Brückner U, Klingelhöffer H, Portella P

THE LONG-TERM CREEP PROPERTY OF NICKEL-BASE SINGLE-CRYSTAL SUPERALLOYS I 327
Koizumi Y, Harada H, Yokokawa T, Kobayashi T

INFLUENCE OF SOLIDIFICATION CONDITIONS ON HOMOGENISATION HEAT TREATMENT AND MECHANICAL PROPERTIES IN SINGLE CRYSTAL NICKEL-BASE SUPERALLOYS I 335
Lamm M, Volek A, Luesebrink O, Singer R F

PREDICTION OF THERMAL MECHANICAL FATIGUE PROPERTIES OF NI-BASE SINGLE CRYSTAL SUPERALLOYS I 347
Ohata H, Yokokawa T, Kobayashi T, Ro Y, Harada H

DEVELOPMENT OF A HIGH STRENGTH NI-BASED SUPERALLOY FOR CONVENTIONAL CASTING I 355
Tamaki H, Yoshinari A, Doi H

HIGH TEMPERATURE PROPERTIES OF SELECTED NI-BASE SUPERALLOYS I 365
Hakl J, Vlasák T

HOT ISOSTATIC PRESSING PROCESS TO REJUVENATE SERVICED CAST NICKEL-BASE SUPERALLOY IN738 TURBINE BLADES I 377
Wangyao P, Zrnik J, Polsilapa S, Nisaratanaporn E, Homkrajai W

DEVELOPMENT OF NEW SUPERALLOYS FOR TURBINE DISK APPLICATIONS I 385
Gu Y, Cui C, Ping D, Harada H, Sato A, Fujioka J

INFLUENCE OF CARBIDES AND OXIDATION ON THERMAL FATIGUE BEHAVIORS OF TWO NICKEL-BASE SUPERALLOYS I 393
Li Y L, Yuan C, Guo J T, Hou J S

LOW CYCLE FATIGUE BEHAVIOR OF WROUGHT NICKEL BASED SUPERALLOY GH413 I 403
Guo X G, Guo J T, Yuan C, Yang H C

EFFECT OF CARBIDES ON THERMAL FATIGUE PROPERTY OF K465 CAST SUPERALLOY I 413
Guan H R, Yang J X, Zheng Q, Wang Y L, Sun X F, Hu Z Q

ENVIRONMENTAL EFFECT ON HIGH TEMPERATURE FATIGUE BEHAVIOUR OF A NICKEL BASE SUPERALLOY FOR TURBINE DISCS I 423
Marchionni M, Onofrio G, Osinkolu G A

INFLUENCE OF SOLUTION HEAT TREATMENT CONDITIONS ON GAMMA PRIME CHARACTERISTICS IN A HOT CORROSION RESISTANT SUPERALLOY I 435
Hou J S, Guo J T, Zhou L Z, Li J Z, Qin X Z, Li Y L, Ye H Q

Contributed papers: Microstructure

MORPHOLOGICAL EVOLUTION OF GAMMA PRIME AND $M_{23}C_6$ CARBIDE IN A CAST NI-BASE SUPERALLOY IN THE DIFFERENT TREATMENT CONDITIONS I 447
Qin X Z, Guo J T, Yuan C, Hou J S, Ye Q H

DISLOCATION SUBSTRUCTURE IN γ-CHANNEL OF SINGLE CRYSTAL NICKEL-BASED SUPERALLOY, CMSX-4, CREPT AT 1273 K, 160 MPA I 455
Kondo Y, Miura N, Matsuo T

DISLOCATION SUBSTRUCTURE AT γ/γ' INTERFACE OF SINGLE CRYSTAL NICKEL-BASED SUPERALLOY CMSX-4 CREPT AT 1273 K, 250 MPA I 465
Miura N, Tanaka F, Kurita K, Kondo Y, Matsuo T

MODELLING OF RAFTING AND ITS INFLUENCE IN NI-BASE SUPERALLOYS I 475
Fedelich B, Künecke G, Epishin A

TEM MICROSTRUCTURAL ANALYSIS OF CREEP DEFORMED CM186LC SINGLE CRYSTAL NI-BASE SUPERALLOY I 485
Dubiel B, Blackler M, Barnard P M, Czyrska-Filemonowicz A

ATOM PROBE MICROANALYSIS OF FIFTH-GENERATION NI-BASE SINGLE-CRYSTAL SUPERALLOYS I 495
Kitashima T, Ping D H, Harada H, Kobayashi T

MICROSTRUCTURAL STABILITY OF CMSX-4 AND CMSX-10 UNDER HIGH TEMPERATURE CREEP CONDITIONS I 507
Epishin A, Link T, Brückner U

X-RAY TOMOGRAPHY FOR POROSITY ANALYSIS IN SINGLE-CRYSTAL NI-BASE SUPERALLOYS I 521
Link T, Zabler S, Haibel A, Epishin A

DEFORMATION BEHAVIOR AND MICROSTRUCTURE EVOLUTION DURING HOT WORKING PROCESS OF NICKEL-BASE ALLOY GH742 I 533
Zhang B, Zhao G, Xu G, Feng D

ORIENTATION DEPENDENCE OF SECONDARY REACTION ZONES IN SURFACE MODIFIED NI-BASED SINGLE CRYSTAL SUPERALLOYS I 541
Murakami H, Sakai T, Shibata M, Yamaguchi A, Kuroda S

STUDY ON THE INVESTMENT CASTING PROCESS OF K418 SUPERALLOY TURBINE I 549
Li J, Zhao M, Shao C, Kong S, Wu J, Li W

STUDY ON CASTING PROCESS OF K4537 SUPERALLOY GAS TURBINE I 555
Shao C, Li J, Zhao M, Li W, Wu J, Kong S

DIFFUSION COEFFICIENT OF REFRACTORY ELEMENTS IN MULTI-COMPONENT NI-ALLOY I 561
Murata Y, Hattori M, Efendi, Goto N, Koyama T, Morinaga M

MICROSTRUCTURAL DEGRADATION OF HAYNES 230 COMBUSTOR HARDWARE I 571
Marchant G, McColvin G, Strang A

SHOT PEENING INDUCED RECRYSTALLIZATION IN A DIRECTIONALLY SOLIDIFIED NI-BASE SUPERALLOY I 583
Zhang J, Wang L, Xie G, Sun C, Lou L H

AUTHOR INDEX I

KEYWORD INDEX VII

Part II

ADVANCED GAS TURBINE MATERIALS

Contributed papers: Modelling

MICRO-MECHANICAL MODELLING OF THE SINGLE CRYSTAL NICKEL-BASE SUPERALLOY CMSX-4 II 595
Tinga T, Geers M G D, Brekelmans W A M

MODELLING THE CONSTANT AND VARIABLE LOADING / TEMPERATURE CREEP BEHAVIOUR OF UDIMET 720LI II 607
Maldini M, Lupinc V

A GENERAL APPROACH TO MICROSTRUCTURAL MODELLING OF CREEP II 619
Pein C, Kozeschnik E

Contributed papers: Joining technology

THE CREEP RUPTURE BEHAVIOUR OF A NICKEL-BASE SINGLE-CRYSTAL SUPERALLOY AFTER TLP BONDING II 627
Liu J D, Jin T, Zhao N R, Wang Z H, Sun X F, Guan H R, Hu Z Q

NANOINDENTATION AND ORIENTATION MEASUREMENTS IN SINGLE CRYSTALLINE BRAZING JOINTS OF NICKEL – BASE SUPERALLOYS II 633
Dinkel M, Pyczak F, Göken M, Heinz P, Volek A, Singer R F, Ott M, Affeldt E, Vossberg A

Contributed papers: Oxidation and hot corrosion

LONG-TIME HIGH-TEMPERATURE OXIDATION OF MA 6000 AND PM 3030 ODS SUPERALLOYS II 645
Maresca P, Pratesi F, Terzigli V, Innocenti M, Giorni E

OXIDATION RESISTANCE OF SILICON-CONTAINING 5TH GENERATION NICKEL-BASE SINGLE CRYSTAL SUPERALLOYS II 655
Sato A, Harada H, Ang J, Yutaka K, Toshiharu K, Kawagishi K, Imai H

ESTIMATION OF THE RISK OF HOT CORROSION IN GAS TURBINES BY THERMODYNAMIC MODELLING II 665
Müller M

Contributed papers: Coating technology

MICROSTRUCTURAL INVESTIGATIONS AND MODELLING OF INTERDIFFUSION BETWEEN MCRALY COATING AND IN738 SUPERALLOY II 675
Dahl K V, Hald J

DEVELOPMENT OF EQ COATINGS FOR A NEW TBC COATING SYSTEM IN NI-BASE SUPERALLOYS II 691
Kawagishi K, Sato A, Matsumoto K, Ang J, Harada H

COATINGS BY LASER CLADDING AGAINST LIQUID DROPLET EROSION II 699
Giannozzi M, Giorni E, Giovannetti I, Pratesi F, Zonfrillo G

A NEW DEVICE FOR TESTING COATINGS UNDER THERMAL SHOCK II 707
Zonfrillo G, Giannozzi M, Pratesi F, Giorni E

CHARACTERIZATION OF THERMAL BARRIER COATINGS BY MEANS OF FURNACE CYCLE TESTING II 717
Cappuccini F, Zonfrillo G, Pratesi F, Giannozzi

ACOUSTIC EMISSION ANALYSIS USED AS MONITORING TOOL FOR BURNER RIG TESTS OF THERMAL BARRIER COATINGS II 727
Mack D E, Casu A, Traeger F, Vaßen R, Stöver D

PRACTICAL APPLICATIONS OF TEMPERATURE ESTIMATION MODELS BASED ON SUPERALLOY BASE METAL AND MCRALY COATING MICROSTRUCTURE EVOLUTION IN SERVICE GAS TURBINE COMPONENTS II 737
Hussain K, Daleo J A

NUMERICAL SIMULATION OF TBC DELAMINATION UNDER THERMAL CYCLIC LOADING II 747
Białas M, Bednarz P, Herzog R

OXIDATION AND HOT CORROSION BEHAVIOUR OF ALUMINIZED PT-IR COATINGS ON NI-BASED SUPERALLOYS TMS-82+ II 757
Yamaguchi A, Wu Y N, Suzuki A, Murakami H, Kuroda S, Imai H

Contributed papers: Intermetallics and ceramics

CREEP BEHAVIOR OF ORTHORHOMBIC Ti_2AlNb-BASED ALLOYS II 767
Hagiwara M, Emura S, Mao Y

COMPARISON OF THE ISOTHERMAL FATIGUE BEHAVIOUR OF TIMETAL 6242 AND γ-TIAL ALLOYS AT 700°C II 773
Cempura G, Penkalla H J, Schubert F, Czyrska-Filemonowicz A

TIAL OXIDATION PROTECTION IMPROVEMENTS USING THE HALOGEN EFFECT II 783
Masset P, Zschau H-E, Schütze M

THERMAL EXPOSURE EFFECTS ON THE MECHANICAL PROPERTIES OF TIAL INTERMETALLIC II 793
Holdway P, Lucas K, Wisbey A

DIRECTIONALLY SOLIDIFIED MULTIPHASE NI_3AL-BASED INTERMETALLICS FOR HIGH TEMPERATURE APPLICATIONS II 803
Lapin J, Pelachová T, Mareček J

SUPERPLASTIC DEFORMATION AND MECHANISM OF EXTRUDED EUTECTIC NIAL/CR(MO) ALLOY DOPED WITH DY II 819
Guo J T, Du X, Li G

FEM STUDY OF A CMC SHROUD II 829
Del Pugliaa P, Lanese N, Zonfrilloa G

ADVANCED STEAM TURBINE MATERIALS

Invited papers

THE EUROPEAN EFFORT IN DEVELOPMENT OF NEW HIGH TEMPERATURE ROTOR MATERIALS – COST 536 II 843
Kern T -U, Staubli M, Mayer K H, Donth B, Zeiler G, DiGianfrancesco A

THE EUROPEAN EFFORTS IN DEVELOPMENT OF NEW HIGH TEMPERATURE CASING MATERIALS – COST 536 II 855
Staubli M, Hanus R, Weber T, Mayer K H, Kern T-U

WELDABILITY AND PROPERTIES OF NEW CREEP RESISTANT MATERIALS FOR USE IN ULTRA SUPERCRITICAL COAL FIRED POWER PLANTS II 871
Bauné E, Cerjak H, Caminada S, Jochum C, Mayr P, Pasternak J

US PROGRAM ON MATERIALS TECHNOLOGY FOR ULTRASUPERCRITICAL STEAM-COAL FIRED POWER PLANTS II 893
Viswanathan R, Henry J F, Tanzosh J, Stanko G, Shingledecker J P, Vitalis B

METALLOGRAPHY AND ALLOY DESIGN IN THE COST 536 ACTION II 917
Hald J

MATERIALS DEVELOPMENT FOR ADVANCED STEAM BOILERS II 931
Helmrich A, Chen Q, Stamatelopoulos G, Scarlin B

COATINGS FOR PROTECTION OF HIGH TEMPERATURE NEW GENERATION STEAM PLANT COMPONENTS: A REVIEW II 949
Aguero A

METALLURGY FOR LONG-TERM STABILIZATION OF FERRITIC STEELS FOR THICK SECTION BOILER COMPONENTS IN USC POWER PLANT AT 650^{O}C II 965
Abe F

Contributed papers: Mechanical properties

CONTRIBUTION TO THE INVESTIGATION OF ADVANCED LOW-ALLOY P23 STEEL CREEP BEHAVIOUR II 985
Hakl J, Vlasák T, Brziak P, Zifcak P

EFFECT OF TEMPERING TIMES ON CREEP STRENGTH IN ASME GR 23 (2 25CR-1 6W STEEL) II 997
Komai N, Imazato T

CREEP OF 0.5CrMoV STEEL AT VERY LOW STRAIN RATES II 1011
Kloc L, Sklenica V

IMPROVEMENT IN CREEP STRENGTH OF HEAT RESISTANT FERRITIC STEEL STRENGTHENED BY INTERMETALLIC COMPOUND II 1019
Toda Y, Kushima H, Kimura K, Abe F

SUPERIOR LONG-TERM CREEP BEHAVIOUR AND MICROSTRUCTURAL EVOLUTION OF 9%CR-STEELS WITH BORON II 1031
Kager F, Böck N, Spiradek-Hahn K, Höfinger S, Brabetz M, Zeiler G

ALLOY DESIGN AND CREEP STRENGTH OF ADVANCED 9%CR USC BOILER STEELS CONTAINING HIGH BORON II 1041
Semba H, Abe F

IMPROVEMENT OF CREEP STRENGTH OF 650 °C FERRITIC/MARTENSITIC SUPER HEAT RESISTANT 11-12 % CR STEELS II 1053
Mayer K-H, Berger C, Scholz A, Wang Y

STATUS OF DEVELOPMENT OF THE VM12 STEEL FOR TUBULAR APPLICATIONS IN ADVANCED POWER PLANTS II 1065
Gabrel J, Bendick W, Vandenberghe B, Lefebvre B

MICROSTRUCTURAL DEVELOPMENT OF VM12 STEEL CAUSED BY CREEP DEFORMATION AT 625ºC II 1077
Zielińska-Lipiec A, Bendick W, Cempura G, Vandenberghe B, Ennis P J, Czyrska-Filemonowicz A

REGENERATIVE HEAT TREATMENT OF L21HMF CAST STEEL AFTER LONG TERM OPERATION II 1087
Golanski G, Kupczyk J, Stachura S, Gajda B

LONG TERM CREEP STRENGTH DEGRADATION IN T122/P122 STEELS FOR USC POWER PLANTS II 1095
Igarashi M, Yoshizawa M, Iseda A, Matsuo H, Kan T

DEGRADATION BEHAVIOUR AND LONG-TERM CREEP STRENGTH OF 12CR FERRITIC CREEP RESISTANT STEELS II 1105
Kimura K, Sawada K, Kushima H, Toda Y

CREEP CURVE ANALYSIS USING THE MODIFIED Ω METHOD II 1117
Yin Y F, Faulkner R G

EFFECT OF NON STEADY LOADING ON CREEP BEHAVIOUR OF ADVANCED 9-12 % FOSSIL POWER PLANT STEELS II 1127
Sklenicka V, Kucharova K, Svoboda M, Kloc L, Kudrman J

CREEP AND CREEP FATIGUE PROPERTIES OF TURBINE STEELS FOR APPLICATION TEMPERATURES UP TO 625 °C II 1137
Berger C, Schwienheer M, Scholz A

LOW CYCLE FATIGUE BEHAVIOUR OF SANDWICH STRUCTURES OF P92 AND NICROFER 6025 HT II 1147
El-Magd E, Stuhrmann J, Gebhard J

CAUSES OF CREEP FRACTURE MECHANISM CHANGE IN 9CR-1 8W-0 5Mo-VNb STEEL II 1157
Lee J S, Arnaki H G, Maruyama K, Muraki T, Asahi H

AUTHOR INDEX I

KEYWORD INDEX VII

Part III

ADVANCED STEAM TURBINE MATERIALS

Contributed papers: Microstructure

MICROSTRUCTURAL CHARACTERIZATION OF MODERN BORON CONTAINING 9-11 % CR STEELS DEVELOPED IN THE FRAMEWORK OF THE COST PROGRAM III 1171
Kauffmann F, Mayer K H, Straub S, Zies G, Scheu C, Willer D, Ruoff H, Maile K

QUANTITATIVE MICROSTRUCTURAL ANALYSIS ON THE STABILITY OF MX AND M2X IN 9-12 % CR STEELS BY AFM, SEM, TEM III 1181
Seibert T, Durst K, Chilukuru H, Göken M

SIMULATION OF THE PRECIPITATION KINETICS DURING HEAT TREATMENT AND SERVICE OF CREEP RESISTANT MARTENSITIC 9-12% CR STEEL III 1191
Holzer I, Rajek J, Kozeschnik E, Cerjak H

MICROSTRUCTURAL ANALYSIS ON A CREEP RESISTANT MARTENSITIC 9-12% CR STEELS USING THE EBSD METHOD III 1199
Sonderegger B, Mitsche S, Cerjak H

DISLOCATION MOBILITY IN 9% CHROMIUM STEELS EXPOSED TO CREEP III 1207
Böck N

EFTEM INVESTIGATIONS ON PRECIPITATES IN A CREEP RESISTANT 9-12% CR STEEL III 1217
Sonderegger B, Kothleitner G, Rechberger W, Cerjak H

PRECIPITATION BEHAVIOR OF Z PHASE AFTER LONG-TERM CREEP IN HIGH CHROMIUM FERRITIC HEAT RESISTANT STEELS III 1227
Sawada K, Kushima H, Kimura K

ON THE ROLES OF M2X AND Z-PHASE IN TEMPERED MARTENSITIC 9-12% CR-STEELS III 1241
Chilukuru H, Durst K, Göken M, Blum W

ELECTRON DIFFRACTION STUDIES ON (Nb,V)CrN PARTICLES IN 12CrMoVNbN STEELS III 1251
Vodarek V, Danielsen H, Grumsen F, Hald J, Strang A

AN EFTEM STUDY OF Z-PHASE NUCLEATION IN MARTENSITIC CHROMIUM STEELS III 1267
Golpayegani A, Andren H O

Z-PHASE IN 9-12%CR STEELS - OBSERVATIONS AND THERMODYNAMIC MODELLING III 1275
Danielsen H K, Hald J

MICROSTRUCTURE AND STEAM OXIDATION RESISTANCE OF LAVES PHASE FORMING 12%CR STEELS AT 600-650°C III 1285
Pirón Abellán J, Ennis P J, Singheiser L, Quadakkers W J

Contributed papers: Modelling

CDM MODELLING OF POWER PLANT FERRITIC STEELS III 1299
Yin Y F, Faulkner R G

AN EFFECTIVE PARAMETRIC STRAIN MODEL FOR CREEP III 1309
Holmström S, Auerkari P, Holdsworth S

ADVANCED ALLOY DESIGN TOOLS APPLIED TO THE DEVELOPMENT OF VANADIUM NITRIDE STRENGTHENED HIGH-TEMPERATURE STEELS III 1319
Gaude-Fugarolas D, Yardley V, Lardon J-M, Montagnon J, De Carlan Y

Contributed papers: Welding technology

APPLICATION OF BAINITIC CREEP RESISTING STEELS FOR SUPERCRITICAL PARAMETERS AND PROPERTIES OF WELDED JOINTS III 1331
Brózda J, Zeman M, Pasternak J

INVESTIGATIONS ON OPTIMISATION OF WELD CREEP PERFORMANCE IN MARTENSITIC STEELS III 1341
Bauer M, Klenk A, Maile K, Roos E, Jochum C

STRUCTURAL STABILITY AND PROPERTIES OF WELD JOINTS OF NEW CREEP-RESISTANT STEEL GRADES WITH 9 OR 12% CR CONTENTS APPLIED IN OPERATION OF POWER GENERATIONS SECTOR OVER 30000 h III 1357
Moskal G, Hernas A, Pasternak J

WELDABILITY AND HIGH TEMPERATURE BEHAVIOR OF 12% CR-STEEL FOR TUBES AND PIPES IN POWER PLANTS WITH STEAM TEMPERATURES UP TO 650 °C III 1369
Vekeman J, Dhooge A, Huysmans S, Vandenberghe B, Jochum C

EXPECTED CREEP LIFE OF WELDED 9-12% CR STEELS III 1381
Auerkari P, Holmström S, Salonen J

STUDY OF THE SIMULATED HAZ OF A BORON ALLOYED CREEP RESISTANT 9% CHROMIUM STEEL III 1393
Mayr P, Cerjak H

MICROSTRUCTURAL STUDIES OF SIMILAR AND DISSIMILAR WELDS OF P91 III 1401
Jandova D, Kasl J, Folkova E, Kanta V

PHYSICAL SIMULATION AND NUMERICAL MODELLING OF X10CRMOVNB 9 10 (P91) STEEL REPAIR WELDING III 1417
Lomozik M, Tasak E

DISSIMILAR WELDED JOINTS WITHOUT A BUFFER AREAS OF STEEL TYPE 9CR WITH 1CRMOV TO BE USED FOR STEAM BOILER PIPELINES III 1427
Tasak E, Hernas A, Pasternak J, Fudali S

CREEP PROPERTIES OF HETEROGENEOUS P91/P23 WELDS AT 550 AND 600 °C III 1437
Kuboň Z, Vodárek V, Toušová D

STRUCTURAL STABILITY OF HETEROGENEOUS WELD JOINT OF 6CRMOV 8-3-2 AND X12CRMOV 10-1 STEELS WITH INCREASED NITROGEN CONTENT III 1449
Foret R, Zlámal B, Sopoušek J, Buršík J

Contributed papers: Oxidation and coatings

OXIDATION OF CANDIDATE CHROMIUM STEELS IN STEAM ENVIRONMENT III 1461
Cizner J, Hakl J

OXIDE SCALE GROWTH AND SPALLATION IN STEAM ENVIRONMENTS – AN ASSESSMENT OF DIFFERENT MODELLING APPROACHES III 1469
Fry A T, Osgerby S

THE INFLUENCE OF OXIDATION ON LONG TERM CREEP RUPTURE STRENGTH DATA III 1479
Allen D J, Harvey B

NEW EXPERIENCE IN THE FIELD OF APPLICATION OF CORROSION RESISTANCE PROTECTION IN FLUE GAS DESULPHURISATION PLANT ABSORBERS III 1491
Hernas A, Imosa M, Pasternak J, Fudali S

CORROSION AND OXIDATION EXPERIENCES IN AVEDØRE II MULTIFUEL BOILER III 1503
Montgomery M, Jensen S A, Biede O, Larsen O H, Andersson A

HEAT EXCHANGER CORROSION IN BIOMASS AND COAL CO-FIRED POWER PLANTS III 1513
Simms N J, Kilgallon P J, Oakey J E

HOT CORROSION MONITORING OF ALLOY 617 IN MOLTEN CHLORIDES USING ELECROCHEMICAL TECHNIQUES III 1523
Pérez, F J, Hierro M P, Nieto J

METAL WASTAGE IN LOW ALLOY STEELS UNDER ALTERNATING ATMOSPHERES AT ELEVATED TEMPERATURE III 1533
Osgerby S, Gohil D D

DEVELOPMENT OF ALUMINIDE DIFFUSION COATINGS FOR HEAT EXCHANGER MATERIALS AND THEIR CREEP-CORROSION RESISTANCE IN SIMULATED COAL FIRING ENVIRONMENT III 1543
Rohr V, Weber T, Schütze M, Ennis P J, Quadakkers W J

DEVELOPMENT AND VALIDATION OF ADVANCED OXIDATION PROTECTIVE COATINGS FOR SUPER CRITICAL STEAM POWER PLANT III 1553
Henderson M B, Scheefer M, Aguero A, Allcock B, Norton B, Tsipas D N, Durham R

IMPROVEMENT OF OXIDATION RESISTANCE OF TUBES BY PULSED SILICONISING III 1571
Maile K, Berreth K, Lyutovich A

INFLUENCE OF SURFACE TREATMENT ON THE OXIDATION KINETICS OF ADVANCED STEELS IN FLOWING STEAM AT 650 °C III 1581
Knoedler R, Straub S

LONG TERM STEAM OXIDATION RESISTANCE OF SHOT-BLASTED STAINLESS STEEL TUBING III 1589
Minami Y, Fukui T

Contributed papers: Austenitics and Ni-base alloys

QUALIFICATION OF NI-BASED MATERIAL FOR TUBES AND PIPING OF 700°C POWER PLANT III 1597
Klenk A, Maile K, Theofel H, Helmrich A, Husemann R U, Lüdenbach G

AN INVESTIGATION ON STRUCTURE STABILITY AND ITS IMPROVEMENT ON A NEW DEVELOPMENTAL NI-CR-CO-MO-NB-TI-AL SUPERALLOY FOR USC POWER PLANT APPLICATION AT TEMPERATURE ABOVE 750ºC III 1609
Xie X, Zhao G, Dong J, Smith G D, Baker B A, Patel S J

CHEMISTRY MODIFICATIONS OF INCONEL 706 FOR IMPROVED MICROSTRUCTURAL STABILITY III 1619
Del Genovese D, Mukherji D, Rösler J, Kindratschuk V, Wabderka N, Banhart J

CRACK GROWTH BEHAVIOUR OF WASPALOY AT 700°C IN DIFFERENT ATMOSPHERES III 1629
Penkalla H J, Schubert F, Singheiser L

ASSESSMENT OF THE INFLUENCE OF LASER-DRILLED HOLES ON THE DAMAGE BEHAVIOUR OF ALLOY 617 III 1639
Mülders B, Wessel E, Schubert F

DEFORMATION BEHAVIOUR OF ALLOY INCONEL 617 TUBES IN THE TEMPERATURE RANGE 600°C TO 850°C III 1651
Makhele-Lekala L, Ennis P J, Schubert F

FIELD TESTING OF TP 347H FG AT ULTRA SUPERCRITICAL STEAM CONDITIONS III 1663
Hansson A N, Montgomery M

AN IMPROVED METHOD TO CALCULATE THE CREEP-FATIGUE ENDURANCE OF TYPE 316H STAINLESS STEEL III 1673
Spindler M

WEB-ENABLED DATABASES OF JRC PETTEN-EFFECTIVE TOOLS FOR EUROPEAN KNOWLEDGE MANAGEMENT III 1683
Over H H, Dietz W

ADDENDUM
These papers arrived too late for reviewing and are reproduced as received

ADVANCED COATINGS FOR GAS TURBINES III 1696
Nicholls J R, Bordenet B

APS-TBC FOR GAS TURBINES: FAILURE MODES, DAMAGE EVOLUTION AND LIFE-TIME ASSESSMENT III 1722
Herzog R, Bednarz P, Trunova O, Steinbrech R W, Wessel E, Quadakkers W J, Schubert F, Singheiser L

AUTHOR INDEX I

KEYWORD INDEX VII

Part II

Advanced Gas Turbine Materials

Advanced Steam Turbine Materials

Part II

Advanced Gas Turbine Materials

Contributed Papers

Modelling

MICRO-MECHANICAL MODELLING OF THE SINGLE CRYSTAL NICKEL-BASE SUPERALLOY CMSX-4

T. Tinga[*], M.G.D. Geers[+], W.A.M. Brekelmans[+]

[*] National Aerospace Laboratory NLR, P.O.Box 153, 8300 AD Emmeloord, The Netherlands, tinga@nlr.nl.
[+] Eindhoven University of Technology, Mechanical Engineering, Mechanics of Materials, Eindhoven, The Netherlands.

Abstract

A multi-scale micromechanical model for a Ni-based superalloy is presented. The unit cell on the material point level incorporates the two-phase γ/γ'-microstructure of the material and the role of the γ/γ'-interfaces in the mechanical behaviour is emphasized. A crystal plasticity framework is used to model the constitutive behaviour of the γ-matrix phase. The limited number of unit cell constituents and the micromechanical simplifications make the framework particularly efficient in a multi-scale approach. The model is implemented in a commercial finite element code and adequately simulates the material response for the alloy CMSX-4. The effect of microstructural changes on the mechanical response is demonstrated.

Keywords: Micromechanics; constitutive model; superalloy; crystal plasticity.

Introduction

The very high resistance against high temperature inelastic deformation is the main reason for the extensive use of single crystal nickel-based superalloys as gas turbine blade materials. This superior behaviour is attributed to the two-phase composite microstructure consisting of a γ-matrix containing a large volume fraction of γ'-particles (see Figure 1). Cubic Ni_3Al (γ') precipitates, with a typical size of 0.5 μm, are more or less regularly distributed in a Ni-matrix (γ-phase). The typical size of the matrix channels in between the precipitates is only 60 nm.

For both gas turbine component design and maintenance it is important to have the ability to perform a reliable life time assessment . Therefore, a lot of models were developed to describe the superalloy mechanical behaviour. The earlier models assumed the material to be a homogeneous single phase material [1-8]. In these approaches crystal plasticity theory was used to model the material response, which means that constitutive laws were defined on the slip system level. The formulation of the slip law ranges from purely phenomenological [1,5] to more physically based approaches [2-4,6]. Since these models are defined on a macroscopic level, they can easily be applied as a constitutive description in a finite element (FE) analysis, which is nowadays the common method used for component stress analysis and life time assessment.

However, to be able to accurately model the material behaviour, the two-phase nature of the superalloy must be taken into account. Therefore, a lot of models have been developed that consider the microstructural morphology (shape, dimensions and properties of both phases) as a model parameter. But completely modelling a macroscopic component on a microscopic level would ask for an enormous computational effort.

There are two ways to reduce this effort. The first way is to use a multi-scale approach in which an appropriate homogenization method is applied to connect the microscopic to the macroscopic level [9-15]. The second way is to use microstructural models that predict the material response in a closed-form set of equations on the level of the material point [16-22]. The microstructural results are then used to develop constitutive descriptions that fit in traditional methods at the macroscopic level. All these microstructural models are based on a unit cell approach, in which a characteristic volume is defined that contains both γ and γ'-phase material with their respective properties and dimensions. The FE based unit cell models are detailed but usually too complex to be used efficiently in a multi-scale analysis of structural components.

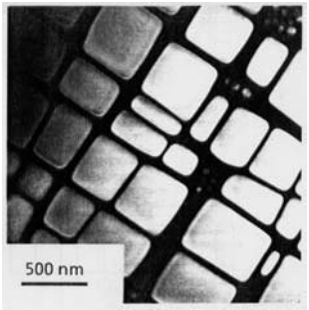

Figure 1 Micrograph of a superalloy microstructure showing the cube-like γ'-precipitates in a γ-matrix.

The model [23] described in this paper combines the merits of the previously mentioned models. The material response is described by a crystal plasticity formulation for the matrix material. Further, a new and efficient unit cell model is used, in which the role of the γ/γ'-interfaces is emphasized. The limited size of the unit cell and the micromechanical simplifications make the framework particularly efficient in a multi-scale approach.

The multi-scale model is described in the next section, providing definitions of the unit cell and the interaction laws. Then the constitutive models are described and the implementation in an FE code is discussed. Finally the model is applied to the Ni-based superalloy CMSX-4. Simulated stress-strain curves are compared to experimental results and the effect of changing microstructural dimensions is demonstrated.

Multi-scale approach

The multi-scale approach used for the prediction of the superalloy mechanical behaviour is shown schematically in Figure 2a . The *macroscopic* level is the engineering level on which a finite element (FE) model is commonly used to solve the governing equilibrium problem. The *mesoscopic* level is the level of the microstructure within a macroscopic material point. At this level the material is considered as a compound of two different phases: γ'-precipitates embedded in a γ-matrix. Finally, the crystallographic response of the individual material phases is described on the *microscopic* level, using a crystal plasticity framework.

Definition of the unit cell

On the material point level the Ni-based superalloy microstructure, consisting of γ'-precipitates in a γ-matrix, is represented by a unit cell containing 16 regions (see Figure 2b):

- 1 γ'-precipitate region
- 3 γ-matrix channel regions (γ_j, j = 1… 3) with different orientations (normal to the [001], [010] and [100] direction)
- 12 interface regions (I_k^m and I_k^p, k = 1… 6) containing the γ/γ'-interfaces. A matrix and a precipitate region together form a bi-crystal, which is located on each face of the γ'-precipitate.

The interface between the two different phases plays an important role in the mechanical behaviour of the material. Therefore, special interface regions were included in the model to take into account the processes that take place at the γ/γ'-interfaces.

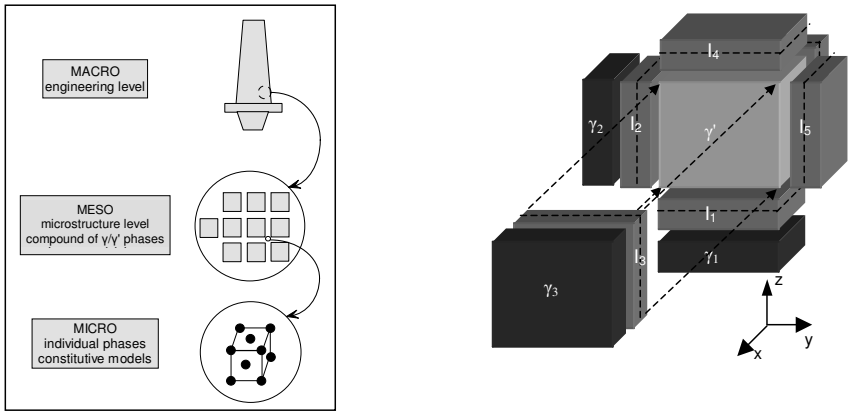

a) b)

Figure 2 Schematic overview of the model, showing (a) the multi-scale character and (b) the multi-phase unit cell, consisting of one precipitate (γ'), three matrix (γ_i) and six double interface(I_i) regions.

Scale transitions and interaction law

In a conventional approach, a finite element method is used on the macroscopic level to solve the engineering problem with its boundary conditions. In the present multi-scale approach the usual standard procedure to obtain the stress response for a given deformation (i.e. a local closed-form constitutive equation) is replaced by a mesoscopic calculation at the unit cell level. The deformation (total strain) for a certain macroscopic material point during a time increment is provided by the macro scale and the stress response is returned after the computations at the mesoscopic level. The quantities used for this macro-meso scale transition are denoted as the mesoscopic average strain ($\bar{\boldsymbol{\varepsilon}}$) and the mesoscopic average stress ($\bar{\boldsymbol{\sigma}}$). The stress tensor $\bar{\boldsymbol{\sigma}}$ is

determined from the strain tensor $\bar{\boldsymbol{\varepsilon}}$ based on the specified mesoscopic configuration and the local constitutive equations of the different phases at the micro level.

The mesoscopic strain is obtained by averaging the microstructural quantities in each of the regions, defined as

$$\sum_{i=1}^{N} f^i \boldsymbol{\varepsilon}^i_{tot} = \bar{\boldsymbol{\varepsilon}}_{tot} \qquad i = \gamma', \gamma_1, \gamma_2, \gamma_3, \mathrm{I}^{\mathrm{p}}_1, \mathrm{I}^{\mathrm{m}}_1, \mathrm{I}^{\mathrm{p}}_2, \mathrm{I}^{\mathrm{m}}_2, \mathrm{I}^{\mathrm{p}}_3, \mathrm{I}^{\mathrm{m}}_3 \tag{1}$$

where f^i are the volume fractions, $\boldsymbol{\varepsilon}^i_{tot}$ the total strain tensors in the different regions and N indicates the effective number (10) of regions in the model.

The constitutive models, which relate the stress tensors to the individual strain tensors for all 10 regions, provide the relation between the mesoscopic and microscopic level

$$\boldsymbol{\varepsilon}^i \rightarrow \text{constitutive box} \rightarrow \boldsymbol{\sigma}^i \qquad i = \gamma', \gamma_1, \gamma_2, \gamma_3, \mathrm{I}^{\mathrm{p}}_1, \mathrm{I}^{\mathrm{m}}_1, \mathrm{I}^{\mathrm{p}}_2, \mathrm{I}^{\mathrm{m}}_2, \mathrm{I}^{\mathrm{p}}_3, \mathrm{I}^{\mathrm{m}}_3 \tag{2}$$

The constitutive model on the micro level, for each phase, is based on a crystal plasticity theory and will be described in the next section.
Both stress and deformation are assumed to be uniform inside each of the different regions. To specify the coupling between the regions an interaction law has to be defined. For the present model a modified Sachs approach is used, which means that in the γ and γ'-regions the stresses are required to be equal to the mesoscopic stress. In each pair of interface regions however, only the *average* stress is enforced to be equal to the mesoscopic stress. This results in the following equations:
- Sachs interaction between γ' and γ-regions

$$\boldsymbol{\sigma}^{\gamma'} = \boldsymbol{\sigma}^{\gamma_1} = \boldsymbol{\sigma}^{\gamma_2} = \boldsymbol{\sigma}^{\gamma_3} = \bar{\boldsymbol{\sigma}} \tag{3}$$

- Modified Sachs interaction for the bi-crystal interfaces

$$f^{\mathrm{I}^{\mathrm{p}}_k} \boldsymbol{\sigma}^{\mathrm{I}^{\mathrm{p}}_k} + f^{\mathrm{I}^{\mathrm{m}}_k} \boldsymbol{\sigma}^{\mathrm{I}^{\mathrm{m}}_k} = \left(f^{\mathrm{I}^{\mathrm{p}}_k} + f^{\mathrm{I}^{\mathrm{m}}_k} \right) \bar{\boldsymbol{\sigma}} \qquad k = 1,2,3 \tag{4}$$

where $\boldsymbol{\sigma}^{\mathrm{i}}$ are the stress tensors in the different regions, $\bar{\boldsymbol{\sigma}}$ is the mesoscopic stress tensor and f^i are the volume fractions of the respective regions.

In the interface regions additional requirements are set. Both stress continuity (across the interface) and kinematical compatibility (in the plane of the interface) are required, resulting in the following equations:
- Compatibility between the matrix $(\mathrm{I}^{\mathrm{m}}_k)$ and the precipitate side $(\mathrm{I}^{\mathrm{p}}_k)$ of the k^{th} interface:

$$\boldsymbol{\varepsilon}^{\mathrm{I}^{\mathrm{p}}_k} \cdot \left(\mathbf{I} - \vec{n}^k \vec{n}^k \right) = \boldsymbol{\varepsilon}^{\mathrm{I}^{\mathrm{m}}_k} \cdot \left(\mathbf{I} - \vec{n}^k \vec{n}^k \right) \qquad k = 1,2,3 \tag{5}$$

- Stress continuity at the same interface:

$$\boldsymbol{\sigma}^{\mathrm{I}^{\mathrm{p}}_k} \cdot \vec{n}^k = \boldsymbol{\sigma}^{\mathrm{I}^{\mathrm{m}}_k} \cdot \vec{n}^k \qquad k = 1,2,3 \tag{6}$$

where $\boldsymbol{\sigma}$ and $\boldsymbol{\varepsilon}$ are the stress and strain tensors in the different regions and $\vec{n}^k$ is the unit normal vector on the k^{th} interface.

For the material point model the mesoscopic deformation (total strain) is provided by the macro scale analysis and the mesoscopic stress must be calculated. Since the model consists of 10 distinct regions in which the deformation and stress are homogeneous, and the symmetric stress and strain tensors contain 6 independent components, a total of 120 unknowns results. Equations

(1) and (3) to (6) yield a total of 60 equations and the constitutive model (2) another 60 equations, which completes the system of equations.

Constitutive models

A crystal plasticity approach is used to model the constitutive behaviour of the two phases. The elastic material behaviour is described by a standard formulation for orthotropic materials with cubic symmetry. The three independent components of the elastic tensor $^4\mathbf{C}$ of both phases in CMSX-4 at 850 °C are given in Table 1 [24].

Table 1 $^4\mathbf{C}$ elastic tensor components for CMSX-4 at 850 °C [24].

	γ-matrix	γ'-precipitate
C_{1111} (GPa)	190.9	216.9
C_{1122} (GPa)	127.3	144.6
C_{1212} (GPa)	100.2	105.2

Matrix constitutive model

The basic ingredient of the crystal plasticity framework is the relation between the slip rates $\dot{\gamma}^\alpha$ and the resolved shear stresses τα for all the slip systems α. The following formulation is used:

$$\dot{\gamma}^\alpha = \dot{\gamma}_0 \left\{ \frac{\left|\tau^\alpha_{eff}\right|}{s^\alpha} \right\}^m \left\{ 1 - \exp\left(-\frac{\left|\tau^\alpha_{eff}\right|}{\tau^{or}} \right) \right\}^n \text{sign}\left(\tau^\alpha_{eff}\right) \qquad (7)$$

where τ^{or} denotes the Orowan stress, s^α the actual slip resistance and τ^α_{eff} the effective stress on slip system α, defined as the combination of the resolved shear stress and the misfit stress.

$$\tau^\alpha_{eff} = \tau^\alpha + \tau^\alpha_{misfit} \qquad (8)$$

Recalling that the elastic properties of γ and γ' are very similar and assuming that the size of both phases is in the same order, it is assumed that the misfit is accommodated equally by both phases, leading to a misfit strain

$$\varepsilon_{misfit} = \frac{\frac{1}{2}\left(a_{\gamma'} - a_\gamma\right)}{a_\gamma} \qquad (9)$$

in the matrix (in the two directions in the plane of the interface) and the same strain with opposite sign in the precipitate. The lattice parameters $a_{\gamma'}$ and a_γ refer to the γ' and γ-phases respectively. The misfit stress and strain tensor are related to each other by a modified elastic stiffness tensor, which ensures that only the stress components parallel to the interface are non-zero.
The resolved shear stress τ^α is obtained from the Cauchy stress tensor $\boldsymbol{\sigma}$ by

$$\tau^\alpha = \boldsymbol{\sigma} : \mathbf{P}^\alpha \qquad (10)$$

where $\mathbf{P}^\alpha$ is the symmetric Schmid tensor defined as

$$\mathbf{P}^\alpha = \frac{1}{2}\left(\vec{s}^\alpha \vec{n}^\alpha + \vec{n}^\alpha \vec{s}^\alpha\right) \qquad (11)$$

The unit length vectors $\vec{n}^\alpha$ and $\vec{s}^\alpha$ are the slip plane normal and slip direction respectively. The (projected) misfit stress is obtained from the corresponding stress tensor in the same way.

The Orowan stress, which is the stress required to bow a dislocation line into the channel between two precipitates, is given by [25] as

$$\tau^{or} = \frac{\mu b}{2\pi d} \ln\left(\frac{d}{r_0}\right) = \alpha \frac{\mu b}{d} \tag{12}$$

where μ is the shear modulus, b the length of the Burgers vector, d the spacing between two precipitates (equal to the channel width) and r_0 the dislocation core radius (in the order of b). There is no generally accepted value for the constant α. A value of $\alpha = 0.80$ is taken here.

The slip resistance is related to the availability of mobile dislocations and the resistance of sessile / forest dislocations and therefore depends on the total dislocation density. The relation between the slip resistance and the dislocation density is defined according to

$$s^{\alpha} = c\mu b \sqrt{\left|\rho^{\alpha}\right|} \exp\left[\frac{Q}{kT}\right] \tag{13}$$

where ρ^{α} is the dislocation density on slip system α, c is a material constant, Q is an activation energy for overcoming the barriers, k is the Stefan-Boltzmann constant and T the absolute temperature.
The dislocation densities are calculated on the basis of an appropriate evolution equation [26], starting from their initial value ρ_0 :

$$\dot{\rho}^{\alpha} = \frac{1}{b}\left(\frac{1}{L^{\alpha}} - 2 y_c \rho^{\alpha}\right)\left|\dot{\gamma}^{\alpha}\right| \quad , \quad \rho^{\alpha}(t=0) = \rho_0 \tag{14}$$

which is the net effect of dislocation accumulation (left term) and annihilation (right term). The parameter y_c represents the critical annihilation length, i.e. the average distance below which two dislocations of opposite sign annihilate spontaneously. The accumulation rate is linked to the average dislocation segment length of mobile dislocations on system α, which is determined by the current dislocation state through

$$L^{\alpha} = \frac{K}{\sqrt{\left|\rho^{\alpha}\right|}} \tag{15}$$

where K is a material constant.

Precipitate constitutive model

In the present model, the precipitate in the superalloy is assumed to be elastic. This assumption is only acceptable under certain conditions. The precipitate may deform inelastically when it is sheared by a dislocation or bypassed by dislocation climb. However, these processes have considerable thresholds in terms of stress and temperature. Therefore, at temperatures below 950 ^{o}C and moderate stress levels the simplification of an elastically deforming precipitate is justified. The development of an enhanced constitutive model that includes crystal plasticity in the precipitate for more extreme conditions, is subject of future work.

Application

The framework described in the previous sections was implemented, as a material subroutine, in the commercial finite element code MSC.Marc. The subroutine is called for every material point and a fully explicit time-integration is performed. An implicit method would be unconditionally

stable, but would also require a significantly larger implementation effort. Therefore an explicit method was selected and limiting the time step yields accurate results within acceptable computation times. The local variables like dislocation densities and plastic strains in the individual regions are stored in state variables and updated at the end of each increment. The integration of the multi-scale model with an FE code in this way enables application of the material model to any structural component for which a FE model is available.

The model has been applied to simulate the mechanical response of the single crystal Ni-based superalloy CMSX-4, for which the model parameters are given in Table 2. In the remainder of this section, first the characteristics of the proposed slip law are demonstrated and then the influence of a change in the microstructural dimensions is shown.

Table 2 Model parameters for the matrix phase of CMSX-4.

Model parameter	Symbol	Value	Unit	Used in equation
Reference slip rate	$\dot{\gamma}_0$	1.4×10^{-4}	s^{-1}	(7)
Rate sensitivity Orowan threshold	n	3		(7)
Rate sensitivity exponent slip resistance	m	7		(7)
Lattice constant matrix	a_γ	0.3590	nm	(9)
Lattice constant precipitate	$a_{\gamma'}$	0.3586	nm	(9)
Boltzmann's constant	k	1.38×10^{-23}	$J\ K^{-1}$	(13)
Reference activation energy	Q	0.0	J	(13)
Strength parameter	c	0.426		(13)
Shear modulus	μ	100.2	GPa	(13)
Burgers vector length	b	0.25	nm	(12),(13),(14)
Parameter in Orowan stress	α	0.50		(12)
Critical annihilation length	y_c	2.31	nm	(14)
Initial SSD density	ρ_0	8.1×10^{14}	m^{-2}	(14)
Material constant	K	10		(15)

Slip law features

The slip law for the matrix material, equation (7), reflects that for each slip system two thresholds must be overcome before plastic slip can occur, associated with the slip resistance and the Orowan stress. Plastic slip will only occur when both thresholds are exceeded by the effective resolved shear stress.

The slip rate as a function of the effective resolved shear stress was calculated for two cases to demonstrate the slip law characteristics. The results are shown in Figure 3 for the Orowan stress below (τ^{or} = 147 MPa) and above (τ^{or} = 368 MPa) the initial slip resistance (s^{α} = 305 MPa). The plots show that the slip rate in both cases reaches the reference slip rate $\dot{\gamma}_0$ when the resolved shear stress exceeds both thresholds.

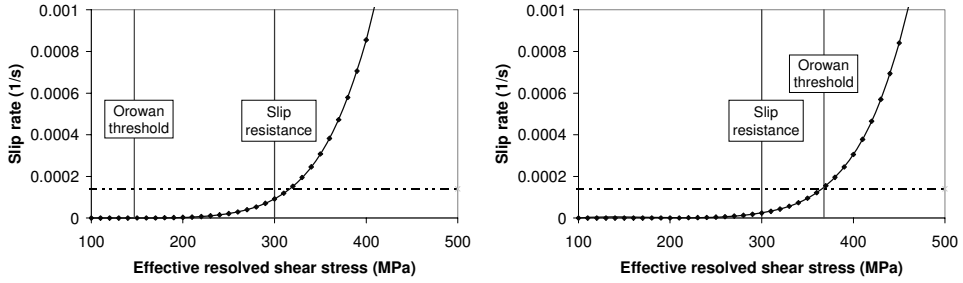

Figure 3 Activation of the proposed slip law for different values of the Orowan threshold.

Effect of microstructural changes

Nickel-based superalloys show a clear size dependence, which means that the mechanical behaviour changes when proportionally increasing or decreasing the microstructural dimensions while keeping all volume fractions constant. The present framework is able to simulate these microstructural size effects, since the Orowan threshold, which is inversely proportional to the γ-channel width h, is incorporated in the model. Before analysing the effects of microstructural changes, a reference case was studied by simulating a tensile test at 850 ^{o}C at a strain rate of 10^{-3} s^{-1}. The microstructural dimensions used are L = 500 nm and h = 60 nm. The result is shown in Figure 4, together with an experimentally determined stress-strain curve for CMSX-4 at the same conditions [24].

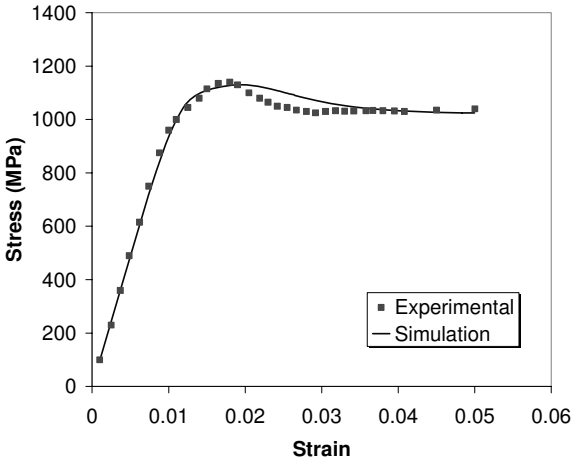

Figure 4 Simulated stress-strain curve for CMSX-4 at 850 ^{o}C at a strain rate of 10^{-3} s^{-1} compared to an experimentally determined curve.

The model parameters from Table 2 lead to an initial slip resistance (s^{α} = 305 MPa) which is considerably higher than the Orowan stress (τ^{or} = 147 MPa). This means that the slip resistance

threshold is the decisive threshold in this case. Downsizing the complete unit cell by a factor 2 or 4 increases the Orowan threshold by the same factor, which means that it approaches or even supersedes the slip resistance and becomes an active threshold. The unit cell dimensions were varied to quantify this size effect. *Figure 5* shows the stress-strain curves for the reference case and for three other cases with all unit cell dimensions multiplied by a factor 0.5, 0.75 and 2. This figure shows that the shape of the curves for the different unit cell sizes remains the same, but the maximum stress shifts to a higher level with a decreasing matrix channel width, i.e. smaller is stronger.

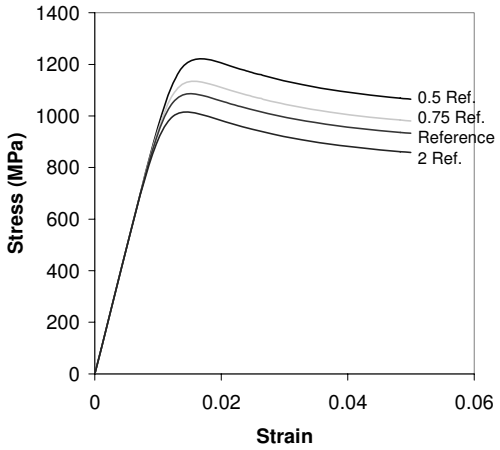

Figure 5 Effect of changing microstructural dimensions on the stress-strain curve. The reference case is L = 500 nm and h = 60 nm.

Conclusions

A physically motivated crystal plasticity framework is presented to describe the mechanical behaviour of the nickel-based superalloys. The framework has the following characteristics:

- The material response is predicted accurately by using a crystal plasticity model for the matrix material. A threshold term related to the Orowan stress is included, as well as the effect of lattice misfit between the two phases.
- The limited size of the unit cell and the micromechanical simplifications make the framework particularly efficient in a multi-scale approach. The unit cell response is determined numerically on a material point level within a macroscopic FE code, which is computationally much more efficient than a detailed FE-based unit cell discretization.
- Special interface regions have been included in the unit cell, since the role of the γ/γ'-interfaces is believed to play an important role in the material deformation behaviour. In the interface regions internal stresses will develop as a result of the lattice misfit between the two phases. Also conditions requiring stress continuity and strain compatibility across the γ/γ'-interfaces have been specified in these regions.

The model was implemented in the commercial FE code MSC.Marc and was applied to the Ni-based superalloy CMSX-4. It was shown to be capable of accurately describing the material stress-strain curve and the influence of changing microstructural dimensions was demonstrated. Therefore, it can be concluded that the present framework is able to accurately describe the material response, while being computationally much more efficient than complex FE unit cell models.

Acknowledgements

The author wants to acknowledge the Dutch Ministry of Defence for funding part of this research under contract NTP N02/12.

References

[1] Jordan, E. H., Shi, S., and Walker, K. P.; *The viscoplastic behavior of Hastelloy-X single crystal*; International Journal of Plasticity, 9 (1993), 119-139.

[2] Daniel, R., Tinga, T., and Henderson, M. B.; *Deformation modelling of the single crystal superalloy CM186LC*; Materials for Advanced Power Engineering, Liège, Belgium, 2002.

[3] Ghosh, R. N., Curtis, R. V., and McLean, M.; *Creep deformation of single crystal superalloys - modelling the crystallographic anisotropy*; Acta Metallurgica et Materialia, 38 (1990), 1977-1992.

[4] Pan, L.-M., Shollock, B. A., and McLean, M.; *Modelling of high-temperature mechanical behaviour of a single crystal superalloy*; Proceedings of the Royal Society London A, 453 (1997), 1689-1715.

[5] Cailletaud, G., Chaboche, J. L., Forest, S., and Remy, L.; *On the design of single crystal turbine blades*; La Revue de Metallurgie, 100 (2003), 165-172.

[6] Busso, E. P., O'Dowd, N. P., and Dennis, R. J.; *A rate dependent formulation for void growth in single crystal materials*; 5th IUTAM symposium on creep in structures, Japan, 2000.

[7] Yue, Z. and Lu, Z.; *Self-consistent constitutive modeling of the creep behaviour of nickel-base directionally solidified superalloys with different grain orientations*; Journal of Material Science and Technology, 14 (1998), 15-19.

[8] MacLachlan, D. W., Gunturi, G. S. K., and Knowles, D. M.; *Modelling the uniaxial creep anisotropy of nickel base single crystal superalloys CMSX-4*; Computational Materials Science, 25 (2002), 129-141.

[9] Eshelby, J. D.; *The determination of the elastic field of an ellipsoidal inclusion, and related problems*; Proceedings of the Royal Society London A, 241 (1957), 376-396.

[10] Ponte Casteñeda, P. and Suquet, P.; *Nonlinear composites*; Advances in Applied Mechanics, 34 (1998), 171-302.

[11] Miehe, C., Schröder, J., and Schotte, J.; *Computational homogenization analysis in finite plasticity. Simulation of texture development in polychrystalline materials*; Computer Methods in Applied Mechanics and Engineering, 171 (1999), 387-418.

[12] Kouznetsova, V. G., Geers, M. G. D., and Brekelmans, W. A. M.; *Multi-scale constitutive modelling of heterogeneous materials with a gradient-enhanced computational*

homogenization scheme; International Journal of Numerical Methods in Engineering, 54 (2002), 1235-1260.

[13] Evers, L. P., Parks, D. M., Brekelmans, W. A. M., and Geers, M. G. D.; *Crystal plasticity model with enhanced hardening by geometrically necessary dislocation accumulation*; Journal of the Mechanics and Physics of Solids, 50 (2002), 2403-2424.

[14] Fedelich, B.; *A microstructure based constitutive model for the mechanical behavior at high temperatures of nickel-base single crystal superalloys*; Computational Materials Science, 16 (1999), 248-258.

[15] Fedelich, B.; *A microstructural model for the monotonic and the cyclic mechanical behavior of single crystals of superalloys at high temperatures*; International Journal of Plasticity, 18 (2002), 1-49.

[16] Busso, E. P., Meissonnier, F. T., and O'Dowd, N. P.; *Gradient-dependent visco-plastic deformation of two-phase single crystals*; Journal of the Mechanics and Physics of Solids, 48 (2000), 2333-2361.

[17] Busso, E. P. and McClintock, F. A.; *A dislocation mechanics-based crystallographic model of a B2-type intermetallic alloy*; International Journal of Plasticity, 12 (1996), 1-28.

[18] Meissonnier, F. T., Busso, E. P., and O'Dowd, N. P.; *Finite element implementation of a generalised non-local rate-dependent crystallographic formulation for finite strains*; International Journal of Plasticity, 17 (2001), 601-640.

[19] Choi, Y. S., Parthasarathy, T. A., and Dimiduk, D. M.; *Numerical study of the flow responses and the geometric constraint effects in Ni-base two-phase single crystals using strain gradient plasticity*; Materials Science and Engineering A, 397 (2005), 69-83.

[20] Svoboda, J. and Lukas, P.; *Modelling of recovery controlled creep in nickel-base superalloy single crystals*; Acta Materialia, 45 (1997), 125-135.

[21] Svoboda, J. and Lukas, P.; *Creep deformation modelling of superalloy single crystals*; Acta Materialia, 48 (2000), 2519-2528.

[22] Kuttner, T. and Wahi, R. P.; *Modelling of internal stress distribution and deformation behaviour in the precipitation hardened superalloy SC16*; Materials Science and Engineering A, 242 (1998), 259-267.

[23] Tinga, T., Brekelmans, W. A. M., and Geers, M. G. D.; *A strain-gradient crystal plasticity framework for single crystal nickel-based superalloys*; Journal of the Mechanics and Physics of Solids, submitted (2006),

[24] Busso, E. P., Meissonnier, F. T., and O'Dowd, N. P.; *Gradient-Dependent Visco-Plastic Deformation of Two-Phase Single Crystals*; Journal of the Mechanics and Physics of Solids, 48 (2000), 2333-2361.

[25] Yuan, C., Guo, J. T., and Yang, H. C.; *Deformation mechanism for high temperature creep of a directionally solidified nickel-base superalloy*; Scripta Materialia, 39 (1998), 991-997.

[26] Evers, L. P., Brekelmans, W. A. M., and Geers, M. G. D.; *Non-local crystal plasticity model with intrinsic SSD and GND effects*; Journal of the Mechanics and Physics of Solids, 52 (2004), 2379-2401.

MODELING THE CONSTANT AND VARIABILE LOADING/TEMPERATURE CREEP BEHAVIOUR OF UDIMET 720Li

M. Maldini and V. Lupinc

CNR – IENI, Via Cozzi 53, 20125 Milano, Italy

Abstract

Constant load creep tests on isothermally forged Udimet 720Li, an advanced superalloy for gas turbine disc application, were run in the stress/temperature intervals 900-450MPa/ 650-700°C resulting in rupture times from 20 to 5000 h.
Creep curves are generally dominated by a long accelerating/tertiary creep that follows a small, often negligible, decelerating/primary creep. No steady state stage has been observed. Analysis of the creep curves has shown that, at low stresses, the accelerating creep stage is due to a strain softening damage whereas, at higher stresses, the accelerating creep is mainly caused by the increase of the applied stress with the strain as it happens in constant load tests.
A model has been introduced to rationalize the different behaviours at low and high stresses and it has been validated with variable stress and temperature creep tests.

Keywords: creep, superalloy, constitutive equation

Introduction

The knowledge of creep behaviour is becoming more and more necessary for designing discs of advanced gas turbines. In fact the introduction of single-crystal blades can bring about a significant increase of disc operating temperature.

This paper reports the creep behaviour and its modeling of an isothermally forged Udimet 720Li superalloy to be utilised for aeronautical turbine disc. The examined stress range overlaps two remarkably different creep behaviours at the chosen temperatures.

Material and experimental procedures

The alloy Udimet 720Li is an advanced wrought superalloy for gas turbine disc applications. The chemical composition of the examined alloy is given in Table 1.

The test piece blanks have been cut from an isothermally forged and heat treated disc by Thyssen Umformtechnik. The heat treatment sequence was:

4 h / 1110°C / oil quench + 24 h / 650°C / air cool + 16h / 750°C / air cool

Table 1 - Udimet 720Li nominal chemical composition (wt.%).

Elem.	Al	Co	Cr	Mo	Ti	W	Zr	Fe	C	Ni
wt(%)	2.5	14.7	16	3.0	5.0	1.25	0.40	0.5	<0.015	bal.

The microstructure of the isothermally forged and heat treated material, examined by SEM and TEM consists of uniformly distributed equiaxed γ grains (~10 μm) and primary γ' particles (~ 3 μm). The primary γ' particles (volume fraction ~ 12 %) are of irregular shape and size and, confirming their stabilising role of the grain size during the first stage of the heat treatment, they are located mainly at grain boundaries, Fig. 1a.

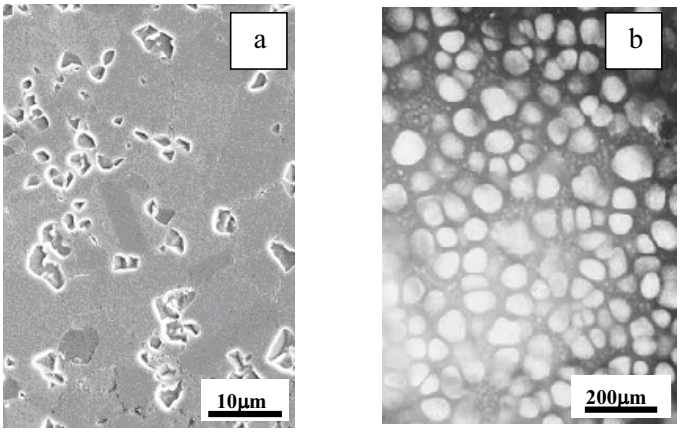

Fig. 1 – Isothermally forged and heat treated Udimet 720Li: the SEM microphotograph (a) points out the primary γ' phase and its role of stabilising grain boundaries, and the TEM microphotograph (b) shows the intra-granular bi-modal distribution of secondary and tertiary γ' particles.

Examination by TEM, Fig. 1b, shows that intra-granular secondary and tertiary γ' particles are spheroidal and their sizes lie, respectively, in the range of 50-100 nm and 5-15 nm, [1]. The bi-modal distribution of the intra-granular γ' appears during oil quenching from solution treatment: at the highest temperatures the precipitation of the large secondary γ' particles is favoured, whereas the precipitation of small tertiary γ' particles occurs at intermediate temperatures [2]. The subsequent standard two stage ageing treatment ripens the tertiary γ' precipitates while it has no apparent influence on the size of secondary γ' particles.

Constant load creep tests were performed on specimens having cylindrical symmetry with a gauge diameter of 4.0 mm and 20 mm gauge length. Three thermocouples were placed in the gauge length allowing control of temperature gradients. Before the start of each test, cold (room temperature) and hot (testing temperature) loading was carried out to check the bending of the specimen due to deviations from axial loading. The specimens were not allowed to spend more than three hours and less than an hour at the testing temperature before commencement of each test.

Experimental results and discussion

Constant load tensile creep tests have been performed at 650 and 700°C and the stresses were selected in the 450-900 MPa range to produce times to rupture up to 5,400 hr. Figs. 2 show examples of the $\log \dot{\varepsilon}$ vs. ε behaviour at both testing temperatures. The creep curves of Figs. 2 are generally not congruent, i.e. it is impossible to overlap them simply by translation. As a consequence the creep curve shape, in a plot ε vs. t/t_r, time normalised with the time to rupture, depends on the test conditions. The substantial part of each creep curve consists of an accelerating stage where the strain rate increases from the minimum creep rate, obtained after a short and small decelerating primary creep stage. That is very apparent in the tests performed at low stresses.

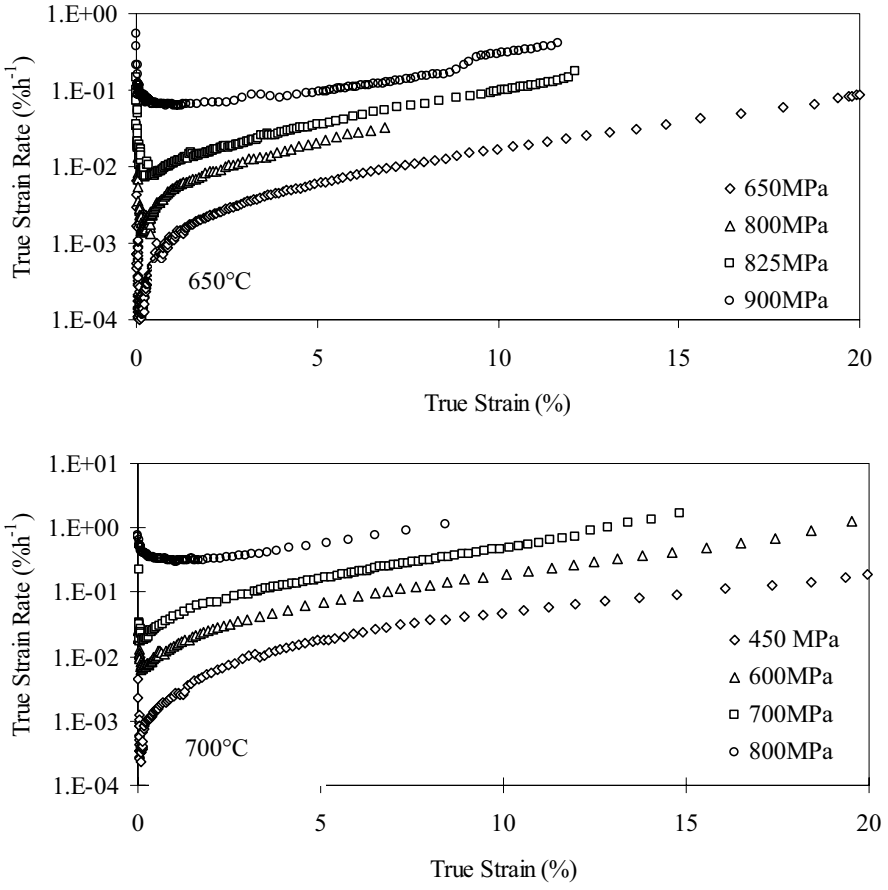

Fig.2 Examples of true strain rate vs. strain for tests performed at 650 and 700°C.

Considering the very low contribution of the primary stage to the total creep strain and time to rupture, this work is focused on the analysis of the minimum creep rate and the following accelerating stage.

Modelling of minimum creep rate

The creep strain rate depends on the mobile dislocation density, ρ, and their average velocity, v, according to the Orowan equation:

$$\dot{\varepsilon} = b\rho v \tag{1}$$

where b is the Burgers vector. During creep, processes of multiplication and annihilation of dislocations can or cannot reach a steady state characterised by a constant creep strain rate $\dot{\varepsilon}_{SS}$.

The stress, σ, and temperature, T, dependence of the steady state creep rate has been often physically modelled by the following equations:

$$\dot{\varepsilon}_{SS} \propto \sigma^n \exp(-Q/RT) \tag{2}$$

or, mainly for alloys reinforced by particle precipitation, by:

$$\dot{\varepsilon}_{SS} \propto [\sigma - \sigma_o(\sigma,T)]^n \exp(-Q/RT) \tag{3}$$

where n is the Norton exponent, having a value between 3 to 7, Q is the activation energy depending on the creep mechanism, R has the usual meaning, and σ_o is an internal or threshold stress reducing the effective stress acting on the dislocations [3].

The equations 2 and 3 have been developed to describe the steady state. Their use to describe the minimum creep rate, in tests where the state does not exist, can be useful to have a phenomenological description of the creep. From a physical point of view, such approximation can be acceptable only if the minimum creep rate is representative of the steady state. In other words, when, in correspondence of the minimum creep rate, the balance between dislocation annihilation and multiplication has produced a constant dislocation structure and the damage mechanisms have not significantly influenced the creep strain rate yet.

A different approach, that seems valid for nickel base superalloys reinforced with a large fraction of second phase particles, considers the minimum creep rate, not a "degraded" steady state due to damage mechanisms, but as the result of two concomitant processes:

1. An increment, during creep, of the mobile dislocations density, from an initial low value, ρ_o, producing a continuous strain acceleration [4].
2. A rapid decrement of the dislocation velocity, due to the development of an internal stress during the first creep and producing the small primary/decelerating creep [5,6].

Such approach leads to a dependence of the minimum creep rate, on the stress, reflecting the dependence of the dislocation velocity, i.e. a hyperbolic sine function, reducing to an exponential for sufficiently high stresses [6]:

$$\dot{\varepsilon}_{min} \propto \mathrm{Sinh}(\beta\sigma) \cong \exp(\beta\sigma) \qquad (4)$$

It is supposed the dislocation density does not significantly increase during the small primary stage.

In principle, the observation of the minimum creep rate in $\log \dot{\varepsilon}_{min}$ vs. $\log\sigma$ or $\log \dot{\varepsilon}_{min}$ vs. σ could discriminate between the two models but, as usual, the scatter of the experimental results does not allow to evaluate which equation can better represent the experimental results. It is important to note the Norton coefficient of Eq. 2 results unacceptably too high (n=20 for the tests at T=650°C). In [7] has been shown that the introduction of the internal stress of Eq. 3 allowed to describe the experimental results with n= 4 and Q close to the self diffusion energy.

Modelling of accelerating creep

Among all damage mechanisms producing a strain acceleration, the grain boundary cavitation cannot explain the convex shape of the accelerating stage exhibited in Fig 2 by the low stress tests, specifically it cannot be responsible of the rapid increment of strain rate after having accumulated only a small creep strain. The cavitation, with the localised necking seems to play an important role in a more advanced stage, producing strong creep acceleration close to the final fracture.

The ripening/dissolution of the tertiary γ' is compatible with the experimental results (the primary and secondary γ' particles are stable in the times/temperatures here explored [8]). In order to quantify the effect of tertiary γ' ripening, creep specimens were heat treated so as to completely dissolve the tertiary creep particles. In Fig. 3 it is shown that the creep tests

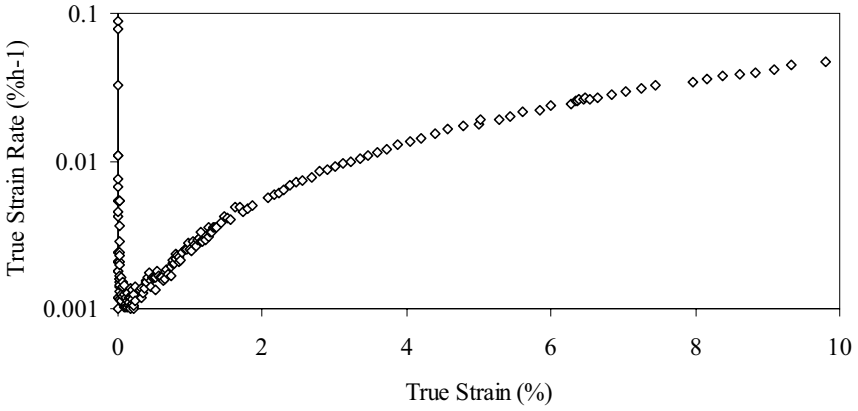

Fig. 3 True strain rate vs. strain in overaged Udimet 720Li alloy (700°C/450MPa).

performed on such material still present a large accelerating stage, showing the ripening of the γ' particles during creep can have only a secondary effect in accelerating the creep deformation.

A creep acceleration, not associated to a real damage in the material, is due to the increment of the applied stress with the strain in the creep tests performed at constant load. The applied stress, σ, increases with the true strain as follows:

$$\sigma = \sigma_a e^{\varepsilon} \tag{5}$$

where σ_a is the engineering stress, provided the reduction of the cross section area is homogeneous along the gauge length and the volume fraction of the specimen during the test is constant. Analysis of specimens in interrupted creep tests and the experimental creep curves shows that both the conditions are satisfied for most of the creep life. Only in the last few per cent of the specimen life does the localized necking begin to influence significantly the creep strain rate.

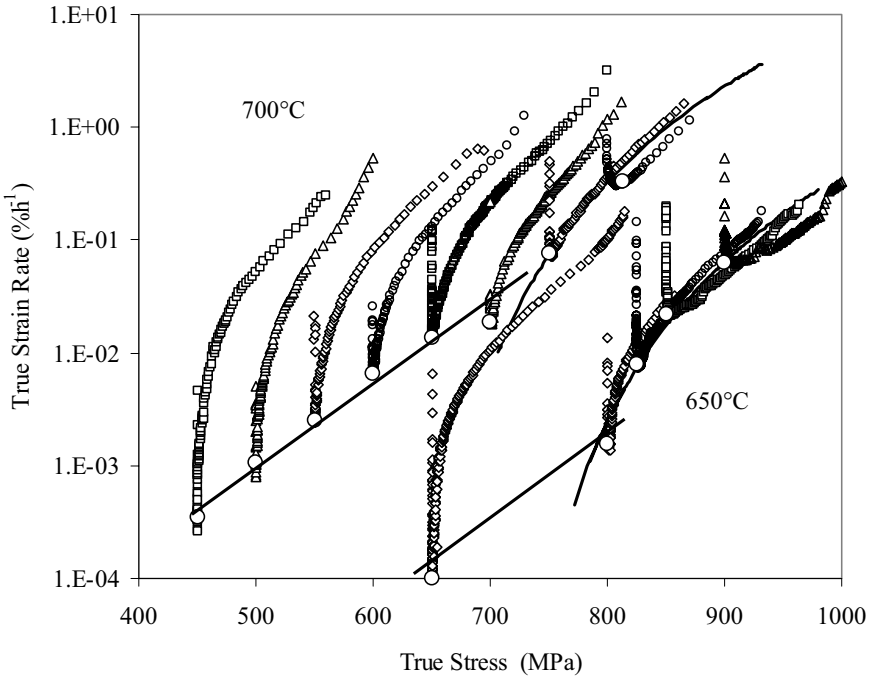

Fig.4 True strain rate as a function of the true stress and interpolation of the minimum creep rate values using the Eq. 3 respectively for the tests performed at high stresses at 650 and 700°C and the Eq. 4 for the tests at low stresses at 700°C.

The contribution of the increasing applied stress with strain in the accelerating creep stage, can be evaluated in a plot of the experimental creep strain rate as a function of the true stress σ of Eq. 5 as shown in Fig. 4. The creep curves at high applied stresses, $\sigma_a \geq 700$MPa, almost overlap the curve interpolating the minimum creep rate [7]. It means that, at high stresses, the accelerating creep is not due to a material damage, but it is mostly due to the increment of the stress with the strain: in other words, creep tests performed at constant stress should present a steady state. Then, at high applied stress, $\sigma_a \geq 700$MPa at both the temperatures, the minimum creep rate followed by the accelerated creep can be modelled by Eq. 3 taking into account the stress increase with the strain according to the Eq. 5. At low applied stress, instead, the contribution of the applied stress increment with strain on the creep acceleration is low, indicating that a material damage mechanism produces most of the strain rate increment. Since at low stresses we are not in a steady state regime, the minimum creep rates of the tests performed at 700°C have been interpolated by Eq. 4.

Model validation by single step variable load creep tests

Following various authors, the creep damage is associated to an increment of the mobile dislocation density [4,9] and the creep acceleration has been modelled by the following couple of differential equations [9,10]:

$$\dot{\varepsilon} = \dot{\varepsilon}_o(\sigma,T)\,[1 + W] \tag{6}$$

$$\dot{W} = C(\sigma)\,\dot{\varepsilon} \tag{7}$$

where $\dot{\varepsilon}_o$ is obtained back-extrapolating to t=0 the strain rate in the accelerating stage. In this paper, the parameter $\dot{\varepsilon}_o$ has been approximated with the minimum creep rate. The approximation can be justified by the very small primary creep for the tests performed at low stresses. W is the damage parameter, related to the dislocation density increase, that is proportional to the creep strain accumulated during the accelerating stage through the constant of proportionality C.

The experimental values of the parameter C has been obtained interpolating the experimental creep curves (Fig. 5) and reported in Fig. 6 for the tests performed at 700°C. The value of the parameter C turned out to be a monotonic decreasing function of applied stress, rapidly reducing at the highest stresses when the creep acceleration is mainly due to the increment with the strain, of the applied stress. In the tests at 650°C results C=0 with the exception of the test at 650MPa.

In Fig. 5 it is shown that the proposed constitutive equations 6 and 7 can adequately describe the constant load creep tests through the "damage" parameter $W = C(\sigma,T)\varepsilon$. Of course this is not a proof the parameter W is really related to the actual damage operating during creep since also equations with totally empirical parameters can excellently interpolate experimental creep curves. However only a constitutive equation capable to follow the actual damage arising in the creeping material as a function of the stress/temperature and accumulated strain is expected to adequately describe the creep behaviour for variable stress/temperature conditions.

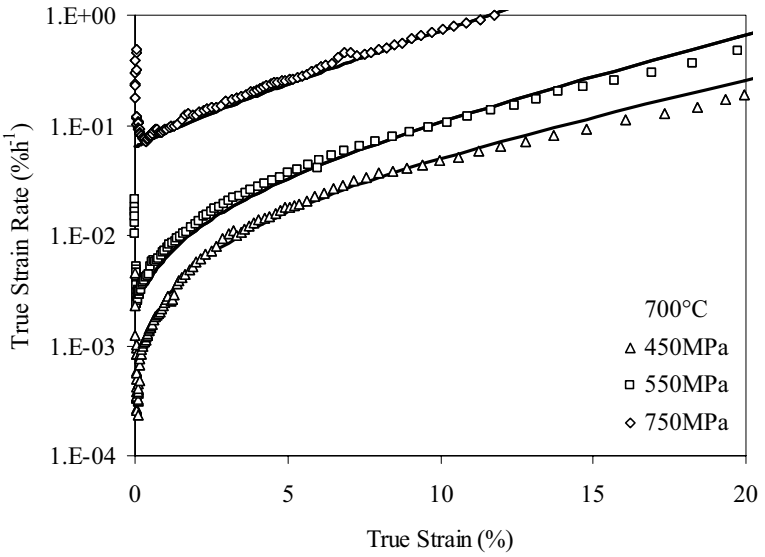

Fig. 5 Examples of true strain rate vs. true strain relation for experimental data and the continuous lines of the model calculation using Eq. 6 and 7.

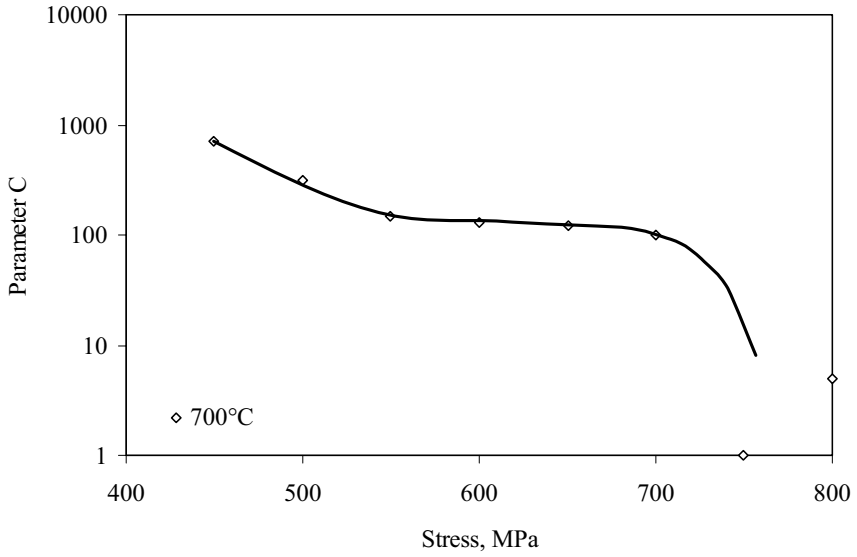

Fig. 6 Stress dependence of the parameter C for the tests at 700°C.

In order to test the proposed model, single step-like variable load and temperature creep tests have been performed and the experimental creep curves have been compared with the prediction of the Eqs. 6 and 7.
To predict the creep response in tests with sharp step or a continuous change in stress/temperature, the set of Eqs 6 and 7 must be numerically integrated, continually updating the values of σ, T and, consequently, the parameters $\dot{\varepsilon}_o$ and C.
Fig. 7a shows constant load tests at 750 and 500 MPa performed at 700°C in addition to the step-like variable load creep test. After the load decrease from 750 to 500 MPa, the experimental creep curve exhibits lower strain rate compared to the reference constant load test. In the figure the description by the proposed equations (continuous line) appears predicting correctly the experimental behaviour. Similar creep behaviour occurs also in Fig. 7b where a large stress decrease occurs simultaneously with the temperature increase from 650 to 700°C.
Since C is generally a monotonic decreasing function of the applied stress, the damage ($W = C\varepsilon$) is not only a function of the strain, as implicit in the Strain Hardening Rule, but it also depends on the stress history. Then a creep strain, ε_1, accumulated at high stress with a low value of parameter C, is less damaging compared to the same amount of strain accumulated at lower stress having a higher parameter C.
Of course, in the steady state stress range, e.g. within 800-900 MPa at 650°C, where the effect of damage W on creep acceleration is negligible compared to the effect of stress increase due to cross-section reduction in constant load tests, the predictions of Eqs. 6 and 7 and the prediction of the Strain Hardening Rule (SHR) are equivalent. Then after a load change both the SHR and the proposed equations predict that the creep curve must overlap the relevant constant load creep data, as it has been experimentally confirmed in Fig. 7c.

Conclusions

An analysis of the creep behaviour of Udimet 720Li alloy in the 650-700°C/900-450 MPa range shows the following:

- The primary stage of the creep curves is relatively small and short and most of the creep strain is caused by accelerating creep.
- A change of the dominant creep mechanism occurs in the 700-800 MPa stress range. This change appears in a discontinuity in the minimum creep rate stress sensitivity and a change in the creep curve shape.
- The accelerating creep in the constant load tests is due to: 1) the strain softening damage in the material and 2) the increase of the applied stress with strain in constant load test.
- The strain softening is the most important material damage mechanism at low stresses and becomes less important at high stresses where the effect of reduction of the cross-section area of the specimen tends to prevail.
- While Strain Hardening Rule holds only within the steady state stress range, the Continuum Damage Mechanics creep law correctly describes experimental behaviour of the accelerating creep under variable load also when creep damage occurs.

Acknowledgements - Part of this work was done within the EC Brite EuRam II project BREU 6021 for which CEC financial support is acknowledged.

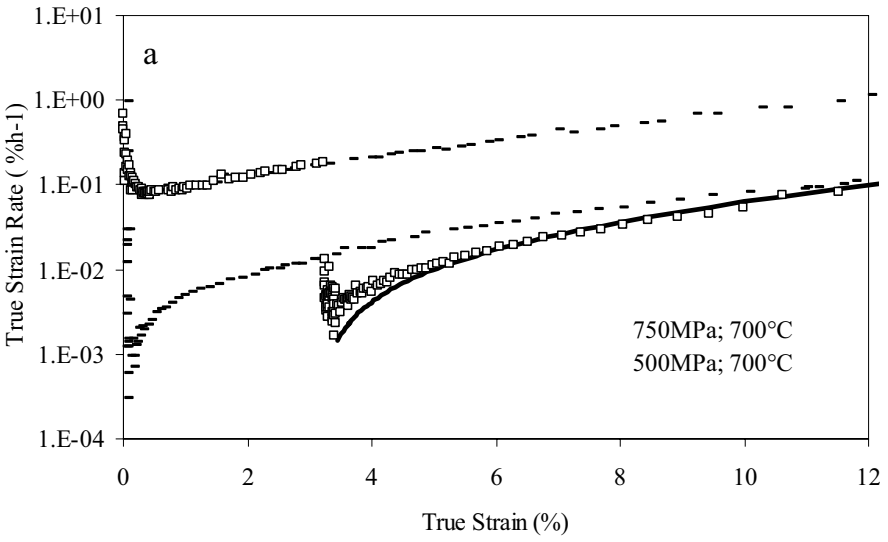
a
1.E+01
1.E+00
1.E-01
1.E-02
1.E-03
1.E-04
True Strain Rate (%h-1)
0
2
4
6
8
10
12
True Strain (%)
750MPa; 700°C
500MPa; 700°C

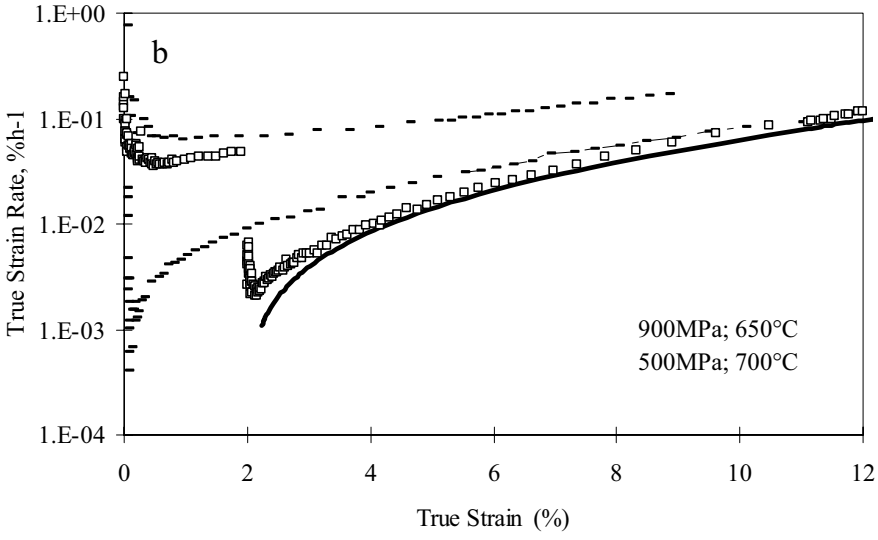
b
1.E+00
1.E-01
1.E-02
1.E-03
1.E-04
True Strain Rate, %h-1
0
2
4
6
8
10
12
True Strain (%)
900MPa; 650°C
500MPa; 700°C

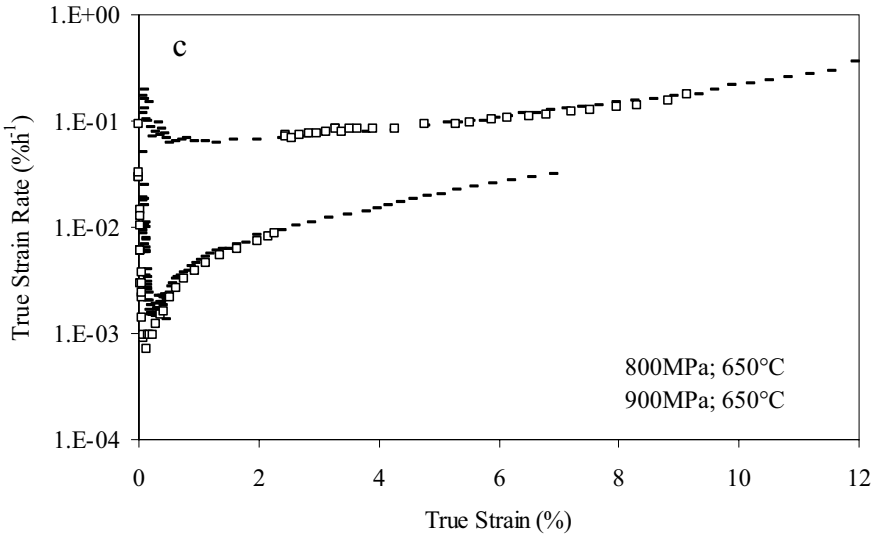

Fig. 7 Comparison between experimental and calculated creep curves. Two experimental constant load and temperature creep curves (dashed curves) are represented togheter with an experimental creep curve where the stress and the temperature was steply changed (□). The prediction (continuous line) of the Eq. 6 and 7 can correctly describe the experimental results. For the variable load test performed in the steady state regime, the creep curve after the load change, overlap the relevant constant load creep curve, as predicted by the proposed model and the strain hardening rule.

REFERENCES

[1] L.Z. Zhou, V. Lupinc, J. Guo, Evolution of microstructure and mechanical property during long-term aging in Udimet 720Li, J. Mater. Sci. Technol., 17, (2001), 633-637.

[2] M.P. Jackson, R.C. Reed, Heat Treatment of UDIMET 720Li: the effect of microstructure on properties, Mater. Sci. Eng. A259 (1999) 85-97.

[3] J. Čadek, Creep in Metallic Materials, Elsevier, Amsterdam, 1988.

[4] B.F. Dyson, M. McLean, Particle-coarsening, σ_o and tertiary creep, Acta Metall. 31 (1983) 17-27.

[5] B.F. Dyson, Creep mechanism transition in precipitation strengthened alloys. Theory and validation, in R.S. Mishra, A.K. Mukherjee, K.L. Murty (Eds.), Creep Behaviour of Advanced Materials for the 21st Century, TMS, Warrendale, Pennsylvania, 1999, 3-12

[6] B.F. Dyson, Modelling Creep Rupture Ductilities and Lifetimes in a Commercial Allumunium Alloy, in R.S. Mishra, J.C. Earthman, S.V. Raj (Eds.), Creep Deformation: Fundamentals and Applications, TMS, Warrendale, Pennsylvania, 2002, 309-318.

[7] M. Maldini, V. Lupinc, Modelling of Creep Strain Behaviour of Udimet 720Li Wrought Superalloy, in R. Townsend, M. Winstone, M. Henderson, J.R. Nicholls, A. Partridge, B. Nath. M. Wood R. Viswanathan (Eds.), Proc. of the *Life Assessment of Hot Section Gas Turbine Components* Conference, IOM Comunications, London UK (2000) 109-118.

[8] V. Lupinc, L.Z. Zhou, M. Maldini, Scatter of Creep Behaviour and Microstructure of Isothermally Forged Udimet 720Li Superalloy, in Proc. of *EUROMAT 2001*, AIM, Milan, (2001) paper 394.

[9] M.F. Ashby, B.F. Dyson, Creep Damage Mechanics and Mechanisms, in S.R. Valluri, D.M.R. Taplin, P.R. Rao, J.F. Knott, R. Dubey (Eds.), Advances in Fracture Research, Pergamon Press, 1984, 3-30.

[10] A.Barbosa, N.G. Taylor, M.F. Ashby, B.F. Dyson and M. McLean, A Model Based Computer Analysis of Creep Data (Crispen): Application to Nickel-base Superalloys, in D. Duhl, C. Maurer, S. Antolovich, C. Lund (Eds.), Proc. 6th Int. Symp. on Superalloys, Metall. Soc. A.I.M.E., New York (1988) 683-692.

A GENERAL APPROACH TO MICROSTRUCTURAL MODELLING OF CREEP

C. Pein[1], E. Kozeschnik[1,2]

[1] Institute for Materials Science, Welding and Forming, Graz University of Technology, Kopernikusgasse 24, A-8010 Graz, Austria.
Ph. 43-316-873-4304 Fax 43-316-873-7187
[2] Materials Center Leoben Forschungsgesellschaft mbH, Franz-Josef Straße 13, A-8700 Leoben, Austria. Ph. 43-3842-459221 Fax 43-3842-459225

Abstract

In materials science, many computational models of inelastic deformation processes on a statistical basis have been developed in order to understand and predict inelastic materials behaviour. To quantify creep, models with high complexity must be used, because, in many cases, experience has shown that creep in advanced materials is a phenomenon far too complex to be modelled on basis of mean or average parameters. It has turned out that the physical processes that occur during creep have to be taken into account on a local basis. The most important mechanisms of creep include self-diffusion of vacancies, the kinetics of dislocation and grain boundary movement, precipitates as well as the mutual interactions among them. In this paper, a corresponding physically-based, comprehensive approach to understand and predict creep behaviour is proposed. In a first step, diffusional creep in bulk and along grain boundaries in the local stress field of a poly-crystalline, multi-phase microstructure is investigated.

Keywords: modelling, creep, microstructure, stress, diffusion

Introduction

Computational studies and models in the area of material science have made major contributions to the current understanding of the material response to mechanical and thermal load. To describe processes occurring on the microstructure scale, in particular, mesoscale mechanics is being used to model and simulate basic mechanisms of material behaviour which are difficult, if not impossible, to analyze by analytical techniques, direct atomistic analysis or a conventional scale independent continuum analysis [1].

A major subject in the field of materials modelling is the understanding and prediction of creep. Creep is defined as the time-dependent deformation of a material under the influence of mechanical stress [2,3]. With regard to power plant applications, creep is a very important issue in terms of component safety and residual lifetime estimation. Therefore, major attention is paid to it in the current COST actions throughout Europe, but also northern America and Japan.

In the effort to quantify the creep behaviour of materials, traditional methods are based on experiments to determine short-term creep rates and creep rupture data and subsequently use more or less sophisticated models to extrapolate these results to longer times. However, despite the huge effort made to improve the prediction and extrapolation models, reliable data can only be evaluated in rare cases. It has been pointed out repeatedly [4,5] that extrapolation of short-term creep data to longer times is only valid if the physical mechanisms of creep remain the same. As soon as a change in creep mechanism occurs over the region of extrapolation, e.g. dislocation creep switches to predominantly diffusional creep, substantial overestimation of the creep strength and creep rupture time will be the consequence and fatal component failure can occur.

In the recent past, a number of attempts have been undertaken to predict the creep behaviour of 9-12% Cr steels on basis of microstructural models. A comprehensive summary of established approaches is given in the thesis of P. Weinert [6]. Moreover, this author has developed a new approach promoting the idea of physically based modelling of creep [7]. Based on a superposition of differential equations for the operational physical mechanisms of creep deformation with time, he was able to relate the macroscopic creep behaviour to the microstructural processes such as dislocation dynamics or vacancy diffusion. However, in the course of this work, it was also recognized that creep must be treated on a local basis rather than on a statistical, macroscopic scale.

If a polycrystalline, multi-phase microstructure is exposed to macroscopic load, the resulting microscopic stresses within the specimen will usually show a complex pattern of areas with alternating compressive and tensile stresses. This pattern strongly depends on the local microstructure and its elements, such as grain boundaries, precipitates, micro-pores etc. In our opinion, phenomenological and statistical approaches cannot capture the essential microstructural changes that occur in the material on a local scale. Important physical processes in creep, such as nucleation and growth of micro-voids or dissolution of precipitates, operate on a local basis, and, therefore, an appropriate model must take these local events into account. Only by these means can modelling and simulation support our conception of creep.

In the effort to understand and even predict creep in a more accurate way, we try to develop a physically based model, which includes all basic mechanisms of creep. These comprise the self-diffusion of vacancies, the kinetics of dislocation and grain boundary movement, the evolution of precipitates in a multi-component multi-phase environment as well as the mutual interactions among them.

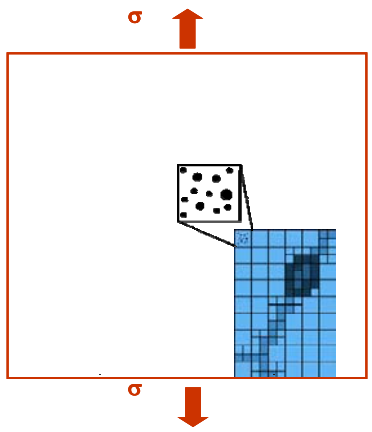

Figure 1: Schematic representation of the proposed microstructure modelling approach.

Figure 1 presents a sketch of our local microstructure approach illustrating the basic mechanisms and interactions which are causing or influencing creep. For instance, if macroscopic stress is applied on this microstructure, the flux of vacancies from regions of high tensile stress to low tensile stress and the resulting mass transport is indicated by arrows. The movement of dislocations as a consequence of local shear stresses is also shown. This

factor will be taken into account in the form of a continuums-mechanical flux that causes deformation of the material. Moving grain and subgrain boundaries and the influence of precipitates will also be considered in a later stage of the present modelling activity.

The project that is introduced in this paper will be mainly concerned with creep in 9-12% Cr power plant steels, but the scientific approach itself is general and it is not limited to a special type of material. Due to the universality of the mathematical and physical formulation of the problem, the proposed approach offers a huge potential for improving understanding and prediction of the creep behaviour of complex materials. The first step in this effort, which is described in this paper, is the microstructural based modelling of diffusional creep.

Diffusional creep and micromechanics

At low applied stresses, the main physical mechanism of creep deformation involves diffusion [8]. Diffusion is the net movement of matter (flux) in a potential or concentration gradient, usually from higher concentration to lower concentration. The net flux of vacancies J_{Va} can be described by Fick's first law

$$J_{Va} = -D\nabla c_{Va} = -J_{LA}. \tag{1}$$

where D is the diffusion coefficient, c is the concentration and ∇ is the gradient operator. The flux of vacancies is counterbalanced by the flux of lattice atoms J_{LA} in the opposite direction. This flux causes a net transport of matter and, thus, deformation of the sample.

In a stressed body, the equilibrium concentration of vacancies can be written as

$$c_{Va}^{equ} = \exp(-\frac{\Delta H_{Va} - PV}{RT}). \tag{2}$$

R is the Universal Gas Constant, T is the absolute temperature, P is the excess local pressure and ΔH_{Va} is the enthalpy of formation of one mole of vacancies in the unstressed state. The value of ΔH_{Va} in iron is typically 135 kJ/mol. According to equation (2), the equilibrium concentration of vacancies depends on a thermodynamic component related to ΔH_{Va} and a component that takes into account local differences in the stress state. In a uniaxially stressed lattice, the concentration of vacancies is increased due to the positive exponent of PV/RT. Thus, the diffusive flux of vacancies goes from regions with tensile stress to regions with compressive stress and matter is transported into the opposite direction. The net result of the diffusional flux is a time dependent deformation of the sample.

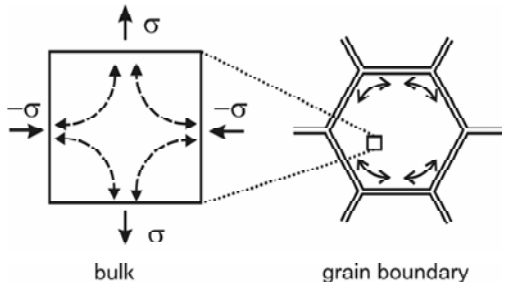

Figure 2: Two-stage Finite Element approach for simulation of diffusional creep.

In our simulation, the local stress state is evaluated by an elastic analysis based on rectangular Finite Elements. Details on this issue are reported in a later chapter. The diffusion of vacancies is then evaluated in two steps: (i) The time-dependent deformation of each finite element, which is treated in the classical way [9], to describe bulk diffusion of vacancies (Nabarro-Herring creep). (ii) Diffusion of vacancies along grain boundaries (Coble creep), which is then overlaid the bulk diffusion solution.

Figure 2 schematically shows the two phases of simulation. The left image represents a volume element, where the local stresses lead to diffusion from high stress to low stress regions and, thus, creep deformation. The right image indicates diffusion occurring along grain boundaries, which is evaluated in a separate step.

Grain boundary diffusion and Coble creep

If a polycrystalline material is loaded with external tensile stress, a small volume which includes a grain boundary will show different response to the local stress than a volume within a grain. The main reason is that grain boundaries cannot withstand parallel shear stresses and two grains loaded with shear will glide along the separating grain boundary. The common approach to simulate the mechanical behaviour of polycrystalline microstructures is to develop a close-to-reality Finite Element representation of the microstructure and to take the weak grain boundary into account by proper mechanical properties of the elements or appropriate contact conditions.

In the present approach, the local stress within a grain boundary is considered as an additional component of mechanical load that is further denoted as the 'inner pressure' P_{GB} of the grain boundary. The value of this inner pressure is dependent on the angle θ between the local effective stress and the direction of the grain boundary. If the grain boundary is located normal to the stress direction, the inner pressure reaches a maximum value, because the entire load of the volume element must be sustained by the grain boundary. If the grain boundary runs parallel to the stress direction, the inner pressure is zero, because the load is assumed to be carried entirely by the relatively stronger, surrounding lattice. The effective inner pressure of the grain boundary P_{GB} can then be defined as

$$P_{GB} = f(\theta) \cdot \tau_{eff} \,. \tag{3}$$

where τ_{eff} is the effective tensile stress in the volume element and $f(\theta)$ is an appropriate function taking into account the angle between the direction of grain boundary and stress. The effective flux of vacancies along the grain boundary is evaluated by inserting the value of P_{GB} into equation (2).

After introduction of the model ingredients for evaluation of the diffusional flux of vacancies in the bulk and along grain boundaries, in a next step, the local stresses of a stress-loaded microstructure are evaluated.

Microstructure

In our simulation, the poly-crystalline, multi-phase microstructure is discretized with rectangular cells, each of them corresponding to a representative volume of the simulation domain. Each element can be one single phase, e.g. matrix, carbide or a grain boundary and, accordingly, material properties such as Young's modulus, shear modulus etc. are assigned to

it. In a first approach, the mechanical properties are assumed to be isotropic. In addition, our treatment is restricted to small stresses and small strains, i.e., we are only performing a fully elastic analysis with an additional diffusional creep component. Plastic deformation and dislocation movement will be considered in future work.

The finite element method is widely used to solve physical problems in engineering analysis and design. First, the physical problem is idealized and cast into a mathematical model, which requires certain assumptions, which finally lead to differential equations governing the process under investigation. As a final part of the geometrical modelling, boundary conditions, such as applied forces, fixed nodal points etc., are taken into account.

Then, for each element, the equilibrium requirements are established in terms of state variables, such as stress and displacement. These are stored into the so-called 'element stiffness matrix' $\mathbf{K}^{(i)}$. Finally, the n element matrices are coupled in the large 'stiffness matrix' $\mathbf{K}$, with

$$\mathbf{K} = \sum_{i=1}^{n} \mathbf{K}^{(i)} . \tag{4}$$

Combined with the boundary conditions of the problem and the vector of displacements $\mathbf{U}$, the elastic analysis is performed on the set of equations

$$\mathbf{KU} = \mathbf{R} . \tag{5}$$

where $\mathbf{R}$ is the vector of the applied forces.

First results

As a first example for an elastic analysis, we consider a hard lens-shaped precipitate within a homogeneous soft matrix. The displacements of the lower boundary of the grid is fixed to zero in y-direction and the sample is loaded with a constant displacement at the upper boundary. The right boundary is fixed in x-direction. This setup represents a specimen loaded with a uniaxial tensile stress in y-direction.

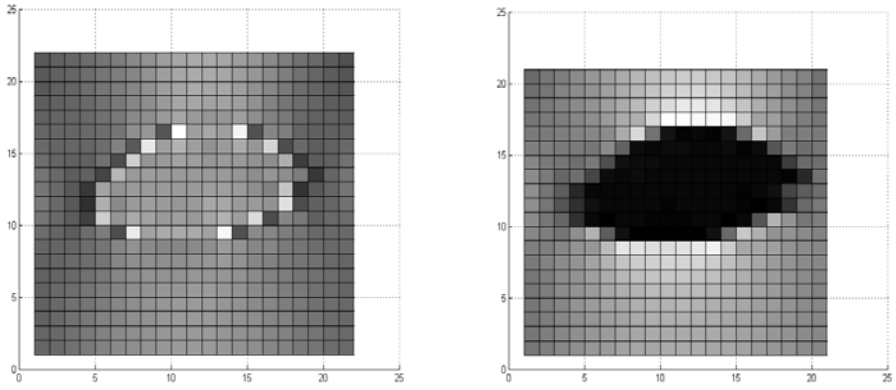

Figure 3: Elastic analysis of a hard carbide precipitate in a soft isotropic matrix. Von Mises stress (left image, dark colours indicate regions of compressive stress) and relative volume change of elements (right image, dark colour indicates no volume change).

Figure 3 shows first results of our simulations with regard to the analysis of local stresses. The images clearly demonstrate that high tensile stresses occur on top and bottom of the precipitate and compressive stresses on its left and right sides. According to the stress gradients, creep will occur and the soft matrix will finally elongate with the hard particle in the center remaining almost unaffected. In addition to the creep deformation in the bulk elements, diffusion along the phase boundary and grain boundaries connected to the precipitate will overlay volume diffusion and speed up the creep process.

Summary and outlook

The proposed approach gives rise to a systematic multi-scale simulation methodology for predicting the microstructure evolution during creep processing of metals in general. In the present project, special focus is put on complex 9-12 % chromium steels. It is expected that this new multi-scale approach advances the current understanding of microstructure evolution, which is still dominated by statistical/empirical techniques.

In the present work, the semi-empirical microstructural relationships are replaced by numerically accurate physically-based models at the mesoscopic length scale. These models take into account the most important mechanism for creep, i.e., diffusion of vacancies, movement of grain and subgrain boundaries, local stresses, pore formation and interaction with precipitates. The approach will be implemented into a microstructure modelling system, which combines mesoscopic microstructural algorithms with continuum-based macroscopic FEM formulations.

References

1 A. Needleman, *Computational mechanics at the mesoscale*, Acta Mater. 48 (2000) 105-124.
2 R.W. Evans and B. Wilshire, *Creep of Metals and Alloys*, The Institute of Metals, 1985.
3 J. Cadek, *Creep in Metallic Materials*, Materials Science Monographs, Elsevier, 1988.
4 G. Dimmler, *Quantifizierung der Kriech- und Zeitstandfestigkeit von 9- 12 % Cr-Stählen*, PhD Thesis, Graz University of Technology, 2003.
5 G. Dimmler, P. Weinert, H. Cerjak: Extrapolation of short-term creep rupture data – The potential risk of over-estimation, ECCC conference “Creep and Fracture in High Temperature Components – Design and Life Assessment Issues”, London, UK, September 2005
6 P. Weinert: *Microstructural Modelling of Creep in Ferritic/Martensitic 9-12% Cr-Steels*, PhD thesis, Graz University of Technology, 2001.
7 P. Weinert and B. Buchmayr, A hierarchical approach for the creep modeling of 9-12% Cr steels, Proc. *CreepDeformation: Fundamentals and Applications*, TMS Annual Meeting, Seattle, USA, 2002, 257-66.
8 F.R.N. Nabarro, *Creep at Very Low Rates*, Met. Mater. Trans., Vol 33A, 2002, 213-218.
9 K.-J. Bathe, *Finite element procedures*, Prentice Hall, Upper Saddle River, 1996.

Part II

Advanced Gas Turbine Materials

Contributed Papers

Joining Technology

THE CREEP RUPTURE BEHAVIOUR OF A NICKEL-BASE SINGLE-CRYSTAL SUPERALLOY AFTER TLP BONDING

J.D.LIU[a,b], T.JIN[a], N.R.ZHAO[a], Z.H.WANG[a], X. F. SUN[a], H.R.GUAN[a], and Z.Q.HU[a]

([a]Department of Superalloys, Institute of Metal Research, Chinese Academy of Sciences, Shenyang 110016, China
[b]Graduate School of Chinese Academy of Sciences, Beijng 100039, China)
E-mail address: jdliu@imr.ac.cn (J.D.Liu)

Abstract

The creep rupture behaviour of a nickel base single-crystal superalloy after TLP (transient liquid-phase) bonding was investigated. Creep rupture tests of the TLP bond and the matrix without TLP bonding were conducted at 1010℃/248MPa. Fracture surfaces and rafting microstructures of TLP bond and the matrix were observed by scanning electron microscopy (SEM). The ductility of the TLP bond is lower than that of the matrix, although the creep rupture life of TLP bond is comparable to that of matrix. There exist obvious differences in the morphology of rafting microstructure between the TLP bond and matrix sample after creep rupture tests. Observation of the fracture surfaces indicates ductile fracture mechanism occurred in all samples.

Keywords: TLP bonding; single-crystal superalloy; creep rupture

1. Introduction

It is very important to develop high quality electric power systems that have excellent energy efficiency. With this in minds, electric power systems combining gas and steam turbines must be improved to increase energy efficiency. A key requirement for land gas turbines is that higher inlet gas temperature can be applied. Single crystal material is one of the most suitable candidate materials for high quality land gas turbines. Ni-base single-crystal superalloys with a high volume fraction (>40%) of $L1_2$-type ordered γ' phase are currently used for blade materials in gas turbine engines due to their anomalous enhancement of mechanical strength at elevated temperatures [1]. However, there is a limited factor that this kind of alloy is very sensitive to hot cracking during fusion welding owing to high content of γ' former such as Al and Ti [2]. Transient liquid-phase (TLP) bonding has been developed to join nickel-base superalloys. It has the advantage of not requiring the rather high pressure needed in typical solid-state diffusion bonding processes. Like brazing, it employs an “interlayer” material as bonding agent. However, the process occurs isothermally. The interlayer melts and solidifies as a result of interdiffusion with the base materials, all at a constant temperature. As a result, the solidified bond region consists of a primary solid solution similar in composition to the base material itself [3]. Many investigations have been done to apply TLP bonding to various kinds of single crystal superalloys because it can produce a strong, interface-free joint [4-8]. However there is little research that studied the creep properties of TLP joints of single crystal superalloys in detail to date. The aim of this work is to investigate the creep rupture behaviour of TLP joint at elevated

temperature.

In the present paper, the creep rupture behaviour at 1010℃/248MPa of TLP joint of a kind of Ni-base single crystal superalloy and the matrix without bonding has been studied, and the microstructures which play an important role in creep deformation and the fracture surfaces have been investigated.

2. Experimental

In this work a kind of nickel-base single crystal superalloy of Ni-Cr-Co-W-Mo-Al-Ti-Ta system was used as base metal for TLP bonding. The nickel-base single crystal superalloys were produced by means of crystal selection method in a vacuum directional solidification furnace under a high thermal gradient. Longitudinal orientation of all specimens was within 10° deviation from [001] which was always aligned perpendicular to the joint interface. The faying surfaces of single crystal samples were mechanically polished using 800 grade emery paper to make the surfaces smooth. A kind of Ni-Cr-B amorphous foils that were prepared by the melt spinning process was used as the interlayer alloy. The thickness and width of amorphous foils were about 40-60μm and 4-10mm respectively。The nominal composition of the interlayer alloy is listed in Table 1.

Table 1 Nominal composition of the interlayer alloy (wt.%)

B	Cr	Ni
3.5	15	Bal

The TLP bonding was carried out in a vacuum of 3×10^{-3}Pa with an applied bonding pressure of about 2.7MPa. The bonding condition was 1250℃ for 8h. After bonding, the specimens were cooled in the vacuum chamber. Prior to the mechanical testing, all test specimens were subjected to a heat treatment procedure consisting of a three-step solution treatment (1295℃/8h AC+1305℃/8h AC+1310℃/8h AC) and a two-step aging treatment(1080℃/4h AC+870℃/24h AC). The heat-treated specimens were machined into creep rupture specimens with gauge length of 25mm and a gauge diameter of 5mm.

Creep rupture tests of TLP joint and matrix sample were carried out in air in a FC-20 constant load high temperature creep-testing machine, and the test condition was 1010℃/248MPa. Microstructures were examined on JSM 6301F scanning electron microscopy, and fracture surface observations were made on SSX-550 scanning electron microscopy.

3. Results and discussions

3.1 Microstructures of TLP joint

The microstructure of longitudinal sectioned TLP joint after bonded at 1250℃ for 8h is shown in Fig. 1. It can be seen that a typical TLP joint consists of bonding zone and substrate zone (Fig.1(a)). The bonding zone is composed of finer and global γ′ phases (Fig.1(b)), because these γ′ precipitates were formed during the cooling process from the bonding temperature that is relatively lower. No grain boundary is found in the bonding zone. There exists lots of γ/γ′ eutectics in the interdendritic region of the substrate

zone.

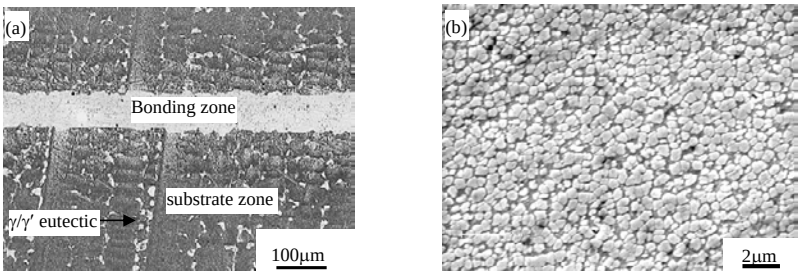

Fig. 1 Microstructure of longitudinal sectioned TLP joint after TLP bonded at 1250℃ for 8h: (a) morphology of TLP joint after TLP bonding; (b) microstructure in bonding zone after bonding

After heat treatment, the microstructure of bonding zone and substrate zone is illustrated in Fig.2. The microstructures are all composed of γ and γ′ phase, and the morphology of γ′ phase from different parts of the joint are similar. The total γ′ volume fraction of the bonding zone is determined to be more than 65%.

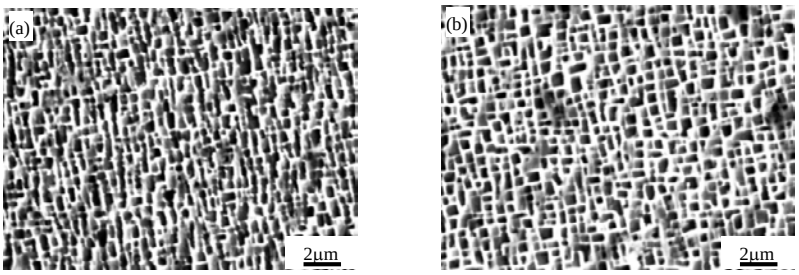

Fig. 2 Microstructures of TLP joints:(a) bonding zone;(b) dendrite core region of substrate zone

3.2 Creep rupture properties at 1010℃/248MPa

The creep rupture properties and creep strain rate curves of TLP joint and matrix sample at 1010℃ /248MPa are shown in Fig.3. The creep rupture life of TLP joint is comparable to that of matrix sample, but the elongation of TLP joint is significantly lower than that of matrix sample (Fig.3(a)). The poor ductility of TLP joint may result from the solid hardening of B and slight mismatch in orientation existed in bonding zone. Compared with TLP joint, the creep strain of matrix is higher, and reaches tertiary stage faster than that of TLP joint (Fig.3(b)). Although the primary and steady creep strain rate of TLP joint and matrix are almost same, tertiary creep strain rate of matrix is significantly higher than that of the TLP joint. This indicates that the TLP joint may have stronger resistance to creep deformation than matrix sample. All TLP samples failed at the bonding zone of the joint.

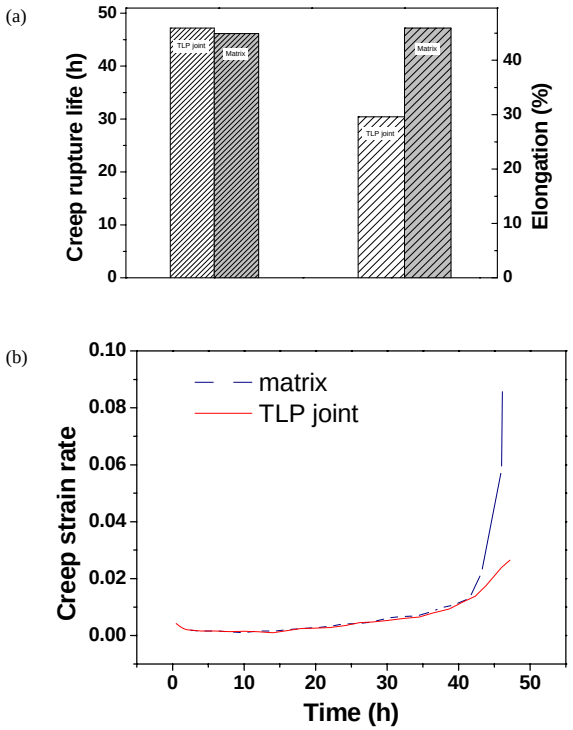

Fig.3 The creep rupture life and elongation of TLP joint and matrix:(a) creep rupture properties of TLP joint and matrix; (b) creep strain rates of TLP joint and matrix

3.3 Directional coarsening of γ′ phase after test

It is well known that N-type raft which is perpendicular to the stress axis can form in alloy with negative lattice misfit during high temperature creep tests and can provide a beneficial structure for creep resistance [9-11]. After creep rupture at 1010℃/248MPa, N-type rafts formed in both TLP joint and matrix. Fig. 4 shows the morphologies of directional coarsening of γ′ phase of TLP joint and matrix sample. At the position near fracture surface, the direction of rafted γ′ phase is not perpendicular to the tensile load axis, and significant thickening of γ′ phase happened. From the view of previous research [12], in the necking zone, the effective loading cross section of specimen decreases and multiaxial stress appears. This makes contribution to the lattice rotation and the thickening of γ′ phase. In present test, obvious necking appears in matrix sample after test, and this may lead to the significant thickening and the rotation of the direction of rafted γ′ phase near fracture surface (Fig. 4(b)). However, the deformation near fracture surface of TLP joint is homogeneous and the necking is not obvious. Therefore, the thickening and rotation of rafted γ′ phase near the fracture surface can not be observed (Fig. 4(a)). As mentioned above, the deformation of TLP joint in tertiary stage is less than that of matrix sample, and this may play an important role in

morphology of rafted γ′ phase.

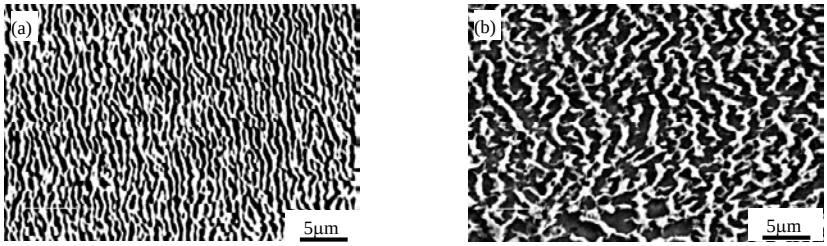

Fig.4 Rafts formed in TLP joint and matrix sample after test:(a) at 2mm away from the fracture surface of TLP joint; (b) at 2mm away from the fracture surface of matrix sample

3.4 Fracture surfaces observations

The fracture surfaces of TLP joint and matrix samples are shown in Fig.5. Although they are all ductile fracture, there are many square-shaped facets in the fracture surfaces (Fig.5(a)). It is noted that the amount and area fraction of the facets in fracture surface of TLP joint are higher than those of the matrix sample. According to literature [13,14], microcracks initiate at shrinkage porosity, and the crack growth by alternate shearing of the γ matrix and quasi-cleavage of γ′ phase results in reduction of effective cross-section area. The final failure processes is initiated once the effective cross-sectional area is reduced to an extent where the resolved shear stress on the most highly stressed slip system is equal to the critical resolved shear stress of the material. It is possible that amounts of creep cavities formed in bonding zone of TLP joint during the last stage of creep rupture test, and these cavities became favorable location for crack initiation. Lots of microcracks propagate on {001} planes rapidly. Once the cracks interconnect, abrupt failure of TLP joint occurs while the ductile deformation is not obvious. This may play an important role in the reduction of elongation of the TLP joint.

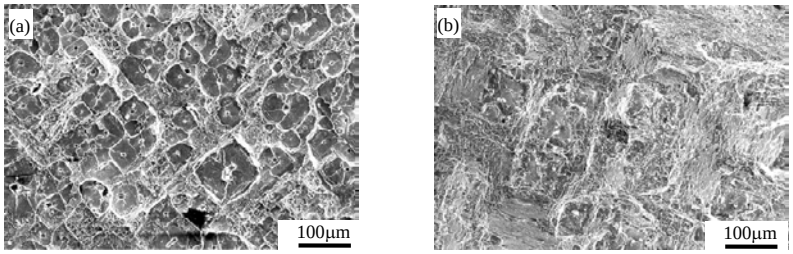

Fig.5 Fracture surfaces of TLP joint and matrix sample: (a) fracture surface of TLP joint;(b) fracture surface of matrix sample

4. Conclusion

(1) After TLP bonding and successive heat treatment, the creep rupture strength of TLP joint is comparable to that of matrix, but the elongation of TLP joint is much lower.

(2) During creep rupture test, long, flat and fine-spaced rafts were formed near fracture surface of TLP joint, and this may result from the much less creep deformation of TLP joint in tertiary stage.

(3) From the observation of the fracture surfaces, it indicates that the reduction of elongation of TLP joint might be due to an amount of creep cavities formed during creep test in the bonding zone of TLP joint.

Acknowledgement

This project is supported by the National Natural Science Foundation of China with Grant No: 50474058.

References

[1] Z.P.Luo, Z.T.Wu, D.J.Miller, The dislocation microstructure of a nickel-base single-crystal superalloy after tensile fracture, Mater. Sci. Eng. A,354,2003,358.

[2] Z.C.Ruan, S.C.Wang, Y.R.Zheng, Microstructure and bonding behavior of a new Hf-bearing interlayer alloy for single crystal nickel-base superalloy, Scripta Mater. ,34 ,1996,163.

[3] I.T.Poku, M.Dollar, T.B.Massalski, A study of the transient liquid phase bonding process applied to a Ag/Cu/Ag sandwich joint, Metall. Trans. A,19,1988,675.

[4] Y.Zheng, L.Zhao , K.R.Tang, Microstructure of Ni-10Co-8Cr-4W-13Zr alloy and its bonding behavior for single-crytal nickel-base superalloy, J. Mater. Sci., 28,1993,823.

[5] W.Li, T.Jin, X.F.Sun, Y.Guo, H.R.Guan, Z.Q.Hu, TLP bonding of Ni-base single crystal superalloy, Acta Metall. Sinica 37 ,2001,1165. (in Chinese)

[6] W.Li, T.Jin, X.F.Sun, Y.Guo, H.R.Guan, Z.Q.Hu, Transient liquid phase bonding of Ni-base single crystal superalloy,J. Mater. Sci. Tech.,18,2002,54.

[7] D.U.Kim, K.Nishimoto,Creep rupture and fatigue properties of transient liquid phase bonded joints of Ni base single crystal superalloy, Mater. Sci. Tech ,19,2003,456.

[8] W.Li, T.Jin, X.F.Sun, Y.Guo, H.R.Guan, Z.Q.Hu, Study of Ni-Cr-Co-W-Mo-B interlayer alloy and its bonding behavior for a Ni-base single crystal superalloy, Scripta Mater., 48,2003,1283

[9] T.Ichitsubo, K.Ianaka, Interpretation in elastic regime for rafting of Ni-base superalloy based on the external-stress-free dimensional change due to internal-stress equilibration, Acta Mater.,53,2005,4497.

[10] D.D.Pearson, F.D.Lemkey, B.H.Kear, Stress coarsening of γ′ and its influence on creep properties of a single crystal superalloy,Superalloys,1980,513.

[11] R.A.MacKay, L.J.Ebert, The development of γ-γ′ lamellar structure in a nickel-base superalloy during elevated temperature mechanical testing,Metall. Trans. A,64,1985,1969.

[12]L.R.Liu, T.Jin, N.R.Zhao, X.F.Sun, H.R.Guan, Z.Q.Hu, Formation of carbides and their effects on stress rupture of a Ni-base single crystal superalloy, Mater. Sci. Eng. A,361,2003,191.

[13]A.A.Hopgood, J.W.Martin, The creep behavior of a nickel-base single-crystal superalloy, Mater. Sci. Eng. A,82,1986,27.

[14]A.H.Sherry, R.Pilkington, The creep fracture of a single-crystal superalloy, Mater. Sci. Eng. A,172,1993,51.

NANOINDENTATION AND ORIENTATION MEASUREMENTS IN SINGLE CRYSTALLINE BRAZING JOINTS OF NICKEL-BASE SUPERALLOYS

M. Dinkel, F. Pyczak, M. Göken
P. Heinz[1], A. Volek[1], R. F. Singer[1]
M. Ott[2], E. Affeldt[3], A. Vossberg[4]

Department of Materials Science and Engineering, Institute I
[1]Department of Materials Science and Engineering, Institute II
University Erlangen – Nürnberg,
Martensstr. 5, D-91058 Erlangen Germany

[2]Siemens AG Power Generation, Mellinghofer Strasse 55, D-45473 Mülheim
[3]MTU Aero Engines GmbH, Dachauer Str. 665, D-80995 München
[4]MTU Maintenance Hannover GmbH, Münchner Strasse 31, D-30855 Langenhagen

Abstract

Due to the high price of single crystalline turbine blades used in industrial gas turbines and aircraft engines, repair processes for these materials are gaining more and more interest. A widely used technique is brazing of narrow cracks. The standard brazing techniques use boron and silicon containing alloys. They tend to create a polycrystalline brazing zone with according loss of creep strength and fatigue resistance. Another detrimental effect of these boron and silicon containing brazing alloys is the development of brittle phases which reduce the ductility.

Current research has shown the possibility of single crystalline repair of nickel – base superalloys by a new brazing process. Such single crystalline joints produced by diffusion brazing are characterized with nanoindentation and orientation measurements. Electron Back Scattering Diffraction (EBSD) – measurements proved epitaxial growth in the brazing zone. Nanoindentation measurements are used to measure the hardness evolution of the brazing filler and the base material.

It can be shown that it is possible to solidify the joints in a monocrystalline way and that the hardness condition of the joint area is equal to that of the substrate. Also the indentation modulus of the joint region is comparable to the substrate.

Keywords: Single Crystalline, Brazing, Diffusion, Nanoindentation, EBSD

Introduction

Single crystalline turbine blades are currently used both in aircraft engines as well as in industrial gas turbines, although the costs for single crystalline parts are very high. A disadvantage of these single crystalline parts is the high amount of investment due to the rather high price of these parts. Therefore it is crucial to keep these parts in service as long as possible. But temperature changes superimposed by changing stress or strain lead to fatigue cracking as one of the most prominent damage mechanisms in these materials. Periodic maintenance can prevent fatal damage by complete replacement of defective parts, but this poses very high costs. So a repair instead of replacement is desirable. Unfortunately, if the single crystalline microstructure is not preserved by the repair process the properties of the part degrade. Commercially applied repair processes use brazing alloys which create polycrystalline joints with brittle intermetallic compounds within the joint region. These intermetallic phases are a consequence of the application of silicon and boron containing brazing alloys. Due to the limited solubility of both boron and silicon in nickel within the

brazing joint nickel borides, nickel silicides and chromium silicides precipitate [1]. As a consequence the development of a novel repair technique, which does not comprise of these disadvantages, is desired.

Diffusion brazing

In this work the joint microstructure produced by a monocrystalline repair of single crystalline turbine parts is examined. The chosen technique is Transient Liquid Phase (TLP) bonding, [2,3] The main mechanism of this method is the diffusion of a melting point depressing element out of the brazing alloy into the surrounding base metal which leads to an interface free single crystalline joint.
The whole process of Transient Liquid Phase bonding can be subdivided into three stages [3,4]. First the melting point depressing element diffuses into the base metal, which leads to limited dissolution of the latter and respective widening of the liquid interlayer until both phases reach an equilibrium state. (Figure 1) After this process isothermal solidification takes place. Now the solid-liquid interface reverses its direction of movement due to the further inter-diffusion of the melting point depressing element into the base metal, which raises the melting point of the liquid interlayer (point 3 in figure 1). Due to the continuous diffusion of the melting point depressant the volume of the liquid phase decreases and the mating solid–liquid interfaces move toward the centre of the joint until all liquid volume is solidified (point 4 in figure 1). This stage is the time controlling step of the process due to the slow diffusion [3]. Subsequently in order to homogenize the joint region an annealing treatment could be applied, which resembles the third stage (point 5 in figure 1).

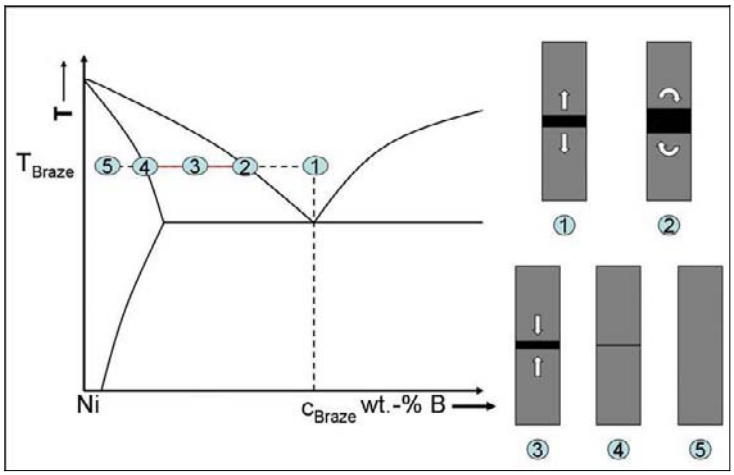

Figure 1: Principle of the TLP Process in the binary Ni-B system. 1 :Dissolution of the base metal, 2: Widening of the liquid interlayer until 3: reversal of the direction of the solid-liquid interface due to isothermal solidification. 4: Shrinkage of the gap until the liquid interlayer is fully solidified. 5: subsequent annealing treatment (if necessary). After [2].

Current research has shown that Transient Liquid Phase bonding, especially the solidification rate and evolving microstructure, is strongly dependent on the temperature and time [5,6]. However, other than in most diffusion controlled processes a rise in temperature does not necessarily lead to a decrease in process time, which would be expected due to an increased diffusion rate. This effect is partly ascribed to the back diffusion of light elements like

Titanium and Aluminium into the liquid interlayer. But it is also necessary to consider that with the diffusion of the melting point depressant the local melting temperature of the substrate is lowered and could be as low as the process temperature for a particular melting point depressant concentration, which would lead to an increased widening of the brazing gap with increasing temperature and therefore extended process times.

Experimental

All experiments were conducted with PWA 1483 as substrate material. The nominal composition is given in table 1. Two different experimental brazing alloys were used. Unfortunately, composition and process details cannot be disclosed here due to patent concerns. But the main focus of the paper lies on the crystallographic and mechanical properties of the different joint microstructures. Hence the value of the presented results is not reduced, if no information is given how these joint microstructures were processed.

Table 1: Composition of PWA 1483 (nickel content is balanced)

Element	Ni	Cr	Co	Mo	W	Al	Ti	Ta	C
wt.-%	Bal.	12,2	9,0	1,9	3,8	3,6	4,1	5,0	0,07

Specimens of 5x5 mm size were cut using a diamond saw and trenches were prepared with a diamond wire saw to obtain a test geometry for brazing experiments with a deformation free surface without any heat affected zones. The trench width was approximately 200 µm. After application of the brazing alloy the samples were then brazed and subsequently cut perpendicular to the trench orientation. After grinding and diamond polishing the samples were polished in an ultrasonic polisher for 24 hours using a 0,1 µm SiO_2-slurry. This is necessary to obtain the almost deformation free surface required for both Nanoindentation and EBSD measurements.

Nanoindentation

The nanoindentation measurements shown in this work were performed with a MTS Nanoindenter XP. All measurements were done with a three-sided Berkovich tip. The Berkovich geometry has a tip area function equivalent to the Vickers pyramid. The Berkovich tip was calibrated using fused silica as a reference material and the tip area function was monitored throughout the whole investigation. The machine compliance was taken into account.

The positioning of the indentation is done with an optical microscope. The machine is equipped with a continuous stiffness module, which applies an additional oscillating force at a frequency of about 45 Hz to the load during indentation. The contact stiffness is continuously evaluated during loading and the hardness and reduced modulus are calculated as a function of the indentation depth using the Oliver / Pharr method [7].

It is very important to mention that the indentation modulus results do not represent the anisotropic Young's Modulus in the direction parallel to the indentation direction. The results are rather comparable to the modulus of a polycrystalline sample, or a single crystal in a <110> direction [8,9].

A measurement array, schematically shown in figure 2, was applied to the specimens. The array was chosen in such a way that the distance between the single indents guarantee

independent measurements with neighbouring indents. The penetration depth was chosen as 2000 nm.

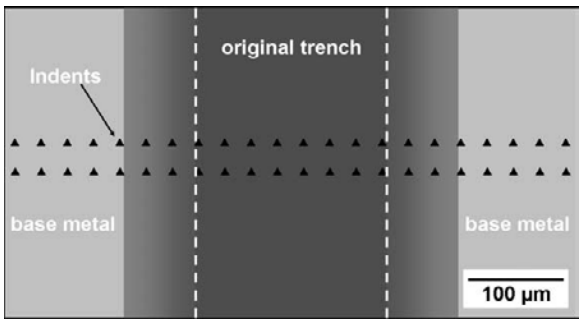

Figure 2: Schematic measurement array over the joint region. The distance between the indents is sufficient to guarantee independent results

Electron Back Scattering Diffraction – measurements

Electron Back Scattering Diffraction (EBSD) is a diffraction technique for obtaining crystallographic information from bulk samples in the scanning electron microscope (SEM). This technique uses an electron beam which interacts with a tilted sample to produce a electron backscattering diffraction pattern (figure 3), which resembles the Kikuchi patterns well known from transmission electron microscopy. For further information the authors refer to Wilkinson et al. [10].

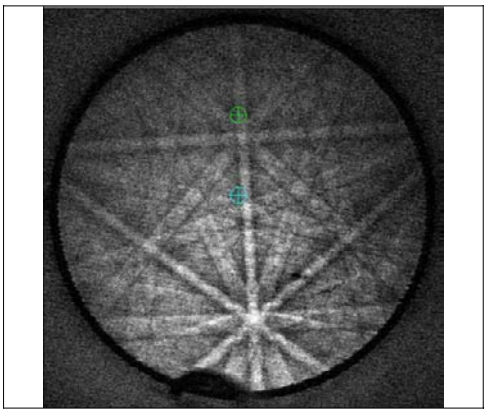

Figure 3: EBSD Pattern,

Each of these patterns corresponds to a definite crystallographic orientation of the crystal. This technique is also known as Orientation Image Microscopy (OIM). The crystallographic orientation of an area is given in terms of a colour change, where each colour stands for a definite direction in the orientation triangle. Each pixel represents a measurement point. Black pixels in the images represent unresolved patterns. Unfortunately only grayscale images can be published here. Accordingly the information is not as easily accessible as in colour images.

Hence, for a better understanding, if necessary the data is also shown in terms of the inverse pole figures, where the orientations for each pixel are displayed. In these figures an accumulation of measured, i.e. a number of measurements with nearly identical crystallographic orientation, can be interpreted as grains. As mentioned before EBSD measurements requires a very smooth and distortion free surface for precise measurements.

Results and discussion

Figure 4 shows the Nanoindentation results for a fully isothermally solidified brazing joint (sample 1). In the graph the indentation modulus and the hardness is shown over the joint area and the neighboring base metal.

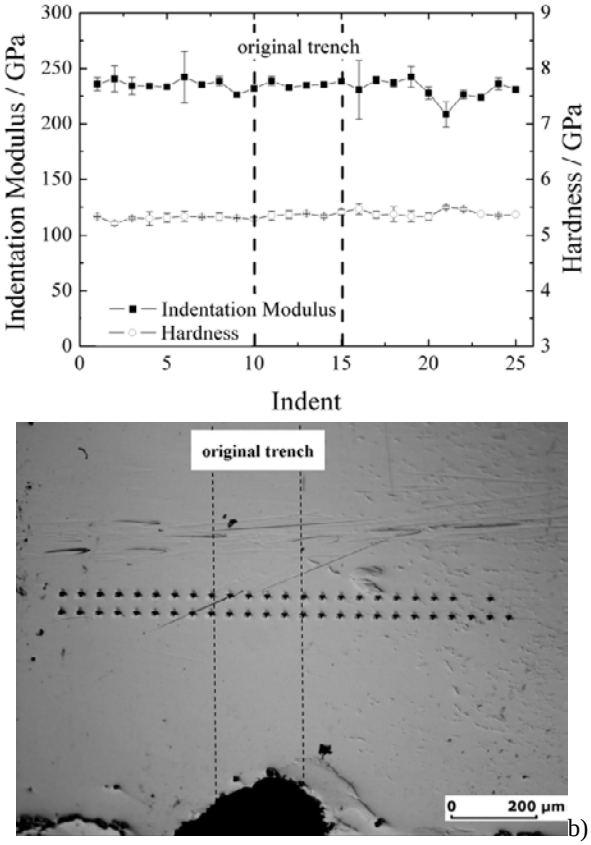

Figure 4: Nanoindentation of a fully single crystalline brazing joint (sample 1): a) Hardness and indentation modulus course over the joint area. b) Light microscope micrograph of the joint region with the visible residual indents

The values for the modulus represent typical values for single crystalline nickel base alloys [11].The measurement on the brazing specimen shows modulus values of about 240 GPa for the modulus in the base metal and about 5.3 GPa for the hardness, respectively. The rather high scatter can be attributed to surface phenomena like porosity.

There is no distinct change neither in the indentation modulus nor in the hardness visible, if the values inside the original trench area compared with the base metal. This is easily understandable, because the initial widening of the liquid interlayer causes a fast homogenization between brazing alloy and base material. Therefore differences in the brazing alloy composition and the substrate composition are no more as pronounced as the starting constitutions would indicate. The element distribution is also homogenized further during the subsequent isothermal solidification process. These two effects then result in the nearly equal mechanical properties at room temperature. The light microscope image (figure 4 b) displays the microstructure in the unetched state. The impressions from of the nanoindentation measurements are clearly visible. No second phase particles are visible and there is a smooth transition from the base metal to the brazing joint. Besides the edge of the specimen and the remaining trench the only feature that indicates the former trench, is the porosity. The newly solidified area, i.e. the joint itself shows virtually no porosity, whereas the cast base metal shows a regular casting porosity.

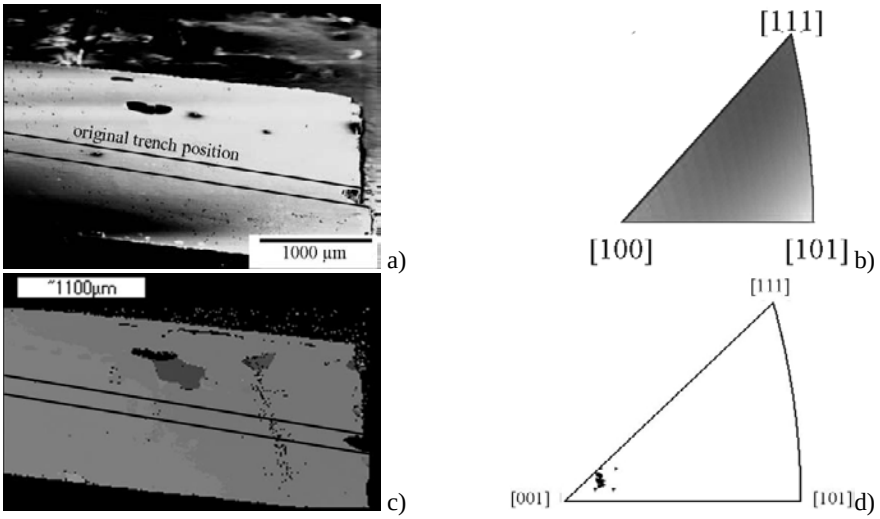

Figure 5: EBSD Results for the fully single crystalline brazing joint: a) Secondary electron image of the sample in the tilted measurement position; b) orientation triangle with the colours indicating the different direction;c) orientation map in the sample normal direction, d) inverse pole figure

Figure 5 shows the results of the orientation measurements. In the SE image (Figure a) the sample is shown in the specific tilted measurement position. The two lines indicate the former trench position. In this picture also a rather big pore can be seen in the upper half of the specimen. From the orientation map (figure 5c) it is visible that there is no contrast change at the former trench position. But close to the afore mentioned pore in the upper part of the sample there is a rather big recrystallised grain visible and also at the edges of the sample there are small new grains apparent. This generation of recrystallised grains at free surfaces sometimes occurs after heat treatments [12]. Due to the position of these grains it is also clear that this is not a direct consequence of the trench production and the subsequent brazing process, i.e. the isothermal solidification process. In figure 5d) the inverse pole figure is shown for measurements in the direct vicinity of the joint. Three measurements with 16 spots were done, above, within and below the original joint position. The result clearly shows that there is no difference to the visual appearance of the orientation map, i.e. the orientation

distribution is in the range of 5 to 10°, which is equal to the orientation distribution normally found in a single crystal cast structure.
In figure 6 the results for a not fully isothermally solidified joint (sample 2) are shown (the brazing process was interrupted prematurely). Here the values of the modulus and hardness in the base metal are slightly lower with values of about 220 GPa for the modulus and 4.5 GPa for the hardness compared to the sample discussed before. This difference can be ascribed to a different temperature treatment during the TLP process and also to the different orientation of the specimen.

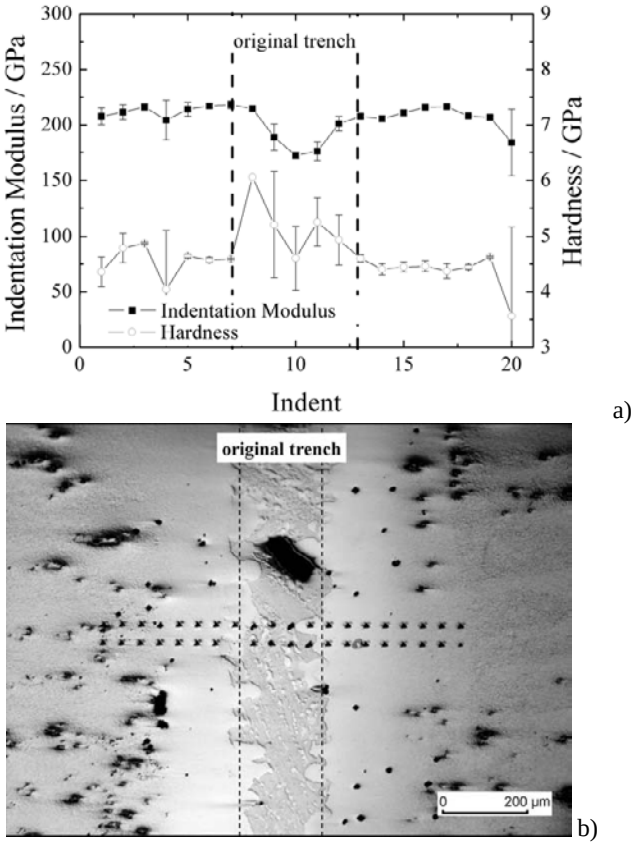

Figure 6: Nanoindentation measurement of a not fully single crystalline solidified brazing joint (sample 2): a) Hardness and indentation modulus in the joint area. b) Light microscope micrograph of the joint region with indents and a clearly visible residual eutectic

The drop in the indentation modulus and also the corresponding rise in hardness within the joint can be explained with the microstructure obtained with the light microscope. Rather high deviations in the hardness result from the fact that within the joint there are some particles as well as residual eutectic, which can result in a strong measurement scatter. These particles are of the same phase, but oriented differently. A clear transition from the base metal to the joint region is obvious, especially for the modulus. Also even in this unetched state a rather wide diffusion zone is visible. In contrast to sample 1 some pores are visible within the diffusion

zone. By comparing the hardness and the modulus results relative to the original trench position it seems that the values for hardness and the modulus stay rather constant until the inner part of the joint region. This is most probably due to the fact that the brazing alloy remained liquid in the joint area until the final cooling of the sample and therefore no isothermal solidification has taken place.
Already the light microscope image reveals that the inner joint region is not solidified in a single crystalline orientation, so an overview of the whole sample with EBSD-measurement would not provide additional information. It is more interesting to take a closer look at the borderline of the solid/liquid interface and evaluate the orientation situation there. Therefore two measurements were made, one at the base of the trench and one in the centre. Figure 7 shows the EBSD results for a measurement made at the bottom of the trench of sample 2. Figure 7a) shows the SE image of this region. The resulting orientation map in the sample normal direction is displayed in figure 7b).

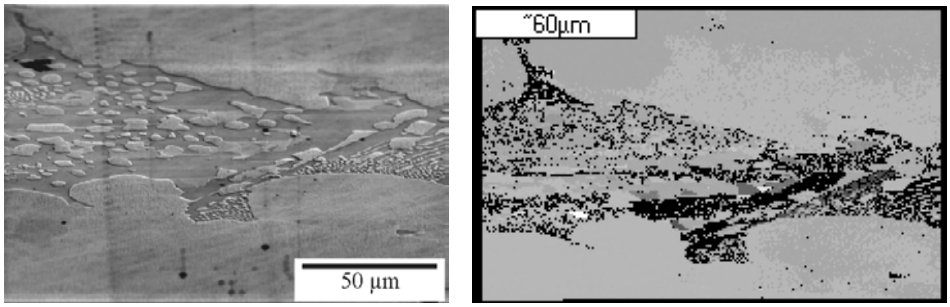

a) b)

Figure 7: EBSD measurement at the trench base of sample 2: a) electron image, b) orientation map in the sample normal direction,

The measurement shows that all protrusions which start to grow into the trench are in fact single crystalline. Moreover it is visible that within the joint a rather large fraction of the remaining liquid interlayer during rapid cooling also solidified in the same orientation as the substrate. But there are some areas with different orientations, as indicated by the contrast changes and also some regions with unsolved patterns. Considering the fact that the measurement was made at the trench bottom, here the liquid interlayer in fact has interfaces with the substrate on three sides. This might lead to different solidification conditions, which results in the high amount of eutectic, oriented identically with the substrate. The grains inside the eutectic, visible in the electron image, also have the same orientation as the substrate.
The EBSD-measurement of the centre region of the trench is shown in figure 8. Here the situation is different from figure 7. Again the protrusions are grown epitaxially into the joint, but within the joint all the liquid interlayer solidified in a different orientation than the base metal. So it seems that the more oriented solidification seen in figure 7 is a consequence of the special position, located at the bottom of the trench. The visible marks in the electron image (figure 8a) are the result of carbon contamination from a previous EBSD-measurement.

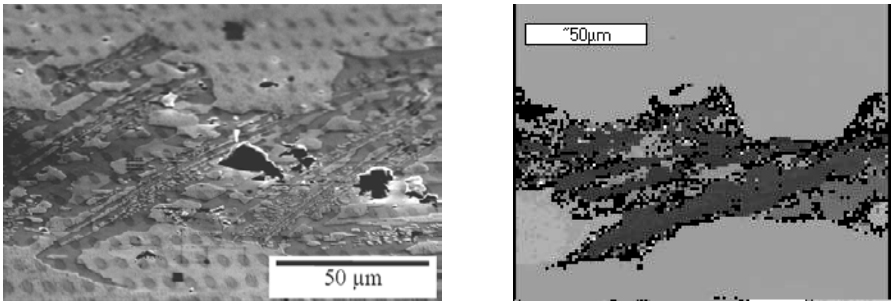

a) b)

Figure 8: EBSD – measurement at the trench centre of sample 2: a) electron image, b) orientation map in the sample normal direction.

For a comparison of the two different measurements the resulting inverse pole figures are displayed in figure 9 a) and b). The high fraction of measurements not oriented closely to the [001]-direction is clearly visible in figure 9b), whereas only a few small misoriented areas, corresponding to the small grains visible in the centre of Figure 7b), are apparent in figure 9a).

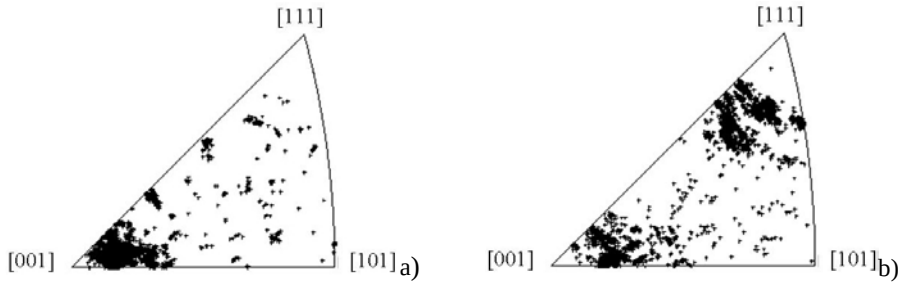

Figure 9: Inverse pole figures: a) corresponding to figure 7; b) corresponding to figure 8

Conclusions

In this work the microstructure generated by a novel technique for the single crystalline repair of turbine parts was evaluated by means of Nanoindentation and Orientation Measurements.
It could be shown that in the case of a fully single crystalline brazing joint all the values derived through nanoindentations, i.e. the indentation modulus and hardness show only small deviations which lie within the scattering band of the measurements itself. The results within the joint are comparable to the values of the substrate material. In contrast a not fully single crystalline joint shows a decrease in the modulus and an increase in hardness within the inner joint region. Inside the joint region some particle/grains, whose origin remains unclear, lead to a rather high scatter of the results especially for the hardness.
The methods of Nanoindentation and Electron Back Scattering Diffraction have proofed to be valuable tools for evaluating the quality and orientation of the brazing joint. With this method the feasibility of a fully single crystalline repair achieved by Transient Liquid Phase bonding can be proven. This process not only results in a single crystalline joint, but additionally due

to the specific properties of the TLP-process, i.e. the dissolution of the base material in the first stage of the brazing process, the mechanical response of the joint is homogenous and comparable to the base material.

References

[1] Tung, S.K., Lim, L.C. and Lai, M.O.: Solidification Phenomena in Nickel Base Brazes containing Boron and Silicon. Scripta Mat. 34, 1,1996, 763-769

[2] Duvall, D.S., Owczarski, W.A and Paulonis, D.F.: TLP Bonding: A new Method for Joining Heat Resistant Alloys. Welding Journal, 53, 1974: 203-214

[3] Tuah-Poku, I., Dollar, M. and Massalski, T.B.: A study of the Transient Liquid Phase Bonding Process Apploed to a Ag/Cu/Ag Sandwich Joint. Metall. Trans. A. Vol 19A, 1988: 675-686

[4] Nakao, Y., Nishimoto, K., Shinozaki, K. and Kang, C.: Theoretical research on transient liquid insert metal diffusion bonding of nickel base alloys. In: Proceedings Superalloys 1988, edited by S. Reichman, D.N. Duhl, G. Maurer, S. Antolovich and C. Lund, p. 775-783

[5] Wikstrom, N.P., Ojo, O.A. and Chaturvedi, M.C.: Influence of process parameters on microstructure of transient liquid phase bonded Inconel 738LC superally with Amdry DF-3 interlayer, MSE A 417, 1-2, 2006, 299-306

[6] Idowu, O.A., Richards, N.L., Chaturvedi, M.C.:Effect of bonding temperature on isothermal solidification rate during transient liquid phase bonding of Inconel 738LC superalloy. MSE A 397, 2005, 98-112

[7] Oliver, W.C. and Pharr, G.M.: An Improved Technique for Determining Hardness and Elastic Modulus using Load and Displacement Sensing Indentation Experiments. J. Mater. Res. 7, 1992, 1564-1583

[8] Durst, K. and Goeken, M.: Micromechanical characterisation of the influence of rhenium on the mechanical properties in nickel-base superalloys. MSE A 387-389, 2004, 312-316

[9] Goeken, M. and Kempf; M.: Microstructural properties of superalloys investigated by nanoindentations in an atomic force microscope. Acta Mat. 47, 3, 1999, 1043-1052

[10] Wilkinson, A.J. and Hirsch, P.B.: Electron Diffraction Based Techniques in Scanning Electron Microscopy of Bulk Materials. Micron, 28, 4, 1997, 279-308

[11] Durst, K. Franke, O. and Goeken M.: Nanoindentations as a local Probe for the mechanical properties and alloying influences in Nickel-base superalloys and aluminide coatings, In: Proceedings Superalloys 2004,edited by: K.A. Green, T.M. Pollock, H. Harada, T.E. Howson, R.C. Reed, J.J. Schirra, and S. Walston, p.467-476

[12] Bond, S.D. and Martin, J.W.: Surface recrystallization in a single crystal nickel-based superalloy. J. Mat. Sci. 19, 1984, 3867-3872

Part II

Advanced Gas Turbine Materials

Contributed Papers

Oxidation and hot corrosion

LONG-TIME HIGH-TEMPERATURE OXIDATION OF MA 6000 AND PM 3030 ODS SUPERALLOYS

P. Maresca[1], F.Pratesi[1], V.Terzigli[1], M. Innocenti[2], E. Giorni[2]

[1] Department of Mechanics and Industrial Technologies, University of Florence, Italy.
[2] GE Oil & Gas – Nuovo Pignone S.p.A., Florence, Italy.
pasquale.maresca@np.ge.com; franco.pratesi@unifi.it

Abstract

The most efficient method for high-temperature strengthening of metals is to combine the known effect of precipitates in a Ni-base superalloy with that of dispersed particles: ODS superalloys are thus produced, usually by mechanical alloying from a powder mixture of a Ni-base superalloy and a refractory oxide. With a large enough amount of Al and Ti, ODS superalloys are strengthened by coherent γ' precipitates, similar to the ordinary superalloys, and - differently from them - they keep the additional contribution to strength from the dispersed particles when the temperature becomes too high for the γ' precipitates. For two such alloys - MA 6000 TM and PM 3030 TM - the oxidation mechanism has been investigated, and information has been obtained for a limited range of temperatures and times. In this communication, results of isothermal oxidation of MA 6000 TM and PM 3030 TM at higher temperatures and longer times are reported; in particular, selected values are 980, 1100, 1170 °C, and 24, 150, 500, 1000 hours, respectively. All the samples have been analysed with optical microscopy and micro-hardness; the most interesting samples with SEM and EDS microanalysis too. The results obtained are discussed with reference to published oxidation models for these ODS superalloys. Even in the most severe conditions (exposure to 1170 °C for 1000 h) oxidation resistance of these materials was compatible with their use in gas turbines. Differences in oxidation behaviour of the two alloys are reported; indicating that either of them may be preferred in given situations of working temperature and times.

Keywords: Oxidation, high-temperature, ODS, superalloys, MA 6000, PM 3030

1. Introduction

The family of oxide dispersion strengthened alloys (ODS) was developed to improve mechanical properties above the solubilisation temperature of the γ' precipitates. The excellent properties of ODS alloys are due to the very fine dispersion of stable, incoherent oxide particles - typically yttrium oxide - formed by mechanical alloying. These particles act as barriers to the movement of dislocations. Typically this effect becomes dominant above 1000 °C; as a consequence, ODS alloys are at present considered to be the best alloys for high-temperature applications.
ODS materials show good oxidation properties too, thanks to the formation of adherent protective layers of Al_2O_3 and/or Cr_2O_3: their adherence, in fact, is improved by the presence of yttria. Moreover, the presence of Y_2O_3 dispersed particles produces a change in the mechanism of oxide scale formation. Generally oxide scale growth takes place by simultaneous inward diffusion of oxygen and outward diffusion of metal cations, so that the oxide layer grows both at the alloy-scale interface and on the external surface of the scale. The presence of yttria induces a reduction of the outward diffusion of cations and consequently scale adherence is improved compared to the conventional (non-ODS) alloys of the same basic composition [1].

To investigate the oxidation properties and to find the upper temperature limit for using commercial ODS alloys, a series of static oxidation tests has been carried out on MA 6000 and PM 3030 alloys. The oxidation mechanism of these two alloys has already been investigated by Angermann [2] and by Guttman [3] in a limited range of temperatures and times. The aim of this work is to extend previous results up to 1170 °C and 1000 h, in order to ascertain oxidation behaviour and its mechanism.

2. Experimental procedure

The materials under investigation are MA 6000 (INCO Alloys International, Ltd.) and PM 3030 (Plansee AG). Their nominal compositions are listed in Table 1.

	Ni	Cr	Al	W	Ti	Mo	Ta	C	B	Zr	Y_2O_3
MA 6000	Bal	15	4.5	4	2.5	2	2	0.05	0.01	0.1	1.1
PM 3030	Bal	17	6	3.2		2	2	0.05	0.01	0.1	1.1

Table 1: Nominal composition of MA 6000 and PM 3030

The specimens were obtained from cylindrical bars of 34 mm diameter. A series of disks of 2 mm thickness was cut and then divided into four equal parts (Fig. 1).

Figure 1: Specimen of MA 6000

Oxidation tests were performed in air at three different temperatures: 980 °C, 1100 °C, and 1170 °C. For each temperature, the materials were exposed for three different times: 24 h, 150 h, and 1000 h. In the test at 1170 °C a fourth specimen was exposed for 500 h. The oxidation test conditions are summarised in Table 2.

Temperature (°C)	Time (h)			
980	24	150	1000	
1100	24	150	1000	
1170	24	150	500	1000

Table 2: Oxidation tests

After each test the specimens were observed by optical microscopy. The most interesting samples were also analysed with SEM and their chemical composition was identified by EDS X-rays analysis.

3. Results and discussion

3.1 MA 6000

In the previous studies [2, 3], the oxidation mechanism of MA 6000 was described and discussed. The main characteristic feature for MA 6000 is the formation of an external scale essentially composed of Cr_2O_3 and a substrate of Al_2O_3 separated by a Ni-rich thin layer. Fig. 2 shows the specimen after the 1000 h 980 °C oxidation test. Fig. 3, 4, and 5 respectively show the chemical compositions of the three layers mentioned.

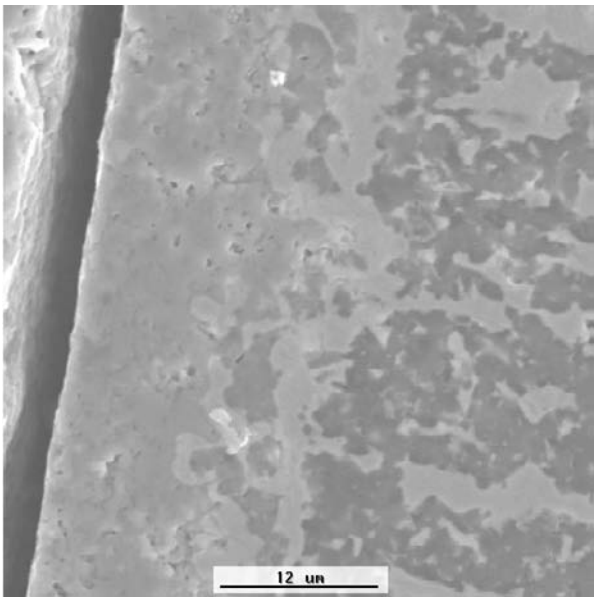

Figure 2: SEM image (cross-section) of MA 6000 980 °C 1000 h

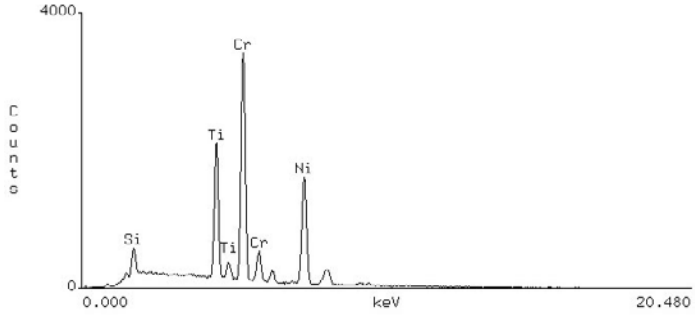

Figure 3: External oxide scale (EDS-spectrum)

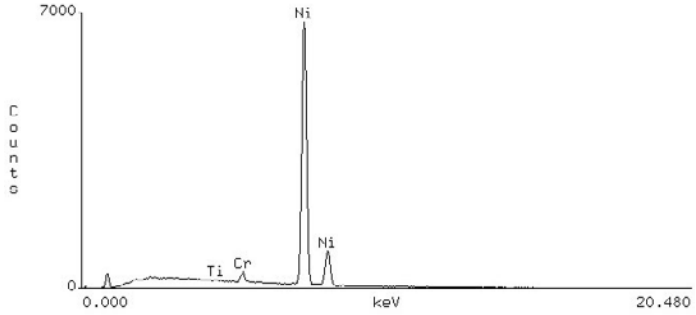

Figure 4: Intermediate Ni layer (EDS-spectrum)

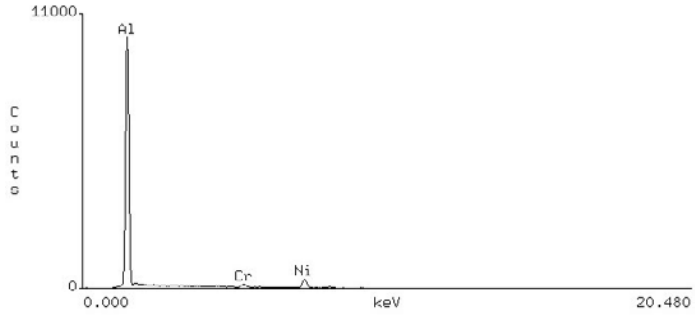

Figure 5: Internal alumina layer (EDS-spectrum)

The basic mechanism of oxidation is well known in this case, so that the oxidation tests can be related to the influence of temperature on oxide growth. To evaluate the influence of temperature it is useful to analyse the very first oxidation stages. For the 980 °C oxidation test, the first

oxidised areas are visible after 150 h, as shown in Fig. 6(a), while for the 1100 °C test Fig. 6(b) shows Al_2O_3 particles after only 24 h.

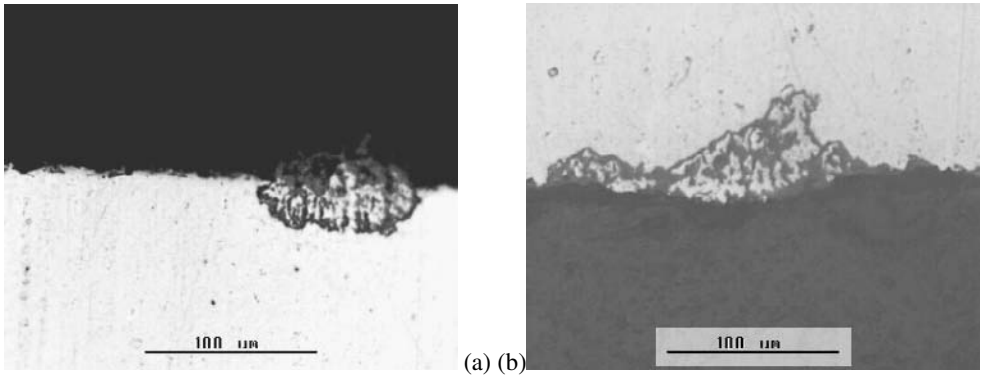

(a) (b)

Figure 6: Comparison between oxidation area after 150 h at 980 °C (a) and oxidation area after 24 h at 1100 °C (b)

At the lower temperature, the final stage of oxidation after 1000 h is the one described before in which the external layer consists of Cr_2O_3, the substrate of Al_2O_3 and with a thin Ni layer placed between them. At higher temperature there is a change in oxide morphology, due to Cr_2O_3 volatilisation. In fact the following reaction can happen above 1000°C:

$$Cr_2O_3\,(s) + \frac{3}{2}\,O_2\,(g) = 2\,CrO_3\,(g)$$

The Cr_2O_3 scale decomposes and delaminates, thus exposing the alumina substrate. Fig. 7 shows how this effect lays bare the primary oxidation areas completely composed of Al_2O_3.

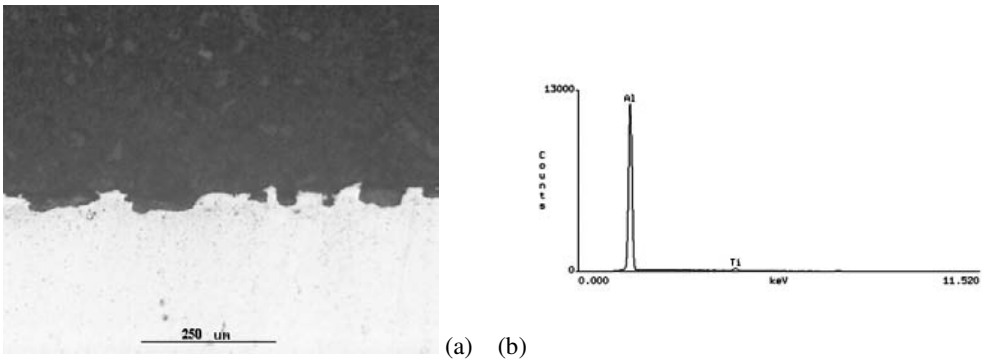

(a) (b)

Figure 7: Cross-section of MA 6000 after 1000 h at 1170 °C (a) and chemical composition of the scale measured by EDS (b)

From this analysis we can see that the Al_2O_3 substrate effectively ensures surface protection in high-temperature applications.

3.2 PM 3030

To understand the oxidation mechanism of PM 3030, it is useful to refer to the lower temperature test for the range of times considered. The effect on the oxidation mechanism of using a higher temperature is just an increase in the rate of oxide growth [2].

The most interesting feature of PM 3030 is the formation of a thin Al_2O_3 layer due to the higher concentration of Al in the matrix, with respect to MA 6000, so that Cr does not take part in the oxidation process.

After 24 h at 980 °C no oxide intrusions were formed. After 150 h, Fig. 8 shows the formation of the first oxidised intrusions. They are composed principally of Al_2O_3 and less of Cr_2O_3 while the sub-scale regions are low in Al and Cr as shown in Fig. 9 and 10.

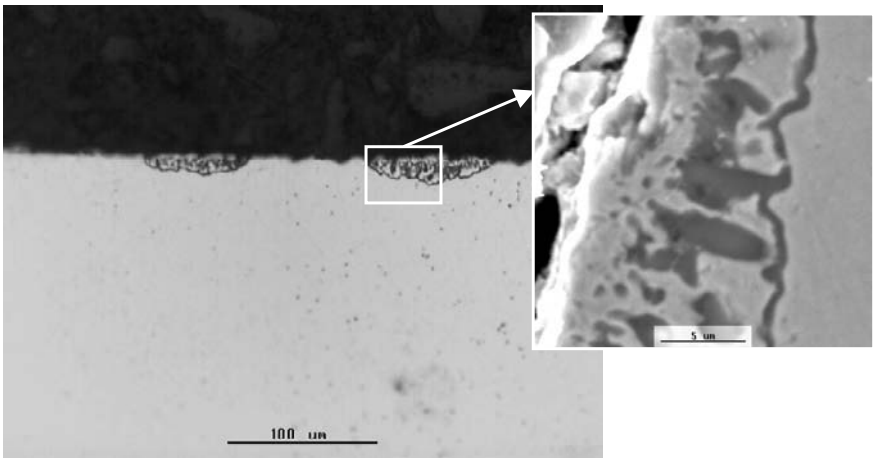

Figure 8: First oxidised areas in PM 3030 after 150 h at 980 °C

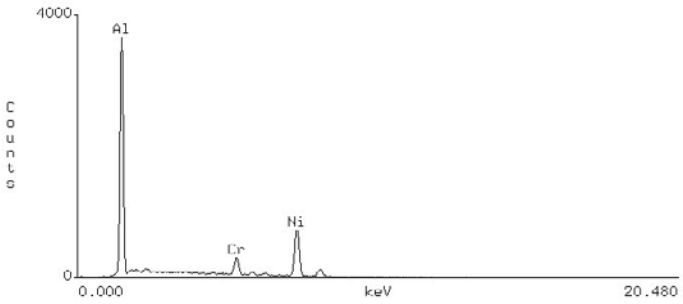

Figure 9: Oxide chemical composition of PM 3030 after 150 h oxidation at 980 °C in air

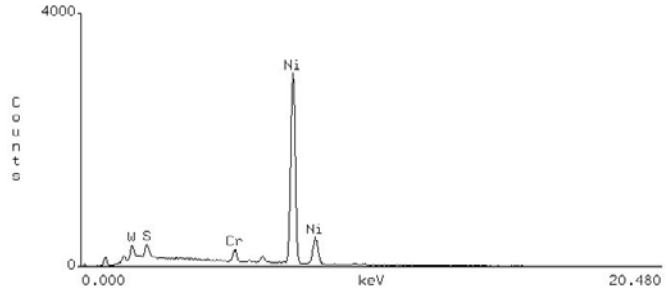

Figure 10: Alloy chemical composition beneath the oxide intrusions

After 1000h at 980°C the surface is completely covered by a thick scale of Al_2O_3, as Fig. 11 shows.

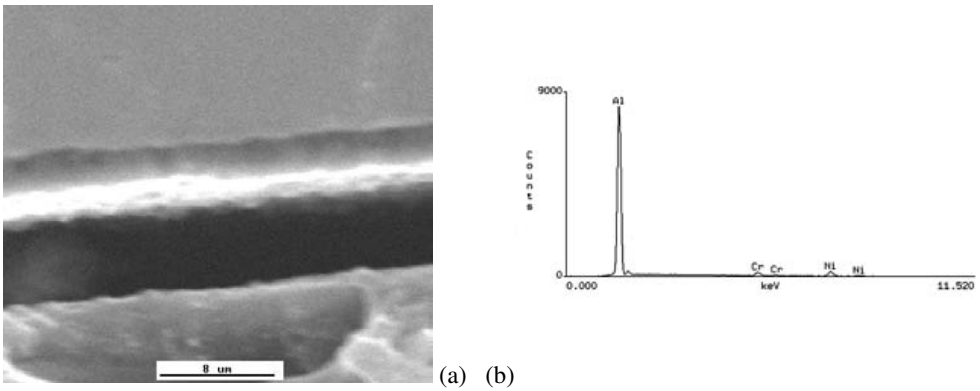

(a) (b)

Figure 11: PM 3030, 980 °C 1000 h air oxidation. (a) SEM cross-section (b) EDS-spectrum of the scale

The previous study [2] does not give any information about the oxide scale adherence for long-time high-temperature oxidation. In MA 6000, Al_2O_3 acts as a protective barrier under the external Cr_2O_3 scale at any time when high temperature induces volatilisation and detachment of Cr_2O_3. To understand the behaviour of the Al_2O_3 scale it is useful to investigate the 1170 °C oxidation after that at 1000 °C. The analysis reveals that the external alloy surface is almost entirely covered by the Al_2O_3 scale. In a few points the scale is a mixture of chromium and aluminium oxides, with a compact layer of alumina formed underneath as shown in Fig. 12.

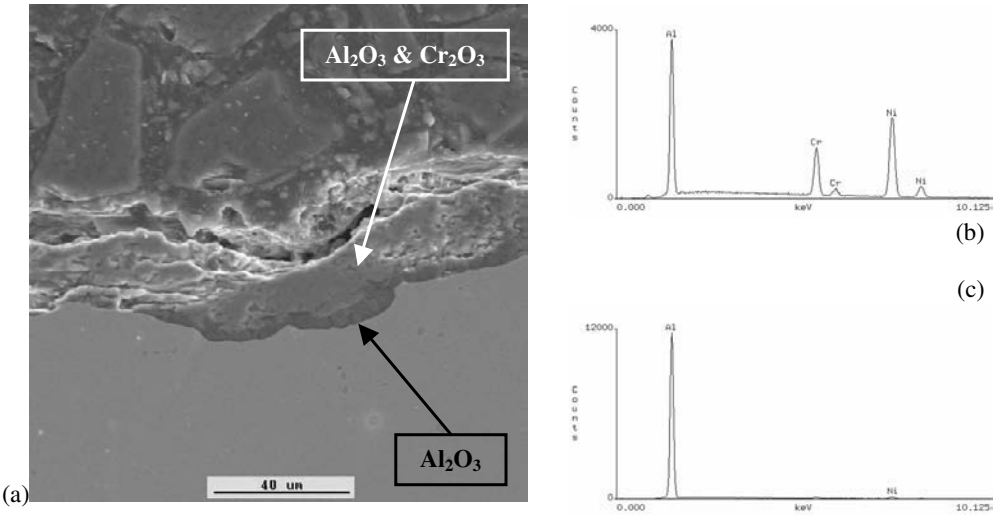

Figure 12: Oxidation of PM 3030 1170 °C 1000 h: (a) SEM cross-section, (b) (c) EDS spectra of the areas marked in (a)

It is noteworthy that in the whole specimen surface there is no evidence of any catastrophic oxidation. Results show that Al_2O_3 scale is adherent almost everywhere or, in the case of detaching, there is a rapid formation of new oxide, in spite of the low diffusivity of aluminium in a nickel matrix.

Comparing results obtained in our 1170 °C 1000 h oxidation test with Angermann's 1150 °C 200 h test [2], we see a lower amount of chromium oxide. This effect may be imputed to oxide volatilisation. The Cr_2O_3 evaporation happens above 1000 °C and depends on temperature and time. Fig. 13 shows the evolution of chromium oxide for different temperatures [4].

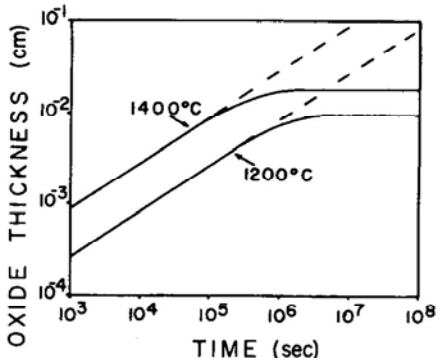

Figure 13: Chromium oxide evolution

In the initial stage oxide growth is faster than evaporation so that oxide thickness increases. As Fig. 13 shows, at 1200 °C equilibrium is reached after 280 h so that in Angermann's test performed at 1150 °C the Cr_2O_3 scale growth is apparently faster than evaporation. In our tests we see a lower amount of Cr_2O_3 because Al_2O_3 acts as a barrier to Cr diffusion, protecting the matrix from serious Cr depletion.

3.3 Comparison

The oxidation tests confirm a suitable behaviour of both ODS alloys, and from the analysis there is no evidence of any catastrophic damage.

At low temperature, the differences in the oxidation mechanism entail a greater oxidation for MA 6000 than for PM 3030. This effect is due to the higher concentration of Al in PM 3030: aluminium, in fact, inhibits chromium oxidation. In PM 3030 a thin layer of Al_2O_3 protects the material from internal oxidation; in MA 6000 the early oxidation of Cr does not prevent the internal oxidation of Al so that a double layer of oxide scale is formed. For this range of temperatures PM 3030 and generally high-Al alloys are preferable. Fig. 14 shows the oxide scale of MA 6000 after 150h at 980 °C formed by external oxidation of Cr and internal oxidation of Al. For the same test conditions, PM 3030 does not show any evidence of Cr oxidation, because the external Al_2O_3 layer acts as a barrier to oxygen diffusion.

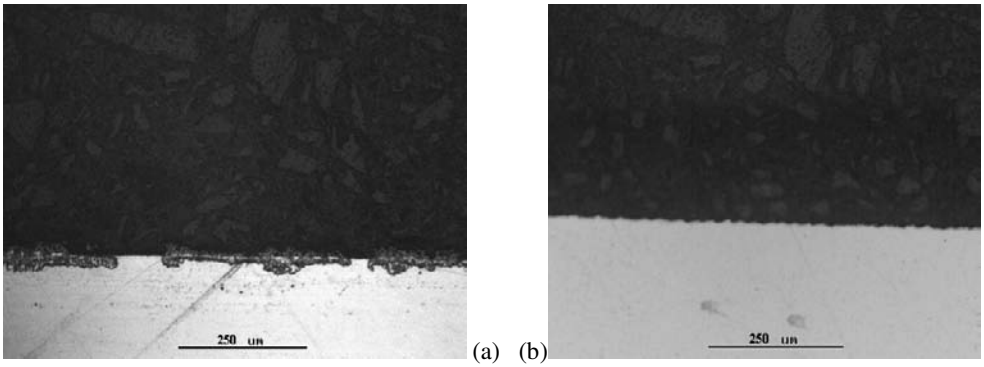

(a) (b)

Figure 14: MA 6000 (a) and PM 3030 (b) after 980 °C 150 h test

For higher temperatures and longer exposures, the same oxidation mechanism leads to different evaluation of the oxidation resistant properties of the two alloys. For PM 3030 at high temperature alumina scale is not as adherent as at lower temperatures so that it gets detached and cannot protect the alloy matrix although a new scale is soon re-formed. In MA 6000 the double-layer scale has a significant role in protecting the alloy. Cr_2O_3 scale is soon created at the external surface while an adherent layer of alumina grows underneath. Just after volatilisation or delamination of Cr_2O_3 scale Al_2O_3 layer starts to play its protective role assuring a better oxidation resistance of the alloy. Fig. 15 shows the oxide scale thickness of the two alloys after 1000 h oxidation test at 1170 °C.

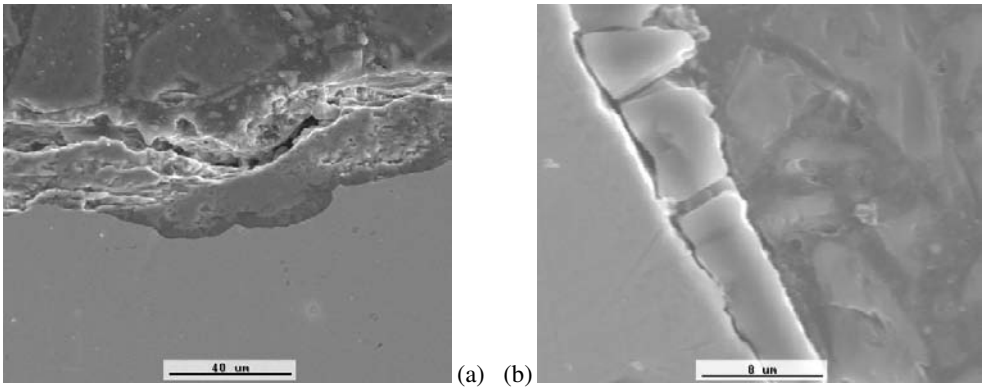

(a) (b)

Figure 15: comparison between oxide scale of PM 3030 (a) and MA 6000 (b) after 1170 °C 1000 h oxidation test

4. Conclusion

Oxidation tests were performed on MA 6000 and PM 3030 alloys to understand their oxidation mechanisms and to compare their oxidation resistance in the 980 °C – 1170 °C range of temperature and for times up to 1000 h. The whole series of tests shows that both alloys maintain good properties up to the maximum temperature tested. The 980 °C tests show that PM 3030 is better than MA 6000. Thanks to high Al concentration PM 3030 does not show significant oxidation, while on MA 6000 a double layer of oxide – external Cr_2O_3 and internal Al_2O_3 – grows noticeably. From 1170 °C tests show however that MA 6000 is to be preferred to PM 3030. The adherent double layer scale on MA 6000 in fact acts as a barrier to oxygen penetration, while in PM 3030 the Al_2O_3 scale is prone to delamination. The comparison between the two alloys investigated has shown different properties derived from different oxidation mechanisms. The presence on the surface of one or two oxide layers gives best results in different ranges of time-temperature exposure. Of course this result is valid for the two alloys, but it can reasonably be extended to other alloys with a similar composition.

References

[1] S. Weinbruch, A. Anastassiadis, H.M. Ortner, H.P. Martinz, *On the mechanism of high-temperature oxidation of ODS superalloys: significance of yttrium depletion within the oxide scale*. Oxidation of Metals Vol. 51, No. 1/2 (1999), 111-128.

[2] H.-H. Angermann, K. Nishi, Y. Aono, M. Inagaki, H. Kodama, *Evolution of oxides on Ni-base ODS superalloys*. Oxidation of Metals Vol. 48, No. 1/2 (1997), 1-39.

[3] V. Guttmann, J.L. Gonzalez-Carrasco, H. Fattori, *Oxidation behaviour of ODS alloy MA 6000.* Oxidation of Metals Vol. 51 No. 1/2 (1999), 159-180.

[4] C. Sims, N. Stoloff, W. Hagel, *Superalloys II - High-temperature materials for aerospace and industrial power.* J. Wiley & Sons, New York, 1987.

OXIDATION RESISTANCE OF SILICON-CONTAINING 5TH GENERATION NICKEL-BASE SINGLE CRYSTAL SUPERALLOYS

Atsushi Sato[1, 2], Hiroshi Harada[2], Jestine Ang[2, 3], Koizumi Yutaka[2], Kobayashi Toshiharu[2], Kyoko Kawagishi[2] and Hachiro Imai[1,2]

[1] Department of Materials Science and Engineering, Shibaura Institute of Technology, Minato, Tokyo 108-0023, Japan
[2] National Institute for Materials Science, 1-2-1 Sengen, Tsukuba-city, Ibaraki 305-0047, Japan
[3] Department of Materials Engineering, The University of British Columbia, Vancouver, V6T 1Z4, Canada

Abstract

A strategy was developed to improve the oxidation resistance of a 5th generation Ni-base single crystal (SC) superalloy, TMS-173, by adding Si to its composition. TMS-173 possesses unrivaled high temperature mechanical properties due to its high Re and Ru content. On the other hand, the addition of such elements considerably degrades the oxidation resistance, and effective measures to prevent this degradation are required.

1.0 - 1.9wt.% Si was added to TMS-173, and Ta content was substituted out in order to minimize the precipitation of topologically close packed (TCP) phases. The oxidation resistances of these Si-containing superalloys were evaluated through a 50-cycle oxidation test at 1100°C. Cross-sections of oxidized samples were analyzed by SEM and EDX.

Alloys of the TMS-173 +Si -Ta system showed excellent oxidation resistance that was much better than that of Rene'N5. Remarkably, an exclusive Al_2O_3 layer was formed on the 1.9wt.%Si alloy.

Keywords: 5th generation Ni-base superalloys, Si, oxidation, high temperature properties

Introduction

The superior high temperature mechanical properties of Ni-base superalloys make them the best candidates for use in jet engines and industrial gas turbines. As higher operating temperatures are required to increase turbine output and efficiency, improvements in the high temperature strength of superalloys are being actively sought.

Recently, it has been found that the addition of platinum group metals, such as Ru, can control the precipitation of Topologically Close Packed (TCP) phases effectively [1-2]. Their addition allows for an increase in solid solution strengthening elements, such as Re, that can be incorporated during the design of the latest Ni-base superalloys [3-5].

Conversely, this increase in Ru and Re content decreases the cyclic oxidation resistance of an alloy[6]. Additionally, Cr_2O_3, the typical protective oxide formed by earlier generation superalloys designed for use of up to 900ºC, would further oxidize to CrO_3 at current substrate temperatures of 1100ºC. CrO_3 has a large vapor pressure [7], and its vaporization would noticeably decrease the long-term oxidation resistance of an alloy. At present, superalloys

containing Ru and Re have rather poor oxidation resistances. When exposed at 1100ºC, spallation-prone Ni oxide and Ni-rich spinels are formed instead of a protective oxide layer. These superalloys rely on protective bond coats to provide protection against oxidation; however, catastrophic failure of the underlying component would be imminent if the bond coat were to fail. Hence there is a need to design the latest superalloys with careful consideration to their resultant oxidation resistance.

Si is known to form the $L1_2$ intermetallic phase with Ni [8]. Its oxide, SiO_2, has been shown to effectively serve as a protective oxide layer for Ni-alloys [9]. This study was carried out to explore the effects of Si addition on has on the oxidation resistance and microstructure of 5th generation Ni-base superalloys.

First approach of Si-containing superalloys

Alloy design

A 5th generation Ni-base SC superalloy TMS-173, which contains 6.9 wt.% Re and 5.0 wt.%Ru, was used as the base alloy. By adding 1.0, 1.4 and 1.9 wt.% Si to TMS-173, three other superalloys were cast. However, TMS-173 contains solid solution strengthening elements at levels that are well above the solubility limit imposed by the solvus of the γ/γ' two-phase region, and the sole addition of Si would unavoidably lead to TCP phase precipitation. In order to minimize this precipitation, Ta was substituted out accordingly. Si forms Ni_3Si with Ni [8], and this led us to suspect that Si might preferentially partition to the Al site in the γ' phase. To facilitate Si addition with minimal solid solution strengthening element loss, the strongest γ'-partitioning element, Ta [10], was removed from the alloy. The Solubility Index (SI) of all Si-containing alloys in this paper were designed to be equivalent to that of TMS-173. The SI concept [11-12] can be described as:

$SI=\Sigma (X_i / X_{i, \mathrm{lim}}) (i=1 \rightarrow n)$

where X_i is the concentration (at.%) of element i in the γ' phase of a Ni-Al-i ternary system, and $X_{i, \mathrm{lim}}$ is the concentration (at.%) of element i in the γ' phase at its solubility limit. Element i represents any substitutional element, such as Cr, Mo, W and Ta, that can occupy the Al site in the γ' phase. The substitution ratio between Ta and Si was determined to equal the ratio between the solubility limit of Ta (at.%) in the γ' phase of Ni-Al-Ta system at 1100ºC, and the solubility limit of Si (at.%) in the γ' phase of Ni-Al-Si system at 1100ºC. As the partitioning behavior of Si is unknown, it was assumed to be equivalent to that of Ta in this alloy design. Alloy compositions are shown in Table 1 and their respective heat treatment conditions are shown in Table 2. It should be noted that TMS-208 has been included in all illustrations, but will be discussed in a last section. TMS-208 is the alloy with best balanced properties of oxidation resistance and creep strength obtained in this study.

Table1 Nominal compositions (wt.%, Ni-bal.) of the superalloys designed in this study.

	Co	Cr	Mo	W	Al	Ta	Hf	Re	Ru	Si
TMS-173	5.6	2.8	2.8	5.6	5.6	5.6	0.1	6.9	5.0	0.0
+1.0Si	5.7	2.8	2.8	5.7	5.7	2.8	0.1	7.0	5.1	1.0
+1.4Si	5.8	2.9	2.9	5.8	5.8	1.4	0.1	7.1	5.2	1.4
+1.9Si	5.8	2.9	2.9	5.8	5.8	0.0	0.1	7.2	5.2	1.9
TMS-208	6.5	3.3	2.4	5.3	5.3	2.4	0.1	7.1	5.9	1.0

Table2 Heat treatment conditions of the superalloys designed in this study.

	Solution treatment	Aging 1	Aging 2
TMS-173	1300ºC1h→1330 ºC10hAC	1100 ºC4hAC	870 ºC20hAC
+1.0Si	1270ºC1h→1300 ºC10hAC	-	-
+1.4Si	1270ºC1h→1300 ºC10hAC	-	-
+1.9Si	1230ºC1h→1260 ºC10hAC	1100 ºC4hAC	870 ºC20hAC
TMS-208	1270ºC1h→1300 ºC10hAC	1100 ºC4hAC	870 ºC20hAC

Experimental procedure

Oxidation test

5 mm thick and 10 mm diameter discs were sliced from heat-treated SC bars of each alloy. They were mechanically polished up to SiC#600, and rinsed with ethanol. A 50-cycle oxidation test was performed, with each cycle lasting 1h at 1100ºC. They were air-cooled after each cycle, and the weight change per unit surface area (mg/cm^2) were measured. The cross-sections of the oxidized samples were analyzed by Scanning Electron Microscope (SEM) equipped with Energy Dispersive X-ray Spectroscopy (EDX). The oxides were also identified by X-ray Diffractometry (XRD).

γ and γ' phases in Si-containing superalloys

As the particle sizes of the γ and γ' phases in heat-treated SC superalloys are too small for compositional analysis, recrystallization was needed to coarsen the alloy's microstructure. 5 mm thick SC specimens of Si-containing SC alloys were highly work-hardened to increase distortion energy, and immediately heated to 1240ºC to induce recrystallization. To obtain the equilibrium compositions, the samples were exposed at several temperatures for different exposure times. In this paper, only the results from 900ºC/1500h and 1100ºC/500h will be shown. Compositional analysis was performed by SEM-EDX.

Results and discussion

Cyclic oxidation results

Specimen weight changes incurred during cyclic oxidation are shown in Fig.1. Increasing Si content decreases specimen mass change dramatically, with the +1.9Si alloy showing the least weight change of +0.3 mg/cm^2 after 50 cycles, as compared with -25.5 mg/cm^2 of the original alloy, TMS-173.

Fig.2 shows the cross-sections of oxide structures formed on Si-containing and

non-Si-containing specimens after a 50-cycle exposure. TMS-173, the original non-Si-containing alloy, formed a 20μm thick NiO layer, together with voluminous Ni-rich spinels (Fig.2 (a)); these Ni-rich oxides are prone to spallation during thermal cycling. TMS-173's inability to form a Al_2O_3 layer in the initial stages of oxidation allowed Ni to diffuse out from matrix to form these non-protective oxides.

In contrast, Si-containing alloys did not have a large increase in weight (Fig.1), and managed to form thin oxide layers instead of thick NiO layers (Fig.2 (b-d)). In the alloys with lower Si content (1.0 & 1.4 wt.%), a 2μm Al_2O_3 layer was found with an overlying 3μm thick $NiAl_2O_4$ layer, along with intermittent small NiO particles. In the 1.9wt.%Si alloy, a fairly thin 3-4μm Al_2O_3 layer formed exclusively. From these results, it is apparent that Si can keep both NiO and $NiAl_2O_4$ formation in check. Furthermore, since Al_2O_3 thickness is seen to increase with increasing Si content (Fig.2), Si seems to promote the Al_2O_3 formation. Evidently, a low Si content (1wt.% ~) in a Ni-base superalloy can dramatically improve its oxidation resistance.

The EDX analysis of the cross-sections of Si-containing and non-Si-containing alloys are summarized in Fig.3. With the addition of Si, the diffusion of Ni from the matrix to the oxide surface, together with the diffusion of oxygen from the surroundings into the matrix, is seen to be controlled (Fig.3 (a)). As well, Si addition increases the Al content in the innermost oxide layer that lies at the oxide/matrix interface (Fig.3 (b)). From these results, it is clear that Si induces the formation of Al_2O_3 layer, and this Al_2O_3 layer works as a diffusion barrier against Ni and oxygen transport.

Si promotes the formation of Al_2O_3. Si distributed uniformly in Si-containing alloys. A means of determining Al_2O_3 stability is to compare the equilibrium oxygen pressure of non-Si-containing alloy ($P_{O2,\ TMS\text{-}173}$), with that of a Si-containing alloy ($P_{O2,\ +1.9Si\ alloy}$). In this case, the chemical equation becomes as follows:

$(4/3)Al_{(TMS\text{-}173)} + O_2 \rightarrow (2/3)Al_2O_3$

$(4/3)Al_{(+1.9Si\ alloy)} + O_2 \rightarrow (2/3)Al_2O_3$

When the oxidation of an element in a multi-component system can be described as $(2x/y)M + O_2 \rightarrow (2/y)\ M_xO_y$, then

$K_T = (a^{2/y}_{MxOy} / (a^{2x/y}_{M} \times P_{O2}))$ (Eq.1)

where a_{MxOy} is the activity of the oxide of element M, and a_M is the activity of element M in a Ni-base superalloy. By obtaining K_T at 1100ºC from a thermodynamic database [13], and using the value of a_M calculated by ThermoCalc^{TM}, the equilibrium P_{O2} can be calculated. $P_{O2,\ TMS\text{-}173}$ to form Al_2O_3 is 1.74×10^{-33} Pa, and $P_{O2,\ +1.9Si\ alloy}$ to form Al_2O_3 was almost one magnitude less, at 5.01×10^{-34} Pa. The addition of Si to an alloy significantly decreases the equilibrium P_{O2} required for Al_2O_3 formation, causing the product in Eq.1 (Al_2O_3) to be even more thermodynamically favoured, resulting in its increased stability.

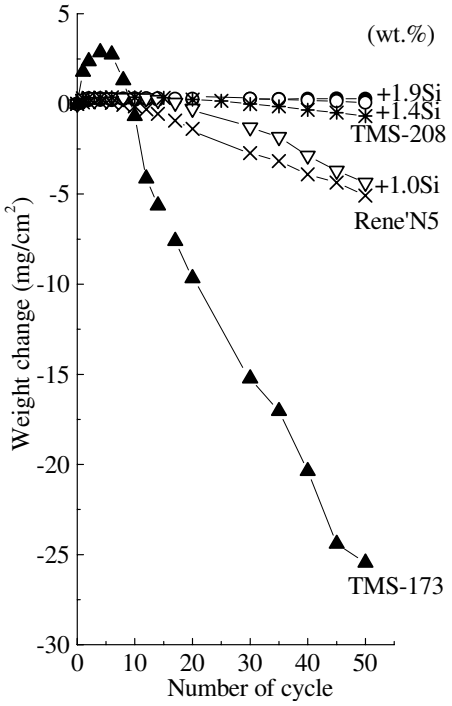

Fig.1 Cyclic oxidation profiles of various silicon-containing alloys.

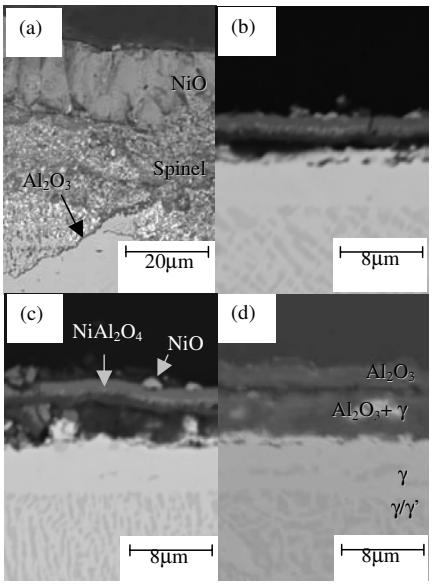

Fig.2 Micrographs of alloy cross-sections after 50 cycles at 1100°C (a)TMS-173, (b)+1.0Si alloy, (c)+1.4Si alloy and (d)+1.9Si alloy.

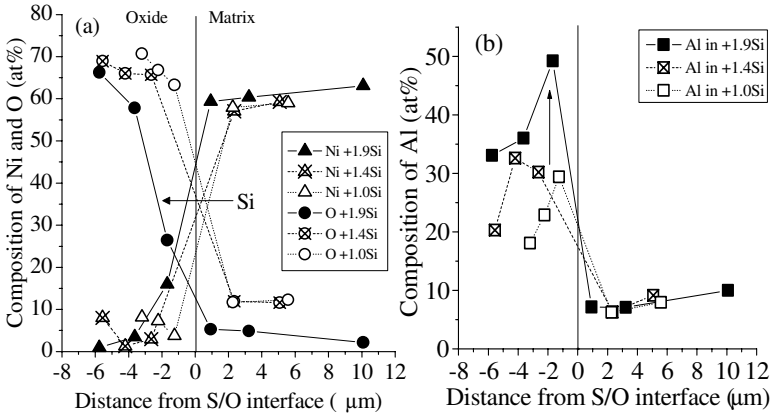

Fig.3 EDX chemical composition profiles of the cross-sections of various Si-containing alloys. (The substrate/oxide interface has been set as 0μm to serve as the reference point)

Although Si was added to the composition of TMS-173, the formation of SiO_2 as a protective oxide was not observed; instead, exclusive Al_2O_3 formation was induced. This can be explained by comparing the standard free energies of formation for pure Al_2O_3 and pure SiO_2. The standard free energy of formation of an oxide is described as:

$$\Delta G=\Delta G_0+RT\ \ln K_T$$

where, ΔG_0 is the standard free energy of formation for 1 mol of O_2, R is the gas constant, T is the absolute temperature, and K_T is the equilibrium coefficient. The equations for Al_2O_3 and SiO_2 formation are as follows:

$$(4/3)Al_{(+1.9Si\ alloy)}+ O_2 \rightarrow (2/3)Al_2O_3$$

$$Si_{(+1.9Si\ alloy)}+ O_2 \rightarrow SiO_2$$

K_T can be calculated from Eq.1 by assuming P_{O2} to be 23% of atmospheric pressure. The value of ΔG_0 is obtained from thermodynamic data [13] at 1100ºC. Reactant activities (Al and Si) were obtained the calculated result of Thermo-Calc™. The standard free energies of Al_2O_3 and SiO_2 formation were thus calculated to be -566.31 kJ and -473.40 kJ respectively. From this, it is suspected that the formation of Al_2O_3 from +1.9wt.%Si alloy was more stable than that of SiO_2.

Since Ta was removed to incorporate Si; hence, any findings in this paper should be interpreted as a result of the combined effects of Si addition and Ta removal. It has been reported that Ta removal degrades the oxidation resistances of 4th generation Ni-base superalloys [6]. This indicates that Si's positive contribution to oxidation resistance outweighs the negative effects of Ta removal.

Microstructure

The microstructures after heat-treatment are shown in Fig.4. TMS-173 has an aligned, coherent γ/γ' structure (Fig.4 (a)) that is typical of advanced Ni-base superalloys. The +1.9Si alloy has a semi-coherent structure (Fig.4 (b)), and precipitates of TCP phases can be seen. One startling fact about the microstructure of this +1.9Si alloy is that it also has β-phase precipitates in the inter-dendritic regions (Fig.5), which has not been seen advanced superalloys. It is suspected that Si addition encouraged β phase formation.

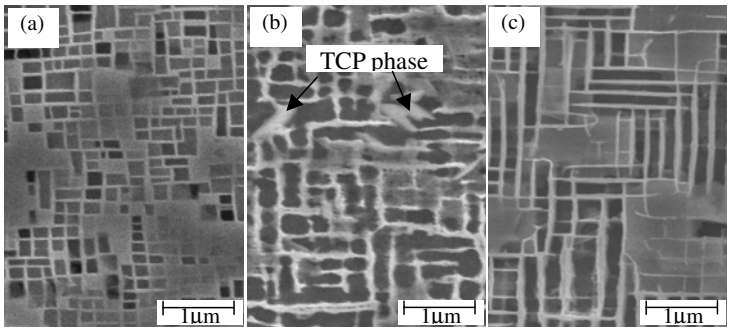

Fig.4 Microstructures of the heat treated alloys: a)TMS-173, b) +1.9Si alloy, c)

+1.9Si alloy had a semi-coherent microstructure even after heat-treatment. In this study, Ta was substituted to Si. The atomic radius of Ta is larger than that of Ni, and also Ta partition to γ'phase strongly. By removing Ta, the lattice misfit δ between γ and γ' phase in the +1.9Si alloy become more negative than that of TMS-173.

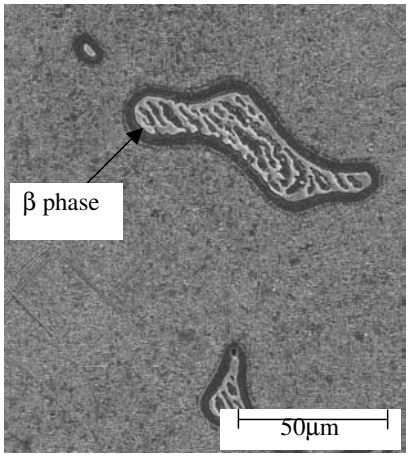

Fig.5 β phase precipitated in heat-treated +1.9Si alloy around inter-dendritic regions.

The initial efforts to control the solubility limit of these new Si-containing superalloys were quite effective, although some precipitation of TCP phases still occurred. This can be explained using the concept of interaction energies between elements [10]. As Ta strongly partitions to γ' preferentially, the Ni-Ta interaction energy is considered to be lowest. W, Re and Cr are known to partition to the γ' phase in Ta-containing superalloys slightly. With the removal of Ta, the interaction energies of Ni-W, Ni-Re and Ni-Cr all decrease; thus causing W, Re and Cr to partition to γ' phase more strongly, which increases the solubility index of γ' in these Si-containing superalloys, resulting in the precipitation of TCP phases.

The equilibrium compositions of γ and γ' in Si-containing alloys at several temperatures are listed in Table 3. The partitioning coefficient K_i of element *i* in Si-containing alloy is calculated from Table 3. K_i is defined as:

$K_i = X_{i,\gamma} / X_{i,\gamma'}$

where $X_{i,\gamma}$ is the concentration of element *i* in γ phase (at.%), and $X_{i,\gamma'}$ is the concentration of element *i* in γ' phase (at.%). The partitioning coefficient of Si between 900ºC and 1100ºC was constant, at about 0.7, meaning that Si slightly partitions to the γ' phase.

Table3 Chemical compositions (wt.% Ni-bal) of γ/γ' phase in silicon-containing superalloys.

		Temp. (ºC)	Time (h)	Co	Cr	Mo	W	Al	Ta	Re	Ru	Si	Analysis methods
+1.9Si	γ	1100	500	7.7	4.5	3.6	5.3	4.0	-	8.1	7.7	1.7	EPMA
				7.6	4.2	3.8	6.6	3.3	-	8.7	7.5	1.7	EDX
+1.9Si	γ'	1100	500	5.2	1.7	1.9	4.7	7.8	-	1.7	4.0	2.3	EPMA
				5.1	1.6	2.0	6.8	6.7	-	1.9	3.9	2.0	EDX
+1.9Si	γ	900	1500	9.3	5.5	4.3	5.6	1.4	-	10.0	7.7	1.5	EDX
+1.9Si	γ'	900	1500	5.1	1.8	2.4	7.5	6.0	-	1.3	2.8	2.0	EDX

Many changes in microstructure, together with the absence of Ta, led to the poorer creep properties of the +1.9Si alloy: precipitation of the β-phase in inter-dendritic region, precipitation

of TCP phases in dendrite regions, and an increase in γ' volume fraction. Too many factors came into play to allow for a proper evaluation of the effects of Si; thus, another Si-containing ni-base superalloy, TMS-208, was designed with more consideration to its microstructure, as described in the following section.

Microstructure-controlled Si-containing superalloys

Alloy design

Our newest silicon-containing alloy, TMS-208, was engineered by integrating the information gathered from the Si groundwork experiments as described above, with the original superalloy, TMS-173. The $\gamma_{TMS\text{-}208}$ composition was derived from averaging the compositions of $\gamma_{TMS\text{-}173}$ and $\gamma_{1.9Si\ alloy}$; likewise, the $\gamma'_{TMS\text{-}208}$ composition was derived from averaging the compositions of $\gamma'_{TMS\text{-}173}$ and $\gamma'_{1.9Si\ alloy}$. The γ and γ' compositions of the +1.9Si alloy at 1100ºC were obtained through SEM/EDX analysis, and that of TMS-173 at 1100ºC were obtained from the alloy design program (ADP) at NIMS.

The resultant composition of TMS-208 and its heat treatment conditions are shown in Table 1 and Table 2 respectively. TMS-208 is a 1wt.%Si superalloy, and this Si content was chosen to prevent β-phase precipitation; previous experiments showed that alloys with higher Si content (1.4 and 1.9wt.%) precipitate the brittle β-phase. The γ' volume fraction of TMS-208 is designed to be 50% at 1100ºC. The γ and γ' of the alloys used to obtain the composition of TMS-208 were in thermodynamic equilibrium with all precipitates that were present in the said alloys. Since γ and γ' were co-existing with the TCP and/or β precipitates, this indicates that the SLs of all elements in γ' are at their maximum possible values.

As explained in a previous paper [5], a superalloy with high refractory element content, when cast, would inevitably have refractory segregation in its dendrite cores. This results in the SI of these regions to be exceeded, which induces TCP precipitation. For this reason, in the design of TMS-208, a factor of safety was introduced by reducing its SI by 0.05 through a 0.5wt.% reduction of Mo content.

With this alloy design strategy, the precipitation of β-phase and TCP phases is eliminated, and the γ' volume fraction is controlled. Accurate evaluation of the high temperature properties of this Si-containing Ni-base superalloy could thus be carried out.

Results and Discussion

TMS-208 has an heavily isotropically rafted microstructure after heat treatment (**Fig**.4 (c)) that is typical of an alloy with a very large lattice misfit between γ and γ'; in fact, it has a larger lattice misfit than TMS-173. No precipitates of TCP phases were observed in this alloy.

TMS-208 is the first step taken towards optimizing the mechanical properties of a Si-containing Ni-base superalloy, and not all factors have been taken into account while designing it. This novel strategy of introducing Si to the composition of a Ni-base superalloy has produced very

promising results. By merely exercising preliminary control of the alloy's microstructure, high temperature properties and oxidation resistances were satisfied. In near future, Si-containing superalloys will be designed with optimal lattice misfit and excellent oxidation resistance.

Conclusion

Si was incorporated into the composition of a 5th generation Ni-base superalloy, TMS-173, to improve its oxidation resistance, and the conclusions can be summarized as follows:

1) Si addition eliminated NiO formation and suppressed $NiAl_2O_4$ formation in TMS-173
2) Si addition induces Al_2O_3 formation.
3) The suppression of voluminous Ni-rich oxides, accompanied by the production of adherent Al_2O_3, improved the superalloy's oxidation resistance dramatically.
4) Si slightly partitions to the γ' phase

Acknowledgements

I was privileged to attain the invaluable advice of Mr.A.Sato of Ishikawajima Heavy Industry Corp, together with Dr.J.Fujioka, Dr.T.Yokokawa, Dr.S.Nakazawa in High Temperature Materials group at National Institute for Materials Science.

References

[1] K.S.O'hara, W.S.Walston, E.W.Ross and R.Darolia: Ni Base Superalloy and Article, U.S.Patent 5,482,789A, (1996).
[2] T.Kobayashi, Y.Koizumi, S.Nakazawa, T.Yamagata and H.Harada: Design of High Rhenium Containing Single Crystal Superalloys with Balanced Intermediate and High Temperature Creep Strengths, Proc. Fourth International Charles Parsons Turbine Conf., (1997), 766-773.
[3] Y.Koizumi, T.Kobayashi, T.Yokokawa, H.Harada, Y.Aoki, M.Arai, S.Masaki and K.Chikugo: Development of 4th Generation Ni-base Single Crystal Superalloys. 2nd International Symposium, "High Temperature Materials 2001". Tsukuba: National Institute for Materials Science, (2001), 30
[4] Y.Koizumi, T.Kobayashi, T.Yokokawa, J.Zhang, M.Osawa, H.Harada, Y.Aoki and M.Arai: Development of Next-Generation Ni-Base Single Crystal Superalloys, Superalloys 2004, (2004) 35-43.
[5] A.Sato, H.Harada, T.Yokokawa, T.Murakumo, Y.Koizumi, T.Kobayashi and H.Imai: The effects of ruthenium on phase stability of fourth generation Ni-base single crystal superalloys, Scr. Mater., (2006), in press.
[6] K.Kawagishi, A.Sato, T.Kobayashi and H.Harada: Effect of Alloying Elements on the Oxidation Behavior of 4th Generation Ni-base Single-crystal Superalloys, TMS Letters, 2, (2005), 23-24.
[7] D.Caplan and M.Cohen: The Volatilization of Chromium Oxide, J.Electrochem. Soc, 108, (1961), 438-442.
[8] D.M.Wee and T.Suzuki: The Temperature Dependence of Hardness of $L1_2$ Ordered Alloys, Mater. Trans., 20, (1979), 634-646.

[9] Y.Saito, K.Kiriu, T.Kimura, T.Amano and S.Yajima: Spalling of the Surface Oxide Formed on Ni-20Cr Alloys with Small Additions of Cerium and Si, J.Japan Inst.Metals, 39, (1975), 1110-1117.
[10] H.Murakami, H.Harada and Y.Saito: Design and Analysis of Ni-base Superalloys on an Atomistic Basis, J.Japan Inst.Metals, 63, (1999), 723-732.
[11] H.Harada and M.Yamazaki: Alloy Design for γ' Precipitation Hardening Ni-base Superalloys Containing Ti, Ta and W, Tetsu-to-Hagane, (1979), 1059-1068.
[12] H.Harada, T.Yamagata, S.Nakazawa, K.Ohno and M.Yamazaki: DESIGN OF HIGH SPECIFIC-STRENGTH NI-BASE SINGLE CRYSTAL SUPERALLOYS, Proc. of conf. held in Liege, HIGH TEMPERATURE MATERIALS FOR POWER ENGINEERING 1990, (1990), 1319-1328.
[13] M.W.Chase,Jr., C.A.Davies, J.R.Downey,Jr., D.J.Frurip, R.A.McDonald and A.N.Syverud: JANAF Thermochemical Tables Third Edition, (1986).

ESTIMATION OF THE RISK OF HOT CORROSION IN GAS TURBINES BY THERMODYNAMIC MODELLING

Michael Müller

Forschungszentrum Jülich, IWV-2, D-52425 Jülich, Germany
mic.mueller@fz-juelich.de

Abstract

Different types of coal fired combined cycle power systems are under development. However, the direct use of hot flue gases originating from coal combustion or gasification for driving a gas turbine requires a hot gas cleanup to prevent corrosion of the turbine blading. One of the main problems are the alkalis released during the coal conversion process. During development of a hot gas cleanup it is necessary to check its effectiveness for preventing hot corrosion. Thermodynamic modelling was used to estimate the risk of hot corrosion. The coexistence of alkali sulphates and $NiSO_4$ or the formation of liquid alkali sulphates were taken as the criterion for a risk of hot corrosion. In addition, the results for the coal based processes were compared with thermodynamic calculations for a gas turbine burning fuel oil. The calculations were performed for 2nd Generation Circulating Pressurized Fluidized-Bed Combustion (2nd-Gen.CPFBC) and Pressurized Pulverized Coal Combustion (PPCC). In both processes, the corrosion risk, if there is any, should be much lower than in a gas turbine burning fuel oil.

Keywords: thermodynamic modelling, hot corrosion, gas turbines, CPFBC, PPCC

Introduction

The limitation of fossil fuel resources and the necessity of reducing CO_2 emission require an increase of the efficiency of power plants by using combined cycle power systems. Up to now efficiencies in excess of 50 per cent are only achievable by using ash free fuels for example natural gas or oil in gas and steam power stations. Coal constitutes 80 per cent of the world's total fossil fuel resources. Today it is mostly fired in steam power stations. Even if supercritical steam parameters are used, these coal fired power plants only reach efficiencies below 50 per cent, so that further development is essential. Therefore, different types of coal fired combined cycle power systems are under development.

The direct use of hot flue gases originating from coal combustion or gasification for driving a gas turbine requires a hot gas cleanup to prevent corrosion of the turbine blading. One of the main problems is the alkali release during the coal conversion process. The alkali metals are mainly bound in the mineral matter of the coal as salts and silicates. The alkali release leads to an alkali concentration in the flue gas significantly higher than the specifications of the gas turbine manufacturers (<0.01 mg Na+K/Nm^3).

During development of hot gas cleanup it is necessary to check its effectiveness for preventing hot corrosion. Corrosion tests are expensive, time-consuming, and need to represent the conditions in a gas turbine as good as possible to generate reliable results. The specifications of the gas turbine manufacturers are mainly based on experiences with ash free fuels and do not take into consideration the interactions with other gaseous species or ash particles. Thermodynamic modelling is able to generate results within less time at lower costs. It is possible to compare the complex systems occurring during coal conversion with systems

occurring in gas or oil fired gas turbines. Moreover, former investigations have already shown the potential of thermodynamic calculations for the prediction of condensed and gaseous phases in gas and oil fired gas turbines. [1, 2]

In the present work, thermodynamic modelling was used to estimate the risk of hot corrosion in gas turbines driven by cleaned coal based flue gases. Thus, the effectiveness of the hot gas cleanup concerning alkali removal was evaluated.

Hot corrosion

Hot corrosion is initiated by deposition or condensation of corrosive species, for example sulphates. The condensation of sulphates on gas turbine blades takes place due to high concentrations of alkalis in combination with high concentrations of sulphur. Even at high concentrations of chlorine, alkali sulphates are formed, because these are the least volatile alkali species.

The typical temperature range for hot corrosion in gas turbines is 600 – 950 °C. The upper temperature limit is given by the dew point of the alkali sulphates. The lower temperature limit is given by the melting point of eutectics formed by the deposits and the corrosion product scale of the blade material.

Hot corrosion has been characterised as type I (high temperature) and type II (low temperature) corrosion. Type I hot corrosion mainly occurs at 800 – 950 °C. It is caused by the formation of liquid alkali sulphates above their melting points leading to basic dissolution of the oxide scale of the blade material. Type II hot corrosion mainly occurs at 600 – 800 °C. It is caused by the formation of an eutectic melt of $NiSO_4$ or $CoSO_4$ and alkali sulphates above the eutectic temperature. $NiSO_4$ and $CoSO_4$ are formed by reaction of the oxide scale of the blade materials with SO_3 in dependence of the SO_3 partial pressure in the hot flue gas.

Therefore, in the following estimations, the coexistence of alkali sulphates and $NiSO_4$ or the formation of liquid alkali sulphates were taken as the criterion for a risk of hot corrosion.

Thermodynamic modelling

The thermodynamic stability of the sulphates and other species in the gas turbine was calculated with the computer program FactSage 5.3.1 and the FACT database [3] using different reactor models. The calculation of the thermodynamic equilibrium is done in this program by minimising the Gibbs free energy of chemical reaction systems. The amount and composition of compounds in complex chemical reaction systems can be calculated for a wide temperature and pressure range. The particular boundary conditions for the calculations are given in the examples.

For comparison, the dew point of sodium sulphate was also calculated for a gas turbine burning light fuel oil with 0.2 % sulphur and 0.5 ppm sodium. There is a lot of experience in the corrosion behaviour of such turbines. Thus, it is possible to calculate at least a corrosion risk (in a “coal” driven gas turbine) relative to a well known corrosion risk (in an oil driven gas turbine), even if the available thermodynamic data are not sufficient to calculate the exact

values. In addition, the calculated dew points were compared with a typical temperature/ pressure profile of a gas turbine operating under full load to determine the area with hot corrosion risk. Kinetic aspects, part load operation, starts and shutdowns, and turbine parts with temperatures different from the typical profile were not taken into consideration.

Hot corrosion risk in 2nd Generation Circulating Pressurized Fluidized-Bed Combustion

The 2nd Generation Circulating Pressurized Fluidized-Bed Combustion (2nd-Gen.CPFBC) is a lignite fired combined cycle concept which is able to achieve efficiencies in excess of 50 % [4]. A schematic flow diagram is given in Figure 1. The system mainly consists of a two stage combustion operating at a pressure of 10-16 bar. In the first stage, the coal is gasified under reducing conditions (air/fuel ratio of $\lambda < 1$) at temperatures of 650-750 °C. After leaving the first stage, the flue gases pass a gas-cleaning section, which consists of ceramic filters for ash removal and an alkali sorption unit. The cleaned gas is then mixed with a secondary air stream and either burned in a second combustion chamber or directly inside the gas turbine, in both cases at $\lambda > 1$. The residual thermal energy of the gas stream leaving the turbine is finally transferred to a steam cycle.

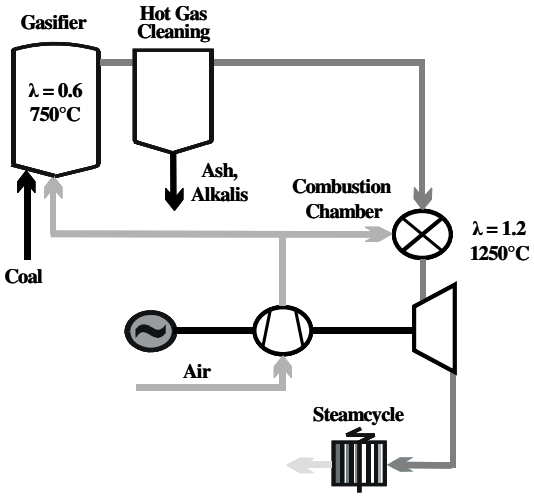

Figure 1 Schematic flow diagram of the 2nd-Gen.-CPFBC

Laboratory investigations were conducted to assess the potential for the reduction of alkali metals from hot gas by different aluminosilicate sorbents, such as silica, bauxite, bentonite, and mullite, under reducing atmospheres at a temperature of 750 °C [5]. Using a flow channel reactor, an alkali chloride-laden gas stream was passed through a bed of aluminosilicate sorbents. Qualitative and quantitative analysis of the hot gas downstream of the sorbent bed was performed using high-pressure mass spectrometry (HPMS). The investigations revealed the possibility of reducing the overall alkali concentration in the hot gas under 2nd-Gen. CPFBC conditions to values of <50 ppb_{vol} through the use of bentonite and activated bauxite.

Based on the experimental results, the thermodynamic stability of the sulphates and other species in the gas turbine was calculated using a four-staged reactor model. The calculations were performed for two types of lignite, "Lausitzer Braunkohle WBK 1778" (53% C, 4% H, 17% H_2O, 20% O_2, 0.8% S, 5% ash, 0.2% Cl) and "Rheinische Braunkohle HKN" (55% C, 4% H, 15% H_2O, 23% O_2, 0.4% S, 5% ash, 0.2% Cl). Figure 2 shows a scheme of the reactor model. Thermodynamic equilibrium was calculated for the reactors gasifier (G), hot gas cleaning (HGC), combustion chamber (CC) and gas turbine (GT). The boundary conditions for the calculations are given in the scheme. In HGC the alkali partial pressure in the gas was set to $4*10^{-8}$ bar according to the experimentally obtained values. Finally the thermodynamic stability of the sulphates results from the equilibrium calculation of GT. For comparison these values were also calculated for a gas turbine burning fuel oil (light fuel oil, 0.2 % S, 0.5 ppm Na).

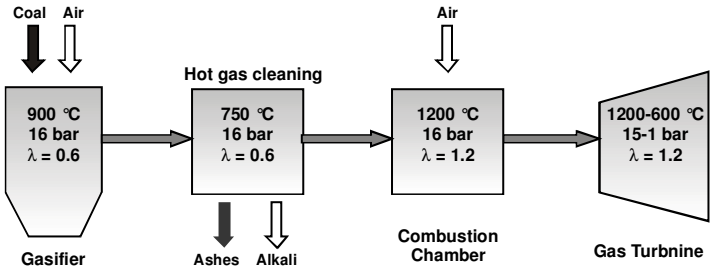

Figure 2 Reactor model used for thermodynamic calculations for 2nd-Gen. CPFBC

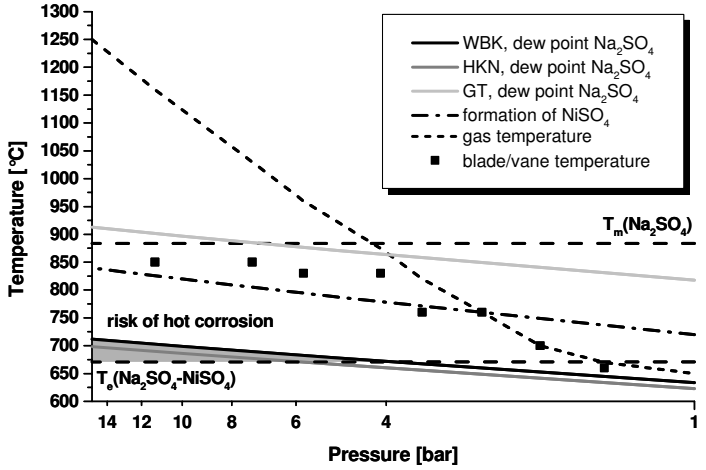

Figure 3 Results of thermodynamic calculations for estimation of hot corrosion risk in 2nd-Gen. CPFBC

The main results of the thermodynamic calculations are shown in Figure 3. The calculated dew points of Na_2SO_4 are much lower in case of 2nd-Gen. CPFBC than those in case of a gas

turbine burning fuel oil. Therefore, the corrosion risk should be much lower. In case of HKN, the dew point of Na_2SO_4 is lower than in case of WBK due to the minor amount of sulphur in the coal and subsequently in the flue gas. The formation of $NiSO_4$ also occurs at lower temperatures in case of HKN, which is not shown in Figure 3. However, this result indicates, that one has not only to look at the alkali concentration in the flue gas to estimate the corrosion risk. Anyway, Na_2SO_4 condenses much below its melting point of 884 °C, so that there isn't any risk of hot corrosion type I. The shadowed area marks the region in which both Na_2SO_4 and $NiSO_4$ are stable above the eutectic temperature of 671 °C, where type II hot corrosion may occur. However, there is no blade operating at these critical conditions under full load. Furthermore, there should be no condensation of Na_2SO_4 on the gas turbine blades operating under full load at all, because the calculated dew points are lower than the temperature of each blade. Therefore, no hot corrosion should take place during full load operation. Even during part load operation no blade should operate at critical conditions. At the worst, the first blades operate at critical conditions. However, these blades are covered by thermal barrier coatings.

Hot corrosion risk in Pressurized Pulverized Coal Combustion

The Pressurized Pulverized Coal Combustion (PPCC) is a coal fired combined cycle concept which is able to achieve efficiencies in excess of 50 per cent [6]. A schematic flow diagram is given in Figure 4. Combustion of pulverised coal takes place at temperatures of about 1600 °C under a total pressure of about 15 bar. The produced flue gas is routed through a column of ceramic balls as a liquid slag separation unit at an average temperature of 1450 °C. A separate alkali removal ($T \leq 1400$ °C) is the last clean up step before the flue gas enters the gas turbine. The residual thermal energy of the gas stream leaving the turbine is finally transferred to a steam cycle.

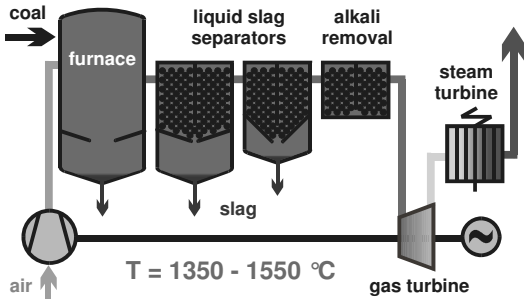

Figure 4 Schematic flow diagram of PPCC

Laboratory investigations were conducted to find a sorbent material for alkali removal at 1400 °C under PPCC conditions sufficient to fulfil the demands of the gas turbine manufacturers [7]. In laboratory-scale flow channel / HPMS experiments at 1400 °C, similar to those mentioned above, kaolin and silica enriched bauxite have shown the best ability to sufficiently remove the alkalis. The alkalis are bound in a melt/glass phase formed during alkali sorption. The total NaCl concentration can be reduced to values < 30 ppb_{vol}.

Based on the experimental results, the thermodynamic stability of the sulphates and other species in the gas turbine was calculated using a three-staged reactor model. The calculations were performed for a typical hard coal (79% C, 5% H, 2% H_2O, 7% O_2, 1% S, 6% ashes, 0.1% Cl). Figure 5 shows a schematic of the reactor model. Thermodynamic equilibrium was calculated for all reactors. The boundary conditions for the calculations are given in the scheme. In "Hot gas cleaning" the alkali partial pressure in the gas was set to $24*10^{-9}$ bar according to the experimentally obtained values. Finally the thermodynamic stability of the sulfates results from the equilibrium calculation of "Gas Turbine".

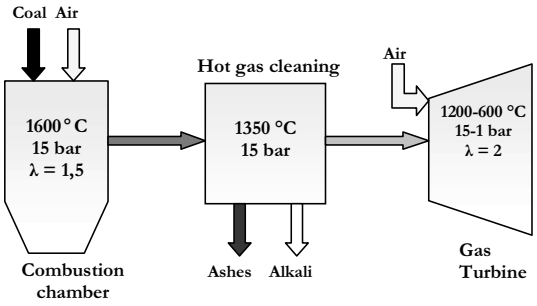

Figure 5 Reactor model used for thermodynamic calculations for PPCC

The results of the thermodynamic calculations are shown in Figure 6. The dew point of Na_2SO_4 is similar to those in 2nd-Gen. CPFBC and much lower than those in a gas turbine burning fuel oil. The dew point of $K_3Na(SO_4)_2$, which is the thermodynamic stable sulphate containing potassium, is about 20 K lower. For the same reasons explained for 2nd-Gen. CPFBC no hot corrosion should take place in case of PPCC.

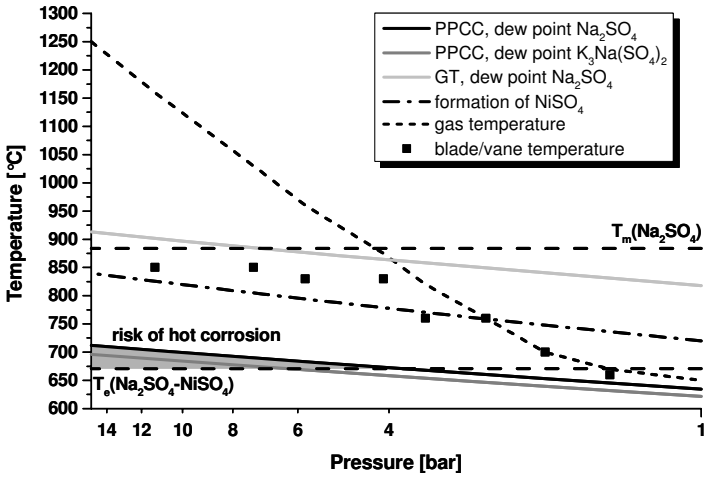

Figure 6 Results of thermodynamic calculations for estimation of hot corrosion risk in PPCC

Conclusions

Thermodynamic modelling was successfully used to estimate the risk of hot corrosion in 2nd-Gen.CPFBC and PPCC using the state of the art alkali removal. The coexistence of alkali sulphates and $NiSO_4$ or the formation of liquid alkali sulphates were taken as the criterion for a risk of hot corrosion. In addition, the results for the coal based processes were compared with thermodynamic calculations for a gas turbine burning fuel oil.

The results of the thermodynamic calculations are similar for both processes. The calculated dew points of Na_2SO_4 are much lower in case of the coal based processes than those in case of a gas turbine burning fuel oil. Moreover, there should be no condensation of sulphates on the gas turbine blades at all, because the calculated dew points are lower than typical blade temperatures. Therefore, no hot corrosion should take place in both coal based processes.

References

[1] Singheiser, L., Grünling H.W., Hochtemperaturkorrosion in stationären Gasturbinen bei alternierender Betriebsweise, Report for BMFT, Germany (1990).

[2] Bordenet, B., High Temperature Corrosion in Gas Turbines: Thermodynamic Modelling and Experimental Results, PhD-thesis, RWTH-Aachen, Germany (2004).

[3] Bale, C.W., Chartrand, P., Degterov, S.A., Eriksson, G. Hack, K., Ben Mahfoud, R., Melancon, J., FactSage Thermochemical Software and Databases, Calphad, 26, N.2 (2002), p. 189-228.

[4] Rombrecht, H.B., Ristau, H., Krautz, H.J., Ein braunkohlenbasierter Kombikraftwerksprozeß (ZDWSF) – Versuchsergebnisse und –erfahrungen, 22. Deutscher Flammentag, VDI-Berichte Nr. 1888, VDI-Verlag, Düsseldorf (2005), p. 49-56.

[5] Wolf, K.J., Müller, M., Hilpert, K., Singheiser, L., Alkali Sorption in Second-Generation Pressurized Fluidized-Bed Combustion, Energy & Fuels, 18 (2004), p. 1841-1850.

[6] Hannes, K., Neuman, F., Thielen, W., Pracht, M., Kohlenstaub-Druckverbrennung, VGB-Kraftwerkstechnik, 77 (1997), p. 393-400.

[7] Escobar, I., Oleschko, H., Müller, M., Einbindung von Alkalien bei der Druckkohlenstaubfeuerung, 22. Deutscher Flammentag, VDI-Berichte Nr. 1888, VDI-Verlag, Düsseldorf (2005), p. 57-62.

Part II

Advanced Gas Turbine Materials

Contributed Papers

Coating Technology

MICROSTRUCTURAL INVESTIGATIONS AND MODELLING OF INTERDIFFUSION BETWEEN MCRALY COATING AND IN738 SUPERALLOY

K. V. Dahl and J. Hald

Materials Technology, Dept of Manufacturing Engineering and Management,
Technical University of Denmark, DTU, Lyngby, Denmark.
kvd@ipl.dtu.dk

Abstract

Interdiffusion at the interface between a Co-36.5Ni-17.5Cr-8Al-0.5Y, MCrAlY coating and the underlying IN738 superalloy was studied in a large matrix of specimens isothermally heat treated for up to 12,000 hours at temperatures 875°C, 925°C or 950°C. Microstructural investigations and calculated phase fraction diagrams show that a precipitate free zone forms between the coating and superalloy and grows with time. Measured composition profiles across the interface were compared with modelled results obtained using the finite difference software DICTRA. The simulated results were able to qualitatively predict the phase-transformations occurring at the interface. The microstructural studies showed that a layer of continuous γ′ was formed on the superalloy side of the interface. This was found in the simulated results as a very high fraction of γ′.

Keywords: MCrAlY, Superalloy, Interdiffusion, DICTRA

Introduction

In the gas turbine, hot section components such as blades and vanes are protected against the aggressive high temperature environment by one or several coatings. Two of the major degradation mechanisms are oxidation and hot corrosion. The MCrAlY (M= Ni,Co) type coating provides good protection against these phenomena by forming stable aluminium and chromium oxides at the outer surface. As long as the coating contains enough aluminium and chromium to form these oxides, the structural part of the blade (the underlying superalloy) remains intact. When e.g. the amount of aluminium in the coating becomes low (after long service time) the coating has to be stripped of and a new coating applied.

The life time of the coating therefore depends on the availability of the oxide forming elements. The formation of protective oxides is however not the only mechanism, removing aluminium and chromium from the coating. At the interface between the coating and underlying superalloy, compositional differences can lead to significant loss of the active elements through interdiffusion.

The behaviour at the interface is complex and will depend on the compositions of the specific coating/ superalloy system chosen for the component. Typically phase transformations occur in both coating and superalloy as a result of the interdiffusion. Thermodynamic and kinetic modelling software may help in understanding these transformations and at the same time provide a tool for predicting the behaviour of specific coating/ superalloy combinations. Using the finite difference software DICTRA [1] to solve the diffusion equations, combined with

multicomponent diffusion mobility and thermodynamic databases allows us to predict phase fractions and interface behaviour of the many different elements present in commercial superalloys and metallic coatings.

In order to test the accuracy of the modelled results, detailed experimental data needs to be available for comparison. Normally when using EDS or WDS methods for composition profiling in multiphase systems there will be a large scatter in the measurements depending on the position of the electron microprobe and whether it hits the γ-matrix or one of the precipitate-phases e.g. β, γ', MC or $M_{23}C_6$. In contrast the compositions calculated by DICTRA will be an average of all the phase compositions. An experimental approach developed in previous work [2] allows for the measurement of true average composition profiles across the interface that can be directly compared to calculated results.

Material

Microstructural investigations were done for a matrix of isothermally heat treated MCrAlY/ IN738 specimens. Average composition profiles were calculated from experimental x-ray elemental maps using an approach described in [2].

Average compositions of the IN738 specimens and the MCrAlY coating are shown in tables 1 and 2. The MCrAlY coating was applied by low pressure plasma spraying after which, the specimens received a standard two step heat treatment:

1) 1120ºC for 2 hours then air cooled with an average cooling rate of 35ºC/min to 650ºC.
2) 845 ºC for 24 hours then air cooled with an average cooling rate of 20ºC/min to 650ºC.

In the following the as-coated condition refers to specimens having received this initial heat treatment.

Table 1: Average composition of MCrAlY coating.

MCrAlY	Ni	Cr	Al	Y	Co
Mass%	36.5	17.5	8	0.5	bal

Table 2: Average composition of superalloy IN738

IN738	Cr	Co	Al	Ti	W	Ta	Mo	C	Zr	B	Nb	Ni
Mass%	16.0	8.5	3.4	3.4	2.6	1.75	1.75	0.11	0.04	0.01	0.85	bal

Specimens were then isothermally heat treated in air at 925ºC or 950ºC for 250, 500, 1,000, 2,000, 4,000, 8,000 and 12,000 hours or at 875 ºC for 500, 1,000, 2,000, 4,000 and 8,000 hours.

Standard metallographic procedures were used to cut, mount and polish the specimens in cross-section. Specimens were ground and then diamond polished to 1 μm finish. The metallographic specimens were then coated with approximately 50 nm evaporated carbon for observation in a JEOL 5900 scanning electron microscope (SEM) equipped with an INCA 400 EDS system from Oxford Instruments.

The interface between coating and superalloy was studied in cross-section both in polished and etched condition using backscatter contrast.

Microstructural observations

Diffusion of aluminium from coating into the IN738 substrate results in the formation of a precipitate free layer in the interdiffusion zone and the formation of a γ'-rich layer on the superalloy side of the interface.

During the first, high temperature step of the initial heat treatment an interdiffusion zone between the coating and the substrate is formed as aluminium is transported into the substrate. During the second step of the initial heat treatment, fine γ'-particles precipitate in the interdiffusion zone and with time further transport of aluminium into the substrate results in the formation of the precipitate free zone.

Fig. 1 shows the microstructure at the interface in a specimen isothermally heat treated at 925°C for 250 hours. The precipitate free zone is visible between the bulk coating and a zone with increased volume fraction of γ' on the superalloy side.

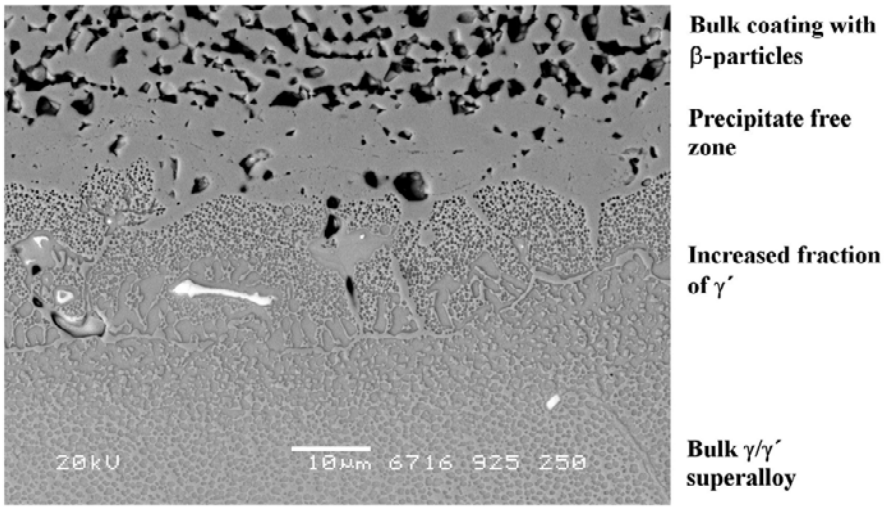

Fig. 1: Interface between coating and substrate for a specimen heat treated for 250 hours at 925°C. The precipitate free zone is visible

For comparison with modelled results average composition profiles across the interface were obtained for all the isothermally heat treated specimens. Fig. 2 shows measured composition profiles for specimens heat treated at 875°C. The behaviour at 925 and 950°C is similar to the behaviour observed at 875°C, except that the precipitate free zone grows faster as a result of the higher temperature.

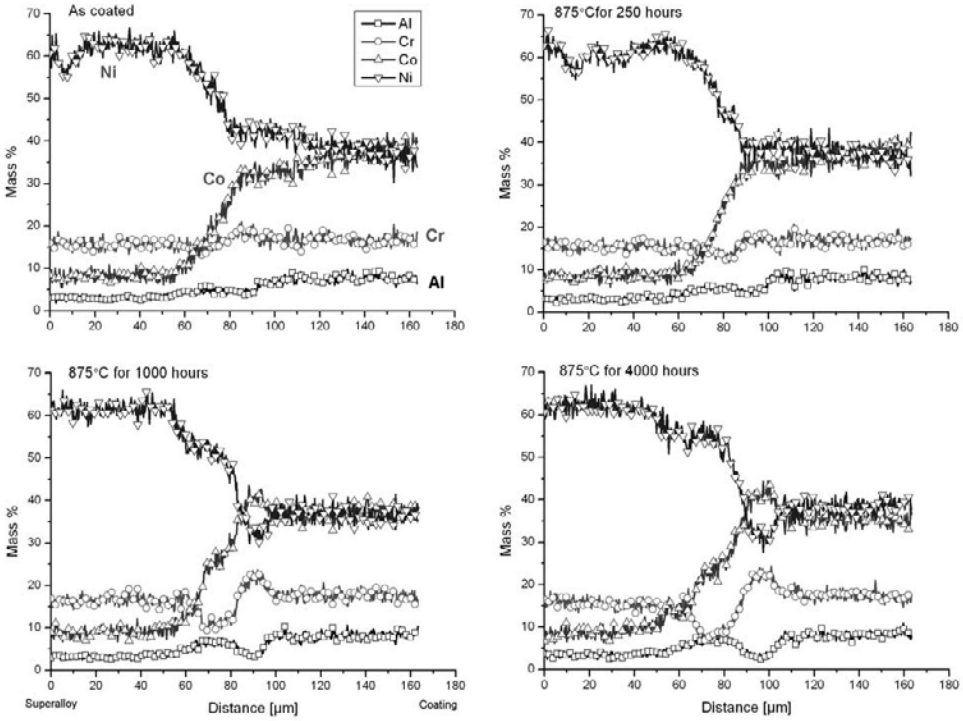

Fig. 2: Measured composition profiles for major elements for the as-coated specimen and specimens heat treated at 875°C for 250, 1,000 or 4,000 hours.

From the experimental composition profiles, phase fraction diagrams were calculated using Thermo-Calc. This was done by first applying a smoothening procedure to the measured profiles and then calculating equilibrium phase fractions for each data-point using the Thermo-Calc software. Thermodynamic data was obtained from the nickel-alloy database Ni-data v. 4 by Thermotech Ltd. [3].

Phase-fraction diagrams calculated from the composition profiles in Fig. 2 are shown in Fig. 3. Since the profile for carbon was unknown (can not be measured using EDS), carbon was not included in the calculations. Therefore Cr-rich σ-phase is predicted to appear at the location where Cr-rich $M_{23}C_6$ carbides are found in the actual microstructure (see Fig. 4).

The calculated phase fraction diagrams nicely illustrate the formation of the precipitate free zone (where the γ-fraction is almost 1).

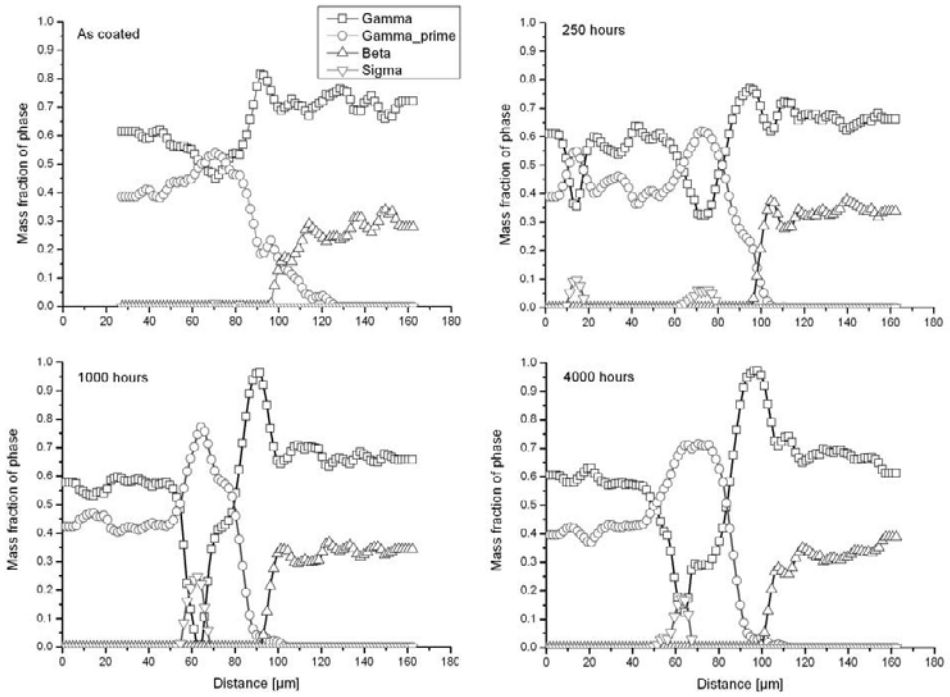

Fig. 3: Phase fraction diagrams calculated from the composition profiles presented in Fig. 2.

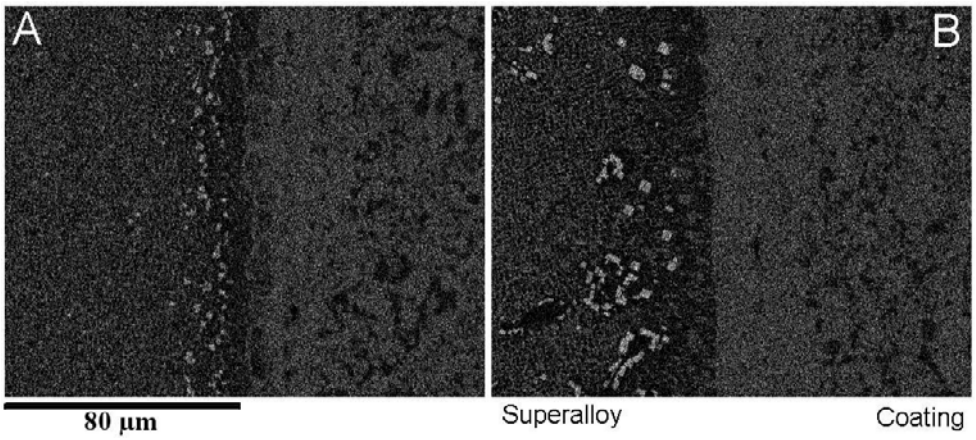

Fig. 4: EDS Cr x-ray maps showing Cr-rich $M_{23}C_6$ carbides on the substrate side of the interface; A: 8,000h at 875°C; B: 8,000h at 925°C.

Modelling

Modelling was performed using the DICTRA software from Thermo-Calc AB.

DICTRA employs a finite difference approach to solve flux and conservation equations between node-points. Temperature and concentration dependent diffusion coefficients are obtained from multicomponent thermodynamic factors and diffusion mobilities. Thermodynamic factors are calculated within each time step in the Thermo-Calc software that also calculates phase fractions in each node point based on the chemical composition in the node-point. The phase fractions are therefore calculated under the assumption of local equilibrium. Thermodynamic data was obtained from the nickel-alloy database Ni-data by Thermotech [3]. Kinetic mobilities were obtained from work by Campbell et al. [4].

In the DICTRA software the atomic mobility coefficient, M_B of an element B is described by an expression derived from absolute-reaction rate theory:

$$M_B = M_B^{\circ} \exp\left(\frac{-Q_B}{RT}\right)\frac{1}{RT}$$

where the mobility coefficient is divided up into an activation enthalpy Q_B and a frequency factor M_B°. Both the activation enthalpy and the frequency factor will in general depend upon composition, temperature and pressure. The composition dependency is represented with a linear combination of the values at each endpoint in composition space and a Redlich-Kister expansion, in spirit with the Calphad approach [5]:

$$\Phi_B = \sum_i x_i \Phi_B^i + \sum_i \sum_{J>i} x_i x_j \left[\sum_{r=0}^{m} {}^r\Phi_B^{i,j}(x_i - x_j)^r\right]$$

where Φ_B represents the composition dependent parameter (M_B° or $-Q_B$), Φ_B^j is the value of Φ_B for pure i, ${}^r\Phi_B^{i,j}$ are binary interaction parameters where the comma separates different species interacting with each other, and x_i is the mole fraction of element i. [6]

The atomic mobility coefficient can be related to the tracer diffusion coefficient by

$$D_B^* = RTM_B$$

The chemical diffusivity is given by a more complex expression where the concentration of one element has been chosen to be dependent on the others. The reduced chemical diffusivity is given by [7]

$$D_{kj}^n = \sum_i (\delta_{ik} - x_k) x_i M_i \left(\frac{\partial \mu_i}{\partial x_i} - \frac{\partial \mu_i}{\partial x_n}\right)$$

where n, k and j are the dependent, the diffusing and the gradient element, respectively, δ_{ik} is the Kronecker delta ($\delta_{ik} = 1$ if i=k and $\delta_{ik} = 0$ otherwise), x_k is the mole fraction of element k and μ_i is the chemical potential of element i.

Initial concentration profiles were entered using an error function expression as shown below:

$$c_1 + \frac{c_2 - c_1}{2}\left[1 + erf\left(\frac{x - x_i}{s}\right)\right]$$

where c_1 and c_2 are the initial concentrations on different sides of the interface, x is the position on the x-axis, x_i is the position of the interface (typically in the centre of the calculation region) and s is a constant used to adjust the smoothness of the transition between the two concentrations in the vicinity of the interface.

The average specified compositions from Table 1 and Table 2 were entered as start values. The actual composition of the specimens may deviate somewhat from the average specified composition. The purpose with the current work is however to use DICTRA as a predictive tool for the behaviour of coated gas turbine components and for such components typically only the specified compositions are available.

Diffusion calculations were done considering the elements *Al*, *Ti*, *Cr*, *Co*, *Ni*, *Mo*, *Ta, W and C*. Phases considered in the calculation were γ-fcc, γ', β, σ, bcc, MC and $M_{23}C_6$.

There is one consideration that should be mentioned concerning the inclusion of carbon in the calculations. During the initial high temperature heat treatment the $M_{23}C_6$ Cr-rich carbides are not thermodynamically stable and carbon is instead found in Ti-Ta rich primary carbides. These primary carbides are not thermodynamically stable at the three isothermal heat treatment temperatures (875, 925 and 950ºC), and in the calculations carbon will therefore immediately be "free" to form $M_{23}C_6$ carbides. In the actual microstructure, the primary carbides are only very slowly dissolved, thus limiting the amount of "free" carbon available to form $M_{23}C_6$ carbides.

The simulation

The initial heat treatment was incorporated as part of the interdiffusion calculation. After the initial heat treatment the isothermal heat treatments at 875, 925 and 950ºC were simulated. The time step was chosen to fit the experimental details; a short time step was used for the initial high temperature treatment and during simulation of the cooling procedures, while a larger time step could be used when the temperature was held constant during the final isothermal heat treatments.

In the calculations the total region was 650 µm wide with the interface between coating and superalloy located at x = 150 µm. The coating region was assumed to be 150 µm wide, which is half the thickness of the original coating. This was entered as a first approximation since aluminium will not only be depleted by interdiffusion but also by oxidation at the surface. Using

150 µm as the size of the region in the calculations therefore corresponds to assuming that depletion of aluminium occurs at the same rate for the two mechanisms.

The standard DICTRA model developed by Engström et al. [8] is a so-called disperse phase model that only takes into consideration diffusion in the matrix phase while particles are handled as non-diffusion phases. The model therefore assumes that the γ-phase is a continuous phase and that diffusion only takes place in this phase. The other phases present are implemented as dispersed phases that act as point sinks or sources for solute atoms as the fraction of the phases grow or shrink in response to the simulated composition in specific node-points.

This means that all other phases than the continuous matrix phase are considered as obstacles for the diffusion in the calculations. This is implemented by multiplying the diffusion parameters for the pure matrix phase with a resistance parameter also called a labyrinth factor that is a function of the volume-fraction of particles.

Concerning the diffusion, the system is thus approximated as a two-phase system consisting of matrix and particles. All particles are assumed to have the same influence on the diffusion, neglecting differences due to different crystal structures of different particles etc. For the present case we have β-particles on the coating side of the interface and γ'-particles on the substrate side of the interface. These different particles may in reality have a different influence on the diffusion but in the calculations they are assumed to slow down the diffusion in the exact same way, only depending on volume fraction. This treatment also means that for instance the influence of coarsening of particles is not taken into consideration in the calculations. These limitations may seem severe, one of the purposes of the current work was however to find a tool to predict the behaviour at the interface without using excessive computation time so that the model would be directly applicable to practical cases from the industry. With more complicated models it would probably be necessary to do calculations with a reduced system (fewer elements) in order to keep the simulations within a reasonable time-frame, which means it may be hard to apply the models directly to service exposed components where the complex phase-transformations and precipitations taking place are an effect of all the elements present.

A common choice for the labyrinth factor is a simplified version of the bounds derived by Hashin and Shrtrikman [9]. Hashin and Shrtrikman used variational methods to derive upper and lower bounds for the effective magnetic permeability of macroscopically homogenous and isotropic multiphase materials. The bounds are also applicable to diffusion and have been used by Engström et al. [10] and Gómez-Acebo et al. [11].

Under the assumption that $D_\gamma > D_{particles}$ the following expression for upper and lower bounds for the effective diffusivity can be applied:

$$D_{eff}^{upper} = D_\gamma + \frac{f_{particles}}{\frac{1}{D_{particles} - D_\gamma} + \frac{f_\gamma}{3D_\gamma}} \qquad D_{eff}^{lower} = D_{particles} + \frac{f_\gamma}{\frac{1}{D_\gamma - D_{particles}} + \frac{f_{particles}}{3D_{particles}}}$$

When $D_\gamma >> D_{particles}$ and $f_\gamma > f_{particles}$ then the upper bound can be simplified to:

$$D_{eff}^{upper} = D_\gamma \left(\frac{2 f_\gamma}{3 - f_\gamma} \right)$$

This expression was used by Gomez-Acebo et al. [11] in their calculations and is equivalent to the expression derived by Raleigh [12] for the influence of spherical particles.

In the present calculations the volume-fraction of γ' reaches a very high value at the interface between coating and superalloy because of diffusion of aluminium into the substrate. During the initial heat treatment the presence of σ-phase, β-phase and the high volume fraction γ' causes the volume fraction of γ-fcc to go to zero at the interface. If the *Raleigh* expression is used, the labyrinth factor will then be zero, causing the diffusion to stop and the calculations to break down.

Therefore a different expression for the labyrinth factor had to be used in order to make the calculations run. In the actual microstructure, when the γ-fraction goes to zero, the effective diffusion at the interface will depend on the diffusion parameters of the γ'-phase. These parameters are not accessible in the DICTRA disperse phase model, where only diffusion in the γ-fcc is treated; it does however seem safe to assume that diffusion in the γ'-phase will be significantly slower than diffusion in γ-fcc, because of the ordered crystal structure of γ'.

Therefore as a first approximation a labyrinth factor was used where it was assumed that when the volume fraction of γ-fcc approached zero, the diffusivity would be approximately an order of magnitude slower than in the γ-fcc ($D_{particles} = 0.1 D_\gamma$). Inserting this expression into the above equations, leads to the following expressions, where the term in brackets can be used as labyrinth factor in the calculations:

$$D_{eff}^{upper} = D_\gamma \left(1 + \frac{3 - 3 f_\gamma}{f_\gamma - \frac{10}{3}} \right) \qquad D_{eff}^{lower} = D_\gamma \left(0.1 + \frac{0.9 f_\gamma}{4 - 3 f_\gamma} \right)$$

In the present calculations the expression for the upper bound is used. It must however be emphasized that the used expression is an upper bound for a two-phase system where the diffusivity in the particle-phases is one tenth of the diffusivity in the matrix phase, it is not an upper bound for diffusion in the actual system. In order to employ the correct expressions for the system a model that could directly take the diffusion inside the precipitate phases into account would be needed.

Results and discussion of simulated results

Modelling was performed for the initial heat treatment and it was found that at the start of the simulation the thermodynamics predicted the formation of γ′ in the interface almost immediately, which results in a large volume fraction of γ′ to be predicted in a single node-point. This was inconsistent with the available experimental data, and therefore γ′ was suspended from the calculations during the high temperature part of the initial heat treatment (the first two hours at 1120ºC). In the actual interface microstructure it will take some time for the γ′ to nucleate and grow and the only way to implement this in the calculation is not to allow the *γ′* to form immediately. During the following cooling, *γ′* was then taken into the calculation and allowed to form.

Fig. 5 and Fig. 6 present modelled and measured composition profiles after the initial two-step heat treatment (as-coated condition), for 4,000 hours at 875 and 925ºC. A good fit is obtained and the correct behaviour is observed for all elements.

In the DICTRA software, the calculated profiles can be directly converted into phase fraction diagrams. From the experimental composition profiles, phase fraction profiles can be calculated in Thermo-Calc by performing equilibrium calculations for the composition in each data-point along the profiles as was shown in Fig. 4. This allows for comparison of phase-fractions calculated from the experimental profiles and phase-fractions calculated from the DICTRA profiles. This is presented in the right column of Fig. 5 where the solid lines are calculated from the experimental data while the dotted lines are phase fractions predicted by DICTRA.

Overall, there is a nice consistency between the simulated and the experimental results. The modelled results are able to predict the formation of the precipitate free layer between coating and substrate, formation of the zone enriched in *γ′*, and also the increased volume fraction of secondary carbides seen in Fig. 4. Qualitatively the modelled results are therefore able to predict the interface behaviour in terms of correct trends in both composition profiles and phase-fraction diagrams.

The fit to the experimentally measured layer widths (see right column of Fig. 5) is quite good, which is in fact a bit surprising since the result is obtained without any input of the true diffusion parameters for the γ′-phase that reaches a high volume fraction at the interface. The reason for the nice fit is probably that diffusion in the γ′-phase is very slow compared to γ-fcc and therefore it works as an effective block for diffusion both in the actual microstructure and in the simulations.

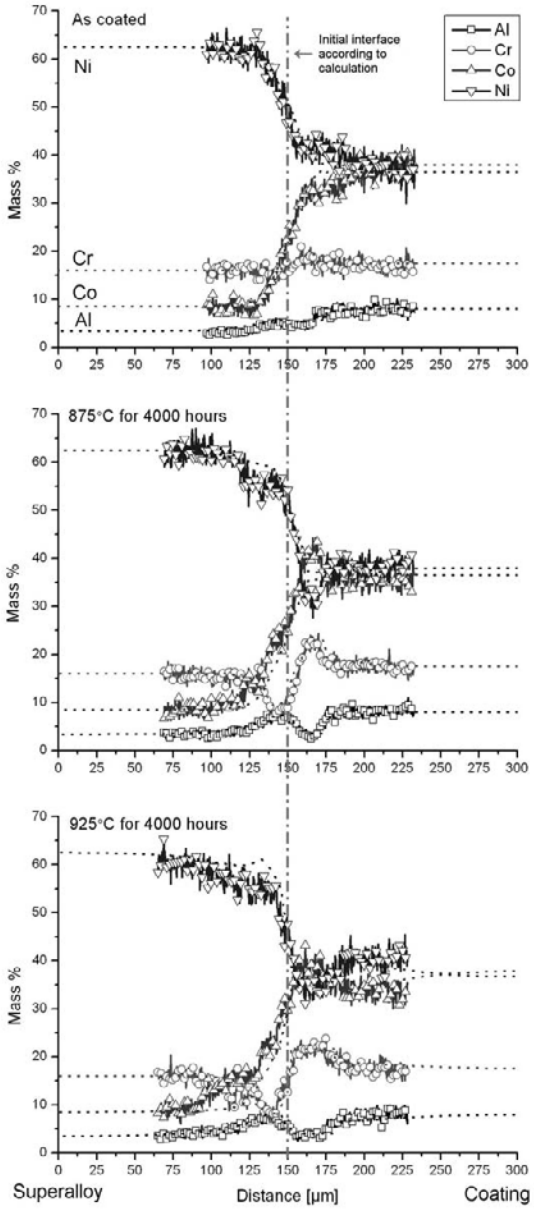

Fig. 5: Measured and modelled composition profiles for major elements across the interface.

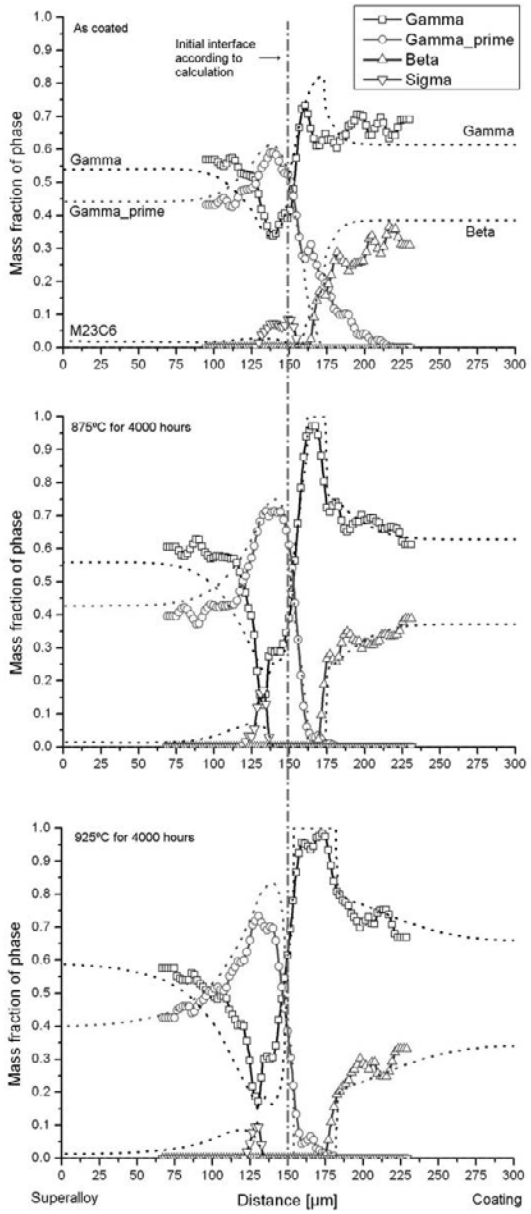

Fig. 6: Phase fraction diagrams; solid lines with symbols are calculated from the measured composition profiles and dotted lines are calculated from the modelled composition profiles.

Fig. 7 shows the calculated increase in γ′-volume fraction at the interface and retraction of β-phase. For the high temperature of 950ºC the fraction of β-phase at x=300 begins to drop and the coating can therefore no longer be considered as semi-infinite. This implies that the β-phase retraction will also depend on the Al-loss due to oxidation at the outer surface.

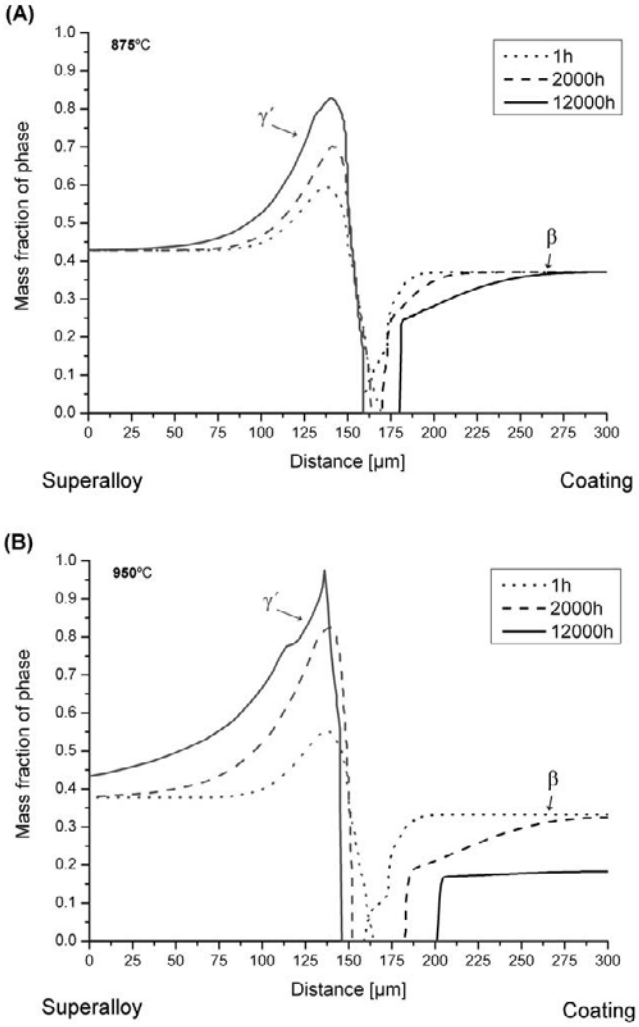

Fig. 7: Simulated *β*- and γ′-phase behaviour at A) 875 and B) 950ºC; profiles are plotted for 1, 2,000 and 12,000 hours of isothermal heat treatment.

The DICTRA model assumes that the γ-fcc phase is the continuous matrix phase at all locations but the microstructure investigations indicate that the γ′-phase becomes the continuous phase at the interface as can be seen in Fig. 8. In order to model this correctly a model allowing for more than one matrix phase to be present in the calculations would have to be used. The correct treatment of diffusion inside the γ′-phase and the implementation of a boundary condition taking into account the Al-loss due to oxidation at the outer surface are left for future work.

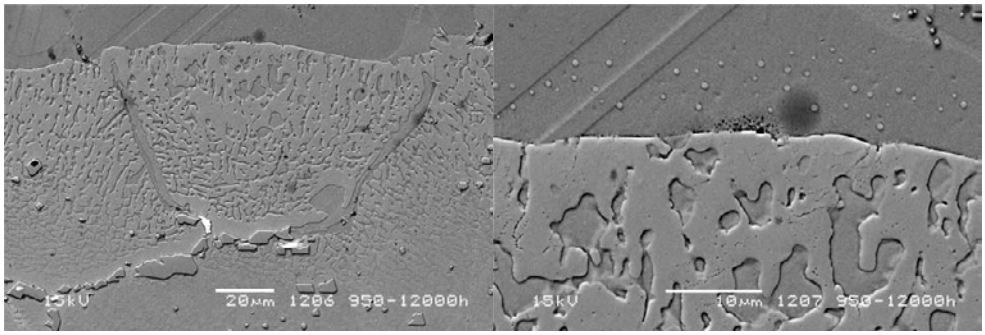

Fig. 8: SEM BSE images for the same location at different magnifications of the γ′-enriched zone at the interface after isothermal heat treatment at 950ºC for 12,000 hours. The precipitate free zone is visible at the top of the micrographs. The large bulky particles grey particles are $M_{23}C_6$ carbides; the Ti-Ta rich primary carbides that appear white in the image have almost been totally dissolved.

Conclusion

Microstructural investigations showed the interdiffusion between the Co-36.5Ni-17.5Cr-8Al-0.5Y, MCrAlY coating and the underlying IN738 superalloy resulted in complex phase transformations at the interface. A precipitate free layer formed in the interdiffusion zone and an increased amount of γ′ and $M_{23}C_6$ were found on the superalloy side of the interface. All these features were successfully predicted by the composition and phase fraction profiles simulated in DICTRA.

Normally the DICTRA disperse phase model can only be used when the volume fractions of the dispersed phases are low compared to the matrix phase. In this specific case it goes well, since diffusion in the γ'-phase is low compared to diffusion in the matrix γ-fcc. The γ' therefore works as an effective block for diffusion both in the actual microstructure and in the calculations. To treat the diffusion inside the γ′-phase correctly and to allow for the shift in continuous phase at the interface it would be necessary to use a model able to take into account multiple matrix phases.

In the calculations it was assumed that the coating region was of a finite thickness (150 µm) and that the β-depletion in this region only occurred because of interdiffusion with the underlying substrate superalloy. In the actual system the depletion may occur both due to interdiffusion and due to oxidation from the surface.

Future work would therefore naturally lead to the use of a numerical model capable of handling multiple matrix phases and also implementation of a boundary condition taking into account the Al-loss due to oxidation at the outer surface.

Acknowledgements

The present research was carried out under the research consortium IMPRESS and is also a part of the European COST 538 action: *High Temperature Plant Lifetime Extension*.

The authors wish to acknowledge the financial support from Energy E2 A/S and the Danish Research Agency (Grant no. 26-03-0275), and also wish to thank ERA Technology for providing heat treated specimens making this investigation possible.

Useful discussions with Henrik Larsson from the Department of Materials Science and Engineering at the Royal Institute of Technology in Stockholm are gratefully acknowledged.

References

[1] A. Borgenstam, A. Engström, L. Höglund and J. Ågren: *Journal of Phase Equilibria*, 2000, **21**, 3, 269-280.
[2] K. V. Dahl, J. Hald and A. Horsewell: Material submitted to *Journal of Microscopy*.
[3] N. Saunders, *SUPERALLOYS 1996 - Procedings of the Eight International Symposium on Superalloys*, Champion, Pennsylvania, 1996, 101-110. Edited by R. D. Kissinger et al.
[4] W. J. Boettinger, U. R. Kattner and C. E. Campbell: *Acta Materialia*, 2002, **50**, 775-792.
[5] J. Ågren: *Current Opinion in Solid State & Materials Science*, 1996, **1**, 355-360.
[6] DICTRA User´s guide Version 23 by Thermo-Calc software:
http://www.thermocalc.se/Download/Man_ex_Dictra.html
[7] B. Jönsson: *ISIJ International*, 1995, 35 (11), 1415-1421.
[8] A. Engström, L. Höglund and J. Ågren: *Metallurgical and Materials Transactions A*, 1994, **25A**, 1127-1134.
[9] Z. Hashin and S. Shtrikman: *Journal of Applied Physics*, 1962, **33**, 10, 3125-3131.
[10] A. Engström: *Scandinavian Jorunal of Metallurgy*, 1995, **24**, 12-20.
[11] T. Gómez-Acebo, B. Navarcorena and F. Castro: *Journal of Phase Equilibria and Diffusion*, 2004, **25**, 3, 237-251.
[12] L. Raleigh: *Philosophical Magazine,* 1892, **34**, 481-502.

DEVELOPMENT OF EQ COATING FOR A NEW TBC COATING SYSTEM IN NI-BASE SUPERALLOYS

K. Kawagishi[1], A. Sato[1, 2], K. Matsumoto[1], J. Ang[1, 3] and H. Harada[1]

[1]National Institute for Materials Science, 1-2-1 Sengen, Tsukuba-shi, Ibaraki 305-0047, Japan
[2]Ishikawajima-Harima Heavy Industries Co., Ltd., 3-5-1 Mukodai-cho, Tanashi-shi, Tokyo 188-8555, Japan
[3]The University of British Columbia, 2329 West Mall Vancouver, BC Canada V6T 1Z4

Abstract

Ni-base single crystal (SC) superalloys containing high concentrations of refractory elements prone to generate a diffusion layer called Secondary Reaction Zone (SRZ) beneath their bond coating during exposure at high temperatures. SRZ cause a reduction of the load bearing cross section and it is detrimental to the creep properties of thin-wall turbine airfoils. In this study, a new bond coat system, "EQ coating" which is stable and suppressing SRZ is proposed. The characteristic of EQ system is that the coating stays in equilibrium state and never reacts with the substrate. Diffusion couples of coating materials and substrate alloys were made and were heat treated at 1100 °C for 300 h and 1000 h. The concentration profiles of alloying elements in these diffusion couples were analyzed by EPMA to investigate the existence of the diffusion zone. Cyclic oxidation examinations were carried out at 1100 °C in air and the oxidation properties of EQ coating materials were discussed.

Keywords: bond coat, equilibrium, interdiffusion, SRZ, oxidation resistance.

Introduction

Ni-base superalloys which have excellent high-temperature strength and oxidation resistance are required for high output and high efficiency of gas turbines and jet engines. Advanced generation Ni-base superalloys, which contain large amount of strengthening elements and platinum-group metals, realize excellent high-temperature strength and suppression of TCP phase formation [1, 2]. However, these alloys are required to be applied with oxidation-resistant coating on the surface for the practical use because they are likely to have lower oxidation resistance than the previous generations of superalloys due to the nature of the alloying elements.

Applying the conventional coatings such as Pt-Al or MCrAlY to Re containing advanced generation single-crystal superalloys, a harmful layer so called secondary reaction zone (SRZ) is formed at the interface of coating and substrate [3-5] due to the interdiffusion during the high temperature exposure and the oxidation resistance of the coating layer and the mechanical properties of the substrates result in degradation [6]. Various techniques such as "diffusion barrier" [4, 7-9] and "carburization" [5] have been employed to minimize interdiffusion between the bond coat and the substrate, but these techniques still have some problems in complicated manufacturing process and long-time exposure in high-temperature.

In our previous research [10, 11], a new coating system, "EQ coating" has been developed. In this system, stable phases in equilibrium thermodynamically with substrate such as γ' phase are used as coating materials, and SRZ formation between the coating and the substrate is suppressed. Interdiffusion is minimized because chemical potentials of alloying elements in the substrate and coating in equilibrium state are equal. In this study, γ and γ' phases of Ni-

base superalloy are used as coating materials and the interdiffusion at the interface of substrate and coating material are investigated. Oxidation resistance of coating materials are measured to evaluate the potential of EQ coating as bond coat. β phase EQ coating systems using β phase coating material in equilibrium with γ/γ' Ni-base superalloy were also examined to obtain higher oxidation resistance than γ/γ' phase EQ coasting.

γ/γ' Phase EQ Coating

Conventional Ni-base superalloys consist of regularly-arranged γ phase and γ' phase. These two phases are in thermodynamical equilibrium, and so chemical potential μ_i of alloying elements *i* (*i*=Ni, Al, etc…) in each phase are equal, and expressed as following equation.

$$\mu_i^{\gamma} = \mu_i^{\gamma'}. \qquad (1)$$

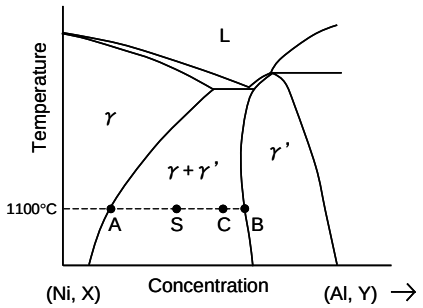

Fig. 1: (Ni, X)-(Al, Y) pseudo-binary phase diagram

γ phase and γ' phase alloys and γ/γ' tie-line alloys which have completely same composition as γ phase and γ' phase of Ni-base superalloy substrate are able to be used as EQ coating material. Fig. 1 shows (Ni, X)-(Al, Y) pseudo-binary phase diagram. Substrate S on a broken line, which means γ/γ' tie-line, consists of γ phase of composition A and γ' phase of composition B. Concentration of alloying element *i* in alloy C on the tie-line is expressed as

$$c_i^{C} = (1-f)c_i^{A} + fc_i^{B}, \qquad (2)$$

where *f* is mole fraction of γ' phase. Seeing microstructure, γ phase of composition A and γ' phase of composition B are intermingled with the ratio (1-*f*): *f* and the chemical potential of alloying element *i* is expressed as

$$\mu_i^{A(\gamma)} = \mu_i^{B(\gamma')} = \mu_i^{C(\gamma+\gamma')} . \qquad (3)$$

Substrate S has different *f* but same structure as alloy C, so the following equation is also given.

$$\mu_i^{S(\gamma+\gamma')} = \mu_i^{A(\gamma)} = \mu_i^{B(\gamma')} = \mu_i^{C(\gamma+\gamma')}. \qquad (4)$$

From this equation, it is obtained that alloys A, B and C are in equilibrium with substrate S and there is no driving force of interdiffusion because the difference of the chemical potential of element *i* is zero between substrate S and alloys A, B and C. In other words, using alloys A, B and C as bond coat, SRZ formation due to the interdiffusion of alloying elements is expected to be suppressed. In this study, this concept of EQ coating is investigated and

Table 1 : Nominal compositions of γ / γ ' phase EQ coating

Alloy	Composition (wt %, Ni balance)									
	Co	Cr	Mo	W	Al	Ti	Ta	Hf	Re	Ru
TMS-82+	7.7	4.6	1.8	8.6	5.3	0.5	6.3	0.09	2.4	-
TMS-82+ γ	10.5	7.6	2.6	10.0	2.9	0.2	3.4	0.03	4.2	-
TMS-82+ γ'	4.7	1.4	0.9	7.2	7.9	0.7	9.5	0.16	0.5	-
TMS-173	5.6	3.0	2.8	5.6	5.6	-	5.6	0.10	6.9	5.0
TMS-173 γ'	4.2	1.5	1.5	5.3	7.8	-	8.0	0.15	2.6	3.9

oxidation resistance of EQ coating is evaluated.

2nd generation Ni-base single-crystal superalloy TMS-82+ and 5th generation Ni-base single-crystal superalloy TMS-173 were used as substrates. The compositions of γ phase and γ' phase at 1100 °C were calculated by Alloy Design Program [12] and these compositions were used for coating materials. Compositions of samples used in this study are shown in Table 1.

β Phase EQ Coating

β phase in Ni-base superalloys has BCC structure and generally contains large amount of Al and Cr. Consequently, formation of Al_2O_3 protective scale and improvement of oxidation resistance compared with γ/γ' EQ coatings is expected. Fig. 2 illustrates phase diagram of Ni-Al-Cr ternary system at 1100 °C. In the region of γ+γ'+β equilibrium state (triangle DEF), the following equation

$$\mu_i^{D(\gamma)} = \mu_i^{E(\gamma')} = \mu_i^{F(\beta)} \quad (5)$$

is given. If a substrate is located on γ/γ' tie-line DE, then this substrate consists of γ phase at point D and γ' phase at point E. Thus, the following is obtained.

$$\mu_i^{substrate(\gamma+\gamma')} = \mu_i^{D(\gamma)} = \mu_i^{E(\gamma')} = \mu_i^{F(\beta)}. \quad (6)$$

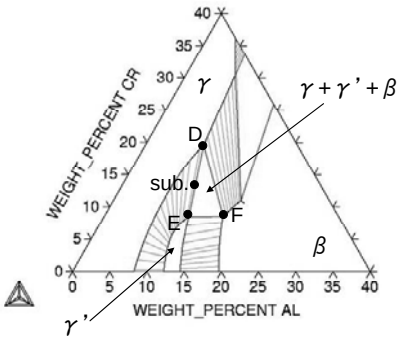

Fig. 2: Ni-Al-Cr ternary phase diagram at 1100 °C.

From this equation, it is concluded that using β phase coating on point F against γ/γ' substrate on line DE, the interdiffusion at the interface of substrate and coating is suppressed in theory. Moreover, mixed phase of γ, γ' and β for example β+γ' or β+γ'+γ are able to be used as coating if they are in equilibrium state, so the design of the coating is possible considering not only the oxidation resistance but also the mechanical properties. However, in the conventional Ni-base superalloys, alloy in equilibrium state with β phase does not exist. In this study, Ni-base superalloy in equilibrium with β phase is developed and the possibility of β phase as EQ coating is investigated.

Compositions of the substrates and coating materials were determined by using thermodynamic calculation software, Thermo-Calc Software (Thermo-Calc Software,

Table 2: Nominal compositions of β phase EQ coatings and substrates.

Alloy	Composition (wt %, Ni balance)						
	Co	Cr	Mo	W	Al	Ta	Hf
S-1	-	14.1	-	-	9.6	-	-
C-1	-	8.5	-	-	16.0	-	-
S-2	-	13.0	3.0	-	8.6	6.0	-
C-2	-	7.1	0.26	-	16.9	4.9	-
S-3	-	12.1	4.0	4.1	8.6	3.0	-
C-3	-	7.3	0.35	0.05	17.4	2.9	-
S-4	8.8	11.9	2.3	5.8	7.3	6.7	0.23
C-4	5.3	5.4	0.21	0.08	17.4	8.3	0.11

Sweden). γ+γ'+β three-phase equilibrium composition at 1100 °C were calculated for Ni-Al-Cr ternary system, Ni-Al-Cr-Mo-Ta, Ni-Al-Cr-Mo-Ta-W and Ni-Al-Co-Cr-Hf-Mo-Ta-W system. Substrates were designed as consisting of γ phase and γ' phase with mole ration of 0.5 and the compositions of coating materials were determined as the compositions of β single phase. Nominal compositions of the substrate alloys and coating alloys used as samples are shown in Table 2.

Experimental Procedure

Samples listed in Table 1 and 2 were prepared by arc melting, except for single-crystal TMS-82+ tie-line alloys. After homogenization, each sample was cut into 10mm in diameter and 5 mm in thickness. Sample surfaces were polished by 0.05μm-φ Al_2O_3 particles into mirror surface and cleaned. Diffusion couples of substrate alloy and coating alloy were made and heated at 1100 °C for 300 h and 1000 h in air. Oxidation resistance of coating materials were examined by 1h cyclic oxidation examination at 1100 °C in air. Cross sections of each diffusion couple were observed by Scanning Electron Microscope (SEM) and concentration profiles were analyzed by Energy Dispersive X-ray Spectroscopy (EDX) and Electron Probe Microanalyzer (EPMA). Oxides formed on the surface after the oxidation examinations were observed and oxidation mechanisms were discussed.

Results and Discussion

Cross sections of diffusion couples of TMS-82+ and coating materials (a) AMDRY962, (b) TMS-82+γ and (c) TMS-82+γ' after diffusion at 1100 °C for 300 h are shown in Fig. 3. Coating material (a) was prepared using same composition as conventional bond coat for comparison. In this diffusion couple, a 150μm thick diffusion layer and a 82μm thick SRZ were observed at the substrate TMS-82+ side of the interface. On the other hand, in (b) γ phase diffusion couple and (c) γ' phase diffusion couple, SRZ was not found and very thin diffusion layers were only observed. In γ' phase alloy, little amount of disk-like TCP phase was found but these particles disperse uniformly throughout the whole sample and it is estimated that the reason of this TCP formation is not due to the diffusion but heat treatment condition. In the concentration profiles of Al and Co in (a) TMS-82+γ/TMS-82+ and (b) TMS-82+γ'/TMS-82+ diffusion couples analyzed by using EPMA shown in Fig. 4, the thickness of diffusion layers were evaluated as 5μm and 15μm, respectively. From these results, using γ and γ' phase of TMS-82+ as coating of TMS-82+ substrate, it is concluded that the thickness of the diffusion layer between the coating and the substrate will be

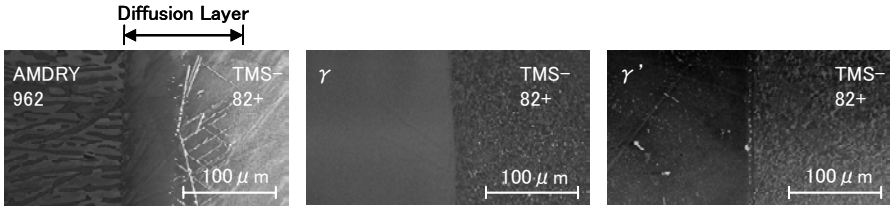

(a) AMDRY962/TMS-82+ (b) TMS-82+ γ /TMS-82+ (c) TMS-82+ γ' /TMS-82+

Fig. 3: Cross sections of (a) conventional bond coat, (b) γ phase coating and (c) γ' phase coating and TMS-82+ diffusion couples diffused at 1100 °C for 300h.

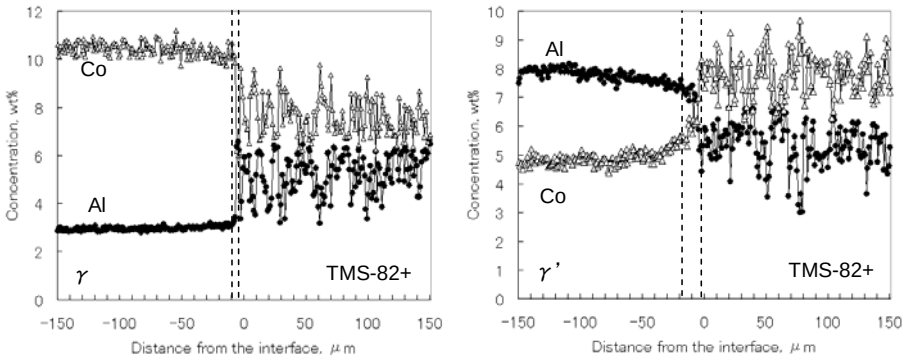

(a) TMS-82+ γ /TMS-82+ (b) TMS-82+ γ' /TMS-82+

Fig. 4: Concentration profiles of Al and Co in (a) TMS-82+γ/TMS-82+ and (b) TMS-82+γ'/TMS-82+ diffused at 1100 °C for 300h.

suppressed drastically.
The effect of γ' EQ coating on 5th generation superalloy was also investigated using the diffusion couple of 5th generation superalloy TMS-173 and its γ' phase. As shown in Fig. 5, diffusion layer of 2μm thick was obtained after the diffusion at 1100 °C for 1000h. Thus, it is confirmed that the concept of EQ coating is able to be applied to Ru-containing 5th generation Ni-base superalloy.

Results of the cyclic oxidation examination performed to evaluate the oxidation resistance of EQ coatings are shown in Fig. 6. The examination was performed at 1100 °C in air, using TMS-82+, TMS-82+γ and TMS-82+γ'. It is clarified from this result that alloys of TMS-82+γ shows largest mass increase in the first few cycles and decrease in the following cycles due to fast oxidation and spallation. TMS-82+γ' shows most excellent oxidation resistance in 50 cycles' examination and it is obviously improved from that of TMS-82+. Thus, it is concluded that γ' phase is promising material for oxidation-resistant coating.

Difference of the oxidation property of γ phase and γ' phase is due to the structure of oxide. While γ' phase forms Al_2O_3 layer, γ phase mainly forms thick NiO and particles of Al_2O_3 inner oxide [13]. More precise investigation about the oxidation mechanisms of γ and γ' phase are necessary in further studies.

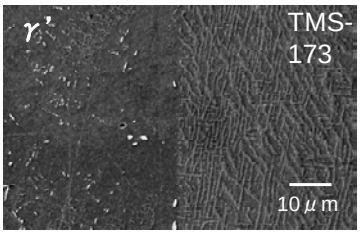

Fig.5: Cross section of TMS-173γ'/TMS-173 diffusion couple diffused at 1100 °C for 1000h.

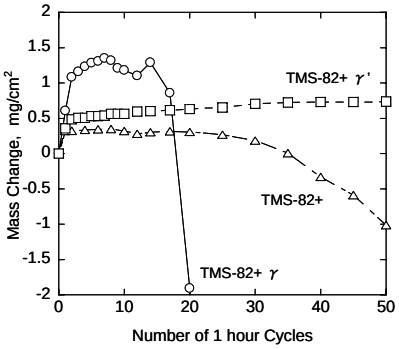

Fig. 6: Cyclic oxidation properties of TMS-82+ tie-line alloys at 1100 °C.

The idea of EQ coating is now developed into β phase coating. Fig. 7 indicates a cross section of C-1/S-1 Ni-Al-Cr ternary system diffusion couple listed in Table 2 diffused at 1100 °C for 300h. Particles of β phase were observed in γ/γ' structure of S-1 alloy, and particles of γ' phase were dispersed in β phase of C-1 alloy. The compositions in Table 2 were calculated to be γ/γ' two phases structure for S-1 and β single phase for C-1, but such mixed phases were formed because the results of Thermo-Calc calculation differed from accurate equilibrium composition. In the concentration profiles of Al and Cr analyzed by EDX, less than 2μm thick diffusion layer was obtained. Considering the special resolution of EDX, it may be concluded that the interdiffusion of Al and Cr was almost suppressed.

Fig. 8 shows a cross section of Ni-Al-Cr-Mo-Ta diffusion couple C-2/S-2 diffused at 1100 °C for 300h. Because difference between the result of Thermo-Calc calculation and actual equilibrium state is larger than C-1/S-1, the dispersion of large amount of β phase in γ/γ' of S-2 and γ' phase in β of C-2 were found. The chemical potentials of alloying elements in S-2

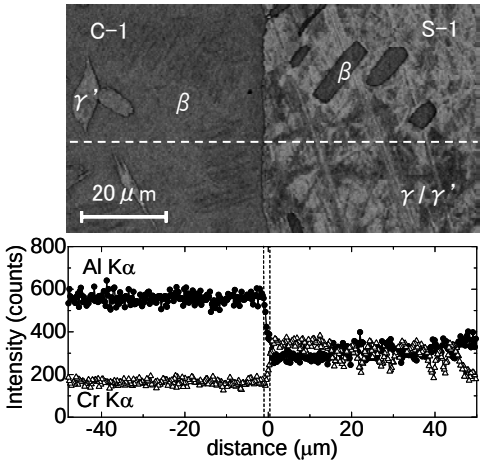

Fig. 7: Cross section and concentration profile of Al and Cr for Ni-Al-Cr diffusion couple diffused at 1100 °C for 300h.

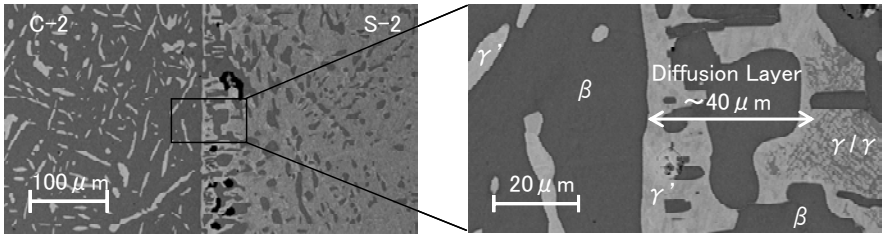

Fig. 8: Cross section of Ni-Al-Cr-Mo-Ta diffusion couple diffused at 1100 °C for 300h.

and C-2 were not equal completely, thus the interdiffusion at the interface occurred but the thickness of the diffusion layer was suppressed to less than about 40μm. The diffusion layers of C-3/S-3 and C-4/S-4 system containing more alloying elements were also obtained as less than 50μm. Analysing precise concentration of γ+γ'+β three phase equilibrium state in future work, the accurate equilibrium composition can be determined without using Thermo-Calc, and the thickness of the diffusion layer will be minimized by the same concept as γ/γ' phase EQ coating. From these results above mentioned, it is confirmed that the concept of EQ coating is possible to be applied to β phase coating and Ni-base superalloy in equilibrium with β phase.

β phase alloys and γ/γ' alloys developed in this study have high Al and Cr concentration and they indicated very excellent oxidation resistance as shown Fig. 8. The clarification of the oxidation mechanism of β phase and significance of β phase coating as oxidation-resistant coating is necessary in further investigation. Moreover, examination of high temperature strength of γ/γ' Ni-base superalloy in equilibrium with β phase developed in this study and practicality of them as high temperature materials is required.

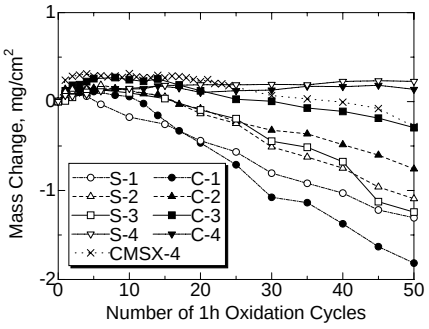

Fig. 9: Cyclic oxidation properties of β phase equilibrium alloys at 1100 °C.

Conclusion

The effect of EQ coating technique using γ phase and γ' phase of 2nd generation Ni-base single-crystal superalloy TMS-82+ and 5th generation Ni-base single-crystal superalloy as bond coat materials were investigated by diffusion experiments using diffusion couples of γ or γ' phase alloys and Ni-base superalloy substrates. From the results of the diffusion

experiments, it is confirmed that the interdiffusion at the interface of EQ coating and substrate was minimized and SRZ formation was suppressed. The possibility of β phase EQ coating was also suggested, and the development of coating systems which has much higher oxidation resistance will be expected. Further investigations will be performed using plasma-sprayed EQ coatings on the advanced generation superalloys.

References

[1] Y. Koizumi, T. Kobayashi, T. Yokokawa, H. Harada, Y. Aoki, M. Arai, S. Masaki and K. Chikugo, "Development of 4th Generation Single Crystal Superalloys", Proc. of 2nd International Symposium on High Temperature Materials 2001, Tsukuba, Japan (2001), p.30.

[2] J. X. Zhang, T. Murakumo, Y. Koizumi, T. Kobayashi, H. Harada and S. Masaki Jr., "Interfacial Dislocation Networks Strengthening a Fourth-Generation Single-Crystal TMS-138 Superalloy", Metall. Mater. Trans. A, Vol. 33, No. 12 (2002), pp. 3741-3746.

[3] W. S. Walston, J. C. Schaeffer and W. H. Murphy: Superalloy 1996, (TMS, 1996) pp.9-18.

[4] Y. Matsuoka, Y. Aoki, K. Matsumoto, A. Sato, T. Suzuki, K. Chikugo and K. Murakami, "The Formation of SRZ on a Fourth Generation Single Crystal Superalloy Applied with Aluminide Coating", Superalloy 2004 (2004), pp. 637-642.

[5] I. E. Locci, R. A. Mackay, A. Grag and F. J. Ritzert, "Successful Surface Treatments for Reducing Instabilities in Advanced Nickel-Base Superalloys for Turbine Blades", NASA/TM-2004-212920, March (2004).

[6] O. Lavigne, C. Ramusat, S. Drawin, P. Caron, D. Boivin and J. –L. Pouchou, "Relationships Between Microstructural Instabilities and Mechanical Behavior in New Generation Nickel-Based Single Crystal Superalloys", Superalloy 2004 (2004), pp.667-675.

[7] T. Narita, S. Hayashi, H. Yukawa, M. Noguchi and M. Miyasaka, "Alloy Coating, Method for Forming the Same, and Member for High Temperature Apparatuses", U. S. Patent 6830827 (2004).

[8] I. T. Spitzberg, R. Darolia, M. R. Jackson, J. C. Zhao and J. C. Schaeffer, "Diffusion Barrier Layer", U. S. Patent 6306524 (2001).

[9] R. G. Wing, "Method of Aluminising a Superalloy", U. S. Patent 6080246 (2000).

[10] H. Harada, A. Sato and K. Kawagishi, Japanese Patent Pending, Tokugan 2005-092542 (2005).

[11] A. Sato, H. Harada and K. Kawagishi, "Development of New Bond Coat 'EQ Coating' System", Metall. Mater. Trans. A, Vol. 37, No. 2 (2006).

[12] H. Harada, K. Ohno, T. Yamagata, T. Yokokawa and M. Yamazaki, "Phase Calculation and Its Use in Alloy Design Program for Nickel-Base Superalloys", Superalloys 1988 (1988), pp. 733-742.

[13] J. Ang, A. Sato, K. Kawagishi and H. Harada, "The Oxidation Characteristics of the γ-γ' Tie-Line Alloys of a Nickel-Based Superalloy", Mater. Trans., Vol. 47, No. 2 (2006).

COATINGS BY LASER CLADDING AGAINST LIQUID DROPLET EROSION

M.Giannozzi[1], E.Giorni[1], I.Giovannetti[2*], F.Pratesi[2], G.Zonfrillo[2]

[1] GE-Nuovo Pignone, Florence, Italy
[2] Department of Mechanics and Industrial Technologies, Univ. of Florence, Italy
[*] Iacopo.Giovannetti@ge.com

Abstract

In steam turbines the highest power output in simple and combined cycles is obtained by lowering the condensing pressure. In such conditions, low-pressure rotor blades are subject to liquid droplets erosion, due to the combined presence of condensed water in the steam and high peak speed of the blades.
Remedies against liquid erosion involve improvements in both design and materials. From a material point of view, blade life can be extended by suitable surface treatments, decreasing the rate of metallic erosion by liquid impingement. In the past this improvement has been accomplished by local hardening or by brazed-on Stellite shields. Recently, several coatings applied by thermal spray or by laser cladding have been studied. In particular Stellite 6, applied by laser cladding, showed a significantly higher erosion resistance than brazed Stellite 6, which was considered the best solution against liquid impingement.
Starting from these results, the work has been continued aimed at increasing erosion resistance by modifying the chemical composition of powders used to produce the laser claddings. Concentrations of carbide forming and solid solution strengthening elements have been varied in a wide range, in order to establish their effects on liquid droplet erosion.
Several samples have been coated and subjected to a liquid erosion test following the recommendations of ASTM G73-93 standard. The machine used consists of a rotating arm that supports the sample. The sample rotates at high speed through water droplets of defined dimensions. The test result is expressed in terms of volume loss as a function of the number of impacts.
In this communication, results of the erosion tests and chemical analysis on the samples are reported, with a discussion on the effects of the different elements on erosion resistance.

Keywords: liquid erosion, turbines, laser cladding, superalloys, Stellite.

Introduction

This study is the continuation of a previous study by Giorni et al. [1], in which the possibility of applying a new erosion-resistant coating on steam turbine blades was investigated.
Cobalt-base superalloy powders were used to produce coatings by laser cladding technique. A very high increase in erosion resistance was obtained by cladding a Stellite 6 coating, as shown in Fig. 1.
The chemical composition of Stellite 6 is reported in Table 1.

Stellite 6	Co	Cr	C	W	Si	Mn	Ni	Fe
	Bal.	28.0%	1.2%	4.6%	1.1%	1.0%	< 3.0%	< 3.0%

Table 1 – Stellite 6 chemical composition.

This study is aimed at improving the liquid droplet erosion resistance of these coatings through modification of their chemical composition and investigating the influence of alloying elements.

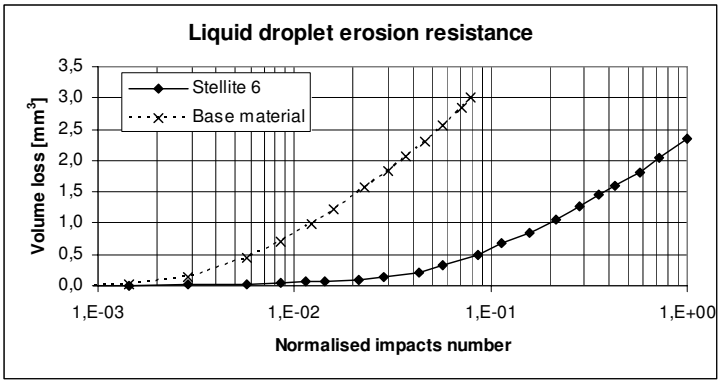

Fig. 1 – Erosion resistance comparison with and without Stellite 6 coating.

Experimental

Preliminary study

Starting from Stellite 6 the concentration of some elements has been modified, in order to obtain the best balance between erosion resistance and weldability. It is well known from the literature [2-3] that these alloys are reinforced by carbide forming and solid solution strengthening elements: the higher the concentration of alloying elements, the lower is material weldability.

Fe: it preserves the toughness and ductility of the matrix. Its concentration however should not be too high, in order not to hamper the action of hard elements Cr, W, and Mo. In common concentrations, it does not decrease the erosion resistance.

Ni: it stabilises the FCC phase. From the literature, it appears to increase erosion resistance, but this needs confirmation.

Si: its actual concentration should balance two contrasting trends. From our tests, it appears that its presence increases erosion resistance; on the other hand, it is well known from the literature [2] that its concentration should not exceed 1%, in order to avoid formation of brittle phases, such as the Laves one.

C: it is required for the formation of hard phases, such as M_6C; an excess however introduces weldability problems. After our preliminary results, the highest concentration has been fixed at 1.3%.

Starting from this information, the decision was made to proceed in two directions, either adding carbide forming elements without Nickel or adding Nickel too, as shown in Fig. 2.

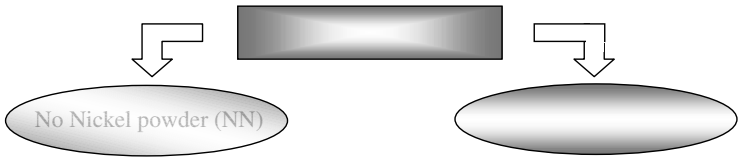

Fig. 2 – Modifications from Stellite 6.

Tests were carried out according to the ASTM G73-93 standard. The testing machine basically consists of a rotating arm that supports the sample. The sample rotates at high speed through water droplets sprayed at a speed that is negligible with respect to that of the sample.
The main test parameters were selected considering typical working conditions of a steam turbine: in particular, parameters chosen were a peak speed of 433 m/s and a drop diameter of 200 μm.
Test results are reported as eroded volume in mm^3 versus number of impacts, considered to be the same as the number of rotations.
Erosion results obtained on the samples show an increase with respect to the Stellite 6 coated material (see Fig. 3); in particular, Nickel content appears to provide a significant improvement in erosion resistance. The number of impacts is normalised to its maximum value.

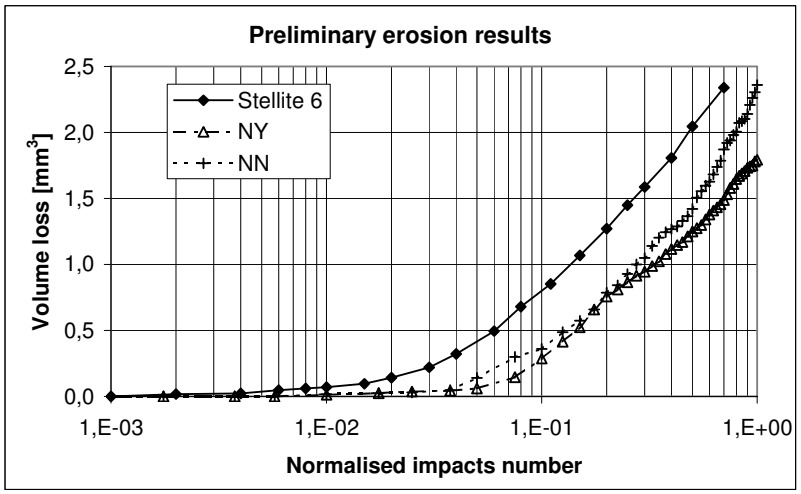

Fig. 3 – Preliminary erosion results.

From these basic tests a significant increase of liquid erosion resistance has been found for both compositions used if compared with plain Stellite 6.
A further step in development has been looked for by varying the chemical composition of new powders in a range within their process capability: new powders have been produced with compositions close to the Lower Specification Limit (LSL), or the Upper Specification Limit (USL), or corresponding to mean values (MEAN) between them.
Seven different materials have been produced: two use the same powders as preliminary experiments (NY, NN) for reference and test confirmation and five (A, B, C, D, E) are modified as indicated in Table 2. For each material, two samples have been obtained and tested for erosion resistance.

NN base			
Element	Material A	Material B	Material C
Cr	LOW	MEAN	HIGH
W	LOW	MEAN	HIGH
C	LOW	MEAN	HIGH

NY base		
Element	Material D	Material E
Cr	MEAN	HIGH
W	MEAN	HIGH
C	MEAN	HIGH
Ni	LOW	MEAN

Table 2 – New materials.

NN materials

Samples have been produced by cladding powders onto the raw material. After cladding, a dye penetrant test has been performed, in order to check for any surface cracks. Moreover, the chemical composition of the samples has been determined by EDX. Three measurements have been performed on each sample; for each element, its average concentration has been calculated and results obtained are summarised in Table 3. The number of impacts required to produce 2 mm^3 of volume eroded has also been reported for each material; complete test results are reported in Fig. 4.

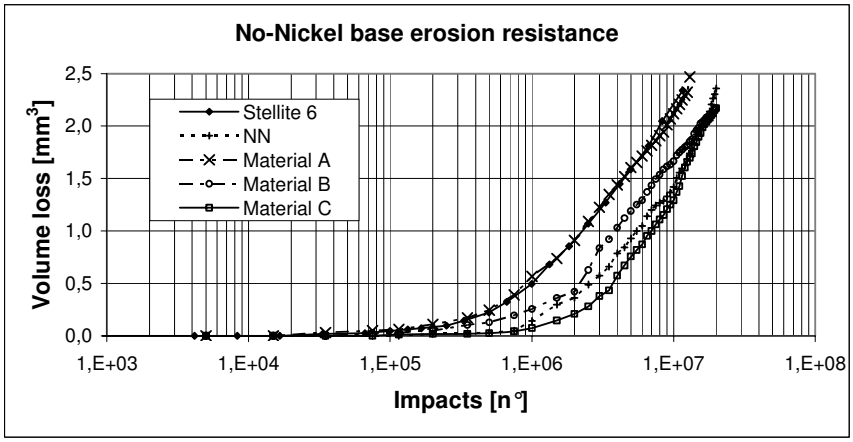

Fig. 4 – Erosion resistance results of samples without Nickel content.

Element wt%	Materials			
	NN	A	B	C
Fe	1.0%	7.5%	3.3%	6.9%
Cr+W+Si	38.2%	32.5%	37.4%	37.8%
Impacts No.	15.7×10^6	8.9×10^6	16.2×10^6	16.2×10^6

Table 3 - Test results on samples without Nickel.

It is worth noting that some samples show an Iron concentration in excess of the powder specification limits. This is mainly due to Iron dilution from the substrate, which occurred during the manufacturing process. Despite this unwelcome result, it has been possible to obtain some useful information on the erosion resistance of these samples.
Considering the materials "NN" and "C", the main difference is in their Iron content. In this case, Iron does not seem to have any influence on erosion resistance and this appears to be justified by the fact that the concentration of carbide forming elements is approximately the same. On the contrary, if addition of Iron decreases the concentration of carbide forming elements (NN and A, or C and A) its effect is detrimental.
The influence of other alloying elements has been studied too. For instance, the presence of Cr, W and Si shows a positive influence improving erosion resistance.

NY materials
Three Nickel-rich powders, NY, Material D and Material E have been tested.
In Fig. 5 the composition difference between Material D and Material E is reported: a high concentration of Iron is found in Material D.
Samples have been analysed by EDX, in order to check their real chemical composition. Three measurements have been performed on each sample; the average value has been calculated for each element, and results obtained are summarised in Table 4, together with the number of impacts required to produce 2 mm^3 of volume eroded.

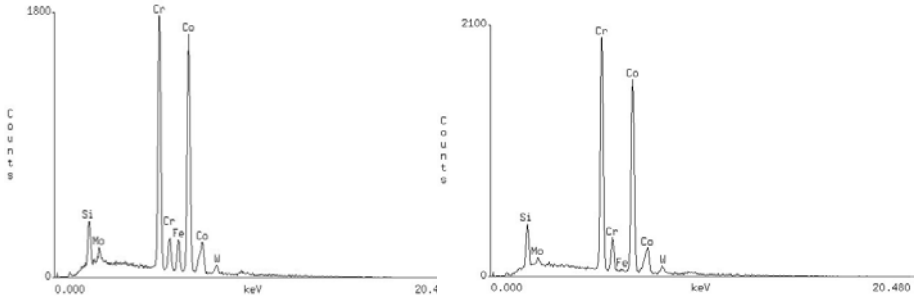

Fig. 5 – Chemical analysis results on material D (on the left) and material E (on the right).

Element wt%	Materials		
	NY	D	E
Ni	4.0%	4.3%	3.0%
Fe	0.9%	5.0%	0.4%
Cr+W+Si	39.1%	38.0%	42.4%
Impacts n°	24.6 x 10^6	18.5 x 10^6	23.7 x 10^6

Table 4 – Test results on samples with Nickel.

While comparing “NY” and “E” materials, it is possible to observe that they have nearly the same erosion resistance; however, the presence of Ni seems to give a benefit: “NY” material has a higher erosion resistance, with lower levels of carbide forming elements such as Cr and W, but with a high Ni content. It is important to note, however, that material D has the highest level of Iron, due to the laser manufacturing process: comparing “D” and “E” materials, the only difference between them is in their Iron content and its presence at higher concentration decreases erosion resistance a great deal. A higher Iron concentration induces a decrease in erosion resistance, as confirmed in the following diagram.

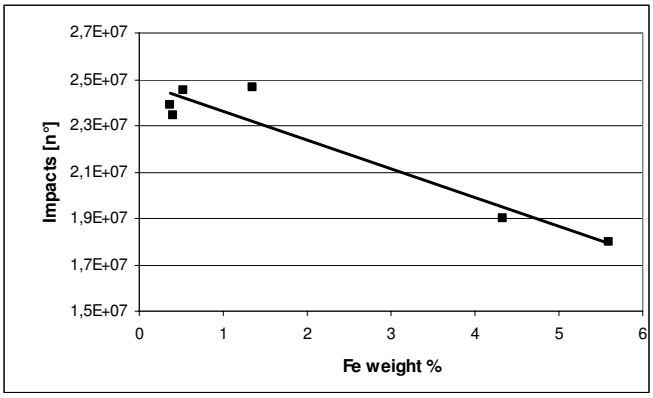

Fig. 6 – Erosion resistance versus Iron content.

In order to complete the study, a comparison between erosion results on the new powders tested and on the Stellite 6 reference one has been performed: a high increase in erosion resistance has been detected and confirmed for all the new powders (Fig. 7).

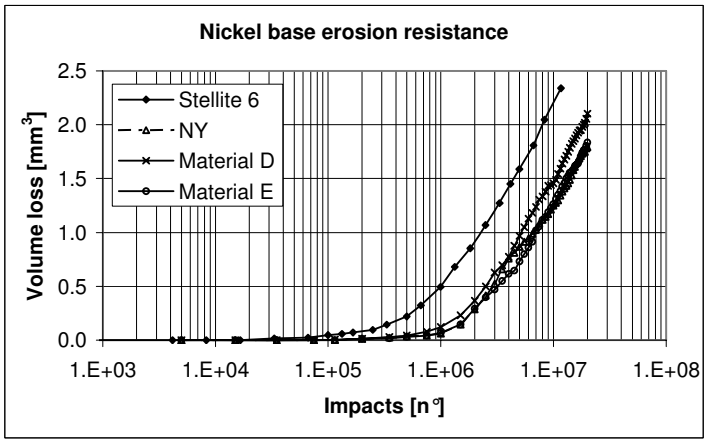

Fig. 7 – Erosion resistance results for samples with Nickel.

Comparison of NY-NN materials

A comparison has been performed between the materials obtained in the two directions investigated, with and without Nickel content. Results for materials with nearly the same content of carbide forming elements have been plotted in the following diagram.

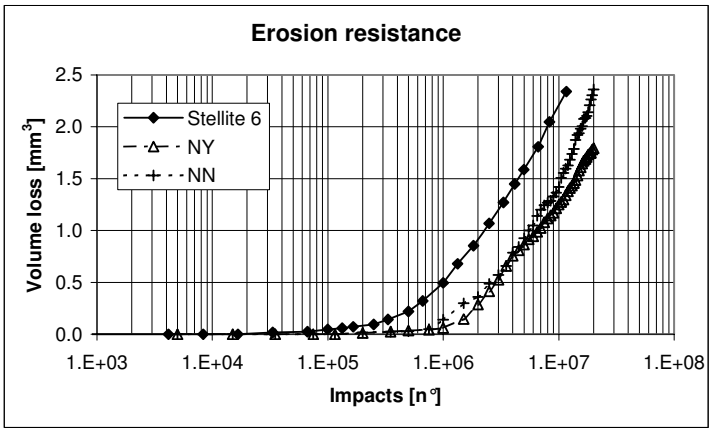

Fig. 8 – Erosion resistance between materials with (NY) and without Nickel (NN).

It is evident that Nickel samples have the highest erosion resistance; this is confirmed by Table 5, where the main difference between the two materials is their Nickel concentration, because the weight percentage of carbide forming elements is nearly the same.

Element wt%	Materials	
	NY	NN
Ni	4.0%	0.0%
Fe	0.9%	1.0%
Cr+W+Si	39.1%	38.1%
Impacts n°	24.6×10^6	15.7×10^6

Table 5 – Comparison between Nickel and no-Nickel samples.

It is possible to note that all the materials tested have a higher resistance to liquid droplet erosion than Stellite 6 material. Nickel's positive influence is also confirmed by considering Table 6, where the average values are reported for all the samples tested, with and without Nickel. It is moreover possible to note that Nickel presence generally permits also an increase in the weight percentage of the carbide forming elements, with respect to the highest concentration allowed for the "NN" materials [2-3], because of Nickel's positive effect on toughness, which reduces crack problems in the cladding process.

Element wt%	Materials		
	Nickel powders	No Nickel powders	Stellite 6
Ni	3.7%	0.0%	0.0%
Fe	2.1%	4.7%	9.5%
Cr+W+Si	39.8%	36.5%	33.7%
Impacts n°	22.3 x 10^6	14.3 x 10^6	8.2 x 10^6

Table 6 – Comparison of test results.

Conclusions

In this communication the possibility has been investigated of increasing liquid-droplet erosion for steam turbine application by using modified Stellite 6 coatings, obtained by laser cladding.

It has been shown that – with respect to Stellite 6 powder – a significant increase in erosion resistance occurs when using modified Stellite 6 coatings (see Table 6).

Iron influence is rather complex: with Nickel, it decreases erosion resistance, without Nickel it seems to have no significant effect on the material.

Nickel content improves erosion resistance a great deal and permits an increase in the concentration of carbide forming elements without crack problems during the manufacturing process.

In conclusion, an improvement in liquid droplet erosion resistance has been established and the two best powder compositions – with Nickel [4] and without Nickel [5] – have been patented.

References

[1] E. Giorni, M. Cecconi, M. Giannozzi, F. Pratesi, F. Sciacchitano, *"Erosion-resistant coatings for low-pressure steam turbine blades"*, Proceedings EUROMAT 99, Munich.

[2] C. T. Sims, W. C. Hagel *"The superalloys"*, Wiley-Interscience, New York, 1972.

[3] W. H. Jiang, X. D. Yao, H. R. Guanz, Z. Q. Hu, *"Secondary M_6C precipitation in a cobalt-base superalloy"*, Journal of Materials Science Letters 303-303, 1999.

[4] US Patent n° 6,986,951 Cobalt-based alloy for the coating of organs subject to erosion by liquid, 2006.

[5] US Patent n° 6,984,458 Method for treating organs subject to erosion by liquids and anti-erosion coating alloy, 2006.

A NEW DEVICE FOR TESTING COATINGS UNDER THERMAL SHOCK

G. Zonfrillo[1], M. Giannozzi[2], F. Pratesi[1], E. Giorni[2]

[1] *Department of Mechanics and Industrial Technologies, University of Florence, Italy – giovanni.zonfrillo@unifi.it.*
[2] *GE-Nuovo Pignone, Florence, Italy.*

Abstract

This communication describes a new device that has been designed and produced by GE-Nuovo Pignone, in cooperation with the University of Florence. The equipment was designed to run automatic tests with thermal fatigue cycles. During a cycle, the sample is subject to heating on the coated side, using a combustion flame, up to the selected temperatures value, followed by a holding time at this temperature and a subsequent fast cooling by forced-air, down to room temperature. The reasons behind the final design of the machine are explained in some detail and adjustments required for correct working are described.
The test-machine is based on a brushless motor, which lets a sample holder rotate stepwise with four or eight coin-shaped samples. The flame originates from a methane-air mixture, enriched with oxygen. Fuel flow is independent of pressure and temperature thanks to mass-flow controllers. The highest reachable temperature is higher than 1200°C. Temperatures of the heated face and of the opposite one are measured with two pyrometers, calibrated taking sample emissivity and its variation during cycling into account. Sample conditions are constantly monitored with a digital camcorder that records some images of the sample surface for each cycle.
Preliminary results from a series of tests (between 1200°C and room temperature) on superalloy samples coated with a standard TBC (B class) are discussed. The new device is able to perform flame thermal cycling tests on any kind of ceramic coating.

Keywords: coatings, high-temperature, thermal barriers, thermal shock, flame thermal cycling.

Introduction

The improvements in performance of gas turbines in the last decade have been mostly due to two factors that made it possible to increase working temperatures: introduction of complex cooling systems (taken from aeronautical practice) and use of thermal barriers.
Thermal barriers coatings, TBCs, usually consist of two layers: the top-coat is the external one, formed by a ceramic material, often yttria-stabilised zirconia; the bond-coat is the intermediate layer, usually an oxidation-resistant metal alloy with the task of firmly connecting the top-coat to the matrix.
These coatings are subject to various types of damage, such as wear from gases, oxidation at the interface with the bond-coat, corrosion. Failure often occurs through spallation or fatigue.
Low-cycle thermal fatigue has one of the main damaging effects on TBCs and ceramic coatings in general; it derives from severe temperature changes occurring during the start-up and shut-down stages, when mechanical stresses in the material arise from the different thermal properties of the metal and ceramic parts of the coatings.
Use of TBCs is continuously increasing and it is necessary to collect information on their behaviour. Observation on working components requires a long-term investigation. In order to obtain reliable results in a reasonable time, accelerated tests are indicated at the lab level. Several devices have been designed to this aim [1-6], but as yet no device has been acknowledged as a standard test-machine. Existing devices are based on variously selected criteria and have been taken into account in this project, with special attention to a particular

case [6].
A new device has been designed and produced by GE-Nuovo Pignone, in cooperation with the University of Florence; it provides experimental results on the life of various thermal barriers in controlled and reproducible conditions and has already been used for testing TBCs for several months.
The design chosen for the device had three aims, as follows.
- Performing a direct comparison of similar coatings; for instance, the same coating coming from different suppliers.
- Obtaining data that may be used by designers – considering the test as an accelerated procedure with respect to actual working conditions. In particular, easy modification of test parameters (such as highest temperature and holding times) is required, so that both low and high-cycle numbers can be investigated for determining fatigue behaviour.
- Providing a contribution toward the establishment of a standard test for checking the resistance of TBCs.

Design of a testing device for thermal shocks

Technical requirements and device scheme
Essential points of the project are flexibility of use, capability of automatic working, and a relatively low cost. The task is to submit superalloy specimens coated with TBCs to tests with thermal cycles consisting in heating the coated surface, holding at high temperature, rapid cooling. Specimens have the shape of a coin (25 mm diameter), with only one side coated with the TBC.
The following parameters have been considered as the most important.
- Set-point temperature. A maximum value of 1200°C has been chosen; the minimum value can be set at room temperature and is not considered a test variable.
- Holding time in a cycle is fixed, but its value can be differently selected for any test, in order to allow investigation of both thermal stresses and oxidation at high temperatures. Any value between 20 seconds and 60 minutes can be selected.
- Number of thermal cycles performed.

For economic reasons and on the basis of locally available facilities, a flame – originating from a methane-air mixture, enriched with oxygen – has been selected for heating and forced air for cooling.
A circular shape has been adopted for locating the samples, as shown in Fig.1. They are mounted on a disk, through pincers provided with sample holders. An intermittently working motor lets the disk rotate stepwise with constant rotation steps.
Samples are tested together and cycled in a constant sequence, each after the adjacent one. They can be either eight or four; the rotation steps are thus either 45 or 90 degrees, respectively.
For each rotation cycle of the system (corresponding to one complete revolution of the motor), the sample is submitted to the various phases of the test cycle.
Let us examine the situation in the case of four samples tested together – namely with clockwise rotation steps of 90°. Starting from position 1 in Fig. 1, the first sample is heated and held at high temperature for the time set. Then we have the first rotation step and the sample passes to position 2, where its forced-air cooling occurs; at the same time, a new sample enters position 1 for its heating phase. The following rotation step brings the first sample to position 3, where a digital camcorder records some images of the sample surface. Position 4 (as for all the unnumbered intermediate positions in the eight samples) is a waiting

position.
The main components of the device are described below, together with the reasons that led to their selection.

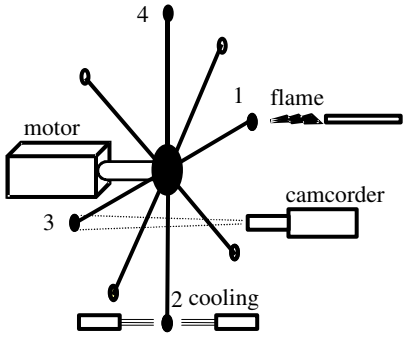

Fig. 1 – Scheme of the test equipments.

Movement of the specimens
The rotation-step movement of the samples into the next position must be carried out with high accuracy. The solution has been found by applying a brushless motor with permanent magnets, owing to its several advantages for this application. It has an internal position sensor, so that rotation speed is controlled by a feedback system; it is suitable for discontinuous application with a high angular precision in its interruptions, which is necessary in this case.
A 1:50 speed reducer has been applied to obtain both a higher couple and a low rotation speed. A disk (Fig. 2) is positioned at the top of the shaft, and pincers are assembled onto it with screws. As a shield from the flame, a steel sheet has been placed behind this disk.

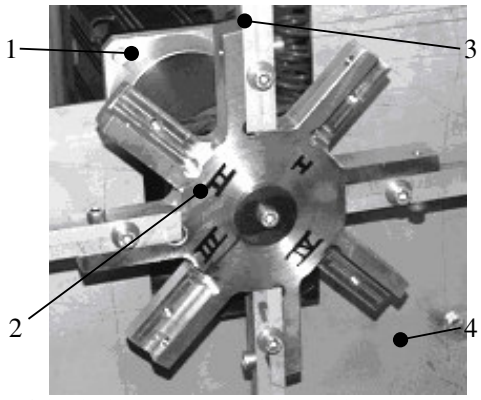

Fig. 2 - View of the devise: motor (1), disk (2), pincer (3), steel sheet (4).

Sample holding
Pincers keeping the samples in place are exposed, as the sample is, to temperature cycles that

can produce significant thermal stresses. Oxidation is a significant factor too.
The solution chosen (shown in Fig. 3) is to use pincers longitudinally divided into two parts, each having its top curved and with a groove inside, where the sample is placed. The two parts are connected onto one another with a screw, and this allows easy mounting and dismounting of the samples.

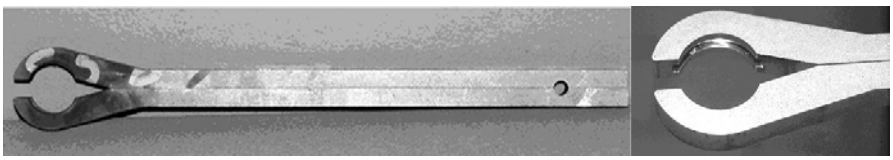

Fig. 3 – Photo of a pincer, with detail on the right.

The material selected is Haynes 230, thanks to its excellent oxidation resistance at mean to high temperatures.
A FEM study has been carried out with the aim of determining the stress distribution. Results show that the highest stresses remain within acceptable limits and are located at the sections where the bars change their shape, near the part where the sample is held. Moreover, as confirmed by the simulation, the pincers do not induce stresses in the sample during heating.

Cooling
As mentioned above, cooling needed for applying thermal shocks occurs by forced air blown onto the front face of the sample. It is controlled by a solenoid valve (driven by a PLC) and jet pressure is controlled by common pressure reducers.
Cooling pipes arrive at both positions following that of heating, corresponding to rotations of 45 or 90° (with eight or four samples respectively). Before each test starts, either set is chosen by means of a manual selector.
Moreover, another nozzle has been positioned behind the sample at its heating position in order to increase the thermal gradient within the sample by cooling the back face, uncoated, when the sample is held at high temperature.

Heating torch
In Nuovo Pignone, both methane and forced-air piping are available and have thus been chosen.
Initially a commercial air-methane torch has been used with a swirler in the shape of a toroidal spiral for pre-mixing the two gases. Several heating tests have been carried out using this burner with different combustion volume ratios. Stable conditions have been obtained up to a temperature value of about 965°C on the sample.
Two possible ways have then been tried in order to further increase temperature: 1) air pre-heating up to 250°C, with a muffle furnace; 2) enriching the gas mixture with additional oxygen amounts.
With the help of pre-heating, a temperature of 1150°C has been obtained, not yet high enough. Adding oxygen produces the problem that – owing to gas pre-mixing – combustion occurs within the torch, with the result that the nozzle of the torch gets heated up to very high temperatures. Therefore, a new torch has been designed, in which fuel and supporter of combustion are kept separated up to the exit nozzle.
Fig. 4 shows a complete view of the torch. It is provided with two coaxial pipes, each ending up with its nozzle. Fuel passes through the inner pipe. Air and oxygen, which support

combustion, are mixed before entering the torch and pass through the outer pipe.

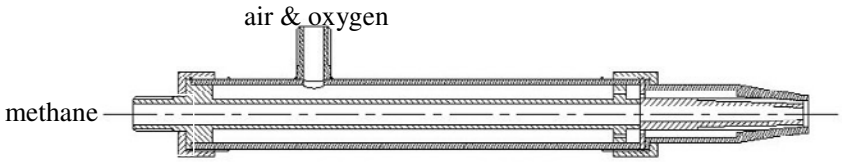

Fig. 4 – Heating torch.

These adaptations have allowed a flame to be obtained with all the properties required, first of all the temperature value on the sample, but also fitness with the sample's dimension and shape. In particular, in order to avoid heating the pincers excessively, the flame must not be irregular and jagged and its dimension must be compatible with that of the samples (Fig. 5).

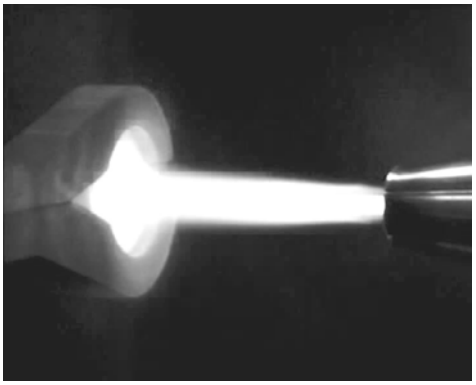

Fig. 5 – Sample heating.

Flow regulation

Once the problem of a suitable torch for optimum combustion has been solved, it remains to introduce a control in order to obtain a suitable slope for increasing temperature and then keeping it constant at the selected set-point. A gas flow control has been used allowing thermal power from the torch – and consequently thermal power absorbed by the sample – to be varied.

Flow regulation has been obtained thanks to mass flow controllers (MFC), which perfectly satisfy our requirements; it occurs through a closed-loop system, on the basis of a measurement with a "hot wire" system of the real flow passing through the MFC. This allows the alimentation system to be uncoupled from pressure and temperature conditions existing both up and down-hill with respect to the MFC.

On the basis of actual flows expected during the tests, three MFCs have been used, located on air, oxygen, and methane lines, respectively.

To link the various flows, it has been decided to keep the flow of methane as the free parameter to set up and to relate oxygen and air flows to through two constants. In particular the oxygen percentages in the air-oxygen mixture and combustion volume ratio are set by the

operator at the beginning of the test. Controlling software can thus calculate the MFCs opening percentages of air and oxygen on the basis of the values set and methane flow. Methane flow is the parameter actually modified by the temperature control system.

Temperature measurement

An infrared optical pyrometer has been selected for measuring temperatures, because moving parts are hardly compatible with the application of thermocouples. The main problem derives from the fact that the emissivity of these materials is not known accurately enough; if wrong values are assumed, they may introduce large errors in the indication of temperature.
Thermal barriers have been studied from this viewpoint, but a general agreement has not yet been reached. Several authors have concluded that TBCs show a very high reflectivity at commonly used wavelengths (1-2 μm) and it is uncertain in which region zirconia approaches the behaviour of a black body [7, 8]. After various preliminary tests, our experience has led to the choice of a special pyrometer working at 7.9 μm, with measurement scale from 400 to 1600°C.
A second pyrometer (2 μm wavelength) is used to measure temperature on the uncoated back face of the sample.

Temperature regulation

Temperature is controlled with a closed-loop scheme using the pyrometer signal as feedback. The driving signal is adjusted with a PID (proportional, integrative, derivative) procedure, and acts on methane flow through the difference between actual and set values of temperature.
Control by means of PID must be continuous. When the sample makes one rotation step, a temperature jump is read and consequently unacceptable jumps in gas flows occur. At the end of each cycle the PID procedure is therefore interrupted and activated again as soon as the sample change has occurred. PID procedure acts both in heating and holding stages but with different sets of parameters, both experimentally determined.

Inspection of coating condition

One of the requirements is that the test should be performed automatically. However, defining the exact condition of failure or delamination is very hard to do in an automatic way. For this reason we used an automatic detecting and recording system capable of indicating the situation after each cycle, so that results can be analysed after the test is finished.
The solution has been found by using a digital camcorder – provided with macro lenses; data obtained are recorded on a dedicated hard disk.
The sample is observed for a few seconds in the intermediate position immediately after that of cooling (because in the heating position it is too bright and in the cooling position the air pipes cover part of the image).
When images are saved, each file name has the date and hour (seconds included) of image recording, so that it is easy to reconstruct the chronological sequence during the following analysis.

Device management

The various parts of the device are controlled by a Programmable Logic Controller (PLC), which is linked to a personal computer and is tasked with performing the whole test and interrupting it in the case of functioning problems. To attain this last goal several controls have been introduced.
The operator sets the main data for the test via computer, namely:

- number of samples used;
- number of cycles to perform;
- temperature set point;
- high-temperature holding time;
- forced-air cooling time;
- cooling or not cooling sample's back side;
- values of PID parameters for temperature regulation;
- combustion volume ratio;
- value of oxygen concentration in the air mixture.

Once the test has started, it continues automatically without any assistance from the operator.
An image of the whole apparatus in reported in Fig. 6.
The value for the number of cycles corresponding to the end of the test can be chosen according to several criteria:
1 – A time is selected long enough for failure of all the specimens; then one opens the image data base and reads the exact time of delamination for each coating.
2 - A given cycle number is set for the end of the test, and specimens still unaffected by delamination can be considered as valid for application.
3 - Standard values are initially set for the number of cycles at which the test is interrupted for visual inspection. The damage evolution of the specimens can thus be monitored and its life assessed. As before, the image database can provide exact times of failure for the specimens.
Moreover, at any time during the test, the operator can observe the images recorded and decide to interrupt the test manually.

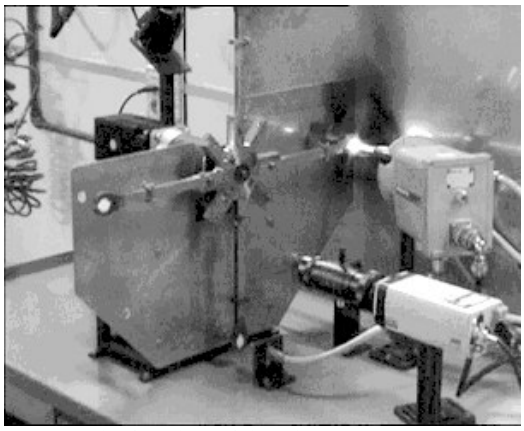

Fig 6 – View of the whole apparatus.

2 Testing of the device

Determination of the emissivity
Testing a new TBC requires a preliminary determination of its emissivity (at the wavelength used by the pyrometer), defined as the ratio between its energy emission and the energy emission of a black body at the same wavelength, taken as 1. As for the pyrometer focused on the back face of the sample, emissivity can be taken from the lists of values existing in the

technical literature for uncoated materials. For the pyrometer located in front of the sample, the emissivity of the TBC must be determined experimentally, because these are relatively new materials with values not yet listed in the literature.
An electric furnace with a maximum temperature of 1200°C has been used for measurements. It has been provided with a ceramic support for the samples. The temperature of the furnace has been initially measured with both a certified pyrometer and a thermocouple located at the bottom of the furnace (comparable with a black body): both methods gave the same values, thus confirming that the thermocouple measurements currently used were reliable.
The furnace is then heated with a sample at its bottom coated with a class B TBC. When the sample is at the same temperature as the furnace, emissivity value is manually changed on the control pyrometer until the temperature value read is the same as that indicated by the thermocouple.
Measurements have been carried out at 1200°, 1100°, 1000°, and 900°C. To evaluate measurement dispersion, four nominally identical samples have been examined (Tab. 1).

Tab. 1 – Values of TBC emissivity at various temperatures.

Temperature (°C)	Emissivity					
	sample 1	sample 2	sample 3	sample 4	average	regression on all data
1200	0.996	0.997	0.996	0.999	0.997	0.997
1100	0.990	0.994	0.991	0.997	0.993	0.993
1000	0.984	0.991	0.986	0.992	0.988	0.988
900	0.978	0.988	0.981	0.988	0.984	0.984

Average values are reported in the last but one column. The last column shows the corresponding values as deduced from the regression curve computed using all the 16 measured values. Up to the precision level used, the two sets of values are exactly the same.
The possibility of emissivity variations following thermal shocks of the samples is another aspect that has been investigated: emissivity has been measured again after 50 and 100 cycles (with 120 s hold time, temperature max 1200°C) with results shown in Tab.2.

Tab.2 – Variation of TBC emissivity (average of four samples) with cycling.

temperature (°C)	average emissivity		
	0 cycles	50 cycles	100 cycles
1200	0.997	0.990	0.990
1100	0.993	0.986	0.988
1000	0.989	0.982	0.983
900	0.983	0.977	0.977

Change from 0 to 50 is greater than from 50 to 100. Probably there is a change during the first cycles and then the value remains almost constant. This may be due either to a change of the physical properties of the coating or to some deposition of combustion products on first heating.
New measurements have been made at 1200°C, with 5-cycle intervals. Results reported in Tab. 3 show that a change already occurs after five cycles, while subsequent variations are very limited and mainly connected with the statistical distribution of measurement values.

Tab. 3 - TBC emissivity at 1200°C as a function of cycle number.

cycle	0	5	10	15	20	25
sample 1	0.993	0.984	0.984	0.981	0.984	0.984
sample 2	0.992	0.981	0.981	0.985	0.984	0.983
sample 3	0.996	0.984	0.983	0.984	0.985	0.985
sample 4	0.993	0.984	0.984	0.984	0.986	0.984
average	*0.994*	*0.983*	*0.983*	*0.984*	*0.985*	*0.984*

Micrographical examination of a barrier submitted to thermal shocks

Metallography has been used to assess damage and its evolution in the TBCs tested. The mechanism involves growth and coalescence of porosities and oxide particles, gradually leading to crack formation parallel to the interface and ultimately to detachment of the coating.

Some porosity is already present at the start, see Fig. 7. The amount is the result of a compromise solution: more porosity would allow an easier and deeper oxidation attack into the bond-coat; less porosity would make the coating too brittle.

With an increasing number of cycles, isolated oxide particles change into small oxide internal layers: in the TBC section, increasingly longer lines are observed. Fig. 8 shows the situation after 1200 cycles at 1200°C, with 120 s hold time, 90 s cooling time and cooling of the back side of the sample. At this stage, formation of extended cracks leading to disconnection is close to starting or already started, depending on the particular case.

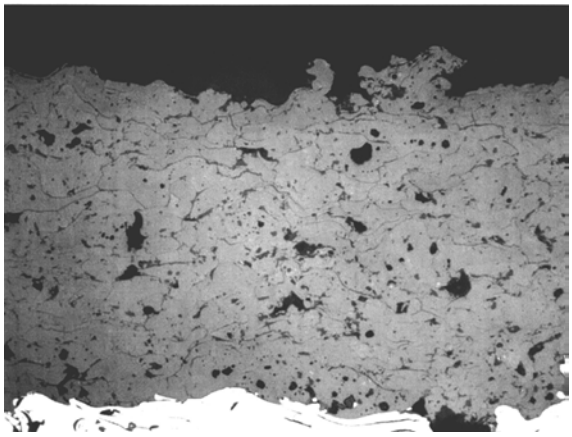

Fig. 7 – Sample before cycling.

Conclusions

An acknowledged test for assessing thermal and mechanical damage in TBCs is still missing. The testing device here described fulfils the aims mentioned in the introduction. Its operation has been verified. It can be used to improve technical and scientific knowledge. In the former case, it may be used for:

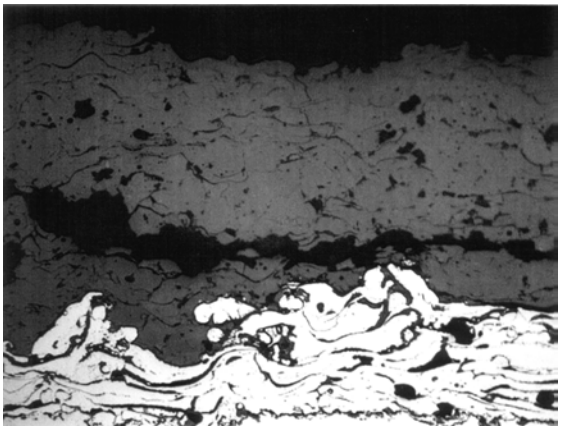

Fig. 8 – Sample after 1200 cycles.

- comparing different TBCs in experimental conditions similar to working ones;
- comparing the same TBCs coming from different makers;
- comparing the same kind of TBCs deposited with different techniques;
- defining a testing procedure for quality control of any TBC supply.

In scientific research, this device may be used for:

- monitoring damage evolution and life of a given TBC in different selected conditions of temperature, cooling, and so on;
- finding the upper temperature limits for any TBC – above 1200°C;
- checking properties of new coatings.

Moreover, the device described may be seen as a contribution toward the general aim of introducing a standard test for TBCs, which is largely required for their characterisation.

References

1. B.Windelband, K.Kleefeldt, D.Munz, B.Schinke, *Thermal cycling and isothermal tests on black-coated specimens*. Fusion Engineering and Design, v.28, 1995, pp. 90-96.
2. V.Teixeira, M.Andritschky, H.Gruhn, W.Maltener, H.P.Buchkremer, D.Stover, *Failure of physical vapor deposition/plasma-sprayed thermal barrier coatings during thermal cycling*. Journal of Thermal Spray Technology, v.9, n.2, 2000, pp. 191-197.
3. M.A.Zamzam, A.S.El-Sabbagh, M.M.Milad, *Study of thermal cycling effects of Al-Ni turbine blades on their lifetime*. Materials and Design, v.23, n.2, 2002, pp. 161-168.
4. A.Kawasaki, R.Watanabe, *Thermal shock fracture mechanism of functionally gradient materials as studied by burner heating test*. Proceedings of 3rd International Symposium on Structural and Functional Gradient Materials, 1995, p 397-404.
5. P.K.Panda, T.S.Kannan, J.Dubois, C.Olagnon, G.Fantozzi, *Thermal shock and thermal fatigue study of alumina*. Journal of the European Ceramic Society, v.22, n.13, 2002, pp. 2187-2196.
6. G.Gualco, S.Corcoruto, A.Camporo, R.Taylor, D.Schwinghel, S.Oswald, *Highly porous thick thermal barrier coatings produced by air plasma spraying of a plastic-ceramic mixed powder*. Thermal Spray: A United Forum for Scientific and Technological Advanced, ASM International, 1997.
7. J.A.Ruud, R.D.Lillquist, D.M.Gray, *Surface temperature measurement of thermal barrier coatings using infrared pyrometry*. Proc. of the 1996 International Gas Turbine and Aeroengine Congress & Exhibition *ASME* 96-GT-281, 1996.
8. D.Zhu, R.A.Miller, *Investigation of thermal high cycle and low cycle fatigue mechanisms of thick thermal barrier coatings***.** Materials Science & Engineering A: Structural Materials: Properties, Microstructure and Processing, v.A245, n.2, 1998, pp. 212-223.

CHARACTERIZATION OF THERMAL BARRIER COATINGS BY MEANS OF FURNACE CYCLE TESTING

F.Cappuccini[1], G.Zonfrillo[2], F.Pratesi[2], M.Giannozzi[3]

[1] *Industrial Engineering Department, University of Perugia*
[2] *Mechanical and Industrial Technologies Department, University of Florence*
[3] *GE-Nuovo Pignone, Florence*

Abstract

In the present communication, four TBC systems consisting of ZrO_2-7wt%Y_2O_3 top coats, MCrAlY bond coat and a nickel base superalloy Hastelloy-X, obtained by APS (air plasma spray) were tested by furnace cycle test (FCT).
The coatings were sprayed using two APS equipments and powders produced by two different suppliers.
Characterization was carried out by means of furnace cycle tests at two temperatures, 1100°C and 1150°C, for 1-hour cycles consisting of 10 minutes heating, 45 minutes holding and 5 minutes forced-air cooling.
After determining the coating life of each TBC system, micrographic examination and adhesion tests were performed on as-sprayed samples, and on samples at 35% and 70% of their coating life.
This investigation led to definition of TBC-BC adhesion as a function of the number of thermal cycles.

Keywords: Thermal cycles, high temperature, zirconia, TBC, APS

Introduction

The efficiency and the specific output of gas turbines are strongly influenced by their operating temperature. Substantial performance gains can be realized by increasing the operating temperature.
To accomplish this there are two realistic options:

- Higher temperature resistant turbine materials, e.g. single crystal nickel base superalloys.
- The use of thermal barrier coatings applied to cooled turbine parts, so that the base materials operate at lower temperatures.

Thermal barrier coatings (TBCs) are widely used on combustion components as liners or transition pieces, both on heavy duty gas turbines for power generation as well as for mechanical driving applications, but despite considerable efforts, the highly desirable prediction of their lifetime is still a demanding task [1].
The TBC concept permits an increase in operating temperature and/or to reduction in the cooling gas flow due to the temperature gradient across the coating, that permit better thermodynamic performance and lower emissions without requiring major alloy development.
TBCs traditionally consist of a thick partially stabilized Zirconia top coating, frequently deposited by air plasma spraying (APS) on superalloy precoated with a metallic bond coat (MCrAlY) produced by vacuum or air plasma spray (VPS,APS).
The partially stabilized ZrO_2 top coat has a porous and laminar structure and consist of splats and cracks perpendicular and parallel to the surface, this porous structure gives increased thermal insulation and the cracks permit better stress accommodation. The metallic bond coat reduces the

diffusion of contaminants and the mismatches of the thermal expansion between top coat and substrate [2].
In order to achieve designed protection of coated component substrates, TBCs must show high reliability and long lifetime under severe conditions, such as high temperature cyclic exposure in an oxidizing environment.
Damage of TBCs occurs during service as a result of thermal stresses and oxidation attack. Thermal stresses are induced by CTE (coefficient of thermal expansion) mismatch between top coat and bond coat /base material; oxidation occurs at the "top coat – bond coat" interface, resulting in higher stress and lower adhesion. It is therefore mandatory to characterize the TBC systems not only by micrographic means but also with tailored tests, able to predict high-temperature and cyclic behavior.
The aim of the investigation presented here is to detect the damage mechanism under thermal fatigue in four thermal barrier coatings systems by using furnace cycle test (FCT) and adhesion tests, comparing results obtained at different damage steps.

Experimental procedures

Durability of TCB systems is dependent on many factors, including type of substrate alloy and chemistry, processing methods and microstructures of bond coat and top coat. Furthermore, the durability can be significantly influenced by test method used. Therefore the selection of test methods for evaluation of TBC durability is very important. The test conditions must be well characterized and the testing must mimic the service operation; otherwise the usefulness of the test data is limited and extrapolation outside the test range can be unreliable.
In the present communication, four TBC systems consisting of ZrO_2-7wt%Y_2O_3 top coats (YSZ), NiCrAlY bond coat on nickel base superalloy Hastelloy-X, obtained by APS (air plasma spraying) were tested. The coatings were sprayed using two APS equipments and spheroidized powders with different granulometry (A: 90-16 μm, B: 125-11 μm) produced by two suppliers, for this reason TBC Systems were named using two letters: first indicating APS plant (F or P), second indicating powders supplier (A or B) as shown in Table 1.

Sample	APS plant	Powders
FA	F	A
PA	P	A
FB	F	B
PB	P	B

Table 1 - Sample nomenclature

As underlined in the introduction, TBC on combustion systems during service is subjected to the combined influence of thermal stresses and oxidation attack; for this reason, in order to evaluate systems durability, two tests were used: furnace cycle test and adhesion test.

Furnace cycle test

FCT predominantly characterizes oxidation dependent failure of thermal barrier coating. TBC coated buttons (25 mm diameter x 3 mm thick) were used for furnace cycle testing conducted in static air furnaces. A representative thermal cycle selected for FCT is shown in Figure 1.

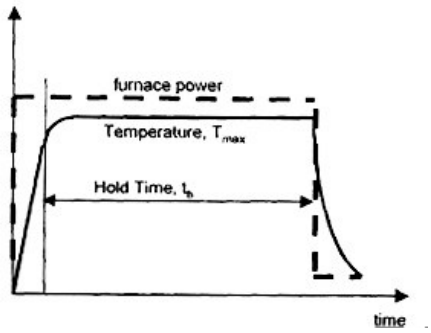

Figure 1 - A schematic diagram showing thermal cycle experienced by TBC during FCT

Tests were carried out at two temperatures, 1100°C and 1150°C, on three samples for each TBC system. The maximum temperature was held constant for a period equal to the hold time t_h. The test specimens were air-cooled outside of the furnace during cooling down portion of the cycle. The total time for the temperature ramp-up and ramp-down was approximately 15 minutes. Thus a 45 minute hold time test resulted in a total cycle duration of one hour. Test specimens were visually inspected periodically for indication of TBC spallation. The test was terminated when ≥20% area of the ceramic coating spalled on the test specimens. The corresponding number of cycles was documented as TBC spallation life [3].
Once the coating lifetime had been determined, other specimens for each system were tested to reach 35% and 70% of their life, and all samples were examined by means of Optical Microscope and SEM, to determine its oxidation levels.

Adhesion test

A tensile test was conducted on samples FA and PA according to ASTM C633. This test method covers the determination of the degree of adhesion (bonding test) of a coating to a substrate, or the cohesive strength of the coating in a tension normal to the surface. The adhesion test consist of bonding the coating to the face of a loading fixture, and subjecting this assembly of coating and fixture to a tensile load normal to the plane of the coating (Figure 2). The test specimen, button 25 mm diameter x 3 mm thick, is attached to the loading fixture using high strength epoxy with a strength at least of 69 MPa. The test was performed at ambient temperature, with an imposed rate of deformation of 0.2 mm/min. Adhesion tests were performed for systems FA and PA on as-sprayed samples and on samples at 35% and 70% of their coating life to evaluate in service adhesion variation, at different degradation steps [4]. Samples after detachment were observed in order to reveal if fracture has occurred at the top coat/bond coat interface or fully within the YSZ layer.

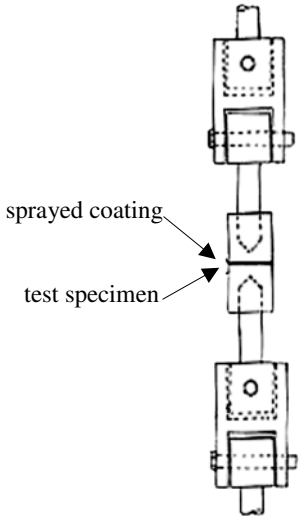

Figure 2 - Adhesion test, tensile test system

Results and discussion

Furnace cycle test

FCT data obtained from Hastelloy X coated samples are summarized in Table 2 and Figure 3.

TBC	TBC life (cycles) 1100°Cx1h	TBC life (cycles) 1150°Cx1h
FA	601	178
PA	612	212
FB	772	210
PB	995	284

Table 2 - FCT results

TBC life is strongly influenced by the thermal cycle selected. Comparing data obtained from the systems analyzed, it can be observed that life before spallation strongly increases with a decrease in maximum temperature; coating life at 1100°C is about double than life at 1150°C. Higher temperature causes both higher thermal strain per cycle and greater oxidation in the bond coat over time, reducing the TBC spallation life.

The data show that systems PB and FB, sprayed using coarser powders, had the best results in terms of spalling life, both at 1100°C and 1150°C, demonstrating higher performance of powders B.

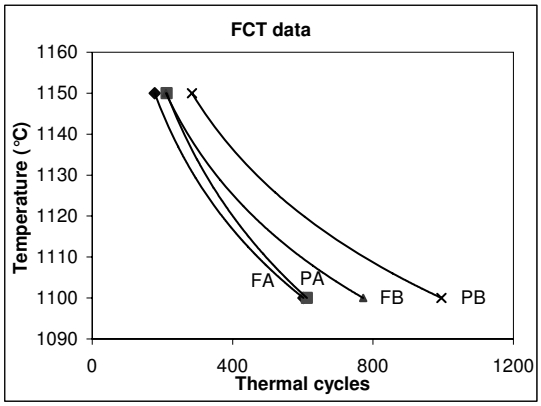

Figure 3 - Graph of FCT results

Adhesion test

Adhesion data obtained from Hastelloy X samples coated with NiCrAlY bond coat and YSZ top coat are summarized in Table 3 and Figures 4, 5. The test was performed only on systems sprayed with finer powders A.

TBC	Adhesion as coated (MPa)	Adhesion after FCT 1100°Cx1h (MPa)		Adhesion after FCT 1150°Cx1h (MPa)	
		35%	70%	35%	70%
FA	11.09	9.43	5.61	9.77	6.58
PA	9.23	7.72	4.08	8.07	6.22

Table 3 - Adhesion test results

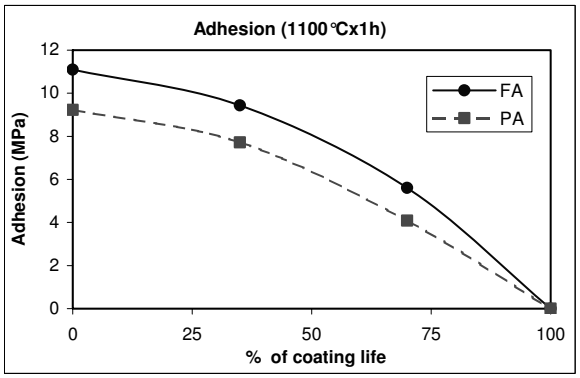

Figure 4 - Adhesion vs. coating fraction life (1100°C x 1h cycle)

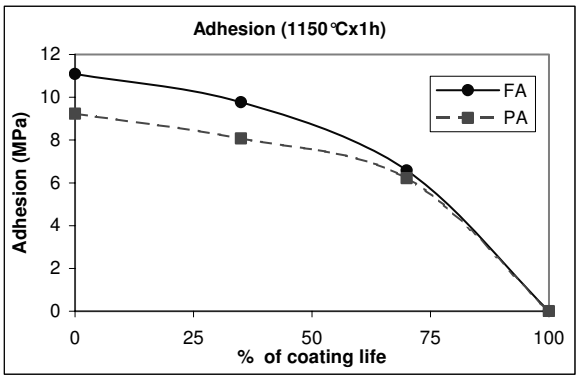

Figure 5 - Adhesion vs. coating fraction life (1150°C x 1h cycle)

The adhesion test, conducted on samples spayed with A powders, showed best performance of system FA, as a result of preeminent characteristics of "F" APS plant in terms of top coat adhesions.

Micrographic investigation

Micro investigation was performed, by means of optical and electron microscopy on samples as coated in order to verify the compliance with specification of TBC systems, and on aged samples to understand damage progress to failure. Attention was focused on oxidation phenomena affecting NiCrAlY bond coat (by means of EDS analysis on oxide scales), and on crack propagation at TBC-BC interface, considered the most important reason for TBC failure. TBC porosity was measured using an image analysis microscope on sixteen fields for each sample. Figures 6 and 7 show two TBC systems as coated.

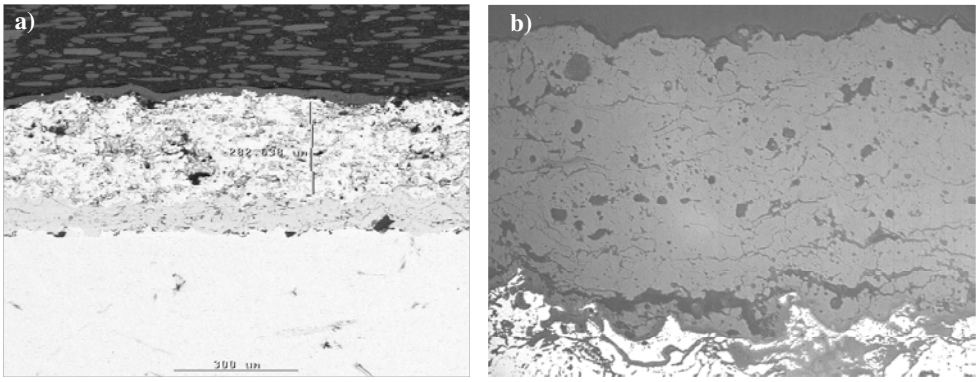

Figure 6 - a) PA as coated. b) PA as coated, TBC porosity.

Figures 8 and 9 show the oxide scale evolution in one of the four systems analyzed PA.

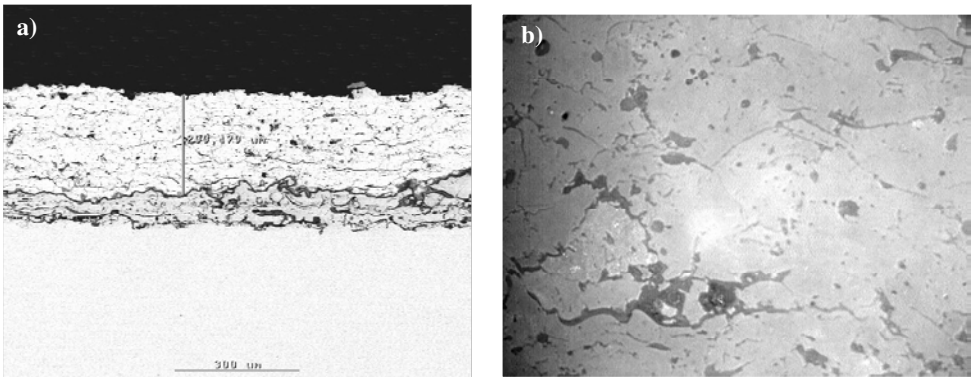

Figure 7 a) FA as coated. b) FA as coated, TBC porosity

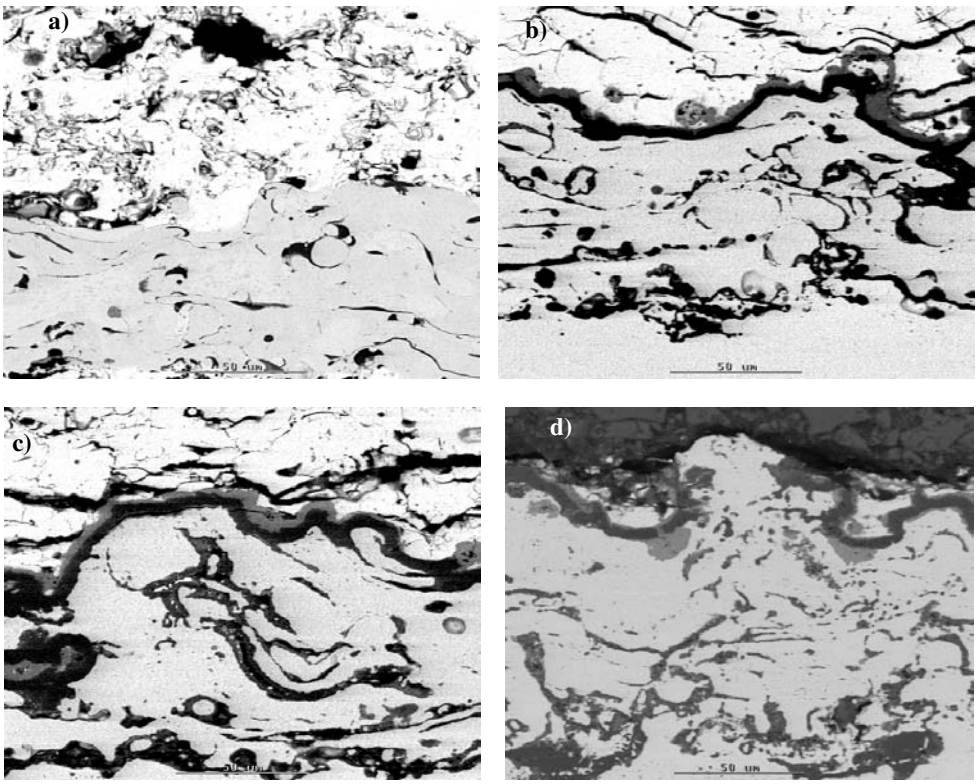

Figure 8 - a) PA as coated. b) PA after 74 cycles (35% TBC life) at 1150°C.
c) PA after 148 cycles (70% TBC life) at 1150°C. d) PA after failure

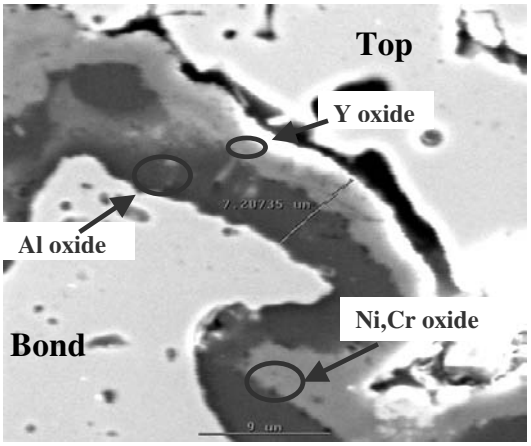

Figure 9- Oxide scale (PA after 428 cycles at 1100°C)

From micrographs on samples as coated it is plain that porosity is in compliance with specifications (5-15%). The bond coat's thickness is 100 μm, while for top coat's is 280 μm. No cracks were found either on the surface or at the BC-TBC interface, which it is actually free from harmful oxides.
After 35% of coating life at 1150°C, no changes in TBC thickness were observed while an oxide scale of 7,5 μm proved a degradation of interface adhesion characteristics.
After 70% of coating life, porosity level had not changed, revealing no traces of sintering at this temperature; the oxide scale observed was not significantly thicker, while its composition was changing towards a higher concentration of Chromium, Yttrium, and Nickel oxides. Some cracks in TBC were also evident.
The failure occurred at the BC-TBC interface; the bond coat appears very oxidized even if the surface oxide scale is still 8 μm, revealing the tendency of oxide to grow very quickly at the beginning and slowly afterwards.

TBCs life modeling
Based on FCT and adhesion results a TBC life model was developed. The model, based on Larson-Miller parameter, aims to find a relation to assess residual life of TBC systems, given service time (Figures 10 and 11).

$$LM = [T(°C) + 273] \times (\log t + C)$$

The value for constant C in Larson-Miller equations was chosen to have the best data fit. Using this equation for a known service time of a TBC system is therefore possible to estimate the residual life of a coating using only adhesion tests.

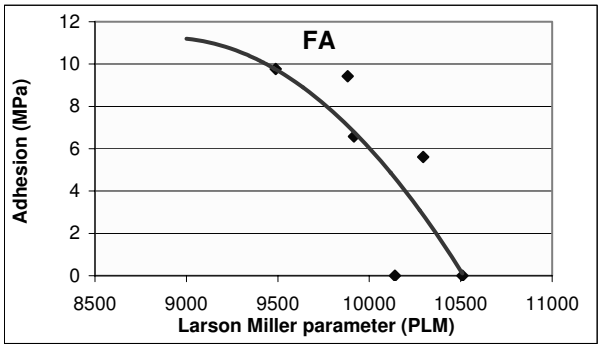

Figure 10 - Larson-Miller vs. adhesion data system FA

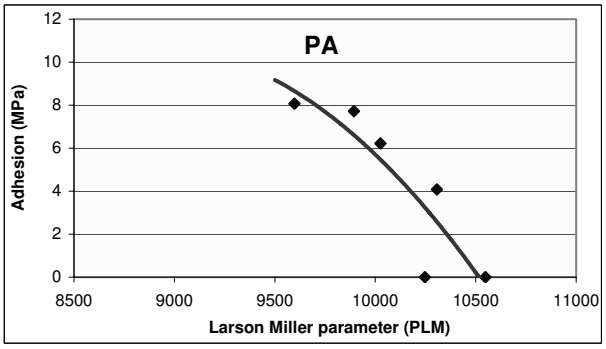

Figure 11 - Larson-Miller vs. adhesion data system PA

Conclusion

The durability of TBC is dependent on many factors, including the test methods used to estimate coating spallation life. Furnace cycle test showed that TBC failure occurs by thermal fatigue, due to concurrent presence of two main mechanisms: mechanical stress induced by thermal cycling and heavy oxidation attack due to high temperature. The adhesion test confirms that TBC degradation at the interface increases with rising test temperature. Bond coat and TGO (Thermally grown oxide) evolution was characterized by means of optical and electronic microscopy.

The PB system was demonstrated to be the best powders-plant compatible in terms of thermal cycle life, showing higher performance in FCT at 1100°C and 1150°C, while system FA was shown to have the best top coat/ bond coat adhesion characteristics.

The tests used are interesting tools to estimate TBC spallation during high temperature service.

References

[1] F.Traeger, M.Ahens, R.Vaben, D.Stover, “A lifetime model of ceramic thermal barrier coatings”, Materials Science and Engineering, A358, 2003, 11.
[2] A.Portinha, V.Teixeira, J.Carneiro, J.Martins, M.F.Costa, R.Vassen, D.Stoever, “Characterization of thermal barrier coating with a gradient of porosity”, Surface and Coating Technology, 2004, 7.
[3] R.Annigeri, P.S.Di Mascio, R.M.Ornstein, J.R.Zuiker,“ Life assessment of thermal barrier coatings for as turbine applications”, ASME Turboexpo, 2000, 8.
[4] “Standard test method for adhesion or cohesive strength of Flame-Sprayed coatings”, ASTM, C633-79, 1993, 5.

Acoustic emission analysis used as monitoring tool for burner rig tests of thermal barrier coatings

D.E. Mack[1], A. Casu[1], F. Traeger[2], R. Vaßen[1], D. Stöver[1]

[1]IWV1, Forschungszentrum Jülich GmbH,
Leo Brandt Str., 52425 Jülich, Germany
[2]Lehrstuhl für Phys. Chemie I, Ruhr-Universität Bochum,
Universitätsstr. 150, D - 44780 Bochum, Germany

Abstract

One major problem in the thermal barrier coatings applied to gas turbine components is the spallation of the ceramic coating under mechanical gradients and thermal cycling environments. In order to study the evolution of failure and the expectancy of lifetime under realistic conditions cycling burner rig tests are a well-established matter of choice. In the same way, the technique of acoustic emission (AE) testing has been widely proven to provide insight to microscopic crack formation. The aim of this study is to expand the use of AE testing as a rugged in-situ monitoring tool for combustion driven cycling rigs and to predict the failure of TBC in those tests.

For a successful application of the AE testing to an experiment using a gas fired and air cooled burner rig, it is necessary to overcome some limitations which are mainly due to the high level of interfering signals under those experimental conditions. A discrimination of signals originating from different sources of the setup has been undertaken by an analysis of the AE source location and the characteristics of the waveforms. In our experiments, AE signals from the ceramic coating are detected from the first cycle on. At least two processes can be differentiated by means of analysis of the AE waveforms. An evaluation of the correlation to experimental conditions and to subsequent metallographic failure inspection has been undertaken.

Keywords: acoustic emission, thermal cycling, thermal barrier coating, burner rig test

Introduction

Thermal barrier coatings (TBC) are frequently used in thermally high loaded parts of gas turbines as turbine blades and vanes. From an economic point of view and to fulfil the demand of optimal technical reliability it is necessary to explore and to improve the lifetime of all components. Despite their frequent use, there is a need for further development of TBCs, and research is being done at a large number of public and industrial places. This may lead to the possibility of further extending the operation conditions to higher working temperatures and therefore a thermodynamically more efficient regime.

For high-temperature applications, e.g. in the case of TBCs in aeronautical applications, the resistance to cyclic thermal loading is at least as important as the cyclic mechanical loading test for the lower temperature regime. For this purpose, a thermal cycling method for lifetime tests has been introduced [1], where the test rig is optimised for thermal barrier coatings designed for gas-turbine applications. In this test rig a thermal gradient is applied through the sample consisting of a ceramic layer on a metallic bond coat and a metallic substrate. To get insight into the exact evolution of microscopic defects in advance to the apparent failure the technique of acoustic emission (AE) can be utilized. Indirectly, this knowledge allows to test and to extend lifetime models, which are based on stress arguments.

The technique of AE testing has been widely proven to provide insight to microscopic crack formation [2-20]. Experiments have been done in combination with thermal mechanical bending tests [2-9], as well as in combination with cyclic oxidation tests [10-19]. However, one has to note, that nearly all experiments have been done with heating methods not-introducing additional mechanical noise at the time of the AE recording, such as movable tube furnaces or optical heaters. Only Kawasaki and Watanabe report from experiments with a combustion driven burner rig [12,15].

In respect to the interpretation of AE data, most work has been concentrated onto the evaluation of time or load dependent accumulation of AE events, counts and energy. This has been shown to be sufficient to monitor the evolution of cracks and delamination in absence of interfering noise. Less work has been done, so far, aiming a detailed analysis of AE signal form including amplitude distribution [6,12,13,15] or Fourier analysis of the signal trace [3,11,12]. Finally, a simulation of signals resulting from cracking in TBCs has been performed by Ma et al. [5,14]. The aim of this study is to expand the use of AE testing as a rugged in-situ monitoring tool for the above-described combustion driven cycling rigs and to try to predict the failure of TBC in those tests. Therefore, it is necessary to overcome some limitations, which are mainly due to the high level of interfering signals under those experimental conditions.

Experimental

Thermal Cycling

In the testing facility disc shaped samples are periodically heated by a natural gas/oxygen burner and cooled in a current of pressured air. Typical dimensions of the samples made from a Ni-based superalloy are 30 mm in diameter for a substrate of 3 mm thickness. During heating the reverse side of the sample is cooled by compressed air to maintain a temperature gradient of typically 0.4-1.0 $K\mu m^{-1}$ across the sample. The samples are clamped within a two-part metallic shield, which is necessary to prevent a perturbation of the burner flame by the backside cooling. Due to the independent regulation of the gas fluxes of natural gas, oxygen and compressed air by means of mass flow controllers the sample temperatures can be adjusted nearly independently in the range from 1050-1400 °C in the surface temperature and 950-1100 °C in temperature at the bond coat for a 300 µm thick TBC system. The surface temperature is measured with an infrared pyrometer operating in the spectral range 8-11.5 µm. The substrate temperature is measured using a NiCr/Ni thermocouple inside a hole, which is drilled radially into the substrate's center. After the high temperature phase, the burner (mounted on an air-driven slide) is removed and the sample is cooled from both faces by compressed air. The air fluxes are high enough to reach a sample temperature below 100 °C within 60-80 s. The cycles usually comprise 5 min of heating and 2 min of cooling and are repeated until a visible failure occurs. In the left part of fig. 1 a photography of the test rig is shown, which has been described in more detail in [1]. After testing, some specimens were cut perpendicular to the surface and polished to observe the cracking morphology in the cross-section of every specimen by means of SEM and optical microscopy.

Figure 1: Photographs of the gas fired and air cooled burner rig (left) and a detail view of the acoustic wave guides spot welded at the backside of the sample.

Acoustic Emission Processing

Degradation of the TBC system has been monitored by analysing acoustic emission events, which were recorded via acoustic conductor wires of about 30 cm length and 2 mm diameter. Those had been spot weld at the backside of the TBC coated samples and at the backside of the metallic sample holder. The use of wave-guides has been necessary to prevent damage to the piezoelectric AE transducers from the elevated sample temperatures in the experiment. Equipment used is based on an AMSY-4 acquisition and processing hardware of Vallen Systems (Icking, Germany). Up to three transducers of the model VS2M-P were attached to the acoustic conductor wires by stainless steel pyramids, which have been welded to the cold ends of the wires. The pyramids acted as a transition from the transducer diameter to the wave-guide with a diameter of 2 mm. During data acquisition, a 34 dB preamplifier of model AEP4 and a high pass filter were applied to the transducer signal before digitalisation with a maximum frequency of 10 MHz. This results in a transmitted frequency range from 350 to about 2000 kHz with a maximum amplification near frequencies of 320 and 790 kHz, respectively, which are typical for this type of transducer.

A number of parameters from the recorded AE waveforms are used to describe an AE event and are evaluated with the software package VisualAE of Vallen Systems. These include: (1) time of threshold crossing, (2) time to peak amplitude, rise time; (3) peak amplitude: (4) duration of the event and (5) the number of peaks that cross the threshold value, referred to as "counts." The most descriptive parameter is acoustic energy (E_{AE}). E_{AE} is estimated by integrating the rectified event signal over its duration and is thus sensitive to the amplitude and duration of the event. Additionally the temperatures of the surface and the substrate of the sample are recorded for any event to correlate the AE events with the given experimental condition. In addition, for some experiments the time dependent transient amplitude data of AE events have been logged, to evaluate the signal shape of different types of events.

In order to localize the sources of AE signals within the TBC sample, a standard localization technique based on run-time differences of AE signals, has been applied. Acoustic conductor wires have been spot welded with a triangular geometry onto the backside of the TBC sample, and AE signals collected from those three sensors have been evaluated. Figure 1 shows in the right part a photograph of the backsides of sample holder and TBC sample with conductor wires applied.

Results & Discussion

Interference of AE noise

For a successful application of the AE testing to an experiment using a gas fired and air cooled burner rig, it is necessary to discriminate signals coming from different sources of the setup. Signals originating from RF electronic noise or from mechanical resonance of the vibrating rig do not fall into the sensitivity range of the chosen transducers or can be easily cut off by a suitable threshold level. More severe interference of signals is found to originate from the metallic sample holder.

Figure 2 shows the time dependency of the acoustic energy of single AE events for several thermal cycles plotted together with the surface temperature for a TBC sample clamped within the sample holder (left) and only loosely fixed behind the sample holder (right). It is found that both, the rate of events as well as the average acoustic energy, are remarkably increased for the clamped sample if compared to the loosely fixed. This is in line with literature, where the amplitude of signals originating from the ceramic TBC is found to be smaller than that of signals correlated to cracking of the metallic bondcoat [6]. Additionally, the damping of an elastic wave can be expected to be increased in a medium having a lower Young's modulus, which is the ceramic TBC in our case.

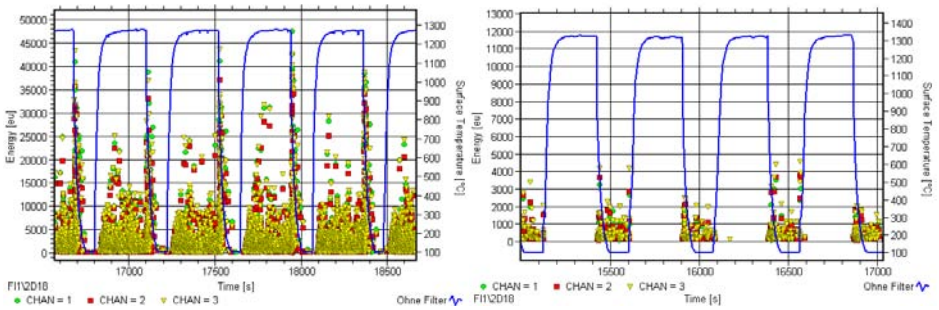

Figure 2: Time dependency of the acoustic energy of single AE events for several thermal cycles plotted together with the surface temperature for a TBC sample clamped within the sample holder (left) and only loosely fixed behind the sample holder (right).

Looking again at fig. 2, the main acoustic activity is found during the heating phases for the clamped sample, where it is found while cooling for the loosely fixed. This observation for the loosely fixed sample is also in accordance with findings previously reported in the literature [2,3,5,11,14,15,19], where preferential those events could be correlated with detrimental cracking and spallation of the TBC, which have been recorded while cooling. Therefore, it can be anticipated that most of the signals recorded from the clamped sample originate from the contact with the sample holder. Unfortunately, a free standing sample cannot be used in long lasting cycling experiments of several thousand cycles in the given cycling rig. So, the acoustic events from degradation of the metallic base material of the sample holder under heavy thermal load as well as those from mechanical friction of sample

holder parts and sample under thermal shock conditions have to be sorted out by a suitable filtering process.

However, when analysing the characteristics of signals recorded under different experimental conditions with and without close fixation between sample holder and sample, at least two processes can be differentiated. Figure 3 shows the correlation of acoustic energy and duration of acoustic events broken down for different phases of cycling by means of temperature ranges, e.g. cooling below 660 °C, intermediate, and heating above 1200 °C. Two trends can be observed from this figure: first, with increasing temperature a decreasing maximum duration of AE events is found; second, signals recorded from the loosely fixed sample emit a maximum of acoustic energy within shortest time if compared to the signal collected from the clamped sample. At first, this seems to be in contrast to the afore mentioned finding, that AE events from the ceramic TBC possess a smaller amplitude than those from the metallic bondcoat.

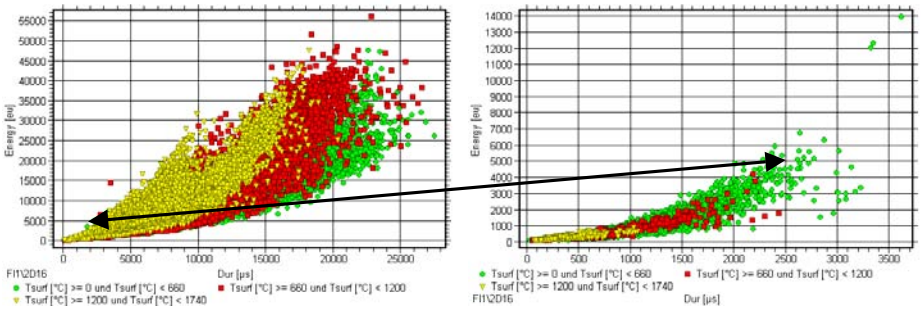

Figure 3: Correlation between acoustic energy and duration of acoustic events from a TBC sample clamped within the sample holder (left) and only loosely fixed behind the sample holder (right) for different temperature ranges. Corresponding coordinates of both graphs are marked with an arrow.

For a more detailed analysis of the correlation between acoustic energy and duration of acoustic events from the clamped sample, the left graph of fig. 3 has been broken apart into separate graphs for each temperature range and is shown in fig. 4. At least two types of AE processes can be differentiated in this view. First, there is one type of event found, which is characterized by relative quick release of considerable acoustic energy and of maximum average amplitude. By comparison of the left diagram of fig. 4 (cooling at low temperature) with the right diagram of fig. 3 (signals from the loosely fixed sample), this type of event can be identified as being originated from the sample.

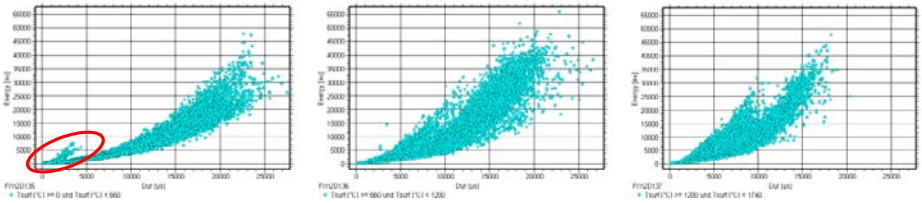

Figure 4: Correlation between acoustic energy and duration of acoustic events from a TBC sample clamped within the sample holder for different temperature ranges (detail).

Other events recorded from the clamped sample show a noticeable slower release of energy. Nevertheless, due to the normally longer duration the total energy of these events mostly exceeds that of the short events attributed to be from the sample itself. An increase of signal amplitudes can be stated for long lasting events with increasing temperature, as a comparable amount of acoustic energy is released in shorter time. At high temperatures a differentiation between both types of events based on the analysis of energy, duration, and amplitude is no longer practicable due to the shift of the long lasting events. It can be supposed that those long lasting acoustic emissions can be attributed to events of friction or plastic deformation nature [13], which gain energy from the thermal reservoir.

Localization of AE events and correlation to cracking and delamination

The localization of an AE source is based on the analysis of run time differences for AE signals originating from the same emission act but recorded at different AE transducers. Thereby a homogeneous and isotropic propagation velocity of sound is anticipated. For the successful application of this method, a measurement of the signal arrival times with an accuracy is prerequisite, which is better than the maximum run time difference of signals given by the distance between the sensor locations and the velocity of sound.

In this experiment, acoustic wave guides of equal length of about 30 cm have been spot welded with a triangular geometry onto the backside of the TBC sample of 30 mm diameter. The distance of the sensors to each neighbour in this arrangement is about 20 mm. The velocity of sound, v_s, can be calculated from the well-known relation $v_s = \sqrt{E / \rho}$, where E is

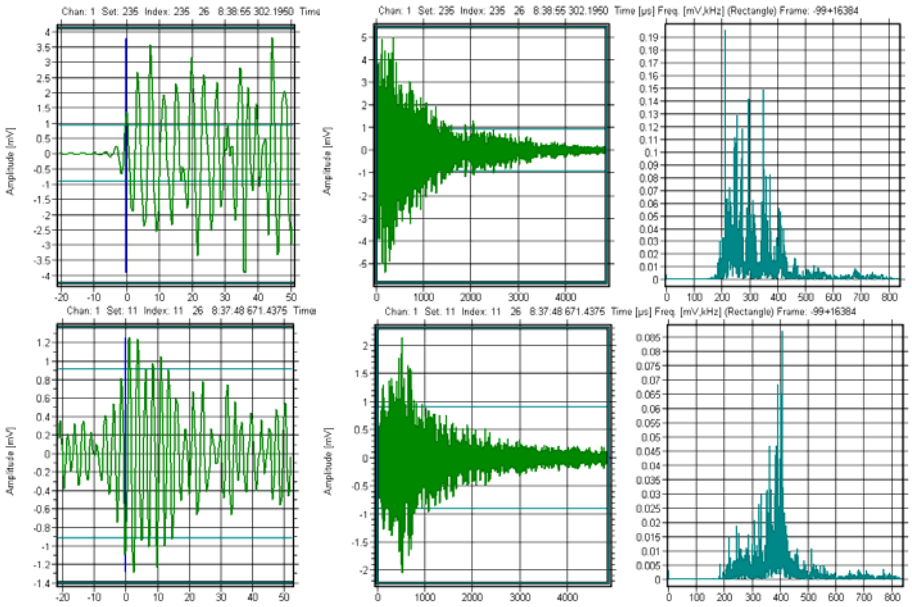

Figure 5: Transient signal forms and Fourier spectra of a typical high amplitude event recorded at low temperatures during cooling (upper part) and of a high amplitude event recorded at elevated temperatures during heating (lower part).

the Young's modulus and ρ is the density of the materials. Given a density of roughly 6 g/cm^3 and a Young's modulus of 40 GPa [21] a velocity of sound of about 2500 m/s is found for an APS TBC used in this study. Taking into account the distance between the sensor spots, run time differences of less than 10 µs have to be measured to allow a meaningful determination of the source's location. In fact, due to the higher Young's modulus of the metallic substrate the effective velocity of sound within the layered sample might be expected to increase, thus the run time differences might be decreased.

From the theoretical point of view, such accuracy can be easily achieved, as the time resolution of the data acquisition system is better than 0.5 µs. As well, the signal rise time of single burst events in an APS TBC has been found to be in the range of a few µs by Ma et al. [5,14]. Thus, the rise time to threshold crossing, which defines the uncertainty of the events arrival time, should be well below the critical value of 10 µs. Figure 5 shows the transient signal forms of a typical high amplitude event recorded at low temperatures during cooling (upper part) and of a high amplitude event recorded at elevated temperatures during heating (lower part). The arrival time as determined by the acquisition system is set to zero in the transient graphs. As can be seen from the upper part of fig. 5, a rise time to threshold crossing below 10µs is experimentally hardly found, even in the case of a well isolated low temperature event. In the case of an event, which suffers from an increased background noise at higher temperatures, the desired accuracy cannot be expected. In fig. 6 transient signal forms are shown, which have been recorded for an artificially generated calibration burst. As can be deduced, even in a case of an optimal signal to noise ratio, the rise times to threshold

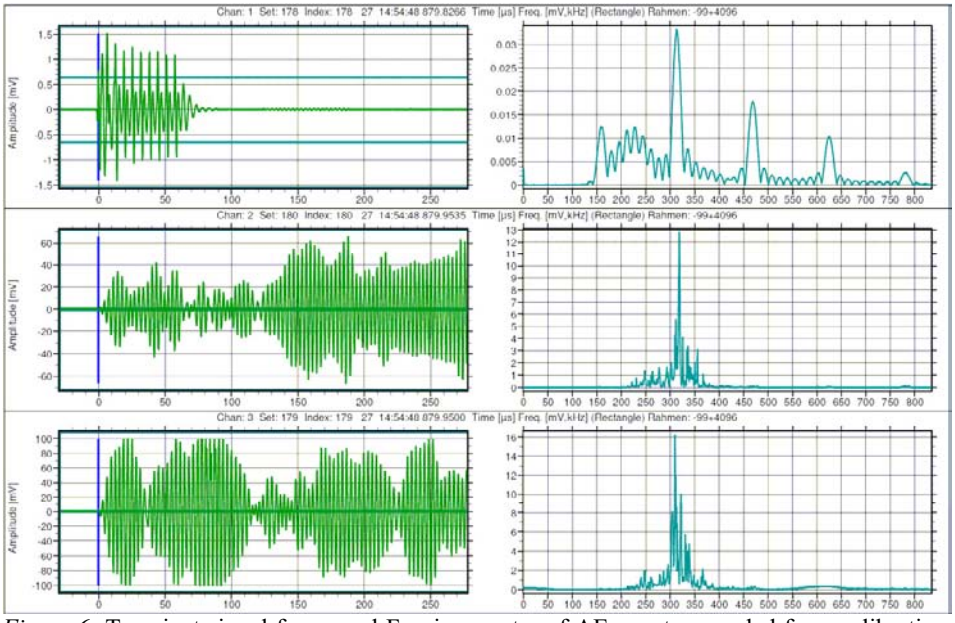

Figure 6: Transient signal forms and Fourier spectra of AE events recorded for a calibration burst of 10 pulses generated by the first piezoelectric AE transducer: signal form of generated calibration burst (upper part), signal form recorded at two different sensor locations (middle and lower part).

crossing are in the order of a few microseconds. Thus, the spatial resolution in this type of experiment is limited to about 5 mm even under optimal conditions. Comparable uncertainties have also been found in bending test experiments by Herzog [6].

Two other observations can be seen from fig. 5 and 6. First, when looking at the transient data of the lower part of fig. 5 and of fig. 6, the disturbation of signal forms due to the reflections and perturbations in the course of transmission through the layered sample and through the acoustic wave guides can lead to a remarkable shift of the maximum amplitude in time. Therefore, even AE signals arising from single burst events in absence of interfering additional events or noise may show rise times to the signals maximum amplitude of more than 100 µs. This makes it more difficult to distinguish between single or multi burst events arising from cracks of brittle material and near continuous signals arising from shear and creep from ductile materials. Second, when looking at the Fourier transforms of the AE transients, main intensity is found in the range from about 200 to 500 kHz. This is not only due to the maximum of the transducer's sensitivity around 320 kHz as higher frequencies can be found in pencil test experiments. However, Fourier transform from the burner rig experiment show a rather broad distribution, what makes it difficult to improve the discrimination of signals arising from different type of AE source. Nevertheless, the comparison of Fourier transforms in fig. 5 indicates that small differences might be sufficient for discrimination after a more thorough analysis of the data.

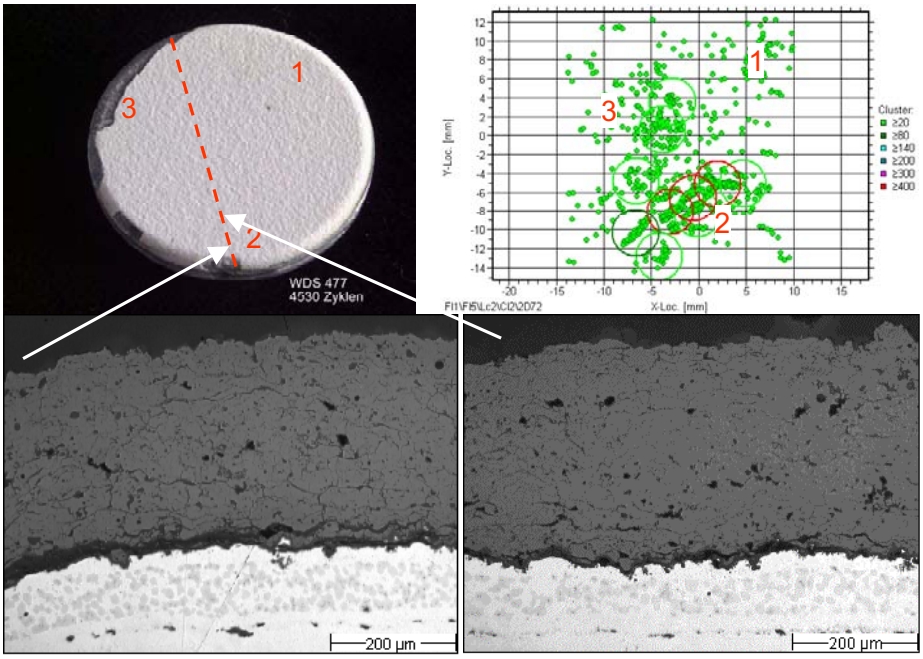

Figure 7: Photograph of a sample with damaged TBC after cycling in the burner rig facility together with results from localization analysis of logically filtered AE data and optical micrographs of regions having shown heavy acoustic activity.

Summing up what has been learned in this burner rig test experiment on the characteristics of AE events originating from the TBC sample an attempt to localize of AE sources has been undertaken after logical filtering of the data. Only those AE events have been considered, which have been recorded at low temperatures during cooling and which possess high amplitudes as well as signal rise times below 150 µs.

Figure 7 shows a photograph of a sample with damaged TBC after cycling in the burner rig facility together with results from localization analysis of logically filtered AE data and optical micrographs. The regions of heavy acoustic activity are located near sensor position 2. The optical micrographs of this region in the lower part of fig. 7 confirm the occurrence of large area delamination at this position and nearby. As is obvious from the photograph, delamination and complete spallation has been occurred to large extend near sensor position 3, too. Unfortunately, for this region no distinguished AE activities have been recorded during the course of the experiment. It remains open at the current state of analysis if this misfit is due to an unsuitable filtering of AE data or if it is due to the above discussed limitations of the localization processing of AE events, which might make it impossible to differentiate different origins of AE within the sample. In any case, more work is needed to improve both the signal to noise ratio during the experiment and the signal analysis to discriminate and correlate the different types of AE events found in the experiment.

Conclusion

A discrimination of signals originating from different sources of the setup has been undertaken by an analysis of the AE source location and the characteristics of the waveforms. In our experiments, AE signals from the ceramic coating are detected from the first cycle on. At least two processes can be differentiated by means of analysis of the AE waveforms. An evaluation of the correlation to experimental conditions and to subsequent metallographic failure inspection has been undertaken. It is encouraging to note that large delaminations could be correlated to a maximum of AE activity through the course of the experiment in one case. Nevertheless, the results cannot be stated to be sufficient at the current state for an application as monitoring tool during cycling in the burner rig experiment.

References

[1] F. Traeger, R. Vaßen, K.-H. Rauwald, and D. Stöver, “Thermal Cycling Setup for Testing Thermal Barrier Coatings”, Advanced Engineering Materials, 5 (6), 2003, 429-32.

[2] P. Robin, F.Gitzhofer, and M.I. Boulos, “Acoustic Emission Techniques for the Nondestructive Evaluation of TBCs under Thermal Cycling Conditions”, Proceedings of the International Thermal Spray Conference 2000, 1255-63

[3] P. Robin, F.Gitzhofer, and M.I. Boulos, “Acoustic Emission Techniques for Life Prediction of TBCs under Thermal Cycling Conditions”, Proceedings of the International Thermal Spray Conference 2001, 1247-53

[4] M.E. Walter, and B. Eigenmann, „The mechanical response of three EB-PVD thermal barrier coating microstructures“, Materials Science and Engineering, A282, 2000, 49-58

[5] X.Q. Ma, S. Cho, and M. Takemoto, “Acoustic emission source analysis of plasma sprayed thermal barrier coatings during four-point bend tests”, Surface and Coatings Technology, 139, 2001, 55-62

[6] R. Herzog, P. Majerus, J. Mönch, R.W. Steinbrech, F. Schubert, and L. Singheiser, "Study of Crack Development in APS and EB-PVD TBCs with Bending Tests using Acoustic Emission and In-Situ Visual Observation", Ceramic Engineering and Science Proceedings, 24 (3), 2003, 483-90.

[7] D. Renusch, H. Echsler, and M. Schütze, „Progress in Life Time Modelling of APS-TBC Part II: Critical strains, macro cracking, and thermal fatigue", Materials at High Temperatures, 21(2), 2004, 77-86

[8] M. Tanno, K. Ogawa, and T. Shoji, "Effect of Cerium and Silicon Additions to McrAlY on the High-Temperature Oxidation Behavior and Bond Strength of Thermal Barrier Coatings", Key Engineering Materials, 261-263, 2004, 1061-66

[9] A.K. Ray, D.K. Das, B. Venkataraman, P.K. Roy, B. Goswami, N. Roy, S.K. Das, N. Parida, S. Tarafder, S. Chaudhuri, S.K. Sahay, and R.N. Ghosh, "Characterization of rupture and fatigue resistance of TBC superalloy for combustions liners", Materials Science and Engineering, A405, 2005, 194-200

[10] C.C. Berndt, and H. Herman, „Failure during thermal cycling of plasma-sprayed thermal barrier coatings", Thin Solid Films, 108, 1983, 427-37

[11] J. Voyer, F. Gitzhofer, and M.I. Boulos, "Study of the Performance of TBC under Thermal Cycling Conditions using an Acoustic Emission Rig", Journal of Thermal Spray Technology, 7(2), 1998, 181-90

[12] A. Kawasaki, and R. Watanabe, "Cyclic Thermal Fracture Behavior and Spallation Life of PSZ/NiCrAlY Functionally Graded Thermal Barrier Coatings", Materials Science Forum, 308-311, 1999, 402-9.

[13] D.J. Andrews, and J.A.T. Taylor, "Quality Control of Thermal Barrier Coatings Using Acoustic Emission", Journal of Thermal Spray Technology, 9(2), 2000, 181-90.

[14] X.Q. Ma, and M. Takemoto, "Quantitative acoustic emission analysis of plasma sprayed thermal barrier coatings subjected to thermal shock tests", Materials Science and Engineering, A308, 2001, 101-10

[15] A. Kawasaki, and R. Watanabe, "Thermal fracture behavior of metal/ceramic functionally graded materials", Engineering Fracture Mechanics, 69, 2002, 1713-28.

[16] Y.C. Zhou, and T. Hashida, "Thermal fatigue failure induced by delamination in thermal barrier coating", International Journal of Fatigue, 24, 2002, 407-17

[17] D. Renusch, H. Echsler, and M. Schütze, „Progress in Life Time Modelling of APS-TBC Part I: Residual, thermal and growth stresses including the role of thermal fatigue", Materials at High Temperatures, 21(2), 2004, 65-76

[18] Z. Gan, and H.W. Ng, "Experiments and inelastic finite element analysis of plasma sprayed graded coatings under cyclic thermal shock", Materials Science and Engineering, A385, 2004, 314-24

[19] M.J. Stiger, G.H. Meier, F.S. Pettit, Q. Ma, J.L. Beuth, and M.J. Lance, „Accelerated cyclic oxidation testing protocols for thermal barrier coatings and alumina-forming alloys and coatings", Materials and Coatings, 57(1), 2006, 73-85

[20] U.T. Schmidt, O. Vöhringer, and D. Löhe, „ The Creep Damage Behavior of the Plasma-Sprayed Thermal Barrier Coating System NiCr22Co12Mo9-NiCoCrAlY-ZrO_2/7%Y_2O_3", Journal of Engineering for Gas Turbines and Power, 121, 1999, 678-82

[21] R. Vaßen, G. Kerkhof, and D. Stöver, "Development of a micromechanical life prediction model for plasma sprayed thermal barrier coatings", Materials Science and Engineering, A303, 2001, 100-9

PRACTICAL APPLICATIONS OF TEMPERATURE ESTIMATION MODELS BASED ON SUPERALLOY BASE METAL AND MCRALY COATING MICROSTRUCTURE EVOLUTION IN SERVICE RUN GAS TURBINE COMPONENTS

K. Hussain and J.A. Daleo
BWD Turbines Limited
1-601 Tradewind Drive.
Ancaster, Ontario, Canada L9G 4V5
hussain@bwdturbines.com, daleo@bwdturbines.com,

Abstract

The level of service damage accumulated in gas turbine hot section components is directly proportional to the peak and steady state metal temperatures and stress experienced in service. It is now possible to accurately estimate the actual operating metal temperature by characterizing the evolution of the base metal and coating microstructures. The gamma prime precipitate coarsening kinetics of the single crystal alloy PWA-1483 were examined over the temperature range of 845°C to 1010°C and used to construct a temperature estimation model. The model was successfully used in conjunction with temperature estimates obtained from previously developed coating/base alloy inter-diffusion models and/or solid state phase changes that occur in MCrAlY coating systems to improve the accuracy of our finite element heat transfer models that support component life and repair limit calculations.

The limitations of using temperature estimation models based on gamma prime growth/rafting kinetics for single crystal alloys are also discussed.

Keywords: single crystal, gamma prime, coating, temperature estimation, gas turbine

Introduction

Life assessment of turbine hot section components is a complex process involving non-destructive evaluations, metallurgical analysis of representative components and finite element modeling for temperature and stress analysis. When available, metallurgical temperature estimates from service-exposed blades and vanes can be used to improve the accuracy of finite element heat transfer models that support component life and repair limit calculations [1].

The commonly used methods by materials engineers to estimate the local service temperatures of turbine components are (a) the rate of gamma prime precipitate (γ') coarsening [2,3] and (b) the rate of inter-diffusion zone growth kinetics between the applied MCrAlY coating and the base alloy [4,5]. The rate of β phase depletion in the coating has also been used [6]. More recently, Ellison et. al [7] proposed a temperature estimation technique based on change in volume fraction of different phases in the SICOAT 2453 [8] overlay coating system.

All of these methods, when properly applied, have proven to be very useful tools for metallurgical life assessment of service-run blades and vanes. Each method of temperature estimation however has limitations. For instance, the rate of gamma prime precipitate coarsening cannot be applied in the analysis of cobalt-based superalloys, since they do not form the gamma

prime strengthening phase, or in second, third and forth generation single crystal materials where the temperature and stress levels induce rafting of the gamma prime precipitates. Furthermore, the diffusion zone growth/beta depletion techniques have proven difficult to apply for certain NiCoCrAlY coating types. Because inter-diffusion is limited, the inter-diffusion zone microstructures are complex and undergo significant constitutional changes over the range of service operating temperatures. Finally, all of these methods of temperature estimation require or assume that the subject blade or vane has operated for thousands of hours at a constant load/temperature level, which is often not the case.

This work constitutes part of a larger BWD Turbines Limited program to develop advanced life analysis techniques, including temperature estimation models for currently used MCrAlY coatings and nickel-based superalloys. The metallurgical temperature estimates can be used to calibrate finite element models which support component life and repair calculations.

Materials and Experiments

The material used for this study was sectioned from a thermal barrier coated Siemens V84.3A2 single crystal PWA 1483 first stage turbine blade, casted in [001] direction. The nominal chemical composition of PWA 1483 alloy is presented in Table I.

Table I: Principal elements in PWA-1483 alloy.

Element	**Cr**	**Co**	**Mo**	**W**	**Ta**	**Al**	**Ti**	**Ni**
Wt.%	12.8	9	1.9	3.8	4	3.6	4.0	Bal.

In order to evaluate the growth kinetics of gamma prime and inter-diffusion zone between SICOAT 2453 bond coat and the substrate, samples of single crystal PWA-1483 were aged in the range of 845°C to 1010°C for times up to 16,000 hours. The gamma prime growth samples were machined from the root form and the coating samples were cut from the airfoil. The SICOAT 2453 coating was applied by a low pressure plasma spray (LPPS) process.

The samples were removed from the furnace, air cooled, mounted and prepared for optical and scanning electron microscopy at preset time intervals. An image analyzer was used to evaluate multiple image fields that were acquired from each sample. The size and distribution of the gamma prime particles were measured and used to calculate the gamma prime growth kinetics and to estimate the activation energy. Similarly, multiple optical images were acquired, evaluated and used to measure the depth of inter-diffusion zone between SICOAT 2453 coating and PWA 1483 substrate.

Results and Discussion

Gamma Prime Growth Kinetics

The starting microstructure of a blade is a product of the chemical composition, the casting

parameters, heat treatment and coating used to manufacture the component. Figure 1, illustrates the starting microstructure of the material used in this experiment. Two different populations of particles can be distinguished, a main population consisting of larger cubidal shaped primary γ′ particles having a mean size of about 0.43 µm surrounded by very small spherical secondary γ′ particles. The primary γ′ size is the average cubidal axis measured by image analysis.

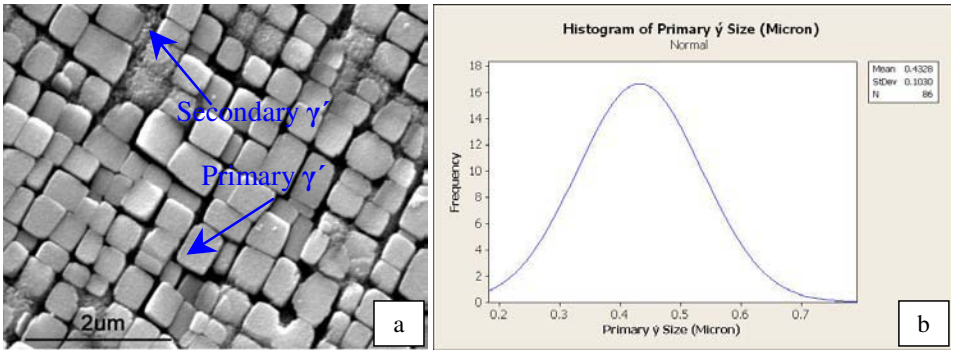

Figure 1: Initial microstructure (a) and γ′ particles size (b) distribution in as cast SX PWA 1483 alloy.

During aging at elevated temperature the most significant changes in the gamma prime (γ́) morphology were the shape and the size of γ′ precipitates. The amount of γ′ growth at 1,000, 3,000 and 8,000 hours at 845°C and 955°C is shown in Figure 2. Two main phenomena can be distinguished, the coarsening and changing in shape of the primary γ′ particles, different from the original cubidal to more round morphology and the dissolution of secondary γ′ particles. The dissolution of secondary γ′ particles was faster at the highest temperature and much slower at lower and intermediate test temperatures, as some particles had not disappeared even after thousands of hours of exposure. At higher temperature, 1010°C exposures, the gamma prime started to raft instead of growing in size. The rafting was also observed at 845°C and 900°C after 16,000 hours of exposure and was not accounted in growth kinetics calculations.

Figure 3 shows the average γ′ size measured from image analysis at the different times and temperatures. It can be seen that growth of γ′ with time follows a linear relationship and is in good agreement with the theory presented by Lifshitz and Slyozov [9], as the proportionality of the γ′ particles size to the cubic root of aging time is followed in all the investigated range of temperatures. The Lifshitz and Slyozov [9] model, also known as Lifshitz-Slyozov-Wanger model, proposes that the mean particle size increases according to the following equation.

$$d_t^3 - d_o^3 = K.t \qquad (1)$$

$$K = 64\,\gamma_e\, D\, C_e\, V_m^2 / 9RT$$

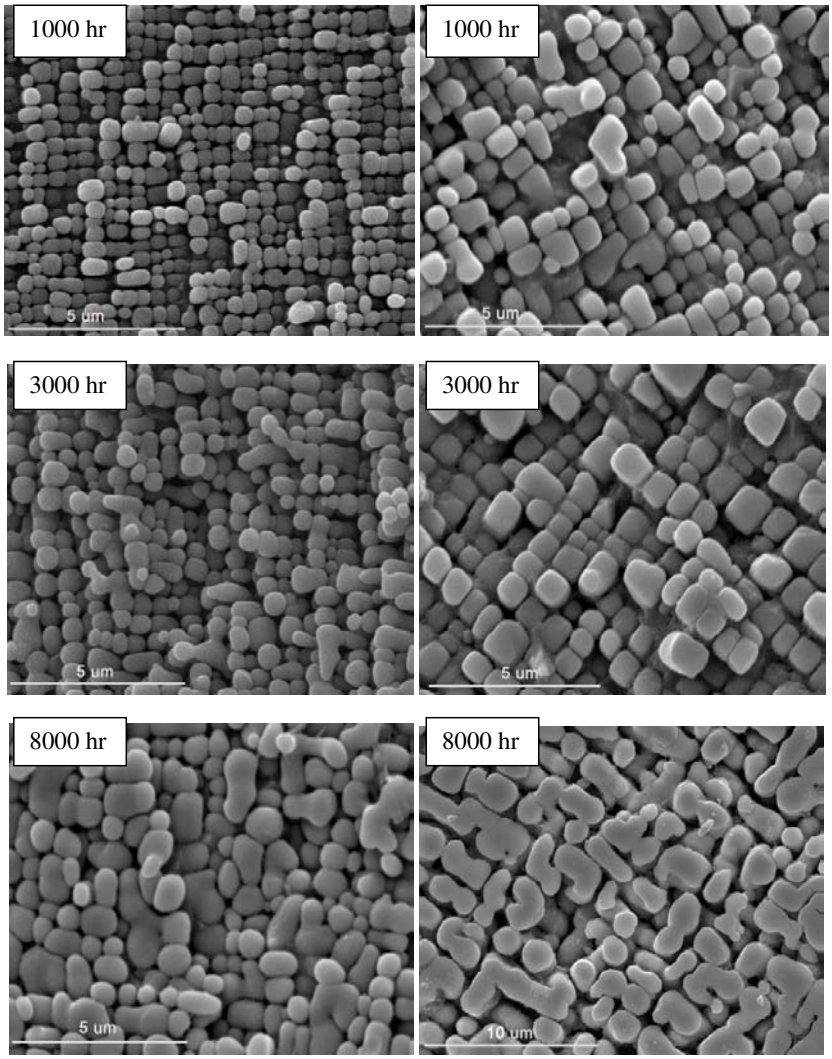

Figure 2: Growth of γ′ at 845°C (left column) and 955°C (right column) for 1,000, 3,000 and 8,000 hours of aging.

where, d_t is average γ′ mean size of aged PWA-1483, d_o is average γ′ mean size of pre aged PWA-1483, γ_e is specific γ/ γ′ interfacial free energy, D is diffusion coefficient of γ′ solutes in γ, C_e is equilibrium molar concentration of γ′ solutes in γ, V_m is molar volume of γ′, R is Bolzmann constant, T is aging temperature in °K and t is aging time. From the slopes of the curves presented in Figure 3, it is possible to calculate the activation energy of the γ′ coarsening process.

Reconsidering Eq.1 and making explicit the dependence of the diffusion coefficient D on temperature i.e.

$$D = D_o e^{-Q/RT} \quad (2)$$

where, D_o is the frequency factor and Q is the activation energy. Figure 4 shows the plot of ln(KT) versus 1/T. Good linearity is also observed in the plot and calculated activation energy is 221kJ/mole. By using this activation energy, the calculated γ′ size is compared with measured size in Figure 5 and estimated temperature is compared with actual aging (test) temperature in Figure 6.

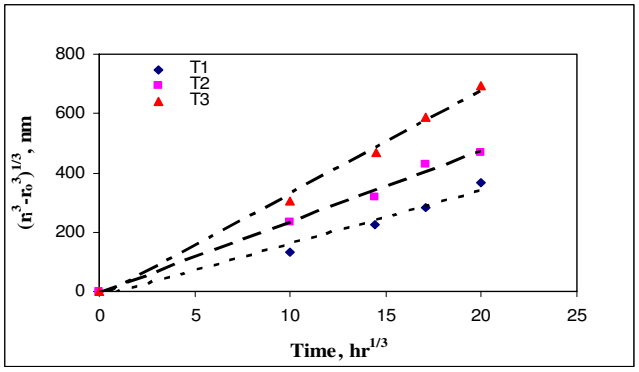

Figure 3: Change in γ′ mean size in PAW-1483 during aging.

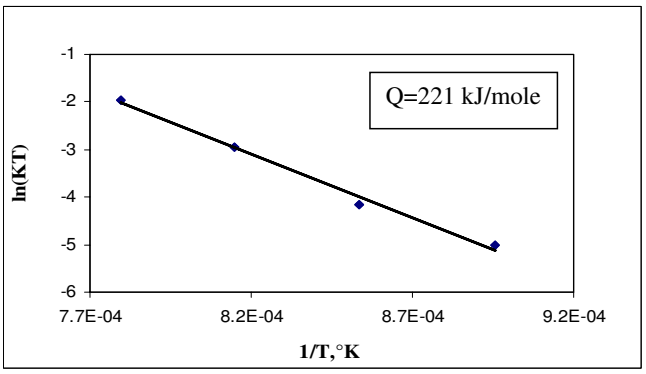

Figure 4: Temperature dependence of rate constant KT.

Coating Inter-diffusion

The growth of inter-diffusion zone is a diffusion controlled process related to the aluminum diffusion between the coating and the base alloy. The growth of inter-diffusion zone in SICOAT 2453 coating and PWA1483 base alloy is depicted in Figure 7.

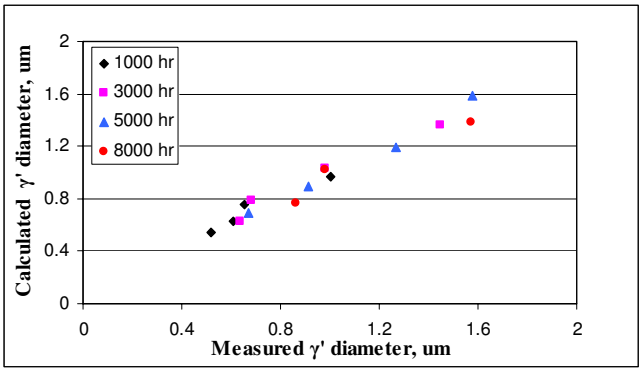

Figure 5: Comparison of measured and calculated γ′ size.

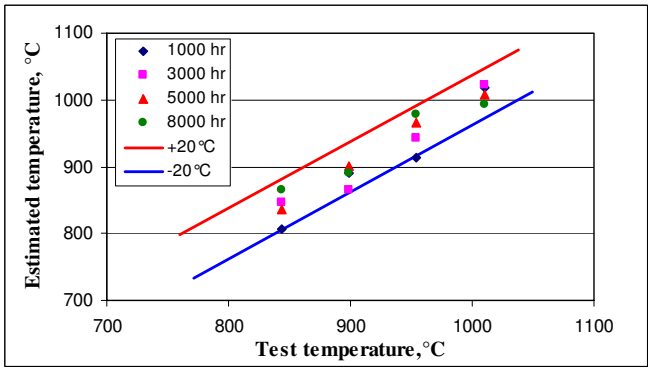

Figure 6: Comparison of test (aging) and estimated temperature along with ±20°C variation band.

Figure 8 shows the average diffusion zone depth measured from image analysis at different times and temperatures. It can be seen that the diffusion zone grows linearly with the square root of time. This may be expressed as:

$$D - D_o = k_p t^{0.5} \tag{3}$$

where k_p is a constant, $(D - D_o)$ is the change in depth of inter-diffusion zone and t is time. The growth is a thermally activated process and may then be related to the Arrhenius equation by:

$$\frac{(D-D_o)^2}{t} = k_p = A\exp\left[\frac{-Q}{RT}\right] \tag{4}$$

where A is a constant, Q is the activation energy, R is the gas constant and T is the temperature in °K. The values of A and Q were determined experimentally and are shown in Figure 9. The calculated activation energy for inter-diffusion growth process is 190 kJ/mole. By using this

activation energy, the calculated temperatures for growth to different depths with time are compared with the actual test (aging) temperatures in Figure 10. In general good correlation is obtained and particularly at longer aging times and higher temperatures.

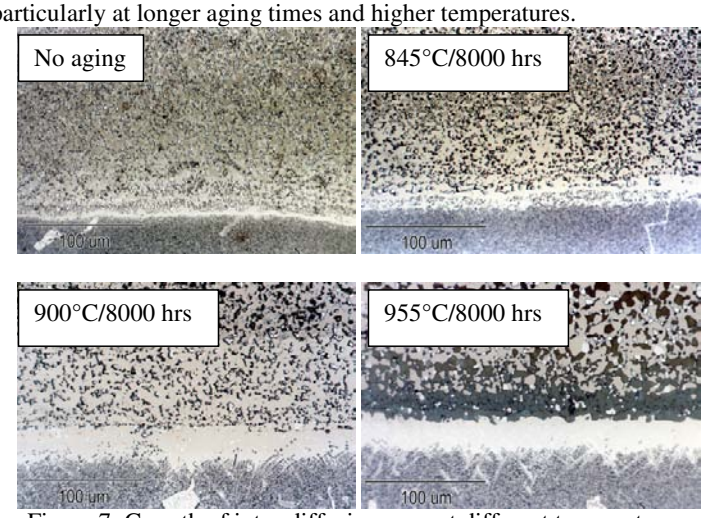

Figure 7: Growth of inter-diffusion zone at different temperatures.

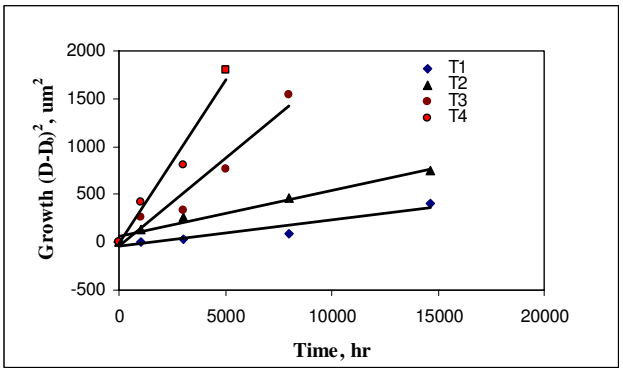

Figure 8: Growth of inter-diffusion zone between SICOAT 2453 and base alloy PAW-1483.

Accuracy of Temperature Estimation

Growth of gamma prime and inter-diffusion zone during aging are modeled by equations 1 and 3. By using these equations, it is possible to estimate the metal temperature of service exposed components. The variation co-efficient between aging temperatures estimated from gamma prime size and coating inter-diffusion zone was calculated by using following equation [10]:

$$V_c = \left| T_{\exp} - T_{est} \right| / T_{\exp} \qquad (5)$$

where T_{exp} is experimental aging temperature and T_{est} is estimated temperature. The average value of the variation co-efficient, V_c, (for each aging time) versus aging time is presented in Figure 11. The Figure shows that the estimated temperature by gamma prime growth is more accurate than the diffusion zone growth method, in general, but diffusion zone growth shows almost no difference in temperature estimation at around 1,000 hours. This could be attributed to the rounding of the gamma prime instead of growth at shorter aging times. In the case of longer aging times, the gamma prime grows and increases the accuracy of the measurement. At higher temperatures and longer exposure, where rafting is the dominant phenomenon, the gamma prime growth model can not be used to predict the service temperature of the components. In such cases, the diffusion zone growth model is a better choice than the gamma prime growth model.

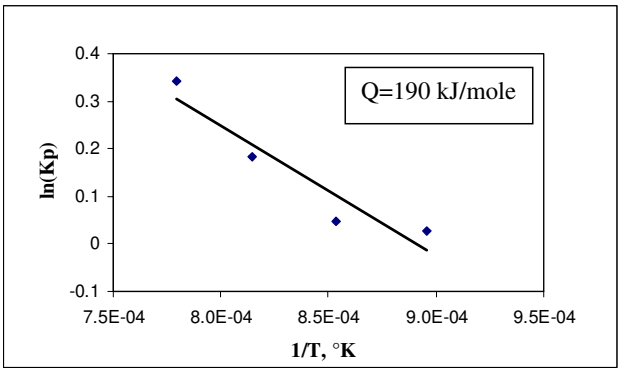

Figure 9: Temperature dependence of rate constant (K_p) of inter-diffusion growth.

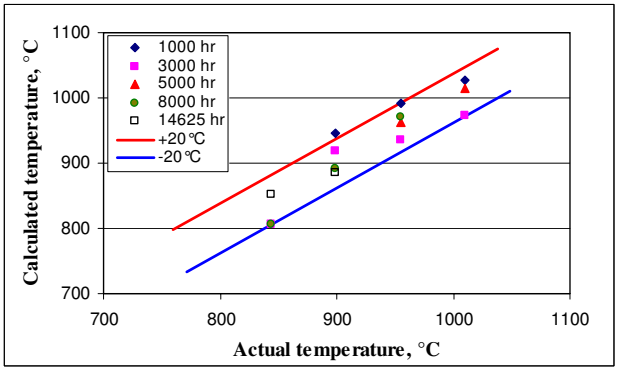

Figure 10: Comparison of test (aging) and calculated temperature of inter-diffusion zone depth at different aging times along with ±20°C variation band.

Estimation of Service Exposed Temperature

Two service exposed PWA1483 SX blades, removed from a V84.3A turbine after 3,000 hr and 9,283 hrs of service were selected to compare estimated temperature by using different

techniques. The metallurgical analysis at 60% airfoil height of the row 1 blade exposed for 3,000 hours showed that estimated temperature by the gamma prime growth model varied between 770-810°C on the suction side, while the SICOAT 2453 inter-diffusion zone growth model showed that the estimated temperature varied between 770-825°C on the suction side of the airfoil. In the same row 1 blade Ellison et al[7] estimated service temperature between 790-855°C based on change in volume fraction of different phases of SICOAT 2453 coating.

The metallurgical analysis of the other row 1 blade after 9,284 hours of service showed that the estimated service temperature by the gamma prime growth model varied between 775-835°C on the suction side, while the SICOAT 2453 inter-diffusion zone growth model showed that the estimated temperature varied between 780-840°C on the suction side of the airfoil. Figure 12 shows the service exposed row 1 blade and the points where temperature was estimated.

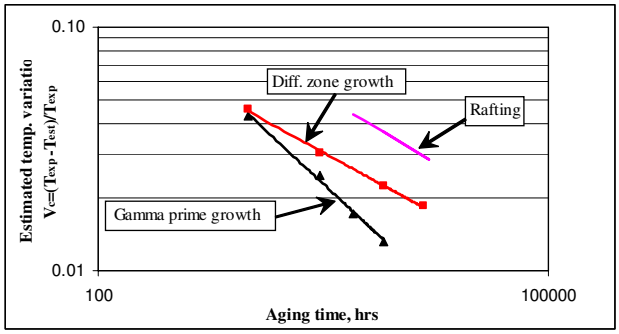

Figure 11: Effect of aging time on variation coefficient of estimated temperature.

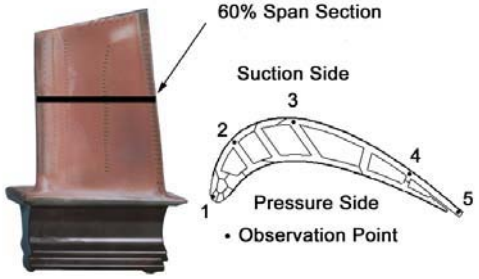

Figure 12: Service exposed V84.3A turbine blade.

Conclusions

Service temperature estimation methods were investigated and verified to be applicable to actual gas turbine components. The results are summarized as follows.

1. Average growth/change in gamma prime size in PWA1483 SX is proportional to one third power of aging time.

2. Coating inter-diffusion growth is proportional to square root of aging time.
3. Comparison of estimated temperature by gamma prime growth and coating inter-diffusion zone growth is in good agreement and comparable to phase change in coating with time and temperature.
4. Longer exposure results show that in this base metal and coating system, the estimated temperature by gamma prime growth is more accurate than the diffusion zone growth method, as temperature variation coefficient is smaller than diffusion zone growth.
5. If rafting is the dominant phenomenon, gamma prime growth model can not be used to predict the service temperature of the components. In such cases, either the diffusion zone growth model or the temperature estimation techniques based on change in volume fraction of different phases in the SICOAT 2453 overlay coating system can be used.

References

[1] J. A. Daleo and D. H. Boone, in Failures 96, Risk, Economy and Safety, Failure Minimization and Analysis, R.K.Penny, Editor, p. 187, A. A. Balkema, Rotterdam (1996).

[2] D.J. Chellman and A.J. Ardell, The Coarsening of γ´ Precipitates at Large Volume Fractions, Acta Metallurgica, 22 (1974), 577-588.

[3] R.A. Stevens and P.E.J. Flewitt, The effects of γ´ Precipitate Coarsening During Isothermal Aging and Creep of Nickel-Base Superalloy IN-738, Materials Science and Engineering, 37 (1979), 237-247.

[4] K.A. Ellison, J.A. Daleo and D.H. Boone, Metallurgical Temperature Estimates Based on Interdiffusion Between CoCrAlY Overlay Coating and a Directionally Solidified Nickel Base Superalloy Substrate, Materials for Advanced Power Engineering 1998, ed. J. Lecomte-Beckers et al, 1523-1534.

[5] K. A. Ellison, and J. A. Daleo, "Microstructural Evaluation of MCrAlY / Superalloy Interdiffusion Zones", Life Assessment of Hot Section Gas Turbine Components, ed. R. Townsend et al. (London, UK: The Institute of Materials, Edinburgh, 2000), 311-327.

[6] V. Srinivasan, N.S. Cheruvu, T.J. Carr and C.M. O'Brien, Degradation of MCrAlY Coating and Substrate Superalloy During Long Term Thermal Exposure, Materials and Manufacturing Processes, 10 (1995), 955-969.

[7] K.A. Ellison, J.A. Daleo and K. Hussain, A New Method of Metal Temperature Estimation for Service-Run Blades and Vanes, Superalloys 2004, ed. K.A. Green et al, TMS,759-768.

[8] United States Patent 5,154,885, Oct 13 1992. Highly Corrosion and/or Oxidation-Resistant Protective Coating Containing Rhenium, N. Czech et al., Siemens Aktiengesellschft, Munich, Fed Rep. of Germany.

[9] M.Lifshitz, V.V. Slyozov, The Kinetics of Precipitation from Supersaturated Solid Solutions, J.Phys. Chem. Solids, 19 (1961), 35-50.

[10] Y. Yoshioka, N. Okabe, T. Okamura, D. Saito, K. Fujiyama and H. Kasiwaya, Service Temperature Estimation for Heavy Duty Gas Turbine Buckets Based on Microstructure Change, Superalloys 1996, Edit. R.D. Kissinger, D.J. Deye et al, (1996) 173-179.

NUMERICAL SIMULATION OF TBC DELAMINATION UNDER THERMAL CYCLIC LOADING

M Białas, P Bednarz, R Herzog

Research Centre Jülich, Institute for Materials and Processing in Energy Systems, IWV-2, D-52425 Jülich, Germany

Abstract

A numerical simulation of crack development within TBC systems is presented. Periodic unit cell is used to examine the effect of interfacial asperity on the stress distribution and subsequent delamination of TBC. Cohesive zone elements within the oxide – ceramic layers model the development of micro-cracks and their subsequent linking leading to the spallation of the protective layer. Cyclic temperature loading combined with oxide growth is assumed.

Keywords: Cohesive zone modelling, Thermal cycling, De-cohesion

1. Introduction

The improvements in increasing the efficiency of gas turbines within the past 20 years have been partially achieved by applying thermal barrier coatings (TBCs) on components such as turbine blades of the first and second rows, where the high temperature loading is dominant. However, the mechanisms leading to failure and the parameters limiting coating lifetime have not been fully revealed so far. Therefore, the full potential of thermal barrier coatings as an important factor allowing for further increase in the gas turbine inlet temperature is still not fulfilled.

Under normal operation conditions coated turbine blades experience rather complex loading, combined with the existence of residual stresses and oxidation processes. Therefore, it is difficult to predict the dominant driving force to cause the failure. Additionally, the microstructure of the constituents, namely TBC, bond coat (BC) and the substrate, continuously changes and modifies the mechanical response. Only lab-scale testing offers the opportunity to define ideal loading profiles. Early experimental investigations into failure mechanisms of TBC identified de-lamination at the top coat-bond coat interface as the primary failure mode, leading ultimately to spallation of the coating (Miller and Lowell [1]). They hypothesized that the failure mechanisms involve residual stresses induced into the coating during the cool down of a thermal cycle. The stresses were due to arise from the expansion mismatch between the top coat and the bond coat. A formation of a thin oxide film at the top coat – bond coat interface during exposure to elevated temperatures influenced substantially the failure process. Especially oxidation processes at the BC/TBC interface modified significantly the damage evolution. Based on the observed location of delamination the interface's irregularity was thought to play a role.

Many researches reported results of numerical simulations of stress development in TBC systems due to rough interface, oxide film and thermomechanical property mismatch on the spallation mechanism. Chang et al. [2] conducted finite element analysis of coatings on cylindrical substrates with sinusoidally varying interfaces simulating cool-down from a

stress-free temperature. Based on this study a model was proposed for failure events leading to spallation. Freborg et al. [3] subsequently conducted validation of the model. They employed cyclic thermal loading that closely simulated actual in-service thermal loading, modelled explicitly oxide film growth and used a creep model for the inelastic behaviour of the TBC constituents. The results demonstrated the evolution of a non-zero stress component normal to the interface. Due to stress relaxation during the hold period of a heat-up/hold/cool-down thermal cycle, this stress component becomes tensile at the interface's crest upon cool-down, setting up a de-lamination initiation site at this location. In the trough region, due to stress relaxation, the normal stress becomes compressive. The growth of the oxide film at the top coat/bond coat interface subsequently changes the normal stress sign in the trough region, facilitating horizontal delamination. This formation of a long-range tensile zone can be interpreted as a possible crack path.

The concept of a cohesive zone ahead of a crack tip, stemming from works by Barenblatt [4] and Dugdale [5], has been extensively used to simulate crack nucleation and propagation in composites and brittle materials. Camacho and Ortiz [6] used a cohesive law fracture model to simulate propagation of cracks along arbitrary paths. Surface-like cohesive elements were introduced at the interfaces between standard volume elements. Simulation of dynamic crack propagation has been presented in the papers by Pandolfi et al. [7] and Zhou and Molinari [8,9] in three-dimensional problems. Tijssens et al. [10] used the damaging cohesive surfaces to study concrete fracture. Caliez et al. [11] used a de-bonding model based on the work of Tvergaard [12] to simulate spallation of EB PVD coatings.

Of particular interest in the present contribution is the experimental work on TBC in which superalloy hollow cylindrical specimens were tested [13]. The specimens were plasma sprayed with yttria-stabilised zirconia on NiCoCrAlY bond coat. Coated specimens were then exposed to cyclic temperature changes simulating a turbine loading profile. Experimentally determined data for TBC and bond coat creep served as an input for material modelling of the constituents. The development of cracks due the thermal loading was simulated using cohesive zone elements.

2. Methodology

2.1. Mesh and the loading profile

Figure 1(a) illustrates the modelling concept. The test cylinder is sufficiently long compared to its diameter for the problem to be approximated by a two-dimensional generalized plane-strain case. It has been assumed that the strain in the axial direction is uniform. As proposed in Figure 1(a) interfaces are idealised as circular segments within a unit cell. Symmetry of the problem allows meshing only one half of the undulation. The assumed boundary conditions put constraints on the displacement field in the cylindrical direction, only radial displacements are allowed to take place along lines OA and OB in Figure 1(a). The cylinder was subjected to cyclic temperature loading. A single loading cycle is presented in Figure 1(b). It consists of heating from 20°C to 1050°C in 103 seconds. Subsequently follows a dwelling period at 1050°C for a time of 7200 seconds. Next we have a cooling from 1050°C down to 20°C in 103 seconds. The last step is a dwell-time at low temperature (20°C) for 900 seconds.

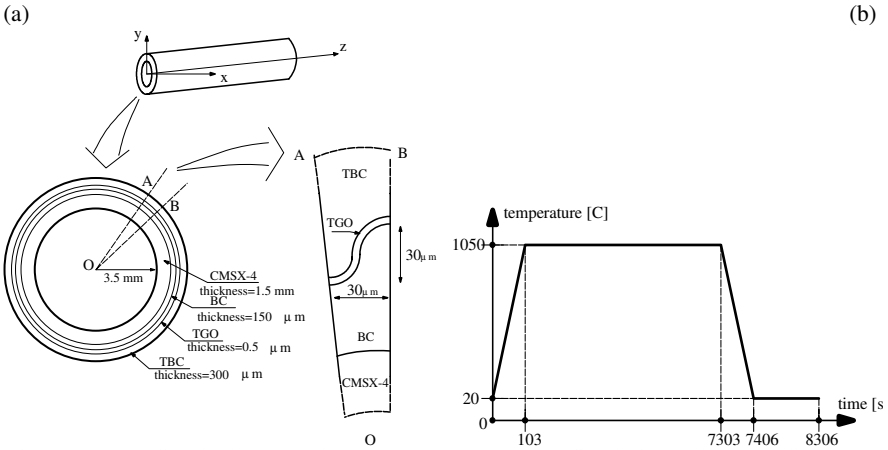

Figure 1. (a) Cylindrical test specimen. (b) Temperature profile during a single loading cycle.

2.2. Materials

Large deformations are assumed for the constituents of the TBC system. The substrate material (CMSX-4) is considered as a pure elastic medium, the bond coat, the thermally grown oxide and the thermal barrier coating are treated as elastic and viscous materials (including creep and stress relaxation). Their mechanical properties are functions of temperature as listed in Table 1. The value of temperature loading equal to 200°C was chosen for the initial stress free state. It matches approximately with the coating stress free temperature for the air plasma spraying process.

Temperature [°C]	Youngs Modulus [MPa]	Poisson ratio	Coefficient of Thermal Expansion	Youngs Modulus [MPa]	Poisson ratio	Coefficient of Thermal Expansion
	Substrate			TGO		
20	123286.	0.359632	1.20023e-05	380365.	0.27	5.07939e-06
220	115546.	0.365476	1.2105e-05	369060.	0.27	5.90395e-06
420	107806.	0.370447	1.25212e-05	361225.	0.27	6.72851e-0
620	100066.	0.374547	1.34314e-05	351876.	0.27	7.55307e-06
820	92326.	0.377774	1.46843e-05	336032.	0.27	8.37763e-06
1020	84586.	0.380129	1.57968e-05	308708.	0.27	9.2022e-06
1220	76846.	0.381613	1.59538e-05	264922.	0.27	1.00268e-05
	Bond coat			TBC		
20	151857	0.31886	1.23579e-05	17500.	0.2	9.68e-06
220	150746	0.32701	1.30407e-05	16340	0.2	9.67479e-06
420	145253.	0.334345	1.39115e-05	15181	0.2	9.70578e-06
620	132337.	0.340863	1.49703e-05	14022	0.2	9.80975e-06
820	108921.	0.346566	1.62171e-05	12863	0.2	1.00235e-05
1020	71890.6	0.351452	1.76519e-05	11704	0.2	1.03837e-05
1220	18090.7	0.355522	1.92747e-05	10545	0.2	1.09271e-05

Table 1. Elastic and thermal expansion properties of CMSX-4, TGO, bond coat and TBC.

Time dependent features of BC and TBC are characterised in the present modelling by primary and secondary creep stages. The creep data were experimentally determined by compression creep test with stand-alone coatings (TBC, BC) and shear deformation experiments on TBC composites [14,15,16]. The data were implemented using the following equation

$$\dot{\varepsilon}_{creep} = A' \cdot \sigma^{n'} \cdot e^{-\frac{\varepsilon}{\varepsilon'}} + A'' \cdot \sigma^{n''} \cdot e^{-\frac{\varepsilon}{\varepsilon''}} + A \cdot \sigma^{n} \quad (1)$$

using user subroutine CREEP within ABAQUS finite element package [17]. Table 2 presents the dependence of material parameters A', n', ε', A'', n'', ε'', A, n used in Equation (1) on temperature. The TGO time dependent behaviour is represented by the secondary creep stage with the following relation between stress and the rate of creep strain:

$$\dot{\varepsilon}_{creep} = A \cdot \sigma^{n} \quad (2)$$

The dependence of material parameters A and n on temperature in this particular case is presented in Table 3.

T [°C]	A’	n’	ε’	A”	n”	ε”	A	n
	Bond coat							
750	1.25e-9	4.5	0.09	1.25e-12	4.5	0.24	1.25e-14	4.5
850	1.4e-6	3.8	0.08	1.4e-9	3.8	0.23	1.4e-11	3.8
950	2.3e-4	3.1	0.07	2.3e-7	3.1	0.22	2.3e-9	3.1
1050	9.5e-3	2.55	0.06	9.5e-6	2.55	0.21	9.5e-8	2.55
	TBC							
750	1.0e-10	4.5	0.01	2.2e-18	4.5	0.05	2.0e-22	4.5
850	1.0e-10	4.32	0.02	2.0e-16	4.32	0.08	2.0e-20	4.32
950	3.0e-10	4.15	0.03	9.0e-15	4.15	0.12	3.0e-18	4.15
1050	3.77e-11	3.98	0.04	3.02e-13	3.98	0.18	3.77e-16	3.98
1150	1.44e-10	3.8	0.05	4.8e-12	3.8	0.25	4.8e-14	3.8

Table 2. Creep data for BC and TBC

T [°C]	A	n
	$\dot{\varepsilon} = A \cdot \sigma^{n}$	
750	7.3e-4	1
1050	7.3e-4	1

Table 3. TGO creep data.

Growing of the alumina scale at high temperature at the BC/TBC interface is simulated using the swelling option in ABAQUS. The oxidation process is considered in the temperature range 950°C --- 1050°C. It is modeled as an orthotropic swelling strain of the TGO layer. Its initial thickness was assumed to be equal to 0.5 μm. The oxidation kinetic was experimentally determined for three different temperatures [18] and approximated by the following equation

$$d_{Oxid}(t) = \left[A^o \cdot e^{\left(\frac{-E_a}{RT}\right)} \cdot t\right]^n \quad (2)$$

with T being temperature, and t time. The values of coefficients A^0, n, E_a and R are listed in Table 4.

T [C]	$A°$	N	E_a	R
950	1.57e-15	0.33	18000	8.314
1000		0.325		
1050		0.3225		

Table 4. Parameters for oxidation kinetic.

(a) (b)

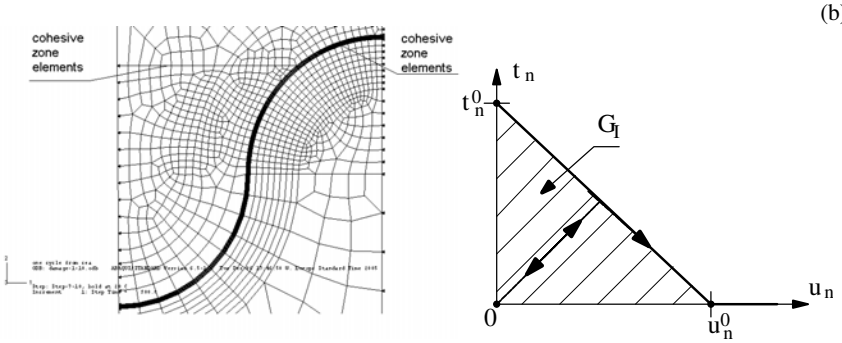

Figure 2. (a) Location of cohesive zone elements. (b) Linear damage evolution.

2.3. Modelling of crack development

As observed in [11] we assume here that the cracks leading to the spallation of the TBC are in a large majority localized at the bond coat/oxide interface. To simulate the damage initiation and propagation cohesive zone elements are located there. The location of cohesive elements within the TBC is suggested by the distribution of radial stresses obtained from a simulation performed only with solid elements [19] and is presented in Figure 2(a). The constitutive law for cohesive elements is formulated in terms of the normal and shear components of tractions on the interface plane $t=\{t_n, t_t\}$ and their corresponding relative displacements across the interface $u=\{u_n, u_t\}$. Interface models offer the advantage that they combine a stress criterion with respect to damage initiation moment with an energy criterion with respect to the failure development (the area under the de-bonding curve corresponds to the critical energy release rate). We use in this work the following quadratic nominal stress criterion to model damage initiation:

$$\left(\frac{< t_n >}{t_n^0}\right)^2 + \left(\frac{t_s}{t_s^0}\right)^2 = 1$$

where t_n^0 and t_s^0 are interface critical stresses respectively in opening or sliding modes. The following relation is used between the traction and separation during monotonic loading

$$t_n = -\frac{t_0^2}{2G_I}u + t_0, \quad u \le \frac{2G_I}{t_0}$$

$$t_n = 0, \quad u > \frac{2G_I}{t_0}$$

with G_I being the critical energy release rate in mode one. The reloading phase is also approximated by a linear function as presented in Figure 2(b). It is assumed that cohesive elements do not undergo damage under pure compression. The value of critical energy release rate G_{II} and the value of critical stress in shear t_s^0 was chosen to be high in comparison with respectively G_I and t_n^0: $G_{II}>>G_I$, $t_s^0>> t_n^0$. Thus, crack development was driven mostly by the opening mode. As reported in the literature [11,13,20] the following material data was used for BC/TGO interface G_I=20 J/m^2, t_n^0=200 MPa. The cohesive zone elements used for TBC are characterized by G_I=5 J/m^2, t_n^0=100 MPa.

3. Results

Figure 3 presents a distribution of radial stresses and configuration of cracks at room temperature after 1, 2, 10, 100, 200 and 300 loading cycles. It can be observed that a zone of tensile stresses forms within the bond coat in the place where the sign of the curvature of undulation changes. Both, the area of this zone and the values of tensile stresses increase as the loading progresses. As already indicated in Figure 2(a) the cohesive elements are located at the interface between thermally grown oxide and the bond coat as well as in the TBC where the material is subjected to maximal tensile stresses. During the first stage of loading a rapid increase in the cracks length is observed. Later on it stabilizes at a constant value and remains unchanged, only an opening mode can be observed as the loading progresses. This effect is particularly strong in the case of TGO/TBC interface crack.

Interesting is the effect of crack development on the stress distribution within bond coat and TBC. In the paper [19] similar analysis is performed for different material laws without taking into account crack development. The aforementioned zone of tensile stresses growing within the bond coat in the place where the undulation curvature changes its sign is not present in the analysis without cohesive zone elements. It can be deduced that the crack development at TGO/TBC interface influences this stress perturbation. On the other hand, the tensile stresses within bond coat below the interface crack have lower values than in the case where the interface crack is not present. This is an obvious effect of crack development.

Local perturbation of the stress field can be also observed in the TBC layer in the vicinity of the crack. The radial stresses become lower close to the fully opened crack faces and reach higher values at the crack tips. This is particularly seen in the region where the TBC crack reaches the TGO layer. The development of damage within the TGO is not modeled here, but the obtained results indicate a location of TGO crack connecting the fully open cracks at the TGO/BC interface with the TBC crack.

Figure 4 presents the lengths of the TBC and BC/TGO interface cracks as a function of time. In accordance to the above statement, the TBC crack grows fast and reaches the value of 12 μm during the first four loading cycles (9 hours). Subsequently it becomes arrested and further increase in its length cannot be observed up to 350 cycles (about 810 hours). The growth of the TBC/BC interface crack is also rapid at the beginning of the loading. Within four cycles the crack reaches the length of 4.5 μm. Its further growth is very slow, though. During the next 340 cycles its length increases up to 7 μm. Similar as in the case of TBC

crack we can treat it as a stabilization period of the failure development within the TBC system.

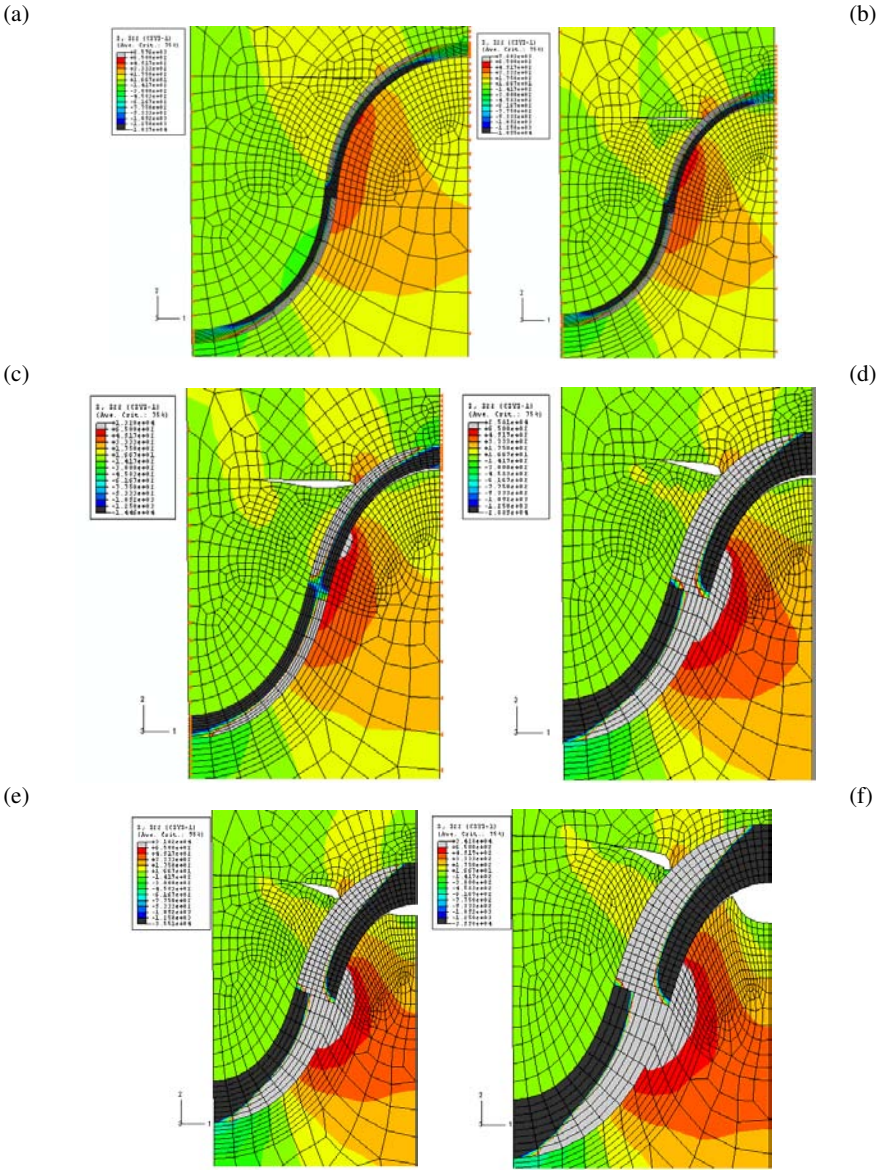

Figure 3. Radial stresses [MPa] and crack development close to the interface asperity after (a) one, (b) two, (c) ten, (d) one hundred, (e) two hundred and (f) three hundred loading cycles.

(a) (b)

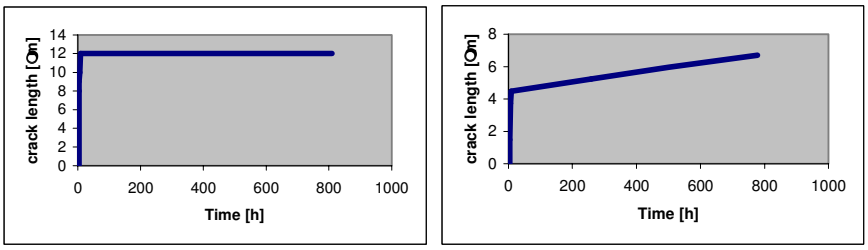

Figure 4. Crack development as a function of time: (a) TBC crack, (b) BC/TGO interface crack.

3. Discussion

The presented results are in an agreement with experimentally observed crack patterns after150 with 2h dwell at 1050°C as presented in Figure 5. This type of failure is typical for oxidation loading and was also reported by Evans et al. [20]. The fact, that the observed micro cracks are located in the TGO and not directly at the TGO/bond coat interface could be explained by progressive oxidation taking place after the initial formation of cracks. The formation of cracks within TGO is not considered in the contribution, the linking of TBC and TGO/BC interface cracks observed in experiments will be considered as a next step. The present results indicate where to place the cohesive elements within the TGO layer. Moreover, it can be deduced that the shear mode in TBC plays a significant role in the failure. Analysis in which only an opening mode is considered reveals a crack arrest after its initial rapid growth. It must be the shear loading at the crack ends that promotes further development and linking of cracks growing from neighbouring asperities.

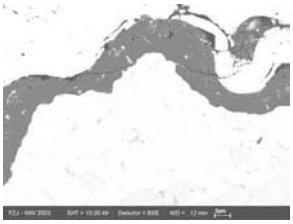

Figure 5. Crack patterns after 150 cycles (after Herzog et al. [21]).

Acknowledgments

The financial support of European Commission (Contract No.~MEIF-CT-2003-501636) is gratefully acknowledged.

References

[1] R.A. Miller, C.E. Lowell. Failure mechanisms of thermal barrier coatings exposed to elevated temperatures. Thin Solid Films 95 (1982) 265-273.

[2] G.C. Chang, W. Phucharoen, R.A. Miller. Behavior of thermal barrier coatings for advanced gas turbine blades. Surface and Coatings Technology 30 (1987) 13-28.
[3] A.M. Freborg, B.L. Ferguson, W.J. Brindley, G.J. Petrus. Modeling oxidation induced stresses in thermal barrier coatings. Materials Science and Engineering A245 (1998) 182-190.
[4] G.I. Barenblatt. The mathematical theory of equilibrium cracks in brittle fracture. Advances in Applied Mechanics 7 (1962) 55-129.
[5] D.S. Dugdale. Yielding of steel sheets containing slits. Journal of Mechanics and Physics of Solids 8 (1960) 100-104.
[6] G.T. Camacho, M. Ortiz. Computational modelling of impact damage in brittle materials. International Journal of Solids and Structures 33 (1996) 2899-2938.
[7] A. Pandolfi, P.R. Guduru, M. Ortiz, A.J. Rosakis. Three dimensional cohesive-element analysis and experiments of dynamic fracture in C300 steel. International Journal of Solids and Structures 37 (2000) 3733-3760.
[8] F. Zhou, J.F. Molinari. Stochastic fracture of ceramics under dynamic tensile loading. International Journal of Solids and Structures 41 (2004) 6573-6596.
[9] F. Zhou, J.F. Molinari. Dynamic crack propagation with cohesive elements: a methodology to address mesh dependency. International Journal for Numerical Methods in Engineering 59 (2004) 1-24.
[10] M.G.A. Tijssens, , B.L.J. Sluys, E. van der Giessen. Numerical simulation of quasi-brittle fracture using damaging cohesive surfaces. European Journal of Mechanics A/Solids 19 (2000) 761-779.
[11] M. Caliez, J.-L. Chaboche, F. Feyel, S. Kruch. Numerical simulation of EBPVD thermal barrier coatings spallation. Acta Materialia 51 (2003) 1133-1141.
[12] V. Tvergaard. Effect of fiber debonding in a whisker-reinforced metal. Materials Science and Engineering A125 (1990) 203-213.
[13] P. Majerus. Neue Verfahren zur Analyse des Verformungs- und Schädigungsverhaltens von MCrAlY-Schichten im Wärmedämmschichtsystem. Schriften des Forschungszentrums Jülich, Reihe Energetechnik 34 (2004).
[14] S. Heckmann, R. Herzog, R. Steinbrech, F. Schubert, L. Singheiser, "Visco-Plastic Properties of Separated Thermal Barrier Coatings under Compression Loading", Proceedings of the 7th Liege Conference 2002, 30. September - 2. October 2002, Liege, Belgium, Materials for Advanced Power Engineering 2002, ISBN 3-89336-213-2, Vol. 21, Part 1, pp. 561-568
[15] P. Majerus, R.W. Steinbrech, R. Herzog, F. Schubert, "Deformation Behaviour of a Low Pressure Plasma-Sprayed NiCoCrAlY Bond Coat under Shear Loading at Temperatures above 750°C", Proceedings of the 7th Liege Conference 2002, 30. September - 2. October 2002, Liege, Belgium, Materials for Advanced Power Engineering 2002, ISBN 3-89336-213-2
[16] E. Trunova, R. Herzog, T. Wakui, R.W. Steinbrech, E. Wessel, L. Singheiser, "Micromechanisms Affecting Macroscopic Deformation of Plasma-Sprayed TBCs", Ceramic Engineering and Science Proceedings, Volume 25, Issue 4,2004, 28th International Conference on Advanced Ceramics and Composites, B. pp. 411-416
[17] ABAQUS/Standard, Version 6.5. Hibbitt, Karlsson and Sorensen, Inc.;2006.
[18] H. Echsler, "Oxidationsverhalten und mechanische Eigenschaften von Waermedaemmschichten und deren Einfluss auf eine Lebensdauervorhersage", Dissertation RWTH Aachen,2003, ISBN 3-8322-1895-5
[19] P. Bednarz, R. Herzog, E. Trunova, R. W. Steinbrech, H. Echsler, W. J. Quadakkers, F. Schubert, L. Singheiser. Stress distribution in APS-TBCs under thermal cyclic loading

conditions, Proceedings of the 29th International Conference on Advanced Ceramics and Composites - Advances in Ceramic Coatings and Ceramic-Metal Systems, Ceramic Engineering and Science Proceedings 26 (2005) 73-80.
[20] A.G. Evans, D.R. Mumm, J.W. Hutchinson, G.H. Meier, F.S. Pettit. Mechanisms controlling the durability of thermal barrier coatings. Progress in Materials Science 46 (2001) 505-553.
[21] R. Herzog, P. Bednarz, E. Trunova, V. Shemet, R.W. Steinbrech, F. Schubert, L. Singheiser. Simulation of stress development and crack formation in APS-TBCs for cyclic oxidation loading and comparison with experimental observations, Proceedings of the 30th International Conference and Exposition on Advanced Ceramics and Composites, January 22-27, 2006, Cocoa Beach (in press).

OXIDATION AND HOT CORROSION BEHAVIOR OF ALUMINIZED Pt-Ir COATINGS ON Ni-BASED SUPERALLOY TMS-82+

A.Yamaguchi[a], Y.N.Wu[b], Aya.Suzuki[c], H.Murakami[b], S.Kuroda[b] and H.Imai[a]

[a] Department of Materials Science and Engineering, Faculty of Engineering, Shibaura Institute of Technology, 3-9-14 Shibaura, Minato-ku, Tokyo, Japan
[b] Thermal Spray Group, Materials Engineering Laboratory, National Institute for Materials Science: 1-2-1, Sengen, Tsukuba-City, Ibaragi, 305-0047, Japan
[c] Department of Materials Science and Metallurgy, University of Cambridge, Pembroke Street, Cambridge, CB2 3QZ, UK

Abstract

Recent demand in increasing the efficiency of gas turbines has led the component materials, ie. coated Ni-base superalloys, to be exposed at much higher operating temperatures. Therefore there is a great demand for improving the protective performance of bond coat materials. The authors have proposed Ir-based alloys as bond coat materials because Ir has excellent oxidation and corrosion resistance and has the highest melting temperature of 2716K among platinum group metals. Ir addition to Ni-base superalloys is also reported to increase the melting temperature thus may enhance the high temperature mechanical properties. In this study, sputtered Pt-Ir films with various compositions were coated on Ni-based single crystal superalloy TMS-82+ followed by the conventional Al-pack cementation process. The effects of Pt-Ir alloy compositions on the oxidation resistance and hot corrosion resistance were investigated. The cyclic oxidation test performed at 1423K for 1h as one heating cycle and NaCl-Na_2SO_4 at 1173K revealed that 30-50 at% addition of Ir to Pt demonstrated the good combination of oxidation and corrosion resistances.

Keywords: Pt-Ir alloy, bond-coat, sputtering, aluminizing, Ni-base superalloy

Introduction

From the viewpoint of global warming, increasing operating temperature of gas turbines has been required in order to get higher heat efficiency. However, higher operating temperature would lead to the component materials to be exposed at much severe environment. Although there is still a continuous effort being done to enhance creep and oxidation resistances of Ni-based superalloys that are used as the substrate materials, inlet combustion gas temperature of latest gas turbines has reached 1500 ºC, well above the melting point of the substrates. Therefore, it is essential to improve thermal barrier coatings (TBCs) for Ni-based superalloys. TBCs have widely been used for turbine blades since 1960s [1-4]. TBCs generally consist of two coating layers; a metallic coat layer called “bond-coat” to have oxidation and hot corrosion resistances, and a ceramic coating layer called “top-coat” to insulate heat conduction. Typically, An aluminum enriched layer such as PtAl [5] and MCrAlY is used as a bond-coat, and yttria stabilized zirconia (YSZ) is used as a top-coat, respectively.

Among bond-coat materials, PtAl has led to the widespread application for TBCs, and some excellent properties were reported, such as to enhance Al diffusion in the coating, and to suppress void formation along the scale[6]. However, recent increase in exposed temperature of the components has brought about following problems. i) Inward diffusion of Pt decreases melting point of the substrate Ni-based superalloys,

resulting in the degradation of creep properties of the components. ii) Brittleness of β-PtAl and $PtAl_2$ phases shown on the surface gives rise to the crack initiation at bond-coat/top-coat interfaces and thus deteriorates fatigue properties of the components. iii) Phase transformation caused by the depletion of Al at the surface would lead to the rumpling of surface [7,8] and accelerate precipitation of topologically close packed (TCP) phase[9,10]. iv) In addition, probably most importantly, industrial usage of Pt is limited because of its high price.

In order to develop novel bond-coat materials with enhanced oxidation and hot corrosion properties, the authors have proposed Ir-based alloys[11-13], because Ir has the highest melting point (2716K) among platinum group metals, higher mechanical strength than Pt, excellent chemical stability, low oxygen diffusivity[14], and low inter-diffusion coefficient into Ni ($\tilde{D}_{Ir,Ni} < \tilde{D}_{Pt,Ni}$) [15]. To make the best use of these beneficial characteristics and to enhance the oxidation resistance will lead to the development of novel bond-coat materials. In this study, Ir addition to the conventional Pt modified aluminide coatings were examined. Pt-Ir films with varied alloy compositions were deposited on Ni-base single crystal superalloy TMS-82+ by the magnetron sputtering method, followed by the diffusion treatment and the aluminizing treatment. Cyclic oxidation tests and salt coated hot corrosion tests were conducted to evaluate the oxidation and hot corrosion resistance of Pt-Ir modified aluminide coatings.

Experimental

As a substrate material, so-called “second generation” Ni-based single crystal superalloy TMS-82+ [16, 17] was selected. Its nominal composition is Ni-7.8Co-4.9Cr-1.9Mo-8.7W-5.3Al-0.5Ti-6.0Ta-0.1Hf-2.4Re (mass%). Substrates were prepared from <001> oriented single crystal bars with 25 mm diameter and 150 mm long. They were cut along {100} direction into 2 mm thick discs, and some of the discs were further cut into 8 mm × 8 mm × 2 mm plates. These substrates were polished with SiC paper up to #800 and cleaned with acetone for 15 min in an ultrasonic bath. Then the magnetron sputtering method was applied to Pt-Ir alloy deposition. In order to control film composition, triangular plates of Pt or Ir were placed on an Ir or a Pt target, respectively. Prior to deposition, inverse sputtering for substrate cleaning and pre-sputter cleaning for the targets were respectively conducted under the following conditions; output power: 400 W, Ar pressure: 5.0 $x10^{-1}$ Pa, time; 1 min. Sputtering deposition was then conducted under the following conditions substrate temperature: 873 K, output power: 800 W, Ar pressure: 5.0 $x10^{-1}$ Pa, time: 1.25 to 2 hours. In this manner, Pt-Ir alloys (Ir = 0, 30, 50, 80, 100 at%) with the thickness of 8-10 μm were deposited. SEM analysis revealed that all the coating were dense, flat, without any cracks. After the deposition, annealing and aluminizing treatments were conducted to evaluate the oxidation and hot corrosion resistances. Discs with 25 mm in diameter and 2 mm in thickness that were used for the oxidation test were annealed at 1423K for 1 hour in vacuum, while plates with 8 mm × 8 mm × 2 mm that were used for hot corrosion test were annealed at 1373K for 1 h in Ar. A conventional Al pack cementation process then was carried out where samples were embedded in a retort consisting of $24.5Al+24.5Fe+49Al_2O_3+2NH_4Cl$ (mass%) powder mixture, and heated at 1273K for 5 hours in atmospheric pressure under

flowing Ar. Together with the Pt-Ir coated specimens, simple aluminizing to the substrate TMS-82+ without any coatings was also conducted for comparison.

Oxidation resistance of aluminized Pt-Ir coating was evaluated by the cyclic oxidation test, where 1 heating cycle was defined as heating at 1423K for 1hour followed by air cooling for 10min, and sample mass was measured after each heating cycle. For evaluating hot corrosion resistance the specimens, the salt-coating hot corrosion test was conducted, where the specimens coated with Na_2SO_4+10mass%NaCl molten salt ($0.2kg/cm^2$) were exposed at 1173K in a muffle furnace. Interval was set up when the total heating time reached 1, 5, 20, 40, 60, 80, 100 hours. At every interval, samples were put out from the furnace, cooled to the room temperature and carefully washed in hot distilled water. After thoroughly dried, the samples were weighed, recoated with the salt, and put into the furnace. The corrosion kinetic curves of the specimens were plotted up to 100 hours of the total heating time.

Phase constitutions of specimens were identified by X-ray diffractmeter. Surface and cross sectional images and corresponding element concentration profiles were analyzed by a field emission scanning electron microscope equipped with X-ray energy dispersive spectrometer.

Results and discussions

Microstructure of aluminized specimens

Although there are some differences in annealing conditions between the oxidation and hot corrosion test pieces, SEM analysis did not indicate any significant differences in the two types of specimens. Therefore, surface and cross sectional morphologies for hot corrosion test pieces will be discussed in this section.

SEM observation confirmed that the annealing treatment was successfully conducted for all the specimens, with coating layer being intact to substrate and without any voids.

Phase constitutions of the five kinds of aluminized Pt-Ir coatings, identified by the XRD analysis, were summarized in Table.1. The single β-NiAl layer was detected on the surface of simply aluminized substrate. With the addition of Pt and/or Ir, the phase composition became complicated.

Table.1 Phase compositions of aluminized Pt-Ir specimens and aluminized specimens

Aluminized specimens	Phase costitution	
	Major phase	Minor phase
Substrate TMS-82+	NiAl	-
Pt	(Ni,Pt)Al, $PtAl_2$	-
Pt-30Ir	(Ni,Pt,Ir)Al, $PtAl_2$	-
Pt-50Ir	(Ni,Pt,Ir)Al	Pt_2Al
Pt-80Ir	(Ni,Pt,Ir)Al	IrAl, $IrAl_3$, Ir_2Al_9
Ir	(Ni,Ir)Al	IrAl, $IrAl_3$, Ir_2Al_9

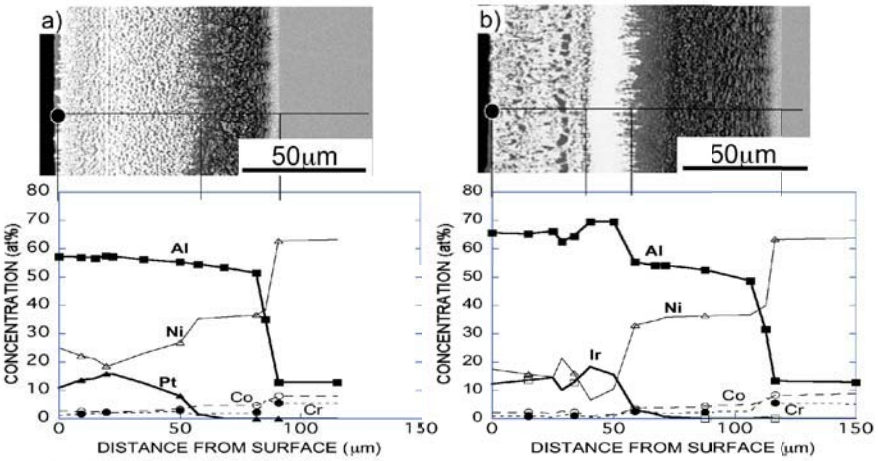

Fig.1: Cross sectional BSE images and corresponding concentration profiles of as-aluminized (a) Pt and (b) Ir.

Typical cross sectional microstructures and corresponding concentration profiles of Pt-Ir coated and aluminized specimens were shown in Fig. 1.
Pt-einriched Pt, Pt-30Ir and Pt-50Ir coated and aluminized specimens shows three layer structure as shown in Fig. 1(a), β-(Ni,Pt,Ir)Al and $(Pt/Ir)_xAl_y$ mixed layer, β-NiAl layer, inter-diffusion zone and substrate. For the Ir-rich specimens such as Ir, Pt-82Ir coated and aluminized specimens consisted of four layers. The Ir, and Al enriched layer was clearly observed between β-(Ni,Pt,Ir)Al and $(Pt/Ir)_XAl_Y$ mixed layer and β-NiAl layer as shown in Fig.1(b).

Formation of this Ir, and Al enriched layer is attributed to the lower diffusivity of Ir and high affinity between Ir and Al. When the sample is annealed, interdiffusion of elements occur, however, Ir tends to stay in the vicinity of substrate surface thus forms an Ir-enriched layer. Due to the high affinity between Ir and Al, IrAl enriched zone easily formed only by the annealing process when Ir content becomes higher. The additional Ir-Al enriched zone observed in the Ir-rich coatings was thus originated by the annealing treatment.

Oxidation resistance

Figure 2 shows the mass change of the specimens as a function of oxidation cycles. In this graph, mass gain indicates formation of oxides on the specimen while mass loss indicates spallation of the oxide and coating layers. That is, a specimen showing smaller mass change can have better oxidation resistance. All the specimen showed mass gains up to 20cycles, attributed to the formation of oxides. However, accelerated mass gain occurred in the Pt aluminized specimen after 20 cycles, followed by a sudden mass loss after 70 cycles. This sudden mass loss is due to spallation of one side of coating layer. There are two possible reasons for this sudden mass loss: one is the bad adhesion between Pt coating layer and substrate, and the other is formation of thick thermally grown oxide (TGO) layer. However, further investigation is necessary to elucidate this phenomenon. On the other hand, Pt-30Ir and Pt-50Ir showed smaller mass change than all the other specimens, and Pt-30Ir showed the smallest mass

change, indicating that Pt-30Ir has the best oxidation resistance of all the specimens evaluated in this study, followed by Pt-50Ir. Mass change of Pt-80Ir and Ir showed accelerated mass gain after 40 cycles and 60 cycles, respectively, followed by the mass loss. These results indicate that Pt addition that is effective to in improving adhesion of oxide [18, 19] is essential to maintain good oxidation resistance for Ir-rich coatings.

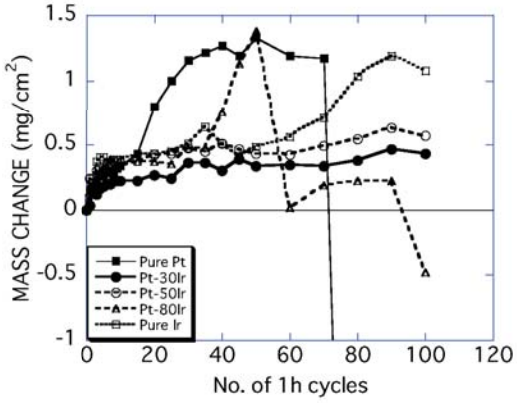

Fig.2: Mass change of specimens as a function of oxidation cycles.

Figure 3 shows the cross sectional image and corresponding concentration profile of specimens tested after 100 cycles. Pt showed undulated surface with 20 μm of maximum surface upheaval, attributable to the rumpling phenomenon, and TGO of this specimen was 5μm thick. Note that the other side of the specimen was completely spalled. Whereas, Pt-30Ir and Pt-50Ir showed much smoother surface, Pt-30Ir was 6μm, Pt-50Ir was 12μm depth of surface upheaval at maximum and TGO were 2-3μm thickness in both specimens. From theses results, Ir addition make surface of coatings retarding surface upheaval. There are possible reasons for the good oxidation resistance and smooth surface in Pt-30Ir and Pt-50Ir. While Pt addition is known to be effective in improving adhesion of oxide scale [18,19], Ir addition can retard the scale growth rate, due to its low permeability of oxygen and low diffusivity into Ni [15], resulting in the decelerated formation of $NiAl_2O_4$ spinel and Nickel oxides. In fact, after 100 cycles of oxidation, surface Ni concentration in the Pt coating layer reached

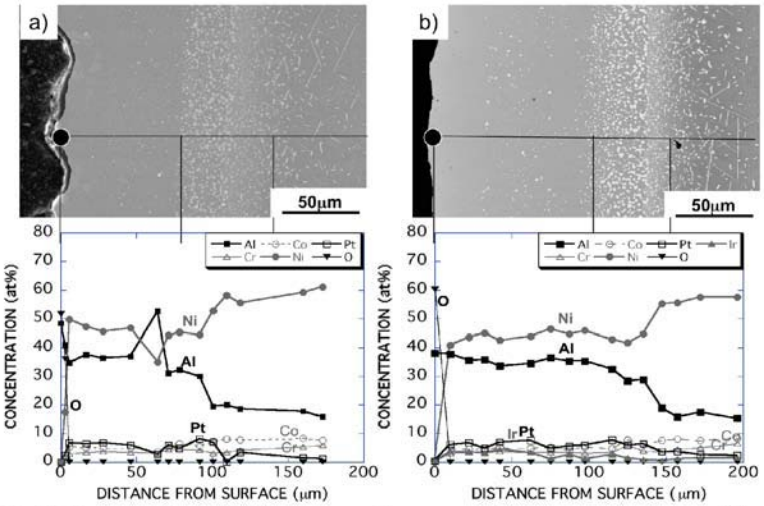

Fig.3: Cross sectional BSE images and corresponding concentration profiles of (a) Pt and (b)Pt-30Ir after 100 cycles of cyclic oxidation.

30 at%, whereas that of Pt-30Ir and Pt-50Ir was only 20-25at%. This higher Ni-concentration at the surface may have promoted the formation of $NiAl_2O_4$ spinel and Nickel oxide in the Pt-coated specimen.

Hot corrosion resistance

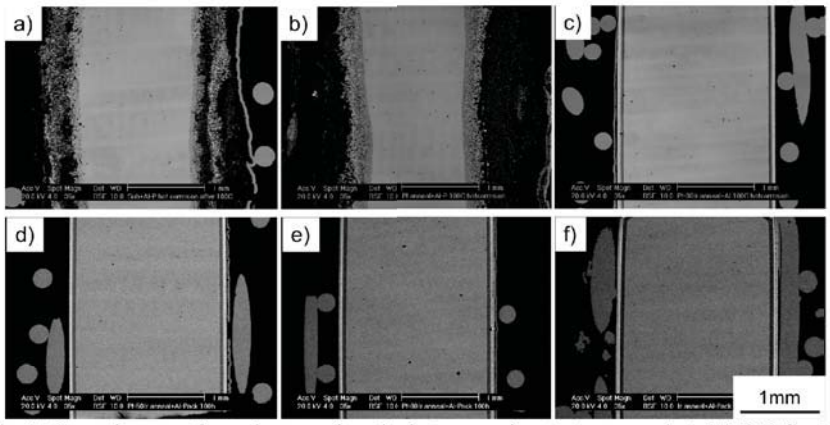

Fig.4: Cross image of specimens after the hot corrosion test exposed at 1173 K for 100 h. (a) Simply aluminized TMS-82+, (b) Pt, (c) Pt-30Ir, (d) Pt-50Ir, (e) Pt-80Ir and (f) Ir.

Figure 4 shows the cross image of specimens after 100 h of hot corrosion test. Figure 5 is the mass change of the specimens as a function of heating time. In this graph, mass gain indicates the formation of oxides and sulfides, while mass loss indicates the surface spallation, or dissolution of oxides and sulfides into molten salts. Therefore, a sample exhibiting smaller mass change can be regarded to have better hot corrosion resistance. All the specimens showed small mass change up to 40 hour. Pt showed dramatic mass increase after 60 hour, whereas Pt-30Ir and Pt-50Ir showed much smaller mass change even after 100 hour of heating. These results indicate that Ir addition improves hot corrosion resistance. Among all the specimens tested, Pt-50Ir showed smallest mass change (0.30mg/cm^2) after 100 hour, suggesting the superior hot corrosion resistance. After 100hour, Pt-30Ir and Pt-50Ir specimens showed mass gain (Pt-30Ir: 1.99 mg/cm^2), whereas, Pt-82Ir and Ir showed mass loss (Pt-82Ir: -2.82 mg/cm^2, Ir: -1.60mg/cm^2). Again, it is indicated that Ir-rich coatings in this study do not demonstrate as good hot corrosion resistance as Pt-30Ir and 50Ir.

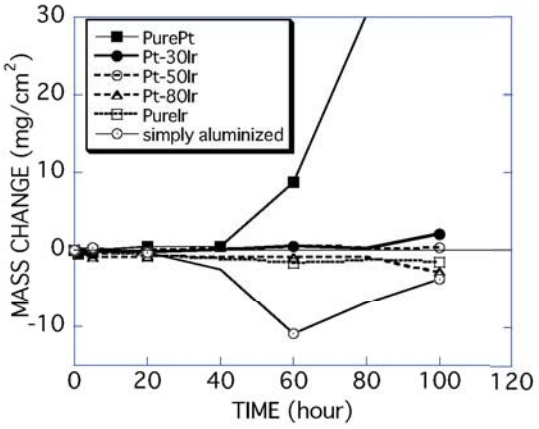

Fig.5: Hot corrosion kinetics of specimens at 1173 K.

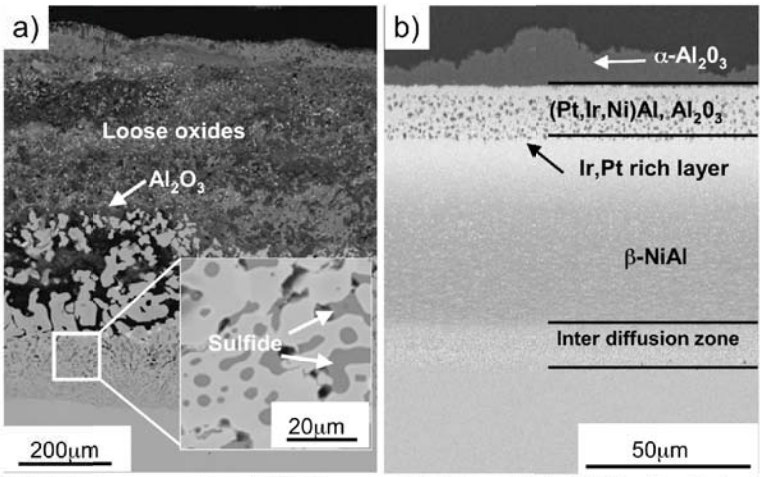

Fig.6 Detailed cross sectional BSE images of (a) Pt and (b) Pt-50Ir after the hot corrosion test for 100 h.

Figure 6 is cross sectional image of specimens after corroded for 100 hours. Thick and porous corrosion products were formed (approximately 400μm) on the surface of Pt, followed by the Al_2O_3 layer, and large number of chromium and nickel sulfides were detected under the Al_2O_3 layer. Formation of these sulfides is caused by the preferential reaction of sulfur with chromium and nickel, due to high diffusivity of sulfur [24]. On the other hand, Pt-30Ir, Pt-50Ir, Pt-80Ir and Ir kept the protective scale layer with 8-13μm thick. It should also be noted that while XRD analysis identified pure α-Al_2O_3, in Pt-30Ir and Pt-50Ir, additional phases were identified for the other specimens, such as α-Al_2O_3, CrS, spinel and NiO in Pt-80Ir, α-Al_2O_3 and CrS. Porous and internal oxide of Al_2O_3 was detected in the β-phase+$(Pt,Ir)_x$ Al_y matrix under the protective scale. However, these internal oxides were seldom observed beneath the Ir, Al enriched layer as described in the previous section, suggesting that the Ir-enriched layer may have blocked the propagation of internal oxidation. In addition, trace amount of tungsten was detected from these two layer (β-phase+$(Pt,Ir)_x$ Al_y matrix and internal oxide layer, Ir rich layer), indicating that Pt and Ir may have hindered the outward diffusion of tugsten which makes the alloy highly susceptible to hot corrosion.

In this study, promoting formation and improve adhesion of the protective Al_2O_3 scale were not obviously shown in Pt-80Ir and pure Ir, although they performed much better hot corrosion resistance than Pt. Synergy effects of Pt and Ir may have improved both oxidation and hot corrosion resistances in this study.

Conclusions

The oxidation and hot corrosion resistance of aluminized Pt-Ir coatings were investigated and following conclusions can be drawn.

(1) Cyclic oxidation test revealed the smallest mass changes for Pt-30Ir and Pt-50Ir aluminized coatings. In addition, these specimens had smoother surfaces than the

others. These results indicate that Ir addition to the Pt-modified aluminide coatings not only enhances the oxidation resistance but also retards surface rumpling.

(2) Hot corrosion test, also revealed that Pt-30Ir and Pt-50Ir aluminized coatings showed small mass change, suggesting that Ir addition enhances hot corrosion resistance. Pt-50Ir aluminized coating demonstrated the smallest mass change ($+0.299 mg/cm^2$) after 100 hour heating time.

(3) From these two tests, Addition of 30 to 50 at% Ir to Pt-modified coatings enhances both oxidation and hot corrosion resistances.

References

[1] J.H. Chen, J.A. Little, Surf: Coatings Technol. 92 (1997) 69-77
[2] A.Nusair Khan, J. Lu, Surf: Coatings Technol. 166 (2003) 37-43
[3] M.J Stinger, N.M Yanar, M.G. Topping, F.S.Pettit, G.H.Meier, Z.Metalkd 12 (1999) 1069-1078
[4] N.M Yanar, G.H.Meier, F.S.Pettit: Scripta Mater. 46 (2002) 325-330
[5] C.Leyens, U.Schulz, B.A.Pint, I.G Wringt: Surf. Coatings Technol, 120-121 (1999) 68-76
[6] G.R.Krishna, D.K.Das, V singh and VJoshi: Materials Science and Engineering A, 251 (1998), 40-47
[7] P.Deb, D.H.Boone, and T.F.Manley: J.of Vacuum Science and Technology A, 5(6), 1987, 3366-3372
[8] V.K.Tolpygo and D.R.Clarke: Acta Materialia, 48, 2000, 3283-3293
[9] T.M.Pollock: Materials Science and Engineering B, B32, 1995, 255-266
[10] Y.Matsuoka, Y.Aoki, K.Matsumoto, A.Sato, T.Suzuki, K.Chikugo, and K.Murakami: Superalloys 2004, ed. By. K.A.Green, T.M.Pollock, H.Harada, T.E.Howson, R.C.Reed, J.J.Shirra, and S.Walston, (The Minerals, Metals, Materials Society, Warrendale, Pittsburg, 2004), 637-642
[11] H.Murakami, A.Suzuki, F.Wu, P.Kuppusami, and H.Harada: Superalloys 2004, ed. By. K.A.Green, T.M.Pollock, H.Harada, T.E.Howson, R.C.Reed, J.J.Shirra, and S.Walston, (The Minerals, Metals, Materials Society, Warrendale, Pittsburg, 2004), 589-596
[12] F.Wu, H.Murakami, Y.Yamabe-Mitarai, H.Harada, H.Katayama, and Y.Yamamoto: Surface and Coatings Technology, 184, 2004, 24-30
[13] A.Suzuki, M.Harada, Y.N.Wu, and H.Murakami: Materials Transactions JIM, 46(8), 2005, 1760-1763
[14] H.Hosoda, T.Takahashi, M.Takehara, T.Kingetsu, and H.Masumoto: Materials Transactions JIM, 10, 1997, 871
[15] M.S.A.Karunaratne and R.C.Reed: Acta Mater, 51, 2003, 2905-2919
[16] T.Hino, T.Kobayashi, Y.Koizumi, H.Harada, and T.Yamagata: Superalloy 2000, ed. K.A.Green, T.M.Pollock, and R.D.Kissinger, (The Minerals, Metals, Materials Society, Warrendale, Pittsburg, 2000), 729-736
[17] T.Hino, Y.Yoshioka, Y.Koizumi, T.Kobayashi and H.Harada: Materials dor Advanced Power Engineering 2002, ed. By J.Lecomte-Beckers et al., 2002, 303-312
[18] E.J.Felten: Oxidation of Metals. 10, (1976), 23-28
[19] E.J.Felten, F.S.Pettit: Oxidation of Metals. 10, (1976), 189-223
[20] P.Hancock: Mater.Sci.Technol. 3, (1987), 536-544

Part II

Advanced Gas Turbine Materials

Contributed Papers

Intermetallics and Ceramics

CREEP BEHAVIOR OF ORTHORHOMBIC Ti_2AlNb-BASED ALLOYS

Masuo Hagiwara, Satoshi Emura, Yong Mao

Titanium Group, Structural Metals Center, National Institute for Materials Science (NIMS)

1-2-1 Sengen, Tsukuba, Ibaraki 305-0047, Japan

HAGIWARA.Masuo@nims.go.jp

Abstract

Titanium intermetallic alloys, based on the ordered orthorhombic Ti_2AlNb phase (O phase), have higher specific strength, greater fracture toughness and better workability than conventional intermetallic alloys, such as TiAl and Ti_3Al. The typical alloy system so far developed is a Ti-22Al-27Nb alloy, consisting primarily of the (O+B2) two-phase microstructure. However, the high temperature mechanical properties, particularly creep, of these alloys must be improved before commercial applications are feasible. To improve the creep behavior of Ti_2AlNb-based alloys, beta-phase stabilizing elements such as Fe, Mo, Cr, W and V were each substituted systematically for a portion of niobium in the Ti-22Al-27Nb system. The effects of each of these modifications on microstructure and creep behavior are reported.

Keywords: Titanium alloy, Ti_2AlNb, compositional modification, microstructure, creep

Introduction

Titanium intermetallic alloys, based on the ordered orthorhombic Ti_2AlNb phase (O phase) [1], have received considerable attention as potential high temperature structural materials, since Ti_2AlNb-based alloys have a higher specific strength, greater fracture toughness and better workability than conventional intermetallic alloys, such as TiAl-based and Ti_3Al-based alloys [2]. The typical alloy system of Ti_2AlNb-based alloys so far developed is a Ti-22Al-27Nb alloy, consisting primarily of the (O+B2) two-phase microstructure. This alloy is reported to have a good balance of tensile, creep and fracture toughness properties [3]. However, the high temperature mechanical properties, particularly creep properties, of the orthorhombic Ti_2AlNb-based alloys must be improved before commercial applications are feasible [4].

In the present study, to improve the creep behavior of Ti_2AlNb-based alloys, the beta (β)-phase stabilizing elements such as Fe, Mo, Cr, W and V were substituted systematically for a portion of Nb in the baseline Ti-22Al-27Nb alloy. The microstructures and creep behaviors of the compositional modified alloys are reported and discussed.

Experimental

The β-phase stabilizing abilities of Fe, Mo, Cr, W and V are stronger than that of Nb. One atomic percent addition of Fe, Mo, Cr, W or V corresponds to the replacement of 7.6, 4.25, 3.9, 3.35 or 1.6 atomic percent of Nb, respectively [5]. To get a proper volume fraction of B2 phase as in the baseline Ti-22Al-27Nb alloy, the total sum of the β-phase stability from each β-stabilizing element in the modified alloy was made equal to that of Ti-22Al-27Nb alloy. According to this guideline, Fe, Mo, Cr, W and V were each substituted for a portion of Nb in the Ti-22Al-27Nb alloy at the respective atomic rates of 1:7.6, 1:4.25, 1:3.9, 1:3.35 and 1:1.6. Six compositional modified alloys were composed as: Ti-22Al-19.2Nb-2Cr, Ti-22Al-12.5Nb-

2W-2Cr, Ti-22Al-10.8Nb-2Mo-2Cr, Ti-22Al-16Nb-2Cr-2V, Ti-22Al-11Nb-2Mo-1Fe and Ti-22Al-16.3Nb-2V-1Fe.

The alloy ingots were prepared by plasma arc melting. Each ingot, with a diameter of 46 mm, was encapsulated in an evacuated stainless steel can and hot rolled into 12 mm square bars at 1100℃ in the single B2 phase region. After the hot processing, the alloys were annealed at 1100℃ for 1 h and then cooled at a controlled rate of 0.03 K/sec to produce a lamellar microstructure. Finally, the alloys were held at 800℃ for 100 h in the (O+B2) two-phase region to stabilize the microstructure. The creep testing specimen had a 4.0 mm diameter and a 25 mm effective gauge length. Creep tests were conducted in air under a constant tensile load, using a dead-weight creep-rupture machine. The phase constitutions of the alloys were identified by the XRD patterns. The microstructures were investigated with optical microscopy and scanning electron microscopy (SEM).

Results and Discussion

Microstructures

The XRD patterns showed that, after being heated at 1100℃ for 1 h and then water-quenched, all of the alloys showed a single B2 phase structure. The grain sizes of the B2 phase (listed in Table 1) were close to each other for these modified alloys (from 162 μm for Ti-22Al-16Nb-2Cr-2V to 195 μm for Ti-22Al-16.3Nb-2V-1Fe). The B2 phase grains along the rolling direction were elongated slightly, to 1.4 times the length in the transverse direction. During the further controlled cooling at a rate of 0.03K/sec, the O and/or α_2 phases precipitated from the previously single B2 phase. The phase constitutions of the compositional modified alloys, after controlled cooling and annealing at 800℃ for 100 h, were identified by XRD patterns and are summarized in Table 1.The density of each alloy is also listed in Table 1. The phase constitutions were (B2+O) phases for Ti-22Al-19.2Nb-2Cr, Ti-22Al-16Nb-2Cr-2V, Ti-22Al-16.3Nb-2V-1Fe and Ti-22Al-27Nb baseline alloys with higher Nb content, whereas the phase constitutions were (B2+O+α_2) phases for Ti-22Al-10.8Nb-2Mo-2Cr, Ti-22Al-11Nb-2Mo-1Fe and Ti-22Al-12.5Nb-2W-2Cr alloys with lower Nb content.

Table 1 Alloy composition, phase constitutions and grain sizes of compositional modified alloys

Alloy	Density (g/cm^3)	Phase constitution	Grain size (μm)
Ti-22Al-19.2Nb-2Cr	5.05	B2+O	187
Ti-22Al-12.5Nb-2W-2Cr	5.02	B2+O+α_2	186
Ti-22Al-10.8Nb-2Mo-2Cr	4.89	B2+O+α_2	181
Ti-22Al-16Nb-2Cr-2V	4.96	B2+O	162
Ti-22Al-11Nb-2Mo-1Fe	4.87	B2+O+α_2	172
Ti-22Al-16.3Nb-2V-1Fe	4.98	B2+O	195
Ti-22Al-27Nb	5.35	B2+O	148

The microstructures of Ti-22Al-12.5Nb-2W-2Cr, Ti-22Al-11Nb-2Mo-1Fe, Ti-22Al-16Nb-2Cr-2V and Ti-22Al-27Nb alloys after controlled cooling and annealing are shown in Fig.1. The volume fractions and morphologies of the constitution phases in these alloys were a little different, depending on the alloy compositions. For the Ti-22Al-12.5Nb-2W-2Cr alloy (Fig.1a), the α_2 phase precipitated continuously at the B2 phase grain boundary, a coarse α_2 colony formed adjacent to the grain boundary, and a fine (B2+O) two-phase lamellar microstructure existed in the grains. In the microstructure of Ti-22Al-11Nb-2Mo-1Fe alloy

(Fig.1b), the α_2 phase also precipitated continuously at the grain boundary, but the size of coarse α_2 colony was less than that in the Ti-22Al-12.5Nb-2W-2Cr alloy. For the Ti-22Al-16Nb-2Cr-2V alloy with higher Nb content (Fig.1c), the O phase precipitated continuously at the grain boundary, very little α_2 phase existed at the grain boundary, and the O phase colony formed adjacent to the grain boundary. No α_2 phase existed in the grains of baseline Ti-22Al-27Nb alloy (Fig.1d), and the coarse O phase colony and fine (B2+O) lamellar microstructure formed in the grains.

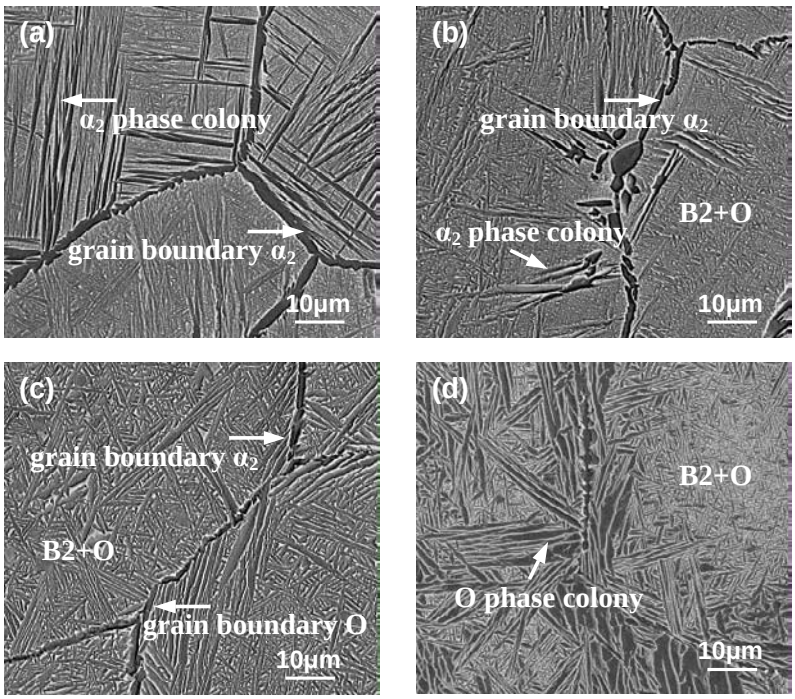

Fig.1 The microstructures of the compositional modified alloys after 1100℃/1h, 0.03K/sec controlled cooling and 800℃/100h. (a) Ti-22Al-12.5Nb-2W-2Cr, (b) Ti-22Al-11Nb-2Mo-1Fe, (c) Ti-22Al-16Nb-2Cr-2V, (d) Ti-22Al-27Nb

Creep behavior

The creep tests were conducted at 650℃ under a tensile load of 310 MPa and at 650 to 750℃ under a tensile load of 200 MPa. The creep strains *vs.* time curves under 650℃/310 MPa conditions of the compositional modified alloys and the baseline Ti-22Al-27Nb alloy are shown in Fig.2. The creep curve is comprised of three normal creep stages: primary transient creep, steady-state creep and accelerating creep. From these creep curves, it is seen that the Mo+Fe- and W+Cr-modified alloys exhibited good creep resistance. The minimum creep rates were much lower than those of other modified alloys or of the Ti-22Al-27Nb alloy.

The creep behaviors of the modified alloys under 650℃/310 MPa and 650 to 750℃/200 MPa conditions are summarized in Table 2. The transient creep time (t_{tr}) is defined as the ending time of transient creep, and the transient creep strain (ε_{tr}) is determined by extrapolating the

steady-state creep line to zero time. The 1% creep-strain lifetime under 650℃/310 MPa condition was prolonged greatly in the Mo+Fe- modified alloy; it was 5.6 times that of Ti-22Al-27Nb alloy. The minimum creep rate of Mo+Fe-modified alloy was 3.1 times less than that of Ti-22Al-27Nb alloy. The transient creep strain of Mo+Fe-modified alloy was also much lower than that of Ti-22Al-27Nb alloy. The data of creep behaviors at 650 to 750℃/200 MPa stress of Mo+Fe-, W+Cr-modified alloys and Ti-22Al-27Nb alloy also revealed that the minimum creep rate, the 1% creep-strain lifetime and the transient creep strain of Mo+Fe-modified alloy were all much better than the Ti-22Al-27Nb alloy under these conditions.

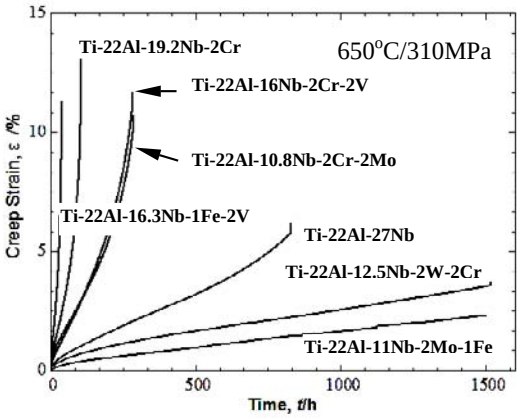

Fig.2 The creep strains *vs.* time curves under 650℃/310 Mpa

Table 2 Creep behaviors of the modified alloys at 650°C/310 MPa and 650 to 750°C/200 MPa

Alloy	Transient Creep Strain, ε_{tr}(%)	Transient Creep Time, t_{tr}(h)	Minimum Creep Rate, $\dot{\varepsilon}_{min}$(%/h)	1% Creep-Strain Lifetime (h)	Failure Lifetime (h)
650°C/310MPa					
Ti-22Al-19.2Nb-2Cr	0.51	10	5.80×10^{-2}	9	106
Ti-22Al-12.5Nb-2Cr-2W	0.90	500	2.08×10^{-3}	150	1519
Ti-22Al-10.8Nb-2Cr-2Mo	0.73	30	2.56×10^{-2}	12	287
Ti-22Al-16.0Nb-2Cr-2V	0.40	28	2.54×10^{-2}	22	283
Ti-22Al-11.0Nb-2Mo-1Fe	0.35	600	1.58×10^{-3}	420	2130
Ti-22Al-16.3Nb-2V-1Fe	0.48	4	1.41×10^{-1}	4	38
Ti-22Al-27Nb	0.72	300	5.88×10^{-3}	75	829
650°C/200MPa					
Ti-22Al-12.5Nb-2Cr-2W	0.74	750	4.10×10^{-4}	700	
Ti-22Al-11.0Nb-2Mo-1Fe	0.49	800	3.32×10^{-4}	1550	
Ti-22Al-27Nb	0.40	250	1.42×10^{-3}	420	
700°C/200MPa					
Ti-22Al-12.5Nb-2Cr-2W	1.42	560	3.75×10^{-3}	85	
Ti-22Al-11.0Nb-2Mo-1Fe	0.32	100	4.06×10^{-3}	160	
Ti-22Al-27Nb	0.75	280	5.00×10^{-3}	95	
750°C/200MPa					
Ti-22Al-12.5Nb-2Cr-2W	0.40	5	1.18×10^{-1}	5	
Ti-22Al-11.0Nb-2Mo-1Fe	0.27	6	6.11×10^{-2}	13	
Ti-22Al-27Nb	0.24	8	5.56×10^{-2}	13	

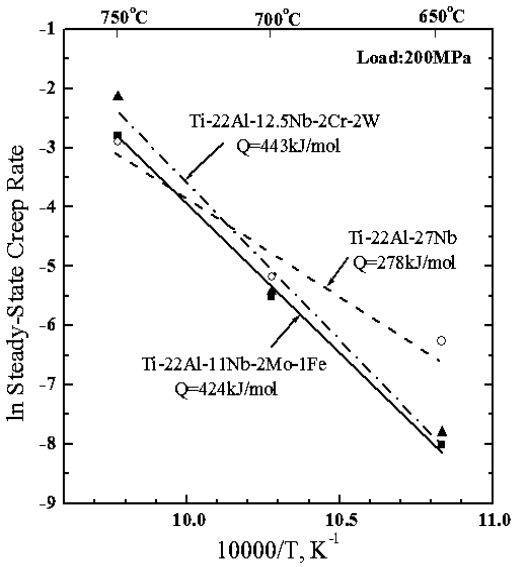

Fig.3 Temperature dependence of $\dot{\varepsilon}_{min}$ for 200 MPa load.

The temperature dependences of minimum creep rate for a 200 MPa tensile load are shown in Fig.3. The minimum creep rate follows the power-law creep equation, $\dot{\varepsilon}_{min}=A\sigma^{n}\exp(-Q_{app}/RT)$, where σ is the tensile stress, A and n are constants, Q_{app} is the apparent activation energy of the creep, R is the gas constant, and T is the absolute temperature. According to the above power-law equation, the value of Q_{app} were calculated from the slope of ln $\dot{\varepsilon}_{min}$ *vs.* 1/T plots. The values of Q_{app} for Mo+Fe- and W+Cr-modified alloys are 424 and 443 kJ/mol, respectively, which is much higher than the 278kJ/mol of the Ti-22Al-27Nb alloy.

For intermediate and high creep stresses (>100 MPa) at intermediate temperatures (650℃ to 760℃), the creep mechanism of grain boundary sliding and dislocation-controlled creep were summarized as the creep behavior of Ti_2AlNb-based alloys [6]. The values 424 and 443kJ/mol of apparent creep active energy of Mo+Fe- and W+Cr-modified alloys corresponded to the dislocation-controlled creep [6], suggesting that the creep process is controlled by dislocation climb.

Fig. 4 shows the crept microstructures of Ti-22Al-11Nb-2Mo-1Fe, Ti-22Al-19.2Nb-2Cr and Ti-22Al-27Nb alloys. These microstructures indicate that grain-boundary sliding and cracking were the main creep deformation mechanisms for the baseline Ti-22Al-27Nb alloy (Fig. 4a), resulting in a medium minimum creep rate. For a Ti-22Al-19.2Nb-2Cr alloy with low creep resistance (Fig. 4b), the main creep deformation mechanisms were the phase-interface sliding and cracking, and also the grain-boundary sliding and cracking. In the crept microstructures of Mo+Fe- and W+Cr-modified alloys such as Ti-22Al-11Nb-2Mo-1Fe alloy (Fig. 4c), no grain-boundary sliding or cracking was observed. This result indicates again that the dislocation-controlled creep was the creep mechanism for the Mo+Fe- and W+Cr-modified alloys.

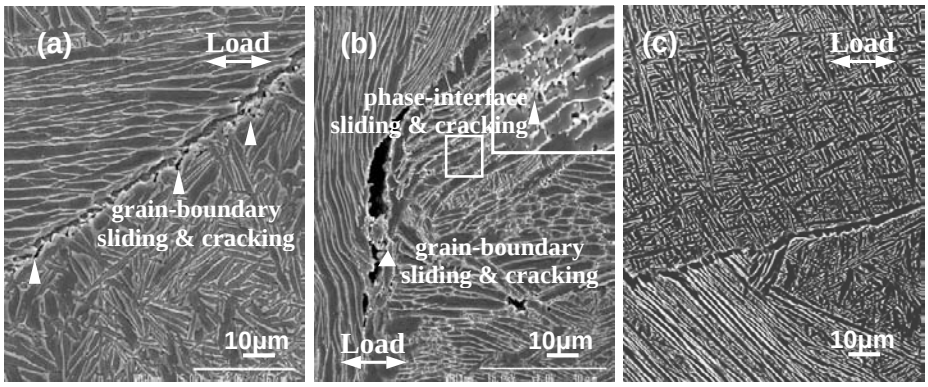

Fig.4 The crept microstructures under 650℃/310 MPa creep conditions in air.
(a) Ti-22Al-27Nb, (b) Ti-22Al-19.2Nb-2Cr, (c) Ti-22Al-11Nb-2Mo-1Fe

Conclusions

Beta-phase stabilizing elements such as Fe, Mo, Cr, W or V were each substituted systematically for a portion of Nb in a Ti-22Al-27Nb alloy system. Six compositional modified alloys were created. The phase constitutions were found to be B2+O or B2+O+α_2 phases, depending on the alloy composition. The microstructures and creep behaviors were investigated under 650℃/310 MPa and 650 to 750℃/200 MPa conditions. Mo+Fe-modified alloys exhibited good creep resistance. The minimum creep rate, 1% creep-strain lifetime and transient creep behavior of Ti-22Al-11Nb-2Mo-1Fe alloy in the temperature range of 650 to 700℃ were better than those of Ti-22Al-27Nb alloy. The dislocation-controlled creep mechanism was suggested to be the creep mechanism for the Mo+Fe- and W+Cr-modified alloys.

References

[1] D. Banerjee et al: "A New Ordered Orthorhombic Phase in Ti_3Al-Nb Alloy," *Acta Metall.* Vol.36 (1988), p.871.
[2] A. K. Gogia et al: "Microstructure and mechanical properties of orthorhombic alloys in the Ti-Al-Nb system", *Intermetallics* Vol.6 (1998), p.741.
[3] R. G. Rowe: "The Mechanical Properties of Titanium Aluminides Near Ti-25Al-25Nb," *Microstructure/Properties Relationships in Titanium Aluminides and Alloys* (TMS-AIME, Warrendale PA, USA 1991), p.387.
[4] F. Tang, S. Nakazawa and M. Hagiwara: "The effect of quaternary additions on microstructures and mechanical properties of orthorhombic Ti_2AlNb-based alloys", *Mater. Sci. Eng.* A329 (2002), p.492.
[5] S. Ankem and S. R. Seagle: *Beta Titanium Alloys in the 1980's* (R. R. Boyer, H. W. Rosenberg, Atlanta 1983), p.107.
[6] C. J. Boehlert and D. B. Miracle: "Part II The Creep Behavior of Ti-Al-Nb O + Bcc Orthorhombic Alloys", *Metall. Mater. Trans.* Vol.30A (1999), p.2349.

COMPARISON OF THE ISOTHERMAL FATIGUE BEHAVIOUR OF TIMETAL 6242 AND γ-TiAl ALLOYS AT 700ºC

G Cempura[1], HJ Penkalla[2], F Schubert[2], A Czyrska-Filemonowicz[1]

[1] *AGH University of Science and Technology, Al. Mickiewicza 30, PL-30059 Kraków, Poland*
[2] *Forschungszentrum Jülich, D-52425 Jülich, Germany*

Abstract

The Ti-based alloy TIMETAL 6242 (Ti-6Al-2Sn-4Zr-2Mo) is at present used for gas turbine components operating up to 538°C (1000°F). A new, 3rd generation γ -TiAl intermetallic alloy with high Nb content (13%) TBN-V2, has been developed for gas turbine components for higher operating temperatures.

The isothermal LCF behaviour at 700˚C of both alloys is compared and microstructural features are presented.

The microstructure of the as-received alloys and the changes in microstructure after isothermal LCF tests performed at 700°C were characterised by means of light microscopy and analytical transmission electron microscopy supported by image analysis. Phase identification was performed using electron diffraction and X-ray spectrometry.

Keywords: γ-TiAl, intermetallic, Ti6242, LCF, structural analysis

1. Introduction

In the last decade, the interest in titanium aluminide based alloys as engineering materials resulted in efforts to understand and to improve the properties of this class of materials. This interest in various branches of modern turbo machine industry is mainly due to attractive combination of low density, high melting point and structural stiffness. The high temperature specific strength made them useful candidates for gas turbine components (jet engines and land based facilities). The room temperature ductility, the minor defect tolerance and the poor hot gas corrosion resistance at very high temperature (above 750ºC) and for former generation the creep resistance are the major barriers for application of γ-TiAl base intermetallics as structural material. Addition of 8-10 at.% Nb significantly improves the oxidation resistance. Thus, TiAl alloys with Nb addition exhibit several desired attributes which give the potential for expanding the service range of titanium aluminides towards higher temperature [1]. Currently used materials (conventional titanium based alloys) can be used up to about 540ºC. Above this temperature, the oxidation rate of these alloys increases very fast. It is documented, that TiAl alloys with high Nb content are oxidation resistant to about 800ºC and addition of Nb to the TiAl base alloy improves the low temperature ductility [2]. The aim of this work was the comparison of low cycle fatigue properties of conventional titanium alloy (Ti6242) and new γ-TiAl alloy with high Nb content (TNB-V2) at 700 ºC.

2. Experiments

2.1. Materials

The LCF behavior of two alloys was examined. One of them is the commercial α+β Ti-alloy Ti6242, developed in late '60's. This alloy is currently used for long term high temperature application (up to 538°C). This alloy is one of the most creep-resistant commercial titanium alloys and is used as material for components like compressor blades, discs, etc [3]. The other investigated alloy is a TNB-V2, 3rd generation γ-TiAl intermetallic alloy with high Nb content (13.1wt.%). The chemical compositions of these alloys are given in Table 1.

Alloy element	γ-TiAl TNB-V2	Alloy element	Ti6242
Ti	55.2 (46.9at. %)	Ti	Bal.
Al	31.5 (47at. %)	Al	6.3
Nb	13.1 (5.7at. %)	Zr	4.3
B	0.1	Mo	2.1
Fe	0.028	Sn	2.1
Si,Sn,Ta,W, Ni,Cr	<0.01	Si	≤0.1
Y, Zn, Mn	0.002		
Zr	0.004		
C	0.092±0.001		
S	<0.001		
N	~0.005		
O	~0.049		

Table 1. Chemical composition of the investigated alloys (wt %)

The specimens for mechanical testing of the alloy Ti6242 have been manufactured from a fully heat treated bar. The heat treatment consists of recrystallisation annealing at 991°C for 1h followed by air cooling and stabilization annealing at 595°C for 8h with subsequent air cooling.

The specimens for mechanical tests of the γ-TiAl intermetallic alloy have been manufactured by spark erosion from hot extruded bar. The heat treatment of TNB-V2 after mechanical working was carried out at 1300˚C for 30 min, air cooling, and then hold at 800˚C for 6h followed by furnace cooling.

The Ti6242 alloy exhibits a dual phase α+β microstructure (α-close packed hexagonal; β-body centered cubic). TNB-V2 alloy exhibit a fine lamellar α_2/γ microstructure (α_2-hexagonal Ti_3Al; γ-tetragonal TiAl phase).

2.2. Fatigue tests

The fatigue behaviour was investigated in strain controlled low cycle fatigue (LCF) test with frequency of 0.1Hz and tension as test start direction. Tests were performed in air at temperature 700°C with different strain ranges from 0.4% up to 1.4%. Test termination criteria was 5% drop in the saturation load.

For fatigue tests standard specimens were used; geometries of the fatigue test specimens are shown below.

Fig. 1. Ti6242 alloy specimen used for fatigue tests

Fig. 2. TNB-V2 alloy specimen used for fatigue tests Type 1 (with measurement ridges)

Fig. 3. TNB-V2 alloy specimen used for fatigue tests Type 2 (without measurement ridges)

For TNB-V2 alloy two types of specimens were used. For standard specimens Type 1 premature failure of a specimen was observed and fracture occurred very close to the ridges. In order to avoid this effect another type of specimens – Type 2, was designed and used. Mechanical fatigue tests were carried out on INSTRON 8500 test machine.

2.3. Microstructural analysis

Specimens in as received condition and after fatigue tests were examined by light microscopy (LM), scanning electron microscopy (SEM) and transmission electron microscopy (TEM). Thin foils for TEM analyses were prepared by mechanical thinning (to about 60μm) and electropolishing (Struers electrolyte A3; temperature +5ºC). Thin foils were examined using Philips CM200 TEM, operated at 200kV. Quantitative microstructural analysis was made with ImageJ software [4] and phase identification was made with JEMS [5].

3. Results and Discussion

3.1. Results of fatigue tests

3.1.1 Ti6242 alloy fatigue tests results

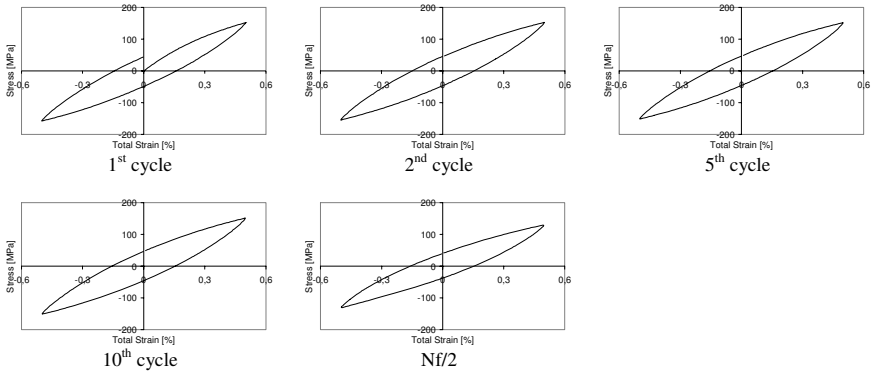

Fig. 4. Stress-strain hysteresis of Ti6242 alloy. LCF tests with constant amplitude, total strain range of ε=1% at 700ºC in air

For Ti6242 alloy there was almost no change in shape of stress-strain hysteresis curves during fatigue tests. Only for specimen deformed with the highest strain rate (ε=1.4%) there was a significant drop in load (Fig. 5).

Fatigue tests with Ti6242 alloy were terminated when 5% drop in load occurred. The specimen was not broken, only cracks were observed. On the surface of all Ti6242 specimens after fatigue tests oxidation products (mostly TiO_2) were observed.

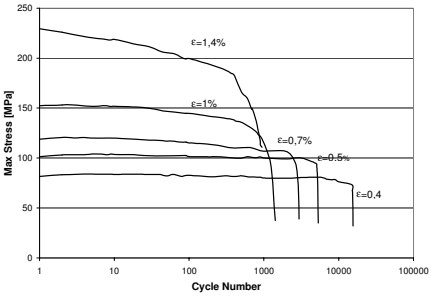

Fig 5. S-N Curve of Ti6242 alloy (700ºC, in air)

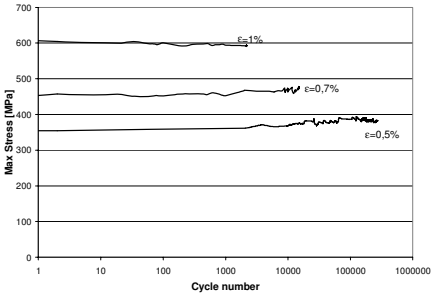

Fig 6. S-N Curve of TNB-V2 alloy (700ºC, in air) Specimens type 2

3.1.2 TNB V2 alloy's fatigue tests results

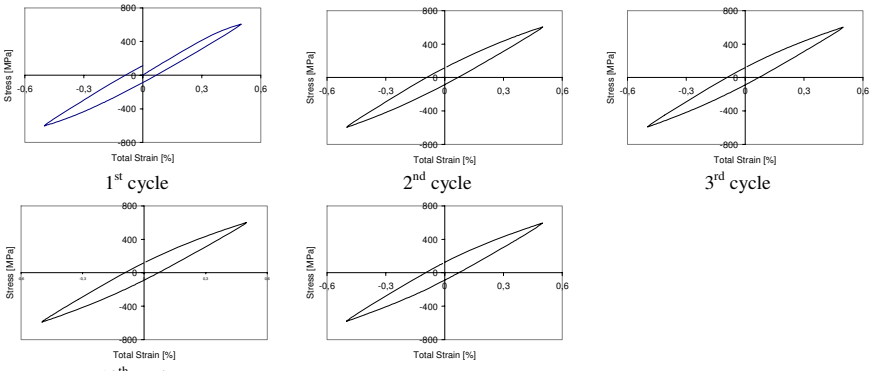

Fig. 7. Stress-strain hysteresis of TNB-V2 alloy. LCF tests with constant amplitude, total strain range of ε=1%, at 700ºC in air

Also for TNB-V2 alloy there was almost no change in shape of hysteresis curve during fatigue tests. Even for the specimen with the highest strain range ε=1%, there was no significant change in the stress amplitude during the tests till the failure of the test specimen (Fig. 6).

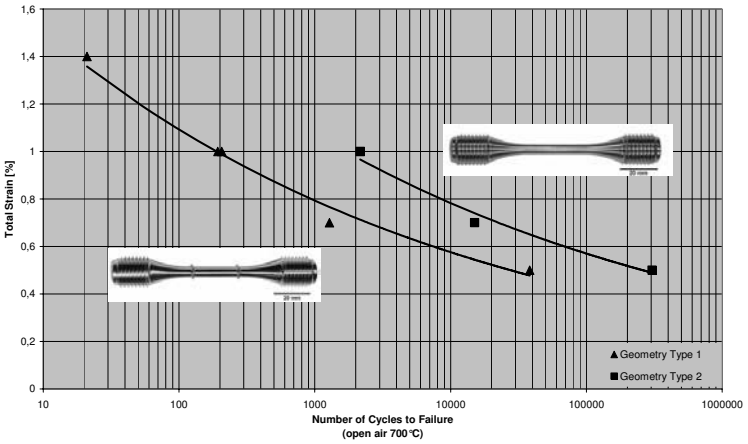

Fig. 8 Comparison of fatigue test results for different geometries of TNB-V2 fatigue specimens (700ºC, in air)

During fatigue tests of TNB-V2 specimens with Type 1 geometry a premature crack occurred directly in the range of the ridges. Specimens with Type 1 geometry exhibit lower fatigue resistance (due to notch sensitivity at the ridges), compared with standard specimens made from Ti6242 alloy. That is an evidence for importance of shape and surface finish for components made from γ-TiAl alloys.

For specimens made from TNB-V2 alloy (ε=0,7% and ε=1%) fracture occurred before 5% load drop. For specimens after 280000 cycles at temperature 700ºC there was no evidence of heavy surface corrosion.

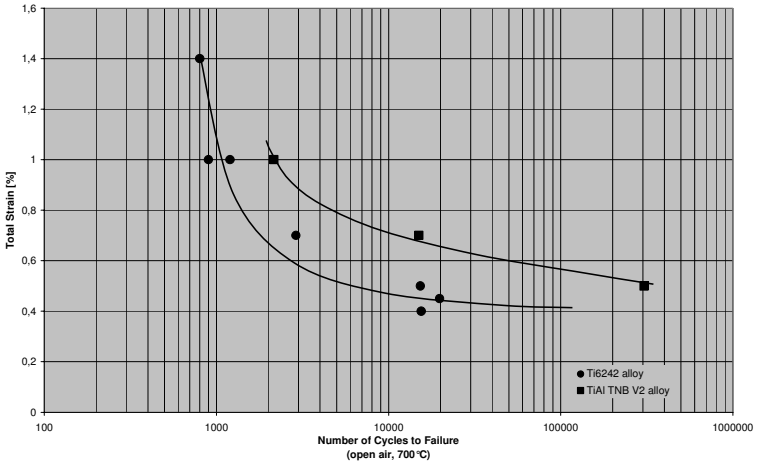

Fig. 9 Comparison of fatigue tests results for Ti6242 alloy and TiAl TNB V2 alloy (700ºC, in air)

3.2 Results of Microstructural analysis

3.2.1 Microstructure of Ti6242 alloy, as received

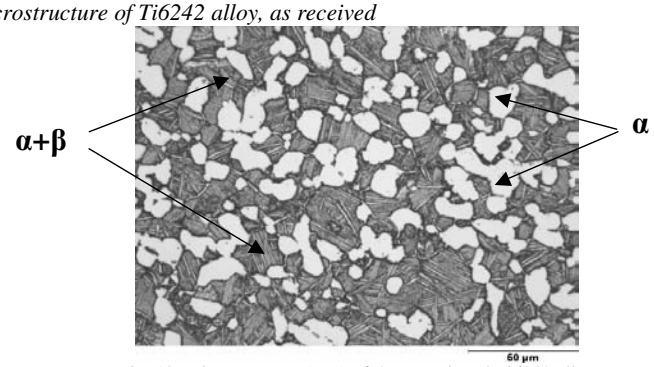

Fig. 10. Microstructure (LM) of the as recieved Ti6242 alloy

Microstructural analysis showed α and α+β phase fraction. Evaluation of phase volume fraction was performed based on LM and SEM micrographs. The volume fraction of the α phase regions were about 27% and α+β phase regions about 63% for Ti6242 alloy. EDX microanalysis made in SEM showed that concentration of such alloying elements as Al, Mo and Zr is higher in areas of α-phase. Concentration of Sn was uniform at the whole observed area.

For titanium based alloys certain alloying elements, particularly transition metals (Mo, V, Nb) stabilizes the cubic beta-phase and decrease the alpha-beta transformation temperature. Al and interstitial solutes (O,N) are alpha-stabilizers and increase the temperature of the alpha-beta transformation. Zr and Sn cause effect on the phase transformation [2].

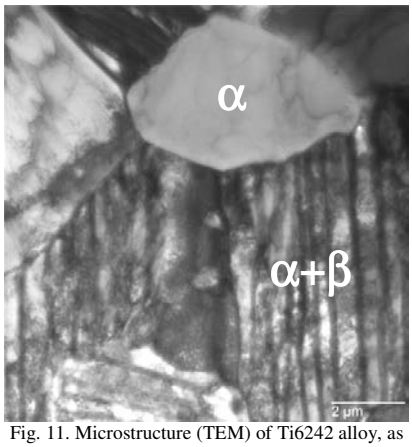

Fig. 11. Microstructure (TEM) of Ti6242 alloy, as received, plates of α +β phase and α phase grains

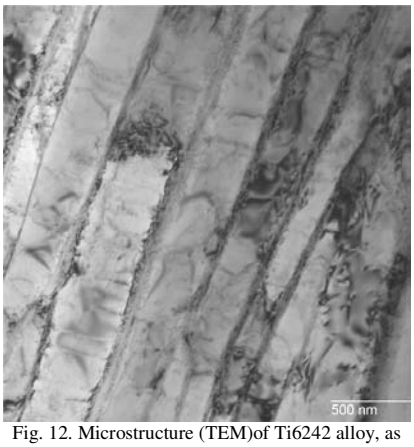

Fig. 12. Microstructure (TEM)of Ti6242 alloy, as received, different plates orientation (α +β region)

TEM observations of thin foils showed a duplex microstructure of Ti6242 alloy, with wide α-phase plates and thin β-phase plates. Sub-grain regions with different plate orientations were observed (Fig. 11). Low dislocation density was observed in as received material. Dislocation density was estimated qualitatively.

3.2.2 Microstructure of Ti6242 alloy after fatigue tests

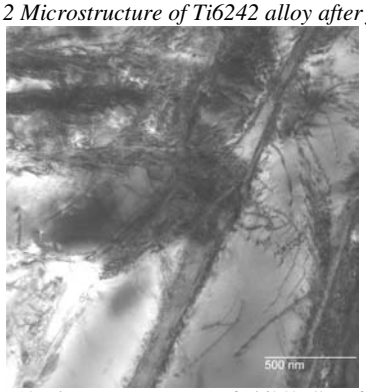

Fig. 13 Microstructure (TEM) of Ti6242 alloy after fatigue test, visible dislocations and dislocation networks

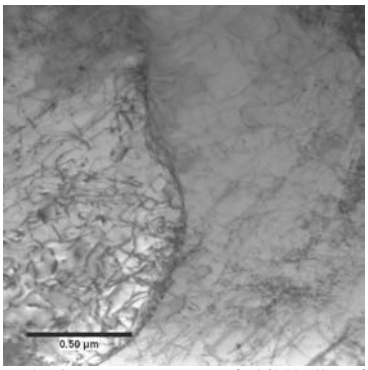

Fig. 14 Microstructure (TEM) of Ti6242 alloy after fatigue test, dislocation networks with higher magnification

After fatigue test, dislocations and dislocation networks were observed (Figs. 13,14). Dislocation density is considerably higher then in the as received material (Fig. 14).

3.2.3 Microstructure of γ-TiAl TNB-V2 alloy, as received

TNB-V2 alloy is the γ-TiAl based alloy with relatively high Nb and B content (13.1 and 0.1 respectively). Around the stoichiometric TiAl composition many phases may exist depending on the Al and of minor alloying elements concentration. Addition of Nb causes a strong strengthening effect in two phase Ti-Al alloys, and Nb additions leads to increase of α_2 phase volume fraction and to refinement of microstructure [1].

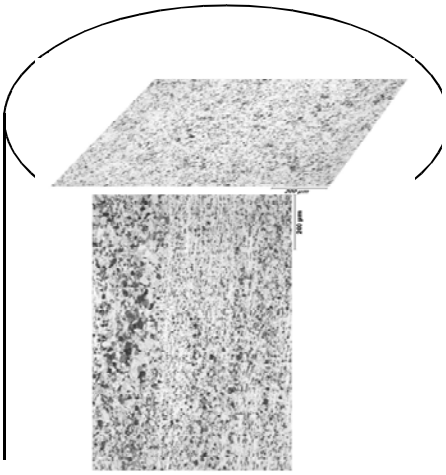

Fig. 15. Microstructure (LM) of the as received TNB-V2 alloy, parallel (below) and perpendicular (above) to a testing axis

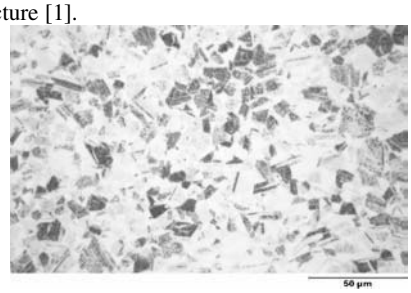

Fig. 16. Microstructure (LM) of TNB-V2 alloy, as received, normal to mechanical working axis

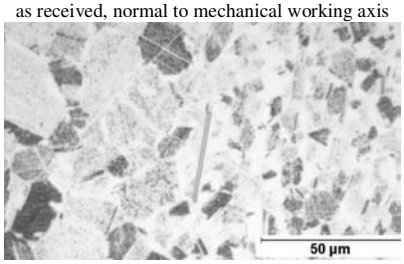

Fig. 17. Microstructure (LM) of TNB-V2 alloy, as received, parallel to mechanical working axis

Light microscopy observation exhibits texture in direction parallel to mechanical working

axis (also direction of fatigue tests).

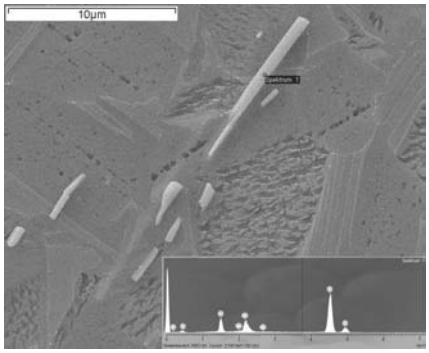

Fig. 18. Microstructure (SEM)of TNB-V2 alloy, as received, parallel to LCF test axis

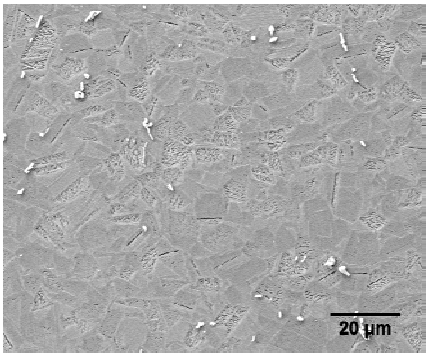

Fig. 19. Microstructure (SEM)of TNB-V2 alloy, as received, perpendicular to LCF test axis

SEM observation showed that in TNB-V2 alloy microstructure there is a large number of boride precipitates. Boride precipitates were identified by EDX technique. The type of boride formed during solidifications (TiB or Ti_2B) depends on the alloying elements and their concentration [6]. Dispersed titanium boride particles are evenly distributed throughout the sample and are elongated in direction parallel to axis of fatigue test.

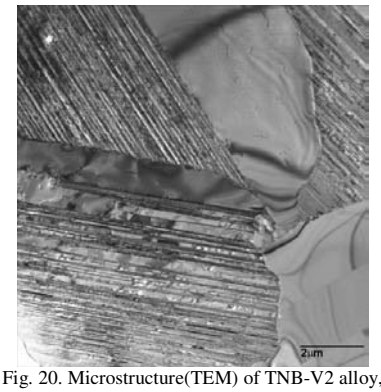

Fig. 20. Microstructure(TEM) of TNB-V2 alloy, as received

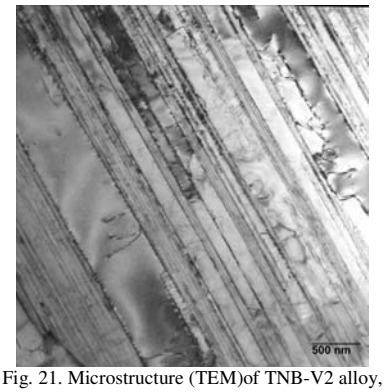

Fig. 21. Microstructure (TEM)of TNB-V2 alloy, as received

Observation of TNB-V2 alloy microstructure at a higher magnification exhibited areas of γ-phase grains and lamellar areas of $\gamma+\alpha_2$ phase with different plate orientations. The measured average plate width in $\gamma+\alpha_2$ phase area was 172nm ±32nm (±18%).

3.2.4. Microstructure of γ-TiAl TNB-V2 alloy after fatigue tests

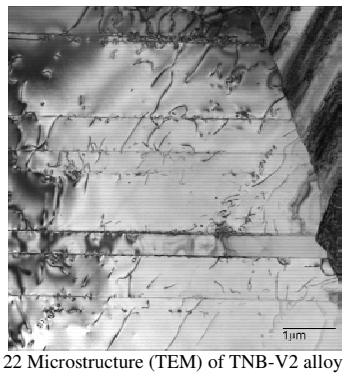

Fig. 22 Microstructure (TEM) of TNB-V2 alloy after fatigue test, visible dislocations inside γ-phase plates

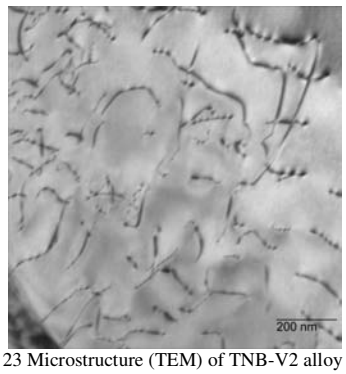

Fig. 23 Microstructure (TEM) of TNB-V2 alloy after fatigue test, dislocations inside γ-phase plates

In TNB-V2 alloy after fatigue test dislocations were present. It was observed that dislocations can traverse through γ/γ phase plates.

3.2.5 Comparison of oxidation resistance of Ti6242 and TNB-V2 alloy

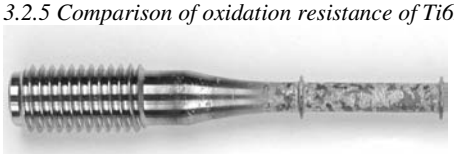

Fig 24. Ti6242 specimen after LCF test with 15000 cycles at 700ºC; oxide layer >2µm

Fig 25. TNB-V2 specimen after LCF fatigue tests with 280000 cycles at 700 ºC; oxide layer <2µm

Specimens made of Ti6242 alloy after LCF tests were considerably more oxidized, compared with these of TNB-2 alloy, although time of fatigue tests for Ti6242 specimens was much shorter than for TNB-V2 specimens. Duration of fatigue test for specimens shown on Fig. 24 was about 25h, and for specimen shown on Fig. 25 was about 470h.

4. Conclusions

The microstructure of the Ti6242 and the TiAl TNB-V2 alloys was characterized. As received Ti6242 alloy exhibits a dual microstructure with low dislocation density inside of α plates. Subgrains with different plate orientations were observed. After fatigue tests in microstructure of the Ti6242 alloy dislocations and dislocation networks were observed.

The as received TNB-V2 alloy, a new 3rd generation γ-TiAl intermetallic alloy with high Nb content (13%), exhibits a fine lamellar microstructure with different plate orientations with average plate width of 172nm. A texture in direction parallel to mechanical testing axis was observed. Because of relatively high boron content, a large number of boron precipitates was observed. Boron precipitates were elongated in direction parallel to direction of fatigue testing.

After fatigue tests on the Ti6242 specimens strong oxidation products were observed. 5% load drop occurred before specimens rupture. For TNB-V2 test specimens fracture occurred before 5% load drop. After LCF tests and 280000 cycles specimen surface was not highly oxidized. The TiAl TNB-V2 alloy exhibit better fatigue properties, in comparison to Ti6242 alloy at 700ºC. Better fatigue properties might be directly connected with oxidation processes and the influence of surface oxidation processes on crack formation and its development. However, the direct relation is not proved at the current state of investigations.

Acknowledgements
The authors would like to thank Dr F Appel (GKSS) and Prof. H.J. Christ (Uni Siegen) for providing the test materials.

References

1. Appel F., Oehring M., Wagner R.; Intermetallics 8 (2000), 1283-1312
2. Shecktman D., Blackburn M.J., Lipsitt H.A.; Metallurgical Transactions 5 (1974) 1373-1381
3. Peters. M.; Titan und Titanlegierungen, (2002), Wiley-VCH, Weinheim
4. http://rsb.info.nih.gov/ij/
5. Stadelmann P.; JEMS Java Electron Microscopy Software, http://cimewww.epfl.ch/people/stadelmann/jemsWebSite/jems.html
6. Hu. D.; Intermetallics 9 (2001) 1037-1042

TiAl OXIDATION PROTECTION IMPROVEMENTS USING THE HALOGEN EFFECT

Patrick Masset*, Hans-Eberhard Zschau, Michael Schütze
Karl-Winnacker-Institut der Dechema e.V., Theodor-Heuss-Alle 25
60486 Frankfurt-am-Main, Germany
* E-mail: masset@dechema.de

Abstract

The effect of fluorine implantation on the oxidation protection of TiAl alloys with Al contents between 10 and 48 at.-% was investigated. As predicted by thermodynamic calculations, it was demonstrated by oxidation tests carried out at 900 °C for 120 hours in laboratory air that the halogen effect promotes the growth of a protective and adherent alumina layer with alloys in which the aluminium content was higher than 40 at.-%. For lower aluminium contents, the halogen effect was not observed. However it was shown that the thickness of the oxide scale decreased and its structure was improved.

Keywords: TiAl, halogen effect, implantation, oxidation.

1. Introduction

γ-TiAl-based intermetallic alloys are of great attraction for structural high temperature applications. These alloys are envisaged for high temperature applications in aeronautics (turbine blades ...) [1] automobile applications (turbocharger...) [2]. However, the use of TiAl alloys is strongly hampered above 750 °C due to their poor oxidation resistance. In the last decade, the effect of chlorine was found to improve oxidation protection whereas it usually enhances corrosion. Since then a lot of work has been devoted to study the effect of halides on TiAl oxidation using different ways of treatment: molten salt, halide-based aqueous solution, gas diffusion, plasma and beam line ion implantation. Using the latter the halide is implanted into the subsurface of the alloy without significantly disturbing the structure (micro alloying). Once implanted the halide reacts preferentially at high temperature with the aluminium to form the expected Al_2O_3 protective layer [3]. Up to now, most of the studies dedicated to the halogen effect were mainly focused on the γ-TiAl composition. Alloys with low Al content were developed to improve their mechanical properties, but often, with drawbacks on the oxidation resistance. The aim of this work is to evaluate the oxidation protection at 900°C of TiAl alloys having lower aluminium contents than 48 at.% using the halogen effect with fluorine. For this study, γ-MET 100 was taken as a reference material as its oxidation behavior is well documented.

2. Thermodynamic predictions

For each $Ti_{1-x}Al_x$ alloy composition ($0.1 < x < 0.5$), the minimum and maximal fluoride partial pressures to get the so-called halide effect were calculated using the program ChemSage [4]. The metal fluoride partial pressures were calculated in the temperature range of typical industrial applications, e.g. 700-1100 °C. Ref. [3] proposed a mechanism to describe the so-called halogen effect. It consists in the preferential reaction of the aluminium with the implanted halogen to form volatile aluminium halides while Ti, which would form fast growing non-protective TiO_2, remains in the metal. The aluminium halides react with the oxygen coming from the environment to establish a protective Al_2O_3 layer free of TiO_2.

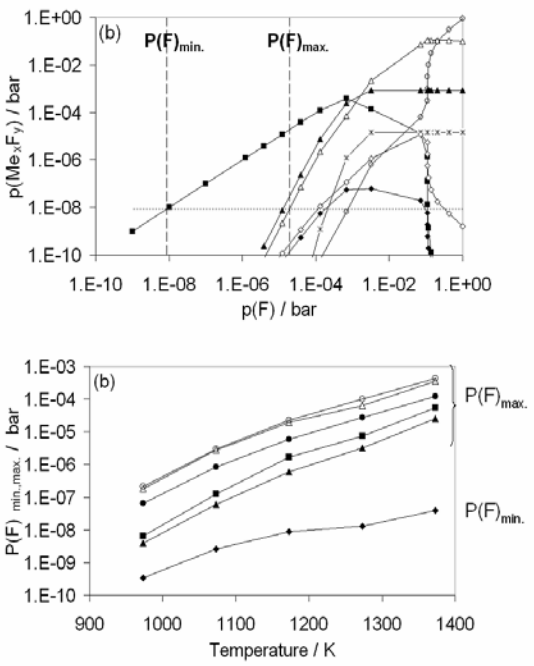

Fig. 1. (a) Evolution of the metal fluoride partial pressure $p(Me_xF_y)$ versus the fluorine pressure p(F) calculated at 900 °C for the $Ti_{0.6}Al_{0.4}$ alloy. (■) AlF, (◆) AlF_2, (▲) AlF_3, (△) TiF_2, (◇) TiF_3, (○) TiF_4, (*) Al_2F_6. (b) Evolution of $p(F)_{max}$ versus the absolute temperature calculated for different TiAl-based alloys. (◆) $p(F)_{min}$ for all alloys regarded in this Fig. (▲) $Ti_{0.9}Al_{0.1}$, (■)$Ti_{0.8}Al_{0.2}$, (●)$Ti_{0.7}Al_{0.3}$, (△)$Ti_{0.6}Al_{0.4}$, (○) $Ti_{0.5}Al_{0.5}$.

The overall mechanism is given by (Eq. 1).

$$2\,Al(s) + X_2 \longrightarrow 2\,AlX(g)$$
$$4\,AlX(g) + 3O_2(g) \longrightarrow 2\,Al_2O_3 + 2\,X_2 \qquad \text{(Eq. 1)}$$

In (Eq. 1), X represents the halogen species (fluoride, chloride, bromide and iodide). Assuming that the Al_2O_3 layer growth follows a parabolic law, the minimum halogen pressure $p(X)_{min.}$ needed to supply sufficient Al via the gas phase AlX for Al_2O_3 growth was calculated by (Eq. 2) [3].

$$p(X)_{min.} = \frac{1}{2124.6} \cdot \left\{ k_p(T) \cdot M_{AlX} \cdot T \right\}^{0.5} \qquad \text{(Eq. 2)}$$

where k_p represents the parabolic rate constant, M_{AlX} is the molecular weight of the AlX compound and T is the absolute temperature. The values of the kinetic constant k_p for the formation of pure alumina were taken from the literature [5]. The halogen pressure p(X) represents the sum of the volatile halide-based species which might be involved in the halogen effect. The upper limit $p(X)_{max.}$ for the operation of the halogen effect is defined when the partial pressure of the most stable TiX compound reaches the value of $p(X)_{min.}$ (Fig. 1a). That is, a partial pressure window exists between $p(X)_{min.}$ and $p(X)_{max.}$ in which the halogen effect can exert its positive role [3]. In our case X is molecular fluorine.

It is well established that oxygen dissolves only little in the γ-TiAl and significantly in α_2-Ti_3Al phases. However, in the literature initially the phases with dissolved oxygen were not included in thermodynamic calculations. The equilibrium pressure of oxygen for the oxides varies with alloy composition as the Al and Ti activities are a function of the alloy composition [6]. It should be also mentioned that the Nb-based phases were not included in the calculations. The activity of Al slightly decreases as Ti and Al are substituted by Nb in the ternary system Al-Nb-Ti [7]. For low aluminium activity the equilibrium pressure of oxygen increases. Therefore the fluorine effect "window" is modified also by the oxygen pressure. From the $Ti_{0.9}Al_{0.1}$ to $Ti_{0.5}Al_{0.5}$ compositions the highest fluorine pressure increases by two orders of magnitude in the 700-1100 °C temperature range (Fig. 1b). Moreover the fluorine effect "window" significantly increases with temperature (Fig. 1b). The temperature enhances the stability of the AlF_x species over that of the TiF_x species. The growth of the layer of alumina is then promoted. Between 40 to 50 at.-% of aluminium the range of applicability of the halogen effect should remain almost unchanged as these theoretical calculations show (Fig. 1b). It means that the implantation parameters optimized in previous investigations with γ-TiAl alloy should be valid and were taken as reference for the implantation process. For smaller amounts of aluminium the corridor where the halogen effect occurs might be strongly modified and the corresponding implantation parameters need to be determined and optimized. For this first screening the dose was fixed on the lowest value in the dose range (1-3 × 10^{17} F cm^{-2}) where the halogen effect is efficient based on the preliminary thermodynamic calculations.

3. Experimental

3.1 Materials

TiAl-based alloys with different alloying elements and mechanical and thermal treatments were used in this study (Table 1).

Table 1. Chemical compositions of the alloys tested (compositions given in at %).

Alloys		Ti	Al	Nb	V	Cr	Mo	Zr	Sn	Si	C	B	Ta	Treatment
A	$Ti_{90}Al_{10}$	90	10	--	--	--	--	--	--	--	--	--	--	VAR technique [8]
B	IMI834	Bal.	10.4	0.4	--	--	0.25	1.8	1.6	0.6	--	--	--	VAR technique
C	Ti6V4	Bal.	10.2	--	4	--	--	--	--	--	--	--	--	Forged + heat treatment
D	Ti6246	Bal.	10.8	--	--	--	3	2.1	0.8	--	--	--	--	Forged + heat treatment
E	$Ti_{80}Al_{20}$	80	20	--	--	--	--	--	--	--	--	--	--	VAR technique
F	Ti_3Al	75	25	--	--	--	--	--	--	--	--	--	--	VAR technique
G	$Ti_{60}Al_{40}$	60	40	--	--	--	--	--	--	--	--	--	--	VAR technique
H	TNBV2A	Bal.	44.5	8	--	--	--	--	--	--	0.2	--	--	Extruded + heat treatment
I	TNBV2B	Bal.	44.5	8		--	--	--	--	--	0.2	--	--	Forged + heat treatment
J	PX3500	Bal.	44.5	2	--	2	--	--	--	--	--	--	--	Fine-cast
K	TNBV3	Bal.	44.5	8	--	--	--	--	--	--	0.2	0.2	--	Fine-cast + HiPed
L	TNBV3A	Bal.	44.5	7	--	--	1	--	--	--	0.2	0.2	--	Fine-cast + HiPed
M	TNBV3B	Bal.	44.5	7	--	--	1	--	--	--	--	0.2	--	Fine-cast + HiPed
N	Ti31Al-2.1(Cr,Nb, Si)	Bal.	44.6	0.9	--	1.3	--	--	--	0.1	--	--	--	VAR technique
O	γ-MET 100	Bal.	46.4	1.1	--	2.5	--	--	--	--	--	0.1	0.5	Powder metallurgy

Samples with dimensions of (10×10×1.5) mm^3 were machined from the materials. Prior to implantation, the specimens were mechanically polished with 4000 grit SiC abrasive paper. Subsequently they were ultrasonically washed in acetone and ethanol for 10 minutes. Ion implantation was undertaken with a gaseous fluorine-based source using a 20 keV acceleration potential and at a nominal dose of 1×10^{17} F cm^{-2}. For the purpose of the

experiment the samples were one-side implanted with fluorine atoms using the ion implanter of the Institute of Nuclear Physics (IKF) of the Johann Wolfgang Goethe University in Frankfurt/Main. The concentration profile in elemental fluorine in the bulk material was supposed to be nearly structure independent. Well defined halide profiles can be achieved by mastering the implantation energy and the implanted doses [9].

The microstructures of the materials were investigated by classical metallographic techniques (Fig. 2). The γ-MET (Fig. 2g) presents a typical near-gamma structure composed of coarse γ grains and lamellar areas of fine α_2–γ grains. Fully lamellar microstructures consist of grains of fine α_2+γ lamellae (Fig. 2b, c, h and i, respectively). The presence of dark needles is ascribed to the presence of boron in the alloy. In Fig. 2c one can observe the effect of the mechanical treatment (vertical line) and the corresponding decrease of the grain size. Fig. 2d depicts a typical duplex structure composed of small γ-grains together with small α_2–γ grains with a fine lamellar structure and some α_2–grains. Alloy IMI834 (Fig. 2a) presents a lamellar structure with remaining areas from the coarse β-phase. Fig. 2f sketches a bimodal structure of the Ti6V4 alloy. The Ti6246 alloy represents a typical martensitic structure resulting from the quench of the β-phase alloy.

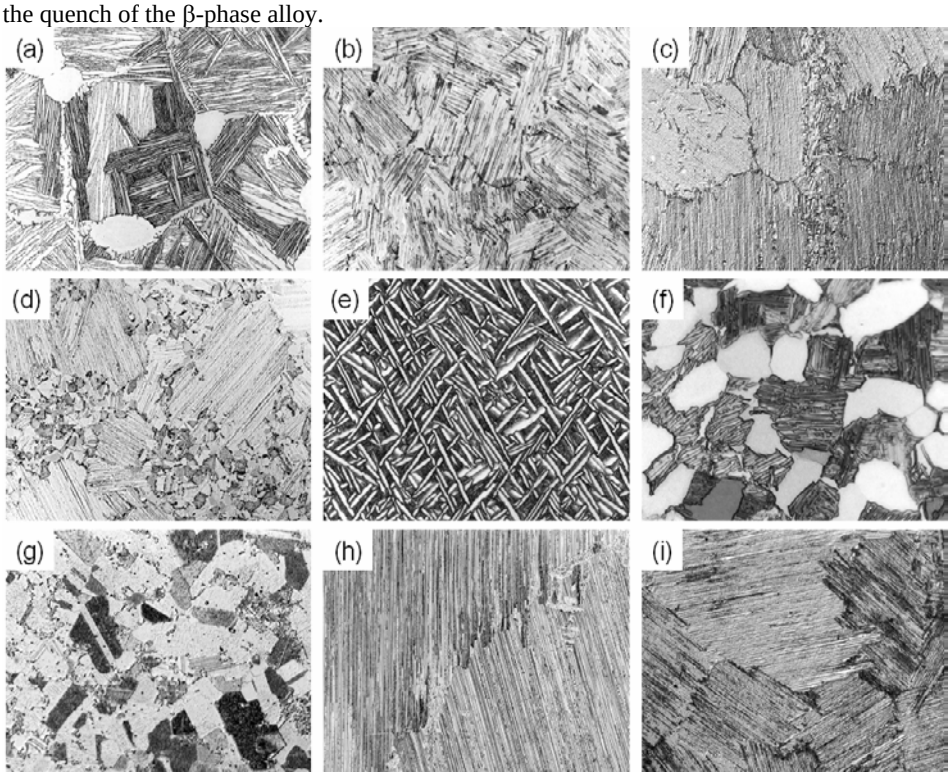

Fig. 2. Typical morphologies TiAl-based alloys used in this study. (a) IMI834, (b) TNBV3,(c) TNBV2A , (d) TNBV2B, (e) Ti6246, (f) Ti6V4, (g) γ-MET 100, (h) Ti-31Al-2.1(Cr,Si,Nb), (i) PX3500.

3.2 Techniques

The mass change of the samples due to oxidation was measured by a thermobalance (Satorius GmbH) under dry synthetic air at 900 °C for 100 hours (precision: ± 1 µg). The oxide scales were post-experimentally investigated by metallography, Scanning Electronic Microscopy (SEM) and microprobe analysis (EPMA). Prior to observation, the samples were gold sputtered, electrochemically coated with Ni and embedded in an epoxy resin. The cross-sections were polished with 4000 grit SiC abrasive paper and silica suspension down to 0.1 µm. SEM images were taken by an XL40 electronic microscope from Philipps/The Netherlands coupled with the EDX probe from EDAX. Elemental mappings with a spatial resolution close to 1 µm were obtained with a SX50 microprobe from Cameca/France. The non-destructive Proton Induced Gamma-Ray Emission technique (PIGE) was also used to determine the fluorine concentration depth profile in the subsurface of the implanted samples before and after the oxidation tests. This method is one of the non-destructive Ion Beam Analysis (IBA) techniques whose depth resolution near the surface is about 20 nm and allows the detection of light trace elements with concentrations in the range of tens of ppm [10]. The PIGE measurements were performed at the 2.5 MV Van de Graaff accelerator of the Institute of Nuclear Physics (IKF) of the Johann Wolfgang Goethe University in Frankfurt/Main using the nuclear reaction $^{19}F(p,\alpha\gamma)^{16}O$.

4. Results and discussion

4.1 Fluorine concentration profiles

The amount of fluorine in the subsurface is well controlled by varying the dose of the implanted fluorine (Fig. 3a). Fig. 3b sketches the fluorine concentration profiles for a typical TiAl alloy for different implantation doses. The fluorine concentration increases deeper in the material with increasing dose as well as fluorine concentration in the near subsurface. The maximum of the curves is nearly dose independent and is located around 40 nm inwards. For higher implantation energy the curve maximum moves inwards into the material. Experimentally, it should be pointed out that the calculated fluorine concentration at the near subsurface is strongly affected by the formation and evaporation of AlF_x and TiF_x volatile compounds during the earlier stage of heating. Therefore the relation between the thermodynamic predictions and the implanted dose is still difficult to establish (Fig. 3c). For the implantation process, a nominal dose of 1×10^{17} F cm^{-2} was fixed.

4.2 Thermobalance experiments

TGA experiments were carried out at 900 °C for 100 h under synthetic air with non-implanted and two-sides implanted samples to measure the kinetics of oxide layer growth (Fig. 4). Without F-implanted the alloys containing niobium present the best oxidation behavior. This is in agreement with previous investigations [11] where it was shown that the optimum niobium content was close to 8-10 at.-%. Assuming a parabolic form for the evolution of the mass with time the kinetic constants were derived from the TGA measurements (Table 2). The results obtained with γ-MET and Ti_3Al alloys agree with previous determinations [1]. The oxidation rate of alloys from the TNB family was found to be in the same order of magnitude as for Ti_3Al-10Nb [1] or orthorhombic Ti-22Al-25Nb [12]. For specimens with low aluminium content the oxidation rate corresponds to the growth kinetics of pure TiO_2.

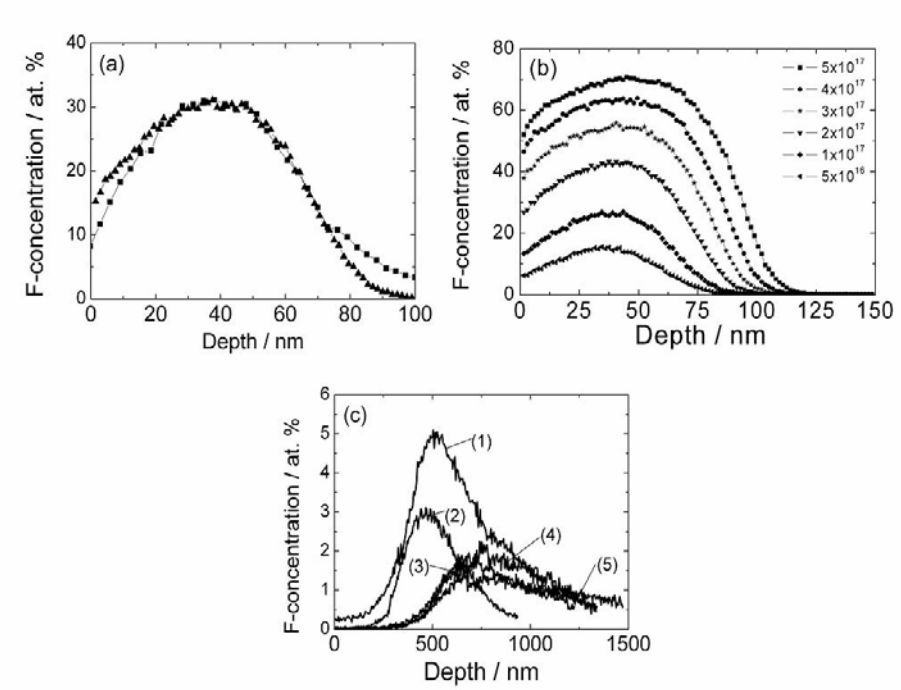

Fig. 3. (a) Comparison of the experimentally (▲) measured with the PIGE probe and calculated (■) fluorine concentration profiles in TiAl alloy with a dose of 1.23×10^{17} F cm^{-2} and acceleration potential of 20 keV. (b) Simulated fluorine concentration profiles in TiAl alloy for different implantation doses (F/cm²) calculated with the T-DYN software [13] for an ion energy of 20 keV. (c) Fluorine concentration in the TiAl alloy measured with the PIGE probe, implantation parameters: dose 1×10^{17} F cm^{-2}, ion energy 20 keV, time of oxidation at 900 °C: (1) 1 h, (2) 12 h, (3) 120 h, (4) 250 h, (5) 500 h.

The TGA curves obtained with two-side implanted specimens show clearly the beneficial effect of the F-implantation. After 100 h of isothermal oxidation at 900 °C under synthetic air with two-side implanted alloys the mass gain does not exceed 0.75 $mg.cm^{-2}$. For non-implanted alloys mass gain after 100 h was at least 1.25 $mg.cm^{-2}$. As seen in Fig. 4, the slope of the curve mass gain versus time is the most important feature to consider. For two-side implanted alloys the slopes of the curves range between 1.4 and 1.8 $\mu g.cm^{-2}.h^{-1}$ whereas it is at least 7.5 $\mu g.cm^{-2}.h^{-1}$ with non-implanted specimens. The oxidation rate is approximately reduced by a factor of 5. These oxidation rates are typical for pure alumina growth kinetics.

Table 2. Kinetic constants of oxidation of different alloys at 900 °C.

	γ-MET	Ti_3Al	TNBV3A	TNBV2A	PX3500
Log k_p ($mg^2.cm^{-4}.h^{-1}$)	- 0.50	- 0.05	-1.86	-1.56	-1.71

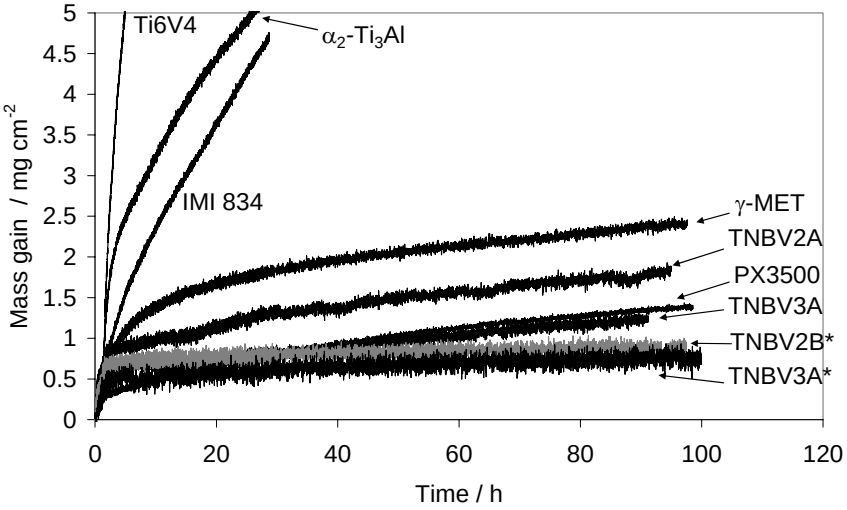

Fig. 4. TGA curves for isothermal oxidation at 900 °C for 100 h under synthetic air of non-implanted specimens, (*) two-side implanted specimens.

4.3 Exposure tests

Isothermal oxidation tests were performed at 900 °C for 120 hours in laboratory air using one-side implanted samples. For this study the alloy γ-MET 100 (alloy O) was chosen as reference material as it has been widely investigated and its oxidation behavior is well documented and understood. After 120 h of isothermal oxidation at 900 °C in laboratory air, a typical yellow and thick layer of TiO_2 on the non-implanted side was observed which agrees with previous investigations whereas a thin (around 2 µm) and adherent alumina layer was formed on the F-implanted surface of the initial material accounting for the halogen effect.

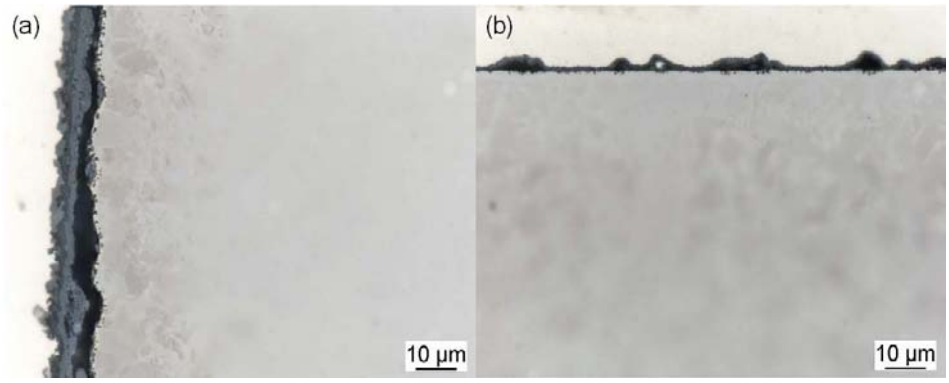

Fig. 5. Comparative SEM images of the oxide scale of the non implanted side (image a) and implanted side (image b) of the sample TNBV2B after 120 h of isothermal oxidation at 900 °C in laboratory air.

For alloys containing at least 40 at.-% (alloys G-O), the halogen effect was well evidenced with the formation of a thin adherent alumina layer for oxidation tests until 120 hours. Cross-sections of the non-implanted and F-implanted side of the alloy H are compared in Fig. 5 a and b, respectively. The layer thickness ranges between 2-5 µm. This is also supported by elemental mappings which show that the thin layer is mainly Al_2O_3 (Fig. 6d and e). The mapping obtained for titanium (Fig. 6f) was taken with a higher sensitivity to enhance the presence of Ti in the scale (Al_2O_3 + ε TiO_2). In Fig. 6e the Al-depleted layer was well evidenced (around 1.5 µm thick) at the subsurface of the original material. One can also observe the layer containing dissolved oxygen (Fig. 6d) located between the Al_2O_3 layer and the bulk material. It should be pointed out that no Nb was detected in the Al_2O_3 layer despite its active participation in the oxidation protection on unimplanted TiAl. The Al_2O_3 surface of F-implanted specimens presents a wave-type oxide layer. This morphology might be ascribed to a certain amount of scale growth stresses building up during oxidation. At oxide "waves" some fluorine was detected at the interface material/oxide. But at that time no correlation can be drawn between the scale morphology and the excess of remaining fluorine at the subsurface.

For the non-implanted side a layer of mixed oxide was formed with a layered structure (50-10 µm thick). On the untreated side the scale formed on the surface spalled whereas the adherence was enhanced through the halogen effect. This is well evidenced in Fig. 5a where a gap (black zone) between the scale and the material can be observed. This was also observed for specimens with low alloying level (alloy N). Under synthetic air (TGA experiment over 100 h) the oxidation of alloys containing at least 40 at.-% leads to an adherent scale. The spallation of the scale under laboratory air was ascribed to water vapor which is known to accelerate the oxidation rate [14]. With the alloy N where the Nb-concentration is low the oxide layer was mainly constituted of TiO_2 on the non-implanted side. Up to now under the present implantation conditions (1×10^{17} F cm^{-2}) for the alloys containing less than 40 at.-%, the positive effect of fluorine implantation was not clearly observed. However the thickness of the scale decreased with the halogen treatment and fewer cracks were observed in the scale itself. It is thought that it also promotes dense layer formation. As predicted by the thermodynamic calculations the corridor width of the halogen effect is strongly decreased with the decrease of the aluminium content. That means that the range of implantation parameters needs further investigation with regards for a potential positive halogen effect also for low Al alloys. As explained in the previous section, the α_2-Ti_3Al(O) was not involved in the calculations. During the earlier stage of oxidation an alumina layer might be formed due to the halogen effect. But as the subsurface is not oxygen-saturated, the oxygen dissolves progressively in the α_2-Ti_3Al phase at the expense of the stability of the alumina layer. In this case the kinetics of oxygen dissolution may influence the alumina layer growth.

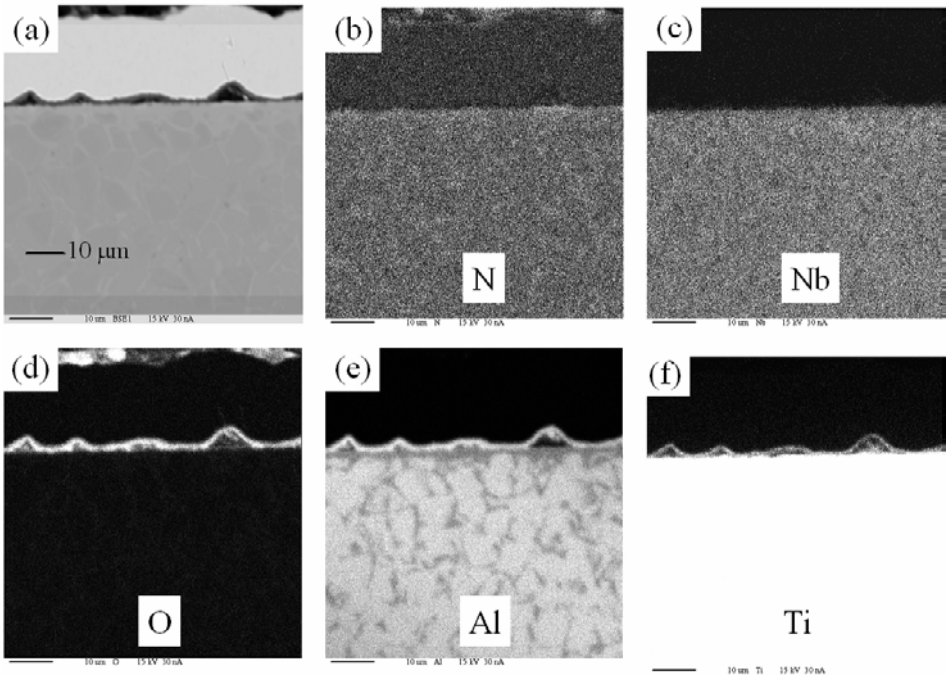

Fig. 6. Typical composition mapping of the cross-section of the F-implanted side (sample TNBV2A) after an oxidation test at 900 °C for 120 h in lab air.

5. Conclusions

The main conclusions of this work are:

1. The halogen effect was obtained with fluorine for alloys whose aluminium content was higher than 40 at. % for up to 120 hours of oxidation in laboratory air.
2. This is in good agreement with the theoretical calculations of this work.
3. On the basis of cross-sectional observations, after 120 h at 900 °C in laboratory air, a pure 3-4 µm Al_2O_3 layer is found on the F-implanted side of the sample whereas a 10-15 µm $Al_2O_3 + TiO_2$ mixed oxide layer is present on the non-implanted side.
4. For the TNB alloy family, the halogen effect was demonstrated with fluorine independent of the alloy processing route (cast, HiPed, extruded, forged…).
5. For the TNB alloys a pure alumina scale is formed with virtually no Nb involved in the scale formation.
6. For alloy with Al contents lower than 40 at.-% the halogen effect was not observed in the experiments. The theoretical calculations predict that the F-concentration corridor for the halogen effect narrows significantly with decreasing Al content when the alloys contain less than 40 at.-%. Future work should therefore aim at potential optimisation of the implantation parameters and the investigation whether the halogen effect can even be used for such alloys when the exactly defined optimum amount of F is applied.

Acknowledgements
The financial support of the Bundesministerium für Wirtschaft und Technologie (BMWi) via the Arbeitsgemeinschaft industrieller Forschungsvereinigungen (AiF) under contract AiF-Nr 177 ZN is gratefully acknowledged. The authors sincerely thank Mr Peter Gawenda (SEM analysis), Ms Ellen Berghof-Hasselbächer (metallographic examinations) and Ms Monica Schorr (EPMA measurements) for the excellent characterization work. GfE Gesellschaft für Elektrometallurgie GmbH/Nuremberg, MTU Aero Engines/Munich, Royce-Royce/Dahlewitz are thanked for providing TiAl-based alloys used in the frame of this project.

References

[1] M. Peters, C. Leyens, J. Kumpfert, „Titan and Titanlegierungen“, ISBN3-88355-244-0 (1996) 139-161
[2] T. Noda, “Application of cast gamma TiAl for automobiles”, Intermetallics, 6 (1998) 709-713.
[3] A. Donchev, B. Gleeson, M. Schütze, “The halogen effect for improving the oxidation resistance of TiAl-alloys”, Intermetallics, 11 (2003) 387-398.
[4] ChemSage program, Version 4.22, GTT-Technologies, Herzogenrath.
[5] J.W. Fergus, “Review of the effect of alloy composition on the growth rates of scales formed during oxidation of gamma titanium aluminide alloys”, Mat. Sci. Eng., 338 (1-2) (2002) 108 -125.
[6] A. Rahmel, P.J. Spencer, “Thermodynamic aspects of TiAl and $TiSi_2$ oxidation”, Oxid. Met., 35(1/2) (1991) 53-68.
[7] M. Eckert, H. Nickel, K. Hilpert, “Determination of thermodynamic activities in the alloys of the Ti-Al and Ti-Al-Nb systems”, Proc. of the 5th European Conference on Advanced Materials and Processes and Applications (1997) 303.
[8] V. Güther, A. Chatterjee and H. Kettner, “Status and prospects of γ-TiAl ingot production”, Gamma Titanium Aluminides 2003.
[9] H.-E. Zschau, M. Schütze, H. Baumann, K. Bethge, “Application of ion beam analysis for the control of the improvement of the oxidation resistance of TiAl at 900 °C in air by fluorine ion implantation and HF-treatment”, Nucl. Meth. In Phys. Res., B240 (2005) 137-141.
[10] J. R. Tesmer, M. Nastasi (Eds.), Handbook of Modern Ion Beam Materials Analysis, Materials Research Society, Pittsburgh 1995, PA, USA
[11] C. Leyens, “Oxidation of orthorhombic titanium aluminide Ti22Al-25Nb in air between 650 and 1000°C”, Journal of Materials Engineering and Performance (2001) 225-229.
[12] C. Leyens, “Environmental Effects on Orthorhombic Alloy Ti-22A1-25Nb in Air Between 650 and 1000°C”, Oxidation of Metals, 5/6 (1999) 52.
[13] J. Biersack, „TRIM-DYNAMIC applied to marker broadening and SIMS depth profiling “Nucl. Instr. & Meth. in Phys. Res. B 153(3-4) (1999) 398-409.
[14] A. Zeller, F. Dettenwanger, M. Schütze, “Influence of water vapour on the oxidation behaviour of titanium aluminides“, Intermetallics, 10 (2002) 59-72.

THERMAL EXPOSURE EFFECTS ON THE MECHANICAL PROPERTIES OF TIAL INTERMETALLIC

P.Holdway, K.Lucas, A.Wisbey

High Temperature Materials, QinetiQ, Farnborough, Hants. GU14 0LX. UK

Abstract

There is considerable interest in the γ TiAl alloys for application into gas turbines, where the low density and high temperature performance of these alloys is attractive. However, previous studies have highlighted the potential problem of reduced mechanical properties with exposure to elevated temperatures. In the work presented here this problem has been explored in terms of the tensile and low cycle fatigue properties of a number of γ TiAl alloys. Significant reductions in the tensile ductility and strengths, as well as fatigue cyclic lives have been shown and this appears to be associated with the surface of components or test pieces. Surface residual stress measurements and chemical analyses have been performed and these suggest that oxygen enrichment of the near surface layers of components or test pieces may be responsible for the property reductions seen. Conventional oxidation studies are not sensitive to these effects and thus the mechanical performance needs to be considered alongside pure oxidation behaviour. These effects are expected to be important in the generation of design data for these alloys and also for some applications where significant surface strains are seen.

Keywords: Gamma TiAl, thermal exposure, fatigue, oxidation

Introduction

There continues to be a requirement to remove mass from industrial gas turbine rotating components, to permit the use of larger low pressure turbine blades for high mass flow engines, whilst maintaining reasonable disc stresses. Clearly there is also a large mass reduction requirement for aerospace gas turbines, seeking higher efficiency and reduced fuel consumption. The γ titanium aluminide alloy system is a promising candidate for these applications and offers weight savings of up to 40% compared with current nickel base alloys and steels. The materials potentially may operate at temperatures of 700-750ºC and they have demonstrated excellent creep and mechanical performance under such conditions, with minimal oxidation. However, a small number of studies have shown that these materials exhibit a reduction in mechanical performance after exposure at typical service temperatures, for example a Ti-48at.%Al-2%Nb-2%Cr alloy had reduced tensile strength after exposure to moist air at 800ºC [1]. An examination of the effect of water vapour/hydrogen atmospheres on the creep and fatigue performance of a Ti-47at.%Al-1%Cr alloy showed reduced fatigue lives and increased minimum creep rates after exposure to these atmospheres [2]. There are thus clear indications that environmental factors may adversely affect the mechanical performance of these materials, with consequent implications for their use in gas turbine applications. This effect was investigated by the present authors within a COST522 action on γ titanium aluminide alloys and has been subsequently followed up with further studies. In the work reported here the effect of thermal exposure on the mechanical properties of a several γ titanium aluminde alloys has been investigated and detailed surface analysis has been undertaken to investigate any chemical changes occurring with exposure to elevated temperatures.

Experimental

Three γ titanium aluminide alloys have been evaluated in this study – extruded Ti-46Al-5Nb-1W (at.%, known as Ti-46-5-1 and similar to Alloy 7) produced by Plansee, Austria, investment cast Ti-46Al-2W-0.5Si-0.5B (at.%, known as ABB-23 or Ti-46-2) produced by Howmet and extruded Ti-46Al-5Nb-0.2C-0.2B (at.%, known as TNB v5 or Ti-46-5) produced by GFE, Germany. The Ti-46-5-1 was produced as vacuum arc re-melted ingot, canned and then extruded at either 14:1 or 18:1 extrusion ratios, at a temperature close to the α transus, to produce bars 30-45 mm in diameter. The analysed composition was close to the nominal, excepting that high levels of oxygen and nitrogen were found (at ~1400 ppm and ~250 ppm respectively). The material was taken and used in the as extruded condition in this study. The cast Ti-46-2 was produced as ~13 mm diameter bars, ~150 mm long and again the material was used in the as cast condition. The analysed composition of this material was very close to that of the nominal values. The Ti-46-5 was produced as vacuum arc re-melted ingot that was canned and extruded to produce bar of ~45 mm diameter. As with the other alloys, this material was used in the as received condition.

Small bars, ~11 mm diameter x 70 mm length were produced from each alloy for mechanical testing. In the case of the Ti-46-2 these bars were simply turned from the cast samples. Whilst for the Ti-46-5-1 and Ti-46-5 these bars were cut from 70 mm lengths of extrusion, with their long axis parallel to the extrusion direction. Previously some of these bars from the Ti-46-2 and Ti-46-5-1 alloys were heat treated at 700ºC for up to 1000 hours, prior to producing tensile test pieces (ground gauge length of ~23 mm and 3.99 mm diameter) to evaluate the effect of bulk microstructural changes on tensile properties [3]. No effect was seen on the room temperature tensile properties and thus this was not repeated for the Ti-46-5 alloy. The remainder of the 11 mm diameter bars were machined into tensile test pieces, with a ground gauge length. These test pieces were degreased in acetone and dried, prior to exposure at 500, 600 and 700ºC for up to 1000 hours in air or vacuum (10^{-5}-10^{-6} torr for 24 hours). A small number of Ti-46-5-1 tensile test pieces were electro-polished to remove the ground surface finish, prior to exposure at 700ºC in air for 24 hours. Following exposure the tensile test pieces were tested at room temperature, using a strain rate of $10^{-4}s^{-1}$ and the extensometry was retained until failure. The curves of stress and strain were plotted to determine the plastic strain to failure. Generally at least three test pieces were tested for each condition, although only two were available for some of the Ti-46-2 test conditions.

In addition to the tensile testing, low cycle fatigue testing has also been undertaken at both room temperature and 700ºC for the Ti-46-5-1 alloy, both with and without thermal exposure (again the test pieces were machined, and degreased in acetone prior to 700ºC, for 24 hours in air). The test pieces were round bar and had a gauge length of 14 mm and diameter of 4 mm; the gauge length has a ground finish. The test pieces for testing at 700ºC were degreased in acetone prior to testing (both as received and pre-exposed conditions) to ensure that there was no extraneous contamination on the test piece surface. All of the testing has been performed in uniaxial strain control, using a triangular waveform and R ratio (minimum strain/maximum strain) of 0. The stress was continuously monitored and recorded throughout the test. Fractography of these fatigue test pieces was undertaken following failure.

In order to study the changes in surface chemistry that occur during thermal exposure (both in air and vacuum), some samples of the Ti-46-5-1 and Ti-46-5 alloys have been subjected to

detailed surface analysis. The Ti-46-5-1 was sectioned and the surface of the material studied using a field emission gun scanning electron microscope (FEG-SEM), along with energy dispersive x ray analysis (EDX). The Ti-46-5 was also examined microstructurally in the FEG-SEM but it was also subjected to x ray photo-electron spectroscopy (XPS) and scanning ion mass spectroscopy (SIMS). The XPS was performed at normal take-off angle with Al Kα incident radiation (1486.6 eV) (under these conditions the sampling depth was ~5-10 nm). SIMS profiling was performed with a 8.5 keV O_2+ and 14.5 keV Cs^+ primary ion beams, for electropositive and electronegative species respectively. Depth scales were derived from a 0.85 μm deep crater made with the Cs^+ ion beam (depths of shallower craters could not be measured due to the high surface roughness) assuming a constant sputter rate. The SIMS interpretation was greatly complicated by the unknown dependence of ion yield on composition.

Results and Discussion

The basic bulk microstructures of the three alloys are shown in Figure 1; these are fairly typical for these alloys with the Ti-47-2 alloy showing a fully lamellar structure, as would be expected with a cast product, whilst the other two wrought materials exhibit a near lamellar structure. All of the material was evaluated in these as received conditions.

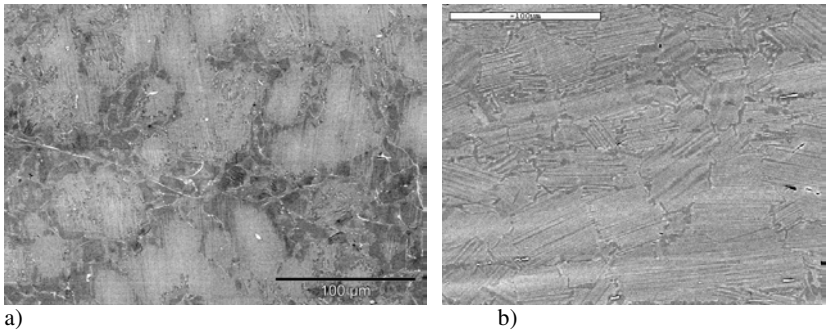

a) b)

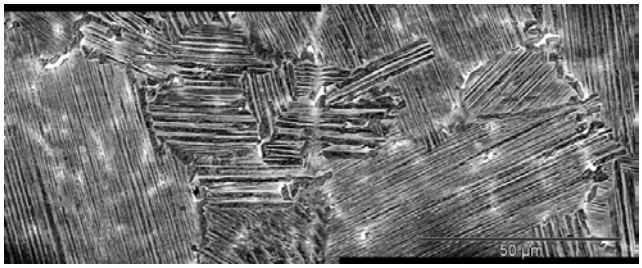

c)

Figure 1 Microstructure of the alloys studied – a) cast Ti-47-2, - b) extruded Ti-46-5, - c) extruded Ti-46-5-1 alloy, showing near lamellar structure (SEM-BEI).

As was noted above there was no discernible effect of heat treatment (thermal exposure) at 700˚C for up to 1000 hours when the test piece was machined following the thermal exposure [3], however, if the tensile test piece was machined and then thermally exposed at 700˚C for up to a 1000 hours then the subsequent room temperature tensile properties were those obtained in Figure 2. Here it can be seen that the Ti-47-2 and Ti-46-5-1 alloy showed an almost immediate and marked reduction in ultimate tensile strength and elongation to failure, with thermal exposure at 700˚C and this was retained through to 1000 hours exposure. This difference in behaviour between the thermally exposing material and then machining test pieces and exposing pre-machined test pieces suggest that the reduced properties are associated with surface modifications occurring during thermal exposure. From this study it can be seen that the reduction in room temperature tensile properties occurs very rapidly, with marked changes after just 1-2 hours exposure and suggests that this effect is unavoidable under normal service conditions.

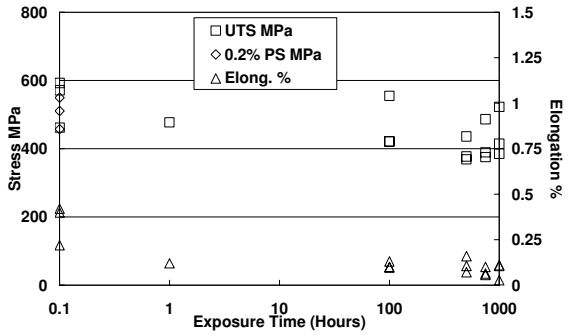

a)

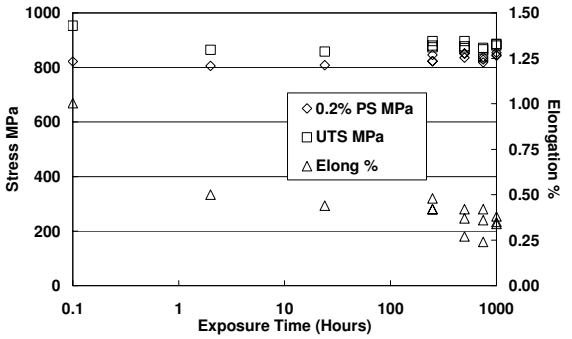

b)

Figure 2. Effect of a prior thermal exposure at 700˚C on pre-machined tensile test pieces of – a) cast Ti-47-2 and – b) extruded Ti-46-5-1.

Following this initial study more detailed investigations have focussed on the extruded Ti-46-5-1 and Ti-46-5 alloy. The effect of exposing the two extruded alloys at a variety of temperatures for 24 hours is shown in Figure 3 and here it can be seen that even after exposure at 500˚C and 600˚C there was some impact on the room temperature tensile

properties, especially with the Ti-46-5 alloy showing markedly reduced elongations. The situation was less clear for the Ti-46-5-1, with moderate tensile elongations after 600˚C, but still with tensile strength reductions. It should be noted that the tensile curves for the as ground condition and following thermal exposure were identical; with the thermally exposed material simply failing significantly earlier than the as ground samples. This is very disappointing for a material aimed at high temperature applications and may have significant implications for the design values to be used for these materials, along with the practical handling of ex service components made from these alloys.

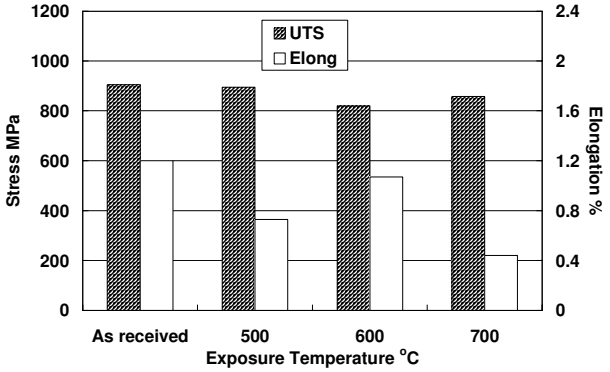

a)

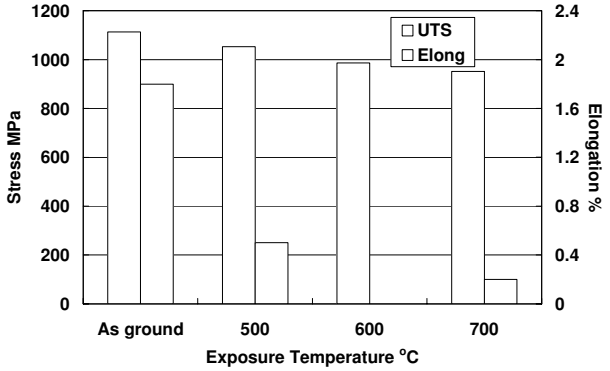

b)

Figure 3 The effect of thermal exposure for 24 hours at various temperatures on the room temperature tensile strength of – a) extruded (18:1) Ti-46-5-1 and – b) extruded Ti-46-5.

In addition to the tensile studies of the impact of thermal exposure, the effect on the low cycle fatigue properties of the Ti-46-5-1 alloy has also been examined and the results of this work is shown in Figure 4. This clearly showed a large decrease in life/strain range during room temperature testing for the samples exposed at 700˚C for 24 hours prior to testing, and compared with the as ground samples. This reduced strain range (or max. strain, since R=0) corresponded with the changes in tensile ductility noted in Figures 2 & 3. Testing of the as

ground test pieces at 700˚C (expected service temperature) also resulted in a marked reduction in life/strain range, compared with the room temperature performance but there appeared to be a yet further reduction in performance after an exposure at 700˚C for 24 hours, prior to LCF testing at 700˚C. Fractography revealed no clear differences between the test pieces in the as ground condition and following thermal exposure.

These changes in fatigue performance with thermal exposure are in contrast to results reported elsewhere for the Ti-46-5- alloy [4], where little change in fatigue strength was measured after exposure at 800˚C for 200 hours in air. This difference is initially somewhat surprising, especially given the much higher exposure temperatures (800˚C) and times than used in the current work. It would also have been thought that the literature testing to 10^6 cycles life [4] would have been sensitive to surface initiation condition and thus more affected than the strain controlled LCF tests here. However, consideration of the fatigue strengths reported in the literature [4] for extruded Ti-46-5 alloy suggest that the accompanying strains would have been well below the point at which an embrittled surface layer would have been effected and thus may mask any impact of thermal exposure on fatigue strength.

Clearly the reduced fatigue performance with thermal exposure is disappointing, however, as suggested, this may not be a significant issue for applications where relatively low stresses and strains occur during service. This work on low cycle fatigue suggests that the effect of pre-exposure should be considered with any fatigue performance testing for γ TiAl alloys for high temperature application.

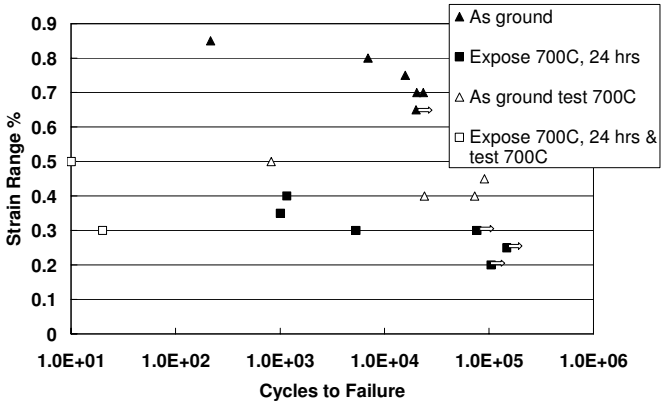

Figure 4 Low cycle fatigue test data for extruded Ti-46-5-1, following room temperature and 700˚C tests, on as ground and pre-exposed (700˚C for 24 hours in air) samples. R=0.

In order to investigate the thermal exposure effects on the mechanical properties, a number of approaches have been used, including – use of heat treatment in controlled atmospheres, surface modification of tensile test pieces, surface residual stress measurement, and detailed chemical analysis. Figure 5 shows the effect of thermal exposure at 700˚C for 24 hours, in both air and vacuum for the extruded Ti-46-5-1 and Ti-46-5 alloys. Very similar behaviour was seen with the two alloys, with the reduction in tensile performance remaining, even after heat treatment in vacuum. It is worth noting that in all cases the test pieces showed no sign of discolouration or other sign of oxidation, indeed the Ti-46-5 alloy was packed in clean Ti

swarf to act as a getter, whilst heat treating in vacuum. This suggests that either the tensile degradation is not related to oxidation or that even very small levels of surface oxygen can have a significant impact on the mechanical behaviour at room temperature.

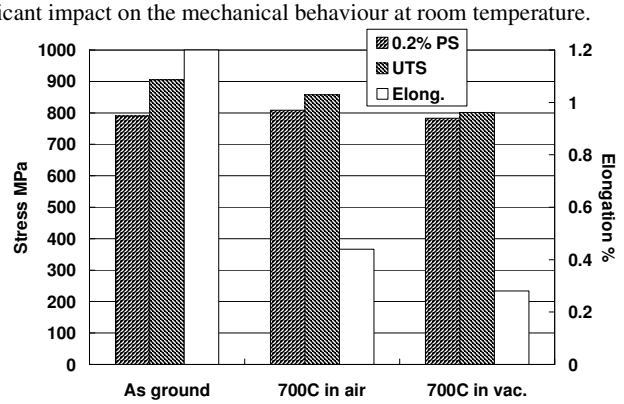

a)

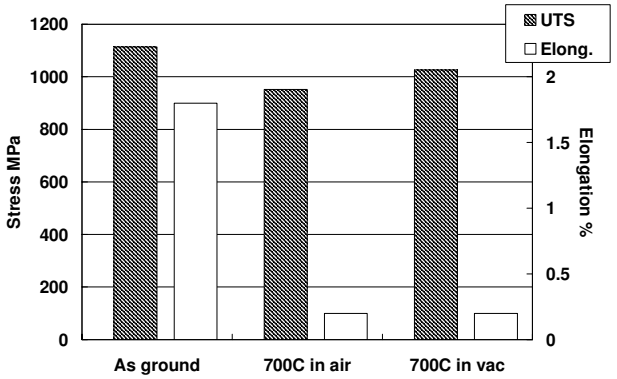

b)

Figure 5 The effect of thermal exposure (700°C for 24 hours) and environment (air or in vacuum) on the room temperature tensile properties of a) extruded (18:1) Ti-46-5-1 alloy and b) extruded Ti-46-5 alloy.

Following this work on atmosphere effects, some trials were conducted with various surface finishes to investigate the potential for machining damage to be associated with the mechanical property changes. Figure 6 summarises the tensile data for the Ti-46-5-1 alloy with various surface finishes and thermal exposure (at 700°C for 24 hours in air). Two electro-polishing regimes have been attempted, the first with minimal surface removal but sufficient to give a polished surface and the second (deep electro-polishing) with ~60 μm of surface removed [5]. In both cases the as electro-polished tensile test pieces gave properties similar to the as ground finish at room temperature, whilst exposure at 700°C for 24 hours gave a marked reduction in strength for all three surface finishes, as seen above. Thus suggesting that

surface damage from machining was not associated with the changes in tensile performance observed.

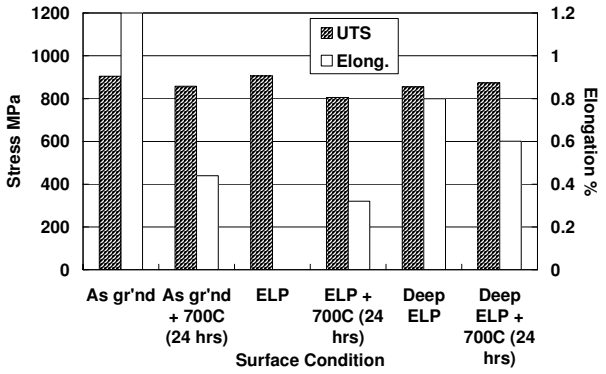

Figure 6 The effect of surface finishes on the tensile properties of extruded (18:1) Ti-46-5-1 alloy after thermal exposure at 700°C for 24 hours in air.

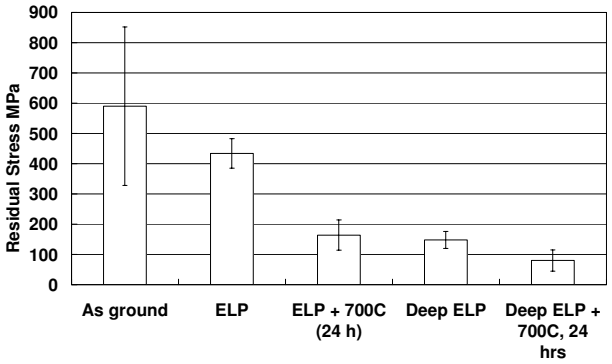

Figure 7 Surface compressive residual stresses measured for Ti-46-5-1 alloy, in various surface conditions – as ground, ELP - electro-polished (minimal surface removal), ELP - electropolished + 24 hrs exposure at 700°C, deep ELP - electropolished (~60 μm removed) and deep ELP - electropolished + 24 hours exposure at 700°C.

Alongside the examination of surface finish and its effect on tensile performance, consideration was also given to the surface residual stress state in the gauge length of the tensile test pieces. Thus Figure 7 shows the surface residual stress of the Ti-46-5-1 alloy in various conditions, consistent with those tensile tested in Figure 6. In the as ground state the surface stress is markedly compressive (~-590 MPa), this was somewhat reduced by the basic electro-polishing (down to ~-430 MPa) but significantly lowered by the deep electro-polishing (down to ~-150 MPa). Interestingly the surface residual stress was also lowered to ~-150 MPa by the thermal exposure at 700°C for 24 hours. Previously it has been noted that

the surface residual stress drops very quickly with thermal exposure, with as little as 2 hours at 700°C significantly reducing the surface residual stress [3]. Thus there appears to be a good correlation between the surface residual stress changes and the tensile reductions, however, the deep electro-polishing reduces the surface residual stress to a similar level, without any deleterious effect. Thus the surface residual stress changes do not appear to be wholly responsible for the tensile property reductions, although they may have a role to play.

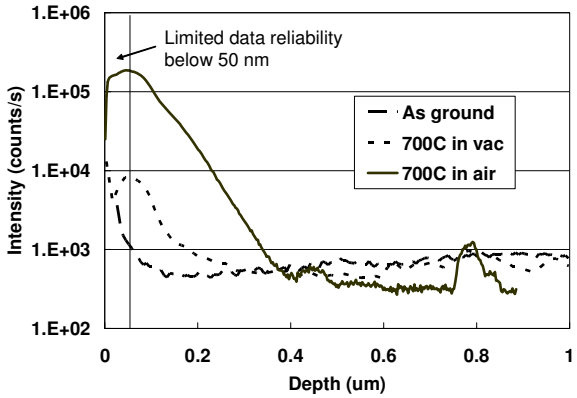

Figure 8 SIMS depth profiling data for oxygen in Ti-46-5 alloy, in various surface conditions.

The final area for study has been the surface chemical states and compositions, along with microstructural considerations. Previous microstructural studies of the surface of Ti-46-5-1 alloy have shown a very thin oxide layer of ~0.5 μm thickness, after 1000 hours at 700°C in air [3]. Even with FEG-SEM studies the oxide layer on the Ti-46-5-1 and Ti-46-5 alloys was not visible and thus attention has switched to alternative techniques to examine the near surface conditions. XPS of the Ti-46-5 alloy indicated that in the as ground condition both Al_2O_3 and Al were found, which was thought to be consistent with an oxide thickness close to the XPS sampling depth (i.e. 5-10 nm). This latter finding is consistent with the difficulty in imaging this layer directly. In the thermally exposed (700°C for 24 hours) Ti-46-5 alloy no Al peak was seen and mainly Al_2O_3 and TiO_2 observed (along with a range of other trace elements). The surface Al/Ti ratio's also changed significantly upon thermal exposure, from 1.7:1 in the as ground condition, to 4.5:1 after heat treatment, which seems at odds with the reported preponderance of TiO_2 upon higher temperature heat treatment [6]. However, it should be noted that much of the oxidation work reported in the literature has been undertaken at higher temperatures than 700°C and this may be responsible for the differences noted. Indeed the Ti-46-5 alloy was thermally exposed at 750°C in reference [6] and this resulted in a significantly thicker oxide layer (>5 μm) than found at 700°C. Further to these XPS studies, depth profiling SIMS of the Ti-46-5 alloy has also been undertaken and the results for oxygen are presented in Figure 8. This data suggests that an increase in surface oxygen occurs, even after heat treatment at 700°C for 24 hours in vacuum (including sample packed in a Ti swarf getter) – although the oxygen increase at the surface is not as marked as for the heat treatment in air. Clearly an improved vacuum would be beneficial in reducing this oxygen pick up during thermal exposure and would assist in isolating the factors associated with property reduction. However, this work tends to support the suggestion made above that

even low levels of oxygen can have an impact on the tensile behaviour of the γ-TiAl alloys, which is clearly a factor to be considered for much component processing (e.g. coatings) or service applications of these materials. In addition it is clear that conventional oxidation studies (e.g. mass gain measurements) of these materials have little relevance to their mechanical performance, for example, the Ti-46-5 alloy is usually considered to have excellent oxidation resistance [6] but clearly suffers from property loss at relatively low temperatures, like 600°C (Figure 3).

Conclusions and Summary

A significant reduction in tensile and low cycle fatigue properties has been found to be associated with thermal exposure at the expected service temperatures for a number of γ TiAl alloys, including Ti-47-2, Ti-46-5-1 and Ti-46-5. It is believed that this effect is related to near surface oxygen enrichment of the surface of components or test samples during thermal exposure and even low levels of oxygen may significantly affect the final mechanical properties. It is possible that changes in the surface residual stress may also affect the properties measured but this may also depend on the surface finish and requires further work. Conventional oxidation studies of the γ TiAl alloys do not appear to give a good indication of the impact of thermal exposure on mechanical properties. These effects need to be considered during the assessment of γ TiAl alloys for application into industrial power generation or aerospace gas turbines.

Acknowledgements

The authors would like to acknowledge the financial support of the UK MOD for this work. In addition Dr.M.Thomas of ONERA is thanked for his assistance with the deep electro-polishing of the Ti-46-5-1 tensile test pieces.

References

1. T.J.Kelly, C.M.Austin, P.J.Fink, J.Schaeffer, 'Effect of elevated temperature exposure on cast gamma titanium aluminde (Ti-48Al-2Cr-2Nb)', Scripta Met. et Mat., 1994, 30, pp1105-1110.
2. A.Zeller, F.Dettenwnager, F.Schultze, 'Influence of water vapour on the creep and fatigue properties of TiAl', Intermetallics, 2002, 10, pp.33-57.
3. R.Pather, W.A.Mitten, P.Holdway, H.S.Ubhi, A.Wisbey, J.W.Brooks, 'The effect of high temperature exposure on the tensile properties of γ TiAl alloys', Intermetallics, 2003, 11, pp1025-1027.
4. S.L.Draper, B.A.Lerch, I.E.Locci, M.Shazly, V.Prakash, 'Effect of exposure on the mechanical properties of Gamma Met PX', Intermetallics, 2005, 13, pp1014-1019.
5. M.Thomas, ONERA, Paris, France, personal communication, 2005.
6. M.-B.Bacos, A.Morel, S.Naveos, A.Bachelier-Locq, P.Josso, M.Thomas, 'The effect of long term exposure in oxidising and corroding environments on the tensile properties of two gamma-TiAl alloys', Intermetallics, 2006, 14, pp102-113.

DIRECTIONALLY SOLIDIFIED MULTIPHASE Ni_3Al-BASED INTERMETALLICS FOR HIGH-TEMPERATURE APPLICATIONS

J. Lapin, T. Pelachová, J. Mareček

Institute of Materials and Machine Mechanics, Slovak Academy of Sciences, Racianska 75, 83102 Bratislava, Slovak Republic
e-mail: ummslapi@savba.sk

Abstract

In recent years, large research effort was devoted to the development and understanding of basic phenomena controlling the microstructure and properties of directionally solidified (DS) multiphase Ni_3Al-based intermetallic alloys with γ'(Ni_3Al)/γ(Ni-based solid solution)-β(NiAl) type of microstructure. The present work summarizes the achieved results for six selected alloys and shows their potential from the point of view of practical applications or perspectives for further development and optimization. In order to achieve optimal balance between room-temperature ductility and high-temperature properties, the basic ternary Ni-(19-22)Al-8Cr (at.%) system was modified by Ti, Ta, Mo, Fe, Zr and B additions. The master alloys were prepared by plasma melting and exo-melt processes and cast into graphite moulds under argon atmosphere. Directional solidification was performed in Bridgman-type apparatus at constant growth rates ranging from $2.78x10^{-6}$ to $1.18x10^{-4}$ ms^{-1} and constant temperature gradients in liquid at the solid/liquid interface ranging from $11x10^3$ to $15x10^3$ Km^{-1}. The effect of several processing parameters including growth rate, temperature gradient in the liquid, annealing temperature and annealing time on the microstructure and mechanical properties of DS alloys was evaluated. Microstructure and phase transformations were studied by scanning electron microscopy, transmission electron microscopy, energy dispersive X-ray spectroscopy and differential thermal analysis. Room- and high-temperature properties were determined by tensile, compression, creep and cyclic oxidation testing.

Keywords: multiphase nickel aluminides, microstructure, mechanical properties, crystal growth, heat treatments

1. Introduction

Intermetallic alloys based on Ni_3Al or NiAl are potential materials for high-temperature structural applications. Although the mechanical properties of Ni_3Al-based intermetallics are attractive, current industrial usage is mainly in corrosion-related structural applications such as heat treating trays, transfer rolls for furnaces, radiant burner tubes, pipes, belt furnace links, forging dies, reaction vessels, pump impellers for slurries and air deflectors for burning of high sulphur fuels [1-4]. Much effort was devoted to utilize NiAl-based alloys for gas turbine applications. Unfortunately, while high-temperature creep strength of single crystalline NiAl was comparable to that of Ni-based superalloy single crystals, ductility, fracture toughness and impact resistance were found to be inadequate for turbine blades but might be sufficient for stationary parts such as vanes and combustor liners [5].

Continuous effort to develop cast Ni-based intermetallics, which might compete with emerging class of cast TiAl based alloys at intermediate temperatures and Ni-based single crystalline superalloys at higher temperatures resulted in a group of multiphase intermetallic alloys [6]. Optimal combination of coexisting phases in multiphase intermetallics can assure room-temperature ductility and required high-temperature mechanical properties [6-13]. Multiphase intermetallic alloys are characterized by good resistance to high temperature oxidation, nitridation and carburisation, high yield strength in a large temperature range and good fatigue resistance.

Among various multiphase systems, Ni-Al-Cr based intermetallic alloys have been

intensively studied for many years due to their potential for high-temperature structural application. In recent years, several new multi-component systems with γ'(Ni_3Al)/γ(Ni-based solid solution)-β(NiAl) type of microstructure were developed and prepared by directional solidification [14-20]. As shown by Jia et al. [21], in equilibrium between γ' and β phases, Cr partitions to the β-phase rather than to the γ'-phase, whereas Ta and Mo concentrate in the γ'-phase. In the case of γ'/γ + β type alloys, Cr concentrates in the following manner: γ > β > γ', whereas Ta and Mo follow γ' > γ > β [21]. Ta, Zr, Ti and Mo are effective solid solution strengtheners of the γ'-phase. Chromium stabilizes the γ-phase and prevents dynamic oxygen embrittlement at elevated temperatures. In addition, spherical and lath-shaped α(Cr) precipitates are effective obstacles to dislocation motion, which improve high-temperature creep resistance. As shown by Aoki et al. [22], small additions of boron are effective in improving tensile ductility of polycrystalline Ni_3Al. The effect of Zr on the properties of Ni-based intermetallics is more complex [23-26]. Besides the solution strengthening, increasing Zr content up to 0.7 at.% improves room-temperature ductility of polycrystalline Ni_3Al. In the case of γ'/β type alloys, Zr increases room-temperature strength and fracture strain [23,24]. On the other hand, Zr can form with nickel low melting point γ+Ni_5Zr eutectic, which can lead to an embrittlement of Ni_3Al alloys after heat treatments [20]. However, there is still lack of information about the effect of directional solidification and heat treatments on the microstructure and mechanical properties of multiphase intermetallic γ'/γ + β type alloys. Directional solidification represents successful approach not only to achieving ductility in Al-rich Ni_3Al but producing complex near-net-shape structural components as well.

The aim of the present work is to characterize microstructure, mechanical properties, some physical properties and oxidation resistance of six multiphase directionally solidified (DS) Ni-Al-Cr based alloys modified with additions of Ti, Ta, Mo, Fe, Zr and B.

2. Experimental procedure

2.1. Alloy preparation and directional solidification

The master ingots of intermetallic alloys with the chemical composition given in Table 1 were prepared by exo-melt and plasma melting processes and cast into graphite moulds in an induction furnace under argon atmosphere. These ingots were machined to rods with a length of 120 mm and placed into high purity alumina crucibles of 11/15 or 8/12 mm diameter (inside/outside diameter). Directional solidification was performed under an argon atmosphere in a modified Bridgman-type apparatus described elsewhere [27]. Specimens were directionally solidified at constant growth rates V ranging from 2.78×10^{-6} to 1.18×10^{-4} ms^{-1} and constant temperature gradients at the solid-liquid interface G_L ranging from 11×10^3 to 15×10^3 Km^{-1}.

2.2. Heat treatments

DS ingots were subjected to various heat treatments including multi-step solution annealing, quenching and ageing. The aim of the heat treatments was to homogenize the microstructure and to optimize mechanical properties of the studied alloys. More details concerning various heat treatments of the studied alloys can be found elsewhere [14-20].

2.3. Mechanical testing

Tensile specimens with a gauge length of 28 mm and gauge diameter of 4 mm were lathe-machined from the DS and heat treated (HT) ingots. The tensile axis of specimens was

Table 1. Chemical composition (in at.%) and processing techniques of investigated Ni-Al-Cr based alloys

Alloy	Ni	Al	Cr	Fe	Ti	Ta	Mo	Zr	B	Processing technique
1	Bal.	20.20	8.20	2.44	–	–	–	–	–	Exo-melt process
2	Bal.	21.71	7.52	–	6.51	–	–	–	–	Exo-melt process
3	Bal.	22.22	8.11	–	5.03	–	0.82	0.58	–	Exo-melt process
4	Bal.	21.29	7.04	–	–	1.46	0.62	0.57	–	Exo-melt process
5	Bal.	21.92	8.13	–	–	4.22	0.89	0.31	–	Plasma melting
6	Bal.	19.05	8.15	–	5.11	–	–	–	2.94	Exo-melt process

parallel to the [001] growth direction of dendrites. After machining, the specimen surface was mechanically polished to a roughness of 0.3 μm. Tensile tests were conducted on a screw-driven Zwick machine at an initial strain rate of $1x10^{-4}$ s^{-1}. The tests were run at temperatures ranging from 20 to 950°C. The offset tensile yield strength was measured at 0.2 % plastic strain and the ductility was evaluated from the total elongation to fracture.

Compression specimens with a diameter of 8 mm and length of 12 mm were machined with the compression axis parallel to the [001] growth direction of dendrites. Compression tests were performed with a computer-controlled universal testing machine at a strain rate of $2.68x10^{-4}$ s^{-1}. The tests were run at temperatures ranging from 20 to 1050°C in air. The offset compressive yield stress was measured at 0.2% plastic strain.

Creep specimens with a gauge length of 20 mm and gauge diameter of 4 mm were lathe-machined from DS ingots. The tensile axis of the specimens was parallel to the [001] growth direction of dendrites. After lathe-machining, the specimen surface was polished to a roughness of about 0.8 μm. Constant load creep tests were performed at temperatures ranging from 700 to 877°C under initial tensile stresses ranging from 150 to 400 MPa. The test temperature was monitored with two thermocouples touching the specimen gauge section and held constant within ± 1°C for each individual test. Specimen displacement was measured using high-temperature extensometer attached to the ledges of the creep specimen. The extensometer was equipped with a linear variable displacement transformer (LVDT). The acquisition of time-elongation data was accomplished by a computer and data processing was performed by a computer program.

2.4. Cyclic oxidation

Cylindrical specimens for oxidation experiments with a diameter of 9 mm and length of 20 mm were machined from DS ingots. After grinding, the surface of the specimens was polished with 1 μm diamond paste. Cyclic oxidation experiments were performed at four temperatures ranging from 700 to 1000°C up to 1000 h in air. Each oxidation cycle included heating of the specimen to oxidation temperature at a heating rate of 5 Ks^{-1}, high-temperature oxidation cycle segment at a given temperature for various time ranging from 5 to 200 h and cooling to room temperature at a cooling rate of 5 Ks^{-1}. The kinetics of the cyclic oxidation was evaluated by weighing of the samples after each oxidation cycle.

2.5. Microstructure characterization

Differential thermal analysis (DTA) was performed in a Netzsch apparatus equipped with alumina crucibles at heating and cooling rates of 0.167 °Cs^{-1} under argon atmosphere. Microstructural analysis was performed by optical microscopy (OM), scanning electron microscopy (SEM), energy dispersive X-ray spectroscopy (EDS) and transmission electron microscopy (TEM). OM and SEM samples were prepared using standard metallographic techniques and etched in a reagent of 150 ml H_2O, 25 ml HNO_3 and 10 ml HF. Samples for TEM were thinned mechanically to a thickness of about 50 μm and then by ion milling until perforation. Volume fraction, size and morphology of coexisting phases were measured by computerized image analyzer.

3. Results and discussion

3.1. Microstructure

Table 2 summarizes results of DTA analysis of the studied alloys. Formation of low-temperature eutectic was identified for the alloys containing 0.6 at.% of Zr. The melting points of these eutectics correspond very well to that of 1170°C determined for $\gamma+Ni_5Zr$ eutectic in a binary Ni-Zr system [28]. As results from Table 2, decreasing content of Zr to 0.3 at.% is shown to be successful to eliminate completely formation of this eutectic in DS Ni-21.9Al-8.1Cr-4.2Ta-0.9Mo-0.3Zr (at.%) alloy.

Due to several similar DS systems studied in this work, detailed microstructure analysis is presented only for DS Ni-21.3Al-7.0Cr-1.5Ta-0.6Mo-0.6Zr (at.%) alloy. This alloy showed complex type of microstructure and promising mechanical properties for further optimization and development.

3.1.1. Microstructure characterization

After directional solidification at constant growth rates ranging from $5.56x10^{-6}$ to $1.18x10^{-4}$ ms^{-1} and temperature gradients in liquid ranging from $11x10^3$ to $15x10^3$ Km^{-1}, the microstructure of the studied alloys consisted of several columnar grains (3-5) elongated in a direction parallel to the ingot axis. The microstructure within the grains was dendritic. Fig. 1a shows the typical example of dendritic microstructure with well developed secondary and tertiary dendritic arms observed in the Alloy 4. As seen in Fig. 1b, the microstructure consists of dendrites and interdendritic region. TEM and EDS observations revealed that the

Table 2. DTA analysis of the studied alloys

Alloy (at.%)	Temperature (°C)				
	Solidus	Liquidus	Freezing range	Peritectic	Eutectic
Ni-20.2Al-8.2Cr-2.4Fe	1310	1325	15	–	–
Ni-21.7Al-7.5Cr-6.5Ti	1270	1395	125	1370	–
Ni-22.2Al-8.1Cr-5.0Ti-0.8Mo-0.6Zr	1270	1380	110	1330	1170
Ni-21.3Al-7.0Cr-1.5Ta-0.6Mo-0.6Zr	1290	1350	60	1345	1162
Ni-21.9Al-8.1Cr-4.2Ta-0.9Mo-0.3Zr	1275	1380	105	1320	–
Ni-19.1Al-8.2Cr-5.1Ti-2.9B	1260	1330	70	1320	–

dendrites are composed of β(NiAl) matrix, few coarse γ'(Ni_3Al) particles, fine γ' needles and spherical α-Cr precipitates (Cr-based solid solution). The interdendritic region contains five microstructurally different areas designated as I, II, III, IV and E, as shown in Figs. 1b, 1c and 1d. The areas I were identified to contain single γ'-phase. Chromium enriched multiphase areas (II) with the typical γ/γ' morphology are usually separated from the β dendrites by a single phase γ' layer. Cellular type of structure (III) was also usually formed between adjacent chromium enriched areas II. In some areas of the interdendritic region, formation of two phase γ/γ' microstructure (area IV) was observed. During directional solidification Zr intensively segregates and form local Zr-enriched eutectic γ+Ni_5Zr regions at the dendrite-interdendritic interfaces (area E). Formation of eutectic regions at the dendritic-interdendritic interfaces was also observed in the Alloy 3. Microstructure observations revealed that the decrease of Zr content to 0.3 at.% in the Alloy 5 eliminates formation of eutectic regions during directional solidification. Table 3 summarizes microstructure features within the dendrites and interdendritic region for selected DS alloys.

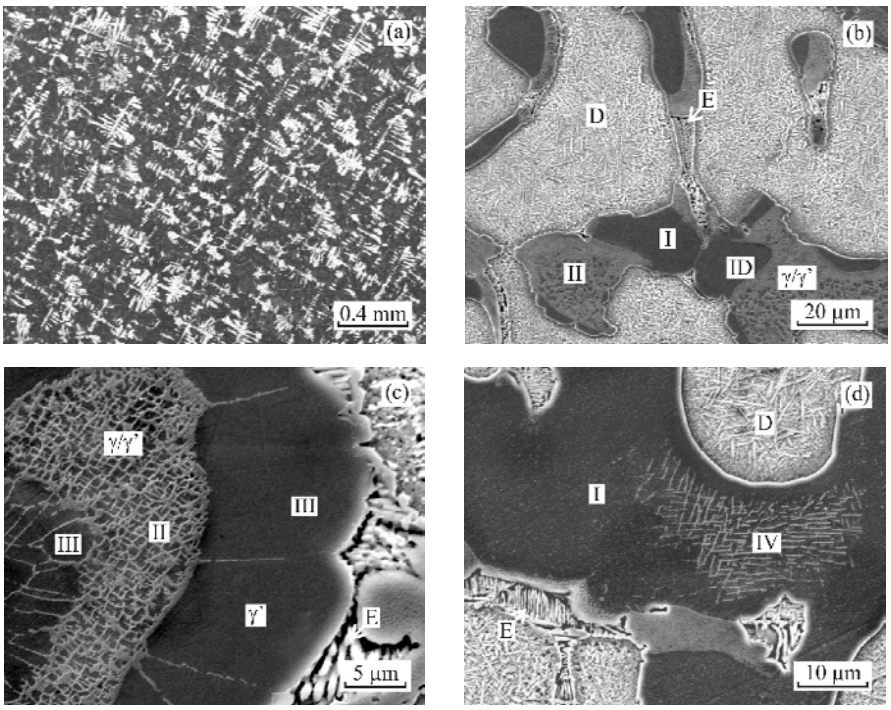

Fig. 1. SEM micrographs of DS Ni-21.3Al-7.0Cr-1.5Ta-0.6Mo-0.6Zr (at.%) alloy, $V = 5.56 \times 10^{-5}$ ms^{-1}: (a) transverse section showing morphology of dendrites within the columnar grains; (b) longitudinal section showing dendrite D, interdendritic region ID, eutectic regions E, single phase area (I), and γ/γ' type of microstructure (II); (c) transverse section showing the typical γ/γ' type of microstructure (II), two types of cellular microstructure (III) and Zr-enriched eutectic regions (E); (d) transverse section showing single phase area (I) and two phase γ/γ' microstructure (IV).

Table 3. Coexisting phases in DS multiphase intermetallic alloys

Alloy (at.%)	β primary solidification phase	
	Dendrites	Interdendritic region
Ni-20.2Al-8.2Cr-2.4Fe	β, spherical α-Cr precipitates	γ + γ' matrix, lath-shaped α-Cr precipitates
Ni-21.7Al-7.5Cr-6.5Ti	β, elongated γ' and spherical α-Cr precipitates	γ + γ' matrix, lath-shaped α-Cr precipitates
Ni-22.2Al-8.1Cr-5.0Ti-0.8Mo-0.6Zr	β, elongated γ' and spherical α-Cr precipitates	γ + γ' matrix, lath-shaped α-Cr precipitates, γ+Ni_5Zr eutectic
Ni-21.3Al-7.0Cr-1.5Ta-0.6Mo-0.6Zr	β, elongated γ' and spherical α-Cr precipitates	γ + γ' matrix, lath-shaped α-Cr precipitates, γ+Ni_5Zr eutectic
Ni-21.9Al-8.1Cr-4.2Ta-0.9Mo-0.3Zr	β, elongated γ' and spherical α-Cr precipitates	γ + γ' matrix, lath-shaped α-Cr precipitates, Cr-32.5Ni-5.9Al-0.5Ta-14Mo-0.7Zr particles

3.1.2. Microstructure evolution during directional solidification

As revealed quenched solid-liquid interfaces of Ni-21.3Al-7.0Cr-1.5Ta-0.6Mo-0.6Zr (at.%) specimens directionally solidified at $V = 1.39\text{x}10^{-5}$ s^{-1} and $G_L = 14\text{x}10^3$ Km^{-1} corresponding to a constant cooling rate of 0.195 $°Cs^{-1}$ and DTA analysis performed in alumina crucibles at a similar cooling rate of 0.167 $°Cs^{-1}$, the solidification starts at a temperature of 1350°C. During directional solidification the β-phase is the primary solidification phase. Since the equilibrium partition ratio coefficient k of Zr in Ni is significantly lower than 1 ($k = C_S/C_L = 0.09$, where C_S and C_L are solid and liquid compositions, respectively), Zr intensively segregates into the interdendritic liquid during solidification. At a peritectic temperature of 1345°C the solid dendrites react with the interdendritic liquid according to reaction $L + \beta \rightarrow \gamma'$. This reaction results in isolation of some dendritic arms with enclosed Zr enriched liquid by the γ'-phase. The γ' layer prevents effective diffusion of Zr from localised regions into the remaining interdendritic liquid. During cooling between 1335 and 1325°C, the reaction $L \rightarrow \gamma + \gamma'$ produces γ/γ' cellular structure. At the final stage in the temperature range from 1325 to 1290°C, the composition of liquid is such that the alloy solidifies as a disordered γ. The Zr enriched regions solidify at 1162°C through an eutectic reaction $L \rightarrow \gamma + Ni_5Zr$. During further cooling to room temperature the disordered eutectic γ transforms to the γ'-phase.

Fig. 2 shows evolution of primary dendrite arm spacing (PDAS) λ with the growth rate V and temperature gradient in liquid at the solid-liquid interface G_L. The primary dendrite arm spacing decreases with increasing growth rate and temperature gradient according to relationship

$$\lambda = KV^{-0.25}G_L^{-0.5} \tag{1}$$

where K is a material constant. Using linear regression analysis, Eq. (1) can be rewritten in the form

$$\lambda = 2.03x10^{-3}V^{-0.25}G_L^{-0.5} \quad (2)$$

As illustrated in Fig. 2, the studied γ'/γ+β alloys growth with higher PDAS than binary Ni_3Al aluminide [29] or classical Ni-based superalloys [30,31] with the γ' or γ primary solidification phase at the identical growth conditions.

As shown in our previous works [18,19], size of α-Cr and γ' precipitates formed within the dendrites affect significantly room-temperature ductility of DS γ'/γ+β type alloys. Fig. 3 shows an example of dependence of mean diameter of α-Cr and γ' precipitates on the growth rate for the Alloy 5. The measured statistical values of mean diameter *d* were fitted to an equation in the form

$$d = K_1 V^a \quad (3)$$

where K_1 is a material constant and *a* is the growth rate exponent. Regression analysis of the data shown in Fig. 3 yields for the mean diameter of α-Cr precipitates $d_{\alpha\text{-Cr}}$ an equation

$$d_{\alpha\text{-Cr}} = 1.68x10^{-9}V^{-0.46} \quad (4)$$

and for the mean diameter of γ' precipitates an equation in the form

$$d_{\gamma'} = 2.34x10^{-9}V^{-0.5} \quad (5)$$

3.1.3. Microstructure evolution during heat treatments

Solution annealing of Zr-containing DS Alloy 3 and Alloy 4 at temperatures of 1210 or 1220°C resulted in a local melting of eutectic regions and formation of porosity at dendritic-interdendritic interfaces connected with a drop of room-temperature tensile ductility. In order to avoid such serious room-temperature embrittlement of the alloys, two different types of heat treatments were applied: (i) ageing at temperatures below the eutectic melting temperature of 1160°C and (ii) heat treatments consisting of dissolution of the metastable eutectic at a temperature below the eutectic melting temperature and solution annealing above this temperature followed by ageing at lower temperatures.

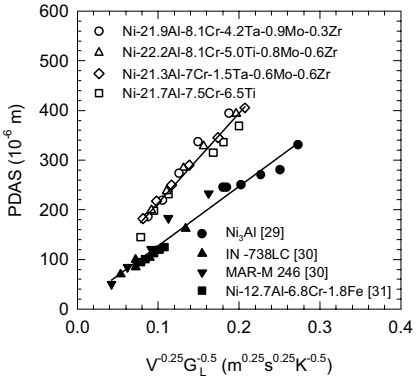

Fig. 2. Comparison of the PDAS for alloys with β and γ or γ' primary solidification phase as a function of $V^{-0.25}G_L^{-0.5}$.

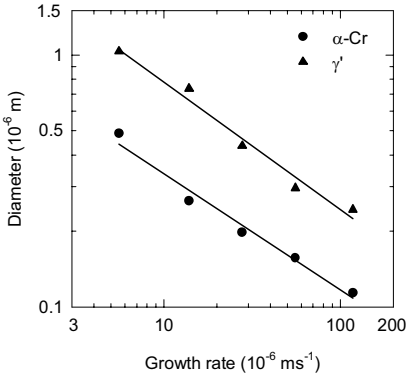

Fig. 3. Evolution of mean diameter of α-Cr and γ' precipitates with growth rate within the β dendrites in the Alloy 5.

Fig. 4 shows evolution of volume fractions of coexisting regions with time during annealing at 1100°C. This first-step annealing below the eutectic melting temperature was applied to dissolve eutectic regions before second-step solution annealing at higher temperatures. As results from Fig. 4 as well as was confirmed by DTA, annealing for 100 h was sufficiently long to eliminate completely the eutectic regions. The second-step annealing at 1210 and 1220°C for 2 h resulted in a complete dissolution of γ' and α-Cr precipitates within the dendrites without forming local porosity at dendritic-interdendritic interfaces. However, this temperature was too low to homogenize completely the interdendritic region.

Fig. 5 shows the typical microstructures of the solution annealed Alloy 5 after ageing. During early stages of ageing in the temperature range from 950 to 1050°C the martensitic β'-phase transforms to the β(NiAl). Beside the transformation of the β'-phase, intensive precipitation and growth of spherical α-Cr and needle-like γ' particles within the dendrites are observed. The size of α-Cr precipitates increases with increasing ageing time and temperature, as summarized in Fig. 6a. The mean diameter $d_{\alpha\text{-Cr}}$ increases with increasing ageing time t according to a relationship

$$d_{\alpha\text{-Cr}} = K_2 t^m \tag{6}$$

where K_2 is a material constant at a given temperature and m is the time exponent. Using linear regression analysis, the time exponent m is determined to vary from 0.31 to 0.32 over the studied temperature range. As results from determined time exponents, the coarsening of α-Cr precipitates can be expressed by $d^p \propto t$ law with an exponent of $p = 1/m \approx 3$ in the form

$$d_{\alpha\text{-Cr}}^3 - d_0^3 = K_3 t \exp\left(-\frac{Q_{\text{Cr}}}{RT}\right) \tag{7}$$

where d_0 is the mean precipitate diameter at time $t = 0$, K_3 is a material constant, Q_{Cr} is the activation energy for α-Cr precipitate coarsening, R is the universal gas constant and T is the absolute temperature. The activation energy for α-Cr precipitate coarsening was calculated to

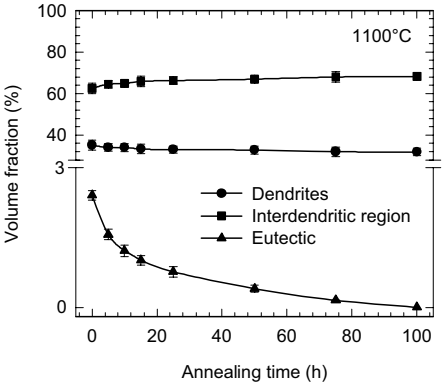

Fig. 4. Variation of volume fractions of dendrites, interdendritic region and eutectic regions with the annealing time at 1100°C for the Alloy 4.

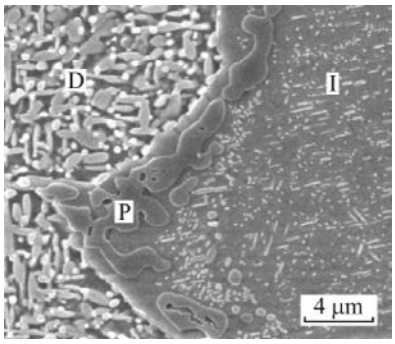

Fig. 5. SEM micrographs showing the typical microstructure after ageing at 1050°C for 100 h for the Alloy 5. D -dendrite, I - interdendritic region, P - Cr-based particles.

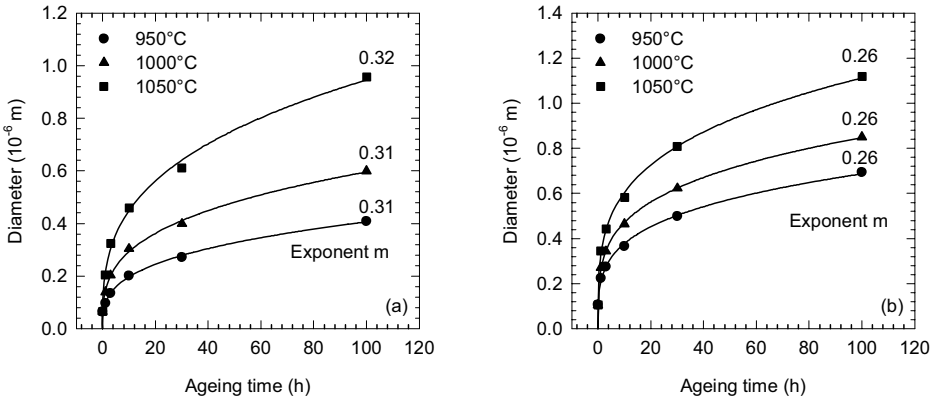

Fig. 6. Variation of mean precipitate diameter with the ageing time within the dendrites for the Alloy 5: (a) α-Cr precipitates; (b) γ' precipitates.

be Q_{Cr} = 337 ± 12 kJ/mol [19].

Mean diameter of the γ' precipitates increases with increasing ageing time and temperature, as summarized in Fig. 6b. As results from the time exponents, the coarsening of the γ' precipitates can be expressed by kinetic equation in the form

$$d_{\gamma'}^4 - d_0^4 = K_4 t \exp\left(-\frac{Q_{\gamma'}}{RT}\right) \tag{8}$$

where $d_{\gamma'}$ is the equivalent diameter of γ' precipitates, K_4 is a material constant and $Q_{\gamma'}$ is the activation energy for γ' precipitate coarsening. The activation energy for the γ'-precipitate coarsening was calculated to be $Q_{\gamma'}$ = 250 ± 9 kJ/mol [19].

During ageing the microstructure within the interdendritic region changed. In the case

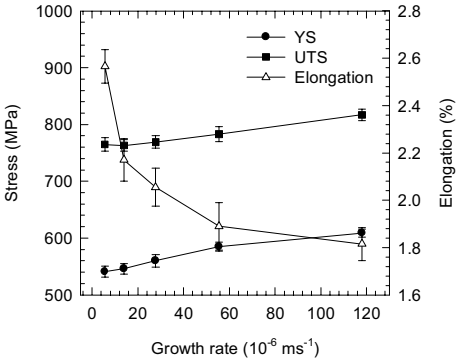

Fig. 7. Dependence of room-temperature tensile yield strength (YS), ultimate tensile strength (UTS) and elongation to fracture on the growth rate for the Alloy 4.

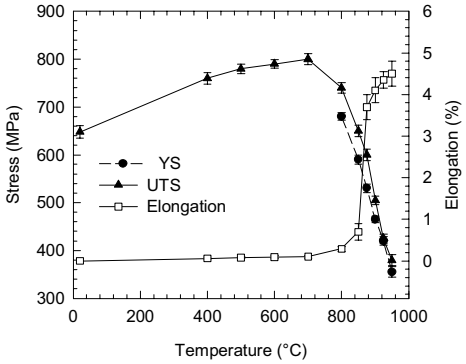

Fig. 8. Temperature dependence of 0.2% offset tensile yield strength (YS), ultimate tensile strength (UTS) and elongation to fracture for the Alloy 5.

Table 4. Room-temperature tensile properties of DS alloys

Alloy composition (at.%)	Growth rate (10^{-6} ms^{-1})	YS (MPa)	UTS (MPa)	Elong. (%)
Ni-20.2Al-8.2Cr-2.4Fe	4.17	460	870	11
Ni-21.7Al-7.5Cr-6.5Ti	5.56-118.1	830-908	960-1040	0.9-1.2
Ni-22.2Al-8.1Cr-5.0Ti-0.8Mo-0.6Zr	5.56-118.1	–	750-890	0-0.1
Ni-21.3Al-7.0Cr-1.5Ta-0.6Mo-0.6Zr	5.56-118.1	540-610	765-820	1.8-2.6
Ni-21.9Al-8.1Cr-4.2Ta-0.9Mo-0.3Zr	5.56-118.1	–	680-830	0
Ni-19.1Al-8.2Cr-5.1Ti-2.9B	27.8	620	830	0.3

of the Alloy 5, the γ matrix with γ' precipitates changed to the γ' matrix, elongated γ particles and irregular shaped Cr-rich precipitates in the interdendritic region, as seen in Fig. 5. In addition, intensive precipitation of lath-shaped α-Cr particles in the γ'/γ regions was observed. Similar microstructure features were observed in all studied alloys.

3.2. Mechanical properties

3.2.1. Effect of directional solidification on tensile properties

Fig. 7 shows evolution of tensile 0.2% offset yield strength (YS), ultimate tensile strength (UTS) and elongation to fracture with the growth rate for the Alloy 4. It should be noted that the data shown in Fig. 7 represent average values from five tensile specimens tested at each growth rate. It is clear that increasing growth rate increases both the YS and UTS but decreases plastic elongation to fracture. Elongation to fracture ranging from of 1.8 to 2.6 % is slightly higher than those reported for DS Ni-21.7Al-7.5Cr-6.5Ti and Ni-21.9Al-8.1Cr-4.2Ta-0.9Mo-0.3Zr (at.%) (no measurable plastic deformation to fracture) alloys but significantly lower than the value of 11 % measured for DS Ni-20.2Al-8.2Cr-2.4Fe (at.%) alloy, as seen in Table 4.

Fig. 8 shows temperature dependence of YS, UTS and elongation to fracture for the Alloy 5. It is clear that the brittle-to-ductile transition occurs at a relatively high temperature of about 875°C. However, elongation to fracture at temperatures above brittle-to-ductile transition temperature (BDTT) is still limited and does not exceed 5%.

3.2.2. Effect of heat treatments on tensile properties

Fig. 9 shows dependence of the YS, UTS and elongation to fracture on the ageing time for the Alloy 4. The data shown in Fig. 9 represent average values from five tensile specimens tested at each ageing time. The dash lines represent average values of the yield strength (YS_{DS}), ultimate tensile strength (UTS_{DS}) and elongation to fracture ($elongation_{DS}$) of DS specimens before the heat treatments. The YS, UTS and elongation to fracture increase with increasing ageing time, reaching maximum values after ageing for 8 h and then decrease with increasing ageing time. Comparing the measured tensile characteristics of the HT specimens to those of DS ones indicates that the YS can be increased by applied heat treatment by 15%

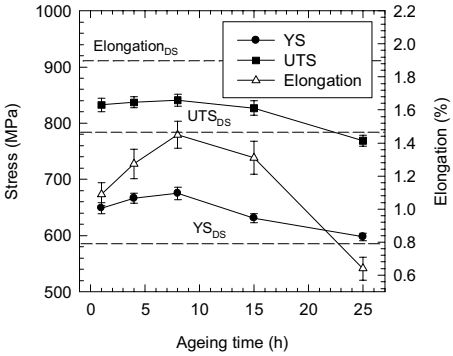

Fig. 9. Dependence of room-temperature tensile yield strength (YS), ultimate tensile strength (UTS) and elongation to fracture on the ageing time at 850°C after prior ageing at 1000°C for 4 h for the Alloy 4.

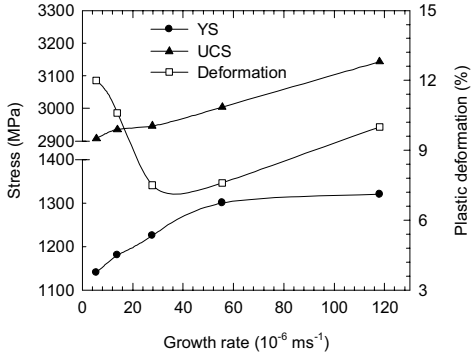

Fig. 10. Dependence of room-temperature compressive yield strength (YS), ultimate compressive strength (UCS) and plastic deformation to fracture on the growth rate for the Alloy 5.

at the expense of the decrease of tensile ductility by 24%. On the other hand, ageing for 25 h leads to a significant decrease of tensile ductility without any positive effect on the YS and UTS.

3.2.3. Compressive properties

Fig. 10 shows dependence of compressive 0.2% offset yield strength (YS), ultimate compressive strength (UCS) and plastic deformation to fracture on the growth rate for the Alloy 5. It should be noted that the data presented in this figure represent average values from four specimens tested at each growth rate. All specimens are ductile in compression, showing plastic deformation to fracture ranging from 7.5 to 12 % and a relatively high UCS up to 3.1 GPa. The YS and UCS increase with increasing growth rate. On the other hand, no definite relationship can be determined between the growth rate and the plastic deformation to fracture.

Fig. 11 shows dependence of compressive 0.2% YS, UCS and plastic deformation to fracture on the ageing time for the specimens solution annealed at 1210°C for 2 h and aged at 1050°C for the Alloy 5. The average YS continuously decreases with the increasing ageing time. On the other hand, the evolution of average UCS and plastic deformation to fracture with the ageing time is not monotonous. A minimum values are achieved after ageing for 10 h and maximum after ageing for 30 h. Ageing at 1050°C decreases the yield strength but increases plastic deformation and UCS when compared to those of 1300 MPa, 3005 MPa and 7.6%, respectively, measured for DS specimens before heat treatments.

Fig. 12 shows temperature dependence of compressive 0.2% YS. The YS initially increases with the temperature reaching a peak values and then decreases with increasing temperature. This anomalous yielding behaviour of the studied multiphase alloys indicates that the yielding is dominated by the interdendritic γ'-phase. The peak yield strength temperature depends on the chemical composition of the γ' matrix and varies from about 700°C for the alloy modified by Fe (Alloy 1) to about 750°C for the alloys modified by Ti or Ta (Alloy 2 and Alloy 4).

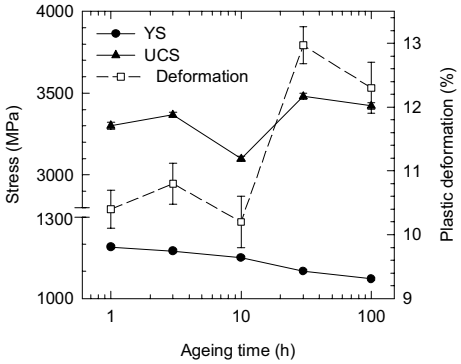

Fig. 11. Variation of compressive yield strength (YS), ultimate compressive strength (UCS) and compressive plastic deformation to fracture with the ageing time for the Alloy 5 aged at 1050°C.

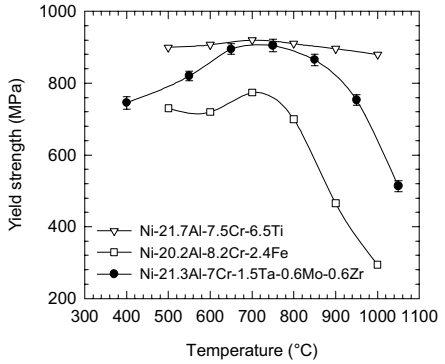

Fig. 12. Temperature dependence of 0.2% compressive yield strength for the Alloy 1, Alloy 2 and Alloy 4.

3.2.4. Creep

In order to evaluate potential of the studied alloys for high-temperature applications, the creep properties including stress exponent n and apparent activation energy for creep Q_a were determined. All of the creep curves obtained in this study have similar basic shape, as shown in Fig. 13 for the Alloy 4. The creep curves exhibit short primary creep stage that is directly followed by the tertiary creep. During the primary creep stage the creep rate decreases with increasing strain. After reaching a minimum at a strain of 0.2-0.4 %, the creep rate increases with increasing strain. No steady-state creep stage was observed in the tests performed between 700 and 800°C with applied stresses ranging from 150 to 400 MPa. The minimum creep rates $\dot{\varepsilon}_{\min}$ and applied stresses σ were fitted to the power law

$$\dot{\varepsilon}_{\min} = A\sigma^n \tag{9}$$

where A is a constant and n is the stress exponent. Fig. 14 shows variation of the minimum creep rate with the applied stress for DS Ni-21.3Al-7.0Cr-1.5Ta-0.6Mo-0.6Zr (at.%) alloy. Using linear regression analysis of the creep data, the stress exponent n is determined to vary from 5.1 to 5.2.

The stress-minimum creep rate-temperature data were also fitted to the power law expression

$$\dot{\varepsilon}_{\min} = B\sigma^n \exp\left(-\frac{Q_a}{RT}\right) \tag{10}$$

where B is a constant and Q_a is the apparent activation energy for creep. Table 5 summarizes the experimentally determined constants B, stress exponents n and the apparent activation energies for creep Q_a for the studied alloys. These parameters can be used for reliable calculation of minimum creep rates according to Eq. (10) taking into account temperature intervals defined for each alloy in Table 5 and applied stresses ranging from 150 to 400 MPa.

Since all studied alloys showed some common characteristic features during tertiary

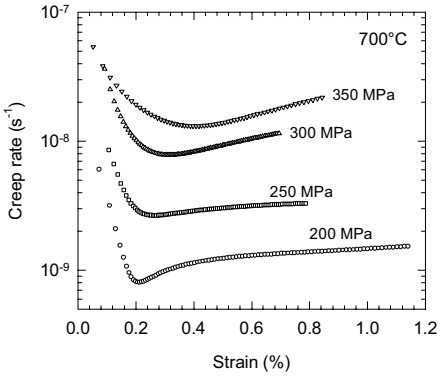

Fig. 13. Examples of creep deformation curves showing evolution of creep rate with the strain at 700°C for the Alloy 4. The applied stresses are indicated in the figure.

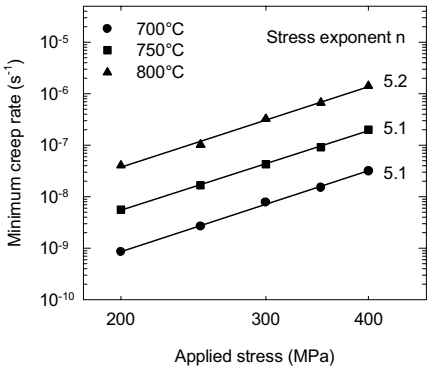

Fig. 14. Dependence of minimum creep rate on the applied stress for the Alloy 4. Creep temperatures and measured stress exponents *n* are indicated in the figure.

creep stage, detailed analysis will be presented for the Alloy 4. During tertiary creep stage the specimens exhibited a plastic deformation ranging from 9% at 700°C/400 MPa to 35% at 800°C/200 MPa. At lower applied stresses (200-300 MPa), the tertiary creep was accompanied by nucleation and growth of cavities at dendritic-interdendritic interfaces. Fig. 15a shows the typical fracture surface of creep specimens with dimples and voids. The dimples with an average diameter of 3 μm are formed within the dendrites by nucleation and growth of microvoids around the spherical α-Cr precipitates. Dimple character of the fracture with average diameter of circular dimples of about 15 μm was also observed in the interdendritic region. In many cases, dimple boundaries corresponded to the cell boundaries observed in the interdendritic region before creep testing. Fig. 15b shows coalescence of the voids formed at the dendritic-interdendritic interfaces and crack propagation in a direction perpendicular to the load direction. At higher applied stresses (350-400 MPa), predominant mechanism leading to the fracture is nucleation and propagation of cracks along the dendritic-interdendritic interfaces in a direction perpendicular to the load axis.

Table 5. Experimentally determined constants *B*, stress exponents *n*, apparent activation energies Q_a and creep temperatures for DS alloys tested at initial applied stresses ranging from 150 to 400 MPa

Alloy composition (at.%)	B ($s^{-1}MPa^{-n}$)	n	Q_a (kJ/mol)	Temperatures (°C)
Ni-20.2Al-8.2Cr-2.4Fe	$1.92x10^{-1}$	4.1	316	773-877
Ni-21.7Al-8.1Cr-6.5Ti	$5.09x10^{2}$	4.3	380	700-850
Ni-22.2Al-8.1Cr-5.0Ti-0.8Mo-0.6Zr	$2.79x10^{4}$	4.4	415	700-800
Ni-21.3Al-7.0Cr-1.5Ta-0.6Mo-0.6Zr	$7.83x10^{-4}$	5.1	326	700-800
Ni-21.9Al-8.1Cr-4.2Ta-0.9Mo-0.3Zr	$1.38x10^{-4}$	7.0	401	700-800

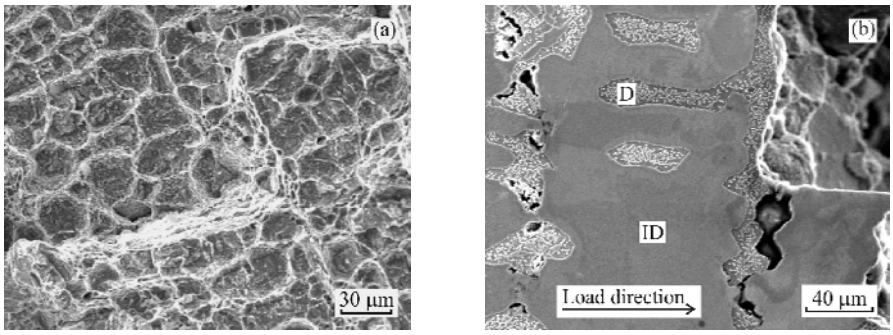

Fig. 15. SEM micrographs showing the typical features of creep fracture: (a) dimple type of fracture surface. Creep test at 750°C and 250 MPa; (b) longitudinal section of the gauge region showing cavity formation and crack propagation at dendritic-interdendritic interfaces. Creep test at 700°C and 300 MPa.

3.3. Cyclic oxidation behaviour

The plots of the weight gain versus the oxidation time for the studied DS alloys are shown in Figs. 16a and 16b. Cyclic oxidation is generally characterized by a mass gain due to oxidation and by scale spallation. In our case, however, no spallation was observed. This was most likely due to limited number of cycles, oxidation time and careful manipulation with the samples. It can be seen that the weight gain due to oxidation is much more rapid for DS Ni-22.2Al-8.1Cr-5.0Ti-0.8Mo-0.6Zr and Ni-19.1Al-8.2Cr-5.1Ti-2.9B (at.%) alloys. As can been seen in Fig. 16b, the cyclic oxidation behaviour of DS Ni-21.7Al-7.5Cr-6.5Ti, Ni-21.3Al-7.0Cr-1.5Ta-0.6Mo-0.6Zr and Ni-21.9Al-8.1Cr-4.2Ta-0.9Mo-0.3Zr (at.%) alloys is comparable to that of binary Ni_3Al and single crystalline CMSX-4 superalloy.

Assuming microstructure stability, room-temperature ductility, tensile and compressive properties, high temperature creep strength and cyclic oxidation resistance, the DS Ni-21.3Al-7.0Cr-1.5Ta-0.6Mo-0.6Zr (at.%) alloy showed the largest potential for some

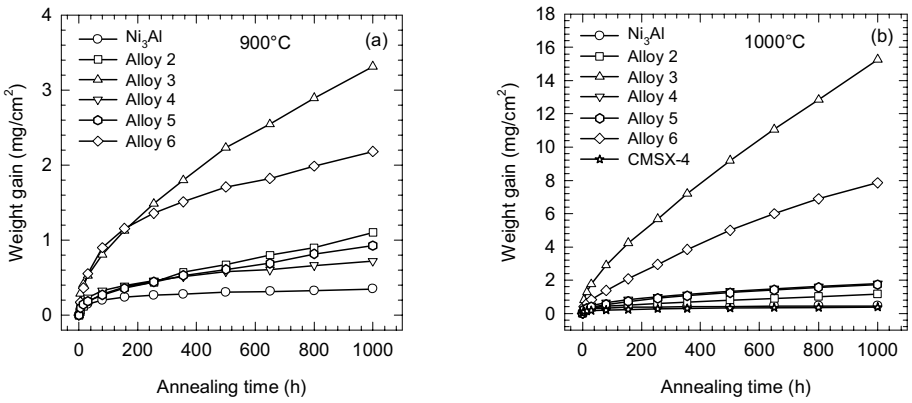

Fig. 16. Dependence of weight gain on the annealing time: (a) 900°C; (b) 1000°C. The studied alloys are indicated in the figures.

structural applications. However, fine tuning of chemical composition and microstructure optimization are still required to achieve full potential of this system.

4. Summary

The present work summarizes the achieved results for six multiphase intermetallic alloys based on ternary Ni-(19-22)Al-8Cr (at.%) system modified by Ti, Ta, Mo, Fe, Zr and B additions. The alloys were prepared by exo-melt or plasma melting processes and directionally solidified in Bridgman type apparatus. The effect of several processing parameters including growth rate, temperature gradient in the liquid at the solid-liquid interface, annealing temperature and annealing time on the microstructure evolution and stability were studied. Room- and high-temperature tensile and compressive properties, creep characteristics including parameters of kinetics creep equation and high-temperature cyclic oxidation behaviour were determined. Among the studied systems, the DS Ni-21.3Al-7.0Cr-1.5Ta-0.6Mo-0.6Zr (at.%) alloy is proposed to have the largest potential for further optimization and high-temperature structural applications.

Acknowledgments

The author gratefully acknowledge the financial support of the Slovak Grant Agency for Science under the contract VEGA 2/4166/24.

References

[1] S.C. Deevi and V.K. Sikka: Nickel and iron aluminides: an overview on properties, processing, and applications. *Intermetallics*, 4, 1996, pp. 357-379.

[2] V.K. Sikka, S.C. Deevi, S. Viswanathan, R.W. Swindeman and M.L Santella: Advances in processing of Ni_3Al-based intermetallics and applications. *Intermetallics,* 8, 2000, pp. 1329-1337.

[3] S.C. Deevi, V.K Sikka and C.T. Liu: Processing, properties, and applications of nickel and iron aluminides. *Progress in Materials Science*, 42, 1997, pp. 177-192.

[4] N.S. Stoloff, C.T. Liu and S.C. Deevi: Emerging applications of intermetallics. *Intermetallics*, 8, 2000, pp. 1313-1320.

[5] R. Darolia: Ductility and fracture toughness issues related to implementation of NiAl for gas turbine applications. *Intermetallics*, 8, 2000, pp. 1321-1327.

[6] R.W. Cahn: Multiphase intermetallics. *Phil. Trans. R. Soc. Lond. A*, 351, 1995, pp. 497-509.

[7] R. Misra, R. Gibala and R.D. Noebe: Optimization of toughness and strength in multiphase intermetallics. *Intermetallics*, 9, 2001, pp. 971-978.

[8] R. Misra and R. Gibala: Plasticity in multiphase intermetallics. *Intermetallics*, 8, 2000, pp. 1025-1034.

[9] G. Sauthoff: Multiphase intermetallic alloys for structural applications. *Intermetallics*, 8, 2000, pp. 1101-1109.

[10] B. Zeumer and G. Sauthoff: Deformation behaviour of intermetallic NiAl-Ta alloys with strengthening Laves phase for high-temperature applications III. Effects of alloying with Cr. *Intermetallics*, 6, 1998, pp. 451-460.

[11] W.F. Gale, Z.A.M. Abdo and R.V. Nemani: Microstructural development in cast and aged Ni-Al-Cr-based alloys derived from the B2 type β-NiAl structure. *J. Mater. Sci.*, 34, 1999, pp. 407-416.

[12] W. Palm, J. Preuhs and G. Sauthoff: Production-scale processing of a new intermetallic NiAl-Ta-Cr alloy for high-temperature application. Part I. Production of master alloy remelt ingots and investment casting of combustor liner model panels. *Journal of Materials Processing Technology*, 136, 2003, pp. 105-113.
[13] N.S. Stoloff and V.K. Sikka: Physical Metallurgy and Processing of Intermetallic Compounds. Chapman and Hall, New York 1996.
[14] J. Lapin: Effect of ageing on the microstructure and mechanical behaviour of directionally solidified Ni_3Al-based alloy. *Intermetallics*, 5, 1997, pp. 615-624.
[15] J. Lapin: High temperature creep of precipitation-strengthened Ni_3Al-based alloy. *Intermetallics*, 7, 1999, pp. 599-609.
[16] J. Lapin, S. Wierzbinski and T. Pelachová: Microstructural stability, hardness and compressive behaviour of directionally solidified intermetallic Ni_3Al-based alloy with $\gamma/\gamma'–\beta$ structure. *Intermetallics*, 7, 1999, pp. 705-715.
[17] S. Wierzbinski, J. Lapin and T. Czeppe: High temperature deformation behaviour of a directionally solidified Ni_3Al-based alloy. *Arch. Metall.*, 44, 1999, pp. 221-237.
[18] J. Lapin, T. Pelachová and O. Bajana: Microstructure and mechanical properties of a directionally solidified and aged intermetallic Ni-Al-Cr-Ti alloy with $\beta–\gamma'–\gamma–\alpha$ structure. *Intermetallics*, 8, 2000, pp. 1417-1427.
[19] J. Lapin and A. Vaňo: Coarsening kinetics of α- and γ'-precipitates in multiphase intermetallic Ni-Al-Cr-Ti type alloy with additions of Mo and Zr. *Scripta Mater.*, 2004, s. 571-575.
[20] J. Lapin: Embrittlement of directionally solidified Zr-doped multiphase intermetallic Ni-Al-Cr-Ta-Mo alloy after heat treatment. *Scripta Mater.*, 51, 2004, pp. 733-738.
[21] C.C. Jia, K. Ishida and T. Nishizawa: Partition of alloying elements between γ (A1), γ' ($L1_2$), and β (B2) Phases in Ni-Al base systems. *Metall. Mater. Trans. A*, 25A, 1994, pp. 473-485.
[22] K. Aoki, K. Ishikawa and T. Masumoto: Ductilization of Ni_3Al by alloying with boron and substitutional elements. *Mater. Sci. Eng. A*, 192/193, 1995, pp. 316-323.
[23] J.H. Lee, B.H. Choe, Z.H. Lee, and H.M. Kim: Effect of zirconium in two phase (NiAl + Ni_3Al) alloy. *Scripta Mater.*, 40, 1999, pp. 853-857.
[24] B.H. Choe, I.H. Kim, B.H. Lee, H.S. Ahn, J.H. Lee, J.H. Lee and H.M. Kim: The enhancement of tensile strength and elongation in two phase (NiAl+Ni_3Al) intermetallics of Zr-doped Ni–20Al–27.5Fe (at.%) alloys. *Mater. Sci. Eng. A*, 323, 2002, pp. 187-191.
[25] T.H. Chuang and Y.C. Pan: On the mechanisms of high-temperature intergranular embrittlements of Ni_3Al-Zr alloys. *Metall. Trans. A*, 23A, 1992, pp. 1187-1193.
[26] H. Li and T.K. Chaki: Incipient melting of grain boundaries in Ni_3Al alloys containing zirconium. *Mater. Sci. Eng. A*, 192/193, 1995, pp. 570-576.
[27] J. Lapin, Ľ. Ondrúš and M. Nazmy: Directional solidification of intermetallic Ti-46Al-2W-0.5Si alloy in alumina moulds. *Intermetallics*, 10, 2002, pp. 1019-1031.
[28] T.B. Massalski: Binary Phase Diagrams. Vol. 3, ASM International, Materials Park, Ohio, 1990, p. 2890.
[29] P.N. Quested and M. McLean: Solidification morphologies in directionally solidified superalloys. *Mater. Sci. Eng.*, 65, 1984, pp. 171-180.
[30] H.K. Kim, J.C. Earthman and E.J. Lavernia: Directional solidification of Ni_3Al. *Acta Metall. Mater.*, 40, 1992, pp. 637-647.
[31] J. Lapin, A. Klimová, R. Velísek and M. Kursa: Directional solidication of Ni-Al-Cr-Fe alloy. *Scripta Mater.*, 37, 1997, pp. 85-91.

SUPERPLASTIC DEFORMATION AND MECHANISM OF EXTRUDED EUTECTIC NiAl/Cr(Mo) ALLOY DOPED WITH Dy

Jianting GUO, Xinghao DU, Gusong LI

Superalloy Department of Institute of Metal Research
The Chinese Academy of Sciences
Email: jtguo@imr.ac.cn, 602@imr.ac.n

Abstract

The superplasticity of cast and hot extruded NiAl-31Cr-3Mo doped with minor Dy is observed as a function of temperature and strain rate, and characterized by a constitutive equation and the deformation microstructure. In the region of strain rate lower than 1.04×10^{-3} s^{-1} at above 1323 K, the alloy exhibits superplastic deformation. The activation energy of deformation is estimated to be Q=143 kJ/mol, half to that of bulk diffusion in NiAl (220~300 kJ/mol). It is suggested that the grain boundary sliding-based mechanism between NiAl and adjacent NiAl or Cr(Mo) grains with local range accommodation, i.e. dislocation climb is responsible for the superplastic deformation for the alloy. The discovery of superplasticity provides a viable way to dissolve the hard-to-machine problem of the alloy.

Keywords: Ni-31Cr-3 Mo (Dy) alloy, Superplasticity, Deformation mechanism, Grain boundary sliding

1. Introduction

B2 type intermetallic compound NiAl is an attractive matrix for high temperature structural materials to replace nickel-based superalloys due to its high melting point, low density, good thermal conductivity and good oxidation resistance [1, 2]. However, poor damage tolerance at ambient temperatures and inadequate strength at high temperatures have prevented its commercial applications. It has found these shortcomings can be improved significantly by the fabrication of NiAl-based eutectic composites involving a refractory metal reinforcement phase, and NiAl/Cr(Mo) alloys display the promising mechanical properties [3,4]. However, these materials are difficult to form by conventional processing routes. Fortunately, it is known that superplasticity can provide the possibility of the high-temperature deformation processing of these brittle materials and has the advantages of improved formability with better dimension accuracy [5].

It is known that many superplastic deformation occurs at strain rates of, typically, lower than ~$10^{-4}s^{-1}$. Obviously, these low rates are unacceptable in practice. However, if the strain rates for superplastic deformation is of ~$10^{-3}s^{-1}$, the production time by superplastic forming is

of the order of 20 to 30 minutes which is acceptable for the fabrication of high-value components having relatively limited application, as in aircraft [6]. On these backgrounds, the deformation behavior and mechanism of extruded eutectic NiAl–28Cr-5.9Mo-0.1Dy alloy under the region of strain rate ~$10^{-4}s^{-1}$–$10^{-2}s^{-1}$ are investigated in this present study.

2. Experimental procedure

The nominal NiAl-31Cr-2.9 Mo-0.1Dy (at.%) alloy, by using high-pure metal elements as starting materials, was induction melted under vacuum conditions and drop cast into cylindrical chill mold. Then the master alloy was homogenized at 1300 for 24 hours. After that, the obtained materials were condensed by extrusion with the area reduction 9:1 at 1000 . The flat tensile specimens, having a gauge section 2×2.5×16mm^3, were electro-discharge machined from the obtained materials. Tensile tests were carried out using a SHIMADZU AG-25KNE testing machine up to 1373 K. Tensile specimens were heated to the deformation temperature at a heating rate of 15 K/min and maintained at the temperature with an accuracy of ±1 K during deformation under the condition of constant crosshead speed. Tensile loads were automatically recorded through a supplement computer. In some cases, deformation was interrupted at a given elongation and specimens were water quenched as fast as possible. The specimens for SEM microscopy were etched in a solution of 5g$FeCl_3$+15mlHCl+65mlCH_3COOH. The foils for TEM observation were taken from the center part of the gage section and prepared by ion milling using argon ion after mechanical polishing to 30μm, and then the samples were examined in a Philips TEM 420 analytical electron microscope operated at 120 kV.

3. Experimental Results

3.1 The tensile properties

Elongations defined as total strains to failure are evaluated on different testing parameters. Concerning the strain rate dependence of the alloys (Fig. 1), it can be observed that maximum elongation (i.e. optimum condition of superplasticity) occurs under the initial strain rate of 1.04×10^{-4} s^{-1} at 1373 K. Figure 2 shows the macrograph of specimens tested at 1323 K and 1373 K under the various strain rates. The results reveal that these specimens deform equally to fracture without obvious necking, which is similar to the character of superplastic deformation of many metallic alloys [7-8].

True stress-true strain curves are drawn from data recorded by the computer under assumption of volume constancy according to the method employed by Oomori et al [9]. Since all the tests are conducted under the condition of constant crosshead speed, the curves of flow stress versus strain may be somewhat different from those under the condition of constant strain rate.

Based on the stress versus strain relation in superplasticity, $\sigma = K\dot{\varepsilon}^m$; where k is a constant, a correlation to transform the stress at non-constant strain rate to that at constant strain rate is developed as

$$\sigma_{c\varepsilon} = \sigma_{cv} e^{m(\varepsilon - 0.002)} \quad (1)$$

$\sigma_{c\varepsilon}$ constant strain rate, 0.002 is true strain corresponding to yielding point, σ_{cv} is the stress under the condition of constant cross head speed. According to the above correlation, the curves of flow stress versus strain were re-plotted in Figure 3. The (2), (4), (6) curves exhibit the true stress-true strain behavior for the alloy under the condition of constant crosshead speed while the (1), (3), (5) are their adjusted curves according to the equation of (1).

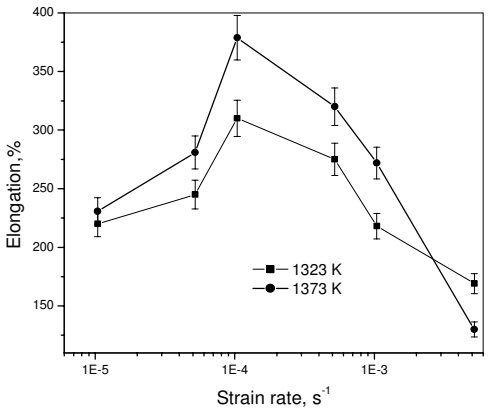

Figure 1. Strain rate dependent of elongation for the tested alloys at 1323 K and 1373 K

1323K, $10^{-3}s^{-1}$, δ =280%。

1323K, $10^{-4}s^{-1}$, δ =290%。

1373K, $10^{-3}s^{-1}$, δ =300%。

1373K, $10^{-4}s^{-1}$, δ =380%。

Figure 2. Macrographs of fracture specimens of NiAl-31 Cr-2.9Mo-0.1Dy alloy

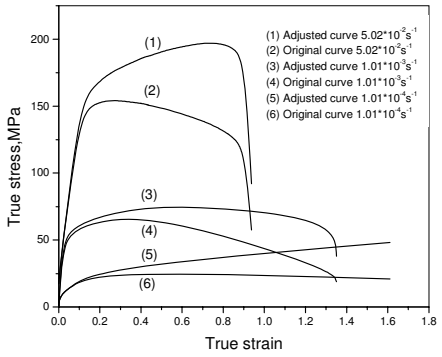

Figure 3. True stress-true strain curves for tested alloy under different strain rates at 1373 K

From Fig. 3, we can observe that at high strain rate, the true stress-true strain curves exhibit modest increase after yield, followed by rapid decrease of stress. As the strain rate decreases, the flow stress decreases. Corresponding to this variation, the steady flow extends to large strain without fracture, being typical of many superplastic materials [7,8]. However, at slow strain rate, the true stress-true strain curves exhibits continuous increase till fracture, which is also common for some materials during superplastic deformation process. The influence of temperature is similar to the influence of strain rate; an increase of temperature leads to the same pattern in the stress-strain curves as that observed by a decrease in strain rate.

3.2 Constitutive equation

High temperature deformation of materials under steady–state conditions can be generally expressed by the relation between flow stress (σ) and strain rate ($\dot{\varepsilon}$):

$$\dot{\varepsilon} = A\sigma^n \exp(-Q/RT) \tag{2}$$

where A *i*s a constant, n is the stress exponent being identical to $1/m$ (m is the strain rate sensitivity index), Q is the apparent activation energy, R is a gas constant and T is the thermodynamic temperature. Fig.4 shows the relationship between the flow stress (ε=0.29) and the strain rate for the tested alloy at various temperatures. Linear relationships are found for the alloy at 1323 K with the strain rate sensitivity index m=0.30, meaning that the alloy exhibits commonly plastic deformation. Generally, the strain rate sensitivity index increases with increasing temperature and attained 0.50 above 1323 K when the strain rate is lower than 1.04×10^{-3} s^{-1}.

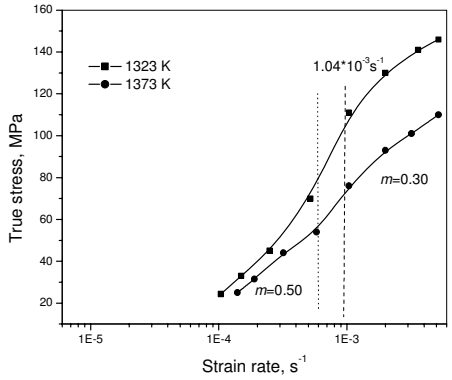

Figure 4 Strain rate dependence of true stress (ε=0.29, corresponding to the steady flow) for the tested alloy

From equation (1) it can be shown that:

$$Q = n \cdot R \cdot \frac{\partial \ln \sigma}{\partial (1/T)} \tag{3}$$

where n=1/m. Fig.5 shows an Arrhenius plot for the flow stress of the tested alloy where the stresses corresponding to the steady flow in the true stress–true strain curves were used as the flow stress. The plot is performed for strain rates of $5.20\times10^{-4}s^{-1}$ (n=2) and $5.20\times10^{-3}s^{-1}$ (n=3). The apparent activation energy is calculated to be about 143 kJ/mol and 324kJ/mol based on the equation (2). The activation energy value for strain rates of $5.20\times10^{-4}s^{-1}$ is about half of the value (220~300 kJ/mol) measured in creep deformation of NiAl, while for the strain rate of $5.20\times10^{-3}s^{-1}$, the apparent activation energy is more than the value measured in creep deformation of NiAl [1]. This indicates that different deformation mechanisms are operative at different strain rate region.

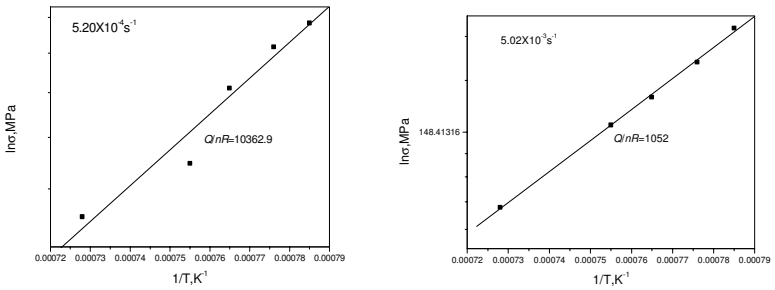

Figure 5 The Arrhenius plot for the alloy in two deformation regime

3.3 Microstructural observations

A typical SEM photograph of the microstructure of the present alloy obtained after hot extrusion is shown in Fig. 6 (a). The NiAl-matrix grains (gray color) are equiaxed and fine. The linear intercept grain size is determined as 3~5 μm. Elongated Cr(Mo) phase (white color) are observed to be distributed in the NiAl matrix. Fig.6(b) shows the SEM image of the alloy after fracture tensile tested at 1373 K under an initial strain rate of 1.04×10^{-4} s^{-1} which corresponds to the continuous work hardening stage on the true stress-true strain curves. The grains of primary β-NiAl matrix in the gage section remain equiaxed but slight coarsening occurs with the mean grain size of more than 10 μm, which is larger than the size of initial grains. The shape of α-Cr (Mo) phase have become more irregular. Similar microstructure can be observed in the fractured specimens tensile tested at 1373 K under an initial strain rate of 5.04×10^{-4} s^{-1} which corresponds to the steady state flow on the true stress–true strain curves.

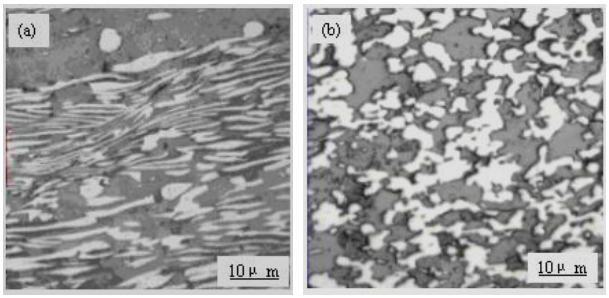

Figure 6 The SEM images of of the specimens obtained at different strains (a) ε=0; (b) ε=0.8 at 1373 K under an initial strain rate of 1.04×10^{-4} s^{-1}

3.4 TEM observations

Based on the value of *m* and activation energy, the deformation process of the alloy at 1323 K can be divided into two regions: one is superplastic deformation process ($\dot{\varepsilon}$ ▪ 1.04×10^{-3} s^{-1}), the other is commonly deformation process ($\dot{\varepsilon}$ ▪ 1.04×10^{-3} s^{-1}). Therefore, the microstructural evolution and fracture shapes are observed for the two regions, respectively.

Figure 7 is the TEM observations of the specimens obtained at different strains corresponding to the strain region of continuous working hardening flow deforming at 1323 K under an initial strain rate of 1.04×10^{-4} s^{-1}. Figure 7 (a) shows that a high density of dislocations around grain boundary of NiAl matrix at the strain of 0.70. These dislocations should be introduced to accommodate stress generated by grain boundary sliding. Fig. 8 (b) shows that the dislocations demonstrate the tendency to form the tangle of dislocations and the cell almost has formed, indicating that dislocations climb behavior has occurred for the alloy during superplastic deformation process. However, almost no dislocation has been observed in Cr(Mo) phase, and this may be due to the higher yield strength of Cr(Mo) phase than NiAl phase at this deformation temperatures.

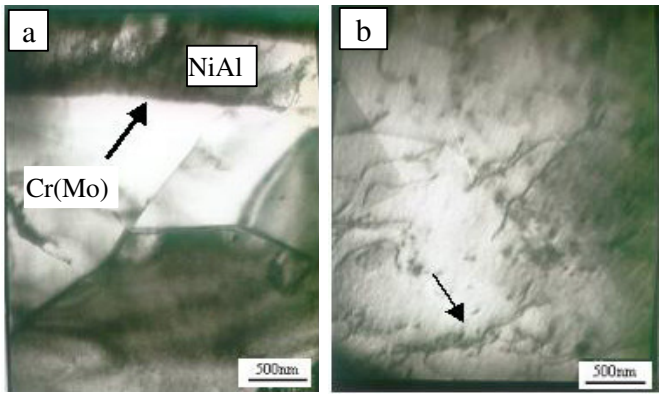

Figure 7 TEM observations of the specimens obtained at different strains (a) ε=0.70; (b) ε=1.40 at 1373 K under an initial strain rate of 1.04×10^{-4} s^{-1}

Fig. 8 is the TEM observations of the specimens obtained at different strains corresponding to the strain region of continuous working hardening flow deforming at 1373 K under an initial strain rate of 5.20×10^{-3} s^{-1}. Numerous dislocation networks or sub-boundary were observed in the specimens with different strains.

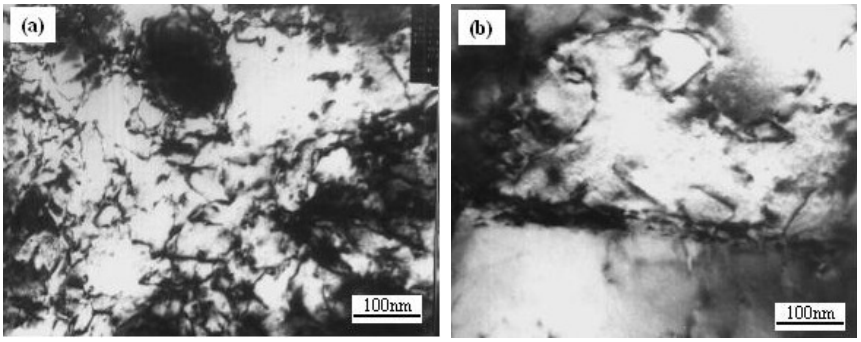

Figure 8 TEM observations of the specimens obtained at different strains (a) ε=0.20; (b) ε=0.80 at 1373 K under an initial strain rate of 5.20×10^{-3} s^{-1}

4. Discussion

Now we can discuss the mechanisms of the elevated-temperature deformation of the present alloy based on both of mechanical and metallographical observations. It is known that the plastic flow of metallic alloys arises from two independent processes at high temperatures

[10]. In one process the grain boundary sliding (GBS) accommodated by dislocation behavior (Glide or climb) occurs in the boundary region, and in the other dislocation slip or diffusion occurs within the core of each grain. Due to the stress exponent *n* measured in strain rate region lower than $1.04\times10^{-3}s^{-1}$ at more than 1323 K in this work was about 1.8~1.9, the mechanisms associated with dislocation slip or diffusional creep may be excluded. On the other hand, a high *m* value of 0.56 implies that grain boundary sliding (GBS) is occurring at grain boundaries between NiAl and adjacent NiAl or Cr (Mo) grains; this trend is also noted in other superplastic materials [7,8]. The apparent energy for the high temperature deformation of the alloy at this strain rate regime is calculated as 143 kJ/mol, which is close to a half of the activation energy of the bulk diffusion of NiAl (220~300 kJ/mol) [1]. Therefore, it is suggested that grain boundary diffusion of NiAl matrix is involved in the process responsible for intermediate strain rate region where superplastic deformation takes place.

In order to investigate the mechanism of superplasticity for the alloy, the tensile tests are also conducted on the specimens of conventional cast alloy with coarse grain with mean grain size more than 200 μm at the same conditions. Figure 9 shows the microstructural shape effect on the true stress-true strain curves of the alloy. The present experiments show that different deformation mechanisms are dominant for the as cast alloy and extruded alloy at same conditions. For the as cast alloy, the flow curve exhibits a narrow stress peak followed by the occurrence of neck- shrinking, and is shown to be associated with dislocation sliding. On the other hand, for the alloy, the flow curve exhibits steady state flow till a large strain. In this case it is assumed that the flow stress is independent of strain and that no necking occurs. Furthermore, the overall level of the flow stress in the extruded alloy is considerable lower than that of material in the conventional coarse grained, i.e cast condition, which is similar to the superplasticity of Al-Cu alloy [11].

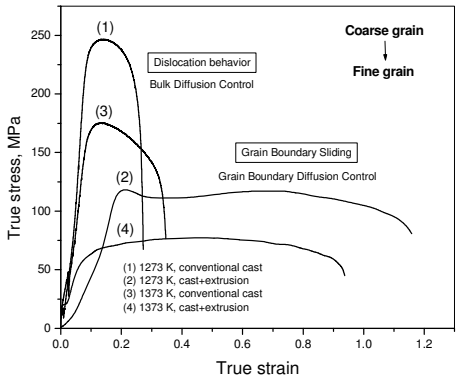

Figure 9 The compare of true stress -true strain curves between conventional cast alloy and the tested alloy under the initial strain rate of 1.04×10^{-3} s^{-1}

Now that the mechanism for the superplastic flow involves grain boundary sliding, it is necessary for an accommodation process to accompany grain boundary sliding. Fig. 7 shows that the dislocations demonstrate climb behavior during superplastic deformation process. This type of dislocation climb is controlled by Ni vacancy diffusion along dislocation cores and may cause dislocation rearrangement at small distances [12]. It is known that thermal vacancy can easily form due to the atomic thermal vibration in B2 type NiAl alloys above 0.33 T_m, and the thermal vacancy concentration can be 2% at the T_m [13]. Therefore, the diffusion coefficient of the atom Ni at NiAl increases significantly due to the presence of high concentration of thermal vacancy at high temperature. In addition, according to the Nesbitt et al [14], the interdiffusion of NiAl and Cr(Mo) phases are significantly higher than the tracer diffusion of Ni, Al. Therefore, the high diffusional coefficient of the NiAl alloy at high temperatures makes the rapid climb of dislocation viable. Dislocations in the grains can be abstracted and absorbed by a dislocation line even sub-boundary, therefore, dislocation climb process can effectively absorb deformation energy and then make the alloy deform in the form of steady flow. On the other hand, the alloy deform by dislocations slid under the high initial strain rate $5.02\times10^{-3}s^{-1}$ at 1373 K (Fig. 8).

It should be noted that similar superplastic phenomena have been observed in FeAl, Fe_3Al, and Fe_3Si alloys [15-18]. The common characteristics of them are that the fracture elongations are not very high. But the elongation beyond 300% is sufficient to make, using superplastic forming technology, extremely complex shapes for most alloys, which only require over 200~300% elongation [19]. In this paper, because the NiAl alloy exhibits superplasticity under the strain rate of the order of ~ 10^{-3} s^{-1}, there is great interest in using the material for engineering structures.

5. Conclusions

The superplastic deformation behavior of hot extruded NiAl-31Cr-3 Mo doped with minor Dy has been characterized. And the conclusions can be given as follow:

(1) The obtained material exhibits superplastic deformation at a strain rate range ($10^{-3}s^{-1}$~10^{-4} s^{-1}) above 1323 K.

(2) Based on the mechanical and microstructural observations, it is suggested that the grain boundary sliding with local range accommodation, i.e. dislocation climb behavior is responsible for the superplastic deformation of the alloy.

(3) The NiAl alloy exhibits superplasticity under the strain rate of the order of ~10^{-3} s^{-1}, there is great interest in using the material for engineering structures.

Acknowledgement

The authors would like to acknowledge National Natural Science Foundation of China (contract No.59895152) and National Advanced Materials Committee of China (No. 863-715-005-0030) for their financial supports.

References

[1] Miracle DB, The physical and mechanical properties of NiAl, Acta Metall Mater, 41(1993) 649.

[2] Noebe D,Bowm an RR, Nathal MV, Physics and mechanical metallurgy of NiAl , NASA technical paper, April (1994)3398.

[3] Johnson, D. R., Chen, X. F., Oliver, B. F., Noebe, R. D.and Whittenberger, J. D., Processing and mechanical properties of in-situ composites from the NiAl-Cr and the NiAl-Cr(Mo) eutectic system , Intermetallics, 3 (1995) 99.

[4] Johnson, D. R., Oliver, B. F., Noebe, R. D. and Whittenberger, J. D., Intermetallics, NiAl-based polyphase in situ composites in the NiAl-Ta-X(X=Cr,Mo,or V) systems ,3(1995) 493.

[5] Y. Sakka, T. Matsumoto, T.S. Suzuki, K. Morita, B.-N. Kim, K. Hiraga, Y. Moriyoshi, Low-temperature and high-strain rate superplastic Zirconia, Advanced Engineering Materials, 5(2003)130.

[6] Terence G. Langdon, Materials Transactions JIM, Developing superplastic properties in an aluminum alloy through severe plastic deformation**,** 40(8) (1999) 716.

[7] Sherby OD, Wadsorth J, Prog Mater Sci., Superplasticity—Recent advances and future directions, 33 (1989) 169.

[8] T. G. Nieh, J. Wadsworth, Fine structural superplasticity of intermetallics, Inter. Mater. Rev., 44(2)(1999) 59.

[9] T.Oomori, T.Yoneyama and H.Oikama, Materials Transactions JIM, 29 (1988) 399.

[10] R. L. Coble, Diffusion-accommodated flow and superplasticity, J. Appl. Phys.34 (1963) 1679.

[11] D.H.Holt, W.A.Backofen, Superplasticity of Zn-Mg alloys, Trans.Quart.A.S.M.59 (1966) 755.

[12] P.Griffiths, C.Hammond, Superplasticity in large grained materials, Acta Met., 12 (1972) 935.

[13] K. Dora, P.K.Longond., Structural basis of solid solution formation during chiral resolution Phil.Mag., 1984, A50, 89.

[14] J.A.Nesbitt and R.W.Heckel., Superplastic behaviour of a Zr-2.5 Wt% Nb pressure tube alloy Metall. Trans.,18A(1987)2061.

[15] Dongliang Lin, Jing Hu and Dongmei Jiang, Superplasticity of Ni-rich single phase NiAl intermetallics with large grains, Intermetallics., 13 (2005)343.

[16] Li D.Q and Lin T.L, Microstructure evolution and activation energy during superplastic deformation of FeAl based intermetallics, Scripta Metall Mater, 36(1997) 1289.

[17] J.Hu and D. Lin, Superplasticity of single-phase Ni–48Al intermetallics with large grains, Mater. Let.,58 (2004)1297.

[18] Kim, W.Y., Hanada, S., Superplastic deformation of boron doped Fe–18at.%Si, Mater Sci Eng., 248 A (1998)78.

[19] N.E.Paton and C.H.Hamilton (editors) Superplastic Forming of Structural alloys, The Metallurgical Society of AIME, Warrendale, PA (1982).

FEM study of a CMC shroud

P. Del Puglia[a], N. Lanese[b], G. Zonfrillo[a]

[a] *Department of Mechanics and Industrial Technologies, University of Florence, Italy.*
[b] *Nuovo Pignone – GE Oil & Gas, Florence, Italy*

Abstract

The quest for more efficient and environment friendly gas turbines demands higher firing temperatures. The employment of Ceramic Matrix Composites (CMCs) in hot components can allow this goal to be attained.
In this study, the possibility of substituting a metallic shroud with an analogous component manufactured using a CMC material is evaluated. The laminate used is composed by long fibres of alumina embedded in a mullite matrix. The study has been carried out with a thermo-mechanical finite element analysis applied to a model of the component. Stresses generally appear to be more remarkable in correspondence to the constraints, which are also the regions with the lowest temperatures. Results show that it would be possible to substitute the metallic shroud with a CMC one, if using a material with slightly better characteristics than that used in this study.

Keywords: Ceramic matrix composites, shroud, laminate, thermal analysis, stress analysis.

Introduction

The aim for development of gas turbines with higher combustion temperatures is to provide a sensible reduction of the air fraction to be tapped for cooling, of the combustible required, and consequently of polluting emissions [1]; moreover, it would also lead to an increase in the overall efficiency.
Ceramic Matrix Composites (CMCs) represent a new class of materials that can represent a substitute for metals in high temperature applications in gas turbines, because of their high melting temperature. Considerable developments in manufacturing processes for CMCs have occurred, so that higher damage tolerance, good behaviour at higher temperatures and weight reduction has been obtained [2, 3].
Qualitatively the introduction of CMC materials should lead to a relevant increase of the combustion temperature. Metallic components can retain their mechanical integrity up to 850-900°C, which can be further enhanced by adoption of impingement cooling, the downside of which is the reduction in efficiency. Thermal barriers placed on the metallic components, extend their operating range to almost 1100°C.
At the moment, 1100°C can be considered the limit for CMCs too. This apparently cannot lead to a great improvement in the engine efficiency, but the possibility of applying a thermal barrier to the CMC component could move this limit to higher values. Moreover, an analysis of the present applications of CMC materials shows that further research is urgently required to satisfy future demands in long-term applications.
To fulfil this task, numerous design problems must be solved, mainly related to material anisotropy and to the interaction between the CMC component and the other metallic parts of the engine.
The development of new materials is a great task for industrial progress. Beside it is important to reach a good level of reliability of the components. Even if nowadays it is possible to manufacture materials with better characteristics at high temperature than metals, they still retain their typical brittleness. A specific thermal-mechanical analysis is then required, alongside with a suitable design of the laminate composition and layout. The finite element

modelling of the components and of the material itself becomes fundamental in order to complete the design phase.
Although the research activity in this field is still limited, the possibility of introducing CMC components in gas turbines has been investigated by several authors [4-7]. This confirms the industrial interest in this area and the possible use of this class of materials, even if manufacturing costs for CMCs are still high.
In this paper, the model of a first-stage shroud is presented and results of its analysis are discussed. For an appropriate design, the component chosen has been modelled including the real working loading conditions.

The component

The component under study is a shroud. It is a ring placed just over the tip of the rotor buckets, where gasses coming from the combustor reach high value of temperature. This component is so mounted as to constitute the external wall of the flow path for gasses. Traditional shrouds are metallic, and they are cooled down by impingement, using cold air from the compressor. To design this component using a CMC laminate, a shroud used in a gas turbine by G.E. Nuovo Pignone Oil & Gas S.p.A. (NP) has been chosen as a reasonable starting point. The design of the component has been performed on the basis of the metallic component in use, and of previous NP design experience with CMC [8-10].
The CMC shroud is composed by eight sectors. The drawing of one of them is shown in Figure 1. The shape of the component derives by an appropriate variation of the radial dimension along the axis: the shroud is placed very close to the tip of the buckets and this shape is necessary to clamp the sectors to the engine. At the extremities in the hoop direction, each sector has half the regular thickness, so that it can be overlapped in that area with the adjacent sectors. The length of the overlap zones is calculated to completely close the ring at the working temperature.

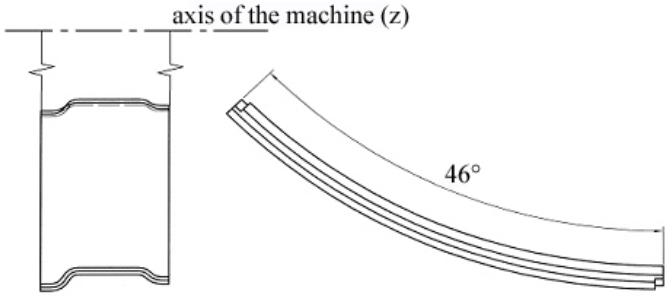

Figure 1 - Schematic drawing of one of the eight sectors constituting the shroud.

Because of the properties of the material, this shroud does not need any internal cooling. The thermal gradient due to hot gasses induces the main load on the component. It causes dilatation and deformations, which should be taken into account: the shroud is mounted at room temperature, and gaps between the sectors are necessary to avoid possible mechanical stresses of compression at hot temperature due to expansion in the hoop direction. Also thermal expansion in the radial direction must be limited to avoid contact of the shroud with the tips of the buckets during functioning.

The CMC shroud is designed to substitute the metallic one, without much changing in the rest of the engine. To constrain the component, surfaces C1 and C2 block radial displacements due to external pressure, and the contact on surface C9 contrasts the axial forces due to gas flow, as shown in Figure 2. This clamping system may be applied in a traditional gas turbine.

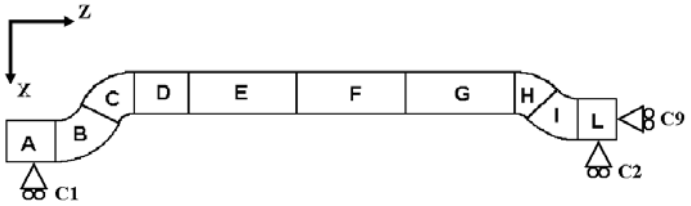

Figure 2 - Section of the shroud on a plane normal to circumferential direction.

The reference system used in defining the model geometry is cylindrical, with the following correspondences:

- x radial direction,
- y hoop direction,
- z axial direction.

The origin of the coordinate system is placed at the ring centre, in correspondence of the first section of the shroud encountered by the gas flow. In the circumferential direction the origin is in the middle plane of the sector.

Material description

The material is a CMC laminate, made of eight laminae. Each lamina is constituted by continuous alumina fibres, with a thickness of 0.225 mm, embedded in a mullite matrix. Fibres are Nextel^{TM} 720 - their properties are described in [11]. Matrix is mullite $3Al_2O_3$-$2SiO_2$ - its properties are reported in [12].
The architecture of the laminate is $[-22.5°/22.5°/67.5°/-67.5°]_S$, with angles referring to the circumferential direction. As first lamina, the internal one is assumed. This configuration is called quasi isotropic; the orientation of the fibres has progressive increments of 45° between adjacent layers, causing a pretty homogeneous distribution of the material elastic properties on the plane of the laminae.

Material strength

To perform a proper structural analysis, the strength of the material has to be known. The tensile strength for the material is 120 MPa at room temperature, and the compressive strength is 214 MPa. The tensile strength decreases to 40 MPa after 200-hours ageing at 1100°C. Inter-laminar shear strength is about 14 MPa [13]. Material strength decreases with increasing temperature. High-temperature experimental data are missing; therefore, as a first approximation, the strength after ageing has been taken as material strength at high temperature, and a linear relation with temperature has been assumed.
These data have been obtained experimentally on samples of the same material, used however in a different architecture. These samples are 12-layer laminates, with a $[0/90]_{6S}$ layout. For a better evaluation of results an experimental investigation would be required on the specific material used. It is however reasonable to suppose that the strength of the selected 8-layer

laminate is higher than that obtained for the $[0/90]_{6S}$, which is taken as reference limit in this work.

Material properties

The values of the elastic properties of the lamina (Young's moduli, Poisson's ratios, and shear stress moduli), and the thermal properties (thermal conductivity) have been provided by the manufacturer [14].

Thermal expansion coefficients for the laminate have been experimentally evaluated by JRC-Institute for Energy. They decrease with temperature, due to micro-porosity of the material.

FEM modelling

The FEM model has been realised and analysed using Ansys software. The study is based on both thermal and structural analysis. The choice of the elements must take the laminate structure of the material into account, as well as the thermal and structural loadings. A coupled-field analysis has been performed, in which a thermal element must be coupled with a structural one.

Choice of elements

The simple case of a thin cylinder under pressure has been preliminarily studied, to chose the type of element, between those available in the Ansys library. The model has been meshed with the following elements:

- SHELL99, with a single element in the thickness including information on the eight layers;
- SOLID46, or SOLID191, with a single element in the thickness including information on the eight layers;
- SOLID46, or SOLID191, with eight elements in the thickness, each one corresponding to a layer of material. This is called stacked configuration. It is more precise, but it has a larger number of elements.

Time for calculation is less when using the SHELL99 element. Although results of axial and hoop stresses are correct, this element does not give any information on the stress distribution through the thickness. Moreover, for the coupled-field analysis of the model, there is not a corresponding thermal element to be coupled with.

Using SOLID46, or SOLID191, elements with a single element on the thickness including information on the eight layers, results correspond to theoretical ones, except in the case of radial stresses.

The best choice is thus to use the stacked configuration, which gives reasonable values of stress in the three main directions. Between SOLID46 and SOLID191, the first element has been chosen, to reduce the calculation time; it has 8 nodes, while SOLID191 has 20 nodes. The mesh distribution is "mapped" and very regular so that the presence of the central nodes on the element edges is not necessary.

The elements used have three degrees of freedom in each node, which are the translations along the three directions. The thermal element (SOLID70) has been chosen accordingly to the structural one. It has 8 nodes, with a single degree of freedom (the temperature) for each one, and it can be used for the steady state analysis or for the transient.

The model of a single sector has been realised. The interaction with the other sectors has been included in the model.

Thermal analysis

The temperature distribution has been calculated through thermal analysis of the model. A steady state analysis has been carried out. The external surface of the shroud is in touch with cold air coming from the compressor, while the internal one is in touch with the hot gasses coming from the combustor; on the sides, the shroud is in contact with the metallic parts of the engine.
While air temperature can be assumed to be constant, the hot gasses in the internal side tend to cool down, so that temperature and thermal exchange coefficients change with the axial direction. To take this situation into account, the shroud is divided into a number of regions (A-L) in the axial direction, as shown in Figure 2, with different boundary conditions.
The temperature of the hot gasses and the thermal exchange coefficients for the CMC shroud have been provided by Heat Transfer & Secondary Flows Group, New Product Engineering Dept. (ING/NPI/NPE) of NP. They were calculated following the G.E. Oil & Gas standard procedure. The thermal exchange coefficients include heat exchanged both by convection and by irradiation [15].
In the overlap region between two sectors it has been considered that, after the expansion due to temperature increase, a little gap always remains between them in the hoop direction. Thermal conductivity coefficients for the laminate have been obtained as step function of temperature. For each temperature range a constant average value has been selected.

Thermal results
The highest temperatures are located on the internal side of the shroud where the hot gas get in touch with the component, as shown in Figure 3. The peak value is 1127°C and the temperature of a large part of the shroud exceeds 1000°C. These values are relatively high and can lead to creep phenomena - this may cause some problems for the performance of the engine for long times.

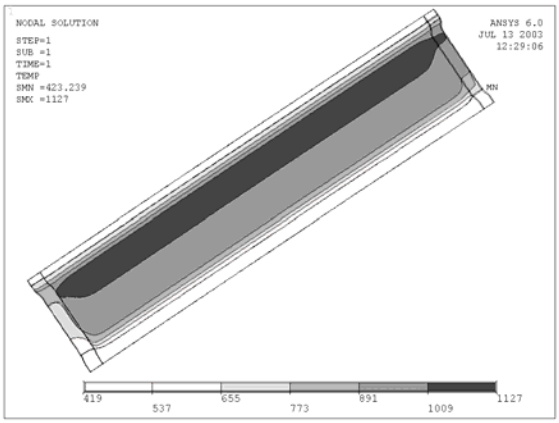

Figure 3 - Temperature distribution on the internal side of the shroud (°C).

In Figure 4 the temperature distribution has also been plotted along two paths of nodes selected on a plane in the centre of the sector, normal to the hoop direction. The nodes of the paths are those on the internal side and on the external side of the shroud, and are selected

with increasing values of an axial coordinate that follows the component shape.
The thermal gradient in the highest-temperature region of the component is shown in Figure 5, where a slice of the sector is shown. The difference of temperature in the radial direction is almost 85°C.

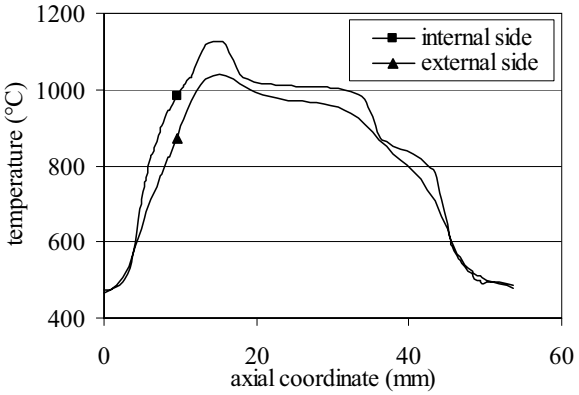

Figure 4 - Temperature vs. axial coordinate on the central section of a sector.

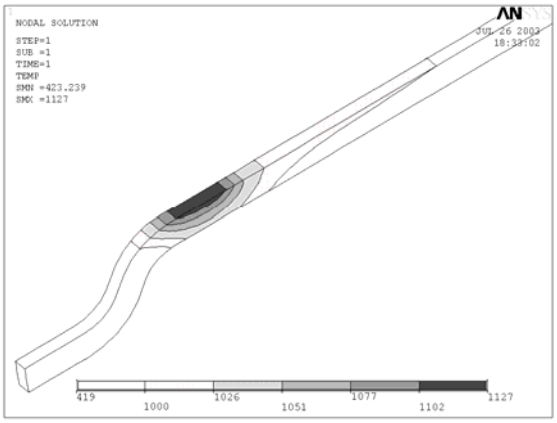

Figure 5 - Thermal gradient in the radial direction in the region of highest temperature (°C).

Structural analysis

Stresses and strains for the component have been calculated through a structural analysis. The temperature distribution obtained with the previous thermal analysis has been applied as body loads. Three hypotheses have been accepted:

- the analysis is static,
- vibrations are not taken into account,
- the problem is linear: deformations are small.

External forces are of two different kinds: thermal loadings, due to temperature gradients, and mechanical loads, due to pressure difference between internal and external gasses. As before,

a gap has been taken into account in the overlap region between sectors, in the hoop direction, to avoid additional stresses.
To apply the given values of pressure on the shroud, it is again necessary to divide it into regions, as previously done in the thermal analysis. While on the external side the gas pressure is almost constant, on the internal side the gas expands and cools down. Actual pressure levels on the shroud have been provided by NP ING/NPI/NPE, evaluated using their standard procedures.
The shroud is pushed by pressure in the radial direction toward the centre of the engine. Gas drag instead tends to move the component in the axial direction away from the combustor.
The COMBIN14 element has been used to constraint the FE model. This element represents a spring with a damper. It has two nodes and is generally defined by two damping coefficients - which are not required in a static analysis - and by an elastic constant in its longitudinal direction.
The nodes corresponding to the constrained surfaces have been duplicated, and linked to their copy, specifying the constraining direction: radial for surfaces C1 and C2, and axial for surface C9, with labels referring to Figure 2.

Results

The displacements of the model have been calculated in the three directions. Those on the internal side, along the same axial path of nodes previously defined, are plotted in Figure 6. The largest displacement is of about 0.27 mm radially toward the engine axis. The clearance between the shroud and the tip of the buckets in a standard gas turbine is usually comparable to the displacement calculated, so that there is a risk of rubbing between the two components.
On the component, stresses mainly change according to geometry, temperature distribution, and through the thickness due to fibres direction. Stresses are compared with the material strength values discussed above. The last values are only indicative, because of the lack of suitable experimental data. The distribution of stresses and their gradients are instead significant.
Stresses in the directions of the coordinate system have been analysed to give a general view of the behaviour of the component; this is the classical engineering approach for evaluating results. Values in the same directions may also be interesting for comparison with those of metallic components.
The distribution of radial stresses is almost constant and with small values in the laminate - since the thickness is very low, the shroud is subjected to a plane state of stress.
Hoop stress (Figure 7) is compressive in the central region, where the temperature reaches its highest value, and tensile in the regions of the constraints, which are colder. The level of stresses is higher in the external laminae of the composite, in agreement with the fibre orientation in the layers.
The stresses in the axial direction are generally smaller than the hoop stresses (Figure 8), and reach the maximum values in the central region of the shroud, while they are pretty small in the region of the constraints.
Two parallel effects influence the axial stress distribution: temperature (lower values in the central layers) and fibre orientation results in high stresses in the external layers (oriented at ±67,5°).
It is also interesting to observe the stresses in each lamina, in the direction of the fibres, and normal to them. The external layers have fibres oriented nearly in the hoop direction, while

the central layers have fibres oriented almost parallel to the axial direction.

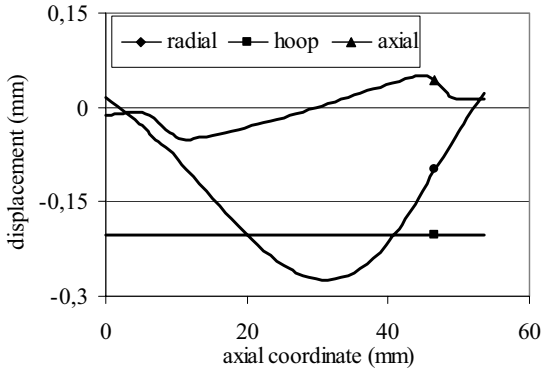

Figure 6 - Nodal displacements in the plane y = 0 on the internal side of the shroud.

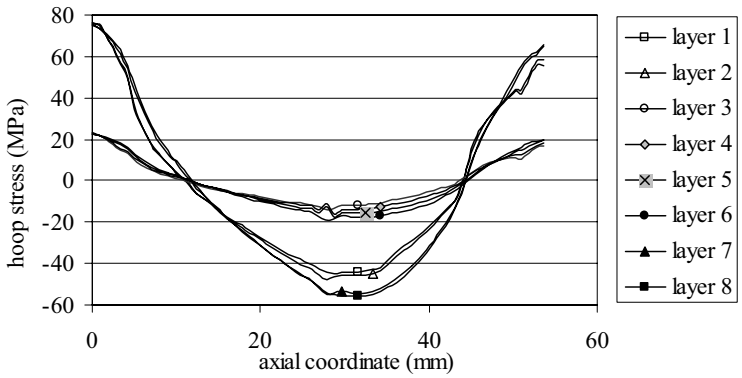

Figure 7 – Hoop stress vs. axial coordinate in the layers (inner to outer radii) of the laminate.

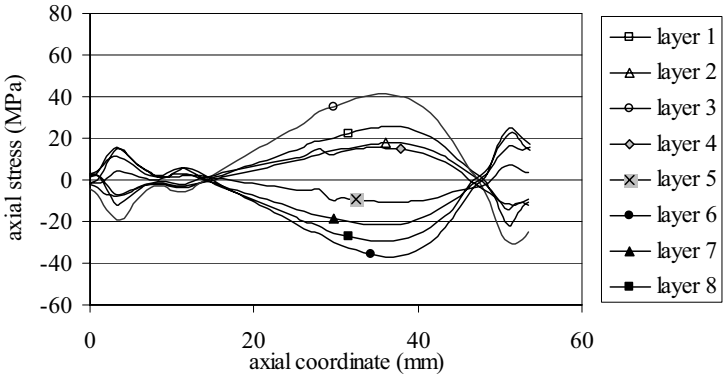

Figure 8 – Axial stress vs. axial coordinate in the eight layers of the laminate.

The stresses in the direction of the fibres are the highest. The external layers show a similar behaviour as that of the plot of the hoop stresses, with maximum values that are tensile and located near the constraints, while in the central region the stresses are compressive. Central layers are less loaded and follow the behaviour of the axial stresses previously presented.
Analogous is the situation for the stresses normal to the fibre direction: the external layer behaves with the stresses in the axial direction and the central layers tend to the hoop stress behaviour.
The most stressed layer is the external one on the outer side. In this layer the stress values in both directions - normal and parallel to the fibres - have comparable values, as shown in the Figure 9.

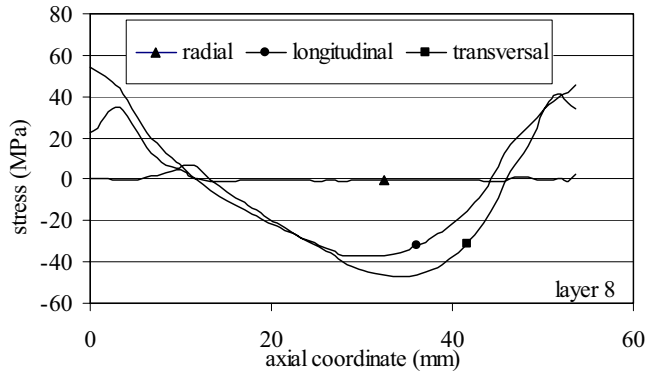

Figure 9 - Stress distribution on the internal surface of the shroud (layer 8).

The data show that the larger critical stresses occur at the regions where temperature values are relatively low. Due to this, assuming the maximum stress as failure criterion, the stresses are generally lower than the limit values. Only for shear, in some zones, the limiting strength is exceeded, especially on the external side of the shroud.

Conclusions

The possibility of substituting the metallic shroud of the first rotor stage in a gas turbine manufactured by NP with an analogous component made of CMC has been studied with a FEM model.
From analyses of thermal and structural results some comments can be made:
– If the shroud is not cooled, the temperature distribution is such that a large part of the component reaches a temperature higher than 1000°C, which can be considered the limit for avoiding creep problems.
– The maximum displacement in the radial direction is comparable to the clearance between shroud and buckets tips, so that a rubbing between these components can occur, especially during transients.
– Radial stresses are small and almost constant through the laminate. Axial stresses are mainly influenced by the thermal gradient, while hoop stresses depend on geometry too.
Stresses in the direction of fibres and normal to them can be compared with the limit values experimentally obtained, although they have been evaluated on samples of the selected

material, but with a $[0/90]_{6S}$ architecture. The stresses are high in the region of the constraints, where the temperature is low. Only for shear stress the limit is surpassed in some layer.
A solution can be the development of new materials with improved high-temperature properties. At the present stage it appears not to be convenient to replace the metallic shroud with a CMC component, although future developments are expected by work in this direction. The resulting values are not far from those of the metallic shroud, which has been developed and improved for years; moreover, the whole engine is not designed taking this specific CMC component into account. The employment of CMC components should thus correspond to a deep revision of the whole machine, in order to take advantage of the good qualities of the CMCs in a complete way.

Acknowledgements
This study has been partially performed within the framework of the R&D programme BRITE/EURAM, "Ceramic Components for Industrial Gas Turbines - CERCO" of the European Commission. The authors thank the other partners of this R&D programme: EADS/Dornier GmbH, JRC - Institute for Energy and University of Patras, Dept. of Mechanical Engineering and Aeronautics.

References

1. Lefebvre AH. Gas turbine combustion, Hemisphere Publ. Corporation, New York, 1993.
2. Holmquist M, Lundberg R, Sudre O, Razzell AG, Molliex L, Benoit J, Adlerborn J. Alumina/alumina composite with a porous zirconia interphase – Processing, properties and component testing. J. of European Ceramic Society 2000; 20: 599-606.
3. Evans AG, Naslain R, editors. High-temperature ceramic-matrix composites II: manufacturing and materials development. Ceramic Transaction 58, The American Ceramic Society, 1995.
4. Shi J, Andrew PD. Finite element modelling and analysis of a ceramic matrix composite combustor. J. Ceramic Eng. and Science Proceedings1998; 19 (4): 225-232.
5. Shi J, Andrew PD. CMC combustor with a thick thermal protection system - A detailed stress analysis. J. Ceramic Engineering and Science Proceedings 1999, 20 (4): 543-550.
6. Kozi N, Ken-Ichiroh I, Koji T, Takeshi S. Development of a combustor liner composed of ceramic matrix composite (CMC). 1998 Int. Gas Turbine & Aeroengine Congress & Exhibition Proceedings, Stockholm (Sweden). ASME Paper 98-GT-104, 1998.
7. Gottler RW, Hindman DL, DeBellis CL, Edwards MJ. Oxide-oxide continuous fiber ceramic composites for gas turbine applications. 1995 Int. Gas Turbine & Aeroengine Congress & Exposition Proceedings, Houston (USA). ASME Paper 95-GT-386, 1995.
8. Dean AJ, Corman GS, Bagepalli B, Luthra K, Di Mascio P, Orenstein R. Design and testing of CFCC shroud and combustor components. ASME Paper 99-GT-235, 1999.
9. Bresciani S, Citti P, Pecchioli M, Tognarelli M. Progetto di uno shroud in composito ceramico per turbina a gas: problematiche e criteri. XXIX AIAS Conf. Proceedings, Lucca (Italy). DMTI University of Florence, 2000, p. 925-934.
10. Corman GS, Dean AJ, Brabetz S, Brun MK, Luthra KL, Tognanelli L, Pecchioli M. Rig and engine testing of melt infiltrated ceramic composites for combustor and shroud applications. J. of Engineering for Gas Turbines and Power 2002; 124: 459-464.
11. Wilson DM, Visser LR. High performance oxide fibers for metal and ceramic composites. Composites – Part A: Applied Science and Manufacturing 2001, 32 (8): 1143-1153.
12. Mazdiyashi KS, Brown LM. Synthesis and mechanical properties of stoichiometric aluminium silicate (mullite). J. of the American Ceramic Society 1972; 55 (11): 548-552.
13. Innocenti M, Del Puglia P, Pappas YZ, Dassios CG, Steen M, Kostopoulos V, Vlachos D. Properties of oxide/oxide CMCs for high temperature applications in gas turbines, In: Leconte-Beckers J and al. editors. Materials for advanced power engineering 2002. Jülich: Forschungszentrum Jülich GmbH, 2002, p.769-780.
14. EADS/Dornier GmbH, Private communication.
15. Hottel HC. Radiant heat transmission. Chapter 4 of McAdams WH. Heat Transmission, 3rd edition, New York, McGraw-Hill, 1954, p.55-125.

Part II

Advanced Steam Turbine Materials

Invited Papers

THE EUROPEAN EFFORT IN DEVELOPMENT OF NEW HIGH TEMPERATURE ROTOR MATERIALS – COST 536

T.-U. Kern [1)], M. Staubli [2)], K.H. Mayer [3)], B. Donth [4)], G. Zeiler [5)], A. DiGianfrancesco [6)]

[1)] Siemens Power Generation, Muelheim/R, Germany [2)] Alstom Power, Baden, Switzerland
[3)] Alstom Power, Nuremberg, Germany [4)] Saarschmiede, Voelklingen, Germany
[5)] Boehler Schmiedetechnik, Kapfenberg, Austria [6)] CSM, Roma, Italy

Abstract

Improved ferritic-martensitic 9-12%Cr steels are under development worldwide. In COST 536 the European turbine manufacturers are aiming for development goals in terms of material properties, fabrication techniques (forging, casting, welding) and non-destructive examination for application temperatures up to 650°C.
First steps for improvements were made in the previous round COST 522 by defining several alloy types. Testing has shown that the most favourable outcome is a Cobalt-Boron containing steel without Tungsten, FB2. Three full-size trial rotors with this composition have been produced and are currently under long-term investigation. In COST 536 further trial melts have shown that there is a strong interaction between the whole processing route and the composition for the achievable property level. The role of Boron is now being looked at in more detail by varying the B/N ratios for Cr-contents of 10 to 11.5% having streamlined at the same time the chemical composition of the alloys. New strategies have been developed to widen up the window for a further increase of the application temperature to the desired 650°C.

Keywords: COST 536, 10Cr steels, high-temperature application, creep strength, material development

1 Introduction

Energy is the source of general well-being and the standard of living in each country. Energy production itself is faced with the introduction of increasingly stringent emission regulations to safeguard health and preserve the environment for future generations.

In the decades to follow, there will continue to be heavy reliance on fossil fuels, such as coal, oil and natural gas. Because the reserves of oil and natural gas are unlikely to be sufficient to satisfy fully the projected increased power demands, coal may be the only fuel available in substantial quantities around the world. This will force power plant utilities to increase the efficiency of their plants.

In the near future, the demand for coal-fired power plants will continue to expand due to the indigenous deposits of coal in large developing countries like India and China. In Europe coal or lignite will also play an important role in the foreseeable future.

The improvement in efficiency of modern steam power plants is related to raising the temperature as well as the pressure of the steam generated in the boiler. To withstand these advanced operating conditions, materials are required with improved high-temperature capability. In order to minimise investment costs (which also influence the effective cost of electricity generation), the greatest possible use must be made of martensitic steels for all major components in both the boiler and turbine. Specifically, steels of the 9 to 12%Cr class are required with high long term creep strength and oxidation resistance in steam, along with ease of fabrication for large forgings, castings and pipe sections.

This article describes the work performed in Europe within COST 536 to develop improved steels for large rotor forgings.

2 Rotor Materials Requirements

For power ranges up to 1,000MW, several basic steam turbine types with the following characteristics are possible:

- High pressure (HP) turbines with high temperature and pressure (≥ 530°C/180bar)
- Intermediate pressure (IP) with high temperature and reduced pressure (≥ 530°C/30bar)
- Low pressure (LP) turbines (≤ 350°C/10bar)

Combined HP-IP and IP-LP turbines for the smaller power range for Combined Cycle Power Plants (CCPP), in monoblock or welded rotor design, complete the solutions for power generation with steam turbines.

Specific design requirements have to be met by the materials in order to offer a certain flexibility to fulfil the various customer needs for the power plant.
The single components in steam power turbo-sets like rotors, casings, valves, bolts, blades and pipes are differently loaded. Therefore their property profiles also have to be specific.

The material properties of the steam turbine components under consideration take into account steam pressure and the surrounding medium. A short summary is given in *Tab. 1.*

Requirements	HP- & IP-Rotors	LP-Rotors, LP-Discs	HP- & IP-Casings	HP- & IP-Blades	LP-Blades	HP- & IP-Bolts
Static strength:						
tensile strength	●	●	●	●	●	●
Creep rupture strength:						
creep behaviour	●		●	●		●
Toughness:						
fracture toughness	●	●	●	●	●	●
Fatigue properties:						
Low cycle fatigue (LCF)	●	●	●	●	●	●
High cycle fatigue (HCF)	●	●		●	●	
Crack growth:						
static - Creep CG	●		●			●
alternating - Fatigue CG	●	●	●			●
Corrosion						
local corrosion		●		●	●	●
stress corrosion cracking		●			●	●
corrosion fatigue		●			●	
Erosion behaviour	●	●	●	●	●	
Oxidation behaviour	●		●	●		●

HP = High Pressure turbine IP = Intermedium Pressure turbine LP = Low Pressure turbine

Table 1: Design requirements and material properties for steam turbine components

As shown, the HP and IP rotor forgings, which can reach diameters of up to 1,200mm, need to be made in well-selected material in order to meet all property requirements.
The creep behaviour plays an important role for areas such as the rotor centre and the blade attachment, whereas the fatigue resistance is mainly considered in the surface regions.

A material class incorporating many advantageous properties was identified with the 9-12%CrMoV steels. They meet all boundary conditions relevant for a flexible design:

- A good through-hardenability up to 1,200mm diameter
- Balance between strength and toughness (short and long term)
- Weldability
- Potential for high oxidation resistance
- Lower cost than Austenites and Ni-base alloys
- Ease of fabrication

Their mechanical and physical property profile has enabled us to go for temperatures T≥600°C. The aim of material development in Europe, defined as follows, was met:

- 100,000 h creep rupture strength at 620°C/600°C of about 100 MPa
- Good creep rupture ductility (>10% elongation) and no notch sensitivity
- Through-hardening up to at least 1,200 mm diameter
- Minimum 0.2-yield strength of 600 or 700 MPa
- Other properties such as toughness and susceptibility to embrittlement should not be worse than with conventional 12%CrMoV and 1%CrMoV rotor steels

Details about the achievements are described in the following chapters.

3 Materials Development in Europe

In Europe the efforts to improve the available 9-12%CrMoV steels are concentrated in the COST programmes, starting with COST 501 in 1986 [1]. **COST** (**CO**-operation in **S**cience and **T**echnology) is a long-established European programme aimed at co-ordinating pre-competitive research activities in numerous areas of science and technology. Participants include turbine and boiler makers, manufacturers of forgings, castings, pipework and welding consumables, as well as testing institutes and utilities. The work has spanned the entire range, from basic research and development, through non-destructive and destructive testing of small experimental batches and large scale components, to standardization of specific steels and full-scale practical application in currently operating power plants.
Today there is established a strong trans-European network in this field running now the 4th action: COST 536 (2004-2009). The effectiveness of the past COST actions is exemplified by the introduction of newly developed martensitic steels for forgings, castings and pipework from the COST 501 and COST 522 actions, "Materials for Power Engineering." These improved steels are in commercial operation in advanced European power stations and have made it possible to increase the operating steam temperatures from widely known 530-565°C up to 580-610°C with a corresponding increase in thermal efficiency.

The outcome of the previous round, COST 522, is the demonstration of the manufacturability of large rotor forgings in the highest potential alloy for 625°C application. It is a 9Cr-1Mo-1Co-100ppm Boron type material tested first with a 500kg trial melt up to currently 72,000 h.
As designation the name FB2 is currently used to describe the new material.
After having determined the long-term stability of toughness and strength of the trial melt FB2 after exposure at 600°C and 650°C, it was shown that the behaviour is better than for

conventional 12%Cr steel at 530°C [2]. Therefore the decision was confirmed to start the production of large scale prototype rotor forgings in this alloy composition.

Trial rotor forgings in FB2

Three trial rotor forgings have been manufactured in Europe. The forgemasters Boehler Kapfenberg/Austria, Saarschmiede/Germany and Societa delle Fucine, Terni/Italy, started with the same material specification but have followed different steelmaking routes.

Boehler/Austria has used a 29to ingot made by Boehler-BEST, a pouring process with special measures to improve the homogeneity of the ingot [3].
SdF Terni/Italy has applied the steelmaking process VCD with an ingot weight of 53to.
Saarschmiede/Germany have used their wide experience in ESR melting practice by making an ingot of 56to weight.

An impression of the manufacturing and a summary of the main prototype rotor dimensions are given in *Fig. 1* and *Fig. 2*.

Fig. 1: COST trial rotor forging FB2 made by Saarschmiede, Germany

Heat treatment parameters have been chosen to fulfil strength requirements of 0.2YS(RT) >700MPa. The heat treatment conditions used for final quality heat treatment are given below. The double-tempering applied already for the 600°C alloys of the COST material family was again applied to ensure a fully tempered martensitic microstructure.

- Austenitizing: 1,100°C/ 10h/ water-air spraying (Boehler)
  1,100°C/ 17h/ oil (SdF Terni)
  1,100°C/ 16h/ water spraying (Saarschmiede)
- 1st Tempering: 590°C/ 22h/ air (Boehler)
  570°C/ 24h/ air (SdF Terni)
  570°C/ 22h/ air (Saarschmiede)
- 2nd Tempering: 700°C/ 22h/ air (Boehler)
  700°C/ 24h/ air (SdF Terni)
  700°C/ 22h/ air (Saarschmiede)

The NDT results show a minimum detectable flaw size of 1.5-2.0mm for the rotor body location. These results are within the expected range and ensure the application for the practice, see *Fig. 3.*

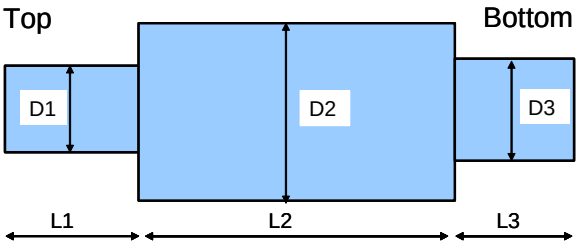

Forge-master	Process	D1 mm	D2 mm	D3 mm	L1 mm	L2 mm	L3 mm
Boehler/A	BEST	770	1180	865	1350	930	1110
Terni/I	EAF+ ASEA	925	1110	790	800	2750	830
Saarschm/ D	ESR	800	1215	1050	1085	2130	800

Fig. 2: COST trial rotor forgings in FB2, dimensions

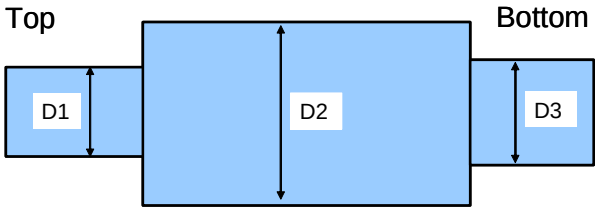

Forgemaster	Process	D1 mm	D1-MDFS 2MHz mm	D2 mm	D2-MDFS 2MHz mm	D3 mm	D3-MDFS 2MHz mm
Boehler/A	BEST	770	1,2	1180	1,8	865	1,3
Terni/I	EAF+ ASEA	925	1,0	1110	1,5	790	1,5
Saarschm./D	ESU	800	1,5	1215	2,0	1050	1,7

MDFS - Minimal Detectable Flaw Size

Fig. 3: COST trial rotor forgings in FB2, NDT results

The quality of the rotor forgings was inspected by determining the basic strength and toughness values at different positions showing the homogeneity in different former ingot locations (top, middle, bottom of ingot) and from surface to centre. As an example, the data for the Saarschmiede rotor are given in *Fig. 4.*

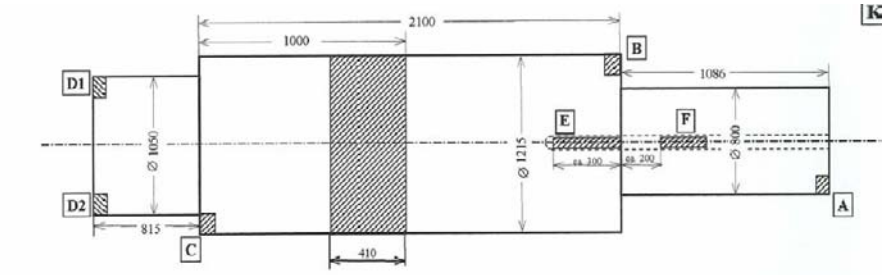

		A	B	C	D1	D2	E	F
0.2 YS [MPa]	RT	722	720	710	718	726	710	710
	625°C	403	392	395	393		396	395
UTS [MPa]	RT	855	846	840	849	860	843	849
	625°C	473	464	463	464		465	467
EL [%]	RT	15,0	15,0	16,0	15,0	15,0	12,5	10,0
	625°C	25,3	26,7	26,0	28,7		22,5	23,0
RA [%]	RT	55,1	56,4	56,4	55,1	53,8	45,3	32,5
	625°C	84,7	83,8	82,1	82,5		70,5	67,4
Impact [J]	RT	35, 27, 26 **29**	37, 36, 35 36	48, 42, 29 **40**	19, 28, 18 **22**	26, 18, 27 **24**	32, 23, 33 **29**	25, 21, 27, 22 **24**
FATT [°C]		51	47	40	50	60	58	40
grain size ASTM		00-2	00-2	00-2	00-2		< 00 = 70%, > 00-2 = 30%	
microstructure		100% martensite						

Fig. 4: Mechanical properties at different positions of trial rotor FB2-Saarschmiede

Today the long-term creep strength determination of the trial rotor forgings is ongoing. Maximum testing times achieved so far are 25,000 h. The results show that all three rotor forgings confirm the behaviour of the 500kg trial melt, as in *Fig. 5*.

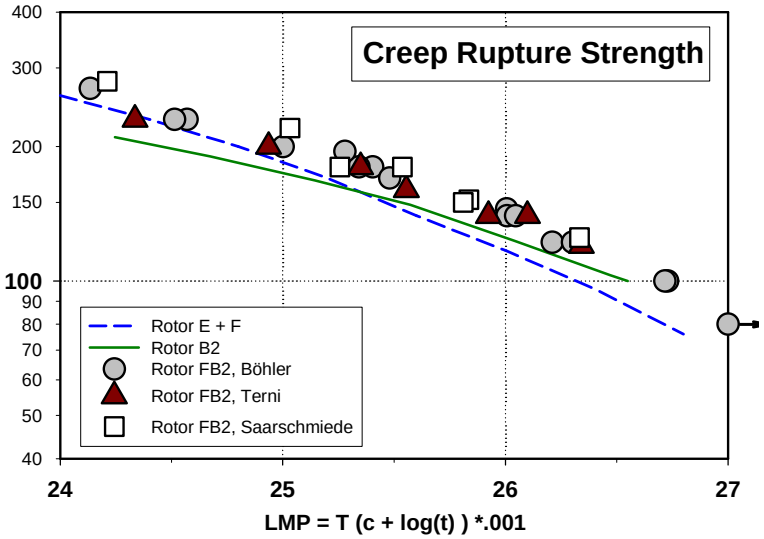

Fig. 5: COST trial rotor forgings FB2, long term creep strength in Larson-Miller plot, position middle of ingot, surface

For comparison, the reference lines are given for the 600°C materials COST Rotor-E (10Cr-1Mo-1W) and COST Rotor-F (10Cr-1,5Mo) together with the line of material B2. Alloy B2 of COST 501 containing 0,18C-1,5Mo-100ppm Boron was the benchmark for further improvements of 9-10%Cr steels. The results show that the FB2 rotor forging data are well above the reference lines offering therefore improved creep rupture strength values for the high temperature design. The rupture ductility is still kept on a high level, which means that notch weakening effects can be excluded.
Other properties like high temperature strength, toughness, Low Cycle Fatigue strength, and fracture toughness are not much different to the known range of 9-12%Cr steels. No changes in design rules have to be made by applying this material.
To summarize, it can be stated that with the chosen balance in chemical composition and the applied manufacturing processes the requirements for high temperature rotor forgings up to 620°C application are well fulfilled.

Materials for Application at Temperatures above 625°C

The improvement of the ferritic-martensitic grades is necessary with respect to creep strength but bearing in mind the increased oxidation occurring at this temperature level.
Experience has shown that steels with higher microstructure stability also show higher long-term creep strength. The further development work was based on the knowledge acquired under the COST 501 and COST 522 programmes, especially the intensive microstructure investigations, the commercially available computing tools such as ThermoCalc and Dictra, the newly developed calculation methods of the equilibrium transformation temperature, and the diffusion parameters of potential candidate test materials.
On the basis of the promising composition FB2, modifications were made in the C-, Cr-, Co-contents and by the addition of W in some cases. Seven trial melts of approx. 150kg and two up-scaled melts of 1,000kg have been produced [4]. The composition ranges investigated are as follows:

- C 0.12 – 0.18%
- Cr 9.9 – 11.2%
- Mo 0.9 – 1.5%
- Co 2.8 – 6.0%
- B 70 – 100ppm
- N 130 – 300ppm
- Ni < 0.20%, Nb 0.06-0.08%, V 0.19-0.22%

Different heat treatments have been carried out to investigate the influence of the austenitizing temperature on the long term properties.
Unfortunately, none of the new melts offers a clear improved behaviour compared to melt FB2. Also the potential of improved oxidation resistance can not compensate the disadvantages in creep compared to the COST 600°C materials. The increased costs caused by the Co-contents above 2.8% play a further detrimental role and provide another reason not to pursue this development path.
Nevertheless, interesting results have been generated concerning the influence of austenitizing temperature and the question of increased Co-content.
As an example, the creep behaviour of the melt FB8 in the conditions 1,080°C and 1,120°C followed by tempering at 570°C/720°C is shown in *Fig. 6.* Details of the chemical composition are given in *Tab. 2.*

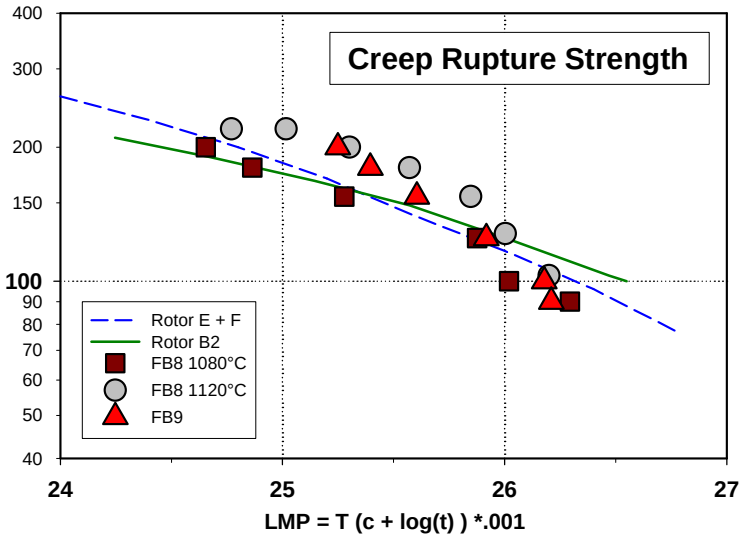

Fig. 6: Creep rupture strength of the COST 522 alloy FB8 and high Co-alloy FB9

Trial Melt	**C**	**Cr**	**Mn**	**Mo**	**Ni**	**B** ppm	**Co**	**N**	**Nb**	**V**
FB 8	0.17	11.1	0.09	1.46	0.20	100	2.94	0.023	0.07	0.21
FB 9	0.18	11.0	0.08	1.48	0.13	90	6.03	0.017	0.06	0.20

Table 2: Product analysis of forged 650°C trial melts in COST 522, in wt%

The data make clear that a higher austenitizing temperature can increase the creep rupture strength for a certain time. Unfortunately, the main microstructure feature of the alloy, meaning the strength stabilizing effects for long term application, have not been affected very much. After about 10,000 h at 625°C, the advantage in creep strength begins to be lost. The alloy FB8 used here seems not to be well balanced in view of the higher Cr-content which was chosen for an improved oxidation resistance. Conclusions have been drawn to use this knowledge for the development work ongoing.
The influence of a higher Co-content of about 6% was investigated with the alloy FB9. The applied quality heat treatment of 1,100°C/570°C/720°C fits with the other alloys. After showing a high strength behaviour at shorter testing times, the rupture times are shifted to shorter values undercutting later on the reference lines of the COST 600°C-materials Rotor-E&Rotor-F and the high Boron alloy of COST 501, material B2 (100ppm Boron).
The main conclusion drawn was not to continue with this chemical balance. The data have been used to sharpen the microstructure modelling tools.
The knowledge and experience gained with the new alloy types underlines the findings that the further increase of the application temperature above 620/630°C for ferritic-martensitic steels has become problematic, thus making it clear that the limit could be near.

The achieved complexity in composition, element balance, melting route, forging procedure and heat treatment of these 9-11%CrMoV alloys is forcing current endeavours to review the design philosophy.
The heat treatment has to be regarded in its entirety, starting from the first stages of the forging process, including preliminary and quality heat treatment.

The decision made by the COST group was to leave within the work package 1 (WP-1) the issue of highest complex alloy types and continue employing already proven alloying elements like C, Cr, Mo, B, N, V and Nb. Based on the composition of former high Boron steels of COST 501 (melts B0 and B2, [5]) and the Japanese TAF steel with about 300-400ppm Boron (known for its high long term creep strength but showing disadvantages in its manufacturability), new ideas have been created. Seven 150kg trial melts have been produced by Saarschmiede. The details of the analysis are given in *Tab. 3*. Apart from an improved creep strength, the manufacturability is also the focus of the work now. The question of which Boron level and which balance in composition still result in a comparable level of strength like the original TAF steel has to be solved.

Melt	**C**	**Si**	**Mn**	**Cr**	**Mo**	**Ni**	**V**	**Nb**	**N**	**B** ppm	**B / N**
B0[*)]	*0.10*	*0.18*	*0.55*	*9.21*	*1.50*	*0.11*	*0.23*	*0.063*	*0.0200*	*180*	*0.900*
B2[*)]	*0.17*	*0.08*	*0.06*	*9.34*	*1.55*	*0.12*	*0.27*	*0.064*	*0.0150*	*100*	*0.667*
FT 1	0.21	0.31	1.02	10.0	1.49	0.12	0.28	0.063	0.0195	98	0.502
FT 2	0.21	0.29	1.04	10.0	1.50	0.13	0.27	0.067	0.0181	180	0.994
FT 3	0.21	0.29	1.02	9.9	1.50	0.11	0.27	0.070	0.0192	275	1.432
FT 4	0.21	0.29	0.92	11.5	1.54	0.11	0.27	0.055	0.0187	80	0.428
FT 5	0.20	0.27	1.00	11.4	1.49	0.10	0.33	0.067	0.0230	182	0.791
FT 6	0.19	0.29	0.98	11.4	1.49	0.12	0.28	0.067	0.0292	200	0.685
FT 7	0.19	0.28	1.01	11.3	1.47	0.11	0.28	0.064	0.0320	252	0.787

Table 3: Trial melts with a streamlined chemical analysis, wt% ([*)] from COST 501 [5])

Compared to the other COST alloys, some major changes have been made:

- higher C-content of about 0.20%
- influence of higher Cr-contents of 10.0 to 11.5% for oxidation reasons
- Si increased to 0.30% for oxidation reasons
- low Ni-contents compensated by a higher Mn-content
- different ratios of Nitrogen to Boron at different Cr-levels ranging from 0.5 to 1.4 for 10%Cr and 0.4 to 0.8 at 11.5%Cr

For the heat treatment a compromise was looked for to get a stable microstructure already at the beginning with a sufficiently high static strength. Heat treatment tests have shown that the preferred annealing range of Ta = 720-740°C has resulted in 0.2YS values lower than 600MPa at RT. Therefore the following heat treatment parameters have been used at first for the quality heat treatment no 1: 1,100°C/oil + 570°C/air + 700°C/air.

The achieved acceptable strength level was in the range of 0.2YS = 635 – 704 MPa, as in *Tab. 4*.

Melt	0.2YS (MPa)	UTS (MPa)	Elongation (%)	Red of Area (%)
FT 1	635	843	17	62
FT 2	650	850	17	62.5
FT 3	654	854	17	59
FT 4	704	908	15.5	58
FT 5	703	893	15	58.6
FT 6	702	890	15	55.5
FT 7	696	885	15.5	56.2

Table 4: Trial melts in COST 536, tensile test results at RT

Based on the experience in former COST rounds, the influence of Boron on the manufacturability was investigated with two alloys, as shown in *Fig. 7*. It became clear again that critical Boron contents reduce the forgeability in such a way that above a border temperature brittle behaviour is observed. Manufacturing these high Boron containing steels means that the number of forging cycles has to be increased and/or higher press forces are required.

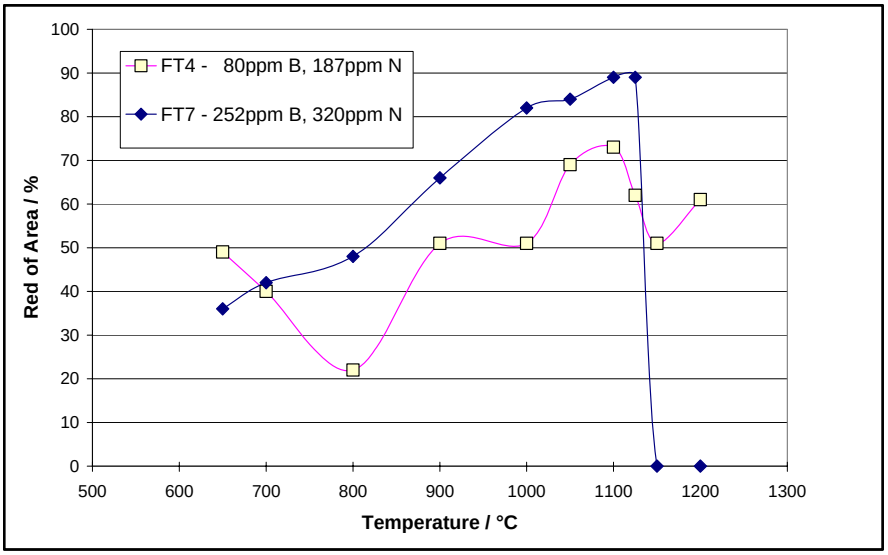

Fig. 7: Simulation test for the forgeability, melts FT4 and FT7

The creep testing has been started recently. First results show that the expected level of creep strength at 650°C can not be reached with the heat treatment no 1. Even with the highest

Boron levels of 250ppm, the reference lines of Rotor B2 of COST 501 and of TAF steel can not be reached, as in *Fig. 8*. Results indicate that with the chosen chemistry and heat treatment the behaviour does not exceed the LMP-line of the 600°C-alloy COST Rotor-F without Boron (10Cr-1.5Mo-VNbN, [1]).

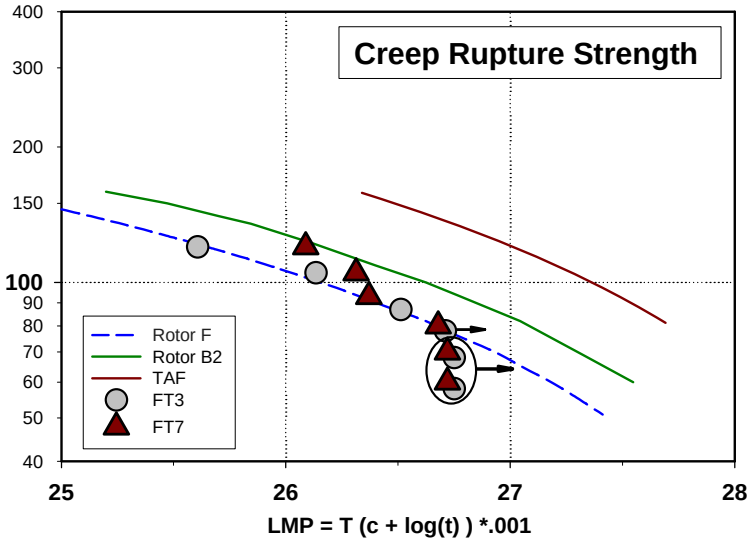

Fig. 8: Creep strength behaviour of COST 536 alloys, type FT3 and FT7

As one reason, the available Boron content in connection with the Nitrogen and Molybdenum level was identified. Detailed analyses are ongoing.
In the next step, a higher austenitizing temperature was used with >1,100°C. Currently running tests are offering improvements in creep elongation limits and creep rupture strength. A final conclusion can not be made yet, but the data points show a tendency to have fracture times above the FB2 reference line.

A second work package (WP-2) is currently dealing with improvements in the FB2 composition of COST 522 [4]. The role of B/N ratio is being studied now. For the successful FB2-composition the B/N ratio is 0.45. Six new trial melts have been set up with B/N ratios of 0.75 to 3.0. In addition, the Si content was increased for improvements in steam oxidation behaviour. The testing will start shortly.

A third work package (WP-3) is working on the role of Tantalum, Copper, Zirconium, Boron and Nitrogen. The B/N ratios cover a range of 1.0 to 2.0. The main goal is

- to stabilize the carbide structure
- to increase the amount of MX particles and improve their localisation and distribution
- to avoid Z-phase precipitation or its fast growing

Trial melt production has been started.

4 Future work

The running work packages WP-1 to WP-3 will be continued. Intensive microstructure investigations are accompanying the ongoing tests and will sharpen the modeling tools. The influence of heat treatment parameters will be covered in a fourth work package WP-4. The manufacturing of a full size 20to rotor forging with streamlined chemical composition has been started in work package WP-5. These two packages are closely linked to each other. The influence of preliminary heat treatment on the results of NDT, such as detectable defect size and sound attenuation, and on creep behavior are going to be investigated.

5 Summary and Conclusions

- After identifying a potential alloy composition for 620°C application, three full-size prototype rotor forgings with different steelmaking routes have been manufactured in Europe. The creep results with currently 25,000 h show that the transformation from the trial melt to the rotor forgings was performed successfully.
- Based on microstructure investigations and modern modelling tools, a series of new compositions was designed. Different steps and investigations have been made resulting in new knowledge about the role of preliminary and final heat treatment parameters as well as the influence of the Boron-Nitrogen ratio.
- The work of COST 536 is continuing in the five work packages WP-1 to WP-5 covering the role of chemical composition, heat treatment, trial rotor production and factors influencing NDT results.

6 Acknowledgements

The authors are grateful to their colleagues and partners in the program for their contributions and many discussions during the course of this endeavour. Many thanks are also extended to the COST Management Committee for their guidance in the program and to the national funding bodies for their financial support of the individual national projects.

7 References

[1] Berger C., Scarlin R.B., Mayer K.H., Thornton D.V., Beech S.M.:
Steam Turbine Materials: High Temperature Forgings,
5th Liège COST Conference, 03.-06. October 1994, Liège, Belgium.

[2] Kern T.-U., Cerjak H., Mayer K.H, Staubli M., Vanstone R.:
Development and Qualification of Rotor Steels for 600 to 650°C Application in COST501/ COST522,
14th Intern. Forgemasters Meeting, 03.-08. September 2000, Wiesbaden, Germany.

[3] Meyer W., Zeiler G., Bauer R.:
Recent Developments on 9 to 12 Chromium Steels Open Die Forgings for Steam and Gas Turbine Applications at Boehler,
14th Intern. Forgemasters Meeting, 03.-08. September 2000, Wiesbaden, Germany.

[4] Kern T.-U., Staubli M., Mayer K.H., Escher K., Zeiler G.:
The European Efforts in Development of New High Temperature Rotor Materials up to 650°C - COST522,
7th COST Conference, 30 Sept -02 Oct 2002, Liége, Belgium.

[5] Berger C., Vanstone R.: Development of 9-12%Cr Steels for Rotor Forgings – COST501/II, 11th Intern. Forgemasters Meeting, 10-12 June 1991, Sheffield, UK.

THE EUROPEAN EFFORTS IN DEVELOPMENT OF NEW HIGH TEMPERATURE CASING MATERIALS – COST 536

M. Staubli[1)], R. Hanus[2)], T. Weber[3)], K-H. Mayer[4)], T-U.Kern[5)]

1) Alstom Switzerland, Baden, Switzerland
2) Voestalpine Giesserei Linz GmbH, Austria
3) PHB Stahlguss, St-Ingbert-Rohrbach, Germany
4) Retired from Alstom Power, Nuernberg, Germany
5) Siemens Power Generation, Muelheim/R, Germany

Abstract

Fossil fuels like lignite and hard coal are expected to stay available in sufficient quantities for quite a long period. Therefore a significant share of energy production worldwide will be based on these fuels in the coming decades. However, the increase in fuel costs on one side and the required limitation of CO_2 emissions on the other side, lead to a strong pressure to make the best use possible of these fuels. With respect to steam power plants this means to increase the efficiency and bring the temperature and pressure parameters to its limits.
Today's state of the art for large fossil-fired steam turbines comprises ultrasupercritical (USC) steam parameters with live steam conditions of up to 600°C/300bar and re-heat temperatures of up to 620°C. These conditions significantly increase the plant efficiency.
The class of the 9-12% Cr steels is currently used for the critical components in such plants since the demand for high operational flexibility of large units requires ferritic materials due to their physical properties.
The COST action " **A**lloy development for **C**ritical **C**omponents of **E**nvironmental friendly **P**ower plan**T**" (ACCEPT, COST536) aims for the further development of these steels with respect to their creep properties but also their steam oxidation resistance.
One of the COST536 working groups is dealing with cast alloys since cast parts such as casings and valves are critical components in USC HP and IP turbines. The development and evaluation of new cast steels from trial melts to pilot components is demonstrated, and the extended investigation of production parts is reported.
A major further step in efficiency requires material suitable up to 700°C and above i.e. the use of Ni-based alloys. These alloys are not included in the scope of COST536. However, there is a strong interest to explore the property limitations of ferritic-martensitic materials in order to keep the amount of expensive alloys in such a ultra high temperature plant at a low level.
To complete the investigations of the cast base materials, similar and dissimilar welds are also included in the action. Matching filler metals and welding procedures are under development for the promising new cast steels, and the related crossweld properties are reviewed.

Keywords: 9%Cr cast steel, creep resistance, experience, application, weldability, COST536

1. Introduction

Fossil fired steam power plants produce some 40% of power worldwide; coal therefore will remain a major backbone of power generation for coming decades. The increasing fuel costs will even strengthen this position. The demand for lower production costs on the one hand and reduced noxious emissions on the other hand is the driving force for utilities to increase the efficiency of their plants. This is not only considered for new plants to cover increasing demands but also for the up-grading or replacement of existing older plants.
Ultrasupercritical (USC) steam conditions are the main key to increased efficiency of steam turbine power plants. An increase from 540°C/180bar in a conventional single reheat power plant up to steam parameters of 600°C/600°C/300bar provides savings of approximately 8% in the heat rate and a corresponding CO_2 reduction. If the steam temperature is further

increased to about 650°C, the heat rate is reduced by more than 10% ensuring even lower CO_2 emission and fuel consumption [1].
An increase in efficiency from ca. 47% to ca. 55% is expected if steam temperatures are brought up to 700°C leading to a reduction of CO_2 emission and fuel consumption of approximately 15%. However, these conditions will require the use of nickel-base materials for a major part of critical components. A temperature of 700°C definitely is outside the application range of ferritic-martensitic steels with respect to their steam oxidation resistance and also their creep strength [2].
The COST programmes are focused on high Cr ferritic-martensitic steels although austenitic materials that meet the requirements for 650°C steam temperature are known.
Experience with austenitics gained in the 60's were unsatisfactory. Due to their physical properties, such as thermal expansion and thermal conductivity, mainly the thick-walled austenitic components suffered from LCF at high temperatures and frequent start-up procedures.

2. International Test Programmes

2.1. Research Programmes in Japan

The long-term research programmes initiated and supported by EPDC (1981-1993) led to a number of new steels with improved creep properties at 600°C and above. A number of USC power plants have been commissioned in Japan using these new materials. The most advanced steam parameters currently used are 605°C/613°C/280bar in the 600MW ISOGO 1 power station. However the target of the EPDC project 1994-2000 was set to 630°C/300bar, and material tests for steam parameters up to 650°C/350bar are currently being carried out.
Research activities for 700°C USC plants have been started (EPDC feasibility study 2000-2002; JSME, 700°C USC project, started 2005). Various industrial partners are involved in R&D of 700°C USC materials including large components in alloy 617, new Ni-based alloys such as LTES700 or FENIX-700 but also the evaluation of modified austenitic steels such as HR6W. [3, 4].

2.2. Research Programmes in the U.S.

The EPRI projects in the US (Projects 1403-15 & 23; 1986-2000) were focused on the development of materials for turbine and boiler components for 1100°F steam plants and in the Projects 1403-50/WO9000-38 the steels HCM12A/P122, NF616/P92 and TB12M were validated. The advanced 9% Cr cast steel (cast version of P91) for large steam turbine components was developed and qualified within the Projects 1403-15 & 23 [5, 6].
DOE Vision 21 project, started in 2002, is targeting USC conditions up to 760°C/760°C/380bar. The focus again has first been on thickwalled components for boiler application [3].

2.3. Research Programmes in Europe

The European activities were concentrated in the COST programmes (COST501: 1986-1997, COST522: 1998-2003). The target steam temperature was increased from initially 600°C to 620°C and then up to 650°C in the course of the programmes. The collaborative effort of a large number of partners (suppliers, manufacturers, utilities and institutes) from 15 European countries led to the qualification of various ferritic steels for forgings, castings and pipework. These steels are commercially in operation in advanced European power stations [7]. The current COST action " **A**lloy development for **C**ritical **C**omponents of **E**nvironmental friendly **P**ower plan**T**" (ACCEPT, COST536, 2004-2009) aims for the further development of these steels with respect to their creep properties but also their steam oxidation resistance. In order

to meet the common requirements with respect to steam parameters for turbine and boiler application, new materials were developed and evaluated in close collaboration between the turbine and boiler sub-groups. The current COST536 programme is also restricted to the development of improved steels as in the previous COST programmes.
The materials for USC conditions of up to 700°C are also dealt with in a number of European projects as listed in Table 1 [8].

AD700/THERMIE	1998-2005 (2013)	Development of materials for 700/720°C, concepts, demo-plant
MARCKO 700	2004-2008	Boiler material development for up to 700/720°C
COMTES 700 E max	2004-2010	Production and testing of components up to 705°C; service experience with test valve at 705°C; Power plant with 700°C/720°C/350bar condition
Operation of test rigs	2004-2008/2010	Service experience for tube materials up to 720°C

Table 1 Important European projects in developing the 700°C power plant

3. Experience with Advanced Cast Ferritic Steels

The contemporary programmes EPRI 1403-15 and COST501 resulted in the development and qualification of the two cast steel grades GX12CrMoVNbN9-1 (cast P91) and GX12CrMoWVNbN10-1-1 [9]. Conclusions from these investigations are:

- Both new cast materials have about the same long-term creep rupture strength at 600°C independent of W-addition or differences in heat treatment
- As compared to conventional cast steel grades such as 1CrMoV (G17CrMoV5-10) and 12CrMoV (GX23CrMoV12-1 / EN10213) a significant improvement in creep strength is reached corresponding to an increase of the application temperature of 30 to 50°C.
- With respect to impact energy, the new W-bearing cast steel GX12CrMoWVNbN10-1-1 is comparable to the widely used GX22CrMoV12-1. The toughness of the W-free steel GX12CrMoVNbN9-1 is considerably higher and exceeds the values of the low alloyed cast steel G17CrMoV5-10.
- The higher creep strength of the new cast steel grades is not accompanied by a lower fracture toughness or by reduced low cycle fatigue strength.

The above programmes included the following development steps:

- Selection of new compositions based on the experience of existing materials and on results of advanced thermodynamic calculation tools
- Production of selected trial melts to identify promising candidate materials by means of mechanical properties, physical properties and manufacturability
- Upscaling for promising materials up to real size pilot components to investigate the influence of production route, size effects, heat treatment effects, quality assurance issues
- Investigation of production parts in order to investigate the scatter in properties due to various production technologies, different suppliers, size and shape of products, variation of chemical composition within the specification, etc.

In each of the above project a full size valve body was investigated. The typical compositions of the two new cast alloys GX12CrMoVNbN9-1 and GX12CrMoWVNbN10-1-1 are given in Table 2 for these two valve bodies.
The benefit of long-term programmes such as the consecutive COST programmes is demonstrated in Figure 1. This figure shows the recently completed creep tests for the valve body in alloy GX12CrMoWVNbN10-1-1. Creep tests in the temperature range 500°C to 650°C have reached maximal duration of >93,600 hours and a total test duration of >98 years has been accumulated!

	C	Mn	Cr	Ni	Mo	V	Nb	N	W
GX12CrMoVNbN9-1	0.10	0.50	9.25	0.12	0.92	0.22	0.068	0.048	0
GX12CrMoWVNbN10-1-1	0.12	0.62	10.51	0.93	0.99	0.22	0.080	0.048	0.99

Table2 Compositions (wt%) of the two valves tested in EPRI1403 and COST501 (wt%)

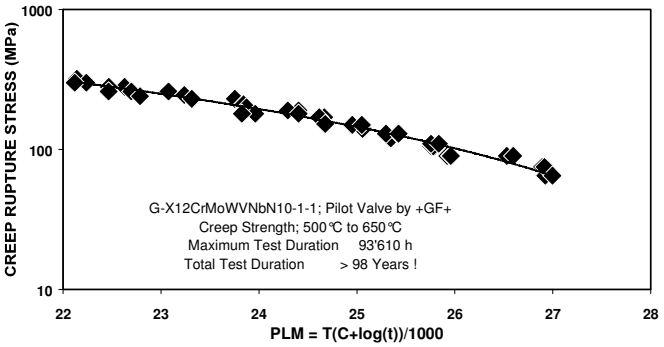

Figure 1
Long-term creep strength of valve body in alloy GX12CrMoWVNbN10-1-1

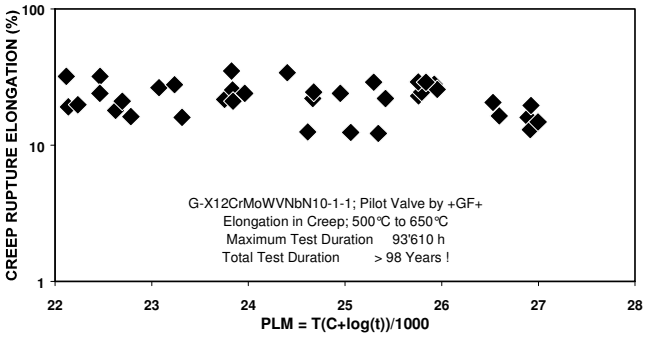

Figure 2
Elongation in long-term creep of valve body in alloy GX12CrMoWVNbN10-1-1

Despite the very long rupture time, the cast alloy GX12CrMoWVNbN10-1-1 exhibits elongation values which do not fall below 10% as shown in Figure 2.
These two new cast steels are meanwhile applied in a series of new European power plants running at elevated steam parameters. The experience the manufacturers of these components have gained sofar is very positive. The acceptance of the new cast steels is demonstrated by the large number of manufactured and installed power plant components not only for steam turbines but also in other turbine applications [10,11].

In order to confirm the long-term properties of these two new steel grades and to establish a comprehensive database for these materials, a programme was launched with the support of VGB in Germany involving the investigation of commercial cast components (Programme No.158). Here 16 castings with weight up to 41t in grades GX12CrMoVNbN9-1 and GX12CrMoWVNbN10-1-1 were produced by different suppliers including the use of different production routes [12, 13]. Since creep is the most important test within the VGB programme, only the current status of these tests at 600°C with durations up to >65,000h is given in Figure 3 for the two alloys GX12CrMoVNbN9-1 and GX12CrMoWVNbN10-1-1.

For both cast steel grades, the results available from these production components confirm the excellent properties measured earlier on the two pilot valves.
However the W-free steel GX12CrMoVNbN9-1 shows a larger scatter reflecting more variation in suppliers and production routes involved. The comparability of the creep strength for both cast steel grades at 600°C/100,000h is confirmed.

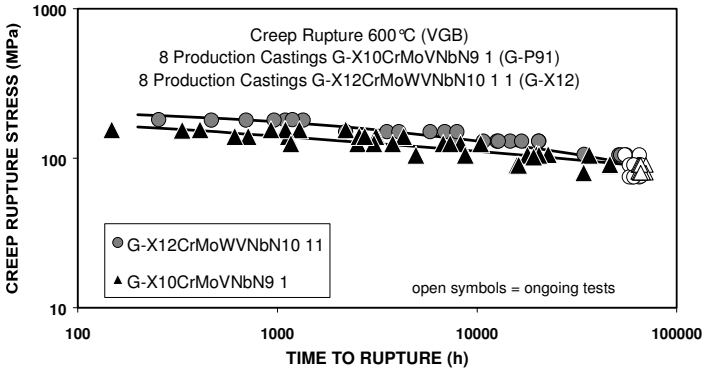

Figure 3
Long-term creep tests at 600°C for new cast alloys within the VGB programme No.158

4. Development of Cast Steels for Application beyond 600°C

4.1 Production and investigation of experimental melts

The target steam inlet temperature of up to 650°C should be reached through the use of ferritic-martensitic steels in order to allow a flexible operating mode in medium-load and peak-load operation of these power plants. Therefore a further improvement of the cast ferritic-martensitic grades is seen to be necessary not only with respect to creep strength but also under consideration of the increased oxidation occurring at this temperature level.
The development work is based on the knowledge previously acquired especially the intensive microstructural investigations, on the commercially available computing tools such as ThermoCalc and Dictra, and on the calculation methods of the equilibrium transformation temperature and diffusion parameters [14,15,16]. The alloy design concept for the modification of cast steels have included:

- Variation of Cr content; improve the steam oxidation behavior
- Limitation of Ni content; improve creep strength
- Addition of Co to avoid formation of delta ferrite; compensate for low Ni content
- Addition of B (with modifying simultaneously the N content); improve creep behavior
- Variation of W content (corresponding modification of Mo); stability and creep strength
- Balancing of the proven elements such as C, Mo, V, Nb, N, B; stability and creep strength

In two steps, totally 11 different trial melts were cast in the form of plates (up to 200mm thick) and 5t stepped blocks (up to 500mm thick) and were subject to large test programmes. These compositions and the corresponding product forms are given in Table 3.
For the trial melts from the first step, creep tests have reached >85,000h; the results are shown in Figure 4. Only two alloys i.e. CB2 and CD2 exhibited higher creep strength than GX12CrMoWVNbN10-1-1. Since the composition of CD2 is close to P92 (except the Co-content), the creep strength of CD2 and CB2 is also compared with the mean value of pipe material P92 according to the evaluation by ECCC (Figure 5). Despite the nearly matching composition, CD2 is not reaching the creep strength of P92 probably due to the different

production route of a thick wall cast component. At lower stresses (or higher temperatures) alloy CB2 is in line with the mean value of P92. It was concluded, that CB2 is the most promising composition from the creep strength point of view. The improvement in creep strength over the grades GX10CrMoVNbN9-1 and GX12CrMoWVNbN10-1-1 is significant and corresponds to another increase of the application temperature of 20-25°C. However the Cr-content of only 9.2% in CB2 was considered improveable to meet the required steam oxidation resistance at temperatures above 600°C.

Alloy	Product	C	Mn	Cr	W	Mo	Co	Ni	V	Nb	N	B(ppm)
Step 1 / Trial melts investigated in COST 501												
CB1	Block	0.12	0.94	9.42	-	1.50	0.93	0.14	0.24	0.08	0.02	40
CB2	Plate	0.12	0.88	9.20	-	1.49	0.98	0.17	0.21	0.06	0.02	110
CD2	Block	0.06	0.88	9.54	1.94	0.43	1.07	0.10	0.21	0.04	0.045	40
CE2	Plate	0.11	0.86	9.39	0.97	0.98	1.52	0.15	0.22	0.05	0.05	-
CF2	Block	0.10	0.77	9.60	-	1.32	0.93	0.22	0.23	0.06	0.04	-
Step 2 / Trial melts investigated in COST 522												
CB5	Plate	0.13	0.20	10.1	-	1.58	2.90	0.16	0.20	0.063	0.035	110
CB6	Plate	0.13	0.19	10.9	-	1.57	2.90	0.15	0.20	0.065	0.025	109
CB8	Plate	0.17	0.20	10.85	-	1.54	2.90	0.16	0.21	0.065	0.025	103
CB9	Plate	0.17	0.19	10.9	-	1.66	5.85	0.16	0.20	0.063	0.022	108
CB10	Block	0.13	0.25	10.24	0.41	0.91	3.14	0.16	0.22	0.058	0.023	84
CB11	Block	0.17	0.17	10.71	0.38	0.84	2.85	0.20	0.22	0.054	0.031	120

Table3 Compositions of the 11 trial cast melts produced for application beyond 600°C (wt%)

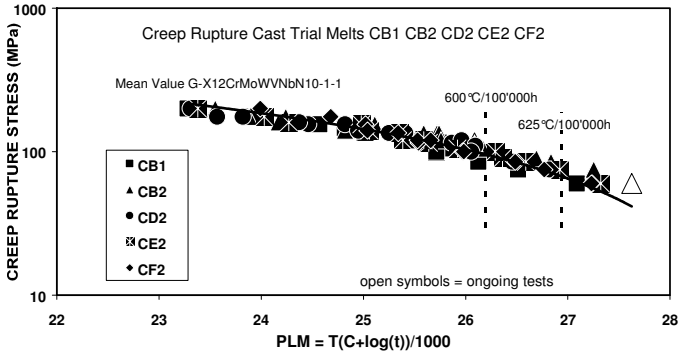

Figure 4
Creep strength of trial melts vs. mean value of GX12CrMoWVNbN10-1-1

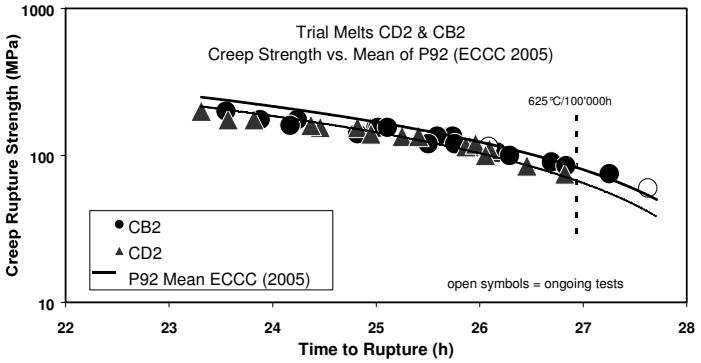

Figure 5
Comparison of creep strength; trial melts CD2 & CB2 vs. mean value of P92 pipe material according to the evaluation by ECCC (2005)

Therefore, the 2nd step included trial melts based on the promising CB2 composition but with higher Cr-contents. The related creep tests have reached >52,000h and some tests are still ongoing. However, Figure 6 shows no significant advantage over CB2 at 625°C for any of these higher Cr & high Co alloyed trial melts due to precipitation of Z-Phase in expense of MX precipitates [17]. Therefore no improvement may be expected also at temperatures above 625°C. Although the increased Cr level may lead to an increased steam oxidation resistance, the limited creep strength and the high level of expensive alloying elements prevent a further development.

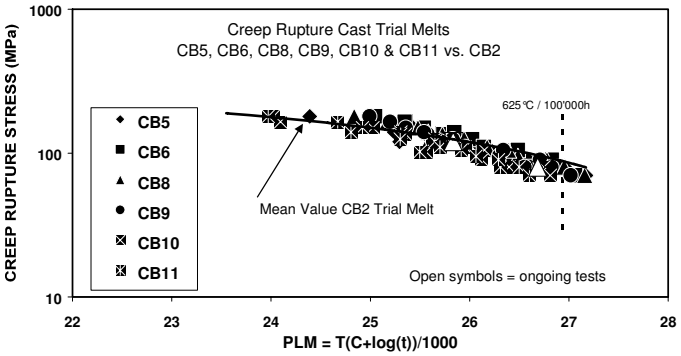

Figure 6
Creep strength of trial melts with higher Cr & Co contents

4.2 Production and investigation of pilot components

The decisions to produce large industrial melts to cast real size components were made quite early in the programme. Therefore not all the long-term results had been available to support these decisions. Based on early promising results, three different foundries produced the large melts given in Tables 4a and 4b. Manufacturing experience is reported in [9,18].

Alloy	C	Mn	Cr	Mo	Co	Ni	V	Nb	N	Al	B(ppm)
CB2P PHB	0.11	0.85	9.14	1.44	0.96	0.22	0.19	0.062	0.021	0.004	112
CB6VO Voest	0.13	0.19	10.35	1.45	2.95	0.18	0.21	0.077	0.029	0.011	140
CB6LU Lucchini	0.12	0.16	10.87	1.54	2.90	0.16	0.21	0.065	0.025	0.005	130

Table 4a Compositions of three large melts produced by different foundaries (wt%)

Alloy	Product forms and weights
CB2P PHB /Germany	1 Pilot Valve / 5t
CB6VO Voest /Austria	1 Pilot Valve / 3.3t, 1 Stepped Block / 3t, 4 Plates 100/50mm, 1 Flange
CB6LU Lucchini/Italy	1 Pilot Valve / 12 t, 2 Stepped blocks /à 4t, 5 Plates 100mm

Table 4b Components and weights for the three large melts produced

Extended test programmes have been carried out on these industrial melts. The present report focuses on the comparison of the creep properties with the corresponding trial melts.

CB2P / PHB Stahlguss, St.Ingbert, Germany

Composition, heat treatment and mechanical properties of this 5t pilot valve are in agreement with the corresponding trial melt CB2. Figure 7 shows the comparison of the creep strength for three positions within the valve and with the trial melt. These results are in line for the positions with equal strength level (A & C). They are slightly lower for position B with somewhat reduced initial strength mainly due to small shrinkages which have a strong influence on the small section of a creep specimen but not on thick wall component..

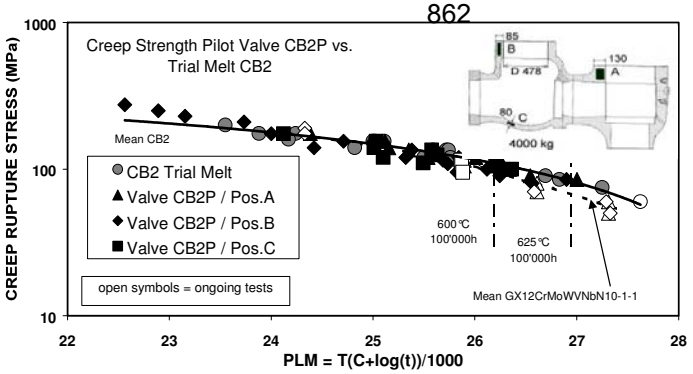

Figure 7
Creep strength of CB2P valve body vs. results of trial melt CB2

CB6VO / Voestalpine Linz, Austria and CB6LU / Lucchini Lovere, Italy

The early creep results of the trial melt CB6 were promising despite the increased Cr content of about 11%. Therefore this composition was selected for the production of upscaled industrial melts by two partner foundries i.e. Voestalpine in Linz, Austria (CB6VO) and Lucchini in Lovere, Italy (CB6LU).

The creep tests in the range 600-650°C have reached >25,000h with several still ongoing tests. Figure 8 shows the current results and a comparison with the results of trial melt CB6. Despite the higher Al-content, melt CB6VO exhibits slightly higher creep strength than CB6LU and is in line with the creep strength of trial melt CB6. However, as mentioned above, trial melt CB6 as well as both industrial melts are below CB2 at temperatures above 625°C.

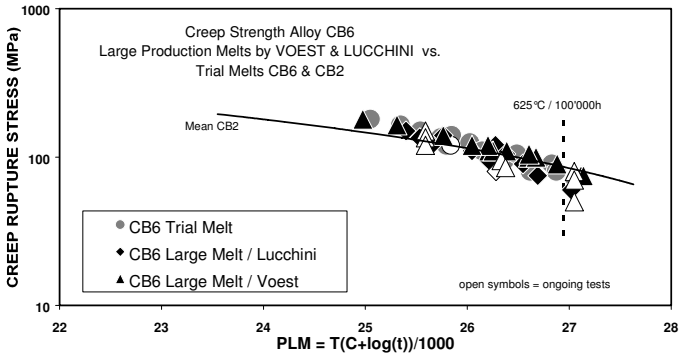

Figure 8
Creep strength of two industrial melts of alloy CB6 produced by two foundry partners vs. results of trial melt CB6 and meanline for CB2

5. Activities within the Current COST 536 Action

From the evaluation of a large number of alloys as given in table 3 it was concluded:

- CB2 is the most promising composition with respect to creep strength for up to 625°C
- CB2 will have reduced oxidation resistance above 625°C due to its low Cr content
- The investigated alloys with higher Cr & Co contents offer no advantage in creep over CB2 at temperatures above 625°C
- The increased oxidation resistance of these alloys requires large amounts of expensive alloying elements

Therefore, further development is needed to reach the targeted application temperature of up to 650°C.

The aims of the current COST536 action (2004-2009) with respect to cast alloys are:

- Development of suitable ferritic cast steels for application up to 650°C
- Optimisation of the newly developed CB2-type alloy and improvements in its data base
- Evaluation of coating systems for cast components at temperatures above 625°C if steam oxidation of base materials is not sufficient for specific areas.

5.1 Development of new alloys

From an early phase of COST there are promising creep results available for a forged steel without W or Co, ca. 9.5% Cr and Boron contents of 100 to180ppm, referred to as B-type rotor steel. New compositions were proposed on the basis of this B-alloyed steel considering the targeted higher temperature and therefore increased Cr-content.

Two compositions CT3 and CT7 as given in Table 5 have been manufactured as small trial melts of ca. 100kg and were cast to plates of ca.400x200x100mm. For comparison, Table 5 also gives the chemistry of two B-type rotors investigated earlier within COST. The only significant difference between CT3 and CT7 is the Cr content of ca. 10% and 11.5% respectively. As compared to CB2 or to the B-type rotor steels, the B content was increased.

Heat	C	Mn	Cr	Ni	Mo	V	Nb	N	B ppm
Trial melt CT3	0.17	0.99	10.0	0.1	1.49	0.26	0.059	0.032	250
Trial melt CT7	0.18	0.96	11.5	0.10	1.49	0.28	0.064	0.035	260
B-type rotor / B0	0.10	0.55	9.21	0.11	1.50	0.23	0.063	0.02	180
B-type rotor / B2	0.17	0.06	9.34	0.12	1.55	0.27	0.064	0.015	100

Table 5 Composition of B-alloyed new cast melts CT3 & CT7 (wt%)

The trial melts CT3 and CT7 were heat treated at 1100°C/8h plus 730°C/10+14h and were given a simulated PWHT of 730°C/12h + 730°C/14h.

The yield strength in the as heat treated condition and after long-term exposure is shown in Figure 9 for CT3 and CT7 together with CB2. Both new trial melts are stronger than CB2 and exhibit no weakening due to long-term exposure.

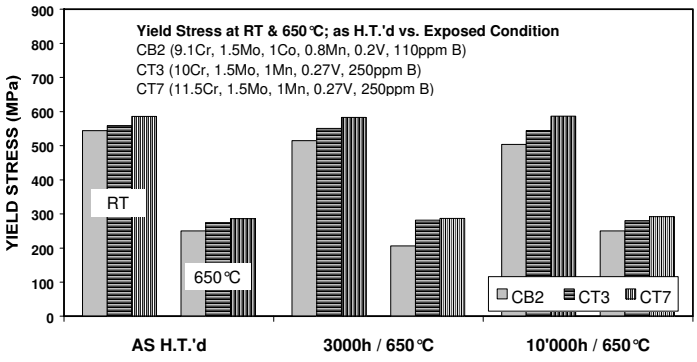

Figure 9
Yield strength at RT & 650°C of trial melts CT3 & CT7 in the as H.T'd condition and after long-term exposure

The impact energy at RT of alloys CT3 and CT7 is significantly lower than for CB2; the toughness of the high Cr melt CT7 is clearly lower than that of CT3 with lower Cr content. During long-term exposure these impact values drop significantly to very low values such as approx. 10Joule for CT7 as shown in Figure 10.

The ongoing creep tests have reached >13,000h and the current results are compared in Figure 11 with trial melt CB2. The values for both melts CT3 & CT7 are approaching the mean line of CB2 at lower stress levels. However, there is no evidence sofar of exceeding this mean line significantly.

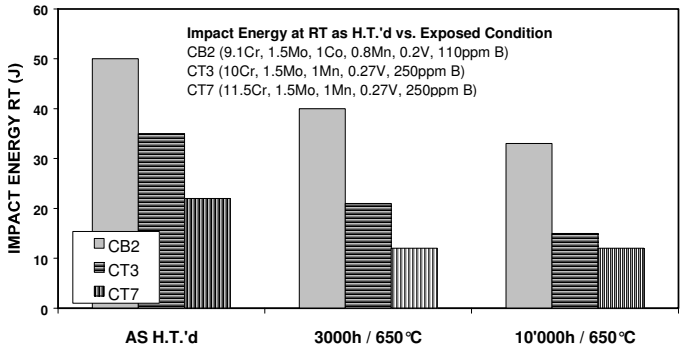

Figure 10
Impact energy at RT of trial melts CT3 & CT7 in the as H.T'd condition and after long-term exposure

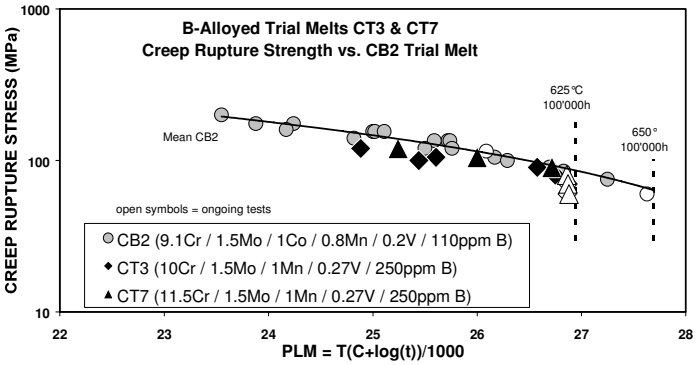

Figure 11
Creep strength of trial melts CT3 & CT7 vs. results of trial melt CB2

Despite the difference in the Cr-content, CT3 and CT7 sofar exhibit quite similar creep properties. However, this creep strength is below the expectation.

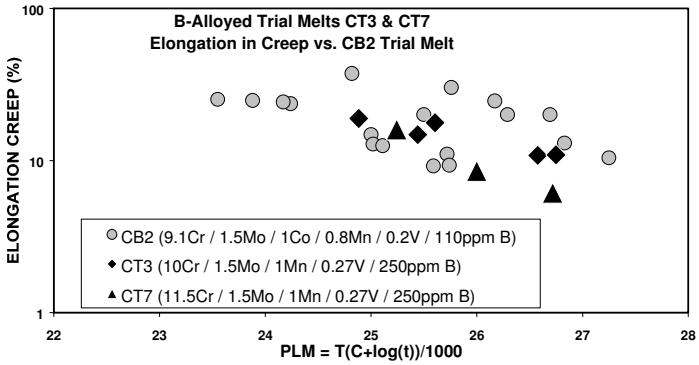

Figure 12
Rupture elongation in creep of melts CT3 & CT7 as compared to melt CB2

The creep ductility of CT7 seems to be lower than for CT3; the comparison to CB2 in Figure 12 shows for both alloys CT3 and CT7 reduced rupture elongation. Microstructure investigations are ongoing to study the unexpected relatively low creep strength of CT3 and CT7.

5.2 Optimisation of alloy CB2

Tables 6a and 6b show the aimed compositions of the modified CB2-type alloys and the products cast by two foundries. CB2VO corresponds to the earlier CB2 melts, the other CB2-type melts have been modified by increasing the B-content while decreasing the N-content and by reducing the contents of Mn and Nb. The B/N ratio is increased to ranges of 1,2 to 1,5.

Alloy	C	Mn	Cr	Mo	Co	Ni	V	Nb	N	Al	$B_{(ppm)}$
CB2 trial melt	0.12	0.88	9.20	1.49	0.98	0.17	0.21	0.06	0.02	0.010	110
CB2P PHB	0.11	0.85	9.14	1.44	0.96	0.22	0.19	0.062	0.021	0.004	112
CB2VO	Standard CB2 composition i.e. range of CB2 trial melt & CB2P PHB										
CB2-3A	9Cr/1Co/1.5Mo/0.3Mn + reduced N, Nb & increased B; low level of Al										
CB2-3B	9Cr/1Co/1.5Mo/0.3Mn + reduced N, Nb & increased B; high level of Al										
CB2-4	9Cr/1Co/1.5Mo/0.3Mn + reduced N, Nb & increased B, V; low level of Al										

Table 6a Aimed compositions of the modified CB2-type alloys

Alloy & Foundry	Products
CB2VO, Voestalpine, Linz	Shell part 4.6t, stepped blocks 2.9t, plates and cast pipes
CB2-3A, PHB, St.Ingbert	Stepped block 2.9t, plates and cast pipes
CB2-3B, Voestalpine, Linz	Trial melt, plates
CB2-4, PHB, St.Ingbert	Trial melt, plates

Table 6b Product forms of the modified CB2-type alloys

In order to improve the steam oxidation behaviour, the Si content is increased to ca. 0.30% as compared to trial melt CB2 with 0.19% Si. In addition to the effect of Si, the influence of the S content on the steam oxidation behavior will also be investigated.
All the new alloys mentioned in Table 6 have been produced recently and an extended test programme has been started.

6. Investigation of Welds

The availability of a suitable weld metal and welding procedure is mandatory for the application of new cast steel grades. Investigations of welds are reported in [9] for cast alloys GX12CrMoWVNbN10-1-1 and GX12CrMoVNbN9-1 and in [18] for alloys CB5 & CB11 welds using Co-modified electrodes. The new welds manufactured within COST and currently under investigation are listed in Table 7a. The corresponding compositions of base materials and filler metals are given in Table 7b.
Figure 13 shows the crossweld creep results for alloy CB6LU welded with electrode WB5.

Base Material	Filler Metal	Welder	Remarks
CB6LU	ElectrodeWB5	Lucchini	SMAW on plates 80mm
CB6VO	Electrode WB2	Voestalpine	Repair weld, valve body
CB2P	Electrode WB2	PHB	SMAW on plates 100mm & repair weld, valve body
CT3 & CT7	Electrode WB2	Voestalpine	Dissimilar weld, plates

Table 7a Details of investigated welds

	C	Mn	Cr	Ni	Mo	Co	V	Nb	N	B ppm	Al
Base Mat CB2P	0.11	0.85	9.14	0.22	1.44	0.96	0.19	0.062	0.021	112	0.004
Base Mat CB6LU	0.12	0.16	10.87	0.16	1.54	2.90	0.21	0.065	0.025	130	0.005
Base Mat CB6VO	0.13	0.19	10.35	0.18	1.45	2.95	0.21	0.077	0.029	140	0.011
Base Mat CT3 & CT7	0.18	0.96	10-11.5	0.10	1.49		0.28	0.064	0.035	260	
Electrode WB5	0.10	0.57	10.80	0.71	1.42	2.90	0.20	0.047		60	
Electrode WB2	0.14	0.56	9.1	0.7	1.4	0.95	0.26	0.05	0.03	38	0.003

Table 7b Compositions of weld metals and base metals investigated (wt%)

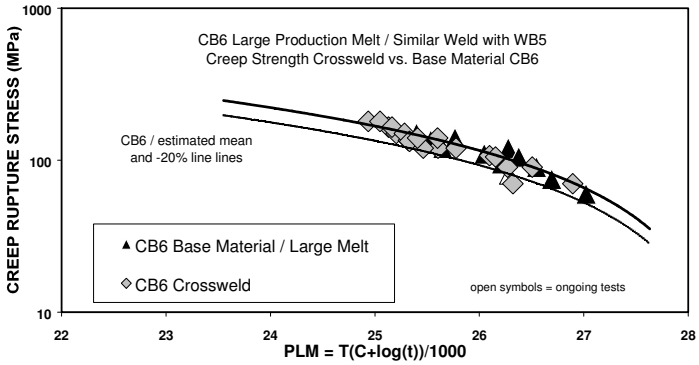

Figure 13
Creep strength of crossweld samples of CB6 welded with WB5. Comparison with mean & -20% lines of CB6

The crossweld results show no significant deteroriation as compared with the base material values, and they are mainly located above the –20% line in creep strength of the base material.

Figures 14 & 15 show the mechanical properties of the repair weld on the CB6VO valve body welded with WB2 filler metal. Due to the higher strength of the WB2 weld metal, tensile rupture occurred in the base material. The weld metal shows about the same impact energy as the base material i.e. above 27Joule at RT; the measured specimens from the HAZ result in an average value of ca.22Joule at RT.

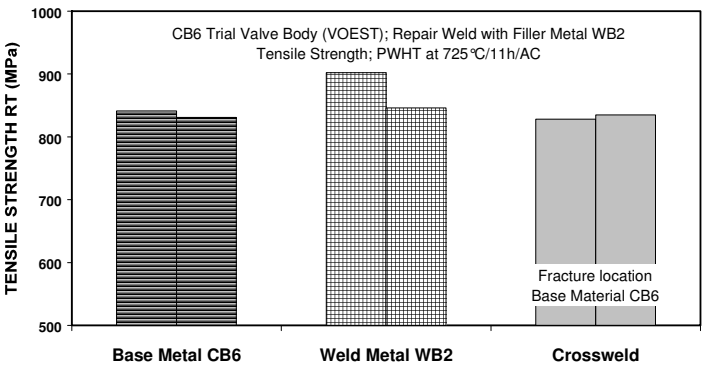

Figure 14
Tensile strength of CB6 welded with WB2 filler metal

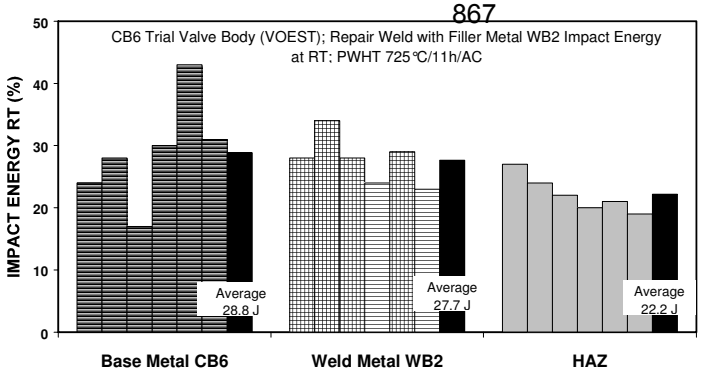

Figure 15
Impact energy at RT of CB6 welded with WB2 filler metal

Alloy CB2P was welded with WB2 filler metal. Similar welds between plates were manufactured and also repair welds on the valve body were carried out. Figure 17 shows the impact energies at RT; these values for weld metal and HAZ are higher than reported for the above mentioned CB6VO weld.

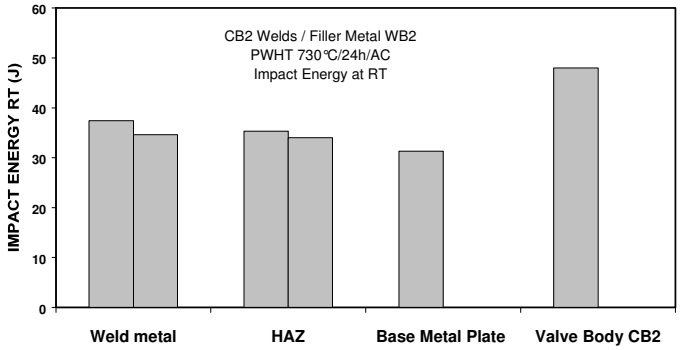

Figure 17
Impact energy at RT of CB2 welded with WB2

Creep tests on crossweld samples have been started and are ongoing. The results sofar show rupture within the 20% scatterband of the base material. The fractographic investigation of ruptured specimens is ongoing.

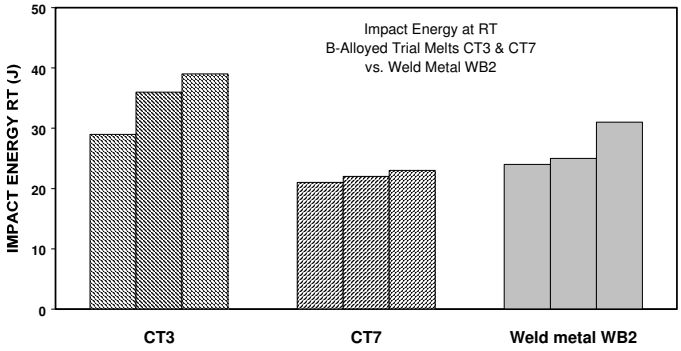

Figure 18
Impact energy at RT, dissimilar weld CT3 & CT7 welded with WB2

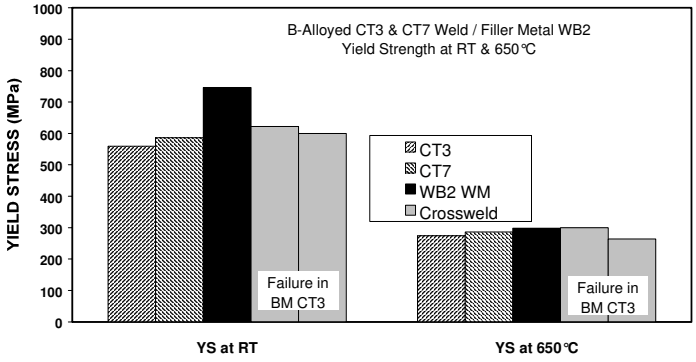

Figure 19
Yield strength at RT & 650°C for the dissimilar weld CT3 & CT7, welded with WB2

The weldability of the high Boron containing melts CT3 & CT7 has been tested with a dissimilar weld between these two alloys. WB2 filler metal was used for this weld (tables 7a & 7b). The mechanical properties are shown in Figures 18 & 19 The impact energy of the weld metal WB2 lies between the values of the two base materials CT3 & CT7 and corresponds to the values measured earlier for this filler metal. The weld metal is stronger than the base materials, and fracture in tensile tests occurred in the CT3 base material.
Dissimilar welds between the new cast alloys of CB2-type and pipe materials such as P92 are currently manufactured within the COST action. These welds are made using P92-type filler metal and with PWHT parameters corresponding to the cast materials.

7. Summary and Conclusions

- The various improvements of 9-12% Cr steels during the last 15-20 years led to an increase in live steam parameters of 600°C/300bar and re-heat temperatures of up to 620°C in recent power plants. This significant step offers an increase in efficiency of about 8% and a related massive reduction in CO_2 emissions.
- However, the creep strength and oxidation resistance of the newly developed cast steels may limit their uncooled or unprotected application in some cases to ca. 625°C.
- A further increase in temperature up to 650°C therefore requires additional development steps. This work has been started within COST536.
- CB2 i.e. the most promising alloy regarding creep should be optimised regarding oxidation resistance. The data base for this steel is currently enlarged by the evaluation of additional industrial and experimental melts with slight modifications in the composition.
- For the CB2-type cast alloys, a matching filler metal has been developed i.e. WB2. The crossweld properties measured sofar are satisfactory. There is no indication that these new cast steels would exhibit a larger strength reduction due to welding than that for the cast materials used previously.

8. Acknowledgement

The authors wish to thank their partners in the entire COST536 working group for their contributions and the discussions during the course of the work. Thanks are also extended to

the partners in the previous COST working groups and to the COST Management Committee and to the national funding bodies for financial support of the individual national projects.

References

[1] Mayer K.H., Bendick W., Husemann R.U., Kern T., Scarlin R.B., New Materials for Improving the Efficiency of Fossil-fired thermal Power Stations, VGB Power Tech 1/98

[2] Blum R., Vanstone R.W., Materials Development for Boilers and Steam Turbines Operating at 700°C, Proceedings of the 6th Int. Charles Parsons Turbine Conf., 16-18 September 2003, Dublin, Ireland

[3] Masuyama.F., Future Development of Materilas for High Efficient Power Plants in Japan; International Workshop "Performance and Requirements of Structural Materials for Modern High Efficient Power Plants"; TU Darmstadt/NIMS/MPA Stuttgart, 6-9. September 2005, Darmstadt, Germany

[4] Abe.F., Actual Status of Improving the Properties of Nickel-based Superalloys for Steam Turbine Applications up to 700°C in Japan, International Workshop "Performance and Requirements of Structural Materials for Modern High Efficient Power Plants"; TU Darmstadt/NIMS/MPA Stuttgart, 6-9. September 2005, Darmstadt, Germany

[5] Touchton G., EPRI Improved Coal-fired Power Plant Project, 1st Int. Conf. on Improved Coal-Fired Plants, 19-21 November 1986, Palo Alto, US

[6] Mayer K.H., Gysel W., Cast Components of Steam Turbines for Improved Coal-Fired Plants, 1st Int. Conf. on Improved Coal-Fired Plants, 19-21 November 1986, Palo Alto, US

[7] Kern T.U., Mayer K-H., Status of the Material Development for Future Steam Turbines – Achievements of COST522, International Workshop "Performance and Requirements of Structural Materials for Modern High Efficient Power Plants"; TU Darmstadt/NIMS/MPA Stuttgart, 6-9. September 2005, Darmstadt, Germany

[8] Tschaffon H., COMTES700-on the way to the 700°C Power Plant, International Workshop "Performance and Requirements of Structural Materials for Modern High Efficient Power Plants"; TU Darmstadt/NIMS/MPA Stuttgart, 6-9. September 2005, Darmstadt, Germany

[9] Staubli M., Mayer K-H., Giselbrecht W., Stief J., DiGianfrancesco A., Kern T-U., Development of Creep Resistant Cast Steels within the European Collaboration in Advanced Steam Turbine Materials for Ultra Efficient Low Emission Steam Power Plant / COST 501-522, 7th COST Conference, 30.Sept-2.Oct. 2002, Liège, Belgium

[10] Mayer K.H., Hanus R., Kern T.U., Staubli M., Thornton D.V., High Temperature Cast Components for Advanced Steam power Plants, 6th COST Conference, 5-7. Oct. 1998, Liège,

[11] Hanus R., Advanced 9-12%Cr Cast Steel Grades, Research-Foundry Process Development-Quality-Experience; EPRI 4th Int. Conf. On Advances in Materials Technology for Fossil Power plants, October 2004, Hilton Head Islands, SC, USA

[12] Mayer K.H., KernT.U., Staubli M., Tolksdorf E., Long-Term Investigations of specimens of 24 Production Components manufactured from the Advanced Martensitic 10%Cr-Steels for 600°C Steam Turbines, 5th Int. Charles Parsons Conference, 3-7. July 2000, Cambridge UK

[13] Mayer K.H., Blum R., Hillenbrand P., Kern T.U., Staubli M., Development Steps of New Steels for Advanced Power Plants; 7th Liège COST Conference, 30.9-3.10. 2002, Liège, B

[14] Vanstone R.W., Cerjak H., Foldyna V., Hald J., Spiradek K., Microstructural Development in Advanced 9-12%Cr Creep Resistant Steels - A Collaborative Investigation in COST 501/3 WP11, 5th Liège COST Conference, 3-6. October 1994, Liège, Belgium

[15] Spiradek K., Bauer R., Zeiler G., Microstructural changes during the Creep Deformation of 9% Cr Steel, 5th Liège COST Conference, 3-6. October 1994, Liège, Belgium

[16] Cerjak H., Hofer P., Schaffernak B., The Influence of Microstructural Aspects on the Service Behaviour of Advanced Power Plant Steels, 1999 ISIJ, P.874ff

[17] Kauffmann F, Mayer K.H., Straub S., Zies G., Scheu C., Ruoff H. and Maile K., Characterization of the precipitates in modern boron containing 9-12%Cr steels by EFTEM and their correlation to the creep strength", 8th COST Conference, 18.-20.9.2006, Liège, Belgium

[18] Contessi A.,Delvecchio D., Ghidini A.,Valenti S., Carosi A., DiGianfrancesco A., Ielpo F.M., The first Industrial Cast of CrMoCoB Advanced Steel for Cast Turbine Components, 7th COST Conference, 30.9.-3.10.2002, Liège, Belgium

[19] Cerjak H., Letofsky E., Jochum C., Nies H., Weldability and Weld Properties for Advanced Power Plant Materials, 7th COST Conference, 30.9.-3.10.2002, Liège, Belgium

WELDABILITY AND PROPERTIES OF NEW CREEP RESISTANT MATERIALS FOR USE IN ULTRA SUPERCRITICAL COAL FIRED POWER PLANTS

E. Bauné[1], H. Cerjak[2], St. Caminada[3], C. Jochum[4], P. Mayr[2], J. Pasternak[5]

1: Air Liquide, Cergy-Pontoise, France
2: Graz University of Technology, Austria
3: Tenaris Dalmine, Italy
4: Böhler Thyssen Schweisstechnik Deutschland, Germany
5: Boiler Engineering Company Rafako S.A., Poland

Abstract

This paper gives an overview about two main points within the work of the Welding Group of COST 536. The present status of filler metal development matching creep resistant steels like T/P 23, T/P 24, VM 12, CB 2 is given, showing actual test results of all weld metals and joints. Creep test programme is going on for all qualities mentioned.
In the second part of this contribution the results of the "matching programme", welding of E 911 Pipe with under-, over- and matching filler metals are presented. Here the focus is on metallographic examination and on creep strength properties of welded joints.

Keywords: filler metals matching to T/P 23, T/P 24, VM 12, Cost CB 2; mechanical properties, welding of pipe E 911, creep properties

Introduction

It is the endeavour of operators of fossil fuel fired power stations to increase the efficiency of their installations through an increase of steam pressure and temperature in order to assure supply of electricity on a low cost level and with reduced CO_2 emission. Increase of service parameter requires adequate materials with sufficient creep strength. This is true for both base materials and welding consumables. All over the world numerous research projects are running to gain this aim. In Europe, one important research project concentrates in the COST Programme, where turbine- and boiler makers, steel makers, producer of filler metals, research and university institutes and finally operating companies of fossil fuel fired power plants work together to improve material properties. At present time COST 536 is running, starting in summer 2004. Within this project about 50 partners of more than 15 European countries joined together in five different work packages: Alloy design, modelling, turbine group, boiler group and welding group. It is their aim to develop and to qualify creep resistant ferritic and martensitic materials for the use up to 650 °C steam temperature.

The focus of this contribution is to present the status of filler metal development which is an important part of the welding group's work. Here, the main materials of interest are grades like: VM 12, CB 2, T/P 23, T/P 24. As an example of a common and ongoing group research work, the results of the so called "matching programme", which was already a major part of COST 522 welding group, are given.

1. New creep resistant base materials

The demand for higher efficiency in fossil fired power plants lead to the development of new creep resistant materials during the last decades. They made it possible to increase the steam temperature up to the range of 625 °C for permanent service, using ferritic and martensitic materials. Further increase up to 650 °C demands martensitic material with better oxidation behaviour. These materials, especially for thick walled components are under development. Striving for higher steam parameters has also led to increased requirements for the tube steels of water walls, which than can no longer be fulfilled with the previously used steels like 13CrMo4-4 or T11/T12. New grades for these applications will be T 23 or T 24.

Table 1 will summarize the chemical composition of above mentioned ferritic – bainitic and martensitic steel grades. For comparison and completeness well known materials like P 22 (11CrMo9-10), X20 (X20CrMoVW12-1) and P91 (X10CrMoVNb9-1) are mentioned, too. For all these materials, matching filler metals are available.

Table 1. Chemical composition of ferritic - bainitic and martensitic base materials including well approved grades like P22, X20 and P91

Grade	Weight-% C	Si	Mn	Cr	Ni	Mo	V	W	Nb	and
Bainitic ferritic steels										
10 CrMo 9-10 (P22)	≤ 0,15	≤ 0,50	0,30 – 0,60	1,90 – 2,60	-	0,87 – 1,13				
HCM2S (T/P23)	0,04 - 0,10	≤ 0,50	0,30-0,60	1,90-2,60	-	≤ 0,30	0,20-0,30	1,45-1,75	0,02-0,08	N ≤ 0,010
7CrMoVTiB10-10 (T/P24) 1.7378	0,05 -0,095	0,15-0,45	0,30-0,70	2,20-2,60	-	0,90-1,10	0,20-0,30	-	-	N ≤ 0,010 B 0,0015-0,0070 Ti 0,05-0,10
Martensitic steels ***(9 - 12 % Cr-)***										
X20CrMoV12-1 1.4922	0,17-0,23	< 0,50	< 1,0	10,0-12,5	0,30-0,80	0,80-1,20	0,25-0,35	-	-	-
X10CrMoVNb9-1 (P91) 1.4903	0,08-0,12	0,20-0,50	0,30-0,60	8,0-9,5	< 0,40	0,85-1,05	0,18-0,25	-	0,06-0,10	N 0,03-0,07
X11CrMoWVNb9-1-1 (E911) 1.4905	0,09-0,13	0,10-0,50	0,30-0,60	8,50-9,50	0,10-0,40	0,90-1,10	0,18-0,25	0,90-1,10	0,06-0,10	N 0,05-0,09
P92 (Nf616)	0,07-0,13	< 0,5	0,30-0,60	8,5-9,5	< 0,40	0,30-0,60	0,15-0,25	1,5-2,0	0,04-0,09	N 0,03-0,07 B 0,001-0,006
VM 12-SHC **[1]**	0,10-0,14	0,40-0,60	0,15-0,45	11,0-12,0	0,20-0,40	0,20-0,40	0,20-0,30	1,30-1,70	0,03-0,08	Co:1,40-1,80 N:0,030-0,070 B:0,0030-0,006
COST Material CB 2	0,11-0,14	0,20-0,30	0,80-1,00	9,00-9,60	0,10-0,20	1,40-1,60	0,18-0,22	-	0,05-0,07	Co:0,9-1,1 N:0,015-0,030 B:0,008-0,015
COST Material CB 5	0,12-0,14	0,20-0,30	0,10-0,30	9,90-10,50	0,10-0,20	1,40-1,60	0,18-0,22	-	0,05-0,07	Co:2,80-3,20 N:0,015-0,030 B:0,008-0,015

2. Development of new creep resistant ferritic and martensitic filler metals

During development of new base materials it is of great importance, that corresponding filler metals with matching creep strength properties will be developed simultaneously. Concerning the alloy concept, it is the easiest way that the chemical composition is identical to those of the base material. That is true for a great number of filler metals, but not for all. Additional micro alloying elements and specialities concerning improvement of weldability and handling are the detailed knowledgement of the individual development departments. Nevertheless within the COST RESEARCH PROGRAMME fabricators, universities, institutes, foundries, competitors, work together as equal partners in order to develop new materials.

2.1 Individual results from the welding group: Air Liquide´s development of matching filler metals for T/P 23 and T/P 24

2.1.1 Girth welding of T/P23 tubing and piping

Grade 23 steel has been identified as a potential solution for its enhanced creep and weldability properties. In the last years Tenaris Dalmine completed the set up of the production cycle and heat treatment for tubes and pipes of this steel grade, in order to obtain and guarantee optimum mechanical and creep properties [2]. Also, Air Liquide Welding developed and optimized a complete range of welding consumables for all new advanced materials for power generation [3, 4]. As such, SMAW and SAW joints were fabricated from seamless tubulars produced in Tenaris Dalmine in the frame of a collaborative research program involving Tenaris Dalmine, the Italian Welding Institute and Air Liquide Welding. The high WT tubes and pipes used for this program were quenched and tempered in order to obtain a tempered fully bainitic microstructure. Light wall tubes are normalized and tempered instead.

SMAW was applied in 2G (tube with vertical axis) and 5G PF conditions (pipe with fixed horizontal axis). SAW was applied in PA condition (rotating pipe with horizontal axis). Welded joints were mechanically and chemically tested in three different conditions: as-welded; and post weld heat treated at 740°C/2h or at 710°C/1.5h. Each of the five girth welded joints prepared was defined with a preliminary welding procedure specification (WPS) according to EN 288-1. Welding energies are reported in Table 2; preheat and interpass temperatures were selected in the 200-250°C range. Weld metal chemical analyses shown in Table 3 match ASTM and ASME requirements for the parent metal. Both transverse (cross weld CW) and longitudinal (all weld AW) tensile tests (at room temperature and 550°C), as well as impact characteristics are reported together with the acceptance criteria in Table 2 for all joints. In addition, no damage occurred at side bend test specimens extracted from P23 joints according to ISO 5173.

In the as-welded 12.5 mm-thick SMAW joint, the impact properties pass the acceptance criterion (>27J in WM, 30J in HAZ). However, the impact properties of the weld metal decrease when increasing the pipe thickness, while hardness increases in the weld metal and in the HAZ. A PWHT is then necessary to restore toughness (increase) and hardness (decrease) properties on pipes of heavier wall thickness. Both PWHT's at 740°C/2h and 710°C/1.5h proved to be effective in this study on 17.5 and 31.75mm pipes.

In SAW joints, the hardness values after PWHT reach acceptable levels. The impact properties at RT are acceptable and over the minimum requirements, although a little bit lower than the values obtained in the SMAW joints, as a probable consequence of slightly coarser microstructures. The impact test results on SAW weld metal obtained on the 17.5 and 31.75 mm wall thickness pipes show that a PWHT at higher temperature seems to be more beneficial to improve the toughness of the weldments (89J at RT at 740°C/2h vs. 53J at 710°C/1.5h).

Table 2. Mechanical characteristics of girth welded joints in the as-welded and PWHT conditions (Oerlikon Cromo SW223 / OP121TT W SAW + Oerlikon Cromocord E223 SMAW + Oerlikon Carborod WF223 GTAW)

Joint / Condition		Test	Zone	Requirement	SMAW	SAW
T23 ODxWT 76x12.5mm (GTAW+SMAW – 2G position – 0.88 kJ/mm)	**As-welded**	UTS at RT [MPa]		UTS >510	652 (CW)*	
		KVC at RT [J]	weld metal	>27J at RT	32	
			fusion line		30	
			FL+2mm		201	
			PM		222	
		HV10 max	WM	NA	310	
			HAZ		364	
			PM	Max 230 HV	214	
P23 ODxWT 219x31.75 mm (GTAW+SMAW – 5G PF– 0.92 kJ/mm ; GTAW+SMAW + SAW –PA – 1.67 kJ/mm)	**As-welded**	tensile RT [MPa]		UTS > 510	641 (CW)*	628 (CW)*
		KVC at RT [J]	weld metal	>27J at RT	17	20
			HAZ		242	215
			PM		395	395
	PWHT 1.5h 710°C	tensile RT [MPa]		UTS > 510	595 (CW)*	615 (CW)*
		KVC at RT (at 0°C) [J]	weld metal	>27J at RT	147 (113)	53 (22)
			HAZ		243 (231)	237 (158)
			PM		395 (377)	395(377)
P23 ODxWT 457x17.5 mm (GTAW+SMAW – 5G PF– 0.92 kJ/mm ; GTAW+SMAW + SAW – PA – 1.67 kJ/mm)	**As-welded**	tensile RT [MPa]		YS > 400	786 (AW)	762 (AW)
				UTS > 510	868 (AW) 601 (CW)*	877 (AW) 615 (CW)*
				E > 20%	11 (AW)	19 (AW)
		KVC at RT [J]	weld metal	>27 J at RT	12	20
			fusion line		30	215
			HAZ		190	219
			PM		399	399
	PWHT 2h 740°C	tensile RT [MPa]		YS > 400	511 (AW)	534 (AW)
				UTS > 510	601 (AW) 555(CW)*	629 (AW) 585 (CW)*
				E > 20%	20.4 (AW)	23.1 (AW)
		KVC at RT (at –20°C) [J]	weld metal	>27 J at RT	161 (39)	89 (15)
			fusion line		197 (61)	127 (31)
			HAZ		226 (196)	183 (24)
			PM		399 (238)	399 (238)
		tensile 550°C [MPa]	YS		339 (AW)	348 (AW)
			UTS		359 (AW) 343 (CW)*	374 (AW) 341 (CW)*

Note: * specimen broken in parent metal

The creep strength of welded joints was also assessed in order to guarantee safety factors for the design and to ensure safe working conditions of components used in high temperature

applications. Creep specimens extracted from welded joints (as-welded and PWHT) were tested in the range 500-600°C, i.e. typical working condition of the T/P23 grade. As seen in Figure 1 which shows the creep behaviour of T/P23 parent material, all ruptures of welded joints creep specimens occurred within the 80% scatter band of the parent material mean line. Examination of the broken creep samples followed, Figures 2 and 3. Ruptures took place in the parent material near the HAZ and most of the ruptures were reported to start on the fusion line and grow between the FGHAZ and ICHAZ. Long-term creep data are still pending on these joints. All above-mentioned results on materials demonstrate satisfactory performances exhibited by grade 23 tubes and pipes and filler metals now available on market according to the relevant current standards.

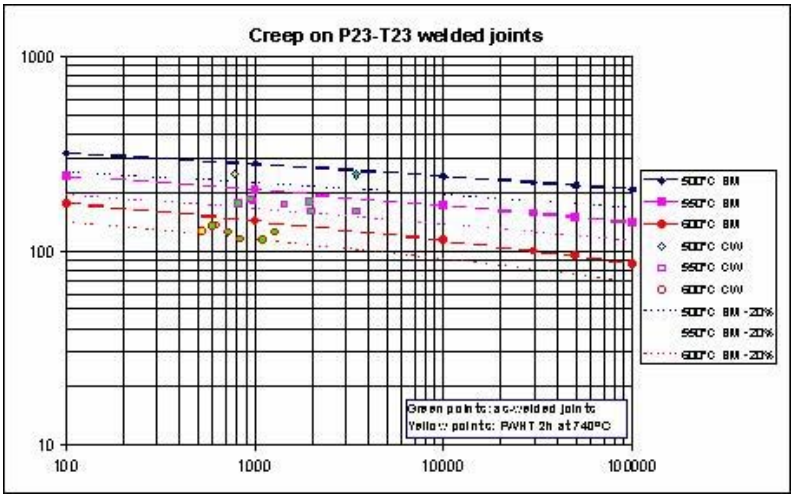

Figure 1. Creep properties of welded joints vs. base metal (x-axis: time in h; y-axis: load in MPa)

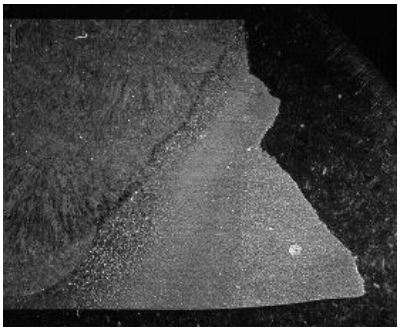

Figure 2 (left). Macrograph of broken creep specimen

Figure 3 (right).

(a) Micrograph of base metal (top);

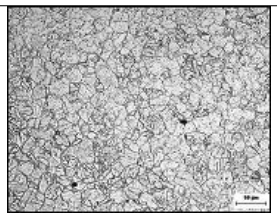

(b) of heat affected zone (bottom).

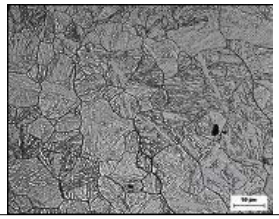

Figure 2 - 3. Pipe P23 from heat n°109194 - 76x12.5, (quench 1050°C + tempered 760°C) Creep specimen tested at 550°C under 179 MPa load with rupture after 1952h (as-welded)

Table 3. Chemical analysis of the joints in different locations (weld metal WM and base metal BM)

	C	Mn	Si	P	S	Ni	Cr	Mo	Cu	Sn	V	Nb	W
ASME	0,04	0,10	0,50	0,03	0,010	-	1,90	0,05	-	-	0,20	0,020	1,45
Req	0,10	0,60	max	max	max		2,60	0,30			0,30	0,080	1,75
T23 tubes (ODxWT 76x12.5 SMAW) :													
BM	0,06	0,47	0,26	0,020	0,004	0,14	2,08	0,10	0,15	0,013	0,21	0,048	1,47
WM	0,05	0,51	0,24	0,011	0,006	0,45	1,94	0,05	0,03	0,005	0,20	0,013	1,28
P23 pipes (ODxWT 457x17.5 SMAW; ODxWT 457x17.5 SAW and ODxWT 219x31.75 SAW) :													
BM	0,06	0,46	0,23	0,008	0,002	0,09	2,09	0,13	0,13	0,011	0,23	0,055	1,54
WM	0,05	0,51	0,23	0,010	0,006	0,49	2,03	0,06	0,03	0,005	0,21	0,015	1,32

2.1.2 *Consumables for T/P 24 welding*

Welding consumables dedicated to welding T/P 24 tubing and piping have also been developed by Air Liquide Welding [3, 4]. Table 4 reports typical weld metal compositions for SMAW electrodes. Table 5 and Figure 4 describe all weld metal characterisation results including hardness, toughness and (hot) tensile both in as-welded and PWHT conditions. In a girth weld carried out on P24 pipe (OD 370x25mm) with SMAW electrodes, toughness lied below the 27J criterion in the as-welded condition, while Hv10 reaches values above 350 both in the weld metal and in the base material HAZ. A PWHT at 730°C/1.5 hour was recommended to obtain Hv10 < 250 and Kv +20°C > 27J.

The all weld metal chemical analysis of the T/P24 sub-arc flux-Ø3.2mm wire combination is shown in Table 6. Welding procedure investigations were carried out throughout the development of this wire to acquire best mechanical performance out of these products, particularly with respect to the Titanium content in the weld, what was found to be essential to guarantee enough creep strength. With preheat and interpass temperatures set at 150 and 230°C respectively, direct current electrode positive polarity was used, with welding parameters of 460A, 31V, a welding speed of 55cm/min, resulting in a heat input of 15.5kJ/cm. A second welding procedure was developed in alternating current too, with 400A, 28V and an energy of 12.2kJ/cm. Mechanical properties including tensile, hardness and toughness data are also enclosed, without and with a PWHT at 740°C for 2 hours, Table 6. The criterion Hv10 < 248 is fulfilled after PWHT 740°C/2h, while both tensile and toughness requirements are met. This wire was then used in the framework of a TNO project to produce a girth weld on a Ø380 x 40mm P24 pipe, in the conditions set forth for DCEP polarity, with PWHT 720°C/2h [5]. Creep evaluation followed. Creep life time of the welded joints was at a level comparable with that of the base metal and rupture was found to occur in the base metal, Figure 5.

Table 4. Weld metal chemical composition of Oerlikon Cromocord E224 electrodes

	C	Mn	Si	P	S	Ni	Cr	Mo	Cu	Sn	V	B	Ti
All weld metal	0.07	0.5	0.5	<0.01	<0.01	0.08	2.4	1.0	-	-	0.25	0.0025	0.06

Table 5. Tensile and hot tensile properties of all weld metal produced using SMAW ALW electrodes

	As-welded	PWHT 740°C/2h (LMP=20565)	PWHT 740°C/8h (LMP=21175)
YS (MPa)	751 at 550°C	640 at 20°C	455 at 550°C
UTS (MPa)	838 at 550°C	736 at 20°C	477 at 550°C

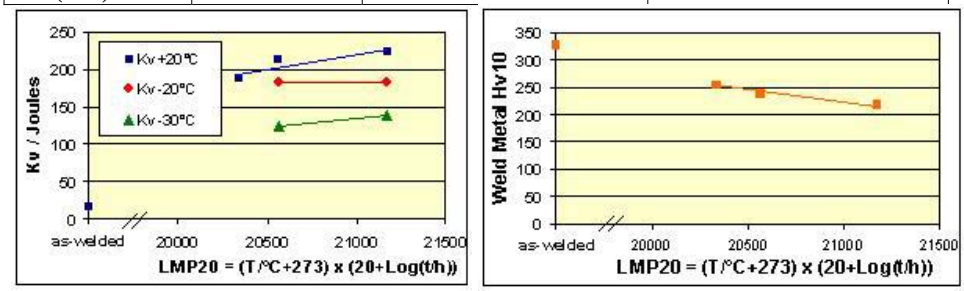

(a) **(b)**

Figure 4. Evolution of (a) all weld metal toughness, (b) hardness of all-weld-metal weld deposits produced using Oerlikon Cromocord E224 SMAW electrodes as a function of Larsen Miller parameter LMP20

Table 6. Typical weld metal properties of OE Oerlikon Cromo SW224 / OP121TT W SAW combination

	C	Mn	Si	P	S	Ni	Cr	Mo	Cu	Sn	V	B	Ti
DCEP	0.055	0.4	0.4	<0.01	<0.01	0.08	2.6	1.0	-	-	0.2	0.0010	0.08
AC	0.055	0.4	0.4	<0.01	<0.01	0.08	2.6	1.0	-	-	0.2	0.0010	0.14

		YS (MPa)	UTS (MPa)	Kv +20°C (J) as-solidified/reheated	Hv10
DCEP	as-welded	-	-	10 / 15	348
	PWHT 740°C/2h	663	750	68 / 163	234
AC	as-welded	-	-	10 / 15	351
	PWHT 740°C/2h	703	790	208 / 251	255

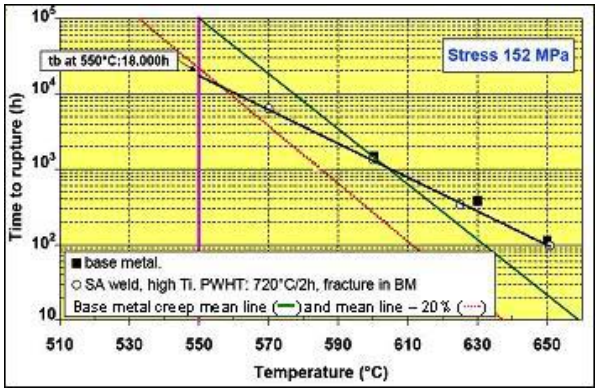

Figure 5. Creep properties of SA-welded pipe vs. P24 base metal at 152MPa

2.2 Individual results from the welding group: Böhler Thyssen Welding´s development of matching filler metals for VM 12 and CB 2

2.2.1 Matching filler metals for welding martensitic the new grade VM 12

During service, the already mentioned base materials E911 and P92 can be used up to max. 620 °C. At higher temperatures, scaling resistance is not sufficient any more. In this high temperature range material with higher Cr content is necessary. In the European research programme COST 536 such a material developed by Vallourec & Mannesmann Tubes [1, 6] – VM 12 (X12CrCoW12 2 2) and suitable up to 650 °C - is under investigation. In comparison to E911 or P92, this grade has a higher Cr content of about 11,5 %. As this will cause formation of ferrite, additional Co as an austenite stabilising element is used. Cobalt will act like Ni, but without influencing the A_{c1b} –temperature. Böhler Thyssen Welding has developed a filler metal matching to VM 12 [7, 8, 9]. The chemical composition of the filler metal matching to the new grade VM 12 is given in table 7.

The development of the base material is not finished so far [1]. Especially for thick walled components optimization of VM 12 is ongoing at V&M in order to reach long term creep strength at least as good as those of P 92 [10]. Nevertheless, main results for the filler metal are already available. The all weld metal can be characterized as a high strength material with YS above 650 MPa and with TS above 750 MPa. Toughness properties of the all weld metal at room temperature are in the range of about 40 to 50 J. This is a level below P92 and E911. Modifications of Ni, as it was carried out successfully with other martensitic fillers like Thermanit MTS 911 or MTS 616, seems not to be very successful with the VM 12 grade. Extension of the PWHT seems to be more successful, at least for GTAW (table 7). Nevertheless the present toughness level is high enough, as the minimum required values are given with ≥ 27 J according European regulations. On the other hand it is clear and necessary, to take outmost care during welding (limitation of heat input, correct choice of electrode Ø, welding thin layers with gentle weaving technique, etc) [12]. A PWHT is necessary for all welding processes at 770 °C – 780 °C. This is higher than with the other 9 % Cr steels, but after a PWHT at 760 °C, sufficient toughness and a small scatter band of values can not be guaranteed. A_{c1b}-temperature of the weld was determined at 800 °C. The following table

shows the chemical composition and the mechanical properties of the all weld metal for Thermanit MTS 5 CoT at different test temperatures and after different PWHT.

Table 7. Chemical composition and mechanical properties of the all weld metal of Thermanit MTS 5 Co T

Chemical composition (weight %)

	C	Si	Mn	Cr	Ni	Mo	V	W	Co	Nb	B	N
GTAW	0,124	0,40	0,46	11,59	0,43	0,03	0,22	1,45	1,65	0,06	0,003	0,046
SMAW	0,134	0,33	0,66	11,28	0,79	0,33	0,24	1,48	1,59	0,068	0,003	0,052
SAW proto type	0,101	0,50	0,60	11,30	0,65	0,29	0,23	1,50	1,60	0,04	0,003	0,060

Mechanical properties of all weld

	Test temp. °C	PWHT °C/h	YS MPa	TS MPa	Elong. %	R. o. A %	Toughness (ISO-V) (RT) J	Hardness (after PWHT) (HV 10)
GTAW	+20	770/2	684	822	18,5	62,1	43 38 50 47 33	297
	+575		416	492	20,4	78,5		
	+600		374	454	20,6	77,3		
	+20	780/2	688	820	17,7	63,2	98 96 122 88 66	290
		790/2	642	788	19,3	65,6	70 84 128 88 88	264
		770/10	628	775	19,6	63,8	64 49 78 90 53	256
SMAW	+20	770/2	689	832	17,2	58,7	49 42 41 40 48	253
	+575		423	509	17,0	68,4		
	+600		330	448	21,0	72,9		
	+20	780/2	594	787	18,3	56,1	51 56 51 48 50	256
		790/2	564	784	19,5	60,0	47 62 58 61 61	258
		770/10	558	771	17,5	56,0	48 54 65 56 48	258
SAW proto type	+20	770/4	688	819	18	59,9	36 48 46	248

Table 8 shows the mechanical properties of a joint VM 12 welded with matching SMAW filler metal Thermanit MTS 5 Co T. From this joint specimen for creep tests have been machined. At present time, these tests are running at 600 and 650 °C. These tests are running in cooperation with Vallourec & Mannesmann Tubes within the COST programme. So far, all samples behave as expected

Table 8. Joint: VM12, pipe-$Ø_a$: 406 mm, wall thickness: 35 mm; filler metal: Thermanit MTS 5 CoT

Root: GTAW - wire-Ø: 2,4 mm;
Fills: SMAW – 2,5 and 3,2 mm;
T pre heat: 220 °C; T inter pass: max. 250 °C

Test temp. °C	PWHT °C/h	Ys MPa	Ts MPa	Fracture location	Toughness (ISO-V) J	Hardness HV10
+20	770/4	576	765	BM	45 41 31	260
600	770/4	293	383	BM	-	-

Table 9 shows results from joints with thin walled tubes (140 x 10 mm) for the welding processes GTAW and SMAW. For both processes creep specimen have been taken out of these joints. Creep tests will start soon.

Table 9. Joint: VM12, pipe-$Ø_a$: 140 mm, wall thickness: 10 mm, Filler metal: Thermanit MTS 5 CoT; rotating tube

weld build-up: root plus 4 layers: wire-Ø: 2,4 mm root pass: 140/13; 1.L: 155/13,5; 2.L: 190/15; 3.L: 180/14,5; 4.L: 180/14,5 T pre heat: 220 °C; T inter pass: 250 – 280 °C						
	Test temp. °C	**PWHT °C/h**	**Ys MPa**	**Ts MPa**	**Fracture location**	**Toughness (ISO-V) J**
GTAW	+20	770/0,5	588	745	BM	40 37 38
	+575		358	431	BM	
	+600		337	396	BM	
weld build-up: root and 1. layer: GTAW; wire-Ø: 2,4 mm; (r):140/13; (1.L.) 170/14 2. fill SMAW - Ø: 3,2 mm (100/23); cap layer: SMAW - Ø: 4,0 mm (135/23) T pre heat: 220 °C; T inter pass: 250 - 280 °C						
SMAW	+20	770/0,5	n.tested	n.tested		29 34 27
	+20	770/2	558	728	BM	47 51 51
	575		310	352	BM	
	600		275	345	BM	

2.2.2 Matching filler metals for welding CB 2 material

In the framework of the turbine group different cast materials CB 2, CB 5, CB 6, CB 8, CB 9, CB 10, CB 11 [11] have been produced and tested. So far, CB 2 materials proved to be the best. For this material matching filler metals have been developed [11] and, with respect to chemical composition, optimized. The foundries PHB Stahlguss and Voest Alpine have manufactured plates and casts and an intensive investigation programme started in order to test weldability, mechanical properties and creep properties.

The all weld metal can be characterized as high strength material with YS in the range of about 630 up to 750 MPa and with TS above 800 MPa. Toughness property of the filler metal at room temperature is – even with the addition of Ni and after PWHT - on a level above 27 J. This level is low but these values are corresponding to those of the base material (table 11). With the knowledge about this behaviour it is obvious to take outmost care during welding (limitation of heat input, correct choice of electrode Ø, welding thin layers with gentle weaving technique, etc) [12]. In order to optimize the weld metal properties, chemical composition of the filler metals has been modified by varying Cr and Ni. The following tables 10 and 11 show the chemical composition and the mechanical properties of the all weld metal for different types of Thermanit MTS 5 Co1. Figure 6 and 7 show toughness properties of the all weld after exposure at 600 and 650 °C for the Cr-content reduced type. The observed reduction of toughness is typical for martensitic weld metals and comparable to those of P91, P92 and E911 filler metals. At present time filler metals with a reduced Cr content of about

9,0 to 9,5 % seems to be best candidates. Ongoing tests are carried out within the COST programme using this type of filler metal composition.

Table 10. Chemical composition and mechanical properties of the all weld metal of Thermanit MTS 5 Co 1, SMAW, different alloying concepts

Chemical composition (weight %)

	C	Si	Mn	Cr	Ni	Mo	V	Co	Nb	B	N
high Cr proto type	0,13	0,22	0,55	10,20	0,58	1,55	0,22	1,05	0,04	0,004	0,040
reduced. Cr content	0,14	0,23	0,55	9,30	0,75	1,50	0,22	1,00	0,06	0,003	0,028
red. Cr&Ni content	0,12	0,27	0,53	9,32	0,06	1,52	0,22	1,07	0,05	0,003	0,057

Mechanical properties of all weld, proto type

Ø mm	Test temp. °C	PWHT °C/h	YS MPa	TS MPa	Elong. %	Red. A %	Toughness (RT) J	Heat Input kJ / cm
4,0	+20	760/2	784	901	16,5	55	25 30 27 37	15 – 18
4,0	+20	740/4	743	869	19,0	61	33 31 31 35	15 – 18
4,0	+20	740/6	722	856	15,5	56	37 40 39	15 – 18
4,0	+20	760/10	699	835	16,2	57	42 46 40	15 – 18
4,0	+20	2 x 730/10	673	814	17,7	55	42 44 35	15 – 18
Mechanical properties of all weld, reduced Cr type								
3,2	+20	2 x 730/12	628	779	17,2	66	28 60 68	15 – 18
4,0	+20	2 x 730/12	688	825	17,0	62	34 40 33	15 – 18
5,0	+20	2 x 730/12	637	777	17,8	67	52 46 48	15 – 18
Mechanical properties of all weld, reduced Cr & Ni type								
4,0	+20	2x730/10	636	795	17,1	60	35 36 40 29 42	15 – 18

Table 11. mechanical properties of the base metal CB 2 and of joint CB 2 welded with Thermanit MTS 5 Co 1

Test temp. °C	PWHT °C/h	Ys MPa	Ts MPa	Elong. %	Red. A %	Toughness J	Fracture location	Rem.
Base metal properties								
+20	730/24	550	698	19,4	55	30 – 34	BM	Tested by Alstom
+20	730/48	530	697	20,0	60		BM	
600	730/48	339	372	23,5	75		BM	
Cross weld properties with the MTS 5 Co 1 proto type								
+20	730/24	650	708	"7,6"	"51,0"	HAZ 20-49 / FL 24-36	BM	Tested by Siemens
+20	730/48	448	669	"14,3"	"62,8"		BM	
600	730/48	305	352	"15,9"	"74,7"		BM	
Cross weld properties with the type MTS 5 Co 1 "reduced Cr-content"								
+20	730/24	654	737	"2,9"	"45,8"		BM	Tested by PHB
+20	730/24	562	716	"14,5"	"54,8"		BM	

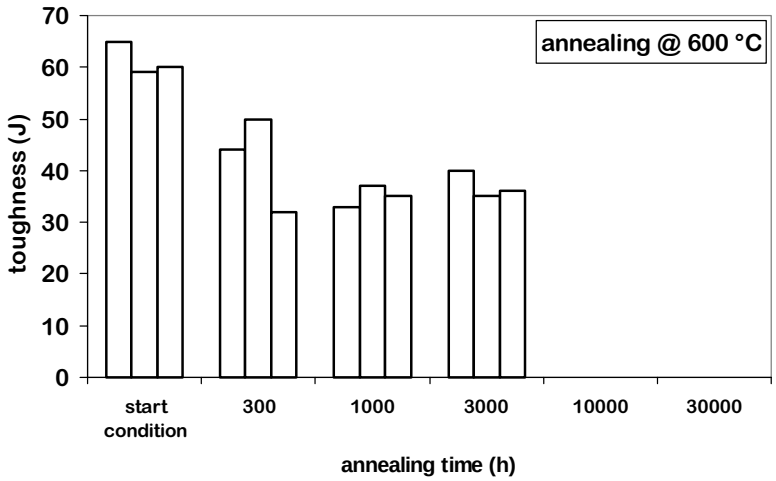

Figure 6. Thermanit MTS 5 Co 1, reduced Cr-content: Influence of exposure at 600 °C on toughness properties of the all weld metal

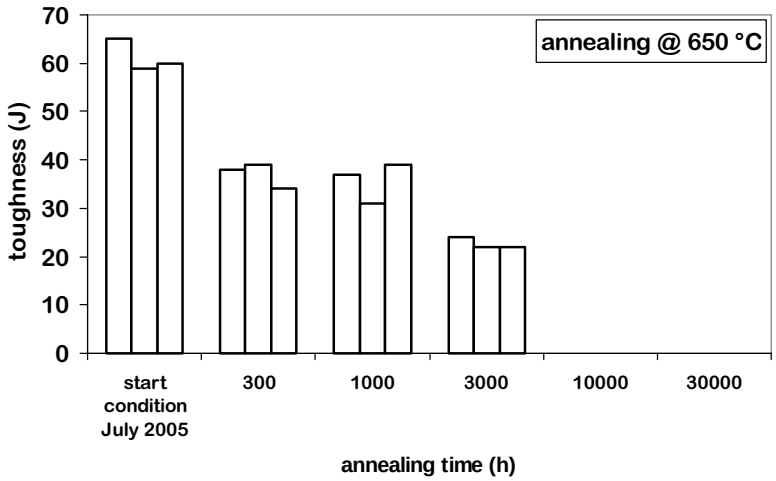

Figure 7. Thermanit MTS 5 Co 1, reduced Cr-content: Influence of exposure at 650 °C on toughness properties of the all weld metal

3. Results of the group research work: "Matching Programme"

Increasing use of newly developed high temperature creep resistant steels requires the employment of adjusted weld filler materials. The mechanical properties of the joints can only be adjusted by the chemical composition of the filler metal, the applied welding procedure and welding parameters and the parameters of the subsequent post weld heat treatment. The raise of creep rupture strength of the weld metal requires significant R&D efforts and causes substantial costs.

Creep testing of crossweld samples and in service behaviour of welded components often revealed the heat affected zone (HAZ) to be the weakest link in this constellation [13, 14]. This cracking mode has been described in literature as "Type IV" cracking [15] reducing the creep strength of welded structures significantly. Abe and co-worker [16] have shown that the decrease of the HAZ width by the use of electron beam welding can significantly increase the creep life of weldments although the fracture also appeared in brittle Type IV mode. This restrained effect can be explained by a mechanically constraint of the deformation of the HAZ by weld metal and base metal.

These results raised the question if the filler material has to have matching or even over matching strength level compared to the base metal or if a filler material of under matching strength level is sufficient. Therefore within COST 522 an extensive research program was started. The program included the welding of a X11CrMoWVNb9-1-1 (E911) pipe with an outside diameter of 355mm and a wall thickness of 43mm using three different welding consumables with different levels of creep strength compared to the base material:

1. Under Matching: Thermanit MTS 3 for GTAW, Thyssen CrMo9V for SMAW (P91 type)
2. Matching: Thermanit MTS 911 for GTAW and SMAW (E911 type)
3. Over Matching: Thermanit MTS 616 for GTAW and SMAW (P92 type)

The welding consumables were provided by Böhler Thyssen Welding and the pipe sections were welded in the fixed horizontal position by Rafako, Poland. Figure 8 shows a schematic of the experimental setup with included weld geometry [17].

3.1 Welding of E 911 Pipe for the matching programme

The objective of COST 522 programme at RAFAKO S.A. was to estimate the correctness of selecting welding parameters, filler metals and heat treatment parameters of welded joints, as well as to estimate the properties. Mastering the processes of welding and heat treatment of creep resisting steels – including E911 with tungsten addition – was based on RAFAKO S.A. experiences gained in 1970s when implementing X20CrMoV12.1 steel [17 19]. The testing material comprised a collector made of E911 steel, diameter ϕ355×45 mm, delivered by the company of Vallourec & Mannesmann Tubes within the frames of COST522 programme.
The examination programme – within COST 522 activities – comprised fabrication of E911 steel joints at RAFAKO S.A., with application of various filler metals used, generally, for welding such steels as P91, E911 and P92. The manufactured welded joints are:

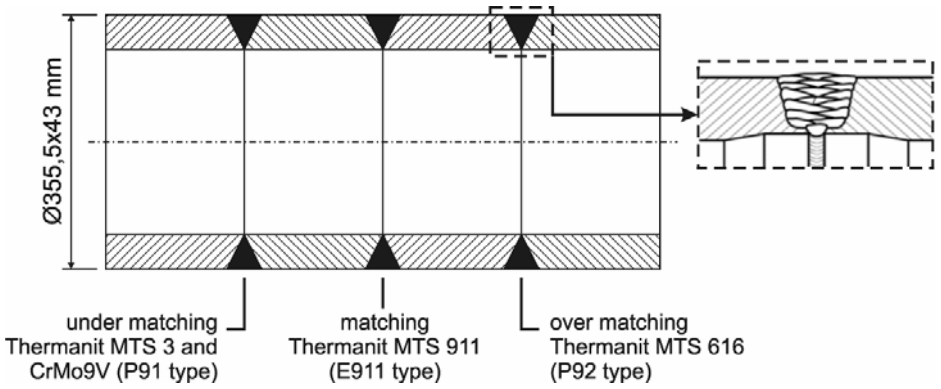

Figure 8. Schematic of experimental setup

- No. 1/COST; filler metal Thermanit MTS3 and electrode Thyssen Chromo 9V in general use for welding steel P91 to steel P91 - under matching joint,
- No. 2/COST; filler metal Thermanit MTS 911, used for welding steel E911 to steel E911 - matching joint,
- and welded joint No. 3/COST; filler metal Thermanit MTS 616, used for welding steel P92 to steel P92 - over matching joint.

The collector – prior to its delivery to RAFAKO S.A. – had undergone non-destructive, strength and technological examinations at the subcontractor's, i.e. those examinations which have to be carried out on tubes to prove their quality. Among others, at RAFAKO S.A. the implementation programme of steels with tungsten addition included:

- evaluation of steel weldability on the basis of thermal cycles simulation,
- selection of welding and heat treatment parameters, non-destructive examinations after welding,
- evaluation of welded joints' quality based on examination results of mechanical and technological properties at ambient temperature and at elevated temperatures,
- evaluation of steel low-cycle fatigue resistance and structural examination of the base metal and welded joints, both directly after welding and heat treatment and after simulation of operating temperature conditions of the boiler superheater components.

Beside the evaluation of steel weldability, the implementation programme of homogeneous and non-homogeneous welded joints' welding technology at RAFAKO S.A. included:

- non-destructive examinations acc. to the requirements of design documentation,
- evaluation of strength properties Rm, R0.2 and HV,
- HAZ macro and micro-structure examinations, deposited metal and welded joints,
- impact strength evaluation on test pieces with V notch,
- bending tests (bending angle 180°),

- fatigue examinations with low number of cycles,
- evaluation of structural changes in base material and welded joints, which occurred in the process of operating temperature conditions simulation on steam superheater components.

3.1.1. Manufacturing technology of E911 steel welded joints

The root bead of all welded joints on ϕ355,5x45mm E911 steel collector was made by means of GTAW method with ϕ2.4 mm wire. For GTAW method the welded joints were made with direct current of reversed polarity. As already mentioned, when manufacturing the joints GTAW and SMAW methods were applied with filler metals Thermanit MTS 3/Chromo 9V for welded joint 1/COST, Thermanit MTS 911 for 2/COST and Thermanit MTS 616 for welded joint 3/COST. The joints were welded with electrode straight polarity, using electrodes ϕ 2.5, 3.2 and 4 mm [20].

The applied heating temperatures and inter-bead temperatures were at all times kept in the range of 200-300^{0}C.

Figure 9 shows the details of welding preparation, welding parameters and the sequence of layers.

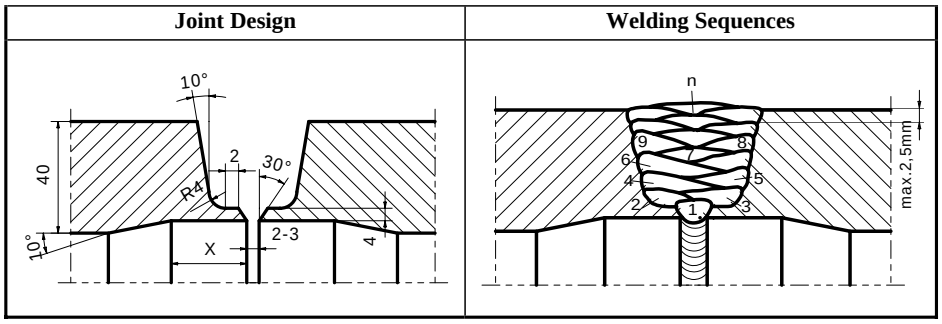

Welding process details

Run	Welding methods	Size of Filler Material	Current [A]	Voltage [V]	Type of current/ Polarity	Wire Feed Speed	Heat input
1	GTAW/ 141	2,4	90 ÷ 100	-	DC"-"	-	-
2 ÷ 3	SMAW/ 111	2,5	70 ÷ 100	-	DC"+"	-	-
4 ÷ 5	SMAW/ 111	3,2	90 ÷ 140	-	DC"+"	-	-
8 ÷ n	SMAW/ 111	4,0	130 ÷ 180	-	DC"+"	-	-

max. thickness of each bead, layer: 2.5mm

Figure 9. Details of welding preparation, wire and electrode diameters and applied welding parameters of butt welded joints on tubes ϕ355,6x45mm steel E911 – for welded joints No. 1/COST, 2/COST and 3/COST

Table 12 presents chemical compositions of filler metals used for welding of joints No. 1/COST, 2/COST and 3/COST.

Table 12. Chemical composition of filler metal used for collector butt welded joints of E911-E911 steel, welded joint No. 1/COST , 2/COST and 3/COST (according to Böhler Thyssen Welding company catalogue)

Joint No / Type of filler metal	Chemical element [%] weight									
	C	Si	Mn	Cr	Mo	Ni	W	V	Nb	N
1/COST Chromo 9V	0,09	0,2	0,6	9,0	1,1	8,8	-	0,2	0,05	0,04
2/COST Thermanit MTS 911	0,11	0,25	0,6	8,8	1,0	0,7	1,0	0,2	0,05	0,05
3/COST Thermanit MTS 616	0,11	0,2	0,6	8,8	0,5	0,7	1,6	0,2	0,05	0,05

In compliance with the agreements made – within COST 522 programme - between Böhler Thyssen Welding, Vallourec-Mannesmann Tubes and RAFAKO S.A., all welded joints were heat-treated at the temperature of 760°C/ 120 min.

3.1.2 Scope of examinations and estimation thereof E911 steel weldability examination

In order to evaluate the correctness of welding parameters' selection, weldability examinations of E911 steel were carried out. They included, among others:

- determining the temperatures of austenite transformations in welding conditions,
- evaluation of material properties in HAZ under the influence of welding thermal cycles at maximum temperature of T_{max} =1250^{0}C with application of cooling times $t_{8/5}$= 6s, 24s, 60s and 300s,
- evaluation of steel annealing crack susceptibility under the influence of heat treatment.

The examinations were carried out by means of a thermal-deformation cycle simulator. The examination results as well as examination methods were implemented in the Welding Institute in Gliwice [18].

Hardness measurements were also taken, together with impact strength and micro-structure of a simulated HAZ on samples having the dimensions of 10x10mm, cut out from the E911 steel tube**.**

3.2 Creep properties of the matching programme

Along with conventional mechanical testing an extensive creep testing program was set up at the Institute for Materials Science, Welding and Forming at Graz University of Technology. Smooth crossweld specimens of the three different welds were machined out of the pipe and exposed to 7 stress levels ranging from 70 MPa to 130 MPa in steps of 10 MPa at a testing temperature of 600°C. Figure 10 shows the actual status (January 2006) of the ongoing creep tests in comparison to the scatter band of creep rupture tests on E911 base material [21]. So far the specimens exposed to 110MPa and 120MPa of all three welds ruptured.

While the specimens with the under matching filler fractured at the lower boundary of the scatter band, the crossweld samples with matching and over matching filler material ruptured at longer times closer to the mean line of the base material scatter band. So far all specimens fractured within the scatter band of the base material and showed sufficient high creep strength.

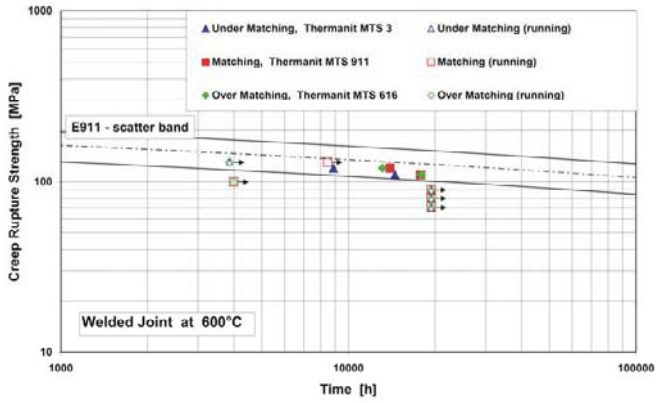

Figure 10. Creep rupture strength of crossweld specimens E911 welded with different filler materials.

All broken specimens were extensively investigated to identify the position of the final fracture within the joint. For this investigation, methods like light microscopy, scanning electron microscopy and hardness testing were utilised to determine the fracture location, mode of fracture and by this the potentially cause of fracture. Figure 11 shows an over view of the up to the present broken samples. Both samples welded with under matching filler metal fractured in the weld metal, while all other samples fractured in the outer part of the heat affected zone close to the unaffected base material.

Figure 12 shows the results of a detailed examination of specimen M2 of the matching series, creep tested at 120MPa and 600°C for 13.945 hours till fracture occurred. The position of fracture can be located in the right HAZ of the weld. Apparently in the HAZ on the opposite side of the weld severe damage in form of cracks and pores has taken place.

	120 MPa	110 MPa
Under Matching	**8.869 h / WM**	**14.519 h / WM**
Matching	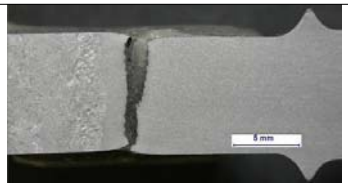 **13.945 h / HAZ**	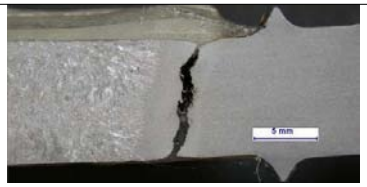 **17.819 h / HAZ**
Over Matching	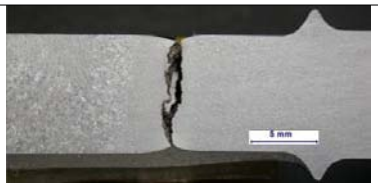 **13.150 h / HAZ**	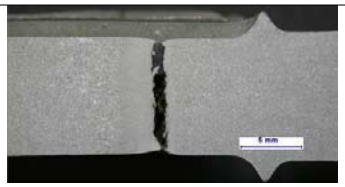 **17.931 h / HAZ**

Figure 11. Investigation of fracture location of creep tested samples with designated time to rupture and position of fracture.

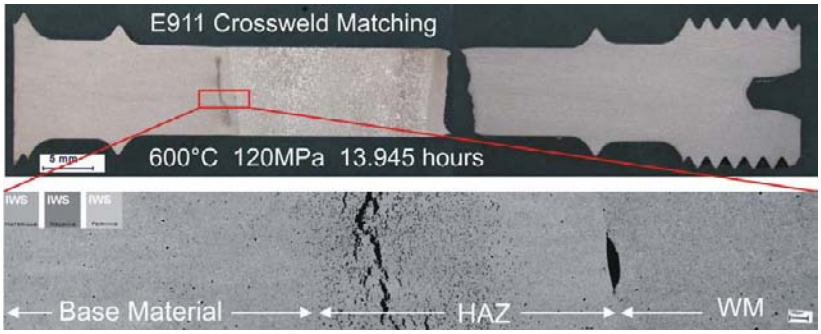

Figure 12. Investigation of fracture location of creep tested crossweld specimen M2, overview (top) and detailed SEM damage study (bottom)

At the fusion line a slag inclusion is clearly visible but didn't cause further damage during creep testing. The complete HAZ has a width of approximately 2 mm. In a region from 1.5 mm to 2 mm away from the fusion line extensive pore formation, agglomeration of pores to pore chains and micro cracks and finally the formation of sizeable cracks was shown by SEM investigations.

The hardness characteristic across the complete specimen width shows a minimum of the hardness (soft zone) in this special part of the HAZ (Figure 13).

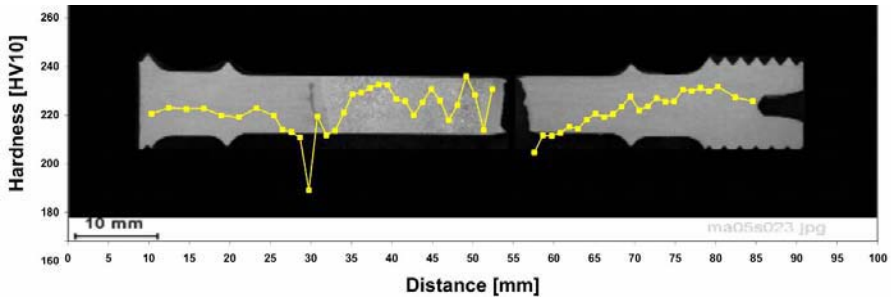

Figure 13. Hardness characteristic across creep tested crossweld specimen M2

4. Conclusion

Within the COST 536 welding group Air Liquide and Böhler Thyssen Welding are active in filler metal development. Both offer matching filler metals for all grades mentioned in this contribution. Concerning T/P 24 filler metals, there is one difference between both suppliers: AL is working with the Ti-alloying concept, BTS is favouring Nb instead of Ti, due to burn-off effects. The new filler metals for VM 12 and for CB 2 show toughness properties, which are lower than those of the well known 9 % Cr-martensitic grades. This requires a more carefully welding, respecting all rules such as: choice of proper diameter and adequate heat input. The mechanical properties meet the requirements and that, not only when welding under laboratory conditions. Creep tests are running and show, that fractures observed so far occur within the scatter band limits of the base materials.

Concerning the matching programme, this investigation showed that the creep behaviour of joints of advanced 9-12% Cr steels can be influenced by the selection of the creep strength of the weld deposit. When using matching or over matching creep strength the fracture occurs in the soft zone of the HAZ. If under matching weld deposit is used the fracture location moves into the weld deposit. This effect shall be taken into account already in the design stage by selection of appropriate weld consumables taking into account the actual stress situation of the welded joint under consideration i.e. circumferential, longitudinal or repair weld.

References

[1] Preliminary datasheet of Vallourec & Mannesmann Tubes for VM12 SHC, WBL 439 draft

[2] Poli, A.; Caminada, S.; Rosellini, C.; Bretoni, A. and Liberati,G.: Fabrication and weldability of Grade 23 tubing and piping, AIM-CSM 1st International Conference "Super-high Strength Steels", Rome, Italy, Nov. 2-4, 2005.

[3] Hahn, B.; Bendick, W.; Heuser, H.; Jochum, C.; Vaillant, J.C.; Weber, J.: Use of modern heat resistant steels like T/P91, T/P23, T/P24 for the retrofitting of power station components – experience, welding and application potential 2nd International Conference "Integrity of High Temperature Welds", 10.-12. November 2003, London; ISBN 1-86125-160-2.

[4] Bauné, E.; Leduey, B.; Bonnet, C. and Bertoni, A.:Development of welding consumables dedicated to the welding of new generation 2 ¼ Cr-1 % Mo pipe materials P23 and P24 for power generation and hydrogen service, in the Proceedings of 2nd International Conference "Integrity of High Temperature Welds", London, UK, Nov. 10-12, 2003, pp. 95-108.

[5] Van Wortel, H.:New generation 2 ¼ Cr-1 % Mo pipe material P23 and P24 for power generation and hydrogen service, within framework of research program, TNO, 2002-2005.

[6] W. Bendick .; B. Hahn, B. Vandenberghe: Entwicklung eines neuen 12 % Cr-Stahles für Rohre in Kraftwerksanlagen mit Dampftemperaturen bis 650 °C FVW/FVHT – 26. Vortragsveranstaltung 28.11.2003.

[7] Jochum, C; Heuser, H: Alloy design for similar and dissimilar welding and their behaviours, AIM-CSM 1st International Conference "Super-high Strength Steels", Rome, Italy, Nov. 2-4, 2005.

[8] Heuser, H.; Schweißzusätze für das Schweißen warmfester Stähle, Jahrbuch Schweißtechnik 2003, S. 72-90, DVS-Verlag, Düsseldorf, ISSN 0935-0292.

[9] Adam, W.; Heuser, H.; Jochum, C.: Neuartige Schweißzusätze für bainitische und martensitische Stähle, DVS Bericht 237, 2005.

[10] J.Gabrel, W.Bendick, J-C. Vaillant, B.Vandenberghe and B.Lefebvre, "VM12 – A new 12%Cr steel for boiler tubes, headers and steam pipes in ultra supercritical power plants", 4th EPRI Int'l Conf. on advances in Materials Technology for Fossil Power Plants, U.S.A., Oct.2004.

[11] Cerjak, H; Letowsky, E; Jochum, C; Nies, H; Weldability and weld properties for advanced power plant materials. Proceedings of the 7th Liege Conference. European Commission, University de Liege, Vol. 21. p. 1081-1090 (Part II). Liege 2003

[12] Blume, R.; Heuser, H.; Leich, K.E.; Meyer., F.: Verbesserungen der mechanisch-technologischen Eigenschaften von Schweißverbindungen an CrMoVNb-Stählen mit 9 % Cr durch Optimierung von Schweißzusätzen und Schweißparametern, DVS Bericht 162, S. 206-210.

[13] Letofsky, E.: Das Verhalten von Schweißverbindungen moderner Kraftwerkswerkstoffe, PhD Thesis, Graz University of Technology (2001).

[14] Takemasa, F. et. al.: Type IV creep damage analysis for full size component test on welded boiler hot reheating piping. in Elevated temperature design and analysis, nonlinear analysis, and plastic components, PVP-Vol. 472 (2004), p.p. 69 – 74.

[15] Schüller, H.J., Hagn, L. and Woitschek, A.: Risse im Schweißnahtbereich von Formstücken aus Heißdampfleitungen – Werkstoffuntersuchungen, Der Maschinenschaden 47, Heft 1 (1974), p.p. 1 – 40 .

[16] Abe, F. and Tabuchi, M.: Microstructure and creep strength of welds in advanced ferritic power plant steels, Science and Technology of Welding and Joining, Vol. 4, No.1 (2004), p.p. 22 – 30.

[17] Hernas A., Kiełbus A., Cieśla M., Rodak K.: „Assessment of large thickness welded joints made of P91, P92 steel grades and T23 base material", Research work P/IX-2/01, September 2001.

[18] J. Brózda, M. Zeman, J. Pasternak. The first supercritical power unit in Poland. Weldability evaluation of new martensitic chromium steels with tungsten additions and properties of welded joints. Proceedings of the 7th Liege Conference. European Commission, University de Liege, Vol. 21. p. 1711-1720 (Part III).

[19] J. Brózda, M. Zeman, J. Pasternak. The first supercritical power unit in Poland. Weldability evaluation of new martensitic chromium steels with tungsten additions and properties of welded joints. Proceedings of the 7th Liege Conference. European Commission, University de Liege, Vol. 21. p. 1711-1720 (Part III).

[20] J. Pasternak, A. Kiełbus "Stability of similar and dissimilar welded joints, high-temperature creep resistant martensitic steels containing 9% Cr". Proceedings of the EPRI Fourth International Conference on Advances in Materials Technology for Fossil Power Plants. October 25 – 28, 2004

[21] ECCC Data Sheets 2005, High alloy ferritic steels - X11CrMoWVNb9-1-1 (E911) (2005).

U.S. PROGRAM ON MATERIALS TECHNOLGY FOR ULTRASUPERCRITICAL STEAM COAL-FIRED POWER PLANTS

R.Viswanathan, EPRI
J.F Henry, Alstom Power
J.Tanzosh, Babcock & Wilcox
G.Stanko, Foster Wheeler Development Corporation
J.P. Shingledecker, Oak Ridge National Laboratory
B.Vitalis, Riley Power

Abstract

One of the pathways for achieving the goal of utilizing the available large quantities of indigenous coal, at the same time reducing emissions, is by increasing the efficiency of power plants by utilizing much higher steam conditions. The US Ultra-Supercritical Steam (USC) Project funded by US Department of Energy (DOE) and the Ohio Coal Development Office (OCDO) promises to increase the efficiency of pulverized coal-fired power plants by as much as nine percentage points, with an associated reduction of CO_2 emissions by about 22% compared to current subcritical steam power plants, by increasing the operating temperature and pressure to 760°C (1400°F) and 35 MPa (5000 psi), respectively. Preliminary analysis has shown such a plant to be economically viable. The current project primarily focuses on developing the materials technology needed to achieve these conditions in the boiler. The scope of the materials evaluation includes mechanical properties, steam-side oxidation and fireside corrosion studies, weldability and fabricability evaluations, and review of applicable design codes and standards. These evaluations are well underway, and have provided the confidence that currently-available materials can meet the challenge.

Introduction and Background

In the 21st Century, the world faces the critical challenge of providing abundant, cheap electricity to meet the needs of a growing global population, while at the same time, preserving environmental values. Most studies of this issue conclude that a robust portfolio of generation technologies and fuels should be developed to assure that the United States will have adequate electricity supplies in a variety of possible future scenarios. Traditional methods of coal combustion emit pollutants (including CO_2) at high levels relative to other generation options. Maintaining coal as a generation option will require methods for addressing these environmental issues.

This project, through a government/industry consortium, is undertaking a five-year effort to evaluate and develop materials technologies that allow the use of advanced steam cycles in coal-based power plants. These advanced cycles, with target steam temperatures up to 760°C (1400°F) will increase the efficiency of coal-fired boilers and reduce emissions substantially. In addition to a reduction in all fuel-related emissions, there are additional benefits to higher efficiency that favorably impact carbon management. Studies have shown that the unit could be designed to allow startup with air, but operate with oxygen and recirculated flue gas blend (to replace the nitrogen). This so-called oxy-fuel combustion option produces a concentrated stream of carbon dioxide which greatly improves the economics of capture. This oxy-fuel option also requires little additional equipment, and may actually eliminate some of the currently-required air quality

control equipment, depending on the purity requirements for carbon capture and sequestration. The USC technology is thus completely compatible with the goals of achieving near-zero emissions in future energy systems.

More than a dozen plants are operating at steam conditions close to 593°C (1100°F)/27 MPa (4000 psi) are in operation worldwide, and plant operation at 620°C (1150°F) appears to be a near-term possibility.(1) Research, development and demonstration programs have been underway in Europe and Japan aimed at materials capable of withstanding steam conditions up to 650°C (1200°F), and over the next decade to 700°C (1300°F). It is imperative that the US boiler manufacturers match those capabilities in this advanced technology area. This is one of the objectives of the US DOE/OCDO project. Furthermore, materials technology is generic in nature and cuts across many energy systems operating at high temperatures. Consequently, materials technology developments for high-temperature applications are expected to be of enduring value. In the near term, materials developed for USC plants can be confidently used for retrofit applications in currently-operating plants to increase their reliability.

In contrast to the European union project (AD 700)[17]. the steam conditions chosen in the US USC Project are more ambitious, and are anticipated to result in higher efficiencies. Further, operating parameters and design practices differ in different countries, and European results cannot be translated directly to operating conditions in the US. For instance, while European plants generally burn low-sulfur coals, coal quality is widely variable in the US. The US program, therefore, calls for evaluation of materials under several different levels of sulfur contents in the coal. Many new alloys have come into the market place since the inception of the original European USC steam project (Thermie). These alloys are among those being evaluated in the US USC program. Also, some results from the European program are available only to the European participants and not to the US domestic boiler manufacturers, so that there is a need to develop indigenous capabilities in the US.

The U.S. DOE/OCDO project is based on an R&D plan developed jointly by the US-based boiler manufacturers and the Electric Power Research Institute (EPRI). It supplements the recommendations of several DOE-organized workshops on the subject of advanced materials, and DOE's vision of clean coal generation technologies. The project originally was planned to be of five years duration, from 6/1/2001 to 12/31/2006. The total project funding is approximately $20 million, with the DOE providing nearly $15 million, the OCDO providing $2 million and the rest being secured in the form of cost sharing by a consortium of EPRI and the major domestic boiler manufacturers (Alstom Power, McDermott Technology, Babcock & Wilcox, Riley Power, and Foster Wheeler Development Corporation). Energy Industries of Ohio (EIO) provides overall program management, and fosters participation by other Ohio entities such as the Edison Welding Institute. The Oak Ridge National Laboratory has been separately funded by the DOE to provide augmenting efforts to the project in the areas of mechanical property measurement, metallurgical evaluations, and steam oxidation data. Co-operation of utility stakeholders, alloy vendors and other National Laboratories has also been secured via advisory roles for their staff.

The project objectives are addressed through the eight tasks listed below:

Task 1. Conceptual Design and Economic Analysis
Task 2. Mechanical Properties of Advanced Alloys
Task 3. Steamside Oxidation and Resistance
Task 4. Fireside Corrosion Resistance
Task 5. Weldability
Task 6. Fabricability
Task 7. Coatings
Task 8. Design Data and Rules

Progress made to date on each of these tasks is described below.

Results

Conceptual Design and Economic Studies

Figure 1 shows a heat balance diagram for a conceptual design of a USC plant.[3] It was concluded that throttle temperature increase would be much more advantageous than throttle pressure increase for improvement of efficiency at minimal cost impact.[2, 3] Based on metal

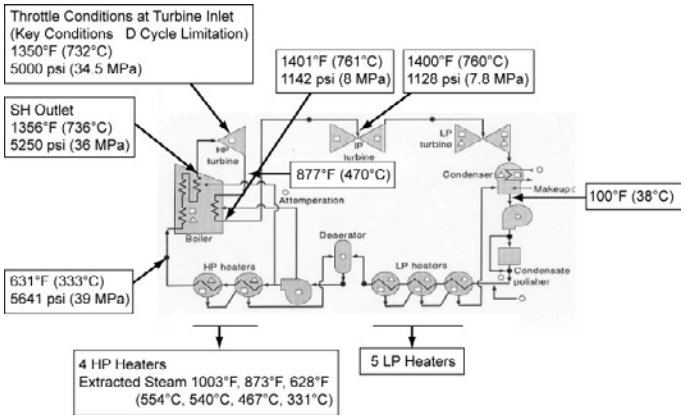

Figure 1. Heat balance diagram for a conceptual 750 MW USC boiler[3]

temperature calculations performed for various sections of a conceptual boiler[2-4], possible materials selections for various sections of the boiler have been performed and are summarized in Fig. 2.[4] Based on creep strength, allowable stress, and data availability considerations,

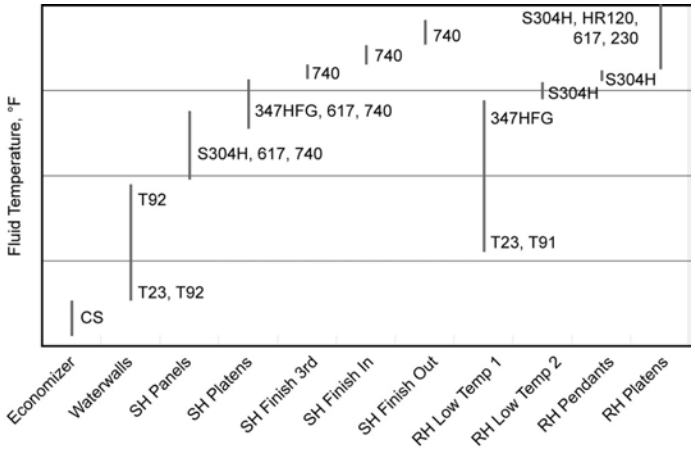

Figure 2. Alloy choices for components of a conceptual USC boiler

Haynes® 230, Inconel® 740 and CCA 617* were selected for the highest-temperature, heavy-section applications as well as tubular components; the austenitics HR 6W and SUPER 304H were selected for tubular applications; and ferritic alloy SAVE 12 was selected for heavy sections at lower temperatures. Alloys T92, T23 and HCM 12 were considered for application in waterwall tubing. The compositions and intended applications of the alloys are shown in Table 1.

Overall, the feasibility of designing an ultra-supercritical 750 MW boiler operating at 732°C (1350°F)/35 MPa (5000 psi) throttle steam conditions with existing material technology is encouraging. The initial goal of 760°C (1400°F) 38.5 MPa (5000 psi) for the main steam was temporarily held in abeyance in view of the need for large thicknesses for the tubing and piping systems. Reheat temperature could however be maintained at 760°C (1400°F), since reheat pressure is only 7.8 MPa (1128 psi). It was estimated that this design will increase the plant

* CCA617: **C**ontrolled **C**ompositional **A**nalysis, a modified composition of Alloy 617

Table 1. Candidate Alloys

Alloy	Nominal Composition	Developer	Application
Haynes 230	57Ni-22Cr-14W-2Mo-La	Haynes	P, SH/RH Tubes
INCO 740	50Ni-25Cr-20Co-2Ti-2Nb-V-Al	Special Metals	P, SH/RH Tubes
CCA 617	55Ni-22Cr-.3W-8Mo-11Co-Al	VDM	P, SH/RH Tubes
HR6W	43Ni-23Cr-6W-Nb-Ti-B	Sumitomo	SH/RH Tubes
Super 304H	18Cr-8Ni-W-Nb-N	Sumitomo	SH/RH Tubes
Save 12	12Cr-W-Co-V-Nb-N		P
T92	9Cr-2W-Mo-V-Nb-N	Nippon Steel	WW Tubes
T23	2-1/4Cr-1.5W-V	Sumitomo	WW Tubes
HCM12	12Cr-1Mo-1W-V-Nb	----	WW Tubes
P - pipe			

efficiency from an average of 37% (HHV)* (current domestic sub-critical steam fleet) to approximately 45% (HHV).[2,3] For a double reheat configuration the efficiency will reach 47%. Expressed in terms of European parameters, this could be as high as 52% LHV*. The efficiency increase from 37 to 47% HHV is expected to save nearly $16.5 million annually in fuel costs, or $330 million over a 20-year plant life for a 750MW plant operating at an 80% capacity factor at a coal cost of $1.5/MBtu. The CO_2 and other fuel-related emissions will be reduced from 0.85 to 0.67 tonnes/MWh, a reduction of nearly 22%. This amounts to an annual reduction of nearly 700,000 tons [Q: tons or tonnes?] of CO_2.[5]

Based on a 20-year break-even consideration, an assumed capacity factor of 80%, and coal cost of $1.42/G J. ($1.50/MBtu), the fuel cost savings over the 20-year period, are sufficient to allow an ultra-supercritical plant to be cost competitive even if the total plant capital cost is 12 to 15% more than a comparable scale facility built using conventional subcritical boiler and cycle designs, as shown in Fig. 3[6]. Balance-of-plant (BOP) costs are expected to be 13 to 16% lower than those for existing boiler and cycle designs due to smaller coal handling and pollution control systems, resulting from the improved plant efficiencies. As a result of these reductions in fuel and BOP costs, boiler and steam turbine capital costs can be permitted to be higher compared to subcritical plant by 40 to 50%. It should be noted that the above economic trade-off

* HHV and LHV: Higher Heating Value and Lower Heating Value, respectively (related to the assumption regarding recovery of heat of vaporization of moisture). Efficiency calculations were based on typical US plant siting and operating practices.

study does not take into account benefits resulting from reduction of emissions due to increased efficiency. If a potential "carbon tax" were also taken into account, the advantage of the USC plant becomes even more substantial. For an assumed tax of $7 per ton of CO_2 emitted, the total annualized savings from increasing efficiency from 37% for a subcritical plant to 47% for an USC plant is estimated to be $4.9 million. The allowable capital cost for a USC plant in this case is considerably higher than when the carbon tax is not taken into account.

Based on the materials specifications listed earlier, a materials trade-off was developed.[3] To obtain the total boiler cost, current market level pricing was applied to the standard ASME materials used in the design. For the non-ASME nickel-based superalloys, vendor-estimated pricing was used; the costs used for the superalloy materials were $20/lb for both Haynes 230 and Inconel 740.[3] The superalloy pricing is the greatest unknown in this analysis, because of the difficulty of estimating the ultimate commercial mass-produced pricing. Other unknowns are the fabrication and construction costs associated with the new superalloys. For the purposes of this study, the fabrication costs were assumed to be equal to the fabrication costs of a conventional supercritical boiler. The construction costs were based on the cost of a conventional supercritical unit increased proportionally by the weight ratio of the ultra-supercritical to a conventional supercritical unit.

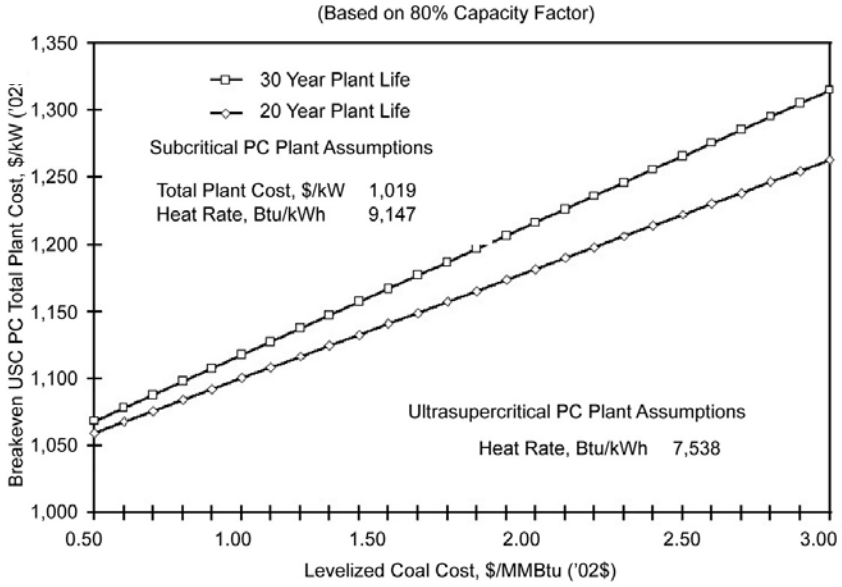

Figure. 3 Break-Even Total Plant Cost and Fuel Cost – 20 vs 30 Year Life[5,6]

The materials tabulation for the ultra-supercritical unit was compared to both a subcritical and conventional supercritical unit of approximately the same power rating.[3] The ultra-supercritical boiler was found to have approximately 7% more suspended weight than a conventional supercritical boiler with the same plant output, despite the smaller size of the ultra-supercritical boiler. Since the ultra-supercritical unit is nearly 20% narrower than a conventional supercritical unit, the total header and piping weight is not increased over a conventional supercritical unit. However, there is an approximately 13% increase in overall tubing weight for the ultra-supercritical unit.

Ultimately the ultra-supercritical design was found to have approximately a 28% increase in cost over a PC subcritical unit.[3] As noted above, the cost comparison was based on a delivered and erected price for the boiler island only. While this analysis indicates that the cost differential over a PC subcritical unit is below the 40% value for economic viability, the assumptions stated and the preliminary nature of the evaluation must be taken into account when drawing any conclusions.

An alternative design consideration that mitigates the high cost of the superalloys is a design with increased throttle temperature without a major increase in throttle pressure. As mentioned earlier, the costs involved in increasing steam temperature are lower than for raising steam pressure. Reducing throttle pressure may allow the more extensive use of standard austenitic materials, while maintaining the plant efficiency gains due to higher throttle temperature. This approach of using lower pressure (in combination with the better than expected material properties observed for some alloys and the lower stresses calculated from the reference stress approach[7] as described later), favors the possibility of achieving the initial goal of 760°C (1400°F) throttle steam.

900

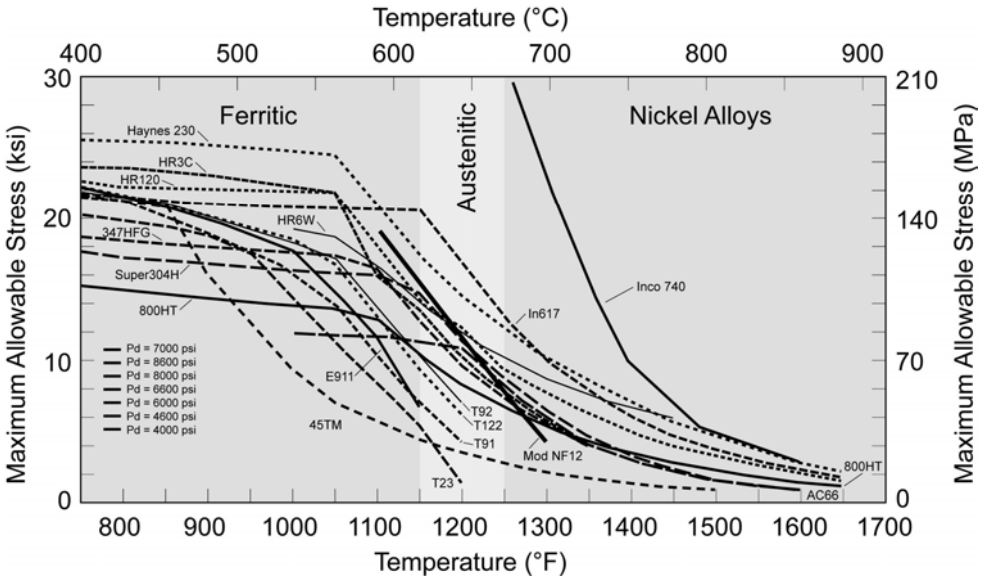

Figure. 4 Allowable stresses for various classes of alloys [8]

Mechanical Properties

Figure 4 is a plot of the allowable stresses as a function of temperature used to compare and determine the temperature capabilities of various classes of alloys.[8] The figure also shows the actual stresses at several steam pressures.[8] The nickel-based alloys Inconel 740, Haynes 230, Inconel 625, Inconel 617, HR6W and HR 120 have much higher temperature capability in decreasing order as listed compared to austenitic steels, followed by the ferritic steels. Purely from the creep strength point of view, at a pressure of 35 MPa (5000 psi) for a 5 cm (2 in) by 1.25cm (0.5 in.) tube (stress 60 MPa or 8.7 ksi), ferritic steels are useful up to about 620°C (1150°F) (metal temperature) and austenitic steels up to about 675°C(1250°F). At metal temperatures higher than this, Ni-based alloys are required.

Creep rupture testing is in progress for SAVE 12, Super 304H, Haynes 230, CCA617, and Inconel 740. Creep-rupture tests on HR6W tubing are complete, and the results confirm earlier predictions (based on short-term data) that indicated the alloy had poorer creep strength than expected from literature. Figure 5 compares the expected and measured 100,000 hour rupture strength as a function of temperature for HR6W. The measured values are 20 to 30% lower than expected. When compared to Super 304H, the creep strength of HR6W is inferior below ~675ºC while it shows an improvement over Super 304H above 675ºC.

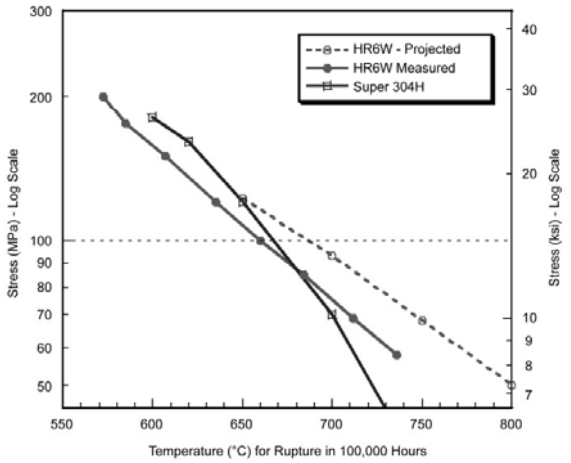

Figure 5. 100,000 hour rupture life for austenitic tubing (extrapolations based on data up to ~20,000 hours). Measured strength of HR6W is significantly lower than projected values from material supplier.

Creep tests on CCA617 have exceeded expectations in the lower temperature regime (650°C to 700°C), but above 750°C the creep strength was indistinguishable from that of the standard Inconel 617. Microstructural studies suggest that this strength difference is due to the precipitation of gamma prime, but at 750°C these precipitates were found to coarsen significantly with time, and at 800°C contributed little to the hardening of the material. [9] This suggests that at 750ºC and above, no long-term strength advantaged is expected for CCA617 due to gamma prime precipitation. Figure 6 show the extrapolated 100,000 hour rupture strengths of 617 and CCA617. The 100 MPa-100,000 hour rupture strength for CCA617 is estimated at 725ºC compared to ~700ºC for 617. Creep testing and isothermal aging continue beyond 23,000 hours at 650 to 750ºC to determine the long-term stability of the alloy for service at USC conditions.

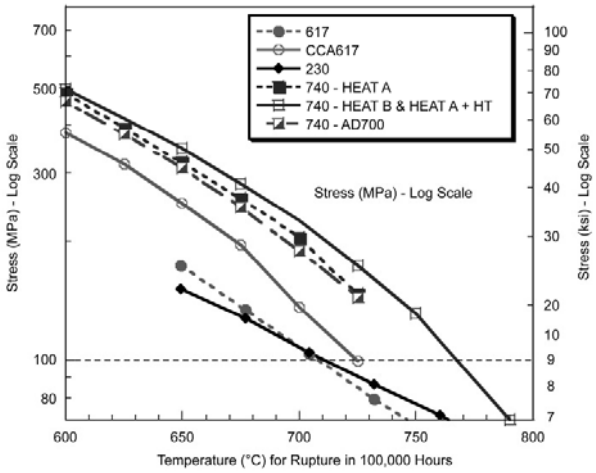

Figure. 6. 100,000 hour rupture life for nickel-based tubing and plates (extrapolations based on data up to ~23,000 hours). CCA617 shows improved strength compared to 617 (725ºC at 100MPa). Inconel 740 rupture strength shows heat-to-heat and heat-treatment variations. All the data suggests better strength than AD700 program reported values.

Creep testing of Inconel 740 is being performed on both tubing and thick plate. Creep-rupture tests on two heats of material and two heat-treatments have shown some data scatter for rupture life as shown in figure 6. All material was given a standard 800ºC-16hr heat-treatment before testing. Heat 'A' shows behavior similar (although slightly improved) to that reported on the AD700 program[17]. However when Heat 'A' was subjected to an additional solution heat-treatement, its rupture behavior followed that of Heat 'B' which was significantly better than that reported by the AD700 program. Heat 'B' has a 100MPa-100,000hr estimated rupture life greater than 760ºC, which meets the aggressive strength requirements of this project. The Inconel 740 data in figure 6 is based on rupture lives up to ~10,000 hours. A number of tests are ongoing with projected rupture times of 10-20,000 hours at 750ºC. For ASME code qualification, data is required on a minimum of three heats of material. A third heat of 740 has been obtained for the required testing.

To evaluate the fabrication and welding processes developed on the program, testing is being performed on welds, weldments, and cold-bent tubes. Cross-weld creep tests on HR6W and on Super 304H have shown that 'overmatching' filler metals have superior creep strength compared to the base metal with most ruptures in the base metal at expected base metal lives. Cross-weld tests on Haynes 230 tubes and thin plates show the weld metal to be approximately 80% the strength of the base metal with all cross-weld failures in the weldments. Current cross-weld creep studies are focused on thick plate weldments in CCA617 (specimens up to 37mm in

thickness), tube weldments in 617, dissimilar metal welds (DMW) in CCA617/Super 304H, and plate weldments in Inconel 740. The cross-weld tests on Inconel 740 are in support of the welding development efforts on this alloy and include matching 740 filler metal and Nimonic 263 filler metal. To examine cold-work effects, pressurized creep tests on tube bends have been performed on Haynes 230 and HR6W. At relatively high levels of cold work (20 to 35% outer fiber strain) after 8,000 hours in test, neither alloy showed large reductions in rupture life at 775ºC indicating the ASME code rules for cold-work will be conservative for the solid solution nickel-based alloys. Tests on Inconel 740 tubes bends are currently underway to examine cold-work effects in age-hardenable nickel-based alloys.

In support of design rules and model development, LCF, thermal fatigue (thermal shock experiments), and creep-fatigue tests are being performed on some alloys. These data will be used primarily to determine the effect thermal transients will have on thick-section components. This is important because the current experience for most boilers is with ferritic steels which have different physical properties compared to the nickel-based alloys.

Steamside Oxidation Tests

Task 3 is designed to determine the steam-side oxidation behavior and temperature limits of commercially-available ferritic steels, austenitic stainless steels, and Ni-based alloys. Experimental testing is being conducted to supplement available data from the literature to increase understanding of the steam-side oxidation behavior, especially the effects of variables such as alloying content and environmental conditions.[10]

The test environments used are: (1) high-purity water with 100-300 ppb of dissolved oxygen and addition of 20-70 ppb ammonia to produce a pH value of 8.0-8.5, used for tests at 1 atm.; and (2) de-aerated, high-purity water (specific conductivity 0.2 µmho) used for testing at 17 atm. Inside the test rigs used, the test solution flashes to steam and passes into a retort that contains the test specimens. The specimens are flat coupons (typically 20 x 10 x 2 mm) that are hung from a test frame and oriented parallel to the flow stream[10].

In general, four to six coupons are tested from each material at each temperature and pressure, and exposures are made to 4000h. The coupons are measured and weighed prior to testing. At each shutdown, the coupons from each material are removed and weighed to determine the weight change. One of the coupons from each material is cross-sectioned and metallographically examined by optical microscopy, and/or by scanning electron microscopy (equipped with energy dispersive x-ray analysis capabilities) to determine oxide morphology and composition, and to allow thickness measurements to be made. Some coupons are descaled and reweighed to determine the descaled weight loss experienced by each material.

Steamside oxidation testing has been completed at 650°C (1 and 17 atm); 700°C (17 atm); and 800°C (1 and 17 atm). The oxidation rates primarily followed a parabolic rate law, and the rate constants derived were found to be in agreement with literature data (where this information is available). Among the ferritic steels, two new steels: MARB2 (developed by NIMS) and VM12 (developed by V&M Tubes) displayed the lowest weight gains/metal loss, whereas all other 2-

9% steels were subject to rapid oxidation. Ferritic steels that showed the lowest weight loss also exhibited the lowest tendency to spall. Clear evidence of spallation was observed for alloys T23, T91 and T92. Ferritic material MARB2 and austenitic material 304H displayed the formation of oxide islands, indicative of the development of a non-protective oxide at some location. The highest tendency among the austenitics for scale exfoliation was found in 347HFG. Shot blasting was found to be beneficial in both Super 304H and in 347HFG steel. The oxidation behavior of some nominally 12%Cr steels (for example, T122) was very variable, with anomalous temperature dependence apparently resulting from the fact that their ability to form a consistently-protective scale was unusually sensitive to minor changes in factors such as levels of minor alloying elements, surface condition, and test variables. However, one nominally 12%Cr steel (VM12) was able to reliably form a protective scale, and performed as well as some austenitic and Ni-based alloys.

No spallation was observed from the austenitic steels or Ni-based alloys in the 650°C (1200°F) tests. Of the austenitic and Ni-based alloys, the Co-containing alloys Nimonic 263, CCA 617 and Inconel 740 exhibited the best oxidation behavior. All of the austenitic and Ni-based materials tested formed a dense layer of chromium oxide that will result in low oxidation rates at this temperature. The Ni-based alloys that contained between 0.5 and 1.3% Al formed near-surface intergranular aluminum oxide penetrations beneath the external (protective) chromia scales, which effectively increased the thickness of load-bearing section lost.

Results from tests at 650 and 600°C in 1 atm steam, shown in Fig. 7, indicate that the oxidation susceptibility appears to be independent of Cr level, once a threshold level of about 10% is reached.

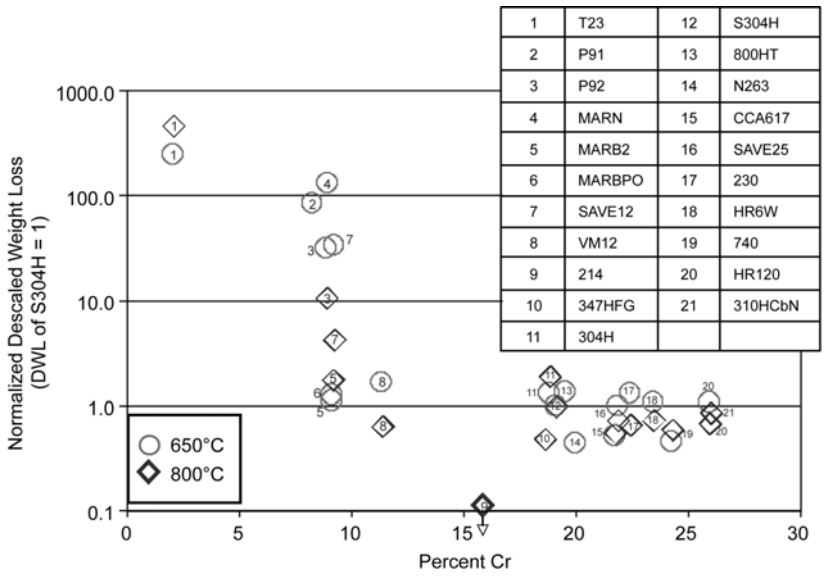

Figure 7. Normalized weight loss of sample after steamside oxidation 1000 hr at 800°C[10]

Among the diffusion coatings tested, SiCr and FeCr coatings performed much better than AlCr coatings. Based on calculated oxidation rates, it appears that the life of austenitic and Ni-based tubing was unlikely to be controlled by steamside oxidation rates rather than fireside corrosion. The primary concern with respect to steamside oxidation is oxide exfoliation.

Fireside Corrosion

The objective of this task is to evaluate the relative resistance of various candidate alloys to fireside corrosion over the full temperature range expected in an USC steam plant.[11] The testing involved the corrosive environments representative of three different domestic coal types: Eastern (E), Midwestern (MW), and Western (W). Also, three types of testing were undertaken: (1) laboratory testing simulating conditions expected at the waterwalls and superheater/reheaters, using appropriate deposit compositions and gas mixtures; (2) steam loops formed by welding together spool pieces of the various materials and inserted into the superheater circuit to be exposed to the actual boiler conditions; and (3) retractable air-cooled probes inserted inside operating boilers.

In the case of the waterwall corrosion testing, specimens tested under MW and E conditions exhibited more wastage than those tested under W-coal conditions (see Fig. 7[11]). The difference in the amount of wastage between the MW/E and W conditions was greater at

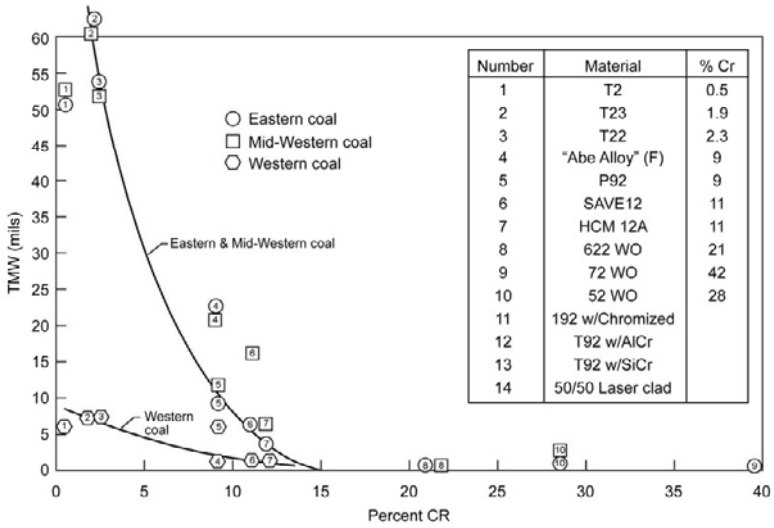

Figure 8. Total metal wastage for alloys under waterwall conditions at 525°C (975°F), 1000 hr[(11)]

454°C (850°F) and 525°C (975°F) than at 593°C (1100°F). The MARB2 and SAVE12 alloys (which contain Co) exhibited higher wastage rates than did the P92 and HCM12A alloys at all three temperatures.

The Inconel-622, -52, and -72 weld overlays and laser clad 50/50 displayed significant improvement in corrosion resistance compared to the wrought alloys at all temperatures, although the Inconel-622 overlay started to show more attack at 593°C (1100°F) compared to -52 and -72. With regard to the diffusion coatings (on T92), they also exhibited significantly improved corrosion resistance compared to the wrought alloys. The chromized coating displayed the best performance, followed by the SiCr and the AlCr. As in the SH/RH tests, the AlCr coating exhibited the most subsurface attack.

Figure 9 provides an illustration of data obtained under superheater/reheater simulation at 650°C (1200°F)[(11)].

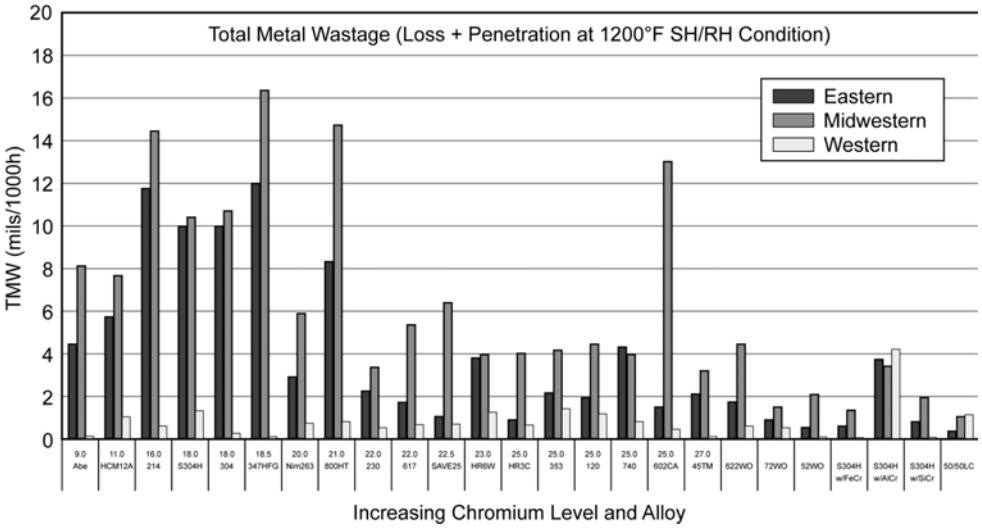

Figure 9. Illustration of fireside corrosion under superheater conditions after 1000 hr at 650°C (1200°F) [11]

The results for superheater/reheater corrosion so far confirm that:

- As noted by others, the environments characteristic of US Midwestern and Eastern coals are much more corrosive than the environment typical of a Western coal.
- Corrosion behavior was a function of Cr level, with corrosion decreasing rapidly as the chromium level increased to 22-27%, and then leveling off.
- Fe-Ni-Cr and Ni-Fe-Cr alloys HR3C (53Fe-25Cr-20Ni), 353 (36Fe-35Ni- 25Cr-1Si), 120 (37Ni-35Fe-25Cr), and HR6W (40Ni-25Fe-23Cr-6W) performed better than the Ni-based alloys tested.
- Of the Ni-based alloys, Inconel 740 exhibited better corrosion resistance than Haynes 230 and CCA617.
- Weld overlays Inconel-72 (42% Cr) and Inconel-52 (28% Cr) performed better than Inconel-622 (21% Cr).
- Diffusion coatings of Cr and Cr-Si displayed better corrosion resistance than Al-Cr and were comparable to weld overlays, but because they are thinner will be breached sooner.

Of the weld overlays, Inconel-72 (typically 42 Cr) and Inconel-52 (typically 28 Cr) performed better than Inconel-622 (typically 21 Cr) at all temperatures, with 72 performing better than the

52. At 650°C (1200°C) and 704°C (1300°C), the 72 and 52 were better than the wrought alloys in the 22-27 Cr range. With regard to the diffusion coating (on Super 304H), the FeCr and SiCr compositions performed better than the AlCr, which exhibited the most extensive subsurface penetration. The FeCr and SiCr coatings were comparable to the weld overlays but, because they are thinner, will be breached sooner.

Figure 10 shows one of two steam loops being hydrotested prior to installation in a boiler, which burns high sulfur coal.[12,13] USC boiler design operating conditions are simulated by throttling the steam flow to achieve metal temperatures up to 760°C (1400°F). Operating parameters during the test are monitored remotely. Physical monitoring of the tubes is accomplished during outages at the plant by means of diameter measurements for hot corrosion wastage, and photographs of the surface condition.

Weldability Studies

The scope of this task includes study of six alloys: SAVE12, Super 304H, HR6W, Haynes 230, Inconel 740, CCA 617. Two product forms, tubing and pipe or plate, are being studied, and welding procedures for 15 materials/product forms/welding processes combinations are being developed. Welding procedures are being developed for three dissimilar metal weld configurations, and weldments for each of the combinations are being evaluated[14].

Preliminary results indicate that submerged arc welding (SAW), a high deposition rate process favored by boilermakers for thick sections, might not be feasible for Ni-based materials; tests on Haynes 230 and Inconel 740 have been unsuccessful. A 7.5cm (3 in.) thick plate of Haynes 230 was successfully welded using pulsed gas metal arc welding (GMAW) technique, as shown in Figure 11.[15] Hot wire gas tungsten arc welding tests conducted on 2-inch thick Inconel 740 plates using a 25% Helium/75% Argon shielding gas and matching filler wire gave encouraging results. There were very few microfissures compared to earlier samples using a pulsed gas metal arc process. Bend and tensile tests will be conducted for further evaluation of this plate in an attempt to fully qualify a welding procedure.

Figure 10. Steam loop assembly being hydrotested prior to installation and hot corrosion testing in a boiler at the Niles, Ohio power station

Figure 11. End view of completed 7.5cm (3 in) thick Haynes 230 alloy weld

An orbital gas-tungsten arc welding (GTAW) process has been qualified for Super 304H and test specimens are being fabricated. While attempts to weld tubing using an automatic GMAW process were unsuccessful, type 347 filler produced acceptable welds. An orbital GTA process was qualified for tubing of alloy CCA 617, and a SAW process was qualified for plate and test specimens are being fabricated. Attempts to perform shielded metal arc welding (SMAW) using matching filler were unsuccessful due to slag control problems with CCA 617 electrodes. On the other hand, successful SMAW welds were achieved using conventional 617 electrodes. Collaboration is being pursued with the alloy vendor (Special Metals Corp.) in view of their experience in welding 2.5 cm (1 in) thick plates of Inconel 740 using GMAW. Summary results of welding trials to-date are presented in tabular form; an example is illustrated in Table 2 for SAVE12.

Table 2. Illustration of the type of weldability data obtained [14]

SAVE 12

Product Form	Weld Type	Process	Filler	Comments
2-inch OD Tube	Butt	Manual GTAW	Grade 92	Qualified
		Manual GTAW	SAVE 12	First sample failed bend testing. Second sample completed using modified PWHT, awaiting results of qualification tests.
		SMAW	SAVE 12	First sample failed bend testing. Second sample completed using modified PWHT, awaiting results of qualification tests.
13.78-inch OD Pipe	Butt	Manual GTAW	SAVE 12	Sample welded, PWHT pending results of tube qualification tests.
		SMAW	SAVE 12	Sample welded, PWHT pending results of tube qualification tests.
		SAW	SAVE 12	Sample welded, PWHT pending results of tube qualification tests.

Fabricability Studies

The primary objective of this task is to conduct fabrication studies on the alloys of interest and to assess the effects of fabrication on material properties, so that potential fabrication problems may be identified.[16] Experience in welding, machining, cutting, boring and grinding of Haynes 230, Inconel 740, HR6W, CCA 617 and Super304H stainless steel has been gained in the course of fabrication of two steam test loops. Protective weld overlay claddings using alloys Inconel 52, Inconel 72 and Inconel 622 were successfully applied to the tube sections that form the test

loops. Field welding was additionally demonstrated during installation of the test loops in the boiler. Samples of strained material required for characterizing the recrystallization/precipitation behavior of USC steam alloys were made by controlled straining (ranging from 0 to 50%) of special tapered tube specimens. Fabrication of multiple U-bends from Haynes 230 and HR6 W. tubing (2 in. OD X 0.4 in. MW) was successfully demonstrated using production equipment. Tube U-bends with strains of 15%, 20% and 35% were produced as shown in Fig. 12.

USC Alloy	Evaluation Planned	Results & Status	Comments	Follow-on Activities
Alloy 230 – B&W –	Cold U-Bend Trials	13.3% 20% & 33.3%	Good; Some ovality	P-Creep at ORNL
	Tubewelding Trials	625 Filler, 622, 52, 72 WOL	Good; Field Test Loops Fabricated	Fabricate Demo Article
	Machining Trials	Completed	Good; Field Test Loops Fabricated	Fabricate Demo Article
	Strain/Rx/Pptn Trials	1500°F & 1600°F	100, 250, 400 & 550 hrs.	Fabricate Microstructures
	Swaging Trials	Planned Spring 2005	Machined Tubes to 0.2" Wall	Assess Microstructures
	Demo Article Fab	Planned Spring 2005	Design Completed	Fabricate; Display TBD

Figure 12. Current Status of Workplan Activities – Alloy 230

Swaging trials of two of the USC steam alloys have been completed. Data on recrystallization behavior, phase precipitation and dissolution in the Ni-based alloys are being compiled to assist in the understanding and development of fabrication procedures. Summary of results for one of Alloy 230 are shown in the table in Figure 12.[16]

As a demonstration of the fabrication capabilities achieved in the course of this project, a mock up section of a header was fabricated, see Figure 13. The mock up illustrates capabilities with

respect to fabrication of CCA 617 alloy into the header shape by bending of plate; girth welding; seam welding; socket welding machining; swaging; hole drilling; and dissimilar welding between CCA 617 and Super304H and T91 tubing.

Fabrication Process

Forming
- Press forming of headers and piping
- Bending of tubing
- Swaging of tube ends

Machining
- Weld grooves for header and pipe longitudinal and circumferential seams
- Socket weld grooves for tube-to-header joints
- Weld grooves for tube circumferential seams

Welding
- Submerged arc welding (SAW) for header and pipe longitudinal and circumferential seam
- Gas tungsten arc welding (GTAW) for tube-to-tube joints
- Shielded metal arc (SMAW) and gas tungsten arc welding (GTAW) for tube-to-header socket joints
- Dissimilar welds

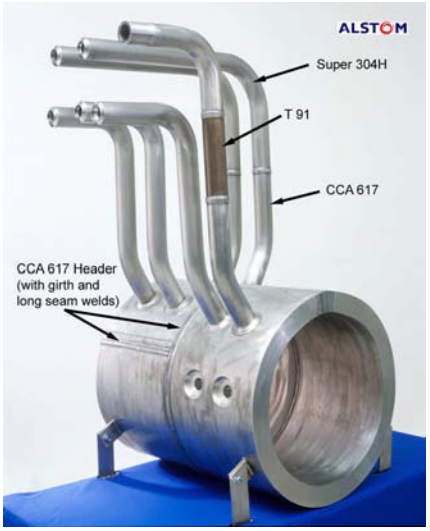

Figure 13. Demonstration of fabrication capabilities with alloys of interest for an USC steam boiler

Coatings

Several specimens with claddings, sprayed coatings [cold spray, high-velocity oxygen/fuel (HVOF)] and diffusion chromium, chromium-silicon, chromium-aluminum coatings have been prepared using commercially-viable processing.[(4)] Results show that ferritic steels benefit most from coatings; austenitic steels may benefit; while Ni-based alloys are not likely to need coatings at all. Process scale-up activities are being pursued. The scale-up tests for the chromizing process have been completed, and the evaluation of results revealed excellent reproducibility for both types of materials, Super304H and T 92. Development of parameters for depositing HVOF and cold spraying techniques for 50Ni/50Cr coatings also has been completed. Optimal parameters have been selected and used to coat Haynes 230 tubes. For the other coating processes of interest, parameters for deposition of 50Ni/50Cr by plasma-transferred arc and laser cladding are being measured.

Design Data and Rules

A new set of design equations has been developed for cylindrical components (tubes, pipes, headers, shells and drums). Since these are based on analysis, they are less conservative than those used in conventional design practice.[7] The impact of the new design equations will be that a consistent failure criterion will be applied to all sizes and types of cylindrical sections. This criterion incorporates a limit load approach in the time-independent regime, and a reference stress approach in the time-dependent regime. It is expected that these proposed rules will permit the use of thinner-walled components than would be permitted under the current ASME and European rules, without compromising component reliability and safety. It is estimated that in ultra-supercritical boilers, where expensive materials are required, a 12% reduction of the cost of boiler pressure parts can be achieved. Also, thinner-walled components would be less subject to thermal fatigue, and therefore the plant would be less susceptible to damage from cyclic operation. This less conservative approach also would permit use of materials with lower creep strengths under a given set of conditions, thus offering a wider selection of alloys for use at high temperatures. Proposed revisions to Section I of the ASME code to permit the use of simplified and more technically-defensible design equations were submitted to Subcommittee I, and accepted by them in September 2004. Subsequent to that, the revisions were included in the Main Committee ballot.

Summary

The technical and economic feasibility of designing an ultra-supercritical steam 750 MW boiler operating at 732/760°C (1350/1400°F) and 35 MPa (5000 psi) with existing materials technology is encouraging. This plant would be capable of achieving a net plant efficiency of about 45 % HHV, based on US design and operating practice. With a double-reheat configuration, a plant efficiency of 47% could be achieved. The materials needed for construction of various parts of the boiler have been identified. Studies pertaining to mechanical properties, steamside oxidation resistance, fireside corrosion resistance, weldability, fabricability and the use of coatings/claddings are nearing completion. Design approaches that are less conservative and more robust have been explored, with a view to extending the range of applicability of available materials to higher temperatures/stresses.

Acknowledgements

The sponsorship and guidance of this work by Dr. Romanosky and Dr. Udaya Rao of NETL, and by Jackie Bird of OCDO is gratefully acknowledged. The project manager is Robert Purgert of EIO. The technical results reported are based on contributions by numerous investigators including Paul Weitzel, Mark Palkes, George Booras, Robert Swindeman, John Shingledecker, Jeff Sarver, Ian Perrin, John Sanders, Mike Borden, Walt Mohn, Steve Goodstine, John Fishburn, and many others. Their contributions are gratefully acknowledged.

References

[1] R. Viswanathan, A.F. Armor and G. Booras, “A Critical Look at Supercritical Plants”, Power Magazine, April 2004, p 42-49.

[2] M. Palkes, "Task 1A, Conceptual Design – ALSTOM Approach, "Boiler Materials for Ultra-supercritical Coal Power Plants", DOE Grant DE-FG-26-01NT41175, OCDO Grant D-00-20, Topical Report USC T-3, February 2003.

[3] "Task 1 B, Conceptual Design – Babcock and Wilcox Approach, "Boiler Materials for Ultra-supercritical Coal Power Plants", DOE Grant DE-FG26-01NT41175, OCDO Grant D-00-20, Topical Report USC T-3, February 2003.

[4] S.L. Goodstine and D.C. Nava, "Use of Surface Modification of Alloys for Ultra-supercritical Coal-fired Boilers", in Proc. of the 4th International Conference on Advances in Materials Technology for Fossil Power Plants, Hilton Head Island, SC, October 2004, ASM International, in press.

[5] G. Booras, "Task 1 C, Economic Analysis", Boiler Materials for Ultra-supercritical Coal Power Plants, DOE Grant DE-FG26-01NT41175, OCDO Grant D-00-20, Topical Report USC T-1, February 2003.

[6] G. Booras, N. Holt and R. Viswanathan, "Economic Analysis of New Coal-fired Generation Options", in Proc. of the 4th International Conference on Advances in Materials Technology for Fossil Power Plants, Hilton Head Island, SC, October 2004, ASM International, in press.

[7] John D. Fishburn, and I. Perrin, "A Single Technically Consistent Design Formula for the Thickness of Cylindrical Sections Under Internal Pressure", PVP2005-71026, Proceedings of PVP2005, 2005 ASME Pressure Vessels and Piping Division Conference, July 17-21, 2005, Denver, Colorado.

[8] B. Vitalis, Private Communication to R. Viswanathan, Riley Power Inc., 2003.

[9] J.P. Shingledecker, R.W. Swindeman, Q. Wu, and V.K. Vasudevan, "Creep Strength of High-Temperature Alloys for Ultra-supercritical Steam Boilers". Proceedings to the 4th International Conference on Advances in Materials Technology for Fossil Power Plants, October 25-28, 2004. ASM International, in press.

[10] J.M. Sarver and J.M. Tanzosh, "An Evaluation of the Steamside Oxidation of Candidate USC Materials at 650°C and 800°C, in Proc. of the 4th International Conference on Advances in Materials Technology for Fossil Power Plants, Hilton Head Island, SC, October 2004, ASM International, in press.

[11] G. Stanko, unpublished work, Foster Wheeler Inc., 2004.

[12] D.K. McDonald and E.S. Robitz, "Coal Ash Corrosion Resistant Material Testing Program", in Proc. of the 4th International Conference on Advances in Materials Technology for Fossil Power Plants, Hilton Head Island, SC, October 2004, ASM International, in press.

[13] J.M. Tanzosh, D.J. DeVault and W.R. Mohn, "Engineering Design and Fabrication of USC Test Loops, in Proc. of the 4th International Conference on Advances in Materials

Technology for Fossil Power Plants, Hilton Head Island, SC, October 2004, ASM International, in press.

[14] M.P. Borden, "Weldability of Materials for USC Boiler Application", in Proc. of the 4th International Conference on Advances in Materials Technology for Fossil Power Plants, Hilton Head Island, SC, October 2004, ASM International, in press.

[15] J. Sanders, Babcock and Wilcox and F.L. Flower, Haynes Corp., unpublished work, 2004.

[16] W.R. Mohn and J.M. Tanzosh, "Considerations in Fabricating USC Boiler Components from Advanced High Temperature Materials, in Proc. of the 4th International Conference on Advances in Materials Technology for Fossil Power Plants, Hilton Head Island, SC, October 2004.

[17] R. Blum, R.W. Vanstone. "Materials Development for Boilers and Steam Turbines Operating at 700°C." *Parsons 2003 - Proceedings of the Sixth International Charles Parsons Turbine Conference*, Institute of Materials, Minerals, and Mining, London, 2003. 489-510.

METALLOGRAPHY AND ALLOY DESIGN IN THE COST 536 ACTION

J. Hald, Elsam/Energy E2/TU Denmark

Department of Manufacturing Engineering and Management, Technical University of Denmark, Kemitorvet b. 204, DK-2800 Kgs. Lyngby, Denmark

e-mail: joh@ipl.dtu.dk

Abstract

The overall aim of the COST 536 ACCEPT action is to develop new (ferritic) high temperature steels with improved creep and oxidation properties, which will allow increases in steam parameters of thermal power plants to above 300 bar/600°C.

An essential part of the work in the COST 536 action is concerned with the definition of new alloy compositions, which will show improvements compared with today's best available steels, i.e. P92 for steam pipes and FB2/CB2 for forgings and castings. This is done in the Nano Scale WP of COST 536, which involves collaboration between 17 European partners.

Studies in the WP concentrate on improving the understanding of metallurgical stability of the high temperature steels including the following main points:

- Understanding long-term precipitate stability
- Improvement of thermodynamic phase stability databases
- Kinetic modelling of microstructure evolution and creep modelling

The studies aim to develop and validate models, which will allow the prediction of influences of chemical composition and heat treatment on the microstructure stability and creep strength. These models should serve as basic tools for alloy design.

The paper reviews ongoing activity and major results of the work in the Nano Scale WP.

Key-words: 9-12%Cr steels, Microstructure and modelling, Z-phase, Boron, Alloy design

Introduction

Over the past 40 years martensitic creep resistant 9-12 % Cr steels have found increasing application in thick section components of steam power plants, i.e. steam piping and large forgings and castings. Beginning with the 12CrMoV steel introduced in power plant in the mid 1960s alloy development over the past 30 years has led to a number of new stronger steels. These include the 9Cr steam pipe steels: P91 introduced in plant in 1988, and the tungsten-modified 9Cr grades P92 introduced in plant in 2001 and E911 introduced in 2002. The development of cast and forged alloys for steam turbines took place in the COST Actions 501 and 522. This led to the 10Cr1.5Mo steel F, to the 10Cr1Mo1W steel E, to the high Boron 9Cr1.5MoB steel B and to the Co modified 9Cr grades FB2 for forgings and CB2 for castings. The creep properties of all of these alloys are well documented by long-term testing up to 80,000 to 100,000 hours at application temperatures. The long-term creep testing has been

undertaken in the COST Actions [1] as well as in joint projects under the European Creep Collaborative Committee - ECCC [2] and the German association of large boiler operators - VGB [3]. Currently, the best available alloys are the P92 for steam pipes and the FB2 for forgings and CB2 for castings, see tables 1 and 2.

	Steam pipe steels				Turbine rotor steels		
Mass %	**12CrMoV**	**P91**	**E911**	**P92**	**Steel E**	**Steel F**	**Steel B**
C	0.2	0.1	0.1	0.1	0.1	0.1	0.2
Cr	11	9	9	9	10	10	9
Mo	0.9	0.9	1	0.5	1	1.5	1.5
W	-	-	1	1.8	1	-	-
Ni	0.5	0.1	0.3	0.05	0.6	0.7	0.1
V	0.3	0.2	0.2	0.2	0.2	0.2	0.2
Nb	-	0.05	0.05	0.06	0.05	0.05	0.05
N	-	0.06	0.07	0.06	0.05	0.05	0.02
B	-	-	-	0.001	-	-	0.01
Austenitisation	1050°C	1050°C	1060°C	1065°C	1070°C	1120°C	1120°C
Pre tempering	-	-	-	-	570°C	570°C	590°C
Tempering	750°C	750°C	770°C	770°C	690°C	690°C	700°C
$\sigma_{B/10^5h/600°C}$	59 MPa	85-90 MPa*)	98 MPa	113 MPa	≈95 MPa	≈95 MPa	≈125 MPa

*) A new evaluation of steel P91 is being made at present by the ECCC.

Table 1. *Chemical composition and heat treatment of a number of 9-12% Cr steels. The quoted creep rupture strength values for the pipe steels E911 and P92 are from the most recent evaluations by the ECCC.*

The steadily improved creep rupture strength of the martensitic 9-12% Cr steels has enabled the construction new advanced fossil fired steam power plants with higher efficiency. Increases in steam parameters from subcritical 180 bar/530-540°C to ultra supercritical values of 300 bar and 600°C have been realised. Furthermore, a number of new coal or lignite fired steam power plants with unit size up to 1100 MW are now under construction or planning in Europe with extensive use of the newly developed materials to their full potential.

The mentioned increase in steam parameters has led to efficiency increases from the previous 30-35% to current 42-47%, equivalent to approximately 30% reduction in specific CO_2 emissions. With the expected continuous increase in the demand for coal for electricity production, especially in the fast developing Asian countries, this technology progress has clearly the potential to become one of the most (if not the most) significant countermeasures against global CO_2 emissions in the coming decades.

Further developments of coal fired plants aim at increasing steam parameters to 350 bar and 700°C within the next decade leading to efficiencies in the range of 53-55%. This will however only be achieved by use of Nickel based alloys for the most highly stressed components. Since the price of these alloys is approximately 10 times higher than for steels, this will lead to

increased investment costs, which must be outbalanced by the efficiency increase. In order to reduce investment costs of the "700°C" power plant, there is thus a strong incentive for development of a heat resistant steel capable of operating at steam temperatures up to 650°C, which could replace part of the expensive Nickel alloys. If this steel development is successful it will also allow construction of a steel based power plant operating at steam conditions 325 bar and 650°C and with an efficiency above 50% without significant increases of the investment costs.

In order to allow steam temperatures up to 650°C another doubling of the creep rupture strength of the 9-12%Cr steels is demanded on top of the impressive development described above. Further, the increased temperature means that steam oxidation will become increasingly severe, and this has to be considered in alloy design.

In the COST 501/3 and 522 Actions and elsewhere many attempts have been made to design martensitic steels with a creep rupture strength approaching 100 MPa at 650°C and at the same time possessing sufficient resistance against steam oxidation. The alloys designed in COST 522 were all based on chromium contents of 10%, and above for oxidation stability. Most of these alloys showed promising behaviour in short term creep rupture tests up to approximately 10,000 hours, but in long-term tests they all collapsed to strength levels below the previously developed alloys FB2 and CB2 [1]. Similar behaviour has been found for alloys developed elsewhere like e.g. the TAF650 [4] for turbines and the pipe and tube steels NF12, HCM12 and HCM12A, see table 2.

	COST 501/3		**COST 522**			**Others**	
Mass %	**FB2**	**CB2**	**FB6**	**FB8**	**FB11**	**TAF 650**	**NF12**
C	0.13	0.12	0.14	0.17	0.19	0.10	0.09
Mn	0.82	0.88	0.10	0.09	0.10	0.50	0.44
Cr	9.32	9.20	11.2	11.1	11.2	10.88	11.60
Mo	1.47	1.49	1.45	1.46	0.90	0.14	0.14
W	-	-	-	-	0.42	2.55	2.68
Ni	0.16	0.17	0.15	0.20	0.17	0.51	0.17
Co	0.96	0.98	2.93	2.94	3.03	2.90	2.48
V	0.20	0.21	0.22	0.21	0.21	0.19	0.20
Nb	0.05	0.06	0.08	0.07	0.07	0.10	0.08
N	0.019	0.02	0.016	0.023	0.020	0.025	0.045
B	0.0083	0.011	0.010	0.010	0.007	0.013	0.0026

Table 2. *Chemical composition of the most successful alloys FB2 and CB2 from the COST 501/3 Action together with examples of unstable alloys from COST 522 and elsewhere.*

The disappointing results of the recent steel development have clearly demonstrated that the ideas behind the alloy design have been based on a lack of understanding of the long-term microstructure stability of this class of alloys. However, new understanding of basic mechanisms behind the observed collapses in long-term creep strength has recently emerged,

which could possibly point to new directions in alloy design of the 9-12%Cr steels. Based on this it was decided to launch the new COST 536 ACCEPT Action in 2004 with the overall aim to develop new (ferritic) high temperature steels with improved creep and oxidation properties, which will allow increases in steam parameters of thermal power plants to above 300 bar/600°C.

An essential part of the work in the COST 536 action is concerned with the definition of new alloy compositions, which will show improvements compared with today's best available steels, i.e. P92 for steam pipes and FB2/CB2 for forgings and castings. This is done in the Nano Scale WP of COST 536, which involves collaboration between 17 European partners.

Current understanding of strengthening mechanisms and microstructure instability of the 9-12%Cr steels is presented below together with ongoing activities and major results of the work in the Nano Scale WP of COST 536.

Microstructure instability of 9-12%Cr steels

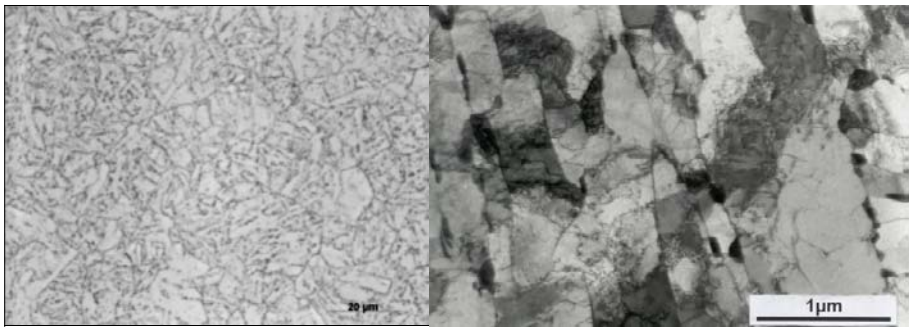

Figure 1. Tempered martensite in steel P92. Light optical (left) and transmission electron micrographs (right)

Microstructure of the 9-12%Cr steels

The microstructure of the 9-12% Cr steels is tempered martensite formed during a final normalising and tempering heat treatment, figure 1. After normalising at 1050°C-1150°C air hardening will lead to a martensitic transformation in sections up to approximately 100-mm thickness due to the chromium content. Tempering in the range 680°C-780°C leads to recovery of ductility. Tempering temperatures in the low end of the range are generally used for components like turbine rotors, where high tensile strength is required. The high end of the range is used for pressurised components like steam pipes, where high toughness is necessary. Cr-carbides (M_7C_3 and finally $M_{23}C_6$) and different nitrides (Cr-rich M_2X followed by (V, Nb)-rich MX) precipitate in the steels during tempering, on prior austenite grain boundaries, ferrite subgrain boundaries and on dislocations inside subgrains. When the steels are put into operation in power plant at temperatures below the final tempering temperature, further particles may precipitate, which are thermodynamically unstable at the tempering temperature, like e.g. the intermetallic $Fe_2(Mo,W)$ Laves phase.

Creep strengthening mechanisms

The technically relevant stresses and temperatures for creep testing and service exposure of the 9-12% Cr steels are in the range 300 MPa/500°C–50 MPa/650°C. Relevant loading conditions in this range will lead to rupture times between 100 and 300,000 hours and minimum creep rates between $3 \cdot 10^{-6}$ and $5 \cdot 10^{-12}$ s^{-1}. There are strong indications that the controlling creep mechanism in the whole of the technically relevant stress/temperature range is dislocation creep. Microstructural sources of creep deformation are then the migration of dislocations and subgrain boundaries [5,6]. This indicates that microstructural explanations for the improved creep strength of the new 9-12%Cr steels should be found in mechanisms which retard the migration of dislocations and subgrain boundaries, and thus delay the accumulation of creep strain with time. Such mechanisms include i) solid solution strengthening by formation of clouds of solute atoms around dislocations, and ii) interactions with precipitate particles.

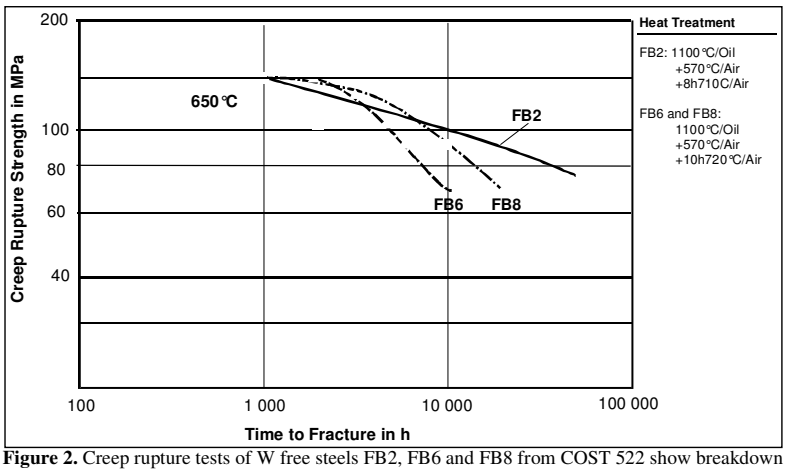

Figure 2. Creep rupture tests of W free steels FB2, FB6 and FB8 from COST 522 show breakdown in long-term stability at 650°C of the high Cr steels [8].

Solid solution strengthening has often been referred to in discussions of the effect of Mo and W on creep strength of 9-12%Cr steels**.** It has since long been clear that during creep exposure at temperatures around 600°C-650°C most of the Mo and W in the steels will precipitate as intermetallic Laves phase ($(Fe,Cr)_2(Mo,W)$). The dominating opinion was that this was the cause for observed creep instabilities in the steels because the solid solution strengthening effect from Mo and W would be lost. This seemed to be supported by the breakdown of long-term creep strength of some W alloyed 10-12%Cr steels, and by the excellent long-term stability of Mo alloyed 9CrB turbine materials (Steel B, FB2 and CB2) from the European COST project (Mo causes less Laves phase precipitation than W). However, the excellent long-term stability of the W alloyed 9Cr steel P92 seemed to contradict the opinion, and Laves phase particle size measurements in steel P92 and other high W steels demonstrated stable particles with sizes of the same order as for $M_{23}C_6$ carbides [7]. Further, a number of W free experimental alloys from the COST 522 action have shown a similar breakdown to some of the W alloyed steels, see figure 2 [8].

It now seems clear that solid solution strengthening from W and Mo has no significant effect on long-term microstructure stability of the 9-12%Cr steels. Precipitation hardening by pinning of dislocations and subgrain boundaries should be regarded as the most significant strengthening mechanism, which controls the microstructure stability in 9-12%Cr steels [9]. This is consistent with two findings: a) the compositional changes, which have improved the creep strength of the 9-12%Cr steels, have also resulted in clear changes in the precipitate populations (introduction of MX and Laves phase). And b) breakdowns in creep stability presented below can be explained by unexpected precipitate reactions.

Z-phase precipitation

As mentioned a large number of test alloys with 11-12%Cr, and with or without W, intended for operation at 650°C have been produced and tested in COST and elsewhere. All of these, which have been tested to long times, show a severe breakdown in creep stability between 5,000 and 30,000 hours at 650°C, figure 2. Many investigators have recently identified Z-phase precipitation as the root cause of this instability in the 10-12%Cr steels, as summarised in [10]. The Z-phase (Cr(V,Nb)N) can completely dissolve the MX carbonitrides, which are major contributors to creep strength. It grows to very large particles, which will not contribute to precipitation hardening, and which may each consume more than 1000 fine MX particles, figure 3.

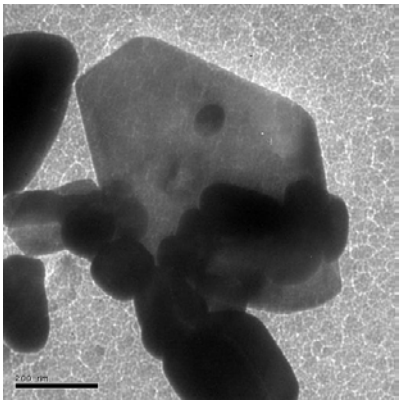

Figure 3. *Z-phase particle surrounded by $M_{23}C_6$ carbides in a 11CrWCoVNbNB steel*

The Z-phase nitride in the form CrNbN has been known from Nb alloyed austenitic stainless steels since the 1950s. In martensitic 9-12%Cr steels alloyed with V and Nb the Z-phase in form Cr(V,Nb)N was first observed in 1986 in the 12%Cr bolting steel X19CrMoVNbN 11 1 [11]. In 1996 detailed investigations of creep specimens of older 12CrMoVNb steels showed that the Z-phase precipitated after 10,000-30,000 hours of creep at 600°C, and that MX (V,Nb)-carbonitrides dissolved. It was concluded that the Z-phase precipitation reaction was responsible for observed creep instabilities in the steels [12]. However, the older 12%CrVNb steels including the X19CrMoVNbN 11 1 have Nb contents, which are app. 5 times higher than the new generation of high strength 9-12%Cr steels, and it was not considered that Z-phase precipitation would occur in the new steels.

Thus, the observed Z-phase precipitation in the 11-12%Cr test steels represent a serious problem to the long-term microstructure stability of the new generation of 9-12%Cr steels, in which a major part of the high creep strength is obtained by particle strengthening with MX (V,Nb)-carbonitrides.

At the onset of the COST 536 action it was unclear, which elements in chemical composition and microstructure would affect the Z-phase precipitation. Consequently, the understanding of Z-phase precipitation has been a central element in the investigations of the Nano Scale WP in COST 536.

Activities of the Nano Scale WP of COST 536

17 partners participate in the metallography and alloy design activity in the Nano Scale WP of COST 536, see Table 3. The objective of the WP is to improve the detailed understanding of metallurgical stability of 9-12%Cr steels under creep conditions with the purpose to propose new alloy compositions or heat treatments leading to improved creep properties for applications up to 650°C steam temperatures.

		Microstructure characterisation			
		Dislocations/ subgrains	Precipitates		Cavities
Partner	Project	TEM	TEM	EFTEM	
TU Graz	AT1	X+EBSD	X	X	X
ARCS	AT4	X	X	X	X
Skoda	CZ1B	X	X	Electroch.	
IPM Brno	CZ2	X	X		
Vitkoice V.R.I	CZ3	X	X		
MPA	DE9	X	X	X	
Elsam	DK1	X	X	X	
Risø	DK2	X	X	X	
CEA	FR3	X	X		
CSM	IT1	X	X		
AGH Krakow	PL1	X	X	TEM/EDS	X
Chalmers/KTH	SE2	X	X	X	
TU Kosice	SK3	X	X	SANS	X
SAS	SK4				
Loughborough	UK1		X		
Leicester	UK8		X		
CORUS	UK4	Alloy production			

Table 3. Partners in the Nano Scale WP of COST 536, and their activities concerning microstructure characterisation

The studies to improve the understanding of metallurgical stability include the following main points:

- Understanding long-term stability of precipitates
- Improvement of thermodynamic phase stability databases
- Kinetic modelling of microstructure evolution and creep modelling

The studies aim to develop and validate models, which allow the prediction of influences of chemical composition and heat treatment on the microstructure stability and creep strength. These models should serve as basic tools for alloy design.

The activities in the WP are grouped under the following headlines:

- Microstructure characterisation
- Modelling
- Alloy design

Microstructure characterisation
The partners of the microstructure characterisation activity have access to a number of advanced analytical electron microscopy techniques, which allow detailed analysis of:

- Quantitative size evolution of individual precipitate phases (EFTEM;TEM-EDS; SEM)
- Evolution in dislocation and subgrain microstructures (TEM)
- Precipitation kinetics (Phase identification after heat treatment or creep)
- Location of Boron (APFIM)

Furthermore, the partners have access to a large selection of (long-term) creep specimens from the previous rounds of the COST collaboration with testing times up to more than 100,000 hours. This gives unique opportunities to study the microstructure evolution of both successful alloys like the FB2 and CB2 and less successful alloys like the FB6 and FB8.

Modelling
Previous attempts to develop high Cr ferritic/martensitic steels have mainly been based on empirical evaluation of a large number of test results [13]. However, the disappointing results of the recent developments have made it clear that a deeper understanding is needed of links between chemical composition, heat treatment and microstructure stability. Moreover, the increasing complexity of the steels means that it is impossible to guess optimum compositions from empirical studies of test alloys. Even the design of systematic variations of test alloy compositions to provide information on important influences of elements, may be impossible based on empirical evaluations. The only way forward is to develop and validate models to predict the complex effects of chemical composition and heat treatment on microstructure stability.

		Modelling				
		Microstructure modelling			Creep modelling	
Partner	Project	TC/DICTRA	TC Database development	Other models	Strain-time	Damage
TU Graz	AT1	X		MatCalc	X	
ARCS	AT4	X			X	
IPM Brno	CZ2	X	X		X	X
MPA	DE9	X				
Elsam	DK1	X	X			
Risø	DK2	X				
CEA	FR3	X	X	Neural network		
CSM	IT1	X	X			
Chalmers/KTH	SE2	X	X	Ab initio	X	
SAS	SK4		X			
Loughborough	UK1	X		X	X	X
Leicester	UK8	X				

Table 4. Modelling activities in the COST 536 Nano Scale WP

In COST 536 attempts will be made to use neural network models to identify hidden effects in the large databases of long-term creep tests on test alloys from the previous COST Actions 501 and 522. However, the multiscale interpolation in the neural network models have no ability to describe effects of alloying elements, which have not been included in the previous test

programs. This means that the neural network models must be supplemented with physically based models of microstructure stability.

The partners in the Nano Scale WP have access to and experience with a wide range of models to predict microstructure stability, see table 4. The most fundamental models in this respect are the thermodynamic phase stability models like the Thermocalc [14], which predict phase stability from chemical composition based on minimisation of the system free energy. The accuracy of these predictions is critically dependent on the quality of the thermodynamic databases, which are based on experimental results. An important task for the Nano Scale WP is to improve the databases with respect to phase descriptions, which are of critical importance to the stability of the 9-12%Cr steels, i.e. Mo-Laves phase, Z-phase, Nitrides and Boron effects.

However, since the microstructures of the 9-12%Cr steels do generally not reach equilibrium during heat treatment, creep testing or service exposure, models of microstructure stability must include kinetic effects like phase precipitation (nucleation and growth) and coarsening of precipitates. In this area multicomponent diffusion models like the DICTRA [15] and the comprehensive precipitate model MatCalc under development at TU Graz [16] are highly useful, see figure 4.

Finally, partners are active in the development of creep models to predict strain-time behaviour based on information on the microstructure evolution.

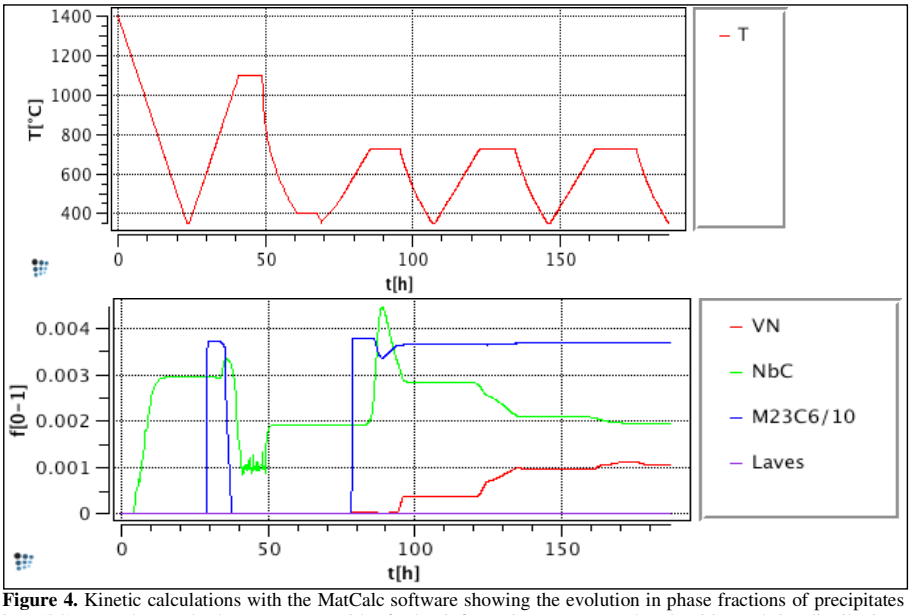

Figure 4. Kinetic calculations with the MatCalc software showing the evolution in phase fractions of precipitates in a 10CrMoVNbN steel. The program provides further information on e.g. number densities and size distributions of the precipitates [16].

Results from the Nano Scale WP

Z-phase precipitation
As mentioned, at the onset of the COST 536 Action very limited information was available about the influencing factors in chemical composition and heat treatment, which control Z-phase precipitation. Studies of a large number of alloys by many partners in the COST Action and elsewhere have confirmed that Z-phase precipitation and MX dissolution can have a deleterious effect on the creep strength of 9-12%Cr steels. In fact, it seems that Z-phase precipitation accompanied by progressed MX dissolution is the most important mechanism to explain the observed unexpected breakdowns in long-term strength of the modern 9-12%Cr steels. [10]

A thermodynamic model has been developed for the Z-phase stability, and this has demonstrated that Z-phase is the most stable nitride in steels containing its constituents Cr, V, Nb and N in sufficient amounts. This is essentially all of the 9-12%Cr Steels [17], and this means that it is the kinetics of Z-phase nucleation and growth, which is important to creep stability and which need to be studied. The thermodynamic model allows initial estimates of the precipitation speed by calculations of the thermodynamic driving forces for Z-phase precipitation. A high driving force indicates fast precipitation of Z-phase. These model calculations show good accordance with observations of Z-phase in the microstructure and with long-term creep stability of the steels, figure 5.

With the model it is possible to investigate the influence of alloying elements on Z-phase precipitation speed. It is found that since the content of V and Nb varies only very little in the modern 9-12%Cr steels it is the content of Cr and N, which play the crucial roles in stability against Z-phase precipitation. High content of Cr and N accelerate Z-phase precipitation, which explains the observed breakdowns in long-term strength of 11-12%Cr steels FB6, FB8, TAF650, NF12 and others as well as the good long-term stability observed for the 8.5-9.5%Cr steels P91, P92, B2, FB2 and CB2.

High content of C is found to slow down Z-phase precipitation since it ties up Cr in $M_{23}C_6$ carbides, which do not transform to Z-phase. Extremely low carbon content as found in a number of new test alloys may be expected to accelerate Z-phase precipitation even in steels with only 9%Cr.

Crystallographic investigations of Z-phase particles have revealed that the tetragonal crystal structure found in the CrNbN many years ago is not adequate to describe the crystal structure of the modified Z-phases Cr(V,Nb)N and CrVN. The modified Z-phases consist of a complex mixture of tetragonal and FCC crystal structures. It is currently assumed that the FCC crystal acts as a precursor to the tetragonal crystal in the Z-phase precipitation reaction [18]

Studies are ongoing to clarify the nucleation sites and nucleation mechanism of the Z-phase. Further, a number of model alloys have been designed and produced in COST 536 with the purpose to follow the crystal transition from FCC to tetragonal by X-ray diffraction studies as well as effects of Cr and Ni on the kinetics of Z-phase precipitation.

The nucleation studies are now being combined with MatCalc calculations in order to predict combined effects of heat treatment and chemical composition on Z-phase precipitation.

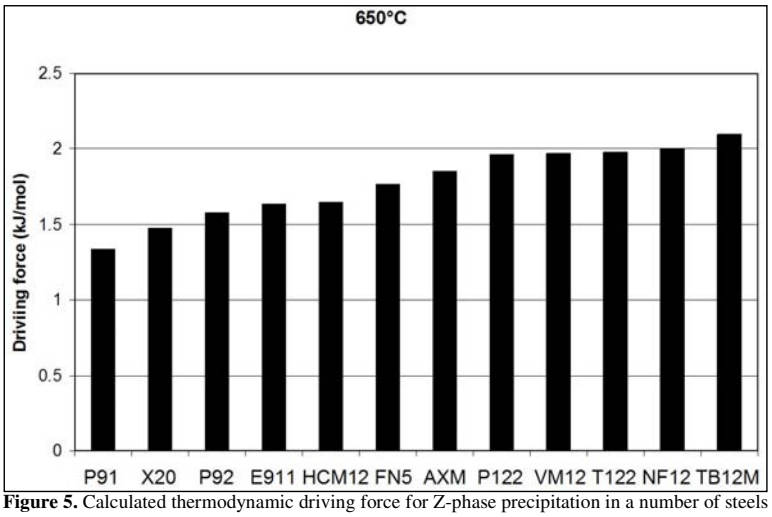

Figure 5. Calculated thermodynamic driving force for Z-phase precipitation in a number of steels at 650°C. The calculations show good accordance with experimental observations [17].

Effect of Boron

The most successful alloys, which have emerged from the alloy developments in the COST actions, are the 9CrB steels B, FB2 and CB2, which show excellent long-term stability. All of these alloys contain high amount of Boron (app. 100ppm) together with 9%Cr and approximately 0.02%N, see tables 1 and 2. A review of available results in literature demonstrate that the TAF steel developed by Fujita in the 1950s is actually the strongest 10%Cr steel ever produced [19]. It contains 300ppm Boron, 0.2%C and 0.02%N, see figure 6.

Detailed investigations including TEM and APFIM of creep specimens from these steels with very long exposure times [20,21,22] have indicated that boron increases the microstructure stability by a reduction of the coarsening rate of $M_{23}C_6$ carbides. Even though detailed studies of the Boron distribution with APFIM have demonstrated that most of the Boron is dissolved in these carbides it is still unclear how this can affect the coarsening rate, since Boron is expected to diffuse interstitially at a high rate.

Recently, studies of BN precipitates in 9-12%Cr steels by NIMS have shown that not all of the Boron added to the steels will be active in the $M_{23}(C,B)_6$ carbides, since part of it can be tied up in large BN precipitates [23]. Furthermore, primary Borides rich in Mo and Nb have been identified in some of the steels, which may similarly reduce the active Boron content. Increasing the austenitizing temperature during heat treatment of such steels improves the creep strength since it will dissolve increasing amount of primary Boron rich precipitates and BN and release Boron to form useful precipitates.

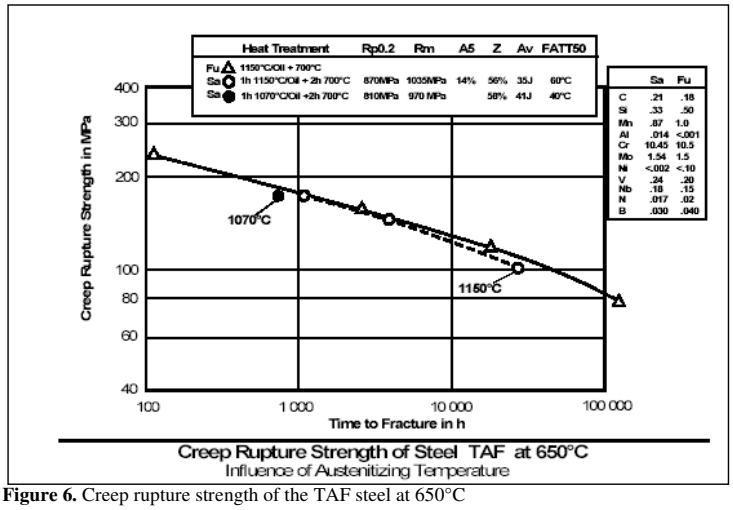

Figure 6. Creep rupture strength of the TAF steel at 650°C

Further investigations of precipitates in the steels B, FB2, CB2 and TAF have shown strong dynamic precipitation of fine stable MX (VN) particles in the steels during creep exposure [20,21]. This should be regarded as a further important strengthening mechanism in these steels, but it is currently unclear how to control this reaction by changes in chemical composition or heat treatment.

Clearly, further studies of the effect of Boron on carbide stability and dynamic VN precipitation are needed. Especially, our ability to model phase stability including Boron in BN, complex Mo and Nb borides and $M_{23}(C,B)_6$ should be improved.

Alloy design in COST 536

The findings described above on microstructure stability have been implemented in a first set of test alloys in COST 536, and these alloys are now being produced and tested. The basic alloy design ideas are:

- Optimise Boron and Nitrogen (modified FB2)
- Avoid Z-phase, (Low Cr)
- Laves phase strengthening (Cu + W)
- Other nitrides Ti, Ta, Zr, Hf

A series of alloys have been designed based on the successful steel FB2 with systematic variation of Boron and Nitrogen in order to avoid formation of BN precipitates according to the findings at NIMS, see figure 7. Further, the developed thermodynamic model of the Z-phase has been used to modify the chemical composition to suppress Z-phase precipitation. This means that so far only steels with 9%Cr are considered, and oxidation stability must be obtained by surface coating.

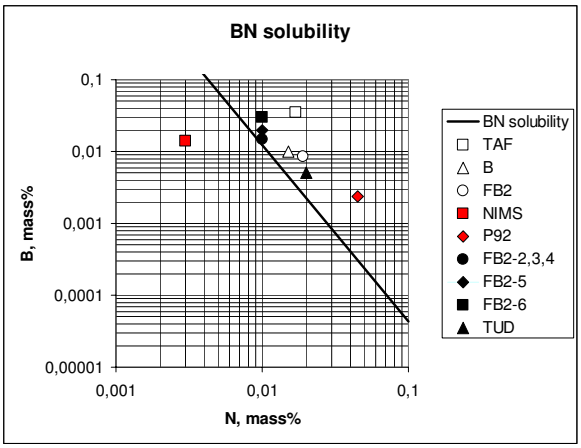

Figure 7. *BN Solubility at 1150°C according to NIMS [21].*
B and N content of test alloys in COST 536.

Further alloys are designed to investigate the effect of enhanced Laves phase precipitation by addition of Cu and W as well as effects of other carbonitride formers like Ta, Zr and Hf.

It is expected that a second set of test alloys can be designed in the COST 536 Action when more results of the microstructure studies and modelling become available.

Summary

In the Nano Scale WP of the COST 536 ACCEPT Action 17 European organisations work together to design new steels with improved creep and oxidation properties, which will enable the construction of power plants with steam parameters higher than 300 bar and 600°C.

The basis for the alloy development is an improved understanding of effects of chemical composition and heat treatment on long-term creep stability of the steels derived from microstructure investigations combined with physically based models of microstructure stability.

Previous attempts to develop alloys for 650°C steam temperature based on 11-12%Cr steels for high oxidation resistance have all failed due to Z-phase precipitation, which causes dissolution of beneficial strengthening MX precipitates. The understanding of the Z-phase precipitation has been significantly improved through microstructure studies and development of thermodynamic and kinetic models.

Studies of stable 9-10%Cr alloys like the FB2 and TAF steels have demonstrated that Boron retards the coarsening of $M_{23}C_6$ carbides. However, Boron may form primary precipitates, like BN or (Mo, Nb)-rich borides, which may limit the effectiveness of the Boron alloying.

Further, dynamic precipitation of fine MX (mainly VN) particles has been identified as an important strengthening mechanism in the stable alloys B, FB2 and TAF.

The understanding of the mechanism of Boron strengthening and controlling factors in the dynamic VN precipitation should be improved through model development.

A first series of test alloys has been designed in COST 536 based on the most recent progress in understanding of microstructure stability. At present all of these alloys are based on 9%Cr and need coating for oxidation protection.

Acknowledgements
The author wishes to acknowledge the fruitful collaboration with partners in the COST 536 action, in particular the 17 partners in the Nano Scale WP.

References

[1] M. Staubli, B. Scarlin, K.-H. Mayer, T.-U. Kern, W. Bendick, P. Morris, A. Di Gianfrancesco, H. Cerjak in proc. Sixt International Charles Parsons Turbine Conference, Dublin 16-18 September 2003. A. Strang et. al. (Eds.), IOM, London 2003, 305-324.
[2] J. Hald: in Proc. 1st International Conf. *Super-High Strength Steels*, Rome, Italy, 2-4 November 2005, AIM and CSM, Rome 2005.
[3] K-H. Mayer, T. -U. Kern, M. Staubli, E. Tolksdorf in proc. Fifth International Charles Parsons Turbine Conference, Cambridge, 3-7 July 2000. A. Strang et. al. (Eds.), IOM, London 2000, 372-385.
[4] T. Uehara, A. Toji, S. Komatsubara, T. Fujita, in Proc. Conf. "Materials for Advanced power Engineering", Liege, September 2002, J. Lecomte-Beckers et. al. (Eds.), Julich, 2002, Part 3, 1311-1320.
[5] S. Straub: Verformungsverhalten und Mikrostruktur warmfester martensitischer 12%-Chromstähle, VDI Forschungsberichte 5, VDI Verlag, Düsseldorf (1995), 405
[6] P. Polcik: Modellierung des Verformungsverhalten der warmfesten 9-12% Chromstähle in Temperaturbereich von 550-650°C, Shaker Verlag, Aachen (1999), 92
[7] J. Hald, L. Korcakova, *ISIJ International,* 43 (2003), No. 3, 420
[8] K.-H. Mayer, Internal COST presentation, 2004
[9] J. Hald, *VGB PowerTech,* 12 (2004), 74
[10] H. K. Danielsen, J. Hald, *Energy Materials,* 1 (2006), 49
[11] E. Schnabel, P. Schwaab, H. Weber, *Stahl u. Eisen,* 107, (1987), II, 691
[12] A. Strang, V. Vodarek, *Mater. Sci. Tech.,* 12 (1996), 552
[13] R. W. Vanstone, in Proc. Conf. "Materials for Advanced power Engineering", Liege, September 2002, J. Lecomte-Beckers et. al. (Eds.), Julich, 2002, Part 2, 1035-1047
[14] B. Sundman, B. Jansson, J.-O. Andersson, *Calphad,* 9, 1985, 153
[15] J.-O. Andersson, L. Höglund, B. Jönsson, J. Ågren in: Fundamentals and Application of Ternary Diffusion, C. R. Purdy (Ed.), Pergamon Press, New York (1990), 153
[16] J. Rajek, E. Kozeschnik, H. Cerjak in Proc. Conf: „ Advances in Materials Technology for Fossil Power Plants", R. Viswanathan, et. al. (Eds.), Hilton Head Island, USA, October 2004, ASM International (2005), 1064-1070
[17] H. Danielsen, J. Hald in Proc. Conf: „ Advances in Materials Technology for Fossil Power Plants", R. Viswanathan, et. al. (Eds.), Hilton Head Island, USA, October 2004, ASM International (2005), 999-1012
[18] H. K. Danielsen, J. Hald, F. B. Grumsen, M. A. J. Somers, submitted to *Metall. Mater. Trans.*
[19] T. Fujita, N. Takahashi, *Trans. ISIJ,* 18, (1978), 702-711
[20] F. Kaufmann, G. Zies, D. Willer, C. Scheu, K. Maile, S. Straub, 31. MPA-Seminar, Stuttgart, 13. And 14. October 2005, lecture 27.
[21] P. Nowakowski, PhD Thesis, TU WIEN, 2000
[22] A. Golpayegani, M. Hättestrand, H.-O. Andrén, in proc. Sixt International Charles Parsons Turbine Conference, Dublin 16-18 September 2003. A. Strang et. al. (Eds.), IOM, London 2003, 365-377.
[23] K. Sakuraya, H. Okada, F. Abe, in Proc. Conf: „ Advances in Materials Technology for Fossil Power Plants", R. Viswanathan, et. al. (Eds.), Hilton Head Island, USA, October 2004, ASM International (2005), 1270-1279

Materials development for advanced steam boilers

A. Helmrich, ALSTOM Boilers, Stuttgart, Germany
Q. Chen, ALSTOM Boilers, Stuttgart, Germany
G. Stamatelopoulos, ALSTOM Boilers, Stuttgart
B. Scarlin, ALSTOM Switzerland Ltd, Baden, Switzerland

Abstract

A number of international programmes have been initiated to develop and exploit new materials for high temperature application for example in the 9-12%Cr steel range (>600°C), for austenitic steels and for nickel-based alloys (>700°C).

For 9-12%Cr steels aspects of the progress in Europe are reviewed:

- in the previous and ongoing COST programmes (alloy design, mechanical properties, oxidation resistance, component manufacture and welding)
- in testing and qualification of manufacturing processes, investigation of creep properties and microstructure related to base material, welds and bends (Marcko 700)
- in manufacturing and qualification based on code requirements determining oxidation resistance and microstructural stability (Komet650, Esbjerg test rigs)

For austenitic steels and nickel-based alloys there is a much greater potential for temperature and efficiency increase but also additional questions concerning fabrication of large components (pipes, tubes and forgings) and minimising the use of the expensive nickel-based alloys.

These questions are being addressed

- in the AD 700 (Thermie) project through manufacture of test melts, components, the installation of test rigs for membrane walls and superheater tubes and their nondestructive and destructive mechanical testing
- in testing and qualification of manufacturing processes, investigation of creep properties and microstructure related to base materials, welds, bends and manufactured components (Marcko 700)
- in the COMTES 700 test facility water walls, superheater tubes, headers, steam pipes and control valves have been manufactured and installed in a section of a power plant which will operate at 700°C for up to 4 years.

In addition a government/industry supported project is ongoing in the US, in which materials for boiler and turbine are under investigation. Target steam temperature is 760°C, so that more complex nickel-based alloys may be required than in AD700, along with increased challenges in the area of manufacturing, welding and heat treatment.

Keywords: Boiler, materials, steam power plant, supercritical

Background

There is an ongoing activity to improve the operating efficiency of fossil fuel fired steam power plants. To a large extent this is achieved through use of materials with a higher temperature and pressure capability than those previously employed. Power plant components for which such materials were not available and where materials had to be specifically developed, qualified and introduced were heavy turbine components such as forged rotors and cast casings and boiler components such as thick-walled main steam pipes and headers and thin-walled tubes for use in water walls and reheaters / superheaters.

Main steam pipes and headers
The best available materials in terms of creep strength at typical steam temperatures of 600°C are P92 (developed in Japan) and E911 (from the COST 501 Programme). The requirement here was primarily for improved creep strength, so as to minimize wall thickness and improve cycling capability, but also for improved oxidation resistance to reduce tendency to growth and spalling of oxide layers, which can lead to solid particle erosion in the turbine and loss of aerodynamic efficiency.

Reheaters and superheaters
At the highest temperatures austenitic steels with improved creep strength are employed. To ensure good resistance to steam oxidation these have particularly high chromium content or are additionally shot peened or used in a fine-grained condition to improve diffusivity of chromium.

To limit the additional costs of high temperature RH / SH use should be made of martensitic steels to the highest possible temperatures (above which austenitic steels are required). These martensitic steels need both high oxidation resistance and high creep strength.

Water walls
Materials require sufficient creep strength and oxidation resistance at temperatures in excess of 530°C also without the need for post weld heat treatment on site.

Easy manufacturing, including bending and welding, and low cost are essential requirements to ensure the efficiency increase with advanced cycles leads to a major reduction in the cost of electricity generated.

There are basically two parallel development trends in the quest for higher steam temperatures and improved operating efficiency

- the development of new improved steels
  The challenge lies in the identification of new compositions which will provide the desired microstructural stability at increased temperature, along with adequate oxidation resistance.
  Development, testing and qualification are carried out in the COST, Komet650 and Esbjerg programmes
- the application of nickel based alloys
  The challenge here lies in the production of components of the required size for large steam power plant at acceptable cost
  In Europe testing and demonstration are performed in the AD700 (Thermie), Marcko and COMTES activities.
  In the US activities are ongoing in the USC Boiler Materials Consortium project.

COST 536 Programme

The current Action entitled “Alloy development for critical components of environmentally friendly steam power plant” was initiated in 2004 and is planned to run for 5 years. There are 69 partners from 17 countries participating in R&D, steel manufacturing, manufacturers of turbine and boiler components and utilities, providing competence in all required areas.

The work is based on achievements in COST 522 and on the most recent status of activities elsewhere in the world.
It comprises activities on

- alloy design
- forgings for turbine components
- castings for turbine components
- boiler materials (pipes and tubes)
- welding
- steam oxidation testing

The boiler working group comprises 20 partners (R&D organizations, steel, tube and pipemakers, and component manufacturers). Table 1 lists the partners and their types of activity. Most partners have concentrated their programmes on 9-12%Cr steels and austenitic steels. Support to the boiler materials group is also provided by the groups:

- Alloy design, providing new compositions designed to either suppress the formation of recently characterized Z phase ($Cr_2(Nb,V)_2N_2$) which nucleates and coarsens in higher Cr steels at the expense of the beneficial MX and $M_{23}C_6$ precipitates or alternatively to produce nucleation in a fine stable form (see separate contributions to this conference, e.g. Golpayegani and Andren). Model alloys have being prepared to investigate the precipitation kinetics to permit the inclusion of all phases, for example, in the Thermocalc alloy design programme. Alloy compositions with the potential for use as thick-walled steam pipes have been identified.
- Welding group performs welding and mechanical testing of tubes and pipes produced from steels with the most promising mechanical properties (tensile, impact and creep strength). Basic information for the design of headers and pipework is also provided by cross-weld testing of joints made with matching, overmatching and undermatching weld consumables and by high-temperature creep testing of welded components under internal pressure
-

COST 536 "ACCEPT" / Alloy Development for Critical Components of Environmental friendly Power PlanT

Country & Project	Organisation	Main activity
CZ4A	SVUM Prague	determination of creep behaviour for advanced steels
DE1/FR1	V&M/MFI Duisburg	manufacturing of test materials and pilot components
DE2	IWM Freiburg	investigation and simulation of welds and welded components
DE4	Alstom Power Generation AG Mannheim	Microstructural investigations
DE8	Siempelkamp	investigation of application relevant longterm behavior - pipes FEM and model testing (multiaxiality) of welded and notched parts FEM and model testing (multiaxiality) of notched pipes
DE11	Alstom Boilers, Stuttgart	testing of welded pipe materials 12CrCoMo
FI1	VTT Industrial Systems, VTT	Creep & oxidation testing & subsequent microstructure investigation
FR4	Air Liquide / Cergy Pontoise	development of filler metals and welding technology
IT1	CSM / Roma	creep of welded joint for boiler material
IT5	Centro Sviluppo Materiali	creep testing of tube/pipe material
IT9	Dalmine	manufacturing of test materials and pilot components
NL1	KEMA / Arnhem	creep strain modelling of heat affected zones in welds
PL2	IFM / Gliwice	investigation of application-relevant longterm behaviour
PL3	Inst. of welding / Gliwice	welding and mechanical testing of low and high alloyed pipe steels
PL4	Rafako / Raciborz	welding & testing of similar / dissimilar welds in new 12%Cr steels
SK1+2	VUZ / Bratislava, SES / Timace	weldability, establish test parameters and welding technologies investigation of test welds and welded components
UK1	Loughborough University	microstructural modelling and validation
UK2	Mitsui Babcock/ Renfrew	stress rupture testing for similar / dissimilar ferritic/austenitic welds
UK4	Corus / Rotherham	manufacturing of test materials
UK7	Ratcliffe on Soar	develop miniature specimen for HT testing / integrity assessment

Table 1: Partners in the COST 536 boiler materials group

9-12%Cr Steels
The steel VM12 [1] has been investigated in the COST 522 programme. It was intended to provide both improved oxidation resistance and creep strength compared with P92. Whereas oxidation resistance has been greatly improved by increase of Cr and Si contents, the additions of Co and W did not result in the desired creep strength improvement. Nevertheless applications are already seen in the lower temperature range, where high oxidation resistance is required. Many tests are still ongoing. Induction bend samples tested in creep after full normalisation and tempering are not inferior to the mother pipe. Results are shown in a separate contribution to this conference (Bendick et al)

A number of other organisations in the boiler group are also performing tests on VM12 similar and dissimilar welds:

- similar TIG (root) and SMAW (fill-up) welds - pipes with 12mm and 35mm wall thickness welded followed by mechanical tests and metallography of base material and weldment, as weld as creep tests at 600°C , 625°C and 650°C
- dissimilar welds between VM12 and IN617 for numerical and experimental investigations (component testing under internal pressure, residual stress measurements and FE calculations).

3 further composition modifications (steel VM12+) have also been manufactured with reduced Co content (reduced cost) increased C and Mn and decreased N content. Improved creep strength is required along with maintained high oxidation resistance.

An alternative approach for thick walled piping could be the use of a 9%Cr steel along with a coating to prevent steam oxidation.

Austenitics
A number of melts of improved versions of Esshete 1250 have been produced. The best results were obtained for a W-containing alloy. Background information was provided at the last Liege Conference [2]. The same creep strength as IN709 is observed at 650°C. A 5 ton batch has also been manufactured and creep tests have been performed at 650, 675 and 700°C. At all temperatures creep rupture tests to 10’000h meet expectations. Oxidation tests and metallographic investigations are planned.

Similar welds have been made and cross-weld creep testing at 650°C is in progress.

Dissimilar welds (austenite – austenite and austenite – 9-12%Cr steel) together with metallography and all mechanical and creep testing are planned.

KOMET650

In addition newly developed materials and coatings from the COST 501 and COST 522 programmes have been exposed to steam oxidation “field testing” in the Komet650 steam bypass and in the Esbjerg test loops. These results are compared with those of long-used materials and of laboratory screening tests.

In the power plant Westfalen a steam bypass was installed in which samples of new alloys can be tested under practical conditions. The goal is to identify materials and coatings with a temperature capability of at least 620 °C. KOMET 650 is a programme which is jointly run by VGB, VEW/RWE, Technip, Babcock and Alstom. It is partly funded by the Bundesministerium für Wirtschaft und Technologie.

Test conditions**:**
- 2 temperatures: nominally 620 and 650 °C *(only 595 and 630 °C reached in general)*
- steam flow: 4 t/h
- pressure: 96 / 180 bar respectively
- Cylindrical specimens are exposed in the steam flow (Fig 1).

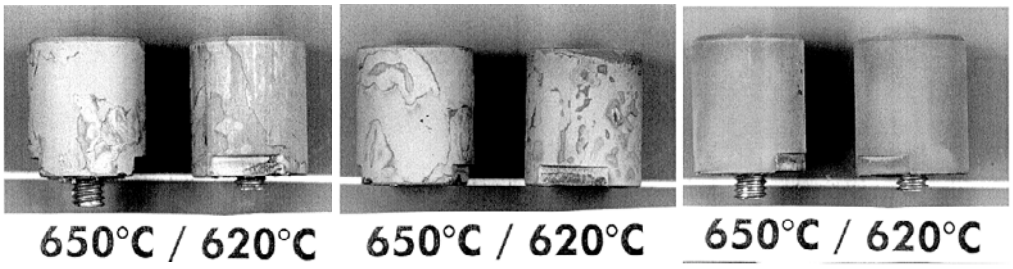

P92 **X20** **Al Slurry Coating**

Fig.1: The appearance of specimens after 6500h of steam exposure.

Figure 2 shows values of the total oxide thickness for samples exposed for >10’000 hours at approximately 600°C. Oxidation rates are larger for the 9%Cr steels.

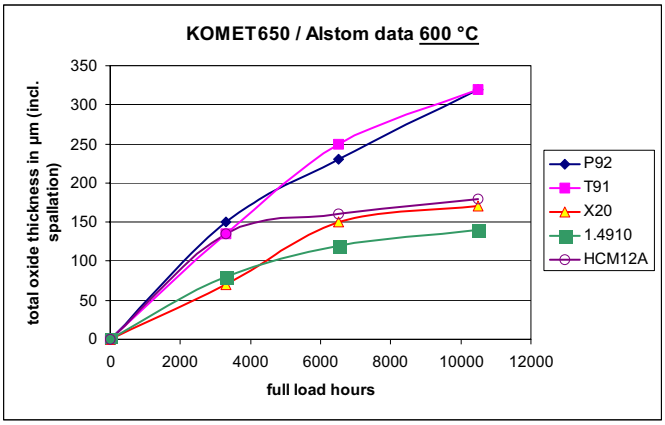

Fig. 2: Total oxide thickness (incl. loss by spallation) for the Komet samples at 600 °C

Fig. 3 shows cross sections of an austenitic steel after 4.300 h exposure. For austenitic steels the penetration of the oxidation layer is highly irregular.

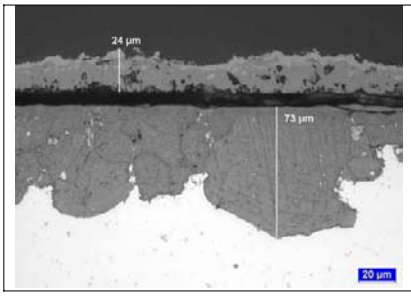

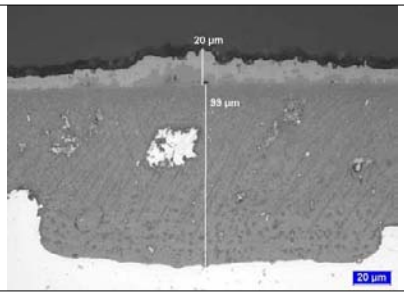

F23 (ESSHETE)
Left: 595 °C
Right: 630 °C

Fig. 3: Cross sections of Esshete 1250

In the following, micrographs of HVOF and slurry coatings on P92 are shown in the as-received state (Fig. 4). They have been prepared within the EU-project "Supercoat". Corresponding samples have been inserted into the bypass for longterm exposure. High oxidation resistance is expected due to the high chromium content.

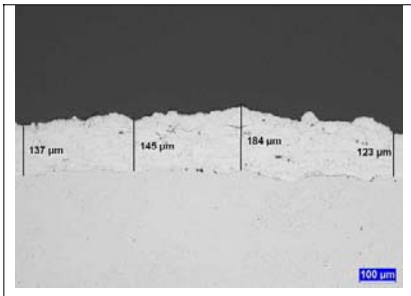

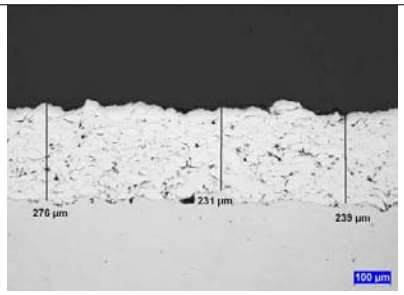

LEFT:
Ni-20Cr-**HVOF** coating, as received

RIGHT:

CrCoWC **HVOF** coating, as received

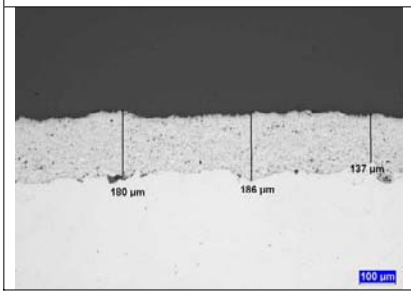

LEFT:
NiCr 80/20 + 25% CrC – **HVOF** coating, As received

Fig. 4: Cross sections of HVOF coatings on 9% Cr substrate

ESBJERG Test Loops

Background

For superheater and reheater tubes of the boiler, the creep rupture strength of the materials should be high enough at relevant pressure and temperature range. Additionally to this requirement, the corrosion resistance of the materials on the flue gas side and the steam oxidation resistance on the steam side have to be taken into consideration. Through steam oxidation an oxide layer is formed which leads to higher material temperatures and could cause creep damage. External corrosion of the tubes leads to certain losses of material on the flue gas side.

The mechanisms of flue gas corrosion and steam oxidation are not extensively clarified. On the flue gas side, not only the material aspect, but also the operational aspects play an important role. The flue gas temperature, steam temperature, the flue gas and ash composition, the dynamic behaviour of the plant are all factors of influence. On the steam side, the oxidation growth rate and the physical properties of the oxide layer can have an effect on the material temperature increase. The lack of knowledge in these areas can only be improved by operating tests in existing boilers which should be carried out at high steam temperatures and over long operating times.

Such tests have been performed in the Danish Power Plant Esbjerg Unit 3 since 1995. The goal of the tests is not only the investigation of high temperature corrosion and oxidation resistance of the new materials, but also a detailed analysis of the effect of different operating parameters on the long time behaviour of the materials.

Esbjerg Test Tig

The test rig was originally built in the framework of the Brite-Euram project in 1995. In the test rig, a total of three different test superheaters can be installed in the boiler. Fig 5 shows the steam side integration of the test rig in the power plant. The steam is taken from the connecting pipe between IT- superheater and final superheater of the existing boiler before the last spray water injection with a steam temperature of approximately 495 °C. In the test loop, the steam is heated to the desired outlet temperature. The mass flow through the test loop is controlled by a control valve at the inlet of the test loop. After the test loop, the hot steam is cooled down to 560 °C by a mixing piece where the hot steam is mixed with a cold bypass steam. This steam flows finally to the hot standby pipe of the high-pressure bypass system of the existing boiler.

On the flue gas side the test superheater is located in the boiler between the final superheater and the final reheater at a flue gas temperature of approx. 920 °C. At one side, the testing tubes are connected to the boiler water wall by means of sleeves. The tube coils lie transversely on the final superheater tubes of the existing boiler which ensures a free expansion of the test tubes. Fig. 6 shows the test superheaters installed in the boiler and the tube samples after dismantling of the test loops from the boiler.

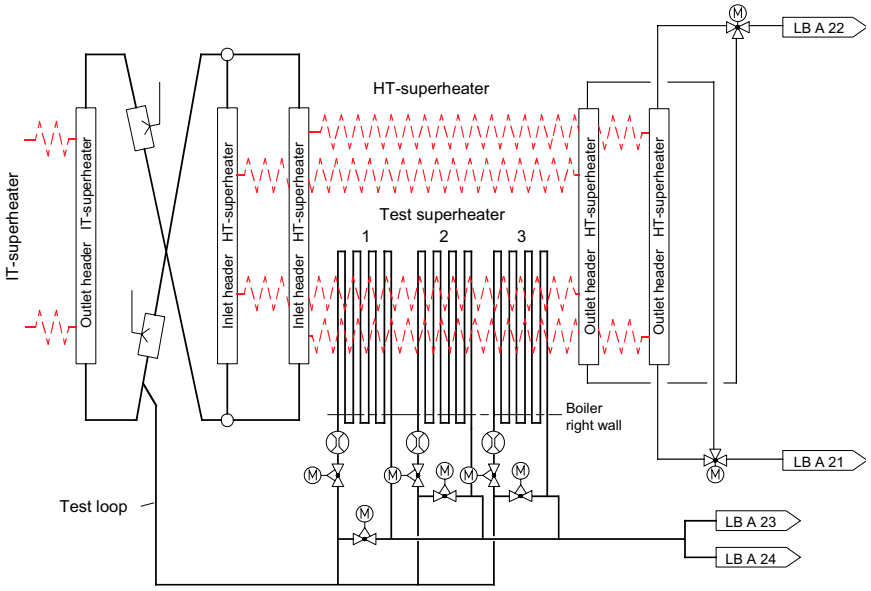

Fig. 5: Esbjerg Test Rig for investigations of advanced materials

Fig. 6: Test superheaters before and after dismantling

Since the first commissioning of the test rig in 1995, various test loops have been installed. Fig 7 shows the operating time of the different test loops in the Esbjerg Test Rig. During the Brite-Euram project, which was partly funded by the European Commission, three test superheaters were installed in 1995 in the existing boiler with a steam temperature at outlet of 620 °C. The three test superheaters have been dismantled, each after a one-year, a three-year and a seven-year exposure time. In the subsequent project, which was a co-operation between Elsam, EDF and ALSTOM, a test superheater with a steam temperature at outlet of 635 °C was installed in 1998 and has been dismantled in 2001. The next test loop, which was fully

funded by ALSTOM, had an outlet steam temperature of 700 °C. This test superheater was installed in 2000 and has been dismantled recently.

In the summer of 2004, a new test loop with a steam temperature at outlet of 720 °C was installed. This project is fully funded by the VGB Initiative Emax Group. The planned operating time is four years (approximately 30000 h exposure time). After dismantling of the test loop, the material samples will be investigated extensively concerning the changes of microstructure, the mechanical properties and especially the corrosion and the oxidation behaviour. Not only base materials but also similar and dissimilar welds will be investigated.

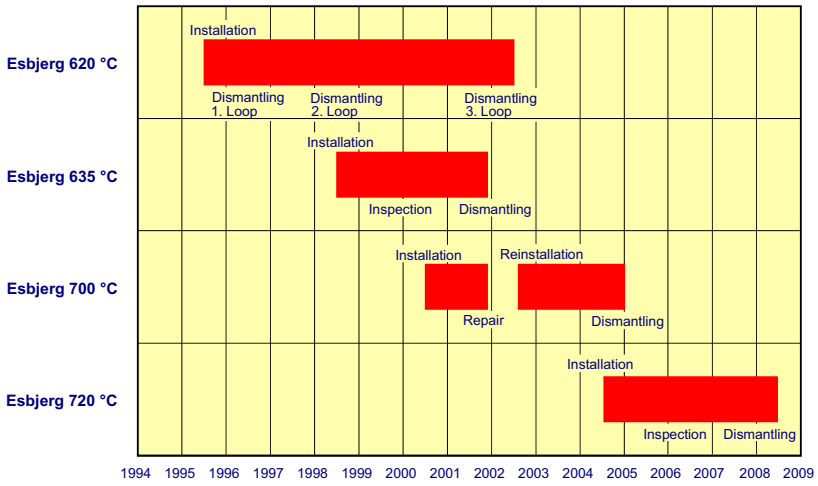

Fig. 7: Test superheaters installed in Esbjerg Test Rig

Material Selection

The purpose of the Esbjerg Test Rig is to test potential candidate materials for the superheater and reheater tubes at high temperatures. Table 2 shows the materials, which have been or are being tested in the test loops. From the group of ferritic steels, martensitic steels, austenitic steels and Ni-based alloys, different representative materials have been tested at different temperature levels.

Ferritic steels (steam temperature 500 - 525 °C)	T 23, T 24
Martensitic steels (steam temperature 500 - 580 °C)	X 20, T 91, T 92, HCM 12, HCM 12A, NF 12
Austenitic steels (steam temperature 510 - 690 °C)	1.4988, TP 347HFG, SUPER 304H, SUPER 304H (SB), NF 709, NF 709 R, Tempaloy A 3, Tempaloy AA 1 (SB), SAVE 25, TP 310 N, HR3C, Alloy 174 (Sanicro 25), HR6W
Ni-based alloys (steam temperature 635 - 720 °C)	Alloy 617, Alloy 617 mod., Alloy 4020, Alloy 740

Table 2: Materials tested in test loops

It is well known that the chemical composition has the largest impact on the corrosion and oxidation behaviour of the materials. The most important parameter here is the chromium content. Therefore, austenitic steels with 16 % to 26 % Cr content have been installed. Additionally, fine grained and shot-blasted austenitic steels, which have much better resistance to steam oxidation have been used.

The results of steam oxidation rates for T92 are shown in Fig. 8.

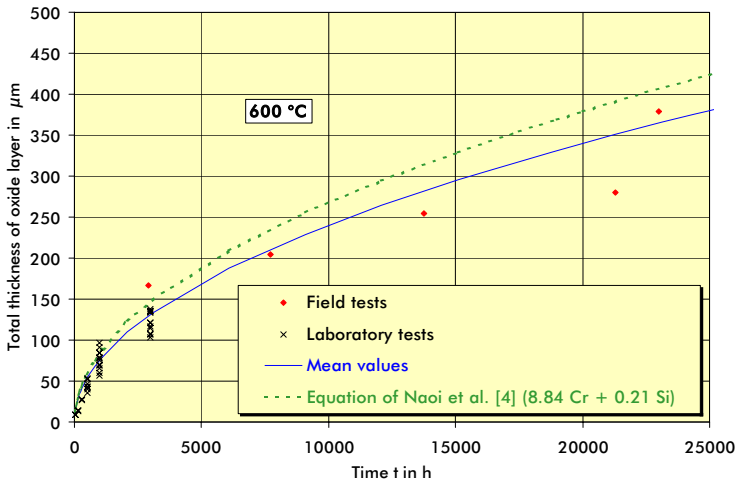

Fig. 8: Steam oxidation rates for T92

Marcko 700

Objectives

The ongoing Marcko 700 project was set up as a basis for the qualification of materials for future 700°C Power Plants. The project follows on from projects finalised in the framework of Marcko , AVIF and AIF as well as on material developments which have been done within COST 522 (Table 3). Overall objective is to create a basis for comprehensive assessement and qualification of the investigated materials, in order to achieve the official approval in the frame of the European Pressure Equipment Directive (PED).

Completed R&D-Projects	**Materials Investigated**
AVIF A77 , A129	T24 , E911
Marcko DE2 , AVIF A130	Alloy 617 mod.
AVIF A180	VM12
AIF P297	E911 , P92
Cost 522	VM12 , E911

Table 3: Previous material qualification projects.

Materials

For the increase of steam parameters up to 700°C, great significance must be attached to materials behaviour. Although martensitic steels with 9-12%Cr as well as 2 ½%Cr steels with improved creep properties can not be used for the high temperatures at the final superheater and reheater level, they still represent structure materials for essential components of the boiler. From this material group, materials such as T24 , T92/P92 and VM12 will be investigated for application of headers, pipes and membrane walls. Exceeding the temperature range of ferrites and martensites, austenitic steels and Ni-based alloys have to be used. For the components headers, pipes and membrane walls, the modified version of the Ni-based material Alloy 617mod., which was developed in the frame of Marcko DE2, will be tested and investigated in more detail.

Austenitic materials are not part of this programme since material properties and corrosion behaviour are already part of programmes such as Komet or Esbjerg.

Table 4 gives an overview of the materials investigated in Marcko 700 and the corresponding application as boiler component.

Material	C	Si	Mn	P	S	Al	Cr	Co	Ni	Mo	V	Nb	Ti	W	N	B	Cu	Fe	Sn
X10CrWMoVNb9-2 (P92)	0.07 - 0.13	0.5	0.3 - 0.6	0.02	0.01		8.5 - 9.5		0.4	0.3 - 0.6	0.15 - 0.25	0.04 - 0.09		1.5 - 2	0.03 - 0.07	0.001- 0.006			
7CrMoVTiB10-10 (T24)	0.5 - 0.95	0.15 - 0.45	0.3 - 0.7	0.02	0.01	0.02	2.2 - 2.6			0.9 - 1.1	0.2 - 0.3		0.05 - 0.1		0.01	0.0015 - 0.007			
Alloy 617 mod.	0.05 - 0.08	0.3	0.3	0.012	0.008	0.8 - 1.3	21 - 23	11 - 13	Rest	8 - 10			0.3 - 0.5		0.05	0.002 - 0.005	0.05	1.5	
VM12	0.11 - 0.13	0.4 - 0.6	0.15 - 0.35	0.02	0.03	0.02	11.2 - 11.7	1.5 - 1.7	0.2 - 0.4	0.2 - 0.4	0.2 - 0.3	0.04 - 0.06		1.4 - 1.6	0.05 - 0.08		0.2		0.02

Material	Application
P92	Piping, Header
T24	Membrane Wall
Alloy 617 mod.	Membrane Wall, Header, Piping
VM12	Membrane Wall, Header, Piping

Table 4: Materials investigated in the Marcko project

Working Packages

The working packages are mainly related to qualify and to demonstrate fabrication based on industrial conditions and European Code Requirements (PED) as well as investigations in laboratory and component tests. In detail the programme specifies the following steps:

- Fabrication and supply of tubes and pipes as well as filler metals.
- Fabrication of similar welds and inductive bends based on usual boiler manufacturing conditions as shown in Table 5.
- Mechanical-technological tests, NDT, macro and micro sections.
- Material properties after ageing.
- Creep tests (base metals, welds, bends)
- Metallurgical investigations of microstructure and development of failure mechanism.
- Component tests on membrane walls in laboratory, based on boiler-relevant loads.

Fabrication steps	Dimensions	Materials
Butt welds for header and pipes	OD 460 x 80mm	P92, VM12, Alloy 617 mod.
Butt welds for tubes	OD 38 x 7,1mm	T24, VM12, Alloy 617 mod.
Nozzle welds at header	OD 460 x 80mm / OD 38 x 7,1mm	P92 / T92, VM12, Alloy 617 mod.
Tube-fin-welds for membrane walls	OD 38 x 7,1mm	T24, VM12, Alloy 617 mod.
Inductive Bends	OD 460 x 80mm	P92, VM12, Alloy 617 mod.

Table 5: Fabrication of pipe welds and bends.

Fabrication of tubes and pipes as well as fabrication of welds and bends was finished at beginning of 2006. Impressions from welding of pipes are shown in Fig. 9. Tests and investigations in the laboratory are in progress.

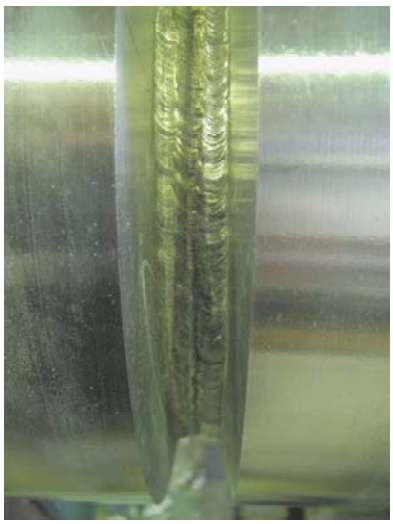

Filler passes, weld build-up

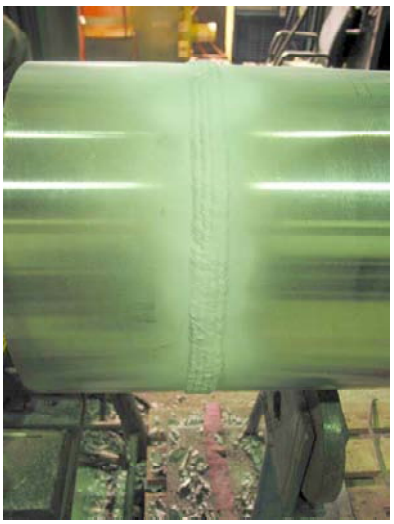

Penetration test at cover pass

Fig.9: Steps in the manufacture of pipe welds.

Further Development stages towards the 700 °C technology

Today´s state-of-the-art provides efficiencies of over 45 % and 43 % (LHV) for bituminous coal and lignite-fired power plants respectively (corresponding to steam outlet temperatures of 600 / 620 °C), compare to a 35 % average in the 1970s. In the mid 1990s manufacturers and utilities decided to make the step towards the 700 °C technology for coal-fired power plants, a step that is equivalent to a net efficiency of over 50 % (LHV) for coal-fired power plants. The advantages of this development are obvious: Increased efficiency offers a

satisfactory response to the requirements for lower Cost of Electricity (CoE), reduction of all primary emissions, saving resources and reduction of CO_2 emissions.

From a technical point of view, the main processes involved in the construction and operation of coal-fired power plants do not change and thus the 700 °C technology can benefit in terms of reliability and availability from the experience gained over decades. Therefore the risk related to the introduction of a new technology is minimised and limited to a number of critical components that need to be tested in advance.

AD700 Project

The testing of the critical components for the 700 °C technology was the reason for launching the AD700 project in 1998 [3]. This phased-programme aims at covering design, materials and demonstration issues linked with this technology. The first phases were jointly funded by the EU and the participating partners.

The formation of the E_{max} initiative by VGB, consisting of major European utilities (RWE, E.ON, EnBW, EDF, Vattenfall, Electrabel, Energi E2, Elsam and PPC) accelerated the identification of additional development needs that require a minimum operational time and shall thus be demonstrated. These needs include:

- long term creep behaviour linked with real plant dimensions and other design features
- determination and evaluation of residual service life
- in-service inspections
- operational testing of Ni-based alloys for pipes and valves
- steam oxidation and hot gas corrosion under real operating conditions.

COMTES Project

In order to fulfil the above needs, the project COMTES700 was launched in 2004 and aims at the demonstration of the critical boiler components, of a turbine inlet valve, of a safety valve and a high pressure (HP) bypass valve for a 700 °C temperature. The project is partly funded by the EU and the partners including the utilities named above and ALSTOM, Siemens, Babcock Hitachi Europe and Burmeister & Wain Energy. ALSTOM has developed the concept and has the technical leadership of the project. Figure 10 shows the flow diagram of the Component Test Facility (CTF).

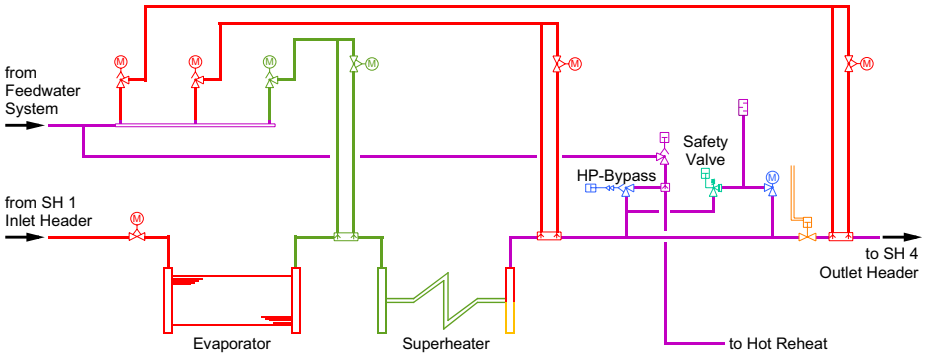

Figure 10: CTF Flow Scheme

The CTF has been installed in the 750 MW_{el} bituminous coal-fired power plant Scholven F. Steam for testing (12 kg/s) is taken from the inlet header of the first superheater stage (SH1) and is led to the membrane wall panel, where it is heated to 600 °C. Between the membrane wall panel and the superheater, an injection is foreseen, which can quickly control the temperature level before the test superheater inlet. The steam is heated in the test superheater at 705°C and will then either enter the HP bypass test valve, or will be cooled down to SH3 temperature level and mixed with the main superheater steam. In the first case the steam after leaving the HP bypass test valve will be cooled and led to the final reheater outlet header.

Figure 11 shows the arrangement of the boiler critical components of the CTF in the existing boiler in Scholven F [4].

The CTF was successfully placed in operation in early summer 2005 and the demonstration will last for at least three years. After completion of the demonstration, secure operational data with the implemented materials will be available that will enable the construction of the first full scale 700 °C power plant. From the technical point of view, the CTF demonstration is the final step that will prove the 700 °C technology concept. The subsequent construction of a commercial, or demonstration full scale coal-fired power plant applying this technology will then depend on economic considerations related to the development of the materials, coal prices, and the value for the avoided CO_2 emissions.

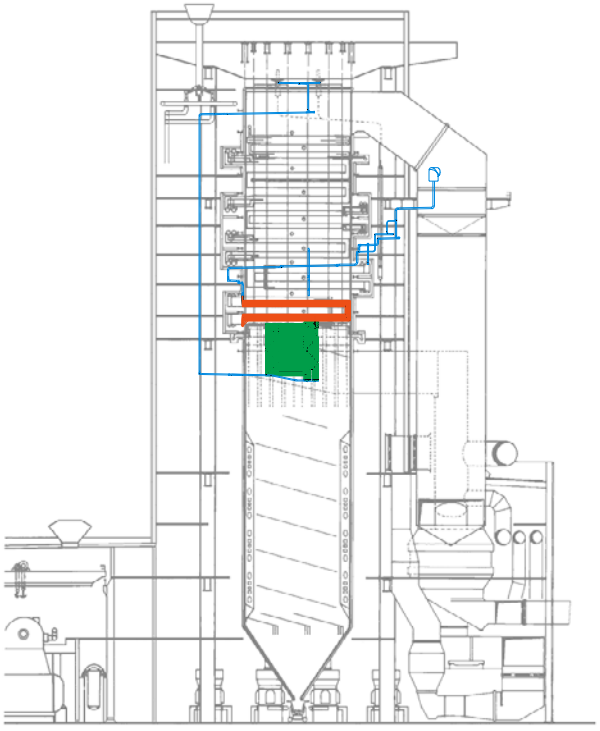

Figure 11: CTF Implementation into existing boiler

DOE USC Boiler Materials Consortium Project

In parallel to the EU-sponsored Thermie project (700/720°C), the USC Boiler Materials Consortium programme to develop a 730/760°C plant, sponsored by the US Department of Energy (DOE) and the Ohio Coal Development Council (OCDC) was initiated in 2003. In the framework of this program ALSTOM designed a 700 MW steam generator with steam turbine throttle conditions of 38.5 MPa/730°C/760°C, and the materials that would be required for the high temperature pressure part components were identified on the basis of those conditions. Figure 12 shows the surface arrangement of the conceptual boiler design. The unit is configured as a once through, two-pass gas design with pendant heating surfaces located in the upper furnace and the tunnel and the horizontal surfaces in the rear pass [5]. The arrangement is similar to that for more conventional steam conditions.

Welded furnace walls, referred to as waterwalls, provide the enclosure around a combustion chamber. Compared to lower pressure steam conditions, ultra-supercritical steam generation takes place at higher temperatures. This is due to a number of factors; each one of which has a significant impact upon the design of the waterwalls. The first factor is the high feedwater temperature at the economizer inlet and outlet, which results in higher fluid temperature entering the furnace walls. The second factor is the high operating pressure, which requires tubes with thicker walls. The third factor relates to the reduced cooling flow associated with improved cycle efficiency. The effect of the higher fluid temperature and pressure on the furnace walls must be mitigated by increased mass velocity or/and higher strength alloy for tubes.

Adequate mass velocity is achieved by using the spiral waterwall construction that has been used by ALSTOM on many supercritical power plants built in Europe and Asia. One important benefit of spiraling tubes around the furnace is that every tube forms part of all four walls. Therefore, every tube acts as a heat integrator around the walls of the furnace, thus minimizing the heat absorption imbalance between individual tubes. This design requires application of T23 (2Cr) alloy in the lower portion of the lower furnace and a material with the strength of T92 (9Cr) in the upper portion of the lower furnace. Due to very high heat fluxes, some sections of the furnace tubes have outer diameter metal temperature near 593°C. Generally, because of metal oxidation concerns, the practice is to limit application of 9Cr alloys not to exceed 650°C. While the estimated metal temperatures are below this limit, such high temperature in the waterwalls fall outside practical operating experience. Experience has shown that some coals produce complex sulfates ash which is extremely corrosive in the temperature range 565-690°C. Therefore, it is anticipated that the application of protective coating to some sections of the furnace walls will be necessary to mitigate corrosion effects.

The primary superheat duty is performed by the roof and backpass wall tubes. Similar to the furnace walls, the likely candidate material of construction is T92. Next, the superheat panels are constructed of 50.8mm OD tubes. Materials of construction and wall thickness vary depending on metal temperatures. Materials proposed for use in superheater panels are Super 304H, IN 617, and IN 740. The estimated maximum tube outside temperature can reach as high as 720°C in some parts of the panel. As was the case with the panels, materials of construction and wall thickness will vary depending on metal temperatures.

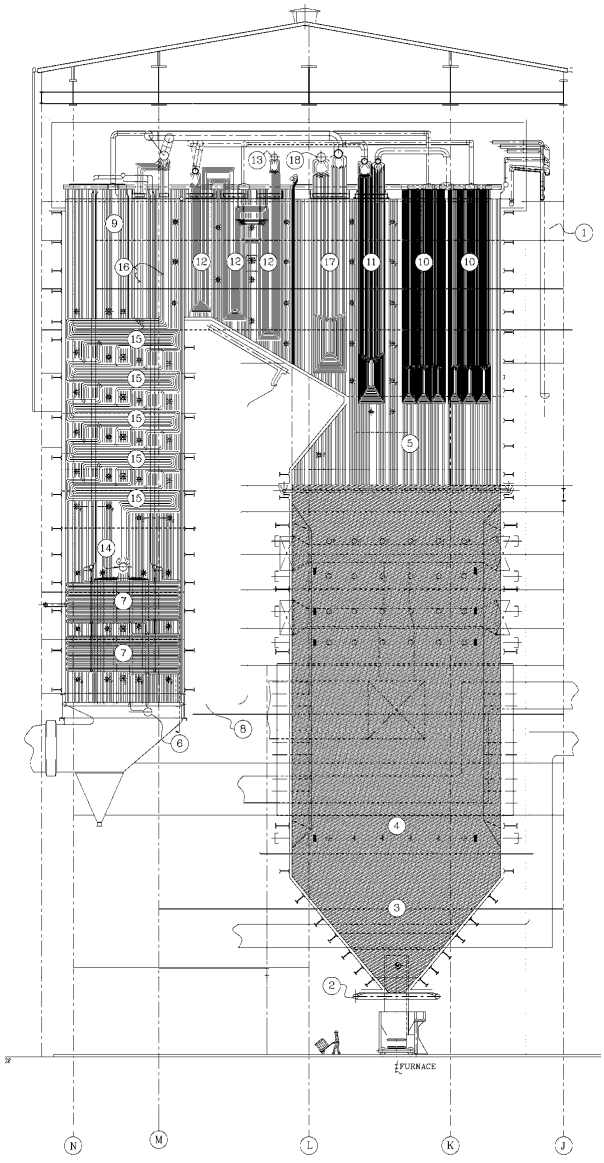

FIGURE 1

Legend

1. Separator
2. Furnace lower ring header
3. Furnace hopper tubes
4. Furnace spiral waterwall tubes
5. Furnace vertical waterwall tubes
6. Economizer inlet header
7. Economizer assemblies
8. Backpass lower ring header
9. Backpass sidewall tubes
10. S.H. division panelettes
11. S.H. platten assemblies
12. S.H. finish assemblies
13. S.H. outlet header
14. R.H. inlet header
15. R.H. horizontal assemblies
16. R.H. low temp. pendant assemblies
17. R.H. finisching assemblies
18. R.H. outlet header

Figure 12: Illustrating the Surface Arrangement of ALSTOM's Conceptual Boiler Design Developed for the US-DOE Ultra-Supercritical Project

Proposed materials are TP347HFG, IN 617, and IN 740. The maximum tube outside temperature of about 743°C was calculated for the wrapper tubes (first tube in the assembly). While the superheat finishing surface is predominantly constructed of IN 740, the IN 617 will be applied for some sections of the tubing. Outside metal temperatures for some tube sections are above 760°C.

Reheat duty is carried out in two sections: a primary reheat horizontal surface installed in the rear pass and a finishing surface located above the arch. Since the reheater operates at relatively low pressure, a range of materials are available with adequate strength to operate up to 760°C.

In the selection of headers and piping, the following five parameters must be considered: pressure drop, flow distribution, design temperature, operating pressure and mode of operation. For the finishing superheater outlet header and the main steam line piping, the candidate alloy is IN 740. For the intermediate temperature headers and links the pool of available materials is much wider. Possible candidate alloys are IN 617, HR6W, SAVE 25, Haynes 230 and HR120. The alloy IN 740 is also applied for the construction of the finishing reheater outlet header and piping.

Conclusions

Through the sum of the activities described in this paper major progress is being made towards the achievement of high steam power plant efficiencies. Figure 13 illustrates the steps

- in steel development in Europe (600 → 620 → 640°C) originating from the COST actions, with further validation through field testing of samples
- in the application of nickel alloys in Europe (to 720°C and in the USA (to 760°C).

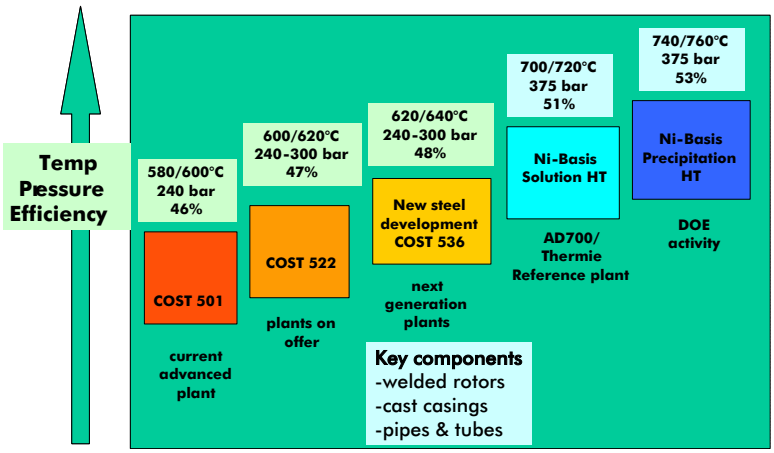

Figure 13: Steps in the development of high temperature steam power plant

An essential step in the introduction of nickel alloys lies in the construction and operation of component test facilities and demonstration plants to ensure customer acceptance.

Acknowledgements

The authors would like to thank their colleagues for many contributions to this work and also the COST Management Committee for their guidance in the programme and to the national funding bodies for their financial support.

References

[1] Gabrel, J.; Bendick, W.; Vaillant, J.C.; Vandenberghe, B.; Lefevre, Bo: VM12- A new 12%Cr steel for boiler tubes, headers and steam pipes, 4th international conference on Advances in Materials Technology, October 25-28, 2004, Hilton Head Island, pp 919-929.

[2] Scarlin, R.B.; Stamatelopoulos, G.N.: New Boiler Materials for Advanced Steam Conditions, Materials for Advanced Power Engineering, Liege 2002, pp 1091 - 1108

[3] Kjaer, S; Klauke, F.; Vanstone, R.; Zeijseink, A.; Weissinger, G.; Kristensen, P.; Meier, J.; Blum, R.; Wieghardt, K.,: The Advanced Supercritical 700°C Pulverised Coal-fired Power Plant, PowerGen Europe, Belgium, May 2001, pp 29.-31

[4] Bauer, F.; Stamatelopoulos; G.-N.; Vortmeyer, N.; Bugge, J.: Driving Coal-fired Power Plants to over 50% Efficiency, VGB PowerTech 12/2003, pp 97-100

[5] Henry, J.F.; Fishburn, J.D.; Perrin, I.J.; Scarlin, B.; Stamatelopoulos, G.N.; Vanstone, R.: Advanced Supercritical Technology - A Vital Component of Future Power Generation, The 29th International Technical Conference on Coal Utilization & Fuel Systems, 18.-22. April 2004, Clearwater, Florida, U.S.A.

COATINGS FOR PROTECTION OF HIGH TEMPERATURE NEW GENERATION STEAM PLANT COMPONENTS: A REVIEW

Alina Agüero
Instituto Nacional de Técnica Aeroespacial (INTA)
Ctra. Ajalvir Km. 4
28850 Torrejón de Ardoz (Madrid)
SPAIN
email: agueroba@inta.es

Abstract

Since 1998 during the European Action COST 522 coatings were developed for the first time in Europe to be used in future supercritical high temperature steam turbines to prevent component oxidation. Slurry applied, pure and Si modified aluminide coatings, electroless Ni and a series of thermal sprayed alloys (FeAl, FeCrAl, NiCr and AlFeCoCr) were deposited on P92. Most of these coatings showed excellent behaviour up to at least 10,000 h for the thermal spray coatings and to 20,000 h for the plain aluminides when exposed to steam at 650ºC in the laboratory. Since then, other researchers in Europe, North America and Japan have also begun to look at coatings for steam oxidation protection including a number of alternative deposition techniques such as pack cementation, electro-plating, CVD (fluidized bed and organometallic as well as thermal), etc. A summary of all available results, including steam oxidation and other testing data will be presented together with a critical analysis of the different alternatives both from the materials behaviour and deposition techniques suitability perspectives.

Keywords: Steam power plant, high temperature, ferritic/austenitic steels, oxidation resistance, coatings.

1. Introduction and Background

Future high efficiency coal-fired steam power plants will operate at higher temperatures. Under steam atmosphere, existing ferritic and austenitic alloys, commonly employed in steam plants, form Cr containing oxides which become less protective at temperatures higher than 550º C. New alloy development activities have been very successful in improving the creep strength at higher temperatures, generally by lowering the chromium content [1, 2]. However, when the Cr content is lower that 10 w%, such as P92, very thick oxide scales form, consisting of a top layer of and an inner zone mainly $(Fe, Cr)_3O_4$ spinels (figure 1a). These scales spall causing metal cross-section loss (figure 1b), blockage and erosion of components located down-stream and also produce a thermal insulating effect resulting in overheating [3, 4].

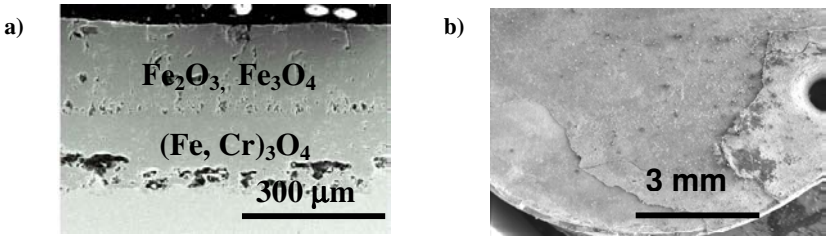

Figure 1: SEM images of uncoated P92 exposed to steam at 650º C for 10,000 h: a) cross-section and b) top view

A similar situation occurred for gas turbine many years ago and was resolved by employing protective coatings. For steam power plants, some work was performed in the US around 30 years ago, particularly addressing the protection of boiler tubes of 2.25 wt.% Cr steels and austenitic stainless steels. The range of coatings and surface treatments investigated included chromizing [5], chromate conversion, application of a Cr_2O_3 ceramic coating, and application of layers of aluminium, electroless nickel or silicon [6, 7]. It was concluded that the only satisfactory behaviour was achieved using chromizing and chromate conversion. However, there is increasing resistance to use chromate conversion processes due to the health and environmental hazards related to Cr^{+6}, and on the other hand pack cementation is carried out at temperatures too high (>800º C) for the steels currently employed in the manufacture of steam turbine components.

After a gap of some 20 years, no other published work appeared in the literature, until 1998, when as part of the activities carried out in COST 522, a feasibility study regarding the use of coatings to prevent component oxidation in future supercritical high temperature steam plants (650º C) was initiated for the first time in Europe [8]. Since then, several groups have begun exploring a number of coating process and materials including formers of all three known protective oxides, Al_2O_3, Cr_2O_3 and SiO_2. This paper includes a summary of available results, including steam oxidation and other testing data along with a critical analysis of the different alternatives both from the materials behaviour and deposition techniques suitability perspectives.

2. Coating Materials and Processes

2.1 Diffusion Coatings

2.1.1 Slurry Aluminide Coatings

Slurries are suspensions of particles (metallic or ceramic) on a binder solvent system that can be applied on a substrate by means of a brush or by spraying. After application, the coated specimen is subjected to a curing heat treatment to eliminated liquids and set the coating.

In the framework of COST Actions 522 and 536 and of the on-going European project “Coatings for Supercritical Steam Cycles” (SUPERCOAT), commercially available aluminium slurries have been applied on several substrates such as P91 [9], P92 [8, 10-13], P22 and P23 [14], following the manufacturer's recommendations to be subsequently heat treated at 700º C under flowing Ar. The resulting coating cross section microstructure is shown in figure 2. Thicknesses of 40-100 μm can be deposited and electron microprobe analysis as well diffraction carried out in a Transmission Electron Microscope, confirmed the presence of an outer Fe_2Al_5 zone with Cr rich precipitates, and an inner and thinner FeAl layer on top of a zone containing acicular precipitates of AlN [8]. The lower Cr substrates P22 and P23 exhibited a similar microstructure with less Cr containing precipitates and no precipitation of AlN within the substrate (both substrates have lower N content than P91 and P92) [14].

Such formed aluminides exhibit stress relieving cracks, present already after the initial diffusion heat treatment, probably due to brittleness of the Fe_2Al_5 phase and to thermal expansion coefficients mismatch. On exposure to steam, the coating develops a protective Al_2O_3 layer and the cracks do not propagate into the base material, nor become sites of

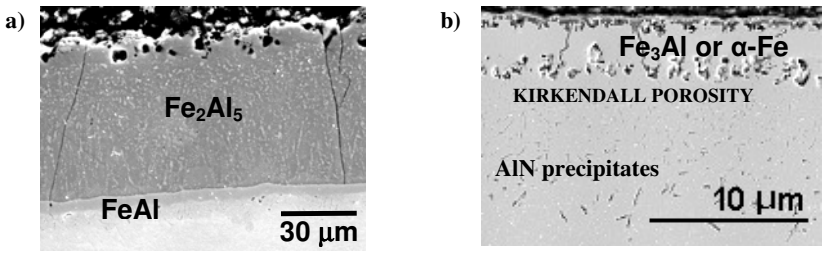

Figure 2: Slurry aluminide coating on P92: a) before exposure and b) after 30,000h of steam oxidation at 650º C

preferential attack by steam. However, slow degradation is observed by a reduction of the Al surface concentration by Al inwards diffusion rather than by spallation and regeneration of the protective scale. In steels with a N content > 0.040 wt.%, the diffused Al causes precipitation of AlN within the substrate as shown in the cross section of a specimen exposed to pure flowing steam for 30,000 h at 650º C (figure 2b). The coating has recently surpassed 40,000 h of exposure without evidence of substrate attack and cracks did not propagate into the substrate after 2,000 cycles (1 cycle: 1 h at 650º C cooling to 100º C for 5 min in 5 min, heating in 5 min) [13]. Moreover, on exposure to high steam pressures both in the laboratory at TU Darmstadt (300 bar) [9] and in a test tube connected to a steam turbine operating at 640º C (180 bar) in Westfalen, Germany [11], the behaviour was similar to that observed in the 1 bar laboratory tests. In addition, creep and Thermo-Mechanical Fatigue (TMF) testing of coated specimens have indicated that these coatings do not affect the properties of P91 at 650º C [15].

A similar process was also developed and patented by Schmitz but thinner and very irregular, non uniform coatings were obtained [16].

Some elements, such as Si and Ni were added to the aluminide coating in an attempt to stabilize the intermetallic phases to retard aluminium interdiffusion from the coating into the substrate, and therefore degradation of the aluminide coatings. The coatings microstructure was modified with new phases rich in Si and Ni. However, after exposure to steam at 650º C, the degree of Kirkendall porosity at the coating-substrate was much higher than that of a pure aluminide after the same exposure. This indicate that both Si and Ni contributed to retard Al inwards diffusion but without significant reduction of Fe outwards diffusion with the consequent generation of pores which with time increase in number and size until coating detachment is caused as shown in figures 3a and b respectively [9, 13].

2.1.2 Chemical Vapour Deposition (CVD) Coatings

In CVD, one or two vapour phase precursor species are brought in contact with a heated substrate and on its surface said vapours decompose or react among themselves respectively, resulting in the deposition of a coating and the release of volatile by-products. In the cases of metals being deposited, if the deposition temperature is sufficiently high, said metal(s) will interdiffuse with the substrate as it is being deposited resulting in an intermetallic diffusion coating.

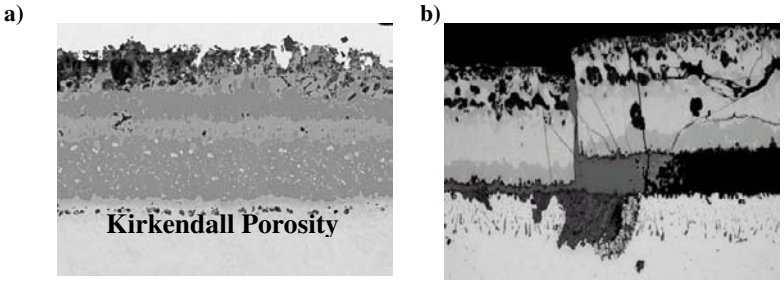

Figure 3: SEM image of the cross section of a (20 wt.%) Si modified aluminide coating on P92: a) after 72 h and b) after 4500 h of exposure to steam at 650º C

Pint, Zhang and co-workers have deposited aluminide coatings on ferritic and austenitic steel substrates by CVD from $AlCl_3$ and H_2 at 900-1100º C [17]. The resulting structure consist of two crack free layers, the top thinner (3-25 µm depending on the temperature) and richer in Al (25 at.%) while the most inner layer is thicker (60-275 µm), with a gradually decreasing Al content and exhibiting acicular AlN precipitates (figure 4). Cyclic oxidation testing of these coatings in air containing up to 10 vol.% of H_2O was carried out at 700-800º C. After 2000 short term cycles (1 cycle: 1 h at 700º C, 10 min at room temperature) thickness through cracks that propagated into the substrate could be observed as well as substrate oxidation through said cracks. However, at a longer cycle length (1 cycle: 100 h and 10 min at R.T.) the coatings were still protective after 14,000 h [18-20].

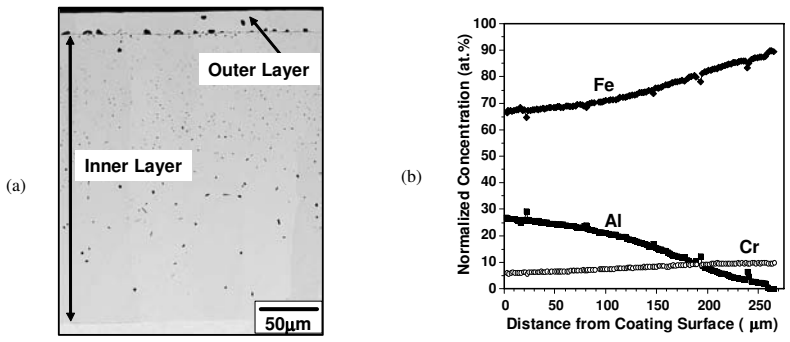

Figure 4: CVD aluminide coating on Fe9Cr1Mo deposited at 1050ºC: a) back scattered electron image and b) compositional profiles of the principal elements [21]

Aluminide, silicide and Si modified aluminide diffusion coatings have also been deposited by Pérez and collaborators employing lower temperatures by means of Fluidised Bed CVD (FBCVD) under atmospheric pressure [22-24]. In FBCVD the specimens to be coated are placed in contact with a fluidised mixture of powders comprising the precursors (Al and/or Si) and inert filler through which HCl is flowed. In this manner transport of the vapours (Al and/or Si chlorides) to the substrates is enhanced. For instance aluminide coatings could be

obtained at 550º C as opposed to the much higher temperature required by the above mentioned CVD process. As shown in figure 5a, the aluminide coating deposited by FBCVD is similar in microstructure to those obtained by slurry deposition, but without stress relieving cracks and significantly thinner (10 μm). After 10,000 h of isothermal steam oxidation laboratory testing at 650º C, the coating began to fail, showing "islands" of Fe_3O_4/(Fe, $Cr)_3O_4$ spinel as seen in figure 5b. The subscale Al content in zones where attack has not begun, was 4.5 wt.%. This observation is in agreement with recent works that indicate that if Cr is present, the critical Al concentration required to form a protective may be lower 5 wt.% [25, 26].

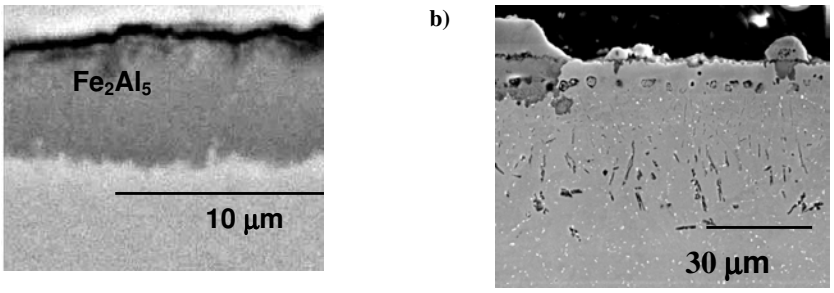

Figure 5: Aluminide coating deposited on P91 by FBCVD at 550º C: a) as deposited and b) after 10,000 h of steam oxidation testing at 650º C [27].

Pure Al coatings have been deposited by Metal-Organic CVD (MOCVD) at 300º C. In this modality of CVD, organometallic precursors are employed and as this type of compounds is less stable than halides typically used in conventional CVD, the deposition can take place at lower temperature. After a diffusion heat treatment at 650º C, a coating similar to that obtained by slurry deposition was obtained [28]. Thicknesses higher than 50 μm (after diffusion) are easily achieved at coatings time of 1 h or less and long exposure testing (over 10,000 h at 650º C) have also indicated excellent behaviour.

High temperature CVD has also been employed to deposit Si inside tubes by K. Berreth and K. Maile and collaborators [29]. At 1050º C, Si was deposited on the inner surfaces of T91 tubes (∅ 42 mm) from $SiCl_4$ and H_2. No prior surface machining was necessary as "in situ" H_2 cleaning is possible. The resulting coating consists of a crack free 20-30 μm diffusion layer containing 4-6 at.% of Si as well as excess Si which was converted to Si_3N_4 employing NH_3. Moreover, the process allows to increase the Si content of inner surfaces of tubes without needing to machine to remove the original scale resulting form the tube's production process (figure 6). Tensile testing up to 700º C indicated that there was only a minor influence on the strength of the base material and exposure to a 10 % water vapour atmosphere at 600º C shows a protective behaviour up to at least 1100 h of exposure.

2.1.3 Pack Cementation Coatings

In Al pack cementation, components to be coated are "buried" in a mixture of powders including Al, an activator which is usually NH_4Cl and inert filler (Al_2O_3). Upon heating, Al reacts with NH_4 producing aluminium chlorides vapours that reach the hot surface of the component reacting with H_2 to deposit Al (by CVD) which diffuses as it is being deposited.

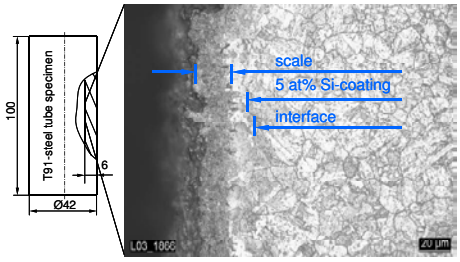

Figure 6: Inner tube surface enriched with Si deposited by CVD [30]

Rohr and Shütze have explored pack cementation as a method to coat the inner surfaces of heat exchanger tubes and they have shown that diffusion coatings essentially consisting of Fe_2Al_5, can be produced at 650º C. Their results also showed that glass bead blasting prior to coating resulted in a thicker and denser coating [31, 32]. Chromizing was also carried out at 1000º C resulting in a Cr enriched 30-50 µm layer [33]. Moreover, chromizing at 1000º C followed by aluminizing at 650º C resulted in 10 µm of Al_4Cr over a Cr rich layer as seen in figure 7. Cr enrichment reached 45 at.% below the surface of the P91 substrate [24]. Pack siliconizing was also carried out and the resulting coating consisted of a porous 10 µm Si rich (24 at.%) layer [24].

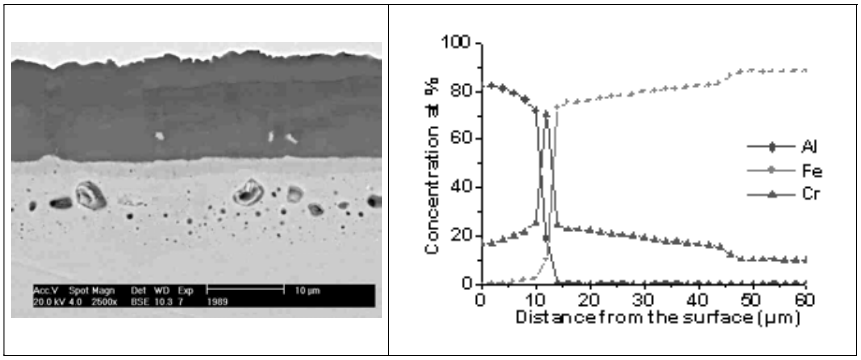

Figure 7: Two step Cr+Al pack cementation coating on P91. 1st step Cr deposition at 1000 °C for 2 hours in Ar followed by a rapid cooling . 2nd step Al deposition at 650° C for 1h in Ar-10 %H2 [34]

Xiang, Datta and co-workers have also deposited suitable thickness aluminide coatings by low temperature pack cementation (700º C) in a reasonably short period of time (a few hours) within the frame of the already mentioned SUPERCOAT project [35, 36]. These pack cementation coatings exhibit a smooth surface in contrast with slurry deposited aluminides as shown in figure 8 but although it is not shown on the figure, these coatings also develop

thickness through cracks. XRD indicated that the "as deposited" coating consist of $Fe_{18}Al_{84}$, differing from Rohr and Shütze Fe_2Al_5 coatings, also deposited by pack cementation as mentioned earlier. Laboratory testing under pure flowing steam at 650º C has shown a similar behaviour to that of slurry deposited aluminides for at least 5000 h and degradation also occurs by coating-substrate interdiffusion.

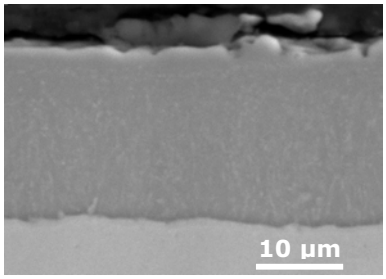

Figure 8: Aluminide coating deposited on P91 by pack cementation at 700º C [37]

Low alloyed steels have been boro-aluminized by Tsipas and co-workers at 715º C [34, 38]. In these 20-30 µm crack-free coatings, B is localized at the coating-substrate interface but does not seem to retard Al interdiffusion as illustrated in figure 9, where a sample exposed to steam at 650º C for 300 h is shown. Results of steam cyclic oxidation testing at 650º C for up to 1,000 h are very satisfactory.

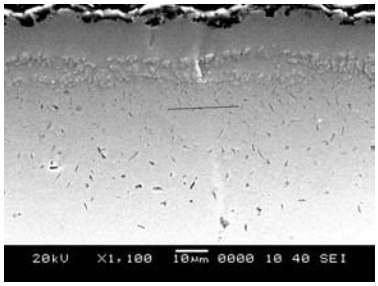

Figure 9: Boron-aluminide coating deposited by pack cementation at 715º C after 300h of steam oxidation at 650º C [39]

Nava and collaborators have also explored Cr, Cr-Si and Cr-Al diffusion coating deposited by pack cementation but at higher temperatures [40]. For instance, pack chromizing of T92 at 1140-1200º C results in a 360 µm Cr rich layer, free of Cr-carbide precipitates as seen in figure 10, with a surface Cr concentration of 30 wt. % which gradually decreases down to 9 wt.% (Cr content of P92). After short periods of exposure to steam at 750º C, there were no apparent signs of attack as well as no indication of breakaway corrosion.

2.2 Overlay Coatings

2.2.1 Thermal Spray Coatings

During thermal spray, finely divided molten or semi-molten droplets of the coating material are accelerated towards the surface to be coated. The particles hit the surface deforming and coalescing on cooling forming a coating.

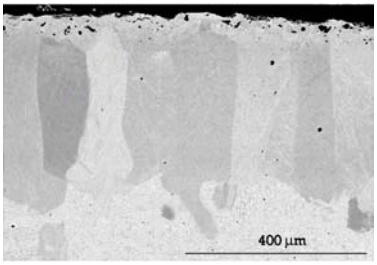

Figure 10: As deposited Cr diffusion coating on T92 by pack cementation at 1200º C [41]

Several intermetallic coating materials have been deposited both by Atmospheric Plasma and High Velocity Oxyfuel Thermal Spray (APS and HVOF respectively) in the framework of COST Actions 522 and 536 and of the European project SUPERCOAT [8-11, 13]. In APS, material particles are passed through an electric plasma supported by an inert gas and/or H_2 and produced by low voltage, high current electric discharges. Fe30Cr5Al, Ni20Al and Al25Fe coatings with a significant degree of porosity were deposited and exposed to steam at 650º C with satisfactory results at least for 500 h [8].

During HVOF, a fuel gas as well as oxygen are mixed in the combustion chamber of a specially designed spray gun. Powders are injected, heated and accelerated to hypersonic gas velocities. As a result of the significantly higher kinetic energy, very dense coatings can be obtained. Fe30Cr5Al, Ni20Cr and Al20Co11Fe11Cr have been deposited and tested at 650ºC under pure steam for periods of at least 10,000 [9, 10]. The first two coatings did not show signs of degradation and formed protective Al_2O_3 and Cr_2O_3 oxide scales respectively. Remarkably, in Ni20Cr there is no evidence of Cr depletion near the protective scale interface as the Cr content remains unchanged except in the zone near the substrate interface where some coating-substrate interdiffusion has taken place (figure 11).

On the other hand, Al20Co11Fe11Cr lost Al by interdiffusion causing phase transformations and Kirkendall porosity [12]. Cermet coatings such as WCCoCr as well as CrCNiCr have also been tested with satisfactory results [9, 11] and more recently, inexpensive Fe12Cr, Fe50Cr, Fe16Al and Fe32Al have also been deposited by HVOF. Both Fe12Cr and Fe50Cr are very stable under steam at 650º C and while Fe50Cr develops a thin Cr_2O_3 protective layer, Fe12Cr the scale also contains Fe (figures 12a and b respectively). Both Fe16Al and Fe32Al form protective Al_2O_3 but Fe32Al develop thickness through cracks that cause substrate attack and eventually spallation probably due to the very brittle nature of FeAl intermetallics with high Al content, exhibiting high resistance to steam oxidation at 650º C [13].

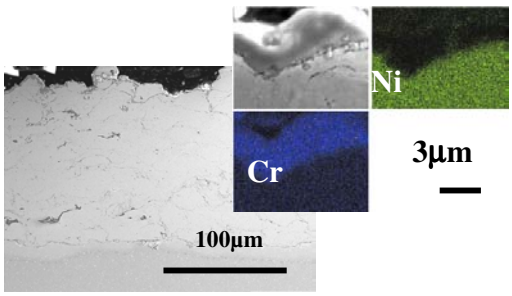

Figure 11: Cross-section of Ni20Cr deposited by HVOF after exposure to steam for 10,000 h at 650º C

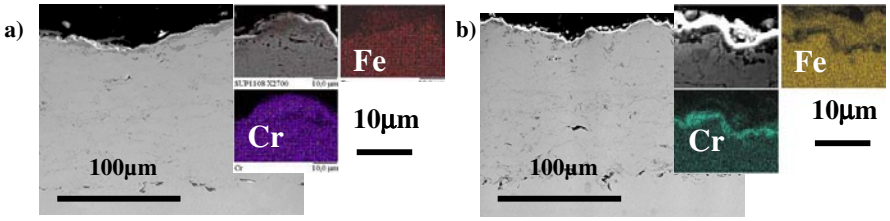

Figure 12: Cross-section of: a) Fe50Cr and b) Fe12Cr deposited by HVOF after exposure to steam for 1,000 h at 650º C

Sundararajan and co-workers have also explored APS and HVOF thermal spray to deposit Al and NiCr coatings for steam oxidation protection. The APS Al coatings deposited on T91 [40] interdiffuse on exposure to steam at 600 and 750º C forming FeAl intermetallic phases similar to those obtained in the already mentioned diffusion aluminide coatings. However, since the APS deposited Al coating exhibits some degree of porosity, steam reaches the substrate surface before the interdiffusion process has been completed resulting in a partially oxidised aluminide layer. The same behaviour was observed when an Al slurry coating was exposed to steam without a prior diffusion heat treatment [9]. Ni20Cr as well as Ni50Cr were also deposited by both APS and HVOF [43-45] exhibiting good steam oxidation resistance up to 750º C for at least 1,000 h. However at 700 and 750º C Fe diffuses from the substrate and through the coating in Ni20Cr, and Ni also diffused into the substrate (see figure 13). A similar behaviour was observed for Ni50Cr but to a significantly lower extent.

The effect of Mn and Si present in NiCr coatings in small concentrations was also studied by Sundararajan and collaborators and the results indicated that $MnCr_2O_4$ and Mn_2SiO_4 spinels formed at the coatings surface on top of the Cr_2O_3 scale at 750ºC in Ni20Cr but were not observed in Ni50Cr [47]. The APS "as deposited" NiCr coatings were very porous and partially oxidised, and after steam exposure at 750º C developed a scale at the coating-substrate interface. In the HVOF deposited coatings, Cr carbide was found at the coating-substrate interface.

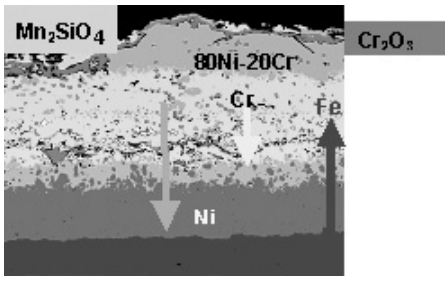

Figure 13: Cross section of Ni20Cr deposited by HVOF exposed to steam for 1,000 h at 750º C [46]

2.2.2 Electroless Nickel Coatings

Electroless nickel with a P-content of 12wt.% was applied onto E911 with a thickness of 40 – 60 µm by Scarlin and Knoedler [11]. After exposure times of up to 5000 h in the laboratory at 600 and 650º C, the oxidation stability of these coatings is high although the presence of cracks that reached the substrate was observed. Figure 14 shows that only thin oxide layers (predominantly Fe-oxides) grow on top of the coating. This is most pronounced in the vicinity of cracks in the nickel coating, and it is therefore important for future work to make efforts to avoid such cracks. At the interface between nickel and base alloy also thin oxides has been formed around the crack. These inner oxides are formed by Fe, Ni and Cr oxides.

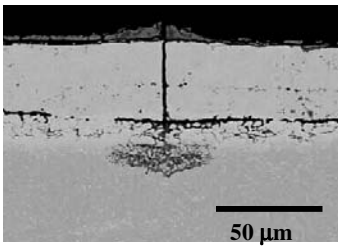

Figure 14: Electroless nickel on E911 after 4350 h at 600° C exposed to steam. Near the crack, thin oxide scales can be seen [48]

2.2.3 Sputtered Coatings

Itagaki and collaborators have coated ferritic steel with Pd and Pt by magnetron sputtering. These very thin coatings (1 µm) where heat treated at 750º C for 50 h in vacuum. Subsequently, the coated samples were strained by hammering on 320 grit SiC paper. An unidentified protective oxide layer formed after exposure to steam at 650º C for 100h. This oxide was more protective in the Pd sputtered sample than in the Pt specimen. These coatings require the straining process to be protective [49].

2.2.4 Dual layer Coatings

Two-layered coatings with a topcoat of Al on Ni20Cr were also deposited by APS and steam oxidation tested for 3,000 h at different temperatures comprised in the 600-750º C range by T.

Sundararajan and co-workers [50, 51]. After 3,000 h, the Al topcoat transformed in a non-continuous NiAl layer over the originally deposited NiCr layer and a thick outer Al oxide layer containing small amounts of Ni and Cr and presenting a "grainy like" appearance. Even at a temperature of 750º C, chosen in order to accelerate the oxidation process, no evidence of substrate oxidation could be observed.

Scarlin and collaborators have patented another two-layer coating system for steam oxidation protection comprising a thin primer layer deposited on top on the component over which a thicker overlay is deposited [52]. The primer coating must be very ductile and oxidation resistant whereas the top layer can be a low cost, less ductile oxidation material. The preferred primer coating are MCrAlY (M = Ni, Co of Fe), stellite or WC-Co over which Ni electroless, Al, Al-Si or Cr alloys can be deposited. The primer coating can be deposited by thermal spray (HVOF or plasma) and prevents steam from reaching the substrate through cracks and/or any other defects present in the top lower-cost layer.

3. Discussion

The various coating materials and deposition techniques that have been explored for this application show advantages and disadvantages, and a number of factors must be taken into consideration when selecting the most appropriate coating and deposition method for a specific steam plants component. Some of these factors are: coating type and composition, application temperature, component size/weight and geometry capacity for coating "in situ" and cost among others.

For instance, diffusion coatings based on Al, Cr or Si are unexpensive and do not have adhesion problems, but on the other hand, require heat treatments, which in some cases are carried out at temperatures too high for the ferritic materials such as P91 and P92 which are subjected to annealing at 730-780º C to reduce stresses. For some components, such as heat exchanger tubes, the high temperature coating process such as $AlCl_3$ and Si CVD, as well as Cr and Si pack cementation can be combined with the base material austenitisation heat treament (see figure 15). However, other components, such as casings, valves, etc. can not be subjected to such high temperatures after having been machined to avoid distorsion.

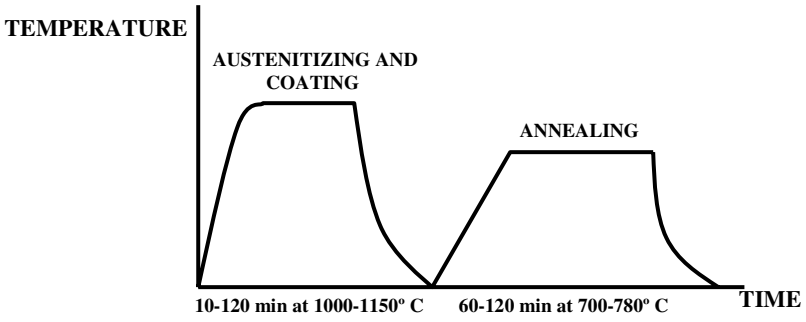

Figure 15: Combination of coating and the typical heat treatment of 9Cr ferritic steels

Moreover, diffusion aluminides degrade by coating substrate interdiffusion which not only reduces the subscale Al content but also may also affect the base materials mechanical properties. Cracks present in the high Al content coatings may propagate into the substrate although there is no evidence of such behaviour in the results available to present [14, 15]. Nitrogen is added to ferritic substrates such as P91 and P92 to improve their high temperature strength, and as mentioned in the previous parragraphs, when N containing substrates such as P91 and 92 are aluminized, AlN acicular precipates form, reaching 500 µm and more within the substrate. This loss of soluble N may therefore affect the materials strenght [11, 53]. Attempts to prevent or slow coating-substrate inerdiffusion have failed so far.

Less data is availabe regarding Si and Cr diffusion coatings, which should be more stable regarding degradation by interdiffusion. High temperature chromizing would only be possible for components that can be subjected to their corresponding heat treatment after they have reached their final shape. Siliconizing can take place at lower temperatures but there is evidence that SiO_2 based coatings are very soluble in high pressure steam [9].

Most studied Al and Cr oxide former overlay coatings deposited by thermal spray, are very resistant to steam, do not require heat treatment, and testing results published up to date do not indicate problems related to coating adhesion. Their higher cost may be justified by their higher stability and also because post coating heat treatments are generally not required. However, thermal spray is a "line-of-sight" deposition technique precluding it for certain complex geometries. Moreover, for some specific coating compositions, and for operating temperatures higher than 650º C, a significant degree of coating substrate interdifussion may result in coating degradation. Overlay Ni electroless coatings are easy to apply and low cost but the process is not reliable enough as thickness through cracks that cause substrate oxidation are often present [11]. On the other hand, Pd and Pt sputtered coatings are certainly not cost-effective for steam power plants.

Regarding the choice of a deposition technique, those that require placing the component in chambers (low or atmospheric pressure) such as CVD, pack cementation, and sputtering, or tanks as electroless plating, are suitable for small components, in particular blades where a smooth surface finishing is required. However, for large and heavy components such as rotors and casings these techniques may perhaps not be very practical as chambers with the required large sizes are not readily available and the fixturing could be quite complex. On the other hand, thermal spray or slurry deposition seem more appropriate as no containment is required and in addition, both techniques can be applied at the component manufacture site or at the plant, reducing transportation costs significantly. Finally, to coat the internal surfaces of heat exchanger tubes, CVD and pack cementation could be suitable as well as the application of slurries by inmersion. However, removing the scale present in the internal surfaces of "as manufactured" tubes may be quite challenging and it is required for most of the deposition techniques.

5. Conclusions and Outlook

Available results have demonstrated that coatings can significantly reduce steam oxidation at 600-750º C. Al, Cr and Si oxide former coatings have been deposited using a variety of deposition techniques and tested for steam oxidation resistance. However, a number of issues are still pending before oxidation resistant coatings can be used in steam turbines. For instance, most of the coatings described in this paper have not been tested under high steam

pressure and moreover, their effects on the mechanical properties of the base materials have not been determined. In addition, although limited work has been carried out, there isn't enough data correlating laboratory and field testing results and there is no standard methodology for carrying out the steam laboratory testing. For instance, differences in steam chemistry (oxygen content and pH of feedwater for instance), flows, temperature cycles, etc. may also play a role. Another very important aspect that needs to be looked at is surface preparation and cleaning. As already mentioned, removing thick scales from inner surfaces of very long tubes is quite challenging.

Another important but little studied aspect is coating repairability. Limited work has been carried out in the EC project SUPERCOAT addressing the repair of slurry aluminide coatings with promising results but to present there are no other published or available results for other type of coatings and/or deposition techniques.

From a more fundamental perspective, such as understanding the degradation mechanisms, some work is already being carried out, for instance, in the frame of the EC project SUPERCOAT [9]. These aspects are of significant importance as the results can provide important tools for better coating design and for establishing life prediction, and therefore more work is required. Coating substrate interdiffusion, protective oxide stability in high pressure steam, protective scale as well as overlay coating spallation mechanisms, etc. are some of the very important aspects that need further in-depth studies.

Acknowledgements

The author wishes to acknowledge all the members of the Metallic Materials Area at INTA for their contribution to the work presented in this paper, in particular F.J. García de Blas, M. Gutiérrez and R. Muelas for their help in the preparation of this manuscript. The authore is grateful to the EC for financial support through the SUPERCOAT project and to Drs F.J. Pérez, M. Schütze, D. Xiang, D. Tsipas, J.C. Nava, K. Berreth, T. Sundararajan, B. Scarlin and Y. Zhang for sending images and information on their current work. Finally, the Management Committee of COST 536 is thanked for the invitation to participate in the Liege conference (Materials for Advanced Power Generation 2006).

References

[1] R. Knoedler, P.J. Ennis, BALTICA V Conference, Porvoo, June 2001, Proceedings p. 355

[2] F. Abe, H. Okada, S. Wanikawa, M. Tabuchi T. Itagaki, K. Kimura and K. Yamaguchi, Proc. First Int. Conf. on Advances in Structural Steels, NIMS, Tsukuba, Japan (2002)

[3] P.J. Ennis and W.J. Quadakkers, Materials for Advanced Power Engineering 2002, (2002) 1131-1142

[4] W.J. Quadakkers, P.J. Ennis, J. Zurek and M. Michalik, Materials at High Temperature, 22 (2005) 47-60

[5] A.J. Blazewics and M. Gold, ASME, 78-JPGC-7 (1978)

[6] I.M. Rehn, W.R. Applet and J. Stringer, Corrosion 80, Chicago, Il., March 1980, paper No. 192

[7] EPRI Report CS-1811, Project 644-1, Corrosion problems in coal-fired boiler superheater tubes: Steam-side oxidation and exfoliation, April 1981
[8] A. Agüero, F.J. García de Blas, R. Muelas, A. Sánchez y S. Tsipas, Materials Science Forum, 369-372 (2001) 939-94
[9] M Scheefer, R. Knödler, B. Scarlin, A (Agüero) Bruna, D.N. Tsipas, Materials and Corrosion, 56 (2005) 907-915
[10] A. Agüero R. Muelas and A. Román., Surface Modification Technologies XIV, T. S. Sudarshan and M. Jeandin Eds., (ASM International, Materials Park, Ohio, (2001), 92-99
[11] A. Agüero, R. Muelas, B. Scarlin and R. Knödler, Materials for Advanced Power Engineering 2002, (2002) 1143-1158
[12] A. Agüero, R. Muelas, A. Pastor y S. Osgerby, Surf. & Coat. Technol., 200 (2005) 1219-1224
[13] A. Agüero, R. Muelas and M. Gutiérrez, Materials Science Forum, 522-523 (2006) 205-212
[14] A. Agüero and R. Muelas, Materials Science Forum, 461-464 (2004) 957-964
[15] A. Agüero, M. Gutiérrez, R. Muelas. R. Van Vulpen, S. Osgerby and L. Brown, Sent to Surf. & Coat. Technol.
[16] F. Schmitz, Us Patent No. 6,755,613 B1 (2004)
[17] B.A. Pint, Y. Zhang, P.F. Tortorelli, J.A. Haynes and I.G. Wright, Materials at High Temperature, 18 (2001) 185-192
[18] Y. Zhang, B.A. Pint, J.A. Haynes and P.F. Tortorelli, Oxidation of Metals, 62 (2004) 103-120
[19] Y. Zhang, B.A. Pint, g. Garner, K. M. Cooley and J.A. Haynes, Surf. & Coat. Technol. 188-189 (2004) 35-40
[20] Y. Zhang, personal communication, (2006)
[21] Reproduced with permission of the author Y. Zhang
[22] F.J. Perez, M.P. Hierro, J.A. Trilleros, M.C. Carpintero, L. Sánchez, J.M.Brossard and F.J. Bolívar, Intermetallics, *in press*
[23] F.J. Bolívar, DEA, Universidad Complutense de Madrid, May 2005
[24] V. Rohr, M. Schütze, E. Fortuna, D.N. Tsipas, A. Milewska and F.J. Pérez, Materials and Corrosion, 56 (2005) 874-881
[25] B.A. Pint, L.R. Walker, I.G. Wright, Mater. High. Temp., 21 (2004) 175-185
[26] G. Strehl, R. Beaven and B. Lesage, Materials and Corrosion 56 (2005) 778-784
[27] Reproduced with permission of the author, F. J. Pérez
[28] A. Agüero, M. García and M. Gutiérrez, Materials and Corrosion, 56 (2005) 937-941
[29] K. Berreth, K. Maile and A. Lyutovich, Materials and Corrosion, 56 (2005) 916-922
[30] Reproduced with permission of the authors K Maile and K. Berreth
[31] V. Rohr and M. Shütze, Proc. Of the Eurocorr 2003 Conference, Sept 2003, Budapest, Hungary, paper No.230 (2003)
[32] V. Rohr and M. Shütze, Surface Engineering, 20 (2004) 266-274
[33] V. Rohr and M. Shütze, Materials Science Forum, 461-464 (2004) 401-408
[34] Reproduced with permission of the author M. Shütze
[35] Z.D. Xiang and P.K. Datta, Surf. And Coat. Technol., 184 (2004) 108-114
[36] Z.D. Xiang S. Rose and P.K. Datta, Intermetallics, *in press*
[37] Reproduced with permission of the author Z.D. Xiang
[38] N.E. Naragoudakis, S.D. Tsipa, G. Stergioudis, H. Omar and D.N. Tsipas, The Journal of Corrosion Science and Engineering, 6 (2003) Paper No. H025
[39] Reproduced with permission of the author D.H. Tsipas

[40] J.C. Nava, S. Goodstine and E. Sylva, Materials at High Temperature, 22 (2005) 87-91
[41] Reproduced with permission of the author J.C. Nava
[42] T. Sundararajan, S. Kuroda, T. Itagaki and F. Abe, Thermal Spray 2003: Advancing the Science and Applying the Technology, ASM International, Materials Park, Ohio, USA (2003) 503-508
[43] T. Sundararajan, S. Kuroda, T. Itagaki and F. Abe, Thermal Spray 2003: Advancing the Science and Applying the Technology, ASM International, Materials Park, Ohio, USA (2003) 495-502
[44] T. Sundararajan, S. Kuroda, T. Itagaki and F. Abe, ISIJ International, 43 (2003) 95-103
[45] T. Sundararajan, S. Kuroda, T. Itagaki and F. Abe, ISIJ International, 43 (2003) 104-111
[46] Reproduced with permission of the author T. Sundararajan
[47] T. Sundararajan, S. Kuroda, K. Nishida, T. Itagaki and F. Abe, ISIJ International, 44 (2004) 139-144
[48] Reproduced with permission of the author B. Scarlin
[49] T. Itagaki, H. Kutsumi, M. Igarashi and F. Abe, Materials for Advanced Power Engineering 2002, (2002) 1639-1648
[50] T. Sundararajan, S. Kuroda, T. Itagaki and F. Abe, The Journal of Corrosion Science and Engineering, 6 (2003) paper No. H050
[51] T. Sundararajan, S. Kuroda and F. Abe, Corrosion Science, 47 (2005) 1129-1147
[52] B. Scarlin and R. Knoedler, World Patent No. WO03029508 (2003)
[53] Y. Zhang, B.A. Pint K.M. Cooley and J.A. Haynes, Surf. & Coat. Technol. 200 (2005)1231-1235

METALLURGY FOR LONG-TERM STABILIZATION OF FERRITIC STEELS FOR THICK SECTION BOILER COMPONENTS IN USC POWER PLANT AT 650°C

Fujio Abe
National Institute for Materials Science, 1-2-1 Sengen, Tsukuba 305-0047, Japan
E-mail : ABE.Fujio@nims.go.jp

Abstract

This paper describes recent advances in the analysis of specific microstructure instability causing a loss of creep strength and key metallurgy for the improvement of long-term creep strength for tempered martensitic 9 to 12Cr steels at 650°C, including welded joints. Many researchers have demonstrated that the dissolution of fine M_2X and MX carbonitrides and the precipitation of Z phase, M_6X carbonitrides and Fe_2(W, Mo) Laves phase during creep cause a loss of creep strength at long times at 550°C and above. The loss of creep strength is also observed in a 9Cr steel with no addition of nitrogen. The stabilization of lath martensitic microstructure in the vicinity of prior austenite grain boundaries (PAGBs) is essential for the improvement of long-term creep strength. This can be achieved by the addition of boron without any formation of boron nitrides. The addition of boron reduces the coarsening rate of $M_{23}C_6$ carbides in the vicinity of PAGBs during creep, resulting in stabilization of martensitic microstructure. The stabilization of martensitic microstructure retards the onset of acceleration creep up to long times, resulting in a decrease in minimum creep rate and an increase in creep life. The addition of small amount of boron and nitrogen, which causes no formation of boron nitrides during normalizing, effectively decreases the creep rates in the transient region by precipitation strengthening due to fine MX and it also retards the onset of acceleration creep by the effect of boron. But excess addition of boron and nitrogen causes the formation of large amount of boron nitrides during normalizing, which significantly decreases effective boron concentration for the microstructure stabilization. The addition of boron also suppresses the Type IV cracking strength loss in welded joints by suppressing the formation of fine-grained heat affected zone.

Key Words: creep, martensitic microstructure, boron, $M_{23}C_6$ carbide, MX carbonitride

1. Introduction

Energy security and lower carbon dioxide emissions are increasingly seen as key factors in protecting the global environment. Research and development of heat resistant steels and alloys for high-efficient USC power plants at 650°C and above are being now promoted in Europe, USA and Japan [1-6]. Since 1997, the National Institute for Materials Science (NIMS, Japan) has been conducting the research and development of advanced ferritic steels for application to large diameter and thick section boiler components such as main steam pipe and header of ultra-supercritical (USC) power plant at 650 °C [5-6]. Critical issues for the development of ferritic steels for 650 °C USC boilers are the improvement of oxidation resistance as well as long-term creep rupture strength. The resistance to Type IV cracking in welded joints is also serious for construction of thick section boiler components. Furthermore, the thermal cycling capabilities of thick section components in USC plant would be severely restricted by fatigue damage. Tempered martensitic 9 to 12%Cr steels can offer the highest potential to meet the required flexibility, because of their smaller thermal expansion and larger thermal conductivity than austenitic steels and Ni base superalloys.

Further advanced steam conditions of 700°C and above have been already initiated to gain net efficiency higher than 50% at Thermie AD700 project [3] aiming at 700°C in Europe and at DOE Vision 21 project [4] aiming at 760°C in the US. These projects involve the replacement of 9 to 12Cr steels by Ni base superalloys for the highest temperature

components. It should be noted that Ni base superalloys are much more expensive than ferritic/martensitic steels. To minimize the requirement of expensive Ni base superalloys, 9 to 12Cr steels can be applied to the next highest temperature components of these very high temperature plants. Therefore, 9 to 12Cr steels are strongly desired to expand the present temperature range up to 650°C and more.

This paper describes recent advances in the analysis of specific microstructure instability causing a loss of creep strength at long times and key metallurgy for the improvement of long-term creep strength for tempered martensitic 9 to 12Cr steels, including welded joints.

2. Loss of creep strength at long times

The loss of creep rupture strength has extensively been investigated for a number of 9 to 12 Cr steels [7]. The proposed mechanisms are due to the occurrence of microstructure degradation during creep exposure and are classified as (a) dissolution of fine M_2X and MX carbonitrides and precipitation of new phases, (b) preferential recovery of microstructure in the vicinity of prior austenite grain boundaries (PAGBs), (c) loss of creep ductility and (d) recovery of excess dislocations. The precipitation of Z phase, M_6X carbonitrides and $Fe_2(W,Mo)$ Laves phase during creep causes a loss of creep strength at long times, because they consume existing fine M_2X and MX and or $M_{23}C_6$ precipitates. Z phase is a complex nitride of the form Cr(Nb,V)N. Figure 1 shows the sigmoidal behavior in creep rupture data for 0.1C-0.55Mn-0.07Si-10.84Cr-0.14Mo-2.63W-2.86Co-0.55Ni-0.19V-0.06Nb-0.016N-0.019B steel (TAF 650) at 650°C, comparing with the data for original TAF and Mod.9Cr-1Mo (T91) [8] and the formation of Z phase [9]. The synergetic effect of Z phase precipitation and tungsten depletion of solid solution due to Fe_2W Laves phase formation could be the reason for the sigmoidal shape of creep rupture data of TAF 650 steel [8].

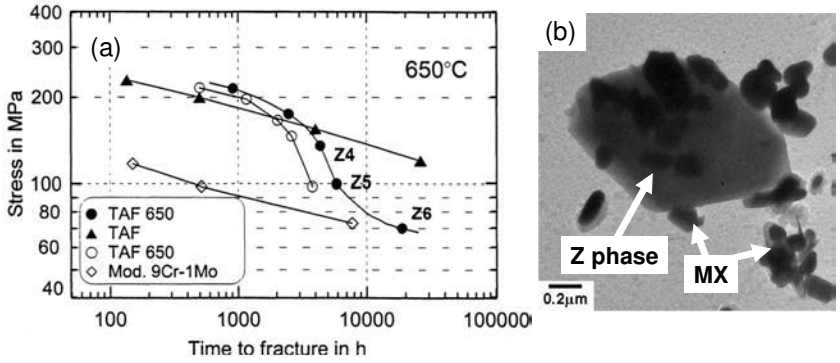

Figure 1 (a) Comparison of stress versus time to rupture curves for various martensitic steels at 650°C [8] and (b) formation of Z phase in NF12 [9].

The coarsening of $M_{23}C_6$ carbides in 12CrMo(W)VNbN steels is accompanied by dissolution of fine MX carbonitrides due to the precipitation of coarse M_6X and or Z phase [10]. Increase in Ni content in 12CrMoV steel results in accelerated microstructure degradation

with more rapid coarsening of $M_{23}C_6$, dissolution of MX, precipitation of coarse M_6X and Fe_2Mo [11]. The formation of Z phase is also observed in T91 steel at 600 and 650°C [12]. Increase in nitrogen content in 9Cr steel results in accelerated microstructure degradation during creep at 650°C with more rapid precipitation of Z phase [13]. The loss of creep rupture strength in T91 steel is reported to be due to preferential recovery of the martensitic microstructure in the vicinity of PAGBs, as shown in Figure 2 [14]. The dissolution of MX and the precipitation of Z phase promote the preferential recovery [12]. Blum and Chilukuru [15] stated that creep life is limited by the continuous increase of creep rate in the tertiary or acceleration stage of creep and that the life-limiting increase of creep rate stems from global changes in the dislocation and phase structure of the high-Cr steels. They reviewed microstructure development in tempered martensitic 9 to 12Cr steels during creep with focus on the differences in stability of different precipitate phases and on their consequences on creep resistance. Large M_2X particles at subgrain boundaries can constitute favorable nucleation sites for Z phase due to their high phase boundary energy and their composition being similar as that of Z phase.

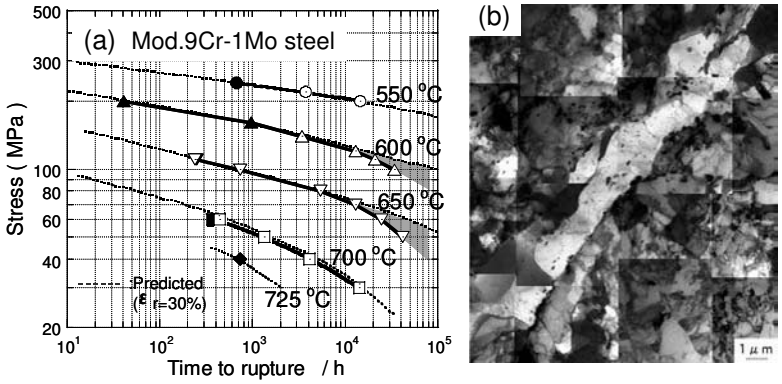

Figure 2 (a) Stress versus time to rupture curves for Mod.9Cr-1Mo steel (T91) and (b) TEM micrograph after creep rupture testing for 34,141 h at 600°C and 100MPa.

Recently, Semba and Abe [16] reported that the loss of creep rupture strength was also observed for a 9Cr-3W-3Co-0.2V-0.05Nb steel with 0.08% carbon but no addition of nitrogen, at long times above about 10^3 h at 650°C as shown in Figure 3. The residual nitrogen content of the steel was only 0.0019% (19ppm), suggesting an extremely low amount of MX carbonitrides and hence an extremely low driving force for the Z phase formation during creep. Therefore, the dissolution of fine M_2X and MX carbonitrides and the precipitation of Z phase can be excluded from the main explanation for the loss of creep rupture strength. The proposed mechanism is the coarsening of $M_{23}C_6$ carbides and the recovery of lath martensitic microstructure in the vicinity of PAGBs.

The tempered martensitic microstructure of the recent high-strength 9 to 12Cr steels consists of lath, block and packet subgrains in prior austenite grains after tempering, as shown schematically in Figure 4. The lath, block and packet subgrains contain high density of dislocations and fine precipitates of $M_{23}C_6$ mainly along various boundaries and of MX

carbonitrides mainly in the matrix. Enhanced diffusion along PAGBs promotes the preferential recovery of the lath-block microstructure in the vicinity of PAGBs during exposure at elevated temperature. This causes localized creep deformation in the vicinity of PAGBs Thus the stabilization of the lath-block microstructure and hence the stabilization of lath and block boundaries up to long times during creep are key issues for the suppression of loss of creep rupture strength.

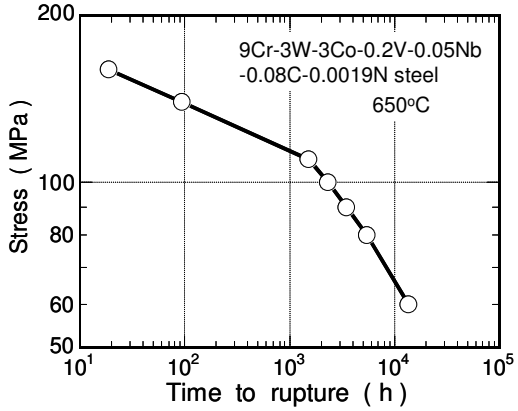

Figure 3 Creep rupture data for 9Cr-3W-3Co-0.2V-0.05Nb-0.08C-0.0019N steel at 650°C.

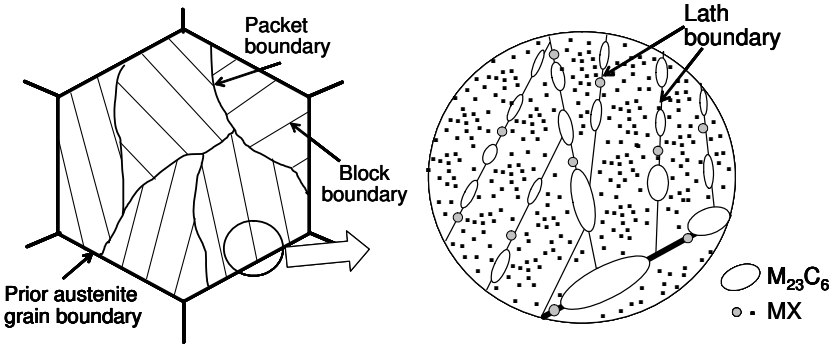

Figure 4 Schematic illustrations of tempered martensitic microstructure.

3. Controlling factor for creep life

Figure 5 shows schematic illustrations of creep and creep rate curves of tempered martensitic 9 to 12Cr steels under constant load. The creep and creep rate curves usually consist of the primary or transient creep region, where the creep rate decreases with time, and of the tertiary or acceleration creep region, where the creep rate increases with time after reaching a minimum creep rate. There is substantially no steady-state region, where the creep rate is constant. The present author has revealed for martensitic 9Cr steels that the transient creep

is basically a consequence of the movement and annihilation of a high density of dislocations produced by martensitic transformation during cooling after normalizing and that the acceleration creep is a consequence of gradual loss of creep strength due to the microstructure evolution [17, 18]. The time to rupture is inversely proportional to the minimum creep rate, $\dot{\varepsilon}_{min}$, times the acceleration of creep rate, $d\ln\dot{\varepsilon}/d\varepsilon$, in the acceleration creep region as given by [18, 19]

$$tr = c / [\ \dot{\varepsilon}_{min}\ (d\ln\dot{\varepsilon}/d\varepsilon)\ ], \qquad (1)$$

where c is a constant given by about 1.5. The minimum creep rate is inversely proportional to the duration of transient creep region and hence inversely proportional to the onset time of acceleration creep [19]. The migration of lath or block boundaries, causing the coarsening of lath or block, is closely correlated with the onset of acceleration creep and the coarsening of lath or block by the migration of their boundaries with absorbing excess dislocations is the major process in the acceleration creep. The migration of lath or block boundaries can be suppressed by a dispersion of carbonitride particles, which exert pinning force for migrating boundaries.

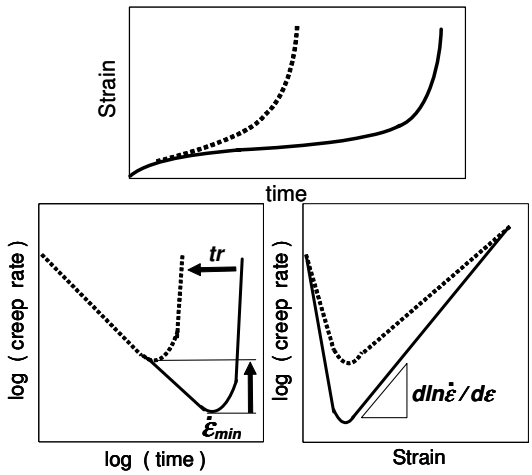

Figure 5 Creep, creep rate versus time and creep rate versus strain curves of tempered martensitic 9 to 12Cr steels under constant load.

4. Stabilization of tempered martensitic microstructure

4.1 Stabilization of $M_{23}C_6$ carbides and martensitic microstructure by boron addition

Figure 6 shows the effect of boron addtion on the creep rupture strength of 9Cr-3W-3Co-0.2V-0.05Nb steel with different boron contents (0, 48, 92 and 139ppm) at 650°C, where the steel with 0ppm boron is the same as that in Fig.3 [6]. Nitrogen was not added in the steels to avoid the formation of boron nitrides. The residual nitrogen content was 11-34 ppm. With decreasing stress below 100 MPa, the time to rupture significantly increases with incrasing boron content. In other words, the degradation in creep rupture strength at long

times becomes more significant with decreasing boron content. The present results suggest that the addition of boron scarcely improves the short-term creep rupture strength but that it effectively suppresses the degradation in creep rupture strength at long times.

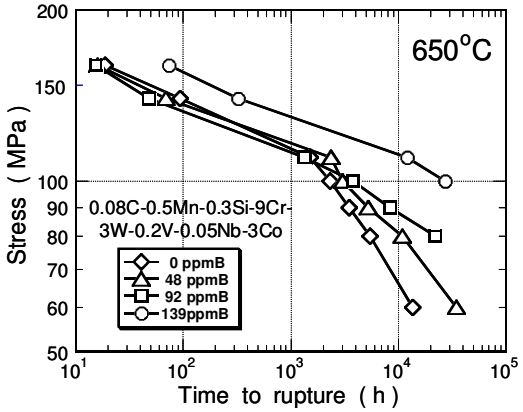

Figure 6 Effect of boron on creep rupture strength of 9Cr-3W-3Co-VNb steel at 650°C.

Figure 7 shows the creep rate versus time curves and the creep rate versus strain curves of the boron-series steels at 650°C and 80 MPa. In the initial stage of creep, the creep rates are approximately the same among the different steels except for the steel with 139ppm boron. The 139ppm boron steel contained a little bit higher nitrogen of 34 ppm than the other steels (11-19 ppm nitrogen). The transient creep region of the steels with boron continues for up to longer times than that of the steel without boron, resulting in lower minimum creep rate and

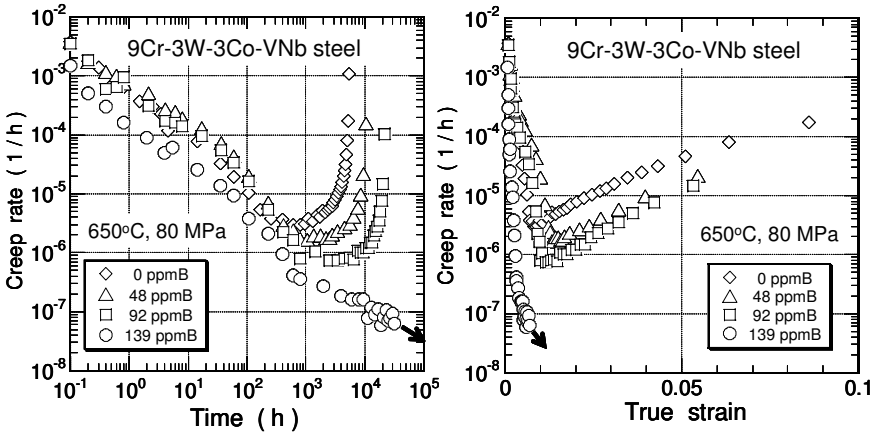

Figure 7 Effect of boron on creep rate versus time curves and creep rate versus strain curves of the steels at 650°C and 80 MPa.

longer rupture time. The logarithmic creep rate increases linearly with strain for a wide range of strain in the acceleration creep region after reaching a minimum creep rate. The value of $d\ln\dot{\varepsilon}/d\varepsilon$ in Eq.(1), corresponding to the slop of the logarithmic creep rate versus strain curves, in the acceleration creep region and the strain to reach a minimum creep rate are approximately the same among the different steels containing different boron contents, although the addition of boron significantly decreases the minimum creep rate.

The analysis by Auger spectroscopy for the 139ppm boron steel after aging at 650°C for 10,300 h shows that boron is enriched in the $M_{23}C_6$ carbides, which is more significant in the vicinity of PAGBs [20]. No evidence is found for the enrichment of boron in the Fe_2W Laves phase, which precipitated during creep. The fine distribution of $M_{23}C_6$ carbides along PAGBs is still maintained in the 139ppm boron steel during creep. The fine distribution of $M_{23}C_6$ carbides is also observed in the 0B steel after tempering, but extensive coarsening takes place during high-temperature exposure. This indicates that boron decreases the rate of Ostwald ripening of $M_{23}C_6$ carbides during creep. The addition of boron improves the reduction of area as well as the long-term creep strength [6]. The improved reduction of area results from that the creep deformation does not concentrate only near PAGBs, because the preferential recovery of martensitic microstructure near PAGBs is retarded for up to long times.

4.2 Effect of instability of MX carbonitrides on creep deformation behavior

The effect of nitrogen concentration on microstructure stability and creep strength has been investigated for the 9Cr-3W-3Co-0.2V-0.05Nb steel with a very low carbon content of 0.002% [13, 21]. The nitrogen concentration was varied in the range of 0.05 to 0.1 mass%. The increase in nitrogen concentration decreases the creep rupture strength at 650°C as shown in Figure 8, although the creep rupture strength of the 0.07N and 0.10N (mass%) steels is still much larger than that of conventional steels P92 and T91.

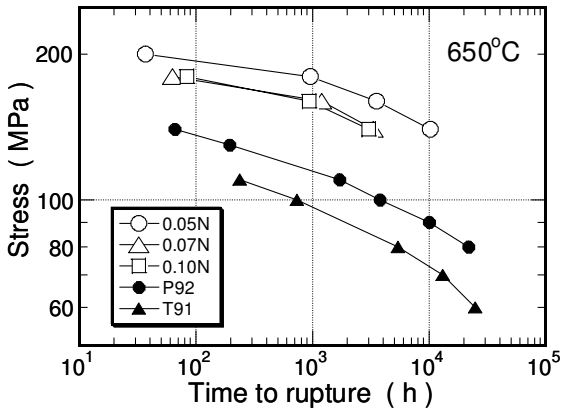

Figure 8 Creep rupture data for 9Cr-3W-3Co-0.2V-0.05Nb-0.002C steel with 0.05N, 0.07N and 0.10N at 650°C, comparing with those for P92 and T91.

After tempering, large Cr_2N as well as fine MX nitrides were distributed along lath, block,

packet and prior austenite grain boundaries in the high nitrogen 0.07N and 0.10N steels, although the amount of Cr_2N was slight [13]. As shown in Figure 9, the mean size of MX is only a little bit smaller in the 0.05N steel than in the 0.07N and 0.10N steels after tempering. During creep at 650°C, the coarsening rate of MX nitrides is larger in the high nitrogen 0.07N and 0.10N steels than in the low nitrogen 0.05N steel. The formation of Z phase is observed even in the 0.05N steel after creep rupture testing for 10285 h at 650°C, although the amount of Z phase is slight. The precipitation of Z phase takes place at shorter times in the high nitrogen 0.07N and 0.10N steels than in the low nitrogen 0.05N steel during creep at 650°C.

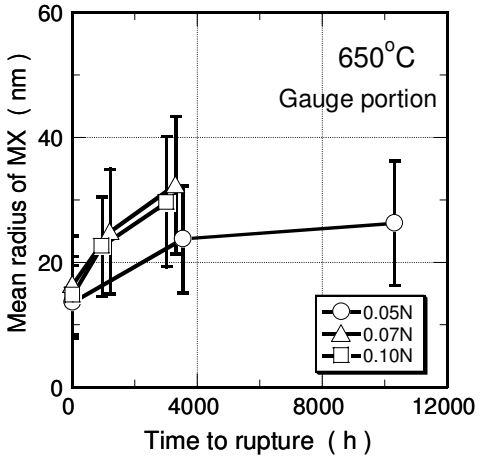

Figure 9 Mean radius of MX nitrides for the 9Cr-3W-3Co-0.2V-0.05Nb-0.002C steel with 0.05N, 0.07N and 0.10N during creep at 650°C.

Recently, Gustafson and Hättestrand [22] reported that the increase in nitrogen content in P92 from 0.05 to 0.06 mass% decreased the coarsening rate of MX carbonitrides during aging at 600 and 650°C. The enhanced coarsening of MX nitrides observed in the present high nitrogen 0.07N and 0.10N steels during creep is thought to be mainly due to an effect of the Z phase formation, which dissolve the small MX particles. Another possibility is the formation of Cr_2N as well as MX nitrides in the present high nitrogen 0.07N and 0.010N steels during tempering. The coarsening rate of Cr_2N during exposure at elevated temperature is usually larger than that of MX.

Figure 10 compares the creep rate versus time curves among the 0.05N, 0.07N and 0.10N steels at 650°C and 140 MPa [13]. The creep rates in the transient region are only a lit bit larger in the high nitrogen 0.07N and 0.10N steels than in the 0.05N steel. It should be noted that the onset of acceleration creep takes place at shorter times in the high nitrogen 0.07N and 0.10N steels than in the 0.05N steel. This results in higher minimum creep rate and shorter time to rupture in the high nitrogen 0.07N and 0.10N steels. Enhanced coarsening of MX nitrides and enhanced formation of Z phase in the high nitrogen steels during creep promote the onset of acceleration creep.

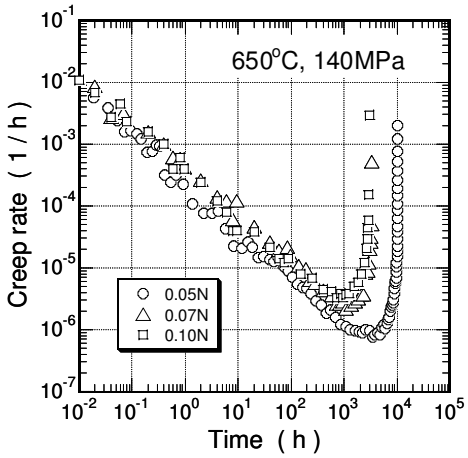

Figure 10 Creep rate versus time curves of 9Cr-3W-3Co-0.2V-0.05Nb-0.002C steel with 0.05N, 0.07N and 0.10N at 650°C and 140 MPa.

4.3 Combination of boron-strengthening and MX nitride-strengthening

The addition of nitrogen causes the precipitation of fine MX nitrides. However, excess addition of boron and nitrogen causes the formation of boron nitrides during forging and heat treatments at high temperature, which offsets the benefit due to boron and nitrogen. Figure 11 shows the relationship between boron and nitrogen concentrations to form boron nitrides for various 9 to 12Cr steels at normalizing temperatures of 1050 to 1100°C [23]. The solubility product for boron nitrides is given by

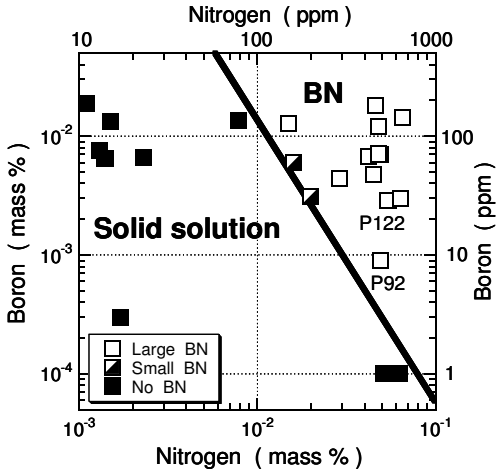

Figure 11 Solid solubility for boron nitride BN in 9-12Cr steels at normalizing temperatures of 1050-1100°C.

$$log\,[\%B] = -2.45\,log\,[\%N] - 6.81, \quad (2)$$

where [%B] and [%N] are the concentration of boron and nitrogen in mass%. At a nitrogen concentration of 100ppm (0.01%) or less, 100ppm boron can dissolve in the matrix without any formation of boron nitrides during normalizing.

The effect of nitrogen addition on the creep rupture strength for the 9Cr-3W-3Co-0.2V-0.05Nb steel containing 0.014% boron (140 ppm boron) are shown in Figure 12 [16]. The steel containing 0.0034N is the same as the 139ppm boron steel in Fig.6. The creep rupture strength significantly increases with increasing nitrogen content from 0.0015 to 0.0079 %, but the excess addition of nitrogen as high as 0.065% decreases the creep rupture strength. Taking the solubility product for boron nitrides given by Eq.(2) and the results shown in Fig.12 into account, the addition of small amount of nitrogen without any formation of boron nitrides significantly improves the creep rupture strength of the boron steel. However, excess addition of nitrogen (0.065%) causes the formation of large amount of boron nitrides and reduces the strengthening effects due to boron and nitrogen.

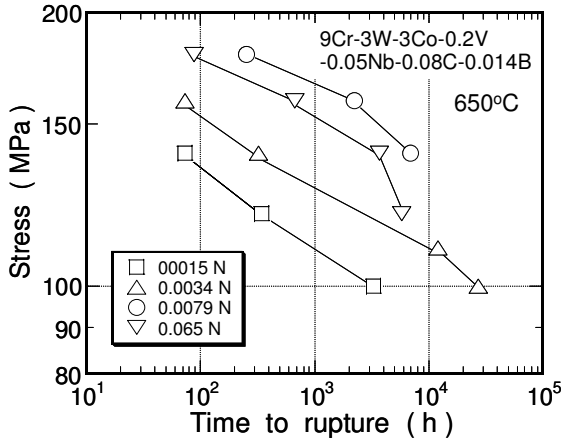

Figure 12 Effect of nitrogen on creep rupture strength of 9Cr-3W-3Co-VNb steel with 140 ppm boron at 650°C.

Figure 13 shows the effect of nitrogen addition on the creep rate versus time curves and creep rate versus strain curves of the steel at 650°C and 120 MPa. The addition of nitrogen, 79ppm (0.0079%) and 650ppm (0.065%) drastically decreases the creep rate in the transient region. Although the creep rates in the transient region are substantially the same between the two steels with 79 and 650 ppm nitrogen, the onset of acceleration creep is promoted in the steel containing higher nitrogen of 650 ppm. This results in higher minimum creep rate and shorter creep life in the 650 ppm nitrogen steel than in the 79 ppm nitrogen steel. The value of $d\ln\dot{\varepsilon}/d\varepsilon$ in the acceleration region after reaching a minimum creep rate is approximately the same between the two steels containing 79 and 650 ppm nitrogen. Again, the main reason for the difference in creep life between the two steels containing 79 and 650 ppm nitrogen is attributed mainly to the difference in minimum creep rate.

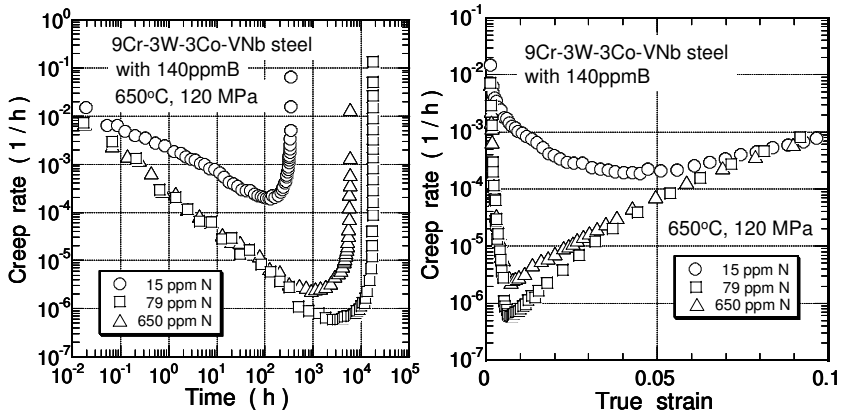

Figure 13 Effect of nitrogen on creep rate versus time curves and creep rate versus strain curves of the steels at 650°C and 120 MPa.

The enrichment of boron in $M_{23}C_6$ carbides was much lower in the steel with 140 ppm boron and 650 ppm nitrogen than in the steel with 140 ppm boron and 15 ppm nitrogen, as shown in Figure 14 [16]. All the added boron in the steels with 15, 34 and 79 ppm nitrogen can be dissolved in the matrix at the normalizing temperature, as can be seen from Fig.11. On the other hand, most of the added boron in the steel with 650 ppm nitrogen formed coarse boron nitrides during normalizing. Therefore, the amount of effective boron in the steel with 650 ppm nitrogen is much less than that in the steels with 15, 34 and 79 ppm nitrogen. The reduced amount of effective boron may lead to large coarsening rate of $M_{23}C_6$ in the steel with 650 ppm nitrogen, resulting in advancing the onset time of acceleration creep and reducing the time to rupture.

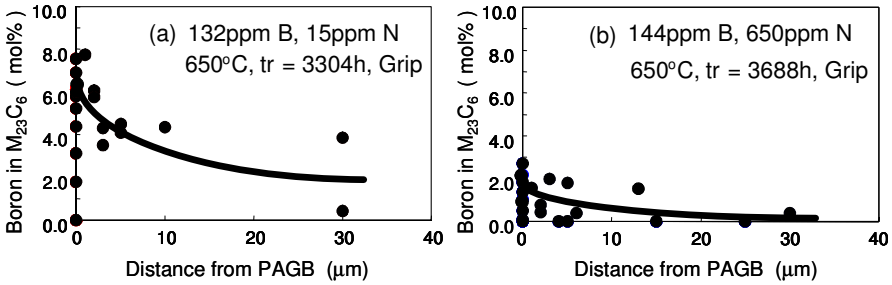

Figure 14 Boron content in $M_{23}C_6$ carbides in the steels after creep rupture testing at 650°C for 3000-4000 h, as a function of distance from prior austenite grain boundary.

Figure 15 shows schematically the creep rate versus time curves of the 9Cr-3W-3Co-0.2V-0.05Nb steel with various combinations of boron and nitrogen contents. Based on the 0B-0N steel, the addition of 140ppm boron but no addition of nitrogen, the curve 2 in Fig.15,

retards the onset of acceleration creep, which effectively decreases the minimum creep rate and increases the creep life. The retardation is caused by the stabilization of martensitic microstructure near PAGBs by an enrichment of boron in $M_{23}C_6$ carbides. The addition of 140ppm boron and small amount of nitrogen of 80ppm, which causes no formation of BN during normalizing, decreases the creep rates in the transient region by precipitation strengthening due to fine MX and it also retards the onset of acceleration creep by the boron effect due to microstructure stabilization described above. However, the addition of 140 ppm boron and excess nitrogen of 650ppm, which causes the formation of large amount of BN during normalizing, decreases the creep rates in the transient region similar as that in the steel with 80ppm nitrogen but it promotes the onset of acceleration creep in comparison with the steel with 80ppm nitrogen. The formation of large amount of BN during normalizing significantly reduces the effective boron concentration and hence reduces the enrichment of boron in $M_{23}C_6$ carbides.

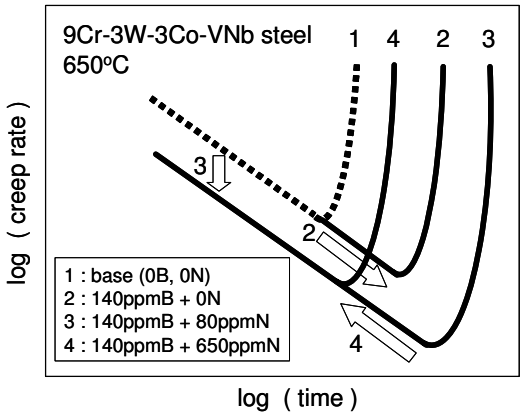

Figure 15 Schematic creep rate versus time curves of the 9Cr-3W-3Co-VNb steel with various combinations of boron and nitrogen contents.

The creep rupture data for several 9 to 12Cr steels at 650°C are shown in Figure 16. The MARN (Martensitic 9Cr steel strengthened by MX nitrides) and MARBN (Martensitic 9Cr steel strengthened by boron and MX nitrides) are the same as the 0.05N steel in Fig. 8 and the 0.0079N steel in Fig. 12, respectively. The 12Cr-2.6W-2.5Co-0.5Ni-0.2V-0.05Ni steel (NF12) [24] and 12Cr-3W-3Co-0.2V-0.05Nb-0.1Ta-0.1Nd-0.05N steel (SAVE12) [25] were developed by Japanese steelmaking companies as upgrade versions of P92 and P122, respectively. The MARN and MARBN steels exhibit much higher creep rupture strength than T91, P92, NF12 and SAVE12. The creep rupture strength at 650°C and 10^5 h is estimated to be about 100 MPa for the MARN and MARBN steels.

The present 9Cr steel MARBN shown in Figure 16 is promising as thick section weld components such as main steam pipe and header of USC boilers, because of no grain refinement in heat affected zone (HAZ) and hence no Type IV fracture in welded joints as will be described later. On the other hand, MARN steel is promising as high temperature bolting material which requires enough creep strength but not welding.

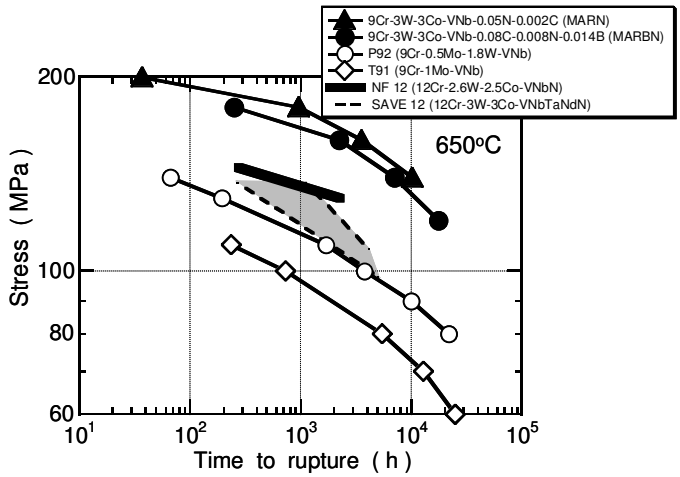

Figure 16 Creep rupture data for the present steels MARN and MARBN, comparing with those for NF12, SAVE12, P92 and T91 at 650°C.

4.4 Effect of HAZ microstructure on long-term stability of welded joints

The P92 and P122 welded joints are fractured in the fine-grained region of HAZ at low stresses, indicating Type IV fracture [26]. Reducing the width of HAZ by electron beam welding is effective for the extension of creep life of welded joints, but the brittle Type IV fracture takes place at low stresses. Multi-axial stress condition in the fine-grained HAZ with lower creep strength, resulting from mechanical constrain effect by the surrounding weld metal and base metal with higher creep strength, is essential for the formation of creep voids and brittle Type IV fracture.

The addition of boron combined with minimized nitrogen as low as 10-20 ppm suppresses the Type IV fracture in HAZ at low stresses, which improves the long-term creep rupture strength of welded joints [27-30]. Figure 17(a) shows the creep rupture data for the welded joints of 9Cr steel with 130ppm boron and P92 at 650°C, comparing with those for their base metals. There is substantially no degradation of creep rupture strength in the boron steel welded joints comparing with the base metal, while the degradation of creep rupture strength in P92 welded joints becomes more significant with increasing test duration due to Type IV fracture. We have systematically examined the effect of boron and nitrogen contents on the grain refinement behavior for a number of 9 to 12Cr steels during heating at temperatures between 900 and 1100°C. The results are summarized in Fig. 17(b). The boron addition of 100 ppm or more combined with low nitrogen below 80ppm causes no grain refinement. On the other hand, no addition of boron causes grain refinement at around Ac_3 temperature, irrespective of nitrogen content. Excess addition of nitrogen also causes grain refinement even if the steel contains high boron. Based on the experimental results, the boron addition suppresses the grain refinement but the nitrogen addition reduces the effect of boron.

There are two possibilities for the production of same grain size between HAZ and base metal in the boron steel welded joints. One of the possibilities is austenite memory effect, which

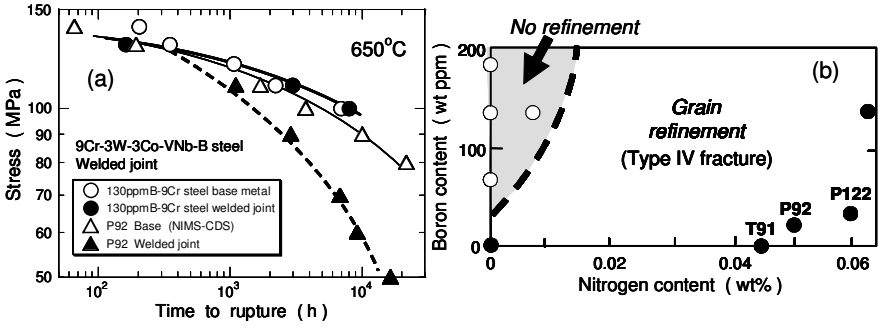

Figure 17 (a) Creep rupture data for welded joints of 9Cr steel with 130ppm boron and P92 at 650°C and (b) grain refinement and no grain refinement regions in 9 to 12Cr steels during heating at 900 to 1100°C.

has been shown to be a direct consequence of the existence of retained austenite in starting bainitic or martensitic microstructure [31, 32]. Another possibility is the effect of martensitic reverse transformation and suppression of subsequent recrystallization during austenitization in heat cycle of welding. Martensitic reverse transformation based on shear mechanism has been reported in 18%Ni maraging steel [33]. Grain boundary segregation of boron can reduce grain boundary energy, which suppresses nucleation of α/γ diffusive transformation at grain boundaries. Suppression of subsequent recrystallization can reproduce the same grain size as the original austenite. Further investigation will be required to make clear the mechanisms responsible for the production of same grain structure between HAZ and base metal in the boron steel.

5. Conclusions

1) The loss of creep strength in 9 to 12Cr steels at 550°C and above is shown to be sometimes due to the dissolution of fine M_2X and MX carbonitrides during creep exposure, which is driven by the precipitation of coarse Z phase which are thermodynamically more stable than the M_2X and MX. The loss of creep strength is also observed in a 9Cr steel with no addition of nitrogen. The proposed mechanism is the coarsening of $M_{23}C_6$ carbides and the recovery of lath martensitic microstructure in the vicinity of PAGBs.

2) The addition of boron up to 140 ppm but no nitrogen addition retards the onset of acceleration creep, resulting in lower minimum creep rate and longer time to rupture for the 9Cr-3W-3Co-0.2V-0.05Nb steel at 650°C. The effect of boron results from the stabilization of martensitic microstructure during creep through the reduction of coarsening rate of $M_{23}C_6$ carbides in the vicinity of PAGBs.

3) The addition of small amount of nitrogen of 80ppm to the steel with 140 ppm boron, which causes no formation of BN during normalizing, decreases the creep rates in the transient region by precipitation strengthening due to fine MX and it also retards the onset of acceleration creep by the effect of boron. The addition of excess nitrogen of 650ppm to the steel with 140 ppm boron causes the formation of large amount of BN during

normalizing, which significantly decreases the effective boron concentration.

4) The addition of boron suppresses the formation of fine grains in the HAZ of welded joints and suppresses the Type IV fracture. Approximately no difference in microstructure between the HAZ and base metal produces no mechanical constrain effect in the HAZ.

5) The present 9Cr steel MARBN is promising as thick section weld components such as main steam pipe of USC boilers, because of improved long-term stability in base metal and no Type IV fracture in welded joints. On the other hand, the MARN steel is promising as high temperature bolting material which requires enough creep strength but not welding.

References

[1] B. Scarlin, T.-U. Kern and M. Staubli, 'The European efforts in material development for 650°C USC power plants' Proc. 4th Int. Conf. on Advances in Materials Technology for Fossil Power Plants, Hilton Head Island, SC, USA (2004), p.80.

[2] T.-U. Kern, K. Wieghardt and H. Kirchner, 'Material and design solutions for advanced steam power plants', as in [1], p.20.

[3] R. Blum, R. W. Vanstone and C. Messelier-Gouze, 'Materials development for boilers and steam turbines operating at 700°C', as in [1], p.116.

[4] R. Viswanathan, J. F. Henry, J. Tanzosh, G. Stanko, J. Shingledecker and B. Vitalis, 'U.S. program on materials technology for USC power plants', as in [1], p.3.

[5] F. Abe, H. Okada, S. Wanikawa, M. Tabuchi, T. Itagaki, K. Kimura, K. Yamaguchi and M. Igarashi, 'Guiding Principles for Development of Advanced Ferritic Steels for 650°C USC Boilers', Proc. 7th Liege Conference on Materials for Advanced Power Engineering 2002, Liege, Belgium (2002), p.1397.

[6] F. Abe, 'Alloy design of creep and oxidation resistant 9Cr steels for thick section boiler components operating at 650ºC', as in [1], p.202.

[7] F. Abe, 'Bainitic and martensitic creep-resistant steels', Current Opinion in Solid State and Mater. Sci. 8, (2004), p.305.

[8] V. Sklenicka, K. Kucharova, M. Svoboda, L. Kloc, J. Bursik and A. Kroupa, 'Long-term creep behavior of 9-12%Cr power plant steels', Mater. Character. 51 (2003), p.35.

[9] H. Danielsen and J. Hald, 'Z-phase in 9-12%Cr steels', as in [1], p.999.

[10] A. Strang and V. Vodarek, 'Z phase formation in martensitic 12CrMoVNb Steel', Mater Sci Technol 12 (1996), p.552.

[11] V. Vodarek and A. Strang, 'Effect of nickel on the precipitation processes in 12CrMoV steel during creep at 550°C', Scripta Mater, 38 (1998), p.101.

[12] K. Suzuki, S. Kumai, H. Kushima, K. Kimura and F. Abe, 'Precipitation of Z-phase and precipitation sequence during creep deformation of Mod.9Cr-1Mo steel', Tetsu-to-Hagane, 89 (2003), p.691. (in Japanese)

[13] K. Sawada, M. Taneike, K. Kimura and F. Abe, 'Effect of nitrogen content on microstructural aspects and creep behavior in extremely low carbon 9Cr heat-resistant steel', ISIJ International, 44 (2004) p. 1243.

[14] H. Kushima, K. Kimura and F. Abe, 'Degradation of Mof.9Cr-1Mo steel during long-term creep deformation', Tetsu-to-Hagane, 85, (1999), p.841. (in Japanese)

[15] W. Blum and H. Chilukuru, 'Tertiary creep of tempered martensitic 9-12%Cr steels', Proc. of International Conference & Exhibition on Pressure Vessels and Piping OPE 2006, Chennai, India, (2006), CD-ROM.

[16] H. Semba and F. Abe, 'Creep deformation behavior and microstructure in high boron containing 9%Cr ferritic heat resistant steels', as in [1], p.1229.
[17] F. Abe, S. Nakazawa, H. Araki and T. Noda, 'The role of microstructural instability on creep behavior of a low radioactivation martensitic 9Cr-2W steel', Metall. Trans. 23A, (1992), p.469.
[18] F. Abe, 'Creep Rates and Strengthening Mechanisms in Tungsten-Strengthened 9Cr Steels', Materials Science and Engineering, A319-321 (2001), p.770.
[19] F. Abe, 'Effect of Quenching, Tempering and Cold Rolling on Creep Deformation Behavior of a Tempered Martensitic 9Cr-1W Steel', Metallurgical and Materials Transactions A, 34A, (2003), p.913.
[20] T. Horiuchi, M. Igarashi, F. Abe, 'Improved utilization of added B in 9Cr heat-resistant steels containing W", ISIJ International, 42 (2002), p.S67.
[21] M. Taneike, F. Abe and K. Sawada, "Creep-strengthening of steel at high temperatures using nano-sized carbonitride dispersions", Nature, 424 (2003), p.294.
[22] Å. Gustafsson and M. Hättestrand, 'Coarsening of precipitates in an advanced creep resistant 9% chromium steel – quantitative microscopy and simulations', Materials Science and Engineering A333 (2002), p.279.
[23] T. Sakuraya, H. Okada and F. Abe, "Coarse size BN type inclusions formed in boron bearing high Cr ferritic heat-resistant steel", as in [1], p.1270.
[24] F. Masuyama, in 'Landolt-Bornstein Numerical Data and Functional Relationships in Science and Technology, Group VIII: Avdabced Materials and Technologies', (eds) Yagi K, Merkling G, Kern T U, Irie H, and Warlimont W, Vol.2 Springer-Verlag; Berlin, Heidelberg, New York (2004) p.200.
[25] F. Masuyama, as in [24], p.204.
[26] F. Abe and M. Tabuchi, 'Microstructural and Creep Strength of Welds in Advanced Ferritic Power Plant Steels', Materials Science and Technology of Welding and Joining, 9 (2004), p.22.
[27] M. Tabuchi M. Kondo, T. Watanabe, H. Hongo, F. Yin and F. Abe, 'Improvement of type IV cracking resistance of 9Cr heat resisting steel weldment by boron addition', Acta Metall. Sinica, 17 (2004), p.331.
[28] S. K. Albert M. Kondo, M. Tabuchi, F. Yin. K. Sawada and F. Abe, 'Improving the creep properties of 9Cr-3W-3Co-NbV steels and their weld joints by the addition of boron', Metallurgical and Materials Transactions A, 36A (2005), p.333.
[29] F. Abe, M. Tabuchi, M. Kondo and S. Tsukamoto, 'Improvement of creep strength of advanced ferritic steel welded joints', Welding in the World, 49 (2005), p.58.
[30] M. Kondo, M. Tabuchi, S. Tsukamoto, F. Yin and F. Abe, 'Suppressing type IV failure via modification of heat affected zone microstructures using high boron content in 9Cr heat resistant steel welded joints', Science and Technology of Welding and Joining, 11 (2006), p.216.
[31] S. T. Kimmins and D. J. Gooch, 'Austenite memory effect in 1Cr-1Mo-0.75V(Ti,B) steel', Metal Science, 17 (1983), p.519.
[32] R. K. Shiue, K. C. Lan and C. Chen, 'Toughness and austenite stability of modified 9Cr-1Mo welds after tempering', Mater. Sci. Eng., A287 (2000), p.10.
[33] T. Maki, H. Morimoto and I. Tamura, 'Recrystallization of the austenite transformed reversely and structure of martensite in 18Ni Maraging steel', Tetsu-To-Hagane, 65 (1979), p.1598. (in Japanese)

Part II

Advanced Steam Turbine Materials

Contributed Papers

Mechanical Properties

CONTRIBUTION TO THE INVESTIGATION OF ADVANCED LOW-ALLOY P23 STEEL CREEP BEHAVIOUR

Jan Hakl[1], Tomáš Vlasák[1], Peter Brziak[2], Peter Zifčák[2]

[1]SVUM a.s., Prague, Czech Republic, hightempmat@svum.cz
[2]VUZ-PI SR, Bratislava, Slovakia

Abstract

Ferritic steels T23/P23 are potential candidate materials for water wall components as well as for thick walled pipes. Results of P23 creep testing conducted as a contribution of SVUM Prague to development of new materials in COST cooperation are presented. Material of P23 pipe dia 219x30 mm made by Vallourec & Mannesmann was investigated at creep condition under constant load at temperature and stress range 500 – 600°C/105 - 290 MPa. A part of the paper is an analysis of microstructural changes caused by creep exposition.

Keywords: power plants, ferritic steel, creep properties, microstructure, carbides.

1. Introduction

Requirements for reducing emissions and growth of the efficiency of coal-fired power plants are the driving force in development of new high-temperature steels. For current power engineering, the characteristic steam temperature at the turbine inlet is 540-565°C. However, in the past years, temperatures have grown above 565°C, up to around 600°C. When comparing the current steam parameters (540°C/18 MPa) with the steam ultra supercritical conditions (610°C/30 MPa), the efficiency can be increased by about 8% while decreasing of the CO_2 emissions is about 20% [1,2].

For components operating in the creep region, key usage properties are the creep resistance and resistance to high-temperature corrosion (oxidation) in the water steam environment. Austenitic CrNi(Mo) steels could be a potential material for these purposes. Their use is prevented by a low temperature conductivity and high thermal expansion, which means the danger of component damage by the mechanisms of thermal fatigue. Apart from this, the high price of these materials plays a role.

In industrially developed countries, considerable attention has been paid to the development and technological management of the new types of martensitic steels on the basis of (9-12) %Cr, modified with other elements (Mo, W, Co, N, B, V). In the EU, this evolution proceeds in the COST projects and one can expect that this group of steels will enable applications at the operating temperatures up to 650°C [3-6]. Apart from this, there is progress in low alloy steels based on 3Cr-0.5Mo hydrogen resistant materials. Results of Japanese and German research are steels T23 (2.25Cr-0.18Mo-0.25V-1.6W,Nb, B) and T24 (2.4Cr-1Mo-0.25V,Ti, B) used for water walls and superheaters [7-9]. The maximum application temperature is 580°C for both steels [12].

Application properties of the thin walled tubes made of T23 and T24 material are already well known [10]. The continuing research focuses on the properties of thick walled pipes made of P23 [10-12]. Our paper aims to these issues.

2. Summary of basic information on T23/P23

The chemical composition of both steels is indicated in Tab. I [10,13]. It is obvious that the composition of both steels is identical. The only difference represents the fact that in case of P23, the low limit of B content is not specified. The main information on T23 will therefore be valid also for P23.

Tab. I Chemical composition of T23, P23 steels and heat No. 73 220 [10,12] (wt.%).

Element	T23 according to ASTM A 213	P23 according to ASTM A 335M	Heat No. 73 220
C	0,04 – 0,10	0,04 – 0,10	0,07
Mn	0,10 – 0,60	0,10 – 0,60	0,54
P	max 0,030	max 0,030	0,008
S	max 0,010	max 0,010	0,004
Si	max 0,50	max 0,50	0,28
Cr	1,9 – 2,6	1,9 – 2,6	2,08
Mo	0,05 – 0,30	0,05 – 0,30	0,08
V	0,20 – 0,30	0,20 – 0,30	0,22
W	1,45 – 1,75	1,45 – 1,75	1,65
Nb	0,02 – 0,08	0,02 – 0,08	0,03
B	0,0005 – 0,0060	max 0,0060	0,002
N	max 0,030	max 0,030	0,011
Al	max 0,030	max 0,030	0,018

The basic physical properties of T23 and the ARA diagram are in [10]. Transformation temperatures A_{C1} are between 800 to 820°C, A_{C3} between 960 and 990°C. It is obvious from diagram ARA that in a wide range of cooling temperatures, a bainitic-martensitic structure will arise. The T23 heat treatment is carried out by normalization at 1060±10°C and tempering at 760°C±15°C, during which carbides precipitate in optimum dispersion.

In comparison with T22 (2.5Cr-1Mo) and P91 (9Cr-1Mo), the basic mechanical characteristics of the T23 steel at 20°C are as follows:

Standard	Steel	$R_{p0,2\ min}$ (MPa)	$R_{p\ min}$ (MPa)	A_{min} (%)	Hardness HB max
ASTM A 213	T 22	205	415	30	163
ASTM A 213 Code Case 2199	T 23	400	510	20	220
ASTM A 213	T 91	415	585	20	250

The temperature dependencies of the $R_{p0,2}$ and R_m limits are graphically illustrated for T 23 in [10], where the heat resistance and allowable design stresses are given for this material.

3. Experimental procedure and creep results

Tested material P23 was produced by Vallourec and Mannesmann Tubes. It was supplied under heat marking 73220 in form of the ∅219x30 mm seamless tube after heat treatment

1060°C/water+760°C/2 h procedure. The chemical composition according to the test [13] is indicated in Table I, basic mechanical characteristics are given in Table II.

Tab. II Attest values of material properties at room temperature.

	$R_{p0,2}$ (MPa)	R_m (MPa)	A (%)	KCV* (J)
Attest	496	597	23,3	185
Requirement	400	510	20	

* Mean value from 3 measurements, specimen oriented in longitudinal direction

The heat resistance tests were carried out on air on specimens with a nominal diameter and length of ∅5x50 mm for temperatures 500, 550 and 600°C and the 320-105 MPa stress. Altogether, 21 tests were carried out.

The one of the most important characteristics of the creep process is dependence of time to rupture on temperature and stress. For a mathematical evaluation of this quantity the procedure in accordance with [14,15] was used

$$\log t_i = A_{1i} + A_{2i} \cdot \log\left|\frac{1}{T} - \frac{1}{A_{5i}}\right| + C_{3i} \cdot \log\left[\sinh\left(A_{6i} \cdot \sigma \cdot T\right)\right] + A_{4i} \cdot \log\left|\frac{1}{T} - \frac{1}{A_{5i}}\right| \cdot \log\left[\sinh\left(A_{6i} \cdot \sigma \cdot T\right)\right] \quad (1)$$

where is

T	temperature,
t_i	i=1 the time to rupture,
	i=2 the time to 1% creep strain,
	i=3 the minimum creep rate,
σ	stress,
$A_{1i} - A_{6i}$	material constants (see Tab.III).

A graphical interpretation of creep strength evaluation by regression model (1) is shown in Fig. 1.

Data from series of creep curves were evaluated by the following model [15]

$$\varepsilon_c = \varepsilon_0 \cdot \left[\left[\frac{\varepsilon_m}{\varepsilon_0}\right]^{[g(\pi(t))]} - 1\right], \quad (2)$$

$$g(\pi(t)) = \pi^N \cdot \left[\frac{1 + \exp\left(-2 \cdot \pi^K\right)}{1 + \exp(-2)}\right]^M, \quad (2a)$$

$$\pi = \frac{t}{t_r}, \quad (2b)$$

$$\varepsilon_0 = \frac{\sigma}{E(T)} \cdot 10^2, \quad (2c)$$

$$E(T) = E_1 + E_2 \cdot \exp\left(\frac{E_3}{T}\right), \tag{2d}$$

where ε_c is total creep strain (%), t is time (h), t_r is time to rupture(h), ε_o is elastic deformation (%), K,M,N, ε_m, $E_{1\text{-}3}$ are material constants. Examples of evaluated creep curves are given in Fig.2.

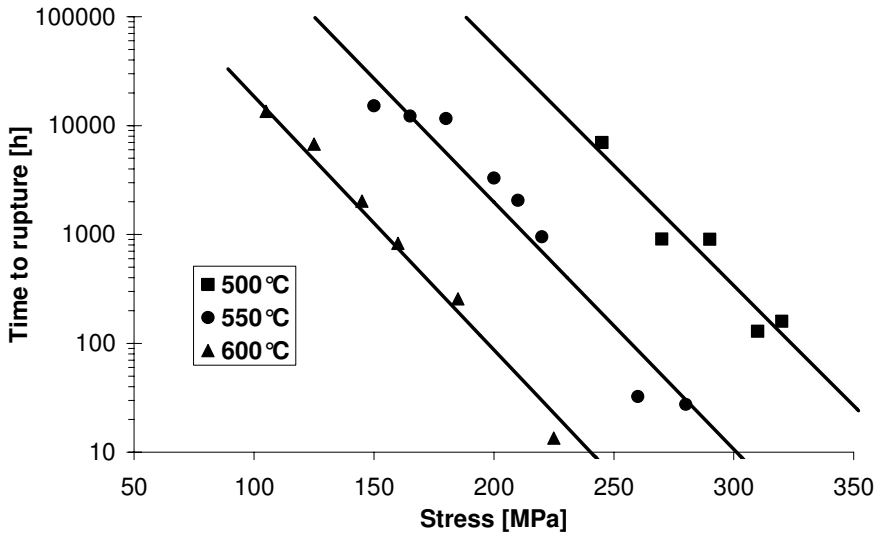

Fig.1 Creep strength evaluation of P23 steel

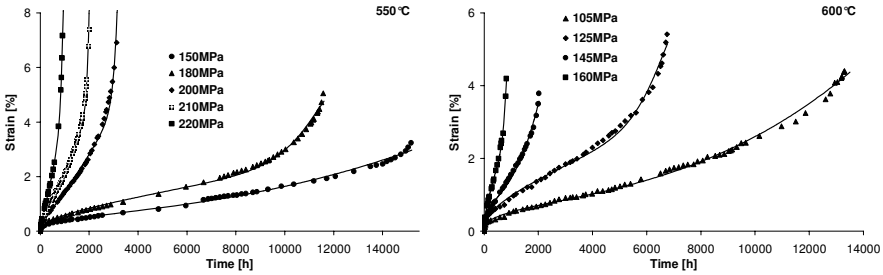

Fig.2 Examples of evaluated creep curves of P23 steel

From the evaluated creep curves is possible to determine time to specific creep strain and minimum creep rate. The same regression model (1) as for time to rupture was used for evaluation of time to 1% creep strain and the minimum creep rate in dependence on temperature and stress [14,15]. Dependence of time for reaching 1% creep strain is shown in Fig.3. Dependence of the minimum creep rate on stress and temperature is graphically shown on Fig.4.

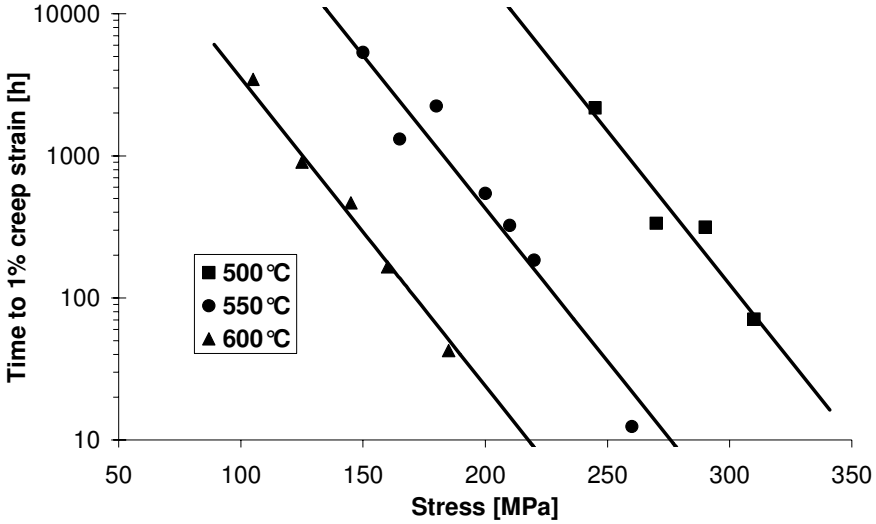

Fig. 3 **Time to 1% creep strain of P23 steel**

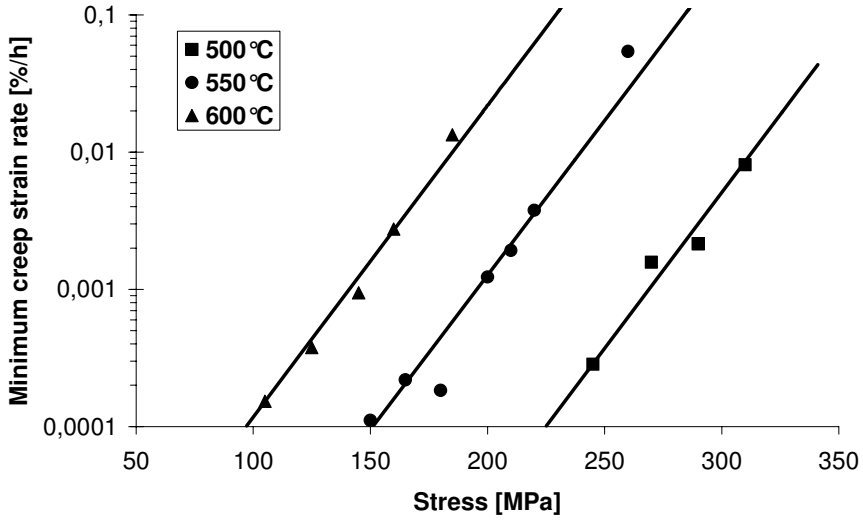

Fig.4 **Minimum creep rate of P23 steel**

Tab. III Material constants of regression model (1) – valid for σ [MPa], T [K] and t_r [h].

Constant	Value	Constant	Value	Constant	Value
A_{11}	1,42704919E+02	A_{12}	-5,69592121E+01	A_{13}	4,49381109E+01
A_{21}	4,59079345E+01	A_{22}	-1,90043873E+01	A_{23}	1,51109664E+01
A_{31}	-7,91971568E-02	A_{32}	1,71470918E-01	A_{33}	-2,27402543E-02
A_{41}	-2,96835347E-01	A_{42}	3,59789868E-01	A_{43}	-4,34530452E-02
A_{51}	1,61283784E+04	A_{52}	6,05017172E+02	A_{53}	6,41491039E+02
A_{61}	9,89855160E-04	A_{62}	2,78389691E-04	A_{63}	1,78679422E-03

4. The influence of creep conditions on microstructure and carbide formation.

The recently published time-temperature precipitation diagrams of carbide evolution are based on tungsten- free low-alloy steel [16]. In P23 steel, the tungsten is added (along with Cr, Nb, N and B) at the detriment of molybdenum to increase the creep strength [10]. According to the author's present knowledge, the precisely evaluated precipitation diagrams of tungsten bearing steels are still missing; and the main degradation mechanism operating during creep exposition is not established yet.

The aim of following chapter is to determine the influence of both testing temperature and time to fracture on the development of microstructure and secondary particles in selected ruptured specimens. The work involves the study of chemical composition and distribution of carbide particles in the steel studied.

One as-delivered and four creep exposed conditions were studied by means of light microscopy (LM) and transmission electron microscopy (TEM), see Tab.IV.

For TEM observations, the JEOL 200CX microscope (equipped with EDX EDAX 9900 chemical analyser) operating at 200 kV was used. The carbide particles, extracted on carbon replicas were identified by EDX and electron diffraction technique. The IMAGE PRO 3.1 image analyser was used for TEM image processing. For this purpose, the TEM images were digitalized; and, when necessary, the carbides were manually separated by adding white lines in between.

Tab.IV Specimens for microstructural study and demonstration of creep exposition

Condition	Specimen location	Detected carbides
As received	-	MX, $M_{23}C_6$, M_7C_3
550°C/200MPa /3 269h	head	MX, $M_{23}C_6$, M_7C_3
	gauge length	MX, $M_{23}C_6$, M_7C_3, M_6C
550°C/150MPa /15 199h	head	MX, $M_{23}C_6$, M_7C_3, M_6C
	gauge length	MX, $M_{23}C_6$, M_7C_3, M_6C
600°C/145MPa /2 021h	head	MX, $M_{23}C_6$, M_7C_3, M_6C
	gauge length	MX, $M_{23}C_6$, M_7C_3, M_6C
600°C/105MPa /13 503h	head	MX, $M_{23}C_6$, M_7C_3, M_6C
	gauge length	MX, $M_{23}C_6$, M_7C_3, M_6C

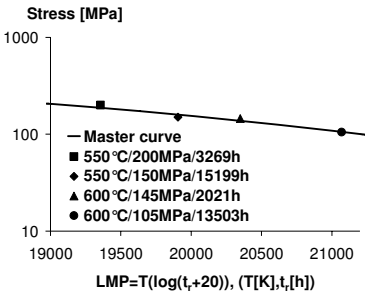

4.1 Microstructure of as-delivered condition

The tempered bainitic-martensitic microstructure of as-delivered condition is shown in Fig.5a (LM) and Fig.5b (TEM). In extraction replica, three types of carbides were identified: $M_{23}C_6$ and M_7C_3 precipitated both in the grain and on grain and subgrain boundaries; and small MX particles precipitated in the grain. The detected carbides are summarized in Tab.IV.

4.2 Microstructure of exposed conditions

Two principal types of microstructure were observed:

1) Microstructure similar to the as-delivered condition was observed in specimens tested at 550°C; the lath microstructure is clear and particles can be resolved only occasionally. A typical example is shown in Fig.5c (LM) and Fig. 5d (TEM).
2) The high-tempered microstructure; only signs of former lath microstructure are visible; and carbides, as a product of decomposition of martensite and bainite, are clearly visible in feritic matrix, see Fig. 5e and Fig. 5f.

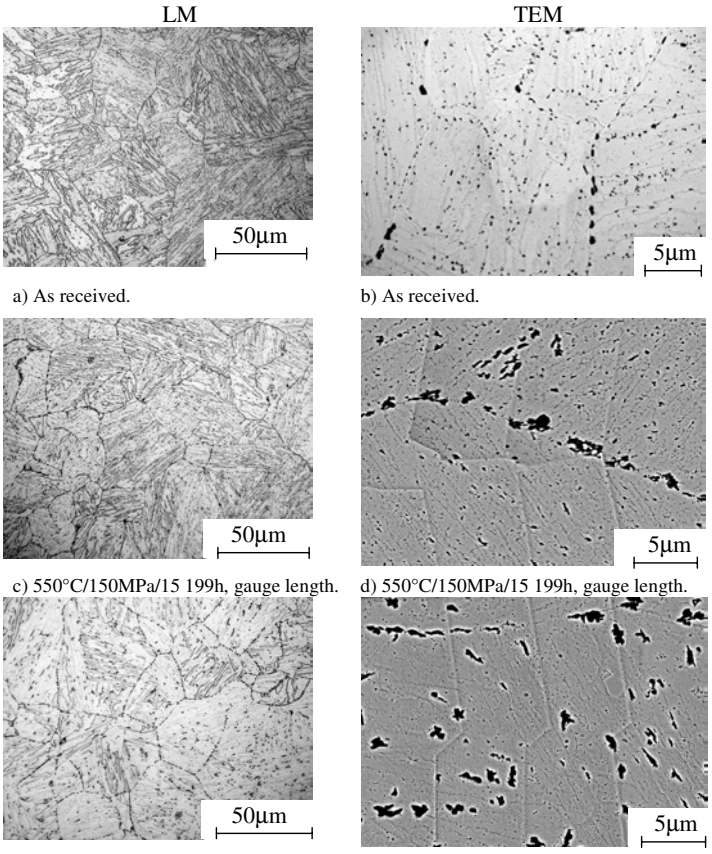

Fig.5 Microstructure of selected specimens.

The detected carbides are summarized in Tab.IV. As in as delivered condition, three types of carbides were identified: $M_{23}C_6$ and M_7C_3 precipitated both in the grain and on grain and subgrain boundaries; and small MX particles precipitated in the grain. Additionally, new M_6C carbide was found on grain boundary in several specimens.

4.3 Chemical composition of carbides

The $M_{23}C_6/M_7C_3/M_6C$ carbides were selected for chemical composition measurements. Approximately 60 carbides of each type were measured in specimens given in Tab.IV. The MX particles were detected in all conditions investigated in this study. They were app.20-30 nm in diameter and contained app. 80 wt % of V, Cr, Nb, W and Mo.

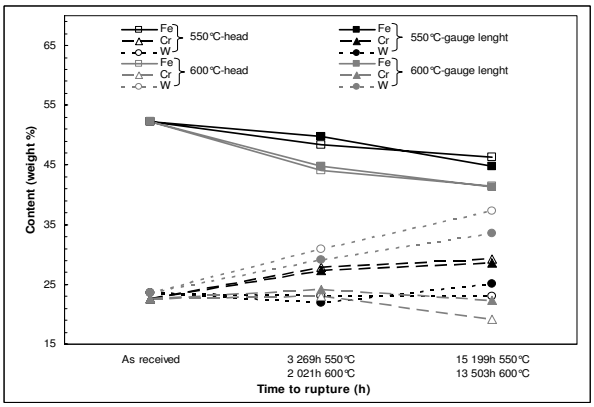

a) $M_{23}C_6$

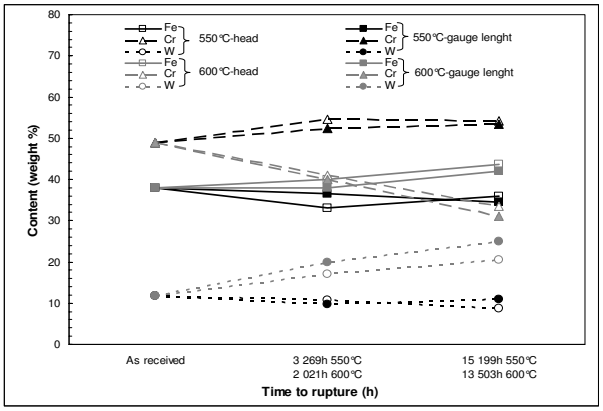

b) M_7C_3

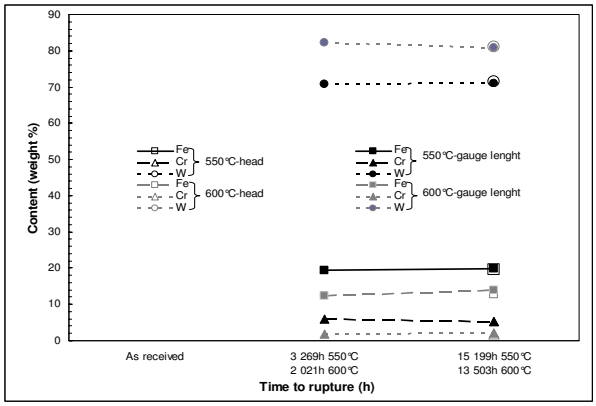

c) M_6C

Fig.6 The chemical composition of carbide particles.

Only those elements were taking into account with weight content more than 2 %. From each fractured specimen, the chemical composition of carbides was measured on carbon replicas prepared from both, head of specimen (only tempering effect) and gauge length (tempering and stress effect) to determine the influence of stress exposure on carbide formation. The results are summarized in Fig. 6a ($M_{23}C_6$ carbides), Fig. 6b (M_7C_3 carbides) and Fig. 6c (M_6C carbides).

During the creep exposition at 550°C, the chromium and tungsten content in $M_{23}C_6$ carbides is increasing on detriment of iron. During creep exposure at 600°C, the rate of iron depleting in $M_{23}C_6$ is much faster when compared to 550°C. Tungsten content is increasing from app. 23 weight % (as-delivered) to app. 37 weight % measured in gauge length of specimen tested for 15 199 h at 550°C. The overall level of tungsten enrichment is the most visible difference in $M_{23}C_6$ carbides kinetics at two temperatures investigated, see Fig.6a.

At 550°C, the M_7C_3 carbides seem chemically very stable, only slight differences in composition were measured, see Fig.6b. On contrary, at 600°C, tungsten content is increasing from app. 11 weight % (as-delivered) to app. 20 weight % measured in gauge length of specimen tested for 13 503 h at 600°C.

The M_6C carbides were not observed in as-delivered condition and in the head of specimens tested at 550°C/200MPa, see Tab.IV. The M_6C carbide remains chemically stable since the beginning of precipitation, see Fig.6c.

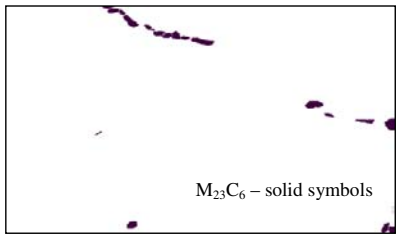

As delivered.

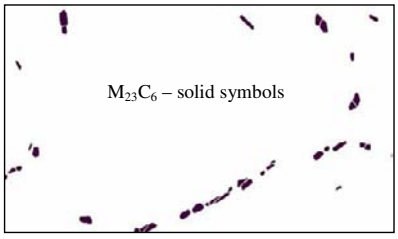

550°C/200MPa/3269h, head

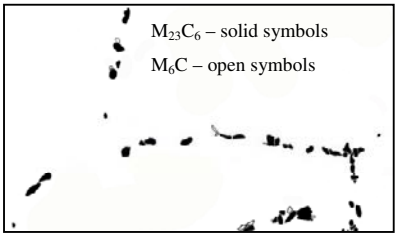

550°C/200MPa/3269h, gauge length

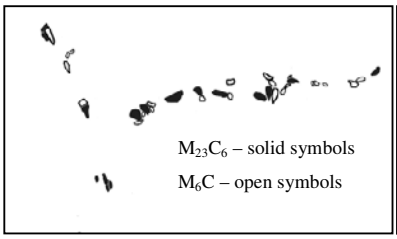

550°C/150MPa/15199h, head

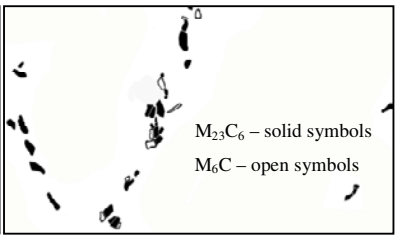

550°C/150MPa/15199h, gauge length

Fig.7 The development of grain boundary carbides during creep exposure.

5. Discussion

The results achieved can be summarized and interpreted as follows.

5.1 Exposition at 550°C

During creep exposure at 550°C, additional tempering accompanied by carbide reactions takes place in formerly tempered martensite – bainite microstructure. This effect is slight; and even after 15 199 h of exposure, lath microstructure is visible. During early stages of creep exposure, they MX/$M_{23}C_6$/M_7C_3/ particles are stable. Additional precipitation of M_6C was identified predominantly on grain boundary in gauge length of specimen tested at 550°C/200MPa for 3 269 h. Fig. 7 shows that the M_6C carbides grow at the detriment of $M_{23}C_6$ ones and the newly precipitated M_6C carbides always grow in close vicinity of $M_{23}C_6$ ones and replace them progressively. The changes in chemical composition of evaluated carbides are slight only. Regarding the chemical composition of carbides, there were found only slight differences between the head and gauge length. The size of $M_{23}C_6$ carbides drops

from app. 450 nm (as delivered) to app. 360 nm (ruptured after 15 199h), which is by app. 20 % less, see Fig. 8. On the other hand, during the creep exposure, the size of M_7C_3 carbides increases from appr. 170 nm to app. 200 nm, see Fig. 8. The precipitation and fast growing of new coarse M_6C particles seems to be the most evident feature of degradation.

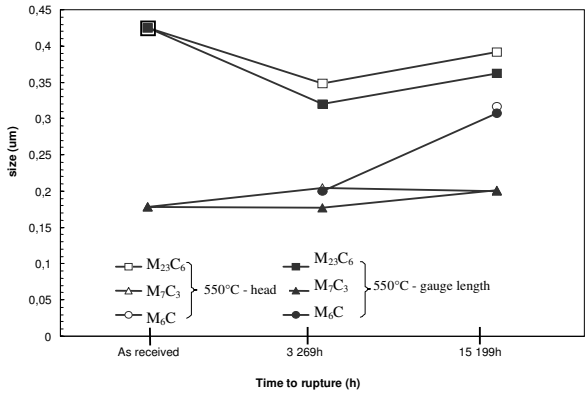

Fig.8 The size of carbide particles in as received condition and after creep exposure at 550°C.

5.2 Exposure at 600°C

During the creep exposure at 600°C, the tempering effect is more visible; the former lath microstructure progressively changes to ferrite carbide mixture. This massive tempering is accompanied by a significant drop in iron content in $M_{23}C_6$ carbides accompanied by increased tungsten content, see Fig. 6**.** At 600°C, the intense diffusion of tungsten from matrix to carbides is obvious. M_6C carbides also contain more tungsten. Regarding the chemical composition of carbides, there were found only slight differences between the head and gauge length. The carbide sequence is the same as for microstructure exposed at 550°C. The precipitation and fast growing of new coarse M_6C, along with tungsten depletion in matrix seem to be the most evident features of degradation.

6. Conclusions

1) The creep strength, time to 1% creep strain and minimum creep rate of P23 steel, the most important characteristics of creep process were determined.
2) Microstructural tempering, accompanied with carbide reactions, takes place during the creep exposure.
3) The precipitation and fast growing of new coarse M_6C, along with tungsten depletion in matrix seem to be the most evident features of degradation.
4) In both above mentioned cases, the M_6C carbide precipitates on detriment of $M_{23}C_6$.

REFERENCES

[1] MARLOW,B.A.: Advanced Steam Turbines. Proc.conf. Advances in Turbine Materials, Design and Manufacturing. p.36. Newcastle upon Tyne, 1997, Eds. A.Strang et al., IOM and IME, London 1997.

[2] KEHLHOFER,R.: Power engineering, status and trends. Proc.conf. Materials for Advanced Power Engineering 1998. p.3. Eds. J.Lecomte-Becker et al., Forschungszentrum Jülich GmbH, 1998.

[3] STAUBLI,M.E.-MAYER,K.H.-KERN,T.V.-VANSTONE,R.W.: COST 501/COST 522. The European Collaboration in advanced steam turbine materials for ultra efficient, low emission power plants. Proc.conf. PARSON 2000: Advanced materials for 21st Century Turbines and power plants. p.98. Eds. A.Strang et al. IOM, London 2000.

[4] VODÁREK,V.: Fyzikální metalurgie modifikovaných (9-12)%Cr ocelí. VŠB - Technická univerzita Ostrava. Ostrava 2003.

[5] KERN,T.V.-SCARLIN,B.-VANSTONE,R.W.-MAYER,K.H.: High temperature forged components for advanced steam power plants. See [2], p.53.

[6] MAYER, K.H.-HANUS,R.-KERN,T.-STAUBLI,M.-THORTON,D.V.: High temperature cast components for advanced steam power plants. See [2], p.71.

[7] DESHAYES,F.-BENDICK,W.-HAARMANN,K.-VAILLANT,J.C.: New 2 – 3% Cr steel grades for waterwall panels and superheaters. See [2], p.499.

[8] JAKOBOVÁ,A.-FOLDYNA,V.-VODÁREK,V.-KUBOŇ,Z.-FILIP,M.: Creep resistant ferritic steels containing 0,5 to 12%Cr. Proc.conf. Creep resistant metallic materials, Prague 2001 p.117. Ed. Vítkovice RD, Ostrava 2001.

[9] HRIVŇÁK,I.: Zvaritelnosť nových ocelí. Zvárač I (2004), č.1, s.3-7.

[10] ARNDT,J.-HAARMANN,K.-KOTTMANN,G.-VAILLANT,J.CJ.-BENDICK,W.-KUBLA,G.-ARBAB,A.-DESHAYES,F.: The T23/T24 Book. New Grades for Waterwalls and Superheaters. Vallourec and Mannesmann Tubes. 2nd Edition, October 2000.

[11] STAUBLI,M.: Final summary report of turbine group. COST 522 – steam power plant. Alstom Switzerland, Baden, 2003.

[12] VAILLANT, J.C.-VANDENBERGHE, B.-HAHN,B.-HEUSER,H.-JOCHUM, C.: T/P23,24,911 and 92: New Grades for Advanced Coal-Fired Power Plants-Properties and Experience. Creep and Fracture in High Temperature Components-Design and Life Assessment, p.87. Ed. I.A.Shibli, S.R.Holdworth, G.Merckling, ECCC Creep conference, Sept. 12-14, 2005 London.

[13] Vallourec and Mannesmann Tubes. Inspection Certificate No.RO2392/02.

[14] PECH, R.-KOUCKÝ, J.-BÍNA, V.: Matematizace hodnot pevnosti při tečení česko-slovenských žárupevných ocelí pro výrobu trub. Strojírenství 29 (1979), č.7, s.389.

[15] BÍNA, V.-HAKL, J.: Relation between creep strength and strength for specific creep strain at temperatures up to 1200°C, Materials Science and Engineering A234-236 (1997), pp. 583-586.

[16] JANOVEC, J., SVOBODA, M., VÝROSTKOVÁ, A., KROUPA, A.: Time-temperature precipitation diagrams of carbide evolution in low alloy steels, Materials Science and Engineering A 402 (2005) 288-293.

This work was supported by Ministry of Education, Youth and Sports of Czech Republic – COST 536 (1P05 OC020).

Effect of tempering times on creep strength in ASME Gr.23(2.25Cr-1.6W steel)

Nobuyoshi Komai and Toshiyuki Imazato
Nagasaki Research & Development Center, Mitsubishi Heavy Industries, Ltd.
5-717-1 Fukahori-machi, Nagasaki 851-0392, Japan
nobuyoshi_komai@mhi.co.jp

Abstract

ASME Gr.23 (2.25Cr-1.6W) steel was originally developed as an improvement on conventional 2.25Cr-1Mo steel for boilers, and has 1.8 times greater creep strength than 2.25Cr-1Mo steel at 600°C. Although normalizing and tempering for thick wall components are needed after hot bending, long tempering for thick components does influence the creep strength of this steel. Consequently, the effect of tempering times on the creep strength of ASME Gr.23 was investigated in this study.

Test materials were tempered at 770°C for 1, 3 and 10h after normalizing at 1050°C for 1h, and long creep rupture testing was conducted primarily at 600°C. Creep rupture strength in longer tempered materials tended to be lower under high stress creep conditions, but the creep rupture strength of all the materials showed similar creep strength under low stress creep conditions.

Longer tempering promotes not only coarsening of precipitates, but also decreased dislocation density due to recovery. It is possible that these microstructural changes effectively improve creep strength under low stress creep conditions due to prevention of non-homogeneous recovery of bainitic laths.

Key words: low alloy steel, T/P23, heat treatment, oxidation, minimum creep rate

Introduction

ASME Gr.23 (2.25Cr-1.6W) steel was developed as an improvement on conventional 2.25Cr-1Mo steel for boilers, and has 1.8 times greater creep strength than 2.25Cr-1Mo steel at 600°C [1]. This steel is already widely used for boiler pressure parts such as tubes for superheater and reheater panels, main steam piping, high temperature reheat piping and headers[2-4]. Long-term creep strength is very important due to use of this steel in applications up to 575°C for more than 10^5h. Although normalizing and tempering are needed after hot bending, long tempering for thick wall components does influence the creep strength, and the effect of tempering times on the creep strength of ASME Gr.23 was accordingly investigated in this study.

It is well known that the long-term creep strength of 2.25Cr-1Mo steel depends on the initial microstructure, i.e., martensite, tempered martensite, bainite and ferrite + pearlite. Yukitoshi et al.[5] and Kushima et al.[6] reported that the creep strength of a fully annealed microstructure consisting of ferrite + pearlite was found to be higher than others. This improving effect is attained by means of less mobile dislocation[7,8].

A remarkable decrease in creep rupture strength at 600°C and 650°C has been observed in the long-term region of greater than approx. 10,000h in Mod.9Cr-1Mo steel[9,10]. It has been concluded that preferential recovery in the vicinity of the prior austenite grain boundary is a major factor in degradation during long-term creep deformation[9,10]. The effect of

tempering temperature on creep properties in Mod.9Cr-1Mo steel was considered by Suzuki et al.[11], who found that lowering the tempering temperature promotes substantial degradation in the long-term region of preferential recovery in the vicinity of the prior austenite grain boundary, thus resulting in greater degradation of the creep strength. Similarly, higher temperature tempering improves the long-term creep strength in 12Cr-1Mo-1W-V-Nb steel[12].

Normalized and tempered 2.25Cr-1.6W steel exhibits a tempered bainite structure having MX type precipitates, serving to dramatically improve creep strength. This microstructure, having bainite laths and fine precipitates, is similar to that of tempered 9 to 12Cr steel containing V and Nb.

Test Material

Two varieties of commercially available large-diameter thick-walled steel pipes (ASME SA-335 P23) measuring 350mm in diameter and having a thickness of 50mm were used as test materials[2]. The chemical compositions are shown in Table 1. There were no remarkable differences in chemical composition between them, and the compositions satisfied their specifications. The as-received materials were austenitized at 1050°C for 1h, then mist-cooled and tempered at 770°C for 1h. Heat A steel was used for the creep and creep rupture tests, while other tests were carried out on Heat B.

Additional tempering at 770°C for 2h and 9h was conducted on the as-received Heat A material to prepare for investigation of the effect of tempering time on the creep strength. Furthermore, simulated heat treatment for post weld heat treatment at 715°C for 4h was carried out on the comparison materials.

Fig. 1 shows the optical microstructure of the as-received (tempered at 770°C x 1h) and 770°C x 10h tempered materials. Both materials show a similar tempered bainite microstructure, and there is no remarkable microstructural change after the additional 9h of tempering at 770°C. Although these steels contain a small amount of polygonal ferrite, it is difficult to distinguish this by optical microscope[13]. The additional 9h of tempering lowered the hardness from 186HV to 162HV.

To consider the effect of the microstructural changes during long-term creep on the creep strength and creep deformation behavior, additional aging heat treatment was conducted on Heat B materials at 600°C for 10,000h and 30,000h, and at 500°C, 550°C, 600°C and 650°C up to 30,000h.

Table 1 Chemical composition of steel tested

(mass%)

Heat	C	Si	Mn	Cr	Mo	W	V	Nb	B	N
A	0.05	0.26	0.51	2.42	0.11	1.56	0.26	0.05	0.0045	0.006
B	0.05	0.21	0.49	2.17	0.11	1.59	0.23	0.05	0.0042	0.008

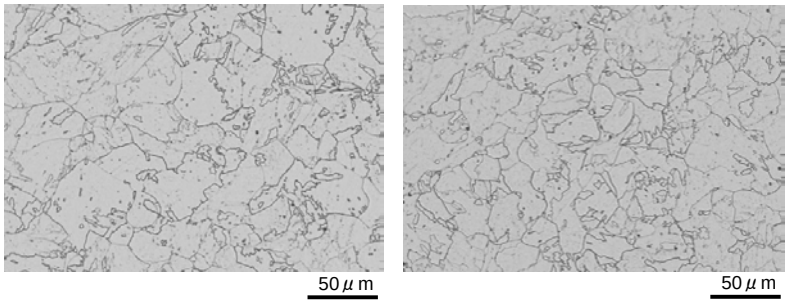

(a) As-received (770℃ × 1h) (b) 770℃ × 10h

Fig.1 Optical microstructures of as-received (tempered at 770°C x 1h) and 770°C x 10h tempered materials

Test procedure

Creep and creep rupture tests

Creep rupture test were conducted in air using uniaxial test specimens 25mm in gauge length and 6~8.5mm in diameter. Simulated post weld heat-treated materials (715°C x 4h) were creep rupture tested in a temperature range from 550°C to 650°C at 25°C intervals. Other materials were creep rupture tested primarily at 600°C. Creep-interrupted specimens at 600°C for 80MPa were prepared from tube materials having a similar chemical composition to measure the change in hardness due to creep deformation[14].

Creep tests were conducted at 600°C under constant load conditions in air. The specimens were 5mm in diameter and 20mm in gauge length.

Tensile tests

Tensile tests were conducted using specimens 6mm in diameter and 30mm in gauge length to measure the 0.2% offset yield stress and elastic limit. The initial strain rate was $10^{-4}s^{-1}$ and the cross head speed was fixed.

Precipitates

Long aged materials at 550°C, 600°C and 650°C up to 30,000h were used. To clarify the precipitates after aging, chemical analysis and X-ray diffraction of the extracted residue were undertaken.

Creep rupture strength

As-received and 715°C x 4h materials

Stress vs. time to rupture curves of the as-received (770°C x 1h) and 715°C x 4h materials are shown in Fig. 2. Both materials had creep strength superior to that of conventional 2.25Cr-1Mo steel. The differences in creep strength between the as-received and 715°C x 4h materials are very small, and it was thus considered that heat treatment at 715°C for 4h did not influence the creep strength. Although a linear relationship between logarithmic stress and logarithmic time to rupture was seen at 550°C and 575°C, creep strength deterioration was

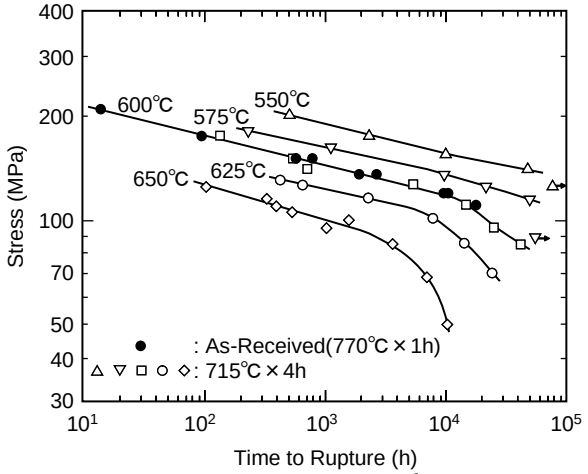

Fig.2 Stress vs. time to rupture curves of 2.25Cr-1.6W steels

observed in the long-term region at over 600°C.

Substantial reductions in creep rupture strength at 600°C and 650°C have been reported in the long term region greater than approx. 10,000h in Mod.9Cr-1Mo steel due to preferential recovery in the vicinity of the prior austenite grain boundary[9,10]. Half of the 0.2% offset yield stress was considered to be a boundary condition between short-term and long-term, where changes in the stress dependence of creep rupture strength and the inflection of the stress vs. time to rupture curve took place[15]. The figures corresponding to half of the 0.2% offset yield stress in the 715°C x 4h materials were 166MPa, 146MPa and 119MPa at 550°C, 600°C and 650°C, respectively. No inflection at the 550°C and 575°C curves in Fig. 3, and

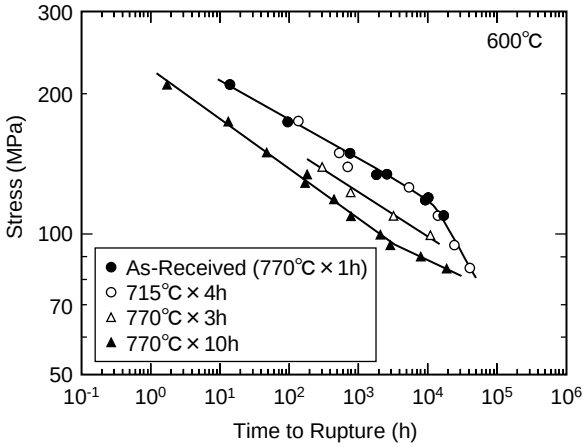

Fig.3 Comparison of stress vs. time to rupture at 600°C in 2.25Cr-1.6W steels tempered at 770°C x 3h and 770°C x 10h comparing with as-received and 715°C x 4h materials

the inflection observed at the 600°C, 625°C and 650°C curves were observed at lower stress than half of 0.2% offset yield stress at the test temperature. Although good correspondence between the elastic limit and half of the 0.2% offset yield stress has been reported for Mod.9Cr-1Mo steel[15], the elastic limit of 715°C x 4h material at 600°C was found to be 193MPa, which is greater than half of the 0.2% offset yield stress at the same temperature. Hence, it was considered that the creep curve inflection behavior in 2.25Cr-1.6W steel was different from that reported for Mod.9Cr-1Mo steel.

The influence of oxidation during long-term creep testing at low stress is quite severe in 2.25Cr-1Mo steel[16], producing an excessively short time to rupture due to load-bearing cross section area reductions by surface oxidation. 2.25Cr-1.6W steel should also be affected by oxidation during long-term creep, since it has the same content as chromium as 2.25Cr-1Mo steel and similar oxidation properties. Consideration of oxidation influence during creep is discussed subsequently.

770°C x 3h and 10h tempered materials

Creep rupture properties at 600°C in materials tempered at 770°C for 3 and 10h are compared in Fig.3 with as-received and 715°C x 4h materials. Creep rupture strength at 770°C for 3 and 10h is seen to be lower than that of the as-received and 715°C x 4h materials, indicating that longer tempering tends to reduce creep strength. However, reverse inflection was observed in the stress vs. time to rupture curve at 95MPa for the 770°C x 10h material, and the slope of the stress vs. time to rupture curve is gentle below this stress level. On the other hand, the slope corresponding to the 715°C x 4h material is steep at levels under 110MPa. Consequently, the extrapolated creep rupture strengths at 600°C for 10^5h among 715°C x 4h, 770°C x 3h and 770°C x 10h materials are asymptotic.

Discussion

Oxidation during creep rupture tests

Fig. 4 shows the cross-sectional macrostructure of a creep-ruptured specimen at 650°C for 10,172.7h in 715°C x 4h material. Oxidation scale was observed only on the small creep deformation portion; there was no oxidation scale near the fracture portion because of exfoliation due to creep deformation. The oxidation scale thickness was approximately 360μm, showing that the specimen was heavily oxidized during creep at the higher test temperature in the long-term test.

Nakashiro et al.[16] developed oxidation correction factors for 2.25Cr-1Mo steel through diameter reductions, taking oxidation during creep into account. Another oxidation correction procedure has also been proposed[17, 18], but perfect oxidation correction would be difficult because oxidation behavior has not yet been completely clarified near the fracture portion in the case of substantial creep deformation.

If oxidation correction were applied to the data for the 715°C x 4h and 770°C x 10h materials, the slope of stress vs. time to rupture curve would be slighter. Consequently, 10^5h creep rupture strengths at 600°C taking into account the effect of specimen oxidation during creep for 715°C x 4h and 770°C x 10h would be nearly the same.

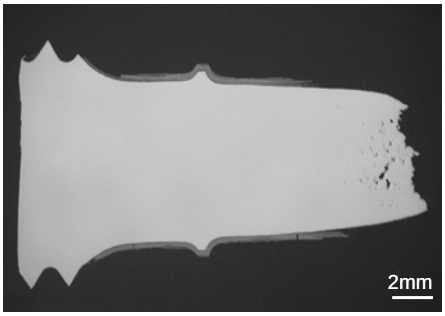

Fig.4 Cross-sectional macrostructure of creep-ruptured specimen at 650°C for 10,172h in 715°C x 4h material

Microstructural degradation during creep

Since microstructural change during creep affects the creep deformation resistance, creep strength was influenced by microstructural degradation. Fig. 5 shows the expected creep damage in accordance with creep time. It should be noted that the creep damage mechanisms were different in short-term creep and long-term creep. The primary damage was derived from creep deformation in short-term creep, and other damage was caused by microstructural change such as coarsening of precipitates, change in precipitation and recovery of dislocation substructure due to having been maintained at high temperature during long-term creep.

Change in hardness

Variation of dislocation density, bainite lath structure and precipitates during creep are considered to change the hardness. Fig. 6 shows hardness changing due to aging in Heat B materials. There is no change in hardness up to 30,000h aged at 500°C and 550°C. On the other hand, substantial reduction in hardness was observed in aged materials beyond 10,000h

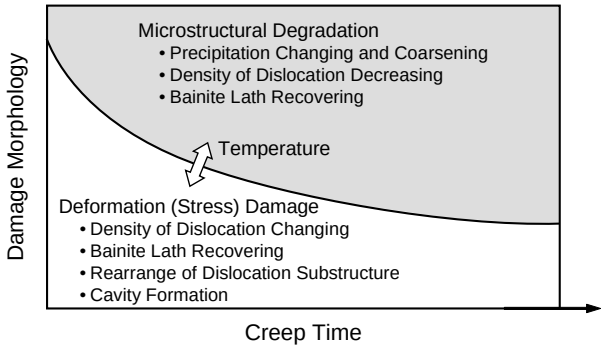

Fig.5 Damage morphology during creep in 2.25Cr-1.6W steel

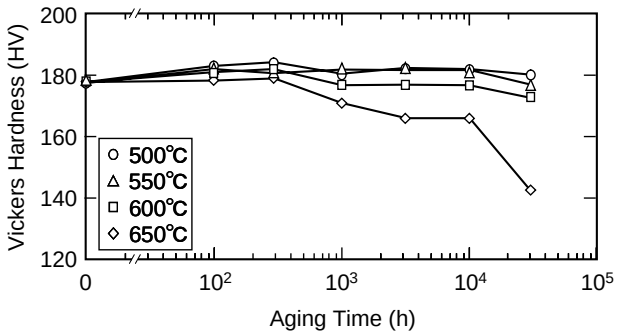

Fig.6 Vickers hardness changes due to aging at 500˚C, 550˚C, 600˚C and 650˚C

and 300h at 600˚C and 650˚C respectively. Notable microstructural change will thus occur at 600˚C in creep test conditions over 10,000h.

Dislocation

The relationship between creep interrupted strain and hardness in the gauge portion at 650˚C -80MPa is shown in Fig. 7. Small creep deformation decreases the hardness, with 0.05 in creep strain corresponding approximately to 140HV. This reduction in hardness is caused by recovery of lath to subgrain and decreasing dislocation density accompanying creep deformation[14]

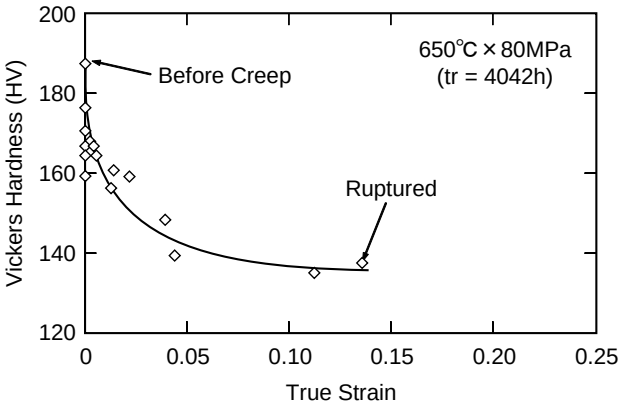

Fig. 7 Relationship between creep interrupted strain and hardness in the gauge portion of a 650˚C - 80MPa creep specimen

Precipitates

Extracted residues obtained from aged materials were identified by X-ray and chemical analysis. $M_{23}C_6$, M_7C_3 and MX type precipitates were identified in the as-received material. M_7C_3 disappeared after aging at 550˚C ~650˚C, and M_6C containing W became apparent. This precipitation behavior is consistent with the results of a previous study[19].

Fig. 8 shows the amount of extracted residues in the aged materials. Long aging at 550˚C to 650˚C promotes precipitates containing W, which are identified as M_6C. However, increased amounts of precipitates containing Fe and Cr is also somewhat due to aging. These analysis results show M_6C type precipitates increasing due to aging. The amount of extracted residue does not change greatly in materials tempered at 770˚C for 1 and 10h, and the amount of precipitates reached equilibrium when tempered at 770˚C for 1h .

Creep properties of long tempered and aged materials

To investigate the effect of the microstructural evolution during creep on creep behavior and strength, materials aged at 600˚C for 10,000h and 30,000h and tempered at 770˚C for 10h were tested for creep at 600˚C. Fig. 9 presents the minimum creep rate against stress. Fig. 10 shows the relationship between minimum creep rate and time to rupture, data for which satisfied the Monkman-Grant relation. Accordingly, it was considered that the minimum creep rate governs time to rupture.

600 ˚C aged materials

The minimum creep rate in 600˚C aged materials was greater than that in as-received materials in the high stress region shown in Fig.9. Nevertheless, the minimum creep rate in the material aged at 600˚C for 30,000h is smaller than that in the as-received material in the low stress region. This property was interpreted by taking into account the decreased dislocation density and increased number of precipitates due to aging before creep. Low

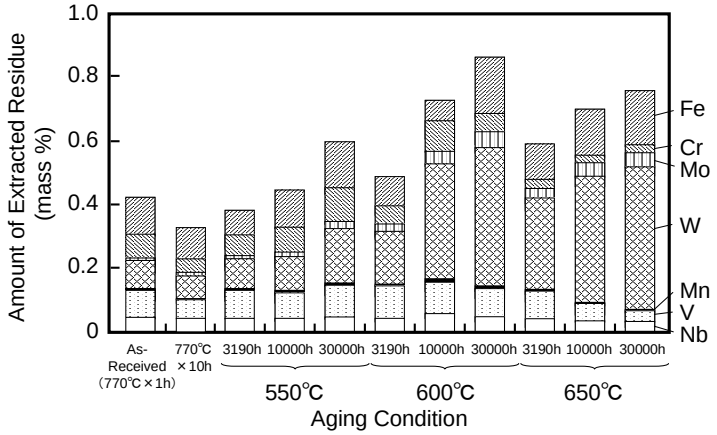

Fig. 8 Amount of extracted residue in aged materials

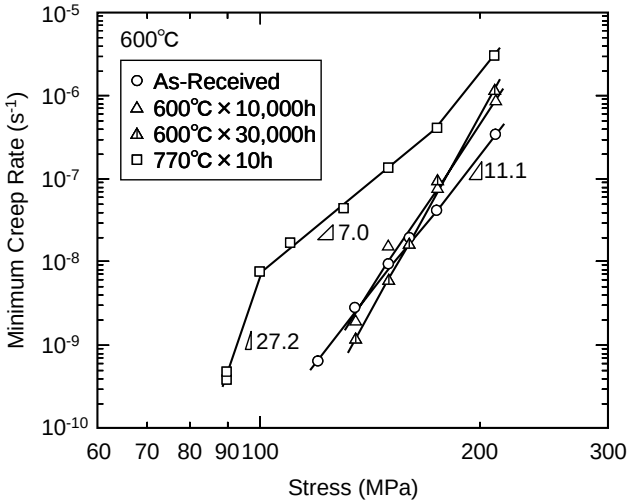

Fig. 9 Stress dependence of minimum creep rates in as-received(770°C x 1h), 600°C x 10,000h and 30,000h aged, and 770°C x 10h tempered materials

dislocation density increases the minimum creep rate in the high stress region, fine dispersion of MX precipitates is maintained, and new precipitates such as M_6C effectively decrease the minimum creep rate in the low stress region. It was concluded that the effect on the creep strength of microstructural change induced hold at 600°C during creep is not especially great in this steel.

770 °C x 10h tempered material

The minimum creep rate in the material tempered at 770°C for 10h was the highest, corresponding to the shortest time to rupture. The stress exponent, shown as the slope in Fig. 9, changed from 7.0 to 27.2 at 100MPa, suggesting a change in the creep deformation mechanism. This boundary stress is consistent with the inflection of stress vs. time to rupture curve as shown in Fig. 3.

The stress exponent was reported to be discontinuous in fully annealed 2.25Cr-1Mo steel consisting of ferrite and pearlite. The stress exponent increases suddenly to 9~15, decreasing applied stress at critical stress, which is stress/Young's modulus = 6~7 x 10^{-4}, and similar inflection is seen at the minimum creep rate vs. stress curve at 500°C, 550°C and 600°C [20]. However, the stress exponent in Mod.9Cr-1Mo and 9Cr-0.1Mo-1.8W-V-Nb steels below critical stress at each test temperature is smaller than that in the high stress region[21]. The creep rate in particle-strengthened materials is dramatically reduced in the low stress region[22]. It was considered that fully annealed 2.25Cr-1Mo and 770°C x 10h tempered 2.25Cr-1.6W steel have low dislocation density but have fine precipitates, and the creep deformation mechanism controlling the minimum creep rate was the same as for particle-strengthened materials in the low stress region. It is possible that these microstructural changes effectively improve creep strength under low stress creep conditions

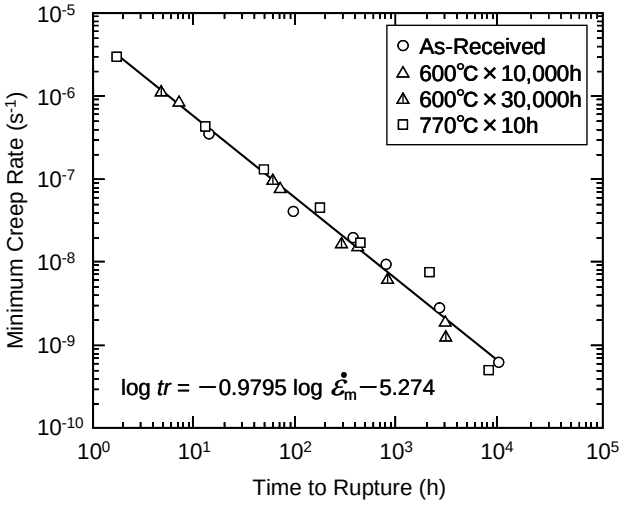

Fig.10 Relationship between minimum creep rates and time to rupture

due to prevention of inhomogeneous recovery of bainitic laths.

Fig. 11 shows the creep rate against creep strain for 770°C x 10h material. The creep deformation behavior is similar to that in the as-received materials above 100MPa. Only the creep deformation behavior at 90MPa was different, which supports the changing stress exponent and creep deformation mechanism in the low stress region.

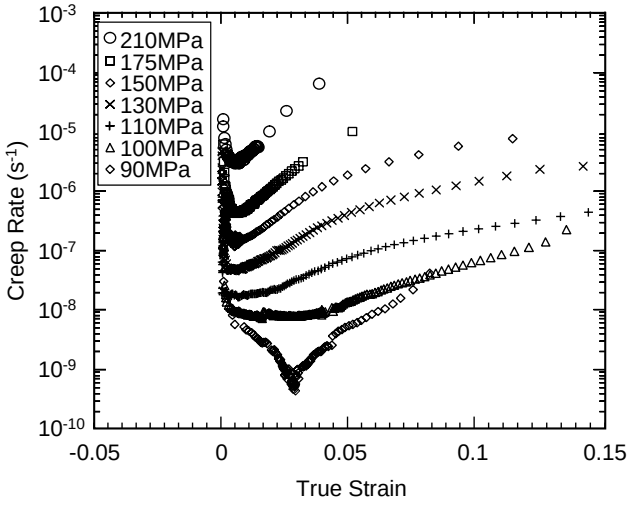

Fig.11 Relationship between true strain and creep rate in 770°C x 10h material

Conclusion

Long-term creep rupture tests were conducted on ASME Gr.23 (2.25Cr-1.6W steel) tempered at 770°C for 1h, 3h and 10h, and the effect of tempering time on creep strength was investigated. The results are summarized as follows.

(1) The effect of heat treatment at 715°C for 4h simulating post weld heat treatment for as-received material on the creep strength at 600°C was very small. A linear relationship between logarithmic stress and logarithmic time to rupture was seen at 550°C and 575°C in the 715°C x 4h material, and creep strength deterioration was observed at over 600°C in the long-term region. Inflection stress observed at stress vs. time to rupture curves was lower than half of the 0.2% offset yield stress and the elastic limit at the test temperature. This inflection behavior differs from that of Mod.9Cr-1Mo steel.

(2) Long-term creep strength at 600°C decreased with increased tempering time at 770°C. However, inflection of the stress vs. time to rupture curve at 95MPa for the 770°C x 10h material was observed, and the slope of the stress vs. time to rupture curve was gentle below this stress level. Consequently, the extrapolated creep rupture strengths at 600°C for 10^5h among 715°C x 4h, 770°C x 3h and 770°C x 10h materials are asymptotic.

(3) The effect of the microstructural evolution during creep on creep behavior and strength was considered using aged materials at 600°C for up to 30,000h. Long aging at 550°C to 650°C promotes precipitates containing W, identified as M_6C. It was concluded that the effect on creep strength of microstructural change induced hold at 600°C during creep is not especially great.

(4) The relationship between minimum creep rate and time to rupture satisfied the Monkman-Grant relation. The minimum creep rate for the material tempered at 770°C for 10h was the highest at high stress region, corresponding to shortest time to rupture.

(5) The creep stress exponent of 770°C x 10h tempered material suddenly changed from 7.0 to 27.2 at 100MPa at 600°C. This suggests that the creep deformation mechanism changed, and this behavior has been previously reported for fully annealed 2.25Cr-1Mo steel. 770°C x 10h tempered material has low dislocation density due to recovery with long tempering but have fine precipitates, and the creep deformation mechanism controlling the minimum creep rate was thus the same as for particle-strengthened materials in the low stress region.

References

[1] F. Masuyama, T. Yokoyama, Y. Sawaragi and A. Iseda : Development of a Tungsten Strengthened Low Alloy Steel with Improved Weldability, *D. Coutsouradis et al.(eds.), Materials for Advanced Power Engineering, Part I*, (1994), 173-181

[2] N. Komai, F. Masuyama, I. Ishihara, T. Yokoyama ,Y. Yamadera, H. Okada, K. Miyata

and Y. Sawaragi : Development and Application of 2.25Cr-1.6W(HCM2S) Steel Large Diameter and Thick Section Pipe, *Advanced Heat Resistant Steel for Power Generation*, IOM communications Ltd., London, (1999), 96-108

[3] N. Komai, F. Masuyama and M. Igarashi : 10-year Experience with T23(2.25Cr-1.6W) and T122(12Cr-0.4Mo-2W) in a Power Boiler, *Journal of Pressure Vessel Technology*, 127(2005), 190-196

[4] S. Sato, M. Matsuda, T. Hashimoto, Y. Wakabayashi and A. Hashimoto : Design Features and Commissioning of the 700MW Coal-Fired Boiler at the Tsuruga Thermal Power Station No. 2, *Mitsubishi Heavy Industries, Ltd. Technical Review*, 38(2001), 106-110

[5] T. Yukitoshi and K. Nishida : Creep Properties of Low Alloy Steels in Relation to Microstructure, The *Sumitomo Search*, No. 8, Nov. 1972, 45-60

[6] H. Kushima, K. Kimura, F. Abe, K. Yagi, H. Irie and K. Maruyama : Effect of Initial Microstructure on Long-term Creep Strength Properties of 2.25Cr-1Mo Steel(in Japanese), *Tetsu to Hagané*, 85(1999), 848-855

[7] K. Kimura, H. Kushima, E. Baba, T. Shimizu, Y, Asai, F. Abe and K. Yagi : Effect of Initial Microstructure on Long Term Creep Strength of a Low Alloy Steel(in Japanese), *Tetsu to Hagané*, 86(2000), 542-549

[8] K. Kimura, T. Watanabe, H. Hongo, M. Yamazaki, J. Kinugawa and H. Irie : Effect of Full Annealing Heat Treatment on Long-term Creep Strength of 2.25Cr-1Mo Steel Welded Joint, *Quarterly Journal of Japan Welding Society*, 21(2003), 195-203

[9] K. Kimura, H. Kushima and F. Abe : Heterogeneous Changes in Microstructure and Degradation Behaviour of 9Cr-1Mo-V-Nb Steel during Long Term Creep, *Key Engineering Materials*, 171-177(2000), 483-490

[10] H. Kushima, K. Kimura and F. Abe : Degradation of Mod.9Cr-1Mo Steel during Long-term Creep Deformation(in Japanese), *Tetsu to Hagané*, 1999, 841-847

[11] K. Suzuki, S. Kumai, H. Kushima, Y. Toda and K. Kimura : Effect of Tempering Temperature on Creep Properties in Mod.9Cr-1Mo Steel(in Japanese), *CAMP-ISIJ*, 15(2002), 1245

[12] A. Iseda, H. Teranishi and F. Masuyama : Effects of Chemical Compositions and Heat Treatment on Creep Rupture Strength of 12wt%Cr Heat Resistant Steels for Boiler(in Japanese), *Tetsu to Hagané*, 76(1990), 1076-1083

[13] N. Komai, T. Imazato and F. Masuyama : Continuously Cooled Microstructure and Creep Rupture Strength of Low C-2.25Cr-1.6W-V-Nb Steel, *ISIJ international*, 41(2001),Supplement(March), S91-S96

[14] N. Komai and F. Masuyama : Microstructural Degradation of Advanced Low Alloy Steel(T23) during Creep, *EPRI/DOE-Conference on Advanced in Life Assessment and Optimization of Fossil Power Plants*, Mar. 11-13, Orland FL, (2002)

[15] K. Kimura, K. Sawada, K. Kubo and H. Kushima : Influence of Stress on Degradation and Life Prediction of High Strength Ferritic Steels, *Proc. 2004 ASME Pressure Vessels and Piping Conference*, San Diego CA, PVP2004-2566, (2004), 11-18

[16] M. Nakashiro, S. Kihara, F. Kishimoto and T. Fujimori : Evaluation of Long-term Creep Strength of 2.25Cr-1Mo Heat Transfer Tube in Actual Service Stress Level Range, *ISIJ international*, 30(1990), 823-828

[17] R. Viswanathan and J. Foulds : Acceralated Stress Range Testing for Creep Life Prediction-Its Value and Limitation, *Journal of Pressure Vessel Technology*, 120, May 1998, 105-115

[18] T. Endo, J. Shi, H. Yoshizu and Y. Monma : Effect of Oxidation on the Long-term Creep Behavior of a 2.25Cr-1Mo Steel(in Japanese), *Tetsu to Hagané*, 83(1997), 742-747

[19] K. Miyata and Y. Sawaragi : Effect of Mo and W on the Phase Stability of Precipitations in Low Cr Heat Resistant Steels, *ISIJ international*, 41(2001), 281-289

[20] K. Maruyama, K. Sawada, J. Koike, H. Sato and K. Yagi : Examination of Deformation Mechanism Maps in 2.25Cr-1Mo Steel by Creep Tests at Strain Rate at 10^{-11} to 10^{-6} s^{-1}, *Materials Science and Engineering*, A224(1997), 166-172

[21] G. Dimmer, P. Weinert and H. Cerjak : Analysis of Steady State Creep Behaviour of 9-12% Chromium Ferritic-Martensitic Steels, *Materials Science and Technology*, 20(2004), 1525-1530

[22] R. W. Lund and W. D. Nix : High Temperature Creep of Ni-20Cr-2ThO_2 Single Crystals, *Acta Metallurgica*, 24(1976), 469-481

CREEP OF 0.5CrMoV STEEL AT VERY LOW STRAIN RATES

Luboš Kloc and Václav Sklenička

Institute of Physics of Materials
Academy of Sciences of the Czech Republic
Žižkova 22, CZ-61662 Brno, Czech Republic
e-mail: ⟨kloc@ipm.cz⟩

Abstract

Creep of 0.5CrMoV steel was investigated experimentally at temperatures from 560 to 625 ˚C and stresses below 100MPa. The conditions are similar to that of technical application of the steel, so creep rates are very low and beginning parts of creep curves can be only measured. The high sensitivity helicoid spring specimen technique was employed to record very small creep strains accurately.

The data are important for better description of the creep process, since the creep damage elements are nucleated during this very early creep stages. Extrapolation capability of a constitutive models of creep process are to be validated against the data; more precise description of the creep will lead to better estimation of design and residual creep lives of plant parts. In some special cases, where the creep strain itself is limiting the creep life of the part rather than creep failure the data are also valuable.

Keywords: low stress creep; primary creep; stress exponent; creep resistant steel; low alloy steel

Introduction

Current procedures for estimation of creep life of creep resistant steels are not reliable enough. The creep process is too slow at stresses and temperatures corresponding to industrial use of the steels, so laboratory experiments are accelerated by application of higher temperature and/or stress. Results have to be extrapolated to the application conditions, which is a source of potentially dangerous errors.

Since the creep damage elements like cavities and voids, which are able to growth to dangerous sizes, are nucleated during primary creep, the primary stage is important indicator of overall creep properties. Primary creep can be measured experimentally even at conditions close to application ones, if high strain sensitivity creep technique is employed. The results can be used for validation of creep constitutive models. The models should be able to describe the primary creep stage correctly. In other case, their reliability is questionable.

Evidences of changes in creep deformation mechanisms at conditions typical for the industrial application of creep resistant steels have been presented [1-4]. The aim of this work is to collect low strain rate creep data of the widely used (though obsolete) 0.5CrMoV creep resistant steel as a basis of improved creep life modelling under action COST-538.

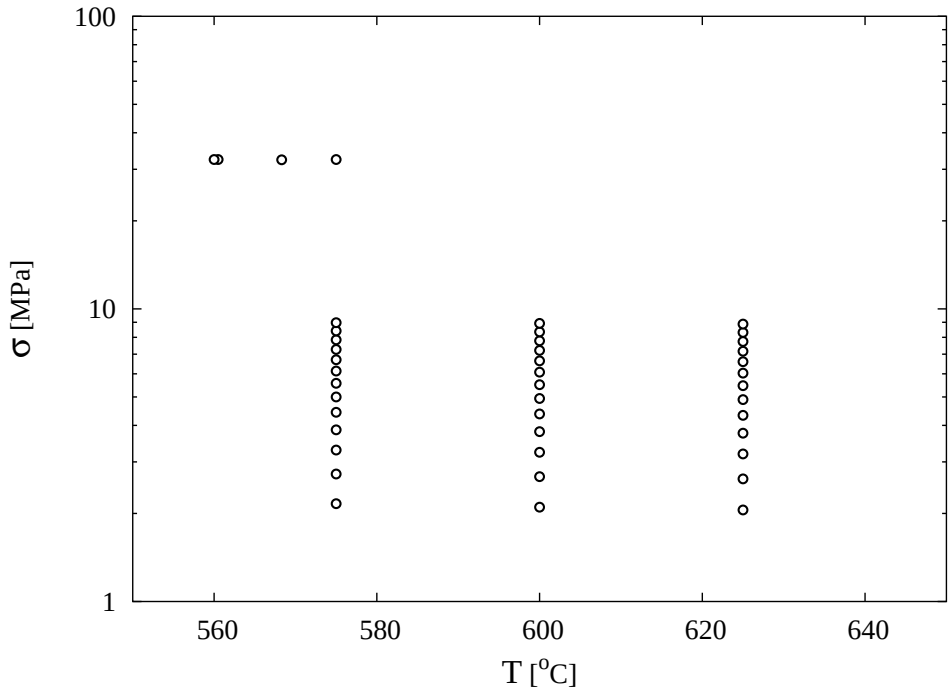

Fig. 1: *Stresses and temperatures of the creep tests*

Experimental material and procedure

Pipes of 0.5CrMoV low alloy steel (Czech designation ČSN 41 5128) was provided by Vítkovice Steel in "ready to use" condition. Chemical composition of the steel is summarized in the table I.

Cr	Mo	Si	Mn	V	C	Al	P	S
0.58	0.52	0.26	0.61	0.29	0.14	0.015	0.02	0.015

Table I: *Chemical composition of the steel in mass %*

Helicoid spring specimen technique [5] was used for creep testing. Purified argon was used for protective atmosphere to prevent oxidation since the technique is sensitive to surface quality. Helicoid spring specimens with square cross section of the "wire" were prepared by careful machining from the pipes to preserve original microstructure of the steel. Creep tests were conducted at temperatures from 560 to 625 °C and stresses from 3 to 32 MPa, testing conditions are plotted in figure 1. Since the stress and strain in the testing technique are essentially the shear ones, they were recalculated to the equivalent tensile quantities using von Mises criterion, that is $\sigma = \sqrt{3}\tau$ and $\varepsilon = \gamma/\sqrt{3}$.

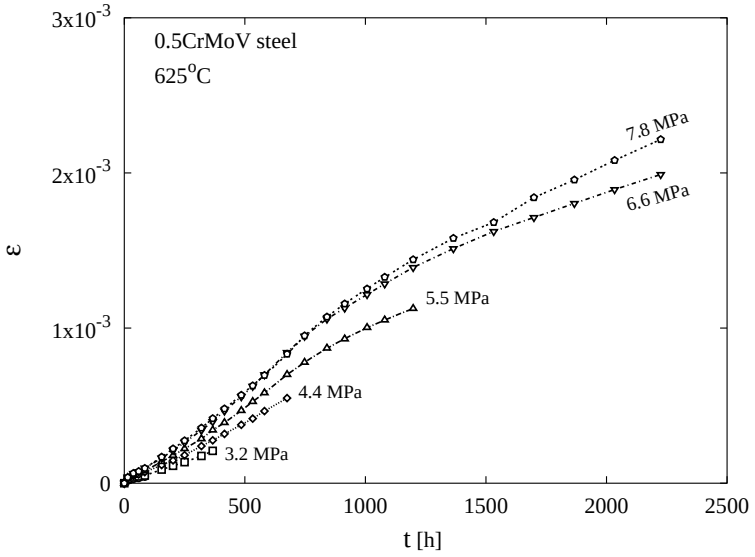

Fig. 2: *Primary creep curves at* $625\,^{\circ}\mathrm{C}$ *and stresses below* $10\,\mathrm{MPa}$.

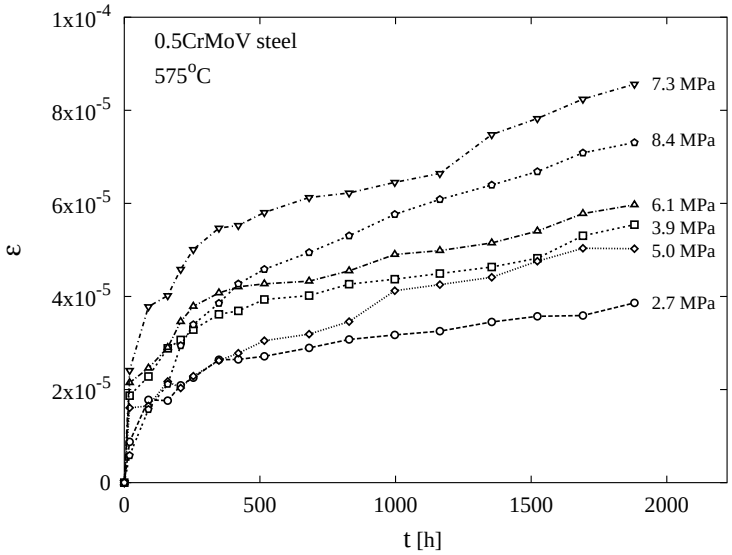

Fig. 3: *Primary creep curves at* $575\,^{\circ}\mathrm{C}$ *and stresses below* $10\,\mathrm{MPa}$.

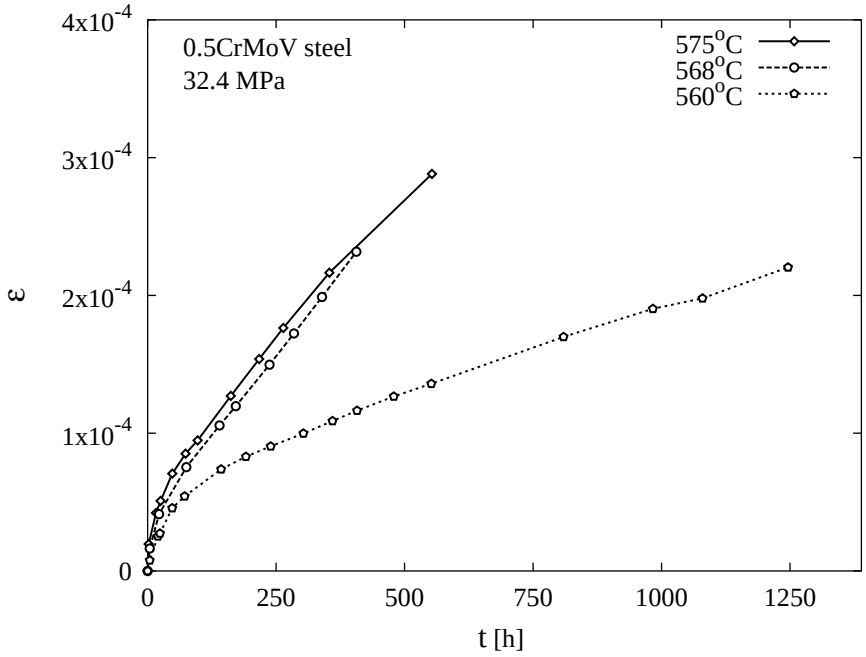

Fig. 4: *Primary creep curves at* $32.4\,\mathrm{MPa}$.

Results

Primary creep flow is measurable for all selected temperatures and stresses. Examples of creep curves recorded in the experiments are depicted in figures 2 to 4. At stresses around 30 MPa, the creep curves exhibit "normal" primary behaviour with decreasing creep rate. Contrary, with low stress experiments below 10 MPa the shape of creep curves is sigmoidal, mainly at temperatures above $600\,^{\circ}\mathrm{C}$.

Discussion

Creep curves

Creep curves of the 0.5CrMoV steel are more complicated than that of P-91 steel [4] and exhibit creep acceleration stage after initial decrease of creep rate. It can be seen from figure 5, that this acceleration occurs at low stresses at all tested temperatures, though it is most pronounced at highest tested temperature of $625\,^{\circ}\mathrm{C}$. On the other hand, the effect is missing at higher stresses of 32.4 MPa. The acceleration clearly indicate the microstructural insability of the steel mainly at higher temperatures. There is no detailed explanation for the effect in the moment; testing of aged specimens is considered as next step.

Creep rate

Creep rate of the steel is about eight times higher than that of P-91 steel at the same conditions.

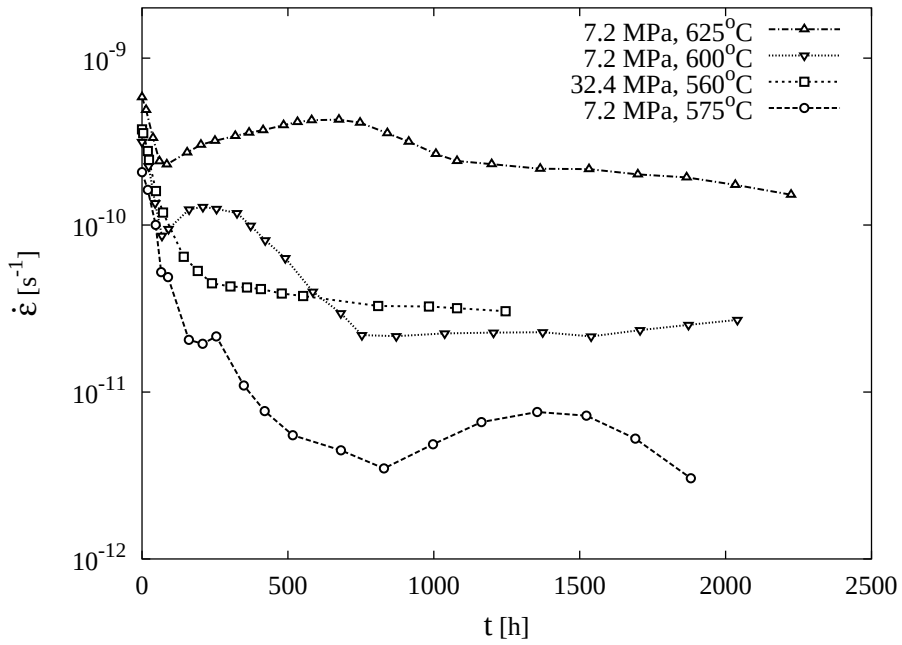

Fig. 5: *Creep rates evolving in time.*

Stress and temperature dependencies of "stabilized" creep rates after approximately 2000 hours of testing are plotted in figures 6 and 7, respectively.

The apparent stress exponent is close to 1 for low stresses and temperatures 600 °C and lower, while at 625 °C the value is about 2.5. Transition to power-law creep with higher stress exponent at stresses around 30 MPa is indicated. Temperature dependence of the creep rate can be expressed by apparent activation energy Q_a defined as

$$Q_a = \frac{\partial \left(\ln \left(\dot{\varepsilon}\right)\right)}{\partial \left(\frac{1}{RT}\right)}.$$

Apparent activation energy seems to be stress dependent and the values are clearly higher than that obtained with previously tested steels P-91 and AISI-316H [4].

The results indicate that there is transition between various creep deformation mechanisms at selected conditions, depending on both stress and temperature values.

Conclusion

Primary creep of 0.5CrMoV steel was investigated at stresses below 35 MPa and temperatures between 560 and 625 °C . Results can be summarized as follows:

- Creep rate is about eight times higher than that of P-91 steel at the same conditions.

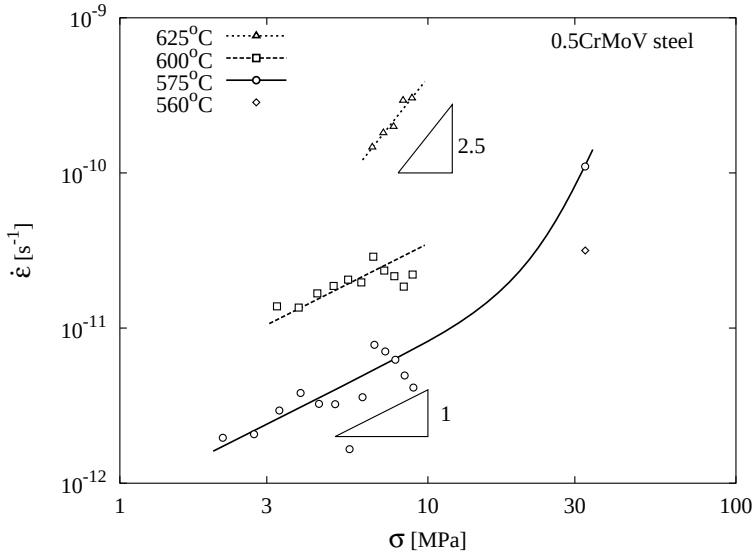

Fig. 6: *Stress dependencies of creep rates.*

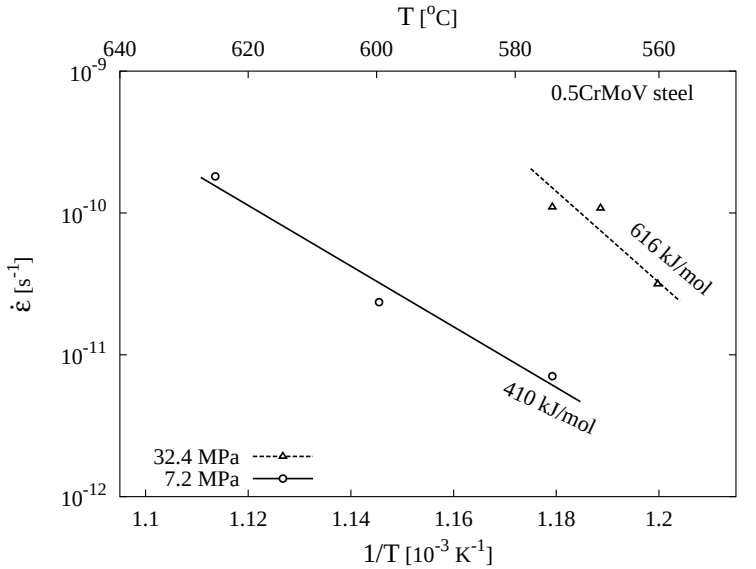

Fig. 7: *Temperature dependencies of creep rates with corresponding Q_a values.*

- After initial decrease of the creep rate, some acceleration of the creep process occurs at stresses below 10 MPa, while no such effect was observed at higher stresses.
- "Viscous" creep with stress exponent about 1 occurs at lowest stresses and temperatures, but higher values of stress exponent are obtained when either stress or temperature is higher.
- The temperature dependence of the creep curves shapes observed makes large difference from previously investigated steels of P-91 and AISI-316H types.
- The stress and temperature range seems to cover complex transitions of creep deformation mechanisms. Correct modelling of the processes may be very difficult.

Acknowledgment

This work was supported by the Ministry of Education of the Czech Republic under contract no. 1P05OC006.

References

[1] T. Sritharan and H. Jones: The creep of type 304 stainless steel at low stresses, Acta Metall. 28 (1980), 1633
[2] T. Sritharan and H. Jones: Creep of type 316 stainless steel at low stresses, Metal Sci. 15 (1981), 365 the Metals Society, London 1984, p. 291
[3] J. Fiala, L. Kloc and J. Čadek: Creep in Metals at Intermediate Temperatures and Low Stresses - A Review, Mater. Sci. Eng. A 137, (1991), 163
[4] L.Kloc, V. Sklenička and J. Ventruba: Comparison of low stress creep properties of ferritic and austenitic creep resistant steels, Mater. Sci. Eng. A319-321 (2001), 774
[5] J. Fiala and J. Čadek: Diffusional creep in iron at homologous temperatures in the vicinity of 0.53, Kovove Mater. 20 (1982), 277

IMPROVEMENT IN CREEP STRENGTH OF HEAT RESISTANT FERRITIC STEEL STRENGTHENED BY INTERMETALLIC COMPOUND

Yoshiaki Toda[(a)], Hideaki Kushima[(a)], Kazuhiro Kimura[(b)], Fujio Abe[(a)]

[(a)]National Institute for Materials Science
1-2-1, Sengen, Tsukuba, Ibaraki 305-0047, Japan
[(b)]National Institute for Materials Science
2-2-54, Nakameguro, Meguro-ku, Tokyo 153-0061, Japan
TODA.Yoshiaki@nims.go.jp

Abstract

The effects of nickel content and heat treatment conditions on the creep strength of precipitation-strengthened 15Cr ferritic steel were investigated. The creep strength of the 15Cr ferritic steel was drastically improved by solution treatment and water quenching. However, over the long term, the detrimental effect of nickel on the creep strength was pronounced for water-quenched steels. The volume fraction of martensite phase increased with increased nickel content in both the furnace-cooled and water-quenched steels. The volume fraction of martensite phase in the water-quenched steel was smaller than that in the furnace-cooled type, even for the same nickel content. Fine particles, smaller than 500 nm, were precipitated homogeneously within the ferrite phase of the water-quenched steel. On the other hand, coarse block-like particles 1 μm in size were precipitated sparsely within the martensite phase, and the recovery of martensitic microstructure was accelerated. The creep strength of the steels decreased with increased volume fraction of the martensite phase caused by furnace cooling and nickel addition. The lower creep strength and microstructural stability of the martensite phase is attributable to less precipitation strengthening. To enable this steel to be put to practical use, it will be necessary to suppress the formation of the martensite phase caused by addition of nickel by optimizing the chemical composition and heat treatment conditions.

Keywords: creep; ferrite matrix; furnace cooling; intermetallic compound; martensite phase; nickel content; recovery; water quenching

1. Introduction

To save fossil fuel resources and reduce CO_2 emissions, considerable efforts have been directed towards the research and development of high-strength, creep-resistant steels and alloys to improve the energy efficiency of power plants [1]. Since the energy efficiency of fossil fuel-burning power plants can be improved by increasing their steam temperature and pressure, high-strength, heat-resistant materials need to be developed. Ferritic heat-resistant steel is suitable for large and thick structural components that are exposed to high temperatures, such as headers and main steam pipes, so it is in wide use in power plants. The microstructure of conventional ferritic heat-resistant steel is usually tempered martensite strengthened by numerous precipitates of carbide and MX-type carbonitride. However, microstructural degradation due to preferential recovery at the vicinity of prior austenite grain boundaries results in decreased creep strength, especially in the long term [2-4]. Both creep strength and oxidation resistance need to be improved in high-temperature structural materials to enable them to withstand higher steam temperatures and pressures. Although chromium is the most effective alloying element for improving oxidation resistance, maximum chromium concentration is restricted to about 11 mass% and below in conventional high strength ferritic

heat-resistant steel to avoid the formation of δ-ferrite, a phase that is detrimental to creep strength and fracture toughness. Improvements in both long-term creep strength and oxidation resistance are important for the development of high strength ferritic heat-resistant steel.

The improvement in long-term creep strength of a 15Cr ferritic steel with an annealed ferrite matrix instead of a tempered martensitic microstructure in conventional ferritic heat-resistant steels has been investigated from the above perspectives [5-11]. Kimura et al. reported that the creep strength of 15Cr ferritic steel could be improved by additions of tungsten and cobalt through precipitation-strengthening effects of intermetallic compounds [5-8]. Toda et al. found that concentrations of carbon and nitrogen strongly affect the stability of microstructures in precipitation-strengthened 15Cr ferritic steel [9]. It has been discovered that higher long-term creep strength in the 15Cr steel than that of conventional steels could be obtained by optimizing carbon and nitrogen content through small coarsening rates of fine particles and homogeneous distribution of those without precipitation-free zones [9]. Moreover, it was found that the addition of nickel and an increase in cooling rate from the annealing temperature improved the impact toughness of precipitation-strengthened 15Cr ferritic steel, although it has been pointed out that 15Cr steel has the drawback of poor toughness due to the presence of ferrite matrix [10, 11]. However, the effects of nickel content and rapid cooling on creep strength of the 15Cr steel have not yet been sufficiently elucidated. The aim of the present study is, therefore, to investigate the effects of nickel content and heat treatment conditions on the creep strength of a precipitation-strengthened 15Cr ferritic steel.

2. Experimental procedure

The chemical compositions of the steels used in the present study are shown in **Table 1**. The base material was nickel-free 0.05C-15Cr-1Mo-0.2V-0.05Nb-6W-3Co-0.04N-0.003B (mass%) steel, which possessed superior creep strength [9]. The other five steels used contained 0.4, 0.8, 1.2, 1.6 and 2.0 mass% nickel. These steels were prepared in a vacuum induction furnace. Ingots with a weight of 10 kg were hot forged into bars 15 mm in diameter and solution-treated for 30 min at 1473 K followed by furnace cooling. Water-quenched steels were also used to investigate the effects of heat treatment on the creep strength.

Table 1. Chemical compositions of the steels used in the present study (mass%).

	C	Ni	Cr	Mo	W	V	Nb	Co	N	B
Base	0.046	<0.01	15.00	1.00	6.07	0.19	0.043	2.97	0.033	0.0030
0.4Ni	0.047	0.42	14.93	1.00	6.05	0.20	0.050	2.96	0.041	0.0029
0.8Ni	0.048	0.78	15.00	1.00	6.05	0.20	0.050	2.96	0.042	0.0029
1.2Ni	0.049	1.21	15.02	1.00	6.04	0.20	0.051	2.96	0.042	0.0028
1.6Ni	0.048	1.60	15.00	1.00	6.03	0.20	0.050	2.95	0.044	0.0026
2.0Ni	0.048	2.00	14.96	0.99	6.07	0.20	0.050	2.98	0.036	0.0029

The dimensions of the creep test specimen were 6 mm in gauge diameter and 30 mm in gauge length according to Type 14A of the Japanese Industrial Standard (JIS) Z 2201 [12]. Creep tests were conducted at 923 K and over a range of stresses from 100 MPa to 240 MPa up to about 25000 h in air. Creep deformation was measured using an extensometer attached to the gauge portion of the specimen. The microstructure of the specimens was examined under an optical microscope (OM), a scanning electron microscope (SEM), and a transmission electron

microscope (TEM). Concentrations and structures in the matrix and precipitates were measured using energy-dispersive X-ray fluorescence spectrometry (EDX) and X-ray analysis. "Thermo-Calc" thermodynamic calculation software was used to predict the mole fractions of equilibrium phases in the steels.

3. Results

3.1. Creep strength

Figure 1 shows stress vs. time-to-rupture curves at 923 K of the furnace-cooled and the water-quenched steels with various nickel contents. The curve for 9Cr-0.5Mo-1.8W-V-Nb steel (ASME T92), which is conventional ferritic heat-resistant steel with a tempered martensitic microstructure, and which possesses the highest creep strength of the conventional steels [13], is also shown by the dashed curve in the same Figure. Regardless of nickel content, the creep strength of the furnace-cooled steels was slightly higher than that of ASME T92 [13]. Moreover, the creep strength of the 15Cr steel was drastically improved by solution treatment and water quenching regardless of Ni content; notably, the creep rupture life of the water-quenched 0.4Ni steel was 9203.6 h at 200 MPa. The creep strength at 10^4 h of this steel was double that of the conventional version, and the creep rupture life at 200 MPa was extended by a factor of approximately 1000. However, time to rupture of the water-quenched steels tended to decrease with increased nickel concentration, and the slope of the curves increased under low stress over the long term.

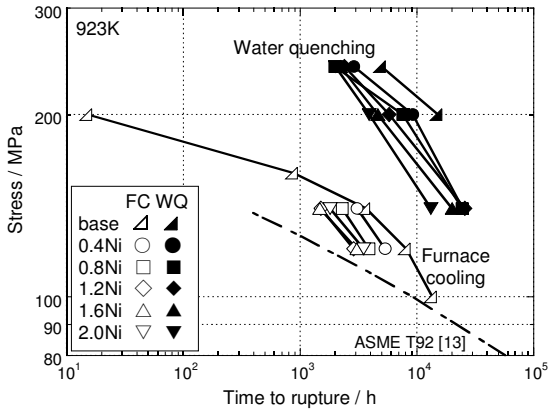

Fig. 1. Stress vs. time to rupture curves of the furnace-cooled and the water-quenched steels with the various nickel contents and the conventional heat resistant steel [13] at 923 K.

Figure 2 shows creep rate vs. time curves of the furnace-cooled base steel and the water-quenched steels with various nickel contents at 140 MPa and 923 K. The water-quenched base steel had not yet ruptured after 16000 h under these stress conditions. The creep rates of the water-quenched steels were about one tenth that of the furnace-cooled version just after loading, and continued to decrease during the transient creep stage. The creep rupture lives of the water-quenched steels extended to longer than those of the furnace-cooled versions.

However, among the water-quenched steels, the onset time of the accelerating creep stage and creep rupture lives tend to shorten with increased nickel content.

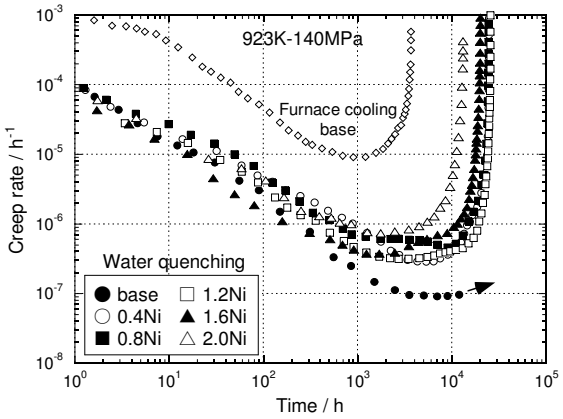

Fig. 2. Creep rate vs. time curves of the furnace-cooled base steel and the water-quenched steels with the various nickel contents at 140 MPa and 923 K.

Figure 3 shows rupture elongation and reduction of area of the water-quenched steels ruptured at 923 K and the various stress conditions as a function of time to rupture. It was found that the addition of nickel improved the elongation and slightly improved the reduction of area.

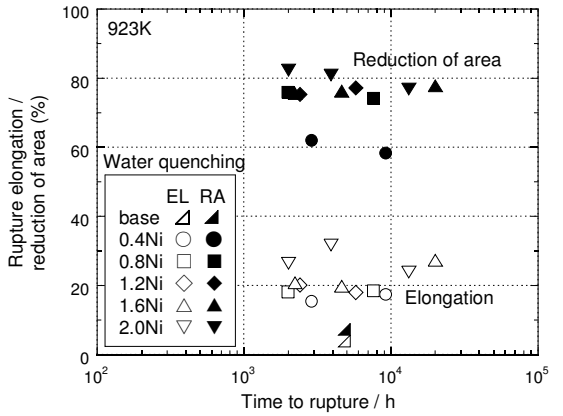

Fig.3. Rupture elongation and reduction of area of the water-quenched steels ruptured at 923 K and the various stress conditions as a function of time to rupture.

Creep strength of the precipitation-strengthened 15Cr ferritic steel was drastically increased by the solution treatment and water quenching, and nickel addition improved rupture elongation and slightly improved the reduction of area of the steel. However, nickel content was found to be detrimental to the creep strength of the water-quenched steel over the long term.

3.2. Microstructure

3.2.1. Effect of heat treatment

Figure 4 shows OM images of (a) 0.0Ni; (b) 1.2Ni; (c) 2.0Ni steels after furnace cooling, and (d) 0.0Ni; (e) 1.2Ni; (f) 2.0Ni steels after water quenching. V_f marked on each photo indicates the volume fraction of the martensite phase. After furnace-cooling, a dense distribution of precipitates along the grain boundaries and coarse particles within the grains was observed in the base steel (Fig. 4 (a)). Some coarse block-type precipitates were formed on the grain boundaries of Ni-added steels (Fig. 4 (b), (c)). These precipitates in the furnace-cooled steels appear to have been formed during furnace cooling. On the other hand, precipitates were not clearly observed in the water-quenched steels, regardless of nickel content (Fig. 4 (d)–(f)). Rapid cooling appears to suppress the formation of coarse precipitates in the water-quenched steels.

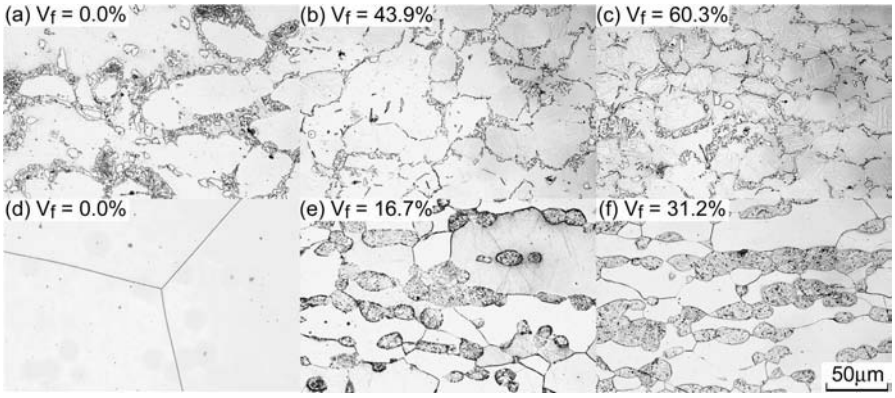

Fig. 4. OM images of (a) base; (b) 1.2 %Ni; (c) 2.0 %Ni steels in the as furnace-cooled condition and (d) base; (e) 1.2 %Ni; (f) 2.0 %Ni steels in the as water-quenched condition. V_f inserted into each photo stand for the volume fractions of martensite phase.

X-ray diffraction analysis and concentration measurement by EDX were conducted to identify the precipitates in the furnace-cooled base steel aged isothermally for 1000 h and 923 K. By comparing the profiles of **Fig. 5** with the Joint Committee on Powder Diffraction Standards cards, the peaks were identified as those from the χ-phase ($Fe_{36}Cr_{12}W_{10}$), the μ-phase (Fe_7W_6), the Laves phase (Fe_2W), which are intermetallic compounds classified into a topologically close-packed (TCP) phase [14], and a carbide ($M_{23}C_6$). **Figure 6** shows the concentrations of precipitates measured by EDX with TEM, and each horizontal bar indicates the concentration of each precipitate. These chiefly comprised iron, chromium, molybdenum and tungsten, and were identified by X-ray analysis and concentration measurement as the χ-phase or Laves

phase, in which where chromium is in solid solution. The same intermetallic compounds appeared to be present in the furnace-cooled and nickel-added steels.

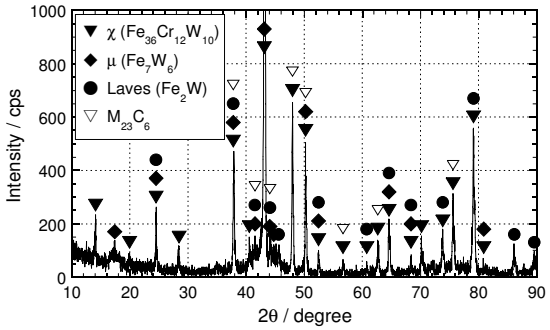

Fig. 5. X-ray diffraction profile of electrolytically extracted residue of the furnace-cooled base steel aged isothermally for 1000 h at 923 K.

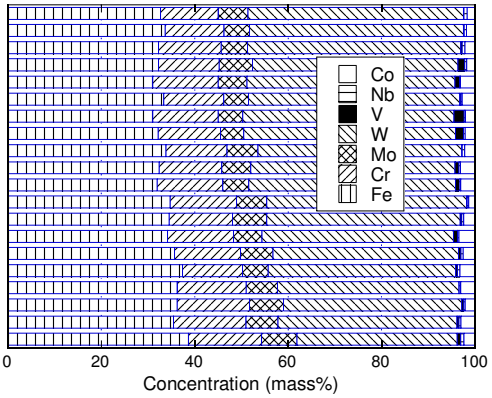

Fig. 6. Concentrations of the precipitates measured by EDX with TEM for the furnace-cooled base steel aged isothermally for 1000 h at 923 K. Each horizontal bar stands for concentrations of each precipitates.

Although the martensite phase was not observed in the furnace-cooled base steel (Fig. 4 (a)), it was observed within some grains with contrasts of block or packet boundaries in nickel-containing steels, and the volume fraction of martensite phase increased with increased nickel content (Fig. 4 (b), (c)). No martensite phase was detected in the water-quenched base steel (Fig. 4 (d)). However, many martensite phase grains 20–30 μm in diameter were observed along the grain boundaries of coarse ferrite grains with dark contrast in both the water-quenched and nickel-containing steels (Fig. 4 (e), (f)). As with the furnace-cooled steels, an increase in the volume fraction of the martensite phase was observed with increased nickel

content in the water-quenched steels. The martensite phase was clearly observable in the water-quenched steels by its dark contrast; however, unlike in the furnace-cooled steels, the volume fraction of martensite phase in the furnace-cooled steels was about double that in the water-quenched version, even for the same nickel concentration.

It is thought generally that martensitic transformation requires a high cooling rate. The reason for the volume fraction of the martensite phase in the furnace-cooled steels being higher than that in the water-quenched steels can be assumed from temperature-dependence of the equilibrium fraction of the austenite phase. The solid curves in **Fig. 7** show calculated mole fractions of the austenite phase in these steels with the various nickel concentrations over a range of temperatures between 800 K and 1600 K. The open circles in the same Figure show the experimental volume fraction of martensite phase after water quenching from the solution-treated temperature of 1473 K. The mole fractions of the austenite phase at 1473 K were calculated to be about 5% in 1.2%Ni steel and 18% in 2.0%Ni steel, and were found to correspond to the experimental volume fractions of the martensite phase under water-quenched conditions. Moreover, it was indicated by calculation that the maximum mole fraction of the austenite phase was formed at the range of temperatures from 1173 K for 2.0%Ni steel to 1313 K for base steel. Therefore, the volume fraction of austenite phase increased during furnace cooling from the annealing temperature of 1473 K, and was followed by martensitic transformation at low temperature. On the other hand, the specimens were cooled quickly before the forming of the austenite phase in the water-quenched steels, which resulted in a higher volume fraction of martensite phase being seen in the furnace-cooled steels than in the water-quenched versions.

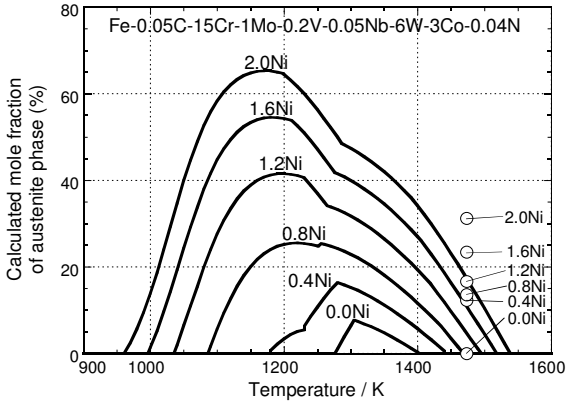

Fig. 7. The solid curves show changes in the calculated equilibrium mole fractions of austenite phase of the steels containing the various nickel contents with temperature. Open circles show the experimental volume fractions of martensite phase after water quenching.

3.2.2. Effect of Ni content on water-quenched steels

Figure 8 shows SEM images of the water-quenched (a) 0.4%Ni; (b) 1.2%Ni and (c) 2.0%Ni steels creep-ruptured at 923 K and 200 MPa. t_r marked on each image indicates times to

rupture. The grains 20–30 μm in size observed in the bottom half of each photo of Fig. 8 (b) 1.2%Ni steel and (c) 2.0%Ni steel are martensite phase that appears to have been transformed from the austenite phase at 1473 K or during water quenching. All of the matrix except for the martensite phase is the ferrite phase. Many particles smaller than 500 nm, which were supposed to have been precipitated during creep exposure, were observed homogeneously within the ferrite matrix in all the steels and remained small, even after several thousand hours of creep exposure. On the other hand, coarsened block-like particles 1 μm in size were precipitated sparsely within the martensite phase. With increased nickel content, the volume fraction of martensite phase increased, and the microstructure of the steels became markedly heterogeneous.

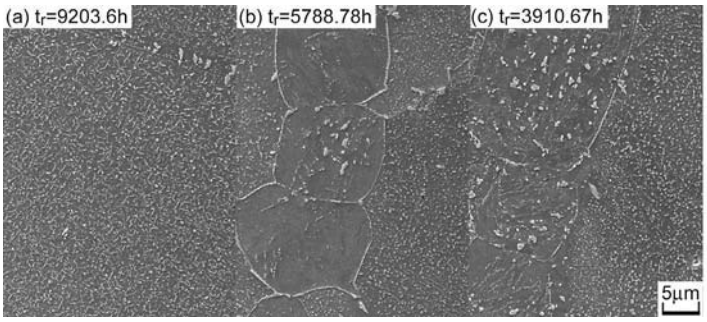

Fig. 8. SEM images of the water-quenched (a) 0.4% Ni; (b) 1.2% Ni; (c) 2.0% Ni steels creep-ruptured at 923 K and 200 MPa. t_r inserted into each photo stand for the time to rupture.

Table 2 shows the average compositions of the ferrite and the martensite phase in the 2.0%Ni steel after water-quenching measured by EDX. Elements accounting for less than 1 mass% were not measured. As a result, the concentration of nickel, which is an austenite former element, was higher in the martensite phase, and concentrations of tungsten and molybdenum, which are ferrite former elements, were lower than those in the ferrite phase. It is assumed that these elements were distributed to each phase at the solution treatment temperature of 1473 K.

Table 2. Average compositions of the martensite and the ferrite phase of 2.0 %Ni steel in the as water-quenched condition (mass%).

	Fe	Ni	Cr	Mo	W	Co
Martensite phase	71.5	3.7	13.8	0.9	6.9	3.2
Ferrite phase	66.3	1.6	14.5	1.7	13.3	2.6

The precipitates of the 15Cr ferritic steel shown in Fig. 8 have been identified as topologically close-packed (TCP) phases, such as the Laves phase, χ phase and μ phase [5-9]. **Figure 9** shows changes at 923 K in the calculated equilibrium mole fractions of TCP phases with nickel concentration of the steels containing different tungsten content. The equilibrium mole fractions of TCP phases decreased in proportion as nickel concentration increased to 1.2

mass%. It was no surprise that the mole fractions of these phases were small in steels with a low tungsten content. Therefore, since the driving force available for precipitation of TCP phases decreased through the high content of nickel and the low content of tungsten by element distribution at the solution treatment temperature, the coarsened precipitates were formed heterogeneously in the martensite phase.

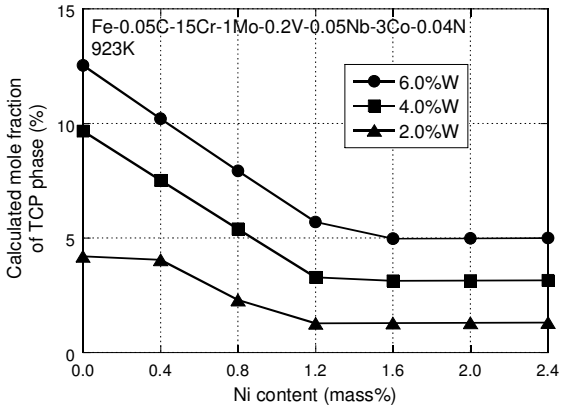

Fig. 9. Changes in the calculated equilibrium mole fractions of TCP phases with nickel concentration of the steels containing various tungsten contents at 923 K.

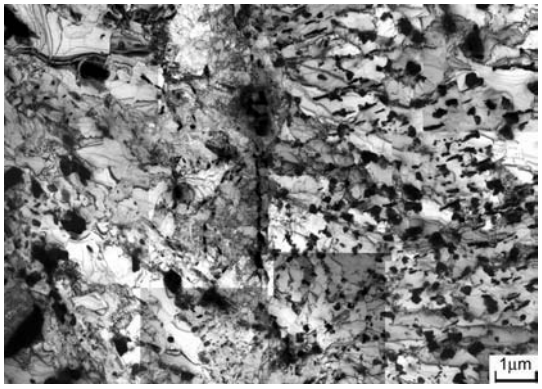

Fig. 10. TEM image of the 0.4 mass% Ni steel creep-ruptured at 923 K and 200 MPa for 9203.6 h.

Figure 10 shows a TEM image of 0.4%Ni steel creep-ruptured at 923 K and 200 MPa. A grain boundary can be observed vertically in the middle of the image. The grain on the right of the boundary is ferrite phase, and on the left is martensite phase. Numerous precipitates

smaller than 500 nm were formed homogeneously within the ferrite grain. Also, many dislocations, which appeared to be formed during martensitic transformation, are observed within the martensite grain. However, microstructural recovery progressed in parts of the martensite phase, and areas without precipitates and dislocations were also observed.

The creep strength of the furnace-cooled steels and the nickel-added steels, the volume fraction of the martensite phase in which was relatively large, was inferior, and the recovery of the martensitic microstructure was observed in the creep-ruptured steels. Therefore, martensitic recovery appears to be a cause of the decrease in creep strength of the precipitation-strengthened 15Cr ferritic steels.

4. Discussion

The results of the creep tests and microstructural observations in the present study show that the creep strength of the precipitation-strengthened 15Cr ferritic steel was closely related to the martensite phase and precipitates, i.e., creep strength was weakened with increased volume fraction of the martensite phase and coarse block-type precipitates.

It is generally believed that intermetallic compounds such as the Laves phase are ineffective in improving creep strength in conventional ferritic heat-resistant steels using tempered martensite because of the large coarsening rate of the Laves phase [15, 16]. However, in the 15Cr ferritic steel based on ferrite matrix, the coarsening of intermetallic compounds is slower than that in conventional steels, and their thermal stability is high [9], as is clear from Fig. 8. The precipitation-strengthening effect of fine precipitates and their thermal stability in the ferrite matrix are assumed to be effective in the extension of the creep rupture lives. However, the sparse distribution of coarse block-type particles in the martensite phase reduces the precipitation strengthening effect. Therefore, the solution treatment and water quenching were particularly effective in improving the creep strength, since the faster cooling rate than furnace cooling suppresses the formation of coarse block-type precipitates and the martensite phase. The addition of nickel, which is effective in improving the impact toughness of the 15Cr ferritic steel [10, 11], had no effect of extending the creep rupture life, since nickel is an austenite former element, and nickel addition increases the volume fraction of the martensite phase and reduces the precipitation strengthening effect.

Almost all these previous studies noted the detrimental effect of nickel on long-term creep strength, as has the present study. However, the addition of more nickel than 1 mass% was required to maintain the high impact toughness of the 15Cr ferritic steel [10, 11]. Therefore, to apply the precipitation-strengthened 15Cr ferritic steel to practical use, it is necessary for the formation of the martensite phase to be suppressed in the solution-treated steels with the addition of nickel by optimization of the chemical composition and heat treatment conditions, such as by reduction of other austenite former elements from the chemical composition or solution treatment at higher temperatures.

5. Conclusions

The effects of nickel content and heat treatment conditions on the creep strength of the precipitation-strengthened 15Cr ferritic steel were investigated and the following conclusions obtained.

(1) The creep strength of the 15Cr ferritic steel was drastically improved by the solution treatment and water quenching. The creep strength at 10^4 h of 0.4%Ni steel was doubled, and the creep rupture life at 200 MPa was extended by a factor of about 1000 over the conventional version. However, for the water-quenched steels, over the long term, the detrimental effect of nickel on the creep strength was pronounced.

(2) Although coarse block-type precipitates were observed in the furnace-cooled steels, they were not clearly detectable in the water-quenched steels. The volume fraction of the martensite phase increased with increased nickel content in both the furnace-cooled and water-quenched steels. The volume fraction of the martensite phase in the water-quenched steel was smaller than that in the furnace-cooled version, even at the same nickel content.

(3) Fine particles smaller than 500 nm were precipitated homogeneously within the ferrite phase of the water-quenched steel. On the other hand, coarse block-like particles 1 μm in size were precipitated sparsely within the martensite phase. Recovery of the martensitic microstructure was accelerated.

(4) The martensitic recovery appears to be a cause of decrease in creep strength of precipitation-strengthened 15Cr ferritic steel. Therefore, to enable this steel to be put to practical use, it will be necessary to suppress the formation of the martensite phase caused by addition of Ni by optimizing the chemical composition and heat treatment conditions.

Acknowledgments
This work was supported by Industrial Technology Research Grant Program in 2003 from the New Energy and Industrial Technology Development Organization (NEDO) of Japan.

References

[1] F. Masuyama: “History of Power Plants and Progress in Heat Resistant Steel”, ISIJ Int., Vol. 41, (2001), p. 612.
[2] T. Matsuo, K. Kimura, R. Tanaka and M. Kikuchi: “Degradation of Cr-Mo-1/4V Steel at High Temperatures”, Proc. of the 4th Int. Conf. on Creep and Fracture of Engineering Materials and Structures, Institute of Materials, London, (1990), p. 477.
[3] K. Kimura, H. Kushima and F. Abe: “Heterogeneous Changes in Microstructure and Degradation Behavior of 9Cr-1Mo-V-Nb Steel During Long Term Creep”, Key Eng. Mater., Vol. 171-174, (2000), p. 483.
[4] K. Kimura, H. Kushima, F. Abe, K. Suzuki, S. Kumai and A. Satoh: “Changes in Precipitates of Modified 9Cr-1Mo Steel During Long-Term Creep Deformation at 873K and 923K”, Proc. of the 7th Int. Conf. on Creep and Fatigue at Elevated Temperatures, JSME, Tokyo, (2001), p. 335.
[5] K. Kimura, K. Seki, Y. Toda and F. Abe: “Development of High Strength 15Cr Ferritic Creep Resistant Steel with Addition of Tungsten and Cobalt”, ISIJ Int., Vol. 41, (2001), p. S121.
[6] K. Kimura, K. Seki, Y. Toda and F. Abe: “Development of High Strength 15Cr Creep Resistant Steel for Low Emission Power Plant”, J. of Advanced Sci., Vol. 13, (2001), p. 294.

[7] Y. Toda, K. Seki, K. Kimura and F. Abe: “Effects of W and Co on the Microstructure and Creep Strength of the Precipitation Strengthened 15Cr Ferritic Steels”, JSME Int. J., Vol. A45, (2002), p. 25.
[8] Y. Toda, K. Seki, K. Kimura and F. Abe: “Effects of W and Co on Long-term Creep Strength of Precipitation Strengthened 15Cr Ferritic Heat Resistant Steels”, ISIJ Int., Vol. 43, (2003), p. 112.
[9] Y. Toda, H. Tohyama, H. Kushima, K. Kimura and F. Abe: “Improvement in Creep Strength of Precipitation Strengthened 15Cr Ferritic Steel by Congrolling Carbon and Nitrogen Contents”, JSME Int. J., Vol. A48, (2005), p. 35.
[10] Y. Toda, H. Kushima, K. Kimura and F. Abe: “Improvement in Creep Strength and Impact Toughness of Advanced Creep Resistant Steel Based on Ferrite Matrix”, Trans. Mater. Res. Soc. Jpn., Vol. 29, (2004), p. 3485.
[11] Y. Toda, H. Tohyama, H. Kushima, K. Kimura and F. Abe: “Influence of Chemical Composition and Heat Treatment Condition on Impact Toughness of 15Cr Ferritic Creep Resistant Steel”, JSME Int. J., Vol. A48, (2005), p. 125.
[12] Japanese Industrial Standard, “Test Pieces for Tensile Test for Metallic Materials: JIS Z 2201”, Japanese Standard Association, Tokyo, (1998).
[13] Data Package for NF616 Ferritic Steel (9Cr-0.5Mo-1.8W-Nb-V), Second Edition, Nippon Steel Corporation, Tokyo, (1994).
[14] F. C. Frank and J. S. Kasper: “Complex Alloy Structures Regarded as Sphere Packings. I. Definitious and Basic Principles”, Acta Cryst., Vol. 11, (1958), p. 184.
[15] H. Cerjak, P. Hofer and B. Schaffernak: “The Influence of Microstructure Aspects on the Service Behaviour of Advanced Power Plant Steels”, ISIJ Int., Vol. 39, (1999), p. 874.
[16] K. Kimura, H. Kushima, F. Abe, K. Suzuki, S. Kumai and A. Satoh: “Microstructural Change and Degradation Behaviour of 9Cr-1Mo-V-Nb Steel in the Long Term”, Proc. of the 5th Int. Charles Parsons Turbine Conf., Institute of Materials, London, (2000), p. 590.

SUPERIOR LONG-TERM CREEP BEHAVIOUR AND MICROSTRUCTURAL EVOLUTION OF 9%Cr-STEELS WITH BORON

F. Kager[1)], N. Böck[1)], K. Spiradek-Hahn[1)], S. Höfinger[1)], M. Brabetz[1)], and G. Zeiler[2)]
[1)]ARC Seibersdorf research GmbH, A-2444-Seibersdorf, Austria
[2)]G. Zeiler, BÖHLER EDELSTAHL GmbH, Kapfenberg, Austria

franz.kager@arcs.ac.at

Abstract

To improve the long-term creep resistance of the steel grades containing 9-12%Cr numerous materials concepts have been proposed. However, the realisation of the desired materials properties is very difficult because of a high complexity of factors influencing the material stability during exposure. Therefore the long-term experimental creep tests in combination with the systematic investigation and evaluation of microstructural changes during creep will give the basis for understanding of creep mechanisms and for further improving of the materials in respect to creep strength. This paper concentrates on 9%Cr steels alloyed with boron. Very long-term creep strength data (up to about 99000h) at 600 and 650°C will be presented with the appropriate analysis of the creep behaviour (e.g. creep rate analysis). The qualitative and quantitative examinations of microstructure will be carried out after different periods of creep deformation in order to describe the microstructural stability of the material. The analysis of microstructural data in correlation with the experimentally observed creep behaviour enables the understanding of on going processes and mechanisms during creep and shows how the microstructural elements on submicro- and nano- scale can steer the macroscopic materials behaviour. It will be shown that the expected excellent creep strength of forged 9%Cr steels with boron has been realised. The reasons for this behaviour will be discussed.

Keywords: 9-12% Cr steels, creep, microstructure, boron

1 Introduction

A lot of work has been done in recent years to improve the long term creep resistance of 9-12%Cr steels for power plant applications. Different material concepts were proposed. However, the realisation of the expected materials requirements is very difficult because of a high complexity of factors influencing the material stability. In recent years especially 9% Cr steels alloyed with Boron and Cobalt are investigated. In the working group COST 501 creep strength of 100MPa at 600°C for 100000h was defined as development goal, this goal was extended to 650°C in the working group Cost 522.

The two boron (about 100ppm) alloyed steels B2 and FB2, which seems most promising to reach at least the first of these goals (100 MPa, 600°C), have reached until now testing times of approximately 99500 hours (B2) respectively 65800 (FB2).
The results of creep test evaluation and microstructural characterisation at shorter loading where already published elsewhere [1], [2], [3], [4]. In these papers it has been demonstrated that FB2 exhibits better creep behaviour than B2 at 650°C. In the following the actual data of creep test evaluations and microstructural characterisations are presented. Based on these novel long-term data further insight concerning the creep behaviour of the considered steels is now possible and will be discussed.

2 Material

The chemical composition of B2 and FB2 is shown in Table 1; both steels where manufactured by BÖHLER EDELSTAHL GmbH. The forged B2 was austenized at 1100°C/2h and then tempered in two steps at 590°C/8h and 700°C/16h. The forged FB2 was austenized at 1100°C/4.5h and then tempered in two steps at 570°C/8h and 710°C/8h.

Steel	C	Si	Mn	Al	Cr	Mo	V	W	Co	Nb	B	N
B2	0,17	0,07	0,06	0,013	9,32	1,55	0,27	---	---	0,064	0,010	0,02
FB2	0,13	0,07	0,86	0,007	9,42	1,5	0,21	---	0,96	0,065	0,009	0,02

Table 1: Chemical composition of the 9%Cr-steels examined (wt%)

3 Experimental Procedure

Creep tests are carried out at 600°C and 650°C at air under different stress levels between 60 MPa to 250 MPa under constant loads according to DIN 50118. The creep strain versus time, the creep strain rate versus creep strain, and the creep strain rate versus time were evaluated.

Detailed microstructural investigations (martensitic structure, precipitates and dislocation structure) were carried out to determine quantitatively and qualitatively the microstructure of this material. Light optical and transmission electron microscopy (Philips CM20 STEM equipped with EDX detector) and the software package AnalySIS 3.2 (for image analysis) were used**.** Energy dispersive X-ray analysis (EDX) from the carbon extraction replicas and selected area diffractions were performed to specify chemical composition and identify precipitated phases. Specimens at different loading times (as-received, after long-term creep and after rupture) and from different sample sections (head section and gauge length) were selected.

4 Results

4.1 Creep Tests

For comparison of the creep behavior of the two steels B2 and FB2 the creep tests at 600°C and 650°C were chosen. The creep tests at 600°C were carried out at a stress level of 100 MPa and the creep tests at 600°C were carried out at a stress level of 80 MPa. Due to specification of the test parameters within the COST group, only the stress level of 80 MPa at 650°C is used for comparison of the two steels (for B2 steels there are no data available at 100 MPa and 650°C).

Creep data at 100MPa and 600°C:

The creep strain versus time curve is shown in Figure 1, the creep strain rate versus creep strain curve is shown in Figure 4. In addition to the steel type the legends show the specimen numbers which are used for further discussion in brackets, the value “t” stands for terminated that means the test is terminated before rupture for microstructural investigations.

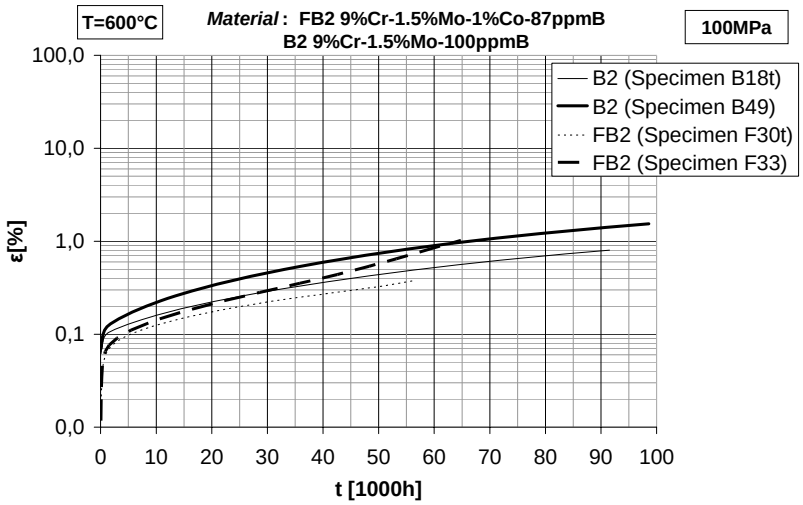

Figure 1: Creep strain versus time at 100MPa and 600°C for B2 and FB2

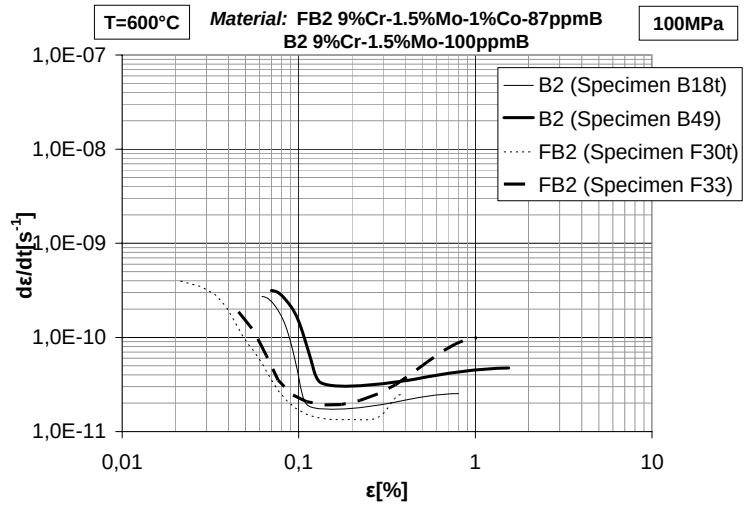

Figure 2: Creep strain rate versus creep strain at 100MPa and 600°C for B2 and FB2

Up to the testing time of approximately 30000 hours the creep strain of B2 is higher than that one of FB2. After 30000 hours the creep strain of FB2(F33) rise above the creep strain of B2. The creep strain rate of the terminated FB2(F30) does not rise over the values of B2 during the testing time, but the creep strain rate increases significant at a creep strain level of 0.3%.

The minimum creep strain rate of the FB2 (averaged over the different specimens) is lower than that of B2.

Although the creep strain curves and the creep strain rate curves of the B2 and FB2 specimens are overlapping, the diagrams show that at lower loading times FB2 seems to be more creep resistant, while above a loading time of approximately 30000 hours to 50000 the situation seems to converse.

Creep data at 80MPa and 650°C:

Figure 3 shows the development of the creep strain during the testing time and Figure 4 the development oft the creep strain rate. In addition to the steel type the legends shows the specimen numbers which are used for further discussion in brackets, the value "r" stands for "ruptured".

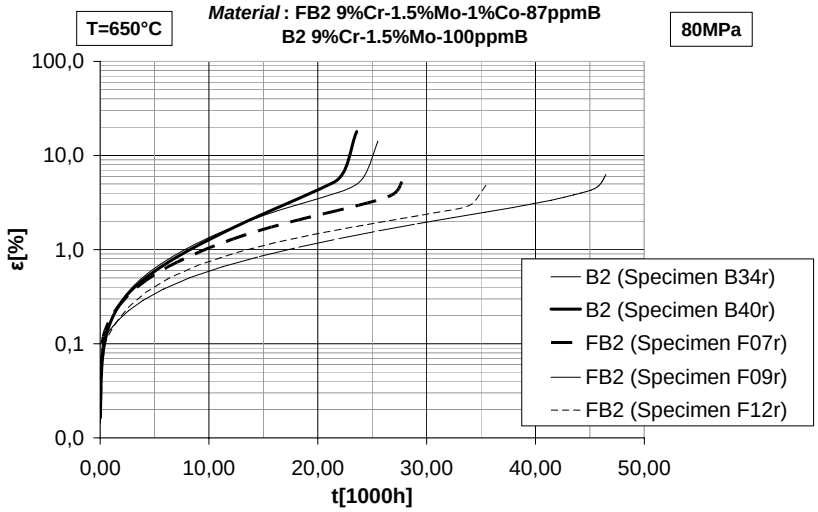

Figure 3: Creep strain versus time at 80 MPa and 650°C for B2 and FB2

The creep strain of B2 at 80 MPa and 650°C is higher than that one of FB2 at the same exposure time. Also the time to rupture is shorter for all B2 specimens compared to the FB2 specimens. The time to rupture of FB2 scatters from 28000 hours to 47000 hours. For both steels the time to rupture at 80 MPa and 650°C is shorter than at 100 MPa and 600°C. Since the specimens tested at 600°C and 100MPa are not ruptured until now, the comparison of the rupture strain at 600°C and 650°C of these two steels could not be performed now.

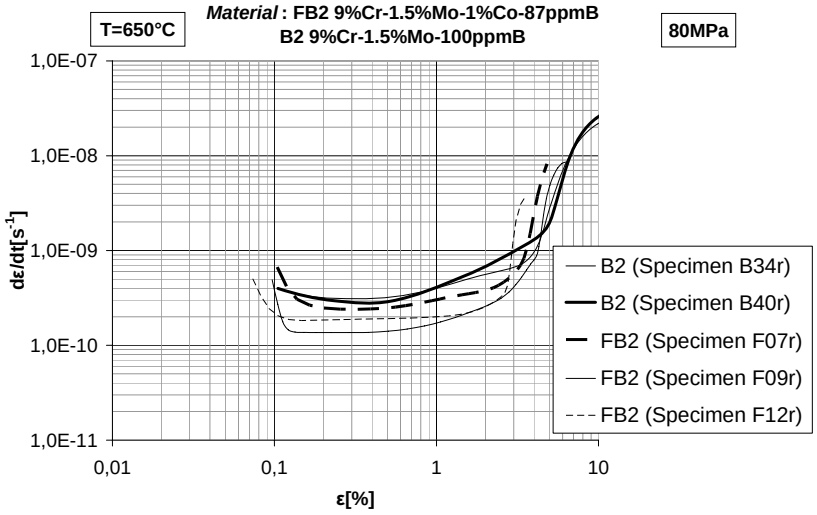

Figure 4 Creep strain rate versus creep strain at 80 MPa and 650°C for B2 and FB2

(Be aware of the logarithmic scales in Figure 2and Figure 4, curvature of the graphs near the minimum strain rate in Figure 4 is greater than Figure 2.)

4.2 Microstructural Investigations

The microstructure of B2 and FB2 in the as-received state is described in papers [1]-[4]. We restrict our description in the following to the material condition after 91500 hours (B2) and 56500 hours (FB2) (i.e. the specimens which are exposed to 100 MPa at 600°C, since the evaluation of specimens exposed to 80 MPa at 650°C is just in progress).

B2 Steel

Figure 5 shows the microstructure of B2 in the as received condition (a), head section (b) (only temperature exposure) after 91500 hours and in the gauge section (c) (temperature and stress exposure) after 91500 hours. In the as received condition the precipitates (mainly $M_{23}C_6$) are uniformly distributed. The size distribution of the precipitates is shown in Figure 6. The particles are placed on the primary austenite grain boundaries, the martensit lath boundaries and also (to a smaller amount) inside the lath. A high dislocation density is observed in most areas of the sample.

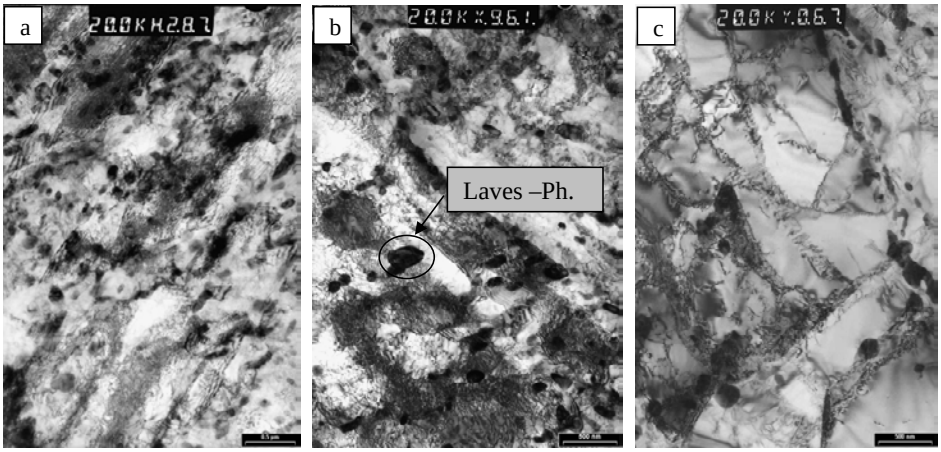

Figure 5: Microstructure of B2: As received condition (a); head section (b) (600°C, no stress) after 91500 hours; gauge section (c) (600°C, 100 MPa) after 91500 hours

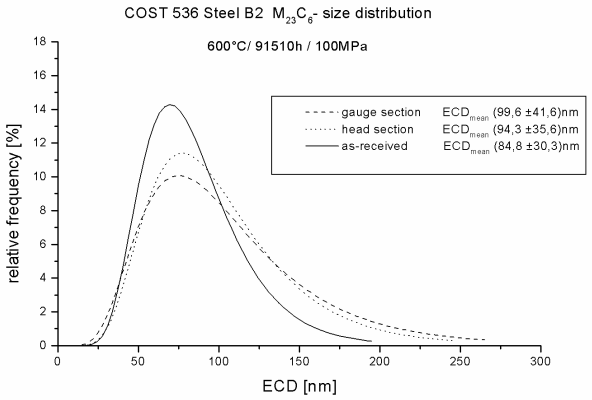

Figure 6: Precipitates size distribution in B2

After 91500 hours in the head section of the creep specimens, there is still a high dislocation density and only a marginal growth of precipitates was observed, except of the Laves phase.

In the gauge section, there is already an advanced formation of subgrains and a large fraction of recovered areas (approximately 42%). The laths width is grown significantly, Figure 5 (c) and Table 2.

Table 2 shows the results of quantitative evaluation of microstructural parameters in the as-received condition and after 91500 hours of creep deformation.

Specimen	As-received	B18	
Stress[MPa] / time [h] / ε [%]		100MPa / 91 500h / 0,8%	
		Head	Gauge length
M23C6:			
ECD / σ [nm]	84,83 ± 30,32	94,31 ± 35,56	99,58 ± 41,61
Area fraction [%]	5,39	5,07	3,75
N_A [1/µm²]	7,74	6,30	4,04
N_v [1/µm³]	30,24	23,77	14,93
I [nm]	242,90	256,95	328,76
Subgrain ECD [nm]	-	288,57 ± 90,14	478,33 ± 176,29
Lath width [nm]	318,55 ± 120,15	293,60 ± 117,74	482,12 ± 224,46

Table 2: Microstructural data of B2 in as-received condition and after 91500 hours creep test

Figure 6 shows, that only a small fraction of precipitates is grown in both the head section and the gauge section, but the size of most particles still lies in the range of 60-70nm.

FB2 Steel:

Figure 7 shows the microstructure of steel FB2 in the as-received condition (a), and in the gauge section (b) (temperature and stress exposure) after 56500 hours. In the as-received condition the precipitates (mainly $M_{23}C_6$) are not so uniformly distributed as in B2. The size distribution of the precipitates is shown in Figure 8. The particles are placed on the martensit lath boundaries and also (to a smaller amount) inside the lath. A high dislocation density is observed in most areas of the sample.

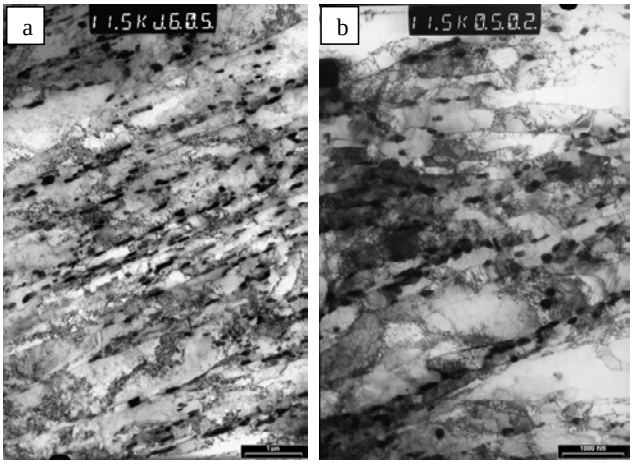

Figure 7: Microstructure of FB2: As received condition (a); gauge section (b) (600°C, 100 MPa) after 56500 hours

In the gauge section the martensite laths become much wider (Figure 7 and Table 3). Also an advanced formation of subgrains can be observed. The measured precipitates size was also much higher (Figure 8).

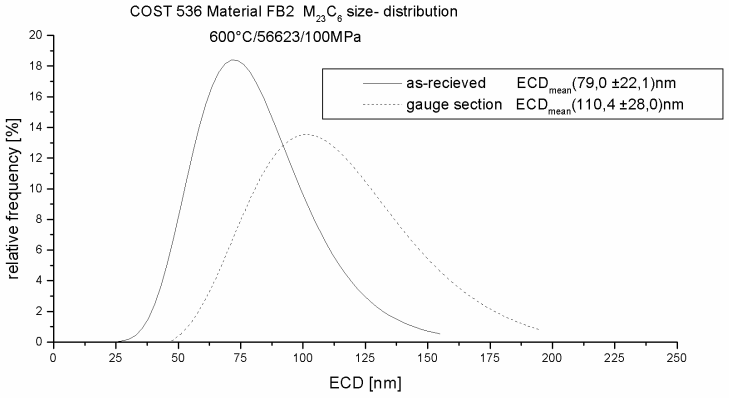

Figure 8: Precipitates size distribution in steel FB2

Figure 8 shows the change of size distribution of the precipitates in steel FB2. After 56500 hours the size of the precipitates shifts significantly towards larger values (compared to the as received state). There are nearly no precipitates with the size below approximately 50 nm. (Remark: The MX particles with an averaged ECD of approximately 10 nm are not included in these evaluations).
Table 3 shows the measured microstructural parameters in the as received condition and after 56500 hours.

Specimen	As-received	F30
Stress [Mpa] / Zeit [h] / ε [%]		100 / 56500 / 0,38
		Gauge length
$M_{23}C_6$:		
ECD / σ [nm]	78,96 ± 22,11	110,40 ± 27,96
Area fraction [%]	5,75	3,66
N_A [1/µm²]	10,83	3,59
N_v [1/µm³]	43,34	12,74
I [nm]	205,81	331,42
Subgrain ECD / σ [nm]	-	436,67 ± 144,80
Lath width / σ [nm]	318,30 ± 180,57	433,32 ± 248,90

Table 3 Microstructural data of FB2 in as -received condition and after 56500 hours creep test

5 Discussion

The long-term creep results of steel B2 have already shown very good creep behaviour at 100MPa and 600°C. The creep exposure times have achieved the defined goal (COST project) of 100000 hours without significantly changes in creep rate over the last 70000 hours.

Considering the low progression of strain rate curve of B2 at 99500 hours, and the fact, that the testing time is very close to the demanded goal of 100000 hours at 100MPa and 600°C, it can be stated that the required creep strength will be exceeded by far. An additional confirmation of that fact bring the creep tests at 110MPa and 600°C, which reached the duration of 100 000h up to now, without any sample rupture (results are not presented within this paper). The very good creep behaviour is a result of the high microstructural stability of this material. The microstructural investigations have revealed only a slow coarsening rate of the $M_{23}C_6$ carbides. The stable $M_{23}C_6$ carbides are important for preserving of narrow martensite laths structure, since they pin the lath boundaries and hinder grain (lath) to grow. It was confirmed that this mechanisms works also for very long testing times (boron influence on stabilisation of $M_{23}C_6$ carbides).
There was relatively large fraction (42%) of recovered areas in the examined specimens, nevertheless it has to be noted that this area fraction occurs not so high compared to other 9-12% Cr steels after long-time tests. Therefore it will be more convenient to call this a large fraction of *non-recovered* areas. This large fraction of non-recovered areas is mainly caused by the martensite structure (stable, narrow laths due to the stable $M_{23}C_6$ carbides). The narrow martensite laths are a hindrance for the evolution and growth of the subgrains. The subgrains evolve and grow during the recovery process. The hindrance of there evolution and growth is the reason for the slow increase of the creep strain and therefore the superior macroscopic long-term creep strength.
In addition, the presence and the stability of very fine V(C,N) is responsible for a high dislocation density in the B2 steel, at the exposure time of 91500 hours. The evaluation of interactions between V(C,N) and dislocations is still under progress.

It is well known that in the mechanical and thermal loaded gauge section the $M_{23}C_6$ carbides grow faster than the $M_{23}C_6$ carbides in the only thermal loaded head section of the creep specimen. This is again shown within this paper, Table 2. There is still not enough attention paid to the influence of the stress level (mechanical loading) on the microstructural evolution in the papers published in the recent years, especially when the numerical simulation of the microstructural evolution is taken into account.

The steel FB2 tested at 600°C and 100 MPa has not shown such good creep behaviour as the steel B2 has. Nevertheless it was shown in [3] that at higher stresses (and therefore shorter times to rupture) the FB2 has a better creep behaviour than B2. At 100 MPa and 600°C, the material concept used for FB2 seems not to fulfil the expected improvements compared to B2. The different causes could be responsible for this behaviour. The microstructural investigations showed that, the $M_{23}C_6$ carbides in FB2 coarsen faster during the creep exposure than those ones in steel B2. This fact also implies the faster broadening of martensite laths in the FB2 material. It could be expected that one of the reasons could be the lower concentration of boron in M23C6 in steel FB2 in comparison to B2. Another point is the role of cobalt. Also the density of small, stable V(C,N) precipitates was significantly lower in the FB2 than in B2. The microstructural work to clear these points is in progress.

At 650°C and 80 MPa steel FB2 shows better creep performance (longer times to rupture) than B2. From the other side as the test temperature was higher the tests duration was also respectively shorter.
It is to emphasize that the manufacturing route of the material (inclusive the heat treatment) is the most important factor (beside the chemical composition) determining the microstructure and in following the materials behaviour during the long-term creep tests.

6 Summary and Conclusion

The results of the long-term creep tests and the relevant microstructural investigations of two, boron alloyed 9% Cr steels were presented.

The following main results were derived:

- The B2 steel has achieved a creep time of 99500 hours at 100MPa and 600°C up to now. The evaluation of the creep strain rate shows that it will definitely reach the goal of 100000 hours, defined as a requirement in the COST group, without significantly changes in creep rate over the last 70000 hours.
- The FB2 steel has not achieved the goal of 100000 at 100MPa and 600°C, although it achieves higher times to rupture than B2 for higher creep loads/applied stresses (shorter exposure time until rupture).
- The better creep behaviour of B2 can be directly related to the microstructural evaluations, which show a very stable behaviour of the $M_{23}C_6$ carbides and martensite laths, and high dislocation densities after long exposure time.
- The creep behaviour of the FB2 steel at 650°C and 80MPa is better than that of the B2 steel.

Microstructural investigations concerning the influence of MX on dislocation motion at 100MPa and 600°C and exposure time of 99500 hours are still in progress, also the microstructural investigations of the specimens which were exposed to 650°C and 80MPa. Using these data the numerical model which is now under construction [5] will be checked.

A part of the work has been done in the frame of COST- projects 501, 522 and 536. The financial support was provided by the *Austrian Research Promotion Agency (FFG)* under *ACCEPT - COST 536*, Proj. No. *808.789*, and *ARC Seibersdorf research Gmbh*. This support is gratefully acknowledged.

[1] K. Spiradek, R. Bauer, G. Zeiler, Microstructural changes during the creep deformation of 9% Cr-steel. Proceedings of Materials for advanced Power Engineering part 1, Liège 1994, 251-262.
[2] P. Nowakowsky, H. Straube, K. Spiradek, G. Zeiler, Microstructural Evolution during creep of a new modified 9%Cr-steel with boron and cobalt, Proceedings of the 6th Liège Conference, Part I, 1998, 567-574.
[3] K. Spiradek-Hahn, P. Nowakowski, G. Zeiler, Boron added 9%Cr steels for forged components in advanced power plants, 3rd EPRI conference on Advancees in Materials Technology for Fossil Power Plants. University of Swansea (United Kingdom), 1-6 Apr 2001, 165-175.
[4] C. Stocker, K. Spiradek, G. Zeiler, Microstructural features influencing the creep properties of 9-12% Cr-steels focusing on Laves Phase precipitation. Proceedings of the 7th Liège Conference, Part III, 2002, 1459-1468.
[5] N. Böck. Dislocation mobility in 9% chromium steels exposed to creep load. Proceedings of the 8th Liège Conference. These proceedings. 2006.

ALLOY DESIGN AND CREEP STRENGTH OF ADVANCED 9%Cr USC BOILER STEELS CONTAINING HIGH BORON

Hiroyuki Semba* and Fujio Abe

National Institute for Materials Science (NIMS)
1-2-1 Sengen, Tsukuba, Ibaraki 305-0047, Japan

*Present address: Sumitomo Metal Industries
1-8 Fuso-cho, Amagasaki, Hyogo 660-0891, Japan
semba-hry@sumitomometals.co.jp

Abstract

In the R&D project of NIMS for advanced ferritic heat resistant steels for 650°C-USC plants, it has been revealed that the addition of boron more than 0.01mass% to the 0.08C-9Cr-3W-3Co-VNb-<0.003N steel remarkably improves long-term creep strength. The boron enriched in $M_{23}C_6$ carbides near prior-austenite grain boundaries suppresses coarsening of these carbides during creep deformation, leading to excellent microstructural stability and creep strength. Further improvement of creep strength is achieved by the addition of appropriate amount of nitrogen which enhances precipitation of fine MX. Excess addition of nitrogen to the high-boron containing steel reduces creep rupture lives and ductility. This degradation of creep strength is due to a decrease in the amount of effective boron, which is dissolved in $M_{23}C_6$ and suppresses its coarsening, resulting from the formation of coarse BN at normalizing temperature. The highest creep strength is obtained with the 0.08C-9Cr-3W-3Co-0.2V-0.05Nb-0.008N-0.014B (mass%) steel, resulting in excellent creep strength in comparison with that of P92. The 10^5 hours extrapolated creep rupture strength at 650°C is about 100MPa. This steel also shows good creep ductility even in the long term. It is, therefore, concluded that this high-boron bearing 9Cr-3W-3Co-VNb steel with the addition of nitrogen in the order of 0.008mass% is the promising candidate which shows superior creep strength without impairing creep ductility for thick section components in the 650°C-USC plants.

Keywords: 9%Cr martensitic steel, creep, microstructural stability, $M_{23}C_6$, MX

Introduction

It is required to improve the efficiency of fossil-fired power plants in order to reduce the CO_2 emission. Therefore, development of ultra-super critical (USC) power plant aiming for steam temperatures of 650-750°C has been forwarded in Japan, USA and EU countries. Successful development of new advanced heat resistant steels and alloys which can be applied at those temperatures, especially for thick section components is a key to attain this advanced USC plant. Many research and development projects on advanced USC steels were launched in recent years [1-4]. Austenitic steels are advantageous in terms of high temperature strength; however, ferritic steels having tempered martensitic microstructure are favourable for thick sections in boilers such as main steam pipes in terms of thermal fatigue resistance. Hence, development of new ferritic heat resistant steels having excellent creep strength is the most important issues.

Tempered martensitic 9-12%Cr steels bearing tungsten, such as P92 and P122 showing higher creep rupture strength than the conventional steel P91, have been developed for thick section components in USC boilers [5]. However, their creep strength is not sufficient for applying at 650°C and above. Since 1997, NIMS has carried out the research and development on

advanced ferritic heat resistant steels which can be applied at 650°C/35MPa as boiler components with large diameter and thick section [6]. In this project, it has been revealed that the addition of boron more than 0.01mass% to the 0.08C-9Cr-3W-3Co-VNb steel remarkably improves long-term creep strength [7-9], resulting in excellent creep strength in comparison with that of P92. It has also been demonstrated that Type IV failure does not occur during creep tests at 650°C performed on welded joints of these high-boron containing steels even at the stresses in which P92 shows Type IV fracture [10]. In this paper, alloy design and creep properties of the developed steel are described.

Alloy design

Suppressing degradation of long-term creep strength by addition of boron

Drastic degradation of long-term creep rupture strength in 9-12%Cr ferritic heat resistant steels is a crucial problem. It has been revealed that inhomogeneous recovery of lath martensitic microstructure in the vicinity of prior austenite grain boundaries causes a sudden decrease in long-term creep rupture lives [11]. The authors have tried to stabilize the martensitic microstructure by the addition of large amount of boron more than 0.01mass%. Table 1 shows the chemical compositions of the steels examined in order to clarify the effect of boron. 0.08C-9Cr-3W-3Co-0.2V-0.05Nb (mass%) is the base composition of the steels. The boron content is changed from 0 to 0.0139 (mass%). No nitrogen was added in order to avoid the formation of coarse boron nitrides. The resultant nitrogen content is less than 0.0034mass%. Normalizing was carried out at 1050°C (the 0B, 0.0048B and 0.0092B steels) and 1080°C (the 0.0139B steel) for 1 hour, followed by tempering at 790°C (the 0B, 0.0048B and 0.0092B steels) and 800°C (the 0.0139B steel) for 1 hour.

Table 1. Chemical compositions of the steels tested (mass%).

	C	Si	Mn	Cr	W	Co	V	Nb	N	B
0B	0.078	0.31	0.50	8.94	2.94	3.03	0.19	0.050	0.0019	<0.0001
0.0048B	0.077	0.29	0.51	8.95	2.93	3.03	0.19	0.050	0.0011	0.0048
0.0092B	0.075	0.29	0.50	8.96	2.92	3.01	0.19	0.049	0.0016	0.0092
0.0139B (0.0034N)	0.078	0.30	0.51	8.99	2.91	3.01	0.19	0.050	0.0034	0.0139

Fig.1 shows creep rupture strength of the 0B, 0.0048B, 0.0092B and 0.0139B steels at 650°C. It is noted that the 0.0139B steel shows the highest and stable long-term creep rupture strength. It is about one order of magnitude longer than that of the P92 steel [12], which is the current advanced ferritic heat resistant steel. It also shows excellent rupture ductility even in the long term. Reduction of area for the crept specimen ruptured at more than 10000h is about 69-75%, in which P92 shows insufficient ductility of less than 50%. This superior ductility of the high-boron bearing steel also leads to good creep-fatigue resistance [13]. Although there is no substantial difference between the 0B, 0.0048B and 0.0092B steels at higher stresses than 100MPa, only the 0.0139B steel exhibits longer rupture time. This may be related with the difference in the amount of dissolved nitrogen. At lower stresses than 100MPa, the 0.0139B steel still shows stable creep rupture strength, while time to rupture in the lower boron bearing steels remarkably falls down with decreasing boron content. These results indicate that boron mainly suppresses the degradation in the long-term creep rupture strength of 9Cr-3W-3Co-VNb steels.

Fig. 2 shows the creep rate versus time curves of these boron containing steels at 80MPa. There is no major difference in creep rates through the primary creep region except the 0.0139B steel. The creep rate of the 0.0139B steel is lower than other steels in the primary region. It is noted that the addition of boron retards the onset time of tertiary creep, resulting in the lowest minimum creep rate and the longest time to rupture in the 0.0139B steel. It is also demonstrated that minimum creep rate of the 0.0139B steel is lower than that of the 0B and lower boron containing steels by almost one to two orders of magnitude. Similar results are obtained at higher stresses. Azuma *et al*. [14] have reported that boron does not affect Ac_1, Ac_3, Ms and M_f temperatures in the 0.1C-10.2Cr-0.7Mo-1.8W-3Co-VNbN steel. This designates that there is little difference in initial lath width and dislocation density, which can be affected by transformation temperature, in spite of the boron content. Fig. 3 shows the

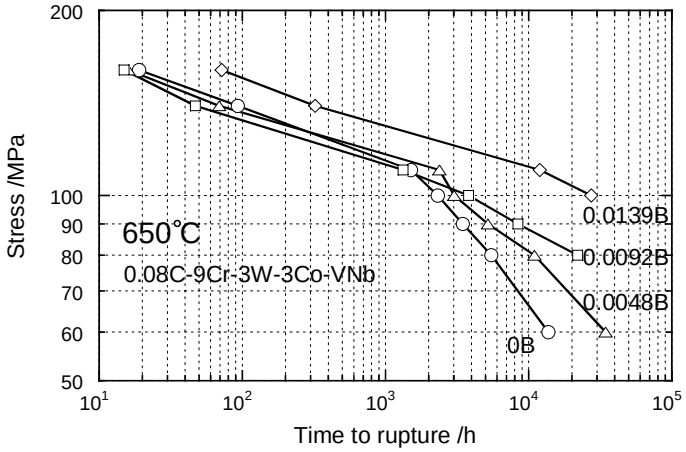

Fig. 1. Creep rupture strength of the various boron-containing 9C-3W-3Co-VNb steels at 650°C.

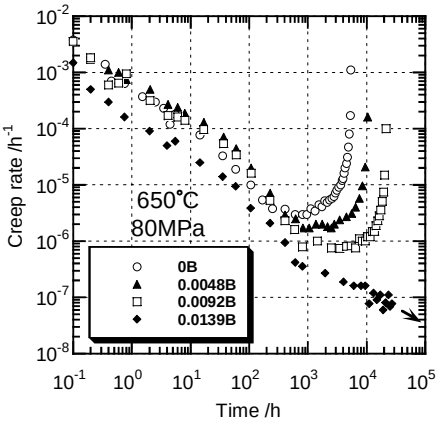

Fig. 2. Creep rate vs. time curves of 9Cr-3W-3Co -VNb steels.

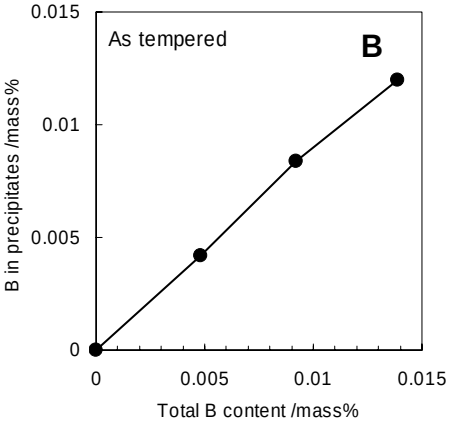

Fig. 3. Chemical analysis results of extracted residues in as tempered steels.

chemical analysis results of extracted residues in as tempered steels. It can be seen that about 90% of added boron is contained in precipitates after tempering.

In order to reveal the effect of boron on the stability of carbides, mean diameter of $M_{23}C_6$ is measured by image analysis of FE-SEM micrographs for the as tempered and aged steels. Fig. 4 shows the measurement results of the 0B and 0.0139B steels. The area of 'near prior austenite grain boundaries (PAGB)' is defined as that within 10μm from PAGB. There is no difference in the mean diameter of $M_{23}C_6$ in the near PAGB and center of prior austenite grain (PAG) areas between the 0B and 0.0139B steels. However, coarsening of $M_{23}C_6$ on PAGB after long-term aging is drastically suppressed in the 0.0139B steel. Fig. 5 shows mean diameters of $M_{23}C_6$ on PAGB in the 0B, 0.0048B, 0.0092B and 0.0139B steels. Coarsening of $M_{23}C_6$ on PAGB after aging for 10300h is suppressed with increasing boron content. This corresponds to the trend of suppressing the degradation of creep rupture strength at around 10000h. As mentioned above, almost 90% of added boron precipitates after tempering. This precipitated boron may mainly exist as $M_{23}(C,B)_6$. Boron concentration in $M_{23}C_6$ in the 0.0139B steel after aging for 10300h has been analyzed by field emission scanning Auger spectroscopy (FE-AES). It has been revealed that boron is enriched in the $M_{23}C_6$ on the prior austenite grain boundaries and in its vicinity (within 5μm) [7]. Therefore, this may suppress the coarsening of $M_{23}C_6$ on the grain boundaries during creep deformation, resulting in the excellent creep rupture strength in the 0.0139B steel through stabilizing lath martensitic microstructures and preventing inhomogeneous deformation in the vicinity of PAGB.

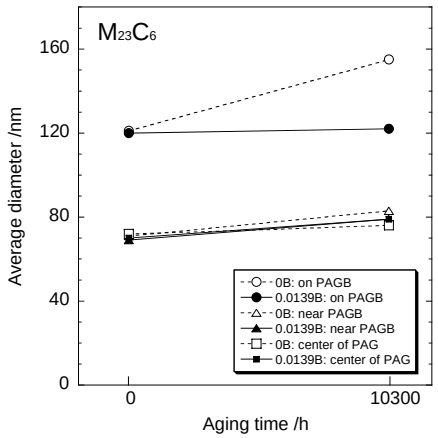

Fig. 4. Effect of boron on mean diameter of $M_{23}C_6$ in the 0B and 0.0139B steels. (PAGB: Prior austenite grain boundaries)

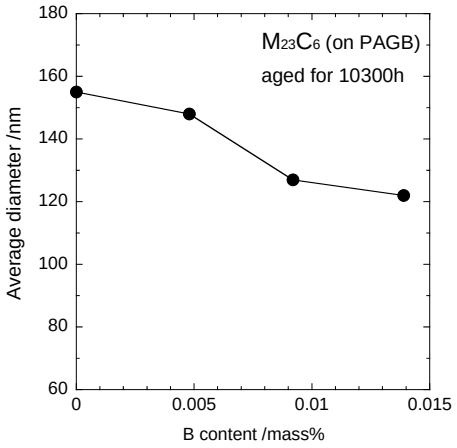

Fig. 5. Effect of boron content on mean diameter of $M_{23}C_6$ on prior austenite grain boundaries.

Improvement of creep strength by addition of nitrogen

The 0.08C-9Cr-3W-3Co-0.2V-0.05Nb (mass%) steel containing more than 0.01mass% boron shows very high and stable creep rupture strength at 650°C. However, further improvement of creep strength is required in order to achieve the target 10^5 hours rupture strength of 100MPa at 650°C. The results mentioned above also suggest that small amount of nitrogen affects creep strength of these steels. Therefore, the effect of nitrogen content on creep

strength was investigated for 0.08C-9Cr-3W-3Co-0.2V-0.05Nb-0.014B steels. Table 2 shows the chemical compositions of the steels tested. The nitrogen content is changed from 0.0015 to 0.065 (mass%). Normalizing was carried out at 1150°C for 1 hour, followed by tempering at 770°C for 4 hours. Normalizing temperature is higher than those for the steels in Table 1 in order to avoid the formation of tungsten borides and enhance the precipitation of MX.

Table 2. Chemical compositions of the steels tested (mass%).

	C	Si	Mn	Cr	W	Co	V	Nb	N	B
0.0015N	0.076	0.30	0.51	9.00	3.02	3.02	0.19	0.053	0.0015	0.0132
0.0079N	0.078	0.31	0.49	8.88	2.85	3.00	0.20	0.051	0.0079	0.0135
0.065N	0.081	0.31	0.51	8.90	3.07	3.00	0.20	0.054	0.065	0.0144

Fig. 6 shows creep rupture strength of these steels containing nitrogen from 0.0015 to 0.065 (mass%). The 0.0034N steel is the same one as the 0.0139B steel shown in Fig. 1. It is noted that creep rupture strength remarkably increases with increasing nitrogen content from 0.0015 to 0.0079 (mass%). The 10^5 hours extrapolated rupture strength of 100MPa at 650°C, which is the target strength, can be accomplished by the 0.0079N steel. However, excess addition of nitrogen in the order of 0.065mass% reduces creep rupture strength. That of the 0.065N steel is lower than the 0.0079N steel in the short term and suddenly falls down in the long term more than 4000h. Minimum creep rate of these steels at 650°C and 120MPa is exhibited in Fig. 7. It decreases with increasing nitrogen content and the lowest creep rate is obtained with the 0.0079N steel. Further addition of nitrogen increases minimum creep rate. It is, therefore, concluded that the highest creep strength of this 0.014mass% boron bearing steel is obtained by the addition of around 0.008mass% nitrogen. Creep rate versus time curves of these 9Cr-3W-3Co-0.2V-0.05Nb-0.014B (mass%) steels at 650°C and 120MPa are shown in Fig. 8. The addition of nitrogen drastically decreases creep rate in the primary region and minimum creep rate by almost two orders of magnitude. The resultant onset time

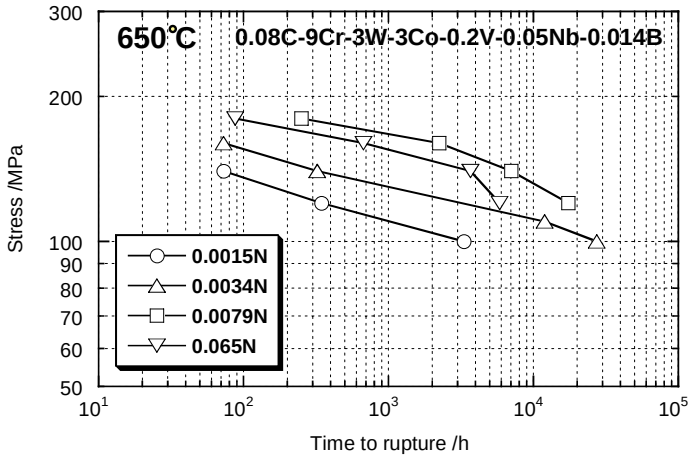

Fig. 6. Creep rupture strength of 9Cr-3W-3Co-VNb-0.014B steels containing 0.0015-0.065 (mass%) nitrogen at 650°C.

of tertiary creep is significantly retarded and creep rupture lives increase by one to two orders of magnitude. There is no difference in the creep rate of the primary region between the 0.0079N and 0.065N steels. However, the onset time of tertiary creep in the 0.065N steel is earlier than that in the 0.0079N steel, resulting in shorter time to rupture.

Chemical analysis of extracted residues was carried out for as tempered steels in order to clarify the effect of nitrogen on precipitation behavior. Fig. 9 shows the amount of dissolved nitrogen calculated from the amount of extracted residues and the total amount of nitrogen. Those of the 0.0079N and 0.065N steels are much higher than the 0.0015N steel. This result indicates that more MX precipitates in the 0.0079N and 0.065N steels during creep at 650°C and contributes to creep strength. Indeed, very fine V-rich MX was confirmed in the

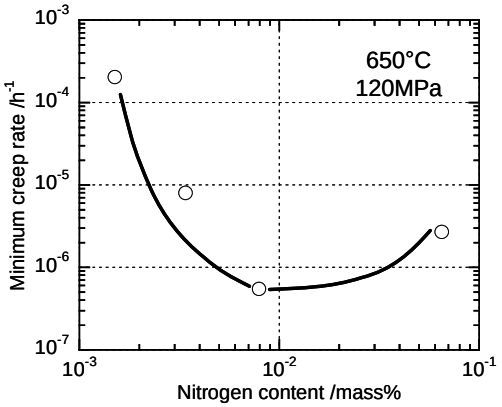

Fig. 7. Minimum creep rate of 9Cr-3W-3Co-VNb-0.014B steels containing 0.0015-0.065 (mass%) nitrogen at 650°C and 120MPa.

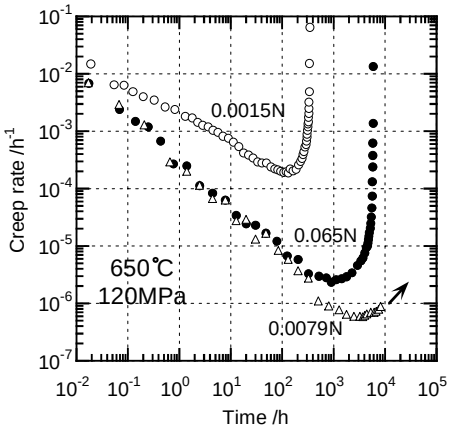

Fig. 8. Creep rate vs. time curves of 9Cr-3W-3Co-VNb-0.014B steels.

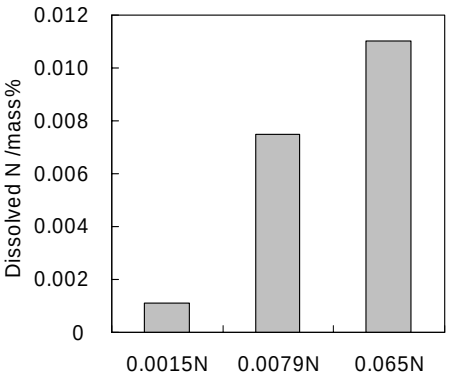

Fig. 9. Dissolved N in as tempered steels.

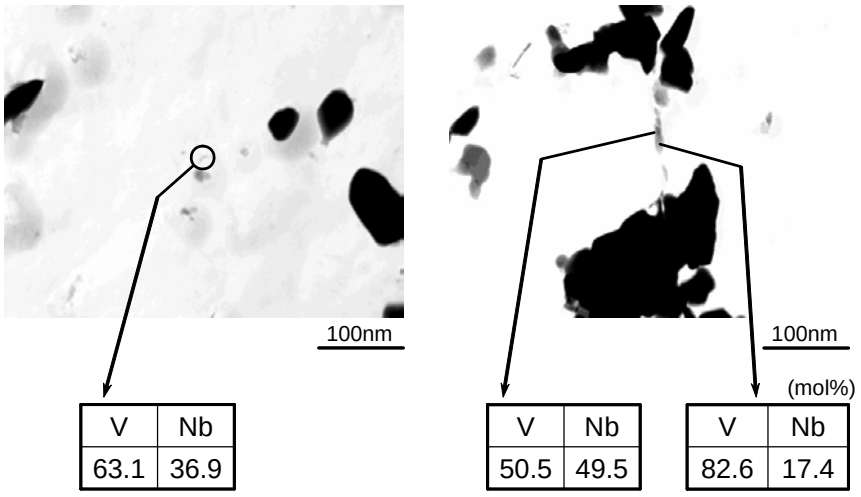

Fig. 10. TEM micrographs of the extracted replica for the 0.0079N steel aged at 650°C for 1000h.

0.0079N steel aged at 650°C for 1000h by TEM observation of extracted replica (Fig. 10). These fine precipitates of MX in the higher nitrogen containing steels drastically decrease creep rate in the transient creep region, resulting in lower minimum creep rate than the 0.0015N steel by almost two orders of magnitude. However, excess addition of nitrogen in the order of 0.065mass% decreases creep rupture strength as shown in Figs. 6 and 8. Coarse BN is observed in the as tempered 0.065N steel (Fig. 11). This is consistent with the observation results of BN in high-Cr steels at normalizing temperatures by Sakuraya *et al* [15]. They have reported the solubility product for boron nitrides as follows:

$$\log [\%B] = -2.45 \log [\%N] - 6.81 \quad (1)$$

where [%B] and [%N] are concentration of boron and nitrogen in mass% respectively. Solution limit of nitrogen is obtained with equation (1) as 0.0095mass% for 0.014mass% boron. Hence, all the added boron in the 0.0079N steel can be dissolved in the matrix or

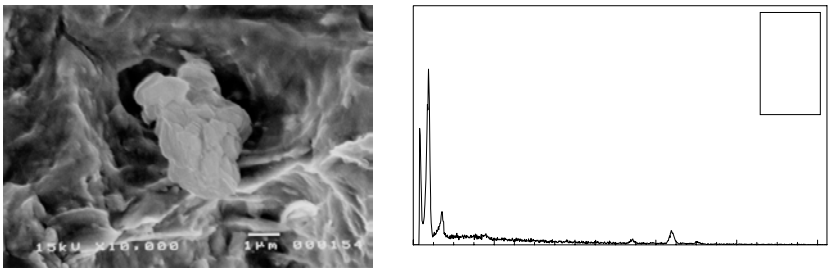

Fig. 11. BN observed in the as tempered 0.065N steel.

$M_{23}C_6$ without formation of coarse BN at the normalizing temperature. On the other hand, most of the added boron may be consumed as coarse BN in the 0.065N steel. Therefore, the amount of effective boron, which is dissolved in $M_{23}C_6$ and suppresses its coarsening, in the 0.065N steel may be less than that in the lower nitrogen containing steels. Table 3 shows the equilibrium composition of $M_{23}C_6$ at 650°C calculated with Thermo-Calc considering the formation of BN. It is noted that the dissolved boron within $M_{23}C_6$ in the 0.065N steel is less than that in the 0.0015N and 0.0079N steels. This supports the above estimation and indicates that the amount of effective boron in the 0.065N steel is less than the 0.0015N and 0.0079N steels. The difference in the amount of effective boron may lead to large coarsening rate of $M_{23}C_6$ in the 0.065N steel, resulting in advancing onset time of acceleration creep and reducing time to rupture.

Table 3. Equilibrium compositions of $M_{23}C_6$ computed by Thermo-Calc (650°C).

	Cr	Fe	Mn	W	V	Co	C	B
0.0015N	64.88	12.26	1.39	0.32	0.33	0.12	15.59	5.11
0.0079N	64.89	12.15	1.41	0.36	0.38	0.11	15.99	4.71
0.065N	64.03	12.20	1.72	1.10	0.15	0.11	18.45	2.24

Chemical composition of the matrix:
0.08C-0.3Si-0.5Mn-9Cr-3W-3Co-0.2V-0.05Nb-0.0135B (mass%

Microstructure and creep strength of the developed steel

The nominal composition of the developed steel is 0.08C-0.3Si-0.5Mn-9Cr-3W-3Co-0.2V -0.05Nb-0.008N-0.014B (mass%). Plates of the developed steel were produced from a 180kg-ingot by hot forging and employed for creep tests. Microstructures of the developed

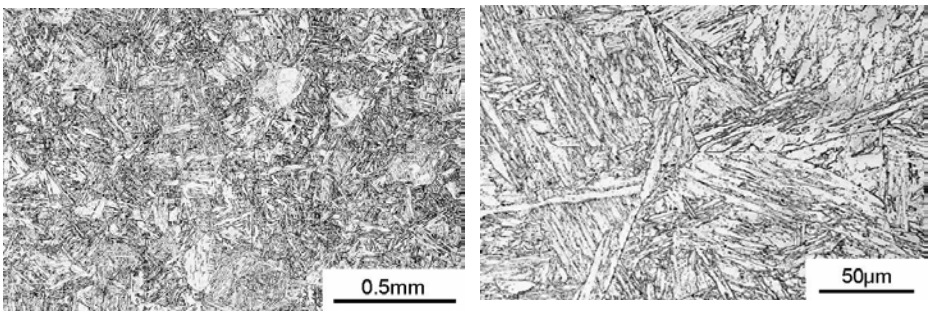

Fig. 12. Optical micrographs of the developed steel (as tempered).

steel after normalizing at 1150°C for 1 hour, followed by tempering at 770°C for 4 hours are shown in Fig. 12. The developed steel has a single phase microstructure of tempered martensite. No δ-ferrite was observed. Transformation temperatures are shown in Table 4.

Table 4. Transformation temperatures of the developed steel (°C).

Ac1	Ac3	Ms	Mf
818	902	445	238

Fig. 13 shows creep rupture strength of the developed steel at 650°C compared with that of P92 [12] and T91 [16]. This developed steel shows stable long-term creep strength. Its rupture strength is more than one order of magnitude longer than that of the P92 steel. The 10^5 hours extrapolated rupture strength of 100MPa may be accomplished by the developed steel. Elongation and reduction of area after creep tests are shown in Figs. 14 and 15. It is noted that the developed steel has good creep ductility even in the long term especially compared with P92. It has been revealed that excess addition of nitrogen to these high-boron bearing steels reduces creep ductility [17]. Formation of coarse BN is considered to be responsible for a decrease in the creep ductility. Excellent creep strength and sufficient creep ductility are accomplished by the optimized balance of boron and nitrogen content as mentioned in the previous section.

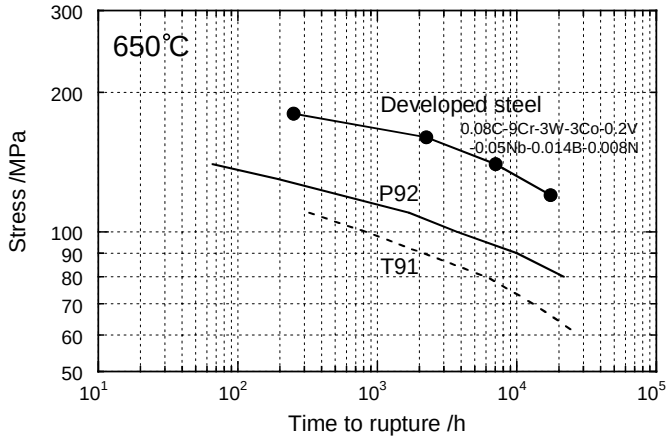

Fig. 13. Creep rupture strength of the developed steel.

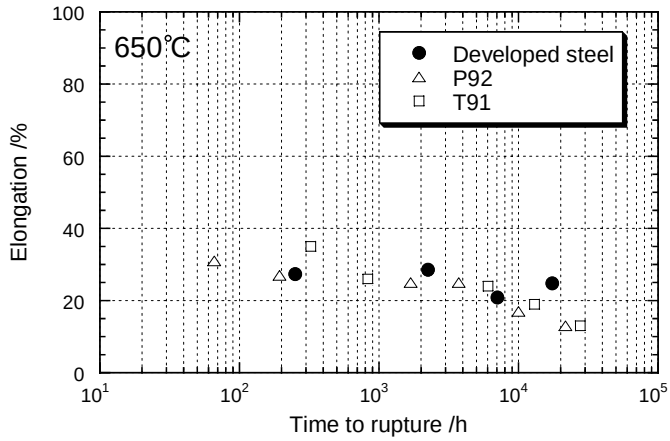

Fig. 14. Creep rupture ductility of the developed steel (Elongation).

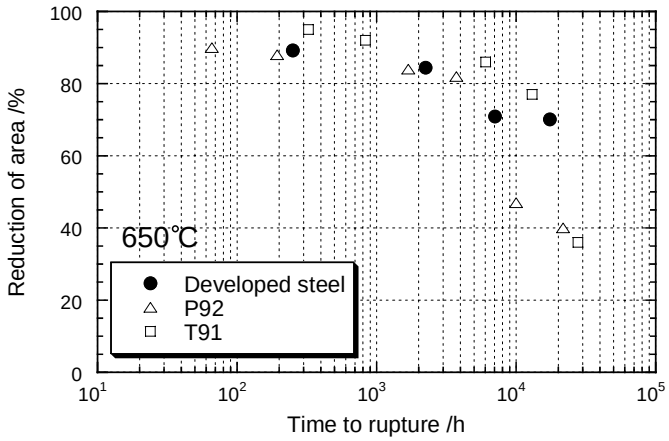

Fig. 15. Creep rupture ductility of the developed steel (Reduction of area).

Conclusions

The addition of boron more than 0.01mass% to 0.08C-9Cr-3W-3Co-0.2V-0.05Nb steels remarkably improves long-term creep strength. It retards the onset time of tertiary creep, resulting in increasing time to rupture. Boron stabilizes the lath martensitic microstructure of 9Cr-3W-3Co steels during creep deformation at 650°C through the stabilization of $M_{23}C_6$ in the vicinity of prior austenite grain boundaries by an enrichment of boron in the $M_{23}C_6$ carbides. Further improvement of creep rupture strength in this high-boron containing steel is accomplished by the addition of appropriate amount of nitrogen enhancing precipitation of fine MX. The highest creep strength is obtained with the 0.08C-9Cr-3W-3Co-0.2V-0.05Nb -0.008N-0.014B (mass%) steel, resulting in excellent creep strength in comparison with that of P92. This steel shows good creep-rupture ductility even in the long term. Hence, it is concluded that this developed steel is the promising candidate which shows superior creep strength without impairing creep ductility for thick section components in 650°C-USC plants.

Acknowledgement

The creep tests were performed by the Creep Group in Materials Information Technology Station, NIMS. The authors are grateful to member of the Creep Group for their sincere efforts. Kind support by Dr. T. Hara in the TEM observation is acknowledged.

References

[1] R. Viswanathan, J.F. Henry, J. Tanzosh, G. Stanko, J. Shingledecker and B. Vitalis, 'U.S.Program on materials technology for USC power plants', Proceedings of the 4th International Conference on Advances in Materials Technology for Fossil Power Plants, 2004, Hilton Head Island (USA), p.3

[2] F. Masuyama, 'Alloy development and materials issues with increasing steam temperature', Proceedings of the 4th International Conference on Advances in Materials Technology for Fossil Power Plants, 2004, Hilton Head Island (USA), p.35.

[3] B. Scarlin, T.U. Kern and M. Staubli, 'The European efforts in material development for 650°C USC power plants – COST522', Proceedings of the 4th International Conference on Advances in Materials Technology for Fossil Power Plants, 2004, Hilton Head Island (USA), p.80.

[4] R. Blum, R.W. Vanstone and C. Messelier-Gouze, 'Materials development for boilers and steam turbines operating at 700°C', Proceedings of the 4th International Conference on Advances in Materials Technology for Fossil Power Plants, 2004, Hilton Head Island (USA), p.118.

[5] F. Masuyama, 'New developments in steels for power generation boilers', Advanced Heat Resistant Steels for Power Generation, R. Viswanathan and J. Nutting (eds.), The Institute of Materials, London, 1998, p.33.

[6] F. Abe, M. Tabuchi, K. Sawada, S. Kuroda, H. Okada and S. Muneki, 'Development of advanced 9Cr steels for thick section boiler components of USC power plant at 650°C', Proceedings of the second International Conference on Advanced Structural Steels, 2004, The Chinese Society for Metals, p.757.

[7] T. Horiuchi, M. Igarashi and F. Abe, 'Improved utilization of added B in 9Cr heat-resistant steels containing W', ISIJ International, 42(2002), Supplement, p.S67.

[8] K. Sawada, T. Horiuchi, K. Kimura and F. Abe, 'Effect of B content on creep behavior in high Cr ferritic steel', Current Advances in Materials and Processes, Report of the ISIJ Meeting, 15(2002), p.1248.

[9] F. Abe, T. Horiuchi, M. Taneike and K. Sawada, 'Stabilization of martensitic microstructure in advanced 9Cr steel during creep at high temperature', Mat. Sci. Eng. A, 378(2004), p.299.

[10] M. Kondo, M. Tabuchi, S. Tsukamoto, F. Yin and F. Abe, 'Improvement of weld creep life by high-B low-N 9Cr-3W-3Co-NbV Steel', Proceedings of the second International Conference on Advanced Structural Steels, 2004, The Chinese Society for Metals, p.834.

[11] K. Kimura, H. Kushima and F. Abe, 'Heterogeneous changes in microstructure and degradation behaviour of 9Cr-1Mo-V-Nb steel during long term creep', Key Engineering Materials, 171-174(2000), p.483.

[12] NIMS Creep Data Sheet No.48, National Institute for Materials Science, Tsukuba, (2002)

[13] M. Kimura, K. Kobayashi and K. Yamaguchi, 'Creep and fatigue properties of newly developed ferritic heat-resistant steels for ultra super critical (USC) power plants', Mat. Sci. Res. Int., 9(2003), p.50.

[14] T. Azuma, K. Miki, Y. Tanaka and T. Ishiguro, 'Effect of combined addition of W, Nb and V with B on the creep strength in high Cr ferritic heat resistant steel', Tetsu-to-Hagané, 89(2003), p.349.

[15] K. Sakuraya, H. Okada and F. Abe, ‘Coarse size BN inclusions formed in high Cr ferritic heat resistant steel’, Proceedings of the Second International Conference on Advanced Structural Steels, 2004, The Chinese Society for Metals, p.772.
[16] NIMS Creep Data Sheet No.43, National Institute for Materials Science, Tsukuba, (1996)
[17] H. Semba and F. Abe, ‘Creep deformation behavior and microstructure in high boron containing 9%Cr ferritic heat resistant steels’, Proceedings of the 4th International Conference on Advances in Materials Technology for Fossil Power Plants, 2004, Hilton Head Island (USA), p.1229.

IMPROVEMENT OF CREEP STRENGTH OF 650°C FERRITIC/MARTENSITIC SUPER HEAT RESISTANT 11-12%CR STEELS

Karl-Heinz Mayer [b], Christina Berger [a], Alfred Scholz [a], Yan Wang [a]

[a] Institute for Materials Technology (IfW) at the Darmstadt University of Technology, Germany

[b] ALSTOM Energie GmbH, Nürnberg

e-mail address: Berger@mpa-ifw.tu-darmstadt.de

Abstract

The investigations of advanced ferritic/martensitic steels for 650 °C power plant components focus on the improvement of high-temperature creep properties with respect to chemical composition. The claim of the present DFG research work is the development of new heat-resistant 12%Cr ferritic-martensitic steels with sufficient creep and oxidation resistance for a 650°C application by using basic principles and concepts of physical metallurgy on the basis of the state of art and to overcome the usual trial and error industrial alloy development. Efforts are focussed on a 100 000h creep strength of 100MPa at 650°C in combination with a sufficient corrosion resistance by a Cr content of 12% with contents 4-5%W, 3.4-5,5%Co,**V,** B and 1%Cu as well as the choice of Ta or Ti instead of Nb. The results demonstrate that the aim is not to realize with the used alloying concept. In the long term range all 12%Cr melts have a lower creep rupture strength than the advanced piping steel P92. A high creep strength could be reached with a 0.06% Ta alloyed 11%Cr melt, which is in addition alloyed with a higher C and B content and as well as with lower W and Co portions. The results indicate in accordance with the finding of other steel researcher that a lower Cr content allows more effectiveness for the alloying partners respectively for the generation of more stable precipitates.

Keywords: Creep behaviour 11-12% CrWCo(Cu)B(V,Ta,T) steels

1. Introduction

The improvement of thermal efficiency and the reduction of environmental influences led to developments of new ferritic-martensitic 9-10%Cr steels with improved high-temperature properties in order to comply the world-wide demands for higher steam parameters of Ultra Super Critical (USC) Power Plants. The aim of the present DFG research work is the development of new heat-resistant 12%Cr ferritic-martensitic steels with sufficient creep and oxidation resistance for a 650°C application by using basic principles and concepts of physical metallurgy on the basis of the state of art and to overcome the usual trial and error industrial alloy development. Alloy development, testing and analysis of microstructure are carried out by partners of a working group. (MPI E Duesseldorf, IWW 1 Erlangen, IWV 2 Juelich and IfW Darmstadt) [1] Efforts are focussed on a 100 000h creep rupture strength of 100MPa at 650°C in combination with a sufficient corrosion resistance by a Cr content of 12%. Series of model alloys were designed, produced and mechanically tested. Theoretical simulations and transmission electron microscopy investigations were part of the development work of model alloys. Results of creep tests of various 11-12%Cr test melts are presented in this work.

2. Development background of 650°C ferritic-martensitic steels

In the last decades significant improvements of the creep properties of 9-12%Cr steels were achieved by minor changes of the chemical compositions compared with well proven steels like X20CrMoV 12 1 [2-6].

The important changes in alloy chemistry are:

- balancing of the V, Nb and N contents for the generation of stable MX precipitates
- increased contents of Mo and W for solution hardening, $M_{23}C_6$ and Laves phase precipitates
- suppression of delta-ferrite with Co, Cu, Mn and C
- nucleation of Laves phase at Cu precipitates
- alloying with boron for the stabilisation of the $M_{23}C_6$ precipitates

The research work confirmed that alloying with boron is the most effective way for the improvement of the creep strength of the 9-12%Cr steels. T. Fujita found already in the sixties a substantial improvement of the creep strength by 0.027 to 0.040% of boron [2]. Meanwhile T. Fujita [3] confirmed the positive effect of boron by test results of an alloy with 0.040% boron (TAF steel) up to 130 000 h. The creep strength of these steels is not far away from the aimed creep rupture strength of 100MPa at 650°C and 100000h. The disadvantage of the high boron content is a reduced forgeability of large components. **Figure 1** exhibits the 100 000h creep strength of the TAF steel versus test temperature in comparison to the steel X20CrMoV 12 1 and to the two rotor steels X12CrMo(W)VNBN 10 1 (1) and X18CrMoVNbB 9 1, developed in the COST 501 research programme [6].

A further key element is Cr which dominates on one hand the oxidation resistance of the heat resistant ferritic-martensitic steels and on the other hand also the creep strength. Experiences demonstrate that a sufficient oxidation resistance occurs with a Cr content of min. 12% and that the highest creep strength is given by a Cr content of about 9.5%. **Figure 2** for example reveals the 100MPa creep strength at 650°C versus the Cr content of newly developed ferritic-martensitic steels of international programmes during the last decades[6]. The overall trend is the increasing of the creep strength with decreasing Cr content. An outstanding position in this comparison have test melts of the above mentioned TAF steel with a relatively high Cr content of 10.5 to 10.7% and a boron content of 0.027 to 0.040%.

Steel	C	Cr	Mo	W	V	Nb	N	B (W.-%)
a)	.28	1.0	0.9	-	.30	-	-	-
b)	.21	12.0	1.0	-	.30	-	-	-
c)	.12	10.0	1.5	-	.20	.05	.05	-
d)	.12	10.0	1.0	1.0	.20	.05	.05	-
e)	.18	9.0	1.5	-	.25	.05	.02	.010
f)	.20	10.5	1.5	-	.22	.15	.02	.040

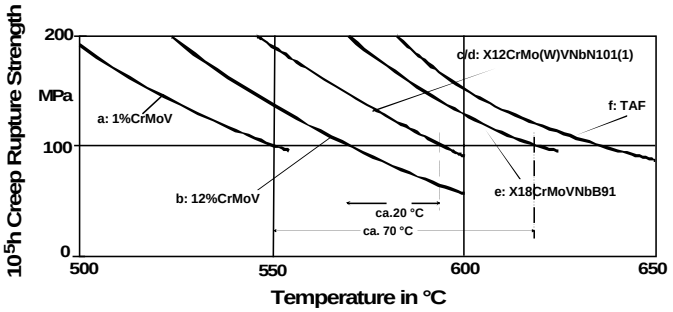

Figure 1: 100 000h creep strength of turbine steels

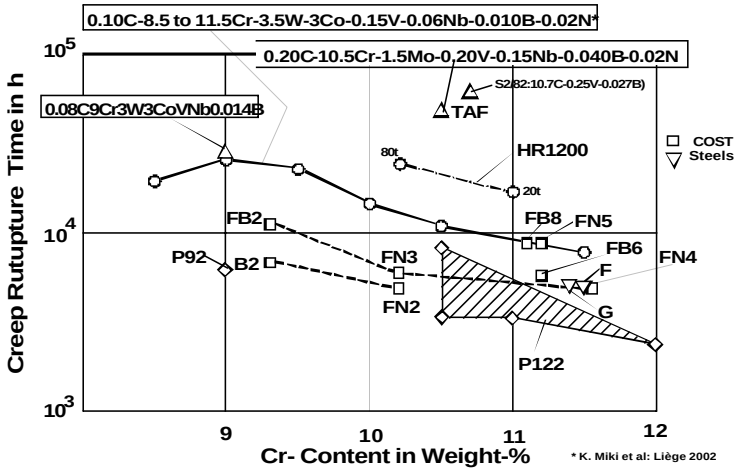

Figure 2: Creep rupture time of new developed ferritic-martensitic steels versus the Cr content for a test stress of 100MPa at 650°C

3. Alloying Concept

An overview of the chemical composition of 11 selected test steels of about 80 melts of the DGF programme is provided in Table 1. As a rule the Cr content is fixed to about 12%Cr to generate a sufficient oxidation resistance. The further elements have been selected to generate a ferritic-martensitic microstructure with precipitations of $M_{23}(C, B)_6$, MX and Laves phase. Further alloying principles are:

- balancing the ferritic-martensitic microstructure by 4-5.5%Co and by ca. 0.30%Mn; 0.13-0.20C; in some cases also by 0.7-1.0Cu
- strenghtening of $M_{23}C_6$ precipitates by 2-5%W; 0.007-0.022% B and 0.13-0.20%C
- strengthening of Laves phase by W
- in some cases supporting a fine distribution of Laves Phase by 0.7-1.0%Cu
- strengthening of MX precipitates by V and/or Ta; Nb and Ti.
- improvement of oxidation resistance by 0.30 to 0.40%Si

Table 1: Chemical composition of selected test steels of the DFG programme (weight-%)

Steel	C	Si	Mn	**Cr**	Mo	**W**	**Co**	**Cu**	V	Nb	Ta	Ti	N	B
5A	.16	.47	.10	**12.0**	.20	**1.99**	**4.81**	-	.22	.07	-	-	.032	<.001
6A	.18	.09	.10	**8.4**	.20	**1.93**	**4.84**	-	.21	.06	-	-	.034	<.001
41Cs	.13	.39	.30	11.9	-	**4.00**	**3.43**	-	-	-	**.20**	-	.050	.0080
52Cs	.15	.38	.32	11.8	-	**4.07**	**5.50**	-	**.39**	-	-	-	.049	.0066
53A	.16	.43	.36	11.9	-	**4.75**	**5.50**	-	**.68**	-	**.25**	-	.044	.0076
46Cs	.14	.40	.29	11.9	-	**3.97**	**4.44**	**1.0**	**.22**	-	-	-	.066	.0068
57A	.16	..42	.35	12.0	-	**4.86**	**4.85**	**1.0**	-	-	**.22**	-	.057	.0087
58A	.14	.42	.35	12.0	-	**4.84**	**4.79**	**1.0**	-		-	**.07**	.040	.0076
71As	.13	.37	.49	12.0	-	**4.00**	**4.00**	**1.0**	.20	-	**.14**	-	.045	.009
59As	**.19**	.37	.30	**11.0**	.50	**2.10**	**1.20**	**.71**	.27	-	**.09**	-	.030	**.020**
62As	**.20**	.28	.32	**10.8**	.51	**2.00**	**1.17**	**.76**	.28	**.04**	-	-	.030	**.022**

The test melts were melted by MPI Düsseldorf (5A and 6A) and by the forgemaster Saarschmiede. The heat treatment has been carried out by IfW Darmstadt. The heat treatment data, specified after a ThermoCalc calculation, are :

- Steels 5A and 6A: 0.5h 1070°C/air + 2h 760°C/air
- Steels 41Cs to 58A: 0.5h 1150°C + 2h 760°C/air
- Steel 71A: 0.5h 1150°C + 2h 730°C/air
- Steels 59As and 62As: 0.5h 1150°C + 2h 765°C/air

4. Results of creep tests

The creep rupture strength versus test time of the tests at 650°C are plotted in Figures 3 to 6. The gained data for the evaluation of the test results are compared with the creep strength of the TAF steel and of the advanced piping steel P92 [7].

Figure 3 demonstrates the negative influence of a high Co content of 4.8% and an increase of the Cr content from 8.4 to 12%Cr on the long term creep rupture strength of the piping steel type P92. The negative influence of Co was not expected due to the knowledge that Co slows down diffusion processes.

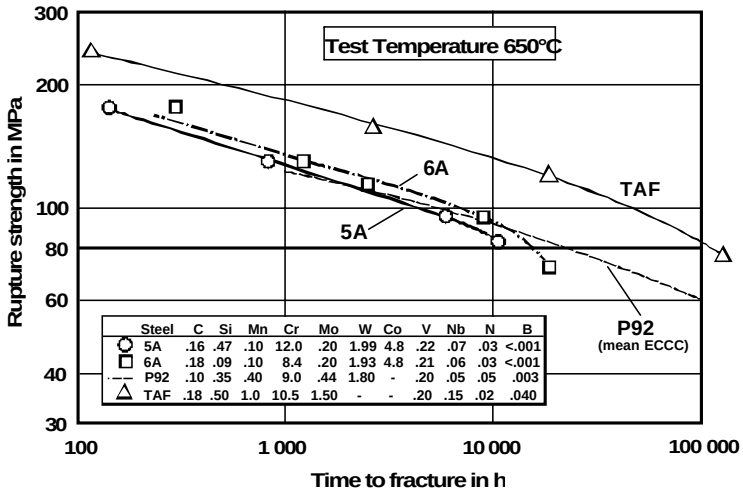

Figure 3: Creep rupture strength versus test time of the test steels 5A and 6A in comparison to the reference steels P92 and TAF at 650°C

Figure 4 gives an overview about the effect of Ta-MX, V-MX and V-Ta-MX on the creep rupture strength of the 12%CrWCo melts 41Cs, 52Cs and 53A. In the long time range all three types exhibit a lower creep strength than P92. The steel 52Cs with a V content of 0.39% has the highest strength**.** The weakest one is the test melt 41Cs with 0.20%Ta.

Figure 5 presents an overview about the effect of Ta-MX, V-MX, Ti-MX and V-Ta-MX on the creep rupture strength of the 12%CrWCo melts 46Cs, 57A, 58A and 71As which are alloyed in addition with about 1% Cu for the generation of finely distributed Laves phase particles. The results are in accordance with the results given in Figure 4. All four test melts reveal a lower creep strength than P92 in the long term range.

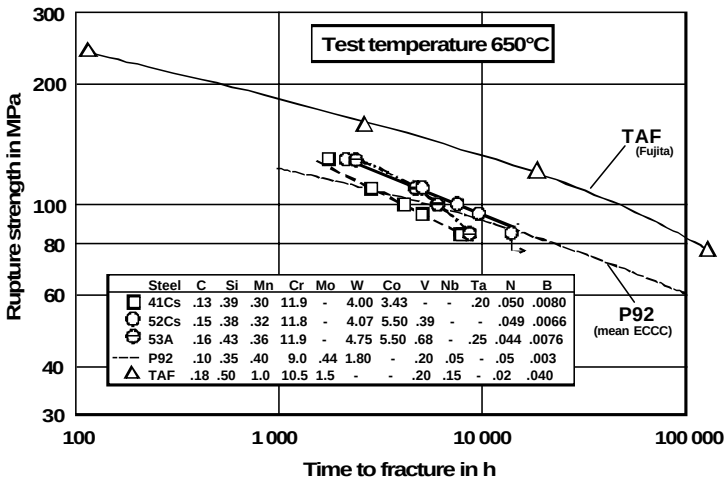

Figure 4: Creep rupture strength versus test time of the test steels 41Cs, 52Cs and 53A in comparison to the reference steels P92 and TAF at 650°C

The best behaviour was found again for a V-alloyed test steel (46Cs) and the weakest behaviour owns the Ta-alloyed test melt 57A. The creep rupture strength curve of the Ti-alloyed test melt 58A shows a sigmoidal shape and allows speculations about a slight better creep rupture behaviour above 10 000h. The accordance of the results of the Figures 4 and 5 indicates that the alloying with 1%Cu does not result in to the expected improvement of the creep rupture strength of the 12%CrWCo steels at 650°C.

In Figure 6 test results are plotted for the 11%Cr steels 59As and 62As which are alloyed with a different concept. They have higher C and B contents (about 0.20%C respectively 0.02%B) and significantly reduced W and Co contents. The distinction in the chemical composition of these two melts is a Ta content of 0.06% of the type 59As and a Nb content of 0.043% of the type 62As. This difference in the composition has obviously a substantial influence on the creep strength. The long term results of the Nb-variant 62As undercut the P92 curve whereas the results of the Ta-variant 59As indicate a rupture shape curve with a substantial higher creep strength in the whole test time range and probably moreover above 10000h. This tendency to a significant higher creep strength of the test melt 59AS is also clear to recognize at the pattern of the creep rate curves of the melts 59As, 62 As and P92(a specific investigated test melt) as demonstrated in Figure 7 for a stress of 100MPa. Long-term testing of steel 59As and 62 As is financed by German industry and BMWA with COST Action 536.

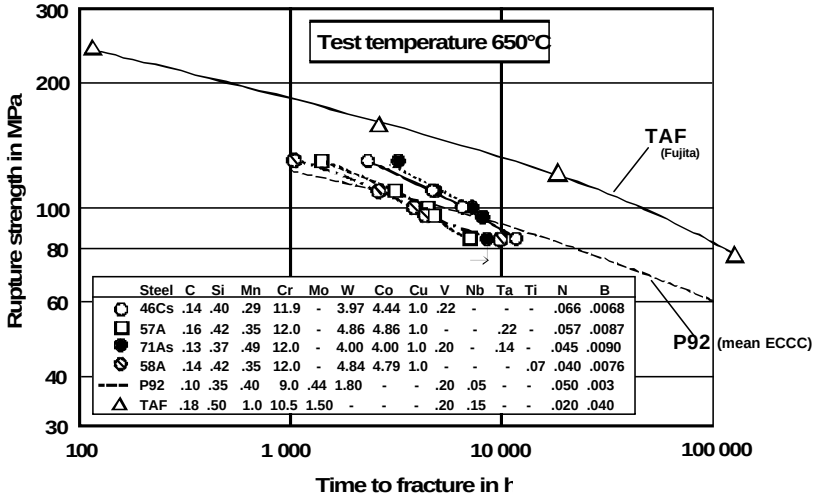

Figure 5: Creep rupture strength versus test time of the test steels 46Cs, 57A and 58A and 71A in comparison to the reference steels P92 and TAF at 650°C

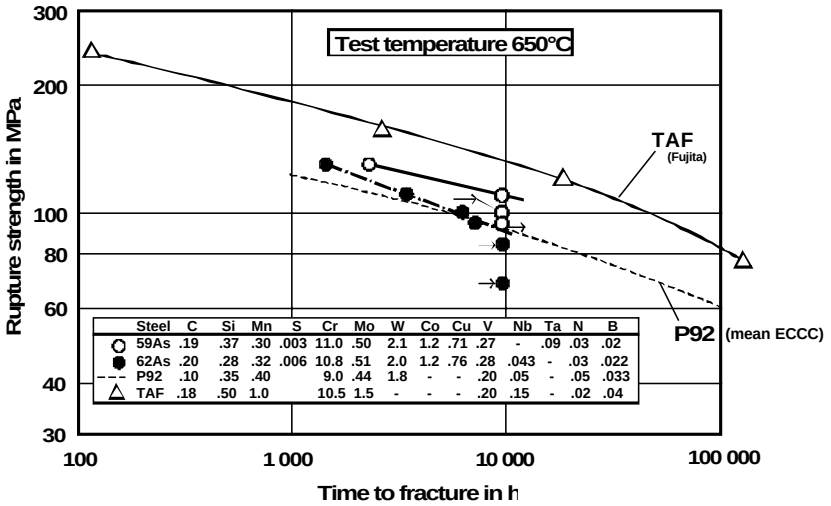

Figure 6: Creep rupture strength versus test time of the test steels 59As and 62As in comparison to the reference steels P92 and TAF at 650°C

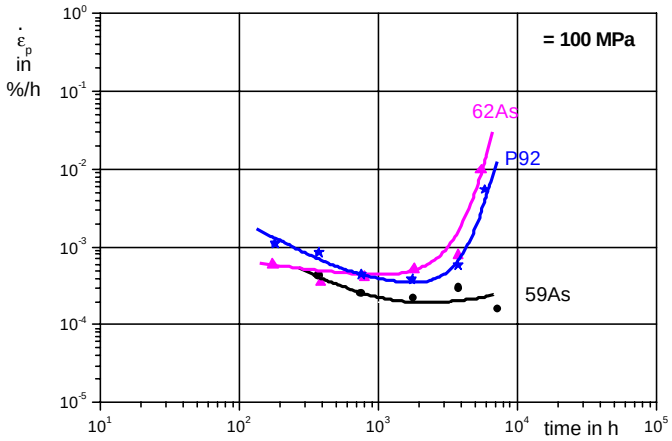

Figure 7: Creep rate $\dot{\varepsilon}_p$ versus test time of the test steels 59As and 62As in comparison to the reference steel P92 at 650°C

5. Discussion of the test results

The gained test results demonstrate that the aim of a 100000h creep rupture strength of 100MPa at 650°C is not to be realized with the used alloying concept, which is characterized particularly by a Cr content of 12%. In the long term range all 12%Cr test melts have a lower creep strength than the advanced piping steel P92, which can be used for a application temperature up to about 620°C. This outcome is in general line with the results of Figure 2, in spite of the high W content of 4-5% , the choice of Ta and Ti instead of Nb and the alloying with Cu for the generation of a finer distribution of the Laves phase particles. The most effective MX precipitates are obviously VX precipitates, which contribute to a higher creep strength without additional alloying with Ta. The results further indicate that a high Co content, used to avoid delta-ferrite in the presence of the high Cr content of 12%Cr and to slow down the diffusion processes, does not has a positive effect on the creep strength at 650°C. Also the B contents of 0.007-0.009% on the stabilization of the microstructure of the 12%Cr steels is questionable. The investigation of the microstructure evolution, which allows the reasons for the low long term creep strength to be understood, is on-going and will be presented later on. A highlight of this investigation is the positive creep behaviour of the Ta alloyed 11%Cr steel 59As, which is in addition alloyed with a higher C and B contents as well as with lower W and Co amounts. The results indicate again that a lower Cr content allows more effectiveness for the alloying partners respectively for the generation of more stable precipitates. But the comparison with the weaker Nb-alloyed partner 62As also demonstrates clearly that the replacement of only one element can completely change the creep behaviour. Behind of this behaviour can only be an additional contribution to the creep strength by finely distributed Ta(C,N).
Astonishing is the low creep strength of the test melt 62As, if we compare the chemical composition of this melt with the composition of the high strength TAF steel, see Table 2.

Table 2: Chemical composition of the test melts 62As and of the Steel TAF

Steel	C	Si	Mn	Cr	Mo	W	Co	Cu	V	Nb	Ta	N	B
62As	.20	.28	.32	10.8	.51	2.0	1.2	.76	.28	.043	-	.03	.022
TAF	.18	.50	1.0	10.5	1.5	-	-	-	.20	.15	-	.02	.04

The main difference between TAF and the weak melt 62As is probably the alloying of 62As with 1.2% Co and Cu as well as the lower B content. All the other elements have in respect to the already available knowledge no significant disadvantage on the creep strength. Due to the 2.0% W there is more Laves phase in 62As, which should not result in a lower creep strength if we also consider that Cu precipitates support a finer distribution of Laves phase. The higher V and the lower Mn and Nb amounts should promote and not reduce the creep strength. Already on-going microstructure investigations of the creep specimens of 59As and 62As will probably disclose the causes of the different creep behaviour of these melts. Results of a comprehensive microstructure investigation of creep specimens of the TAF steel are already available for this purpose [8].

In the context of the relatively high creep strength of the 11%Cr test melt 59As, we have in addition to consider the influence of the Cr content on the oxidation resistance in a steam atmosphere, because the general requirement of a sufficient oxidation resistance is a Cr content of min. 12%. In the framework of the DFG programme the partner IWV 2 Jülich has investigated among other test melts specimens of the 11%Cr melts 59As and 62As as well as specimens of the 12%Cr melt 71As and of the piping steel P92 in an environment of Ar-50%H_2O at 600 and 650°C[9]. The results of Figure 8 show that the oxidation resistance of the 11%Cr test melts 59As and 62 As are even a bit higher than the oxidation resistance of the 12%Cr test melt 71As and all three test steels of the DFG programme exhibit as expected a significantly better oxidation resistance than the 9%Cr piping steel P92.

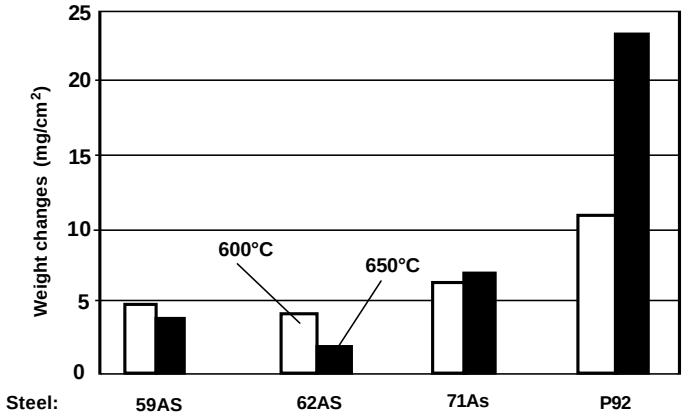

Figure 8: Comparison of the oxidation behaviour of the test melts 59As, 62As, 71As and steel P92 at 600°C and 650°C in Ar-50H_2O, data from [9]

The gained test results demonstrate that the aim of a 100000h creep rupture strength of 100 MPa at 650°C is not to be realized with the used alloying concept, which is characterized particularly by a Cr content of 12%, a high W and Co content and the choice of Ta and Ti instead of Nb as well as in some cases with the alloying by Cu for the generation of fine distributed Laves phase particles. Also the B amounts of 0.007-0.009% did not appearently lead to the stabilization of the microstructure of the 12%Cr steels [10]. In the long term range all 12%Cr test melts have a lower creep strength than the advanced piping steel P92, which can be used for a application temperature up to about 620°C.

A highlight of the investigation is the positive behaviour of the Ta alloyed 11%Cr melt 59As, which is in addition alloyed with a higher C and B content as well as with lower W and Co portions. The results indicate in accordance with the finding of other researcher that a lower Cr content allows more effectiveness for the alloying partners respectively for the generation of more stabile precipitates. The creep test results of the test melt 59As show a significant superiority to the steel P92 at 650°C in the whole investigated test time range and obviously also in the long time range above 10000h. The investigation of the microstructure evolution, which allows the reasons for the different long term creep strength to be understood, is on-going and will be presented by the project partners later on.

Acknowledgement
The financial support by the Deutsche Forschungsgemeinschaft is gratefully acknowledged. Further companies in the working group are kindly acknowledged for providing test material.

7. References

[1] R. Agamennone, C. Berger, W. Blum, J. Ehlers, P.J. Ennis, J. Granacher, G. Inden, V. Knezevic, J. W. Quadakkers, G. Sauthoff, A. Scholz, L. Singheiser, J. Vilk and Y. Wang: "Martensitic/Ferritic Super Heat-Resistant 650°C Steels", in: Materials for Advanced Power Engineering 2002 (Proc. 7th Liége Conference), Hrsg. J. Lecomte-Beckers, M. Carton, F. Schubert und P.J. Ennis, Forschungszentrum Jülich (2002) III. 1279-1288.

[2] T. Fujita: "Effect of Mo,V, Nb, and N on creep rupture strength of TAF steel", Trans JIM, Vol. 9 (1968) pages 167 –169.

[3] T. Fujita: "Twenty-first century electricity generation plants and materials", International Workshop on Development of Advanced Heat Resistant Steels, 8th November 1999, Yokohama, Japan (1999).

[4] F. Abe: "Alloy design of creep and oxidation resistant 9Cr steels for thick section boiler components operating at 650°C", 4th EPRI Conference on Advances in Materials Technogy for Fossil Power Plants,25.-28.October 2004, Hilton Oceanfront Resort, Hilton Head Island, SC, USA (2004) 273 pages 202-216.

[5] M. Hättestrand: "Precipitation reactions at high temperature in 9-12%Cr steels", Doctorial thesis for the degree of Doctor of Philosopy, Chalmers University of Technology and Göteborg University, Sweden, 2000.

[6] K. H. Mayer: "Einfluß des Cr-Gehaltes auf die Zeitstandfestigkeit der modernen 9-12%Cr-Stähle.", 29. MPA Seminar-Stuttgart, 9-10. Oktober 2003.

[7] J. Hald: “ECCC E911-P92 Assessment”, ECCC Data Sheet published in Sept. 2005 at the ECCC creep conference, Sept. 12-14, 2005, London, UK.

[8] F. Kauffmann, G. Zies, C. Scheu, H. Ruoff, K. Maile, S. Straub and K.H. Mayer: “Microstructural characterization of modern Boron containing 9-11%Cr steels developed in the frame of the COST program”, 8th Liège COST Conference Materials for Advanced Power Engineering, 18.-20. September 2006, Liège, Belgium.

[9] J. Pirón Abellán, P. J. Ennis, L. Singheiser, W. J. Quadakkers: Microstructure and steam oxidation resistance of Laves phase forming 12% Cr steels at 600-650°C, 8th Liège COST Conference Materials for Advanced Power Engineering, 18.-20. September 2006, Liège, Belgium.

[10] C. Berger, A. Scholz, Y. Wang, K.-H. Mayer: Creep and creep rupture behaviour of 650°C ferritic/martensitic super heat resistant steels, Zeitschrift für Metallkunde 96 (2005), 6, S. 668-674.

STATUS OF DEVELOPMENT OF THE VM12 STEEL FOR TUBULAR APPLICATIONS IN ADVANCED POWER PLANTS

J. Gabrel, Centre de Recherche Vallourec, Route de Leval, F-59620 Aulnoye
W. Bendick, Salzgitter-Mannesmann Forschung GmbH, Ehinger Str. 200, D-47259 Duisburg
B. Vandenberghe, V&M France, 37 rue Henri Barbusse, 59880 Saint-Saulve, France
B. Lefebvre, V&M France, ZI du Galibot, 59880 Saint-Saulve, France

e-mail address : jean.gabrel@vallourec.fr

Abstract

New design power plants require high pressure and high temperature steam parameters in order to reach higher efficiencies and minimize harmful emissions. This evolution has lead to the development of new families of ferritic steels with improved creep rupture strength values together with a good oxidation resistance in steam at high temperature.
Recently, Vallourec and Mannesmann Tubes started the development of a new 12%Cr-steel, called VM12, to be used as tubes and pipes for steam temperature up to 650°C. Manufacturing of this grade has been proved by production of several heats and rolling of tubes and pipes in several dimensions and with different rolling processes. Beside of base metal properties investigations – including creep tests and high temperature oxidation behaviour – welding, cold bending and hot induction bending qualifications took place. This paper summarises the results of the investigations and presents the first findings for processing.

Keywords: 9-12% Cr steels, VM12, Creep properties, Steam side oxidation, Processing

Introduction

The development of steels like T/P911 and T/P92 has achieved an increase of creep rupture strength of 10 to 25% in comparison with modified 9% chromium steel T/P91. Their use allows operating temperatures up to about 610°C for live steam and 620°C for hot reheat steam [1 - 3] limited by their oxidation and corrosion resistance.
Worldwide activities aim at further improvement of plant efficiency by continuing to increase the steam temperature. Also new ferritic steels are needed for use at higher operating temperature between 610 and 650°C.
The aim of the R&D project initiated by Vallourec & Mannesmann Tubes (V&M) was to develop a new 12% Cr steel with improved oxidation resistance to allow an application up to 650°C [4, 5]. In addition the strength properties of the new steel should be close to the best ferritic steel T/P92.

Tube and Pipe production

Based on the positive results of the 7 lab heats [6], V&M decided to take the next step of alloy development, i.e. industrialization of the new steel grade under the name VM12. The following table gives the different processes and products.

Steel plants	*Process*	*Quantity tons*	*Round bar*	*Mills*	*Process*	*Products*
1	*Electric Arc Furnace - Vacuum degassing*	*20*	*Ingot Forging*	*A*	*continuous mandrel rolling*	*Tubes 60.3 x 8.8 mm*
				E	*push bench*	*Tubes 51 x 4 mm*
			Ingot	*B*	*pierce and pilger rolling*	*Pipes 406.4 x 35 mm*
2		*80*	*Continuous Casting + Forging*	*A*	*continuous mandrel rolling*	*Tubes 38 x 6.3 mm 38 x 7.1 mm 44.5 x 10 mm 51 x 4 mm*
				E	*push bench*	*Tubes 51 x 4 mm*
				C	*continuous mandrel rolling*	*Tubes 140 x 12 mm*
3		*65*	*Ingot*	*D*	*pierce and draw rolling*	*Pipes 460 x 80 mm*
				B	*pierce and pilger rolling*	*Pipes 460 x 60 mm*

Table 1: Status of the Industrial production of VM12 grade

Whatever the tube or pipe sizes and processes, no problems occurred during production. The cast and rolling revealed a comparable behaviour to T/P91.

Chemical composition

The chemical composition of the three VM12 industrial heats is given in table 2 and compared with the Lab heat F and ASTM A213 for grades T92 and T122.

Grades	*C %*	*Mn %*	*P %*	*S %*	*Si %*	*Cr %*	*W %*	*Mo %*	*V %*	*Nb %*	*Co %*	*N %*	*B %*	*Al %*	*Ni %*	*Cu %*
A213 T92	*0.07 0.13*	*0.30 0.60*	*- 0.020*	*- 0.010*	*- 0.50*	*8.50 9.50*	*1.5 2.00*	*0.30 0.60*	*0.15 0.25*	*0.04 0.09*		*0.030 0.070*	*0.001 0.006*	*- 0.04*	*- 0.40*	
A213 T122	*0.07 0.14*	*- 0.70*	*- 0.020*	*- 0.020*	*- 0.50*	*10.0 12.5*	*1.50 2.50*	*0.25 0.60*	*0.15 0.30*	*0.04 0.10*		*0.040 0.100*	*0.0005 0.005*	*- 0.04*	*- 0.50*	*0.30 1.70*
Lab Heat F	*0.110*	*0.20*	*0.013*	*0.002*	*0.45*	*11.50*	*1.40*	*0.28*	*0.24*	*0.065*	*1.30*	*0.056*	*0.0030*	*0.015*	*0.23*	*0.013*
Industrial Heat 1	*0.115*	*0.35*	*0.018*	*0.001*	*0.49*	*11.50*	*1.50*	*0.29*	*0.26*	*0.050*	*1.62*	*0.065*	*0.0049*	*0.008*	*0.29*	*0.080*
Industrial Heat 2	*0.106*	*0.32*	*0.015*	*0.002*	*0.45*	*11.25*	*1.44*	*0.24*	*0.26*	*0.047*	*1.55*	*0.055*	*0.0044*	*0.012*	*0.26*	*0.045*
Industrial Heat 3	*0.110*	*0.18*	*0.018*	*0.002*	*0.48*	*11.25*	*1.44*	*0.27*	*0.23*	*0.051*	*1.50*	*0.053*	*0.0035*	*0.010*	*0.23*	*0.080*

Table 2: Chemical composition of the three industrial heats (mass - %)

VM12 has high chromium and silicon content in order to meet the requirement for good oxidation resistance. Vanadium, niobium and nitrogen have been introduced in quantities

similar to the 9% Cr-steels in order to achieve precipitation strengthening by MX particles. Other strengthening elements such as molybdenum, tungsten and boron have also been added. VM12 is a tungsten bearing steel with 1.4% W and only 0.3% Mo, using the strengthening effect of Laves phase precipitation similar to T/P92.

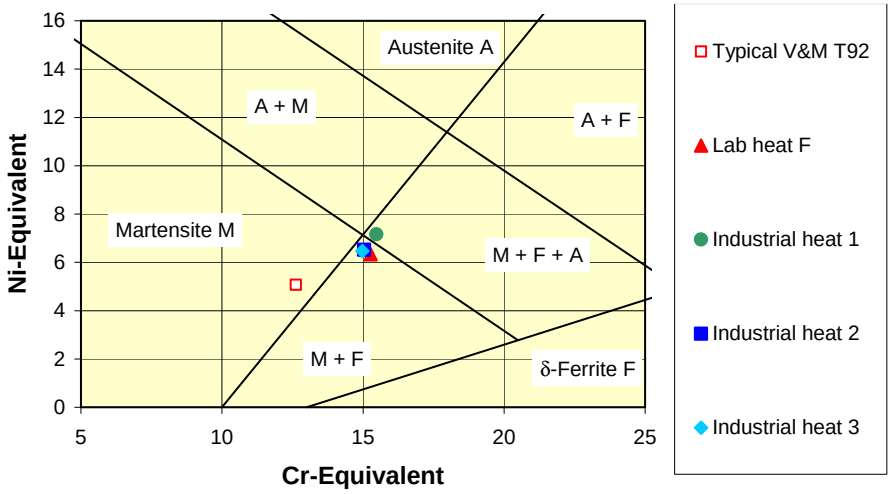

Figure 1: modified Schaeffler diagram
Cr_{Eq} = Cr + 2Si + 1.5Mo + 5V + 5.5Al + 1.75 Cb + 1.5Ti + 0.75W
Ni_{Eq} = Ni + Co + 0.5Mn + 30C + 0.3Cu + 25 N

The chromium and nickel equivalents for the three industrial heats have been calculated and plotted into the figure 1 allowing a rough estimation of the phase stability of these heats. All heats are located near the martensite area where the Cr_{Eq} is maximum to obtain a fully martensitic structure. For comparison the figure 1 gives the location of the typical V&M T92.

Heat treatment and structure

VM12 steel is used in the normalized and tempered condition. The typical heat treatment after hot rolling is:

- Normalization: 1040-1080°C (1905-1975°F) / air cooling
- Tempering: 750-800°C (1380-1470°F) / air cooling

Depending on chemical composition, A_{C1} temperature was found to be between 820°C (1510°F) and 830°C(1525°F), and A_{C3} around 890°C (1635°F).

The structure is composed of tempered martensite. A small amount of δ-ferrite (less than 2%) could be present as illustrated by Figure 2. This low amount of δ-ferrite had no influence on the rolling behaviour and mechanical properties.

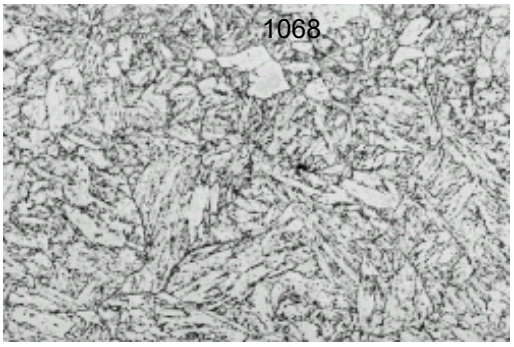

Figure 2 : Microstructure (pipe 406.4 x 35 mm)
after normalization and tempering

Mechanical properties

Tensile Properties

Yield and tensile strength values at room and elevated temperature are plotted in the figure 3. Actual results are distinctly located above the minimum curves of T/P92. Tensile properties of VM12 are similar to T/P92 as illustrated.

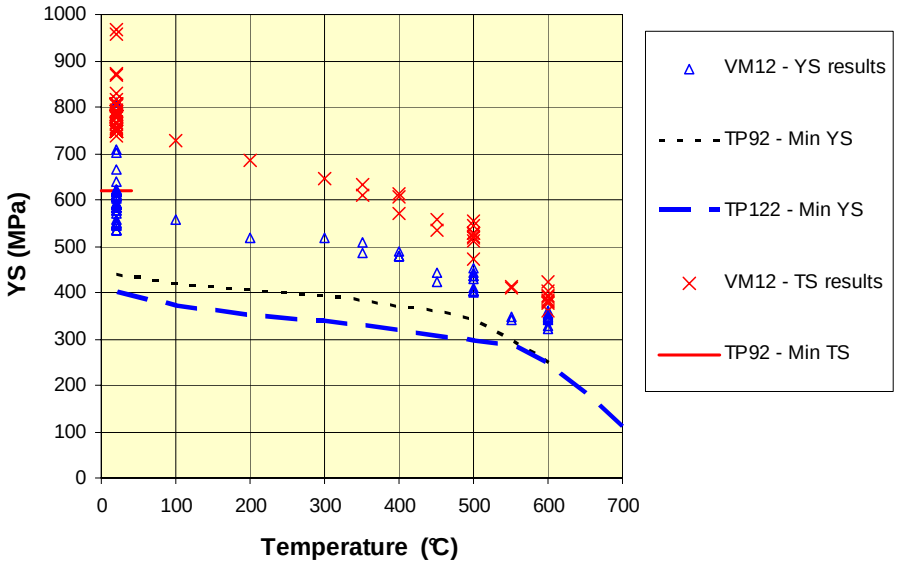

Figure 3 Yield and tensile strength of VM12 compared to TP92 and TP122

Impact tests

As illustrated by the figure 4 both VM12 tube and pipe from the first industrial heat show good impact properties. For example at room temperature the absorbed energies are 119 J (tube) and 103 J (pipe)

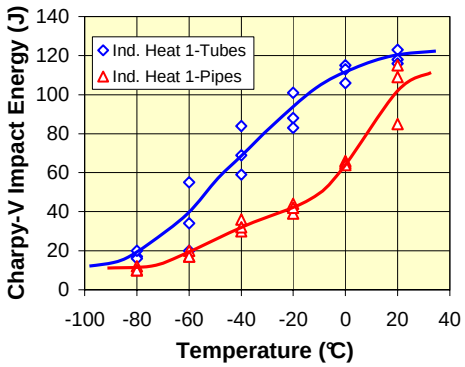

Figure 4 Charpy-V notch results of VM12 tubes and pipes from the first industrial heat (5)

Creep tests

A creep testing program has started for 550, 600, 625 and 650°C (1020, 1110, 1155 and 1200°F) temperatures. Currently the longest tests are now greater than 22 000 hours; the cumulated duration is close to 820 000 hours.

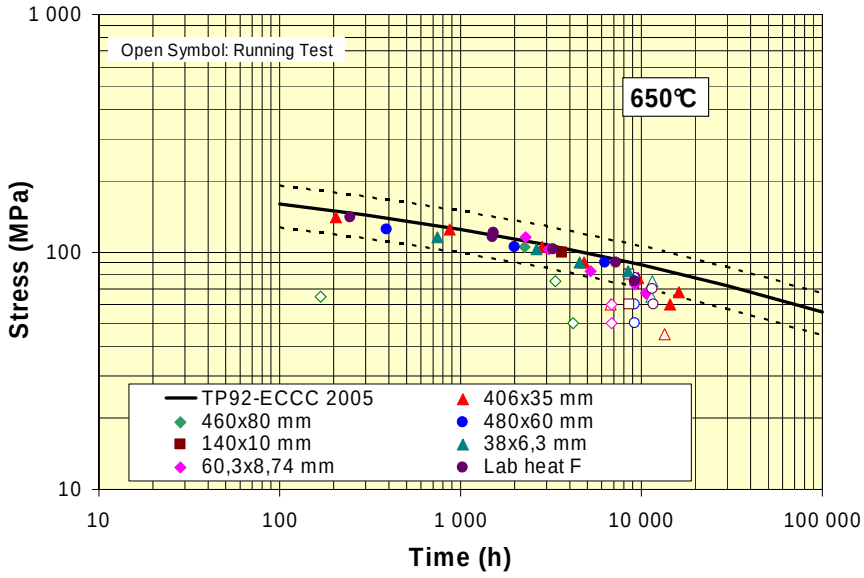

Figure 5 Creep test results at 650°C

The current status at 650°C is given in the figure 5. A first estimation gives a mean rupture stress at 600°C (1110°F) for 100,000 hours of 100 MPa. In comparison with the assessment performed in 2005 by the European Creep Collaborative Committee (ECCC) for T/P92 (113MPa) and T/P911 (98 MPa), VM12 seems to behave like T/P911 and a little lower than

TP92. However, the current status of testing does not allow a final judgment on creep strength.

Steam side oxidation

Inner steam oxidation is the cause of various problems in power plants, such as:

- The increase in the metal temperature during operating due to the formation of an insulating layer of oxide between the internal tube surface and the steam.
- The formation of oxide layers reducing the tube thickness and increasing the stress
- Exfoliation of the oxide layers, sealing tubes or causing erosion inside the turbine.

As everybody knows, steam side oxidation resistance is a limitation of the design temperature of 9%Cr steels. In spite of the fact that T/P92 steel has good mechanical properties at elevated temperature, its steam oxidation resistance is similar to T91. Consequently the operating temperature of such steels found its limit at around 610°C (1130°F).
Improved oxidation behaviour was one of the key requirements for the new VM12 steel.

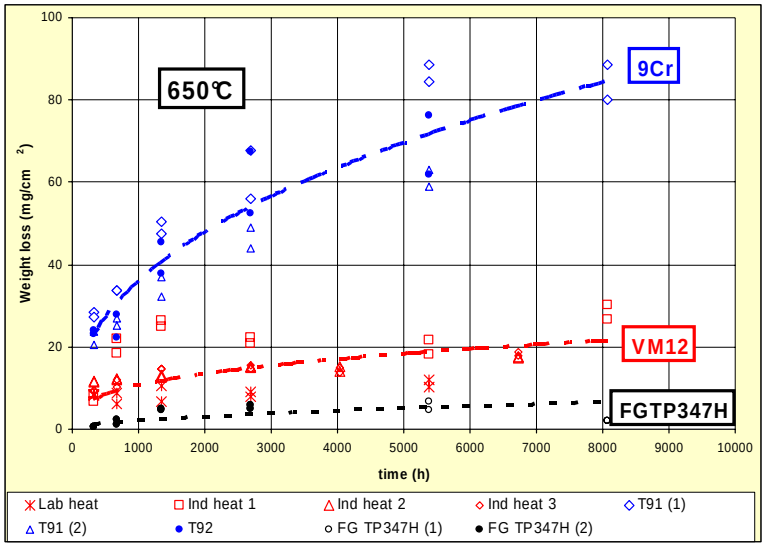

Figure 6: Steam side oxidation at 650°C in pure vapour [7]

Therefore oxidation tests were performed at 600 (1110°F) and 650°C (1200°F) in pure water vapour (Tests made by Ecole des Mines-Douai-France). Test duration of 8,000 h has been reached. As an example the results at 650°C (1200°F) are represented in figure 6. In addition to the new steel, material from T91, T92 and TP347 FG were also exposed for comparison. The weight change measurements indicate a distinct better oxidation resistance of the new VM12 steel compared to T91 and also to T92. On the other hand results are close to the austenitic steel TP347FG.
For all test durations and temperatures, two different types of corroded surfaces were observed:

- The first one is characterized by a relatively homogeneous two-oxide layer: The scale thickness grows with temperature and time of exposure. A typical example is T/P91.

- The second one shows localised nodules of corrosion products beneath which the steel is attacked: this type is the best represented by TP347FG. In the locations of the nodules, the oxide thickness increases with the time but simultaneously the corrosion attack expands onto the whole surface.

VM12 steel revealed a very thin homogenous oxide layer, whereas T91 and T92 partly showed severe local attack. Additional tests on VM12 were performed in an argon atmosphere with 50 vol.-% steam in a second laboratory (Tests made by Forschungszentrum-Jülich-Germany). More recently Alstom Germany inside the COST project and Babcock & Wilcox in the frameworks of the DOE program [8] and [9] have confirmed the excellent steam oxidation resistance of the VM12 independently of the specific test conditions.

Processing:

Welding

Welding consumables (coated electrode, solid wire and flux) and welding procedures have been developed by partner companies.
In weldability tests [10], neither hot cracks nor end crater cracks have been observed. Also the material did not show any susceptibility to stress relief cracking. Main conclusions from weld simulations are:

- The lowest toughness and highest hardness can be expected in the coarse grained HAZ
- Fulfilling the hardness criteria (<350HV) seems easily achievable with a post welding heat treatment at 770°C.

First industrial welds (SMAW and SAW) were performed on pipe 406.4 x 35 mm from the first industrial heat. After post welding heat treatment performed at 770°C / 2 hours, microstructure and mechanical properties (tensile, impact, hardness and creep) showed satisfying results. Figure 7 shows the status of creep tests on the SMA-weld at 625°C.

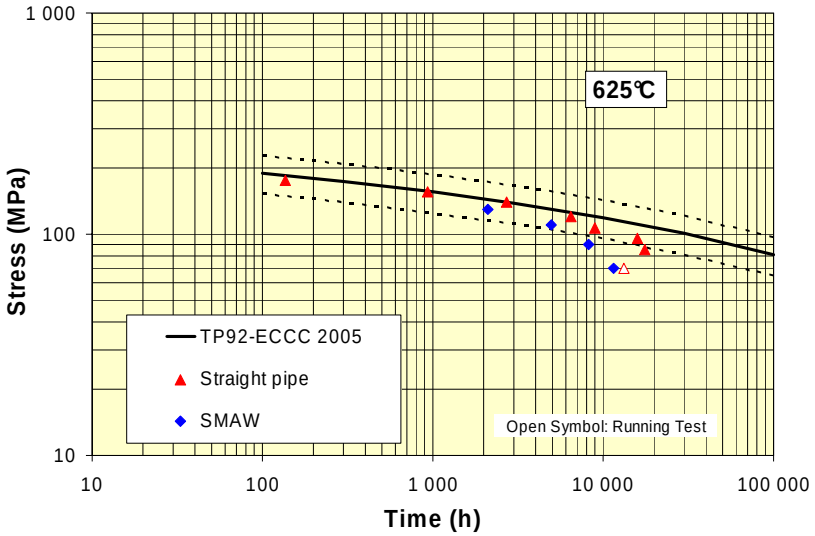

Figure 7: Cross weld creep tests on SMAW joint

Induction bending

An induction bend has been made from the same pipe used for welding trials. After complete heat treatment (normalization and tempering), microstructure and mechanical properties are very similar to the parent pipe as illustrated by figures 8 and 9.

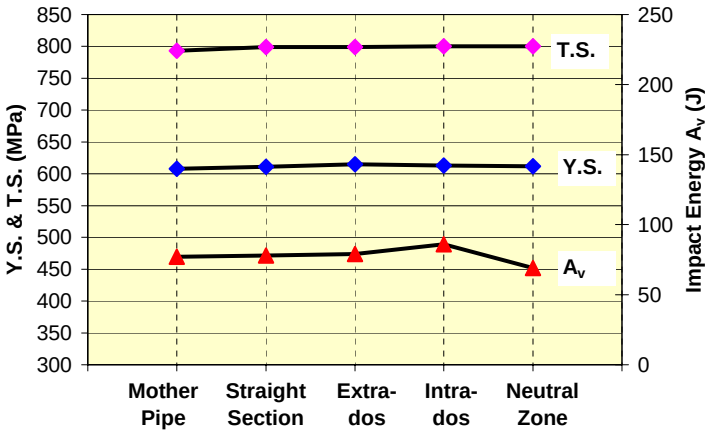

Figure 8: Mechanical properties at RT after hot bending, normalizing and tempering

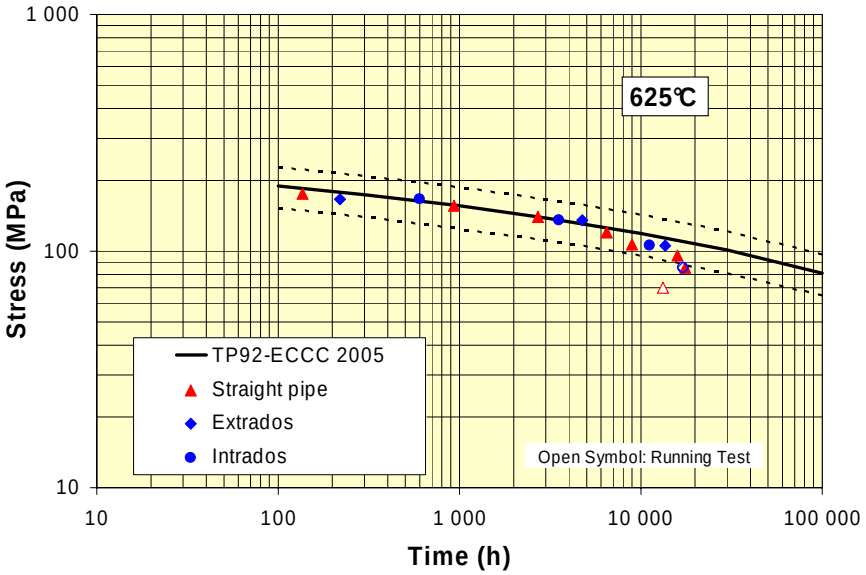

Figure 9: Creep results after hot bending, normalizing and tempering

Cold bending

For this purpose V&M worked with two partner companies to perform cold bending qualifications. Thanks to their facilities (Schwarzewirtz machines 100DB with back thrust jack), cold bends were performed on tubes 38 x 6.3 mm and 60.3 x 8.8 mm with a radius between 3 and 1.3 times the outside diameter (figure 10).
After bending without any problem, each bent tube was controlled by dye penetrant method. No external defects were detected. Variation in wall thickness as illustrated below (figure 11) and behaviour during bending were very comparable to T91 or T92. Hardness and microstructure were satisfying in the as bent condition and after stress relief treatment (SRT) at 750°C.

Figure 10: Cold bending operation

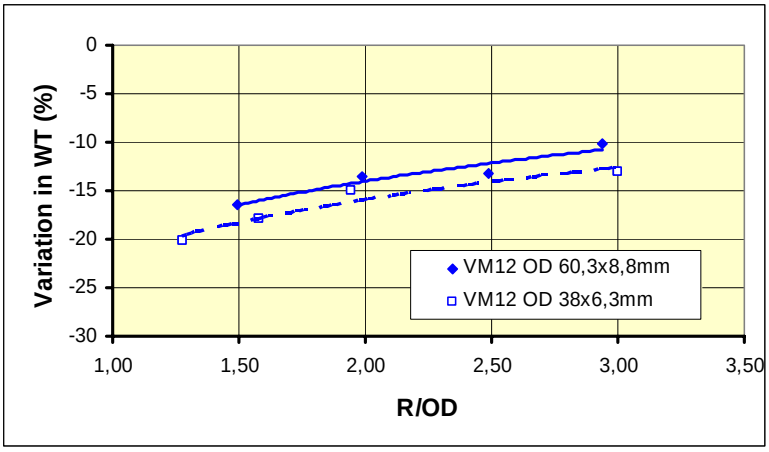

Figure 11: Variation in wall thickness in extrados versus the ratio radius/outside diameter

Principally, no recrystallization has been observed showing the very stable structure of the VM12 steel. Moreover this observation was confirmed after cold deformation of up to 35% followed by SRT. Creep tests after bending and cold deformation show similar results to those obtained on the parent tube. Even though the results were satisfying, we recommend

performing a stress relief treatment at 750°C to eliminate or reduce residual stresses for most severe bending radii.

Conclusion:

Results on industrial tubular products confirm the first results obtained with lab heats.
Thanks to a good adjustment of chemical composition, tubes and pipes have been rolled without any trouble in accordance with mill procedures used for T/P91.
Structure and mechanical properties at room and elevated temperatures are similar to T/P92.
With industrial heats, we also get excellent steam side corrosion behaviour at 650°C (1200°F); it is close to austenitic steels.
Welding and bending trials with boiler maker partners show that recommendations defined for 91 and 92 grades will be similar for the new grade, especially for welding, cold and induction bending operations.
The creep properties seem to behave like T/P911 and are not as high as initially expected in comparison with TP92. However the creep results are clearly upper than other 12%Cr steels with comparable oxidation resistance.

Because of its excellent steam-side oxidation resistance and good processing, VM12 has been recently chosen for a German project. For this special application a TÜV approval is ongoing, although the development of the steel grade has not been finished yet.

Outlook:

For improving creep properties and keeping the excellent oxidation resistance, three new lab heats with slight modification of the chemical composition have been produced. Presently the steam oxidation results are located in the same scatter-band and the creep tests, which have reached 7 000 h, are too short to allow a reliable judgment.

Acknowledgement:

Part of this work was performed within the frame of the European COST Action 536 with funding by the German BMWA under Contract No. 0327705F.

List of references

[1] W. Bendick, F. Deshayes, K. Haarmann, and J.-C. Vaillant, EPRI Conf. Advanced Heat Resistant Steels for Power Generation, San Sebastian, Spain, 27-29 April, 1998

[2] D. Richardot, J.-C. Vaillant, A. Arbab, and W. Bendick, *The T92/P92 Book*. Vallourec & Mannesmann Tubes, 2000

[3] A. Arbab, J.-C. Vaillant, and B. Vandenberghe, 3rd EPRI Conference “Advances in Material Technology for Fossil Power Plants”, 5-6 April, 2001, Swansea, UK, ed. by R. Viswanathan et al., The Institute of Materials, London, 2001, pp. 99-112

[4] J. Gabrel, W. Bendick, JC. Vaillant, B. Vandenberghe and Bo. Lefebvre, 4th Int. Conference on advances in Materials Technology for fossil Power Plants, “VM12-A new

12%Cr steel for boiler tubes, headers and steam pipes in ultra-super- critical power plants.”, 15-28 Oct. 2004, 10 pages

[5] B. Vandenberghe, J. Gabrel, JC. Vaillant and Bo. Lefebvre, AFIAP conference, “Development of a new 12%Cr steel for tubes and pipes in power plants with steam temperatures up to 650°C”, Paris 28-30 Sept 2004, 12 pages

[6] W. Bendick, J. Gabrel, JC. Vaillant and B. Vandenberghe, Liège conference, “Development of a new 12%Cr steel for tubes and pipes in power plants with steam temperatures up to 650°C”, Liege 30 Sept- 2 Oct. 2002, 10 pages

[7] V. Lepingle, G. Louis, D. Petelot, B. Lefebvre, B. Vandenberghe, « Long term exposure of new 12% Cr boiler steels in steam high temperature ». Eurocorr 2005 - Lisbon - 4-8 Sept 2005

[8] J.M. Sarver, J.M. Tanzosh, “Preliminary results from steam oxidation tests performed on candidate materials for ultra supercritical boiler” EPRI International Conference on Materials and Corrosion Experience for Fossil Power Plants, Charleston, 2003

[9] J.M. Sarver, J.M. Tanzosh, 4th Int. Conference on advances in Materials Technology for fossil Power Plants, “An Evaluation of the Steamside Oxidation of Candidate USC Materials at 650°C and 800°C”, 15-28 Oct. 2004

[10] A. Dhooge, S. Huysemans, B. Vandenberghe, J. Vekeman , New 12%Cr steel for tubes and pipes in power plants with steam temperature up to 650°C - Weldability and high temperature behaviour- Welds 2005 - Geesthacht - 8-9 Sept 2005

MICROSTRUCTURAL DEVELOPMENT OF VM12 STEEL CAUSED BY CREEP DEFORMATION AT 625 °C

A Zielińska -Lipiec[1], W Bendick[2], G Cempura[1], B Vandenberghe[3], P J Ennis[4], A Czyrska-Filemonowicz[1]

[1] AGH University of Science and Technology, PL-30 059 Kraków, Poland
[2] Salzgitter Mannesmann Forschung GmbH, D-47251 Duisburg, Germany
[3] V&M France CTIV, F-59880 Saint-Saulve, France
[4] Research Centre Jülich, Institute for Materials and Processes in Energy Systems, IWV-2, D-52425 Jülich, Germany

Abstract

The microstructure of the as received and long-term creep deformed new martensitic 12% Cr steel, VM12, has been characterised using analytical transmission electron microscopy (TEM). Statistical quantitative analyses of VM12 steel microstructure, based on TEM micrographs, were undertaken to determine the dislocation density within the subgrain, the width of the martensite laths/subgrain and the precipitates parameters (shape, size, distribution). Phase identification was performed using electron diffraction and X-ray spectrometry.

The TEM results showed that the as received VM12 steel microstructure consists of elongated sub-grains with various precipitates. Sub-grains boundaries were pinned by $M_{23}C_6$, while fine MX were precipitated within the sub-grains. The dislocation density within the subgrain was high. Thermal exposure and creep deformation at 625°C caused some changes of the VM12 steel microstructure. Statistical quantitative analyses of the microstructural parameters, based on TEM micrographs, showed that the sub-grains size and $M_{23}C_6$ parameters slightly increased after exposure up to 16 000h. Microstructure changes in the creep deformed specimens were much more pronounced than in the thermal exposed (annealed) specimens. These findings are correlated with long-term rupture strength of VM12 steel.

Keywords: 12%Cr steel, VM12, creep, microstructure, analytical TEM

Introduction

In the European COST Actions 501 and 522, martensitic 9-12% chromium steel for advanced coal-fired power stations, which can be operated reliably at higher temperatures and pressures, were developed. The research programmes were set to establish the basic guidelines for achieving new steels with enhanced creep rupture strength and improved steam-oxidation resistance to be used for supercritical steam conditions.

Creep deformation of martensitic steels during service exposure at high temperature is controlled by recovery and softening processes of the tempered martensite, which strongly depends on the microstructure and its change with time. Also the alloying elements strongly influence the thermodynamic stabilization and strengthening of martensitic matrix. Combined addition of the ferrite-stabilizing elements such as Mo, W is effective both to increase thermodynamic stability of matrix and to increase the creep rupture strength. Additions of V and Nb are necessary for precipitation hardening of the matrix. For satisfactory creep and

stress rupture strength, Cr contents of around 9-10% allows the desired fully martensitic microstructure to be obtained. For satisfactory resistance to steam oxidation, Cr contents of at least 11% are necessary [1, 2].

The present study is focused on the detailed characterisation of the VM12 steel, a new high chromium martensitic steel developed for advanced coal-fired power station operating around 650 ˚C [3]. The microstructure of the as-received steel and its changes during annealing and creep deformation at 625 ˚C for about 16 000 h is described. Microstructural stability, which influences the long-term rupture strength of the VM12 steel, is discussed.

Experimental details

The VM12 steel was delivered by Vallourec & Mannesmann Tubes as a pipe of 406.4 x 35 mm. The steel chemical composition is as follows (wt %): 0.115 C, 11.50 Cr, 1.62 Co, 1.50 W, 0.29 Mo, 0.29 Ni, 0.26 V, 0.05 Nb, 0.08 Cu, 0.005 B, 0.066 N. Its heat treatment consisted in austenitisation at 1060 ºC /0.5 h followed by tempering at 780 ºC /2 h.

Creep tests were carried out at 625 ºC. The experimental data of specimens selected for microstructure investigations are listed in Table 1.

Table 1 Creep tests on VM12 pipe 406.4 x 35 mm specimens at 625 °C

Stress MPa	Time h	Status[1)]	Rupture	
			Elongation %	Red. of Area %
175	137	R	32.0	88
155	927	R	19.6	80
140	2706	R	24.2	83
120	6511	R	23.1	76
107	8931	R	14.6	62
96	15788	R	20.7	68
85	17487	R	24.3	72
70	12096	C		

1) C: Continuing, R: Ruptured

As received, thermally exposed and crept specimens were investigated by optical metallography and transmission electron microscopy (TEM) of thin foils and extraction double-replicas. The foils were prepared by mechanical thinning and electrolytic polishing in a 10% perchloric acid and 90% acetic acid solution at 10 ˚C. The extraction double-replicas were produced according to the procedure described by Czyrska-Filemonowicz et al. [4]. The TEM investigations were performed by JEOL JEM 200CX and JEM-2010 ARP equipped with scanning transmission electron microscopy attachment (STEM) and energy dispersive X-ray spectrometer (EDS). Thin foils were used for statistical determination of the sub-grain width and the dislocation density. The latter was estimated according to the method described by Ham [5]. Phase identification was performed using electron diffraction supported by JEMS

software [6] and STEM/EDS spectrometry. Image analyses of TEM micrographs were performed using AnalySIS 3.1 software.

Results

Creep tests

Creep tests were carried out at 625 ºC; the experimental data are listed in Table 1.

Figs 1-3 show the results of the VM12 creep tests.

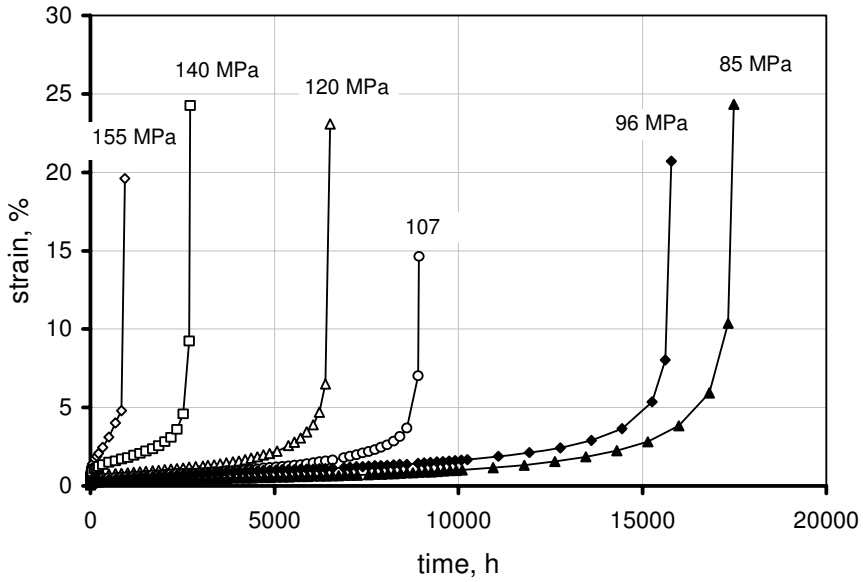

Figure 1 Creep curves for VM12 tested at 625 ºC

The results show that the primary stage of decreasing creep rate is relatively short. A very short secondary creep stage is followed by relatively long tertiary one, representing the major of the test duration and the major part of total creep strain.

Figure 3 shows a comparison the VM12 stress rupture strength with that of the E911 steel at 625 °C.

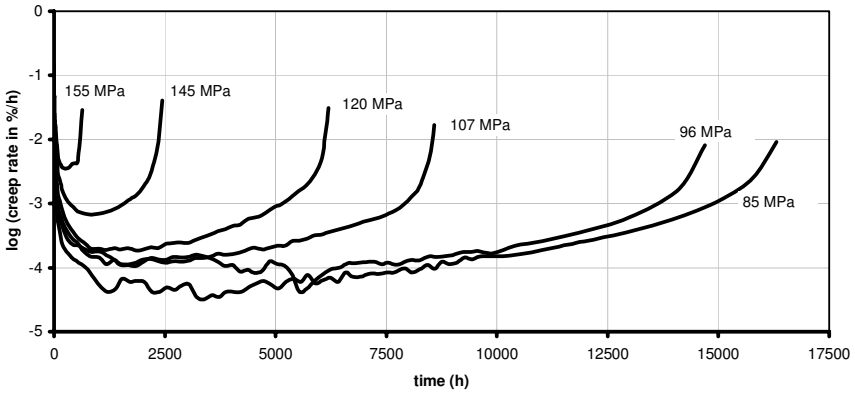

Figure 2 Strain rate as a function of time at 625 ºC

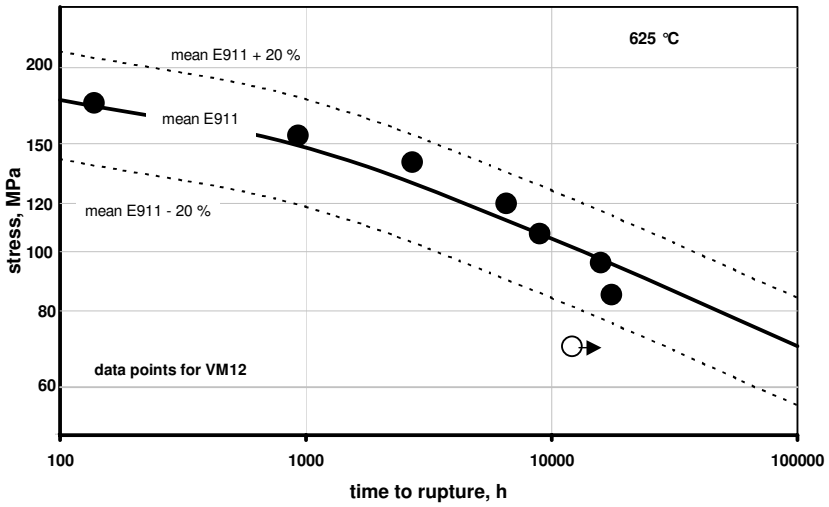

Figure 3 Stress rupture strength of VM12 steel as compared with E911 steel

For creep testing shorter than 15 000 h, all rupture points lie above or on the average creep curve of the E911 steel. Only specimen creep deformed at 85 MPa exhibited a shorter time to rupture than E911 steel at the same stress.

Microstructure of the as received VM12 steel

Figures 4 a, b show the VM12 steel microstructure after austenitisation at 1060 ºC /0.5 h followed by tempering at 780 ºC /2 h.

a) b)

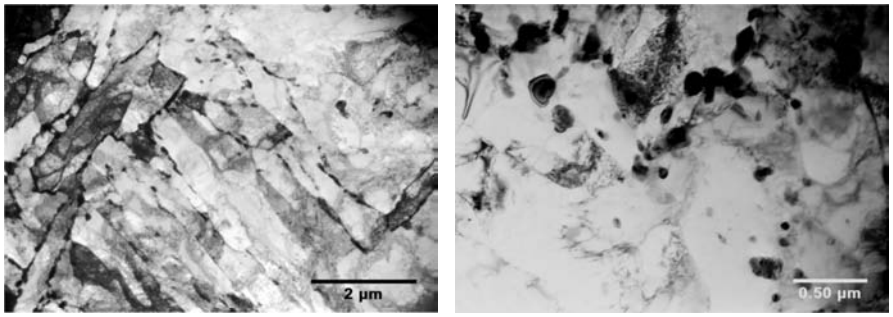

Figure 4 Microstructure of the as received VM12 steel showing a) elongated sub-grains with $M_{23}C_6$ carbides, b) fine MX within tempered martensite sub-grain

The microstructure of the as received steel consisting of tempered martensite with a high dislocation density and finely distributed carbides or carbonitrides (Figure 4a). The dominant particles are the $M_{23}C_6$ carbides, where (M= Cr, Fe, Mo). These precipitates are mainly located at prior austenite grain boundaries and sub-grain boundaries, however also appear within martensite laths. The strengthening precipitates that are important for the mechanical properties of high chromium steels are the fine M(C, N) with forming elements V and Nb. The morphology of these small precipitates is shown in Figure 4b. Very high dislocation density was observed inside of sub-grains ($6.57\pm1.4x10^{14}m^{-2}$). The results of the quantitative measurement of the microstructural parameters (sub-grain width, dislocation density and precipitate dimensions) are given in the Table 2.

Table 2
Quantitative TEM measurements for VM12 steel

condition	exposure type	sub-grain width, µm	dislocation density, 10^{14} m^{-2}	$M_{23}C_6$ mean diameter, µm
as received	-	0.6 ±0.2	6.5	110 ± 36
2706 h /625 °C	thermal	0.7 ±0.3	2.6 ± 0.4	170 ± 120
2706 h/625 °C/140 MPa	creep	1.0 ±0.4	1.9 ± 0.5	170 ± 80
15788 h/625 °C	thermal	0.8 ± 0.3	2.1 ± 0.7	180 ± 80
15788 h/625 °C/96 MPa	creep	1.1 ± 0.4	1.3 ± 0.9	250 ± 110
17487 h/625 °C	thermal	1.1 ± 0.5	2.0 ± 1.2	190 ± 80
17487 h/626 °C/85 MPa	creep	1.4 ± 0.7	1.2 ± 0.9	280 ± 130

Microstructural evolution during thermal exposure and creep deformation

Thermal exposure at 625 ˚C as well as creep deformation at this temperature caused some changes in the VM12 steel microstructure. The degree of changes is dependent on the duration of the creep test and the creep deformation. The typical microstructures of VM12 steel after thermal exposure and after creep deformation at 625˚C are shown in Figures 5-7.

a) b)

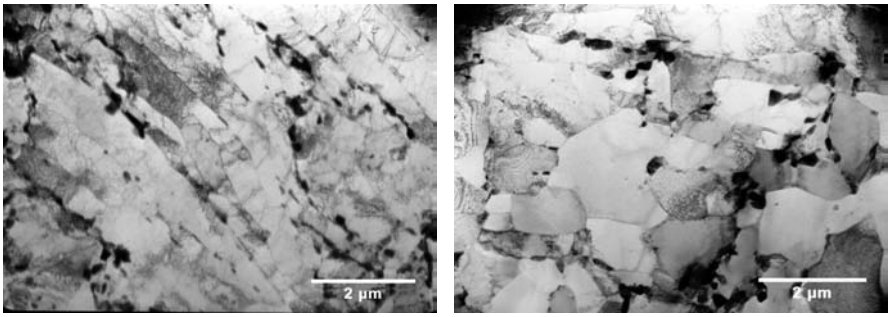

Figure 5 TEM micrographs of the VM12 microstructure after a) thermal exposure, b) creep deformation at 625 ºC for 2 706 h

a) b)

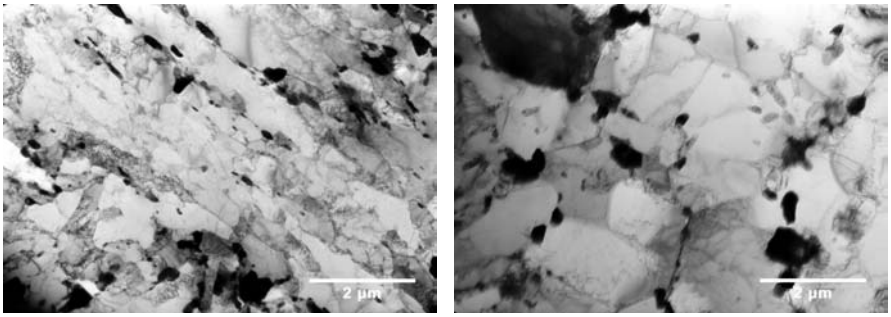

Figure 6 TEM micrographs of the VM12 microstructure after a) thermal exposure, b) creep deformation at 625 ºC for 15 788 h

a) b)

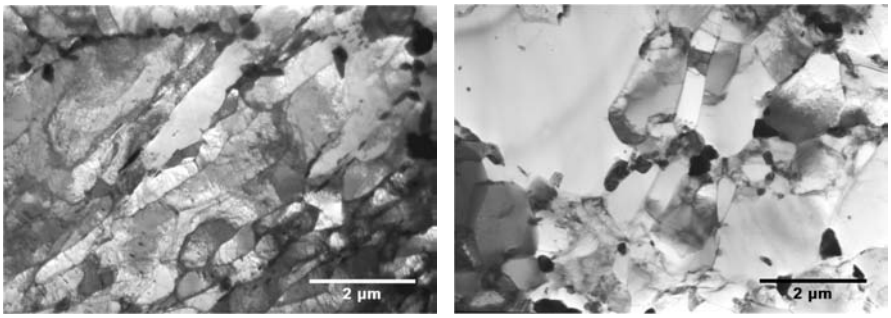

Figure 7 TEM micrographs of the VM12 microstructure after a) thermal exposure, b) creep deformation at 625 ºC for 17 487 h

Well developed sub-grains of low dislocation density in the interiors are characteristic features of the long–term exposed specimens. The results of quantitative measurements of sub-grain size and dislocation density within the sub-grains with prolongation of thermal exposure and creep deformation are given in the Table 2. The results show that in the first 3 000h of exposure there is a rapid reduction in the dislocation density and an increase of the sub-grain width. It was also found that in thermally exposed specimens, the elongated shape of the sub-grains (resulting from the lath martensite structure) was preserved, i.e. sub-grain shape coefficient was low.

TEM microstructure investigations as well as the quantitative data given in Table 2 show that the recovery processes are faster during during creep exposure. In creep deformed specimens, some very large sub-grains were observed (Figure 7b), which may be the result not only of recovery but also of *in situ* recrystallisation processes. Furthermore, the sub-grains had become more equiaxed in form.

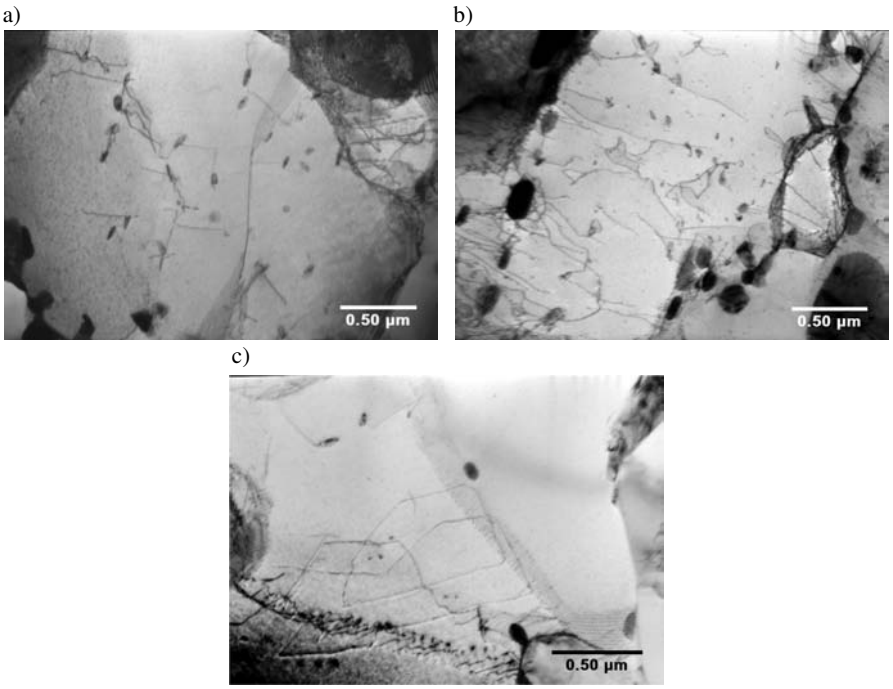

Figure 8 Fine MX particles within the sub-grains of the VM12 steel after creep deformation at 625 °C for a) 140 MPa/ 2706 h, b) /96 MPa/ 15788 h, c) 85 MPa/ 17487 h

The various precipitates play an important role in microstructure stabilization. The $M_{23}C_6$ carbides are precipitated at the prior austenite grain boundaries, martensite lath and inside the laths. The fine MX particles, precipitated intragranularly, act as obstacles for moving dislocation (Figure 8 a,b,c) . The effectiveness of these precipitates in hindering dislocation movement is related to the particle size and volume density. The precipitate size, morphology and distribution all changed during thermal exposure and creep deformation. Quantitative particle measurements of the VM12 steels show that the coarsening of the $M_{23}C_6$ carbides is significantly low (Table 2).

Another phase that precipitates in high chromium steels is the Laves phase, $Fe_2(W,Mo)$. This takes place after long term thermal exposure or creep at 600 - 650 °C [2, 7]. In the investigated VM12 steel, the Laves phase was found after 2 706 h creep deformation at 625 ºC. With increasing creep duration, growth of the Laves phase was observed. As shown in Figure 11, in the specimens creep deformed for about 17 500 h, the Laves phase particles were very large (larger than 0.5 µm in diameter).

Discussion

The normalised and tempered steel microstructure, which provides the optimum creep strength, is characterized by a dislocation substructure and a dispersion of phases in a solid-solution hardened matrix.

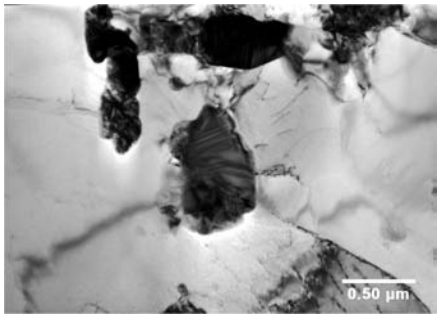

Figure 11 TEM micrographs of the steel VM12 after creep deformation at 625 ºC for 17 487 h showing large particle of the Laves phase

For the VM12 steel, TEM investigations and the results of the structural parameters (sub-grain size, dislocation density, carbide dimensions) measurements show that this steel has a stable microstructure during thermal exposure at 625 ºC. Creep deformation under external stress caused an acceleration of the microstructure changes, especially reflected in a decreasing mobile dislocation density within the sub-grains and an increase in the sub-grain size.

In the case of dislocation creep, creep rate is controlled by the Orowan mechanism, and thus depends on mobile dislocation density and rate of their motion. The precipitated particles act as effective barriers to the glide and climb of dislocations, but also interact with and stabilize

the sub-grain boundaries (low energy planar dislocation networks) [8, 9]. Prolongation of thermal exposure causes the formation of sub-grains with very different sizes. In the areas of higher particle density, the sub-grains are smaller than in the areas where there are not so many precipitates. Carbide particles of $M_{23}C_6$ carbides, where (M= Cr, Fe, Mo), precipitated on the sub-grain boundaries, stabilize the sub-grain microstructure. The precipitates that are important for retarding the movement of dislocations in VM12 are the fine MX particles. Additionally, the precipitation of intermetallic phase particles, mainly Fe_2(W,Mo) Laves phase, which precipitate more slowly during creep deformation than the carbides, may decrease matrix solution hardening of W-modified steels [10,11].

All processes described above, were also observed in the VM12 steel during thermal exposure and creep deformation at 625 ºC. In the specimen creep tested at 85 MPa for about 17 500 h, the microstructure indicated an acceleration of the recovery processes, withsignificant sub-grain growth and the appearance of sub-grains of very different sizes (Figure 7). This suggests a decrease in the effectiveness of sub-grain boundary pinning by the $M_{23}C_6$ carbides.

An increase in the creep deformation duration also resulted in the precipitation of much larger particles of the intermetallic Laves phase, influencing the matrix solution hardening. Some of the Laves particles precipitated in the specimen deformed for 17 500 h were particularly coarse, up to about 1 μm diameter. The precipitation of the Laves phase removes Mo and W from the matrix solid solution and therefore may cause a weakening of the matrix.

These microstructural changes were reflected in the results of the creep tests; in comparison with the 10 % Cr steel E911, the stress rupture curves exhibited a steeper decrease with increasing test duration.

Conclusions

A new martensitic chromium steel, VM12, developed for advanced ultra-supercritical steam power plants operated at about 650 ºC, was studied using optical metallography and analytical transmission electron microscopy techniques. The purpose of the work was to characterise the steel microstructure and identify the microstructure parameters influencing its stability during long-term thermal exposure and creep deformation at 625 ºC.

The microstructure of the VM12 steel in the as received condition consisted of narrow tempered martensite sub-grains with high dislocation density within the sub-grains. After thermal exposure and creep testing at 625 ºC, the steel microstructure exhibited recovery processes (reduction of dislocation density, sub-grain growth, $M_{23}C_6$ particle growth and coarsening).

Various precipitates were present in the VM12 steel. The dominating precipitates were the $M_{23}C_6$ carbides, which formed on prior austenite grain boundaries and on sub-grain boundaries. The precipitates that are important for the long-term mechanical properties of VM12 are the fine MX particles. Precipitation of the intermetallic Laves phase may lead to a decrease in the matrix solution hardening, and was observed in the specimen creep tested for about 2000 h. Long-tem exposure of VM12 caused significant growth of Laves phase

particles. The microstructural changes were reflected in the results of the creep tests, with decreasing strength at longer test duration, compared with the 10 % Cr steel E911.

Acknowledgements

The study was performed under co-operation of the COST Action 536. The authors from the AGH University of Science and Technology also gratefully acknowledge the support of the Ministry of Education and Science (project nr SPB-COST536).

References

1. P J Ennis, W J Quadakkers, The Oxidation Behaviour of Chromium Steels in Supercritical Steam Power Plant, in Proceedings of the 7th Liège Conference 'Materials for Advanced Power Engineering', 30 Sept – 2 Oct 2002, Liège, Belgium; ed J Lecomte-Beckers, M Carton, F Schubert, P J Ennis, Forschungszentrum Jülich, Energy Technology Series, Volume 21, Part II, pp 1131-1142, ISSN 1433-5522, ISBN 3-89336-312-2, 2002
2. Czyrska-Filemonowicz A, Ennis PJ, Zielińska-Lipiec A, High Chromium Creep Resistant Steels for Modern Power Plant Applications, in "Metallurgy on the Turn Of 20th Century", K. Świątkowski (ed.), The Committee of Metallurgy of the Polish Academy of Sciences, Krakow, 2002, 193-218
3. Bendick W, Gabrel J, Vaillant J C, Vandenberghe B, Development of a new 12% Cr steel for tubes and pipes in powwer plants with steam temperatures up to 650 °C, EPRI Int. Conf. on Materials and Corrosion Experience for Fossil Power Plants, Nov. 18-21, 2003, Wild Dunes Resort, Isle of Palms, SC, USA
4. Czyrska-Filemonowicz A, Spiradek K, Gorczyca S, Extraction Double Replica Technique for Electron Microscopy Studies of Precipitates, Praktische Metallograpie, 29, 1992, 35-43
5. Ham RK, Determination of Dislocation Densities in Thin Films, Philosphical Magasine, 6, 1961, 1183-1184
6. Stadelmann P. JEMS Java Electron Microscopy Software, http://cimewww.epfl.ch/people/stadelmann/jemsWebSite/jems.html.
7. Ennis PJ, Zielinska-Lipiec A, Wachter O, Czyrska-Filemonowicz A, Microstructural Stability and Creep rupture Strength of the Martensitic Steel P92 for Advanced Power Plant, Acta Materialia, 45, 1997, 4901-4907
8. Zielińska-Lipiec A, The Analysis of a Microstructural Stability of Modified Martensitic 9% Cr Steels during Thermal Exposure and Creep Deformation, Reports of the AGH-UST No 146, Krakow 2005, in press (in Polish)
9. Eggeler G, The Effect of Long-Term Creep on Particle Coarsening in Tempered Martensite Ferritic Steels. Acta Metallurgica, 37, 1989, 3225-3234
10. Orlova A, Bursik J, Kucharova K, Sklenicka V, Microstructural Development during High Temperature Creep of 9% Cr Steel. Mater. Sci. Eng., A245, 1998, p 39
11. Pesicka J, Kuzel R, Dronhofer A, Eggeler G, The Evolution of Dislocation Density during Heat Treatment and Creep of Tempered Martensite Ferritic steels. Acta Materialia, 51, 2003, 4847-4862

REGENERATIVE HEAT TREATMENT OF L21HMF CAST STEEL AFTER LONG TERM OPERATION

Golański G., Kupczyk J., Stachura S., Gajda B.

Institute of Materials Engineering, Czestochowa University of Technology,
42 – 200 Czestochowa, Armii Krajowej 19, Poland
e-mail:grisza@mim.pcz.czest.pl

Abstract

This paper presents the results of investigation of influence of regenerative heat treatment on the structure and properties of long - term serviced L21HMF cast steel (symbol according to Polish Standard). It has been shown that the structure of tempered bainite ensures high mechanical properties and impact energy KV > 100J in the cast steel with degenerated structure caused by long - time operation at elevated temperatures. Obtained mechanical properties in regenerated cast steel exceed the requirements for new castings.

Key words: cast steel, regenerative heat treatment, bainitic structure, impact energy

Introduction

Cylinders and valve chambers of high power steam turbines are made of Cr – Mo and Cr – Mo – V cast steel. The steel castings have been mostly normalized and tempered. The result of such treatment is a mixture of ferritic-perlitic and ferritic-bainitic microstructures.

Operation of casts for over 100 000 hours in creep conditions causes structural changes and deformations which lower the functional properties. Impact energy decreases drastically, markedly below the required level of 27J, e.g.: 6 ÷ 10J. Additionally there is an increase of transition temperature, often above 60 ^{o}C. The changes of functional properties of cast steel during long-term operation are caused by the following structural features [1÷5]:

- ✓ preferencial precipitation of carbides on grain boundaries and change of morphology and dispersion of precipitates;
- ✓ segregation of phosphorus and other micro-elements to grain boundaries;
- ✓ disintegration of perlite or/and bainite areas.

Experiences of private research [6], carried out on samples taken from a few dozen cylinders and valve chambers, have shown that the decrease of impact energy caused by long-term operation at elevated temperature depends to a large extent on the initial structure of cast steels. The decrease of impact energy is the smallest in the case of tempered bainite initial structures.

However, changes in the functional properties of casts caused by long-term operation do not limit the possibilities of their further service, because in the cast steel investigated here, no irreversible creep changes have been found. The basic condition of prolonging the time of safe operation of the casts is the revitalization process [7, 8]. The process of cast steel revitalization consists in post-operational repairs through welding and heat treatment of the frames in order to regenerate the structure and properties.

Regenerative heat treatment, at expenses not larger than 40% of the new frame price, allows to obtain the functional properties (yield point, impact energy, transition temperature) comparable to those of the new casts. Regenerated frame can operate further for at least another 100 000 hours [8].

Research material

The materials for research, i.e. samples of L21HMF cast steel, were taken from the inner cylinder of the turbine after long-term operation - over 186 000 hours at the temperature of 540 ^{o}C and the pressure of 13.5MPa. Chemical composition of the investigated cast steel is shown in the Table 1.

Table 1. Chemical composition of the investigated L21HMF cast steel (wt.%)

C	Mn	Si	P	S	Cr	Mo	V
0.19	0.74	0.30	0.017	0.014	1.05	0.56	0.28

In the post-operational condition the structure of the cast was ferritic – perlitic (Fig.1). Inside the grains, and mainly on ferrite grain boundaries, numerous carbides were observed. They often formed a continuos network of precipitates. In perlite, however, the process of fragmentation and spheroidization of carbides could be seen (Fig. 1b). The identification of precipitates by means of extraction carbon replicas revealed $M_{23}C_6$ carbides on ferrite grain boundaries and in the areas of degraded perlite. Inside ferrite grains, apart from $M_{23}C_6$ carbides, VC and M_6C carbides were identified. The size of ferrite grain in the investigated cast steel was diverse, from 88 to 31μm, which corresponds to grain size of 4-7 according to the ASTM standards. After operation the cast steel was characterised by very low impact energy of 10J and hardness of 156HV30. Investigated cast steel met the requirements concerning tensile strength and elongation limit for new products (according to the Polish Standard PN - 89/ H – 83157), only the yield point was lower by 15MPa than the minimum requirements of the norm (table 4).

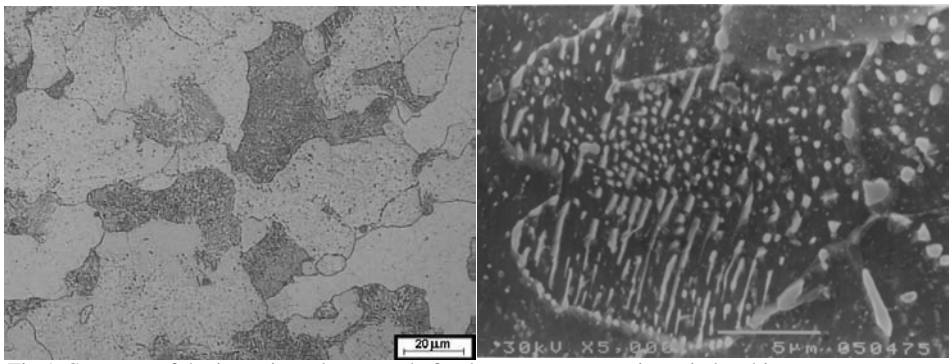

Fig.1. Structure of the investigated cast steel after long – term operation, nital etching

Results

The basis for determining the optimum parameters for heat treatment of the L21HMF cast steel, was determining the critical temperatures A_{c1} and A_{c3}, which amounted to 775 ^{o}C and 906 ^{o}C respectively. These temperatures were measured according to Polish Standard PN – 68/H – 04500 for the heat up rate 0.05 $K \cdot s^{-1}$.

Selection of the optimum parameters of austenitization required determining of the influence of austenitization temperature during 3 hours of heating on the cast steel grain size after long-term operation (Fig. 2, Table 2).

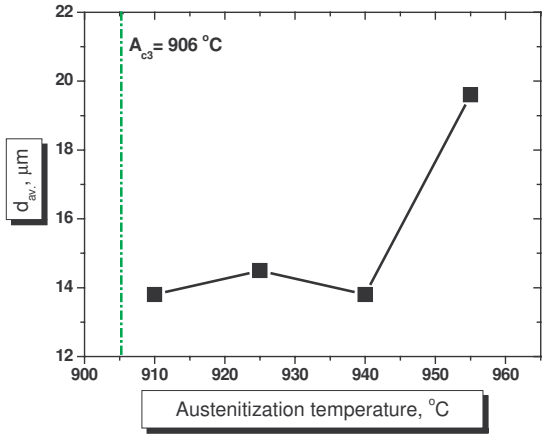

Fig. 2. Changes of the austenite grains mean diameter depending on the austenitization temperature, t=3h

Table 2. Sizes of the austenite grain of the cast steel, austenitized at different temperatures for 3 hrs

Statistic parameters	*Austenitization temperature, °C*			
	910	***925***	***940***	***955***
Amount of grains counted	506	485	502	630
$d_{av.}$, µm	13.78	14.51	13.83	19.54
$\Sigma d_{av.}$, µm	6971	7039	6944	12 311
$\Sigma(d_{av.} - d_i)^2$ µm^2	19 670	17 879	18 962	54 240
S^2	38.95	36.94	37.85	86.23
Standard deviation, σ	6.40	6.05	7.12	9.27
d_{max}, µm	35	35	39	59
d_{min}, µm	2	2	2	2
min. test number (for $\alpha = 0.05$), u	150	142	145	331

Austenitization in the temperature range of 910 ÷ 940 °C allows to get fine austenite grain with grain mean diameter of 14 ÷ 15 µm, which corresponds to 9/10 grade according to ASTM standards. Austenitization within this range of temperatures permits to get the grain of similar size, which is shown by the comparable variation values (table 2). Austenitization temperatures higher than 940 °C contribute to thick austenite grain obtainment. At the temperature of 955 °C austenite grains mean diameter increased by about 50% in relation to the grain sizes specified in 910 ÷ 940 °C temperature range. Influence of

austenitization temperature on the properties (impact energy and hardness) after tempering at 720 ^{o}C is shown in Fig. 3.

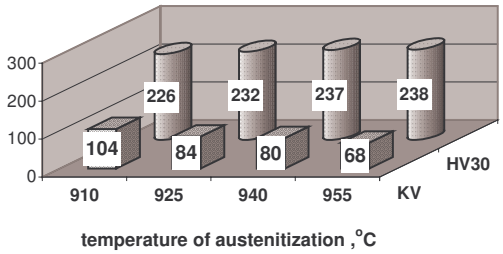

Fig. 3. Influence of austenitization temperature (holding time 4h) on the impact energy and hardness after tempering at 720 ^{o}C temperature – holding time 3h

The structure of tempered bainite, on the one hand, ensures high mechanical properties and impact energy of KV >100J in low-alloy cast steels, and on the other hand, guarantees the smallest decrease of plastic properties during long-term operation at elevated temperatures. In order to determine the cooling rate, which allows to obtain the bainitic structure in the investigated cast steel after austenitization process, a CCT diagram has been drawn (Fig. 4). The CCT diagram was made on the basis of dilatometric curves data taken from optical dilatometer LS – 4. M_s temperature was characterized on the basis of the chemical composition of the cast steel, using the relations mentioned in the work [9].

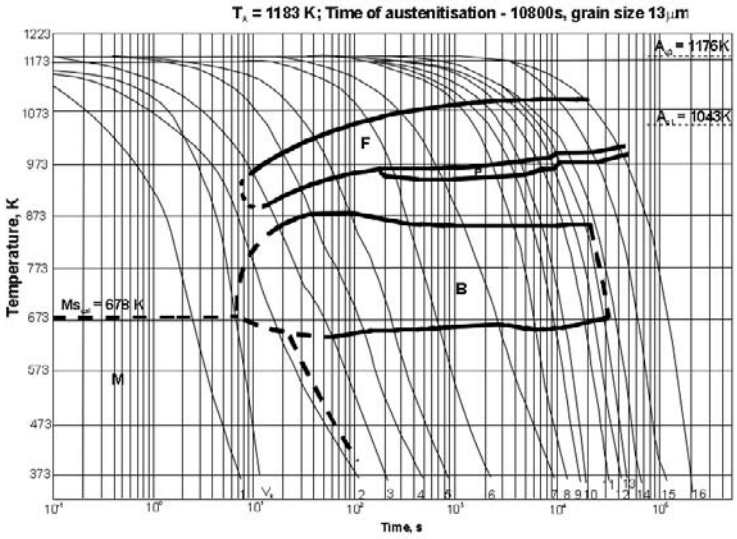

Fig. 4. CCT diagram for the L21HMF cast steel

The influence of selected cooling rates on the type of structure and on the change of hardness in L21HMF cast steel is presented in Table 3.

Table 3. The influence of the cooling rate on the type of structure and hardness of cast steel

No.	V_{8-5} $K \cdot s^{-1}$	HV 30	Type of microstructure/ percentage
1	183.490	500	martensite/100
V_k	71.430	------	martensite
2	33.330	463	bainite/100
3	13.636	333	bainite/90, ferrite/10
4	5.332	315	bainite/81, ferrite/19
6	0.869	280	ferrite/53, bainite/44, single grains of perlite/2
8	0.093	191	ferrite/80, perlite/16, bainite/4
10	0.040	181	ferrite/76, perlite/21, bainite/3
13	0.017	161	ferrite/74, perlite/26
14	0.013	158	ferrite/74, perlite/26

Heat treatment consisted in austenitization of the samples for 3 hours at the temperature of 910 ^{o}C and the cooling rate of $v_{8-5} \sim 33.330\ K \cdot s^{-1}$. Then samples were tempered for 4 hours at temperatures: 690, 700, 710 and 720 ^{o}C. Bainitic hardening with tempering enabled to obtain tempered bainite structure in the investigated cast steel with numerous carbide precipitates on the prior austenite grain boundaries and on subgrain boundaries within the bainite lath (Fig. 5).

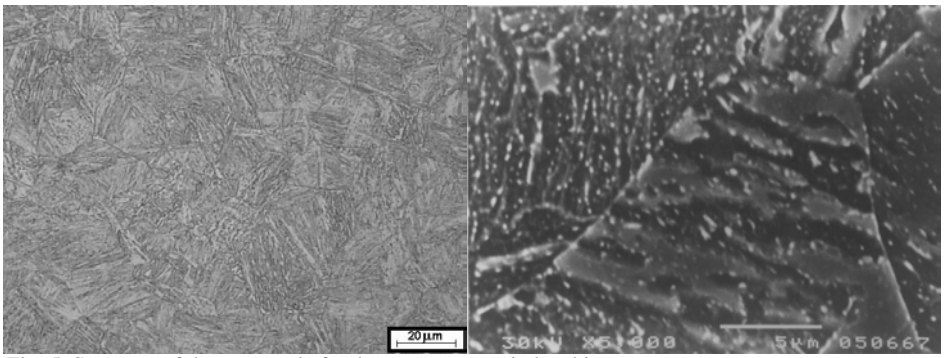

Fig. 5. Structure of the cast steel after heat treatment, nital etching

Figure 6 shows the influence of tempering temperature on the changes of impact energy and hardness after bainitic hardening from the temperature of 910 ^{o}C.

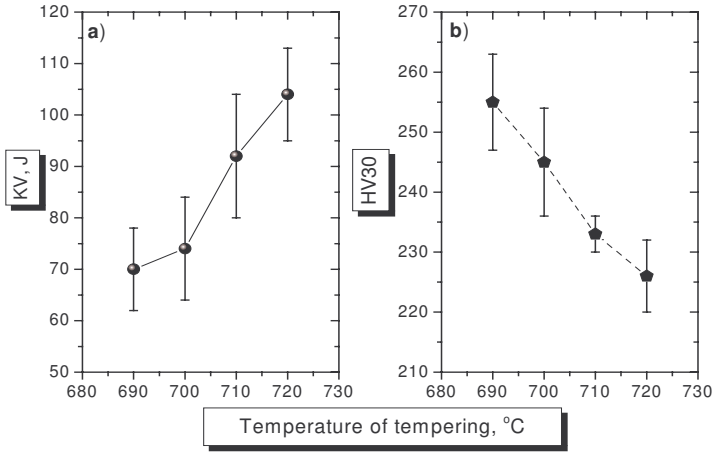

Fig. 6. Influence of tempering temperature on impact energy (a) and hardness (b)

Tempering of the L21HMF cast steel at the temperature of 690 °C permits to obtain hardness of 255HV30 at the KV impact energy of 68J. Raising the tempering temperature up to 710 °C (maximum temperature suggested by the Polish Standard PN - 89/ H - 83157) and to 720 °C, contributes to impact energy increase above 100J, although with the hardness decrease by about 10%, in comparison with tempering at the temperature of 690 °C.

Cast steels as products having diverse thickness of sides on intersections, require long times of holding during the heat treatment. For that reason it has been determined, how the heating time at the austenitization temperature (Fig. 7a), and the tempering temperature (Fig. 7b), influence the change of impact energy and hardness.

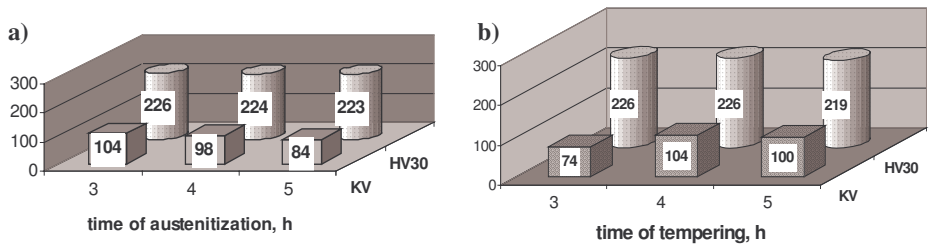

Fig. 7. Influence of heating time on hardness and impact energy: a) at austenitization temperature of 910 °C with followed tempering at 720 °C/4h; b) at tempering temperature of 720 °C after austenitization at 910 °C/3h

It has been proved that the increase of holding time at austenitization temperature of 910 °C from 3 to 5 hours, does not influence hardness and contributes to impact energy decrease by about 20% after tempering process. Moreover, increase of holding time at the temperature of 720 °C from 3 to 5 hours, influences the impact energy growth by about 30% with only slight hardness decrease.

In order to compare the influence of other cooling rates after austenitization process on the properties and structure of L21HMF cast steel after long-term operation, the heat treatment was performed with parameters presented in Table 4. Results of the research confirmed that the structure of tempered bainite ensures optimum combination of high mechanical properties and very high impact energy. Plastic properties, elongation in particular, can be increased by applying higher tempering temperatures (730 or 740 ^{o}C).

Table 4. Structure and properties of the cast steel after heat treatment

Parameters of heat treatment	**TS MPa**	**YP MPa**	**El %**	**KV J**	**HV30**	**Structure**
after operation	545	305	26	10	156	ferritic-perlitic
910 ^{o}C/3h/33.330 K · s^{-1} + 720 ^{o}C/4h	728	620	18	104	228	bainitic
910 ^{o}C/3h/2.791 K · s^{-1} + 720 ^{o}C/4h	721	594	17	62	220	bainitic-ferritic
910 ^{o}C/3h/0.017 K · s^{-1} + 720 ^{o}C/4h	558	336	27	26	153	ferritic-perlitic
acoording to Polish Standrad *	500 ÷ 670	min. 320	min. 20	min. 27	140 ** ÷ 197	___

*- PN - 89/ H - 83157
** - hardness according to Brinell

Conclusions

1. L21HMF cast steel after long-term operation does not reveal increased tendency to austenite grain growth. Austenite grain remains fine, up to temperatures higher by 10 ÷ 30 ^{o}C than A_{c3} temperature.
2. In regenerative heat treatment of the casts, bainitic structure is the optimum one. It ensures high level of mechanical properties and high impact energy. The bainitic-ferritic structure with about 20 percentage of ferrite, reveals similar mechanical properties at the impact energy lower by about 40%. The ferritic – perlitic structure is not recommended, as it ensures mechanical properties and impact energy on the level of minimum requirements described by the norm.
3. Cooling rate of the casts higher than $v_{8-5} > 13.636$ K · s $^{-1}$ ensures obtaining of the bainitic structure.

Scientific work funded by the Ministry of Education and Science in the years 2006 ÷ 2008 as a research project No. DWM/46/COST/2005.

Literature

1. Pigrova, G. D.; Tchyzhik, T. A. - "Phase composition of 1.5Cr-1.0Mo-0.3V rotor steel as a factor of cooling rate from austenitic region", Materials at High Temperatures, 13, 3, 1995, 121

2. Ševc, P.; Janovec, J.; Koutník, M.; Výrostková, A. - "Equilibrium grain boundary segregation of phosphorus in 2.6Cr-0.7Mo-0.3V steels", Acta Metallurgica Et Materialia, 43, 1, 1995, 251
3. Perhácová, J.; Výrostková, A.; Ševc, P.; Janovec, J.; et. al. - "Phosphorus segregation in CrMoV low-alloy steels", Surface Science, 454, 6, 2000, 642
4. Viefhaus H., Richarz B. – „Phosphor in eisen und Stahl – Ein Überblick über grenzflächenanalytische Untersuchungen am Max – Planck – Institut für Eisenforschung zum Segregationsverhalten des Phosphorus an äußeren und inneren Grenzflächen von Eisen und Stahl", Materials and Corrosion, 46, 1995, 306
5. Islam M. A., Knott J.F., Bowen P. - "Kinetics of phosphorus segregation and its effect on low temperature fracture behaviuor in 2.25Cr - 1Mo pressure vessel steel", Materials Sc. and Techn., vol.21, No.1, 2005, 76
6. Golanski G., Stachura S., Kupczyk J., - not published
7. Stachura S., Trzeszczynski J. - "The choice of the regenerative thermal treatment of the Cr - Mo and Cr - Mo - V cast steel casings", Inzynieria Materiałowa, 1997, 6, 233 (in Polish)
8. Trzeszczynski J., Grzesiczek E. - "To exchange or to revitalise", Energetyka, 3, 1998, 133 (in Polish)
9. "Steel A Handbook for Materials Research and Engineering" - edited by Verein Deutscher Eisenhüttenleute, Springer - Verlag, 1993

LONG-TERM CREEP STRENGTH DEGRADATION IN T122/P122 STEELS FOR USC POWER PLANTS

M. Igarashi[1)], M. Yoshizawa[1)], A. Iseda[2)], H. Matsuo[3)] and T. Kan[3)]

[1)] Corporate Research and Development Laboratories
1-8 Fuso-cho, Amagasaki, Hyogo, 660-0891, JAPAN.
igarashi-msa@sumitomometals.co.jp
[2)] Tubular Products Technology Department
1-8-11 Harumi, Chuo-ku, Tokyo, 104-6111, JAPAN.
[3)] Quality Control & Technical Service Department, Steel Tube Works
1 Higashi-Mukojima, Amagasaki, Hyogo, 660-0856, JAPAN.
Sumitomo Metal Industries, Ltd.

Abstract

Creep rupture and deformation behavior of KA-SUS410J3 type steels (equivalent to ASME P122/T122) with different Cr content and the resultant matrix phases such as **α'** (martensite) and **α'+ δ** (martensite and delta-ferrite) has been studied using creep testing and a detailed TEM observation. New allowable tensile stress values of the steels with two different Cr content levels set using the region splitting method in Japan are tabulated. Long-term creep rupture strength, in particular, of the **α'+ δ** dual phase steel is found to be lower than that expected from the short-term creep testing. Fine grain microstructure is found to enhance the creep deformation at lower stress region and decrease in fine MX and unequal distribution of MX in the ferrite matrix are to be the major causes of the strength degradation in the **α'+ δ** dual phase steel with the higher Cr content. It is concluded that the heterogeneous creep deformation is much more pronounced at lower stress level in the dual phase steel, which is due to inhomogeneous microstructure consisting of **α'+δ** phase matrix and the relevant heterogeneous distribution of fine precipitates such as MX and $M_{23}C_6$ in the **δ** ferrite matrix and near the interface between the soft **δ** ferrite and the hard martensite (**α'**) phases. Homogeneous microstructure is a key for achieving the long-term creep strength in the advanced ferritic steels at elevated temperatures over 600°C. KA-SUS410J2TB steel (designated as HCM12) is found to exhibit a similar creep strength degradation, which is mainly due to a similar microstructure of KA-SUS410J3 type steel with the higher Cr content.

Keywords: P122, T122, HCM12, allowable stress, heterogeneous creep

Introduction

Advanced high Cr ferritic steels such as ASME P92/T92 and P122/T122 have successfully been used for large diameter and thick section boiler components such as main steam pipe and header in ultra-supercritical pressure (USC) boilers in fossil-fired power plants [1-3]. These steels are characteristically strengthened by the combination of W substituting Mo in ASME P91/T91 and the addition of B. Recently, long-term creep strength of the advanced high Cr ferritic steels has been discussed regarding the instability of their microstructures at high temperatures over 600°C [4-8]. In Japan, the allowable tensile stresses for these steels have been reviewed according to the update creep rupture data and been lowered based on a new assessment method adapted by the committee on establishing allowable stress value etc. of High Cr Ferritic Steels for Ministry of Economy, Trade and Industry (hereafter SHC) set up in Japan since 2004 [9].

In this paper, the updated creep rupture data of KA-SUS410J3 type steels (equivalent to

ASME P122/T122) have first been reviewed and the new allowable tensile stress values of the steels with two different Cr content levels set in Japan are tabulated. We investigate the long-term creep deformation behavior of these steels with different matrix phases such as martensite (**α'**) and martensite with delta-ferrite (**α'**+**δ**) at different stress levels to clarify the major causes of the long-term creep strength degradation of the advanced ferritic steels. We find that at lower stress level the heterogeneous creep deformation takes place in these steels whose matrix is strengthened too much by the combination of MX and W, and this is enhanced in the area along the interfaces between the soft **δ** and the hard **α'** phases in the **α'**+**δ** steel with higher Cr content. We conclude that the homogeneous microstructure is a key for achieving the long-term creep strength in the advanced ferritic steels at elevated temperatures over 600°C. We also find that KA-SUS410J2TB steel (designated as HCM12) exhibits a similar creep strength degradation which is mainly due to a similar microstructure of the **α'**+**δ** matrix phases comparing with that of KA-SUS410J3 type steel with the higher Cr content.

Experimental

KA-SUS410J3TP (P122) pipes with Cr less than 11.5% and KA-SUS410J3DTB (T122) tubes with Cr more than 11.5% were produced using a conventional manufacturing process. The chemical compositions of KA-SUS410J3 type steels defined by the specification and the materials used in this study are given in **Table 1**. Model steels with different matrix phases, a martensitic single phase steel denoted as **α'** and a martensite with delta-ferrite dual phase steel denoted as **α'**+**δ** were prepared and normalized for 0.5 h at 1050°C followed by air-cooling, and tempered for 2 h at 780°C. The microstructures of the specimens crept and creep interrupted were examined using a transmission electron microscopy (JEOL 2000EX) operated at 200kV. KA-SUS410J2TB (HCM12) tubes were also prepared using a conventional process and their chemical compositions are given in **Table 1**.

Table 1 The chemical compositions of the steels used (mass%, Bal.Fe)

	C	Si	Mn	Ni	Cr	Mo	W	Cu	V	Nb	Al	B	N
KA-SUS410J3	0.07				10.0	0.25	1.50	0.30	0.15	0.04		0.0005	0.04
Specification	–	≤	≤	≤	–	–	–	–	–	–	≤	–	–
(P122/T122)	0.14	0.50	0.70	0.50	12.5	0.60	2.50	1.70	0.30	0.10	0.040	0.005	0.10
KA-SUS410J3TP	0.11	0.01	0.55	0.26	10.15	0.33	1.79	0.49	0.18	0.04	0.001	0.0011	0.052
pipes used	–	–	–	–	–	–	–	–	–	–	–	–	–
(Cr<11.5%)	0.14	0.34	0.64	0.35	11.02	0.44	2.03	0.95	0.22	0.07	0.022	0.0037	0.074
KA-SUS410J3DTB	0.07	0.28	0.52	0.21	11.73	0.32	1.85	0.43	0.19	0.04	0.002	0.0015	0.048
tubes used	–	–	–	–	–	–	–	–	–	–	–	–	–
(Cr≥ 11.5%)	0.11	0.34	0.66	0.37	12.22	0.42	2.14	0.99	0.21	0.06	0.017	0.0029	0.066
α' model steel	0.13	0.31	0.61	0.34	10.6	0.34	1.84	0.87	0.21	0.06			0.07
α'+δ model steel	0.10	0.31	0.53	0.35	12.2	0.36	1.88	0.86	0.20	0.05			0.05
KA-SUS410J2TB	0.09	0.20	0.51		11.70	0.98	0.90		0.21	0.02			
tubes used	–	–	–	N/A	–	–	–	N/A	–	–	N/A	N/A	N/A
(HCM12)	0.13	0.35	0.59		12.70	1.06	1.06		0.30	0.19			

Results and discussion

Fig.1 shows the creep rupture data of KA-SUS410J3 type steels with two different Cr content levels. There are two different matrix microstructures existing in this steel; one is the α' single phase matrix and the other is the α'+δ dual phase matrix, since the steel is allowed to change a large variation in Cr content in its original chemical compositions. It is obvious from these updated rupture data that the creep rupture strength should be analyzed separately for this steel according to the Cr content levels. **Fig.2** shows the updated creep rupture data

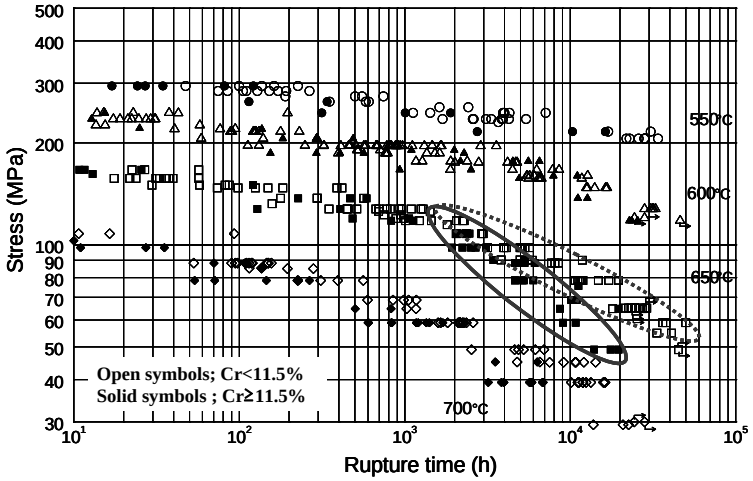

Fig.1 Creep rupture data of KA-SUS410J3 type steels with two different Cr content levels.

of KA-SUS410J3TP pipes with the lower Cr content less than 11.5%. Three different fitted curves are the ones based on the LMP method with the original data and with the updated data, and the one determined by the region splitting method by Kimura [9] adopted in the SHC. Using the region splitting method, the allowable tensile stresses obtained are much lowered

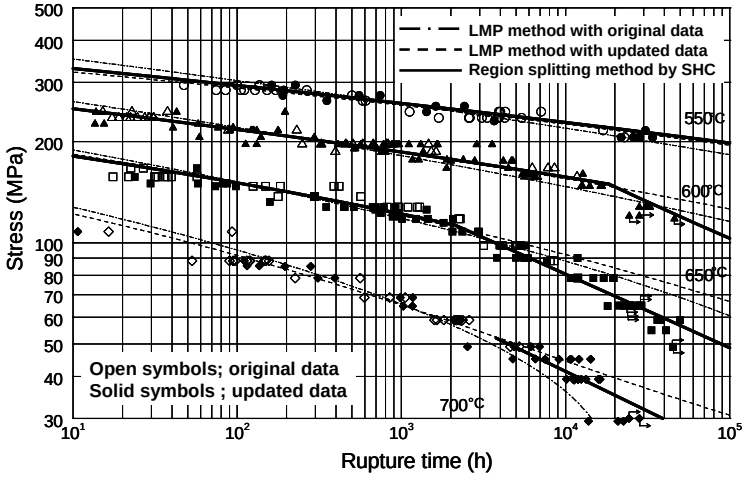

Fig.2 Updated creep rupture data of KA-SUS410J3TP pipe with Cr less than 11.5%.

comparing with those originally proposed as given in **Table 2**.

Table 2 Allowable tensile stress values of METI KA-SUS410J3 type steels revised according to the region splitting method adopted in the SHC in 2005. There are two steels designated according to different Cr content in the corresponding METI specification.

Temperature, °C	575	600	625	650
ASME CC2180-2(P122)*	107	83	61	(45)
KA-SUS410J3TP pipe with lower Cr	100	68	46	27
KA-SUS410J3DTB tube with higher Cr	94	52	25	16

* Allowable stress of ASME P122/T122 has been being reassessed in ASME subcommittee and would be revised soon according to the revision in Japan.

Fig.3 shows the updated creep rupture data of KA-SUS410J3DTB tubes with the higher Cr content more than 11.5%. The fitted curve is the one determined using the region splitting method adopted in the SHC. The resultant allowable tensile stresses obtained are much lowered as given in **Table 2**. The detailed analysis and the master curves for life assessment by Kimura in the SHC are described elsewhere [9].

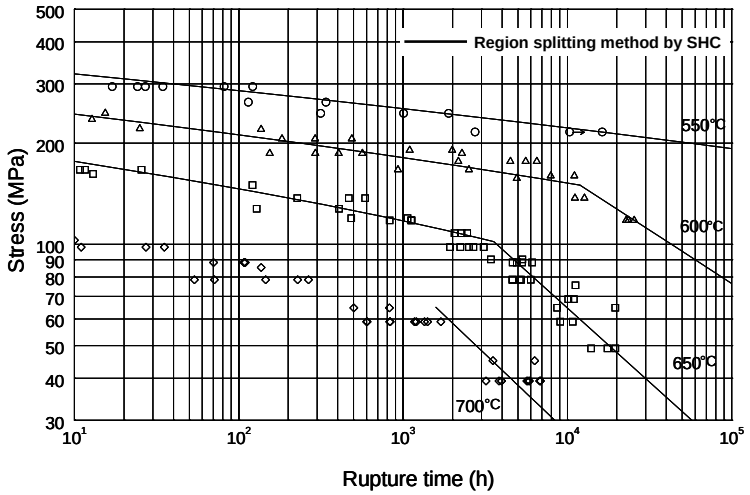

Fig.3 Updated creep rupture data of KA-SUS410J3DTB tubes with Cr more than 11.5%.

To clarify the effect of different matrix microstructure on the long-term creep strength degradation of KA-SUS410J3type steels, the creep deformation behavior has been examined for the **α'** single phase and the **α'**+δ dual phase matrix model steels. **Fig.4** shows the creep rupture data of the **α'** single phase and **α'**+δ dual phase steels crept at 650°C as a function of the applied stress. It is seen that the **α'** steel exhibits monotonous increase in rupture life with decreasing the applied stress, while the **α'**+δ steel does a peculiar change in rupture life resulting in a sort of sigmoidal behavior. This difference indicates that the creep deformation process of the **α'**+δ steel is completely different from that of the **α'** steel. To clarify the mechanism of long term creep strength degradation observed in this type of steel

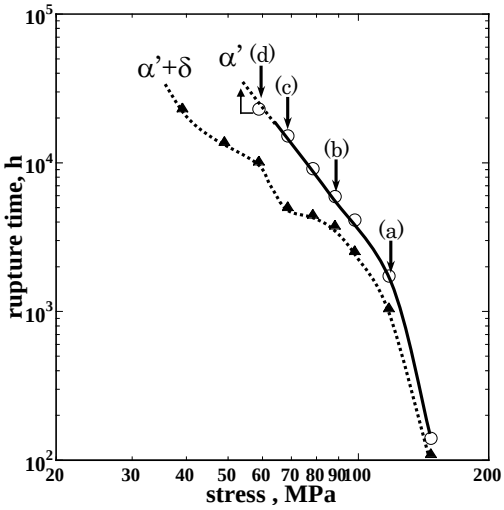

Fig.4 Creep rupture data of the α' and α'+ δ steels crept at 650°C.

and the effect of the matrix microstructures with changing Cr content on the creep strength, we examined the creep rate vs. creep strain curves of both steels. These figures are very useful for understanding the creep deformation mechanism involved. The parameters to be considered are the slopes of the curve in both transient and acceleration creep regions and the onset strain giving the minimum creep rate that indicates the transition to the acceleration creep. **Fig.5** shows the corresponding creep rate vs. strain curves of the specimens labeled (a) to (d) in **Fig.4**. The initial and minimum creep rates of both steels decrease in general with decreasing the applied stress. There seems to be no large difference in the creep deformation behavior between the α' and α'+δ steels crept at 118MPa labeled (a) except the slight difference in the initial creep rate and the resultant minimum creep rate. At a lower stress, 88MPa, where the rupture life of the α'+δ steel starts to deviate from a straight line, the creep rate of the α'+δ steel decreases sharply with strain in the transient creep region and then increases sharply with strain in the acceleration creep region, giving a small on-set strain from the transient creep to the acceleration creep. The creep rate of the α' steel, on the other hand, decreases sharply with strain in the transient creep region but increases gradually with strain in the acceleration creep region, giving a large on-set strain. At a further low stress, 69MPa, where the rupture life of the α'+δ steel deviates most from the straight line, the creep rate of the α'+δ steel decreases sharply with strain in the transient creep region but at a very small strain the acceleration creep starts and the creep rate turns out to increase with strain sharply, resulting in the short rupture life. The creep rate of the α' steel crept at 69MPa decreases sharply with strain in the transient creep region but increases gradually with strain in the acceleration creep region, giving a large on-set strain. At the lowest stress, 59MPa, where the rupture life of the α'+δ steel recovers toward the straight line, the creep rate of the α'+δ steel decreases very sharply with strain in the transient creep region and after reaching a low minimum creep rate at a very small strain the acceleration creep starts and the creep rate increases with strain rather gradually, resulting in the creep rupture life prolonged. It is

noted that in the **α'** steel the creep rate in the transient creep region decreases gradually with strain and the on-set strain from the transient to acceleration creep does not change much with decreasing the applied stress.

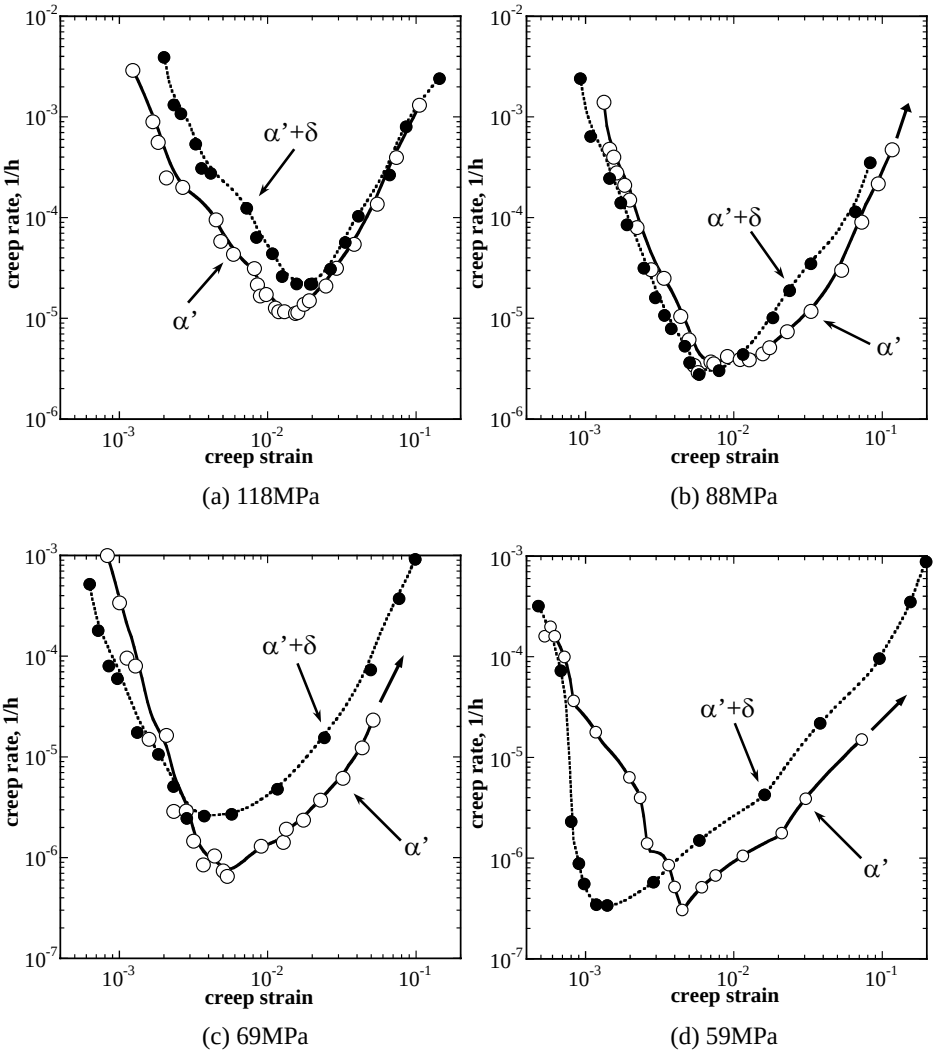

Fig.5 The corresponding creep rate vs. strain curves of the specimens labeled in **Fig.4.**

Fig.6 shows the stress dependence of the minimum creep rate and the offset strain to the acceleration creep of the **α'** and **α'**+ **δ** steels shown in **Fig.5**. It is seen that the minimum creep rate of both steels decreases with decreasing the applied stress. The **α'** steel exhibits the smooth change in the minimum creep rate with stress. It is found that in the **α'** steel the

power-law creep is relevant at higher stress regime above 60MPa where the stress exponents are high enough from 5 to 15, while the viscous creep is at lower stress where the stress exponent is as low as 1. This behavior is very similar to those observed in P91 steel by Kloc and Sklenicka [10, 11]. The **α'**+ **δ** steel, on the other hand, exhibits the deviation from the expected smooth change in the minimum creep rate around the critical stress, where the rupture life of the **α'**+**δ** steel starts to deviate from the straight line. At lower stress a sudden drop in the minimum creep rate has been observed, indicating that the creep deformation mechanism has changed explicitly from the high stress regime and the viscous creep becomes dominant at lower stress regime. It is noted in the **Fig.6 (b)** that the change in the on-set strain of the **α'**+ **δ** steel with stress is completely different from that of the **α'** steel, in particular, at lower stress where a sudden drop in the minimum creep rate has been observed. This suggests that in the **α'**+ **δ** steel at a particular stress level the heterogeneous creep deformation takes place as a consequence of the prohibition of the ordinary homogeneous deformation and the enhancement of the localized deformation which gives rise to the acceleration creep even at a very small strain by a very small creep rate.

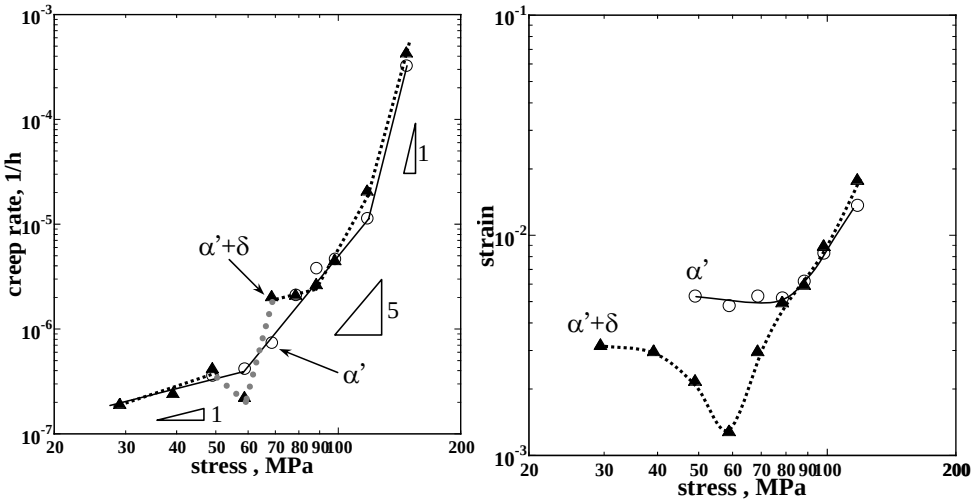

(a) minimum creep rate **(b)** on-set strain

Fig.6 Stress dependence of the minimum creep rate and the on-set strain to the acceleration creep of the **α** and **α'**+**δ** steels.

Figs.7 and **8** show TEM micrographs showing the microstructural evolution during creep deformation of the **α'**+**δ** steel crept and interrupted at 650°C with the stresses of 118 and 59 MPa, respectively. It is seen in the specimens crept at higher stress regime shown in **Fig.7** that dislocations are introduced inside the **δ** ferrite grains during creep deformation in the transient creep region, while the excess dislocations are reduced much inside **α'** martensite lath-grains. Once the dislocation starts to rearrange into a sub-grain structure preferentially along the **α'** / **δ** interfaces, the transition to the acceleration creep takes place. This sub-grain formation propagates rather inside the lath-martensite grain and also inside the **δ** ferrite grain

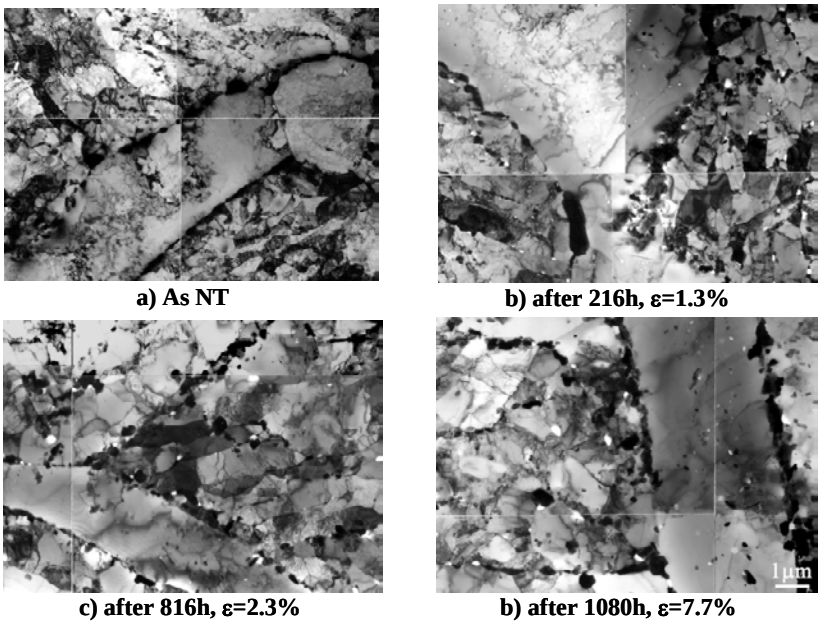

a) As NT **b) after 216h, ε=1.3%**

c) after 816h, ε=2.3% **b) after 1080h, ε=7.7%**

Fig.7 TEM micrographs showing the microstructural evolution during creep deformation of the α'+δ steel crept and interrupted at 650°C with 118 MPa.

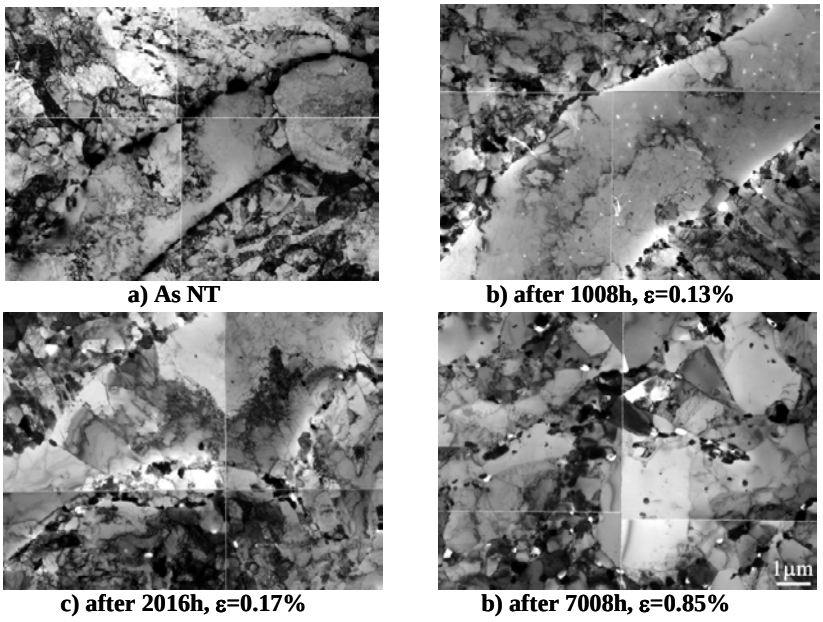

a) As NT **b) after 1008h, ε=0.13%**

c) after 2016h, ε=0.17% **b) after 7008h, ε=0.85%**

Fig.8 TEM micrographs showing the microstructural evolution during creep deformation of the α'+δ steel crept and interrupted at 650°C with 59 MPa.

in the acceleration creep region. The similar creep deformation process has been identified in the specimens crept at a lower stress as shown in **Fig.8**. It is, however, noted that at a low stress the sub-grains formation is much more localized along the **α'** / **δ** interfaces, which indicates the heterogeneous creep deformation is pronounced, giving a very small on-set strain. This is understood in such a way that in the dual phase steel soft **δ** ferrite grains scattered in the hard **α'** martensite serve as an embryo of sub-grain formation when crept at a lower stress which cannot activate the dislocation generation homogeneously, and this causes a heterogeneous viscous creep deformation via an easy deformation mode, resulting in the early transition to the acceleration creep at a very small creep strain and the shorter creep rupture life. It is thus concluded that the viscous creep is relevant creep deformation mechanism in the **α'+δ** steel, in particular, at lower stress regime. The detailed strength degradation mechanism of this type of steel is described elsewhere [12, 13].

Fig.9 shows the creep rupture data of KA-SUS410J2TB (HCM12) steels with the fitted curve determined using the region splitting method adopted in the SHC in 2006. It is found that KA-SUS410J2TB steels also exhibit a similar creep strength degradation which is mainly due to a similar microstructure of the **α'+δ** matrix phases comparing with that of KA-SUS410J3 type steel with the higher Cr content.

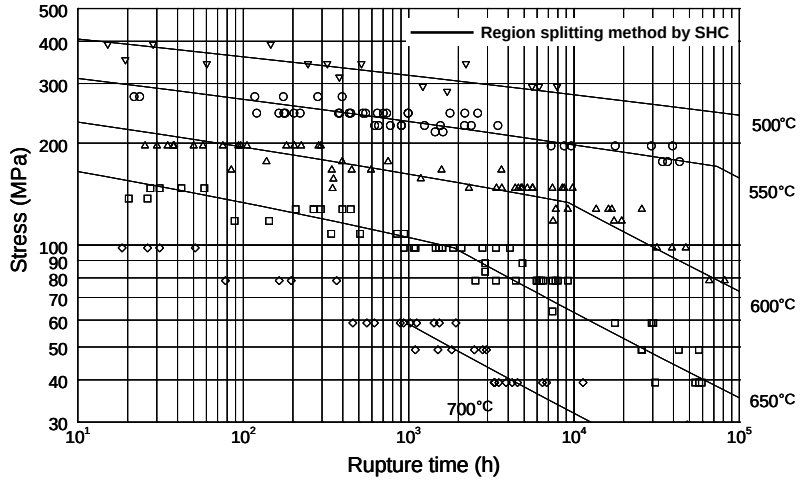

Fig.9 Updated creep rupture data of KA-SUS410J2TB (HCM12) tubes with the fitted curve determined using the region splitting method adopted in the SHC.

Conclusion

The updated creep rupture data of KA-SUS410J3 type steels (equivalent to ASME P122/T122) have been reviewed and the new allowable tensile stress values of the steels with different matrix phases such as martensite (**α'**) and martensite with delta-ferrite (**α'+δ**) according to two different Cr content levels set in Japan are tabulated. It is found that at lower stress level the heterogeneous creep deformation takes place in these steels whose

matrix is strengthened too much by the combination of MX and W, and this is enhanced in the area along the interfaces between the soft δ and the hard α' phases in the α'+δ steel with higher Cr content. It is thus concluded that the homogeneous microstructure is a key for achieving the long-term creep strength in the advanced ferritic steels at elevated temperatures over 600°C. It is also found that KA-SUS410J2TB steel (designated as HCM12) exhibits a similar creep strength degradation which is mainly due to a similar microstructure of the α'+δ matrix phases comparing with that of KA-SUS410J3 type steel with the higher Cr content.

Acknowledgments

The authors would like to express their sincere gratitude to Dr. Hiroyuki Semba and Hirokazu Okada for their useful discussion on the creep deformation, and Kenichi Murata, Shunichi Tenokuchi and Masatoshi Saito for their sincere collaboration in experiments.

References

[1] F. Masuyama, I. Ishihara, T. Yokoyama and M. Fujita: The Thermal and Nuclear Power, **46** (1995), 498.
[2] K. Muramatsu: Proc. Advanced Heat Resistant Steels For Power Generation, edited by R. Viswanathan and J. Nutting, The University Press, Cambridge, (1998), 543.
[3] F. Masuyama: Proc. Advanced Heat Resistant Steels For Power Generation, edited by R. Viswanathan and J. Nutting, The University Press, Cambridge, (1998), 33.
[4] K. H. Mayer: Proc. 28th MPA seminar, Stüttgart, (2002), Paper No.47.
[5] J. Hald: Proc. 28th MPA seminar, Stüttgart, (2002), Paper No.54.
[6] F. Abe, H. Okada, S. Wanikawa, M. Tabuchi, T. Itagaki, K. Kimura, K. Yamaguchi and M. Igarashi: Proc. the 7th Liege Conf. on Materials for Advanced Power Engineering, edited by J. Lecomte-Beckers, F. Schubert and P.J. Ennis, Forshungszentrum, Jülich GmbH, (2002), **III**.1397.
[7] K. Kimura, H. Kushima and F. Abe: Proc. 8th Int. Conf. On Creep and Fracture of Engineering Materials and Structures, edited by T. Sakuma and K. Yagi, Trans Tech Publications, Switzerland, **171-174** (2000), 483.
[8] M. Igarashi, S. Muneki and F. Abe: Proc. 8th Int. Conf. On Creep and Fracture of Engineering Materials and Structures, edited by T. Sakuma and K. Yagi, Trans Tech Publications, Switzerland, **171-174** (2000), 505.
[9] K. Kimura: PVP2005-71039(2005).
[10] L. Kloc and V. Sklencka: Proc. the 6th Liege Conf. on Materials for Advanced Power Engineering, edited by J. Lecomte-Beckers, F. Schubert and P.J. Ennis, Forshungszentrum, Jülich GmbH, (1998), **I**. 215-222.
[11] L. Kloc and V. Sklencka: Mater. Sci. Eng., **A** 234-236 (1997), 962.
[12] M. Igarashi and M. Yoshizawa: Proc. 4th Inter. Conf. on Advances in Materials Technology in Fossil Power Plants, South Carolina, USA (2004) *in press*.
[13] M. Yoshizawa and M. Igarashi: International Journal of Pressure Vessels and Piping, (2006) *in press*.

DEGRADATION BEHAVIOUR AND LONG-TERM CREEP STRENGTH OF 12CR FERRITIC CREEP RESISTANT STEELS

K. Kimura*, K. Sawada**, H. Kushima** and Y. Toda**

National Institute for Materials Science
* 2-2-54 Nakameguro, Meguro, Tokyo 153-0061, Japan
** 1-2-1 Sengen, Tsukuba, Ibaraki 305-0047, Japan

Abstract

Creep strength and life prediction have been investigated on ASME Grade 122 type high chromium ferritic creep resistant steels. In the high stress and short-term region, stress and temperature dependences of creep rupture life is extremely large and rupture ductility is high. On the other hand, inflection of stress vs. time to rupture curve results in overestimation of long-term creep rupture strength and remarkable decrease in rupture ductility is observed in the long-term. Inflection of the curve is more significant for dual phase steel containing delta-ferrite, and long-term creep strength of it is significantly lower than that of the others. Inflection of the curve corresponds to stress condition of 50% of 0.2% offset yield stress. Accuracy of creep rupture strength evaluation is drastically improved by region splitting analysis in consideration of 50% of 0.2% offset yield stress. Delta ferrite produces concentration gap due to difference in equilibrium composition of austenite and ferrite at the normalizing temperature. It increases driving force of diffusion and promotes recovery of tempered martensite adjacent to delta-ferrite. Concentration gap may be produced also in heat affected zone (HAZ), especially in fine grain HAZ similar to dual phase steel, and it has possibilities to promote recovery and, therefore, to decrease in creep strength. The advantage has been confirmed on region splitting analysis for creep rupture strength of high chromium ferritic creep resistant steels. It is important to avoid a generation of concentration gap in order to improve stability of microstructure and to maintain high creep strength for long-term.

Keywords: creep, high chromium ferritic steel, long-term creep strength, life prediction, delta-ferrite

1. Introduction

Increasing energy demand for development and economical growth is requested to harmonize well to global environment. That is critical issue to realize sustainable development and society. Thermal power plant is steady and reliable dominant source of electricity supply. On the other hand, combustion of fossil energy resources such as oil, coal and natural gas, is a principal emission source of carbon dioxide gas, which is thought to be the most likely cause of global warming. Consequently improvement in energy efficiency of thermal power plant is desired, and Ultra Supercritical (USC) power plant with operating condition of higher steam temperature and pressure is one of the key technologies. Higher steam condition has been attained by introduction of creep strength enhanced ferritic steels for large scale thick components, such as header and main/reheat steam pipes. However, a risk of remarkable drop of long-term creep strength has been pointed out on those ferritic steels [1-3]. In this paper, creep strength and life prediction with region splitting method [4-6] is investigated on high chromium ferritic creep resistant steels, and degradation mechanism in the long-term is discussed.

2. Experimental procedure

The steels used in the present study are KA-SUS410J3 type steels [7-9] corresponding to ASME Grade 122, and chemical compositions of those are listed in Table 1. Product form,

heat treatment condition and microstructure of those are shown in Table 2. Optical micrographs of the steels in the as heat treated condition are shown in Figure 1. Microstructure of the steels is tempered martensite, except for KA-SUS410J3DTB which contains about 5 vol% of delta-ferrite due to higher chromium concentration and hereinafter referred to as dual phase steel. Creep rupture strength and microstructural change during creep exposure have been investigated, especially on influence of delta-ferrite phase. Creep rupture data of the steels has been analyzed by region splitting method [4-6].

Table 1 Chemical composition (mass%) of the steels studied.

Steels	C	Si	Mn	Cr	Mo	W	Cu	V	Nb	B	Al	N
KA-SUS410J3TP	0.12	0.30	0.60	10.65	0.34	1.89	0.85	0.19	0.05	0.0029	0.007	0.054
KA-SUS410J3	0.12	0.28	0.61	10.50	0.36	2.05	0.97	0.21	0.06	0.0029	0.005	0,069
KA-SUS410J3TB	0.13	0.31	0.60	10.65	0.33	1.87	0.86	0.19	0.05	0.0024	0.007	0.057
KA-SUS410J3DTB	0.11	0.27	0.59	12.10	0.34	1.82	0.82	0.19	0.06	0.0030	0.012	0.066

Table 2 Product form, heat treatment condition and microstructure of the steels studied.

Steels	ASME Code	Form	Normalizing	Tempering	Microstructure
KA-SUS410J3TP	P122	pipe	1050°C x 60min. /AC	770°C x 6h /AC	Tempered martensite (TM)
KA-SUS410J3	Grade 122	plate	1050°C x 100min. /AC		
KA-SUS410J3TB	T122	tube	1050°C x 10min. /AC		
KA-SUS410J3DTB	-	tube	1050°C x 10min. /AC	790°C x 3h /AC	TM + δ ferrite

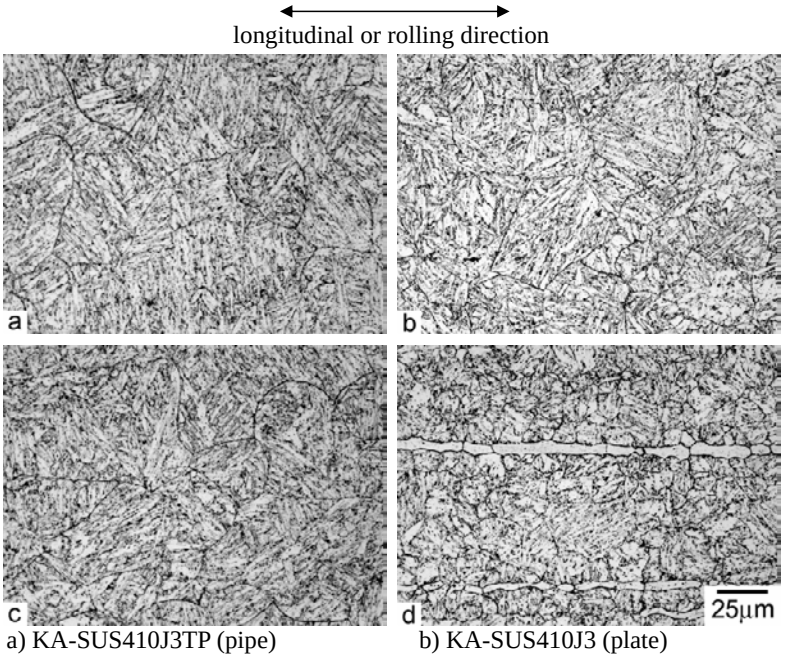

a) KA-SUS410J3TP (pipe) b) KA-SUS410J3 (plate)
c) KA-SUS410J3TB (tube) d) KA-SUS410J3DTB (tube)

Fig.1 Optical micrographs of the steels in the as heat treated condition.

3. Results and Discussion

3.1 Tensile test

Tensile strength and 0.2% offset yield stress of the steels are plotted against temperature and shown in Figure 2. Those values were evaluated under strain rate of 1.25 x 10^{-3} s^{-1} and 5 x 10^{-5} s^{-1}, respectively. Tensile strength and 0.2% offset yield stress decrease remarkably with increase in temperature in excess of 500°C, especially for plate steel whose values are lower than those of the others. A 50% of 0.2% offset yield stress evaluated for each steels was used for region splitting analysis of the creep rupture data. Rupture elongation and reduction of area are shown in Figure 3. Rupture ductility slightly decreases with increase in temperature up to 400°C, and it turns to increase with increase in temperature.

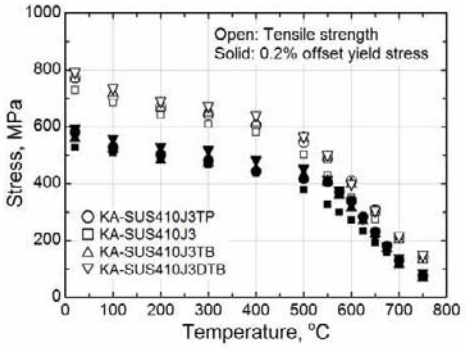

Fig.2 Tensile strength and 0.2% offset yield stress of the steels.

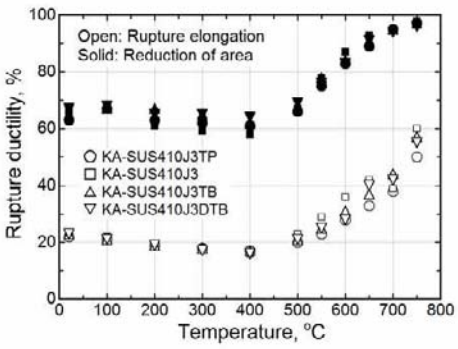

Fig.3 Rupture elongation and reduction of area for tensile test of the steels.

3.2 Creep rupture strength

Creep rupture strength of ASME Grade 122 type single phase pipe, plate and tube steels are shown in Figure 4. Although a little difference in creep rupture life is observed in the short-term at lower temperatures of 550 and 600°C, creep rupture strength of these steels are almost the same. Stress dependence of creep rupture life is large in the short-term, however, it decreases with increase in time to rupture and slope of the stress vs. time to rupture curves becomes steeper in the long-term.

Creep rupture strength of single phase and dual phase tube steels are compared in Figure 5, with open and solid symbols, respectively. Short-term creep rupture strength is almost the same for both steels, however, slope of the stress vs. time to rupture curve of dual phase steel is much steeper than that of single phase steel in the long-term and long-term creep rupture strength of dual phase steel is lower than that of single phase steel.

Rupture elongation and reduction of area of the steels is plotted against time to rupture and shown in Figure 6 (a) and (b). Rupture ductility is high enough in the short-term, however, it indicates remarkable decrease with increase in time to rupture. Large drop in rupture ductility corresponds to increase in slope of the stress vs. time to rupture curve and it is thought to be associated with preferential recovery at the vicinity of prior austenite grain boundary [3, 4].

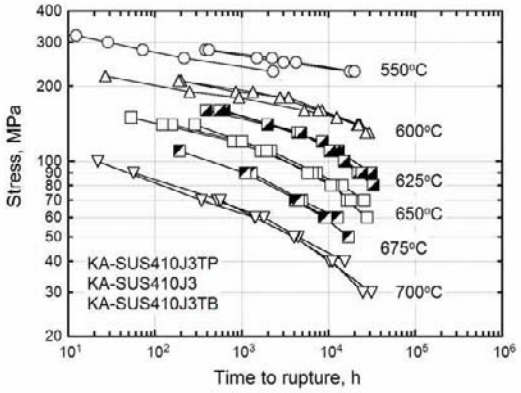

Fig. 4 Creep rupture strength of ASME Grade 122 type single phase steels.

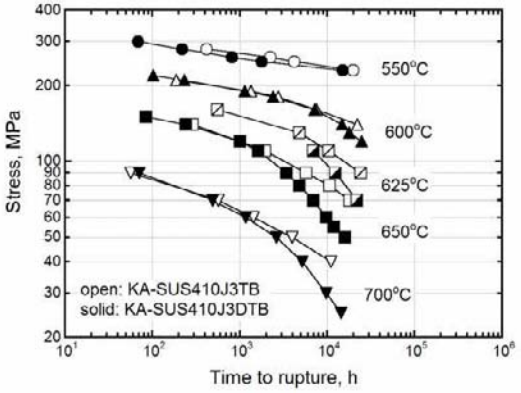

Fig.5 Comparison of creep rupture strength of single phase and dual phase steel tubes.

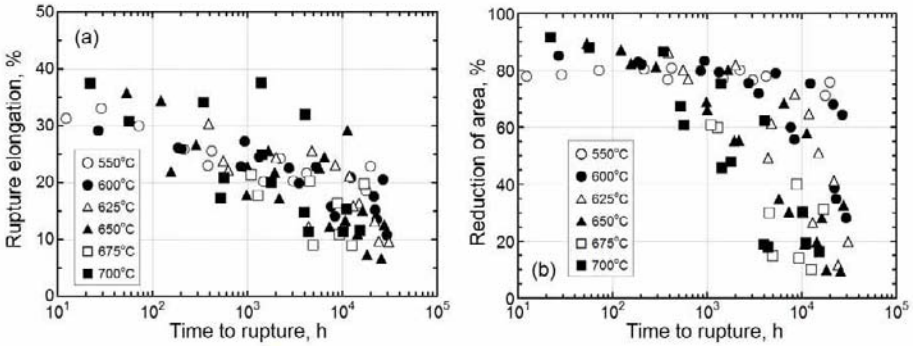

Fig.6 Rupture elongation (a) and reduction of area (b) plotted against time to rupture of the steels.

Creep rupture strength of the steels shown in Figs 4 and 5 are plotted against a ratio of stress to 0.2% offset yield stress and shown in Figure 7 for individual steel. Relation between stress to 0.2% offset yield stress ratio and time to rupture indicates inflection and slope of the curve changes from gentle in the high ratio region to steeper in the low ratio region. Moreover, inflection of the relation is observed at the ratio of stress to 0.2% offset yield stress is about 0.5 for each steels. It should be indicated that an extrapolation of the short-term creep rupture data in the high ratio region over 0.5 results in overestimation of long-term creep rupture strength in the low ratio region under 0.5. Based on this feature of stress dependence of creep rupture strength, creep rupture strength should be evaluated separately for high and low stress regions by considering a boundary condition of 50% of 0.2% offset yield stress.

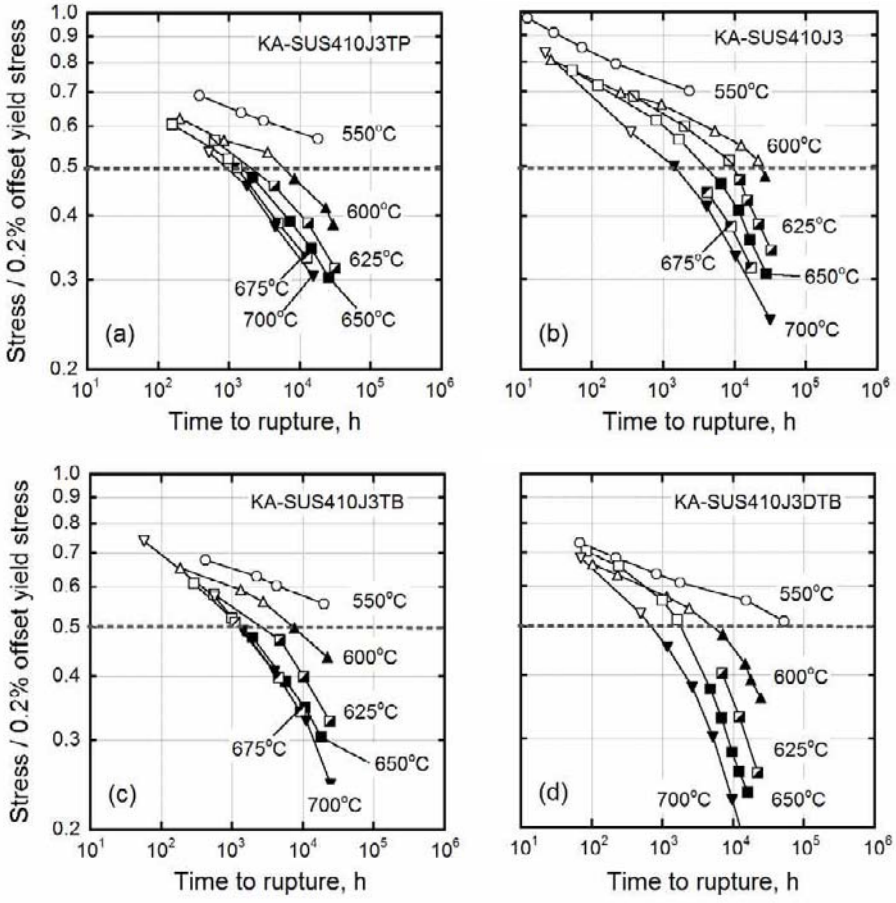

Fig.7 Creep rupture life of the steels plotted against ratio of stress to 0.2% offset yield stress.

3.3 Evaluation of creep rupture strength

Creep rupture data of ASME Grade 122 type single phase steels and creep rupture life curves predicted by Larson-Miller parameter (P_{LM}) by means of conventional manner with whole data (dotted lines) and region splitting method [4-6] (solid lines) are shown in Figure 8. Quadratic function of logarithm stress was used for curve fitting with P_{LM} for both methods, and best fit parameter constant of P_{LM} was 30.8, 39.8 and 20.6 for conventional whole data analysis, short-term and long-term of region splitting method, respectively. Master creep rupture life curves obtained by these analyses are expressed by the following equations.

Conventional analysis with whole data

$$P_{LM} = 24{,}778 + 14{,}151 \log \sigma - 5{,}339 (\log \sigma)^2, \ C = 30.8 \quad (1)$$

Region splitting method for short-term

$$P_{LM} = 20{,}218 + 28{,}171 \log \sigma - 9{,}098 (\log \sigma)^2, \ C = 39.8 \quad (2)$$

Region splitting method for long-term

$$P_{LM} = 29{,}161 - 2{,}601 \log \sigma - 408 (\log \sigma)^2, \ C = 20.6 \quad (3)$$

Conventional life assessment with whole data indicates overestimation of 10^5h creep rupture strength at 600, 625 and 650°C. On the other hand, region splitting method analyze creep rupture data in short-term and long-term independently, that is divided by 50% of 0.2% offset yield stress, and it evaluates long-term creep data accurately. The effectiveness of the respective master equation to represent observed creep rupture life, t_{Robs} was examined by the following relationship proposed by European Creep Collaborative Committee (ECCC) [10].

$$\log t_{Rprd} = \log t_{Robs} \pm 2.5 \ SE = \log t_{Robs} \pm \log(Z) \quad (4)$$

where t_{Rprd} is predicted creep rupture life, t_{Robs} is observed creep rupture life and SE is a standard error of estimate, and for a normal distribution, about 99% of the observed creep

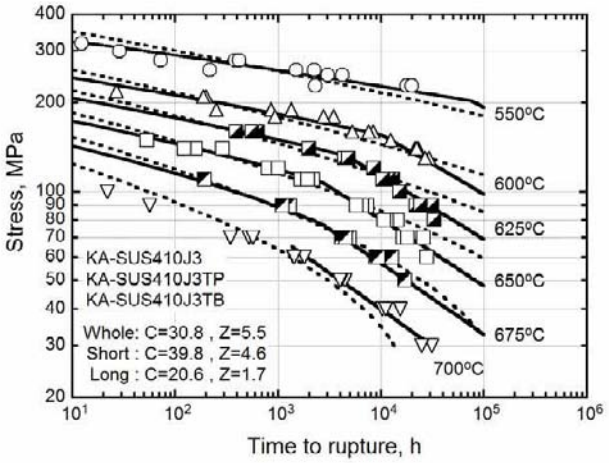

Fig. 8 Creep rupture strength of ASME Grade 122 type single phase steels and creep rupture life curves predicted by Larson-Miller parameter (P_{LM}) by means of conventional manner with whole data (dashed lines) and region splitting method (solid lines) [4-6].

rupture lives would be expected to exist within the boundaries defined by the equation (4). Comparisons of predicted and observed creep rupture lives are shown in Figures 9 and 10 for conventional analysis and region splitting method, respectively. Dashed lines defined by the equation (4) with Z value are also shown in the figures. Z value is 5.5 for conventional whole data analysis and that is 4.6 and 1.7 for short-term and long-term of region splitting method.

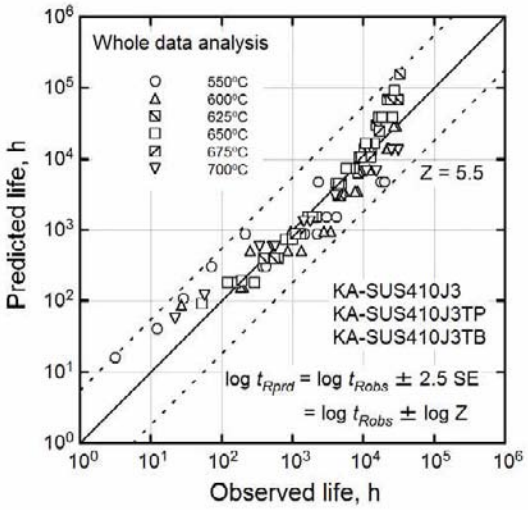

Fig. 9 Comparison of predicted and observed creep rupture lives for ASME Grade 122 type single phase steels by means of conventional whole data analysis.

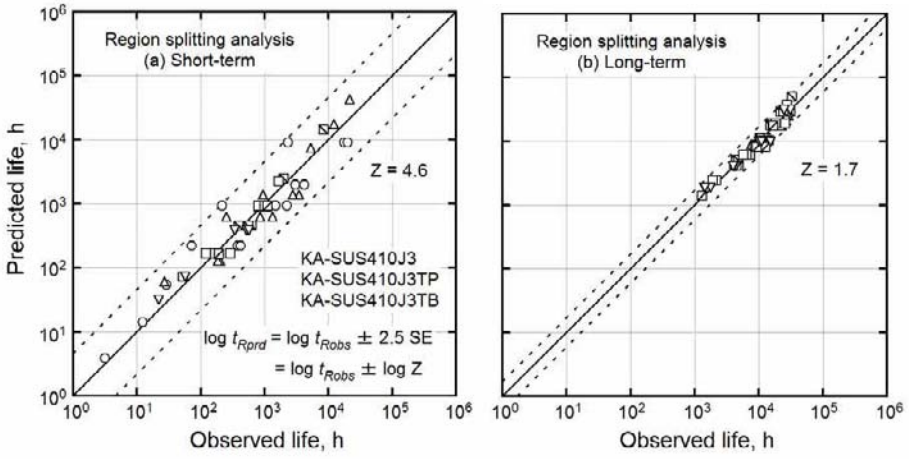

Fig.10 Comparisons of predicted and observed creep rupture lives for ASME Grade 122 type single phase steels by means of region splitting method for short-term (a) and long-term (b).

For Z value of 2, almost 99% of the observed creep rupture lives lie within factor of 2, and Z value of smaller than 2 is recommended for a reliable prediction by ECCC [10]. Z value for long-term creep life prediction by region splitting analysis is 1.7 and effectiveness of region splitting analysis has been confirmed, especially on long-term. Z value of 4.6 for the short-term should be caused by heat-to-heat variation of 0.2% offset yield stress.

Creep rupture data of dual phase steel and creep rupture life curves predicted by P_{LM} similar to the other steels are shown in Figure 11. Master creep rupture life curves obtained by these analyses are expressed by the following equations.

Conventional analysis with whole data

$$P_{LM} = 20{,}755 + 9{,}184 \log \sigma - 3{,}613 (\log \sigma)^2, \; C = 23.4 \quad (5)$$

Region splitting method for short-term

$$P_{LM} = 13{,}324 + 32{,}367 \log \sigma - 9{,}918 (\log \sigma)^2, \; C = 37.8 \quad (6)$$

Region splitting method for long-term

$$P_{LM} = 22{,}864 - 4{,}924 \log \sigma + 695 (\log \sigma)^2, \; C = 13.6 \quad (7)$$

Comparisons of predicted and observed creep rupture lives are shown in Figures 12 and 13 for conventional analysis and region splitting method, respectively. Dashed lines defined by the equation (4) with Z value are also shown in the figures. Z value is 7.2 for conventional analysis and that is 2.1 and 1.6 for short-term and long-term of region splitting method.

Creep rupture data was analyzed by both methods for individual steels and obtained best fit parameter constant of P_{LM} and Z value is listed in Table 3. For conventional whole data analysis, Z value is in a range of 2.8 - 7.2 and unacceptable results, however, it could be reduced to be less than 2 for long-term data by region splitting method. The availability of

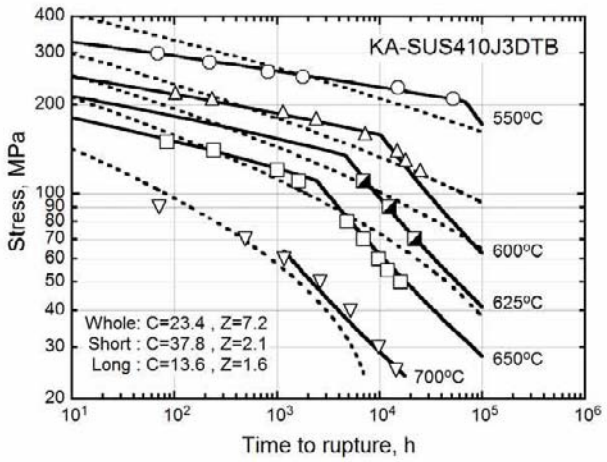

Fig. 11 Creep rupture strength of dual phase steel and creep rupture life curves predicted by Larson-Miller parameter (P_{LM}) by means of conventional manner with whole data (dashed lines) and region splitting method (solid lines).

region splitting method for long-term creep strength prediction is clearly demonstrated. Best fit parameter constant of P_{LM} for the single phase steels are about 20 and that of dual phase steel of 13.6. The parameter constant of 20 means temperature dependence of creep rupture life roughly corresponds to that of self diffusion of iron, and long-term creep strength is governed by diffusion controlled phenomena. Small parameter constant value of the dual phase steel should be caused by presence of delta-ferrite phase.

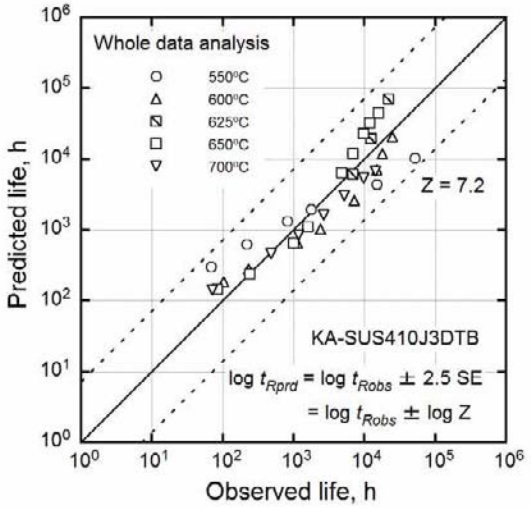

Fig.12 Comparison of predicted and observed creep rupture lives for dual phase steel by means of conventional whole data analysis.

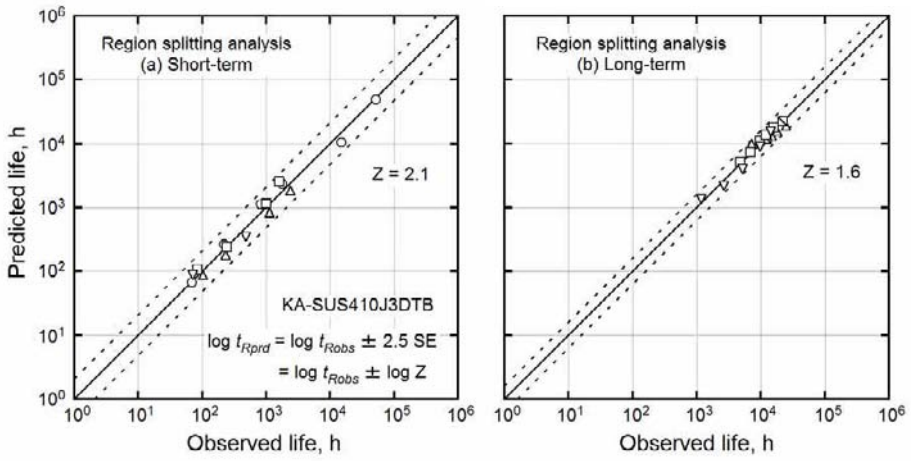

Fig.13 Comparisons of predicted and observed creep rupture lives for dual phase steel by means of region splitting method for short-term (a) and long-term (b).

Table 3 Summary of creep rupture data evaluation of the steels.

Steels	Constant of P_{LM}			Z		
	Whole data	Region splitting		Whole data	Region splitting	
		Short-term	Long-term		Short-term	Long-term
3 single phase steels	30.8	39.8	20.6	5.5	4.6	1.7
KA-SUS410J3TP	29.4	42.3	24.0	2.8	1.9	1.4
KA-SUS410J3	29.6	36.4	18.4	4.5	2.3	1.5
KA-SUS410J3TB	29.7	42.8	21.7	3.0	1.8	1.5
KA-SUS410J3DTB	23.4	37.8	13.6	7.2	2.1	1.6

3.4 Influence of delta-ferrite

Bright field TEM image at a vicinity of grain boundary between delta-ferrite (upper right) and tempered martensite grain (bottom left) of the dual phase steel crept for 500h at 700°C and 50MPa is shown in Figure 14. A lot of coarsened precipitates are observed at a cross point of block boundary and grain boundary between delta-ferrite and tempered martensite grain.

Equilibrium chemical composition of austenite and ferrite phases in KA-SUS410J3DTB steel at normalizing temperature of 1050°C is calculated by Thermo-Calc [11] and compared in Figure 15. Austenite phase stabilizing elements such as carbon and nitrogen are poor in ferrite phase, and ferrite phase stabilizing elements are enriched in ferrite phase. Equilibrium carbon and nitrogen concentrations in austenite phase are about six times higher than those in ferrite phase. Consequently, diffusion of carbon and nitrogen atoms from tempered martensite grain toward delta-ferrite along block boundaries should be enhanced by large concentration gap between delta-ferrite and tempered martensite grain, and it promotes coarsening of precipitate on grain boundary between delta-ferrite and tempered martensite grain and recovery of tempered martensite microstructure.

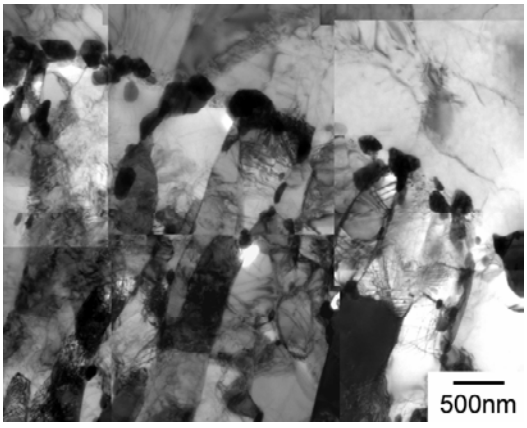

Fig.14 Bright field TEM image of the dual phase steel crept for 500h at 700°C and 50MPa.

Creep rupture strength of cross weld specimen of ASME Grade 122 type plate steel at 650°C [12] is shown in Figure 16, together with those of KA-SUS410J3TB and KA-SUS410J3DTB steels. Cross weld specimen indicates significant drop in long-term creep strength with similar slope to that of dual phase steel. Distribution of alloying elements should be caused in HAZ and it could be factors of large drop in long-term creep strength.

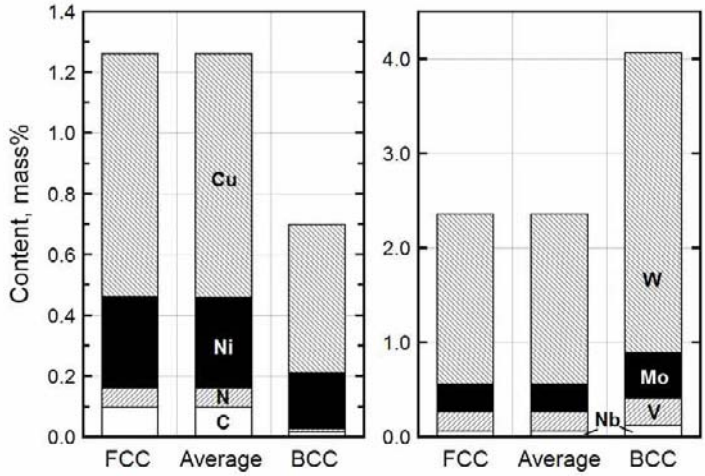

Fig.15 Equilibrium chemical composition of austenite and ferrite phases in dual phase steel at 1050°C calculated by Thermo-Calc. [11].

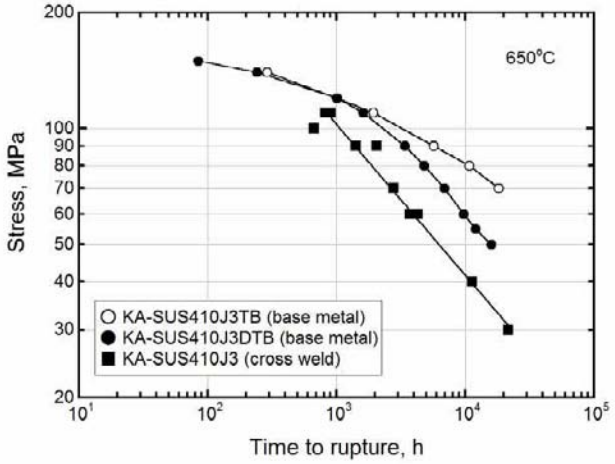

Fig. 16 Stress vs. time to rupture curves at 650°C of base metal of single and dual phase steels and cross weld specimen of ASME Grade 122 type steel plate [12].

4. Conclusions

Creep strength and life prediction with region splitting method have been investigated on creep strength enhanced ferritic steels and degradation behavior during long-term creep exposure has been discussed. The following results are obtained.

1. Inflection of stress vs. time to rupture curve is observed at 50% of 0.2% offset yield stress for all the steels studied.
2. The availability of region splitting method for long-term creep strength prediction is clearly demonstrated by means of Z value proposed by ECCC. It has been speculated that long-term creep strength is governed by diffusion controlled phenomena.
3. Decrease in long-term creep strength is promoted by delta-ferrite phase, since diffusion of carbon and nitrogen atoms may be promoted by large concentration gap, and it enhances coarsening of precipitates and recovery of microstructure. It has been supposed that significant drop in creep strength of cross weld specimen should be also caused by distribution of alloying elements formed in a fine grain HAZ.

References

[1] V. Foldyna, Z. Kuboň, A. Jakobová and V. Vodárek, 'Development of Advanced High Chromium Ferritic Steels', *Microstructural Development and Stability in High Chromium Ferritic Power Plant Steels*, A. Strang and D.J. Gooch eds., The Institute of Materials, London, (1997), 73-92.

[2] A. Strang and V. Vodárek, 'Microstructural Stability of Creep Resistant Martensitic 12%Cr Steels', *Microstructural Stability of Creep Resistant Alloys for High Temperature Plant Applications*, The Institute of Materials, London, (1998), 117-133.

[3] K. Kimura, H. Kushima, and F. Abe, 'Heterogeneous Changes in Microstructure and Degradation Behaviour of 9Cr-1Mo-V-Nb Steel During Long Term Creep', *Key Engineering Materials*, 171-174(2000), 483-490.

[4] K. Kimura, H. Kushima and F. Abe, 'Degradation and Assessment of Long-term Creep Strength of High Cr Ferritic Creep Resistant Steels', Proc. Int. Conf. Advances in Life Assessment and Optimization of Fossil Power Plants, Orland, Florida, USA, Mar. 11-13, (2002).

[5] K. Kimura, K. Sawada, K. Kubo and H. Kushima, 'Influence of Stress on Degradation and Life Prediction of High Strength Ferritic Steels', ASME PVP-Vol.476, (2004), 11-18.

[6] K. Kimura, 'Assessment of Long-term Creep Strength and Review of Allowable Stress of High Cr Ferritic Creep Resistant Steels', ASME PVP2005-71039, (2005).

[7] Thermal Power Standard Code, Ministry of Economy, Trade and Industry (METI), 2005.

[8] NIMS Creep Data Sheet, National Institute for Materials Science, No.51, (2006).

[9] NIMS Creep Data Sheet, National Institute for Materials Science, No.52, (2006).

[10] ECCC Recommendations - Volume 5, Part 1a, 'Generic recommendations and guidance for the assessment of full size creep rupture datasets', ECCC Document AC/MC/35 [Issue 5], ed: Holdsworth, S.R., August-2003.

[11] B. Sundman, B. Jansson and J-O. Andersson, Calphad, 9(1985), 153.

[12] M. Tabuchi, M. Matsui, T. Watanabe, H. Hongo, K. Kubo and F. Abe, 'Creep Fracture Analysis of W Strengthened High Cr Steel Weldment', Mat. Sci. Res. Int., 9(2003), 23-28.

CREEP CURVE ANALYSIS USING THE MODIFIED Ω METHOD

You Fa Yin, Roy G Faulkner
Institute of Polymer Technology and Materials Engineering, Loughborough University,
Loughborough, Leicestershire LE11 3TU, UK
y.yin@lboro.ac.uk; r.g.faulkner@lboro.ac.uk

Abstract

Parameters such as the minimum creep rate are very useful in estimating the remanent life of power plant metals in engineering applications. However, in most cases, problems occur when determining these parameters using methods such as the moving average. In this paper, different methods of analysing creep curves have been studied and compared against a large set of creep curves. It is found that a modified version of the Ω method can describe creep curves of a number of power plant metals very well. In addition, the methods can directly give an estimation of the rupture life. The method has been used to analyse creep curves of several power plant steels and good correlation between predicted rupture life and strain rate and creep damage has been found.

Key words: Creep damage; creep strain; Ω method; remanent life; creep rate

1. Introduction

Analysis of creep strain curves can yield useful information with regard to the material and its application. During the European COST 522 programme, efforts had been made to clarify how creep damage development is associated with the creep strain curve and hence provide useful information for the development of better consumables for advanced plant [1-3]. The widely recognised and used Monkman-Grant relationship correlates the failure time to the minimum creep rate [4], thereby can be used to estimate rupture life from the minimum creep rate. However, the determination of creep curve characteristics, such as the minimum creep rate is not straight forward due to the large scatter involved in the measurement of creep strain. It becomes very difficult when the creep strain curves are produced by interrupted creep tests and the data points are limited. Here we describe and compare some methods for quantitative analysis of creep strain curves and their application to power plant metals.

2. Methods for creep curve analysis

Three methods used to analyse creep curves in this study are introduced below.

2.1 Moving average

It is desirable from the engineering point of view that there is an easy and reliable way to analyse the creep curves. In most cases, the analysis of creep curves is performed by obtaining the creep rate as a function of time, so that parameters such as the minimum creep rate and time for tertiary creep to start can be found. In such cases, the analysis is basically the differentiation of the creep curves and can be carried out easily using the Excel worksheet. Generally speaking, the differentiation of creep curves is the execution over the creep data of the following equation:

$$\dot{\varepsilon}_i = \frac{\Delta\varepsilon}{\Delta t} = \frac{\varepsilon_{i+n} - \varepsilon_{i-n}}{t_{i+n} - t_{i-n}} \tag{1}$$

where n specifies the time interval used to carry out the differentiation. In our particular case, we used n = 7, *i.e.* the creep rate at ith data point was calculated as:

$$\dot{\varepsilon}_i = \frac{\varepsilon_{i+7} - \varepsilon_{i-7}}{t_{i+7} - t_{i-7}} \tag{2}$$

It is clear that after this calculation, the first and the last 7 data points are lost. Also, $\dot{\varepsilon}_i$ calculated using Eq. (2) is dependent on the size of Δt used. It is hoped that the larger time intervals used here would somehow smooth the results. However, due to the nature of the experimental creep data, the calculated creep rate scatters markedly. Therefore, the calculated $\dot{\varepsilon}_i$ is smoothed using a moving average method, *i.e.*,

$$\dot{\varepsilon}_j = \frac{1}{2n_1 + 1} \sum_{i=j-n_1}^{j+n_1} \dot{\varepsilon}_i \tag{3}$$

Here, the creep rate has been smoothed twice with n_1 = 6 and n_1 = 12, *i.e.*,

$$\bar{\dot{\varepsilon}}_j = \frac{1}{13} \sum_{j-6}^{j+6} \dot{\varepsilon}_i \quad \text{and then} \quad \bar{\bar{\dot{\varepsilon}}}_k = \frac{1}{25} \sum_{k-12}^{k+12} \dot{\varepsilon}_j \tag{4}$$

It is evident that during these smoothing processes, a further 12 and 24 data points are lost. Therefore, a total of 50 data points are lost during the whole process of differentiation and smoothing. In most cases, there are thousands of data points. Therefore this is not a big problem. However, if the experimental data are limited, the application of this approach is not feasible. Finally, the calculated creep rate is fitted with a polynomial up to the 6th order.

2.2 Model Equations

An alternative to the moving average method is to fit the experimental creep data to a model equation and then find the creep rate by differentiating the model equation. There are several model equations available in the literature [5-8]. However, we found that the following equation best fits the creep data:

$$\varepsilon = \varepsilon_L \left[1 - \exp(-mt)\right] + \dot{\varepsilon}_s t + \varepsilon_T \exp(ht) \tag{5}$$

where ε_L, m, $\dot{\varepsilon}_s$, ε_T and h are fitting parameters. The three terms in the above equation have clear meanings. The first term describes primary creep. The second describes the steady state or secondary creep, therefore $\dot{\varepsilon}_s$ is the secondary creep rate. The last term is tertiary creep. Differentiation of Eq. (5) gives the creep rate:

$$\dot{\varepsilon} = \varepsilon_L m \exp(-mt) + \dot{\varepsilon}_s + \varepsilon_T h \exp(ht) \tag{6}$$

Therefore, creep rate at any given time can be calculated using Eq. (6) if parameters in Eq. (5) have been determined by fitting of Eq. (5) to the creep data. Unlike the moving average approach, no data points are lost when differentiating the creep curve.

2.3 The Ω method [9, 10]

A common application of the Ω method is to predict the rupture life of a material using short-term creep testing. In engineering practice, the creep curves are first differentiated using an approach formulated in Eq. (1). Then the creep rate is plotted against the true strain on a natural logarithm scale. At longer creep test times, this may give a linear relation. Fit of the linear part of the curve to the following equation

$$\ln(\dot{\varepsilon}) = \ln(\dot{\varepsilon}_0) + \Omega\varepsilon \tag{7}$$

will give the values of $\dot{\varepsilon}_0$ and Ω. The rupture life can then be calculated from these two parameters as follows.

$$t_r = \frac{1}{\Omega \dot{\varepsilon}_0} \tag{8}$$

Clearly, this approach is easy to use. However, the linear region is not so clear in some cases due to the scatter in the creep data and due to the limited number of data available. In such cases, the predicted rupture life may be very different when even just one data point is removed or added into the fitting set.

Eq. (7) implies that the creep behaviour at later stages of creep obeys the following equation:

$$\varepsilon = -\frac{1}{\Omega}\ln\left(1 - \Omega \dot{\varepsilon}_0 t\right) \tag{9}$$

or in another form using the rupture life, t_r:

$$\varepsilon = -\frac{1}{\Omega}\ln\left(1 - \frac{t}{t_r}\right) \tag{10}$$

Therefore, if the Ω method is applicable, the creep data should fit Eqs. (9) or (10) reasonably well at later stages of creep. In such a case, both Ω and t_r can be obtained by fitting the data to Eq. (10) and $\dot{\varepsilon}_0$ can then be calculated using Eq. (8). The creep rate can also be expressed as a simple function of creep time:

$$\dot{\varepsilon} = \frac{1}{\Omega\left(t_r - t\right)} \tag{11}$$

The advantage of this approach is that there is no need to differentiate the creep curve and this therefore limits the possible errors generated in the analysis. In addition, it can use all the data points. This is particularly useful when there are only limited data available.

Although Eq. (10) gives zero strain at $t = 0$, it does not fit the initial part of the creep curves well. In addition, Eq. (10) seems to give much higher creep rate at later stages. Therefore, it is modified as follows.

$$\varepsilon = \varepsilon_L\left[1 - \exp\left(-mt\right)\right] - \frac{1}{\Omega}\ln\left[1 - \left(\frac{t}{t_r}\right)^{\alpha}\right] \tag{12}$$

It is clear that the first term in Eq. (12) is a representation of the primary creep and uses the same formula as discussed in section 2.2. An exponent, α, has been added to the original Ω term to adjust the creep rate at later stages of creep. From Eq. (12), as t approaches t_r, the creep strain will approach infinity. Therefore, these modifications have not altered the description of t_r as the creep rupture life. It also can be seen that Eq. (12) reduces to Eq. (10) when $\varepsilon_L = 0$ and $\alpha = 1$. In other words, Eq. (12) is inclusive of Eq. (10). As Eq. (12) has three more fitting parameters than Eq. (10), it is expected that Eq. (12) will fit the data better than Eq. (10). The method using Eq. (12) is called the modified Ω method thereafter in this paper.

The equation for calculating creep rate corresponding to Eq. (12) is

$$\dot{\varepsilon} = \varepsilon_L m \exp\left(-mt\right) + \frac{\alpha}{\Omega}\frac{t^{\alpha-1}}{t_r^{\alpha} - t^{\alpha}} \tag{13}$$

Again, it reduces to Eq. (11) when $\varepsilon_L = 0$ and $\alpha = 1$.

3 Results and Discussion

3.1 Model Equation fits of creep curves

Two examples of the creep curves obtained from the interrupted creep tests of some 9-Cr weldments (for composition and welding procedures, please refer to reference [1-3]) are shown in Fig. 1. For clarity, there are only a small fraction of the experimental data points (symbols) plotted. Lines shown in Fig. 1 are the best fits of Eq. (5) to the experimental data.

Fig. 1(a) and (b) show two different situations. In Fig. 1 (a), the specimen is well into the tertiary regime, while in Fig. 1(b) the specimen has just entered tertiary creep. However, the model creep equation fits both creep curves extremely well, though Fig. 1(b) shows that the model predicts higher strain in primary creep.

Similar good fits have been found for all creep curves studied, including those from 9-Cr weldments, parent materials such as P92 and CMV specimens. This demonstrates that the model equation, Eq. (5), can accurately describe creep behaviour of many power plant steels and therefore can be used relatively accurately to analyse creep properties of such materials.

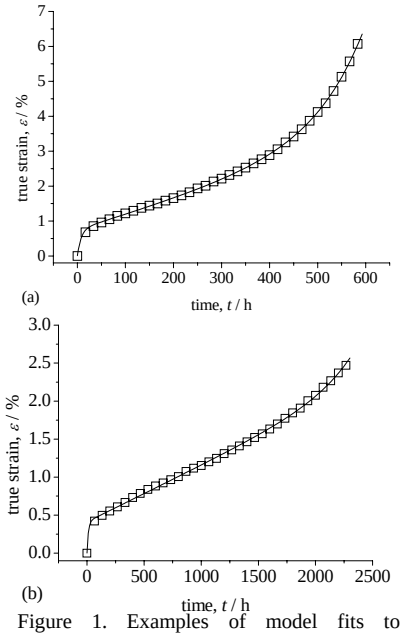

Figure 1. Examples of model fits to experimental creep curves of 9-Cr weldments at 650 °C 83 MPa (a) post weld heat treatment at 755 °C for 1 h and aged at 760 °C for 30 h; (b) post weld heat treatment at 755 °C for 1 h. Only a fraction of the data is plotted in the figure. Symbols are experimental data and the lines are the best fits.

3.2 Comparison between model equation fit and moving average method

The creep rate as a function of time of the two specimens in Fig. 1 is presented in Fig. 2. The symbols in Fig. 2 are creep rate calculated according the moving average routine set up in Section 2.1. The solid lines are polynomial fits to the 6^{th} order to the data points in Fig. 2 and the dashed lines are creep rate calculated using the creep model, *i.e.* Eq. (6). According to our practice, the 6^{th} order is necessary and enough to obtain reasonably good fits for all specimens studied.

There is much scatter in the creep rate calculated using the moving average approach, even after the two smoothing operations, as clearly demonstrated in Fig. 2(b). Note that the model fits to the raw creep data of specimen in Fig 2(b) is as good as that in Fig. 2(a) (see Fig. 1), the differentiation of the creep data using Eq. (2) results in considerable scatter in the case of (b) due to the errors in the raw strain data. However, both the model and the polynomial fit to the strain rate reasonably well, especially the central and the long time region.

However, unlike the model calculations, the polynomial fits are somehow wavy in both cases as shown in Fig. 2, makes it difficult to determine the minimum creep rate. In fact, this is common in all the specimens studied. The situation may be improved by cutting off the data

at the initial and/or the final parts of the creep curves. This of course leads to the loss of more data and useful information such as the onset time of secondary creep. In addition, there are a number of factors which will affect the results and have to be determined subjectively. For example, the number of points to be cut off and the orders of the polynomials to use have to be determined and are very subjective.

The model calculation does not have such problems and therefore the results are less subjective and more reproducible. However, the problem with the model calculation is also clearly shown in Fig. 2. It seems to be the nature of the model used that the decrease in creep rate at the beginning of the curves in Fig. 2 is too steep, thereby leading to the underestimation of the onset time for secondary creep. In other words, the term that describes the primary creep in Eq. (5) overestimates the change of creep rate. Unfortunately, we are unable to find a simple and more effective formula for the primary creep, although addition of another term similar to the one used in Eq. (5) for description of primary creep may improve the situation as did in the situation of θ-projection method applied to low creep ductility materials by Evans [11].

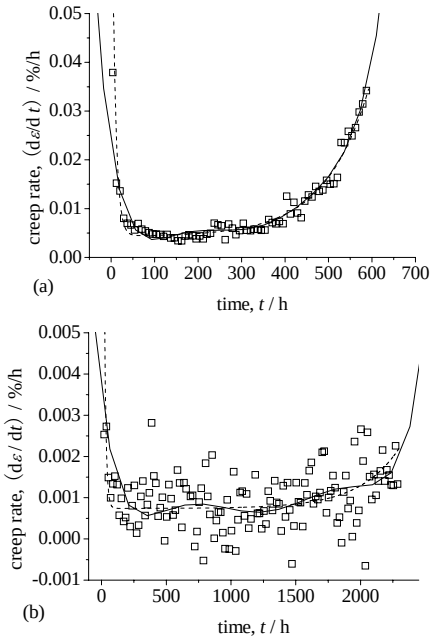

Figure 2. Example plots of the creep rate as a function of time calculated from creep curves in Fig. 1. Symbols are values calculated using the moving average approach, solid lines are the polynomial fits (6th order) and dashed lines are creep rates calculated according to the model, Eq. (6). (a) post weld heat treatment at 755 °C for 1 h and aged at 760 °C for 30 h; (b) post weld heat treatment at 755 °C for 1 h.

The minimum strain rate determined using both the moving average method and the model equation calculations are shown in Fig. 3 by the symbols and the line is a linear fit. The minimum creep rate determined using the two methods agrees with each other reasonably well. The corresponding equation of the fitted line is

$$\log\left(\dot{\varepsilon}_{\min,MA}\right) = \left(1.09 \pm 0.05\right)\log\left(\dot{\varepsilon}_{\min,Model}\right) + \left(0.12 \pm 0.14\right) \qquad (14)$$

It is clear that the two values are very close to each other if we also consider the errors involved in the parameters determined. Therefore, both methods can be used to estimate the minimum creep rate. However, the minimum strain rate determined using the moving average method is generally lower than that determined using the model, as indicated in Eq. (14).

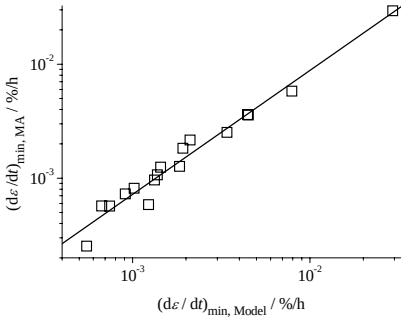

Figure 3. Comparison of the minimum creep strain rate determined using the moving average method (denoted as MA and in Y-axis) and the model calculations (denoted as Model and in X-axis).

Both methods are ineffective when they are used to determine the onset time for secondary creep. Therefore, the results are not presented here. Nevertheless, we used the model to determine the secondary creep time. Here, we define the onset time for secondary creep is when the creep rate decreases to 110% of the minimum creep rate. Similarly, we define the onset time for the tertiary creep is when the creep rate increases to 110% of the minimum strain rate. The secondary creep duration is then the difference of the two onset times. The results of all specimens tested are shown in Fig. 4 in the form of a Monkman-Grant type plot. The symbols are the determined values and the line is the best fit of the following Monkman-Grant type equation:

$$\dot{\varepsilon}_{\min} t_S = C \qquad (15)$$

It is clear that the results fit to the equation well and the constant of the best fit is $C = 1.16\%$.

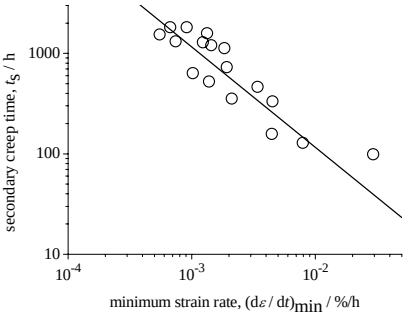

Figure 4. Secondary creep time as a function of minimum creep rate in the form of the Monkman-Grant type plot for two 9-Cr weldments with different post weld heat treatment and creep test conditions. The line is a best fit of the Monkman-Grant type Equation: $\dot{\varepsilon}_{\min} t_S = 1.16\%$.

3.3 The Ω method

The modified Ω method, Eq. (12) fits to the experimental creep data very well, as shown in Fig. (5) for the specimens presented in Fig. 1. In Fig. 5, symbols are experimental measurements and the lines are the fits. The fits nearly pass through all the data points as in the case of the model fits in Fig. 1 and this is true for all the specimens studied. Therefore, it is concluded that the modified Ω method can be used to analyse the creep curves as accurately as using the model equation, Eq. (5). In addition, the modified Ω method can give more accurate results than the model equation when the creep curve contains a substantial tertiary creep. Fig. 6 demonstrates such a case. The specimen here was tested to a higher level of creep damage development and therefore the experimental creep curve (symbols) shows a clear and substantial tertiary creep. From Fig. 6(a), the model fit to such a creep curve does not agree with the experimental measurements well. During the primary creep and early secondary creep stage, the model seems to underestimate the creep strain; the model overestimates the creep strain during later stages of secondary

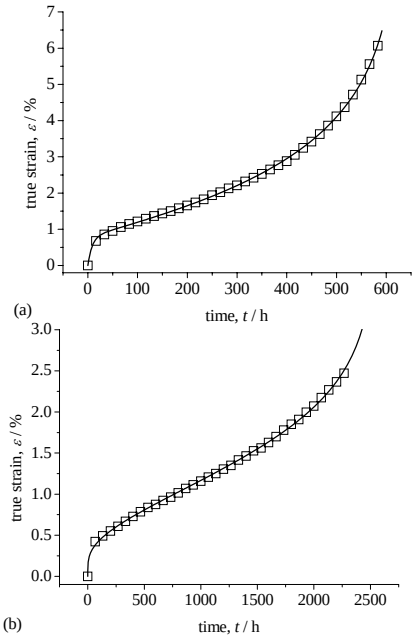

Figure. 5. Examples of fits of the modified Ω method, Eq. (12), to the creep data of 9-Cr weldments at 650 °C 83 MPa (a) post weld heat treatment at 755 °C for 1 h and aged at 760 °C for 30 h; (b) post weld heat treatment at 755 °C for 1 h. Only a fraction of the data is plotted in the figure. Symbols are experimental data and the lines are the best fits.

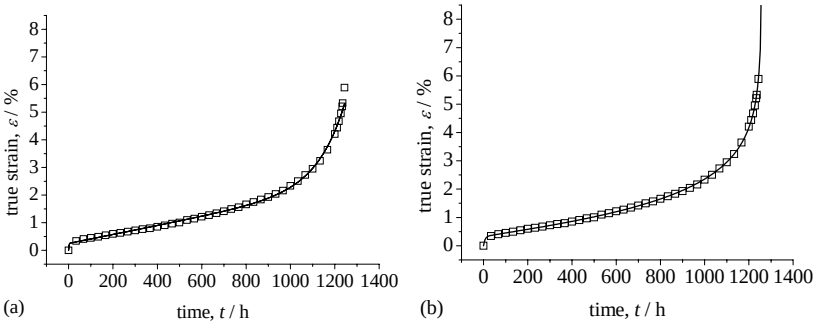

Figure 6. Comparison of the fits of the modified Ω-method (b) and the model equation (a). The specimen is a 9-Cr weldments post weld heat treated at 755 °C for 1 h and then creep tested at 650 °C 104 MPa.

creep; during tertiary creep stage, the model sometimes overestimates and sometimes underestimates the creep strain. Most importantly, the model gives much lower creep strain and strain rate at later stages of tertiary creep. In contrast, the fit using the modified Ω method (Eq.(12)) agrees with the experimental measurements very well over the whole range of the creep test (Fig. 6(b)). Some more examples demonstrating the good fitness of the method are shown in Fig. 7.

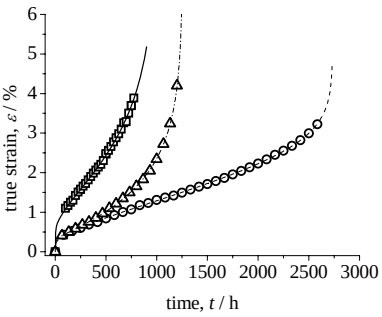

Figure 7. More examples of creep curves fitted using the modified Ω method.

The differentiation of the fitted equations in the form of Eq. (12) gives the creep rate as a function of time, Eq. (13). An example calculated using Eq. (13) is shown in Fig. 8, together with strain rates calculated using the moving average approach (symbols), fitted polynomial to the results calculated using the moving average approach (solid line), and calculated using the model (dashed line). The strain rate calculated using the Ω method differs only slightly from the values calculated using the model. Therefore, the curves calculated using these two methods are difficult to distinguish in Fig. 8. However, at the final part of the curves, the Ω method gives higher strain rate than the model calculation. It is therefore natural to conclude that the Ω method gives similar results as discussed above and presented in Figs. 3 and 4. Indeed, calculations carried out using the Ω method are similar to those

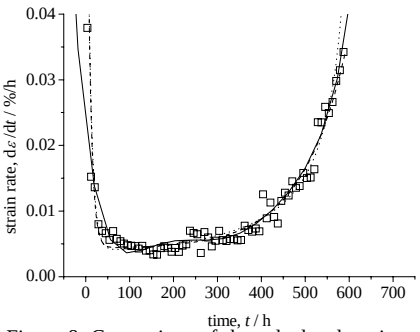

Figure 8. Comparison of the calculated strain rate using the moving average approach (symbols and solid line), the model calculations (dashed line) and the Ω method (dotted line). Note, the Ω method gives nearly identical results as the model calculations; therefore the two are hardly distinguishable in the figure.

calculated using the model calculations. Therefore, they are not presented here. However, the following section presents more results using the modified Ω method.

3.4 Creep damage, remanent life and creep rate

As discussed above, one of the advantages of the modified Ω method over the model calculations is that it can give more accurate results when the creep curves contain a substantial tertiary part. Another advantage of the application of the modified Ω method is that it can give a prediction of the total life of the specimen under the test conditions. Therefore, it enables more analysis to be done. There follows some examples of this.

3.4.1 Creep damage and strain rate

The creep damage level of a specimen is closely related to its straining and is thought to be a function of the strain rate. Here we use the Ω method to calculate the strain rate when the creep test was interrupted (termed as final strain rate here) and make an attempt to correlated the damage levels with the final strain rate. The results are shown in Fig. 9.

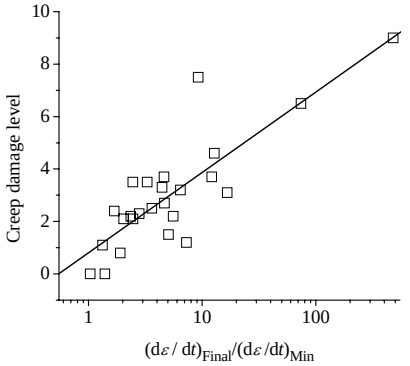

Figure 9. Creep damage level as a function of the ratio of the final and the minimum strain rate. Both the final and the minimum strain rates are calculated using the modified Ω method. Creep damage level from 0: no damage to 10: broken.

Creep damage levels presented in Fig. 8 are determined using a semi-quantitative rating system defined by Allen (3). The damage levels are from 0 to 10 with Level 0 representing no creep damage at all and with Level 10 meaning a broken specimen at the interruption of the test. Fig. 9 shows a clear correlation between the damage ratings and the ratio of final strain rate over the minimum strain rate. The correlation is remarkable when we take into consideration the subjectivity involved in the rating of creep damage and possible errors involved in the fitting of experimental creep data using the modified Ω method, though there are scatters in the experimental data. Although there are not many data points at very low and very high damage levels, following conclusions can be drawn from Fig. 9: (1) Creep damage level is closely related to strain rate and increases sharply with increasing strain rate at lower strain rates. (2) Appreciable creep damage can be observed only when the strain rate is much higher than the minimum strain rate. This suggests that the development of creep damage is associated with tertiary creep.

3.4.2 Consumed life and strain rate

The predicted total rupture life is one of the five fitting parameters in Eq. (12). Therefore, the fraction of the total life that has been consumed up to the time when the test is interrupted is then simply the ratio of the test duration over the predicted rupture life. Fig. 10 shows the consumed life as a function of the strain rate, expressed as the ratio of the final strain rate over the minimum strain rate. The symbols in Fig. 10 are the calculated results. It is clear that the consumed life increases sharply with increasing final strain rate at lower final strain rate as expected. This increase in consumed life continues until the final strain rate reaches about 10 times the minimum strain rate. Then there is little further increase and the consumed life is very close to 100% of the total rupture life.

The correlation between the consumed life and the final strain rate determined using the modified Ω method is very good. It is interesting that this relation can be described approximately by the following equation:

$$\frac{t_c}{t_r} = \frac{\left(\dot{\varepsilon}_F / \dot{\varepsilon}_{Min}\right)^{3/2}}{1+\left(\dot{\varepsilon}_F / \dot{\varepsilon}_{Min}\right)^{3/2}} \times 100\% \qquad (16)$$

Where $\dot{\varepsilon}_F$ and $\dot{\varepsilon}_{Min}$ are the final and the minimum strain rate respectively, t_c and t_r are the consumed and the total rupture life respectively. The solid line in Fig. 10 is a plot of Eq. (16) and it is clear that it fits to the data very well.

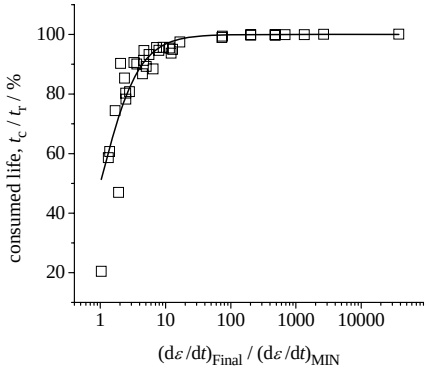

Figure 10. Predicted percentage of consumed life in total rupture life as a function of the final strain rate. Symbols are calculated results. The line is a plot of Eq. (16).

If we set $\dot{\varepsilon}_F = \dot{\varepsilon}_{Min}$ in Eq. (16), then $t_c = 50\% t_r$. This is about right as compared to the results from the creep rupture tests reported in reference [3]. It also can be shown form Eq. (16) that over 95% of the total life has been consumed when the strain rate reaches about 4.5 times the minimum strain rate.

3.4.3 Remanent life and creep damage level

Creep damage level may be used to monitor the remanent life of power plant component, because it is a good indicator of the microstructural degradation. It is therefore interesting to look at the possible correlations between the predicted remanent life and the creep damage levels presented in Fig. 9.

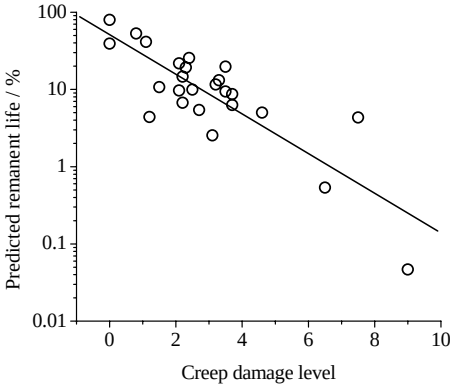

Figure 11. Predicted remaining life using the Ω method as a function of the creep damage rating. Symbols are the data and the line is the best linear fit.

Fig. 11 shows the predicted remanent life using the modified Ω method as a function of the creep damage levels. The circles are the data points and the line is a best linear fit showing roughly the trend. First of all, it is clear that there is a good correlation between the predicted remanent life and the creep damage levels. Secondly, as the vertical axis is a logarithmic scale, the remaining life of the specimens decreases sharply with increasing damage level. Finally, Fig. 11 shows that there would be only a few percent of the total life left when the damage level exceeds about 4. Therefore, Fig. 11 may provide a useful means to estimate the remanent life of power plant components.

4 Conclusions

The moving average approach, the model equation calculation and the modified Ω method can be used in the analysis of creep curves. The strain rate determined using the moving average approach is often wavy and may involve much subjectivity. The modified Ω method can give more accurate fits to creep curves which contain a substantial portion of tertiary creep and can yield an extra and useful parameter, *i.e.* the rupture life. Therefore it is the preferred method for analysing creep curves where it is applicable.

Creep damage level is very much dependent on the strain rate. Appreciable creep damage can be observed optically only when the strain rate is appreciably higher than the minimum strain rate. In this sense, creep damage is a product of tertiary creep. The consumed creep life of the specimens increases sharply with increasing strain rate. This dependence can be described by a simple equation. When tertiary creep sets in, nearly half of the creep life is consumed. And when the strain rate reaches about 4.5 times the minimum strain rate, about 95% of the total life has been consumed.

The predicted remanent life correlates with the creep damage level very well. Therefore, it is possible to use the damage rating or similar microstructural parameters as an approximate indicator of the remanent life of power plant components.

Acknowledgements

We would like to thank EPSRC for funding part of the work under the RAIS (Research Associate Industrial Secondment) scheme (Grant number GR/S77523) and Metrode and Mitsui Babcock for collaboration. The authors are also grateful to Dr David Allen of Power Technology, E.ON UK for hosting one of the authors (YFY) during the above scheme.

References

[1] ALLEN, D J, COST 522 UK6 progress report 1 (PTC), 2002.
[2] ALLEN, D J, COST 522 UK6 progress report 2 (PTC), 2002.
[3] ALLEN, D J, COST 522 UK6 final report (PTC), 2004.
[4] Li, Y. D., A new creep lifetime prediction method: the C-project concept, Int. J. Pres. Ves. & Piping 69 (1996) 161-167.
[5] Evans, R. W. and Wilshire, B., Creep of metals and alloys, Institute of Metals, 1985
[6] Evans, H. E., Mechanisms of creep fracture, Elsevier Applied Science, London, 1984.
[7] Evans, R. W., and Scharning, P. J., The theta projection method applied to small strain creep of commercial aluminium alloy, Materials Science and Technology, 17(5), 2001, 487-493.
[8] Evans, R. W., A constitutive model for the high temperature creep of particle hardened alloys based on the theta projection method, Proceedings of the Royal Society of London Series A — Mathematical Physical and Engineering Sciences, 456(1996), 2000, 835-868.
[9] Prager, M., The Omega method - An engineering approach to life assessment, Journal of Pressure Vessel Technology – Transactions of the ASME, 122(3), 2000, 273-280.
[10] Fujibayashi, S., Endo, T., Creep analysis of a service-exposed 1.25Cr-0.5Mo steel using the omega method, TETSU TO HAGANE-Journal of the Iron and Steel Institute of Japan, 88(7), 2002, 406-412.
[11] Evans, R. W., The theta projection method and low creep ductility materials, Materials Science and Technology, 16(1), 2000, 6-8.

EFFECT OF NONSTEADY LOADING ON CREEP BEHAVIOUR OF ADVANCED 9-12% FOSSIL POWER PLANT STEELS

Vaclav Sklenicka[1], Kveta Kucharova[1], Milan Svoboda[1], Lubos Kloc[1], Jiri Kudrman[2]

[1] Institute of Physics of Materials, Academy of Sciences of the Czech Republic, CZ-616 62 Brno, Czech Republic
[2] UJP Praha a.s., CZ-156 10 Prague, Czech Republic
sklen@ipm.cz

Abstract

Creep behaviour and degradation of creep properties of advanced 9-12%Cr ferritic steels are phenomena of major practical relevance, often limiting the lives of power plant components and structures. Because life expectancy is, in reality, based on the ability of the material to retain its high-temperature creep strength for a period of at least twice the projected design life, methods of creep property assessment based on physical changes in the material that are likely to occur during service exposure rather than simple parametric extrapolation of the short-term data are necessary.

Further, critical high temperature components of machines and structures are often subjected to complicated load and temperature histories. The closest laboratory simulation involves creep under nonsteady temperatures and stresses. For example, the start up and shut down cycles can be well simulated by temperature variation by use of intermittent heating tests. Another types of nonsteady loading are the isothermal loading with stress cycling and creep/fatigue interaction. In order to consider the above effects of different loading, one needs to design experimental methods for simulating the operating state which has many cycles of heating/cooling and nonsteady stressing. This work attempts to highlight the problem areas just in this respect. The proposed approaches are illustrated by recent experimental results on advanced high creep strength 9-12%Cr ferritic-martensitic steels (P91, P92 and E911).

Keywords: 9-12%Cr steels, creep behaviour, variable creep loading, intermittent heating, microstructural changes.

1. Introduction

Many fossil power plant performance improvements can be attributed primarily to advances in materials and their manufacturing technology. Worldwide research has resulted in a number of new 9-12%Cr steels with improved creep strength [1-7]. Optimization of C, Nb, Mo and V and partial substitution of W for Mo in the 9-12%Cr steels have resulted in new steels (e.g. P91, P92 and E911), capable of operating up to 620°C. However, for the long-term applications of the new steels a better understanding of the materials behaviour is necessary to provide the basis for more sophisticated designs for high-temperature service. At present only partial solutions of these problems are available.

Although the development and evaluation of 9-12%Cr steels have proceeded on the basis of simple short-term laboratory-type tests, it is widely recognized that the realistic application of these materials is under conditions far different from those for which they were developed. When applied in service, the material is likely to be subjected to stress variation, temperature variation, and the combined effects of these variables. Periodic applications of excessive loads and intermittent heating are normally absent when the steel is evaluated.

Thus the object of the present paper is an attempt to obtain some information on the effects of intermittent heating on the creep behaviour of P91, P92 and E911 steels to simulate the service regime which has many cycles of heating/cooling.

2. Experimental materials and procedures

The P91 tempered martensitic-ferritic steel produced by Vitkovice Steel, Czech Republic, was subjected to the two-stage heat treatment: 1060°C/1h/air + 750°C/2h/air. Its chemical composition (in wt.%): 0.09 C, 0.56 Mn, 0.20 Si, 0.021 P, 0.009 S, 0.05 Cu, 0.46 Ni, 8.36 Cr, 0.86 Mo, 0.20 V, 0.06 Nb, 0.065 N and 0.007 Al. The P92 steel was produced by Nippon Steel, Japan, and received in the form of a seamless pipe with the following heat treatment: 1065°C/2h/air + 770°C/2h/air. Its chemical analysis (in wt.%): 0.08 C, 9.0 Cr, 0.5 Mo, 1.8 W, 0.2 V, 0.06 Nb, 0.05 N, 0.003 B, <0.04Al. The E911 was produced by Mannesmann Röhrenwerke AG, Germany, and received in the form of a pipe having the diameter of 390 mm after the following heat treatment: 1060°C/1h/air + 770°C/2h/air. Its chemical composition (in wt.%): 0.115 C, 8.85 Cr, 0.20 Si, 0.50 Mn, 0.017 P, 0.002 S, 0.007 Al, 0,24 Ni, 0.96 Mo, 0.22 V, 0.07 Nb, 0.95 W and 0.084 N.

Constant load tensile creep tests were carried out at 600°C and uniaxial applied stresses ranging from 125 to 200 MPa. The effect of temperature variation during the creep test has been investigated by intermittent heating under constant load. Simultaneously, for comparison purposes, the standard creep tests with the same creep testing temperature were performed. In all cases the initial load (tensile stress) was maintained during the entire test.

Following creep testing, samples were prepared for examination by means of both transmission (Philips CM 12 TEM/STEM) and scanning (Jeol 6460) electron microscopy.

3. Experimental results

The effect of intermittent heating at constant load

In the creep testing at nonsteady temperature, the creep specimens in one cycle were moved first from room temperature to the testing temperature (600°C), then creep loaded (the holding time after stabilization of the testing temperature was about 144 hours) and finally the specimens were cooled under load down to room temperature. The same type of temperature cycle was repeated after 24 h without removal of load during the whole creep test up to the final fracture of specimen.

Two elongation ε vs. time t creep curves for steel P91, for uniaxial tensile creep tests conducted at 600°C, with different loading history under the same level of the applied stress σ of 125 MPa are shown in Fig. 1a. The first curve represents the standard creep test which was run at constant load and temperature to the final fracture of the crept specimen. The second curve in Fig. 1a shows the creep behaviour of specimen with intermittent heating, resulting in the fracture of specimen after 67 cycles. More clear comparison of these two creep curves follows from Fig. 1b where the creep curve for non-monotonic creep encompasses the time at the testing temperature only. The results of cycled and standard creep tests of steel P92 and E911 are shown in Figs. 2 and 3 for the same testing temperature and the applied stress of 150 MPa. As shown in these figures, the cycled specimens failed after 77 cycles (steel P92) and 107 cycles (steel E911), respectively.

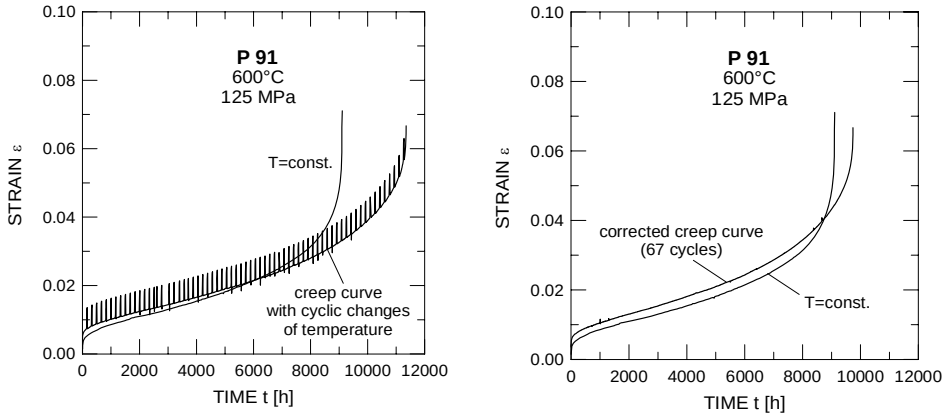

Fig. 1 Creep curves of P91 steel with different loading histories at 125 MPa with the curve for cyclic creep: (a) uncorected (b) corrected

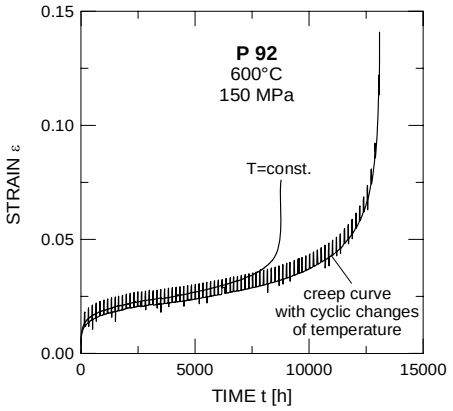

Fig. 2 Creep curves of P92 steel with different loading histories at 150 MPa.

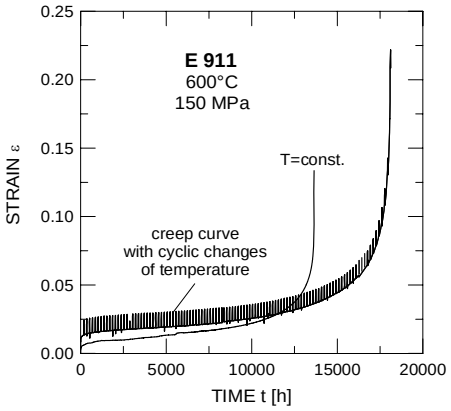

Fig. 3 Creep curves of E911 steel with different loading histories at 150 MPa.

As demonstrated by the figures, no detrimental effect of intermittent heating on the creep behaviour of the specimens during the cycled tests was found. The cycled specimens exhibit a little longer times to fracture than those of the specimens crept at constant temperature, as can be seen from Table 1. A possible explanation for this difference may lie in a serial addition of holding and cooling periods for cycled specimens which overestimates the time to fractures in Figs. 1a, 2 and 3. In fact, the time to fracture for the specimen of P91 steel subjected to standard loading at 125 MPa is about 9100 h whereas the test piece endurance for a cycled specimen is ~ 9700 h when derived from holding periods only. Thus, it is clear from these experiments that the creep resistance of the investigated steels is not deteriorated by intermittent heating.

Table 1. Time to fracture for standard creep tests, t_f, cyclic creep, t_{fc}, and corrected time for cyclic tests, t_{fcor}, at temperature 600 °C and various applied stresses.

Steel	σ [MPa]	t_f [h]	t_{fc} [h]	t_{fcor} [h]
P91	125	9111	11350	9742
P92	150	8773	13088	11240
E911	150	13647	18120	15552

Microstructural and fractographic investigations

All three steels exhibited similar microstructures after the creep exposures. Microstructure of P91 steel is documented in Figs. 4 and 5. The prior austenite grain boundaries are decorated by a network of $M_{23}C_6$ particles. Particles of this phase are also observed on subgrain boundaries as well as inside subgrains. Further, there are tiny precipitates of minor phase, present both on grain boundaries and on former martensitic laths. Careful examination revealed also very small particles inside the former martensitic laths.

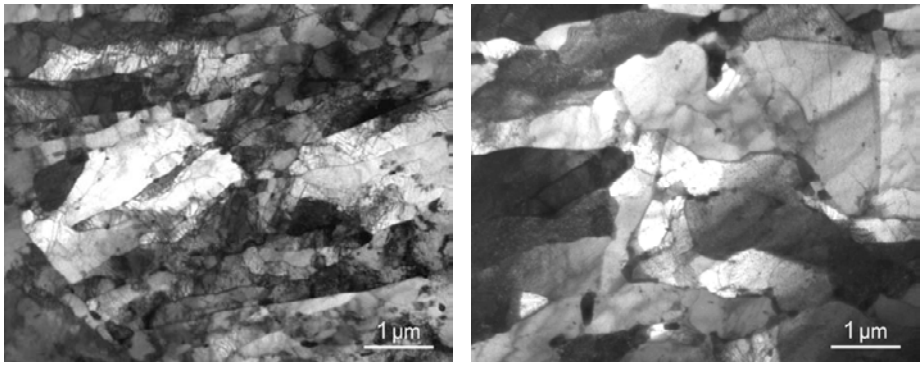

Fig. 4 TEM micrographs of P91 steel subjected to monotonic creep at 125 MPa: (a) head location, (b) gauge length location.

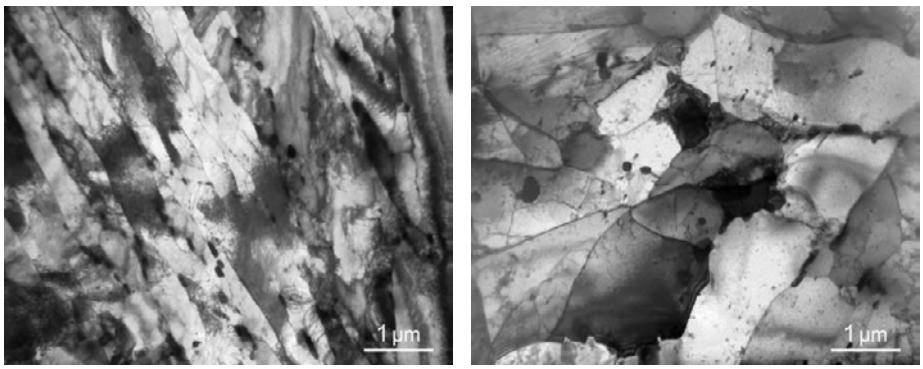

Fig. 5 TEM micrographs of P91 steel subjected to cyclic creep at 125 MPa: (a) head location, (b) gauge length location.

The similar situation was found out also for P92 and E911 steels, see TEM micrographs in Figs. 6 – 9. Clearly defined subgrains are evident in both the head and gauge length of test pieces. In comparison with the as-received states, the subgrain structure evolution exhibits the growth of the mean subgrain size in the gauge length of the crept specimens, which is supported by the influence of the applied stress and is more pronounced than the subgrain growth in the specimen heads subjected only to the influence of temperature. It should be noted that this "subgrain coarsening" is more intensive in the specimens crept under constant testing temperature in comparison with the intermittently heated specimens. The observed differences in the subgrain microstructure may be explained by possible additional precipitation reactions during intermittent heating. New precipitate particles on subgrain boundaries and dislocations may block the migration of subgrain boundaries or the movement of mobile dislocations, which contribute to the microstructural stability and consequently to the creep strength of the investigated steels. Simultaneously with the subgrain coarsening

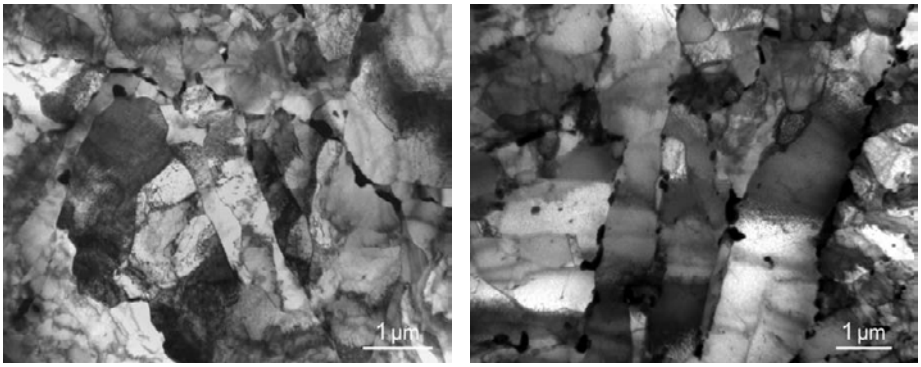

Fig. 6 TEM micrographs of P92 steel subjected to monotonic creep at 150 MPa:
(a) head location, (b) gauge length location.

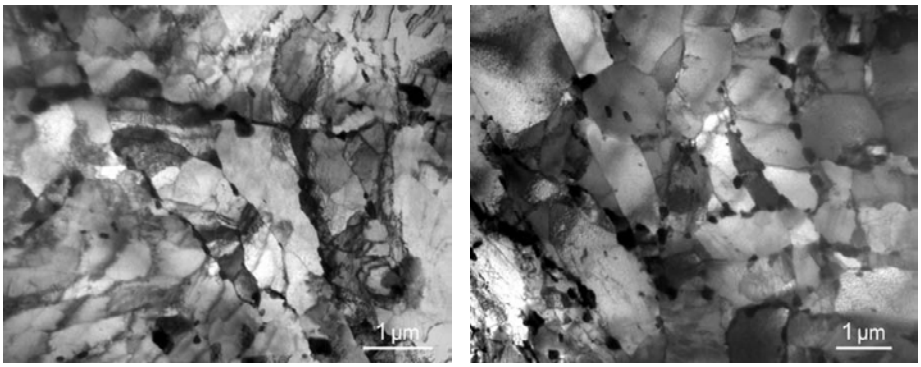

Fig. 7 TEM micrographs of P92 steel subjected to cyclic creep at 150 MPa:
(a) head location, (b) gauge length location.

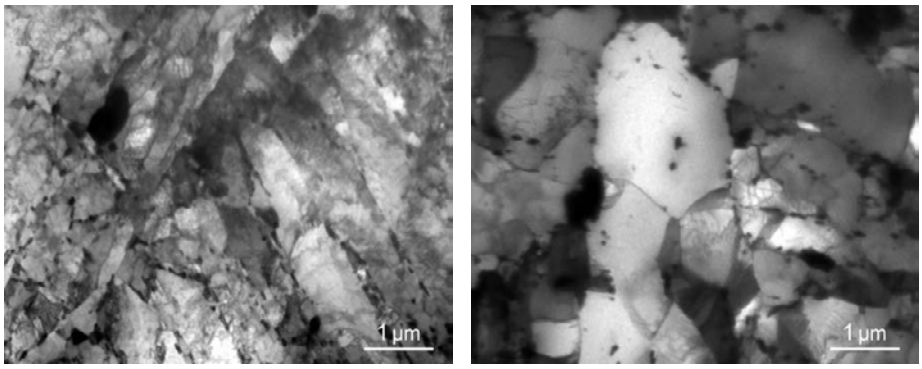

Fig. 8 TEM micrographs of E911 steel subjected to monotonic creep at 150 MPa: (a) head location, (b) gauge length location.

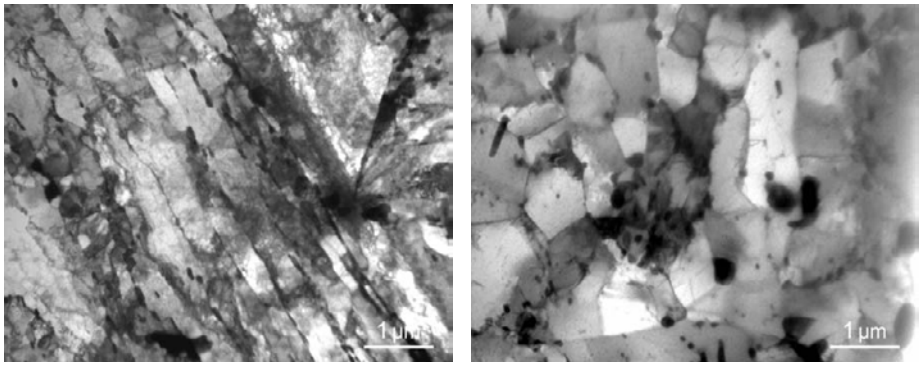

Fig. 9 TEM micrographs of E911 steel subjected to cyclic creep at 150 MPa: (a) head location, (b) gauge length location.

a change in the subgrain shape factor occurs indicating that the subgrains try to approach the equiaxed shape. Again this change is strongly accelerated by the influence of the applied stress.

On examining the creep fracture surfaces of the investigated steels (Fig. 10) it was found that the failure is always of the ductile transgranular mode regardless of the creep loading history.

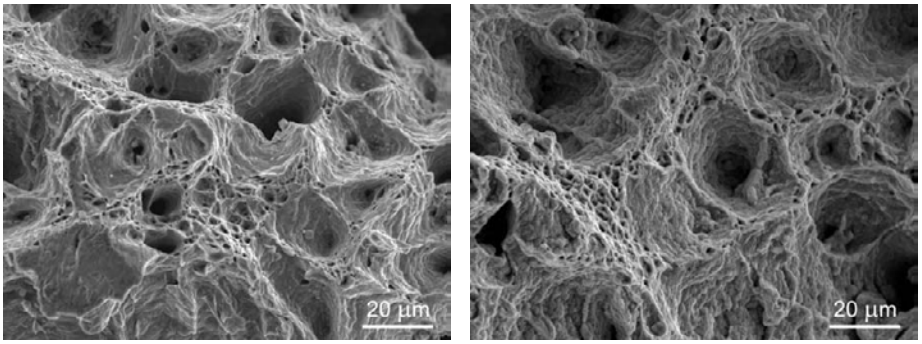

Fig. 10 SEM micrographs showing the creep fracture surface of P91 steel after creep at 125 MPa: (a) monotonic creep, (b) cyclic creep.

4. Discussion

At present we are still some distance from a more complete description and understanding of significant microstructural features and deformation mechanisms responsible for the enhanced creep strength of tempered martensitic ferritic 9-12%Cr steels in dislocation (power-law) creep. The movement of dislocations through the matrix is at first resisted by (a) the dislocation substructure distribution (dislocation strengthening mechanism), (b) intragranular particles, mainly MX (particle strengthening), and (c) the strain fields associated with elements in solid solution (solid solution strengthening). As creep progresses the dislocation substructure changes to form subgrains whose boundaries are stabilized by $M_{23}C_6$ and MX particles and possibly also by Laves phases [7-10]. However, as these particles form and coarsen they denude the surrounding matrix of elements in solid solution, thus reducing the contribution of solid solution strengthening to creep resistance. Thus it seems likely that, as these changes progress, creep resistance becomes less and less dependent on resistance to the movement of individual dislocations through the matrix and more and more dependent on the resistance to subgrain growth through boundary migration [7].

Recently, Sklenicka et al. [11], Cadek et al. [12] and Orlova et al. [13] reported extensive studies and analyses of creep behaviour and microstructure of the P91 steel in the region of the power-law (dislocation) creep. The analyses suggested strongly that: (i) the creep rate is not recovery controlled, (ii) neither is the creep rate controlled by dislocation climb around carbide particles provided no interaction of dislocations with carbide particle takes place; and finally (iii) the Rösler-Arzt model [14] assuming an attractive interaction of dislocations with dispersed particles and thermally activated detachment of the dislocations from the particles, failed to account for the creep data of the P91. A metallographic analysis had shown that the effect of the rearrangement of dislocations and subgrain coarsening on creep may be more important than the effect of precipitation strengthening [11-13]. However, some evidence has been found for suppression or retardation of subgrain boundaries motion by the particles. A similar conclusion has also been convincingly demonstrated by Kucharova et al. [15] using a novel approach in which creep specimens of P91 steel (in the as-received state) were

subjected to additional thermo-mechanical treatments to change the subgrain and particle structures.

The contributions of the various microstructural features (dislocation density, subgrain size, carbide, carbonitride and intermetallic precipitates) to the creep strength of P92 steel have been extensively studied. Ennis [16] reported that in P92 steel, during the first 3000 h of exposure at 600 – 650°C, a rapid reduction in the dislocation density and increase in size of $M_{23}C_6$ precipitates occur. The fine carbides, nitrides and carbonitrides are stable and do not coarsen significantly. Hattestrand and Andren [17] studied an isothermally aged P92 and found that coarsening of $M_{23}C_6$ carbides is accelerated by the strain, while the effect of strain on VN precipitates is insignificant. According to these authors, MX (mainly VN) precipitates appear to be relatively stable during ageing for up to 10000 h at 600 and 650°C. With $M_{23}C_6$ precipitates the situation is different. At 600°C, no coarsening appears to take place during 10000 h of ageing, while in creep the particles coarsen to about 20% larger size. The role of tungsten (P92 steel has the addition of 1.8 wt% tungsten in comparison with P91 steel) was studied by Hald [18]. It was found that W precipitates as intermetallic Laves phase during creep exposure, but the loss of tungsten from solid solution does not seem to affect long-term creep stability. Subgrains in steel P92 grow as a function of creep strain and stress following a general function for all 9-12%Cr steels, which indicates that the precipitate stability may control the creep strength of the steels. While MX (VN) particles coarsen very slowly during creep exposure, precipitation of new MX particles during creep could not be confirmed.

From the above discussion, it can be concluded that the creep behaviour and the creep strength in the power-law creep region are controlled by the coexistence of dislocation substructure and precipitates, the latter mainly acting as subgrain stabilizer. Thus, the role of dislocation substructure dominates the role of precipitation strengthening due to carbide particles.

The temperature changes consisting in cooling the specimen from the testing temperature of 600°C down to the room temperature and heating up again to the testing temperature may cause some additional strain generated by the thermal stresses created during temperature changes. However, this phenomenon seems to have no substantial effect on the creep behaviour of the specimen. Provided that the microstructures of specimens subjected to both monotonic and cyclic loading are relatively similar there is no reason for substantially different creep behaviour of uninterrupted and cycled creep specimens.

5. Conclusions

The creep behaviour and the creep strength of advanced 9-12%Cr steels in the power-law (dislocation) creep regime are controlled by the coexistence of dislocation substructure and precipitates, the latter mainly acting as subgrain stabilizer. Thus, the role of dislocation substructure dominates the role of precipitation strengthening due to carbide particles. Consequently, any difference in the creep resistance of those steels may be explained by taking account of the change of dislocation substructure during creep loading.

No significant deterioration of the creep properties was found for the steels P91, P92 and E911 under temperature-cycled creep loading in power-law creep. Provided that the microstructures of specimens subjected to both monotonous and cyclic loading are very

similar there is no reason for their markedly different creep behaviour in a regime of power-law (dislocation) creep. However, detailed understanding of the mechanism of microstructure coarsening and precipitation reactions seems to be a key to understanding of the microstructural stability and the creep behaviour of the 9-12%Cr steels.

As mentioned previously creep resistant materials are frequently subjected to various structural changes accompanying creep in their service-temperature range. The creep behaviour will be influenced by these structural changes as well as by those mechanisms applicable to stable materials. We need such investigations, which reveal the gross influence of temperature and load variations, such as might be encountered in service. Unfortunately, no particular cycle can be considered typical of all service conditions, and the selection of a test programme is somewhat arbitrary.

6. Acknowledgements

Financial support for this work was provided by the Ministry of Education, Youth and Sport of the Czech Republic under Grant No.1P05OC007 (COST 536).

7. References

[1] B. Scarlin, R. Vanstone and R. Gerdes, Materials developments for ultrasupercritical steam turbines, In: Proc. 4th Int. Conference on Advances in Materials Technology for Fossil Power Plant, eds. R. Viswanathan et al., ASM International, 2005, pp. 51-67.

[2] B. Scarlin, T.-U. Kern and M. Staubli, The European efforts in material development for 650°C USC power plants – COST 522, ibid, pp. 80-99.

[3] R.W. Vanstone, Alloy design and microstructural control for improved 9-12%Cr power plant steels. In: Materials for Advanced Power Engineering 2002, eds. J. Lecomte-Beckers et al., Forschungszentrum Jülich GmbH, 2002, part. II, pp. 1035-1048.

[4] K.H. Mayer, R. Blum, P. Hillenbrand, T.-U.Kern and M. Staubli, Development steps on new steels for advanced steam power plants, ibid, part III., pp. 1385-1396.

[5] F. Abe, H. Okada, S. Wanikawa, M. Tabuchi, T. Hagaki, K. Kimura, K. Yamaguchi, M. Igarashi, Guiding principles for development of advanced ferritic steels for 650°C USC boilers, ibid, part III., pp. 1397-1408.

[6] T. Fujita, Advances in 9-12%Cr heat resistant steels for power plant. In: Proc. 3rd Conf. on Advances in Material Technology for Fossil Power Plants, eds. R. Viswanathan. W.T. Bakker, and J.D. Parker, The Institute of Materials, London, 2001, pp. 33-65.

[7] V. Sklenicka, K. Kucharova, M. Svoboda, L. Kloc, J. Bursik and A. Kroupa, Long-term creep behaviour of 9-12%Cr power plant steels, Materials Characterization, 51 (2003), pp. 35-48.

[8] M. Svoboda, I. Podstranska, A. Kroupa, V. Sklenicka and K.-H. Mayer, Creep resistance and microstructural stability of TAF 650 steel, In: Proc. 10th Int. Conference on Creep Resistant Metallic Materials, ed. J. Purmensky, Vitkovice R&D Ltd., Ostrava, 2001, pp. 196-203.

[9] Y. Hasegawa, T. Muraki, M. Ohgami and H. Mimura, Optimum tungsten content in high strength 9 to 12%Cr containing creep resistant steels, Key Eng. Materials, 171-174 (2000), pp. 427-436.

[10] L. Korcakova, Microstructure evolution in high strength steel for power plant application: Microscopy and modelling. PhD Thesis, Technical University of Denmark, Lyngby, August 2002.
[11] V. Sklenicka, K. Kucharova, A. Dlouhy and J. Krejci, Creep behaviour and microstructure of a 9%Cr steel. In: Proceedings of the Conference on Materials for Advanced Power Engineering, eds. D. Coutsouradis, J. H. Davidson, J. Ewald, P. Greenfield. Kluwer Academic Publishing, 1994, pp. 435-444.
[12] J. Cadek, V. Sustek and M. Pahutova, An analysis of set of creep data for a 9Cr-1Mo-0.2V (P91 type) steel. Mater. Sci. Eng., A 225, (1997), pp. 22-28.
[13] A. Orlova, J. Bursik, K. Kucharova and V. Sklenicka, Microstructural development during high temperature creep of 9%Cr steel. Mater. Sci. Eng. A 245, (1998), pp. 39-48.
[14] J. Rösler and E. Arzt, A new model-based creep equation for dispersion strengthened materials, Acta Met. Mater., 38, (1990), pp. 671-683.
[15] K. Kucharova, J. Nemec and A. Dlouhy, Microstructure and creep strength of tempered martensitic ferritic steel. In: Proc. Int. Conference on Creep and Fracture of Engineering Materials and Structures, eds. J.C. Earthman and F.A. Mohamed, University Press, Irvine (1997), pp. 79-88.
[16] J. P. Ennis, Creep strengthening mechanisms in high chromium steels. In: Proc. 3rd Conference on Advances in Material Technology for Fossil Power Plants, eds. R. Wiswanathan, W.T. Bakker and J.D. Parker, The Institute of Materials, London, (2001), pp. 187-194.
[17] M. Hattestrand, H.-O. Andren, Evaluation of particle size distributions of precipitates in a 9%Cr steel using energy filtered transmission electron microscopy. Micron 22, (2001), pp. 789-797.
[18] J. Hald, Microstructure stability of steel P92 and P122. In: Proc. 3rd Conference on Advances in Material Technology for Fossil Power Plants, eds. R. Wiswanathan, W.T. Bakker and J.D. Parker, The Institute of Materials, London, (2001), pp. 115 – 124.

CREEP AND CREEP FATIGUE PROPERTIES OF TURBINE STEELS FOR APPLICATION TEMPERATURES UP TO 625 °C

Christina Berger, Michael Schwienheer and Alfred Scholz
Institute of Materials Technology
Darmstadt University of Technology
Germany
e-mail: berger@mpa-ifw.tu-darmstadt.de

Abstract

Advancing the efficiency and availability and reducing the fuel consumption is one of the most important topics of the current development of steam power plants. Therefore the material requirements increases and new steels for heavy turbine components e.g. rotors and casts are needed for application temperatures of 600 °C and higher. Within the COST 501/522/536 research projects several martensitic 9-12% Cr-steels with suitable production properties and promising long term behaviour were developed. In order to employ the full potential of these steels and to obtain reliable design parameters the long term behaviour under creep and creep fatigue loading of COST steel type E, COST steel type F and the new cobalt and boron alloyed steels of type FB2/CB2 were investigated. With phenomenological equations the strength behaviour and the deformation behaviour under static and cyclic loading were described on the basis of different casts. Scatter within the steel grades can be analysed in order to develop more reliable design data. The results of the investigations reveal a suitable material behaviour of the 10% Cr-steels with and without tungsten for 600 °C application. At present, an acceptable capability of the new cobalt and boron alloyed steels can be confirmed for applications up to 625 °C.

Key words: 9-12% Cr steels, creep rupture, creep equations, creep fatigue

1. Introduction

The development of new fossil power plants aims at reducing the fuel consumption in order to increase the environmental compatibility. Therefore the steam parameters have to be raised up to maximum pressure of 300 bar and temperatures above 600°C which means a significant increase in the requirements for creep resistance and fatigue strength of the materials. During the last decades martensitic 9-12%Cr-steels were developed within the COST projects. Modern 10%Cr-steels e.g. COST steel type E and F with and without tungsten are able to increase the application temperature up to 600°C [1, 2, 3]. The material development activities within the COST 522 and 536 projects have demonstrated that a further increase of the application temperature of above 600°C is involved with many challenges concerning long term stability of microstructure [4], creep rupture behaviour and low cycle fatigue behaviour and ductility as well as oxidation resistance [5].

Hint: with regard to the interests of the industrial partners no quantitative values are shown in the following figures

2. Materials

Within the German MARCKO research project [6], the European COST 501/522 projects [3] and the German VGB project [7], different casts of the 600°C steels with and without tungsten content were investigated under static and cyclic long term conditions. The chemical composition and the heat treatment of typical casts are given in Table 1 and 2.

No	*Steel*	*Chemical Composition (wt-%)*										
		C	Cr	Mo	W	Ni	V	Nb	N	Mn	Si	P
1A	X12CrMoWVNbN10-1-1	0.12	10.7	1.04	1.04	0.76	0.16	0.05	0.06	0.42	0.1	0.007
2A	GX12CrMoWVNbN10-1-1	0.13	9.51	1.02	1.02	0.52	0.19	0.06	0.04	0.82	0.29	0.014
		Heat Treatment										
1A	X12CrMoWVNbN10-1-1	1050°C 7h/oil + 570°C 10.25h/air + 690°C 10h/air										
2A	GX12CrMoWVNbN10-1-1	1070°C 12 h/air + 730°C 12h/air + up to 300°C 10 h/furnace										

Table 1. 600°C steels with tungsten (COST Steels Type E)

No	*Steel*	*Chemical Composition (wt-%)*										
		C	Cr	Mo	W	Ni	V	Nb	N	Mn	Si	P
3A	X12CrMoVNbN10-1	0.14	9.99	1.40	-	0.56	0.17	0.06	0.04	0.55	0.08	0.011
4A	GX12CrMoVNbN9-1	0.12	9.04	0.86	-	0.12	0.20	0.1	0.06	0.54	0.41	0.011
		Heat Treatment										
3A	X12CrMoVNbN10-1	1070°C 20h/oil + 570°C 27h/air + 675°C 25h/air										
4A	GX12CrMoVNbN9-1	1050°C 10h/fan cooled + 740°C 14/air + 730°C 10h/air + 720°C 8h/air										

Table 2. 600°C steels without tungsten (COST Steels Type F)

These steels were produced as components under near-service conditions with large dimensions, e.g. rotors or valves.
The forged steel FB2 and the cast steel CB2, containing boron and cobalt were identified for the new challenge of 625°C applications of large components of fossil power plants [8]. Three casts of these steels were also investigated in the German MARCKO project (s. Table 3).

No	**Steel**	**Chemical Composition (wt-%)**										
		C	Cr	Mo	Co	Ni	V	Nb	N	Mn	Si	B
5A	X12CrMoCoVNbB9-1	0.13	9.03	1.42	1.28	0.16	0.22	0.05	0.02	0.33	0.1	0.0083
5B	X11CrMoCoVNbB9-2	0.14	9.28	1.51	1.33	0.15	0.19	0.05	0.00	0.31	0.08	0.0091
6A	GX12CrMoCoVNbB9-1	0.12	9.14	1.47	0.95	0.22	0.19	0.06	0.02	0.86	0.29	0.0121
		Heat Treatment										
5A	X12CrMoCoVNbB9-1	1100°C 10h/water + 590°C 22h/air + 700°C 22h/air										
5B	X11CrMoCoVNbB9-2	1100°C 16h/water + 570°C 22h/air + 700°C 22h/air										
6A	GX12CrMoCoVNbB9-1	1100°C 9h + 740°C 10h +730°C 12h+12h/air										

Table 3. 625°C steels (COST Steels Type FB2 and CB2)

3. Creep Rupture Behaviour

The knowledge of the material long term rupture behaviour is an essential basis for the design of turbine components. In this case the mean behaviour of the material type and its behaviour at the lower scatter band is of special interest in order to determine reliable design parameters. A comprehensive creep testing programme was performed on the 600°C steels with tungsten (COST steels type E) and on the 600°C steels without tungsten (COST steels type F).

Different casts of each steel type were considered. Up to now the creep tests have reached about 75 000 h duration.

To determine the mean creep rupture behaviour numerical scatter band methods based on time-temperature parameters e.g. Larson Miller [9] as well the more flexible but time consuming graphical cross plotting method [10] were used.

The steel type E shows a consistent creep rupture behaviour for temperatures from 500 to 625°C (Fig 1a). On the other hand the determined 650°C isothermal runs different to the curve family. This behaviour also can be demonstrated in a Larson-Miller plot, whereby significant differences of master curves for different temperature ranges were identified (Fig. 1b).

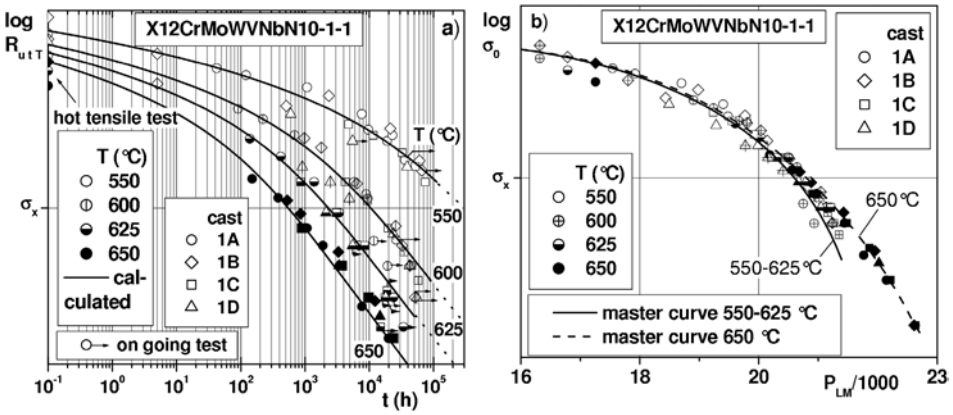

Fig. 1. Isothermals of mean creep rupture behaviour (a) and master curve of temperature range of 550- 625°C and 650 °C (b), COST steel type E with tungsten content

The different creep rupture behaviour at 650°C indicates a change in the microstructure [11] while increasing the temperature from 625 to 650°C. The determined isothermal at 650°C is not representative for the material behaviour at lower temperatures and a consideration of these data in numerical assessments could overestimate the creep rupture strength at the application temperature of 600°C. It can be concluded that creep rupture data assessments always should be examined by material experts with regard to the determination of reliable design parameters. The current discussion on the devaluation of creep strength values of important martensitic steels confirms this conclusion.

Further, also of industrial relevance is the comparison of the creep rupture isothermals of forged and cast steels. The numerical as well as the graphical creep rupture data assessments of type E steels show that the forged steel grade starts with a higher strength level at short terms than the cast steel grade, but the lost of strength during long term loading is more pronounced. In the long term region the creep rupture strength of the forged steel is expected to be similar or even lower than the cast steel grade (Fig. 2).

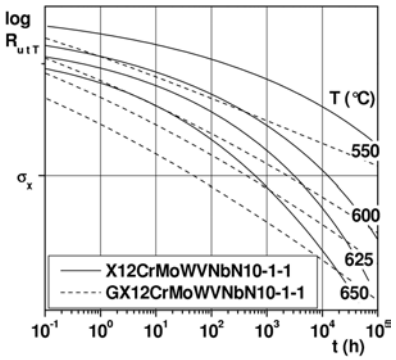

Fig. 2. Comparison of mean curves of creep rupture strength of forged steel and cast steel, COST type E

On the one hand this unexpected result can be explained with different chemical compositions of the forged steels with a higher content of Chromium and Nickel. Investigations of Hald [11] have shown an increase of Z-phase precipitation during creep loading caused by higher chromium contents at higher temperatures in the long term range. This phase decreases the creep rupture strength by reducing the MX and MX_2 particle quantity in the microstructure of 9-12% Cr-steels. On the other hand the heat treatment influences the long term behaviour of creep rupture strength. The forge steels were optimized for a high elastic limit with a relatively low tempering temperature (Table 1). Microstructural investigations [12, 13] show a lower content of $M_{23}C_6$ particles and a faster growth of in addition existing M_2X particles and subgrain during creep loading of the forge steels in comparison to the cast steels. Therefore a balanced compromise of initial strength values and long term stability supported by an optimized heat treatment seems to be important for improved 9-12% Cr steels.

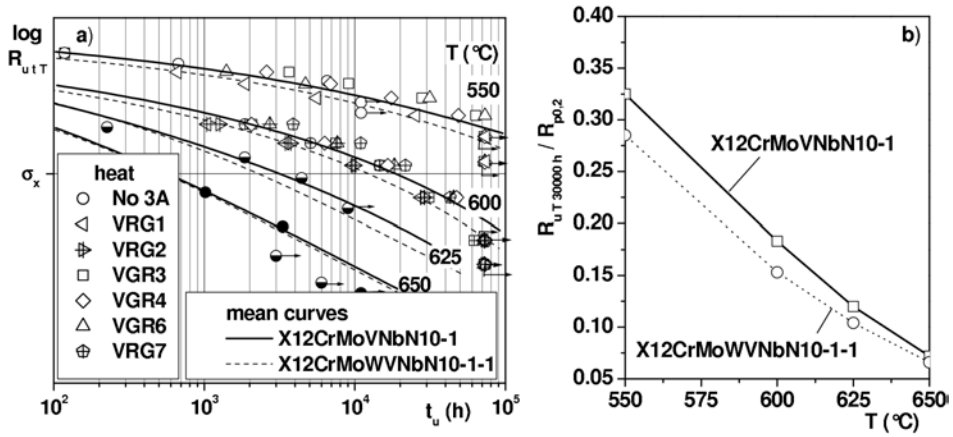

Fig. 3. Creep rupture behaviour of COST steels type F in comparison of type E (a) and creep rupture strength ($R_{u\ T\ 30000\ h}$) at 30 000 h related to the yield strength ($R_{p0.2}$) (b)

These effects also can be observed on the COST steels type F without tungsten. The forged steels without tungsten show significant higher mean values of creep rupture strength than the

steels with tungsten (Fig. 3a). Also a comparison of the creep rupture strength after 30 000 h related to the yield strength (Fig. 3b) supports this statement for temperatures up to 625 °C.

The data basis of the new 625°C steels with boron and cobalt content includes creep tests with test durations of about 10 000h. A first assessment of the creep rupture strength indicates an improved behaviour in comparison to the 600°C steels (Fig 4).

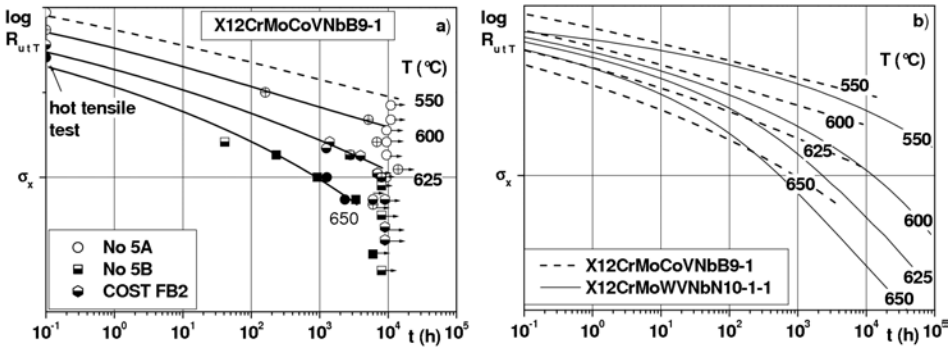

Fig. 4. Creep rupture behaviour of forge steels X12CrMoCoVNbB9-1 (a) and comparison of creep rupture strength of 625°C steels with 600°C steels (b).

Because of the relatively small data set the assessment can only deliver preliminary values. The current status of the creep tests on the 625°C cast steels (COST type CB2) indicates a lower strength level than the cast steels, but also an improved creep rupture strength behaviour in comparison to the 600°C cast steels. Again this assessment is strongly influenced by the given data set and the heat treatment conditions.

4. Creep Strain Behaviour

The knowledge of the time dependent deformation is very important for the design of high temperature components. Simple creep equations e.g. Norton-Bailey are easy to use, but a parameter set is only valid for a discrete temperature and a limited range of time and stress. More powerful phenomenological model such as the Graham Walles equation and the Theta projection method can describe primary, secondary and tertiary creep. The modified Garofalo equation [14, 15]

$$\varepsilon_{per} = \varepsilon_i + \varepsilon_{f1} + \varepsilon_{f2} + \varepsilon_{f3} = \varepsilon_i + \varepsilon_{f1max} \cdot \left[1 - e^{-D(t/t_{12})^u}\right] + \dot{\varepsilon}_{pmin} \cdot t + C_{23} \cdot \left(t / t_{23}\right)^f \qquad (1)$$

is of special interest because this equation is flexible due to its modular structure and often forms the best solution [16]. A key feature deals with the temperature dependence of parameters. Activities on creep modelling of the 600°C steel No 1A document a well applicability of this equation to describe the complex creep deformation [6].

Three steps were identified in order to determine the parameters of eq. (1) for material grade:

i. Numerical scatter band assessment of creep rupture data and of specific times to strain

ii. Determination of parameters of master curves for creep rupture and times to specific strain representing a consistent curve family. These optimized curves can be used for the calculation of data points for creep curves, which describes the mean creep strain behaviour of the material grade (Fig 5a).
iii. Determination of parameters of eq. (1) on the basis of mean creep curves derived from steps i. and ii.

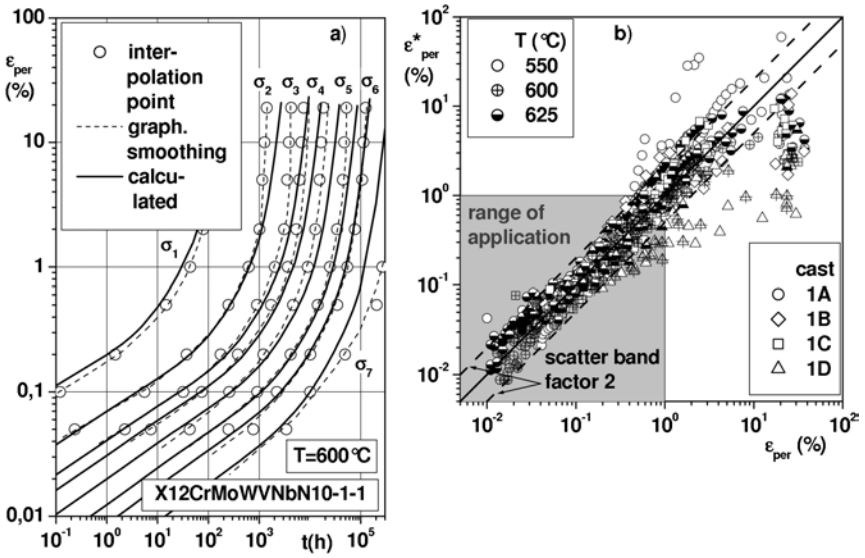

Fig. 5. Comparison of creep curves determined with scatter band assessment and creep calculated with mod. Garofalo equation (a) and comparison of measured (ε_{per}) and calculated (ε^*_{per}) creep curves (b), material grade X12CrMoWV-NbN10-1-1

As observed in foregoing investigations [15], the martensitic 10% Cr steels show a complex creep behaviour especially concerning the function stress-strain-time. Investigations demonstrated that the modified Garofalo equation is able to reproduce the creep behaviour of the material grade X12CrMoWVNbN10-1-1 in the application range of 550-625°C and up to 1% permanent strain in an acceptable way (Fig. 5b). In this range the scatter band factor of measured and calculated strain values is about 2. For higher strain values, the scatter band increases, which is mainly caused by one heat (No D) which shows a lower creep rupture strength.

The creep behaviour of the new 625°C steels also was investigated. Because of the relatively small data basis, the Norton-Bailey and Graham-Walles equation was used in a first step to describe the creep behaviour.

These new steel types also show a complex stress-strain-time dependence. Therefore the simple creep laws are not able to fit the high stress and low stress region with one single parameter set (e.g. Fig. 6a and 6b). In further investigations it is planed to validate the more powerful creep equation of type modified Garofalo for the description of the 625°C forged steel and cast steel.

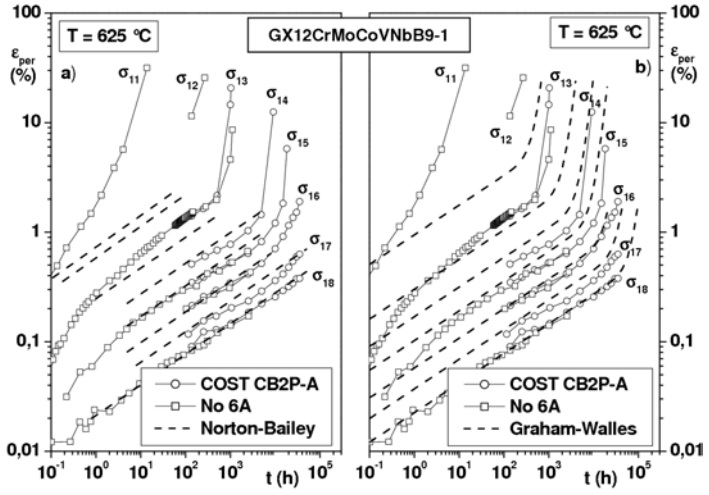

Fig. 5. Measured and calculated creep curves at 625°C of new 625°C cast steel GX12Cr-CoVNbB9-1, a) calculated with Norton-Bailey equation, b) calculated with Graham-Walles equation.

5 Fatigue and Creep Fatigue Behaviour

At the heated surface of turbine components, temperature transients at start-up and shutdown-phases cause strain cycling with variable thermal (secondary) stresses. In addition, pressure loading and, for rotors, centrifugal loading, leads to quasistatic (primary) stresses. Strain cycling and the corresponding low cycle fatigue (LCF) behaviour is relevant for crack initiation at critical locations of massive turbine components. In order to simulate creep fatigue loading conventional fatigue and creep fatigue tests with tensile and compression hold time ($t_{Ht} = t_{Hc}$ = 3 min or 10 min) at the main test temperature were carried out at different values of total strain range $\Delta\varepsilon$. The tests were performed with the laboratory-typical strain rate at the ramps of $\dot{\varepsilon}_r$ = 6 %/min.

The crack initiation behaviour of the 600°C steels was investigated on different casts at the main application temperatures 550°C, 600°C and also at 625°C. The data of number of cycles to crack initiation N_i were used as a basis for modelling the fatigue life curves (Fig. 6a and b) with the Manson-Coffin-Equation [17].

The result of the investigations indicates a comparable fatigue life behaviour of the forged steels types with and without tungsten (Fig. 6a). Both 600°C forged steel grades show a scatter band factor of 2.5 of number of cycles to crack initiation data. As a conclusion, a systematic different behaviour of these two steel grades cannot be observed.

The data set of the 600°C cast steels indicates a lower fatigue strength of the tungsten-free cast steels (Fig. 6b). This corresponds with the creep rupture behaviour of the investigated 600°C steels. However the different tensile strength of the casts has to be considered, which affects the fatigue life especially in the short term range.

The observed cyclic stress strain behaviour also confirm this result. While the flow curve at test start reflects the tensile behaviour, the stress strain curves of the 600°C steels at mid term cycle are very similar (Fig. 7).

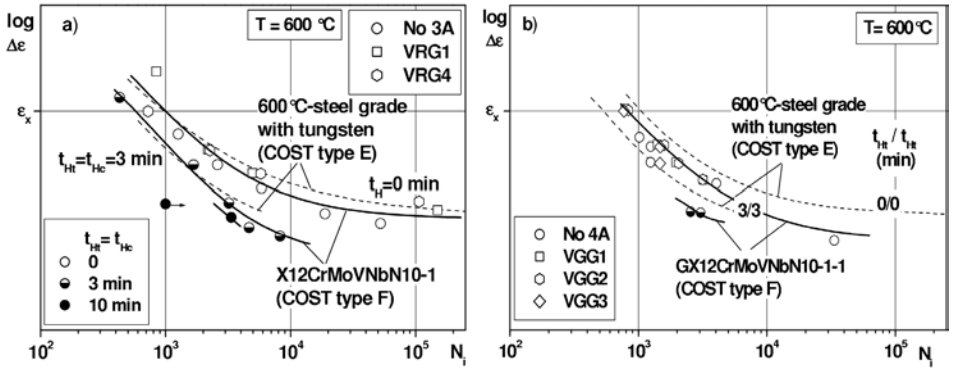

Fig. 6. Comparison of fatigue and creep fatigue life of 600°C-steels, a) forge steels, b) cast steels.

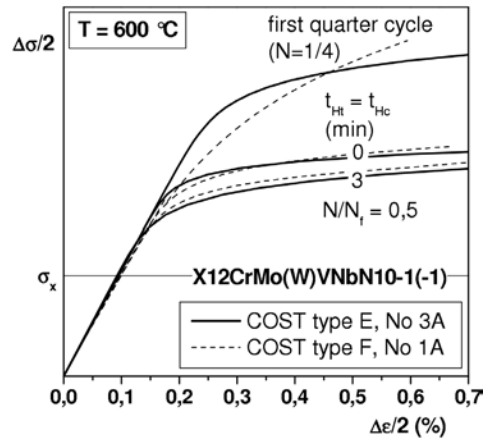

Fig. 7. Cyclic stress-strain curve at mid term cycle (N/N_i =0.5) for fatigue and creep fatigue, steel X12CrMoVNbN10-1/3A and X12CrMoW-VNbN10-1-1/1A

The stress-strain was modelled by the Ramberg-Osgood-equation as

$$\varepsilon = \sigma / E + (\sigma/K')^{1/n'}, \quad (4)$$

whereby the parameters E, K' and n' are temperature and strain-rate dependent as well as dependent on the ratio N/N_i. The effect of hold time on cyclic strength is somewhat smaller for the rotor steel compared to the cast steel.

Also the fatigue and creep fatigue behaviour of the 625°C steels was investigated (Fig. 8). Summarising, the 625°C forge steels of type FB2 show no difference to the 600°C forged steels. This was observed for fatigue life as well as for cyclic stress-strain behaviour. However, the 625°C cast steel No 6A shows a lower fatigue strength for 600 and 625°C. Because of the relatively small data basis, a statement for the material grade cannot be made yet.

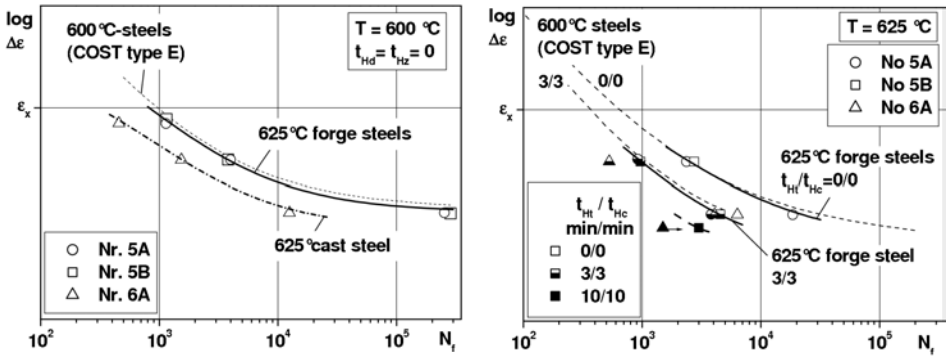

Fig. 8. Comparison of fatigue and creep fatigue life of 625°C-steels, a) T=600°C, b) T=625°C.

6. Conclusions

Within a research programme on martensitic 600°C steels and new 625°C steels, the behaviour of strength, deformation and damage under near-service conditions was determined and described with different phenomenological methods. Among single casts the behaviour of the material grade was of special interest. It can be summarised that these martensitic steels show a clear influence of heat treatment on tensile strength, creep rupture strength, creep fatigue strength and microstructural stability in the long term range. The 600°C steels with and without tungsten show an acceptable creep and creep fatigue strength up to temperatures of 600°C and the already available data of the 625°C steels indicate an application up to a temperature of about 625°C. The superposition of fatigue and creep demonstrate interaction effects with dominant influence on crack initiation behaviour.
The generation of relevant long term data and modelling of creep, fatigue and cyclic stress strain behaviour contributes to knowledge on steels for industrial applications.

7. Acknowledgement

The results are based on the research project No 032753A of the German Bundesministerium für Wirtschaft und Technologie (BMWi). The authors would like to thank the BMWi for funding and the companies working in the research groups for funding and technical support. The responsibility for the content belongs to the authors.

8. Literature

[1] Mayer, K.H., R. Hanus, T.-U. Kern, M. Staubli, D.V. Thornton: High temperature cast components for advanced steam power plant, Procedings of the 6th COST Conf. "Materials for Advanced Power Engineering 1998", Part I, Lecomte-Beckers, Schubert, Ennis (Ed), 1998, Liège, Belgium, S. 71-85.

[2] Mayer, K.H., T.U. Kern, K.-H. Schönfeld, M. Staubli, E. Tolksdorf: Long-term investigations of specimens of 8 production rotors manufacturers of the Advanced

Martensitic 10 % Steels X12CrMo(W)VNbN10-1(1), Proc.of the 14th Int. Forgemasters Meeting, 3-8 September 2000, Wiesbaden, S. 277-282.

[3] Staubli, M., K.H. Mayer, T.U. Kern, R.W. Vanstone, COST 501/COST522 - The European Collaberation in Advanced Turbine Materials for Ultra Efficient, Low Emission Steam Power Plant, Proc. of the 5th Int. Charles Parson Turbine Conf., Cambridge, UK, 2000, p. 98-122.

[4] Hald, J.: Microstructure of 9-12% Cr Steels, Presentation on the International Workshop on Performance and Requirements of Structural Materials for Modern High Efficient Power Plants, 5^{th} –7^{th} Sept. 2005, Darmstadt University of Technology, Proceedings.

[5] Mayer, K.H.: Modern 9-12% Cr-Steels for Power Plant Application, Proc. of the 28 th MPA Seminar „Worldwide Development of new 9-12% Cr-Steels for Advanced Power Stations, Safety and Reliability in Energy Technology“, MPA Universität Stuttgart, Vol. 2, 2002, p. 47.1-47.24

[6] Schwienheer, M., Haase, H., Scholz, A., Berger, C.: Long Term Creep and Creep Fatigue Properties of the Martensitic Steels of Type (G)X12CrMoWVNbN10-1-1, Proc. of the 6^{th} COST Conference "Materials for Advanced Power Engineering 1998", Part I, Lecomte-Beckers, Schubert, Ennis (Ed), 1998, Liège, Belgium, p. 1409-1418.

[7] Mayer, K. H.: VGB Rearch Project No 158, „Neue Werkstoffe für Dampfturbinen – Qualifizierung neuer Werkstoffe im Einsatz bei Dampfturbinen mit erhöhten Temperaturen zur Verbesserung des thermischen Wirkungsgrads“, final report (in German), 2001.

[8] Staubli, M., K.H. Mayer, T.U. Kern, R.W. Vanstone, R. Hanus, J. Stief, K.H. Schönfeld: COST 522-Power Generation into the 21st Century; Advanced Steam Power Plant, 3th EPRI Conf. on Advances in Material Technology for fossile Power Plants, 1-6 April 2001, University of Wales, Swansea.

[9] Larson, F. R., J. Miller: A time-temperature relationship for rupture and creep stresses, Trans. ASME 74 (1952), S. 765-775.

[10] Holdsworth, S.R. (Ed.) ECCC-WG1 Recommendations Volume 5. Guideline for the assessment of creep rupture, creep strain and stress relaxation data. ECCC Doc. 5524/MC/38 [Issue 3, 1996].

[11] Hald, J.: Z-Phase in 9-12%Cr-Steels. In: Proceedings of the 4th International EPRI Conference on Advances in Materials Technology for Fossil Power Plants. Hilton Head Island, South Carolina : EPRI, Oktober 2004.

[12] Goetz, G.: Langzeitentwicklung der Mikrostruktur neuer 9-12Chromstähle für den Einsatz in fossilen Kraftwerken, Universität Erlangen-Nürnberg, Dissertation, 2003.

[13] Dubey, J. S. ; Chilukuru, H. ; Blum, W. ; Chakrartty, J. K. ; Schwienheer, M. ; Scholz, A.: On effects of cyclic deformation on subgrain structure evolution and creep behaviour in tempered martensitic 9-12 In: Material Science and Eng. A

[14] Garofalo, F., Fundamentals of Creep and Creep-rupture in Metals, Macmillan, New York, 1965.

[15] Kloos, K.H., Granacher, J. and Monsees, M., Creep equations for heat resistant steels, steel research 69 (1998) p. 447 453.

[16] Granacher, J., H. Moehlig, M. Schwienheer, C. Berger, Creep Equations for High temperature Materials, Creep 7, the seventh International Conference on Creep and Fatigue at Elevated Temperatures, June 3 - 8, 2001, NRIM, Tsukuba, Japan, Proceedings p. 609-616.

[17] Coffin, L. F., Jr.: Fatigue at high temperature-prediction an interpretation, Procedings IME 188 (1994), S. 109-27.

LOW CYCLE FATIGUE BEHAVIOUR OF SANDWICH STRUCTURES OF P92 AND NICROFER 6025HT

Essam El-Magd, Jan Stuhrmann, Jürgen Gebhard

Institute of Material Science (LFW), Technical University of Aachen
E-mail: Jan.Stuhrmann@iwk.rwth-aachen.de

Abstract

A further improvement of the thermal efficiency in modern steam turbines can be achieved by increasing the steam operating temperature which demands the application of new cooling systems, such as effusion cooling.
Within the scope of the Collaborative Research Center 561 of Aachen University, a new cooling component for steam turbine casing parts has been developed. The so called grid sheet, a welded sandwich structure composed of a woven wire mesh layer covered with sheets, fulfils both the mechanical and the functional requirements. In order to employ the full potential of this cooling concept, the knowledge of its mechanical long term behaviour as well as the low cycle fatigue behaviour close to service conditions is essential.
On the one hand the structures were produced from the martensitic steel P92 and on the other hand from the nickel-base alloy Nicrofer 6025HT. In this work the Low Cycle Fatigue behaviour of those sandwich structures was investigated. Modified testing methods were introduced in order to characterize the cyclic behaviour of the complex structure with loading transverse to the intermediate layer.
Fully reversed and pulsating Low Cycle Fatigue tests were carried out at room temperature and at 650°C. Further more the influence of the test frequency on the fatigue life at 650°C was investigated.
The results show a strong cyclic softening of the complete sandwich structure because of successive weldment failure with increasing number of cycles. Structures of the nickel-base alloy show in all cases better fatigue properties than the structures of the martensitic steel.

KEYWORDS: low cycle fatigue, sandwich-structures, P92, 6025HT

Introduction

This study is carried out in the frame of the collaborative Research program „Thermally Highly Loaded, Porous and Cooled Multi-Layer Systems for Combined Cycle Power Plants" of Aachen university. The goal is to increase the efficiency in combined cycle power plants from 58 % up to 65% during the next 25 years.
In order to obtain higher efficiency in the modern combined cycle power plants temperature and pressure have to be increased. To achieve steam operating temperatures around 680°C and steam pressures about 350 bar a new layout of steam turbines is necessary.
In a preliminary investigation a cooling system was developed which combines an interlayer of a woven wire mesh between two plane face sheets. This sandwich structure enables cooling steam to pass without severe losses (Figure 1) [1].
Current developments of 9-12% chromium steels, such as P92, have sufficient oxidation resistance in steam and good creep resistance up to approximately 600°C [2]. For higher temperatures it is necessary to use nickel base alloys, such as Nicrofer 6025HT. Since this material has been brought onto the market in the year 1992 the popularity increased rapidly in the application areas kiln engineering, automotive and chemicals industry [3, 4, 5].
In order to increase the cooling efficiency of the sandwich structure, the sheet facing the inside of the turbine is planned to be perforated. However, the low cycle fatigue behaviour was investigated on non-perforated sandwich structures out of P92 and Nicrofer 6025HT for the first instance.

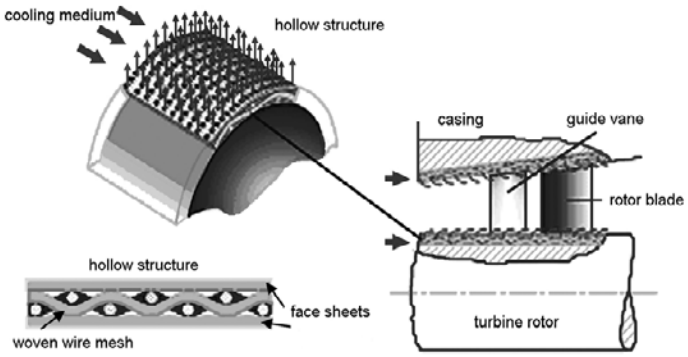

Fig. 1: The new cooling concept of the rotor and the housing surfaces

Investigated Materials

The Low Cycle Fatigue tests have been carried out on sandwich structures with sheet metals and wire mesh manufactured from P92 and the second time from Nicrofer 6025HT.

Ferritic Martensitic Chromium Steel P92

In order to increase the formability of the cold rolled metal sheets for the further bending process of the complete sandwich structure, the sheet metals were annealed at 850°C for 5 minutes before welding. To achieve better mechanical properties of the sandwich structure after manufacturing, a hardening heat treatment at 1065°C for one hour followed by air cooling and tempering at 760°C for 45 minutes was carried out.

The chemical composition of the P92 steel is listed in table 1.

C	Mn	P	S	Cr	Mo	Ni	Nb	V	W	B	Fe
0,076	0,468	0,009	0,006	9,05	0,437	0,058	0,067	0,191	2,052	0,001	87,5

Tab. 1: Chemical composition of P92 steel after cold rolling

Nicrofer 6025HT

The cold rolled sheets were solution annealed in a continuous annealing furnace at approximately 1170°C for 2 minutes followed by solution annealing in a vacuum furnace at 1220°C for 1h and cooled in nitrogen with a cooling rate of approximately 10 K/min. The grain size has been measured and found around 80 µm whereas also much smaller grains are existent.The chemical composition of the alloy is given in table 2.

Ni	Cr	Fe	C	Al	Ti	Zr	Y
Rest	24,0 – 26,0	8,0 – 11,0	0,15 – 0,25	1,8 – 2,4	0,1 – 0,2	0,01 – 0,10	0,05 – 0,12

Tab. 2: Chemical composition of Nicrofer 6025HT (2.4633)

Sandwich Structure

For joining, structure capacitor discharge resisting welding was used. This joining method was suitable for manufacturing the sandwich structure. Capacitor pulse resistance welding is characterized by a low thermal effect on the joined parts compared with the conventional resistance welding process [6]. Before welding, the wire was pulled through a copper bath to get a better current conduction during the welding process. Due to the weaving, the sandwich structure contains warp and weft wires. A cross section and a schematic drawing of the sandwich structure geometry is shown in figure 2.

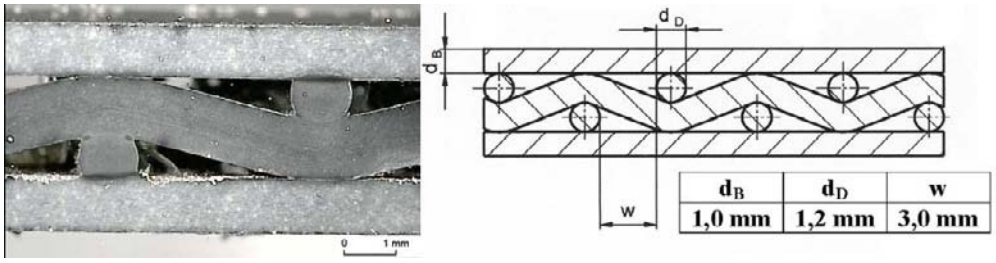

d_B	d_D	w
1,0 mm	1,2 mm	3,0 mm

Fig. 2: Cross section and schematic drawing of the sandwich structure geometry

Low Cycle Fatigue Test Specimen and Test Arrangement

In order to investigate the Low Cycle Fatigue behaviour of the sandwich structure by loading transversely to the intermediate layer, a new kind of test sample was developed. The new test specimen and test arrangement is presented in figure 3. A steel cube with an inside thread is joined together with the metal sheets by a filled weld around the complete circumference (figure 3). In this arrangement, the samples can be connected to the force line of the Low Cycle Fatigue testing machine and placed into a resistor furnace. The temperature is controlled by a regulator with a deviation less than +/− 1 K.

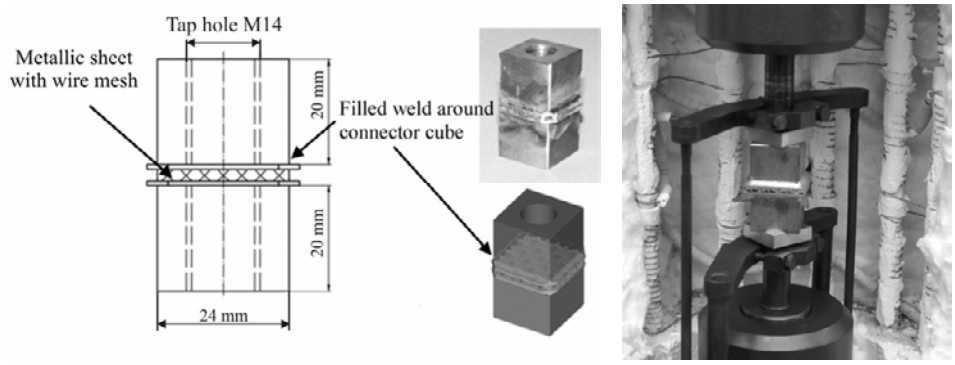

Fig. 3 Sandwich structure LCF test specimen for loading across to the intermediate layer

It is to mention that joining the connector cube to the sheet metal affects slightly the mechanical properties of the test specimen. The heat affected zone of such a welding process is small in comparison to the dimensions of the test sample, as shown in figure 4. This effect was eliminated by hardening and tempering of the test specimens.

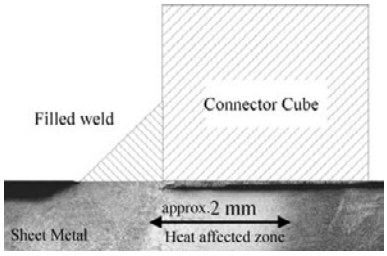

Fig. 4: Filled weld joint of connector cube and sheet metal with heat affected zone

Elongation-controlled Low Cycle Fatigue Tests

To determine the fatigue life of the sandwich structures of P92 and 6025HT under cyclic loading, elongation controlled LCF tests have been carried out at room temperature with a test frequency of 0,2 Hz and at 650°C with test frequences of 0,2 and 0,02 Hz. Table 3 shows the summary of the separate test parameters.

material	**temperature**	**frequency**	**elongation ratio** $R = \frac{\Delta u_u}{\Delta u_o}$
P92 structure	RT	f = 0,2 Hz	R = 0
P92 structure	650°C	f = 0,2 Hz	R = 0
P92 structure	650°C	f = 0,02 Hz	R = 0
6025HT structure	RT	f = 0,2 Hz	R = 0 and R = −1
6025HT structure	650°C	f = 0,2 Hz	R = 0
6025HT structure	650°C	f = 0,02 Hz	R = 0

Tab. 3: LCF-test parameters

Behaviour of the Sandwich Structures under Cyclic Elasto-Plastic Deformation

Elongation-controlled LCF-tests have to be accomplished with a constant strain. For metallic solid materials the curve progression of the force as a function of the applied elongation for separate cycles of fully reversed LCF tests (R = −1) shows the typical hysteresis loop, where a similar behaviour is found in the tension region and in the compression region. In contrast to this due to the build up of the investigated sandwich structures the behaviour under tensile load differs clearly from the behaviour under compression load. As an example figure 5 shows the plot of the first and the second cycle of a LCF test of a sandwich structure of 6025HT under fully reversed elongation with an amplitude of 0,2 mm carried out at room temperature. Additionally, figure 5 shows a quasi-static tensile and compression test at room temperature.

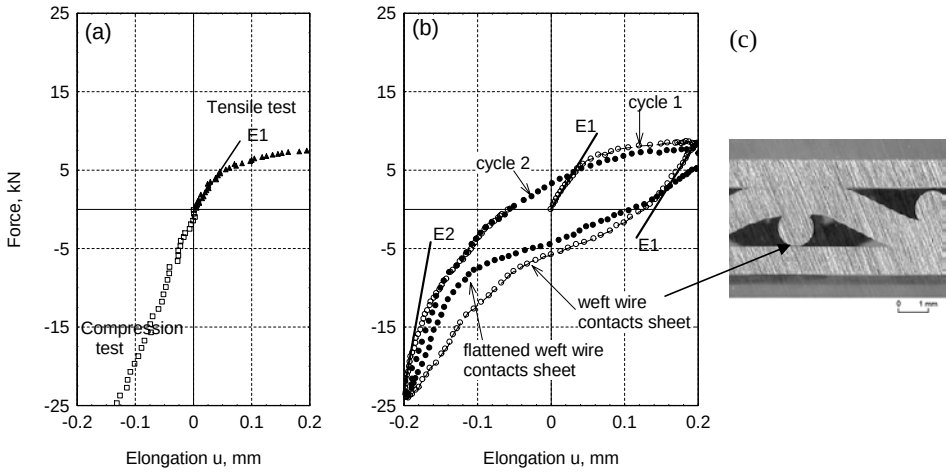

Fig. 5:
a) quasi-static tensile and compression test on 6025HT structures at RT
b) fully reversed LCF-test (R = −1) on 6025HT structures at RT
c) 6025 HT structure

At the beginning of the first cycle of the LCF test, according to the gradient of the Young`s Modulus, there is an elastic deformation of the structure in direction of tension. Afterwards a plastic deformation of the warp wires between the separate spot welds can be observed. After the direction of velocity has been reversed the structure is elastic released followed by the beginning of plastic compression of the warp wires. Due to the lack of connection to the sheets the weft wires can pass the explained deformation procedure with a minium of resistance. However at a certain point of time they come into contact with the sheets, which produces a spontaneous increase of the force. Thereby the wire material is plastically compressed. After the direction of velocity has changed again the warp wires are elastic released by a significant increase of the Young`s modulus followed by a second plastic bending. In the second cycle, due to the permanent plastic deformation, the contact of the weft wires with the sheets and so the increase of the compression force takes place at a later point of time.

The hysteresis loops of sandwich structures under pulsating elongation (R = 0) show a curve progression similar to solid materials. Figure 6 shows an example for a 6025HT structure.

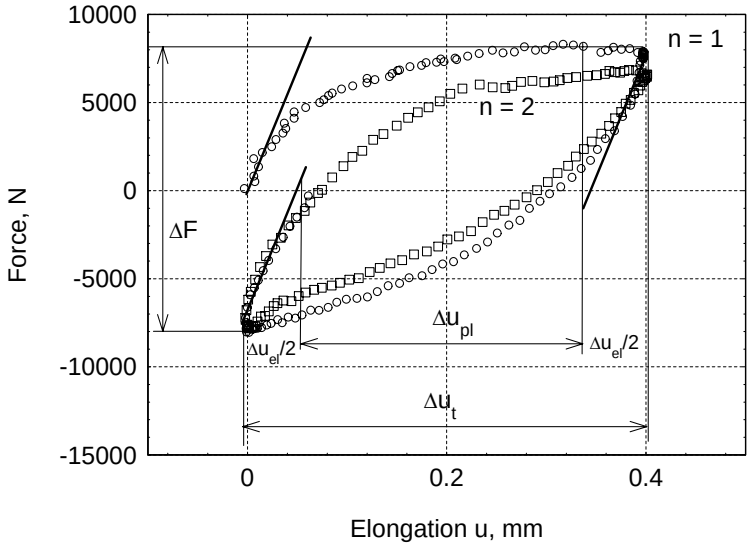

Fig. 6: Hysteresis loops of a LCF test under pulsating elongation for a 6025HT structure (R=0)

Definition of a failure criterion

In contrast to normal specimen of bulk material the sandwich structures do not fail due to a spontaneous rupture, so that an adequate failure criterion for the sandwich structures has to be defined. The maximum force in direction of tension decreases continuously till the last spot weld has failed. A cycle-dependent stiffness S according to eq. 1 is defined:

$$S = \frac{F_{max/n}}{u_a} \tag{1}$$

$F_{max/n}$ is the maximum force in the specific cycle n and u_a is the applied elongation amplitude of the test.
The stiffness at failure is determined from the quasi-static tensile test. Figure 7 represents the force displacement curve and the corresponding stiffness F/u curve. The stiffness at maximum force $F_{max/n}$ is considered as the critical value.

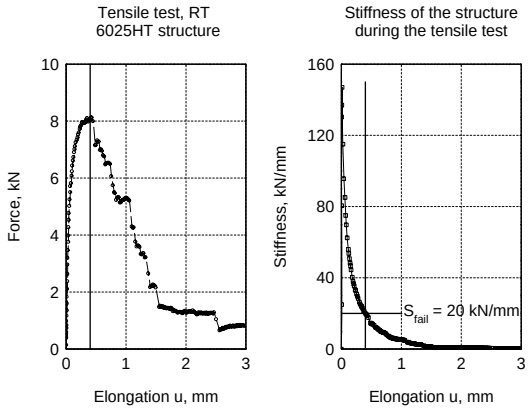

Fig. 7: Definition of failure of the structures on the basis of quasi-static tensile tests

With this failure criterion the dependence of the elongation amplitude on the number of cycles till failure can be determined. This is shown exemplary in figure 8 for 6025HT structures, which were tested at 650°C with a frequency of f = 0,2 Hz.

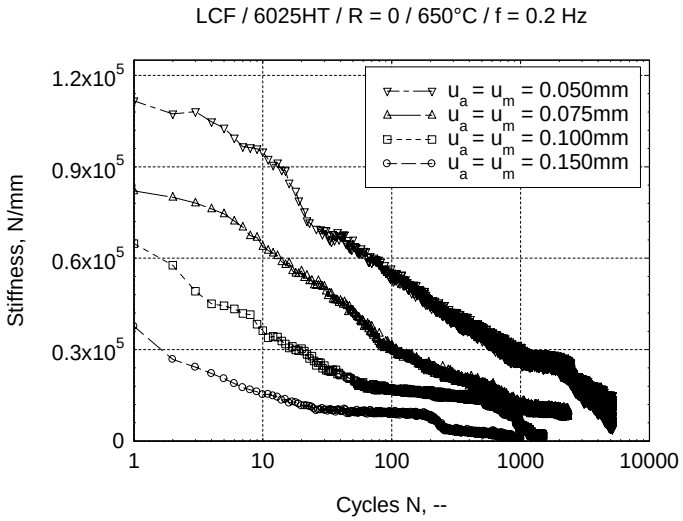

Fig. 8: Stiffness depending on the number of cycles for LCF tests on 6025HT structures at 650°C with a frequency of 0,2 Hz

Results of the Low Cycle Fatigue Tests

6025HT structures

The range of displacement can be divided into a plastic and an elastic part:

$$\Delta u_t = \Delta u_{el} + \Delta u_{pl} \tag{2}$$

If the dependences $\Delta u_{pl}(N_B)$ and $\Delta u_{el}(N_B)$ are plotted double logarithmic, both functions can be linearised and described by a power law. For the Low Cycle Fatigue region a correlation between the plastic part $\Delta\varepsilon_{pl}$ of the elongation amplitude (u_a) and the number of cycles to rupture N_B was determined for bulk materials by Manson and Coffin [7, 8]:

$$\Delta\varepsilon_{pl} = B \cdot N_B^{-m} \tag{3}$$

The characterisation of the elastic part is based on the approximation of Basquin [9]:

$$\Delta\varepsilon_{el} = A \cdot N_B^{-n} \tag{4}$$

This leads to the correlation:

$$\Delta\varepsilon_t = A \cdot N_B^{-n} + B \cdot N_B^{-m} \tag{5}$$

Based on common theoretical approximations [10, 11] for solid material n and m can be taken as n = 0,10 and m = 0,5 [12]. However, the application of such constants can lead to major deviation from the real material behaviour.

In the case of sandwich structures, a similar relation can applied for the displacement instead of strain:

$$u_a = C \cdot N_B^{-e} + D \cdot N_B^{-f} \tag{6}$$

The relation between the displacement amplitude (u_a) and the number of cycles at fracture is represented in figure 9 and described by eq. 6.

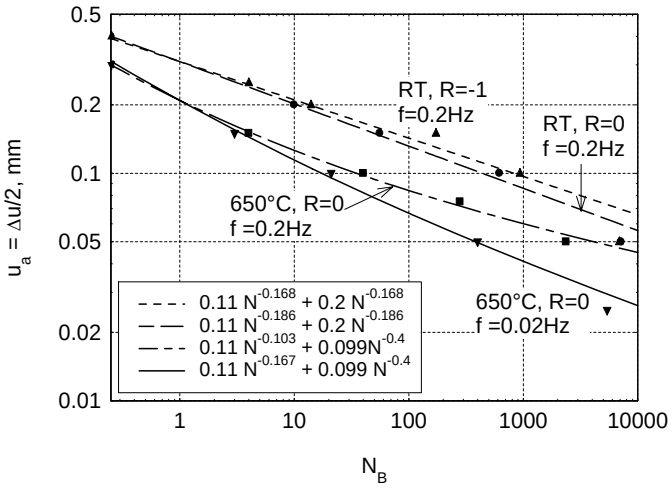

Fig. 9: Fatigue life curves for 6025HT structures

As expected the durability of the 6025HT structures decreases with an increase of the applied test temperature. A remarkable influence of the test frequency is observed. Due to creep contribution during the cycle, the fatigue life is reduced when the frequency decreases. According to eq. 6 the description of the LCF test results for the investigated frequencies f = 0,2 Hz and f = 0,02 Hz at 650°C show that with exception of the parameter n all other parameters remain equal.
Again for the description of the results the constants C and D from eq. 6 for R = 0 and R = -1 can remain equal.

P92 structures

The fatigue life curves for the P92 structures are shown in figure 10. In analogy to the 6025HT structures the fatigue life decreases on the one hand with an increasing applied test temperature and on the other hand with decreasing test frequencies. In contrast to the 6025HT structures a description of the LCF results for the P92 structures with eq.6 is not possible. Due to the relative low ductility of the P92 structures in dependence on the cycles two different regions can be distinguished. In this case each region is described separately by a power law.

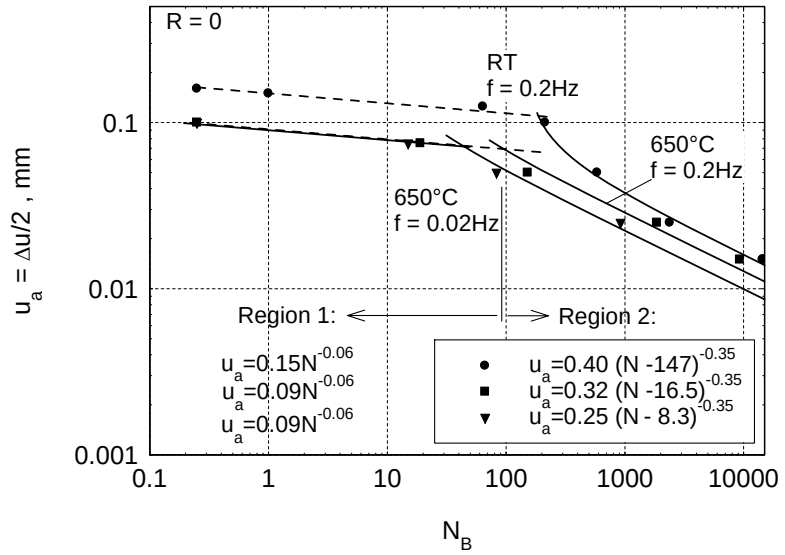

Fig. 10: Fatigue life curves for P92 structures

At low amplitudes the decrease of the durability becomes less distinct. The results in the second region can be described by the power function

Region 1: $$u_a = D_1 \cdot (N_B)^{-f_1} \quad (7)$$

Region 2: $$u_a = D_2 \cdot (N_B - M)^{-f_2} \quad (8)$$

Again a constant value for the exponent for all test temperatures and test frequencies can be used.

Conclusion

- Due to the greater ductility of weld spots in the nickel base alloy 6025HT structures, they show a higher fatigue resistance than P92 structures.
- The LCF-life at high temperatures decreases with decreasing frequency as a result of the greater influence of creep deformation.
- The dependence of the number of cycles to rupture on the elongation amplitude of the 6025HT structures can be described by the usual relations used for bulk materials.

Acknowledgement

The authors gratefully acknowledge the financial support of the Deutsche Forschungsgemeinschaft (DFG) within the Collaborative Research Center (SFB561) „Thermally Highly Loaded, Porous and Cooled Multi-Layer Systems for Combined Cycle Power Plants" at the RWTH Aachen University.

References

[1] U. Dilthey, B. Hachmann, R. Kopp, U. Marek, J. Rappen, VDI-Berichte 1994,1080,657.
[2] O. Wachter, P.J. Ennis, VGB Kraftwerkstechnik 1997,77(9)
[3] U. Brill, G. Giersbach und H.-W. Kettler: Effizienzsteigerung kontinuierlicher Wärmebehandlungsanlagen durch den Einsatz ungekühlter Ofenrollen aus dem neuen Werkstoff Nicrofer 6025 HT (2.4633), VDI-Berichte Nr. 1151, 1995
[4] U. Brill: Praktische Erfahrungen mit dem neuen Werkstoff Nicrofer 6025 HT im Ofen- und Wärmebehandlungsanlagenbau, Verlag Stahleisen GmbH, Düsseldorf, 1995, 37 – 40
[5] U. Brill: Ergebnisse mit dem Werkstoff Nicrofer 6025 HT im Ofen- und Wärmebehandlungsanlagenbau, Verlag Stahleisen GmbH, Düsseldorf, 1999, 54 – 56
[6] U. Dilthey, A. Ghandehari, R. Kopp, Hohmeyer P., Beiss P., Iglesias Figuerdo E., El-Magd E., Kranz A., „Development of Porous Steel Structures for Steam Turbines" ADVANCED ENGINEERING MATERIALS, 2001,3,No.3
[7] L. F. Coffin: A Study of the Effect of Cyclic Thermal Stresses on a Ductile Metal, Trans. ASME, 76 (1954), pp. 931 – 950
[8] S. S. Manson: Interfaces between Fatigue, Creep and Fracture, International Journal of Fracture Mechanics, 2 (1966), pp. 327 -363
[9] O. H. Basquin: The Experimental Law of Endurance Test, Proc. ASTM, Vol. 10, Part II (1910), pp. 685
[10] S.S. Manson: Fatigue: A Complex Subject – some Simple Approximations, Experimental Mechanics, 5 (7) (1965), pp. 193 – 226
[11] H. Zenner: Niedrig-Lastwechsel-Ermüdung (low cycle fatigue), VDI-Bericht Nr. 268, (1976) S. 101 – 112
[12] E. El-Magd: Hochtemperaturwerkstofftechnik Vorlesungsumdruck SS/2005

CAUSES OF CREEP FRACTURE MECHANISM CHANGE IN 9Cr-1.8W-0.5Mo-VNb STEEL

Jae Seung Lee[1,2], Hassan Ghassemi Armaki[1], Kouichi Maruyama[3], Taro Muraki[4] and Hitoshi Asahi[4]

[1] Graduate School of Engineering, Tohoku University, 6-6-02 Aobayama, Sendai 980-8579, Japan
[2] Now with Wire Rod Research Group, POSCO, Pohang 790-785, Korea
[3] Graduate School of Environmental Studies, Tohoku University, 6-6-02 Aobayama, Sendai 980-8579, Japan
[4] Steel Research Laboratories, Nippon Steel Corporation, Futtsu 293-8511, Japan
maruyama@material.tohoku.ac.jp

Abstract

Quick decrease, namely breakdown of creep strength often occurs in long term creep of advanced high Cr ferritic steels. Causes of the breakdown were examined paying special attention to fracture mechanism change observed in such steels. The material studied was grade 92 steel crept at 550 to 650 ^{o}C for up to 63151 h. The steel shows ductility drop with increasing rupture life, and the breakdown coincides with the occurrence of brittle intergranular fracture. Creep cavities are nucleated at coarse precipitates of Fe_2W Laves phase along grain boundaries. The coarsening of Laves phase particles triggers the intergranular fracture and the consequent breakdown of creep strength. The coarsening of Laves phase can be detected non-destructively by means of hardness testing of a material exposed to elevated temperature without stress.

Keywords: Grade 92 steel; Premature breakdown of creep strength; Intergranular fracture; Coarsening of Laves phase; Non-destructive evaluation

Introduction

Structural materials in high temperature plants are usually used for a duration longer than 10^5 h. The long term rupture lives are evaluated from short term rupture data with the aid of Time-Temperature-Parameter (TTP) method [1]. In the case of Orr-Sherby-Dorn (OSD) method [2], a linear relation is assumed between $\log t_r$ and $1/T$ as shown in Fig.1 (a), where t_r is the rupture life, and T the testing temperatures. In other words, the $\log t_r - \log\sigma$ curve measured at T_1 is simply shifted to longer life according to the activation energy Q (dotted line in Fig.1 (b)). The linear extrapolation is based on a crucial assumption that the activation energy determined by the short term data does not change in long term creep. However, the activation energy for rupture life sometimes decreases in long term creep as shown by the dashed line in Fig.1 (c), and the linear extrapolation (open circles) overestimates the true rupture life (solid circles). The earlier fracture than the prediction has been called “premature failure” [3-5]. The premature failure may bring about an unexpected shutdown of plants. If we can postpone the transition from the mechanism with high activation energy to that with low activation energy, we can extend rupture life of the material. The decrease in activation energy is always accompanied by a decrease in stress exponent for rupture life from n to a lower value of n’.

This aspect of the transition, namely quick decrease in creep strength has been named as "premature breakdown of creep strength" [6,7]. Thorough understanding of the transition in creep behavior is necessary for detecting and preventing the premature failure and the premature breakdown.

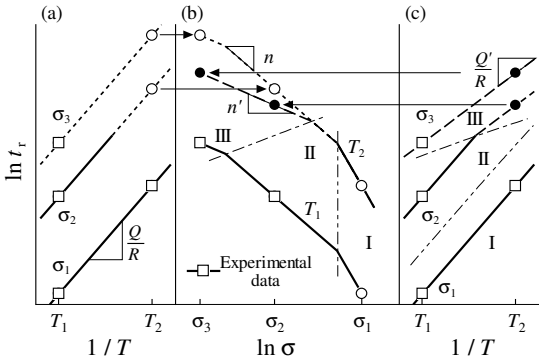

Fig. 1 Evaluation procedure of long term creep rupture life, and explanations of premature failure and premature breakdown of creep strength.

Advanced high Cr ferritic steels, for example 9Cr-1.8W-0.5Mo-VNb steel, are strengthened by a combination of several strengthening mechanisms, such as precipitation hardening due to MX carbonitrides, $M_{23}C_6$ carbide and Laves phase [8,9], and solid solution hardening due to W and Mo [10-13]. The dislocation hardening due to tempered martensitic lath structure is another important strengthening mechanism [4]. Sustenance of the hardening mechanisms is a fundamental requirement for good long term creep properties. However, recovery of the lath structure [4], coarsening of precipitates [14-17] and loss of supersaturated solid solution elements [18,19] often occur during creep exposure. These degradation processes can bring about the breakdown of creep strength. MX carboniterides are one of the most effective strengthening elements in the advanced high Cr ferritic steels. However, Z phase is formed at the expense of MX carbonitrides during high temperature exposure. Z phase grows rapidly and cannot contribute to strengthening. The premature breakdown has often been explained by the disappearance of MX carboniteride [6,7,14]. Ferritic rotor steels tempered at a low temperature (below 700 ^{o}C) have been studied in those researches. In such steels, M_2X carboniterides are formed, thereby promoting the formation of Z phase. However, this is not the case in ferritic boiler steels tempered at a temperature close to 800^{o}C. Semba et al. [20] have found a similar breakdown of creep strength in the high Cr ferritic steel in which Z phase cannot be formed because of the absence of nitrogen atom. Kushima et al. [21] have found a recovered zone along prior austenite grain boundaries in Mod.9Cr-1Mo steel, and have proposed the enhanced recovery as the cause of the premature failure reported in the steel. However, positive and sufficient proof supporting their proposal has not been given yet. Transition from ductile transgranular fracture to brittle intergranular fracture often occurs in long term creep of advanced high Cr ferritic steels for boiler. It has been well demonstrated in the fracture mechanism maps [22] that the change in fracture mechanism brings about decreases in activation energy and stress exponent for rupture life, and therefore results in premature failure. Maruyama et al. [4,23] have explained the premature failure of 11Cr-2W-

0.4Mo-1Cu-VNb steel (grade 122) by the change in fracture mechanism. However, the ductile to brittle transition does not occur in ferritic rotor steel tempered at a low temperature [4].

The causes of the premature failure and the premature breakdown of creep strength have not been fully understood yet. The major cause may be different depending on alloy composition and heat treatment condition. 9Cr-1.8W-0.5Mo-VNb steel (grade 92) is practical advanced high Cr ferritic steel used extensively in USC power plants. In this paper, the cause of the premature breakdown in grade 92 steel is studied paying special attention to precipitation and growth of Laves phase. Non-destructive evaluation by means of hardness testing is applied for detecting the breakdown. More details have been reported elsewhere [24].

Table 1 Chemical composition of the steel studied (mass %)

C	Si	Mn	Cr	W	Mo	V	Nb	N
0.10	0.20	0.44	9.2	1.82	0.45	0.20	0.05	0.05

Experimental procedure

The chemical composition of the steel studied is listed in Table 1. The steel was normalized at 1050 ^{o}C for 1 h, followed by tempering at 780 ^{o}C for 3 h. Creep specimens, 6 mm in diameter and 30 mm in gage length, were tested at 550, 600 and 650 ^{o}C under constant load for up to 63151 h in air. Microstructures of crept specimens were analyzed with field emission scanning electron microscopy (FESEM) and field emission transmission electron microscopy (FETEM) equipped with energy dispersive X-ray spectroscopy (EDS). The specimens for SEM analysis were etched with a etching solution. Size distribution of Laves phase precipitates was determined through measurement of 300 - 1000 particles.

Cause of premature breakdown

Creep rupture life

Creep rupture lives of the grade 92 steel studied are plotted in Fig.2 as a function of creep stress. The stress σ and temperature T dependence of rupture life t_r is expressed as

$$t_r = t_o \, \sigma^{-n} \exp\left(\frac{Q}{RT}\right) \quad (1)$$

where t_o is a constant, n is the stress exponent, Q is the apparent activation energy, R is the gas constant, and T is the absolute temperature. There are two regions with different values of Q and n in the figure, and the two regions are bounded by the dash-dot line: Q = 667 kJ/mol and n = 17 in the short term and high stress region H, and Q = 624 kJ/mol and n = 8.4 in the long term and low stress region L. The values of Q and n decrease in the long term region, and the breakdown (quick decrease) of creep strength is evident in region L. However, the difference in Q between the two regions is not so significant as compared with grade 122 steel [23]. The decrease in Q value generally suggests the overestimation of long term rupture life, but the overestimation is not so serious in the grade 92 steel.

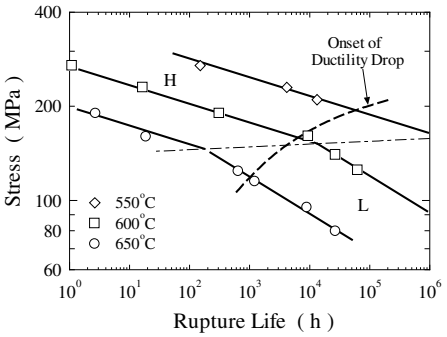

Fig. 2 Stress versus rupture life plot of 9Cr-1.8W-0.5Mo-VNb steel studied.

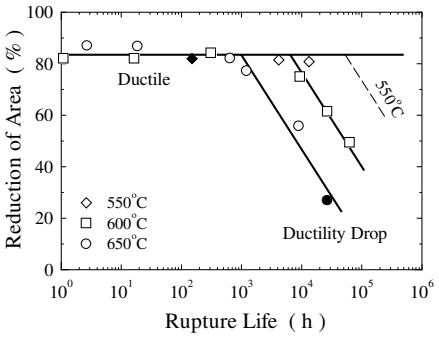

Fig. 3 Reduction of area after creep rupture of the steel studied

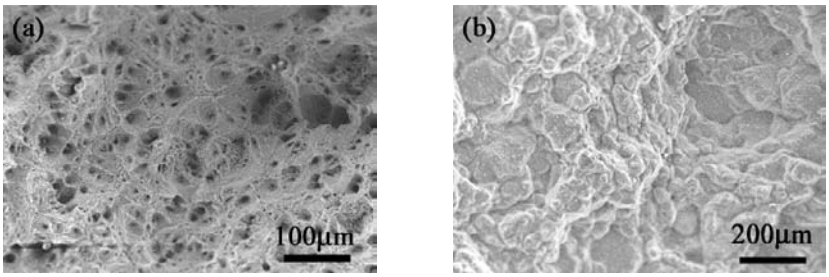

Fig. 4 Fracture surfaces of specimens after (a) 150.2 h creep at 550 ºC and 270 MPa and (b) 26783 h at 650 ºC and 80 MPa.

Fracture mode

Reduction of area measured after creep rupture is plotted in Fig.3 as a function of rupture life. The rupture ductility drops beyond a critical point, suggesting a change in fracture mechanism. The dashed line of 550 °C was predicted from the measurements at 600 and 650 °C. The onset of the ductility drop is indicated by the dashed curve in Fig.2. The onset of ductility drop accords fairly well with the boundary between regions H and L.

Figure 4 shows the representative fractographs taken (a) before and (b) after the ductility drop. The corresponding data points are indicated in Fig.3 with the solid symbols. The dimple pattern is typical of ductile transgranular fracture. The fracture appearance shown in Fig.4 (b) is obviously different from Fig.4 (a). The absence of dimple pattern suggests brittle intergranular fracture, though the fractured surface is oxidized.

Results of the examination of creep fracture modes are summarized in Fig.5. The fracture modes are classified into two types; transgranular and intergranular fracture. The intergranular fracture region is further divided into two domains according to the location of cavity

formation. Secondary electron (SE) and back scatted electron (BSE) images of the same area are shown in Fig.6. Laves phase with a higher average atomic number takes a bright contrast in the BSE image and is easily identified. The other particles seen in the figures are mostly $M_{23}C_6$ carbides. At higher stresses in the intergranular fracture region (Fig.6 (a) and (b)), cavities are formed at the triple grain junction at which a high density of Laves phase particles are present. This type is called "wedge crack" in Fig.5. The other type is "isolated cavity" formed independently at coarse Laves phase particles on prior austenite grain boundaries (arrows in Fig.6 (c)). This type is mainly observed after long term creep in the intergranular fracture region as shown in Fig.5. Though $M_{23}C_6$ carbide and Lave phase particles are potential nucleation sites of cavities, many cavities are attached to Laves phase.

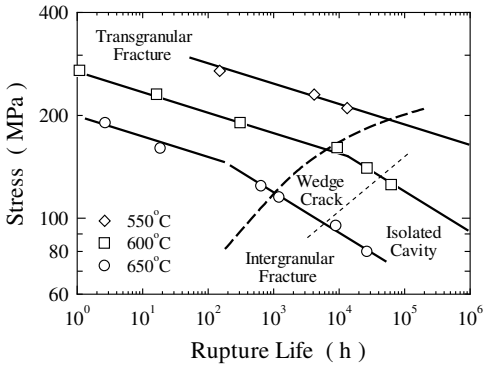

Fig. 5 Fracture mechanism map of the steel studied.

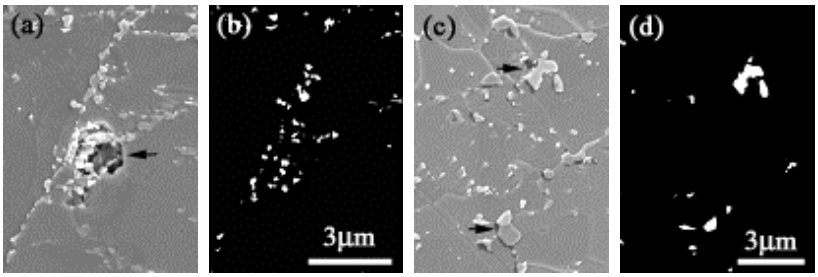

Fig. 6 Cavity formation in specimens crept (a)(b) for 26875h at 600ºC and (c)(d) for 26783h at 650ºC.

Evolution of Laves phase particles

Evolution process of Laves phase is depicted in Fig.7: (a) mean diameter of Laves phase and (b) amount of W in precipitates. The latter has been reported in Ref. [25] on grade 92 steel. Figure 7 (a) includes the measurements in gage and grip portions, but there is not obvious difference between the two portions. The coarsening of particles is known as Ostwald ripening and described by the following equation [26,27]:

$$d^{\mathrm{m}} - d_{\mathrm{o}}^{\mathrm{m}} = K_{\mathrm{d}}\, t \qquad (2)$$

where d and d_o are the average diameter of particles before and after high temperature exposure, respectively, t is the exposure time, and K_d is a material constant proportional to diffusivity. When d_o is negligibly small, Eq. (2) can be simplified to

$$d^m = K_o\, t \exp(\frac{-Q_d}{RT}) \qquad (3)$$

where Q_d is the activation energy for particle coarsening, and K_o is a constant. The exponent m characterizes the coarsening mechanisms of precipitates; for example, m = 3 for the coarsening controlled by lattice diffusion, and 4 for grain boundary diffusion [25].

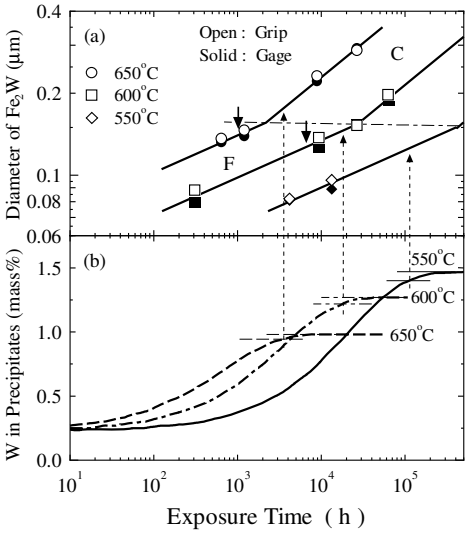

Fig. 7 (a) Coarsening of Laves phase in gage and grip portions, and (b) amount of W in precipitates [25] as a function of exposure time.

It is evident in Fig.7 (a) that there are two stages F and C with different exponents m on the log$d$ vs. log$t$ curves. Apparent activation energies Q_d and exponent m obtained are Q_d = 348 kJ/mol and m = 7 in stage F, and Q_d = 342 kJ/mol and m = 4 in stage C. The amount of W in precipitates increases with increasing exposure time, and saturate at an equilibrium value as shown in Fig.7 (b). The points at which 95% of W has precipitated are indicated in Fig.7 (a) with the upward arrows. In stage C, W precipitation has finished and the basic assumption of Ostwald ripening is fulfilled. The Q_d value of 342 kJ/mol is close to that for lattice diffusion of W in 9Cr steel [28]. Therefore, it can be concluded that the growth of Laves phase is controlled by lattice diffusion in stage C, though m = 4 is larger than the expected value of 3 for this mechanism. In the early stage, nucleation and coarsening of Laves phase proceeds simultaneously. Since the delay of W precipitation at lower temperature raises apparent activation energy, the true activation energy should be smaller than 348 kJ/mol in stage F. From this fact one may speculate grain boundaries as diffusion path in this stage.

Segregation of W to grain boundary

Segregation of W was analyzed by EDS attached to FETEM in a grip portion after 646 h and

8955 h exposure at 650 °C. The two exposure durations are in stage F (646 h), at which the supersaturated W is still present, and stage C (8955 h), after finishing the precipitation of Laves phase, respectively. In stage F, the W peaks measured at grain boundary is obviously higher than those from the matrix. This result suggests that a part of supersaturated W segregates to grain boundaries. The segregated W is consumed to form precipitates of Laves phase on grain boundaries. The path of W flow for the precipitation can be grain boundaries as speculated in the last section. The W peaks almost disappear in stage C after finishing the precipitation. In this stage, Ostwald ripening of Laves phase probably proceeds through lattice diffusion, as suggested by the activation energy for the ripening.

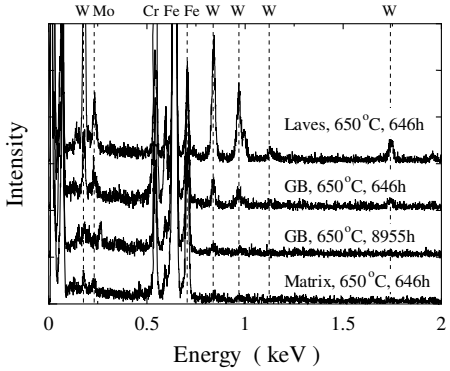

Fig. 8 EDS analyses of matrix, Laves phase and grain boundary after 646 h exposure at 650 ºC (stage F), and of grain boundary after 8955 h at 650 ºC (stage C).

Cause of fracture mechanism change

The stress exponent *n* for rupture life of the grade 92 steel decreases in long term region L. The boundary between the two regions H and L is indicated by the dash-dot line in Fig.2. The breakdown (quick drop) of creep strength in region L is typical of advanced high Cr ferritic steels containing W. Transition from ductile transgranular fracture to brittle intergranular fracture occurs in the grade 92 steel. The onset of ductility drop is represented by the dashed line in Fig.2. The two boundaries of the breakdown and the fracture mode change coincide fairly well with each other, confirming that the change in fracture mechanism is the cause of the breakdown of creep strength. Similar good correlations have been reported on grade 122 steel [23] and austenitic stainless steel [29]. The breakdown at the boundaries between different fracture mechanisms has been well recognized in the fracture mechanism maps published by Ashby and his co-workers [22].

Creep cavities are formed on grain boundaries in the brittle intergranular fracture region. The cavities are usually attached to coarse particles of Laves phase suggesting that the precipitation and coarsening of Laves phase are responsible for the intergranular fracture. The onset of ductility drop is indicated in Fig.7 (a) with the downward arrows. The points correspond to average diameter of Laves phase of 130 nm (127 nm at 600 °C and 140 nm at 650 °C). This fact together with the nucleation site of cavities suggests that coarsening of Laves phase particles over a critical size triggers the intergranular fracture in the present steel studied. Creep cavities are nucleated on coarse particles of Laves phase in brittle intergranular

fracture region of grade 122 steel also [23]. This agreement suggests that the major cause of the ductility drop is the same in grade 92 and 122 steels for boiler application.

Non-destructive evaluation of transition to intergranular fracture

Advanced high Cr ferritic steels with W have been widely used in electric power plants [30]. Accurate evaluation of their creep lives is necessary for safe and efficient operation of power plants, and detection of the breakdown (quick drop) of creep strength is crucially important. The breakdown is caused by the transition from transgranular to intergranular fracture, and coarsening of Laves phase particles triggers the transition of fracture mechanism. Therefore, measurements of cavity density and particles size of Laves phase are essential for the residual life assessment. The measurements can be done with replica sampling. However, it is more practical if the transition can be detected more easily, for example, by hardness testing.

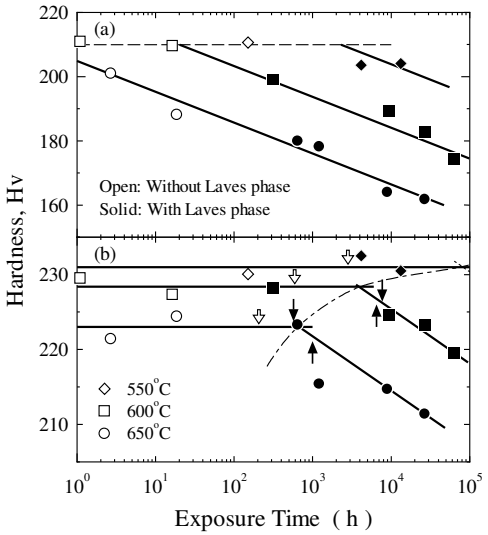

Fig. 9 Change of Vickers hardness in (a) gage and (b) grip portions of the steel studied.

Figure 9 shows the changes of Vickers hardness as a function of exposure time. The hardness was measured in gage and grip portions after creep rupture. The solid symbols indicate the detection of Laves phase after the exposure. The high Cr ferritic steel has a tempered martensitic lath structure, and recovery of the dislocation substructure primarily brings about the decrease in hardness after creep deformation in the gage portion [31]. However, any signal indicating the breakdown or the fracture mechanism change can be detected on the softening curve. As seen in Fig.9 (b), the hardness changes even in the grip portion, and the curves reveal two stages. The hardness remains almost constant during the short term exposure, and decreases gradually after the long term exposure. The points at which Laves phase particles have grown to average size of 130 nm are indicated by the solid downward arrows in Fig.9 (b). The onset of ductility drop is also indicated in the figure by the upward arrows. These points well accord with the drop of hardness in grip. So, the drop of hardness can be a useful signal

of the particle coarsening and the consequent fracture mechanism change. The drop of hardness can reasonably be correlated to coarsening of Laves phase.

The steel was tempered at 780 ^{o}C for 3 h. In grip portion without creep deformation, recovery of tempered martensitic lath structure does not proceed evidently, since the recovery is strain assisted process [4]. Loss of solid solution hardening and/or precipitation hardening should be the cause of the hardness decrease in the grip portion. Laves phase precipitates during the high temperature exposure at the expense of W in the matrix. Removal of W should result in decrease of hardness. The points at which 0.5 mass% W has precipitated are indicated in Fig.9 (b) by the downward open arrows. However, the drop of hardness does not start at those points. Precipitation hardening due to fine Laves phase particles can compensate the loss of solid solution hardening in the early stage of Laves phase precipitation as reported in literatures [19]. This is why the hardness is maintained constant after the precipitation of Laves phase. Laves phase grows faster than $M_{23}C_6$ and MX particles. The hardness starts to drop when Laves phase particles have grown and cannot compensate the loss of solution hardening. Therefore the hardness drop in grip portion accords with the coarsening of Laves phase particles.

Conclusion

The cause of premature breakdown (quick drop) of creep strength in 9Cr-1.8W-0.5Mo-VNb steel was examined. The results are summarized as follows:
1. Stress exponent for rupture life decreases from 17 to 8.4 in long term creep, indicating the breakdown of creep strength typical of advanced high Cr ferritic steel. Transition from ductile transgranular fracture to brittle intergranular fracture is the major cause of the breakdown.
2. Evolution processes of creep cavities during the intergranular fracture are classified into two types. One is wedge cracking observed at high stress during shorter term creep, and the other is formation and coalescence of isolated cavities under long term creep conditions. Most of the cavities are nucleated at coarse Laves phase particles.
3. Cavity formation at coarse particles of Laves phase triggers the brittle intergranular fracture. The intergranular fracture starts when Laves phase has reached an average diameter of 130 nm.
4. Supersaturated W atoms segregate to grain boundaries. Laves phase are formed by gathering such W atoms. Coarsening of Laves phase is controlled by lattice diffusion in the latter stage of particle growth.
5. One can non-destructively detect the coarsening of Laves phase particles and the consequent intergranular fracture by hardness testing during high temperature exposure without stress.

References

1. R. Viswanathan: Damage Mechanisms and Life Assessment of High Temperature Components, ASM Intern., Metals Park, Ohio, (1989), Chap. 3.
2. R.L. Orr, O.D. Sherby and J.E. Dorn: Trans. ASM, 46 (1954), 113.
3. H. Cerjak, P. Hofer and B. Schaffernak: ISIJ Intern., 39 (1999), 874.

4. K. Maruyama, K. Sawada and J. Koike: ISIJ Intern., 41 (2001), 641.
5. K. Kimura, H. Kushima and K. Sawada: Proc. 6th International Charles Parsons Turbine Conference, Ed. by A. Strang et al., (2003), p.443.
6. H. Danielson and J. Hald: Proc. 4th EPRI International Conference on Advances in Materials Technology for Fossil Power Plants, (2004), CD-ROM.
7. R. Agamennone, W. Blum, C. Gupta and J. K. Chakravartty: Acta Mater, (2006), in press.
8. K. Iwanaga, T. Tsuchiyama and S. Takaki: Key Eng. Mater., 171-174 (2000), 477.
9. M. Taneike, M. Kondo and T. Morimoto: ISIJ Intern., 41 (2001), Suppl., S1111.
10. Y. Tsuchida, K. Okamoto and Y. Tokunaga : ISIJ Intern., 35 (1995), 317.
11. K. Sawada, M. Takeda, K. Maruyama, R. Ishii, M. Yamada, Y. Nagae and R. Komine: Mater. Sci. Eng., A 267 (1999), 19.
12. Y. Kadoya and E. Shimizu: J. Iron Steel Inst. Jpn., 86 (2000), 74.
13. T. Muraki, Y. Hasegawa and M. Ohgami: Key Eng. Mater., 171-174 (2000), 499.
14. A. Strang and V. Vodarek: Mater. Sci. Tech., 12 (1996), 552.
15. K. Suzuki, S. Kumai, H. Kushima, K. Kimura and F. Abe: J. Iron Steel Inst. Jpn., 86 (2000), 52.
16. H. Kushima, K. Kimura and F. Abe: Proc. 7th Liege Conference on Materials for Advanced Power Engineering 2002, Ed. by L. Beckers et al., (2002), p.1581.
17. J.S. Lee, K. Maruyama, I. Nonaka and T. Ito: Creep Deformation and Fracture, Design, and Life Extension, Ed. by R.S. Mishra et al., Mater. Sci. Tech. 2005, (2005), p.139.
18. V. Foldyna, A. Jakobova, V. Vodarek and Z. Kubon: Proc. Conf. on Materials for Advanced Power Engineering, Ed. by D. Contsouradis et al., Kluwer Academic Publishers, Dordrecht, (1994), p.453.
19. F. Abe: Mater. Sci. Eng., A 319-321 (2001), 770.
20. H. Semba and F. Abe: Symp. on USC Steels for Fossil Power Plants 2005, Beijing, China, (2005), p.157.
21. H. Kushima, K. Kimura and F. Abe: J. Iron Steel Inst. Jpn., 85 (1999), 841.
22. M. F. Ashby, C. Gandihi and D. M. R. Taplin: Acta Metall., 27 (1979), 699.
23. K. Maruyama and J. S. Lee: Creep & Fracture in High Temperature Components - Design & Life Assessment Issues, Ed. by I.A. Shibli et al., DEStech Publications, Lancaster, PA., (2005), p.372.
24. J.S. Lee, H. Ghassemi Armaki, K. Maruyama, T. Muraki and H. Asahi: Mater. Sci. Eng. A, (2006), in press.
25. J. Hald: EPRI / National Power Conference, New Steels for Advanced Plant up to 620 ^{o}C, Ed. by E. Metcalfe, (1995), p.152.
26. I. M. Lifshitz and V. V. Slyozov: J. Phys. Chem. Solids, 19 (1961), 35.
27. C. Wagner: Z. Electrochem., 65 (1961), 581.
28. J. Cermak, J. Ruzickova and A. Pokorna: Acta Mater., 12 (1996), 5007.
29. H. Nakakuki, K. Maruyama, H. Oikawa and K. Yagi: J. Iron Steel Inst. Jpn., 81 (1995), 220.
30. F. Masuyama: Materials for Advanced Power Engineering 1998, Ed. by J. Lecomte-Beckers et al., Forschungszentrum Julich GmbH, Julich, (1998), p.1807.
31. K. Sawada, K. Maruyama, Y. Hasegawa and T. Muraki: Key Eng. Mater., 171-174 (2000), 109.

AUTHOR INDEX

A

Abe F, II 965, II 1019, II 1041
Affeldt E, II 633
Aguero A, II 949, III 1553
Allcock B, III 1553
Allen D J, III 1479
Andersson C, III 1503
Andren H O, III 1267
Ang J, II 655, II 691
Armaki H G, II 1157
Asahi H, II 1157
Auerkari P, III 1309, III 1385

B

Baker B A, III 1609
Banhart J, III 1651
Barnard P M, I 485
Batfalsky P, I 69
Bauer M, III 1341
Baune E, II 871
Bednarz P, II 747, III 1722
Bendick W, II 1065, II 1077
Berger C, II 1053, II 1137
Bernasovský P, I 261
Berreth K, III 1571
Bhanu Sankara Rao K, I 121
Białas M, II 747
Biede O, III 1503
Birnbaum U, I 161
Blackler M, I 485
Blum L, I 69
Blum R, I 41
Blum W, III 1241
Böck N, II 1031, III 1207
Bolt H, I 81
Bordenet B, GT103
Brabetz M, II 1031
Brekelmans W A M, II 595
Brózda J, III 1331
Brückner U, I 317, I 507
Brziak P, I 261, II 985
Buršík J, III 1449

C

Caminada S, II 871
Cappuccini F, II 717
Casu A, II 727
Cempura G, II 773, II 1077
Cerjak H, II 871, III 1191, III 1199, III 1217, III 1393
Chen Q, II 931
Chilukuru H, III 1181, III 1241
Cizner J, III 1461
Cui C, I 385
Czyrska-Filemonowicz A, I 485, II 773, II 1077

D

Dahl K V, II 675
Daleo J A, II 737
Danielsen H K, III 1251, III 1275
De Carlan Y, III 1319
De Maria L, I 217
Dechamps P, I 25
Del Genovese D, III 1651
Del Puglia P, II 829
Dhooge A, III 1369
Dietz W, III 1683
DiGianfrancesco A, II 843
Dinkel M, II 633
Doi H, I 355
Dong J, III 1609
Donth B, II 843
Du X, II 819
Dubiel B, I 485
Durham R, III 1553
Durst K, III 1181, III 1241

E

Efendi, I 561
El-Magd E, II 1147
Emura S, II 767
Ennis P J, III 1285, II 1077, III 1543, III 1651

Epishin A, I 205, I 317, I 475, I 507, I 521

F

Faulkner R G, II 1117, III 1299
Fedelich B, I 475
Feng D, I 533
Folkova E, III 1401
Foret R, III 1449
Fry A T, III 1469
Fudali S, III 1427, III 1491
Fujioka J, I 385
Fukui T, III 1589

G

Gabrel J, II 1065
Gajda B, II 1087
Gaude-Fugarolas D, III 1319
Gebhard J, II 1147
Geers M G D, II 595
Giannozzi M, II 699, II 707, II 717
Giorni E, II 645, II 699, II 707
Giovannetti I, II 699
Gohil D D, III 1533
Göken M, II 633, III 1181, III 1241
Golanski G, II 1087
Golpayegani A, III 1267
Goto N, I 561
Grumsen F, III 1251
Gu Y, I 385
Guan H R, I 413, II 627
Guo J T, I 189, I 393, I 403, I 435, I 447, II 819
Guo X G, I 403

H

Hagiwara M, II 767
Haibel A, I 521
Hake J F, I 161
Hakl J, I 365, II 985, III 1461
Hald J, II 917, II 675, III 1251, III 1275
Hansson A N, III 1663
Hanus R, II 855
Harada H, I 287, I 309, I 327, I 347, I 385, I 495, II 655, II 691
Harvey B, III 1479
Hashizume R, I 273
Hattori M, I 561
Heinemann J, III 1597
Heinz P, II 633
Helmrich A, II 931, III 1597
Henderson M B, III 1553
Henry J F, II 893
Hernas A, III 1357, III 1427, III 1491
Herzog R, II 747, III 1722
Hierro M P, III 1523
Höfinger S, II 1031
Holdsworth S R, I 91, III 1309
Holdway P, II 793
Holmström S, III 1309, III 1385
Holzer I, III 1191
Homkrajai W, I 377
Hou J S, I 393, I 435, I 447
Hu Z Q, I 189, I 413, II 627
Husemann R U, III 1597
Hussain K, II 737
Huysmans S, III 1369

I

Igarashi M, II 1095
Imai H, II 655, II 757
Imazato T, II 997
Imosa M, III 1491
Innocenti M, II 645
Iseda A, II 1095

J

Jandovà D, III 1401
Jensen S A, III 1503
Jin T, II 627
Jochum C, II 871, III 1341, III 1369

K

Kager F, II 1031
Kakehi K, I 299
Kan T, II 1095
Kanta V, III 1401
Kasl J, III 1401
Kauffmann F, III 1171
Kawagishi K, II 655, II 691
Kern T -U, II 843, II 855
Kilgallon P J, III 1513
Kimura K, II 1019, II 1105, III 1227

Kindratschuk V, III 1619
Kitashima T, I 495
Kiyono T, I 273
Klenk A, III 1341, III 1597
Klingelhöffer H, I 317
Kloc L, II 1011, II 1127
Knoedler R, III 1581
Kobayashi T, I 287, I 309, I 327, I 347, I 495
Koizumi Y, I 309, I 327
Komai N, II 997
Kondo Y, I 455, I 465
Kong S, I 549, I 555
Kothleitner G, III 1217
Koyabu H, I 299
Koyama T, I 561
Kozeschnik E, II 619, III 1191
Kuboň Z, III 1437
Kucharova K, II 1127
Kudrman J, II 1127
Kunecke G, I 475
Kupczyk J, II 1087
Kurita K, I 465
Kuroda S, I 541, II 757
Kushima H, II 1019, II 1105, III 1227

L

Lamm M, I 335
Lanese N, II 829
Lapin J, II 803
Lardon J M, III 1319
Larsen O H, III 1503, I 245
Lee J S, II 1157
Lefebvre B, II 1065
Li G, II 819
Li J, I 549, I 555
Li W, I 549, I 555
Li Y L, I 393, I 435
Li Z J, I 435
Link T, I 205, I 317, I 507, I 521
Linssen J, I 161
Liu J D, II 627
Lomozik M, III 1417
Lou L H, I 583
Lucas K, II 793
Lüdenbach G, III 1597
Luesebrink O, I 335
Lupinc V, II 607
Lyutovich A, III 1571

M

Mack D E, II 727
Maier H, I 81
Maile K, III 1171, III 1341, III 1571, III 1597
Makhele-Lekala L Z, III 1651
Maldini M, II 607
Mao Y, II 767
Marchant G, I 571
Marchionni M, I 423
Mareček J, II 803
Maresca P, II 645
Maruyama K, II 1157
Masset P, II 783
Masuyama F, I 175
Mathieu P, I 143
Matsumoto K, II 691
Matsuo H, II 1095
Matsuo T, I 455, I 465
Mayer K H, II 843, II 855, II 1053, III 1171
Mayr P, III 1393
McColvin G, I 571
Menzler N H, I 69
Meyr P, II 871
Minami Y, III 1589
Mitsche S, III 1199
Miura N, I 455, I 465
Montagnon J, III 1319
Montgomery M, I 245, III 1503, III 1663
Morinaga M, I 273, I 561
Moskal G, III 1357
Mukherji D, III 1619
Mülders B, III 1639
Müller M, II 665
Murakami H, I 541, II 757
Muraki T, II 1157
Murakumo T, I 287
Murata Y, I 273, I 561

N

Nazmy M, I 205
Nicholls J R, III 1696
Nieto J, III 1523
Nisaratanaporn E, I 377
Norton B, III 1553

O

Oakey J, I 233, III 1513
Ohata H, I 347
Onofrio G, I 423
Osgerby S, I 217, III 1469, III 1533
Osinkolu G A, I 423
Ott M, II 633
Over H H, III 1683

P

Pasternak J, II 871, III 1331, III 1357, III 1427, III 1491
Patel S J, III 1609
Pein C, II 619
Pelachová T, II 803
Penkalla H J, II 773, III 1629
Pérez F J, III 1523
Ping D, I 385, I 495
Pirón Abellán J, III 1285
Polsilapa S, I 377
Portella P, I 317
Pratesi F, II 645, II 699, II 707, II 717
Pyczak F, II 633

Q

Qin X Z, I 435, I 447
Quadakkers W J, III 1285, III 1543, III 1722

R

Raj B, I 121
Rajek J, III 1191
Rechberger W, III 1217
Rinaldi C, I 217
Ro Y, I 347
Rohr V, III 1543
Roos E, III 1341
Rösler J, III 1619
Ruoff H, III 1171

S

Sakai T, I 541
Salonen J, III 1385
Sato A, I 287, I 385, II 655, II 691
Sawada K, II 1105, III 1227
Scarlin B, II 931
Scheefer M, III 1553
Scheu C, III 1171
Scholz A, II 1053, II 1137
Schubert F, II 773, III 1629, III 1639, III 1651, III 1722
Schütze M, II 783, III 1543
Schwienheer M, II 1137
Seibert T, III 1181
Semba H, II 1041
Shao C, I 549, I 555
Shibata M, I 541
Shingledecker J P, I 107, II 893
Simms N J, III 1513
Singer R F, II 633, I 335
Singheiser L, III 1285, III 1629, III 1722
Sklenicka V, II 1011, II 1127
Smith G D, III 1609
Sonderegger B, III 1199, III 1217
Sopoušek J, III 1449
Spindler M W, III 1673
Spiradek-Hahn K, II 1031
Stachura S, II 1087
Stamatelopoulos G, II 931
Stanko G, II 893
Staubli M, I 205, II 843, II 855
Steinbrech R, I 69, III 1722
Stöver D, II 727
Strang A, I 571, III 1251
Straub S, III 1171, III 1581
Stuhrmann J, II 1147
Sun C, I 583
Sun X F, I 413, II 627
Suzuki A, II 757
Suzuki T, I 309
Svoboda M, II 1127

T

Tamaki H, I 355
Tanaka F, I 465
Tanzosh J, II 893
Tasak E, III 1417, III 1427
Terzigli V, II 645
Theofel H, III 1597
Tinga T, II 595
Toda Y, II 1019, II 1105
Toshiharu K, II 655

Toušová D, III 1437
Traeger F, II 727
Trunova O, III 1722
Tschaffon H, I 61
Tsuno N, I 299
Tsipas D N, III 1553

V

Vandenberghe B, II 1065, II 1077, III 1369
Vanstone R W, I 41
Vaßen R, II 727
Vekeman J, III 1369
Viswanathan R, II 893
Vitalis B, II 893
Vlasák T, I 365, II 985
Vodarek V, III 1251, III 1437
Volek A, I 335, II 633
Vossberg A, II 633

W

Wabderka N, III 1651
Walbeck M, I 161
Wall G, I 5
Wang L, I 583
Wang Y, II 1053
Wang Y L, I 413
Wang Z H, II 627
Wangyao P, I 377
Weber T, II 855, III 1543
Wenglarz R, I 233
Wessel E, III 1639, III 1722
Willer D, III 1171
Wisbey A, II 793
Wright I G, I 107
Wu J, I 549, I 555
Wu Y N, II 757

X

Xie G, I 583
Xie X, III 1609
Xu G, I 533

Y

Yamaguchi A, I 541, II 757
Yang H C, I 403
Yang J X, I 413
Yardley V, III 1319
Ye H Q, I 435, I 447
Yeh A C, I 287
Yin Y F, II 1117, III 1299
Yokokawa T, I 287, I 309, I 327, I 347
Yoshinari A, I 273, I 355
Yoshizawa M, II 1095
Yuan C, I 393, I 403, I 447
Yutaka K, II 655

Z

Zabler S, I 521
Zeiler G, II 843, II 1031
Zeman M, III 1331
Zhang B, I 533
Zhang J, I 287, I 583
Zhao G, I 533
Zhao M, I 549, I 555
Zhao N R, II 627
Zhao S, III 1609
Zheng Q, I 413
Zhou L Z, I 435
Zielińska-Lipiec A, II 1077
Zies G, III 1171
Zifcak P, II 985
Zlámal B, III 1449
Zonfrillo G, II 699, II 707, II 717, II 829
Zrnik J, I 377
Zschau H E, II 783

KEYWORD INDEX

(Nb,V) CrN particles: III.1251
10Cr steels: II.843
12% Cr steel: II.1077, III.1285, III.1369
12CrMoVNbN steels: III.1251
3DAP: III.1619
5th generation Ni-base superalloys: II.655
6025HT: II.1147
9% Cr steels: III.1393, III.1553
9% Cr cast steel: II.855
9% Cr martensitic steel: II.1041
9-12% Cr steels: II.917, III.1207, II.1031, II.1065, II.1127, II.1137, III.1181, III.1199, III.1241, III.1267, III.1275, III.1357, III.1543
9-12Cr ferritic steels: I.107
Acoustic emission: II.727
Activation energy: I.533
AD700: I.41
Advanced creep laws: III.1341
Advanced power plant materials: III.1479
Advanced power plants: I.143
AFM: III.1181
Allowable stress: II.1095
Alloy 617 welds: III.1597
Alloy 617: III.1597, III.1639
Alloy composition: I.347
Alloy design: II.917
Alloy-80A: I.91
Alloys: III.1683
Alternating atmospheres: III.1533
Aluminising: I.541, II.757, III.1553
Analysis routines: III.1683
Analytical TEM: II.1077
Anisotropy: I.299
Application: I.161, II.855
APS: II.717
Atom-probe field-ion microscopy: I.495
Bainitic structure: II.1087
Biomass: I.245, III.1513
Blading: I.205
Boiler tube: III.1589
Boiler: I.41, II.931
Boron alloyed: III.1393
Boron: II.917, II.965, II.1031
Brazing: II.633
Burgers vectors: I.465
Burner rig test: II.727
Carbides: I.393, I.413, II.985
Carbon and nitrogen redistribution: III.1449
Cast steel: II.1087
CDM modelling: III.1299
Ceramic matrix composites: II.829
Ceramic membranes: I.143
Chemistry modification: III.1619
Chlorination: I.245
Chromium steel: III.1461, III.1469
CM186LC: I.485
CMSX-10: I.507
CMSX-4: I.317, I.507
CO_2 capture: I.143
CO_2 emissions mitigation: I.143
CO_2: I.25
Coal: III.1513
Coarsening of laves phase: II.1157
Coatings: I.217, I.583, II.707, II.737, II.893, II.949
Co-firing: I.245, III.1503, III.1513
Co-free: I.309
Cohesive zone modelling: II.747
Compositional modification: II.767
Conceptual design: II.893
CoNiCrAlY: I.541
Constitutive equation: II.607, III.1341, III.1651
Constitutive model: II.595, III.1207
Conventional Casting (CC): I.355
Cooling time: III.1417
Corrosion resistance: II.893, III.1427, III.1491
Corrosion: III.1533, III.1683
COST536: II.843, II.855
CPFBC: II.665
Crack growth: I.413
Crack initiation: I.403, III.1639
Crack propagation: I.403

Crack: I.393
Cr-diffusion: III.1663
Creep behaviour 11-12%CrWCo(Cu)B(V,Ta,T) steels: II.1053
Creep behaviour: II.1127
Creep damage: II.1117, III.1299, III.1673
Creep equations: II.1137
Creep failure: I.175
Creep fatigue: II.1137
Creep properties: I.365, II.871, II.985, II.1065
Creep rate: II.1117
Creep resistance: II.855, III.1171
Creep resistant steel: II.1011, III.1217, III.1449
Creep resisting steels: III.1331
Creep rupture: II.627, II.1137
Creep strain: II.1117
Creep strength: I.273, II.843, III.1267
Creep testing: III.1401
Creep: I.107, I.287, I.299, I.317, I.455, I.475, I.485, I.507, I.521, II.607, II.619, II.767, II.965, II.1019, II.1031, II.1041, II.1077, II.1105, III.1309, III.1319, III.1369, III.1381, III.1437, III.1479
Creep-fatigue: III.1673
Creep-resistance: III.1357
Cr-steel: III.1319
Crystal growth: II.803
Crystal plasticity: II.595
CVD: III.1571
Cyclic strain: I.403
Damage parameter: III.1341
Damage: III.1639
De-cohesion: II.747
Deformation mechanism: II.819
Degradation: I.205, I.571
D-electrons concept: I.273
Delta ferrite: II.1105, III.1393
Development of FBR materials: I.121
DICTRA: II.675
Diffusion coatings: III.1543
Diffusion coefficient: I.561
Diffusion: II.619, II.633
Directional solidification: I.335
Directionally solidified (DS): I.355
Disk application: I.385
Dislocation dynamics: III.1207
Dislocation Substructure: I.465
Distribution: I.161
Document management system: III.1683
Documentation database: III.1683
Dynamic recrystallisation: I.533
EBSD: II.633, III.1199
ECCC Data sheets: I.91
ECCC: III.1309
Ecological engineering: I.5
EFTEM: III.1217
Electrochemical impedance: III.1523
Electron diffraction: III.1251
Energy alternatives: I.121
Energy and natural resources: I.5
Energy supply chain: I.161
Energy: I.25
Energy-filtered TEM: III.1267
Environmental effect: I.423
Environmental sciences: I.5
Equilibrium: II.691
Esshete 1250: III.1503
European Commission: I.25
Exergy: I.5
Experience: II.855
Experimental data: III.1683
ExtreMat Integrated Project: I.81
Fatigue and creep fatigue crack growth: III.1629
Fatigue crack propagation: I.423
Fatigue: I.317, I.335, II.793
Ferrite matrix: II.1019
Ferritic steel: I.69, II.985, III.1299, III.1309, III.1401
Ferritic/austenitic steels: II.949
Filler metals matching to T/P 23, T/P 24, VM 12, Cost CB 2: II.871
Fireside corrosion: III.1503, III.1513
Flame thermal cycling: II.707
Flow behaviour: I.533
Flue gas desulphurisation plants: III.1427, III.1491
Fossil fuels: I.25
Free energy: I.447
Frequency-Scanning Eddy Current: I.217
Furnace cooling: II.1019

Gamma channel: I.455
Gamma prime: I.205, II.737
Gamma prime precipitate: I.435, I.447, I.465
Gamma TiAl: II.773, II.793
Gas turbine: I.189, I.217, I.423, II.665, II.737
GH2984 superheater alloy: I.189
GH690 alloy tube: I.189
Glass ceramics: I.69
Grade 92 steel: I.91, II.1157
Grain boundary sliding: II.819
Growth stresses: III.1663
HI.2530: I.571
Halogen effect: II.783
Hardness: I.571
Hastelloy alloys: III.1427
HAZ-toughness: III.1393
HCM12: II.1095
Heat affected zone: III.1417
Heat exchanger materials: III.1543
Heat exchanger: III.1513
Heat resistant alloy: I.175
Heat treatment: I.435, II.803, II.997, III.1191
Heterogeneous creep: II.1095
Heterogeneous weld: III.1437
High alloy steel: III.1479
High chromium ferritic steel: II.1105
High efficiency power plant: III.1597
High heat flux materials: I.81
High temperature corrosion: I.245, III.1543
High temperature materials: I.189
High temperature properties: II.655
High temperature: I.61, II.645, II.707, II.717, II.949
High-temperature application: II.843
Homogenisation: I.335
Hot corrosion resistance: I.273
Hot corrosion resistant superalloys: I.189
Hot corrosion: II.665
Hot isostatic pressing (HIP): I.377
Hot working: I.533
Hydrogen effects: III.1663
Hydrogen generation: I.161
Impact energy: II.1087
Implantation: II.783
IN706: III.1619
Inconel 617: III.1651
Inconel 740: III.1609
Industrial gas turbine: I.485
Influence of multiaxiality of the stress state: III.1341
In-situ observation in SEM: III.1639
Interdiffusion: II.675, II.691
Intergranular fracture: II.1157
Intermetallic compound: II.1019
Intermetallic: II.773
Intermittent heating: II.1127
Issues: I.233
K418 superalloy turbine: I.549
K4537 turbine: I.555
K465 cast superalloy: I.413
Laminate: II.829
Larson-Miller parameter: I.327
Laser back-Scattering: I.217
Laser cladding: II.699
Lattice misfit: I.287, I.309
Laves phases: III.1285
LCF: II.773
Life prediction: II.1105
Life: III.1381
Lifetime extension: I.261
Lifing: I.365
Liquid erosion: II.699
Liquid metal cooling: I.335
Long term aging: I.447
Long term exposure: I.377
Long-term creep strength: II.1105
Long–term creep: I.327, III.1227
Low activation materials: I.81
Low alloy steel: II.997, II.1011
Low alloy steels: III.1533
Low cycle fatigue: I.403, I.423, II.1147
Low stress creep: II.1011
LPPS: I.541
M23C6 carbide: I.447, II.965, II.1041
MA 6000: II.645
Martensite: III.1199, III.1417
Martensitic microstructure: II.965
Martensitic phase: II.1019
Material compatibility: I.69

Material development: II.843
Materials database: III.1683
Materials properties data: III.1683
Materials: I.41, I.233, II.931
Mathematical models: I.365
MCrAlY: II.675
Mechanical properties data: III.1683
Mechanical properties of weld joints: III.1357
Mechanical properties: I.347, I.555, II.803, II.871, II.893
Microhardness: I.435
Micromechanics: II.595
Microporosity: I.521
Microstructural changes: II.1127
Microstructural evolution: III.1299
Microstructural parameter: I.347
Microstructural stability: II.1041
Microstructure and modelling: II.917
Microstructure evolution: III.1191
Microstructure: I.507, I.571, II.619, II.767, II.803, II.985, II.1031, II.1077, III.1181, III.1393, III.1401, III.1427, III.1437, III.1491, III.1619
Minimum creep rate: II.997
Mismatched weld materials: III.1341
Mod. Z-phase: III.1217
Model: III.1309
Modelling: I.261, I.475, II.619, III.1469
Modified Z phase: III.1251
Molten salt corrosion: III.1523
Morphological evolution: I.447
Morphology instability: I.435
Multiphase nickel aluminides: II.803
MX and M2X Phase: III.1241
MX carbonitride: II.965
MX precipitates: III.1285
MX: II.1041
Nanoindentation: II.633
NDE: I.217, I.261
Neural network: III.1319, III.1469
Ni-31Cr-3 Mo (Dy) alloy: II.819
Ni-base single crystal superalloy: I.287, I.309, I.347
Ni-base superalloy: I.327, I.385, II.757
Ni-based alloy: I.107, I.561
Ni-based superalloy: I.273, I.299, I.377, I.423, I.455, I.465, I.475, I.533, I.541, I.583
Nickel alloys: III.1491
Nickel based materials: I.61
Nickel content: II.1019
Nickel-base single-crystal superalloy: I.495
Ni-Co-base superalloy: I.385
Ni-YSZ cermet: I.69
Non-conventional sand case: I.549
Non-destructive evaluation: II.1157
Nuclear fission: I.81
Nuclear power programme: I.121
Nuclear technology: I.121
Numerical simulation: I.549, I.555
ODS: II.645
Omega method: II.1117
Outlet header: III.1597
Oxidation resistance: III.1571, I.273, I.287, II.691, II.949
Oxidation: I.107, I.393, I.413, II.645, II.655, II.783, II.793, II.997, III.1461, III.1479
Oxide growth: III.1469
Oxide scale: III.1581
Oxyfuel: I.143
P122: II.1095
P23 steel: III.1437
P91 steel: III.1417, III.1437
P92 steel: II.1147
Pack cementation: III.1543
Partitioning ratio: I.309
PBMR: I.309
Phase computation: III.1609
Photo-luminescence piezospectroscopy: I.217
Plasma facing materials: I.81
Plastic properties: III.1417
PM 3030: II.645
Porosity: III.1319
Power generation: III.1331, III.1357
Power plant: I.61, I.175, III.1369, II.985
PPCC: II.665
Precipitates: III.1217
Precipitation analysis: III.1171
Precipitation kinetics: III.1191
Precipitation site: III.1227

Premature breakdown of creep strength: II.1157
Primary creep: I.299, II.1011
Processing: II.1065
Protective coatings: III.1553
Pt-Ir alloy: II.757
R5: III.1673
Rafting: I.475
Recovery: II.1019
Recrystallization (RX): I.583
Regenerative heat treatment: II.1087
Regression analysis: I.347
Remanent life: II.1117
Research: I.25
Rhenium: I.561
Ruthenium or Iridium addition: I.495
Ruthenium: I.561
SAGBO effect: III.1629
Sandwich-structures: II.1147
Second generation: I.327
SEM and TEM: III.1629
SEM: III.1181, III.1619
Short-range ordering: I.495
Shot peening: I.583, III.1581
Shot-blasted tube: III.1589
Shroud: II.829
Si: II.655
Siliconising: III.1571
Simulation of diffraction patterns: III.1251
Simulation: III.1191, III.1207
Single crystal superalloy: I.335
Single crystal: I.205, I.299, I.317, I.327, I.455, I.465, I.475, I.485, II.737
Single crystalline: II.633
Single-crystal superalloy: II.627
Size distribution: III.1217
Slip system: I.455
SNMS: III.1285
Solid oxide fuel cell: I.69
Spallation: III.1581
Sputtering: II.757
SRZ: II.691
Stainless steel: III.1589
Steam environment: III.1461
Steam oxidation: I.175, III.1285, III.1553, III.1581, III.1589, III.1663
Steam power plant: I.261, II.931, II.949
Steam side oxidation: II.1065
Steam turbine: I.41
Steam: III.1469
Steamside oxidation and resistance: II.893
Steamside oxidation: III.1503
Steel tubes: III.1571
Steel: III.1381
Stellite: II.699
Storage: I.161
Strain rate: III.1651
Strain: III.1309
Straw: I.245
Strength: III.1381
Stress analysis: II.829
Stress and/or strain effect: III.1227
Stress exponent: II.1011
Stress: II.619
Structural analyses: II.773, III.1449
Structural stability: III.1357
Structure analysis: I.377
Structure degradation: I.377
Structure stability: III.1609
Superalloy: I.205, I.317, I.355, I.365, I.393, I.435, I.507, I.521, II.595, II.607, II.645, II.675, II.699, III.1609
Supercritical: II.931
Superheater tubes: III.1597
Superplasticity: II.819
Surfaces: III.1581
Sustainable development: I.5
Syngas: I.233
T/P23: II.997
T122: II.1095
TBC: II.717
TCP phase: I.541
TEM: III.1171, III.1181, III.1401, III.1619
Temperature estimation: II.737
Tensile test: III.1651
Testing: III.1479
Thermal analysis: II.829
Thermal barriers: II.707
Thermal barrier coating: II.727
Thermal cycles: II.717
Thermal cycling: II.727, II.747
Thermal exposure: II.793

Thermal fatigue: I.175, I.393, I.413
Thermal mechanical fatigue: I.347
Thermal shock: II.707
Thermal spraying: III.1553
Thermal welding cycle: III.1417
Thermo mechanical fatigue: I.287
Thermodynamic and kinetic modelling: III.1449
Thermodynamic modelling: II.665
Thermo-physical properties data: III.1683
Ti2AlNb: II.767
Ti6242: II.773
TiAl: II.783
Titanium alloy: II.767
TLP bonding: II.627
Tomography: I.521
TP347H FG: III.1503
Tungsten: I.561
Turbine: I.233, I.365, II.699
Type 316H: III.1673
U720Li: I.385
Ultrasupercritical: I.107
USC plant: III.1589
USC: III.1609
Variable creep loading: II.1127
VM12: II.1065, II.1077, III.1369
VN precipitation: III.1319
Wallpapering: III.1491
Waspaloy: III.1629
Waste incineration: III.1523
Water quenching: II.1019
Web-enable data: III.1683
Web-services: III.1683
Weld joints: III.1449
Weld: III.1381
Weldability: II.855, II.893, III.1331
Welded joints: III.1331
Welding of pipe E911: II.871
Welding: III.1369, III.1401
Woodchip: I.245
Wrought Ni-based superalloy: I.403
YH61: I.355
Z phase: II.917, III.1171, III.1227, III.1241, III.1267, III.1275
Zirconia: II.717

Schriften des Forschungszentrums Jülich
Reihe Energietechnik / Energy Technology

1. **Fusion Theory**
   Proceedings of the Seventh European Fusion Theory Conference
   edited by A. Rogister (1998); X, 306 pages
   ISBN: 3-89336-219-3

2. **Radioactive Waste Products 1997**
   Proceedings of the 3rd International Seminar on Radioactive Waste Products
   held in Würzburg (Germany) from 23 to 26 June 1997
   edited by R. Odoj, J. Baier, P. Brennecke et al. (1998), XXIV, 506 pages
   ISBN: 3-89336-225-8

3. **Energieforschung 1998**
   Vorlesungsmanuskripte des 4. Ferienkurs „Energieforschung“
   vom 20. bis 26. September 1998 im Congrescentrum Rolduc und
   im Forschungszentrum Jülich
   herausgegeben von J.-Fr. Hake, W. Kuckshinrichs, K. Kugeler u. a. (1998),
   500 Seiten
   ISBN: 3-89336-226-6

4. **Materials for Advances Power Engineering 1998**
   Abstracts of the 6th Liège Conference
   edited by J. Lecomte-Beckers, F. Schubert, P. J. Ennis (1998), 184 pages
   ISBN: 3-89336-227-4

5. **Materials for Advances Power Engineering 1998**
   Proceedings of the 6th Liège Conference
   edited by J. Lecomte-Beckers, F. Schubert, P. J. Ennis (1998),
   Part I XXIV, 646, X pages; Part II XXIV, 567, X pages; Part III XXIV, 623, X
   pages
   ISBN: 3-89336-228-2

6. **Schule und Energie**
   1. Seminar Energiesparen, Solarenergie, Windenergie. Jülich, 03. und
   04.06.1998
   herausgegeben von P. Mann, W. Welz, D. Brandt, B. Holz (1998), 112 Seiten
   ISBN: 3-89336-231-2

7. **Energieforschung**
   Vorlesungsmanuskripte des 3. Ferienkurses „Energieforschung“
   vom 22. bis 30. September 1997 im Forschungszentrum Jülich
   herausgegeben von J.-Fr. Hake, W. Kuckshinrichs, K. Kugeler u. a. (1997),
   505 Seiten
   ISBN: 3-89336-211-8

8. **Liberalisierung des Energiemarktes**
   Vortragsmanuskripte des 5. Ferienkurs „Energieforschung“
   vom 27. September bis 1. Oktober 1999 im Congrescentrum Rolduc und
   im Forschungszentrum Jülich
   herausgegeben von J.-Fr. Hake, A. Kraft, K. Kugeler u. a. (1999), 350 Seiten
   ISBN: 3-89336-248-7

9. **Models and Criteria for Prediction of Deflagration-to-Detonation Transition (DDT) in Hydrogen-Air-Steam-Systems under Severe Accident Conditions**
   edited by R. Klein, W. Rehm (2000), 178 pages
   ISBN: 3-89336-258-4

10. **High Temperature Materials Chemistry**
    Abstracts of the 10th International IUPAC Conference, April 10 - 14 2000, Jülich
    edited by K. Hilpert, F. W. Froben, L. Singheiser (2000), 292 pages
    ISBN: 3-89336-259-2

11. **Investigation of the Effectiveness of Innovative Passive Safety Systems for Boiling Water Reactors**
    edited by E. F. Hicken, K. Verfondern (2000), X, 287 pages
    ISBN: 3-89336-263-0

12. **Zukunft unserer Energieversorgung**
    Vortragsmanuskripte des 6. Ferienkurs „Energieforschung“
    vom 18. September bis 22. September 2000 im Congrescentrum Rolduc und
    im Forschungszentrum Jülich
    herausgegeben von J.-Fr. Hake, S. Vögele, K. Kugeler u. a. (2000),
    IV, 298 Seiten
    ISBN: 3-89336-268-1

13. **Implementing Agreement 026**
    For a programme of research, development and demonstration on advances fuel cells
    Fuel Cell Systems for Transportation
    Annex X. Final Report 1997 - 1999
    edited by B. Höhlein; compiled by P. Biedermann (2000), 206 pages
    ISBN: 3-89336-275-4

14. **Vorgespannte Guß-Druckbehälter (VGD) als berstsichere Druckbehälter für innovative Anwendungen in der Kerntechnik**
    Prestressed Cast Iron Pressure Vessels as Burst-Proof Pressure Vessels for Innovative Nuclear Applications
    von W. Fröhling, D. Bounin, W. Steinwarz u. a. (2000) XIII, 223 Seiten
    ISBN: 3-89336-276-2

15. **High Temperature Materials Chemistry**
    Proceedings of the 10th International IUPAC Conference
    held from 10 to 14 April 2000 at the Forschungszentrum Jülich, Germany
    Part I and II
    edited by K. Hilpert, F. W. Froben, L. Singheiser (2000), xvi, 778, VII pages
    ISBN: 3-89336-259-2

16. **Technische Auslegungskriterien und Kostendeterminanten von SOFC- und PEMFC-Systemen in ausgewählten Wohn- und Hotelobjekten**
    von S. König (2001), XII, 194 Seiten
    ISBN: 3-89336-284-3

17. **Systemvergleich: Einsatz von Brennstoffzellen in Straßenfahrzeugen**
    von P. Biedermann, K. U. Birnbaum, Th. Grube u. a. (2001), 185 Seiten
    ISBN: 3-89336-285-1

18. **Energie und Mobilität**
    Vorlesungsmanuskripte des 7. Ferienkurs „Energieforschung“
    vom 24. September bis 28. September 2001 im Congrescentrum Rolduc und im Forschungszentrum Jülich
    herausgegeben von J.-Fr. Hake, J. Linßen, W. Pfaffenberger u. a. (2001),
    205 Seiten
    ISBN: 3-89336-291-6

19. **Brennstoffzellensysteme für mobile Anwendungen**
    von P. Biedermann, K. U. Birnbaum, Th. Grube u. a. (2002)
    PDF-Datei auf CD
    ISBN: 3-89336-310-6

20. **Materials for Advances Power Engineering 2002**
    Abstracts of the 7th Liège Conference
    edited by J. Lecomte-Beckers, M. Carton, F. Schubert, P. J. Ennis (2002),
    c. 200 pages
    ISBN: 3-89336-311-4

21. **Materials for Advanced Power Engineering 2002**
    Proceedings of the 7th Liège Conference
    Part I, II and III
    edited by J. Lecomte-Beckers, M. Carton, F. Schubert, P. J. Ennis (2002),
    XXIV, 1814, XII pages
    ISBN: 3-89336-312-2

22. **Erneuerbare Energien: Ein Weg zu einer Nachhaltigen Entwicklung?**
    Vorlesungsmanuskripte des 8. Ferienkurs „Energieforschung“
    vom 23. bis 27. September 2002 in der Jakob-Kaiser-Stiftung, Königswinter
    herausgegeben von J.-Fr. Hake, R. Eich, W. Pfaffenberger u. a. (2002),
    IV, 230 Seiten
    ISBN: 3-89336-313-0

23. **Einsparpotenziale bei der Energieversorgung von Wohngebäuden durch Informationstechnologien**
    von A. Kraft (2002), XII, 213 Seiten
    ISBN: 3-89336-315-7

24. **Energieforschung in Deutschland**
    Aktueller Entwicklungsstand und Potentiale ausgewählter nichtnuklearer Energietechniken
    herausgegeben von M. Sachse, S. Semke u. a. (2002), II, 158 Seiten, zahlreiche farb. Abb.
    ISBN: 3-89336-317-3

25. **Lebensdaueranalysen von Kraftwerken der deutschen Elektrizitätswirtschaft**
    von A. Nollen (2003), ca. 190 Seiten
    ISBN: 3-89336-322-X

26. **Technical Session: Fuel Cell Systems of the World Renewable Energy Congress VII**
    Proceedings
    edited by D. Stolten and B. Emonts (2003), VI, 248 pages
    ISBN: 3-89336-332-7

27. **Radioactive Waste Products 2002 (RADWAP 2002)**
    Proceedings
    edited by R. Odoj, J. Baier, P. Brennecke and K. Kühn (2003), VI, 420 pages
    ISBN: 3-89336-335-1

28. **Methanol als Energieträger**
    von B. Höhlein, T. Grube, P. Biedermann u. a. (2003), XI, 109 Seiten
    ISBN: 3-89336-338-6

29. **Hochselektive Extraktionssysteme auf Basis der Dithiophosphinsäuren: Experimentelle und theoretische Untersuchungen zur Actinoiden(III)-Abtrennung**
    von S. A. H. Nabet (2004), VI, 198 Seiten
    ISBN: 389336-351-3

30. **Benchmarking-Methodik für Komponenten in Polymerelektrolyt-Brennstoffzellen**
    von Matthias Gebert (2004), 194 Seiten
    ISBN: 3-89336-355-6

31. **Katalytische und elektrochemische Eigenschaften von eisen- und kobalthaltigen Perowskiten als Kathoden für die oxidkeramische Brennstoffzelle (SOFC)**
    von Andreas Mai (2004), 100 Seiten
    ISBN: 3-89336-356-4

32. **Energy Systems Analysis for Political Decision-Making**
edited by J.-Fr. Hake, W. Kuckshinrichs, R. Eich (2004), 180 pages
ISBN: 3-89336-365-3

33. **Entwicklung neuer oxidischer Wärmedämmschichten für Anwendungen in stationären und Flug-Gasturbinen**
von R. Vaßen (2004), 141 Seiten
ISBN: 3-89336-367-X

34. **Neue Verfahren zur Analyse des Verformungs- und Schädigungsverhaltens von MCrAlY-Schichten im Wärmedämmschichtsystem**
von P. Majerus (2004), 157 Seiten
ISBN: 3-89336-372-6

35. **Einfluss der Oberflächenstrukturierung auf die optischen Eigenschaften der Dünnschichtsolarzellen auf der Basis von a-Si:H und µc-Si:H**
von N. Senoussaoui (2004), 120 Seiten
ISBN: 3-89336-378-5

36. **Entwicklung und Untersuchung von Katalysatorelementen für innovative Wasserstoff-Rekombinatoren**
von I.M. Tragsdorf (2005), 119 Seiten
ISBN: 3-89336-384-X

37. **Bruchmechanische Untersuchungen an Werkstoffen für Dampfkraftwerke mit Frischdampftemperaturen von 500 bis 650°C**
von L. Mikulová (2005), 149 Seiten
ISBN: 3-89336-391-2

38. **Untersuchungen der Strukturstabilität von Ni-(Fe)-Basislegierungen für Rotorwellen in Dampfturbinen mit Arbeitstemperaturen über 700 °C**
von T. Seliga (2005), 106 Seiten
ISBN: 3-89336-392-0

39. **IWV-3 Report 2005. Zukunft als Herausforderung**
(2005), 115 Seiten
ISBN: 3-89336-393-9

40. **Integrierter Photodetektor zur Längenmessung**
von E. Bunte (2005), XI, 110 Seiten
ISBN: 3-89336-397-1

41. **Microcrystalline Silicon Films and Solar Cells Investigated by Photoluminescence Spectroscopy**
by T. Merdzhanova (2005), X, 137 pages
ISBN: 3-89336-401-3

42. **IWV-3 Report 2005. Future as a challenge**
(2005), 115 pages
ISBN: 3-89336-405-6

43. **Electron Spin Resonance and Transient Photocurrent Measurements on Microcrystalline Silicon**
by T. Dylla (2005), X, 138 pages
ISBN: 3-89336-410-2

44. **Simulation und Analyse des dynamischen Verhaltens von Kraftwerken mit oxidkeramischer Brennstoffzelle (SOFC)**
von M. Finkenrath (2005), IV, 155 Seiten
ISBN: 3-89336-414-5

45. **The structure of magnetic field in the TEXTOR-DED**
by K.H. Finken, S.S. Abdullaev, M. Jakubowski, M. Lehnen, A. Nicolai, K.H. Spatschek (2005), 113 pages
ISBN: 3-89336-418-8

46. **Entwicklung und Modellierung eines Polymerelektrolyt-Brennstoffzellenstapels der 5 kW Klasse**
von T. Wüster (2005), 211 Seiten
ISBN: 3-89336-422-6

47. **Die Normal-Wasserstoffelektrode als Bezugselektrode in der Direkt-Methanol-Brennstoffzelle**
von M. Stähler (2006), VI, 96 Seiten
ISBN: 3-89336-428-5

48. **Stabilitäts- und Strukturmodifikationen in Katalysatordispersionen der Direktmethanolbrennstoffzelle**
von C. Schlumbohm (2006), II, 211 Seiten
ISBN: 3-89336-429-3

49. **Eduktvorbereitung und Gemischbildung in Reaktionsapparaten zur autothermen Reformierung von dieselähnlichen Kraftstoffen**
von Z. Porš (2006), XX, 182, XII Seiten
ISBN: 3-89336-432-2

50. **Spektroskopische Untersuchung der poloidalen Plasmarotation unter dem Einfluß statischer und dynamischer Ergodisierung am Tokamak TEXTOR**
von C. Busch (2006), IV, 81 Seiten
ISBN: 3-89336-433-1

51. **Entwicklung und Optimierung von Direktmethanol-Brennstoffzellstapeln**
von M. J. Müller (2006), 167 Seiten
ISBN: 3-89336-434-X

Schriften des Forschungszentrums Jülich
Reihe Energietechnik / Energy Technology

52. **Untersuchung des reaktiven Sputterprozesses zur Herstellung von aluminiumdotierten Zinkoxid-Schichten für Silizium-Dünnschichtsolarzellen**
von J. Hüpkes (2006), XIV, 170 Seiten
ISBN: 3-89336-435-8

53. **Materials for Advanced Power Engineering 2006**
Proceedings of the 8th Liège Conference
Part I, II and III
edited by J. Lecomte-Beckers, M. Carton, F. Schubert, P. J. Ennis (2006),
Getr. Pag.
ISBN: 3-89336-436-6

COST is supported by the EU framework programme

COST is an intergovernmental European framework for international cooperation between nationally funded research activities. COST creates scientific networks and enables scientists to collaborate in a wide spectrum of activities in research and technology. COST activities are administered by the COST Office.

ESF provides and manages the scientific and technical secretariat for COST

Forschungszentrum Jülich
in der Helmholtz-Gemeinschaft

50 Jahre / Zukunft

Band / Volume 53, Part II
ISBN 3-89336-436-6

Energietechnik
Energy Technology

Forschungszentrum Jülich
in der Helmholtz-Gemeinschaft
50 Jahre / Zukunft

J. Lecomte-Beckers, M. Carton,
F. Schubert and P. J. Ennis (Editors)

Materials for Advanced Power Engineering 2006

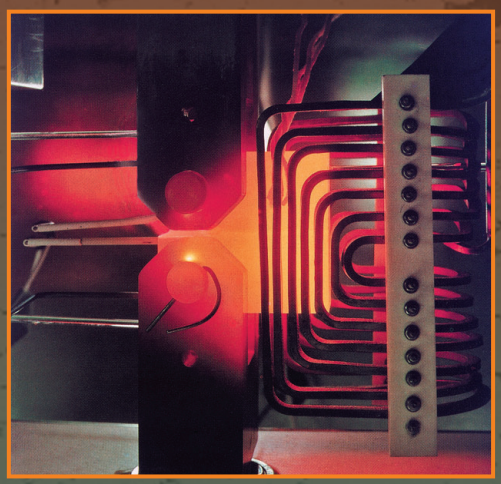

Proceedings Part III

Energietechnik
Energy Technology

Schriften des Forschungszentrums Jülich
Reihe Energietechnik / Energy Technology Band/Volume 53, Part III

Forschungszentrum Jülich GmbH
Institut für Energieforschung

Jacqueline Lecomte-Beckers, Marc Carton,
Florian Schubert and Philip J. Ennis (Editors)

Materials for Advanced Power Engineering 2006

Proceedings of the 8th Liège Conference

Part III

Université de Liège
European Commission
COST
European Science Foundation

Schriften des Forschungszentrums Jülich
Reihe Energietechnik / Energy Technology Band / Volume 53, Part III

ISSN 1433-5522 ISBN 3-89336-436-6

Bibliographic information published by Die Deutsche Bibliothek.
Die Deutsche Bibliothek lists this publication in the Deutsche Nationalbibliografie; detailed bibliographic data are available in the Internet at <http://dnb.ddb.de>.

Publisher and Distributor:	Forschungszentrum Jülich GmbH Zentralbibliothek, Verlag D-52425 Jülich Telefon (02461) 61-5368 · Telefax (02461) 61-6103 e-mail: zb-publikation@fz-juelich.de Internet: http://www.fz-juelich.de/zb
Cover Design:	Grafische Medien, Forschungszentrum Jülich GmbH
Printer:	Grafische Medien, Forschungszentrum Jülich GmbH
Copyright:	Forschungszentrum Jülich 2006

Schriften des Forschungszentrums Jülich
Reihe Energietechnik / Energy Technology Band / Volume 53, Part III

ISSN 1433-5522
ISBN 3-89336-436-6

Neither this book nor any part may be reproduced or transmitted in any form or by any means, electronic or mechanical, including photocopying, microfilming, and recording, or by any information storage and retrieval system, without permission in writing from the publisher.

FOREWORD

The European Co-operation in the field of Scientific and Technical Research (COST) is a well-established organisation for the co-ordination of national research and development programmes on the European level. The series of Liège conferences began in 1978 with the aim of disseminating the results of the COST Action 50 in which materials for gas turbines were investigated. Since then, a Liège Conference has been held every four years and the results of COST Actions 501 and 522, which were concerned with materials for power generation plant, reported. At this, the Eighth Liège Conference, the materials research and development work being carried out in the current COST Actions 536 'Alloy Development for Critical Components of Environmentally Friendly Steam Power Plant' with the acronym ACCEPT and 538 'High Temperature Plant Lifetime Extension' will be reported.

Reliable energy supply at reasonable cost is one of the most important factors in the development and maintenance of the modern industrial society, but there are increasing concerns about the environmental impact of energy production as well as about the need to conserve valuable energy resources for future generations. New and emerging energy technologies are of great interest, but fossil fuels will continue to make a considerable contribution to energy requirements into the foreseeable future. The emphasis in this field is therefore on the most efficient use of fossil fuels, which can be achieved by increasing the thermal efficiency of the energy conversion process. For steam power plant and gas turbines, this means raising the temperature and pressure of the process. This in turn requires the application of improved materials that are able to withstand the increasingly arduous service conditions.

In the COST Actions, the materials research and development activities that are necessary for the critical components of advanced, highly efficient power generation plant have been based on the principle of work-sharing, bringing together materials scientists and engineers, plant designers, alloy producers, component manufacturers, plant constructors and plant operators. This constellation of expertise reflects the need to match materials properties to component behaviour.

In order to put the European efforts into a world-wide scenario, there are in this conference a number of invited papers that will discuss the energy perspectives and the development of power plant materials in the USA, Japan, India and China.

The Conference Proceedings are organised as follows:

Part I: INAUGURAL SESSION
Invited papers

EUROPEAN ENERGY MATERIALS RESEARCH
Invited papers

ENERGY PERSPECTIVES
Invited papers

ADVANCED GAS TURBINE MATERIALS
Invited papers
Contributed papers
Mechanical properties
Microstructure

Part II: ADVANCED GAS TURBINE MATERIALS
Contributed papers
Modelling
Joining technology
Oxidation and hot corrosion
Coating technology
Intermetallics and ceramics

ADVANCED STEAM TURBINE MATERIALS
Invited papers
Contributed papers
Mechanical properties

Part III: ADVANCED STEAM TURBINE MATERIALS
Contributed papers
Microstructure
Modelling and alloy design
Welding technology
Steam oxidation and coatings
Austenitic and nickel-base alloys

ADDENDUM

The Technical and Editorial Board members would like to express their gratitude to all the members of the COST 536 and COST 538 Management Committees, for their supervision and support of the considerable research and development efforts, both in their own countries and across national borders. Those who were involved in the reviewing of the submitted papers are also sincerely thanked for their important contribution to the production of the Proceedings.

Research Centre Jülich - 50 Years of Innovation

Addressing society's challenges, questions and expectations and delivering solutions with the aid of excellent, strategically positioned research: this is the mission that Research Centre Jülich has been involved in ever since its foundation 50 years ago. Over the course of the years, it has undergone a huge transition, moving from research focused on the peaceful uses of nuclear energy to a research enterprise run on a multi-programmatic and interdisciplinary basis with an internationally unrivalled profile.

The key to this profile is the close linking of Jülich's traditional core competence, physics, to the other sciences. The basic insights gained in physics contribute decisively to a better understanding of the complex systems in energy, chemistry, biology, medicine and the geosciences, while the questions encountered in these fields extend the approaches adopted in physics. A further core competence that has evolved in Jülich with a remarkable momentum over the last few years is scientific computing. The operation of medium and large-scale equipment and a well-developed scientific and technical infrastructure round off the profile. This leads to the co-operation between and mutual enrichment of the different areas of expertise in Jülich, which remains internationally unparalleled in both nature and intensity. The positive effect of this cross-linking is further enhanced through strategic alliances with other centres in the Helmholtz Association, as well as with universities, industrial companies and research institutions worldwide.

The Research Centre Jülich will use this profile as a focal point for its research over the next two decades, making thus significant future contributions to the following four grand challenges: responsible management of the environment's natural resources, sustainable and comprehensive energy supply, securing food for and the health of a growing world population, and the provision and solutions-orientated linking of large quantities of information.

TABLE OF CONTENTS

Part I

Foreword iii
Table of Contents vii

INAUGURAL SESSION

ENGINEERING SUSTAINABILITY 5
Wall G

THE EU RESEARCH STRATEGY TOWARDS ZERO EMISSION FOSSIL FUEL POWER PLANTS 25
Dechamps P

EUROPEAN ENERGY MATERIALS RESEARCH

MATERIALS DEVELOPMENT FOR BOILERS AND STEAM TURBINES OPERATING AT 700 °C I 41
Blum R, Vanstone R W

THE EUROPEAN WAY TO 700°C COAL FIRED POWER PLANT I 61
Tschaffon H

MATERIALS ASPECTS OF SOLID OXIDE FUEL CELLS I 69
Steinbrech R, Menzler N H, Batfalsky P, Blum L

MATERIALS FOR EXTREME ENVIRONMENTS IN FUSION APPLICATIONS I 81
Bolt H, Maier H

DEVELOPMENT AND CURRENT STATUS OF ECCC CREEP PROPERTY DATA SHEETS I 91
Holdsworth S R
(see also Part III 1722, Addendum)

ENERGY PERSPECTIVES

EVALUATION OF THE MATERIALS TECHNOLOGY REQUIRED FOR A 760°C POWER STEAM BOILER I 107
Shingledecker J P, Wright I G

CURRENT AND 2050 ENERGY PERSPECTIVES IN INDIA: OPPORTUNITIES FOR MATERIALS SCIENTISTS AND TECHNOLOGISTS I 121
Baldev Raj, B S Rao Kota

MATERIALS CHALLENGES IN CO_2 CAPTURE AND STORAGE I 143
Mathieu P

THE HYDROGEN ECONOMY I 161
Birnbaum U, Hake J-F, Linssen J, Walbeck M

ADVANCED POWER PLANT DEVELOPMENTS AND MATERIAL EXPERIENCES IN JAPAN I 175
Masuyama F

DEVELOPMENT OF HIGH TEMPERATURE MATERIALS FOR ENERGY MARKET IN CHINA I 189
Hu Z Q, Guo J T

ADVANCED GAS TURBINE MATERIALS

Invited papers

DEGRADATION IN SINGLE CRYSTAL NICKEL-BASE SUPERALLOYS – A REVIEW I 205
Nazmy M, Epishin A, Link T, Staubli M

RECENT ADVANCES IN NDT TECHNIQUES FOR GAS TURBINE COATINGS I 217
Osgerby S, Rinaldi C, De Maria L

GAS TURBINE ISSUES IN ADVANCED GASIFICATION SYSTEMS I 233
Wenglarz R, Oakey J

MATERIALS PROBLEMS AND SOLUTIONS IN BIOMASS FIRED PLANTS I 245
Larsen O H, Montgomery M

RE-QUALIFICATION OF BOILER DRUMS IN THERMAL POWER PLANT I 261
Brziak P, Bernasovský P

(see also Part III 1696, Addendum)

Contributed papers: Mechanical properties

DEVELOPMENT OF NI-BASED SINGLE CRYSTAL SUPERALLOYS FOR POWER-GENERATION GAS TURBINE BLADES I 273
Hashizume R, Yoshinari A, Kiyono T, Murata Y, Morinaga M

A 5TH GENERATION NI-BASE SINGLE CRYSTAL SUPERALLOY WITH SUPERIOR ELEVATED TEMPERATURE PROPERTIES I 287
Sato A, Yeh A C, Kobayashi T, Yokokawa T, Harada H, Murakumo T, Zhang J

EFFECT OF PLASTIC ANISOTROPY ON CREEP STRENGTH OF SINGLE CRYSTAL NI-BASED SUPERALLOYS I 299
Koyabu H, Tsuno N, Kakehi K

DEVELOPMENT OF CO-FREE NI-BASE SINGLE CRYSTAL SUPERALLOY I 309
Yokokawa T, Kobayashi T, Suzuki T, Koizumi Y, Harada H

THE EFFECT OF HIGH TEMPERATURE CREEP DAMAGE ON LOW CYCLE FATIGUE IN CMSX-4 I 317
Epishin A, Link T, Brückner U, Klingelhöffer H, Portella P

THE LONG-TERM CREEP PROPERTY OF NICKEL-BASE SINGLE-CRYSTAL SUPERALLOYS I 327
Koizumi Y, Harada H, Yokokawa T, Kobayashi T

INFLUENCE OF SOLIDIFICATION CONDITIONS ON HOMOGENISATION HEAT TREATMENT AND MECHANICAL PROPERTIES IN SINGLE CRYSTAL NICKEL-BASE SUPERALLOYS I 335
Lamm M, Volek A, Luesebrink O, Singer R F

PREDICTION OF THERMAL MECHANICAL FATIGUE PROPERTIES OF NI-BASE SINGLE CRYSTAL SUPERALLOYS I 347
Ohata H, Yokokawa T, Kobayashi T, Ro Y, Harada H

DEVELOPMENT OF A HIGH STRENGTH NI-BASED SUPERALLOY FOR CONVENTIONAL CASTING I 355
Tamaki H, Yoshinari A, Doi H

HIGH TEMPERATURE PROPERTIES OF SELECTED NI-BASE SUPERALLOYS I 365
Hakl J, Vlasák T

HOT ISOSTATIC PRESSING PROCESS TO REJUVENATE SERVICED CAST NICKEL-BASE SUPERALLOY IN738 TURBINE BLADES I 377
Wangyao P, Zrnik J, Polsilapa S, Nisaratanaporn E, Homkrajai W

DEVELOPMENT OF NEW SUPERALLOYS FOR TURBINE DISK APPLICATIONS I 385
Gu Y, Cui C, Ping D, Harada H, Sato A, Fujioka J

INFLUENCE OF CARBIDES AND OXIDATION ON THERMAL FATIGUE BEHAVIORS OF TWO NICKEL-BASE SUPERALLOYS I 393
Li Y L, Yuan C, Guo J T, Hou J S

LOW CYCLE FATIGUE BEHAVIOR OF WROUGHT NICKEL BASED SUPERALLOY GH413 I 403
Guo X G, Guo J T, Yuan C, Yang H C

EFFECT OF CARBIDES ON THERMAL FATIGUE PROPERTY OF K465 CAST SUPERALLOY I 413
Guan H R, Yang J X, Zheng Q, Wang Y L, Sun X F, Hu Z Q

ENVIRONMENTAL EFFECT ON HIGH TEMPERATURE FATIGUE BEHAVIOUR OF A NICKEL BASE SUPERALLOY FOR TURBINE DISCS I 423
Marchionni M, Onofrio G, Osinkolu G A

INFLUENCE OF SOLUTION HEAT TREATMENT CONDITIONS ON GAMMA PRIME CHARACTERISTICS IN A HOT CORROSION RESISTANT SUPERALLOY I 435
Hou J S, Guo J T, Zhou L Z, Li J Z, Qin X Z, Li Y L, Ye H Q

Contributed papers: Microstructure

MORPHOLOGICAL EVOLUTION OF GAMMA PRIME AND $M_{23}C_6$ CARBIDE IN A CAST NI-BASE SUPERALLOY IN THE DIFFERENT TREATMENT CONDITIONS I 447
Qin X Z, Guo J T, Yuan C, Hou J S, Ye Q H

DISLOCATION SUBSTRUCTURE IN γ-CHANNEL OF SINGLE CRYSTAL NICKEL-BASED SUPERALLOY, CMSX-4, CREPT AT 1273 K, 160 MPA I 455
Kondo Y, Miura N, Matsuo T

DISLOCATION SUBSTRUCTURE AT γ/γ' INTERFACE OF SINGLE CRYSTAL NICKEL-BASED SUPERALLOY CMSX-4 CREPT AT 1273 K, 250 MPA I 465
Miura N, Tanaka F, Kurita K, Kondo Y, Matsuo T

MODELLING OF RAFTING AND ITS INFLUENCE IN NI-BASE SUPERALLOYS I 475
Fedelich B, Künecke G, Epishin A

TEM MICROSTRUCTURAL ANALYSIS OF CREEP DEFORMED CM186LC SINGLE CRYSTAL NI-BASE SUPERALLOY I 485
Dubiel B, Blackler M, Barnard P M, Czyrska-Filemonowicz A

ATOM PROBE MICROANALYSIS OF FIFTH-GENERATION NI-BASE SINGLE-CRYSTAL SUPERALLOYS I 495
Kitashima T, Ping D H, Harada H, Kobayashi T

MICROSTRUCTURAL STABILITY OF CMSX-4 AND CMSX-10 UNDER HIGH TEMPERATURE CREEP CONDITIONS I 507
Epishin A, Link T, Brückner U

X-RAY TOMOGRAPHY FOR POROSITY ANALYSIS IN SINGLE-CRYSTAL NI-BASE SUPERALLOYS I 521
Link T, Zabler S, Haibel A, Epishin A

DEFORMATION BEHAVIOR AND MICROSTRUCTURE EVOLUTION DURING HOT WORKING PROCESS OF NICKEL-BASE ALLOY GH742 I 533
Zhang B, Zhao G, Xu G, Feng D

ORIENTATION DEPENDENCE OF SECONDARY REACTION ZONES IN SURFACE MODIFIED NI-BASED SINGLE CRYSTAL SUPERALLOYS I 541
Murakami H, Sakai T, Shibata M, Yamaguchi A, Kuroda S

STUDY ON THE INVESTMENT CASTING PROCESS OF K418 SUPERALLOY TURBINE I 549
Li J, Zhao M, Shao C, Kong S, Wu J, Li W

STUDY ON CASTING PROCESS OF K4537 SUPERALLOY GAS TURBINE I 555
Shao C, Li J, Zhao M, Li W, Wu J, Kong S

DIFFUSION COEFFICIENT OF REFRACTORY ELEMENTS IN MULTI-COMPONENT NI-ALLOY I 561
Murata Y, Hattori M, Efendi, Goto N, Koyama T, Morinaga M

MICROSTRUCTURAL DEGRADATION OF HAYNES 230 COMBUSTOR HARDWARE I 571
Marchant G, McColvin G, Strang A

SHOT PEENING INDUCED RECRYSTALLIZATION IN A DIRECTIONALLY SOLIDIFIED NI-BASE SUPERALLOY I 583
Zhang J, Wang L, Xie G, Sun C, Lou L H

AUTHOR INDEX I

KEYWORD INDEX VII

Part II

ADVANCED GAS TURBINE MATERIALS

Contributed papers: Modelling

MICRO-MECHANICAL MODELLING OF THE SINGLE CRYSTAL NICKEL-BASE SUPERALLOY CMSX-4 II 595
Tinga T, Geers M G D, Brekelmans W A M

MODELLING THE CONSTANT AND VARIABLE LOADING / TEMPERATURE CREEP BEHAVIOUR OF UDIMET 720LI II 607
Maldini M, Lupinc V

A GENERAL APPROACH TO MICROSTRUCTURAL MODELLING OF CREEP II 619
Pein C, Kozeschnik E

Contributed papers: Joining technology

THE CREEP RUPTURE BEHAVIOUR OF A NICKEL-BASE SINGLE-CRYSTAL SUPERALLOY AFTER TLP BONDING II 627
Liu J D, Jin T, Zhao N R, Wang Z H, Sun X F, Guan H R, Hu Z Q

NANOINDENTATION AND ORIENTATION MEASUREMENTS IN SINGLE CRYSTALLINE BRAZING JOINTS OF NICKEL – BASE SUPERALLOYS II 633
Dinkel M, Pyczak F, Göken M, Heinz P, Volek A, Singer R F, Ott M, Affeldt E, Vossberg A

Contributed papers: Oxidation and hot corrosion

LONG-TIME HIGH-TEMPERATURE OXIDATION OF MA 6000 AND PM 3030 ODS SUPERALLOYS II 645
Maresca P, Pratesi F, Terzigli V, Innocenti M, Giorni E

OXIDATION RESISTANCE OF SILICON-CONTAINING 5TH GENERATION NICKEL-BASE SINGLE CRYSTAL SUPERALLOYS II 655
Sato A, Harada H, Ang J, Yutaka K, Toshiharu K, Kawagishi K, Imai H

ESTIMATION OF THE RISK OF HOT CORROSION IN GAS TURBINES BY THERMODYNAMIC MODELLING II 665
Müller M

Contributed papers: Coating technology

MICROSTRUCTURAL INVESTIGATIONS AND MODELLING OF INTERDIFFUSION BETWEEN MCRALY COATING AND IN738 SUPERALLOY II 675
Dahl K V, Hald J

DEVELOPMENT OF EQ COATINGS FOR A NEW TBC COATING SYSTEM IN NI-BASE SUPERALLOYS II 691
Kawagishi K, Sato A, Matsumoto K, Ang J, Harada H

COATINGS BY LASER CLADDING AGAINST LIQUID DROPLET EROSION II 699
Giannozzi M, Giorni E, Giovannetti I, Pratesi F, Zonfrillo G

A NEW DEVICE FOR TESTING COATINGS UNDER THERMAL SHOCK II 707
Zonfrillo G, Giannozzi M, Pratesi F, Giorni E

CHARACTERIZATION OF THERMAL BARRIER COATINGS BY MEANS OF FURNACE CYCLE TESTING II 717
Cappuccini F, Zonfrillo G, Pratesi F, Giannozzi

ACOUSTIC EMISSION ANALYSIS USED AS MONITORING TOOL FOR BURNER RIG TESTS OF THERMAL BARRIER COATINGS II 727
Mack D E, Casu A, Traeger F, Vaßen R, Stöver D

PRACTICAL APPLICATIONS OF TEMPERATURE ESTIMATION MODELS BASED ON SUPERALLOY BASE METAL AND MCRALY COATING MICROSTRUCTURE EVOLUTION IN SERVICE GAS TURBINE COMPONENTS II 737
Hussain K, Daleo J A

NUMERICAL SIMULATION OF TBC DELAMINATION UNDER THERMAL CYCLIC LOADING II 747
Białas M, Bednarz P, Herzog R

OXIDATION AND HOT CORROSION BEHAVIOUR OF ALUMINIZED PT-IR COATINGS ON NI-BASED SUPERALLOYS TMS-82+ II 757
Yamaguchi A, Wu Y N, Suzuki A, Murakami H, Kuroda S, Imai H

Contributed papers: Intermetallics and ceramics

CREEP BEHAVIOR OF ORTHORHOMBIC Ti_2ALNB-BASED ALLOYS II 767
Hagiwara M, Emura S, Mao Y

COMPARISON OF THE ISOTHERMAL FATIGUE BEHAVIOUR OF TIMETAL 6242 AND γ-TIAL ALLOYS AT 700°C II 773
Cempura G, Penkalla H J, Schubert F, Czyrska-Filemonowicz A

TIAL OXIDATION PROTECTION IMPROVEMENTS USING THE HALOGEN EFFECT II 783
Masset P, Zschau H-E, Schütze M

THERMAL EXPOSURE EFFECTS ON THE MECHANICAL PROPERTIES OF TIAL INTERMETALLIC II 793
Holdway P, Lucas K, Wisbey A

DIRECTIONALLY SOLIDIFIED MULTIPHASE NI_3AL-BASED INTERMETALLICS FOR HIGH TEMPERATURE APPLICATIONS II 803
Lapin J, Pelachová T, Mareček J

SUPERPLASTIC DEFORMATION AND MECHANISM OF EXTRUDED EUTECTIC NIAL/CR(MO) ALLOY DOPED WITH DY II 819
Guo J T, Du X, Li G

FEM STUDY OF A CMC SHROUD II 829
Del Pugliaa P, Lanese N, Zonfrilloa G

ADVANCED STEAM TURBINE MATERIALS

Invited papers

THE EUROPEAN EFFORT IN DEVELOPMENT OF NEW HIGH TEMPERATURE ROTOR MATERIALS – COST 536 II 843
Kern T -U, Staubli M, Mayer K H, Donth B, Zeiler G, DiGianfrancesco A

THE EUROPEAN EFFORTS IN DEVELOPMENT OF NEW HIGH TEMPERATURE CASING MATERIALS – COST 536 II 855
Staubli M, Hanus R, Weber T, Mayer K H, Kern T-U

WELDABILITY AND PROPERTIES OF NEW CREEP RESISTANT MATERIALS FOR USE IN ULTRA SUPERCRITICAL COAL FIRED POWER PLANTS II 871
Bauné E, Cerjak H, Caminada S, Jochum C, Mayr P, Pasternak J

US PROGRAM ON MATERIALS TECHNOLOGY FOR ULTRASUPERCRITICAL STEAM-COAL FIRED POWER PLANTS II 893
Viswanathan R, Henry J F, Tanzosh J, Stanko G, Shingledecker J P, Vitalis B

METALLOGRAPHY AND ALLOY DESIGN IN THE COST 536 ACTION II 917
Hald J

MATERIALS DEVELOPMENT FOR ADVANCED STEAM BOILERS II 931
Helmrich A, Chen Q, Stamatelopoulos G, Scarlin B

COATINGS FOR PROTECTION OF HIGH TEMPERATURE NEW GENERATION STEAM PLANT COMPONENTS: A REVIEW II 949
Aguero A

METALLURGY FOR LONG-TERM STABILIZATION OF FERRITIC STEELS FOR THICK SECTION BOILER COMPONENTS IN USC POWER PLANT AT 650^{O}C II 965
Abe F

Contributed papers: Mechanical properties

CONTRIBUTION TO THE INVESTIGATION OF ADVANCED LOW-ALLOY P23 STEEL CREEP BEHAVIOUR II 985
Hakl J, Vlasák T, Brziak P, Zifcak P

EFFECT OF TEMPERING TIMES ON CREEP STRENGTH IN ASME GR 23 (2 25CR-1 6W STEEL) II 997
Komai N, Imazato T

CREEP OF 0.5CrMoV STEEL AT VERY LOW STRAIN RATES II 1011
Kloc L, Sklenica V

IMPROVEMENT IN CREEP STRENGTH OF HEAT RESISTANT FERRITIC STEEL STRENGTHENED BY INTERMETALLIC COMPOUND II 1019
Toda Y, Kushima H, Kimura K, Abe F

SUPERIOR LONG-TERM CREEP BEHAVIOUR AND MICROSTRUCTURAL EVOLUTION OF 9%CR-STEELS WITH BORON II 1031
Kager F, Böck N, Spiradek-Hahn K, Höfinger S, Brabetz M, Zeiler G

ALLOY DESIGN AND CREEP STRENGTH OF ADVANCED 9%CR USC BOILER STEELS CONTAINING HIGH BORON II 1041
Semba H, Abe F

IMPROVEMENT OF CREEP STRENGTH OF 650 °C FERRITIC/MARTENSITIC SUPER HEAT RESISTANT 11-12 % CR STEELS II 1053
Mayer K-H, Berger C, Scholz A, Wang Y

STATUS OF DEVELOPMENT OF THE VM12 STEEL FOR TUBULAR APPLICATIONS IN ADVANCED POWER PLANTS II 1065
Gabrel J, Bendick W, Vandenberghe B, Lefebvre B

MICROSTRUCTURAL DEVELOPMENT OF VM12 STEEL CAUSED BY CREEP DEFORMATION AT 625°C II 1077
Zielińska-Lipiec A, Bendick W, Cempura G, Vandenberghe B, Ennis P J, Czyrska-Filemonowicz A

REGENERATIVE HEAT TREATMENT OF L21HMF CAST STEEL AFTER LONG TERM OPERATION II 1087
Golanski G, Kupczyk J, Stachura S, Gajda B

LONG TERM CREEP STRENGTH DEGRADATION IN T122/P122 STEELS FOR USC POWER PLANTS II 1095
Igarashi M, Yoshizawa M, Iseda A, Matsuo H, Kan T

DEGRADATION BEHAVIOUR AND LONG-TERM CREEP STRENGTH OF 12CR FERRITIC CREEP RESISTANT STEELS II 1105
Kimura K, Sawada K, Kushima H, Toda Y

CREEP CURVE ANALYSIS USING THE MODIFIED Ω METHOD II 1117
Yin Y F, Faulkner R G

EFFECT OF NON STEADY LOADING ON CREEP BEHAVIOUR OF ADVANCED 9-12 % FOSSIL POWER PLANT STEELS II 1127
Sklenicka V, Kucharova K, Svoboda M, Kloc L, Kudrman J

CREEP AND CREEP FATIGUE PROPERTIES OF TURBINE STEELS FOR APPLICATION TEMPERATURES UP TO 625 °C II 1137
Berger C, Schwienheer M, Scholz A

LOW CYCLE FATIGUE BEHAVIOUR OF SANDWICH STRUCTURES OF P92 AND NICROFER 6025 HT II 1147
El-Magd E, Stuhrmann J, Gebhard J

CAUSES OF CREEP FRACTURE MECHANISM CHANGE IN 9CR-1 8W-0 5Mo-VNb STEEL II 1157
Lee J S, Arnaki H G, Maruyama K, Muraki T, Asahi H

AUTHOR INDEX I

KEYWORD INDEX VII

Part III

ADVANCED STEAM TURBINE MATERIALS

Contributed papers: Microstructure

MICROSTRUCTURAL CHARACTERIZATION OF MODERN BORON CONTAINING 9-11 % CR STEELS DEVELOPED IN THE FRAMEWORK OF THE COST PROGRAM III 1171
Kauffmann F, Mayer K H, Straub S, Zies G, Scheu C, Willer D, Ruoff H, Maile K

QUANTITATIVE MICROSTRUCTURAL ANALYSIS ON THE STABILITY OF MX AND M2X IN 9-12 % CR STEELS BY AFM, SEM, TEM III 1181
Seibert T, Durst K, Chilukuru H, Göken M

SIMULATION OF THE PRECIPITATION KINETICS DURING HEAT TREATMENT AND SERVICE OF CREEP RESISTANT MARTENSITIC 9-12% CR STEEL III 1191
Holzer I, Rajek J, Kozeschnik E, Cerjak H

MICROSTRUCTURAL ANALYSIS ON A CREEP RESISTANT MARTENSITIC 9-12% CR STEELS USING THE EBSD METHOD III 1199
Sonderegger B, Mitsche S, Cerjak H

DISLOCATION MOBILITY IN 9% CHROMIUM STEELS EXPOSED TO CREEP III 1207
Böck N

EFTEM INVESTIGATIONS ON PRECIPITATES IN A CREEP RESISTANT 9-12% CR STEEL III 1217
Sonderegger B, Kothleitner G, Rechberger W, Cerjak H

PRECIPITATION BEHAVIOR OF Z PHASE AFTER LONG-TERM CREEP IN HIGH CHROMIUM FERRITIC HEAT RESISTANT STEELS III 1227
Sawada K, Kushima H, Kimura K

ON THE ROLES OF M2X AND Z-PHASE IN TEMPERED MARTENSITIC 9-12% CR-STEELS III 1241
Chilukuru H, Durst K, Göken M, Blum W

ELECTRON DIFFRACTION STUDIES ON (Nb,V)CrN PARTICLES IN 12CrMoVNbN STEELS III 1251
Vodarek V, Danielsen H, Grumsen F, Hald J, Strang A

AN EFTEM STUDY OF Z-PHASE NUCLEATION IN MARTENSITIC CHROMIUM STEELS III 1267
Golpayegani A, Andren H O

Z-PHASE IN 9-12%CR STEELS - OBSERVATIONS AND THERMODYNAMIC MODELLING III 1275
Danielsen H K, Hald J

MICROSTRUCTURE AND STEAM OXIDATION RESISTANCE OF LAVES PHASE FORMING 12%CR STEELS AT 600-650°C III 1285
Pirón Abellán J, Ennis P J, Singheiser L, Quadakkers W J

Contributed papers: Modelling

CDM MODELLING OF POWER PLANT FERRITIC STEELS III 1299
Yin Y F, Faulkner R G

AN EFFECTIVE PARAMETRIC STRAIN MODEL FOR CREEP III 1309
Holmström S, Auerkari P, Holdsworth S

ADVANCED ALLOY DESIGN TOOLS APPLIED TO THE DEVELOPMENT OF VANADIUM NITRIDE STRENGTHENED HIGH-TEMPERATURE STEELS III 1319
Gaude-Fugarolas D, Yardley V, Lardon J-M, Montagnon J, De Carlan Y

Contributed papers: Welding technology

APPLICATION OF BAINITIC CREEP RESISTING STEELS FOR SUPERCRITICAL PARAMETERS AND PROPERTIES OF WELDED JOINTS III 1331
Brózda J, Zeman M, Pasternak J

INVESTIGATIONS ON OPTIMISATION OF WELD CREEP PERFORMANCE IN MARTENSITIC STEELS III 1341
Bauer M, Klenk A, Maile K, Roos E, Jochum C

STRUCTURAL STABILITY AND PROPERTIES OF WELD JOINTS OF NEW CREEP-RESISTANT STEEL GRADES WITH 9 OR 12% CR CONTENTS APPLIED IN OPERATION OF POWER GENERATIONS SECTOR OVER 30000 h III 1357
Moskal G, Hernas A, Pasternak J

WELDABILITY AND HIGH TEMPERATURE BEHAVIOR OF 12% CR-STEEL FOR TUBES AND PIPES IN POWER PLANTS WITH STEAM TEMPERATURES UP TO 650 °C III 1369
Vekeman J, Dhooge A, Huysmans S, Vandenberghe B, Jochum C

EXPECTED CREEP LIFE OF WELDED 9-12% CR STEELS III 1381
Auerkari P, Holmström S, Salonen J

STUDY OF THE SIMULATED HAZ OF A BORON ALLOYED CREEP RESISTANT 9% CHROMIUM STEEL III 1393
Mayr P, Cerjak H

MICROSTRUCTURAL STUDIES OF SIMILAR AND DISSIMILAR WELDS OF P91 III 1401
Jandova D, Kasl J, Folkova E, Kanta V

PHYSICAL SIMULATION AND NUMERICAL MODELLING OF X10CRMOVNB 9 10 (P91) STEEL REPAIR WELDING III 1417
Lomozik M, Tasak E

DISSIMILAR WELDED JOINTS WITHOUT A BUFFER AREAS OF STEEL TYPE 9CR WITH 1CRMOV TO BE USED FOR STEAM BOILER PIPELINES III 1427
Tasak E, Hernas A, Pasternak J, Fudali S

CREEP PROPERTIES OF HETEROGENEOUS P91/P23 WELDS AT 550 AND 600 °C III 1437
Kuboň Z, Vodárek V, Toušová D

STRUCTURAL STABILITY OF HETEROGENEOUS WELD JOINT OF 6CRMOV 8-3-2 AND X12CRMOV 10-1 STEELS WITH INCREASED NITROGEN CONTENT III 1449
Foret R, Zlámal B, Sopoušek J, Buršík J

Contributed papers: Oxidation and coatings

OXIDATION OF CANDIDATE CHROMIUM STEELS IN STEAM ENVIRONMENT III 1461
Cizner J, Hakl J

OXIDE SCALE GROWTH AND SPALLATION IN STEAM ENVIRONMENTS – AN ASSESSMENT OF DIFFERENT MODELLING APPROACHES III 1469
Fry A T, Osgerby S

THE INFLUENCE OF OXIDATION ON LONG TERM CREEP RUPTURE STRENGTH DATA III 1479
Allen D J, Harvey B

NEW EXPERIENCE IN THE FIELD OF APPLICATION OF CORROSION RESISTANCE PROTECTION IN FLUE GAS DESULPHURISATION PLANT ABSORBERS III 1491
Hernas A, Imosa M, Pasternak J, Fudali S

CORROSION AND OXIDATION EXPERIENCES IN AVEDØRE II MULTIFUEL BOILER III 1503
Montgomery M, Jensen S A, Biede O, Larsen O H, Andersson A

HEAT EXCHANGER CORROSION IN BIOMASS AND COAL CO-FIRED POWER PLANTS III 1513
Simms N J, Kilgallon P J, Oakey J E

HOT CORROSION MONITORING OF ALLOY 617 IN MOLTEN CHLORIDES USING ELECROCHEMICAL TECHNIQUES III 1523
Pérez, F J, Hierro M P, Nieto J

METAL WASTAGE IN LOW ALLOY STEELS UNDER ALTERNATING ATMOSPHERES AT ELEVATED TEMPERATURE III 1533
Osgerby S, Gohil D D

DEVELOPMENT OF ALUMINIDE DIFFUSION COATINGS FOR HEAT EXCHANGER MATERIALS AND THEIR CREEP-CORROSION RESISTANCE IN SIMULATED COAL FIRING ENVIRONMENT III 1543
Rohr V, Weber T, Schütze M, Ennis P J, Quadakkers W J

DEVELOPMENT AND VALIDATION OF ADVANCED OXIDATION PROTECTIVE COATINGS FOR SUPER CRITICAL STEAM POWER PLANT III 1553
Henderson M B, Scheefer M, Aguero A, Allcock B, Norton B, Tsipas D N, Durham R

IMPROVEMENT OF OXIDATION RESISTANCE OF TUBES BY PULSED SILICONISING III 1571
Maile K, Berreth K, Lyutovich A

INFLUENCE OF SURFACE TREATMENT ON THE OXIDATION KINETICS OF ADVANCED STEELS IN FLOWING STEAM AT 650 °C III 1581
Knoedler R, Straub S

LONG TERM STEAM OXIDATION RESISTANCE OF SHOT-BLASTED STAINLESS STEEL TUBING III 1589
Minami Y, Fukui T

Contributed papers: Austenitics and Ni-base alloys

QUALIFICATION OF NI-BASED MATERIAL FOR TUBES AND PIPING OF 700°C POWER PLANT III 1597
Klenk A, Maile K, Theofel H, Helmrich A, Husemann R U, Lüdenbach G

AN INVESTIGATION ON STRUCTURE STABILITY AND ITS IMPROVEMENT ON A NEW DEVELOPMENTAL NI-CR-CO-MO-NB-TI-AL SUPERALLOY FOR USC POWER PLANT APPLICATION AT TEMPERATURE ABOVE 750°C III 1609
Xie X, Zhao G, Dong J, Smith G D, Baker B A, Patel S J

CHEMISTRY MODIFICATIONS OF INCONEL 706 FOR IMPROVED MICROSTRUCTURAL STABILITY III 1619
Del Genovese D, Mukherji D, Rösler J, Kindratschuk V, Wabderka N, Banhart J

CRACK GROWTH BEHAVIOUR OF WASPALOY AT 700°C IN DIFFERENT ATMOSPHERES III 1629
Penkalla H J, Schubert F, Singheiser L

ASSESSMENT OF THE INFLUENCE OF LASER-DRILLED HOLES ON THE DAMAGE BEHAVIOUR OF ALLOY 617 III 1639
Mülders B, Wessel E, Schubert F

DEFORMATION BEHAVIOUR OF ALLOY INCONEL 617 TUBES IN THE TEMPERATURE RANGE 600°C TO 850°C III 1651
Makhele-Lekala L, Ennis P J, Schubert F

FIELD TESTING OF TP 347H FG AT ULTRA SUPERCRITICAL STEAM CONDITIONS III 1663
Hansson A N, Montgomery M

AN IMPROVED METHOD TO CALCULATE THE CREEP-FATIGUE ENDURANCE OF TYPE 316H STAINLESS STEEL III 1673
Spindler M

WEB-ENABLED DATABASES OF JRC PETTEN-EFFECTIVE TOOLS FOR EUROPEAN KNOWLEDGE MANAGEMENT III 1683
Over H H, Dietz W

ADDENDUM
These papers arrived too late for reviewing and are reproduced as received

ADVANCED COATINGS FOR GAS TURBINES III 1696
Nicholls J R, Bordenet B

APS-TBC FOR GAS TURBINES: FAILURE MODES, DAMAGE EVOLUTION AND LIFE-TIME ASSESSMENT III 1722
Herzog R, Bednarz P, Trunova O, Steinbrech R W, Wessel E, Quadakkers W J, Schubert F, Singheiser L

AUTHOR INDEX I

KEYWORD INDEX VII

Part III

Advanced Steam Turbine Materials

Contributed Papers

Microstructure

MICROSTRUCTURAL CHARACTERIZATION OF MODERN BORON CONTAINING 9-11 % CR STEELS DEVELOPED IN THE FRAMEWORK OF THE COST PROGRAM

F. Kauffmann[1], K. H. Mayer[2], S. Straub[3], G. Zies[1], C. Scheu[1,4], D. Willer[1], H. Ruoff[1] and K. Maile[1]

[1] Materialprüfungsanstalt, University of Stuttgart, Stuttgart, Germany
Email: florian.kauffmann@mpa.uni-stuttgart.de
[2] Schwarzenbruck, Germany
[3] ALSTOM Power Generation AG, Mannheim, Germany
[4] now at: Institute for Physical Metallurgy & Materials Testing, University of Leoben, Leoben, Austria

Abstract

New ferritic-martensitic 9-12 wt.% Cr steels for the usage in steam power plants are currently under development with the aim to further enhance the creep properties and thermal resistance of these materials. Those improved materials would allow higher steam inlet temperatures and pressures in the power plants. Thereby the thermal efficiency could be increased and the CO_2 emission decreased. One important method to improve the creep properties is to control and optimize the microstructural features of the materials. In the present work, a combination of various microscopy techniques, ranging from optical microscopy to transmission electron microscopy, is used to investigate the microstructural features relevant for the creep-resistance. These include the quantitative measurement of the subgrain-size, the number of free dislocations, the chemical composition and the crystallographic structure of the precipitates, as well as their density and size distribution. Small precipitations with a high precipitation density and especially a high thermal stability are of great benefit to improve the creep strength. The results of these investigations on new boron containing 9-11 % Cr steels investigated within the COST program are presented.

Keywords: creep resistance, precipitation analysis, Z-phase, TEM

Introduction

During the last decades new ferritic-martensitic 9-12 wt. % Cr steels for modern steam power plants were developed with the aim to raise the steam inlet temperature from 540 - 550 °C up to temperatures of 600 - 650 °C [1]. This increased inlet temperature would lead to a significantly improved rate of efficiency and reduced CO_2 emission. The traditionally used X20(2)CrMoV-12-1 has been improved with the development of 9-12 % CrMo(W)VNbN steels yielding a significantly enhanced creep resistance. This improvement has its origin in a thermally stabilised $M_{23}C_6$, vanadium and niobium carbonitrides and the precipitation of the Laves phase. These steels are already applied in nearly 30 power stations, operating at maximum steam inlet temperatures of 610 °C. Typical examples for these steels are the X10CrMoVNbN-9-1 (P91), X12CrMoVNbN-10-1 and X12CrMoWVNbN-10-1-1 (E911) [1].

For a further stabilization of the $M_{23}C_6$ precipitates 30 to 100 ppm boron has been added to the 9 wt.% Cr steels. The nitrogen content has to be reduced in these cases to avoid the formation of primary boron nitride on the expense of vanadium carbonitrides. These boron steels are suited for applications up to 625 °C [1]. Alloys representing this second development step are X10CrWMoVNbNB-9-2 (P92) and X14CrMoVNbB-9-1 (FB2). Recent research results suggest that the creep properties can be further improved by increasing the boron content and adjusting the nitrogen content accordingly. This should lead to an increased amount of fine vanadium carbonitrides and prevent the formation of boron nitride at the same time [2, 3].

The potential for the improvement by alloying boron is demonstrated by the development of the 10.5 wt% Cr TAF steel by Fujita and coworkers about 30 years ago [4, 5]. Figure 1 exhibits the 100 000 h creep rupture strength of the TAF steel versus test temperature in comparison to the above mentioned rotor steels. The drawback of the TAF steel is the high B content of about 300 to 400 ppm. In accordance with the current experiences it reduces for example the hot workability of large turbine components dramatically. Nevertheless, the quantitative investigations of the microstructure of this steel with modern analysis techniques are of great importance for the development of new 9-12 wt. % Cr steels with moderate boron contents. The available data for the microstructure of the TAF steel, dated from 1982, give only a qualitative view of the observed phases [6].

Steel	C	Cr	Mo	W	V	Nb	N	B (W.- %)
a)	.28	1.0	0.9	-	.30	-	-	-
b)	.21	12.0	1.0	-	.30	-	-	-
c)	.12	10.0	1.5	-	.20	.05	.05	-
d)	.12	10.0	1.0	1.0	.20	.05	.05	-
e)	.18	9.0	1.5	-	.25	.05	.02	.010
f)	.20	10.5	1.5	-	.22	.15	.02	.040

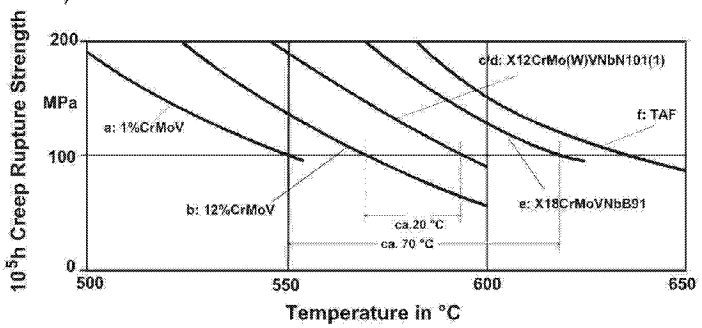

Figure 1: 100 000 hour creep rupture strength of turbine steels.

For our own investigations, we used a TAF test melt from Saarschmiede in Völklingen, produced in the framework of the COST 501 research project. Long-term creep tests have been performed on this material. Some of the tested specimens were characterized in detail within the framework of the COST 536 project and the results of the experiments at 650 °C are compared with the results of the COST steels B0 and FB8 which are different in the B, Cr, Co and C content as well as in the heat treatment condition. The chemical composition of the investigated melts of the TAF, the B0 and the FB8 alloys are given in Table 1.

Table 1: The chemical composition of the TAF test melt F35 by Saarschmiede and of the B0 and the FB8 COST test melts.

Test melt	C	Si	Mn	Cr	Co	Mo	Al	Ni	V	Nb	N	B
TAF (F35)	.21	.33	.87	10.5	-	1.54	.014	<.02	.24	.18	.017	.03
B0	.14	.20	.53	9.2	-	1.43	.008	.11	.23	.06	<.02	.018
FB8	.17	.09	.09	11.1	2.94	1.46	.005	.20	.21	.07	.023	.010

Microstructural Characterization

Optical microscopy and scanning electron microscopy

The optical microscopy (OM) analysis was done using a Leitz Aristomet. The specimens were prepared by standard metallographic methods such as cutting, grinding and polishing. To develop the microstructure the specimen were etched by 3% HNO_3. Scanning electron microscopy (SEM) investigations were carried out using a JEOL JSM 6400 operated at 10 kV for the analytical measurements and at 25 kV for acquiring images. For the analytical measurements the SEM is equipped with an energy-dispersive X-ray spectrometer (EDX) system (TN5500 from NORAN) which allows the detection of elements with an atomic number ≥ 5 (Boron).

Transmission electron microscopy

Conventional transmission electron microscopy (TEM) investigations were performed using a JEOL JEM 2000 FX operated at 200 kV to determine the subgrain size and dislocation density. For analytical measurements the TEM is equipped with an EDX detector (Kevex Sigma 1 from NORAN, capable for detection of elements with an atomic number ≥ 11) and with a GATAN energy filter. The latter was used for acquiring elemental maps. A detailed description of energy filtered TEM (EFTEM) measurements can be found for example in [7, 8]. For the quantitative evaluation of the precipitate state (type, size, shape and distribution) a digital image processing system (SEM-IPS 500, Kontron) was used to analyze the EFTEM images and/or TEM bright field micrographs. For each specimen an area of about 40 μm^2 was quantitatively analyzed.

For the conventional TEM measurements metal foils were prepared by mechanical cutting, grinding and chemical etching using a Tenupol-3 from Struers. Most of the analytical TEM investigations were performed on formvar extraction replica. Detailed information about the two applied preparation techniques is given in [9]. Each precipitation type was characterised by electron diffraction to determine the crystallographic structure and by EDX measurements to determine the chemical composition. EDX was done on approximately 80% of all particles visible in the TEM micrographs. The electron diffraction experiments were performed on selected particles using either a parallel beam for selected area diffraction or by convergent beam electron diffraction (CBED). A detailed description of the applied methods can be found in [10].

Test material

For the microstructural investigations material in the initial state and creep-ruptured samples tested at 650 °C were used. The creep test of the TAF steel has been performed at 650 °C with a load of 100 MPa which lead to failure after 26 931 hours. The B0 material has been tested at 650 °C for 18 788 h with a load of 80 MPa, the FB8 steel has been tested at 650 °C for 19436 h with a load of 70 MPa. The chemical composition of the test melts, the heat treatment data and the 0.2 limit at RT after heat treatment of the samples TAF, B0 and FB8 are presented along with the creep data for these two alloys in Figure 2. The heat treatment of the TAF steel is typical for bars which are used for the manufacturing of blades and bolts. The heat treatment of the Steels B0 and FB8 represents the heat treatment procedure of large forgings.

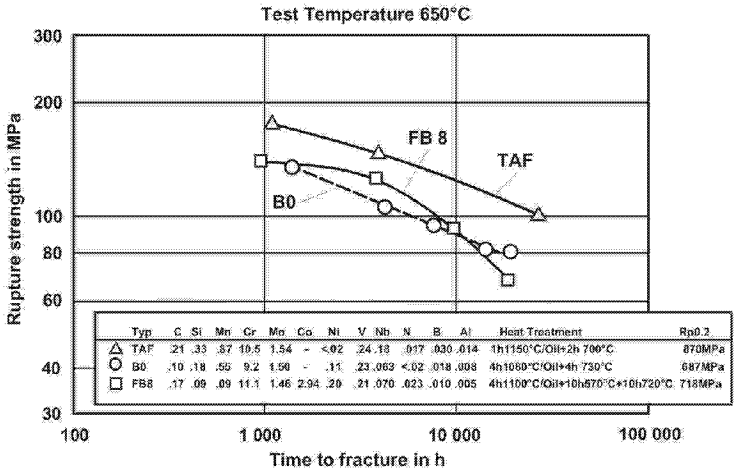

Figure 2: Creep resistance of the TAF, the B0 and the FB8 steels tested at 650 °C.

As no initial material was available for the microstructural characterization of the TAF specimen, the original heat treatment has been applied again to one specimen head of the sample. The hardness values obtained after heat treatment are in accordance with the tensile strength during the initial tests, which suggests that the initial state was successfully reproduced.

Results

Microstructure

The initial state of the TAF steel as observed by OM is shown along with the creep tested condition in Figure 3. This steel has a ferritic-martensitic microstructure. Prior austenite grain boundaries and martensite laths can be observed. For the creep tested specimen a small increase in grain size was observed along with several creep pores.

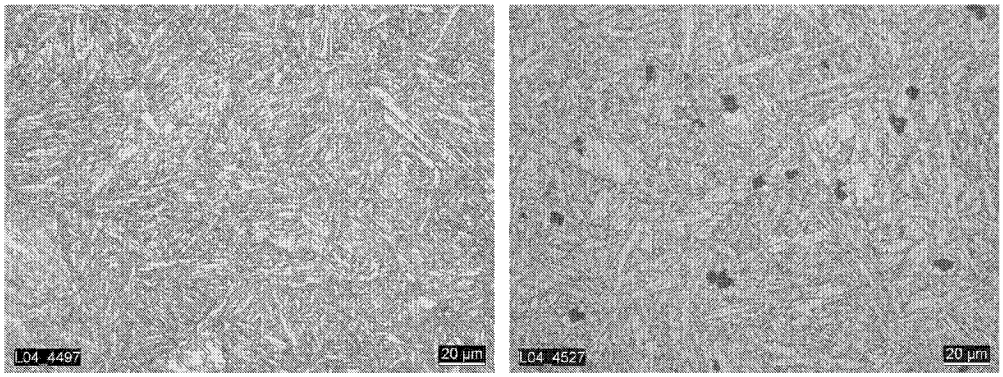

Figure 3: OM images of the TAF material in the initial state and after creep.

The former austenite boundaries and also to a lesser extent the subgrain boundaries are decorated with precipitates, which can be observed by SEM (Figure 4). The particles were analyzed by EDX in the SEM and most of them show Cr enrichment compared to the neighbouring matrix. Additionally, several primary niobium containing particles were observed. Large Laves phase particles containing mainly iron and molybdenum were found in the creep tested condition.

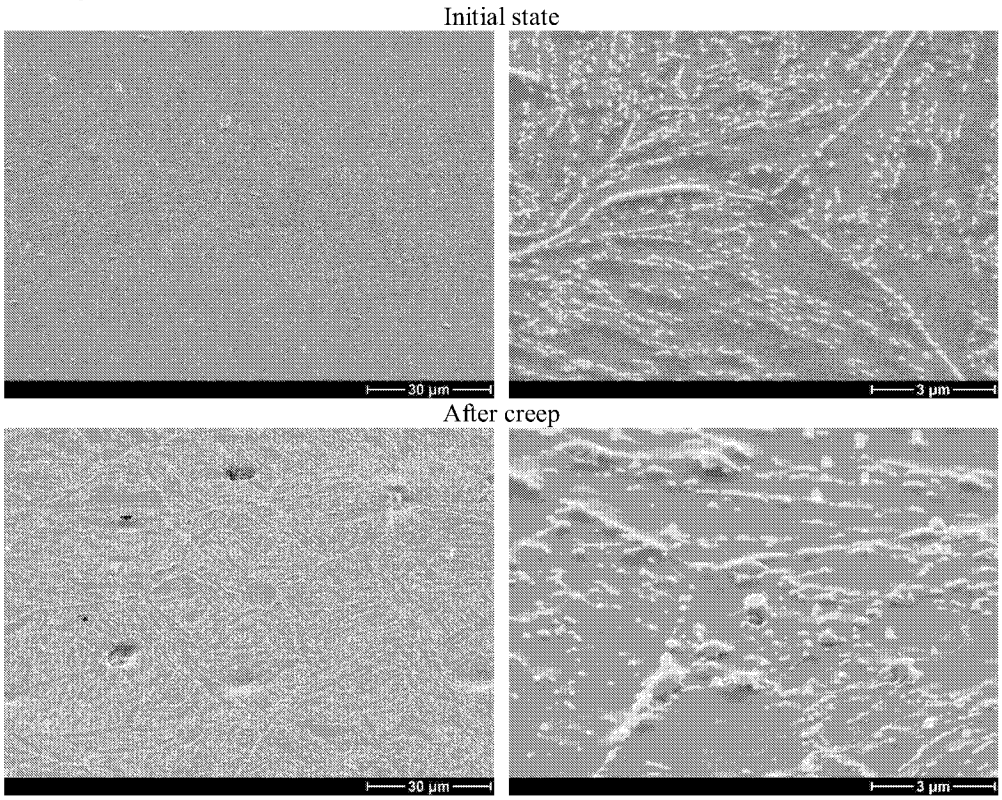

Figure 4: SEM images of the TAF material in the initial state and after creep.

Since it is not possible to study the chemical composition of particles with sizes of 1 µm and less by EDX in the SEM due to the large interaction volume in which X-rays are generated, the quantitative study of these particles was carried out in the TEM. Figure 5 shows a montage of four low magnification TEM micrographs of an extraction replica of the TAF material in the initial state.

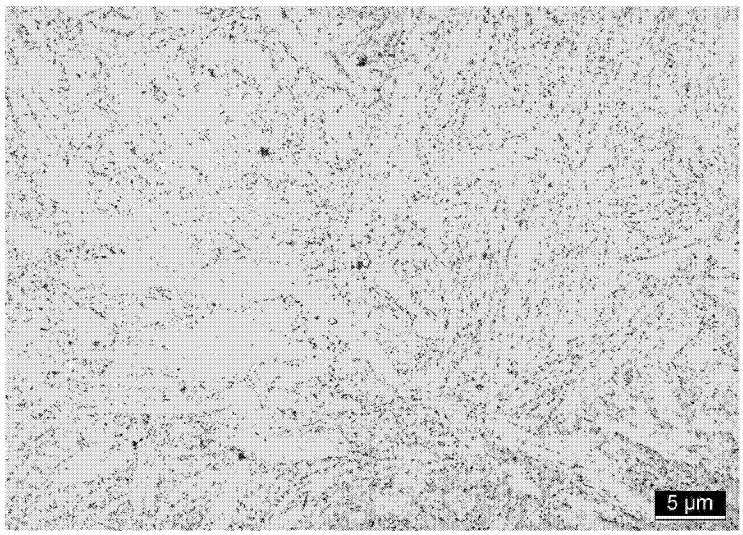

Figure 5: Montage of four TEM low magnification bright field images of an extraction replica produced from the TAF material in the initial state.

Precipitation analysis

The analysis of the particle sizes and size distributions has been carried out at extraction replica. In Figure 6 a TEM bright-field image and the corresponding elemental maps showing the chromium and the vanadium distribution of the particles are depicted. The Cr-rich particles have been identified by EDX and electron diffraction experiments as $M_{23}C_6$ phase and the V-rich particles as MX-phase. Some particles are not visible in the two elemental maps. These particles have all been analysed by EDX and can be attributed to either Nb(C, N), or to the Laves phase (particles containing mainly iron and molybdenum; present only after thermal exposure or creep testing). The particle sizes and their distributions have been analysed from 10 of these EFTEM images, corresponding to an analysed area of 40 µm², for each condition.

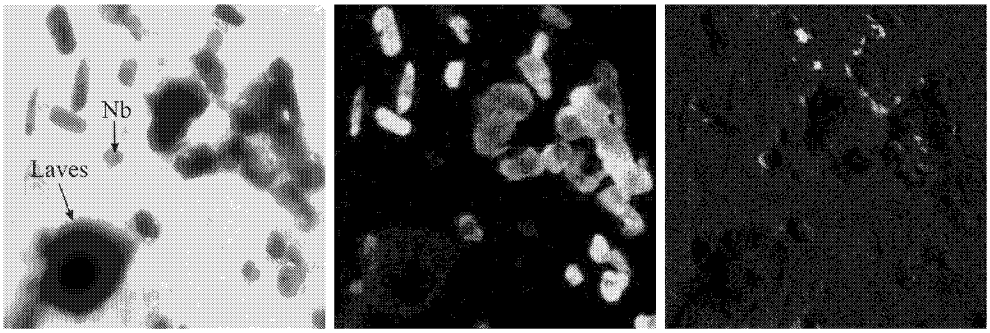

Figure 6: Bright field TEM, Cr and V EFTEM images of the TAF material after creep. The field of view of these images is 2 μm * 2 μm.

The results of the quantitative precipitation analysis of the three different steels are presented in Figure 7. The fraction of the different precipitate types observed are given in relation to the total precipitation number. In all samples, the most prominent precipitates are from the $M_{23}C_6$ type. Their fraction ranges from 62 % in case of the creep tested B0 steel to about 99 % for the initial state of the TAF material. Remarkable is the low initial size of these precipitates in the TAF steel of only about 75 nm. But of even greater importance for the creep stability of the TAF material is the slow coarsening rate of these particles, which reached of 138 nm after 26 931 hours. This slow growth prevents the creep properties from degrading. A further positive effect on the creep strength is the dynamic precipitation of the fine VN particles during creep. The B0 steel exhibited a very comparable precipitation behaviour in relation to the TAF steel, but to a lesser extent. The $M_{23}C_6$ particles in the B0 steel also had a low initial diameter of about 80 nm. The growth rate was significantly higher and resulted in a particle diameter of 143 nm after 18 788 hours, more than 9 000 hours less than in the case of the TAF steel. In accordance with the results of the TAF steel, the B0 steel exhibits also a dynamic precipitation of VN particles, but as it was the case with the $M_{23}C_6$ precipitations, the growth rate was significantly higher. The analysis of the FB8 steel yielded different results. The initial size of the $M_{23}C_6$ was relatively high with 98 nm, and they coarsened quickly. But of greater importance is the existence of the Z-phase in this steel. This relatively large phase consumed all fine MX particles during creep, which is very detrimental for the creep stability. In all steels, Laves-phase has been found after creep.

Figure 8 gives an overview of the growth rate of $M_{23}C_6$ at 650 °C in different steels developed within the COST projects along with data for the P92 steel [12]. This graph demonstrates that both, the absolute size and the growth rate, are quite low for the B0 steel, but even lower for the TAF test materials. This is usually attributed to the relatively high boron content of this material. The boron is built-in in the $M_{23}C_6$ particles and reduces their rate of Oswald ripening (e.g. [2, 13]).

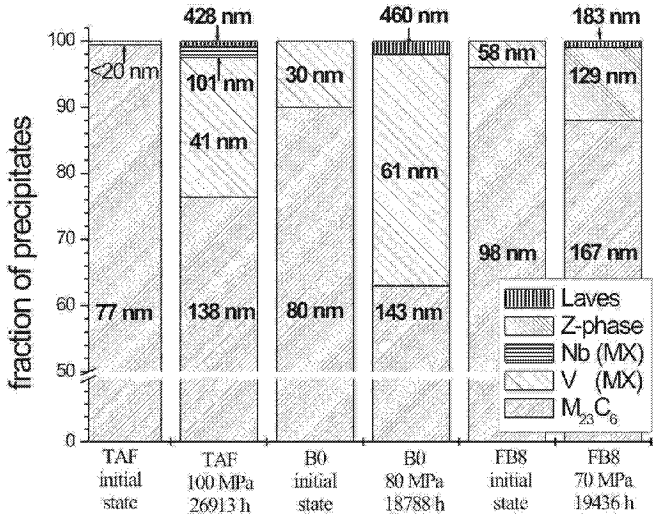

Figure 7: Precipitations smaller than 1 µm present in the investigated steels.

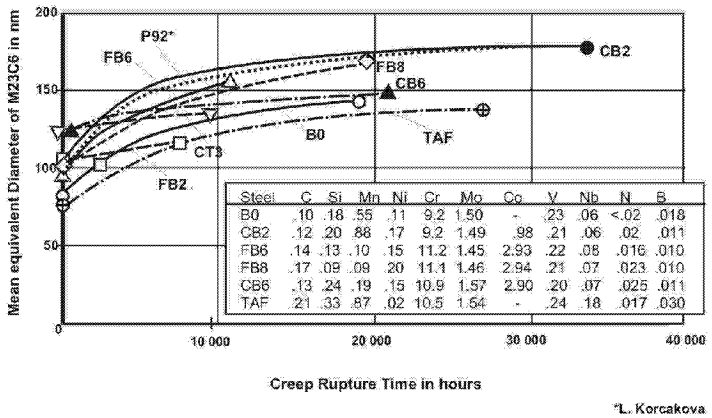

Steel	C	Si	Mn	Ni	Cr	Mo	Co	V	Nb	N	B
B0	.10	.18	.55	.11	9.2	1.50	-	.23	.06	<.02	.018
CB2	.12	.20	.88	.17	9.2	1.49	.98	.21	.06	.02	.011
FB6	.14	.13	.10	.15	11.2	1.45	2.93	.22	.08	.016	.010
FB8	.17	.09	.09	.20	11.1	1.46	2.94	.21	.07	.023	.010
CB6	.13	.24	.19	.15	10.9	1.57	2.90	.20	.07	.025	.011
TAF	.21	.33	.87	.02	10.5	1.54	-	.24	.18	.017	.030

Figure 8: Coarsening of $M_{23}C_6$ precipitates in 9-12 % Cr steels at 650 °C.

Additionally to the slowly coarsening $M_{23}C_6$ precipitates, MX-type vanadium nitrides precipitate during the heat treatment and even more during creep of the TAF steels. The initial size and the growth of these particles is summarized in Figure 9 for the three test steels and other COST steels. The MX particles in the TAF steel exhibit the smallest initial size of less then 20 nm in the initial state and still only 41 nm after creep testing. Additionally, the amount of MX precipitates increased significantly during exposure and even more during the creep testing of the TAF material. These fine MX-type particles increase further the creep resistance of the material. The present niobium carbonitrides have no significant role in the strengthening of the material. The effect of the precipitation of the Laves phase on the creep properties is probably small due the low number and relatively large size of the precipitates in

comparison to the $M_{23}C_6$ and VN precipitates. The same effects found for the TAF steel are also true for the B0 steel, but to a lesser extent. The main reason may be the lower boron content of this steel, which leads to a lower creep strength, but it also enhances the hot workability of the steel. The decrease of the mean diameter in the cases of FB8 and FB6 is due to the nucleation of the Z-phase in these steels. This Z-phase coarsens quickly and consumes the fine MX particles in this process. In the case of the CB6 steel, the slight decrease in MX size can also be attributed to the beginning nucleation of the Z-phase (fraction 2 %).

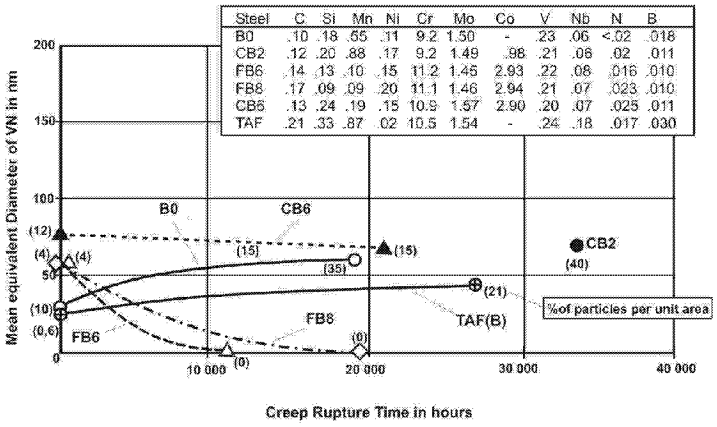

Figure 9: Coarsening of MX precipitates in 9-12 % Cr steels at 650 °C.

Conclusions

The investigated specimens of the TAF steel exhibit the precipitates which generate the high creep strength of this steel. It is on one side the small initial size and slow coarsening of the $M_{23}C_6$ precipitates and on the other side the dynamic precipitation of small VN particles which strengthen the material during deformation. The origin of the slow coarsening of the $M_{23}C_6$ precipitates can be mainly attributed to the high boron content of this material. The embedding of Boron in $M_{23}C_6$ particles reduces the growth rate. The reason for the dynamic precipitation of the VN particles could be the relatively short tempering time of 2 hours at 700 °C and the high austenitizing temperature of the TAF material (1150 °C) which promote probably the dynamic precipitation during the creep process.

The B0 steel exhibits a comparable evolution of the microstructure, but always with slightly worse properties than the TAF material with regard to creep resistance. Higher initial precipitation diameters and a faster growth rate (although both at very good values) lead to a lower creep strength as evidenced by Figure 2.

The 11.1 wt.% Cr FB8 steel, alloyed in addition with 2.94 % Co, reveals more coarsening of the $M_{23}C_6$ precipitates and forms Z-phase during the creep process in expense of the beneficial fine MX particles. Both effects are responsible for the low long time creep strength.

Acknowledgement
The authors wish to thank their partners of the COST projects for the creep test specimens and Dr. Wang from the University of Darmstadt for the additional heat treatment for reproducing the initial state of the TAF material. Thanks are also extended to the German COST partners and to the German Government for the financial support of the investigations.

Literature

[1] T.-U. Kern, K.H. Mayer, C. Berger, G. Zies, M. Schwienheer: „Stand der Entwicklungsarbeiten in COST 522 für Hochtemperatur-Dampfturbinen," 27. Vortragsveranstaltung FVHT, VDEH, 26. 11.2004, Düsseldorf.

[2] F. Abe: „Alloy Design of Creep and Oxidation Resistant 9Cr Steels for Thick Section Boiler Components Operating at 650°C", 4th EPRI International Conference on Advanced in Materials Technology for Fossil Power Plants", Hilton Oceanfront Resort, Hilton Head Island, SC, USA, October 25-28, 2004, 273-283

[3] K. Sakuraya, H. Okada, F. Abe: „Coarse Size BN Type Inclusions formed in Boron Bearing High Cr Ferritic Heat Resistant Steels", 4th EPRI International International Conference on Advanced in Materials Technology for Fossil Power Plants", Hilton Oceanfront Resort, Hilton Head Island, SC, USA, October 25-28, 2004, 1325-1338

[4] T. Fujita, N. Takahashi: The Effect of Boron on the Long Period Creep Rupture Strength of the modified 12%Cr heat-resisting Steel", Transaction of ISIJ 18, 1978, 702-711

[5] T. Fujita: „Twenty–first Century Electricity Generation Plants and Materials", International Workshop of Advanced Heat-resisting Steels, Yokohama, Japan, 8. November 1999

[6] I-M. Park, T. Fujita: „Long Term Creep Rupture Properties and Microstructure of 12% Cr Heat resisting Steels", Transaction of ISIJ 22, 1982, 830-837

[7] F. Hofer, P. Warbichler, W. Grogger: „Imaging of nanometer-sized precipitates in solids by electron spectroscopic imaging," Ultramicroscopy 59, 1995, 15-31

[8] F. Hofer, W. Grogger, G. Kothleitner, P. Warbichler: „Quantitative analysis of EFTEM elemental distribution images," Ultramicroscopy 67 (1997) 83-103

[9] J.S. Brammer, M.A.P. Dewey: „Specimen Preparation for Electron Metallography," Blackwell Scientific Publications, Oxford, 1966

[10] C. Scheu, F. Kauffmann, G. Zies, K. Maile, S. Straub, K.H. Mayer: „Requirements for microstructural investigations of steels used in modern power plants," Metallkunde 06, 2005, 653-659

[11] G. Zies, K. Maile, A. Klenk, S. Straub and K.H. Mayer: "Determination of Microstructural Parameters Influencing Creep Behaviour of 9-12%Cr Steels", 27. MPA-Seminar, Stuttgart, 4. and 5. October 2001

[12] K.H. Mayer: „Vergleichende Bewertung des Einflusses der Mikrostruktur auf die Kriechfestigkeit der borlegierten COST-Stähle mit erhöhtem Cr- und Co-Gehalt," Interner COST 536-Bericht, 14. 9. 2004

[13] L. Lundin: „High Resolution Microanalysis of Creep Resistant 9-12%Cr Steels," Doctoral Thesis for the Degree of Doctor of Philosophy, Department of Physics, Chalmers University of Technology and Gothenbourg University, Sweden, 1995

QUANTITATIVE MICROSTRUCTURAL ANALYSIS ON THE STABILITY OF MX AND M_2X IN 9-12% Cr STEELS BY AFM, SEM AND TEM

T. Seibert*, K. Durst, H. Chilukuru, M. Göken

* Framatome ANP GmbH, Freyeslebenstr. 1, 91058 Erlangen, Germany
University Erlangen-Nürnberg, General Material Properties, Martensstr. 5, 91058 Erlangen, Germany
durst@ww.uni-erlangen.de

Abstract

The evaluation of mean diameter and volume fraction of individual phases with the analysis of carbon extraction replica has been studied on 9-12% Cr steels. Moreover, the thermal stability of MX and M2X phase to coarsening has been studied in annealing experiments. Extraction replicas were analyzed by SEM and TEM. In order to compare information obtained from different high resolution microscopic techniques, atomic force microscopy (AFM), scanning electron microcopy (SEM) and transmission electron microscopy (TEM) were used to analyze the same area on a TEM thin foil, as prepared by jet polishing. It turned out that the particle size distribution from all techniques is relatively similar. Furthermore it is found, that in an extraction replica, the information depth is approximately given by the mean diameter of the individual phase. By considering the mean diameter of the individual phase, its volume fraction can thus be quantified within certain limits. In the annealing experiments at 700°C it is found, that M_2X is found at subgrain boundaries and coarsens quite rapidly. While Z-phase nucleation is detected it does not occur in expense of carbonitrides.

1 Introduction

9-12% Cr-steels play an important role in Gas and Steam Power Plants and have been focus of several research programs [3]. Two important aspects of the material behaviour are the high temperature stability and the resistance to creep deformation. The materials have a good creep resistance mainly due to the tempered martensite structure and precipitation hardening. As the creep and deformation behavior are directly correlated with the evolution of the microstructure the characterization of the precipitate and dislocation structure is of great importance for understanding and improving the creep resistance of these materials. The present paper focuses on the quantification of the particle size distribution of individual phases and their long term stability. Within the frame of a research program both ageing experiments and microstructural analyses were performed on the model alloys 1A and 5E. The microstructure was analyzed with Transmission Electron Microscopy (TEM) using extraction replica and thin foil as well as Atomic Force Microscopy (AFM) and Scanning Electron Microscopy (SEM). Aim of these investigations was to gain more information about the extraction replica process and the determination of the volume fraction of precipitates from replicas. The nucleation of Z-phase and the subsequent loss in precipitation hardening in grain interior is considered to be one of the main reasons for the degradation in creep resistance in 9-12% Cr steels [2,6,7]. Therefore, the stability of alloys containing MX and M_2X phase was studied in an annealing experiment at 700°C.

2 Characterization of the microstructure

The investigations were performed on the experimental model alloy 1A, 5E having the compositions given in Table 1. Due to the chemical composition and the performed heat treatment precipitates like $M_{23}C_6$ ($Mn_{23}C_6$, $Cr_{23}C_6$), Laves-Phase (Fe_2W, Fe_2Mo), M_2X ($Cr_2(CN)$), MX (VX, NbX) and Z phase (Cr(V,Nb)N) are found in these steels [1,2]. $M_{23}C_6$ and Laves phase are mostly found at grain and subgrain boundaries whereas small secondary M_2X and MX are found in the grain interior [5]. The phases have very different size distributions with mean diameters ranging from only a few nanometers up to nearly one micrometer.

Table 1: Chemical composition of the model alloy 1A, 5A

weight %	Fe	C	Si	Mn	Cr	Mo	W	V	Nb	N
1A	bal.	0.12	0.10	0.42	10.7	1.07	1.04	0.16	0.05	0.056
5E	bal.	0.12	0.33	0.04	11.6	0.2	2.00	0.21	0.06	0.034

The individual phases stabilize the grain and subgrain structure and act moreover as obstacles to dislocation motion. The coarsening kinetics during high temperature deformation of these steels is very different for the individual phases and its understanding is one key for determining the creep behaviour of these alloys. Therefore volume fraction and diameter of individual phases were characterized by analyzing carbon extraction replica in a TEM. Additionally, a TEM foil of the model alloy was prepared. This foil is investigated in TEM, SEM and AFM at the same location. By comparing these three methods and considering the results of the extraction replica a reliable determination of the volume fraction of the different phases should be possible.

2.1 Carbon extraction replica

For the extraction replica, the surface of the material is first ground and polished to 1 µm. Etching of the surface is done with picric acid, which only attacks the Fe-matrix and not the Carbon precipitates. After coating the surface with carbon the replica is stripped by using nitrohydrochloric acid. The replica is put on a copper grid and imaged in STEM mode in a TEM (Philips CM200), where each single particle is investigated by EDX-analyses (Figure 1). By the characteristic spectrum of the different phases the particles can be assigned to the different phases [8]. In Figure 1 lower picture the different phases are marked with different colors. The mismatch of some marked particles with the replica is due to the separation of the single precipitates. Shown is the microstructure of material 5E after heat treatment (see chap. 3), where a high volume fraction of large M_2X particles is found at the subgrain.

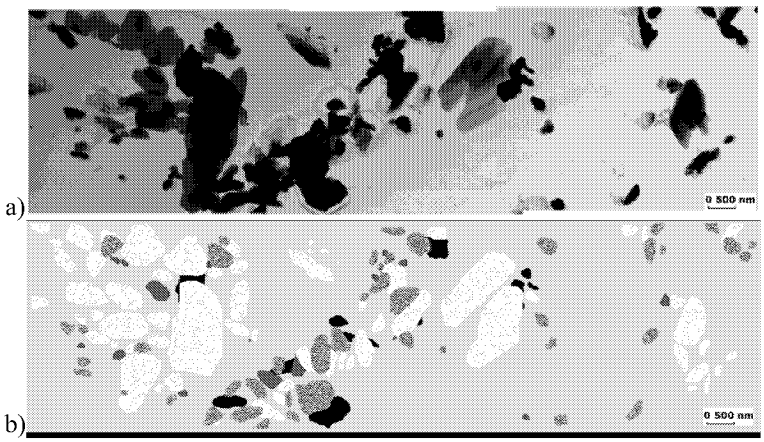

Figure 1: Extraction replica in TEM, STEM mode (a); marking of the different phases (b). White: M_2X, Pepper: $M_{23}C_6$, Black: Laves phase, Dark grey: Z phase.

The shape of the different phases is marked with image processing software and an equivalent circle diameter *d* is calculated from the projected area of the precipitate using Image C. The individual phases are then characterized by their particle size distribution and mean diameter. To determine the volume fraction from these data and accordingly the coarsening kinetics of the individual phases, the etching depth for the particles needs to be analyzed (Figure 2).

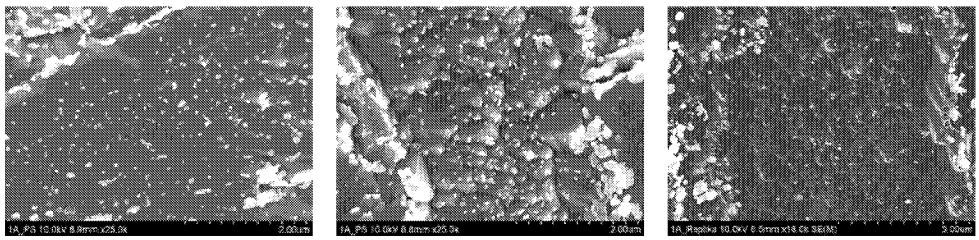

Figure 2: Microstructure of the specimen surface after etching with picric acid (a, b) and of the corresponding replica (c). Pictures taken with SEM (measure a, b: 2000 nm, c: 500 nm).

The left and middle picture shows the microstructure of the steel material after picric acid etching. In both pictures a grain including its grain boundary is visible. It is striking that both grains show a completely different etching behavior resulting from the different grain orientations. The SEM image of the corresponding replica is shown in the right picture. From these images it becomes quite clear, that the microstructure of the etched surface is transferred to the replica with nearly no loss. Due to the selective etching process, the matrix is removed, leaving the particles bared on the surface. After cleaning, most of the particles are removed and only particles which stick in the surface remain. This surface profile with the particles is then transferred to the replica. The carbonitrides are mainly found in the grain interior and

$M_{23}C_6$ and Laves Phase are mostly found at the subgrain boundaries. The mean diameter of the carbonitrides is moreover much smaller compared to the other phases. The information depth for an individual species of particles thus corresponds approximately to the mean particle diameter.

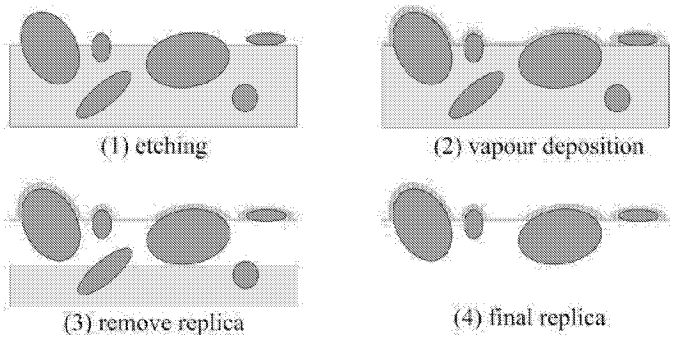

Figure 3: Schematics of the extraction replica process.

As can be seen from Figure 3, the replica process does not correspond to a simple section through the material. The particles are fully removed and in the TEM, the projection of the full particles is analyzed. The projected area is thus bigger compared to a simple section through the microstructure. Some experimental details are not fully considered in this simple model. It is found that particles can stick to each other, specifically big particles at grain boundaries. The information depth there is thus bigger compared to the mean particle diameter. The etching process within the grain is moreover inhomogenous, leading to a rough surface and the number density of particles is larger, compared to a flat surface.

2.2 Determination of the volume and area fraction

For comparing the results of different method for calculating the volume fraction of the individual phases, the mean area fraction and mean volume fraction is determined. The area fraction of a phase k is simply the summation of all particle areas, calculated from the individual particle diameter $d_{k,j}$, divided by the observed area A. The volume fraction of the individual phases f_p is calculated similar to volume calculations for TEM thin foils:

$$f_p = \frac{\sum_j V_{p,j}}{A \cdot (h_{foil} + d_p)}, \qquad \text{Eq. 1}$$

where $V_{p,j}$ are the volumes of individual precipitates j =1, 2, ... and the denominator is the sampling volume given by the product of the investigated area A and the mean precipitate size d_p plus the foil thickness h_{foil}. To determine the volume fraction the thickness of the foil h_{foil} of about 100 nm has to be considered for TEM thin foils. This value seems to be a good estimate to determine the volume fraction in TEM-foils. In a previous work, this value has also been used for calculating the volume fraction from carbon extraction replica [7]. It is proposed here, that a foil thickness = 0 nm is more appropriate for describing the extraction replica process and calculating the volume fraction (Figure 7).

2.3 Investigation of a TEM foil in TEM, SEM and AFM

In Figure 4, a characteristic grain boundary in a thin TEM steel foil is imaged with the SEM (left), the AFM (middle) and the TEM (right).

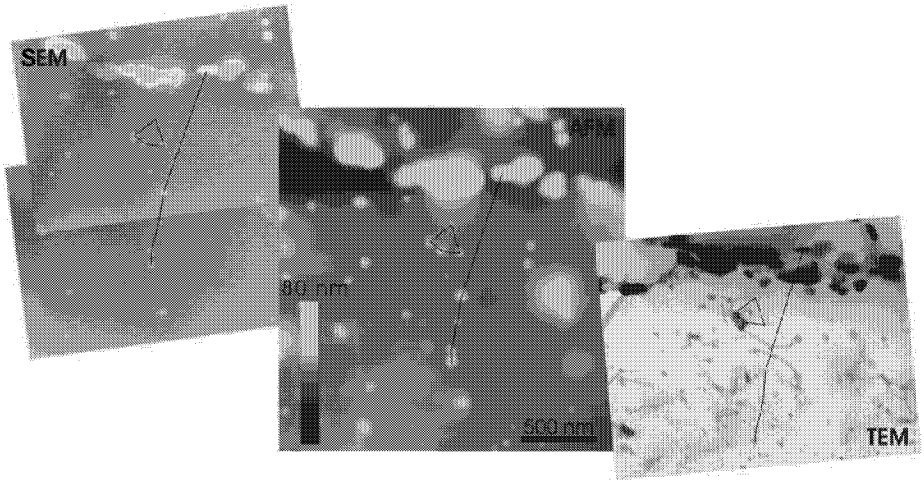

Figure 4: Investigation of a TEM-foil in TEM (STEM mode), SEM (FEG-SEM) and AFM (tapping mode).

The direct comparison of the same area in microscopes that represent only the surface of the specimens like AFM and SEM and microscopes that represent a volume like TEM makes clear that some precipitates are only visible in TEM.

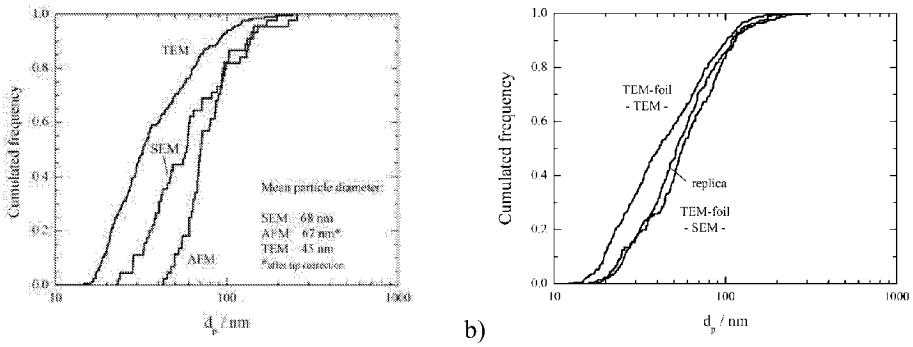

a) b)

Figure 5: Particle size distribution of the pictures of Figure 4 (a). Particle size distribution of the montages of Figure 6 (b).

Especially in the grain interior (lower part of the pictures) the density of precipitates in TEM is significantly higher than in SEM and AFM due to the investigation of a volume and not only a plane. The particles shown in the AFM and SEM picture are identical. Because of the

convolution of the AFM tip with the sample surface, particles in AFM are imaged larger than in SEM. By considering the tip geometry with a tip radius of about 10 nm [6] this effect can be corrected. The discrepancy of the particle size distribution between the pictures taken in TEM, SEM and AFM is relatively high for particles smaller than 100 nm. For larger particles the agreement is good (Figure 5). This is mostly due to the fact, that in TEM a volume is imaged and the two other techniques mainly image the surface. Particles which are within the foil or on the other side of the thin foil can only be imaged in transmission.
The AFM picture shows that it is necessary to distinguish between particles in grains and at the grain boundary. The surface topography shows that particles at a grain boundary (upper area of the picture) stick out further of the surface (~50 nm) than small particles in the grain interior (~10 nm). It is therefore proposed, that for the TEM foil, the particle etching depth needs also to be considered. As the investigated area for this analyzes was relatively small the statistic is not very good. Therefore, montages of the pictures taken in TEM and SEM are analyzed and a corresponding replica was included in this comparison. The focus in this comparison is put on the volume and area fraction.

2.4 Comparison of volume and area fraction of TEM, SEM and replica montages

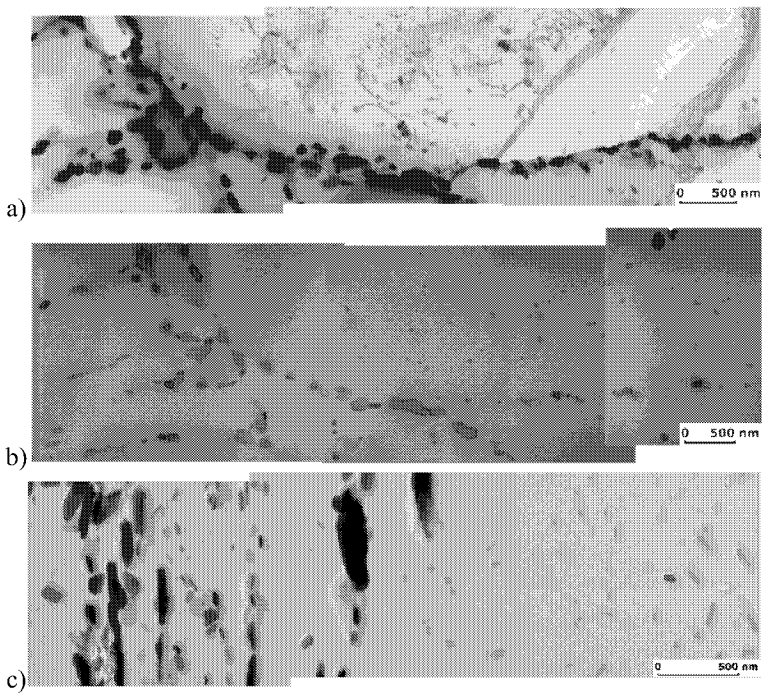

Figure 6: Montages of the investigation of the TEM-foil in (a) TEM and (b) SEM and (c) the corresponding replica.

The volume fraction both in replica and TEM foil of particles larger than 70 nm is higher than for the small particles in grain interior. Nevertheless, the volume fraction of the replica is

twice as high as the volume fraction of the foil but much better than the first calculation (Table 2).

Table 2: Volume and area fraction of the montages of Figure 6.

		Replica	TEM	SEM
V_V / %		16.9	4.54	/
A_A / %		12.7	/	4.4
V_V / %	$d_p > 70$ nm	7.5	4	
	$d_p <$ 70 nm	2.8	1.1	

3. Annealing experiments

For studying the thermal stability of M_2X and MX phase annealing experiments were performed on material 5E (Table 3). Small samples of the material were heat treated for obtaining a microstructure with M_2X and MX phase in the material. Although the different heat treatments (WB1, WB2) should lead only to one type of precipitates, a certain number of the other phase was found. Therefore, the ratio of particles after heat treatment MX/M2X is included. After heat treatment, the materials were annealed at 700°C for ~2000 h. The evolution of microstructure was investigated by carbon extraction replica in TEM.

Table 3: Heat treatment and fraction of MX/M2X particles.

	Austenitization			MX/M_2X
WB1	1000°C@0.5h	570°C@10h	690°C@10h	1:200
WB2	1000°C@0.5h	760°C@6h	Oven cooling	1:17

The volume fraction was determined for each phase by Eq. 1. Figure 7 shows the volume fraction for the M_2X phase as calculated by the new formula (h=0nm) and the old formula (h=100nm). It is expected, that after conventional heat treatment of these alloys, the carbides are nucleated and no or only a small change in volume fraction occurs in subsequent thermal annealing. With the old formulae, an increase in the volume fraction of M_2X is found with tempering, while after applying the modified volume calculation, a nearly constant volume fraction is obtained. The volume fraction for M_2X and $M_{23}C_6$ as determined here is too high compared to thermodynamic calculations (Figure 8). For MX a reasonable volume fraction of ~ 0.001 is found. This discrepancy in quantification of volume fraction is due to the location of the phases at subgrain boundaries. Particles located at subgrain boundaries might stick to each other and the overall information depth might be bigger than the diameter of the individual phase. Moreover, the analysis was mainly focused on subgrain boundaries and the neighboring grain interior. The overall statistic, even so two montages as presented in figure 1 were analyzed, is limited.

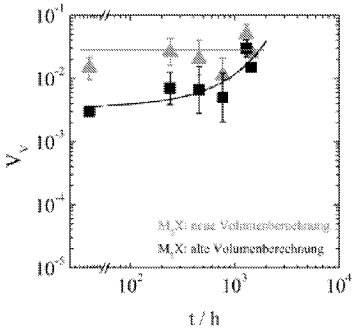

Figure 7: Volume fraction of M_2X particles after thermal annealing as determined by new and old formula.

The new formula is thus used to study the evolution of the different phases during annealing treatment (Figure 8). For WB2 heat treatment only MX particles are expected and vice verca for WB2 heat treatment. Nevertheless some M_2X (MX) particles are found, having a relatively small volume fraction. The corresponding data points are therefore doted in Figure 8. It is found, that the volume fraction of M_2X and MX is approximately constant throughout the annealing experiments, while Z-phase precipitates during the treatment. It should be noted that due to the small volume fraction of Z-phase, initially only a small number of particles is found. This leads to a high standard deviation in volume fraction. M_2X coarsens strongly and MX remains quite stable. While M_2X is found mostly at subgrain boundaries, MX is found mostly in the grain interior. Z-phase grows rapidly, but not on the expense of M_2X or MX particles. A similar coarsening of M_2X-phase has been observed during creep deformation at 600°C for 20 kh [9]. It is there concluded, that the coarsening of M_2X at subgrain boundaries is one important factor for the degradation of creep strength in 9-12% Cr steels. $M_{23}C_6$ is observed on the subgrain boundaries and precipitation of Laves phase occurs during annealing treatment. Due to the lack of space, this data is not shown here.

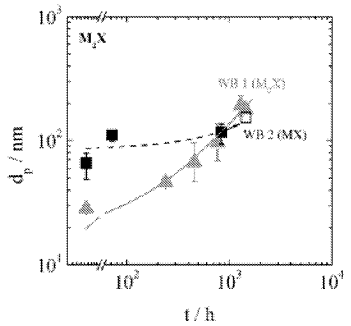

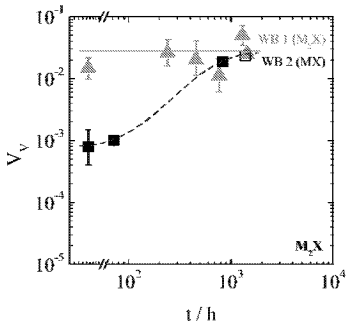

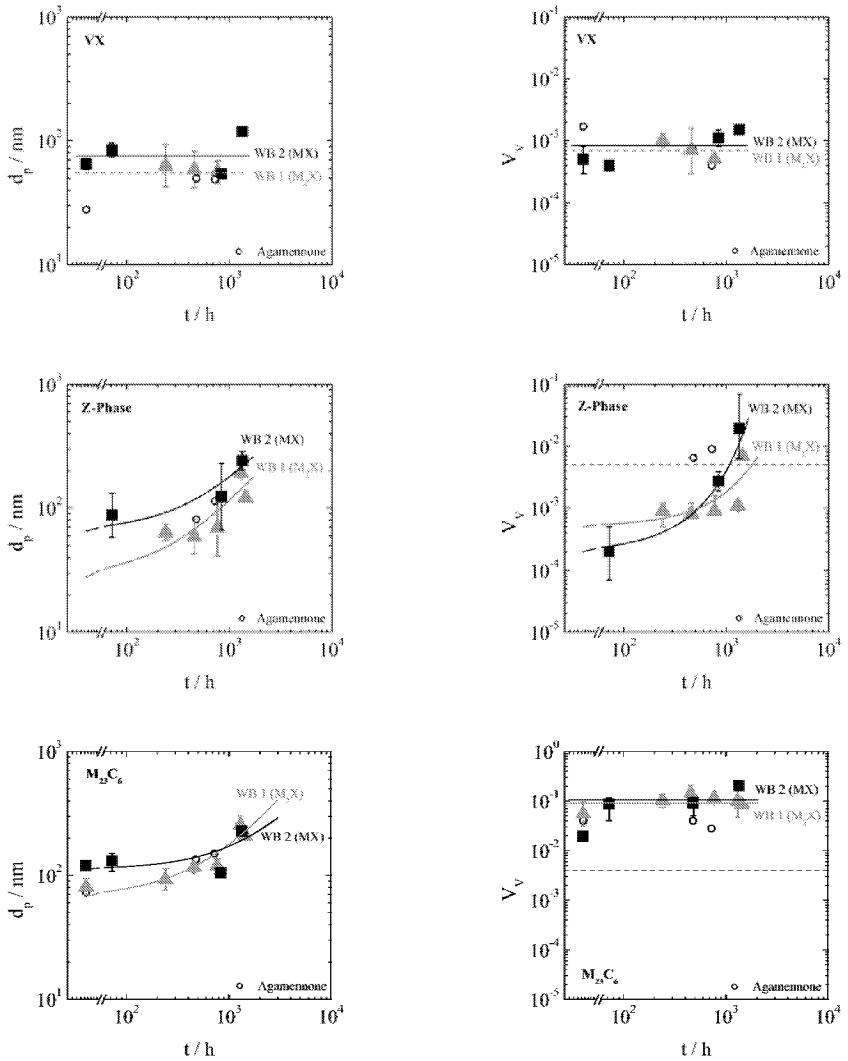

Figure 8: Mean particle diameter and volume fraction of M2X, MX, Z-phase and $M_{23}C_6$ for the different heat treatments WB1 and WB2.

4 Conlusions

The analysis of carbon extraction replica allows a quantification of microstructure using EDX analysis in a TEM. It is found, that by considering the mean diameter of the particles, the volume fraction can be determined within reasonable limits. During thermal annealing treatment at 700°C MX remains the most stable phase. While Z-phase precipitates, no change in volume fraction of M_2X or MX is found, whereas M_2X phase is coarsening strongly on subgrain boundaries.

5 Literature

[1] J.D. Robson, H.K.D.H. Bhadeshia: Modelling precipitation sequences in power plant steels Part 2 - Application of kinetic theory, Mater. Sci. Technol. 13 (1997) 640.

[2] A. Strang, V. Vodarek: Z phase formation in martensitic 12CrMoVNb steel, Mater. Sci. Technol. 12 (1996) 552.

[3] V. Knezevic, G. Sauthoff, J. Vilk, G. Inden, A. Schneider, R. Agamennone, W. Blum, Y. Wang, A. Scholz, C. Berger, J. Ehlers, L. Singheiser, Martensitic/ferritic super heat restistant 650°C steels – Design and testing of model alloys, ISIJ International 42, 2002, pp. 1505-1514.

[4] P. Polcik, S. Straub, W. Blum, in: The 4th European Conference on Advanced Materials and Processes, Associatione Italiana di Metallurgia, Mailand, 1995, pp. 313–318.

[5] D. Henes, H. Möhlig, S. Straub, J. Granacher, W. Blum, C. Berger, in: H. Mughrabi, G. Gottstein, H. Mecking, H. Riedel, J. Tobolski (Eds.), Microstructure and Mechanical Properties of Metallic High-Temperature Materials, Wiley-VCH, Weinheim, 1999, pp. 179–191.

[6] H. Danielsen and J. Hald. Z-Phase in 9-12%Cr Steels. Technical Report M4313, Värmeforsk Service AB, 10153 Stockholm, February 2004.

[7] R. Agamennonel, W. Blum, C. Gupta, J. K. Chakravartty: Evolution of microstructure and deformation resistance in creep of tempered martensitic 9–12%Cr-2%W-5%Co steels, submitted to Acta. Mat., 2006

[8] K. Durst , M. Göken: Quantitative Microstructural Characterisation by Atomic Force Microscopy and Electron Microscopy - A Comparative Study on the Superalloy Waspaloy, Prakt. Metallogr., 38 (2001), 197-215

[9] G. Götz, W. Blum, Influence of thermal history on precipitation of hardening phases in tempered martensite steel of type X12CrMoWVNbN10-1-1, Mater. Sci. Eng. A 348/1-2, pp. 201-207, 2003.

[10] K. Sawada, H. Kushima, and K. Kimura. Precipitation behavior of Z phase during aging and creep in 9-12 %Cr ferritic heat resistant steels. In International workshop on performance and requirements of structural materials for modern high efficient power plants, pages 96–104, Darmstadt, September 6-9 2005.

[11] H. Chilukuru, K. Durst, M. Göken, W. Blum: On the Roles of M_2X and Z-Phase in Tempered Martensitic 9-12% Cr-Steels, Liege conference 2006.

SIMULATION OF THE PRECIPITATION KINETICS DURING HEAT TREATMENT AND SERVICE OF CREEP RESISTANT MARTENSITIC 9-12% CR STEEL

I. Holzer[1], J. Rajek[1], E. Kozeschnik[1,2], H. Cerjak[1]

[1] Institute for Materials Science, Welding and Forming, Graz University of Technology, Kopernikusgasse 24, A-8010 Graz, Austria.
Ph. 43-316-873-7181 Fax 43-316-873-7187
[2] Materials Center Leoben Forschungsgesellschaft mbH, Franz-Josef Straße 13, A-8700 Leoben, Austria. Ph. 43-3842-459221 Fax 43-3842-459225

Abstract

Based on the software package MatCalc, the evolution of precipitates during the complete thermal history of the COST 522 steel CB8 is simulated, including cooling after cast solidification, heat treatment and service. At definite points, the results of the calculation are compared with experimental results. The comparison shows good agreement. Thus, these results illustrate the potential of implementing advanced simulation techniques into the process of alloy development and prediction of the service behaviour of this type of steels.

Keywords: Microstructure evolution, heat treatment, precipitation kinetics, simulation.

Introduction

In the past years, a lot of effort was made to enhance the efficiency of fossil fired power plants with the goal of decreasing the CO_2 exhaust due to environmental protection. One of the most promising ways to reach this goal is to further improve the material properties of the newly developed 9-12%Cr steels. Thus, the steam parameters, namely pressure und temperature, can be increased. However, long-term application of these materials at higher temperature and pressure is extremely challenging in terms of the stability of the highly optimized microstructure, which provides the superior creep resistance of these materials.

A major ingredient for a stable tempered martensite microstructure is strengthening with a high number of finely dispersed precipitates. The physical mechanism behind this strategy is, that precipitates, which are located on the grain- and subgrain boundaries and dislocations, work as obstacles for the movement of boundaries and dislocations and, thus, effectively pin and stabilize the microstructure. In all the efforts to improve the properties of 9-12% Cr-steels, a stable microstructure with minimized precipitate coarsening, minimal grain and subgrain growth and dislocation recovery is aspired.

By application of numerical simulation software, it became possible to predict some aspects of the evolution of the microstructure on the researcher's desktop. This provides the possibility to study variations of the chemical composition and/or the heat treatment conditions on the computer and allows drawing conclusions on the changes in mechanical properties of the investigated material. Subsequently, the evolution of precipitates in a typical modern heat resistant complex 9-12% Cr steel is simulated through the entire heat treatment, starting from casting until the end of the design lifetime at more than 10^5h. To carry out the numerical simulations, the software MatCalc [1], which is developed at the Institute for

Materials Science, Welding and Forming (IWS) of the Graz University of Technology, is utilised. For details on the model and its implementation in the software, the reader is referred to refs. [2-4].

Numerical Simulation

Material

The steel CB8 is a test-melt designed during the COST 522 project on the development of 9-12% Cr steels for application in 650°C *USC* steam power plants. The chemical composition of CB8 steel is summarized in table 1.

Table 1: Composition of CB8 utilised in the kinetic simulations.

wt%	Al	C	Co	Cr	Mn	Mo	N	Nb	Ni	Si	V
CB8	0.028	0.17	2.92	10.72	0.20	1.40	0.0319	0.06	0.16	0.27	0.21

Simulation settings

For the following heat treatment simulation, the time temperature sequence has been designed to closely resemble the typical industrial heat treatment for this type of steel. The time temperature sequence including heat treatment and service at 650°C is shown in figure 1. It is important to emphasize that, in the course of the production process, the material undergoes several austenite/ferrite phase transformations. These are taken into account in the present simulation.

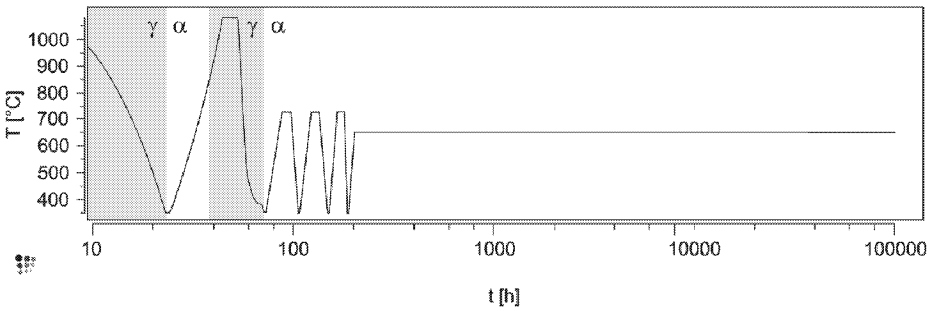

Figure 1: Time temperature sequence for the kinetic simulation

The numerical calculation starts closely below the solidus temperature of CB8 at 1400°C in an austenitic matrix. Then, the ingot cools down slowly to 350°C. At this temperature, the austenite matrix decomposes into martensite. It is assumed that no precipitation reactions occur below this temperature due to the sluggish diffusion. In the next simulation step, the temperature is increased again. The simulation is performed in a ferritic matrix up to the calculated A_1 temperature of this steel at 847°C. Then, the matrix is switched to austenite again and austenitisation takes place at 1080°C with subsequent cooling to 350°C. The three

quality heat treatment cycles take place again in a ferritic matrix and at temperatures of 730°C. Service is simulated for 100000 hours at 650°C.
In the present simulation, the precipitate phases $M_{23}C_6$, M_7C_3, MX, Laves and the so-called modified Z-phase [5] were considered in accordance with experimental findings. The experiments also showed that two types of MX precipitates are present in this steel, i.e. a vanadium and nitrogen-rich phase and a niobium and carbon-rich phase. Figure 2 presents the calculated phase fraction diagram with all precipitates except Z-phase. The separation of the complex (NbV)-carbonitride into VN and NbC is clearly observed.
In order to bring the simulation and experiment in accordance, a slight adjustment of the interfacial energy of the Laves phase and the modified Z-phase has been necessary. The calculated interfacial energy [6] of Laves phase was decreased by 25%, the interfacial energy of the Z-phase increased by 10%. We assume that these corrections had to be made due to some incomplete thermodynamic description of these phases.

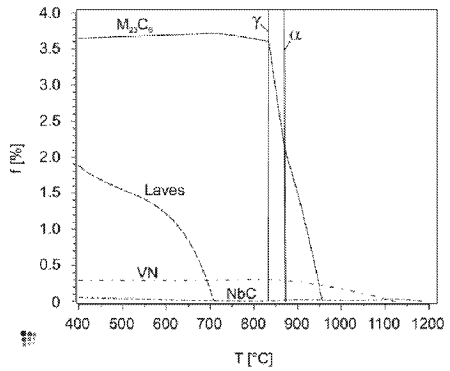

Figure 2: Phase fraction diagram of the simulated CB8 steel.

During the simulation, all precipitates interact with each other by exchanging atoms with the matrix phase. The kinetics of this process is controlled by the multi-component diffusivities of all elements, which are available through kinetic databases, such as the mobility database of the software package DICTRA [7]. The thermodynamic parameters for calculation of the chemical potentials are taken from the TCFE3 database [8] with some modifications specific to this type of steel [6].
Apart from accurate thermodynamic and kinetic data, a very important input parameter for the simulation is the type of heterogeneous nucleation site for each of the precipitate phases, such as grain boundaries, subgrain boundaries, dislocations, grain boundary edges and/or grain boundary corners. For the present simulation, the nucleation site for each precipitate was defined according to experimental observation. The number of nucleation sites, which are actually available at each instant of the simulation, is defined by the microstructural quantities grain size, subgrain size and dislocation density as well as the grain or subgrain elongation factor. The latter takes into account the geometrical elongation, for instance, of a martensite lath. All relevant parameters for the entire heat treatment simulation are shown in tables 2 and 3 and described in detail in ref. [6].

Table 2: Microstructural parameters of the matrix phase

	Austenite	Ferrite
Grain size [m]	$700 \cdot 10^{-6}$	$700 \cdot 10^{-6}$
Subgrain size [m]	-	$0{,}5 \cdot 10^{-6}$
Subgrain size elongation factor	1	1
Dislocation density [m^{-2}]	$1 \cdot 10^{11}$	$1 \cdot 10^{14}$

Table 3: Prescribed nucleation sites for the precipitate phases

	Matrix phases	Precipitate phases					
		$M_{23}C_6$	M_7C_3	NbC	VN	Laves phase	mod. Z-phase
Casting	Austenite	GB	GB	GB	GB	GB	GB
Austenitising (350°C-847°C)	Ferrite	GB, SGB	GB, SGB	GB, SGB, D	GB	GB, SGB	GB, SGB, D
Austenitising (847°C-1080°C-350°C)	Austenite	GB	GB	GB	GB	GB	GB
Heat treatment	Ferrite	GB, SGB	GB, SGB	GB, SGB, D	GB, SGB, D	GB, SGB	GB, SGB, D
Service	Ferrite	GB, SGB	GB, SGB	GB, SGB, D	GB, SGB, D	GB, SGB	GB, SGB, D

GB… Grain boundary, SGB… Subgrain boundary, D… Dislocations

In the simulations, it is assumed that the transformation from austenite to martensite and back occurs instantaneously and that the parent and product phase have the same chemical composition. The precipitate population does not change during this transformation. When the simulation starts at 1400°C, all elements are initially assumed to be in solid solution.

Results and Discussion

Simultaneously to the development of the heat treatment simulation model, the complex microstructure of the CB8 steel was characterized by a number of investigations at the IWS [9]. Special attention in this experimental program has been directed towards the microstructural evolution before long-term service at 650°C. The specimens were simulated in the furnaces of the IWS laboratory in accordance with the heat treatment described above. The microstructural analysis was accomplished using the EFTEM method. More detailed information is given in an accompanying paper [10]. The results of the heat treatment simulation are shown in figure 3. The phase fraction of the $M_{23}C_6$ and Laves Phase is divided by a factor of ten to get a more concise diagram.

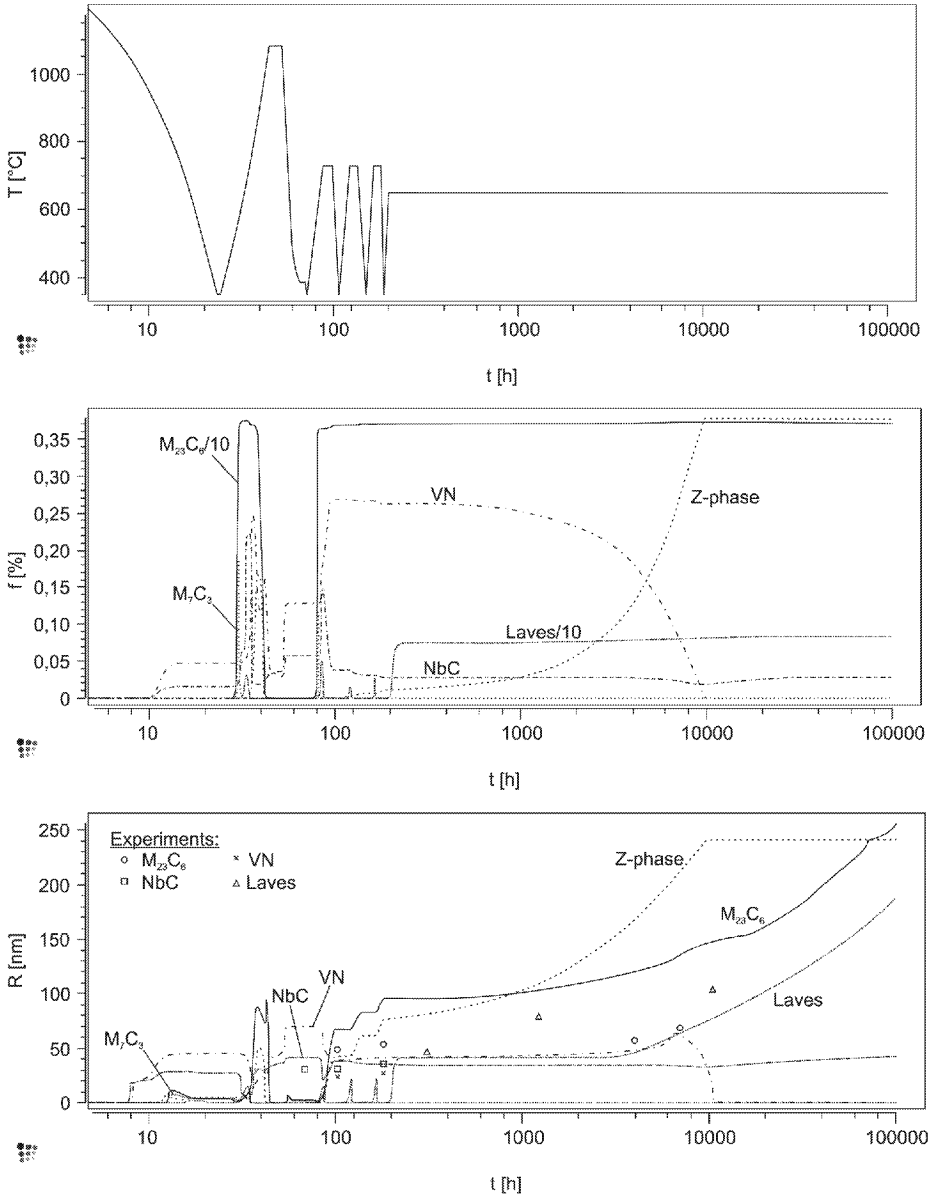

Figure 3: Results of the kinetic simulation of CB8.

Casting

During cooling from 1400°C, the first NbC and VN nucleate at approximately 1050°C. At around 830°C, $M_{23}C_6$ and M_7C_3 also nucleate as well as Laves phase at around 680°C. The casting simulation ends after 23,3h. At this point small amounts of NbC, VN, $M_{23}C_6$, M_7C_3 and Laves phase are present.

Austenitising

Before beginning the austenitising simulation, the matrix is switched from austenite to ferrite and kept unaltered during reheating from 350°C to the calculated A_1 temperature at 874°C. Up to about 500°C, diffusion processes are too slow to cause major changes in the precipitate microstructure. The phase fractions and radii of the present precipitate phases remain almost constant. Above this temperature, the amount of $M_{23}C_6$ and NbC as well as the amount of VN, M_7C_3 and Laves phase rise sharply. The latter precipitate phases dissolve again already at temperatures around 700°C. At 874°C, the matrix phase is switched back to austenite.
With increasing temperature the $M_{23}C_6$ start to grow until they dissolve again after exceeding their solubility temperature. After a short intermediate increase of the phase fractions of NbC and VN, the amount of these phases decreases until the equilibrium phase fraction at austenitising temperature is reached. During the subsequent cooling, additional VN nucleate as well as $M_{23}C_6$ and M_7C_3 carbides. After the austenitising process, a mean radius of NbC of 31.5 nm was measured. The simulation delivers a calculated radius of 41.9 nm. This accordance is considered as good. No experimental information on the other phases was available in this state.

Quality heat treatment

Similar to reheating during the austenitisation, the phase fractions of $M_{23}C_6$, M_7C_3, NbC, VN and Laves phase are increasing during heating to annealing temperature. Again, the latter are dissolving at temperatures around 700°C. Nucleation, growth and subsequent dissolution of Laves phase is observed in all three annealing cycles. The high number of newly precipitated VN causes a sharp increase of the VN phase fraction and a decrease of the mean radius. From this point on, the phase fractions of VN as well as the phase fractions of NbC and $M_{23}C_6$ remain close to their equilibrium value. The measured precipitate radius of NbC, VN, $M_{23}C_6$ and Laves-phase is indicated by open symbols in figure 3. The experimental data were taken from references [10] and [11]. In contrast to the good agreement of NbC, VN and Laves-phase, the mean radius of $M_{23}C_6$ shows some deviation. Nonetheless, agreement of simulation results and experimental data is considered as good, since only the interfacial energy of the Laves-phase and Z-phase have been modified.
During the three annealing cycles, coarsening of the $M_{23}C_6$ precipitates is observed. Interestingly, occurrence of the modified Z-phase is visible already during the first annealing cycle. However, the phase fraction and number density is very low (≈0.002%, $6{,}4 \cdot 10^{16} m^{-3}$) and the mean radius is still small (≈40nm). Experimental characterisation of precipitates in this stage is rather difficult, particularly because Z-phase and VN precipitates can hardly be distinguished by composition differences. Therefore, no experimental points for Z-phase are available for the heat treatment period.

Service

In addition to the previously discussed heat treatment, a service period at 650°C was carried out for 100.000h. Coarsening of all precipitate phases is clearly observed, with NbC and VN having significantly slower kinetics. The phase fraction of Z-phase is increasing constantly,

while, simultaneously, the VN phase dissolves. According to our simulations, at approximately 10500h, the VN have disappeared completely and the Z-phase has reached its maximum phase fraction. The same phenomenon has been observed experimentally in the investigated specimens, where, after 16000h, no more VN were observed. In the same specimen, modified Z-phase was detected [9].

Summary and Outlook

The possibility to simulate precipitation kinetics during the whole production and service of materials used in power plant applications is of particular importance, especially for the development of modern 9-12% Cr steels with advanced creep strength at enhanced service temperature and pressure. On basis of the newly developed multi-component multi-phase precipitation kinetics model, which is implemented into the software MatCalc, simulations are carried out for the COST steel CB8.
The results of the simulation show good agreement with new experimental data characterising the precipitate microstructure in the production stages, i.e. casting, austenitization and heat treatment.
Despite the complexity of the alloy composition and the time temperature-sequence which was simulated, only slight changes of some input quantities have been necessary to obtain reasonable agreement with experiments. It is hoped that improved thermodynamic databases for kinetic simulation make these adjustments unnecessary in the future.

Acknowledgement

This work was part of the Austrian research cooperation "ARGE ACCEPT – COST 536" and was supported by the Austrian Research Promotion Agency Ltd. (FFG) which is gratefully acknowledged. Financial support by the Austrian Kplus program within the strategic projects SP11 and SP16 of the Materials Center Leoben is gratefully acknowledged.

References

1 E. Kozeschnik and B. Buchmayr, Mathematical Modelling of Weld Phenomena 5 (London, Institute of Materials, Book, 734, 2001), 349-361.
2 J. Svoboda, F. D. Fischer, P. Fratzl, and E. Kozeschnik, Modelling of kinetics in multi-component multi-phase systems with spherical precipitates I. – Theory, *Mater. Sci. Eng. A*, Vol 385 (No. 1-2), 2004, p 166-174.
3 E. Kozeschnik, J. Svoboda, P. Fratzl, and F. D. Fischer, Modelling of kinetics in multi-component multi-phase systems with spherical precipitates II. – Numerical solution and application, *Mater. Sci. Eng. A*, Vol 385 (No. 1-2), 2004, p 157-165.
4 E. Kozeschnik, J. Svoboda, and F. D. Fischer, Modified evolution equations for the precipitation kinetics of complex phases in multi-component systems, *CALPHAD*, Vol 28 (No. 4), 2005, p 379-382.
5 V. Vodarek, A. Strang, "*Z Phase Characteristics in Martensitic 12CrMoVNb Steels*", Proc. Materials for advanced power engineering, Liege (2002), 1223-1231.
6 J. Rajek, PhD thesis, Computer simulation of precipitation kinetics in solid metals and application to the complex power plant steel CB8, Graz University of Technology, 2005.

7 J.O. Andersson, L. Höglund, B. Jönsson, and J. Ågren, Computer simulations of multicomponent diffusional transformations in steel, in: *Fundamentals and Applications of Ternary Diffusion*, G.R. Purdy (ed.), Pergamon Press, New York, NY, 1990, p 153-163.
8 TCFE3 thermodynamic database, Thermo-Calc Software AB, Stockholm, Sweden, 1992-2004.
9 B. Sonderegger, PhD thesis, Characterisation of the substructure of modern power plant materials using the EBSD method, Graz University of Technology, 2005 (in German).
10 B. Sonderegger, S. Mitsche, H. Cerjak, Microstructural analysis on a creep resistant martensitic 9-12% Cr steel using the EBSD method, at this conference.
11 G. Dimmler, PhD thesis, Quantification of creep resistance and creep fracture strength of 9-12%Cr steel on microstructural basis, Graz University of Technology, 2003 (in German).

MICROSTRUCTURAL ANALYSIS ON A CREEP RESISTANT MARTENSIC 9-12% CR STEEL USING THE EBSD METHOD

B. Sonderegger[1,2], S. Mitsche[3], H. Cerjak[1]

1: Institute for Materials Science, Welding and Forming, Graz University of Technology, Kopernikusgasse 24, 8010 Graz, Austria
2: Materials Center Leoben, Franz Josef Straße 13, 8700 Leoben, Austria
3: Research Institute for Electron Microscopy, Graz University of Technology, Steyrergasse 17, 8010 Graz, Austria

Abstract

9-12% chromium steels are well established materials for high temperature components in ultra efficient power plants. One important impact factor for the creep resistance are the parameters of martensite laths and subgrains, namely lath width, subgrain size, interfacial energies and the interfacial mobility. In this work, the morphology and crystallography of the martensitic creep resistant 9-12% Cr steel CB8 was examined by EBSD (Electron BackScatter Diffraction). This technique, applied for the first time for these types of steels, makes it possible to analyse the size of the microstructural elements, as well as the misorientations on internal interfaces as function of ageing and creep deformation. This information can then be further used for simulations of the microstructural evolution in the course of heat treatment, thermal ageing and creep loading.

Keywords: Martensite, EBSD, 9-12% Cr steel

Introduction

In high temperature components of caloric power plants, high creep resistance is indispensable for the application of the material. One of the main reasons for the creep process is the dislocation movement, which is most effectively depressed by precipitates and internal matrix interfaces. In order to keep the high creep resistance, it is of particular interest, how far these structures coarsen during tempering and creep loading.

Because of the low mobility of martensite lath boundaries (amongst other parameters), ferritic - martensitic steels are ideal for the application as creep resistant material. Also contributing to the hindering of dislocation movements are subgrain boundaries, which are low angle boundaries located in the martensite laths. These boundaries are expected to have a higher mobility, which is leading to a higher coarsening rate.

While the misorientation of martensite laths and the lath width have been examined by transmission electron microscopy [1, 2], EBSD is a rarely used method on this topic [3]. The reason is the lateral resolution of the technique (roughly 0,2 - 0,5µm) – many martensite laths are about the same size. As a consequence it is not sure if a sufficiently high number of laths can be resolved in order to detect coarsening effects.

In the following, misorientations of martensite laths are studied by using the EBSD method on the example of an advanced creep resistant 9-12% Cr steel. Not only the "as received" condition is considered, also several samples after tempering and creep loading were measured to examine the evolution of the boundary properties.

Experimental

Material

The investigated material is an advanced creep resistant martensitic 9-12% Cr cast steel, the chemical composition is given in Table 1.

Table 1: Chemical composition of the steel testmelt. Element concentrations are given in wt%

Fe	C	Cr	Mo	V	Nb	N	B	Co	Si
Bal	0.17	10.86	1.42	0.21	0.061	0.024	0.01	2.94	0.22

The steel was cast, austenitized (8h, 1100°C) and heat treated (730°C for 10h, 12h and 14h, consecutively). After the full heat treatment, samples were thermally aged or exposed to a creep load at 650°C for times up to 16.000h. Table 2 summarises the sample codes used subsequently:

Table 2: Investigated Samples

Sample name	Additional treatment
t2000	Tempered, 650°C, 2000h
t4000	Tempered, 650°C, 4031h
t7000	Tempered, 650°C, 7063h
t16000	Tempered, 650°C, 16000h
c2000	Creep loaded, 650°C, 110MPa, 2000h
c4000	Creep loaded, 650°C, 100MPa, 4031h
c7000	Creep loaded, 650°C, 100MPa, 7063h
c16000	Creep loaded, 650°C, 80MPa, 16000h

Measurements

All EBSD analysis were performed at the Austrian Centre for Electron Microscopy and Nanoanalysis (FELMI) at TU Graz, the sample preparation was partially carried out at FELMI, partially at the Institute for Materials Science, Welding and Forming (IWS).
In order to obtain EBSD-measurements with high quality a routine of the specimens preparation was applied, which was introduced by Katrakova and Mücklich [4]. The samples were embedded cylindrically with the Technovit 4071 encapsulant (dimensions: diameter 2.5 cm, height 1 cm). After the surface grinding and the fine grinding till to a granulation of 4400 the sample surface was polished in three steps with a diamond paste of 6 µm, 1 µm and 0.25 µm granulation a few minutes each. The final step was a surface polishing with an alkaline colloidal silica solution (0.04 µm granulation) for 2h. The surface of the encapsulant was covered with a conductive silver layer and the sample itself was conducted with a carbon strip to avoid charging during the long analysis time.
All measurements were performed on a Zeiss DSM 982 Gemini equipped with an EBSD-system from EDAX-TSL. The microscope was operated with an accelerating voltage of E_0 = 20 keV and a specimen current of I_{sp} = 2.8 nA. Three micrographs with a stepsize of 0.05, 0.25 or 1µm respectively were produced of each sample. These used step sizes permits a

resolution, which is high enough to resolve single martensite laths, and low enough to receive good statistic by covering a high number of laths in one investigation field. To make sure no misinterpreted pixels were considered in the examinations, only subgrains and laths greater than the area of 5 Pixels were counted. For better statistic of the misorientation of neighbouring points, hexagonal rastering was chosen because of the higher number of nearest neighbours per pixel.
For the evaluation of the EBSD maps, misorientations were calculated for every pixel-neighbouring pixel combination. If the misorientation showed a rotation angle less than 1.5°, the two points were interpreted to belong to the same lath and subgrain, and consequently neglected in the statistics. If the rotation angle was higher than 1.5°, the misorientation was added to the statistics of the sample. This procedure created statistics on the type and frequency of misorientation of internal interfaces for every sample.

Results

General

All samples show the typical martensitic lath structure, even the longest running samples are no exception (Figure 1). In nearly all micrographs, numerous laths are arranged to bundles. The laths have a length of roughly 10-100µm (although one has to consider the micrographs are only a cut through the sample) and a width of 0,5-10µm. One former austenite grain contains only few (5-7) main directions of the longest diameter of the martensite laths. The crystal orientation of the matrix appears to correlate with the direction of the martensite lath itself – when analysing parallel laths, one finds only 2-3 main crystal orientations.

Within a martensite lath numerous small angle boundaries exist. Approximately half of these boundaries surround a subgrain completely. The other half seem to end in the matrix, although this is probably an effect of the measurement tolerance of 1,5°.

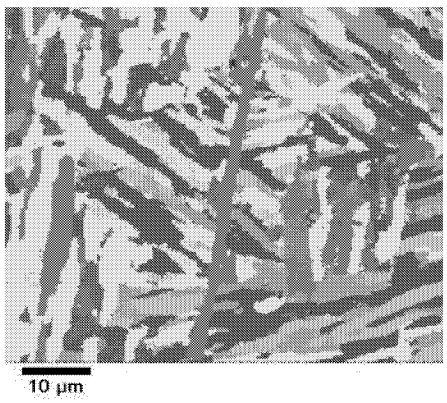

Figure 1: EBSD map of sample c16000
(16.000h at 650°C, 80MPa)
Stepsize: 0.25µm/Pixel

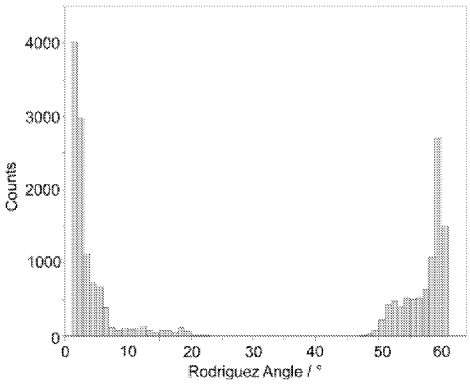

Figure 2: Histogram of rotation angles of internal interfaces in sample c16000

Figure 2 shows an analysis of the misorientation angles of boundaries in sample c16000. Only two groups of boundaries exist: boundaries below 20° misorientation and boundaries with

more than 50° misorientations. This finding confirms the categorisation between small angle grain boundaries and martensite lath boundaries. The next section gives a more detailed analysis of the detected boundaries.

Misorientation of boundaries

Following analysis uses the axis-angle representation. The misorientation of a boundary is not fully given by the angle (called "Rodriguez angle") alone, also the rotation axes has to be considered (for definitions, see [5]). For example, a low energy Σ3 twin is denoted as [1,1,1], 60° boundary, a rotation of 60° regarding to the space diagonal of the unit cell. This special boundary is expected to form during martensitic transformation, thus leading to a low mobility. As Figure 2 shows, high angle grain boundaries show a peak at 59° - if they also have a peak at a rotation axes of [1,1,1], one can be sure the interpretation of martensite lath boundary is correct.

Figure 3a and 3b show the analysis of the rotation axes of low-angle and high-angle boundaries, respectively, of sample t2000. Here, the axes is represented in a reduced polefigure. It shall be emphasised, that *Figure 3a and 3b do not show the orientation of crystals, but the misorientation of boundaries*. While the analysis approve the rotation axes of small angle grain boundaries to be completely random (Figure 3a), high angle grain boundaries posses two main peaks, according to two main misorientations, one with a rotation axes at [0,1,1], the second with an axes near [1,1,1] (Figure 3b).

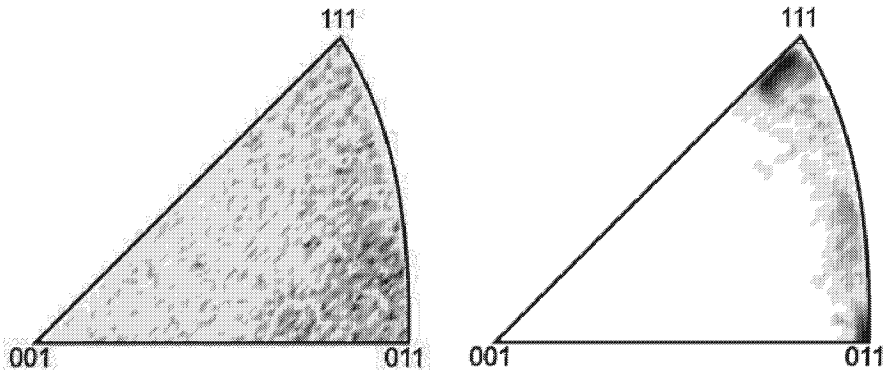

1.5°-20° **47°-63°**

Figure 3a, b. Sample t2000, 0.25µm stepsize. The reduced polar figures provide the orientations of the rotation axes. Left image: small angles (1-20°), right: large angles (47-63°)

Detailed numerical analysis finds even three peaks, namely at [0,1,1] 55°, [0,1,1] 59° and [1.2,1,1] 59°, beside some boundaries with fuzzily spread misorientations between these main directions. Originally, these boundary misorientations were not expected and do not coincide with values calculated by the classical models for martensitic transformation (Kurdjumov-Sachs [6], Nishiyama-Wassermann [7]). However, a model for martensitic transformation combining the two classical approaches has been developed [8], which confirms the findings presented here with high accuracy. It can thus be assumed, that all high angle grain boundaries can be interpreted as martensite laths, apart from a few former austenite grain boundaries, found in roughly half of the samples and representing only a small amount of the

overall boundaries. Now, after a simple criterion has been found to decide between martensite lath and small angle grain boundaries, an automatic determination of the laths width and subgrain size is possible.

Martensite lath width and subgrain size

The task of automatically determining subgrain size and martensite lath width was handled by a MatLab program specially designed for this exercise [8]. Each area of the map surrounded by a boundary was interpreted to be a martensite lath or a subgrain, if some of the boundary provided a misorientation angle below 20°, the area was defined as a subgrain. In order to cover as much size classes as possible, all three maps with their different resolutions were included and overlapped in the calculations. In each map, the number of subgrains and martensite laths were normalised to number per square meter. Figure 4 and Figure 5 shows two representative results of the measurement of subgrain sizes, with the size distribution encoded in a histogram.

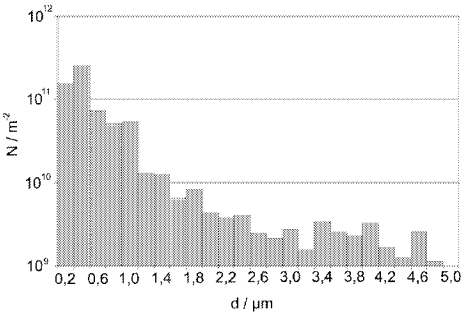

Figure 4: Subgrains per m², Sample t2000

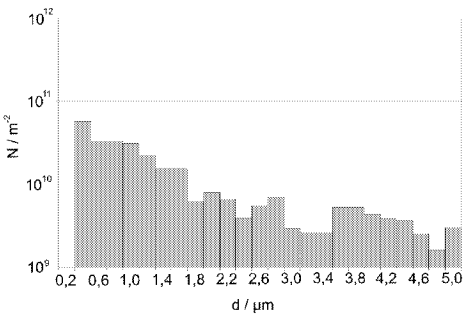

Figure 5: Subgrains per m², Sample c16000

Here, the shortest running tempered sample (t2000) is compared to the longest running creep loaded sample (c16000). It can be clearly seen, that the size distribution is much less left-shifted in the long running sample. This comparison qualitatively reproduces the process of subgrain coarsening. In order get quantitative information, one has to follow the evolution of the mean diameters. For this task, equation 1 was applied:

$$\overline{D} = \frac{\sum_i g_i \cdot D_i}{\sum_i g_i}, \text{ with } g_i = \frac{1}{A_{map,i}} \qquad \text{Equation 1}$$

Equation 1 does not only provide mean diameters measured in one micrograph, but includes several micrographs with different resolutions, by the factor g_i. i denotes one subgrain, g_i is the surface area of the map, in which the subgrain was found in. The mean martensite lath width was calculated analogously. However, one has to keep in mind that only microstructural elements larger than the detection limit of 0,2µm were considered in these statistics. The results are shown in Figure 6 and 7:

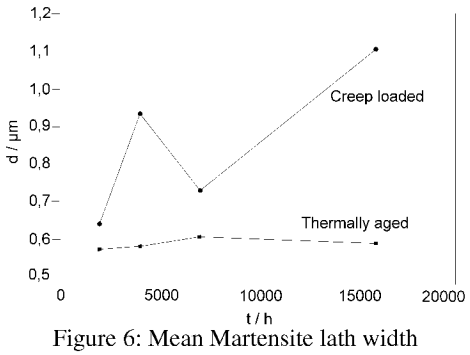

Figure 6: Mean Martensite lath width

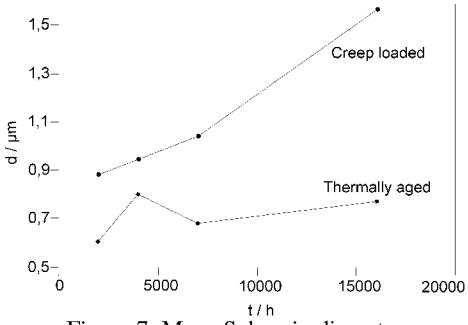

Figure 7: Mean Subgrain diameter

The effect of tempering on the martensite lath width is statistically not significant, and the impact on subgrain growth is only minimal. On contrary, when additionally applying mechanical strain, subgrain growth and lath widening are both pronounced strongly and to a similar extent (martensite laths: factor 2.0; subgrains: factor 2.7 after 16000h of creep compared to the shortest running tempered sample). The comparable mobility of martensite lath and subgrain boundaries are probably the result of the misorientation of the martensite lath boundaries, which are not identical to the more stable Σ3 twins.

Conclusion

The EBSD method has been applied successfully on martensitic/ferritic samples in order to measure misorientation, martensite lath widths and subgrain sizes. It was shown, that martensite lath boundaries and small angle grain boundaries can be differed by simple criteria, thus making it possible to detect both by automatic routines. While the misorientations of small angle grain boundaries are completely random, martensite lath boundaries show some preferential axes-angle combinations. The specific results do not coincide with the expected misorientations of low energy Σ3 boundaries, but show systematic deviations. These findings can be explained with high precision by applying an advanced model for martensitic transformation. Both, tempering and creep loading do not have any effect on the misorientation of martensite laths.

Due to the automatic differentiation between martensite lath and subgrain boundaries it was also possible to measure martensite lath widths and subgrain diameters automatically. As a result, it turned out that tempering alone did not have a statistically significant effect on lath widening, and only little effect on subgrain growth. In contrary to these findings, creep loading leads to a pronounced evolution of both effects. Furthermore, coarsening of subgrains and martensite laths have similar values. This effect is probably caused by the not ideal misorientation of martensite laths.

Because of the lack of other literature data, no final conclusions can be brought up at this moment. Nevertheless, this study should motivate similar investigations on other steels, in order to find further correlations on boundary misorientations and coarsening effects. If a variation of the chemical composition or the parameters of heat treatment lead to different initial misorientations, this can be a first step to lower boundary mobilities and thus leading to a better creep resistance.

Acknowledgment

This work was supported by the Austrian Federal Ministry of Transport, Innovation and Technology, the Province of Styria and the Austrian Research Promotion Agency (FFG), which are gratefully acknowledged.

References

[1] A. Dronhofer, J. Pesicka, A. Dlohy, G. Eggeler: On the nature of internal interfaces in tempered martensite ferritic steels, Z. Metallk., 94 (5) (2003), pp. 511 - 520

[2] P . Hofer: Mikrostrukturelle Analyse als Basis für die Entwicklung neuer Kraftwerkswerkstoffe am Beispiel von G-X12 CrMoWVNbN 10-1-1, PhD thesis, Graz University of Technology, 1999

[3] S. Morito et al.: The morphology and crystallography of lath martensite in Fe-C alloys, Acta Materialia 51 (2003), pp. 1789 - 1799

[4] D. Katrakova, F. Mücklich: Specimen preparation for electron backscatter diffraction Part 1: Metals, Praktische Metallographie 38 (2001) 10, pp. 547 - 565

[5] U.F. Kocks, C.N. Tome, H.R. Wenk: Texture and Anisotropy, Cambridge University Press 1998

[6] G. V. Kurdjumov, G. Sachs: Über den Mechanismus der Stahlhärtung, Z. Phys. 64 (1930), pp. 325 - 343

[7] Z. Nishiyama: X-Ray investigations of the mechanism of the transformation from face- centered cubic lattice to body- centered cubic, Sc. Rep. Tohoku Imp. Univ. 23 (1934), pp. 637 - 664

[8] B. Sonderegger: Charakterisierung der Substruktur in modernen Kraftwerkswerkstoffen mittels der EBSD Methode, PhD thesis, Graz University of Technology, 2005

DISLOCATION MOBILITY IN 9% CHROMIUM STEELS EXPOSED TO CREEP

N. Böck
ARC Seibersdorf research GmbH, A-2444-Seibersdorf, Austria
nikolaus.boeck@arcs.ac.at

Abstract

The macroscopic creep deformation of 9% Cr-steels at their usual application temperature and load is primarily caused by the motions of dislocations. These motions occur primarily due to dislocation climbing. The numerical simulation of dislocation motion and its dependence on local microstructure is a promising approach for predicting the creep behaviour. The simulation offers the possibility to avoid long term creep tests. Further it allows a more rigorous approach for alloy development. There exist several estimations of the mobility of dislocations during climbing. These estimations include on the one hand material parameters like the diffusion coefficient but on the other hand they include rather intuitive parameters like averaged distances between dislocations. The notation "estimation" is used, because in most cases they are based on the description of single dislocations in homogeneous stress fields and are used for complex dislocation arrangements in arbitrary stress fields. Since the results of these estimations are not very satisfactory, if the microscopic inhomogeneous structure of the 9% chromium steels is considered, there is a more physical based approach applied in the following. For some test arrangements of dislocations, the stress field due to the dislocations are calculated by use of the finite element method and Green's functions. Further the vacancy flow will be calculated. Based on the results of these calculations dislocation velocities are calculated. The results of these calculations are compared with the mentioned estimations. These simulations provide a first step for large scale simulation of realistic dislocation assembles.

Keywords: 9-12% Cr steels, dislocation dynamics, simulation, constitutive model

1. Introduction

A crucial point during development of heat resistant 9-12% Cr steels is the evaluation of the creep behaviour of the examined alloys. In operation the steels are exposed to loads which act well beyond 10^5 hours. It is common to perform creep tests over a loading time of 10^5 hours, [1], which is not conservative since it is known that relevant micromechanical processes, for example dissolution of precipitates, occur after 3.10^4 and even more hours, [2]. To avoid unsuccessful development cycles, including such time consuming and expensive long term tests, it seems promising to enhance the use of simulation techniques.

The prediction of the creep behaviour of 9-12% Cr steels by means of simulation techniques can roughly be divided in two important tasks. One task is the prediction of the long term stability of precipitates which have major influence on the creep resistance of the steels. The other task is the prediction of the creep strains based on the information about the microstructure. Today in the field of the first task the major effort is made, since some commercial software packages exist, which allow the calculation of phase equilibria and phase transformations with satisfactory accuracy, based on proper thermodynamic formulations.

In the field of the second task there is a lack of such accurate prediction tools. There exist a number of macroscopic constitutive models, for example the well known Dorn relation, which are useable for description of the creep strain evolution. Since these macroscopic evolution laws of creep strains are mostly based on empirical parameters and numerical fitting

parameters, they are rather useful to describe the creep behaviour after the parameters have been evaluated in long term creep tests, than to *predict* the long term creep behaviour [3]. Another shortcoming of this class of empirical macroscopic laws is that they use averaged microstructural variables, like dislocation densities, which do not allow taking into account the microscopic very inhomogeneous development of dislocation interaction and patterning. These local interactions of dislocations with precipitates and the evolution of subgrains need special attention, since they mainly influences the overall creep behaviour.

During the last decade there was much work done in the field of so called *dislocation dynamics* simulation [4], [5]. The dislocation dynamics approach is a continuum mechanical approach. The displacements, stresses, and strains caused by the dislocations are calculated by means of linear elastic constitutive relations and Green's functions. The forces acting on the dislocations are described as so called material forces (Peach-Koehler forces, $\mathbf{F}_{pk}$). Material forces are not forces in Newton's sense, but forces which relate the motion of material defects to the change of total energy of a considered body (like J-integral in linear fracture mechanics), [6], [7]. This approach leads to a description which relates the degrees of freedom of the considered system to the degrees of freedom of dislocation segments. This description reduces the amount of necessary degrees of freedom of the microscopic model, since it is not necessary to evaluate the dislocation (strain, stress) field in every material point, which is theoretically necessary in a continuum mechanical description in strong form. The description of the dislocations via degrees of freedom of dislocation segments which are related to the Peach-Koehler forces, allows the application of the finite element method. The displacements of a dislocation segment are defined at discrete nodes and the displacement field between the nodes via interpolation functions. The overall solution of the problem can be calculated in weak form.

The pure mechanical part of the dislocation dynamics approach is well developed. Nevertheless there are still some remaining questions especially the efficient handling of interaction with boundary surfaces and the consideration of anisotropic elasticity [4].

In the field of constitutive modelling further improvement is necessary for the description of local interactions of dislocations, since near the core of a dislocation the linear elastic description is not longer valid. For constitutive modelling of dislocation glide it is common to use a so called drag coefficient, B, which describes the material dependent resistance against dislocation motion, $\mathbf{F}_{pk}=B\cdot\mathbf{v}$ ($\mathbf{v}$ is the velocity vector related to a dislocation segment). There are several values of this drag coefficient published in literature, e.g. [5], but not for the steels which are considered within this paper and the considered temperature range.

In the temperature range from 600°C to 650°C the dislocation motion comprises glide and climb (i.e. dislocation creep). The portion of glide motion and climb motion on the whole dislocation motion is not well known. It is often mentioned in literature that during dislocation creep, the resistance against glide is rather low compared to the resistance against climb, see for example [8]. But this obviously depends on the considered material, mechanical load range and temperature. Therefore this assumption cannot be ad hoc stated for the heat resistant 9-12% Cr steels.

To apply the dislocation dynamics method to the simulation of the creep behaviour of 9-12% Cr steels it is necessary to get quantitative values for the constitutive relations. The

quantitative calculation of drag forces against glide needs molecular dynamics simulation. The climb velocities can be calculated by means of continuum thermodynamical diffusion simulation, since it is related to vacancy diffusion.

For simulation of the vacancy diffusion some further investigations concerning the availability and mobility of vacancies in real microstructures are necessary. In the following some models are discussed which quantifies the influence of vacancy diffusion on dislocation motion. The results of the performed simulations are discussed with respect to their usability in dislocation dynamics simulation. Further they are compared with analytical estimations of climb velocities which are published in literature [9], [10].

2. Peach-Koehler force and driving force for diffusion

In this section the influence of the Peach-Koehler force on vacancy diffusion and some limitations of statistical thermodynamics and continuum thermodynamics are shortly discussed.

If two load cases are considered, and in both cases the material dependent resistance against dislocation motion is the same, that load case that causes the higher driving force for dislocation motion (i.e. Peach-Koehler force), will cause a higher dislocation velocity. From this simple statement it follows, that, if climb motion is considered, the vacancy flow must increase, if the Peach-Koehler force increases. Therefore the Peach-Koehler force can be related to the driving force of diffusion.

As mentioned above the Peach-Koehler force can be associated to the change of energy (in this case strain energy) with respect to the motion of the dislocation, $\mathbf{F}_{pk}=dE/d\mathbf{x}$. A climb motion of a dislocation caused by $\mathbf{F}_{pk}$ in a finite medium will lead to a reduction of free energy in the considered body, and this reduction of free energy will act as a driving force for diffusion.

In the following gradients of free energy are defined and related to the motion of single vacancies. If a crystal is in thermodynamic equilibrium at finite temperatures it contains an equilibrium concentration of vacancies. The number of vacancies can be calculated by means of statistical thermodynamics. It is obvious that the number of atoms in the considered system must be large enough that the statistical approach makes sense and that inside of this system the vacancies can not be assigned to an exact position. In a continuum thermodynamic approach the amount of vacancies is described by means of concentrations and also not by position vectors of single vacancies. Using this continuum approach the flow has to be integrated over position and time to get the information which averaged time passed until a vacancy meets the dislocation.

In the real physical process a single vacancy is moving through the lattice, which cannot be modelled directly neither by the statistical thermodynamics approach nor by the continuum thermodynamics approach. Nevertheless, having these limitations in mind, in the following the statistical thermodynamics approach is used for calculation of equilibrium concentration, and the continuum thermodynamics approach is used for calculation of the vacancy flow caused by the Peach-Koehler force.

If only the area near the dislocation is considered, where only a limited number of atoms are situated, both approaches reach their limitations. They are useable, but should not be over-interpreted in the core region of the dislocation. In the next section it is estimated how many real (single) vacancies exist around the dislocation core.

In the models used within this paper it is estimated that the continuum elastic description of the material is useable outside a certain distance from dislocation core. This distance is estimated to be five Burgers vectors. This definition is also used for the continuum diffusion simulation. The diffusion flux at the boundary of this adjusted dislocation core is calculated and related to the dislocation climb motion.

The stress field and Peach-Koehler force of an arbitrary formed dislocation is usually calculated by means of Green's functions [4], [9], or Fourier series [13].

3. Quantitative estimations

In the following quantitative estimations will be performed which serve as a basis for proper model assumptions in large scale simulations. The usability of the results will be discussed in the last section. The main goal is, to make an estimation, how the availability and mobility of vacancies influences the climb motion of dislocations in the considered temperature and stress range, and which major effects have to be taken into account in large scale simulations.

There are several sources and sinks of the vacancies which are produced or annihilated during the climb process. The mentioned availability of the vacancies includes their production/annihilation rate and their transport rate. Further it includes the available vacancies which already exist within the matrix material or can be assembled in the matrix material. They first question which arises, is whether there is a sufficient number of vacancies within the matrix to allow dislocation climb. With a vacancy formation enthalpy of ΔH_v^f=1.4 eV (for Fe, [12]) the equilibrium vacancy concentration at T=600°C is: $c_{v0}^{eq} = K_v \exp(-\Delta H_v^f / k_B T) = 2.5e-8$ (K_v includes the entropy of formation term which is almost constant, [12], here the value K_v =3, is used for the first estimation, [13]; k_B is the Boltzmann constant and T is the temperature).

The following discussion is related to the edge component of a dislocation (i.e. the parts of the dislocation which are able to climb). To clarify the problem the mechanical description is based on a plain strain formulation. An edge dislocation causes a hydrostatic stress which influences the equilibrium vacancy concentration, see for example [9]. To estimate the available vacancies in equilibrium the vacancy concentration around a dislocation is integrated over a cylindrical domain, including the influence of the hydrostatic stress, figure 1. The dislocation lies on the cylinder axis and the inner boundary is a cylinder with a radius of approximately five Burgers vectors (R=1.25e-9 m). The length of the cylinder is 1.25e-7 m. As discussed above the statistical approach requires a sufficiently large domain, nevertheless this integration is applied to give an estimation. Figure 1 shows the number of vacancies as a function of the outer boundary radius. The number of vacancies which occurs if an additional hydrostatic stress of =100 MPa is applied (at 600°C) is also shown.

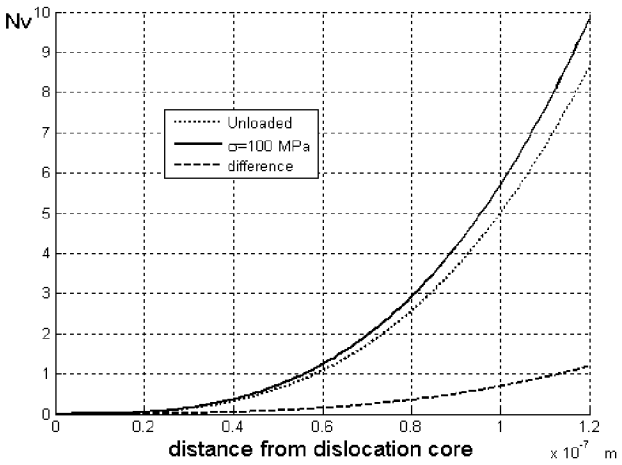

Figure 1: Number of vacancies in a cylindrical domain around an edge dislocation.

The climb component of the Peach-Koehler force drives these vacancies to the dislocation (or away). On the other hand, addition or subtraction of vacancies drives the matrix away from equilibrium, which leads to an opposite force, which is called osmotic force. Figure 1 shows, that even in that case that all vacancies in the matrix are driven to the dislocation, the number of equilibrium vacancies in the matrix is not sufficient to contribute significant to dislocation climbing, having in mind, that the dislocation in the above example has a length of 1.25e-7 m. (A dislocation with the length of 1e-7 m in a cuboid which edges have a length of 1e-7 m gives a dislocation density of 1e-14 m/m³, which is approximately the value of dislocation density in the steels which are discussed within this paper).

From the above simulation it follows that the vacancies which are produced or annihilated during climb have to be provided by other sources or sinks, for example dislocations or grain boundaries. The next question which arises is, how large is the vacancy flow from the sources and sinks to the considered dislocation which is exposed to the Peach-Koehler force, since this directly influences the climb velocity. To discuss this question some finite element simulations are performed. The following two test configurations are considered:

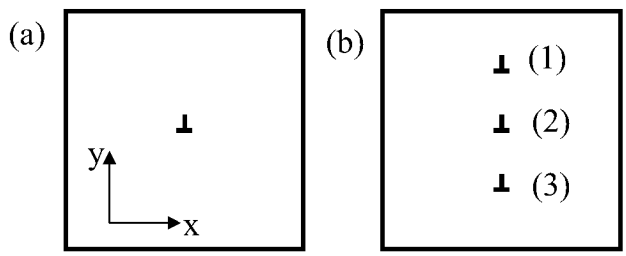

Figure 2: Dislocation configurations for climb velocity estimation.

The squares have a length of 100 nm and are discretised with 100x100 2D-solid finite elements with a thickness of 100 nm.

A vacancy diffusion coefficient of D_v=1e-11 m^3/ms is used based on self diffusion coefficients calculated in [14] and the above calculated vacancy concentration. An applied stress of σ_{xx}= -100 MPa is considered.

In a two dimensional plain strain assemble, as in shown in figure 2 the component of the Peach-Koehler Force acting in y direction (i.e. the climb direction) is $F_{PKy} = -\sigma_{xx} bl$, (l is the length of the dislocation). If the length of the dislocation is defined as l=b and the dislocation moves the length b (0.25nm) forward, this leads to an strain energy release of $\Delta\mu = F_{PKy} b = 1.56e-21\ J = 0.01\ eV$, which lies in a reasonable range.

The free energy release is applied to a continuum model of diffusion. For the finite element simulation the assumption is made that this energy release is allocated within the above cited core region. For case of simplicity in the finite element simulation a concentration c_v^{eq} is defined which leads to the same difference in chemical potential. This leads with the above definitions for F_{PKy}, and $\Delta\mu$, to the formulation $c_v^{eq} = c_{v0}^{eq} \exp(\sigma_{xx} b^3)/k_B T)$ at the inner boundary. A similar formulation is also derived in [9] p.559, based on a somewhat other argumentation. On the outer boundary it is estimated that the vacancy concentration is always in equilibrium, (which lead to the assumption of an instantaneous availability of vacancies on the outer boundary). For the simulations the finite element program ABAQUS is used.

The above assumptions leads to a Peach-Koehler force per unit length of F_{pk}/l=2.50e-2N/m for configuration (a), figure 2, and to a simulated climb velocity of v_c=2.2e-10 m/s. The results for configuration (b), figure 2, are shown in figure 3.

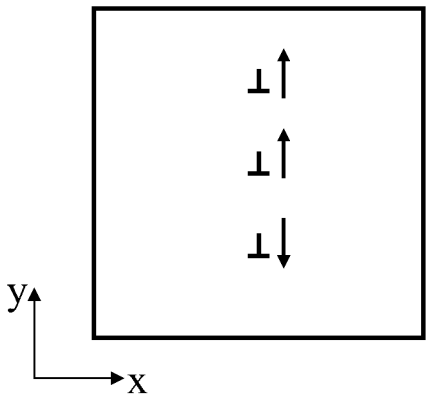

(1) σ_{xx}= -325 N/mm²; F_{pk}/l=8.12e-2N/m , v_c=5.1e-10 m/s

(2) σ_{xx}= -100 N/mm²; F_{pk}/l=2.50e-2N/m , v_c=1.9e-10 m/s

(3) σ_{xx}= 125 N/mm²; -F_{pk}/l=3.12e-2N/m , v_c= -5.4e-10 m/s

Figure 3: Stress, Peach-Koehler force and steady state climb velocity for configuration (b) according to figure 2.

The steady state concentration of vacancies related to the equilibrium concentration for configuration (b) is shown in figure 4. The equilibrium concentration is inhomogeneous due to the inhomogeneous stress field, therefore in some areas uphill diffusion occurs. It can be seen that dislocations (1) and (2) are vacancy sinks while dislocation (3) is a vacancy source

(numbers according to figure 2). Therefore dislocation (3) gains the largest vacancy flux although the largest (absolute value) driving force is acting on dislocation (1).

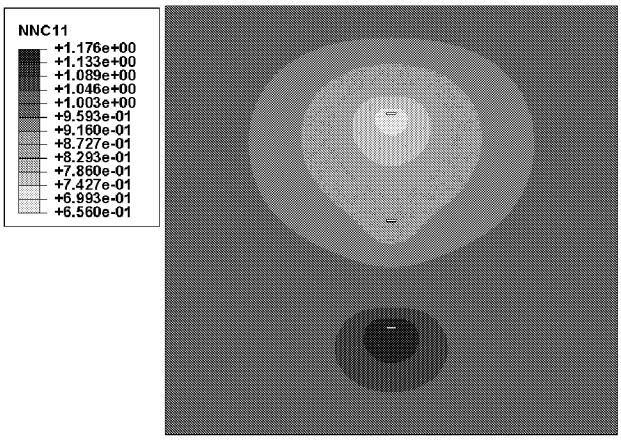

Figure 4: Vacancy concentration at steady state (related to equilibrium concentration) for configuration (b) according to figure 2.

Dislocation (2) in configuration (b) has a smaller climb velocity than the dislocation in configuration (a), although both are exposed to the same driving force. This is caused by the different availability of vacancies. In both configurations the steady state is reached in approximately 300 seconds. The amount of vacancy flow fits well to analytical estimations which a based on a one dimensional rod with the same gradient of chemical potential.

The calculated velocity values lies within the range which can be calculated using analytical estimations of, for example, [9] or [10], but are very high compared to the values which are expected based on the results of creep test and microstructural investigation.

4. Summary and Discussion

The above performed estimations show very high dislocation climb velocities compared to the expected dislocation velocities during creep. There are several aspects of the model which have to be discussed with respect to the unexpected amount of the calculated velocities.

(i) The material dependent mobility of the vacancies (described by the vacancy diffusion coefficient) lies within an expected range. The value of the vacancy diffusion coefficient is based on the self diffusion coefficients calculated in [14]. The approximations which are made in the models concerning the availability of the vacancies i.e. the properties of the sources and sinks are not so reliable.

The most important sources or sinks of vacancies in the considered steels are grain boundaries and dislocations, but these sources have very different properties. In the used model there is an instantaneous availability of vacancies at the boundaries proposed. That means an equilibrium concentration of vacancies (see above discussion of continuum approach at this

length scale). This high availability seems to be realistic at large angle grain boundaries (in the considered steels these are former austenite grain boundaries or boundaries between lath packages (not between the laths themselves), and some of the boundaries between the matrix and M23C6 precipitates). At small angle grain boundaries (boundaries between the martensite laths for example) there is a larger resistance against the integration or rejection of vacancies, also at boundaries with coherent or semicoherent precipitates like MX, or $M_{23}C_6$ in early stages of precipitation.

Even more obvious is this difference of the source properties of dislocations. If a dislocation is exposed to a load which causes the production of vacancies it is a very effective source of vacancies for another dislocation which needs vacancies for its movement. If the dislocation has a stable position or even needs vacancies for its motion it will not be very useable source of vacancies. The usability of dislocations as source or sink of vacancies can be related to the Peach-Koehler force acting on them (the part of the Peach-Koehler force which causes climb) and is therefore taken into account in the above model.

For the grain boundaries an equivalent quantitative calculation is not so obvious, but it seems clear that it has also to be related to the driving force for grain growth. Even in the simple estimation which is performed above it can be seen, that the different availability of vacancies causes different velocities for the single dislocation in configuration (a) and dislocation (2) in configuration (b), which are both exposed to the same driving force.

(ii) There are several other important driving forces for vacancy diffusion which can be acting against the Peach-Koehler force driven diffusion.

Since the vacancies themselves causes positive residual stresses they will diffuse due to a stress fields. Therefore the local stress fields caused for example by inclusions, stable dislocation arrangements (for example subgrain boundaries) or simple the different orientation of neighbouring (anisotropic) grains can reduce the vacancy flow to a dislocation which is exposed to a Peach-Koehler force.

In addition grain growth and dissolution or precipitation, which occur during creep exposure, cause substitutional diffusion, which is based on vacancy diffusion. Therefore the driving forces for these processes can also be competing with the Peach-Koehler force.

(iii) The Peach-Koehler forces acting on the dislocations depend on the stress state, which is on a microscopic scale very inhomogeneous. The loading stress itself is inhomogeneous due to stress concentrations caused by precipitates and due to the anisotropic material behaviour of the grains. In addition the self stress of the considered dislocation and the stresses caused by other dislocations have to be taken into account. Further there are many sources of residual stresses as for example the misfit strains caused by precipitates. If the microstructure is as inhomogeneous as in the considered 9%Cr steels, the forces acting on the dislocations vary at short distances. The formation of stable dislocation arrangements, for example subgrain boundaries, also influences the Peach-Koehler on a dislocation inside such a stable arrangement, but these effects (influence of other dislocations) are considered within the dislocation dynamics simulation (as it is shown in the above calculation of the Peach-Koehler forces in arrangement (b)).

Hence, to make a useable dislocation dynamics simulation including dislocation climb, the different driving forces acting on the vacancies, the different locations and "quality" of sources and sinks and the local stress fields which influences the Peach-Koehler forces have to be taken into account. The use of averaged parameters will not allow to build models which describe the local physical behaviour because the microstructure is locally to inhomogeneous. Such averaged parameters always have empirical or even only numerical character.

5. Summary and conclusion

The dislocation dynamics simulation seems to be very useful tool for prediction of dislocation arrangements and creep strain evolution (despite of the fact that there are some aspects as short range interactions between dislocations, or useable methods of calculating Green's functions in finite anisotropic areas etc., which need further improvements). The use of averaged microstructural parameters in connection with empirical evolution laws does not offer the possibility of further improvement based on thermodynamical relations.

The performed simulations provide some basic estimations for the coupling of dislocation dynamics simulation with continuum simulation of diffusion. The proper calculation of vacancy diffusion is a basis for a usable description of dislocation motion due to climb. Due to the local very inhomogeneous microstructure the estimation of averaged dislocation velocities will not allow to gain further knowledge about the quantitative influences of microstructure on the motion of the dislocations. But this knowledge is necessary for optimising the microstructure with respect to creep resistance. Therefore based on the presented simulation models further improvements, related to the above discussed aspects, will be implemented to get useable models for dislocation dynamics simulation.

Thanks go to my colleagues at *Competence Centre of Micro and Nanocharacterisation* at *ARC Seibersdorf research Gmbh* for helpful discussions and providing of the test results of long term creep tests, including microstructural characterisation. Financial support was provided by the *Austrian Research Promotion Agency Ltd. (FFG)* under *ACCEPT - COST 536*, Proj. No. *808.789,* and *ARC Seibersdorf research Gmbh*. This support is gratefully acknowledged.

[1] K. H. Mayer, R. Blum, P. Hillenbrand, T.-U. Kern, M. Staubli. Development Steps of new steels for advanced steam power plants. Materials for advanced power engineering 2002: Proceedings of the 7th Liège Conference, Part III, 2002, 1385-1396.

[2] F. Kager, K. Spiradek-Hahn, N. Böck, S. Höfinger, M. Brabetz, G. Zeiler. Superior long-term creep behaviour and microstructural evolution of 9%Cr-steels with boron. Materials for advanced power engineering 2006: Proceedings of the 8th Liège Conference, (these proceedings), 2006.

[3] N. Böck, F. Kager. Finite element simulation of the creep behaviour of 9% chromium steels based on micromechanical considerations. *Creep Deformation and Fracture, Design, and Life Extension.* Edited by R.S. Mishra, J.C. Earthman, S.V. Raj, and R. Viswanathan. Materials Science & Technology Conference , Pittsburgh 2005, p 149-158.

[4] N. M: Ghoniem, E. P. Busso, N. Kioussis. Multiscale modelling of nanomechanics and micromechanics: an overview. Philosophical Magazine, 2003, Vol. 83, Nos. 31-34, 3475-3528.

[5] H. M. Zhbib, M. Hiratani, M. Shehadeh. Multiscale discrete dislocation plasticity. Continuum scale simulation of engineering materials. Edited by Dierk Raabe et al. Wiley 2004.

[6] R. Phillips. Crystal, defects and microstructures, modelling across scales. Cambridge university press. 2002.

[7] J. D. Eshelby. The elastic energy momentum tensor. Journal of elasticity, Vol. 5, Nos. 3-4, November 1975.

[8] R. Bürgel. Handbuch Hochtemperaturwerkstofftechnik. Vieweg 2001.

[9] J. P. Hirth, J. Lothe. Theory of dislocations. Krieger Publishing Company, 1992.

[10] N. M. Ghoniem, J. R. Matthews, R. J. Amodeo. A dislocation model for creep in engineering materials. Res Mechanica 29 (1990) 197-219.

[11] T. Mura. Micromechanics of defects in solids. Kluwer academic publishers. 1998.

[12] M. E. Glicksman. Diffusion in solids, Field theory, solid-state principles, and applications. Wiley. 2002.

[13] D. A.. Porter, K. E. Easterling. Phase transformations in Metals and Alloys. Chapman&Hall. 1996.

[14] H. Cerjak, P. Hofer, B. Schaffernak. The influence of microstructural aspects on the service behaviour of advanced power plant steels. ISIJ international. Vol. 39 (1999), No. 9, pp874-888.

EFTEM INVESTIGATIONS ON PRECIPITATES IN A CREEP RESISTANT 9-12% CR STEEL

B. Sonderegger[1], G. Kothleitner[2], W. Rechberger[2], H. Cerjak[1]

1: Institute for Materials Science, Welding and Forming, Graz University of Technology, Kopernikusg. 24, A- 8010 Graz, Austria
2: Research Institute for Electron Microscopy and Fine Structure Research, Graz University of Technology, Steyrerg. 17, A-8010 Graz, Austria

Abstract

9-12% chromium steels are well established materials for high temperature components in ultra efficient power plants. One important parameter for the creep resistance of these steels is the formation and interaction of different precipitate populations like NbC, VN, $M_{23}C_6$, Laves phase and modified Z-phase. Energy filtered TEM (EFTEM) studies were carried out on samples of the European COST steel CB8. Enhanced analysis methods were applied to determine the size, volume fraction and number frequency of precipitates with arbitrary size distribution in samples of varying thickness. The results show growth, coarsening and dissolution of precipitates during in-service exposure. The dissolution of VN precipitates at long running times was identified as the most likely reason for the drop of creep resistance of the steel CB8. Furthermore, the drop in the number density of VN precipitates corresponds with the first appearance of the V- and N- containing modified Z-phase Cr(V,Nb)N.

Keywords: EFTEM, precipitates, size distribution, creep resistant steel, mod. Z-phase

Introduction

Creep resistant 9-12% Cr steels are used for high temperature components in fossil power plants. Amongst other parameters like oxidation resistance, ductility etc., high temperature creep resistance is one of the key factors for the reliability and long life of these components. State-of-the-art steels withstand temperatures of 600-620°C at mechanical stresses of 100MPa for over 10 years (10^5h). However, further increase of the operation temperature allows constructing more efficient power plants with less emission of CO_2. The European Cooperation in the field of Scientific and Technical Research (COST) is aiming at this goal in Action 536 [1].

The creep resistance is mainly influenced by the presence and the stability of different kinds of precipitates at service conditions. According to the backstress concept [2], a high number of small precipitates are the best precondition for improved creep properties. Most importantly, this high number density must not decrease distinctively during service. Effects like coarsening and dissolution of precipitates accelerate the number density decrease, and thus the drop of creep resistance.

In the European COST program 522 (the predecessor of 536), several types of Boron alloyed test melts have been developed [3]. One of the most promising candidates for creep resistance, the test melt CB8, was chosen for long-term creep tests. It turned out that CB8 shows a drop in creep resistance at times greater than 10^4h, although the initial microstructure shows all properties needed for a good performance. Therefore, extensive studies of the microstructure were carried out to help understanding this effect.

Due to the different sizes of precipitates, several experimental techniques have to be used to fully quantify precipitate parameters. Techniques commonly used are SEM phase contrast imaging [4], TEM/EFTEM [5, 6] and atom probe [7]. This paper focuses on EFTEM

measurements of precipitates in heat treated, creep loaded and thermally aged specimens. The investigations on the steel CB8 are complemented by SEM studies [8] and thermodynamic simulations [9, 10], published elsewhere.
The measured precipitate parameters and their evolution in the course of heat treatment and creep loading give valuable indications for the reason of the drop in creep resistance, which is the first step to further improve the material.

Experimental

Materials

Two test melts of the cast steel CB8 (G-X17CrCoMoVNbB), namely Heat 1 and Heat 2, were produced by voestalpine Giesserei Linz GmbH, Austria, in 1998 [11] and 2004 [12], respectively. A high amount of Co is supposed to reduce the self-diffusion coefficients in the martensitic matrix, the high amount of Boron is intended to stabilise matrix-precipitate interfaces. Other alloying elements such as V, N, Nb and C are added to form precipitates to achieve the desired properties. Table 1 gives the nominal and the measured chemical compositions of the test melt CB8 in wt%.

Table 1: Chemical Composition of the Test Melt CB8, wt%

	C	Si	Mn	Cr	Ni	Mo	V	Nb	Co	Al	B ppm	N
Nom.	0,16	0,2	0,1	10,7	0,1	1,4	0,18	0,05	2,8	0,01	80	0,015
	0,18	0,3	0,3	11,3	0,2	1,6	0,22	0,07	3,2	0,02	150	0,030
Heat 1	0,17	0,27	0,2	10,86	0,15	1,42	0,21	0,061	2,94	0,026	106	0,024
Heat 2	0,17	0,27	0,2	10,72	0,16	1,4	0,21	0,06	2,92	0,028	112	0,032

The material of Heat 2 was heat treated, heat 1 additionally thermally exposed and creep loaded. Heat treatment of steel 2 was carried out by W. Plimon [13]. After casting, the steel was austenitised at 1100°C for 8h, tempered at 730°C for 10h and stress relieved two times at 730°C for 12h and 14h, respectively. The creep experiments were carried out by G. Dimmler [14]. The samples were creep exposed up to 16564h, at a temperature of 650°C and stresses of 80-100MPa. By taking samples of the head and the central region of the creep loaded specimen, thermally aged and creep exposed samples were generated. 10 samples were chosen for detailed TEM studies. Each thermally aged sample was complemented with a creep exposed sample of similar loading time. The mechanical stress was chosen such that the sample was expected to rupture soon after the pick.

Table 2 Heat treated samples

Sample	Condition
As cast	Solidified melt
Austenitised	After austenitising (1100°C, 8h)
Heat treated	After first heat treatment cycle (730°C, 10h)
As received	After the full heat treatment

Table 3: Thermally aged samples (all samples were heat treated before ageing, see Table 2)

Sample	t/h	t/s
A4000	4031	$1.45.10^7$
A7000	7063	$2.54.10^7$
A16000	16564	$5.96.10^7$

Table 4: Creep loaded samples (all samples were heat treated before creep loading)

Sample	t/h	t/s	Stress/MPa
C4000	4031	$1.45.10^7$	100
C7000	7063	$2.54.10^7$	100
C16000	15802	$5.69.10^7$	80

EFTEM

All samples were mechanically pre-polished and thinned and then milled to the final thickness by employing a Gatan PIPS Argon ion mill, operated at a voltage of 4 kV and a milling angle of 3-4 degrees. The typical sample thicknesses were estimated by the log-ratio method and were in the range of the inelastic mean free path of the material which amounted to about ~30-150nm.

The investigations were carried out on a Philips CM20 at a primary energy of 200kV. A Gatan Imaging Filter model 678 was used for all EFTEM experiments. For elemental mapping and ratio imaging [5] the microscope was operated in imaging mode employing a condenser aperture, which limited the convergence angle to less than 1.5 mrad. Furthermore, an objective aperture restricted the according collection angles to about 7.6mrad. On the spectrometer a 3mm entrance aperture was used for imaging and a 2mm aperture for energy-loss spectroscopy. The system was equipped with a high sensitivity CCD detector with a 14bit dynamic range, operated in a dark current subtracted and gain normalised mode.

Precipitates of NbC, VN, $M_{23}C_6$ and modified Z-phase were visualised by taking jump ratio images and elemental maps of Cr, N, C and V. Additionally, jump ratio images and elemental maps of Fe, B, Nb and Mo were generated. Zero loss images and unfiltered bright field images were produced to display the morphology of the microstructure and to calculate thickness maps. The drift correction for the image series was carried out with a statistically determined spatial drift correction program [15]. Table 5 gives the experimental parameters used for the acquisition of the element specific micrographs. Depending on the size of area that was suitable for EFTEM investigation, 8-14 image series per sample were taken.

Table 5 Window Energies for the Acquisition of Jump Ratio Images and Elemental Maps

Z	Element	Edge type	Edge /eV	Post edge/eV	Pre edge 1 / eV	Pre edge 2 / eV	Window width / eV	Aquisition time / s
5	B	K	188.0	198	156	176	20	3
6	C	K	283.8	295	249	274	20	10
7	N	K	401.6	412	371	391	20	20
23	V	$L_{2,3}$	513.0	523	481	501	20	30
24	Cr	$L_{2,3}$	574.0	591	525	560	30	45
26	Fe	$M_{2,3}$	54.0	64	-	48	8	1
41	Nb	$M_{4,5}$	204.6	225	170	195	20	5
42	Mo	$M_{4,5}$	227.0	320	192	214	20	5

Evaluation of precipitate parameters

The precipitates found in the elemental maps and jump ratio images were analysed with Gatan´s Digital Micrograph software package. In this software, mean equivalent circle diameters of the precipitates projections, its XY-positions and shape parameters can be calculated. Together with the normalised thickness maps, these datasets were used to determine volume fraction, number of precipitates per volume, mean and median diameter and size distributions of the second phases.

These analyses were carried out using mathematical routines programmed in the commercial software MatLab. As a basis for the calculation, the stereologic evaluation equations of Underwood [16], Hättestrand and Andren [17] were applied in a slightly modified manner: These authors derived mean correction factors from mean diameters and mean sample thicknesses, and applied these factors to all precipitates. This approach works perfectly well for a population of precipitates with constant size in a sample of constant thickness. In this work, the sequence of evaluation was reversed: First, correction factors for each particle were calculated by using the diameter of the particle and the sample thickness at the position of the particle. Afterwards, a statistical analysis for calculating the parameters of the precipitate populations was performed. Using individual correction factors for every single particle instead, enables the evaluation of parameters for precipitate populations with different size distributions in a sample of varying thickness. The following equations were used:

$$f_V = \frac{V_V}{V_{Sample}} = \frac{1}{A_{Sample}} \cdot \sum_i A_i \frac{2d_{m,i}}{2d_{m,i} + 3t_i} \qquad \text{Equation 1}$$

where f_V is the total phase fraction. f_V is calculated with the parameters V_V (absolute volume of the phase in the examined sample volume), V_{Sample} (sample volume), A_{Sample} (sample area), A_i (measured area of precipitate i), $d_{m,i}$ (measured equivalent circle diameter of precipitate i) and t_i (foil thickness at the position of precipitate i).

$$N_V = \frac{1}{A_{Sample}} \cdot \sum_i \frac{1}{t_i + d_i} \qquad \text{Equation 2}$$

where N_V is the number of precipitates per unit volume. The real diameter d_i is calculated with equation 3:

$$d_i = \frac{2}{\pi}\left(d_{m,i} - t_i\right) + \sqrt{\left(\frac{2}{\pi}\left(d_{m,i} - t_i\right)\right)^2 + \frac{4d_{m,i} \cdot t_i}{\pi}} \qquad \text{Equation 3}$$

Huge particles are more likely to intersect a sample, when having the same number density as small particles. This can be considered by the factor w_i, which gives the probability of a spherical precipitate having its centre located inside the sample volume, when intersecting the sample:

$$w_i = \frac{t_i}{t_i + d_i} \qquad \text{Equation 4}$$

d_i is the real diameter of the precipitate i, calculated by equation 3. By using this probability w_i, one finds for the mean precipitate diameter $\bar{d}$:

$$\bar{d} = \frac{\sum_i d_i \frac{t_i}{t_i + d_i}}{\sum_i \frac{t_i}{t_i + d_i}}$$ Equation 5

When calculating size distributions, the probability factor given in equation 4 is used for each precipitate.

Results and Discussion

Qualitative Description of Precipitate Evolution:

The as cast condition of the steel showed no statistically spread precipitates in the matrix. Some string-shaped precipitates located on former austenite grain boundaries were identified as Mo-rich M_3B_2 phases by Selected Area Diffraction (SAED) [12].

The first precipitates in the matrix appear after austenitising and were determined to be NbC particles. These bulky precipitates showed a low number density (10^{18} m^{-3}) and a size of roughly 70nm. Both parameters stay practically constant during the rest of the heat treatment, thermal ageing and creep loading.

The most noticeable change in microstructure happens after the first heat treatment cycle. High numbers of Cr-rich $M_{23}C_6$ (confirmed by SAED) and VN (confirmed by ELNES) precipitates form at subgrain boundaries and martensite lath boundaries [12, 18]. Though statistical deviation blur the results, both precipitate phases appear to have already reached most of their equilibrium phase at this point of time.

During tempering and creep loading, $M_{23}C_6$ and VN precipitates stay the most common types. Mo-rich Laves phase forms after 50h of tempering at 650°C and was examined by SEM [8]. As shown in the next section, $M_{23}C_6$ precipitates coarsen, while VN particles keep their initial size for at least 7000h.

A very small number of precipitates containing Cr and V were detected only in the thermally aged sample A16000 and the creep sample C16000, both with the longest running times of roughly 16000h. According to literature, this phase was also found in similar steels after long creep and ageing times and is assumed to be modified Z-phase Cr(V,Nb)N by a number of authors due to its chemistry [17, 19-21], and approved to be so by measurements of the crystallography with CBED of TEM samples (Papst-Letofsky et al [23]) and SAED of extraction replicas (Vodarek and Strang [24]). Figure 1 shows a micrograph of sample A16000 with $M_{23}C_6$ and VN precipitates, as well as a precipitate of the Cr- and V-rich phase.

Simultaneously with the first appearance of the modified Z-phase, the number density of VN precipitates decreases consistently. This coincidence, which lowers the overall number frequency of precipitates, was also found in similar 9-12% Cr steels [25]. At the same time, the creep resistance of the steel CB8 drops drastically. The obvious correlation in time of these three incidences strongly suggests the modified Z-phase as one of the reason for the deterioration of the materials properties.

As the number density of the modified Z-phase was to low for accurate statistical evaluations, a detailed quantitative study of the most common precipitates, namely $M_{23}C_6$ and VN, was carried out in order to further clarify the precipitate evolution.

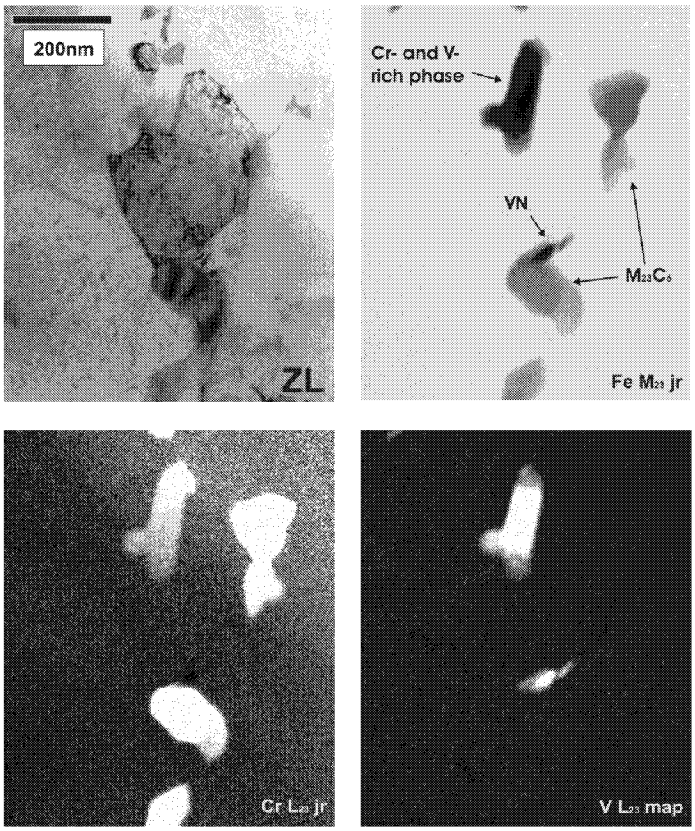

Figure 1: Cr-carbides, VN and Cr- and V-rich phase (presumably mod. Z-phase) found in thermally aged sample A16000

Quantitative Evaluation of Precipitate Parameters:

To obtain statistics for the precipitate populations of $M_{23}C_6$ and VN, Cr jump ratio images and V elemental maps were used. The numbers of Laves phase, NbC and mod. Z-phase were too low for a proper statistic. The number of $M_{23}C_6$ detected per sample was between 49 and 154, the number of VN between 18 and 101, respectively.

Figure 2a and 2b show the size distribution of $M_{23}C_6$ and VN precipitates in heat treated and thermally aged samples, calculated with equations 3 and 4, from their first appearance in sample "heat treated" up to sample A16000. Nearly all distributions are left shifted with one single peak. Analysing the $M_{23}C_6$ particles, one clearly recognises the shift of the peak position from 60nm in the sample "heat treated" to 120nm after 16000h of tempering. In contrary to this behaviour, VN precipitates only seem to grow until 4000h of tempering. After this sample condition no clear tendency is obvious. For further analysis it is inevitable to determine mean diameters, the volume fraction and, most important, the number density in the course of the experiments.

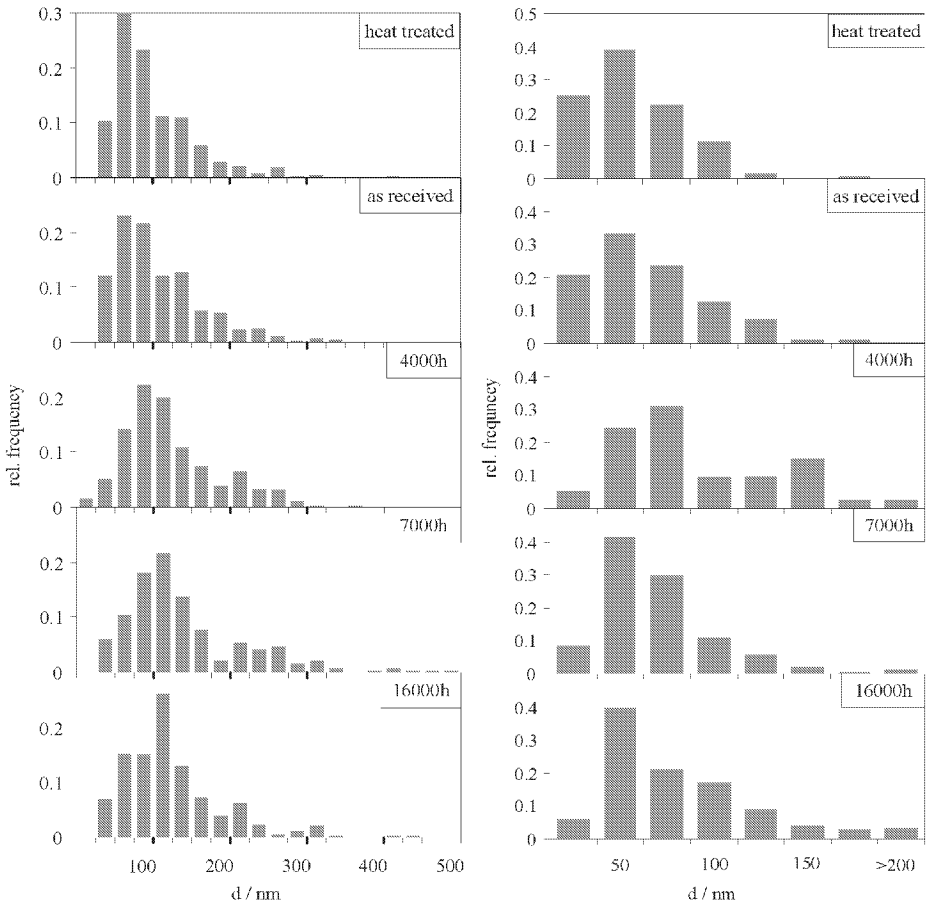

Figure 2a, b: The left diagram shows the measured size distribution of $M_{23}C_6$ precipitates, the right image the distribution of VN precipitates.

Very definite trends can be found when analysing the number of precipitates per unit volume. For thermally aging and creep loaded samples, the number density of the precipitates is decreasing for both precipitate types (Figure 3 and 4).

Although the statistic errors are larger when analysing the fewer VN precipitates (compared to $M_{23}C_6$), the drop of the number density is eye-catching here: for the longest running aged and creep exposed samples the number goes down by a factor of 20 (creep exposed) and 10 (aged), respectively (Figure 4). This striking decline is probably one of the main reasons for the deteriorating long-term creep resistance.

When analysing the precipitate volume fractions, the amount of $M_{23}C_6$ precipitates stays moreless constant from the heat treated sample to the longest running thermally aged and creep loaded conditions (Figure 5). In contrary, the volume fraction of VN is clearly decreasing after 16.000h in both, thermally aged and creep loaded samples (Figure 6). This is clearly a result of the decreasing number density.

Analysing the evolution of the $M_{23}C_6$ mean diameters, this parameter increases for thermally aged and creep loaded samples (Figure 7). Additionally considering the constant volume fraction and decreasing number density, these precipitates clearly show the effect of coarsening.
In contrary, the VN moreless keep their initial size (Figure 8), except for a slight tendency in the thermally aged sample to grow.

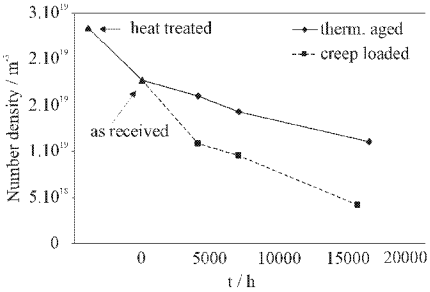

Figure 3: Number density of $M_{23}C_6$ prec.

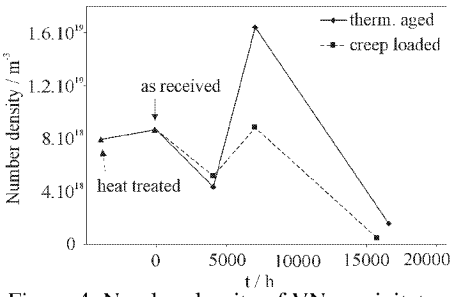

Figure 4: Number density of VN precipitates

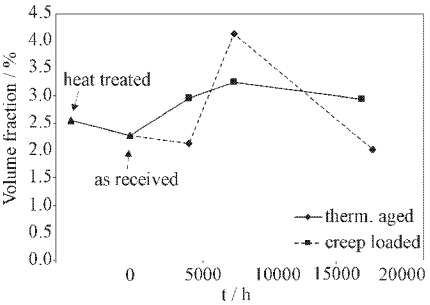

Figure 5: Volume fraction of $M_{23}C_6$ phase

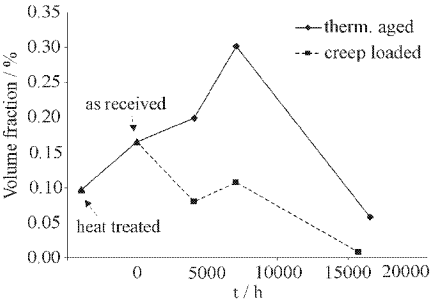

Figure 6: Volume fraction of VN phase

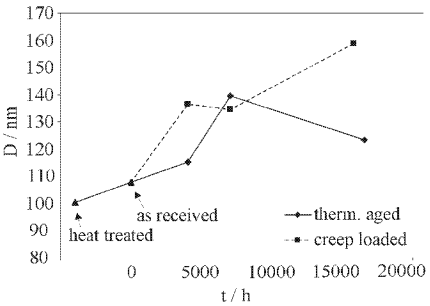

Figure 7: Mean diameter of $M_{23}C_6$ prec.

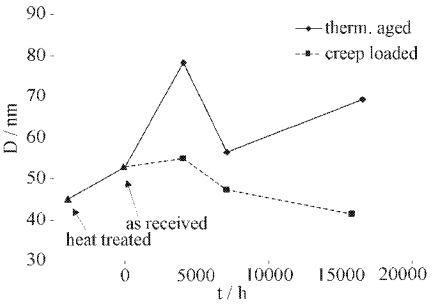

Figure 8: Mean diameter of VN precipitates

Discussion:

As shown by the quantitative evaluation, the $M_{23}C_6$ particles coarsen continuously (constant volume fraction, decreasing number density, increasing mean diameter). This process is found in the thermally aged and, even more pronounced, the creep loaded samples.
In contrary, the parameters of the VN precipitates show no clear tendency at first – until the longest running samples A16000 and C16000. At this loading time of 16000h, the number

frequency drops dramatically. At the same moment, the V- and N- containing mod. Z-phase appears for the first time, consuming the nitrogen formerly bound in VN precipitates. The precipitates of this phase were found to have greater diameters than VN (by a factor of 2), and therefore producing a much lower number frequency, when consuming the same amount of Nitrogen. Conspicuously, the creep properties deteriorate at the same moment.

This behaviour is also found in similar steels [25]. The mod. Z-phase is known to coarsen fast [26], and thus further degrading the creep properties. Numerical thermodynamic studies based on new databases [26, 27] show that this phase in fact is an equilibrium phase, and displacing VN in the long run. First kinetic simulations, carried out on the software MatCalc, also approve this behaviour [27]. The slow coarsening of $M_{23}C_6$ precipitates additionally contributes to the overall decrease of the precipitates number density.

Conclusion

The formation and interaction of precipitates in the course of heat treatment, thermally ageing and creep loading were measured successfully by TEM/EFTEM for the COST steel CB8. The precipitate types VN and $M_{23}C_6$ were studied in detail by evaluating the evolution of their size (distribution), volume fraction and number density. As most remarkable effect, the decrease in the number density of VN by a factor of 10-20 in the longest running samples was identified. This corresponded to the first appearance of V- and N- containing mod. Z-phase Cr(V,Nb)N. The formation of mod. Z-phase is found as the most likely reason for the drop of the VN number density, and therefore the drop of long-term creep resistance of the steel CB8.

For future developments, the emphasis must be laid on suppressing the formation of mod. Z-phase as long as possible. For this goal it is inevitable to associate the microstructural investigations with thermodynamic kinetic simulations of the precipitate evolution, in order to find improved chemical compositions of 9-12% Cr steels.

Acknowledgements

The authors want to thank the Austrian Federal Ministry of Transport, Innovation and Technology, the Province of Styria and the Austrian Research Promotion Agency (FFG) for their financial support.

References

[1] COST - European Cooperation in the field of Scientific and Technical Research, Action 536: Alloy development for Critical Components of Environmental friendly Power planT (ACCEPT); http://cost.cordis.lu/src/action_detail.cfm?action=536

[2] B. Reppich: Ein auf Mikromechanismen abgestütztes Modell der Hochtemperaturfestigkeit und Lebensdauer für teilchengehärtete Legierungen, Zeitschrift für Metallkunde, 73 (11), 1982, pp. 697-805

[3] B. Schaffernak: Charakterisierung von 9-12% Cr Stählen Mittels Thermodynamischer Modellrechnungen, PhD thesis, Graz University of Technology, 2000

[4] L. Korcakova, J. Hald, M. A. J. Somers: Quantification of Laves phase particle size in 9CrW steels, Materials Characterisation, 47, 2001, pp. 111-117.

[5] F. Hofer, P. Warbichler: Improved imaging of secondary phases in solids by energy-filtering TEM, Ultramicroscopy, 63 (1), 1996, pp. 21-25.

[6] M. Hättestrand, H.-O. Andren: Influence of strain on precipitation reactions during creep of an advanced 9% chromium steel, Acta Mater., 49, 2001, pp. 2123-2128.

[7] A. Gustafson, M. Hättestrand: Coarsening of precipitates in an advanced creep resistant 9% chromium steel-quantitative microscopy and simulations, Materials Science and Technology, 333 (1-2), 2002, pp. 279-286.
[8] G. Dimmler, P. Weinert, E. Kozeschnik, H. Cerjak: Quantification of the Laves phase in advanced 9-12% Cr steels using a standard SEM, Materials Characterisation, 51, 2003, pp. 341-352.
[9] J. Rajek, E. Kozeschnik, H. Cerjak: Simulation of precipitation in a complex 9-12% Cr steel for modern steam power plants, Proc. Mat. Sci. Tech. 2003, USA 2003
[10] J. Rajek, E. Kozeschnik and H. Cerjak: Computer simulation of precipitation in a complex 9-12% Cr-steel during fabrication heat treatment, Proc. "EPRI 4th Int. Conf. Adv. in Mat. Tech. for Fossil Power Plants", Hilton Head Island, USA, 2004
[11] R. Hanus: COST Report VOEST Alpine Gießerei Linz GmbH, COST 522, 2000
[12] B. Sonderegger: Charakterisierung der Substruktur in modernen Kraftwerkswerkstoffen mittels der EBSD Methode, PhD thesis, Graz University of Technology, 2005
[13] S. W. Plimon: Simulation einer großtechnischen Wärmebehandlung und begleitende mikrostrukturelle Untersuchung an einem modernen 9-12% Cr Stahl, Diploma thesis, Graz University of Technology, 2004
[14] G. Dimmler: Quantifizierung der Kriech- und Zeitstandfestigkeit von 9-12% Cr Stählen auf Mikrostruktureller Basis, Ph.D. thesis, Graz University of Technology, 2003
[15] B. Schaffer, W. Grogger, G. Kothleitner: Automated spatial drift correction for EFTEM image series, Ultramiscroscopy 101, 2004, pp. 123-128
[16] E. E. Underwood: Quantitative Stereology, London, 1970, pp.174
[17] M. Hättestrand, H.-O. Andren: Evaluation of particle size distribution in a 9% Cr steel using energy filtered transmission electron microscopy, Micron, 32 , 2001, pp. 789-797
[18] F. Hofer, P. Warbichler, A. Scott, R. Brydson, I. Galesic, B. Kolbesen, J. Microscopy, 204 (2), 2001, pp.166.
[19] K. Kimura, K. Suzuki, Y. Toda, H. Kushima, F. Abe: Precipitation of Z-phase and degradation behaviour of mod. 9Cr-1Mo steel, Proc. Materials for advanced power engineering, Liege, 2002, pp. 1171-1180.
[20] A. Strang, V. Vodarek: Microstructural stability of high chromium ferritic power plant steels, Proc. Microstructural development and Stability in high Chromium ferritic power plant steels, Cambridge, 1995, pp. 31-51.
[21] J. Bursik, N. Merk: Quantitative microstructural assessment of P91 ferritic steel after long term creep at high temperature, Proc. Mechanical Behaviour of Materials at High Temperature, Sesimbra, 1995, pp. 1-12.
[22] P. Hofer: Mikrostrukturelle Analyse als Basis für die Entwicklung neuer Kraftwerks-werkstoffe am Beispiel von G-X12CrMoWVNbN 10-1-1", PhD thesis, Graz University of Technology, 1999.
[23] I. Papst, P. Warbichler, F. Hofer, B. Schaffernak, E. Letofsky: Identifizierung der modifizierten Z-Phase mittels konvergenter Elektronenbeugung, Metallographietagung Dortmund, Germany, 6.-10. September 1999
[24] V. Vodarek, A. Strang: Z Phase characteristics in martensitic 12CrMoVNb steels, Materials for advanced power engineering, Liege, 2002, pp. 1223-1231.
[25] K. H. Mayer: Vergleichende Bewertung des Einflusses der Mikrostruktur auf die Kriechfestigkeit der borlegierten COST-Stähle mit erhöhtem Cr- und Co-Gehalt, Internal COST Report, 14.9.2004
[26] H. Danielsen, J. Hald: Z-phase in 9-12% Cr steels", ISSN 0282-3772, Värmeforsk Service AB, Stockholm, 2004
[27] J. Rajek: Computer simulation of precipitation kinetics in solid metals and application to the complex power plant steel CB8, PhD thesis, Graz University of Technology, 2005

PRECIPITATION BEHAVIOR OF Z PHASE AFTER LONG - TERM CREEP IN HIGH CHROMIUM FERRITIC HEAT RESISTANT STEELS

K. Sawada, H. Kushima and K. Kimura

Materials Reliability Center, National Institute for Materials Science,
1-2-1, Sengen, Tsukuba, 305-0047, Japan
sawada.kota@nims.go.jp

Abstract

The precipitation behavior of the Z phase was investigated after long-term creep exposure in ASME-T91, T92, T122 without δ-ferrite, and T122 with δ-ferrite through elemental mapping using EF-TEM. The Z phase was identified by comparing the Cr map with the V map. Most of the Z phase was observed around prior austenite grain boundaries and/or packet boundaries in all of the steels examined. In T122 with δ-ferrite, the Z phase also precipitates around the δ-ferrite. In particular, the number of MX carbonitrides was very small in T122 with a large amount of the Z phase. The main metallic composition of the Z phase in T91 was the same as that in T92. In T122, the Z phase contained a lower Nb content. The main metallic composition of the Z phase around the δ-ferrite was the same as that in the other areas. There was no large difference in the size distribution of the Z phase among the steels. The mean diameter of the Z phases for T122 with δ-ferrite was relatively large in spite of a shorter creep exposure in contrast with T91 and T92. The number density of the Z phases increased with increasing creep exposure time except in the case of T91. The order of the number density was T122 with δ-ferrite, T91, T122 without δ-ferrite, and T92. In crept samples, the amount of Z phase in the gauge portion was higher than that in the grip portion, meaning that stress and/or strain promotes the formation of a Z phase during creep exposure.

Keywords: Z phase, long-term creep, precipitation site, stress and/or strain effect

1. Introduction

Steam power plants need high chromium ferritic steel with higher creep strength to improve thermal efficiency. In order to improve the creep resistance of high chromium ferritic steels, we need to retard microstructural changes, such as the recovery of martensitic lath structures and the coarsening of precipitates. In particular, creep strength at long terms abruptly decreases due to microstructural degradation. New phases such as Laves and Z phase appear after long-term creep exposure. [1-4] In 9-12% Cr ferritic steels, the Z phase precipitates after creep exposure for about 10,000 h at 650°C. It is assumed that the formation of the Z phase causes an abrupt decrease in the creep strength since Z phase formation consumes MX carbonitrides, which are important strengtheners. [5,6] Suzuki et al. reported that the Z phase is formed around prior austenite grain boundaries, and that Nb-rich MX disappears after long-term creep exposure in Mod.9Cr-1Mo steel. [7] Thus, we need to know the precipitation behavior of the Z phase to improve creep strength at the long term.

In actual power plants, Type IV cracking has been found in heat-affected zones in a modified 9Cr-1Mo steel after long-term service. [8] The creep strength of weld joints is related to that of the base material. It is necessary to assess accurately the long-term creep strength of the base material to maintain the safety of components in power plants. An abrupt drop in the creep strength at the long term is a problem in high chromium ferritic steels. [9] Recently, an assessment of the long-term creep strength and a review of the allowable stress of high Cr ferritic heat resistant steels have been conducted in Japan. [10] In order to assess accurately the long-term creep strength of high chromium ferritic steels, it is important to clarify the degradation mechanism of the creep strength by the formation of Z phase.

In high chromium ferritic steels, a Z phase was found after long-term creep by Strang et al.. [3] A great deal of information about the Z phase such as the presence of a Z phase, the orientation relationship between the Z phase and the matrix [11], the main metallic composition of the Z phase [12-15] and the size distribution of the Z phase [16] has been reported by many researchers. Additionally, it has been observed that the Z phase precipitates after creep in both weld metals and the heat-affected zone. [17,18] Danielsen et al. has established a thermodynamic model for the Z phase using experimental data and a literature survey. [19] We need to explain how the Z phase affects creep strength degradation based on previous work regarding the Z phase. However, the precipitation behavior of the Z phase mentioned above is different among various steels. The existing information on the Z phase is not enough for a discussion on the degradation mechanism of the creep strength.

To remedy this lack of information, this paper systematically clarifies the precipitation sites, main metallic composition, size distribution, number density of Z phases, and the effect of stress and/or strain on Z phase behavior in four kinds of 9-12% Cr ferritic heat resistant steels. In addition, in order to clarify the effect of Z phase precipitation on creep strength over a wide range of temperatures, TTP diagram of Z phase was investigated.

2. Experimental procedure

The steels examined were ASME-T91[20],T92[21] and T122[22,23] with and without δ-ferrite. The chemical compositions and heat treatment conditions of the steels are given in Table 1. All steels have a tempered martensite structure. T122[22]with 10.65 mass% in Cr content (T122-s) includes no δ-ferrite, while T122[23] with 12.10 mass% in Cr content (T122-d) contains δ-ferrite. The volume fraction of δ-ferrite was evaluated to be about 5%. [24] Creep tests were performed under a constant load in air using specimens 6 mm in gauge diameter and 30 mm in gauge length. The microstructures were observed using a conventional TEM and an energy-filtered TEM (EF-TEM) at 200 kV. Extracted carbon replicas were prepared from the gauge and grip portions of crept samples for TEM observation. The compositions of the precipitates were analyzed by energy dispersive X-ray spectrometry (EDS). The diameters and number densities of the precipitates were evaluated in a selected area of 255 μm^2 for each sample.

3. Results and Discussion

3.1 Creep rupture strength of the steel studied at 600°C

Figure 1 shows the applied stress and rupture time diagram of the steels studied at 600°C. The creep strengths of T92 and T122 with tungsten are higher than that of T91. However, in the

long-term region, the creep strength decreases in all of the steels. In particular, the drop in creep strength for T122-d is larger than that in the other steels. It has been reported that the Z phase precipitates after 10,000 h of creep at 600°C. [12] We selected samples crept at 600°C for about 7,000 to 40,000 h to analyze the precipitation behavior of the Z phase in order to compare the precipitation behavior of Z phase among the steels studied.

Table1 : Chemical compositions(in mass%) and heat treatment conditions of the steel studied.

	C	Si	Mn	P	S	Ni	Cr	Mo	W	Cu
ASME-T91	0.0900	0.29	0.35	0.009	0.002	0.28	8.70	0.90	—	0.032
ASME-T92	0.0980	0.29	0.42	0.007	0.0013	0.13	9.50	0.36	1.74	—
ASME-T122-s	0.1300	0.31	0.60	0.017	0.001	0.36	10.65	0.33	1.87	0.86
ASME-T122-d	0.1100	0.27	0.59	0.015	0.002	0.33	12.10	0.34	1.82	0.82

	V	Nb	Al	B	N	Normalizing	Tempering
ASME-T91	0.22	0.072	0.001	—	0.044	1050°C, 10min A.C.	765°C, 30min A.C.
ASME-T92	0.19	0.062	0.009	0.0020	0.0462	1100°C, 12min A.C.	780°C, 60min A.C.
ASME-T122-s	0.19	0.050	0.007	0.0024	0.057	1050°C, 10min A.C.	770°C, 360min A.C.
ASME-T122-d	0.19	0.060	0.012	0.0030	0.066	1050°C, 10min A.C.	790°C, 180min A.C.

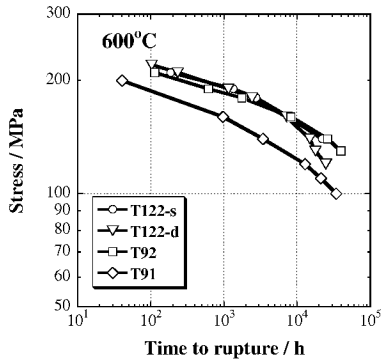

Figure 1 : Creep rupture strength of the steel studied.

3.2 Identification method of Z phase

The Z phase contains mainly V, Nb, Cr and N [3], while MX carbonitrides include V, Nb, C, N and a small amount of Cr. [12] We can distinguish the Z phase from MX carbonitrides by elemental mapping. Several researchers have reported [25,26] that the Z phase can be identified by comparing Cr, V and N maps using EDS or EF-TEM methods. Bright field and energy-filtered images of Cr, V and N in the crept samples are shown in Figure 2. The high contrast particles in the Cr map are $M_{23}C_6$ since $M_{23}C_6$ contains mainly Cr and Fe. MX

carbonitrides can be seen in the V and N maps. However, several particles are present in both the Cr and V maps as indicated by the arrows. Figure 3 is the EDS spectrum for the particles indicated by the arrows. This spectrum is in good agreement with typical EDS spectra of Z phases previously reported in the literature. [27,28] In order to confirm whether the particles with strong contrast in the Cr and V maps are Z phase or not, the electron diffraction pattern of the particles was analyzed. Figure 4 shows the electron diffraction pattern for the particles that were regarded as a Z phase by elemental mapping. The particles were observed in crept samples for T92 and T122-d. A Z phase was identified based on electron diffraction patterns of the selected areas. The Z phase possessed a tetragonal unit cell with a = 0.286 nm and c = 0.739 nm, as reported by Strang et al. [3] In short, we can use elemental mapping as an identification method for the Z phase. In this study, we also obtained an EDS spectrum for all of the Z phases to investigate their metallic compositions.

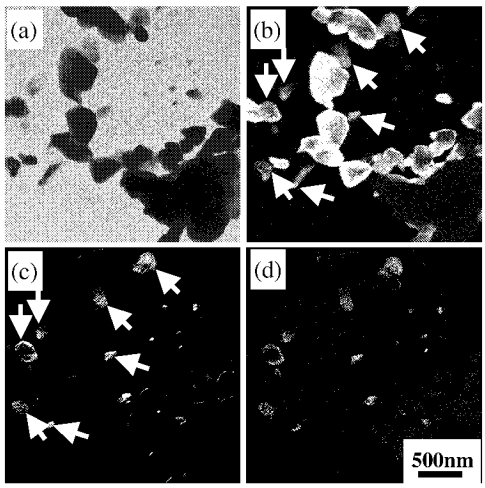

Figure 2 Bright filed image (a) and energy filtered image of (b)Cr, (c)V, and (d) N. 600°C, t_r = 34,141.0h

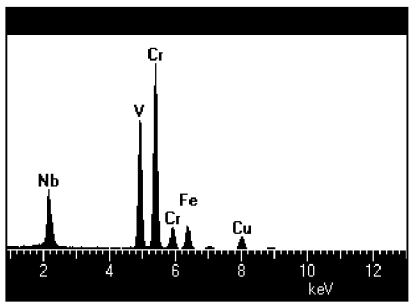

Figure3 EDS spectrum of the particle indicated by arrow in Fig.2.

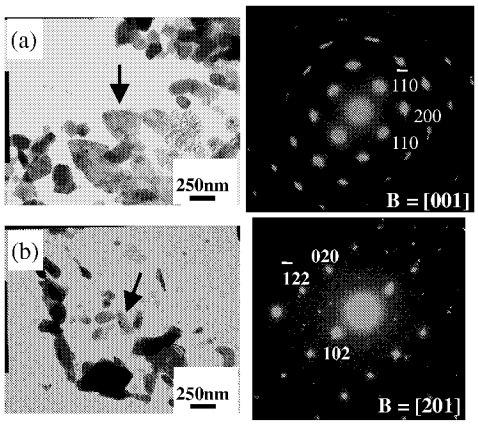

Figure4 Electron diffraction pattern analysis of Z phase. (a)T122-d (600°C, 24,656.4h) (b) T92 (600°C, 39,539.9h).

3.3 Distribution of Z phase particles

The distribution of precipitates before creep exposure for all of the steels is shown in Figure 5. The particles were colored based on the elemental maps of Cr, V and N. Prior austenite grain boundaries and/or packet boundaries predicted by the distribution of precipitates are also shown as dashed lines in the figure. $M_{23}C_6$ (black particles) and MX carbonitrides (grey

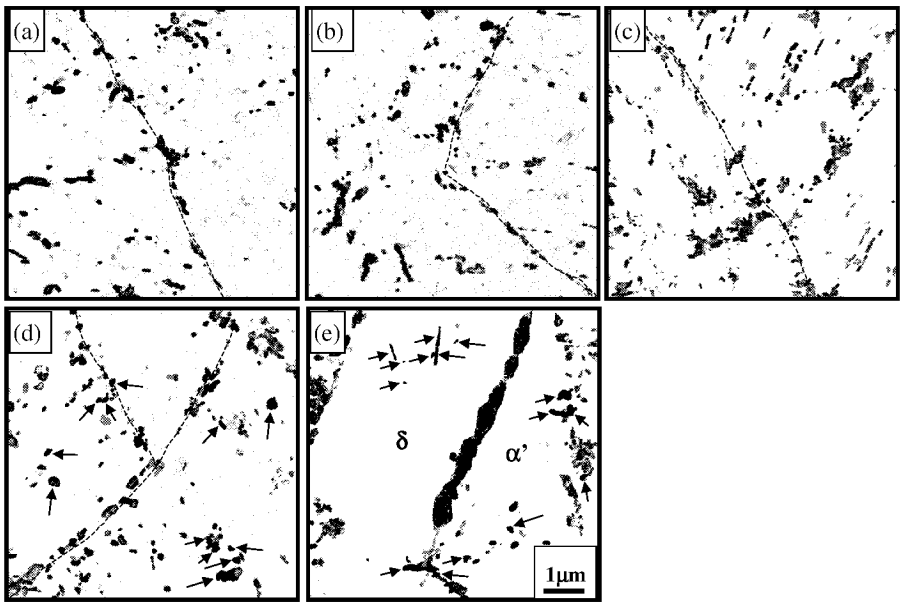

Figure5 Precipitates distribution before creep. (a)T91, (b)T92, (c)T122-s, (d),(e) T122-d Grey particles indicate MX carbonitrides. Arrows indicate M_2X.

particles) were observed in all steels. M_2X(with arrow) was also seen in T122-d. It has been assumed that MX carbonitrides are located inside lath grains. However, a recent study indicated that MX carbonitrides are present not only inside lath grains, but also at prior austenite grain boundaries, packets and block boundaries. [15,29] In Figure 5, MX carbonitrides are also distributed around prior austenite grain boundaries and/or packet boundaries in all of the steels. In addition, MX carbonitrides were also present at boundaries between martensite and δ-ferrite in T122-d.

Figure 6 shows the precipitate distributions in the gauge portion of crept samples for all of the steels. The dashed lines are the predicted prior austenite grain boundaries and/or packet boundaries. The Laves phases are not shown in the figure since it is difficult for EF-TEM to provide elemental maps of W and Mo forming Laves phases. The grey particles indicate Z phases identified by comparing the Cr and V maps. It was confirmed by EDS that all of the grey particles have a typical spectrum for the Z phase. In all of the steels, the Z phase is mainly located around prior austenite grain boundaries and/or packet boundaries. A large number of Z phases are also present around the δ-ferrite in T122-d. The Z phase formation consumes the MX carbonitrides, since the main metallic composition of the Z phase is similar to that of MX carbonitrides. Indeed, the number of MX carbonitride particles is very small in T122-d, which has many Z phases. Therefore, MX carbonitrides at prior austenite grain boundaries and boundaries between martensite and δ-ferrite, shown in Figure 5 contribute to the formation of Z phases after long-term creep. Consequently, Z phase formation after long-term creep can decrease the strength of the area around prior austenite grain boundaries and δ-ferrite due to the disappearance of MX carbonitrides.

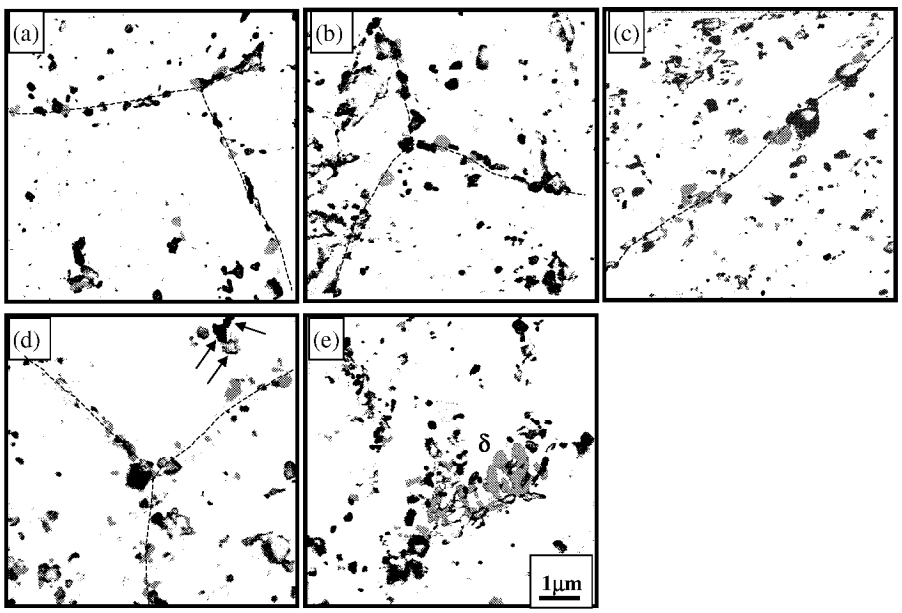

Figure6 Precipitates distribution after creep exposure. (a) T91 : 600°C - 34,141h, (b) T92 : 600°C - 39,539.9h, (c) T122-s :600°C - 22,002.9h, (d)-(e) T122-d : 600°C - 24,656.4h Grey particles indicate Z phase. Arrows indicate M_2X.

3.4 Metallic composition of the Z phase

The Nb-V-Cr balance of all Z phase particles of crept samples in all steels are compared in Figure 7, although the Z phase contains several mass percent of Fe, as discussed later. The main metallic composition of the Z phase in T91 is in good agreement with that in T92. On the other hand, a Z phase with a lower Nb content is observed in T122-s and T122-d in contrast with T91 and T92. The mean metallic compositions of the Z phases are summarized in Table 2. The Nb and Cr contents of T122 are lower and higher than those of T91 and T92, respectively. The main difference between T122, T91 and T92 is in the Cr content of the steel, indicating that Z phase behavior depends on the Cr content of the steel. It has been reported [13] that M_2X changes to a Z phase during creep exposure. In T122-d, several M_2X particles were observed before creep, as shown in Figure 5, leading to the acceleration of Z phase formation during creep exposure. The mean metallic compositions of the Z phases and M_2X for T122-d after creep exposure are listed in Table 3. If the V and Nb contents increase in the M_2X, M_2X can change to a Z phase. The presence of a Z phase with lower Nb content in T122 may be related to the previous existence of M_2X. There is no difference in the metallic composition of the Z phases around the δ-ferrite areas and in other areas.

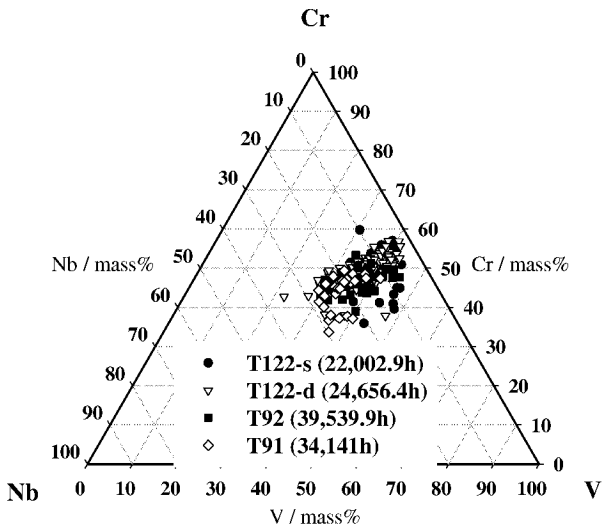

Figure7 Nb-V-Cr balance of Z phase in all steels.

Table 2 : Mean metallic composition of Z phase. (mass%)

	T91	T92	T122-s	T122-d
V	32.4	34.8	36.8	33.7
Cr	44.0	44.2	46.9	49.6
Nb	19.4	16.3	11.4	11.0
Fe	4.2	4.7	4.9	5.7

Table 3 : Mean metallic composition of Z phase and M_2X in T122-d. (mass%)

	V	Cr	Nb	Fe
M_2X	17.0	79.9	-	3.1
Z phase	33.7	49.6	11.0	5.7

creep condition : 600°C, tr = 24,656.4h

3.5 Size distribution and number density of Z phase

Figure 9 shows the size distributions of the Z phase around prior austenite grain boundaries and/or packet boundaries for crept samples in all of the steels. The creep exposure time of the samples was between 22,000 and 40,000 h. The mean diameters of the Z phases are also indicated in the figure. The size distributions are not different among the steels. However, the mean diameter of Z phase in T122-d is relatively large in spite of the shorter creep exposure time in contrast with those of T91 and T92. Danielsen et al. [19] reported that the driving force of Z phase formation depends on the Cr content in high Cr ferritic steels. In T122-d, Z phase formation should be faster, since the Cr content of T122-d is the highest among the steels studied. The difference in the driving force for Z phase formation can be predicted to lead to differences in the mean size of the Z phases shown in Figure 9. The size of the Z phases is obviously larger than that of the MX carbonitrides shown in Figure 6. Therefore, the contribution of the Z phase itself to strengthening of the material will be smaller than that of MX carbonitrides.

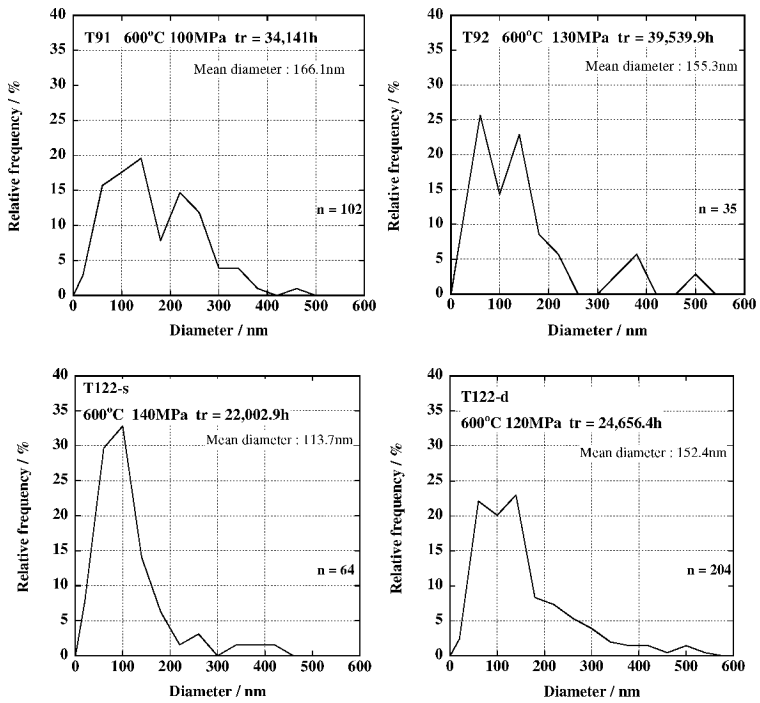

Figure8 Size distribution of Z phase in all steels.

The number densities of the Z phases around prior austenite grain boundaries and/or packet boundaries for samples crept for long-term are listed in Table 4. The number densities estimated on replica is not absolute value. However, the inter-particle spacing of the Z phases, λ, was roughly calculated from the number density p using the equation $\lambda = 1/\sqrt{p}$. The

inter-particle spacing of the Z phases was evaluated to be between 1.1 and 2.7 μm in all of the steels. It was reported [30] that typical inter-particle spacings of $M_{23}C_6$, MX, and Laves phases are 0.26, 0.32, and 0.41 μm, respectively. The inter-particle spacing of the Z phases observed here is much larger than those of other precipitates. Z phase formation itself cannot give rise to higher Orowan stress, in contrast with other precipitates. Figure 10 shows the change in the number density of the Z phases during creep exposure at 600°C. All data was obtained from samples ruptured after about 7,000 to 40,000 h. The number density of T92, T122-s, and T122d increased with increasing time to rupture, while the number density of T91 did not change during creep exposure. The order of the number densities of the Z phases is T122-d (12.10 mass% Cr), T91 (8.70 mass% Cr), T122-s (10.65 mass% Cr) and T92 (9.50 mass% Cr). This order corresponds to that of the Cr content of the steels, except for T91. This result is in good agreement with the prediction by Danielsen et al. [19] In the next section, we will discuss the reason for the higher number density of Z phases in T91 in spite of the smaller Cr content. In T122-d, the strengthening effect of MX carbonitrides abruptly decreases after long-term creep exposure in contrast with other steels, in which a large number of Z phases consume many MX carbonitrides around prior austenite grain boundaries. The disappearance of MX carbonitrides promotes a preferential recovery of lath structures [9] around prior austenite grain boundaries. This can lead to an abrupt drop in creep strength, shown in Figure 1.

Table 4 : Number density and inter-particle spacing of Z phase.

	T91	T92	T122-s	T122-d
p / 10^{11}m^{-2}	3.3	1.4	2.6	8.0
λ / μm	1.7	2.7	2.0	1.1

T91 : 600°C - 34,141.0h
T92 : 600°C - 39,539.9h
T122-s :600°C - 22,002.9h
T122-d : 600°C - 24,656.4h

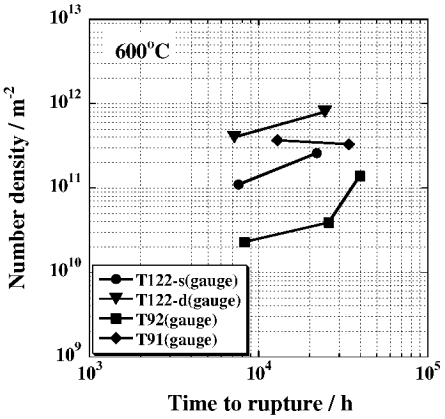

Figure 9 : Change of number density of Z phase during creep.

3.6 Effect of stress and/or strain on precipitation of Z phase

Change of number densities of Z phase in the gauge and grip portions of T91 and T122-d are shown in Figure 10. A large number of Z phases can be clearly seen in the gauge portions in contrast with the grip portions for both steels. The number density of the Z phase in the gauge portion is two to four times larger than that in the grip portion, indicating that stress and/or strain accelerates Z phase precipitation during creep exposure. In Figure 9, the number density of the Z phases in T91 is higher in spite of a lower Cr content. If creep strain

accelerates Z phase formation, it can be predicted that the amount of Z phase is higher in largely deformed material. Figure 11 compares rupture elongations among the steels at 600°C. The rupture elongation in T91 is higher than those in T92 and T122 at almost the same time. This indicates that the amount of creep deformation in T91 may be larger than those in other steels. In short, it is likely that the number density of the Z phases in T91 may be higher due to the large amount of creep strain. We compared the metallic composition of the Z phases in the gauge and grip portions. However, we did not find a difference in the metallic compositions between the gauge and grip portions.

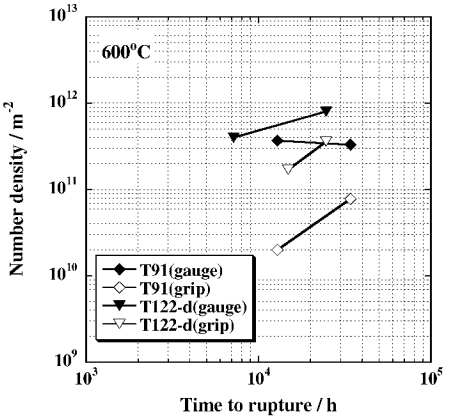

Figure 10 : Number density of Z phase in gauge and grip portions.

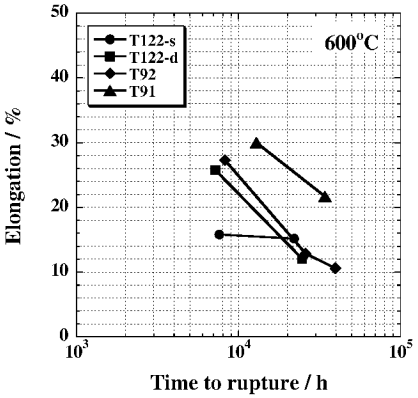

Figure 11 : Rupture elongation of all steels.

3.7 Temperature dependence of precipitation behavior of Z phase

Figure 12 shows TTP diagram of Z phase for T91. The crept samples corresponding to solid and open marks were investigated. Solid mark is plotted when the Z phase is observed in an area of 255μm^2 by the method shown in Fig.2. The Z phase forms after creep exposure at not only 600°C and 650°C but also 550°C. However, we can not detect the Z phase after creep exposure for 62475.0 h at 500°C and for 14106.5 h at 700°C. Danielsen et al. predicted by thermodynamic models that Z phase precipitation takes place at the temperatures lower than 800°C in ASME-T122 steel [19]. We may find Z phase after creep exposure for much longer time at 500°C and 700°C. T91 is used at around 550°C in steam power plants. Besides, high Cr ferritic steels are candidate material for components in fast breeder reactor.[31] In that case, the steel is also supposed to be used at 550°C [31]. Therefore, it is important to evaluate how the Z phase decreases creep strength at 550°C. The Z phase was mainly located around prior austenite grain boundaries and/or packet boundaries at 550°C. However, MX carbonitrides consumed by Z phase formation at 550°C will less than that at 600°C since almost all the Z phase formed at 550°C was smaller than that at 600°C. Nb-V-Cr balance of all Z phase particles of crept samples are simply compared in Fig.13. The Nb and V content of Z phase decreases and increases with decreasing temperature. The same tendency was reported in other steels by Vodarek et al. [11]. Suzuki et al. reported that number of Nb-rich MX

carbonitrides decreases due to the Z phase formation at 650°C in T91 [7]. It can be predicted that not only Nb-rich MX carbonitride but also V-rich one disappears after creep exposure at 550°C since the V content of Z phase is larger at the temperature. The morphology and precipitation site of V-rich MX carbonitride is different from Nb-rich one [32]. Therefore, the effect of Z phase formation on creep strength degradation may depend on temperatures. Figure 14 demonstrates change of number density of Z phase particle during creep exposure. All data points were obtained from samples ruptured under several stresses. The number density of the Z phase at 550°C is lower than that at 600°C. It is predicted from the tendency of amount of Z phase at 550°C that the creep strength degradation due to the Z phase formation will be remarkable at long time more than 100,000h.

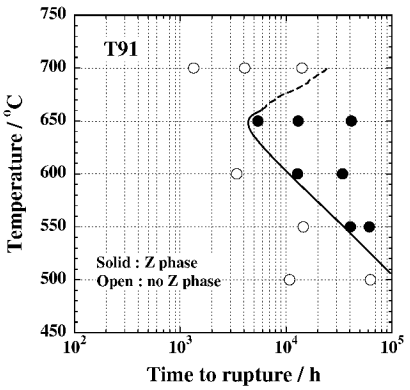

Figure12 TTP diagram of Z phase for T91 steel.

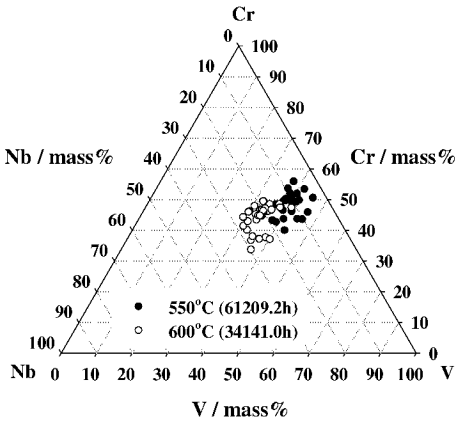

Figure13 Temperature dependence of main metallic composition of Z phase particles in T91.

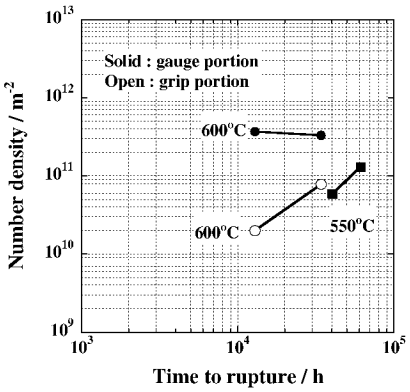

Figure14 Change of number density of Z phase during creep exposure in T91.

4. Conclusions

Z phase precipitation behavior was investigated after long-term creep exposure in T91, T92, T122 without δ-ferrite and T122 with δ-ferrite using elemental mapping through EF-TEM. The results are summarized as follows.

(1) Z phases precipitate around prior austenite grain boundaries and/or packet boundaries after creep exposure in all steels. In T122 with δ-ferrite, a large number of Z phases are also located around δ-ferrite regions. The MX carbonitrides around prior austenite grain boundaries and/or packet boundaries seem to be consumed by Z phase formation.

(2) The Z phase mainly consists of Cr, V and Nb. The main metallic composition of the Z phase is not different between T91 and T92 after creep exposure. The Nb content of the Z phase in T122 is lower than those in T91 and T92. The main metallic composition of the Z phase does not depend on precipitation sites such as prior austenite grain boundaries or δ-ferrite regions.

(3) The size distribution of the Z phases is almost the same among the steels studied. The mean diameter of the Z phases in T122 with δ-ferrite is relatively large in spite of the shorter creep exposure time compared with T91 and T92. The number density of the Z phases is 1.4 to 8.0×10^{11} m^{-2} in samples crept for 22,000 to 40,000 h at 600°C. The number density increases with increasing time to rupture except for T91. The order of number density of the Z phases is T122 with δ-ferrite, T91, T122 without δ-ferrite, and T92. This order relates to the Cr content of the steel. The highest number density of Z phases in T122 with δ-ferrite contributes to an abrupt decrease in creep strength since Z phase formation consumes a large number of MX carbonitrides.

(4) In crept samples, the number density of Z phases in the gauge portion is two to four times larger than that in the grip portion. Stress and/or strain accelerate Z phase precipitation during creep exposure. Stress and/or strain do not influence the main metallic composition of the Z phase.

(5) The Z phase was found in specimens crept at 550°C to 650°C in T91. However, we did not find the indication of the Z phase formation at 500°C and 700°C. The Nb content of Z phase observed at 550°C is lower than that at 600°C in T91. The number density of Z phase measured at 550°C is lower than that at 600°C, indicating that the preferential recovery of lath structure around prior austenite grain boundary is not so pronounced at 550°C.

References

[1] J. Hald : Steel Res., 67 (1996), 369.

[2] P. J. Ennis, A. Zielinska-Lipiec, O. Wachter and A. Czyrska-Filemonowicz : Acta mater., 45 (1997), 4901.

[3] A. Strang and V. Vodarek : Mater. Sci. Technol., 12 (1996), 552.

[4] J. Bursik and N. Merk : Proc. 'Mechanical Behavior of Materials at High Temperature', NATO Advanced Study Institute, Sesimbra, (1995), 1.

[5] V. K. Sikka : Proc. Topical Conf. on Ferritic Alloys for Use in Nuclear Energy Technologies, Warrendale PA, TMS-AIME, (1984), 317.

[6] M. Taneike, F. Abe and K. Sawada : Nature, 424 (2003), 294.

[7] K. Suzuki, S. Kumai, H. Kushima, K. Kimura and F. Abe : Tetsu-to-Hagane, 89 (2003), 691.

[8] S. J. Brett, D. L. Oates and C. Johnston : Proc. Creep and Fracture in High Temperature Components – Design and Life Assessment Isuues, ed. by I. A. Shibli et al., DE*Stech* Publications, Inc., (2005), 563.

[9] H. Kushima, K. Kimura and F. Abe : Tetsu-to-Hagane, 85 (1999), 841.
[10] K. Kimura : Proc. Creep and Fracture in High Temperature Components – Design and Life Assessment Isuues, ed. by I. A. Shibli et al., DE*Stech* Publications, Inc., (2005), 1009.
[11] V. Vodarek and A. Strang : 7th Liege Conf. on 'Materials for Advanced Power Engineering, ed. by J. Lecomte-Beckers et al., Forshungs-zentrum, Jülich GmbH, Jülich, (2002), II.1223.
[12] K. Suzuki, S. Kumai, H. Kushima, K. Kimura and F. Abe : Tetsu-to-Hagane, 86 (2000), 550.
[13] R. Ishii, Y. Tsuda, M. Yamada and K. Kimura : Tetsu-to-Hagane, 88 (2002), 36.
[14] M. Svoboda, J. Bursik, I. Podstranska, A. Kroupa, V. Sklenicka and K. H. Mayer : 7th Liege Conf. on 'Materials for Advanced Power Engineering, ed. by J. Lecomte-Beckers et al., Forshungs-zentrum, Jülich GmbH, Jülich, (2002), III.1521.
[15] K. Sawada, M. Taneike, K. Kimura and F. Abe : ISIJ Int., 44 (2004), 1243.
[16] H. Cerjak, E. Letofsky, R. Hanus, H. Heuser and C. Jochum : Proc. 5th International Charles Parsons Turbine Conference, ed. by A. Strang et al., IOM Communications Ltd, (2000), 386.
[17] H. Heuser and C. Jochum : Proc. 3rd Conference on Advances in Material Technology for Fossil Power Plants, ed. by R. Viswanathan et al., The Institute of Materials, (2001), 249.
[18] M. E. Abd El-Azim, A. M. Nasreldin, G. Zies and A. Klenk : Mater. Sci. Tecnol., 21 (2005), 779.
[19] H. Danielsen and J. Hald : Proc. 4th International Conference on Advances in Materials Technology for Fossil Power Plants, ed. by R. Viswanathan et al., ASM International, (2004), 999.
[20] NRIM Creep Data Sheet, No.43, National Research Institute for Metals, Tsukuba, Japan, 1996.
[21] NIMS Creep Data Sheet, No.48, National Institute for Materials Science, Tsukuba, Japan, 2002.
[22] NIMS Creep Data Sheet, No.51, National Institute for Materials Science, Tsukuba, Japan, 2006.
[23] NIMS Creep Data Sheet, No.52, National Institute for Materials Science, Tsukuba, Japan, 2006.
[24] M. Yoshino, Y. Mishima, K. Sawada, Y. Toda, H. Kushima and K. Kimura : CAMP-ISIJ, 18 (2005), 1623.
[25] M. Igarashi, H. Semba, H. Okada, H. Okubo, S. Muneki, K. Yamada and F. Abe : Proc. 9th Ultra-Steel Workshop, National Institute for Materials Science, (2005), 96.
[26] M. Hättestrand and H. O. Andrén : Micron, 32 (2001), 789.
[27] G. Götz and W. Blum : Mater. Sci. Eng. A348 (2003), 201.
[28] I. Letofsky-Papst, P. Warbichler, F. Hofer, E. Letofsky and H. Cerjak : Z. Metallkd., 95 (2004), 18.
[29] K. Sawada, K. Kubo, T. Hara and F. Abe : 7th Liege Conf. on 'Materials for Advanced Power Engineering, ed. by J. Lecomte-Beckers et al., Forshungs-zentrum, Jülich GmbH, Jülich, (2002), II.1181.
[30] K. Maruyama, K. Sawada and J. Koike : ISIJ Int., 41 (2001), 641.
[31] T. Onizawa, T. Wakai, M. Ando and K. Aoto: Proc. Creep and Fracture in High Temperature Components – Design and Life Assessment Issues, ed. by I.A. Shibli et al.,

DE*Stech* Publications, inc., (2005), p.130
[32] K. Suzuki, S. Kumai, Y. Toda, H. Kushima and K. Kimura: ISIJ Int. Vol. 43 (2003), p. 1089

ON THE ROLES OF M_2X AND Z-PHASE IN TEMPERED MARTENSITIC 9-12% Cr-STEELS

H. Chilukuru, K. Durst, M. Göken, W. Blum

University Erlangen-Nürnberg, General Material Properties, Martensstr. 5, 91058 Erlangen, Germany

Abstract

Z-Phase precipitation accompanied by dissolution of the fine M_2X and MX type of precipitates is believed to be the primary cause for the accelerated degradation of creep strength in 9-12% Cr steels used in steam power plants. Current investigations show that after the precipitation of Z-Phase no complete dissolution of M_2X precipitates was observed after 50 kh at 600 °C. EDX analysis was carried out on the extraction replicas in STEM to identify the individual type of precipitate phases and to quantify their sizes and volume fractions. M_2X coarsens much faster than VX, forming large M_2X precipitates at subgrain boundaries at the expense of fine M_2X precipitates in the subgrain interior. This reduces the precipitation hardening of the subgrain interior. It has been demonstrated with the composite model of creep Mikora that loss of hardening in the subgrain interior leads to an increase of creep rate by an order of magnitude. M_2X may thus be another reason for the degradation in creep strength.

1 Introduction

In pursuit of materials that sustain high temperatures in steam power plants several Cr-steels (Table 1) were designed for the project MARCKO DT1/2. W-bearing steels 1A and 2A, W-free steels 3A and 4A were developed for use at 600°C and B- and Co-bearing steels 5A and 6A for use at 625°C. Table 1 shows their chemical compositions. In the present work we focus on the influence of precipitates, in particular the phase M_2X (M: metal, X: C, N) and the Z-phase, on the long-term creep resistance.

Alloys	1A	2A	3A	4A
C	0.12	0.13	0.14	0.115
Si	0.10	0.29	0.8	0.41
Mn	0.42	0.82	0.55	0.54
Ni	0.76	0.52	0.56	0.12
Cr	10.7	9.51	9.99	9.04
Mo	1.07	1.02	1.40	0.86
W	1.04	1.02		
Co				
V	0.16	0.19	0.17	0.20
Nb	0.05	0.059	0.059	0.10
B		0.0005		
N	0.056	0.041	0.041	0.058
Al				0.021

Table 1: Alloys investigated in the project and their compositions in mass%

In-situ TEM experiments were carried out with the equipment and support kindly provided by U. Messerschmidt at MPI für Mikrostrukturforschung, Halle, Germany. To our knowledge this is the first time that an in-situ TEM investigation was done on 9-12 % Cr steels to show dislocation motion during deformation at elevated temperature of 650 °C. Fig. 1 shows still pictures from the investigation. Dislocations are bowed out between obstacles under the stress acting in the thin foil. Precipitates evidently act as strong obstacles (Fig. 1a). The dislocation activity at the free end of a subgrain boundary pinned by precipitates suggests dissolution of the boundary. Fig. 1(b) shows dislocations leaving a subgrain boundary which is heavily loaded with precipitates.

These in-situ findings support the basic assumptions in the model Mikora [12], in particular pinning of subgrain boundaries by precipitates, knitting-out of dislocations from subgrain boundaries, stress concentration at subgrain boundaries and precipitation hardening in the subgrain interior.

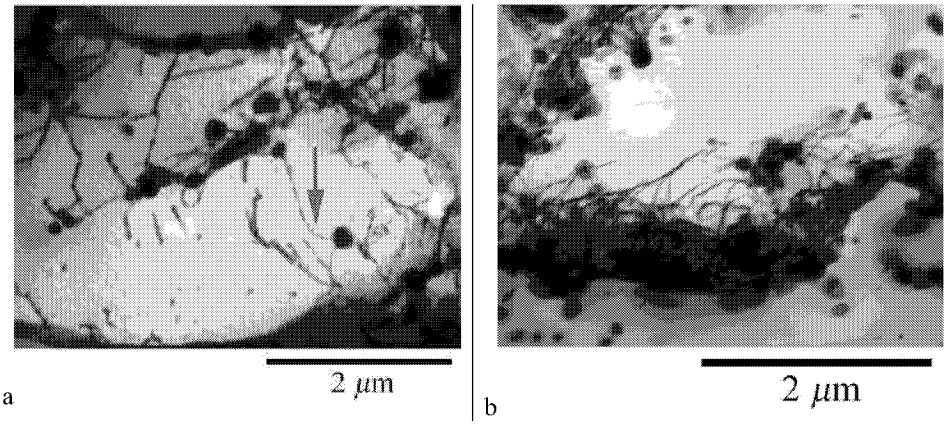

a b

Figure 1: TEM micrograph of steel 2A during in-situ deformation at 923 K (a) showing strong bowing of a dislocation at a precipitate and free end of subgrain boundary (center) which probably is in process of dissolution. (b) Dislocations bowing out from a subgrain boundary.

2 Influence of prior austenite grain size

The prior austenite grain size d_{aust} in 9-12 % Cr steels depends on the austenitisation treatment. Table 2 shows that d_{aust} increases with increase in austenitisation temperature, time and decrease of cooling rate. Differences in d_{aust} do not affect the long-term deformation behavior significantly. For instance, d_{aust} in 2A is larger than in 1A by a factor 20, but the long-term deformation behavior of 2A is better than that of 1A (compare Fig. 9 and Fig. 10).

Table 2: Austenite grain sizes as a result of austenitisation treatment

Alloys		1A	2A	3A	4A
Austenitisation	T / °C	1050	1070	1070	1050
	t/ h	7	12	20	10
	cooling	oil	air	oil	blower
d_{aust} /μm		57	1107	362	62

This supports the view that long-term deformation behavior is significantly dependent on strengthening contributions from other microstructural elements such as dislocations, subgrains and precipitates.

3 Precipitates

An essential contribution to the deformation resistance comes from particle hardening. The initial state does not provide full insight into the deformation resistance of the alloy at elevated temperatures, as this state is changed by the coarsening of phases, formation of new and dissolution of existing phases. In the following we report the method of quantification of the precipitate structure and present results on changes in the precipitate structure which lead to distinct loss of initially high creep resistance.

3.1 Replica analysis

The method of extracting the precipitates from the matrix has been found successful for analyzing the precipitate structure [1 - 3]. Besides the precipitate size, the volume fraction f_p of precipitates is a most important parameter, not only for estimating precipitation hardening, but also as input for thermodynamic data bases. In the past an empirical formula has been used to provide a rough estimate of f_p [5]. As described in [2], this formula needs to be modified on the basis of scanning electron microscopic (FEG-SEM) investigations of the etched steel surface as

$$f_p = \frac{\sum_j V_{p,j}}{A \cdot d_p},$$

where $V_{p,j}$ are the volumes of individual precipitates j =1, 2, ... and the denominator is the sampling volume given by the product of the investigated area A and the mean precipitate size d_p (see [13]).

3.2 M_2X

In 9-12 % Cr steels, the phases M_2X and MX are important contributors to deformation resistance as they precipitate in large numbers within the subgrain interior restricting the dislocation motion there. Z-phase has been proposed [4 - 8] to exert a deleterious effect by dissolution of VX and M_2X being thermodynamically less stable than Z-phase. This leads to loss of subgrain strengthening in the subgrain interior which is not compensated by hardening, because Z-phase precipitates on the subgrain boundaries (Fig. 4).

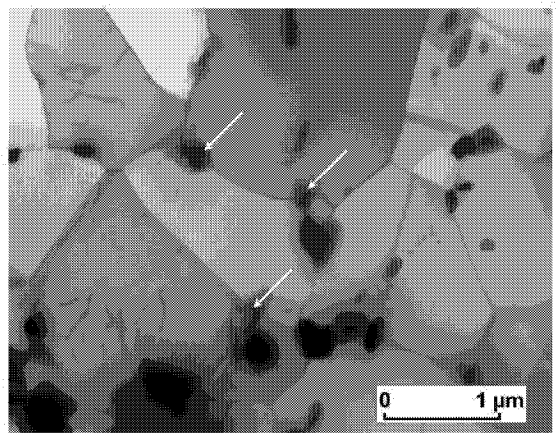

Figure 4: Z-phase particles located at the subgrain boundaries (from [3])

In their initial states 1A and 3A contain M_2X as a result of tempering below 700 °C in agreement with findings in [5]. In the course of deformation Z-phase precipitates in these alloys (Fig. 5). However, this is not related to fast disappearance of M_2X. Rather, numerous large M_2X particles were found especially on the subgrain boundaries. These particles were confirmed by analysis of chemical composition and crystal structure. The chemical composition of M_2X is distinctly different from that of Z-phase so that both phases can be clearly separated [12]. Fig. 6 shows that it is independent of the particle size, excluding the possibility of phase transformation during particle coarsening. The lattice constant of the hexagonal crystal structure determined from electron diffraction agrees well with literature data for M_2X [9]. The coarsening of M_2X at subgrain boundaries is quite fast in comparison to VX (Fig. 5). It must be related to dissolution of fine M_2X inside the subgrains, as there is no reason to assume that the volume fraction of M_2X increases.

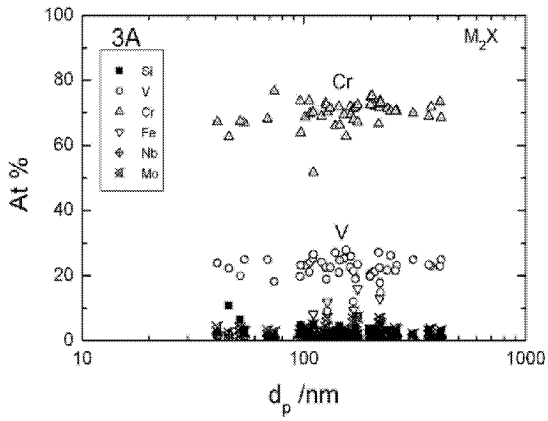

Figure 6: M_2X chemical composition is independent of particle size (EDX analysis in TEM replica)

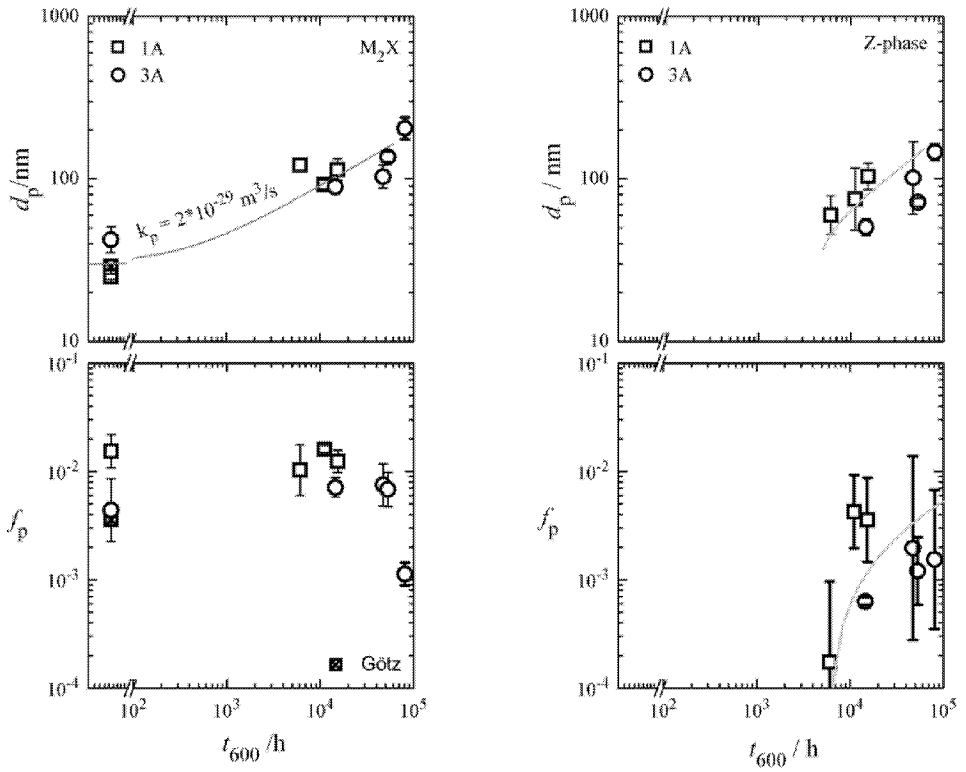

Figure 5: left: evolution of M_2X; right: evolution of Z-phase. Coarsening but no dissolution of M_2X by in the presence of Z-phase in 1A and 3A.

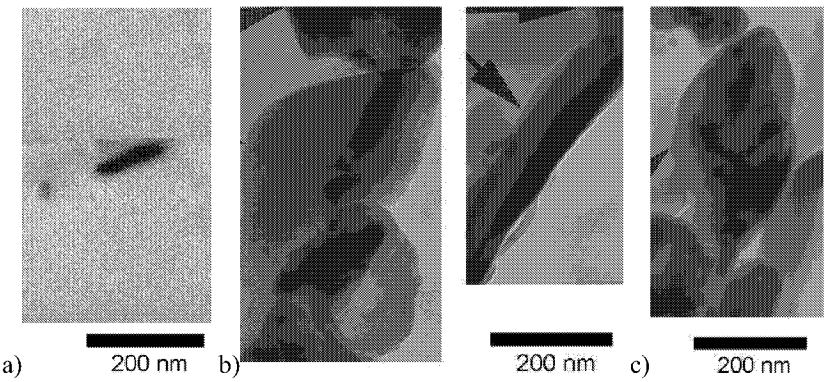

Figure 7: Evolution of M_2X particle size and shapes, suggesting a change in coherency (a) needle, (b) plate and plate tilted, (c) rod.

Why does M_2X coarsen so rapidly? Investigations on the shape of M_2X might provide the answer. In the initial state, M_2X precipitates are small, coherent, needle-shaped particles. In the course of deformation they become plate-shaped particles which may be semicoherent, and □nally large rod-shaped particle are found on the subgrain boundaries which are incoherent (Fig. 7). This loss in coherency increases the interfacial energy and therefore increases the coarsening rate.

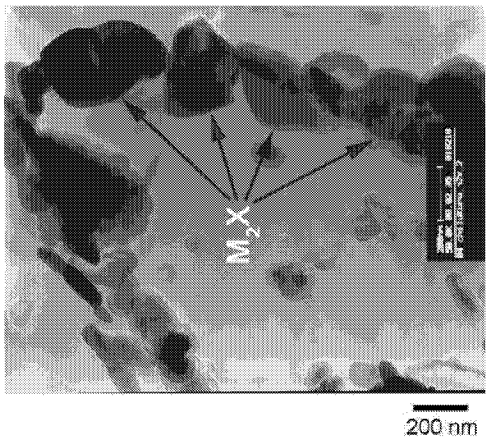

Figure 8: Steel 1A after 20 kh @ 600 ◦C; subgrain boundary decorated with few large M_2X particles precipitated at the expense of small M_2X particles that were present inside the subgrain.

Coarsening of different phases has specific consequences on the deformation resistance. For instance, coarsening of $M_{23}C_6$ will destabilize the subgrain boundaries (lower resistance against migration). Coarsening of M_2X particles at subgrain boundaries at the expense of □ne M_2X precipitates in the subgrain interior (Fig. 8) reduces the precipitation hardening of the subgrain interior and thereby deteriorates the deformation resistance. The microstructural model Mikora, which accounts for hardening by precipitates, subgrains free dislocations (see e.g. [10, 11]), predicts a factor of 10 increase in creep rate as the loss precipitation hardening in the subgrain interior gets lost [10], adding to the normal increase of creep rate with strain by subgrain coarsening.

If the phase M_2X is responsible for enhanced degradation of creep resistance, the question arises why Z-phase is usually found under conditions of anomalously fast degradation of creep resistance. The answer may lie in a correlation between M_2X and Z. Large, incoherent M_2X particles at the subgrain boundaries with high interfacial energy, large interface and high V-content constitute favorable nucleation sites for Z-phase. Consequently, M_2X may not only initiate the anomalous degradation of creep resistance, but also cause nucleation of stable Z at the subgrain boundaries, which will then enhance the degradation because it contributes to reduction of precipitation hardening in the subgrain interior by V-containing phases. Thus M_2X may be a clue in the understanding of enhanced degradation of the creep resistance of 9-12%Cr steels.

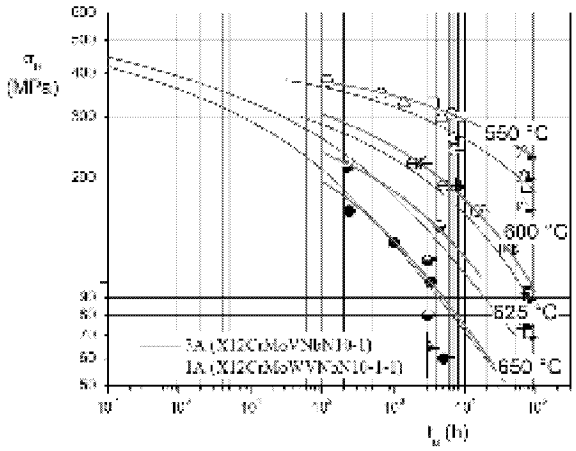

Figure 9: 1A blue (X12CrMoWVNbN1011) and 3A red (X12CrMoVNbN101) creep rupture curves from IfW Darmstadt

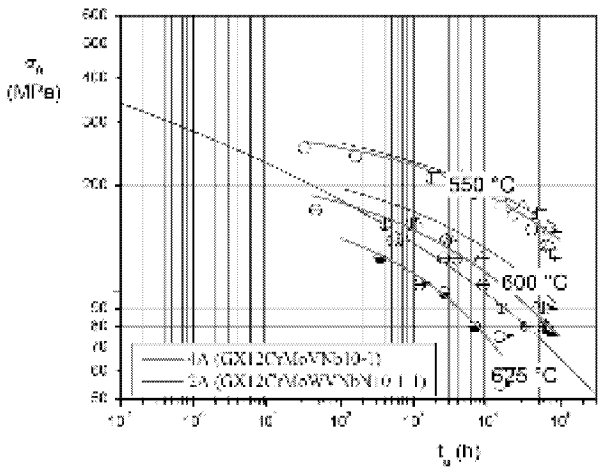

Figure 10: 4A red (X12CrMoWVNbN1011) and 2A blue(X12CrMoVNbN101) creep rupture curves from IfW Darmstadt

The technological consequence of these considerations is that the thermal treatment of steels designed for long term use at high temperature should be such as to avoid precipitation of V in the form of M_2X. This means in particular that low temper temperatures must be avoided.

6 Microstructural interpretation of the creep rupture behavior

This section provides the microstructural interpretation for the experimental creep rupture curves from IfW Darmstadt displayed in Figs. 9 and 10. The W-based steels 1A, 2A and W-free 3A, 4A are designed for operation at 600°C. The forged steels 1A and 3A show better initial creep resistance due to their small initial subgrain size w_0 and numerous fine M_2X particles in comparison to larger w_0 and MX particles in the cast steels 2A and 4A. As evident from the creep rupture curves, the deterioration of creep resistance with increasing rupture time is faster in 1A and 3A in comparison to 2A. This is primarily due to the relatively rapid coarsening of M_2X (section 4.2). According to the Ostwald ripening law, the coarsening of precipitates occurs at a certain constant rate of increase of precipitate volume with time. This coarsening becomes relevant only at a time where the increase of volume is significant relative to the initial volume of the precipitates. This time decreases when the initial size of precipitates $d_{p,0}$ is small and the coarsening rate is high. Smaller $d_{p,0}$ and higher coarsening rate of M_2X in comparison to MX explain why the creep resistance of 1A and 3A degrades faster than that of 2A and 4A. Consistent with the thermal activation of coarsening the degradation by coarsening of M_2X sets in at lower times for higher temperature. This explains why the point of intersection of the curves for 1A (with M_2X) and 2A (with MX) shifts to smaller times with increasing temperature.

The initial subgrain sizes in 1A and 3A are similar, giving no reason for a difference in creep rupture behavior. Yet the creep rupture strength of the W free 3A is better than that of W based 1A. Laves phase in the W-bearing steels is expected to stabilize the subgrain boundaries and increase the creep life of 1A. Obviously, this effect is not dominant here, but is masked by other changes in the microstructure probably related to carbonitride precipitates.

In the case of the cast steels the expectation of a positive effect of W is fulfilled. However, the W-free steel 4A shows abnormal fracture behavior with low fracture strain. For instance, the investigated 4A-specimen crept at 90 MPa at 600 °C has only 4.0 % fracture strain whereas a 3A-specimen crept at 125 MPa at 600 °C has 17.5 % fracture strain. This embrittlement may have to do with grain boundaries, for instance in relation with localized strain at grain boundaries, which may be due to locally coarsened microstructure, or to impurity segregation at the boundaries. However, there are no data to clarify this issue.

7 Summary

Precipitation hardening is essential for creep resistance of tempered martensite Cr steels to suppress dislocation glide and coarsening of the subgrain structure. If the steels are heat treated to be hardened by M_2X, they show relatively high initial creep resistance at temperatures around 873 K due to fine M_2X in the subgrain interior, but relatively low long-term creep resistance as M_2X coarsens rapidly at subgrain boundaries and dissolves in the subgrain interior.

8 Acknowledgments

Financial support of the DFG in the DT1/2 project is gratefully acknowledged. We thank Prof. Messerschmidt and his coworkers, MPI, Halle, Germany, for performing the in-situ TEM deformation experiments at high temperature.

9 References

[1] G. Götz, Y. Qin, and W. Blum. Investigation of precipitation in cast martensitic annealed steel X12 CrMoVWNbN 1011 by semiautomatic EDX analysis in the scanning transmission electron microscope. In R. Viswanathan, W.T. Bakker, and J. D. Parker, editors, Advances in materials technology for fossil power plants, Proc. of the 3rd Conference held at University of Wales Swansea, 5th April 6th April 2001, pages 155–163, London, 2001. The Institute of Materials.

[2] T. Seibert, K. Durst, H. Chilukuru, W. Blum, and M. Göken. Quantitative Gefügeanalyse von 912%Cr Stählen mittels AFM, REM und TEM. in M. Göken, editor, 37. Praktischen Metallographie Sonderbände, Fortschritte in der Metallographie, page 73, Erlangen, Sept. 2005. DGM.

[3] R. Agamennone, W. Blum, C. Gupta, and Chakravartty. Evolution of microstructure and deformation resistance in creep of tempered martensitic 9-12%Cr2W5%Co steels. Acta Mater., to be published.

[4] K. Kimura, K. Suzuki, H. Kushima, and F. Abe:Precipitation of Z-phase and its effect on creep strength of Mod.9Cr1Mo steel. In R. Gladi□ A. Jakobov′na Z. Kubo□J. Purmensk′y M. Filip, V. Foldyna and J. Sobotka, editors, Proceedings of the 10th joint International Conference on Creep & Fracture of Engineering Materials and Structures, Creep Resistant Metallic Materials, 811 April 2001, pages 186– 195, Prag, Czech Republic, 2001. VitkoviceResearch and Development and TERIS 2002.

[5] G. Götz and W. Blum. In□uence of thermal history on precipitation of hardening phases in tempered martensite steel of type X12CrMoWVNbN1011. Mater. Sci. Eng. A, 348/12:201–207, 2003.

[6] H. Danielsen and J. Hald. Z-Phase in 9-12%Cr Steels. Technical Report M4313, Värmeforsk Service AB, 10153 Stockholm, February 2004.

[7] J. Hald. Long-term Stability of 912% Cr Steels Current Understanding and Future Perspectives. In Werkstoffe und Qualitätssicherung 2004, Dortmund, March 2004. VGB.

[8] I. Letofsky, Papst, P. Warbichler, F. Hofer, E. Letofsky, and H. Cerjak. On the occurrence of Z-phase in a creep tested 10% Cr steel. Z. Metallkd., 95(1):18, 2004.

[9] L. Lundin, S. Fällman, and H.O. Andr′en. Microstructure and mechanical properties of a 10% chromium steel with improved creep resistance at 600◦C. Mat. Sci. Tech., 13(3):232–242, 1997.

[10] X. H. Zeng and W. Blum. Modelling the In□uence of Microstructure on Creep Strength of GX12CrMoWVNbN 1011. In 29th MPA Seminar, Safety and Reliability in Energy Technology, Oct 2003, Stuttgart, 2003.

[11] D. Henes, H. Möhlig, S. Straub, J. Granacher, W. Blum, and C. Berger. Microstructure Based Modelling of the Long Term Monotonic and Cyclic Creep of the Martensitic Steel X 20(22) CrMoV 12 1. In H. Mughrabi, G. Gottstein, H. Mecking, H. Riedel, and J. Tobolski, editors, Microstructure and Mechanical Properties of Metallic HighTemperature Materials, pages 179–191, Weinheim, 1999. WileyVCH.

[12] K. Sawada, H. Kushima, and K. Kimura. Precipitation behavior of Z phase during aging and creep in 9-12 %Cr ferritic heat resistant steels. In International workshop on performance and requirements of structural materials for modern high efficient power plants, pages 96–104, Darmstadt, September 6-9 2005.

[13] T. Seibert, K. Durst, H. Chilukuru, M. Göken: Quantative microstructural analysis on the stability of MX and M2X in 9-12% Cr steels by AFM, SEM, TEM submitted to Liege 2006

ELECTRON DIFFRACTION STUDIES ON (Nb,V)CrN PARTICLES IN 12CrMoVNbN STEELS

Vlastimil Vodárek*, Hilmar K. Danielsen**, Flemming B. Grumsen**, John Hald**, Andrew Strang***

* VÍTKOVICE – Research and Development Ltd., Ostrava, Czech Republic
** TU of Denmark, Lyngby, Denmark
*** University of Leicester, Leicester, United Kingdom

Abstract

Electron diffraction studies on (Nb,V)CrN particles in 12CrMoVNbN steels revealed that most diffraction patterns were composed of zone axes belonging to a tetragonal unit cell with dimensions a=0.286nm, c=0.739nm and a FCC unit cell with the parameter a=0.404nm. The established lattice correspondence between the FCC and tetragonal unit cells is identical with that of the FCC subcell in the proposed tetragonal unit cell of the modified Z phase. Diffraction results indicate that small FCC and tetragonal microdomains are irregularly intermixed inside (Nb,V)CrN particles. Generally, the intensity of spots belonging to the FCC unit cell decreased with time of thermal exposure, and spots related to the tetragonal unit cell become more intensive. This can be regarded as an evidence of a descending volume fraction of FCC microdomains in (Nb,V)CrN particles with prolonged time of exposure. It can be expected that the FCC unit cell plays an important role in the formation of (Nb,V)CrN particles in 9-12%Cr martensitic steels. In situ transformation of the FCC unit cell into the tetragonal unit cell with prolonged time of exposure can take place by ordering of metal atom layers along the $[001]_{FCC}$ // $[001]_Z$ direction.

Keywords: 12CrMoVNbN steels, (Nb,V)CrN particles, electron diffraction, simulation of diffraction patterns, modified Z phase.

1. Introduction

(Nb,V)CrN particles were originally referred to as modified Z phase [1]. This minor phase has been recognised as an undesirable phase in creep resistant 9-12%Cr steels [1-4]. Precipitation of this complex nitride is accompanied by dissolution of both primary and secondary MX particles, which slow down the processes of recovery and recrystallisation of the matrix. Precipitation of the modified Z phase in 9-12%Cr steels usually results in a pronounced drop in creep rupture strength [1].

1.1 Structure of Z phase, NbCrN

Z phase was firstly detected in 1950's in austenitic steels containing niobium and nitrogen [5]. The structure of Z phase was studied by Ettmayer [6] and by Jack and Jack [7]. Ettmayer [6] studied the syntesized complex nitrides NbCrN and reported a tetragonal unit cell with parameters a=0.4283 nm and c=0.7361nm, space group F4bm.

Jack and Jack [7] studied Z phase in an austenitic steel and interpreted all the X-ray data by a tetragonal cell of dimensions a=0.3037nm, c=0.7391nm. The relationship between this unit cell and that of the Ettmayer's cell in the basal plane is $\sqrt{2}\mathbf{a}_{JACK} = \mathbf{a}_{ETTM.}$. For the unit cell proposed by Jack and Jack [7] systematic absences occur for hk0 when h + k = 2n + 1. Trial and error methods showed that Z phase is a complex nitride with ideal cell contents $Nb_2Cr_2N_2$ and an atomic arrangement shown by Fig. 1.

Both proposed structures for Z phase are identical within experimental error, even though that authors claim different unit cells and different space groups. The P4bn space group reported by Ettmayer [6] does not give systematic absences for hk0 with h+k=2n+1 (indexed on the unit cell proposed by Jack and Jack), and Ettmayer explains his observed absent reflections as the result of structure amplitudes which are coincidentally negligible or zero.

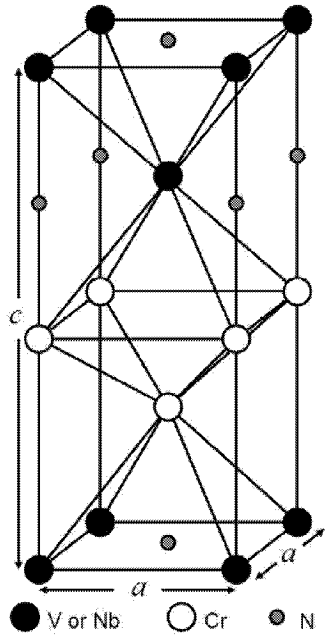

Fig. 1 Structure of Z phase, NbCrN, as proposed by Jack and Jack [7]

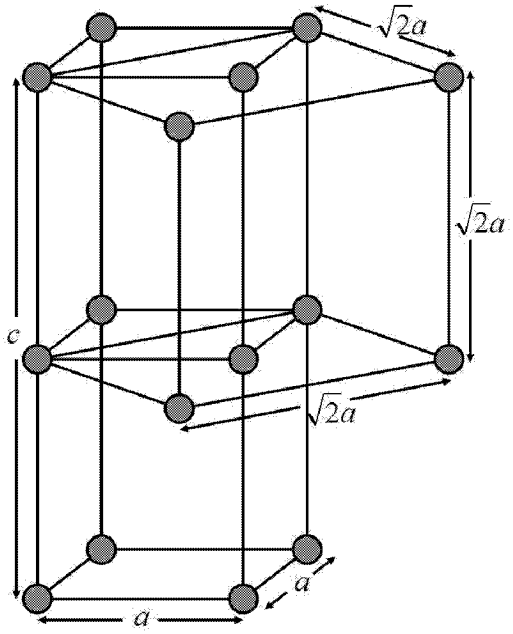

Fig. 2 The correspondence between the Z phase unit cell and the FCC subcell. Nitrogen and some metal atoms have been left out for clarity, [8].

The metal atom arrangement is characterized by double layers of similar atoms alternating along the c axis of the unit cell to give an AABBAABB... sequence. As can be seen in Fig. 2 in the upper part of the tetragonal unit cell the arrangement of metal atoms corresponds to the alignment of atom layers in the FCC cell. This might be the consequence of the general tendency to form the close-packed structures [6]. Nitrogen atoms occupy octahedral interstices. Each occupied site is one in which the nitrogen can be coordinated by a maximum number (five) of niobium and a minimum number (one) of chromium atoms. Interstitial nitrogen is important in stabilising the double layer transition metal nitrides [7].

It is considered that in specimens from steels of different composition and different thermal history there will be differences in atomic ordering among the structural sites, and that there may well be substitution for niobium and chromium by atoms of other transition metals [7]. In this case the differences in unit cell dimensions and reflected intensities are not unexpected.

1.2 Modified Z phase, (Nb,V)CrN

Investigations on minor phase evolution in martensitic 12CrMoVNbN steels using X-ray diffraction revealed apart from diffraction lines belonging to $M_{23}C_6$ and MX phases an additional strong diffraction peak corresponding to an interplanar spacing of d=0.226nm [9].

This diffraction line had an asymmetric shape and was found to be present only in records related to long-term exposures at testing temperatures of 550 and 600°C. The presence of this additional strong diffraction peak indicated that a substantial amount of another minor phase had formed in these steels during long-term thermal/creep exposure. Identification of this minor phase was however not possible because all other diffraction lines belonging to this phase were overlapped by either $M_{23}C_6$ or MX phases. Detailed analytical electron microscopy studies revealed that particles of this phase had a tetragonal unit cell with dimensions of a=0.286nm and c=0.739nm [10]. Based on the broad asymmetric diffraction peak in X-ray records some variability in unit cell dimensions is to be expected. These particles were rich in vanadium, chromium, niobium and nitrogen. Chemical composition of individual particles was very variable. It was proposed that vanadium partly substituted niobium in the original NbCrN phase and this resulted in the reduction of the lattice parameter in the basal plane. This (Nb,V)CrN phase was referred to as *modified Z phase* [10]. Chemical composition of the modified Z phase was found to be dependent on both chemical composition of steels and temperature of thermal/creep exposure [11]. The solution temperature of (Nb,V)CrN particles is significantly lower (T=800-830°C) than that of NbCrN phase (T=1200-1250°C) [4,5]. Dissolution of (Nb,V)CrN particles in 9-12%Cr martensitic steels during annealing at temperatures 800-830°C is accompanied by the formation of MX phase with a FCC unit cell of the dimension about a=0.420nm [4].

Electron diffraction studies performed by Danielsen [12] demonstrated that some diffraction patterns taken on (Nb,V)CrN particles in 9-12%Cr martensitic steels were consistent with a FCC unit cell with lattice parameter a=0.404nm. The size of this FCC unit cell is related to the basal plane of the tetragonal unit cell of the modified Z phase as $\mathbf{a}_{FCC} = \sqrt{2}\mathbf{a}_Z$ and the lattice correspondence between the FCC and tetragonal unit cells, as established from electron diffraction patterns, is shown in Fig. 3.

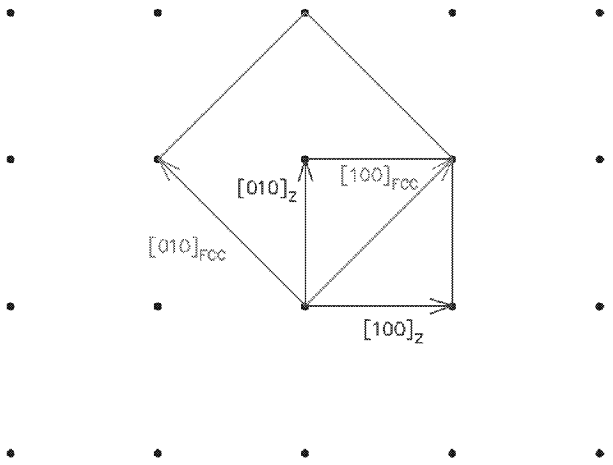

Fig. 3 The lattice correspondence between the FCC unit cell and the tetragonal unit cell of the modified Z phase in the basal plane, $\mathbf{a}_{FCC} = \sqrt{2}\mathbf{a}_Z$

The relationship between coordinate axes of the modified Z phase and the FCC phase can be expressed as follows:

$$[100]_Z = \frac{1}{2}[1\bar{1}0]_{FCC}$$

$$[010]_Z = \frac{1}{2}[110]_{FCC}$$

$$[001]_Z = \frac{c_Z}{a_{FCC}}[001]_{FCC} = 1.83[001]_{FCC}$$

These equations determine elements of transformation matrices, which can be applied for transformation of Miller indices of any vector $\vec{\mathbf{r}}$ in real space:

$$\left[\mathrm{FCC},\vec{\mathbf{r}}\right] = \left(\mathrm{FCC}\mathbf{T}_Z\right)\left[Z,\vec{\mathbf{r}}\right] \qquad \left[FCC,\vec{\mathbf{r}}\right] = \begin{pmatrix} 0.5 & 0.5 & 0 \\ -0.5 & 0.5 & 0 \\ 0 & 0 & 1.83 \end{pmatrix}\left[Z,\vec{\mathbf{r}}\right]$$

$$\left[Z,\vec{\mathbf{r}}\right] = \left(Z\mathbf{T}\ \mathrm{FCC}\right)\left[\mathrm{FCC},\vec{\mathbf{r}}\right] \qquad \left[Z,\vec{\mathbf{r}}\right] = \begin{pmatrix} 1 & -1 & 0 \\ 1 & 1 & 0 \\ 0 & 0 & 0.546 \end{pmatrix}\left[FCC,\vec{\mathbf{r}}\right]$$

For transformation of Miller indices of vector $\vec{\mathbf{g}}$ in reciprocal space following transformation matrices can be used:

$$\left[Z,\vec{\mathbf{g}}\right]^* = \begin{pmatrix} 0.5 & -0.5 & 0 \\ 0.5 & 0.5 & 0 \\ 0 & 0 & 1.83 \end{pmatrix}\left[FCC,\vec{\mathbf{g}}\right]^* \qquad \left[FCC,\vec{\mathbf{g}}\right]^* = \begin{pmatrix} 1 & 1 & 0 \\ -1 & 1 & 0 \\ 0 & 0 & 0.546 \end{pmatrix}\left[Z,\vec{\mathbf{g}}\right]^*$$

Transformation matrices were applied for calculations of all possible variants of diffraction patterns of Z phase corresponding to the zone axes of the FCC phase with low Miller indices. Kinematical SAD patterns for both phases were simulated using the computer programme provided by the Centre for Microanalysis of Materials, University of Illinois, USA (http://emaps.mrl.uiuc.edu). It was supposed that positions of individual atoms in the unit cell of the modified Z phase were the same as those in the NbCrN phase. In calculations of kinematical intensities of Z phase reflections niobium atoms were replaced by vanadium, i.e.

calculations were performed for VCrN phase. The results of calculations are shown in Table 1. It has been proved that in a number of zone axes the differences between the corresponding FCC and Z phase diffraction patterns are so small that these zone axes cannot be used for a reliable differentiation between both unit cells by electron diffraction techniques. In such patterns the differences in the lengths of corresponding reciprocal vectors of the FCC and tetragonal unit cells are mostly less than 3% and differences in angles between the corresponding reciprocal vectors are less than 2.5°. It means that for some orientations all spots related to the FCC unit cell are very close to those belonging to the tetragonal unit cell of the modified Z phase. Only in a limited number of Z phase orientations there are extra spots in SAD patterns, i.e. spots belonging solely to the tetragonal Z phase. Such diffraction patterns make it possible to differentiate reliably between the tetragonal and FCC unit cells. It is worth noting that in many cases simulated intensities of extra spots are very weak and therefore it might be difficult to observe some of these spots in experimental diffraction patterns. The results of SAD simulations suggest that reliable discrimination between the FCC and tetragonal unit cells under consideration requires a series of diffraction patterns taken on each (Nb,V)CrN particle investigated. Examples of simulated patterns for zone axes $[101]_{FCC}$, $[102]_{FCC}$, $[114]_{FCC}$ and the corresponding patterns of the tetragonal Z phase are shown in Tables 2, 3 and 4, respectively.

Table 1 Transformation of the FCC low index zone axes into the tetragonal unit cell of the modified Z phase

$\langle uvw \rangle_{FCC}$	$[uvw]_{FCC}$	$[uvw]_Z$	Extra Spots*
<100>	[100]	[110]	Yes
	[001]	[001]	No
<110>	[110]	[010]	Yes
	[101]	[221]	No
<111>	[111]	[041]	Yes
<210>	[102]	[111]	Yes
	[210]	[130]	Yes
	[201]	[441]	Yes
<211>	[112]	[021]	Yes
	[211]	[261]	No
<310>	[103]	[223]	No
	[310]	[120]	Yes
	[301]	[661]	No
<321>	[213]	[263]	Yes
	[312]	[241]	Yes
	[321]	[2.10.1]	No
<411>	[411]	[6.10.1]	Yes
	[114]	[011]	Yes
<433>	[433]	[2.14.3]	No
	[334]	[031]	Yes

* the occurrence of extra spots in diffraction patterns of the tetragonal Z phase compared to the corresponding diffraction pattern of the FCC phase

FCC	Zone axis: $[101]_{FCC}$
$R_1 = 4.950\ nm^{-1}$ $R_2 = 4.287\ nm^{-1}$ $\angle R_1R_2 = 54{,}7°$	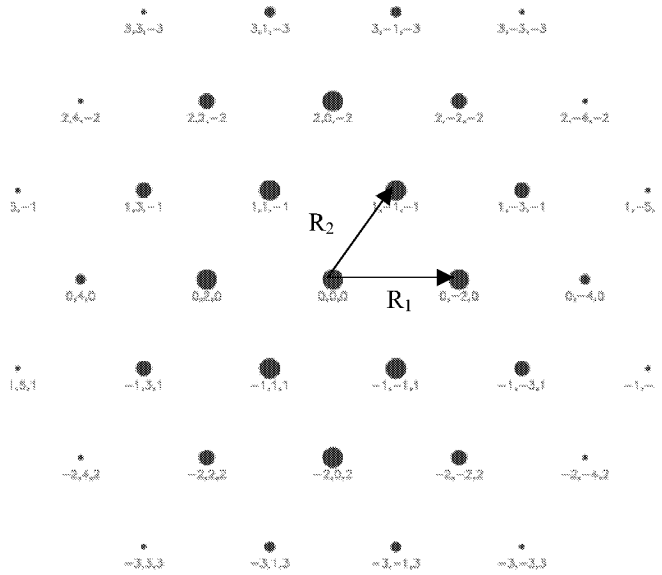
Z phase	**Zone axis: $[221]_Z$**
$R_1 = 4.945\ nm^{-1}$ $R_2 = 4.421\ nm^{-1}$ $\angle R_1R_2 = 56°$	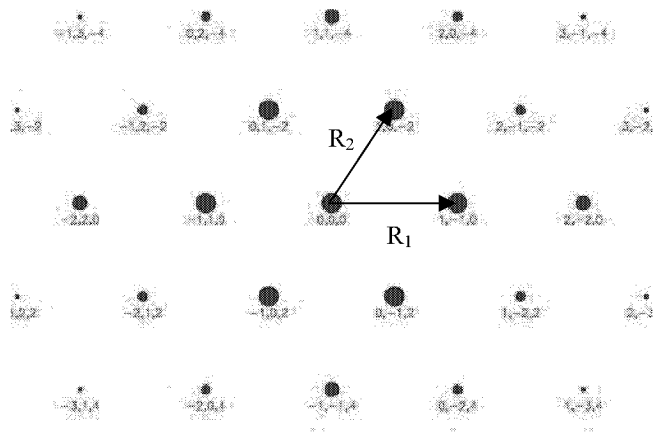

Table 2 Simulated diffraction patterns $[101]_{FCC}$ and $[221]_Z$

FCC	Zone axis: $[102]_{FCC}$
$R_1 = 4.950\ nm^{-1}$ $R_2 = 11.069\ nm^{-1}$ $\angle R_1R_2 = 90°$	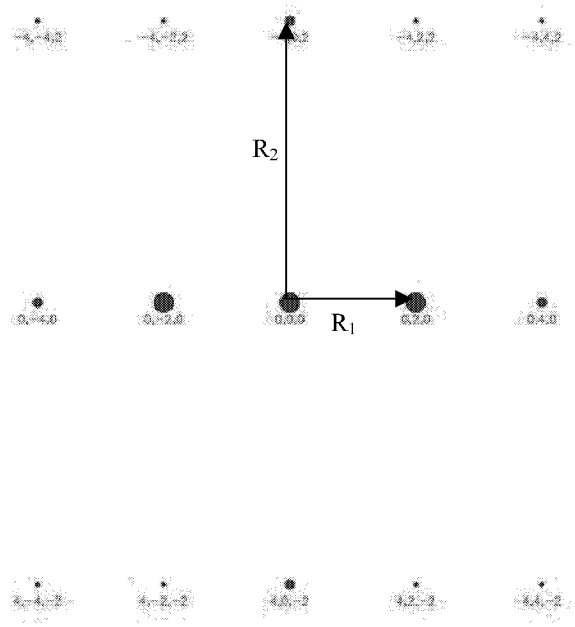
Z phase	**Zone axis: $[111]_Z$**
$R_1 = 4.945\ nm^{-1}$ $R_2 = 11.274\ nm^{-1}$ $\angle R_1R_2 = 90°$	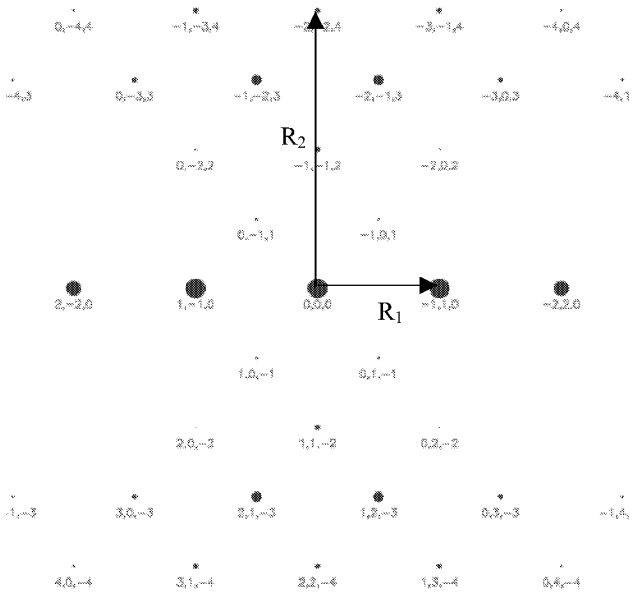

Table 3 Simulated diffraction patterns $[102]_{FCC}$ and $[111]_Z$

FCC	Zone axis: $[114]_{FCC}$
$R_1 = 4.950\ nm^{-1}$ $R_2 = 8.209\ nm^{-1}$ $\angle R_1R_2 = 64.8°$	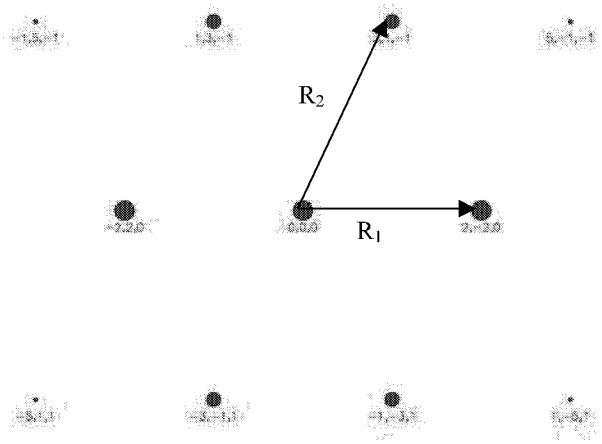
Z-phase	**Zone axis: $[011]_Z$**
$R_1 = 4.945\ nm^{-1}$ $R_2 = 8.274\ nm^{-1}$ $\angle R_1R_2 = 65°$	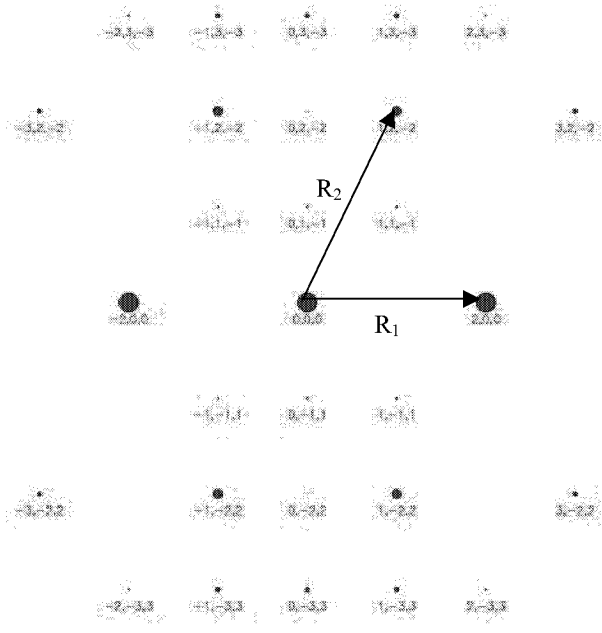

Table 4 Simulated diffraction patterns $[114]_{FCC}$ and $[011]_Z$

2. Experimental Materials and Technique

The studies were carried out on three commercial casts of a 12CrMoVNbN steel. Details of chemical composition of the steels are shown in Table 5. Quality heat treatment of these steels consisted of normalizing and tempering in the temperature range of 650-700°C [1].

Table 5 Chemical compositions of the 12CrMoVNbN steels (wt.%)

Cast	C	Si	Ni	Cr	Mo	V	Nb	N
ME	0.16	0.28	0.52	11.2	0.61	0.28	0.29	0.074
LD	0.14	0.37	0.76	11.1	0.57	0.36	0.32	0.062
FM	0.14	0.13	1.15	11.7	0.50	0.29	0.30	0.064

Creep rupture tests on these casts with different nickel contents were conducted at temperatures of 550 and 600°C for durations up to 100 000 hours. The results described in this paper were obtained on heads of the creep rupture testpieces where the microstructural changes corresponded mainly to the effects of thermal exposure. Electron microscopy studies were performed on specimens described in Table 6.

The specimens were chosen with the intention to reveal the effect of following variables on the lattice structure of (Nb,V)CrN particles:

- temperature
- time of exposure
- effect of Nb content in the particles.

Table 6 Exposure parameters of specimens investigated

Specimen	Temperature [°C]	Time of exposure [hours]
ME42	550	100 538
FM7*	600	7 247
LD27	600	16 000
LD49	600	67 200

* the first appearance of Z-phase in the FM heat at 600°C

Electron microscopy studies were carried out on carbon extraction replicas and thin foils using a JEOL 3000F FEGTEM, equipped with INCA EDX system. The goniometer of the microscope enabled double tilt in the range of angles x=±30°, y=±19°. Both SAD and CBED patterns were taken. Diffraction studies were accompanied by quantitative EDX microanalysis. The thin foils were prepared by twin jet electropolishing in a solution of 5%$HClO_4$ in glacial acetic acid at room temperature and a voltage of 80V.

Diffraction experiments revealed that Kikuchi patterns from (Nb,V)CrN particles in low index orientations close to $[001]_Z$ are very similar to Kikuchi patterns of FCC crystals. This fact made it possible to use Kikuchi patterns of a FCC crystal for controlled navigation from one zone axis to another one [13]. Controlled tilting of particles into required orientations was very important in order to perform a reliable identification of the unit cell of particles investigated. The analysis was focused on getting diffraction patterns exhibiting some reflections belonging solely to the tetragonal Z phase, i.e. extra spots. The ideal starting orientation was found to be $[001]_{FCC}$ /$[001]_Z$. Tilting from this orientation using Kikuchi lines to zone axes $[114]_{FCC}$ /$[011]_Z$ and $[102]_{FCC}$ /$[111]_Z$ provides important data for a reliable

identification of the tetragonal unit cell. Furthermore, (Nb,V)CrN particles were tilted to orientations where diffraction patterns for both unit cells are very dissimilar, e.g. $[100]_{FCC}$ /$[110]_Z$.
(Nb,V)CrN particles in martensitic 9-12%Cr steels form thin plates with habit planes parallel to the $(001)_{FCC}$ // $(001)_Z$ basal plane, Fig. 5. That is why many (Nb,V)CrN particles on extraction replicas are oriented approximately parallel to the (001) planes.

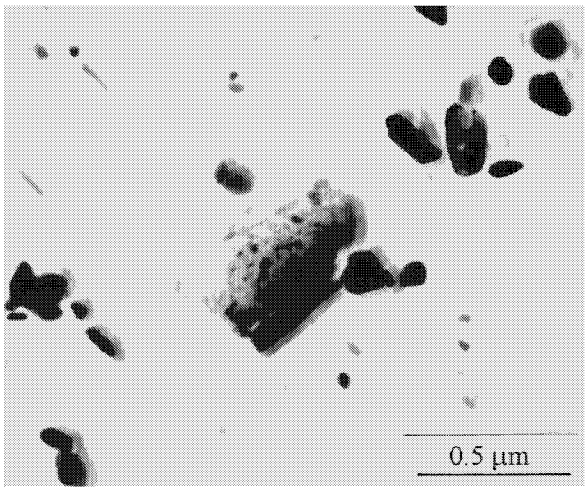

Fig. 5 A (Nb,V)CrN thin plate on extraction replica

3. Results of diffraction studies

Electron diffraction studies on (Nb,V)CrN particles in 12CrMoVNbN steels revealed that most diffraction patterns were composed of zone axes belonging to a FCC unit cell with the parameter a=0.404nm and a tetragonal unit cell with dimensions a=0.286nm, c=0.739nm. Figs. 6a, b show CBED patterns composed of $[100]_{FCC}$ and $[110]_Z$ zone axes which were recorded on specimens FM7 and LD 49, respectively. Computer simulations of these zone axes are given in Table 7. In Fig. 6a spots corresponding to the $[100]_{FCC}$ are much more intensive than those belonging to the $[110]_Z$. In Fig. 6b spots corresponding to the $[110]_Z$ have become much stronger compared to Fig. 6a. Specimen FM7 exhibited the first appearance of (Nb,V)CrN particles in the FM heat during exposure at 600°C while specimen LD49 was exposed at the same temperature for a very long period of time. Generally, intensities of the spots belonging to the zone axes of the FCC unit cell decreased with time of exposure, while those of the zone axes of the tetragonal unit cell increased. After long time exposures the spots belonging to the tetragonal unit cell become more intensive than those of the FCC unit cell which become weaker and diffuse. The evidence of the FCC unit cell in (Nb,V)CrN particles also represents a $[111]_{FCC}$ zone axis revealing a three fold rotation axis in the cubic unit cell, Fig. 7 and Table 8.

It can be speculated that small FCC and tetragonal microdomains are intermixed inside individual particles. Diffraction results give an indication that the ratio of FCC/tetragonal microdomains is for a given temperature dependent on time of exposure. A gradual transformation of the FCC unit cell into the tetragonal unit cell seems to be realistic. In situ

transformation of the FCC cell into the tetragonal unit cell can take place by ordering of metal atom layers along the $[001]_{FCC}$ /$[001]_Z$ direction, see Figs. 1 and 2. The Nb/V content also varied within the particles investigated, but no evident effect on the lattice structure was observed. No streaking was observed along $[001]_Z^*$ directions.

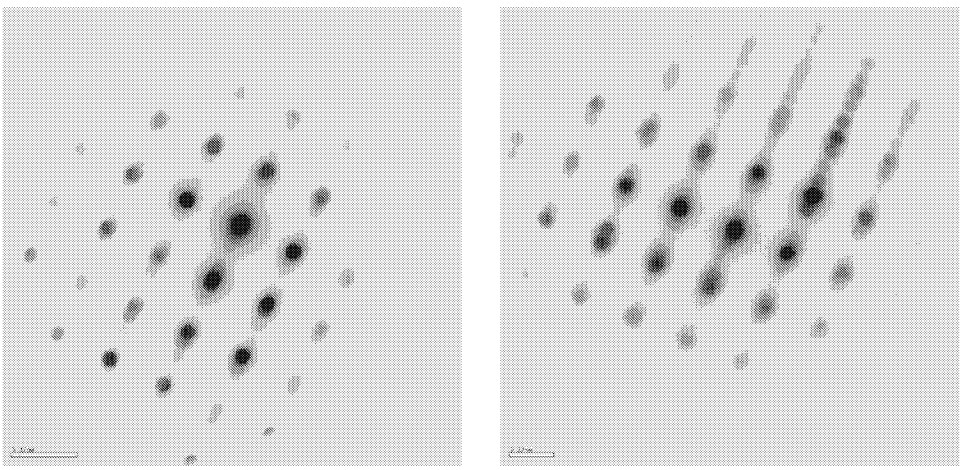

a. b.

Fig. 6 The composed CBED patterns $[100]_{FCC}$ and $[110]_Z$, a. specimen FM7, $[100]_{FCC}$ zone axis predominates, b. specimen LD49, $[110]_Z$ zone axis is clearly visible

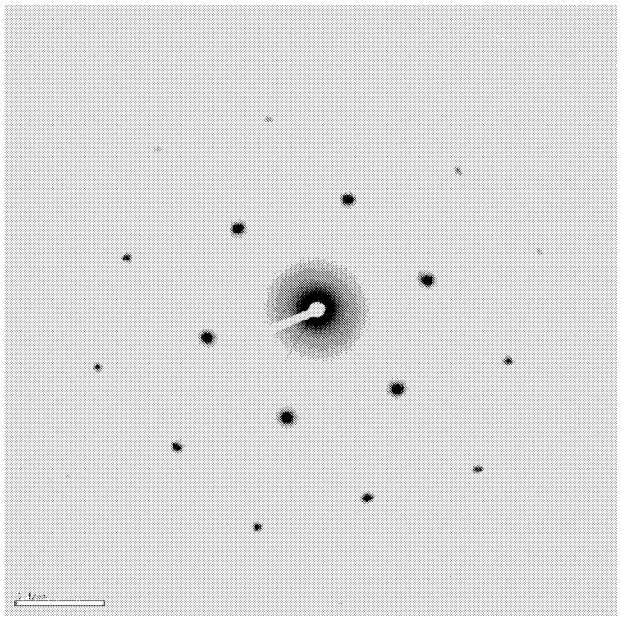

Fig. 7 SAD pattern showing a $[111]_{FCC}$ zone axis, specimen LD27

FCC	Zone axis: $[100]_{FCC}$
$R_1 = 4.950\ nm^{-1}$ $R_2 = 4.950\ nm^{-1}$ $\angle R_1R_2 = 90°$	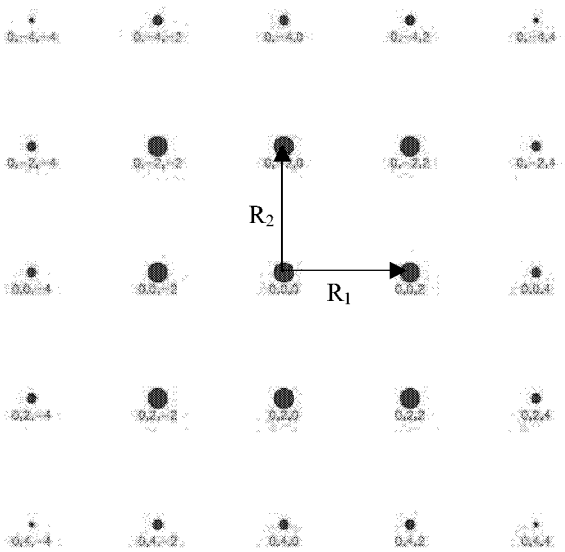
Z-phase	**Zone axis: $[110]_Z$**
$R_1 = 5.413\ nm^{-1}$ $R_2 = 4.945\ nm^{-1}$ $\angle R_1R_2 = 90°$	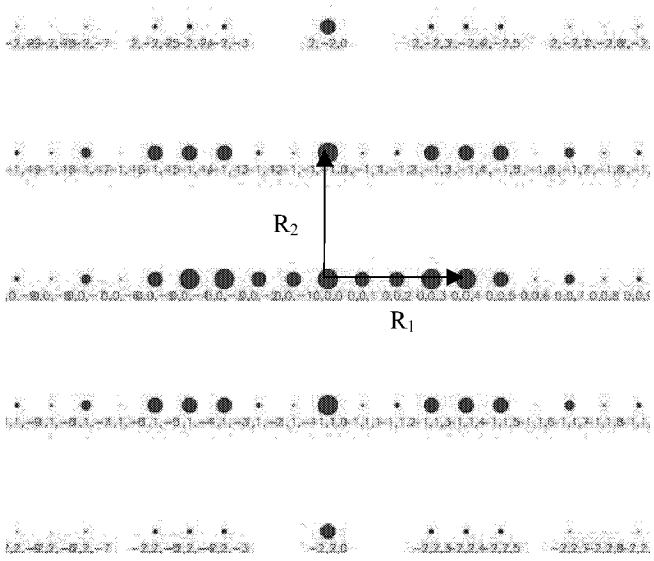

Table 7 Simulated diffraction patterns $[100]_{FCC}$ and $[110]_Z$

FCC	Zone axis: $[111]_{FCC}$
$R_1 = 7.001\ nm^{-1}$ $R_2 = 7.001\ nm^{-1}$ $\angle R_1R_2 = 60°$	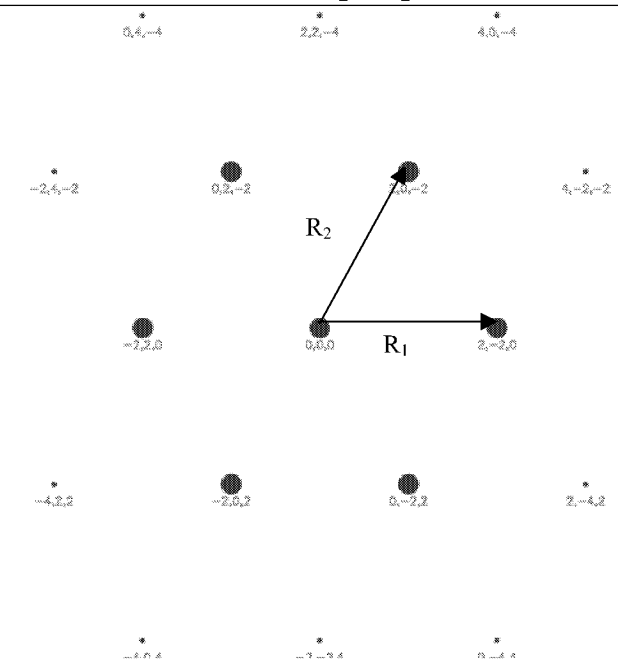
Z phase	**Zone axis: $[041]_Z$**
$R_1 = 6.993\ nm^{-1}$ $R_2 = 7.331\ nm^{-1}$ $\angle R_1R_2 = 61.5°$	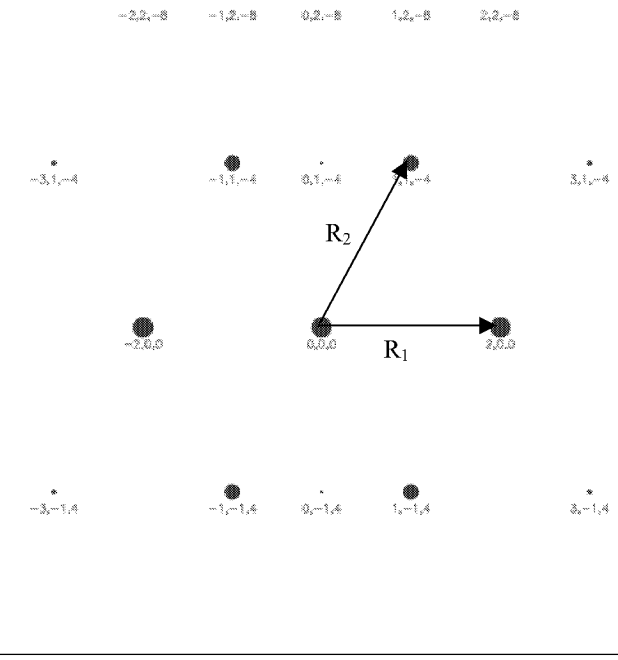

Table 8 Simulated diffraction patterns $[111]_{FCC}$ and $[041]_Z$

A high volume fraction of FCC microdomains in (Nb,V)CrN particles can explain why in some series of diffraction patterns recorded on the same particle individual diffraction patterns exhibit only very weak spots belonging solely to the tetragonal unit cell and the exact geometry of diffraction patterns showing only intensive spots is identical with the FCC unit cell. These small deviations from the tetragonal unit cell were typical mainly for CBED patterns taken from small areas of particles investigated.
It has been observed that intensity of potentially overlapping FCC/Z spots in diffraction patterns recorded on (Nb,V)CrN particles is much stronger than that of other spots. Generally, the calculated kinematical intensities of reflections in simulated Z phase diffraction patterns did not show the same effect. A typical example of this phenomenon is illustrated in Fig. 8. The correct indexing of the diffraction pattern is evident from simulated patterns shown in Table 3. Strong rows of reflections (the 4th row) resemble a slightly distorted $[102]_{FCC}$ zone axis. Intensities of individual spots in the rows marked by arrows (the 2nd row) were very weak, in many cases these rows of spots were not visible in diffraction patterns. In fact this diffraction pattern represents a composed $[111]_Z$ and $[102]_{FCC}$ diffraction pattern. The intensity difference between overlapping and extra spots in such composed diffraction patterns is expected to be proportional to a ratio of FCC/tetragonal microdomains in (Nb,Cr)VN particles.

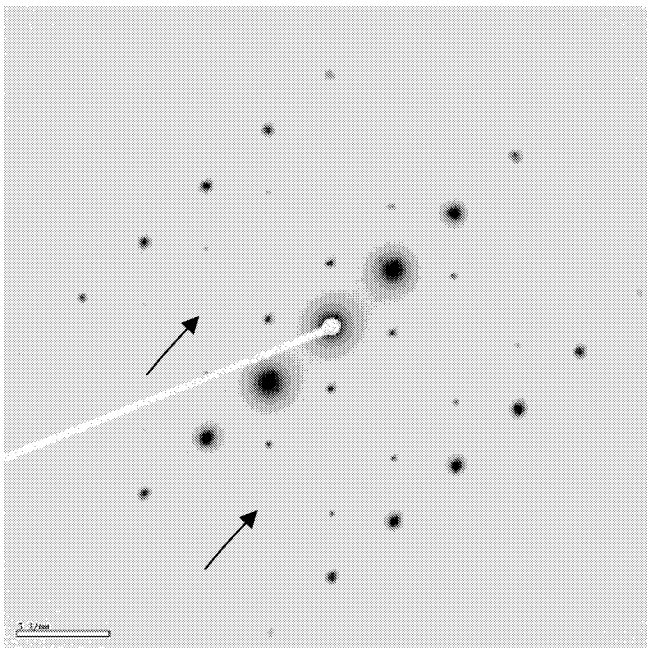

Fig. 8 Composed SAD pattern showing the $[111]_Z$ and $[102]_{FCC}$ zone axes, specimen LD27

The diffraction pattern in Fig. 9 is another example of the differences in intensities of overlapping (potentially common spots of the FCC and tetragonal unit cells) and extra reflections of the tetragonal Z phase. In this orientation the positions of spots in the corresponding FCC and the modified Z phase patterns again occur in almost identical positions, see Table 4. It is evident that spots belonging potentially to both the FCC and tetragonal unit cells are much stronger than the extra spots. The differences in spot intensities

decreased with increased time of exposure. This can be regarded as an evidence of a descending volume fraction of FCC microdomains in (Nb,V)CrN particles with prolonged time of exposure.

Strong intensities of reflections corresponding potentially to both the FCC and tetragonal unit cells make it clear why Kikuchi patterns from (Nb,V)CrN particles are very similar to Kikuchi patterns of a FCC crystal.

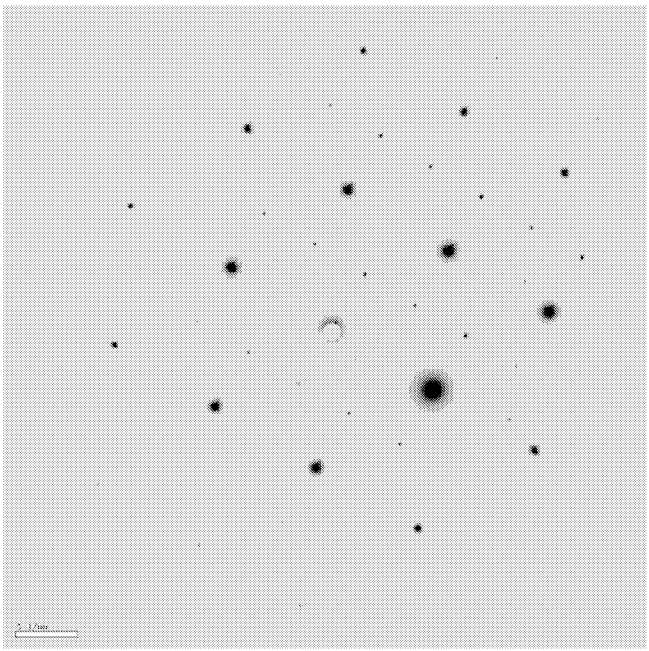

Fig. 9 Composed SAD pattern showing the $[011]_Z$ and $[114]_{FCC}$ zone axes, specimen LD 27

4. Conclusions

- Electron diffraction studies on (Nb,V)CrN particles in 12CrMoVNbN steels revealed that most diffraction patterns were composed of zone axes belonging to a tetragonal unit cell with dimensions a=0.286nm, c=0.739nm and a FCC unit cell with the parameter a=0.404nm. The established lattice correspondence between the FCC and tetragonal unit cells is in accordance with that of the FCC subcell in the proposed tetragonal unit cell of the modified Z phase. Generally, the intensity of spots belonging to the FCC unit cell decreased with time of thermal exposure, and spots related to the tetragonal unit cell become more intensive. This can be regarded as an evidence of a descending fraction of FCC microdomains in (Nb,V)CrN particles with prolonged time of exposure.
- It can be speculated that FCC and tetragonal microdomains are irregularly intermixed inside (Nb,V)CrN particles. In situ transformation of the FCC unit cell into the tetragonal unit cell with prolonged time of exposure can take place by ordering of metal atom layers along the $[001]_{FCC}$ // $[001]_Z$ direction.

- Based on the diffraction results it can be expected that the FCC unit cell, whose lattice correspondence with the tetragonal unit cell is identical to that of the FCC subcell in the tetragonal unit cell of the modified Z phase, plays an important role in the formation of (Nb,V)CrN particles in 9-12%Cr martensitic steels. The tetragonal unit cell predominates in diffraction patterns only after long-term exposure.

References

[1] Strang, A., Vodarek,V, The effect of microstructural stability on the creep properties of high temperature martensitic 12Cr steels, Proc. of the 7th Int. conf. on creep and fracture of engineering materials and structures, Irvine 1997, 415.

[2] Letofsky, E., Cerjak, H., Papst, L., Warbichler, P., The use of light and electron microscopy investigations to characterise the creep behaviour of welded joints in modern power station materials, Proc. of the 3rd EPRI conference on advances in materials technology for fossil power plants, R. Viswanathan et al. Eds., IOM Swansea, 2000, 133.

[3] Svoboda, M., Buršík, J., Podstránská, I., Kroupa, A., Sklenička, V., Mayer, K.H., High temperature creep behaviour and microsrtructural changes of TAF 650 steel, Proc. of Materials for advanced power engineering, J. Lecomte-Beckers, et al. Eds., Forschungszentrum Jülich, Liege 2002, III/1521.

[4] Danielsen, H.K., Hald, J., Energy Materials, 1, 2006, in press.

[5] Hughes, H., J. Iron Steel Institute, 205, 1967, 775.

[6] Ettmayer, P., Monatshefte für Chemie, 102, 1971, 858.

[7] Jack, D.H., Jack, K.H., J.Iron Steel Institute, 1972, 209, 790.

[8] Danielsen, H.K., Hald, J., Grumsen, F.B., Somers, M.A.J., On the crystal structure of Z-phase, Cr(V,Nb)N, submitted to Metallurgical and Materials Transactions.

[9] Chickwanda, H. : Microstructural stability of 12CrMoVNb power plant steels, PhD Thesis, Imperial College, London 1994.

[10] Strang, A., Vodárek, V., Mater. Sci. and Technology, 12, 1996, 552.

[11] Vodárek, V., Strang, A.: Z phase characteristics in martensitic 12CrMoVNb steels, Proc. of Materials for advanced power engineering, J. Lecomte-Beckers, et al. Eds., Forschungszentrum Jülich, Liege 2002, II/1223.

[12] Danielsen, H., Report of the STSM, TU of Denmark, 2004.

[13] Loretto, M., Electron Beam Analysis of Materials, Chapman and Hall, New York, 1984

Acknowledgements

The Management Committee of the COST 536 programme is kindly acknowledged for funding of the STSM missions to Ostrava and Risoe.

The authors wish to acknowledge the financial support from MSMT of the Czech Republic (contract no. OC 099-COST 536), Elsam A/S and the Danish Research Agency (grant no. 26-03-0275). The work by H. K. Danielsen was carried out under the IMPRESS research consortium.

AN EFTEM STUDY ON Z-PHASE NUCLEATION IN MARTENSITIC CHROMIUM STEELS

Ardeshir Golpayegani and Hans-Olof Andrén

Microscopy and Microanalysis
Department of Applied Physics
Chalmers University of Technology
SE-412 96 Gothenburg, Sweden
agolpa@fy.chalmers.se

Abstract

9-12% Cr martensitic steels that are used in crucial parts of steam power plants have been found liable to the precipitation of Z-phase after long time at service temperature. This complex nitride consumes vanadium nitrides and leaves the matrix with a relatively big vanadium poor region causing the creep strength of material to fall drastically after several thousand hours. It is of great importance to monitor the initial stages of precipitation of this phase to understand the factors promoting it and to get ideas about ways to suppress or eliminate it. In this work, Z-phase has been characterized using energy-filtered TEM. It has been found that VN provides the most suitable nucleation site for Z-phase since its lattice has the minimum misfit for starting the nucleation and it also provides vanadium for the growth. It has also been observed that the presence of niobium carbide close to the nucleation site is crucial for the nucleation and growth of this phase.

Keywords: 9-12% chromium steel, Z-phase, creep strength, Energy-filtered TEM

Introduction

The microstructure of the 9-12%Cr steel used in boilers and turbines of steam power plants generally consists of tempered martensite formed during a final normalizing and tempering heat treatment. A fine distribution and high thermal stability of carbides and nitrides provides the high creep strength in these materials and it has been shown that changing the type and distribution of the precipitates can double the creep strength of these steels [1]. It has been found that the precipitation of Z-phase, the complex nitride Cr(V,Nb)N, happens during creep [2] and it has now been realized that it may have the most detrimental effect on the creep strength. One example of this is steel TAF650 which showed a large creep instability after several thousand hours (see figure 1)[3].

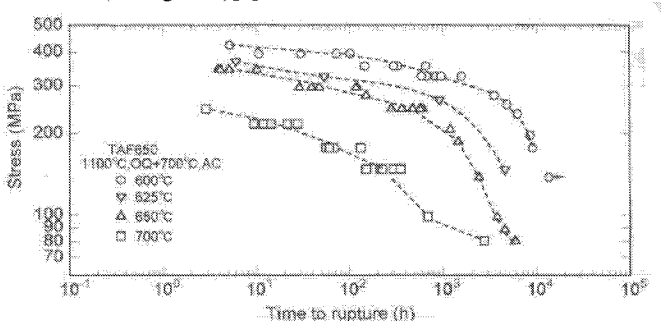

Figure 1. Creep rupture strength of steel TAF 650 [3]

This steel was originally developed to improve the successful example of trial steel TAF with relatively similar composition which had shown excellent creep properties [4]. The Z-phase precipitates at service temperature while other nitrides such as MX or M_2X are present. It forms large particles and it does not contribute to the creep strength. Instead, the loss of MX particles will have a detrimental effect on the creep strength [1, 5]. High Cr steels and Nb containing steels are more liable to Z-phase precipitation [2, 6]. However, not so much effort has been put on studying the nucleation of this phase yet. Investigating the nucleation sites and crystallographic orientation relationship between Z-phase, other precipitates and matrix would create not only a better understanding of precipitation of this phase, but also provides valuable insights in ways to suppress its formation.

Investigated materials

Three different 9-12% Cr steels have been used in this study. Steel designated as KP, was supplied by Siemens Industrial Turbomachinery in the form of tensile and creep specimens. This steel was produced by hot isostatic pressing of gas-atomized powders and has been studied in detail in reference [7]. It has been austenized at 1150°C for one hour and tempered at 730°C for 5 hours and then subjected to creep testing at 600°C for approximately 54,000 hours. Steel X19CrMoNbVN11-1 was taken from a 994 mm turbine blade and has been austenized at 1160°C for one hour followed by two temperings at 620°C and 650°C for 4 hours and then air-cooled. It has been creep tested at Siemens Industrial Turbomachinery at 550°C for 40 000 hours and at 650°C for 13,189 hours. This steel has been selected for this study mainly due to high Nb content which makes it more liable to Z-phase precipitation. Steel T122, aged at 660°C for 12,000 hours, has also been used in this study as a comparison with steel X19. This steel is also believed to be liable to Z-phase precipitation due higher chromium content. The chemical composition of these steels is given in Table 1.

Table 1. Chemical composition of the investigated steels (wt%, bal. Fe).

	C	Si	Mn	Cr	Ni	Mo	W	V	Nb	N	B
T122	0.09	0.25	0.60	12.20	0.18	0.35	1.97	0.25	0.06	0.06	
KP	0.15	0.11	0.49	10.6	0.58	1.07	1.05	0.23	0.05	0.064	0.0009
X19	0.14	0.32	0.71	10.50	0.75	0.62		0.21	0.23	0.05	

Experimental methods – Characterization of Z-phase

Presence of different types of precipitates with similar size and shape makes the interpretation of bright field images of transmission electron microscope (TEM) difficult. On the other hand, methods like Energy-filtered TEM (EFTEM) and jump ratio maps have been proven very useful in revealing quantitative spatial data [8-10]. Imaging of different precipitates and Z-phase was performed with a Philips CM 200 field emission gun TEM instrument operating at 200 kV equipped with a Gatan image filter. For determining the chemical composition of Z-phase by energy-dispersive X-ray spectroscopy (EDX), a Link ISIS system attached to the TEM has been used.

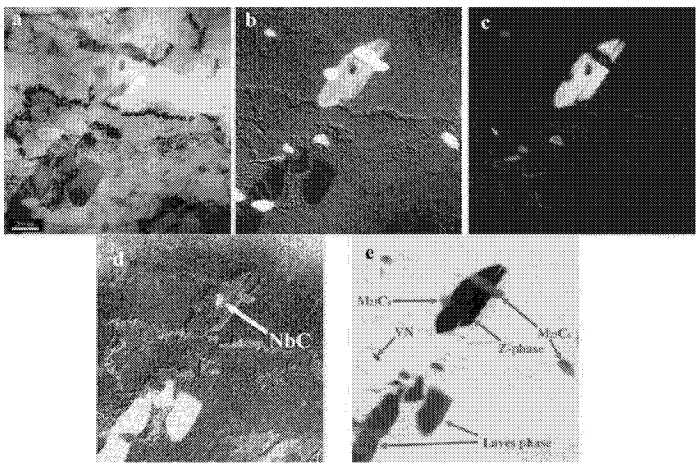

Figure 2. a) Zero-loss image of steel KP. Jump ratio images of b) chromium, c) vanadium, d) niobium and e) iron-M

Filtering for iron provides a comprehensive overview of the distribution of all precipitates (see figure 2-e). The large phases in figure 2-d are most probably Laves phase and contain molybdenum but due to the overlap with niobium in the energy-loss spectrum, they have provided the contrast in the niobium image. One can use filtering for tungsten in order to image the Laves phase but this has not been done here due to high energy-loss characteristic peaks of this element which require longer acquisition times and Laves phase has not been in the interest of this work. Many aspects of characterization of this phase has been studied references [11, 12]. The experimental conditions for acquiring energy-filtered images are given in Table 1.

Table 1. Experimental parameters used for acquisition of jump ratio images [13, 14]

Element	Edge	Edge onset (eV)	Pre-edge window	Post-edge window	Window width (eV)	Acquisition time (sec.)
Fe	$L_{2,3}$	708	692	724	30	20
Fe	$M_{2,3}$	54	49	62	10	3
Cr	$L_{2,3}$	575	559	591	30	20
V	$L_{2,3}$	512	497	531	30	20
Mo (Nb)	$M_{4,5}$	227(205)	190	270	30	3

Specimens were prepared with a combination of conventional electropolishing and ion milling and thickness in the order of 60-70 nm has been found to be suitable for a successful EFTEM process [14].

Results and discussion

Z-phase precipitation was not observed in steel X19 at 550°C, even after relatively long aging time (40,000 hours). Instead, the high amount of niobium in this material has contributed to the formation of large carbo-nitrides of type (Nb,V)(C,N) which have consumed the VN precipitates, causing the observed drop in the creep strength of this material at this temperature. Although Z-phase does not form in this high niobium steel at 550°C, this phase has been observed in some other steels with slightly higher chromium content at temperatures between 475°C and 600°C [15]. The absence of Z-phase is probably due to the lack of suitable nucleation sites. It is shown below that VN acts as nucleation site for Z-phase in steels with lower Nb content, but in this steel no pure VN precipitates were observed.

Figure 2 shows the observed Z-phase in steel KP aged at 600°C after 54,000 hours. The observed Z-phase in this figure has the typical sharp-edge lamellar morphology. This phase is hardly recognized in the bright field image and this makes the use of EFTEM necessary. In many cases, an $M_{23}C_6$ chromium-rich carbide has been observed in contact with large Z-phase (see figures 2-b, 3-a and 4-b). Since the growth of Z-phase involves dissolution of both VN and NbC, carbon is released which leads to growth of nearby $M_{23}C_6$ precipitates. It is believed that Z-phase and $M_{23}C_6$ make contact during growth and consequently $M_{23}C_6$ is not involved in nucleation of Z-phase.

The strong contrast that is observed in the chromium images clearly indicates the difference in the chromium content of Z-phase and chromium carbides. The high content of chromium in the material also promotes nucleation. It can be noted that the presence of niobium carbide in the vicinity of a specific site seems essential for triggering the nucleation of this phase since it acts as the source of niobium. This has also been noted by Strang and Vodarek [2].

The comparison between chromium and vanadium image in figure 3 indicate the presence of a relatively coarse Z-phase in this imaging area. This large phase has been formed at almost half of the life of the material and has presumably consumed high number of VN particles (note the size of VN poor region marked with circle).

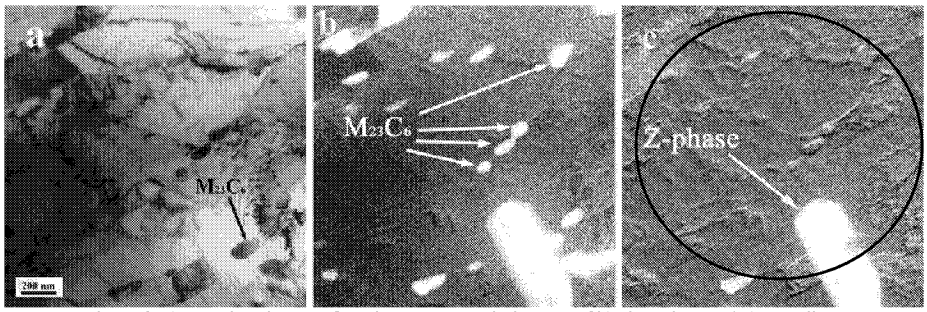

Figure 3. a) Zero-loss image of steel KP. Jump ratio images of b) chromium and c) vanadium

At the even higher temperatures, a vast number of Z-phase is observed in both steel T122 (after 13,000 hours) and X19 (after 40,000 hours) where Z-phase has grown to roughly 600-700 nm in size (see figures 4 and 5).

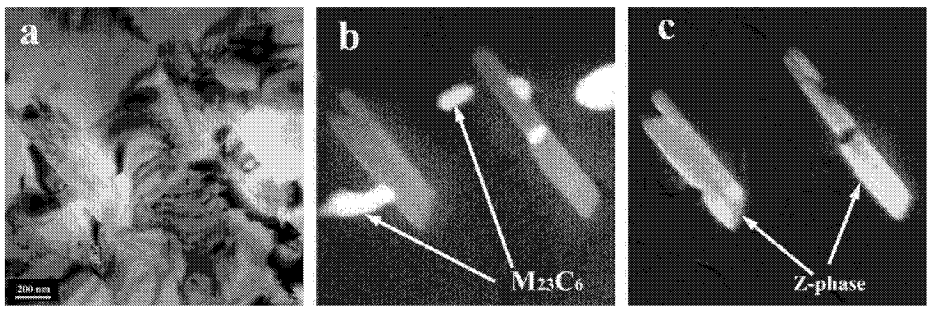

Figure 4. a) Zero-loss image of steel X19 aged at 650°C. Jump ratio images of b) chromium and c) vanadium

Figure 5 shows a possible nucleation stage for Z-phase in steel T122 where a relatively large NbC is seen very close to Z-phase. At two sites Z-phase has obviously nucleated as a thin layer on existing VN precipitates.

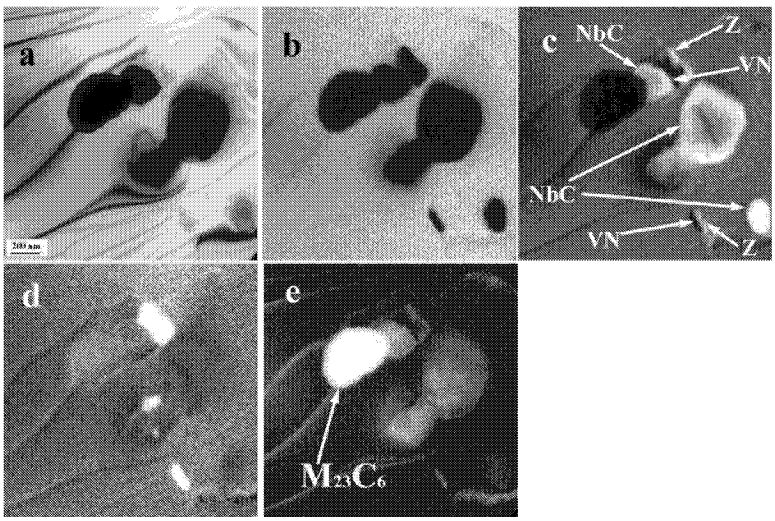

Figure 5. a) Zero-loss image of steel T122 aged at 660°C. Jump ratio images of b) iron, c) niobium, d) vanadium and e) chromium

It has been shown by Baker and Nutting [16] that VN has the following orientation relationship with the matrix

$$[110]_\alpha // [100]_{VN} \text{ and } [001]_\alpha // [001]_{VN}$$

and also Z-phase has a parallel orientation relationship with matrix [15] after all the VN is consumed i.e. the base planes of cubic ferrite and tetragonal Z-phase unit cells are parallel. The very small misfit in the base plane and the larger misfits along the tetragonal c-axis of Z-phase makes it grow large in one plane and this explains its plate-like morphology.

Combining the orientation relationships of VN and Z-phase, we get the following orientation relationship between Z-phase and VN in the nucleation stage

$$[110]_Z//[100]_{VN} \text{ and } [001]_Z//[001]_{VN}$$

or in other words, the base planes of VN and Z-phase are also parallel with each other, only it is rotated with 45° so that [110] in Z-phase is parallel to [100] in VN. It should be noted that the misfit between the lattice parameters of tetragonal Z-phase and VN is about 2.8% (lattice parameter of modified tetragonal Z-phase and VN is 2.86Å [15] and 4.16Å) which makes the nucleation of Z-phase on this nitride very favorable. Also, the diffusion lengths of both nitrogen and vanadium become short. It is difficult to spot the nucleation stage of Z-phase in the microstructure as small VN are quickly dissolved. Figure 5 shows an early stage of nucleation and figure 6 shows a vanadium nitride surrounded by Z-phase in the steel X19 aged at 650°C along with the corresponding jump ratio images. The latter is one the few cases that VN has not been completely consumed by Z-phase.

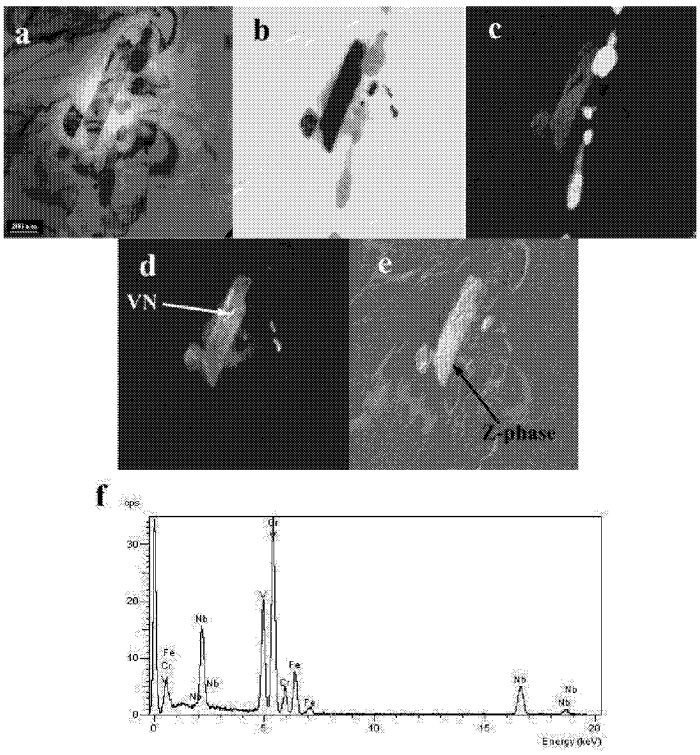

Figure 6. a) Zero-loss image of steel X19 aged at 650°C. Jump ratio images of b) iron, c) chromium, d) vanadium and e) niobium. f) a typical EDX spectrum obtained from Z-phase to confirm the chemical composition of Z-phase.

Conclusion

1. VN precipitates in the vicinity of NbC precipitates act as nucleation sites for Z-phase in modified 9-12% chromium steels due to a small misfit in the (100) planes of VN and Z-phase.
2. The small misfit between ferrite and tetragonal Z-phase in the (100) plane results in a plate-like morphology of Z-phase.
3. The growth of Z-phase leads to large VN-free areas in the microstructure and causes the decrease in the creep strength while $M_{23}C_6$ carbides grow due to the release of carbon from dissolution of NbC carbides.
4. In the steel with high niobium content, no Z-phase precipitation was observed at 550°C. Instead, coarse (Nb,V)(C,N) grow at the expense of VN causing the observed drop in the creep strength.

Acknowledgements

Hilmar Danielsen and John Hald of Technical University of Denmark are thanked for fruitful collaboration. Lennart Johansson of Siemens Industrial Turbomachinery is thanked for providing the X19 material. The authors would also like to thank the KME Consortium as well as Swedish Foundation for Strategic Research (SSF) and the Research Foundation of VGB in Germany for financial support of this project.

References

1. J. Hald and S. Straub. *Microstructural stability of 9-12% CrMo(W)VNbN-steels.* in *Materials for advanced power engineering.* 1998. Liege: Forschungszentrum Jülich GmbH, 1998.
2. A. Strang and V. Vodarek, *Z phase formation in martensitic 12CrMoVNb steel.* Materials science and technology, 1996. **12**: p. 552-556.
3. T. Uehara, T. Ohno, R. Watanabe and T. Fujita, *Development of high strength 12 % Cr ferritic heat-resistant steel.* in *Materials engineering in turbines and compressors.* 1995. Newcastle upon Tyne: The Institute of Materials, London, 1995.
4. T. Fujita and N. Takahashi, *The effect of boron on the long period creep rupture strength of the modified 12%Cr heat-resisting steel.* Transaction of ISIJ, 1978. **18**: p. 702-711.
5. H. Danielsen and J. Hald, *Z-phase in 9-12% Cr Steels*. 2004, Värmeforsk Service AB: Stockholm, Sweden.
6. J. Hald. *Long-term stability of 9-12%Cr steels - Current understanding and future perspectives*. in *VGB W6Q*. 2004. Dortmund.
7. L. Lundin, M. Hättestrand, and H.-O. Andrén. *Redistribution of elements during ageing and creep testing of 9-12% chromium steels*. in *Parsons 2000 Advanced materials for 21st century turbines and power plants*. 2000. Cambridge: The Institute of Materials, London, 2000.
8. P. Hofer, H. Cerjak, B. Schaffernak and P. Warbichler, *Quantification of precipitates in advanced creep resistant 9-12% Cr steels.* Steel Research, 1998. **69**(8): p. 343-348.
9. F. Hofer, P. Warbichler, and W. Grogger, *Imaging of nanometer-sized precipitates in solids by electron spectroscopic imaging.* Ultramicroscopy, 1995. **59**: p. 15-31.

10. P. Warbichler, F. Hofer, P. Hofer and E. Letofsky, *On the application of energy-filtering TEM in materials science: III. Precipitates in steel.* Micron, 1998. **29**(1): p. 63-72.
11. L. Korcakova, J. Hald, and M.A.J. Somers, *Quantification of Laves phase particle size in 9CrW steel.* Materials Characterisation, 2001. **47**: p. 111-117.
12. G. Dimmler, P. Weinhert, E. Kozeschnik and H. Cerjak, *Quantification of the Laves phase in advanced 9-12% Cr steels using a standard SEM.* Materials Characterization, 2003. **51**(5): p. 341-352.
13. I. Letofsky-Papst, P. Warbichler, F. Hofer, E. Letofsky and H. Cerjak, *On the occurrence of Z-phase in a creep-tested 10% Cr steel.* Zeitschrift fur Metallkunde, 2004. **95**(1): p. 18-21.
14. M. Hättestrand and H.-O. Andrén, *Evaluation of particle size distributions of precipitates in a 9% Cr-steel using energy filtered transmission electron microscopy.* Micron, 2001. **32**: p. 789-797.
15. V. Vodarek and A. Strang, *Z phase precipitation in martensitic 12CrMoVNb steels.* Journal de Physique IV (Proceedings) International Conference on Martensitic Transformations, 10-14 June 2002, 2003. **112**(pt.1): p. 445-8.
16. R.G. Baker and J. Nutting. *The tempering of a Cr-Mo-V-W steel and a Mo-V steel.* in *Precipitation Processes in Steels*. 1958. Sheffield, UK: The Iron and Steel Institute, London, 1959.

Z-PHASE IN 9-12%CR STEELS
OBSERVATIONS AND THERMODYNAMIC MODELLING

H. K. Danielsen, J. Hald

Dept. of Manufacturing Engineering and Management
Produktionstorvet, DTU – Building 204, 2800 Kgs. Lyngby, Denmark
Hilmar@ipl.dtu.dk

Abstract

Precipitation of the modified Z-phase Cr(V,Nb)N has recently been identified as a major cause for premature breakdown in creep strength of a number of new 9-12%Cr martensitic creep resistant steels, as it dissolves beneficial MX particles.
A thorough investigation on the presence of Z-phase in 12 different 9-12%Cr martensitic steels showed that high Cr content (11-12%) increase the precipitation speed of the Z-phase, which is consistent with observed creep instabilities of high Cr steels.
The dissolution temperature of the modified Z-phase in these steels was found to be 800°C which is considerably lower than the 1200-1250°C dissolution temperature for the unmodified CrNbN Z-phase. The existence of a Nb free version of the Z-phase, CrVN, was confirmed.
The crystal structure of modified Z-phase was found to consist of coexisting cubic and tetragonal lattices.
A thermodynamic model of the Z-phase was developed based on results from current investigations and literature. Model predictions including, driving force calculations show good agreement with the observations and allow optimisations of chemical composition in order to delay Z-phase precipitation.

Keywords: Z-phase, 9-12%Cr steels

Introduction

The development over the last decades of new creep resistant martensitic 9%Cr steels grades such as the P91 and P92 for steam power plant applications has allowed increases in operating steam temperatures up to 600°C. New alloys are under development in order to increase the temperature further up to 650°C for better efficiency. This high temperature calls for improved steam oxidation resistance besides improved creep strength, and the majority of test alloys have thus been based on 11-12%Cr contents. Short-term creep tests have indicated improvements but after longer testing times all of the new 11-12%Cr alloys have experienced dramatic breakdowns in microstructure stability [1], which could not be explained.

Z-phase

Recent microstructural investigations after creep testing of many of the experimental steels developed for 650°C have shown extensive presence of large particles of the complex nitride Z-phase, Cr(V,Nb)N. The MX carbonitrides, Nb(C,N) or V(C,N), which precipitate as small and densely distributed particles, are one of the major contributors to the creep strength of new 9-12%Cr martensitic steels. The Z-phase contains the same elements as the MX carbonitrides, and its precipitation is accompanied by dissolution of the beneficial MX particles [2]. The Z-phase precipitates as large particles, which do not contribute to precipitate strengthening, and thus the creep strength of the steel is considerably lowered.

Very little is known about the behaviour of Z-phase in 9-12%Cr steels [2] since it has only been observed to precipitate after long times of exposure in plants or after long-term creep testing.

The present investigations including microstructure observations and thermodynamic modelling of the Z-phase are made with the aim to investigate controlling factors in chemical composition and microstructure of 9-12%Cr steels, which may trigger Z-phase precipitation.

Experimental

12 commercial as well as experimental steels were investigated for Z-phase, see table 1. The Z-phase could not be found in as-received condition, it only appeared after prolonged exposure to temperatures in the range 585-660°C, either by power plant service, creep testing or isothermal heating in furnaces.

	P91	**E911**	**P92**	**AXM**	**HCM12**	**P122**	**T122**	**NF12**	**FN5**	**TB12M**	**VM12**	**X20**
C	0.10	0.11	0.11	0.11	0.10	0.11	0.09	0.085	0.11	0.113	0.12	0.19
N	0.053	0.065	0.049	0.05	0.025	0.053	0.0609	0.045	0.027	0.055	0.078	0.025
Si	0.36	0.18	0.17	0.08	0.18	0.02	0.25	0.25	0.06	0.01	0.48	0.23
Mn	0.37	0.46	0.43	0.42	0.51	0.56	0.60	0.44	0.55	0.51	0.37	0.49
Cr	8.30	8.61	9.27	10.48	12.20	11.0	12.20	11.60	11.20	11.33	11.61	11.5
Mo	0.95	0.92	0.48	1.04	1.00	0.42	0.35	0.14	0.26	0.5	0.28	0.91
W	-	0.995	1.701	0.99	0.99	1.94	1.97	2.68	2.63	1.98	1.58	-
Ni	0.15	0.21	0.25	0.77	0.01	0.32	0.18	0.17	0.40	0.96	0.31	0.66
Nb	0.07	0.089	0.067	0.043	0.05	0.05	0.06	0.08	0.065	0.082	0.044	-
V	0.21	0.19	0.197	0.18	0.24	0.19	0.25	0.20	0.22	0.18	0.251	0.31
Cu	-	-	-	0.04	-	0.87	0.43	0.01	-	0.06	0.06	0.054
Al	0.15	0.013	0.005	0.008	-	0.012	0.004	-	-	0.004	-	0.016
B	-	-	0.0026	0.0002	-	0.0011	0.0021	0.0026	0.0010	-	0.0045	-
Co	-	-	-	-	-	-	-	2.48	2.66	-	1.56	0.021
Heat treatment	1050°C/ 1h 780°C/ 1h	1060°C/ 1h 770°C/ 2h	1060°C/ 1h 770°C/ 2h	1070°C/ 17h 570°C/ 22h 700°C/ 24h	1050°C/ 1h 800°C/ 1h	1050°C/ 1h 770°C/ 3h	1050°C/ 0.2h 790°C/ 3h	1100°C/ 0.2h 760°C/ 1h	1100°C/ 4h 570°C/ 8h 715°C/ 24h	1080°C/ 2.5h 775°C/ 2h	1060°C/ 0.5h 780°C/ 2h	1050°C/ 1h 750°C/ 2h
Exposure	8,000h 650°C	10,000h 650°C	31,000h 650°C	43,000h 600°C	85,000h 585°C	10,000h 650°C	12,000h 660°C	17,000h 650°C	8,000h 650°C	10,000h 650°C	16,000h 625°C	150,000h 600°C

Table 1: *Compositions (wt%), heat treatment and exposure conditions of the steels investigated during the course of this work.*

Sample preparation

Carbon extraction replicas were prepared by chemical etching of polished surfaces in Vilellas etchant (1% picric acid and 5% conc. hydrochloric acid in ethanol) for about 15 seconds. A carbon film was deposited onto the specimens by carbon evaporation, using a Quorum Technologies CC7650. Thereafter the film was cut into pieces and the sample was dissolved in a mixture of 10% bromium in methanol, leaving the carbon extraction replica in the solution. The replicas were cleaned with ethanol and caught on small copper grids.

X-ray powder diffraction investigations of extracted precipitates were made of a number of samples. Precipitates were extracted from the steel by electrolysis using a 95% ethanol and 5% conc. HCl mixture as electrolyte. This dissolved the matrix, while leaving all of the particles intact. The particles where then fixed on a silicon single crystal and investigated using a Philips PW1820/3711 X-ray diffractometer.

Electron microscopy

Transmission electron microscope (TEM) observations were carried out using a Philips EM 430 with an EDAX PV9760/20 EDS and a JEOL 3000F FEG TEM with an Oxford Instruments Inca energy dispersive spectrometer (EDS) and a GIF electron energy loss

spectrometer (EELS). The examined particles were identified as Cr(V,Nb)N using EDS in the TEM. Occasionally, particles were investigated with EELS as to assess the nitrogen content.

Results

Most of the investigations were based on TEM observations of carbon extraction replicas. Precipitate compositions were analysed with EDS, which formed the basis of the phase identification of the particles. Since it is not possible to measure the N content with EDS, the Z-phase was identified by its metallic composition, approximately 50 at% Cr+Fe and 50 at% V+Nb. This was found to be an easy and reliable method to distinguish Z-phase from other particles, since no other particles in the 9-12%Cr steels have such a composition.

Z-phase was found in all of the investigated steels, which had been exposed for several thousand hours at 585-660°C. This indicates that the modified Z-phase is a stable phase in all of the 9-12%Cr martensitic steels, which contain its constituents. There was great variation in the quantity of Z-phases found in the different steel types, as well as in the time necessary to precipitate them.

Table 2 shows the Z-phase quantity in the steels. Care should be taken when interpreting the results, as the steels have had different exposure conditions. Investigations of 11-12%Cr steels, which had suffered breakdowns after exposure at ca. 650°C, revealed high quantities of Z-phase as expected. For steels, which had been exposed for more than 10,000 hours, only few MX particles were observed. Three commercial 9%Cr steels, P91, E911 and P92 were investigated although no drastic breakdowns in strength had been observed. Z-phase was found in all of these steels, but there were very few of them, even in the P92 samples, which had been exposed for 31,000 hours at 650°C. All of the 9%Cr samples still contained a considerable amount of MX particles. In general the Z-phase was present in much greater quantity in 11-12% Cr steels, such as T122, NF12, VM12 and TB12M, compared to the 9% Cr steels, P91, P92 and E911.

Steel type	Cr content, wt%	Exposure	Observed Z-phase quantity
P91	8.30	8,000h / 650°C	Very low
X20	11.5	150,000h / 600°C	Low
E911	8.61	10,000h / 650°C	Low
P92	8.96	31,000h / 650°C	Low
P122	11.0	10,000h / 650°C	Medium
AXM	10.48	43,000h / 600°C	Medium
FN5	11.20	8,000h / 650°C	Medium
HCM12	12.20	85,000h / 585°C	Medium
VM12	11.61	16,000h / 625°C	High
TB12M	11.33	10,000h / 650°C	High
T122	12.20	12,000h / 660°C	High
NF12	11.60	17,000h / 650°C	High

Table 2: *An overview of the estimated degree of Z-phase precipitation in the investigated steels.*

Composition of Z-phase

As mentioned the identification of the modified Z-phase was based on a composition with approximately 50 at% Cr+Fe and 50 at% V+Nb, see table 3. EELS measurements confirmed presence of N in amounts indicating Z-phase composition. The Cr/Fe ratio was always very uniform, with around 45 at% Cr and 5 at% Fe. The V and Nb contents was mostly around 40

at% V and 10 at% Nb, but there were relatively large variations when looking at different particles in the same extraction replica samples, and even within the particles themselves. Generally, it appears that the niobium content in the Z-phase is higher in samples which only contain few Z-phases, usually 9%Cr steels. Many literature sources indicate small Mo concentrations in the modified Z-phase, but this could not be confirmed during the course of this work [3,4].

Steel type	Observed Z-phase quantity	Cr		Fe		V		Nb	
		Obs.	Calc.	Obs.	Calc.	Obs.	Calc.	Obs.	Calc.
P91	Very low	Not enough particles observed for statistics							
X20	Low	40	45.4	6	4.6	54	50.0	-	-
E911	Low	46	44.0	4	6.0	27	39.6	23	10.4
P92	Low	48	44.3	5	5.7	33	41.1	14	8.9
P122	Medium	45	44.6	5	5.4	33	43.4	17	6.6
AXM	Medium	43	44.6	5	5.4	44	43.9	8	6.1
FN5	Medium	47	45.0	6	5.0	38	45.0	9	5.0
HCM12	Medium	49	44.7	4	5.3	37	42.0	10	8.0
VM12	High	48	44.8	5	5.2	40	45.5	7	4.5
TB12M	High	47	44.3	5	5.7	37	39.5	11	10.5
T122	High	46	44.8	5	5.2	42	43.5	7	6.5
NF12	High	47	44.5	5	5.5	37	39.5	10	10.5

Table 3: *The average metallic composition (at %) of Z-phases found in the different steels compared to equilibrium calculations of the Thermo-Calc model.*

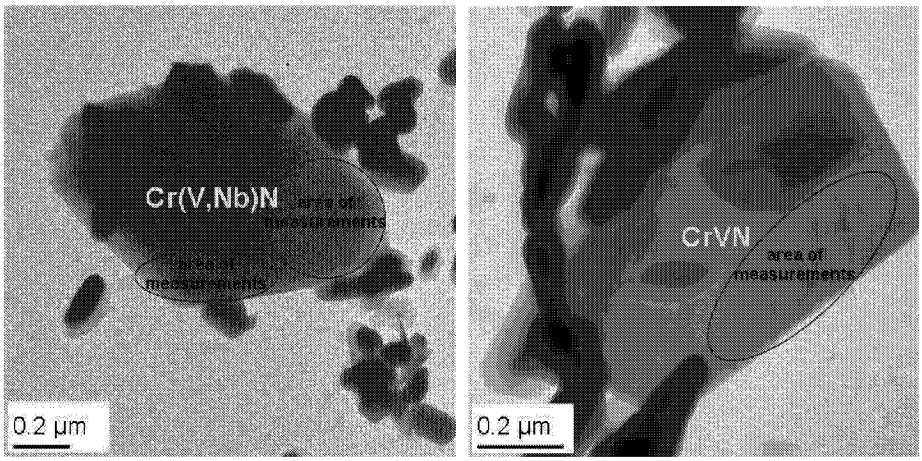

Figure 1: *A) A modified Z-phase found in an NF12 sample exposed at 650°C for 17,000h. B) A CrVN Z-phase found in an X20 sample exposed at 600°C for 150000h.*

CrVN

As work with the thermodynamic model progressed, it predicted Z-phase to be stable in 9-12%Cr steels, which contain vanadium but no niobium, but this could not be confirmed by literature. This Z-phase would have the empirical formula CrVN and to our knowledge had never been observed before. Several samples of the 12CrMoV steel X20 (CrMoV 12 1), which does not contain Nb, were investigated. In one of these samples, exposed at 600°C for 150,000h, Z-phase was found, see figure 1. Even though this sample had a very long exposure time, only very few Z-phase particles were found, and MX particles were still present. EELS

measurements confirmed presence of N in amounts indicating Z-phase composition. Except for what appears to be a very slow precipitation speed, the CrVN phase seems to be identical to the modified Z-phase.

Crystal structure of modified Z-phase

As there had been no previous reporting of a Nb free modified Z-phase, electron diffraction investigations were carried out to verify the crystal structure. These investigations showed discrepancies in the tetragonal modified Z-phase structure reported by Strang and Vodarek [3]. Electron diffraction investigation clearly showed the presence of fcc patterns in the Z-phase particles. It is assumed these patterns derive from a cubic NaCl type crystal structure consisting of an fcc sublattice occupied by metal atoms and N atoms in half the available octahedral sites. This crystal structure was found to coexist with the tetragonal Z-phase structure in CrVN and Cr(V,Nb)N particles, see figure 2, with the orientation relationship [5]:

$(001)_{tetragonal}//(001)_{cubic}$

$[010]_{tetragonal}//[110]_{cubic}$

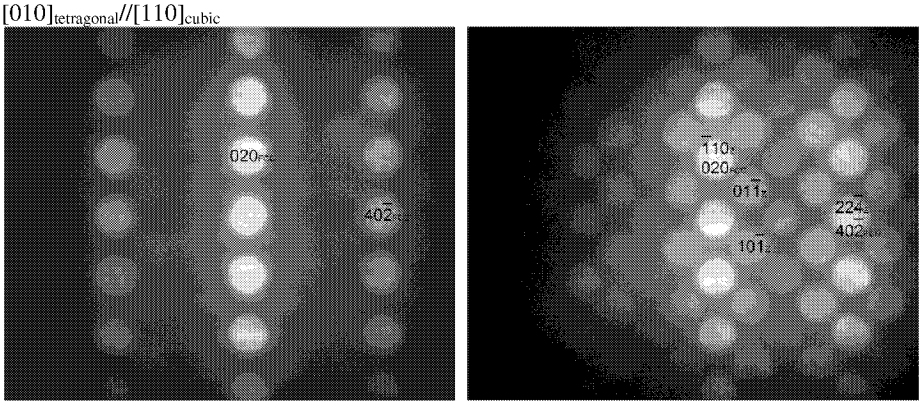

Figure 2: *Two CBED patterns taken at the same tilt angles but at different locations on the same Cr(V,Nb)N particle. The left picture shows a [102] FCC pattern and the right a [111] Z-phase pattern. Notice how the FCC spots overlap with the Z-phase spots. [5]*

Heat treatment experiments

The original Z-phase, CrNbN, is known to be stable at temperatures up to 1200°C-1250°C in austenitic steels, but no information has been found on the solution temperature of the modified Z-phase Cr(V,Nb)N. As this information was vital for the modelling of modified Z-phase, some experiments were carried out to determine the solution temperature. Steels which had already developed Z-phase during long-term exposure in power plants or test facilities were heated up to 700-850°C for 100h in order to dissolve the Z-phase. The used materials included T122 exposed at 660°C for 12,000h and NF12 exposed at 650°C for 17,000h, where Z-phase had replaced nearly all MX particles, see figure 3. Later investigations of the CrVN Z-phase were carried out on an X20 sample exposed for 150,000h/600°C.

Using electron microscopy and X-ray diffraction, these experiments gave a solution temperature of the modified Z-phase between 800°C and 850°C. In the samples where the Z-phase had been dissolved, it had been replaced by large particles consisting mainly of V and Nb. The composition of the metallic elements was (at%): 66% V, 20% Nb, 13% Cr, which

suggests this to be MX particles. X-ray diffraction also verified these results, see figure 3, as MX peaks (fcc crystal structure, lattice parameter 0.416nm) start appearing at 800°C.

In the 800-850°C interval the newly formed MX particles seemed to coexist with the Z-phase, but this could be because of insufficient time to dissolve the Z-phase. In the opinion of the authors the modified Z-phase has a thermodynamic solution temperature of ca. 800°C in martensitic steels. This is a very large difference in stability compared with the 1200°C-1250°C for the original CrNbN Z-phase.

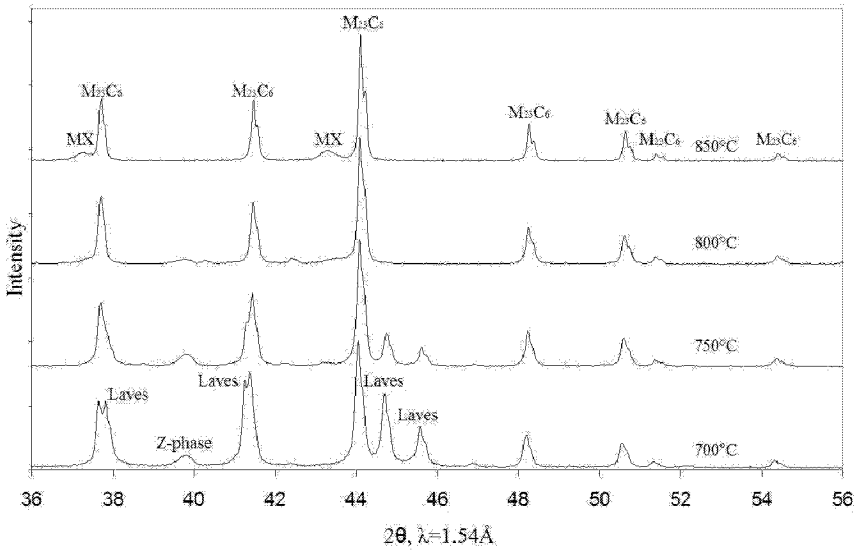

Figure 3: *Powder diffraction spectrum of precipitates from T122 after exposure 660°C/12,000h, and further heat treatment at 700-850°C for 100h. The Z-phase peak disappears around 800°C.*

The thermodynamic Z-phase model

A thermodynamic model of the Z-phase was created using the Thermo-Calc software. This is based on the regular solution model developed by Hillert and Staffanson [6] and extended by Ågren and Sundman [7]. Thermo-Calc calculates the Gibbs energy for every phase in a multi-component system, and can then tell which phases will be stable at certain temperatures and in which quantity and composition they will appear.

An extensive literature survey was conducted with the intention to find solid results, which could be used in the model, i.e. the composition of the Z-phase and its solution temperature, together with the overall composition of the steel. Information of both the original Z-phase, CrNbN, and the modified Z-phase, Cr(V,Nb)N, was gathered in order to make a comprehensive model [8].

The current model is under development using the commercial TCFE3 database, with version Q of Thermo-Calc. The model is based upon results from the literature as well as from own

experiments. The Z-phase is considered to consist of three sublattices, the major elements being Cr, V, Nb and N, the empiric formula being Cr(V,Nb)N. As small quantities of Fe and Mo are frequently reported in the Z-phase and some sources indicate the presence of C [9,10], these element have been included in the model, the total composition being (Cr,Fe)(V,Nb,Mo)(N,C).

Equilibrium calculations

Overall, the model seems to correspond well to the general observations of the Z-phase. The calculations done on the solution temperatures all coincide within 50°C of the measured values from the literature research and own experiments. The calculations of Z-phase compositions also fit generally well with measurements, although there are some deviations in steels with low Z-phase content, see table 3. As the measured compositions of Z-phase in steels with low concentration of Z-phase generally have a higher Nb contents, it is assumed the Z-phase has not yet reached equilibrium in these steels.

The model predicts the Z-phase to be stable in practically all 9-12%Cr steels containing V and N. The experiments so far have all confirmed these calculations, including the presence of Z-phase in steels without Nb. According to equilibrium calculations, Z-phase will eventually replace all VN particles. It is important to recognise Z-phase precipitation as a kinetic problem in these steels, its precipitation can be significantly slowed down, but probably not avoided altogether.

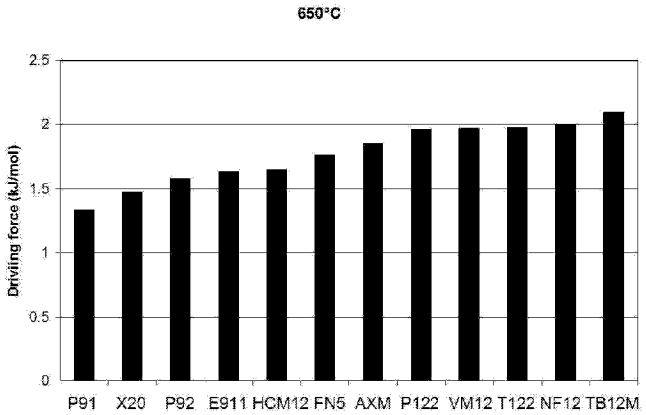

Figure 4: *The calculated driving force of Z-phase precipitation in the investigated steels.*

Driving force calculations

Thermo-Calc is mostly used to calculate systems at equilibrium, but it can also calculate the driving force for the Z-phase precipitation reaction, which is exclusively dependent upon the chemical composition of the steel. The driving force is calculated by comparing the change in Gibbs energy for a steel with Z-phase to the same steel without Z-phase. This effectively means that the driving force is the stability difference between Z-phase and VN, the second most stable nitride. Steels with higher driving forces are likely to precipitate Z-phase faster compared to steels with lower driving forces.

The driving force has been calculated for the steels investigated in this work, see figure 4, and give the approximate order of steels, which should most readily precipitate Z-phase. The high Cr steels, which show relatively fast Z-phase precipitation, generally have higher driving

forces compared to the low Cr steels, where Z-phase precipitation has been observed to be significantly slower. There are slight inconsistencies, e.g. the driving force for P122 should probably be a bit lower and for HCM12 a bit higher, but overall the results correspond well with the observations. Care should generally be taken when comparing the driving force directly with the Z-phase precipitation speed, as other factors, including microstructure and heat treatments, may have an effect on the kinetics of Z-phase precipitation.

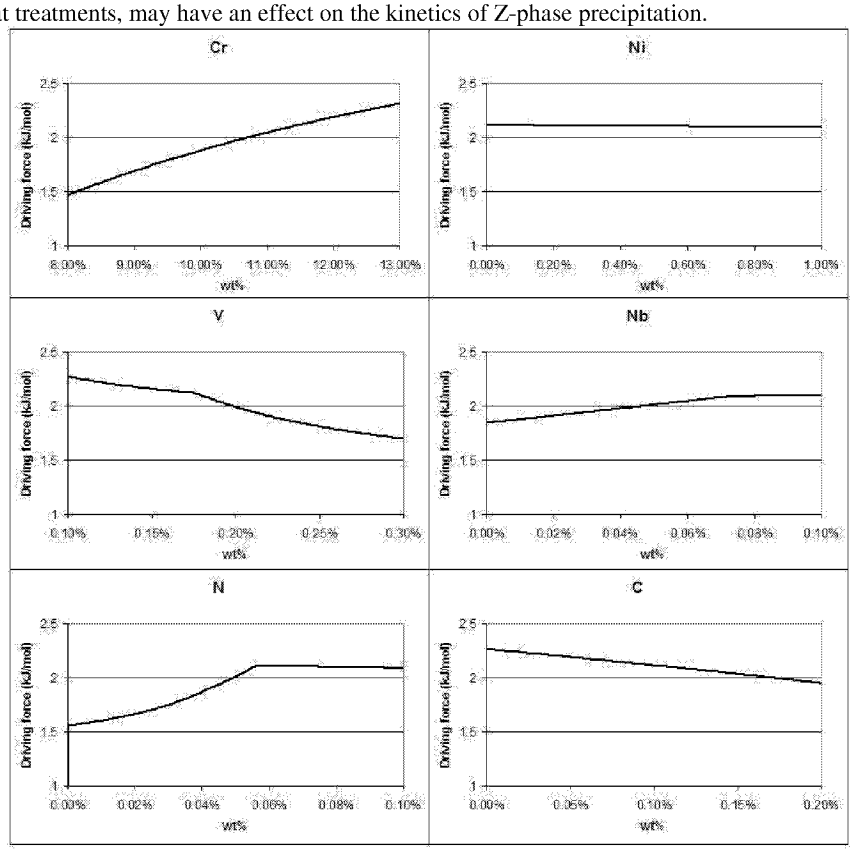

Figure 5: *By varying the content of one element, the influence on the driving force can be seen, here on TB12M.*

Driving force calculations with systematic variation of single elements give indications as to which elements affect the Z-phase precipitation speed, see Figure 5. Increasing the Cr content will increase the driving force of Z-phase, as it contains much more Cr compared to VN. Cr seems to be the most influential element, as seen in experimental observations. As C will form chromium carbides, and thus remove Cr from the system, a higher concentration of C will reduce the driving force. Adding Nb will stabilise the Z-phase compared to VN, over stoichiometric alloying Nb with respect to N (shown by the kink in the line in figure 5) will result in the formation of NbC. Decreasing the V content will destabilise the VN, while the Z-phase will become more Nb rich. Over stoichiometric alloying V with respect to N (kink in line) will result in stabilisation of V(N,C). Low nitrogen content will also stabilise V(N,C),

over stoichiometric alloying N with respect to Nb+V (kink in line) will lead to the formation of chromium nitrides (M_2X). Strang and Vodarek [11] have suggested that Ni should have an accelerating effect on the precipitation of Z-phase, but the model does not show any indications of this.

Summary

A thorough investigation into the presence of modified Z-phase, Cr(V,Nb)N, in creep resistant martensitic 9-12%Cr steels has been carried out, and a thermodynamic model of the Z-phase has been created using the Thermo-Calc software. The model predicts the Z-phase being stable in all of the 9-12%Cr martensitic steels, provided they contain its constituents. This is verified by experimental investigations, as twelve different commercial and experimental steels with varying composition have been investigated, and modified Z-phase has been found in all of these steel types in varying quantities.

The chromium content in 9-12%Cr martensitic steels has a strong influence on the precipitation of modified Z-phase. The higher chromium (11-12%) steels have a much higher rate of Z-phase precipitation compared to steels with around 9% Cr. The high Cr steels have all shown a premature breakdown in creep strength in the same time-temperature range as the Z-phase precipitation, whereas the low Cr steels have demonstrated good long-term creep stability up to more than 50,000 hours at 650°C [1]. This clearly demonstrates that accelerated Z-phase precipitation has a crucial influence on the premature breakdown in creep strength observed in the high Cr steels.

Since Z-phase was found in all of the investigated steels, the presence of Z-phase in itself does not have a direct influence on the creep strength. Z-phase precipitation is accompanied by dissolution of the beneficial MX particles, and has to precipitate in large enough quantities to dissolve an appreciable amount of MX particles in order to affect the creep strength. In the high Cr steels the MX dissolution was all but complete after ~10,000h at 650C°, this can be measured using both X-ray diffraction, see figure 3, and TEM microscopy.

The presence of niobium also appears to accelerate Z-phase precipitation. In the 12CrMoV steel X20 with high Cr but no Nb, Z-phase was found after exposure for 150,000h at 600°C. Even after such extended time, there were only very few Z-phase particles present. The empirical chemical composition of these Z-phases was CrVN, and is not known to be observed before.

The crystal structure of modified Z-phase was investigated, and was found to consist of coexisting tetragonal/cubic crystal structures [5].

The solution temperature of the modified Z-phases Cr(V,Nb)N and CrVN has been determined to be close to 800°C in 11-12%Cr martensitic steels, which is much lower than the 1200-1250°C solution temperature for CrNbN. Above the solution temperature the modified Z-phase is replaced by MX particles.

Driving force calculations of the Z-phase generally show the steels with higher Cr contents to have higher driving force compared to the steels with low Cr content, which also correspond well with experimental observations. Driving force calculations show the major elements of

the modified Z-phase, Cr, V and N, to have the largest effect on the Z-phase driving force. Other elements, such as Nb and C also appear to have an effect on the Z-phase driving force. Ni has been suspected of having an accelerating effect on Z-phase precipitation, but no clear tendencies in support of this could be observed in the present investigations, neither with experimental observations nor modelling.

Acknowledgements

G. Freville and C. Messelier-Gouze, EdF, France; the ECCC WG3A; the KME-114 project; Elsam, Esbjerg and Studstrup Power Plants are kindly acknowledged for providing samples for the investigations
The present work was carried out under the IMPRESS research consortium. The authors wish to acknowledge the financial support from Elsam A/S and the Danish Research Agency (Grant no. 26-03-0275).
The project is part of the European COST action 536 and the Swedish CROX project supported by the SSF (Stiftelsen för Strategisk Forskning) and the VGB Research Foundation.

References

[1] J. Hald: in Proc. 1st International Conf. *Super-High Strength Steels*, Rome, Italy, 2-4 November 2005, AIM and CSM, Rome 2005.

[2] H. K. Danielsen, J. Hald: *Energy Materials*, 1, 2006, pp. 49-57.

[3] A. Strang, V. Vodarek: *Materials Science and Technology*, 12, July 1996, pp. 552-556.

[4] R. Ishii, Y. Tsuda, M. Yamada, K. Kimura: *J. Iron and Steel Institute of Japan,* 88, 2002, pp. 36-43.

[5] H. K. Danielsen, J. Hald, F. B. Grumsen, M. A. J. Somers: Submitted to *Metallurgical and Materials Transactions.*

[6] M. Hillert, L-I. Staffansson: *Acta Chem. Scand.*, 24, 1970, pp. 3618-3626.

[7] B. Sundman, J. Ågren: *J. Phys. Chem. Solids*, 42, 1981, pp. 297-301.

[8] H. Danielsen, J. Hald: in Proc. Conf. *Advances in Materials Technology for Fossil Power Plants*, Hilton Head, USA, 25-28 October 2004, R. Viswanathan et al. (Eds.), ASM International, 2005, pp. 999-1012.

[9] L. Karlsson, A. Henjered, H-O. Andren, H. Norden: *Materials Science and Technology,* 1, 1985, pp. 337-343.

[10] V. H. Gerlach, E. Schmidtmann: *Archiv fur das Eisenhuttenwesen,* 39, 1968, pp. 139-149.

[11] V. Vodarek, A. Strang: in Proc. Conf. *Materials for Advanced Power Engineering*, Liege, Belgium, September 2002, J. Lecomte-Beckers et al. (Eds.), Julich, 1998, Part 2, pp. 1223-1232.

MICROSTRUCTURE AND STEAM OXIDATION RESISTANCE OF LAVES PHASE FORMING 12%CR STEELS AT 600-650°C

J Pirón Abellán, P J Ennis, L Singheiser, W J Quadakkers
Forschungszentrum Jülich, Institute for Materials and Processes in Energy Systems
D-52425 Jülich Germany

Abstract

Tempered martensitic/ferritic 12%Cr steels can be considered as candidate materials for Ultra Super Critical (USC) Power Plants from the point of view of long-term oxidation resistance. However, microstructure degradation of the high Cr-steels leads to poorer creep strengths compared with 9%Cr steels. The effect of elements, such as Co, Cu, Mn and Si on the alloy microstructure and oxidation resistance at 600 and 650°C have been investigated on various 12%Cr model alloys, containing high W additions that correspond with the assumption that the contribution of the Laves phase to the creep strength is higher than that of the MX particles. During long-term exposure it has been also observed the beneficial effect of combined additions of Co/Cu on the oxidation resistance allowing the formation of protective Cr-rich oxide scales at exposure temperatures of 600 to 650°C.

Keywords: 12%Cr steels, steam oxidation, Laves phases, MX precipitates, SNMS.

Introduction

In recent years the demand for steam power plants with increased efficiencies has led to the development of materials capable of operating at steam temperatures and pressures significantly higher than those employed in current power plants [1]. The use of low-Cr steels, such as 2¼ %Cr-1% Mo steels is limited to boiler service at temperatures around 550 °C both on grounds of insufficient creep strength and the relatively high oxidation rates in steam at higher temperatures around 600 °C [2]. Martensitic steels containing around 9% Cr are capable of use up to 600 °C at the stress levels of interest [3]. The commercial 9% Cr grades P91, P92 and E911 possess high creep strengths; unfortunately, these steels exhibit poor oxidation resistance in high water vapour containing atmospheres at 600-650 °C [4] and are therefore unsuitable for thin-walled components, such as boiler tubes. The oxidation resistance of the steels may be improved by increasing the chromium content, frequently up to levels of around 12% Cr. This, however, results in a decrease in creep strength at higher Cr concentrations [5], possibly due to the formation of Z-phase [6] and the fact that during austenitising the material may not be fully austenitic with the result that after quenching the steel is ferritic/martensitic rather than fully martensitic. To overcome the latter problem, the steels are frequently alloyed with substantial amounts of Co [7]. Recently, a number of developments have aimed at the partial replacement of Co by Cu additions, mainly to reduce the alloy cost.

The new steel compositions mostly contain minor amounts of Si and Mn because these elements are used to reduce the oxygen and sulphur content during alloy manufacturing. From both elements, it is also known that they affect the oxidation behaviour [8]. Additionally, Mn can partly replace the austenite stabilizing effect of the costly alloying element Co.

The aim of the present paper is the investigation of the microstructural features and the steam oxidation resistance of a number of recently developed Laves phase strengthened 12%Cr steels. The as-received microstructures of the materials were studied to determine the possible formation of the deleterious δ-phase [9], which is reported to adversely affect the steel toughness. The oxidation mechanisms were evaluated by detailed oxide scale characterization

after long-term exposure at 600 and 650 °C using secondary neutrals mass spectrometry (SNMS) and transmission electron microscopy (TEM).

Experimental

Small casts of a number of model alloys were produced at Forschungszentrum Jülich and at the Max-Planck Institute for Iron Research (Düsseldorf) by vacuum-induction melting followed by a standard heat treatment (austenization: 1070 °C/30 min and subsequent air-cooling; tempering: 780 °C/2h and subsequent air-cooling). The chemical compositions of the studied alloys, determined by ICP-OES, are shown in Table 1.

From these materials, specimens with a size of 20x10x2 mm were machined and progressively ground to 1200 grit surface finish. Oxidation tests were performed for 1000 h at temperatures ranging from 600 and 650 °C in a high water vapour containing atmosphere, i.e. Ar-50 vol % H_2O [8]. The samples were cooled to room temperature every 250 h under argon for mass gain measurements. After oxidation the samples were prepared for conventional metallographic investigation and the scales formed on the material surface were subsequently examined by optical microscopy, X-ray diffraction (XRD) and scanning electron microscopy (SEM) equipped with energy dispersive X-ray spectroscopy (EDX). Additionally, the steel microstructure in the as-cast and heat treated condition was investigated using a Philips CM200 transmission electron microscope (TEM) operated at 200 kV and equipped with an EDX (Oxford INCA) analytical system.

To obtain a higher accuracy for the precipitate compositions, extraction replicas were prepared from thin foils. These were obtained by evaporating a carbon film onto both sides of the metal foil. The metal matrix between both carbon films was then dissolved by exposing the coated foil to a 10 % solution of bromide in ethanol, which dissolves the matrix but does not attack the precipitates. Finally the replicas were cleaned and picked up using Au-grids, instead of conventional Cu-grids. The precipitates on the extracted replicas were identified and analysed by EDX and EELS. The compositions of the oxide scales formed on the material surface after steam oxidation were investigated by secondary neutrals mass spectroscopy (SNMS) and in selected cases by TEM of thin foils prepared by focussed ion beam (FIB).

Model alloys	Fe	Cr	Mn	Si	Co	Cu	Ta	W	C	N
Co (low Mn)	Bal.	11.5	0.31	0.41	9.3	-	2.2	4.6	0.026	0.1
Co (high Mn)	Bal.	11.0	1.1	0.38	8.7	-	1.4	3.0	0.06	0.006
Cu (low Mn)	Bal.	11.6	0.34	0.43	-	3.9	2.3	4.5	0.006	0.09
Cu (high Mn)	Bal.	12.5	1.3	0.45	-	4.3	2.0	3.1	0.06	0.005
Co/Cu (Low Mn)	Bal.	11.7	0.31	0.45	6.0	3.9	2.2	6.5	0.05	0.06
Co/Cu (High Mn)	Bal.	11.8	1.1	0.45	6.3	4.1	1.5	3.5	0.06	0.005

Table 1. Chemical compositions of studied model alloys in mass %.

Results and discussion

Microstructure

The etched (V2A-Pickle) microstructure of the studied alloys in the as-cast and heat treated condition revealed that the microstructure of the Cu (high Mn) containing alloy was predominantly ferritic, whereas the Co/Cu (high Mn) and Co (high Mn) alloys exhibited a ferritic/martensitic microstructure. Detailed studies of the microstructure performed by FIB/TEM analysis are shown in Figure 1 for the Co/Cu- containing alloys with high and low Mn additions. The Co/Cu (high Mn) alloy is characterized by the formation of relatively large precipitates of W-rich phase Laves phase. It is important to note that the Laves phase does not, as previously reported, solely contain W, Fe and/or Cr but additionally substantial amounts of Ta and Cu. Additionally, near the Laves phase particles, very small and quite finely distributed metallic Cu-rich particles were found (Figure 1a).

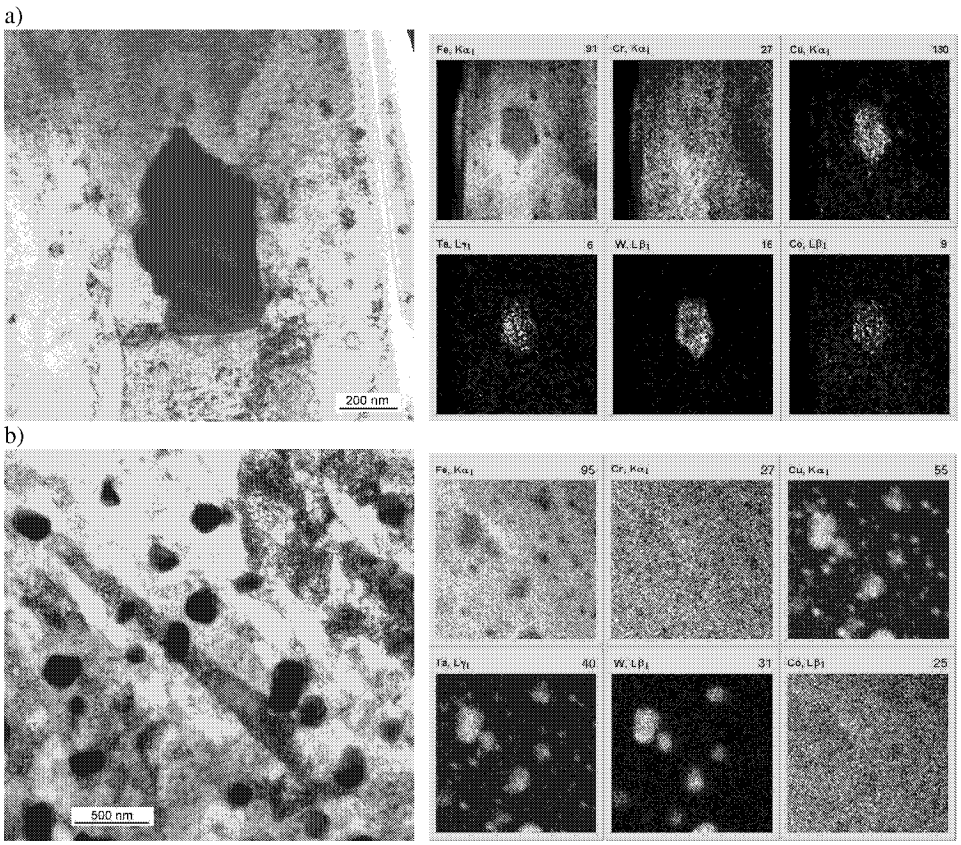

Figure 1 FIB/TEM analysis and EDX-mapping of the elements for the Co/Cu- containing alloys with a) high and b) low Mn additions in the as-received condition.

The precipitates of the Laves phases in the Co/Cu (low Mn) alloy were more homogeneously distributed than in the high Mn containing alloy. In the steel matrix a large numbers of tiny precipitates of a Cu,Ta-rich phase were found (Figure 1b). These precipitates were additionally analysed by EELS (not shown here), which revealed large amounts of nitrogen, thus indicating that the precipitates consist of Cu-containing Ta-nitrides or carbo-nitrides.

Analysis of the different precipitates in the extraction replica showed that the Laves phases (Figure 2) contained relatively large amounts of Cr and Fe, of the order of 4 and 20 wt% respectively. The amount of Ta varied from 4 to 15 wt % and the shape of the Laves phases seemed to change from bulky to rod-like with increasing amount of Ta in the intermetallic phase (Figure 2). Interestingly, the amount of Cu in the Laves phases and the Ta-rich MX particles was found to be quite high at around 23 to 25 wt %. Extraction replicas confirmed the results obtained from the mapping of the elements shown in Figure 1 with respect to the presence of Cu and Ta in the Laves phase and the formation of Ta,Cu-rich MX particles.

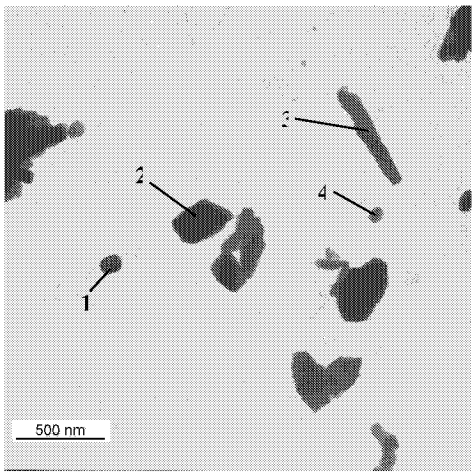

	Point 1	Point 2	Point 3	Point 4
Fe	12.5	20.7	19.4	12.1
Cr	3.5	4.3	4.4	3.3
Si	4.9	0.6	3.2	6.5
W	7.0	43.5	35.1	7.7
Cu	25.4	24.4	23.2	24.2
Ta	46.6	6.0	14.7	46.2

Figure 2 Extraction replica and EDX analysis (in wt %) of different precipitates formed in a Cu- added alloy in the as-cast and heat treated condition

The presence of Cu in the Laves phase and the formation of (Ta,Cu)X-particles have been clearly observed and further studies are needed to examine their effect on creep strength. However, first results on similar steel compositions have confirmed the positive influence of partial substitution of Co by Cu in alloys containing Ta [11]. Other studies performed by Ku and Ju [11] pointed to the beneficial results of Cu additions on creep rupture strength by increasing the solid solution strengthening effect in high W containing steels.

Oxidation resistance in high water vapour atmosphere

Figure 3 shows the weight changes for the Laves phase forming model alloys during oxidation at 600 and 650 °C in Ar-50 vol % H_2O compared with various commercial ferritic steels. At the lower temperature of 600 °C, additions of Cu or Co led to low oxidation resistances comparable in case of the Co (high Mn) alloy to the commercial P92 steel, whereas the alloys with combined Co/Cu additions exhibited low oxidation rates similar than those observed for the 12 % Cr steel X20CrMoV 12 1. However, at higher temperatures, the studied alloys show similar oxidation

rates as consequence of the faster outward diffusion of oxide scale forming elements. At the higher temperature both commercial ferritic P92 and X20CrMoV 12 1 steels exhibited much higher oxidation rates than the model alloys.

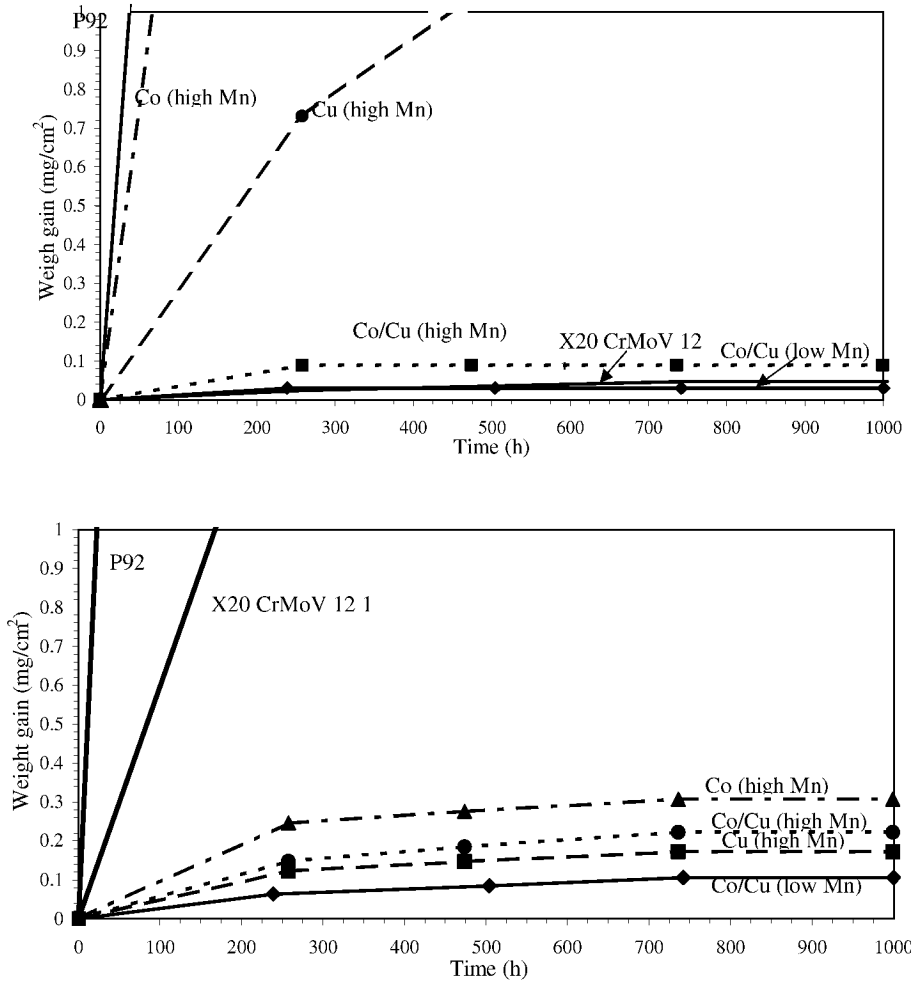

Figure 3 Weight changes of Laves-phase forming model alloys compared with the commercial ferritic P92 and X20CrMoV 12 1 steels during oxidation in Ar-50 vol % H_2O at 600 and 650 °C

To observe the effect of manganese content on the oxidation resistance, model alloys were prepared containing 0.3 and 1 wt % Mn (Table 1). The steels with combined additions of Co/Cu, showed at both temperatures very low scaling growth rates, irrespective of the manganese content (Figure 4). At 600 °C the alloys with single additions of Cu or Co exhibited high mass gains but additions of 1 mass % Mn were very effective in reducing the oxidation rate, especially at 650 ° (Figure 4b).

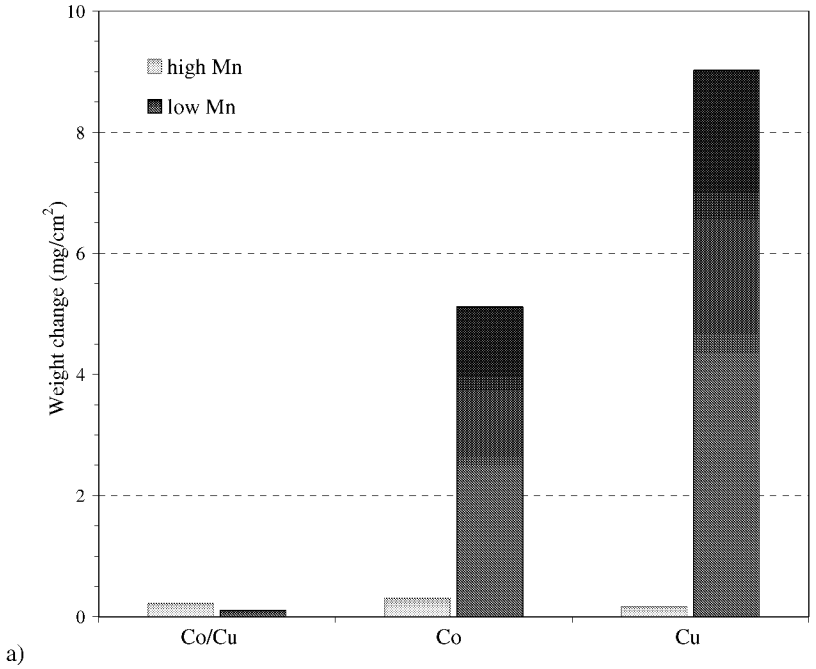

a)

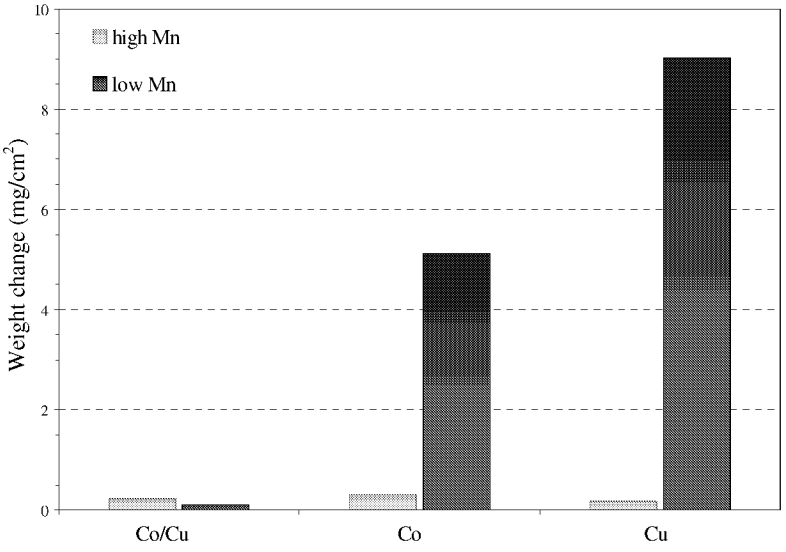

b)

Figure 4 Effect of manganese additions on the weight gains of Co, Cu and Co/Cu- model alloys after 1000 h oxidation in Ar-50 vol % H_2O at a) 600 and b) 650 °C

Figure 5 shows the SEM pictures of the various alloys after 1000 h oxidation at 600 and 650°C in Ar-50 vol % H_2O. The Co (high Mn) containing alloy (Figure 5a) formed a non-protective scale, which was prone to spalling, clearly visible by the formation of a large gap at the interface external/internal spinel layer, whereas increasing the exposure temperature lead to the formation of a protective Cr-rich oxide scale (Figure 5b), with the presence of some localized attack in form of iron-rich oxides, whose composition was similar to that of the continuous oxide scale formed at 600 °C. The Co/Cu added alloys (high Mn) formed at both temperatures very thin scales (Figure 5c, d) that were identified using XRD as a chromium-rich oxide. Therefore, by increasing the operation temperature an increase of the oxidation resistance for this type of "intermediate Cr-containing alloys" can be achieved, as was proposed by Ehlers et al [8].

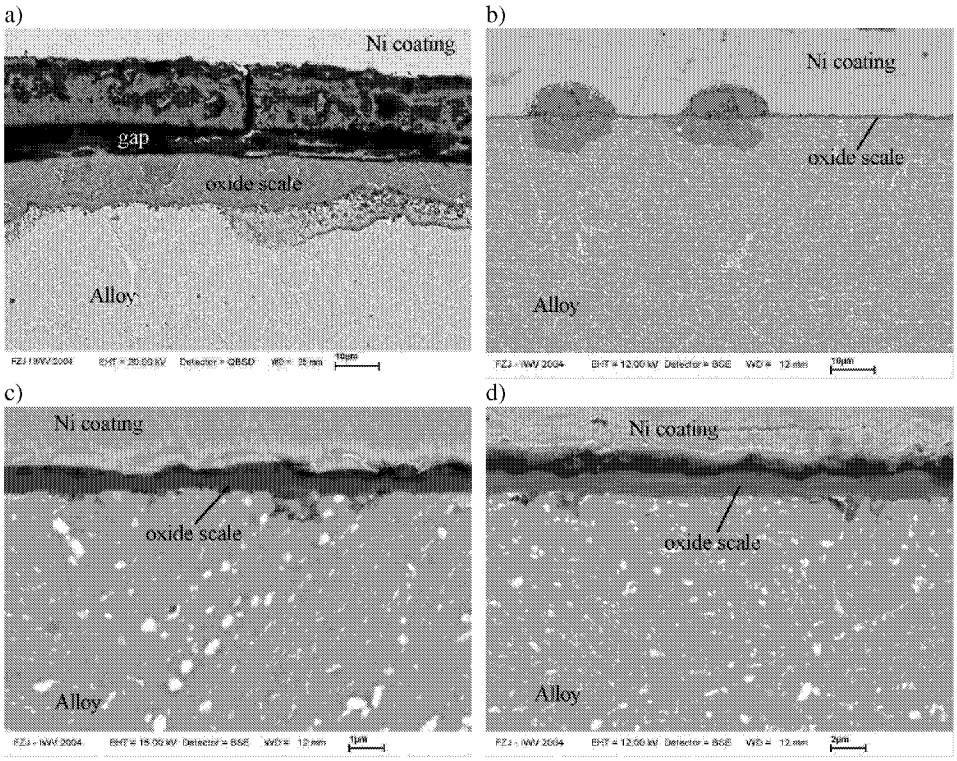

Figure 5 Metallographic cross section of (a,b) Co (high Mn) and (c,d) Co/Cu (high Mn) model alloys after 1000 h oxidation at 600 (a,c) and 650°C (b,d) in Ar-50 vol % H_2O

An attempt to get an insight of the oxidation resistance of the studied model alloys was done carrying out SNMS analysis on selected samples oxidized for 1000 h at 600 and 650 °C respectively. The Co/Cu-containing steel formed at 600°C a thin oxide scale consisting mainly of Cr- rich oxide (Figure 6a). The low O/M-ratio observed the gas/oxide scale interface is related to the formation of another oxide of the spinel type. This external layer consists mainly of Mn, Si and small amounts of Cr and Fe. For this steel an enrichment of Cu could not be observed in the scale surface and in the same way, Co was not incorporated into the oxide scale. At 650 °C (Figure 6b) the SNMS profile shows that the scale was slightly thicker than that formed at 600 °C but the scale composition remained similar. The external layer seemed also to be thicker

than at 600 °C, and the amount of iron present was significantly reduced. The amounts of Mn and Si in the external spinel layer at 600 and 650°C were similar, whereas the Cu content was much higher at 600 °C.

a)

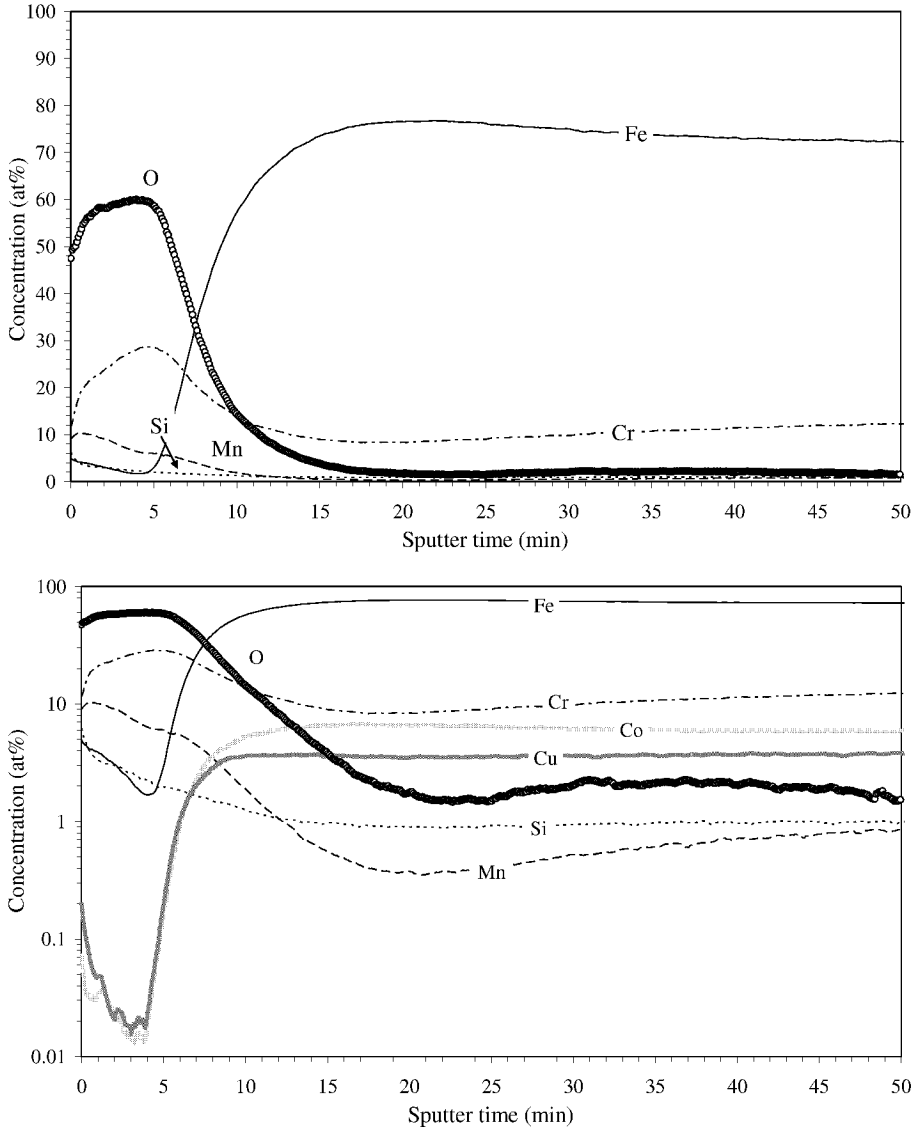

Figure 6 *SNMS analysis of Co/Cu (high Mn) Laves-phase forming model steel after 1000 h oxidation at 600 °C*

b)

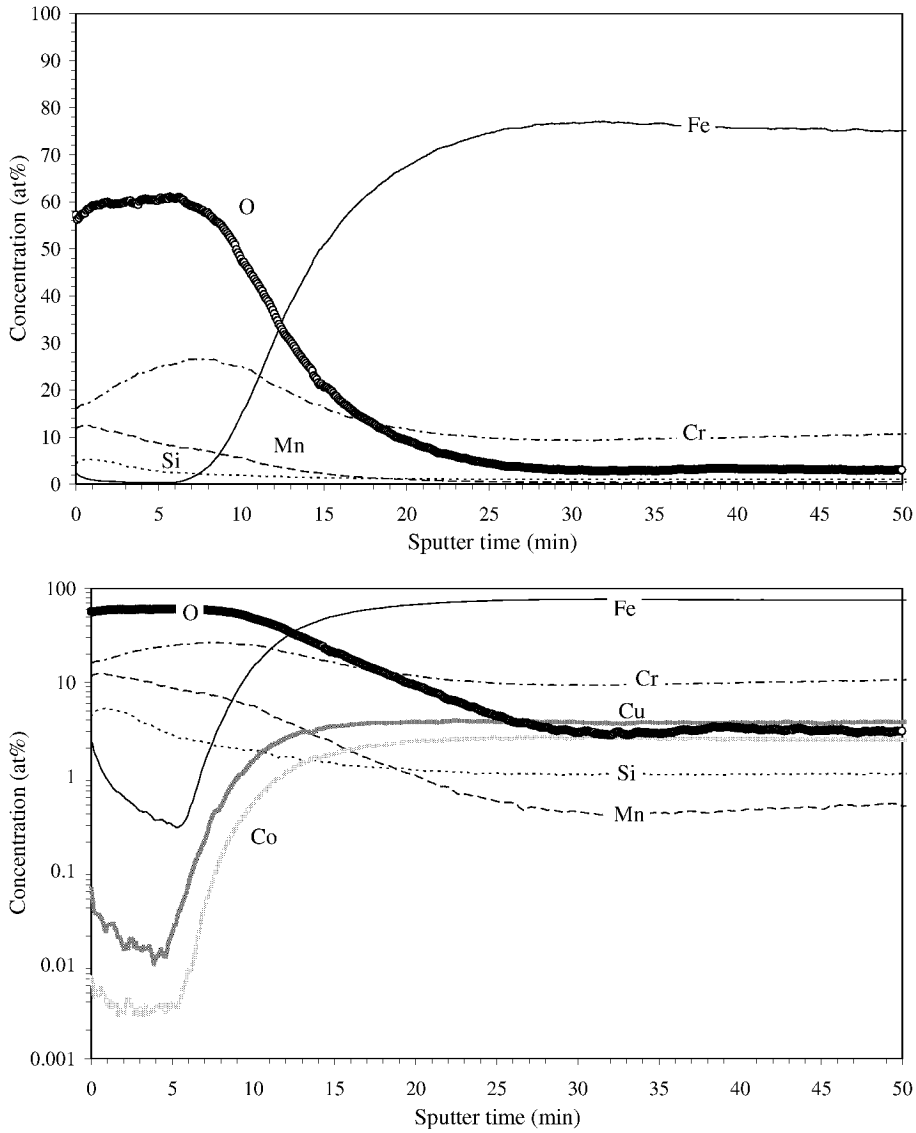

Figure 7 SNMS analysis of Co/Cu (high Mn) Laves-phase forming model steel after 1000 h oxidation at 650 °C

Further studies on the oxide scale composition were performed by TEM analysis (Figure 8), in this case a Co/Cu (low Mn) alloy was selected. A very thin oxide scale could be observed consisting of an external spinel layer and a Cr-rich oxide scale. At high magnification (Figure 9b), a white layer at the interface oxide scale/alloy was found, which corresponds with the formation of Si-oxide. Also, some white particles were observed at the oxide scale surface; these were identified by EDX analysis as Si-oxide. A possible explanation of the formation of external Si-oxides could be found in the high evaporation rates of Si, most likely in the form of oxy-hydroxides [12] such as, $Si(OH)_{4(g)}$, at higher temperatures and in atmospheres of low low pO_2.

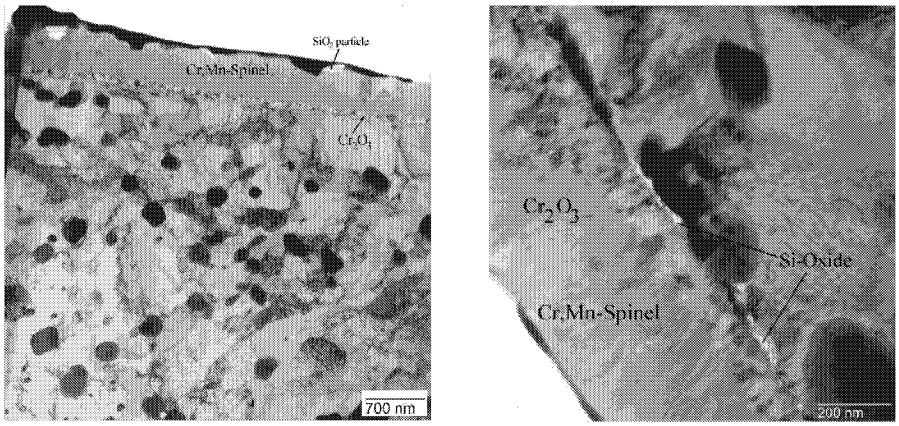

Figure 8 TEM pictures of Co/Cu (low Mn) model alloy after 1000 h oxidation at 600 °C in Ar-50 vol % H_2O

Conclusions

The steam oxidation resistance of 12% Cr steels can be significantly improved by suitable additions of minor alloying elements, such as Mn, Co, Si and Cu, confirming that not only the chromium content in the alloy is the factor determining the long-term oxidation resistance. TEM investigations have revealed that copper is incorporated into MX particles and it is also enriched in Laves phase precipitates, thus the amount of "free" metallic copper particles in the alloy matrix is reduced strongly. Therefore, in order to modelling the alloy microstructure of Cu-containing alloys, the databases must be modified according with these new findings.

Acknowledgement

The financial support by the Deutsche Forschungsgemeinschaft (DFG) is gratefully acknowledged. The authors are grateful to their colleagues D.Dreschers, P. Lersch and J. Bartsch for their assistance in carrying out the oxidation studies, the XRD and optical metallography. They also acknowledge HJ. Penkalla and D. Esser for carrying out the TEM and FIB analyses.

References

[1] F Abe, M Igarashi, N Fujitsuna, K Kimura, S Muneki, Alloy design of advanced ferritic steels for 650 deg C USC boilers, Advanced Heat Resistant Steel for Power Generation, San Sebastian, Spain; 27-29 April, 1998, pp 84-95

[2] I G Wright and B A Pint, NACE Corrosion 2002, Paper 02-377, Denver, CO, March 2002

[3] P J Ennis, A Zielinska-Lipiec, O Wachter O, A Czyrska-Filemonowicz, Acta Materialia, Volume 45,Number 12, December 1997, pp 4901-4907

[4] P J Ennis, W J Quadakkers, 9-12% chromium steels: application limits and potential for further development, PARSONS 2000: Fifth International Charles Parsons Turbine Conference; Cambridge; UK; 3-7 July, 2000, pp 265-275

[5] V Sklenička, K Kuchařová, M Svoboda, L Kloc, J Buršk, A Kroupa, Materials Characterization 51 (2003), pp 35-48.

[6] H Danielsen and J Hald, Z-phase in 9-12%Cr steels, Fourth International Conference on Advances in Materials Technology for Fossil Power Plants, Hilton Head Island, South Carolina, 25-28 October, 2004

[7] B Jiang, K Xu, X Qi and W Zhou, Effects of cobalt content on martensitic transformation and shape memory effect in Fe-Mn-Si-Cr-Ni alloys, J. Phys. IV France, 112 (2003), p 393

[8] J Ehlers, W J Quadakkers, Report Forschungszentrum Jülich, Jülich, FRG, Jül-3883, ISSN 0944-2952, June 2001

[9] V Knezevic, G Sauthoff, J Vilk, G Inden, A Schneider, R Agamennone, W Blum, Y Wang, A Scholz, C Berger, J Ehlers, L Singheiser, ISIJ International, Vol 42 (2002), No. 12, pp 1505-1514

[10] V Knezevic, G Sauthoff, Improvement of creep strength of heat-resistant martensitic - ferritic 12% Cr steels, Fourth International Conference on Advances in Materials Technology for Fossil Power Plants, Hilton Head Island, South Carolina, 25-28 October, 2004, pp 1256

[11] B S Ku, J Yu, Scripta Materialia, 45, 2001, pp 205-211

[12] N Jacobson, D. Myersb, E. Opila, E. Copland, Interactions of water vapor with oxides at elevated temperatures, Journal of Physics and Chemistry of Solids 66 (2005), pp 471-478

Part III

Advanced Steam Turbine Materials

Contributed Papers

Modelling and Alloy Design

CDM MODELLING OF POWER PLANT FERRITIC STEELS

You Fa Yin and Roy G Faulkner
Institute of Polymer Technology and Materials Engineering, Loughborough University,
Loughborough, Leicestershire LE11 3TU, UK
y.yin@lboro.ac.uk; r.g.faulkner@lboro.ac.uk

Abstract

A new continuum creep damage mechanics (CDM) modelling based on Monte Carlo simulations of precipitation kinetics has been developed to predict the creep behaviour of power plant steels. The output of the microstructural evolution simulation, including inter-particle spacing (owing to particle coarsening) and depletion of solution hardening atoms from matrix (due to the formation of laves phase), is fed to a CDM modelling program to calculate creep curves and creep rupture strength. The combined modelling technique has been validated by applying it to a 9wt.% Cr ferritic steel, P92, and using the microstructural data published in the literature and creep data supplied by our collaborators. Reasonably good agreement with experimental observations has been found. The approach has also been used to study the effects of different creep damage mechanisms on the creep behaviour. The new approach shows promise to provide a useful tool for both new alloy development and component life prediction.

Keywords: CDM modelling; Creep damage; Microstructural evolution; Ferritic steels

1. Introduction

Prediction of long term creep behaviour of power plant steels from short term experimental observations or from using models has been of great interest to both academics and engineers for many years [1, 2]. Recently, Dyson reviewed the application of CDM in materials modelling and component creep life prediction and showed that this method provides a unifying framework for some of the other methods [3]. Different creep damage mechanisms can be integrated into the model, provided that the damage mechanism is understood and the evolution of the particular damage with time is known. Therefore, models of different creep damage mechanisms have to be used. For example, Wagner's model has to be used to derive the evolution of the damage due to particle coarsening. Limitations of such an approach are that the model is only applicable to intra-granular spherical particles. We have recently developed a technique to simulate the microstructural evolution of power plant steels using Monte Carlo simulations [4, 5]. This technique is different from many previous approaches to this problem [6-8] and can give important information about particle coarsening and solute depletion from the matrix. Therefore, the combination of this approach with Dyson's CDM modelling would eliminate some limitations of Dyson's approach. Here we report the results of our CDM modelling using this combined approach.

2. Simulation of precipitation kinetics

The Monte Carlo based precipitation kinetics simulation technique employed in this study has been reported elsewhere [4, 5]. However, a summary of the technique is provided below.

The simulation is carried out in a representative bulk of the material which includes both matrix and grain boundaries. Segregations to grain boundaries is then calculated according to the model developed by Faulkner *et. al.* [9] to give the solute concentration in grain boundaries. The pre-service heat treatment and service (or test) durations at different

temperatures are divided into many small time intervals, Δt. In each time interval, possible phase transformations, including nucleation, growth and dissolution, are considered. The nucleation of precipitates has been considered using a classical nucleation theory and nuclei are generated both on grain boundaries and inside the grain according to the corresponding critical activation energies for nucleation. The growth or dissolution of a nucleated particle is determined by the solute concentration gradient around the particle. If the gradient is positive the particle grows, otherwise the particle dissolves. The gradient is determined by the average solute concentration, solute concentration at the surface of the particle and the average inter-particle spacing.

Thus, the increase of the volume of a intra-granular particle, ΔV, in time interval $t \sim t + \Delta t$ is

$$\Delta V = D_V S g \frac{\rho_\theta}{C_\theta \rho_\theta - C_r \rho_\alpha} \Delta t \tag{1}$$

where $S = 4\pi r^2$ is the surface area of the spherical particle with a radius of r, g is the solute gradient at the interface, D_V is the volume diffusion coefficient, ρ_θ and ρ_α are the densities of the precipitate phase and the matrix respectively, C_r is the solute concentration at the interface and C_θ is the solute concentration in the precipitate phase. Similarly, the increase of the volume of a grain boundary particle in time interval $t \sim t + \Delta t$ can be calculated using

$$\Delta V_{GB} = \left(D_V S_M g_M + D_{GB} S_{GB} g_{GB}\right) \frac{\rho_\theta}{C_\theta \rho_\theta - C_r \rho_\alpha} \Delta t \tag{2}$$

Where S_M and S_{GB} are the surface areas of the parts of grain boundary particle within the matrix and inside the grain boundary respectively and therefore $S_M + S_{GB}$ is the total surface area of the inter-granular particle, D_{GB} is the grain boundary diffusion coefficient, g_M and g_{GB} are solute gradients at the surface of the grain boundary particle from the matrix and along the grain boundary respectively. The process is then repeated for the required time duration.

3. Continuum creep damage mechanics modelling

The continuum creep damage mechanics model in this paper follows the approach of Dyson [3]. Two types of damage are considered here: (1) thermally induced damage, including damage due to particle coarsening and due to solute depletion from the matrix; (2) strain induced damage, including damage due to cavity nucleation and growth and due to multiplication of mobile dislocations. These are briefly reviewed below.

The effect of precipitation hardening of alloys is related with the inter-particle spacing of the hardening particles. Therefore, creep damage due to particle coarsening is defined as [3]

$$D_P = 1 - \frac{P_0}{P_t} \tag{3}$$

where P_0 and P_t are the inter-particle spacing at the beginning of coarsening and at any time t respectively. Supposing that the coarsening of the particles obeys Lifshitz-Wagner equation, the following relationship can be derived:

$$\dot{D}_P = \frac{k_P}{3}\left(1 - D_P\right)^4 \tag{4}$$

where k_P is a constant. It should be noted that Eq. (4) only applies to intra-granular spherical particles, such as MX, but is not applicable to $M_{23}C_6$ particles as they are mainly situated at the grain boundaries in high Cr ferritic steels.

The level of damage due to solute depletion from the matrix is defined as

$$D_S = 1 - \frac{\overline{C_t}}{C_0} \tag{5}$$

where C_0 is the initial solute concentration in the matrix and $\overline{C_t}$ is the average solute concentration at time t. The evolution of D_S can be described by the Wert-Zener equation

$$\dot{D}_S = K_S D_S^{1/3}(1 - D_S) \tag{6}$$

where K_S is a material parameter.

The model uses a dimensionless parameter H to model primary creep. H is defined as

$$H = \frac{\sigma_i}{\sigma} \tag{7}$$

where σ is the uniaxial stress and σ_i is an internal back stress generated during stress redistribution within "hard" regions of the microstructure (particles, sub-grains, etc.) as inelastic strain accumulates. The evolution of H is as follows:

$$\dot{H} = \frac{h'}{\sigma}\left(1 - \frac{H}{H^*}\right)\dot{\varepsilon} \tag{8}$$

The constant $h' = E\phi$, where E is the Young's modulus and ϕ is the volume fraction of all phases giving rise to the stress redistribution.

The damage parameter for grain boundary cavitation, D_N is defined as the fraction of grain boundary facets cavitated. When cavities nucleate continuously, the evolution of D_N can be described by the following equation:

$$\dot{D}_N = \frac{k_N}{\varepsilon_{fu}}\dot{\varepsilon} \tag{9}$$

where ε_{fu} is the uniaxial strain at fracture and k_N has an upper limit of $\approx 1/3$. This implies that damage due to cavitation is directly proportional to strain rate, *i.e.* $D_N = A\varepsilon$. We found that this is too simple in some cases and if vacancy condensation plays a role in grain boundary cavitation, creep damage due to cavitation would increase with increasing temperature. Recently, Khaleel *et. al.* quantitatively determined creep damage as a function of creep strain by measuring the area fractions of grain boundary cavities in a modified aluminium alloy [13]. Their results show that creep damage increases slowly at low strains but quickly at higher strains with increasing creep strain. Chabaud-Reytier *et. al.* have also made a quantitative study of inter-granular damage in heat affected zones in Type 321 stainless steels [14]. The damage parameter in their study is defined as the percentage of the cracked grain boundary length in the total boundary length in the area of measurement. The damage parameter for the unaged material increases sharply at low creep strains and then very slowly at higher strains with increasing creep strain. On the other hand, the relationship between creep damage and strain for the aged material is nearly linear. Taking account of these, we modified the expression to

$$D_N = A\varepsilon^B \tag{10}$$

where both A and B can be functions of temperature. Therefore, the modified damage evolution associated with cavitation is

$$\dot{D}_N = A'\varepsilon^{B'}\dot{\varepsilon} \tag{11}$$

Where $A' = AB$ and $B' = B-1$. Eq. (11) is a special case of this equation when $B = 1$.

Damage due to the multiplication of mobile dislocations and its evolution can be described by

$$D_d = 1 - \frac{\rho_0}{\rho_t} \tag{12}$$

$$\dot{D}_d = C(1-D_d)^2\dot{\varepsilon} \tag{13}$$

where ρ_0 and ρ_t are dislocation density at t = 0 and at any time instant, t, C is a material constant.

Considering all the damage mechanisms discussed above, the creep strain rate at any instant is then given by

$$\dot{\varepsilon} = \frac{\dot{\varepsilon}_0}{(1-D_d)(1-D_S)}\sinh\left[\frac{\sigma(1-H)}{\sigma_0(1-D_P)(1-D_N)}\right] \tag{14}$$

The two parameters $\dot{\varepsilon}_0$ and σ_0 are related to temperature

$$\dot{\varepsilon}_0 = \dot{\varepsilon}_0' \exp\left(1 - \frac{Q_{d/j}}{RT}\right) \tag{15}$$

$$\sigma_0 = \sigma_{o,m}\left\{1 - \exp\left[-\frac{\Delta H}{RT_S}\left(\frac{T_S}{T} - 1\right)\right]\right\} \tag{16}$$

where $\dot{\varepsilon}_0'$ is a constant, $Q_{d/j}$ is the combined activation energy for diffusion and jog formation, T_S the solvus temperature when $\sigma_0 = 0$ and ΔH is the enthalpy of solution.

4. Application of the combined precipitation/CDM models

The uniqueness of this work lies in taking the precipitation and solute depletion data from the precipitation simulation and inserting it into the CDM models directly. This gives the evolutions of both inter-particle spacing and the matrix solute concentration and therefore negates the need to use the analytical equations (4) and (6).

The material studied in this paper is a creep resistant 9wt.% chromium steel used in power plant, namely P92. The composition of the steel is shown in Table 1 [12]. The steel is austenitised at 1070 °C for two hours and air cooled, followed by tempering at 770°C for two hours and then air-cooling.

Table 1. Chemical composition of steel P92 in wt% (Fe balance)

Cr	Mn	Ni	Mo	W	V	Nb	C	B	N	Si	P
8.96	0.46	0.06	0.47	1.84	0.20	0.07	0.11	0.001	0.05	0.04	0.008

We apply our simulation to VN, $M_{23}C_6$ and laves phase precipitates in this material under the heat treatment conditions discussed above, assuming that $M_{23}C_6$ is both inter-granular (i.e. at

prior-austenite grain boundaries and sub-grain boundaries) and intra-granular (i.e. inside sub-grains), VN is intra-granular and laves phase is inter-granular. The parameters used in the

Table 2 Main parameters used in the simulation of precipitation kinetics.

Parameter	Unit	Value			Reference
		$M_{23}C_6$	VN	Laves Phase	
a : lattice parameter	nm	0.2866			13
V_θ : molar volume, precipitate	$m^3\ mol^{-1}$	1.82×10^{-4}	1.11×10^{-5}	3.35×10^{-5}	13
V_α : molar volume, matrix	$m^3\ mol^{-1}$	9.05×10^{-6}			14
D_{b0}: grain boundary diffusion Pre-exponential term	$m^2\ s^{-1}$	502	N/A	502	15*
Q_b : grain boundary diffusion Activation energy	$kJ\ mol^{-1}$	283.1	N/A	283.1	15
D_{V0} : volume diffusion pre-exponential term	$m^2\ s^{-1}$	8.5×10^{-4}	1.0×10^{-3}	8.5×10^{-4}	16
Q_V : volume diffusion Activation energy	$kJ\ mol^{-1}$	240	240	240	16
ψ : contact angle	degree	57	90	90	17
ΔH : enthalpy of solution	$kJ\ mol^{-1}$	102.9	17.8	26.1	§
ΔS :entropy of solution	$J\ mol^{-1}\ K^{-1}$	-109.3	-103.9	-2.65	§

* calculated from triple product taking grain boundary width $\delta = 5\times10^{-10}$m and segregation factor $k = 1$.
§ calculated using MTDATA

simulations are summarised in Table 2. For $M_{23}C_6$ and VN, Cr and V have been chosen as the rate-control element respectively, as C and N diffuse much faster than the substitutional element. For laves phase, W and Mo are rate-control elements as Fe is available in sufficient amount everywhere. The interfacial energies are taken as fitting parameters.

Creep modelling has been carried out using our own simulation results. This means there is no need to solve Eq. (4) as the simulation directly gives the inter-particle spacing at any instant, t. Therefore, Eq. (3) is used when we use the simulation results. The coarsening effects considered are due to VN and $M_{23}C_6$. Similarly, solute depletion due to the formation and growth of laves phase is a direct result of the simulation approach. Eq. (5) was used to model the effects of laves phase on creep behaviour. The parameters used are summarised in Table 3. It is clear that the parameter set for both 600 and 650°C are the same except those describing the cavitation process. The larger values of both A' and B' for 650 °C indicate a much faster cavity nucleation and growth process at 650 °C than that at 600 °C (see Eq. (11)). All CDM modelling is conducted under constant load condition, in accordance with experimental measurements.

Table 3 Main parameters used in creep modelling.

Parameter	Unit	Value
$\dot{\varepsilon}_0'$	s^{-1}	7400
Q_{dj}	$kJ\ mol^{-1}$	300
$\sigma_{o,m}$	MPa	33
$\Delta H/RT_S$	/	0.35
T_S	K	1350
h'	MPa	6000
H^*	/	0.57
A'	/	2.9(4.5)*
B'	/	0.95(1.02)*
C	/	50

* values are different for 600 and 650 °C; those in ( ) are for 650 °C.

5. Results and discussion

5.1 Precipitation kinetics

The precipitation curves of VN, $M_{23}C_6$ and laves phase particles are shown in Figs. 1 - 3 respectively. The lines in these figures represent the number average of equivalent particle radius as a function of time from our simulation, and the symbols are experimental results reported in the literature [12, 18-19]. The equivalent particle radius is defined as the radius of the circle which has the same area as the cross section perpendicular to the grain boundary of the particle. Therefore, it equals to the radius for spherical particles and is directly comparable with experimental measurements. Some of the experimental observations are made on isothermally aged samples and others are made on creep tested samples. There is no significant difference between the two cases. The agreement between the simulation results and the experimental observations is fairly good in all the cases of VN, $M_{23}C_6$ and laves phase particles.

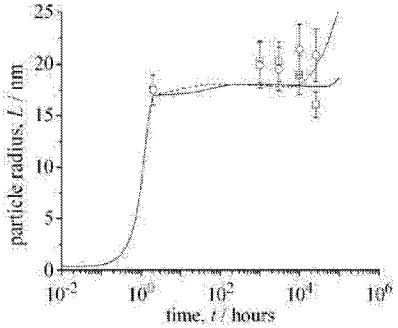

Figure 1. Precipitation kinetics of VN in P92. Lines: simulated (solid, 600 °C; dash 650 °C). Symbols: experimental (ref. 12 and 18. Squares, 600 °C; circles, 650 °C).

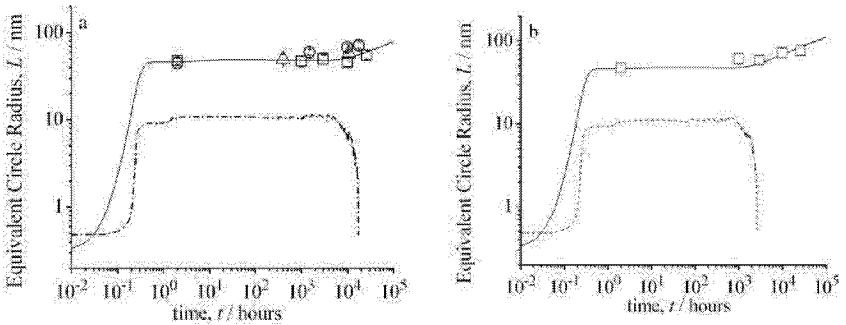

Figure 2. Precipitation kinetics of $M_{23}C_6$ in P92 at 600 °C (a) and 650 °C (b). Lines: simulations (solid: inter-granular; dash: intra-granular); symbols: experimental measurements (squares: ref. 15 and 18, isothermally aged; circles: ref. 19, creep tested; triangles: ref. 12 and 18, creep tested at 160 MPa).

The tempering temperature of the steel is too high for the formation of laves phase particles. Therefore, there is no laves phase present during tempering. When the tempered steel is exposed to much lower temperatures, appreciable number of laves phase particles are formed after a few hundred hours of the exposure. The number of laves phase particles formed at 650 °C is much smaller than that formed at 600 °C. However, the size of the formed particles is much bigger, about four times. Because the number of laves phase

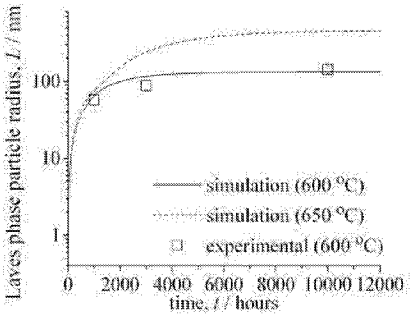

Figure 3. Precipitation kinetics of laves phase particles in P92. Experimental data are after reference (18).

particles is much less when compared with both $M_{23}C_6$ and VN, the coarsening of laves phase particles is relatively less profound over long times.

The inter-particle spacing as a function of ageing time from our simulations is shown in Figs. 4 and 5 for VN and inter-granular $M_{23}C_6$ particles respectively. The inter-particle spacing decreases sharply, corresponding to the sharp increase in the number of precipitates nucleated, at the beginning of tempering as the initial part of the curves in Figs. 4 and 5 shows. The minimum inter-particle spacing is reached at (VN) or before ($M_{23}C_6$) the end of tempering, indicating that no new VN or $M_{23}C_6$ particles are nucleating during service. The inter-particle spacing increases sharply after a few thousand to ten thousand hours as a result of coarsening. The effect of higher ageing temperature on coarsening rate is also clearly demonstrated here with a much earlier and sharper increase in inter-particle spacing at 650 °C than at 600 °C in both cases of VN and $M_{23}C_6$. Comparison of Figs. 4 and 5 shows that the increase of inter-particle spacing is much more marked in the case of $M_{23}C_6$ than in the case of VN, indicating that VN is much more stable than $M_{23}C_6$.

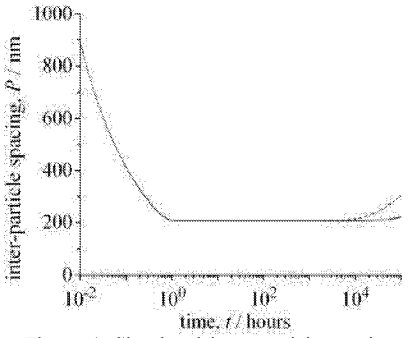

Figure 4. Simulated inter-particle spacing for VN in P92 at 600 °C (solid) and 650 °C (dash).

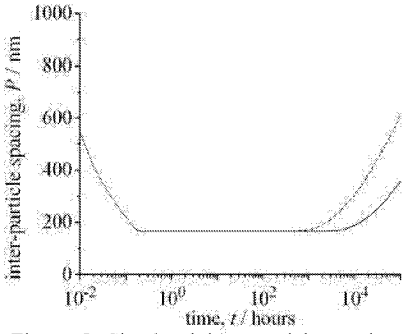

Figure 5. Simulated inter-particle spacing for $M_{23}C_6$ in P92 at 600 °C (solid) and 650 °C (dash).

The predicted volume fraction of laves phase particles at both 600 °C and 650 °C is shown in Fig. 6 as a function of exposure time. The volume fraction of laves phase at 650 °C is lower than that at 600 °C. This is because that the solubility of W and Mo in the matrix is higher at higher temperatures, therefore less solute is available for precipitation. Also that the formation of laves phase at 650 °C is delayed by several hundred hours as compared with the formation at 600 °C due to lower nucleation rates.

The amount of W and Mo used and creep damage due to W and Mo depletion by laves phase formation and growth is directly proportional to the volume fraction of laves phase. Therefore solute depletion induced creep damage increases with ageing time in the same way as is shown in Fig. 6. In such a case, the effect of solute depletion on creep behaviour rises sharply with ageing time before about 10,000 hours, but is nearly stable thereafter.

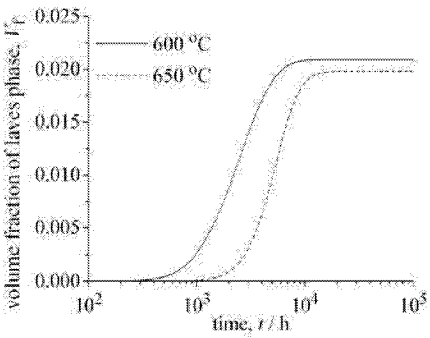

Figure 6. Predicted volume fraction of laves phase in P92 as a function of time.

5.2 CDM modelling

Results of experimental creep rupture tests on P92

at 600 and 650 °C are shown in Fig. 7 (symbols). The data points presented here are averages from a large data set that was supplied by Corus. The lines are the results of CDM modelling using the parameters presented in Table 3 at the corresponding temperatures and the rupture criterion of 100% creep strain. It is evident that the modelling results fit to the experimental measurements reasonably well, although a more conservative prediction at very low stress is given by the modelling. The discrepancy between the modelling and the experiments is due to the limitations present in the current version of the precipitation simulation. Straining effects on precipitate coarsening are not included in the current model. It is widely accepted that straining may result in some kind of decohesion between the precipitates and the matrix and therefore accelerate the coarsening rate. This in turn reduces the rupture life of the material. It is expected that the effects of straining increase with increasing applied stress. Thus the effect will be more marked at higher stresses (or shorter lives) and less marked at lower stresses (or longer lives). This will reduce the life predicted in Fig. 7 and the reduction in life is more severe at higher stresses. Therefore, the inclusion of straining effect will flatten curves in Fig. 7 and much better fits can be obtained at lower stresses by altering the parameter set.

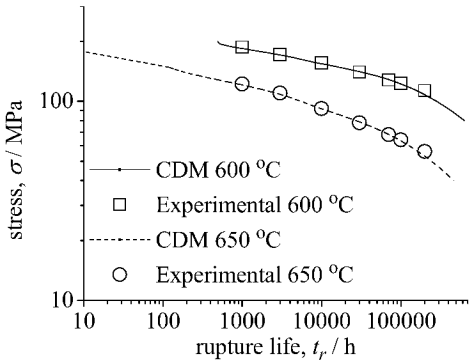

Figure 7. Experimental creep rupture data (symbols) used to analyse the parameter set. Lines are results from CDM modelling using parameters in Table 3.

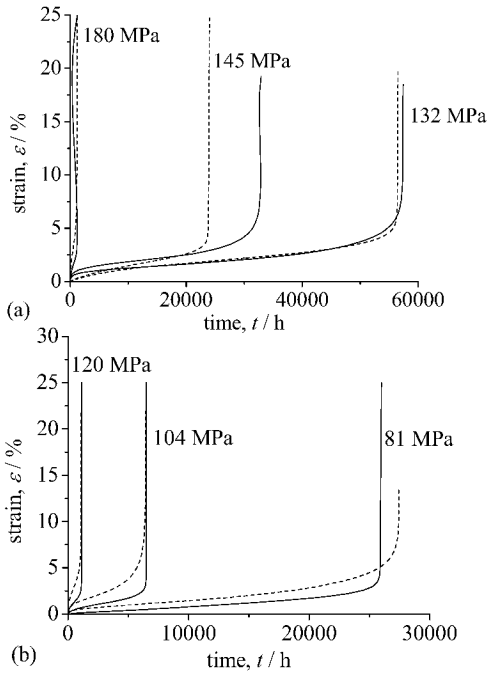

Figure 8. Examples of experimental measured (dashed lines) and CDM predicted (solid lines) creep curves for P92 at (a) 600 °C and (b) 650 °C at various applied stresses.

Fig. 8 shows some predicted creep curves of P92 using the parameters listed in Table 3 (solid lines) compared with the experimental ones (dashed lines) at both 600 (a) and 650 °C (b). All creep curves here were obtained from a single heat of P92 manufactured by Nippon Steel Corporation. The creep tests were carried out in single-specimen machines with continuous strain measurements under constant load. The experimental creep curves show very typical three-stage creep behaviour. The CDM predicted creep curves agree with the experimental observations reasonably well with regard to both the rupture life and the shape of the curves when considering that the scatter in experimental measurements can be large. Noting that the time scale in Fig. 8 is from a few thousand to several tens of thousand hours, we conclude that the parameter set listed in Table 3 describes the creep behaviour of

P92 well. In view of the stochastic nature of creep curves, these results suggest that the predictions made using the approach proposed here are extremely good.

In above discussions, all four creep damage mechanisms are included in the CDM modelling. In order to study the severity of each different damage mechanism, CDM modelling has been carried out with individual creep damage mechanism being considered while setting the damage due to the remaining three mechanisms to zero. The applied stress was set at 132 MPa and temperature was 600 °C. For comparison, the creep behaviour of P92 under the same conditions without any creep damage has been also computed. The results are shown in Fig. 9.

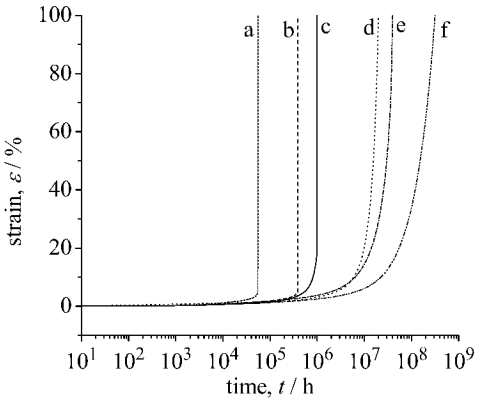

Figure 9. Creep curves for comparing effects of different creep damage mechanism. The applied stress is 132 MPa and the temperature is 600 °C. a: all damage considered; b: only grain boundary cavitation considered; c: only particle coarsening considered; d: only dislocation multiplication considered; e: only solute depletion due to laves phase formation considered; f: no damage considered.

In Fig. 9, curve a is the creep curve with all four damage mechanisms considered and therefore has the shortest rupture life. Curve f is the result with no creep damage was considered, and therefore has the longest rupture life. Therefore, if all creep damage mechanisms are present, the creep life of the material can be several orders of magnitude shorter than the creep damage-free case. All other creep curves lie between these two as is expected. Curve b shows the effect of grain boundary cavitation. Therefore, grain boundary cavitation is the most severe type of creep damage mechanism and will result in considerable reduction in the creep rupture life of the material. Particle coarsening is the second most important creep damage mechanism, as indicated by curve c. The effects of both solute depletion and dislocation multiplication are much less significant than those of grain boundary cavitation and particle coarsening. In the long term, dislocation multiplication (curve d) has slightly more severe effects than that of solute depletion (curve e). However, over shorter time scales, such as the normal lifetimes of power plant component, the contribution of solute depletion to creep degradation is much bigger than that of dislocation multiplication. This is because the depletion of W and Mo from the matrix occurs mainly during the nucleation and growth of laves phase. The depletion rate is much lower during coarsening stage.

6. Conclusions

The simulation technique for modelling of precipitation kinetics in power plant steels developed by the authors has shown excellent agreement with experimental measurements published in the literature. Therefore, the method is promising in providing a means to predict the microstructural evolution. The CDM creep damage model can be used to consider a variety of both thermally and strain induced creep damage mechanisms and shows very useful information on the predicted creep behaviour of the material. When the CDM creep damage model is used with the simulation precipitation kinetics results, it predicts the creep life and creep curves of the material well when the stochastic nature of creep curves is taking into

consideration. This kind of approach can also be used to provide useful information for alloy designers on the effects on creep of using different compositions.

Acknowledgements

We would like to thank the Engineering and Physical Science Research Council (EPSRC) for funding the project (grant number GRN 13074, GRS 77523) and Powergen and Innogy, UK for co-funding. The authors also acknowledge the financial support from The Department of Trade and Industry (DTI) of UK (Grant 409). We are also grateful to Mr Philip Clarke of Corus for supplying the experimental data of creep rupture life of P92 (Figure 7) and Mr Phil Ennis of Institute for Materials and Processes in Energy Systems, Jülich, Germany for supplying the experimental data of the creep curves (Figure 8).

References

1. B. J. Cane, and P. F. Aplin, *Journal of Strain Analysis for Engineering Design*, 1994, **29**(3), 225-232.
2. R. W. Evans, *Proceedings of the Royal Society of London Series A- Mathematical Physical and Engineering Sciences*, 2000, **456**(1996), 835-868.
3. B. Dyson, *Journal of Pressure Vessel Technology*, 2000, **122**(3), 281-296.
4. Y. F. Yin and R. G. Faulkner, *Materials Science and Technology*, 2003, **19**, 91-98.
5. Y. F. Yin and R. G. Faulkner, *Power Technology*, J. Lecomte-Beckers *et. al.* (eds.), 2002, **19**(II), 1247-1256.
6. J. D. Robson, H. K. D. H. Bhadeshia, *Materials Science and Technology*, 1997, **13**(8), 631-639.
7. Y. F. Yin and R. G. Faulkner, *Materials Science and Engineering A*, 2003, **344**, 92-102.
8. G. Ghosh, and G. B. Olson, *Metallurgical and Materials Transactions A*, 2001, **32**(3), 455-467.
9. R. G. Faulkner, *International Materials Reviews*, 1996, **41**(5), 198-208.
10. M. A. Khaleel, H. M. Zbibb, and E. A. Nyberg, *International Journal of Plasticity*, 2001, **17**, 277-296.
11. M. Chabaud-Reytier, L. Allais, D. Poquillon, C. Cäes-Hogrel, M. Mottot, and A. Pineau, *Materials at High Temperatures*, 2001, **18**(2), 71-80.
12. Å. Gustafson, and M. Hättestrand, *Materials Science and Engineering A*, 2002, **333**(1-2), 279.
13. W. B. Pearson, A handbook of Lattice Spacings and structures of metals and alloys, Pergamon Press, London 1958.
14. E. A. Brandes and G. B. Brook, Smithells Metals Reference Book, Butterworth-Heinemann, Oxford, 1992.
15. Zs. Tőkei, K. Hennesen, H. Viefhaus and H. J. Grabke, *Materials Science and Technology*, 2000, **16**, 1129-1138.
16. T. Gladman, in Microstructural Stability of Creep Resistant Alloys for High Temperature Plant Applications (ed. Strang, A. *et al.*), IOM, 1998, 49.
17. R. A. Carolan, and R. G. Faulkner, *Acta Metall.* 1988, **36**(2), 257.
18. M. Hattestrand, and H. O. Andren, ACTA MATERIALIA, 2001, **49** (12), 2123-2128.
19. P. J. Ennis *et al.*, 'Quantitative Comparison of the Microstructures of High Chromium Steels for Advanced Power Stations', *Microstructural Stability of Creep Resistant Alloys for High Temperature Plant Applications*, Strang, A. *et al.*(eds.), IOM, 1998, 135-143.

AN EFFECTIVE PARAMETRIC STRAIN MODEL FOR CREEP

Stefan Holmström[1], Pertti Auerkari [1], Stuart Holdsworth [2]

1) VTT Technical Research Centre of Finland
P.O.Box 1000
FI-02044 VTT, Finland
Stefan.Holmstrom@vtt.fi

2) EMPA, Materials Science & Technology
Überlandstrasse 129
CH-8600 Dübendorf, Switzerland

Abstract

Within the European Creep Collaborative Committee (ECCC), the effectiveness of numerous creep strain models has been reviewed, ranging from simple-phenomenological to complex-constitutive models fitted to large sets of uniaxial creep data. In this paper, a parametric model called MHG (Manson-Haferd-Grounes) is considered and compared in terms of performance with other models, when applied to two steels, 10CrMo9-10 (P22) and X10CrMoVNb9-1 (P91). The MHG model has the ability to describe the deformation characteristics in primary, secondary and tertiary creep. The model performed better than many more complex models and the fitting effectiveness was very good for both steels. The recommended procedure to apply the MHG model requires pre-assessment in the form of investigating the general quality of the creep curves. In case of multi-heat data, heat-specific fitting to the raw data should be performed with intermediate evaluation of the fitting efficiency. In the case of inhomogeneous creep data, a balanced intermediate data set can be constructed by extracting stress-temperature-time values for selected strains using heat-specific MHG equations. This intermediate data is then re-fitted to produce the final master equation. For well-behaving single heat data this iteration step is not needed. In its simplest form the MHG model can perform well with only four fitting constants in the master curve (MHG-4). More complex MHG models with more fitting constants can naturally provide even better fits but with potential disadvantages in model robustness and extrapolation. A low number of required fitting constants for the MHG-4 implies robustness of the master curves, which also showed good applicability for the whole strain range of uniaxial creep tests, including time to rupture.

Keywords: creep, strain, model, ferritic steel

Introduction

Creep strain is typically addressed in materials standards only to fixed limits such as rupture or 1% strain. However, analysis of component behaviour beyond simple design code treatment will require more detailed strain descriptions for transferring the uniaxial creep properties to multi-axial behavior. For this purpose, the uniaxial creep curves need to be evaluated for creep strain modeling. Such modeling is also of interest for extrapolation from shorter term test data to longer term component lifetimes, both for design and later life assessment purposes.

To predict the time to a given creep strain, or stress to reach a given creep strain at some combination of time and temperature, several approaches have been used for selecting the creep models and fitting the available creep test data [1-6].

One of the more simple approaches is to apply time-temperature parameters (TTP), widely used for predicting the time to creep rupture, extended to describe the time to given creep strain. This

is possible because the original derivation of the TTPs for rupture makes use of models for minimum creep strain rate, which can be further correlated with primary creep.

Here, the principle of classical TTP's is extended to predict time to given strain [2,3,4]. The resulting model is shown to hold considerable promise in predicting the creep strain response of both single- and multi-heat creep data. The model and the assessment procedure have been developed during the strain assessment exercises of ECCC (European Creep Collaborative Committee).

Modelling

Most simple creep models attempt to provide a single function, where strain or strain rate is given as an expression separable in stress and temperature. Simplicity in the modelling is of value not only in fitting of the experimental creep data and in derivation of analytical modifications, but also and more importantly because it can make it easier and faster to apply the results in numerical (finite element) component analysis. However, simplicity should not excessively compromise the required predictive accuracy. What is excessive in this respect is not well defined in common standards, and it is therefore of interest also to assess the model performance.

For a generalised TTP concept [1] the mechanical property x can be seen to depend on the material state (factor of microstructural change) s, temperature T, stress σ and operating mechanisms (number of processes n and mechanism factor m). As a result, one can write

$$x = F(n, s, T, \sigma, m) \tag{1}$$

Assuming that the mechanism (here creep) remains the same and that the temperature dependence follows an Arrhenius type of behaviour,

$$dx/dt = F(x, T, \sigma, s) \cdot exp[H(T,\sigma)/RT] \tag{2}$$

Assuming that the microstructural change can be related to the accumulated strain, and integrating with $x = 0$ at $t = 0$, and $x =$ constant when $t = t_\varepsilon$, gives

$$T[ln(t_\varepsilon) + P(T, \sigma, \varepsilon)] = Q(T, \sigma) \tag{3}$$

This can be rewritten as

$$ln(t_\varepsilon) = Q(T, \sigma)/T - P(T, \sigma, \varepsilon) \tag{4}$$

Here t_ε is the time to strain ε at temperature T and stress σ, and the functions $P(T, \sigma, \varepsilon)$ and $Q(T,\sigma)$ are to be selected for the model. The equation (4) is further modified as for the Manson-Haferd parameter, yielding

$$[log(t_\varepsilon) - C]/T = F(T, \sigma, \varepsilon) \tag{5}$$

where C is a constant.

In this work the F(T, σ, ε) is restricted to multi-linear combinations of T, σ and ε. For this modified TTP (here called Manson-Haferd-Grounes or MHG) the function F(T, σ, ε) is selected here so that

$$[log(t_\varepsilon)-C]/T = a_0+a_1 \cdot ln(\sigma)^x+a_2 \cdot ln(\varepsilon)^y \quad (6)$$

where a0, a1, a2, x and y are fitting constants; here x and y are in fact low non-negative integers. This is the simple form of the MHG model (MHG-4) with four fitting constants. In a further expansion of the model (MHG-10) it is formulated as

$$MHG\text{-}10= b_0+b_1 \cdot \sigma+b_2 \cdot ln(\varepsilon)+b_3 \cdot \sigma^2+b_4 \cdot ln(\varepsilon)^2+b_5 \cdot \sigma \cdot ln(\varepsilon)+b_6 \cdot \sigma^3+b_7 \cdot ln(\varepsilon)^3+b_8 \cdot \sigma \cdot ln(\varepsilon)^2+b_9 \cdot \sigma^2 \cdot ln(\varepsilon) \quad (7)$$

where b_0 - b_9 are fitting constants.

Fitting efficiency

The model accuracy can be described by the root mean square (RMS) value calculated from the actual and predicted logarithmic time at the same levels of stress and temperature

$$RMS = \sqrt{\frac{\sum \left(\log(t_{\varepsilon-actual}) - \log(t_{\varepsilon-predicted})\right)^2}{n}} \quad (8)$$

where n is the number of data points. The fitting efficiency is the better the smaller is the scatter factor Z, defined as

$$Z = 10^{2.5 \cdot RMS} \quad (9)$$

When calculating the fitting efficiency it is important to report which actual data has been used. In this work all tabulated Z values are on raw data.

Creep test data and fitting

The first data set involved a single-heat steel 10CrMo9-10 (P22), constant stress creep testing results, provided by ECCC, up to about 3000 h of testing time. The data set contained 30 creep curves with five isotherms (510-600°C) containing six tests each at different stress levels (120-280 MPa). As noted below, closer examination of the creep curves suggested some anomalous creep curves with clear cross-over behaviour, but these were not excluded from the modelling.
A data set consisting of the strain values of interest, i.e. 0.1%, 0.2%, 0.5%, 1%, 2%, 5%, 10%, 15% and maximum reported strain, were extracted from the raw data by log-log interpolation between actual data points. These data points were then fitted to the MHG-4 and MHG-10 models.

The second data set, also provided by ECCC, included both interrupted and continuous constant load creep tests for six heats of the P91 steel, containing 101 constant load creep curves up to about 50 000 h of testing time (450-700°C, 39-528 MPa). Two heats were divided into two sub-heats each due to clearly differing creep behaviour. The amount of data per creep curve varied

widely between heats, suggesting that some balancing is required to avoid bias in the fitting due to differences in the number of data points in each represented creep curve. First the data from each data heat batch with no data reduction were fitted to MHG-4 model. This resulted in poor fitting, with $Z > 10$ largely due to one heat with inconsistencies such as strain jumps and questionable initial strain values. For all data excluding this heat, the combined $Z = 4.18$ using individual models for each sub-heat, and this Z-value was considered as a reference target for a combined master curve. To produce a balanced master curve for the whole data set, the initial models for each sub-heat were utilised for producing a new more balanced synthetic data set of creep curves at temperatures and stresses representative of sub-heat data, each curve consisting of the strain values of interest, i.e. 0.1%, 0.2%, 0.5%, 1%, 2%, 5%, 10%, 15%, however limited to the maximum strain in the original data. The resulting synthetic creep curve data set was then refitted to the MHG model to provide the final master curve surface.

The data were fitted to the model of Eqs. (6) and (7) using iteratively usual standard fitting routines of program Tablecurve 3D (Systat Software Inc.), supported by purpose-built functions in Origin (OriginLab Corp.).

The fitting results were compared with parallel results obtained from the same data sets using other models tested within ECCC [1, 6].

Fitting results

The fitting constants for the MHG-4 model on the single heat P22 data are shown in Table 1, and the fitting results in Fig. 1 and 2. An intercomparison of the MHG model performance with other models, as tested in the ECCC excercise, is shown in Table 2.

Table 1. Fitting constants for MGH-4 of Eq. (6) / P22 data (x = y = 2)

Constant	$\mathbf{a_0}$	$\mathbf{a_1}$	$\mathbf{a_2}$	**C**
Value	-33.2	-0.95	-0.2	55.62

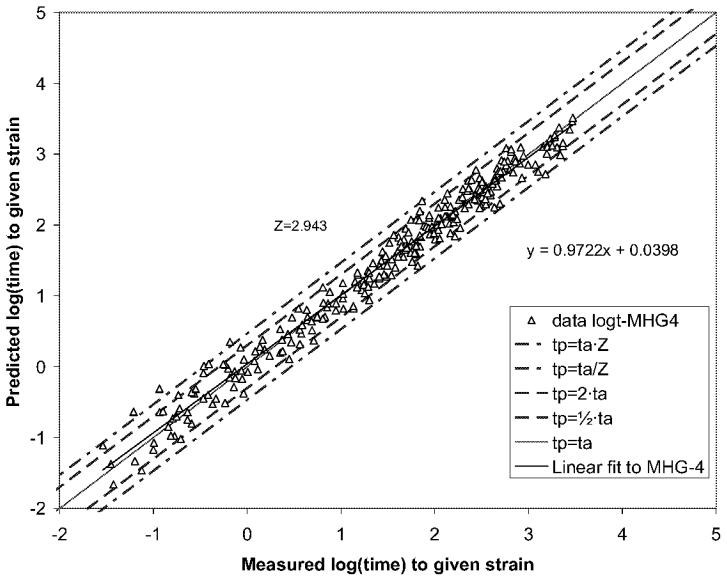

Fig. 1. Single heat fit for P22 to all data from 0.2% strain to rupture (MHG-4 model)

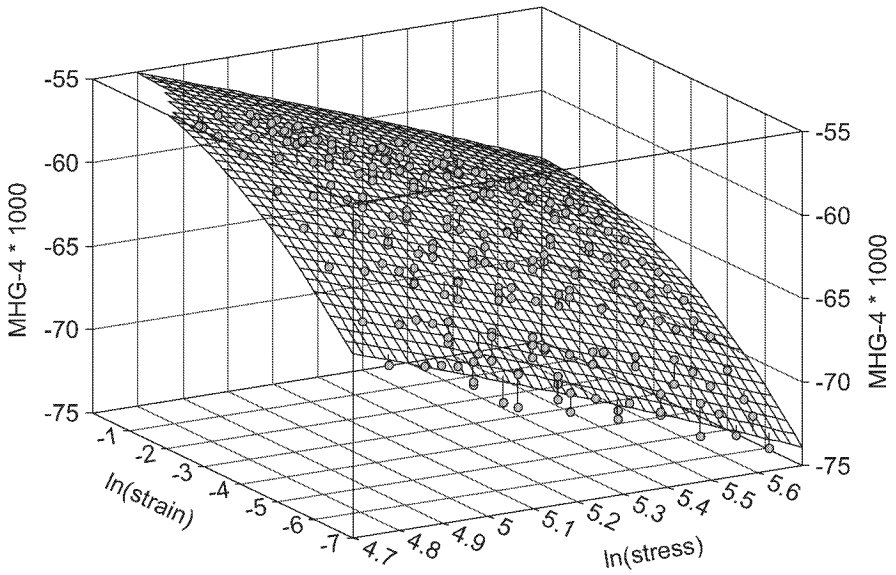

Fig. 2. Fitted MHG-4 master curve surface for P22 steel (single heat data)

Table 2. Comparison of strain models for steel P22 (single heat data) [1]; P/S/T = primary / secondary / tertiary

Model equation	Creep regimes	Z for time to specified strain (all temperatures)				
		0.2%	0.5%	1 %	2 %	5 %
Omega model	S/T	468	39	10		
BJF model	P/S	15	6	4		
Theta model	P/S/T	17	3	2		
Modified Theta	P/S/T	10		4		
Creep strength ratio model	P/S/T	4	8	7		
Dyson-McClean	P/S/T	12	7	3		
Baker-Cane	P/S/T	5		2		
Bartsch model	P/S	3	2	4		
Modified Garofalo model	P/S/T	2	2	2		
Modified Graham-Walles	P/S/T	3	3	2	2	2
Strain law (Modified Nadai/VTT)	P/S/T	3	2	2	2	2
MHG-4	P/S/T	3	3	3	3	3
MHG-10	P/S/T	3	2	2	2	2

The fitting constants for the MHG-4 model on the multi heat P91 data are shown in Table 3. The fitting performance is shown in Fig. 3 between predicted and actual raw data. The master curve surface from the raw data fit is presented in Fig. 4 to be compared with the balanced synthetic data fit in Fig. 5.

A comparison of the MHG model performance with other models, as tested in the ECCC excercise, is shown in Table 4.

Table 3. Fitting constants for the P91 (balanced) data, MHG-4 master curve (x=2, y=3).

Constant	a_0	a_1	a_2	C
Value [1)]	-54.0639	-1.04837	-0.02944	77.25199

1) F multiplied by 1000

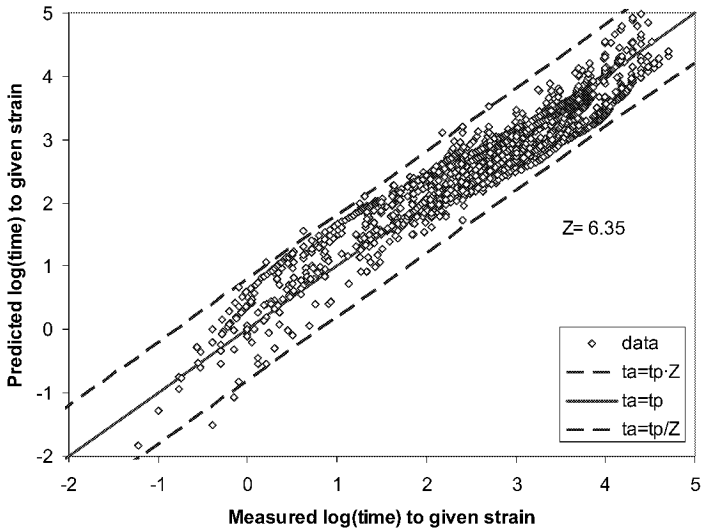

Fig. 3. MHG-4 master curve fit on P91 with 1559 raw data points.

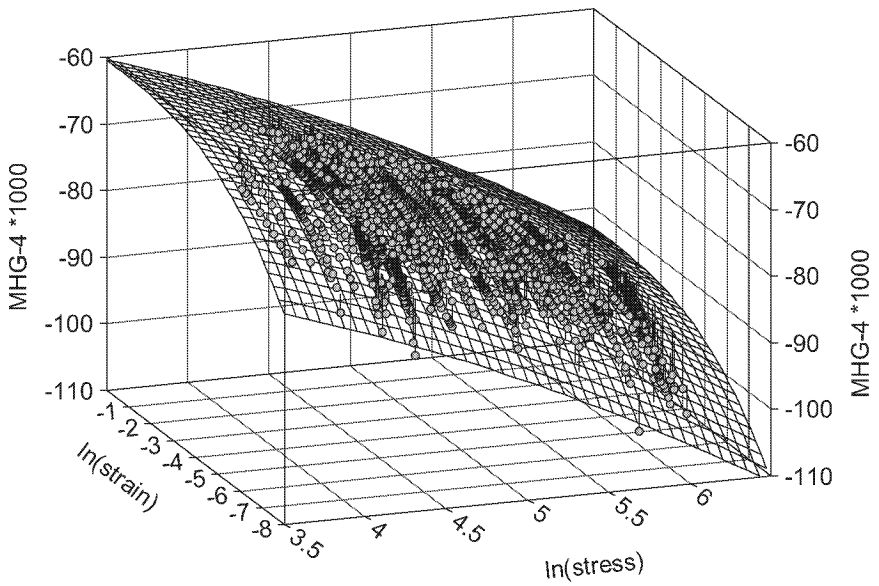

Fig. 4. MHG-4 model fit to all uncensored raw creep data on P91.

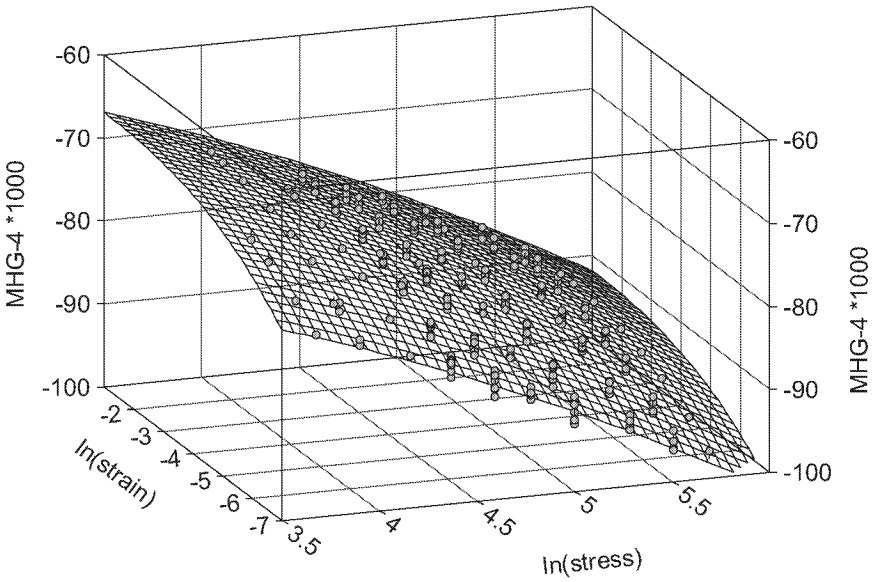

Fig. 5. The fitted MHG-4 master curve surface for P91 steel with the balanced synthetic data.

Comparing fitting efficiency (Z-values) when using the new master curve on the original data showed that adding the balanced synthetic data of the problematic P91 heat into the overall fit did not remove the incompatibility of the problematic heat. Therefore, the master curve without this heat was selected as the preferred model.

Table 4. Intercomparison of strain models for steel P91 (multi-heat data) [1]

Model equation	**Creep regimes**	**Z-value for time to specified strain (all temperatures)**				
		0.2%	**0.5%**	**1 %**	**2 %**	**5 %**
BJF model	P/S/T	113	104	50	32	11
Modified Theta model	P/S/T	74	19	17	8	12
Li & Akulov model	P/S/T	143	42	18	6	4
Modified Omega model	S/T	138	19	11	8	5
Creep strength ratio model	P/S/T	38	7	7	6	5
Modified Sandstrom	P/S/T	11	7	6	6	6
Modified Graham-Walles	P/S/T	7	7	6	7	5
MHG-4	P/S/T	6	7	6	6	5

Discussion and conclusive remarks

As can be seen from Tables 2 and 4, in spite of its simplicity the MHG-4 model has a very competitive performance in predicting time to given creep strain of the tested steels. throughout the strain range of uniaxial creep testing (0.1 - 30%). The MHG-10 model with 10 fitting constants does improve the fitting performance somewhat but at a cost of complexity in the stress-strain function, and additional uncertainty in extrapolation. For most practical purposes, the MHG-4 model appears quite adequate.

Because of good performance throughout the strain range, the MHG models can also be used to predict time to rupture. Results for the P22 data are shown in Table 5.

Table 5. Comparison of predicted stress to creep rupture (the rupture strain is assumed to be 30% for P22 at 10 000 h). Rupture stress involves extrapolation by a time factor of 3.

Model	500°C	525°C	550°C
MHG-4 [1)]	197	163	135
MHG-10 [1)]	190	158	133
MH04 [2)]	196	164	135
EN 10216-2	195	150 [3)]	111

1) whole creep curve modeled
2) Manson-Haferd TTP fit according to PD6605 [7], only rupture data used
3) interpolated value

Considering the inherent heat-to-heat scatter in the original multi-heat P91 data, the MHG model appears to produce reasonably good results in predicting the time to given creep strain (creep curves). For reasonable results it was however necessary to censor the data by excluding one clearly deviant heat with multiple anomalous creep curves. The preliminary master curve models when fitted to individual heats resulted in Z-values ranging from 2.9 to 4.3 when calculated from the original raw data. The corresponding Z = 6.35 for the master curve for all final data is considered a good result.

The predicted stress levels to selected strain levels at 100 000 h and 200 000 h at 500°C, 550°C and 600°C are shown in Table 6.

The results suggest that the MHG model performs well and is robust with minimal number of fitting constants. The approach is theoretically applicable with both constant stress and constant load creep tests. Although the MHG model performed better than even quite complex other models, some room for further improvement is possible, as is seen from the apparent systematic S-shaped trend in the P91 raw data presented in Fig. 3.

Table 6. Predicted stress to given strain using the MHG model for P91 at 100 and 200 kh. For comparison, results are shown from a rupture assessment using the MC model of PD6605 [7] on the same data set.

Limit strain	500°C		550°C		600°C	
	100 kh	200 kh	100 kh	200 kh	100 kh	200 kh
0.2%	119	108	69	62	40	36
0.5%	154	141	92	84	55	50
1%	177	163	107	98	66	60
2%	196	180	120	110	74	68
5%	213	197	132	122	83	76
15% (assumed rupture)	225	208	140	129	88	81
MC (rupture)	227	214	149	138	88	80
EN 10216-2 (rupture)	258	246	166	154	94	86

References

1. Holdsworth, S.R., Askins, M., Baker, A., Gariboldi, E., Holmström, S., Klenk, A., Merckling, G., Sandström, R., Schwienheer, M., Spigarelli, S. (WG1/ECCC) Factors Influencing Creep Model Equation Selection. Proc. ECCC Conf. on Creep & Fracture in High Temperature Components, Design & life assessment issues, 12-14/9/2005, London, UK
2. Manson, S. S., Haferd, A. M. A linear time-temperature relation for extrapolation of creep and stress rupture data, NASA TN 2890, 1953.
3. Grounes, M. A. Reaction-Rate Treatment of the Extrapolation Methods in Creep testing, Journal of Basic Engineering, Series D, Trans. ASME, 1969.
4. Holmström, S. & Auerkari, P. Prediction of creep strain and creep strength of ferritic steels for power plant applications. Proc. Baltica Conf. on Life Management and Maintenance for Power Plants, VTT Symposium 234, 8-10/6/2004, Espoo, Finland.
5. Holdsworth S. R. & Merckling G. ECCC developments in the assessment of creep-rupture data. Proc. 6th Int. Charles Parsons Conf. on Engineering Issues in Turbine Machinery, Power Plant & Renewables, Trinity College, Dublin, 16-18 Sept, 2003.
6. Holdsworth S. R. Developments in the assessment of creep strain and ductility data. Materials at High Temperatures 2004;21(1):125-132.
7. BS PD6605, Guidance on Methodology for the Assessment of Stress-Rupture Data, British Standard Institution (1998).
8. Mannesmann Data Sheet 435R, 1993

ADVANCED ALLOY DESIGN TOOLS APPLIED TO THE DEVELOPMENT OF VANADIUM NITRIDE STRENGTHENED HIGH-TEMPERATURE STEELS

D. Gaude-Fugarolas[1*] V. Yardley[1,3] J-M. Lardon[2] J. Montagnon[2]
Y. De Carlan[1]

1.- CEA Saclay
SRMA/LA2M bât 453
91191 Gif Sur Yvette CEDEX (France)
2.- Aubert et Duval
Parc Technologique La Pardieu 6 r Condorcet
63063 Clermont Ferrand CEDEX 1 (France)
3.- Now at Tohoku University (Japan)

Abstract

The modern power generation industry is constantly seeking to attain higher efficiency levels to obtain better environmental and economic performance. In order to achieve these goals, materials are needed with sufficiently high creep resistance to withstand operation under more demanding conditions, particularly higher service temperatures. A new generation of Fe8-12Cr ferrito-martensitic steels have the potential to become optimal candidates for various critical applications in the thermal and nuclear power generation and petrochemical industries.

One effective method of enhancing the creep resistance of an alloy is by producing a fine precipitate distribution that minimises deformation at service temperatures. MX precipitates such as VN are especially suitable for this task, due to their morphology, homogeneous distribution and slow coarsening (especially in comparison with $M_{23}C_6$-type carbides). Moreover, VN is stable to higher temperatures than $M_{23}C_6$, allowing an increase in the working temperature of the alloy.

An alloy with a high nitrogen content is not devoid of potential problems, and therefore careful design of the alloy composition and heat treatments are needed. The occurrence of porosity related to high nitrogen content has been noted. The maximum nitrogen content (both in absolute terms and relative to other elements, e.g. V/N, V/C) needs to be optimised in order to obtain the best possible mechanical performance whilst minimising the risk of porosity after casting.

In the work described here, thermodynamic software packages based on the CALPHAD method, together with advanced statistical analysis using neural networks, were used to suggest optimum compositions, microstructures and heat treatments to obtain improved creep properties in a new set of alloys for the nuclear power industry. The computational work was complemented by the use of experimental castings and characterisation of a selection of alloys of various compositions and with a wide range of nitrogen contents. This also enabled the development of a criterion to predict the

*Corr. Author: dgaude@cantab.net Tel: +33 (0)1 69 08 22 69 Fax: +33 (0) 169 08 71 30

formation of nitrogen-induced porosity during casting; this should be useful both to research and to the steel-making industry.

Keywords: Cr-Steel; Creep; VN Precipitation; Porosity; Neural Networks

Introduction

In order to satisfy more demanding efficiency requirements and to achieve better environmental and economic performance, the modern power generation industry requires a continuous process of improvement. New materials able to outperform present ones in safety, mechanical properties and service temperature are a continuous need in this process. In the past, the process of designing a new material was mostly heuristic, requiring repeated experimental trial and error, but the accuracy of current scientific knowledge in thermodynamics and transformation kinetics enables us to design successful new alloys using minimal empirical feedback. The design process is, however, still somewhat iterative, each stage leading to a more refined definition of the final alloy. The difference from the traditional approach is that most of the process is performed theoretically or computationally, involving the production of only a few essential trial casts to verify the suitability of the product material.

Design methodology and discussion

To illustrate the potential of modern materials design methods, a new family of alloys for the nuclear power industry has been developed. Ferritic-martensitic steels are known to perform well as low-activation materials, due to their low swelling under radiation and long service life at high temperatures [1]. An Fe8-12Cr ferritico-martensitic alloy was selected as the basis for this new type of alloy, due to its good balance between mechanical properties and oxidation resistance [1, 2, 3]. A neural-network model based on a large database of creep properties of alloys used in high-temperature applications was then used to narrow the range of suitable compositions. An alloy containing carbon, chromium, tungsten, vanadium and nitrogen was chosen.

Creep damage involves several competing mechanisms, but under typical power plant conditions, the main mechanism consists of the easy glide of dislocations along slip planes, and the subsequent, thermally activated dislocation climb into a different slip plane when dislocations encounter an obstacle (for instance, an incoherent precipitate). Providing a fine distribution of precipitates that remain stable at service temperature is therefore a suitable strategy to improve the creep behaviour of an alloy [4].

The composition selected provides the possibility of reinforcing the microstructure with a nanometric distribution of MX-precipitates. VN precipitates, for instance, are stable at higher temperatures than other MX precipitates or $M_{23}C_6$ carbides, and are less prone to coarsening than $M_{23}C_6$ [2, 5]. Calculations of the stability of phases were performed using thermodynamic models based on the CALPHAD method [6, 7]. When dealing with high nitrogen contents, there is a risk of developing a small amount of porosity in the material. Sometimes this kind of problem is not obvious at the first stages of the process of alloy design, but it clearly needs to be taken into account nonetheless. Obviously, there is a demand to find suitable criteria that could be applied in research and industrial environments to predict the occurrence of such porosity. One such criterion for the occurrence of porosity in high-nitrogen alloys is presented in this work.

The optimal heat treatment to obtain the desired distribution of precipitates in a suitable microstructure was determined using a thermodynamic and kinetic model based on the CALPHAD method and the

Onsager extremum principle [8, 9, 10]. The alloy designed in this way was cast at the *Aubert et Duval* steelworks and its properties are being characterised at CEA Saclay.

General composition

Many alloys for high temperature applications, especially in the power generation industry, are based on the Fe8-12Cr system. This family of alloys presents a good compromise between mechanical properties (especially creep resistance) and oxidation resistance [1, 2, 3]. The optimal structures for high temperature nuclear applications are the body-centred cubic ferritic or martensitic phases, usually as a matrix with a complex arrangement of reinforcing precipitates. Austenitic alloys lack the capability of ferritic alloys of withstanding the radiation damage, especially swelling [1, 2, 3].

A balance between ferrite-stabilising (or α-gen) elements and austenite-stabilising (or γ-gen) elements needs to be achieved in the alloy composition to avoid the formation of δ-ferrite at the austenitisation temperature. This phase would produce brittleness in the final component, and unless the structure could be fully transformed into austenite, the subsequent transformation to martensite on quenching would be incomplete [3, 11].

Some alloying elements, such as Mo, Ni, Nb, Si, Mn, Co and B, which are commonly used to improve the properties of steels for the conventional power generation industry and other high-temperature applications, need to be reduced or even excluded entirely from alloys intended for use in the nuclear industry because of their behaviour under neutron irradiation. They are commonly substituted by W, V and Ta in alloys intended for operation under radiation [1, 2, 3].

Starting from the general criteria found in the literature, a first set of compositions was defined, and then a thermodynamic calculation software package was used to select the ones that would fit to the microstructure requirements imposed. The thermodynamic software packages MTDATA and Thermocalc were used to perform this type of calculation on the thermodynamic stability of the phases of interest [3, 11]. A general range of possible compositions including the elements Fe, Cr, W, V, N, and C but with limited contents of Ni, Si, Mn and B was therefore selected following the above criteria.

At the same time, and in order to analyse the effect of small variations of each element on the creep resistance of the alloy (and the respective interactions), an advanced statistical method was used, a Bayesian-based neural network [12, 13]. Cole *et al.* had trained a neural network describing the creep properties of a wide range of steels [14]. This model is publicly available at the Materials Algorithms Project website [15]. Using this tool, the effect of variations in composition on the creep rupture strength after 100,000 hours was analysed and a well-defined composition was defined that would potentially maximise creep resistance.

In all figures showing the predictions obtained with the neural network model (Figures 1 to 6), the predictions for each set of conditions are plotted in solid lines and surrounded by dashed lines representing the *errorbar* or confidence estimate of the prediction [12, 13].

According to the predictions using the neural network trained by Cole *et al.* [14], for some elements there was an optimal composition range (represented by a maximum in the predicted creep rupture strength at 10,000 hours). This was the case for Cr and W, elements for which the optimal contents were around 9.5 wt.% (Figure 1) and 2 wt.% (Figure 3) respectively. In the case of chromium, this value lies in the lower end of the range of compositions traditionally used for high-temperature applications, and therefore it will be necessary to pay special attention to aspects such as the corrosion resistance of the alloy. Tungsten is usually added to produce solid solution strengthening of the matrix, but it is also a strong α-gen element.

Carbon has a strong solid solution strengthening effect, and according to the neural network predictions (Figure 2), the creep rupture strength of the alloy increases monotonically with its carbon content.

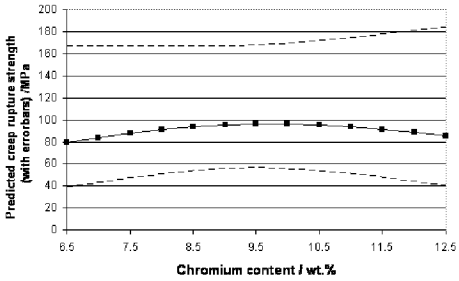

Figure 1: Creep rupture strength predicted using a neural network as a function of chromium content.

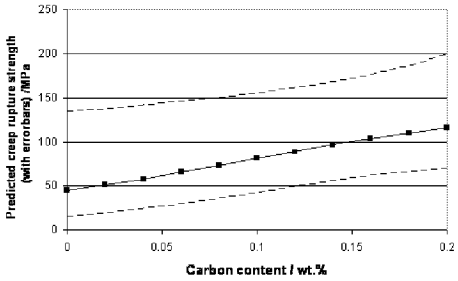

Figure 2: Creep rupture strength predicted using a neural network as a function of carbon content.

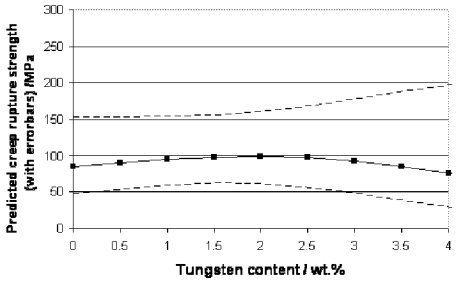

Figure 3: Creep rupture strength predicted using a neural network as a function of tungsten content.

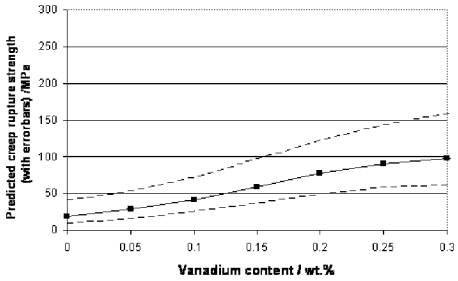

Figure 4: Creep rupture strength predicted using a neural network as a function of vanadium content.

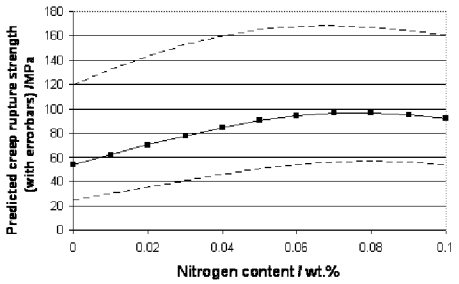

Figure 5: Creep rupture strength predicted using a neural network as a function of nitrogen content.

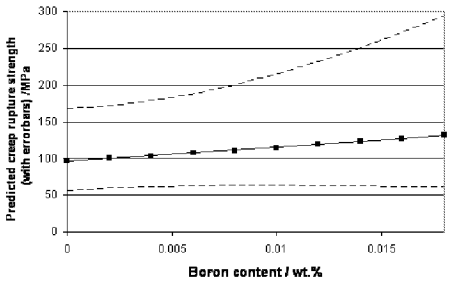

Figure 6: Creep rupture strength predicted using a neural network as a function of boron content.

Carbon is also a strong γ-gen element, which helps to compensate for the increase in α-gen elements such as W or V. However, this trend needs to be treated with caution, as not all the carbon stays in solid solution; instead it tends to precipitate as $M_{23}C_6$. $M_{23}C_6$ precipitates have rapid coarsening kinetics and therefore produce little improvement in the mechanical properties. In addition, they 'steal' Cr from the matrix of the alloy, reducing its oxidation resistance. Better results are expected from a fine distribution of MX precipitates (*i.e.* VN), which not only coarsen more slowly, allowing for a potential improvement in creep resistance and toughness, but are also stable at higher temperatures. VN precipitates are able to play that strengthening role, and so it would seem at first to be advantageous to increase the content in both V and N. Indeed, the creep rupture strength increases with the vanadium content (Figure 4) but this element is at the same time a strong α-gen element, and an excess of it would prevent the complete austenitisation of the alloy. The predictions of the neural network suggest that the optimal nitrogen content lies around 0.07wt.%, as shown in Figure 5, but an excessive N content could lead to porosity in the cast, as will be described in a later section [11, 5].

Last but not least, Figure 6 shows that the predicted creep rupture strength increases with boron content. Even small additions of boron have an important influence on the creep behaviour of Cr-steels, as it diffuses to the surfaces of $M_{23}C_6$ precipitates, especially to those close to prior austenite grain boundaries, and slows down their coarsening [16, 17]. In the natural form of boron, the isotope B^{10} predominates. This has a deleterious effect in alloys exposed to irradiation, because it transforms to helium. However, since only small amounts of boron are necessary for improved creep properties, the less common isotope B^{11}, which does not exhibit this problem, could be isolated and used in alloys for nuclear applications, so that the beneficial effect of boron could still be obtained [11].

To conclude, after examining the related literature and analysing the possible compositions with the help of advanced statistical methods, an alloy composition optimised to maximise the creep rupture strength, while presenting good oxidation properties, was chosen. The proposed composition was (all compositions are in wt.%) Fe 9.5Cr 0.14C 2.5W 0.35V with up to 0.07N and with the possibility of small (less than 0.1 wt.%) additions of B^{11}.

Microstructure and heat treatments

Once the composition of the alloy has been selected, the heat treatments to obtain the desired microstructure need to be carefully designed. In order to obtain the fine precipitation of vanadium nitrides we need first to austenitise the alloy and dissolve all existing precipitates. Then one or more annealing treatments will allow the precipitation of VN in the austenitic matrix. Subsequent quenching to transform the austenite matrix to martensite and tempering to relieve internal stresses and to precipitate $M_{23}C_6$ and therefore to stabilise the microstructure will finish the treatment. Using a thermo-mechanical treatment would also be feasible, adding stages of hot rolling prior to annealing to increase the density of precipitate nucleation sites and hence to accelerate the precipitation reaction and reduce the average size of the precipitates. The optimisation of the heat treatment parameters (temperature and duration of each stage of the heat treatment) is possible using a software package such as 'MatCalc' developed by TU Graz, Austria, which combines equilibrium phase stability calculations with simulations of the kinetics of precipitation, (nucleation, growth and coalescence of precipitates), and predictions of the size distribution obtained with each set of conditions [8, 9, 10]. The package uses thermodynamic, mobility and physical property databases expressed in a standard CALPHAD-type format. The calculations for the present work were made using the database "IWS_Steel", developed at TU Graz.

Figure 7 shows the calculated phase stability diagram as a function of temperature for steel VY1. Using this diagram we can define the temperatures for the different stages of the heat treatment to obtain the optimal microstructure.

Using Figure 7 as a reference, we can define the austenitisation temperature at 1175°C, and then a

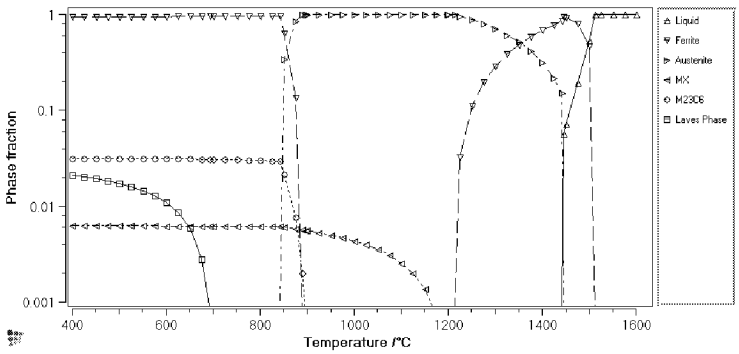

Figure 7: Phase distribution as a function of temperature for designed alloy. Diagram calculated using MatCalc.

subsequent annealing at 900°C for 1 hour to produce a distribution of VN precipitates. At this temperature, the driving force for precipitation of vanadium nitrides is large and the equilibrium phase fraction of precipitates is close to the maximum it is possible to reach at any temperature. Parameters such as austenite grain size and dislocation density could be modified to account for different starting conditions of recrystallisation, grain size and hot work. In the example shown in Figures 8 to 10 an austenite grain size of 100 μm and two different dislocation densities, representing annealed and hot worked microstructures, have been used. After the MX-precipitation annealing, the alloy should be quenched to transform austenite to martensite and finally a last stage of stabilisation tempering is performed at 700°C for 3 hours to reduce internal stresses and to precipitate $M_{23}C_6$.

Using a software package that includes at the same time thermodynamics and precipitation and coarsening kinetics simplifies considerably the selection of optimal heat treatment conditions to obtain the desired microstructure and precipitate distribution, while avoiding incomplete precipitation reactions or excessive precipitate coarsening. In the present case, the duration of the MX precipitation annealing is chosen to ensure that the equilibrium fraction of MX has been reached. On Figures 8 to 10 we see that 30 minutes would suffice but an hour has been chosen to ensure that reaction is complete but that there is no significant coarsening. The same procedure is applied to the stabilisation annealing and the precipitation of $M_{23}C_6$. The final distribution of reinforcing phases predicted comprises in both cases coarser particles of $M_{23}C_6$ than MX, but the effect of the initial density of dislocations (and therefore of nucleation sites) makes a large difference in the scale of MX precipitates. A similar calculation could be performed to study the evolution of the microstructure during service conditions, for instance to predict the excessive coarsening of some of the reinforcing phases or to anticipate deleterious phases that have very slow kinetics, like Z-phase.

Undesirable phase: Nitrogen gas

As the nitrogen content of the alloy is increased to produce a larger extent of precipitation of the reinforcing phase VN, there is an increased risk that the matrix of the alloy will not be able to keep in solution all the nitrogen and some will be released as gas, resulting in the formation of porosity. Some alloys with very high nitrogen content can even present macroscopic porosity, as shown in Figure 11. The nitrogent content of the alloy shown in Figure 11 is 0.073wt.% .

Some Cr-steels with substantial nitrogen contents develop porosity (*e.g.* the alloy designated A2, in

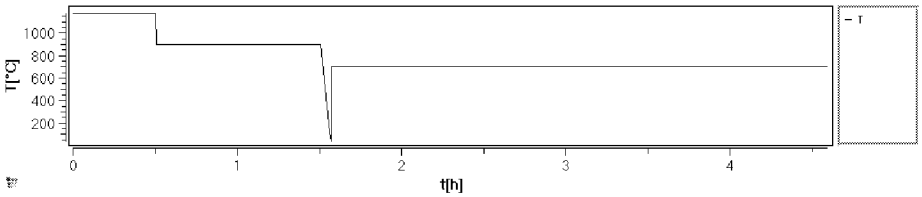

Figure 8: Simulated heat treatment on the designed alloy: Fe9.5Cr0.14C2.5W0.35V0.07N (wt.%).

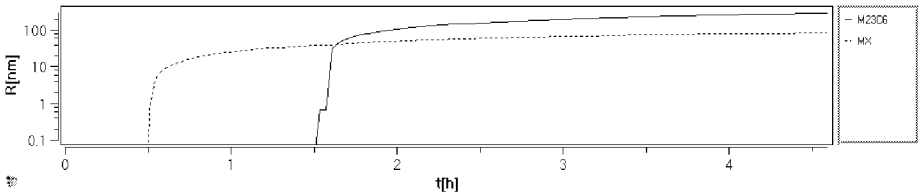

Figure 9: Simulation of the evolution of the average radius of MX and $M_{23}C_6$ precipitates on the designed alloy with dislocation density in austenite of $10^{11}\mathrm{m}^{-2}$ and in martensite of $10^{14}\mathrm{m}^{-2}$ (*i.e.* as annealed).

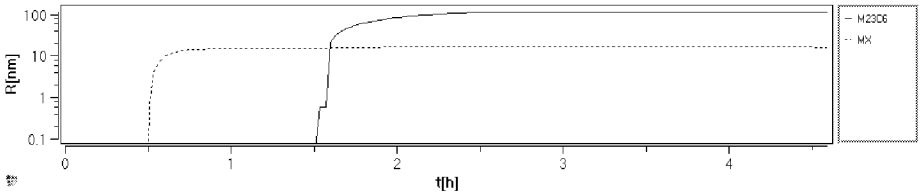

Figure 10: Simulation of the evolution of the average radius of MX and $M_{23}C_6$ precipitates on the designed alloy with dislocation density in austenite of $10^{14}\mathrm{m}^{-2}$ and in martensite of $10^{15}\mathrm{m}^{-2}$ (*i.e.* as hot worked).

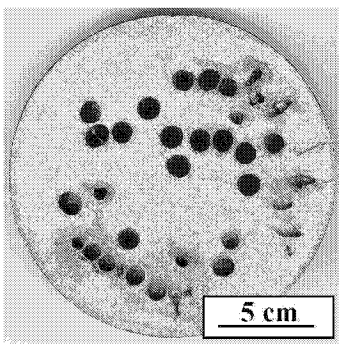

Figure 11: 'A2' steel showing nitrogen-induced porosity (in wt.% Fe 7.9Cr 0.1C 2.5W 0.3V 0.005Nb 0.073N).

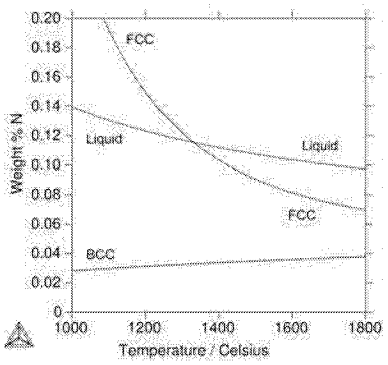

Figure 12: Nitrogen solubility limit for liquid, δ-ferrite, and austenite equilibrium with nitrogen gas, calculated using Thermocalc.

wt.% Fe 7.9Cr 0.1C 2.5W 0.3V 0.005Nb 0.073N), as shown in Figure 11, but others of similar composition do not (*e.g.* alloy T91, in wt.% Fe 8.24Cr 0.1C 0.43Si 0.37Mn 0.97Mo 0.2V 0.13Ni 0.075Nb 0.05N). The issue of porosity in the development of any industrial alloy is of severe importance as it can render an otherwise perfectly designed alloy completely useless. There is need to find a suitable criterion to find out which compositions are susceptible to porosity.

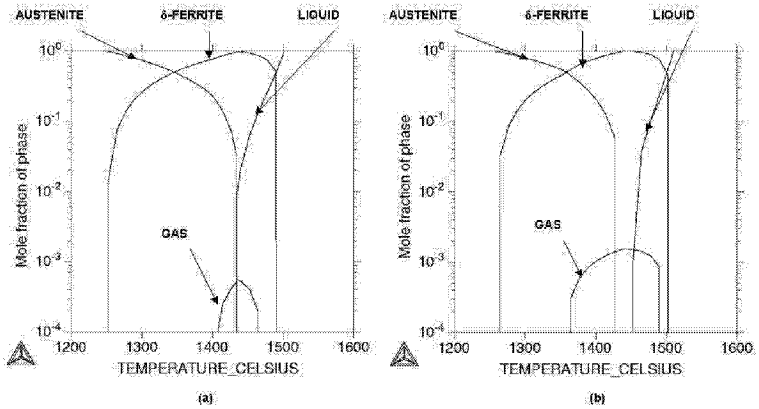

Figure 13: Phase stability diagrams for steels (a) T91 (in wt.% Fe 8.24Cr 0.1C 0.43Si 0.37Mn 0.97Mo 0.2V 0.13Ni 0.075Nb 0.05N) and (b) A2 (in wt.% Fe 7.9Cr 0.1C 2.5W 0.3V 0.005Nb 0.073N), showing the thermodynamic stability of the gas phase and the different equilibrium transformation path in each case.

The phase diagrams as a function of temperature of the two alloys mentioned above, A2 and T91, are shown in Figure 13. These diagrams have been calculated using Thermocalc and its standard database TCFE3. It can readily be observed that in both cases the nitrogen gas is predicted to be a stable phase. On the other hand, the series of transformation reactions from liquid to austenite under equilibrium conditions would follow a different route in each case. For the T91 alloy the transformation proceeds as [liquid + δ-ferrite] $\rightarrow$ [δ-ferrite + austenite(γ)]. In the case of alloy A2 however, the transformation traces a different path: [liquid + δ-ferrite] $\rightarrow$ [δ-ferrite] $\rightarrow$ [δ-ferrite + austenite(γ)]. The transformation path followed by the alloy presenting severe porosity has crossed a phase field containing only δ-ferrite, while in the other alloy there is always a second phase (either liquid or austenite) accompanying δ-ferrite.

The nitrogen solubility limits in each of the three phases liquid, δ-ferrite, and austenite have been calculated in equilibrium with nitrogen gas using Thermocalc (Figure 12). The maximum solubility of nitrogen in δ-ferrite is much lower than in the liquid phase or in austenite, and while in the case of alloy T91 the nitrogen partitioning from δ-ferrite can still be dissolved in the liquid phase or in austenite, this is not possible in the case of alloy A2, and therefore an excess of nitrogen will appear in the form of gas and create bubbles that become trapped in the matrix of the alloy. Moreover, as nitrogen and vanadium are increased in parallel in the alloy to produce a larger distribution of VN precipitates, and as vanadium is an α-gen element, the risk of producing an alloy presenting porosity problems increases twofold.

The limiting (maximum) amount of nitrogen that the alloy can contain in equilibrium conditions can be determined by calculating the minimum amount that the whole microstructure can dissolve at any one temperature (*i.e.* the *bottleneck* of keeping all nitrogen in solution). We can express that value as,

$$[N]^{alloy}_{max} = MIN\left([N]^{\delta}_{max} \cdot X^{\delta} + [N]^{Liq.}_{max} \cdot X^{Liq.} + [N]^{\gamma}_{max} \cdot X^{\gamma}\right)\{T\} \quad (1)$$

where X^i is the fraction of each phase (δ-ferrite, liquid and austenite) and $[N]^i_{max}$ is the maximum solubility of nitrogen in the alloy or in phase i, as a function of temperature T.

Nevertheless, the process of forming a gas bubble in the alloy is not immediate, and the effect of kinetics needs to be taken into account. The formation of gas porosity is not unlike other phenomena governed by nucleation and growth [18]. In this case, nitrogen and vacancies need to coalesce in sufficient quantity to nucleate a *"bubble-nucleus"*, with the creation of new gas/matrix interfaces, and subsequently this nucleus needs to be able to grow above a certain critical size, becoming energetically stable instead of redissolving again in the matrix. The difference with the classical nucleation and growth scenario, however, is that in this case there is a term related to the pressure of the gas in the bubble that will contribute to its overall energy. Consequently, and with respect to the criterion described by Equation 1, there will be a region where the nitrogen gas will remain dissolved in the matrix in metastable conditions. For instance, it would be feasible to keep in solution an amount of nitrogen larger than the minimum of $[N]_{max}$ but lower than most of the curve as long as it was only for a short time. Likewise, it could be possible to keep in solution for a long time an amount of nitrogen that was only marginally higher that that described by Equation 1.

All parameters in Equation 1 can be calculated using a CALPHAD-based thermodynamic software package. From this expression it is clear that an alloy which presents a δ-ferrite single-phase region will not tolerate nitrogen content much higher than 300ppm (Figure 12) without producing a porous cast. Alloys that do not form δ-ferrite or in which this phase is part of a dual microstructure with either liquid or austenite at all temperatures will be more tolerant to large nitrogen contents.

Conclusions

The work presented here is a case study on how the current accuracy of thermodynamic and kinetic calculations allow new alloys to be designed to respond to demanding operating conditions, while avoiding most of the experimental trial and error needed in the past. Software tools based on the CALPHAD method and various kinetic models are available, allowing the prediction not only of the feasibility of a target microstructure but also of its evolution during various heat treatments.

In the present study a new reduced activation ferritic/martensitic alloy has been designed that should be able to sustain service temperatures of 650°C. This alloy has been cast and treated and is being characterised microstructurally and in terms of mechanical properties.

Acknowledgements:

The authors are grateful to Ms. A. Petit and Mr. F. Vivier for their collaboration in the development of this work and to Prof. H. K. D. H. Bhadeshia and Dr. E. Kozeschnik for their invaluable advice on the use of the various methods employed in the present work.

References

[1] J. L. Séran, J-C. Brachet, and A. Alamo. Fast reactor cores, ferritic-martensitic steels for. In *Enciclopedia of Materials: Science and Technology*, pages 2863 2866. Elsevier Science Ltd., 2001.

[2] H. K. D. H. Bhadeshia. Design of heat resistant alloys for the energy industries. In *5th International Charles Parsons Turbine Conference*, pages 3 39, 2000.

[3] Y. De Carlan, M. Murugananth, T. Sourmail, and H. K. D. H. Bhadeshia. Design of new Fe-9CrWV reduced-activation martensitic steels for creep properties at 650°C. *Journal of Nuclear Materials*, 329-333:238–242, 2004.

[4] R. W. Hertzberg. *Deformation and fracture mechanics of engineering materials.* John Wiley & sons, inc., New York, 1996.

[5] V. A. Yardley and Y. de Carlan. Design criteria for high-temperature steels strengthened with vanadium nitride. *Journal of Phase Equilibria and Diffusion*, 27, 2006.

[6] D. A. Porter and K. E. Easterling. *Phase transformations in metals and alloys.* Chapman & Hall, London, 1981.

[7] N. Saunders and A. P. Miodownik. *CALPHAD, calculation of phase diagrams, a comprehensive guide.* Pergamon Press, Oxford, 1998.

[8] J. Svoboda, F. D. Fischer, P. Fratzl, and E. Kozeschnik. Modelling of kinetics in multi-component multi-phase systems with spherical precipitates I: Theory. *Materials Science and Engineering A*, A385:166 174, 2004.

[9] E. Kozeschnik, J. Svoboda, P. Fratzl, and F. D. Fischer. Modelling of kinetics in multi-component multi-phase systems with spherical precipitates II: Numerical solution and application. *Materials Science and Engineering A*, A385:157–165, 2004.

[10] E. Kozeschnik, J. Svoboda, and F. D. Fischer. Modified evolution equations for the precipitation kinetics of complex phases in multi-component systems. *Computer Coupling of Phase Diagrams and Thermochemistry*, 28:379 382, 2004.

[11] V. A. Yardley and Y. De Carlan. Progress in fabrication of experimental 9cr steel compositions optimised for creep resistance, thermodynamic and statistical analysis and proposed solutions. Technical report, CEA (France), 2005.

[12] D. J. C. MacKay. Bayesian non-linear modelling with neural networks. In H. Cerjak, editor, *Mathematical modelling of weld phenomena 3*, pages 359–389. The Institute of Materials, London, 1997.

[13] D. J. C. MacKay. Probable networks and plausible predictions - a review of practical Bayesian methods for supervised neural networks. In http://wol.ra.phy.cam.ac.uk/mackay/.

[14] D. Cole, C. Martin-Moran, A. G. Sheard, H. K. D. H. Bhadeshia, and D. J. C. MacKay. Modelling creep rupture strength of ferritic steel welds. *Science and Technology of Welding and Joining*, 5:81 89, 2000.

[15] Materials Science and Metallurgy Department - University of Cambridge and National Physical Laboratory. *Materials Algorithms Project.* University of Cambridge, http://www.msm.cam.ac.uk/map/mapmain.html, 1995.

[16] T. F. Kelly, D. J. Larson, M. K. Miller, and J. E. Flinn. Three dimensional atom probe investigation of vanadium nitride precipitates and the role of oxygen and boron in rapidly solidified 316 stainless steel. *Materials Science and Engineering A*, A270:19 26, 1999.

[17] F. Abe, T. Horiuchi, M. Taneike, and K. Sawada. Stabilisation of martensitic microstructure in advanced 9Cr steel during creep at high temperature. *Materials Science and Engineering A*, A378:299–303, 2004.

[18] J. W. Christian. *Theory of transformations in metals and alloys, Part I.* Pergamon Press, Oxford, 1975.

Part III

Advanced Steam Turbine Materials

Contributed Papers

Welding Technology

APPLICATION OF BAINITIC CREEP RESISTING STEELS FOR SUPERCRITICAL PARAMETERS AND PROPERTIES OF WELDED JOINTS

Jerzy Brózda[1)], Marian Zeman[1)], Jerzy Pasternak[2)]
[1)] Instytut Spawalnictwa, 16/18 Bł. Czesława Str, 44-100 Gliwice, Poland
[2)] Fabryka Kotłów RAFAKO S.A., 33 Łąkowa Str, 47-400 Racibórz, Poland
jerzy.brozda@is.gliwice.pl

Abstract

Short characteristics of the Polish power generation system are given from the point of view of the necessity of pollutant reduction in the next years. In order to prepare the power industry for the application of new creep-resisting steels to be applied for the boiler and pipe systems operating at supercritical parameters, weldability examinations on selected heat-resisting steels have been performed at the Institute of Welding in cooperation with RAFAKO Boiler Engineering Company and REMAK – Opole. This paper contains examination results of bainitic heat resistant steels, completed in cooperation with the COST 522 research program.
The basic characteristics of the T/P23 and T/P24 steels is given and their transformations under welding thermal cycles, which reveal no need of preheating and PWHT of tube welded joints. Mechanical properties at room and elevated temperatures and impact strength of welded P23 steel pipe (ϕ 219 x 30 mm) are given, which show a tensile strength not less than that of the base material and high notch toughness after PWHT.
Dissimilar P91 + P23 joints welded by using fillers matching both steels were tested in the as welded state and after exposure at 550 °C and 600 °C for 3000 and 10 000 hours. Mechanical properties at room temperature and 600 °C are given and impact strength of the base materials, welds and HAZ's.

Keywords: power generation, creep resisting steels, weldability, welded joints

1. Introduction

The production of electrical energy in Poland is based on bituminous coal and lignite, which, with their rich deposits shall continue to be the main energy source for the next decades. Combustion of coal in power boilers is the source of emission into the atmosphere of a great number of pollutants such as CO_2, SO_2, NO_x and various kinds of particulate matter. European Parliament and European Council Directive 2001/80/EC "on the limitation of emissions of certain pollutants into the air from large combustion plants" sets acceptable limits on pollutants emission values [1]. The power and heat generating plants will have to reduce the emission of SO_2, NO_x and particulate matter in a strictly defined timetable [2, 3]. The reduction of SO_2 emission shown in Figure 1 [3] is especially important.

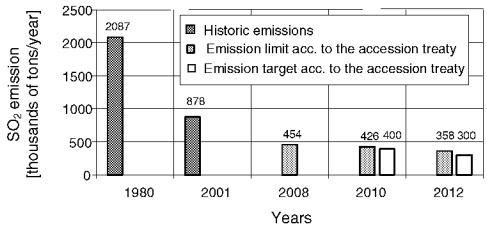

Fig. 1. SO_2 emission into the air from large combustion plants in Poland [3]

Figure 1 demonstrates that SO_2 emission has to be almost halved during six years, which is related to much higher costs than hitherto incurred [3]. New power units operating at supercritical parameters have to be built in the near future. The supercritical operating parameters require new creep-resisting steels to be applied for the boiler and pipe systems. In order to

prepare our power industry for the new task, weldability examinations have been performed at the Institute of Welding on selected heat-resisting steels. RAFAKO Boiler Engineering Company and REMAK - Opole (Power Installations Modernisation Company) have executed tube/pipe test weld joints, followed by heat treatment and examination of weldment properties in order to select proper fabrication conditions. Test results of martensitic steels have been presented on the 7th Liège conference [4]. This paper contains examination results of bainitic heat resistant steels, performed in cooperation with the COST 522 research program [5].

2. Basic characteristics of T/P23 and T/P24 steels

Higher steam parameters have also led to increasing requirements for the tube steel of water walls, which can no longer be fulfilled with the hitherto used 10CrMo 9-10 (T22) steel. T/P23 and T/P24 bainitic steels have been developed. Carbon content in both steels is much lower than in the 10CrMo9-10 steel, which has a positive influence on their application (forming and welding). The creep strength of these steels has been increased by addition of carbide forming elements V, Nb and Ti (table 1). The T/P23 steel was additionally alloyed with tungsten by simultaneous reduction of molybdenum content.

Table 1. Chemical composition of ferritic heat-resisting steels (mass %)

Element	T/P23	T/P24[1)]	T/P91	E911	P92	HCM12A
C	0,04-0,10	0,05-0,10	0,08-0,12	0,09-0.13	0,07-0.13	0,07-0.13
Si	≤0,50	0,15-045	0,20-0,50	0,10- 0.50	≤0.50	≤0.50
Mn	0,10-0,60	0,30-070	0,30-060	0,30-0,60	0.30-0,60	≤0.70
Ni	-	-	max 0,40	0,10-0,40	≤0,40	≤0.50
Cu	-	-	-	-	-	0,30-1.70
Cr	1,90-2,60	2,20-2,60	8,00-9,5	8,50-9,50	8,50-9.50	10,0-12.5
Mo	0,05-0,30	0,90-1,10	0,85-1,05	0,90-1.10	0.30-0,60	0,25-0.60
W	1,45-1,75	-	-	0,90-1.10	1,50-2,00	1.50-2,50
V	0,20-0,30	0,20-0,30	0,18-0,25	0,18-0,25	0,15-0,25	0,15-0.30
Nb	0,02-0,08	-	0,06-0,10	0.06-0,10	0,04-0,09	0.04-0,10
N	≤0,030	≤0,01	0,030-0,070	0,05-0,09	0,03-0,07	0.06[2)]
B	0,0005-0,006	0,0015-0,007	-	0,0005-0,005	0.001-0,006	0.002[2)]

[1)] 0,05-0,10% Ti, [2)] nominal chemical composition

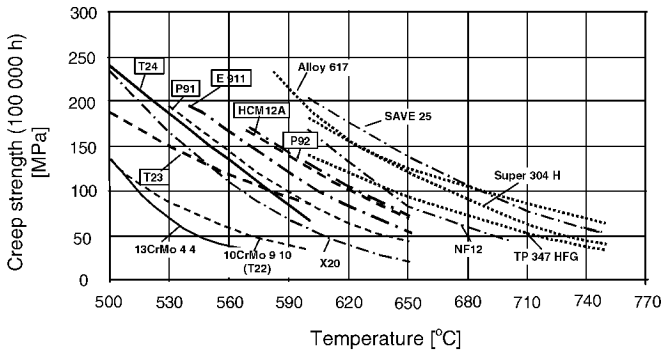

Fig. 2. Creep strength of heat-resisting materials (ferritic & austenitic steels and nickel alloys) used in the power generation industry

The creep strength of both steels is much higher than that of the T22 steel (Fig. 2), and in the lower temperature range the long-term values of T/P24 are only slightly below those of P91.

The values of T/P23 steel are lower, however, approach the T92 curve at 600 °C. But due to the limited resistance to oxidation, as a result of low chromium content, the maximum operation temperature is only about 575 °C [6].
The steels are delivered in the normalized or quenched (for greater thicknesses) and tempered conditions and have a bainitic microstructure.
From the CCT – diagrams (Fig. 3) it can be concluded, that in the heat affected zone (HAZ) of welded joints bainitic microstructures will be formed with a maximum hardness not exceeding 350 HV, for all the practically possible cooling times $t_{8/5}$ in the 800-500 °C temperature range.

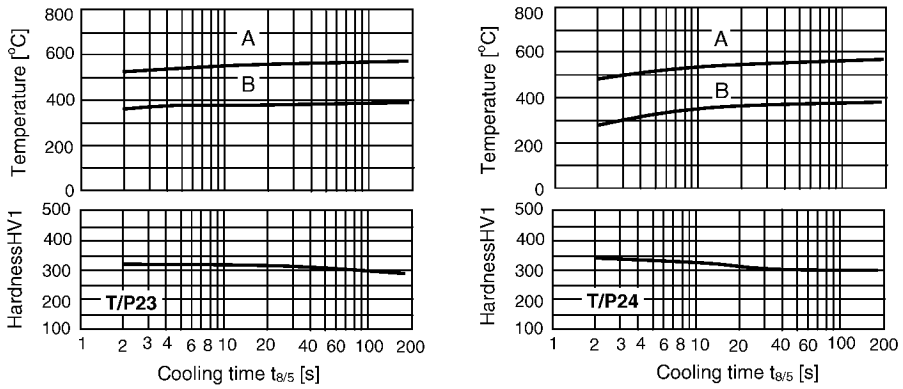

Fig. 3. CCT – diagrams for welding purposes (austenitizing temperature 1250 °C) for T/P23 and T/P24 steels [5]

Thus T23 and T24 steel tubes can be welded without preheating or with only low preheating temperatures. There is no need either for post weld heat treatment (PWHT) of GTA welded thin-walled tube joints. The main application of those steels are therefore water walls, where PWHT is very difficult and often impossible to perform.
Matching filler metals for welding of both steels were developed by Böhler Thyssen Schweisstechnik and properties of weld metal have been published [6].

3. P23 steel pipe welded joint and its properties

The test joint has been welded in the fixed vertical position (PC) on a pipe (ϕ 219 x 30 mm) delivered by Vallourec & Mannesmann with the following chemical composition: 0,07% C, 0,28% Si, 0,54% Mn, 0,008% P, 0,004% S, 2,08% Cr, 0,08% Mo, 1,65% W, 0,22% V, 0,002% B, 0,011% N, 0,03% Nb and 0,018% Al. For the TIG welded root pass the Union ICr2WV wire (ϕ 2,4 mm) was used and Cr2WV covered electrodes (ϕ 2,5 mm and 3,2 mm), delivered by Böhler Thyssen Schweißtechnik, for the filling and cap layers. The preheating temperature was 150 °C and the interpass temperature did not exceed 250 °C.
Non destructive examination performed by radiography did not reveal any essential imperfections (quality level B acc. to the standard PN-EN 25817). From the welded test joint a small segment was cut out to perform metallographic examination and impact tests in the as welded conditions. The remaining part of the welded pipe joint was heat treated at 740 °C for 2 hours in an electric resistance furnace.

Results of tensile tests, performed on specimens (ϕ 10 mm) at room temperature acc. to PN-EN 895, are given in table 2.

Table 2. Tensile test results of P23 parent material and welded joint

Specimen	$R_{0.2}$ [MPa]	R_m [MPa]	A_5 [%]	Z [%]	Remarks
Parent material	486,5	584,3	24,0	79	Without visible defects
	494,5	594,4	23,8	79	Without visible defects
Cross-weld	525,2	617,5			Ruptured in parent material
	526,3	620,2			Ruptured in parent material

The cross-weld tensile tested specimens ruptured in the parent material at a tensile strength R_m=618 MPa, which is higher than the minimum value specified for the P23 steel (510 MPa). The side-bend test completed acc. to PN-EN 910 by using a 75 mm plunger (d=4t), to reach the 130 ° bend angle, shows good plastic properties of the welded joint.

Notch toughness tests have been performed acc. to PN-EN 875 on Charpy V specimens with notches machined in the parent material, central part of the weld and in the HAZ (≈ 1 mm from the fusion line). Test results presented in Figure 4 show good toughness levels of both the weld and HAZ after PWHT. In the as welded conditions the notch toughness of the weld is very low. The maximum hardness of the welded pipe joint without PWHT is 345 HV (Fig. 5) and after PWHT it decreases to about 250 HV.

The P23 parent material and welded joints (cross-weld specimens) were also tensile tested at elevated temperatures in accordance with PN-EN 10002-5 (cylindrical specimens). The test results presented in Figures 6 and 7 show, that the mechanical properties ($R_{0,2}$, R_m) of the welded joint are not lower than that of the base material (all specimens ruptured at the base material)

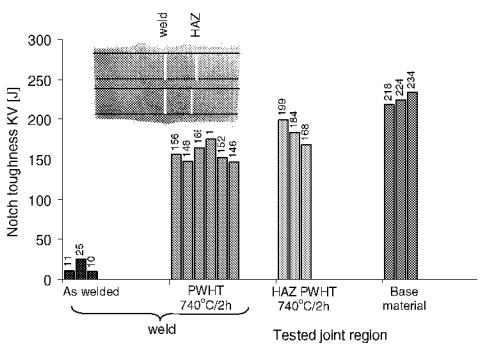

Fig. 4. Notch toughness KV of the P23 pipe welded joint

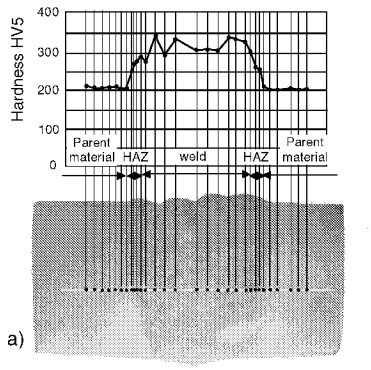

Fig. 5. Macrostructure and hardness profile of the welded pipe joint without PWHT

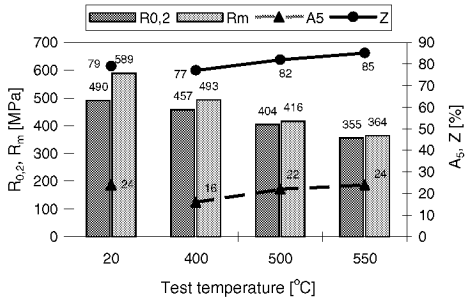

Fig 6. Mechanical properties of P23 base material at elevated temperatures (mean values of 2 specimens).

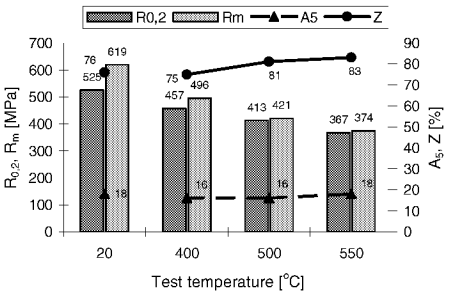

Fig 7. Mechanical properties of P23 pipe welded joint at elevated temperatures (mean values of 2 specimens).

4. Dissimilar P91+P23 pipe joints welded with different filler metals and their properties

P91 + P23 steel pipe joints (ϕ 219 x 30 mm) have been welded at SES Kotly in Tlmače (Slovakia) with P91 and P23 matching filler metals [7]. Welding parameters are given in table 3.

Table 3. Welding parameters of dissimilar P91 + P23 steel pipe joints [8]

Layer	Welding method	Filler metal	Diameter [mm]	Welding current [A]	Voltage [V]	Layout of layers
Welded with P91 matching filler 9Cr, 1Mo						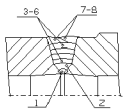
1	141 (TIG)	W CrMo91	2,4	120-140	15-22	
2	111 (E)	E CrMo91 B	3,2	110-130	20-25	
3-6	111 (E)		4,0	140-160	20-25	
7-8	111 (E)		4,0	140-160	20-25	
Welded with P23 matching filler 2,25Cr, 0,25V, 1,5W						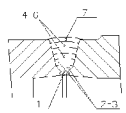
1	141 (TIG)	W ZCr2WV	2,5	125-140	15-22	
2-3	111 (E)	E ZCr2WV	2,5	75-90	20-25	
4-6	111 (E)		4,0	150-180	20-25	
7	111 (E)		4,0	150-180	20-25	

The preheating temperature was ca. 180 °C and the interpass temperature did not exceed 350 °C. The test joints were post weld heat treated at 750 °C for 2 hours [7]. Impact test results for the HAZ's and welds are given in Figures 8 - 12 as the "not exposed" values.

Two welded joints were delivered to the Institute of Welding in Gliwice and samples for exposure testing (tensile and Charpy V impact tests) were machined. Additionally small samples were taken for metallographic examination and hardness measurements in the as received conditions.

Macrostructures of the welded joints and results of Vickers hardness measurement are shown in Fig. 8. In both welded joints the maximum hardness did not exceed 260 HV5, at the weld - for P91 matching filler metal joint (Fig. 8a), and at the P91 steel HAZ – for P23 matching filler metal joint (Fig. 8b). To reveal an eventual reactive diffusion of carbon into the Cr rich areas (from P23 material to 9Cr weld metal and from 2,25Cr weld metal to P91 steel), micro hardness HV 0,05 has been measured.

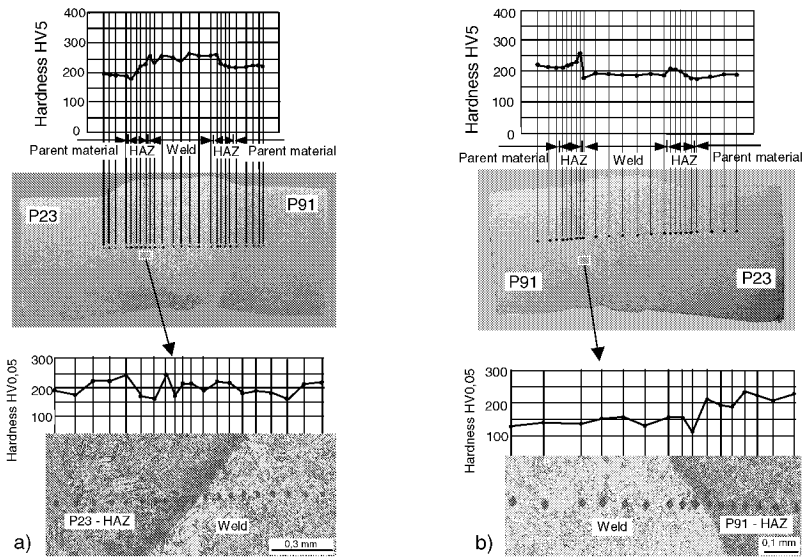

Fig. 8. Macrostructure and Vickers hardness profiles of P91+P23 welded pipes
a) Pipe joint welded with P91 matching fillers (9 %Cr, 1 %Mo)
b) Pipe joint welded with P23 matching fillers (2,25 %Cr, 0,25 %V, 1,5 %W)

Local, very narrow carbon enrichment (darker etching band) is observed close to the fusion boundary in both cases. In the P91 matching filler joint the carbon enriched band is located in the weld metal and is characterized by a slight increase of micro hardness and a narrow zone in the P91steel HAZ with small hardness decrease due to carbon depletion (Fig. 8a). In the P23 matching filler joint the carbon enriched darker band is located in the HAZ of P91 steel (Fig. 8b).

5. Properties of dissimilar P91 + P23 pipe joints after exposure test at 550 °C and 600 °C

From both test joints samples were taken for impact tests and cross-weld tensile tests. Exposure testing was performed at the Institute for Ferrous Metallurgy in Gliwice at 550 °C and 600 °C in multi-specimen furnaces used for creep testing [8]. After 3000 and 10 000 hours of exposure batches of samples were removed from the furnaces and tested according to the agreed procedure.
After machining the bars for impact test specimens, their surface was etched to mark the exact location of the Charpy V notches in the narrow HAZ and weld centre. Results of impact tests at room temperature are presented in Figures 9 – 12 (single values). The graphs include also impact test results of joints in the as received condition (not exposed).
The tensile tests of the cross-weld specimens have been performed at room temperature and 600 °C. Examination results can be seen in Figures 13 and 14 as ultimate yield stress ($R_{0,2}$), tensile stress (R_m) and elongation (A_5). All specimens ruptured at the P23 parent material. The graphs contain also tensile test results (at 20 °C and 550 °C) of the P23 parent material not exposed to high temperatures.

In Figures 15 and 16 microstructures of base materials P91, P23, HAZ's and both welds in the not exposed condition and after exposure testing are presented.

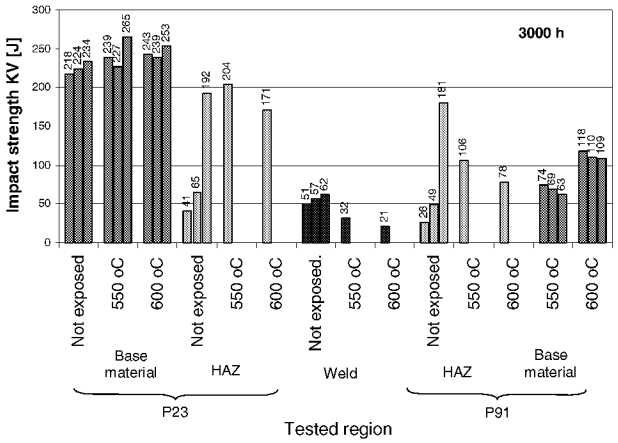

Fig. 9. Impact strength of P91+P23 pipes welded with P91 matching fillers (9 %Cr, 1 %Mo) after exposure test at 550 °C and 600 °C for 3000 hours

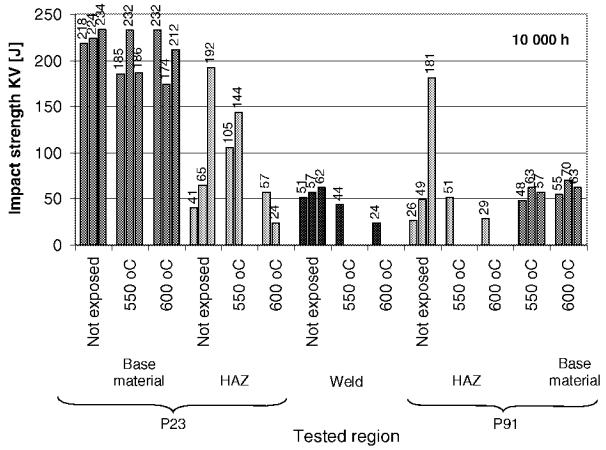

Fig. 10. Impact strength of P91+P23 pipes welded with P91 matching fillers (9 %Cr, 1 %Mo) after exposure test at 550 °C and 600 °C for 10 000 hours

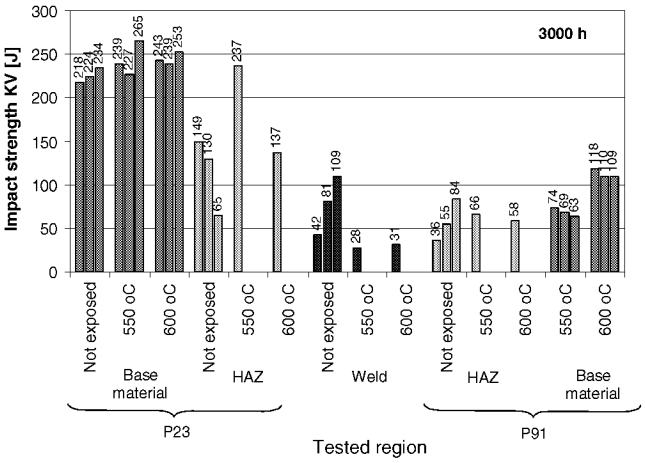

Fig. 11. Impact strength of P91+P23 pipes welded with P23 matching fillers (2,25%Cr, 0,25%V, 1,5%W) after exposure test at 550 °C and 600 °C for 3000 hours

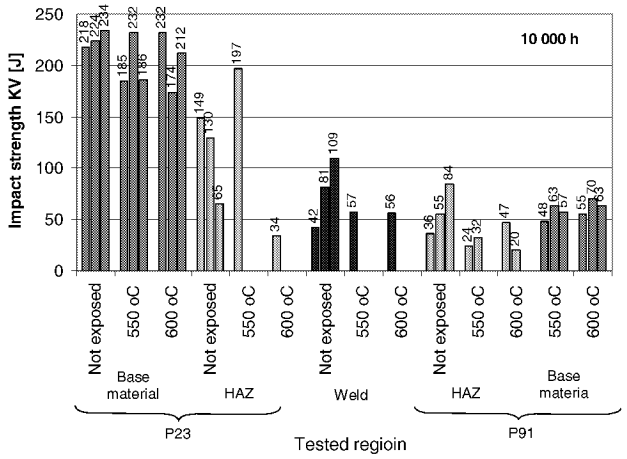

Fig. 12. Impact strength of P91+P23 pipes welded with P23 matching fillers (2,25%Cr, 0,25%V, 1,5%W) after exposure test at 550 °C and 600 °C for 10 000 hours

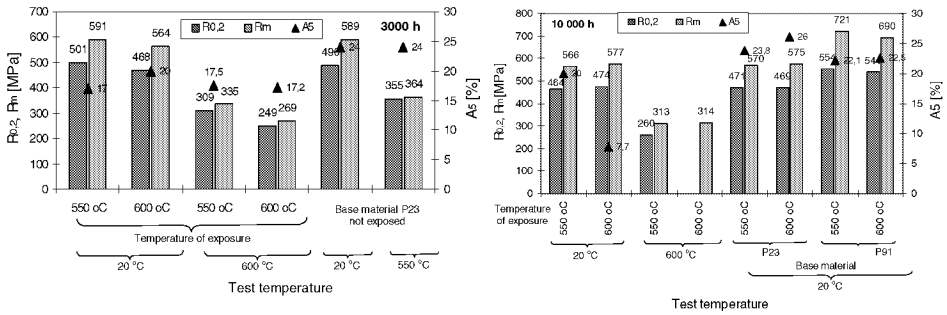

Fig. 13. Mechanical properties at 20 °C and 600 °C of P91 + P23 pipes welded with P91 matching fillers (9 %Cr, 1 %Mo) after exposure test at 550 °C and 600 °C for 3000 and 10 000 hours

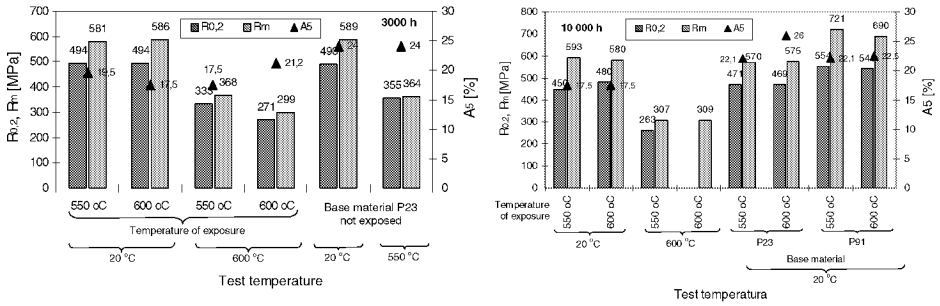

Fig. 14. Mechanical properties at 20 °C and 600 °C of P91 + P23 pipes welded with P23 matching fillers (2,25 %Cr, 0,25 %V, 1,5 %W) after exposure test at 550 °C and 600 °C for 3000 and 10 000 hours.

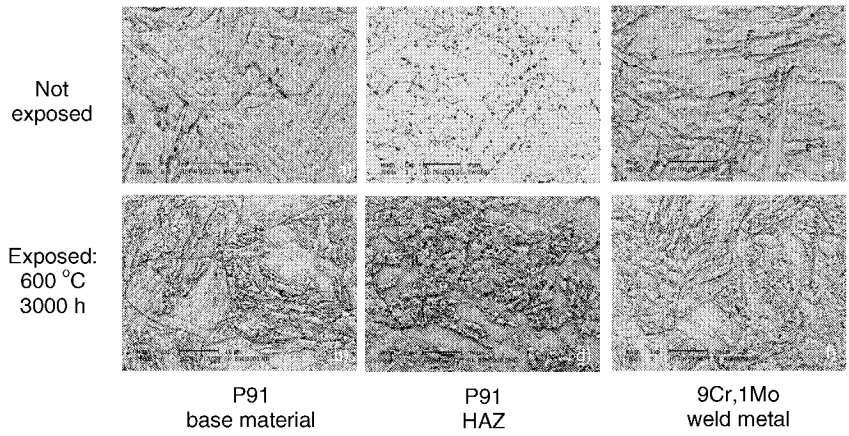

Fig. 15. Microstructures of P91 steel, its HAZ and P91 matching weld metal

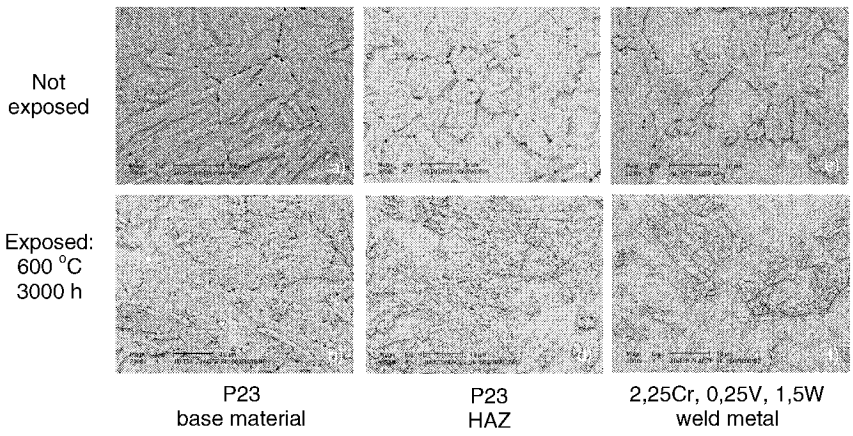

Fig. 16. Microstructures of P23 steel, its HAZ and P23 matching weld metal

5. Discussion of results

Hardness not exceeding 350 HV in the HAZ of T23 and T24 steel tube joints as well as high toughness of the GTA weld metal in the as welded conditions [6], are a good basis for the application of those steels for water walls in supercritical boilers, without the need of PWHT. Pipes with greater wall thicknesses in P23 and P24 steels require PWHT to get the required impact strength of the HAZ and weld metal. Mechanical properties at room and elevated temperatures of the P23 pipe welded joint are not lower than that of the base material.
For welding dissimilar P91 + P23 pipe joints the P23 steel matching filler is a better choice, because its weld metal has a higher toughness than the P91 matching weld metal. The tensile strength of welded joints is not lower than that of the P23 steel.
The high Charpy V notch toughness of the P23 steel does not change much after exposure at 550 °C and 600 °C for 3000 h and 10 000 h (Fig. 9-12). The influence of the ageing temperature and time on the toughness of P91 steel is also not too big. After 10 000 h of exposure at 550 °C and 600 °C the impact strength of the P23 steel matching weld shows still a value of 56 J (Fig. 12). The scatter of the HAZ's test results is more evident than of the base material and weld. It is caused by difficulties in the exact location of the Charpy V notch in the narrow HAZ region. The lowest toughness values are observed in the HAZ of P91 steel.
The cross-weld specimens tensile tested at room temperature show no significant differences in the proof stress $R_{0,2}$ and tensile strength R_m after exposure at 550 °C and 600 °C for both ageing times (Fig. 13, 14). Tensile tests performed at 600 °C revealed some lower mechanical properties of both welded joints after 3000 h exposure at 600 °C. No differences are seen after 10 000 h exposure. All specimens ruptured in the P23 base material.

References

[1] Directive 2001/80/EC of the European Parliament and of the Council of 23 October 2001. http://europa.eu.int/eur-lex/pri/en/oj/dat/2001/l_309/l_30920011127en00010021.pdf

[2] Najgebauer E, Patrycy A.: Commitment of the Polish power industry to the EC (in Polish). http://www.geoland.pl/dodatki/energia_xxxv/energ_belch.html

[3] Preliminary evaluation of the realizability of the 2001/80/EC Directive accession treaty by large combustion plants in Poland (in Polish) http://www.geoland.pl/dodatki/energia_xxxv/energoprojekt.html

[4] Brózda J., Zeman M., Pasternak J.: The first supercritical power unit in Poland. Weldability evaluation of new martensitic chromium steels with tungsten additions and properties of welded joints. Proceedings of the 7th Liege Conference. European Commission, University de Liege, Vol. 21. p. 1711-1720 (Part III).

[5] Brózda J.: Weldability characteristics and welding technology guidelines of the advanced heat resisting steels. COST 522 Final Report. Gliwice, 07. 2003.

[6] Bendick W., Fuchs R., Hahn B., Heuser H., Vaillant J., Weber J.: Application capability and welding of modern heat-resistant steels (T/P91, T/P23, T/P24) for the maintenance and refurbishment of power station components. Paper presented on a seminar at RAFAKO (Poland), 2003.

[7] Pecha J., Kaszásová E., Bobonič M.: Welding test welds of P23 steel and P23 + P91 steel. COST 522 Progress Report No 2, SES Kotly s.r.o. Tlmače, Slovakia, 02. 2002.

[8] Brózda J., Maciosowski A.: Weldability characteristics and welding technology guidelines of the advanced heat resisting steels. COST 522 Progress Report No 5. Gliwice, 05. 2003.

INVESTIGATIONS ON OPTIMIZATION OF WELD CREEP PERFORMANCE IN MARTENSITIC STEELS

M. Bauer[1)], A. Klenk[1)], K. Maile[1)], E. Roos[1)], C. Jochum[2)],
[1)] MPA University of Stuttgart, [2)] Böhler-Thyssen Schweißtechnik
email: mathias.bauer@mpa.uni-stuttgart.de

Abstract

Under service conditions, for a number of heat resistant materials e.g. new martensitic steels, the fine grained or intercritical heat affected zone (HAZ3) has poorest creep strength since the heat input of the welding affects the microstructure of this zone. Furthermore the stress situation and multiaxiality of the stress state in the weld region changes permanently due to creep and relaxation. Experimental results show a strong influence of the factor of multiaxiality of a stress state on the creep behaviour of components especially of welded components. Metallographic investigations clearly show a higher creep damage close to the centre of a crossweld creep specimen, where the multiaxiality of the stress state has its maximum. Numerical investigations offer the possibility to characterise the influence on the stress distribution and degree of multiaxiality by a specific variation of the weld metals creep strength. A modified Graham-Walles creep law with a multiaxiality dependant damage term is used for the Finite - Element simulations. As a result of these simulations, it can be stated that by using an undermatched weld metal with specific creep strength, two beneficial effects on the lifetime of welded components can be achieved. On the one hand, the multiaxiality of the stress state in the intercritical HAZ was reduced which led to a reduction of damage in this area. On the other hand, the relatively sharp stress gradients between the different zones were smoothened resulting in a more homogeneous stress distribution. Numerous experiments (components and specimens) are being conducted to validate the numerical results.

Keywords: constitutive equations, advanced creep laws, damage parameter, mismatched weld materials, influence of multiaxiality of the stress state

1 Introduction

Raising thermal efficiency of fossil fired power plants is besides the reduction of greenhouse gases the major aim in modern power plant construction. In general, this can be achieved by increasing steam temperature and pressure. Therefore plants with steam and process parameters ranging from 300bar/620°C to 300bar/720°C are under detailed design investigation at the moment, using new improved materials, see Figure 1.

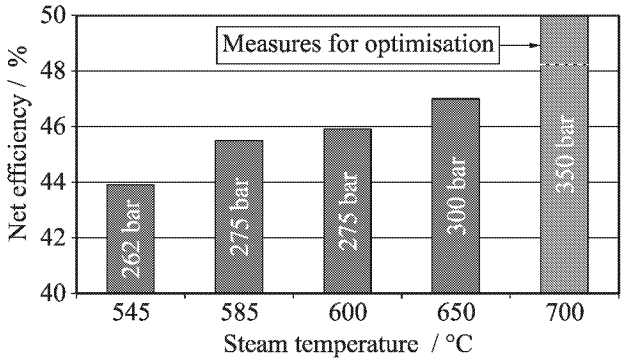

Figure 1: Increasing efficiency by development of new materials for optimization of components [1], potentials

For the temperature range questioned, new improved modified martensitic 9 to 11% Cr steels like P91 (X10CrMoVNb9-1) and the tungsten and boron alloyed P92 (X10CrWMoVNb9-2) and E911 (X11CrMoVNb9-1-1), are used or planned to be used in components of modern plants. There have been numerous investigations on the long term behaviour of the base materials of those steels [2]-[4]. However welds in these materials are more critical with respect to the long term behaviour due to the complex stress situation, the multiaxiality of the stress state and the interaction of the different material zones in that region. For the materials considered here, several research projects [5]-[7] have identified the intercritical heat affected zone (HAZ3) as the "weakest link" in welded components under service conditions. The heat input during the welding procedure affects the microstructure of this zone, (Figure 2).

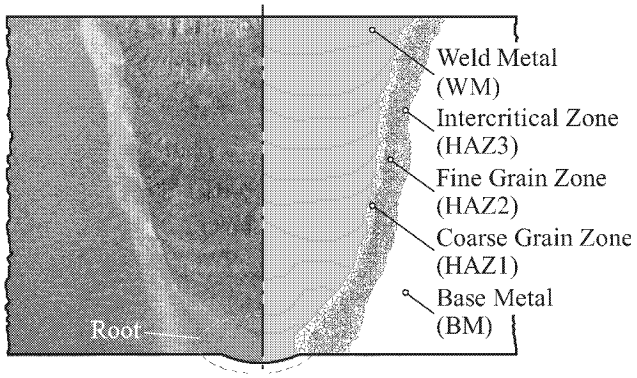

Figure 2: Five zone weld discretisation.

Furthermore the stress situation and multiaxiality of the stress state in the weld region during operational exposure changes permanently due to creep and relaxation. Experimental results indicate in general a strong influence of the factor of multiaxiality of the stress state on the creep damage behaviour of welded components. This correlation can be derived from microstructural examinations of an E911 cross weld creep specimen under high temperature loading ($\vartheta = 600\,°C$, $\sigma_{ax} = 90\,MPa$, $t_r = 19800\,h$, type 4 failure). A higher creep damage i.e. higher creep cavity density can be found close to the centre of the specimen, where the multiaxiality of the stress state has its maximum. In comparison to areas close to the surface of the specimen (upper part of Figure 3) where only sporadic creep cavities can be found, cavity chains perpendicular to the loading direction indicate a severe state of damage in the centre of the specimen.

In anticipation of chapter 3, Figure 3 shows on the right a comparison of FE - results (top) and the micrograph (not etched) of the E911 creep specimen (bottom). The correlation of cavity density (creep damage respectively) and the multiaxiality of the stress state q within the specimen becomes obvious. Please note that low numbers of q describe a high level of multiaxiality.

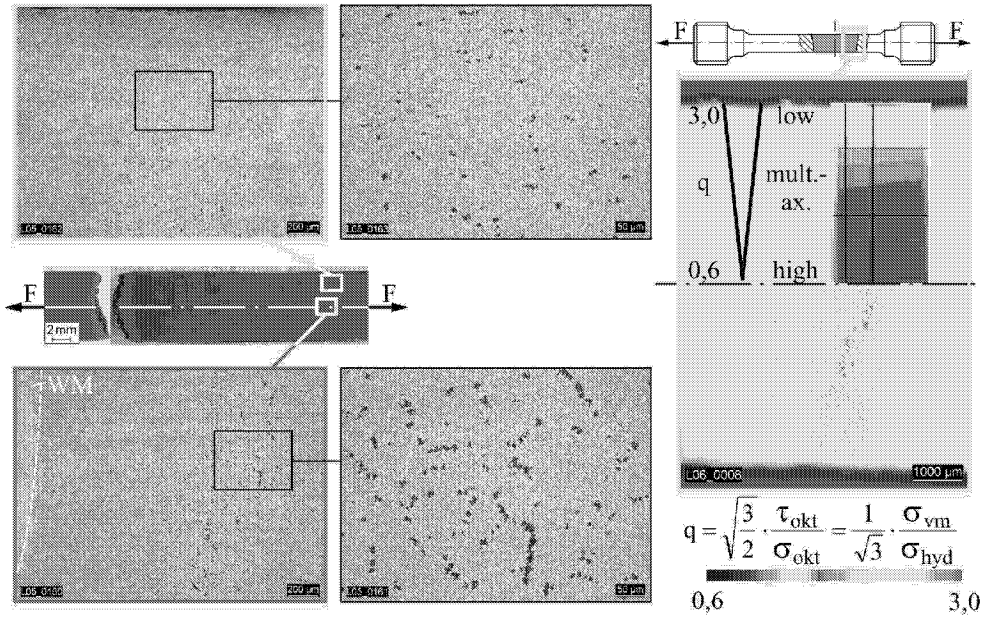

Figure 3: Creep cavities in an E911 crossweld tensile specimen – influence of multiaxiality of stress state.

As mentioned above, the heat affected zone of creep resistant materials e.g. new martensitic steels like P91, P92 and E911 is assumed as an area of premature failure under long term creep loading, due to unfavourable heat input during welding. An extension of the lifetime of welded components can be achieved by the reduction of the factor of multiaxiality and the relevant local stress in the intercritical HAZ. Therefore different weld configurations - using filler materials of specific creep strength – are investigated.

By arranging different stiffness/creep ductility of both, weld metal as well as base metal, a reduction of critical multiaxial stress states and local stresses and furthermore a shift of the failure location to base or weld metal can be realized. Numerical investigations offer the possibility to study the influence of the stress distribution and of the degree of multiaxiality by a parametric variation of the weld metals creep strength. The simulation tools which are developed and verified in the project, help to avoid the premature creep failure in components.

The research presented here focuses on longitudinally welded E911 pipes with the following weld configurations:

- undermatched weld metal (Thermanit MTS 3, P91 WM),
- overmatched weld metal (Thermanit MTS 616, P92 WM),
- matching E911 weld metal as reference (Thermanit MTS 911).

The chemical composition of the base and weld metals is given in Table 1.

	Chemical composition (melt analysis) in mass / %															
	C	Si	Mn	P	S	Cr	Mo	Ni	V	W	Al	B	Cu	N	Nb	Ti
E911 VdTÜV min.	0.090	0.10	0.30	-	-	8.50	0.90	0.10	0.180	0.900	-	0.0005	-	0.050	0.060	-
E911 VdTÜV max.	0.130	0.50	0.60	0.020	0.010	9.50	1.10	0.40	0.250	1.100	0.040	0.0050	-	0.090	0.100	-
E911 BM (specific melt)	0.120	0.20	0.47	0.015	0.002	8.62	0.94	0.24	0.203	0.959	0.016	0.0018	-	0.075	0.084	-
MTS 3 Böhler Thyssen Welding	0.110	0.30	0.60	-	-	8.90	0.98	0.75	0.200	-	-	-	-	0.050	0.050	-
MTS 3 (specific melt)	0.087	0.25	0.64	0.006	0.006	8.69	0.96	0.64	0.190	-	0.020	-	0.037	0.035	0.046	0.001
MTS 616 Böhler Thyssen Welding	0.090	0.38	0.60	-	-	8.70	0.43	0.60	0.200	1.650	-	-	-	0.050	0.050	-
MTS 616 (specific melt)	0.087	0.35	0.56	0.007	0.005	8.79	0.40	0.51	0.180	1.650	0.016	<0.001	0.043	0.040	0.056	0.001
MTS 911 Böhler Thyssen Welding	0.100	0.35	0.60	-	-	8.90	0.96	0.70	0.200	1.050	-	-	-	0.050	0.050	-
MTS 911 (specific melt)	0.093	0.32	0.56	0.007	0.005	8.92	0.97	0.58	0.200	0.960	0.017	<0.001	0.047	0.042	0.046	0.001

Table 1: Chemical composition [8], [9].

2 Experiments

In the framework of the research project presented here, two component tests of longitudinal welded pipes and tests with standard specimens are carried out, (see Table 2). The standard specimen tests include creep and tensile tests of all materials (zones resp.) involved, as well as crossweld tests extracted from the welded pipes. The results of these tests are needed as an input for the material laws, and the crossweld specimens and component tests are used to validate the numerical results. The pipes have been loaded with internal pressure. All tests were carried out at 600 °C.

Component Test 1 (15 kh)	Component Test 2 (15 kh)
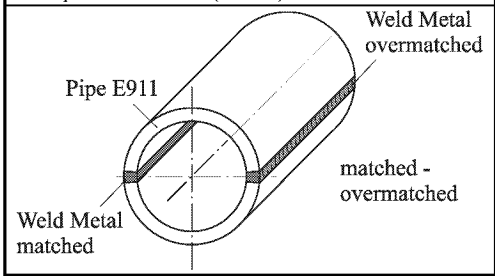	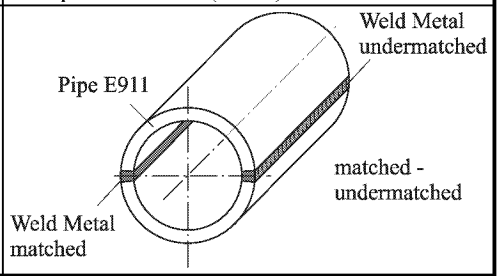
Creep Tests (1 - 35 kh)	Tensile Tests
E911 BM, E911 WM, P91 WM, P92 WM, HAZ 1, HAZ 2, HAZ 3, ϑ_{peak} 780°C, ϑ_{peak} 800°C, ϑ_{peak} 820°C, ϑ_{peak} 880°C Crossweld matched, over- & undermatched	E911 BM, E911 WM, P91 WM, P92 WM, HAZ 1, HAZ 2, HAZ 3, ϑ_{peak} 780°C, ϑ_{peak} 800°C, ϑ_{peak} 820°C, ϑ_{peak} 880°C

Table 2: Experimental overview.

Thermal simulation of HAZ material

For the numerical simulations, the weld is divided into five zones (comp. Figure 2). To be able to fit the constitutive equations to the material behaviour of the different heat affected zones, E911 base material was heat treated (inductive heating) with different peak temperatures, see Figure 4. For the weld geometry (narrow-gap) and welding method (submerged arc welding, SAW) considered here, the size of the different heat affected zones can be estimated and implemented in the geometrical model of the weld. The peak temperatures given in Table 3 can be estimated as representative for the respective zone for 9-Cr steels from previous research work.

Weld-zone	Microstructure	Simulation temperature / °C	Peak temperature / °C
HAZ1	coarse grain	$\vartheta_{peak} > A_{C3}$	1300 °C
HAZ2	fine grain	$A_{C3} > \vartheta_{peak} > A_{C1}$	1100 °C
HAZ3	intercritical	$\vartheta_{peak} > A_{C1}$	850 °C

Table 3: Peak temperatures for HAZ simulation.

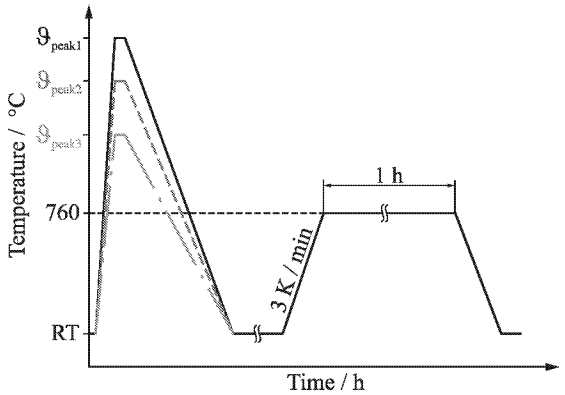

Figure 4: Thermal simulation of heat affected zone material.

Current research [10], [11] indicate that 850 °C may not be the peak temperature which represents the intercritical zone structure with weakest properties. Therefore a parameter study with various peak temperatures from 780 °C to 880 °C is included in this research. Besides five creep tests with a state of the art heat treatment for HAZ3 (ϑ_{peak} 850°C), three experiments with 880 °C peak temperature and two creep tests for 780 °C, 800 °C and 820 °C will be conducted. All thermally treated specimens were tempered at 760 °C for 1h.

Tensile tests

Results of tensile tests at 600 °C are given in Table 4. Yield and tensile stress of the different heat simulated HAZ3 materials lie within a narrow scatter band. So far no conclusions can be drawn concerning the creep resistance of those materials.

Material	Value	$R_{p0,2}$ / MPa	R_{pl} / MPa	R_m / MPa	A_5 / %	Z / %	E / GPa
E911 BM	VdTÜV min.	231	-	267	-	-	-
	$\bar{x}$	322	356	376	30.8	90.0	135
MTS 911	Böhler Thyssen min.	300	-	360	-	-	-
	$\bar{x}$	316	343	365	28.3	81.5	129
MTS 3	Böhler Thyssen min.	304	-	373	-	-	-
	$\bar{x}$	306	321	338	26.5	83.0	123
MTS 616	Böhler Thyssen min.	290	-	350	-	-	-
	$\bar{x}$	326	340	357	25.0	82.5	146
HAZ1	$\bar{x}$	436	468	489	27.8	83.0	141
HAZ2	$\bar{x}$	342	373	397	31.0	89.5	137
HAZ3	$\bar{x}$	312	341	361	42.3	90.5	137
ϑ_p 880°C	$\bar{x}$	310	328	343	37.6	90.3	141
ϑ_p 820°C	-	320	349	366	36.6	90.0	139
ϑ_p 800°C	-	327	351	368	29.6	90.0	131
ϑ_p 780°C	-	318	347	367	32.4	90.0	138
$\bar{x}$:= mean value							

Table 4: Tensile tests at 600 °C.

Creep tests

Comparable to the tensile tests, creep tests are conducted for all materials investigated in this research, in order to fit the material laws for numerical simulation. Exemplary results of these tests are shown in Figure 5. Creep rupture data of the different weld metals (matched, under- and overmatched) is plotted together with literature data. As far as can be seen from the tests with short durations which are finished, the creep strength of the undermatched weld material is comparable to previous experiences [5]. There are still two running tests with undermatched weld material at low stresses. A final classification of this weld material in the scatter band will be possible when these tests are finished.

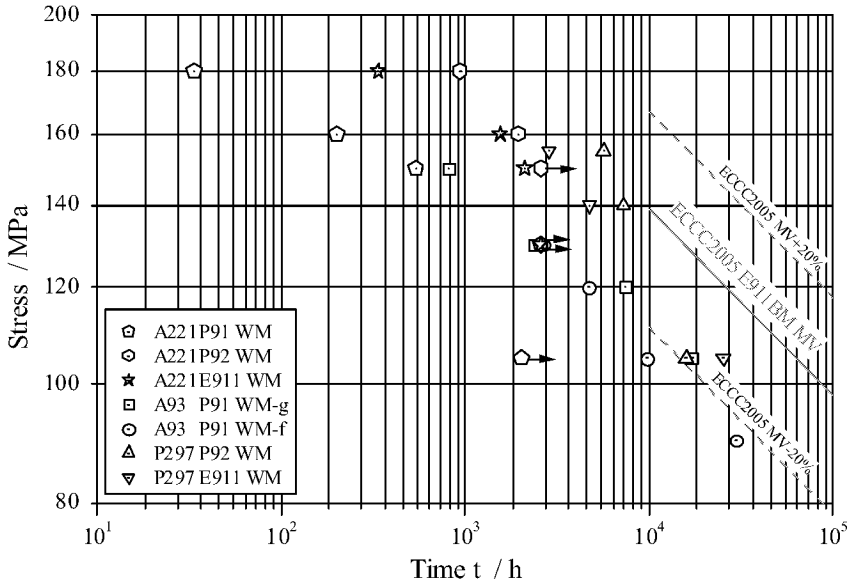

Figure 5: Weld metal creep diagram (A221 P91 undermatched, A221 P92 overmatched, A221 E911 matched WM, $\vartheta = 600°C$) [12], [13].

Component tests

To validate the developed simulation tools, two feature tests are an essential part of the experimental investigations within this research project. As mentioned above, the component tests consist of two longitudinally welded pipes loaded with internal pressure under 600 °C. In a first step, an E911 pipe (D = 355 mm, d = 269 mm, L = 2900 mm) was divided in two parts and then cut into four half shells. After milling the weld bevels, the half shells were adjusted and welded as specified in Table 2. Two segments of the welded pipes were sawed off for the preparation of the crossweld creep specimen. To minimize the volume of the pressurized air needed for the experiments, two solid fillers were inserted in the pipes before girth welding the spherical heads, see Figure 6. After welding, the pipes and the segments were heat treated at 760 °C for 4 h.

High temperature capacitive strain gauges are positioned on the pipes to measure the integral hoop strain in the base metal and over the complete welds. Special strain gauges with small measuring lengths of about 2 mm are mounted on the pipes to measure the strain in the HAZ. Furthermore speckle interferometry of the partner KEMA (Arnheim, NL) is used to investigate the creep behaviour of the material in that region. In contrast to the high temperature strain gauges, which "only" allow an integral strain measurement due to the measuring length, the outcome of the speckle interferometry are local strains.

To be able to check whether the online strain measurement with high temperature strain gauges produces reliable data, plastic strain will be measured in defined time intervals (3, 5, 10 kh) and post test. Therefore little pocket holes are drilled into the pipe and hard metal spheres were driven into the holes. By using a special slide calliper and measuring the distance between the spheres pre-test and at the time intervals as well as post-test, the plastic strain can be determined. Changes in diameter and the influence of potential out-of-roundness is examined using a special measuring device at the planned time intervals. Thermocouples are used to control the temperature and to measure the temperature distribution over the pipes during the test.

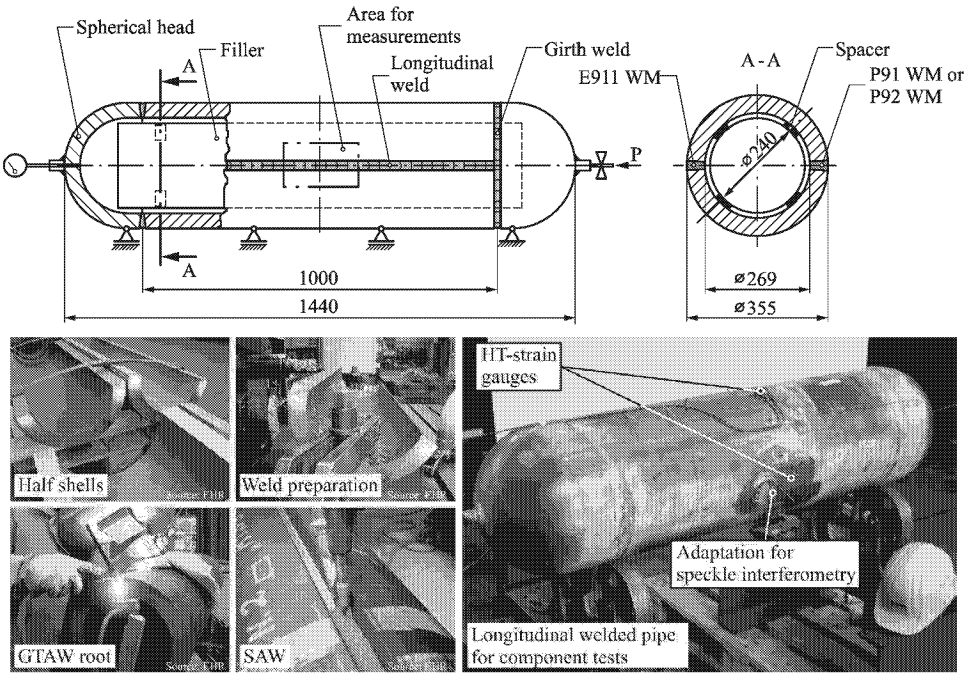

Figure 6: Weld preparation, welding and delivery of welded pipes

3 Numerical Investigations

In typical technical applications, it is often sufficient to describe the primary and secondary creep state because the tertiary creep regime is not generally of interest for design of these components. In this case a modified Garofalo [14] creep model can be used to describe the behaviour of the component under high temperature loading. If consideration of advanced life time assessment and modelling of damage and failure behaviour is planned, the inelastic finite element calculations must be based on constitutive models covering all three creep stages. In the research presented here, a modified creep law of Graham and Walles is used [15]. In its general form, the Graham-Walles material law reads as follows:

$$\dot{\varepsilon}_{cr} = A_1 \sigma^{n_1} \varepsilon_{cr}^{m_1} + A_2 \sigma^{n_2} \varepsilon_{cr}^{m_2} + A_3 \sigma^{n_3} \varepsilon_{cr}^{m_3}$$

The tertiary creep behaviour can also be represented by an effective stress concept with a damage parameter D. As mentioned above, the material laws are fitted phenomenologically to creep data from uniaxially loaded creep tests. Therefore an additional parameter quantifying the multiaxiality of the stress state in real components is required. The constitutive formulation of the modified Graham-Walles creep law is given below:

$$\dot{\varepsilon} = 10^{A1} \cdot \left(\frac{\sigma_{Mises}}{(1-D)} \right)^{n1} \cdot \varepsilon_{eq}{}^{m1} + 10^{A2} \cdot \left(\frac{\sigma_{Mises}}{(1-D)} \right)^{n2} \cdot \varepsilon_{eq}{}^{m2}$$

with:

$$\dot{D} = 10^{AD1} \cdot \left(\left(\frac{\sqrt{3}}{q} \right)^{\alpha} \cdot \sigma_{vm} \right)^{nD1} \cdot \tilde{\varepsilon}^{mD1} + 10^{AD2} \cdot \left(\left(\frac{\sqrt{3}}{q} \right)^{\alpha} \cdot \sigma_{vm} \right)^{nD2} \cdot \tilde{\varepsilon}^{mD2}$$

and the factor of multiaxiality of the stress state:

$$q = \sqrt{\frac{3}{2}} \cdot \frac{\tau_{okt}}{\sigma_{okt}} = \frac{1}{\sqrt{3}} \cdot \frac{\sigma_{vm}}{\sigma_{hyd}} \quad \text{with} \quad \sigma_{hyd} = \frac{1}{3} \cdot (\sigma_1 + \sigma_2 + \sigma_3)$$

In Figure 7 the normalized results of a finite element simulation of a crossweld specimen are shown. If compared to the metallographic findings of a crossweld specimen subjected to high temperature loading plotted in Figure 3, correspondence between numerical calculation and experiment can be found. By coupling the damage parameter to the factor of multiaxiality, the damage parameter D can be used for the calculation of the failure location.

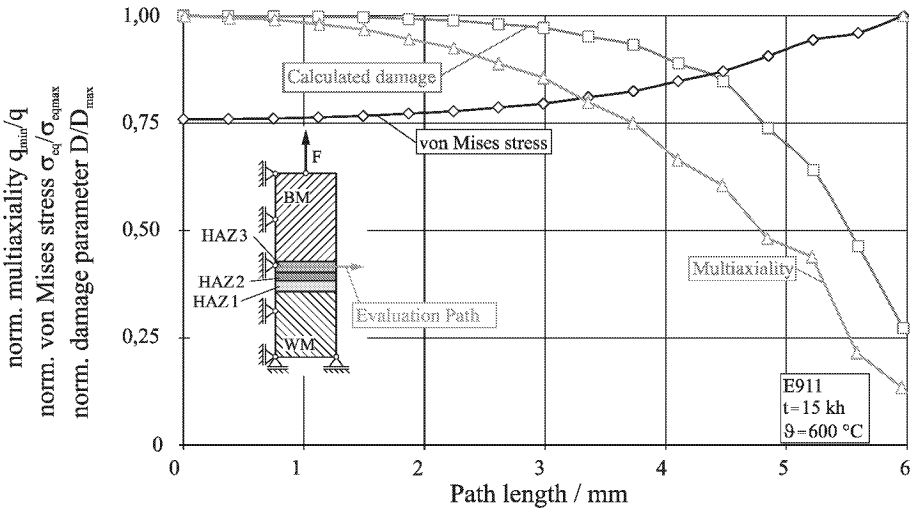

Figure 7: FE evaluation along a path length in the HAZ3 of a crossweld specimen

FE simulations of crossweld specimens

The influence of the different weld metals' creep strength on the overall behaviour of the weld can very nicely be shown when simulating crossweld specimens by means of FE method.
Since the data base of creep curves for P92 weld metals is small at the moment, this report emphasizes on the influence of undermatched and matched weld metal on creep weld performance, where sound material models could be determined.

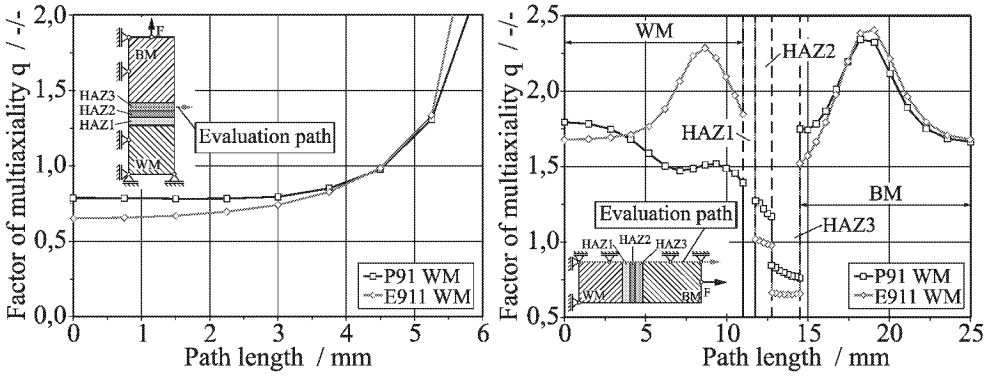

Figure 8: Factor of multiaxiality for different WM in crossweld specimens (left: radial; distribution in HAZ 3; right: axial, simulation time: 10kh)

The beneficial effect of the weld metal with reduced creep strength compared to E911 base metal is clearly visible in Figure 8 and Figure 9. The reduction of severe multiaxial stress state in the centre of the specimen in the intercritical HAZ led also to a reduction of damage in that area. It has to be mentioned, that with the use of less creep resistant filler material, the multiaxiality of the stress situation in the weld metal and thus the damage accumulation will increase there – but the overall performance of the weld will improve as long as the weld metal is strong enough to avoid premature weld failure in the weld metal.

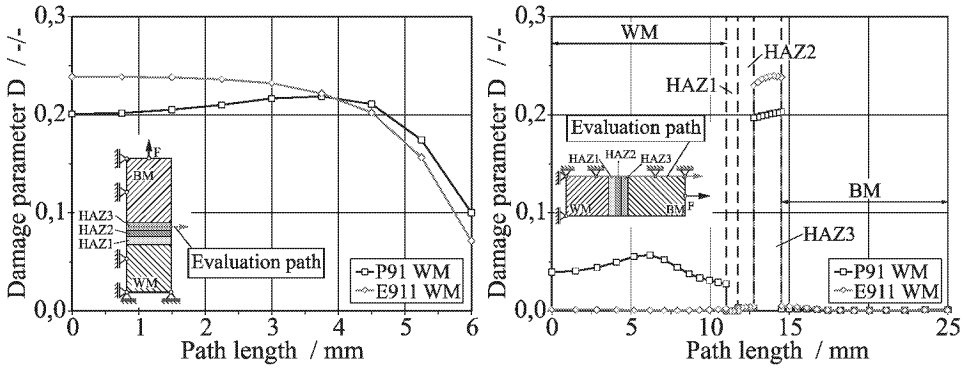

Figure 9: Damage parameter for different WM in crossweld specimens (left: radial in HAZ3, right: axial, simulation time: 10kh)

Taking the time history into consideration, the permanent changes of the stress situation and the multiaxiality of the stress state in the weld region due to creep and relaxation can be shown, see Figure 10. The higher stresses in the beginning of the simulation diminish due to relaxation processes with time. Nevertheless the multiaxiality – and thus the accumulation of creep damage – increases with ongoing time. Here, the specimen welded with P91 filler metal shows higher stresses in the HAZ3. The simulation was run for 20.000 h at 600 °C and 100 MPa.

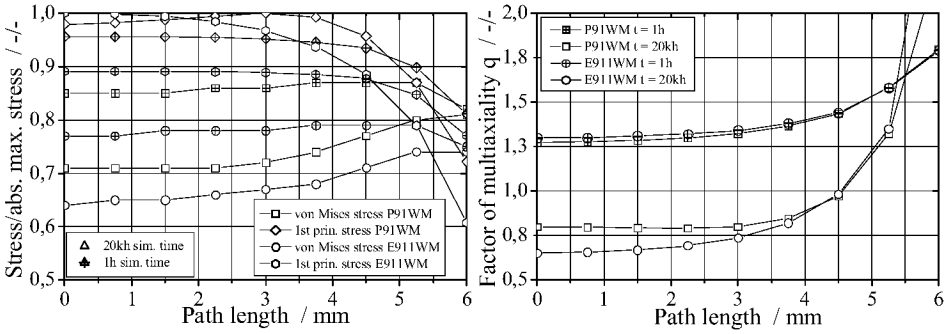

Figure 10: Time history of normalized stress and quotient of multiaxiality of tensile specimens in the HAZ3 for 1h and 20000h of simulation time.

FE simulations of components

In a next step, the developed material law is applied to a more complex geometry. A quarter model of the longitudinally welded pipe presented in Figure 6 was simulated under service conditions with similar weld configurations as presented for the crossweld specimens above. In contrast to the axis symmetrical crossweld specimens where 2D-finite elements could be used to model the geometry, plain stress or plain strain approaches are not appropriate for the components due to the longitudinal seams. Hence, a three dimensional, computation time consuming model is required here. To ensure the integrity of the end caps and the girth welds, simulations of those were included in this research, see Figure 11.

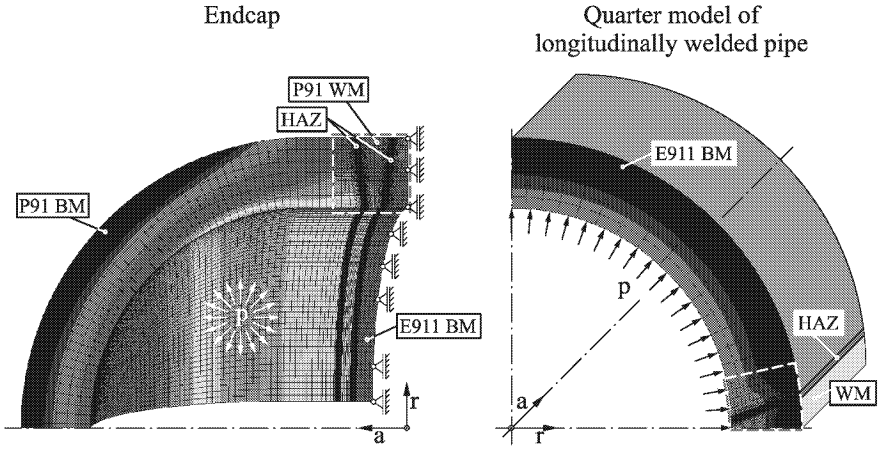

Figure 11: Geometric models of end cap and quarter pipe

The results presented below result from simulations of longitudinally welded pipes with various filler metals under internal pressure of 200 bar (250 bar), 600 °C, and 15.000 h of simulation time. The trend observed with the crossweld specimens – a reduction of the weld metals creep strength leads to a smaller factor of multiaxiality in the intercritical heat affected zone i.e. a higher level of multiaxiality – can also be found here, see Figure 12. To determine the boundary conditions for the experiment, simulations with various internal pressures were carried out for the matching weld metal configuration.

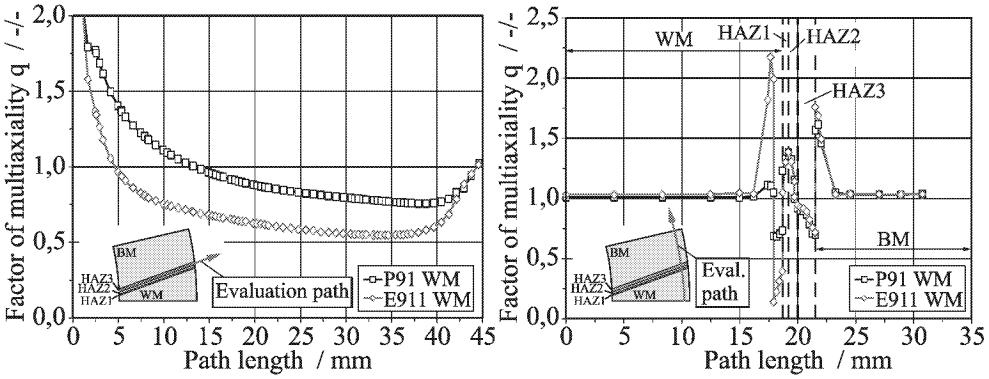

Figure 12: Factor of multiaxiality for different WM in longitudinally welded pipes under internal pressure (left: radial in HAZ3, right: circumferential, sim. time 1.5kh).

The damage distribution for different internal pressures in the HAZ3 and along a circumferential path trough weld metal, HAZ1-3 and base metal is shown in Figure 13. As expected, the increase of the internal pressure from 200 bar to 250 bar resulted in an severe increase in damage too. Although it is not visible in the graphs presented here, there is also damage in the other material zones (WM, HAZ1-2, BM), but very low compared to the one in the HAZ3. The failure location (here maximum of damage) – for pipes under high temperature loading (internal pressure) in general close to the outer surface [16] – is represented well by the simulations, especially when loads increase.

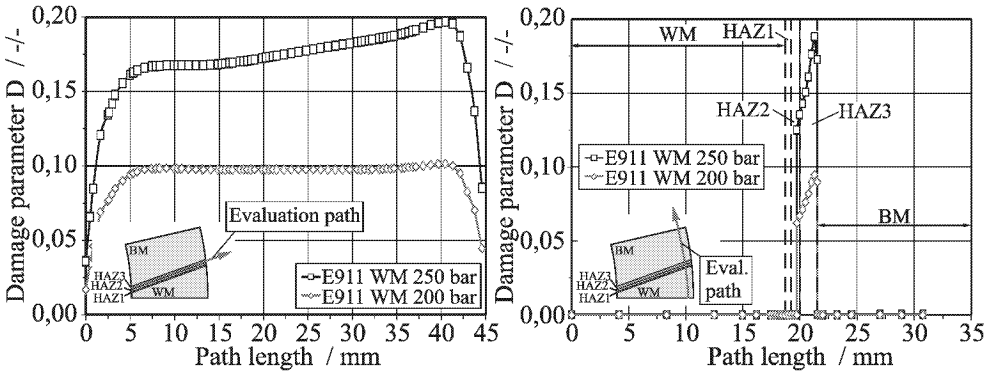

Figure 13: Damage parameter for different internal pressures in longitudinally welded pipes under internal pressure (left: radial; right: circumferential, sim. time 1.5kh).

Results of the FE-simulations of the end caps are presented in Figure 14. As expected, the intercritical heat affected zone in the P91 semi-spherical head is the location of maximum creep strain because of the poor creep strength of this zone compared to flanking materials. Nevertheless there is no doubt concerning the integrity of the heads as maximum strains remain well below 0.5 %.

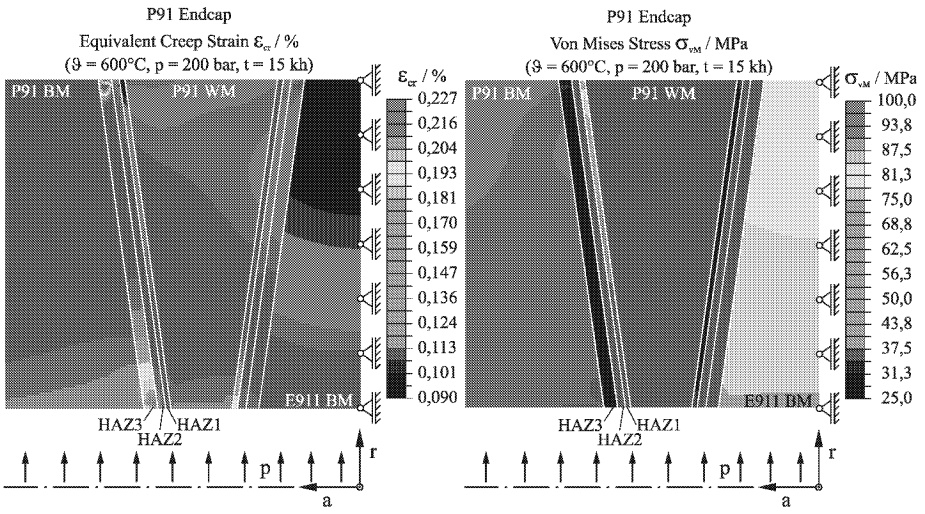

Figure 14: Equivalent plastic strain and von Mises stress in the circumferential endcap weld, P91 BM and WM

4 Conclusions and Outlook

After evaluating the numerical results extracted from an ongoing R&D programme, an extension of the lifetime of welded components seems realistic, by avoiding premature failure in the intercritical heat affected zone, due to a specified variation of the weld metals creep strength. A reduction of the multiaxiality of the stress state and thus of damage can be observed if a weld metal with lower creep resistance compared to the base metal is chosen. The results are very promising concerning uniaxially loaded crossweld specimens. Drawing conclusions from these cylindrical specimens on welded components with more complex geometries seems not necessarily applicable. Nevertheless simulations also show for complex geometries that replacing the matching weld metal by a weld metal with lower creep strength, a reduction of the multiaxiality of the stress state can be achieved. The beneficial effects of this reduction on the damage of components is main subject of the ongoing research.
Numerical investigations on the influence of overmatching weld metal have been postponed so far due to a lack of reliable data. These simulations will be started as soon as the experimental results of the running creep tests are available and implemented in the constitutive equations.
Finally, the presented numerical tools will be optimized and verified so a desired optimum of different material behaviour between weld metal and base metal can be found and realized in technical applications.
On the experimental side, the longitudinally welded pipes for the component tests are prepared for testing (installation of high temperature strain gauges, thermo couples etc.). From the feature, tests results will be obtained which can be used for the verification of effects determined by numerical simulation. Furthermore, creep tests on tensile and crossweld specimens will be carried out to enhance the material data base. Especially the influence of the peak temperature when simulating HAZ material will be clarified when these experiments are finished.

5 Acknowledgement

Main parts of the investigations presented in this paper are supported by the Research Association of the Iron and Steel Manufacturing Industry (AVIF) in Germany under contract no. A221 -MISMATCH. The support is highly acknowledged. Furthermore the investigations are supported by the COST group – mainly in the framework of COST 536 and by the members of the Work Group W1 of the German Creep Group. These contributions are appreciated.

6 References

[1] Tschaffon, H.:
COMTES700 – on the way to 700°C Power Plant.
Int. Workshop: Performance and Requirements of Structural Materials for Modern High Efficient Power Plants, Sept. 2005, Darmstadt, Germany

[2] Hahn, B., V. Baumhoff and M. Zschau:
Use of X10CrMoVNb9-1 Steel in Power Plant Retrofitting Applications - Experience and Application Potential
Advanced Heat Resistant Steel for Power Generation. Eds. R. Viswanathan and J. Nutting. Conference Proceedings. 27-29 April. 1998. San Sebastian. Spain

[3] Bendick, W., K. Haarmann and M. Zschau:
E911 Ein neuer Werkstoff für Dampfleitungen im Kraftwerksbau
VGB Kraftwerkstechnik 5/2000

[4] Hald, J.:
Long-term Stability of 9- to 12% Cr Steels – Current Understanding and Future Perspectives
VGB PowerTech 12/2004

[5] Maile, K. et al.:
Zeitstandverhalten von P91-Schweißverbindungen.
19. Vortragsveranstaltung AGW/AGHT, Düsseldorf, 1996, Germany

[6] Husemann, R. U. et. al.:
Langzeiteigenschaften von Schweißverbindungen moderner Stähle für Dampferzeuger
23. Vortragsveranstaltung AGW/AGHT, Düsseldorf, 2000, Germany

[7] Maile, K. et. al.:
Behaviour of similar welds in T24 Tubes and E911 pipes
3rd HIDA and Integrity Conference, Integrity of High Temperature Repair Welds, Oeiras-Lisabon, Portugal, 16-18 September, 2002, pp. 69/80

[8] TÜV Rheinland/Berlin Brandenburg:
VdTÜV-Werkstoffblatt 522/2 and 522/3

[9] Böhler Thyssen Welding:
Schweißzusätze
Böhler Tyssen Schweisstechnik, 2002, Hamm, Germany

[10] Ennis, P. J.:
The mechanical properties and microstructures of 9% chromium Steel P92 weldments.
OMMI (Vol. 1, Issue2), 2002

[11] Schubert, J., A. Klenk and K. Maile:
Determination of weld strength factors for the creep rupture strength of welded joints.
European Creep Collaborative Committee (ECCC) Conference: Creep and fracture in High Temperature Components – Design and Life Assessment Issues, 2005,
London, UK

[12] Heuser, H., et. al.:
Ermittlung der Langzeiteigenschaften artgleicher Schweißgüter neuer warmfester Stähle
Forschungsbericht P 297, 2000, Düsseldorf, Germany

[13] Theofel, H., K. Maile and E. Roos:
Untersuchung einer artgleichen Schweißverbindung für 9%Cr 1%Mo-Stähle unter besonderer Berücksichtigung des Langzeitkriechverhaltens
Abschlussbericht AiF-Nr. 9300, 1997, Stuttgart, Germany

[14] Granacher, J. and A. Pfenning:
Kriechgleichungen II – rechnergestützte Beschreibung des Kriechverhaltens ausgewählter hochwarmfester Legierungen.
FVV Forschungsvorhaben Nr. 432, 1991

[15] Graham, A. and K. F. A. Walles:
Relationships between Long- and Short-Time Creep and Tensile Properties of a Commercial Alloy
Journal of The Iron and Steel Institute, Vol. 179, pp. 104-121, 1955

[16] Rauch, M. et. al.:
Numerical Calculation and Experimental Validation of Damage Development in 9 Cr Steels
30. MPA-Seminar: Safety and Reliability in Energy Technology, Vol. 2, 2004,
Stuttgart, Germany

STRUCTURAL STABILITY AND PROPERTIES OF WELD JOINTS OF NEW CREEP-RESISTANT STEEL GRADES WITH 9 OR 12% CR CONTENTS APPLIED IN OPERATION OF POWER GENERATIONS SECTOR OVER 30 000H

Grzegorz Moskal[1], Adam Hernas[1], Jerzy Pasternak[2],
[1] The Silesian University of Technology, 8 Krasińskiego Str, 40-019 Katowice, Poland
[2] Boiler Engineering Factory RAFAKO S.A., 33 Łąkowa Str, 47-400, Racibórz, Poland
jerzy.pasternak@rafako.com.pl

Abstract

Continuously developing power generation sector, including boilers with supercritical parameters, requires the applications of new creep-resistant steel grades for pressure components in construction of boilers, turbo-generators and steam piping. This paper presents RAFAKO S.A. experience within the field of research and implementation of a new group of creep-resistant steel grades with tungsten and cobalt contents for applications on elements of steam superheaters boilers with supercritical parameters – including the selection of filler metal, welding procedures and selected results of mechanical properties carried out during implementation of the welding process.

The article presents the results of examinations of steam superheater coils, with 38 mm diameter and wall thickness 4,4 or 6,3 mm, made of martensitic, creep-resistant steel grades containing 9% and 12% Cr with the addition of Mo, V and additional tungsten contents, after more than 20 and 30 thousand hours of operation in actual operational conditions.

In order to compare the required parameters of examined steel grades after extended operation period, the research was focused on structure degradation processes, which are mainly manifested in the form of: disintegration of martensitic areas, release of $M_{23}C_6$ type carbides, release of Laves phase, steel recrystallization and recovery processes. The scope of examinations included microstructure examinations (LM, SEM, TEM) and assessment of mechanical properties at ambient temperature and at 600°C. Such examination program enabled for the assessment of steel structure stability during operation. It was clearly shown that 20 thousand hours of operation have little impact on changes occurring in microstructure and other properties of the examined steel grades.

The examinations were performed by RAFAKO within the framework of European COST 522 and COST 536 programs.

Keywords: power generation, mechanical properties of weld joints, creep-resistance, 9-12%Cr steel, structural stability,

Introduction

The average efficiency of local utilities amounted to c.a. 33% while the efficiency values of new power-generating units in Europe approached the range of 42-46%. In line with the decision to build a 440MW power-generating unit in Pątnów Power Plant, the main guidelines of country's energy policy stipulate construction of another 440MW power-generating unit in Łagisza Power Plant and a 840MW power-generating unit in Bełchatów Power Plant, both operating with supercritical parameters of the medium, i.e. steam temperature reaching 580°C-620°C, steam pressure amounting to 26-30 MPa and design unit efficiency of 43-46 %. These newly designed boilers shall also meet very stringent requirements concerning availability and environment protection resulting from the provisions of European Directive no. 80/2001/EU [1-3].

Such boiler design parameters require application of new generation martensitic steel grades with 9-12% Cr contents and tungsten addition in manufacturing of outlet superheater

elements. This clear tendency to increase power plant efficiency - and, in particular, the efficiency of power-generating units with supercritical steam parameters – has resulted in the last 10 years in development of a whole series of new creep-resisting steels grades, which can be used in outlet steam temperatures of c.a. 620°C (650°C). In case of a typical "supercritical" unit, with steam temperature of c.a. 600°C and steam pressure of c.a. 270 bar – with steam reheat in secondary part up to 600°C – applied creep-resisting steel grades have to assure the required creep resistance of individual boiler components in design temperatures, as follows [4-6]:

- up to 500°C – for elements of boiler membrane walls,
- up to 600 (620)°C – for large thickness boiler elements located outside the flue gas zone,
- up to 630 (650)°C – for steam superheater elements located within the flue gas zone [6-10].

Considerable European contribution, which has helped to determine the directions of development and the scope of modifications of new martensitic steel grades consist in European COST 522 – currently COST 536 – program "Power Generation into the 21st Century; Advanced Steam Power Plant". Already in the year 2000, RAFAKO S.A., in co-operation with Welding Institute and IMŻ Gliwice, commenced its participation in COST 522 program quickly becoming one of the major participants [3]. The objective of RAFAKO S.A. participation in COST 522 program was to recognize current directions of development of creep-resisting steel grades combined with use of its large manufacturing and implementation capacities in applications of new materials, optimizing of manufacturing process such as welding, plastic forming as well as implementation of new techniques of examinations of power-generating equipment for both local and European Community markets [5,6]

1. Materials and scope of examinations

Examinations were carried out on martensitic steels grades containing 9 and 12% Cr with tungsten addition such as P92, HCM12 and HCM12A. Materials subjected to testing, i.e. elements made of the new generation creep-resisting steel grades with the following dimensions:

- ϕ38×4 mm made of HCM12 steel,
- ϕ38×6,3 mm made of T122 (HCM12A) steel
- ϕ38×6 mm made of T91 steel

Specification of chemical composition of steel grades subject to examinations is shown in Tab.1.

This article shows only the selected results of strength and metallographic examinations within the field of assessment of base material properties and structure stability in both similar and dissimilar joints of welded joints of steam superheater coils elements made of HCM12, T122 (HCM12A) and T91 steels:

- after welding and heat treatment,
- after 20 000 and 30 000 hours of operation in actual operating conditions of boiler no. 7 in Bełchatów Power Plant,
- after annealing simulating actual steam superheater operating conditions – comparing to actual operating condition.

Tab.1. Specifications of chemical composition of steel grades – in accordance with the requirements of standards – (upper lines of chemical compositions) and specification of chemical analyses of applicable tubes, basis of data originating form material certificates (lower lines of chemical compositions) [6].

Steel grade		Contents [%]														
		C	Si	Mn	P	S	Ni	Cr	Mo	W	Cu	V	Nb	Al	B	N
HCM12	Stand.	<0,14	<0,5	0,3 ÷ 0,7	<0,03	<0,03	-	11 ÷ 13	0,8 ÷ 1,2	0,8 ÷ 1,2	-	0,2 ÷ 0,3	<0,2	-	-	-
	Cert.	0,1	0,26	0,53	0,028	0,02	-	11,93	1,01	1,02	-	0,24	0,04	-	-	-
T122 (HCM12A)	Stand.	0,07 ÷ 0,14	<0,5	<0,7	<0,02	<0,01	<0,5	10 ÷ 12,5	0,25 ÷ 0,6	1,5 ÷ 2,0	0,3 ÷ 1,7	0,15 ÷ 0,1	0,04 ÷ 0,1	<0,04	< 0,005	0,04 ÷ 0,1
	Cert.	0,13	0,31	0,6	0,014	0,001	0,35	10,65	0,35	1,92	0,94	0,22	0,06	0,009	0,0009	0,061
T91	Stand.	0,08 ÷ 0,12	0,2 ÷ 0,5	0,3 ÷ 0,6	<0,02	<0,01	<0,4	8,0 ÷ 9,5	0,85 ÷ 1,05	-	-	0,18 ÷ 0,25	0,06 ÷ 0,1	<0,04	-	0,03 ÷ 0,07
	Cert.	0,10	0,45	0,44	0,015	0,001	0,13	8,16	0,94	-	-	0,21	0,07	0,04	-	0,06

2. Results of microstructure and hardness distribution of 9 and 12% Cr steel grade in delivery condition and after welding and heat treatment

T91 steel

The microstructure of T91 steel in delivery condition includes tempered martensite of slat structure (fig.1a,b). Areas of $M_{23}C_6$ and MX were detected – they are visible at the limits of δ-ferrite grains and primary austenite grains as well as at the limits of martensite slats (fig.1b). Measured steel hardness amounts c.a. 225HV and its impact resistance equals kV ~ 145 J/cm^2 [8].

T122 (HCM12A) steel

T122 (HCM12A) steel in delivery after normalization at a temperature 1050ºC/60min. and tempering at a temperature of 750ºC/60min. show a tempered martensite structure with a small amount of δ-ferrite (c.a.3%) and release of $M_{23}C_6$ carbides, within the area of tempered martensite grain and at the limits of martensite slats (fig.2a,b). Measured hardness of examined material ranges from 260 to 265HV [4,6].

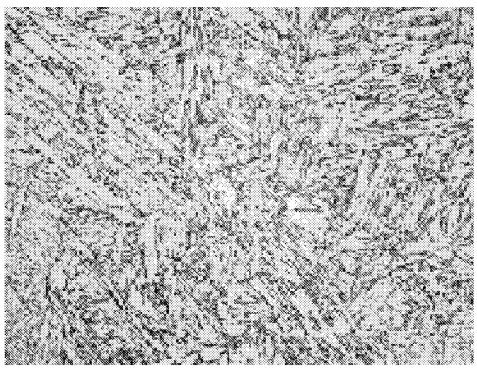

Fig.1a. T91 steel grade – tempered martensite of slat structure LM, magn. 500×

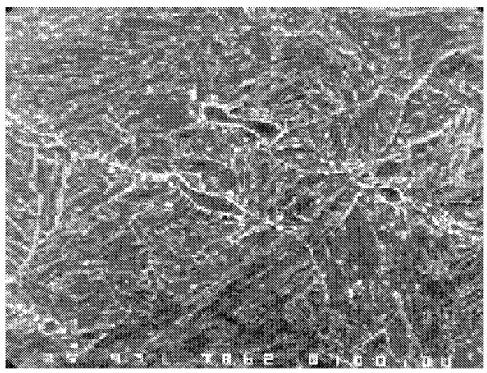

Fig.1b. T91 steel grade – detail of structure from fig.1a, δ-ferrite areas in martensitic SEM, magn. 470×

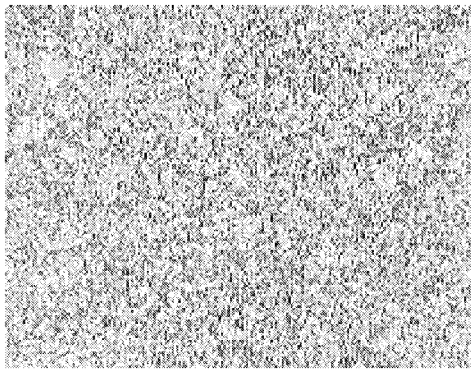

a) LM magn.150×

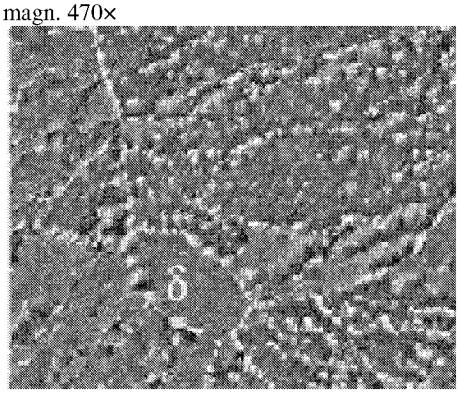

b) SEM magn. 3000×

Fig.2. T122 (HCM12A) steel microstructure after austenitization at a temperature of 1050°C/60min. and tempering at a temperature 750°C/60min. Tempered martensite with ferrite δ. – 2a). LM magn. 150×, 2b). SEM magn. 3000×

All of the joints designated for Bełchatów Power Plant have been welded at RAFAKO S.A. The tube joints ϕ38×6,3 mm were TIG welded using T-HCM12A ϕ1,6 mm Sumitomo wire with a preheating temperature of 250°C. Microstructure of tube welded joints, measured hardness and hardness distribution of joint ϕ38×6,3 mm is presented in fig.3.

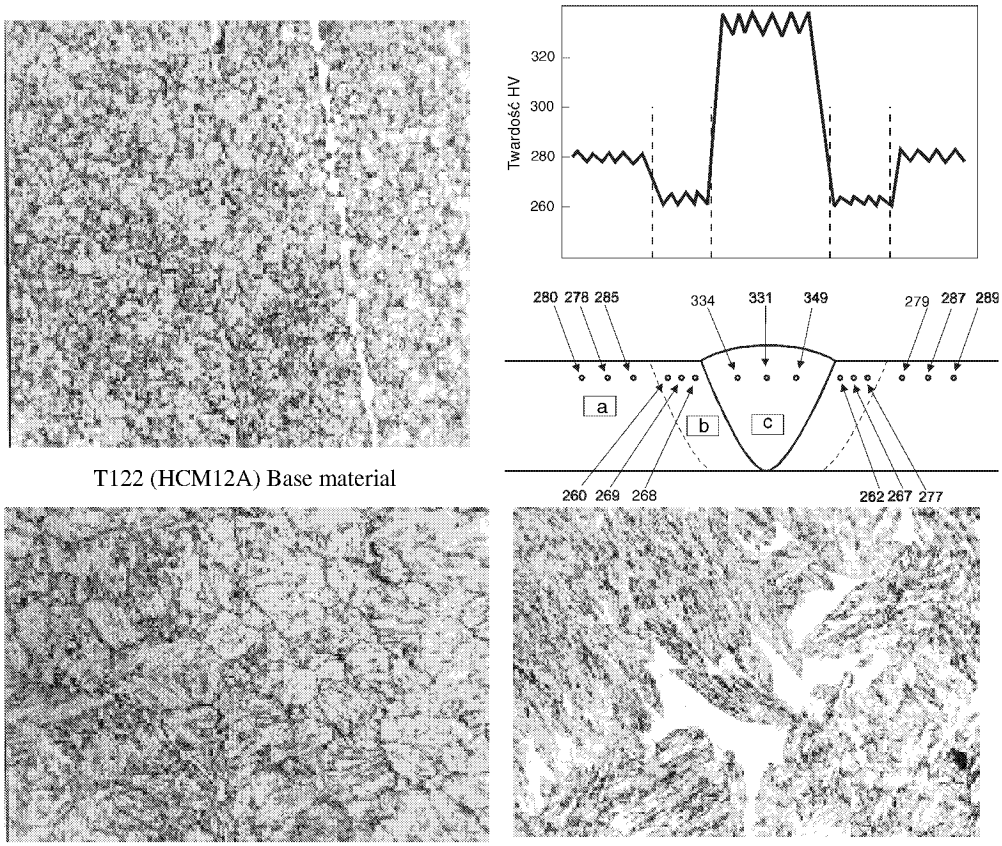

T122 (HCM12A) Base material

HAZ

Weld deposit A

Fig 3. Microstructure, measured hardness and hardness distribution of weld T122 (HCM12A- T HCM12A -HCM12A) steel grade

3. Assessment of mechanical properties examinations of steel grades with 9 and 12% Cr contents after c.a. 20 000 and 30 000 hours of operation in actual operating conditions

The examined material consisted of steam superheater tubes made of HCM12, HCM12A and P91 steel grades, with ϕ38 mm diameter and wall thickness 4, 4 and 6,3 mm respectively. Analyzed tubes were operated for c.a. 20 000 and over 30 000 hours in a P3 superheater of the boiler no. 7, type BB-1150 in Bełchatów Power Plant. Examinations were carried out both at ambient temperature and at a temperature of 600ºC. Results of examination carried out at ambient temperature are shown in Tab.2, and results of those carried out at the temperature 600ºC are shown in Tab.3.

Tab.2. Results of mechanical property of welded joint. Static test at ambient temperature

	20 000h			30 000h		
Steel grade	$R_{0,2}$ MPa	R_m MPa	A_5 %	$R_{0,2}$ MPa	R_m MPa	A_5 %
HCM12	450/454	716/691	20,5/21	434	673	19
HCM12A	600/503	774/651	40/22	554	664	20
P91	608/600	815/810	14,4/14,4	584	753	16

Tab.3. Results of welded joint static test at temperature of 600ºC.

	20 000h	30 000h
Steel grade	$R_{0,2}^{600°C}$ MPa	$R_{0,2}^{600°C}$ MPa
HCM12	244/262	320
HCM12A	277/291	303
P91	286	350

4. Assessment of microstructure examinations of steel grades with 9 and 12% Cr contents after c.a. 20 000 and 30 000 hours of operation in actual boiler operating conditions

T122 (HCM12A) steel

HCM12A steel grade after 20 000h of operation shows a tempered martensite structure with a small amount of ferrite δ (<5%). Few $M_{23}C_6$ carbide releases were observed at grain limits (fig.4,a-b). The measured hardness of material reaches the level of 223HV.

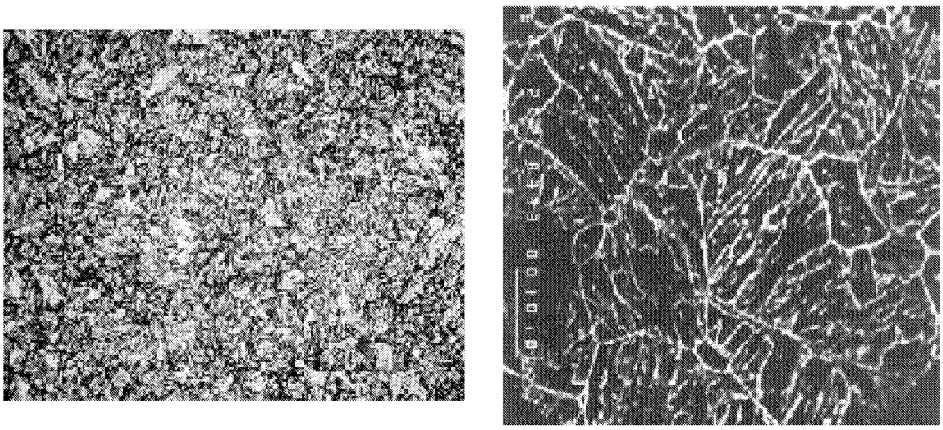

a) LM magn. 500× b) SEM magn. 2000×

Fig. 4. T122 (HCM12A) steel grade microstructure after 20 000 hours of operation. LM, SEM.

T122 (HCM12A) steel grade substructure after 20 000h of operation shows well-formed polygonal sub-grains (fig.6a), inside which we observe a very low dislocations density – results of combined temperature and time effect. We also observe the release of $M_{23}C_6$ carbide, mainly at the limits of equiaxial sub-grains (fig.5b,c,d). The released carbides have characteristic elongated and coagulated form. In the vicinity of the coagulated $M_{23}C_6$ carbide

we observe the elongated Laves phases particles (fig.5e,f). However, the occurrence of such phases is rarely seen and frequently such elongated releases are $M_{23}C_6$ carbide particles. MX-type releases occur inside sub-grains.

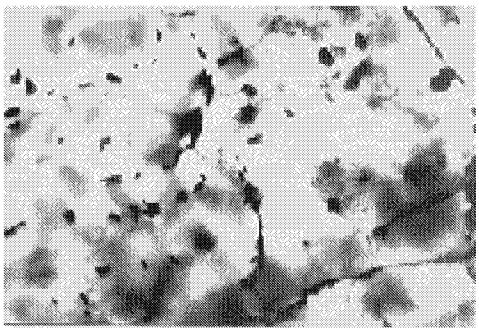

a) sub-granular structure with numerous carbide release at limits magn. 6700×

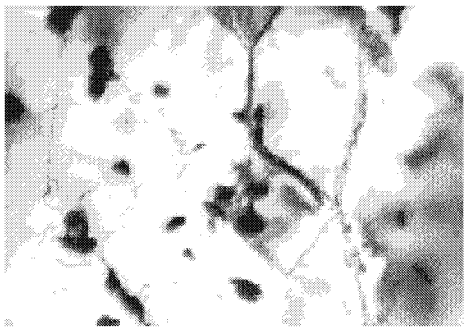

b) diversified morphology of $M_{23}C_6$ release magn.17000×

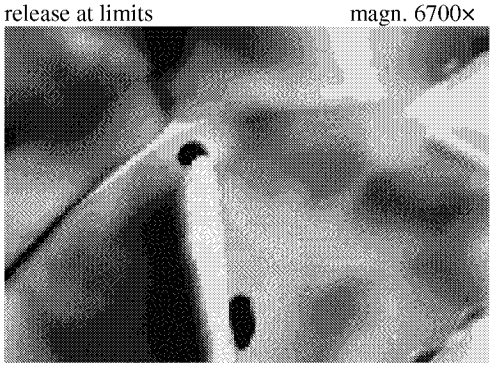

c) elongated Laves phase release in HCM12A steel grade. DF TEM magn. 33000×

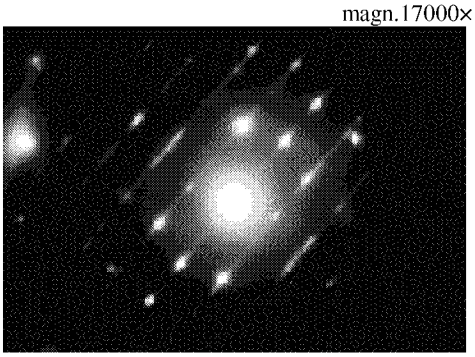

d) diffraction from fig c)

e) $M_{23}C_6$ carbide release in HCM12A steel grade, LF TEM magn. 33000×

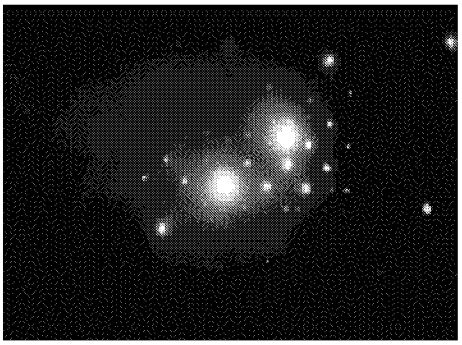

f) diffraction from fig e)

Fig.5. HCM12A steel sub-structure after 20 000h of operation - TEM.

Microstructure of the analyzed steel grade after 30 000h of operation has not changed considerably versus the condition after 20 000h. Also in this case, the tempered martensite structure dominates, with little amount of δ ferrite. A slight increase of carbide releases were

observed at martensite grain limits (fig. 6, a-b). The measured hardness of material reaches the level of 217HV after another 10 000h of operation.

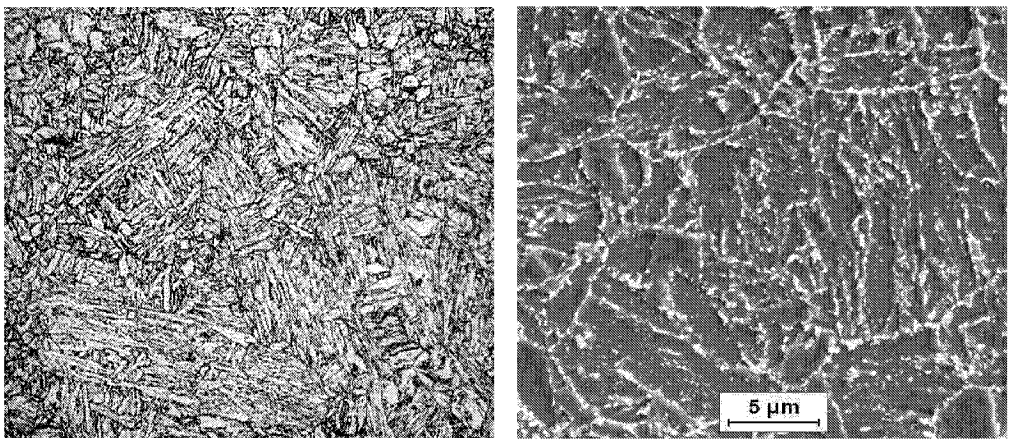

a) LM magn. 400× b) SEM magn. 2000×

Fig.6. HCM12A steel microstructure after 30 000h of operation - LM, SEM.

Metallographic examinations of other steel grades HCM12 and P91 also showed little influence of the time of operation on microstructure of the examined steel. In the case of HCM12 steel grade, a tempered martensite structure with a small amount of δ ferrite and numerous carbide releases dominated at grain limits (fig. 7, a-d). The measured hardness of the examined steel reached the level of 213HV.

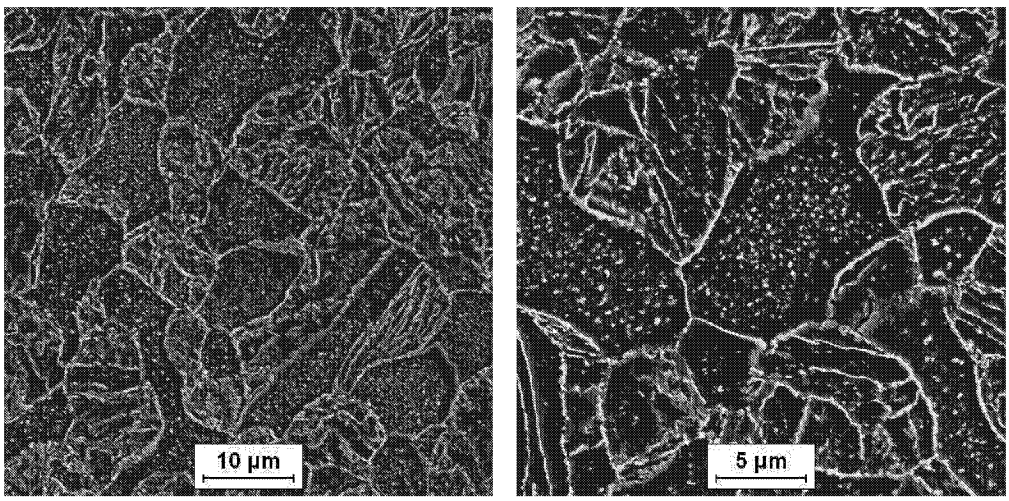

a) SEM magn. 1000× b) SEM magn. 2000×

Fig.7. HCM12 steel microstructure after 30 000h of operation - LM, SEM.

P91 steel grade is characterized by a tempered martensite structure with little amount of carbide releases (fig. 8a, b). Hardness after 30 000h of operation reached the level of 240HV.

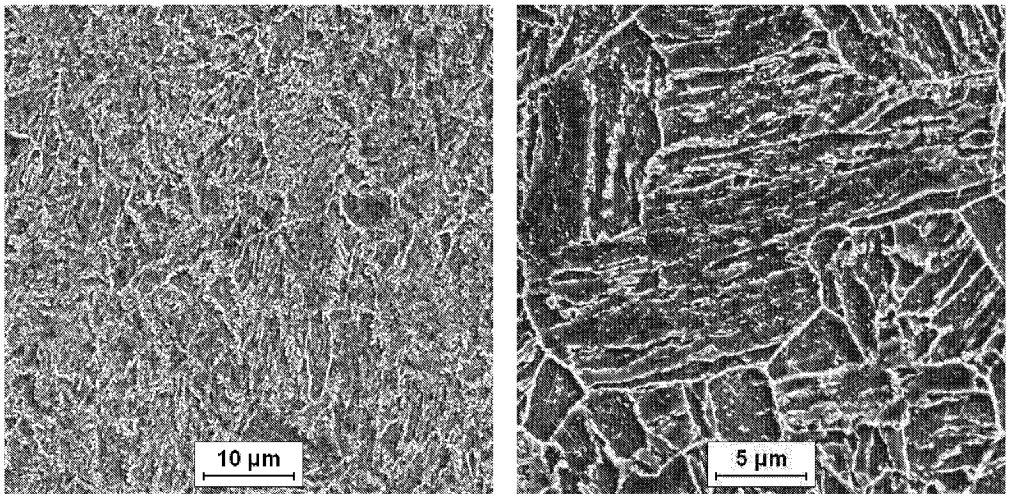

a) SEM magn. 1000× b) SEM magn. 2000×

Fig.8. P91 steel microstructure after 30 000h of operation - LM, SEM.

5. Summary and conclusions

During mechanical examinations, it was clearly stated that the lowest field point – both at ambient temperature and at the temperature of 600°C – is characteristic for HCM12 steel grade. P91 and HCM12A steel have similar yield point and tensile strength values, not depending on the temperature of examination, and similar A_5 elongation, which meet the required material properties level expected during a boiler operation process.

T91 steel grade in delivery condition has a characteristic tempered slat martensite structure with δ ferrite areas and $M_{23}C_6$ carbides release. Sub-structure shows the elongated arrangements of tempered martensite sub-grains with high dislocation density as well as $M_{23}C_6$ and MX carbide release at the limits and inside the sub-grains. Materials hardness reaches the level of 225 HV and impact strength amounting to ~ 145 J/cm^2.
After annealing, T91 steel grade shows a coarse-needled martensite structure with δ ferrite areas. Release of coagulated carbides form a δ ferrite islands. In a sub-structure we observe very intensive processes of recovery and traversing as well as the increase of number and size of carbide release. Polygonal sub-grains are dislocation-free. Phase composition examination has shown the occurrence of $M_{23}C_6$, MX, M_2X release and Laves phase. The measured steel hardness of 200 HV is lower than in delivery condition whereas the impact resistance on kV samples amounted to ~ 75 J/cm^2.

T122 (HCM12A) steel grade in delivery condition shows tempered martensite grains with low number of δ ferrite and few $M_{23}C_6$ carbide releases at the limits of martensite grains and blocks as well as MX release inside the said blocks. The measured hardness of examined material in delivery condition is slightly higher – by c.a. 40 HV – when compared with HCM12 steel and amounts 263 HV. Impact resistance on kV samples amounted to ~ 95 J/cm^2.

After annealing at the temperature of 700°C/100h, the structure of HCM12A steel demonstrates the increase of the size of carbides released at grain limits as well as diversified dislocation density when compared to delivery conditions. After annealing at the temperature of 700°C/200h this process is further continued with clear coagulation of carbide released at the limits of primary austenite grains. It was also demonstrated that the processes of accelerated carbide release and further spheroidising occur due to the annealing. Steel hardness is lower – when compared to delivery condition – and amounts to 232 HV. Completed examinations demonstrate that HCM12A steel grade is characterized with relatively high stability of structure and properties.

HCM12A steel grade after c.a. 20 000h of operation shows a tempered martensite structure with low δ ferrite contents (<5%). Moreover, few $M_{23}C_6$ carbide releases were observed at grain limits. Sub-structure is characterized with well-formed polygonal sub-grains, inside which we observe a low dislocation density resulting from the combined temperature and time effect. $M_{23}C_6$ carbide releases were observed mainly at the limits of equiaxial sub-grains. Released carbides have a characteristic elongated and coagulated form. MX – type release occur inside the sub-grains. Material hardness amounts to 123HV.

P91 steel grade after 30 000h did not show any major effects of microstructure degradation either. Typical for that steel grade tempered martensite structure with carbide releases was observed at and outside grain limits, as well as higher than the minimum required hardness at the level of 200HV - 240 HV. Mechanical characteristics fulfill the requirements of the relevant standards – plastic properties at ambient temperature higher than 390 MPa; plastic properties at the temperature of 600°C higher than 250 MPa and elongation lower than minimum 20%

T122 (HCM12A) steel grade after 30 000h showed typical of that steel grade two-stage tempered martensite structure with few δ ferrite releases and few carbide releases at grain limits, as well as higher than the minimum required hardness at the level of 200HV - 214÷220 HV. Mechanical characteristics fulfill the requirements of the relevant standards – plastic properties at ambient temperature higher than 400 MPa; plastic properties at the temperature of 600°C slightly lower than 310 MPa and elongation equal minimum 20%.

HCM12 steel grade after 30 000h also showed typical of that steel grade two-stage tempered martensite structure with few δ ferrite releases but considerable amount of carbide releases at grain limits. Higher than the minimum required hardness was observed, at the level of 200HV - 211÷214 HV. Similarly as before, mechanical characteristics fulfill the requirements of the relevant standards – plastic properties at ambient temperature higher than 390 MPa; plastic properties at the temperature of 600°C higher than 250 MPa and elongation lower than minimum 20%.

Final conclusion

In all examined cases, the materials condition show a minimum degree of degradation, related to the occurrence of few carbide releases within and at grain limits. The analyzed structure is correct and stable; the level of mechanical properties considerably exceeds minimum values. Walls thickness measurements do not show any wear effect or losses of the steam superheater coils walls. Analysis of the carried out examinations results showed that 30 000h of operation had little impact on microstructure and level of characteristics of coils made of HCM12, T122 (HCM12A) and P91 steel grades.

The examined steel grades show considerable stability of microstructure at the temperature of approximately 585°C, which was measured in the experimental sections of steam superheater coil elements.

References

[1]. Development study of the electric energy production subsystem until 2020. Polish Electric Networks S.A., Warszawa , 1994 (in Polish)

[2]. The Energy Market Agency S.A.: Assumptions for the Polish energy policy until 2020. Working draft –version 2. Warszawa, 1999 (in Polish).

[3]. Pasternak J., Hernas A., Miliński P.: New martensitic steels for supercritical boilers. Energetyka No. 4, 1997 (in Polish).

[4]. Zeman M., Brózda J., Pasternak J.: Weldability evaluation of the HCM12A steel assigned for elements of supercritical power boilers. Przegląd Spawalnictwa No. 6, 1999, p. 1-7 (in Polish).

[5]. Brózda J.: Weldability characteristics and welding technology guidelines of the advanced heat resisting steels. COST 522 Progress Report No. 1 (12.03.2001) and No. 2 (28.09.2001).

[6]. Pasternak J. Analysis of process and structural factors determining the properties and applicability of steel grades with 9-12% Cr-Mo-V with tungsten in construction of boilers with supercritical steam parameters, April 2000

[7]. Hernas A., Cieśla M., Niewielski G., Kiełbus A., Lalik S: Assessment of delivery condition properties of selected new Cr-Mo-V-W-(Cu) steel grades used for boiler tubes and their welded connections to be operated in supercritical parameters, Research work NB-200/RM-7/98, November 1998.

[8]. Hernas A., Kiełbus A., Cieśla M., Rodak K.: Assessment of large thickness welded joints made of P91, P92 steel grades and T23 base material, Research work P/IX-2/01, September 2001.

[9]. A.Kiełbus, J.Pasternak: Structural stability of creep-resisting steel grades with 9% Cr contents", XI Scientific Seminar: New technologies and materials in metallurgy and material engineering, Katowice, May 2003.

[10] J. Pasternak, A. Kiełbus: Stability of similar and dissimilar welded joints, high-temperature creep resistant martensitic steels containing 9% Cr. Proceedings of the EPRI Fourth International Conference on Advances in Materials Technology for Fossil Power Plants. October 25 – 28, 2004

Weldability and high temperature behavior of 12% Cr-steel for tubes and pipes in power plants with steam temperatures up to 650 °C.

Johan Vekeman[1], Alfred Dhooge[1], Staf Huysmans[2], Bruno Vandenberghe[3], Claus Jochum[4]

[1]Belgian Welding Institute, St-Pietersnieuwstraat 41, 9000 Gent, Belgium
[2]Laborelec, Rodestraat 125, 1630 Linkebeek, Belgium
[3]Vallourec & Mannesmann Tubes, rue H. Harbusse 37, 59880 Saint-Saulve, France
[4]Böhler Thyssen Welding, Unionstraße 1, 59067 Hamm, Germany
Johan.Vekeman@soete.UGent.be

Abstract

Nowadays, high efforts are undertaken to increase efficiency and thereby minimizing harmful emissions of power plants. This can be achieved by increasing the steam temperature and pressure to supercritical conditions. Presently martensitic 9% Cr-steels, e.g. P91, E911 and P92 are used for power plants with advanced steam parameters. While these materials have the highest creep rupture strength values of ferritic steels, their oxidation resistance is lower than 12% Cr-steels, such as X20CrMoV12-1. With increasing steam temperature (target: 650°C) the lifetime of components made of 9% Cr-steel becomes limited not only by creep but also by oxidation.

The present paper is about a new martensitic steel developed by Vallourec & Mannesmann, that is designed for use at temperatures up to 650 °C. Test results obtained in a Belgian collective research project in collaboration with Laborelec and with industrial partners are given. The focus is on weldability, welding aspects and properties of welded joints (similar and dissimilar welds).

Keywords
VM12 – 12%Cr steel – Power plant - Welding - Creep

1. Base material [1 - 2]

Within the project thinwalled tubes, with a wall thickness of 8,8 mm and an outside diameter of 60,3 mm, and a thickwalled pipe, with a wall thickness of 35 mm and an outside diameter of 406,4 mm were tested. Both tubes and pipe were from the same heat 53 058 and have a tempered martensitic microstructure. The chemical composition is shown in table 1.

Austenizing temperature: 1060 °C - Holding time: 20min. (tubes), 30 min. (pipe) - air cooled Tempering temperature: 780 °C - Holding time: 2 h – air cooled														
C	**Si**	**Mn**	**P**	**S**	**Cr**	**Mo**	**Ni**	**Al**	**Nb**	**V**	**N**	**Co**	**B**	**W**
0,12	0,49	0,35	0,018	0,001	11,5	0,29	0,29	0,008	0,05	0,26	0,067	1,62	0,005	1,50

Table 1: chemical composition of VM12

2. Basic Weldability Study – weld simulations

Weld simulation tests were performed to study the weldability of the 12Cr steel and to be used as input data for making the welded joints under field conditions. An extensive simulation program was carried out to determine the influence of the welding parameters and a Post Weld Heat Treatment (PWHT) on the microstructure, hardness and the toughness of the Heat Affected Zone (HAZ).

2.1. Experimental procedure

In weld simulation, impact test specimens are subjected to weld thermal cycles by computer controlled dynamic resistance heating and simultaneous cooling via water-cooled jaws. A programmed heating and cooling thermal cycle is thereby applied to the central working zone of the specimen. The microstructures obtained in the central zone correspond to the microstructures of the HAZ obtained in welded joints under field conditions.
Single weld cycles were simulated with different peak temperatures (T_{p1} = 1350°C, 1200°C and 1000°C). Cooling times $t_{8/5}$ between 800°C and 500°C of 10 and 60 seconds for the tubes and 10, 30 and 60 seconds for the pipes were selected. Besides the single weld thermal cycles, also double cycles were applied with T_{p1} = 1350°C and a second peak temperature T_{p2} of either 850°C or 1000°C. All specimens received a PWHT in a furnace at 770°C, one hour for the tubes and four hours for the pipe, with a heating/cooling rate of 150°C/hour.

After simulation and heat-treating of four specimens in the same condition, one specimen was used to measure the Vickers Hardness HV10 and to perform microstructural investigations. The other three specimens were used for Charpy V - impact tests, according to EN 10045-1, to determine the impact toughness at room temperature.

The test results were evaluated using the following criteria:

- maximum hardness 350HV10 (power generation application),
- minimum impact energy at room temperature according to EN 13445-2 in conjunction with the Pressure Equipment Directive refers to:
  27 J for full-size specimen (10 x 10 x 55 mm – pipe specimens)
  22 J for sub-size specimen (7,5 x 10 x 55 mm – tube specimens)
  The mean value of the three specimens shall be at least equal to the impact energy requirement. Only one specimen may show a lower value, but this value shall not be less than 70 % of this requirement.

2.2. Test results and discussion

A similar behaviour for the tubes and pipe was found.
Typical test results from the pipe are shown in figures 1 and 2.

The hardness remained always below 350 HV10 and the hardness variation with different cooling rates was not very pronounced. The lowest toughness and highest hardness were found in the coarse grained heat affected zone.

The mean impact toughness was always above 27 J, but individual impact values below 27 J were found for the longest cooling time, 60 seconds. The impact toughness increases with faster cooling rates.

Applying a double weld cycle with T_{p2} = 1000°C (T_{p1} = 1350°C) resulting in a grain refinement, improves the coarse grained HAZ toughness, but T_{p2}= 850°C has a negative effect (no grain refinement) resulting in lower impact toughness.

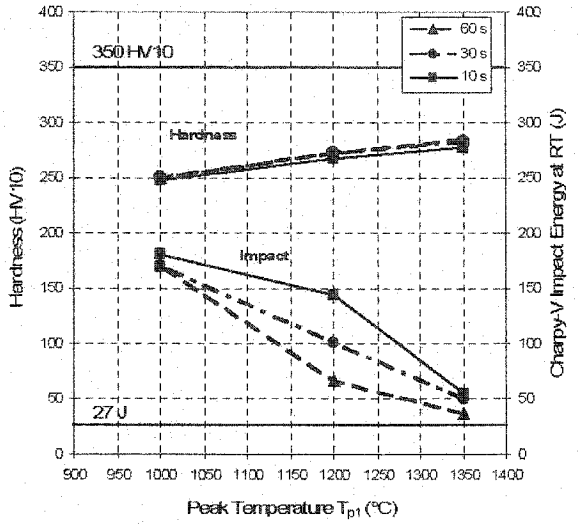

Figure 1: Influence of peak temperature and cooling time on hardness and impact toughness

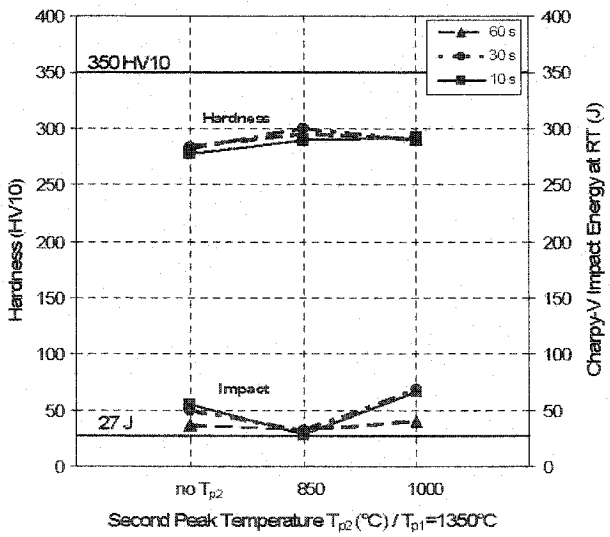

Figure 2: Influence of second weld cycle on hardness and impact toughness

Microstructures revealed the presence of delta-ferrite in the coarse grained heat affected zones (T_{p1} = 1350°C). Less delta-ferrite was found for lower cooling rates corresponding to higher heat inputs (Table 2). Applying a second weld cycle with T_{p2} = 1000°C reduced the delta-ferrite content. More delta-ferrite was found in pipe compared to tube specimens.

	Delta-ferrite (%) mean (maximum)		
$t_{8/5}$ (s)	T_{p2}		
	no T_{p2}	850°C	1000°C
10	3,4 (3,8)	1,5 (2,4)	1,0 (2,0)
30	1,8 (2,6)	2,6 (3,9)	0,6 (1,2)
60	1,5 (2,7)	1,4 (3,6)	0,4 (1,0)

Table 2: Influence of heat input and second weld cycle on delta-ferrite content

2.3. Conclusions

- ***The lowest toughness and highest hardness can be expected in the coarse grained heat affected zone.***
- ***Fulfilling the hardness criteria (< 350 HV10) is achievable with a Post Weld Heat Treatment at 770°C.***
- ***Welding requires an adequate heat input to limit grain growth in order to obtain the required toughness at room temperature (27 J) in the coarse grained heat affected zone and to reduce the amount of delta-ferrite.***
- ***Multilayer welding is necessary for obtaining fine grained HAZ microstructures with acceptable toughness.***

3. Reheat Cracking susceptibility

Reheat cracking, also called stress relief cracking, is a possible cause of weld failures in creep-resistant, precipitation-strengthened alloys such as ferritic alloy steels. Reheat cracking is defined as an intergranular cracking phenomenon occurring in the heat affected zone and occasionally in the weld metal of a welded joint, being initiated during a post-weld heat treatment or during high temperature service. A susceptible microstructure is a coarse prior austenite grain size with strong grain interiors that resist plastic deformation and weak grain boundaries. Therefore the coarse grained heat affected zone (CGHAZ) is the most susceptible region of a weldment.

3.1. Experimental Procedure

At the Research Centre of the Belgian Welding Institute, a lot of experience has been gathered with the isothermal slow strain rate tensile test. In this test, cylindrical specimens are given a weld simulation cycle with peak temperature T_{p1} = 1350°C to simulate the CGHAZ. After cooling to room temperature ($t_{8/5}$ = 30 seconds), the specimen is heated to and held at the test temperature between 600°C and 800°C. As soon as this temperature is obtained, the specimen is slowly strained to fracture at a strain rate of 0.5 mm/min. After the specimen is fractured, its reduction in area is measured to assess the ductility. Below 20% the material is considered to be susceptible to reheat cracking.

The tests were performed using a Gleeble 1500/20 thermo mechanical simulator. Cylindrical test samples, 110 mm long and with a diameter of 6 mm (tubes), respectively 12 mm (pipes),

with threaded ends were used. The samples were taken in axial direction. After simulation, a zone of 10 mm in the centre of the specimen was machined to 4 mm (tubes), respectively 6 mm (pipes) so that specimen fracture during tensile testing occurred in the simulated zone.

The influence of double weld cycles, second peak temperature T_{p2} = 850 or 1000°C, has been compared to single weld cycles.

3.2. Test results and discussion

Figure 3 shows the reduction in area and the ultimate tensile strength as a function of the peak temperature.

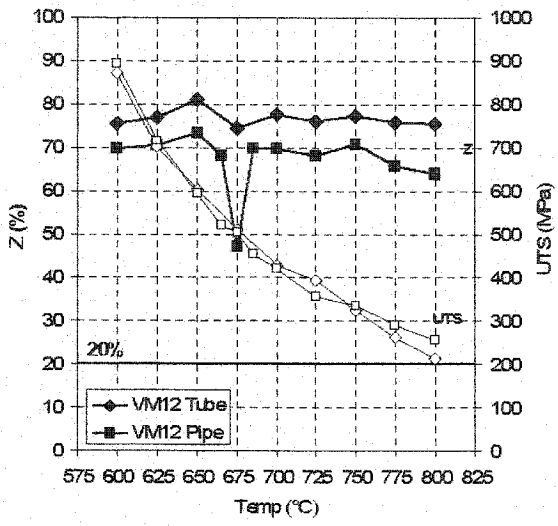

Figure 3: Reheat cracking susceptibility of VM12

Specimens from the VM12 Pipe showed a very high ductility, above 60%, in the whole temperature range (600°C - 800°C). There is only a small drop at 675°C where the reduction in area decreases to 47 %. For the specimens from the VM12 Tube, a reduction of area above 70% was found. At 675°C, a second weld cycle with a peak temperature at 1000°C increases the reduction in area from 47 to 62 %. A double weld cycle with a second peak temperature at 850°C increased the reduction in area to 77 %. Multi-pass simulation increases the ductility of the specimens. According to the above criterion, the material is considered not susceptible to reheat cracking. This confirms the trend that high alloyed ferritic steels are not susceptible to embrittlement at high temperature after post weld heating.

3.3. Conclusion

- ***VM12 is not susceptible to reheat cracking***

4. Welding

VM12 is an air hardening martensitic steel used in the normalized and tempered condition. By cooling from high temperature to room temperature, the structure of VM12 undergoes complete transformation into martensite with a maximum hardness of 510 HV10. This means that the matching weld metal and HAZ will have a hard, brittle microstructure if no special precautions are taken. In the case of storage after welding and before PWHT, the maximum time should be one week and during this time the components must be kept dry, as for the standard steels such as P91 and P92. An appropriate preheat and post weld heat treatment are necessary to obtain acceptable ductility and to avoid cold cracking.

Welding consumables (coated electrode, solid wire and flux) and welding procedures have been developed. VM12 was welded with the standard welding processes: GTAW, SMAW and SAW to homogeneous and heterogeneous (T/P91) materials. Welding tubes and pipes in the martensitic regime with matching filler metal, designated Thermanit MTS 5 CoT from Böhler Thyssen Welding Germany, was realised by using a preheat temperature below the Ms temperature (start of martensitic transformation around 300°C). After each weld bead was deposited, the weld metal and HAZ were allowed to transform partially to martensite. Part of this martensite is tempered during the deposition of the subsequent weld bead, which means that when welding is completed, part of the martensite is already tempered. The tubes were preheated at 200°C, the pipes at 200°C-250°C. After welding, the welded joint was allowed to cool down to room temperature and subjected to a heat treatment. The welding parameters are summarized in table 3.

Joint	Preheat (°C)	Interpass (°C)	Layer	Process	Diam. (mm)	Heat Input (kJ / cm)	k* x H I (kJ / cm)	PWHT (°C / h)
Homogeneous joints VM12-VM12								
GTAW (on tube 60,3 x 8,8 mm)								
I	200	200-300	6	GTAW	2,4	13-28	8-17	760-770-780 / 2
II	200	200-300	3	GTAW	2,4	n.a.	-	770 / 2
SMAW (on pipe 406,4 x 35 mm)								
I	250	250-300	1-2	GTAW	2,4	19-22	11-13	760-770-780 / 4
			3-7	SMAW	2,5	8-9	6-7	
			8-40	SMAW	3,25	11-17	9-14	
II	250	250-300	1-2	GTAW	2,4	10-29	6-17	770 / 4
			3	SMAW	2,5	7	6	
			4-33	SMAW	3,25	13-20	10-16	
SAW (on pipe 406,4 x 35 mm)								
I	200	200-300	1-2	GTAW	2,4	17-25	10-15	760-770-780 / 4
			3-40	SAW	3	7-11	7-11	
II	200	200-300	1-2	GTAW	2,4	17-27	10-16	770 / 4
			3-56	SAW	3	8-11	8-11	

Table 3: Welding parameters (* k: thermal efficiency according EN1001-2)

Joint	Preheat (°C)	Interpass (°C)	Layer	Process	Diam. (mm)	Heat Input (kJ / cm)	k* x H I (kJ / cm)	PWHT (°C / h)
Heterogeneous joints VM12-T/P91								
GTAW (on tube 60,3 x 8,8 mm)								
II	200	200-300	3	GTAW	2,4	n.a.	-	770 / 2
SMAW (on pipe 406,4 x 35 mm)								
II	250	250-300	1-2	GTAW	2,0	10-17	6-10	770 / 4
			3-4	SMAW	2,5	9-15	7-12	
			5-33	SMAW	3,2	12-20	10-16	

Table 3 continued: Welding parameters (* k: thermal efficiency according EN1001-2)

4.1. Test results and discussion

4.1.1 Homogeneous joints VM12-VM12

Joints I were post weld heated at 760 °C, 770 °C and 780 °C under laboratory conditions to optimise the PWHT. After evaluation of the hardness measurements and impact tests on these joints, it was concluded that the hardness criteria (<350 HV10) and the requirements for impact toughness, as can be seen in Figure 4, could be fulfilled with a PWHT at 770 °C and 780 °C during two hours for the tubes and four hours for the pipes.

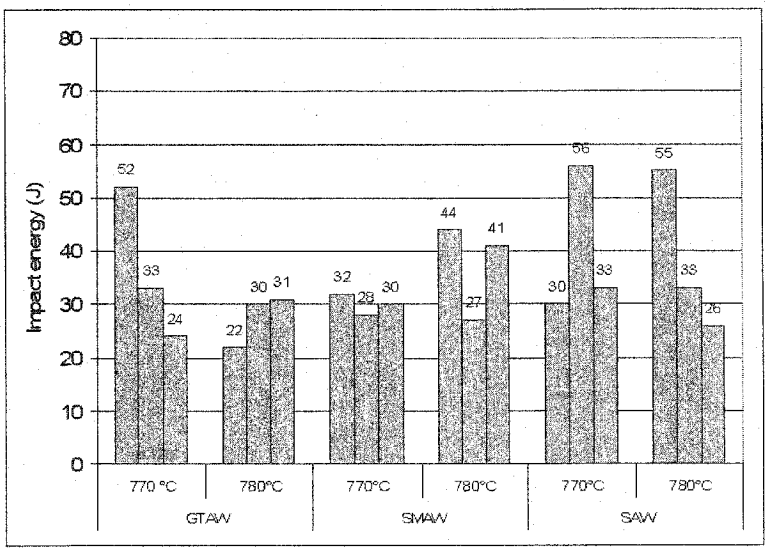

Figure 4: Charpy-V impact energy in weld metal

Joints II, post weld heat treated at the selected optimum parameters, were tested according to EN ISO 15614-1. The welded joints fulfilled the requirements regarding strength (rupture in base material), bending (no cracks greater than 3 mm in each direction after 180° bending) and hardness (lower than 350 HV10). The highest hardness was found in the coarse grained HAZ, the lowest hardness in the fine grained HAZ (Table 4).

	Hardness HV10			
Welding process	**BM**	**IC-HAZ**	**CG-HAZ**	**WM**
	Mean	Min.	Max.	Mean
GTAW	246	230	285	276
SMAW	242	225	287	266
SAW	242	224	279	249

Table 4: Hardness across welded joints

A low toughness was found in the weld metal for the pipe welded with electrodes (39 J / 28 J / 30 J). A toughness below the requirements of the PED was found for the TIG (13 J / 51 J / 43 J) and submerged arc welded joints (15 J / 31 J / 17 J). The heat affected zone showed good impact toughness with values above 120 J. One must remark here that the notch is not only sampling HAZ, but also weld metal and base metal (V-joint preparation).

Although VM12 normally has a fully martensitic microstructure, the chemical composition is such that it is close to the borderline of delta-ferrite formation. As a result, weldments which are subjected to elevated temperatures and rapid cooling can contain delta ferrite in the weld metal and HAZ.

Optical micrographs of the weld metal revealed the presence of delta-ferrite in the GTAW and SAW welded joints. Islands of delta-ferrite were found and the delta-ferrite was aligned on the grain boundaries. More delta-ferrite was found near the cap layers. For the TIG welded joint most of the delta-ferrite was found in the cap layer (Figure 5). Impact specimens of 5 mm thickness, not including the cap layer, revealed a good toughness. No delta-ferrite was found in the weld metal of the SMAW joint, neither in the heat affected zone of all three joints. When looking at the chemical composition of the filler metal, a higher Ni-content was found in the deposited weld metal from the SMAW joint (0,51%), a lower Ni-content in the GTAW (0,16%) and SAW (0,18%) joint. Nickel, which is a strong austenitizer, has a positive effect on impact toughness.

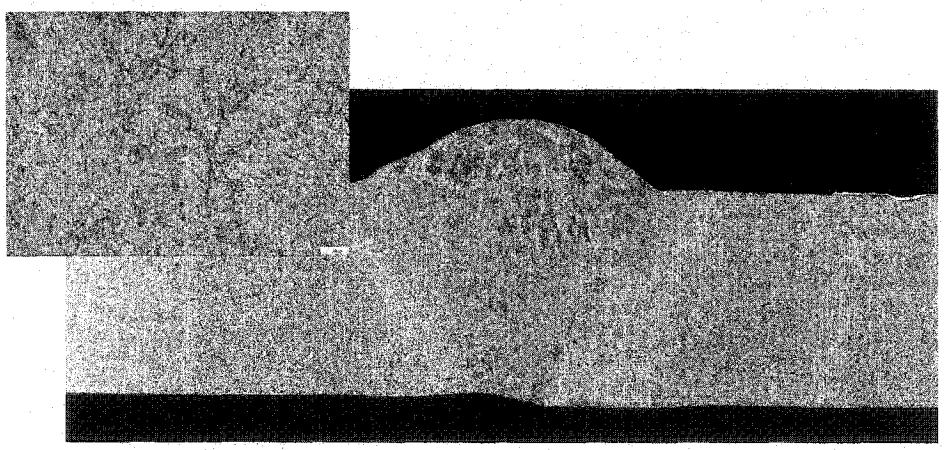

Figure 5: Macro of the GTAW joint (Etching with Villella) with optical micrograph of weld metal showing delta-ferrite in cap layer

4.1.2. Heterogeneous joints VM12-T/P91

The welded joints fulfilled the requirements regarding strength (rupture in T/P91 base material), bending (no cracks greater than 3 mm in each direction after 180° bending), hardness (lower than 350 HV10) and toughness (minimum 27 J at room temperature).

The lowest hardness, 206 HV10 for the GTAW and 203 HV10 for the SMAW joint, was found in the fine grained HAZ of T/P91 and the weld metal mean hardness was respectively 280 HV10 and 297 HV10.

The weld metal and heat affected zones showed no delta-ferrite, due to dilution with the 9%Cr steel, and good impact toughness. In the weld metal of the TIG welded joint a very good toughness (70 J / 63 J / 67 J) was found compared to the homogeneous joint welded with the same parameters. For the SMAW welded joint the impact toughness is still low (41 J / 38 J / 37 J), but sufficient according to the PED.

4.2. Conclusions

- ***The GTAW, SMAW and SAW homogeneous welds fulfilled the strength, bending and hardness requirements. Low impact toughness is found in the weld metal (average below 40 J).***
- ***The GTAW and SMAW heterogeneous welds to T/P91 fulfilled the strength, bending, hardness and toughness requirements.***
- ***The chemical composition of the weld metal and the welding parameters determine the delta-ferrite content in the weld metal after welding. Delta-ferrite in the weld metal is responsible for the scatter in impact toughness. Lower bound values can be found due to the presence of delta-ferrite.***
- ***In general, increasing heat input and preheat temperature cause a reduction in weld metal delta-ferrite level. On the other hand, the heat input must be limited to avoid grain coarsening and low impact toughness in the coarse grained heat affected zone.***
- ***Welding with a preheat between 200°C-250°C for the tubes, 250°C for the pipes is preferred, and a heat input between10kJ/cm and 18 kJ/cm is recommended.***

5. Creep test results

Uniaxial, isostress creep rupture tests on VM12 pipe base material and the welded pipe joints were performed by Laborelec. The specimens with a diameter of 5 mm were machined at the outside surface from the 35 mm thick pipe and crossweld specimens were taken out for the pipe joints The specimens were heated up to the selected test temperatures in the range 650-720°C and a constant load was applied corresponding to an initial stress of 78 MPa. The time to rupture was measured and for the pipe joints the location of fracture was determined by metallographic examination.

5.1. Test results and discussion

The isostress test results can be found in figure 6 and were used for extrapolation towards a temperature of 625°C. An extrapolation up to three times the longest testing time is generally allowed.

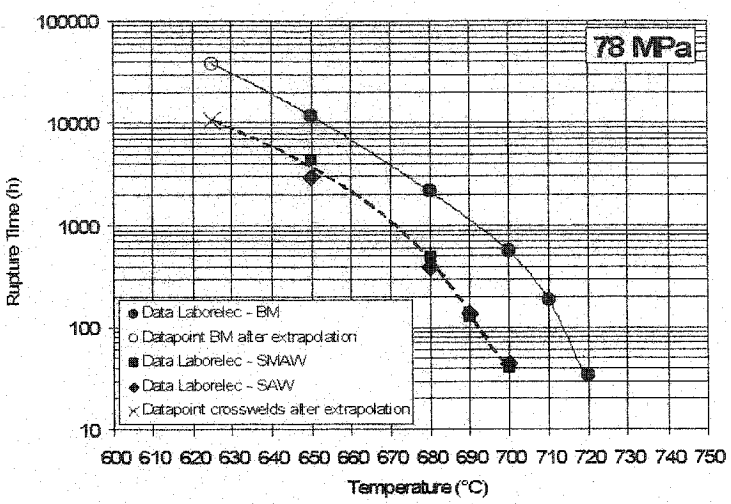

Figure 6: Isostress creep data (78 MPa) of VM12 base material and pipe cross welds

The creep rupture strengths are compared with creep data from Vallourec & Mannesmann and the specifications for E911 (ECCC 2005) in the isotherm diagrams in figure 7 and 8. A scatterband of 20% is assumed on the VM12 and E911 data.

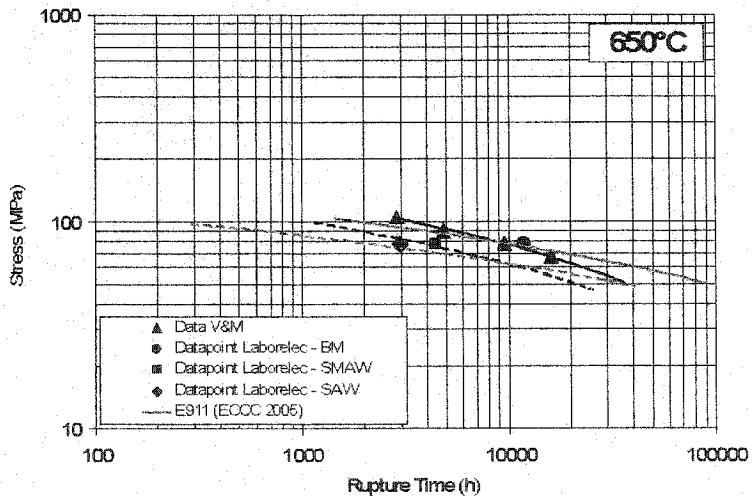

Figure 7: Isotherm creep data (650°C) of VM12 base material and pipe cross welds

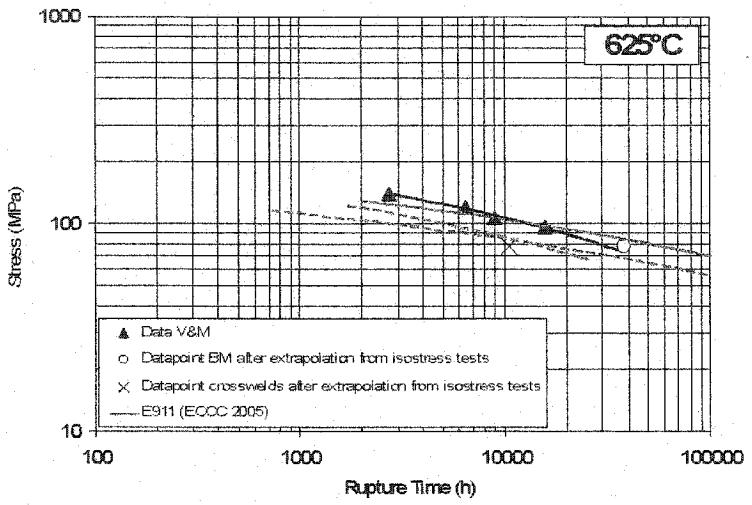

Figure 8: Isotherm creep data (625°C) of VM12 base material and pipe cross welds

Test results on base material confirmed the creep results from Vallourec & Mannesmann It can be seen that the creep rupture strength of VM12 at 650°C is close to the mean value of E911 and lies within the scatterband of E911 at 625°C.

The crossweld creep specimens have lower creep rupture strengths than the base material and specimens broke in the small, soft, fine grained heat affected zone close to the base material (InterCritical HAZ – 'Type IV' zone), which is also the case in other ferritic/martensitic steels like E911. At 650°C, the creep rupture strength of both welds is within the scatterband of the E911 base material, near the scatterband of VM12 base material. The rupture strength of the IC-HAZ at 625°C as obtained through extrapolation from the rupture times of the welded joints falls outside the scatterbands.

5.2. Conclusions

- ***The creep rupture strength of VM12 lies within the scatterband of E911(ECCC 2005).***
- ***Welding resulted in a creep strength loss for the VM12 crosswelds with ruptures occurring in the IC-HAZ ('Type IV' zone).***

Acknowledgements

The authors would like to thank the Federale Overheidsdienst Economie, KMO, Middenstand en Energie and WTCM for their financial support of the prenormative research project. Also the industrial partners are gratefully acknowledged: Carnoy Industrial Piping, Cockerill Mechanical Industries, Fabricom, Stork Mec, Böhler Thyssen Welding Germany, Vallourec & Mannesmann Tubes, AIB Vinçotte, VCL, Tractebel and WTCM.

References

[1] Gabrel J, Bendick W, Vaillant JC, Vandenberghe B, Lefebre B.
VM12 – A new 12Cr steel for boiler tubes, headers and steam pipes in ultra supercritical power plants.
EPRI fourth International Conference on Advances in Materials Technology for Fossil Power Plants. October 26-28, 2004, South-Carolina.

[2] Vandenberghe B, Gabrel J, Vaillant JC, Lefebvre B.
Development of a new 12%Cr-steel for tubes and pipes in power plants with steam temperatures up to 650 °C.
Journées d'Etudes Européennes sur les Equipements sous Pression. Paris 28,29 and 30 Septembre

EXPECTED CREEP LIFE OF WELDED 9-12% CR STEELS

Pertti Auerkari, Stefan Holmström, Jorma Salonen

VTT, Espoo, Finland

Abstract

The damage mechanisms affecting engineering steels at high temperatures include creep cavitation and cracking that can form the path for final failure in susceptible locations such as welds. The useful experience of the in-service damage is not readily available from the newer heat resistant 9-12% chromium steels that are used in hot steam lines of power plants.

Inspection experience shows very modest creep cavitation in the conventional 11% Cr steel X20CrMoV11-1 (X20) even after long term service. This is of interest because early creep failures have been reported from high temperature components of X10CrMoVNb9-1 (P91), a newer martensitic high chromium steel.

Assessments of cross-weld creep rupture data of some 9% Cr steels suggest that the weld strength can fall below the traditionally assumed 80% of the parent material level, at least at the high temperature end of the testing range. This can result in non-conservative (too long) predicted creep life for structures subjected to significant loading across the welds. For robust modeling of creep rupture strength of welds, two new procedures are proposed using the parent material master curve as a baseline. The first approach, or rigidity parameter correction (RPC), is designed to suit for small data sets, and is always conservative by nature. The second method, called logistic prediction (LP), accepts the apparent sigmoidal behaviour from the transition of failure location in welds, and is less conservative in extrapolation. Both procedures can be used to predict cross-weld rupture strength and weld strength factors (WSF) from any type of parent material master curve. These procedures can be used to predict WSF for design and life assessment purposes.

Keywords: creep, weld, steel, strength, life

1. Creep damage in high chromium steels

Creep cavitation and subsequent cracking can limit component life when such damage gradually forms the path of final failure. The bright side of the damage is that the observed extent of it can also be used to indicate the material condition in the in-service inspections, particularly for welds that are common weakest links in creep. As a result, in-service inspections can be safely limited to a small fraction of a large structure such as pipework between boilers and turbines, and the inspection experience has facilitated guidelines on setting safe inspection periods [1]. However, such experience is not available for new materials that may deviate from the usual course of creep damage evolution.

In addition to creep cavitation and cracking, high temperature damage involves parallel effects of other mechanisms such as creep straining, strain-dependent damage (e.g. softening), thermal degradation as microstructural changes, and related redistribution of constitutive elements and phases. However, although creep cavitation and cracking only represent a part of the total damage, creep cavitation also to some extent reflects the impact of other mechanisms that are weakening the material.

Unfortunately, plant service-like creep cavitation damage can be tedious to reproduce in the laboratory. This is particularly true for steels with good creep ductility, such as low-alloy steel 10CrMo9-10 (P22) or many higher alloyed 9-11% Cr steels including X20CrMoV11-1 (X20),

X10CrMoVNb9-1 (P91), X11CrMoWVNb9-1-1 (E911) and P92 (NF616). Consequently, characteristic signature of creep damage is normally obtained from long-term service experience in plant. This is inconvenient for relatively new materials for which there is no long term testing data or service experience.

An example of observed in-plant creep damage in steel X20 is shown in Fig 1. This is a relatively rare case in this steel, where inspections usually show little or no indications of cavitation damage.

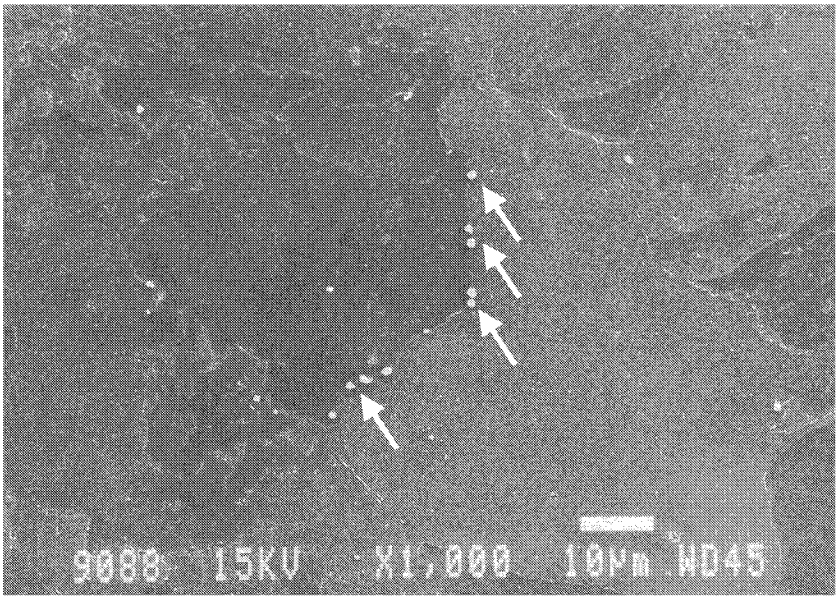

Fig 1. Example of in-service (>100 000 h) creep cavitation damage (arrows) in an X20 steam line, observed from a surface replica of a branch weld.

There are some peculiarities in the observed in-service damage of 9-11% Cr steels. While the creep cavitation damage is easily found particularly in the welds of vintage steam systems made of low alloy steels, the same is not true for components or welds made of X20. In general, the service and maintenance experience suggests that this steel performs extremely well [2,3]. Much of the reported creep damage in this material is most probably due to misinterpretation due to incorrect etching in replica inspections [4]. Although some plants where X20 is used in headers, steam lines and turbine parts have exceeded a service time of 200 000 h, lack of damage and creep cracking means that it is still somewhat unclear how long would be the actual technical lifetime for these components.

Lack of definite cavitation damage in the welds of X20 after long term service appears somewhat surprising, as recent reports suggest that relatively early creep damage is possible in welds of P91 [5]. Both steels belong to the same general class of ferritic steels, first heat treated to martensitic state and then tempered to the required level of mechanical properties, and with a significant contribution of precipitate strengthening by carbides and carbonitrides.

From design point of view, the actual creep life should not be very much materials dependent for a given design life, because the design aims to compensate for the materials properties. When this is not the case, either some of the materials properties are not as expected or there is other bias in the features that determine the actual creep life. The steel X20 was introduced nearly half a century ago, and with generally good results until present. It could be seen a little disappointing if a comparable relative performance were not provided by newer steels like P91, first introduced some 30 years later. Since the alloy design is comparable, the differences could also imply early creep failures in steels like E911 and P92, for which even less service experience is available.

2. Design aspects of steels subjected to long term creep

For common steels intended for high temperature service, characteristic creep strength values are given in public standards and guidelines (Fig 2). The creep strength indicated by e.g. EN 10216-2 is considerably higher for P91 than for X20, which itself once was at least a similar improvement to the low alloy steel 14MoV6-3 (0.5CMV).

The differences between steel types are also reflected in the maximum allowed service temperatures. For example, X20 has been applied to steam temperatures up to about 560-565°C, and P91 in newer plants slightly higher, up to about 570-580°C. The actual service temperatures are usually somewhat lower for both steels, typically in the range 500-550°C. This is often because of other design limits, such as the limited inlet gas temperatures in HRSG's, hot corrosion limits in biomass and process boilers, or other conservatism in process design. Even if such factors were not specifically considered, the temperature difference between systems made of X20 and P91 is only partly due to the limits in material strength. Another reason is related to design codes and design practices, resulting generally in somewhat lower temperatures in the geographical regions where X20 has been used for otherwise similar plant.

More detailed differences can be seen in the chemical composition: X20 has higher carbon content than P91 and no specified nitrogen, with resulting differences in the composition of MX precipitates. Higher carbon content in X20 also results in higher martensite hardness and lower toughness before tempering, though this is an issue for manufacturing rather than for in-service properties. X20 may be somewhat less sensitive than P91 to deviations in heat treatment, but requires more care in welding in both original fabrication and repairs. Additional scatter factors can be expected e.g. from variations in section thickness or production via rolling, drawing, forging, casting etc.

Comparing the long-term (200 000 h) creep rupture strength of different 9-11% Cr steels (Fig 2) shows that at the usual levels of service temperatures the relative improvement from X20 to P91 is roughly similar as was the improvement from the traditional low-alloy steels to X20. However, the relative improvement from P91 to newer steels like P92 is less impressive. Particularly small difference now appears between P91 and E911.

As noted above, the plant experience with the X20 steel has been excellent. The reasons are probably at least partly due to relatively low service temperatures and often also low stresses in comparison with the allowed maximum levels. However, there are also other factors

involved, as can be seen from Figs 3 and 4. For this purpose, the relative 200 000 h creep strength ratio sr is here defined as

$$sr = \frac{R_{u/200kh/T}(material)}{R_{u/200kh/T}(P22)} \tag{1}$$

This ratio describes the relative 200 000 h rupture strength of the steel to be compared, in relation to the corresponding 200 000 h creep rupture strength of steel P22. The 200 000 h values are here selected because they are likely to be closer to actual service life than the 100 000 h values which were common design basis for plants that are now or soon retiring, and utilizing steels like P22 and/or X20.

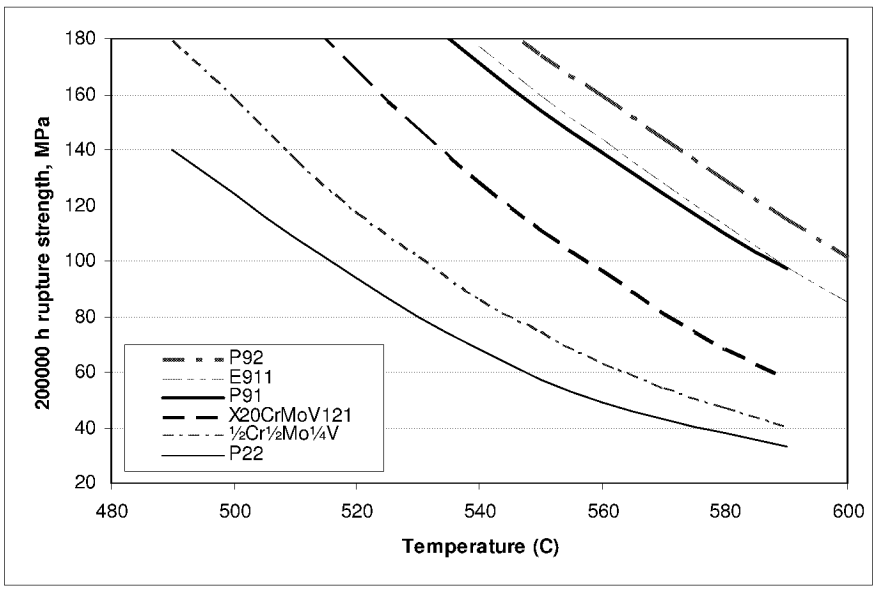

Fig 2. Comparison of the 200 000 h creep rupture strength of selected 9-11% Cr steels according to EN 10216-2 and ECCC data sheets; also the corresponding strength values of the low-alloy steels 0.5CMV(½Cr½Mo¼V) and P22 are shown.

Fig 3 shows for the steels of Fig 2 the relative improvement in 200 000 h rupture strength from the corresponding strength of P22, as a function of temperature. This creep strength ratio essentially shows the improvement due to precipitate strengthening, suggesting for example that the improvement in 0.5CMV is practically constant by a factor of about 1.2-1.3, independent of temperature. In case of X20, the relative improvement factor is between 1.5 and 2.0. However, for X20 the ratio is less constant and shows an apparent maximum at about 550-560°C, decreasing slightly towards both lower and higher temperatures. Remarkable features in case of the 9% Cr steels P91, E911 and P92 are not only the large values of the creep strength ratio but also its increasing trend towards higher temperatures, to values of about 3 or even higher.

The high values of the creep strength ratios for the newer steels imply a high potential loss in creep strength, if the intended precipitation hardening is not achieved in manufacturing (heat treatments) or is lost by in-service degradation. The resulting adverse consequences for materials such as P91 can therefore be expected to be much more pronounced than for steels with lower strength ratios, like X20. As the difference in these ratios between P91 and X20 is clearly increasing with temperature, the problems could be exacerbated for P91 or other newer steels if used at the high end of the service temperature range.

This reasoning is roughly in line of the concept of "inherent creep strength", which implies that the asymptotic very long term creep strength would be mainly due to solid solution strengthening by elements such as Mo and W, when all contributing particles have been precipitated and coarsened [6].

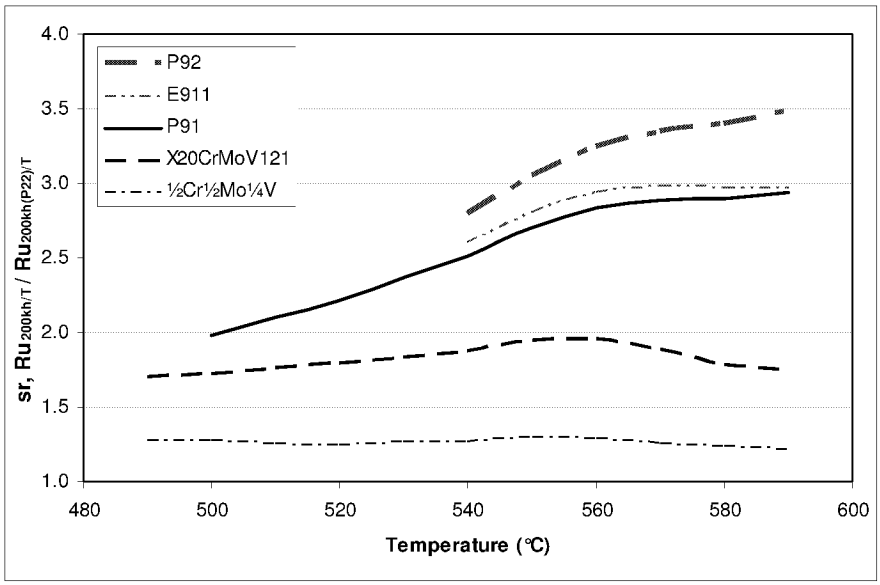

Fig 3. The 200 000 h creep strength ratio for the steels of Fig 2, using the rupture strength of P22 (10CrMo9-10) as a baseline for the comparison.

It can also be noted that at temperatures above 570-580°C only for P91 and P92 the creep strength ratios appear to be still increasing. Even for the steel E911, for which there is a recent updated assessment of recommended creep strength values by ECCC, the ratio appears to be leveling off for increasing temperatures. It could perhaps be speculated whether future reassessments of longer term test data of P91 and P92 might change this situation.

It is an unfortunate but common feature in the development of new steels and materials standards that the early recommended values of creep strength tend to be somewhat overly optimistic, requiring downward correction in later amendments. This was the case for nearly all low alloy steels and has been also seen for E911, for example. Apparently the past or current assessment methods are not able to fully accommodate the degradation mechanisms

that are affecting the long-term mechanical properties, when extrapolated beyond the range of uniaxial rupture data. Such non-conservative assessment results can be also expected for the new steels. In Fig 3, the 200 000 h creep strength values for P91 are from extended extrapolation (by a factor > 3 in time), and therefore changes would not be unexpected in later reassessment of longer term data.

Here the nominal "time safety margin" or design life ratio dlr without additional safety factors is defined as an isothermal time factor as follows:

$$dlr = \frac{t_{u/0.8\cdot\sigma(200kh)/T}}{200kh} \tag{2}$$

where $t_{u/0.8\cdot\sigma(200kh)/T}$ is the predicted rupture time at 80% of the 200 000 h rupture stress.

Fig 4 gives this time factor as a function of temperature for the same steels as Figs 2 and 3. It is apparent that the steels fall into two distinct groups. The low-alloy steels and X20 form here one group, with a dlr ≈ 2 - 4 at temperatures above 510°C. The second group includes the 9% Cr steels P91, E911 and P92, for which dlr is much higher and strongly increases with decreasing temperature (Fig 4).

The higher values of dlr for P91, E911 and P92 than for X20 would suggest higher inherent safety margins for the 9% Cr steels, which as intact material should perform well. However, this could be more than compensated for, should the creep strength of the 9% Cr steels collapse due to lacking precipitate strengthening. Such a collapse would have less drastic effects on X20, which is in this respect more comparable to the low alloy steels.

Welds of classical steels tend to show cross-weld rupture strength reduced by about 20% from the level of the parent material. For newer 9% Cr steels, higher strength reduction appears possible. However, the additional strength reduction could mainly apply to the high temperature end of the application range, and for many applications the classical 20% rule would still work reasonably well. As long as creep failure of welds remains in the heat affected zone or parent material, the above reasoning would largely apply to welds as well.

3. Prediction of weld strength factors (WSF)

In general the weld creep strength factor (WSF) is defined according to ECCC recommendations [7] as

$$WSF = \frac{R_{u(W)/t/T}}{R_{u/t/T}} \tag{3}$$

where $R_{u(W)/t/T}$ is the rupture strength of the weld at specified time and temperature, and $R_{u/t/T}$ is the corresponding strength of the parent material at the same time and temperature.

Fitting the cross-weld rupture data to a range of different models and then selecting the "best" model according to these fitting results can lead to problems when predicting WSF. If the resulting model is different from that for the parent material, differences in the extrapolated predictions can accumulate due to the differences in the mathematical expressions, rendering predicted values of WSF even more uncertain than the predictions on rupture strength (Fig 5). The problem is often amplified by relatively small data sets on welds, and shorter maximum testing time than for parent material. Therefore it would be best to apply similar models for welds and parent material, and this also could be otherwise justified when the welds fail in the HAZ, i.e. in the parent material with only microstructural deviation from the unaffected parent material.

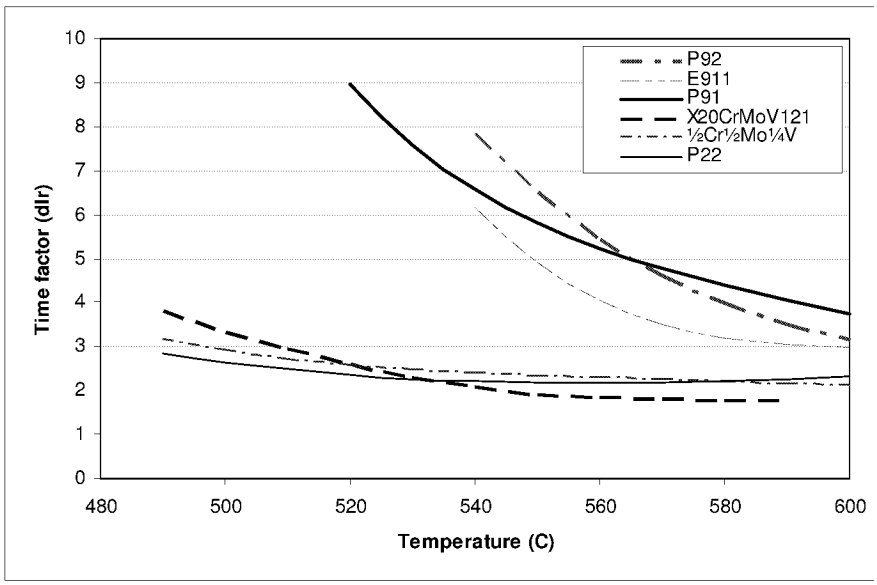

Fig 4. Nominal design life ratios (time factors, dlr) for the same steels as in Fig 2.

Applying this principle, methods have been developed for predicting creep strength values for welded 9% chromium steels. The methods are here demonstrated for P91. The methods include the rigidity parameter correction method (RPC) and the logistic prediction method (LP) [8-10]. Both methods are tools for modifying the master curve of the parent material to represent the cross-weld creep rupture data, aiming to counter the typical problems of mismatching and small data sets in case of cross-weld testing.

The RPC is defined as follows:

$$\log(tr_R) = \frac{\log(tr_m) - \log(t_p)}{1 + R \cdot (\log(tr_m) - \log(t_p))} + \log(t_p) \tag{4}$$

where R is the rigidity parameter, tr_m is the time to rupture in parent material (model), tr_R is the predicted time to rupture of the weld, and t_p is the pivot point in time. In Fig. 5 the calculated WSF curves are presented using a traditional master curve CW assessment. The model mismatch can be seen as WSF curve cross-over. In Fig. 6 the RPC correction has been applied to the same data as in Fig 5.

The LP approach, which assumes sigmoidal behaviour of the cross-weld data, is defined through a parametric reduction so that

$$LP(LMP) = \left(\frac{1-L}{1+(\frac{LMP}{x_0})^p} + L \right) \cdot \sigma_{PM} \tag{5}$$

where tr is time to rupture for the weld, T is temperature (K), σ_{PM} is the stress to cause a rupture in the parent material at time tr predicted by the parent material master curve, LMP is the Larson-Miller expression for temperature compensated time, and L, x_0, p and C are fitting constants. The resulting predicted WSF for P91 is shown in Fig 7.

The predicted WSF values using the three different approaches, direct independent fitting to cross-weld data (master), RPC and LP methods, are shown for 600°C and 650°C in Figs 8 and 9.

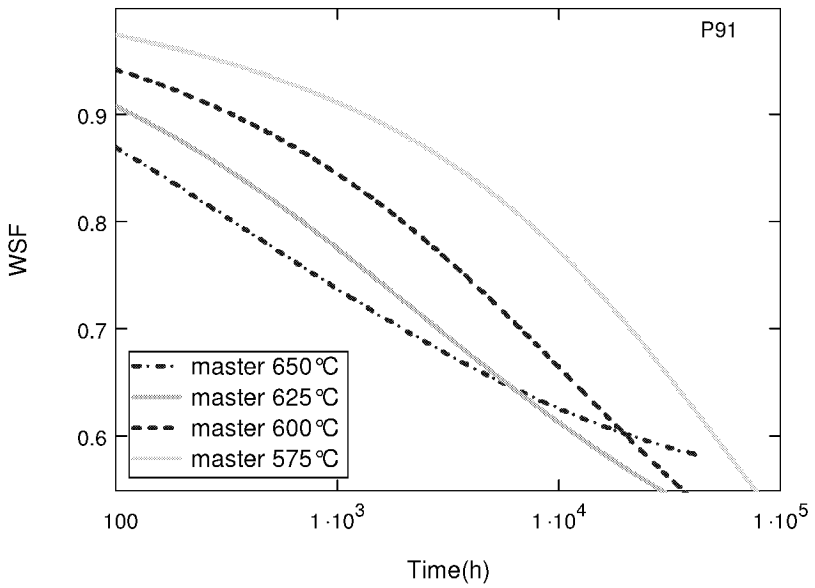

Fig. 5. WSF of P91 showing the effect of mismatching models of PM and CW data.

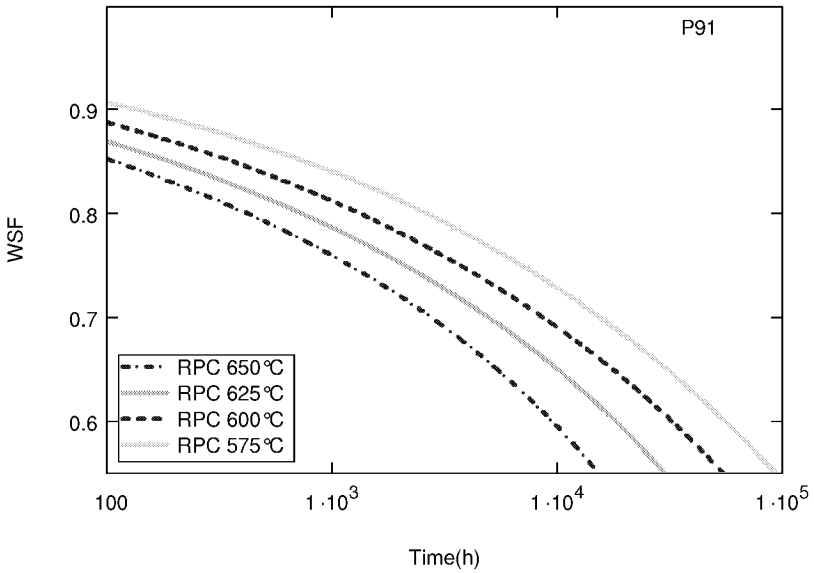

Fig. 6. WSF for P91 steel using the RPC approach.

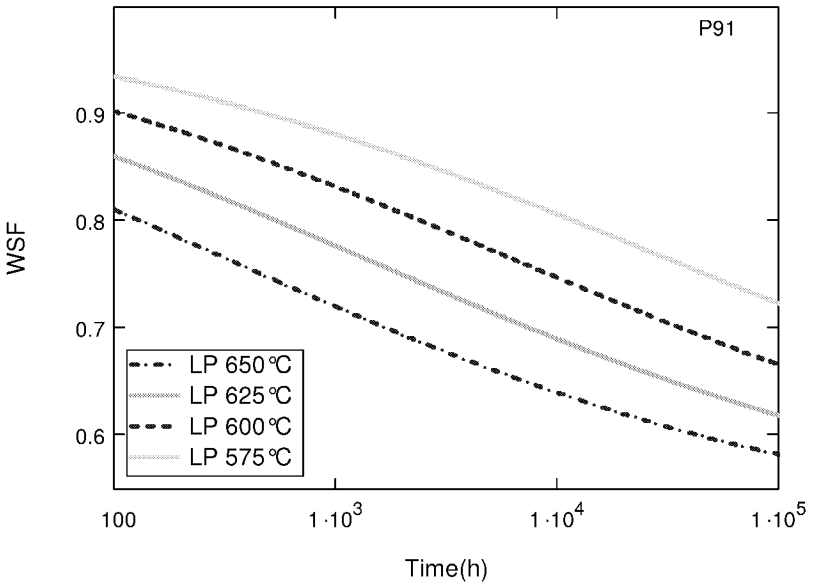

Fig. 7. WSF for P91 steel using the LP approach.

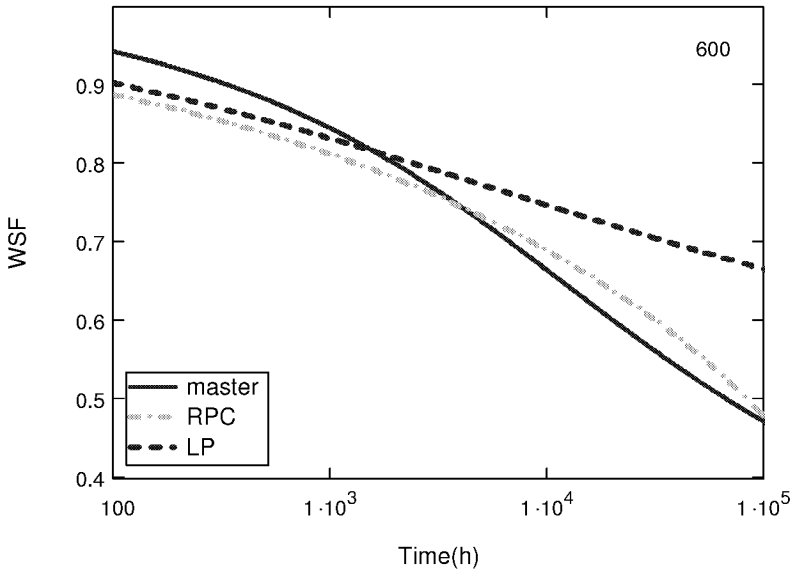

Fig. 8. Comparison of WSF for P91 steel using independent fitting (master) and RPC and LP approaches at 600°C.

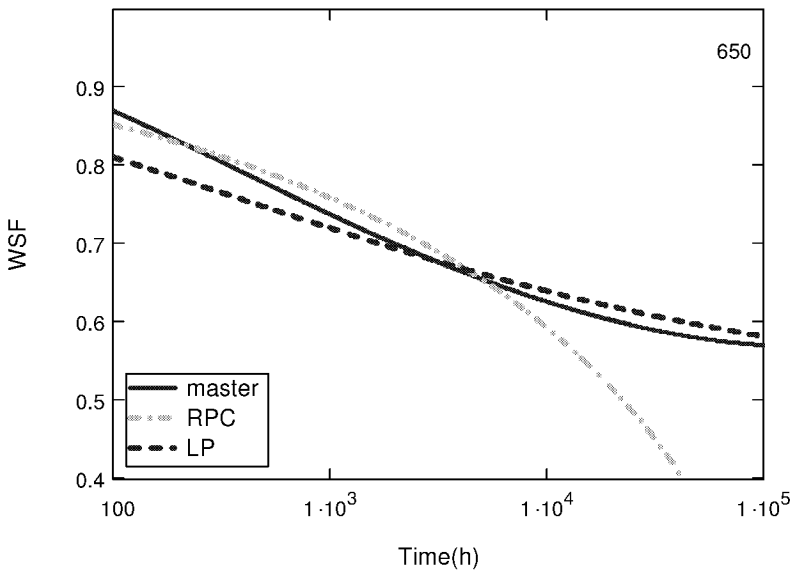

Fig. 9. Comparison of WSF for P91 steel using independent fitting (master) and RPC and LP approaches at 650°C.

4. Discussion and conclusive remarks

Creep damage is unavoidably inflicted to materials at high temperature, and reflected as limited life and gradual degradation of material properties. Creep damage can also be used as a monitoring tool, when experience on damage accumulation is available. This approach is widely applied for low-alloy steels and their weldments. However, the service history of most 9-11% Cr steels is much shorter, particularly for newer steels. The inspection experience suggests that the only vintage steel in this class, X20, shows slower damage accumulation than conventional low alloy steels, and records of creep failures are rare even after long term service. The reasons of good performance are of interest also for plants where this steel is replaced by P91 that has reportedly shown early creep failures.

To check for the potential for creep cavitation damage, a relatively convenient technique has been developed using high tensile multi-axiality for damage acceleration [2,11,12]. The method appears particularly useful for the new and relatively ductile 9% Cr steels, where creep cavitation may develop only slowly and where no in-service inspection results can be used to support life assessment.

The relative extent of the applied precipitation strengthening, combined with modest design temperatures, may explain much of the excellent service records of plants where X20 has been used in the steam systems. Similar examination suggests a relatively higher potential of strength loss in 9% Cr steels like P91, if the intended precipitation strengthening is lost. Fortunately, also a significant fraction of P91 applications do not fully utilize the capability of the material, and this will reduce the potential impact of e.g. deviations in heat treatment.

The recently developed RPC and LP approaches can be used on any parent material creep rupture model to obtain predictive models for cross-weld strength and weld strength factors (WSF) of the same material. The RPC modification will force the curvature of the parent material master curve to fit the weld data by finding a pivoting point and reducing life after this point, whereas the LP approach assumes a sigmoidal behaviour for the welds. In the example cases of cross-welded P91, the predicted WSF curves are smooth with isotherms that do not cross as can happen with independently assessed cross-weld master curves. Both methods have good potential for reducing the mismatching effect in WSF assessment.

Examples of obtained WSF values for the steel P91 at 600°C are shown in Table 1, using LP, RPC and independently evaluated models (master curves) for cross-weld data. For this isotherm the differences are not very large between the independent and RCP methods, but the LP approach will pick up the high temperature indications of the transition in failure locations and predicts higher (less conservative) values of WSF.

In comparison with traditional evaluation of cross-weld and parent material rupture data to obtain WSF, the RPC and LP methods have several advantages. First, no independently assessed cross-weld master curve is needed for WSF evaluation. Only a small number of fitting constants (2 for RPC and 4 for LP) are needed in addition to the parent material master equation. Also, smooth WSF isotherms are guaranteed without cross-over or turn-back, and less cross-weld data are required than in traditional independent assessment. The LP approach has particular additional advantages, as it can accommodation the (sigmoidal) transition of failure locations in welds, and is inherently less conservative than RPC.

Table 1. Predicted WSF at 600°C using three different approaches for cross-welded P91

HAZ failure time	WSF (600°C)		
	Independent	RPC	LP
30 000 h	0.56	0.60	0.71
100 000 h	0.47	0.48	0.67
(200 000 h)	(0.43)	(0.38)	(0.65)

References

1. Auerkari, P., Salonen, J. & Borggreen, K. Guidelines for evaluating in-service creep damage. Nordtest TR 302, 1995. VTT, Espoo, 24 p.
2. Bendick, W., Hahn, B. & Schendler, W. Development of creep damage in steel grades X10CrMoVNb9-1 (P/T91) and X20CrMoV12-1. 9th Int. conf on Creep and Fracture of Engineering Materials & Structures, Swansea 1-6 April 2001.
3. Storesund, J., Borggreen, K., Zang, W., Nilsson, H. & Samuelson, Å. Creep damage in welds of steel X20CrMoV121 (in Swedish). Värmeforsk Rep. 874, Stockholm 2004. 20 p.
4. Borggreen, K. Storesund, J. Creep behaviour of welds in X20 CrMoV 12 1 evaluated from replica inspection results. Proceedings of Baltica VI – Int. Conf. on Life Management for Power Plants. Helsinki-Stockholm 2004. Vol 2, p. 449-463.
5. Brett, S. J., Bates, J.S. & Thomson, R.C. Aluminium nitride precipitation in low strength Grade 91 power plant steels. 4th EPRI Int Conf on Advances in Materials Technology for Fossil Power PlantsOct 26-28, 2004, Hilton Head Island, S.C. 15 p.
6. Kimura, K., Kushima, H. & Abe, F. Degradation and assessment of long-term creep strength of high Cr ferritic creep resistant steels. Proc. Of the EPRI Int. Conf. on Advances in Life Assessment and Optimization of Fossil Power Plants. EPRI 2002.
7. ECCC Recommendations, 2003. Volume 2 Part 2b [Issue 2], Terms and terminology for weld creep testing .
8. Holmström, S, Auerkari, P. 2005. Effect of short-term data on predicted creep rupture life, pivoting effect and optimized censoring. International Conference on Creep & Fracture in High Temperature Components – Design and Life Assessment Issues. London.
9. Holmström, S., Auerkari, P., 2005, Predicting weld creep strength reduction for 9Cr steels, International Conference WELDS 2005, Geestschacht.
10. Holmström, S. Auerkari, P. Enhanced weld creep strength modeling based on parent material master curves, International Conference OPE 2006, Chennai 7-9.2.2006.
11. Rantala, H., Hurst, R.C., Auerkari, P., Bendick, W., Holdsworth, S.R. & Nikbin, K. Predicting long term creep behaviour using the LICON methodology. 9th Int. conf on Creep and Fracture of Engineering Materials & Structures, Swansea 1-6 April 2001.
12. Auerkari, P., Holdsworth, S.R., Rantala, J.H., Hurst, R., Coussement, C. & Hack, R. Modelling the development of creep damage: the LICON experience. Proceedings of Baltica V: Int. Conf. on Condition and Life Management for Power Plants, Porvoo, Finland, 2001. Vol 2, p. 609-620.

STUDY OF THE SIMULATED HAZ OF A BORON ALLOYED CREEP RESISTANT 9% CHROMIUM STEEL

Peter Mayr and Horst Cerjak

Institute for Materials Science, Welding and Forming
Graz University of Technology
Kopernikusgasse 24, 8010 Graz, Austria
Email: peter.mayr@tugraz.at

Abstract

A basic study on the weldability of a boron alloyed advanced 9% Cr steel was performed applying the so-called 'Heat Affected Zone Simulation' technique using a Gleeble 1500 thermo-mechanical testing machine. Changes in the microstructure and in the materials properties of the HAZ were examined, before and after a postweld heat treatment (PWHT) of 730°C for 12 hours by applying light-microscopy, scanning electron microscopy (SEM), different methods of analytical transmission electron microscopy, hardness measurements and Charpy-V notched bar impact tests. The microstructures at representative points during a typical welding cycle and ensuing post-weld heat treatment were studied in detail. The evolution of precipitates during a characteristic welding cycle and subsequent PWHT was observed, showing the complete dissolution of all precipitates during the weld thermal cycle and re-precipitation during the PWHT. Delta-ferrite formation was observed for welding cycles with high enough peak temperatures causing retained delta-ferrite in the material after PWHT.

Keywords: 9 Cr steel, boron alloyed, microstructure, delta-ferrite, HAZ-toughness

Introduction

Within the last decades worldwide, increased R&D effort was put into the development of advanced creep resistant 9-12% chromium steels. These steels are strongly required for the construction of critical components of coal fired power plants operating at much higher efficiencies than the current generation of supercritical plants. This increase in efficiency is mainly driven by the use of ultra supercritical steam conditions (USC). Within research programs in the USA, Japan and Europe, several types of creep resistant martensitic 9-12% chromium steels have been developed and brought into service. These steels are capable of live steam temperatures up to 600°C and a steam pressure up to 290 bar [1]. Welding is the most important joining process for these components. Research [2,3] and in-service experience [4] have shown that the heat affected zone (HAZ) of weldments is often the weakest part in these constructions. Microstructural changes within this zone caused by the influence of the weld thermal cycle lead to inferior mechanical properties of this zone compared to the base material. Reduced toughness values generated by the formation of a brittle and coarse grained microstructure and accelerated pore formation in softened regions after welding and subsequent post-weld heat treatment (PWHT) often result in a final fracture in the HAZ [5]. The method of thermo-mechanical simulation is widely used to generate the microstructure of the different parts of the HAZ and subsequently investigate these microstructures metallographically and by mechanical testing. In this work, apart from conventional investigation methods, also advanced electron microscopy methods were utilised. All work performed should lead to a better understanding of the complex processes

taking place in the HAZ during welding and subsequent PWHT and their effects on the mechanical properties.

Experimental

Material

For this investigation a 100 kg test melt of a modified steel grade X10CrMoVNb9-1 was cast at Voestalpine Foundry Linz, Austria. The chemical composition of the test melt "CB2A" is similar to a forged rotor steel designated "B2" developed within the framework of the European COST 501 programme, which showed a good combination of strength and toughness. The results of creep tests running up to 90.000 hours are very promising and allow a prediction of the 100.000 hours creep rupture strength at 600°C of about 120 MPa [6]. Table 1 shows the chemical composition of both steels.

Table 1: Chemical composition of steels.

wt%	C	Si	Mn	Al	Cr	Mo	Ni	V	Nb	B	N
B2	0.170	0.07	0.06	0.016	9.34	1.55	0.12	0.27	0.063	0.0100	0.0150
CB2A	0.168	0.23	0.22	0.003	8.85	1.54	0.18	0.29	0.057	0.0092	0.0161

In the as-received condition, i.e. after casting, austenitization at 1100°C for 8 hours and quality heat treatment at 730°C for 10 hours, the base material of CB2A showed a tempered martensitic cast microstructure with precipitates at the prior austenite grain boundaries and martensite lath boundaries. No delta-ferrite was observed in the base material (see Figure 1).

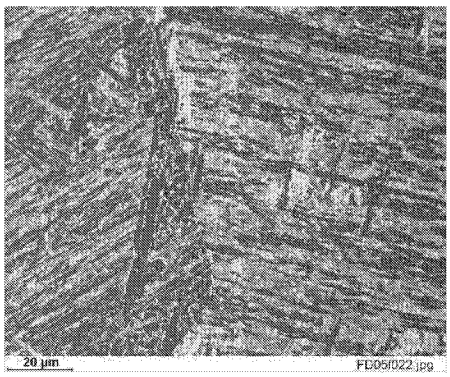

Figure 1: Base material CB2A – as-received condition (etchant LBIII).

Analytical electron microscopic methods like EDX, EFTEM and EELS were used to identify the different precipitate populations and their size distribution. TEM brightfield images and corresponding elemental maps and jump ratio images of the elements Fe, Cr, V, Nb, C and N were taken of CB2A in as-received condition, see Figure 2. The following precipitate types were identified: Cr-carbides (bulky, 100 – 200 nm), V-nitrides (globular, 2 – 20 nm) and (Nb,V)(C,N) precipitates (globular, 30 – 50 nm).

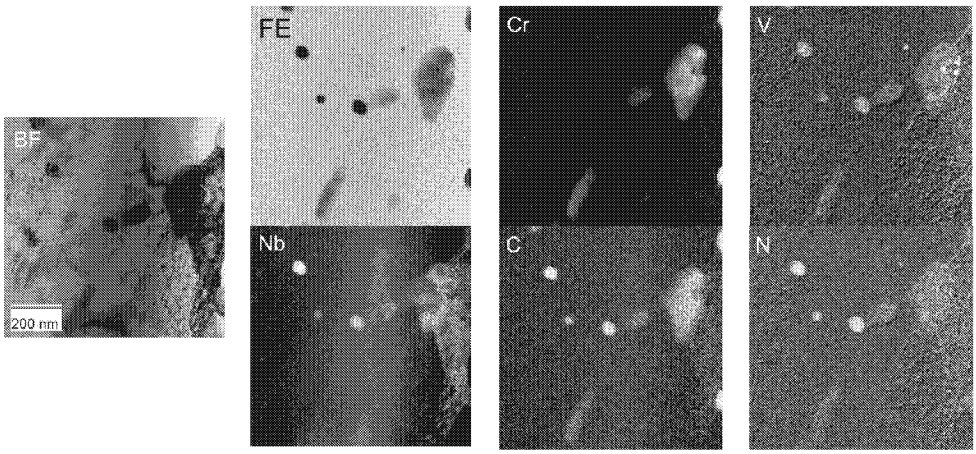

Figure 2: TEM image and elemental maps of base material CB2A (as-received condition).

The transformation temperatures during the welding cycle were determined by dilatometry with 979°C for A_{c1} and 1066°C for A_{c3}. During cooling, martensite formation starts at 380°C [7].

Gleeble simulation

To study the influence of different weld thermal cycles on the microstructure and the mechanical properties, square specimens with dimensions 10 x 10 x 100 mm were used for the thermo-mechanical simulation on a GLEEBLE 1500. Characteristic time-temperature cycles experienced in the HAZ of a submerged arc weld were used for the simulation process. For the simulation of the different regions of the HAZ, single weld thermal cycles with different peak temperatures ranging from 950°C to 1300°C in steps of 50°C and a representative cooling time between 800°C and 500°C – $t_{8/5}$ – of 40 seconds were utilized.
After the weld cycle, a PWHT at 730°C for 12 hours was applied. All specimens went through microstructural examination, hardness testing and micro hardness testing. ISO-V impact testing was performed on the PWHT samples.

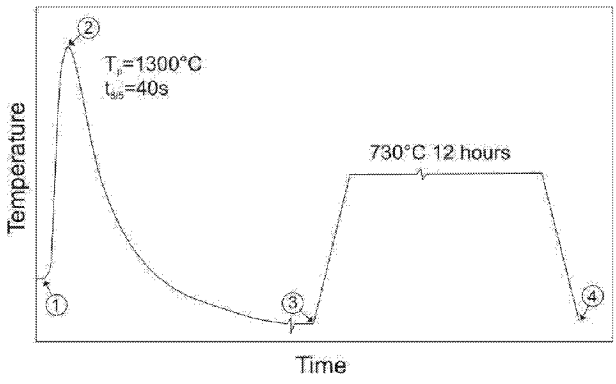

Figure 3: Schematic of thermal history of samples investigated by TEM.

Apart from the as-received condition (Pos. 1), three more material states were chosen for detailed TEM investigations. One sample was quenched after reaching the peak temperature of 1300°C (Pos. 2), one specimen was taken after a welding cycle of T_p=1300°C and $t_{8/5}$=40s in the as-welded condition (Pos.3) and one sample after the subsequent PWHT of 730°C/12h (Pos.4). Figure 3 shows a schematic of the thermal history of the samples investigated by TEM.

Results and Discussion

Microstructural characterisation

Base material, weld simulated specimens and additionally PWHT samples were extensively investigated using light microscopy, scanning electron microscopy and transmission electron microscopy. A combination of these three techniques, covers the entire precipitate size distribution ranging from 2 nm up to the largest precipitates.

Single weld thermal cycle with varying peak temperature

Microstructural investigations were performed on GLEEBLE simulated specimens. After the simulation in the as-welded condition, samples exposed to peak temperatures higher than 1000°C showed a homogenisation of the cast microstructure. Precipitates at martensite lath boundaries started to dissolve at 1000°C.

This finding was supported by analytical Transmission Electron Microscopy (TEM) of sample 2, which was quenched by a water jet at the time reaching the peak temperature of 1300°C. Investigations showed that nearly all precipitates visible in the as-received condition have been dissolved during the heating period of the weld thermal cycle. The only exceptions were fine NbC, where the heating period was not long enough to completely dissolve them (Pos. 2).

Figure 4 shows a TEM image and corresponding elemental distribution maps of Fe and C of the specimen in as-welded condition, sample 3 (T_p=1300°C and a cooling time of $t_{8/5}$=40s).

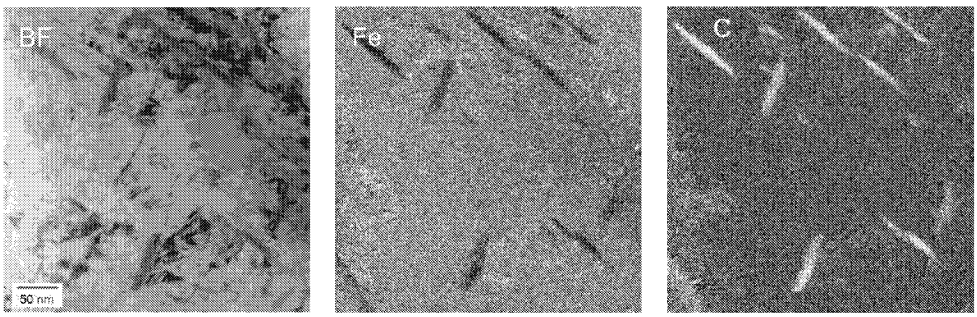

Figure 4: TEM image and elemental distribution maps of sample 3 (as-welded, T_p=1300°C and a cooling time of $t_{8/5}$=40s) showing needle shaped iron carbides.

In the as-welded condition (Pos. 3) all precipitates found in the base material as well as the retained NbC in the quenched specimen have been dissolved. The only newly formed precipitate type were needle shaped iron carbides (Figure 4).

After PWHT at 730°C for 12 hours, the cast microstructure was no longer visible. Precipitate populations similar to those in the as-received condition formed again at prior-austenite grain boundaries and martensite lath boundaries. The iron carbides visible in the as-welded condition dissolved completely during the PWHT.

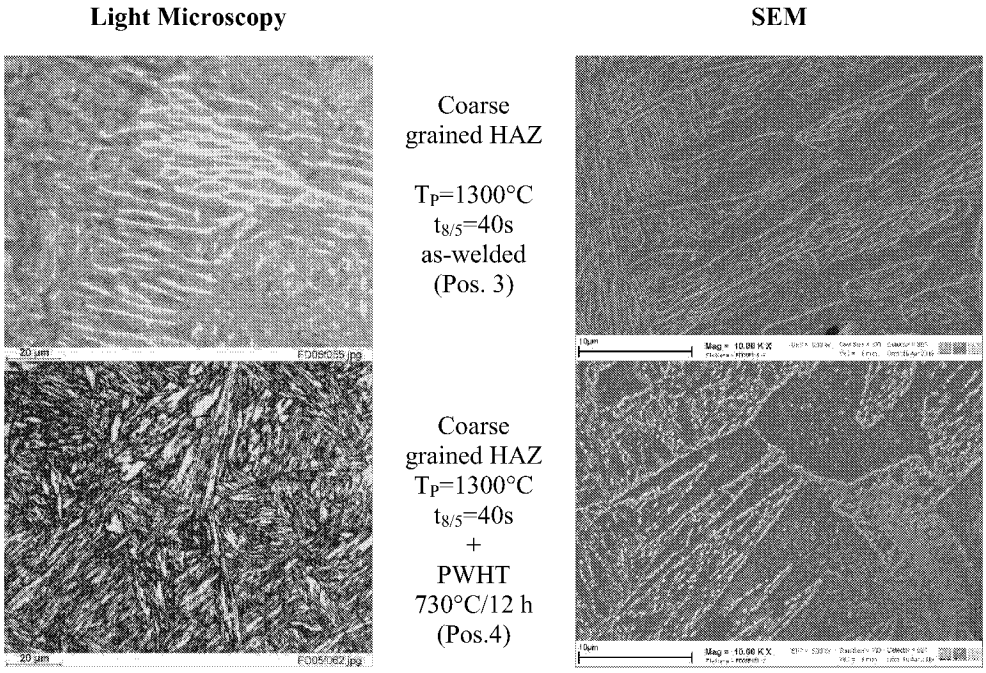

Figure 5: Microstructural characterisation by means of light microscopy and scanning electron microscopy of simulated specimens representing CGHAZ in as-welded (top) and PWHT condition (bottom)

The weld thermal cycles with peak temperatures higher than 1150°C generated a coarse, virgin martensite microstructure because of complete austenitization. Large areas of delta-ferrite occurred in a compact shape in segregated regions as well as in elongated shape between the martensite laths. The compact shape of delta-ferrite occurred at peak temperatures above 1200°C. Delta-ferrite laths in between the martensite laths appeared for the first time at a peak temperature of 1150°C.

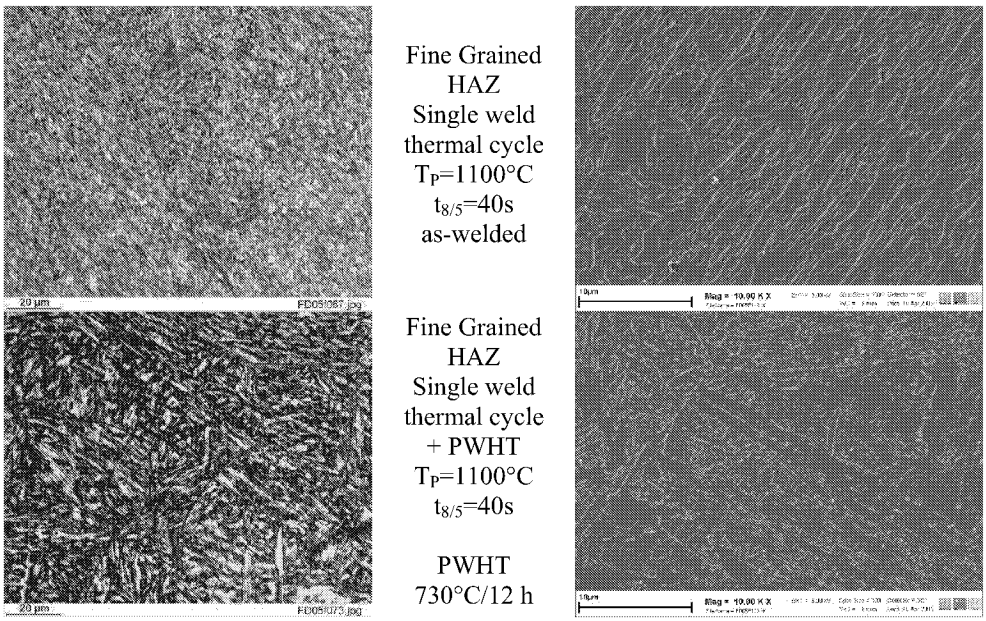

Figure 6: Microstructural characterisation by means of light microscopy and scanning electron microscopy of simulated specimens representing FGHAZ in as-welded (top) and PWHT condition (bottom).

For specimens simulated with peak temperatures higher than 1250°C, after PWHT, precipitates were also identified along and in between the delta-ferrite regions (see Figure 5 bottom).

Mechanical properties

Hardness

CB2A base material shows a hardness of about 250HV10 in the as-received condition. Hardness measurements on samples exposed to single weld cycles with varying peak temperatures revealed a strong increase in hardness for samples exposed to peak temperatures higher than the A_{c1} temperature. The maximum hardness of 513 HV10 was reached at a peak temperature of 1250°C and a cooling time $t_{8/5}$ of 40s. The increase in hardness can be explained by the new formation of untempered martensite by these cycles. Above 1250°C, the hardness dropped to values of 450 HV10, which was a result of the dissolution of existing precipitates at these temperatures.

PWHT of 730°C for 12 hours reduced the hardness of all simulated specimens to the level of the base material or even below for specimens simulated with peak temperatures below the A_{c1} temperature.

Micro-hardness

Micro-hardness measurements in the as-welded and PWHT condition supported the results of the light microscopical investigations. The phase designated as delta-ferrite showed

hardnesses of 130 to 188 HV10p, whereas the martensite exhibited clearly higher hardness values of 370 to 660HV10p (Figure 7) in as-welded condition. The wide range of hardness values for the martensite can be explained by the coexistence of virgin and tempered martensite regions in samples simulated with peak temperatures in between the transformation temperatures A_{c1} and A_{c3}.

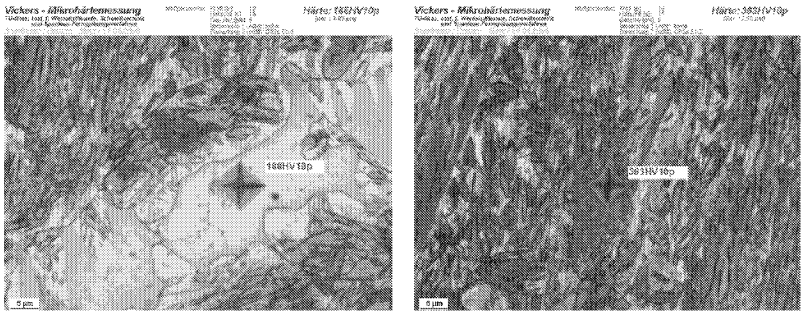

Figure 7: Micro-hardness of 188HV10p in delta-ferrite region (left) and 363HV10p in martensitic region (right) of simulated specimen T_p=1300°C, $t_{8/5}$=40s, as-welded).

ISO-V impact toughness tests

The impact toughness values of the base material at room temperature were in the order of 70 Joules. The impact toughness values of simulated specimens were determined after the PWHT and were in the range of 37 to 100 Joule. Above peak temperatures of 1150°C, the toughness values dropped significantly (see Figure 8). These toughness characteristics can be attributed to a coarse grained microstructure and the appearance of delta-ferrite, which appears for the first time in the peak temperature range of 1150°C to 1200°C. The delta-ferrite fraction rises with increasing peak temperature. The well-known negative effect of delta-ferrite on the toughness is maintained after PWHT [8].

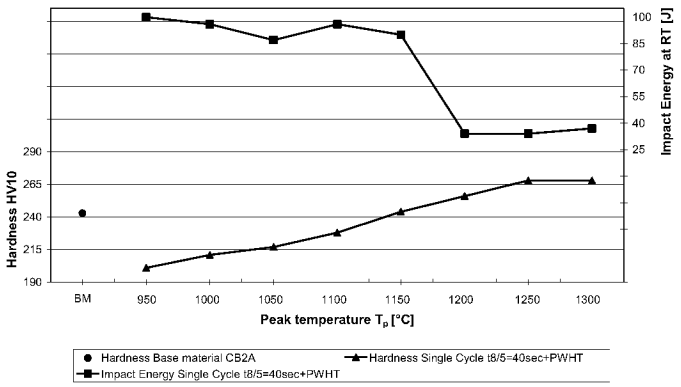

Figure 8: Mechanical properties after single welding cycle with different peak temperatures and subsequent PWHT

Summary

A microstructural study of base material and heat affected zone of a boron alloyed advanced 9% Cr steel was performed applying the so-called 'Heat Affected Zone Simulation' technique using a Gleeble thermo-mechanical testing machine. Hardness and impact testing on simulated specimens gave information about the mechanical properties in the different parts of the HAZ.
Analytical TEM studies at representative points during a characteristic welding cycle and the ensuing PWHT revealed the complete dissolution of precipitates, i.e. Cr-carbides, V-nitrides and (Nb,V)(C,N) during the weld thermal cycle. During PWHT, re-precipitation takes place resulting in a similar precipitate distribution compared to the as-received condition. In specimens simulated with peak temperatures higher than 1150°C, retained delta-ferrite was observed in the as-welded condition. With micro-hardness measurements areas of tempered martensite and virgin martensite could be distinguished, whereas delta-ferrite regions showed a much lower hardness level. A drop of impact energy for samples simulated with peak temperatures higher than 1150°C can be directly attributed to the formation of delta-ferrite. The present study shows that the boron containing steel CB2A has a good weldability.

Acknowledgement

This work was part of the Austrian research cooperation "ARGE ACCEPT – COST 536" and was supported by the Austrian Research Promotion Agency (FFG) which is gratefully acknowledged.

References

[1] Scarlin, B., Kern, T.U. and Staubli, M.: The European efforts in material development for 650°C USC power plants – COST522, Proc. 4th International Conference on Advanced Materials Technology for Fossil Power Plants (2004), pp. 80 - 99
[2] Albert, S.K. et al: Microstructural investigations on Type IV cracking in a high Cr steel, ISIJ International, Vol. 42, No. 12 (2002), pp. 1497 - 1504
[3] Masuyama, F., Komai, N. and Sasada, A.: Creep failure experience in welds of advanced steel boiler components, IIW Doc. XI-795-04 (2004)
[4] Tezuka, H. and Sakurai, T.: A trigger to Type IVdamage and a new heat treatment procedure to suppress it. Microstructural investigations of long-term ex-service Cr-Mo steel pipe elbows. International Journal of Pressure Vessels and Piping, Vol. 82 (2005), pp. 165 -174
[5] Komai, N. and Masuyama, F.: Microstructural degradation of the HAZ in 11Cr-0.4Mo-2W-V-Nb-Cu steel (P122) during creep, ISIJ International, Vol.42, No. 12 (2002), pp. 1364 - 1370
[6] Private Communication, Dr. K. Spiradek-Hahn, Austrian Research Centers GmbH – ARC, 2444 Seibersdorf (2005)
[7] Schalber, E.: Master Thesis, Graz University of Technology, Graz, Austria (1998)
[8] Letofsky, E.: PhD Thesis, Graz University of Technology, Graz, Austria (2001)

MICROSTRUCTURAL STUDIES OF SIMILAR AND DISSIMILAR WELDS OF P91

Dagmar Jandová[1], Josef Kasl[1], Eva Folková[2], Václav Kanta[1]

[1] SKODA RESEARCH s.r.o., Tylova 57, Pilsen, CZ 316 00, Czech Republic

[2] SKODA POWER a.s., Tylova 57, Pilsen, CZ 316 00, Czech Republic

dagmar.jandova@skoda.cz

Abstract

Creep testing of two trial weld joints of 9Cr-1Mo steel (similar weld joint and dissimilar 9Cr-1Mo / 2.25Cr-1Mo weld joint with filler metal on the base of 2.25Cr-1Mo steel) were carried out at temperatures ranging from 525°C to 625°C and stresses from 40 to 240 MPa. The weld joints were prepared using the GTAW & SMAW methods. Post-weld heat treatment was applied. Creep rupture strength was evaluated according to the Larson-Miller parametric equation. Fractographic analysis, hardness measurement and detailed microstructural study of the creep tested specimens were performed using light, scanning and transmission electron microscopy. Critical zones of creep failure were determined in dependency on conditions of the creep exposure. At higher temperatures and lower stresses fracture of the dissimilar weldment occurred in the weld metal while rupture of the similar weld was located in the heat affected zone of the parent material. The processes of recovery in connection with fine carbide dissolution and high grain boundary diffusion in fine prior austenitic grain zones seem to be the main causes of the decrease in creep rupture strength of both weld joints in comparison to the corresponding parent materials.

Keywords: ferritic steels, welding, creep testing, microstructure, transmission electron microscopy.

1. Introduction

In the last two decades great efforts have been made to improve efficiency and reduce harmful emissions in fossil fuel power plants. Both can be achieved by increasing the temperature and pressure of the steam. The components of the boilers and the turbines operating under severe service conditions have to be produced from advanced materials with high strength, corrosion and creep-resistance and adequate fatigue properties. To meet these requirements, modified (9-12)%Cr martensitic steels were developed and some of them, such as ASTM Grades 91, 92 and 911 are currently used in new power plants [1-3].

Long-term creep resistance depends on a high structural stability. Since welding effects the steel structure and causes a decrease in the creep strength, great attention has to be paid to welding methods and the selection of suitable welding metals. Weld joints are commonly susceptible to fracture especially if different materials are welded. Fracture is usually initiated in a specific microscopic region which forms as a result of cyclic thermal and stress loading after each weld pass [4]. Structures that form after single and double rapid induction heating have been described and mechanical properties have been tested using standard bulk specimens [5]. Detailed microstructural study of heat affected zones in real weld joints after extended service was also performed [6,7]. In this study the long-term creep testing and microstructural investigation of trial weld joints were carried out within the verification of a new welding method for steam piping.

Steam piping belongs to the most exposed parts of power plant. For the production of pipes which are exposed to temperatures above 550°C tempered martensitic (9-12)%Cr steels are favoured due to their excellent combination of mechanical and oxidation-resistant properties. The other parts of the piping can be made from creep-resistant low alloy Cr-Mo or Cr-Mo-V steels [8]. In SKODA POWER a.s. the steam piping for inlet steam up to temperatures of 600°C and pressures of 100 MPa is produced from P91 steel. Parts of piping operated at lower temperatures and pressures (up to 525°C and 10 MPa, exceptionally to 540°C and 6.3 MPa) are made from low alloy P22 steel. Pipes must be joined with caution using an appropriate welding method, filler metals and with particular emphasis placed on welding parameters.

2. Experimental procedures

Two trial weld joints were fabricated from creep-resistant 9Cr-1Mo steel known as P91 or X10CrMoVNb9-1 steel and 2.25Cr-1Mo steel marked as P22 or 10CrMo9-10 steel. Straight pipes with external diameter 324 mm, thickness 25 mm and length 400 mm were jointed together by GTAW & SMAW in PC position (manual welding under argon atmosphere with a coated electrode). The chemical composition of the parent and the welding materials used is given in Table 1. The parent steels were used in normalised and tempered conditions.

Welding was carried out using internal protection of the weld root by inert gas. Inductive heating with thermal insulation ensured a preheating temperature in the range from 200 to 250°C. The interpass temperature was kept below 300°C. Filler metals on the base of 2.25Cr-1Mo steel were used for welding P91 and P22 steels. Root pass was formed with Union I CrMo910 wire (∅ 2.4 mm) and SH Chromo 2KS (∅ 3.2 mm) was used as an electrode. In the case of the P91/P91 weld joint, the chemical composition of filler metals (Thermatit MTS3 wire and Chromo 9V electrode) corresponded to 9Cr-1Mo steel. Post-weld heat treatment (PWHT) was carried out in an electric furnace for 2.5 hours at 730°C for the dissimilar weld joint and 760°C for the similar one.

Table 1. Chemical composition of weld joints investigated (wt.%).

Steel	C	Mn	Si	P	S	Cr	Ni	Mo	V	Nb	N
P91	0.116	0.50	0.29	0.010	0.004	8.50	0.27	0.93	0.20	0.08	0,066
P22	0.114	0.46	0.25	0.013	0.002	2.24	-	0.95	-	-	-
Union I CrMo910	0.08	0.93	0.51	0.008	0.006	2.55		0.98	-	-	-
SH Chromo 2KS	0.06	0.70	0.22	0.008	0.006	2.22	-	0.99	-	-	-
Chromo 9V	0.10	0.62	0.24	0.009	0.006	9.05	0.73	1.05	0.20	0.05	0.040
Thermatit MTS3	0.126	0.61	0.24	0.007	0.002	8.93	0.67	0.99	0.18	0.069	0.058

Creep-testing was carried out using cross-weld specimens with a length of 92 mm and a diameter of 8 mm. Fracture surfaces was observed using a scanning electron microscope (SEM). Then specimens were cut along their longitudinal axis. Macrostructure was revealed using Vogel´s reagent and location of fracture in different regions of weldment was specified.

Vickers hardness was measured along the line across the weld joint using selected specimens before and after creep tests. Metallographic samples were prepared in the longitudinal section. Regions of 9Cr-1Mo steel were etched with Vilella´s reagent while 3% nital was used for 2.25Cr-1Mo steel. Changes in chemical composition across the dissimilar weldment were measured using energy dispersive X-ray (EDX) and wave dispersive X-ray (WDX) microanalyses.

The substructure of weldments was observed using transmission electron microscopy (TEM) at the accelerating voltage of 120 kV or 200 kV. Thin foils were prepared from selected critical regions of the weldments. Slices with a thickness of 0.8 mm were cut in parallel longitudinal sections of creep test specimens and were slightly etched to find fusion lines and heat affected zones. Then mechanical grinding and electropolishing were performed and 3mm diameter discs were punched. Final thinning was carried out by a jet electropolishing in 6% solution of perchloric acid in methanol at the temperature of - 40°C.

3. Results

3.1. Long-term creep properties

Creep tests were carried out at temperatures in the range from 525 to 625°C and stresses from 40 MPa up to 240 MPa. Creep rupture strength was evaluated using the Larson-Miller parametric equation [8]

$$P = T \cdot (C + \log \tau),$$

where T represents temperature (°K), C is a specific constant for a given material (C = 25 for 9Cr-1Mo steel, C = 20 for 2.25Cr-1Mo steel) and τ means time to fracture (hrs). The creep rupture strength of cross-weld specimens is graphically represented in Fig. 1. The creep rupture strength of the similar and dissimilar weld is compared to the creep rupture strength of P22 steel and P91 steel, respectively. The creep rupture strength of the P91/P22 weldment falls into the –20% scatter band of the creep rupture strength of the parent material. At lower temperatures measured values are placed at the bottom margin of the -20% scatter band of creep rupture strength of the parent material. At higher temperatures creep properties of the weldment approach those of the parent material. On the contrary, the creep rupture strength of the similar weldment is comparable to the parent steel at lower temperatures and some decrease in comparison to the parent material was detected at higher temperatures. At creep exposures above 575°C creep rupture strength of cross-weld specimens falls below the -20% scatter band of the creep rupture strength of the parent material. Two creep tests at 625°C are still running.

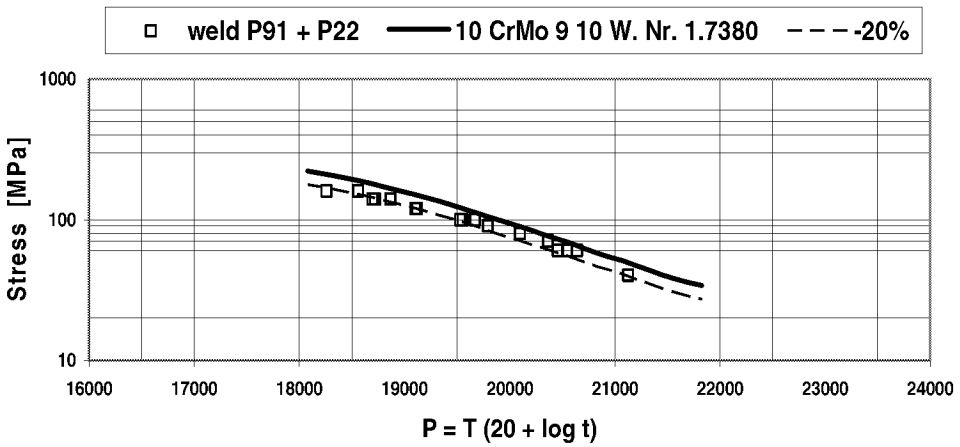

(a)

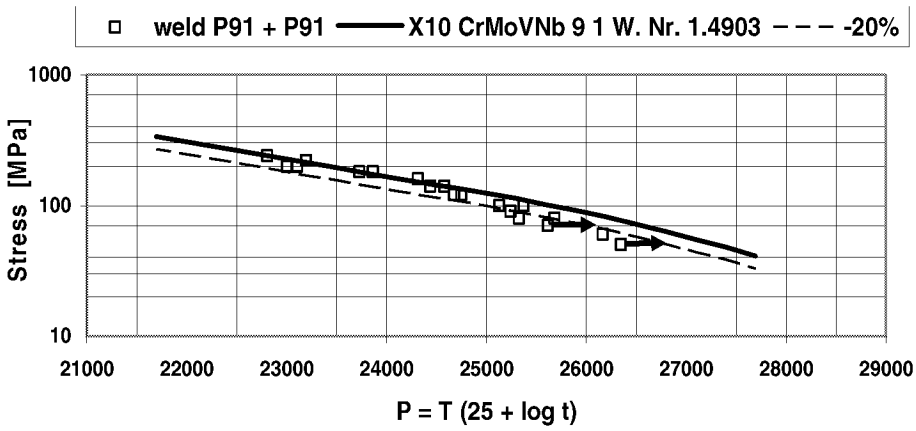

(b)

Fig. 1. Creep rupture strength of cross-weld specimens in dependency of the Larson-Miller parameter: a) dissimilar weld joint and b) similar weld joint.

3.2. Fractography

Location of fracture surfaces in individual cross-weld creep test specimens depended on the materials of weldment and on the creep test conditions and is represented graphically in Fig.2. In the dissimilar weld joint tested at relatively low temperatures and high stresses, fracture occurred in the unaffected P22 parent material. At higher temperatures and lower stresses the cracks formed in the weld metal. In the case of the similar weld joint, fracture was located in the weld metal after creep exposure at lower temperatures and higher stresses and in the heat-affected (HAZ) of the P91 parent material after creep test at higher temperatures.

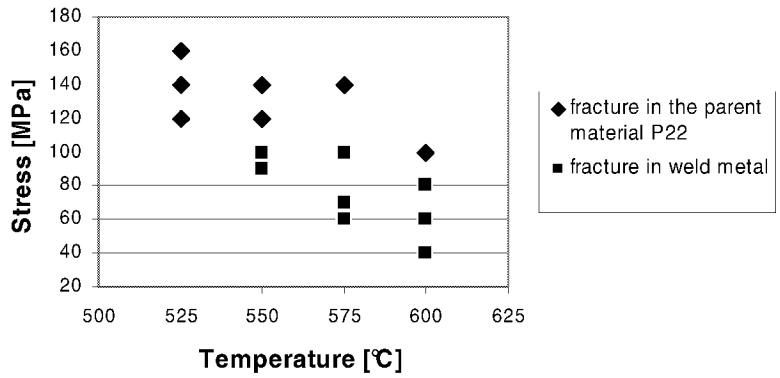

(a)

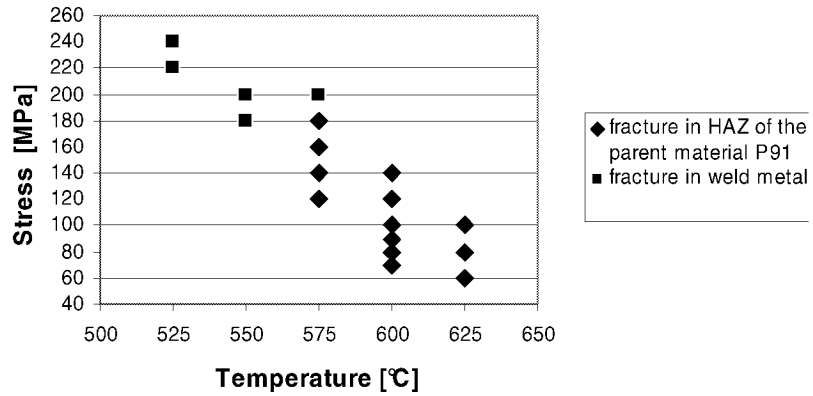

(b)

Fig. 2. Graphical representation of fracture locations in the creep test specimens: a) P91/P22 weld joint, b) P91/P91 weld joint.

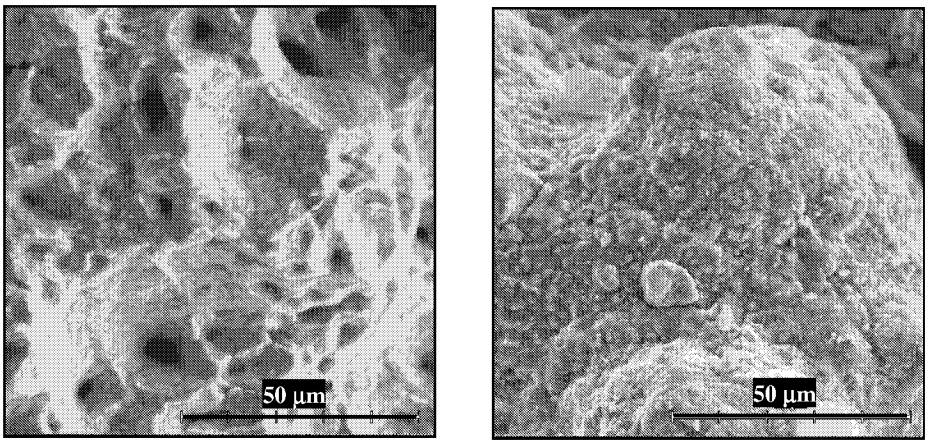

(a) (b)

Fig. 3. SEM micrographs of fracture surfaces of P91/P22 cross-weld specimens after creep tests: a) 525°C/120 MPa/8,695 hrs to rupture, b) 575°C/70 MPa/10,279 hrs to rupture.

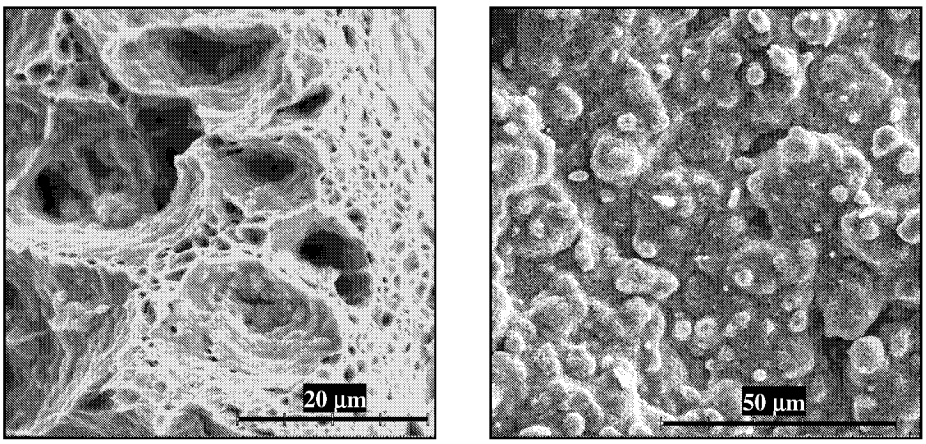

(a) (b)

Fig. 4. SEM micrographs of fracture surfaces of P91/P91 cross-weld specimens after creep tests: a) 575°C/180 MPa/960 hrs to rupture, b) 625°C/60 MPa/13,673 hrs to rupture.

Fracture surfaces of both weld joints creep tested at 525°C and 550°C revealed a dimpling morphology, which is typical for ductile transcrystalline fracture (Fig 3a, 4a). After creep exposures at higher temperatures surfaces were covered with thick oxide layers, which made impossible to specify the rupture mechanism (Fig 3b, 4b). Differences between similar and dissimilar weld joint were found in contraction and elongation of specimens creep tested at temperatures above 550°C; much higher contraction and elongation corresponded to the P91/P22 cross-weld specimens.

3.3. Macrostructure and hardness measurement

The macrostructure of one of the trial weld joints is shown in Fig. 5. Geometry and also width of heat affected zones, which ranged from 3 to 4 mm, were identical in both the weld joints.

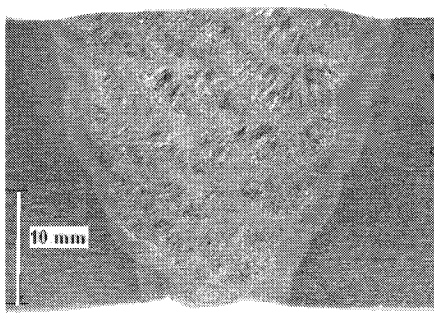

Fig. 5. Macrostructure of P91/P91 weld, Vogel´s reagent.

The hardness distribution across the weld joint was determined using the HV scale with a 10 kg load in weld joints before creep testing and after the creep exposure at different temperatures for approximately ten thousand hours.

P91/P22 weld. A typical hardness profile across P91/P22 weld is shown in Fig. 6. The hardness HV10 of unaffected parent materials after post-weld heat treatment corresponded to 225 and 150 for P91 steel and P22 steel respectively. Local maximum was found in the prior austenite coarse grained HAZ of P91 steel. In the weld bead adjacent to parent material P91, which was enriched with alloying elements from P91 steel, hardness was about 200. Hardness in the remaining parts of the weld metal corresponded to that of unaffected P22 steel. After creep tests any important changes of hardness were not detected in chromium rich P91 steel while in low alloyed regions hardness decreased to 135.

P91/P91 weld. Hardness HV10 across the weld joint varied from about 180 to 240. Hardness of the unaffected parent material was 200, about 25 lower than the hardness of the same parent material in the P91/P22 weld. This is a result of the higher temperature of post weld heat treatment in comparison with the dissimilar weld joint. Hardness of coarse prior austenite grained HAZ did not exceed 237. Minimum hardness was found in the parent material 2 mm from the fusion line. Creep exposures at temperatures ranging from 525 to 575°C and at 625°C did not significantly influence hardness, while exposure at 600°C resulted in an increase in hardness by about 20 (Fig. 7).

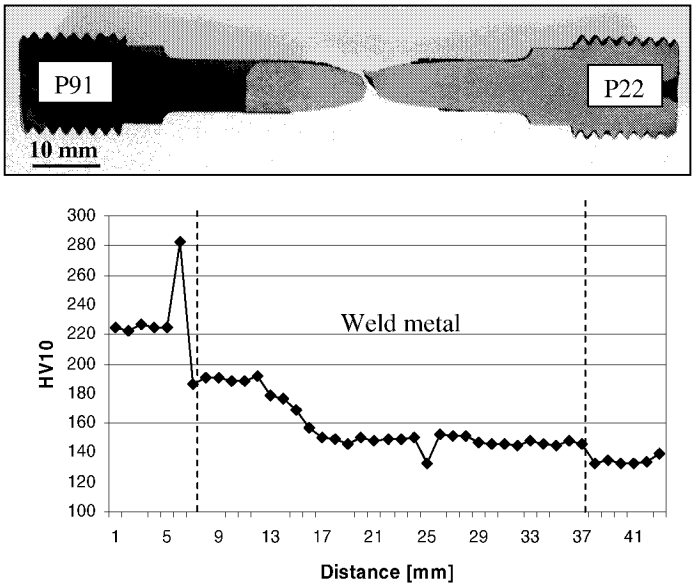

Fig. 6. Macrograph of longitudinal section of cross-weld specimen and hardness profiles across P91/P22 weldment after creep test 550°C/90MPa/11,190hrs.

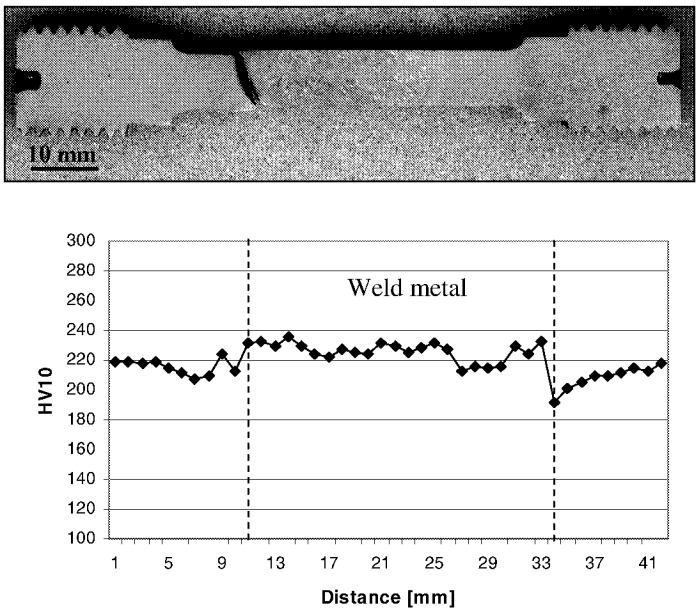

Fig. 7. Macrograph of longitudinal section of crossweld specimen and hardness profiles across P91/P91 weldment after creep test 600°C/80MPa/10,181hrs.

3.4. Microstructural study

Microstructural study was concentrated on critical zones of the weldments after long-term creep exposures at high temperatures. Microstructures before and after the creep testing were compared.

P91/P22 weld. The parent material of P22 steel consisted of a mixture of ferrite and pearlite. The parent material of P91 steel was tempered martensite. Microstructures of the weld metal (WM) and the HAZ of P22 steel were formed of bainitic structures. Decarburized zones with ferritic grains containing a low number of carbides were observed along the WM/P91 fusion line on the low-alloy side (Fig. 8a). A similar effect was also found in the weld metal along the fusion line of the bead adjacent to the chromium rich parent material (Fig. 8b); overlaying welding resulted in an increase in chromium content from 2.5 wt.% to 3.0 wt.%. Consequently two significant interfaces in relation to the chemical composition arose: P91/WM fusion boundary, where chromium concentration decreased from 8.85 wt.% to 3.0 wt.% and the second bead/the third bead fusion boundary, where Cr content decreased from 3.0 wt.% to 2.50 wt.%. The carburization of P91 steel reached 0.35 wt.% (WM/P91 fusion line) and carburization of weld metal 0.16 wt.% (boundary of weld beads). Carbon concentration in the depleted zones decreased below a limit of measurability of WDX method (~0.1 wt.%).

The carbon-denuded zones were associated with the changes in the chromium concentration. It is well known that carbon atoms cross the fusion line from low alloy material to high alloy material as a result of different carbon activity in different solid solutions. Decarburized zones, which can be formed during welding and especially during long-term exposures at high temperatures, are often called "soft zones" and they often cause a decrease in creep rupture strength [9,10]. However in this study no fracture was located in these regions. Fracture at high temperatures occurred close to the fusion line of two weld beads with identical chemical composition.

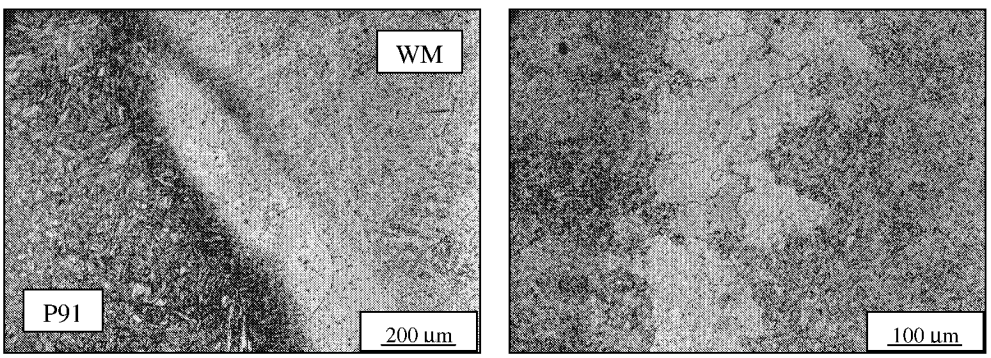

(a) (b)

Fig. 8. Carburized and decarburized zones in P91/P22 weld after creep exposure 625°C/40MPa/15,875hrs: a) P91/WM fusion line, b) weld metal.

Substructures of the non creep tested cross-weld specimen and the specimen after the longest creep exposure at the highest temperature (600°C/40 MPa/15,875 hrs) were observed using

TEM. Thin foils were prepared from the central part of weld metal (unaffected weld metal) and from the critical region of the weld metal.

The microstructure of the unaffected weld metal before creep test was composed of typical bainitic lath with relatively coarse chromium rich $M_{23}C_6$ carbide particles on the lath boundaries and small particles within ferritic laths (Fig. 9a). According to incomplete diffraction patterns (interplanar distances d_{111} = 0.255 nm, d_{040} = 0.232 nm and d_{114} = 0.222 nm) these fine particles could correspond to orthorhombic M_3C_2 carbides (Cr_3C_2 or Cr_2VC_2). Ring diffraction patterns which corresponded to interplanar distances from 0.252 nm to 0.257nm were often detected. They could give evidence of the occurrence of fine M_3C_2 or $(Cr,V)_2C$ carbides.

In the critical region of weld metal the microstructure consisted of small grains and subgrains with a low dislocation density and also of bainite laths with a relatively high dislocation density. Sporadic coarse carbides were observed on grain and/or subgrain boundaries (Fig.9b).

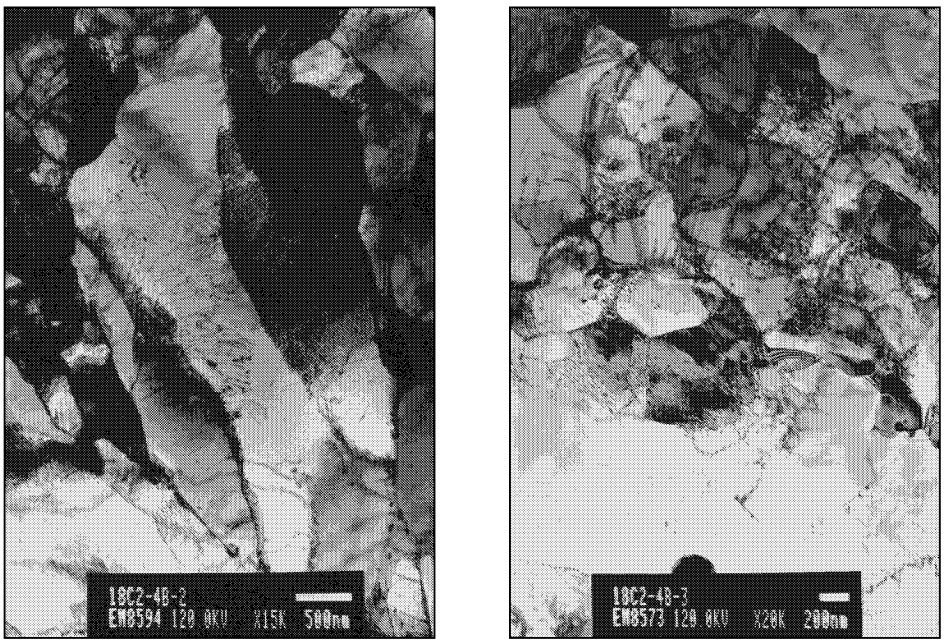

(a) (b)

Fig. 9. TEM micrograph of P91/P22 weld after PWHT: a) weld metal in central weld bead, b) critical region of weld metal.

After long-term creep exposure at 600°C an increase in the dislocation density was observed within the small ferritic grains and subgrains near the fracture surface (Fig. 10). Subgrain boundaries became thicker as a result of a high dislocation density. In addition, coarsening of carbides occurred. Most of the fine carbides were dissolved.

P91/P91 weld. All regions of the weldment were formed by severely tempered martensitic structures. Fracture at creep exposures at temperatures above 575°C occurred predominantly in the HAZ of the parent material, at a distance of about 1.5 mm from the fusion line. Microstructure observed in this critical zone using a light microscope consisted of fine grained martensite. Cavities were observed near fracture surfaces. Their size and density increased with increasing temperature and duration of creep tests. A lot of cavities appeared also in the HAZ on the opposite side of the cross-weld creep test specimen after creep exposure at 625°C/60MPa/13,673h (Fig.11). Most of the cavities were located on prior austenite grain boundaries.

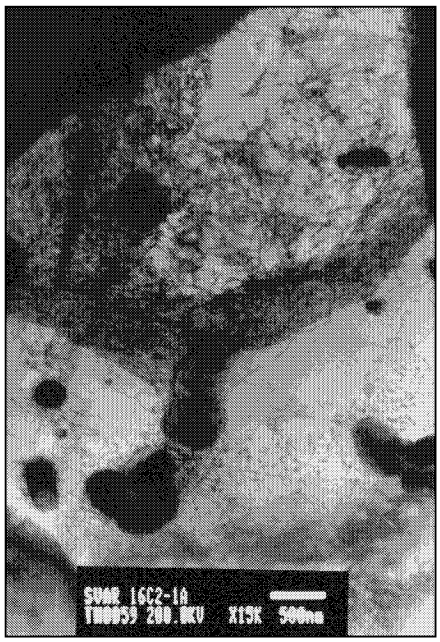

Fig. 10. TEM micrograph of a critical region of weld metal in P91/P22 weld after creep test 600°C/40MPa/15,875hrs.

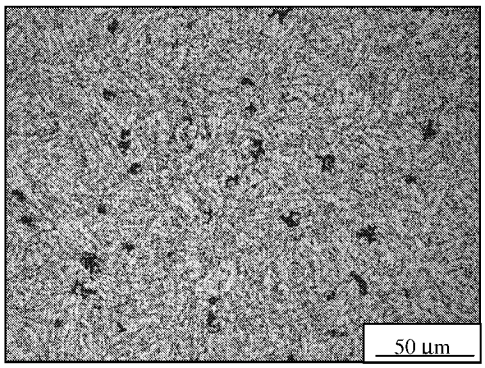

Fig. 11. Cavities in prior austenite fine grained zone of HAZ after creep test 625°C/60MPa/13,673hrs.

A lath-like microstructure with a large number of coarse $M_{23}C_6$ carbide particles on grain and subgrain boundaries was observed in the foils prepared from unaffected parent material after post-weld heat treatment. Density of these precipitates was much higher than in the weld metal of the P91/P22 weld. Fine precipitates of hexagonal Mo_2C carbide and cubic V(C,N) carbonitride (a = 0.416 nm) were found in some of the laths. After creep exposure at 600°C for about 16,000 hours fine Mo_2C carbides were dissolved while coarse particles on grain and subgrain boundaries built up. A slight increase in particle size was proved by quantitative evaluation of particles with a diameter above 10 nm. Vanadium carbonitride particles were still detected.

Foils were also prepared from a cross-weld creep test specimen under conditions 625°C/60MPa/13,673hrs. Typical lath-like martensitic structure of the weld metal close to the

fusion line is shown in Fig. 12a. Coarse particles of secondary phases were observed sporadically because they were dissolved during welding. In regions close to the fracture surface (at a distance of about 1.5 mm from the fusion line) the microstructure consisted of small ferritic grains and subgrains almost free of dislocations (Fig. 12b). Fine precipitates were not found. The density of coarse particles was lower in comparison to the unaffected parent material. Some of them were identified using selected-area diffraction as $M_{23}C_6$ carbide. About 50 particles in foil were analyzed and underwent EDX microanalysis. Four of the analyzed particles revealed a high content of molybdenum, in the others chromium dominated. The high content of molybdenum increases the probability of the Laves phase occurrence, while the high chromium content demonstrates the $M_{23}C_6$ carbide.

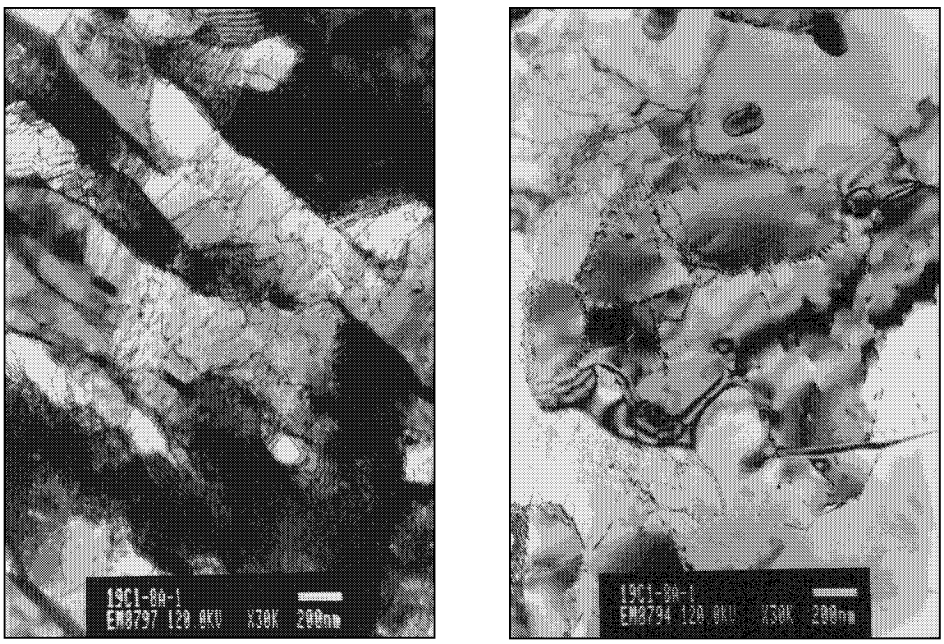

(a) (b)

Fig. 12. TEM micrograph of HAZ of P91/P91 weld after creep test 625°C/60MPa/13,673hrs: a) coarse grained HAZ, b) fine grained HAZ close to the fracture surface.

4. Discussion

Samples of dissimilar weld joint were creep tested at a wide temperature range up to 600°C, although parent P22 steel is usually used only at temperatures below 550°C. Creep testing shows that at 525°C the P91/P22 weldment has a higher strength than the parent P22 steel. At higher temperatures the weld metal seems to be more susceptible to rupture than both parent materials; fractures were located in the weld metal with the exception of creep exposures at stresses above 100 MPa. Cracks located in the weld metal always propagated in the heat affected regions in the weld bead adjacent to the parent P22 steel. Although decarburized zones were observed along the P91/WM fusion line and also along the fusion line between

weld beads (chromium enriched weld bead and low-alloyed bead), they did not influence rupture propagation.

Ductile transcrystalline fracture was the main rupture mechanism in all cross-weld creep test specimens of dissimilar weldment. After the creep test at 625°C/40MPa/15,875hrs some cavities were observed near the fracture surface. Fractures located in the weld metal occurred in the fine-grained heat-affected regions of the low-alloyed weld metal, in normalized and intercritically reheated structures. The microstructure in this region consisted of small ferritic grains and subgrains with a low dislocation density. After post-weld heat treatment the ferritic matrix was hardened particularly by fine chromium rich carbide precipitates. Lath and subgrain boundaries were stabilized with coarse $M_{23}C_6$ carbides. Long-term creep testing at temperatures above 550°C resulted in the dissolution of fine precipitates, a slight coarsening of $M_{23}C_6$ carbides and structure recovery. As a result, hardness of low-alloyed regions decreased by about 20 HV10 while hardness in regions with high chromium content did not change.

Fracture in the weld metal occurred in the fine grained HAZ of low-alloyed steel. At high temperatures a low yield stress supported intensive slip and formation of steps on grain boundaries. These steps served as the nuclei of cavities. Many cavities were formed on a large area of the grain boundaries and their growth was promoted by high grain boundary diffusion.

Creep testing of the similar weld joint revealed satisfactory creep rupture strength at temperatures up to 575°C. At long-term exposures at 600°C and 625°C a significant decrease in comparison to the parent material was found. At 525°C and 550°C fracture occurred in the weld metal while at higher temperatures ruptures were localized in the HAZ of the weld joint. Ductile transcrystalline fracture with a dimpling morphology was observed, when rupture occurred in the weld metal. Cross-weld specimens creep tested above 575°C had significantly lower ductility than specimens creep tested at lower temperatures. Fractures at these temperatures occurred in fine-grained HAZ, in regions where hardness measurement revealed a local minimum in all of the tested cross-weld specimens.

Microstructural examination of structures in the similar weldment after the post-weld heat treatment and after long-term creep exposures at 600°C and 625°C revealed some differences although no significant changes in hardness were found. The microstructure of the creep non-tested weldment consisted of a lath-like structure of severely tempered martensite with coarse $M_{23}C_6$ carbides and fine Mo_2C and V(C,N) precipitates. The density of individual phases depended on the region of the weldment. Plenty of coarse particles were present in the unaffected parent material and the prior austenite fine-grained HAZ, a remarkably lower coarse particle density was observed in the coarse-grained HAZ. After creep exposures fine particles of Mo_2C carbide were dissolved and coarse carbides built up slightly. Within the subgrains fine V(C,N) precipitate was detected. It is known that vanadium carbonitride is a very stable phase at the creep exposures up to 650°C and for times up to 60,000 hrs [12].

Fracture surfaces of P91/P91 cross-weld specimens creep tested at 600°C and 625°C were located in the prior austenite fine-grained and intercritically reheated HAZ of the parent material as a result of dislocation and diffusion creep. High grain boundary diffusion is a controlling factor of the fracture propagation.

4. Conclusions

Microstructural and creep studies of P91/P22 and P91/P91 weldments led to the following conclusions.

1. Both weld joints investigated can be used in temperature and pressure ranges in which the parent materials are usually used. This means exposures below 550°C for the dissimilar weld joint and 600°C for the similar one. At 600°C the creep strength of the similar weld joint decreased by about 20% in comparison to the parent material.
2. Critical zones from the point of view of the creep rupture at high temperatures were located in the prior austenite fine grained normalized and intercritically reheated zones in the weld metal in the case of the dissimilar weld joint and in the prior austenite fine grained normalized HAZ of the parent material in the similar weld joint.
3. The main causes of decrease in creep rupture strength were found in the processes of recovery, dissolution of fine precipitates and diffusion on grain boundaries taking place during creep exposures at high temperatures.

Acknowledgements

This work was supported by Grant project number 1P05OC024 COST 536 from the Ministry of Education, Youth and Sports of the Czech Republic.

References

[1] J. Pasternak, A. Kielbus: "Structural Stability of New Creep-Resisting Steel Grades with 9 and 12% Cr Contents Applied in Power Generation Sector in Industrial Condition". In: Proceedings of 1st International Conference Super-High Strength Steels, Italy. Associazione Italiana di Metalurgia. [CD-ROM]. November 2005.ISBN 88-85298-56-7.

[2] J. Hald: "Creep Resistant 9-12% Cr Steels – Long-Term Testing, Microstructure Stability and Development Potentials". In: Proceedings of 1st International Conference Super-High Strength Steels, Italy. Associazione Italiana di Metalurgia. [CD-ROM]. November 2005. ISBN 88-85298-56-7.

[3] L. Cipolla, J. Gabrel: "New Creep Rupture Assessment of Grade 91". In: Proceedings of 1st International Conference Super-High Strength Steels, Italy. Associazione Italiana di Metalurgia. [CD-ROM]. November 2005. ISBN 88-85298-56-7.

[4] R. Mythili, P. V. Thomas, S. Saroja, M. Vijayalakshmi, V. S. Raghunathan: "Microstructural Modification Due to Reheating in Multipass Manual Arc Welds of 9Cr-1Mo Steel". Journal of Nuclear Materials. Vol. 312, 2003, 199 - 206.

[5] A. Moitra, P. Parameswaran, P. R. Sreenivasan, S. L. Mannan: "A Toughness Study of the Weld Heat-Affected Zone of a 9Cr-1Mo Steel". Material Characterization, Vol. 48, 2002, 55-61.

[6] J. R. Yang, C. Y. Huang, C. N. Yang, J. L. Horng: "Microstructural Examination of 2.25Cr-1Mo Steel Steam Pipes After Extended service".Material Characterization, Vol. 30, 1998, 75-88.

[7] C. D. Lundin, K. K. Khan, D. Yang: "Effect of Carbon Migration in Cr-Mo Weldments on Metallurgical Structure and Mechanical Properties". WRC Bulletin, Vol. 407, 1995, 1-48.

[8] H. K. D. R. Bhadeshia: "Design of Creep–Resistant Steel Welds". In: Trends in Welding Research. Ed. S. A. David, T. DebRoy, J. A. Jonson, H. B. Smartt, J. M. Vitek. ASM International. Ohio. 1999, 795 – 804.

[9] R. Foret, B. Million, M. Svoboda, K. Stránský: "Structural Stability of Dissimilar Weld Joints of Steel P91". Science and Technology of Welding and Joining, Vol. 6, No. 6, 2001, 405 – 411.

[10] K. Laha, S. Latha, K. Bhanu Sankara Rao, S. L. Mannan, D. H. Sastry: "Comparison of Creep Behaviour of 2.25Cr-1Mo/Cr-1Mo Dissimilar Weld Joint with Its Base and Weld Metals". Materials Science and Technology, Vol. 17, 2001, 1265 – 1272.

[11] A. Di Gianfrancesco, L. Cipolla, F. Cirilli: "Microstructural Stability and Creep Data Assessment of Tenaris Grades 91 and 911. In: Proceedings of 1th International Conference Super-High Strength Steels, Italy. Associazione Italiana di Metalurgia. [CD-ROM]. November 2005.ISBN 88-85298-56-7.

PHYSICAL SIMULATION AND NUMERICAL MODELLING OF X10CrMoVNb 9.10 (P91) STEEL REPAIR WELDING

Mirosław Łomozik [1)], Edmund Tasak [2)]

[1)] Instytut Spawalnictwa (Institute of Welding), Poland
ul. Bł. Czesława 16/18, 44-100 Gliwice,
e-mail: Miroslaw.Lomozik@is.gliwice.pl
[2)] AGH University of Science & Technology, Poland

Abstract

The characteristics of a welding thermal cycle is presented as well as phenomena which occur in the HAZ during multi-pass welding. Examples of examination results aimed at the determination of HAZ properties in P91 steel by using the simulation technique are given and also some results of numerical modelling of thermal fields and cycles in the HAZ by means of ANSYS 5.6 programme.

Keywords: thermal welding cycle, Heat Affected Zone, P91 steel, cooling time, martensite, plastic properties

1. Introduction

Safety during operation of welded structures is strictly connected with the quality and mechanical properties of welded joints. At operating conditions, where the welded joint is subjected to alternating and often dynamic loads, one of its most important characteristics, besides mechanical properties, is toughness, and especially in the region of the heat affected zone (HAZ).

Due to degradation of welded structures, for instance welded installations in the power industry, their failures take place at present, and it should be reckoned with the possibility that they will occur also in future. The best solution in that case would be the replacement of old structures by new ones. Due to technical and economic reasons such a solution is most often impossible. Therefore repair of welded constructions is necessary.

The next important problem is the necessity of post weld heat treatment (PWHT), as is the case for example at pressure vessel welding in the power industry. The objective of PWHT is the improvement of the HAZ and weld metal toughness and maximum reduction of welding residual stresses. But in the case of repair welding of big objects PWHT may cause serious difficulties.

In situations, where due to technical reasons conventional PWHT is restricted or impossible, an effective means for ensuring proper high HAZ toughness is the application of so-called "temper bead welding". The method consist in such a means and sequence of laying individual weld beads, to temper the martensitic microstructure in the HAZ of previously welded beads by the controlled welding thermal cycle. The temper bead welding technique enables lowering of hardness of martensitic and upper bainitic microstructures, which occur in the coarse grain region of the HAZ, and in consequence toughness improvement of these welded joint regions.

2. Phenomena accompanying multi-pass welding in HAZ area

During multi-pass welding, while making successive beads (or layers) of a weld, an HAZ area is subject to an effect of successive thermal cycles and, consequently, the creation of metallographic structures characterised by various mechanical (strength and plasticity-related) properties takes place. In addition, during multi-pass welding, in some HAZ areas, tempered structures are formed. As far as plastic properties and especially impact strength are concerned, the most unfavourable HAZ area is CGHAZ (i.e. *Coarse Grain Heat Affected Zone*). As a result of the overlaying of successive thermal cycles, some areas of CGHAZ are reheated to intercritical temperatures from the range of A_{C1} and A_{C3}. The area formed as a result there of (after cooling) continues to have a coarse grain structure known as ICCGHAZ (i.e. *Intercritically Reheated Coarse Grained HAZ*). The area of ICCGHAZ is characterised by similarly unfavourable plastic properties as is the case of the CGHAZ area. The location of various structural areas in HAZ is presented in Figure 1.

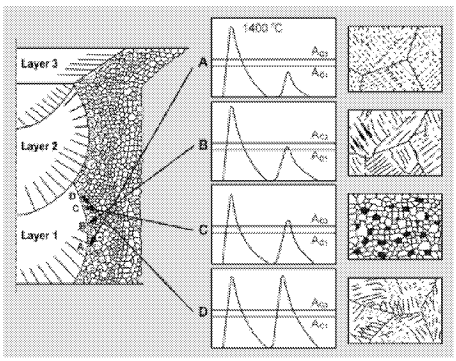

Fig. 1 Diagrammatic presentation of HAZ area microstructures in multi-pass welding in function of maximum temperatures of successive thermal cycles [1 ÷ 5].

Short characteristics of the areas shown in Figure 1:

A ⇒ the HAZ area reheated by the cycle of the maximum temperature lower than A_{C1} temperature; the area has a coarse grain structure and is designated as SRCGHAZ (i.e. *Subcritically Reheated CGHAZ*);

B ⇒ the reheated coarse grain HAZ area designated as ICCGHAZ, for which the maximum temperature of a successive thermal cycle was contained within the temperature range between A_{C1} and A_{C3};

C ⇒ the fine grain HAZ area designated as FGHAZ, for which the maximum temperature of a successive thermal cycle exceeded the temperature value of A_{C3};

D ⇒ the coarse grain HAZ area, for which every successive thermal cycle has a temperature exceeding 1150 °C.

3. Use of simulation of welding thermal cycles in examinations of structural changes and testing of properties of various HAZ areas

To a great extent, the practical usability of a welded joint depends on HAZ properties influenced by HAZ microstructure, which, in turn, is dependent upon the chemical

composition of a welded material and a welding thermal cycle. A simulation technique was used in order to examine the properties of HAZ of P91 steel affected by many thermal cycles. The methodology of examinations consisted in exposing small-sized samples to overlaying thermal cycles of various maximum temperatures (T_{max}) and various cooling times ($t_{8/5}$); as a result, the said methodology enabled the obtaining of simulated HAZ areas of various morphological structure in the steel used in tests. The device used for the simulation of welding thermal cycles is presented in Figure 2.

a) 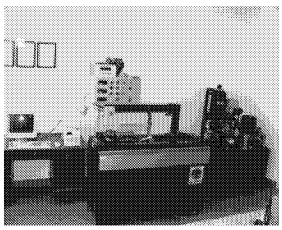 b) 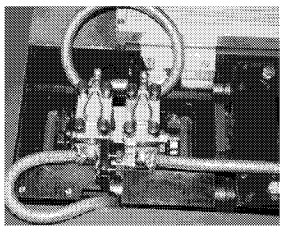

Fig. 2 Simulator of welding thermal and strain cycles at Instytut Spawalnictwa, Gliwice:
a) general view,
b) heated specimen in simulator jaws.

In HAZ of an actual welded joint, areas differing in structural morphology and properties are characterised by very small width values (in fractions of millimetres), which results in the fact, that while testing impact strength, the radius of a notch cut in a sample amounts to 0.25 mm and is often bigger than the width of a tested zone. For this reason, simulation has proved very useful. The use of simulation technique for obtaining various HAZ areas corresponding to the areas in an actual welded joint is characterised as follows:

1. it enables the simulation in a steel of an area of a selected HAZ structure of such a width which does not create any difficulty in making a notch in a sample used for the testing of impact strength;
2. it facilitates the performance of microscopic metallographic examinations of individual HAZ areas for specific parameters of thermal cycles;
3. it enables the determination of the tendency of structural and plastic properties (impact strength and hardness) in the function of multiple thermal cycles without the necessity of making real welded joints.

It should, however, be taken into consideration, that in an real welded joint, HAZ areas of the most unfavourable plastic properties (CGHAZ, ICCGHAZ, SRCGHAZ) are surrounded by areas of a more plastic structure and beneficial effect on the HAZ tested. For that reason, impact strength values are higher in a welded joint in comparison to those obtained in samples with simulated HAZ areas (for the same parameters of thermal cycles).

4. Examination of plastic properties of simulated HAZ areas in P91 steel [6]

The examinations incorporated the use of alloy martensitic steel X10CrMoVNb 9.10 (P91); the chemical composition of the steel is presented in Table 1.

Table 1 Chemical composition of steel X10CrMoVNb 9.10 (P91).

Steel	Chemical content in [%]										
	C	Mn	Si	P	S	Cr	Ni	Mo	V	$Al_{solub.}$	Nb
P91	0.10	0.41	0.33	0.018	0.001	8.27	0.25	0.876	0.18	0.007	0.08
wg ASTM A335	0.08 ÷ 0.12	0.30 ÷ 0.60	0.20 ÷ 0.50	max. 0.015	max. 0.010	8.00 ÷ 9.50	max. 0.40	0.85 ÷ 1.05	0.18 ÷ 0.25	max. 0.04	0.06 ÷ 0.10

The steel was sampled and the specimens were used for the simulation of welding thermal cycles. The samples had the shape, size and Charpy V notch i.e. appropriate for impact strength testing. Afterwards, by means of a simulator for thermal and strain cycles, HAZ areas of various structures and properties were simulated in the samples in conditions of multiple welding thermal cycles. The simulation scheme for P91 steel is presented in Table 2.

Table 2 Parameters of simulated welding thermal cycles in P91 steel.

HAZ area	Cycle temperature T_{max} [°C]			Cooling time $t_{8/5}$ [s]		
	T_1	T_2	T_3	6	24	60
CGHAZ	1250	-	-	×	×	×
FGHAZ	1250	950	-	×	×	×
ICCGHAZ	1250	860	-	×	×	×
SRCGHAZ	1250	750	-	×	×	×
Temper bead	1250	790	550	×	×	×

Where:

CGHAZ - coarse grain HAZ; single cycle;

FGHAZ - fine grain HAZ; T_{max} of the second cycle higher than the A_{C3} temperature;

ICCGHAZ - reheated coarse grain HAZ; T_{max} of the second cycle situated in the range temperature between A_{C1} and A_{C3};

SRCGHAZ - reheated coarse grain HAZ; T_{max} of the second cycle lower than the A_{C1} temperature;

Temper bead - triple cycle; T_{max} of the second and third cycle lower than the A_{C1} temperature.

The samples with simulated HAZ areas were subjected to impact strength tests in the ambient temperature, microscopic metallographic examinations and measurements of hardness by means of Vickers method, with the load of 1kG (HV1).

The examples of results of microscopic metallographic examinations are presented in Figure 3; the examples of results related to tests of absorbed energy and hardness measurements are presented in Figures 4 ÷ 6. Microstructures of P91 steel presented in Figure 3 were revealed by means of ferric chloride $FeCl_3$ and the photographs were taken at 1000× magnification.

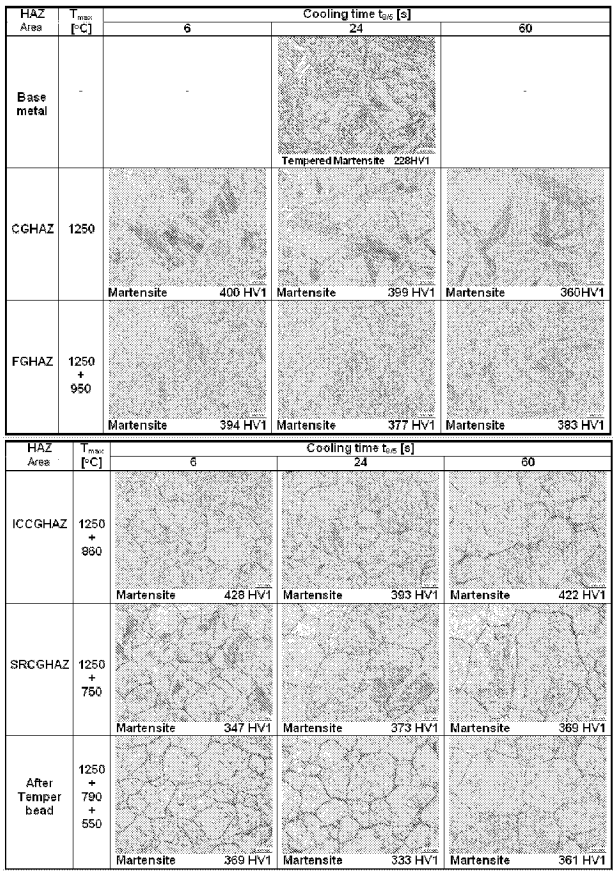

Fig. 3 Example of results of microscopic metallographic examinations of simulated HAZ areas in P91 steel.

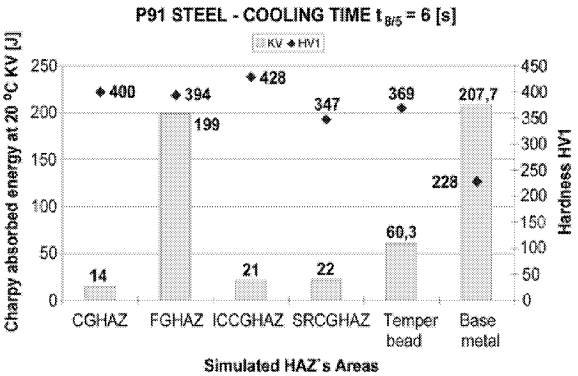

Fig. 4 Comparison of absorbed energy (KV) and hardness (HV1) of various HAZ areas in P91 steel for cooling time $t_{8/5}$ = 6 s.

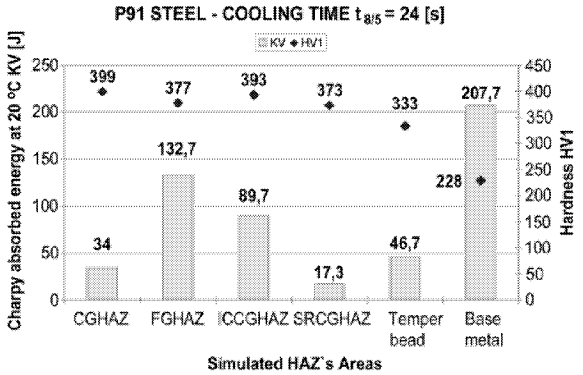

Fig. 5 Comparison of absorbed energy (KV) and hardness (HV1) of various HAZ areas in P91 steel for cooling time $t_{8/5}$ = 24 s.

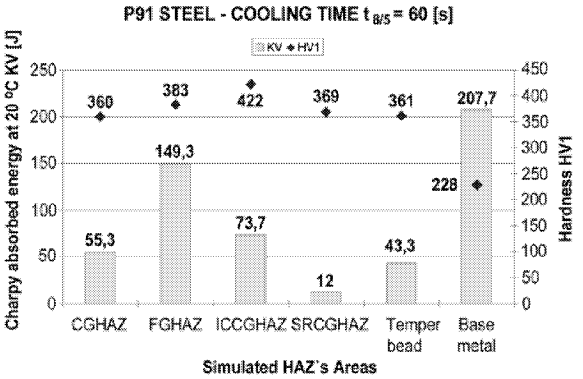

Fig. 6 Comparison of absorbed energy (KV) and hardness (HV1) of various HAZ areas in P91 steel for cooling time $t_{8/5}$ = 60 s.

In P91 steel, irrespective of the type of a thermal cycle and cooling time $t_{8/5}$, a substantial part of microstructure is composed of martensite. In the parent metal, the martensite is tempered. In the simulated HAZ areas, the morphology of martensite varies. For instance, the coarse grain martensite with a distinctly formed acicular structure occurs in the HAZ simulated with a thermal cycle of T_{max} = 1250 °C and the cooling time of $t_{8/5}$ = 6, 24 and 60 seconds (CGHAZ). An acicular structure, however, disappears in such HAZs as ICCGHAZ, SRCGHAZ or after a tempering cycle; the disappearance of the acicular structure is accompanied by the occurrence of grain boundaries with carbid precipitation along them.

While analysing the influence of cooling time ($t_{8/5}$) on hardness and absorbed energy of the simulated HAZ areas in P91 steel, it is possible to observe the following phenomena:

a) the increase of cooling time ($t_{8/5}$) does not entail a significant decrease of hardness,
b) the highest values of absorbed energy characterise the fine grain HAZ area (FGHAZ) obtained after a double thermal cycle, for which the maximum temperature of the second cycle was higher than the A_{C3} temperature;

c) it is difficult to observe unquestionable effect of the cooling time on the absorbed energy of coarse grain HAZ areas (ICCGHAZ and SRCGHAZ).

The explanation of this phenomenon is presented below.
While considering the issue in question, two terms for designating martensite types in P91 steel were used i.e. the martensite existing in the structure of steel as delivered was called "primary", whereas the martensite formed in the structure as a result of transformations taking place in a solid state due to successive thermal cycles was called „secondary". Due to the fact that during the action of welding thermal cycles the heating time is short and the maximum temperatures of successive thermal cycles are not too high (around A_{C1} temperature), not all of the "primary" martensite is transformed into austenite but only its part. On the other hand, the cooling process is accompanied by an opposite transformation, during which the "secondary" martensite appears in the matrix of the "primary" one. Due to the heterogeneity of its chemical composition, the "secondary" martensite becomes enriched in alloying components and is more supersaturated with carbon. In addition, the extension of cooling time ($t_{8/5}$) increases the occurrence of hardening precipitation, for instance, in the form of carbonitrides located mainly along the grain boundaries. The presence of both the "secondary" martensite as well as separations in the steel structure impairs the plastic properties of coarse grain HAZ areas.

In order to confirm the rightness of the adopted interpretation of the phenomena related to the changes of martensite, examinations were performed by means of a transmission electron microscope (TEM); the result of examinations of the simulated HAZ areas of P91 steel are presented in Figure 7.

Thin foil magnification 10 000×
1 – not transformed martensite ("primary")
2 – newly formed martensite ("secondary")

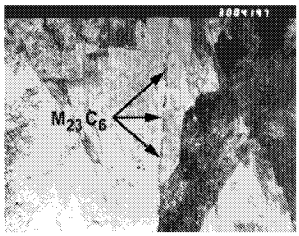

Thin foil magnification 30 000×
Carbid precipitation ($M_{23}C_6$) on boundary of former austenite grain

Fig. 7 HAZ area in P91 steel reheated to temperatures within range $A_{C1} \div A_{C3}$ (ICCGHAZ) with visible areas of secondary martensite.

5. Numerical modelling of thermal fields and thermal cycles in multi-pass welding conditions [7]

The shape of a geometrical model adopted in numerical calculation was determined by practical aspects reflected both in welding practice and regulations pertaining to principles of repairing welded joints by means of temper bead welding. Due to the foregoing, the reasoning adopted included the following issues. In a currently used hypothetical structural element (e.g. an element of a power industry) a crack hazardous to further safe operation was detected. The repair work must be performed by means of a welding technology.

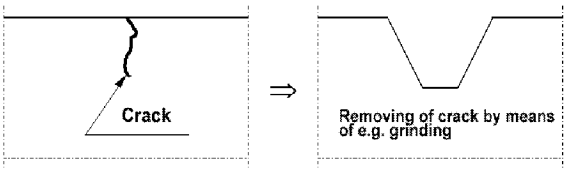

Fig. 8 Example of crack in hypothetical construction and removal of defect through mechanical working.

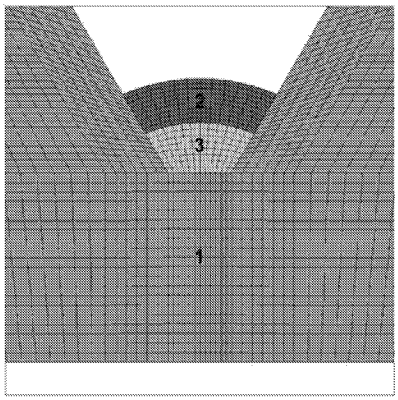

Fig. 9 A geometrical model adopted for numerical calculation after division into finite elements:
1 – parent metal,
2 – molten metal (liquid state),
3 – deposited metal after solidification (dendritic form).

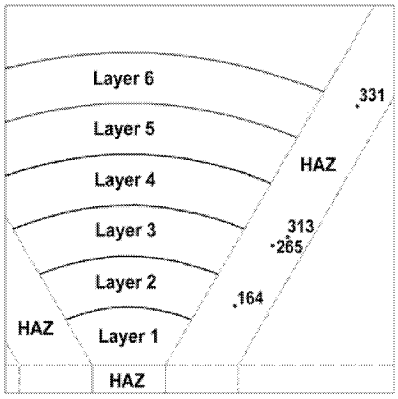

Fig. 10 Scheme of selection of characteristic points selected in order to determine thermal cycles.

The following input data were used for numerical calculation:

a) parent metal: alloy steel – type 91,
b) welding filler metal: filler metal-like material similar to P91 steel,
c) welding method: TIG, no preheating, six layers in a weld,
d) physical properties such as mass density [kg/mm^3], thermal conductivity λ [cal/(mm×s×°C)] and specific heat c [cal/(kg×°C)] were adopted for alloy steel and alloy deposited metal accordingly.

The purpose of numerical modelling was to present thermal phenomena occurring in HAZ areas in the vicinity of a weld groove affected by multiple welding thermal cycles. The adopted procedure was as presented below. First, a thermal field in the temperature range 1100 ÷ 1500 °C was selected. Then, for a model containing six welded layers, characteristic points situated in HAZ were selected (as presented in Fig. 10). Next, for the aforementioned points, thermal cycles were determined successively for individual layers of a weld.

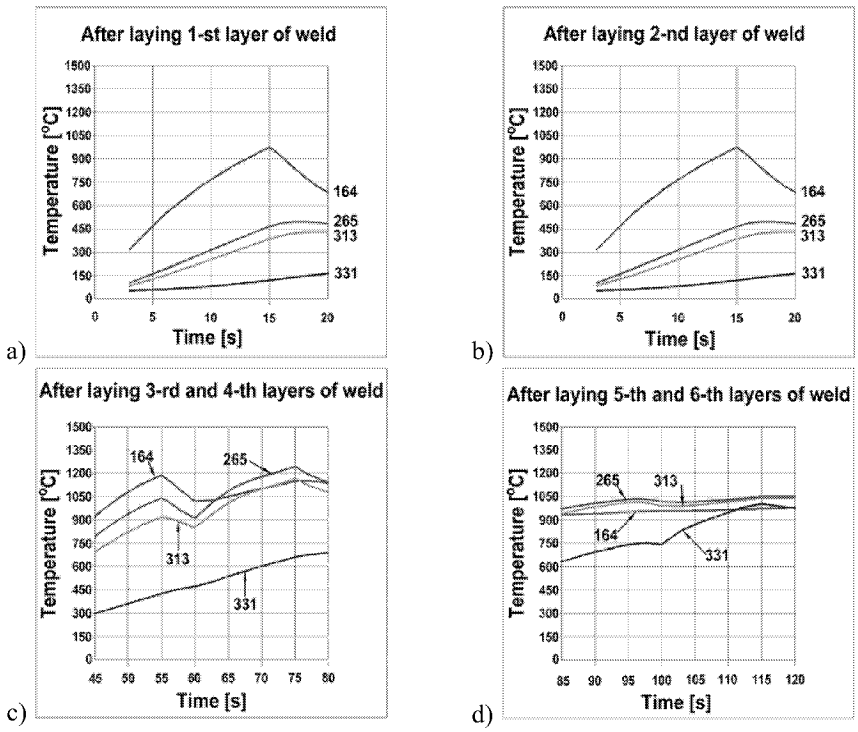

Fig. 11 Thermal cycles after laying successive layers of weld.

While analysing the results of examinations obtained on the basis of numerical calculation, it is possible to follow the tendencies of the changing parameters of welding cycles (see Figure 12).

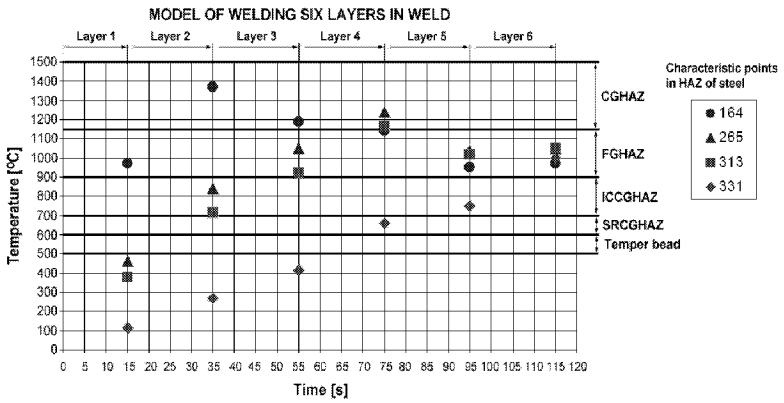

Fig. 12 Distribution of temperatures for thermal cycles in characteristic points located in HAZ area next to faces of third and sixth layers of weld for P91 alloy steel.

The distribution of temperatures of thermal cycles in selected points of HAZ in P91 steel after making successive layers of a weld shows that the maximum temperatures of cycles become stabilize between the fourth and sixth layers (Figure 12). The said temperatures are situated in the temperature range corresponding to a fine grain HAZ, which leads to the conclusion that the improvement of plastic properties of coarse grain HAZs during repair welding may be obtained after making three or four layers of a weld.

6. Summing up

As a result of examinations conducted it was possible to obtain very important information related to plastic properties of HAZ areas of different microstructures and the knowledge about the course and parameters of welding thermal cycles in the conditions of multiple welding thermal cycles. Both the examinations performed by means of a simulator for thermal and strain cycles and numerical calculation made by means of ANSYS 5.6 programme proved useful and efficient as despite the great complexity of phenomena accompanying an actual welding process they made it possible to predict tendencies of changes of structural morphology of steel, plastic properties and the parameters of thermal cycles.

7. References

[1] Haze T., Aihara S.: Metallurgical Factors Controlling HAZ Toughness in HT50 Steels. IIW Doc. IX-1423-86.

[2] Guide to Weldability and Metallurgy of Welding of Steels Processed by Thermomechanical Rolling or by Accelerated Cooling. IIW Doc. IX-1649-91.

[3] Devillers L., Kaplan D., Testard P.: Predicting the microstructure and toughness of weld HAZs. Welding International, nr 9, 1995, s. 128 ÷ 138.

[4] Matsuda F. et al.: Review of Mechanical and Metallurgical Investigations of M-A Constituent in Welded Joint in Japan. IIW Doc. No IX-1782-94.

[5] Łomozik M.: Investigations on welding thermal cycles in temperbead welding process for ductility improvement. Tarasaki R&D Center, Japan Power Engineering and Inspection Corporation, Hitachinaka, Japan, August 2000 - July 2001,

[6] Łomozik M.: Badanie zmian własności SWC stali pod wpływem wielokrotnych cykli cieplnych w oparciu o technikę symulacji. Praca badawcza Instytutu Spawalnictwa Nr Id-115, 2003.

[7] Łomozik M.: Modelowanie pól temperatur w obszarach strefy wpływu ciepła złączy spawanych stali przy pomocy programu ANSYS. Praca badawcza Instytutu Spawalnictwa Nr Da-99, 2004.

DISSIMILAR WELDED JOINTS WITHOUT A BUFFER AREAS OF STEEL TYPE 9CR WITH 1CRMOV TO BE USED FOR STEAM BOILER PIPELINES

Edmund Tasak*, Adam Hernas**, Jerzy Pasternak***, Stanisław Fudali***
* Academy of Mining, 30 Mickiewicza Str., 30-059 Kraków, Poland
** KALLA Sp. z o.o., 17 Barbary Str., 40-053 Katowice, Poland
*** Boiler Engineering Company RAFAKO S.A., 33 Lakowa Str, 47-400 Raciborz, Poland
tasak@metal.agh.edu.pl

Abstract

The main material which is used in Poland in fabrication of steam pipelines is steel grade 1CrMoV. Modernisation of the national power plants, among others through the use of P91 steel grade for pipelines, requires the application of proper technologies when joining the two very different steels.
This paper includes the evaluation of strength properties, characteristics of low-cycle fatigue and technological, evaluation of welded joints' structure, HAZ and deposited metal by means of LM, SEM and TEM techniques.
Conclusions were presented regarding the manufacturing process, recommended welding technology and heat treatment of pipeline welded joints of steel 1CrMoV to steel P91, ensuring full implementation thereof in modernisation works of the existing 360MW units. This technology may also be applied in erection of the supercritical power unit at Belchatow Power Station.

Keywords: Hastelloy alloys, flue gas desulphurisation plants, corrosion resistance, microstructure.

Introduction

The objectives of the Polish power policy include erection of power units with supercritical parameters at the following power stations: PAK, Lagisza and Belchatow P.S. Moreover, de-capitalisation of the vast majority of the power units requires modernisation and prompt rehabilitation of units with conventional parameters, as well as increase of their efficiency, also including modernisation of steam pipelines [1,2].
The dominant steel grade applied in fabrication of steam pipelines is 13HMF steel (equivalent of 14MoV63 acc. to DIN Standard), which contains approx. 1%Cr, 1%Mo and up to 0.25%V. Therefore, some research works were taken up in order to gain more knowledge indispensable for modernisation works at the national power stations and production of dissimilar welded joints on steam pipelines. The basic technological issues accompanying fabrication of this type of joints cover the increased brittleness in P91 steel heat-affected zone, resulting from so-called "reactive" diffusion. The diffusion results from a considerable difference between Cr concentration in the P91 steel HAZ material and the welded joint made with electrodes characterised by 1CrMoV steel chemical composition. Formation of coal enriched and impoverished zones has a considerable impact on mechanical and functional properties of a welded joint [3].
Technological experiments and examinations were carried out on three thick-wall butt test welded joints on P91 – 1CrMoV tubes. The applied welding materials, welding and heat treatment parameters of the pipeline joints were determined on the basis of tests performed at RAFAKO S.A.[2,3]

1. Selection of materials and fabrication of welded joints

In order to verify the assumed welding technology, three butt test welded joints of 13HMF steel tube to P91 steel tube, dim. Ø325x36mm, were manufactured. The shape and dimensions of the test joints corresponded to standard EN 288-3.
The selection of welded joints was made taking into consideration the evaluation of filler metal chemical composition influence on the welded joint properties, especially the heat-affected zone. The joints were fabricated with the application of the following filler metals:

- high-alloy, with higher strength properties, type C9MV-IG/ Fox C 9 MV, used in welding P91 type steel,
- low-alloy, with lower strength properties level, type DMV 83-IG/ Fox DMV 83 Kb, used in welding 13HMF type steel,
- and high-nickel filler metal type Thermanit Nicro 82.

The welded joints were made according to WPS, instructions and WPAR prepared in RAFAKO S.A. The joints were made on tubes having the wall thickness of 36 mm and diameter of 325 mm. The root beads in all these welded joints were made using GTAW (141) method, whereas the filling beads were made using SMAW (111) method. Before welding, the joints were heated to the temperature of 300÷350°C. During welding, constant inter-pass temperature of 200÷300°C was maintained. All welded joints underwent heat treatment – i.e. stress relief annealing – for 3 hours at the temperature of 730°C.
The welding conditions and parameters of the joints were determined on the basis of manufacturing experiences of RAFAKO S.A., as well as those gained during the co-operation between RAFAKO S.A. and Silesian Technical University in Katowice [2,3].

The details of welding preparation, welding parameters and the sequence of the welded joint beads with the use of filler metal having higher alloy element content, i.e. type C9MV-IG/ Fox C9MV, are presented in figure/ table 1.

Joint Design	Welding Sequences
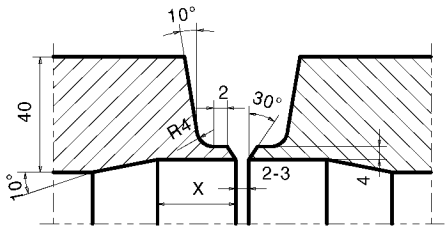	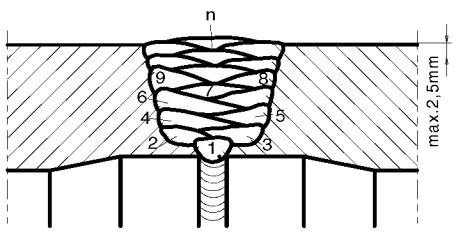

Welding process details

Run	Welding methods	Size of Filler Material	Current [A]	Voltage [V]	Type of current/ Polarity	Wire Feed Speed	Heat input
1	GTAW/ 141	2,4	90 ÷ 100	-	DC"-"	-	-
2 ÷ 3	SMAW/ 111	2,5	70 ÷ 100	-	DC"+"	-	-
4 ÷ 5	SMAW/ 111	3,2	90 ÷ 140*	-	DC"+"	-	-
8 ÷ n	SMAW/ 111	4,0	130 ÷ 180*	-	DC"+"	-	-

*max. thickness of each bead, layer: 2,5mm

Figure/Table 1. Details welding preparation, wire and electrode diameters and applied welding parameters of ϕ325x36mm tube butt welds.

The chemical composition and types of the filler metals applied in welding the aforementioned joints are contained in Table 2.

Table 2. Chemical composition of filler metals used in butt welds of 13HMF to P91 acc. to Bohler-Thyssen Welding company catalogue.

Type of Filler Metal	Chemical composition [%] Weight									
	C	Si	Mn	Cr	Mo	Ni	W	V	Nb	Fe
Fox C 9 MV	0.09	0.3	0.5	9.0	0,9	0.9	-	0.2	0.05	n.a.
Fox DMV 83 Kb	0.05	0.4	1.1	0.4	0.9	-	-	0.5	-	n.a.
Thermanit Nicro 82	0.02	0.2	2.8	19.5	-	> 67	-	-	2.5	<2.0

2. Examination programme

The examination programme of the welded joints made included among other things:

- selection of welding and heat treatment parameters and after-welding non-destructive examinations,
- evaluation of the welded joints quality based on the mechanical and technological properties testing results at ambient temperature and at elevated temperatures,
- evaluation of the welded joint strength and technological properties,
- macro- and micro-structure examinations of the base material,
- experimental heat treatment and evaluation of decarburisation processes in the welded joint area.

2.1. Examination methodology

The evaluation of strength, tensile and technological properties of the welded joints made was carried out through the executed non-destructive examinations, which were performed following the heat treatment and non-destructive examinations of the joints.

The results of mechanical and technological properties of RAFAKO SA experiments - after welding, heat treatment and non-destructive examination are demonstrated in table 3.

Table 3. The results of mechanical and technological properties of butt welds, 13HMF to P91 steel connection - including properties of base material, HAZ, and weld metal.

Type of welded joints	Base material								Weld metal		
	13HMF				P91						
	Tens Str. [MPa]	Yield Point [MPa]	Alon [%]	Impact Energy [J]	Tens Str. [Mpa]	Yield Point [Mpa]	Alon [%]	Impact Energy [J]	Tens Str. [Mpa]	Yield Point 350^0C [Mpa]	Impact Energy [J]
Fox C 9 MV	532	376	28,8	48,42,36	670	516	26,2	208 192 190	571 569	337	90,84,78 82,88,80
Fox DMV 83 Kb	538	377	-	46,54,42	663	506	-	190 192 186	574 568	347	186,176,190 198,210,206 158,178,184
Thermanit NICRO 82	524	359	27	38,32, 38	663	505	28,4	166 148 160	562 556	281	76,88,92 98,88,90 90,90,86

	HAZ 13HMF		HAZ P91		
Fox C 9 MV	-	78,202,72 210,142,178 122,130,142	-	70,42,94 78,94,64 216,206,216	-
Fox DMV 83 Kb	-	190,198,242 266,264,262 254,192,236	-	150,158,132 110,176,82 144,86,110	-
Thermanit NICRO 82	-	190,170,118 100,160,116 142,128,126	-	118,140,110 198,246,226 152,198,192	-

Static tensile test of the base materials was executed in accordance with PN-EN 10002-1:1998 + AC1/ PB.5.4.52 standard, that of the welded joints – according to the requirements of PN-EN 895 standard.
Static tensile test of the welded joint at elevated temperatures was performed according to PN-EN 10002-5:1998 standard.
Static bending test on the welded joints was carried out according to PN-EN 910 standard on a bending mandrel having the diameter equal to 3 thickness of a sample.

Impact test of the base materials used in welding of the test welded joints and testing of the impact strength of the samples cut out from the thick-walled tube welded joints were performed on normalised impact samples, having the dimensions of 10x10x55 mm – with Charpy V-notch cut on the depth of 2 mm.
Hardness measurements of the welded joints with Vickers method: according to EN 1043-1 and EN 288-3 standards, with the load of 98.1kG (HV10).
The neatly planned fatigue testing at ambient temperature and at 550^0C are just being executed.

3. Influence of heat treatment on structural changes in welded joints of 13HMF steel to P91 steel

In accordance with the technological instruction, after welding, 13HMF to P91 welded joints are annealed at the temperature range of 720÷750°C, in order to temper the martensite formed during the welding process. In manufacturing conditions there is sometimes a necessity to perform heat treatment several times, when the welding process parameters are not always maintained. Therefore, on the welded joints, heat-treated in the industrial conditions, another heat treatment at the temperatures of 730, 750 and 780°C, and for 3, 5 and 10 hours were performed. The temperature of 780°C is beyond the admissible level for 13HMF steel. The purpose of the examinations was to show unfavourable changes to the structure and properties during heat treatment at various temperatures and time, as well as in overheat conditions and seeking ways of foreseeing such changes [4,5].
After the renewed heat treatment, metallographic micro-sections were made and thorough analysis of structural and properties changes was carried out in the area where different materials were joined. The width of the decarbonised zone was measured, as well as the micro-hardness in the decarbonised and carbonised zones. Moreover, an attempt was made to calculate the width of the decarbonised zone with the use of Recarb programme.
Examples of typical microstructures following heat treatment are shown in drawings 2 to 7.
Microscopic examinations proved that another heat treatment at the temperature of 730°C and lasting 3÷10 hrs does not have any significant impact on the structure change. Only some slightly brighter areas are visible on the 13HMF steel side or the side of welded joint made by means of Fox DMV 83 Kb electrode. It is the heat treatment, which lasts 10 hours, which results in appearance of decarbonised areas with large ferrite grain (Figure 2).

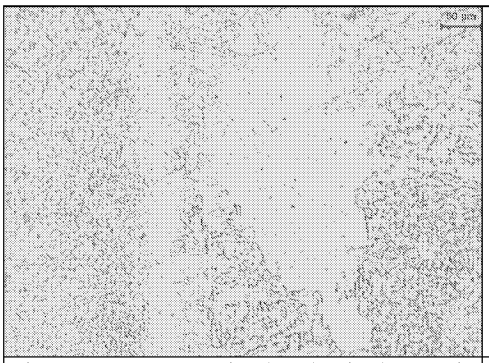

Figure 2. Coarse grain decarbonised zone in welded joint made with electrode having 13HMF composition. Annealing temperature 730°C, time 10 hrs.

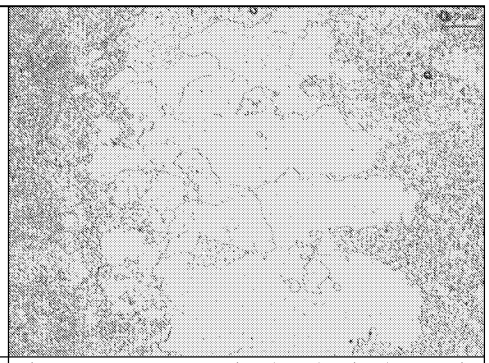

Figure. 3. Coarse grain decarbonised zone in welded joint made with electrode having 13HMF composition. Annealing temperature 730°C, time 5 hrs.

At the temperature of 750°C, after only 3 hours, there occur distinct decarbonised areas, the length of which cab be measured easily. Time extension and temperature increase result in formation of intensely decarbonised areas with large ferrite grain having the width of up to 0.35 mm (Figure 3). Simultaneously, in 13HMF steel and the welded joint made with Fox DMV 83Kb electrode with this filler metal at the temperature of 750°C there occur traces of "fresh" martensite in a pour-out arrangement. These effects are even more significant after heat treatment at the temperature of 780°C (Figures 4 and 5). Such structure causes considerable decrease of tensile properties, particularly in impact resistance.

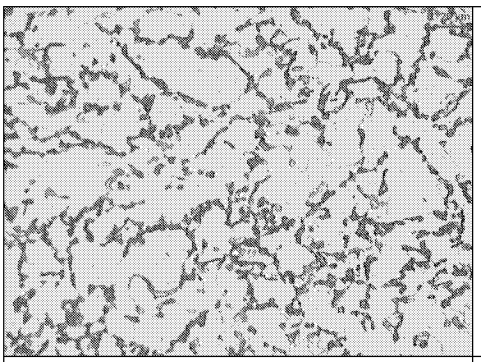

Figure 4. Ferrite-martensitic structure of 13HMF steel. Annealing temperature 780°C/3h.

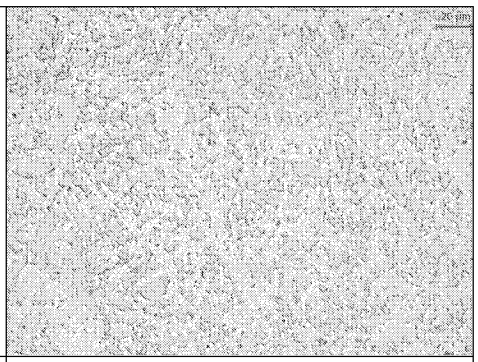

Figure 5. Ferrite-martensitic structure of welded joint made with electrode with 13HMF composition. Annealing temperature 780°C/3h.

In the area of welded joint fusion penetration, made with Thermanit NICRO 82 filler metal, there are no significant changes in the structure. However, in the welded joint made with this filler metal, we can observe a distinct heterogeneity of the structure. This is a normal phenomenon, though, which does not have any significant influence on the welded joints properties.

4. Presentation of test results

1. The tests executed showed that heat treatment of 13HMF to P91 steel welded joints at the temperature of 730°C, within the tested range of p to 10 hrs, does not cause any crucial changes of structure in the joint area. Higher temperatures, i.e. 750 and 780°C, lead to formation of a clearly decarbonised zone on the material side below alloy. The longer the heat treatment time, the larger the width of the decarbonised layer. The measured width of the decarbonised coarse-grain layer for the temperature of 780°C and 10 hours of annealing is 0.37 mm. The calculated widths of the decarbonised layer are not compliant with the experimental data and are considerably larger (Table 4). Such difference may result from the fact that decarbonisation occurs not only in the coarse-grain area of ferrite (which is measured), but also in the areas with fine acicular structure. This is shown in Figure 6. Evaluation of the actual width of the decarbonised zone can be made on a micro-probe. This is, however, a time-consuming method and practically useless [4-7].

2. 13HMF to P91 steel welded joints must not be annealed at the temperature of 750°C or higher, since A_{c1} temperature may be exceeded and, after cooling, "fresh" martensite is obtained in the structure. This would lead to the considerable decrease in tensile properties of both the parent metal and the welded joint.

Table 4. Properties of fusion penetration line area and decarbonised zone width.

Temperature [°C]	Time [h]	Medium hardness of carbonised zone [μHV]	Medium hardness of de-carbonised zone [μHV]	Measured width of decarbonised zone [μm]	Calculated width of decarbonised zone [μm]
730	5	250	132	no distinct zone	-
730	10	253	131	no distinct zone	-
750	3	234	136	40	547
750	5	246	134	250	746
750	10	242	130	500	1,067
780	3	253	126	330	808
780	5	257	128	350	1,044
780	10	246	132	375	1,470

3. The decarbonised zone can be characterised by low hardness and strength and, therefore, they may contribute to numerous cracks and failures of constructions operating at given stresses and at elevated temperatures.

4. 13HMF steel is highly prone relaxation cracks (Figure 7). Therefore, the mode of heating during heat treatment of dissimilar welded joints of 13HMF to P91 steel ought to be changed. Heating should be disrupted at the temperature of 530-550°C in order to allow preliminary

relaxation of stresses (Figure 8). The duration of preliminary annealing at the temperature of 530-550°C should be twice longer than the heat treatment time at the temperature appropriate for this type of welded joint (730-740°C).

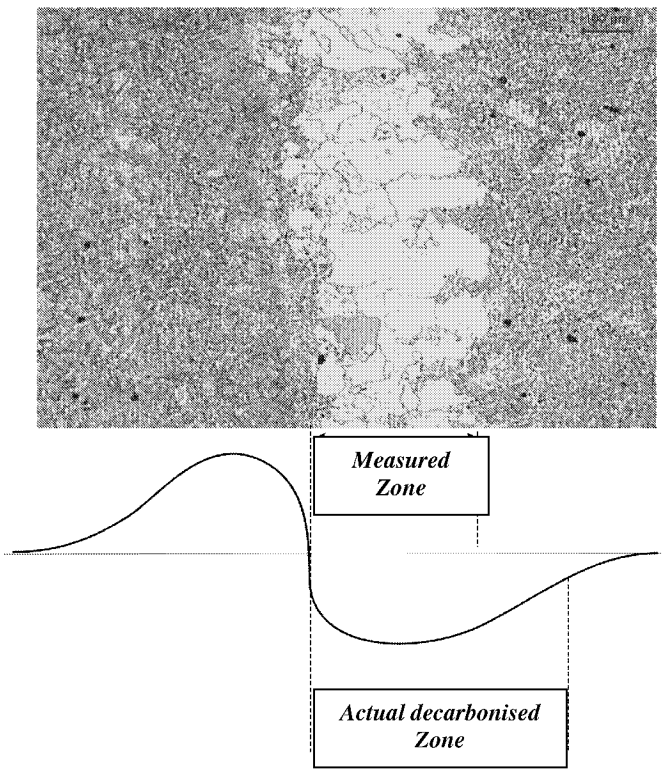

Figure 6. Probable reason of difference between experimental and calculation data.

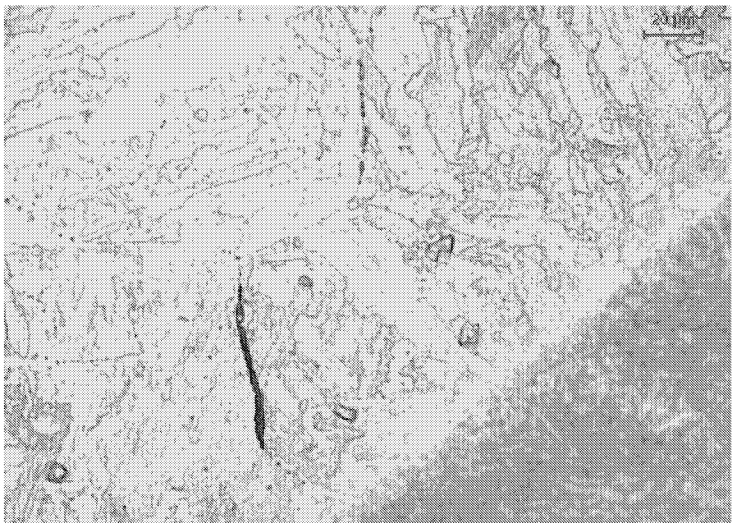

Figure 7. Relaxation cracks in HAZ of 13HMF steel.

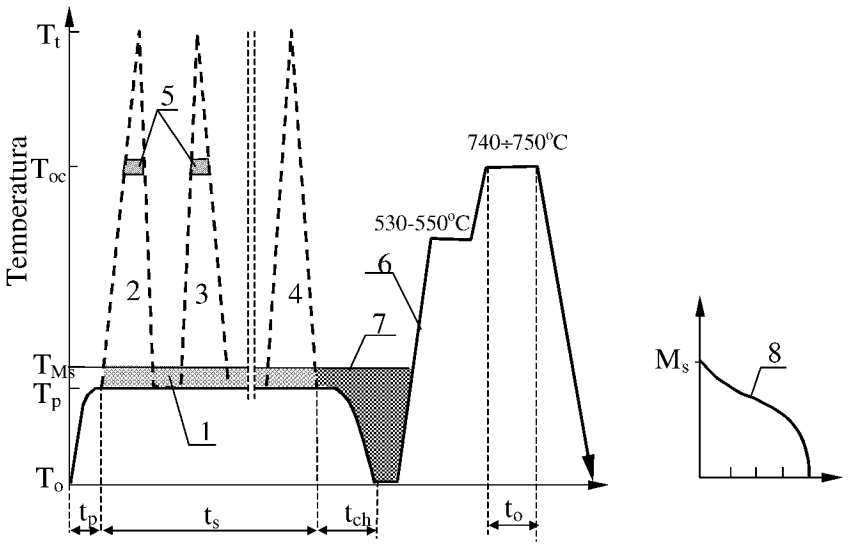

Figure 8. Proposed diagram of heat treatment for dissimilar welded joints of 13HMF to P91 steels

6. Conclusions

It was unquestionably found out that the technologies of welding and heat treatment, which are applied in the manufacturing process, in case of pipeline welded joints of 13HMF to P91 steel, can be largely used in modernisation works of the existing standard boilers, as well as guarantee their full application for supercritical parameters Unit 13 which is to be erected at Belchatow Power Station [4,5].
Introduction of P91 steel enables to decrease the design wall thickness of tubes, the weight of superheaters and, thus, the investment and operational costs of a unit, with vast improvement of the unit efficiency, on condition that:

- the experiences regarding chosen techniques and technologies of welding 13HMF steel to P91 steel tubes are made available to the power plant technical personnel,
- training shall be provided for welders from Belchatow Power Station, regarding the required welding techniques of P91 steel.

7. References

[1]. Pasternak J., Hernas A., Miliński P.: New martensitic steels for supercritical boilers. Energetyka No 4, 1997 (in Polish only).
[2]. Hernas A., Cieśla M., Niewielski G., Kiełbus A., Lalik S: „Assessment of delivery condition properties of selected new Cr-Mo-V-W-(Cu) steel grades used for boiler tubes and their welded connections to be operated in supercritical parameters", Research work NB-200/RM-7/98, November 1998.
[3]. Hernas A., Kiełbus A., Cieśla M., Rodak K.: „Assessment of large thickness welded joints made of P91, P92 steel grades and T23 base material", Research work P/IX-2/01, September 2001.
[4] Tasak E., Hernas A.: Report No P/XII-4/ 2004, RAFAKO SA, Poland
[5] Tasak E., Ziewiec A., Brzeziak: Przegląd Spawalnictwa, nr 9, 2002
[6]Pilous V., Stransky K.: Zvaranie 32, nr 8, 1983 i Zvaranie 33, nr 1 , 1984
[7]Stransky K., Milion B., Kucera J.: Zvaranie 32, nr 1 1983

CREEP PROPERTIES OF HETEROGENEOUS P91/P23 WELDS AT 550 AND 600°C

Zdeněk Kuboň, Vlastimil Vodárek, Denisa Toušová

VÍTKOVICE – Research and Development, Ltd., Ostrava, Czech Republic
creep.lab@vitkovice.vz

Abstract

The experience indicates, that in majority of cases where high temperature failure of power plant components occurs, defects predominate in the vicinity of weldments. P91 and P23 steels represent prospective materials for applications in boilers of modern power plants. The use of heterogeneous welds made of these steels seems to be unavoidable. Practical application of such heterogeneous welds does require detailed knowledge about their creep properties at design temperatures and stresses.

Heterogeneous welds made of tubes P91/P23 with dimension ϕ219x25mm were prepared by combination of GTAW and SMAW technologies. Two different filler materials were used: E CrMo91 B and Thyssen Cr2WV. The paper summarises results of creep rupture tests on crossweld specimens of heterogeneous welds P91/P23 at temperatures 550 and 600°C. Furthermore, results of metallographic investigations on longitudinal sections of ruptured test pieces and hardness profiles are discussed. The analysis of preferential failure locations of heterogeneous welds in relation to the type of the filler material, temperature of testing and applied stress is performed.

Keywords: heterogeneous weld, P23 steel, P 91 steel, creep, microstructure

Introduction

The demand for the improvement of thermal efficiency of fossil fuelled power plants by means of increasing the operating parameters of boilers has recently led to the development of new creep-resistant steels like chromium modified steel grades T/P91 (X10 CrMoVNb 9-1 according to EN 10216-2), E911 (X 11CrMoWVNb 9-1-1) and T/P92. They have improved mechanical properties at high temperatures and in particular creep strength. The new grades of low alloyed heat resistant steels T/P23 and T/P24 (7CrMoVTiB10-10) with substantially higher creep resistance compared to the Grade 22 steel are designed for the water wall panels for USC boilers but can be also used for the superheaters of conventional boilers.

Mechanical properties including long-term creep resistance of all new boiler materials have been studied extensively and at the present time these steels are routinely used in construction of the new as well as remedy of the existing power plant units. In all these structures it is inevitably necessary to make weldments, either among materials with the same chemical composition or heterogeneous welds to join materials with different chemical composition. As weldments are widely recognized as the life-limiting part of many high temperature components, special attention should be paid to the long-term creep behaviour of the welds. Moreover, the reliability of the heterogeneous welds is affected not only by the complex of design, technology and service parameters [1], but also by the change of the chemical composition through the weld joint due to the different chemical composition of the individual base metal [2, 3]. Therefore, it is necessary to study creep resistance, failure mode and failure locality of welded joint besides the parent materials.

Weldments made of modified 9-12% chromium steels and low alloy creep resistant steels belong to the most important ones [4-6]. However, the chemical heterogeneity of these welded joints influence negatively their structural stability especially during long-term creep exposure. Due to the gradient in the chemical potential interstitially dissolved atoms (typically carbon and nitrogen) diffuse through the fusion line from the low alloy steel to the chromium modified steel. As a result the formation of carburised (or nitrided) zone in the more alloyed steel is observed and on the other hand the depleted zone in the low alloyed steel [6-8]. The extent of degradation of the material properties depends on the type of parent materials, filler metal as well as the parameters of creep exposure.

The presented paper deals with creep properties and microstructure of the heterogeneous weldments made of P91/P23 steels.

Experimental materials and procedures

Two dissimilar weld joints made of P23 and P91 steel pipes of the dimensions Ø219x25 mm were fabricated in SES Tlmače [9, 10] by using different filler metal based on low-alloyed and chromium modified steel. Pipe of P91 steel has been produced in ESW Röhrewerke GmbH while the pipe of P23 steel was delivered by Vallourec&Mannesmann Tubes. The chemical analysis of applied base materials (as specified in the material standards and by heat analysis) is stated in table 1.

Table 1: Chemical composition of P91 and P23 base materials, mass. %

Steel	C	Si	Mn	P	S	Cr	Mo	Al	Nb	V	N	B	W
P23	0.04	max.	0.10	max.	max.	1.90	0.05	max.	0.02	0.02	max.	max.	1.45
	0.10	0.50	0.60	0.030	0.010	2.60	0.30	0.030	0.08	0.08	0.030	0.006	1.75
	0.07	0.28	0.54	0.008	0.004	2.08	0.08	0.018	0.03	0.22	0.011	0.002	1.65
P91	0.08	0.20	0.30	max.	max.	8.00	0.85	max.	0.060	0.18	0.030	-	-
	0.12	0.50	0.60	0.020	0.015	9.00	1.05	0.040	0.100	0.25	0.070		
	0.10	0.38	0.49	0.020	0.001	8.50	0.94	0.018	0.069	0.23	0.043	-	-

Hot rolled pipes made of P91 steel were normalized at 1050°C followed by air cooling and tempering at 750°C. Heat treatment of P23 steel pipes was carried out by quenching from 1050°C into water with subsequent tempering at 760°C. The mechanical properties of both pipes after heat treatment is given in table 2.

Table 2: Mechanical properties of delivered pipes

Steel	Mechanical properties at 20°C		
	R_e [MPa]	R_m [MPa]	A_5 [%]
P23	496	597	23.3
P91	564	715	20

As the combined joints of this type can be made by using filler metal having chemical composition corresponding either to high or to low alloy parent metal, there were chosen two different filler metals based on 9%Cr and 3%Cr steels, respectively. Wire made of Thermanit MTS 3 was used in the root and Thyssen Chromo 9V electrode for the filler in the first case

(marked in the following as **WELD A**). The second weldment marked as **WELD B** was based on 3%Cr weld metal, namely Union I Cr2WV wire for root in combination with Thyssen Cr2WV electrode for filler.

Both weldments were fabricated by using GTAW (141) in combination with SMAW (111) welding as a part of COST 522 project in SES Tlmače (Slovakia). The details of welding process, used parameters and the results of non-destructive as well as mechanical testing were stated in [9]. After welding were both welds post weld heat treated at 750°C for 2 hours. Cross weld creep specimens were machined so that they include both base materials, heat affected zone and weld metal (due to the fact that GTAW was used only for the first weld bead in the root, weld metal corresponded to the SMAW filler material composition). Uniaxial creep rupture tests were performed at temperatures 500, 550 and 600°C and in the stress interval from 75 to 170 MPa. Hardness profiles were measured in some ruptured creep tests as well as microstructure analysis of fracture zone and the other parts of weldment after creep exposure.

Results of creep tests of both weldments

The results of creep tests of both welds are stated in Figs. 1 and 2 for welds A and B, respectively in the form of stress dependence of Larson-Miller parameter with L-M constant C=25. Still running creep tests are marked with arrows.

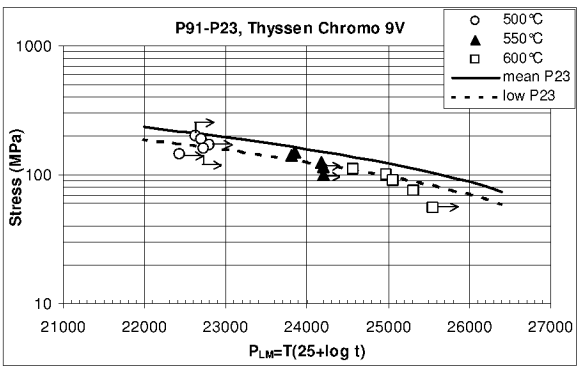

Fig. 1: Creep rupture strength results of Weld A

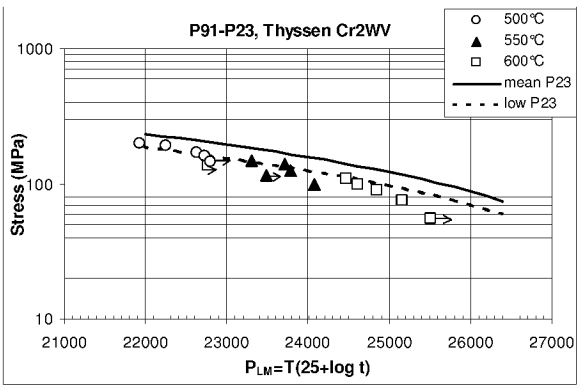

Fig. 2: Creep rupture strength results of Weld B

Together with the results of experimental materials, the mean and minimum (-20% of the mean value) standardized creep rupture strength of steel P23 is stated there expressed in the same way by stress dependence of Larson-Miller parameter. Although the testing is not finished yet, the results indicate that the creep rupture strength of weldments in both cases lie close to and even under the minimum standardized value for steel P23. Most creep tests run at 550 and 600°C at stresses under 100 MPa showed low reduction of area, typically under 8%.

Structural analysis

Microstructure analysis of the fracture locality and surrounding heat affected zone, weld metal and basic material of a set of broken creep tests of both weldments with different reduction of area levels was made together with the measuring of hardness profile of the weld.

Weld A

The principal testing parameters and results of ruptured creep tests of weld A together with the location of fracture are stated in Table 3.

Table 3: Testing parameters and location of fracture of Weld A

Specimen	Temperature °C	Stress MPa	Time to rupture, h	R.A. %	Fracture location
A1	500	200	18 802	50.8	BM P23
A2	**550**	**150**	**9 715**	**26.3**	**IC HAZ of P23**
A3	550	140	8 665	4.1	FL WM/P23, CG HAZ P23
A4	550	125	23961	4.1	FL WM/P23, CG HAZ P23
A5	600	110	1 384	2.1	CGHAZ of P23
A6	600	100	4 056	1.8	FG HAZ of P91
A7	**600**	**90**	**5 171**	**8.2**	**FL WM/P23, CG HAZ**
A8	**600**	**75**	**9 852**	**0.6**	**FG HAZ of P91**

Microstructure of the steel P91 and weld metal (E CrMo91 B) was martensitic, while microstructure of the base material of steel P23 consisted of tempered bainite. Narrow carburised zone in the fusion line of P23 steel is a result of carbon redistribution from low alloy P23 steel to the higher alloyed weld metal. Typical width of the heat affected zone varied from 3 to 3.5 mm.

Detailed microstructural analysis was made in three crept specimens highlighted in table 3 by bold text in shadowed cells. The first specimen analysed (specimen A2) had relatively high reduction of area and the fracture occurred in fine grained part of heat affected zone of steel P23 (Fig. 3). At the same time cracks spreading perpendicularly to the surface along the prior austenite grains in coarse grained HAZ of steel P23 were detected, too (Fig. 4).

Specimen A7 ruptured in the fusion line of steel P23, see Fig. 5. The rupture line run partly (approx. 50%) through coarse grained part of HAZ, partly through weld metal. Large amount of cavities was detected in the intercritical part of HAZ of steel P91, Fig. 6.

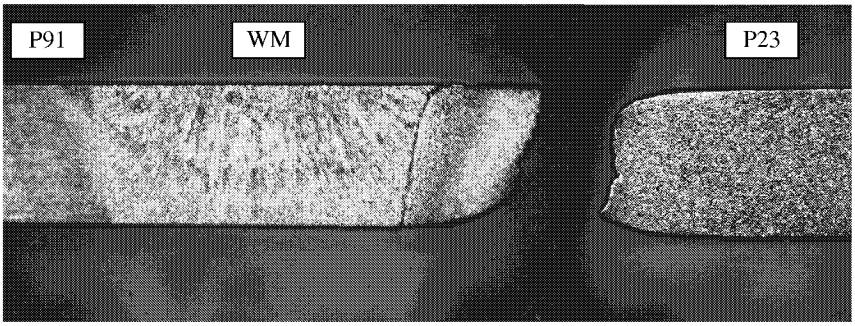

Fig. 3: Longitudinal sections of ruptured testpiece A2

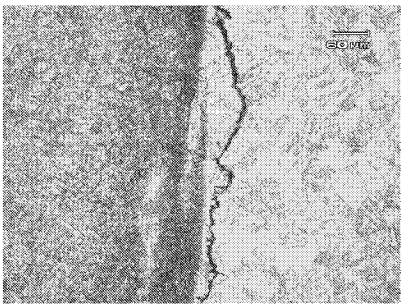
Fig. 4: Crack propagation in fusion line of testpiece A2

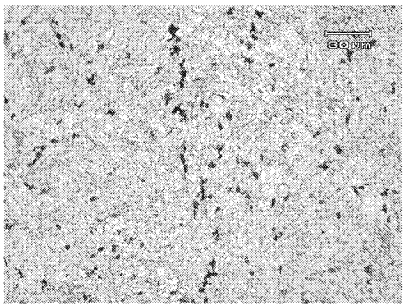
Fig. 6: Cavities in intercritical region of HAZ in specimen A7

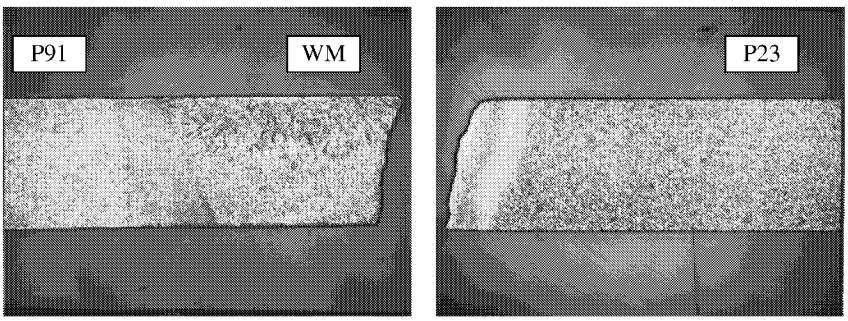

Fig. 5: Longitudinal sections of ruptured testpiece A7

Specimen A8, tested also at 600°C but at lower stress, ruptured in fine grained aprt of HAZ on side of steel P91 – see Fig. 7. Similarly as in case of specimen A2 cracks spreaded perpendicularly to the surface preferentially along the prior austenite grains in coarse grained HAZ of steel P23 were detected – see Fig. 8.

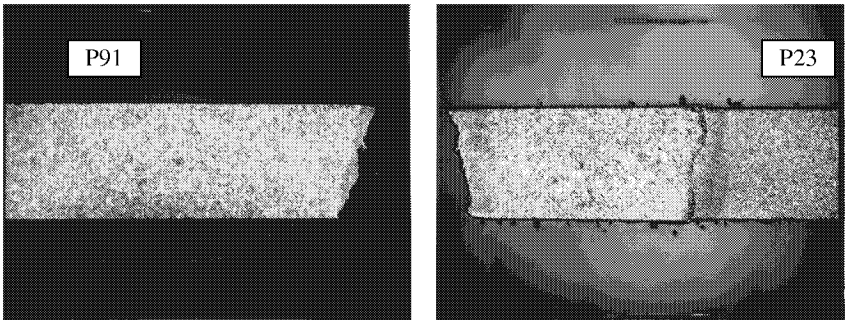

Fig. 7: Longitudinal sections of ruptured specimen A8

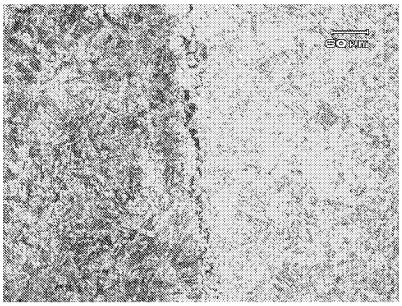
Fig. 8: Cracks in CG HAZ of P23 steel, specimen A8

Results of metallographic investigations prove that preferred locality of failure in Weld A is a complex function of testing parameters (temperature, stress) and local microstructural parameters. Three critical localities prone to the development of creep damage were identified as follows:

a) intercritical part of heat affected zone (IC HAZ) of P23 steel
b) fusion line and coarse grained HAZ on the side of P23. In this coarse grain area decarburization took place during PWHT and creep exposure.
c) intercritical and/or fine grain regions of heat affected zone (IC HAZ, FG HAZ) of P91 steel.

In the course of creep exposure the development of creep damage can simultaneously take place in several critical areas but the location of the final failure is determined by the "weakest area" for given testing parameters.

Weld B

The testing parameters and results of ruptured creep tests of weld B including the location of fracture are stated in Table 4.

Microstructure of the steel P91 was again martensitic, while both weld metal (Cr2WV and base material of steel P23 consisted of tempered bainite. On the contrary to the previous weld A, there is a pronounced transition area between weld metal and heat affected zone of steel

P23 and narrow carburised zone in P91 steel along the fusion line. Typical width of the heat affected zone varied from 2 to 4 mm.

Table 4: Testing parameters and failure location of Weld B

Specimen	Temperature °C	Stress MPa	Time to rupture, h	R.A. %	Fracture location
B1	500	200	2 327	76.0	IC HAZ of P23
B2	500	190	6 065	66.0	IC HAZ of P23
B3	**500**	**170**	**18 679**	**59.3**	**IC HAZ of P23**
B4	550	150	2 064	1.0	WM (close to FL WM/P91)
B5	550	140	6 390	1.5	WM (close to FL WM/P91)
B6	**550**	**125**	**7 778**	**2.5**	**WM (close to FL WM/P91)**
B7	550	115	3 395	7.3	WM (close to FL WM/P91)
B8	600	110	1 090	3 9	WM (close to FL WM/P91)
B9	600	100	1 538	4.2	WM (close to FL WM/P91)
B10	600	90	2 917	3.8	WM (close to FL WM/P91)
B11	**600**	**75**	**6 550**	**4.6**	**WM (close to FL WM/P91)**

Microstructural analysis was made also in three crept specimens highlighted in table 4 by bold text in shadowed cells. The first analysed specimen (specimen B3) had the lowest testing temperature, the longest time to rupture and also high reduction of area. The fracture occurred in fine grained part of heat affected zone of steel P23 (Fig. 9) and was accompanied by the extensive cavitation in IC HAZ of steel P23.

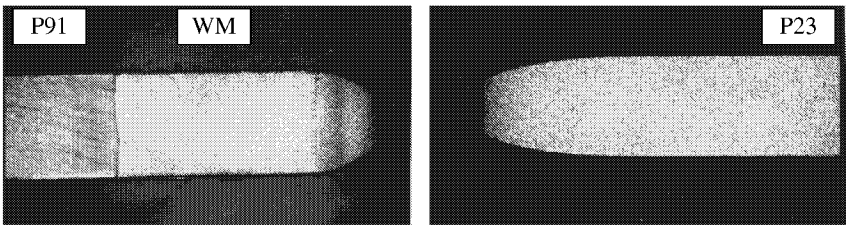

Fig. 9: Longitudinal sections of ruptured testpiece B3

Specimen B6 tested at 550°C for 6390 hours had the lowest reduction of area of all specimens examined in detail (see Table 4). The fracture line lies in the weld metal very close to the fusion line with steel P91 (Fig. 10). In Fig. 11 there is a detail of transverse crack found in the transition area between weld metal and HAZ of steel P23.

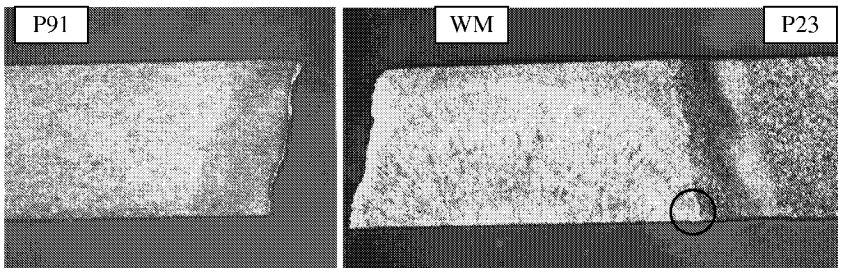

Fig. 10: Longitudinal sections of ruptured specimen B6 (crack in circle)

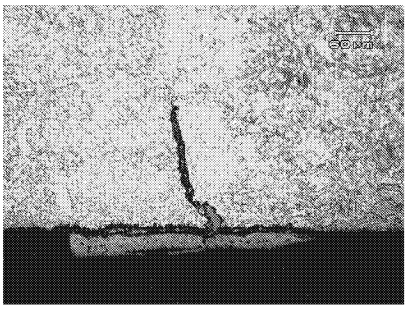
Fig. 11: Detail of crack in fusion line with steel P23, specimen B6

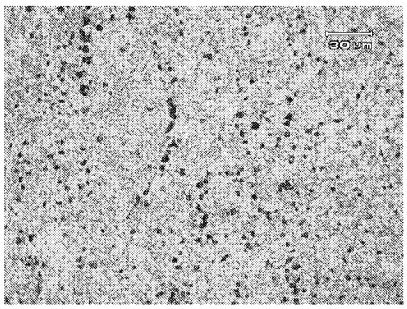
Fig. 13: Cavitation in IC HAZ of steel P23 in specimen B11

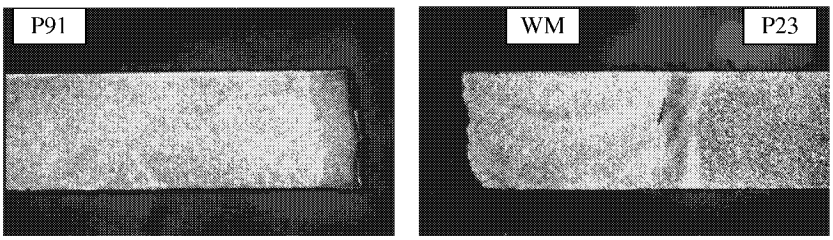

Fig. 12: Longitudinal sections of ruptured specimen B11

Microstructural analysis of creep tests prepared from weld B revealed that also in this case fracture locality depended on the parameters of creep exposure. At lowest temperature 500°C the critical locus of weldment was intercritical part of HAZ while at temperatures 550 and 600°C the preferred area of failure was partly decarburised layer of 2%Cr weld metal in the close vicinity of fusion line WM/P91 steel.

Hardness profiles

Hardness profiles HV 10 were measured in all ruptured creep testpieces and the results are stated in Table 5 compared to the original hardness measured in the state after post weld heat treatment [9]. Moreover, two examples of hardness profile are shown in Figs. 14 and 15 for specimen A8 and B11.

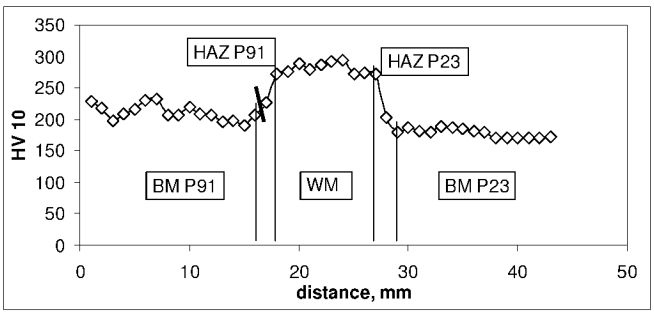

Fig. 14: Hardness profile of specimen A8

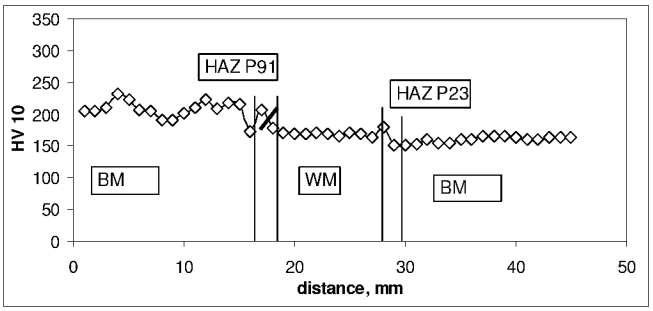

Fig. 15: Hardness profile of specimen B11

Table 5: Results of hardness HV 10 measurements of analysed specimens

Specimen	Temp.	Stress	Time to	HV	Locality	HV	Locality
	°C	MPa	rupture, h	max.		min.	
-	after PWHT			285	CG HAZ P91	185	IC HAZ P23
A1	500	200	18 802	339	WM	183	BM P23
A2	550	150	9 715	287	WM	157	IC HAZ P23
A3	550	140	8 665	281	CG HAZ P91	167	IC HAZ P23
A4	600	110	1 384	343	WM	182	BM P23
A5	600	100	4 056	319	WM	167	BM P23
A7	600	90	5 171	260	WM	153	IC HAZ P23
A8	600	75	9 852	294	WM	171	BM P23
-	after PWHT			260	CG HAZ P91	175	IC HAZ P23
B1	500	200	2 327	256	BM P91	183	WM,BM P23
B2	500	190	6 065	-	-	-	-
B3	500	170	18 679	216	CG HAZ P91	143	BM P23
B4	550	150	2 064	273	CG HAZ P91	-	-
B5	550	140	6 390	236	CG HAZ P91	146	BM P23
B6	550	125	7 778	235	BM P91	147	IC HAZ P23
B7	550	115	3 395	-	-	-	-
B8	600	110	1 090	238	BM P91	168	BM P23
B9	600	100	1 538	236	BM P91	168	IC HAZ P23
B10	600	90	2 917	216	BM P91	136	IC HAZ P23
B11	600	75	6 550	231	BM P91	150	IC HAZ P23

Weld metal is the part of Weld A where the maximum hardness was found in most cases, while in Weld B it was either base metal of steel P91 or coarse grained part of HAZ in steel P91. The weakest part of weldment is then mostly the intercritical part of heat affected zone of steel P23 and in some cases also base metal of steel P23. In weld A the weakest part of the weldment corresponded to the failure locality. On the contrary, the most rupture loci in weld B was not the place of minimum hardness, which is typically IC HAZ of steel P23, but the decarburised part of weld metal adjacent to steel P91 (Fig. 15).
So far, there is no detectable dependence of hardness HV 10 on the testing parameters of creep tests, although the clear secondary hardening of 9Cr-1Mo weld metal in weld A is evident at least at shorter times to rupture. No such clear evidence of secondary hardening can be found in weld B, as the only case where the hardness was higher after creep exposure than after welding was specimen B4 tested at 550°C/150 MPa for 2064 hours. Hardness measurement of minimum values in intercritical part of HAZ or base metal of steel P23 did not revealed signs of secondary hardening in both welds. The only exception was testpiece B1 (500°C/200 MPa/2327 h).

Summary and conclusion

The results of creep tests of two dissimilar weld joints made of P91 and P23 steels with either 9Cr-1Mo base weld metal (THYSSEN Chromo 9V – weld A) or 2Cr-W-Mo (THYSSEN Cr2WV – weld B) conformed that:

- creep rupture strength of both welds lie close to the lower bound of ±20% scatterband round the mean creep rupture strength curve of steel P23
- low reduction of area (below 8%) is typical for creep tests run at 550 and 600°C at stresses lower than 100 MPa
- creep deformation and final fracture occurred in several critical parts of weldment according to the creep exposure parameters, namely:
  - IC HAZ of steel P23
  - close to the fusion line between weld metal and P23 steel (weld A)
  - close to the fusion line between weld metal and P91 steel (weld B)
  - IC HAZ and FG HAZ of steel P91
- creep deformation can develop simultaneously in several parts of weldment, fracture then occurs in the "weakest" locality, which has not to be necessarily the locus with the lowest hardness values
- in order to get relevant information about deformation and failure mechanisms of heterogeneous weldments of advanced creep resistant steels, it is necessary to prolong the creep testing of both weldments at stresses that are comparable to those used in real high temperature components.

Acknowledgement

The authors would like to express thanks to Ministry of Education, Youth and Sport of Czech Republic for the financial support in the frame of the projects OC099 and OC 100.

References

[1] Price, A. T., Williams, J. A.: The Influence of Welding on the Creep Rupture Properties of Steeels, in Recent Advances in Creep and Fracture of Engineering Materials and Structures, Ed. B. Wilshire, D.R.J. Owen, Pineridge Press, Swansea, U.K., 1982, p. 265

[2] Kučera, J., Million, B., Stránský,K.: Chemical Diffusion of Al, Cr, Fe, Ni in Steel Weldments in the Temperature Range of 500-1100 Degrees C. Kovove Mater. 41, 2003, p. 325

[3] Bhadeshia, H.K.D.H.: Design of Heat Resistant Alloys for the Energy Industries, in Parsons 2000–Advanced Materials for 21st Century Turbines and Power Plants, IOM, London, U. K., 2000, p. 1

[4] Laha, K., et al.: Comparison of Creep Behaviour of 2.25Cr-1Mo/9Cr-1Mo Dissimilar Weld Joint with its Base and Weld Metals, Material Science and Technology, 17, 2001, p. 1285

[5] Allen, D. J.: Creep Performance of Dissimilar P91 to Low Alloy Weldments, in Parsons 2003, Engineering Issues in Turbine Machinery, Power Plant and Renewables, IOM, London, UK., 2003, p. 281

[6] Kozeschnik, E.: Dissimilar 2.25Cr/9Cr and 2Cr/0.5CrMoV Steel Welds, Science and Technology of Welding and Joining, 7, 2002, p. 63

[7] Vodárek, V. Fyzikální metalurgie modifikovaných (9-12)%Cr ocelí, Ostrava, VŠB TUO, 2003, p. 169

[8] Pilous, V., Stránský, K.: Strukturní stálost svarových spojů pro energetiku, Studie ČSAV, Academia Praha, 1989

[9] Pecha, J., Bošanský, J.: Welding of similar and dissimilar steels, COST 536 Progress Report, SES Tlmače-WRI Bratislava, 2002

[10] Pecha, J., Kaszásová, E., Bobonič, M.: Welding test welds steel P23 and steel P23 with steel P91, COST 536 Progress Report, SES Tlmače, 2002

STRUCTURAL STABILITY OF HETEROGENEOUS WELD JOINT OF 6CrMoV 8-3-2 AND X12CrMoV 10-1 STEELS WITH INCREASED NITROGEN CONTENT

Rudolf Foret [a], Bronislav Zlámal [a], Jiří Sopoušek [b], Jiří Buršík [c]

[a] Brno University of Technology, [b] Masaryk University,
[c] Institute of Physics of Materials, AS CR; Czech Republic
foret@fme.vutbr.cz; zlbr@email.cz; sopousek@chemi.muni.cz; bursik@ipm.cz

Abstract

Heterogeneous weld joints of creep-resistant steels are used with increasing frequency in the construction of new or repair and reconstruction of existing facilities of power generating and chemical industries. The structural instability of these weld joints appearing during PWHT and in the course of subsequent operation shows by carbon redistribution and subsequent sequence of changes in the structure that lead to the formation of a carbon and nitrogen-depleted zone (CNDZ) in low-alloy steel and, on the contrary, the appearance of a carbon- and nitrogen-enriched zone (CNEZ) in high-alloy steel, with the differences in chromium content having the greatest significance. The paper includes the results of a study of structural changes taking place in laboratory weld joints of the 6CrMoV 8-3-2 (T25) and X12CrMoVNb 10-1 (P91) steels annealed at temperatures of 600 and 900 °C. The nitrogen content in both steels was increased by ion-nitriding and subsequent homogenization. Carbon and nitrogen redistribution measurement by the EPMA method was complemented with detailed structural analyses aimed at the phase and chemical composition of coexisting carbides and carbonitrides.
Results of experimental work were compared with thermodynamic and kinetic calculations using the Thermo-Calc and DICTRA software. A good agreement between the calculations and the experiments was obtained in particular for the phase composition of individual areas of the weld joints.

Keywords: creep-resistant steel, weld joints, structural analyses, thermodynamic and kinetic modelling, carbon and nitrogen redistribution

Introduction

Structural stability of dissimilar welds of creep-resistant steels

An integral part of the development of creep-resistant steels with ferritic matrix is the study of the degradation processes occurring during their operation in power generating and chemical plants, inclusive of the structural instability of both the steels themselves and their weld joints. The term structural instability usually refers to the successive microstructural changes towards equilibrium state, when the Gibbs energy is minimal and when in creep-resistant steels the metastable minority phases dissolve and the stable ones precipitate, and the density of dislocations and the size of grain boundary area (phase interface) decrease. An example of the effect of structural instability on the creep properties of some modified 9-12% Cr steels is the sigmoidal form of the stress-rupture plots [1].

In view of the exhausted service life of a number of power generating blocks (2 x 10^5 and more hours of operation) and with regard to the growing power demand, increased capital investment activities are expected in the area of constructing conventional power plants. It can be expected that in the construction of new power generating blocks and in the reconstruction of existing blocks attention will focus on increasing their efficiency, which will entail continuous development of creep-resistant steels with ferritic matrix, as given, for example, in [2, 3]. Both nuclear and conventional power plants are complex systems, in which it is practically impossible to rule out welding different kinds of creep-resistant steel. In the case

of heterogeneous weld joints of the type of austenite/ferrite or ferrite/ferrite it is already in the stage of their heat treatment (PWHT) or in the course of subsequent exploitation that in particular interstitials (C, N and H) are redistributed, which leads to the appearance of carbon-depleted zones (CDZ) on the part of low-alloy steels, and on the contrary the appearance of carbon-enriched zones (CEZ) on the part of high-alloy steels, both of them in a close vicinity of the fusion zone. The appearance of the above zones is determined by the type of steels being welded, by the conditions of PWHT and by the exploitation itself. The structure of the carbon-depleted zone is usually formed by ferritic grains without any apparent carbidic precipitate [4-6], in which the localization of plastic deformation may occur and the state of tri-axial stress appears. In [7] it is stated that the following three principal cracking mechanisms affecting CrMoV welds had been identified: reheat cracking, type IV cracking and type IIIa cracking. In [4] a detailed description is given of the differences between reheat cracking and type IIIa cracking, adding that type IIIa cracking is due to the above carbon migration.

The authors of [8] observe that the influence of the CDZ on the creep strength of the weld has been the subject of some controversy over the years. Some authors suggest that it has a significant influence on the mechanical properties [9], while others consider the influence negligible [10]. Also ambiguous are the results of the effect of the time of operation (creep tests) on the occurrence of type IIIa failure. While in the case of a weld of the type of 1%CrMoV/12%CrMoV studied in [9] the CDZ shows negatively for short annealing times, in the case of welds of 2.25%CrMo/12%CrMoWV steels type IIIa failure was observed only after longer creep stress times [8]. Likewise Albert et al. [11] report that the occurrence of CDZ and CEZ in heterogenous weld joints is of pronounced negative effect on their toughness at room temperature. As regards the creep characteristics, this effect is ambiguous in the case of type ferrite/ferrite welds while in the case of type ferrite/austenite welds the degradation of these characteristics predominates.

The effect of CDZ on mechanical properties, inclusive of the creep characteristics, must be considered comprehensively. Besides the carbon depletion itself, assessed by the zone width and carbon concentration, it is also necessary to examine the occurrence of carbides or nitrocarbides not only in the CDZ but also in the carbon-enriched (hard) zone of high-alloy steel and then evaluate the mechanical properties of the weld joint as a whole, i.e. with the corresponding stress concentration and level of internal stress. The need for an appropriate prediction of the redistribution of interstitials and subsequent structural changes is thus obvious.

Modelling of structural stability of weldments

The CALPHAD approach [12] can be used for the solution of both local and global phase equilibrium problems concerning the base material and weld joints. The approach enables the calculation of chemical compositions of equilibrated phases at a given temperature as well as any of the phase diagram cross-sections. Also important is the possibility to calculate the chemical potentials/activities of elements.

The brief literary analysis given above concerned the redistribution of carbon in heterogenous weld joints of heat-resistant steels. Grade P91 steel and the follow-up "generation" of 9-12% Cr steels contain, in addition to carbon, also not negligible amounts of nitrogen, as reported, for example, in [6]. Nitrogen increases markedly the creep strength and structural stability of the above steels, which is exploited also in the case of low-alloy steels and filler metals (see Table 1 and Table 2). It is thus obvious that in the case of heterogeneous weld joints of

advanced low- and high-alloy heat resistant steels it is meaningful to study simultaneous diffusion (redistribution) of the two interstitial elements, i.e. carbon as well as nitrogen.

Table 1 Chemical composition of advanced low-alloy creep-resistant steels [wt. %]

Steel	C	Mn	Si	Cr	Mo	V	W	Nb	Ti	N	B	Al
T23	0.04 0.10	0.10 0.60	max. 0.50	1.90 2.60	0.05 0.30	0.20 0.30	1.45 1.75	0.02 0.08	-	max. 0.030	0.0005 0.0060	max. 0.03
T24	0.05 0.10	0.30 0.70	0.15 0.45	2.20 2.60	0.90 1.10	0.20 0.30	-	-	0.05 0.10	max. 0.012	0.0015 0.0070	max. 0.02

Table 2 Chemical composition of filler metals for the welding of steels T/P24 and T/P23 for the SMAW, SAW, GTAW methods [wt.%]

Filler met.	C	Mn	Si	Cr	Mo	V	Ti	Nb	W	Ni	N	B
T/P24	0.050 0.091	0.49 0.72	0.20 0.47	2.26 2.39	0.97 1.01	0.22 0.24	0.015 0.073	0.007 0.046	-	-	0.009 0.016	0.0010 0.0037
T/P23	0.05 0.08	0.26 0.27	0.46 0.55	2.04 2.28	0.02 0.11	0.19 0.28	-	0.031 0.043	1.55 1.72	0.04 0.12	0.007 0.017	0.001 0.002

*) filler metal for welding by the SMAW method, with increased Nb content and no Ti

The DICTRA program [14], which contains subroutines for the CALPHAD method, is widely used as a conductive tool to simulation of processes in dissimilar welds. The benefits of using the DICTRA program are described in [15]. This program embodies the assumption of local condition of phase equilibrium, the assumption that diffusion is the controlling process of the phase transformation rate [16, 17], the theory of multi-component bulk diffusion [18] and, of course, the gradients of chemical potentials/activities of the elements are considered for mass flux evaluations.

Aim of the work

The contribution deals with the theoretical modelling and experimental studies of the kinetics of the development of chemical composition and phase profiles of heterogeneous laboratory weld joints of creep-resistant steels from the point of view of their long-term stability. The T25 (6 CrMoV 8-3-2) creep-resistant ferritic steel currently being developed [19] and the advanced P91 (X10CrMoVNb 10-1) chromium steel, both steels after ion nitriding, homogenization at 1050 °C and weld joining were the subject of study. The long-term annealing of the T25+0.11wt%N | P91+(0.8±0.064wt)N weld joints were simulated at 600, and 900 °C. The phase diagrams of the investigated materials were calculated using the CALPHAD approach. The activities of carbon, nitrogen, and other elements were calculated by the same method. The CALPHAD approach complemented with an appropriate diffusion model given in the DICTRA code enabled simulating the phase and element profile evolutions inside the diffusion-affected zone of weld joint.

Experimental procedures

Samples of coin-like shape (about 4 mm in width and 12 mm in diameter) were prepared from the T25 ferritic steel being developed and from the P91 chromium steel (see Table 3 for initial composition). The samples were ion-nitrided and homogenized at 1050 °C for 24 h. A subsequent analysis of the nitrided samples (materials T25+N and P91+N) informs us that the homogenization was successful in the case of material T25+N but not for P91+N. The nitrogen content in the P91+N material remained higher on the surface after homogenization

and the exponential function $N^{**} = 0.80 \cdot e^{(-1.830x)}$ fits best the experimental over-all nitrogen content in P91+N (nitride case and bulk, x in mm gives the distance from the surface for the P91+N material).

Table 3 Chemical compositions of the initial steels P91 and T25 and nitrided materials T25+N and P91+N (N* gives the nitrogen content in initial steels, N** represents the nitrogen content in the nitrided material)

Wt%	C	Mn	Si	P	S	Cr	Mo	V	W	B	Al	N^*	Nb	N^{**}
T25	0.06	0.42	0.34	0.012	0.011	1.91	0.31	0.22	0.01	0.003	0.009	0.024	0.058	0.1129
P91	0.12	0.38	0.44	0.010	0.003	9.96	0.89	0.22	-	-	0.010	0.069	0.07	$0.8e^{-1.83x}$

Each of these coin-like samples was ground and polished, and pairs were welded to form „sandwich"-type couples. Welding was conducted using an electric current pulse in a protective argon atmosphere. These samples were sealed into evacuated quartz ampoules and annealed. Experimental results presented in this paper are those obtained for 600ºC/240h and 900ºC/18h.

After annealing the joints were cut perpendicularly to the weld interface. Analyses of microstructure were then carried out on these surfaces, with Vilella´s reagent and 2% nital reagent being used to reveal the microstructure. The carbon motion across the welds was measured by means of wavelength dispersive X-ray analysis (WDX) in a Jeol JXA-8600 electron probe microanalyzer (EPMA). A transmission electron microscope working in the scanning mode (STEM), energy dispersive X-ray analysis (EDX), and selected area electron diffraction (SAED) were used to determine the characteristics of microstructure, especially the carbides (Philips CM12 TEM/STEM equipped with Phoenix EDX, carbon extraction replicas). A combination of diffraction data and chemical composition were used for phase identification.

Model calculations were conducted using the Thermo-Calc and the DICTRA software and utilizing the STEEL 16.tdb database [20] and the Dif.tdb kinetics database.

Experimental results

The measured carbon and nitrogen concentration profiles across the weld interface are given in **Fig. 1**. As expected, carbon diffused from the T25 low-alloy steel into the P91 high-alloy steel. Also in the case of nitrogen its so-called up-hill diffusion can be observed, but in comparison with carbon the amount of redistributed nitrogen is substantially lower. The maximum and minimum carbon and nitrogen concentrations in the CNEZ (C_{max}, N_{max}) and in CNDZ (C_{min}, N_{min}) are given in **Table 4**, together with estimates of CNDZ and CNEZ widths. If during annealing the matrices of the two steels are austenitic (a temperature of 900 °C), the redistribution of carbon is little pronounced. If, however, the above matrices are ferritic, the redistribution of carbon is considerable. From the C and N profiles measured in CNEZ, a "competition" between C and N can be inferred since carbon is expulsed by nitrogen to a greater distance from the weld interface.

Table 4 Carbon and nitrogen concentrations in the CNEZ and in CNDZ

Annealing	With of CDZ And CEZ, μm		$N_{C\ min}$, wt. %	$N_{C\ max}$, wt. %	With of NDZ and NEZ, μm		$N_{N\ min}$, wt. %	$N_{N\ max}$, wt.%
900 °C/18 h	> 500	275	~ 0.10	0.16	50	-	0.099±0.071	1.05
600 °C/240 h	> 500	175	0.026±0.021	0.35	35	-	0.081±0.011	1.10

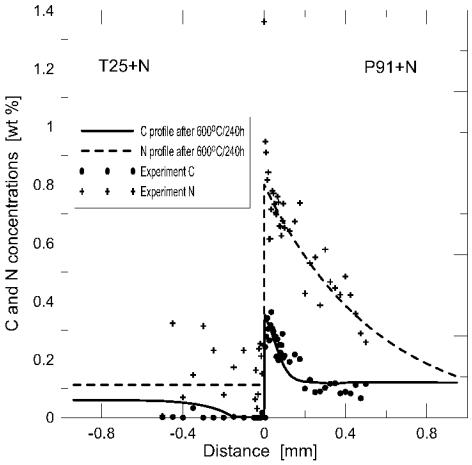

Fig. 1a Redistribution of C and N across the weld interface (600 °C/240 h)

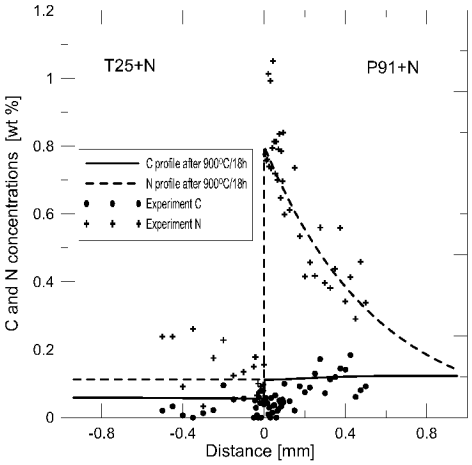

Fig. 1b Redistribution of C and N across the weld interface (900 °C/18 h)

At annealing temperatures of 900 °C, when the matrix of the two steels is austenitic, subsequent cooling in air results in martensitic transformation of the P91 steel and predominantly bainitic transformation of the T25 steel. In these structures, CNDZ and CNEZ are difficult to observe. A typical structure of the weld interface of a sample annealed at a temperature of 600 °C can be seen in **Fig. 2** The CNDZ of the T25 steel is formed by ferritic grains, in which relatively coarse precipitates can be seen to occur (**Fig. 2b**). A high density of precipitates can be observed in the CNEZ of the P91 steel (**Fig. 2a**).

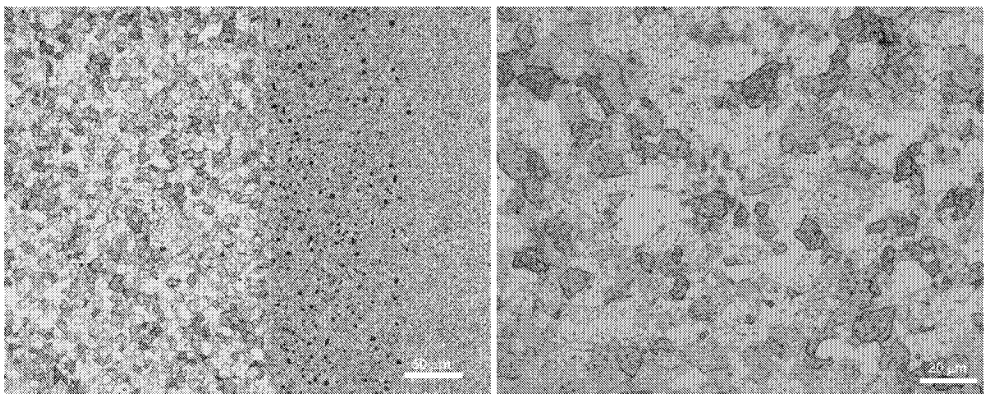

a) b)

Fig. 2 Microstructure of CNDZ and CNEZ (annealed at 600 °C/240 h, a) overview, b) detail of the CNDZ in T25 steel)

Results of the analyses of minority phases in individual regions of the weld joints under study are given in Table 5. At a temperature of 900 °C it is only the phase MX (X = C,N) that dominates in the T25 steel, while carbides M_7C_3 occur sporadically. Phases M_2X and MX

could be observed in the P91 steel. At a temperature of 600 °C, M_7C_3 and MX are found in the T25 steel; carbon and nitrogen depletion did not lead to the dissolution of carbides M_7C_3. In the P91 steel at 600 °C, the minority phases are formed by $M_{23}C_6$ + MX + M_2X, with M_2X being dominant in CNEZ; carbide $M_{23}C_6$ does not occur here at all.

Table 5 Chemical composition of precipitates in at.% at the temperatures 900 and 600 °C

Area	Phase	Experiment					Calculation						
		V	Cr	Fe	Nb	Mo	V	Cr	Fe	Nb	Mo	C	N
BMT	**MX**	33.3 ±5.9	7.7 ±2.5	-	8.6 ±5.4	0.5 ±0.2	31.3	14.2	-	4.6	0.1	0.5	49.3
	M_7C_3	6.8	58.4	-	0.5	2.7							
CNDZ	**MX**	33.0 ±3.33	10.3 ±3.8	-	6.1 ±3.0	0.6 ±0.2	33.0	12.1	-	5.1	0.1	-	49.7
	M_7C_3	3.5 ±1.30	62.1 ±2.6	1.8 ±1.3	0.8 0,3	1.9 ±0,3							
CNEZ	**M_2X**	3.3 ±1.1	6.9 ±1.4	1.2 ±1.0	0.8 ±0.3	1.5 ±0.5	0.4	58.5	5.3	0.1	2.6	5.0	28.1
	MX	6.9 ±1.4	39.6 ±1.5	0.4 ±0.2	2.4 ±0.7	0.7 ±0.4	6.4	41.7	-	1.1	1.1	0.3	49.4
BMP	**M_2X**	5.7 ±0.3	54.9 ±0.6	2.6 ±0.7	0.9 ±0.3	2.8 0.5							
	MX	30.0 ±1.6	12.3 ±2.1	-	7.0 ±1.2	0.5 ±0.1	30.1	15.2	-	5.7	0.1	2.7	46.2

BMT–base material, steel T25; BMP–base material, steel P91

Area	Phase	Experiment					Calculation						
		V	Cr	Fe	Nb	Mo	V	Cr	Fe	Nb	Mo	C	N
BMT	**M_7C_3**	1.9 ±0.7	41.8 ±1.2	24.1 ±0.8	0.5 ±0.1	1.8 ±0.2	-	56.5	12.5	-	1.0	30.0	-
	MX [1]	39.0 ±2.1	2.8 ±0.9	0.5 ±0.2	7.2 ±2.3	0.5 ±0.1							
	MX [2]	25.2	19.7	0.4	3.7	1.0	25.6	20.8	-	3.7	0.1	1.8	48.0
CNDZ	**M_7C_3**	1.9 ±1.4	43.5 ±1.0	22.0 ±2.1	0.6 ±0.2	2.1 ±0.3							
	MX	33.8 ±4.4	8.8 ±4.6	-	6.4 ±3.2	0.6 ±0.2	26.3	20.0	-	3.8	0.1	0.5	49.3
CNEZ	**M_2X**	1.9 ±1.1	59.1 ±2.1	1.3 ±0.3	0.9 ±0.4	2.9 ±1.1	2.5	62.1	1.5	0.1	1.0	12.4	20.4
	MX	11.8 ±6.8	33.1 ±6.4	0.6 ±0.1	3.7 ±1.4	0.8 ±0.4	23-33	11.5-23	-	2.9	0.1	0.5	49.2
BMP	**M_2X**	6.4 ±1.2	52.9 ±2.3	-	1.4 ±0.8	5.3 ±1.9							
	$M_{23}C_6$	1.8 ±0.9	59.4 ±4.2	12.3 ±6.1	-	5.3 1.2	0.1	62.5	12.5	-	4.2	20.7	-
	MX	20.7	25.9	-	2.4	1.0	24.4	21.9	0	4.3	-	0.2	49.2

Equilibrium and diffusion simulations, discussion

The CALPHAD approach [12] and the STEEL thermodynamic database [20] were used for the solution of both local and global phase equilibrium problems concerning the initial steels (T25, P91), nitrided materials (T25+N, P91+N), and weld joints ((T25+N) | (P91+N)). The approach enables the calculation of chemical compositions of equilibrated phases at a given temperature as well as the chemical potentials/activities of elements too.

The calculated phase composition (types of phases and their chemical composition) of the base materials and individual affected areas is given in **Table 5**, together with experimental results. It can be seen from a comparison of the calculations with the experimentally established values that the agreement is very good, inclusive of the chemical composition of individual carbides and nitrides. Experimentally established, however, was also the occurrence of phases not predicted by calculations, such as carbides M_7C_3 in steel T25 at a temperature of 900 °C and in CNDZ of the same steel at 600 °C, and also the M_2X phase at both temperatures in P91 steel that had not been affected by redistribution. The above differences are related to the insufficient annealing times for reaching equilibrium states.

An important result of phase equilibrium calculations is the evaluation of the activities of individual elements in the steels with respect to standard element reference (SGTE) [23]. The activity difference of the given element in two different materials can be used as a first approximation for weld joint stability judgement [24] because each element diffuses to a place with its lower activity and this diffusion flux is roughly proportional to the absolute value of the activity difference. In the case of the microstructure evolution of dissimilar weld joints of steels interstitial elements (such as carbon, nitrogen and hydrogen) are of the most importance because they diffuse more quickly than substitution elements and thus the diffusion of the metal elements can be neglected. Along with the carbon and nitrogen redistribution the redistribution of Fe, Cr and Mo was also measured. These analyses confirmed that width of the fusion zone and the diffusion zone of substitution elements does not exceed the value 5 μm and can thus be neglected.

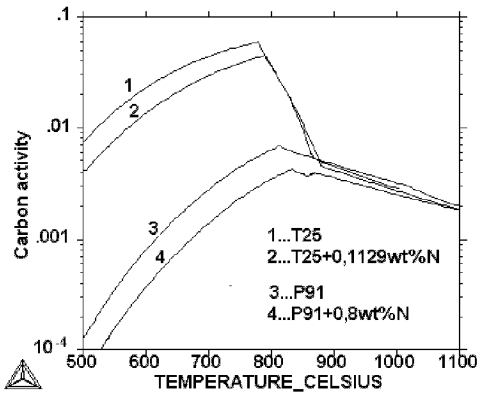

Fig. 3 Simulated temperature dependence of carbon activity of investigated initial steels and nitrided materials.

The temperature dependence of the carbon activity for the examined steels is given in **Fig. 3**. Fig. predicts that the carbon will diffuse from T25 to P91 at low temperatures, ranging from 500-870ºC (i.e. carbon up-hill diffusion). At temperatures higher than 870 °C, when the matrices of the two steels are completely austenitic, the differences in activities are substantially smaller; consequently, the carbon redistribution is also markedly lower, as was experimentally confirmed (**Fig. 1**).

The carbon mass transport is much more intensive than the nitrogen transport in the T25+N and the P91+N materials. The calculated nitrogen activity differences for diffusion couples of the initial steels and nitrided materials are very low (10^{-10}-10^{-7}).

The nitrogen mass transport does not play a great role in the T25+N | P91+N joints in the monitored temperature range.

The results of the diffusion simulations at 600ºC/240h are given in **Figs 1 and 4.** The carbon up-hill diffusion can be observed at this temperature. The carbon diffused from the T25+N material to the P91+N material in accordance with the carbon activity difference given in **Fig. 3.** The carbon depleted zone inside the T25+N material and the carbon enriched zone inside the P91+N material are formed in the vicinity of the T25+N | P91+N weld joint interface. **Fig. 4** shows the M_7C_3 carbide dissolution given by the displacement of carbon from the T25+N material. The carbon overflow replaces nitrogen in M_2X carbonitride in the P91+N material. The nitrogen diffusion is very slow and the initial nitrogen profile remains stable. The high thermodynamic stable MX carbonitride can be found in the carbon depleted as well as in the carbon enriched zones. The M_2X carbonitride can be found in the P91+N material with high nitrogen content (in the position of the original nitride case). The simulated and experimental carbon profiles can be found in **Fig. 1**.

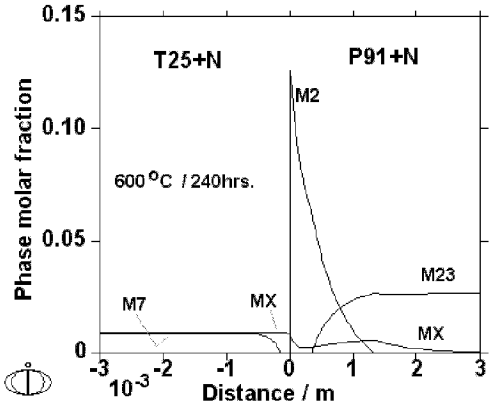

Fig. 4 Simulated phase profiles of T25+N | P91+N weld joints after annealing at 600ºC/240h.

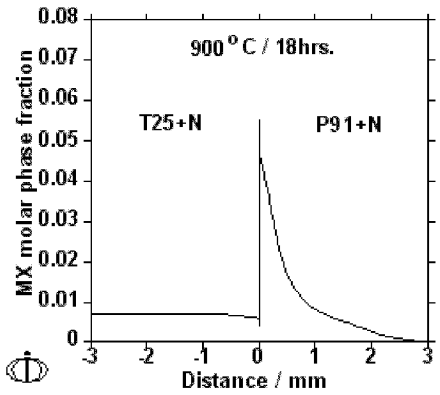

Fig. 5 Simulated phase profile of T25+N | P91+N weld joint after annealing 900ºC/18h.

Figs 1 and **5** refer to simulation results at 900 ºC. The carbon and nitrogen diffusion is small and can be neglect in the T25+N | P91+N diffusion couple (consider carbon activity from **Fig. 3**). **Fig. 5** shows that the MX carbonitride could be present in the weld joint at 900ºC only. The MX molar phase fraction is fixed in accordance with the initial nitrogen content.

The thermodynamic and kinetic stability of the weld joints of dissimilar materials can be estimated from the carbon activity temperature dependence similar to that given in **Fig. 3**. More precise results can be attained on the basis of weld joint simulations described in this paper (see **Figs 1, 4** and **5**). The simple knowledge of the activity dependences is sometimes sufficient to estimate the effect of nitrogen on weld stability of heat resistant steels. In our case the nitriding decreases the carbon activities of both the T25 and the P91 ferrite steels (see **Fig. 3**).

A correct judgement of the weld stability of heat resistant steels alloyed with carbon and nitrogen is not possible on the basis of carbon activity temperature dependence alone but it is necessary to perform more precise kinetic simulations. The simulations performed for the

T25+N | P91+N weld joint show a great difference in the diffusion and phase stability at 600 °C and at 900 °C. The T25+N | P91+N diffusion joint reveals the formation of carbon depleted zone and carbon enriched zone at 600°C, which is confirmed by the experiment. This weld joint combination represents much risk in practical service conditions at 600 °C.

The weak point of heterogeneous weld joints of heat-resistant steels is CDZ, in which in the cases of welding only CrMo steels there is an almost complete carbon depletion and a practically perfect dissolution of carbidic phases. In this area, a rapid recrystallization of the ferritic matrix then follows. In more advanced steels, which are usually alloyed with vanadium, niobium and nitrogen there is in the CDZ non-dissolved carbonitride MX (M = V, Nb, Cr,...), which provides precipitation hardening and, at the same time, deacelerates recrystallization processes. In advanced creep-resistant steels the appearance of a CDZ does not necessarily lead to failure by type IIIa cracking.

High diffusion stability is reached at 900°C. The diffusion is negligible at this temperature but it has to be noted that the matrix is formed by the FCC phase (austenite) at this temperature, which is above the temperature range of the applications of the steels under study.

Conclusion

The simulation results enable understanding the processes taking place in the diffusion-affected zone of the studied weld joint under different temperature conditions. It was found that the nitriding of both heat resistant steels decreased their carbon activities. The kinetic simulation of the T25+N | P91+N weld joint has confirmed it. It can be concluded that the method used provides results that are in good agreement with experimental observations.

The simulation procedure used can be transferred to weld joints of heat resistant steels with simultaneous carbon/nitrogen diffusion. In this case, the simulation method can offer results that can be used for the evaluation of long-term microstructural stability of weldments at high temperatures.

Acknowledgement

The present work was supported by the Ministry of Education, Youth and Sports, project No MSM0021630508.

References

[1] STRANG, A., VODÁREK, V. Microstructural degradation of martensitic 12%Cr power plant steel during prolonged high temperature creep exposure. *Proc. of the 6th Liege Conference Materials for Advanced Power Engineering. 1998,* eds. J. Lecomte-Beckers et al., p.601, Jülich Forschungszentrum.

[2] MASUYAMA, F. Trends in power engineering in Japan and requirements for improved materials and components. *Proc. of the 7th Liège Conference Materials for Advanced Power Engineering 2002*, eds.J. Lecomte-Beckers et al. pp. 1767-1782. Jülich Forschungszentrum.

[3] MAYER, K.H. et al. Development of new steels for advanced steam power plants. *Proc. of the 7th Liège Conference Materials forAadvanced Power Engineering 2002*, eds. J. Lecomte-Beckers et al. pp. 1385-1397.Jülich Forschungszentrum.

[4] BRETT, S.J. Type III cracking in 1/2CrMoV steam pipe work systems. *Science and Technology of Welding and Joining,* 9, 2004, 1, pp.41-45.

[5] FORET, R. et al. Structural stability of dissimilar weld joints of steel P91. *Science and Technology of Welding and Joining*. 6, 2001. 6, pp. 405-411.
[6] SUDHA, C. et al. Systematic study of formation of soft and hard zones in dissimilar weldments of Cr-Mo steels. *Journal of Nuclear Materials*. 302, 2002, 4), pp. 193-205.
[7] BRET, S.J. 1998. In-service cracking mechanism affecting 2CrMo welds in1/2CrMoV steam pipe work system. *Proc. of int. con. Integrity of high-temperature Welds*. pp.3-14. Professional Engineering Publishing Limited London.
[8] HELANDER, T, ANDERSSON, C.M., OSKARSSON, M. 2000. Structural changes in 12-2.25 weldments – an experimental and theoretical approach. *Materials at High Temperatures,* 17, 2000, 3, pp. 389-396.
[9] BUCHMAYR, B. et al. Experimental and numerical investigations of the creep behavior of the dissimilar weldment GS-17 CrMoV 5 11 and X 20 CrMoV 12 1. *Steel Research.* 61, 1990, 6, pp. 268-273.
[10] ROBERTS, D.I., RYDER, R.., VISWANATHAN, R. 1985. Performance of dissimilar welds in service. *Journal of Pressure Vessel Technology*. 107, 1985, 3, pp. 247-254.
[11] ALBERT, S.K. et al. 1997. Soft zone formation in dissimilar welds between two Cr-Mo steels. *Welding Journal.* 76, 1997, 3, pp. 135-142.
[12] SAUNDERS, N., MIODOVNIK, A.P. *CALPHAD (Calculation of phase diagram – A Comprehensive Guide)*. Amsterdam 1998, Elsevier Science Publishing.
[13] VISWANATHAN, R., PURGERT, R., RAO, U. Materials Technology for Advanced Coal Power Plants. In Proc. of Conf. *Super-High Strength Steels* [CD-ROM]. Rome, Italy, November 2-4, 2005.
[14] ANDERSON, J.O. et al. Thermo-Calc and DICTRA, computational tools for materials science. *CALPHAD.* 26, 2002, pp. 273-312.
[15] BORGENSTAM, A., et al. 2000. DICTRA, a tool for simulation of diffusional transformations in alloys. *Journal of Phase Equilibria*, 21, 2000, 3, pp. 269-280.
[16] KIRKALDY, J.S., YOUNG, D.J. *Diffusion in the Condensed State*, London 1985, The Institute of Metals.
[17] ENGSTRŐM, A, HŐGLUND, L., ÄGREN, J. Computer simulation of diffusion in multiphase system. *Metallurgical and Materials Transactions A*. 25A, 1994, 2, pp. 1127-1134.
[18] ANDERSSON, J.O. et al. Computer simulation of multicomponent diffusional transformations in steel. *Proc. Fundamentals and Applications of Ternary Diffusion*. Eds. G. R. Purdy, pp.153-163. Pergamon Press, New York 1990.
[19] FOLDYNA, V. et al. Microstructure and properties of modified 3%Cr steels. *Proc. of the 7th Liège Conference Materials for Advanced Power Engineering 2002*, eds. J. Lecomte-Beckers et al. pp. 1477-1486. Jülich Forschungszentrum.
[20] KROUPA, A. et al. Phase diagram in the iron-rich corner of the Fe-Cr-Mo-V-C system below 1000 K. *Journal of Phase Equilibria.* 22, 2001, 3, pp. 312-323.
[21] SOPOUŠEK, J., JAN, V., FORET, R. Simulation of dissimilar weld joints of steel P91. *Science and Technology of Welding and Joining*. 9, 2004, 1, pp. 59-63..
[22] KUBOŇ, Z., FOLDYNA, V., VODÁREK, V., Optimized chemical composition of 9-12%Cr steels with respect to maximum creep resistance. . *Proc.of the 6th Liege Conference Materials for Advanced Power Engineering. 1998.* eds. J. Lecomte-Beckers et al., pp.311-325, Jülich: Forschungszentrum.
[23] DINSDALE, A.T. SGTE data for pure elements. *CALPHAD* 15, 1991, 4, pp. 317-425.
[24] JAN, V., SOPOUŠEK, J., FORET, R. Weld joint simulation of heat-resistant steels *Archives of Metallurgy and Materials.* 49, 2004, 3, pp. 439-480.

Part III

Advanced Steam Turbine Materials

Contributed Papers

Steam Oxidation and Coatings

OXIDATION OF CANDIDATE CHROMIUM STEELS IN STEAM ENVIRONMENT

Josef Cizner, Jan Hakl

SVÚM a.s., Prague, Czech Republic

Abstract

Laboratory tests of ferritic chromium steels and model alloys in steam environment at testing temperature 600 and 650 °C. Gravimetric evaluation performed minimal differences between ferritic steels. Metallography analysis made it possible to separate steels with low-grade oxidic safety layer. Model alloys with higher content of chromium or Ni+Cr alloys had the best results.

Keywords: Oxidation, steam environment, chromium steels

Introduction

For development of advanced steam boilers of a new generation it is necessary to have material data for steels to be used at high temperatures and pressure regimes. These materials, apart from having excellent creep properties, have to be resistant against corrosion attack (both on the combustion gas - outer side of tubes - as well as the steam side).

Low alloy steels are applicable up to temperature 560 °C. For higher temperatures it is necessary to use more highly alloyed elements steels- ferritic steels (8 - 12% Cr base) and/or austenitic steels. These steels are usually alloyed with additional elements (Mo, W, V, Co, Nb etc) which positively influence creep properties. However in some cases, this could negatively influence high temperature corrosion resistance.

For this reason, it is necessary to test candidate materials in laboratory conditions and later in the field. The question of steam oxidation resistance in candidate steels at the temperatures 600 and 650 °C was investigated in COST 522 „Steam power plant" programme [1] and now is also being further studied in COST 536. Project of SVUM is located in section „Oxidation", marked as CZ4b SVUM.

Testing programme

Long - term testing of candidate steels and model alloys were performed at SVÚM. Chemical composition of tested materials is shown in table 1. There is a group of ferritic steels in their wrought and cast states with different alloying elements. Chromium content is 11,5 wt%, molybdenum content is 1,5 wt% and other alloying elements like Nb, V, N and B improve the strength of metal basic material. In VM 12 steel are also present Co, Cu and W.

Model alloys tested were Fe10Cr, Fe20Cr, Ni10Cr and Ni25Cr. Long - term testing conditions are shown in table 2.

For these tests, superkanthal furnaces with metal gas proof muffles made from AISI 310 steel were utilized with programmable temperature control.

Table 1 Materials selected for tests in SVÚM a.s.

Steel	FZJ-Id	C	Mn	Si	Cr	Mo	W	Ni	Co	Nb	V	N	B	Cu
FT1	KJL	0.200	1.04	0.29	9.95	1.48		0.11		0.065	0.28	0.022	0.10	
FT2	KJM	0.200	1.02	0.29	10.00	1.50		0.13		0.067	0.27	0.021	0.017	
FT3	KJN	0.200	1.00	0.27	9.85	1.48		0.11		0.070	0.26	0.023	0.026	
FT4	KJP	0.200	0.86	0.23	11.45	1.47		0.11		0.058	0.24	0.018	0.008	
FT5	KJR	0.200	0.98	0.25	11.40	1.50		0.11		0.065	0.33	0.026	0.019	
FT6	KJS	0.190	0.94	0.26	11.40	1.49		0.13		0.065	0.27	0.030	0.018	
FT7	KJT	0.190	1.00	0.25	11.40	1.51		0.11		0.066	0.27	0.035	0.025	
CT3*	KJU	0.200	1.00	0.30	11.00	1.50				0.060	0.20	0.020	0.020	
CT7*	KJW	0.200	1.00	0.30	11.00	1.50				0.06	0.20	0.020	0.020	
VM12	KJY	0.120	0.37	0.48	11.61	0.28	1.58	0.31	1.56	0.044	0.25	0.078	0.005	0.06
Fe10Cr	BEP	0.003			10.33									
Fe20Cr	BEU	0.011			20.09									
Ni10Cr	BEY	0.013			10.28									
Ni25Cr	BEZ	0.015			25.25									

* Nominal composition

Table 2 Conditions for laboratory tests

1	Test environment:	50 % Ar + 50 % steam
2	Test temperatures:	600 and 650 °C
3	Total exposure:	max. 5000 h
4	Time interval between sample removals for corrosion evaluation:	50, 100, 200, 500, 1000, 1500, 2000, 2500 etc.
5	Gas flow rate:	300 ml/min.
6	Number of samples:	max 10 samples from one steel
7	Max. number of samples in furnace: 100	

Results of experiments

High temperature steam oxidation resistance of steels and alloys is mainly connected with creation of protective layer. The outer oxidizing layer is formed during oxidation of diffused metal elements - Fe, Cr, Mn, Si, etc - on the surface of specimens as well as on the inner oxidizing layer, which to forms due the reaction of oxygen with metal elements. Both these layers are different due to morphology and chemical composition. It is very important to have a compact corrosion layer, firmly bonded to the surface that protects diffusion of other elements through this layer.

We carried out our experiments at temperatures 600 and 650 °C. Evaluation of gravimetric measurements is shown in Fig. 1 and 2 for temperature 600 °C and in Fig. 3 and 4 for temperature 650 °C. For up to 2500 hours exposure, there is no difference between ferritic steels. The highest weight gains were found for the model steel Fe10Cr.

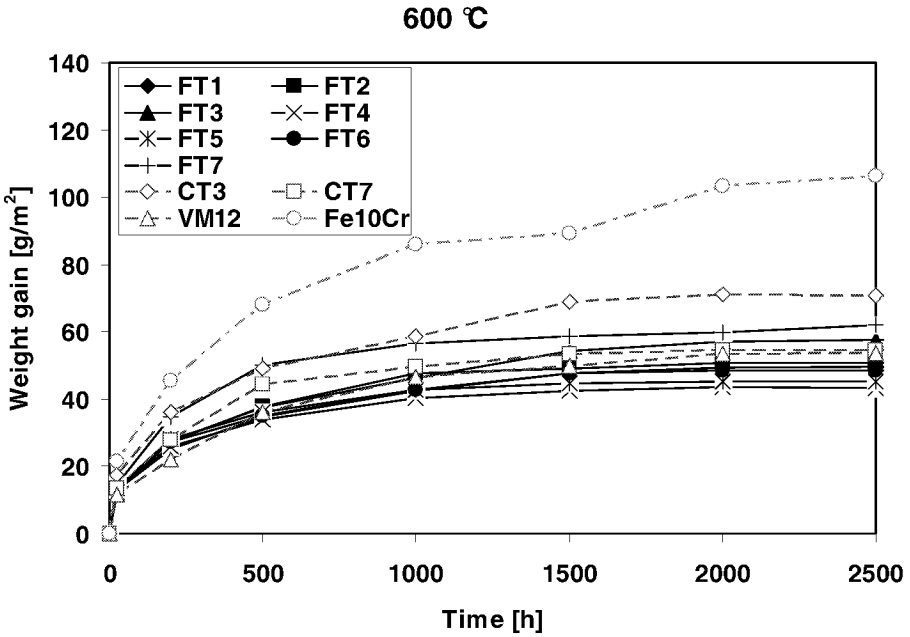

Fig. 1 Weight gains for various steels at 600 °C

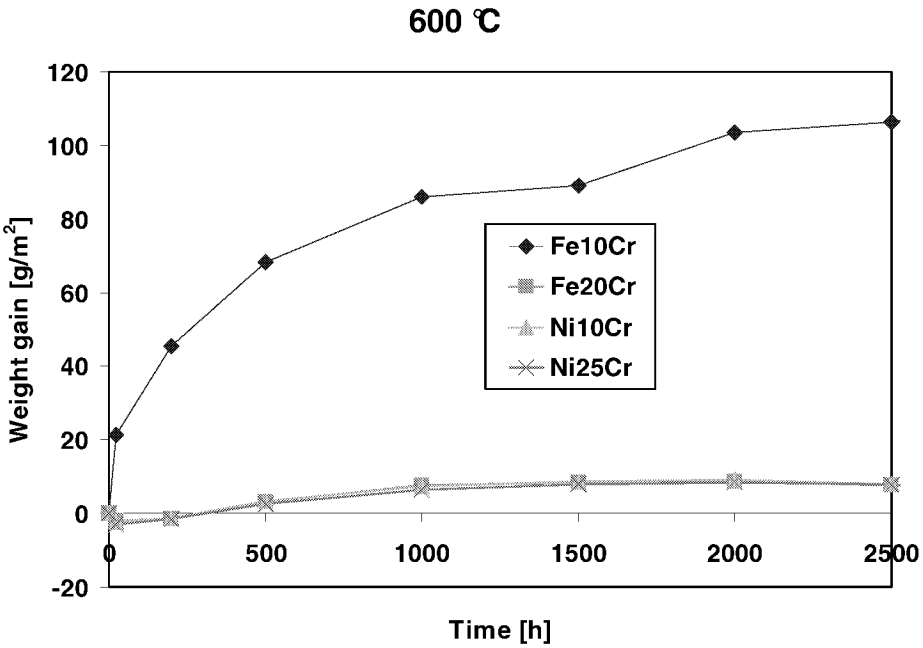

Fig. 2 Weight gains for model binary Fe-Cr and Ni-Cr alloys at 600 °C

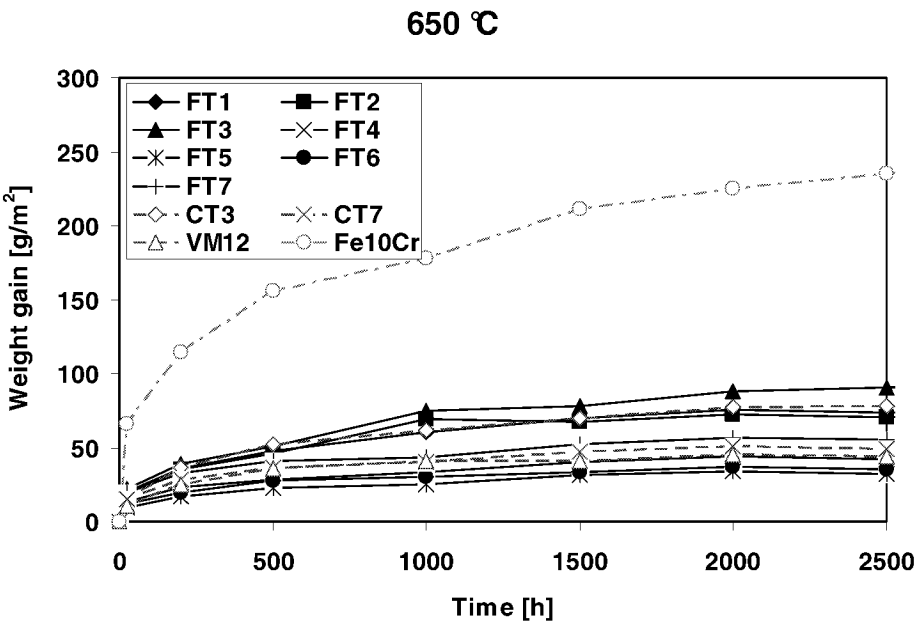

Fig. 3 Weight gains for various steels at 650 °C

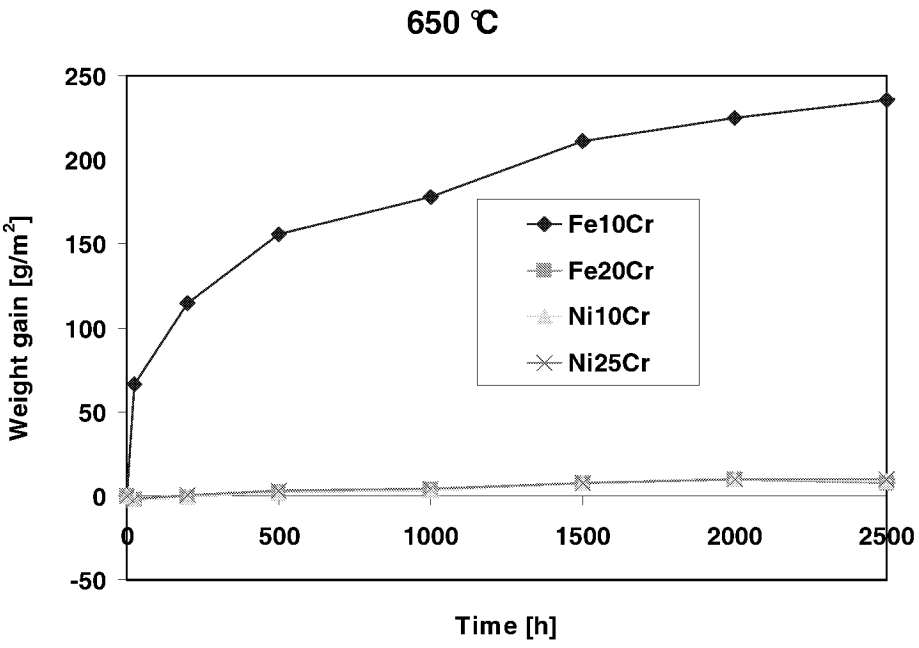

Fig. 4 Weight gains for model binary Fe-Cr and Ni-Cr alloys at 650 °C

Metallographic evaluation was used to examine the quality of oxidizing layers. The morphologies of corrosion layers of candidate steels are shown in Fig. 5 and 6. In steels FT3 and FT4 we observed the cracks on surface layers (Fig. 7 and 8). These steels are not subject to further consideration.

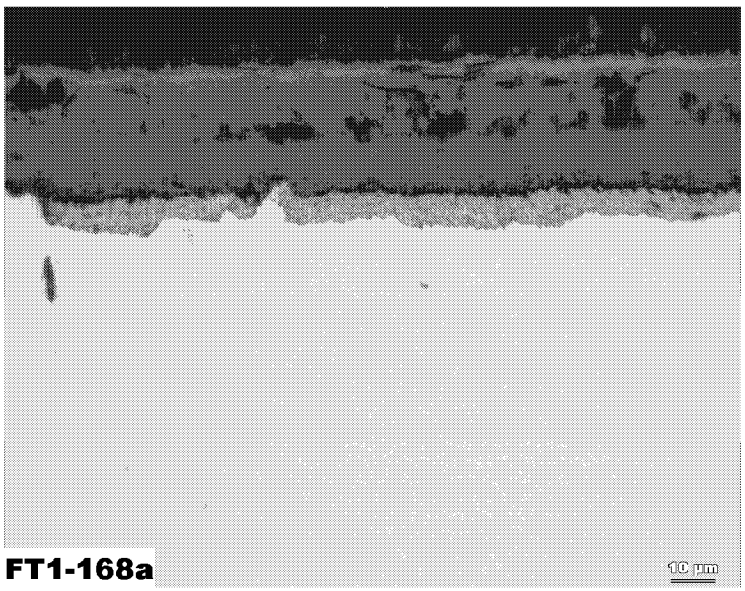

Fig. 5 Microstructure of oxide layer on Fe10Cr1.5MoV NbN steel, temperature 650 °C, time 1000 h, 50%Ar + 50%H_2O

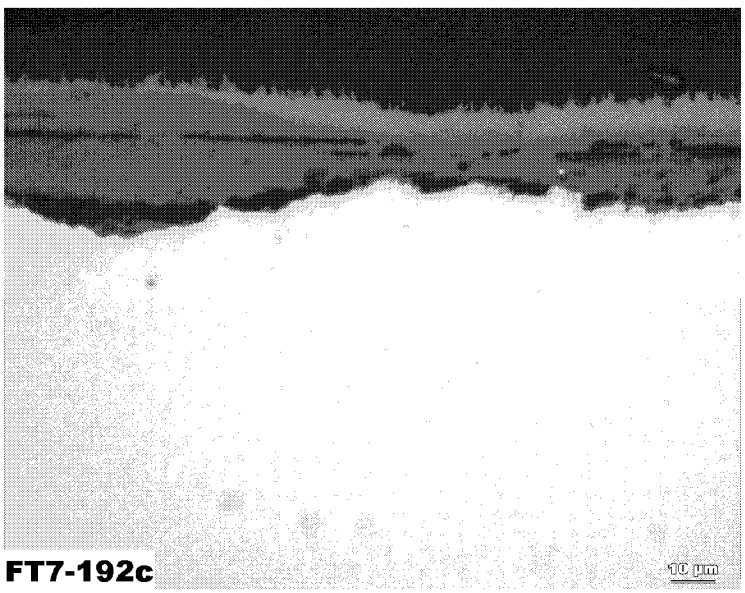

Fig. 6 Microstructure of oxide layer on Fe11.5Cr1.5MoVNbN steel, temperature 650 °C, time 1000 h, 50%Ar + 50%H_2O

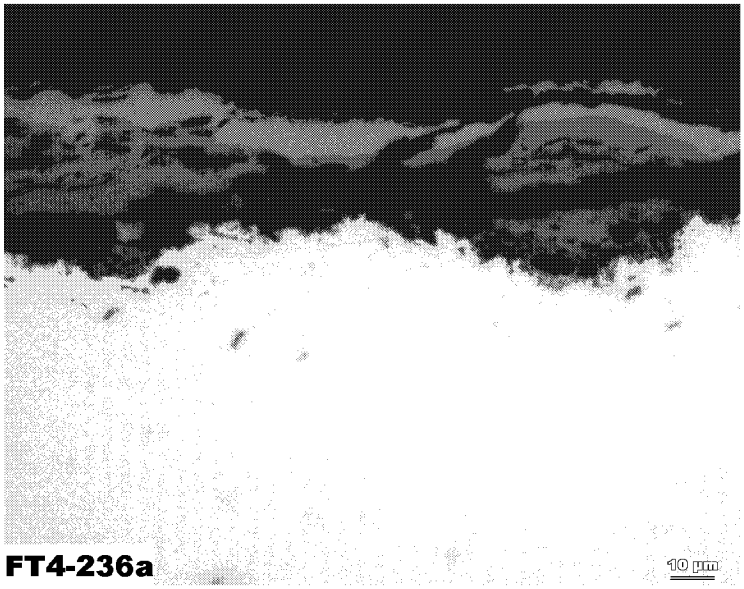

Fig. 7 Microstructure of oxide layer on Fe11.5Cr1.5MoVNbN steel, temperature 650 °C, time 1000 h, 50%Ar + 50%H_2O

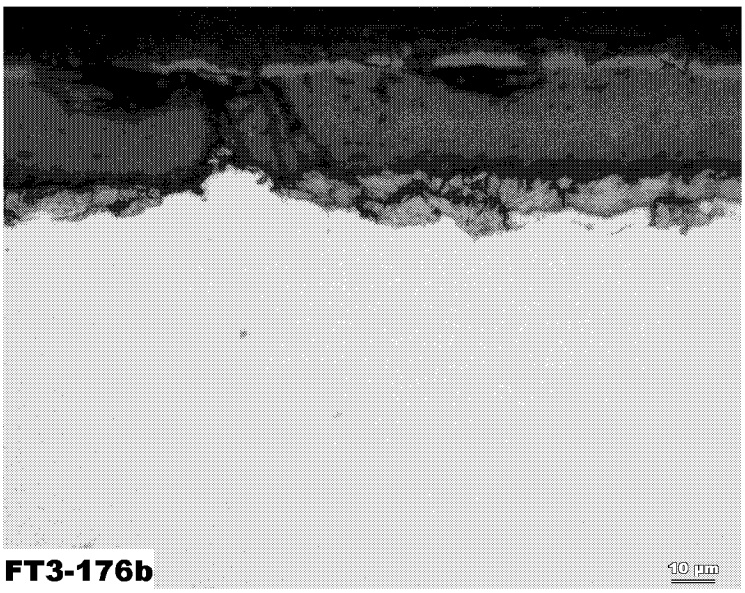

Fig. 8 Microstructure of oxide layer on Fe10Cr1.5MoVNbN steel temperature 650 °C, time 1000 h, 50%Ar + 50%H_2O

Microanalysis of corrosion layers was carried out on a CAMEBAX analyzer. External corrosion layer consists mainly of iron oxide. Below the outer corrosion layer, there was an increase in the chromium percentage in the oxide from 18 wt% to 50 wt%. In addition, the

penetrated layer contained 30 wt% chromium. Concentration profiles of basic elements - Fe, Cr and O are shown in Fig. 9.

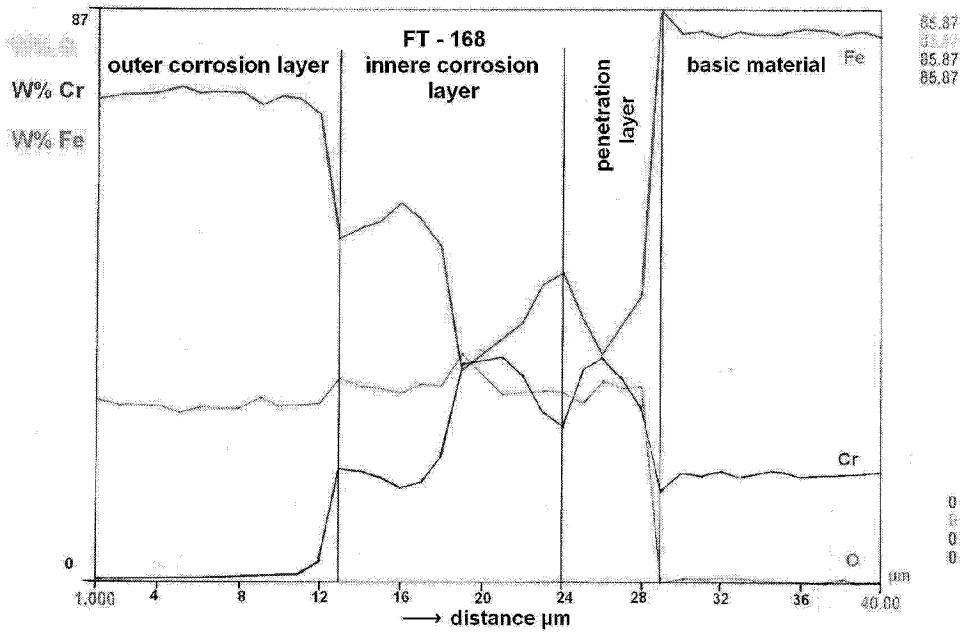

Fig. 9 Concentration profile of corrosion layer

Conclusions

1. The best results were achieved in at model alloys with higher content of Cr or Ni+Cr. The oxidizing layers were too thin and metallographic evaluation could not be used.
2. The gravimetric evaluation of ferritic steels demonstrated no significant differences. FT3 and FT4 showed cracks on protective oxidizing layers.

Final results will be given after the end of experiments - with exposition up to 5000 hours.

Literature

[1] Cizner J., Hakl J.; COST 522, WPCA4 – Final report of project CZ, July 2003
[2] P. J. Ennis et al.: Steam oxidation of chromium steels and its implications for service life of components, International Conf. High Temperature Plant Integrity Life Extension, April 2004, Cambridge

OXIDE SCALE GROWTH AND SPALLATION IN STEAM ENVIRONMENTS – AN ASSESSMENT OF DIFFERENT MODELLING APPROACHES

A T Fry, S Osgerby
National Physical Laboratory, Hampton Road, Teddington, UK
tony.fry@npl.co.uk

Abstract

The ability to model accurately the oxide scale growth of materials in high temperature and pressure steam environments is an attractive and desirable tool for designers and utility managers. A number of techniques have been used to develop models to predict the oxide scale growth and scale spallation for a range of high temperature materials. These include an oxide grain growth model which uses experimental thermogravimetric data to calculate instantaneous values for the oxidation kinetics, which can then be used to determine the oxide growth mechanism; an analytical model which uses key composition variables to model the growth kinetics and neural networks which form relationships based on experimental data. Although all of the techniques can be used for oxide growth modelling, not all are applicable for predicting the onset of spallation. The results from these different approaches have been compared and the relative merits and disadvantages discussed.

Keywords: Modelling, Neural Network, Oxide Growth, Chromium Steel, Steam

Introduction

All modelling techniques have a basic requirement of either fundamental understanding of the processes occurring with mathematical expressions that describe them, or a set of data that can be analysed to establish trends and relationships, which can then be modelled. This latter technique does not require any knowledge of the processes occurring, although this is, of course preferable. Since oxidation is a time dependant process it can take exposures of many thousands of hours to degrade the material to such an extent that metal loss and spallation become problematic. Thus the evaluation of materials purely based on accelerated laboratory tests, whilst very beneficial, does not always supply enough information. This is particularly the case with very oxidation resistant materials where oxide growth can be very slow. With steam power plants typically designed for a lifetime of 25 years, and with the economic pressure to extend this life further, long-term performance is a very important issue. Thus the use of modelling techniques is advantageous.

Three techniques have been used to develop a model for predicting the specific mass change of 9-12% (by weight) chromium containing steels. Some of these models can also be used to predict the likelihood of spallation occurring. The following describes the different techniques used and presents the results obtained. The merits and disadvantages of each technique are discussed.

Oxide Growth Model

Basis

This model assumes that the rate-determining factor in the steam oxidation of martensitic steels is the diffusion of the reactive species through the oxide scale. This is controlled

through a combination of bulk and grain boundary diffusion. Thus the overall rate (K_p) is defined by the sum of the contributions from bulk and grain boundary diffusion.

$$K_P \propto D = D_B + \delta D_{GB} \quad (1)$$

Where D is the overall diffusion coefficient, D_B is the coefficient for bulk diffusion, D_{GB} is the coefficient for grain boundary diffusion and δ is the effective width of the grain boundary. Atkinson [1] reviewed the development of grain structure in thermally grown oxides, reporting a $t^{1/3}$ law for grain growth. Using this relationship, it follows that equation (1) can be rewritten to give a general expression.

$$K_P = K_1 + K_2 t^{-\frac{1}{3}} \quad (2)$$

Where K_1 and K_2 are the growth rates due to bulk diffusion and grain boundary diffusion respectively. The scale growth kinetics therefore become sub-parabolic as the controlling grain size in the oxide increases with time.

Results

Thermogravimetric tests were performed on samples of P91 and P92 in a gas mixture of Ar/15%H_2O, at 650 °C and 850 °C for durations of 150 hours. The specific mass change with time data generated are shown in Figure 1. At both temperatures P91 showed lower mass change than P92, consistent with results reported previously [2]. These data were then used to calculate instantaneous values for the oxidation rate constant K_p. Figure 2 shows the agreement between the model expressed by equation 2, and the experimental data. It can be seen that, after an initial period the form of the expression follows the data for the remainder of the exposure. The initial deviation from the model is believed to be due to the initial formation of the scale, which is controlled by a different (and as yet undefined) mechanism.

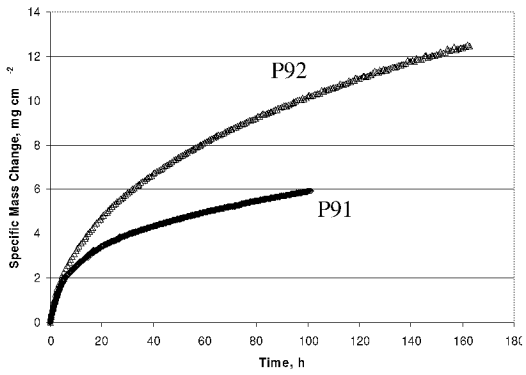

Figure 1 Mass change with time for P91 and P92 exposed to Ar/15%H_2O at 650 °C

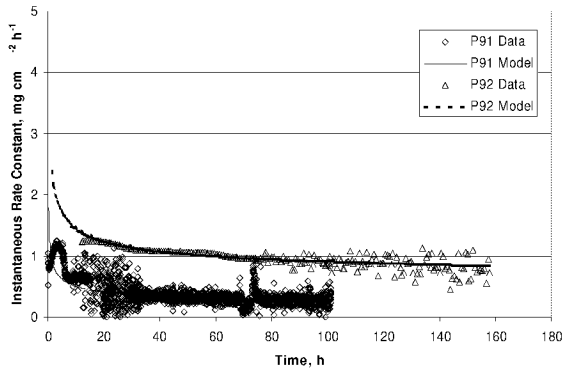

Figure 2 Instantaneous rate constant as a function of time for P91 and P92 exposed to Ar/15%H2O at 650 °C

The oxide scales formed on P92 were examined using electron back-scattered diffraction (EBSD). Images of the magnetite and spinel layers produced are shown in Figure 3, where it is clear that the magnetite grain size is much larger. The growth of the oxide grain size with time is demonstrated in Figure 4. The growth rate in both cases follow a power law but the exponent is lower than the 0.33 expected. Nevertheless these results provide good evidence for the validity of the model.

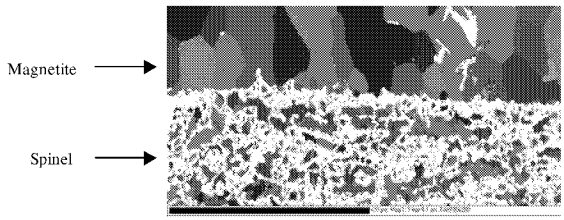

Figure 3 Colour orientation contrast image of magnetite and spinel layers formed on P91 after exposure to argon/15% H_2O for 100 h at 650 °C

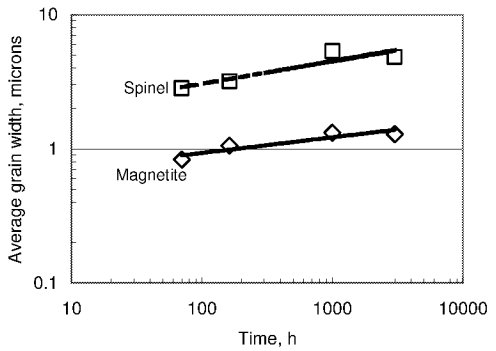

Figure 4 Oxide grain growth as a function of time for P92 exposed to argon/15% H_2O at 650 °C

Chromium Equivalent Model

Basis

It is known one of the major contributors to the steam oxidation resistance of steels is the amount of chromium they contain [3,4]. However chromium is not the only alloying addition that affects the behaviour of these materials in steam environments. Ennis and Quadakkers [5] for instance noted the beneficial effects of high levels of silicon and manganese on the observed mass change of a series of 9-12%Cr steels exposed to steam for 2000 h at 600 and 650 °C.

Analysis of experimental results has shown that the scale growth kinetics of martensitic steels containing 9-12% chromium (by weight) can be correlated with the silicon, manganese, molybdenum and tungsten contents of the alloy [6]. Increased silicon, manganese and molybdenum contents appear to enhance the steam oxidation resistance whereas tungsten appears to have a detrimental effect. This effect has been quantified by analysis of experimental data and the subsequent development of a concept of 'chromium equivalent', which can be defined for 9-12% Cr steels as:

$$Cr_{eq} = <Cr> +3.86<Si> +15.94<Mn> +16.42<Mo> -10.45<W> \qquad (3)$$

where $\langle\ \rangle$ refers to the wt% of the individual elements in the alloy.

Results

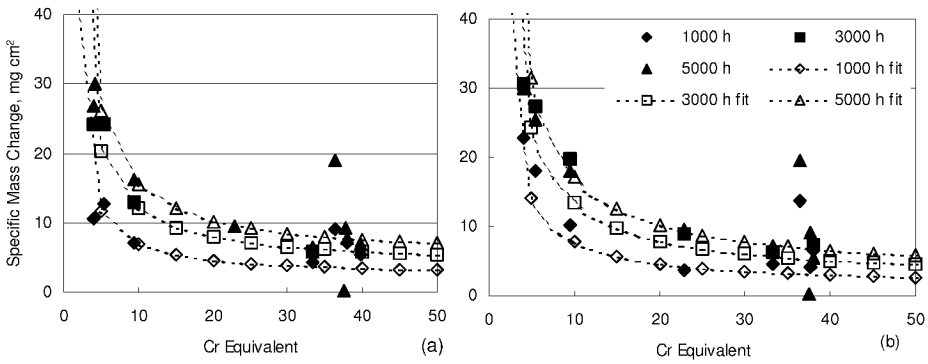

Figure 5 Correlation between empirical Cr equivalent model and experimental data at (a) 600 °C and (b) 650 °C

Figure 5 shows the chromium equivalent modelled specific mass change curves for 9-12% Cr steels exposed to flowing steam at 600 and 650 °C for 1000, 3000 and 5000 h. These curves are compared with experimental data obtained from laboratory-based exposures. The chromium equivalent approach shows good agreement with the experimental data and thus could be used to provide guidance on the influence of alloy composition on steam oxidation performance.

Whilst the agreement shown in Figure 5 is encouraging, unless there is a mechanistic explanation for the influence of the individual components of the chromium equivalent parameter, the approach remains purely empirical. To counter this potential criticism an attempt has been made to relate the proposed effects to published mechanisms of steam oxidation [7].

Metallographic investigation of three steels after laboratory-based exposure to steam environments was performed to determine the distribution of each element after the exposure. Detailed analysis of the distribution of each element revealed that Si forms an additional oxide layer beneath the spinel; Cr, Mo and W concentrate in the spinel and only Mn diffuses outward from the original metal surface into the magnetite [7]. These latter observations are consistent with the mechanism proposed by Cox et al [8] who used crystal field theory to characterise elements according to their preference for diffusion using octahedral sites.

Analysis of several proposed mechanisms for steam oxidation showed that diffusion of the oxidant gas through microcracks and the modification of the oxide defect structure are the most appropriate mechanisms that are able to explain the observed effects of alloy composition [7]. The latter mechanism is consistent with the oxide growth model.

Neural Network Model

Basis

An alternative approach to predict material behaviour under multi-variable conditions is by using neural network modelling. The main requirements to generate a reliable model are that the dataset used to train the network should be as large as possible and contain reliable and complete data. In order to achieve this, data generated at NPL and by other COST partners using 9-12% Cr steels have been used to train the neural network.

For the purpose of this work a commercial neural network software package has been used. This package allows several different types of neural network to be used. To establish which of these would be the most appropriate, a series of trials were performed using the complete data set to rank the 'goodness of fit' of the networks prediction. The initial trials indicated that using a Fuzzy Logic (NFZ) approach gave the best agreement to the experimental data.

During the training process the NFZ network initially uses all of the input variables presented to it. The software then performs a series of optimisations such that only 'key' parameters with appropriate weightings and interdependencies are used in the final trained network to predict the final target value. This feature makes the NFZ network attractive to use as it can cut down the number of input variables required but still be successful.

Results

Initially the network was presented with 18 individual parameters that were derived from the exposure technique, temperature, exposure time and alloy composition. The network constructed the necessary weighted neurons and established a set of 'rules' based on only 6 of these parameters. These were the exposure technique, temperature, time, and the wt% content of Mn, Cr and N. Using these relationships the neural network was able to predict the specific mass change, the results of this are presented in Figure 6, which shows a plot of the specific mass change as predicted by the network compared with the actual experimental

value, this figure illustrates the good agreement between the neural network and observed data.

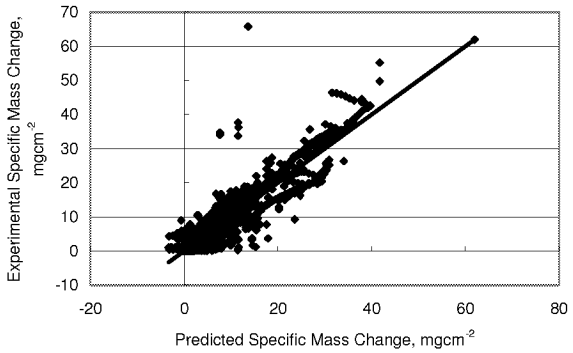

Figure 6 Comparison of predicted specific mass change of 9-12% Cr steels with the observed experimental value.

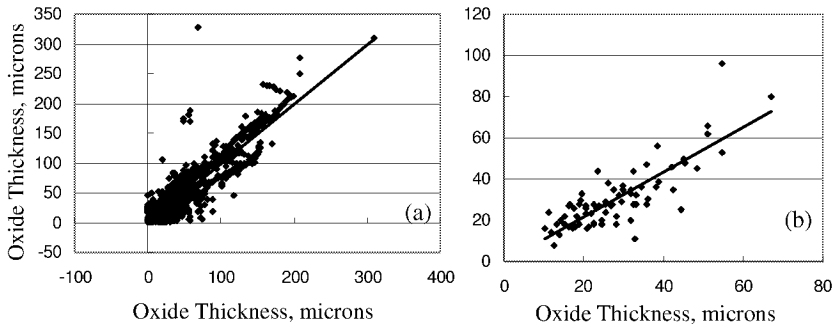

Figure 7 The predicted oxide outward growing (a) and inward growing (b) oxide thickness compared with the experimental values for a range of 9-12% Cr steels.

Further networks were trained to predict the thickness of the outward growing oxide layer and the inward growing oxide layer, with a view to using these parameters to give an indication of whether spallation was likely to occur with a given alloy composition, in specific atmospheres at a given temperature and time. The predicted target values matched well with the experimental data as shown in Figure 7. It should be noted that the data used to train the inward growing oxide was less abundant as these values are often not reported.

The prediction of spallation events is also encouraging however the limited data in terms of spallation observations is preventing extensive training and testing of the network. More complete datasets would help with this situation. Table I shows the success rate of the neural networks with the prediction of spallation events, with the network achieving a success rate of 88% when it uses the thickness of the outward growing oxide layer to predict spallation, and a

success rate of 50% when the thickness of the inward oxidation layer is used. This suggests that the outward growing oxide is the better parameter to follow as it provides a more sensitive measure of spallation events.

Table I Prediction of spallation based on the thickness of the outward growing oxide (88% Success rate) and the thickness of the inward growing oxide (50% success rate).

Network Prediction, Spallation?	Based on thickness of outward growing oxide		Based on thickness of inward growing oxide	
	Experimental Observation Spallation		Experimental Observation Spallation	
	Yes	No	Yes	No
Yes	**11**	0	**39**	712
No	87	**1164**	50	**472**
Maybe	43	32	11	215

Discussion

Each method of modelling oxidation under steam atmospheres has both advantages and disadvantages. Therefore the most appropriate technique applied depends on the data available for the model development and the aim of the final model developed. For example if the prediction of an event is required then the neural network technique is the most appropriate technique to use.

The oxide growth model has the advantage of being based on physical mechanisms that can be observed and measured. Also it requires a limited amount of data for the initial development of the model. Further data is obviously required for validation purposes, but this is true of all the models discussed. Whilst this model cannot be used to assess the effect of changes to the alloy composition, unlike the chromium equivalent model and the neural network model, it does give an indication of the dominant diffusion process taking place during the exposure.

The predicted specific mass change from the chromium equivalent model is based on the specific alloy composition, as described in equation 3 and based on experimental observations. Whilst this limits the information required to use the model there is a concern that important interactions from other minor element additions have not been taken into account. Although from our studies we have at least identified the major contributors and verified their interaction in the oxidation process through micro probe analysis. However, this technique has shown that it is possible to at the least gauge the effect of changes to the alloy composition and thus rank alloy compositions. The accuracy of this technique is however dependant on the range of alloy composition used to formulate the curves, thus a relatively large set of data is required for a robust set of curves, which it should also be noted are only applicable for one exposure time.

A large data set is also a requirement of the neural network model, both to ensure the accuracy of the model and to extend its applicability to different alloy compositions and exposures (type, time and temperature). Having trained the neural network with a range of data, it is possible to use the network to obtain specific mass change values for specific conditions outside of the training data set, although extreme caution is recommended in

applying this data to critical components. It is also possible to use the same data set to model other experimental observations, such as oxide thickness or spallation, which increases the value of the data; this is of course dependant on the completeness of the data set.

Table II summarises the advantages and disadvantages of each method.

Table II summary of the advantages and disadvantages of the different model techniques described previously.

Method	Advantages	Disadvantages
Oxide Growth Model	Based on physical mechanisms. Does not require a large dataset for development. Gives an indication of the dominant diffusion mechanism.	No extrapolation to other alloy compositions. No facility to model spallation. Requires an assumption regarding the grain growth law.
Chromium Equivalent Model	Requires limited information on the composition. Basis drawn from experimental observations. Possible to assess the influence of different alloy compositions via the Cr equivalent parameter.	Does not use the whole composition of the alloy, and consequently may miss important interactions. Requires a large data set for the developing curves for different exposures times. No extrapolation in terms of exposure time and temperature.
Neural Network Model	Uses only the most influential input parameters. Can be used for extrapolation for composition, temperature and time, provided the extrapolation does not exceed the bounds of the neural network. Can be used to model other observations from the same data set, e.g. oxide thickness.	Requires a large data set for adequate training. 'Black Box' computation. Tendency to only work within the bounds of the training data.

Figure 9 shows the predicted mass change from the three developed networks, for P92 exposed to 100% flowing steam at 650 °C, plotted with experimental results for the same material and experimental conditions. As this figure clearly illustrates there are some differences in the predicted values from the three models. However it is also evident that with the experimental data there is a large amount of variability in the recorded specific mass change, for example at an exposure time of 300 hours the specific mass change covers a range of 20 $mgcm^{-2}$, with some of the data points being due to spallation (see Figure 9). It is possible that not all spallation occurrences were reported, as there appears to be a region of data after 4000 hours that deviates from the experimental data population. This could be due to mass loss through spallation.

The chromium equivalent model has a tendency to over predict, and this may be due to the chromium equivalent parameter of 5, being near the limit of the models applicability. The neural network model also over predicts in the initial stages of the exposure, but performs well within the region encompassed by the experimental data. This model also appears to show a plateau of the specific mass change after an exposure time of around 20,000 hours, which could be an indication of the spallation limit.

The oxide growth model appears to model the mass change well, and fits the experimental data excellently up to an exposure time of around 3000 hours. After this point the predicted values are towards the upper limit of the experimental data and continues to rise. It is worth noting that it is around 3000 hours where the frequency of spallation events increases.

Interestingly the oxide growth and neural network models coincide at exposures between 3000 and 8000 hours, and it could be that the point at which the two curves diverge could be used as a measure of the oxidation limit point, although this is a subject for future work.

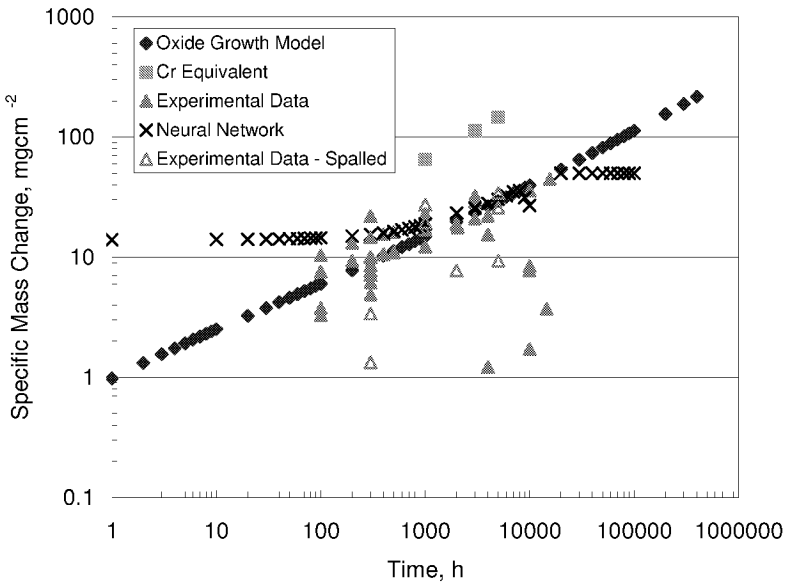

Figure 9 Results from the three developed models compared with the experimental results from exposures in flowing steam at 650 °C of P92.

Conclusion

It has been demonstrated that there are different techniques that use experimental data to develop models which can predict the material behaviour of 9-12% Cr alloys in oxidation studies. Whilst each technique has is benefits and weaknesses no one technique has been shown to fully model the oxidation behaviour, although the oxide growth model does an excellent job up to around 20,000 hours. As Figure 9 illustrates, the models become more 'powerful' if used in a combination. For example, the oxide growth model could be used to describe the behaviour of the oxide growth up to 10,000 hours in combination with the neural network model which predicts spallation and a plateauing of the mass change after 20,000 hours.

Acknowledgements

This work was part of the COST536 collaboration, Alloy development for Critical Components of Environmentally friendly Power plant (ACCEPT). Funding for the work was provided by the UK Department of Trade and Industry.

References

[1] H V Atkinson, Mater. Sci. Technol.1988 4 1052-1063

[2] P J Ennis and W J Quadakkers, Parsons 2000 Advanced Materials for 21st Century Turbines and Power Plant, eds A Strang, W M Banks, R D Conroy, G M McColvin, J C Neal and S Simpson, IOM Communications Ltd 2000 pp 265-275
[3] H.L.Solberg, G.A. Hawkins and A.A. Potter, *Transactions of the American Society of Mechanical Engineers*, 1942, 64, 303.
[4] F. Eberle and C.H. Anderson, *Journal of Engineering Power*, 1962, 84, 223.
[5] P J Ennis and W J Quadakkers in Materials for Advanced Power Engineering 2002, eds J Lecomte-Beckers, M Carton, F Schubert and P J Ennis, pub Forschungszentrum Julich GmbH 2002 pp 1131-1142.
[6] S Osgerby and A T Fry, Advance in Materials Technology for Fossil Power Plants, Proceeding from the Forth International Conference, October 25-28, 2004, 388-397.
[7] S Osgerby and A T Fry, International Symposium on High Temperature Oxidation and Corrosion, Nara, Japan, Nov 2005
[8] M G C Cox, B McEnaney and V D Scott, *Nature Physical Science*, 1972 237 140

THE INFLUENCE OF OXIDATION ON LONG TERM CREEP RUPTURE STRENGTH DATA

D J Allen[1] and B Harvey[2]

E.ON UK, Power Technology, Ratcliffe-on-Soar, Nottingham, NG11 0EE, UK[1]
Mitsui Babcock Energy Ltd, Porterfield Rd., Renfrew, PA4 8DJ, UK[2]
david.allen@eon-uk.com

Abstract

Long term creep tests on ferritic steels in air often show substantial oxidation. This may act to shorten creep life and produce over-conservative long term strength data. A recent E911 cross-weld test failed in just below 70,000 hours, less than half the predicted life, but the presence of a thick oxide layer gave rise to concern. Failure examination included measurement of metal and oxide thickness variations along the gauge length and correlation of diametral contraction data with measured axial elongation. This made it possible to separate out the effects of creep strain and hence determine metal loss due to oxidation. The results then indicated relatively small metal loss values, probably because the oxide was highly porous, and therefore occupied a large volume while consuming relatively little metal. The effect of oxidation on long term creep strength values in this high alloy steel thus appears to be a fairly small factor, but it is not negligible. For less oxidation-resistant materials, the development of appropriate oxidation correction techniques and their validation by inert atmosphere testing may be essential to obtain reliable long term creep strength values.

Keywords: Creep, testing, oxidation, high alloy steel, advanced power plant materials

Introduction

Recently, the final high alloy steel E911 cross-weld creep rupture test specimen from the Mitsui Babcock (MBEL) "ACCTS" project [1], tested at 650°C and 26 MPa, failed after 69,334 hours. This was over twice the duration of the previous longest failed test in the European Creep Collaborative Committee (ECCC) E911 weld data set. Its rupture life was below half that predicted [2] from previous ECCC data, but considerable oxidation was evident. A simple calculation based on overall diameter measurement suggested that the life shortfall might be largely due to oxidation-induced loss of section. This gave rise to the concern that even in high alloy ferritic steels, long term creep test results or data extrapolations to realistic end-of-life conditions might be seriously compromised by oxidation effects.

Initial measurements indicated a 0.6mm increase in specimen diameter at the weld. On the conventional assumption of a Pilling-Bedworth ratio of two, this suggested an oxide thickness of 0.6mm (single layer), with the total diameter thus increased to 8.57mm, and the metal diameter reduced by oxidation (ignoring the additional effects of creep strain) to 7.37mm. On such an assumption, the effective stress would be increased by 17% at the end of the test.

Many workers have modelled the effects of oxidation on creep life, with differing results. For example, Hart [3] attempted to allow for the fact that as oxidation progresses, the net section stress on the remaining metal increases, and so the enhancement in rate of creep life consumption increases throughout the test. This analysis produced a rather complex formula and introduced a factor described as the "creep life fraction at failure". This was treated as an

adjustable parameter which need not (as might have been assumed) necessarily be 100%. Whilst it is true that oxidation causes an increasing stress enhancement, it can be argued that we have no real knowledge of how this affects creep behaviour - for example, how the creep life in a test at a constant 80MPa might differ from a test at a stress increasing linearly from 75MPa at the start to 85MPa at the finish. Consequently, the value of modelling the varying life consumption rate is questionable. It is much simpler to calculate the time-averaged stress enhancement from a model of oxidation kinetics. Arguably, this is not truly less rigorous, and it avoids the uncertainty which an adjustable parameter would introduce.

It is then necessary to assume an appropriate oxide growth law. Parabolic kinetics apply when diffusion through the oxide is rate controlling, whereas linear or pseudo-linear growth can occur in different circumstances [4]. If oxidation is parabolic, a simple calculation shows that the mean diameter reduction during the test is 2/3 of its final value (since parabolic growth implies faster growth in the early part of the test). Thence, the mean increase in effective stress due to oxidation during this long term creep test would be about 11%.

Clearly, if this estimate proved to be correct and representative, it would imply that oxidation has a substantial influence on assessed long term creep strength values in high alloy steels. Broadly, the test condition is representative of thermal exposure at end of life in an operating plant, since 69,334h at 650°C equates (using a Larsen-Miller parametric conversion with C=20) to about 470,000 hours at a more realistic operating temperature of 620°C. Hence, the implication would be that long term creep strength values may be underestimated by figures of the order of 10% if testing is carried out (as, of course, is usual) in air. This is clearly a substantial and unwelcome source of uncertainty.

Indeed, the uncertainty makes it difficult to use the long term data point at all. A stress increase by 11% corresponds to a much larger percentage decrease in creep life. Simple calculations show that if oxidation is ignored, this long term data point falls far below the prediction [1] from shorter term data, suggesting a considerable need to revise the prediction for the longer term. However, if the above oxidation correction is instead applied, the shortfall largely disappears. It is ironic that a primary aim of ECCC has been to extend creep data out to 70,000 hours: but that when such a data point is generated, its interpretation may be so subject to ambiguity that it seems to be almost unusable.

Experimental

The cross-weld creep test used a 44mm parallel length, 40mm gauge length, 7.97mm actual diameter cross-weld specimen. The weld, of width approximately 16mm, was centrally located. The series of eight tests all showed HAZ "Type IV" zone failure. The long term test specimen examined here had failed in the HAZ on one side of the weld and had a large secondary crack in the HAZ on the opposite side. Its measured elongation, 5.98% and reduction in area, 18.4%, were toward the upper end of the range for the test series. Chemical composition data are given in Table 1.

	C	Si	Mn	P	S	Al	Cr	Ni	Mo	V	W	Nb	N
Parent	0.115	0.19	0.35	0.007	0.003	0.006	9.10	0.22	1.00	0.23	0.98	0.069	0.069
Weld	0.110	0.20	0.61				8.71	0.77	0.95	0.20	0.94	0.046	0.055

Table 1. Chemical composition

After failure, the specimen diameter within the gauge portion of each broken half was measured, using a micrometer, at 2.5mm intervals along its axis. For precision, the measurement intervals were reduced to 1mm in the necked regions close to the failure and to the secondary crack.

The two broken halves were each then sectioned along their centrelines and mounted and polished to preserve the surface oxide layer. Diametral measurements were then repeated at the same axial positions, using an optical microscope eyepiece graticule. This allowed two sets of measurements to be made: the total diameter (metal plus oxide where present), comparable to the micrometer measurements; and the metal-only diameter.

It was expected that the sections would not be perfectly located at the centreline. However, excellent agreement was obtained with the micrometer data, indicating that the sections were sufficiently close to the centreline to require no data correction. The only major discrepancy was that the micrometer data were the higher at the actual failure location, presumably because of the difficulty of gripping the specimen at its minimum diameter. Hence, the microscopical measurements were then the more accurate. The results are shown in Table 2.

	Distance from fracture mm	Diametral measurements mm			Oxide thickness (two layers)
		Micrometer	Optical – Metal only	Optical – Metal and oxide	
Parent metal	32.5	8.11			
Parent metal	30	8.09	7.975	8.1	0.13
Parent metal	27.5	8.14	7.95	8.075	0.12
Parent metal	25	8.24	7.95	8.125	0.18
Parent metal	22.5	8.13	7.975	8.125	0.15
Edge of HAZ	20	7.56	7.55	7.55	
HAZ crack	19	7.3			
HAZ / Weld metal	17.5	7.5	7.55	7.55	
Weld metal	15	7.61	7.6	7.6	
Weld metal	12.5	7.76	7.6	7.6	
Weld metal	10	8.58	7.725	8.6	0.88
Weld metal	7.5	8.53	7.775	8.55	0.78
Weld metal	5	8.54	7.725	8.6	0.88
Weld metal	4	8.52	7.65	8.625	0.98
Weld metal	3	8.55	7.725	8.5	0.78
HAZ	2	8.61	7.6	8.55	0.95
HAZ	1	8.67	7.325	8.45	1.13
Fracture, long side	0	7.92	6.75	6.75	
Fracture, short side	0	7.16	6.8	6.8	
Edge of HAZ	-1	7.52	7.4	7.4	
Parent metal	-2	7.55	7.45	7.45	
Parent metal	-3	7.52	7.45	7.45	
Parent metal	-4	7.5	7.45	7.45	
Parent metal	-5	7.52	7.375	7.375	
Parent metal	-6	7.34	7.375	7.375	
Parent metal	-7.5	7.34	7.3	7.3	
Parent metal	-10	7.37	7.425	7.425	
Parent metal	-12.5	7.6			

Table 2. Diametral data

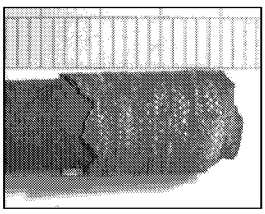

Fig. 1. Thick oxide on part of weld metal

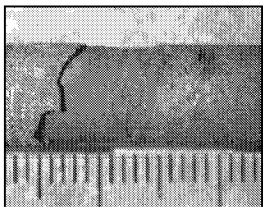

Fig. 2. Thick oxide (weld, left); no oxide (cracked HAZ, centre); thin oxide (parent, right.)

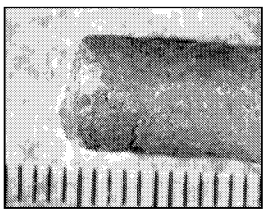

Fig. 3. Small retained oxide patch on strained parent material

Metallographic examination of the broken halves showed that a thick oxide layer had been retained on much but not all of the weld metal region, Figure 1. A thinner oxide layer was also visible on the parent material on the longer broken half, this being the parent material not adjacent to the actual failure, Figure 2. The shorter broken half, consisting mainly of the parent material adjacent to the failure, also had an isolated retained oxide patch, Figure 3. Elsewhere, including both the failed and the secondary cracked regions, all the surface oxide had spalled off, either during the test or on removal of the specimen from the machine.

Results

Broadly, three different types and thicknesses of oxide were observed at different locations on the specimen.

The parent material on the unfailed side of the weld, which had accrued very little creep strain (Table 2), showed the thinnest oxide layer. This was typically 0.07mm thickness, and rather variable, with pits corresponding to protrusions, Figure 4. A duplex oxide structure, with an inner spinel and an outer magnetite layer, was evident.

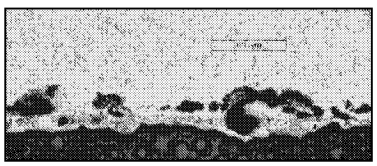

Fig. 4. Oxide on unfailed side parent material (scale 200μm)

The parent material on the failed side, which had accrued quite substantial creep strain, showed an oxide layer of about 0.13mm thickness, in the small area where it had not spalled away. Its morphology, Figure 5, was fairly similar to that found on the unfailed side parent material, though with a more consistent thickness. These results thus suggest that tensile creep strain accelerates oxidation.

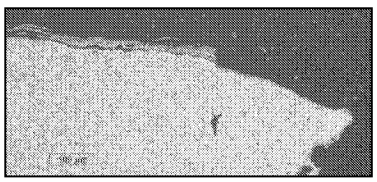

Fig. 5. Oxide on failed side parent material (scale 500μm)

The oxide which covered about half of the weld metal was much thicker, Figure 6. Its typical total thickness (as measured on a single face of the specimen) was estimated as 0.435mm, based on average data. The oxide structure was rather more complex, Figure 6.

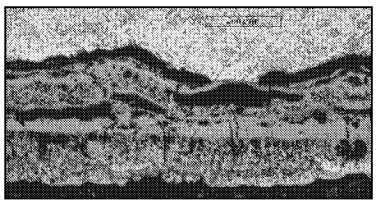

Fig. 6. Thick oxide on weld metal (scale 200μm)

An outer magnetite layer (probably capped with haematite) can be identified, growing outward from a very flat boundary, which can thus be identified as representing the original surface of the specimen before testing. However, the oxide on the inner side is not simply an inward-growing spinel, but contains multiple layers, thought to be successive duplex-layer bands, each comprised of an inner spinel and outer magnetite layer. It thus appears that as the oxide thickened, it became increasingly liable to disbond from the metal, allowing oxygen easy access to the fresh surface via the cracks and voids in the oxide, and repeatedly re-starting the duplex oxidation process. This would have tended to promote pseudo-linear rather than parabolic oxidation kinetics, with less retardation in the oxidation rate in the later stages. It is also notable that the oxide has a high content of porosity, voidage, and cracking.

The observations on the oxide which extends just beyond the weld metal to cover part of the HAZ close to the failure, Figures 7 and 8, are puzzling. It would seem evident that chemical composition differences must be the reason why the oxide on the weld metal is so much thicker than that on the parent material. However, on crossing the fusion boundary from the weld metal into the HAZ, the observed oxide structure hardly changes. The HAZ is clearly a weaker region, and the metal surface thus shows rapidly increasing diametral shrinkage due to creep strain. In response to this, the oxide layer merely becomes even more fragmented, whilst maintaining or even increasing in thickness. Moving even closer to the failure, Figure 8, it is evident that the oxide finally breaks up and spalls away entirely, no doubt due to the high creep strain. However, about a 1mm axial length of the HAZ surface does include a retained oxide layer, of thickness quite similar to that on the weld metal.

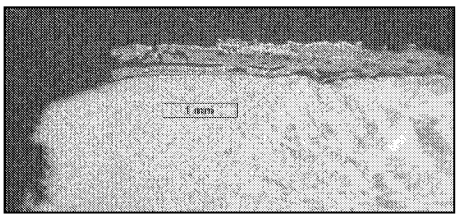

Fig. 7. Thick oxide extending from weld metal into HAZ (scale 1mm)

Fig. 8. Thick oxide extending from weld metal into HAZ (scale 500μm)

Analysis

Creep Strain

If a creep specimen is assumed to deform homogeneously at constant volume, and oxidation is either neglected or correctly compensated for, then its radial contraction can be used to determine its corresponding local axial (engineering) creep strain:

$$EL = [(d_0^2 / d^2) - 1] \times 100\%$$

where d_0 is initial diameter and d is measured final diameter.

If these local strain measurements (weighted to correspond with their axial spacing) are averaged over the gauge portion (here taken as a 42.5mm length, to allow for the axial 5.98% elongation on the original gauge portion of 40mm), then in the absence of oxidation, the result should equal the measured elongation. It will be noted that, since diametral measurements are

being used to predict an axial elongation measurement, the exercise is, in principle, an effective test of the accuracy of the two different methods of creep strain measurement.

Because of oxidation, however, the diametral measurements do not predict axial elongation correctly. If metal-only diameter data are used, the prediction is +9.5% elongation, an overestimate because oxidation has contributed to the reduction in diameter. If metal-plus oxide data are used where available, the prediction is +3.3% elongation, an underestimate (even though retained oxide is only present for about half these measurement points).

Calculated local axial creep strain values, one series based on the metal-only data and a second series based on the metal-plus-oxide data, are plotted as a function of axial location in Figure 9. It can be seen, for example, that the metal-only data would apparently suggest a high tensile creep strain in the (oxide covered) weld metal, whereas the metal-plus-oxide data would suggest a high compressive creep strain. Both of these uncorrected result series are evidently inaccurate.

Oxidation

The interaction between oxidation and creep strain may be analysed on the basis of a simple assumption, that:

K = (thickness of metal consumed / thickness of oxide layer formed) is a constant

For an assumed Pilling-Bedworth constant of 2, the value of K would be 0.5. However, the following analysis provides a means of determining K from the metallographic information. The effective final diameter at each location, d_{eff}, can be determined from measurements on the failed specimen as:

d_{eff} = metal-only diameter + K(metal-plus-oxide diameter minus metal-only diameter)

i.e. d_{eff} = metal-only diameter + K (thickness of two oxide layers)

Then, d_{eff}, and hence K, can be determined as those values which correctly predict the measured axial elongation from diametral data. Hence, it is possible to calculate the thickness loss due to oxidation (as opposed to creep strain) at the failure location, and thereby determine the effective increase in stress due to oxidation.

When retained oxide is not present, its thickness must be estimated. Fortunately, there is enough information available in this case to enable reasonable estimates to be made. For the unfailed-side parent / HAZ region, the estimated thickness of two oxide layers is based on the average of the measured values on the unfailed parent region, 0.14mm. For that part of the weld metal where no oxide was retained, the corresponding thickness is based on the average of the values measured elsewhere on the weld metal, 0.87mm. For the HAZ location at 1mm from the fracture, actual oxide thickness data were available. Turning to the parent material on the fractured side of the weld, the estimated thickness of two oxide layers is taken as 0.26mm, as indicated by the small patch of retained oxide shown in Figure 3.

The most problematic question to decide is what oxide thickness allowance to assume at the failure location itself, just inside the HAZ. It seems most probable that the highly strained

HAZ region all maintains or exceeds the high oxidation rate shown by the weld metal, whereas the oxide thickness on the less severely strained parent material falls to the much lower value determined for the surviving patch shown in Figure 3. In this work, it has been arbitrarily assumed that the thickness change occurs at the fracture face, so that the oxide thickness allowance at the (+0mm) position is taken as 0.87mm, while that at the (-0mm) position is taken as 0.26mm. Whilst these are simplistic assumptions, their accuracy is not very important in terms of an overall calculation of the constant K, as they characterise oxidation losses only over a small region of the specimen.

Oxidation and Metal Loss

The value of K, taken as a simplifying approximation to be the same constant for all the materials, may then be calculated as that which predicts the overall elongation of 5.98%. The result is that K=0.253. Using this value, revised values of local axial creep strain have been calculated by correcting the "metal-only" data for oxidation losses. These are plotted in Figure 9 as "metal corrected" results.

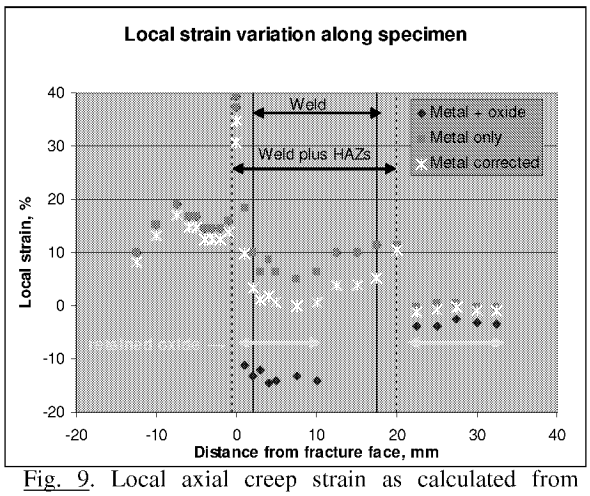

Fig. 9. Local axial creep strain as calculated from diametral measurements

The acceptability of the calculations, and the simplifying assumption that K is the same for all materials, can be assessed by examining whether the "metal corrected" results are physically realistic. Figure 9 shows that the calculated axial creep strain in the weld metal then becomes low (about 1%) and tensile. This is entirely plausible for a region within the specimen which is not creep damaged. The same applies to the parent material on the unfailed side. There is a local tensile strain peak of about +35% at the fractured HAZ, with a secondary peak of about +10% at the opposite cracked but not completely failed HAZ, both of which are again plausible results, though they are not very sensitive to the oxidation correction. In the parent material on the failed side, there is evidently a considerable tensile creep strain, rising to a maximum of about +20% at some 10mm from the fusion boundary. These results cannot primarily be due to any underestimate of oxidation losses, as the oxidation correction here is very much smaller than the calculated creep strain. They therefore indicate that the parent E911 material had also reached a substantial fraction of its creep life. The high tensile creep strain in the parent material, extending over a substantial part of the specimen length, also probably accounts for the higher than usual specimen elongation in this test.

The calculated "metal corrected" strain values for the oxide-spalled region of the weld metal are a little more questionable, the average value being higher than for the unspalled regions, at

around 4%. It is conceivable that these regions did accrue greater strains than the oxide-unspalled weld metal, but it is more probable that the oxidation losses have been somewhat underestimated. If the metal losses in the spalled region were in fact some 50% greater than those in the unspalled region, then the creep strain data on the two regions would be brought into line. This seems credible, as spallation exposes a fresh surface which can oxidise more rapidly. It thus seems likely that oxide spallation does increase the metal loss rate, albeit to a fairly moderate extent. To test sensitivity to the assumptions made, the K calculation was repeated with weld metal strain values adjusted to 1% for the spalled weld metal regions. This gave only a marginal reduction in the calculated K value, from 0.253 to 0.235.

The result that K=0.253 can thus be confirmed as a reasonable best estimate for this specimen. There is some uncertainty, but it is clearly more appropriate than the conventional (and very different) assumption that K=0.5. The main explanation is probably that the oxide layer is highly porous and fractured, and therefore occupies more space. In consequence, the true metal loss is much smaller than would be calculated on the K=0.5 assumption.

Effect of Oxidation on Applied Stress

The derived K value may then be used to calculate the extent of metal loss, at the failure location, at the end of the test. This, however, is the stage at which the most critical assumption is required. It is necessary to assume a value for the oxide layer thickness at the failure, given that no retained oxide is present in this highly strained region.

As noted earlier, the oxide layer on the HAZ seems to become somewhat thicker, but also more porous or fractured, than that on the weld metal. It seems reasonable, therefore, to adopt the average thickness value (two oxide layers) of 0.87mm which was obtained for the weld metal. On that assumption, and with K = 0.253, the metal loss is 0.22mm. This acts to reduce the diameter from 7.97mm to 7.75mm by the end of the test, and thus to increase the stress by 5.8%. As noted earlier, however, the mean stress increase during the course of the test is, if oxidation is parabolic, 2/3 of the final value. Hence, the effect of oxidation is to increase the mean applied stress by 3.8%. This equates to a change in the applicable stress value from 26 MPa (applied engineering stress) to 26.98 MPa. (For a linear oxidation model, the mean stress would be half of the final value, and so the effect would be somewhat less.)

The assumptions on oxide thickness at the position of failure, however, can only be best guesses. A higher value will apply if repeated oxide spallation and regrowth causes faster metal loss in the rapidly straining zone close to the failure. The calculated effect of oxidation therefore probably represents a lower bound estimate. The real effect could be greater.

Implications

E911 cross-weld data assessment

According to this analysis, the long term creep strength value in this test is underpredicted by slightly less than 4%. This is equivalent [2] to an underprediction of about 18% in terms of mean creep life. These are not entirely negligible figures, but they are considerably smaller than the 11% strength underprediction figure previously suggested on the basis of simple estimates from the overall diametral measurements. Micrometer measurement alone is therefore not sufficient to assess the effects of oxidation with any accuracy.

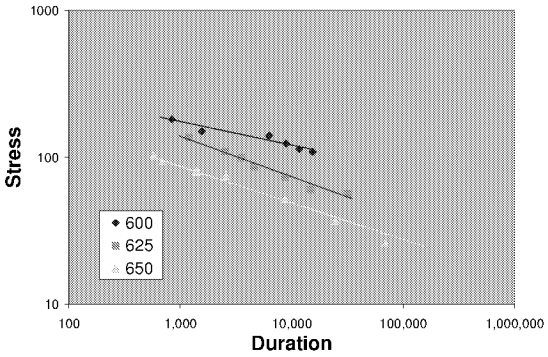

Fig. 10. ACCTS data and trendlines from [1]

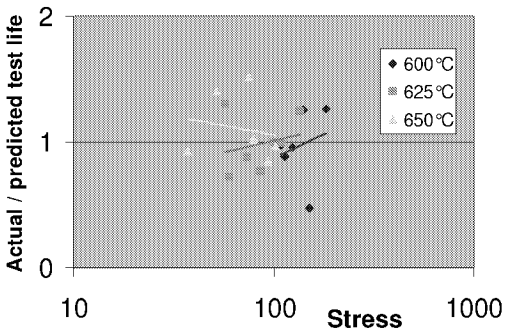

Fig. 11. ACCTS data replotted excluding long term failure

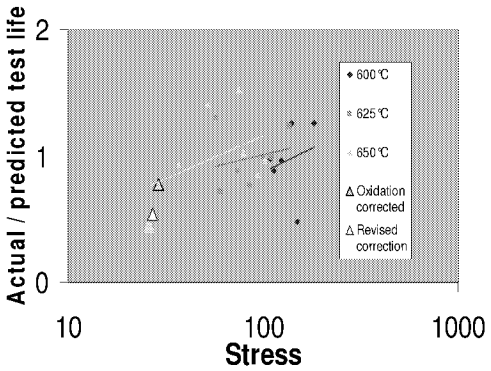

Fig. 12. ACCTS data replotted, including long term failure

The effects of including this long term data point in analysis, and of applying an oxidation correction, are shown in Figures 10 -12. Figure 10 shows all the ACCTS cross-weld data (points) on the E911 cast tested by MBEL, and compares these with the predicted mean life values [2] (trend lines) from the ECCC data set. Figure 11 includes all the ACCTS data points except the longest term point, and shows the ratio of actual to predicted [2] life, plotted against stress for each of the three test temperatures employed. The ACCTS data were not themselves included in the data set used [2] to produce a cross-weld creep rupture life assessment. Figure 11 suggests that the prediction parametric nevertheless fits quite well, in that the mean ratio is close to unity, and there is no clear trend with stress, although there is some data scatter. However, addition of the uncorrected new data point in Figure 12 alters the situation, and suggests that the Servetto and Allen parametric [2] systematically tends to overpredict life at lower stresses.

Figure 12 also includes the original and revised "corrected" values for the new data point, with the effective stress adjusted for oxidation. The original correction, based on micrometer measurements, would have raised the data point from the very low actual / predicted life ratio of 0.44 to a more typical figure of 0.78. The revised, much lesser correction now derived produces a life ratio of only 0.54. It does not appear, therefore, that the relatively poor result of this test can be just an artefact caused by oxidation. Whether it truly indicates a long term downturn in creep strength is a different question. The low value obtained in this one very long test might perhaps be only due to random scatter in the data. It may be noted that the next lowest stress test in the ACCTS series, at 37 MPa, produced a life ratio only just

below unity. An assessment including the data point would, of course, give it due weight in determining the most probable trend line.

Oxidation and creep data extrapolation

The application of an oxidation correction to the long term test data point alone is, however, very questionable. Oxidation also affects shorter term tests, if to a lesser degree. It may be argued that a viable oxidation correction procedure, if it is adopted, should be applied to all the data points.

The apparent proportional reduction in creep strength caused by oxidation increases, for a given temperature and a fixed specimen diameter, as the rupture life increases. If the oxidation kinetics are known, the relationship is predictable and continuous. Hence, it does not seem reasonable to suppose that the creep data analyst can "hide" away from the oxidation problem, simply by avoiding long term testing. If it is long term strength data that are needed, then an extrapolation from short term data (with a slight oxidation error, if left uncorrected) through medium term data (with a moderate error) should, in principle, correctly predict what data a long term test would produce – including the oxidation error. Hence, the long term ACCTS test did not introduce a new problem of data interpretation. Rather, it served to highlight a problem which had hitherto gone largely unrecognised.

Creep data on high alloy steels

The ACCTS long term test corresponds, using a Larson-Miller parameter calculation with C=20, to approximately 470,000 hours at a realistic service temperature of 620°C. Hence, although the test was on a weld, the stress was so low that the level of oxidation should be at least representative of expected end-of-life conditions for high alloy steels in power plant. An implication is therefore that end-of-life creep strength values for high alloy steels in general are probably underestimated, as a result of oxidation, by figures of the order of 4%. This is of course a moderately low figure, and is smaller than the recent (downward) revisions in ECCC strength values for P92, E911 and P91. However, it is not entirely negligible. It is, of course, a very tentative conclusion based on a single creep test.

A number of the uncertainties should be noted. First, the very different oxidation responses of the E911 weld metal and parent material may be due to chemical composition differences. Thus, for example, higher chromium steels may be less affected. Secondly, it cannot be excluded that the 4% figure is substantially too low because of faster oxidation at the rapidly straining failure location. Better information should be obtained by repeating this type of detailed investigation on a long term parent material test specimen, where compositional variations will not complicate the analysis, and by comparison with inert atmosphere testing. Thirdly, it might be that oxidation rate increases more sharply with temperature than does creep rate, although this remains to be explored.

General Implications

Most notably, if the oxidation issue is at all significant for high alloy steels, it is likely to be major for low alloy steels under end-of-life conditions.

A common working assumption in the operation of high temperature plant is that whereas creep rupture strength data may be used for design purposes, such data are of lesser value in the assessment of component remaining life after long term operation. Thus, creep rupture

data on as-manufactured materials inevitably relate to short and medium term exposure, whereas remaining life may perhaps be better investigated by testing the actual long term exposed material. However, this approach does place reliance on obtaining and testing specific samples with differing service histories, while making less use of established information databases on creep rupture properties.

Recent developments, for example references [5, 6], suggest that creep rupture data assessment is now – if rather belatedly - becoming a reasonably exact science. With the abandonment of unsuitable techniques and the development of more accurate models, it may no longer be appropriate to ignore what can be done to predict component remaining life from the data on as-manufactured materials. For example, a creep rupture database on a large number of different casts of a specified steel should, in principle, provide a good way of identifying its lower bound material characteristics and properties. Remanent life testing, which will inevitably be limited to a restricted selection of samples taken from aged plant, may not easily pick out the particular cast from a wide range of components which will have the lowest remaining life.

Oxidation remains a substantial stumbling block. Even for the E911 example, an uncertainty of the order of 18% in predicted mean life would significantly impair predictive capabilities. Thus for example, if an E911 component that had run for 220,000 hours had a predicted lower bound rupture life of 250,000 hours, it would be reasonable to schedule it for replacement. This could be wasteful if a better lower bound life prediction, correcting for oxidation effects, was in fact 305,000 hours, as would be implied by an 18% life underprediction figure. Indeed, much effort would probably be put into alternative approaches, such as in-service monitoring and remanent life assessment testing, to stave off any premature replacement. For low alloy steels, the uncertainties are larger. Research to reduce these uncertainties could potentially bring large savings in component replacement costs.

Acknowledgements

This paper is published by permission of E.On UK plc and Mitsui Babcock Energy Ltd.

References

[1] MITSUI BABCOCK ENERGY LTD, (2000), "A New Creep-Resistant Ferritic Steel for Improved Energy Efficiency", Future Practice Report No. 66, prepared for the Energy Efficiency Best Practice Programme, ETSU, Harwell.

[2] SERVETTO, C, and ALLEN, D J, (2002) "An Assessment of Creep Rupture Data on E911 Steel Weldments", 7th Liege Conference on Materials for Advanced Power Engineering, 2002, pp. 1661-1670.

[3] HART, R V, (1985), "The Effect of Test Piece Oxidation on Creep Life Predictions of Thick Components", CEGB, unpublished report.

[4] NICHOLLS, T, (2000), "Oxidation Correction in Creep Life Assessment", M. Res. Thesis, Swansea University.

[5] MERCKLING, G, (2005), “Long Term Creep Rupture Strength Assessment: The Development of the European Creep Collaborative Committee Post Assessment Tests”, Proc. Conf. “Creep and Fracture in High Temperature Components”, London, Sept 12-14, pp. 3-19.

[6] BENDICK, W, and GABREL, J, (2005), “Assessment of Creep Rupture Strength for the New Martensitic 9%Cr Steels E911 and T/P92”, Proc. Conf. “Creep and Fracture in High Temperature Components”, London, Sept 12-14, pp. 406-418.

NEW EXPERIENCE IN THE FIELD OF APPLICATION OF CORROSION RESISTANCE PROTECTION IN FLUE GAS DESULPHURISATION PLANT ABSORBERS

Adam Hernas[1], Macin Imosa[1], Jerzy Pasternak[2], Stanisław Fudali[2]
[1] Silesian University of Technology, 8 Krasińskiego Str, 40-019 Katowice, Poland
[2] Boiler Engineering Company RAFAKO S.A., 33 Lakowa Str, 47-400 Raciborz, Poland
jerzy.pasternak@rafako.com.pl

Abstract

Absorbers form the main part of the flue gas desulphurisation plants for 360MW units at Belchatow Power Station. The plant working cycle and service life depend on the material grades of the absorber lining corrosion-resistance protection materials in its individual zones. The objective of manufacturer activities in this field is to extend the service life of the flue gas desulphurisation plant by implementation of the "wallpapering" technology in the absorber cylindrical part with plate sheet having the thickness from 0.5 to 1,6mm, made of Hastelloy type nickel alloys. The experiment carried out on Hastelloy nickel alloys, grades C-22 and C-2000, among others by means of evaluation of corrosion resistance of the base material, "wallpaper" plate sheet, welded joints and HAZ.

The corrosion tests were executed for three different conditions of corrosive environment:

1. The environment of actual chemical composition of boiler outlet flue gases, with 10% weight addition of K_2SO_4. Test temperature 70^0C, testing time up to 1,000 hrs.
2. The environment of actual chemical composition of boiler outlet flue gases, with 6% weight addition of K_2SO_4 and 4% weight addition of NaCl. Test temperature 70^0C, testing time up to 1,000 hrs.
3. Simulation of the actual conditions of waste incineration environment, pertaining during thermal utilisation of wastes with the following chemical composition: $N_2 + 9\%O_2 + 0.08\%SO_2 + 0.2\%$HCL. Test temperature 450 and 600^0C, testing time up to 1,150 hrs.

For the purpose of comparison, corrosion resistance tests were carried out on boiler steel types T22, E911, HCM12 and TP347H.

This document includes the results of evaluation of welded joints structure and HAZ (Heat Affected Zones), joint corrosion resistance characteristics, corrosion product test results, as well as requirements and recommendations with regard to fabrication of welded joints, the preparation degree of lining plate join surfaces, and requirements in field of weld joints.

Keywords: nickel alloys, flue gas desulphurisation plants, wallpapering, corrosion resistance, microstructure

Introduction

The development of the power sector plays a dominant role in the welfare of each country, however, its development has become the main cause of degradation of the natural environment. Degradation of the environment – which in consequence leads to deterioration of the living conditions – must not be neglected by a power equipment manufacturer. Therefore, in the 90-th years has been taken up some environmental activities, i.e. limitation of sulphur emissions, and offers our customers, among others:

- various techniques of sulphur emissions reduction in the boiler furnace chamber by means of so-called primary methods,
- designing and erection of fluidised bed boilers,
- boiler outlet flue gas cleaning installations, reducing sulphur oxides by means of secondary methods, including the most efficient desulphurisation method, i.e. wet limestone method.

Owing to considerable costs of plant shutdown and time-consuming repairs, if any, the plant operational cycle should not be shorter than 100,000hrs. The service life of a flue gas desulphurisation plant depends on the type of applied absorber corrosion resistance materials in its selected parts [6-10].

The objective of this elaboration is to show activities aimed at increasing the service life of flue gas desulphurisation plants, including implementation of stainless steels and alloys based on nickel contents, used as absorber protective lining in the wet limestone desulphurisation plants. This paper includes selection of materials, preparation of WPS (Welding Procedure Specification), elaboration and requirements of welding technology, "wallpapering" technology (sheet lining using the high nickel alloyed, corrosion resistance plates in absorber surfaces), as well as the evaluation of welded joints and HAZ (Heat Affected Zones) corrosion resistance.

1. Examples of selected applications for corrosion resistance lining in flue gas desulphurisation plants

Flue gas desulphurisation by means of the wet limestone method is the most common and efficient method of SO_2 removal from the flue gases. The desulphurisation efficiency of this method ranges between 90-95%. The flue gas desulphurisation process takes place in the absorber, which is the main part of the flue gas desulphurisation plant. The absorber is a tower-type washer designed for SO_2 removal, as well as almost complete removal of HCl from the flue gases. This method is to rinse the flue gases with lime slurry (or limestone slurry) in the absorption tower [1]. As the slurry is of acid reaction, the absorber bottom and sides have to be lined inside with a material to resist the influence of the absorber environment. Therefore, the materials applied have to be resistant, among others, to the temperatures of 55-75^{0}C, condensate including dissolved acids or salts with pH value equal to 1-2, to influence of gases, i.e. SO_2, HCl, HF and NO_x, surface abrasion, influence of steam and formation of deposits.
It is assumed that the following corrosion resistance types of constructional steels protection can be used in the flue gas desulphurisation plants [2,3], e.g.:

- special types of rubber,
- ceramic materials or plastic materials,
- application of stainless steels or high-alloy materials with nickel and chromium.

The experiences of manufacturer have had so far; reveal some parallel concepts of application of corrosion resistance lining made of high-alloy steels or nickel alloys in the absorber working area. One of them is manufacture of complete austenitic material elements – especially ones having not too large dimensions. Another offer includes surfacing by welding with austenitic electrodes. Still another one is the promotion of "wallpapering" technology (sheet lining using the high alloyed, corrosion resistance material in absorber, scrubber surfaces). This is the technology highly recommended in order to provide protection for large surfaces exposed to chemically aggressive substances [6-9]. The areas where such materials are applied include absorber inlet stubs, bottom and lower part of the absorber, damper and flue gas ducts. The lining is fixed to the absorber casing, made of carbon steel, by means of some welding techniques [2,3].

2. Selection of materials and technologies of welded joints fabrication

The objective of any reliable manufacturer, is to extend the effected service life of any flue gas desulphurisation plant by implementation of new materials and technologies for absorber protection, including "wallpapering" with lining of plate sheet, having the thickness of 0.5 – 1,6mm, made of Hastelloy nickel alloys, grades C-22 and C-2000 [2-5,7,8].
The experiment to implement the new corrosion resistance protection technology, included among others:

- selection of materials and preparation of corrosion resistance protection welding technologies,
- fabrication of qualification welded joints for individual stages of „wallpapering" technology,
- evaluation of the welded joints quality using, among others, the estimation of base material corrosion resistance, that of „wallpapering" plate sheet, welded joints and HAZ.

Below, there are exemplary constructional solutions with WPS (Welding Procedure Specification)of "wallpapering" process, chemical composition of base materials used, welding materials and welding process parameters.
The details of welding preparation, welding parameters and the sequence of layers of welded butt and fillet joint beads, with the use of filler metal are presented in figure 1 and figure 2.

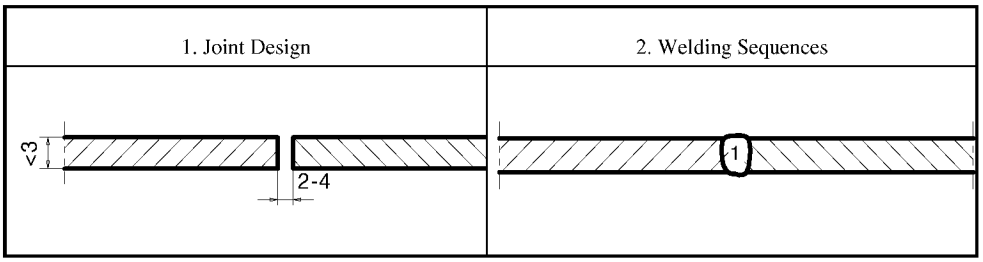

1.Welding Process Details – 141 Method

Run number	Welding methods	Size of Filler Material	Wire's classification	Current [A]	Voltage [V]	Type of current/ Polarity	Inter-pass temperature
1	141	1,2	Hastelloy C-2000	60 ÷ 90	-	DC "-"	max 100 °C
2. Welding Process Details – 131 Method							
1	131	1,2	Hastelloy C-2000	70 ÷ 90	18 ÷ 20	DC "+"	max 100 °C

Figure 1. Details of welding preparation, wire diameter and applied welding parameters of butt welds.

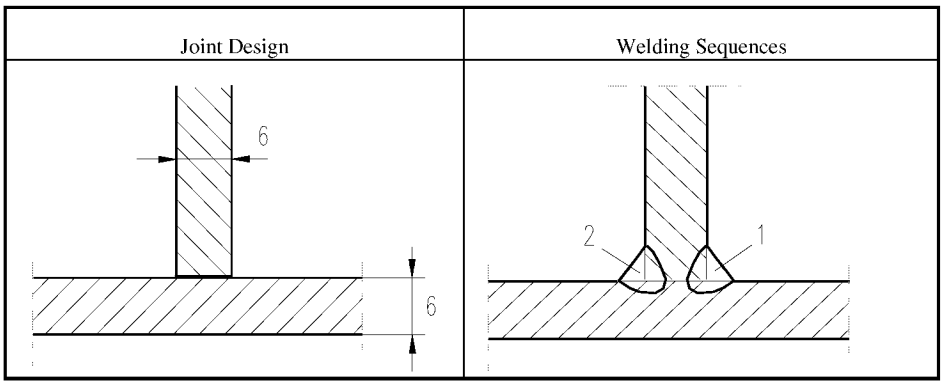

2.1. Welding Process Details - for 141 Method

Run	Welding methodes	Size of Filler Material	Wire's classification	Current [A]	Voltage [V]	Type of current/ Polarity	Inter-pass temperature
1	141	1,2	Hastelloy C-2000	70 ÷ 90	-	-	max 100 °C
2	141	1,2	Hastelloy C-2000	70 ÷ 90	-	-	max 100 °C
3. Welding Process Details - for 131 Method							
1	131	1,2	Hastelloy C-2000	70 ÷ 90	18 ÷ 20	18 ÷ 20	max 100 °C
2	131	1,2	Hastelloy C-2000	70 ÷ 90	18 ÷ 20	18 ÷ 20	max 100 °C

Figure 2. Details of welding preparation, wire diameter and applied welding parameters of fillet welds.

The chemical composition of plates applied in welding, C-276, C-22 and C-2000 grade and critical crevice, critical pitting temperatures – acc. to Haynes specification – of aforementioned joints are contained in table 1.

Table 1. The chemical composition of plates C-276, C-22 and C-2000 grade and the selected properties – acc. to Haynes specification.

Type of alloys	Ni	Cr	Mo	Fe	Other
Hastelloy C-276	57	16	16	5	4W
Hastelloy C-22	56	22	13	3	3W
Hastelloy C-2000	59	23	16	2	1.6Cu
Type of alloys	Critical Crevice Temperature, ^{0}C		Critical Pitting Temperature, ^{0}C		
316L	0		0		
Hastelloy C-276	55		>120		
Hastelloy C-22	80		>120		
Hastelloy C-2000	80		>120		

3. Analysis of corrosion resistance conditions

The analysis of the flue gas desulphurisation plant working conditions showed that the main factor contributing to the deterioration of materials with the influence of raw glue gases is high-temperature chlorine-sulphuric corrosion, with the presence of such compounds as SO_2 and HCl.
Whereas, the conditions prevailing inside the absorber would rather cause damage due to electro-chemical corrosion with sulphate and chloride ions. On the basis of the aforementioned analyses of the operating conditions, quick corrosion tests were carried out in the conditions resembling the actual ones, but with many times higher destructive conditions of the corrosive environments.

The evaluation of the corrosive service life was performed on welded joint cutouts with two surface condition (i.e. raw after welding and polished) and on welded joints. The testing conditions were as follows:

- The environment of actual boiler outlet flue gas chemical composition, with addition of 10% K_2SO_4 by weight. Test temperature 70^0C, testing time up to 1,000 hrs.
- The environment of actual boiler outlet flue gas chemical composition, with addition of 6% K_2SO_4 by weight and 4% NaCl by weight. Test temperature 70^0C, testing time up to 1,000 hrs.
- The environment simulating flue gas chemical composition in a waste incineration plant: N_2 + 9%O_2 + 0,08%SO_2 + 0,2%HCL. High-temperature corrosion at 450 and 600^0C, testing time up to1,150 hrs.

Simultaneously, for the purposes of comparison, the corrosion resistance examinations were carried out – in a flue gas desulphurisation plant conditions – on HCM12 and TP347H boiler steel types.

4. Analysis of electrochemical corrosion test results

The analysis of the potentials-static (Figure 3b and Table 2) and galvanostatic examinations of test samples made of C-22 and C-2000 alloys in 0.2% HCl solution and at the temperature of 70^0C shows the tendency to surface passivity. Surface damage in the solution including Cl^- ions should not lead to acceleration of corrosion processes.

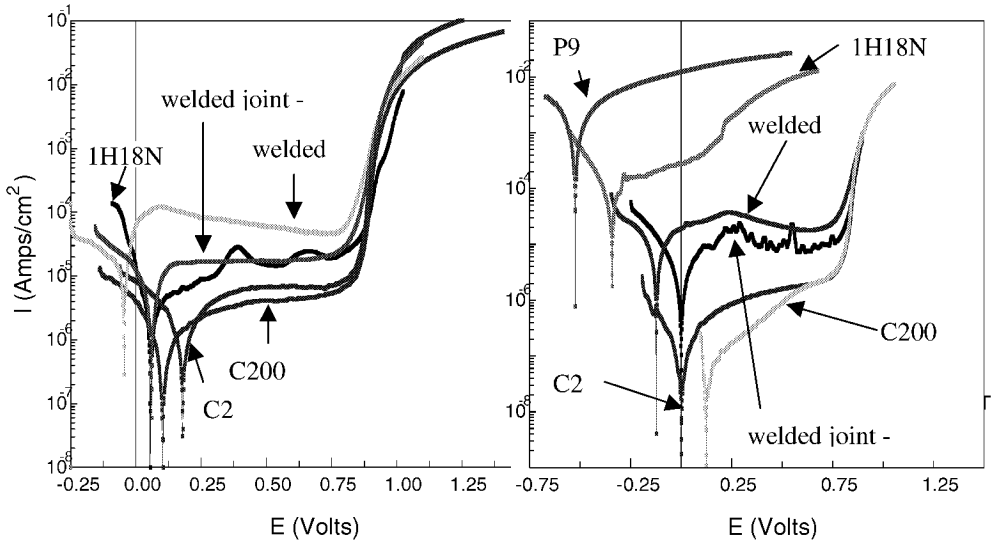

Figure 3. Potentio-dynamic curves of test pieces made of C-22 and C-2000 alloys and 1H18N9T and P92 steels at temperature 70^0C:
a) in 3% H_2SO_4 solution b) in 0.2% HCl solution

Table 2: Results of investigations the potentio-dynamic in 0.2% HCl solution

Sample	E_{cor} [mV]	I_{cor} [μA/cm^2]	I_{pas} for E=250 mV [μA/cm^2]	I_{pas} dla E=750 mV [μA/cm^2]	$E_{breakdown}$ [mV]
C-2000 – 1	123,16	0,013	0,17	2,9	783,0
C-22 – 2	1,72	0,048	0,86	2,82	782,0
Welded joint C22 – C2000 – 3	122,5	4,70	-68,0	18,7	718,4
Welded joint – polishing C-22 – C-2000 – 4	0,01	1,08	114,4	9,54	767,4
Steal P92	-524,17	488,53	18 983,0	—	—
Sample	E_{cor} [mV]	I_{cor} [μA/cm^2]	E_{pas} [mV]	I_{pas} [μA/cm^2]	$E_{breakdown}$ [mV]
Steal 1H18N9T	-341,68	39,48	-286,7÷ -170,0	162,5	195,7

The passive range was observed on the potentio-dynamic curves of all the tested samples. All tested samples made of C-22 and C-2000 alloys were characterised by a similar breakdown potential, above which the current density, as well as the corrosion rate increased rapidly. The condition of samples after corrosion – lack of significant pitting (Figure 4) – proves uniform characteristics of the course of corrosion processes. However, in case of 1H18N9T steel, a considerably lower breakdown potential was observed. Thus, this steel reveals low resistance to pitting corrosion at 0.2% HCl and at the temperature of 70^0C. On the basis of very high potential values, achieved on the potentio-dynamic curve, it can be assumed that even slight polarisation of the steel, owing to formation of, for example, a concentration cell; will result in fast, uncontrolled deterioration of the material.

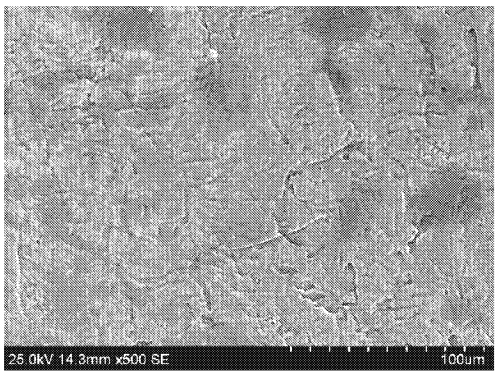

Figure 4. Microstructure of sample No. 2 surface of C-22 alloy after examinations by means of potentiostat in 0.2% HCl solution.

Among the samples made of C-22 and C-2000 alloys, C-2000 alloy showed the highest resistance to corrosion. This is proved by the lowest value of the corrosive and passive current. The disadvantage, however, lies with somehow smaller width of the passive range, in comparison with that of C-22 (i.e. also smaller resistance to the influence of concentration cells) as well as the fact that in the passive range the potentio-dynamic curve is not ideally flat

which may prove that the passive layer formed is not ideally tight which, in turn, contributes to gradually faster pacing corrosion speed with the growth of the potential, which should not take place.

The analysis of the potentiostatic (Figure 3 and Table 3) and galvanostatic tests, executed in 3% H_2SO_4 solution, showed that the samples made of C-22 alloy and the samples without a polished welded joint could be characterised by a tendency to surface passivity. In case of these materials, it can be assumed that a surface defect would not result in acceleration of corrosion processes. In case of samples made of C-2000 alloy and comparatively tested 1H18N9T and P92 steels, after the initial passivity there occurred surface activation, followed by passivity, etc. Possible damage to the material surface exposed to corrosion in the solution including SO_4^{2} ions – may result in acceleration of corrosion processes. Solely in case of the sample made of C-22 and C-2000 alloys with a polished welded joint, the proneness for surface activation was detected.

Table 3: Results of investigations the potentio-dynamic in 3% H_2SO_4 solution

Sample	E_{cor} [mV]	I_{cor} [μA/cm^2]	E_{pas} [mV]	I_{pas} [μA/cm^2]	$E_{breakdown}$ [mV]
C-2000 – 1	103,16	0,491	207,2	4,14	806,4
C-22 – 2	178,92	0,980	270,0	6,72	825,1
Welded joint C-22 – C-2000 – 3	45,22	9,53	94,6	65,5	782,0
Welded joint – polishing C-22 – C-2000 – 4	59,77	4,56	144,0	15,2	790,0
Steel 1H18N9T	560,97	2,19	457,71	26,70	757,0
Steel P92	-496,98	4 486,0	—	—	—

Similarly as in case of tests in 0.2% HCl solution, passive range was observed on the potentio-dynamic curves. The breakdown potential was slightly lower for the samples with a welded joint. The examinations of the sample surface condition (Figure 4), following corrosion tests, showed no pitting, which proves the uniform characteristics of corrosion and can be considered highly advantageous. In case of samples made of 1H18N9T steel, pitting was found. The most disadvantageous was the condition of samples made of P92 alloy, where the quench annealing effects were detected. The samples made of C-2000 alloy showed the highest corrosion resistance, which can be backed up by the lower corrosive and passive current density value.

5. Test results analysis of electrochemical corrosion on welded joints and HAZ

The macro and micro-structure tests of the welded joints, both and fillet ones, made of C-22 and C-2000 nickel alloys, show the proper base material structure – HAZ properties, as well as the correct joint shapes. In the both C-22 and C-2000 nickel alloys tested, there were partial structural uniformities, which is due to the plate plastic deformation. In case of C-2000 alloy, some lamer extractions were observed, which are characteristic for the plate material supplied. How ever, the extractions in C-22 alloy are of pointwise character, with uniform distribution.
The welded samples, in comparison with monolithic ones, were characterised with lower corrosion resistance, which was proved especially by higher value of the corrosion and passive current, i.e. also by faster corrosion rate. The samples with polished welded joints showed higher corrosion resistance than the samples without polished welded joints. The

considerable difference in corrosive (i.e. corrosion rate) and passive current density proves the purposefulness of this treatment in case of welded components made of C-22 and C-2000 alloys, which are susceptible to SO_4^{2-} ions influence at elevated temperatures.
The difference in the density value of corrosion and passive current is so significant, that this treatment may be considered purposeful and with crucial influence on the material corrosion resistance.

6. Analysis of high-temperature corrosion test results

The expected application of high nickel alloys in thermal waste utilization boilers, the additional laboratory tests of high-temperature corrosion were carried out at the temperature of 600°C for 1,100 hours, with the simulated corrosive atmosphere having the following chemical composition: N_2 + 9%O_2 + 0.08%SO_2 + 0.2% HCl, selected with the purpose of simulating the extreme operating conditions.
The analyses of the corrosion kinetics diagrams (Figure 5 and 6) of the examined C-22 and C-2000 alloys, welded joints and, comparatively T22, E911, P92 and TP347H steels showed that at the testing temperature of 600°C the resistance of Hastelloy type alloys and welded joints is many times higher than that of the tested steels. In case of austenitic steel, TP347H the corrosion resistance in relation to the tested alloys C-22 and C-2000 is even up to ten times lower, however, in case of an unpolished welded joint, the difference in the corrosion resistance diminishes almost twice. The negative changes in weight, observed in the diagrams of C-22 and C-2000 alloys and welded joints, may result due to chipping of the scale formed, but also owing to sublimation of the corrosion products, formed on a sample surface.

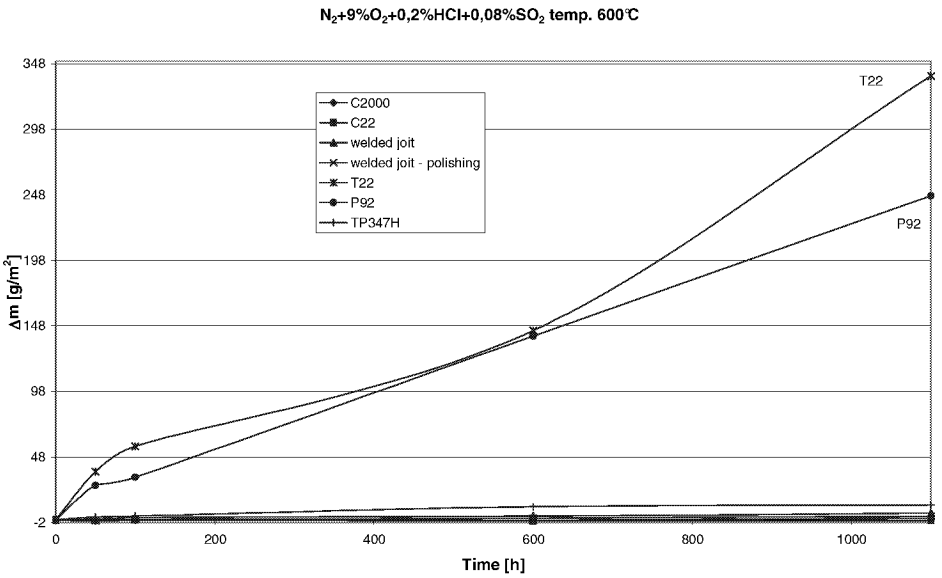

Figure 5. Corrosion resistance test results obtained at corrosion test workplace in model corrosive atmosphere with the following chemical composition:
N_2 + 9%O_2 + 0.08%SO_2 + 0.2% HCl at temperature 600°C.

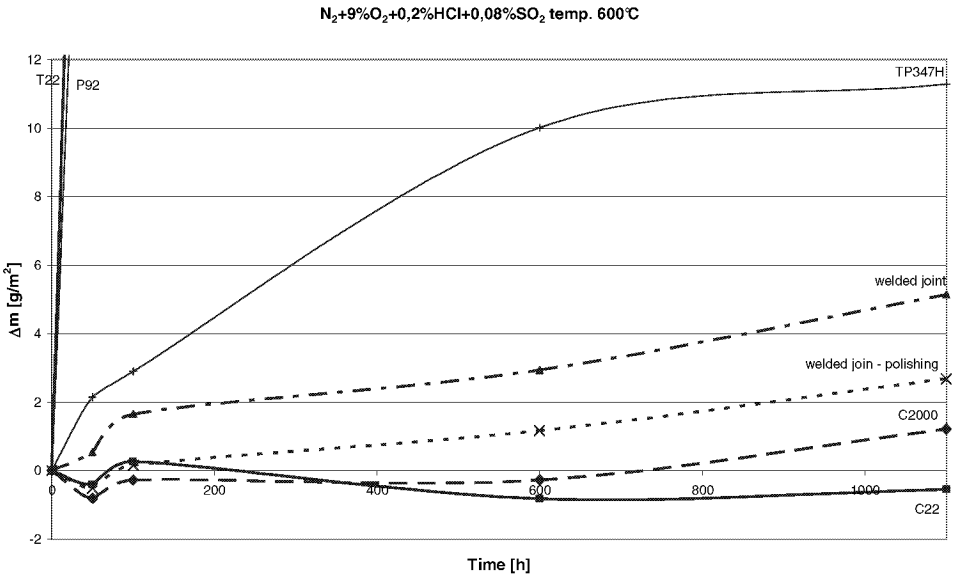

Figure 6. Corrosion resistance test results obtained at corrosion test workplace in model corrosive atmosphere with the following chemical composition:
N_2 + 9%O_2 + 0.08%SO_2 + 0.2% HCl at temperature 600°C

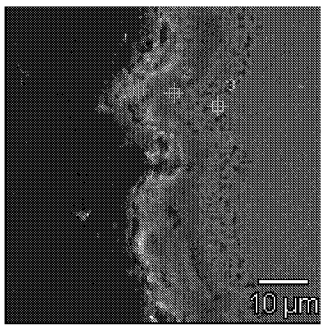

Table 4. Radiographic microanalysis results of areas from figure 7.

	Al	*S*	*Cl*	*Cr*	*Fe*	*Ni*	*Mo*
1	0.98	2.24	0.44	90.82	1.74	3.78	
2				77.74		9.30	12.96
3				4.71		74.31	20.98

Figure 7. Microstructure of corrosion products formed in model atmosphere at temperature of 600°C on C-2000 alloy after 1,100 test hours, with marked spots of chemical composition analysis

The analysis of the structure and chemical composition of corrosion products after 1 100 testing hours in model atmosphere at the temperature of 600°C proves that the scale on the tested samples is very thin, with its maximum thickness of 10 µm (e.g.: TP347H, on average 50µm) and is not continuous. However, the analysis of the chemical composition of the corrosion products on the tested samples, in both the variants, showed that the dominant chemical elements included in the scale are, most of all, chromium, as well as nickel and molybdenum. The presence of sulphur and chloride was also found. The presence of chromium is highly advantageous as far as corrosion resistance is concerned, since it proves the existence of chromium oxide Cr_2O_3 and chromium-nickel spinel, which form a scale with

protective properties. The sulphur and chlorine found in the scale accelerate the corrosion processes, however, they appear in an insignificant quantity and, as one should expect, their presence is bound to diminish with the growing thickness of the oxide protective layer. The tested samples also show the presence of internal oxidation zone (Figure 7 and Table 4), in which mostly chromium is oxidised, forming a scale layer consisting of Cr_2O_3 above the solid scale zone. The existence of such internal oxidation zone is beneficial, since it allows the formation of an adherent protective layer. This also proves that the corrosion processes on C-22 and C-2000 alloy samples and welded joints are in the incubation phase. Based on these test results, it can be stated, with high probability, that further execution of tests in the aforementioned atmosphere would lead to formation of a compact adherent scale, consisting of Cr_2O_3, with further sequence of corrosion processes undergoing the logarithmic law.

Conclusions

- Application of austenitic steels or nickel alloys in flue gas desulphurisation plants, guarantees very high chemical resistance and long service life of the plant.
- C-22 and C-2000 nickel alloys have shown very good resistance to electrochemical corrosion, both in 3% H_2SO_4 solution and 0.2% HCl solution at the temperature of 60^0C. The values of corrosive and passive current density – in range of micro-amperes and, in some cases, hundredths of micro-amperes, gives reasons to assume that these alloys will be capable of being operated throughout a considerable period of time. Their advantage is that their main deterioration mechanism is uniform corrosion, not pitting corrosion or quench annealing as in the case of the materials tested for comparison purposes.
- Corrosion resistance of welded joints in the environment of electrochemical corrosion is lower than C-22 and C-2000 parent material, however polishing of the welded joint surfaces can improve it.
- C-22 and C-2000 alloys and their welded joints can also be characterised by very high resistance to high-temperature chloride – sulphur corrosion which, in simulated the thermal west utilisation conditions, is ten times higher than that for TP347H austenitic steel, being even several time higher in case of E911, P92 and T22 steels.
- The limitation for general application of the "wallpapering" technology may lie with its high investment costs.

References

[1] Rataj Z, Wasilewski A, Wojnar B: Maksymalizacja stopnia wykorzystania potencjału energii odpadowej spalin kotłowych. Ocena sprawności i bilansowanie. Publishing by Silesians Technical University Gliwice,1998. (In polish only)
[2] Van Gansbeke. L., L.Paul, D. Kingseet: Experience with the new Ni-Cr-Mo alloy HASTELLOY C-2000 in Flue Gas Desulphurisation (FGD) System.
[3] Van Gansbeke. L, D.C. Pattison: Scrubber duct lining project at Louisville gas electric company's mill creek station units 1-4.
[4] Zidr M, Debeljak B, Dermond J: Application of different limestone qualities for wet flue gas desulphurisation. VGB Power Tech, 11,2002.
[5] Schutttenhelm W, Braun W: Most recent development and optimisation aspect for FGB technologies. PowerGen Conference 2004
[6] Hernas, A.; Imosa, M.; Formanek, B.; Cizner, J.: „High-temperature chlorine–sulfur corrosion of heat-resisting steels", Journal of Materials Processing Technology, Volume: 157-158, Complete, December 20, 2004, pp. 348-353.

[7] A. Hernas, M. Imosa, J. Cizner: „ High-temperature corrosion resistance of new creep-resisting steels", Proc. Mezi. Konf. Kotle, energeticka zarizeni a spalovny odpadu, Brno 2002.
[8] Khanna A.S. High Temperature Oxidation and Corrosion, ASM International 2002.
[9] Cahn R.W. Haasen P. Kramer E.J. Corrosion and Environmental Degradation, Materials Science and Technology Series, WILEY – VCH 2000.
[10] Neumann J., Kautz H.R.: „Evaluation of international literature on fireside corrosion in coal-fired power plants and waste-to-energy plants", VGB Kraftwerkstechnik 77(1997),

CORROSION AND OXIDATION EXPERIENCES IN AVEDØRE II MULTIFUEL BOILER

M. Montgomery[1], S.A. Jensen[2], O. Biede[2], O.H. Larsen[3], C. Andersson[4]
[1]Energi E2/Elsam/IPL - DTU, Kemitorvet, 2800 Lyngby, Denmark (mm@ipl.dtu.dk)
[2]Energi E2 Power Company, Teglholmen, AC Meyers Vænge 9, 2450 København, Denmark.
[3]Elsam A/S, Kraftværksvej 53, Skærbæk, 7000 Fredericia, Denmark,
[4]Vattenfall Nordic Heat AB, 81426 Älvkarleby, Sweden.

Abstract

Avedøre II was commissioned in 2001, and since then corrosion and oxidation have been investigated each year. In the first year heavy oil and gas were used as fuels and in the following years, heavy oil + gas + wood pellets have been utilised. Superheater 3 is fabricated in TP347H FG, however part of the superheater is a test section which has alternate sections of TP347H FG and Esshete 1250. The reason for this was to compare the fireside corrosion and steamside oxidation of the two steels in the actual plant. After 1 years exposure where the boiler had been fuelled with heavy oil and gas, the deposit on the specimens was sodium sulphate with particles of vanadium oxide. After the second year, where the fuel had been wood pellets + gas + heavy oil, the deposit consisted of predominately potassium sulphate with sodium sulphate present at the outer part of the deposit. Vanadate particles were still present within the deposit. Fireside corrosion occurred by sulphidation. This was the same after three years exposure, however as well as an enrichment of sulphur present in the corrosion product, there was some attack at grain boundaries. Corrosion morphology and corrosion rates were similar for Esshete 1250 and TP347H FG. Steam oxidation showed similar results for Esshete 1250 and TP347H FG after the first year. However in the following two years, the steam oxide of Esshete 1250 was thicker than that of TP347H FG.

Keywords: TP347H FG, Esshete 1250, fireside corrosion, steamside oxidation, co-firing

Introduction

Avedøre 2 CHP (combined heat and power) plant was commissioned in 2001 and is located south of Copenhagen in the Energi E2 area in Denmark. Avedøre 2 comprises of three modules – a large USC (ultra super critical) plant, two parallel-powered gas turbines and a biomass plant. The steam pressure of the USC boiler is 300 bar and that of the reheater components is 80 bar. The main boiler is a once through tower boiler of the Benson type with single reheat and it is designed for ultra super critical steam data, i.e. 300 bar and 580/600°C. It has a thermal capacity of 800MW. The outlet temperature varies depending on fuel type. On the steamside, the feedwater treatment was alkaline water treatment (AVT) during the first year (3000 hrs) and CWT (combined water treatment) in following years (pH 9.1, O_2 120 ppb and NH_3 used for regulating pH).

Use of biomass as a fuel is an important measure for reduction of CO_2 emissions in Denmark. In addition Energi E2 is committed by the government to use 300,000 tons/year wood pellets in the main USC boiler. A wood pellet manufacturing plant has been built on the coast 30 km from Avedøre, and the pellets are transported to Avedøre 2 by ship. At present the main boiler uses a mixture of heavy fuel oil, gas and wood pellets, however the temperature has been held at 540°C to avoid potential corrosion problems.

Operational Conditions

In superheater 3 at Avedøre 2, a test tube has been welded in with alternate sections of TP347H FG and Esshete 1250 to compare both steamside and fireside oxidation for these two types of steel. The alloy specifications are given in Table 1.

Table 1: Material specifications of sections investigated.

	C	Cr	Mo	Ni	Si	Mn	Others
TP 347H FG	0.04-0.10	17.0-20.0		9.00-13.00	<1.00	<2.00	Nb/Ta x C<1.00
Esshete 1250	0.06-0.15	14.0-16.0	0.8-1.20	9.0-11.0	0.20-1.00	5.5-7.0	Nb 0.75-1.25 V 0.15-0.40

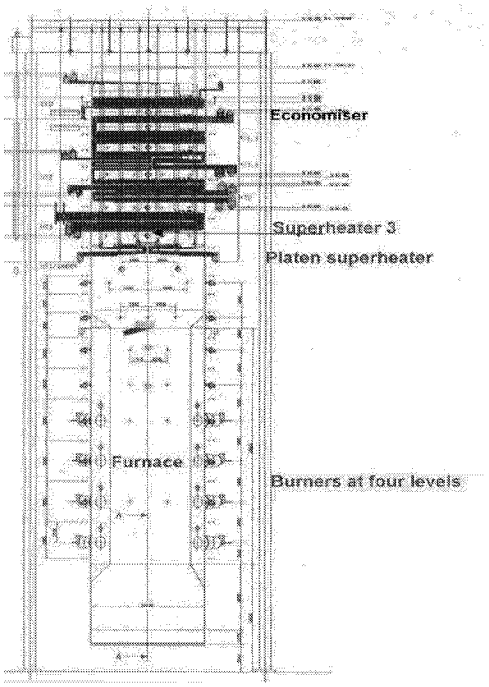

Figure 1: Avedøre 2 main boiler.

The test section investigated (arrow in Figure 1) is on the lower side of superheater 3 and therefore has estimated steam temperatures of 510°C when the outlet temperature of superheater 3 is 540°C. During the first year (3000 hours), the plant was fuelled alternately with natural gas (total 1000 hours) and heavy fuel oil (total 2000 hours). The outlet steam temperature was 580°C during gas firing and 540°C during oil firing [1]. During the 2nd and 3rd years (8000 hours each), the plant was fired simultaneously with heavy fuel oil (2.5% S and max. 120ppm V), gas and wood pellets, and the outlet temperature was 540°C [2,3]. The exact ratios of fuel vary. In the combustion chamber the excess air is 1.2% with oil firing and this is 2.5-3% with wood pellets. Each year during the summer shutdown, a section of this superheater has been removed and investigated at IPL-DTU. Investigations of cross-sectioned specimens were conducted using light optical and scanning electron microscopy.

Results

From the results described in this paper, the fireside corrosion and steamside oxidation can be compared for TP347H FG and Esshete 1250 for the total exposure time of 19,000 hours. The deposits formed are also analysed.

Fireside Corrosion

There was very little deposit after firing with gas and heavy oil; however thicker deposits were present after the 2nd and 3rd years when wood pellets were involved. Soot blowing was used periodically during the 2nd and 3rd year to remove the outer deposits, so only the inner most deposits have been analysed after exposure. During the first year of exposure, with gas and heavy oil, the deposit formed on the surface of the specimens was sodium sulphate matrix and metal vanadate particles - mostly iron vanadate but also some nickel vanadate (Figure 2). The inner deposit from the 3rd year has been analysed as shown in Figure 3. Instead of sodium sulphate matrix, the matrix now contains predominantly potassium and calcium sulphate. Within this matrix there are less iron vanadate particles however now iron oxide needle-like particles are also present.

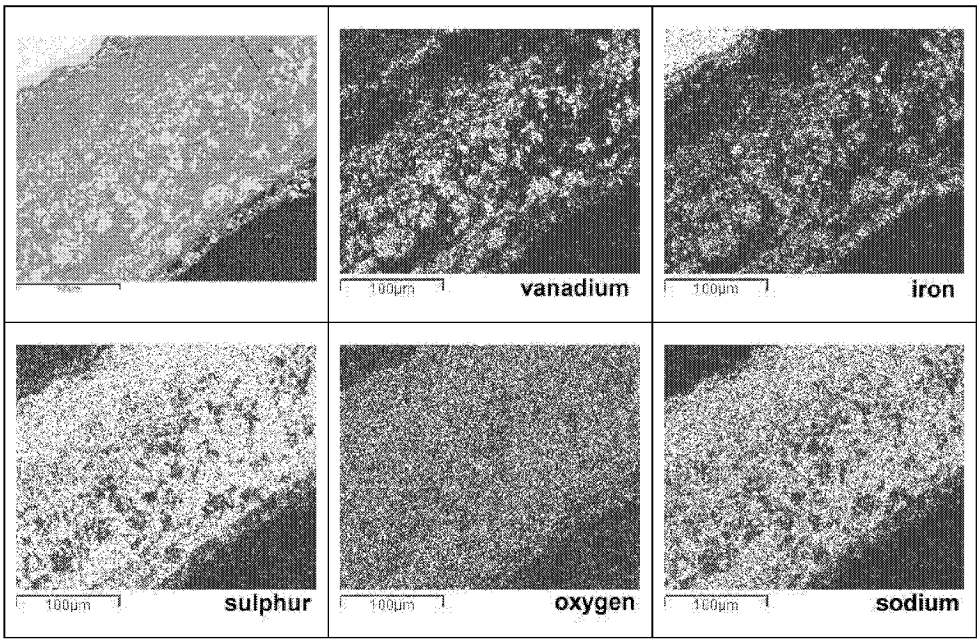

Figure 2: Mapping of deposit from first year (oil + gas) showing the elemental distribution.

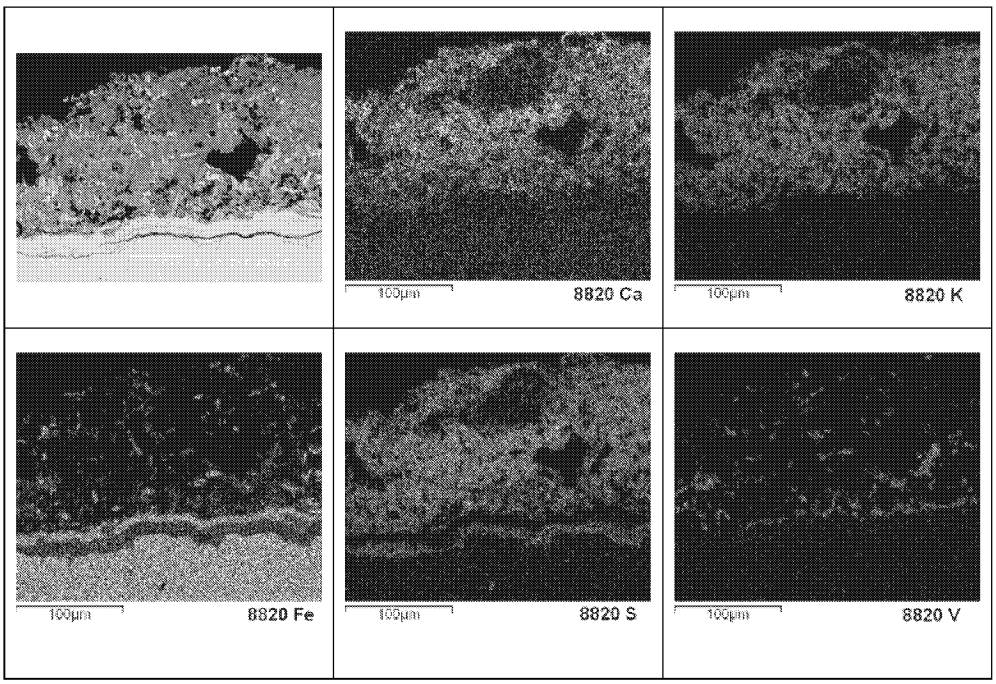

Figure 3: Mapping of deposit from third year (oil + gas + wood pellets) showing the elemental distribution.

The morphology of the fireside oxide was similar for both the Esshete 1250 and the TP347H FG. The fireside oxide after the first year consisted of an inner chromium rich oxide and the outer part of the oxide was iron oxide. On the top of this oxide, there were particles of iron vanadate. Figure 4 shows the elements present in the layers, the elements with highest abundance are named first. Elements have been measured in wt. %.

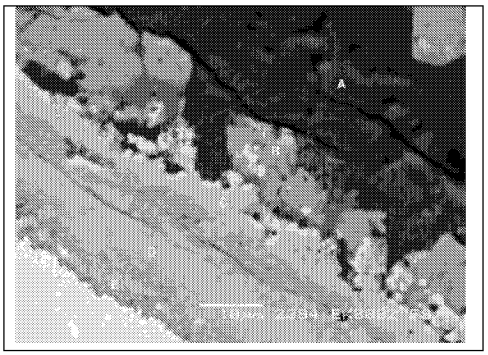

	Main elements	Minor elements
A	O S Na	Ca
B	V Fe O	Ni, Na, Mg
C	Fe O Ni Cr	Zn
D	Fe, Cr, O, Ni	
E	Fe, Cr, O	

Figure 4: Composition of fireside oxide on Esshete 1250 after the 1st year exposure with heavy oil and gas.

Figure 5 is from the oxide after 2 years exposure and shows that adjacent to the oxide the matrix is potassium sulphate with some calcium. Needle like precipitates in the deposit matrix are iron oxide. Some precipitates of iron vanadate are observed close to the oxide surface however not so many as in the first year. The outer oxide is iron oxide and the inner oxide is a more chromium rich iron nickel oxide. In the inner oxide there is more sulphur present than was the case for the previous year.

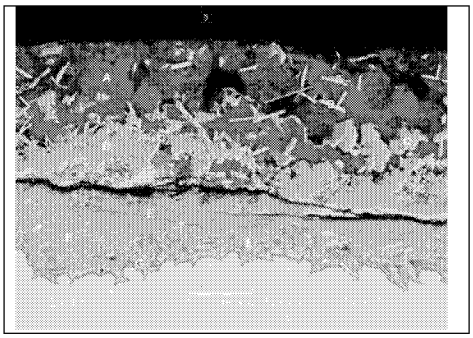

	Main elements	Minor elements
A	S O K	Ca Ni
B	Fe O	S
C	Fe V Ni O	
D	Fe O	
E	Cr Fe O Ni	S
F	Cr Fe O S	Ni
G	Cr Fe O S	Ni Mn

Figure 5: Composition of fireside oxide on TP347H FG after 2 years exposure.

In the third year, similar types of deposit and corrosion products were observed as for the second year. However in addition to this, there were a few areas with grain boundary attack within the metal. Analysis of these grain boundaries revealed the presence of sulphur. This was similar for both Esshete 1250 and TP347H FG. Figure 6 shows the variation in fireside attack on two places on the same specimen (NB different magnifications). There is an increase in the sulphur concentration within the oxide at the oxide-metal interface from <1 in the 1st year, to approx 8% in the 2nd year to 12% in the 3rd year which could be responsible for sulphur grain boundary attack.

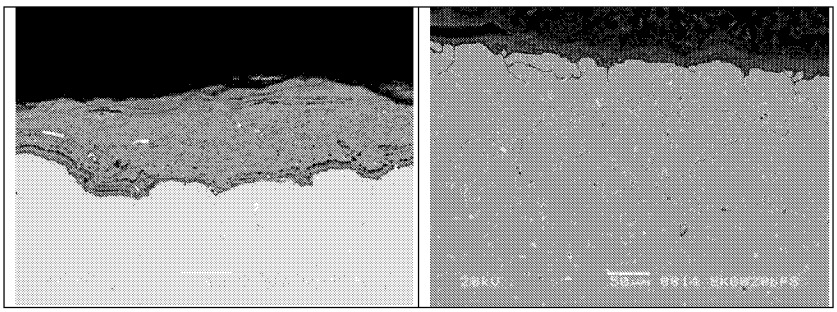

Figure 6: Esshete 1250 exposed for 3 years showing localised grain boundary attack - NB varying magnification.

The corrosion rate is so small for these specimens that measurement of residual metal thickness does not give meaningful results. Thus data for the fireside oxide thickness (without localised grain boundary attack which is approx 100 μm) for the two steels lies between 25-35μm for all the specimens which is acceptable, however extensive grain boundary attack, although very localised would give problems.

Steamside oxidation

The inner and outer oxides were investigated each year and are shown in Figure 7.

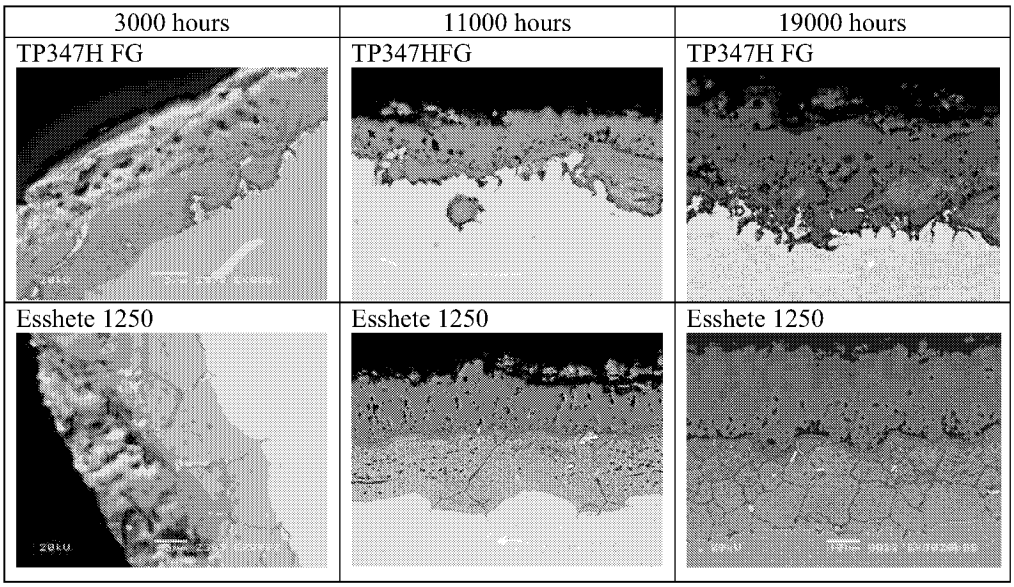

Figure 7: Comparison of steamside oxide for Esshete 1250 and TP347H FG - N.B. varying micron markers.

The outer oxide for TP347H FG was iron oxide and the inner oxide was an iron chromium nickel oxide. In some cases the original grain boundaries could be observed. With longer exposure times there were areas with more chromium rich oxide within the inner oxide. Some chromium depletion at the metal adjacent to the oxide was revealed after the longest exposure

times. For the Esshete 1250 the outer oxide is also iron oxide with a small amount of manganese. The original grain boundaries of the alloy are very clearly observed in the oxide structure and are chromium rich. The oxide within the grains is a chromium iron nickel oxide. In the first 3000 hours of exposure the oxide thickness of the two steels are similar, however with longer exposure times, TP347H FG has a significantly thinner oxide that Esshete 1250 (Figure 8). The inner oxide and outer oxide has approximately the same thickness for both alloys, and in neither was there observed significant spallation.

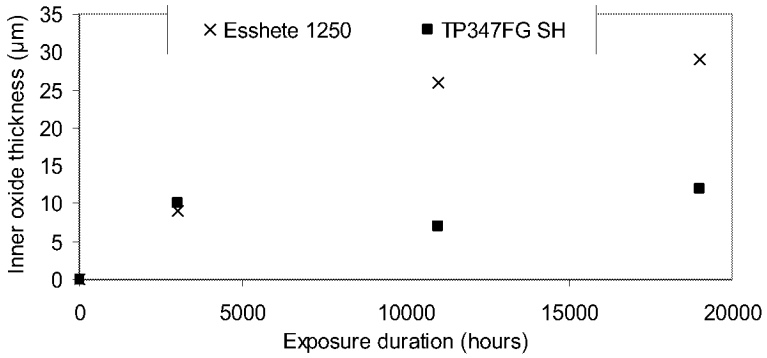

Figure 8: Inner steamside oxide for Esshete 1250 and TP347H FG.

Discussion

Fireside Corrosion

Corrosion mechanism for heavy oil and gas firing

During gas firing the steam temperature of the specimens investigated is estimated to be 540°C and this is lowered to approximately 510°C during oil firing to avoid corrosion. However, despite this there is evidence of hot corrosion.

In the combustion chamber, vanadium from oil is oxidised to V_2O_3, V_2O_4 or V_2O_5, depending on the amount of excess air present. The vanadates with +3 and +4 oxidation levels have high melting points (over 1600°C), and therefore do not contribute to low melting eutectics together with alkalis. The critical excess air level was found to be 3% where vanadium pentoxide is preferentially formed [4]. At the conditions at Avedøre 2 where excess air level is around 1.2%, this should result in vanadium oxides in the lower oxidation states. Vanadium oxide is found in the deposit - however the actual oxidation state of the deposits is not known. If the lower oxidation levels are formed, and deposited in a sulphate matrix, then further oxidation may also occur in the deposit. Phase diagrams depicting the formation of low eutectic melts are with vanadium oxide in the +V oxidation state.

After the first year, the ash layer consists of a sodium sulphate matrix and particles of metal vanadate. Nickel and iron are detected in the vanadate compounds present in the matrix of sodium sulphate which indicates that some fluxing of the oxide has occurred. Trace amounts of sulphur were detected within the oxide at the oxide-metal interface and this indicates that some sulphidation occurs due to the sodium sulphate in the deposit. The lowering of the temperature during oil firing has not removed the threat of sodium and vanadium oxide forming a eutectic melt. Cooling and heating curves of mixtures of sodium sulphate and

vanadate show areas where there are low molten salt combinations [5] and a eutectic melt of sodium vanadate can form at 535°C. During gas firing, the surface metal temperature is probably in this temperature region. Thus sodium sulphate and vanadate components are deposited during oil firing and vanadate corrosion occurs during gas firing.

There is a seemingly protective fireside oxide formed, but the outer oxide contains iron, chromium and nickel and iron vanadium oxide then covers this surface. There is no outer iron oxide layer which suggests that the oxide is reacting with the melt i.e. the outer iron oxide layer has already been removed. In the deposit and oxide surface, there are particles of iron vanadium oxide which substantiates the theory that the iron oxide has been reacted. The following reactions may occur at the oxide-deposit interface [6]. As V_2O_5 is acidic, it will react with basic oxides as follows:

$$V_2O_5 + Fe_2O_3 \rightarrow 2FeVO_4$$
$$V_2O_5 + Cr_2O_3 \rightarrow 2CrVO_4$$
$$V_2O_5 + 3NiO \rightarrow Ni_3V_2O_8$$

In this investigation, it is seen that iron and nickel are present as metal vanadate. There must be continual dissolution and migration of these metal oxide ions to the outer part of the deposit to give precipitation throughout the deposit. There is virtually no vanadium in the sodium sulphate matrix and very little sodium in the vanadate deposits. In the literature, sodium sulphate deposits have been detected [7] at lower temperatures (below 650°C) where there is a high SO_3 partial pressure. At higher temperature, the deposit consists of sodium vanadate.

Corrosion in heavy oil + wood pellets + gas

During 2002-2004, Avedøre II main boiler was fuelled simultaneously with wood pellets, gas and heavy oil. Despite firing with wood pellets, there was no chlorine in the deposits or at the corrosion front. It is assumed that any of the chlorine present as KCl has been converted in the combustion chamber to potassium sulphate according to the following reaction:

$$2KCl + SO_2 + H_2O + ½O_2 \rightarrow K_2SO_4 + 2HCl$$

A similar reaction mechanism was established when co-firing of straw and coal [8]. The large amount of sulphur dioxide required to react with KCl originates from both heavy oil and wood pellets. The potassium sulphate condenses on metal components while HCl remains in the gas stream and has no major effect on corrosion.

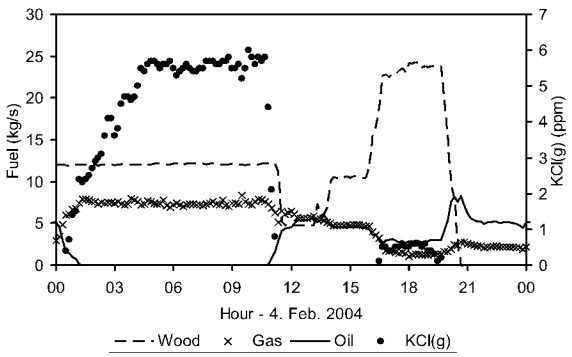

Figure 9: Potassium chloride as measured with IACM with different fuel combinations.

From the extensive amount of research on straw-firing, the fear of potassium chloride deposit corrosion was known. Therefore potassium chloride in the gas phase was measured using an IACM system (In situ alkali continuous Monitor System) developed by Vattenfall which is based on differential optic absorbance spectroscopy [9]. Figure 9 shows the fluctuation of potassium chloride measured in the superheater area when burning different fuel combinations. Thus wood pellets + gas results in high potassium chloride emissions, however the addition of oil removes potassium chloride. The ratio of oil to wood is very important such that it has been decided that wood pellets will only be used with at least 10% heavy fuel oil containing 2% sulphur.

The ash from wood pellets has a high amount of calcium, thus more calcium is also incorporated in the deposit. The deposit consists of a matrix of potassium-calcium-sodium sulphate with particles of vanadate or metal vanadate. However the content of sodium was very small and was only present in the deposit at the gas-deposit interface. The deposit was much thicker than during the first year's operation, which was due to the additional contribution of potassium and other sulphates, which makes up the bulk of the matrix. Hupa [10] describes thick deposits that were formed on a plant with steam temperature at 535°C where bark was fired together with oil. Similar to this investigation, deposits consisted of alkali and alkali earth metal sulphates where the alkali sulphates were present close to the tube. However the presence of vanadium was not seen by Hupa and this may be due to the type of oil used or bark to oil ratio.

Much work has been conducted on the presence of sodium sulphate and vanadium oxides however there is no information on potassium sulphate and vanadium oxide corrosion. From phase diagrams [11], it is seen that potassium oxide together with vanadate can give eutectic melts at even lower temperatures from 390°C. Alkali vanadate corrosion is similar to other sulphate hot corrosion mechanisms where a melt reacts with the oxide and fluxes it away to be precipitated in the deposit [12]. A difference exists in the corrosion rate in that the sulphate corrosion mechanisms have a bell-shaped curve with respect to temperature. Corrosion increases as the temperature to the eutectic melt is approached and then decreases as the components in the eutectic melt decompose. For vanadium corrosion there are many eutectic melts that are present as temperature increases, and finally there is vanadium oxide itself as a melt, so corrosion increases exponentially [7].

For the austenitic specimens described, corrosion is caused by the presence of the ash layer adjacent to the tube. The ash layer consists of predominantly potassium sulphate matrix with a small contribution by calcium. The particles present in the deposit were vanadium oxide and iron oxide, however there were less vanadium compounds in the deposits adjacent the oxide compared with 1st year. Vanadium compounds may have been present in the outer deposit and removed by soot blowing. The tubes were exposed to a lower temperature than the first year so the vanadium compounds are not so mobile within the deposit. In addition, due to the greater amount of ash present, the percentage of vanadium particles has decreased. All factors probably contribute to the fewer metal vanadates present adjacent to the oxide. Sulphur is detected within the oxide at the oxide-metal interface and this indicates that sulphidation occurs due to the alkali sulphate in the deposit. There is little indication of vanadate corrosion, i.e. that vanadates have dissolved the oxide and precipitated them in the deposit as metal vanadates as was the case last year. Instead, there is evidence of some sulphate fluxing of oxide, where iron oxides are precipitated within the matrix.

After 3 years exposure, localised grain boundary attack of approx. 100μm of the metal adjacent the oxide was observed. Since sulphur is present at the oxide-metal interface, it can also diffuse via grain boundaries and form sulphides together with chromium [13]. Internal attack has been observed for especially austenitic alloys at intermediate and low sulphur partial pressures but at higher temperatures of 800°C. The explanation of such behaviour was as follows: at low sulphur pressures, the diffusion rate in the alloy plays an important role in sulphidation kinetics because of preferential sulphidation of chromium to form the surface scale. Chromium diffuses faster at grain boundaries than in the bulk such that the counterflowing will inject vacancies and nucleate voids at the grain boundaries and sulphur can migrate rapidly through these voids, perhaps as gaseous molecules [14]. The sections investigated were close to the soot blower which also could have had some effect.

Both steels have similar low corrosion rates and morphology based on residual metal measurements and fireside oxide thickness. However the localised grain boundary attack needs to be monitored with continued exposure. It must be noted that a corrosion probe has been used to investigate corrosion rates at higher temperatures in this plant with the addition of coal-flyash. The corrosion probe was exposed for a 3 month period and showed that TP347HFG had a better corrosion resistance compared to Esshete 1250 at higher temperatures up to 620°C [9].

Steamside oxidation

Although oxidation for the two steels was similar after the first 3000 hours exposure, subsequent results show a stabilisation of the oxide growth for TP347H FG and a parabolic increase of the Esshete 1250. Esshete 1250 has oxide morphology where there is chromium rich oxide at the original alloy grain boundary and iron chromium nickel spinel within the grains. This is similar to the morphology observed by Osgerby and Fry [15]. Otsuka and Fujikawa [16] showed a higher oxidation rate for Esshete 1250 compared to TP347H FG after only 1000 hours however this was at temperatures of 700°C. This could indicate that the higher temperature leads to more chromium diffusion to form a chromium rich protective layer faster for TP347H FG. Esshete 1250 has insufficient chromium diffusion due to it lower chromium concentration to produce such an oxide. As shown from previous investigations of TP347H FG the oxidation rate of TP347H FG is not parabolic with time, and has a change in kinetics with different temperature ranges. Jianmin et al [17,18] revealed that in this metal temperature of approximately 540°C, the thickness of the inner oxide is almost stable for 30,000 hours of exposure. Hansson et al [19] showed that at temperatures below 520°C, after 60,000 hours exposure, a faster oxidation rate was observed and this needs to be monitored.

Conclusions

Comparisons of the deposits in the different environments show that in oil and gas, the deposit is sodium sulphate and vanadium compounds which can result in fluxing of the oxide. Change of fuel to wood pellets + gas + heavy oil results in a deposit which is predominantly potassium sulphate with only a little vanadate. With this deposit, sulphidation and alkali sulphate attack on the oxides has occurred giving modest corrosion rates. However Esshete 1250 and TP347HFG do not differ in either corrosion morphology or corrosion rates. On the contrary for steamside oxidation, Esshete 1250 has a significantly higher oxidation rate. This could result in spallation problems after longer exposures.

References

[1] "Corrosion Investigations at Avedøre 2 USC Boiler" Internal Energi E2 report, 2002.

[2] "Corrosion Investigations at Avedøre 2 USC Boiler Part II" Internal Energi E2 report, December 2003.

[3] "Corrosion Investigations at Avedøre 2 USC Boiler Part III" Internal Energi E2 report, December 2004.

[4] R.W. Bryers, "Fireside slagging, fouling and high temperature corrosion of heat-transfer surface due to impurities in steam-raising fuels" Progress Energy Combustion Science, Vol 22 pp. 29-130 (1996)

[5] G. Lai "High Temperature Corrosion of Engineering Alloys" Publ ASTM International pp 154-160.

[6] M. Seierstein, H.J. Ratzer-Sheibe, P. Kofstad. "Sodium vanadate induced corrosion of MCrAlY coatings - Burner rig studies" Werkstoffe u Korrosion 38 532-540 (1987)

[7] A. Wong-Moreno, D. Lopez-Lopez L. Martinez L "High temperature corrosion mechanism by combustion products of heavy high sulphur fuel oils: An extension of the Wilson Model" NACE Corrosion 2002 Paper 02734.

[8] M. Montgomery, O.H. Larsen "Field test corrosion experiments in Denmark with biomass fuels Part 2: Co-firing of straw and coal" Materials and Corrosion 53 pp. 185-194 (2002).

[9] J. P. Jensen, K. Nielsen, M. Montgomery, C. Andersson "Ash Chemistry, Corrosion and Heavy Metal Emissions from a 800MW wood pellet + oil+ natural gas fired power plant" 14th European Biomass Conference, Paris, 17-21 October, 2005.

[10] M. Hupa "Ash problems when burning bark with oil" VGB Kraftwerkstechnik 59 H7 July 1979 pp. 568-576.

[11] "Phase diagrams for ceramists" Two oxides, p89. Publ. American Ceramists Society 1964.

[12] R.A. Rapp "Hot corrosion of materials: a fluxing mechanism" Corrosion Science 44, pp 209-221 (2002)

[13] R.E. Lobnig, H.J. Grabke "Mechanism of Simultaneous Sulfidation and oxidation of Fe-Cr and Fe-Cr- Ni Alloys and of the failure of protective chromia scales" Corrosion Science Vol 30, 10 pp.1045-1071 (1990).

[14] T. Narita and T. Ishikawa: "Internal sulphidation phenomena of heat resistant alloys at low sulpur pressures"Materials Science and Engineering, A120 (1989) pp31-38.

[15] S. Osgerby, A.T. Fry "Steam oxidation resistance of selected austenitic steels" Materials Science Forum Vols 461-464 (2004) pp. 1023-1030

[16] N. Otsuka and H. Fujikawa "Scaling of austenitic stainless steels and nickel-base alloys in high temperature steam at 973K" Corrosion April 1991 pp240-248.

[17] J. Jianmin, M. Montgomery, O.H. Larsen, S.A Jensen "Investigation of steam oxidation behaviour of TP347H FG Part 1: Exposure at 256 bar" Materials and Corrosion 56 pp 459-467, 2005

[18] J. Jianmin, M. Montgomery, O.H. Larsen, S.A. Jensen "Investigation of steam oxidation behaviour of TP347H FG Part 2: Exposure at 91 bar" Materials and Corrosion 56 pp. 542-549, 2005.

[19] A.N. Hansson, L. Korcakova, M. Montgomery "Long-term steam oxidation of TP347H FG in power plants" Microscopy of oxidation 6 Conference, Birmingham UK, April 2005.

Acknowledgements: PSO has financially supported the IACM analysis.

HEAT EXCHANGER CORROSION IN BIOMASS AND COAL CO-FIRED POWER PLANTS

N J Simms, P J Kilgallon and J E Oakey

Energy Technology Centre, Cranfield University,
Cranfield, Bedfordshire, MK43 0AL, UK

Abstract

Co-firing of biomass in conventional pulverized coal power generating systems offers a means to rapidly introduce renewable and CO_2 neutral fuels into the power generation market. The existing coal-fired power stations are both much larger and more efficient than potential new biomass power plants; so a few % of biomass fed into an existing large coal fired station will give more biomass derived power than a new dedicated biomass station using the same amount of biomass. The introduction of biomass can be achieved by relatively minor modifications to existing coal-fired plants and so avoids the large capital costs and risks of building a new biomass-only fired power system. However, for the existing coal fired power stations, this gives some potential practical problems: the control of co-firing two fuels; changes to bottom/fly ash chemistry; changes to deposition (fouling and slagging) within the boiler; reduced reliability of key high temperature components (e.g. heat exchangers), due to increased corrosion problems relative to those experienced with coal alone.

This paper reports the results of a series of laboratory corrosion tests that have been carried out to assess the effects of co-firing coal on the fireside corrosion of heat exchangers. The 1000 hour corrosion tests have been carried out using the deposit recoat method in controlled atmosphere furnaces, at typical superheater and evaporator metal temperatures using simulated deposit compositions and gaseous environments (selected on the basis of plant experience and potential fuel compositions). Five materials were exposed in these tests: 1 Cr steel, 2.25 Cr steel, X20CrMoV121, AISI 347H and alloy 625. During the tests, the materials degradation was monitored using mass measurements. However, one of the aims of the work was to produce statistically valid data on the actual metal loss from the materials and so the performance of the material in these tests was determined from dimensional metrology before and after exposure. For each material, these data have been used to determine the sensitivity of the corrosion damage to changes in the exposure conditions (e.g. deposit composition, gas composition). SEM/EDX analyses of selected samples have been used to confirm whether changes in corrosion mechanism were associated with changes in damage levels (e.g. pitting to internal corrosion). Taking the analysis of the numerical data further, models of the corrosion performance of the materials have been produced for the range of test conditions investigated.

Keywords: co-firing; biomass; coal; heat exchanger; fireside corrosion

Introduction

Co-firing of biomass in conventional pulverized coal power generating systems offers a means to rapidly introduce renewable and CO_2 neutral fuels into the power generation market. Interest in this type of co-firing is being stimulated by the search for electricity generation methods that minimise environmental emissions and utilise available sustainable fuel sources, as well as regulatory pressures. The existing coal-fired power stations are both much larger and more efficient than potential new biomass power plants; so a few % of biomass fed into an existing large coal fired station will give more biomass derived power than a new dedicated biomass station using the same amount of biomass. The introduction of biomass can be achieved by relatively minor modifications to existing coal-fired plants and so avoids the large capital costs and risks of building a new biomass-only fired power system. However, for the existing coal fired power stations, this gives some potential practical problems: handling and feeding biomass fuels, the control of co-firing two fuels; changes to bottom/fly

ash chemistry; changes to deposition (fouling and slagging) within the boiler; reduced reliability of key high temperature components (e.g. heat exchangers), due to increased corrosion problems relative to those experienced with coal alone.

The work reported in this paper forms part of an on-going programme of work (throughout the EU COST522 and COST538 programmes) that is developing models to predict the effect on fireside corrosion of heat exchanger (i.e. superheater, reheater and evaporator) materials of changes in fuel compositions resulting from co-firing. Such a model will provide a means of predicting tube lives when different fuels are used and will also allow fuel specifications for coal/biomass blends to be defined.

Biomass Fuel Compositions and Effects on Heat Exchanger Environments

A wide range of different biomass fuels are being considered / used, including:

- Specifically cultivated biomass ('energy crops'), e.g.; coppiced willow (or poplar), miscanthus, reed canary grass
- Waste biomass; various straws, wood waste / forest residues
- World traded biomass products, e.g.; olive residues, pelletised wood, almond waste, cereal co-product (CCP)

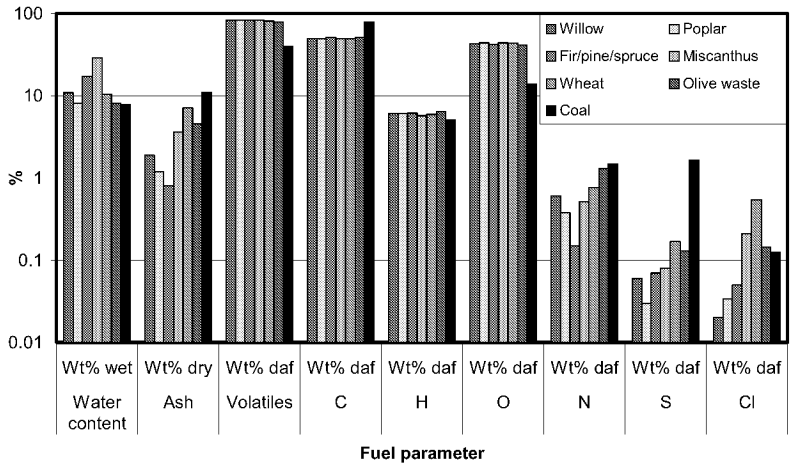

Figure 1 Example fuel properties for a selection of biomass fuels compared to a coal

These different types of biomass inevitably have a range of different properties and compositions that need to be considered during their evaluation as potential fuels. In general the faster growing biomass tends to have high chlorine (and potassium) contents than slower growing biomass. Figure 1 illustrates some of these properties for a selection of biomass fuels. It should be noted that for clarity this figure does not indicate the scatter in fuel properties that are found. For many biomass, the timing of harvesting, harvesting conditions and post-harvest treatment / storage can result in a wide variation of fuel compositions. Figure 2 illustrates the range of potassium and chlorine levels for selected straws.

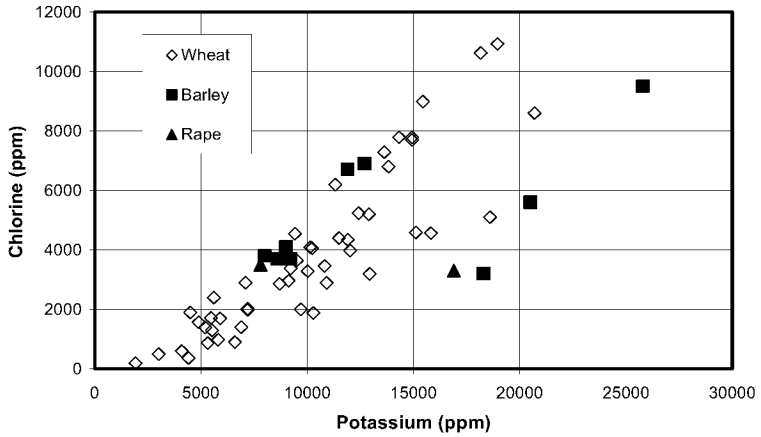

Figure 2 Variation of chlorine with potassium levels in straws

In general biomass contains lower levels of sulphur compared to coal so co-firing of coal with biomass results in reductions in the combustion gas sulphur dioxide (SO_2) levels. Biomass can potentially have high chlorine contents, up to 2.5%. In comparison, significant ranges of both sulphur (~0.65-2.8%) and chlorine (~0.03-0.65%) levels have been reported within the UK by a single power company over a two year period during the 1990s [1]. An assessment of potential gas compositions from using coal with 10% wheat straw or willow wood gave gas compositions that are well within the ranges predicted for firing different coal compositions alone (Figure 3).

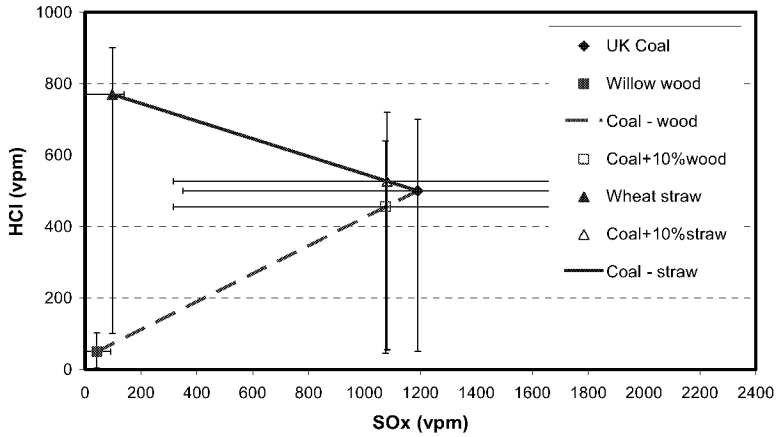

Figure 3 Gas compositions predicted for two biomass and coal-biomass mixtures

A survey of deposit compositions in co-fired combustion systems [2] has been carried out. The high potassium and chlorine levels in some biomass fuels such as straw can lead to deposits rich in KCl, especially in low temperature combustion systems fired solely on

biomass. However in fuels with higher sulphur levels, vapour phase deposition is dominated by sulphate formation. In addition, higher combustion temperatures and/or co-firing with coal can result in a combination of the potassium with alumino-silicate rich ash particles and / or higher levels of K_2SO_4 in deposits. Generic views, based on fuel composition alone, of the relationship between the sulphur and chlorine contents of the fuels and deposit compositions have been produced by US Department of Energy [3] and EU [4] research programmes. These views of deposition from biomass fuels being a balance between chloride and sulphate formation depending on the composition of the fuel are very similar and consistent with earlier work carried out on coal combustion systems. Such an approach to understanding deposition has been utilised in one application [5], where sulphur containing additives have been added to a biomass fired combustion plant. This effectively altered the S/Cl balance in the boiler combustion gas stream and so increased the sulphate / decreased the chloride concentration in the deposit and caused less corrosive deposits to form on heat exchangers in the power plant. As well as fuel composition, combustion temperature and heat exchanger surface temperatures, the relative levels of KCl and K_2SO_4 in deposits also vary with specific boiler designs, as they are dependent on particular vapour and particle deposition mechanisms.

Laboratory Testing

A series of well-controlled laboratory corrosion tests were used to investigate the effect of different exposure parameters on the corrosion performance of common and candidate heat exchanger materials. The heat exchanger materials and compositions are given in Table 1.

Table 1. Nominal chemical composition of alloys

Material	Wt%								Usage
	C	Cr	Ni	Mo	Mn	V	Nb	Fe	
1 Cr	0.1	1.0		0.50	0.5			Bal	*evaporator*
2¼Cr	0.1	2.25		1.0	0.5			Bal	*superheater*
X20CrMoV121	0.2	12.0	0.5	1.0		0.3		Bal	*superheater*
TP347HFG	0.07	18.0	10.0		2.0		1.0	Bal	*superheater*
Alloy 625	≤0.1	21	Bal	9	≤0.5		3.5	≤5	*superheater, evaporator repair*

The test sample geometry was a solid cylinder of 10 mm diameter and 10 mm length. The performance of materials in these tests was determined using a dimensional metrology methodology [6, 7]. This methodology uses accurate pre-exposure contact metrology and post-exposure optical microscopy / image analysis to quantitatively characterise the extent of corrosion damage at a number of points, usually at least 24, around each sample. Statistical analysis of the data produced gives characteristic parameters (e.g. median metal loss, most likely pit depth) from which materials performance models can be derived. This approach to materials corrosion performance assessment was adopted by the EU COST522 and COST538 programme as their standard methodology [8]. To determine the performance of the materials to the accuracy required for modelling purposes, it is necessary to use materials that have been machined to known dimensions / tolerances with a specified surface roughness.

The 1000 hour laboratory corrosion tests were carried out using the well-established deposit re-coat procedure [6-8] with a recoat interval of 100 hours. The deposit compositions, given in

Table 2, were decided by taking into account the range of deposit compositions observed on heat exchangers in Danish biomass and co-fired power plants. The gas SO_X and HCl concentrations (Table 3) were based on 0.1wt% of contaminant in the fuel going to 100ppmw in the gas phase with 100% chlorine and 70% sulphur release and 20% by mass of the biomass being co-firing with coal.

Table 2. Deposit compositions applied in laboratory tests

Component	Deposit Compositions (wt %)								
	D0	**D1**	**D2**	**D3**	**D4**	**D5**	**D6**	**D7**	**D8**
KCl	0	2.5	5	5	10	10	20	0.5	0
K_2SO_4		5	2.5	10	5	20	10	5	0
Fly ash		92.5	92.5	85	85	70	70	94.5	100

Table 3. Target gas compositions for laboratory corrosion tests

Gas	N_2	O_2 (%)	CO_2 (%)	H_2O (%)	CO (%)	SO_x (ppmv)	HCl (ppmv)
1	Balance	4	14	6	0	1420	170
2						460	320
3						1420	
4		0.1			4		

The series of tests were carried out at three temperatures:

- 600°C: for Alloy 625, TP347HFG and X20 steel (Table 1); deposits D0-D8 (Table 2) and gases 1-3 (Table 3); tests 1-3 respectively
- 560°C: for Alloy 625, TP347HFG and 2¼Cr steel (Table 1); deposits D0-D7 (Table 2) and gases 1-3 (Table 3); tests 4-6 respectively
- 425°C: for Alloy 625, 2¼Cr steel and 1Cr steel (Table 1); deposits D0-D7 (Table 2) and gases 3-4 (Table 3); tests 7-8 respectively

Results & Model Development

Cross-sections of all the samples exposed in these corrosion tests were measured to give 24 sets of measurements of metal surface position, depth of internal corrosion and scale thickness. The data on the post-exposure metal surface position were combined with the pre-exposure sample measurements to give metal loss data; with the addition of internal corrosion measurements, this gave good, or sound, metal loss data sets.

These corrosion damage measurements can be used to produce corrosion damage versus probability plots. An example of this type of plot is shown in Figure 4 that shows the sensitivity of the corrosion damage to different deposit compositions. However, even this condensed form of displaying corrosion damage data is too clumsy to use when large volumes of data have been produced, so damage with a 10% probability of being exceeded was selected for comparing the performance of all materials / exposure conditions. All the datasets of materials performance produced in this project have been analysed and these data points extracted. Using these data, Figures 5–7 illustrate the performance of Alloy 625, TP347HFG and 2¼Cr steel to show the effect of the different deposits and gas compositions / test temperatures.

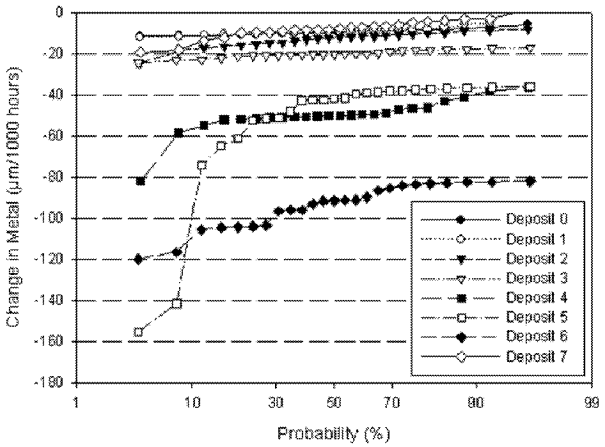

Figure 4. Example of corrosion damage versus probability plot showing the sensitivity of TP347HFG to variations in deposit compositions in Test 3

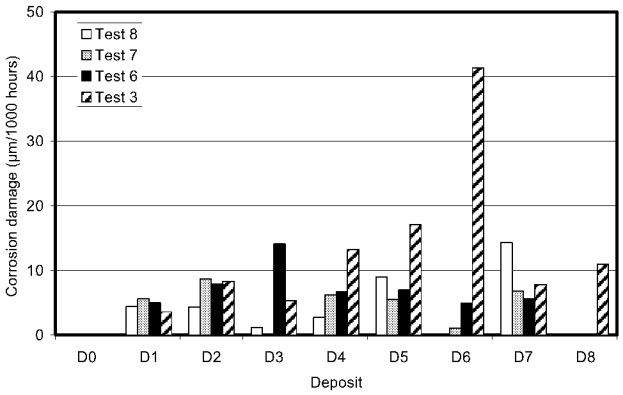

Figure 5. Summary of the performance of alloy 625 as a function of deposit composition and gas composition/temperature (with corrosion damage evaluated at the 10% probability of damage being exceeded)

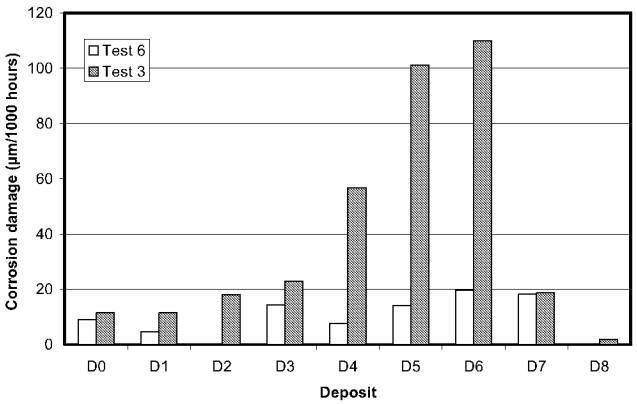

Figure 6. Summary of the performance of TP347HFG as a function of deposit composition and gas composition/temperature (with corrosion damage evaluated at the 10% probability of damage being exceeded)

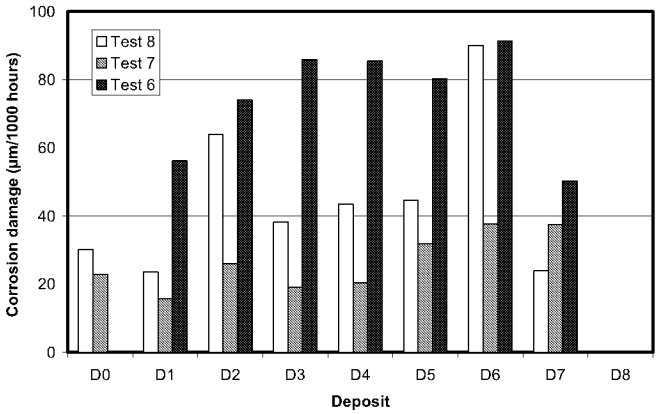

Figure 7. Summary of the performance of 2¼Cr steel as a function of deposit composition and gas composition/ temperature (with corrosion damage evaluated at the 10% probability of damage being exceeded)

These data can be further analysed to quantitatively determine sensitivity of the corrosion damage to changes in the deposit compositions (i.e. weight % of potassium, chloride and sulphate in the deposits) and gaseous environments (i.e. vpm of SOx and HCl at 560 and 600°C (and pO_2 at 425°C)) for each alloy / temperature tested. These sensitivities can then be combined to produce empirical corrosion models that are alloy and temperature specific. Figure 8 illustrates the correlation between predicted and measured corrosion rates for these models. Inevitably there is some scatter in these data. This reflects uncertainties in the measurement of the corrosion damage and in the modelling process, as well as the scatter that is associated with corrosion damage in these types of environments. Given the limited amount of corrosion data used to generate these models, they should be regarded as initial (or first generation) versions. Current testwork (being carried out within COST538) is generating much more data on corrosion damage as a function of exposure conditions for biomass co-fired systems.

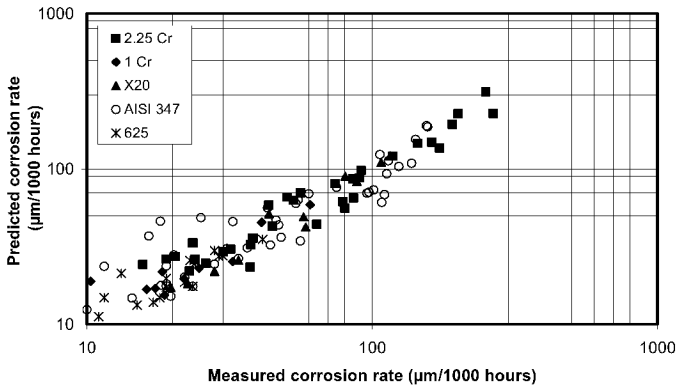

Figure 8. Illustration of the correlation between the measured corrosion damage rates and the predicted corrosion damage rates - with corrosion damage evaluated at the 10% probability of damage being exceeded

In recent years there have been a few publications related to producing empirically based corrosion damage models for coal-fired power systems [1, 6, 7, 8-11]. The majority of these relate to gas turbines and gasification systems, where corrosion damage has the potential to be

critical to the viability of the power system. However, there are now some publications on predicting the corrosion damage in coal-fired pulverised fuel systems from the UK [1, 10-11], the US [12] and COST522 [8, 13]. None of the empirical models produced have been published in sufficient detail to allow comparisons with the models produced in this work.

Comparison with Plant Data

Materials performance data (of corrosion rate as a function of metal temperature) that have been obtained from a range of sources are provided in Figures 9 and 10. It is notable that in these figures there is considerable scatter in the corrosion data: as well as the fuel variability, there are other factors that can contribute to this scatter. Utility boilers, even if operated continuously, unfortunately seldom operate under constant conditions. Combusted gas temperatures vary daily with load, leading to changes in heat flux and steam temperature. In addition, unplanned outages, often caused by problems with auxiliary equipment, give rise to temperature cycling effects. The thermal history of boiler tubing cannot easily be transformed into one alternative temperature, which the material could have been subjected to over its entire period of exposure in the boiler, and still develop the same corrosion. However, the thickness of the steam side layer of magnetite can be used to give an estimate of the thermal history of superheater materials [11, 14]. This method of estimating the thermal history of a material has the advantage of being as direct as possible in the sense that it gives a magnetite thickness on the inside of a tube where the flue gas corrosion is measured on the outside of the tube. The magnetite thickness has to be averaged over a number of points but is one of the more accurate methods available.

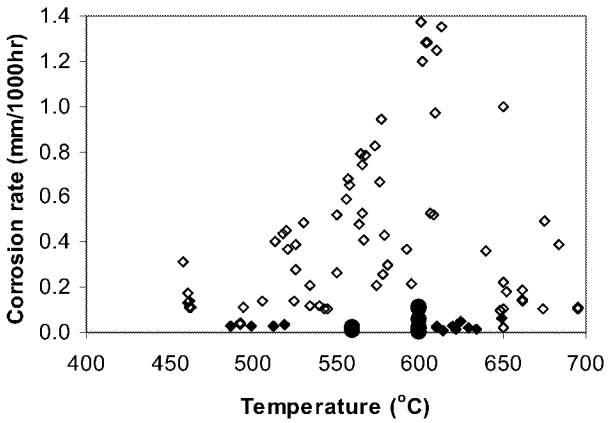

Figure 9. Comparison of Plant Corrosion Data for TP347H and TP347HFG with coal (filled diamond), straw (open diamond) and TP347HFG results from this work shown as filled circles

It is apparent from Figures 9 and 10, that straw is a very aggressive fuel. Plant data show that there is an enormous difference in corrosion rates between straw and wood; with the corrosion rates of steels in straw-fired plant being more similar to those from waste-firing and results from wood-firing bearing more similarity to those from coal with medium to high chlorine contents.

The results from the laboratory corrosion tests have been compared to the plant data (in Figures 9 and 10 they are superimposed as filled circles). The corrosion rates measured in the

laboratory tests are in line with those found for wood or coal firing alone. This is consistent with the information on potential deposits and gas environments that showed the conditions anticipated for coal co-fired with low levels of biomass (wood or straw) were within the scatter band for those found from coal-firing alone.

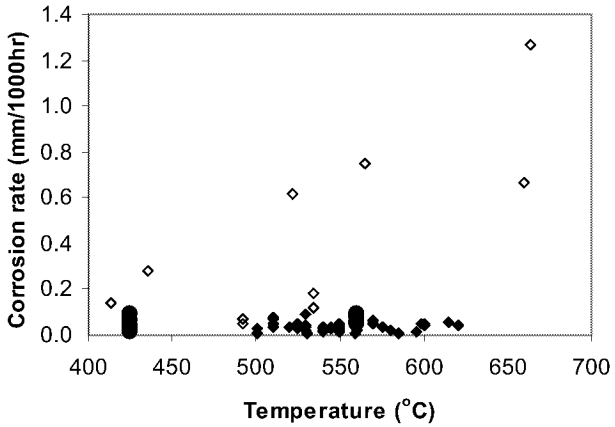

Figure 10. Comparison of plant corrosion data for T22 with coal (filled diamond), straw (open diamond) and 2¼Cr results from this work shown as filled circles.

Further laboratory corrosion tests are underway in COST538 (and other programmes) to generate corrosion rate data under a wider range of controlled laboratory conditions. In addition, a database of materials performance in all types of power plants, which included detailed records of fuels used and operating conditions would be very useful for testing materials performance models and so allow such tools to be validated. COST522 started the development of such a database of materials plant performance in plant environments [8, 13].

Conclusions

A programme of work has been carried out to assess the potential effects of co-firing coal with biomass materials. The activities have covered fuel compositions, the resulting gas environments and deposits formed on heat exchanger tubing, and especially the corrosion damage caused by these operating conditions.

Corrosion tests were carried out on five materials (1Cr steel, 2¼Cr steel, X20CrMoV121, TP347H and alloy 625). Test conditions were targeted at superheater and evaporator conditions, with gas and deposit compositions selected on the basis of plant experience and potential fuel compositions. Laboratory corrosion tests were carried out using the 'deposit recoat' technique in controlled atmosphere furnaces for 1000 hour periods. The performance of the materials in these tests was determined from dimensional metrology before and after their exposure. These data have been used to derive empirically based corrosion models of the materials corrosion performance under these test conditions.

The corrosion data / models obtained from this programme of work have been compared to that available from operating power plants fired on coal, straw or wood fuels. This indicates that the levels of damage anticipated for dilute mixes of biomass in coal are similar to the ranges of damage observed for coal or wood firing alone. The empirical corrosion models

developed within this work are based on a limited set of experimental data. A more extensive set of linked corrosion tests would give rise to a more comprehensive corrosion model, with increased scope in terms of the range of conditions covered and increased confidence in its reliability. This work is being carried out within the on-going COST538 programme.

References

[1] P.J. James and L.W. Pinder, Materials at High Temperature 14 (2/3) (1997) p117

[2] Reliability Improvements For Co-Combustion Plants, Final Report of ECSC Project 7220-PR-080 (2002)

[3] A. Robinson, L. Baxter, H. Junker, C. Shaddix, M. Freeman, R. James and D. Dayton, 'Fireside Issues Associated with Coal-Biomass Co-firing', NREL Report TP-570-25767 (1998)

[4] 'Operational Problems, Trace Emissions and By-Product Management for Industrial Biomass Co-Combustion', Publishable Final Summary Report on EU contract JOR3-CT95-0057 (OPTEB), 1999

[5] P.J. Henderson, J. Hogberg and M. Mattsson, 'Reduction in Fireside Corrosion of Superheater Materials in a Biomass-fired Circulating Fluidised Bed Boiler', Materials for Advanced Power 2002, Eds J Lecomte-Beckers et al (Forschungszentrum Jülich), p883.

[6] 'Erosion/Corrosion of Advanced Materials for Coal-fired Combined Cycle Power Generation', EC JOULE Project, JOUF-0022.

[7] N.J. Simms, J.E. Oakey, D.J. Stephenson, P J Smith and J R Nicholls, 'Erosion/Corrosion of Gas Turbine Materials for Coal-Fired Combined Cycle Power Generation', Erosion by Liquid and Solid Impact, Cambridge, 4-8 September 1994

[8] S.R.J. Saunders, N.J. Simms, S. Osgerby and J.E. Oakey, 'Degradation of Boiler and Heat Exchanger Materials: Data generation, Databases and Predictive Modelling', Materials for Advanced Power 2002, Eds J Lecomte-Beckers et al (Forschungszentrum Jülich,), p801

[9] N.J. Simms, J.R. Nicholls and J.E. Oakey, Materials Science Forum 369-372 (2001) p947

[10] L. Pinder and C. Davis, 'Effect of Fuel Type on the Fireside Corrosion of Boiler Materials for Advanced Clean Coal Technologies', Materials for Advanced Power 2002, Eds J Lecomte-Beckers et al (Forschungszentrum Jülich), p893

[11] P.J. Henderson, A. Karlsson, C. Davis, P. Rademakers, J. Cizner, B. Formanek, K. Goransson and J. Oakey, 'In-situ Fireside Corrosion Testing of Advanced Boiler Materials with Diverse Fuels', Materials for Advanced Power 2002, Eds J Lecomte-Beckers et al (Forschungszentrum Jülich), p785

[12] T.M. Linjewile, J. Valentine, K.A. Davis, N.S. Harding and W.M. Cox, Materials at High Temperatures 20 (2) (2003), pp175-185

[13] N.J. Simms, S.R.J Saunders, S. Osgerby and J.E. Oakey, 'Measurement and and compilation of materials degradation data in the COST522 programme', Materials at High Temperatures 20(2) (2003), pp137-152

[14] M. Montgomery and A. Karlsson, 'Corrosion Investigations at Masnedø Combined Heat and Power Plant', Part 1 (DTU and ELKRAFT, July 1997), Part II (DTU and ELKRAFT, November 1997) and Part V (DTU, ELKRAFT and Elsam, December 1999)

HOT CORROSION MONITORING OF ALLOY 617 IN MOLTEN CHLORIDES USING ELECTROCHEMICAL TECHNIQUES

F. J. Pérez, M.P. Hierro and J. Nieto
Grupo de Investigación de Ingeniería de Superficies. Universidad Complutense de Madrid. Departamento de Ciencia de los Materiales. Facultad de Ciencias Químicas. 28040 Madrid. Spain

Abstract

Molten chloride mixtures are formed in waste incineration plants during waste firing and energy production. These mixtures are responsible for degradation processes like hot corrosion. In order to evaluate the damage of molten salt mixtures in waste incineration environments, the alloy 617 was exposed beneath a molten KCl-$ZnCl_2$ mixture at 650 ºC in air. The corrosion process was monitored by electrochemical impedance spectroscopy (EIS). An extensive microscopy analysis have been done in order to correlate the electrochemical results, and to establish an electrochemical mechanism for such high temperature corrosion process.

Keywords: Waste Incineration, Molten Salt Corrosion, Electrochemical Impedance.

1. Introduction

Incineration plants are recognized as a valid and efficient technology to treat municipal solid wastes, particularly when they are part of integrated treatment plants. Waste incineration reduces the waste volume and weight, thus saving space on the landfill; also the end products are hygienized by transforming organic matter into water and carbon dioxide (CO_2); it is also possible to recover steam and/or energy. The main environmental impact in an incineration plant is due to the residues of the process (solid, liquid and gaseous emissions). Also, these residues cause the corrosion process in boiler superheater tubes used in incinerators and biomass-fired plants. The gaseous species (HCl, Cl_2, SO_2, etc.) and solid impurities as the alkali and heavy metals (K, Na, Zn, Pb, Sn, etc.) can form chlorides and sulphates with a low melting point, these eutectic salts allow the accelerated attack of metallic materials in oxidizing environments [1-5].

In this work the corrosion resistance of Ni-base alloy 617 was studied under the influence of molten KCl(70%mol)-$ZnCl_2$(30%mol) salt mixture at 650 ºC in air atmosphere. This salt mixture has frequently been identified in the ash deposits of waste incinerations. Chlorine played an important role in the degradation of 617 alloy, the material corrosion resistance was altered by loss of structural elements as volatile chlorides ($CrCl_3$, $NiCl_2$).

The corrosion process was monitored by electrochemical impedance spectroscopy. This technique provides a real time monitoring process of the experiment without disturbing the thermodynamic system; so many measurements can be taken at different times to establish the corrosion mechanism.

2. Experimental procedure

The experimental setup used in the present study is shown in Fig. 1. Test electrodes are placed in a crucible containing the salt mixture, KCl70%mol - $ZnCl_2$30%mol. The crucible is within a stainless steel chamber that is heated at 650 ºC in a cylindrical furnace. A two-electrode system was used for the impedance measurements. The working electrode and the reference electrode are both the testing material, Ni- base alloy 617. The alloy composition is shown in table 1.

Ni	Cr	Co	Mo	Fe	Mn	Si	Al	C	Ti	S	N	O
54,8	22,4	11,1	9,0	1,2	0,051	0,050	1,1	0,053	0,49	<0,001	0,0128	0,0015

Table 1. Chemical composition of alloy 617 (%wt.)

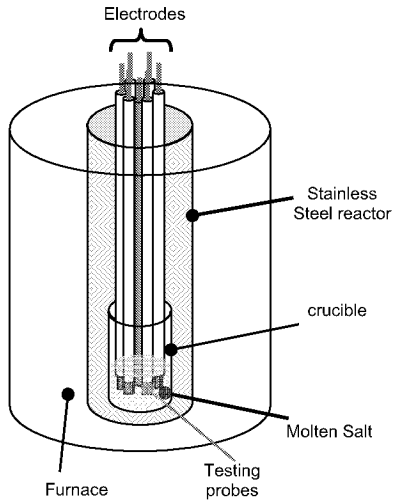

Fig. 1. Experimental setup.

The electrodes were prepared as follows. The metal testing was cut with the size 7 x 3 x 20 mm^3, followed by grinding up to 600 SiC paper. A Ni-Cr wire was spot welded to one of the metal for electric connection.

Impedance measurements were carried out by Voltalab 80 system, the amplitude of input sine-wave was ±10mV, and frequencies from 50KHz to 10 mHz. Software developed by B.A. Boukamp was used to fit the impedance spectra.

Scale morphology and composition were examined using scanning electron microscopy SEM and X-ray diffraction.

3. Results and Discussion

The Ni-base alloy beneath molten chlorides suffered two corrosion mechanisms, for initial stages the material developed an oxide protective scale, in this case the corrosion process was controlled by the transportation of ions in this scale. The impedance spectra are composed of two capacitance loops, a small semicircle at high frequency and a big semicircle at low frequency, the Nyquist diagram of 2 and 8 hours of alloy 617 in KCl-$ZnCl_2$ can be fitted to equivalent circuit of Fig. 2. [6-8]

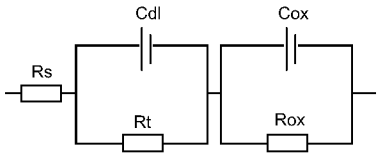

Fig. 2. Equivalent circuit of protective scale model

Where Rs represents the molten salt resistance, Rt the electrochemical transfer resistance, Cdl the double layer capacitance at the alloy-melt interface, Cox the oxide capacitance and Rox the transfer resistance of ions in the scale. Taking into account the dispersion effect, a constant phase angle element CPE = $[Q(j\omega)^n]^{-1}$ was used to describe the element Cdl and Cox in the fitting procedure. Where j is the imaginary number, Q is the frequency independent real constant, $\omega = 2\pi f$ is the angular frequency (rad/s), f is the frequency of the applied signal and n is the CPE exponent[9].

Thus the total impedance of Fig. 2 can be expressed by the equation 1 [8, 9]:

$$Z = R_s + \frac{1}{Y_{dl}(j\omega)^{n_{dl}} + \frac{1}{R_t}} + \frac{1}{Y_{ox}(j\omega)^{nox} + \frac{1}{R_{ox}}} \qquad (1)$$

Where Y_{dl}, n_{dl} and Y_{ox}, n_{ox} are constants representing the element Q_{dl} and Q_{ox} respectively.

After 24 hours a porous scale formed on the metal surface may be considered to be permeable to the molten chlorides, and thus may influence the diffusion direction of oxidants. The Nyquist plot is composed of a semicircle at high frequency and a line at low frequency representing a diffusion-controlled reaction Warburg impedance. The diffusion-controlled reaction of alloy 617 in deep molten salt can be described by the equivalent circuit of Fig. 3. [8, 10]
In Fig. 3, Rs represents the molten salt resistance, Rt the electrochemical transfer resistance, Cdl the double layer capacitance at the alloy-melt interface and W the Warburg resistance.
The impedance can be expressed by the following equation [11]:

$$Z = R_s + \frac{1}{Y_{dl}(j\omega)^{n_{dl}} + \frac{1}{R_t + W}} \qquad (2)$$

For 48, 72 and 100 hours the Nyquist plots are similar to those obtained after 24 hours. The ions transport through the scale and the diffusion of oxidants in the molten salt are the rate limiting process. The impedance diagrams can be fitted to the equivalent circuit of Fig. 3. [6, 8]

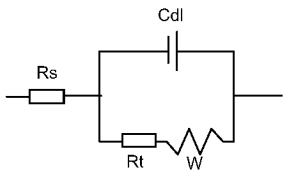

Fig. 3. Equivalent circuit of Porous Scale Model

The parameters in equations (1, 2) were obtained by fitting the impedance spectra on the basis equivalent circuits of Fig. 2 and Fig. 3. and are listed in the table 2.

Time (h)	$\mathbf{R_s}$ (Ω)	$\mathbf{R_t}$ (Ω)	$\mathbf{Q_{dl}}$ ($\Omega^{-1}s^n$)	$\mathbf{n_{dl}}$	$\mathbf{R_{ox}}$ (Ω)	$\mathbf{Q_{ox}}$ ($\Omega^{-1}s^n$)	$\mathbf{n_{ox}}$	**W** (Ω)
2	1.88	304.93	$3.45x10^{-2}$	$7.35x10^{-1}$	20.37	$1.36x10^{-2}$	$6.43x10^{-1}$	
8	1.83	11.55	$4.99x10^{-3}$	$6.81x10^{-1}$	673.70	$2.67x10^{-2}$	$6.29x10^{-1}$	
24	2.02	10.28	$1.74x10^{-3}$	$6.89x10^{-1}$				$5.68x10^{-2}$
48	2.14	5.84	$2.55x10^{-3}$	$6.41x10^{-1}$				$9.19x10^{-2}$
72	2.27	6.67	$2.64x10^{-3}$	$6.19x10^{-1}$				$1.92x10^{-1}$
100	2.39	4.90	$3.61x10^{-3}$	$6.15x10^{-1}$				$2.17x10^{-1}$

Table 2. Fitting results of the impedance spectra for alloy 617 in molten KCl-$ZnCl_2$ at 650 ºC in air.

The fitting results at 2, 8, 24, 48, 72 and 100 hours of alloy 617 in molten KCl-$ZnCl_2$ at 650 ºC in air are shown in Fig. 4.

To corroborate the impedance results, the corroded samples were analyzed by SEM and XRD.
The SEM analysis confirmed the presence of Cr_2O_3 layer on the material surface, this scale was able to protect the material during 24 hours. Fig. 5 shows the chromium oxide growth on the metal surface by the following reactions:

$$2Cr + 3Cl_2 \rightarrow 2CrCl_3 \quad (1)$$
$$2CrCl_3 + 3O_2 \rightarrow 2Cr_2O_3 + 6Cl_2 \quad (2)$$

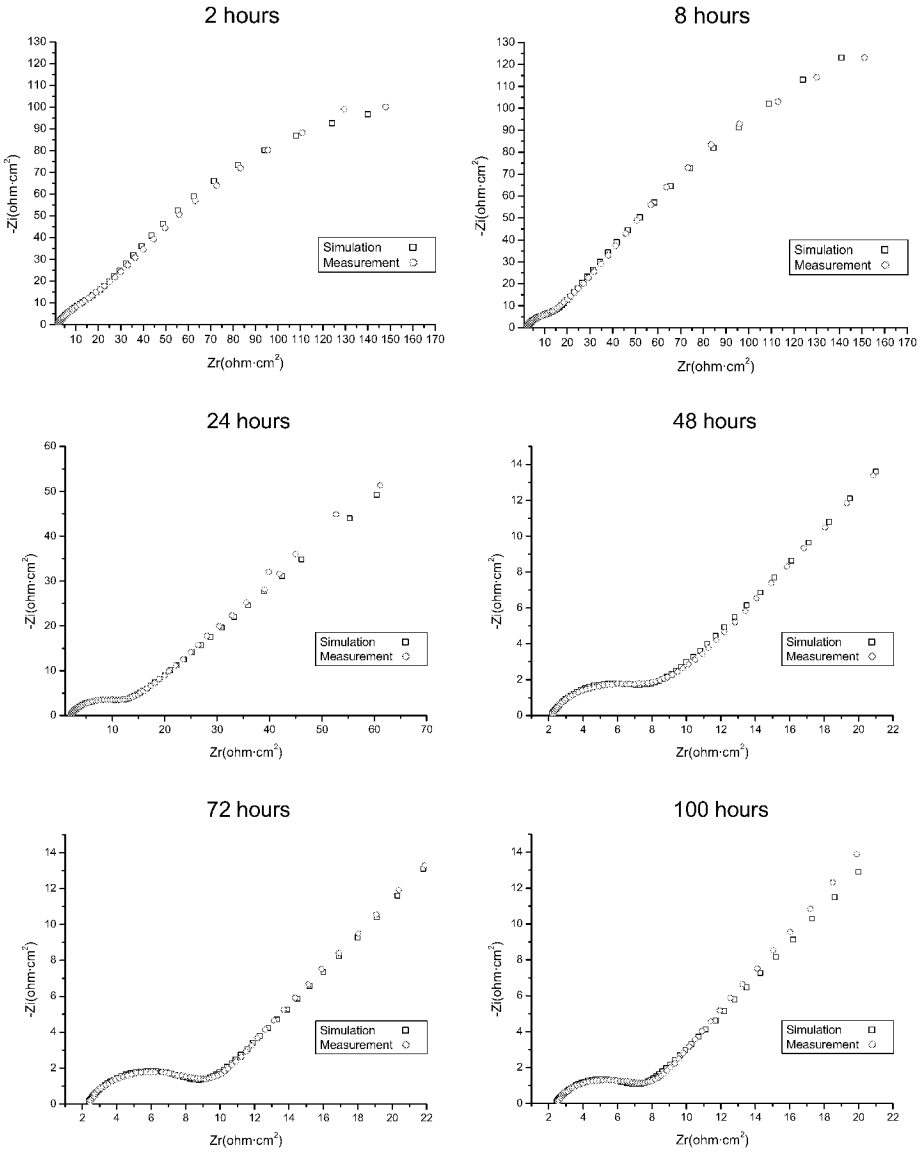

Fig. 4. Nyquist plots for the 617 alloy in molten KCl-$ZnCl_2$ at 650 ºC in air.

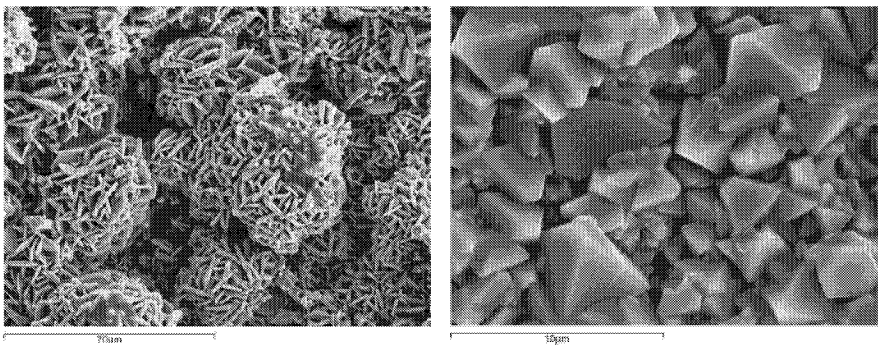

Fig. 5. SEM images of Cr_2O_3 protective scale on alloy 617 surface after 24 hours in molten salts.

The material was protected by Cr_2O_3 layer during 24 hours, after that, molten phases as volatile chlorides $ZnCl_2$, KCl and gas components (HCl, Cl_2, O_2, etc.) penetrated through scale defects into the scale and removed that, in consequence the material lost the corrosion protection in some zones. Fig. 6(a).
In the other hand, while chromium was forming an oxide layer, chlorine reacted with chromium oxide to form a volatile $CrCl_3$, this process was favoured thermodynamically due to evaporation of $CrCl_3$ at high temperature according the reaction (3):

$$2Cr_2O_3 + 6Cl_{2(g)} \rightarrow 2CrCl_{3(g)}\uparrow + 3O_{2(g)} \qquad (3)$$

At the same time, during the corrosion process, $ZnCl_2$ was consumed continuously due to its strong evaporation as well as to its oxidation to form ZnO, which reacted with Cr_2O_3 to form the $ZnCr_2O_4$ spinel Fig. 6(b), by the following reactions[1]:

$$ZnCl_{2(l)} + 1/2O_{2(g)} \rightarrow ZnO_{(s)} + Cl_{2(g)} \qquad (4)$$

$$ZnO_{(s)} + Cr_2O_{3(s)} \rightarrow ZnCr_2O_{4(s)} \qquad (5)$$

Studies on the solubility of oxide scales in molten chlorides can also provide important information on the mechanism of dissolution of protective scales, Ishitsuka [12] measured the solubility of Cr_2O_3 in molten NaCl-KCl mixtures at 727 °C at different basicity levels, by changing the partial pressures of HCl and H_2O and found that the Cr_2O_3 films can easily dissolve in the molten salt forming hexavalent chromium ion according to the reaction (6):

$$Cr_2O_3 + O_2 + 4O^{2-} \rightarrow 4CrO_4^- \qquad (6)$$

The chromium content decreased near the alloy-oxide interface due to evaporation as $CrCl_3$, dissolution as CrO_4^- [13] and formation of $ZnCr_2O_4$ spinel. Thus, the Cr_2O_3 scale lost their protective properties. Subsequently, other alloying elements oxidized forming NiO and MoO_3. The oxide scales formed by this way were rather porous and can hardly provide any effective protection, so that the corrosion rate will be significantly enhanced. Fig 7(a).

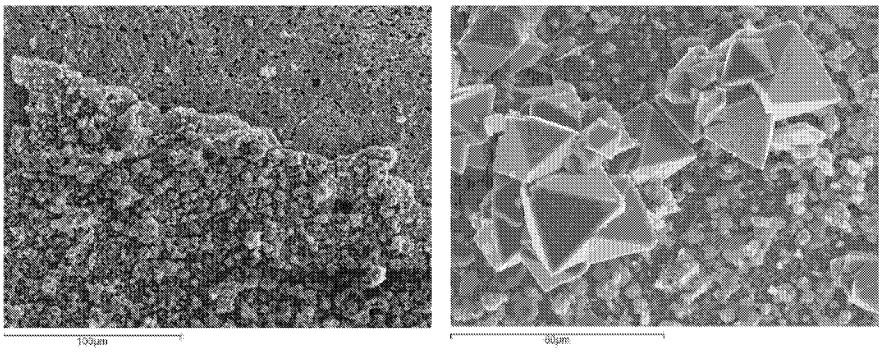

(a) **(b)**

Fig. 6. SEM pictures of 617 alloy surface after 24 hours beneath molten salts.

The Fig. 7(b) shows the cross section morphologies of alloy 617 in molten chlorides after 100 hours, the chromium absence allowed the salt penetration trough the NiO porous scale.

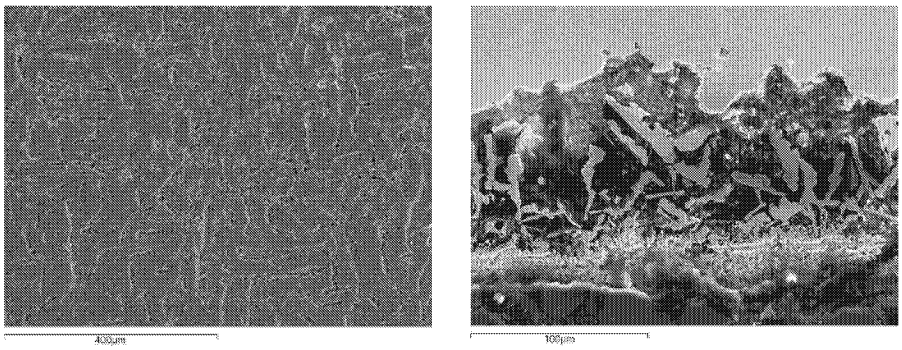

(a) **(b)**

Fig. 7. SEM pictures of 617 alloy surface after 100 hours beneath molten salts. (a) Superficial image. (b) Cross section image.

Kawahara [14] presented a corrosion model for alloy 625 in molten chlorides, under high pO_2 and high pCl_2, the alloying elements reacted as the following reactions:

$$2Cr + 3Cl_2 \rightarrow 2CrCl_3 \quad (7)$$

$$Mo + O_2\ (Cl_2) \rightarrow MoO_2\ (MoCl_2) \quad (8)$$

$$2Ni + O_2\ (Cl_2) \rightarrow NiO\ (NiCl_2) \quad (9)$$

The XRD results confirmed the presence of Cr_2O_3, $ZnCr_2O_4$ and NiO. The presence of MoO_2 was not identified by this technique. Nevertheless, it was possible adjusted some picks in the XRD spectrum at 100 hours (see Fig. 8) to another molybdenum oxide, MoO_3.

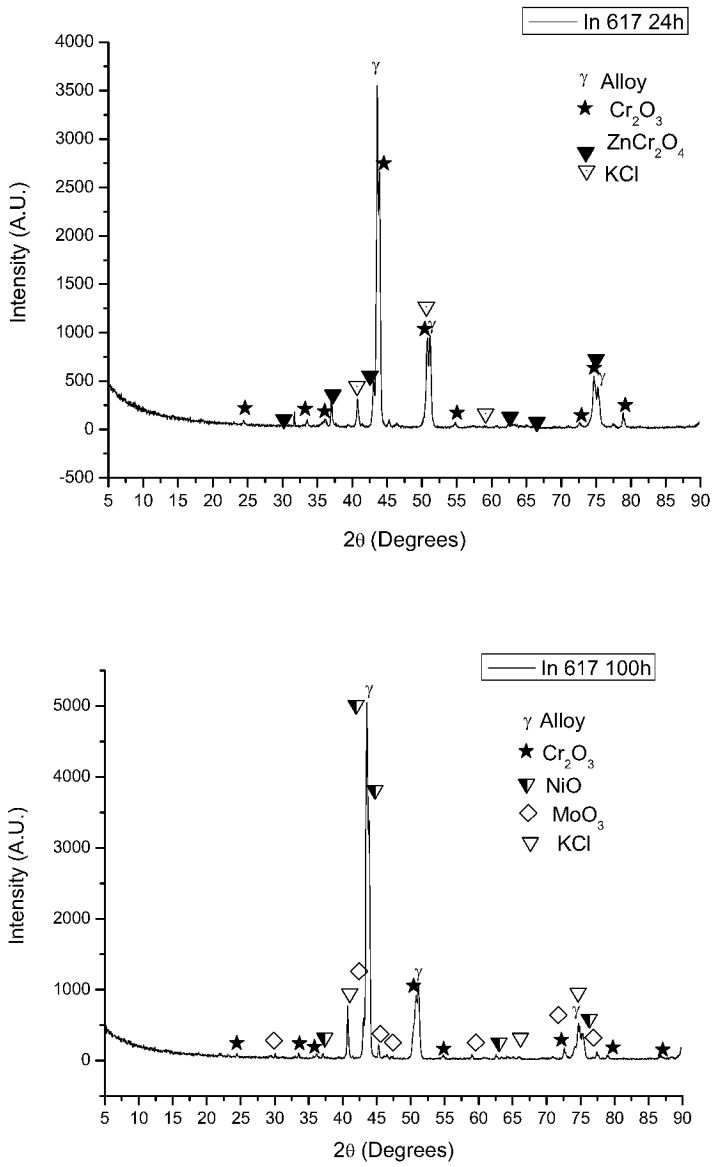

Fig. 8. XRD results for 24 and 100 hours of alloy 617 in molten KCl-$ZnCl_2$ at 650ºC in air atmosphere.

4 Conclusions:

The corrosion behaviour of Ni-base alloy 617 in presence of molten chlorides has been monitored by electrochemical impedance spectroscopy.
This alloy formed a protective oxide scale which became porous after a certain period of time leading to the oxidation and chlorination of alloying elements such Cr, Ni and Mo. In spite of the high chromium content of the alloy 617, it was not an efficiency protection to the corrosion of molten chlorides, due to evaporation and dissolution of Cr as $CrCl_3$ and CrO_4^-. Neither the oxides scales formed by Ni and Mo were enough to protect the alloy in this severity corrosion environment.

The EIS profiles were fitted to a protective scale model before 24 hours and to a porous scale model after that. The monitoring system allowed following the corrosion mechanism in real time.

5. References

1. Li, Y.S., Y. Niu, and W.T. Wu, *Accelerated corrosion of pure Fe, Ni, Cr and several Fe-based alloys induced by ZnCl2-KCl at 450 degrees C in oxidizing environment.* Materials Science and Engineering a-Structural Materials Properties Microstructure and Processing, 2003. **345**(1-2): p. 64-71.
2. Spiegel, M., G. Schroer, and H.J. Grabke, *Corrosion of high alloy steels and Fe-Cr-alloys beneath deposits from waste incinerator plants*, in *High Temperature Corrosion and Protection of Materials 4, Pts 1 and 2*. 1997. p. 527-534.
3. Spiegel, M., *Corrosion mechanisms and failure cases in waste incineration plants*, in *High Temperature Corrosion and Protection of Materials 5, Pts 1 and 2*. 2001. p. 971-978.
4. Spiegel, M., *Salt melt induced corrosion of metallic materials in waste incineration plants.* Materials and Corrosion-Werkstoffe Und Korrosion, 1999. **50**(7): p. 373-393.
5. Li, Y.S. and M. Spiegel, *Models describing the degradation of FeAl and NiAl alloys induced by ZnCl2-KCl melt at 400-450 degrees C.* Corrosion Science, 2004. **46**(8): p. 2009-2023.
6. Zeng, C.L. and J. Li, *Electrochemical impedance studies of molten (0.9Na,0.1K)(2)SO4-induced hot corrosion of the Ni-based superalloy M38G at 900 degrees C in air.* Electrochimica Acta, 2005. **50**(28): p. 5533-5538.
7. Macdonald, J.R., *Impedance Spectroscopy and Its Use in Analyzing the Steady-State Ac Response of Solid and Liquid Electrolytes.* Journal of Electroanalytical Chemistry, 1987. **223**(1-2): p. 25-50.
8. Zeng, C.L., W. Wang, and W.T. Wu, *Electrochemical impedance models for molten salt corrosion.* Corrosion Science, 2001. **43**(4): p. 787-801.
9. Mansfeld, F., H. Xiao, and Y. Wang, *Evaluation of Localized Corrosion Phenomena with Electrochemical Impedance Spectroscopy (Eis) and Electrochemical Noise-Analysis (Ena).* Werkstoffe Und Korrosion-Materials and Corrosion, 1995. **46**(1): p. 3-12.
10. Mansfeld, F., et al., *Evaluation of corrosion protection by polymer coatings using electrochemical impedance spectroscopy and noise analysis.* Electrochimica Acta, 1998. **43**(19-20): p. 2933-2945.

11. Mansfeld, F., *Electrochemical Impedance Spectroscopy (Eis) as a New Tool for Investigating Methods of Corrosion Protection.* Electrochimica Acta, 1990. **35**(10): p. 1533-1544.
12. Ishitsuka, T. and K. Nose, *Stability of protective oxide films in waste incineration environment - solubility measurement of oxides in molten chlorides.* Corrosion Science, 2002. **44**(2): p. 247-263.
13. Rapp, R.A., *Hot corrosion of materials: a fluxing mechanism?* Corrosion Science, 2002. **44**(2): p. 209-221.
14. Kawahara, Y., *High temperature corrosion mechanisms and effect of alloying elements for materials used in waste incineration environment.* Corrosion Science, 2002. **44**(2): p. 223-245.

METAL WASTAGE IN LOW ALLOY STEELS UNDER ALTERNATING ATMOSPHERES AT ELEVATED TEMPERATURE

S Osgerby and D D Gohil

National Physical Laboratory, Teddington, Middlesex, TW11 0LW, United Kingdom
steve.osgerby@npl.co.uk

Abstract

T22 and T23 steels have been exposed to two atmospheres, representative of low NOx combustion conditions, at 540 °C for times up to 4000 h. One atmosphere corresponded to 'base' conditions whilst the other represented a 'high sulphur' environment. Exposures have been carried out in each atmosphere singly and alternating between atmospheres every 250 or 500 h. Significant differences were found in rates of mass change and in scale microstructure between the different exposure sequences in both alloys. Several effects of fluctuating atmosphere have been identified; the occurrence of each in a particular specimen having a degree of stochastic behaviour. The detailed mechanism may be due to transient behaviour in the early stages of exposure to different atmospheres but further investigation is required to fully understand this behaviour.

Keywords: Low alloy steels, corrosion, alternating atmospheres

Introduction

Laboratory exposures are traditionally carried out under conditions that are kept as constant as possible. However industrial plant is operated under conditions where both the thermal and service atmosphere conditions vary with time. Cyclic oxidation testing is well established but the influence of changing the atmosphere during laboratory testing has so far been neglected.

Previous work on metal wastage of low alloy steels in atmospheres that simulate low NOx combustion environments [1] demonstrated that the addition of small amounts of active species in the test environment has a significant effect both on metal wastage rates and on scale composition and microstructure. The current work studies the material response to systematically alternating the gaseous atmosphere.

Experimental

An experimental matrix was set up to expose two low alloy steels, T22 and T23, to two atmospheres at 540 °C. The materials were alternated between the two atmospheres at different intervals. The composition of the steels, the atmospheres and the test schedule are given in Tables I, II and II respectively. Specimens were removed for mass change determination every 250 h.

Table I Composition of the test steels, wt%

Alloy	Fe	C	Si	S	P	Mn	Cr	Mo	V	N	Nb	W	B ppm	Al
T22	Bal	0.10	0.5	0.025	0.025	0.6	2.25	0.54						
T23	Bal	0.07	0.5	0.01	0.03	0.35	20.5	0.17	0.25	0.03	0.05	1.6	6	0.03

Table II Composition of the test atmospheres

Description	Composition, vol%								
	O_2	CO	CO_2	H_2	H_2S	HCl	H_2O	COS	N_2
Base	1.0	3.98	0.97	1.39	0.03	0.01	3.0	-	Bal
High COS	1.0	3.98	0.97	1.39	0.05	0.01	3.0	0.04	Bal

Table III Testing Matrix

Run No.	Sequence of Atmospheres	Time between changes
1	Base	Continuous
2	High COS	Continuous
2	Base → High COS→Base→High COS	250 h
3	Base → High COS→Base→High COS	500 h
5	High COS→Base→High COS→Base	250 h
6	High COS→Base→High COS→Base	500 h

Specimens were withdrawn from the exposure schedule at 1000, 2000, 3000 and 4000 h for metallographic investigation. These specimens were sectioned, mechanically polished and examined in the SEM using both energy-dispersive and wavelength-dispersive X-ray analysis. 'Digimaps' showing the elemental distribution were generated.

One specimen of T22 has been exposed in a continuous microbalance using sequence 2 in order to study the detailed kinetics associated with changing between atmospheres.

Results and Discussion

Mass change data as a function of time and exposure sequence are shown in Figure 1 for T22. Each graph contains data from 4 nominally identical specimens. Figures 1a and 1b show that for exposures to continuous atmospheres the mass change data are similar for the first 1500 h of exposure after which exposure to the High COS atmosphere leads to accelerated mass gain through the growth of a non-protective scale. The measured parabolic rate constant during the initial period is lower under the High COS atmosphere - however the difference is not significant, being ~17%.

When the specimens are switched between atmospheres (Figures 1c-1f) again little difference is seen until the exposures exceed 1500 h. After this period the variation in behaviour between specimens experiencing nominally identical exposure histories apparently increases with the range of mass change measured increasing significantly in most cases.

T23 shows more erratic behaviour with the variation in behaviour between samples that have experienced similar exposure histories starting earlier (after about 750 h exposure) and even in the case of exposure to the same atmosphere. In this case the difference between specimens is attributed to spallation of the corrosion product from some specimens and is a consequence of the higher creep strength of T23 compared to T22.

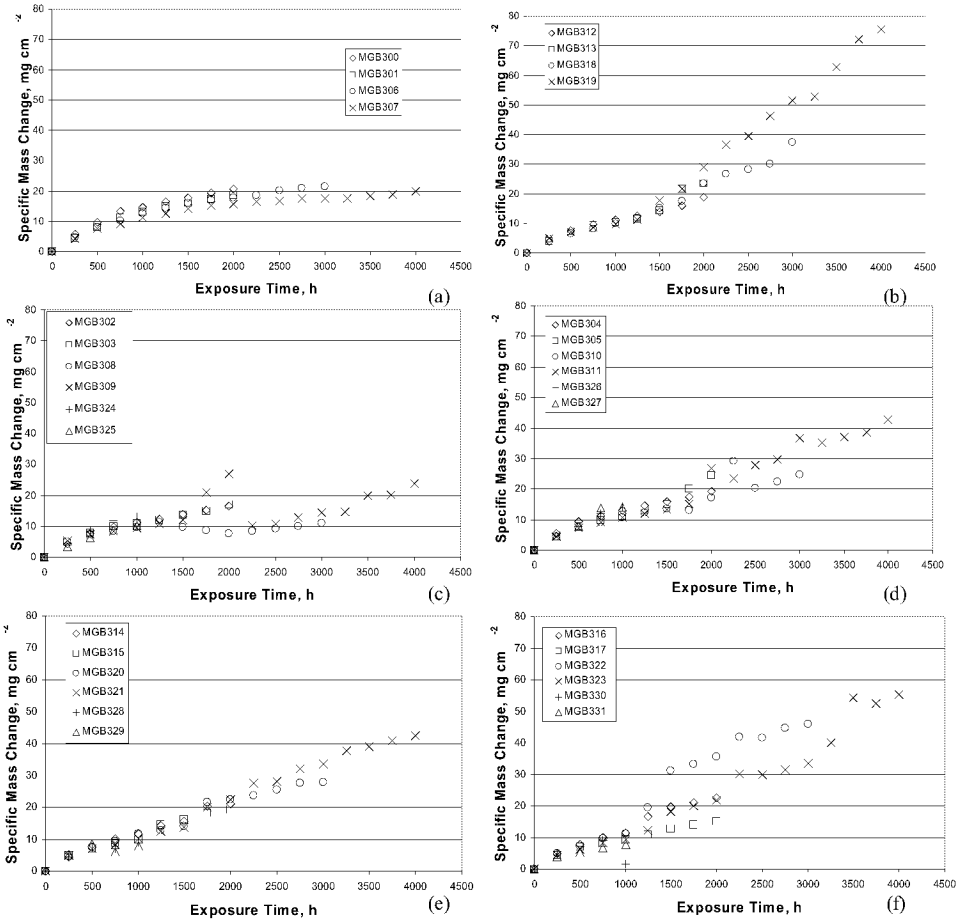

Figure 1 Specific Mass Change as a Function of Time and Sequence of Furnace Atmosphere for T22 Exposed at 540 °C (a) Run 1 (b) Run 2 (c) Run 3 (d) Run 4 (e) Run 5 (f) Run 6 – defined in table III

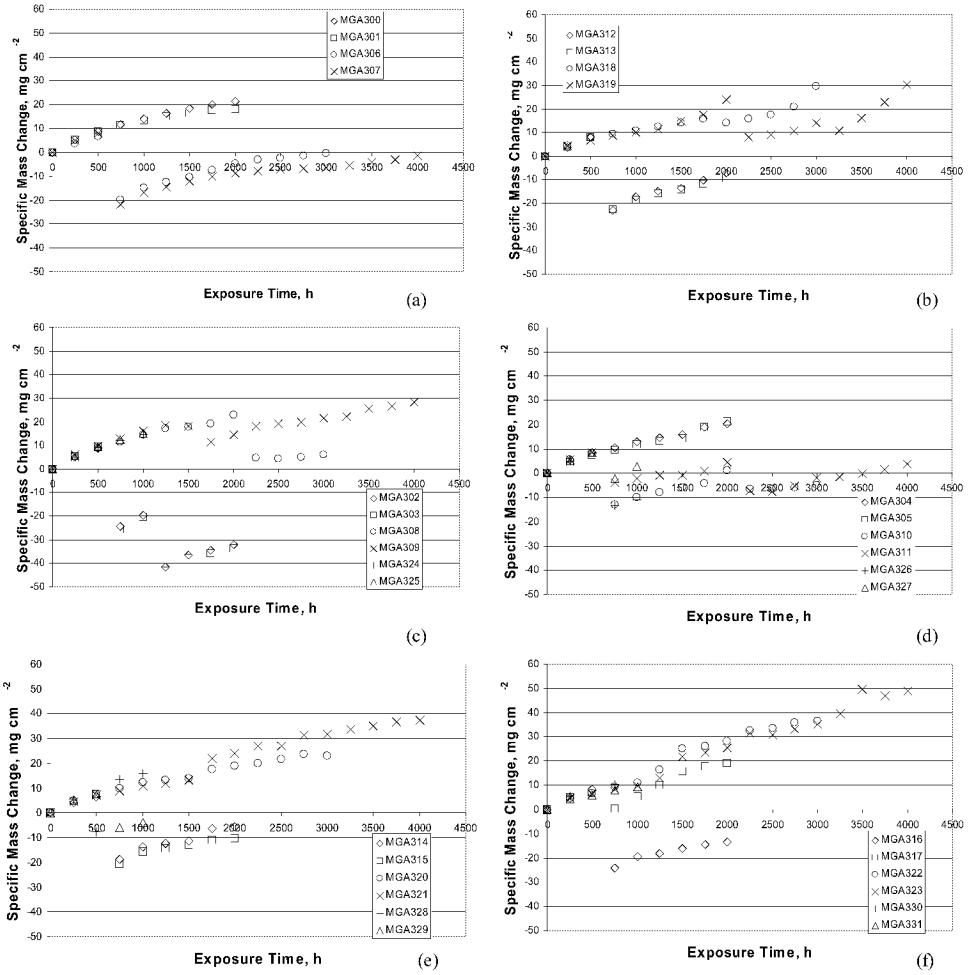

Figure 2 Specific Mass Change as a Function of Time and Sequence of Furnace Atmosphere for T23 Exposed at 540 °C (a) Run 1 (b) Run 2 (c) Run 3 (d) Run 4 (e) Run 5 (f) Run 6 – defined in table III

Specimens were removed from test after 1000, 2000 and 4000 h exposure and sectioned for examination of the corrosion product. Figure 3 shows images of the corrosion product together with distribution maps for oxygen and sulphur for T22 specimens exposed for 2000 h. In all the examples shown the scale has remained protective and unspalled. When the alloy is exposed to a single atmosphere the sulphur is restricted to the inner scale and interface between the two scales. However when the atmosphere fluctuates during the exposure the outer scale becomes disrupted and sulphur is allowed to accumulate within this layer.

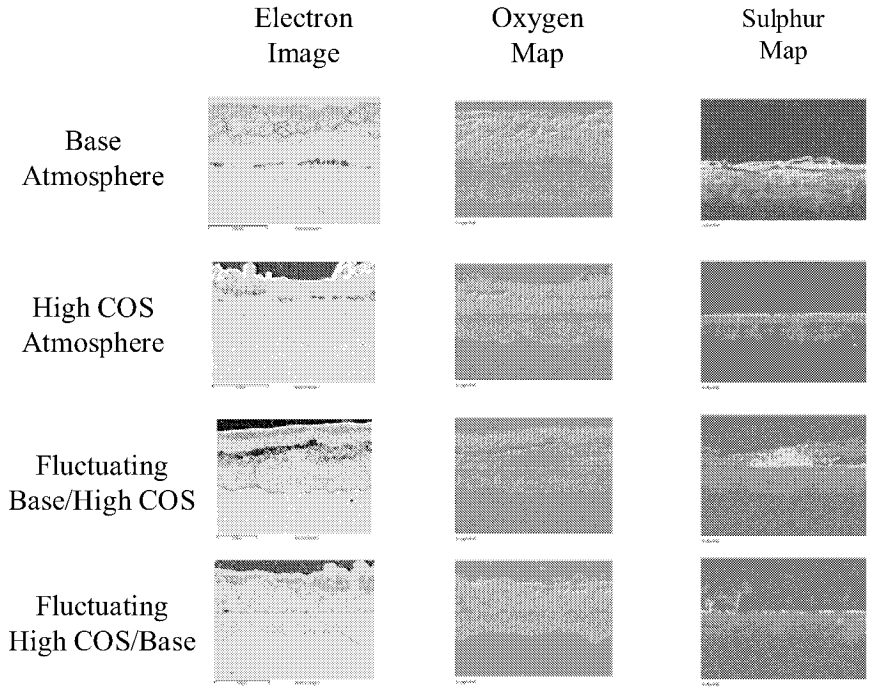

Figure 3 Structure of scale formed on T22 after exposure to various atmospheres at 540 °C for 2000 h.

One can envisage several types of material behaviour that could be induced by alternating atmospheres viz:

i. The behaviour follows a life fraction law where the overall response is a simple average between the behaviour in each individual atmosphere
ii. The behaviour follows the response to the more aggressive atmosphere in that once breakaway is established it continues during further exposure to the less aggressive environment
iii. The protective behaviour remains active for longer periods than predicted by the life fraction rule as the disruptive mechanism associated with the more aggressive environment is relieved during exposure to the less aggressive atmosphere.

iv. The behaviour becomes more complex as additional mechanisms are activated due to the change between atmospheres.

Figure 4 shows examples of these different types of behaviour in T22 - type i is exhibited by specimen MGB311 in figure 4b, type ii by MGB305 in figure 4b, type iii by MGB303 in figure 4a and type iv by MGB308 and MGB309 in figure 4a.

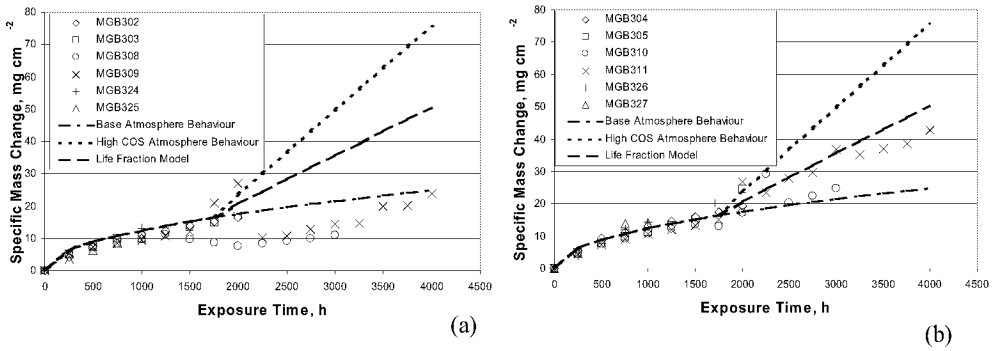

Figure 4 Specific Mass Change of Specimens with superimposed behavior from Continuous Behaviour and Life Fraction Model as a Function of Time for T22 Exposed at 540 °C for (a) Run 3 and (b) Run 4

In both these latter specimens there is a distinct mass loss between consecutive cycles after (a) continuous protective behaviour in the case of MGB308 or (b) a transition to non-protective behaviour for MGB309. The observation of such diverse behaviour in specimens that experienced nominally identical conditions suggests that there is a stochastic element to the onset of both non-protective scale growth and spallation.

Figure 5 shows images and digimaps of the scales where spallation has (MGB308) and has not (MGB302) occurred. Several key differences can be observed. Firstly the secondary electron images show the presence of an interfacial crack in the specimen that has spalled (Figure 5d) but only a layer of defects, at the original surface, in the specimen where spallation has yet to occur (Figure 5a). The interfacial crack is immediately below a layer enriched in sulphur (Figure 5f) and depleted in oxygen (Figure 5e). In contrast, where the scale has not spalled the sulphur is contained beneath the layer of defects (Figure 5c).

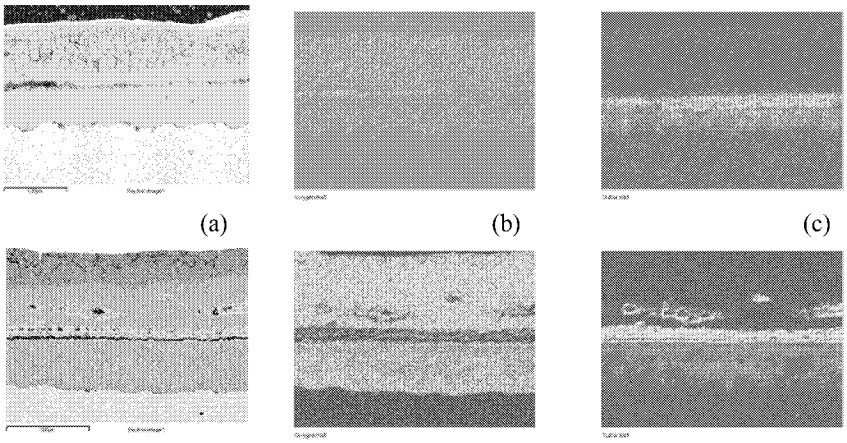

Figure 5 Structure of scale formed on T22 after exposure to alternating atmospheres at 540 °C (a-c) specimen MGB302, run3 (d-f) specimen MGB308, run3; (a,d) electron image (b,e) oxygen map (c,f) sulphur map

It is evident from both Figure 3 and Figure 5 that the migration of sulphur across the boundary between the inner and outer scale is key to the transition from protective scale growth to either spallation or non-protective growth. A clue to the mechanism by which this occurs is given by detailed examination of the data from the exposure in the continuous microbalance. Figure 6 shows the complete mass change data during the exposure. Initially (cycles 1-3) the material shows protective parabolic kinetics, however from cycle 4 onwards the material shows increased rates of mass change when exposed to the 'High COS' atmosphere, consistent with the non-protective behaviour observed after extended exposure to this atmosphere, Figure 1b.

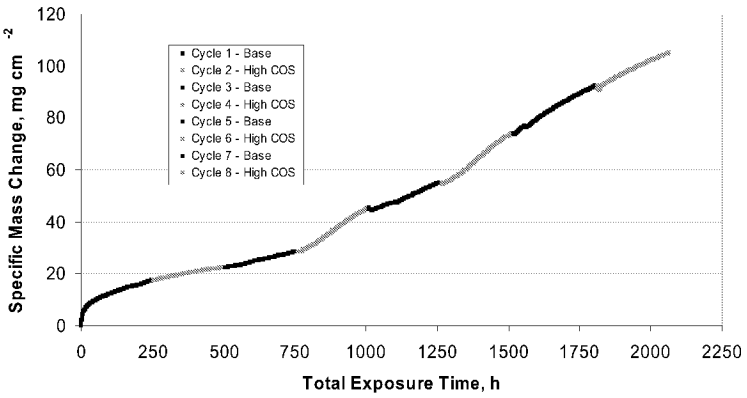

Figure 6 Specific Mass Change as a function of time for T22 exposed under alternating atmospheres in a continuous microbalance

Figure 7 shows the mass change during the initial hours of each cycle. During the first cycle the mass changes shows the expected parabolic behaviour with time, however on subsequent cycles the initial behaviour shows increasing amounts of mass loss at the start of each new cycle. This mass loss is unlikely to be due to spallation but instead can be attributed to chemical transient effects. Further investigation is necessary to understand this behaviour fully.

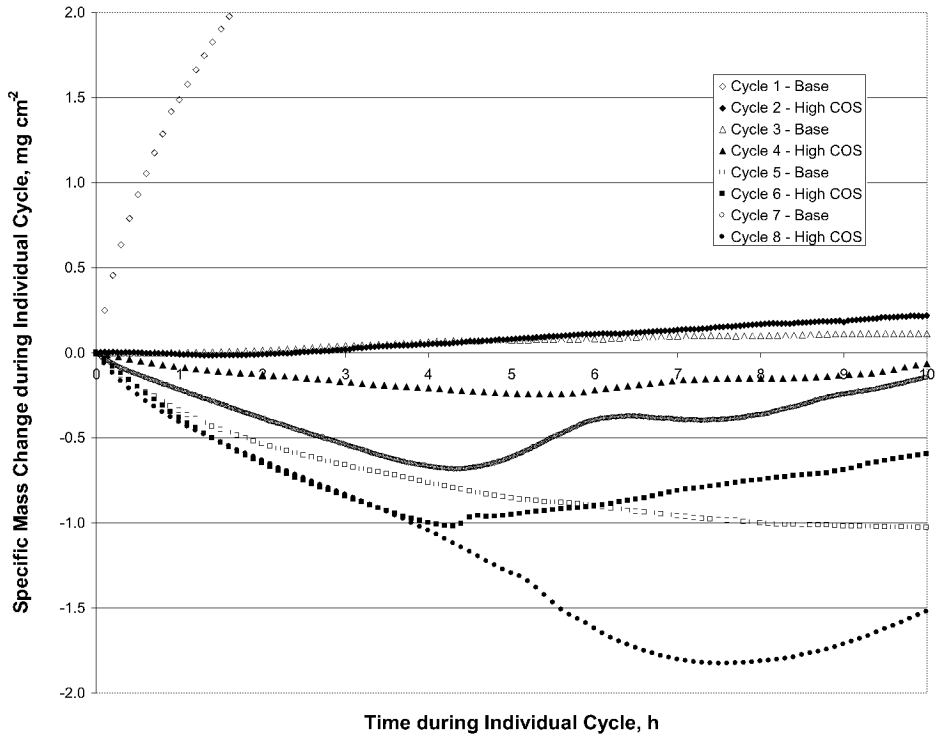

Figure 7 Specific mass change as a function of time at the start of each exposure cycle for T22 exposed to alternating atmospheres at 540 °C

Concluding Remarks

The behaviour of T22 and T23 exposed to two atmospheres based upon low NOx combustion environments at 540 °C has been studied. Significant differences in behaviour were observed between the two materials and the two atmospheres. Additionally when the materials were exposed to alternating atmospheres additional mechanisms began to operate. These mechanism include migration of sulphur across the boundary between the inner and outer scales and may be linked to transient chemical effects in the initial period of exposure to a new atmosphere. Further work is required to explain these effects fully.

Acknowledgements

This work was carried out under the COST538 Collaboration on Plant Life Extension. Funding for the work was provided by Materials – Performance, a programme of underpinning research commissioned by the United Kingdom Department of Trade and Industry.

References

[1] S Osgerby, A T Fry and D D Gohil, "Metal Wastage in Low Alloy Ferritic Steels Exposed to Multi-component Gaseous Atmospheres: Data Representation and Predictive Modelling", Materials at High Temperature (in press)

DEVELOPMENT OF ALUMINIDE DIFFUSION COATINGS FOR HEAT EXCHANGER MATERIALS AND THEIR CREEP-CORROSION RESISTANCE IN SIMULATED COAL FIRING ENVIRONMENT

V. Rohr[1], T. Weber[1], M. Schütze[1], P. J. Ennis[2], J. Quadakkers[2]
[1]*Karl Winnacker Institut der Dechema e.V.*
Theodor-Heuss Allee 25, D-60486 Frankfurt am Main, Germany
[2]*Forschungszentrum Jülich IWV-2, D 52425 Jülich, Germany*
Contact: weber@dechema.de

Abstract

The improvement of the efficiencies of thermal power plants requires an increase of the operating temperatures and thus of the corrosion resistance of heat exchanger materials. Therefore, the present study aimed at developing protective coatings by using the pack cementation process. Two types of heat exchanger steels were investigated: The 17%Cr/13%Ni austenitic steel and three ferritic-martensitic steels with 9 (P91 and P92) and 12 %Cr (HCM12A). The austenitic steel was successfully aluminised at 950 °C. For the ferritic-martensitic steels, the pack cementation temperature was decreased to 650 °C in order to maintain their initial microstructure. Two types of aluminide coatings consisting of Fe_2Al_5 and FeAl were developed.

The corrosion resistance of coated and uncoated steels was compared in simulated coal firing environment for durations up to 2000 h between 650 and 700 °C. It was shown that the coatings offer a significant corrosion protection and, thus, an increase of the component lifetime. The performance of coated 9-12 % Cr steels is no longer limited by corrosion but by interdiffusion between the coating and the substrate. Finally, the influence of interdiffusion on the creep properties of P92 was also evaluated.

Keywords: diffusion coatings, heat exchanger materials, pack cementation, 9-12 % Cr steels, high temperature corrosion.

Introduction

Modern heat exchanger materials for advanced power plants have to withstand operating temperatures in excess of 600 °C and pressures up to 300 bar. The long-term creep resistance and the corrosion resistance are both crucial and unfortunately counteracting factors concerning the materials lifetime. A key issue is the content of chromium as alloying element. Generally speaking, the higher the chromium content, the higher the corrosion resistance and the lower the creep resistance. A comparison between the different mechanical properties of several commercial alloys is shown in Figure 1. Although in short-term testing the higher Cr steels show the higher creep strength, the strength falls steeply after about 5000 h to below that of the 9 % Cr steel P92. The superior mechanical properties of the 9 % Cr steel (P92) against the 12% Cr-steel (HCM12A) and vice versa the superior corrosion resistance of the 12 % Cr-steel compared to the 9 % Cr-steel are obvious. Enhanced mechanical properties and improved corrosion resistance can be obtained using austenitic and Ni-base alloys. However, these materials are costly, they have a lower thermal conductivity and an inferior workability. Thus, the aim of this work was the improvement of the corrosion properties of conventional 9-12% Cr-steels by the application of protective aluminium diffusion coatings which are able to stimulate the formation of thin, well adherent and slow growing oxide scales for long term corrosion protection.

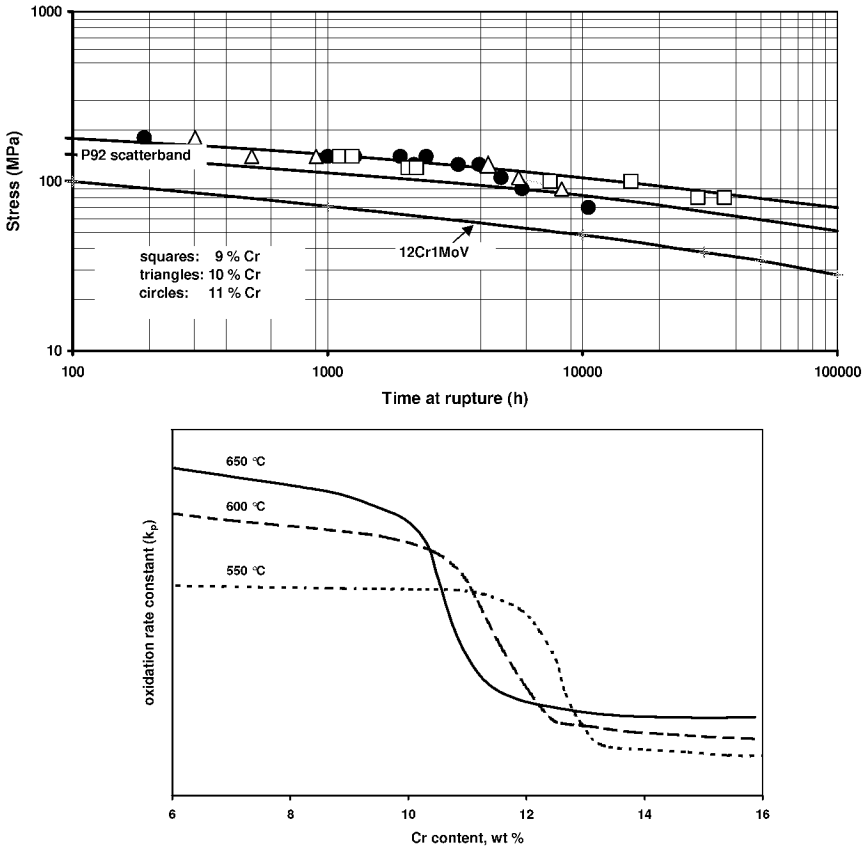

Figure 1: Influence of Cr-content on stress rupture strength (top) and steam oxidation rate constant (bottom) of boiler tubes [1,2]

Experimental

Diffusion coatings

The materials selected to be coated and their nominal compositions are given in Table 1. Diffusion coatings can be applied by the conventional pack cementation process [3,4]. This method allows the enrichment of a metal surface with aluminium, chromium, silicon or other elements by a CVD process. Figure 2 shows the principle of this process.

Table 1: Nominal compositions (wt %) of the investigated alloys

Material	Fe	C	N	Si	Cr	Al	Ni	Mn	Mo	V	Nb	W	Co	Others
Ferritic-martensitic steels														
P91	88.2	0.09	0.05	0.40	9.20	0.01	0.38	0.50	0.90	0.22	0.06	-	0.01	P 0.01
HCM12A	83.5	0.07	0.06	0.25	12.5	0.01	0.34	0.54	0.36	0.21	0.05	1.90		Cu 0.85
P92	88.2	0.11	0.05	0.04	8.96	0.01	0.06	0.46	0.47	0.20	0.07	1.84		P 0.01
Austenitic steel														
17Cr/13Ni	66.8	0.02	0.12	0.27	16.7	-	12.5	1.30	2.20	-				

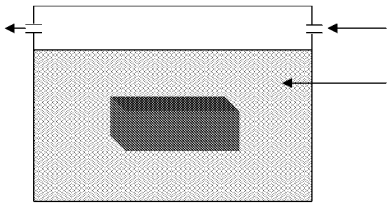

Figure 2: Scheme of the pack cementation process

The work piece to be coated is embedded in a powder mixture of the element to be diffused, a halide activator and an inert filler material to prevent the powder from sintering. During heating under an inert or slightly reducing atmosphere the activator – usually NH_4Cl – decomposes and stimulates the formation of aluminium chlorides. At the surface of the material to be coated these aluminium chlorides decompose and aluminium is deposited which can now diffuse into the subsurface zone. If the activity of the powder pack is very low the element to be diffused is enriched within the surface in solid solution, if higher activities are present new phases are formed; in case of Al-diffusion these are iron aluminides or ferritic substrates. Normally the process is conducted at temperatures around 900 °C to obtain the desired coating thickness within reasonable time. For the 9% and 12% Cr-steels the process temperature is limited to 650 °C; higher temperature treatments would cause degradation of the martensitic-ferritic structure leading to a loss of creep strength.

Coupon specimens of 20 x 10 x 3 mm were ground with 120 grit SiC paper and subsequently glass bead blasted for surface preparation. They were embedded in a powder consisting of Al_2O_3-10Al-1NH_4Cl (wt %) within a covered alumina crucible and subjected to heat treatment at 650 °C for 6 h in a horizontal tube furnace. Prior to heating the furnace tube was evacuated and flushed with Ar-10% H_2. A cross section of the obtained diffusion coating is shown in Figure 3 for P91. On the HCM12A the coating shows the same appearance. The coating is homogeneous and of quite uniform thickness. A quantitative line-scan obtained by electron microprobe analysis (EPMA) shows the presence of the intermetallic phase Fe_2Al_5 nearly without any interdiffusion zone to the base material.

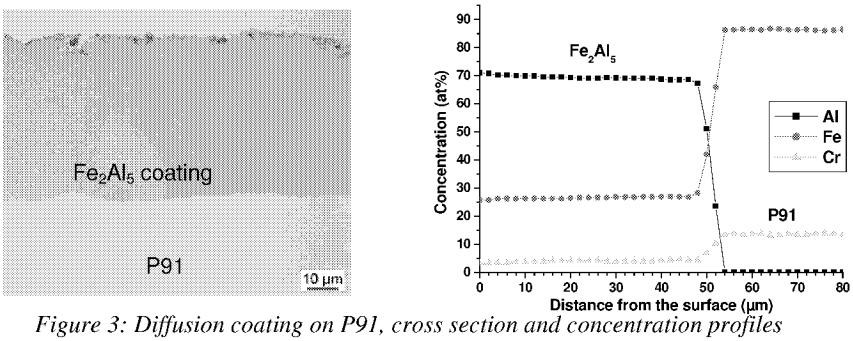

Figure 3: Diffusion coating on P91, cross section and concentration profiles

Since the intermetallic Fe_2Al_5-phase provides only a poor ambient temperature ductility due to its high aluminium content, a coating with lower Al-concentration was also produced. To achieve this, it was necessary to reduce the Al-activity of the powder pack, which can be done by adding a second element to be co-diffused (for example, Si) or by using Fe_2Al_5 as masteralloy as done in the present case. Since a gradient of the chemical potential between powder pack and substrate surface is necessary for the coating deposition process [5,6] one may expect that if Fe_2Al_5 is used as masteralloy a lower Al-containing FeAl-phase is formed. The coating obtained using a powder of Al_2O_3-20Fe_2Al_5-2NH_4Cl heat treated for 24h at 650 °C is shown in Figure 4.

Due to the lower activity, the process duration had to be prolonged to obtain a reasonable diffusion depth. This coating has a thickness of max. 10µm with continually decreasing Al-content as shown by the line scan graph.

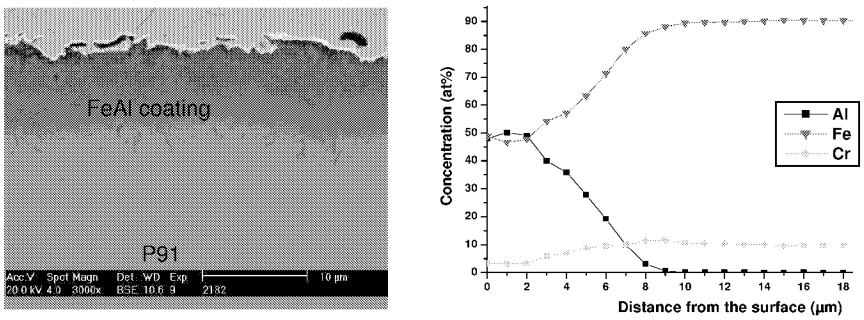

Figure 4: Low activity diffusion coating on P91, cross section and concentration profiles

The coating on the austenitic 17Cr/13Ni steel was produced at a temperature of 950 °C during 8h using a powder of Al_2O_3-5Al-0.5NH_4Cl. The cross section and lines cans are depicted in Figure 5. It consists of an outer uniform (Fe,Ni)Al layer of about 60 µm and an interdiffusion zone of about 70 µm thickness. The interdiffusion zone is characterized by the precipitation of needle shaped Al-nitrides. Obviously chromium was forced to diffuse inwards since a Cr-depletion is present in the outer zone and a Cr-enrichment up to nearly 20% can be found within the interdiffusion zone.

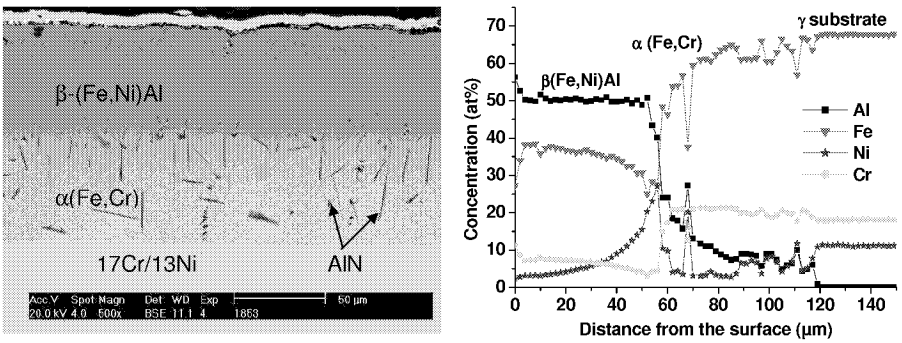

Figure 5: Diffusion coating on 17Cr/13Ni, cross section and concentration profiles

Corrosion experiments

The corrosion experiments were performed at 650 °C in a simulated hard coal firing environment composed of N_2-14CO_2-10H_2O-1O_2-0.1SO_2-0.01HCl (Vol.-%). A scheme of the test rig is shown in Figure 6.

Coated and uncoated specimen were placed each in separate crucibles to collect spalled oxide flakes. The specimen preparation and the weighing procedure before and after corrosion testing was executed following the ISO draft 1122 for discontinuous isothermal corrosion testing [7].

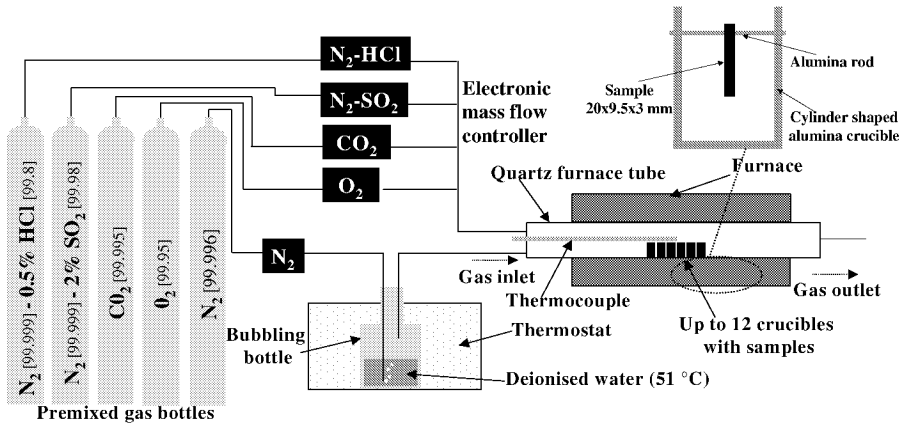

Figure 6: Test rig for discontinuous isothermal corrosion experiments according to ISO draft 1122

All uncoated specimens exhibited to various extents by corrosion attack, as shown in Figure 7. The P91 developed a thick, two-layer oxide scale with the typical post breakaway structure where the outer magnetite layer is only loosely adherent. Due to the higher chromium content of the HCM12A, nodules of iron chromium oxide spinel formed on the surface which eventually coalesced. In principle the same morphology of the corrosion layer

as on P91 may be expected during further exposure. The austenitic alloy 17Cr/13Ni suffered from extensive spallation; inwardly growing nodules were found consisting of $(Fe,Cr)_3O_4$ and $(Fe,Cr)_2O_3$.

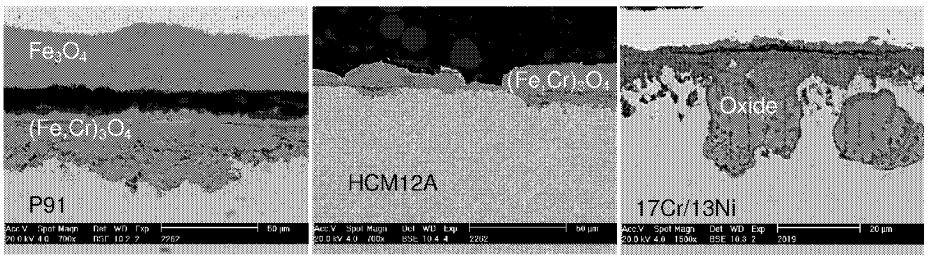

Figure 7: Uncoated P91 and HCM12A after 1000h, uncoated 17Cr/13Ni after 300h at 650 °C

All coated materials showed a significant improvement with respect to their corrosion resistance. The cross sections of the aluminised P91 as well as the mass gain curves after 1000 h and 2000 h are shown in Figure 8.

Under the white nickel layer applied to protect the oxide scale during metallographic preparation, a very thin Al-rich oxide with some intrusions was detected. Obviously a transformation of the Fe_2Al_5-layer into FeAl occurred as consequence of an inward diffusion of Al into the ferritic base material. Due to the growing activity of Fe the amount of hematite incorporated within the oxide scale gradually increased with time. The mass gain plot shows that all aluminised coatings provided significant protection comparable to the behaviour of the Ni-base Alloy 617. The performance of the coated HCM12A specimens is virtually the same. Here also an Al-depletion of the surface zone occurs during exposure due to interdiffusion with the base alloy.

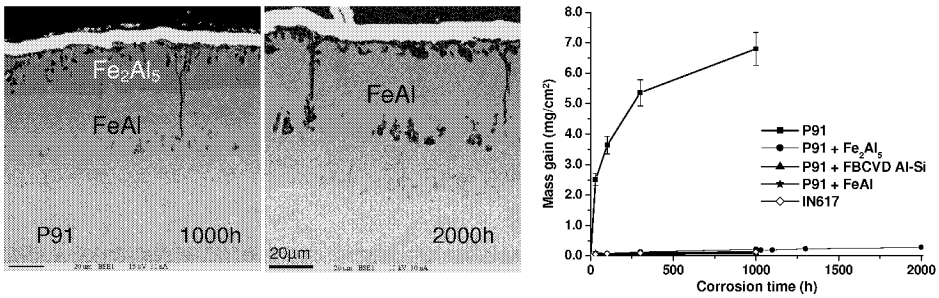

Figure 8: Coated P91 after exposure at 650 °C, cross sections and mass gain curves for coated and uncoated specimens

The aluminised austenitic 17Cr/13Ni alloy showed also a significantly improved corrosion resistance as illustrated by Figure 9. Only a slight mass gain was found for the coated specimen due to the formation of a thin α-alumina layer, which could be identified by XRD. The appearance of the diffusion layer did not change during exposure. Also no tendency of Al inward diffusion could be observed.

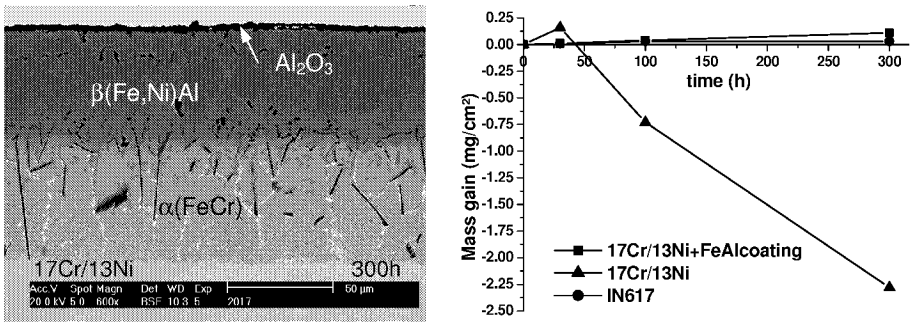

Figure 9: Coated 17Cr/13Ni after exposure at 650 °C, cross sections and mass gain curves for coated and uncoated specimens

Creep experiments

Since a possible deterioration of the mechanical properties of diffusion coated materials is often discussed, creep experiments were performed with coated and uncoated P92 specimens. Since an apparatus allowing creep experiments within corrosive environments was not available, pre-corroded specimens were used for creep experiments in laboratory air at 650 °C under a constant load of 120 MPa. The specimen shape and a schematic of the creep apparatus are shown in Figure 10. Five types of specimens were tested under conditions as follows:

- P92 as received
- P92 heat treated for 1000 h at 650 °C in inert gas
- P92 preoxidised- in Ar - 50% water vapor for 1000 h at 650 °C
- P92 pre-corroded under simulated coal firing environment for 1000 h at 650 °C
- Coated P92 pre-corroded under simulated coal firing environment for 1000 h at 650 °C

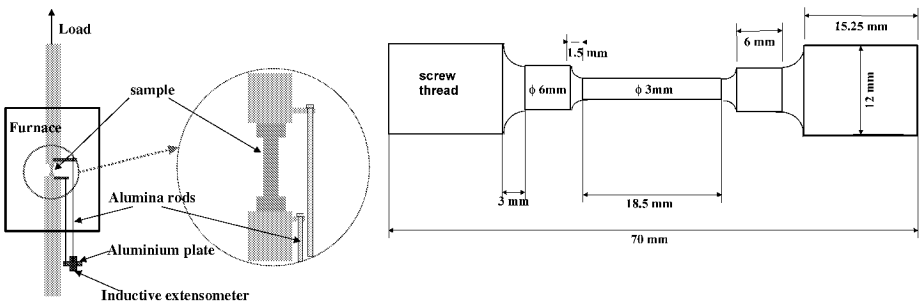

Figure 10: Schematic of the creep apparatus and specimen geometry

For each of these conditions tensile strain versus time curves were averaged for two different specimens and reported in Figure 11. The experiments were generally stopped when 2 % strain had been reached. The creep strength decreased in the following order:
as received > heat treated > Ar-H_2O > coated and pre-corroded > uncoated and pre-corroded
These results suggest that the mechanical behaviour of the material is not negatively influenced by the coating process, coated and pre-oxidised specimens exhibiting similar creep deformation to that of the pre-oxidised specimens.

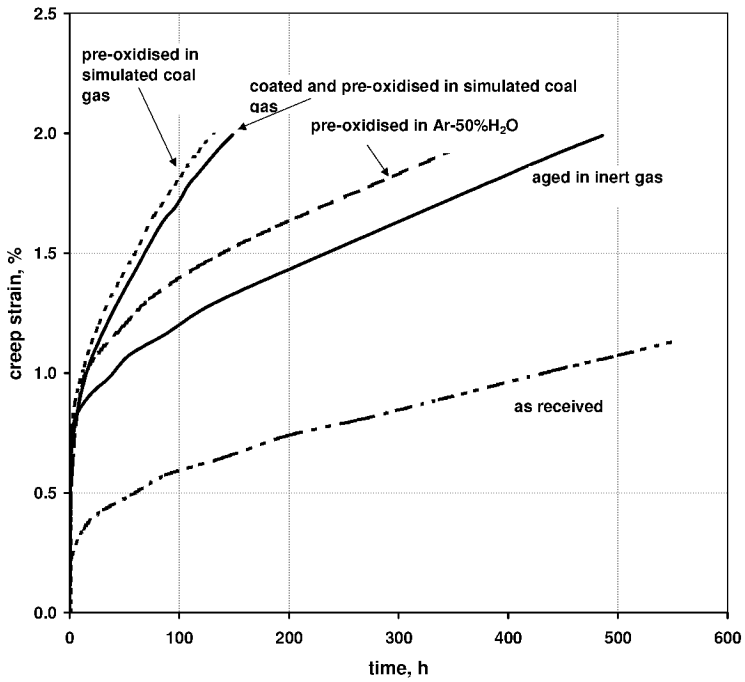

Figure 11: Creep curves for different P92 specimens at 650 °C and 120 MPa

Several conclusions may be drawn from these creep curves. Obviously the heat treatment under inert gas led to a thermal ageing effect which enhances recovery of the tempered martensite and a coarsening of the carbides and carbonitrides leading to accelerated motion of dislocations [8] and reduced precipitation strengthening [9]. The bulk of the specimen heat treated in Ar-H_2O was in the same condition; the corrosion of the surface may provide an additional effect due to the influence of Cr-depletion and oxide scale formation. The latter effect is much more pronounced for the specimen pre-corroded under simulated coal combustion conditions resulting in voluminous oxide scales that significantly reduced the unaffected cross section. The unaffected cross section may be to a similar extent reduced also for the coated specimen but in this case because of the inward diffusion of Al. A comparison between the uncoated and coated material under creep load in corrosive environments including the above mentioned results leads to a hypothetical creep evolution as shown in Figure 12.

The uncoated steel will reach eventually a break-away corrosion mode which will result in a continuously decreasing wall thickness and thus, a continuously decreasing creep strength. For the coated material the initial creep strength is lowered by the formation of the diffusion

coating and a certain degradation will follow during service due to the interdiffusion with the substrate. However, the excellent protective behaviour of the coating will preserve the material for a long time until the Al-content at the surface becomes too low to sustain a slow growing alumina scale, and rapid oxidation will occur. Then the material will fall into the same degradation mode as the un-coated steel.

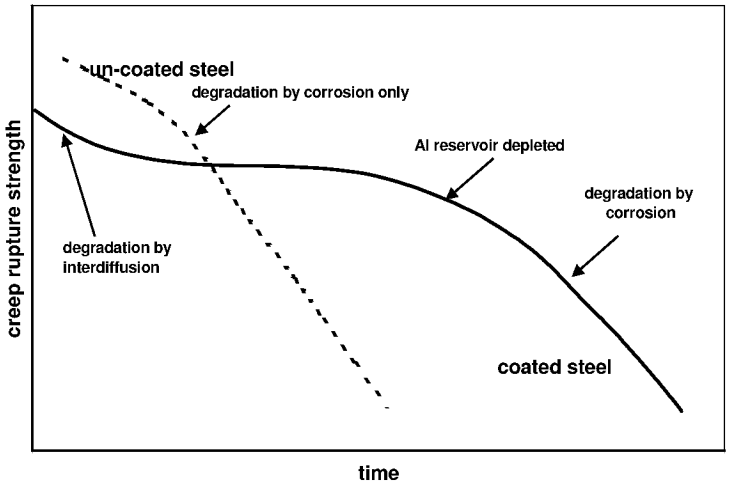

Figure 12: Hypothetical evolution of creep strength with exposure time for un-coated and coated steels

Conclusions

It could be shown that Al-diffusion coatings using a conventional pack cementation process can be applied on ferritic-martensitic steels without affecting the mechanical properties of the base material. This was possible by a reduction of the diffusion temperature down to 650 °C. At the same time the activity of the powder mixture had to be adjusted to obtain homogenous coatings of a reasonable thickness. Generally a Fe_2Al_5 coating with poor room temperature ductility is formed if pure Al is used as diffusion source. If a FeAl coating is desired the Al activity within the pack has to be reduced. The coated materials show a very good corrosion resistance under simulated hard coal combustion conditions compared to the uncoated steels which suffer from the formation of thick oxide scales and scale spallation. The coatings can stimulate the formation of a thin alumina rich oxide scale. During exposure the coating undergoes a certain degradation due to inward diffusion of Al into the base material. Fe_2Al_5 coatings eventually transform completely into FeAl-layers, thus, it may be concluded that interdiffusion is the main degradation mode. The situation is different for the austenitic base materials. The investigated 17Cr/13Ni steel developed a (Fe,Ni)Al coating during the diffusion process. The morphology and the dimensions of this coating remained stable during exposure due to the much lower diffusivity present within the austenitic fcc-lattice.

Creep tests with coated and uncoated differently pre-treated P92 specimens showed that the coating does not negatively affect the mechanical properties of the material and seems to be a promising measure to extend the lifetime of boiler tubes at elevated temperatures.

Acknowledgements

The authors would like to thank for the support of this work in the frame of the SUNASPO network project (RTN project N° HPRN-CT-2001-00201) funded by the European Commission. They also would like to thank all project partners and co-workers for their contributions concerning the experimental work and the post-experimental investigations.

Literature

[1] P.J. Ennis, in Advances in Materials Technology for Fossil Power Plants, Proc 4th International Conference, 25-28 October 2004, Hilton Head Island, South Carolina, USA, ed R Viswanathan, D Gandy, K Coleman, EPRI Report Number 1011381, ISBN 0-87170-818-3, ASM International, Ohio, 2005, pp 1146-1159

[2] J. Zurek, L. Nieto-Hierro, J. Piron-Abellan, L. Niewolak, L. Singheiser, W.J. Quadakkers, Materials Science Forum 2004, 461-464

[3] R. Mévrel, C. Duret, R. Pichoir, Materials Science and Technology 3/1986, 201-206

[4] R.L. Wachtell, Science and Technology of surface coating, B.N. Chapman & J.C. Anderson (eds.), Academic Press London, NY (1974) 105-118

[5] B.K. Gupta, L.L. Seigle, Thin Solid Films 73/1980, 365-371

[6] R.A. Rapp, Proceedings of Corrosion 89, April 17-21, New Orleans 1989, paper 352

[7] Corrosion of metals and alloys – Test method for Isothermal Exposure Testing under High Temperature Corrosion Conditions for Metallic Materials, ISO Document ISO/TC 156 N 1122 - Working Draft

[8] G.E. Dieter, Mechanical Metallurgy, 2. Edition, Int. Student Edition, McGraw-Hill Kogakusha Ltd. (1976) 451-489

[9] O. Wachter, P.J. Ennis, VGB Kraftwerkstechnik 9/1997, 770-785

DEVELOPMENT AND VALIDATION OF ADVANCED OXIDATION PROTECTIVE COATINGS FOR SUPER CRITICAL STEAM POWER PLANT

M. B. Henderson[1], M. Scheefer[1], A. Agüero[2], B. Allcock[3], B. Norton[4], D. N. Tsipas[5], R. Durham[6] and Z Xiang[7]

[1]*ALSTOM Power Ltd., Newbold Road, Rugby, CV21 2NH*
mike.henderson@ power.alstom.com
[2]*Instituto Nacional de Técnica Aeroespacial (INTA), Spain,* [3]*Monitor Coatings Ltd., UK,*
[4]*Indestructible Paints Ltd., UK,* [5]*Aristotle University of Thessaloniki, Greece,*
[6]*FZ Julich, Germany,* [7]*Northumbria University, UK*

Abstract

Increasing the efficiency of coal-fired power plant by increasing steam temperatures and pressures brings benefits in terms of cheaper electricity and reduced emissions, particularly CO_2. In recent years the development of advanced 9%Cr ferritic steels with improved creep strength has enabled power plant operation at temperatures in excess of 600°C, such that these materials are being exploited to construct a new generation of advanced coal-fired plant. However, the move to higher temperatures and pressures creates an extremely hostile oxidising environment. To enable the full potential of the new steels to be achieved, it is vital that protective coatings are developed, validated under high temperature steam and applied to candidate components from the steam path. This paper reviews recent work conducted within the Framework V project "Coatings for Supercritical Steam Cycles" (SUPERCOAT) to develop and demonstrate advanced slurry and thermal spray coatings capable of providing steam oxidation protection at temperatures in excess of 620°C and up to 300 bar. The programe of work has demonstrated the feasibility of applying a number of candidate coatings to steam turbine power plant components and has generated long-term steam oxidation rate and failure data that underpin the design and application work packages needed to develop and establish this technology for new and retrofit plant.

Keywords: 9%Cr steels, steam oxidation, protective coatings, aluminising, thermal spraying

Introduction

Increasing the efficiency of coal-fired power plant by increasing steam temperatures and pressures brings benefits in terms of cheaper electricity and reduced green house gas emissions, particularly CO_2 [1]. As illustrated by Figure 1, over recent years a series of more creep resistant ferritic steels have been developed to meet the demands for high temperature, more efficient and reliable power plant that are cost effective to manufacture and operate. These developments have been achieved through alloy design and long term testing of candidate materials that has led to the introduction of additions such as tungsten, vanadium, niobium and boron [2] and has culminated in the 9%Cr ferritic steels such as P91 (X12CrMoVNbN9-1) and P92 (X10CrWMoVNb9-2) and more latterly the COST steels such as FB2 (X13CrMoCoVNbNB9-2-1) and CB2. These steels now offer the potential for power plant operation at temperatures up to 620°C and are being exploited to construct a new generation of advanced coal-fired plant in Europe, Japan and China. Table 1 sumarises the current state-of-the-art for high performance plant in Europe that offer efficiency levels as high as 49%. The advent of high temperature, super critical steam turbines creates an extremely hostile oxidising environment for the components that may lead to excessive oxide scaling and loss of component profile due to exfoliation and erosion that may impact directly upon plant operation and efficiency, component durability and overhaul procedures [3].

To enable the full potential of the advanced 9%Cr steels to be achieved, it is vital that protective coatings are developed, validated under steam environment and applied to components from the steam path (main and re-heat steam pipe, steam chest & valve assemblies, turbine blades). Without these complimetary advances, the problem of excessive oxidation may offset many of the potential economic, environmental and performance benefits that can be achieved. This paper reviews recent work on processing and testing of selected coatings produced within the FPV "Coatings for Supercritical Steam Cycles" (SUPERCOAT) project, led by ALSTOM Power in collaboration with seven European partner organisations (see Figure 2), to develop and demonstrate candidate slurry and thermal spray coatings that offer the capability of providing increased component reliability, extended plant life and increased performance of supercritical steam turbines operating at temperatures in excess of 620°C and up to 300 bar. The work described has demonstrated the feasibility of applying coatings to advanced steel samples and steam turbine plant components, as follows:

- Slurry aluminising (diffused aluminium paint)
- High velocity oxy-fuel (HVOF) deposition of metallic and Cermet powders (Ni20Cr, Cr Carbide Ni/Cr, Fe50Cr, for example)

Long-term steam oxidation rate and failure data have been generated to underpin the design and process work packages needed to establish this technology for new and retrofit power plant.

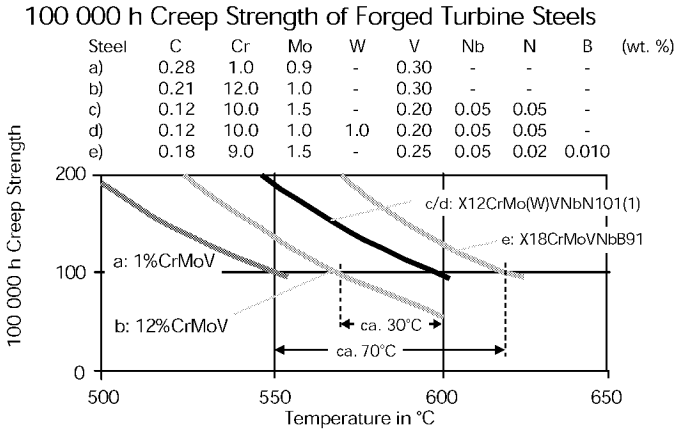

Figure 1. Development in creep strength capability of forged and cast steels (after [4]).

Steam Plant	Output MW_e	Live Steam bar / °C	Reheat Steam °C	Thermal Efficiency %
Skaerbaek	400	290 / 582	580 / 580	49
Nordiylland	400	290 / 582	580 / 580	48
Avedoere	530	300 / 582	600	47
Skopau A,B	450	285 / 545	560	40
Schwarze Pumpe A,B	800	264 / 542	560	40.6
Boxberg Q,R	818	260 / 540	580	41.7
Lippendorf R,S	900	268 / 554	583	42.3
Niederaussem	1050	265 / 576	600	>43
Westfalen (design study)	350	283 / 600	620	>43

Table 1. Summary of European Advanced Steam Power Plant (after [2]).

Project overview

The SUPERCOAT project is aimed at development and implementation of cost effective and environmentally friendly coating technologies for steam power plant. By developing and validating oxidation protective coatings for the high creep strength ferritic steels used in current and future power plant installations the project aims to help facilitate the targeted rise in operating temperature from approximately 550 to 650°C to achieve increased efficiency and reduce operating costs. To achieve these objectives are number of work packages have been undertaken, as summarised in Table 2. As indicated in Figure 2, eight partners from five EC countries have participated and Table 3 summarises the activities and contributions made.

The target components for coating application were identified as the main steam and hot reheat pipe system, steam chest and control valve internals and the high temperature turbine stages. These parts are mainly thick-walled and made of either forged or cast ferritic materials such as P91 or P92. These two alloys have been selected as the main substrate samples and a series of steam oxidation, mechanical property and thermophysical property tests on coated samples have been conducted and the degradation and failure mechanisms characterised and models developed aimed at simulating the breakdown in protective properties of the coatings during high temperature steam exposure. In addition to component demonstration tests and planned field tests with large components, the consortium has been able to take advantage of the KOMET650 programme at KW Westfalen power plant in Hamm, which has two specifically designed by-pass loops incorporated for materials testing purposes. As part of this programme, a number of coated and uncoated SUPERCOAT samples have been tested in live steam at temperatures ranging from 585 to 610°C.

WP 1. Mechanisms	Evaluation of oxidation & corrosion behaviour of uncoated and coated P91 & P92. Develop improved understanding of scale growth and coating degradation.
WP 2. Coatings	Coating application trials (slurry and HVOF) to define optimal process conditions, quality procedures and minimise costs. Pack aluminising, electro less Ni-P and Ni-B, electroplating Cr & Ni and hybrid coatings have also been evaluated.
WP 3. Characterisation	Determination of mechanical and thermophysical properties of coatings (strain to failure, modulus, bond strength, etc.).
WP 4. Laboratory testing	Steam oxidation testing of uncoated and coated P91 and P92 (650°C, ambient and 300 MPa pressure) - isothermal and thermal cycling.
WP 5. Modelling	Prediction of scale formation and coating lifetime. Substrate interdiffusion, analysis of chemistry and stability.
WP 6. Large component coating	Develop methods for coating and testing of steam pipes, chests and turbine parts. Demonstrate feasibility by application to components.
WP 7. Field tests	Selected coatings to be tested on components in a power plant.

Table 2. Summary of SUPERCOAT Work Packages.

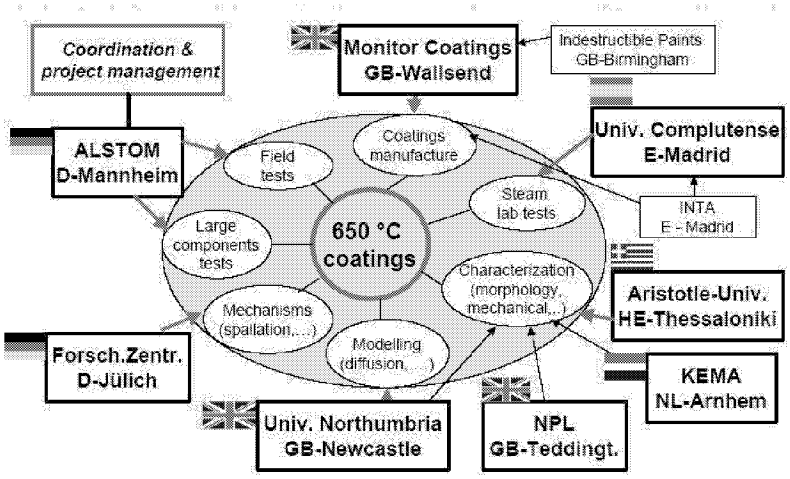

Figure 2. SUPERCOAT consortium (red arrows mark WP-leaders).

Coatings Development

To meet the demanding conditions experienced within an ultra-supercritical steam cycle (oxidation, solid particle erosion, high temperature and pressure cycling), the coating requirements have been summarised as follows:

- Passivation: formation of a protective oxide ceramic layer.
- Impervious to high temperature steam and free of open porosity.
- High resistance to ion-diffusion and high ohmic resistance.
- Coating and its passive layer insoluble in supercritical steam.
- Similar thermal expansion coefficient and superior adhesion to the base material.
- High Erosion-resistance.
- Repairability.
- Lifetime should be at least 50,000 EOHs.
- Resistance against chemical agents used in power plant.

UNN, FZJ, UCM and INTA

The coatings identified consist of thermally sprayed metal powders and Cermets such as chromium carbide, and non-metallic inorganic coatings such as oxide-based overlay or aluminide based diffusion coatings applied using paint or sol-gel slurries. Figure 3 summarises the general scheme for differentiating between different strands of the coating development work plan. Generally, each process aims to provide a barrier to oxygen contacting the steel surface by providing either a physical, stable protective layer that remains largely unreactive with the substrate, or else forms an integral layer diffused into the surface of the steel to provide a reservoir of aluminium for scale formation. Included within the development programme was an evaluation of binders, sealants, repair processes, hybrid coatings (plating & aluminising) and surface modification using borides.

Slurry coatings are suitable for internal and external application to small (e.g. blades) and large components (e.g., steam pipe, casings, valve internals) and can be relatively easily applied to complex shaped objects. HVOF deposition on the other hand, is a line of sight

thermal spray process that is suitable for small and large parts, but application is to some extent limited to external, regularly shaped surfaces. Most other deposition techniques (plating, CVD, PVD etc) are more or less limited to small component coating.

Following an extensive assessment of a number of candidate coatings using ambient and high pressure steam oxidation testing, as well as microstructural and mechanical evaluation, a down-selection of the most promising coatings was possible, as summarised in Table 4. Each of these performed extremely well under steam oxidation and demonstrated satisfactory mechanical integrity and adhesion with the substrate. Figures 4 through to 7 show typical examples of the initial microstructure of each of the down selected coatings listed in Table 4.

Partner	**Business Activity**	**Role in Project**
ALSTOM Power	OEM	**Co-ordinator.** Characterisation and long term testing. Field tests & supply of components. Implementation and exploitation.
Monitor Coatings Ltd	Coatings supplier	**WP2 Leader**. Thermal spray & slurry coating supplier, development of coating processes & repair procedures.
National Physical Laboratory (NPL)	RTO	Determination of properties and adhesion. Modelling of spallation and diffusion. Long term tests under steam.
Aristotle Univ. of Thessaloniki	University	**WP3 Leader.** Microstructural investigations, adhesion testing. Investigations into hybrid (duplex) coatings and boride coatings.
Univ. Complutense Madrid (UCM)	University	**WP4 Leader.** Determination of coating properties & mechanisms of oxide formation. Life models, scale fracture & surface modification.
FZ Jülich (FZJ)	RTO	**WP1 Leader.** Long term testing under steam, diffusion and thermodynamic modelling, characterisation, spallation mechanisms.
Northumbria University (UNN)	University	**WP5 Leader.** Microstructural modelling, interdiffusion & thermodynamics, characterisation (SEM, EDX), FEA.
KEMA	RTO	Test facilities & laboratories, NDT and creep.
Indestructible Paints Ltd.	Sub-contractor	Subcontract to Monitor Coatings for slurry coatings & sealants.
INTA	Sub-contractor	Supplier of slurry and HVOF coatings. Development of coatings, testing and characterisation.

Table 3. SUPERCOAT Consortium overview.

Number	**Coating Type**	**Coating Name**	**Composition**
1	Slurry Aluminide	IPCOAT 9183	H3PP4, Cr_2O_3, Al, Phosphate binder
2	HVOF	Ni20Cr Powder	Cr min 20%, Ni(bal).
3	HVOF	Fe50Cr Powder	Cr min 50%, Fe(bal).
4	Pack Aluminide (PA)	Low Temp. PA	Al
5	Hybrid	ElCr PA	Cr, Al

Table 4. Summary of down-selected coatings for SUPERCOAT.

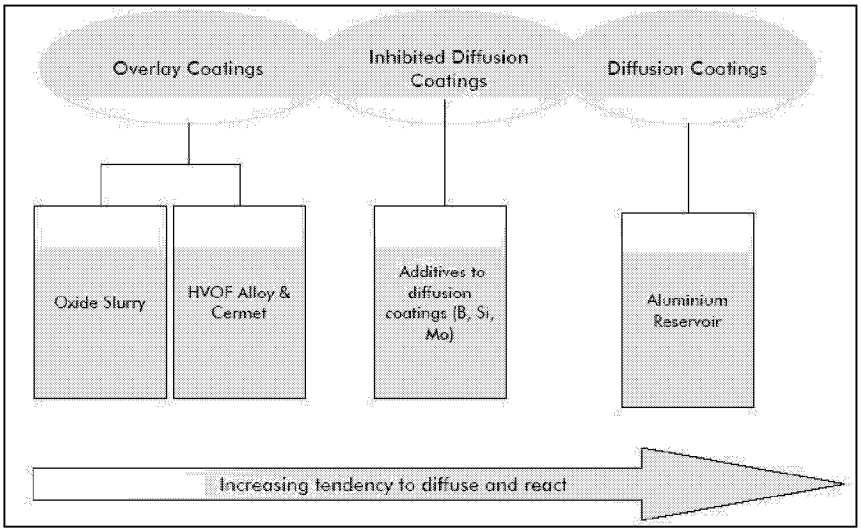

Figure 3. Classification of SUPERCOAT Coating systems

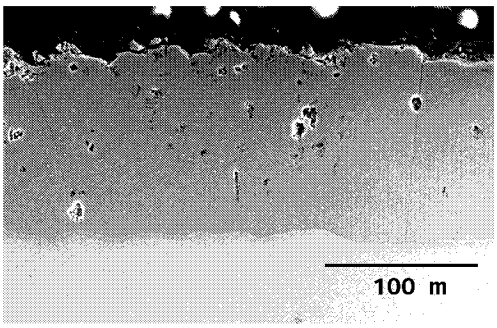

Figure 4. Diffused aluminide coating on P92 substrate.

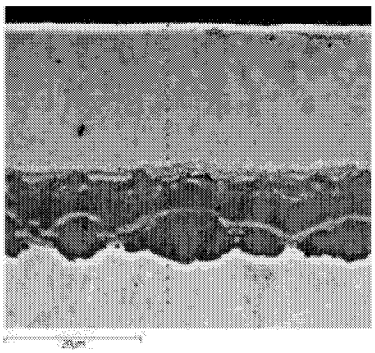

Figure 5. Hybrid aluminide coating on P92 substrate.

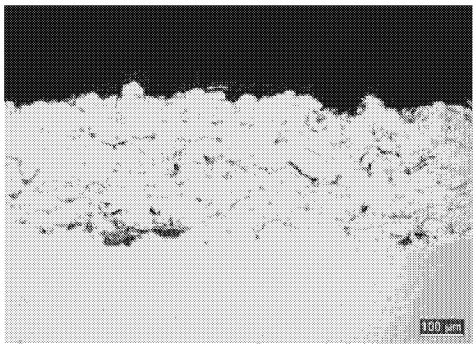

Figure 6. HVOF Ni20Cr coating on P92 substrate.

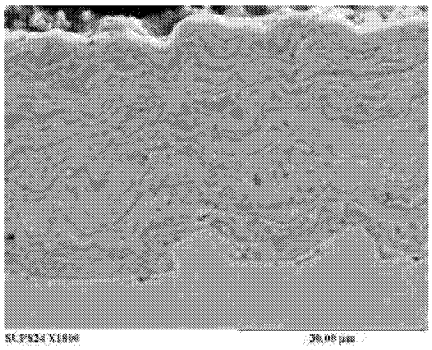

Figure 7. HVOF Fe50Cr coating on P92 substrate.

Concentration of effort on a limited number of candidates has enabled further developments and the application processes to be tailored to the needs of particular components identified by the manufacturer and suppliers. New slurry formulations have also been developed that include metallic powder and boron additions, as well as silicate-free and chromium-free binders. New HVOF coatings have also been evaluated based on FeAl, FeCr, FeCrAl and NiAl. Each has shown good processability and applied successfully to P91 coupons and have performed well under ambient steam oxidation testing. Additional slurry based coatings have also been prepared, such as overlay modified slurry aluminides, B modified diffusion aluminides and electroless Ni-diffusion aluminides. Surface preparation and heat treatment cycles (drying, curing, diffusion treatment) for application of these coatings have been developed and the method of manufacture specified for the requisite quality documentation.

Steam Oxidation, Mechanical Testing and Characterisation

The main thrust of the experimental programme has centred on manufacture of a significant number of uncoated and coated P91 and P92 coupons for steam oxidation testing using gravimetric weight change analysis following incremental long term exposure under ambient and high pressure steam. In addition, samples for thermophysical property measurements (elastic modulus, thermal expansion coefficient, thermal diffusivity), strain to failure, ductile to brittle transition temperature and interfacial bond strength and residual stress measurements have been tested and the data compiled and applied within the modelling work packages. Both pre- and post-test exposure tests have been performed to assess the influence of thermal and steam exposure on coating durability and properties. Publications describing some of these activities can be found elsewhere [5 – 7].

Another main objective has been to evaluate the pre- and post-exposure characteristics and effectiveness of the coatings using optical and electron microscopy (EDX and WDX), NDT (eddy current) and X-Ray diffraction and establish quality control procedures for manufacture and assessment of the coatings produced (thickness, uniformity, morphology, porosity, adhesion and composition). Post-exposure examination has established the protection & degradation mechanisms (element redistribution, scale growth & thickness, porosity, spallation, etc), the nature of the corrosion products and amount of metal loss suffered following steam exposure. Mass spectrometry has been used to study in-situ the role of volatile species in the oxidation of P91 and P92 steels and coatings at 650°C at 1 bar pressure under a range of Ar-H_2O vapour mixtures (10 – 80% H_2O) in conjunction with gravimetric analyses of the kinetics of oxidation behaviour [8].

Steam Oxidation Testing

Steam oxidation testing has formed the basis for the down selection of the coatings produced. The objectives were to define the test parameters such as temperature, gas composition, flow rate, length of exposure, etc., as summarised in Table 5, and conduct rig testing under flowing steam at atmospheric and high pressures. Test conditions were selected to simulate those encountered in actual power plants and were based on prior laboratory test results [9]. Coating performance was determined by weight variation as a function of time and by microscopical analysis of exposed samples. Uncoated P92 and X20CrMoV11-1 steel coupons were tested by each of the partners as a means of benchmarking results generated by different test laboratories (ALSTOM, UNN, FZJ, UCM and INTA). Furthermore, thermal cycling tests have been performed by Aristotle University, Thessaloniki.

Temperature	650°C (long term tests >10,000 hrs) 800°C (accelerated tests up to 3,000 hrs)
Steam Composition	50% Ar, H_2O, de-oxygenated 100% H_2O, de-oxygenated
Flow Rate (ml/min)	1.7, 15.0, 33.3
Pressure	1 bar (long term tests >10,000 hrs) 300 bar (short term tests – 1,500 hrs)

Table 5. Summary of Supercritical Steam Oxidation test conditions

Figure 8 shows the rig set up used for testing in pure, superheated steam at ambient pressure, typically at flow velocities between 150 and 300 ml/h. De-ionised water was de-oxygenated to < 20 ppb by continuous bubbling of nitrogen through the reservoir. During a test run, a series of weight change measurements were taken and when a test was terminated the exposed samples were sectioned for metallographic analysis. Figure 9 summarises the mass change curves obtained for uncoated P91 and P92 tested at 650°C, 1 bar supercritical steam with test results out to >10,000 hrs. The test results for P92 show good reproducibility, but also an accelerated oxidation rate compared with that for P91 as expected from previous results [10]. Figure 10a shows a typical example of a microsection through uncoated P92 after 2,300 hrs exposure to 1 bar supercritical steam at 650°C. A thick, multilayer oxide scale has developed on the surface of the steel that shows irregular internal features between the outer magnetite (Fe_3O_4) and inner Fe, Cr spinel layers and the development of sub-surface porosity adjacent to the steel. The overall thickness of the oxide scale is approximately 170 µm with significant depth of penetration into the steel.

In addition to the ambient pressure tests, a series of high-pressure steam oxidation tests have been carried out at 650°C and 300 bar pressure on behalf of the consortium by TU Darmstadt. The once-through design test facility is shown schematically in Figure 11. As for the ambient pressure tests, mass change measurements and metallographic characterisation have been conducted as a means of tracking the oxidation behaviour of the uncoated and coated P92 samples. In addition, a number of uncoated substrate samples have been tested for comparison (X20CrMoV11-1, Alloy 122, AISI 316 Ti, Inconel 625). The compositions are given in Table 6.

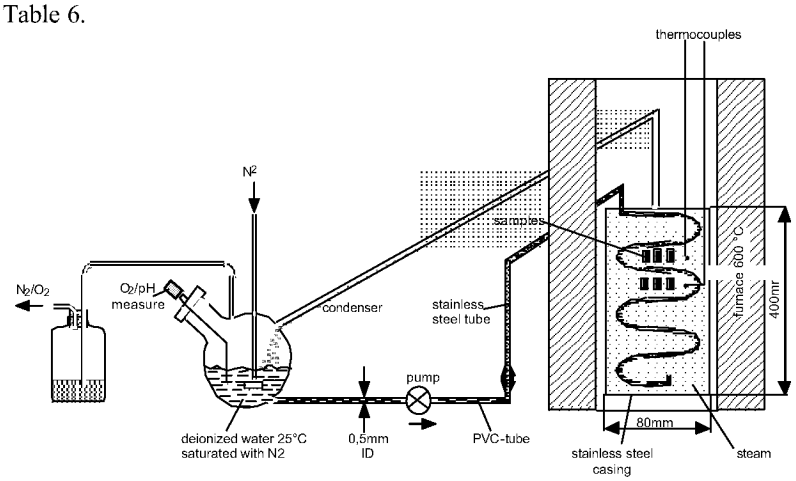

Figure 8. Schematic illustration of the atmospheric pressure, superheated steam test facility.

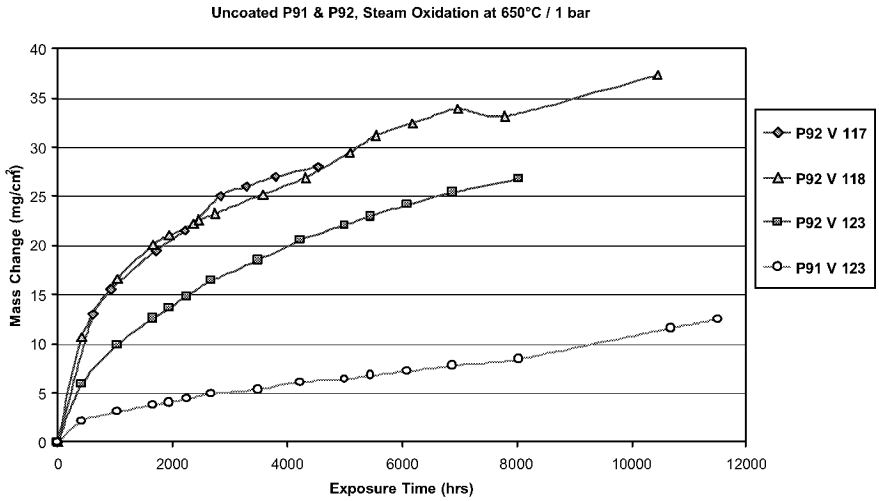

Figure 9. Mass change curves of uncoated P91 and P92 samples exposed to superheated steam at 1 bar, 650°C.

In most cases weight change measurements were found to be reasonably reproducible and in-line with expectations for the uncoated samples. Figure 12 shows the mass change test results for the uncoated samples exposed to 300 bar pressure steam at 650°C for test durations out to 1,500 hrs. These data show a consistent trend in terms of the effect of composition on oxidation resistance, ie., increased Cr content of the steel generally reduces the oxidation rate and the data show the clear advantage of austenitic stainless steels and nickel alloys under these environments (AISI 316 Ti & Inconel 625). These data also demonstrate the significant difference in oxidation resistance between P91 and P92.

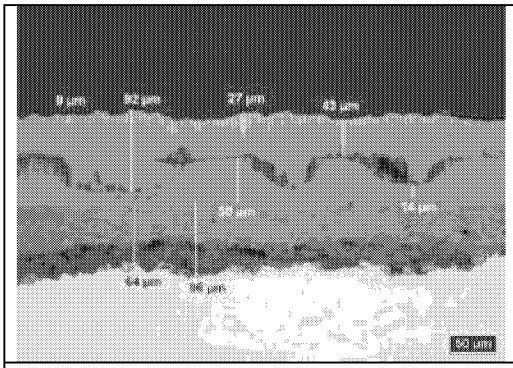

Figure 10a.Cross section through a P92 sample after 2,300 hours exposure to superheated steam at 1bar, 650°C.

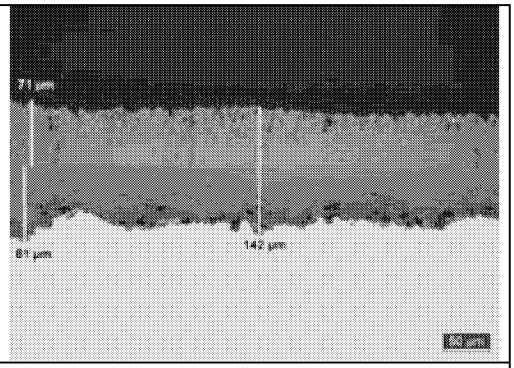

Figure 10b. Cross-section through P92 sample after 1,500 hrs exposure to HP steam at 300 bar, 650°C.

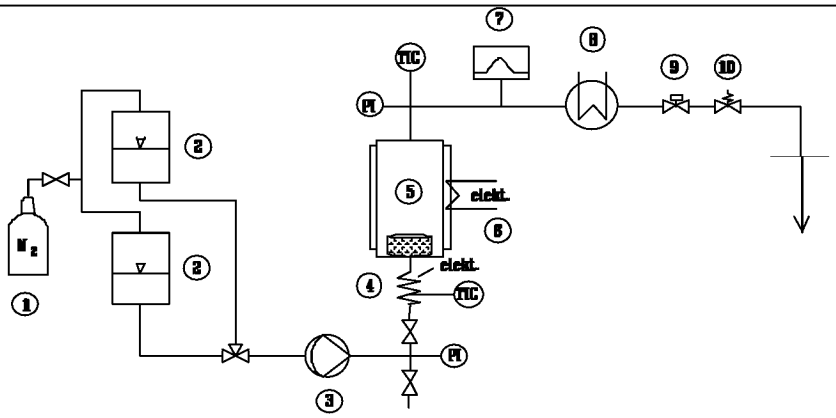

#	Item	Type / Manufacturer
1	Nitrogen	Linde, Specification 4.0
2	Feed water tank	Volume 16 litres
3	HP membrane pump	Orlita Mh/15/5, max. flow 30 g min^{-1}
4	Preheater	Time, ¼"-tube (Inconel 625®), toroidal transformer 3000 VA, 2 x 4 V
5	Autoclave	Self-made TU Darmstadt, Volume 250 ml, Inconel 625®
6	Trace heater	Philips, NiCr 80/20, heat length 600 cm, resistance 3,1 Ω
7	Burst disc	HIP, Linden Ave Erie PA, ¼" (8412 psi)
8	Heat exchanger	Self-made, ¼", Tube length 2 m
9	Control valve	HIP, Linden Ave Erie PA, ¼"
10	Overflow valve	Riegler, 1/8" (red spring, 35 MPa)

Figure 11. High pressure steam oxidation test facility at TU Darmstadt for tests in supercritical steam.

Figure 10b shows a typical microsection through a P92 coupon following 1500 hrs exposure to 300 bar pressure steam at 650°C. The overall coating thickness is approximately 140 µm and shows a more regular internal structure to that seen at ambient pressure (see Figure 10a), though clearly a significant level of metal depth has been oxidised (inner and outer oxide scales are 81 and 71 µm respectively). An outer magnetite scale (Fe_3O_4) and an inner Cr-Fe-spinel have formed and the interface between the two scales remains unchanged during oxide growth. The magnetite grows by iron ions migrating through the two scales and taking-up oxygen from the steam. The spinel grows at the interface to the alloy by taking-up oxygen which migrates through the two scales [11].

Comparison of the ambient and high pressure test results for uncoated and coated samples revealed that for most of the coatings and base materials, the 1 bar test results provide a representative measure of the steam oxidation behaviour at higher pressures and can, therefore, be used for determining the oxidation behaviour and for general selection of candidate coatings. The weight gain curves for P92 at atmospheric pressure are very similar to those derived from high pressure testing (see Figures 9 and 12). A key result, however, was that certain silica-based coatings that performed adequately under ambient pressure steam

were unsuitable for steam turbine plant due to the solubility of SiO_2, which led to the rapid degradation of these coatings under HP steam.

Alloy	Fe	Ni	Cr	W	Mo	Nb	C	Mn	Si	V	B	Others
X20CrMoV11-1	Bal.	0.5*	11.5	2	0.45	0.07	0.1		0.5*	0.25	0.005*	0.04*Al, 0.02*P, 0.01*S
P91	Bal.	0.4	9	-	0.95	0.08	0.1	0.45	0.5*	0.2		0.04*Al, 0.02*P, 0.01*S
P92	Bal.	0.4*	9	1.75	0.45	0.065	0.1	0.45	0.5*	0.2	0.004	0.04*Al, 0.02*P, 0.01*S
Alloy122	Bal.	0.31	11.1	1.94	0.35	0.054	0.12	0.68	0.2	0.22	0.002	1.0Cu, 0.011Co, 0.005Al, 0.01*P, 0.007*S
AISI 316 Ti	Bal.	11	18.	-	2.0		0.1*	<2.0				Ti = 5x%C
Inconel 625	5.0*	58	22		9	3.65#	0.1	0.50 *	0.5*			1.0*Co, 0.4*Ti. 0.4*Al, 0.015*P, 0.015*S

Table 6. Summary of compositions (mid-range for specification) of substrate steel and nickel samples tested under HP steam (* = max. # = plus Ta).

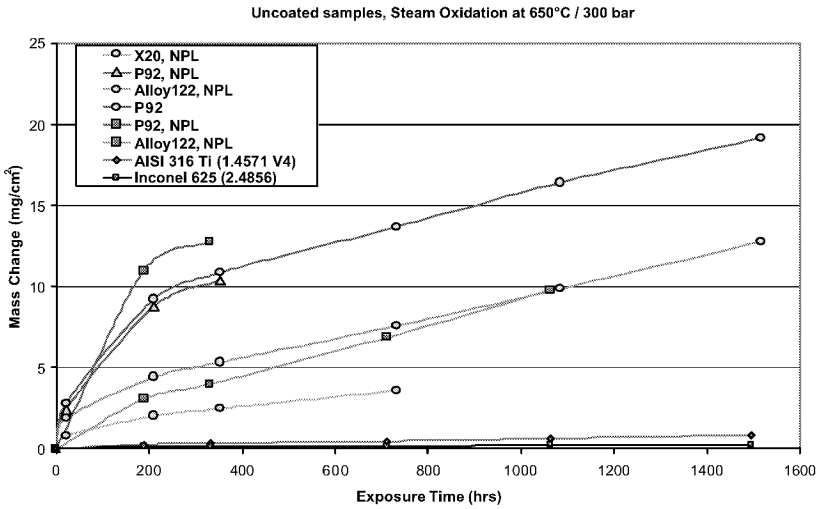

Figure 12. Mass change curves of uncoated substrates, exposed to supercritical steam at 300 bar, 650°C.

Steam oxidation weight change data for aluminised (diffused coating) and HVOF coated P92 samples are shown in Figure 13. In both cases, a significant reduction in oxidation rate is seen compared with uncoated P92, in particular for the diffused aluminide and HVOF Ni20Cr samples.

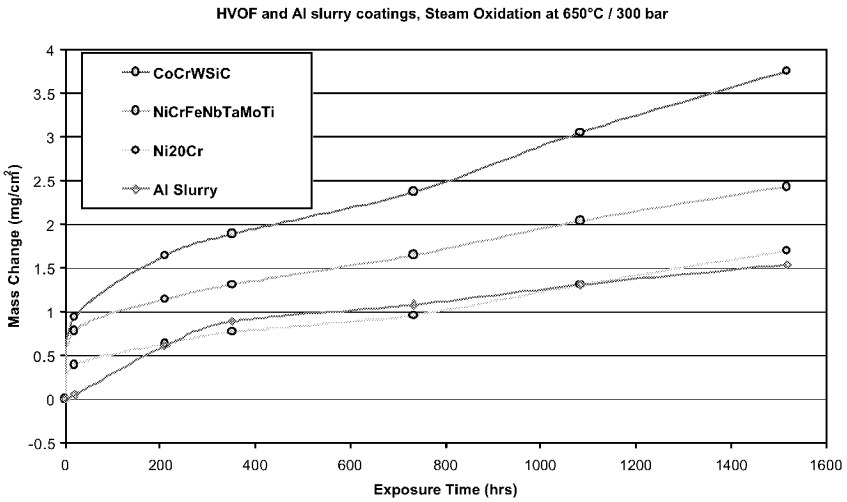

Figure 13. Mass change curves for HVOF and aluminium slurry coated P92 coupons, exposed to supercritical steam at 300 bar, 650°C.

The data for diffused aluminide coatings have been substantiated by long term results, provided by INTA from COST522, on the behaviour of slurry aluminides under ambient pressure steam at 650°C and indicate that these coatings offer the potential for long-term protection. The data for a slurry aluminide are compared with those for uncoated P92 in Figure 14a (coated sample test results out beyond 35,000 hrs) and a significant difference in oxidation behaviour is observed. Figure 14b shows a microsection through a typical diffused aluminide coated sample after 20,000 hours of exposure. By comparison with Figure 4, the coating can be seen to have developed a band of interfacial porosity (Kirkendal interdiffusion between Fe and Al), but has remained intact to form an effective barrier to oxidation of the steel. A secondary reaction zone is also evident immediately below the coating that shows evidence of coarse AlN precipitates, which may indicate the presence of a weakened zone beneath the coating surface (reduced nitride strengthening of the steel). The impact of sub-surface depletion of alloy constituents due to oxidation on the mechanical properties of these steels has been reported previously [12]. Microhardness measurements taken within the current programme do not seem to show a reduction in hardness of the steel after 20,000 hrs exposure, but do indicate a softening of the aluminide coating itself as the level of aluminium in the coating is depleted due to external oxidation and internal diffusion to the steel.

Impact Fatigue Testing of Coated P92

Impact fatigue testing has been conducted at room temperature as a means of evaluating the fatigue strength of the coatings produced within the programme [13 - 16]. Using this method, the surface of the coated specimen is cyclically loaded by repetitive impacts applied using a hard ball indenter until coating failure occurs. The Hertzian pressure field developed induces a complex stress field both within the coating and at the interface with the substrate that induces distinct failure modes either within the coating or at the interface and generates fatigue crack initiation and growth within the coating. The impact testing facility is shown in Figure 15 and Figure 16 illustrates the form of the indent impression and the means by which typical indents are analysed as the number of impact cycles accumulates. The impact crater is examined using

an SEM for microcracking and the constituent elements of the coating and substrate are identified using EDX analysis.

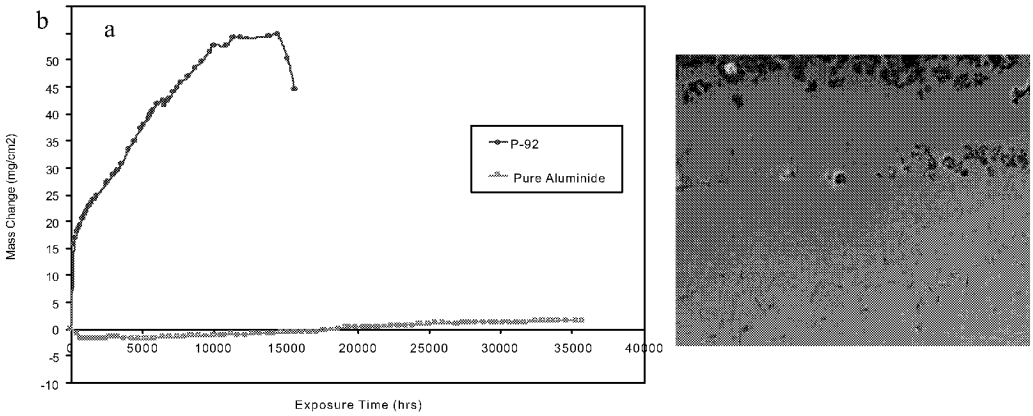

Figure 14. a) Mass change curves for uncoated and slurry aluminide coated P92 coupons exposed to ambient pressure steam at 650°C. b) Diffused aluminide coating after 20,000 hours exposure to ambient pressure steam at 650°C.

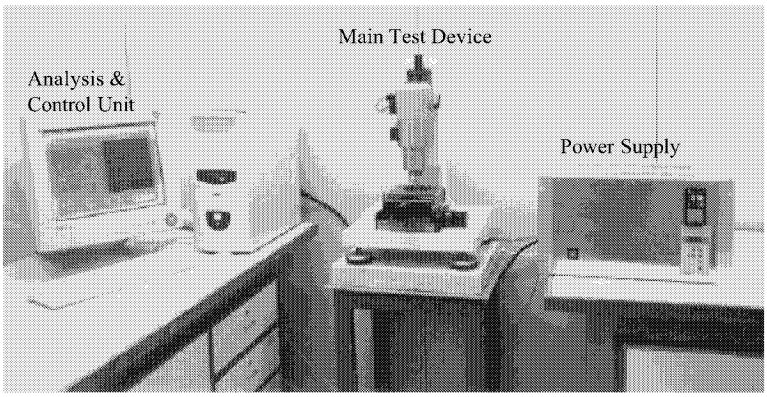

Figure 15. Impact testing system.

Figure 17 shows the fatigue endurance curves (impact load vs. cycles to failure) generated for a number of coatings tested at room temperature using the impact fatigue test method. Under these loading conditions the HVOF sprayed coating WC-CoCr shows superior fatigue threshold and strength to both the Ni20Cr, CrC-Ni25Cr and diffused aluminide coatings (SUP86, SCOAT & SUP76). The slurry overlay type coatings (MB1, MAC1-C and MX1) show an intermediate fatigue threshold level. The pack aluminised coating SCOAT was found to have the lowest fatigue endurance of the coatings tested.

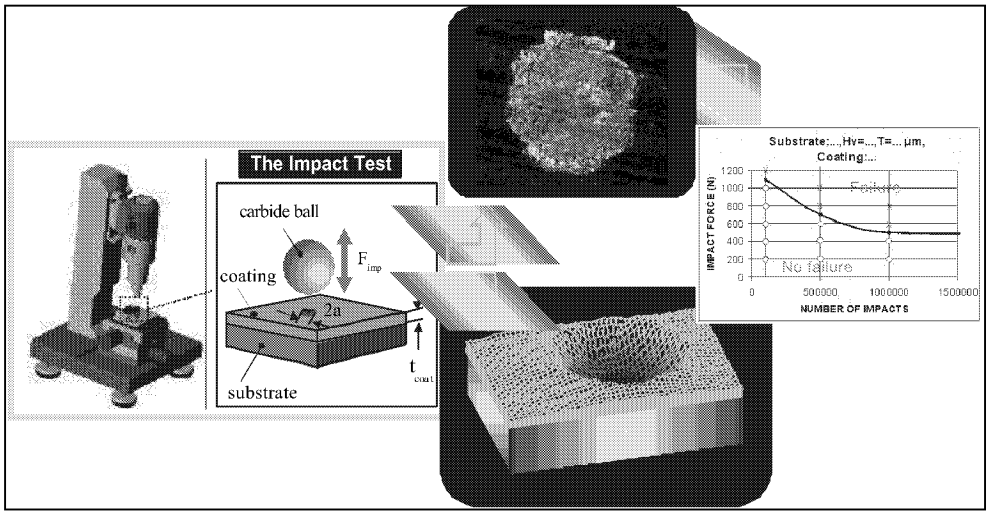

Figure 16. Schematic illustration of impact fatigue endurance and failure mode determination.

Mechanisms and Characterisation

The objectives for this work package were to develop an improved understanding of the mechanisms of scale formation and growth, oxidation protection and the processes responsible for degradation during high temperature exposure. The influence of thermal exposure and cycling on the scale formation and degradation mechanisms such as spallation and breakdown of protective oxide layers have been investigated, as well as interdiffusion of coating and substrate alloying constituents, solution of coating material in supercritical steam (hydrothermal processes, e.g. in the case of silicates) and phase change processes. The most important degradation mechanism in the case of aluminide forming coatings is diffusion of Al into the substrate material, though for some protective layers volatility is a critical issue as the solution of the coating material by supercritical steam was observed, which has been shown to be heavily dependant on the pressure.

Figure 18 shows a typical examination conducted on an HVOF Ni20Cr coating applied to P92 and examined using optical and electron microscopic and EDX analysis techniques. A thin, external chromia scale was found on the coating surface that formed an adherent and stable protective film. Alumina particles were also found at the metal/coating interface, which also showed evidence of a non-continuous chromia layer. Some evidence of Cr-rich particles was also evident as indicated. No evidence of cracking within the coating or along the interface was found and these coatings were seen to provide a stable, protective barrier to the ingress of steam to the steel surface. As a footnote to the experimental measurements made on small coupons, it is evident that the majority of the weight gain measured for the HVOF Ni20Cr samples was due to oxidation of the steel at or around the support hole drilled into the samples, which are difficult to coat using HVOF processes.

Modelling

The objectives for the SUPERCOAT modelling work package are to develop models based on the experimental observations to predict scale formation, scale growth, interdiffusion, phase stability (thermodynamic and kinetic), scale deformation and fracture and enable better

design choices to be made in the development of high performance coatings for protection against steam oxidation. A number of modelling tools have been applied, including DICTRA and Darken (diffusion modelling) and ThermoCalc (thermodynamic phase equilibria calculations) in simulating the phase stability and interdiffusion of the coating layers with the substrate steels. FE calculations of the thermal stresses generated within the protective scale and underlying coating layer have been performed using ABAQUS. This work has not been reported in detail in the present paper, but will be presented at a later date.

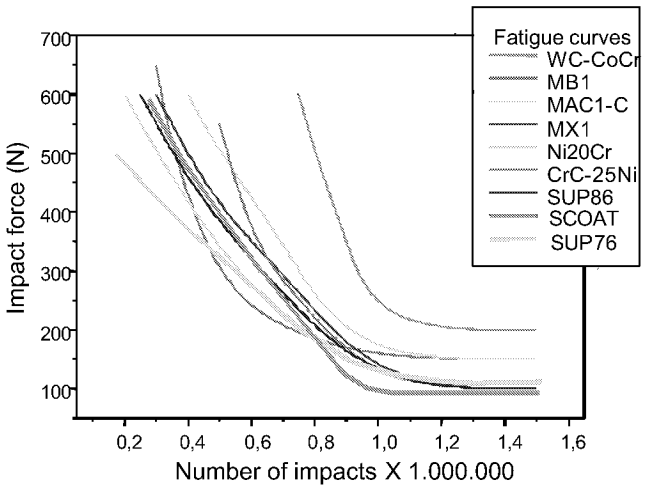

Figure 17. Impact fatigue endurance curves for HVOF and slurry aluminide coated P92 at room temperature.

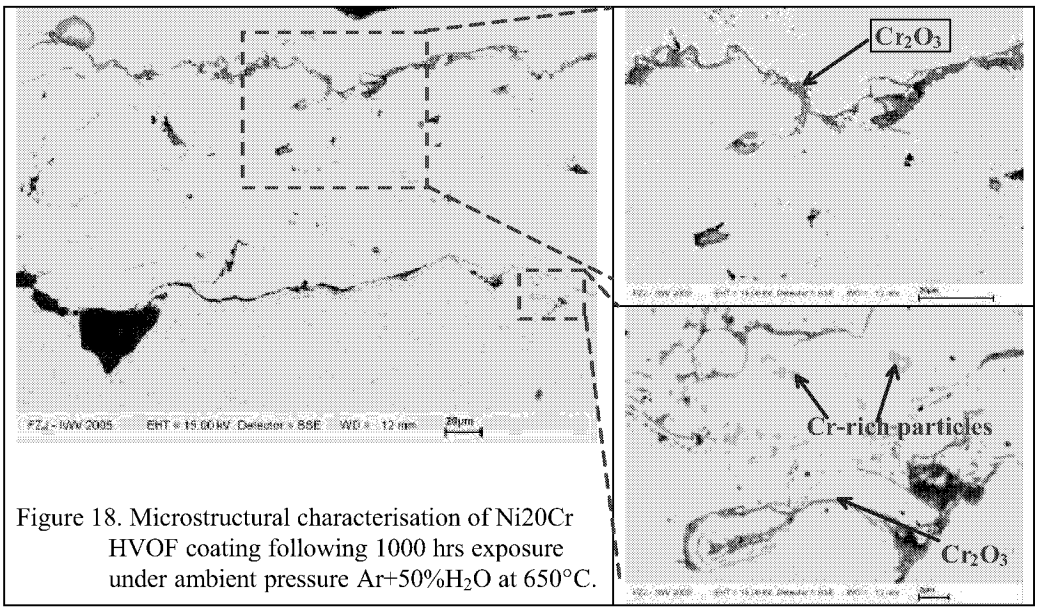

Figure 18. Microstructural characterisation of Ni20Cr HVOF coating following 1000 hrs exposure under ambient pressure Ar+50%H_2O at 650°C.

Component coating trials

The objectives for these trials are to establish the method of manufacture and industrialise the process suitable for steam power plant components. Further optimisation will follow industrial assessments (surface preparation, composition and processes) and establish quality procedures for coating large components. A number of actual and sub-scale components have been coated as a means of demonstrating the feasibility of oxidation protective coatings for steam turbine power generation plant. To date, several steam turbine blades have been coated using pack aluminising, slurry aluminising and HVOF deposition of Ni20Cr, Cr Carbide Ni/Cr and Fe50Cr powders. Figure 19 shows a typical example of a coated turbine blade following surface tumbling treatment and examples of the microsections taken through the leading edge section of the blade. A large section of 400 mm diameter P92 steam pipe has been coated (aluminised inner surface) and is presently being evaluated by means of NDT, sectioning and weldability trials. In addition, a number of small-scale tubes have been coated (aluminised inner walls and HVOF Ni20Cr or Fe50Cr applied to the outer surfaces) for field testing as part of the KOMET650 programme in the power plant KW Westfalen in Hamm.

Field trials

Field tests were conducted to validate the laboratory test results using small test specimens (KOMET650 stub samples as shown in Figure 20), as well as larger components to enable further assessment and optimisation of the coatings to be achieved. The field tests within the KOMET project are carried out in two test bypass tubes at different pressures and temperatures. Conditions in the high temperature bypass are on average 630°C, 180 bar and in the "low temperature" bypass 595°C, 96 bar. Coated samples (HVOF and slurry based) have been tested at KW Westfalen and removed periodically for inspection over the last two years. The exposure started in August 2003, however, due to plant shut-down the exposure periods have been subject to interruption. This work is continuing with results expected for late 2006.

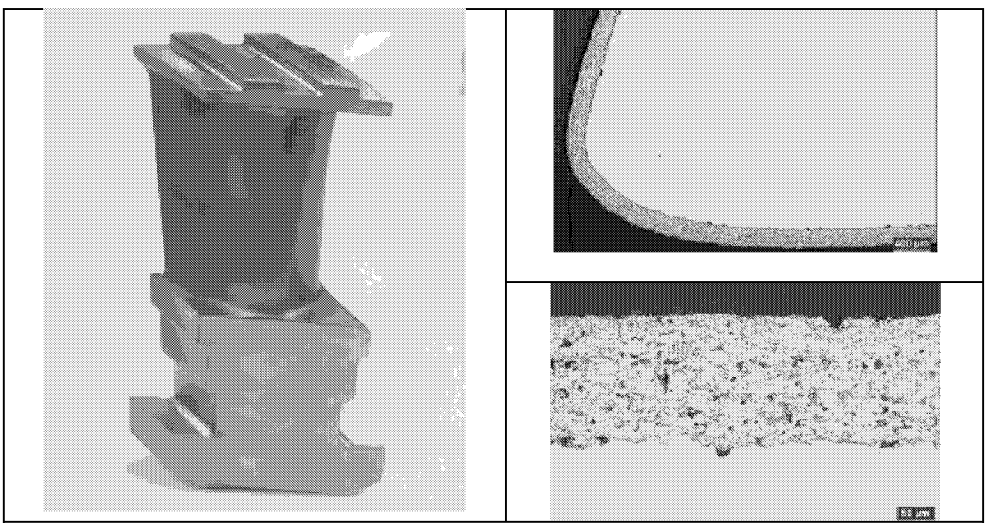

Figure 19. Typical example of HVOF Cr Carbide Ni/Cr coated steam turbine blade.

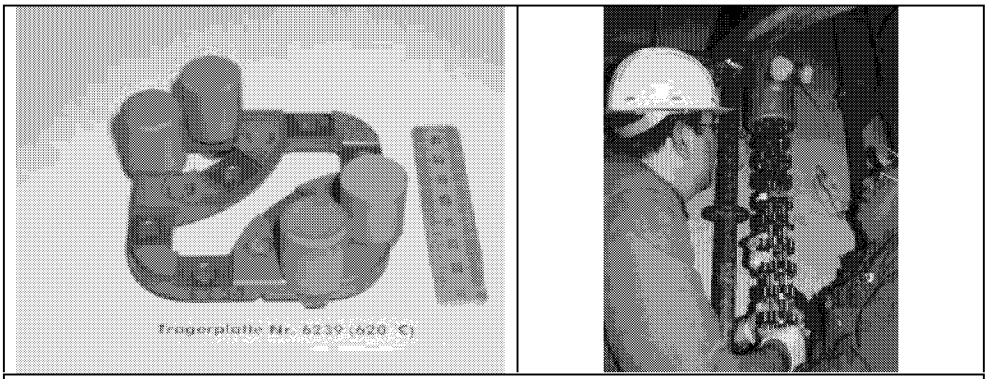

Figure 20.KOMET650 test stubs and carrier (left) prior to assembly and insertion in by-pass loop (right).

Conclusions

1. A brief review of the Framework V project SUPERCOAT has been provided.
2. A significant number of uncoated and coated P91 and P92 samples have been prepared and tested under ambient and high pressure steam oxidising conditions at 650°C. Diffused and pack aluminide coatings and HVOF Cermet and metallic powder coatings have all shown promising results in providing reduced steam oxidation rates
3. A range of mechanical and thermophysical property tests have been conducted on coated samples. These data have been used to down select the most promising candidates for further development and industrialisation studies.
4. An in-depth study of oxide scale formation and coating degradation and failure mechanisms has been conducted by means of mechanical testing and optical and electron microscopy. These analyses have been used to inform coating selection and the development of models for prediction of coating degradation and spallation. Mechanisms of protection and degradation have been identified.
5. Coating process industrialisation and validation continues with application of diffused and pack aluminised and HVOF coatings to components (turbine blades, steam pipe) and field test specimens (test stubs, tubes). Metallographic inspection and characterisation have been used to inform development of quality standards and improved processes.

Acknowledgments

The authors are grateful to the SUPERCOAT project partners for their invaluable efforts during the course of the programme and the kind permission of ALSTOM Power to publish this work. SUPERCOAT is a RTD project, funded by the European Community under the "ENERGY" (EESD) Programme (1998-2002). We express our gratitude to the E.U. for financing this work through Contract No: ENK5-CT-2002-00608.

References

1. N. Otter et al., "A Vision for Clean Fossil Power Generation – Recommendations for a UK Carbon Abatement Programme." UK Advanced Power Generation Technology Forum, May 2004.

2. M. Staubli, B. Scarlin, K. H. Mayer, T.U. Kern, W. Bendick, P. Morris, A. DiGianfrancesco and H. Cerjak, "Materials for Advanced Steam Power Plants: The European COST522 Action." Proc. 6th Int. Charles Parsons Turbine Conf., September 2003, pp. 305 – 324.
3. W.J. Quaddakers and P.J. Ennis, "The Oxidation Behaviour of Ferritic and Austenitic Steels in Simulated Power Plant Service Environments." Proc. 6th Liège Conf., on Materials for Advanced Power Engineering, September 1998, p. 123.
4. "Review of Status of Advanced Materials for Power Generation." Technology Status Report 018, DTI Cleaner Coal Technology Programme, May 2002.
5. A. Aguero, R. Muelas, A Pastor and S. Osgerby, "Long Exposure Steam Oxidation Testing and Mechanical Properties of Slurry Aluminide Coatings for Steam Turbine Components." Surface & Coatings Technology, submitted for publication, 2005.
6. A. Agüero, M. Gutiérrez and R. Muelas, "Steam Oxidation Testing of Coatings For Next Generation Steam Power Plants Components." Proc. International Symposium on High-temperature Oxidation and Corrosion, Nara, Japan, December 2005.
7. A. Agüero, R. Muelas, M. Gutiérrez, R. Van Vulpen, S. Osgerby and L. Brown, "Cyclic Oxidation and Mechanical Behaviour of Slurry Aluminide Coatings for Steam Turbine Components." Proc. TMS Annual Symposium: Effects of Water Vapor on High-Temperature Oxidation and Mechanical Behavior of Metallic and Ceramic Materials, San Antonio TX. March 2006.
8. F. J. Pérez and S. I. Casteñeda, "New Materials Design for Supercritical Steam Turbines: Study by Means of the Mass Spectrometry of Volatile Species in the Oxidation of Cr, Cr_2O_3, Al, Al_2O_3, Si, SiO_2, Fe and Ferritic/ Martensitic Steel Samples at 923K in Ar+(10 to 80%) H_20." Submitted to Journal of Oxidation of Metals, 2005.
9. R. Knödler and P.J. Ennis, Proc. Conf. BALTICA V, Porvoo, June 2001, pp. 355-364
10. A. Agüero, R. Muelas, B. Scarlin and R. Knödler, "Coatings for Steam Power Plants under Advanced Conditions." Proc. 7th Liège Conf., on Materials for Advanced Power Engineering, September 2002, pp. 1143 - 1158.
11. R. Knödler and S. Straub, "Influence of surface treatment on the oxidation kinetics of advanced steels in flowing steam at 650°C." Proc. 8th Liège Conf., on Materials for Advanced Power Engineering, September 2006.
12. L. Nieto Hierro, V. Rohr, P. J. Ennis, M. Schutze and W.J. Quadakkers, "Steam Oxidation and its Potential Effects on the Creep Strength of Power Station Materials." Materials and Corrosion, Volume 56, Issue 12, December 2005, pp. 890 – 896.
13. A.A. Voevodin, R. Bantle, A. Matthews, "Dynamic Impact Wear of TiCxNy and Ti-DLC Composite Coatings." Wear, 185 (1995), pp. 151-157.
14. R. Bantle, A. Matthews, "Investigation Into The Impact Wear Behaviour of Ceramic Coatings." Surface and Coatings Technology, 74-75 (1995), pp. 857-868.
15. W. Heinke, A. Leyland, A. Matthews, G. Berg, C. Friedrich, E. Broszeit, "Evaluation of PVD Nitride Coatings, Using Impact, Scratch And Rockwell-C Adhesion Tests." Thin Solid Films, 270 (1995), pp. 431-438.
16. H. Ziegele, C. Rebholz, A.A. Voevodin, A. Leyland, S. L. Rohde, A. Matthews, "Studies of the Tribological And Mechanical Properties of Laminated CrC-SiC Coatings Produced by r.f. and d.c. Sputtering." Tribology International, Vol. 30, No. 12 (1997), pp. 845-856.

IMPROVEMENT OF OXIDATION RESISTANCE OF TUBES BY PULSED SILICONISING

K. Maile, K. Berreth, A. Lyutovich

Material Testing Institute (MPA), University of Stuttgart,
Pfaffenwaldring 32, D-70569 Stuttgart, Germany
Karl.Maile@mpa.uni-stuttgart.de

ABSTRACT

Tubes for boilers of new conventional power plants with increased steam parameters (T > 600°C) show water-side oxidation. Experimental work was performed to produce and investigate siliconised inner surfaces to improve the oxidation resistance of tubes made of 9-11%Cr-steels. The siliconising process of the internal surface of steel tube specimen represents a combination of standard heat treatment with a CVD coating technology. The coating process works under H_2 atmosphere with pulsed chemical vapour deposition of Si from $SiCl_4$ precursor. The pulsed CVD mode of operation promotes dechlorination, the transition from gas to solid phase, diffusion of Si into the inner surface of the tube and the formation of new phases as Fe-Si, Si-Cr. This new ferritic layer exhibits a Si content of about 5%. The number and duration of cycles influences the thickness of the Si-diffusion layer. A layer thickness up to 200 µm has been achieved. Aging tests in steam with cycling temperatures have been performed. Microstructural investigations by SEM with EDS, EPMA and X-ray diffraction show that oxidation is reduced due to the formation of Cr-oxide and silicides at the surface. Since the new layer is a ductile coherent part of the tube a negative influence on the workability, e.g. bending, could not be assumed. Ongoing creep tests with siliconised specimens also demonstrate that the creep strength is within the scatterband of the base metal.

Keywords: siliconising, steel tubes, CVD, oxidation resistance

Introduction

Ultrasupercritical boilers being considered for future high efficiency fossile fired power plants will require the utilization of advanced steels and alloys with improved creep strength. However, environmental resistance, i. e. internal steam oxidation will be the factor limiting the application of materials with decreased Cr-content. In those cases, the operating range of such 9%Cr-steels can be significantly extended by use of surface modification techniques. Surface modification methods are under review as a way to mitigate alloy degradation and permit the use of less expensive alloy composition.

The requirements for technical application of a surface modification technique could be summarized as follows:

- Sustainable increase of oxidation resistance
- Low costs (no special preparation/cleaning of the tubes)
- No impact on environment using toxic elements
- Applicability to long tubes
- No negative impact on workability (e. g. welding, bending)
- No negative impact on creep strength
- No stripping/debonding of the coating or hard particles e. g. due to erosion, or cyclic thermal loading

Improvement of steam oxidation performance by diffusion coating appears technically feasible, it fulfils the above mentioned requirements and seems to be the best identified option at this time [1].

To fulfil these requirements siliconising is of major technical interest. It is known that silicon promotes the formation of a protective layer with favourable oxidation resistance. The process can be described as follows:

- formation of silicon films
- formation of siliconoxide films
- increased Cr diffusion from the bulk to the surface
- formation of phases as α-Fe, SiO_2, Cr_2O_3, Fe_xSi_y $MoSi_2$, WSi_2
- passivation of the surface by oxidation
- surface diffusion

Recent research results suggest that in martensitic steels the addendum of 0.3 Si together with 11%Cr improve steam oxidation resistance [2].

In [3, 4] it is mentioned that silicon seems to retard breakaway in the presence of water vapour, and that Si may facilitate Cr-rediffusion from the bulk which helps to repassivate the surface after breakaway. In consequence the level of Cr in the alloy of the structure material can be kept lower than for Si-free steels. Since the corrosion resistance is just needed in the near surface area, the structure material can be used as Cr-reservoir. At least not a continuous silica layer is the reason for the improved oxidation behaviour, but the thickness and the difference in the electrical potential of the transition zone.

The positive effect of silicon seems to become stable at values above 0.5% of Si. A possible reason for the influence of silicon seems to be that silicon enhances the diffusion of Cr in the metal matrix.

Experimental Procedures

A single step intergradient pulsed CVD siliconising process for thick surface diffusion zones was developed, which includes cleaning of the scaled inner surface of the tube, pulsed coating, dechlorination, dehydrogenisation and standard heat treatment of the steel [5, 6].

The formation of an effective oxidation resistant Si-diffusion layer can be described as follows:

- cleaning with hydrogen at high temperature
- reduction of Si from $SiCl_4$-precursor
- deposition of free silicon on the surface
- diffusion of silicon to the structure material
- growing of a α-structured silicone enriched zone
- formation of a martensitic structure during cooling down
- Annealing

The precursor $SiCl_4$ is a liquid salt at ambient temperature and dissolves at temperatures corresponding to those of a typical heat treatment of martensitic steels.

At the start of the process the oxygen out of air has to be removed by repeated vacuum application, then a hydrogen atmosphere is introduced and controlled heating cycle to the coating temperature starts. First cleaning in the hydrogen atmosphere occurs. Hydrogen is the carrier gas saturated with $SiCl_4$ that flows into the reactor. The $SiCl_4$ reduces and then the free Si is adsorbed on the surface of the heated tube. Si diffuses into the steel. The chlorine reacts to HCl and can be removed with the help of the hydrogen atmosphere. After this the hydrogen in the steel is removed to the original amount given in the material standard. Then the standard annealing follows, Fig 1.

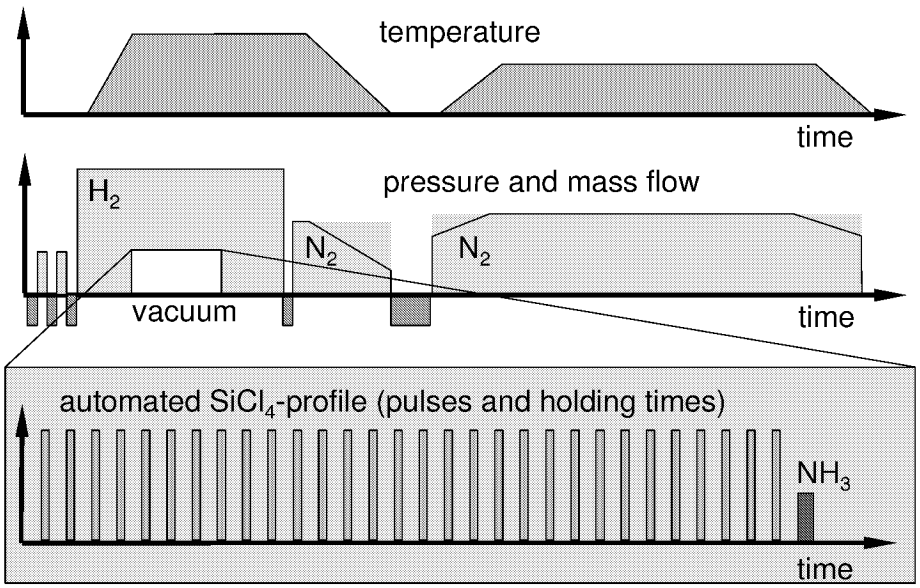

Fig. 1 Schematic representation of the pulsed CVD coating process

The complete pulsed deposition process of Si is automated by SIMATIC PCS7. The heating in a horizontal "Cold Wall" reactor chamber works with HF (high frequency) under atmospheric pressure, Fig. 2. For lower gas consumption and to stimulate the chemical reactions the coating can be performed at low pressure.

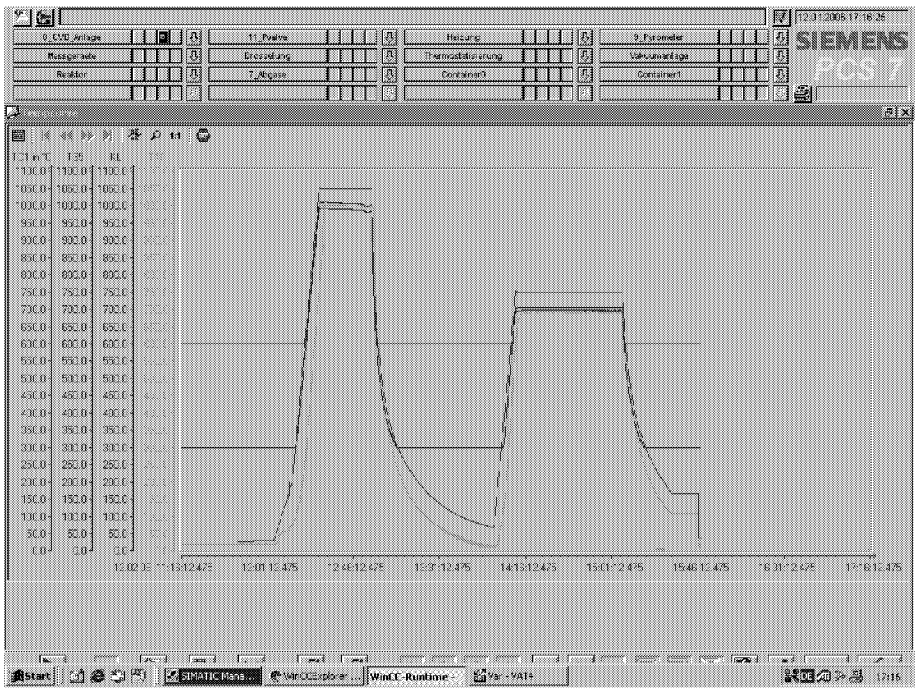

Fig. 2 Temperature profile of the coating process measured with different pyrometers and by thermocouple

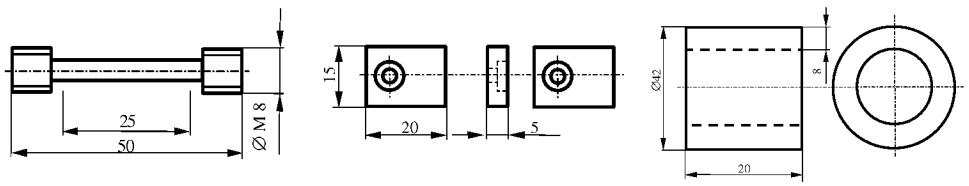

tensile test specimen flat specimen coupons tube specimen

Fig. 3 Shape of the T92 specimen

Specimens of T91 and T92 have been coated, Fig 3. The physical and chemical properties of the modified surfaces were investigated and characterised using the SEM, EDX, electron microprobe and the X-ray diffraction. Also creep tests and tests in water vapour have been carried out.

Results

Microstructural Investigations

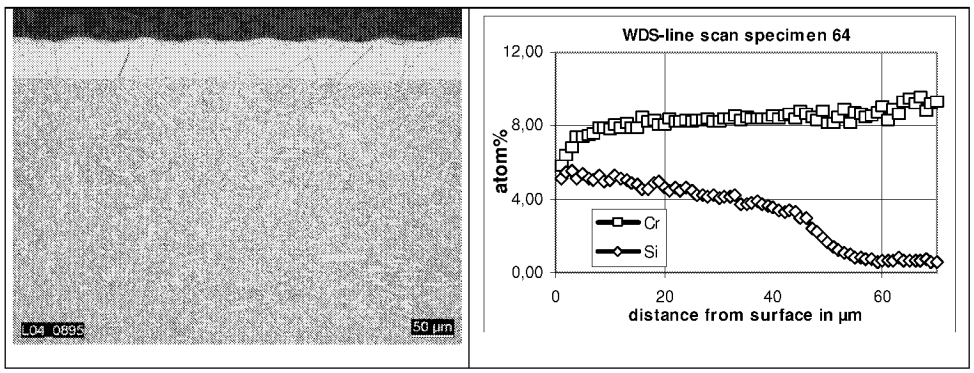

Fig. 4 Siliconised surface with WDS measured element distribution

Fig 4 shows the micrograph (cross section) of a siliconised specimen. The increased silicon content in the ferrite modified zone is about 5% and drops down in the transition zone. It is interesting, that the chromium content has nearly no changes from the original 9%. The chromium reservoir is the base material. The values of the iron content are to balance up to 100%. It could be determined that in this layer Fe is substituted by Si with a concentration of about 5%, however the Cr content is almost constant. A clear martensitic structure is visible in the area without Si.

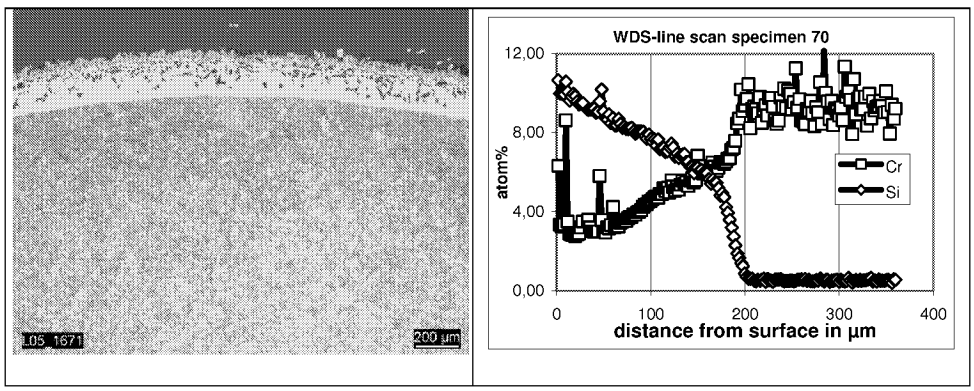

Fig. 5 Siliconised surface with WDS measured element distribution

Fig 5 shows a specimen with a thicker Si-diffusion zone. This zone shows a relatively high Si content of about 10% near the surface. With increasing Si-content also pores in this zone appear.

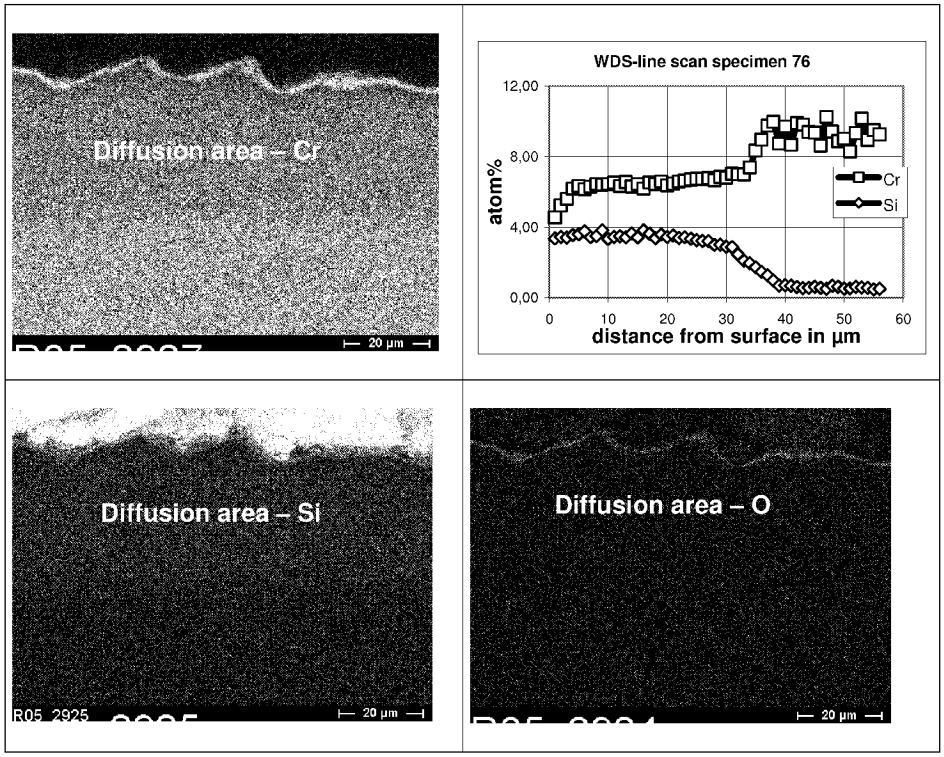

Fig. 6 Diffusion area and line scan after 3000 h annealing

After 3000 h aging in steam atmosphere a stable oxid layer has been formed of Cr, Si, Fe and O, Fig. 6.

Creep test results

Creep tests with coated specimens demonstrate that the creep strength of the material is not negatively influenced by the siliconising process, Fig. 7. The rupture points up to 8000 h are above the lower scatter band of the data given in the standard.

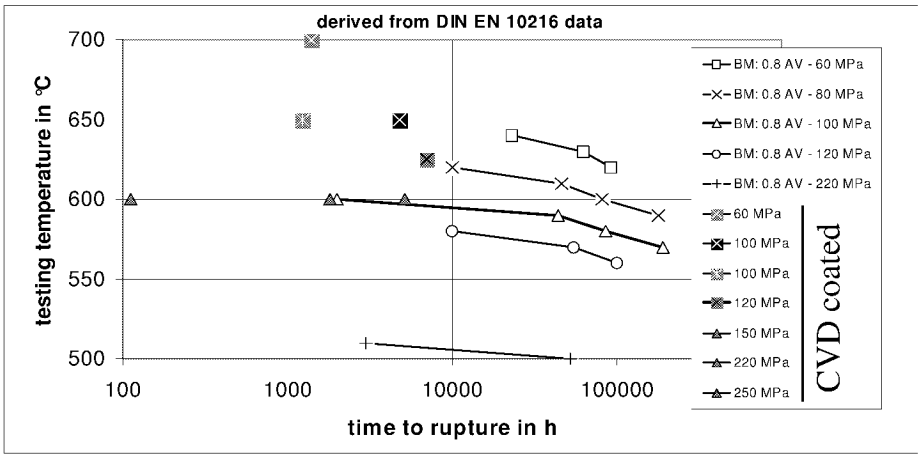

Fig. 7 Creep test results, BM (base material), AV (averaged value)

Oxidation Tests

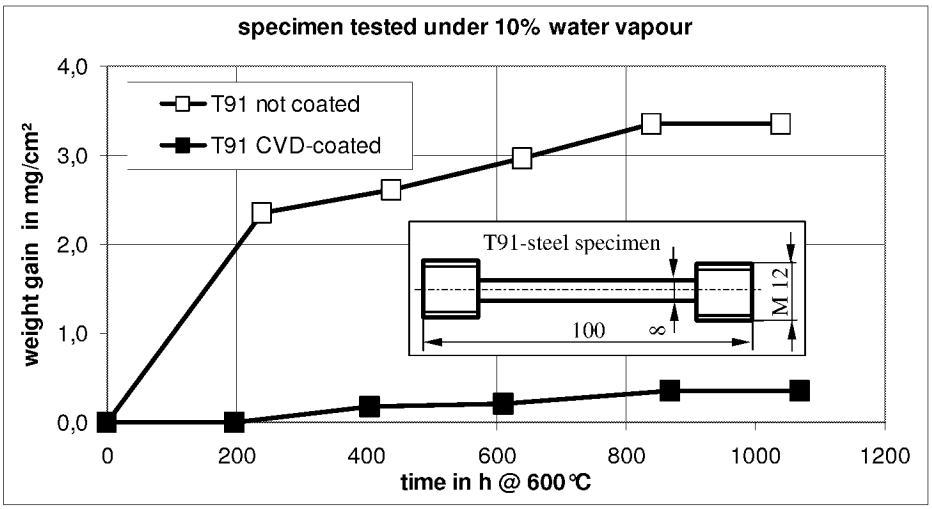

Fig. 8 Comparison of oxidation test results with different specimens: not coated and coated round bar specimen

For the investigation of the oxidation resistance aging tests under steam conditions containing 10% water at 600°C were performed. Test duration was up to more than 1000 h. As it can be seen in Fig 8, the siliconised (modified) surface does not show significant oxidation attack. The increase of weight gain of the coated specimen was significantly less.

Hardness Measurements, Hot Tensile Tests

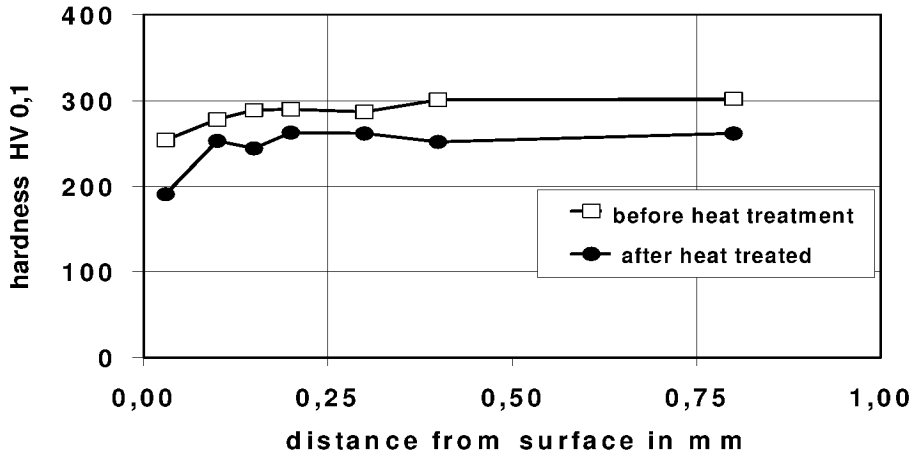

Fig. 9 Hardness measurements before and after siliconising

The hardness of the siliconised surface area represents a typical value for a ferritic structure. The hardness of the martensite structure after siliconising is about 50 units below the initial state, Fig. 9

Performed tensile tests at 600°C with 1%, 2% and 3% plastic deformation show no cracks in the surface due to the ductile behaviour of the siliconised ferritic zone. Tensile testing at temperatures 200°C, 300°C, 400°C, 500°C, 600°C, 700°C shows a neglectable influence on the strength of the base material.

Discussion

The tests proved that siliconised zones with Si content below 5% are already advantageous with regard to oxidation behaviour [7]. An additional effect could be achieved by Si-contents higher than approximately 5%. In this case the microstructure of the steel show a transition from γ (austenite) to α (ferrite) phase at coating temperature. This ferritic phase does not change to martensite during the following cooling down. The ferrite phase has lower hardness and better ductility than the martensite phase of the base material.

Within this concept the surface of the tubes – influenced by the manufacturing process - must not be machined. It will be cleaned during the CVD process with hydrogen at high temperature. The hydrogen that diffuses into the steel will be removed in the frame of the siliconising process by effusion under vacuum keeping the high temperature to avoid embrittlement. In principle silane can be used as precursor, but since silan is toxic and pyrophoric, $SiCl_4$ is easier to handle as precursor. With this precursor also the removal of chlorine from the steel surface could to be done during the process, in order to avoid the effect of chlorine induced corrosion.

The surface modifying siliconising process is at least not a coating process with an additional layer. The strength of the tube materials is not influenced by changing the optimised microstructure of the steel, since the Si-diffusion takes place as a continuous intergradient process within the limits of the standard heat treatment. The temperatures applied during the coating process therefore are in accordance with the given limits of the respective specific steel alloy. In addition the fabricability is not influenced, as the coating is ductile. No problems with bending and welding of long tubes arise. There is no risk that hard particles spalled from coated surfaces may cause damage as blockage or erosion.

Conclusion

A surface modifying CVD coating technology, considering the specific requirements of heat treatment as a single continuous intergradient process has been successfully developed. By means of this technology Si diffusion occurs in a limited zone at the inner surface of tubes.

The thickness of the transformed zone is about 50 µm after 20 minutes of pulsed siliconising.

Experimental investigations modifying the inner surface of tubes of 9%Cr steel via pulsed CVD with silicon containing precursors have been performed to provide improved protection against high temperature oxidation in steam atmosphere.

The diffusion layer consists in a ductile ferritic structure coherent to the original martensitic structure. Fe atoms were substituted by Si with a maximum concentration of approximately 5% Si. No negative impacts on the fabricability of the tubes (bending, welding) could be stated. The strength and creep behaviour of the substrate was not influenced, but oxidation behaviour was improved.

Increased Si content of more than 10% and thicker layers of more than 50 µm could be achieved by optimisation of the pulsing process.

Acknowledgment

The authors performed their work at MPA University of Stuttgart with support from AVIF (project A176) that is gratefully acknowledged here. Thanks are also extended to the German COST 536 partners and to the German Government for the financial support of the investigations (Project 1501 285).

References

[1] S. Goodstine, J. Nava: Use of Surface Modification for Alloys for Supercritical Coal-Fired Boilers. EPRI/DOE Fourth International Conference on Advances in Materials Technology for Fossil Power Plants, October 26 –28, 2004 Hilton Oceanfront Resort – Hilton Head Island, South Carolina

[2] Phil. J. Ennis and W. J. Quadakkers: The Steam Oxidation Resistance of 9-12% Chromium Steels; IWV2, Research Centre Juelich (FZJ); Proceedings of the 7th Liège Conference PART II, Liège, 2002, pp 1131- 1142

[3] V. Rohr, A. Donchev, M. Schütze: Diffusion coatings for the high temperature corrosion protection of 9 – 12% Cr steels, Proc. EUROCORR 2004 Nice, 2004 (CD-ROM), paper no. 237

[4] T. Weber, M. Schütze: Kodiffusionsschichten aus Aluminium, Silizium und Titan zur Verbesserung der Hochtemperatur-Korrosionsbeständigkeit von Apparatebauwerkstoffe, Werkstoffe und werkstofftechnischen Anwendungen (TU Chemnitz) 18 (2004) 181–186

[5] Berreth, K.; Lyutovich, A.; Maile, K.:
Deutsches Patent 10 2004 053 502.7: „Verfahren zur Beschichtung von Innenoberflächen langer Rohre“, Priorität 27.10.2004.

[6] Berreth, K.; Lyutovich, A.; Maile, K.:
Europäische Patentanmeldung und PCT, PCT/EP 2005/011399: „Verfahren zum Korrosionsschutz von Bauteilen aus warmfestem Stahl“

[7] W. Quadakkers; Dampfoxidation von Chromstählen; Beitrag GfKORR-Arbeitskreis, 09.11.05

Influence of surface treatment on the oxidation kinetics of advanced steels in flowing steam at 650 °C

Reinhard Knödler and Stefan Straub,
ALSTOM Power Generation AG, Mannheim, Germany
stefan.straub@power.alstom.com

Abstract

Within the European COST Action 536, the oxidation mechanisms of ferritic-martensitic and austenitic steels in steam-containing environments are being examined, so that steels with increased steam oxidation resistance at temperatures of up to 650 °C can be developed. Preliminary results concerning the influence of surface treatment on oxidation kinetics are reported. It turned out, that austenitic steels are highly susceptible to cold-working of the surface. By this procedure, which can be accomplished by shot-peening or sand blasting, the oxidation rate in steam could be lowered considerably. With the ferritic-martensitic steels no clear dependence on surface treatment was found up to now. Systematic investigations are under way to clarify the role of different treatments like polishing, lathing, grinding, shot peening, etc.

Keywords: Steam oxidation, spallation, oxide scale, surfaces, shot peening.

Introduction

Highly efficient, advanced power plants will operate at high steam temperatures of up to 650 °C. It is necessary at such temperatures to use materials with high creep strength and sufficient oxidation resistance in the service environments [1]. Several high Cr-steels have been developed, which have good mechanical properties at temperatures > 600°C (e.g. E911, HCM12A, P91, P92). However, at these temperatures, the materials suffer from rapid oxidation in steam, which reduces the load-bearing cross-section [2]. Furthermore, thick oxide scales tend to spall, leading to erosion damage of the steam turbine blades.

In several publications a positive effect of work hardening on the steam oxidation of austenitic alloys was described. This effect was attributed to the increase of the number of grain boundaries by the work hardening processes. In turn, this alleviates the diffusion of chromium to the surface, leading to protective chromium oxide scales. A possible mechanism is illustrated in fig. 1. This mechanism was first proposed by [3]. In this work, ferritic and austenitic steels with 10–26 wt. % Cr were cold worked by abrading with 600-grit SiC (1.2 mg/cm2 material removed). It turned out, that the oxidation resistance was increase only for the austenitics (factor of 5), but not with the ferritics. This effect was confirmed by [4] by testing shot-blasted (on the inner side) austenitic tubes for 10 years in a superheater and reheater. The oxide scale thickness on the 18% Cr steel was only about 2 µm at 590 °C. Shot peening of 9 % Cr-steels with Fe- and Cr-particles produced no improvement in oxidation resistance [5]. Only after a 1 h preoxidation in air at 700 °C after shot peening with Cr-particles a considerable reduction in steam oxidation rate could be seen. These publications show that it is worthwhile to investigate the surface effects in more detail in order to improve the oxidation behaviour of steels for advanced temperatures.

In the following, results of tests are reported on oxidation of advanced alloys - developed in COST 522 and COST 536 - with different surface conditions. In addition, scale morphologies are reported.

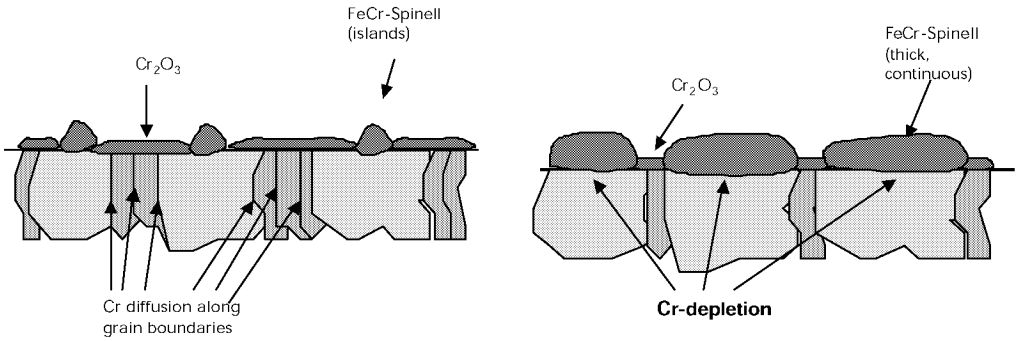

Fig. 1: Mechanism of **slow** oxide growth of cold-worked surface with many grain boundaries (left) and of **rapid** growth at a stress relieved surface (right).

Experimental and test materials

The samples were exposed to superheated steam using a re-circulating arrangement. It works at ambient pressure at 650 °C. The steam has a flow velocity between 150 and 300 ml/h, which corresponds to about 4-8 cm/s (0.01 kg/m^2 s). De-ionized water with no additives was used. By continuous bubbling nitrogen through the reservoir, the oxygen content of the steam was kept below 20 ppb. The arrangement is shown in fig. 2.

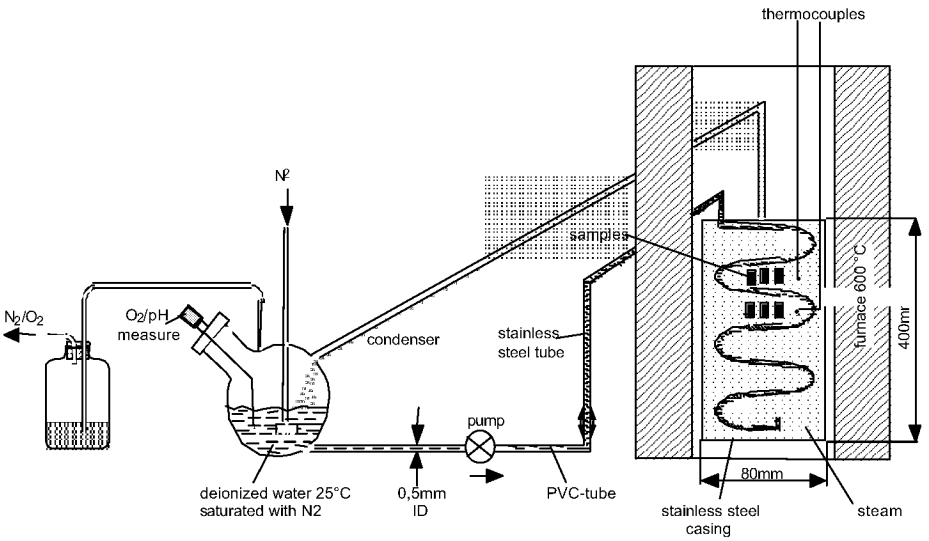

Fig. 2: Experimental arrangement for testing in circulating steam.

The samples had a surface area of about 6 cm^2 and – after milling - were fine-ground until about 50 µm of material was removed. In order to measure the oxygen uptake, the weight of the samples was determined after regular time intervals. For this purpose, they were cooled down slowly in the furnace and again slowly heated up.

The thickness of the oxide scale after exposure was determined by metallographic cross sections. In the case of Cr steels the scale consists of an outer magnetite scale (Fe_3O_4) and an inner Cr-Fe-spinel. The interface between the two scales remains unchanged during oxide growth. Thus, the magnetite grows at the interface to the steam by iron ions migrating through the two scales and taking-up oxygen from the steam. The spinel grows at the interface to the alloy by taking-up oxygen which migrates through the two scales.

The compositions of the materials tested is given in table 1.

Alloy	*Cr*	*Mn*	*Ni*	*Co*	*W*	*Mo*	*V*	*Nb*	*N*	*C*	*Si*	*Al*
TempA1	18	1.5	11							0,08		
CT3	10	1	0,1			1,5	0,2	0,06	0,02	0,2	0,3	
CT7	11,5	1	0,1			1,5	0,28	0,06	0,03	0,18	0,3	
E911	9.2	0.5	0.2		1	1	0.2	0.08	0.07	0.1	0.2	
FB2	9.3	0.8	0.16	1		1.5	0.2	0.05	0.02	0.13	0.05	0.005
FT2	10	1	0,1			1,5	0,27	0,07	0,02	0,2	0,3	
FT6	11,4	1	0,1			1,5	0,3	0,07	0,02	0,2	0,27	

Table 1: Chemical compositions of the investigated steels (wt.-%).

Results

Austenitic steels

A tube from the alloy TEMP A1 was shot blasted at the inner side and exposed to steam for 8000 h at 650 °C. After etching, the non-shot-blasted side showed heavy corrosion attack (fig. 3a), whereas the shot-blasted side was not attacked (fig. 3b). This side showed a dense network of grain boundaries, caused by the shot peening process. Fig. 4 shows the weight change as function of time for this steel. It corresponds well with the cross sections by showing a very low oxidation rate.

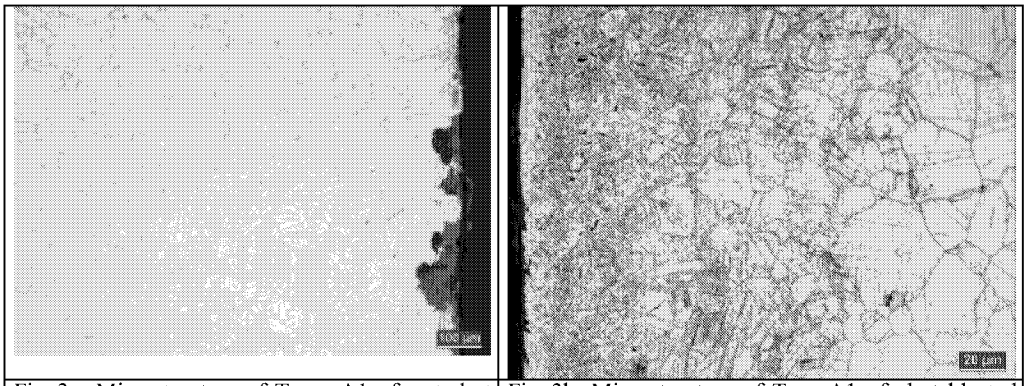

Fig. 3a: Microstructure of Temp A1 of <u>not</u> shot blasted side after 8000 h at 650 °C: deep corrosion attack and oxide growth.	Fig. 3b: Microstructure of TempA1 of <u>shot blasted</u> side after 8000 h at 650 °C: many grains, no attack, no oxide scale. Note different magnification of figs. 3a and 3b!

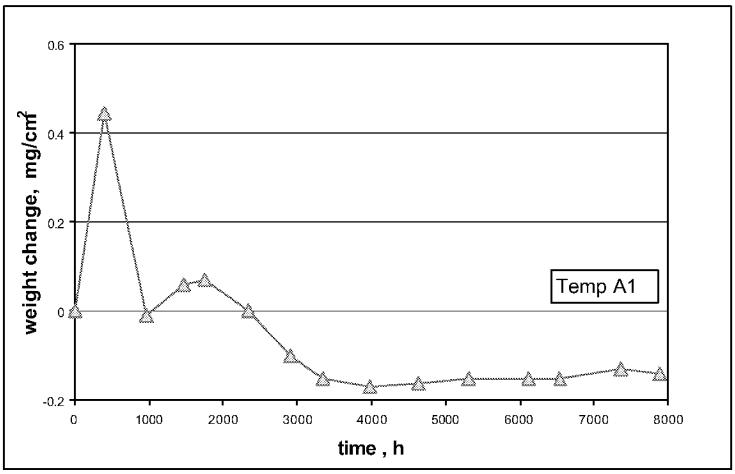

Fig. 4: Oxidation behaviour of TempA1 in steam at 650°C .

<u>Ferritic- and martensitic steels</u>

The following steels were investigated:

- 2 standard (reference) steels with 9 wt. % Cr: E911 and FB2.
- 2 new cast steels: CT3 and CT7.
- 2 new forged steels: FT2 and FT6.

These steels were exposed to the steam in the as-received state (50 µm of material removed by wet fine-grinding with SiC-paper) and after shot peening. Shot peening was done (always after the fine-grinding) with glass beads (called here "glass peened") and with steels beads (here called "steel peened").

Fig. 5 shows the effect of glass- and steel peening after about 1200 h of exposure at 650 °C for FB2 and fig. 6 for E911 (experiment will be continued):

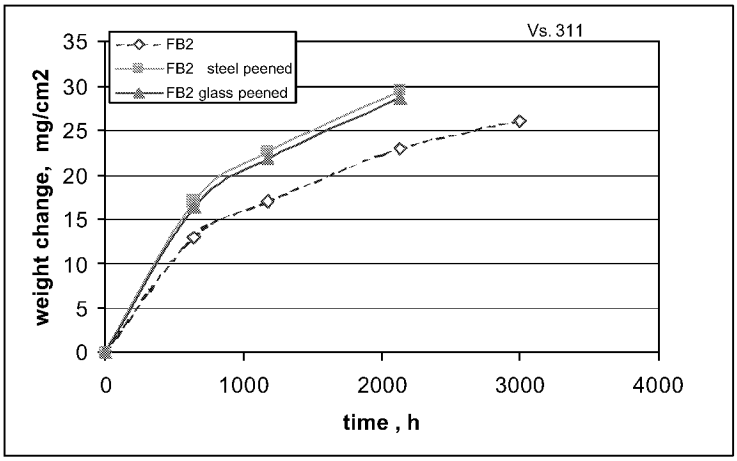

Fig. 5: Oxidation behaviour of FB2 in steam at 650 °C for different surface treatments (dashed line = untreated).

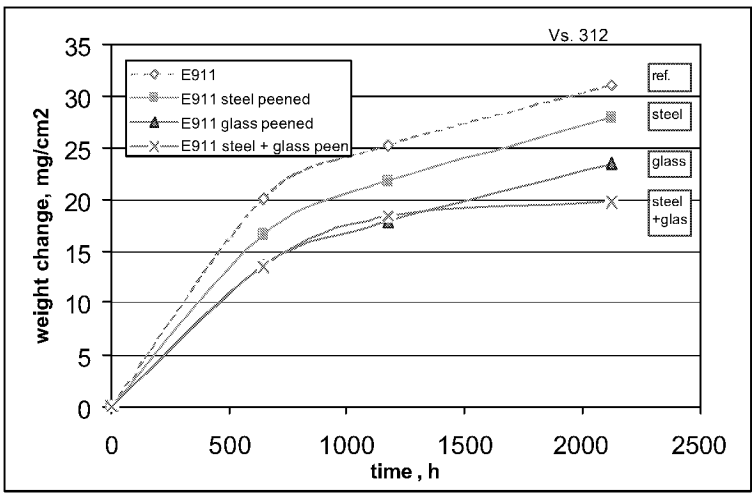

Fig. 6: Oxidation behaviour of E911 in steam at 650 °C for different surface treatments (dashed line = untreated).

It can be seen for E911, that steel- and glass-peening yield lower oxidation rates than the untreated samples. The figures show also, that shot peening with glass beads is more effective than with steel beads. For FB2 no such beneficial effect can be observed.

The effects of the same treatment for the new steels CT3 and CT 7 are shown in fig. 7 and for FT2 and FT6 in fig. 8:

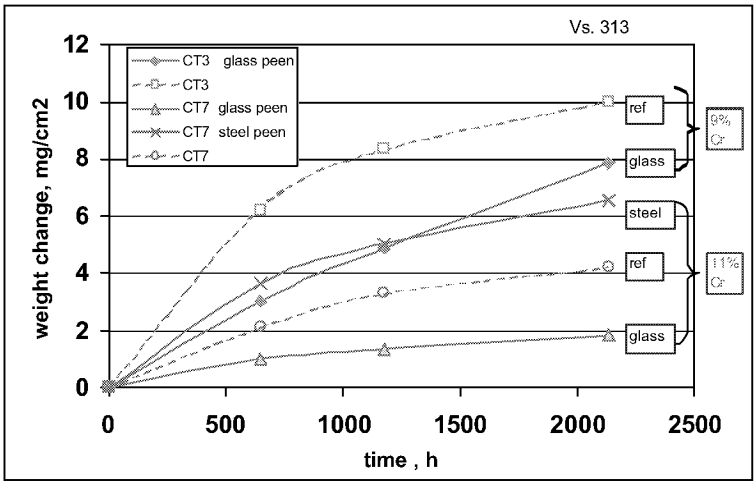

Fig. 7: Oxidation behaviour of CT3 and CT7 in steam at 650 °C for different surface treatments (dashed line = untreated).

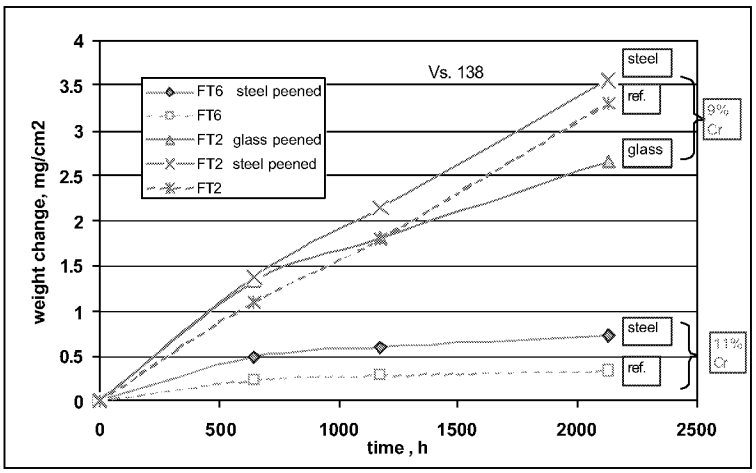

Fig. 8: Oxidation behaviour of FT3 and FT7 in steam at 650 °C for different surface treatments (dashed line = untreated).

Fig. 7 shows, that for both the cast steels CT3 and CT7 shot peening with glass beads yields lower oxidation rates than with the untreated surface. However, steel peening in this case is worse than with the untreated state. Generally, the oxidation rate for the steel CT3 with its lower Cr-content is higher than the steel CT7 with its higher Cr-content, as expected.

In the case of the forged steels FT2 and FT6 no benefit is gained from shot peening as fig. 8 shows. This can not be explained so far and is therefore the focus of further investigations (hardness measurements, microstructure investigations, etc.). As in the case of the cast steels CT3 and CT7, the steel with the higher Cr-content (FT6) exhibit a lower oxidation rate than FT2.

These are preliminary results, which will be supplemented by microstructure and hardness investigations.

Conclusions

- Shot peening of steel surfaces of austenitic steels generally is beneficial for the oxidation behaviour. The reason is martensitic work-hardening and an increase of the number of grain boundaries.
- For some of the 9 % Cr-steels a similar (beneficial) effect is observed. The reason for this behaviour is not yet clear and will be investigated in the future.
- The 10–11.5 % Cr-steels in their cast versions show also an increase in the oxidation resistance after shot peening. However, it is not yet clear, why the forged versions did not follow these observations.
- The increase in the Cr-content from 10 to 11.5 wt % resulted in a doubling of the oxidation resistance of the steels.
- Further investigations are necessary to elucidate the mechanisms by which the work-hardening processes act upon the oxidation behaviour.

Acknowledgement

The authors would like to thank the german Bundesministerium für Wirtschaft und Arbeit for the financial support of the investigations.

References

[1] G. Scheffknecht, Q. Chen, 5th Intl. Parsons Conf., July 2000, Cambridge.
[2] R. Knödler, B. Scarlin, Oxidation of advanced ferritic/martensitic steels and of coatings in flowing steam at 650 °C, Materials for Advanced Power Engineering 2002, Liege , 1601-1611.
[3] D. Caplan, Effect of cold work on the oxidation of Fe-Cr-alloys in water vapor at 600 °C, Corr. Sci. 6 (1966), 509-515.
[4] Y. Minami, A. Tooyama, M. Seki, K. Nonaka, K. Koga, Steam oxidation resistance of shot blasted stainless steel tubing after 10-year service, NKK Techn. Rev. No. 75 (1996), 1-10.
[5] H. Haruyama, H. Kutsumi, S. Kuroda, F. Abe, Effect of shot peening and pre-oxidation treatment on steam oxidation resistance of Mod.9Cr-1Mo steel, EPRI Conf. 2004, 659-667.

LONG TERM STEAM OXIDATION RESISTANCE OF SHOT-BLASTED STAINLESS STEEL TUBING

Yusuke Minami and Toshihiko Fukui
TenarisNKKTubes
1-10 Minamiwatarida, Kawasaki
Kanagawa 210-0855 JAPAN
e-mail:yminami@nkktubes.co.jp

Abstract

According to the increasing of steam temperature in boiler of thermal power plant, large part of super heater (SH) and re-heater (RH) are composed of austenitic stainless steels, especially 18-8 stainless steels. The scale formed on the inner surface of the tubes becomes to be very thick and causes the scale problem after several years' service. It is well known that a shot-blasted tube of 18-8 stainless steel shows enough resistance to steam oxidation. Therefore, many power plants use the shot-blasted tube as SH and RH in boiler. The effect of shot-blasting on a resistance to steam oxidation has been investigated on the tubes used as SH and RH in the boiler for long term service. The scale thickness of the shot-blasted tubes are very thin at 538/566℃ for 10 years and at 593℃ for 6 years. The effect of shot-blasting has been assured to be excellent even at 750℃ by the steam oxidation test.

Keywords: shot-blasted tube, steam oxidation, boiler tube, stainless steel, USC plant

Introduction

The temperatures and pressures of steam boilers are intentionally increased for the purpose of increasing efficiency of power generation and reducing CO_2 emission. Therefore the materials require not only higher creep rupture strength but also better resistance to steam oxidation. The improvements and the study of the steam oxidation resistance of 9-12%Cr steels are performed in many organizations [1]-[3]. On the other hand, regarding 18-8 stainless steels, shot-blasted or fine grained tubes have been used as SH (super heater) and RH (re-heater) tube in the boiler of thermal power plant. However there is the report that the fine-grained tube was prone to scaling during long term service [4]. Therefore, the shot-blasted tube may be more promising for advanced steam conditions. The mechanism of shot-blasting to avoid steam oxidation and the characterization of the shot-blasted tube were investigated and reported [5].

In this report the results of shot-blasted tubes used as SH and RH for long-term service in large thermal power plants are shown. In order to investigate the resistance of shot-blasted tube at higher steam temperatures than that of USC (Ultra super critical) plants operating at present, the laboratory tests were carried out at 750℃. The result is also given in this report.

10 years service in power plant at 538/566℃

The material of shot-blasted tubes for investigation is 18Cr-10Ni-Ti (Type 321H) stainless steel. Tubes are SH size of 45.0mm outer diameter and 8.0mm wall thickness

and RH size of outer diameter 57.0mm and 4.5mm wall thickness. The power plant capacity is 600MW. The steam conditions of the plant are 24.5MPa and 538/566℃ at turbine inlet. The operation period is 78400h, around 10 years.

The scale formed on the inner surface of SH tube is shown in Fig.1. The scale thickness could not be measured by optical microscope and estimated to be below one μm. Figure 2 shows the scale formed on the inner surface of RH tube. The scale thickness of RH tube is thicker than that of SH tube because the metal temperature of RH tube is higher than that of SH tube. However, the average scale thickness of RH tube is measured to be only 1.3 μm by high magnification optical microscopy, although there are few nodular scales.

The result of E.P.M.A. analysis on the scale of SH tube is illustrated in Fig.3. The scale was too thin to analyze on a normal cross section, so after mounting, the scale was polished at an angle of about 6 degree to increase its cross-sectional area and then analyzed. A very high concentration of Cr was detected in the scale. This Cr-rich scale was the reason for the excellent resistance to steam oxidation.

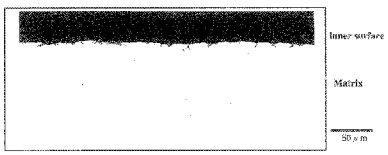

Fig.1 Scale formed on inner surface of SH tube after 10 years service

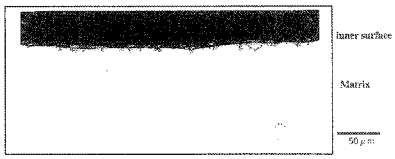

Fig. 2 Scale formed on inner surface of RH tube after 10 years service

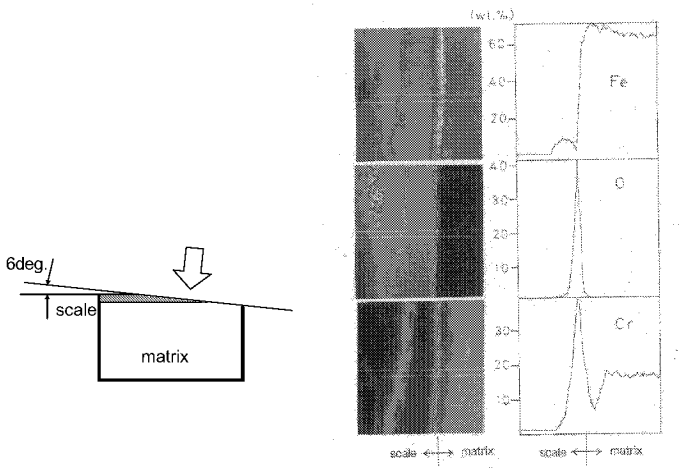

Fig.3 Result of EPMA analysis on steam side scale of SH tube
(Scale was polished at an angle of 6 degree to increase its cross sectional area)

6 years service in power plant at 593℃

The material of shot-blasted tubes for investigation is 18Cr-10Ni-Ti-Nb stainless steel. Tube is RH size of 50.8mm outer diameter and 3.2mm wall thickness. The power plant capacity is 1000MW. The steam conditions of the plant are 24.5MPa and 593/593℃. The operation period was 52000h, around 6 years.
The scale formed on the inner surface and the microstructure of the shot-blasted region is shown in Fig.4. The thickness of the scale formed during 6 years operation is observed to be very thin and measured to be below a few μm by high magnification optical microscopy. The precipitation of carbides on slip bands is clearly observed. The white layer of 10 μm at the inner surface region is the precipitate-free zone.

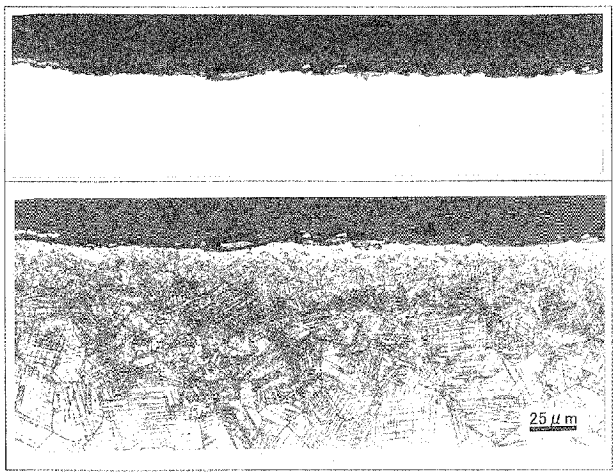

Fig.4 Scale formed on inner surface of shot blasted tube after 52,000h operation (Upper: unetched, Bottom: etched)

Steam oxidation resistance at heat affected zone

The steam oxidation resistance was investigated on the heat affected zone of RH tube weldment used in the same plant (1000MW, 593/593℃) as above after 2 years operation. The inner scale thickness on the heat affected zone is shown in Fig.5 as a function of the distance from weld metal. The microstructure of the 4mm position away from weld metal is given in Fig.6. There is little scale at 4mm position from weld metal. Carbide precipitation on the slip bands became clearer as the distance from weld metal increased. The slip bands caused by shot-blasting of the area near weld metal have disappeared in the weld heat affected zone because the shot-blasting is a cold working. However, as shown in Fig.5, the scale growth is limited to be very narrow area in the vicinity of the weld metal in HAZ. There have not been any problem at all caused by the scale formed on the inner surface of a shot-blasted stainless steel tubing.

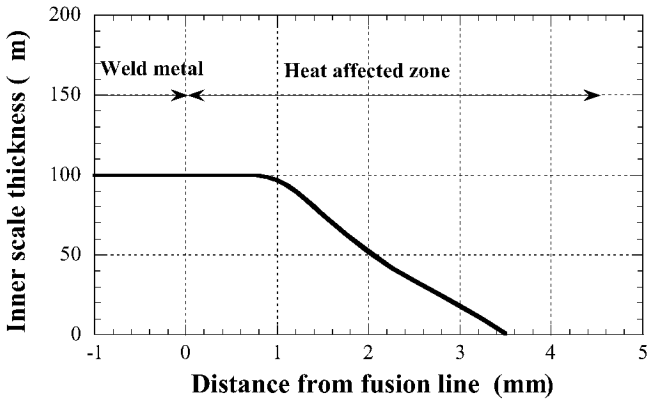

Fig.5 Inner scale thickness at heat affected zone

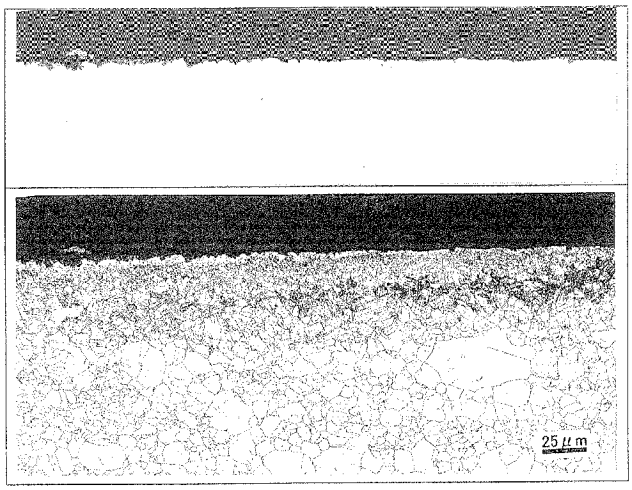

Fig.6 Microstructure of 4mm position away from weld metal
(Upper: no etched, Bottom: etched)

Steam oxidation resistance of shot-blasted stainless steel at 750℃

The steam oxidation test was carried out in order to investigate the resistance of shot-blasted tube at high temperature. The test samples were taken from the shot-blasted tube of 18Cr-10Ni-Ti-Nb steel. The test condition is 750℃ up to for 3000h. The non shot-blasted tube was also tested as a reference material. The test results are shown in Fig.7. The scale thickness of non shot-blasted tube is the inner scale thickness in this figure because a part of the outer scale had exfoliated. The scale thickness of non

shot-blasted tube increased according to the parabolic law and was about 100 μm after 3000h at 750℃. On the other hand the scale thickness of shot-blasted tube is very thin and estimated to be below a few μm. The scales of shot-blasted and non shot-blasted tubes after 3000h steam oxidation at 750℃ are shown in Fig.8 and 9 respectively.

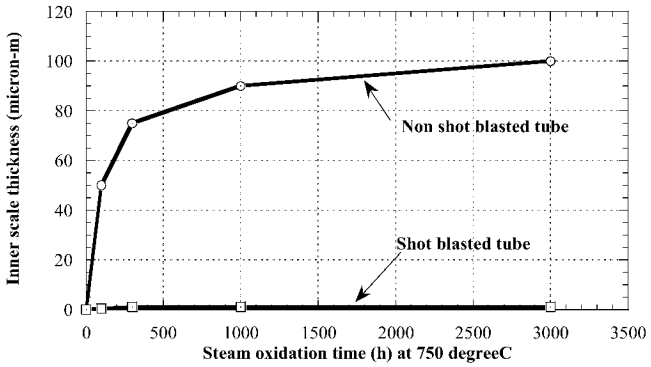

Fig.7 Inner scale thickness of shot-blasted and non shot-blasted tube at 750℃

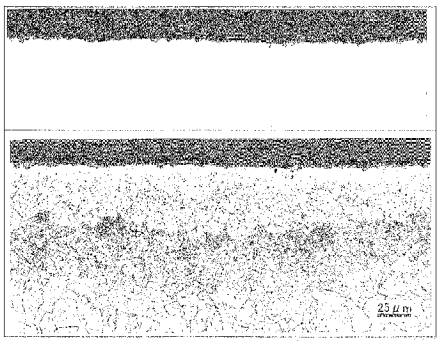

Fig.8 Scale formed on shot-blasted tube after 3000h steam oxidation at 750℃ (Upper: no etched, Bottom: etched)

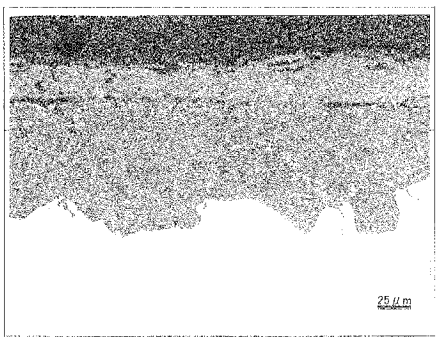

Fig.9 Scale formed on non shot-blasted tube after 3000h steam oxidation at 750℃

Conclusions

The steam oxidation resistance of shot-blasted tubes used as SH and RH tubes in the boiler of power plant for long term was investigated. The steam oxidation test at 750℃ was also conducted on shot-blasted tube. The following conclusions are drawn.

(1) The scale thicknesses of shot-blasted SH and RH tubes after 10 years service at 538/566℃ thermal power plant were below 1 μm and 1.3 μm respectively.

(2) The scale thickness of shot-blasted RH tube at 593℃ plant for 6 years service was below a few μm.

(3) Although the effect of shot-blasting is reduced at HAZ by welding, its region is

within 4 mm from weld metal.

(4) The effect of shot-blasting on steam oxidation has been shown to be effective even at 750℃ for 3000h and the scale thickness was estimated to be below a few μm while the sale thickness of non shot-blasted tube was over 100 μm.

Acknowledgements

The authors greatly acknowledge Babcock-Hitachi K.K. and J-POWER for providing the stainless steel tubes exposed in thermal power plant.

References

(1) H.Kutsumi, H.Haruyama and F.Abe "Application of the pre-oxidation treatment in Ar gas to the NIMS high-strength steels" Proceedings of the 8th Ultra-Steel Workshop, Tsukuba, Japan, July 21-22, 2004

(2) J.M.Sarver and J.M.Tanzosh "Steam Oxidation Behavior of Candidate USC Materials at 650℃ and 800℃" Proceedings of the 8th Ultra-Steel Workshop, tsukuba, Japan, July 21-22, 2004

(3) R.Knodler and B.Scarlin "Oxidation of advanced ferritic/martensitic steels and of coatings in flowing steam at 650℃" Materials for Advanced Power Engineering 2002, PartIII, Liege, 2002

(4) B.Dooley "The Importance of Oxide Growth and Exfoliation" EPRI's International Conference on Materials and Corrosion Experience for Fossil Power Plants, Isle of Palms, SC, Nov. 18-21, 2003

(5) T.Kanero, Y.Minami and H.Ichinose "Shot-blasted Stainless Steel Tubing Resistant to Steam-indused Oxidaition" NIPPON KOKAN TECHNICAL REPORT Overseas No.26 (1979)

Part III

Advanced Steam Turbine Materials

Contributed Papers

Austenitic Steels and Nickel-base Alloys

QUALIFICATION OF NI-BASED MATERIAL FOR TUBES AND PIPING OF 700°C POWER PLANT

Andreas Klenk, Karl Maile, Heinrich Theofel, MPA University of Stuttgart
Andreas Helmrich, Alstom Power Boiler, Stuttgart
Ralf Udo Husemann, Babcock Hitachi Europe, Oberhausen
Josef Heinemann, UTP Schweißmaterial, Bad Krozingen
Gereon Lüdenbach, VGB Power Tech, Essen

Abstract

In order to achieve efficiencies above 50%, live steam temperature of 700°C and pressure of 300 to 375 bar have to be realized. Considering the temperatures imbalances the single tube can reach temperatures of up to 750°C. Therefore for tubes and piping Ni-based alloys need to be qualified for thin- and thick-walled components.
This paper reports on research results on all important aspects which are related to manufacturing and use of piping systems and membrane wall panels e.g. hot forming, weldability, hot and cold bending. The main focus is put on long term properties of base material as fabricated and welded joints of Alloy 617. The aim of the investigations was to qualify this material for use as piping, outlet headers and superheater tubes in fossil fired power plants. First a systematic investigation of alloying elements was undertaken in order to improve and confirm the creep rupture behaviour of a batch with controlled chemical analysis (CCA). Longterm properties for base materials and welded joints were investigated. The corrosion behaviour under fire side conditions and the properties of a weld-on coating system were investigated. Metallographic results from crept specimens as well as a field test in the power plant were carried out.

Keywords: High efficiency power plant, superheater tubes, outlet header, Alloy 617, Alloy 617 welds

1 Introduction

Within the next 20 years the demand for approx. 300 000 MW of electric power will arise in Europe. This demand is primarily due to the substitution of older plants with low efficiency relative to modern ones and increasing concerns over environmental sustainability, **Fig. 1** [1]. The substitution of ageing power plants primarily concerns replacement of fossil fuelled steam power stations with old technology that are also near the end of their operating time. A reasonable efficiency improvement can be achieved by application of new technologies in existing plants which can result in a 20% reduction in CO_2-emissions due to the substitution of old plants by already available technologies.

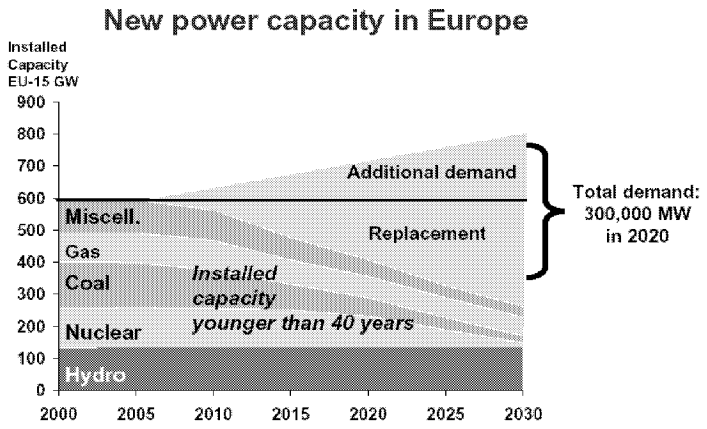

Figure 1: Demand for new power capacity in Europe

A higher thermal efficiency can be achieved in fossil fuelled power plants by process optimisation measures (like e. g. double reheating) and by increasing the steam parameters [1, 2]. The main feature and technology of the 700/720°C power plants lies among others primarily in the significant increase of the live steam temperature to approx. 700°C. Material issues are of vital importance for the increase of the steam parameter to temperatures in the area of up to 720°C. Martensitic 9-12%Cr-steels cannot be used at this temperature. However, they still constitute the structural material in large parts of the boiler and in the power plant in general. For the highest temperature areas though, materials have to be developed and qualified that have not been used for this purpose up to now. The required creep resistance and corrosion resistance can only be achieved by nickel based alloys [3]. The research project described in the following paper therefore deals with the development of a material system for the highest temperature regions of the boiler. A basic objective was the qualification of a material system based on Inconel 617 (Alloy 617) in the fabricated state.

2 Base material for steam generator components operating at 700°C

For the fabrication of boiler components under the defined general conditions (720 up to 750°C) common ferritic/martensitic or austenitic steels are not suitable. The use of nickel based materials is therefore inevitable if these conditions are to be sustained. Among the available alloys, the material Alloy 617 was chosen mainly based on the criteria of manufacturing and weldability as well as creep rupture behaviour. Firstly, a great deal of knowledge already exists concerning this material, e.g. from the field of reactor construction (high temperature reactor, HTR) and the gas turbine technology and secondly the chances that required processability can be achieved are higher. The basic requirements for the application in steam generators like sufficient creep resistance, good processability (deformation, welding) and corrosion resistance have to be proved. An improvement of the creep characteristics, especially in the temperature area up to 750°C, seemed possible. Systematic investigations [4, 5] showed, that by tighter alloy specification and specifying Boron a considerable improvement in creep behaviour is to be expected. Hence the limited analysis (CCA) displayed in **Table 1** was proposed.

Table 1: Chemical analyses of Alloy 617 and 617 welding consumables (comparison)

Chemical composition of Alloy 617, UNS N06617	Analysis range of various standards and manufacturer´s data sheets														
	C	Si	Mn	Cr	Ni	Mo	Co	Al	Ti	Cu	B	Fe	N	S	P
VdTÜV 485	0,050-0,100	max. 0,70	max 0,70	20-23	bal.	8-10	10-13	0,6-1,5	0,2-0,5					max. 0,008	max. 0,012
Material No. 2.4663 DIN EN 10302	0,05-0,10	≤ 0,20	≤ 0,20	20-23	bal.	8,5-10	11-14	0,7-1,4	0,20-0,60					0.010	0.010
Manufacturer 1	0,05-0,1			20-23	bal.	8-10	10-13	0,6-1,5	0,2-0,6						
Manufacturer 2		max 1.0	max 1.0	20-24	min 44.5	8-10	10-15	0,8-1,5	max. 0,6					max. 0.015	
Ltd. Analysis (A130)	0.05-0.08	max. 0.3	max 0.3	21-23	bal	8-10	11.-13.	0.8-1.3	0.3-0.,5	max. 0.05	0.002 - 0.005	max 1.5	0.050	0.008	0.012
Actual Values: Manufacturer 1	0.067	0.13	0.02	22.25	54.30	9.11	12.15	1.14	0.60					0.005	0.005

An evaluation of various data corresponding to this analysis resulted in the mean values for the 10.000 and 100.000 h creep rupture strength displayed versus temperature in **Fig. 2**. For comparison the corresponding averages of the VdTÜV-material sheet are plotted.

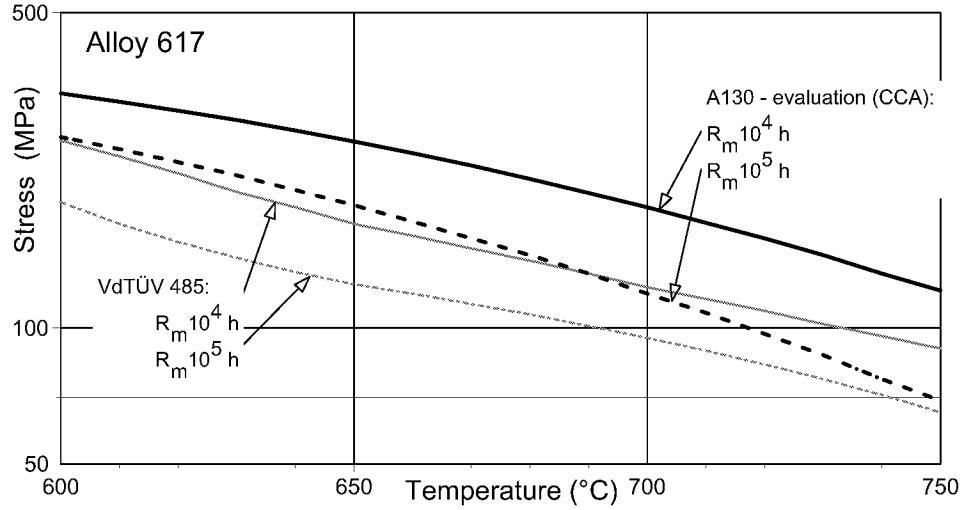

Fig. 2: Newly evaluated creep rupture strength values for the limited analysis and comparison to VdTÜV material sheet 485

Using this limited analysis, boiler tubes (dimensions ø 38 mm x 6.5 mm) and seamless thickwalled pipes (ø 400 mm x 50 mm) were fabricated and investigated further. The creep tests carried out on these melts confirm the evaluation mentioned above. **Fig. 3** shows the comparison of creep rupture strengths determined on boiler tubes, thickwalled pipes and tube elbows fabricated by inductive bending. An average of the 100.000 h creep rupture strengths of 119 Mpa could be determined despite the limited data base. This one lies considerably higher as the one of the previous VdTÜV-material paper at 700°C .

3 Examination of corrosion protection systems

Boiler tubes in the combustion chamber are exposed to extreme conditions of high temperature oxidation and corrosion. In order to be able to provide corrosion protection if necessary, several possibilities to equip the base material with coatings were investigated. Besides weld cladding, coating technologies such as chemical vapour deposition (CVD) and physical vapour deposition (PVD) have been tested for their suitability. Material sheets coated using the different coating techniques were aged in flue gas and ash environment. Primarily due to operational reasons built-up weld cladding proved to be the most promising protection system. For this metal active-gas welding is used. Thus on a weld clad plate of Alloy 617 using two different welding consumables were carried out. The chemical compositions of the consumables are shown in **Table 2**.

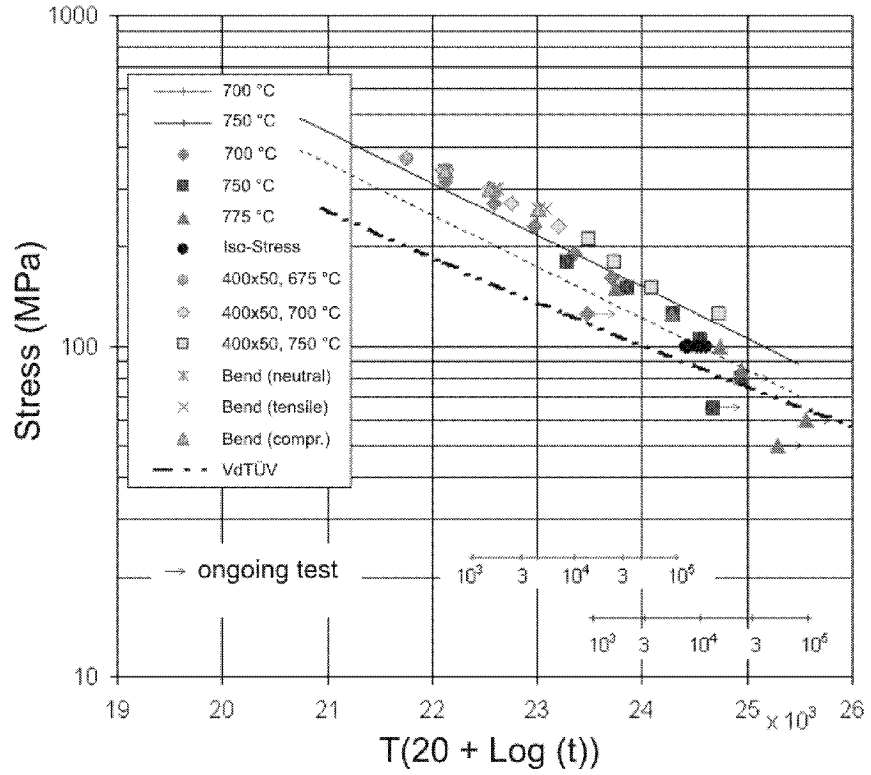

Fig. 3: Creep rupture strength of Alloy 617, test results for different products made from melts with limited analysis /6/

Table 2: Chemical composition of the built-up weldings (weight %)

Cladding Type	Ni	Cr	Fe	Mn	Si	C	S	Cu	Nb
Nicrofer 6030	63	28	8,5	0,14	0,16	0,02	0,003	0,12	
UTP A 3545 Nb	45	35	17	0,8	1	0,45			0,9

On these plates preliminary inspections were carried out that proved both the efficiency of the corrosion protection by ageing up to 3000 h in ash and flue gas at 700°C and a sufficient deformation ability for tube bending. The compositions of the synthetic flue gas and the synthetic ash are: flue gas: SO_2 (0,25 %), O_2 (3,5 %) , CO_2 (15 %), N_2 (bal.); ash: Na_2SO_4 (5 %), K_2SO_4 (5 %), Al_2O_3 (30 %), SiO_2 (30 %), Fe_2O_3 (30 %). The samples were aged under the above mentioned conditions at a temperature of 700°C in presence of a platinum catalyser. After ageing the oxide layer of the built-up welds had a maximum thickness of approximately 30 µm (Nicrofer 6030) or 10 µm (UTP A3545 Nb), resp. The oxide layer thickness of the unprotected material under the same test conditions were up to 400 µm, **Fig. 4**. Both of the overlay built-up welds were tested on boiler tubes and subjected to bending and formality tests, as shown in **Fig. 5,** as well as creep tests. The 6030-cladded material showed sufficient cold forming capabilities, the tubes clad with material containing 45% Nickel could not be cold formed in an appropriate manner.

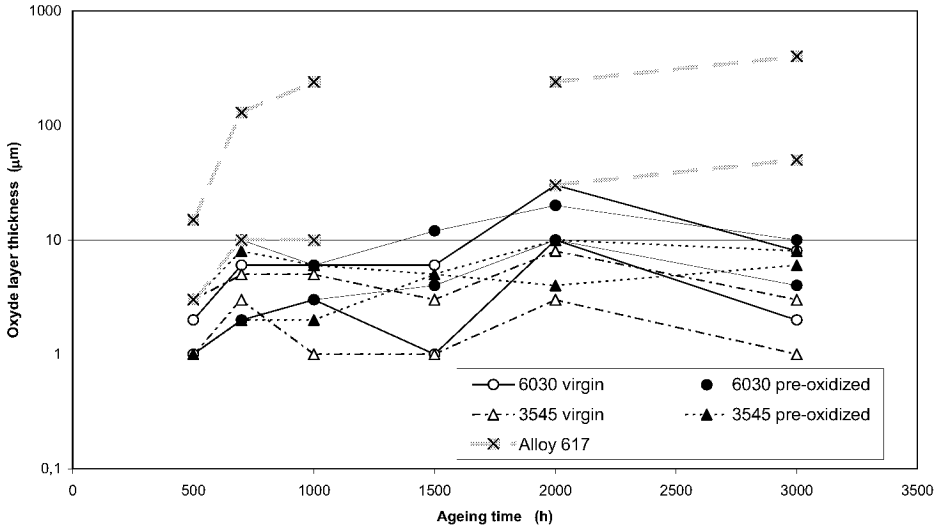

Fig.4: Oxide layer thickness of Alloy 617 with and without built-up welds

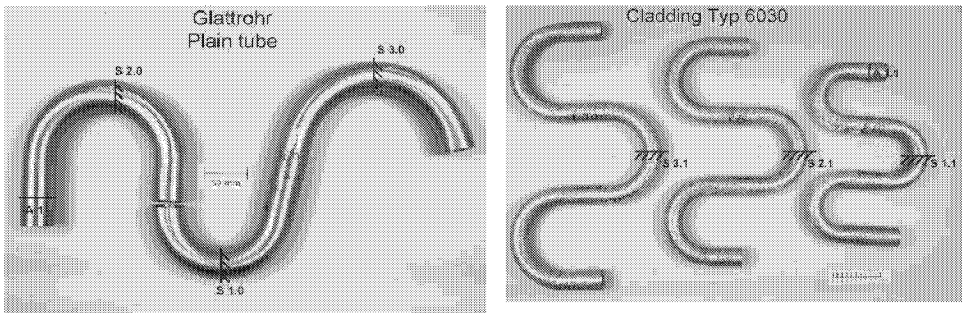

Fig. 5: Bend tests on plain (left) and cladded tubes (right)

4 Welded joints

4.1 Optimisation of the welding consumables

For the welding of Alloy 617 similar welding consumables are used. Similar to the base material large tolerance ranges in the chemical composition presetting exist. As an example, different chemical compositions of welding consumables are included in Table 1. The standard requirements do not contain a minimum value for carbide- or oxide generating elements such as titanium or aluminium. These elements, however, do have a considerable impact on the creep resistance. Concerning various welding procedures such as shielded metal arc welding (SMAW) and especially submerged arc welding (SAW) one has to consider the possibility of significant burn-off and loss of these alloying elements.

Furthermore, the degree of burn-off is influenced by the welding procedure employed. Using welding consumables which are processed under inert gas (argon or argon helium, argon hydrogen mixtures) the burn-off of alloying elements is negligible. The application of electrodes and electrode-flux combinations is indispensable on construction and production sites due to their universal applicability for the processing of Alloy 617. By an adequate cladding concept at the rod electrode the burn-off can be compensated. Additional alloying of the respective alloy elements is also possible. With the electrode-flux combination the burn-off can be influenced by the welding technique /7/.
By an optimisation of the weld metal composition it could be guaranteed that the mechanical property requirements, especially sufficient notch toughness, can be achieved [7], **Fig.6**.

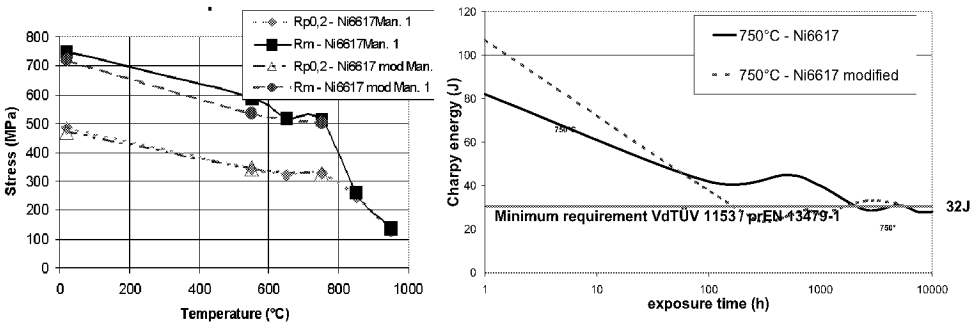

Fig. 6: Comparison of common and modified Alloy 617 weld metal

Samples from a first SAW-joint in a thickwalled pipe produced within the project, showed an insufficient creep resistance in isostress-tests performed at temperatures of 730 - 800°C. The analysis of the chemical composition showed relatively low Al-contents of 0,5 to 0,6%. By improvements to the welding procedure, especially by application of smaller filler wire diameters, higher Al-contents could be achieved. **Fig. 7** shows the analyses for a weld fabricated with different procedures.

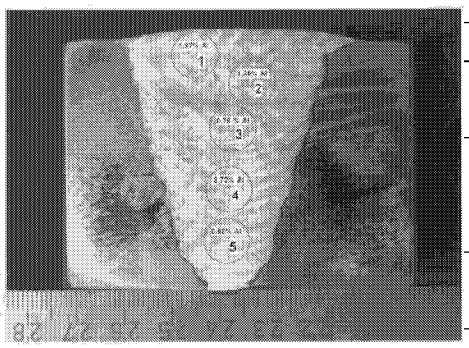

Welding process	Al (weight.-%)
SMAW	1,37
SAW	0,76
	0,72
	0,82
MAG	1,24
	1,23

Fig. 7: Al-content at a weld fabricated with different procedures

Preliminary creep tests on cross weld samples extracted from this weld are currently undergoing iso-stress-testing. In summary, it can be stated that by optimisation of the weld metal for shielded metal arc welding and MAG-welding procedures good Al-concentrations can be achieved and for submerged arc welding the Al-burn off can be reduced significantly.

4.2 Creep tests on welded joints

Cross weld samples were extracted from the thick-walled pipes. Instead of round bar test specimens commonly used for creep tests the cross weld specimens were taken from the boiler tubes as longitudinal strips with a rectangular cross-section (6 x 6.3 mm^2). Test temperatures were 650°C, 700°C and 750°C. Tests at 650°C carried out randomly showed creep resistances lying significantly above the average of the VdTÜV-sheet. The influence of weld position on creep rupture strength was investigated for boiler tubes by tests with samples taken from tubes welded with vertical tube axes and horizontal tube axes, respectively. In the creep rupture diagram for 700°C, **Fig. 8**, the results of the welded joint tests are compared to the base material tests and to the scatterband according to VdTÜV 485 and A130 (limited analysis). The fractured cross weld samples lie significantly above the VdTÜV-scatterband, however at the stress level of 220 MPa the rupture time of the base material was not completely achieved. The fracture positions were located within the heat affected zone or in the weld metal. An unfavourable influence from the welding position is not detectable and the rupture time for samples taken from different positions of the horizontally welded tube were slightly above that for the tube welded in the vertical position. One sample tested at 140 MPa has not yet fractured but has exceeded the upper scatterband boundary of the VdTÜV-values. At 750°C in principle the same creep rupture behaviour can be observed, Fig. 8.

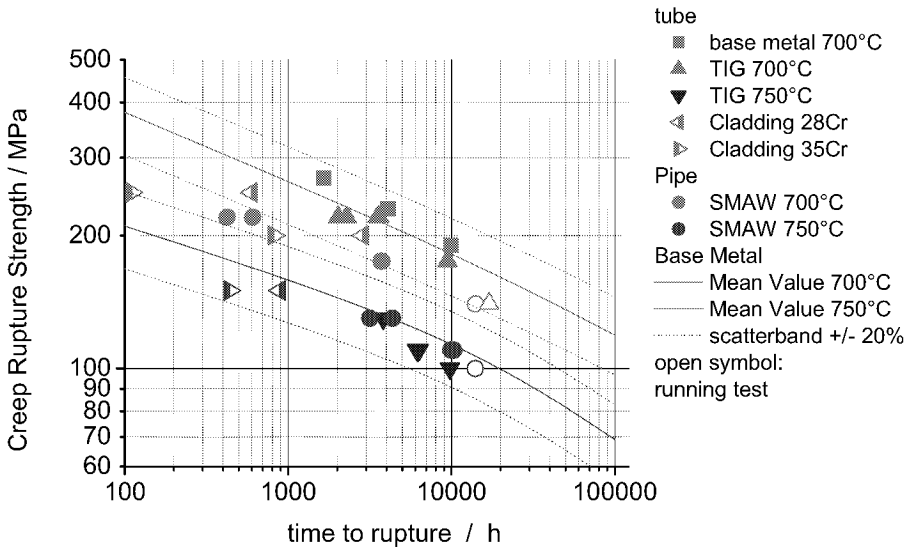

Fig. 8: Results of cross weld creep rupture tests at 700°C and 750°C

For each cladding type three creep tests at 700°C and 750°C each were performed on built-up welded boiler tubes. The results are included in the creep rupture diagram shown in Fig. 8. At 700°C the samples from the cladding type 6030 lie approximately on line with the cross weld samples taken from the uncoated tube. The samples from the cladding type 3545, however, fractured considerably earlier. This weld overlay showed a more unfavourable behaviour during bend tests at room temperature as well. It is emphasized that for both types weld overlay cracks in the heat affected zones appeared, penetrating the whole cladding at high

strains. One has to assume that a long-term corrosion protection is jeopardised if high expansions occur.

Samples were taken selectively from the upper (12 o'clock position) and lower area (6 o'clock position) of the circumferential seam of the shielded metal arc weld, with the sample position in the wall centre. All fractures occurred in the weld metal. The high creep resistance of the base material found for the thick walled pipe was not achieved. All test results at longer testing times lie, however, in the base metal scatterband and the upper scatterband of the VdTÜV-scatterband is still exceeded. The continuing test at 140 MPa has already reached this upper limit. An influence of the sampling position could not be found, i.e. for tests with a stress level of 175 MPa the samples taken in 6 and 12 o'clock position lie nearly congruent in the diagram. The rupture points of the tests at 750°C also lie in the area of the upper limit of the VdTÜV-scatterband. The difference in rupture time between base metal and cross weld samples is less than that at 700°C. An influence of the sampling position could not be detected at this testing temperature either.

5 Further analyses for the qualification of the material

In addition to the analyses mentioned for proving the producibility of components, e. g. fabrication of tube bends (cold bending) and pipe bends by inductive heating, a boiler tube with the dimensions of ø 38 mm x 6.3 mm was integrated into an existing test cycle of the power plant Weisweiler, block G. The boiler tube was supposed to be operated at a pressure of 165 bar and temperature of 720°C. After a leakage occurred the tube was removed from the test cycle in March 2004 after 20000 hrs operating time. The analyses performed showed considerable different local expansions (up to approx. 20%), local significant differences in hardness as well as a damage detection (pore density) that correlated well with the local expansion observed. On the flue gas side flat corrosion depressions could be detected. The wall thickness removal was approx. 1 mm. The leakage was due to a local overheating. Fig. 9 shows the metallographic examination of the service exposed tube.

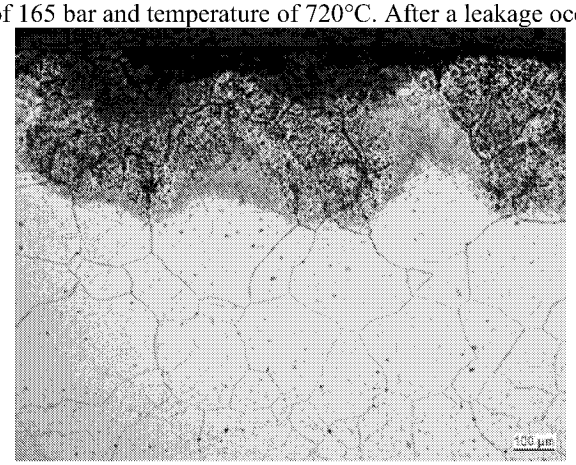

Fig. 9: Oxide layers on a tube service exposed for 20,000 h at 700°C

For the purpose of microstructural characterisation, samples were taken both from the boiler tube and the pipe and subjected to an extensive light and electron microscopical analysis. Beside detailed investigations of grain sizes of different product forms, the microstructure was characterized by transmission electron microscopy to determine the development of the number and size of precipitates, the subgrain size and dislocation density. Thereby, first comparisons with long-term exposed specimens were made.

In order to get information about the long-term damage behaviour and especially about the determination of the degree of damage by replicas taken from components, tests were conducted on creep samples of the material Alloy 617 at different temperatures regarding microstructures and their verifiability by replica technique.

Regarding the damage formation, it shows that the boundaries of the creep damage in the gauge area (uniaxial load) have significant deformation structures, whereas the damage in the radius of the sample head (geometrically caused multi-axiality) does not show a visible deformation. From this different mechanisms of damage formation can be deduced: Concerning the uniaxially loaded gauge area one can assume a slippage of the grain boundaries under deformation of the material such that the heat resistance of the material was locally exceeded. Concerning the multi-axially loaded head area one has to assume a creep pore formation by vacancy condensation without deformation of the material structure that corresponds to a damage mode expected at operational strained components. The available analysis shows that the creep damage of nickel base alloys has to be proved and documented with the already available replica technique. Using etching reagents one has to clarify in advance due to the complex precipitation kinetics of this material if possible phase precipitations will be eliminated by the etching procedure used and thus simulate anomalous creep damage. Hence the results of this analysis can only be used for the available structure and precipitation conditions and cannot be transferred to other alloy types or longer operating times without restrictions.

6 Summary and future prospects

Increased efficiency which is necessary with regard to CO_2-reduction and a more economic use of resources at coal-fired power plants will be achieved by an increase of the steam parameters, especially of the steam temperature up to 720°C. The consequence is that in the area of the highest temperatures other materials for thick walled tubes, headers and boiler tubes have to be employed. According to the present state-of-the-art exclusively nickel base alloys can be used in the temperature range of 650 to 750°C. The objective of the analyses described in this paper was: optimising the alloy composition of the nickel base alloy 617 for application in the component and pipeline construction, thereby proving its suitability. This was achieved by testing the producibility and long-term characteristics in the processed state as well as identifying an adequate protection against fire side corrosion of boiler tubes and testing its suitability for the application purpose under discussion.
Restriction of the chemical analysis specification published in VdTÜV-sheet 485 demonstrably led to a material that met the desired characteristics regarding procucibility and creep resistance. The restricted analysis was realised in industrially fabricated melts and filler metals. With this material the creep strength levels shown in **Table 3** can be achieved.
The producibility was proved by fabrication and examination of boiler tubes (straight tubes and formation of bends of different radii) and thick walled tubes (straight tubes and inductive tube bends).
The fabrication of welded joints for boiler tubes was carried out with the WIG-procedure, for thick walled tubes SMAW and SAW-procedures were employed. Examinations for the optimisation of welded joints showed the necessity to adjust the chemical composition systematically within the designated specification. The welds were achieved with welding consumables and welding procedures optimised in such a way. Parameters for strength,

ductility and notch impact energy fulfilling the employable rules were determined by mechanical testing. The results obtained for the creep tests on welded joints were found, except for an SAW-joint, to be only slightly below the average of the base material with the restricted analysis. Creep rupture occurred mostly in the weld metal.

Table 3: Creep rupture strengths of Alloy 617 with restricted analysis

Temperature/Time	10.000 h	100.000 h
700°C	185 MPa	119 MPa
750°C	121 MPa	69 MPa

Two nickel base built-up welds with differing nickel and chrome concentrations were tested for their applicability as protection against fire-side corrosion. In the tests under flue gas and ash conditions both showed a significant decrease of the oxidation layer thickness compared with the base metal. Regarding the creep resistance and the bending test, the built-up weld layer showed better characteristics with 63% nickel and 28% chrome, the creep resistance of the base material and the welded joints was nearly reached.

Regarding the evaluation of damage in service exposed material, it is important to know about the changes in the material´s microstructure. Therefore for virgin material and material exposed to creep tests, microstructural investigations by light-optical microscope and scanning and transmission electron microscope were carried out. An inspection of ruptured creep specimens showed that cavitation occurs and therefore a determination of creep damage on components of nickel based alloys is in principle possible with the established replica technique.

In summary it can be stated that the described project succeeded in optimising the nickel based alloy 617 and qualifying it for the application in modern high efficiency power plants. This concerns the producibility and – within the time-frame possible within the project time – the required characteristics, especially the creep resistance in the temperature area 700°C up to 750°C. Thus the results form a good base for further examinations that are necessary for an application in the power plant regarding the long-term protection and description of the characteristics. That includes among other things the verification/proof of the long-term creep characteristics of the base material in consideration of the melt caused scatterband behaviour as well as the further, additional qualification of the proposed procedures for the fabrication of welded joints, especially SAW-joints, with the objective of ensuring the required long-term creep behaviour.

With respect to materials technology, the available project results constitute the technical base for the fabrication of highly stressed components in future high-efficiency power plants for the temperature area up to 720°C. As a consequence of the restricted specification analysis a new material is available for the material manufacturers that can be used for the fabrication of pre-materials and components once adequate further qualifications have been completed. The manufacturers of welding consumables can use the project results for the fabrication of optimised and adapted weld metals. The determined parameters enable the component and boiler manufacturers to produce components which are suitable for the economic and safe application in the temperature region. The proof of weldability enables the fabrication of components and component groups and the application of the material in power plant construction is already possible, therefore Alloy 617 tubes and other components are parts of

test loops in various power plants. Components were employed for test purposes in the project COMTES700 and other test loops. Examples are shown in Fig. 10.

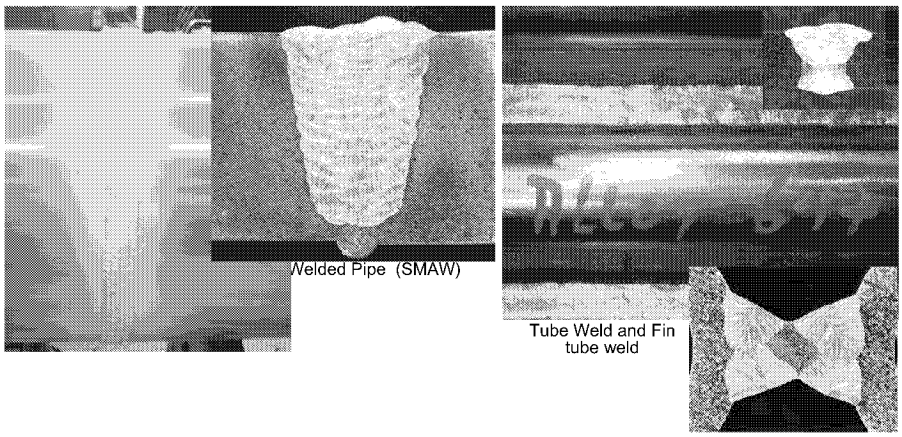

Figure 10: Plant components made of Alloy 617

7 Acknowledgement

The presented report was promoted with funds of the Federal Department of Commerce and Labour (BMWA) under the promotional reference 0327062 and the foundation "Stahlanwendungsforschung" in the foundation association for German Science under the reference AVIF A130. Our gratitude for this is expressed hereby. The technical monitoring of the project was made by a management committee, secretariat of which is with FDBR. Our gratitude is expressed to the committee members for the details originated from further technical discussions.

8 Literature

[1] K. Theis: Cleaner Coal technology: A new Initiative for Europe, VGB, Brussels, 22.03.2002

[2] C. Berger, K.H. Mayer und R.B. Scarlin: Neue Turbinenstähle zur Verbesserung der Wirtschaftlichkeit von Kraftwerken, VGB Kraftwerkstechnik 71 (1991), S. 686-699

[3] R.U. Husemann: Werkstoffe und Werkstoffentwicklungen für die Komponenten Membranwand und Überhitzrohre für zukunftige Dampferzeuger. In. TAM Fachtagung „Kohlekraftwerke im Jahr 2000/2015", Dresden, 30.-31.03.1995

[4] U. Brill and R. Weiß: Vortragsveranstaltung der Arbeitsgemeinschaft warmfeste Stähle und der Arbeitsgemeinschaft für Hochtemperaturwerkstoffe, November 2000, Düsseldorf

[5] D.C. Agarwal and U. Brill: Influence of the Tungsten Addition and Content on the Properties of the High Temperature-High Strength Ni-Base Alloy 617, 4th Int. Conference on Advances in Materials Technology for Fossil Power Plants. EPRI, (Ed.: R. Viswanathan), Hilton Head Island, October 25-28, 2004

[6] A. Klenk, H. Theofel, A. Helmrich, R.U. Husemann, R. Weiß, U. Brill, T. Kremser, . J. Heeschen: MARCKO-DE 2: Neue Rohrwerkstoffe für Dampferzeuger mit Wirkungsgraden über 50% , Final Report, BMWA, AVIF, Stuttgart, 2005

[7] Heinemann, A. Helmrich and R.U. Husemann: Applicability of Ni-Based Welding Consumables for Boiler Tubes and Piping in the Temperature Range up 720°C. 4th Int. Conference on Advances in Materials Technology for Fossil Power Plants. EPRI, (Ed.: R. Viswanathan), Hilton Head Island, October 25-28, 2004

AN INVESTIGATION ON STRUCTURE STABILITY AND ITS IMPROVEMENT ON A NEW DEVELOPMENTAL NI-CR-CO-MO- NB-TI-AL SUPERALLOY FOR USC POWER PLANT APPLICATION AT TEMPERATURE ABOVE 750°C

Xishan Xie[1], Shuangqun Zhao[2], Jianxin Dong[1], G. D. Smith[3], B. A. Baker[3], S. J. Patel[3]

[1] High Temperature Materials Research Laboratories, University of Science and Technology Beijing, Beijing 100083, China
[2] Department of Physics, Ningxia University, Yinchuan 750021, China
[3] Special Metals Corporation, Huntington, WV 25705, USA
E-mail: [1] xishanxie@mater.ustb.edu.cn, [2] shuangqunzhao@sina.com, [3] gsmith@ smcwv.com

Abstract

A new Ni-Cr-Co-Mo-Nb-Ti-Al superalloy INCONEL® 740 is under development for the application of USC boilers above 750°C. This paper introduces the structure stability of this new alloy briefly. Experimental results show that the most important structure changes at high temperatures are γ' coarsening, γ' to η transformation and G phase formation. The coarsening of γ' phase follows a cube rate law: $\bar{r}^3 \propto t$ and the η phase develops to a Widmanstätten pattern structure following long term exposure at elevated temperatures. Phase computation by Thermo-Calc has been adopted to study main influencing factors on precipitates. Chemical composition modifications were attempted to improve the alloys' structure stability. Several suggested new modified alloys in adjustment of Al and Ti contents and/or in control of Si level were designed and melted for experimental study. The preliminary results indicate that the modified alloys exhibit more stable structure stability at 750°C long time aging till 5000h. A bright perspective has been shown for the development of this kind new alloy and for the application in USC power plants in the near future.

Keywords: Superalloy; INCONEL 740; USC; Structure Stability; Phase Computation

Introduction

Increasing demand for more electricity, reduced plant emissions and greater efficiency is forcing power plants to increase steam temperature and pressure of pulverized coal-fired boilers. It has been shown that the efficiency of pulverized coal-fired boilers can be increased to over 50% LHV (lower heating value) when ultra supercritical steam (USC) conditions higher than 300 bar and 600°C are adopted. In these power plants, the superheater/reheater midwall temperature can be 660°C or higher which means the well-established 9-12%Cr steels must be replaced by austenitic stainless steels with higher creep strength and better corrosion resistance.

® INCONEL is trademark of the Special Metals Corporation group of companies.

Recent ultra-supercritical steam conditions up to 35 MPa and 700°C, are being planned by both the European THERMIE AD700 and the German MARCKO DE2 projects, will enhance the efficiencies of coal-fired boilers to about 50% and lead to superheater/reheater midwall temperatures as high as 740°C to 760°C as well. At these temperatures and pressures, the superheater and reheater materials will therefore be required which have a high creep rupture strength ($100MPa/10^5h$) at temperatures of about 750^oC, together with high corrosion resistance ($\leq$2mm cross-section loss in 2×10^5h). For long-term service at these high pressures and temperatures, neither solid solution strengthening austenitic stainless steels nor a currently available nickel-base superalloy, such as NIMONIC 263, INCONEL 617, CCA617, INCONEL 690 and INCONEL 671, can meet the requirements for stress rupture strength and corrosion resistance [1-4]. A new precipitation-hardenable Ni-Cr-Co-Mo-Nb-Ti-Al superalloy, designated as INCONEL 740, is under development at Special Metals Corporation (Huntington) for USC power plant application at temperatures above 750°C. The nominal chemical composition is (in wt.%): Cr 25.0, Co 20.0, Mo 0.5, Al 0.9, Ti 1.8, Nb 2.0, Fe 0.7, Mn 0.3, Si 0.5, Ni balance [5, 6]. In collaboration with Special Metals Corporation, University of Science and Technology Beijing has investigated strengthening mechanism, structure stability and corrosion resistance of this new alloy [7-10]. So far, the preliminary studies prove that the this alloy successfully surpasses the established strength design target as mentioned above and exhibits favorable resistance to coal ash corrosion in laboratory tests designed to simulate boiler conditions as well. Although the alloy keeps a good microstructural stability during prolonged aging at temperatures under 725^oC, the structure stability of the alloy needs to be improved above 750^oC. This paper briefly introduces the important results of structure stability of the alloy during long-term aging at elevated temperatures. On the basis of thermodynamic calculation, the methods for structure stability improvement have been suggested and four experimental heats of modified alloys (two heats made in Beijing and two heats made in Huntington) have been produced and their structure stabilities have been also evaluated at 750°C.

Structure characterization of INCONEL 740

Microstructure of the alloy at standard heat-treatment

Microstructures of the alloy in the state of solution-annealed plus precipitation treatment are shown in Figure 1. SEM micrograph (Figure 1a) of the alloy indicates that carbides precipitated in matrix and at grain boundaries. The blocky particles distributed in the matrix and the grain boundaries are MC and $M_{23}C_6$ carbides mainly, which can be electro-extracted in a solution of HCl and CH_3OH and be ascertained by X-ray diffraction. The exact and detailed results of the precipitates as shown in Tab. 1, which were analyzed by physical and chemical phase analyses, indicate that the precipitates are γ', MC, $M_{23}C_6$ and G phase. The MC and $M_{23}C_6$ are (Nb,Ti)C and $Cr_{23}C_6$ type carbides, respectively. As shown in Figure 1b, the uniformly dispersed fine γ' precipitates are observed in the matrix, which contributes the main strengthening effect for the new alloy. The formation of cubic γ' morphology can be attributed to the medium degree of γ-γ' lattice mismatch. The average radium of γ' is about 15nm. INCONEL 740 is based on Ni-25Cr-20Co with Mo for solid solution strengthening and

with Nb, Ti and Al for γ' precipitation strengthening.

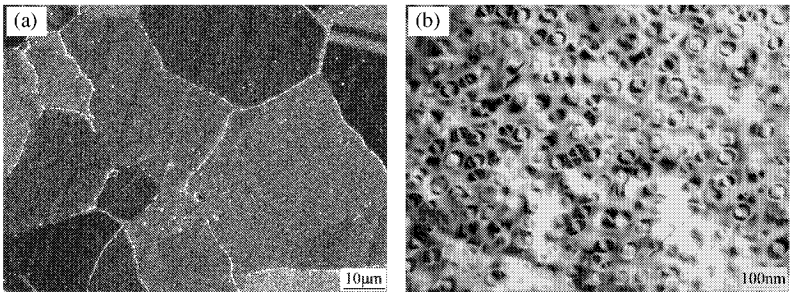

Figure1 Microstructures of the alloy at standard heat-treatment condition

Table 1 Fraction of the precipitates in the alloy (wt.%)

Heat-treatment	γ'	MC	$M_{23}C_6$	G
800°C /16h	12.980	0.183	0.115	0.054

Microstructure evolution during long-term exposures at high temperatures

Figure2 shows SEM images of the alloy aged at 704 and 725°C for 4000h. The morphology and distribution of the precipitates in the samples are quite similar as in Figure 1. Very fine γ' precipitates distribute in the grains. The large particles (MC) distribute in matrix at random. The grain boundary precipitates can be obviously observed after long time exposure at 704°C. Detailed phase analyses indicate that the major carbides MC, $M_{23}C_6$ mixed with a few of G phase. The MC carbide forms from the liquid and it is stable at high temperatures. $M_{23}C_6$ mainly forms at grain boundaries and have no significant variation with prolonged aging time. However, after aging for 4000 h at 725°C, a small quantity of needle-like and blocky η precipitates have formed mainly nearby grain boundaries (Figure 2b).

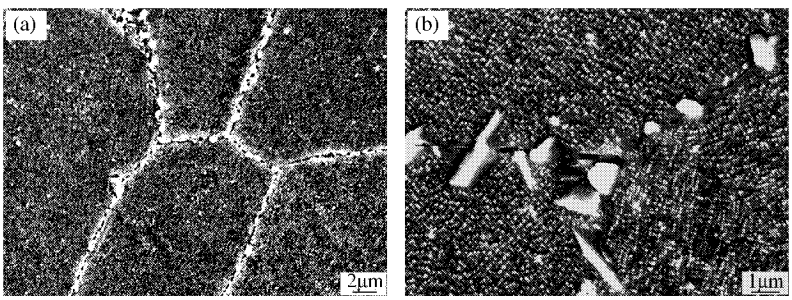

Figure 2 SEM images of the alloy aged at 704 (a) and 725°C (b) for 4000h

Figure 3 shows SEM images of the alloy aged at 750°C for 1000 and 5000h. The same as in Figure 2b, the significant structure change is η-phase formation besides the growth of γ'

particles. After 1000h aging (Figure 3a), a small amount of η phase, especially in the area close to the grain boundaries, has been observed in the sample. The quantity and size of η precipitates rapidly increase with aging time. Till 5000h (Figure 3b), not only η phase initiates at grain boundaries but also a significant amount of η phase forms in the grains as Widmanstätten pattern structure. In addition, there are γ′-free zones surrounding η plates and nearby the grain boundaries. It indicates that the η phase forms at the expense of γ′ phase.

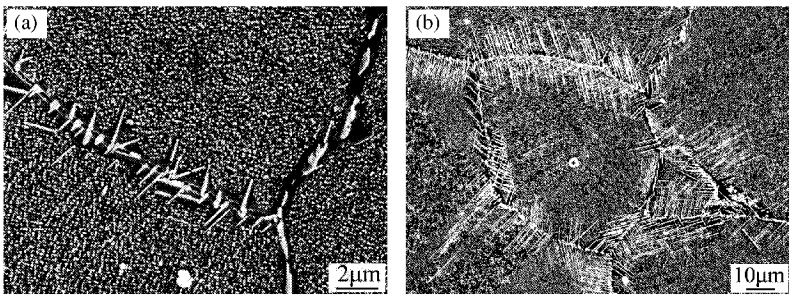

Figure 3 SEM images of the alloy aged at 750°C for 1000 (a) and 5000h (b)

Coarsening of γ′ precipitates

The coarsening behavior of γ′ particles was examined as a function of temperature at 704, 725 and 760°C, and as a function of ageing times up to 4000h for the alloy. The relationship between average effective radius of γ′ precipitates obtained by SAXS in this alloy with various ageing time at three temperatures are plotted in Figure 4. It is clear that the relationships between effective radius $\bar{r}^3$ and ageing time t at different aging temperatures are linear, suggesting that the coarsening of γ′ particles in this new superalloy containing not too high volume fraction of γ′ follows typical $\bar{r}^3 \propto t$ kinetics of diffusion-controlled particle growth (LSW Law). It is also an evidence in Figure 4 that the γ′ particle coarsens more rapidly as the aging temperature increases to 760°C.

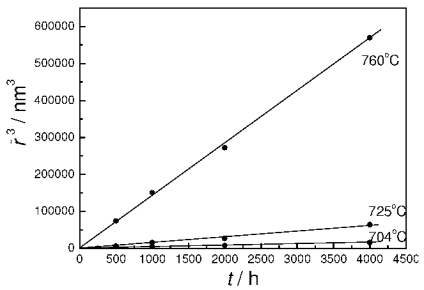

Figure 4 Coarsening of γ′ phase in the alloy

η phase formation

In order to study the η precipitation behavior, the samples as solution-annealed were aged at different high temperatures to investigate when the η phase forms. After aging at 725°C for 4000 h, 800°C for 100h, 900°C for 16h and 950°C for 26h, a small amount of η phase formed at grain boundaries and/or in matrix. In addition, the η phase has not formed in the sample aged at 1000°C for 140h. According to these results, the TTT-diagram for η phase formation

can be given in Figure 5. Though no exact results at temperatures above 950°C, the formation trend of η phase is also given in accordance to the thermodynamics calculation with nominal composition, which indicates the highest stable temperature of η phase is about 1118°C. According to these results, it is likely that the η phase forms in the temperature range of 700~1118°C. The peak temperature of η phase formation is about 900°C.

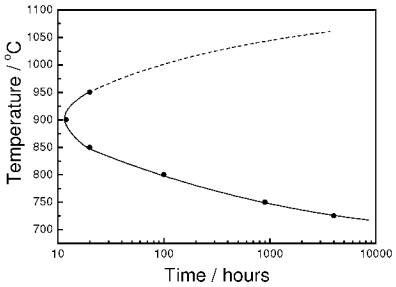

Figure 5 TTT curve of η phase formation in the alloy

G-phase precipitation

The weight fractions of precipitates in the alloy aged at 704 and 760°C for 1000 and 2000 h obtained by physical and chemical phase analyses are given in Tab. 2. The results indicate that the precipitates in the alloy are γ′(+η), MC, $M_{23}C_6$ and G phase. Because of the similar electrochemical property, the γ′ phase and the η phase could not be differentiated by this method. The weight fraction of γ′ precipitates in samples aged at 760°C is total fractions of γ′ and η. The actual fraction of γ′ phase in the samples aged at 760°C is less than that of at 704°C, because a certain amount of γ′ has transformed to η. The fractions of γ′(+η), MC and $M_{23}C_6$ have no large changes with increasing time at temperatures 704 and 760°C. Phase analyses also indicate that the chemical composition of γ′ precipitate is $Ni_3(Ti,Al,Nb)$ and G phase is $A_6B_{16}Si_7$-type $(Nb,Ti)_6(Ni,Co)_{16}Si_7$. It is worth to mention that the fractions of G phase in the samples aged at 760°C are much higher than those of at 704°C.

Table 2 Fraction of precipitates in the alloy (wt%)

Aging	γ′(+η)	MC	$M_{23}C_6$	G
704°C /1000h	16.629	0.154	0.139	0.046
704°C /2000h	16.835	0.151	0.151	0.063
760°C /1000h	14.364	0.161	0.170	0.336
760°C /2000h	14.633	0.154	0.217	0.471

Phase computation for structure stability improvement

Thermodynamic equilibrium phase

Experimental results show that main structure instabilities of the alloy above 750°C aging are rapid coarsening of γ′, η phase transformation, and a certain amount of G phase formation at grain boundaries. Consequently, the structure stability improvement of this alloy should be concentrated on the precipitation behavior of γ′, η and G phase.

Thermodynamic calculation was carried out to predict the phase stability and phase fractions in the alloy using Thermo-Calc software, version M, accompanied with 14-element Ni-database (not include Si and Mn) [11]. The calculated phase diagram of the alloy under

equilibrium condition is shown in Figure6, in which all the predicted equilibrium phases and their weight fractions at each temperature are given. Thermodynamic calculation (Figure6) reveals that the equilibrium phases above 600°C include γ, γ′, η, MC and $M_{23}C_6$, which were observed in the alloy, and σ phase as well, which was not observed and may be formed after longer exposure time. The liquidus, solidus, σ, η and γ′ solvus temperatures of the alloy are about 1369, 1293, 699, 1118 and 850°C, respectively. The predicted solidification temperature range (76°C) of this alloy is in good agreement with the experimental value (74°C). The equilibrium compositions of the precipitates at 700°C are shown in Tab. 3.

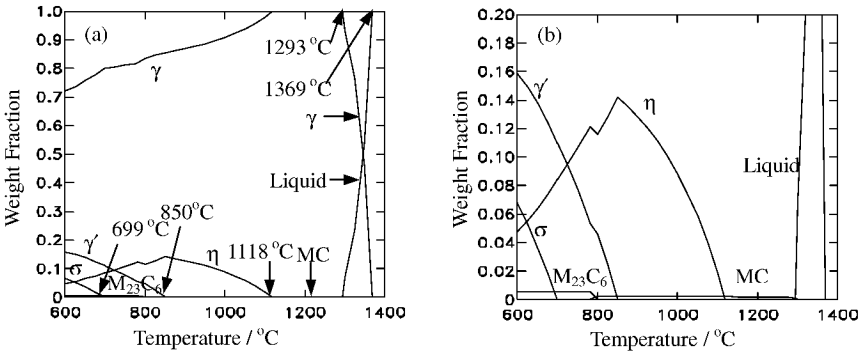

Figure 6 Phase calculation results (a) of the INCONEL 740 and its partial magnification (b)

Table 3 Chemical compositions of equilibrium phases at 700°C (wt%)

Phase	Ni	Cr	Co	Fe	Mo	Al	Nb	Ti	C
γ	45.12	30.52	22.52	0.86	0.52	0.27	0.11	0.08	Trace
γ′	70.51	1.17	7.38	0.06	0.02	4.78	8.63	7.44	-
η	61.74	0.33	13.68	0.05	-	1.92	11.43	10.86	-
$M_{23}C_6$	2.82	74.88	2.88	0.07	14.06	-	Trace	Trace	5.28

Effect of chemical compositions on the precipitation of γ′ phase

Both the physical and chemical phase analysis results and thermodynamic calculation results (as shown in Tab. 3) show the chemical composition of γ′ phase is $Ni_3(Al,Ti,Nb)$, therefore, phase computation should concentrate on Al, Ti and Nb. Figure 7 gives the calculated results of the effect of Al, Ti and Nb content on the weight fraction and solution temperature of γ′ phase. With the increase of Al content, the weight fraction of γ′ phase increases obviously. For example, when the content of Al is 0.7%, 0.9%, 1.1% and 1.5%, the weight percentage of γ′ phase is 1.7%, 7.7%, 13.5% and 23.7% at 750°C, respectively. Simultaneously, the precipitation temperature of γ′ phase is also increase with the content of Al and they are 775°C, 850°C, 904°C and 987°C, respectively. While the content of Ti decreases from 2.4% to 1.4%, the weight fraction of γ′ phase increases slightly and this change is not a simplex decrease with the content of Ti decreasing more. For example, when the content of Ti is 2.4%,

1.8%, 1.4% and 0.8%, the weight percent of γ′ phase is 7.2%, 7.7%, 8.8% and 11.2% at 750°C, respectively. The precipitation temperatures of γ′ phase mildly change and they are in the temperature range of 850~861°C. The content of Nb also have an influence on the precipitation behavior. With the decrease of Nb, the weight percent and the precipitation of γ′ phase increase slightly.

Phase computations also reveal that the effect of Ti on η phase precipitation is more than that of Nb and Al. The effect of Ti on η phase precipitation behavior is shown in Figure 7d. The maximum percentage of η phase in the alloy (Ti 1.8% - nominal composition) will reach to 14.16% at 850°C. When the content of Ti decreases to 0.8%, the maximum percentage of η phase will be 7.33% at 861°C and the precipitation temperature is only limited in the range of 744~1011°C.

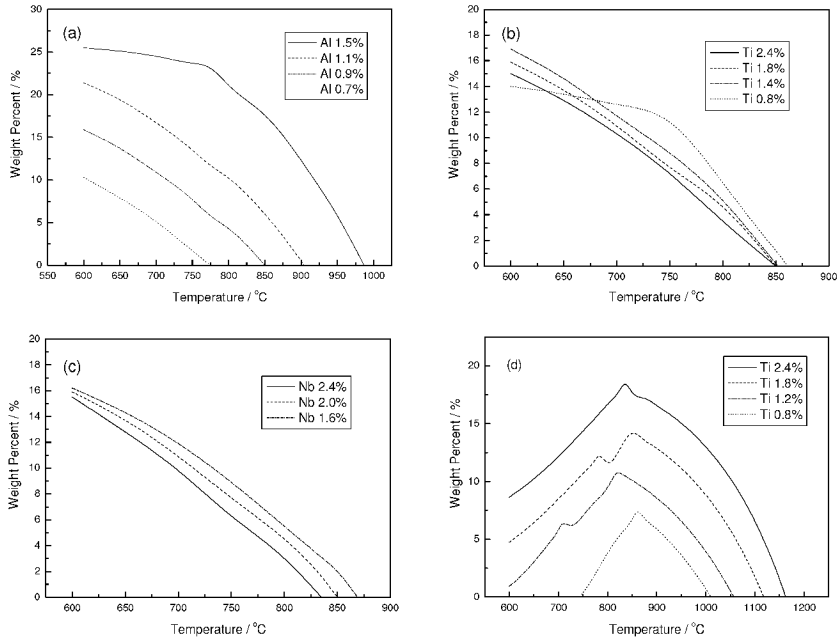

Figure 7 Calculated curves of the effect of Al (a), Ti (b), and Nb (c) on γ′ phase precipitation behavior and the effect of Ti on η phase precipitation behavior (d)

The existence of large blocky G phase at grain boundaries at 760°C may develop embrittlement and will degrade mechanical properties of the alloy, thus the formation of G phase should be restrained. However, due to the lack of Si in the thermodynamic database, the formation of G phase cannot be speculated by Thermo-Calc software.

Experimental results on modified alloys

According to experimental and thermodynamic calculation results, 4 modified alloys were made to investigate the improvement on structure stability. Their chemical compositions are listed in Tab. 4. Heat 1 and Heat 2 were made in Beijing to adjust the contents of Al, Ti and to control Si content to a lower level in the alloys. Heat 3 and Heat 4 were made in Huntington to adjust the contents of Al, Ti only. The manufacture process and heat-treatment conditions of 4 modified alloys are same as former INCONEL 740. All the modified alloys as solution-annealed were aged at 750°C for about 500, 1000, 2000 and 5000h, respectively.

Tab. 4 Chemical compositions of 4 modified alloy (wt.%)

Heat	C	Cr	Co	Nb	Ti	Al	Fe	Mn	Si	Mo	Ni
1	0.016	25.45	20.37	1.99	0.67	1.21	0.066	0.001	0.009	0.001	Bal
2	0.014	25.8	20.4	1.99	1.38	1.25	0.07	0.001	0.011	0.01	Bal
3	0.042	24.5	19.8	2.2	1.12	1.73	0.6	0.29	0.5	0.5	Bal
4	0.031	24.5	19.9	2.37	1.15	1.41	0.1	0.28	0.5	0.5	Bal

Figure 8 shows the SEM images of modified alloys Heat 1 and Heat 2 aged at 750°C for 5018h.

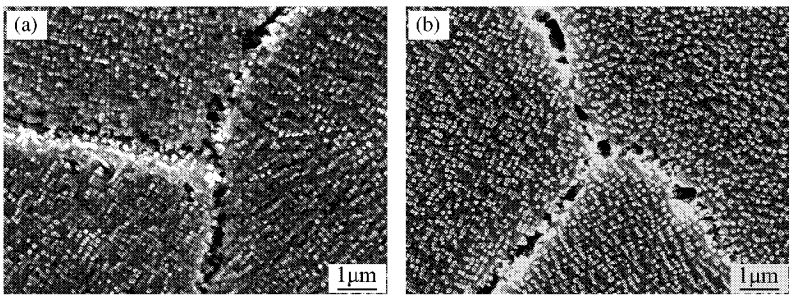

Figure 8 SEM images of the alloy aged at 750°C for 5018h (Heat 1 (a), Heat 2 (b))

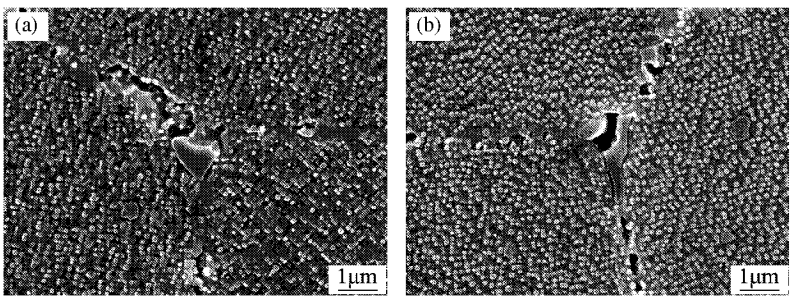

Figure 9 SEM images of the alloy aged at 750°C for 5018h (Heat 3 (a), Heat 4 (b))

The strengthening phase γ′ has been discerned clearly and a small amount of carbides was also found in the grains and at grain boundaries. In comparison with Figure 3, neither η phase in the grains nor G phase at grain boundaries can be found in the modified alloys Heat 1 and Heat 2 after long time aging for 5018h at 750°C. Figure 9 shows the SEM images of modified alloys Heat 3 and Heat 4 aged at 750°C for 5018h. The same as in Figure 8, no η phase was found but blocky carbides and G phase was found at the grain boundary. The more detailed studies on the precipitates, mechanical properties and corrosion resistance of these 4 modified alloys are still in progress.

Thermodynamic calculation was also made to evaluate the precipitates of modified alloys. Tab. 5 gives the results of phase computation. The weight percentages of γ′ phase are almost higher than 15% in the 4 modified alloys. A minimum percentage of 15% was deemed acceptable to gain the stress rupture strength target. The solution temperatures of γ′ phase in 4 modified alloys all have a large increase. Furthermore, both the precipitation temperature scope and percentage of η phase decrease clearly. These results are in accordance with experimental results as shown in Figure 8 and Figure 9.

Tab.5 Phase computation results of 4 modified alloy

Heat	Content of γ′ (η) / %		γ′ Precipitation	ηPrecipitation	σ Precipitation
	700°C	750°C	Temperature / °C	Temperature / °C	Temperature / °C
1	15.2	14.1	930	852-1014	652
2	20.3	19.1	934	749-1100	725
2	22.9	21.9	1018	950-1072	728
3	21.3	19.6	962	824-1079	699
NC*	10.9(8.5)	7.7(10.7)	850	<1118	699

* Nominal composition of INCONEL 740

Conclusions

The main structure instabilities of INCONEL 740 during thermal exposure include the γ′ coarsening, large amount of η formation and certain fraction of G phase existence at grain boundaries after long-term aging above 750°C. The γ′ particle follows a coarsening behavior of the cube rate law: $\bar{r}^3 \propto t$. The η phase can develop to a Widmanstätten pattern structure at higher aging temperatures with long term exposure. The G phase can form as larger block particles at grain boundaries. The γ′ particle growth rate and the η phase formation become fast at 760°C and the fraction of G phase increases rapidly with an increase in aging temperature.

Phase computation results shown that Al, Ti and Nb contents have an obvious effect on precipitation behavior. The improvement of structure stability of this alloy can be achieved by the adjustment of Al, Ti and Si level in the alloy. The modified alloys exhibit more stable

structure at 750°C aging till 5000h as increasing more stable γ' fraction, retarding the transformation of γ' to η and/or eliminating G phase formation.

Acknowledgements

The university authors express their appreciation to Special Metals Corporation, Huntington WV, USA for funding this project and providing the experimental materials.

Reference

[1] R. Blum. Preliminary Considerations for the Design of a Pulverized Coal Fired Steam Boiler with Ultra Supercritical Advanced Steam Parameters. *Advanced (700°C) PF Power Plant, EC Contract No. SF/1001/97/DK (1997).*

[2] G. D. Smith, S. J. Patel, N. C. Farr and M. Hoffmann.. The Corrosion Resistance of Nickel-Containing Alloys in Coal-Fired Boiler Environments. *Corrosion 99*, NACE International, Houston (1999) p.12.

[3] G. D. Smith and H. W. Sizek. Introduction of an Advanced Superheater Alloy for Coal-Fired Boilers. *Corrosion 2000*, NACE International, Houston (2000) p. 00256.1.

[4] P. Castello, V. Guttmann, N. Farr and G. D. Smith. Laboratory Simulated Fuel-Ash Corrosion of Superheater Tubes in Coal-Fired Ultra-Supercritical-Boilers. *Corrosion and Materials*, 51 (2000): p. 786.

[5] INCONEL alloy 740 Bulletin, Special Metals Corporation, Huntington, WV (2004).

[6] B. A. Baker. A New Alloy Designed for Superheater Tubing in Coal-Fired Ultra Supercritical Boilers. *Superalloys 718, 625, 706 and Derivatives 2005*, TMS (2005), p. 601.

[7] S. Zhao, X. Xie, G. D. Smith, and S. J. Patel. Microstructural stability and mechanical properties of a new nickel-based superalloy. *Mater Sci Eng A*, 355 (2003), p. 96.

[8] S. Zhao, J. Dong, X. Xie, G. D. Smith and S. J. Patel. Thermal Stability Study on a New Ni-Cr-Co-Mo-Nb-Ti-Al Superalloy. *Superalloys 2004*, TMS (2004), p. 63.

[9] S. Zhao, X. Xie, G. D. Smith and S. J. Patel. Gamma prime coarsening and age hardening behaviors in a new nickel base superalloy. *Mater Lett*, 58 (2004), p. 1784.

[10] X. Xie, S. Zhao, J. Dong, G. D. Smith and S. J. Patel. An Investigation of Structure Stability and Its Improvement on New Developed Ni-Cr-Co-Mo-Nb-Ti-Al superalloy. *Mater Sci Forum*, 475 (2005), p. 613.

[11] B, Sundman, B, Jansson and J. O. Anderson. The Thermo-Calc databank system. *CALPHAD*, 9 (1985), p. 153.

Chemistry Modifications of Inconel 706 for Improved Microstructural Stability

D. Del Genovese[1], D. Mukherji[1], J. Rösler[1], V. Kindrachuk[2], N. Wanderka[2] and J. Banhart[2]

[1] Institut für Werkstoffe, TU Braunschweig, Langer Kamp 8, 38106 Braunschweig, Germany
[2] Hahn-Meitner-Institut Berlin, Glienickerstr. 100, 14109 Berlin, Germany

Due to its combination of high mechanical strength with good fabricability and machinability, Inconel 706 is under consideration for ultra high temperature steam turbine applications with prospective steam temperatures up to 973 K. The alloy properties directly depend on the precipitation hardening system, which is based on the coherent precipitation of two kinds of A_3B-type compounds: the fcc $Ni_3[Ti,Nb,Al]$ γ' phase and the bct $Ni_3[Nb,Ti]$ γ'' phase. However, the γ' and γ'' precipitates in this alloy exhibit a metastable character, and transform to large laths of η phase (hcp $Ni_3[Ti,Nb]$) upon exposure at $T > 923$ K. This overageing process is accompanied by an unacceptable loss of creep and tensile strength. In order to overcome this impasse, two different stabilization concepts were probed. On the one hand, it was attempted to create a diffusion barrier in the matrix surrounding the γ'/γ'' precipitates by adding Rhenium to the composition of Inconel 706. Rhenium is known to effectively retard the γ' coarsening in cast single crystal Ni-base superalloys, as it strongly partitions to the matrix. On the other hand, the [Ti+Al]/[Nb] ratio of Inconel 706 was specifically refined in order to minimize the thermodynamical tendency to transformation of γ'/γ''. This modification was associated with a redesign of the Inconel 706 chemistry, resulting in a new alloy, named DT706.
The microstructures of Inconel 706, Re-modified 706, and DT706 were investigated by means of electron microscopy (SEM, TEM) and three-dimensional atom probe (3DAP) in the as-heat treated condition as well as after long-term exposure at 1023 K. Results show that Rhenium was homogeneously dissolved in the matrix, but its partitioning ratio is too low to provide an effective obstacle to the γ'/γ'' coarsening. In contrast, the microstructural degradation in DT706 was retarded as compared to Inconel 706, although the formation of η phase was not completely suppressed.

Keywords: IN706, Chemistry modification, microstructure, SEM, TEM, 3DAP

1. Introduction

Although initially conceived as material for gas-turbine components in the aerospace industry, alloy 706 has been successively developed to substitute steels in large forging parts of industrial gas turbines [1, 2]. This development was driven by the quest for higher efficiencies in the electric utility sector, which requires higher operating temperatures and larger machines. Nonetheless, it has provided extreme challenges to the metal processing industry, since the size of the forgings for land based gas turbines exceeds the largest aircraft engine by almost an order of magnitude [3]. The recent need for increased efficiency in the steam turbine industry could jack up the development of 706 one step further. For instance, the objective of the European THERMIE project is to develop an ultrasupercritical (USC) steam turbine operating with steam inlet temperatures of 700°C and higher, aiming at a thermodynamic efficiency of approximately 55% (today 48%). As steam turbine components are uncooled, substitution of currently employed ferritic steels in the hottest turbine sections constitutes a complex proposition. The use of Ni-base wrought superalloys appears as a logical consequence, but indeed the transition from gas turbine to steam turbine uses is not a straightforward enterprise as it may seem. Several challenging requirements are in fact introduced, outpacing significantly the aeroengine needs. In particular, two aspects are of dominant importance: the capability of manufacturing very large forgings (up to 50 tons) and an exceptional long term stability of the microstructure in the aimed temperature range, to ensure stable mechanical performance over the entire operating life of the power plant. Among the commercial wrought nickel-iron-base superalloys, Inconel 706 stands out for this application because it combines high mechanical strength with good fabricability and

machinability. These properties directly relate to the precipitation hardening system of alloy 706, which provides the desirable characteristic of delayed the hardening response during exposure to precipitation temperatures [4]. Similarly to alloy Inconel 718, from which Inconel 706 is derived, the primary precipitation hardening elements of 706 are niobium, titanium and aluminum. The balance between Niobium and Titanium has been judiciously chosen in Inconel 706 to minimize the tendency of segregation during solidification of the ingot, thus allowing the casting of larger ingots than those of Inconel 718. The austenitic Ni-Fe-Cr matrix of Inconel 706 is mainly strengthened by the precipitation of two kinds of coherent A_3B-type compounds: the tetragonal Ni_3Nb γ'' phase (bct, DO_{22} structure) and the cubic $Ni_3[Al,Ti]$ γ' phase (fcc, $L1_2$ structure). The major source of strengthening in Inconel 706 is γ'', resulting from coherency strain and caused by a relatively large lattice misfit between the tetragonal cell of γ'' and the cubic cell of the γ matrix. Further, precipitation of intergranular Ni_3Ti η (hcp, DO_{24} structure) platelets can occur in some heat treatment conditions. The η precipitation is reported to stabilize the grain boundaries against environmental embrittlement and enhances the creep crack growth resistance of Inconel 706 up to three orders of magnitude compared to the unstabilized material [5].

Although Inconel 706 exhibits an excellent manufacturability and adequate mechanical properties, a recent research study [6] has pointed out that Inconel 706 does not fully meet the stringent requirements of the aimed application. Namely, the thermal stability of 706 is insufficient for long term service at 700°C, which leads to a dramatic loss of creep and tensile strength. This deterioration is caused by the metastable character of the strengthening γ' and γ'' precipitates, which rapidly transform upon exposure at temperatures > 700°C into semicoherent η laths.

In order to overcome this impasse, a compositional modification of 706 seems to be necessary. In this article we report on two different strategies for the optimization of the microstructural stability. On the one hand, it was attempted to create a diffusion barrier in the matrix surrounding the γ'/γ'' precipitates by adding Rhenium to the standard composition of Inconel 706. Rhenium is known to effectively retard the γ' coarsening in cast single crystal Ni-Base superalloys, as it strongly partitions to the matrix. On the other hand, the chemistry of Inconel 706 was specifically refined in order to minimize the thermodynamical tendency for the transformation of γ'/γ''. As the stability of the metastable γ' phase depends, among other factors, on the [Ti+Al]/[Nb] ratio of the alloy, a new alloy composition was designed, resulting in the alloy named DT706 presented here.

This article reports on the microstructural characterisation of Inconel 706 and its two derivative variants Re706 and DT706 in the as heat treated condition as well as after an overageing treatment. In order to achieve a precise determination of the phase compositions, three dimensional atom probe (3DAP) was used to complement the measurements from conventional scanning and transmission electron microscopes (SEM and TEM).

2. Experimental

2.1 Material & Heat Treatments

The compositions of the alloys used for this study are given in Tab. 1. The samples of Inconel 706 were cut from a triple melted (VIM, ESR and VAR) and forged turbine disc supplied by Alstom Ltd. Switzerland. DT706 samples were sectioned from a double melted (VIM+VAR) forged bar (final dimensions: 65 x 30 x 900 mm^3) manufactured by Saarschmiede GmbH, Germany. The Re-modified alloy Re706 was a ~ 0.3 kg ingot manufactured in our laboratory. The ingot was VIM melted and cast into a plate-shaped mould. In order to achieve a full recrystallization in the subsequent stabilizing and ageing heat treatment, the plate was first

homogenized under vacuum in three steps (1253 K / 1h, 1353 K/1h and 1453 K/1h), then cold rolled by a number of passes from 3 mm to 2 mm thickness.

Table 1: Chemical composition of the investigated alloys in wt. %.

	Ni	Fe	Cr	Nb	Ti	Al	Re	C
IN706	41.96	36.93	16.01	3.06	1.56	0.21	-	0.01
Re706	45.6	31.3	15.8	3.13	1.69	0.29	1.96	0.01
DT706	53.7	22.72	17.96	3.01	1.84	0.57	< 0.1	0.01

Each block of material was initially heat treated according to the so called modified stabilization treatment (MST) cycle. This heat treatment, derived from the standard stabilization heat treatment (ST) for Inconel 706 [1], was developed by Müller and Rösler [5], aiming to increase the precipitation of intercrystalline η phase. In Inconel 706, the MST treatment results in almost three orders of magnitude higher creep crack growth resistance than the ST condition. The heat treatment parameters of the MST cycle are identical for both IN706 and Re706 alloys but differ for DT706, in order to account for the effects of a slightly higher solutioning temperature due to the corresponding compositional changes. Further, the precipitation ageing step, consists only of a single ageing at 993 K for DT706 (instead of the double aging at 993 K and 893 K for IN706 and Re706). All heat treatments are listed in Table-2.

Table 2: Heat treatment parameters.

	Solutioning	Stabilization	Ageing
IN706, Re706	1253 K / 3h with 240 K / h FC to 1093 K	1093 K / 10 h FC to RT	993 K / 8 h, with 60 K / h FC to 893 K / 8h AC to RT
DT706	1353 K / 3h with 240 K / h FC to 1108 K	1108 K / 10 h FC to RT	993 K / 8 h, AC to RT

In order to simulate the microstructural changes that may occurr on long exposure at the service temperature of the prospected steam turbine components, samples of the investigated alloys were annealed at 1023 K for 5000h. This accelerated treatment aims to artificially approximate the "mid-of-life condition" of a steam turbine (that is 10,000h at 973 K) by assuming a Larson-Miller parameter $P_{LM} = T(22 + \log t)$, with the temperature T in K and the time t in h [6].

2.2 Metallography

Specimens for scanning electron microscopy were prepared by conventional mechanical grinding and polishing. The IN706 and DT706 samples were etched with the "V2A-Beize" mixture [8] at a temperature between 333 K and 343 K. For SEM imaging of the Re706 samples a mixture of 100 ml distilled water, 100 ml HNO_3 (65%), 100 ml HCl (37%) and 3 g of MoO_3 (85%) at ambient temperature was used as etchant. Foils for transmission electron microscopy were prepared by twin jet-polishing at 258 K with a solution of 30 ml ethylene-glycol monobutyl ether, 63 ml ethanol and 7 ml $HClO_4$. A Leo 1550 Gemini SEM with field emission gun and in-lens detector, and a point to point resolution of 3 nm and a Philips CM 12 TEM operating at an acceleration voltage of 120 kV was used for microstructural studies.
The Vickers hardness of the samples was measured according to EN 6507-1, applying a load of 98.1 N for 30 s.

2.3 3-Dimensional Atom Probe (3DAP)

The samples used for 3DAP analyses were cut into rods of 0.2 x 0.2 x 10 mm^3. From these rods tips with radius < 50 nm were prepared by electropolishing in two steps: first in a solution of 15 % perchloric acid in 85 % acetic acid and second in an electrolyte of 2 % perchloric acid in butoxyethanol. The 3DAP analyses were performed in vacuum of 10^{-8} Pa at a temperature of 60 K with a pulse fraction of 20 % and a pulse repetition rate of 1kHz. A CAMECA Three-Dimensional Tomographic Atom Probe was employed.

3. Results

3.1 Electron Microscopy

Microstructures after MST heat treatment

The microstructure of IN706 after the MST heat treatment is presented in fig. 1. The majority of the grain boundaries are decorated with discontinuous platelets having length between 0.5 μm and 3 μm. These particles were identified as hexagonal η phase from the analysis of the selected area diffraction pattern. The composition of the plates (measured by EDS in TEM, see Tab. 3) differs from the stoichiometric Ni_3Ti formula, revealing a large solubility for Nb and other elements such as Fe, Cr and Al. A small fraction of thin needles of η phase is also precipitated in the grain interior. The matrix is mainly hardened by a dispersion of fine γ'/γ" particles, as shown in figure 2. They are present in two morphologies, the "compact" type (consisting of a cuboidal γ' particle mantled on all six facets by shells of γ") and the "non-compact" type (i.e., a core of γ' sandwiched between two discs of γ"). The fraction of non-compact co-precipitates prevails over the compact type. Besides, larger co-precipitates consisting of a coarse γ" disc in epitaxy with an elongated γ' particle are also dispersed in the matrix (see fig. 2).

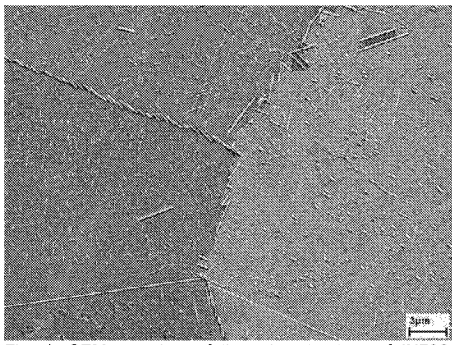

Fig. 1: SEM overview of the microstructure of IN706 after MST heat treatment.

Fig. 2: TEM micrograph of IN706 MST showing the presence of compact and non-compact γ'/γ" co-precipitates. Also visible is a large γ" disc to which a γ' particle is attached.

An overview of the DT706 microstructure is given in fig. 3. The grain boundaries are decorated by cellular η precipitates, which form in some cases large nodules extending into the grain interior. A TEM image of the intragranular structure is shown in fig. 4, displaying a bimodal particle distribution. The larger particles are primary precipitates formed during the η-stabilization step at 1108 K, whereas the finer particles (secondary precipitates) have formed during the final ageing at 993 K. The γ'/γ" particles are generally larger in size and more widely spaced than in IN706. Although both the compact and the non-compact γ'/γ" types have precipitated in DT706, the major fraction of γ'/γ" co-precipitates are of the compact morphology, in

contrast to IN706. No coarse γ'/γ" precipitates were found in DT706. A detailed characterization of the precipitation behaviour of DT706 alloy is reported in [9].

Table 3: Phase composition in at. %, detected by EDS analysis.

Phase	Ni	Fe	Cr	Nb	Ti	Al	Re
η_{IN706}	71.4 ± 1.35	5.7 ± 0.55	1.0 ± 0.55	7.5 ± 0.45	13.5 ± 0.43	-	-
η_{Re706}	62,25 ± 1,0	10,29 ± 1,7	3,13 ± 0,9	8,9 ± 1,2	14,2 ± 1,2	1,16 ± 0,3	0,09 ± 0,07

A SEM image of Re706 is shown in fig. 5. Two types of particles are precipitated intergranularly in this alloy: discontinuous platelets and rounded / blocky particles. The compositions of these particles were analysed by EDS in the SEM. The platelets are identified as $Ni_3(Ti,Nb)$ η phase, whereas the blocky precipitates exhibit an A_2B stoichiometry that can be ascribed to the Laves phase. TEM bright field image and selected area diffraction pattern (SAD), shown in fig. 6, demonstrates that γ'/γ" precipitates are also present in this alloy. However, they are significantly finer than in IN706 and DT706, and are consequently not visible in fig. 5. Due to their extremely small size, a precise determination of the precipitate / co-precipitate morphology was not attempted.

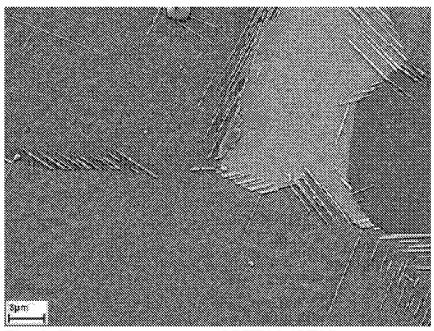

Fig. 3: The microstructure of DT706 (SEM).

Microstructures after overageing

The structure of the MST heat treated Inconel 706 after overage annealing (5000h at 1023K) is shown in Fig. 7. While the intergranular structure does not manifest an evident coarsening as compared to the initial heat treated state, the intragranular γ'/γ" particles have completely transformed into η laths, having a Widmanstätten morphology.

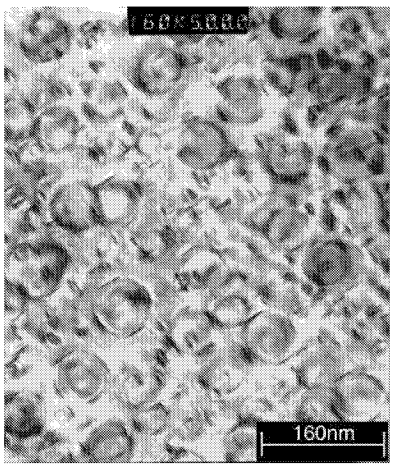

Fig. 4: TEM bright field image showing the distribution of the γ'/γ'' precipitates in DT706.

The overaged microstructures of the DT706 and Re706 samples are presented in figures 8 and 9, respectively. Although both experimental alloys show degradation of the initial microstructure, the

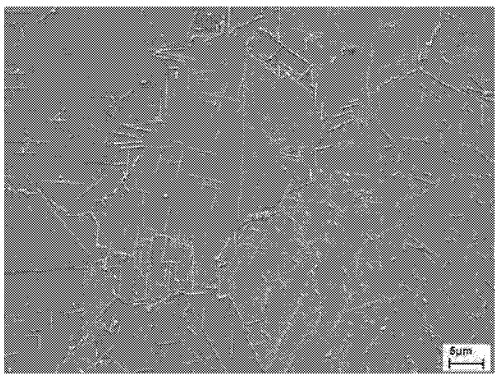

Fig. 5: SEM micrograph of the Re706 sample.

state of coarsening and phase transformation differ from each other. In DT706 only a relatively moderate fraction of the original γ' particles has transformed into η phase after overageing, while the remaining γ' precipitates have grown to a size of about 250 nm, as further documented in fig. 10. The shells of γ", which originally covered the cuboidal γ' particles, are almost completely dissolved. Some remaining γ" phase has the morphology of relatively large discs after overageing, usually in epitaxy with γ' particles. In contrast, the grain interiors of the overaged Re706 sample exhibits a bimodal distribution of long and short Widmanstätten plates, plus a very low fraction of coarse γ' and γ" particles.

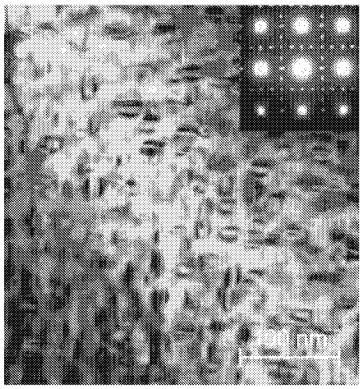

Fig. 6: TEM bright field image of Re706. The SAD pattern in the inset proves that both γ' and γ'' phases are precipitated in the matrix.

Hardness

Figure 11 shows the hardness as a function of the ageing time at 1023K for the investigated alloys. All alloys display a gradual decrease in hardness, which tends to reach a stationary value after prolonged exposure. The hardness of DT706 in the overaged condition is 74% of the initial value, compared to 62% and 57% for IN706 and Re706, respectively.

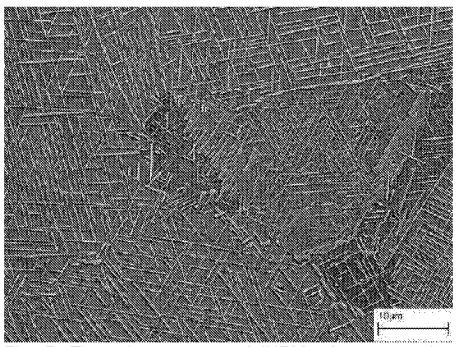

Fig. 7: The microstructure of IN706 after overageing treatment ($18*10^6$ s / 1023K), taken at the SEM.

3.2 Three-dimensional Atom Probing

The composition of different γ' and γ" precipitates after MST heat treatment is measured using 3DAP. The spatial reconstruction of the atom positions detected by 3DAP allows identification of the size, the morphology and the composition of different precipitates in the investigated alloys after heat treatment, revealing sometimes the presence of fine particles which were not clearly resolved in the electron microscope. In IN706, for instance, individual γ' precipitates – but no individual γ'' - were detected by 3DAP. These particles (not seen in the TEM) are extremely small. Non-compact γ'/γ'' co-precipitates were identified, too. The examination of the precipitates in Re706 revealed a mixed distribution of individual and combined γ'/γ'' particles. The typical size of the individual γ' and γ'' particles, and that of the γ'/γ'' co-precipitates are about 10 nm. In the analysed volumes of DT706 large and

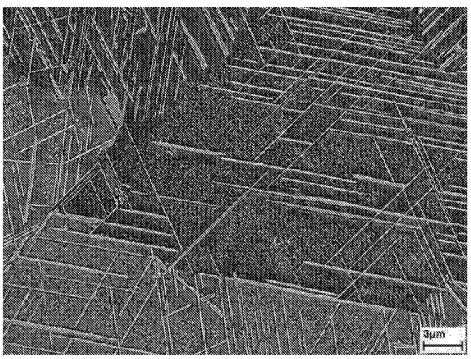

Fig. 8: The microstructure of DT706 after overageing treatment ($18*10^6$ s / 1023K), taken at the SEM.

small γ′ particles, corresponding to the primary and secondary precipitates respectively, were encountered. No shells of γ" were however found in the reconstructed volumes.

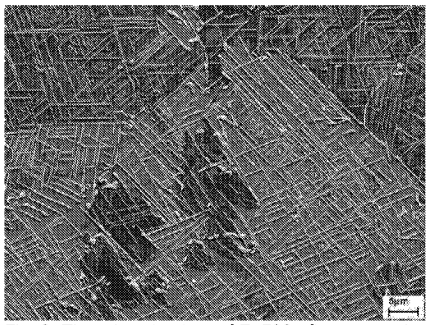

Fig. 9: The microstructure of Re706 after overageing treatment (18*10^6 s / 1023K), taken at the SEM.

The compositions of the γ' and γ" phases for the different alloys after heat treatment are listed in table 4. The γ′ phase in IN706 shows a higher concentration of Ti (~ 17 at. %), regardless of the particle morphology (individual particles or in epitaxy with γ′′). On the contrary, the Al and Nb contents of the individual and combined γ′ are slightly different. The individual γ′ particles contain 5.1 at. % Al, but the Al content is lower in the combined γ′ particle (3.5 at. %). The concentrations of Niobium in the individual and combined particles of □′ are comparable to that of Aluminium, but it shows the inverse partitioning tendency. The γ′′ composition indicates a relatively large solubility for Ti (7.0 at. %).

Table 4: Phase compositions in at. % of the investigated alloys after MST heat treatment, as measured by three-dimensional atom probe. (Ind. = individual precipitate, copr. = co-precipitate, pr. = primary precipitate, sec. = secondary precipitate).

	Ni	Al	Ti	Nb	Cr	Fe	Re
				IN706			
γ	36.8 ± 0.5	0.47 ± 0.1	1.0 ± 0.1	1.0 ± 0.1	16.1 ± 0.6	44.2 ± 0.7	
γ'_{ind}	70.1 ± 0.6	5.1 ± 0.4	17.2 ± 0.5	3.8 ± 0.3	0.4 ± 0.1	3.1 ± 0.3	
γ'_{copr}	70.2 ± 0.6	3.5 ± 0.3	17.0 ± 0.6	6.1 ± 0.3	0.7 ± 0.1	2.1 ± 0.2	
γ''_{copr}	69.9 ± 0.7	-	7.0 ± 0.3	20.6 ± 0.7	0.7 ± 0.1	1.8 ± 0.2	
				DT706			
γ	44.8 ± 0.4	0.46 ± 0.03	0.57 ± 0.01	1.8 ± 0.2	24.3 ± 0.3	28.2 ± 0.6	
γ'_{pr}	70.1 ± 0.8	8.1 ± 0.6	13.7 ± 1	4.9 ± 0.4	0.5 ± 0.1	2.7 ± 0.4	
γ'_{sec}	69.9 ± 3	8.8 ± 2	11.5 ± 2	6.2 ± 2	0.7 ± 0.4	2.8 ± 0.6	
				Re706			
	36.9 ± 1	0.36 ± 0.04	0.38 ± 0.05	0.7 ± 0.2	17.2 ± 1	43.6 ± 0.5	0.79 ± 0.05
γ'_{ind}	76.1 ± 2	3.1 ± 0.3	12.1 ± 2	5.2 ± 1	0.78 ± 0.2	2.6 ± 0.4	0.25 ± 0.1
γ'_{copr}	76.45 ± 3	3.36 ± 0.8	12.63 ± 2	4.67 ± 1	0.38 ± 0.2	2.31 ± 0.3	0.20 ± 0.1
γ''_{ind}	75.26 ± 2	0.11 ± 0.1	9.15 ± 1	12.92 ± 2	0.63 ± 0.3	1.62 ± 0.9	0.32 ± 0.2
γ''_{copr}	75.02 ± 3	0.1 ± 0.1	8.77 ± 2	13.33 ± 3	0.85 ± 0.3	1.66 ± 0.6	0.274 ± 0.2

The compositions of the γ′ and γ′′ phases in Re706 differ only marginally from IN706. The γ' precipitates (both individual and the co-precipitates) have higher Ni but lower Ti. The three-dimensional reconstruction of the various atom distribution shows that the matrix has 3-4 times higher Re content than in the γ' precipitates, and the spatial distribution of Rhenium in the matrix is not homogeneous. However, no preferential Re enrichment at the γ/γ' interfaces were observed.

The results of the 3DAP analysis of DT 706 are listed in Table 4, too. The average compositions of the primary and secondary γ' precipitates are similar, as the differences between the two kinds of particles are maintained within the statistical uncertainties. The γ′ particles contain a similar amount of Ni and Nb as in IN706, but about 5 at.% more Al and correspondingly less Ti.

The concentration ratios (γ/γ') of the various elements for different precipitate morphologies in different alloys are listed in table 5. It may be noted that these values are not partitioning ratios, since the alloys contain more than two phases.

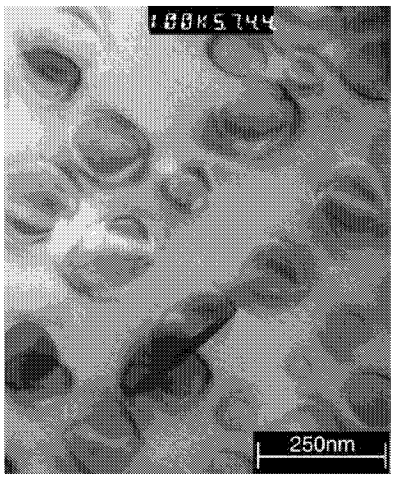

Fig. 10: Detailed Bright Field TEM image of the transgranular particles in DT706 after overageing.

Table 5: γ/γ' Concentration ratios for the different alloying elements calculated from the data presented in table 4.

	Ni	Al	Ti	Nb	Cr	Fe	Re
				IN706			
$\gamma/\gamma'_{ind.}$	0.5	0.09	0.06	0.27	40	14.3	/
$\gamma/\gamma'_{copr.}$	0.5	0.13	0.06	0.16	23	21	/
				DT706			
γ/γ'_{pr}	0.64	0.06	0.04	0.37	48.6	10.4	/
				Re706			
$\gamma/\gamma'_{ind.}$	0.48	0.12	0.03	0.13	22.1	16.8	3.16
$\gamma/\gamma'_{copr.}$	0.48	0.11	0.03	0.15	45.2	18.9	3.95

4. Discussion

The microscopic investigations on Inconel 706 demonstrated that the overageing treatment chosen for this study (which is presumed to approximately simulate the effects of a thermal exposure corresponding to the mid of life condition of a steam turbine disk), leads to an extreme deterioration of the initial microstructure. As the hardening γ' and γ" particles transform into long laths of η phase after 5000h at 1023 K, the mechanical strength of the alloy is dramatically affected. This softening effect is confirmed by the hardness measurements, which shows that the hardness in the overaged state of IN706 is only approx. 2/3 of that in the as heat treated condition.

In contrary to the expectations, the Rhenium modified variant of Inconel 706 does not show a significant increase of the thermal stability. The amount of remaining γ'/γ" precipitates after the overageing treatment is small and the final hardness of Re706 is almost the same as that of IN706. A possible explanation is offered by the results of the 3DAP investigations. It was shown that the partitioning of Rhenium between γ / γ' is not as strong as in the case of new generation single crystal superalloys [10]. In Re706 the matrix has only about 2 to 3 times more Re than in the γ' phase. Further, the Re atoms do not tend to accumulate in the region surrounding the γ/γ' interfaces in the matrix side, and thus do not effectively hinder precipitate growth. The results of this study therefore suggest that alloying with Re is not the right choice in order to stabilize the structure of Ni-Fe wrought superalloys such as Inconel 706.

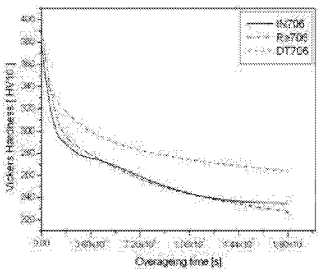

Fig. 11: Hardness profiles of the tested alloys as a function of the overageing exposure at 1023 K.

On the other hand, it was observed that the thermal stability of DT706 is significantly improved. Although the γ' particles have coarsened to larger sizes and have also partly transformed into η phase, a significant fraction of them is retained even after the overageing treatment, thereby preserving a substantial part of the initial strength of the matrix. The improvement is mainly ascribed to the change in composition of the matrix and the precipitate phases which thermodynamically stabilize the γ' phase in DT706. It also leads to a lower γ / γ' lattice misfit value compared to that in Inconel 706 [11]. Beside this aspect, other microstructural factors, like different precipitate morphology and distribution of the γ'/γ" co-precipitates, or the lower fraction of the γ" phase, could also have an influence on the improved stability of the microstructure. The encouraging results demonstrate that the design concept of DT706 represents a successful step forward in the development of new 706 chemistry to meet the requirements of the USC steam turbine application.

5. Acknowledgements

The authors are grateful to the Deutsche Forschungsgemeinschaft (DFG) for the financial support for the Projects: Wa-1378/5-3 and Rö 2045/12-3. Thanks are also due to Alstom LTD, for the kind supply of the IN706 material.

References

[1] P.W. Schilke, R.C. Schwant, Alloy 706 use, process optimization, and future directions for GE gas turbine rotor materials, Superalloys 718, 625, 706 and Various Derivatives, (2001), pp. 25-34.
[2] H.L. Eiselstein, Properties of Inconel alloy 706, ASM tech. Rep. No. C 70-9.5 , Metals Park, Ohio, (1970), pp. 1-21.
[3] S. V. Thamboo, R. C. Schwant, L. Yang, L. A. Jackman, B. J. Bond, R. L. Kennedy, Large diameter 718 ingots for land-based gas turbines, Superalloys 718, 625, 706 and Various Derivatives, (2001), pp. 57-70.
[4] Inconel alloy 706 (technical broschure), Huntington Alloys Inc., (1974).
[5] J. Rösler, S. Müller, D. Del Genovese, M. Götting, Design of Inconel 706 for Improved Creep Crack Growth Resistance, Superalloys 718, 625, 706 and Various Derivatives, (2001), pp.523-534.
[6] J. Rösler, M. Götting, D. Del Genovese, B. Böttger, R. Kopp, M. Wolske, F. Schubert, H.-J. Penkalla, T. Seliga, A. Thoma, A. Scholz, C. Berger, Wrought Ni-Base Superalloys for Steam Turbine Applications beyond 700 °C, Advanced Engineering Materials, Volume 5, (2003), pp. 469 – 483.

[7] D. Mukherji, P. Strunz, D. Del Genovese, R. Gilles, J. Rösler; A. Wiedenmann, Investigation of microstructural changes in INCONEL 706 at high temperatures by in-situ small-angle neutron scattering, Metal. Mater. Trans. A, 34A, (2003), pp. 2781-2792.
[8] G. Petzow, Metallographisches, keramographisches, plastographisches Ätzen, (1994), p. 241.
[9] D. Del Genovese, P. Strunz, D. Mukherji, R. Gilles, J. Rösler, Microstructural Characterization of a Modified 706-type Ni-Fe Superalloy by Small-Angle Neutron Scattering and Electron Microscopy, Metal. Mater. Trans. A, 36A, (2005), pp. 3439-3450.
[10] D. Mukherji and J. Rösler, Effect of the γ' volume fraction on the creep strength of Ni-bae superalloys, Z. Metallkd. **94** (2003) 478-484
[11] M. Hoelzel, D. Del Genovese, R. Gilles, D. Mukherji, D.M. Toebbens, J. Roessler and H. Fuess, Phase analysis and lattice mismatches in superalloys DT706 and Iconel 706, Physica B (2006) in print.

CRACK GROWTH BEHAVIOUR OF WASPALOY AT 700 °C IN DIFFERENT ATMOSPHERES

H.J. Penkalla, F. Schubert, L. Singheiser

Research Centre Jülich, Institute for Materials and Processes in Energy System
D-52425 Jülich, Germany

h.j.penkalla@fz-juelich.de

Abstract:

An investigation of the fatigue and creep fatigue crack growth behaviour at 700 °C in vacuum and in air of the material Waspaloy is presented. Beside the presentation of the mechanical properties in form of crack growth rates a main aspect of this investigation is the observation of the micro structural processes near the crack tip and their dependency on the environment. Particularly hints for the SAGBO effect (stress accelerated grain boundary oxidation) were observed by transmission electron microscopy (TEM). A special method to prepare suitable TEM specimens from CT specimens with focused ion beam (FIB) was developed.

Keywords: Waspaloy, fatigue and creep fatigue crack growth, SAGBO effect, SEM and TEM

1. Introduction

The efficiency of fossil fired steam power plants can be markedly improved by the construction of steam turbines with steam inlet temperatures of 700°C or above. The realisation of ultra supercritical steam cycle plants leads to an efficiency level of about 55% [1].

The application temperatures of advanced ferritic steels are limited to temperatures below 650°C. It seemed to be mandatory to use Ni-base alloys for the hottest parts in an ultra-supercritical steam turbine. Following the trend to large engines (increased power supply) some parts, like the rotors, are increasing loaded by additional higher loadings due to the increased centrifugal forces. A certain number of Ni-base superalloys, which can withstand these high temperature loadings, are known from the use in air-jet-turbine-engines. But due to the expected component size (rotor discs with >1 m diameter) and weights (above 10 tons) the fabricability of this kind of components is still not satisfactorily solved. In a former research program [2] some of the wrought superalloys have been examined concerning their potential for the application for rotors in steam turbine. The alloys are representative for 1) a solid solution hardened material (Alloy 617) 2) for a γ'-precipitation hardened superalloy (Waspaloy) and 3) for the γ'/γ''-precipitation hardened Fe-Ni-base alloys (Inconel 706).

Beside the questions concerning fabricability (melting and remelting procedures, forging procedures) the high temperature behaviour of yield strength, the creep resistance and the crack initiation and the crack growth at high temperature are the most important design criterions for gas and steam turbine rotors. The crack growth behaviour under cyclic and steady loading seems to be very dependent on the microstructural processes in and at the grain boundarie. For alloy 706, the crack growth can be too high due to environmental

embrittlement of the grain boundary [4], referred as SAGBO (Stress accelerated grain boundary oxidation [3,5]), The following examinations may provide an impression, how far the γ´-hardened Ni-base alloy Waspaloy suffers under grain boundary processes of oxidation under mechanical loadings at 700°C. The main effort was concentrated on the metallographic examinations in the regions of the crack path and the crack tip.

2. Experiments

2.1 Test material

Waspaloy is a γ' hardened Ni-base wrought alloy with the chemical composition given in Table 1. The heat treatment results in a microstructure with a bimodal γ´-size distribution with a volume fraction of about 25%. The bimodal γ' precipitates split into about 20 vol-% fine spherical with a mean diameter of about 30 to 50 nm and about 5 vol-% coarse spherical γ' particles with diameters of about 250 to 300 nm. Additionally some primary TiN and Ti(C, N) and some secondary globular Cr-carbides $M_{23}C_6$ at the grain boundaries can be detected. The mean grain size of the tested material was of ASTM 3-4. Fig. 1 includes a typical metallographic image and a TEM dark field image of the bimodal γ' size distribution [4].

element	Ni	Fe	Cr	Ti	Al	Co	Mo	C	B
Weigth-%	Bal.	0,57	19,5	3,05	1,4	13,5	4,25	0,06	0,005

Table 1: Chemical composition of Waspaloy.

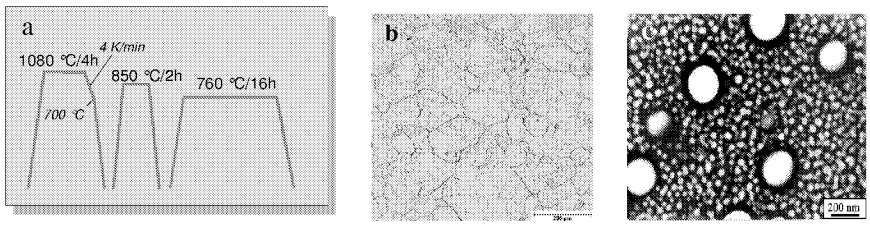

Figure 1: Scheme of the heat treatment a), microstructure after heat treatment: b) light microscopy, c) TEM dark field image with γ' particles distribution

The specimens were machined out of an experimental forging produced by Saarschmiede for the DFG-Programme [2]. All ½ inch CT- specimens for crack growth experiments were fabricated with guide notches.

2.2 Crack growth tests

Fatigue crack growth tests (FCG) and creep fatigue crack growth tests (CFCG) were carried out at 700 °C in a servo hydraulic INSTRON test machine, equipped with an environmental chamber, which allows the usage of different gases or vacuum as test environments. Both types of tests were carried out under vacuum and in air. The specimens were heated by an induction coil and the crack growth was observed by the potential drop method. Before the test at 700 °C, the specimens were cyclic loaded at room temperature in a resonance machine until an initial crack of about 8 mm was generated.

The loading cycles of the FCG tests were of sinus shape with a frequency of 5 Hz.. The loading cycle of the CFCG test was a trapezoid cycle with 300 s dwell time at the maximum tensile load of 5.6 kN, 1 s uploading and downloading and 1 s dwell time at the minimum load of 0.5 kN. The R value was 0.1.

After the crack growth tests at 700 °C the specimens were post cyclic loaded within the high frequency resonance machine at room temperature until final rupture. After the rupture the crack length generated at 700 °C was determined under a light microscope for the normalisation of the potential drop measurements results. After that the K_I values were determined by the program "Cracker" [5].

Two additional CFCG test were carried out to prepare TEM specimens from the area near the crack tip and to demonstrate the change of crack growth rate with changing environment (vacuum and air). The first CFCG test was terminated after 1000 cycles in vacuum and the CT specimen was directly prepared to TEM specimen. The other CFCG test was terminated after 1200 cycles in vacuum, then cooled down to room temperature and deloaded to a minimum load of 0.5 kN. After changing the environment into air, the specimen was reheated and reloaded for further 900 cycles. The resulting crack length during this test was calculated by the observed potential drop curve, which has been calibrated before the experiments with the potential calibration curve. This specimen was also used for the later crack tip preparation for TEM observation.

2.3 Micro structural investigations

The fracture modes and the resulting oxide scales at the surfaces of fracture branches were investigated by light microscopy (LM) and by scanning electron microscopy (SEM). A special software from PROIMAGE for light microscopy was used to create sharp images of the rough fracture surface with high magnification. Using a layer technique, this software reconstructs a sharp image from a set of images with different focal planes. This technique was important to observe the oxide scales near the crack tip of the broken specimens after the FCG and CFCG tests.

For SEM investigations a ZEISS Gemini 1540 scanning electron microscope was used.

2.4 Crack tip preparation by Focused Ion Beam (FIB)

For the investigation of the crack tip of the CFCG tests after the simulation on air ingress and the propagation in air were terminated and not post ruptured at room temperature. In a first step one side surface was grinded and polished to eliminate the crack guide notch. This procedure was applied to observe the penetration depth of the crack under a light microscope. Then the CT specimen was cut under an angle of 45 ° to slices of about 2 mm thickness. By this way each slice contains a part of the crack and the crack front is now oriented about 45 ° to the slice surface. This fact is important for the subsequent cutting of a TEM specimen and prevents a break of the very thin TEM specimen during the subsequent FIB preparation. Fig. 2 demonstrates the procedure of CT specimen machining schematically. Fig. 3 shows the path of the diversified crack in the slice used for subsequent FIB preparation and the marks the prepared crack tip.

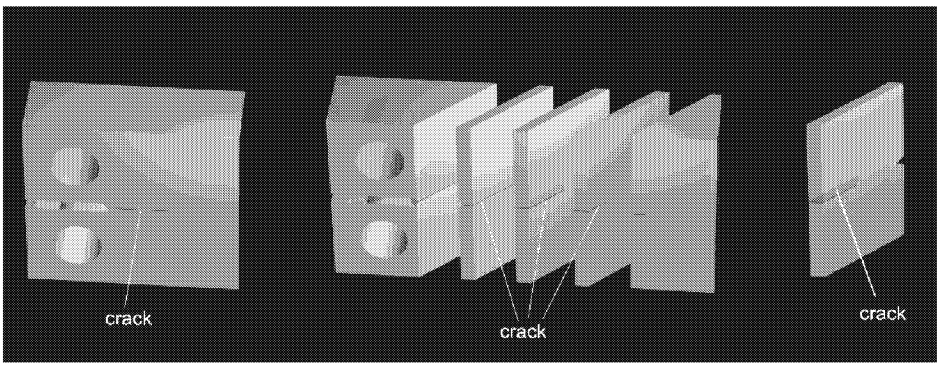

Figure 2: Machining of the CT specimen after crack growth test. The side plane was grinded (a) until the crack is visible. After cutting into thin slices under 45 ° (b) each slice contains a part of the crack (c) ready to prepare by FIB.

The subsequent preparation of a TEM specimen from one of the thin slices was carried out in a ZEISS Cross Beam 1540 dual beam FIB with combined electron and ion source. The focused ion beam with an energy of 30 keV allows the cutting of material in the micron and submicron range. During the cutting with the ion beam the process can be observed by the electron beam simultaneously.

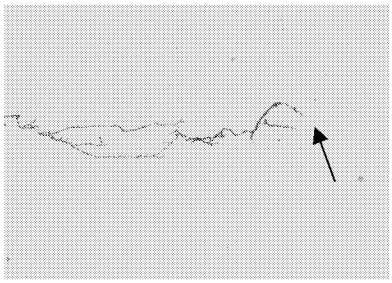

Figure 3: Path of the CFCG crack in the used slice and prepared crack tip (arrow)

Fig. 4 demonstrates the further process of preparation. Below the crack tip observed with the electron beam a rectangular trough of about 15 µm width was cut until the crack tip was just visible in the wall of the tough (Fig. 4a). Then a second trough from the other side was cut until the residual wall or lamella between both troughs exhibited a thickness of about 1 – 2 µm (Fig. 4b).

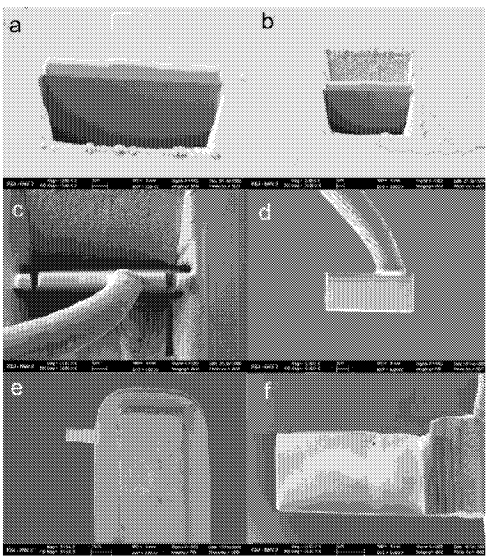

Figure 4: Steps of TEM specimen preparation by FIB with the in-situ lift-out method.

In order to separate the wall between both toughs a micro-manipulator controlled, very thin W needle was fixed at the top of the lamella by W deposition which occurred during the decomposition of W-carbonyl under the influence of the ion beam (Fig. 4c). The lamella was cut on both sides and at the

base of the wall. The lamella fixed at the needle (Fig. 4d) was shifted to an OMNIPROBE specimen holder and fixed in the same manner. Subsequently, the needle was detached from the lamella by cutting with the ion beam (Fig. 4e). In a last step, the lamella was polished by a low current ion beam parallel to the lamella surface until the lamella was electron transparent (Fig. 4f).

3. Results and discussion

3.1 Fatigue and creep fatigue crack growth

The fatigue crack growth rate da/dN of Waspaloy at 700 °C in air and vacuum in dependence on the stress intensity factor ΔK_I is compared in Fig.5. Both curves tend to nearly the same threshold of about 16 MPa $m^{1/2}$. In the range of steady state crack growth the crack growth, rate curves are described by the Paris equation

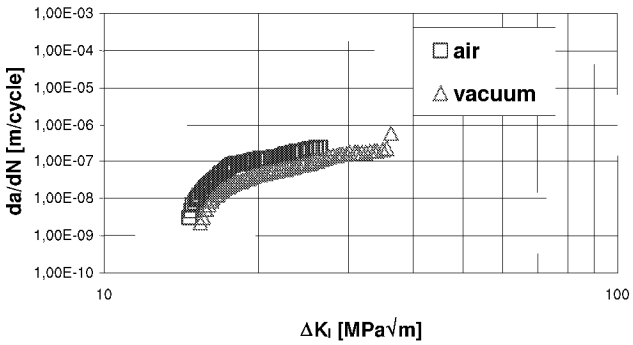

Figure 5: Fatigue crack growth behaviour of Waspaloy at 700 °C in air and in vacuum.

$$\frac{da}{dN} = C \cdot \Delta K_I^{\,n} \qquad \text{(da/dN in m/cycle, } \Delta K \text{ in Mpa}\sqrt{m}\text{)}$$

the constants C and n result to $C = 1.18 \cdot 10^{-11}$ and n =3.143 for vacuum, and $C = 4.32 \cdot 10^{-12}$ and n = 3.103 for air.

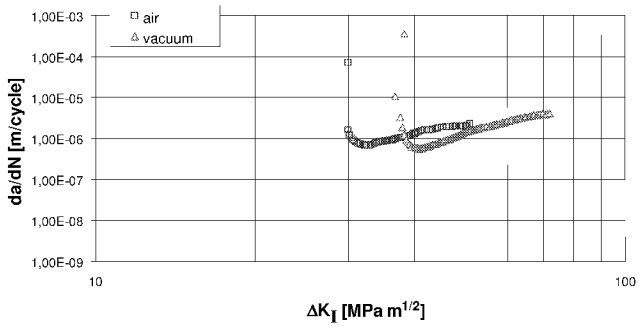

Figure 6: Creep fatigue crack growth behaviour of Waspaloy at 700 °C in vacuum and air, 300s dwell time.

The creep fatigue crack growth rates at 700 °C in air and in vacuum vs. the stress intensity factor ΔK_I are given in Fig. 6. The threshold value for air tends to about 29 MPa $m^{1/2}$ and seems to be lower than the threshold value for vacuum with about 36 MPa $m^{1/2}$. Up to a ΔK_I value of about 55 MPa $m^{1/2}$, the creep fatigue crack growth rate in air is higher than under vacuum. The tendency of both curves indicates that the influence of air on the creep fatigue crack growth disappears at higher ΔK_I values.

The result of the creep fatigue crack growth tests with changing environment are given in Fig. 7. During the first 1200 cycles the specimen was loaded under pure vacuum, then an air ingress is simulated by cooling down after deloading, and finally reloaded and reheated in air. The average crack growth rate da/dN of the specimens increased from $3.1 \cdot 10^{-4}$ mm/cycle under vacuum to $5.55 \cdot 10^{-4}$ mm/cycle in air.

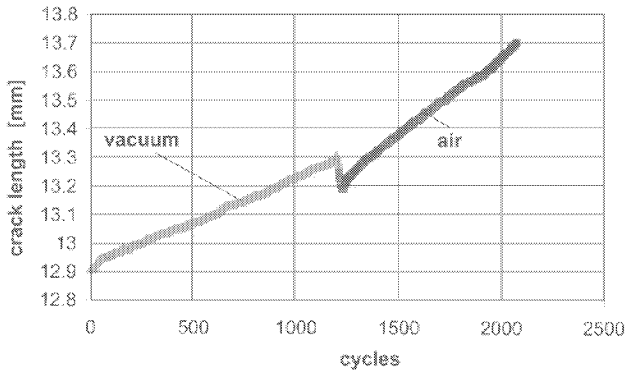

Figure 7: Creep fatigue crack growth of Waspaloy at 700 °C in changing environment.

3.2 Fracture surface and oxide layer

Fig. 8 represents a typical macro image of the CT-specimen fracture surface from crack growth tests in air with clearly visible parts of the crack. Part I is the initial crack generated at room temperature with the resonance machine, part II is the crack generated at 700 °C, part III the crack generated under HCF loading at room temperature, and part IV indicates the final rupture of the specimen. This example of the FCG test showed a strongly oxidised initial crack surface in part I. The surface of the fatigue crack in part II exhibited only a very thin, homogeneously golden-orange coloured oxide layer. Region III and IV are, as expected, free of oxide layers.

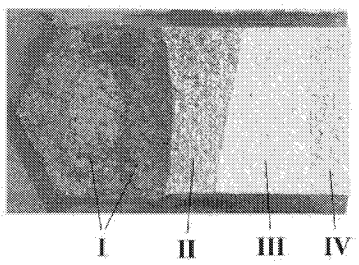

Figure 8: Macro image from the CT-specimen fracture surface from the FCG test in air.

In the following investigation by light microscopy the resulting colours of the thin oxide scale on the fracture surface was used as an indicator for the oxidation around the crack tip. Fig. 9a shows an LM image from the FCG crack front. The parallel path of the oxide scale front indicates a distance between both of about 4 µm. This means that under the given FCG conditions (cyclic loading) no SAGBO effect can be observed.

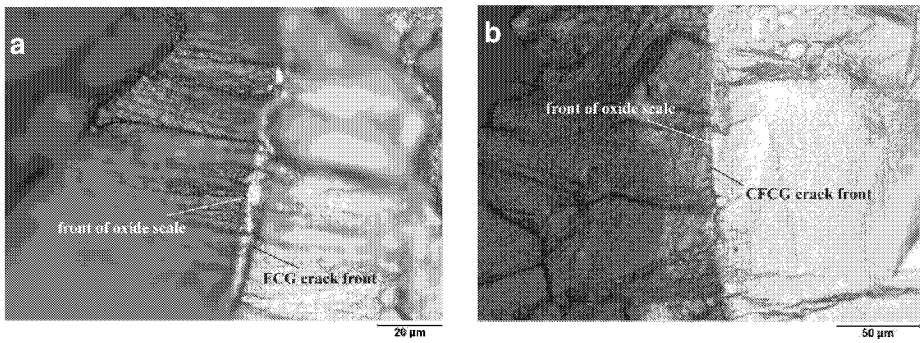

Figure 9: Sharpness corrected LM images from the FCG crack front (a) and CFCG crack front (b).

Another impression is given in Fig. 9b which shows the CFCG crack front after test. The oxide scale is dark gray coloured and thicker than in Fig. 9a. Near the crack front a transition

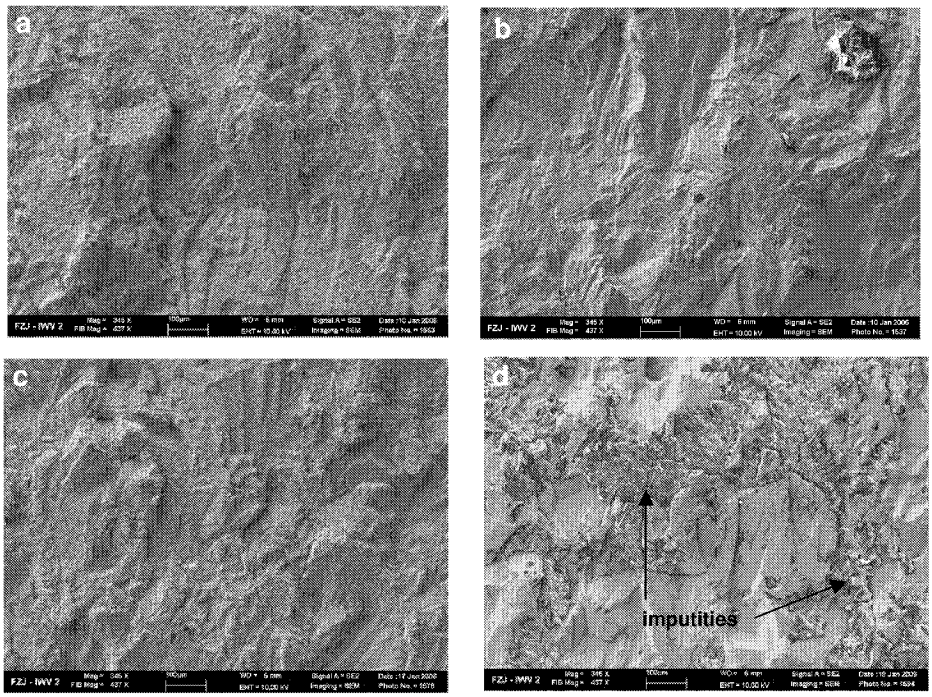

Figure 10: SEM images from the fracture surfaces: (a) FCG test in vacuum, (b) FCG test in air, (c) CFCG test in vacuum, (d) CFCG test in air.

range with a thinner oxide scale was observed but the oxide scale front coincides with the crack front. Under the CFCG loading condition an influence of oxygen on crack growth behaviour could be possible, but the results do not prove the SAGBO effect.

The results of SEM investigations are presented in Fig. 10a to 10d. Both crack surfaces from the FCG tests in vacuum (Fig. 10a) and in air (Fig. 10b) show mainly transcrystalline rupture. The fracture surfaces in Fig 10c (vacuum) and Fig. 10d (air) are caused under CFCG loading conditions and contain higher proportions of intercrystalline ruptures. The fractured specimen after the CFCG test in air provided a certain amount of impurities in the crack branch (Fig. 10d). The chemical analysis by EDX demonstrates the typical elements of slag, possibly caused by the remelting during the material production. This fact must be kept in mind for the interpretation of the creep fatigue crack growth in air as presented in Fig. 6, where the test in air showed a significantly lower threshold than in vacuum.

3.2 Crack tip investigation with TEM

The results of the TEM analysis are shown in Fig. 11. Fig. 11a represents the FIB prepared

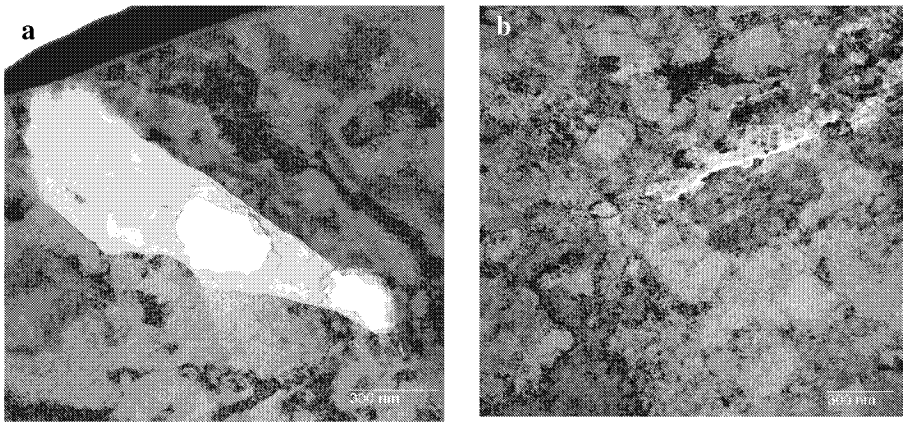

Figure 11: TEM images of CFCG cracks in vacuum (a) and in air (b).

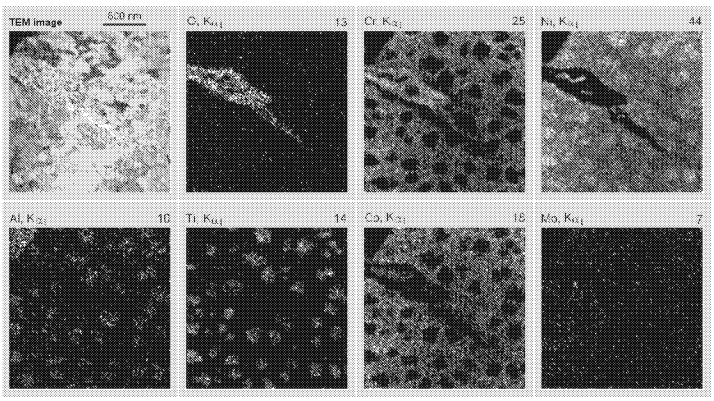

Figure 12: EDX element maps from the crack surrounding. The higher intensity of Cr and O indicate a Cr-oxide scale.

crack tip of the CFCG test under vacuum condition. The interior of the crack was identified as impurity caused by the polishing of the specimen surface before FIB preparation. The rounding of the crack tip indicates a plastic deformation around the crack. The dark fringes around the crack are ranges of high dislocation density and characterise the boundary of a plastic zone at the crack tip.

Fig. 11b shows the course of the CFCG crack generated in air. In order to detect the oxide scale around the crack, an EDX element map was taken (compare Fig. 12). The higher intensity of Cr and O indicate a Cr-oxide scale. The oxide scale, however, has been grown only on one side of the crack. This fact can be a point that the crack growths along the oxide scale and matrix interface, assumed the penetration of the oxide is locally deeper than the penetration of the crack. A detailed analysis of the crack tip is shown in Fig. 13. The crack tip is about 50 nm displaced from the main course of the crack. The oxide scale shows no deeper penetration than the crack tip.

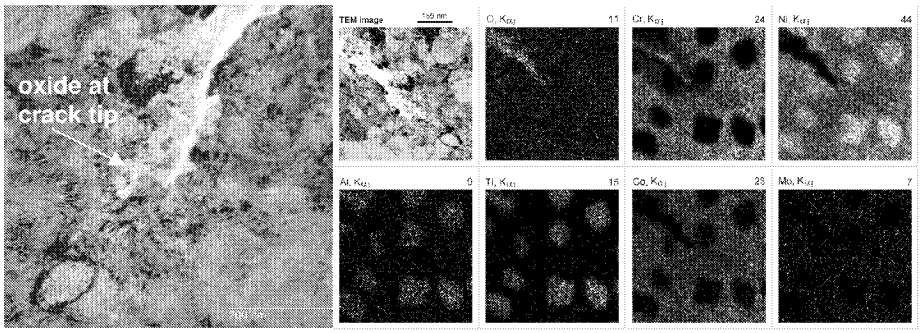

Figure 13: TEM image (left side) and EDX element maps from the crack tip surrounding.

4. Conclusions

The fatigue and creep fatigue crack growth behaviour of Waspaloy at 700°C in vacuum and air have been investigated. Fatigue crack growth in vacuum and air show nearly the same threshold value and the crack growth rate in air is about the factor 2 higher than in vacuum. The threshold value of creep fatigue crack growth in air is lower than in vacuum and the crack growth rate in air is higher than in vacuum, but with increasing ΔK_I value the difference between both crack growth rates disappears.

Structural investigations showed, that the oxide scale inside the crack is homogeneously thin and does not reach the crack tip. Therefore, no interaction of oxygen at the crack tip of FCG specimen could be detected after pure cyclic loading. This result corresponds with the observation of mainly transcrystalline rupture surface.

Creep fatigue crack growth tests showed a mixed rupture surface with higher amounts of intercrystalline rupture surface. Particularly the tests in air led to an oxide scale on along the crack with about the same penetration depth as the crack.

To observe the crack tip in a TEM, a special method for TEM specimen preparation near crack tip by FIB (focused ion beam) was developed. The achievements of TEM investigations

demonstrate that near the crack tip the crack was oxidised only on one side. Near the crack tip a crack growth along the interface of oxide and matrix may be expected..

There are some observations that during CFCG-tests a reaction with oxygen can happen at 700°C. The degree of the influence of these reactions on crack growth rate must be examined further.

5. References

[1] G. Härkegard and J.Y. Guedou, in:
Materials for Advanced Power Engineering, Forschungszentrum Jülich 1998,
Ed by J. Lecomte_Beckers, F. Schubert , P.J. Ennis, Schriften des Forschungszentrums Jülich, ISSN 1433-5522, p. 913.

[2] J. Rösler, B. Böttger, M. Wolske, H.J. Penkalla, C. Berger in „Materialsfor advanced Power Engineering 2002“, Proceedings of the 7th Liège Conference (2002) ed. By J. Lecomte-Beckers, M. Carton, F. Schubert, P.J. Ennis, Schriften des Forschungszentrums Jülich, ISSN 1433-5522, Vol. 21, p.89

[3] W. Carpenter, B.S.J., Kang, K.M. chang: SABGO Mechanism on High Temperature Cracking Behaviour of Ni-base Superalloys in Superalloy 718, 625, 706 and Varius Derivates (11987), p. 679-688

[4] H.J. Penkalla, J. Wosik, W. Fischer, F. Schubert, “Structural investigations of candidate materials for turbine disc applications beyond 700 ºC”, Proc. of Fifth International Symposium on Superalloys 718,625, 706 and Derivates, TMS, June 2001, Pittsburg, Pensilvania USA, Ed. by E.A. Loria, pp 279 - 290

[5] L. Mikulová, “Bruchmechanische Untersuchungen an Werkstoffen für Dampfkraftwerke mit Frischdampftemperaturen von 500 bis 650 °C”, D 82 Diss. RWTH-Achen 2005, Schriften des Forschungszentrums Jülich, Reihe Energietechnik, Band 37.

ASSESSMENT OF THE INFLUENCE OF LASER-DRILLED HOLES ON THE DAMAGE BEHAVIOUR OF ALLOY 617

B Mülders*, E Wessel[1], F Schubert[1]

1.) Institute for Materials and Processes in Energy Systems, Research Centre Jülich, 52425 Jülich, Germany

*Philips Technology GmbH, Philipsstr.8, 52068 Aachen,
E-mail: Barbara.Muelders@philips.com

ABSTRACT

The objective of the Collaborative Research Centre (SFB 561) at the RWTH Aachen uses effusion cooling for very high temperature exposed structures. Investigations on the deformation behaviour of flat specimens (Alloy 617) with laser drilled pores has been carried out at temperatures of 20 and 400°C. The specimens simulate the structure of an effusion cooled high temperature component. The crack initiation and propagation was studied by conducting the tensile tests in the scanning electron microscope chamber. Some theoretical ideas to use the triaxiality for estimating the crack initiation (micro scale) and crack propagation (meso scale) and failure (macro scale) are discussed.

Key words: Alloy 617, crack initiation, damage, in-situ observation in SEM

Introduction

Rising energy demands coupled with the need to reduce emissions lie behind the development of high efficiency, environmentally benign fossil fired advanced power plants, both the USC (ultra super critical) steam plants and the combined cycle plants (combination of gas and steam turbine plants). The objective of the collaborative research centre SFB 561 (Technical University of Aachen, Germany) is to evaluate the scientific and technological basis for raising the thermal efficiency of a combined cycle plant to 65 %. This ambitious target may be achieved by increasing the gas turbine inlet temperature.

Ni-base superalloys are currently under consideration for the structural material of combustion chamber internal walls and for gas turbine blades. Although the expected load of combustion chamber wall is very low compared with the load of rotating blades, the thermally induced stresses may be sufficient to cause crack initiation and failure. In order to avoid much higher (surface) material temperatures, the cooling systems must be improved, but without an increase in the consumption of the cooling gas. The combination of convection and film cooling cannot guarantee a complete protection over the whole structure because of turbulent flow, possibly due to the relatively large distance between the cooling holes. It would be beneficial to increase the number and decrease the spacing between the cooling holes, so that protection of the whole surface can be achieved. This cooling technique is referred to as effusion cooling.
For the assessment of effusion cooled structures, made by laser drilling of cooling pores, the knowledge of the mechanisms controlling the long term integrity (safety and function) of the

components exposed at high temperature are required. The loss of stiffness of a component, that means the loss of function by plastic deformation with consequent ductile fracture of structural material (as a continuum without drilled pores), is controlled either by rate independent or rate dependant plasticity, depending on the temperature. The change in component stiffness caused by the presence of chains of laser drilled cooling pores cannot be estimated by a simple change of the load bearing cross section. The array of cooling pores produces an inhomogeneous local stress-strain situation (meso-scaled) in the material surrounding the cooling pores, which does not allow a simple global (macro-scaled) approach. Therefore the classical fracture mechanics approach does not enable the prediction of the damage behaviour and the theory of damage mechanics has to be used.

The present paper describes a study intended to assess the influence of the laser-drilled cooling holes on the damage behaviour of tensile test specimens of Alloy 617, one of the candidate structural materials for combustion chamber walls. For this, tensile tests were carried out in the scanning electron microscope (SEM) in which in-situ observations of crack initiation and propagation could be made. FE-Element calculations were carried out to determine the local stress-strain situation.

Theoretical background

Face-centred-cubic metals and alloys typically exhibit ductile failure, which is a result of the nucleation, the growth and the coalescence of cavities. For the nucleation process of cavities, the existence of particles or non-metallic inclusions plays a dominant role [2]. Two mechanisms for this heterogeneous nucleation process are possible: i) failure of the particles, if the particle size is greater than a critical size and ii) the separation of particle/ matrix interface due to a low cohesive energy of the interface if the particles are sufficiently small. The latter is caused by the formation and pile–up of dislocations around the non-deforming particles and leads to an inhomogeneous internal stress situation in the material surrounding of the particles. Internal parameters that influence such dislocation arrangements are microstructural features, such as particle size and hardness, volume fraction of precipitates and orientation of grains. External parameters are the deformation temperature and the strain rate; both determine the density of dislocations and their mobility. If the incoming and outgoing dislocation densities are in equilibrium, a pile-up could not be formed [1].

Taking into account all these microstructural features does not allow a feasible quantification of micro-crack initiation to guarantee the integrity of the structural material. In this context a continuums mechanics approach appears to be more appropriate. The damage of the material due to void nucleation, growth and coalescence is strongly influenced by stress triaxiality, it is generally accepted that the stress triaxiality is the controlling parameter for the growth of voids [4-12]. The stress triaxiality ξ is given by

$$\xi = \frac{[\sigma_1 + \sigma_2 + \sigma_3]}{3 \cdot \sigma_{VM}} \qquad (1)$$

With σ_i main stress components and σ_{VM} von Mises stress. The influence of the level of stress triaxiality is shown in Figure 1. The coalescence of growing cavities is then defined as microcrack-initiation. The strong influence of the cooling pores on the local stress-strain distribution in of the material must be taken into account. The classical continuum mechanics

approach of fracture mechanics considers only the macroscopic stress-strain behaviour and does not allow for the inhomogeneous local stress-strain situation.

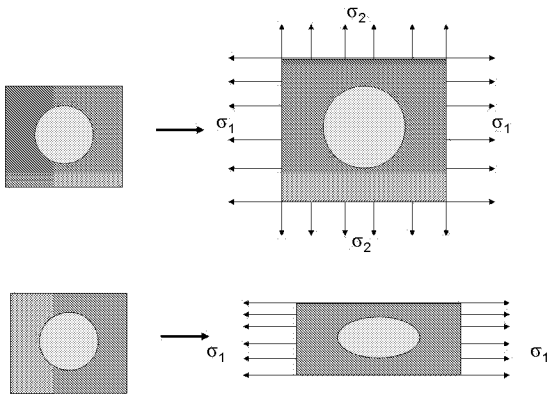

Figure 1: Influence of level of stress triaxiality on the void growth

In contrary to this, the damage mechanics approach includes this inhomogeneous local stress-strain-situation and enables a description of the initiation of the micro-voids and their evolution due to local stress- strain distribution. For the prediction of the damage of technically relevant materials containing particles, so-called failure curves are used, which correlate the stress triaxiality ξ and the equivalent plastic strain σ_{vM}. Therefore the failure curve includes the main influence of the stress triaxiality and the equivalent plastic strain. The material is regarded as a continuum containing damage in a plastic matrix [10]. An applicable tool to describe the damage behaviour in correlation with deformation is the use of phenomenological approaches [5,11,12]. In the past such models have been used for single-notch specimens. The question arises if such a phenomenological prediction could be used to describe the damage behaviour of materials containing chains of cooling pores. The rims of laser-drilled holes do not seem to act as a crack tip in the classical fracture mechanics approaches [3]. In the open literature, there is no recommendation referring the treatment of chains of cooling holes in turbine blades from the view of structural integrity. Therefore for a first assessment a phenomenological approach should be used.

Experiments

Alloy 617 microstructure

The yield stress of flat specimens manufactured out of the Ni-base, single crystal superalloy CMSX-4 or comparable material is much higher than the load that can be applied with the equipment available (maximum load 5000 N). Experiments were carried out on non-deformed Alloy 617, instead of a real turbine blade material. The characterisation of microstructure was done by SEM (Scanning Electron Microscopy). The matrix of Alloy 617 after the usual heat treatment contains small $M_{23}C_6$-particles with a mean diameter of roughly 35 nm. Additionally there are zones of larger carbides on grain boundaries (Figure 2a) and large particles of Ti nitride (Figure 2b).

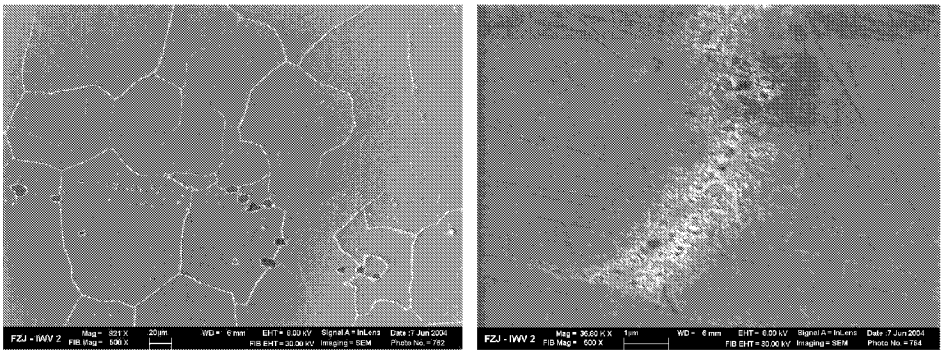

a.) b.)

Figure 2: Microstructure of Alloy 617 (secondary electron image)

SEM investigation

The tensile specimens were manufactured by electrical discharge machining (EDM). Cooling holes were drilled using microsecond Nd/YAG laser radiation. The mean diameter of the cooling holes was 168 µm. Three different arrangements of holes were investigated, see Figure 3. The geometry of the test pieces used for the tensile tests is shown in Figure 3a.

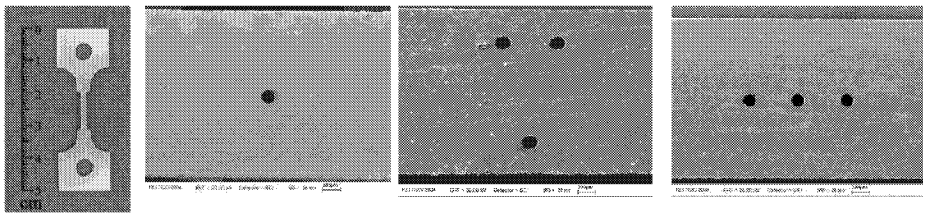

a.) b.) c.) d.)

Figure 3: Test piece geometry (a) and cooling hole arrangements (b, c, d) in tensile specimens

After laser-drilling the specimens were polished and etched with V2A-etchant (H_20 dist., HCl, HNO_3, Vogels Sparbeize) to remove freeze cast products and to make the grain structure of the material visible. The tensile testing was carried out in a mechanical tensile testing device, which was installed in a scanning electron microscope (SEM). The specimens were tested at room temperature and at 400 °C. For experiments at 400 °C the specimens were heated up using a graphite furnace. The temperature was controlled using a NiCr/Ni-thermocouple mounted directly under the tensile sample. The arrangement of the experiment is described elsewhere /3/.

The deformation process was observed online in the SEM. At certain deformation degrees secondary electron images were taken. A typical sequence of the deformation process as function of the mechanical elongation and load is shown in Figure 6. To obtain information concerning the fracture mechanism, additional SEM analysis of the cross-section were carried

out after the mechanical testing procedure. The secondary electron image of the fracture surface is shown in Figure 8.

FE-Calculation

For the large deformation FE-analysis (ANSYS 7.1), a two-dimensional quadrangular 8- node element with two degrees of freedom for each node (ux,uy) was used. The finite element mesh is shown in Figure 6.

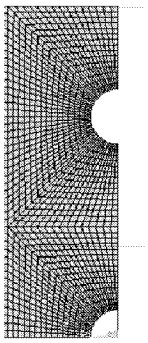

Figure 4: FE-Mesh of a tensile specimen with three cooling holes, reduced to 3/2 holes because of the sake of symmetry.

For the calculation of the local stress-strain state at the location of crack initiation, a material law is needed. To describe material behaviour, tensile tests in SEM were carried out using specimens without holes. From these tests true stress- true strain curves were obtained, which were extrapolated to large deformation. The stress-strain curves and the coefficients for multi-linear regression of the curves as material law are shown in Figure 7 and Table 1.

Results

Typical elongation-load diagrams measured by the in-situ tensile testing for Alloy 617 are shown in Figures 6, 9 and 11. The in-situ observation of crack initiation during tensile deformation is shown for one cooling hole at room temperature (Figure 6) and at 400 °C (Figure 9) . Figure 11 shows the deformation behaviour of a sample with an arrangement of 3 holes in one line at room temperature.

At room temperature the deformation of the 1-hole sample seems to be elastic up to elongations of 100µm (0.1%). When plastic deformation occurs the material starts to form deformation lines mainly at the top and the bottom of the hole indicating the highest stress in this region. The main crack starts to form at the grain boundary (elongation 1500µm). With increasing elongation, the crack propagates approximately perpendicular (intra granular) to the elongation direction following slip planes (Figure 7), because of the higher stress in this region. At an elongation of 3500 µm the sample fails. As shown in Figure 8 the cross fraction is of honeycomb-type indicating a ductile fracture mechanism.

Strain [1]	Stress [MPa]
0.001	215
0.016	415
0.044	529
0.282	1034
0.307	1082
0.367	1198
0.424	1290
0.443	1315
1.24	2173
2.0	2450

a) multilinear regression and extrapolation at room temperature

Strain [1]	Stress [MPa]
0.001	189
0.011	361
0.088	583
0.293	1027
0.345	1107
0.7	1683
0.95	1900
1.4	2000
2.0	2000

b) multilinear regression and extrapolation at 400 °C

Table 1: Mechanical parameters derived from measurement and extrapolation

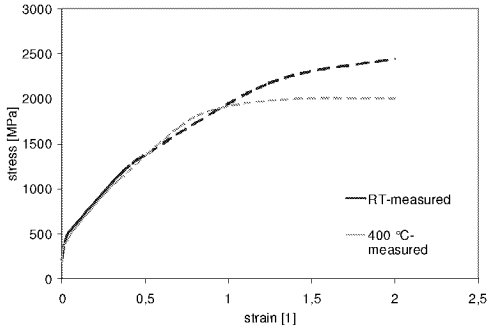

Figure 5: Extrapolation (dashed lines) of measured stress- strain behaviour for room temperature and 400 °C.

In principal the deformation and crack behaviour at 400°C is similar to that at room temperature. The crack formation at the top of the hole is interesting. At first the crack starts to form at the right hand side of the grain located at the top of the hole. Than the crack propagates intergranularly and approximately perpendicular to the elongation direction. After increasing the load, slip planes are formed at the left hand corner of the grain. Due to the formation and the movement of slip planes a weakening of the material occurs and a void forms. The increasing stress at the tip of the void leads to the final failure of the material. The detrimental crack follows the slip planes across the grain.

The experiment with the 3-hole arrangement was carried out at room temperature. Figure 11 shows the load versus the elongation and the corresponding micrographs. The sample failed at the hole positioned at the right hand side of the sample (3rd hole). It is obvious, that in the 3-hole arrangement the stress distribution of the first (left-hand side) and the third cooling hole must be symmetrical. Additionally, the locations at the top and at the bottom of the first or third hole are theoretically identical with respect to the stress state. In the experiment, however, the initiation and propagation of the dominant and critical crack takes place at one certain location, namely the third hole. This is, among other microstructural reasons, due to the specific orientation of the certain grain or sub-grain and the resulting stress located in the grain. This is clearly visible in Figure 12, which shows the situation directly before the sample fails. The dominant and detrimental crack starts at the 3rd hole. It is clearly visible that the grains in the surrounding of the cooling pores do not have similar deformations.

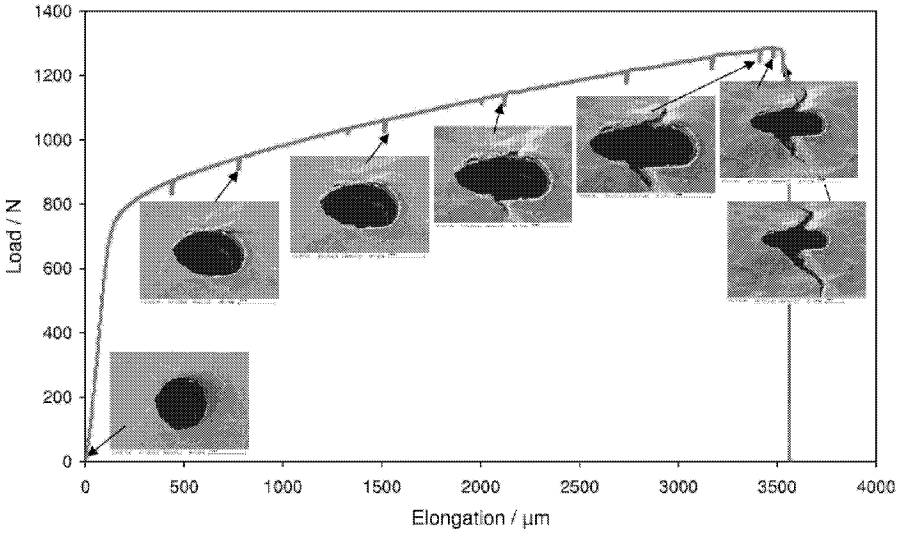

Figure 6: Sequence of deformation process for one cooling hole in a tensile test specimen observed in SEM at room temperature.

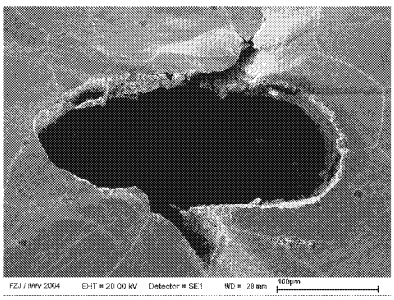

Figure 7: Crack propagating perpendicular to the tensile direction , following slip planes

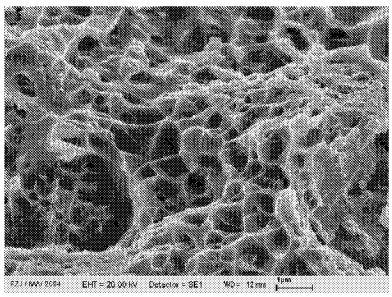

Figure 8: Honeycomb-type fracture indicating a ductile crack behaviour

Discussion

The results of the in-situ observations can be used to decide unambiguously which crack leads to the failure of the specimen and, in combination with the FE-Analysis, it is possible to calculate the local stress-strain-situation (ξ, ε_{vM}) at the starting point (crack initiation) of the crack.

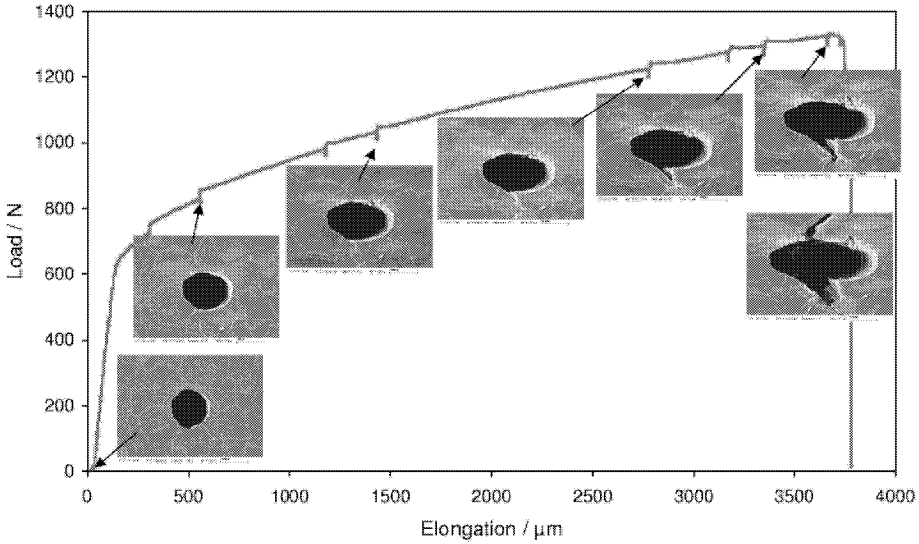

Figure 9: In-situ-observation of crack initiation and propagation at one cooling hole at 400 °C

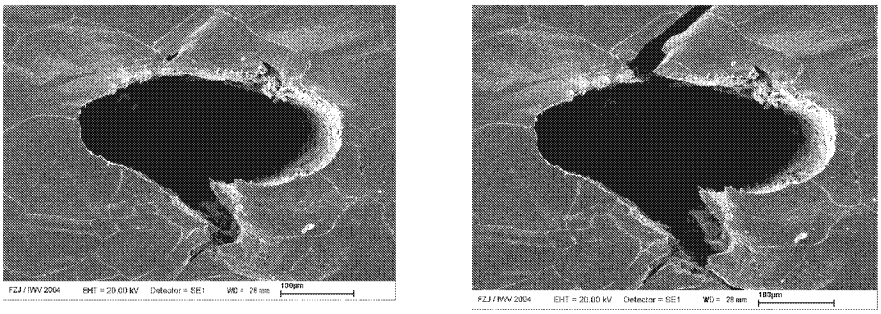

a.) b.)

Figure 10: Crack propagating perpendicular to the tensile direction , following slip planes

It is postulated that the damage behaviour due to the inhomogeneous local stress-strain-situation produced by the cooling pores could be described by a failure curve combing the local stress triaxiality with the deformation degree. The data points are fitted to a phenomenological model [e.g. 11,12]. The model is given in equation 2, the experimental values and the model are shown in Figure 13:

$$\xi = a \cdot \exp(-b \cdot \varepsilon_{vM}) + c \qquad (2)$$

with a=0.8, b=9.6 and c=0.34

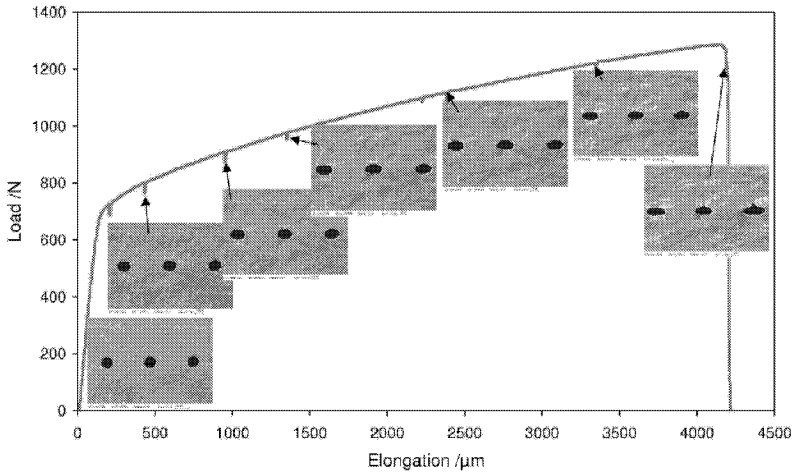

Figure 11: In-situ-observation of crack initiation and propagation for three cooling holes, room temperature

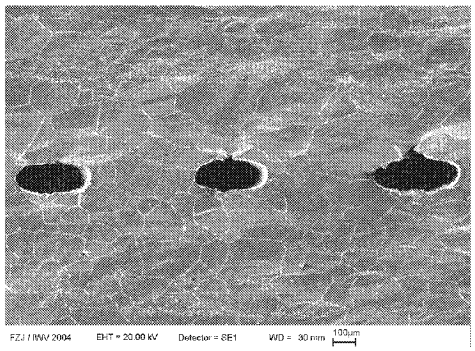

Figure 12: Dominant crack at the 3rd hole from left

Figure 13 shows that the experimental data are in good agreement to model. Because of the very first work concerning this kind of modelling, the predicted experimental data are in the steady-state of the failure curve. In future it is necessary to get data points just in the beginning of the failure curve, i.e. the range of the rising slope of the curve. Of course the continuums mechanical nature of the model does not account the microscopic stress state, which is due to the different grain orientations in the surrounding of the cooling pores. Due to the online-observation in SEM it could be noticed, that the different grains at the rims of the cooling pores perpendicular to the loading direction achieve different deformation degrees as could be seen by slip planes in the grains. This micro structural factor pitch the micro-crack initiation on a special cooling pore in spite of the symmetrical position concerning the local stress situation in comparison with the other cooling pores.

In further work, the model could be extended to take the microstructural influence into account. This could be implemented by considering statistical grain orientations in a two-step

procedure. First, the model should be computed for all possible grain orientations, and second, the damage behaviour should be predicted as a weighted average over all these grain orientations.

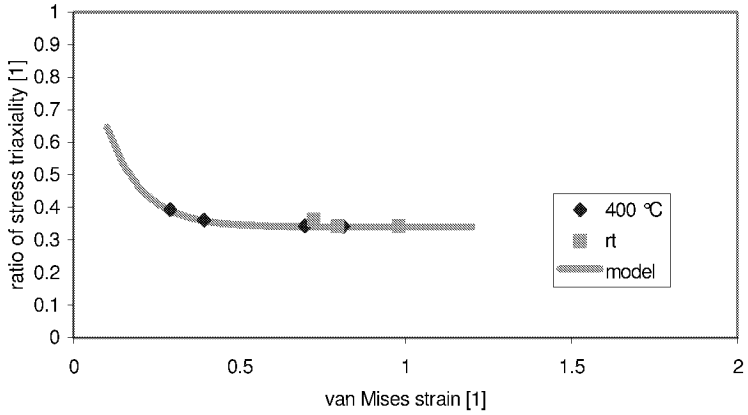

Figure 13: Phenomenological description of the micro-crack-initiation

5. Summary

In this first approach the influence of small, closely spaced holes in a structural material on the micro-crack-initiation and the damage development has been investigated. The main interest was focused on developing and testing a method for observing the initiation of micro-cracks in-situ. It could be shown that the experiment could be carried out in the chamber of a scanning electron microscope at room temperature and at 400°C. Additionally this work shows that a continuum mechanics approach, namely the application of the so-called damage curve, is able to predict the crack initiation, in spite of the fact that the initiation of the micro-cracks is clearly dependent on the microstructure.

Acknowledge

The authors gratefully acknowledge the financial support of the Deutsche Forschungsgesellschaft (DFG) with the collaborative Research Centre (SFB 561) at RWTH Aachen.

References

/1/ Goods S H , Brown L M, Acta Metall. 27, 1979, 1-15
/2/ Argon A S, Im J, Safoglu R, Metallurgical Transactions 6A, 1975, 825-837
/3/ Klabbers J, Wessel E, Schubert F, Proc. of 7th Liége Conference "Materials for Advanced Power Engineering 2002" ed. by J. Lecomte-Beckers, M Carton, F Schubert and P J Ennis
/4/ Seidenfuß , Dissertation, Uni Stuttgart year??
/5/ Arndt, 1997, Dissertation RWTH Aachen
/6/ Navasimham R, Eng. Fract. Mech. 47 (6), 1994, 919-934
/7/ McClintock FA, J.Appl. Mech., 35, 1968, 363-371

/8/ Rice J R, Tracey D M, L.Mech.Phys.Sol., 17, 1969, 201-217
/9/ Jun S, Jie D Z, Jing T M, Eng,Fract.Mech., 39 (6), 1991, 1051-1060
/10/ Hancock J W, Mackenzie A C, J. Mech. Phys. Sol. 24, 1976,147-169
/11/ Achenbach U J, Dissertation RWTH Aachen, Shaker-Verlag 7/99, 1999
/12/ Prahl U, Dissertation RWTH Aachen, Berichte aus der Eisenhüttenkunde, Bd.2003,2 Shaker-Verlag, 2003

DEFORMATION BEHAVIOUR OF ALLOY INCONEL 617 TUBES IN THE TEMPERATURE RANGE 600°C TO 850°C

L.Z. Makhele-Lekala[1], P.J. Ennis and F. Schubert
Research Centre Jülich (FZJ), Germany

Abstract

Tensile tests on tubular test pieces of boiler tube dimensions have been carried out at 600°C, 700°C, 800°C, and 850°C at different deformation rates. The results were used to determine the parameters of constitutive equations for the material. The deformation behaviour at both 700°C and 800°C are different at low and high strain rate.

Keywords: Inconel 617, tensile test, constitutive equation, strain rate

Introduction

There is a world-wide effort to improve fossil fired steam cycle power plants to achieve total efficiencies higher than 50%. This target can be achieved through the production of life steam of 700°C at (30 -35) MPa. That means the materials for the last stage of the superheater (tubing and heaters) in the boiler have to withstand temperatures between 720°C and 730°C,since the superheater or reheater metal can exceed the steam temperature by as much as 28° [1]. For this operational conditions the advanced (9-12)% ferritic Cr-steels are not long term creep resistant enough and have poor steam oxidation resistance. Austenitic steels with Cr-content above 20% may provide the required steam oxidation resistance, but the creep resistance at temperatures above 700°C is insufficient. Moreover these materials have the disadvantage of high thermal expansion and low thermal conductivity. The requirements of high temperature superheater components may be met by Ni-based alloys, which are workable, forgeable and weldable for the manufacture of heat exchange components of hot headers and high temperature resistant tubing.

The alloy Inconel 617 is rich in nickel and chromium, with exceptional high temperature resistance properties. This makes the alloy a candidate material, for example, for boiler tubes in the super heater and re-heater of advanced supercritical steam power plants that are operating at steam temperatures around 700°C. Originally this alloy was developed for use as a sheet material for combustion chambers in gas turbines, and has been qualified in the 1980s for the main components for a He/He-heat exchanger (IHX) in advanced gas cooled high temperature reactors (HTGR) with experimental temperatures of 900°C to 950°C [2]. At that time, the materials qualification was concerned with test temperatures above 850°C. Thus a gap of information is remaining for application temperature in the range 600°C to 850°C. This range of operational temperatures is expected for advanced boilers in the ultra-supercritical (USC) steam cycle power plants with 700°C live steam.

The aim of this paper is to examine the deformation behaviour of the alloy Inconel 617 in the temperature range 600°C to 850°C. To this end hot extruded tubings manufactured for the investigation of HTGR components are used.

[1]Guest Scientist at IWV2 FZJ

Experimental Details

Material

The test material was manufactured by the VDM factory according to the German specification of the "werkstoffblatt". From this material, tubular specimens with physical dimensions given in Table 1 were made for use in the tests. The chemical composition, in mass %, is summerised in Table 2 below and the time-temperature-transformation diagram for Alloy 617 has been reported in [3] .

Table 1: Physical dimensions of the specimens used

Parameter	Dimension
Length	742mm
Outer Diameter	22mm
Wall thickness	2mm

Table 2: Chemical composition for Inconel 617 alloy in mass percentage

Ni	Cr	Co	Mo	Ti	Al	C	N	B
Remainder	22.23	11.58	9.75	0.48	0.74	0.067	0.038	<0.003

Test Procedure

In Fig. 1 a photo of a typical tubular specimen used in this investigation is shown. Specimens described above are bolted between flanges that are fixed to the loading extension gauge. These specimens were tensile tested in four columns Servo hydraulic Instron test machine (Type 1345). The strain rate was cross-head controlled. All tests were interrupted after reaching a total elongation of about 15%.

Experimental Results

Following the procedure outlined above, several tensile tests were carried out on the tubular specimens of the alloy at 600°C, 700°C, 800°C and 850°C; and at different strain rates of 1×10^{-6} s^{-1}, 1×10^{-5} s^{-1}, 1×10^{-4} s^{-1}, and 1×10^{-3} s^{-1}. At 600°C it was sufficient to perform the tests only at 1×10^{-6} s^{-1} and 1×10^{-3} s^{-1}. The measured data was used to determine the constitutive equations for the Inconel 617 for the aforementioned operational conditions.

The experimental true stress-strain results, together with the results obtained from the constitutive equations are plotted in Figures 4. The corresponding experimental data at room temperature (RT) is also shown in Figure 5 for completeness.

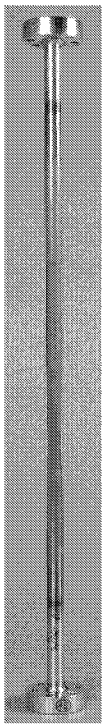

Figure 1: A typical tubular specimen

Constitutive Equations and Modelling

The fundamental basis for modelling the mechanical behaviour of a material is the formulation of appropriate constitutive equations relating stress and strain. These relations depend on the dominant mechanism(s) taking place, which in turn are influenced by the test methods employed. For example, under uniaxial tension and for operational conditions considered in this work the dominant deformation behaviours are plastic and steady state creep. Deformation can either be elastic, plastic, or elastic/viscoplastic

In the case of viscous deformation (creep) (for uniaxial tensile stress) the strain rate $\dot{\varepsilon}$ is related to the stress σ via Norton's power law [4]

$$\dot{\varepsilon} = K\sigma^n \,, \tag{1}$$

where K and n are the material constants. This law is known to yield satisfactory results of creep compared to the experimental data for various materials. Elastic deformation is described by the Hookean constitutive equation

$$\sigma = \mathrm{E}\varepsilon \tag{2}$$

where E is the Young's modulus of elasticity. This is a linear equation of the form $y = mx + c$, which can be used in a straight forward way to obtain the material parameter

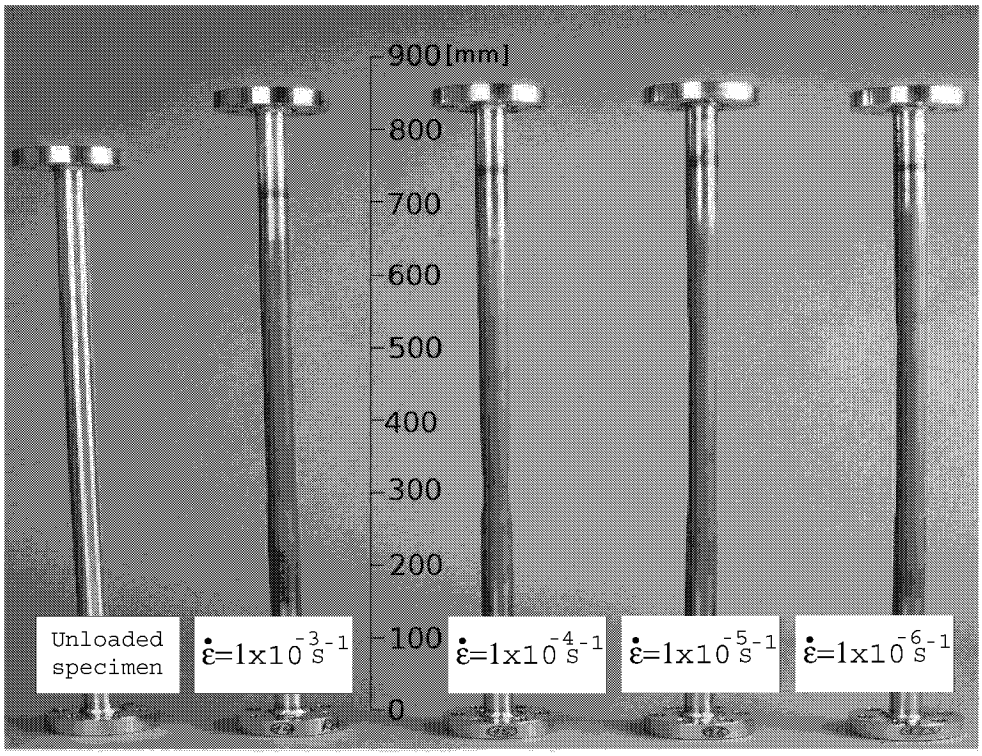

Figure 2: Tubular specimens before and after exposure to 800°C

E. c is expected to be zero or almost zero. For viscoplastic deformations the strain rate is related to the applied stress by [5]

$$\sigma = K_v \dot{\varepsilon}^m \varepsilon^p \tag{3}$$

This leads to the constitutive equation

$$\sigma = \tilde{K} \varepsilon^p \tag{4}$$

where K_v, $\tilde{K}$, m, and p are material constants. For practical reasons Eq. 4 can be linearized as

$$\ln(\sigma) = p \ln(\varepsilon) + \mathcal{C}\,, \tag{5}$$

where $\mathcal{C} = \ln(\tilde{K})$.

Several approaches may be used to determine the material constants E, $\tilde{K}$, and n. The intercept c following from Eq. 2 can also be determined in this way. Examples of the approaches include, e.g. local or global minimization techniques, Levenberg-Marquadt Method [6]. In these and other methods, in general, the objective is to minimize the

function

$$\mathcal{F} = \sum_{i=1}^{N} \frac{[\sigma^i_{\text{exp}} - \sigma^i_{\text{mod}}]^2}{N-2} \tag{6}$$

where N is the number of data points, σ_{exp} is the measured stress, and σ_{mod} is model stress determined via a constitutive equation.

Table 3: Parameters for modelling constitutive equations

Strain rate [s^{-1}]	E	p	K	c
600°C				
1×10^{-6}	112727	0.18	0.7×10^3	3
1×10^{-3}	108334	0.16	0.7×10^3	-1
700°C				
1×10^{-6}	114470	0.10	0.4×10^3	1
1×10^{-5}	103616	0.19	0.7×10^3	1
1×10^{-4}	114092	0.17	0.7×10^3	1
1×10^{-3}	118035	0.17	0.7×10^3	-1
800°C				
1×10^{-6}	110906	0.05	0.2×10^3	0.2
1×10^{-5}	104224	0.03	0.3×10^3	3
1×10^{-4}	103392	0.08	0.4×10^3	3
1×10^{-3}	90543	0.22	0.9×10^3	-13
850°C				
1×10^{-6}	61741	0.03	0.1×10^3	-6
1×10^{-5}	98281	0.02	0.2×10^3	6
1×10^{-4}	105876	0.05	0.3×10^3	1
1×10^{-3}	75005	0.06	0.4×10^3	0.1

In this work a simple Least Square Method using a χ^2 as a criterion for goodness of fit, was used to fit the experimental true stress-strain data to the constitutive equations 2 and 5. The parameters obtained for the different strain rates are listed in Table 3. Once the parameters are determined, the model *vs* experimental data were plotted to check the reliability of the models. The results are shown in Figures 4.

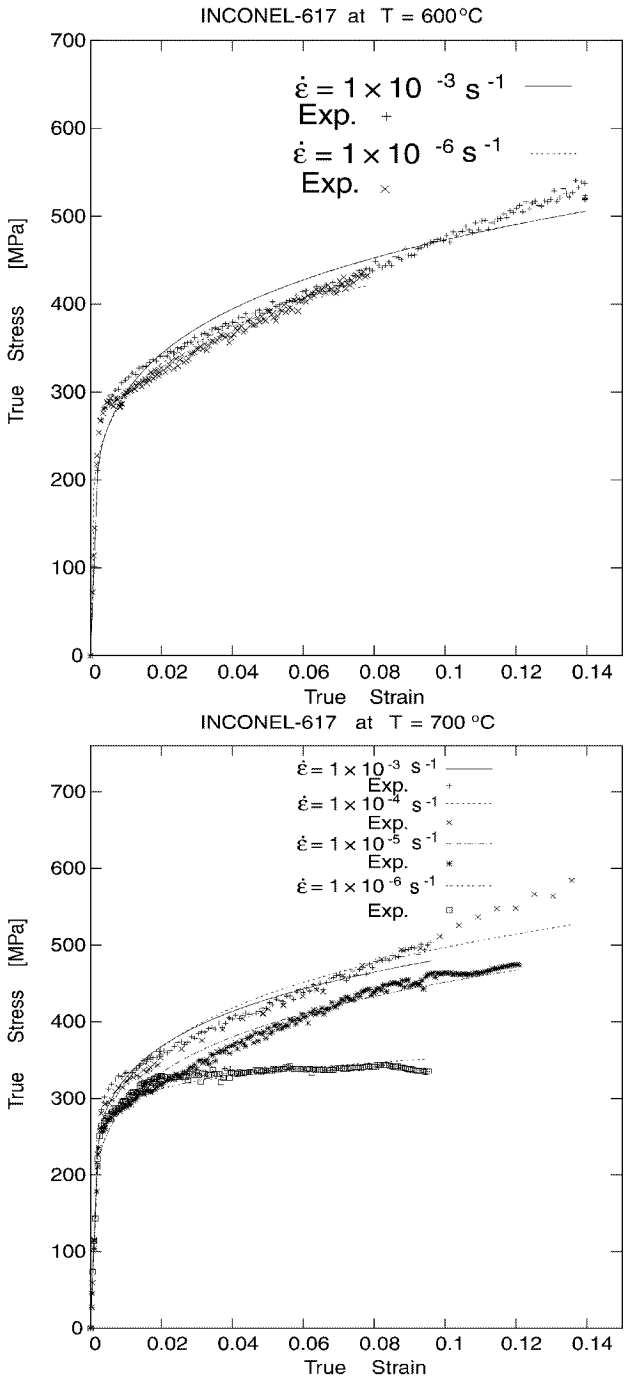

Figure 3: Experimental results and model results for 600°C, and 700°C

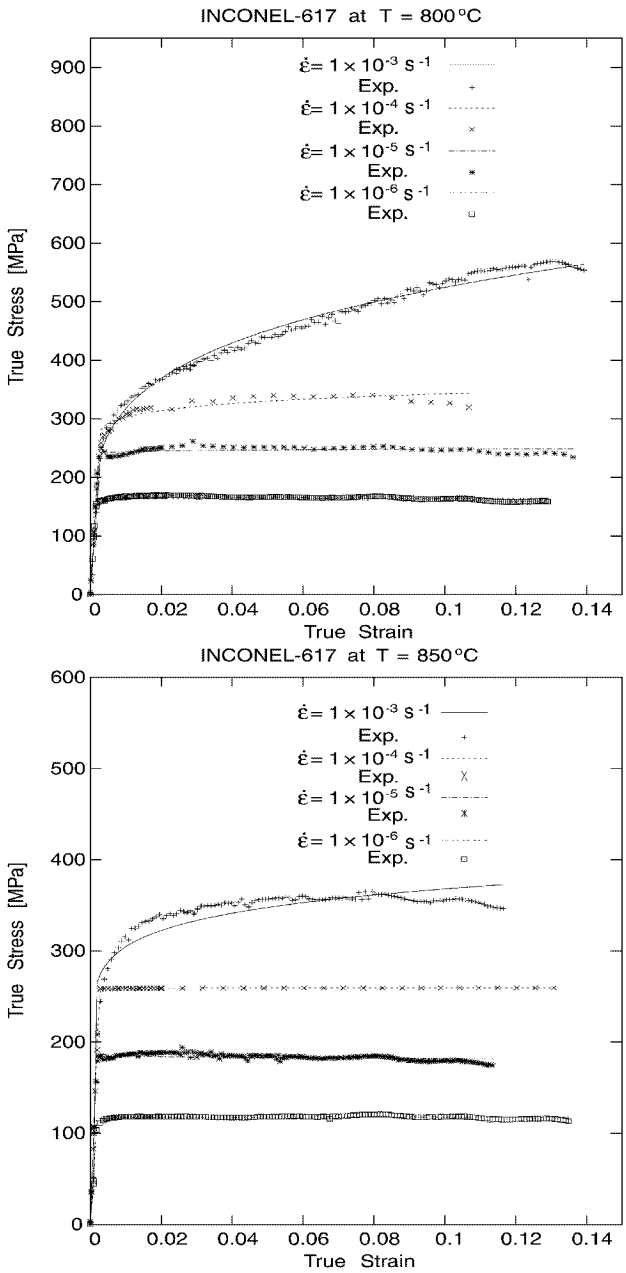

Figure 4: Experimental results and model results for 800°C, and 850°C

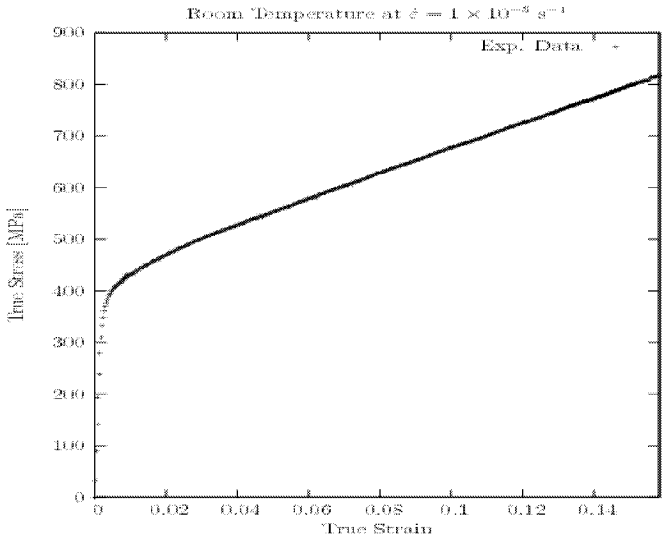

Figure 5: Experimental data for Inconel 617 at room temperature

Discussion

The experimental results obtained show that at 600°C, the deformation behaviour of Inconel 617 is purely plastic at both 10^{-6} s^{-1} and 10^{-3} s^{-1} strain rates. On the other hand, at 700°C and 800°C the deformation shows a somewhat peculiar behaviour. For example, at the highest strain rate the material deforms plastically whilst at the lower strain rate it exhibits a viscoplastic behaviour. This behaviour is, however, similar to the results obtained by Schubert [3] at 750°C as shown in Figure 6. It was shown here that the material deforms plastically and then changes to viscoplastic for the same strain rate compared with the 700°C at 10^{-5} s^{-1}.

Finally, with respect to the modelling of the constitutive equations we mention the following: Our primary focus was to examine whether the deformation behaviour of the alloy Inconel 617 follows the said constitutive laws. To this end we linearized the equations and used a simple Least Squares Algorithm. The results obtained are remarkably good in that they reproduce the experimental data. However, the point out that the values of the parameters can be improved by either (i). using a nonlinear model instead of a linear one, or (ii). by incorporating the errors of the data points in the minimization, or (iii). a combination of (i) and (ii).

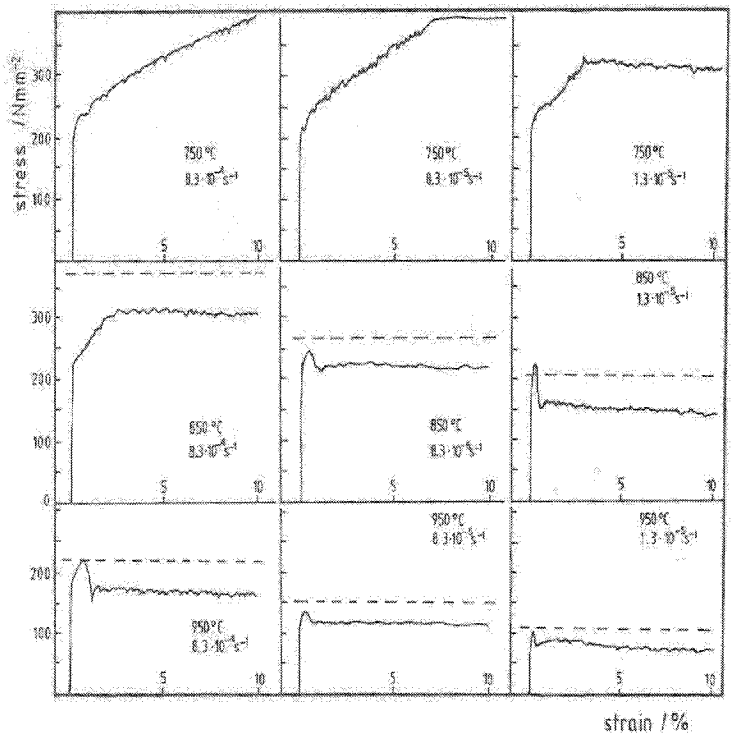

Figure 6: Deformation behaviour for Inconel 617 at different temperatures and strain rates [7]

References

[1] R. Viswanathan, W. Bakker; Journal of materials Engineering and Performance **10**, 81 (2001)

[2] F. Schubert, *et al*; Nuclear Technology **66**, 227 (1984)

[3] H. Kirchhöfer, F. Schubert, H. Nickel; Nuclear Technology **66**, 139 (1984)

[4] W.N. Findley, J.S. Lai, K. Onaram; *Creep and Relaxation of Nonlinear viscoelastic Materials*, Dover Publications, New York (1989).

[5] J. Lemaitre, J.-L. Chaboche; *Mechanics of Solid Materials*, Cambridge University Press, Cambridge, United Kingdom (2000).

[6] W.H. Press, S.A. Teukolsky, W.T. Vetterling, B.P. Flannery; *Numerical Recipes in Fortran 77*, 2nd ed. Cambridge University Press, Cambridge, United Kingdom (2003).

[7] F. Schubert; Habilitation Thesis,"Werkstoffkunliche Gesichtspunkte bei der Auslegung kriechbeanspruchter Hochtemperaturkomponenten morderner Ernegieerzeugungsalagen" Univ. Aachen, German 1990.

FIELD TESTING OF TP 347H FG AT ULTRA SUPERCRITICAL STEAM CONDITIONS

A.N. Hansson[a] and M. Montgomery[b]

Department of Manufacturing Engineering and Management, Technical University of Denmark,

Kemitorvet b. 204, DK-2800 Kgs. Lyngby, Denmark

[a]anh@ipl.dtu.dk, [b]mm@ipl.dtu.dk

Abstract

TP 347H FG was exposed in test superheater loops in a Danish coal-fired power plant. The superheaters were exposed at ultra supercritical steam conditions for 7720 h, 22985 h, 29588 h, and 57554 h. The steam oxidation results from the superheaters with the 3 shortest exposure times have been reported previously [1]. It was found that the thickness of the inner layer did not change significantly with oxidation time and temperature. Instead, the inner layer became more Cr rich at higher temperatures and consequently, it offered a higher protectiveness against oxidation.

In this paper, the steam oxidation results from the superheater exposed for the longest duration are reported. Surprisingly, extensive oxide growth had occurred at the lowest temperatures (506°C and 534°C) as compared to the previous exposures, and the inner layer had become more Fe rich. The microstructure and the average thickness of the inner oxide layer for the samples, which were exposed between 541°C and 620°C, reflected the earlier test results. Considerable oxide growth had also occurred at the highest temperature (648°C) such that the inner layer consisted of a Fe-Ni-Cr spinel layer, which was sandwiched between two Cr_2O_3 layers. The morphology shows that the first formed Cr_2O_3 layer does not remain protective. This paper focuses on the differences in the morphology between the samples exposed for 57554 h and those exposed at shorter times. The results are discussed in terms of hydrogen effects, Cr diffusion and growth stresses.

Keywords: Steam oxidation, Cr-diffusion, hydrogen effects, growth stresses.

Introduction

The goal of increasing the efficiency of steam power plants in order to reduce fuel consumption and the CO_2 emissions has been pursued for many years. It can be achieved by raising the steam temperature and pressure. Higher steam temperatures may result in thicker steamside oxide layers on superheater tubes, which will increase the metal temperature, and thereby the corrosion and creep degradation of the steel tubes [2]. Furthermore, thick oxides are more susceptible to exfoliation, which can cause blockage of the superheater tubes [3]. Therefore, knowledge about the steam oxidation behaviour of the steels is required in order to predict the lifetime of superheater tubes.

The Nb-stabilised austenitic steel TP 347 H has become one of the candidate alloys for superheater tubes at high steam temperatures and pressures. Mitsubishi and Sumitomo have developed a fine-grained version of this alloy, which showed an improved steam oxidation resistance at 650°C and 700°C compared to the coarse-grained version [4]. The increased grain boundary area provided an enhanced Cr transport to the oxide-alloy interface, which allowed the formation of a uniform and protective Cr_2O_3 layer along the inner oxide-alloy interface. In the coarse-grained steel, Cr_2O_3 only formed close to intersections between the inner oxide and the alloy grain boundaries [4,5]. The oxidation behaviour of the fine-grained version was only tested for exposure times up to 2000 h [5]. Thus, field-testing of the fine-grained version was initiated in order to obtain more reliable data on the long term steam oxidation behaviour [2].

The oxidation behaviour of TP 347H FG after 7720 h, 22985 h, and 29588 h exposure has been reported previously. A thin oxide layer, consisting of $MnCr_2O_4$ on top of Cr_2O_3, developed during oxidation at 625°C for 7720 h. On all other samples, double-layered oxides formed [1]. The outer layer consisted of Fe_2O_3 and Fe_3O_4 [6]. The morphology of the inner layer was affected by the metal temperature. Below approximately 585°C, the inner oxide consisted of a continuous network of Fe-Cr oxide (reflecting the grain boundary structure of the alloy), in which regions of Fe-Ni-Cr spinel were embedded. At higher temperatures, a Fe-Cr oxide constituted the main part of the inner layer. The average thickness of the inner layer was not influenced significantly by the metal temperature or the exposure time [1] (see Fig. 1).

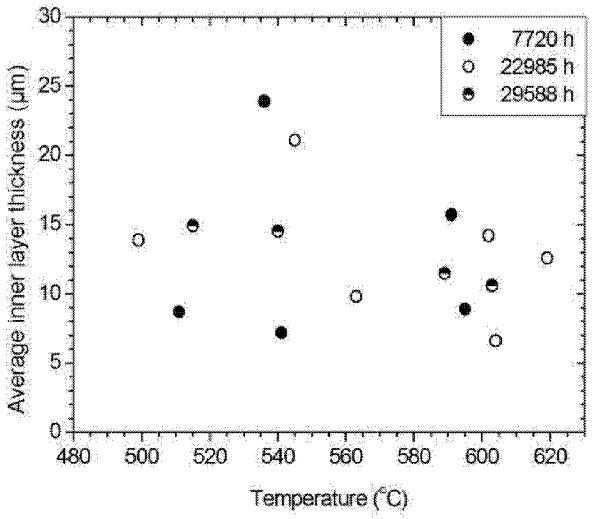

Fig. 1: The average thickness of the inner layer formed during steam oxidation of TP 347H FG at 256 bar, temperatures between 499°C and 619°C, and times between 7720 h and 29588 h.

Experimental

Tubes of TP 347H FG were exposed in 8 locations in a test superheater with 4 loops (see Fig. 2) in a coal-fired Danish power plant for 57554 h. The composition (wt%) and the grain size (ASTM) according to the certificate from the supplier were as follows: C: 0.09, Cr: 18.5-19.3, Ni: 12.3-12.6, Si: 0.5, Mn: 1.6, Nb+Ta: 0.9, and grain size: 8.8-9.2. The inner diameter of the tube was 25 mm, and the wall thickness was 5 mm (in loop 1 to 3) or 9 mm (in loop 4). During the exposure, the steam flow rate, the steam pressure (256 bar), and the inlet and outlet temperatures of each loop were recorded. The metal temperature at the location of each sample was calculated from these data. The temperatures were: 506°C*, 534°C, 541°C*, 566°C*, 567°C, 615°C*, 620°C, and 648°C. The asterisk indicates that the temperature originates from a sample placed in one of the loop outlets (i.e. the samples did not experience heat flux).

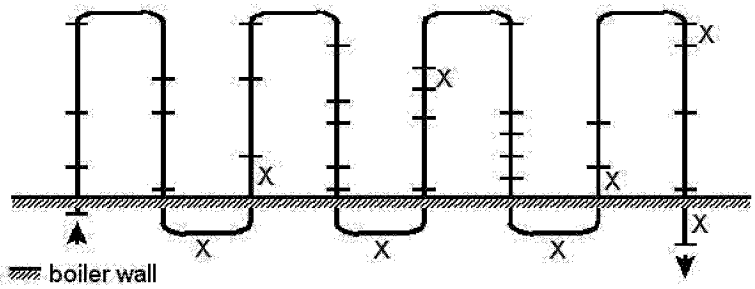

Fig.2: The position (x) of the samples in the superheater.

On selected samples, part of the oxide layer was isolated by cutting, grinding, and etching with 10% bromine in methanol (etching time: minimum three days). The oxide was cleaned in ethanol, dried, pulverised and analysed with X-ray diffraction (XRD). Cross-sections of the tubes were prepared according to normal metallographic techniques. The metal loss measurements were so small that they could not be measured accurately. The steamside oxide was investigated with light optical microscopy (LOM), and scanning electron microscopy (SEM) with X-ray analysis facilities (EDS). The backscatter electron (BSE) detector was used during image recording in the SEM. The thickness of the inner layer reported in this paper was measured as an average of 225 measurements (25 LOM images, 9 random positions on each).

Results

XRD positively identified Cr_2O_3 and Fe_2O_3 in the oxide powder from the samples exposed at 615°C and 648°C. Some Cr_2O_3 may be present in oxide powder from the sample exposed at 506°C. In all three powders, XRD identified a spinel (see the diffractograms in Fig. 3). Fe_3O_4 was not observed, however it may have transformed to Fe_2O_3 during etching.

Microstructure investigations showed that double layered oxides had formed on all samples. The outer layer was Fe rich (a), occasionally with Ni enrichment at the inner part of the outer layer (b)

(Fig. 4: III, V). The morphology of the inner layer was influenced by the metal temperature. The samples, which were exposed at a temperature of 506°C and 534°C, had by far the thickest (inner) oxide layer (Fig. 4: I) and their microstructure was similar. The inner oxide consisted of a continuous network (d), which resembled the grain boundary structure of the alloy. The back-scatter image contrast of the network (d) changes across the inner layer, and EDS-analyses shows that it is rich in Fe in the main part, whereas Cr is also present in the innermost part. Porosities were observed in the Fe rich part of the network (Fig. 4: II). At some locations, the network continued into the metal. Regions of Fe-Cr-Ni spinel (c) were embedded in the network. The regions contained few porosities and small precipitates (Fig. 4: II). The darker back-scatter image contrast of the precipitates suggests that they are rich in Cr. Un-oxidised metal (Fe and Ni) was frequently observed within the inner oxide layer.

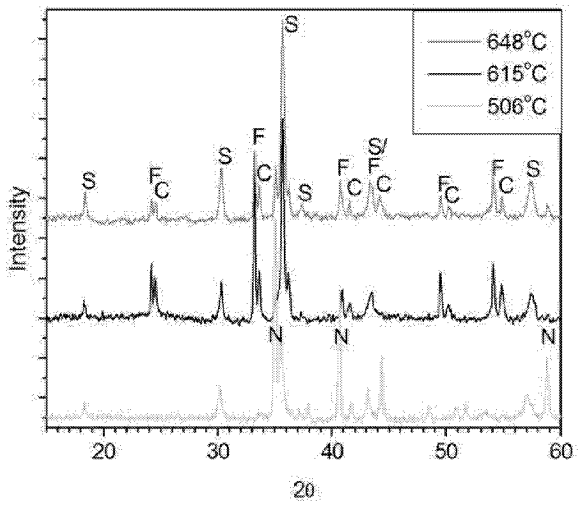

Fig. 3: X-ray diffractograms of the oxide powder from the samples, which were exposed at 506°C, 615°C, and 648°C for 57554 h. S: spinel, F: Fe_2O_3, C: Cr_2O_3, N: NbC.

The inner layer of the samples, which were exposed at 541°C, 566°C (Fig. 4: III), and 567°C (Fig. 4: IV), also consisted of regions of Fe-Cr-Ni oxide surrounded by the continuous network. However, EDS showed that Cr was incorporated in the entire network, though the Cr content was highest closest to the interface between the inner oxide and the metal (Fig. 5, right). The oxide network appeared thicker than for the samples exposed at 506°C and 534°C.

A Fe-Cr oxide layer constituted the main part of the inner layer for the samples exposed at 615°C (Fig. 4: V) and 620°C. EDS showed a very high Cr-intensity closest to the interface between the oxide and the metal, it decreased towards the outer oxide layer (Fig. 5, left). Ni was occasionally incorporated into the Fe-Cr oxide.

The inner layer consisted of three distinct layers for the sample exposed at 648°C (Fig. 4: VI). A Fe-Cr-Ni spinel was sandwiched between two Cr-rich oxide layers. The Fe-Cr-Ni spinel became richer in Cr and poorer in Fe closer to the innermost Cr rich layer.

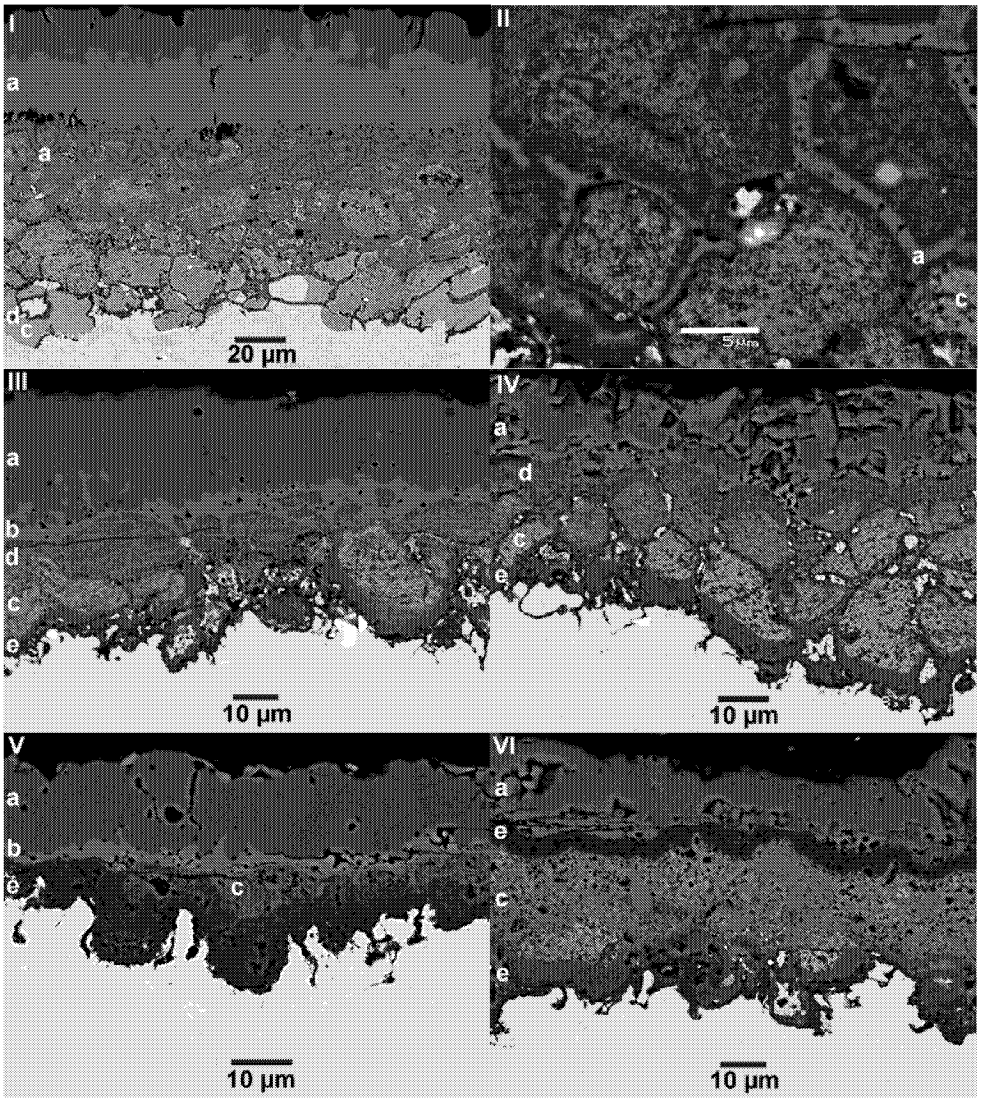

Fig. 4: BSE-SEM cross-section morphology of the oxide layer formed during 57554 h exposure in steam at 256 bar and I, II: 534°C, III: 566°C, IV: 567°C, V: 615°C, VI: 648°C. a: Fe oxide, b: Fe-Ni spinel, c: Fe-Ni-Cr spinel, d: Fe-Cr oxide, e: Cr rich oxide.

The average inner layer thicknesses for the samples are listed in Table 1.

Table 1: The average thickness of the inner layer on TP 347H FG after steam oxidation at 256 bar for 57554 h.

Metal temperature (°C)	506	534	541	566	567	615	620	648
Average inner layer thickness (µm)	69	65	26	22	34	10	22	33

EDS-analyses showed that at all temperatures, the alloy beneath the oxide had become depleted in Cr. The Cr-depletion occurred in localized areas for the samples exposed to the lowest metal temperatures (Fig. 5, left). These areas grew with temperature such that for temperatures above approximately 585°C, the composition of the alloy along the whole oxide-alloy interface was affected (Fig. 5, right). EDS measurements indicated that the Cr content in the metal close to the oxide-alloy interface increased with increasing temperature. Cr-depletion was also identified along grain boundaries for specimens exposed to 566°C and temperatures above; Ni was enriched in the Cr depleted areas.

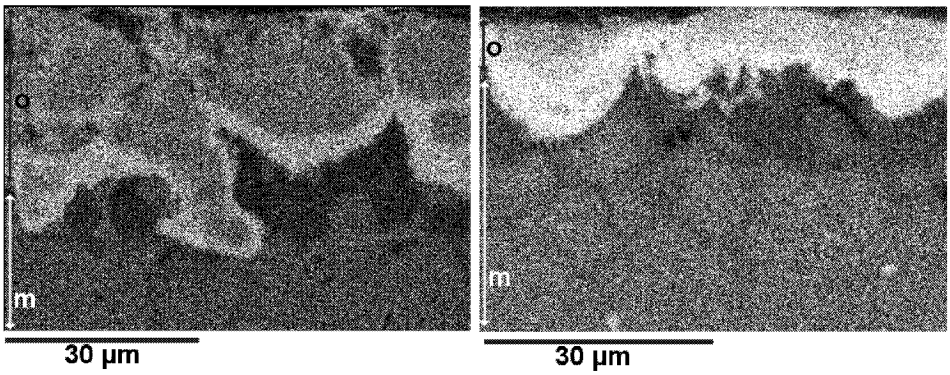

Fig. 5: Cr-EDS map across the inner oxide layer (o) and part of the alloy (m) for the samples, which have been oxidised for 57554 h and, left: 541°C, right: 615°C.

Discussion

The results from the test superheaters, which were exposed for 7720 h, 22985 h, and 29588 h, showed that the thickness of the inner layer did not change significantly with oxidation time and temperature [1]. This behaviour was also observed for the samples, which were exposed at metal temperatures between 541°C and 620°C for 57554 h. The inner layer became more Cr rich at higher temperatures and consequently, it offered a higher protectiveness against oxidation: The morphology changed from a network structure (Fig. 4: IV) to a more homogeneous structure (Fig. 4: V).

Fig. 6 compares the bulk diffusion coefficient of Cr in the alloy (D_L) [7] with the grain boundary diffusion coefficient (D_{gb}) [8] and the effective diffusion coefficient (D_{eff}). It was assumed that the grain boundary width is 0.5 nm and that the grains are cubic with at a size of 15 μm. Fig. 6 shows that the effective diffusion coefficient is more than three orders of magnitude higher than the bulk diffusion coefficient at 500°C. The slow bulk diffusion combined with the large contribution from the grain boundary diffusion to the overall diffusion in the alloy explains why a Cr_2O_3 layer only forms along the former alloy grain boundaries. Furthermore, if the layer loses it protectiveness (see below), healing might be difficult due to the slow bulk diffusion of Cr. Fast oxidation is likely to occur until the oxidation front reaches the next alloy grain boundary in depth (Fig. 4: IV).

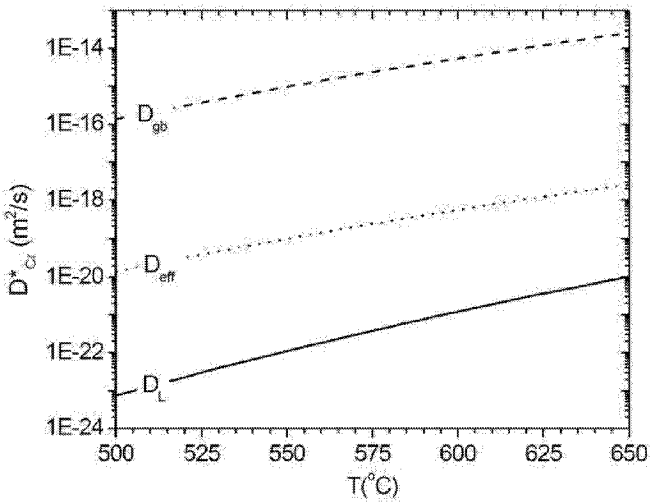

Fig. 6: The tracer diffusion coefficient of Cr (D_{gb} [8], D_{eff}, and D_L [7]) in Fe-18Cr-12Ni as a function of temperature. Grain boundary width ≈ 0.5 nm. Cubic grains with a grain size ≈ 15 μm.

As the temperature increases, the bulk diffusion contributes more and more to the overall Cr diffusion in the alloy. Thus, the change in morphology of the inner layer for temperatures above approximately 585°C may be related to an easier (re)establishment of a Cr_2O_3 layer due to faster Cr-diffusion within the alloy. The observations of a) a higher Cr-content in the alloy just below the oxide layer and b) a larger depth of the Cr-depleted zones (Fig. 5) with increasing temperature do indeed suggest a more significant Cr-transport within the alloy for temperatures above approximately 585°C.

The inner oxide layer of the sample, which was exposed at 648°C for 57554 h, consisted of a Fe-Cr-Ni spinel layer sandwiched between two Cr_2O_3 layers (Fig. 4: VI). The microstructure suggests that a Cr_2O_3 layer initially developed on this sample. This is supported by the observation of the thin Cr-rich oxide layer after 7720 h oxidation at 625°C [1]. Selective incorporation of Cr into this layer has depleted the underlying alloy in Cr (this is supported by the

Cr gradient in the Fe-Cr-Ni spinel layer). At some point the oxidation front has broken through this layer. Chemical breakthrough is generally considered unlikely at the temperatures of interest [9,10] as Cr_2O_3 coexists in equilibrium with an alloy containing $3.5*10^{-5}$ wt% Cr (648°C) [11]. The breakthrough has more likely been caused by localized spallation [10] and/or micro cracking [9] as a result of geometrically induced growth stresses. Fast oxidation of the depleted alloy did occur until a depth was reached, at which the Cr-content was high enough for the protective layer to reform [9,10] (i.e. the innermost Cr_2O_3 layer).

The oxide network was Fe rich and the oxide layer was thicker for the samples exposed at 506°C and 534°C for 57554 h as compared to all the other samples. The cation diffusion rates in Fe-Cr spinels increases with decreasing Cr content [12,13] thus the two observations are probably related. But why has the network become more Fe rich? One reason could be that the network has become more and more depleted in Cr due to the formation of gaseous $CrO_2(OH)_2$. Such a mechanism has been proven detrimental for the oxidation resistance of chromia forming alloys in fast flowing atmospheres with high oxygen and water contents [14,15]. However, thermodynamic calculation suggests that the amount of volatile Cr components in steam is negligible due to the low oxygen content (in the order of 10 ppb) [16].

During oxidation in steam, H_2 develops both at the oxide-gas interface and at the oxide-alloy interface (as a result of the inward growth of the inner layer) [17]. Perhaps, the formed H was accumulated with time within the alloy of the samples, which was exposed at the lowest temperatures (506°C and 534°C) [18]. H is believed to change the defect structure of the spinel [19], leading to an enhanced cation transport [19,20]: Oxidation of Fe and H-induced Fe (i.e. the H-content of Fe was increased by electrolysis of H_2O) at 500°C in O_2 showed faster oxide growth on the H-induced sample [20]. The oxidation rate of ferritic steels with Cr content between 2 and 12 wt% at 600°C in air was enhanced when the steels were exposed to steam on one side and air on the other side as compared to air on both sides. H was found to penetrate through the sample from the steam side to the air side [21]. H_2 desorption occurred at approx. 330°C during cooling in Ar after steam oxidation of Fe-10Cr-0.8C for 1000 h at 650°C. H_2 desorption was not observed at this temperature during heating of the non-exposed steel in Ar. H was believed primarily to dissolve in the Fe-Cr spinel [19]. Preliminary results indicate that the H content of the metal did indeed increase during the 57554 h oxidation at 506°C [22] thus a H-induced, enhanced outward Fe cation diffusion may possibly explain the increased growth for the samples exposed at 506°C and 534°C for 57554 h.

Conclusion

The large contribution from grain boundary diffusion to the Cr transport within the alloy explains why a protective Cr_2O_3 layer is only observed along former alloy grain boundaries at the lowest temperatures. Bulk diffusion contributes more and more to the Cr transport within the alloy with increasing temperature, which eases the (re)formation of a protective Cr_2O_3 layer. This explains the charge in morphology of the inner layer for temperatures above approximately 585°C.
At 648°C the first formed Cr_2O_3 layer has lost it protectiveness during the 57554 h exposure as a result of localized spallation and/or micro cracking. The spallation or cracking occurred as a

result of geometrical induced growth stresses. Fast oxidation of the depleted alloy did occur until a depth was reached, at which the Cr-content was high enough for Cr_2O_3 to reform.

Increased oxide growth was observed for the samples, which were exposed at 506°C and 534°C for 57554 h. Moreover, the oxide network along the former grain boundaries had become Fe-rich. It is suggested that H has accumulated with time within the alloy during steam oxidation, resulting in an enhanced outward Fe cation diffusion.

Acknowledgement

Elsam and Energy E2 are acknowledged for partnership. ELTRA and Elkraft systems are acknowledged for funding (PSO project no. 5293).

References

[1] J. Jianmin, M. Montgomery, O.H. Larsen, and S.A. Jensen, Investigation on steam oxidation behaviour of TP 347H FG. Part 1: Exposure at 256 bar, Materials and Corrosion, 2005, 56(7), 459-467.
[2] Von G. Scheffknecht, R. Blum, Q. Chen, and A. Vanderschaeghe, Ein Vorhaben zur Ermittlung der Hochtemperaturkorrosionseigenschaften verschiedener Dampferzeugerwerkstoffe unter Betriebbedingungen bis 620°C, VGB Kraftwerkstechnik, Vol. 76(10), 1996, 856-862.
[3] O.H. Larsen, R.B. Frandsen, and R. Blum, Exfoliation of Steamside Oxides from Austenitic Superheaters, VGB PowerTech, 84(7), 2004, 89-94.
[4] H. Teranishi, Y. Sawaragi, M. Kubota, and Y. Hayase, Fine-grained TP 347H Steel Tubing with High Elevated Temperature Strength and Corrosion Resistance for Boiler Applications, The Sumitomo Search, 38(5), 1989, 63-74.
[5] N. Otsuka, and H. Fujikawa, Scaling of Austenitic Stainless Steels and Nickel-Base Alloys in High-Temperature Steam at 973 K, Corrosion, April, 1991, 240-248.
[6] Pantleon, K. and Montgomery, M., Phase identification and internal stress analysis of steamside oxides on superheater tubes by means of X-ray diffraction, Värmeforsk report M4-312, 2004.
[7] DICTRA Software, SE.
[8] J. Čermák, Grain Boundary Diffusion of ^{51}Cr in Fe-Cr-Ni Alloys, Zeitschrift für Metallkunde, 81(3), 1990, 193-195.
[9] J.P. Vossen, K. Gawenda, K. Rahts, M. Röhrig, M. Schorr, and M. Schütze, Limits in the Oxidation Resistance of Several Heat-Resistant Steels under Isothermal and Cyclic Oxidation as well as under creep in air, Materials at High Temperatures, 14(4), 1997, 387-401.
[10] H.E. Evans, A.T. Donaldson, and T.C. Gilmour, The Development of Localized Pits During Stainless Steel Oxidation, Oxidation of Metals, 14(3), 1980, 235-247.
[11] Thermo Calc Software, SE.
[12] J. Töpfer, S. Aggarwal, and R. Dieckmann, Point Defects and Cation Tracer Diffusion in $(Cr_xFe_{1-x})_{3-\delta}O_4$ Spinels, Solid State Ionics, 81, 1995, 251-266.
[13] R. Dieckmann, T.O. Mason, J.D. Hogde and H. Schmalzried, Defects and Cation Diffusion in Magnetite (III) Tracer Diffusion of Foreign Tracer Cations as a Function of Temperature and Oxygen Potential, Berichte der Bunsen-Gesellschaft Physik Chemie, 82, 1978, 778-783.

[14] H. Asteman, K. Segerdahl, J.-E. Svensson, and L.-G. Johansson, The Influence of Water Vapour on the Corrosion of Chromia-forming Steel, Materials Science Forum, 369-372, 2001, 277-286.
[15] H. Asteman, K. Segerdahl, J.-E. Svensson, and L.-G. Johansson, Evidence of Chromium Evaporation Influencing the Oxidation of 304L: The Effect of Temperature and Flow Rate, Oxidation of Metals, 57(3/4), 2002, 193-216.
[16] B.B. Ebbinghaus, Thermodynamics of Gas Phase Chromium Species: The Chromium Oxides, the Chromium Oxyhydroxides, and Volatility Calculations in Waste Incineration Processes, Combustion and Flame, 93, 1993, 119-137.
[17] L. Thomlinson and N.J. Cory, Hydrogen Emission during the Steam Oxidation of Ferritic Steels: Kinetics and Mechanism, Corrosion Science, 29(8), 1989, 939-965.
[18] G. Hultquist, private communication with M. Montgomery, December 2005.
[19] M. Nakai, K. Nagai, Y. Murata, M. Morinaga, S. Matsuda, and M. Kanno, Correlation of High-Temperature Steam Oxidation with Hydrogen Dissolution in Pure Iron and Ternary High-chromium Ferritic Steel, ISIJ International, 45(7), 2005, 1066-1072.
[20] D. Wallinder, E. Hörnlund, and G. Hultquist, Influence of Hydrogen in Iron and in Two Stainless Steels on Aqueous and Gaseous Corrosion, Journal of the Electrochemical Society, 149(9), 2002, B393-B397.
[21] K. Nakagawa, Y. Matsunaga, and T. Yanagisawa, Corrosion Behavior of Ferritic Steels on the Air Sides of Boiler Tubes in a Steam/Air Dual Environment, Materials at High Temperatures, 20(1), 2003, 63-73.
[22] Measurements performed by G. Hultquist, Division of Corrosion Science, Department of Materials Science and Engineering, Royal Institute of Technology, Stockholm, Sweden, January 2006.

AN IMPROVED METHOD TO CALCULATE THE CREEP-FATIGUE ENDURANCE OF TYPE 316H STAINLESS STEEL

M W Spindler

British Energy, Barnett Way, Barnwood, Gloucester, GL4 3RS, UK
mike.spindler@british-energy.com

Abstract

Austenitic stainless steels are susceptible to creep-fatigue failures, which arise from thermal cycling. Consequently, life extension of stainless components requires accurate predictions of creep-fatigue endurance. Calculations of creep damage during creep-fatigue cycling are often carried out using either a time fraction approach or a ductility exhaustion approach. In the case of the time fraction approach the rupture strength is used to calculate creep damage, whereas creep ductility is used in the ductility exhaustion approach. This paper examines whether the time fraction approach or the ductility exhaustion approach gives the better predictions of creep damage in creep-fatigue tests on Type 316H steel. In addition, a new creep damage model, which was developed by removing some of the simplifying assumptions that are made in the ductility exhaustion approach, was used. This new creep damage model is a function of the strain rate, stress and temperature and was derived from creep and constant strain rate test data using a reverse modelling technique. It is shown that the new creep damage model gives better predictions of creep damage in the creep-fatigue tests than the time fraction and the ductility exhaustion approaches.

Keywords: R5, Creep-Fatigue, Type 316H, Creep Damage.

1. Introduction

Within the UK's advanced gas cooled reactors, AGR, Type 316H stainless steel has been used for boiler tubes, steam pipework and steam headers. Many of these components experience both thermal cycles and long periods of steady operation, which lead to the accumulation of both fatigue and creep damage. Consequently, life extension of stainless components requires accurate predictions of creep-fatigue endurance. The typical design codes and assessment procedures that address creep-fatigue loading are ASME III [1], RCC-MR [2] and R5 [3]. In ASME III and RCC-MR, calculations of creep damage under conditions of strain control are carried out using a time fraction approach. The R5 procedure uses a ductility exhaustion approach to calculate creep damage. It is usual to validate the approaches used to calculate damage by using isothermal creep-fatigue tests in which a strain controlled dwell is placed at the maximum strain in the cycle. In particular, UKAEA Springfields and latterly AEA Technology Risley have conducted a series of creep-fatigue tests on cast BQ at 570°C [4]. Cast BQ is now the 'best tested' cast of Type 316H at temperatures below 600°C. Thus, it is of particular interest to the operation of AGR and to the validation of R5 Volume 2/3 [3]. Previous analyses of the creep and fatigue damage for cast BQ [4] have been used to show that the ductility exhaustion approach gives more realistic predictions of creep damage than the time fraction approach. In particular, the microstructural evidence of the failure mechanisms corresponded well with the ductility exhaustion approach, in that tests with calculated creep damages of unity and low fatigue damages failed in a wholly intergranular manner. In addition, tests with similar levels of calculated creep and fatigue damages failed with a mixture of transgranular fatigue cracking and intergranular cracking. However, the time fraction approach did not correspond with the microstructural evidence, in that low creep damages were calculated for tests which failed in a wholly intergranular manner and high

creep damages were calculated for tests that failed with a mixture of transgranular fatigue cracking and intergranular cracking.

Recently, it has been shown that a new creep damage model, called 'stress modified' ductility exhaustion gives better predictions of creep damage in the creep-fatigue tests than both the time fraction and the ductility exhaustion approaches [5,6,7]. The 'stress modified' approach was developed by removing some of the simplifying assumptions that are made in the ductility exhaustion approach and the validation tests were conducted on a Type 347 weld metal and on a cast Type 304L stainless steel. This paper examines which of the time fraction, the ductility exhaustion or the 'stress modified' approaches give the best predictions of creep damage in creep-fatigue tests on Type 316H cast BQ at 570°C.

2. Test Data

UKAEA Springfields and latterly AEA Technology Risley (now superseded by Serco Assurance) have conducted fatigue and creep-fatigue tests on cast BQ at 570°C. Many of these data have been analysed and reported previously [4]. Nevertheless, for the purposes of this paper the fatigue and creep-fatigue data have been reinterpreted in order to calculate fatigue and creep damage. The data were provided by Bretherton [8] under a collaborative programme to develop the R5 procedures.

2.1 Fatigue Data

The data from four fatigue tests are available for cast BQ at 570°C. The tests were carried out under diametral strain control with a strain rate of either 0.02 or 0.06 %/s. It can be seen from Figure 1 that the fatigue endurance of cast BQ is close to the mean for Type 316H, which is given in the AGR Materials Data Manual R66 [9]. The definition of fatigue endurance that is used in this report is the number of cycles to give a 25% drop in the peak load, $N_{25\%}$. This corresponds to a crack of 2.6mm in a 7mm diameter specimen.

2.2 Creep-Fatigue Data

Twenty six creep-fatigue tests have been conducted on cast BQ at 570°C with strain ranges of between 1.85 and 0.35% and with dwell times of between ¼ and 48 hours (see Fig. 1). It should be noted that there are differences between the test methods for these creep-fatigue tests. Twenty of the tests (with prefix H or S) were carried out under diametral strain control, whereas six of the tests were carried out under axial strain control. The tests with large strain ranges and diametral control were subject to elastic follow-up as a consequence of the test method. Values for the elastic follow-up factor, Z, have been estimated for these tests and are reported in Table 1.

For the purpose of calculating the creep damage the stress drop during the dwell, $\Delta\sigma$, was fitted to the Feltham equation

$$\Delta\sigma = \sigma_0 - \sigma = \sigma_0 B''.\ln(b.t/Z + 1) \qquad (1)$$

where σ and σ_0 are the instantaneous and initial stresses respectively, t is the time and B'' and b are material constants. The stress relaxation constants that have been obtained are given in Table 1. Typically stress relaxation data were available for only one cycle of each test, usually this was a mid life cycle, i.e. at saturation.

Table 1 – Creep-Fatigue Test and Damage Results for Type 316H Cast BQ at 570°C

Test No.	Strain Range (%)	Dwell Time (h)	σ_0 (MPa)	$N_{25\%}$	Z	B″	b/Z (1/s)	D_f	D_f + Time Fraction, D_c^{TF}	D_f + R5 Approach, D_c^{R5}	D_f + Stress Modified, D_c^{SM}
H76	1.85	3	436	43	1.33	0.0312	0.1568	0.134	1140	0.467	0.711
H77	1.85	10	433	42	1.33	0.0307	1.0000	0.131	150.3	0.562	1.026
H79	1.77	0.25	456	139	1.33	0.0189	7.0990	0.397	4061	0.815	0.740
H81	1.60	0.25	452	136	1.33	0.0257	0.5147	0.316	8222	0.754	0.679
H97	1.39	3	405	74	1.33	0.0320	0.1099	0.126	151.8	0.669	0.868
H85	1.00	1.5	325	194	1.33	0.0215	1.2107	0.139	1.033	0.936	0.566
H82	0.95	1	342	219	1.33	0.0203	0.6228	0.134	4.112	0.927	0.638
T3/70	0.87	2	337	121	1	0.0140	0.3688	0.056	7.424	0.352	0.555
T3/72	0.88	10	312	76	1	0.0222	0.0856	0.036	1.504	0.365	0.733
H95	0.85	1.5	378	200	1.33	0.0271	0.1078	0.085	65.59	1.101	1.094
H96	0.85	2	389	336	1.33	0.0167	0.2711	0.143	746.6	1.472	2.832
H78	0.70	0.5	329	710	1.33	0.0109	2.3280	0.146	9.071	1.488	1.037
R1/9	0.65	24	239	185	1.10	0.0210	0.3347	0.028	0.225	0.808	0.903
S4/7	0.611	47.5	230	241	1	0.0263	0.4867	0.027	0.223	1.241	1.169
H167	0.61	5	297	687	1	0.0214	0.5884	0.077	2.130	2.675	2.597
S4/6	0.607	23.33	249	195	1	0.0301	5.03E-3	0.021	0.506	0.893	1.445
S1/6	0.606	15	207	356	1	0.0467	0.0208	0.039	0.088	2.106	0.474
S4/8	0.60	0.5	288	580	1	0.0125	2.4611	0.06	0.512	0.943	0.434
T2/45	0.60	1	278	725	1	0.0103	1.4877	0.075	0.882	1.137	0.810
T2/36	0.60	1	321	306	1	0.0145	0.4319	0.032	3.592	0.671	0.616
H154	0.60	2	266	566	1	0.0209	0.0483	0.059	0.542	1.492	0.907
S1/2	0.60	10	240	439	1	0.0186	0.0945	0.046	0.432	1.347	1.394
H178	0.59	1	297	916	1	0.0262	0.0325	0.088	2.380	2.561	1.403
H159	0.59	2	248	752	1	0.0330	0.0266	0.072	0.244	2.581	0.801
T2/60	0.35	0.5	183	12700	1	5.40E-3	1.0537	0.045	0.188	6.640	1.221
S2/3	0.35	1	202	5400	1	6.69E-3	1.6151	0.019	0.241	4.247	1.370
								Antilog[Mean [log(total damage)]]	**4.897**	**1.152**	**0.928**
								SD [log(total damage)]	**1.451**	**0.309**	**0.201**

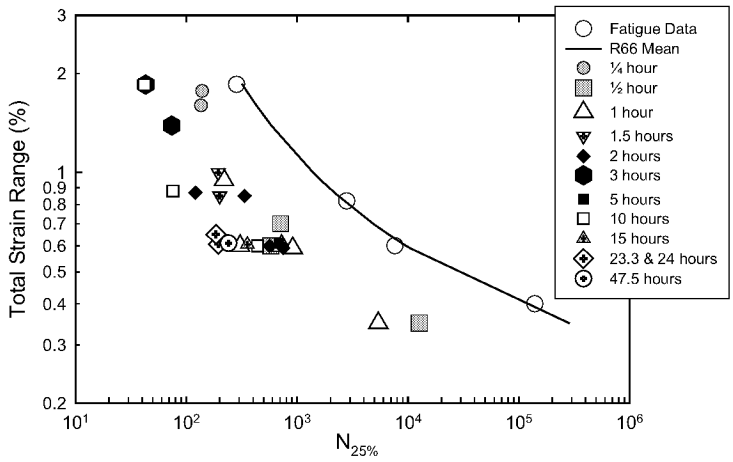

Figure 1 – Fatigue and Creep-Fatigue Endurance of Type 316H Cast BQ at 570°C.

2.3 Creep and Tensile Data

Creep and tensile data for cast BQ were obtained from the ERA Technology Ltd 'Creep of Steels' project [10] and from Bretherton [8]. Reference [10] contains the results of

interrupted creep tests at temperatures of 600 to 700°C in 25°C intervals and tensile tests at room temperature and at temperatures of 100 to 700°C in 100°C intervals. The creep rupture tests were conducted over a wide range of stresses and with durations of up to 158kh (at 600°C). The data from Bretherton [8] contained the results of creep deformation, creep rupture and constant strain rate tests at 570°C. The constant strain rate tests were conduced at lower strain rates than those normally used for tensile tests. The creep tests were conducted over a limited range of stresses and failed with durations of 200 to 2848 hours.

2.3.1 Rupture Strength

The rupture data for cast BQ were analysed following the procedures of BS:PD6605 [11]. The method enables a range of creep rupture models to be fitted and under the guidance of PD6605 the best model is selected on the basis of its deviance and extrapolation behaviour. Twelve models were fitted to the data with a Weibull error distribution. The model which offered the best overall fit and which was amongst the most robust in extrapolation behaviour was the Manson-Haferd 4th order with a temperature offset of zero, given by

$$\ln(t_f) = \begin{bmatrix} -1.75478899 + 3.49290562\log(\sigma_R) - 2.65893531(\log(\sigma_R))^2 \\ +0.894181013(\log(\sigma_R))^3 - 0.112517141(\log(\sigma_R))^4 \end{bmatrix} T + 57.0158348 \qquad (2)$$

where t_f is the failure time in hours, σ_R is the engineering stress in MPa and T is the temperature in Kelvin.

The prediction of Eq. (2) is presented in Figure 2, from which it is clear that Eq. (2) fits the data well for temperatures of 600 to 700°C. However three of the data at 570°C fail with shorter durations that the prediction.

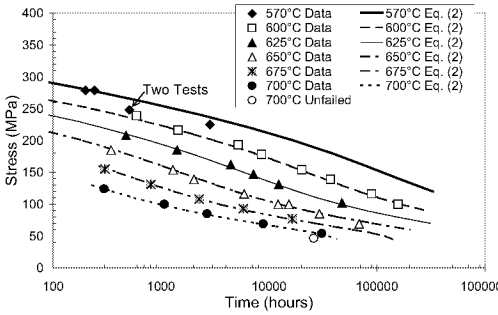

Figure 2 – Creep Rupture Strength of Type 316H Cast BQ at 570 to 700°C.

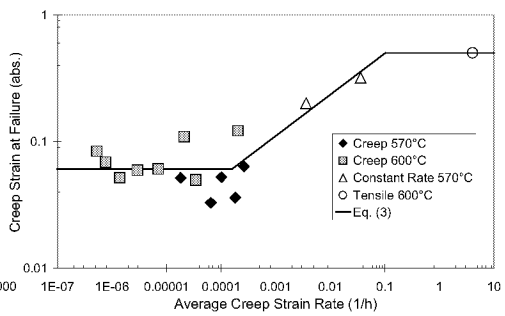

Figure 3 – Creep Ductility of Type 316H Cast BQ at 570 and 600°C.

2.3.2 Creep Ductility

The current approach in R5 Volume 2/3 is to use the creep strain at failure at an appropriate temperature in conjunction with the average creep strain rate to define the relationship between ductility and strain rate. The creep strain at failure has been calculated from the elongation at failure minus the plastic loading strain. Loading strain data were available for two of the tests on cast BQ at 570°C and these have been used to estimated the plastic loading strain of the remaining tests at 570°C. In the absence of plastic loading strain data for the tests at 600 to 700°C [10] this has been estimated from the tensile data on cast BQ.

The relationship between creep strain at failure and average creep strain usually takes the form of a lower shelf at low strain rates and an upper shelf at high strain rates, which are connected by a transition region. In this region the ductility, ε_f, is a function of the average creep strain rate, $\dot{\varepsilon}_c^{av}$, which is given by ε_f / t_f. The ductility on the upper shelf and the transition region has been defined by the elongation at failure measured from tensile tests at 570 and 600°C. The tensile tests at 570°C were conducted at constant strain rate. The upper shelf was set to 0.5, which is the elongation of the highest strain rate tensile test, and the lower shelf was defined by the average of the logarithm of creep strains at failure from the creep data at 570 and 600°C. Regression analysis was then used to define the transition region. The results of the fit to the creep strain at failure and tensile data is shown in Figure 3 and the resulting relationship is given by

$$\varepsilon_f = \mathrm{MIN}\left[0.5, \mathrm{MAX}\left(0.0604, 1.0496\,\dot{\varepsilon}_c^{\,0.3258}\right)\right] \tag{3}$$

were ε_f is in absolute units and the strain rate is in units of h^{-1}.

3. Calculation of Damage

The models to predict creep-fatigue failure that have been investigated in this report calculate the total creep damage, D_c, and the total fatigue damage, D_f, separately. Failure is conceded when the sum of the fatigue and creep damages reaches some failure criterion; for example in R5 [3] a linear damage summation is used and failure is conceded when $D_c+D_f \geq 1$. It is usual for the failure criterion to vary depending on the method used to calculate the creep damage and in ASME III [1] and RCC-MR [2] the interaction diagram that best describes failure of creep-fatigue tests is selected empirically. This presupposes that the calculations of damage have used the optimal method and that the choice of interaction diagram is the main factor determining failure. The bilinear interaction diagram used in [1,2] for Type 316 steel, is shown in Figure 4. The approach adopted in this work was to critically examine the calculation of damage as the main factor determining failure and then to test the hypothesis that the linear interaction is the most appropriate. The methods for calculating fatigue and creep damage are described in the following Sections.

3.1 Fatigue Damage

The approach for the calculation of fatigue damage per cycle, d_f, in ASME III [1], RCC-MR [2] and R5 [3] is simply

$$d_f = 1/N_0 \tag{4}$$

where N_0 is the continuous cycling fatigue endurance to create a crack of depth a_0 at the appropriate total strain range. For the analysis of these tests N_0 is given by $N_{25\%}$ and is calculated from the R66 line (Fig. 1). Thus, for this analysis a_0 corresponds to the crack length that reduces the area of the specimen by 25%, which corresponds to a crack of 2.6mm in a 7mm diameter specimen.

3.2 Time Fraction

The time fraction rule for the estimation of creep damage is widely used in design codes such as ASME III [1] and RCC-MR [2]. The time fraction rule for the creep damage per cycle is

$$d_c^{TF} = \int_0^{t_h} \frac{dt}{t_f(\sigma, t)} \tag{5}$$

where t_f is calculated as a function of the stress and temperature, which prevail for the increment

of time, dt, during stress relaxation and t_h is the dwell time. The creep rupture strength for cast BQ was given by Eq. (2). The stress history during relaxation was calculated from Eq. (1).

3.3 R5 Ductility Exhaustion

The ductility exhaustion approach of R5 for the creep damage per cycle, d_c^{R5}, is given by

$$d_c^{R5} = \int_0^{t_h} \frac{\dot{\varepsilon}_c}{\varepsilon_f(\dot{\varepsilon}_c, T)} dt \tag{6}$$

where $\dot{\varepsilon}_c$ is the instantaneous creep strain rate, $\varepsilon_f(\dot{\varepsilon}_c, T)$ is the corresponding uniaxial creep ductility at the appropriate temperature as a function of the creep strain rate, which for cast BQ is given by Eq. (3). The instantaneous creep strain rate was obtained by differentiating Eq. (1) and replacing $\dot{\sigma}$ by $-\dot{\varepsilon}_c E/Z$, where E is Young's Modulus, so that

$$\dot{\varepsilon}_c = ZB''\sigma_0 b/[E(b.t + Z)] \tag{7}$$

3.4 Stress Modified Ductility Exhaustion

The ductility exhaustion approach of R5 can be modified to include the effect of stress on creep damage by treating the ductility as a function of both strain rate and stress [5,6,7]. The resulting expression for the creep damage per cycle calculated from a ductility exhaustion approach, which includes the effect of stress, d_c^{SM}, is given by

$$d_c^{SM} = \int_0^{t_h} \frac{\dot{\varepsilon}_c}{\varepsilon_f(\dot{\varepsilon}_c, \sigma, T)} dt \tag{8}$$

where $\varepsilon_f(\dot{\varepsilon}_c, \sigma, T)$ is the creep ductility at the appropriate temperature as a function of both strain rate and stress. This approach has been called the 'stress modified' approach. In [5] and in [7] it was shown that the creep ductility of Type 347 weld and the creep ductility of cast Type 304L respectively can be described by

$$\varepsilon_f = A_1 \exp(Q/T)\dot{\varepsilon}_c^{\,n_1}\,\sigma^{-m_1} \tag{9}$$

where A_1, n_1, m_1 and Q are material constants. In this paper the same approach will be applied to Type 316H cast BQ. Furthermore, in [5,6,7] it was shown that the use of 'reversed damage modelling' to determine the relationship between ductility, stress and strain rate gave improvement in the prediction of creep-fatigue failure when compared to the time fraction and the current R5 ductility exhaustion approach. In 'reverse damage modelling' the instantaneous true inelastic strain rate and the true stress as calculated from the available creep curves in conjunction with an appropriate creep ductility model (i.e. the logarithmic form of Eq. (9)) to calculate creep damage using Eq. (8). Thus, the creep damage in each creep test is calculated from

$$d_c^{SM} = \sum_{\varepsilon_c=0}^{\varepsilon_f} \{\delta\varepsilon_c / \exp[\ln(A_1) + Q/T + n_1 \ln(\dot{\varepsilon}_c) + (-m_1)\ln(\sigma)]\} \tag{10}$$

where $\delta\varepsilon_c$ is the inelastic strain increment between test measurements, and includes plastic loading strains. The use of the instantaneous inelastic strain rate and the true stress enables the large differences between the strain rates during loading and creep and the increasing true stress during the tests, to be taken into account. This also enables the constant strain rate tests to be used as well as the constant load tests. The creep damage model, Eq. (10), is then solved by iterating on the constants, to give d_c^{SM} close to one for all of the available tests. This has been achieved using non-linear regression to minimise the sum of $(\log d_c^{SM})^2$. The use of $\log d_c^{SM}$ assumes that like the ductility the creep damage is log normally distributed.

The data that were analysed included all the creep and constant strain rate tests at temperatures from 570 to 700°C. However, on the first attempt it was found that the values of n_1 and $-m_1$, (0.08 and 0.6 respectively) were not physically correct [5]. The value of n_1 should theoretically be $(n-1)/n$, where n is the stress exponent for the minimum creep rate, and $-m_1$ should be negative [5]. Hence, the theoretical value of $(n-1)/n$ [5] has been assumed for n_1. A value of n of 6.1, which gives a value of n_1 of 0.8366, has been determined for cast BQ from the test data at 600°C. Thus, the reverse modelling process only needed to find the best values for $\ln(A_1)$, Q and $-m_1$. These were determined to be 7.1065, 18748 and -4.334 respectively.

3.4 Results of Damage Calculations

The calculation of the fatigue and creep damages for each test were conducted for the mid life cycle and the total creep, D_c, and total fatigue, D_f, damages were calculated from the calculated damages per cycle multiplied by the number of cycles ($N_{25\%}$) in the test. All of the damages in this paper are best estimates as they have been calculated using mean data.

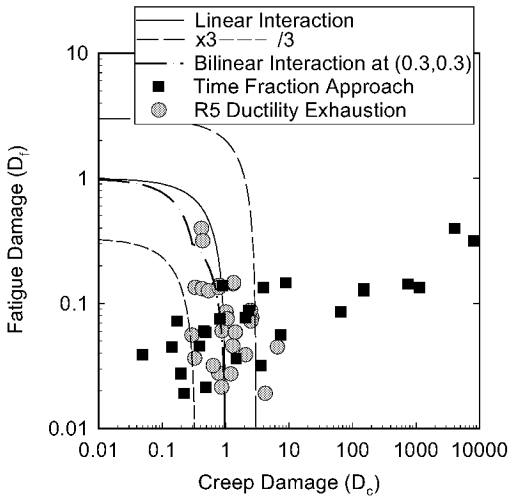

Figure 4 – Interaction Diagram showing the Time Fraction and R5 Approaches.

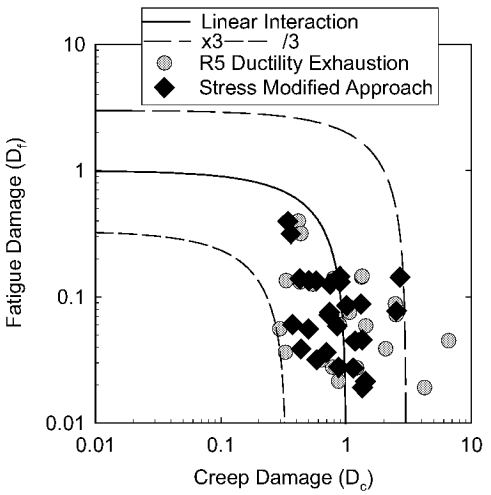

Figure 5 – Interaction Diagram showing the R5 and 'Stress Modified' Approaches.

The results of the creep damage and fatigue damage calculations are presented in Figs 4 and 5. As a guide to the scatter shown by the damage, factors of $^1/_3$ and 3 have been applied to the linear interaction line. Factors of ½ and 2 are generally used for creep-fatigue tests [6,7]; however, the data on cast BQ show a large amount of scatter. This scatter is probably caused by the variety of different test methods which have been used to perform the tests and because stress relaxation data were available for only one cycle of each test. The total damage (D_c plus D_f) for each test are also presented in Table 1 along with the mean values and standard deviations (SD) calculated assuming that the total damage is log normally distributed. These values are used to assess the level of conservatism of each of the cases and to show which give the least scatter.

It can be seen from Figure 4 that the time fraction approach gives unrealistic predictions of creep damage. In particular, very large values of creep damage are predicted for the tests with the largest fatigue damage values. Nevertheless, the current R5 approach, which uses the

creep strain at failure as a function of average creep strain rate, gives a reasonable prediction of creep and fatigue damage at failure for all of the tests (see Figure 5). In particular the mean creep damage is slightly greater than unity and there are no data with total damages less than 1/3 (Table 1). Furthermore, it is shown in Table 1 and Figure 5 that the best predictions of creep damage are achieved when the 'stress modified' approach. In particular the mean total damage is close to unity and the SD is significantly lower than the other approaches that were considered (Table 1).

4. DISCUSSION

The theoretical understanding of the time fraction approach would suggest that the creep damages would be smaller than those predicted using a ductility exhaustion approach [12]. However, when the rupture behaviour is described by Eq. (2) many of the values of creep damage are unrealistically large. This observation is explained by the rupture data on cast BQ and does not invalidate the theoretical understanding of the time fraction approach. As a polynomial Eq. (2) is not trustworthy in extrapolation in terms of stress and since the maximum stress in the rupture data for cast BQ was 279MPa, it should not be used above 306MPa (10% above the maximum stress) [11]. Indeed, it can be seen from Table 1 that the creep damage, which is predicted using the time fraction approach, is unrealistic for the tests with initial stresses greater than about 300MPa. Furthermore, Table 1 shows that for stresses below 300MPa the creep damages are lower than those predicted using ductility exhaustion, which is in accord with the theoretical understanding. The reason that the initial stresses in the creep fatigue tests are so high is due to cyclic hardening.

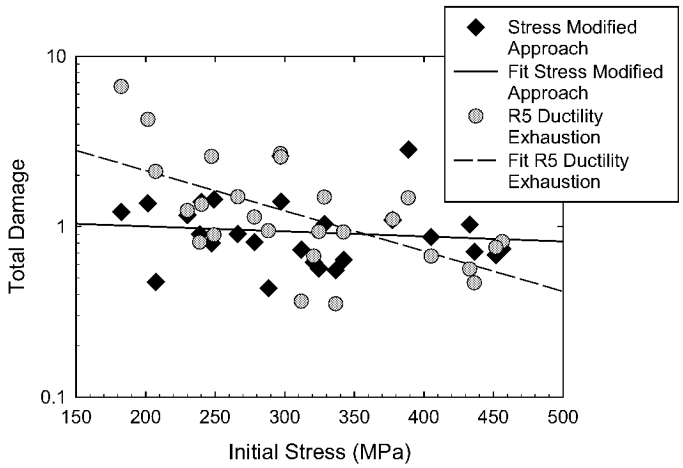

Figure 6 – The Effect of Stress on the Predictions of Total Damage.

The current R5 approach, which uses the creep strain at failure as a function of average creep strain rate, gives a reasonable prediction of creep and fatigue damage at failure for all of the tests (Fig. 5). This validates the current R5 ductility exhaustion approach. Although the current R5 approach gives good predictions of damage at failure it can be seen from Figure 6 that the initial stress has a systematic effect on the calculated damage. In particular, at low initial stresses the ductility exhaustion approach tends to be overly conservative and when the initial stress is high the ductility exhaustion approach tends towards non-conservatism. This

is precisely the type of behaviour that would be expected if the ductility were a function of stress as well as strain rate and temperature, as predicted by Eq. (9). Indeed, the best predictions of creep damage are achieved when the 'stress modified' approach is used, see Figure 5. It can be seen from Figure 6 that the 'stress modified' approach completely removes all of the dependence of the total damage at failure on the initial stress.

The reason why the 'stress modified' approach works so well is shown by the stress relaxation behaviour during creep-fatigue dwells (see Fig. 7). The tests with low initial stress (low strain ranges) experience higher creep strain rates for a given stress than both the creep tests and the tests with high initial stress (large strain ranges) (see Fig. 7). Conversely, the tests with high initial stress (large strain ranges) experience lower creep strain rates for a given stress than the creep tests, the constant strain rate tests and the tests with low initial stress (low strain ranges) (see Fig. 7). Since, n_1 is positive and $-m_1$ is negative, Eq. (9) predicts that the ductility is high for combinations of low stress and high strain rate and that the ductility is low for combinations of high stress and low strain rate.

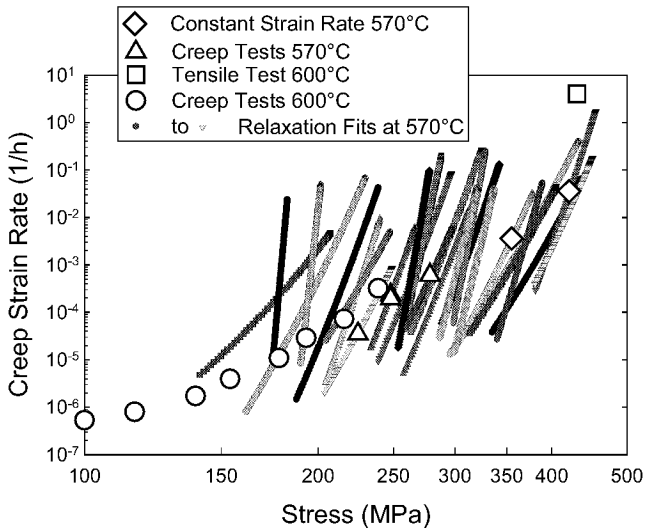

Figure 7 – The Creep Strain Rates for Relaxation Dwells and Creep Rupture Data (the creep data are plotted as $\dot{\varepsilon}_c^{av}$ versus σ_R and tensile and constant rate data are plotted as average total strain rate versus the ultimate tensile strength).

Hence the 'stress modified' ductility exhaustion approach used relatively high ductilities when assessing tests with low initial stress (low strain ranges) and relatively low ductilities when assessing tests with high initial stress (large strain ranges). This was the reason for the reduced scatter when the 'stress modified' ductility exhaustion approach was used. In particular, it reduced the level of scatter in total damage values at failure (Fig. 5) and it also removed the marked dependence of the damage on the initial stress (Fig. 6). The reasons for the differences between the stress relaxation behaviour and the creep strain rates are not considered in detail in this report. Nevertheless, it is likely that the high strain rates in the tests with low initial stresses are caused by primary creep and that the low strain rates in the tests with large initial stresses (high strain range tests) are caused by cyclic hardening, which affects the stress relaxation behaviour.

5. Conclusions

Creep-fatigue data for Type 316H cast BQ at 570°C have been used to investigate different approaches for calculating creep damage. It has been found that:

1. The time fraction approach is inferior to the R5 ductility exhaustion approach for predicting creep damage at failure in Type 316H steel. Indeed the time fraction gives wholly unrealistic and overly conservative predictions of creep damage for creep-fatigue cycles with large strain ranges.
2. The R5 ductility exhaustion approach gives a reasonable prediction of creep damage at failure for all of the tests.
3. The most accurate predictions of creep damage and thus the best approach to be used for life extension studies was the 'stress modified' ductility exhaustion approach.

6. Acknowledgements

This paper is published by permission of British Energy Generation Ltd. The author acknowledges UKAEA and latterly AEA Technology and Serco Assurance for providing the test data. Acknowledgement for permission to publish the creep test results is given to the sponsors of the ERA Technology Project-4080 from which the long term data originate, in particular ALSTOM Power (UK) Ltd, British Energy and E.On UK plc.

7. References

[1] ASME, Section III Div. 1 Sub-Section NH, ASME New York USA, 2001.
[2] RCC-MR, Design and Construction Rules for Mechanical Components of FBR Nuclear Islands, AFCEN, Paris, France, 2002.
[3] R5, Assessment Procedure for the High Temperature Response of Structures Issue 3, British Energy, Gloucester, UK, 2003.
[4] Wareing J, Bretherton I and Livesey V B, Life Prediction for Elevated Temperature Components Subjected to Cyclic Deformation, Proc. IMechE Conf. Engineering Materials and Structures, Sheffield UK, IMechE Paper C269/86, Sept. 1986.
[5] Spindler M W. The prediction of creep damage in Type 347 weld metal: part 1. The determination of material properties from creep and tensile tests. Int. J. of Press. Vess. and Piping, Vol. 82, 2005, pp. 175–184.
[6] Spindler M W. The prediction of creep damage in Type 347 weld metal: part II creep fatigue tests, Int. J. of Press. Vess. and Piping, Vol. 82, 2005, pp. 185–194
[7] Spindler M W, Effects of Dwell Location on The Creep-Fatigue Endurance of Cast Type 304L, in Creep & Fracture in High Temperature Components Conference Proceedings, DEStech, Lancaster, USA, 2005, pp. 615-627.
[8] Bretherton I, Serco Assurance, Private Communication, 2002.
[9] R66, AGR Materials Data Handbook, Issue 6, British Energy, Gloucester, UK, 2004.
[10] Grover H K & Higginbottom A, Final Report on the Elevated Temperature Tensile and Creep Rupture Properties of Type 316 Steel, ERA Technology Report 2A/858, 1983.
[11] PD6605-1998, Guidelines on Methodology for Assessment of Stress Rupture Data, British Standards Institute, 1998.
[12] Takahashi Y, Further Evaluation of Creep-Fatigue Life Prediction Methods for Low-Carbon Nitrogen–Added 316 Stainless Steel, J. of Press. Vess. Techn., Vol. 121, 1999, pp. 142-148.

WEB-ENABLED DATABASES OF JRC PETTEN – EFFECTIVE TOOLS FOR EUROPEAN KNOWLEDGE MANAGEMENT

H. H. Over[1], W. Dietz[2]

[1]Joint Research Centre of the European Commission, Institute for Energy, Petten, The Netherlands, hans-helmut.over@jrc.nl

[2]Consulting Metallurgist / MECS, Lindlar, Germany

Abstract

Materials databases (MDBs) are effective tools to store big amounts of complex materials test data, which are created by modern, computerised test facilities. They guarantee the effective and efficient handling of large amounts of generic and detailed materials properties data related to e.g. fabrication processes. In combination with analysis tools experimental data are necessary for e.g. mechanical design, construction and lifetime predictions of complex components.

An important issue of MDBs for R&D projects is data quality and confidentiality as well as a fast data access in combination with immediate graphical and numerical output as well as data analysis and evaluation. Another advantage would be if data could be uploaded form the post-processing part of a test machine direct into the database. Beside the numerical data a lot of expertise is conserved in documents of R&D projects such as interim and final reports, microstructural images, etc. These documents should be retrievable together with the numerical data.

Most of these objectives are fulfilled by the materials database Mat-DB in combination with the documentation database DoMa accessible through a web-enabled interface on the ODIN portal (*On-line Data Information Network:* https://odin.jrc.nl) of JRC Petten (JRC). ODIN is established on professional hard- and software.

This paper describes the present status of the structure and functionality of Mat-DB and DoMa and gives examples how these tools can be used for the benefit of ongoing European materials research projects and networks such as COST.

Keywords

Materials database, materials properties data, experimental data, mechanical properties data, thermo-physical properties data, Web-enabled database, analysis routines, alloys, corrosion, document management system, documentation database, web-services

Introduction

Fast access and exchange of materials data between research, design and manufacturing teams working on different sites worldwide is a challenging issue to be addressed during the product cycle in materials engineering [1]. Another imported issue is safeguarding high investments made into materials research, which means that experimental data in combination with related documentation must be properly conserved, easily be located and quickly be retrieved. Materials databases (MDBs) are effective tools to address these problems. Various categories of MDBs exist for different requirements, for example containing standards data on metallic alloys [2, 3] and plastics [4] or more complex database applications needed for the design analysis [5]. MDBs are also basic elements for establishing knowledge based and expert systems.

With the emergence of the Internet, the capability of MDBs has further increased. Web-enabled MDBs provide a more centralized management and conservation of the data. Finding and accessing the required data is much faster than to search for them in a traditional manner, from publications and handbooks. In particular the dissemination of research results has improved significantly, as the data are accessible over the World Wide Web. However, only few web-

enabled materials applications exist at present on the market. Examples are the Materials databases of NIMS (National Institute for Materials Science) in Japan [6], which offer a lot of data but their interface guidance is still very limited. Currently, acceptance and use of web-enabled, publicly available MDBs is still hindered by problems such as lack of standardization, ease of handling and availability of free qualified data.

As a contribution to European knowledge preservation which is a goal of the European Research Area, JRC was considering these problems in the development of database applications to support in particular European R&D projects in storing, accessing and evaluating materials data together with related documentation.

Emphasis of this paper will be the introduction into JRC web-enabled database applications for use in European R&D materials projects with a detailed description of their present status. Details of the features of the Mat-DB have been described recently elsewhere [7].

3 ODIN Web Portal

The installation of a professional server infrastructure was a basic condition for the realisation of European R&D related knowledge management. JRC has set up the ODIN (On-line Data Information Network: https://odin.jrc.nl) Web Portal (see figure 1) as a redundant server application to guarantee high availability. A redundant load balancer behind a firewall controls the user access via two application servers, which connect to two redundant database servers behind a second firewall. The documents are stored on powerful raid arrays. The output is encrypted via a secure connection.

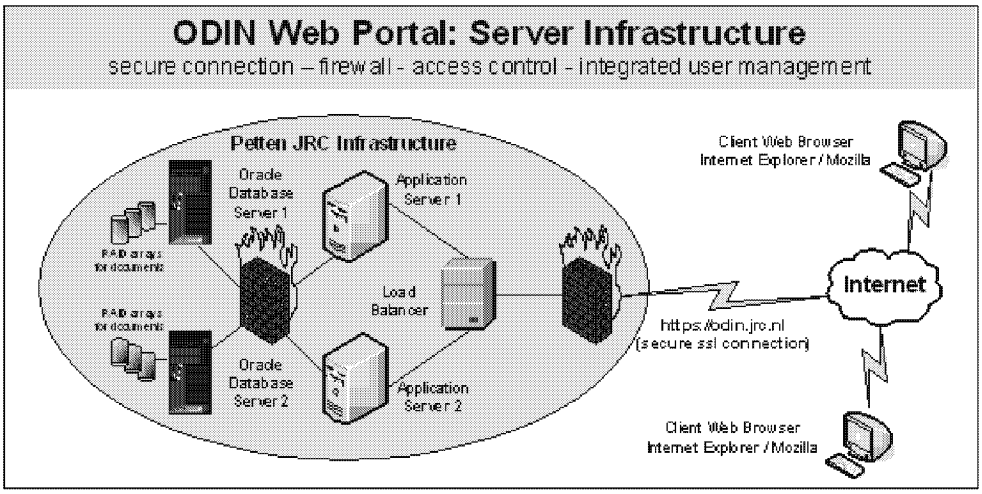

Figure 1: Server infrastructure of the ODIN Web Portal

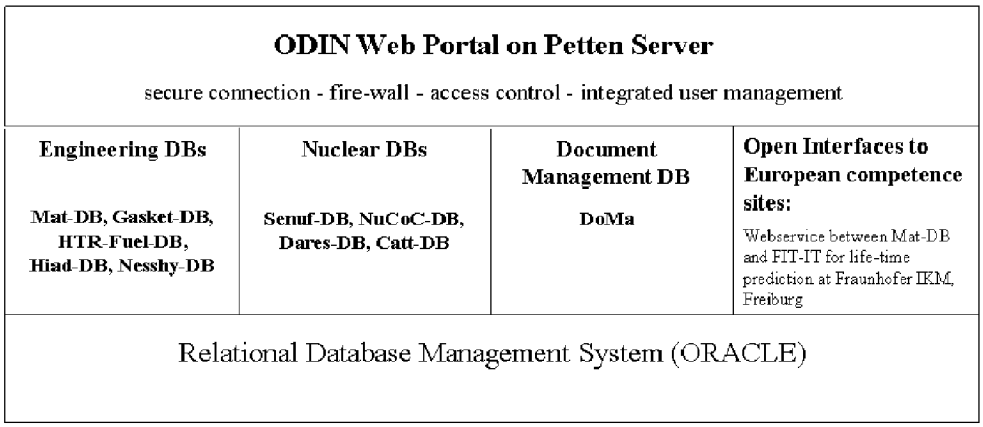

Figure 2: Databases and interfaces within the ODIN Web portal

The various databases within the ODIN Web Portal are shown in figure 2. The application servers control the access rights to public and confidential domains of these databases and also to the linked Fitit web interface. Since Mat-DB and DoMa share this common user management, it is possible to synchronise access to protected areas in both databases, i.e. a user who has access to protected numerical data in Mat-DB can transparently access the corresponding documentation in DoMa and vice-versa.

The databases within ODIN are ever growing. New energy related applications are already requested. The soft- and hardware of server infrastructure is maintained, continuously updated and upgraded. It is the aim of JRC to link together European web competences for the time being within the area of materials properties data such as Fitit complex materials modeling (described in the data retrieval part) and a network of web-enabled Mat-DBs on different customer sites.

4 Mat-DB features

The JRC has been developing a materials database for safeguarding and managing its experimental materials data resulting from in-house research some 20 years ago [8,9]: Mat-DB covers mechanical and thermo-physical properties data of engineering alloys at low, elevated and high temperatures for base materials and joints [10] as well as high temperature corrosion. It includes e.g. irradiation materials testing in the field of fusion and fission, tests on single crystals with thermal barrier coating for gas turbines and mechanical properties testing on a corroded specimen, which refers to weight gain/loss data of high temperature exposed engineering alloys, ceramics and hot isostatic pressed powder materials and covers corrosion tests such as oxidation, sulfidation and nitridation. The Mat-DB database structure has continuously grown and the application developed from the initial mainframe database without graphical user guidance, over stand-alone PC and client/server applications to the new web-enabled application (see section 3). All current applications use an identical database structure simplifying data exchange between the JRC and its external MDB partners. The commercially available Mat-DB is being used as stand-alone PC or client/server applications by a number of European industry and research

organizations to manage their in-house experimental test results. The Web-application presently is only installed at the Petten Server.

Mat-DB is designed for experimental data, which is delivered by the laboratories in defined formats and quality. The emphasis is on data from tests, which comply with existing or pre-normative standards. The data can be entered, stored and accessed with typical database routines and can be evaluated with integrated analysis tools.

The Mat-DB entities (see table 1) contain detailed meta-information and entry of many fields is mandatory to increase data quality. Thesauri are provided for many text and image fields facilitating and improving standardization during data entry and retrieval. All entities contain additional fields (customer internals), which can be used for company-specific purposes. In addition to the numerical and alphanumerical data, any type of binary files can be stored within the database, for example final reports of R&D activities, drawings or large amounts of raw data (unfiltered curve data, basic output of strain gauge measurements).

Table 1: Description of Mat-DB entities

Entity	**Meta-information for e.g.**
Data Source	Organization, laboratory, scientist, R&D project
Material	Material characterisation, chemical composition, heat treatment, process data, microstructure (tests on dissimilar materials joints need a 2nd material entity)
Specimen	Sampling, orientation, type of specimen, geometry, coating layers
Test condition	Test environment, mechanical or thermal pre-exposure, irradiation
Joining	Process method, joining parameters, joining geometry, filler metal
Test result	See table 2

In total, the database structure for base materials contains more than 130 tables and 1850 fields, which are grouped into logical entities: *data source*, *material*, *specimen*, *test condition* and *test result* (see also table 1). The entity *'test result'* is divided into different areas, which contain tables for storing test type specific mechanical (24) and thermo-physical (10) properties and corrosion data (see table 2).

Manuals describing user-guidance and analysis tools including image and text thesauri, curve file structures and test type definitions for Mat-DB can be downloaded by users from the ODIN portal. .

A series of companies and research institutions worldwide are using Mat-DB PC and client/server applications for their own data administration. All database functionalities and object-controlled features for data entry, retrieval and analysis were well tested. There is a permanent user feedback. Since 1999 their remarks and proposals were discussed within annual user meetings and new functionalities, test types, etc were added to Mat-DB.

Table 2: Mat-DB test result entity

MECHANICAL PROPERTIES	*IRRADIATION*
CRACK GROWTH & FRACTURE	Irradiation creep
Creep crack growth	Swelling
Cyclic creep crack growth	*TENSILE*
Fatigue crack growth	Compression
Fracture toughness	Multiaxial tensile
Impact	Uniaxial tensile
CREEP	Small punch tensile
Cyclic creep	*Complex test*
Multiaxial creep	**THERMO-PHYSICAL PROPERTIES**
Torsional creep	Density
Uniaxial creep	Electrical resistivity
Small punch creep	Emissivity
RELAXATION	Linear thermal expansion
Multiaxial relaxation	Poisson's ratio
Uniaxial relaxation	Specific heat
FATIGUE	Shear modulus
High cycle fatigue	Thermal conductivity
Low cycle fatigue (load control)	Thermal diffusivity
Low cycle fatigue (strain control)	Young's modulus
Thermal fatigue	**CORROSION**
Thermo-mechanical fatigue	High temperature corrosion

5 Web-enabled Mat-DB

The emergence of the Internet created new opportunities for materials databases. Therefore the JRC has ported Mat-DB to the Internet. Objectives of the web-enabled application are:

- Facilitating data management, exchange and dissemination within European R&D projects free of charge
- Providing data pools which contain public and restricted data for use in industry, research and education
- Providing the web-enabled Mat-DB to interested multi-national organizations and customers, with which they can make confidential data accessible to authorised employees at different sites via their Intranet.

Any public user can check the presently available materials data content sorted by materials, test types and depending on the test types by temperatures.

All well introduced functionalities and object controlled features of PC and client/server applications for data entry, retrieval and analysis are now implemented in the web-enabled Mat-DB which are described in detail in the following sections.

5.1 Data entry and exchange

Mat-DB provides web-enabled data entry from the machine into the database for European project and network partners (see figure 3) by using XML (eXtensive **M**ark-up **L**anguage). XML is an established standard to exchange data over the Internet between organisations having dissimilar structured databases or between machines and databases. Data are not only assigned by their values but also by their names and units. The nomenclature of the field names within Mat-DB is compatible with the standard MATML (www.matml.org), a library developed by the international materials society and maintained by NIST (US: **N**ational **I**nstitute of **S**tandards and Technology).

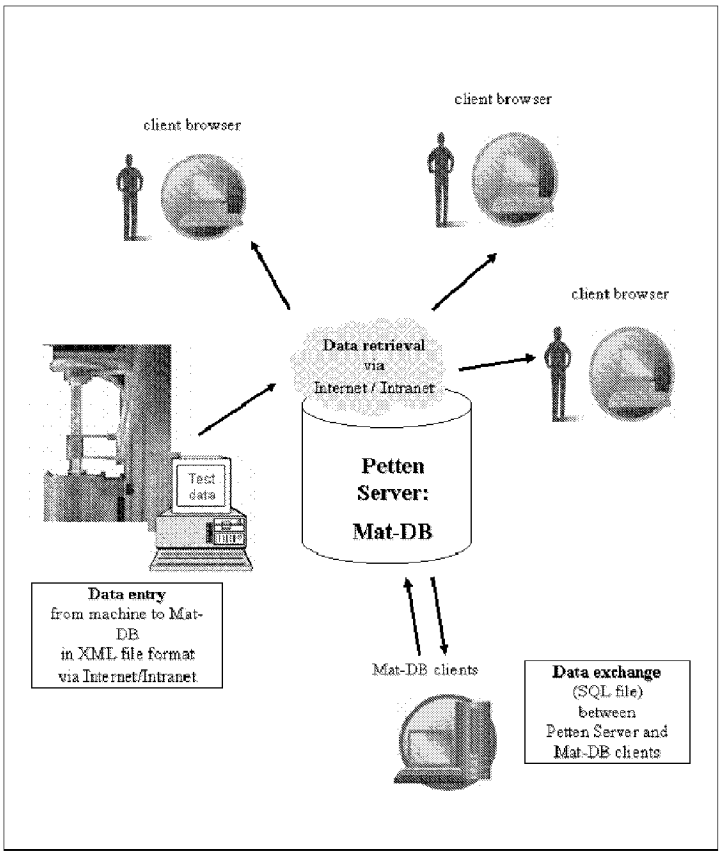

Figure 3: Data flow from machine into Mat-DB

Post processing tools of the machines, which are extended to export into the defined XML format, can transfer the test data in a random order into Mat-DB because the application recognises and applies the data to the assigned database fields. Source, material, specimen, test condition and joining meta-information can be completed within separate steps. The whole data sets can be checked, updated and validated before they are uploaded into the relational database part and released for clients. This XML based data entry procedure [11] with a very user-friendly web-interface similar to the PC client is pilot tested within the European R&D project "TMF-Standard" [12].

Test result data available in CSV files can easily be uploaded into the database. They can be arranged in pre-defined column settings, which are available in the Mat-DB user manual and saved in a separate directory on the clients PC from which the user can transfer it into the web-enabled Mat-DB. The data can be attached to related source, material, specimen and test condition information.

5.2 Data retrieval and analysis

The user interface for web-enabled data retrieval follows the lines of the well-established stand-alone PC and client/server applications, although it is slightly less sophisticated due to the limitations of the HTML protocol [13]. It allows constructing a query to retrieve the test results in three sequential levels. The first level starts with mandatory selections on *source*, *test type* and *material* following a hierarchical order. Data retrieval can then be continued with optional selections of a so-called *combined material*, which characterizes special features of the material such as service exposed, irradiated, low carbon, etc, *batch identifier*, *specimen* (type) and (test) *environment*. Retrieval can be finished with optional selections on test type specific fields such as *time at rupture*, *test temperature*, *elongation* in the case of *uniaxial creep*.

After the mandatory fields have been specified the *Generate report* button is active allowing the user to create an overview report on the selected material tests. The report contains links to detailed information on e.g. source (including documentation), heat treatment, chemical composition, raw data sets or numerical and graphical curve information. Furthermore the report screen allows exporting the selected test data to pre-defined EXCEL charts or starting routines for analysing the test data.

Mat-DB contains a number of the test-type specific analysis routines, which allow a fast evaluation of the retrieved data. The evaluation programme library of the PC and client/server applications (see table 3) contains mathematical models, constitutive equations, parametric expressions and regression functions. The analysis routines allow a comparison of data sets against each other. Database customers often use the analysis results for their publications and reports [14]. For the web-enabled application the analysis routines are re-programmed and implemented as Java servlets. They will be accessible also independent of the Mat-DB with direct data input in a given format. The analysis routines allow user specified extrapolations and interactive manipulations to add or delete data points. Currently, the major part of the analysis methods is implemented. Until end of 2006 all the other analysis routines except the constitutive equations shown in table 3 will be implemented into the web-enabled Mat-DB. The materials parameters calculated by the analysis routines are necessary for inelastic analysis calculations of high temperature exposed components. Figure 4 shows a 2^{nd} order polynomial Larson-Miller extrapolation, which was exported to EXCEL. Triangular symbols belong to the dissimilar welded joint X10 CrMoVNb9 1/ X20 CrMoV12 1 – dj, the rectangular symbols to the similar welded joint X10 CrMoVNb9 1 – sj.

Table 3: JRC MDBs evaluation programme library

Uniaxial creep *Creep relations:* Norton creep law, Prandtl creep law, Soderberg creep law, Monkman-Grant relation, Dobés-Milîcka relation *Extrapolation methods:* Larson-Miller, Manson-Haferd, Manson-Brown, Orr-Sherby-Dorn, Spera, Minimum commitment method *Constitutive creep equations:* Theta projection, Mc Vetty equation, Kachanov equation *Interpolation routines:* Polynomial creep curve fit, Polynomial stress dependence, Isochronous & isostrain determination	**Fatigue** Ludvik law, Manson-Coffin relation, Basquin analysis, Frequency modified Manson-Coffin relation **Crack growth** ASTM compliant creep crack growth analysis, Creep crack growth plot, Fatigue crack growth analysis **HT Corrosion** *Weight gain/loss analysis:* Power law, Power law-time, Parabolic Δm^2, Parabolic $t_{1/2}$, Kp(t), Breakaway

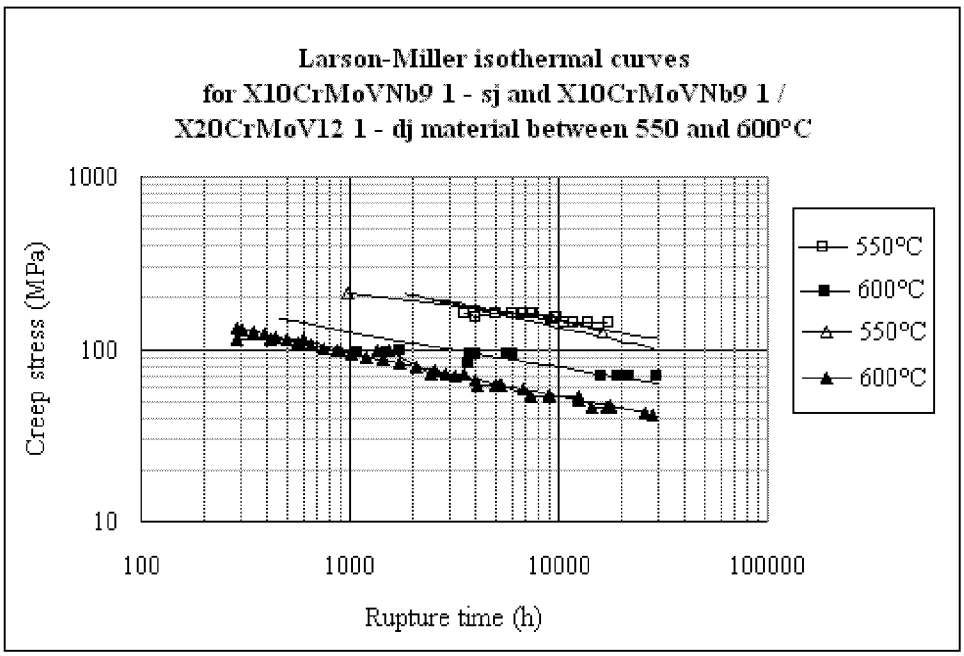

Figure 4: Larson-Miller extrapolation of a Siempelkamp data set: Similar (X10 CrMoVN b9 1 – sj: triangular symbols) and dissimilar (X10 CrMoVNb 9 1/ X20 CrMoV 12 1 – dj: rectangular symbols) welded joints

In addition to the existing database analysis routines, the JRC is currently integrating **Fitit**, - proprietary software of the Fraunhofer Institute in Germany designed for the calculation of complex material models. **Fitit** can be used for models defined as a set of differential equations and analytic functions, e.g. Chaboche and Kachanov. Data selected within the web-enabled Mat-DB can be sent to **Fitit**, which then fits the data to a selected model. The performed job is attached to the users' account.

Once the model parameters have been calculated, they are returned to Mat-DB. The user automatically receives a message and can open his account. He receives information about the number of iterations, the fitted material parameters, the scattering and the numerical and graphical results in comparison to the input data. Figure 5 shows a fitted tensile curve result by using the Chaboche model. The fitted parameters can be applied to Finite Element (FE) lifetime calculations of high temperature exposed components with commercial codes like ABAQUS or ANSYS [15].

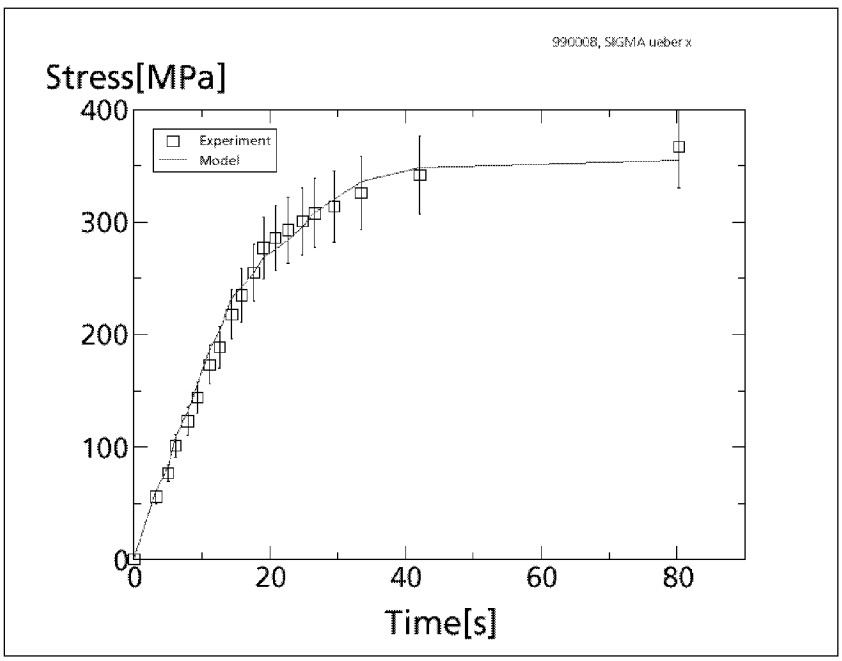

Figure 5: Fitted tensile curve result by using the Chaboche model

6 Documentation database DoMa

One of the ODIN applications which complement Mat-DB by providing controlled access to any kind of supporting documents is the documentation database (DoMa). DoMa is a web-enabled digital document repository designed to enhance the dissemination of information amongst the R&D community in the energy sector. Any type of electronic record (i.e. publications, minutes,

spreadsheet, graphic, etc.) may be stored. Documents are organized in a hierarchical structure as in any standard file system with folders and sub-folders and document retrieval is controlled through access rights: a public document can be retrieved by any registered user, a confidential document requires that the user has been granted specific access rights for the document. Document upload and administration of access rights is delegated to the responsible persons of the various projects, i.e. each project can upload their documents and control the access their area remotely via the DoMa web-interface. DoMa provides an indexed full text search and a very fast search on abstracts, titles, keywords, etc. It contains manuals as well as for the user and the administrator.

7 Benefit for European materials projects

The intention of JRC as a supra-national institution is safeguarding high investments made into European materials research and to conserve the knowledge. As one way in achieving this goal, the JRC offers Mat-DB and DoMa to European R&D projects and other European groups and committees as a free tool to manage and exchange their experimental data and documentation, similar to the Japanese 'Data Freeway', which was set up to exchange data between several research centres [16]. European R&D participants, who are supported by public funding, are encouraged to release their data for public access at the end of the project. Thus, the project benefits from a sophisticated web-enabled database for the management and conservation of materials data and related documentation. The European research community may benefit from the availability of valuable data and analysis routines.

Mat-DB contains the experimental properties data, which are filtered, smoothed, reduced, etc. A complex thermo-mechanical fatigue test for instance could run depending on the loading conditions several hundred or thousands cycles. To store all of them would slow down even the most powerful database. Therefore usually only some specific cycles together with hysteresis information (usually reduced to 200-300 data points per hysteresis) are stored in a database. But, if necessary, the complete raw data sets can be stored as binary objects in Mat-DB. A project partner can conserve for example his original EXCEL file and all other partners who have access rights can then open this file within a Mat-DB retrieval session. Moreover, project documentation related to the data sets such as final reports can be stored in DoMa. Project responsible himself can enter the documentation in DoMa and determines the access rights. The general project description could be publicly available; documentation such as reports accessible only for a chosen group of customers could have a confidentiality level 1 and minutes of project meetings an even more restricted confidentiality level 2. If somebody would request any access to the confidential parts the project responsible receives a mail and can make his decision. DoMa and Mat-DB are linked with each other. Having logged-in in ODIN the user can retrieve data from Mat-DB and related documentation from DoMa and vice versa. The access rights together with password and user identification are administrated in the ODIN application server.

The web-enabled Mat-DB provides access to public, restricted and confidential materials data and documentation from former and current European R&D activities and from extensive material programmes, e.g. the German High Temperature Reactor Programme [17]. It currently contains a pool of with approximately 25000 test results. Public data are open to anybody who registers, restricted data are released after agreement by the data owner and confidential data are accessible by the project participants only. The quality of data is the responsibility of the

laboratory where they have been generated. JRC controls mandatory input, but does not take any liability for the data. Offering a broad range of materials data together with the analysis options and related documentation would make the ODIN platform an address of interest both for research and industry.

However, proprietary data are often very sensitive and/or the data owners invested significant resources for testing the materials. Therefore they do not want to release the data without any return. In such a case, the ODIN portal may act in future as a tool for exchange of materials data and documentation over the Internet or could act as data warehouse [18] for European groups and committees, which retain full control over their own data. Therefore the web-enabled Mat-DB has also been installed at FZ Jülich. FZ Karlsruhe is using the JRC server to upload their data in an own domain, which is totally under their control. Other European research centres such as BAM and CEA Saclay are also interested in the web-enabled Mat-DB. The goal of JRC is to implement a web-enabled data content functionality, which browse through all accessible data on the different Mat-DB servers. The individual sites control the access rights to these data. The added value for these network partners is the use of all implemented analysis routines, the interface to Fitit and DoMa.

Partners from industry and research are represented in COST materials projects. They create a lot of experimental data, which are supported partly by European funding. Therefore they should feel obliged to conserve the gained knowledge in form of data and documentation, especially the public part. On the other hand if there is any interest to commercialise confidential data and documentation, the COST projects as a whole or single partners could make use of the ODIN platform free of charge. Interested partners could upload the data into assigned data pools. Documentation related to the data sets can be implemented linked to DoMa. The data owners can then determine the rules for data exchange or data release, which may include e_commerce and can control the access for those customers who subscribe for the data. JRC is guaranteeing data confidentiality, encryption of the data and maintenance of the ODIN platform free of charge.

A lot of data and documentation of finished COST projects have already been uploaded to DoMa and Mat-DB. Many other R&D projects such as the High Temperature and Generation IV Reactor related ones make meanwhile use of the ODIN Web Portal.

8 Summary and Conclusion

Material databases (MDBs) are important and effective tools for the conservation, exchange and dissemination of data. The potential has even further increased with the emergence of the Internet. The availability of experimental materials data in a defined and traceable quality is necessary for structural integrity and inelastic analysis calculations or complex materials modelling. In combination with FE calculations lifetime predictions can result in a much better use of high temperature exposed components, which improves safety and reliability and saves costs. Therefore the European scientific and engineering community on materials technology and the European Commission itself would have an added value in conserving valuable data and documentation and in establishing an ever-growing data pool promptly accessible via the Internet.

The JRC has a long history of developing material databases and can offer a mature web-enabled Mat-DB to manage mechanical, thermo-physical and corrosion properties data. The database

structure includes detailed meta-information on the *material*, *test condition*, *data source* etc. Mat-DB and the related analysis routines are installed on a powerful and secure server within the Online Data Information Network (ODIN: **https://odin.jrc.nl**). The application is offered at no charge to support European R&D activities as well as European groups and committees for the management and conservation of their experimental materials data. Under the aspect of knowledge conservation the project participants are encouraged by the EU to release their data for public access at the end of the project. Data owners such as COST partners who invested a lot of money for testing the materials and intend to sell restricted materials data and documentation via the Internet could also use ODIN to form a materials data warehouse.

Since ODIN is a central Web Portal to a series of its activities, the JRC intends to ensure a long-term continuation of the related applications including maintenance and further development of the various web-enabled database applications for engineering and nuclear safety.

The web-enabled Mat-DB will be further developed to include the entire cycle of data entry from machine to database, data retrieval and analysis. New test types will be added as required. The structure has already been upgraded to include ceramics and composites.

References

[1] Advanced Engineering Materials Vol. 4, 2002, Nr. 6, pages 317-416: Special Issue "Materials and Process Selection"

[2] Plantfacts Database of the German VDEh (Verein Deutscher Eisenhüttenleute - German Iron and Steel Institute): http://www.vdeh.de/deutsch/arbeit/informat/plantfe.htm

[3] WIAM®-METALLINFO DB, IMA-Dresden: http://www.ima-dresden.de/deutsch/startde.htm

[4] Materials Databases of MBase, Aachen, Germany: http://www.m-base.de/main/en/index.html

[5] MSC.Mvision Databanks, USA: http://www.mscsoftware.com

[6] Materials Databases of NIMS - National Institute for Materials Science, Japan: http://mits.nims.go.jp/db_top_eng.htm

[7] H.H. Over, E. Wolfart, W. Dietz, L. Toth, "A web-enabled materials database to support European R&D projects and network activities", Advanced Engineering Materials, August, 2005

[8] R.C. Hurst, H. Kröckel, H.H. Over, P. Vannson, "The Use of Models in Materials Databanks", Materials 88 - Materials and Eng. Design, The Institute of Metals, London 1988

[9] H. Kröckel, H. H. Over, "The Need for an European Approach to Materials Characterisation and Data Management", International Symposium on Advanced Materials for Lightweight Structures, March 1994

[10] H.H. Over, J. H. Rantala N. Taylor, W. Dietz, "A materials properties database approach to cover welded joints", 2nd International Conference on Integrity of High Temperature Welds, London, UK, 10th – 12th November, 2003

[11] M. Nagy, H.H. Over, A. Smith, "XML related Data Exchange from the Test Machine into the Web-enabled Alloys-DB", 19th International CODATA Conference, "The Information Society: New Horizons for Science", Berlin Germany, 7th - 10th November 2004

[12] Thermo-mechanical fatigue – the route to standardisation', CORDIS R&D project no. GRD2-2000-30014

[13] H.H. Over, E. Wolfart, E. Veragten, "Data Retrieval and Evaluation within the Web-enabled Alloys-DB", 19th International CODATA Conference, "The Information Society: New Horizons for Science", Berlin, Germany, 7-10 November 2004

[14] P.J. Ennis, "Candidate Materials for a Modular High Temperature Reactor Power Plant in Engineering Issues in Turbine Machinery, Power Plant and Renewables", editors A Strang, R.D. Conroy, W.M. Banks, M. Blackler, J. Leggett, G.M. McColvin, S. Simpson, M. Smith, F. Starr, R. Vanstone, Maney, IoM3 Publications, Book Number B0800, ISBN 1-904350-20-8, 2003, pp 1029 – 1037

[15] R. Mohrmann, V. Denner, T. Hollstein, "'Zur Lebensdauervorhersage von Austenit-Ferrit-Mischverbindungen"', Tagungsband FDBR Düsseldorf (2003) Teil 4

[16] 15th International CODATA Conference, M. Fujita, Some Trials on WWW Servers in the "Data Freeway", Scientific Data in the Age of Networking 29 September - 3 October 1996, Tsukuba, Japan

[17] Endbericht zum Verbund-Forschungsvorhaben des BMFT, "Auslegungskriterien für hochtemperaturbelastete metallische und keramische Komponenten sowie des Spannbeton-Reaktordruckbehälters zukünftiger HTR-Anlagen", Teil B: Metallische Komponenten, KFA Jülich, August 1988

[18] Y. Li, "Building the Data Warehouse for Materials Selection in Mechanical Design", Advanced Engineering Materials 2004, 6, No. 1 - 2, pp 92 - 95

Part III

Addendum

Invited papers

These papers arrived too late for reviewing

and are reproduced as received

ADVANCED COATINGS FOR GAS TURBINES

J. R. Nicholls[+] and B. Bordenet[*]
[+] Cranfield University, Cranfield, Bedford MK43 0AL,UK
[*] ALSTOM (Switzerland) Ltd, Brown Boveri, Strasse 7, CH-5401, Baden, Switzerland

Abstract

Coating systems and the associated surface engineering are now key materials technologies in the design of advanced gas turbines. This paper focuses on the concept of the 'coating system' to provide environmental and/or thermal protection to hot gas path components.

This paper provides a review of available coating systems and discusses their relative benefits in terms of performance against manufacturing complexity and therefore cost. Systems may vary from low cost, aluminide diffusion coatings through to the more exotic 'smart' corrosion resistance coatings and 'self diagnostic' thermal barrier coating concepts.

Future trends in the design of environmental protection and thermal protection coatings are discussed including the latest advances in modified aluminide coatings, with the addition of reactive elements, diffusion barrier concepts applicable beneath advanced overlay coatings, the new $\gamma+\gamma'$ strong bondcoat systems and the latest structurally modified, low thermal conductivity thermal barrier coating systems.

Keywords: Gas turbine coatings, diffusion coatings, platinum aluminides, yttrium aluminides, MCrAlY overlay coatings, APS, VPS, HVOF, PVD, EB-PVD, diffusion barriers, thermal barriers, smart coating systems

Introduction and Background

Over recent years, gas turbine based systems have become the equipment of choice for power generation and now form an integral part of modern advanced power plant engineering [1,2]. They are featured in the most efficient of designs, where they are used as a means of converting raw fuel into electrical energy, plus the exhaust residual heat from the turbine can also be used to raise steam. Their versatility allows them to burn many fuel types including natural gas, synthetic gas, produced from coal or other feedstock such as biomass, or a range of liquid fuels. Thus modern power plants designs can be quite complex involving combined cycles, intercoolers, reheat reformers and recuperation to improve the overall efficiency of the plant. Efficiencies up to 55-60% have been projected for combined cycle plant [1-3], requiring heavy duty gas turbine inlet temperatures up to 1450°C [2,3], although many plants may operate at lower temperatures in the range 900-1425°C [2].

The current popularity of gas turbine power plant relates the shorter construction lead times and ease of installation, with the modular nature of such plant design permitting an incremental increase in capacity when growth in demand require it [2]. These design considerations coupled with increased fuel flexibility, low CO_2 projected emissions through projected increased efficiencies and the availability of power units in the 180-400MWe have ensured that future utility power plants will be based on gas turbine technologies as part of a combined cycle application.

Thus strategically, the view is that alternative fuels/operating cycles will play a major role in future world power generation [1,2]. The challenge to the gas turbine sector is to continue to increase turbine efficiency (Siemens Westinghouse ATS has exceeded 60% efficiencies for a

400MWe plant in combined cycle operation [4]), whilst reducing emissions in engines with multi-fuel capability.

Such targets have a major influence on the choice of materials for hot gas path components. Higher firing temperatures and reduced cooling, implies that turbine blades and vanes must be fabricated from single crystal materials with the highest temperature capability, in combination with advanced coating systems. Operation and maintenance (O&M) costs for these, next generation, high firing temperature turbines will be a significant factor. Such replacement costs for hot section components can be expected to exceed 35% of the cost of new units [2]. First stage turbine blades are an area of major concern, as they see the most demanding of service conditions – high temperatures, high stresses, creep, thermo-mechanical fatigue, severe oxidation and hot corrosion conditions. Component lives are short and replacement parts are expensive. It is often coating failure that dictates blade refurbishment intervals, thus protective coating systems are foreseen both as a need and as a major cost for future gas turbine based power plant operations.

Thus, coating life, in the hot section, is one of the most critical areas of concern. With the drive for increased service temperatures, utility turbine material selection and coating technologies have mirrored developments in the aero-gas turbine sector. Coatings have evolved from simple diffusion aluminides, through MCrAlY overlays, more complex duplex designs, to the latest ceramic thermal barrier designs.

This paper, first discusses the historical development in such coating systems, reviewing the relative benefits in terms of performance against manufacturing complexity, and therefore cost. New coating concepts are then reviewed including functionally gradient structures, as evident in 'Smart' overlay coating designs, diffusion barriers, thermal barrier coatings (TBCs) and advanced TBC concepts aimed at lowering the thermal conductivity and increasing the thermal stability of TBC systems.

A Historical Perspective on High Temperature Coating Developments

The evolution of coating technologies for gas turbine blades on vanes, have followed the demand for higher temperature capable materials, coupled with the need to provide improved environmental resistance; albeit from oxidation, cyclic oxidation or high temperature corrosion. The first aluminide coatings were used to protect gas turbine superalloy aero-foils in the 1960's. Since that date, many excellent reviews on high temperature coatings have been published [2,4-12] as coating methods and processing routes have developed to meet industrial needs. One outcome of the development in single crystal, high pressure, turbine blade technology was the recognition that coatings were a necessary component within the system to ensure adequate oxidation and corrosion resistance. This was an inevitable outcome of the reduction of chromium content in the advanced superalloys, necessary to achieve the required improvements in mechanical properties to match the higher desired operating temperatures.

Thus in 1957 [8] the first turbine aero-foils were surface treated using a diffusion process (pack aluminizing) to improve oxidation and hot corrosion performance. Pack aluminizing was widely applied to aero-gas turbines in the early 1960's [5,7-9] and some 10-12 years later, in the early 70's overlay coatings were introduced [5-7,10-13]. In the mid 1970s, type II hot corrosion became a significant problem and modifications to both the diffusion and overlay coating compositions were researched to combat this mode of attack. Aluminide coatings were either

enriched in chromium [5,7-12,14-16] or silicon [17-21] or both [22]. Similarly, high chromium overlay coatings were investigated as an alternative technology [23-24].

Conventionally cast, directionally solidified and first generation single crystal materials could be protected against oxidation and corrosion, to give adequate high pressure turbine blade (HPTB) life using these early diffusion aluminide coatings and MCrAlY overlay coatings [2,4-13]. However, as the turbine entry temperature (TET) increased, platinum aluminides replaced conventional aluminides [7-12,25-27] and improved MCrAlY compositions were developed to offer better high temperature cyclic oxidation resistance [10-12,27,28].

Second generation single crystal alloys, though stronger, have proven to be susceptible to hot corrosion, particularly high temperature sulphidation, and a wide range of alternative coating strategies have been proposed to address these issues [10-12,14,29-33].

The latest development in this drive for improved surface protection, high temperatures, and therefore better performance is thermal barrier coatings applied to turbine aerofoil surfaces and other hot gas path components. New developments in structurally modified low thermal barrier coatings will also be reviewed.

Diffusion Coating Processes

Diffusion coatings can be applied to hot gas components using a range of techniques including pack cementation, slurry cementation, over pack CVD* and vapour phase CVD*. Comprehensive reviews of the methods of deposition of diffusion coatings are given in references [7,8,10-12,14,15,21,34,35]. In pack aluminising, overpack aluminising and vapour phase aluminising the deposition rate and morphology of the coating depends on the aluminium activity in the gas phase, processing time and temperature. Coatings are classified as either 'low activity' when outward diffusion of nickel occurs, or 'high activity' when inward diffusion of aluminium occurs. In the latter case, a surface layer of Ni_2Al_3 forms and a further heat treatment is required to convert this brittle surface layer to NiAl. This step is usually combined with the heat treatment required to recover substrate properties.

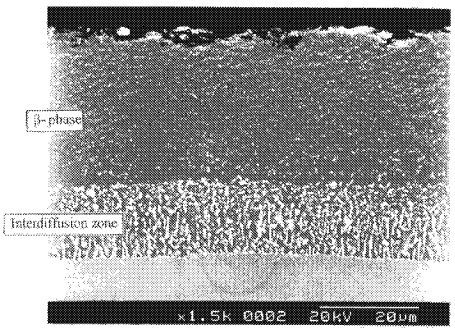

Figure 1 Fully processed pack aluminide coating (high activity) on IN738.

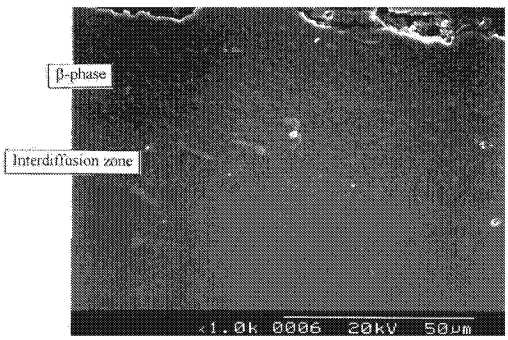

Figure 2 Vapour phase aluminised coating (low activity) on IN738

Footnote * CVD = chemical vapour deposition

Figure 1 illustrates a typical aluminide coating deposited onto a nickel based superalloy using a high activity pack coating process. The coating was deposited using an aluminising pack contains 2.2%Al at 900°C, and was heat treated for 2h at 1120°C, then 24h at 845°C. Figure 2 illustrates a similar aluminide coating produced using vapour phase aluminising.

Clearly, the properties of the aluminide coating (or for that matter any diffusion coating) depend upon the process methodology, the substrate composition and the subsequent heat treatment. Typically, aluminide coatings contain in excess of 30wt%Al and are deposited to thicknesses between 30-100μm depending on the type of aluminide formed. From a mechanical property perspective the most important coating property is its resistance to thermo-mechanical fatigue cracking (TMF) – a property closely related to coating ductility. For aluminide coatings the ductile to brittle transition temperature (DBTT) – defined as the temperature to obtain a fracture strain of 0.6% - lies in the range 650-800°C depending on thickness, aluminium content and base alloy composition. Low activity processes give coatings with lower Al contents and therefore lower ductile to brittle transition temperatures. Such coatings offer satisfactory performance for many applications. However, under severe hot corrosion conditions, or at temperature above 1050°C, these aluminide coatings offer limited protection. To address these issues, modified aluminide coatings and overlay coating (MCrAlY) technologies were developed in the 1970's and development in these two areas continues today to combat the increased demands placed on modern gas turbine power plants.

Modified Aluminide Coatings

Modified aluminide coatings are fabricated [7,8,10-12,14-16,20-22] either by depositing an interlayer – for example 7μm of platinum, by electroplating or PVD (physical vapour deposition) – prior to aluminising, when manufacturing a platinum aluminide (Figure 3), or by pretreating the superalloy before aluminising – for example chromising prior to pack aluminising -, or by co-depositing elements from a pack, slurry or blending them in the vapour phase – Sermaloy J and Sermaloy 1515 are slurry co-deposited silicon aluminide coatings [17-19].

Alloying additions that have been considered include Cr, Si, Ta, various rare earths and precious metals, with many of these coatings now commercially available. To improve the high temperature oxidation performance of aluminides, a most significant advance was made with the development of platinum modified aluminides. This class of coating is now an accepted industrial standard, out performing conventional aluminides under high temperature oxidation, cyclic oxidation and hot corrosion conditions [5,8,10-12,15,16,20,25-27,36]. Much work is continuing in this important area both as environmental protection coatings (EPCs) and as bondcoats to thermal barrier coatings (TBCs) as will be reviewed later in this paper.

Despite numerous studies of platinum modified aluminides [25-27,37-48], the exact mechanism by which platinum improves the performance of β-(Ni,Pt)Al coatings is still a subject of open discussion. It has been well documented, since the mid 1970's [37-39], that platinum additions improve scale adhesion. It has also been proposed that platinum additions reduce the rate of growth of interfacial voids [40,41], can interact with indigenous sulphur [41,42] and also limits the outward diffusion of minor alloying elements (e.g. Ti, Ta, etc) from the superalloy [43], all of which would improve scale adhesion. The role platinum plays in the performance of diffusion coatings is also influenced by the coating manufacturing process, the substrate alloy composition and the resultant coating microstructure and how this may change in service due to oxidation and interdiffusion with the substrate [44,46-48]. Most researchers concur that platinum promotes the

selective oxidation of aluminium and this results in the formation of a purer, slow growing alumina scale.

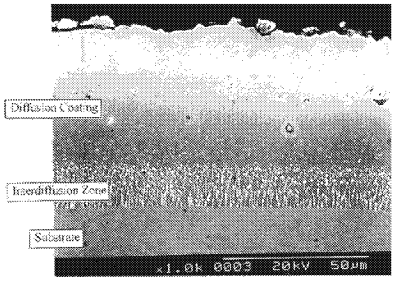

Figure 3 Platinum aluminide coating (RT22LT)

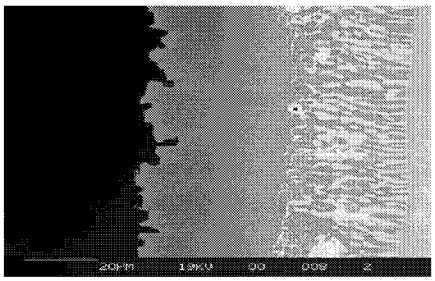

Figure 4 Yttrium modified aluminide [57]

There has been continued interest in the ability to incorporate active elements in β-NiAl, to improve oxide scale adherence. Most of this work has been on model alloys [34,49-53], in particular hafnium, zirconium or yttrium. However, a few papers have researched the incorporation of reactive elements into the CVD coating process [34, 54-57], with one process developed by Howmet at the commercial stage [55]. A micrograph of a yttrium modified aluminide coating, developed at Cranfield, is given in Figure 4. [58], while, Figure 5, provides a comparison of the influence of platinum additions and yttrium additions on the cyclic oxidation of aluminide coated IN738 at 1100ºC, 1h cycles, referenced to the uncoated superalloy and a low temperature high activity aluminide coating, similar to that shown in Figure 1. The uncoated alloy failed (zero net mass gain cross over point) at 30h, the high activity aluminide failed at 220h, while the platinum aluminide lasted 680h and the yttrium modified aluminide had not failed when the test was terminated at 900h and was projected to last over 1000h at 1100ºC [57].

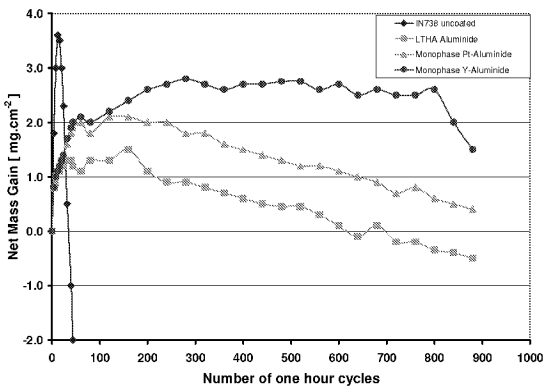

Figure 5 Cyclic oxidation performance of modified aluminide coatings - 1100ºC, 1h cycles [57]

To combat hot corrosion, additions of chromium [14-16,23] and silicon [17-19,21,22] were researched in the 70's and 80's. Although no better than standard aluminides under high temperature oxidation conditions, chromium rich diffusion coatings offered improved performance in industrial and marine turbines burning high sulphur fuels [16,23]. Additions of

silicon were also shown to improve the hot corrosion resistance [21]; at about 10wt%Si addition, silicon modified coatings proved uniquely resistant to Type I and Type II hot corrosion [17-19], if somewhat brittle. This research was the basis for Sermaloy J (Figure 6), a $CrSi_2$ dispersed, β-NiAl diffusion coating [17-19,59,60]. Later as engine technologies advanced and directionally solidified or single crystal alloys were more widely adopted, less chromium was available within the alloy to form the $CrSi_2$, (a critical component within Sermaloy J [38]), thus joint research between Sermatech and Rolls Royce lead to the development of Sermaloy 1515, a layered structure slurry aluminide coating, containing bands of $CrSi_2$, which is capable of providing hot corrosion resistance to low Cr containing single crystal alloys [19,20,59,60].

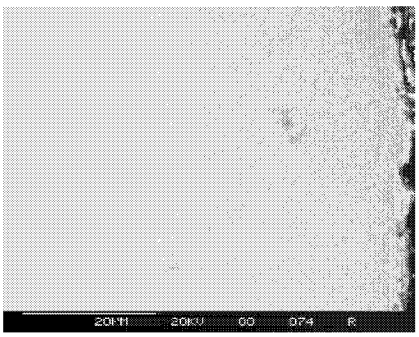

Figure 6 Silicon aluminide coating (Sermaloy J)

Overlay Coatings

Diffusion coatings, by the nature of their formation, imply a strong interdependence on substrate composition in determining their corrosion resistance and mechanical properties, hence, the possibility of depositing a more 'ideal' coating, with a good balance between oxidation, corrosion and ductility has stimulated much research interest, since the early 70's. The early MCrAlY coatings were alloys based on cobalt (CoCrAlY) containing chromium additions in the range 20-40wt%, aluminium additions between 12-20wt% and yttrium levels around 0.5wt% with the most successful coating being Co25Cr14Al0.5Y [13]. Later, NiCrAlY, CoNiCrAlY and NiCoCrAlY compositions were introduced with the aim of balancing the often conflicting needs of cyclic oxidation, hot corrosion and thermo-mechanical fatigue. Generally, under high temperature oxidising conditions NiCrAlY's and NiCoCrAlY's out perform the cobalt based systems [9,61,62]. Coatings offering the best resistance to type I hot corrosion are those high in aluminium and lower in chromium content, typically >11wt%Al, and <23wt%Cr. Whereas, for optimum performance under type II hot corrosion chromium contents greater than 30wt% are beneficial. Thus, now a days, the actual composition of these coatings is engineered to match their intended use, with the most recent coatings of more complex design, based on the M-CrAl-X system, where M is Ni, Co, or a combination of these and X is an oxygen active element, for example Y, Si, Ta, Hf [15,21,30,63-66] or a precious metal, for example Pt, Pd, Ru, Re etc. [28,63,67-70]. The composition of the M-Cr-Al system is selected to give a good balance between corrosion resistance and coating ductility, while the active element addition(s) can enhance oxide scale adhesion and decrease oxidation rates. Current thinking suggests that a combination of active elements is beneficial in reducing coating degradation through their synergistic interaction.

Table 1 [2] summarises the specifications of some current commercial overlay coatings applied to blades and vanes of land based gas turbines. In each case, the chosen coating has been selected to match the expected service environment. Currently, no single commercial overlay coating can offer a balance between oxidation and hot corrosion resistance as well as good mechanical properties for all perceived service conditions [2]. With the aim of meeting this objective, research is underway into innovative functionally gradient structures offering a more optimized solution to these complex design needs, and these approaches will be discussed later in this paper.

Table 1 Nominal composition of MCrAlY overlay coatings used by industrial gas turbine manufactures [2], (compositions in wt%).

OEM	Coating	Ni	Co	Cr	Al	Y	Ta	Si	Re
Alstom	SV20	Bal.	-	25.0	5.5	0.6	1.0	2.7	-
GE	GT29	-	Bal.	29.0	6.0	0.5	-	-	-
	GT33	Bal.	37.0	22.0	9.0	0.5	-	-	-
S-W	CoNiCrAlY	32.0	Bal.	21.0	8.0	0.5	-	-	-
Siemens	SC2231	30.0	31.0	30.0	8.0	0.6	-	-	-
	SC2453	52.0	10.0	23.0	12.0	0.6	-	0.7	3.0
MHI	CoNiCrAlY	32.0	Bal.	21.0	8.0	0.5	-	-	-

Overlay coatings have been deposited using a range of techniques. The earliest production method was electron beam physical vapour deposition (EB-PVD) [13]. However, because of the high capital cost in setting up a commercial EB-PVD plant, plasma spray methods have found wide acceptance, particularly the argon shrouded and vacuum plasma spray processes [16,30,70-72] and more recently high velocity oxy-fuel spraying processes [30,72-75], composite electroplating [65,76-78] and autocatalytic electroless deposition [31,79,80] methods have been used to deposit overlay coating systems. However, coatings produced by EB-PVD processes are still considered the commercial standard against which other process routes are compared. Figure 7 is a micrograph of an EB-PVD CoCrAlY (ATD5B) on MarM002, Figure 8 is an Argon shrouded plasma sprayed NiCoCrAlY and Figure 9 is a NiCoCrAlReY coating produced by the composite electroplate method.

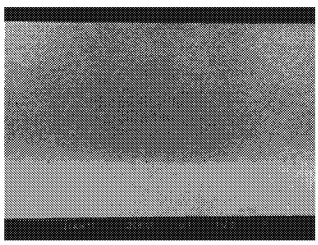

Figure 7 EB-PVD CoCrAlY (ATD 5B) coating on MarM002

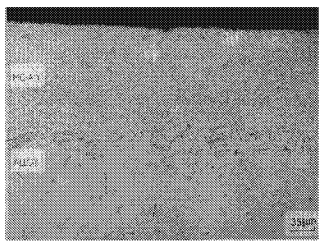

Figure 8 Argon shrouded plasma spray CoNiCrAlY (LCO22)

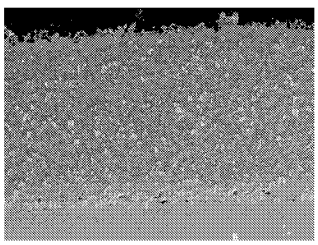

Figure 9 A NiCoCrAlReY, overlay coating produced by the composite electro-plate process.

Overlay coatings of classic design, with 18-22wt%Cr and 8-12wt%Al, generally perform better at higher temperatures where oxidation is the dominant failure mode (above 900°C) reflecting the good adherence of the thin alumina scales which is promoted by the presence of active elements such as yttrium. Various methods have been investigated to improve the traditional MCrAlY performance. New MCrAlXY alloys have been developed with additions of multiple active elements (Ti, Zr, Hf, Ta and Si for example have been researched [15,21,63-66] or the incorporation of precious metal additions (Pt, Pd, Re and Ru have been studied [28,63,67-70]). Surface modifications also have been examined using CVD [81-83], PVD [63,64,84] electroplating [57,85-88] and re-processing with high energy beams [15,66,89-92]. An interesting proposal from such recent processing work is the possibility of depositing a single crystal MCrAlY alloy coating onto a single crystal superalloy [90,91]. The single crystal, epitaxial coating was produced using laser cladding technology, with controlled solidification of the melt pool.

As can be seen from Table 1, many of the overlay coatings in current service follow the classic design as proposed by Talboom [13], 18-22wt%Cr and 8-12wt%Al, but now the alloy base can be nickel, cobalt or a combination of these depending on the desired balance between oxidation, hot corrosion resistance and resistance to thermal mechanical fatigue. More corrosion resistant coatings have higher chromium contents, up to 30wt%, and an associated reduction in aluminium content (6-8wt%). Yttrium is widely used as the active element, at around 0.5wt% level, similar to that originally proposed by Talboom [13], but some overlays are of more complex design containing Y, Ta, Si and Re.

Under TMF loading, the resistance to cracking can be correlated with coating ductility. Most overlay coatings have a ductile to brittle transition temperature significantly below that of any of the diffusion aluminides [2,10,93], with many overlay's having DBTT's below 450°C, and low temperature ductilities often above 0.5-0.6% strain, in the as manufactured and heat treated condition. Figure 10 illustrates the ductile to brittle transition behaviour of selected MCrAlY alloys [2,10,93].

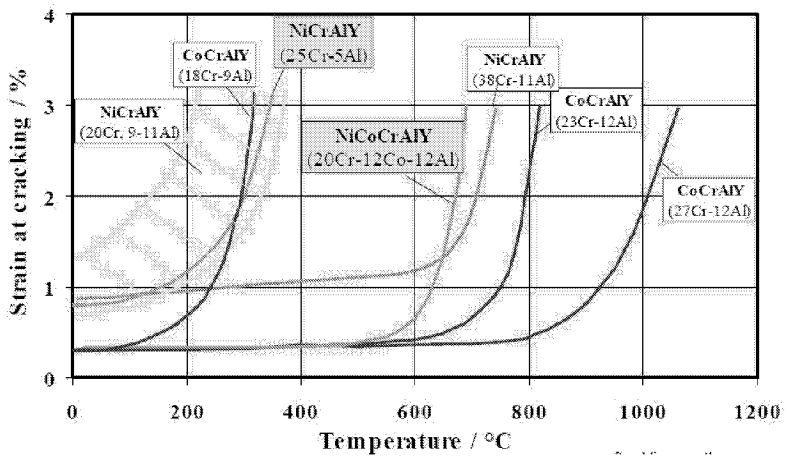

Figure 10 Ductile brittle transition temperatures for various MCrAlXY overlay coatings.

Thus for some coating systems, when strains are low, the DBTT is not an important factor when

selecting the overlay. However, more often if strain levels are such that cracking may occur then it is advantageous to select coatings with low DBTT's. For MCrAlY overlay coatings, an increase in Al content, and to a lesser extent Cr, tends to increase the coatings DBTT. This is most noticeable for CoCrAlY coatings, where as NiCrAlY and NiCoCrAlY systems have lower DBTTs, even when aluminium contents may be as high as 17wt% [2]. This behaviour is attributable to the higher DBTT for β-CoAl, when compared to β-Ni-Al; both of which are major constituents in MCrAlY overlay coatings. In general, to improve ductility, Al contents should be below 12wt%, and under high strain operating conditions levels as low as 5-6wt% may be used.

Additions of silicon or rhenium also increase the DBTT of overlay coatings [2], however, by careful selection of alloy composition it is possible to design coatings with sufficient ductility and a low DBTT that the coating is able to resist cracking in applications where thermal mechanical fatigue is prevalent. Such modelling of TMF behaviour, based on coating composition, is illustrated in Figure 11. Measured and predicted lifetimes agree well (predictions at 800°C and 1000°C are illustrated, based on model datasets of 11 coatings and 18 coatings respectively). In this study, critical composition variables were Ni, Co, Al, Ta and Re at 800°C, and Ni, Cr, Al, Ta and Re at 1000°C.

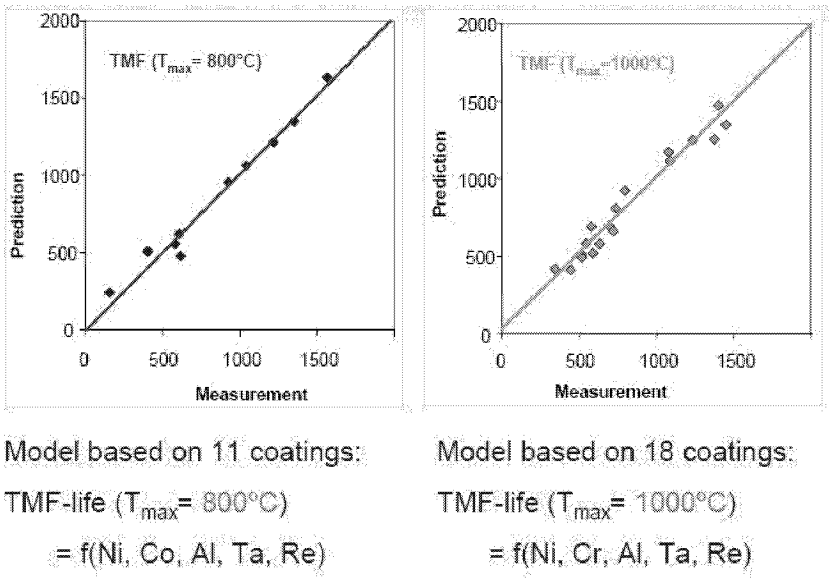

Figure 11 Optimisation of TMF life based on MCrAlXY overlay coating composition

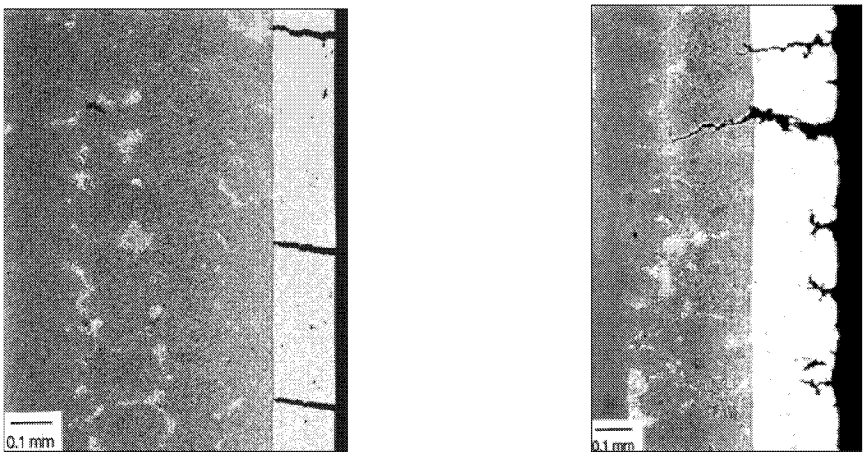

a) Brittle cracking on the first loading cycle of a NiCo20Cr12AlXY coating [TMF out of phase : 400-1000°C : $\Delta\varepsilon_m = 0.67\%$: $N_f = 1000$ cycles]

b) Multiple crack initiation and high crack density, with slow crack through a Ni25Cr5AlXY coating [TMF out of phase : 400-1000°C: $\Delta\varepsilon_m = 0.91\%$: $N_f = 759$ cycles]

Figure 12 TMF cracking in NiCoCrAlXY overlay coatings

Figure 12.a illustrates the early helical brittle cracking, believed to occur on the first loading cycle in an out of phase TMF test. The NiCo20Cr12AlXY alloy was strained to 0.67% and, from DBTT tests, cracks at 0.6%. The more ductile NiCo25Cr5AlXY alloy, Figure 12.b, shows multiple crack initiation with a high density of crack initiation sites. These propagate more slowly through the coating and into the substrate. For this test the strain was 0.91%.

These MCrAlXY overlay coatings exhibit a duplex microstructure consisting of β-(Ni,Co)Al in a γ matrix, whether deposited by EB-PVD, plasma spraying, electroplating or electroless plating. For rhenium containing alloys, for example Sicoat 2453 (see Table 1.), the microstructure is more complex, consisting of α, β,σ and γ phases [2,94,95], where the α-phase is chromium rich and the σ-phase is rich in chromium and rhenium; these latter two phases contain no aluminium [2].

As is well known and documented, both overlay coatings and diffusion coatings degrade in service; by oxidation or hot corrosion at the coating surface and by interdiffusion with the substrate alloy. For MCrAlY overlay coatings, such degradation is manifest by decomposition of the Al rich β-phase into γ', or γ, near either interface; the coarsening of the remaining β-phase in the MCrAlY coating and an enlargement of the interdiffusion zone between the MCrAlY overlay coating and the substrate. This behaviour is illustrated in Figure 13. Thus, progressively the two phase, β + γ, region reduces in thickness and this depletion is often used as a measure of the remnant coating life.

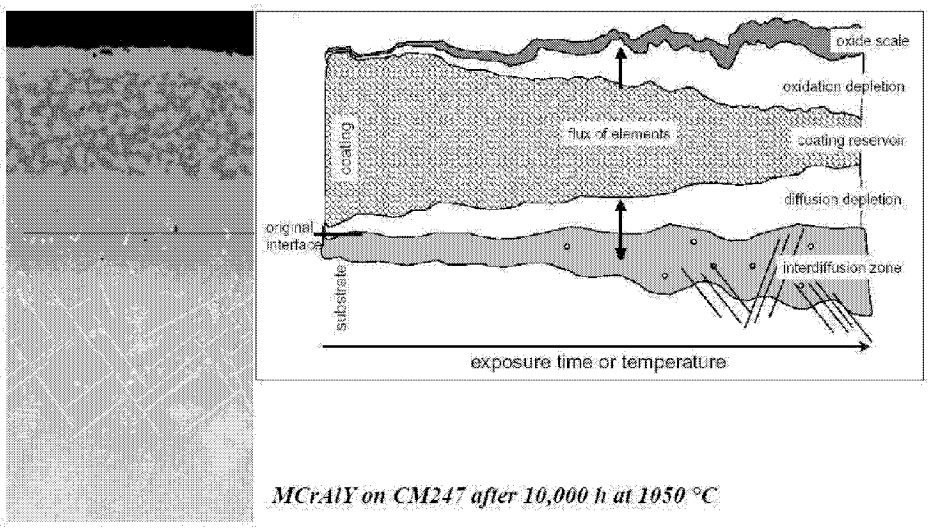

Figure 13 Oxidation and interdiffusion in MCrAlY overlay coatings on Ni-based superalloys.

Using this approach, several investigators have compared the degradation of coated specimens after isothermal and/or cyclic exposure for between 10,000-15,000 h with that of turbine blades after long term service [93,95,96]. Figure 14 illustrates the results of such β-depletion modelling for four different Alstom engines, plotted as an Arrhenius temperature dependence; the temperature of engine operation, T1-T4, have been estimated from ex-service parts by measuring γ' coarsening, to determine wall temperature, and then correlating with β-phase depletion in the coating. Superimposed on Figure 14 is the T ± 25K design curve for 15,000h operation. As can be seen, there is reasonable agreement between engine service data and the oxidation/interdiffusion modelling for the MCrAlY coatings used on Alstom engines, within a ±50K precision (2x std.dev.).

Modified Overlay Coatings

Surface modification of MCrAlY overlay coatings by aluminising was first published in 1984, when Restall and Haymen [97] pulse aluminised overlay coating for improve hot corrosion resistance in marine gas turbines [98]. Such over aluminising of MCrAlY coating systems permits a dual layered coating structure, to be constructed, where the outer layer (the aluminide region), which can contain up to 25wt%Al provides high temperature oxidation resistance, while the MCrAlY base layer C rich in Cr and Co confers improved resistance to hot corrosion. GE29+, GT33+ and GE34+ are proprietary over aluminised MCrAlY overlay coatings with graded aluminium profiles.

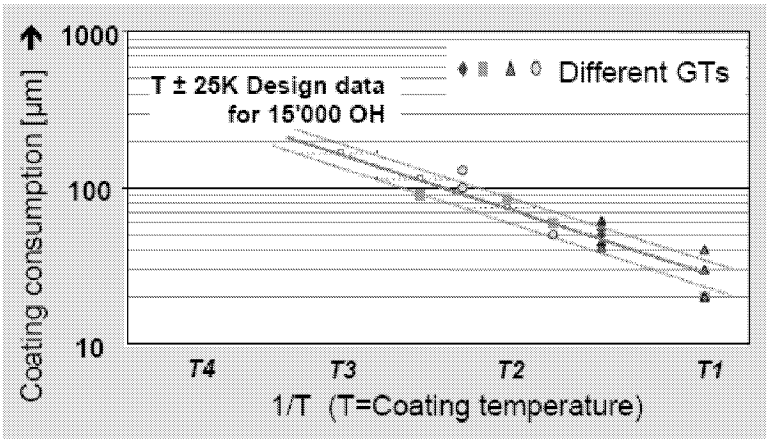

Figure 14 Correlation between oxidation/interdiffusion coating consumption and engine service data.

Recent work has focussed on the modification of the surface of MCrAlY alloys with platinum and other precious metals [57,85-88,99] to improve their performance under high temperature cyclic oxidation conditions [57,85,86]. Such treatments were first proposed in the early 80's as a method of improving the MCrAlY alloy corrosion performance to aggressive deposits from a range of alternate fuel sources [63]. The need for improved cyclic oxidation resistance driven by the pursuit of bondcoats for advanced TBCs has seen recurrent interest in the performance of platinum modified MCrAlY's both as environmental protection coatings and as bondcoats. Figures 15 and 16 illustrate the platinum modified surface microstructures. Platinum modification to the surface of the MCrAlY [57,85,86,99] or just to the superalloy without depositing on MCrAlY [87,88,100,101], improves the cyclic oxidation performance. This advantage of the platinum surface treatment relates to the ability this platinum diffused layer has in providing a smoother, stronger more defect free surface. Both strategies are being pursued as TBC bondcoats and will be discussed further in the section reviewing TBC developments.

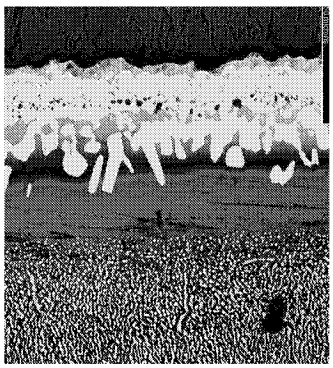

Figure 15 A platinum diffused, $\gamma + \gamma'$ coating on CMSX4

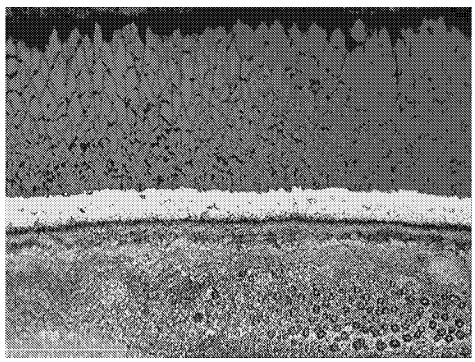

Figure 16 A platinum diffused NiCoCrAlY overlay coating on CMSX4

Smart Overlay Coatings [29,102,103]

Smart overlay coatings are functionally gradient coating systems designed to provide high temperature corrosion protection over a wide range of operating conditions. The SMARTCOAT design consists of a MCrAlY base, enriched first in chromium, then aluminium to provide a chemically graded structure. At elevated temperatures, above 900°C, the coating oxidises to produce a protective alumina scale. However, at lower temperatures, this alumina scale does not reform rapidly enough to confer protection under Type II hot corrosion conditions. The SMARTCOAT is therefore designed with an intermediate chromium-rich interlayer, which permits the rapid formation of chromia, healing areas of Type II corrosion damage. Figure 17 illustrates the microstructure of SMARTCOAT SmC155, produced by surface treating an air plasma sprayed Amdry 995 basecoat. The three layer microstructure can clearly be seen. The outer layer [A] varies in composition between Ni-15Cr-32Al and Ni-10Cr-21Al, as a result of the aluminising treatment, the interlayer [B] is chromium rich with a composition in the range Ni-60Cr-20Al to Ni-35Cr-40Al, over a basecoat of Amdry 995 (Co-32Ni-21Cr-8Al-0.5Y) for this variant of the SMARTCOAT process.

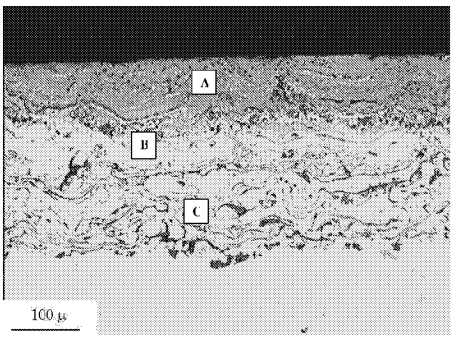

Figure 17 A micrograph of SMARTCOAT SmC155, showing the three layered microstructure that is Characteristic of SMARTCOAT[80]

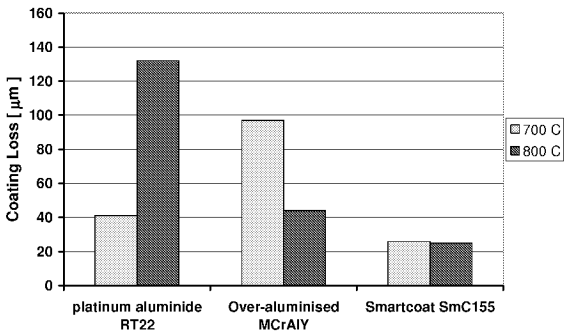

Figure 18 Hot corrosion performance of SMARTCOAT SmC 155, relative to an over aluminised CoNiCrAlY and a Platinum Aluminide (RT22)

The hot corrosion performance of the SMARTCOAT structure is illustrated in Figure 18, where SMARTCOAT SmC155 is compared to a conventional platinum aluminide (RT22) and an over aluminised CoNiCrAlY – a similar process and structure to that of GT29+, a General Electric proprietary coating. The hot corrosion test was a 500 h duration salt recoat procedure, with daily replenishment of an 80% Na_2SO_4/20% K_2SO_4 salt mix at equivalent deposition flux of 0.015 mg/cm^2/h. The tests were conducted at 700 and 800°C in an air-300 vpm SO_2/SO_3 gaseous environment. At both test temperatures, only the outer aluminide region of the smartcoat was attacked, whereas the platinum aluminide coat was consumed down to the interdiffusion zone at 700°C and complete penetrated at 800°C. For all coatings the substrate was a corrosion resistant superalloy, IN738LC.

Diffusion Barrier Concepts

Even within MCrAlX systems and more advanced overlay coating concepts, diffusion of elements between the substrate and coating can have a major influence on coating performance. Therefore to provide long terms stability it is necessary to develop diffusion barrier coatings that can be used to minimise interdiffusion between the coating and the substrate. Some interdiffusion is of course necessary to provide good adhesion, therefore the diffusion barriers must be tailored to limit the movement of particular elements. Both precious and refractory metals [28,63,104], intermetallics [105,106] and ceramics [30] have been proposed as diffusion barriers with varying degrees of success. Figure 19 illustrates the deposition of an intermetallic diffusion barrier at the interface of a high Cr high Al containing overlay coating and a superalloy substrate (MarMOO2). The diffusion barrier was developed to limit chromium movement from the coating into the substrate [105] and hence reduce the likelihood of forming sigma phase within the alloy below the coating. Chromium diffusion rates, reduced by one to two orders of magnitude over the temperature range 750-1150°C. Along similar lines, Narita et al [106] developed a Re-Cr based intermetallic diffusion barrier to limit aluminium diffusion from a β-NiAl coating into TMS-82+ (a single crystal superalloy). The barrier layer was a continuous zone of σ-phase, with composition 35-40%Re, 15-20at%W, 15-25at%Cr, balance Ni. After 100h at 1150°C cyclic oxidation the structure and composition of the sigma phase barrier composition of the sigma phase barrier was little changed. The Re-Cr-Ni layer acted as an effective diffusion barrier against the inward diffusion of Al and outward diffusion of alloying elements. Ceramics [30] such as TiN/AlN, AlON and ZrO_2 have been investigated as part of the COST 501 programme to limit elemental diffusion. These ceramic layers were deposited using sputter deposition. Each of these ceramic systems were able to reduce interdiffusion for several hundred hours at 1100°C, but ultimately failed locally allowing some interdiffusion. Of these ceramic systems ZrO_2 performed best lasting 586h at 1100°C, before cracking in the zirconia layer led to barrier breakdown.

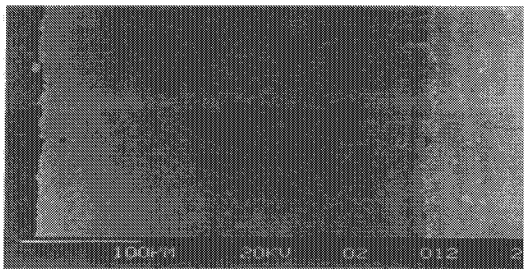

Figure 19 Graded NiCrAlY overlay coating and diffusion barrier (located at the coating/substrate interface) deposited on MarM002, by EB-PVD

Once the concept of a diffusion barrier is accepted as a method of providing good interface stability, one is no longer constrained in the design of the best overlay coating. No longer is substrate alloy compatibility a requirement in specifying the overlay coating composition. By removing this constraint it should be possible to design overlay coatings with optimised oxidation or corrosion [105,107].

THERMAL BARRIER COATING TECHNOLOGIES

An alternative strategy to the development of environmental protection coatings [EPC], based on corrosion resistant alloys and intermetallics, is to design coating systems that a lower the metal surface temperature. Thermal barrier coatings (TBCs) work in this way and provide the potential to drop metal surface temperatures by up to 150°C, using current technologies in conjunction with component cooling. A 150°C reduction in the component surface temperature would have the effect of reducing oxidation rates by an order of magnitude and would provide further benefits by reducing the components propensity to creep and limiting the extent of interdiffusion between the bondcoat and substrate superalloy.

Thermal barrier coatings (TBCs) have been used for this purpose within the aero-gas turbine since the 1970's [85,108-115]. They are now widely used in land based gas turbines for power generation [2,93] to provide thermal protection to hot section components. For aero-applications the TBC is not considered 'prime reliant' to the extent that they can be used with assurance that failure will not occur [116]. However, for some industrial turbine applications, TBCs are used as 'prime reliant' on hot section components [G and H class] while on other classes (D, E and F class) they are applied to extend service life, but are not 'prime reliant' [2].

Commercial TBC systems are typically two layered structures, consisting of a ceramic topcoat and an underlying metallic bondcoat. Between the ceramic topcoat and bondcoat a thin thermally grown oxide (TGO) forms during manufacture and thickens during service. The TGO imparts oxidation resistance and also serves to bond the ceramic topcoat to the substrate/bondcoat system. Oxidation induced failure of the TBC is associated with cracking and spallation of the thickening TGO, above some critical thickness. This is considered the ultimate failure mechanism of commercial TBCs, particularly those produced by electron beam physical vapour deposition (EB-PVD) [117-119]. Since their introduction, PYSZ TBCs have performed well in service, significantly increasing the life of components. For example, the application of 7wt% PYSZ TBC to combustion can walls reduces the thermal stresses in the can and can result in component lives in excess of 20,000 hours [120]. Thus, by virtue of its low thermal conductivity, and good thermal stability at temperatures up 1500°C, 8wt% yttria partially stabilised zirconia TBCs have become the industrial standard to reduce the heat flux into hot path components within gas turbine engines. Their use allows a high thermal gradient to be subtended across the ceramic thickness without any increase in metal surface temperature, potentially allowing up to 150°C increase in turbine entry temperature (TET).

Although plasma sprayed TBCs have performed well in service on annular surfaces in the engine, their microstructure does yield coatings with the necessary strain compliance, erosion resistance or surface finish required for successful application on blade or nozzle guide vane aerofoils within the aero-gas turbine [117]. They are however, used on blades and nozzle guide vanes in large utility gas turbines [2,93,121-123] where service lives up to 24,000h of operation are expected [2,93,122]. An example of the structure of the plasma sprayed TBC is shown in Figure 20. For comparison Figure 21 shows a micrograph of an electron-beam physical vapour deposition (EB-PVD) TBC which, because of their columnar microstructure exhibit very high levels of strain compliance and is most often found on high pressure turbine blades and nozzle guide vanes in aero-gas turbines [11,12,116]. The columnar microstructure is due to the atomistic nature of the deposition process, with nucleation and growth of the coating controlled by condensation from the vapour phase. In addition to their good compliance, EB-PVD TBC systems also offer other benefits over plasma sprayed TBCs in terms of improved adhesion, surface finish and erosion

resistance. The major limitations associated with the EB-PVD microstructures are their high thermal conductivity, the cost of manufacture and the size of parts that can be coated using the EB-PVD process. Table 2 summarises typical properties of an EB-PVD and plasma sprayed thermal barrier coating, as measured at room temperature.

Table 2 Properties of TBCs at Room Temperature

Property/Characteristic	EB-PVD	Plasma Sprayed
Thermal Conductivity (W/mK)	1.5-1.9	0.8-1.1
Surface Roughness (μm)	1.0	10.0
Adhesive Strength (MPa)	400	20-40
Young's Modulus (GPa)	90	200
Erosion Rate (Normalised to PVD)	1	7

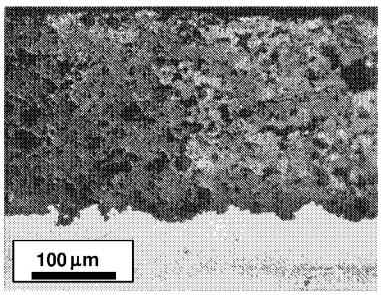

Figure 20 Plasma spraying ZrO_2-8wt%Y_2O_3 thermal coating [93]

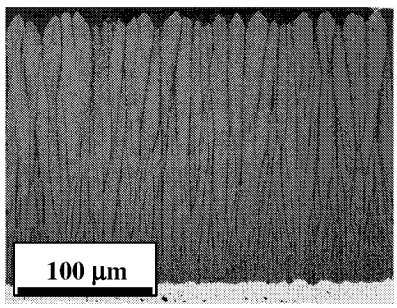

Figure 21 EB-PVD ZrO_2-8wt%Y_2O_3 thermal barrier coating [12]

Bondcoat Oxidation Strain Compliance and Coating Adhesion

Long term durability is a major concern when using TBCs as a prime reliant coating. TBCs may fail from several mechanisms as a result of high temperature exposure and the cyclic strains induced in service. Many experimental and modelling studies [116,121-134] have now collectively started to provide a better understanding of TBC degradation, whether protected by an EB-PVD system [116,124,126-128,134] or APS system [121-123,125,129-133]. The emerging picture is one of progressive degradation, with much of the time spent in various initiation stages, before induced cracks link up to give final failure. Sintering of the TBC, oxidation of the bondcoat and growth of the TGO, formation of delamination cracks, progressive bondcoat rumpling, loss of scale forming elements are all considered contributing factors.

Of these bondcoat oxidation is recognised as a major factor affecting the durability of both plasma sprayed and EB-PVD TBC systems [10,57,85,86,99-101,108-155,120-145]. Maintaining coating integrity for a TBC is significantly more difficult than for a metallic, environment protection coating due to the relatively large change in properties from the metallic substrate through to the

ceramic top coat; important among these are the coefficient of thermal expansion, the elastic modulus/compliance, the fracture toughness, the coating density, and the size and distribution of defects in the coating system.

The microstructure of the coating resulting from plasma spraying (Figure 20) differs from that produced by EB-PVD deposition (Figure 21) and thus the coating failure modes are not the same. Bondcoat oxidation is however, a significant factor in both modes of failure [57,85,86,99-101,108-115,120-145]. The onset of TBC spallation is triggered by some form of microstructural instability at the bondcoat/TGO (thermally grown oxide) or TGO/ceramic interface [99,110,112-115,127-133,142]. The nature of this instability and its influence on TBC life is an area of intense research, which varies from one TBC system to another, differs between EB-PVD and plasma sprayed ceramic top (coats and is also dependent on the nature, chemistry and surface finish of the bondcoat. However, two major contributions to this failure are the extent of bondcoat oxidation and the strain generated by the thermal mismatch between the ceramic topcoat and the metallic components within the system. Other contributing factors include the strength of the bondcoat, changes in bondcoat microstructure and chemistry, the surface roughness of the component and possible sintering of the ceramic that can modify the overall system compliance. For plasma sprayed systems, failure results from delamination cracking, as a result of in-plane compressive stresses that result in significant out-of-plane tensile stresses. The delamination cracks, within the TBC, are parallel to the interface and near the peaks of the rough bondcoat [110,112-115,121-123,125,128-132,143,144,145]. Thus, the rough interface in plasma sprayed coatings, first aids initial adherence through mechanical interlocking, but later drives its delamination due to the generation of out-of-plane stresses as a result of the interaction between bondcoat roughness and oxidation. Thus reducing its final life.

EB-PVD coatings tend to fail at the alumina scale/bond coat interface, unless substantial bondcoat surface rumpling occurs [85,86,99-101,115,120,124-127,133-137,140,141-143] whereupon failures may transfer to the TGO/ceramic interface. This failure at the TGO/bondcoat interface, results from the progressive reduction in adhesion, as microcracks form and grow. Oxidation of the bondcoat is therefore a major driver of the failure of EB-PVD TBCs. The rate of growth of the oxide, provided α-alumina is formed at the ceramic/bondcoat interface, is reasonably constant for all alumina formers (platinum aluminide, MCrAlY, $\gamma + \gamma'$ bondcoat). What differentiates performance is the ability of the TGO to resist spallations as a result of defect formation, microcrack growth and loss of adhesion. Thus critical issues are the ease of void formation at the TGO/bondcoat interface, how readily less protective oxides form beneath the alumina scale and how easily debonding occurs at the TGO/bondcoat interface. This aspect has been extensively studied in the above citations and it has been shown by Meier, Pettit and co-workers [85,86,99] that the surface treatment of an MCrAlY overlay coating by platinum diffusion acts to bury surface 'grit-line' defects and thus improves TBC adhesion, giving improved TBC lives. Figure 22 presents data from the work of Meier, Pettit and co-workers, demonstrating how both over aluminising treatments (a similar treatment to that applied to GT29+ or GT34+) and surface platinum diffusion can be used to improve the cyclic oxidation lives of MCrAlY coatings. In this study, these modified MCrAlY's failed to match the performance of three commercial platinum aluminide coatings, although the platinum overlay coatings gave cyclic lives only a little less than the lowest of the PtAl coatings.

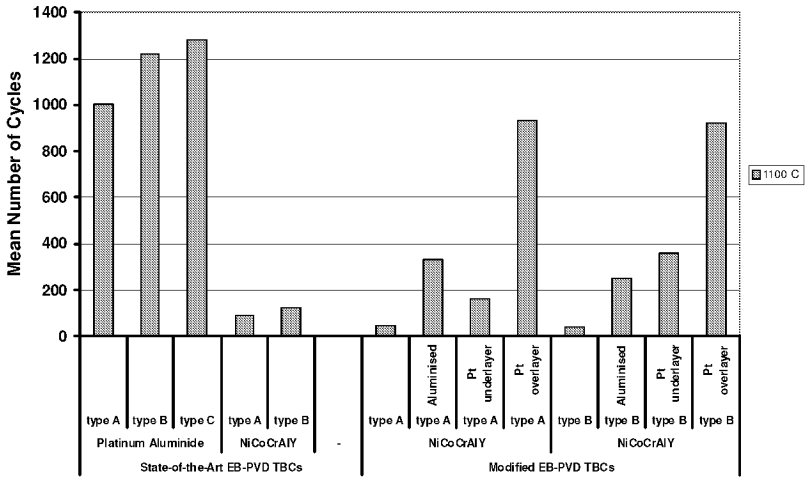

Figure 22 Cyclic Oxidation failure times for various bondcoats with an EB-PVD ZrO_2-8wt%Y_2O_3 top coat test at 1100°C (1h cycles) [data from references 85, 86]

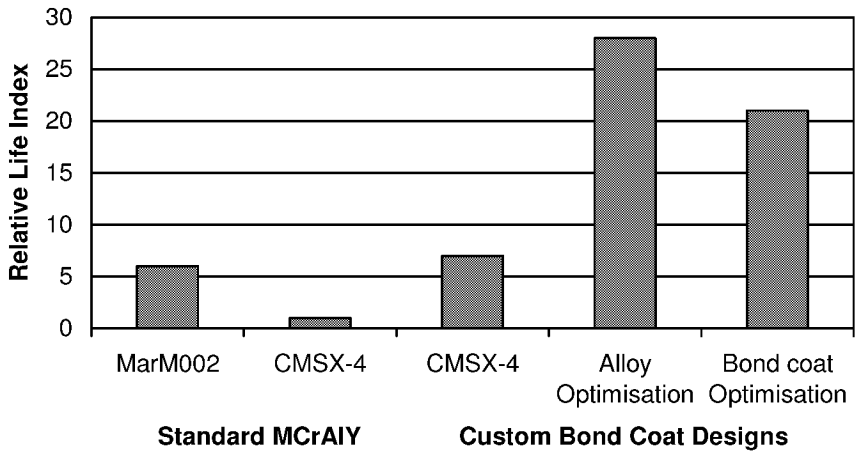

Figure 23 Life improvement through $\gamma + \gamma'$ bondcoat development [EB-PVD ZrO_2-8wt%Y_2O_3 onto NiCoCrAlY coated CMSX4 is taken as the reference]

In recent work, Rolls Royce has developed custom designed bondcoats by diffusing platinum into the single crystal superalloy surface [87,88] - these patented bondcoats have a $\gamma + \gamma'$ microstructure [100, 101,116] – that have been formulated to prevent or delay these degradation

processes. The $\gamma + \gamma'$ bondcoat provide a stronger bondcoat system offer high creep strength thus resisting "rumpling". They also provide a physical barrier and a metallurgical stable

microstructure to limit substrate element diffusion. Figure 23 illustrates such bondcoat development and demonstrates that relative to CMSX4 with a standard NiCoCrAlY bondcoat the new $\gamma + \gamma'$ microstructures provide a 20 fold increase in life for an optimised bondcoat deposited on CMSX4. With further optimisation of the single crystal superalloy (fourth generation alloys) the life can be increased still further.

Low Thermal Conductivity, EB-PVD Thermal Barrier Coatings

As eluded to in the previous sections the first concern of the materials engineer was the thermal stability of the TBC system. Thus, in the early days of TBC research much work was undertaken to determine the best stabilising agent for zirconia. For very high temperature applications (mostly driven by the aero industry) there was broad agreement that 6-8wt% yttria partially stabilised zirconia offered the best solution as it showed the highest resistance to spallation under thermal cycling conditions [114] and excellent thermal stability. Later, explanations of this phenomenon identified the formation of the well know t' phase in partially stabilised zirconia [146] and its toughening mechanism [147]. Thus, yttria stabilised zirconia based thermal barrier coatings are viewed as todays "standard" and will meet the need for thermal protection in the latest generation of high powered, high performance gas turbine engines, whether for aero- or industrial applications.

Having addressed many of the mechanical stability issues, the research focus has now changed and is directed towards future engine performance. From Table 2, it is apparent that although the columnar microstructure of the EB-PVD TBC offers improved mechanical properties its thermal conductivity (1.65 W/mK) is significantly higher than its plasma sprayed counterpart (0.8 W/mK). Therein lies the challenge "How to reduce the thermal conductivity of an EB-PVD TBC to 0.8 W/mK, while still maintaining strain tolerance and thermal stability?"

Many have taken up this challenge [11,12,127,148-156] and a new generation of 'low thermal conductivity' TBC ceramics have been developed based on lanthanide doped zirconia or pyrochlore phases. Research at Cranfield, under Rolls Royce sponsorship, has examined the influence of tertiary and quaternary lanthanide dopants on the thermal conductivity of EB-PVD TBCs [153-155]. The aim was to produce partially stabilised zirconia, within the t' phase field, that contained phonon scattering centres to lower the ceramic thermal conductivity. Further, if the dopants also colours the ceramic this could be beneficial in reducing radiative transport. Following this concept, our work on dopant effects concentrating on the role of high atomic mass additions as these should theoretically provide the more effective scattering centres. Dopants evaluated included: NiO (atomic mass 51), Nd_2O_3 (atomic mass 144) and Gd_2O_3 (atomic mass 157) Er_2O_3 (atomic mass 167) and Yb_2O_3 (atomic mass 173). These five dopants were evaluated both as ternary and quaternary additions by manufacturing custom evaporation rods with known dopant levels; selected from 1.0, 2.0, 4.0 and 8.0 mole % addition. The additions were introduced to maximise lattice strains and discordant lattice vibrations. The thermal conductivity of each doped TBC was measured using a laser flash technique and the results for various ternary additions are presented in Figure 24, at a 4mole% addition of tertiary dopant.

Erbia, gadolinia, neodymia and ztterbia all lower the thermal conductivity of zirconia-4.5 mole% yttria (8wt% yttria), when added at a 4 mole% level. Nickel oxide, the only divalent oxide addition used, produced only a small decrease in contrast to the work of Tamerin et. al [156].

4mole% Erbia reduced the thermal conductivity by 25% and colouring the ceramic pink, Neodymia at 4 mole% lowered the thermal conductivity by 42% and coloured with ceramic blue/lilac. The best system, gadolinia, resulted in a thermal conductivity of 0.88 W/mK, a 47% reduction, achieving thermal conductivities comparable to plasma sprayed TBC, in an EB-PVD

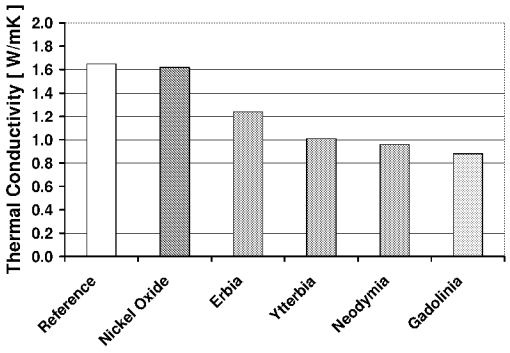

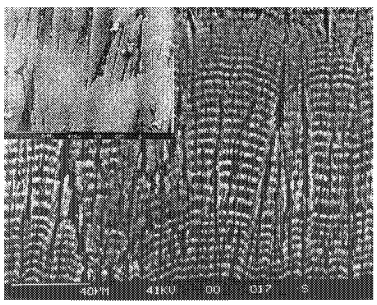

system. In all cases the ceramic crystal structure remains t' phase and the modified EB-PVD TBCs have a columnar microstructure.

Figure 24 Thermal conductivities of dopant modified EB-PVD TBCs at 4mole%addition and 250μm thickness (data measured at 500°C and corrected to a 250μm thickness using the method proposed in reference[113]

Figure 25 Layered structured EB-PVD TBC introduced by PAPVD processing of the ceramic. Insert is detail of a coatings boundary

The foregoing discussion would suggest that to reduce the thermal conductivity of EB-PVD TBCs further one should introduce additional phonon scattering centres into the coating. This is possible by modifying the coating nano-structure. Further, by reducing the mean free path from 250μm (of the order of the thickness of the coating) to 1-2μm would cause a reduction in the radiation contribution to the total thermal conductivity [153]. Thus, layering of the ceramic offers a promising route to further lower the thermal conductivity of an EB-PVD TBC, by modifying both the phonon and photon transport within the coatings.

For photon scattering, the periodicity of the layers should be chosen to act as a quarter wavelength filter (between λ and $\lambda/4$ of the incident radiation). With radiation wavelengths between 0.3-5.0μm, the layer periodicity should lie between 0.2-2.0μm, centred around 0.7μm.

The method of obtaining such structures in practice uses a glow discharge plasma to vary the density of the ceramic during deposition. Figure 25 illustrates a typical micrograph of the morphological changes that can be introduced. The layers were produced by switching the D.C. bias applied to the substrate between high and low levels during deposition. This has the effect of periodically changing the degree of ion bombardment and thus altering the density of the layers deposited. The measured thermal conductivity for this microstructure is significantly lower than that for a coating produced without ion bombardments. Values between 0.95-1.2 W/mK have been achieved [153,154] for a 2μm periodic layer structure, as depicted in Figure 25 manufacture with 'standard' zirconia-8wt% yttria ceramic. Thus reductions of the order of 37-45% compared to state-of-the-art EB-PVD TBCs are possible for these layered structures. Clearly layering at

micron dimensions and the introduction of density change from layer to layer work in combination to reduce the thermal conduction of the coating. The layering periodicity is selected to significantly reduce photon transport, while local changes in layer density act to scatter phonons and thus reduce thermal conduction by lattice vibration as well.

CONCLUDING REMARKS

This paper has reviewed available coating systems to protect hot path components within gas turbines. Trends in the design of environmental and thermal protection coatings have been presented including concepts of smart corrosion resistant coatings, diffusion barriers, new bondcoat technologies and low thermal conductivity thermal barrier coatings.

To the future, one must look towards custom surface engineering with the substrate and coating system designed to compliment each other such that they provide optimal protection, be it environmental, thermal or a combination of both technologies.

REFERENCES

1. Oakey J. E., Allen D. H. and Staubi M. 'Power Generation in the 21st Century – The New European COST Action', Euromat '99
2. Cheruvu N. S., Chan K. S. and Viswanathan R., Energy Materials, 1 (1), 33-347 (2006)
3. Schulenberg 'New Developments in Land Based Gas Turbine Technology' in 'Materials for Advanced Power Engineering, 1988 [eds J. Lecomte-Becker, F. Schubert and P.J. Ennis) part II, p849-859, Forschungszentrum, Julich, Germany (1998).
4. Viswanthan R. and Scheirer S. T., Proc. 7th. Int. Conf. on 'Creep and Fatigue at Elevated Temperatures' 7-21, Tokyo, Japan, 2001.
5. Goward G. W. and Boone D. H., Oxid. Met. 3, (1971), 475.
6. Gupta D. K. and Davall D. S., ' Coatings for Single Crystal Superalloys', TMS, Warrendale, PA (1984).
7. Goward G. W., Surf. Coat. Technol 108-109, 73 (1998).
8. Goward G. W, and Cannon L. W., ASME Paper 87-GT-50 (1988).
9. Streiff R., J. Phys IV, Colloque C9, Suppl. 3, 17-40, 1999.
10. Nicholls J. R., JoM 52, 28 (2000).
11. J. R. Nicholls, 'Advances in Surface Engineering in Gas Turbines', Parsons 2003 Engineering Issues in Turbine Machinery, Maney Publishers, p803-826, Sept 2003.
12. J. R. Nicholls 'Advances in Coating Design for High Performance Gas Turbines' MRS
13. Talboom F. T., Elam R. C. And Wilson L. W., 'Evaluation of Advanced Superalloy Protection Systems' Report CR7813, NASA, Houston TX (1970).
14. Mevrel R., Duret C, and Pichoir R, Mater. Sci. Technol., 2 (1986) 201.
15. Duret C., Davin A, Marrijnissen G and Pichoir R, in "High Temperature Alloys for Gas Turbines", (Conf Proc.) (Eds. R. Brunetaud et al.) p53-87; Dordrecht, D. Reidel Publishing Co. (1982).
16. Malik M., Morbioli and Huber P. In 'High Temperature Alloys for Gas Turbines' Conf Proc. (ed. R. Brunetaud et. al.) 87-98, Dordrecht, D. Reidel Publishing Co (1982).
17. Davis F. N. and Grinell C. E., ASME Pub. 82-GT-244 (1982).
18. Van Roode M. and Hsu L., Surf. Coat. Technol. 37, 461-481 (1989).
19. Berry D., Meelu M. C., McMondie B. G., Kircherin T. A., ASME Pub. 95-GT-359 (1995).
20. Stringer J. and Viswanathan R in "Advanced Materials and Coatings for Combustion Turbines", [Eds. V. P. Swaninathan and N. S. Cheruvu] ASM p6 (1994).

21. Goward G. W., in 'High temperature corrosion' (Conf. Proc. NACE-6), (Ed. R. A. Rapp), p553-560; Houston, TX, NACE (1983).
22. Fitzer F. and Schlichting J., in 'High Temperature Corrosion' NACE-6 p604-614 (1984).
23. Luthra K. L and LeBlanc O. H., Mater, Sci. & Eng. 88 (1987), 329-335.
24. Luthra K. L., J. Electrochem Soc. 132, 1293-8 (1985).
25. Lehnert G. and Meinhardt H., Surf. Treatment 1, 72, (1972).
26. Levin S. R., and Caves R. M., J. Electrochem. Soc. 120, C232 (1973).
27. Pint B. A., Materials Science Forum, 251-254, 397 (1997).
28. Czech N., Schmitz F. and Stamm W., Surf. Coat. Technol. 68-69, 17-21 (1994).
29. Nicholls J. R., Simms N. J., Chan W. Y. and Evans H., E., Surf Coat. Technol. 149, 236 (2002).
30. Peichl L. and Bettridge D. F., in "Materials for Advanced Power Engineering 1994", pt 1, p717-740 (1994).
31. Bacos M. P., Girard B., Josso P. and Rio C. "MCrAlY Coating by an Electrochemical Route" in "Materials for Advanced Power Engineering 2002", [Eds. J. Lecomte-Beckers, M. Carton, f. Schubert and P. Ennos] publisher Forschungzentrum, Julich, Germany, part 1. p429-437 (2002).
32. Chan K. S., Cheruvu N. S, Leverant G.R. and Viswanathan R., in 'Materials Lifetime: Science and Engineering (Ed. P. K. Liaw et al) TMS, San Diego, CA, USA (2003).
33. Viswanathan R. In ,Damage Mechanisms and Life Assessment Techniques for High Temperature Components, ASM, Metals Park, OH (1987).
34. Bianco R. And Rapp R. A., J. Electrochem. Soc. 140, 1181-1191 (1993).
35. Bianco R., Haprer M. A. And Rapp R. A., JoM, 43, 68-73 (1991).
36. Stringer J. and Viswanathan R., 'Gas Turbine Hot-Section Materials and Coatings in Electric Utility Applications' pp1-21 in Proceedings of ASM 1993 Materials Congress Materials Week '93, Pittsburgh, Pennsylvannia, October 17-21, Materials, Park Ohio; ASM International 1993.
37. Felten E. J. and Pettit F. S. , Oxid. Met. 10, 189-223 (1976).
38. Fountain J. G, Golightly F. A., Stott F. S. and Wood G. C., Oxid.Met. 10, 341-345 (1976).
39. I. M. Allam, H. C. Akuezlte and D. P.Whittle, Oxid. Met. 14, 517-530 (1980).
40. Pint B. A., Oxid. Met. 48, 303-333, (1997).
41. Y. Zhang, J. Haynes, W. Y. Lee, I. G. Wright, B. A. Pint, K. M. Cooley and P. K. Laiw, Met. Mater. Tran. A. 32A, 1727-(2001).
42. E. C. Dickey, B. A. Pint, K. B. Alexander and I. G. Wright, in High Temperature Surface Engineering [ed. J. R. Nicholls, and D. S. Rickerby] p115-128, IoM Communications, London, (2000).
43. B. A. Pint, I. G. Wright, W. Y. Lee, Y. Zhang, K. Prüssner and K. B. Alexander, Mat. Sci. Eng. A245, 201-211 (1998).
44. R. Streiff and D. Boone, J. Mater. Eng. 10, 15- (1988).
45. G. H. Meier and F. S. Pettit, Surf. Coat Technol. 39/40, 1- (1989).
46. J. Angenete and K. Stiller, Mater. High Temp 17, 179, (2000).
47. J. Angenete and K. Stiller, Surf. Coat. Technol. 150, 107 (2002).
48. V. K. Tolpygo, D. R. Clarke and K. Murphy, Met. Mater. Trans 32A, 1467- (2001).
49. Pint B. A, More K. L. and Wright I. G., Materials at High Temperature (2002).
50. Bennett I. J. and Sloof W. G., Materials at High Temperature (2002).
51. Schumann E., Yang J. C., Graham M. J., and Ruhle M. , Mater. Corrosion, 47, 631-632 (1996).
52. Pint B. A., Garrett-Reed A. J., and Hobbs L. W., Microscopy of Oxidation, Vol. 2, 463-475 (1993).
53. Pint B. A., Wright I. G., Lee W. Y., Zhang Y., Prussner K. and Alexander K. B.. Mat. Sci.

Eng A245, 201-, 1998.
54. Naveos S., Oberlaender G., Cadoret, Y., Josso. P., and Bacos M-P, Les Embiez (2004).
55. Haynes J. A., Pint B. A., More K. L., Zhang Y., and Wright I. G., Oxid. Met. 58, 513-544 (2002).
56. Haynes J. A., Pint B. A., More, K. A., Zhang Y. and Wright I. G., Oxid. Met. 58, 513- (2002).
57. Nicholls J. R., Wing R., "Advanced Coating Systems for Utility Gas Turbines" in "Materials for Advanced Power Engineering 2002, "[Ed. J. Lecomte-Beckers, M. Carton, F. Schubert and P. J. Ennis], publishers Forschungzcentrum Julich, Germany, Part 1 P57-71 (2002).
58. Amperiawan G., PhD Thesis, Cranfield University, (2002).
59. McMordie B. G. and Weatherill A. in "Turbine Forum", Nice, France (2002).
60. Sermaloy 1515, U. S. Patent 5,547,700
61. Mom, A.J. A., NLR Report MP 81003U, Amsterdam. 1981.
62. Novak R. C. (1994), 'Coatings for High Temperature Structural Materials' NMAB, NRC, National Academy Press, Washington DC (1996).
63. Prater J. T., Patten J. W., Hayes D. D. and Moss R. W, im Proc. 2nd Conf. on 'Advanced materials for alternate fuels capable heat engines', (eds J. W. Firbanks and J. Stringer), Report No. 2639SR, 7/29-7/43; Palo Alto, CA EPRI (1981).
64. Goebel J. A., Giggins C S., Krasij M. and Stringer J, in Proc. 2nd Conf. on 'Advanced materials for alternate fuel capable heat engines', (ed. J. W. Firbanks and J. Stringer), Report No. 2639SR, 7/1; Palto Alto, CA EPRI (1981).
65. Forster J., Cameron B. P. and Carews J. A., Trans. Inst. Metal Finish, 63 (1985) 115.
66. Bornstein N. S. and Smeggil J., in 'Corrosion of Metals Processed by Directed Energy Beams', Met. Soc. AIME, p147-158 (1982).
67. Coupland D. R., Hall C. W. and McGill I. R. Platinum Metal Review 26 (4) 146-157 (1982).
68. Wolff I. M., Iorio L. E., Rumpt T., Scheers P. V. T., Potgieter J. H., Mater. Sci. Eng. A241, 264-276 (1998).
69. Juarez F., Monceau D., Tetard D., Pieraggi B. and Vahlas C., Surf Coating. Technol. 163, 44-49 (2003).
70. Czech N. and Stamm W. in "High Temperature Surface Engineering" [Eds. J. R. Nicholls and D. S. Rickerby] p61-65, IoM Communications, London (2000).
71. Taylor T. A., Overs M. P., Gill B. J., and Tucker R. C., J. Vac. Sci. Tech. 3 (1985), 2526.
72. Herman H., "Powders for Thermal Spray Technology" Thermal Spray Technology. Powder Science and Technology 9: 187-199 1991.
73. Kaufol R. W., Rotolico A. J., Nerz J. and Kushner B. A., "Deposition of Coatings Using a New High Velocity Combustion Spray Gun", pp561-569 in Thermal Spray Research and Applications, T. F. Bernecki ed. Materials Park, Ohio: ASM International 1990.
74. Russo L. and Dorfman M. "High-Temperature Oxidation of MCrAlY Coatings Produced by HVOF. Pp1179-1194 in Proceedings of the International Thermal Spray Conference, A. Ohmori, ed. Japan: High Temperature Society of Japan.
75. Lugscheider E., Herbst C. and Zhao L in "High Temperature Surface Engineering" [Ed. J. R. Nicholls and D. S. Rickerby] p67-76 IoM Communications, London (2000).
76. Kedward E. C., Metallurgia, 79, (1969) 225.
77. Honey F. J., Kedward E. C. and Wride V., J. Vac. Sci. Tech., A4, 2593-(1986)
78. Foster J., Turbine Forum", Nice, France, April 2002.
79. Bacos M-P., Girard B., Josso P. And Rio C., Surface and Coatings Technology 162, 248-260, (2003).

80. Bacos M-P andJosso P. US Patent No. 868267 (2001).
81. Restall J.E. and Hayman C, in 'Coatings for heat engines' (Workshop Proc.,) (ed. R. L. Clarke et al.) 347-357; Washington, DC, US Department of Energy (1984).
82. Chan K. S., Cheruvu N. S. and Leverant G. R., Materials Science Forum,Vol, 369-372, 623-630 (2001)
83. Warnes B. M., Surf. Coat. Technol. 163-164, 106-111 (2003)
84. Swadzba L., Saunders S. R. J., Hetmanczyk M. and Mendala B. in "Materials for Advanced Power Engineering" (2002), Forschungszentrum Julich, Germany, (2002)
85. Steiger M. J., Yanar N. M., Topping M. G., Pettit F. S. and Meier G. H., Z. Metallkund 90, 1069-1078 (1999).
86. Yanar, N. M., Kim G. M., Pettit F. S., and Meier G. H., in 'Turbine Forum', Nice, France (2002)
87. Rickerby D. S. and Wing R. G. "Thermal Barrier Coating for a Superalloy and a Method of Application Thereof" US Patent 5,942,337 Aug (1999).
88. Rickerby D. S, Bell S. R. and Wing R. G., "Article Including Thermal Barrier Coated Superalloy Substrates", U. S. Patent 5,981,901 Nov (1999).
89. Saunders S. R. J. and Nicholls J. R., Thin Solid Films 119, 247- (1984).
90. Bezencon, C, Konter M., Wagniere J-D and Kurz W. "Microstructural Development in Laser Cladding of a Single Crystal Nickel Based Alloy", in Proc. of Lasers in Manufacturing, German Scientific Laser Society, June 2001, Munich, Germany, p580-589 (2001).
91. Bezemcon, C., Wagniere J-D, Hobel M., Schrell A., Konter M., and Kurz W, "Single Crystal Coating of a Single Crystal Turbine Blades by a Laser Cladding Technique" in "Materials for Advanced Power Engineering 2002", [Eds. J. Lecomte-Beckers, M. Carton, F. Schubert and P. Ennis], publisher Forschungszentrum Julich, Germany Part 1, p503-510 (2002).
92. Muller G., and Strauss D. "Improvement of MCrAlY Properties by Pulsed Electron Beams", in "Turbine Forum", Nice, France, April 2002.
93. Bossman H-P, 'Development and Optimisation of High Temperature Turbine Coatings in Turbine Forum, Nice, France, April 2006.
94. Czech N., Schmitz F. and Stamm W., Surf. Coat. Technol. 94-95, 41-45 (1997).
95. Chez N., Schmitz F. and Stamm W., Surf. Coat. Technol. 76-75, 28-33 (1995).
96. Dallio J. A. and Doone D. H., Proc. ASME Conf. on 'Gas Turbine and Aero-engineering', Orlando F1, USA, June 1997, paper 97-GT-486.
97. Restall J. E. and Hayman C., in Proc. Workshop for Heat Engines, [Ed. R. L. Clarke et al] p347-357, Washington DC, US DoE (1984)
98. Nicholls J. R., Stephenson D. J., Hancock P., Wood M. I. and Restall J. E. in Proc. Workshop on Gas Turbine Materials in Marine Environment, Bath UK Ministry of Defence, Session 2, paper 7 (Nov. 1984).
99. Evans A. G., Mumm D. R., Hutchinson J. W., Meier G. H., and Pettit F. S., Progress in Materials Science, 46, 505, (2001).
100. Bouhanek K., Adesanya O A., Stott F. H., Skeldon P., Lees D. G., and Wood G. C, Materials Science Forum Vol 369-372, 615-622 (2001).
101. Adesanya O. A., Bouhanek K., Stott F. H., Skeldon P., Lees D. G. and Wood G. C., Materials Science Forum Vol. 369-372, 639-646 (2001).
102. Nicholls J. R., Simms N. J., Neseyif S., Evans H. E., Ponton C. and Taylor M, J. Electrochem Soc. 99-38, 305-316 (2002).
103. Nicholls J. R., Simms N. J., Taylor M. and Evans H. E., 'Smart Overlay Coatings' "Turbine Forum", Nice, France, April 2002.
104. Young S. G. and Zellars G. R., Thin Solid Films 53, 241-250 (1987).

105. Nicholls J. R., Lawson k. J., Chester G., Yasiri L. H., Hancock P., in 'European Research on Materials Substitution (eds. I. V. Mitchell and H. Nosbuch), p295-307, Elsevier, London (1988).
106. Nartia T., Thosen K. Z., Fengqun L., Murakami H., Gleeson B. and Young D., Surf. Coating Technol. (2004).
107. Nicholls J.R., Lawson K. J., Al-Yasiri L. H. and Hancock P. Corr. Sci. 35, (1993), 1209.
108. Liebert C. H. et al. "Durability of Zirconia Thermal Barrier Coatings on Air Cooled Turbine Blades in Cyclic Jet Engine Operation," report TMX-3410, NASA (1976).
109. Grisaffe S. J., "Thermal Barrier Coatings" report TMX-78848, NASA, (1978).
110. Miller R. A., "Current Status of TBCs – An Overview", Surface Coat. Technol. 30, 1, (1987).
111. Strangman T. E., Thin Solid Films, 127, 93-95 (1985).
112. Meier S. M. and Gupta D. K., J. Eng. Gas Turbine and Power 116, 250, (1994).
113. Soechting F. O., "A Design Perspective on Thermal Barrier Coatings", Thermal Barrier Coating Workshop, NASA-CP-3312 p3, NASA (1995).
114. Bose S., and Demasi-Marcin J., Thermal Barrier Coating Experience in Gas Turbine Engines at Pratt and Whitney, pp63-77, in Thermal Barrier Coatings Workshop, NASA-CP-3312. Cleveland, Ohio, National Aeronautics and Space Administration Lewis Research Centre 1995.
115. AGARD Report 823, "Thermal Barrier Coatings" (1998).
116. Gleeson B., J. Propulsion and Power 22, 375-382 (2006).
117. Meier S. M., and Gupta D. K., Transactions of the ASME 116, 250- (1994).
118. Shillington E. A. G and Clarke D. R., Acta Materialia 47 (4), 1297- (1999).
119. Barber B., Jordon E., Gell N. and Geary A., J. Thermal Spray 8(1), 79-, (1999).
120. Morrell P. and Rickerby D. S., ibid 20-1, (1998).
121. Subranmanian R. and Burns A., 'Turbine forum, 2004' Nice, France, (April 2004).
122. Cheruvu N. S. and Chan K. S., 'Combustion Turbine Hot Section Coating Life Management', EPRI Report, 1011593, Electric Power Research Institute, Palo. Alto, CA, USA (2005).
123. Herzog R., Steinbrech R. W., Singheiser L.,Turbine Forum 2006 Nice, France (April 2006).
124. Stiger M. J., Yanar N. M., Pettit F. S. and Meier G. H., in 'Elevated Temperature Coatings : Science and Technology' [Eds. J. M. Hamkin and N. B. Dahotri] TMS, Warrendale, PA, USA pp51- (1999).
125. Padture N. P., Gell M. and Jordon E. H., Science 296 280- (2002).
126. Peters M., Leyens C., Schutz U. And Kaysser W., Advanced Engineering Materials 3 (4), 193- (2001).
127. Clarke D. R., and Levi C. G., 'Annual Review of Materials Research 33, 383- (2003).
128. Akaa J., Sfar K. and Munz D., Acta Materialia 53, 4399-(2005).
129. Sridharan S., Xie L., Jordon E. J., Gell M. and Murphy K. S., Material Science and Engineering A, A393, 51- (2005).
130. Spitsburg I. T., Mumm D. R. and Evans A. G., Material Science and Engineering A, A394, 176-(2005).
131. Schlichteng K. W., Padture N. P., Jordon E. H. and Gell M., Material Science and Engineering A, A342, 120- (2003).
132. Rabiei A. and Evans A. G., Acta Materialia 48, 3963 (2000).
133. Xu T., He M. Y., Evans A. G., Acta Materialia 51 3807- (2003).
134. Shilling E. A. G. and Clarke D. R., Acta Mater. 47, 1297-1305 (1999).
135. Wright P. K. and Evans A. G., Current Opinions Sol. State and Mater. Sci. 4, 255 (1999).
136. Mumm D. R. and Evans A. G., Acta. Mater. 48, 1815-1827, (2000).

137. Tolpygo V. K., Clarke D. R. and Murphy K. S., Surf. Coat. Technol. 146-147, 124, (2001).
138. Chang G. C., Phuchaeron W., Miller R. A., Surf. Coat. Technol. 32, 307 (1987).
139. Meier S. M., Nissley D. M., and Sheffler K. D., "Thermal Barrier Coating Life Prediction Model Development, Phase II, report CR-18911, NASA, (1991).
140. Pint B. A., Garratt-Reed A. J. and Hobbs L. W., Mater. High Temp. 13, 3 (1995).
141. Smialek J. L., Met. Trans. A22, 739, (1991).
142. Evans H. E. Strawbridge A, Carolan R. A. and Ponton C. B., Mater. Sic. Eng., 1997, A225, 1
143. Atkinson A., Selcuk A. and Webb S. J., Oxid. Met. 54, 371, (2000).
144. Brindley W. J., "Workshop on Thermal Barrier Coatings", Report CP-3312, NASA Cleveland, p189, (1995).
145. Freborg A. M., Ferguson B. L., Brindley W. J. and Petrus G. J., in "Thermal Barrier Coatings", AGARD report 823, 17-1, (1998).
146. Miller R. A., Garlick R. G. and Smialek J. L., Am. Ceram. Soc. Bull, 62, 1355, (1983).
147. Lelait L : cited in Alperine S., Derrien M., Jaslier Y., and Mevrel R. in "Thermal Barrier Coatings" AGARD Report 823.
148. Maloney M. J., US Patent No. 6,007,880 Dec. 1999.
149. Maloney M. J., US Patent No. 6,057,047 May 2002.
150. Levi C. G., Current Opinion in Solid State and Material Science, 8, 77-91 (2004.
151. Zhu D. and Miller R. A., Ceram. Eng. Sci. 23, 457-468 (2002).
152. Zhu D., Chen Y. L. And Miller R. A., Ceram. Eng. Sci. 24, 525-534 (2003).
153. Nicholls J. R., Lawson K. J. Rickerby D.S and Morrell P. in "Thermal Barrier Coatings", AGARD Report, 823; 6-1, (1998).
154. Nicholls J. R., Lawson K. J., Johnstone A. and Rickerby D. S., Mater. Sci. Forum, 369, 595 (2001).
155. Nicholls J. R., Lawson K. J., Johnstone A. and Rickerby D. S, Surf. Coat. Technol. 151-152 383 (2002).
156. Tamarin Y. A., Kachanov E. B. and Zherzdev S. V, Mater. Sci. Forum 251, 949 (1997).

APS-TBCS FOR GAS TURBINES: FAILURE MODES, DAMAGE EVOLUTION AND LIFE-TIME ASSESSMENT

Roland Herzog, Piotr Bednarz, Olena Trunova, Rolf W. Steinbrech, Egbert Wessel, Willem J. Quadakkers, Florian Schubert, Lorenz Singheiser

Research Center Jülich, Institute of Energy Research, IEF-2, 52425 Jülich, Germany

Abstract

Ceramic thermal barrier coatings (TBCs) for hot-section components of advanced gas turbines are exposed to complex thermo-mechanical loads, which may lead to failure in form of macroscopic spallations from the metallic component. The durability of TBCs is limited by the interaction of different processes and parameters, such as bond coat oxidation, sintering of the ceramic top coat, cyclic strains, phase transformations, visco-plastic and relaxation properties, fracture toughness, interface roughness and others. The effect of loading conditions on the activation of different crack propagation paths will be addressed using results from isothermal and cyclic oxidation tests as well as thermal cycle tests. It will be further shown that macroscopic spallation failure of plasma-sprayed TBCs is the final step of a continuous damage evolution and accumulation, which starts before 5% of life-time and is strongly related to bond coat oxidation. Furthermore, a life-time prediction model approach for plasma-sprayed TBCs will be presented, which comprises loading and material parameters such as thermal strain mismatch, oxidation kinetics, interface roughness and slow crack growth. The approach has been developed particularly for cyclic oxidation loading on the basis of experimentally observed crack growth kinetics.

Keywords: Thermal Barrier Coatings, Failure Modes, Damage Evolution

1. Introduction

The development of highly efficient gas turbines in the last two decades was essentially due to optimized construction, advanced cooling techniques and complex material composites. Highly loaded turbine blades of the first stages do not longer consist of a single metallic alloy, but rather of a material composite that has to fulfil several tasks. The load carrying body is frequently manufactured from high temperature resistant nickel-base alloys with optimized strength and fatigue properties. Chemical composition as well as a tailored microstructure achieved by advanced single-crystal casting technology guarantees the high-level mechanical properties. Metallic coatings with high aluminium and chromium contents protect the blades against high temperature corrosion and oxidation. Ceramic thermal barrier coatings on top of the highly loaded, internally cooled blades provide thermal insulation and prevent overheating in order to extend their life-time. With increasing operating temperature of advanced gas turbines, spallation failure of thermal barrier coatings becomes more and more important, since the loss of the thermal barrier causes exposure of the metallic blade material to hot gases. Thus, the understanding of spallation failure and underlying damage mechanisms as well as the development of life prediction concepts is a key issue for further TBC development and a prerequisite for the full integration of TBCs into component design. Over the past two decades a considerable amount of insight into damage mechanisms and factors controlling the life-time has been achieved [e.g. 1,2,3,4,5,6,7,8,9,10,11]. The present paper addresses various failure modes with respect to the activated crack propagation path and their relation to the load profile, the evolution of damage from crack formation at early stages of exposure to macroscopic spallation and a basic concept for calculating the life-time of APS TBCs.

2. Experimental

Isothermal and cyclic oxidation tests as well as thermal cycle tests with and without temperature gradient have been performed on <001>-oriented, cylindrical specimens of single crystal CMSX-4 and on flat specimens, coated with a VPS-NiCoCrAlY bond coat and a thermal barrier coating of zirconia stabilized with 7-8 wt% yttria. The bond coat thickness was appr. 150 µm and the TBC thickness app. 300 µm. Micrographs of the respective structure of the constituents are represented in Fig. 1.
Isothermal and cyclic oxidation tests were conducted partly in a resistance furnace and partly in an infrared furnace with a temperature distribution of ± 5°C within the respective area, the samples where placed. The oxidation cycle was defined as: heating from room temperature to T_{max}, holding the temperature for 2 h, cooling down to 60°C in air within 15 min. T_{max} was predominantly 1050°C. Part of the isothermal tests were carried out up to various fractions of life to analyze the damage evolution. Failure has been defined as the first occurrence of macroscopically visible spallation of the TBC. The thermal cycle tests without dwell time at high temperature were carried out in an infrared furnace as well as those tests with a temperature gradient induced by internal cooling with compressed air. After testing, all specimens were longitudinally and transversally cut and metallografically prepared for microstructural investigations. The thickness of the TGO and the length of microcracks were determined using optical microscopy and SEM.

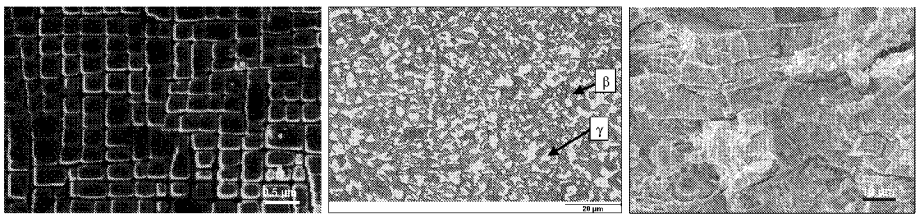

Figure 1: The investigations have been performed on <001>-oriented, cylindrical specimens of single crystal CMSX-4 (left), coated with a VPS-NiCoCrAlY bond coat (middle) and a plasma-sprayed thermal barrier coating of zirconia stabilized with 7-8 wt% yttria (right).

3. Correlation between Damage Mode And Load Conditions

Fig. 2 displays the length section of 4 specimens which were exposed to isothermal oxidation at 1050°C (a), to cyclic oxidation with 2 hours dwell-time at 1050°C (b), to thermal cycling with T_{max} = 1050°C without dwell-time at high temperature (c) and to thermal cycling with 2 hours dwell-time at a bond coat temperature of 1050°C (as cyclic oxidation) but with a temperature gradient resulting in a surface temperature of the TBC of 1150°C (d). The four micrographs illustrate the differences in the location of the major delamination crack paths, which were activated by the respective loading conditions. After isothermal oxidation the TGO was relatively thick and crack path was located predominantly in the TGO (black failure). Cyclic oxidation resulted in a crack path partly located in the TGO and partly in the TBC (grey failure). The TGO was thinner compared to isothermal oxidation. After pure thermal cycling without a dwell-time at high temperature, the TGO was fairly thin and the crack path was located predominantly in the TBC (white failure). After thermal cycling with

a dwell-time of 2 hours at 1050°C and a superimposed temperature gradient the delamination cracks were located in the TBC partly close to the interface and partly close to the surface of the TBC. Additionally, diagonally oriented cracks were observed in the TBC.

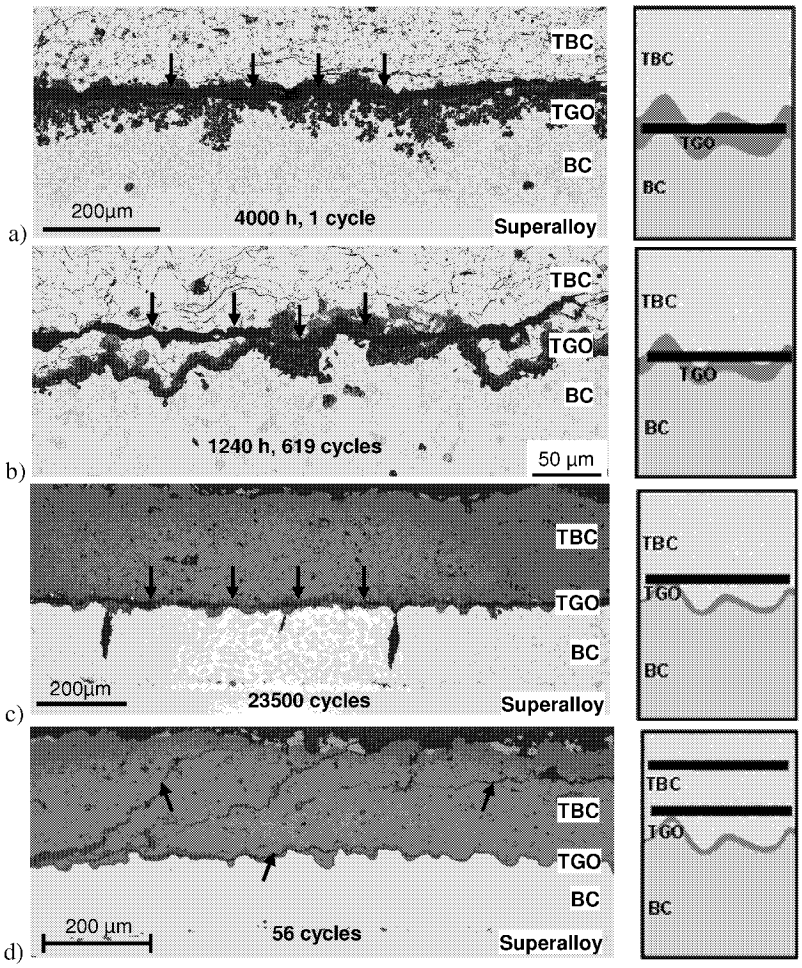

Figure 2: Length section of TBC specimens after isothermal oxidation at 1050°C (a), after cyclic oxidation with 2 hours dwell-time at 1050°C (b), after thermal cycling with T_{max} = 1050°C without dwell-time at high temperature (c) and after thermal cycling with 2 hours dwell-time at a bond coat temperature of 1050°C (as cyclic oxidation) but with a temperature gradient resulting in a surface temperature of the TBC of 1150°C (d). The drawings at the right side display schematically the location of the respective delamination crack paths.

The activation of various crack paths according to the specific load conditions was related to different life-times or number of cycles to failure. It has to be taken into account that different

crack paths are related to different material properties affecting the crack propagation (e.g. fracture toughness) and different stresses as well as strain energy release rates as driving force for crack propagation.

4. Damage Evolution Under Oxidizing Conditions

A serious of isothermal furnace tests on APS TBCs with increased exposure time from 96 up to 4490 hours (spallation failure) at 1050°C was carried out. After each selected exposure time the specimens were cooled to room temperature in order to characterize the damage by means of metallographic and SEM investigations. A series of 8 SEM images with identical magnification was selected for each exposure time at 1050°C. Figure 3 shows examples of the damage state after various exposure times. Cracks were observed already after 96 hours at 1050°C for instance at the TBC/TGO interface. Concurrently some of the pre-existing cracks within the TBC near the TGO were widened (Fig. 3.a, b). After longer times (≥ 1730 h) crack formation appeared increasingly in the TGO and at the TGO/BC interface (Fig. 3.c). In addition, the number density of cracks increased with increasing exposure time. Further exposure (≥ 2780 h) led to linking of individual cracks. The crack length became significantly larger and macroscopic cracks were formed. Those macrocracks were located predominantly in the TGO as mentioned in section 3., but partly also in the TBC (Fig. 3.d).

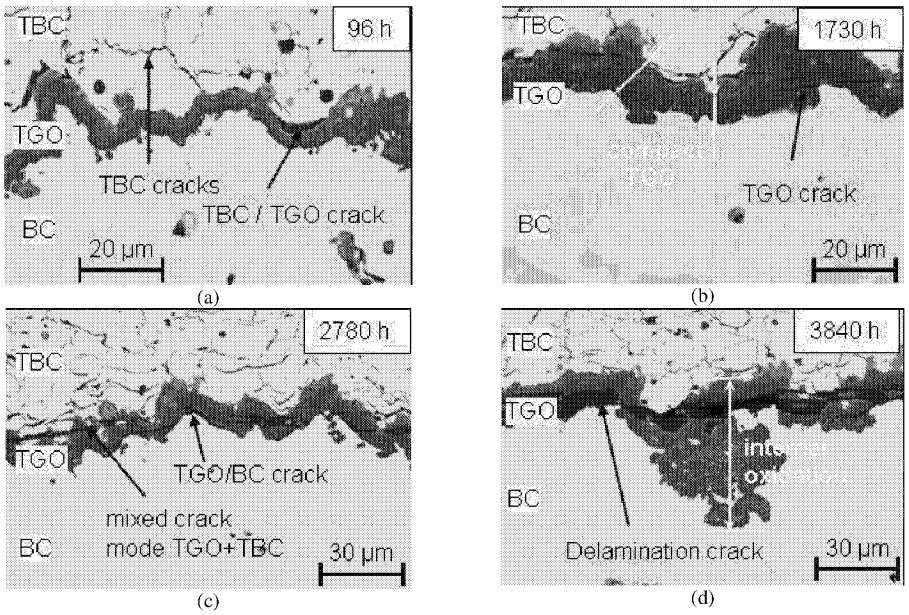

Figure 3: Microcracks near the TGO after various exposure times at 1050°C

The series of 8 SEM images for each exposure time was used to quantify the population of microcracks. All cracks were counted and their length was measured. As an example, the number of cracks after 580 h at 1050°C is shown in Fig. 4 (left) as a function of their length. The bar graph was generated by sorting those cracks which belong to a pre-defined crack

length interval of 1 µm. The resulting distribution was then represented by adjusting a Gaussian distribution function to obtain a smooth correlation. The Gaussian distribution function was furthermore used to define a mean crack length, namely the value corresponding to the peak of the distribution. Fig. 4 (right) displays five distribution functions for different exposure times. The first three distributions (96 h, 580 h, 1730 h) revealed an increase of the number of microcracks. In contrast, during the same range of exposure time the mean crack length increased only slightly from 10µm to 12 µm. Moreover, the maximum crack length was limited to values below 40 µm. For larger exposure times the distribution function became broader. The mean crack length increased up to 18 µm after 2400 h. Again after longer times (> ca 2500 hours) the mean as well as the maximum crack length reached macroscopic values. The distribution function became much broader and extremely flat, while the number density of cracks decreased.

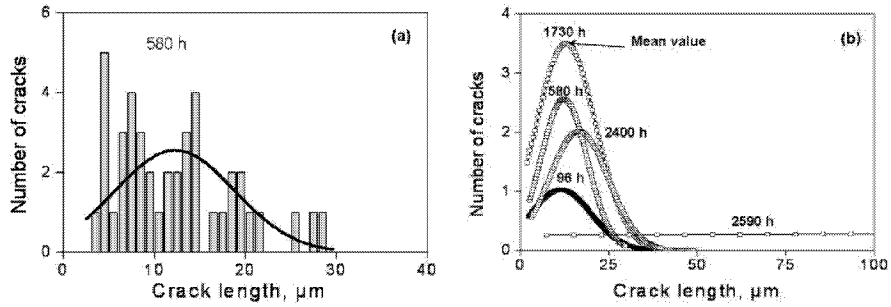

Figure 4: Example of the crack length distribution after 580 h at 1050°C with Gaussian distribution function (left), Gaussian distribution functions for various exposure times at 1050°C (right).

In Fig. 5 the maximum crack length as well as the number of cracks observed within a constant length section of the specimens is represented as a function of exposure time. The maximum crack length was below 40 µm up to 2400 h and then started to increase more rapidly up to several millimetres. The number of microcracks increased up to 2000 h and decreased for larger exposure times. The corresponding micrographs revealed that the decrease of the number of cracks was associated with linking of individual cracks, which contributed to the development of macroscopic cracks.

The results presented in Figs. 3 to 5 comprise complementary information, which document a continuous evolution of damage along the TGO with respect to increasing exposure time at 1050°C. First cracks which were not due to the coating process were observed below 5% of life. No indications were found that the life-time was determined by a critical crack length. The continuous crack growth curve indicates rather that the life-time is affected by the kinetics of the single processes (i) crack formation, (ii) crack linking and (iii) crack growth.
Furthermore, Fig. 5 suggests to discriminate two stages with respect to the underlying evolution of cracks. Within a first stage microcracks were increasingly formed along the TGO, but their length was limited to values below 40 µm. This stage lasted for about 2000 h corresponding to 45% of TBC life. During the subsequent second stage individual microcracks

started to form links and the resulting cracks grew to macroscopic length values until final spallation occurred.

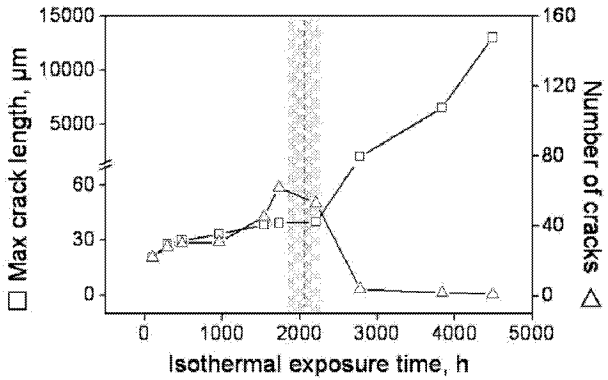

Figure 5: Maximum crack length and number of cracks as a function of exposure time.

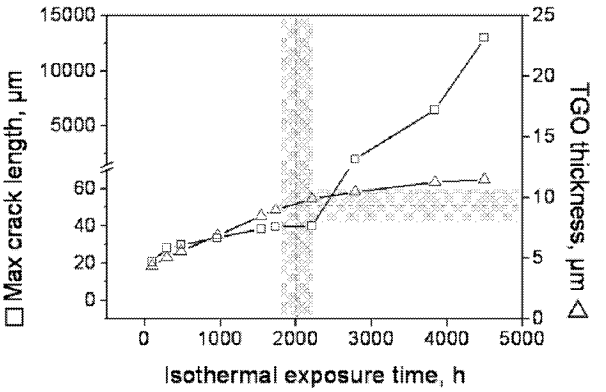

Figure 6: Maximum crack length and uniform or compact TGO thickness as a function of exposure time at 1050°C.

Fig. 6 shows the evolution of maximum crack length in comparison with the evolution of the TGO thickness. Regions where internal oxidation occurred were not considered for the determination of the TGO thickness. Thus, the resulting values reflect the evolution of the uniform or compact TGO thickness. The compact TGO thickness reached 5 µm after about 200 h, 10 µm after 2500 h and was approximately 13 µm for the specimen, which showed complete TBC spallation after 4490 h. At about 2000 h, after which crack linking and rapid growth was observed, the TGO thickness was approximately 9 µm. Thus, a TGO thickness of about 9 µm marks the transition between first and second stage of the evolution of cracks in and near the TGO. No indications were found that a critical TGO thickness controls the spallation failure. If the TGO plays a role in controlling the kinetics of the crack evolution, the

results rather indicate that the TGO thickness affects the transition from the first to the second stage of damage evolution.

4. Basic Approach For Life Prediction

The results represented in the last section were used to develop a life-time prediction approach for plasma-sprayed TBCs. Generally, the approach is limited to oxidizing load conditions according to the experimental observations. Furthermore, it is based on the assumption that spallation failure can be treated as the final step of a continuous process of formation, linking and growth of micro- and macrocracks. This assumption includes that the time-to-spallation is determined by the kinetics of the damage evolution. The second assumption is that the damage evolution can be represented by the growth of the longest crack as displayed in Fig. 5. Thus, the damage evolution is projected on the length of the longest crack (a) as a function of exposure time (t) and number (N) of load cycles:

$$a = a(t, N) \tag{1}$$

The time-to-failure (t_f) is defined by a limiting macroscopic crack length (a_{cr}) at which spallation ocurs. If (a) equals (a_{cr}), failure occurs:

$$t = t_f \qquad \text{if} \qquad a = a_{cr} \tag{2}$$

According to the experimental observations, crack growth is divided into two stages: crack formation and initial growth (stage 1, see section 3) and subsequent crack linking and growth (stage 2). The model approaches for both stages will be discussed separately in the following. Afterwards, the complete model will be described.

Stage 1: crack formation and initial crack growth:
Generally, the formation of microcracks, which contribute to the relevant damage accumulation, was observed in the TGO as well as in the TBC near the TGO or at the interfaces BC / TGO and TGO / TBC due to various mechanisms. Sometimes the formation of microcracks was related to pores in the TBC or in he TGO (Fig. 7, top left). In the TBC, pores and microcracks are already present in the as-coated state due to the thermal spray process. Pores in the TGO are possibly the consequence of the volume change associated with θ- to α-alumina transformation and resulting formation of cavitations. Crack formation was observed also at brittle precipitates like yttria-alumina garnets at the bond coat / TGO interface (Fig. 7: top, right). At early stages of exposure cracks were often observed at the interface bond coat / TGO at roughness peaks (Fig. 7, bottom left at about 10% of life). They pattern suggest that they were formed at the interface and then crossed the TGO at their roughness flanks at both sides and started to penetrate the neighboring TBC.

The presented examples of crack formation in plasma-sprayed TBCs shall document that it is neither a uniform process nor related to a single mechanism. The detailed formation process of each single crack within the population of microcracks which is distributed along the interface region of bond coat, TGO and TBC is not known as well as the detailed initial growth of each crack is not known. However, the development of the whole population of microcracks showed the tendency to form crack pattern comprising cracks in the TGO at roughness peaks

and cracks in the TBC at roughness valleys for oxidizing load conditions. Sometimes the crack propagation path was located more in the TGO, sometimes located more in the TBC depending on the particular TGO thickness and the detailed shape of and microstructure at the interface.

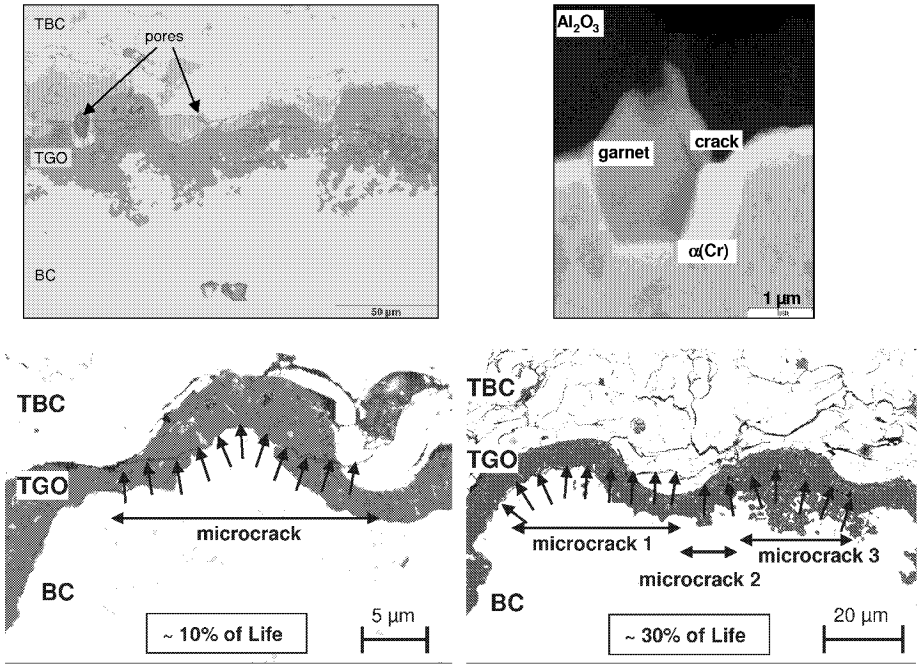

Figure. 7: Examples for microcrack formation at pores (top, left), at brittle yttria-alumina garnets at the bond coat / TGO interface (top, right), after initial growth at about 10% of life at the bond coat / TGO interface and through flanks of the TGO (bottom, left) and at about 30% of life, when cracks propagated through the TBC above roughness valleys and before individual cracks started to form links (bottom right).

For the development of the model approach it is assumed that the similarity of these frequently observed crack pattern results from a stochastic evolution of the microcrack population distributed along the interfacial region. The assumption comprises that the evolution of individual crack length values can be represented by mean or characteristic values of the length distribution independent from single cracks as it is displayed by the crack growth curve in Fig. 5.

One of the major questions is which parameters control the growth kinetics of the population of microcracks at the interface. Chang, Phucharoen and Miller [12] have already in the 80s analyzed the stress distribution in a plasma-sprayed TBC at the rough metal-ceramic interface

by means of FEM calculations. The stochastic roughness profile was approximated by a sinusoidal shape with a single amplitude and wavelength. In particular, the evolution of stress distribution with respect to thermal cycling and growth of the TGO has been studied. It has been shown that during thermal cycling the stress distribution along the interface is characterized by alternating regions of tensile and compressive stresses according to roughness peaks and roughness valleys. Compressive and tensile stresses result from different thermal expansion of TBC and bond coat in combination with the concave (peaks) and convex (valleys) curvature of the interface respectively. The interface can be stress free only at one single temperature. Provided that this temperature is equal to the maximum temperature of the thermal cycle (stress relaxation processes at high temperature may lead to this situation), the peak and valley regions in the TBC showed a characteristic stress distribution. Above roughness peaks out-of-plane tensile stresses and above valleys in-plane and out-of-plane compressive stresses occurred during cooling (out-of-plane = perpendicular to coating plane, in-plane = parallel to coating plane). That means that cracks can be opened under mode 1 load in the vicinity of peaks, but they are not able to penetrate roughness valleys because of local compressive stresses. The situation changed when the TGO got thicker. In this case, the stress state in the TBC was no longer determined by the higher CTE of the bond coat rather than by the lower CTE of the TGO. With increasing TGO thickness, local tensile stresses above roughness peaks decreased and were converted to compressive stresses, when the TGO exceeded a minimum thickness. A similar change but with opposite sign was obtained in the TBC above roughness valleys. Initial compressive stresses decreased with increasing TGO thickness and were converted into tensile stresses at the same TGO thickness value.

Therefore, the authors have deduced the following schematic damage evolution based on a strong correlation between growth kinetics of near-interface TBC cracks and the development of local stress distribution with increasing TGO thickness. Cracks are formed in the TBC above roughness peaks, when the TGO is thin, due to high mode 1 tensile stresses. At this early stage, the cracks cannot penetrate into the adjacent valley regions due to local compressive stresses, i.e. they are formed but their further growth is hindered. When the TGO exceeds a certain thickness, the compressive stresses above roughness valleys are converted into tensile stresses, the cracks can penetrate into the valley regions from both sides and can coalesce. This coalescence process along the interface would lead to macroscopic spallations. These results were confirmed by other authors, e.g. [13,14], and applied also for TGO cracks [15]. The present authors have shown [16] that the influence of creep stress relaxation lead to a more complex evolution of stresses near the TGO as a response to cyclic oxidation loading, but in principal it was concluded that the evolution of local tensile and compressive stress zones with increasing TGO thickness controls the growth kinetics of microcracks. Thus, the crack growth is directly linked to the TGO growth at least within the first stage of damage evolution, what is indicated also in Fig. 6.

Fig. 8 displays a schematic representation of crack evolution according to the current experimental observations. Cracks are formed in the TGO during stage 1 preferentially in mode 1 tensile stress regions. They propagate as far as they are stopped by adjacent compressive stresses. Their further growth is controlled by decreasing compressive stresses. The decrease of compressive stresses is controlled by the growth of the TGO. This interrelationship leads to the principal dependence of crack growth rate on the TGO growth rate.

Furthermore, a criterion for the end of stage 1, i.e. a criterion for the vanishing of compressive stresses over roughness valleys has to be formulated. Chang, Phucharoen and Miller [12] have shown that vanishing of compressive stress regions depends on TGO thickness relative to the roughness amplitude of the interface.

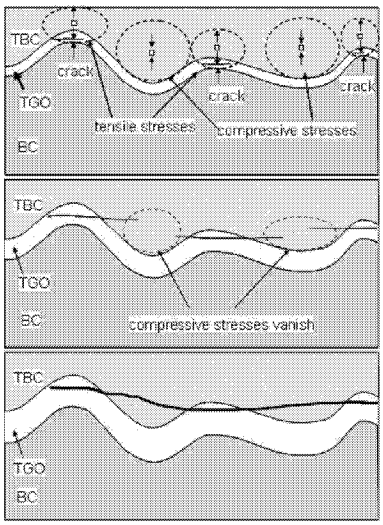

Stage 1:
Formation and initial growth of micro cracks, crack propagation is controlled by decreasing compressive stress values associated with the reduction of compressive stress regions.

Transition from stage 1 to stage 2:
Compression stresses vanish, a long range delamination path is enabled.

Stage 2:
Further crack growth partly in TBC, partly in TGO.

Figure 8: Schematic representation of crack development in plasma-sprayed thermal barrier coatings

The data in Figs. 5 and 6 shows that the transition from stage 1 to stage 2 is associated with a TGO thickness of about 9 µm. The experimentally determined technical roughness amplitude (R_z= measure for the peak-to-valley distance of a roughness profile) of the investigated specimen was about 30-40 µm. In case of a sinus function R_z is two times larger than the amplitude. The experimentally determined TGO thickness at the end of stage 1 was approximately a quarter of R_z. The criterion for the end of stage 1 is thus defined as:

Stage 1 ends, when:
$$d_{TGO} = \frac{R_z}{4} \cdot f(P_i) \qquad (3)$$

with d_{TGO} = TGO thickness e, R_z = technical measure for the roughness amplitude. $f(P_i)$ is a function which shall comprise the influence of the particular load parameters, because it is likely that the influence of a higher amount of thermal cycling or the contribution of cyclic TMF strains could accelerate the evolution of local tensile stresses and the decrease of local compressive stresses so that the TGO thickness at which the linking of individual cracks occur could be smaller. For the first model calculations $f(P_i)$ is set to 1.
The definition in Eq.(3) agrees with FEM calculations by Kerkhoff [13] and analytical results by Fuller [14]. It seems reasonable that the length of the longest crack at the transition point between stage 1 and stage 2 is approximately half of the mean wavelength of the roughness profile, thus the quantitative formulation for the crack growth during stage 1 is:

$$a(t) = \frac{\lambda_r}{2} \cdot \frac{d_{TGO}(t)}{R_z / 4} \qquad \text{for} \quad d_{TGO} < \frac{R_z}{4} \tag{4}$$

with a(t) = crack length, λ_r = mean wavelength of roughness profile.

Eq. (4) expresses that the length of the longest crack increases linearly with the TGO thickness and reaches a value of half of the mean wavelength of the roughness profile, when the TGO thickness equals a quarter of R_z. The evolution of TGO thickness is calculated using a power-law which was adjusted to the experimentally determined oxidation kinetics:

$$d_{TGO} = (k_p t)^{0,5} \tag{5}$$

with k_p = oxidation rate constant.

Another helpful relation can be derived from Eq. (3) by inserting the parabolic oxidation law from Eq. (5) into Eq. (3). It results in an expression for the duration of stage 1 and should be regarded in the following as incubation time (t_i):

$$t_i = \frac{R_z^2}{16\, k_p} \tag{6}$$

The incubation time provides a lower bound for the time-to-spallation of APS TBCs under oxidatizing conditions and can be used to estimate the service life in a conservative manner.

Stage 2: subsequent crack growth:
It has been shown that during cyclic oxidation, delamination cracks propagate partly in the TBC and partly in the TGO. In order to obtain crack growth data for delamination cracks in the TBC, wedge-crack-opening investigations have been carried out on separated TBCs. Details of the procedure will be published elsewhere. Some of the results are represented in Fig. 9. It was shown that slow crack growth of an in-plane crack at room temperature occurred when a load below the critical energy release rate was applied. The correlation between crack growth rate and energy release rate was characterized by a straight line in the log-log plot with a slope of approximately 17 (Fig. 9). After annealing for 100 h at 1000°C, the resistance against slow crack growth was increased. The resulting correlation was likewise characterized by a straight line, but with a slope of approximately 24.

These data were used to calculate the crack growth in stage 2 (when $d_{TGO} > R_z/4$) using a power-law correlation between crack propagation rate and energy release rate:

$$a(t) = \int_{t_0}^{t} \dot{a}\, dt = \int_{t_0}^{t} A \cdot G^n\, dt \qquad \text{for} \quad d_{TGO} > \frac{R_z}{4} \tag{7}$$

$\dot{a}$ = crack growth rate, A = numerical constant, G = energy release rate, n = exponent.

The energy release rate depends generally on the Young's modulus (E), the difference of CTE values ($\Delta\alpha$), the temperature range(ΔT), the fracture mechanical weight function (Y) and the crack length a:

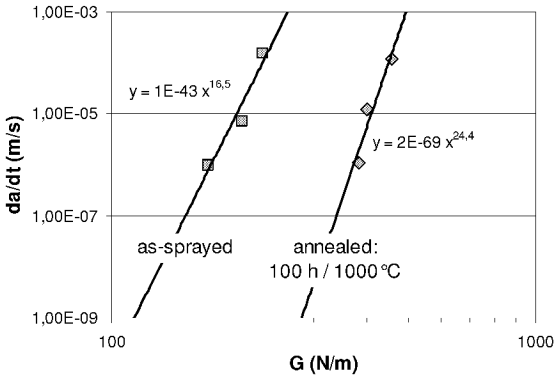

Figure 9: Crack growth rate vs. energy release rate of an in-plane crack in a plasma-sprayed TBC determined by wedge-crack-opening method at room temperature.

$$G = \frac{1}{2} \cdot E_{TBC,TGO}(T,t) \cdot (\Delta\alpha \cdot \Delta T)^2 \cdot Y^2 \cdot a \tag{8}$$

The load cycle, which is defined by upper and lower temperature, heating and cooling rate, dwell times at upper and lower temperature is subdivided in small time segments. For each time step the crack length increment Δa was calculated analytically using Eqs. (4), (5), (7) and (8). The crack length increments per loading step were than summed up for the complete loading cycle and afterwards for all loading cycles for stage 1 and stage 2 using a numerical software code, which has been developed for the present life-prediction concept. Failure occurred when the afore mentioned maximum crack length a_c was reached:

$$\sum_i \frac{a}{a_c} = 1 \tag{9}$$

with i = number of loading cycles, a = crack length, a_c = maximum crack length. The number of cycles i is related to time by the particular cycle definition including high temperature dwell-time as well as heating and cooling times. For the present calculations, the maximum crack length was defined as 1 mm. However, it became apparent that the maximum crack length value did not affect the life-time in a significant manner. This was due to the fact that close to failure at macroscopic crack length values the crack growth rate was comparably high and the time the crack needed to grow from e.g. 1 mm to 5 mm took just a negligible fraction of total life.

The present model for the life-time of thermal barrier coatings allows to study the influence of loading and material parameters on the time-to-failure. The input parameters were experimentally determined (oxidation data, slow crack growth data, CTE and elastic data, roughness amplitude and mean wavelength as well as the load cycle parameters, heating and cooling rate, maximum temperature, dwell time). The load cycle parameters were defined according to cyclic oxidation tests. The calculated life-time for an oxidizing temperature of

T_{max}=1050°C was than calibrated to the measured life at 1050°C by adjusting the fracture mechanical weight function.

Results for the temperature influence on the crack growth curves and thus on the life-time are represented in Fig. 10 (left). The time related to the steep rise at the end of the curve was almost identical to the life-time. The model was calibrated to the observed life-time of 936 h at 1050°C under cyclic oxidation conditions (shortest crack growth curve). The calibration affects generally the crack growth during stage 2, but not the incubation time (duration of stage 1). The incubation time depends only on the input parameters k_p and R_z without any calibration dependency and resulted from the calculations to about 612 h or 65% of the total calculated life-time. Stage 2 took accordingly 324 h or 35% of life-time. The effect of a temperature decrease (T_{max}= 950 and 1000°C) is represented by the two additional crack growth curves in Fig. 10 (left). For the variation of T_{max} no additional adjustment of the model has been done. Only the temperature dependence of the input parameters was used. The calculated life-time for T_{max}=1000°C was 2204 h, whereas the observed life-time was 1728 h. For T_{max}= 950°C a life-time of 12078 h was calculated, whereas no failure has been experimentally observed within 5000 h. However, the direct comparison of predicted and observed life-time is less informative than the relative factor of 13 for the life-time resulting from a temperature decrease of 100°C from 1050 to 950°C. Moreover, the model calculations provided the information that the effect of temperature decrease from 1050°C to 950°C on life-time increase was due to two parameters, namely the oxidation rate (k_p) and the magnitude of thermally induced strains ($\Delta\alpha\Delta T$). The effect of $\Delta\alpha\Delta T$ was slightly higher, than the effect of the oxidation rate.

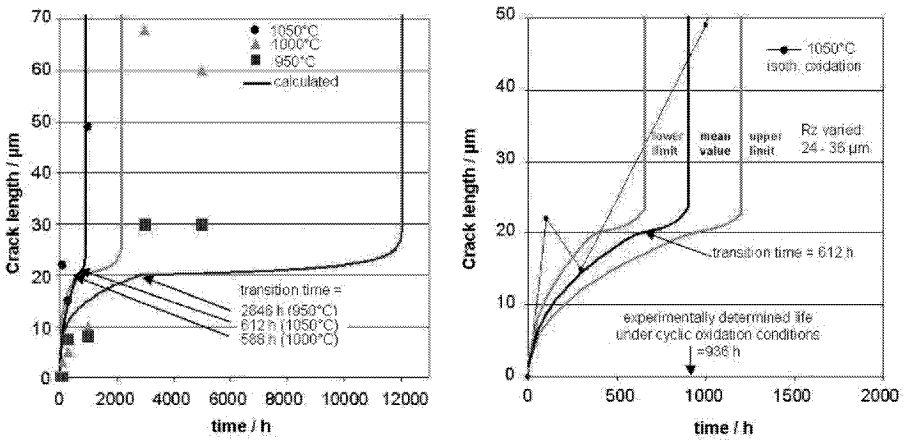

Figure 10, left: calculated effect of temperature on crack growth for cyclic oxidation loading; at first, the model was calibrated to cyclic oxidation data at T_{max}=1050°C, afterwards, the crack growth was predicted for T_{max}=1000 and 950°C; data points from isothermal oxidation tests are displayed for comparison; right: calculated effect of roughness amplitude on crack growth and life-time; the model was calibrated with R_z = 30 µm and crack growth was predicted for R_z = 24 (shorter life-time) and 36 µm (longer life-time).

The calculated influence of roughness amplitude (R_z) on life-time is represented in Fig. 10 (right) for a temperature of 1050°C. A roughness amplitude (R_z) of 30 µm ($R_a \approx 6$µm), has been taken as an experimentally determined input value for the calibration calculation shown in Fig. 10 (left). The variation of R_z from 24-36 µm led to a variation of total life from 694 h to 1244 h (t_i = 370 to 920 h), i.e. roughly ± 30%. This data might be also interpreted as a measure for the scattering in life time due to the stochastic character of the roughness profile.

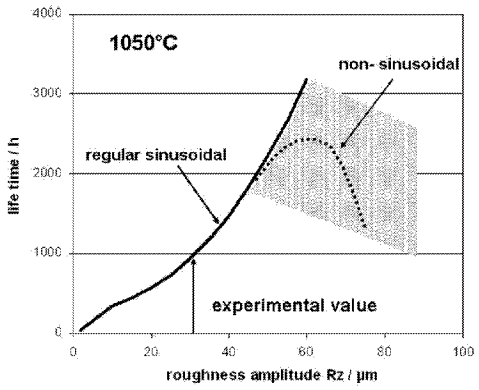

Figure 11: Calculated effect of roughness amplitude on life-time.

Another representation of the effect of roughness amplitude on life-time is displayed in Fig. 11. The calculated life-time is plotted against the roughness amplitude. The experimental roughness amplitude and respective life-time are marked. The calculation resulted in a monotonically increasing life with increasing roughness amplitude. In the range R_z=10-50 µm the life-time increased more than proportionally. However, it has been observed that roughness amplitudes higher than about R_z=50-60µm led to a decrease of life. This effect is indicated in Fig. 11 by the dotted line. It is assigned to increasing irregularities in the shape of the roughness profile, for instance undercuts of metal and ceramic material areas, which affect the beneficial recurrent sequence of local compressive stresses in a detrimental manner.

4. Summary and Conclusions

By comparing the damage after isothermal oxidation tests, cyclic oxidation tests, thermal cycling tests without a dwell-time at high temperature and thermal cycling tests with dwell-time at high temperature and a superimposed temperature gradient across the TBC by internal cooling the effect of loading conditions on the activation of different crack propagation paths was shown. After isothermal oxidation the delamination crack path was located predominantly in the TGO (black or adhesive failure), whereas after thermal cycling without a dwell-time at high temperature the delamination crack path was located predominantly in the TBC (white or cohesive failure). Cyclic oxidation loading (thermal cycling and high temperature dwell-time) resulted in a mixed-mode crack path that was located partly in the TGO and partly in the TGO (grey failure). It was concluded that oxidizing load conditions shift the crack path towards the TGO, whereas thermal cycling shifts the crack path towards the TBC.

Thermal cycling with dwell-time at high temperature (cyclic oxidation) plus a superimposed temperature gradient across the TBC showed delamination cracks in the TBC close to the TGO but also delamination cracks closer to the surface of the TBC and diagonally oriented macroscopic cracks. By comparison with damage after cyclic oxidation it can be concluded that a temperature gradient shifts the activated delamination crack path into the TBC.

Investigations about the damage evolution in APS TBCs using isothermal oxidation tests with increasing exposure time at 1050°C from 100 h up to spallation failure were carried out. It was shown by quantitatively analyzing the population of microcracks distributed along the TGO that spallation failure of APS TBCs is the final step of a continuous evolution and accumulation of damage. Generally, the microcracks showed a statistical distribution of their length values, which could be represented by a Gaussian number distribution over the crack length. The sequence of distribution curves for increasing exposure times revealed a continuous increase of the number density of microcracks along the TGO up to a fraction of 45% of time-to-spallation. At the same time the mean crack length increased only from 10 to 12 µm and the maximum crack length was limited to values below 40 µm. For exposure times > 45% of life-time individual cracks started to form links and the maximum crack length increased rapidly up to macroscopic values. A maximum crack length of 6 mm was observed for a fraction of 90% of time-to-spallation. The observed evolution of cracks suggested that the life-time is governed by the kinetics of crack formation, linking of individual cracks and crack growth. The shape of the crack growth curve revealed decelerated growth before and accelerated growth after 45% of life. The transition point corresponded with a TGO thickness of about 9 µm. Based on these results a general discrimination of two stages for the damage evolution in APS TBCs under oxidation conditions is proposed:
1. stage: Formation and initial, decelerated growth of microcracks: more and more micro cracks are formed along the TGO, but their growth is restricted to values below 50 µm. The TGO thickness was below 9 µm. This stage is regarded as incubation phase.
2. stage: Crack linking and accelerated crack growth: individual microcracks started to form links resulting in accelerated crack growth up to the exposure time at which macroscopic spallations occurred. The TGO thickness was larger than 9 µm. Spallation occurred at a TGO thickness of about 13 µm.

Based on these results a phenomenological life prediction model was developed. It comprises the calculation of crack growth for the incubation phase and the actual crack growth phase. The duration of the incubation phase (incubation time) is related to the oxidation kinetics and the roughness parameters, the calculation of crack growth during stage 2 is based on subcritical crack growth data for the ABS TBC and the calculation of a mean energy release rate as driving force. The transitional crack length was one half of the mean wavelength of the roughness profile according to experimental data. The current model state allowed to calculate for example the influence of T_{max} of cyclic oxidation loading, the influence of the oxidation rate as well as the influence of the roughness amplitude on the time-to-failure. The predictions of their respective influence on life-time are based on physical data, thus the predictions can be validated and used for ranking.

Acknowledgments
The authors gratefully acknowledge the support of Priv.-Doz. Dr. R. Vaßen by manufacturing the coatings at the Institute of Materials and Processes in Energy Systems, IWV 1 (now Institute of Energy Research, IEF 1) of Research Centre Juelich.

References

[1] R.A. Miller, C.E. Lowell. Failure mechanisms of thermal barrier coatings exposed to elevated temperatures. Thin Solid Films 95 (1982) 265-273.

[2] A. G. Evans, D. R. Mumm, J. W. Hutchinson, G. H. Meier and F. S. Pettit: Mechanisms controlling the durability of thermal barrier coatings, *Progress in Material Science* 46 5 (2001), 505-553

[3] L. Singheiser, R. Steinbrech, W.J. Quadakkers, D. Clemens, R. Herzog: Thermal Barrier Coatings – [Properties and Failure Mechanisms, Proceedings of NACE 2000, 26.-31.03.2000, Orlando, Paper No. 231

[4] R. Vaßen, G. Kerkhoff, D. Stöver: *Development of a micromechanical life prediction model for plasma sprayed thermal barrier coatings*, Materials Science and Engineering A303 (2001) 100-109.

[5] D. Renusch, H. Echsler and M. Schütze: Life Time Modeling of High Temperature Corrosion Processes, Workshop of the European Federation of Corrosion (EFC-Event No. 248), Frankfurt am Germany, Feb. 22,23 (2001), Eds. M. Schütze, W. J. Quadakkers, J. K.Nicholls, EFC-Publication No. 34, IoM Publication London (2001)

[6] W.J. Quadakkers, A.K. Tyagi, D. Clemens, R. Anton, L. Singheiser: The Significance of Bond Coat Oxidation for the Life of TBC Coatings, Elevated Temperature Coatings: Science and Technology III, Proceedings of the TMS Annual Meeting in San Diego, California, Feb 28 – Mar 4, 1999, 119-130

[7] E.P. Busso, J. Lin, S. Sakurai: A mechanistic study of oxidation-induced degradation in a plasma-sprayed thermal barrier coating system. Part II: life prediction model, Acta mater. 49 (2001) 1529-1536.

[8] A.M. Karlsson, J.W. Hutchinson, A.G. Evans: A fundamental model of cyclic instabilities in thermal barrier systems, Journal of the Mechanics and Physics of Solids 50 (2002) 1565-1589.

[9] J. Rösler, M. Bäker, K. Aufzug: A parametric study of the stress state of thermal barrier coatings, Part I: creep relaxation, Acta Materialia 52 (2004) 4809-4817.

[10] H. Echsler, D. Renusch, M. Schütze: Bond coat oxidation and its significance for life expectancy of thermal barrier coatings, Mat. Sci. Techn. 20 (2004) pp. 307–318.

[11] R. Herzog, P. Bednarz, E. Trunova, V. Shemet, R.W. Steinbrech, F. Schubert, L. Singheiser: Simulation of Stress Development and Crack Formation in APS-TBCs for Cyclic Oxidation Loading and Comparison with Experimental Observations, Proceedings of the 30th International Conference and Exposition on Advanced Ceramics and Composites, January 22-27, 2006, Cocoa Beach, to be published

[12] G.C. Chang, W. Phucharoen, R.A. Miller: Behaviour of Thermal Barrier Coatings for Advanced Gas Turbine Blades, Surface and Coatings Technology 30 (1987), 13-28

[13] G. Kerkhoff: Reports of Research Centre Jülich, Jül-3784, 2000

[14] E.R. Fuller, M.R. Locatelly: Fracture Mechanics Model of Damage Evolution in Air-Plasma-Sprayed Thermal Barrier Coatings, Proceedings of the 27th Annual International Conference on Advanced Ceramics & Composites, January 26-31, 2003, Cocoa Beach, Florida

[15] K.W. Schlichting, N.P. Padture, E.H. Jordan, M. Gell: Failure modes in plasma-sprayed thermal barrier coatings, Materials Science and Engineering A342 (2003) 120-130.

[16] R. Herzog, P. Bednarz, E. Trunova, V. Shemet, R.W. Steinbrech, F. Schubert, L. Singheiser: Simulation of Stress Development and Crack Formation in APS-TBCs for Cyclic Oxidation Loading and Comparison with Experimental Observations, Proceedings of the 30th International Conference and Exposition on Advanced Ceramics and Composites, January 22-27, 2006, Cocoa Beach

AUTHOR INDEX

A

Abe F, II 965, II 1019, II 1041
Affeldt E, II 633
Aguero A, II 949, III 1553
Allcock B, III 1553
Allen D J, III 1479
Andersson C, III 1503
Andren H O, III 1267
Ang J, II 655, II 691
Armaki H G, II 1157
Asahi H, II 1157
Auerkari P, III 1309, III 1385

B

Baker B A, III 1609
Banhart J, III 1651
Barnard P M, I 485
Batfalsky P, I 69
Bauer M, III 1341
Baune E, II 871
Bednarz P, II 747, III 1722
Bendick W, II 1065, II 1077
Berger C, II 1053, II 1137
Bernasovský P, I 261
Berreth K, III 1571
Bhanu Sankara Rao K, I 121
Białas M, II 747
Biede O, III 1503
Birnbaum U, I 161
Blackler M, I 485
Blum L, I 69
Blum R, I 41
Blum W, III 1241
Böck N, II 1031, III 1207
Bolt H, I 81
Bordenet B, GT103
Brabetz M, II 1031
Brekelmans W A M, II 595
Brózda J, III 1331
Brückner U, I 317, I 507
Brziak P, I 261, II 985
Buršík J, III 1449

C

Caminada S, II 871
Cappuccini F, II 717
Casu A, II 727
Cempura G, II 773, II 1077
Cerjak H, II 871, III 1191, III 1199, III 1217, III 1393
Chen Q, II 931
Chilukuru H, III 1181, III 1241
Cizner J, III 1461
Cui C, I 385
Czyrska-Filemonowicz A, I 485, II 773, II 1077

D

Dahl K V, II 675
Daleo J A, II 737
Danielsen H K, III 1251, III 1275
De Carlan Y, III 1319
De Maria L, I 217
Dechamps P, I 25
Del Genovese D, III 1651
Del Puglia P, II 829
Dhooge A, III 1369
Dietz W, III 1683
DiGianfrancesco A, II 843
Dinkel M, II 633
Doi H, I 355
Dong J, III 1609
Donth B, II 843
Du X, II 819
Dubiel B, I 485
Durham R, III 1553
Durst K, III 1181, III 1241

E

Efendi, I 561
El-Magd E, II 1147
Emura S, II 767
Ennis P J, III 1285, II 1077, III 1543, III 1651

Epishin A, I 205, I 317, I 475, I 507, I 521

F

Faulkner R G, II 1117, III 1299
Fedelich B, I 475
Feng D, I 533
Folkova E, III 1401
Foret R, III 1449
Fry A T, III 1469
Fudali S, III 1427, III 1491
Fujioka J, I 385
Fukui T, III 1589

G

Gabrel J, II 1065
Gajda B, II 1087
Gaude-Fugarolas D, III 1319
Gebhard J, II 1147
Geers M G D, II 595
Giannozzi M, II 699, II 707, II 717
Giorni E, II 645, II 699, II 707
Giovannetti I, II 699
Gohil D D, III 1533
Göken M, II 633, III 1181, III 1241
Golanski G, II 1087
Golpayegani A, III 1267
Goto N, I 561
Grumsen F, III 1251
Gu Y, I 385
Guan H R, I 413, II 627
Guo J T, I 189, I 393, I 403, I 435, I 447, II 819
Guo X G, I 403

H

Hagiwara M, II 767
Haibel A, I 521
Hake J F, I 161
Hakl J, I 365, II 985, III 1461
Hald J, II 917, II 675, III 1251, III 1275
Hansson A N, III 1663
Hanus R, II 855
Harada H, I 287, I 309, I 327, I 347, I 385, I 495, II 655, II 691
Harvey B, III 1479
Hashizume R, I 273
Hattori M, I 561
Heinemann J, III 1597
Heinz P, II 633
Helmrich A, II 931, III 1597
Henderson M B, III 1553
Henry J F, II 893
Hernas A, III 1357, III 1427, III 1491
Herzog R, II 747, III 1722
Hierro M P, III 1523
Höfinger S, II 1031
Holdsworth S R, I 91, III 1309
Holdway P, II 793
Holmström S, III 1309, III 1385
Holzer I, III 1191
Homkrajai W, I 377
Hou J S, I 393, I 435, I 447
Hu Z Q, I 189, I 413, II 627
Husemann R U, III 1597
Hussain K, II 737
Huysmans S, III 1369

I

Igarashi M, II 1095
Imai H, II 655, II 757
Imazato T, II 997
Imosa M, III 1491
Innocenti M, II 645
Iseda A, II 1095

J

Jandovà D, III 1401
Jensen S A, III 1503
Jin T, II 627
Jochum C, II 871, III 1341, III 1369

K

Kager F, II 1031
Kakehi K, I 299
Kan T, II 1095
Kanta V, III 1401
Kasl J, III 1401
Kauffmann F, III 1171
Kawagishi K, II 655, II 691
Kern T -U, II 843, II 855
Kilgallon P J, III 1513
Kimura K, II 1019, II 1105, III 1227

Kindratschuk V, III 1619
Kitashima T, I 495
Kiyono T, I 273
Klenk A, III 1341, III 1597
Klingelhöffer H, I 317
Kloc L, II 1011, II 1127
Knoedler R, III 1581
Kobayashi T, I 287, I 309, I 327, I 347, I 495
Koizumi Y, I 309, I 327
Komai N, II 997
Kondo Y, I 455, I 465
Kong S, I 549, I 555
Kothleitner G, III 1217
Koyabu H, I 299
Koyama T, I 561
Kozeschnik E, II 619, III 1191
Kuboň Z, III 1437
Kucharova K, II 1127
Kudrman J, II 1127
Kunecke G, I 475
Kupczyk J, II 1087
Kurita K, I 465
Kuroda S, I 541, II 757
Kushima H, II 1019, II 1105, III 1227

L

Lamm M, I 335
Lanese N, II 829
Lapin J, II 803
Lardon J M, III 1319
Larsen O H, III 1503, I 245
Lee J S, II 1157
Lefebvre B, II 1065
Li G, II 819
Li J, I 549, I 555
Li W, I 549, I 555
Li Y L, I 393, I 435
Li Z J, I 435
Link T, I 205, I 317, I 507, I 521
Linssen J, I 161
Liu J D, II 627
Lomozik M, III 1417
Lou L H, I 583
Lucas K, II 793
Lüdenbach G, III 1597
Luesebrink O, I 335
Lupinc V, II 607
Lyutovich A, III 1571

M

Mack D E, II 727
Maier H, I 81
Maile K, III 1171, III 1341, III 1571, III 1597
Makhele-Lekala L Z, III 1651
Maldini M, II 607
Mao Y, II 767
Marchant G, I 571
Marchionni M, I 423
Mareček J, II 803
Maresca P, II 645
Maruyama K, II 1157
Masset P, II 783
Masuyama F, I 175
Mathieu P, I 143
Matsumoto K, II 691
Matsuo H, II 1095
Matsuo T, I 455, I 465
Mayer K H, II 843, II 855, II 1053, III 1171
Mayr P, III 1393
McColvin G, I 571
Menzler N H, I 69
Meyr P, II 871
Minami Y, III 1589
Mitsche S, III 1199
Miura N, I 455, I 465
Montagnon J, III 1319
Montgomery M, I 245, III 1503, III 1663
Morinaga M, I 273, I 561
Moskal G, III 1357
Mukherji D, III 1619
Mülders B, III 1639
Müller M, II 665
Murakami H, I 541, II 757
Muraki T, II 1157
Murakumo T, I 287
Murata Y, I 273, I 561

N

Nazmy M, I 205
Nicholls J R, III 1696
Nieto J, III 1523
Nisaratanaporn E, I 377
Norton B, III 1553

O

Oakey J, I 233, III 1513
Ohata H, I 347
Onofrio G, I 423
Osgerby S, I 217, III 1469, III 1533
Osinkolu G A, I 423
Ott M, II 633
Over H H, III 1683

P

Pasternak J, II 871, III 1331, III 1357, III 1427, III 1491
Patel S J, III 1609
Pein C, II 619
Pelachová T, II 803
Penkalla H J, II 773, III 1629
Pérez F J, III 1523
Ping D, I 385, I 495
Pirón Abellán J, III 1285
Polsilapa S, I 377
Portella P, I 317
Pratesi F, II 645, II 699, II 707, II 717
Pyczak F, II 633

Q

Qin X Z, I 435, I 447
Quadakkers W J, III 1285, III 1543, III 1722

R

Raj B, I 121
Rajek J, III 1191
Rechberger W, III 1217
Rinaldi C, I 217
Ro Y, I 347
Rohr V, III 1543
Roos E, III 1341
Rösler J, III 1619
Ruoff H, III 1171

S

Sakai T, I 541
Salonen J, III 1385
Sato A, I 287, I 385, II 655, II 691
Sawada K, II 1105, III 1227
Scarlin B, II 931
Scheefer M, III 1553
Scheu C, III 1171
Scholz A, II 1053, II 1137
Schubert F, II 773, III 1629, III 1639, III 1651, III 1722
Schütze M, II 783, III 1543
Schwienheer M, II 1137
Seibert T, III 1181
Semba H, II 1041
Shao C, I 549, I 555
Shibata M, I 541
Shingledecker J P, I 107, II 893
Simms N J, III 1513
Singer R F, II 633, I 335
Singheiser L, III 1285, III 1629, III 1722
Sklenicka V, II 1011, II 1127
Smith G D, III 1609
Sonderegger B, III 1199, III 1217
Sopoušek J, III 1449
Spindler M W, III 1673
Spiradek-Hahn K, II 1031
Stachura S, II 1087
Stamatelopoulos G, II 931
Stanko G, II 893
Staubli M, I 205, II 843, II 855
Steinbrech R, I 69, III 1722
Stöver D, II 727
Strang A, I 571, III 1251
Straub S, III 1171, III 1581
Stuhrmann J, II 1147
Sun C, I 583
Sun X F, I 413, II 627
Suzuki A, II 757
Suzuki T, I 309
Svoboda M, II 1127

T

Tamaki H, I 355
Tanaka F, I 465
Tanzosh J, II 893
Tasak E, III 1417, III 1427
Terzigli V, II 645
Theofel H, III 1597
Tinga T, II 595
Toda Y, II 1019, II 1105
Toshiharu K, II 655

Toušová D, III 1437
Traeger F, II 727
Trunova O, III 1722
Tschaffon H, I 61
Tsuno N, I 299
Tsipas D N, III 1553

V

Vandenberghe B, II 1065, II 1077, III 1369
Vanstone R W, I 41
Vaßen R, II 727
Vekeman J, III 1369
Viswanathan R, II 893
Vitalis B, II 893
Vlasák T, I 365, II 985
Vodarek V, III 1251, III 1437
Volek A, I 335, II 633
Vossberg A, II 633

W

Wabderka N, III 1651
Walbeck M, I 161
Wall G, I 5
Wang L, I 583
Wang Y, II 1053
Wang Y L, I 413
Wang Z H, II 627
Wangyao P, I 377
Weber T, II 855, III 1543
Wenglarz R, I 233
Wessel E, III 1639, III 1722
Willer D, III 1171
Wisbey A, II 793
Wright I G, I 107
Wu J, I 549, I 555
Wu Y N, II 757

X

Xie G, I 583
Xie X, III 1609
Xu G, I 533

Y

Yamaguchi A, I 541, II 757
Yang H C, I 403
Yang J X, I 413
Yardley V, III 1319
Ye H Q, I 435, I 447
Yeh A C, I 287
Yin Y F, II 1117, III 1299
Yokokawa T, I 287, I 309, I 327, I 347
Yoshinari A, I 273, I 355
Yoshizawa M, II 1095
Yuan C, I 393, I 403, I 447
Yutaka K, II 655

Z

Zabler S, I 521
Zeiler G, II 843, II 1031
Zeman M, III 1331
Zhang B, I 533
Zhang J, I 287, I 583
Zhao G, I 533
Zhao M, I 549, I 555
Zhao N R, II 627
Zhao S, III 1609
Zheng Q, I 413
Zhou L Z, I 435
Zielińska-Lipiec A, II 1077
Zies G, III 1171
Zifcak P, II 985
Zlámal B, III 1449
Zonfrillo G, II 699, II 707, II 717, II 829
Zrnik J, I 377
Zschau H E, II 783

KEYWORD INDEX

(Nb,V) CrN particles: III.1251
10Cr steels: II.843
12% Cr steel: II.1077, III.1285, III.1369
12CrMoVNbN steels: III.1251
3DAP: III.1619
5th generation Ni-base superalloys: II.655
6025HT: II.1147
9% Cr steels: III.1393, III.1553
9% Cr cast steel: II.855
9% Cr martensitic steel: II.1041
9-12% Cr steels: II.917, III.1207, II.1031, II.1065, II.1127, II.1137, III.1181, III.1199, III.1241, III.1267, III.1275, III.1357, III.1543
9-12Cr ferritic steels: I.107
Acoustic emission: II.727
Activation energy: I.533
AD700: I.41
Advanced creep laws: III.1341
Advanced power plant materials: III.1479
Advanced power plants: I.143
AFM: III.1181
Allowable stress: II.1095
Alloy 617 welds: III.1597
Alloy 617: III.1597, III.1639
Alloy composition: I.347
Alloy design: II.917
Alloy-80A: I.91
Alloys: III.1683
Alternating atmospheres: III.1533
Aluminising: I.541, II.757, III.1553
Analysis routines: III.1683
Analytical TEM: II.1077
Anisotropy: I.299
Application: I.161, II.855
APS: II.717
Atom-probe field-ion microscopy: I.495
Bainitic structure: II.1087
Biomass: I.245, III.1513
Blading: I.205
Boiler tube: III.1589
Boiler: I.41, II.931
Boron alloyed: III.1393
Boron: II.917, II.965, II.1031
Brazing: II.633
Burgers vectors: I.465
Burner rig test: II.727
Carbides: I.393, I.413, II.985
Carbon and nitrogen redistribution: III.1449
Cast steel: II.1087
CDM modelling: III.1299
Ceramic matrix composites: II.829
Ceramic membranes: I.143
Chemistry modification: III.1619
Chlorination: I.245
Chromium steel: III.1461, III.1469
CM186LC: I.485
CMSX-10: I.507
CMSX-4: I.317, I.507
CO_2 capture: I.143
CO_2 emissions mitigation: I.143
CO_2: I.25
Coal: III.1513
Coarsening of laves phase: II.1157
Coatings: I.217, I.583, II.707, II.737, II.893, II.949
Co-firing: I.245, III.1503, III.1513
Co-free: I.309
Cohesive zone modelling: II.747
Compositional modification: II.767
Conceptual design: II.893
CoNiCrAlY: I.541
Constitutive equation: II.607, III.1341, III.1651
Constitutive model: II.595, III.1207
Conventional Casting (CC): I.355
Cooling time: III.1417
Corrosion resistance: II.893, III.1427, III.1491
Corrosion: III.1533, III.1683
COST536: II.843, II.855
CPFBC: II.665
Crack growth: I.413
Crack initiation: I.403, III.1639
Crack propagation: I.403

Crack: I.393
Cr-diffusion: III.1663
Creep behaviour 11-12% CrWCo(Cu)B(V,Ta,T) steels: II.1053
Creep behaviour: II.1127
Creep damage: II.1117, III.1299, III.1673
Creep equations: II.1137
Creep failure: I.175
Creep fatigue: II.1137
Creep properties: I.365, II.871, II.985, II.1065
Creep rate: II.1117
Creep resistance: II.855, III.1171
Creep resistant steel: II.1011, III.1217, III.1449
Creep resisting steels: III.1331
Creep rupture: II.627, II.1137
Creep strain: II.1117
Creep strength: I.273, II.843, III.1267
Creep testing: III.1401
Creep: I.107, I.287, I.299, I.317, I.455, I.475, I.485, I.507, I.521, II.607, II.619, II.767, II.965, II.1019, II.1031, II.1041, II.1077, II.1105, III.1309, III.1319, III.1369, III.1381, III.1437, III.1479
Creep-fatigue: III.1673
Creep-resistance: III.1357
Cr-steel: III.1319
Crystal growth: II.803
Crystal plasticity: II.595
CVD: III.1571
Cyclic strain: I.403
Damage parameter: III.1341
Damage: III.1639
De-cohesion: II.747
Deformation mechanism: II.819
Degradation: I.205, I.571
D-electrons concept: I.273
Delta ferrite: II.1105, III.1393
Development of FBR materials: I.121
DICTRA: II.675
Diffusion coatings: III.1543
Diffusion coefficient: I.561
Diffusion: II.619, II.633
Directional solidification: I.335
Directionally solidified (DS): I.355
Disk application: I.385
Dislocation dynamics: III.1207
Dislocation Substructure: I.465
Distribution: I.161
Document management system: III.1683
Documentation database: III.1683
Dynamic recrystallisation: I.533
EBSD: II.633, III.1199
ECCC Data sheets: I.91
ECCC: III.1309
Ecological engineering: I.5
EFTEM: III.1217
Electrochemical impedance: III.1523
Electron diffraction: III.1251
Energy alternatives: I.121
Energy and natural resources: I.5
Energy supply chain: I.161
Energy: I.25
Energy-filtered TEM: III.1267
Environmental effect: I.423
Environmental sciences: I.5
Equilibrium: II.691
Esshete 1250: III.1503
European Commission: I.25
Exergy: I.5
Experience: II.855
Experimental data: III.1683
ExtreMat Integrated Project: I.81
Fatigue and creep fatigue crack growth: III.1629
Fatigue crack propagation: I.423
Fatigue: I.317, I.335, II.793
Ferrite matrix: II.1019
Ferritic steel: I.69, II.985, III.1299, III.1309, III.1401
Ferritic/austenitic steels: II.949
Filler metals matching to T/P 23, T/P 24, VM 12, Cost CB 2: II.871
Fireside corrosion: III.1503, III.1513
Flame thermal cycling: II.707
Flow behaviour: I.533
Flue gas desulphurisation plants: III.1427, III.1491
Fossil fuels: I.25
Free energy: I.447
Frequency-Scanning Eddy Current: I.217
Furnace cooling: II.1019

Gamma channel: I.455
Gamma prime: I.205, II.737
Gamma prime precipitate: I.435, I.447, I.465
Gamma TiAl: II.773, II.793
Gas turbine: I.189, I.217, I.423, II.665, II.737
GH2984 superheater alloy: I.189
GH690 alloy tube: I.189
Glass ceramics: I.69
Grade 92 steel: I.91, II.1157
Grain boundary sliding: II.819
Growth stresses: III.1663
HI.2530: I.571
Halogen effect: II.783
Hardness: I.571
Hastelloy alloys: III.1427
HAZ-toughness: III.1393
HCM12: II.1095
Heat affected zone: III.1417
Heat exchanger materials: III.1543
Heat exchanger: III.1513
Heat resistant alloy: I.175
Heat treatment: I.435, II.803, II.997, III.1191
Heterogeneous creep: II.1095
Heterogeneous weld: III.1437
High alloy steel: III.1479
High chromium ferritic steel: II.1105
High efficiency power plant: III.1597
High heat flux materials: I.81
High temperature corrosion: I.245, III.1543
High temperature materials: I.189
High temperature properties: II.655
High temperature: I.61, II.645, II.707, II.717, II.949
High-temperature application: II.843
Homogenisation: I.335
Hot corrosion resistance: I.273
Hot corrosion resistant superalloys: I.189
Hot corrosion: II.665
Hot isostatic pressing (HIP): I.377
Hot working: I.533
Hydrogen effects: III.1663
Hydrogen generation: I.161
Impact energy: II.1087
Implantation: II.783
IN706: III.1619
Inconel 617: III.1651
Inconel 740: III.1609
Industrial gas turbine: I.485
Influence of multiaxiality of the stress state: III.1341
In-situ observation in SEM: III.1639
Interdiffusion: II.675, II.691
Intergranular fracture: II.1157
Intermetallic compound: II.1019
Intermetallic: II.773
Intermittent heating: II.1127
Issues: I.233
K418 superalloy turbine: I.549
K4537 turbine: I.555
K465 cast superalloy: I.413
Laminate: II.829
Larson-Miller parameter: I.327
Laser back-Scattering: I.217
Laser cladding: II.699
Lattice misfit: I.287, I.309
Laves phases: III.1285
LCF: II.773
Life prediction: II.1105
Life: III.1381
Lifetime extension: I.261
Lifing: I.365
Liquid erosion: II.699
Liquid metal cooling: I.335
Long term aging: I.447
Long term exposure: I.377
Long-term creep strength: II.1105
Long–term creep: I.327, III.1227
Low activation materials: I.81
Low alloy steel: II.997, II.1011
Low alloy steels: III.1533
Low cycle fatigue: I.403, I.423, II.1147
Low stress creep: II.1011
LPPS: I.541
M23C6 carbide: I.447, II.965, II.1041
MA 6000: II.645
Martensite: III.1199, III.1417
Martensitic microstructure: II.965
Martensitic phase: II.1019
Material compatibility: I.69

Material development: II.843
Materials database: III.1683
Materials properties data: III.1683
Materials: I.41, I.233, II.931
Mathematical models: I.365
MCrAlY: II.675
Mechanical properties data: III.1683
Mechanical properties of weld joints: III.1357
Mechanical properties: I.347, I.555, II.803, II.871, II.893
Microhardness: I.435
Micromechanics: II.595
Microporosity: I.521
Microstructural changes: II.1127
Microstructural evolution: III.1299
Microstructural parameter: I.347
Microstructural stability: II.1041
Microstructure and modelling: II.917
Microstructure evolution: III.1191
Microstructure: I.507, I.571, II.619, II.767, II.803, II.985, II.1031, II.1077, III.1181, III.1393, III.1401, III.1427, III.1437, III.1491, III.1619
Minimum creep rate: II.997
Mismatched weld materials: III.1341
Mod. Z-phase: III.1217
Model: III.1309
Modelling: I.261, I.475, II.619, III.1469
Modified Z phase: III.1251
Molten salt corrosion: III.1523
Morphological evolution: I.447
Morphology instability: I.435
Multiphase nickel aluminides: II.803
MX and M2X Phase: III.1241
MX carbonitride: II.965
MX precipitates: III.1285
MX: II.1041
Nanoindentation: II.633
NDE: I.217, I.261
Neural network: III.1319, III.1469
Ni-31Cr-3 Mo (Dy) alloy: II.819
Ni-base single crystal superalloy: I.287, I.309, I.347
Ni-base superalloy: I.327, I.385, II.757
Ni-based alloy: I.107, I.561
Ni-based superalloy: I.273, I.299, I.377, I.423, I.455, I.465, I.475, I.533, I.541, I.583
Nickel alloys: III.1491
Nickel based materials: I.61
Nickel content: II.1019
Nickel-base single-crystal superalloy: I.495
Ni-Co-base superalloy: I.385
Ni-YSZ cermet: I.69
Non-conventional sand case: I.549
Non-destructive evaluation: II.1157
Nuclear fission: I.81
Nuclear power programme: I.121
Nuclear technology: I.121
Numerical simulation: I.549, I.555
ODS: II.645
Omega method: II.1117
Outlet header: III.1597
Oxidation resistance: III.1571, I.273, I.287, II.691, II.949
Oxidation: I.107, I.393, I.413, II.645, II.655, II.783, II.793, II.997, III.1461, III.1479
Oxide growth: III.1469
Oxide scale: III.1581
Oxyfuel: I.143
P122: II.1095
P23 steel: III.1437
P91 steel: III.1417, III.1437
P92 steel: II.1147
Pack cementation: III.1543
Partitioning ratio: I.309
PBMR: I.309
Phase computation: III.1609
Photo-luminescence piezospectroscopy: I.217
Plasma facing materials: I.81
Plastic properties: III.1417
PM 3030: II.645
Porosity: III.1319
Power generation: III.1331, III.1357
Power plant: I.61, I.175, III.1369, II.985
PPCC: II.665
Precipitates: III.1217
Precipitation analysis: III.1171
Precipitation kinetics: III.1191
Precipitation site: III.1227

Premature breakdown of creep strength: II.1157
Primary creep: I.299, II.1011
Processing: II.1065
Protective coatings: III.1553
Pt-Ir alloy: II.757
R5: III.1673
Rafting: I.475
Recovery: II.1019
Recrystallization (RX): I.583
Regenerative heat treatment: II.1087
Regression analysis: I.347
Remanent life: II.1117
Research: I.25
Rhenium: I.561
Ruthenium or Iridium addition: I.495
Ruthenium: I.561
SAGBO effect: III.1629
Sandwich-structures: II.1147
Second generation: I.327
SEM and TEM: III.1629
SEM: III.1181, III.1619
Short-range ordering: I.495
Shot peening: I.583, III.1581
Shot-blasted tube: III.1589
Shroud: II.829
Si: II.655
Siliconising: III.1571
Simulation of diffraction patterns: III.1251
Simulation: III.1191, III.1207
Single crystal superalloy: I.335
Single crystal: I.205, I.299, I.317, I.327, I.455, I.465, I.475, I.485, II.737
Single crystalline: II.633
Single-crystal superalloy: II.627
Size distribution: III.1217
Slip system: I.455
SNMS: III.1285
Solid oxide fuel cell: I.69
Spallation: III.1581
Sputtering: II.757
SRZ: II.691
Stainless steel: III.1589
Steam environment: III.1461
Steam oxidation: I.175, III.1285, III.1553, III.1581, III.1589, III.1663
Steam power plant: I.261, II.931, II.949
Steam side oxidation: II.1065
Steam turbine: I.41
Steam: III.1469
Steamside oxidation and resistance: II.893
Steamside oxidation: III.1503
Steel tubes: III.1571
Steel: III.1381
Stellite: II.699
Storage: I.161
Strain rate: III.1651
Strain: III.1309
Straw: I.245
Strength: III.1381
Stress analysis: II.829
Stress and/or strain effect: III.1227
Stress exponent: II.1011
Stress: II.619
Structural analyses: II.773, III.1449
Structural stability: III.1357
Structure analysis: I.377
Structure degradation: I.377
Structure stability: III.1609
Superalloy: I.205, I.317, I.355, I.365, I.393, I.435, I.507, I.521, II.595, II.607, II.645, II.675, II.699, III.1609
Supercritical: II.931
Superheater tubes: III.1597
Superplasticity: II.819
Surfaces: III.1581
Sustainable development: I.5
Syngas: I.233
T/P23: II.997
T122: II.1095
TBC: II.717
TCP phase: I.541
TEM: III.1171, III.1181, III.1401, III.1619
Temperature estimation: II.737
Tensile test: III.1651
Testing: III.1479
Thermal analysis: II.829
Thermal barriers: II.707
Thermal barrier coating: II.727
Thermal cycles: II.717
Thermal cycling: II.727, II.747
Thermal exposure: II.793

Thermal fatigue: I.175, I.393, I.413
Thermal mechanical fatigue: I.347
Thermal shock: II.707
Thermal spraying: III.1553
Thermal welding cycle: III.1417
Thermo mechanical fatigue: I.287
Thermodynamic and kinetic modelling: III.1449
Thermodynamic modelling: II.665
Thermo-physical properties data: III.1683
Ti2AlNb: II.767
Ti6242: II.773
TiAl: II.783
Titanium alloy: II.767
TLP bonding: II.627
Tomography: I.521
TP347H FG: III.1503
Tungsten: I.561
Turbine: I.233, I.365, II.699
Type 316H: III.1673
U720Li: I.385
Ultrasupercritical: I.107
USC plant: III.1589
USC: III.1609
Variable creep loading: II.1127
VM12: II.1065, II.1077, III.1369
VN precipitation: III.1319
Wallpapering: III.1491
Waspaloy: III.1629
Waste incineration: III.1523
Water quenching: II.1019
Web-enable data: III.1683
Web-services: III.1683
Weld joints: III.1449
Weld: III.1381
Weldability: II.855, II.893, III.1331
Welded joints: III.1331
Welding of pipe E911: II.871
Welding: III.1369, III.1401
Woodchip: I.245
Wrought Ni-based superalloy: I.403
YH61: I.355
Z phase: II.917, III.1171, III.1227, III.1241, III.1267, III.1275
Zirconia: II.717

Schriften des Forschungszentrums Jülich
Reihe Energietechnik / Energy Technology

1. **Fusion Theory**
   Proceedings of the Seventh European Fusion Theory Conference
   edited by A. Rogister (1998); X, 306 pages
   ISBN: 3-89336-219-3

2. **Radioactive Waste Products 1997**
   Proceedings of the 3rd International Seminar on Radioactive Waste Products held in Würzburg (Germany) from 23 to 26 June 1997
   edited by R. Odoj, J. Baier, P. Brennecke et al. (1998), XXIV, 506 pages
   ISBN: 3-89336-225-8

3. **Energieforschung 1998**
   Vorlesungsmanuskripte des 4. Ferienkurs „Energieforschung“
   vom 20. bis 26. September 1998 im Congrescentrum Rolduc und
   im Forschungszentrum Jülich
   herausgegeben von J.-Fr. Hake, W. Kuckshinrichs, K. Kugeler u. a. (1998),
   500 Seiten
   ISBN: 3-89336-226-6

4. **Materials for Advances Power Engineering 1998**
   Abstracts of the 6th Liège Conference
   edited by J. Lecomte-Beckers, F. Schubert, P. J. Ennis (1998), 184 pages
   ISBN: 3-89336-227-4

5. **Materials for Advances Power Engineering 1998**
   Proceedings of the 6th Liège Conference
   edited by J. Lecomte-Beckers, F. Schubert, P. J. Ennis (1998),
   Part I XXIV, 646, X pages; Part II XXIV, 567, X pages; Part III XXIV, 623, X pages
   ISBN: 3-89336-228-2

6. **Schule und Energie**
   1. Seminar Energiesparen, Solarenergie, Windenergie. Jülich, 03. und 04.06.1998
   herausgegeben von P. Mann, W. Welz, D. Brandt, B. Holz (1998), 112 Seiten
   ISBN: 3-89336-231-2

7. **Energieforschung**
   Vorlesungsmanuskripte des 3. Ferienkurses „Energieforschung“
   vom 22. bis 30. September 1997 im Forschungszentrum Jülich
   herausgegeben von J.-Fr. Hake, W. Kuckshinrichs, K. Kugeler u. a. (1997),
   505 Seiten
   ISBN: 3-89336-211-8

8. **Liberalisierung des Energiemarktes**
   Vortragsmanuskripte des 5. Ferienkurs „Energieforschung"
   vom 27. September bis 1. Oktober 1999 im Congrescentrum Rolduc und
   im Forschungszentrum Jülich
   herausgegeben von J.-Fr. Hake, A. Kraft, K. Kugeler u. a. (1999), 350 Seiten
   ISBN: 3-89336-248-7

9. **Models and Criteria for Prediction of Deflagration-to-Detonation Transition (DDT) in Hydrogen-Air-Steam-Systems under Severe Accident Conditions**
   edited by R. Klein, W. Rehm (2000), 178 pages
   ISBN: 3-89336-258-4

10. **High Temperature Materials Chemistry**
    Abstracts of the 10th International IUPAC Conference, April 10 - 14 2000, Jülich
    edited by K. Hilpert, F. W. Froben, L. Singheiser (2000), 292 pages
    ISBN: 3-89336-259-2

11. **Investigation of the Effectiveness of Innovative Passive Safety Systems for Boiling Water Reactors**
    edited by E. F. Hicken, K. Verfondern (2000), X, 287 pages
    ISBN: 3-89336-263-0

12. **Zukunft unserer Energieversorgung**
    Vortragsmanuskripte des 6. Ferienkurs „Energieforschung"
    vom 18. September bis 22. September 2000 im Congrescentrum Rolduc und
    im Forschungszentrum Jülich
    herausgegeben von J.-Fr. Hake, S. Vögele, K. Kugeler u. a. (2000),
    IV, 298 Seiten
    ISBN: 3-89336-268-1

13. **Implementing Agreement 026**
    For a programme of research, development and demonstration on advances fuel cells
    Fuel Cell Systems for Transportation
    Annex X. Final Report 1997 - 1999
    edited by B. Höhlein; compiled by P. Biedermann (2000), 206 pages
    ISBN: 3-89336-275-4

14. **Vorgespannte Guß-Druckbehälter (VGD) als berstsichere Druckbehälter für innovative Anwendungen in der Kerntechnik**
    Prestressed Cast Iron Pressure Vessels as Burst-Proof Pressure Vessels for Innovative Nuclear Applications
    von W. Fröhling, D. Bounin, W. Steinwarz u. a. (2000) XIII, 223 Seiten
    ISBN: 3-89336-276-2

15. **High Temperature Materials Chemistry**
Proceedings of the 10th International IUPAC Conference
held from 10 to 14 April 2000 at the Forschungszentrum Jülich, Germany
Part I and II
edited by K. Hilpert, F. W. Froben, L. Singheiser (2000), xvi, 778, VII pages
ISBN: 3-89336-259-2

16. **Technische Auslegungskriterien und Kostendeterminanten von SOFC- und PEMFC-Systemen in ausgewählten Wohn- und Hotelobjekten**
von S. König (2001), XII, 194 Seiten
ISBN: 3-89336-284-3

17. **Systemvergleich: Einsatz von Brennstoffzellen in Straßenfahrzeugen**
von P. Biedermann, K. U. Birnbaum, Th. Grube u. a. (2001), 185 Seiten
ISBN: 3-89336-285-1

18. **Energie und Mobilität**
Vorlesungsmanuskripte des 7. Ferienkurs „Energieforschung“
vom 24. September bis 28. September 2001 im Congrescentrum Rolduc und im Forschungszentrum Jülich
herausgegeben von J.-Fr. Hake, J. Linßen, W. Pfaffenberger u. a. (2001), 205 Seiten
ISBN: 3-89336-291-6

19. **Brennstoffzellensysteme für mobile Anwendungen**
von P. Biedermann, K. U. Birnbaum, Th. Grube u. a. (2002)
PDF-Datei auf CD
ISBN: 3-89336-310-6

20. **Materials for Advances Power Engineering 2002**
Abstracts of the 7th Liège Conference
edited by J. Lecomte-Beckers, M. Carton, F. Schubert, P. J. Ennis (2002), c. 200 pages
ISBN: 3-89336-311-4

21. **Materials for Advanced Power Engineering 2002**
Proceedings of the 7th Liège Conference
Part I, II and III
edited by J. Lecomte-Beckers, M. Carton, F. Schubert, P. J. Ennis (2002), XXIV, 1814, XII pages
ISBN: 3-89336-312-2

22. **Erneuerbare Energien: Ein Weg zu einer Nachhaltigen Entwicklung?**
Vorlesungsmanuskripte des 8. Ferienkurs „Energieforschung“
vom 23. bis 27. September 2002 in der Jakob-Kaiser-Stiftung, Königswinter
herausgegeben von J.-Fr. Hake, R. Eich, W. Pfaffenberger u. a. (2002), IV, 230 Seiten
ISBN: 3-89336-313-0

23. **Einsparpotenziale bei der Energieversorgung von Wohngebäuden durch Informationstechnologien**
von A. Kraft (2002), XII, 213 Seiten
ISBN: 3-89336-315-7

24. **Energieforschung in Deutschland**
Aktueller Entwicklungsstand und Potentiale ausgewählter nichtnuklearer Energietechniken
herausgegeben von M. Sachse, S. Semke u. a. (2002), II, 158 Seiten, zahlreiche farb. Abb.
ISBN: 3-89336-317-3

25. **Lebensdaueranalysen von Kraftwerken der deutschen Elektrizitätswirtschaft**
von A. Nollen (2003), ca. 190 Seiten
ISBN: 3-89336-322-X

26. **Technical Session: Fuel Cell Systems of the World Renewable Energy Congress VII**
Proceedings
edited by D. Stolten and B. Emonts (2003), VI, 248 pages
ISBN: 3-89336-332-7

27. **Radioactive Waste Products 2002 (RADWAP 2002)**
Proceedings
edited by R. Odoj, J. Baier, P. Brennecke and K. Kühn (2003), VI, 420 pages
ISBN: 3-89336-335-1

28. **Methanol als Energieträger**
von B. Höhlein, T. Grube, P. Biedermann u. a. (2003), XI, 109 Seiten
ISBN: 3-89336-338-6

29. **Hochselektive Extraktionssysteme auf Basis der Dithiophosphinsäuren: Experimentelle und theoretische Untersuchungen zur Actinoiden(III)-Abtrennung**
von S. A. H. Nabet (2004), VI, 198 Seiten
ISBN: 389336-351-3

30. **Benchmarking-Methodik für Komponenten in Polymerelektrolyt-Brennstoffzellen**
von Matthias Gebert (2004), 194 Seiten
ISBN: 3-89336-355-6

31. **Katalytische und elektrochemische Eigenschaften von eisen- und kobalthaltigen Perowskiten als Kathoden für die oxidkeramische Brennstoffzelle (SOFC)**
von Andreas Mai (2004), 100 Seiten
ISBN: 3-89336-356-4

Schriften des Forschungszentrums Jülich
Reihe Energietechnik / Energy Technology

32. **Energy Systems Analysis for Political Decision-Making**
edited by J.-Fr. Hake, W. Kuckshinrichs, R. Eich (2004), 180 pages
ISBN: 3-89336-365-3

33. **Entwicklung neuer oxidischer Wärmedämmschichten für Anwendungen in stationären und Flug-Gasturbinen**
von R. Vaßen (2004), 141 Seiten
ISBN: 3-89336-367-X

34. **Neue Verfahren zur Analyse des Verformungs- und Schädigungsverhaltens von MCrAlY-Schichten im Wärmedämmschichtsystem**
von P. Majerus (2004), 157 Seiten
ISBN: 3-89336-372-6

35. **Einfluss der Oberflächenstrukturierung auf die optischen Eigenschaften der Dünnschichtsolarzellen auf der Basis von a-Si:H und µc-Si:H**
von N. Senoussaoui (2004), 120 Seiten
ISBN: 3-89336-378-5

36. **Entwicklung und Untersuchung von Katalysatorelementen für innovative Wasserstoff-Rekombinatoren**
von I.M. Tragsdorf (2005), 119 Seiten
ISBN: 3-89336-384-X

37. **Bruchmechanische Untersuchungen an Werkstoffen für Dampfkraftwerke mit Frischdampftemperaturen von 500 bis 650°C**
von L. Mikulová (2005), 149 Seiten
ISBN: 3-89336-391-2

38. **Untersuchungen der Strukturstabilität von Ni-(Fe)-Basislegierungen für Rotorwellen in Dampfturbinen mit Arbeitstemperaturen über 700 °C**
von T. Seliga (2005), 106 Seiten
ISBN: 3-89336-392-0

39. **IWV-3 Report 2005. Zukunft als Herausforderung**
(2005), 115 Seiten
ISBN: 3-89336-393-9

40. **Integrierter Photodetektor zur Längenmessung**
von E. Bunte (2005), XI, 110 Seiten
ISBN: 3-89336-397-1

41. **Microcrystalline Silicon Films and Solar Cells Investigated by Photoluminescence Spectroscopy**
by T. Merdzhanova (2005), X, 137 pages
ISBN: 3-89336-401-3

42. **IWV-3 Report 2005. Future as a challenge**
(2005), 115 pages
ISBN: 3-89336-405-6

43. **Electron Spin Resonance and Transient Photocurrent Measurements on Microcrystalline Silicon**
by T. Dylla (2005), X, 138 pages
ISBN: 3-89336-410-2

44. **Simulation und Analyse des dynamischen Verhaltens von Kraftwerken mit oxidkeramischer Brennstoffzelle (SOFC)**
von M. Finkenrath (2005), IV, 155 Seiten
ISBN: 3-89336-414-5

45. **The structure of magnetic field in the TEXTOR-DED**
by K.H. Finken, S.S. Abdullaev, M. Jakubowski, M. Lehnen, A. Nicolai, K.H. Spatschek (2005), 113 pages
ISBN: 3-89336-418-8

46. **Entwicklung und Modellierung eines Polymerelektrolyt-Brennstoffzellenstapels der 5 kW Klasse**
von T. Wüster (2005), 211 Seiten
ISBN: 3-89336-422-6

47. **Die Normal-Wasserstoffelektrode als Bezugselektrode in der Direkt-Methanol-Brennstoffzelle**
von M. Stähler (2006), VI, 96 Seiten
ISBN: 3-89336-428-5

48. **Stabilitäts- und Strukturmodifikationen in Katalysatordispersionen der Direktmethanolbrennstoffzelle**
von C. Schlumbohm (2006), II, 211 Seiten
ISBN: 3-89336-429-3

49. **Eduktvorbereitung und Gemischbildung in Reaktionsapparaten zur autothermen Reformierung von dieselähnlichen Kraftstoffen**
von Z. Porš (2006), XX, 182, XII Seiten
ISBN: 3-89336-432-2

50. **Spektroskopische Untersuchung der poloidalen Plasmarotation unter dem Einfluß statischer und dynamischer Ergodisierung am Tokamak TEXTOR**
von C. Busch (2006), IV, 81 Seiten
ISBN: 3-89336-433-1

51. **Entwicklung und Optimierung von Direktmethanol-Brennstoffzellstapeln**
von M. J. Müller (2006), 167 Seiten
ISBN: 3-89336-434-X

Schriften des Forschungszentrums Jülich
Reihe Energietechnik / Energy Technology

52. **Untersuchung des reaktiven Sputterprozesses zur Herstellung von aluminiumdotierten Zinkoxid-Schichten für Silizium-Dünnschichtsolarzellen**
von J. Hüpkes (2006), XIV, 170 Seiten
ISBN: 3-89336-435-8

53. **Materials for Advanced Power Engineering 2006**
Proceedings of the 8th Liège Conference
Part I, II and III
edited by J. Lecomte-Beckers, M. Carton, F. Schubert, P. J. Ennis (2006),
Getr. Pag.
ISBN: 3-89336-436-6

COST is supported by the EU framework programme

COST is an intergovernmental European framework for international cooperation between nationally funded research activities. COST creates scientific networks and enables scientists to collaborate in a wide spectrum of activities in research and technology. COST activities are administered by the COST Office.

ESF provides and manages the scientific and technical secretariat for COST

Forschungszentrum Jülich
in der Helmholtz-Gemeinschaft

50 Jahre / Zukunft

Band/Volume 53, Part III
ISBN 3-89336-436-6

Energietechnik
Energy Technology